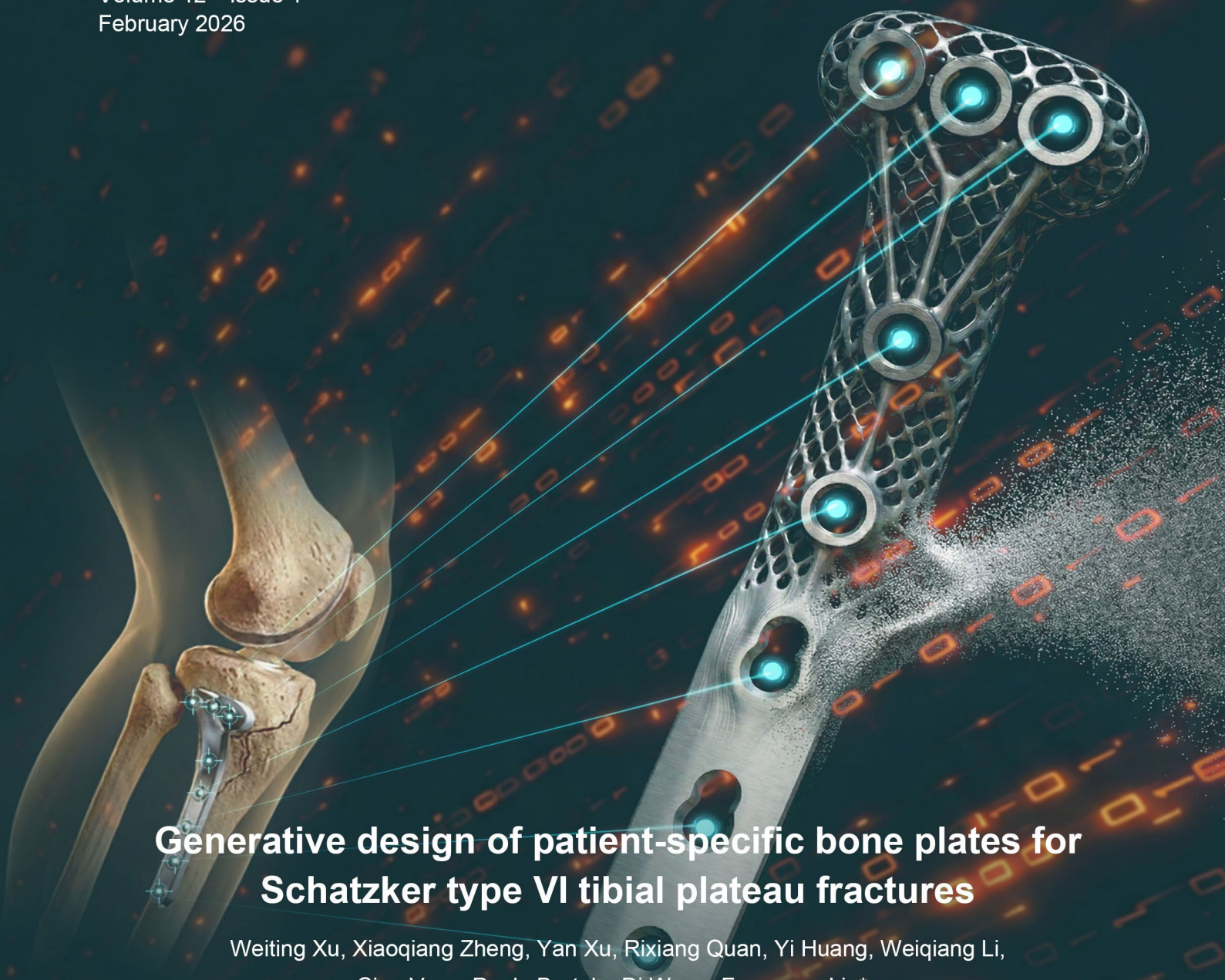
International Journal of
BIOPRINTING

ISSN: 2424-7723 (Print)
ISSN: 2424-8002 (Online)
Volume 12 • Issue 1
February 2026



Generative design of patient-specific bone plates for Schatzker type VI tibial plateau fractures

Weiting Xu, Xiaoqiang Zheng, Yan Xu, Rixiang Quan, Yi Huang, Weiqiang Li, Cian Vyas, Paulo Bartolo, Di Wang, Fengyuan Liu*

ACCSCIENCE PUBLISHING

ACCSCIENCE PUBLISHING

International Journal of Bioprinting

Print ISSN: 2424-7723

Online ISSN: 2424-8002

International Journal of Bioprinting is an international journal covering the technology, science and clinical application of the broadly defined field of Bioprinting. Bioprinting is defined as the use of 3D printing technology with materials that incorporate viable living cells or biological elements to produce tissue or biotechnological products. We are interested in the scientific topics spanning all stages of bioprinting process from concept creation to fabrication and beyond.



Scan to access website:

Scan to submit papers:

About the Publisher

AccScience Publishing is a publishing company based in Singapore. We publish a range of high-quality, open-access, peer-reviewed journals and books from a broad spectrum of disciplines.

Contact Us

Managing Editor
ijb.office@accscience.sg

AccScience Publishing
9 Raffles Place, Republic Plaza 1 #06-00 Singapore 048619.

Volume 12 • Issue 1 • February 2026
ISSN 2424-7723 (print) ISSN 2424-8002 (online)

INTERNATIONAL JOURNAL OF BIOPRINTING

Editor-in-Chief

Chee Kai Chua

Singapore University of Technology and Design, Singapore

ACCSCIENCE PUBLISHING

Access Science Without Barriers

Full issue copyright © 2026 AccScience Publishing
All rights reserved. Without permission in writing from the publisher, this full issue publication in its entirety may not be reproduced or transmitted for commercial purposes in any form or by any means, electronic or mechanical, including photocopying, recording, or any information storage and retrieval system. Permissions may be sought from ijb.office@accscience.sg.

Article copyright © Respective Author(s)
See articles for copyright year. All articles in this full issue publication are open-access. There are no restrictions in the distribution and reproduction of individual articles, provided the original work is properly cited. However, permission to reuse copyrighted materials of an article for commercial purposes is applicable if the article is licensed under Creative Commons Attribution-NonCommercial License. Check the specific license before reusing.

INTERNATIONAL JOURNAL OF BIOPRINTING

ISSN: 2424-7723 (print)
ISSN: 2424-8002 (online)



Editorial and Production Credits

Publisher: AccScience Publishing
Managing Editor: Linda Cui
Editorial Assistants: Puva Ramakrishnan, Flora Kang
Production Editor: Puva Ramakrishnan
Special Issue Commissioning Editors: Shirley Song, Terra Shi
Article Layout and Typeset: Bsmart Publishing (India)

For all advertising queries, contact ijb.office@accscience.sg.

Supplementary file

Supplementary files of articles can be obtained at https://accscience.com/journal/IJB/12/1.

Disclaimer

AccScience Publishing is not liable to the statements, perspectives, and opinions contained in the publications. The appearance of advertisements in the journal shall not be construed as a warranty, endorsement, or approval of the products or services advertised and/or the safety thereof. AccScience Publishing disclaims responsibility for any injury to persons or property resulting from any ideas or products referred to in the publications or advertisements. AccScience Publishing remains neutral with regard to jurisdictional claims in published maps and institutional affiliations.

International Journal of Bioprinting

Editorial Board

Editor-in-Chief

Chee Kai Chua
Singapore University of Technology and Design, Singapore

Executive Editor-in-Chief

Jiankang He

Xi'an Jiaotong University, China

Associate Editors

Wai Yee Yeong
Nanyang Technological University, Singapore

Amit Bandyopadhyay
Washington State University, USA

Liliang Ouyang
Tsinghua University, China

Maling Gou
Sichuan University, China

Yongqiang Hao (Clinician)
Shanghai Jiao Tong University School of Medicine, China

Xiaoxiao Han
Hunan University, China

Editorial Board Members*

Jason A. Burdick, *USA*
Shweta Agarwala, *Denmark*
Eben Alsberg, *USA*
Anthony Atala, *USA*
Douglas B. Chrisey, *USA*
Andrea Barbetta, *Italy*
Mikhael Bechelany, *France*
Martin Birchall, *UK*
Mahdi Bodaghi, *UK*
Mohd Fauzi Mh Busra, *Malaysia*
Paulo J.D.S. Bártolo, *Singapore*
Christian Celia, *Italy*
Elisabetta Ceretti, *Italy*
Ming-Wei Chang, *UK*
Maria Chatzinikolaidou, *Greece*
Jun Chen, *Australia*
Daniel Chen, *Canada*
Boris Chichkov, *Germany*
Dong-Woo Cho, *Korea*
Gianluca Ciardelli, *Italy*
Jeremy Crook, *Australia*
Cédric Delattre, *France*
Rui Domingues, *Portugal*
Dennis Douroumis, *UK*
Nileshkumar Dubey, *USA*
Tal Dvir, *Israel*
Eleonora Ferraris, *Belgium*
Sanjay Garg, *Australia*
Antonio Gloria, *Italy*
Manuela Gomes, *Portugal*
Brunella Grigolo, *Italy*
Dong-Wook HAN, *Korea*
Michinao Hashimoto, *Singapore*
Charlotte A. E. Hauser, *Saudi Arabia*
Dong Nyoung Heo, *Korea*
Raymund E. Horch, *Germany*
Di Huang, *China*
Dietmar W. Hutmacher, *Australia*
Geun Hyung Kim, *Korea*
Richard James Bibb, *UK*
Jinah Jang, *South Korea*
Jingchao Jiang, *China*
Qing Jiang, *China*
Hyun-Do Jung, *Korea*
Lifeng Kang, *Australia*
Ali Khademhosseini, *USA*
Moon Suk Kim, *South Korea*
Keekyoung Kim, *Canada*
Jangho Kim, *South Korea*
Bahattin Koç, *Turkey*
Dimitrios A. Lamprou, *UK*
Junmin Lee, *South Korea*
Jin Woo Lee, *South Korea*
Shulamit Levenberg, *Israel*
Zhong Alan Li, *Hong Kong*
Khoon Lim, *Australia*
Ki-Taek Lim, *South Korea*
Fengyuan Liu, *UK*
Xiao Liu, *Australia*

Veronica MacChi, *Italy*
Carmelo De Maria, *Italy*
Elena Martínez Fraiz, *Spain*
Laurence Meagher, *Australia*
Ferry Melchels, *Australia*
Nikolaos Michailidis, *Greece*
David K. Mills, *USA*
Vladimir Mironov, *Russia*
Mario Moisés Alvarez, *Mexico*
Maurice N Collins, *Ireland*
Makoto Nakamura, *Japan*
Seung Yun Nam, *Korea*
Roger Narayan, *USA*
Insup Noh, *Korea*
Ali Nokhodchi, *UK*
J.M.A.C. de Oliveira, *Portugal*
Aleksandr Ovsianikov, *Austria*
Sang-Hyug Park, *Korea*
Sungsu Park, *South Korea*
Jose Luis Pedraz, *Spain*
Alokesh Pramanik, *Australia*
Aldo R. Boccaccini, *Germany*
Michael Raghunath, *Switzerland*
Anabela Raymundo, *Portugal*
Shinji Sakai, *Japan*
Thomas Scheibel, *Germany*
Vahid Serpooshan, *USA*
Cijun Shuai, *China*
Swee Leong Sing, *Singapore*
Kedong Song, *China*
Jie Sun, *China*
Zhonghua Sun, *Australia*
Ergün Süleyman, *Germany*
Ibrahim Tarik Ozbolat, *USA*
Savas Tasoglu, *Turkey*
S. Vijayavenkataraman, *UAE*
Giovanni Vozzi, *Italy*
Liqiang Wang, *China*
Stephanie M. Willerth, *Canada*
Yin Xiao, *Australia*
Mingen Xu, *China*
Seung-Schik Yoo, *USA*
Barbara Zavan, *Italy*
Ioanna Zergioti, *Greece*
Yu Shrike Zhang, *USA*
Min Zhang, *China*
Yi Zhang, *China*
Wei Zhu, *China*
Ali Zolfagharian, *Australia*
Hala Zreiqat, *Australia*

Assistant Editor

Jia An, *Singapore*

Youth Editorial Board Members

Tanveer Ahmad, *Saudi Arabia*
Shivesh Anand, *USA*
Gokhan Bahcecioglu, *USA*
Bárbara Blanco-Fernández, *Spain*
Gianluca Cidonio, *Italy*
Wangwang Ding, *China*
Giovanni Falcone, *Italy*
Ruben Foresti, *Italy*
Gabriele Maria Fortunato, *Italy*
Farnaz Ghorbani, *UK*
Paola Serena Ginestra, *Italy*
Xulin Hu, *China*
Anna Jezierski, *Canada*
Yiting Lei, *China*
Lan Li, *China*
Huixin Liang, *China*
Elena Marcello, *Italy*
Wei Long Ng, *Singapore*
Egor Osidak, *Russia*
Chenxi Peng, *Australia*
Rúben Pereira, *Portugal*
Mohammadmajid Sepantafar, *USA*
Mahdiyar Shahbazi, *Austria*
João Carlos Silva, *Portugal*
Yogendra Pratap Singh, *India*
Thiago Domingues Stocco, *Brazil*
Binbin Sun, *China*
Aitor Tejo-Otero, *Spain*
Danlei Zhao, *China*
Hui Zhu, *China*

*Editorial Board Members as of February 15, 2026

ACCSCIENCE PUBLISHING

Volume 12 | Issue 1 | February 2026 | Page 1 – 707 |

International Journal of Bioprinting

https://accscience.com/journal/IJB

CONTENTS

REVIEW ARTICLES

1 **Three-dimensional bioprinting in tendon/ligament–bone interface regeneration: From design innovations to performance enhancement**
Ying Ji, Zheng Lv, Hongfu Jin, Jiahui Chen, Xin Tang

19 **Toward functional bone bioprinting: Addressing the overlooked challenges of mechanical compliance**
Amin Ebrahimi Sadrabadi, Payam Baei, Yalda Alibeigian, Mohamadreza Baghaban Eslaminejad, Samaneh Hosseini

38 **Beyond structure: A review of intelligent, bioresponsive, and sustainable design paradigms for three-dimensional-printed metamaterials in drug delivery**
Wanchong He, Qinghua Zeng

71 **Acoustic lithography: Field-directed cell patterning for bio-systems engineering**
Yuyang Li, Dengjie Sun, Chenglin Miao, Yuqi Gao, Bin Zhao, Xu Du, Xiaoming Liu, Tatsuo Arai, Zhongqiang Zhang

102 **Application and prospects of chitosan-based 3D-printed scaffolds in the repair of osteochondral defects**
Jiahui Liang, Jiyang Zou, Yuqing He, Jiyuan Qi, Yihan Wang, Zhaoyang Liu, Weiguo Zhang, Duo Zhang, Xiaolin Cui, Xing Wang, Kang Tian

125 **AI-driven integration of multimodal CT/MRI imaging and 3D printing in medicine: Advances, clinical applications, and future directions**
Weipeng Zhou, Lihua Gao, Meng Wu, Jianhua Liu

145 **Precision hydrogel environments for advanced microbial culture and patterning**
Jeremy Elias, Catherine Klein, Benjamin Wu, Xuesong He, Jirun Sun

173 **3D bioprinting-driven strategies for tissue regeneration and controlled immune modulation**
Jianfeng Zhang, Fujia Ren, Fangtian Bu, Yao Yao, Mengmeng Li

199 **Advances in three-dimensional bioprinted tumor organoids: From model construction to clinical translation**
Yuwen Wang, Jiaqi Shi, Yali Wang, Sihan Zhao, Hui Ren, Huanhuan Huang, Wenyue Lv, Huiheng Feng, Yunxiang Zhou, Kun Ji, Wei Wu

225 **Extracellular matrix-inspired 4D SMART biomaterials for bioprinting in tissue engineering**
Ryan Martin, Haiwei Zhai, Daehoon Han, Fanben Meng, Daeha Joung

RESEARCH ARTICLES

262 **Converging *Pvt1* signaling and 3D bioprinting technology for next-generation biodegradable tracheal replacement constructs**
Wei Zuo, Shao-Xiao Qiu, Jian Cui, Wen-Jian Liao, Jun-Tao Zou, Qing Jie Chen, Fei Xu

283 **Hydroxyapatite/BMP-2–mineralized decellularized amniotic membrane scaffolds for orbital defect repair**
Bing Qin, Yi Wang, Yiyi Chen, Yabo Shi, Wei Liu

302 **Electrohydrodynamically printed microfibrous scaffolds with different pore sizes modulate macrophage polarization and foreign body reaction to enhance bone regeneration**
Junzheng Liu, Zijie Meng, Jiaming Yu, Qin Guo, Jiahao Zhang, Yulin Wang, Le Jia, Jiankang He, Wei Wang

323 **Fibrous bioinks for bioprinting anisotropic micro-and nanoscale scaffolds: A novel strategy for *in vitro* skeletal muscle engineering**
Gerardina Ruocco, Elena Marcello, Camilla Paoletti, Massimo Salvi, Alice Zoso, Mattia Spedicati, Irene Carmagnola, Valeria Chiono

348 **Three-dimensional-printed bionic dual crosslinked drug-loaded hydrogel composite**

scaffolds for large bone defect repair
Xulin Hu, Zhen Zhang, Lijin Ning, Yixuan Lan, Wang Gong, Jiayu Liu, Shuhao Yang, Haoming Wu, Weiming Zhao, Jian He, Kainan Li, Weizong Weng

385 **3D-printed biodegradable hydrogel microrobots for controlled therapeutic delivery**
Pan Liao, Junyang Li, Shuxun Chen, Yi Hou, Guangda Zhu, Dong Sun

398 **3D-bioprinted active gingival hydrogel for periodontal soft tissue regeneration via TGF-β/Smad and Wnt/β-Catenin-mediated extracellular matrix remodeling**
Han Hu, Yue Liao, Jiachen Dong, Mengjun Sun, Xin Sun, Guodong Zhou, Zhongchen Song

413 **3D-printed PETG/BC scaffolds for bone tissue repair**
Evangelos Daskalakis, Mohamed H. Hassan, Abdalla M. Omar, Maria Kapousidou, Dino Freitas, Mehmet Cagirici, Cian Vyas, Hussein Mishbak, Alexandra Lanot, Niel C. Bruce, Prasad Potluri, Wajira Mirihanage, Paulo J.D.S. Bartolo

432 **A visible light-crosslinkable decellularized kidney matrix bioink for 3D bioprinting of organoids and drug testing**
Wenqi Hu, Guohua Wu, Mengjiao Xia, Di Wu, Qijun Du, Qinrui Lu, Jiashu Wang, Ao Xie, Chenwei Sun, Haijie Hu, Litian Zhao, Zipeng Yao, Shuqi Wang

448 **Fabrication of biomimetic corneas featuring epithelial, stromal, and endothelial layers via bioprinting**
Tong Zhu, Renhao Ni, Haowen Sun, Shengkai Yu, Xu Cao, Shang Chen, Jingyu Shi, Cuicui Su, Yang Luo, Lu Yang, Hua Zhang

467 **Three-dimensional-printed hydroxyapatite/zirconium dioxide composite scaffold incorporating bone morphogenetic protein-2 for lumbar vertebral bone defect repair in rhesus macaques**
Rui Qiu, Hua-Teng Zhou, Ren-Fu Quan, Can-Da Xu, Tuo Wang, Wei-Bin Du, Huan-Huan Gao, Xiao-Long Huang, Cai-Yin Xu, Long-Bao Lv, Xi-Cheng Wei, Jin-Fu Wang

485 **Optimization of 3D bioprinting of mouse preosteoblasts using nanofibrillated cellulose hydrogels**
Na Li, LinGe Wang, Roxana Guillen De La Cruz, Zhenyu Jason Zhang

523 **Multimaterial vat photopolymerization: Computational optimization of slicing workflow for complex tissue geometries**
Alejandro González-Santos, Adrian García, Nadina Usseglio, Julián Flores, Daniel Nieto

540 **Psoralen immunomodulation: *In vitro* macrophage reprogramming to enhance osseointegration of 3D-printed porous titanium scaffolds in osteoporosis**
Jian Ji, Jijie Peng, Yilong Wu, Yue Meng, Di Che, Siyan Chen, Jingyang Chen, Xingmao Zhou, Junzhe Wu, Yufeng He, Yuzhu Wang

559 **Generative design of patient-specific bone plates for Schatzker type VI tibial plateau fractures**
Weiting Xu, Xiaoqiang Zheng, Yan Xu, Rixiang Quan, Yi Huang, Weiqiang Li, Cian Vyas, Paulo Bartolo, Di Wang, Fengyuan Liu

586 **Black phosphorus scaffolds for efficient bone defect repair via anti-inflammatory, osteogenic, and photothermal therapeutic effects**
Peng Xue, Hongzhong Xi, Wei Zhang, Anlong Liu, Aoyun Hu, Chenjian Peng, Jianning Zhao, Jun Wang

607 **Antibacterial photocurable resin loaded with cetylpyridinium chloride for vat photopolymerization 3D printing in dental applications**
Tomoe Nishikawa, Yuki Nagamatsu, Yusaku Nishizawa, Yasuhiko Akama, Jun J. Miyamoto, Kaori Gunjigake-Kometani, Tatsuo Kawamoto, Hiroshi Ikeda

637 **Development of an *in situ* 3D bioprinting and laser-assisted wound care model: From leech regeneration to space medicine applications**
Giada Loi, Mariagrazia Zaccara, Francesca Cialdai, Chiara Risaliti, Glenda Leggieri, Lorenzo Notari, Daniele Bani, Michele Conti, Monica Monici

656 **3D-printed nano-hydroxyapatite/polylactic acid scaffold with simvastatin-loaded hydroxyethyl methacrylate/sulfobetaine methacrylate hydrogel for accelerated bone repair**
Yang Qu, Ya-nan Wang, Weiqing Kong, Xiaofan Du, Jianyi Li, Yukun Du, Guanghui Gu, Yongming Xi

672 **Construction of gelatin methacryloyl-based artificial skin substitutes with "small-micro" vascular networks via hybrid double-crosslinked coaxial and extrusion bioprinting**
Yichen Luo, Dan Li, Cai Lin, Bin Zhang, Hao Ding, Xue Zhou

689 **Structural design and multiphase biomechanical evaluation of a topology-optimized metal 3D-printed dual-compression plate for patellar fractures**
Chi-Yang Liao, Shao-Fu Huang, Ya-Han Chan, Hsuan-Wen Wang, Yu-Pin Yang, Chun-Li Lin

CORRECTION

707 Development of an *in situ* 3D bioprinting and laser-assisted wound care model: From leech regeneration to space medicine applications

Giada Loi, Mariagrazia Zaccara, Francesca Cialdai, Chiara Risaliti, Glenda Leggieri, Lorenzo Notari, Daniele Bani, Michele Conti, Monica Monici

ACCSCIENCE PUBLISHING

International Journal of Bioprinting

REVIEW ARTICLE

Three-dimensional bioprinting in tendon/ligament–bone interface regeneration: From design innovations to performance enhancement

Ying Ji[1,2†], Zheng Lv[3†], Hongfu Jin[1,2], Jiahui Chen[1,2], and Xin Tang[1,2*]

[1] Sports Medicine Center, West China Hospital, Sichuan University, Chengdu, Sichuan, China

[2]Department of Orthopedics and Orthopedic Research Institute, West China Hospital, Sichuan University, Chengdu, Sichuan, China

[3]Department of Nuclear Medicine, Fourth Hospital of Harbin Medical University, Harbin, Heilongjiang, China

Abstract

The tendon/ligament–bone (T/L–B) interface represents a critical junction where tendons and ligaments anchor to bone and is characterized by a complex, graded structure. Pathological conditions caused by aging, lifestyle factors, or trauma can severely impair this interface, leading to functional deficits and a significant decline in quality of life. However, replicating the intricate structural and biological features of the native T/L–B interface remains a major challenge with conventional fabrication methods. In this context, three-dimensional (3D) bioprinting has emerged as a promising approach for tissue repair and regeneration. This review aims to summarize the application of 3D bioprinting technologies in the reconstruction of the T/L–B interface. The review first provides a brief overview of the biology of the T/L–B interface. It then examines recent innovations in 3D printing technologies, biomaterials, and gradient structure design applied to interface regeneration. The review also explores strategies for optimizing the mechanical performance and bioactivity of 3D-bioprinted scaffolds for T/L–B interface regeneration. Finally, it highlights current challenges and future directions for advancing 3D bioprinting in this field. This review provides new insights into the clinical translation of 3D-bioprinted T/L–B interface constructs and may inform the future development of next-generation orthopedic implants.

Keywords: Gradient scaffold design; Tendon/ligament–bone interface; Three-dimensional bioprinting; Tissue engineering

†These authors contributed equally to this work.

***Corresponding author:**
Xin Tang
(tangxin9388@163.com)

Citation: Ji Y, Lv Z, Jin H, Chen J, Tang X. Three-dimensional bioprinting in tendon/ligament–bone interface regeneration: From design innovations to performance enhancement.
Int J Bioprint. 2026;12(1):1-18.
doi: 10.36922/IJB025410419

Received: October 11, 2025
Revised: November 2, 2025
Accepted: November 7, 2025
Published online: November 12, 2025

Copyright: © 2025 Author(s). This is an Open Access article distributed under the terms of the Creative Commons Attribution License, permitting distribution, and reproduction in any medium, provided the original work is properly cited.

Publisher's Note: AccScience Publishing remains neutral with regard to jurisdictional claims in published maps and institutional affiliations.

1. Introduction

The tendon/ligament–bone (T/L–B) interface is a critical junction where tendons and ligaments connect to bone tissue, enabling the efficient transmission of muscle-generated forces to the skeleton.[1,2] It has a four-layered gradient structure comprising tendon/ligament, nonmineralized fibrocartilage, mineralized fibrocartilage, and bone tissue.[3,4]

This hierarchical architecture not only exhibits remarkable biomechanical complexity but also reflects a finely tuned gradation of tissue function and mechanical performance. The interface is composed of multiple cell populations and extracellular matrix (ECM) components arranged in a spatially graded manner.[5,6] In addition, tendons and ligaments connect to bone through a fibrocartilaginous transition zone, in which the progressive increase in mineral content and stiffness across layers creates a seamless mechanical and structural continuum.[7] Such a gradation effectively dissipates stress concentrations and enables the interface to withstand substantial external loading. Importantly, each layer is distinguished by specific cell types and ECM compositions, ensuring the structural integrity and biomechanical functionality of the T/L–B interface.[8]

Numerous clinical scenarios, such as common tendon/ligament injuries, rotator cuff tears, and ligament damage, place substantial demands on tissue repair and regeneration. Rotator cuff tears are among the most common sports-related injuries, especially in middle-aged and elderly individuals, and are often accompanied by extensive tendon damage.[9,10] Ligament injuries are common in the knee joint, with anterior cruciate ligament (ACL) ruptures particularly prevalent in competitive sports and high-intensity physical activities.[11,12] These injuries are often associated with severe disruption of the T/L–B interface, compromising joint stability and overall function.[13,14] Suture anchors, ligament reconstruction, and tendon transposition are commonly used clinically to treat T/L–B interface damage. However, the repaired tissue typically exhibits fibrotic scar formation rather than regeneration of the native gradational structure of the interface. As a result, the reconstructed interface frequently suffers from insufficient mechanical performance, suboptimal functional recovery, and a high risk of reinjury.[15–17] Moreover, reestablishing the intrinsic gradient architecture of the T/L–B interface after injury is difficult, as the complex anisotropy and zonal organization do not readily regenerate spontaneously.[18] Therefore, strategies that can replicate the natural anisotropic characteristics of the T/L–B interface and provide cells with appropriate mechanical and biochemical cues are crucial for successful tissue regeneration and functional restoration.[19]

Three-dimensional (3D) bioprinting has attracted considerable attention because of its ability to precisely deposit biomaterials, living cells, and biochemical components to fabricate complex tissue structures.[20,21] Using computer-aided design (CAD), 3D bioprinting enables the layer-by-layer deposition of multiple biomaterials in a spatially and temporally controlled manner, thereby generating engineered constructs with customizable architectures.[22,23] This approach helps overcome many of the limitations associated with conventional repair strategies and has been shown to significantly improve regeneration outcomes.[24,25] Importantly, 3D bioprinting offers the potential to better mimic the biological and mechanical characteristics of the native T/L–B interface. By integrating specific biochemical cues within printed scaffolds, it is possible to recreate a favorable microenvironment that promotes cell survival, differentiation, and tissue integration.[26] Through precise biomimetic design, 3D bioprinting not only allows for the optimization of scaffold mechanical properties and the enhancement of biological activity but also provides a novel and promising solution for T/L–B interface repair.[27–29] Consequently, this technology is emerging as a valuable therapeutic strategy for conditions, such as rotator cuff tears and ligament injuries.[30]

This review provides a comprehensive overview of 3D bioprinting in the repair of the T/L–B interface, with a particular emphasis on performance enhancement. Specifically, we discuss innovations in 3D printing technology, biomaterials, and gradient structure design applied to T/L–B interface regeneration. Furthermore, we also examine the strategies for optimizing the mechanical performance and bioactivity of 3D-bioprinted scaffolds for T/L–B interface regeneration. Finally, we highlight current challenges and future directions for 3D bioprinting in T/L–B interface regeneration. Unlike previous reviews that primarily provide general overviews of bioprinting applications in musculoskeletal tissue engineering, this work focuses on how to improve the mechanical strength, biological activity, and degradation behavior of bioprinted scaffolds for T/L–B interface regeneration. These optimizations help bridge the gap between laboratory experiments and clinical applications. The key topics discussed in this review are summarized in Figure 1.

2. Overview of 3D bioprinting technology and its application at the tendon/ligament–bone interface

2.1. Principles of 3D bioprinting

3D bioprinting is an advanced manufacturing technology that enables the construction of 3D biological structures by precisely depositing biomaterials in a spatially controlled manner.[31,32] The core principle relies on the use of bioinks containing living cells, biomaterials, and bioactive cues, which are deposited layer by layer under CAD guidance to fabricate constructs with predefined geometries and microenvironmental features.[33–35] This method not only enables the creation of scaffolds with highly controlled geometry, porosity, and mechanical

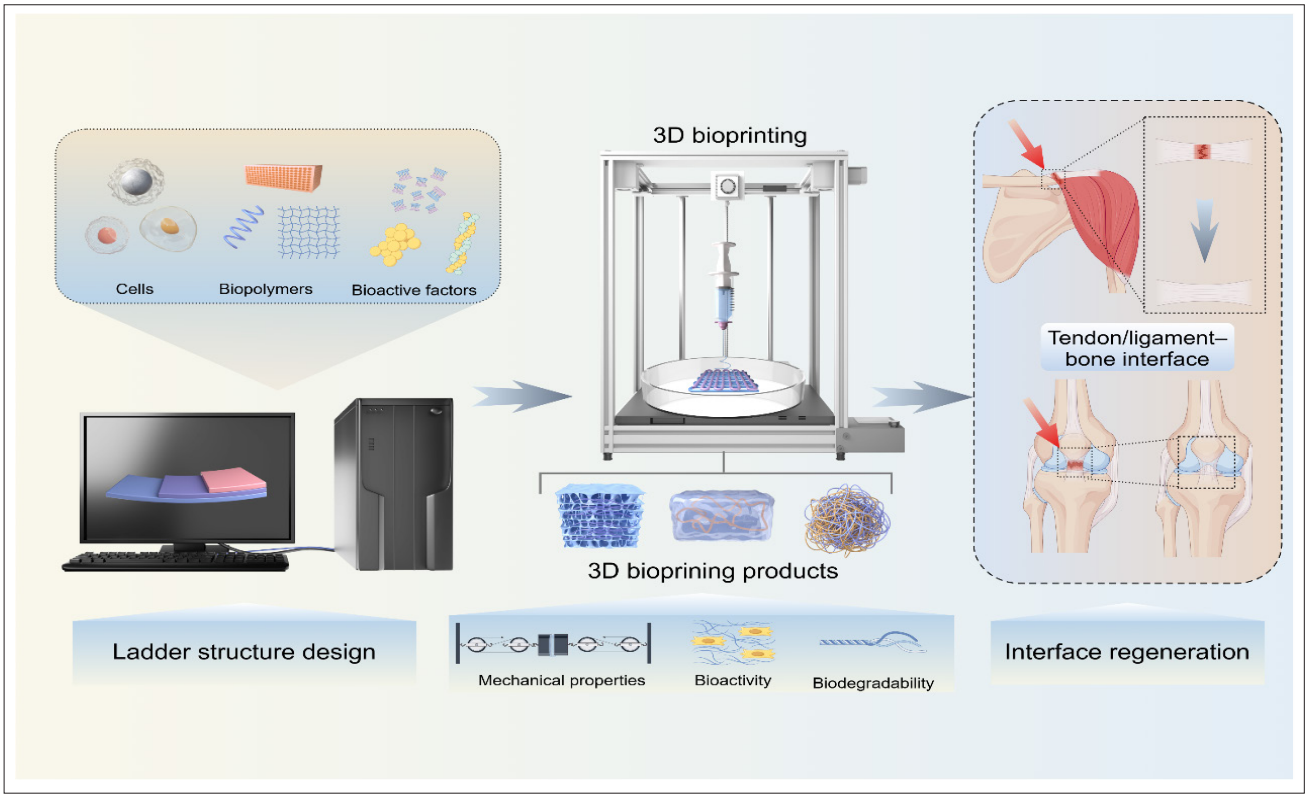


Figure 1. Schematic representation of three-dimensional (3D) bioprinting materials applied to the tendon/ligament–bone interface. Image created using Figdraw.

properties but also facilitates the construction of biomimetic scaffolds incorporating living cells and growth factors.[36,37] Compared with conventional two-dimensional approaches, 3D bioprinting offers greater design flexibility and high spatial resolution. It can more effectively mimic the complex compartmentalization, mechanical gradients, and biochemical environments of natural tissues.[38–41] As such, it opens new avenues in tissue engineering and regenerative medicine.

2.2. Major strategies for 3D bioprinting

Currently, various bioprinting strategies are based on the fundamental principles for fabricating different functional tissue structures. The main modalities are inkjet printing, extrusion bioprinting, stereolithography (SLA), and laser-assisted bioprinting.[42] For example, researchers utilized an extrusion-based 3D bioprinter to print hydrogels containing predifferentiated autologous adipose-derived mesenchymal stem cells (ADMSCs) into region-specific structures, thereby mimicking the architecture of the tendon–bone (T-B) interface.[43] Ker *et al.*[44] used an inkjet-based bioprinter to pattern geometric and biochemical cues that directed musculoskeletal cell alignment and differentiation *in vitro*, in line with fiber orientation and the printed patterns. Additionally, researchers have developed an SLA-based bioprinting platform for the multimaterial fabrication of multiphase hydrogel structures.[45] They validated the system's biocompatibility by introducing gelatin methacryloyl with encapsulated cells into a microfluidic device to fabricate cellular constructs.

2.3. Applications of 3D bioprinting in tendon/ligament–bone interface regeneration

2.3.1. Structural design and gradient material printing

Given the functional complexity of the T/L–B interface, reproducing its hierarchical and gradated structure is critical for successful repair and regeneration.[46] 3D bioprinting enables the fabrication of scaffolds with graded compositions and structures to mimic the natural transitional interface. For instance, Du *et al.*[47] successfully developed a biomimetic gradient scaffold by combining tendon/bone-associated cells with a molybdenum silicate bioceramic to mimic the hierarchical structure and cellular composition of the T-B interface. The scaffold induced tendinogenic and osteogenic differentiation of tendon/bone-related cells *in vitro* and promoted regeneration of the T-B interface *in vivo* (Figure 2A–2D). By integrating 3D cell printing with tailored bioinks, a

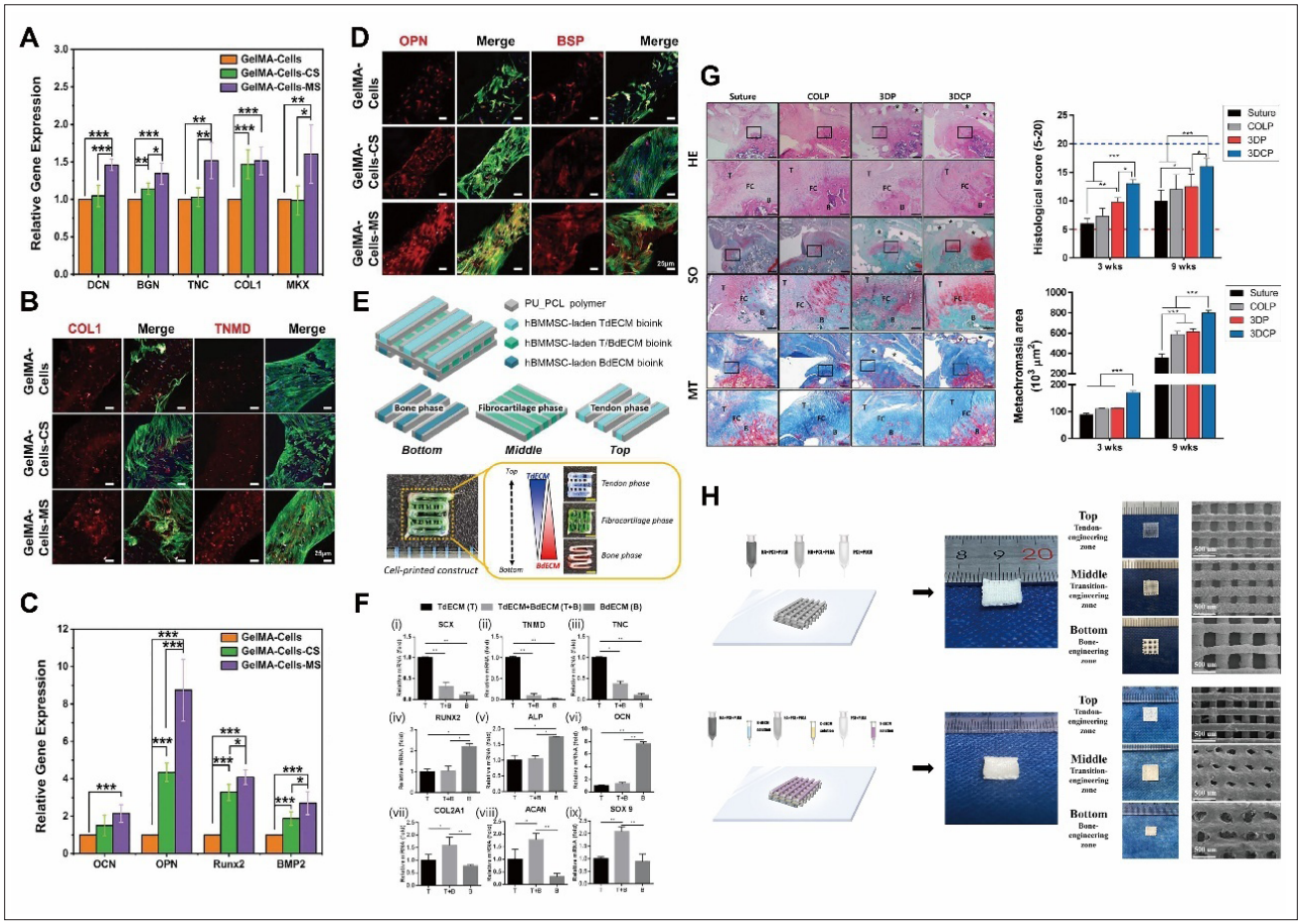


Figure 2. Gradient 3D-bioprinted scaffolds enabling spatial control of tendon-, cartilage-, and bone-lineage differentiation. (A and B) TSPC tenogenic differentiation in biomimetic multicellular scaffolds. Scale bar: 25 μm. Reprinted from.[47] (C and D) BMMSC osteogenic differentiation in biomimetic multicellular scaffolds. Scale bar: 25 μm. Reprinted with permission.[47] (E) Design and fabrication of 3D cell-printed T–B interface patches. Reprinted with permission.[48] Copyright © 2021, IOP Publishing. (F) T–B interface patches induced human BMMSCs to differentiate into tendon, cartilage, and bone at the interface. Reprinted with permission.[48] Copyright © 2021, IOP Publishing. (G) Patches promoted healing at the T–B interface *in vivo* studies. Scale bar: 500 and 200 μm. Reprinted with permission.[48] Copyright © 2021, IOP Publishing. (H) Design, manufacture, and observation of the graded biomimetic scaffold. Reprinted with permission.[51] Copyright © 2023, American Chemical Society. Abbreviations: 3D, Three-dimensional; 3DCP, Three-dimensional printed composite; 3DP, Three-dimensional printing; BdECM, Bone-derived extracellular matrix; BSP, Bone sialoprotein; COL1, Collagen type 1; COLP, Collagen peptide; CS, Cartilage sheets; GelMA, Gelatin methacryloyl; BMMSCs, Bone marrow mesenchymal stem cells; HE, Hematoxylin and eosin; MS, Muscle sheets; MT, Masson's trichrome; OPN, Osteopontin; PU_PCL, Polyurethane–polycaprolactone composite; SO, Safranin O; T–B, Tendon–bone; T/BdECM, Tendon/bone-derived extracellular matrix; TdECM, Tendon-derived extracellular matrix; TNMD, Tenomodulin; TSPC, Tendon stem/progenitor cells.

new therapeutic system has been designed to replicate the spatially graded physiological environment of the T-B interface and promote its functional regeneration.[48] The novel spatially graded T-B interface patch induced region-specific differentiation of encapsulated human bone marrow mesenchymal stem cells (BMMSCs) *in vitro*. *In vivo*, the intervention enhanced T-B interface healing, including regeneration of the transitional zone, improved collagen alignment, and increased biomechanical strength (Figure 2E–2G). Additionally, scaffold pore size and overall porosity play essential roles, as they regulate oxygen and nutrient diffusion, which is essential for cell viability.[49] Moreover, researchers have observed changes in cellular behavior as a function of pore size.[50] Zhang *et al.*[51] fabricated a graded biomimetic scaffold (GBS-E) with structural, compositional, and mechanical hierarchies using 3D bioprinting. The GBS-E scaffold demonstrated zone-specific surface topographies, each approximating the ideal pore dimensions known to promote tenogenic, chondrogenic, or osteogenic differentiation (Figure 2H). Researchers also proposed a multitissue construct with a cell-loading gradient.[52] Using 3D bioprinting technology, an inverse gradient containing T-B interface-specific bioink and stem cells was constructed to simulate the

multitissue structure and phenotype of the T-B interface, providing guidance for complex interface regeneration in animal rotator cuff models.

2.3.2. Integration of cells and bioactive factors

In addition to structural features, 3D bioprinting allows the direct incorporation of cells and bioactive molecules into scaffolds. Mesenchymal stem cells (MSCs), chondrocytes, and osteoblasts can be embedded within printed scaffolds to support proliferation, migration, and lineage-specific differentiation during regeneration.[53–55] For example, a heterogeneous T-B interface was engineered using a 3D-printed multiphasic scaffold, with tendon fibroblasts, BMMSCs, and osteoblasts seeded onto distinct scaffold phases to regenerate tenogenic, fibrocartilaginous, and osteogenic tissues, respectively (Figure 3A).[56] In addition,

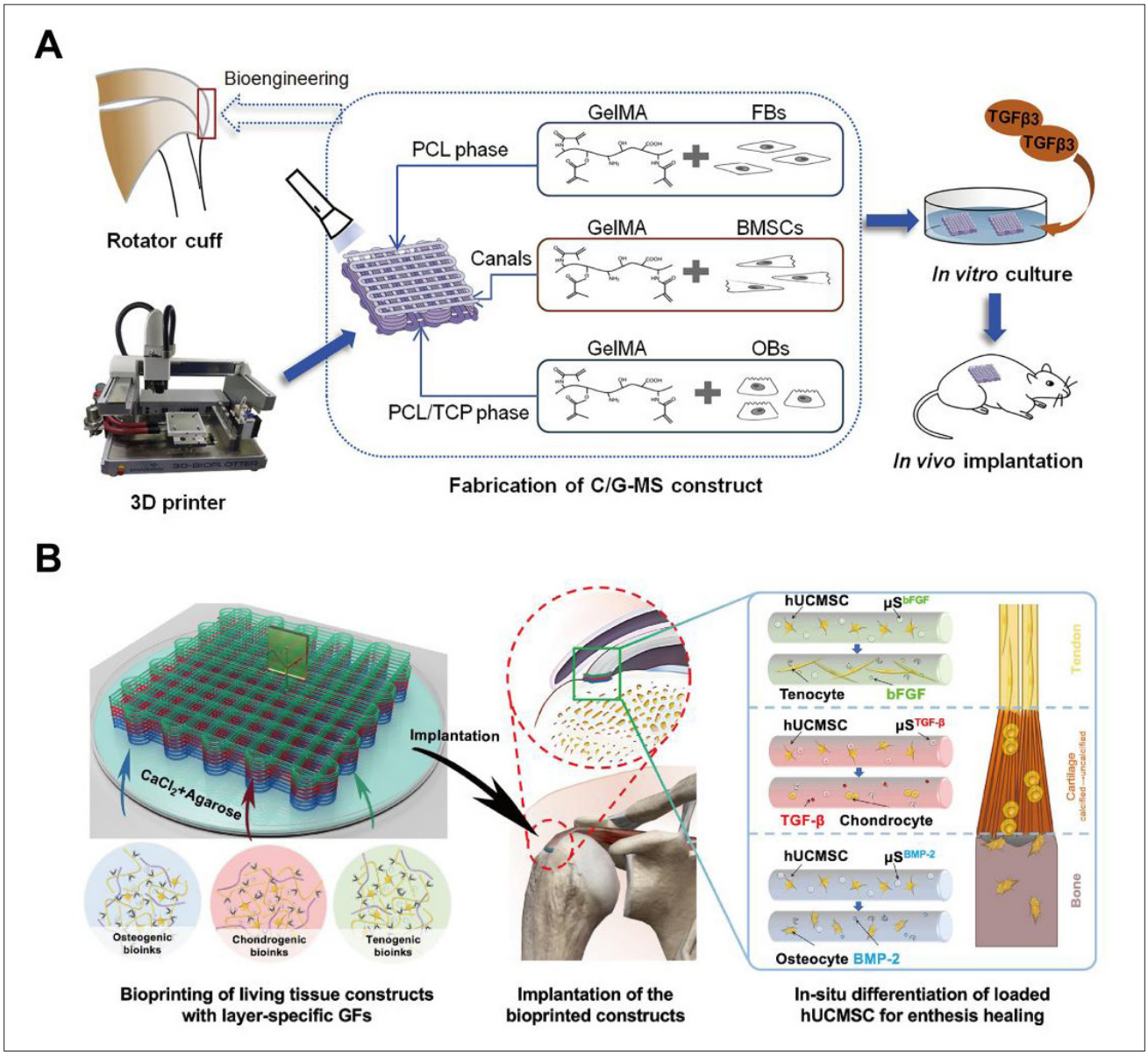


Figure 3. 3D-bioprinted constructs integrating cells, biomaterials, and cues to induce tendon-, cartilage-, and bone-like tissues. (A) Illustration of the use of 3D-printed multiphasic scaffolds to construct heterogeneous tendon-to-bone interfaces. Reprinted with permission.[56] Copyright © 2020, Elsevier. (B) Implantation of bioprinted living tissue constructs with layer-specific GF-loaded μS to facilitate zonal tenogenesis, chondrogenesis, and osteogenesis during the rotator cuff healing process. Reprinted with permission.[58] Copyright © 2022, Elsevier. Abbreviations: 3D, Three-dimensional; bFGF, Basic fibroblast growth factor; BMSC, Bone marrow mesenchymal stem cells; C/G-MS, Collagen/gelatin microspheres; FB, Fibroblast; GelMA, Gelatin methacryloyl; GF, Growth factor; hUCMSC, Human umbilical cord mesenchymal stem cells; OB, Osteoblast; PCL, Polycaprolactone; TCP, Tricalcium phosphate; TGF, Transforming growth factor.

signaling factors, such as bone morphogenetic protein-2 (BMP-2), vascular endothelial growth factor (VEGF), fibroblast growth factor (FGF), and transforming growth factor (TGF), can be spatially loaded or hierarchically distributed to achieve spatiotemporally controlled release, thereby regulating osteogenesis, chondrogenesis, and angiogenesis in specific regions.[57] One bioprinted construct incorporated layer-specific growth factors that directed localized differentiation of embedded stem cells into tendon-, cartilage-, and bone-like cells, significantly improving enthesis healing in a rabbit rotator cuff injury model (Figure 3B).[58] Through this synergistic integration of cells, biomaterials, and signaling molecules, 3D-bioprinted scaffolds can optimize both biofunctionality and mechanical performance during tissue repair. Table 1 summarizes the primary 3D bioprinting approaches, the associated biomaterials and bioactive molecules, and their outcomes.

3. Application of performance-optimized 3D bioprinting strategies in tendon/ligament–bone interface repair

An ideal 3D-bioprinted scaffold for T/L–B interface regeneration should not only mimic the hierarchical, graded architecture of the native interface but also optimize mechanical strength, biological activity, and degradation kinetics, thereby supporting the tissue regeneration process.

3.1. Mechanical performance optimization

The T/L–B interface, as a region subjected to complex biomechanical loads, requires repair scaffolds with robust mechanical properties to ensure that the repaired area can withstand movement and external forces during the healing process.[62–64] By tailoring fiber alignment, porosity, and compositional gradients, 3D-bioprinted scaffolds can reproduce the natural transition from soft tissue to hard tissue, thereby restoring mechanical functionality. To evaluate the mechanical performance of 3D-bioprinted scaffolds, various mechanical testing protocols have been employed. *In vitro* tensile, compressive, and cyclic loading tests are typically used to assess the elastic modulus, ultimate tensile strength, and fatigue resistance of scaffolds under conditions that simulate the physiological mechanical stress at the T/L–B interface. For example, Zhang *et al.*[65] fabricated a mechanically robust, slow-degrading polythiourethane (PHT) elastomer scaffold via a simple and rapid 3D printing method for tendon repair. The 3D-printed PHT scaffold exhibited mechanical properties comparable to those of the human supraspinatus tendon and maintained integrity after undergoing 10 000 cycles of physiological tensile loading (Figure 4A–4E). In another study, polycaprolactone (PCL), poly(lactic-

Table 1. Summary of 3D bioprinting approaches, biomaterials, bioactive molecules, and their principal outcomes

3D printing strategy	Biomaterials	Cells/Bioactive factors	Key findings	References
Extrusion	PCL	hMSCs, CTGF, TGF-β3, BMP-2	Enabled microprecise, spatiotemporal delivery of multiple growth factors.	[59]
	mPCL	Cell sheets, BMP2	Provided scompartmentalization and guided fiber alignment.	[60]
	PCL, hydrogels	ADMSCs	Supported host-cell infiltration into the multilayered scaffold and interaction with implanted autologous ADMSCs.	[43]
	Mo-containing silicate bioceramics, GelMA	TSPCs, BMMSCs	Exhibited bidirectional bioactivity, promoting both tenogenic and osteogenic differentiation.	[47]
Inkjet	Agarose hydrogel	H9C2, HUVEC	Printed heterogeneous constructs with different components.	[61]
	Polystyrene STEP fibers	FGF-2, BMP-2	Controlled stem cell orientation and directed differentiation toward multiple phenotypes.	[44]
SLA	GelMA	MSCs, fibroblasts, osteoblasts	Demonstrated efficient fabrication with noticeable improvement in speed.	[45]

Abbreviations: 3D: Three-dimensional; ADMSCs: Autologous adipose-derived mesenchymal stem cells; BMMSCs: Bone marrow mesenchymal stem cells; BMP-2: Bone morphogenetic protein-2; CTGF: Connective tissue growth factor; FGF: Fibroblast growth factor; GelMA: Gelatin methacryloyl; hMSCs: Human mesenchymal stem cells; HUVEC: Human umbilical vein endothelial cells; mPCL: Methacrylated polycaprolactone; MSCs: Mesenchymal stem cells; PCL: Polycaprolactone; SLA: Stereolithography; STEP fibers: Shear-templated electrospun fibers; TGF: Transforming growth factor; TSPC: Tendon stem/progenitor cells.

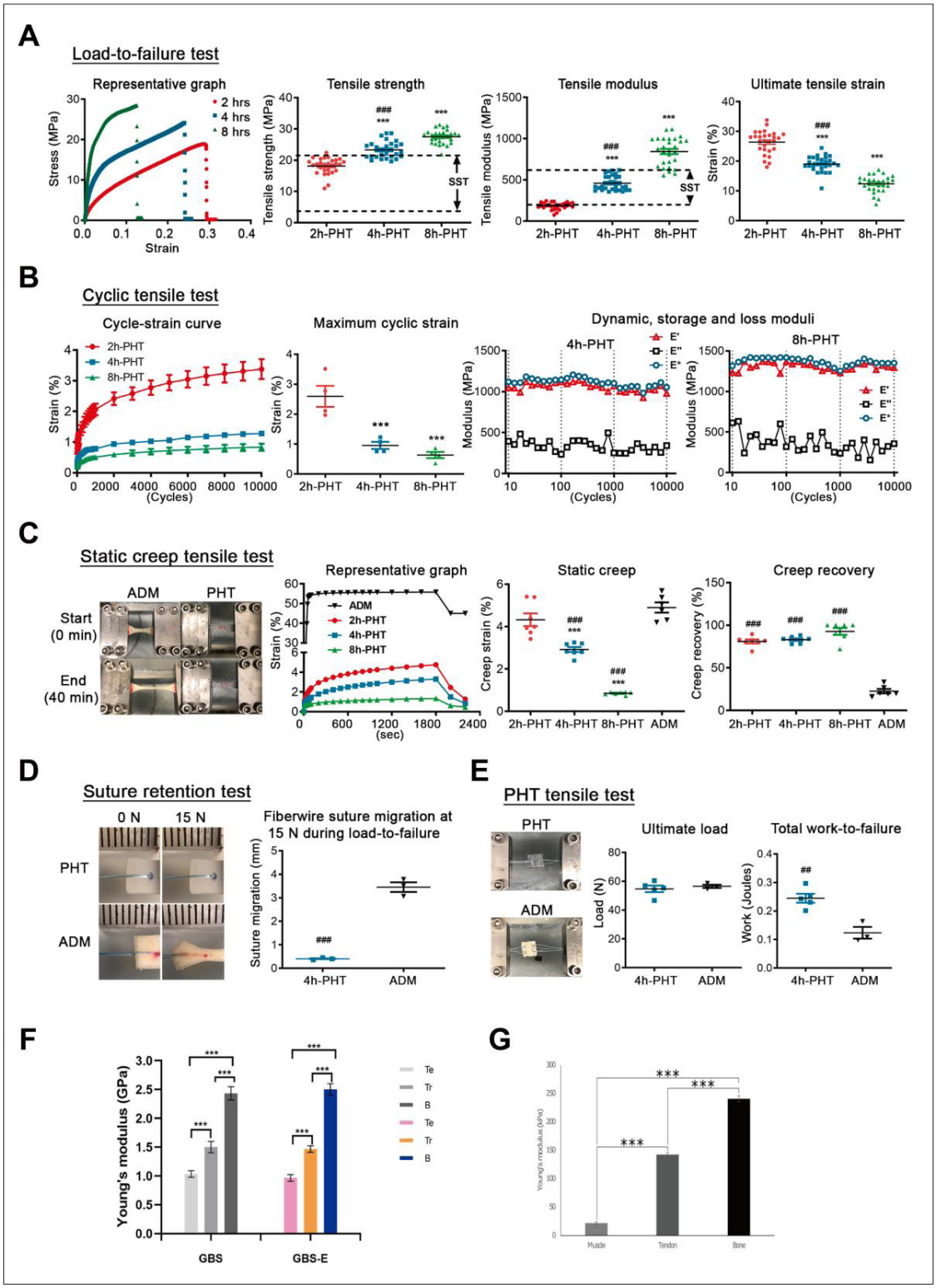


Figure 4. 3D-bioprinted scaffolds with tendon-like mechanics and a continuous stiffness gradient toward bone. (A–E) PHT polymers and 3D-printed PHT scaffolds exhibited mechanically robust, tendon-like properties. Reprinted with permission.[65] Copyright © 2024, Elsevier. (F) Young's modulus increased from the tendon-engineering zone to the bone-engineering zone along with increasing mineral content. Reprinted with permission.[51] Copyright © 2023, American Chemical Society. (G) A stiffness gradient was obtained as the Young's modulus increased. Reprinted from.[71] Abbreviations: 3D, Three-dimensional; ADM, Acellular dermal matrix; PHT, Polyhexahydrotriazine.

co-glycolic acid) (PLGA), and hydroxyapatite (HA) were combined in different ratios to fabricate triphasic scaffolds representing tendon (1:1:0), transition (1:1:2), and bone (1:1:4) regions.[51] The results indicated that the Young's modulus progressively increased from the tendon region to the bone-mimetic region as the mineral content increased (Figure 4F). *In vivo* experiments demonstrated that this scaffold exhibited favorable biomechanical properties, enhancing tendon-to-bone repair. The use of composite materials (such as bioceramic–polymer composites) can enhance the overall mechanical properties of the scaffold.[66,67] HA increases compressive strength and stiffness, whereas polymers, such as polylactic acid (PLA) and PCL, provide flexibility suitable for tendon/ligament regions.[68–70] One study developed a 3D *in vitro* model using collagen and agarose matrices with varying concentrations of HA to simulate a stiffness gradient across muscle, tendon, and bone.[71] The engineered constructs exhibited Young's moduli of 20, 140, and 240 kPa, respectively, successfully mimicking the mechanical transition from soft to mineralized tissues (Figure 4G).

3.2. Biological activity optimization

Beyond mechanical support, scaffolds must also serve as bioactive microenvironments that regulate cell behavior and drive tissue regeneration. The biological activity of 3D-bioprinted scaffolds is typically assessed through both *in vitro* cell-based assays and *in vivo* regeneration models. *In vivo* animal models, such as rabbit rotator cuff tear repair, rat Achilles tendon reconstruction, and ACL replacement, are widely used to assess osteointegration, collagen organization, fibrocartilage regeneration, and vascularization, thereby validating the regenerative efficacy of the scaffold in a physiologically relevant environment. Microchannels or porous architectures within the scaffold provide pathways for neovascularization, facilitate the distribution of angiogenic factors, and thereby improve the blood supply to the repair site.[72–74] For instance, Kim *et al.*[75] developed an innovative bioprinting method utilizing tendon- and bone-specific decellularized ECM-based bioinks supplemented with HA and TGF-β/poly(vinyl alcohol) to enhance construct functionality. The resulting complex construct induced angiogenesis, enhanced ECM formation, and supported functional restoration of full-thickness tendon-to-bone defects, with robust interface integration and improved mechanical function (Figure 5A–5C). Controlled delivery of bioactive factors represents another key strategy for enhancing scaffold bioactivity.[76] For example, osteogenic (e.g., BMP-2) and angiogenic (e.g., VEGF) factors can be loaded onto the bone side, chondrogenic factors (e.g., TGF-β) can be introduced into the cartilage or transition zone, and factors promoting fibroblast activity (e.g., FGF) can be applied to the ligament region.[77–79] Spatially patterned or temporally controlled release systems can recapitulate native biochemical gradients, enabling coordinated multitissue regeneration. One study reported that sustained, spatially regulated release of tenogenic, chondrogenic, and osteogenic growth factors was achieved through microsphere-based delivery systems incorporated into thin, membrane-like scaffolds.[59] *In vitro*, scaffolds incorporating growth factors effectively directed the spatial differentiation of mesenchymal progenitor cells, resulting in the formation of multiphasic tissues resembling tendon, cartilage, and bone regions. *In vivo*, these scaffolds promoted the integrative healing of tendon and bone via the reformation of a strong fibrocartilaginous interface (Figure 5D).

Furthermore, integrating cells with scaffolds is crucial for achieving functional repair. Cells seeded within scaffolds not only deposit ECM components but also modulate the immune microenvironment via paracrine signaling, enhancing both early stabilization and long-term integration at the repair site.[80–82] For example, researchers designed and fabricated two types of scaffolds by combining a 3D-printed PLGA scaffold with cell-laden collagen-fibrin hydrogels.[83] The findings indicated that the printed scaffolds effectively promoted the adhesion, proliferation, and tenogenic differentiation of human ADMSCs. Another study investigated 3D-bioprinted scaffold sleeves seeded with MSCs.[84] These MSC-seeded sleeves significantly enhanced osteointegration between the tendon graft and tunnel bone in a rabbit model. In general, the combined use of cells and growth factors can further augment scaffold bioactivity. A recent study designed a 3D-printed PCL scaffold loaded with basic FGF and BMMSCs (PCLMF) to restore the T–B interface and regulate the local inflammatory microenvironment.[85] This construct not only promoted osteogenesis and inhibited adipogenesis but also regulated macrophage polarization and inflammatory responses in both *in vitro* and *in vivo* settings (Figure 6A–6C).

3.3. Degradation performance optimization

In T/L–B interface repair, the degradation rate of scaffolds must be synchronized with the regeneration rate of newly formed tissues. Excessively rapid degradation may result in insufficient mechanical support, whereas overly slow degradation can trigger chronic inflammatory responses or hinder tissue integration.[86,87] The degradation kinetics can be fine-tuned by adjusting the material composition, molecular weight, and crosslinking density.[88] For example, polyester-based materials, such as PLA and PCL, exhibit predictable degradation profiles, allowing degradation time frames to be tuned by adjusting their compositional ratios.[89] Ni *et al.* analyzed the degradation of composite

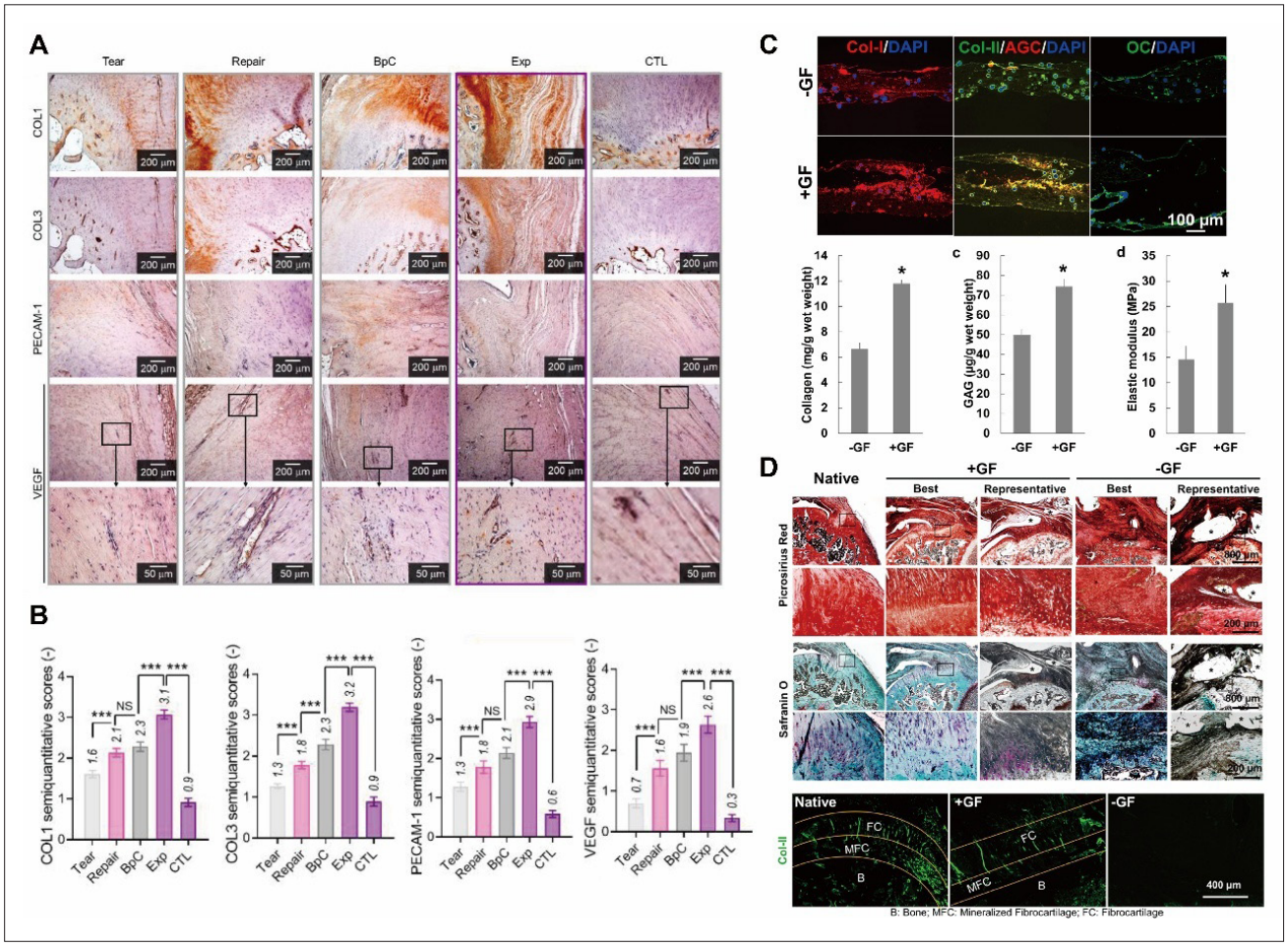


Figure 5. Bioactive 3D-bioprinted constructs enhancing vascularization and tendon–bone interface healing. (A–B) The complex construct promoted regenerative capacity, including tendon-to-bone tissue integration and vascular formation. Scale bar: 200 and 50 μm. Reprinted with permission.[75] Copyright © 2024, Elsevier. (C) Scaffolds embedded in a spatiotemporal delivery system guided the differentiation of hMSCs to form a gradient fibrocartilaginous matrix tissue. Scale bar: 100 μm. Reprinted with permission.[59] Copyright © 2019, IOP Publishing. (D) Spatiotemporal delivery of GFs via 3D-printed scaffolds improved the healing of the tendon-to-bone fibrocartilaginous interface. Scale bar: 800, 200, and 400 μm. Reprinted with permission.[59] Copyright © 2019, IOP Publishing. Abbreviations: 3D, Three-dimensional; BpC, Bone progenitor cells; COL, Collagen; CTL, Control; FC, Fibrocartilage; GAG, Glycosaminoglycan; GF, Growth factor; hMSCs, Human mesenchymal stem cells; MFC, Mineralized fibrocartilage; PECAM-1, Platelet endothelial cell adhesion molecule-1; VEGF, Vascular endothelial growth factor.

scaffolds and reported that degradation was most rapid during the first 2 weeks in both *in vitro* and *in vivo* settings, consistent with the inflammatory period following surgery.[85] Complete degradation occurred at approximately 4 weeks. Furthermore, as the scaffold degraded, its microstructure was disrupted, leading to the gradual release of loaded cytokines (Figure 6D). By the fourth week, nearly all cytokines had been released, which facilitated subsequent tissue repair. Composite scaffold design can also enable region-specific degradation. In another study, novel structural designs integrating biomaterials and stem cells were used to fabricate multilayered scaffolds with *in vivo* degradability via 3D printing.[83] Experimental findings revealed that the solid ends were partially degraded when the scaffolds were harvested. In the middle part, more than 60% of the scaffolds were degraded by the time of harvest. Table 2 summarizes the mechanical, biological, and degradation performance of 3D-bioprinted constructs used in T/L–B interface repair.

4. Conclusion and future perspectives

Although T–B and ligament–bone interfaces differ in their origins and functions, they share striking similarities in histological structure, biomechanical properties, injury repair mechanisms, and tissue-engineering strategies.[94,95] The T/L–B interface is highly specialized transitional tissues characterized by unique gradients in composition,

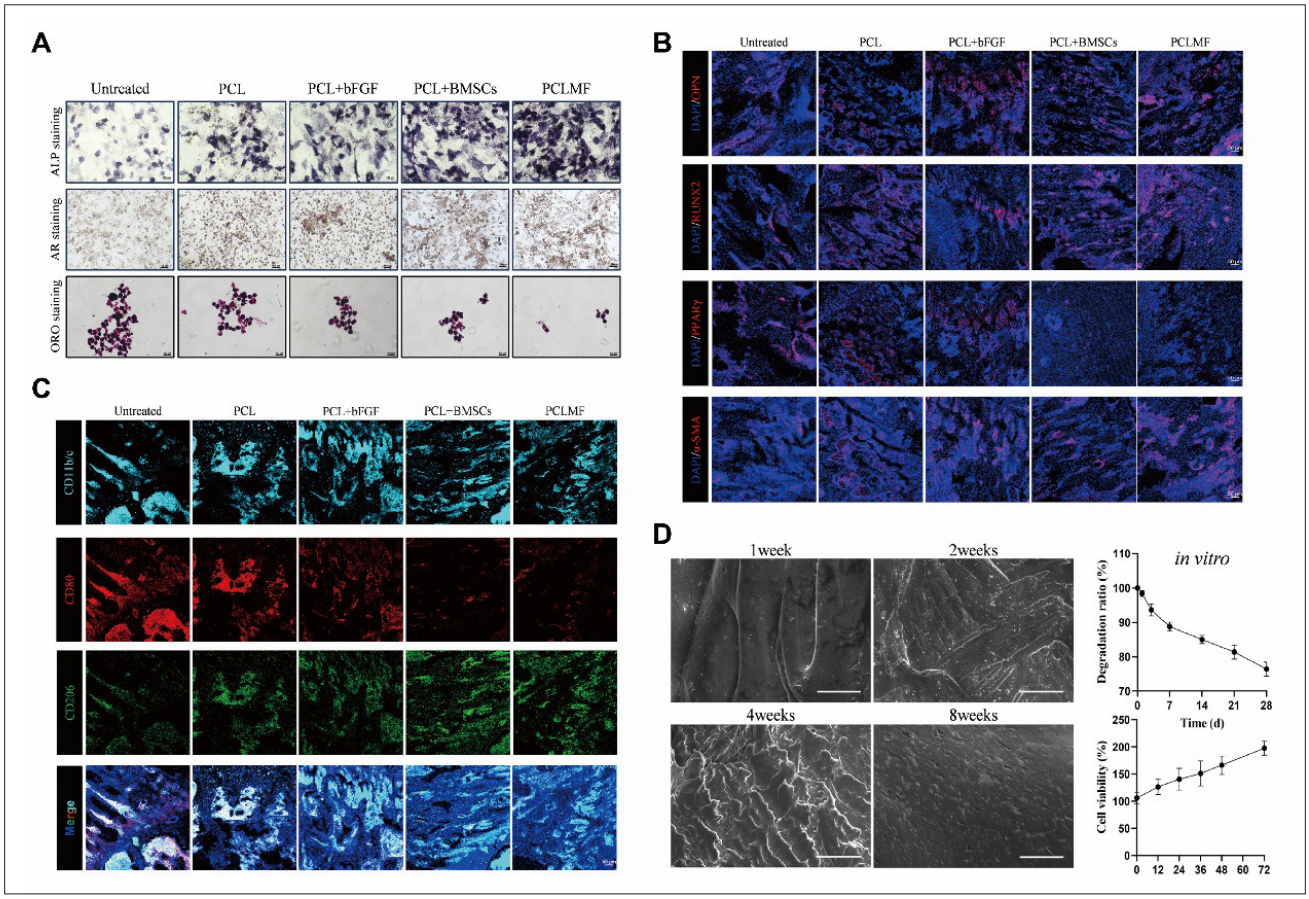


Figure 6. 3D-bioprinted scaffolds promoting osteogenesis, modulating immunity, and allowing controlled biodegradation. (A–B) 3D-printed PCLMF scaffolds promoted osteogenesis and inhibited adipogenesis both *in vitro* and *in vivo*. Scale bar: 100 and 50 μm. Reprinted with permission.[85] Copyright © 2025, American Chemical Society. (C) Modulation of macrophage polarization by 3D-printed PCLMF scaffolds *in vivo*. Scale bar: 50 μm. Reprinted with permission.[85] Copyright © 2025, American Chemical Society. (D) The PCLMF scaffold degradation rate was fastest at 2 weeks. Reprinted with permission.[85] Copyright © 2025, American Chemical Society. Abbreviations: 3D, Three-dimensional; ALP, Alkaline phosphatase; AR, Alizarin red; bFGF, Basic fibroblast growth factor; BMSCs, Bone marrow mesenchymal stem cells; ORO, Oil red O; PCL, Polycaprolactone; PCLMF, Polycaprolactone scaffold loaded with basic fibroblast growth factor and bone marrow mesenchymal stem cells.

structure, and mechanical properties.[96] Understanding the mechanobiological principles underlying these interfaces is essential for guiding effective repair strategies.[97] Current repair strategies include direct repair and graft-based reconstruction. The rapid advancement of tissue engineering has spurred the development of multiple strategies to promote graft repair and regeneration.[98–100] In this context, 3D bioprinting has emerged as a promising technology, offering spatial precision and the ability to integrate cells, bioactive molecules, and biomaterials in a highly controlled manner.[27] By enabling the fabrication of scaffolds with distinct biomechanical properties and hierarchical architectures, 3D bioprinting provides a novel pathway to recapitulate the native structure and function of the T/L–B interface.[101,102] Although the application of biological 3D printing in interface tissue engineering is rare, recent advances are still worth discussing. By emphasizing performance enhancement as the central theme, this work bridges the gap between structural design and functional outcomes, aiming to guide future translational research in T/L–B interface regeneration.

Nevertheless, significant challenges remain before clinical translation can be achieved, and these can be broadly categorized into three domains: (i) design and fabrication challenges, (ii) material challenges, and (iii) biological and translational challenges. In terms of design and fabrication, multifunctional gradient scaffolds remain technically demanding. At present, the generation of physiologically relevant heterogeneous interfaces with functionally graded spatial variations remains constrained by technical limitations.[103] Achieving scaffolds that both accurately mimic the native attachment site and maintain spatial

Table 2. Summary of the performance and outcomes of 3D bioprinted constructs used for tendon/ligament–bone interface repair.

Category	Mechanical properties	Biological activity	Degradation performance	*In vitro*/*in vivo* results	References
Tendon–bone interface	Tensile modulus: 42.94 ± 6.04 kPa; tensile strength: 159.75 ± 1.31 kPa	Increased number of spreading cells from day 4 to day 7	Lost original shape within 12–18 days	Promoted Col-I remodeling, fibrocartilage reconstruction, and osteointegration	[58]
	Tensile toughness: 3 MPa; ultimate load: 54.69 ± 2.26 N; suture migration: 0.4 ± 0.03 mm	Maintained high cell viability	Exhibited little to no mass loss under acidic/oxidizing conditions and 69% mass loss under alkaline conditions	Restored tendon biomechanical function to native levels; regenerated 1 cm of rotator cuff tendon tissue	[65]
	Ultimate load comparable to other patch types	Enhanced proliferation, migration, and tenogenic differentiation of BMMSCs	Scaffold remained only partially degraded at 8 weeks	Promoted BMMSCs' tenogenic differentiation and induced regeneration of tendon tissue	[90]
	Young's modulus increased gradually from the tendon to the bone zones	Demonstrated good cytocompatibility	Biodegradable	Improved tendon-to-bone healing by promoting zone-specific cellular differentiation	[51]
	Tri-layered scaffolds exhibited higher elastic stiffness compared with individually printed single-layer scaffolds	Increased cell proliferation rate within scaffolds	PLGA partially degraded during culture; the collagen–fibrin hydrogel became thinner after 14 days	Supported human ADMSC viability and tenogenic differentiation; showed excellent biocompatibility and *in vivo* degradability	[83]
	Provided reliable mechanical properties	Enabled efficient cell proliferation and adhesion on scaffold fibers	Displayed an appropriate degradation rate	Promoted stratified cell seeding and chondrogenesis	[56]
	Significantly increased strength of regenerated tendon	Showed no cytotoxicity and no adverse effect on rabbit BMMSC proliferation	PLGA mass loss: 25% (4 weeks), 43.3% (8 weeks), 75.7% (12 weeks)	Improved collagen organization and fibrocartilage deposition	[91]
Ligament–bone interface	Linear stiffness: 130.6 ± 12.54 N mm^{-1}; compressive modulus: 29.03 ± 3.35 MPa	Maintained cell viability	Not described	Promoted rapid tissue infiltration, vascularization, and compartmentalization	[60]
	Increased tensile toughness, modulus, and yield stress	Improved cell attachment and homogeneous cell distribution	Supported bone regeneration with simultaneous scaffold degradation	Induced MSC differentiation toward the osteoblast lineage; coordinated bone and periodontal regeneration	[92]
	Facilitated improved integration and enhanced mechanical properties	Demonstrated optimal cellular affinity and osteogenic potential for BMMSC differentiation	Not described	Promoted stem cell differentiation into tendon and bone cells; enhanced ACL repair and healing	[93]

Abbreviations: ACL: Anterior cruciate ligament; ADMSCs: Autologous adipose-derived mesenchymal stem cells; BMMSCs: Bone marrow mesenchymal stem cells; MSC: Mesenchymal stem cell; PLGA: poly(lactic-*co*-glycolic acid).

doi: 10.36922/IJB025410419

continuity with biologically specific gradient distributions will require innovations in material systems and printing strategies. Moreover, reproducing the anisotropic collagen fiber orientation and progressive mineralization patterns of the native interface remains a critical hurdle.[104,105] From a materials standpoint, the native tendons and ligaments endure complex tensile, compressive, and shear forces, demanding scaffolds with high load-bearing capacity, fatigue resistance, and dynamic adaptability.[106,107] Existing biomaterials often struggle to strike a balance between printability and long-term mechanical stability, highlighting the urgent need to develop novel composite or hybrid materials.[108] In addition, integrating diverse biological cues and cell sources is indispensable for engineering optimal multitissue interfaces.[52,109] Scaffolds must not only support cell adhesion, proliferation, and differentiation but also actively coordinate osteogenesis, chondrogenesis, and tenogenesis in a spatially regulated manner.[110] From biological and translational perspectives, several key obstacles continue to impede the clinical application of 3D-bioprinted constructs. The precise spatiotemporal delivery of bioactive signals, such as growth factors, peptides, and extracellular vesicles, remains an area requiring substantial refinement. Additionally, limitations in printing resolution, bioink properties, and immunocompatibility must be addressed to ensure reproducibility and safety.[111,112] Beyond the technical aspects, tissue integration and regulatory approval represent crucial bottlenecks in translating laboratory-scale constructs into clinical-grade therapeutic products. Overcoming these multifaceted challenges is essential for advancing 3D bioprinting from experimental innovation to practical orthopedic applications.

Future progress will depend on continuous innovations in scaffold design, functional materials, and biomanufacturing technologies to engineer musculoskeletal interfaces with native-like gradient mechanics. Future research should place greater emphasis on the role of mechanobiological principles in interfacial regeneration. By integrating materials science, tissue engineering, biomechanics, and computational modeling, it will be possible to better elucidate the dynamic interactions among cells, biomaterials, and their mechanical environment.[113] The development of next-generation multifunctional biomaterials represents another promising direction.[114] These dynamic, stimuli-responsive materials can direct cell growth, alter degradation rates, or release bioactive molecules in response to mechanical stress or inflammatory cues.[115,116] Ideally, such materials should have mechanical strength, bioactivity, and immunomodulatory capacity while offering antibacterial or anti-inflammatory properties to minimize postoperative complications. Beyond this, integrating 3D printing with nanomedicine and synthetic biology aids in optimizing scaffold structures to better mimic the native tissue environment. Just as importantly, establishing specialized regulatory frameworks tailored to bioprinted medical products—including safety, immunogenicity, and standardization guidelines—will be essential to accelerate clinical translation. If these challenges can be addressed, 3D bioprinting may provide transformative therapeutic solutions for common injuries, such as rotator cuff tears and ACL ruptures.

In summary, 3D bioprinting holds tremendous potential for regenerating T/L–B interfaces, with its core strength in precisely reconstructing their complex hierarchical architecture and biological characteristics. The future of this technology relies on interdisciplinary innovations spanning biomaterials science, biomechanics, tissue engineering, and biomanufacturing. By overcoming current barriers in scaffold design, bioactivity, and translational manufacturing, 3D bioprinting could evolve from a conceptual strategy into a clinically viable solution, ultimately enabling functional regeneration of the T/L–B interface.

Acknowledgments

None

Funding

This work was funded by the National Natural Science Foundation of China (Grabt Nos. 82072514 and 82272569).

Conflict of interest

The authors declare that they have no conflicts of interest.

Author contributions

Conceptualization: Ying Ji
Writing–original draft: Ying Ji and Zheng Lv
Writing–review & editing: All authors
Supervision: Xin Tang
Visualization: Hongfu Jin and Jiahui Chen
Funding acquisition: Xin Tang
All the authors have read and agreed to the published version of the manuscript.

Ethics approval and consent to participate

Not applicable.

Consent for publication

Not applicable.

Availability of data

Not applicable.

References

1. Wang D, Zhang X, Huang S, *et al*. Engineering multi-tissue units for regenerative medicine: Bone-tendon-muscle units of the rotator cuff. *Biomaterials*. 2021;272:120789. doi: 10.1016/j.biomaterials.2021.120789
2. Rossetti L, Kuntz LA, Kunold E, *et al*. The microstructure and micromechanics of the tendon-bone insertion. *Nat Mater*. 2017;16(6):664–670. doi: 10.1038/nmat4863
3. Moffat KL, Sun WH, Pena PE, *et al*. Characterization of the structure-function relationship at the ligament-to-bone interface. *Proc. Natl Acad Sci USA*. 2008;105(23):7947–7952. doi: 10.1073/pnas.0712150105
4. Zhu C, Qiu J, Thomopoulos S, Xia Y. Augmenting tendon-to-bone repair with functionally graded scaffolds. *Adv. Healthcare Mater*. 2021;10(9):e2002269. doi: 10.1002/adhm.202002269
5. Wang H, He K, Cheng CK. The structure, biology, and mechanical function of tendon/ligament-bone interfaces. *Tissue Eng Part B Rev*. 2024;30(5):545–558. doi: 10.1089/ten.TEB.2023.0295
6. Zhong S, Lan Y, Liu J, *et al*. Advances focusing on the application of decellularization methods in tendon-bone healing. *J Adv Res*. 2025;67:361–372. doi: 10.1016/j.jare.2024.01.020
7. Lu HH, Thomopoulos S. Functional attachment of soft tissues to bone: Development, healing, and tissue engineering. *Annu Rev Biomed Eng*. 2013;15:201–226. doi: 10.1146/annurev-bioeng-071910-124656
8. Khalak FA, Decuyper JM, Khalak KA, Alonso SR, Saenz-Del-Burgo L, Pedraz Muñoz JL. 3D bioprinting approaches for musculoskeletal interfaces in tissue engineering. *Int J Pharm*. 2025;682:125939. doi: 10.1016/j.ijpharm.2025.125939
9. Maffulli N, Longo UG, Gougoulias N, Caine D, Denaro V. Sport injuries: A review of outcomes. *Br Med Bull*. 2011;97:47–80. doi: 10.1093/bmb/ldq026
10. Bedi A, Bishop J, Keener J, *et al*. Rotator cuff tears. *Nat Rev Dis Primers*. 2024;10(1):8. doi: 10.1038/s41572-024-00492-3
11. Maniar N, Cole MH, Bryant AL, Opar DA. Muscle force contributions to anterior cruciate ligament loading. *Sports Med (Auckland, NZ)*. 2022;52(8):1737–1750. doi: 10.1007/s40279-022-01674-3
12. Bram JT, Magee LC, Mehta NN, Patel NM, Ganley TJ. Anterior cruciate ligament injury incidence in adolescent athletes: A systematic review and meta-analysis. *Am J Sports Med*. 2021;49(7):1962–1972. doi: 10.1177/0363546520959619
13. Font Tellado S, Balmayor ER, Van Griensven M. Strategies to engineer tendon/ligament-to-bone interface: Biomaterials, cells and growth factors. *Adv Drug Deliv Rev*. 2015;94:126–40. doi: 10.1016/j.addr.2015.03.004
14. Lei T, Zhang T, Ju W, *et al*. Biomimetic strategies for tendon/ligament-to-bone interface regeneration. *Bioact Mater*. 2021;6(8):2491–2510. doi: 10.1016/j.bioactmat.2021.01.022
15. Chen S, McCarthy A, John JV, Su Y, Xie J. Converting 2D nanofiber membranes to 3D hierarchical assemblies with structural and compositional gradients regulates cell behavior. *Adv Mater (Deerfield Beach, Fla)*. 2020;32(43):e2003754. doi: 10.1002/adma.202003754
16. Yang R, Zheng Y, Zhang Y, *et al*. Bipolar metal flexible electrospun fibrous membrane based on metal-organic framework for gradient healing of tendon-to-bone interface regeneration. *Adv Healthc Mater*. 2022;11(12):e2200072. doi: 10.1002/adhm.202200072
17. Chen Y, Li Y, Zhu W, Liu Q. Biomimetic gradient scaffolds for the tissue engineering and regeneration of rotator cuff enthesis. *Biofabrication*. 2024;16(3). doi: 10.1088/1758-5090/ad467d
18. Chen K, Liu Z, Zhou X, *et al*. Hierarchy reproduction: Multiphasic strategies for tendon/ligament-bone junction repair. *Biomat Res*. 2025;29:0132. doi: 10.34133/bmr.0132
19. Fang L, Lin X, Xu R, *et al*. Advances in the development of gradient scaffolds made of nano-micromaterials for musculoskeletal tissue regeneration. *Nano-Micro Lett*. 2024;17(1):75. doi: 10.1007/s40820-024-01581-4
20. Ostrovidov S, Salehi S, Costantini M, *et al*. 3D bioprinting in skeletal muscle tissue engineering. *Small (Weinheim an der Bergstrasse, Germany)*. 2019;15(24):e1805530. doi: 10.1002/smll.201805530
21. Mandrycky C, Wang Z, Kim K, Kim DH. 3D bioprinting for engineering complex tissues. *Biotechnol Adv*. 2016;34(4):422–434. doi: 10.1016/j.biotechadv.2015.12.011
22. Mei Q, Rao J, Bei HP, Liu Y, Zhao X. 3D bioprinting photo-crosslinkable hydrogels for bone and cartilage repair. *Int J Bioprint*. 2021;7(3):367. doi: 10.18063/ijb.v7i3.367
23. Fang W, Yang M, Wang L, *et al*. Hydrogels for 3D bioprinting in tissue engineering and regenerative medicine: Current progress and challenges. *Int J Bioprint*. 2023;9(5):759. doi: 10.18063/ijb.759

24. Park W, Gao G, Cho DW. Tissue-specific decellularized extracellular matrix bioinks for musculoskeletal tissue regeneration and modeling using 3d bioprinting technology. *Int J Mol Sci*. 2021;22(15). doi: 10.3390/ijms22157837

25. Altunbek M, Afghah F, Caliskan OS, Yoo JJ, Koc B. Design and bioprinting for tissue interfaces. *Biofabrication*. 2023;15(2). doi: 10.1088/1758-5090/acb73d

26. Bai X, Yang Y, Chu J, Deng Y, Li M, Yang H. 3D bioprinting patient-specific grafts for tendon/ligament repair in motion: Emerging trends and challenges. *Front Bioeng Biotechnol*. 2025;13:1643430. doi: 10.3389/fbioe.2025.1643430

27. Xu T, Rao J, Mo Y, *et al*. 3D printing in musculoskeletal interface engineering: Current progress and future directions. *Adv Drug Deliv Rev*. 2025;219:115552. doi: 10.1016/j.addr.2025.115552

28. Chae S, Cho DW. Biomaterial-based 3D bioprinting strategy for orthopedic tissue engineering. *Acta Biomater*. 2023;156:4–20. doi: 10.1016/j.actbio.2022.08.004

29. Chen P, Cui L, Fu SC, *et al*. The 3D-printed PLGA scaffolds loaded with bone marrow-derived mesenchymal stem cells augment the healing of rotator cuff repair in the rabbits. *Cell Transplant*. 2020;29:963689720973647. doi: 10.1177/0963689720973647

30. Micalizzi S, Russo L, Giacomelli C, *et al*. Multimaterial and multiscale scaffold for engineering enthesis organ. *Int J Bioprint*. 2023;9(5):763. doi: 10.18063/ijb.763

31. Murphy SV, Atala A. 3D bioprinting of tissues and organs. *Nat Biotechnol*. 2014;32(8):773–785. doi: 10.1038/nbt.2958

32. Schwab A, Levato R, D'Este M, Piluso S, Eglin D, Malda J. Printability and shape fidelity of bioinks in 3d bioprinting. *Chem Rev*. 2020;120(19):11028–11055. doi: 10.1021/acs.chemrev.0c00084

33. Lee SJ, Jeong W, Atala A. 3D bioprinting for engineered tissue constructs and patient-specific models: Current Progress and prospects in clinical applications. *Adv Mater (Deerfield Beach, Fla)*. 2024;36(49):e2408032. doi: 10.1002/adma.202408032

34. Malda J, Visser J, Melchels FP, *et al*. 25th anniversary article: Engineering hydrogels for biofabrication. *Adv Mater (Deerfield Beach, Fla)*. 2013;25(36):5011–5028. doi: 10.1002/adma.201302042

35. Derby B. Printing and prototyping of tissues and scaffolds. *Science (New York, NY)*. 2012;338(6109):921–926. doi: 10.1126/science.1226340

36. Li L, Wang P, Liang H, *et al*. Design of a Haversian system-like gradient porous scaffold based on triply periodic minimal surfaces for promoting bone regeneration. *J Adv Res*. 2023;54:89–104. doi: 10.1016/j.jare.2023.01.004

37. Liu X, Hao M, Chen Z, *et al*. 3D bioprinted neural tissue constructs for spinal cord injury repair. *Biomaterials*. 2021;272:120771. doi: 10.1016/j.biomaterials.2021.120771

38. Shapira A, Dvir T. 3D tissue and organ printing-hope and reality. *Adv Sci (Weinheim, Baden-Wurttemberg, Germany)*. 2021;8(10):2003751. doi: 10.1002/advs.202003751

39. Matai I, Kaur G, Seyedsalehi A, McClinton A, Laurencin CT. Progress in 3D bioprinting technology for tissue/organ regenerative engineering. *Biomaterials*. 2020;226:119536. doi: 10.1016/j.biomaterials.2019.119536

40. Wang Z, Kapadia W, Li C, *et al*. Tissue-specific engineering: 3D bioprinting in regenerative medicine. *J Control Rel: Offic J Control Rel Soc*. 10 2021;329:237–256. doi: 10.1016/j.jconrel.2020.11.044

41. Akbari M, Khademhosseini A. Tissue bioprinting for biology and medicine. *Cell*. 2022;185(15):2644–2648. doi: 10.1016/j.cell.2022.06.015

42. Liu W, Zhang YS, Heinrich MA, *et al*. Rapid continuous multimaterial extrusion bioprinting. *Adv Mater (Deerfield Beach, Fla)*. 2017;29(3). doi: 10.1002/adma.201604630

43. Jiang X, Kong Y, Kuss M, *et al*. 3D bioprinting of multilayered scaffolds with spatially differentiated ADMSCs for rotator cuff tendon-to-bone interface regeneration. *Appl Mater Today*. 2022;27:101510. doi: 10.1016/j.apmt.2022.101510

44. Ker ED, Nain AS, Weiss LE, *et al*. Bioprinting of growth factors onto aligned sub-micron fibrous scaffolds for simultaneous control of cell differentiation and alignment. *Biomaterials*. 2011;32(32):8097–9107. doi: 10.1016/j.biomaterials.2011.07.025

45. Miri AK, Nieto D, Iglesias L, *et al*. Microfluidics-enabled multimaterial maskless stereolithographic bioprinting. *Adv Mater (Deerfield Beach, Fla)*. 2018;30(27):e1800242. doi: 10.1002/adma.201800242

46. Xie X, Wang Y, Li Z, *et al*. Recent advances in gradient biomimetic scaffolds for tendon-bone interface regeneration. *Front Bioeng Biotechnol*. 2025;13:1629816. doi: 10.3389/fbioe.2025.1629816

47. Du L, Qin C, Zhang H, *et al*. Multicellular Bioprinting of Biomimetic Inks for Tendon-to-Bone Regeneration. *Adv Sci (Weinheim, Baden-Wurttemberg, Germany)*. 2023;10(21):e2301309. doi: 10.1002/advs.202301309

48. Chae S, Sun Y, Choi YJ, Ha DH, Jeon I, Cho DW. 3D cell-printing of tendon-bone interface using tissue-derived

extracellular matrix bioinks for chronic rotator cuff repair. *Biofabrication*. 2021;13(3). doi: 10.1088/1758-5090/abd159

49. Zhu Y, Yu X, Liu H, *et al*. Strategies of functionalized GelMA-based bioinks for bone regeneration: Recent advances and future perspectives. *Bioact Mater*. 2024;38:346–373. doi: 10.1016/j.bioactmat.2024.04.032

50. Abbasi N, Ivanovski S, Gulati K, Love RM, Hamlet S. Role of offset and gradient architectures of 3-D melt electrowritten scaffold on differentiation and mineralization of osteoblasts. *Biomater Res*. 2020;24:2. doi: 10.1186/s40824-019-0180-z

51. Zhang X, Song W, Han K, *et al*. Three-dimensional bioprinting of a structure-, composition-, and mechanics-graded biomimetic scaffold coated with specific decellularized extracellular matrix to improve the tendon-to-bone healing. *ACS Appl Mater Interfaces*. 2023;15(24):28964–28980. doi: 10.1021/acsami.3c03793

52. Chae S, Yong U, Park W, *et al*. 3D cell-printing of gradient multi-tissue interfaces for rotator cuff regeneration. *Bioact. Mater*. 2023;19:611–625. doi: 10.1016/j.bioactmat.2022.05.004

53. Rak Kwon D, Jung S, Jang J, Park GY, Suk Moon Y, Lee SC. A 3-Dimensional bioprinted scaffold with human umbilical cord blood-mesenchymal stem cells improves regeneration of chronic full-thickness rotator cuff tear in a rabbit model. *Am J Sports Med*. 2020;48(4):947–958. doi: 10.1177/0363546520904022

54. Du L, Wu J, Han Y, Wu C. Immunomodulatory multicellular scaffolds for tendon-to-bone regeneration. *Sci. Adv*. 2024;10(10):eadk6610. doi: 10.1126/sciadv.adk6610

55. Anjum S, Li T, Saeed M, Ao Q. Exploring polysaccharide and protein-enriched decellularized matrix scaffolds for tendon and ligament repair: A review. *Int J Biol Macromol*. 2024;254(Pt 2):127891. doi: 10.1016/j.ijbiomac.2023.127891

56. Cao Y, Yang S, Zhao D, *et al*. Three-dimensional printed multiphasic scaffolds with stratified cell-laden gelatin methacrylate hydrogels for biomimetic tendon-to-bone interface engineering. *J Orthop Transl*. 2020;23:89–100. doi: 10.1016/j.jot.2020.01.004

57. Han J, Han SC, Kim YK, *et al*. Bioactive scaffold with spatially embedded growth factors promotes bone-to-tendon interface healing of chronic rotator cuff tear in rabbit model. *Am J Sports Med*. 2023;51(9):2431–2442. doi: 10.1177/03635465231180289

58. Bai L, Han Q, Meng Z, *et al*. Bioprinted living tissue constructs with layer-specific, growth factor-loaded microspheres for improved enthesis healing of a rotator cuff. *Acta Biomater*. 2022;154:275–289. doi: 10.1016/j.actbio.2022.10.058

59. Tarafder S, Brito JA, Minhas S, Effiong L, Thomopoulos S, Lee CH. In situ tissue engineering of the tendon-to-bone interface by endogenous stem/progenitor cells. *Biofabrication*. 2019;12(1):015008. doi: 10.1088/1758-5090/ab48ca

60. Lui H, Bindra R, Baldwin J, Ivanovski S, Vaquette C. Additively manufactured multiphasic bone-ligament-bone scaffold for scapholunate interosseous ligament reconstruction. *Adv Healthcare Mater*. 2019;8(14):e1900133. doi: 10.1002/adhm.201900133

61. Feng F, He J, Li J, Mao M, Li D. Multicomponent bioprinting of heterogeneous hydrogel constructs based on microfluidic printheads. *Int J Bioprint*. 2019;5(2):202. doi: 10.18063/ijb.v5i2.202

62. Beldjilali-Labro M, Garcia Garcia A, Farhat F, *et al*. Biomaterials in tendon and skeletal muscle tissue engineering: Current trends and challenges. *Materials (Basel, Switzerland)*. 2018;11(7). doi: 10.3390/ma11071116

63. Ma D, Wang J, Zheng M, *et al*. Degradation behavior of ZE21C magnesium alloy suture anchors and their effect on ligament-bone junction repair. *Bioact. Mater*. 2023;26:128–141. doi: 10.1016/j.bioactmat.2023.02.021

64. Dong Y, Li J, Jiang Q, *et al*. Structure, ingredient, and function-based biomimetic scaffolds for accelerated healing of tendon-bone interface. *J Orthop Transl*. 2024;48:70–88. doi: 10.1016/j.jot.2024.07.007

65. Zhang X, Li K, Wang C, *et al*. Facile and rapid fabrication of a novel 3D-printable, visible light-crosslinkable and bioactive polythiourethane for large-to-massive rotator cuff tendon repair. *Bioact Mater*. 2024;37:439–458. doi: 10.1016/j.bioactmat.2024.03.036

66. Liu F, Luo S, Li J, *et al*. Laser-induced 3D graphene enabled polymer composites with improved mechanical and electrical properties toward multifunctional performance. *Adv Sci (Weinheim, Baden-Wurttemberg, Germany)*. 2025:e09039. doi: 10.1002/advs.202509039

67. Huang W, Zhang J, Singh V, *et al*. Digital light 3D printing of a polymer composite featuring robustness, self-healing, recyclability and tailorable mechanical properties. *Addit Manuf*. 2023;61:None. doi: 10.1016/j.addma.2022.103343

68. Wang J, Wu Y, Li G, *et al*. Engineering large-scale self-mineralizing bone organoids with bone matrix-inspired hydroxyapatite hybrid bioinks. *Adv Mater (Deerfield Beach, Fla)*. 2024;36(30):e2309875. doi: 10.1002/adma.202309875

69. Barrera Bernal JL, Gaytán Salvatella Í, Del Campo BIM, Alvarez Perez MA, Masuoka-Ito D. Synthesis of hydroxyapatite-gelatin composite hydrogel for bone tissue application. *Gels (Basel, Switzerland)*. 2025;11(8).

doi: 10.3390/gels11080630

70. Silva M, Gomes S, Correia C, *et al*. Biocompatible 3D-printed tendon/ligament scaffolds based on polylactic acid/graphite nanoplatelet composites. *Nanomaterials (Basel, Switzerland)*. 2023;13(18). doi: 10.3390/nano13182518

71. Balestri W, Hickman GJ, Morris RH, Hunt JA, Reinwald Y. Triphasic 3D in vitro model of bone-tendon-muscle interfaces to study their regeneration. *Cells*. 2023;12(2). doi: 10.3390/cells12020313

72. Gu J, Zhang Q, Geng M, *et al*. Construction of nanofibrous scaffolds with interconnected perfusable microchannel networks for engineering of vascularized bone tissue. *Bioact. Mater*. 2021;6(10):3254–3268. doi: 10.1016/j.bioactmat.2021.02.033

73. Hann SY, Cui H, Esworthy T, *et al*. Dual 3D printing for vascularized bone tissue regeneration. *Acta Biomater*. 2021;123:263–274. doi: 10.1016/j.actbio.2021.01.012

74. Luo Y, Zhang T, Lin X. 3D printed hydrogel scaffolds with macro pores and interconnected microchannel networks for tissue engineering vascularization. *Chem Eng J*. 2022;430:132926. doi: 10.1016/j.cej.2021.132926

75. Kim W, Kwon DR, Lee H, *et al*. 3D bioprinted multi-layered cell constructs with gradient core-shell interface for tendon-to-bone tissue regeneration. *Bioact Mater*. 2025; 43:471–490. doi: 10.1016/j.bioactmat.2024.10.002

76. Zhou B, Jiang X, Zhou X, *et al*. GelMA-based bioactive hydrogel scaffolds with multiple bone defect repair functions: Therapeutic strategies and recent advances. *Biomater Res*. 2023;27(1):86. doi: 10.1186/s40824-023-00422-6

77. Shanto PC, Park S, Fahad MAA, Park M, Lee BT. 3D bio-printed proteinaceous bioactive scaffold loaded with dual growth factor enhanced chondrogenesis and in situ cartilage regeneration. *Bioact Mater*. 2025;46:365–385. doi: 10.1016/j.bioactmat.2024.12.021

78. Choe G, Lee M, Oh S, *et al*. Three-dimensional bioprinting of mesenchymal stem cells using an osteoinductive bioink containing alginate and BMP-2-loaded PLGA nanoparticles for bone tissue engineering. *Biomater Adv*. 2022; 136:212789. doi: 10.1016/j.bioadv.2022.212789

79. Lu J, Gao Y, Cao C, *et al*. 3D bioprinted scaffolds for osteochondral regeneration: advancements and applications. *Mater Today Bio*. 2025;32:101834. doi: 10.1016/j.mtbio.2025.101834

80. Yu K, Huangfu H, Qin Q, *et al*. Application of bone marrow-derived macrophages combined with bone mesenchymal stem cells in dual-channel three-dimensional bioprinting scaffolds for early immune regulation and osteogenic induction in rat calvarial defects. *ACS Appl Mater Interf*. 2022;14(41):47052–47065. doi: 10.1021/acsami.2c13557

81. Liang W, Ao R, Xu M, *et al*. Bifunctional adECM bioscaffold with STIM1-ASCs and IGF-2 promotes functional masseter VML repair via myogenesis and fibrosis suppression. *Bioact Mater*. 2025;54:466–491. doi: 10.1016/j.bioactmat.2025.08.019

82. Thattaruparambil Raveendran N, Vaquette C, Meinert C, Samuel Ipe D, Ivanovski S. Optimization of 3D bioprinting of periodontal ligament cells. *Dent Mater: Offic Publ Acad Dent Mater*. 2019;35(12):1683–1694. doi: 10.1016/j.dental.2019.08.114

83. Jiang X, Wu S, Kuss M, *et al*. 3D printing of multilayered scaffolds for rotator cuff tendon regeneration. *Bioact Mater*. 2020;5(3):636–643. doi: 10.1016/j.bioactmat.2020.04.017

84. Park SH, Choi YJ, Moon SW, *et al*. Three-dimensional bio-printed scaffold sleeves with mesenchymal stem cells for enhancement of tendon-to-bone healing in anterior cruciate ligament reconstruction using soft-tissue tendon graft. *Arthroscopy*. 2018;34(1):166–179. doi: 10.1016/j.arthro.2017.04.016

85. Ni Y, Tian B, Lv J, *et al*. 3D-printed PCL scaffolds loaded with bFGF and BMSCs enhance tendon-bone healing in rat rotator cuff tears by immunomodulation and osteogenesis promotion. *ACS Biomater Sci Eng*. 2025;11(2): 1123–1139. doi: 10.1021/acsbiomaterials.4c02340

86. Wang L, Wang C, Wu S, Fan Y, Li X. Influence of the mechanical properties of biomaterials on degradability, cell behaviors and signaling pathways: Current progress and challenges. *Biomater Sci*. 2020;8(10):2714–2733. doi: 10.1039/d0bm00269k

87. Jia B, Huang H, Dong Z, *et al*. Degradable biomedical elastomers: Paving the future of tissue repair and regenerative medicine. *Chem Soc Rev*. 2024;53(8):4086–4153. doi: 10.1039/d3cs00923h

88. Li C, Guo C, Fitzpatrick V, *et al*. Design of biodegradable, implantable devices towards clinical translation. *Nat Rev Mater*. 2020;5(1):61–81. doi: 10.1038/s41578-019-0150-z

89. L GE, Farias NC, J SC, *et al*. Designing sustainable polymer blends: Tailoring mechanical properties and degradation behaviour in PHB/PLA/PCL blends in a seawater environment. *Polymers*. 2023;15(13). doi: 10.3390/polym15132874

90. Zhang X, Wu Y, Han K, *et al*. 3-Dimensional bioprinting of a tendon stem cell-derived exosomes loaded scaffold to bridge the unrepairable massive rotator cuff tear. *Am J Sports Med*. 2024;52(9):2358–2371.

doi: 10.1177/03635465241255918

91. Chen P, Cui L, Chen G, *et al*. The application of BMP-12-overexpressing mesenchymal stem cells loaded 3D-printed PLGA scaffolds in rabbit rotator cuff repair. *Int J Biol Macromol*. 2019;138:79–88.
doi: 10.1016/j.ijbiomac.2019.07.041

92. Golafshan N, Castilho M, Daghrery A, *et al*. Composite graded melt electrowritten scaffolds for regeneration of the periodontal ligament-to-bone interface. *ACS Appl Mater Interf*. 2023;15(10):12735–12749.
doi: 10.1021/acsami.2c21256

93. Yu C, Chen R, Chen J, *et al*. Enhancing tendon-bone integration and healing with advanced multi-layer nanofiber-reinforced 3D scaffolds for acellular tendon complexes. *Mater Today Bio*. 2024;26:101099.
doi: 10.1016/j.mtbio.2024.101099

94. Luo W, Wang Y, Han Q, *et al*. Advanced strategies for constructing interfacial tissues of bone and tendon/ligament. *J Tissue Eng*. 2022;13:20417314221144714.
doi: 10.1177/20417314221144714

95. Tang Y, Wang Z, Xiang L, Zhao Z, Cui W. Functional biomaterials for tendon/ligament repair and regeneration. *Regener Biomater*. 2022;9:rbac062.
doi: 10.1093/rb/rbac062

96. Steltzer SS, Abraham AC, Killian ML. Interfacial tissue regeneration with bone. *Curr Osteop Rep*. 2024;22(2):290–298.
doi: 10.1007/s11914-024-00859-1

97. Golman M, Abraham AC, Kurtaliaj I, *et al*. Toughening mechanisms for the attachment of architectured materials: The mechanics of the tendon enthesis. *Sci Adv*. 2021;7(48):eabi5584.
doi: 10.1126/sciadv.abi5584

98. Li Y, Zhou M, Zheng W, Yang J, Jiang N. Scaffold-based tissue engineering strategies for soft-hard interface regeneration. *Regener Biomater*. 2023;10:rbac091.
doi: 10.1093/rb/rbac091

99. Chen C, Shi Q, Li M, *et al*. Engineering an enthesis-like graft for rotator cuff repair: An approach to fabricate highly biomimetic scaffold capable of zone-specifically releasing stem cell differentiation inducers. *Bioact Mater*. 2022;16:451–471.
doi: 10.1016/j.bioactmat.2021.12.021

100. Sun Han Chang RA, Shanley JF, Kersh ME, Harley BAC. Tough and tunable scaffold-hydrogel composite biomaterial for soft-to-hard musculoskeletal tissue interfaces. *Sci Adv*. 2020;6(34):eabb6763.
doi: 10.1126/sciadv.abb6763

101. Rose JC, De Laporte L. Hierarchical design of tissue regenerative constructs. *Adv Healthc Mater*. 2018;7(6):e1701067.
doi: 10.1002/adhm.201701067

102. Kang HW, Lee SJ, Ko IK, Kengla C, Yoo JJ, Atala A. A 3D bioprinting system to produce human-scale tissue constructs with structural integrity. *Nat Biotechnol*. 2016;34(3):312–319.
doi: 10.1038/nbt.3413

103. Potyondy T, Uquillas JA, Tebon PJ, *et al*. Recent advances in 3D bioprinting of musculoskeletal tissues. *Biofabrication*. 2021;13(2).
doi: 10.1088/1758-5090/abc8de

104. Xie X, Cai J, Li D, *et al*. Multiphasic bone-ligament-bone integrated scaffold enhances ligamentization and graft-bone integration after anterior cruciate ligament reconstruction. *Bioact Mater*. 2024;31:178–191.
doi: 10.1016/j.bioactmat.2023.08.004

105. Pitta Kruize C, Panahkhahi S, Putra NE, *et al*. Biomimetic approaches for the design and fabrication of bone-to-soft tissue interfaces. *ACS Biomater Sci Eng*. 2023;9(7):3810–3831.
doi: 10.1021/acsbiomaterials.1c00620

106. Aykora D, Taşçı B, Şahin MZ, *et al*. Tendon regeneration deserves better: Focused review on In vivo models, artificial intelligence and 3D bioprinting approaches. *Front Bioeng Biotechnol*. 2025;13:1580490.
doi: 10.3389/fbioe.2025.1580490

107. Gracey E, Burssens A, Cambré I, *et al*. Tendon and ligament mechanical loading in the pathogenesis of inflammatory arthritis. *Nat Rev Rheumatol*. 2020;16(4):193–207.
doi: 10.1038/s41584-019-0364-x

108. Bertsch P, Diba M, Mooney DJ, Leeuwenburgh SCG. Self-healing injectable hydrogels for tissue regeneration. *Chem Rev*. 2023;123(2):834–873.
doi: 10.1021/acs.chemrev.2c00179

109. Li Y, Chen C, Jiang J, *et al*. Bioactive film-guided soft-hard interface design technology for multi-tissue integrative regeneration. *Adv Sci (Weinheim, Baden-Wurttemberg, Germany)*. 2022;9(15):e2105945.
doi: 10.1002/advs.202105945

110. Xiao L, Sun Y, Liao L, Su X. Response of mesenchymal stem cells to surface topography of scaffolds and the underlying mechanisms. *J Mater Chem B*. 2023;11(12):2550–2567.
doi: 10.1039/d2tb01875f

111. Agarwal T, Onesto V, Banerjee D, *et al*. 3D bioprinting in tissue engineering: Current state-of-the-art and challenges towards system standardization and clinical translation. *Biofabrication*. 2025;17(4).
doi: 10.1088/1758-5090/ade47a

112. Raees S, Ullah F, Javed F, *et al*. Classification, processing, and applications of bioink and 3D bioprinting: A detailed review. *Int J Biol Macromol*. 2023;232:123476.
doi: 10.1016/j.ijbiomac.2023.123476

113. Wang Z, Xiang L, Lin F, Tang Y, Cui W. 3D bioprinting of emulating homeostasis regulation for regenerative

medicine applications. *J Control Rel: Offic J Control Rel Soc*. 2023;353:147–165.
doi: 10.1016/j.jconrel.2022.11.035

114. Yuan Z, Bai X, Li S, *et al*. Multimaterial and multidimensional bioprinting in regenerative medicine: Advances, limitations, and future directions. *Adv Healthc Mater*. 2025;14(18):e2500475.
doi: 10.1002/adhm.202500475

115. Mozammal HMD, Lee H. A comprehensive review in the advancements of bioprinting for tissue engineering using polysaccharide biomaterials and a future strategies. *Int J Biol Macromol*. 2025;322(Pt 3):146667.
doi: 10.1016/j.ijbiomac.2025.146667

116. Li Y, Wu J, He C, *et al*. 3D prestress bioprinting of directed tissues. *Adv Healthc Mater*. 2023;12(28):e2301487.
doi: 10.1002/adhm.202301487

ACCSCIENCE PUBLISHING

International Journal of Bioprinting

REVIEW ARTICLE

Toward functional bone bioprinting: Addressing the overlooked challenges of mechanical compliance

Amin Ebrahimi Sadrabadi[1,2], Payam Baei[3], Yalda Alibeigian[1], Mohamadreza Baghaban Eslaminejad[1]*, and Samaneh Hosseini[1,3]*

[1] Department of Stem Cells and Developmental Biology, Cell Science Research Center, Royan Institute for Stem Cell Biology and Technology, ACECR, Tehran, Iran

[2] Department of Tissue Engineering, Faculty of Basic Sciences and Advanced Technologies in Medicine, Royan Institute, ACECR, Tehran, Iran

[3] Department of Cell Engineering, Cell Science Research Center, Royan Institute for Stem Cell Biology and Technology, ACECR, Tehran, Iran

(This article belongs to the *Special Issue*: *Biofabrication Breakthroughs: Innovation and Application in Bioprinting, Biomaterials, and Organoid*)

Abstract

Three-dimensional bioprinting has emerged as a transformative biofabrication technology capable of engineering complex tissue constructs for regenerative medicine. While considerable progress has been made in replicating soft tissues using hydrogel-based bioprinting, the fabrication of mechanically robust bone-mimicking constructs remains a significant challenge. The mechanical heterogeneity of bone, including its anisotropic structure, varying mineral density, and intricate extracellular matrix composition, complicates the development of bioinks that can simultaneously achieve printability, structural integrity, and cellular viability. Recent advancements have focused on optimizing the mechanical properties of bioinks through composite hydrogels, osteoinductive nanomaterials, and bioactive moieties that enhance cell adhesion and differentiation. This review examines the role of mechanical cues in directing mesenchymal stem cell fate, the interplay between material stiffness and osteogenesis, and strategies to enhance bioink performance. We highlight limitations in mechanical compliance and propose novel biomaterial designs, crosslinking strategies, and scaffold functionalization to overcome these barriers. This review aims to bridge the gap between biomaterials science and clinical translation, with the ultimate goal of advancing functional bone graft substitutes.

Keywords: 3D bioprinting; Bioinks; Bone tissue engineering; Extracellular matrix; Mechanical compliance; Regenerative medicine

***Corresponding authors:**
Mohamadreza Baghaban Eslaminejad (eslami@royaninstitute.org)

Samaneh Hosseini (hosseini.samaneh@royaninstitute.org)

Citation: Sadrabadi AE, Baei P, Alibeigian Y, Eslaminejad MB, Hosseini S. Toward functional bone bioprinting: Addressing the overlooked challenges of mechanical compliance. *Int J Bioprint*. 2026;12(1):19-37. doi: 10.36922/IJB025420425

Received: October 15, 2025
Revised: November 26, 2025
Accepted: December 3, 2025
Published online: December 3, 2025

Copyright: © 2025 Author(s). This is an Open Access article distributed under the terms of the Creative Commons Attribution License, permitting distribution, and reproduction in any medium, provided the original work is properly cited.

Publisher's Note: AccScience Publishing remains neutral with regard to jurisdictional claims in published maps and institutional affiliations.

1. Introduction

Three-dimensional (3D) bioprinting is an impressive technology for artificial bone production compared to other engineering approaches. This technology seeks to biofabricate a scaffold in a 3D architecture and mimics the exact positioning of various cell types under controlled 3D gradients of growth factors or biological molecules. As the first ingredient in the process of 3D bioprinting, bioinks need to be adjusted

by combination with growth factors, cells, and different materials, making it a challenging process. Regardless of the precise management of the nano- to macro-scale transformations in the engineered bioinks, it still encounters some difficulties that alter the final constructs and are not thoroughly investigated yet. Achieving mechanical compliance in bioprinted constructs that closely mimic native bone tissue remains a significant challenge in tissue engineering.

Recent advancements have focused on developing composite hydrogels and hybrid scaffolds that integrate multiple materials to replicate the complex mechanical properties of bone. For instance, combining natural polymers like gelatin methacrylate (GelMA) with inorganic components such as hydroxyapatite has shown promise in enhancing the mechanical strength and bioactivity of bioprinted scaffolds. These composite materials not only provide the necessary structural integrity but also support cellular functions, promoting tissue regeneration.[1,2] However, optimizing the composition and fabrication techniques to achieve the desired mechanical properties while maintaining biocompatibility requires further research. Understanding the interplay between material properties and cellular responses is crucial for the successful application of these advanced biomaterials in clinical settings.

Functional biofabrication has been hindered by various biological and nonbiological challenges that include the lack of control over cell shape, size, and orientation, inability to create complex cellular structures, and the difficulty of fabricating and controlling the mechanical properties of the microenvironments surrounding the cells *in vivo*. The mechanical properties of the extracellular matrix (ECM), particularly its stiffness, play a pivotal role in directing the fate of mesenchymal stem cells (MSCs). Studies have demonstrated that MSCs cultured on substrates with stiffness analogous to that of bone tissue (~40 kPa) tend to undergo osteogenic differentiation, whereas those on softer substrates resembling brain tissue (~0.1–1 kPa) are inclined toward neurogenic pathways. Intermediate stiffness levels, similar to muscle tissue (~10 kPa), have been shown to promote myogenic differentiation.[3] This mechanotransduction involves the regulation of gene expression and cellular functions, such as proliferation and migration, mediated through pathways like RhoA/ROCK.[4] Understanding these dynamics is crucial for developing bioinks in 3D bioprinting that not only provide structural integrity but also mimic native tissue stiffness to guide desired cellular behaviors.

Many attempts have been made to optimize the mechanical features of bioink. Utilization of composite hydrogels and additive compounds, such as osteo-promotive materials and active moieties, has transformed hydrogels into advanced materials with improved mechanical characteristics.[5-7] It was found that silver and platinum alloy nanoparticles, as well as zinc ions, improve the biological and mechanical performance of bioink and matrix deposition of MSCs.[8] The thiol-ene or click chemistry makes active moieties an appropriate agent to regulate biological and nonbiological properties of biomaterials.[9] Thiol-ene click chemistry is a robust and efficient reaction between thiol groups and carbon–carbon double bonds (alkenes), typically initiated by light or radical initiators. This reaction proceeds rapidly under mild conditions, making it highly suitable for biomedical applications. One of the key advantages of thiol-ene chemistry is its high specificity and yield, allowing for the precise fabrication of hydrogels with controllable crosslinking densities.[10] This precision enables tuning mechanical properties to match those of native tissues, crucial in tissue engineering and regenerative medicine. Additionally, the reaction's insensitivity to oxygen and its cytocompatibility make it ideal for *in situ* gelation, facilitating the encapsulation of cells and bioactive molecules without compromising their viability or function. Recent studies have demonstrated the successful application of thiol-ene click hydrogels in controlled therapeutic delivery and tissue scaffolding, highlighting their potential in advancing bioprinting technologies.[11] Additionally, the Janus-faced hydrogen bonding moieties coupled to the supramolecular network provide excellent network stability and improved mechanical strength.[12] As a result, hydrogen bonds are more stable due to the presence of active moieties, giving rise to stronger network structures. In addition, thiol-ene click chemistry produces a more efficient and cost-effective way of creating and regulating these moieties, allowing for greater control over the mechanical properties of the bioink.

Superior biofabrication approaches can develop biocompatible and shear-thinning bioinks, which could mimic bone mechanical strength while simultaneously maintaining cell/stem cell viability. Shear-thinning and thixotropic properties have hindered the development of novel mechanically optimized bioinks. These properties describe the nonlinear relationship between shear stress, shear strain, and the time-dependent changes in the viscosity of a fluid after applying force. Additives that are added to bioink to improve its mechanical features can interfere with bioink printability and counteract these features. Viscose biomaterials, such as chitosan and alginate, as well as nanoscale biomaterials, such as clay and hydroxyapatite, increase viscosity excessively, and disrupt printability.[13,14] Therefore, in order to ensure

the printability of bioink, it is important to choose additives carefully and in moderation. For bioprinted bone constructs to successfully integrate and remodel into functional bone tissue, it is imperative that they recapitulate this mechanical environment. Failure to provide an appropriate mechanical environment have significant consequences.[15] Scaffolds that are too stiff may lead to stress shielding, where the implant carries a disproportionate amount of the load, preventing the surrounding native bone and the cells within the construct from experiencing the mechanical stimuli necessary for growth and remodeling. This can result in bone resorption and implant loosening.[16] Conversely, scaffolds that are too weak will fail to provide the necessary support for cell proliferation and differentiation and may collapse under physiological loading. Therefore, the ideal bioprinted bone construct should possess mechanical properties that are not only compatible with the target anatomical location but also tailored to promote a specific cellular response.[17] This concept of "mechano-mimicking" is a central theme in modern bone tissue engineering, and a key focus of this review.

This review explores the complexities of bone bioprinting, focusing on the mechanical challenges in replicating native bone structures. We discuss the factors influencing bone mechanical strength, the influencing factors of printability, the distinct requirements for different bone bioprinting applications, and the potential strategies to overcome current limitations in bioink design (Figure 1).

2. Factors affecting mechanical properties of bone constructs

2.1. Complexity and mechanical strength of bone

Bones, as connective tissues, provide a rigid framework to support soft organs and help balance minerals, such as calcium and phosphate.[18] As a highly dynamic organ, a bone undergoes the process of remodeling that supports the minerals' hemostasis and participates in preserving the integrity of the skeleton through self-renewal.[19-21] Cortical and trabecular bones have been shown to perform these functions accurately. The bone strength, mineral density (BMD), and porosity of cortical and trabecular bone are substantially different.[22] These features are distinct in age, gender, and ethnicity.[23] Specifically, BMD is lower in women than men, decreasing almost linearly with age.[24,25] As measured by finite element analysis (FEA), young women have softer bones than young men, and both genders lose bone strength with aging.[26,27] The bone complexity has also extended to the microarchitecture of the different bone tissues. Trabecular microarchitecture and conformation vary by ethnicity and gender.[28] This variety consists of different ratios of plate-like and rod-like trabeculae morphology, making bone tissue a heterogeneous organ in terms of mechanical strengths (Figure 2A). The difference between the structures of these two types of bones has caused the variation in their mechanical strengths; as the compressive strength of the trabecular bone is estimated to fall in the range of 2–12 MPa with the elastic modulus of 0.1–5 GPa, while this value raises to 100–150 MPa for cortical bone with elastic modulus ranging from 7 to 20 GPa.[29,30] These properties vary between different types of bones as the needed force to break down the femur is around 74131.83 N, which decreases to 5833.99 N, 4412.99 N, and 1882.88 N for the humerus, tibia and patella, respectively.[31] This mechanical and microstructural diversity has raised a desire for a method that provides precise structural control in three dimensions.

2.2. Heterogeneity of bone structure and composition

A bone is a mineralized tissue that is a mixture of collagen and noncollagenous proteins, water, minerals, and some organics, whose mechanical strength can be determined based on various factors.[32] These factors include the type of bone (primary, woven, or both), density, the arrangement of collagen fibers, the amount and type of noncollagenous proteins, and the quantity of minerals and water present in the bone. All of these components work together to provide a bone with its unique strength and flexibility. Each bone is characterized by a randomized distribution of cells, collagen fibers, and osteoids.[33,34] Since lamellar bones participate in fracture repair and embryonic development, they show more rigidity compared to primary bones in the adult skeleton.[33] Cortical bone possesses greater density and resistance to stress, while trabecular bone, with its honeycomb-like structure, is the opposite. Trabecular bone's elasticity increases and its stress resistance decreases to 50 MPa,[35,36] thereby increasing elasticity and decreasing stress resistance. This is because a lamellar bone has a larger quantity of collagen fibers with higher tensile strength than a primary bone. The increased stiffness of lamellar bones is attributed to their greater mineral content, which increases their density and strength. Cortical bone has a greater ratio of mineral to organic matter, which increases its density and resistance to stress. Trabecular bone has a porous structure and a much lower mineral to organic matter ratio, which reduces its density and strength, but increases its elasticity and decreases its stress resistance.[37] The degree and quality of mineralization is another factor that could change related mechanical properties, such as elasticity, plasticity, and viscoelasticity, as low mineralization can lead to the fragility of bones.[38,39] Several studies have delineated that the mineralization pattern of bone plates and their

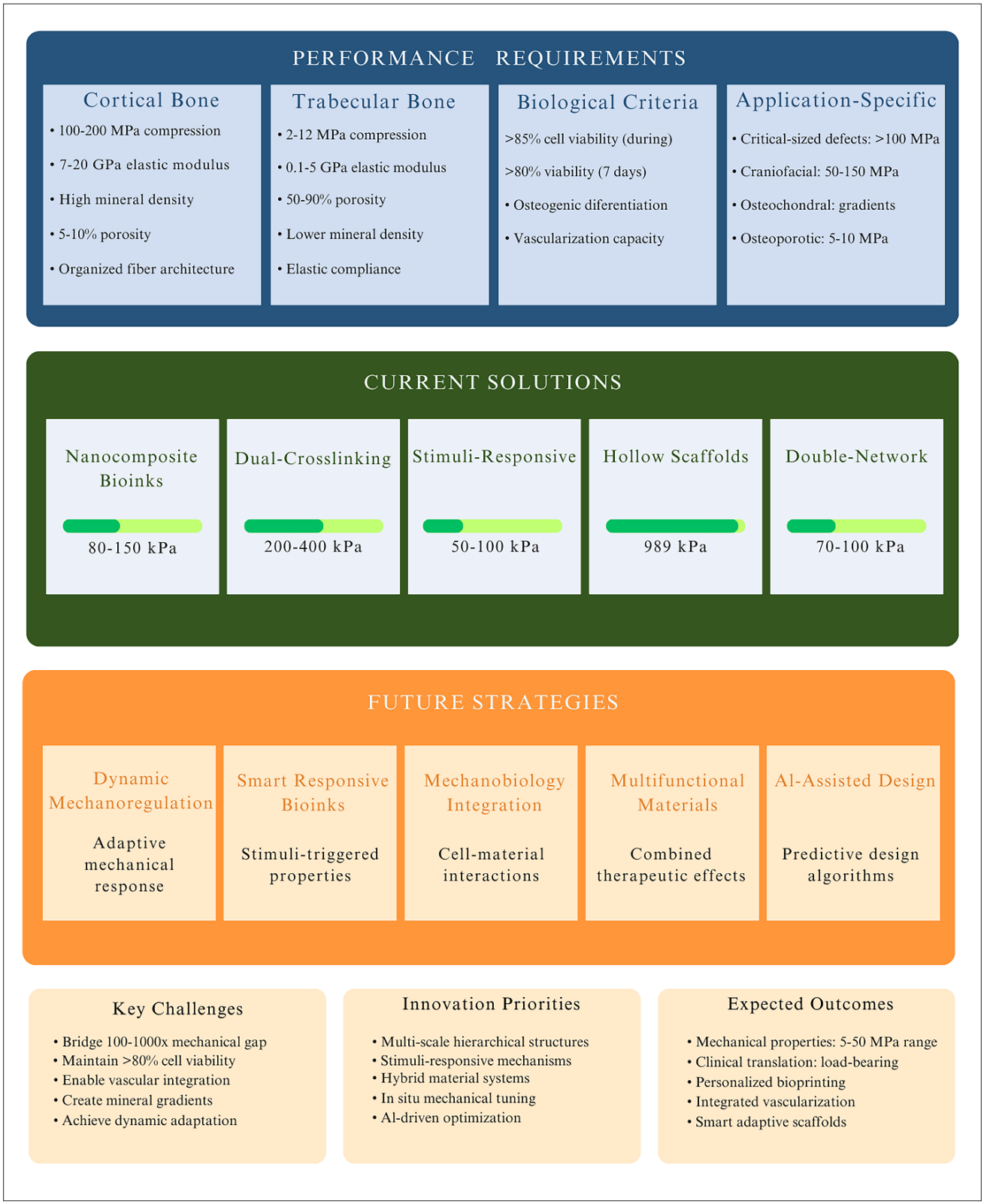


Figure 1. Comprehensive framework for mechanical compliance in bone bioprinting. Top panel presents performance requirements across bone types and clinical applications. Middle panel maps current technological solutions achieving bone mechanical properties. Bottom panel outlines future innovation strategies. Bottom boxes highlight key challenges, innovation priorities, and expected outcomes.

absolute degree of mineralization could determine the mechanical strength.[40] This is because mineralization is important for the deposition of collagen and other proteins, which are necessary for the strength of the bone. As mineralization increases, the collagen is better organized and the bones become stronger. This strength is further enhanced by the formation of hydroxyapatite crystals and other minerals, which add to the overall mineralization of the bones. The other contributing factor is porosity, defined by the distribution and magnitude of pores in bones.[41,42] Trabecular and cortical bones are recognized with a porosity varying from 50% to 90% and 5% to 10%, respectively. A slight change in the porosity significantly affects the stiffness and tolerability of the bones,[43,44] because it affects the ability of the bone to absorb energy, the rate of diffusion of substances through the bone, and the strength of the bone. The interaction and a perfect combination of these factors determine the mechanical properties of bones and make the mechanical strength of bones vary from 12.56 to 16.87 kg/mm^2.[32] Therefore, it is important to understand the correlation between porosity and the mechanical properties of bones, in order to achieve the desired strength and durability (Figure 2B). Thus far, these unique physical properties of bones have not been mimicked by any of the developed scaffolds and these features have never been successfully replicated with the use of any bioink technology. To this end, further research is needed to accurately replicate the structural composition of bones in order to effectively replicate its mechanical properties in tissue engineering scaffolds and bioinks.

2.3. Influence of substrate cues

For a long time, biochemical factors and signals were believed to be the only compounds that affected cell differentiation and determined cellular fate. However, some research has demonstrated that biophysical forces and mechanical stress derived from rigidity, elasticity, and stiffness can also effectively alter proliferation rate, survival, and differentiation and determine cellular fate (Figure 2C).[45,46] In other words, once mechanical forces have been sensed by the cells, during a mechanotransduction process, a cascade of molecular changes and biochemical signals regulate the response of the cells to the physical stimuli.[47] Biophysical stimuli are caused by factors such as surface geometry, fluid shear stress, stain, rigidity,

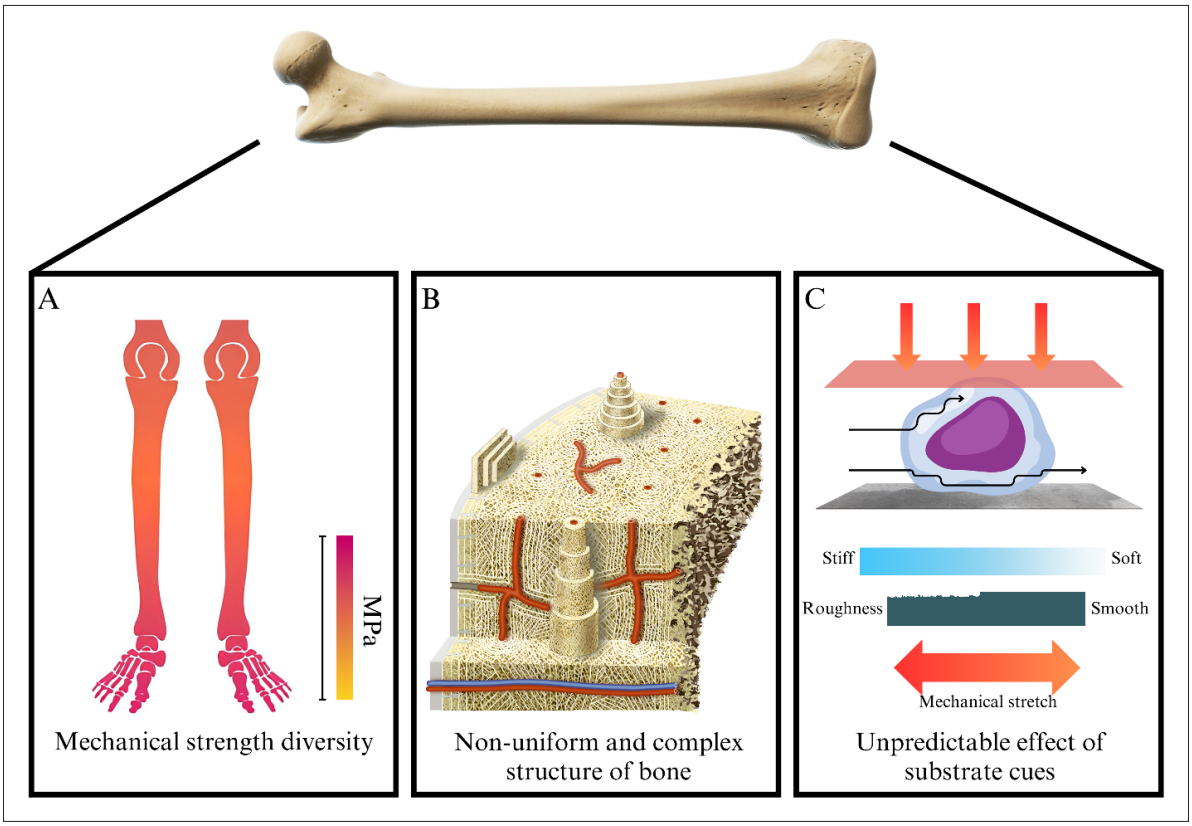


Figure 2. Key barriers for developing mechanically optimized bone mimicking constructs. (A) Diversity in bone mechanical strength; (B) Inhomogeneous and complex structure of bones; (C) Heterogeneity and complexity of substrate cues.

stiffness, and matrix surface topography.[48] The influence of physical changes typically begins with the detection of integrins. This eventually results in alteration of cytoskeleton structure by polymerization or contraction and downstream signaling reaching the nucleus.[49] These changes in cytoskeleton structure and downstream signaling can further lead to changes in gene expression, which can alter the cell's phenotypic response, such as cell shape and motility. In a study, it was shown that MSCs differentiate into neurogenic, chondrogenic, or osteogenic lineages when exposed to a range of materials with varying characteristics, from soft to rigid.[50] Controlling these substrate cues in the desired bioink is obviously not straightforward. Thus, understanding how to control the substrate cues to alter gene expression and drive differentiation is a critical step toward achieving directed differentiation of MSCs in bioinks.

A topological property of substrates may affect the self-renewal properties of stem cells, as murine embryonic stem cells (mESCs) cultured on stiff substances kept expressing Nanog and Oct3/4, as well as preserving self-renewal properties.[51] Furthermore, the expression of Sox2, another stemness-related marker, was also higher on stiff substrates compared to soft ones. This finding indicates a potential role for mechanical forces in stem cell differentiation. However, it is important to note that culturing human mesenchymal stem cells (hMSCs) in a 3D hydrogel that has a stiffness over 1 kPa might have a counterproductive effect, since their proliferation has been shown to decrease.[52] This suggests that there is an optimal stiffness that can be used to achieve the desired cell differentiation while still allowing cells to proliferate and function normally. Thus, the ideal mechanical environment should be tailored to the specific cell type in order to maximize their differentiation potential while still allowing them to proliferate and function.

Nevertheless, in another study, hydrogels with low stiffness and quasihexagonally arranged nanopatterns stimulated mechanotransduction, which led to osteogenic differentiation of MSCs.[53] It was also shown that the mechanotransduction of the nanopatterned hydrogels containing RGD (Arg-Gly-Asp) peptide was able to induce the differentiation of MSCs into osteogenic lineages. These results illustrate that cellular responses to substrate cues are not explicit. It is clear that substrate cues have unpredictable effects on stem cells, which makes it challenging to mimic an ideal bioink. The substrate cues can interact with the cells in complex ways and can trigger a cascade of events that lead to different cell responses.[54] This poses a challenge to predict cell response to a given substrate, making it much difficult to create an ideal bioink that will accurately provoke the desired response.

3. Factors affecting the printability of hydrogels

Printability is the main requirement of the bioprinting process, which refers to the capability of a substance, under specific circumstances of bioprinting, to form a 3D object in a layer-by-layer manner.[55] It could be challenging to control the properties of the hydrogel like surface tension, rheological cues, gelation kinetics, swelling properties, and finally the bioprinting process itself. [56] This is because each of these properties affects the printability of the hydrogel, and the ability to form a 3D object depends on the balance between them (Table 1). Additionally, the bioprinting technique itself can be difficult to control, as it requires precise control of the speed and pressure of the nozzle, as well as the temperature and composition of the materials used. Specifically, rheological behavior is crucial to the formation of droplets in inkjet bioprinting.[57] Therefore, only materials with a viscosity range of 10 mPa·s are considered suitable.[58,59] For instance, cell-laden hydrogels, such as collagen or fibrin, are not suitable for inkjet bioprinting, as their high viscosity (up to 10,000 mPa·s) does not permit the formation of droplets. In contrast, low-viscosity materials such as alginate- or polyethylene glycol (PEG)-based hydrogels (1–2 mPa·s) can be used in inkjet bioprinting, but they require the addition of crosslinkers to increase the viscosity to the appropriate range. Non-Newtonian fluids are most appropriate for extrusion-based bioprinting. For example, thermally sensitive and shear-thinning hydrogels such as alginate can be extruded with high resolution and accuracy due to their low viscosity at low shear rates.[60] As a result, bioink printability can sometimes be contrasted with bioink formulations, and it is impossible to maintain its printability parallel to mechanically optimized features.

The bioink must possess both thixotropic and extrudability characteristics, which determine whether it can be continuously squeezed out of the bioprinting nozzles. These attributes become critical when extra force is needed for hydrogel extrusion, which could diminish cellular viability.[61,62] For instance, to ensure the highest viability of printed cells, the extrusion pressure must be below the threshold value of 1.5 kPa. Additionally, current bioprinters are primarily designed to dispense liquid, or semiliquid materials, limiting the design of an ideal bioink with thixotropic properties.[63] Both thixotropic and extrudability properties directly limit the formulation of bioink and hinder the mechanical strength of the bioprinted

construct. For example, the use of high concentrations of hydrogel precursors, such as alginate, can result in a bioink with high mechanical strength, but this bioink is not extrudable due to its high viscosity.

Embedded cells in bioink influence its printability and indirectly determine its physical properties. Cells embedded in bioink reduce its viscosity, allowing it to be extruded through a 3D printer.[64] However, when the concentration of cells is too high, they can compromise the mechanical strength of the bioink. Therefore, it is critical to find a balance between cell concentration and hydrogel precursors in order to produce a bioink with both high mechanical strength and printability. As in a previous experiment conducted to compare the impact of the presence of hepatocarcinoma cells on the bioprinting of methacrylamide-modified gelatin (Gel-MOD), the rheological properties were modified, and the viscosity of the bioink changed along with the incorporation of the cells.[65] Also, Diamantides *et al.*[66] have investigated the influence of cell density on the rheological and printability properties of collagen bioink, illustrating that moderate cell density could improve printability. Furthermore, the capability to maintain the structural integrity of a bioprinted construct with increasing cell density requires an in-depth understanding of the material properties of the bioinks. Thus, any agent that manipulates the formulation of bioink could directly impact its printability and restrict cellular viability. As such, the formulation of bioink must be carefully designed to enable successful bioprinting and ensure cell viability.

4. Application-specific requirements for bone bioprinting

The clinical translation of bone bioprinting technology requires consideration of diverse application circumstances, each presenting unique mechanical, biological, and structural requirements. Understanding these demands is essential for designing appropriate bioinks and fabrication strategies.[75]

Critical-sized bone defects represent the most mechanically demanding application scenario. These defects, typically beyond 2–3 cm in long bones, result from trauma, tumor resection, osteomyelitis, or nonunion fractures. Bioprinted constructs for these applications must exhibit high compressive strength (100–200 MPa) to bear immediate load-bearing requirements, incorporate proangiogenic factors to support vascularization, and demonstrate controlled degradation kinetics that match new bone formation rates.[75] Recent studies have shown that composite scaffolds combining biodegradable polymers with bioceramics can achieve the necessary mechanical standards while supporting cell viability and osteogenic differentiation.[76]

Craniofacial reconstruction applications, including mandibular defects and calvarial reconstruction, focus on precise anatomical replication and mechanical function. These purposes typically require moderate mechanical properties (50–150 MPa compressive strength) but demand high geometric accuracy and smooth surface.[77] Patient-specific 3D-bioprinted constructs based on computed

Table 1. Main challenges to mechanically optimized hydrogels bioprinting

Limitation	Description	Ideal condition for printing	Possible solution	Acceptable range	Refs.
Viscosity	Hydrogels with high viscosity are difficult to print because they do not flow easily through the printer nozzle.	Low viscosity	Use a printing nozzle with a larger diameter or reduce the viscosity of the hydrogel by adding diluents or using lower-molecular-weight polymers.	100–10,000 Pa·s	[67,68]
Shear stress tolerance	Hydrogels with low shear stress tolerance are easily damaged when they are subjected to the shear stress of printing.	Low shear stress	Use a printing method with lower shear stress, such as extrusion printing or drop-on-demand printing.	0.1–10 Pa	[69,70]
Gelation speed	Hydrogels with fast gelation speeds may subject to very rapid solidification during printing, which can lead to clogging of the printer nozzle.	Slow gelation speed	Use a hydrogel with a slower gelation speed or reduce the gelation speed by adjusting the crosslinking conditions.	1–60 min	[71,72]
Printability resolution	Hydrogels with low printability resolution cannot be used to print constructs with fine details.	High printability resolution	Use a printing method with high resolution, such as stereolithography (SLA) or digital light processing (DLP).	50–500 μm	[73,74]

tomography (CT) imaging have demonstrated superior outcomes compared to conventional approaches by enabling precise anatomical fit.[78] Multimaterial bioprinting creates gradient scaffolds with cortical-like regions transitioning to trabecular-like zones, recapitulating bone's mechanical heterogeneity.[79,80]

Osteochondral tissue engineering presents unique challenges due to the need for gradient structures mimicking the transition from articular cartilage to subchondral bone. This application requires bioprinting of stratified constructs with spatially varying mechanical properties[81]: soft hydrogels (0.5–2 MPa)[82] for the cartilage layer, hydrogels with intermediate stiffness (1–10 MPa)[83] for the calcified cartilage zone, and stiffer substrate (10–20 MPa)[84] for subchondral bone. Dynamic mixing during printing creates seamless transitions, reducing delamination, and improving interfacial integration in *in vivo* models.[85] Organoid-integrated bioprinted constructs combine self-organized tissue structures (diameter 200–500 μm) with hydrogel matrices. Bone organoids demonstrate enhanced mineralization, elevated osteogenic markers and superior performance in osteochondral defect models compared to dissociated cell approaches.[86]

Osteoporotic fracture treatment requires bioprinted constructs that can integrate with mechanically compromised host bone which have reduced mineral density and altered microarchitecture. These applications benefit from bioinks incorporating osteo-promotive factors, such as bone morphogenetic proteins, parathyroid hormone (PTH) peptides, or bisphosphonates that stimulate both construct integration and host bone architecture improvement.[87] Mechanical properties should match the weakened host bone (5–10 MPa) to minimize stress shielding while providing adequate structural support.[88]

Understanding these application-specific requirements enables rational design of bioinks, scaffold architectures, and fabrication strategies tailored to clinical needs, ultimately advancing the translational potential of bone bioprinting technology.

5. Strategies to overcome mechanical challenges

Despite the variety of materials used in the production of bioinks, it seems that without additives, their drawbacks may still compromise their usage. As a result, developing new scaffolds with improved mechanical strength can be fulfilled by adding other materials and creating composite constructs. Several studies have focused on developing new composite scaffolds to promote mechanical properties for bone tissue engineering. In this section, different approaches for improving the mechanical properties of 3D-printed constructs will be discussed (Figure 3).

5.1. Developing composite constructs

5.1.1. Incorporation of bioceramic/polymer composite

A composite scaffold consisting of calcium phosphate and collagen developed using low-temperature 3D printing possesses desirable cytocompatibility, mechanical strength, and bone regeneration in a critical-sized femoral defect. By optimizing the concentration of phosphoric acid-based binder solution and supplemented collagen solution, appropriate cytocompatibility and mechanical strength were achieved. The addition of collagen to the binder solution increases the strength of the 3D-printed construct in a linear fashion, with higher collagen concentrations resulting in stronger constructs. By increasing the concentration of collagen in the solution (0–2 wt%), the maximum flexural strength could improve from 55 to 75 kPa. Implantation of such 3D-printed scaffold into a critical-sized murine femoral defect resulted in a desirable new bone formation.[89] In another study, a composite hydrogel containing alginate, polyvinyl alcohol (PVA) and hydroxyapatite (HA) with optimal rheological properties and appropriate osteoconductivity was designed for reconstruction of bone defects. The addition of HA into alginate-PVA solution enhanced the viscosity of hydrogel and simultaneously promoted the osteoconductivity of the printed scaffold. This optimized formulation represented a storage modulus of 600–1200 Pa following gelation, as depicted by rheological assessments. Moreover, the selected hydrogel revealed the average compressive modulus of 10.3 kPa and this value was continually decreased to 2.4 kPa over 14 days of immersion in culture medium. Encapsulation of mouse calvaria 3T3-E1 (MC3T3) cells within optimal hydrogel exhibited well distribution and high viability through the process of 3D printing.[60]

5.1.2. Addition of inorganic nanofillers

Nanosilicate (nSi) may also be considered as a promising biomaterial, which can be used in composite formation due to its biocompatibility and osteoinductivity features. A biomimetic nanocomposite bioink consisting of gelatin, alginate and nSi was developed for 3D bioprinting of engineered bone constructs. Incorporation of nSi considerably promoted the printability and mechanical strength of the printed constructs and improved the osteogenic differentiation of encapsulated rat bone marrow MSCs without any exogenous osteoinductive factors. Nanocomposite bioink with different concentrations of nSi (0–3%) was evaluated through a uniaxial compression test. Nanocomposites containing 2% and 3% nSi represented significantly higher compressive modulus (101.41 ± 3.11 kPa for 2% nSi and 123.59 ± 2.10 kPa for 3% nSi) in

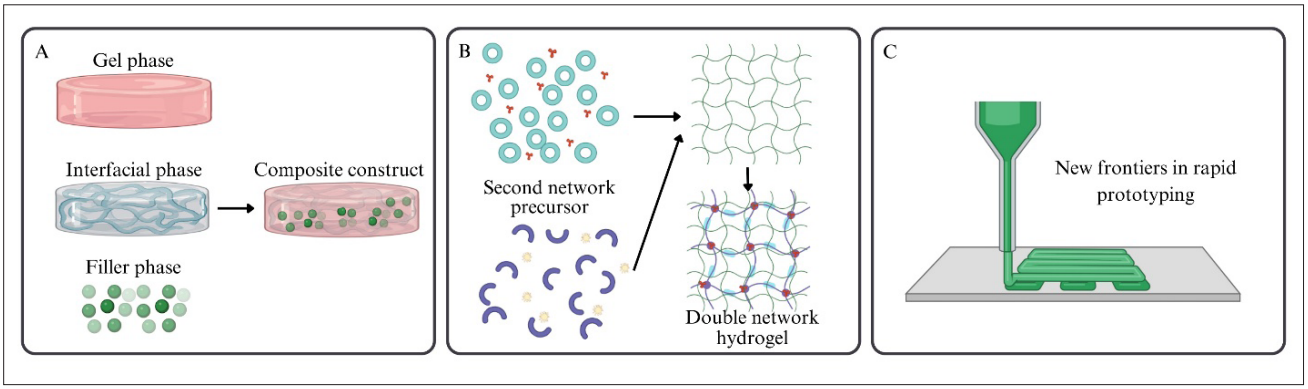


Figure 3. Different approaches for overcoming mechanical challenges in 3D bioprinting. (A) Introducing novel composite hydrogel with improved mechanical features; (B) Designing double-network hydrogel; (C) Developing an emerging technology for rapid prototyping of hydrogel.

comparison with 0% and 1% nSi (46.98 ± 1.54 kPa for 0% nSi and 57.82 ± 1.69 kPa for 1% nSi). The results of rheological and mechanical analysis revealed that the addition of nSi considerably improved the printability of nanocomposite compared to gelatin-alginate alone, and increasing the concentration of the nSi promoted the mechanical strength of the constructs.[90] In an attempt to create a 3D-printed osteogenic nanocomposite, an alginate dialdehyde-gelatin (ADA-GEL) hydrogel containing mesoporous silica–calcia nanoparticles (MSNs) along with icariin drug was developed. Incorporation of MSNs promoted the mechanical stiffness of the constructs as well as cell adhesion and proliferation, as a result of inducing apatite layer formation following immersion in simulated body fluid. The nanocomposite hydrogels represented considerably higher stiffness compared to the neat hydrogel (60 ± 15 kPa for ADA-GEL/MSN vs. 25 ± 10 kPa for ADA-GEL). The covalent interaction between flexible hydrogel and stiff MSNs results in higher stiffness of the hydrogel nanocomposite. Interestingly, the hydrogel nanocomposites containing icariin depicted higher compressive stiffness (160 ± 40 kPa) compared to the neat hydrogel. In these nanocomposites, numerous hydroxyl groups of icariin provide hydrogen bonding with amine groups of gelatin. Moreover, esterification may take place due to the interactions of the hydroxyl groups from icariin and carboxyl groups of gelatin and consequently result in higher mechanical stiffness of icariin-containing hydrogel nanocomposites. Furthermore, it has been shown that such hydrogel nanocomposites improve osteoblast proliferation, adhesion, and differentiation.[91]

In a comparative experiment, osteogenic differentiation, printability, and physiochemical features of common alginate-based bioinks, including alginate-nanocellulose (alg-ncel), alginate-$CaCl_2$ (alg-$CaCl_2$), alginate-gelatin (alg-gel), and alginate-$CaSO_4$ (alg-$CaSO_4$) have been analyzed. Among bioinks, alg-$CaSO_4$ and alg-ncel represented higher storage modulus in comparison with alg-$CaCl_2$ and alg-gel constructs (9.9 ± 4.9 kPa for alg-$CaSO_4$, 7.1 ± 0.6 kPa for alg-ncel, 4.1 ± 0.6 kPa for alg-$CaCl_2$, and 2.6 ± 1.1 kPa for alg-gel). After 7 days in culture, all hydrogels showed declines in stiffness except for the alg-ncel group, which preserved its stability. The reduction in stiffness in the alg-$CaCl_2$ and alg-$CaSO_4$ constructs following 7 days in culture may be attributed to the dissociation of calcium crosslinks. Encapsulation of MSCs in alg-$CaCl_2$ constructs during culture in the osteogenic medium revealed more osteogenic differentiation compared to the other three bioinks mentioned above.[92]

5.2. Developing double-network hydrogels

Double-network hydrogels represent an advanced biomaterial design strategy wherein two interpenetrating polymer networks with distinct crosslinking mechanisms synergistically contribute to mechanical performance. The mechanical superiority of double-network hydrogels derives from their capacity to distribute stress across both networks, with the sacrificial bonds in the first network rupturing preferentially to absorb energy, while the second network maintains overall structural continuity. Recent innovations have focused on incorporating dynamic and reversible crosslinks that enable stress relaxation while maintaining mechanical robustness.[93]

A double-network hydrogel composed of alginate, methacrylated gelatin (GelMA), and polyethylene glycol diacrylate (PEGDA) was developed as a 3D-bioprinted construct for bone reconstruction. Calcium-crosslinked alginate and created a physical network while PEGDA/GelMA formed a chemical network through covalent crosslinking. This unique double network structure provided stretchability in the bioink and enabled desirable strength and stiffness for bone remodeling. The results of

the compression test revealed that the double-network bioink possesses a compressive modulus of 78.1 kPa, strength of 60.4 kPa, strain at break of 33.9%, and toughness of 71.35 kJ/m^3.[94]

In another study, a double-network hydrogel composed of polyurethane (PU) and gelatin with adjustable mechanical features and degradation rates was prepared as bioink. The two-stage double-network structure was formed via Ca^{2+} chelation and thermal gelation at 37°C. The PU-gelatin double-network hydrogel possessed desirable elasticity and mechanical strength and could promote MSC proliferation. The biodegradable waterborne PU was the major constituent of this bioink and provided the essential elasticity, tunable mechanical characteristics, as well as shear thinning feature. However, PU possessed low viscosity, which hampered its printability. Therefore, gelatin was incorporated to improve the viscosity of bioink and provided the stability of printed construct. At room temperature, the static compressive modulus (1.5 ± 0.2 kPa), strength (5.2 ± 0.6 kPa), and deformation (69.6 ± 6.1%) of PU-gelatin hydrogel after the $CaCl_2$ treatment was higher than hydrogel without $CaCl_2$ treatment (static compressive modulus of 0.6 ± 0.1 kPa, strength of 1.3 ± 0.2 kPa, and deformation of 62.3 ± 4.2%). At 37°C, however, the mentioned parameters were 2.6 ± 0.3 kPa, 8.1 ± 1.1 kPa, and 68.8 ± 8.3%, respectively. Moreover, the static tensile modulus (14.7 ± 1.3 kPa), strength (7.3 ± 0.6 kPa), and elongation (105 ± 10.8%) of PU-gelatin hydrogels following 24 h of incubation were significantly higher than the hydrogels before incubation (static tensile modulus of 7.2 ± 0.8 kPa, strength of 3.2 ± 0.3 kPa, and elongation of 94.1 ± 10.3%).[95]

Bone-derived decellularized ECM (dECM) integrated into alginate networks presents another promising double-network strategy that combines mechanical enhancement with biological functionality. An alginate-methacrylated dECM (Alg/Ma-dECM) system demonstrated considerably higher compressive modulus (90.4 ± 14.9 kPa) compared to alginate-$CaCl_2$ hydrogel alone (35.6 ± 8.9 kPa). The improvement in mechanical properties was attributed to the presence of UV-crosslinked Ma-dECM constituent in printed constructs, creating a hybrid physical-chemical crosslinking network. Importantly, the dECM component provided growth factors and ECM proteins that promoted cell adhesion, proliferation, and osteogenic differentiation beyond purely mechanical benefits.[96]

DNA-encoded dynamic hydrogels represent a cutting-edge approach for organoid bioprinting, leveraging the programmable and reversible nature of DNA base pairing to create networks with precisely tunable mechanical properties and stress relaxation kinetics. These systems utilize complementary DNA sequences as dynamic crosslinkers that can repeatedly associate and dissociate, enabling cellular remodeling and mechanoadaptation. For cartilage organoid bioprinting, DNA-silk fibroin (DNA-SF) hydrogel sustained-release systems have achieved remarkable success, supporting development of millimeter-scale organoids with authentic cartilage phenotypes. The programmability of DNA crosslinks enables rational design of stress relaxation timescales matching cellular contractile dynamics (seconds to minutes), facilitating cell spreading, migration, and tissue organization.[97] The mechanical properties, crosslinking mechanisms, and their limitations characteristics of the double-network hydrogel systems discussed in this section are summarized in Table 2.

5.3. Rapid prototyping technology

The various strategies were investigated to develop 3D-bioprinted constructs with desirable mechanical properties for bone regeneration. The scaffolds derived from natural polymers are mechanically weak; therefore, incorporation of inorganic additives may improve mechanical strength and also bioactivity. These materials are printed together with living cells, achieving simultaneous cellular encapsulation and mechanical reinforcement. The incorporation of nanohydroxyapatite (nHAp) and bioactive glass nanoparticles (BGNp) into alginate/gelatin bioinks operates through multiple reinforcement mechanisms. First, the ceramic nanofillers provide direct physical reinforcement through load-bearing interactions within the hydrogel network. Second, nanoparticles serve as nanoscale crosslinking sites, establishing electrostatic interactions with polymer chains and increasing network density. Third, the ceramic nanoparticles release bioactive ions (Ca^{2+}, PO_4^{3-}, Si^{4+}) that promote both ionic crosslinking of the hydrogel matrix and osteogenic differentiation of encapsulated cells.[98,99] When bioprinted using extrusion-based bioprinting systems, these nanocomposite bioinks achieve compressive moduli of 80–150 kPa (compared to 5–10 kPa for unreinforced alginate/gelatin hydrogels), sustained cell viability exceeding 85% postprinting, and improved shape fidelity during and after printing. The nanoparticles create hierarchical interactions with polymer chains, enabling the bioink to maintain high viscosity at low shear rates in the syringe before extrusion while dramatically reducing apparent viscosity during nozzle extrusion.[100] This combination minimizes shear stress experienced by cells while maintaining strand integrity postextrusion.

To achieve both immediate structural stability critical for handling complex printed geometries and long-term mechanical integrity, recent bioprinting approaches employ dual-crosslinking strategies that combine

Table 2. Comparison of double-network hydrogel systems for bone bioprinting

Network components	Crosslinking mechanisms	Compressive modulus	Limitations	Refs.
Alginate (physical), PEGDA/ GelMA (chemical)	Ionic (Ca^{2+}), photopolymerization	78.1 kPa	Moderate strength, potential phototoxicity	[94]
PU (chemical), gelatin (physical)	Covalent, Ca^{2+} chelation, thermal	7.3 ± 0.6 kPa (37°C)	Lower stiffness, complex formulation	[95]
Alginate (physical), Ma-dECM (chemical)	Ionic (Ca^{2+}), photopolymerization	90.4 ± 14.9 kPa	Batch variation, limited strength	[96]
DNA crosslinks, silk fibroin	Programmable base-pairing, physical entanglement	Variable (tunable)	Cost, complexity, primarily for soft tissues	[97]

Abbreviations: GelMA: Gelatin methacrylate; Ma-dECM: Methacrylated decellularized extracellular matrix; PEGDA: Polyethylene glycol diacrylate; PU: Polyurethane.

chemical and ionic crosslinking. Representative dual-crosslinked bioink compositions include alginate (2–3% w/v) providing the backbone for ionic crosslinking, GelMA (8–10% w/v) with methacrylate groups enabling photochemical crosslinking, gellan gum (0.5–1% w/v) enhancing shear-thinning properties, hydroxyapatite nanoparticles (10–15% w/v) providing osteogenic reinforcement, and cell suspensions of SaOS-2 osteoblasts or hBMSCs at 2×10^6 cells/mL. Following 3D bioprinting via extrusion bioprinting, constructs are immediately exposed to ultraviolet (UV) irradiation to induce free-radical polymerization of the methacrylate groups on GelMA, forming covalent C–C bonds between polymer chains and establishing a primary photochemical network. Constructs are subsequently immersed in calcium chloride solution, where Ca^{2+} ions form ionic bridges between guluronate and mannuronate blocks of the alginate polymer and simultaneously crosslink gellan gum polymer chains, establishing a secondary ionic network. The dual-crosslinked networks create robust hydrogel structures with compressive strength ranging from 200 to 400 kPa, featuring increased elasticity while maintaining structural integrity despite cell-mediated extracellular matrix remodeling during culture.[101,102] Furthermore, these dual-crosslinked networks exhibit enhanced stability in physiological conditions demonstrating minimal scaffold degradation, which is crucial for supporting long-term cellular function and tissue development.

A paradigm-shifting approach addresses the critical challenge of achieving bone-level mechanical strength (>500 kPa) while maintaining cell viability during bioprinting. The optimized gelatin methacryloyl/laponite nanoclay/*N*-acryloyl glycinamide (GLN) bioink achieves exceptional mechanical properties with compression modulus of 989 ± 49 kPa and compression strength of 1200 ± 78 kPa. This bioink enables one-step coaxial extrusion bioprinting of hollow hydrogel-based scaffolds (HHS) with tunable architecture (outer diameter 0.4–0.8 mm, inner diameter 0.1–0.6 mm) that can be printed acellularly then loaded postfabrication with 13-fold increased cell loading efficiency, >85% cell viability and uniform cell distribution. The hollow scaffold architecture allows precise spatial segregation of multiple cell types: endothelial cells (HUVECs) populate the hollow channels, forming interconnected vascular networks with a mature endothelial phenotype, while osteogenic cells (hBMSCs) seeded on the solid walls undergo osteogenic differentiation. In critical-sized segmental rat femoral defects (8 mm), HHS-loaded hBMSCs accomplished complete bridging by 12 weeks with 2.1-fold higher new bone volume compared to acellular scaffolds, while HHS-loaded with both hBMSCs and HUVECs demonstrated 2.5-fold higher bone volume with enhanced early vascularization preceding bone formation. Also, in osteoporotic metaphyseal defects, HHS-loaded with hBMSCs achieved robust bone regeneration despite the osteoporotic host environment, demonstrating that cell-laden constructs overcome both the mechanical insufficiency of purely acellular scaffolds and the biological insufficiency of osteoporotic host tissues.[103]

6. Osteo-promotive materials and their roles

Recent investigations have been focused on discovering and utilizing osteo-promoting factors that facilitate the new bone formation and can be used in the preparation of mechanically enhanced scaffolds. In parallel with bone formation, ECM components, dECM particles, and nanoparticles may act as osteo-promoting agents (Table 3). The ECM consists of a network of proteins and polysaccharides that offer an appropriate binding site for growth factors, cytokines, and other molecules involved in bone formation. It allows cells to interact with one another and with the surrounding environment, therefore stimulating osteoblast differentiation. Components of the ECM could also deliver a substrate and a physically

supportive environment for new bone arrangements. The ECM components have been shown to interact with osteoblasts and enhance their survival, proliferation, and differentiation.[104] This leads to increased matrix deposition and consequently reinforces the mechanical strength of the resulting construct. The ECM component can be used in combination with biomaterials to create mechanically enhanced bioinks. For instance, the addition of collagen to a nHAp-based bioink was demonstrated to improve the interconnectivity of the formed construct and its mechanical properties.

Decellularized human ECM could be a promising osteo-promotive material because of its similarity to native bone tissue. It was demonstrated that osteogenic MSC-derived ECM could stimulate osteogenic differentiation and mineralization.[105] Moreover, a comparative experiment between autogenous bone pieces, intramembranous demineralized bone matrix (DBM), and HA was carried out to investigate the mechanical strength of healed rat calvarial defects, trephined into the parietal bones, and then filled with the mentioned materials. The results showed that the defects filled with DBM had better mechanical strength than defects implanted with HA or bone pieces.[106] Although these results have validated the remarkable characteristics of ECM-based biomaterials, batch-to-batch variation hinders their therapeutic application. To address this issue, recent studies have focused on developing standardized decellularization protocols to reduce variability. For example, an automated multitissue decellularization method has been developed to produce ECM biomaterials with reduced batch-to-batch variability, enhancing reproducibility and clinical applicability.[107] Additionally, the use of induced pluripotent stem cells (iPSCs) as a source for cell-secreted ECM has been proposed to offer scalability and potentially decrease batch-to-batch variations that hinder the clinical translation of ECM-based biomaterials. iPSCs can provide a consistent and renewable source of ECM, which may lead to more reproducible outcomes in tissue engineering application.[108]

Incorporating nanoscale materials to provide mechanically enhanced bioinks has offered another opportunity. The osteogenic efficacy and mechanical properties of injectable platelet-rich fibrin (i-PRF) scaffolds can be further enhanced through the addition of laponite, a synthetic nanosilicate clay with disc-shaped morphology (diameter ~25 nm, thickness ~1 nm). The compressive modulus of i-PRF-alginate/gelatin scaffolds increases from approximately 130 kPa to over 200 kPa with the addition of 1% laponite. Also, laponite forms electrostatic interactions with growth factors, enabling their controlled release over extended periods (>14 days), and it releases bioactive ions (Mg^{2+}, Si^{4+}) that directly stimulate osteogenic differentiation.[109] Deng *et al.*[110] reported that polydopamine nanoparticles (PDA NP) were incorporated into fibrous membranes derived from polymerization of dopamine mixed with polycaprolactone (PCL). PDA NP in hybrid membranes, even without added growth factors, promoted osteogenic differentiation and supported MSC cytocompatibility, and successfully induced bone regeneration in mouse models of calvarial critical-sized defects.[110] Furthermore, PDA NP in hybrid membranes has been demonstrated to possess superior osteogenic activity compared to membranes without PDA NP. Metal nanoparticles, such as alloyed silver-platinum nanoparticles (AgPt NP), exhibit osteo-promotive properties, and cross-sectional focused-ion beam analysis has shown that they are internalized by hMSCs, exhibiting low cytotoxicity and antimicrobial activity while simultaneously promoting osteogenic differentiation.[8] Despite their osteopromotive and antimicrobial properties, potential cytotoxic effects of metal nanoparticles, such as silver-platinum nanoparticles (AgPt NPs), at high doses and concentrations must be considered. Studies have shown that AgPt NPs with a silver content above 50 mol% can release silver ions, leading to cytotoxicity in hMSCs. This cytotoxicity is attributed to the dissolution of silver ions from nanoparticles, which can induce oxidative stress and compromise cell viability.[111] Additionally, the cytotoxicity of bimetallic AgPt NPs has been found to be higher than that of monometallic silver nanoparticles. For instance, Ag70Pt30 and Ag50Pt50 nanoparticles exhibited significant cytotoxic effects on HeLa cells at concentrations around 50 μg/mL. This increased toxicity is not solely due to silver ion release, suggesting that the combined presence of silver and platinum in the nanoparticle structure contributes to enhanced cytotoxic effects.[112] These AgPt NP were found to form a protective monolayer on the surface of hMSCs, which then triggered the secretion of osteogenic cytokines and proteins, such as osteocalcin, alkaline phosphatase, and osteopontin. This resulted in increased osteogenic differentiation of hMSCs, enhancing the expression of osteogenic markers and stimulating bone formation. Moreover, the use of nanoglass paste can help with generating new bone in a recent approach, where 200-nm-sized silicate-glass (with Ca, Cu) particles successfully induced osteogenic differentiation of MSCs and promoted angiogenesis.[113] This suggests that nanoparticles can be used to positively influence the osteogenic differentiation of hMSCs, ultimately leading to the production of new bones. Furthermore, they could augment osteoblast functionality and alkaline phosphatase (ALP) activity, consequently increasing the mechanical properties of the bioprinted constructs.

Table 3. Osteo-promotive materials for bone-specific bioink optimization

Candidate material	Mechanism of action	Printability	Disadvantages	Refs.
Hydroxyapatite (HA)	A mineral scaffold that promotes bone growth and mineralization, but can clog the printer nozzle at high concentrations	Printable using a variety of methods, but requires careful handling to prevent clogging	Sterilization challenging, as HA can be damaged by high temperatures and harsh chemicals	[114]
Bone morphogenetic proteins (BMPs)	Growth factors that promote the growth and differentiation of bone cells	Soluble BMPs can be easily incorporated into bioinks	BMPs can be degraded by enzymes in the body, limiting their therapeutic potential	[115]
Collagen	A natural scaffold that provides structure and support for bone cells	A challenging bioink ingredient to print with, as collagen is highly viscous	Collagen could be denatured by the shear stress of printing	[116]
Decellularized extracellular matrix (dECM)	Contains all the essential proteins and molecules for bone regeneration	A complex bioink ingredient that requires careful optimization to print without damaging the ECM	Sterilization can be challenging, as dECM is sensitive to heat and chemicals	[104]
Demineralized bone matrix (DBM)	A bioink ingredient that contains osteo-inductive factors that promote bone growth and differentiation	A versatile bioink ingredient that can be printed using a variety of methods, but requires careful handling	DBM variability can make it difficult to produce consistent results with DBM bioinks	[117]
Polydopamine nanoparticles (PDA NPs)	Nanoparticles that deliver osteo-inductive factors to bone cells and create scaffolds that support bone growth	PDA NPs can be printed at high resolutions, which is important for creating complex bone-shaped scaffolds	PDA NPs can be cytotoxic to cells at high concentrations	[118]
Silver–platinum nanoparticles (*AgPt NPs*)	Nanoparticles that kill bacteria and promote bone growth	AgPt NPs can be incorporated into bioinks at high concentrations without clogging the printer nozzle	AgPt NPs can be expensive to produce at scale	[119]
Silicate-glass	Particles that deliver Ca and Cu ions to bone cells, which are essential for bone mineralization	Easily printable but requires careful optimization to avoid damaging the particles	Silicate-glass particles can form aggregates, which can lead to nozzle clogging of the bioprinter	[120]

7. Conclusion and future perspectives

At present, experimental studies for developing the ideal formulation for bone bioink are in progress. Over the past few years, relevant research has focused on improving different criteria of bioinks. However, significant challenges remain, including achieving compressive strength equivalent to natural bones, replicating complex geometries, maintaining appropriate porosity without compromising other features or properties, and promoting vascularization to support cell survival.[121] To surmount these challenges, various solutions have been attempted, including developing composite hydrogels to fulfill the goal of enforcing mechanical strength and printability, as well as preserving the encapsulated cells in the bioprinting process. Moreover, biodegradability of the constructs has been achieved through the use and development of new formulations.[122] Printing methods and appliances, such as nozzle-based or laser-based printers, with the help of computer-aided design (CAD), have also played an essential role in revolutionizing the production of artificial scaffolds. Other challenges, such as bioink preparation, cell viability and differentiation, and angiogenesis inside the scaffolds require further investigation. Ultimately, it is important to not only sort out the mentioned limitations, but also to reduce the cost of final constructs. Currently, angiogenesis within the scaffolds is stimulated using approaches such as nonviral gene delivery and nanoparticles[123]; however, these strategies have raised ongoing concerns regarding the potential activation of proto-oncogenes and tumorigenesis.[124] Overall, given the increasing demand for 3D-bioprinted constructs driven by high transplantation failure rates and limited availability of donor organs and tissues, there is a pressing need to develop new strategies to address these challenges.

The current review revolves around existing strategies for addressing mechanical challenges, which are primarily addressed by the development of composite bioinks and the optimization of scaffold architecture. While these approaches have shown promise, they are often associated with a trade-off between mechanical

strength and biocompatibility. The next generation of bioprinted bone constructs is expected to embrace a "dynamic mechanoregulation" paradigm, in which scaffold mechanical properties are not static but can be adjusted *in situ* to match the changing needs of regenerating tissue. This will be achieved through the development of "smart" bioinks that can respond to specific biological or physical cues, and the use of advanced bioreactors that can apply controlled mechanical stimuli to the developing construct. Ultimately, the goal is to create a truly living implant that can actively participate in the process of bone regeneration, rather than simply acting as a passive scaffold.

Acknowledgments

None.

Funding

The authors did not receive support from any organization for the submitted work.

Conflict of interest

The authors declare that they have no competing interests.

Author contributions

Conceptualization: Amin Ebrahimi Sadrabadi, Mohamadreza Baghaban Eslaminejad, Samaneh Hosseini

Visualization: Yalda Alibeigian

Writing–original draft Amin Ebrahimi Sadrabadi, Payam Baei

Writing–review & editing: Mohamadreza Baghaban Eslaminejad, Samaneh Hosseini,

Ethics approval and consent to participate

Not applicable.

Consent for publication

Not applicable.

Availability of data

The resources that support this review work are available upon request from the corresponding author.

References

1. Chimene D, Lennox KK, Kaunas RR, Gaharwar AK. Advancedbioinks for 3d printing: a materials science perspective. *Ann Biomed Eng*. 2016;44(6):2090-2102. doi: 10.1007/s10439-016-1638-y
2. Pedroza-Gonzalez SC, Rodriguez-Salvador M, Perez-Benitez BE, Alvarez MM, Santiago GT. Bioinks for 3D bioprinting: a scientometric analysis of two decades of progress. *Int J Bioprint*. 2021;7(2):333. doi: 10.18063/ijb.v7i2.337
3. Engler AJ, Sen S, Sweeney HL, Discher DE. Matrix elasticity directs stem cell lineage specification. *Cell*. 2006;126(4):677-689. doi: 10.1016/j.cell.2006.06.044
4. Chaudhuri O, Gu L, Klumpers D, *et al*. Hydrogels with tunable stress relaxation regulate stem cell fate and activity. *Nat Mater*. 2016;15(3):326-334. doi: 10.1038/nmat4489
5. Bergonzi C, Bianchera A, Remaggi G, Ossiprandi MC, Bettini R, Elviri L. 3D printed chitosan/alginate hydrogels for the controlled release of silver sulfadiazine in wound healing applications: design, characterization and antimicrobial activity. *Micromachines (Basel)*. 2023;14(1):137. doi: 10.3390/mi14010137
6. Wang L, Zhou A, Chen C, Huang X, Zhang S, Chen J. Preparation and properties of composite hydrogels for 3D bioprinting. *Polym Adv Technol*. 2023;34(7):2369-2383. doi: 10.1002/pat.6057
7. Zhang X, Yang X, Wu W, *et al*. Improving the mechanical properties of 3D printed GelMA composite hydrogels by tannic acid. *MedComm–Biomater Appl*. 2023;2(3):e51. doi: 10.1002/mba2.51
8. Breisch M, Grasmik V, Loza K, *et al*. Bimetallic silver-platinum nanoparticles with combined osteo-promotive and antimicrobial activity. *Nanotechnology*. 2019;30(30):305101. doi: 10.1088/1361-6528/ab172b
9. Lu N, Lu Y, Liu S, *et al*. Tailor-engineered POSS-based hybrid gels for bone regeneration. *Biomacromolecules*. 2019;20(9):3485-3493. doi: 10.1021/acs.biomac.9b00771
10. Hoyle CE, Bowman CN. Thiol-ene click chemistry. *Angew Chem Int Ed Engl*. 2010;49(9):1540-1573. doi: 10.1002/anie.200903924
11. Fairbanks BD, Schwartz MP, Halevi AE, Nuttelman CR, Bowman CN, Anseth KS. A versatile synthetic extracellular matrix mimic via thiol-norbornene photopolymerization. *Adv Mater*. 2009;21(48):5005-5010. doi: 10.1002/adma.200901808
12. Mondal S, Lessard JJ, Meena CL, Sanjayan GJ, Sumerlin BS. Janus Cross-links in supramolecular networks. *J Am Chem Soc*. 2022;144(2):845-853. doi: 10.1021/jacs.1c10606
13. Motloung MP, Mofokeng TG, Ray SS. Viscoelastic, thermal, and mechanical properties of melt-processed poly (epsilon-caprolactone) (PCL)/hydroxyapatite (HAP) composites. *Materials (Basel)*. 2021;15(1):104.

doi: 10.3390/ma15010104

14. Chuysinuan P, Nooeaid P, Thanyacharoen T, Techasakul S, Pavasant P, Kanjanamekanant K. Injectable eggshell-derived hydroxyapatite-incorporated fibroin-alginate composite hydrogel for bone tissue engineering. *Int J Biol Macromol*. 2021;193(Pt A):799-808.
doi: 10.1016/j.ijbiomac.2021.10.132

15. Stocco TD, de Carvalho RP, Silva HCO, de Melo Sousa TS. The feasibility of 3D bioprinting for bone regeneration: key challenges and future directions. *Regen Med*. 2025;20(11):625-652.
doi: 10.1080/17460751.2025.2572218

16. Garcia-Aznar JM, Nasello G, Hervas-Raluy S, Perez MA, Gomez-Benito MJ. Multiscale modeling of bone tissue mechanobiology. *Bone*. 2021;151:116032.
doi: 10.1016/j.bone.2021.116032

17. Chmielewska A, Dean D. The role of stiffness-matching in avoiding stress shielding-induced bone loss and stress concentration-induced skeletal reconstruction device failure. *Acta Biomater*. 2024;173:51-65.
doi: 10.1016/j.actbio.2023.11.011

18. Florencio-Silva R, Sasso GRdS, Sasso-Cerri E, Simões MJ, Cerri PS. Biology of bone tissue: structure, function, and factors that influence bone cells. *BioMed Res. Int.*. 2015;2015(1):421746.
doi: 10.1155/2015/421746

19. Raubenheimer E, Miniggio H, Lemmer L, van Heerden W. The role of bone remodelling in maintaining and restoring bone health: an overview. *Clin. Rev. Bone Miner Metab*. 2017;15:90-97.
doi: 10.1007/s12018-017-9230-z

20. Hadjidakis DJ, Androulakis, II. Bone remodeling. *Ann N Y Acad Sci*. 2006;1092(1):385-396.
doi: 10.1196/annals.1365.035

21. Crockett JC, Rogers MJ, Coxon FP, Hocking LJ, Helfrich MH. Bone remodelling at a glance. *J Cell Sci*. 2011;124(7): 991-998.
doi: 10.1242/jcs.063032

22. Ott SM. Cortical or trabecular bone: what's the difference? *Am J Nephrol*. 2018;47(6):373-375.
doi: 10.1159/000489672

23. Reyes KJC, Stanford FC, Singhal V, *et al*. Bone density, microarchitecture and strength estimates in white versus African American youth with obesity. *Bone*. 2020;138:115514.
doi: 10.1016/j.bone.2020.115514

24. Reichert JC, Wullschleger ME, Cipitria A, *et al*. Custom-made composite scaffolds for segmental defect repair in long bones. *Int Orthop*. 2011;35(8):1229-1236.
doi: 10.1007/s00264-010-1146-x

25. Cheung AM, Adachi JD, Hanley DA, *et al*. High-resolution peripheral quantitative computed tomography for the assessment of bone strength and structure: a review by the Canadian Bone Strength Working Group. *Curr Osteoporos Rep*. Jun 2013;11(2):136-146.
doi: 10.1007/s11914-013-0140-9

26. Das D, Zhang S, Noh I. Synthesis and characterizations of alginate-α-tricalcium phosphate microparticle hybrid film with flexibility and high mechanical property as a biomaterial. *Biomed. Mater*. 2018;13(2):025008.
doi: 10.1088/1748-605X/aa8fa1

27. Abelardo E. Synthetic material bioinks. In: *3D Bioprinting for Reconstructive Surgery*. Amsterdam, Netherlands: Elsevier; 2018:137-144.

28. Popp K, Xu C, Yuan A, *et al*. Trabecular microstructure is influenced by race and sex in Black and White young adults. *Osteoporosis Int*. 2019;30:201-209.
doi: 10.1007/s00198-018-4729-9

29. De Mori A, Pena Fernandez M, Blunn G, Tozzi G, Roldo M. 3D printing and electrospinning of composite hydrogels for cartilage and bone tissue engineering. *Polymers (Basel)*. 2018;10(3):285.
doi: 10.3390/polym10030285

30. Morgan EF, Unnikrisnan GU, Hussein AI. Bone mechanical properties in healthy and diseased states. *Annu Rev Biomed Eng*. 2018;20(1):119-143.
doi: 10.1146/annurev-bioeng-062117-121139

31. Karpiński R, Jaworski Ł, Czubacka P. The structural and mechanical properties of the bone. *J Technol Exploitat Mech Eng*. 2017;3(1):43-51.
doi: 10.35784/jteme.538

32. Currey J. The structure and mechanical properties of bone. In: *Bioceramics and Their Clinical Applications*. Amsterdam, Netherlands: Elsevier; 2008:3-27.

33. Vassiliou V, Chow E, Kardamakis D. *Bone Metastases: A Translational and Clinical Approach*. Vol 21. Dordrecht: Springer Science & Business Media; 2013.

34. Shapiro F. Bone development and its relation to fracture repair. The role of mesenchymal osteoblasts and surface osteoblasts. *Eur Cell Mater*. 2008;15:53-76.
doi: 10.22203/ecm.v015a05

35. Kopperdahl DL, Keaveny TM. Yield strain behavior of trabecular bone. *J Biomech*. 1998;31(7):601-608.
doi: 10.1016/s0021-9290(98)00057-8

36. Currey JD. How well are bones designed to resist fracture? *J Bone Miner Res*. 2003;18(4):591-598.
doi: 10.1359/jbmr.2003.18.4.591

37. Osterhoff G, Morgan EF, Shefelbine SJ, Karim L, McNamara LM, Augat P. Bone mechanical properties and changes with osteoporosis. *Injury*. 2016;47 Suppl 2(Suppl 2): S11-S20.
doi: 10.1016/S0020-1383(16)47003-8

38. Boivin G, Bala Y, Doublier A, *et al*. The role of mineralization and organic matrix in the microhardness of

bone tissue from controls and osteoporotic patients. *Bone*. 2008;43(3):532-538.
doi: 10.1016/j.bone.2008.05.024

39. Bala Y, Farlay D, Boivin G. Bone mineralization: from tissue to crystal in normal and pathological contexts. *Osteoporos Int*. 2013;24(8):2153-2166.
doi: 10.1007/s00198-012-2228-y

40. Zumstein V, Kraljević M, Wirz D, Hügli R, Müller-Gerbl M. Correlation between mineralization and mechanical strength of the subchondral bone plate of the humeral head. *J Shoulder Elbow Surg*. 2012;21(7): 887-893.
doi: 10.1016/j.jse.2011.05.018

41. Augat P, Schorlemmer S. The role of cortical bone and its microstructure in bone strength. *Age Ageing*. 2006;35 Suppl 2(suppl_2):ii27-ii31.
doi: 10.1093/ageing/afl081

42. Zebaze RM, Ghasem-Zadeh A, Bohte A, *et al*. Intracortical remodelling and porosity in the distal radius and post-mortem femurs of women: a cross-sectional study. *Lancet*. 2010;375(9727):1729-1736.
doi: 10.1016/S0140-6736(10)60320-0

43. Seeman E, Delmas PD, Hanley DA, *et al*. Microarchitectural deterioration of cortical and trabecular bone: differing effects of denosumab and alendronate. *J Bone Miner Res*. 2010;25(8):1886-1894.
doi: 10.1002/jbmr.81

44. Riggs BL, Melton III LJ, Robb RA, *et al*. A population-based assessment of rates of bone loss at multiple skeletal sites: evidence for substantial trabecular bone loss in young adult women and men. *J Bone Miner Res*. 2008;23(2): 205-214.
doi: 10.1359/JBMR.07102

45. Luu YK, Pessin JE, Judex S, Rubin J, Rubin CT. Mechanical signals as a non-invasive means to influence mesenchymal stem cell fate, promoting bone and suppressing the fat phenotype. *Bonekey Osteovision*. 2009;6(4):132-149.
doi: 10.1138/20090371

46. Guilak F, Cohen DM, Estes BT, Gimble JM, Liedtke W, Chen CS. Control of stem cell fate by physical interactions with the extracellular matrix. *Cell Stem Cell*. 2009;5(1): 17-26.
doi: 10.1016/j.stem.2009.06.016

47. Kirby TJ, Lammerding J. Cell mechanotransduction: stretch to express. *Nat Mater*. 2016;15(12):1227-1229.
doi: 10.1038/nmat4809

48. Yang L, Gao Q, Ge L, *et al*. Topography induced stiffness alteration of stem cells influences osteogenic differentiation. *Biomater Sci*. 2020;8(9):2638-2652.
doi: 10.1039/d0bm00264j

49. Shen B, Delaney MK, Du X. Inside-out, outside-in, and inside-outside-in: G protein signaling in integrin-mediated cell adhesion, spreading, and retraction. *Curr Opin Cell Biol*. 2012;24(5):600-606.
doi: 10.1016/j.ceb.2012.08.011

50. Mousavi SJ, Doweidar MH. Role of mechanical cues in cell differentiation and proliferation: a 3D numerical model. *PLoS One*. 2015;10(5):e0124529.
doi: 10.1371/journal.pone.0124529

51. Chowdhury F, Li Y, Poh YC, Yokohama-Tamaki T, Wang N, Tanaka TS. Soft substrates promote homogeneous self-renewal of embryonic stem cells via downregulating cell-matrix tractions. *PLoS One*. 2010;5(12):e15655.
doi: 10.1371/journal.pone.0015655

52. Wang LS, Chung JE, Chan PP, Kurisawa M. Injectable biodegradable hydrogels with tunable mechanical properties for the stimulation of neurogenesic differentiation of human mesenchymal stem cells in 3D culture. *Biomaterials*. 2010;31(6):1148-1157.
doi: 10.1016/j.biomaterials.2009.10.042

53. Zhang M, Sun Q, Liu Y, *et al*. Controllable ligand spacing stimulates cellular mechanotransduction and promotes stem cell osteogenic differentiation on soft hydrogels. *Biomaterials*. 2021;268:120543.
doi: 10.1016/j.biomaterials.2020.120543

54. Cun X, Hosta-Rigau L. Topography: a biophysical approach to direct the fate of mesenchymal stem cells in tissue engineering applications. *Nanomaterials (Basel)*. 2020;10(10):2070.
doi: 10.3390/nano10102070

55. Godoi FC, Prakash S, Bhandari BR. 3D printing technologies applied for food design: status and prospects. *J Food Eng*. 2016;179:44-54.
doi: 10.1016/j.jfoodeng.2016.01.025

56. Hölzl K, Lin S, Tytgat L, Van Vlierberghe S, Gu L, Ovsianikov A. Bioink properties before, during and after 3D bioprinting. *Biofabrication*. 2016;8(3):032002.
doi: 10.1088/1758-5090/8/3/032002

57. Hospodiuk M, Dey M, Sosnoski D, Ozbolat IT. The bioink: a comprehensive review on bioprintable materials. *Biotechnol Adv*. 2017;35(2):217-239.
doi: 10.1016/j.biotechadv.2016.12.006

58. Saunders RE, Derby B. Inkjet printing biomaterials for tissue engineering: bioprinting. *Int Mater Rev*. 2014;59(8):430-448.
doi: 10.1179/1743280414Y.0000000040

59. Xu T, Jin J, Gregory C, Hickman JJ, Boland T. Inkjet printing of viable mammalian cells. *Biomaterials*. 2005;26(1):93-99.
doi: 10.1016/j.biomaterials.2004.04.011

60. Mancha Sanchez E, Gomez-Blanco JC, Lopez Nieto E, *et al*. Hydrogels for bioprinting: a systematic review of hydrogels synthesis, bioprinting parameters, and bioprinted structures behavior. *Front Bioeng Biotechnol*. 2020;8:776.
doi: 10.3389/fbioe.2020.00776

61. Kyle S, Jessop ZM, Al-Sabah A, Whitaker IS. 'Printability'of candidate biomaterials for extrusion based 3D printing: state-of-the-art. *Adv Healthcare Mater*. 2017;6(16):1700264. doi: 10.1002/adhm.201700264

62. Li M, Tian X, Zhu N, Schreyer DJ, Chen X. Modeling process-induced cell damage in the biodispensing process. *Tissue Eng Part C Methods*. 2010;16(3):533-542. doi: 10.1089/ten.TEC.2009.0178

63. Aljohani W, Ullah MW, Zhang X, Yang G. Bioprinting and its applications in tissue engineering and regenerative medicine. *Int J Biol Macromol*. 2018;107(Pt A):261-275. doi: 10.1016/j.ijbiomac.2017.08.171

64. Shanjani Y, Pan CC, Elomaa L, Yang Y. A novel bioprinting method and system for forming hybrid tissue engineering constructs. *Biofabrication*. 2015;7(4):045008. doi: 10.1088/1758-5090/7/4/045008

65. Billiet T, Gevaert E, De Schryver T, Cornelissen M, Dubruel P. The 3D printing of gelatin methacrylamide cell-laden tissue-engineered constructs with high cell viability. *Biomaterials*. 2014;35(1):49-62. doi: 10.1016/j.biomaterials.2013.09.078

66. Diamantides N, Dugopolski C, Blahut E, Kennedy S, Bonassar LJ. High density cell seeding affects the rheology and printability of collagen bioinks. *Biofabrication*. 2019;11(4):045016. doi: 10.1088/1758-5090/ab3524

67. Gregory T, Benhal P, Scutte A, *et al*. Rheological characterization of cell-laden alginate-gelatin hydrogels for 3D biofabrication. *J Mech Behav Biomed Mater*. 2022;136:105474. doi: 10.1016/j.jmbbm.2022.105474

68. Guo Z, Ma C, Xie W, Tang A, Liu W. An effective DLP 3D printing strategy of high strength and toughness cellulose hydrogel towards strain sensing. *Carbohydr Polym*. 2023;315:121006. doi: 10.1016/j.carbpol.2023.121006

69. Müller SJ, Fabry B, Gekle S. Predicting cell stress and strain during extrusion bioprinting. *Phys Rev Appl*. 2023;19(6):064061. doi: 10.48550/arXiv.2209.13666

70. Boularaoui S, Shanti A, Khan KA, Iacoponi S, Christoforou N, Stefanini C. Harnessing shear stress preconditioning to improve cell viability in 3D post-printed biostructures using extrusion bioprinting. *Bioprinting*. 2022;25:e00184. doi: 10.1016/j.bprint.2021.e00184

71. Lyu J, Johnson M, Creagh-Flynn J, *et al*. Instant gelation system as self-healable and printable 3D cell culture bioink based on dynamic covalent chemistry. *ACS Appl Mater Interfaces*. 2020;12(35):38918-38924. doi.org/10.1021/acsami.0c08567

72. Ashammakhi N, Ahadian S, Xu C, *et al*. Bioinks and bioprinting technologies to make heterogeneous and biomimetic tissue constructs. *Mater Today Bio*. 2019;1:100008. doi: 10.1016/j.mtbio.2019.100008

73. Schwab A, Levato R, D'Este M, Piluso S, Eglin D, Malda J. Printability and shape fidelity of bioinks in 3D bioprinting. *Chem Rev*. 2020;120(19):11028-11055. doi: 10.1021/acs.chemrev.0c00084

74. Oh D, Shirzad M, Kim MC, Chung EJ, Nam SY. Rheology-informed hierarchical machine learning model for the prediction of printing resolution in extrusion-based bioprinting. *Int J Bioprint*. 2023;9(6):308-324. doi: 10.36922/ijb.1280

75. Wu L, Zhao J, Huang J, Huang P, Zhao H. Advances and challenges in 3D bioprinting of bone organoids: materials, techniques, and functionalization strategies. *Int J Bioprint*. 2025;0(0) doi: 10.36922/ijb025190183

76. Khalaf AT, Wei Y, Wan J, *et al*. Bone tissue engineering through 3D bioprinting of bioceramic scaffolds: a review and update. *Life*. 2022;12(6):903. doi: 10.3390/life12060903

77. Lakatos E, Magyar L, Bojtar I. Material properties of the mandibular trabecular bone. *J Med Eng*. 2014;2014(1):470539. doi: 10.1155/2014/470539

78. Luo Y. Toward fully automated personalized orthopedic treatments: innovations and interdisciplinary gaps. *Bioengineering (Basel)*. 2024;11(8):817. doi: 10.3390/bioengineering11080817

79. Zhou J, See CW, Sreenivasamurthy S, Zhu D. Customized additive manufacturing in bone scaffolds-the gateway to precise bone defect treatment. *Research (Wash D C)*. 2023;6:0239. doi: 10.34133/research.0239

80. Varshney S, Dwivedi A, Pandey V. Bioprinting techniques for regeneration of oral and craniofacial tissues: current advances and future prospects. *J Oral Biol Craniofac Res*. 2025;15(2):331-346. doi: 10.1016/j.jobcr.2025.01.019

81. Lai Y, Fan J, Li P, *et al*. Recent advances in 3D bioprinting for cartilage and osteochondral regeneration. *Int J Bioprint*. 2025;0(0). doi: 10.36922/ijb025120098

82. Eschweiler J, Horn N, Rath B, *et al*. The biomechanics of cartilage: an overview. *Life (Basel)*. 2021;11(4). doi: 10.3390/life11040302

83. Petitjean N, Canadas P, Royer P, Noel D, Le Floc'h S. Cartilage biomechanics: from the basic facts to the challenges of tissue engineering. *J Biomed Mater Res A*. 2023;111(7):1067-1089. doi: 10.1002/jbm.a.37478

84. Dąbrowski M, Rogala P, Uklejewski R, Patalas A, Winiecki M, Gapiński B. Subchondralbone relative area and density

in human osteoarthritic femoral heads assessed with micro-CT before and after mechanical embedding of the innovative multi-spiked connecting scaffold for resurfacing THA endoprostheses: a pilot study. *J Clinic Med*. 2021;10(13):2937. doi: 10.3390/jcm10132937

85. Lu J, Gao Y, Cao C, *et al*. 3D bioprinted scaffolds for osteochondral regeneration: advancements and applications. *Mater Today Bio*. 2025;32:101834. doi: 10.1016/j.mtbio.2025.101834

86. Gao D, Li R, Pan J, *et al*. 3D bioprinting bone/cartilage organoids: construction, applications, and challenges. *J Orthop Translat*. 2025;55:75-93. doi: 10.1016/j.jot.2025.08.008

87. Wang J, Chen X, Li R, *et al*. Standardization and consensus in the development and application of bone organoids. Review. *Theranostics*. 2025;15(2):682-706. doi: 10.7150/thno.105840

88. Ohman-Magi C, Holub O, Wu D, Hall RM, Persson C. Density and mechanical properties of vertebral trabecular bone: a review. *JOR Spine*. Dec 2021;4(4):e1176. doi: 10.1002/jsp2.1176

89. Inzana JA, Olvera D, Fuller SM, *et al*. 3D printing of composite calcium phosphate and collagen scaffolds for bone regeneration. *Biomaterials*. 2014;35(13):4026-4034. doi: 10.1016/j.biomaterials.2014.01.064

90. Bendtsen ST, Quinnell SP, Wei M. Development of a novel alginate-polyvinyl alcohol-hydroxyapatite hydrogel for 3D bioprinting bone tissue engineered scaffolds. *J Biomed Mater Res A*. 2017;105(5):1457-1468. doi: 10.1002/jbm.a.36036

91. Monavari M, Medhekar R, Nawaz Q, *et al*. A 3D printed bone tissue engineering scaffold composed of alginate dialdehyde-gelatine reinforced by lysozyme loaded cerium doped mesoporous silica-calcia nanoparticles. *Macromol Biosci*. 2022;22(9):e2200113. doi: 10.1002/mabi.202200113

92. Ojansivu M, Rashad A, Ahlinder A, *et al*. Wood-based nanocellulose and bioactive glass modified gelatin-alginate bioinks for 3D bioprinting of bone cells. *Biofabrication*. 2019;11(3):035010. doi: 10.1088/1758-5090/ab0692

93. Wang LL, Highley CB, Yeh YC, Galarraga JH, Uman S, Burdick JA. Three-dimensional extrusion bioprinting of single- and double-network hydrogels containing dynamic covalent crosslinks. *J Biomed Mater Res A*. 2018;106(4):865-875. doi: 10.1002/jbm.a.36323

94. Zhang X, Yan Z, Guan G, *et al*. Polyethylene glycol diacrylate scaffold filled with cell-laden methacrylamide gelatin/alginate hydrogels used for cartilage repair. *J Biomater Appl*. 2022;36(6):1019-1032. doi: 10.1177/08853282211044853

95. Hsieh CT, Hsu SH. Double- network polyurethane-gelatin hydrogel with tunable modulus for high-resolution 3D bioprinting. *ACS Appl Mater Interfaces*. 2019;11(36):32746-32757. doi: 10.1021/acsami.9b10784

96. Lee J, Hong J, Kim W, Kim GH. Bone-derived dECM/alginate bioink for fabricating a 3D cell-laden mesh structure for bone tissue engineering. *Carbohydr Polym*. 2020;250:116914. doi: 10.1016/j.carbpol.2020.116914

97. Chen Z, Zhang H, Huang J, *et al*. DNA-encoded dynamic hydrogels for 3D bioprinted cartilage organoids. *Mater Today Bio*. 2025;31:101509. doi: 10.1016/j.mtbio.2025.101509

98. Leite AJ, Sarker B, Zehnder T, Silva R, Mano JF, Boccaccini AR. Bioplotting of a bioactive alginate dialdehyde-gelatin composite hydrogel containing bioactive glass nanoparticles. *Biofabrication*. 2016;8(3):035005. doi: 10.1088/1758-5090/8/3/035005

99. Korkeamaki JT, Rashad A, Ojansivu M, *et al*. Systematic development and bioprinting of novel nanostructured multi-material bioinks for bone tissue engineering. *Biofabrication*. 2025;17(2):025005. doi: 10.1088/1758-5090/ada63b

100. Liu B, Li J, Lei X, *et al*. 3D-bioprinted functional and biomimetic hydrogel scaffolds incorporated with nanosilicates to promote bone healing in rat calvarial defect model. *Mater Sci Eng C Mater Biol Appl*. 2020;112:110905. doi: 10.1016/j.msec.2020.110905

101. Mathur V, Agarwal P, Kasturi M, Srinivasan V, Seetharam RN, Vasanthan KS. Innovative bioinks for 3D bioprinting: exploring technological potential and regulatory challenges. *J Tissue Eng*. 2025;16:20417314241308022. doi: 10.1177/20417314241308022

102. Bastos AR, da Silva LP, Maia FR, *et al*. Hydroxyapatite/alginate/gellan gum inks with osteoconduction and osteogenic potential for bioprinting bone tissue analogues. *Int J Biol Macromol*. 2024;271(Pt 2):132611. doi: 10.1016/j.ijbiomac.2024.132611

103. Yang J, Chen Z, Gao C, *et al*. A mechanical-assisted post-bioprinting strategy for challenging bone defects repair. *Nat Commun*. 2024;15(1):3565. doi: 10.1038/s41467-024-48023-8

104. Ebrahimi Sadrabadi A, Baei P, Hosseini S, Baghaban Eslaminejad M. Decellularized extracellular matrix as a potent natural biomaterial for regenerative medicine. *Adv Exp Med Biol*. 2021;(1341):27-43. doi: 10.1007/5584_2020_504

105. Baroncelli M, Van Der Eerden BC, Chatterji S, *et al*. Human osteoblast-derived extracellular matrix with high homology to bone proteome is osteopromotive. *Tissue Eng Part A*. 2018;24(17-18):1377-1389.

doi: 10.1089/ten.TEA.2017.0448

106. Jones L, Thomsen JS, Mosekilde L, Bosch C, Melsen B. Biomechanical evaluation of rat skull defects, 1, 3, and 6 months after implantation with osteopromotive substances. *J Craniomaxillofac Surg*. 2007;35(8):350-357. doi: 10.1016/j.jcms.2007.06.004

107. Biehl A, Gracioso Martins AM, Davis ZG, *et al*. Towards a standardized multi-tissue decellularization protocol for the derivation of extracellular matrix materials. *Biomater Sci*. 2023;11(2):641-654. doi: 10.1039/d2bm01012g

108. Ramos-Rodriguez DH, Leach JK. Decellularized cell-secreted extracellular matrices as biomaterials for tissue engineering. *Small Sci*. 2025;5(2):2400335. doi: 10.1002/smsc.202400335

109. Cao B, Zhang K, Zuo R, *et al*. 3D-bioprinted functional scaffold based on synergistic induction of i-PRF and laponite exerts efficient and personalized bone regeneration via miRNA-mediated TGF-beta/Smads signaling. *Int J Surg*. 2025;111(5):3193-3211. doi: 10.1097/JS9.0000000000002312

110. Deng Y, Yang W-Z, Shi D, *et al*. Bioinspired and osteopromotive polydopamine nanoparticle-incorporated fibrous membranes for robust bone regeneration. *NPG Asia Mater*. 2019;11(1):39. doi: 10.1038/s41427-019-0139-5

111. Grasmik V, Breisch M, Loza K, *et al*. Synthesis and biological characterization of alloyed silver-platinum nanoparticles: from compact core-shell nanoparticles to hollow nanoalloys. *RSC Adv*. 2018;8(67):38582-38590. doi: 10.1039/c8ra06461j

112. Wolff N, Bialas N, Loza K, *et al*. Increased cytotoxicity of bimetallic ultrasmall silver-platinum nanoparticles (2 nm) on cells and bacteria in comparison to silver nanoparticles of the same size. *Materials (Basel)*. 2024;17(15):3702. doi: 10.3390/ma17153702

113. Seo JJ, Mandakhbayar N, Kang MS, *et al*. Antibacterial, proangiogenic, and osteopromotive nanoglass paste coordinates regenerative process following bacterial infection in hard tissue. *Biomaterials*. 2021;268:120593. doi: 10.1016/j.biomaterials.2020.120593

114. Sadeghianmaryan A, Naghieh S, Yazdanpanah Z, *et al*. Fabrication of chitosan/alginate/hydroxyapatite hybrid scaffolds using 3D printing and impregnating techniques for potential cartilage regeneration. *Int J Biol Macromol*. 2022;204:62-75. doi: 10.1016/j.ijbiomac.2022.01.201

115. Seok JM, Kim MJ, Park JH, *et al*. A bioactive microparticle-loaded osteogenically enhanced bioprinted scaffold that permits sustained release of BMP-2. *Mater Today Bio*. 2023;21:100685. doi: 10.1016/j.mtbio.2023.100685

116. Osidak EO, Kozhukhov VI, Osidak MS, Domogatsky SP. Collagen as bioink for bioprinting: a comprehensive review. *Int J Bioprint*. 2020;6(3):270. doi: 10.18063/ijb.v6i3.270

117. Hogan KJ, Oztatli H, Perez MR, *et al*. Development of photoreactive demineralized bone matrix 3D printing colloidal inks for bone tissue engineering. *Regen Biomater*. 2023;10:rbad090. doi: 10.1093/rb/rbad090

118. Im S, Choe G, Seok JM, *et al*. An osteogenic bioink composed of alginate, cellulose nanofibrils, and polydopamine nanoparticles for 3D bioprinting and bone tissue engineering. *Int J Biol Macromol*. 2022;205:520-529. doi: 10.1016/j.ijbiomac.2022.02.012

119. Ghosh S, Webster TJ. Metallic nanoscaffolds as osteogenic promoters: advances, challenges and scope. *Metals*. 2021;11(9):1356. doi: 10.3390/met11091356

120. Palivela BC, Bandari SD, Mamilla RS. Extrusion-based 3D printing of bioactive glass scaffolds-process parameters and mechanical properties: a review. *Bioprinting*. 2022;27:e00219.

121. Badhe RV, Chatterjee A, Bijukumar D, Mathew MT. Current advancements in bio-ink technology for cartilage and bone tissue engineering. *Bone*. 2023;171:116746. doi: 10.1016/j.bone.2023.116746

122. Genova T, Roato I, Carossa M, Motta C, Cavagnetto D, Mussano F. Advances on bone substitutes through 3D bioprinting. *Int J Mol Sci*. 2020;21(19):7012. doi: 10.3390/ijms21197012

123. Bahraminasab M. Challenges on optimization of 3D-printed bone scaffolds. *Biomed Eng Online*. 2020;19(1):69. doi: 10.1186/s12938-020-00810-2

124. Midha S, Dalela M, Sybil D, Patra P, Mohanty S. Advances in three-dimensional bioprinting of bone: progress and challenges. *J Tissue Eng Regen Med*. 2019;13(6):925-945. doi: 10.1002/term.2847

ACCSCIENCE PUBLISHING

International Journal of Bioprinting

REVIEW ARTICLE

Beyond structure: A review of intelligent, bioresponsive, and sustainable design paradigms for three-dimensional-printed metamaterials in drug delivery

Wanchong He* and Qinghua Zeng*

Shandong Key Laboratory of Applied Technology for Protein and Peptide Drugs, School of Pharmaceutical Sciences and Food Engineering, Liaocheng University, Liaocheng, Shandong, China

Abstract

Drug administration involves the precise delivery of therapeutic agents to targeted sites in a controlled manner, maximizing efficacy while minimizing adverse effects. This goal is pursued through drug delivery systems (DDSs), built from synthetic, natural, or hybrid biomaterials, that encapsulate and release drugs via diverse administration routes and mechanisms. Their core purpose is to localize pharmacological activity, reduce systemic toxicity, and protect surrounding healthy tissues. Despite advances, persistent challenges remain, including poor bioavailability, instability in drug loading and release profiles, limited targeting accuracy, undesirable systemic persistence, and inadequate spatiotemporal control. Additional concerns include inadequate chemical stability, patient compliance, and risks of long-term toxicity, all of which hinder clinical translation. To overcome these obstacles, metamaterials—engineered structures with geometry-driven properties—have emerged as promising platforms. By leveraging additive manufacturing and nanoscale design, metamaterials offer tunable architectures and unconventional physicochemical properties, enabling precise control over release dynamics, spatial specificity, and therapeutic outcomes. This review highlights the integration of metamaterials into DDSs, focusing on material selection, structural design strategies, fabrication challenges, and the novel possibilities enabled by three-dimensional printing. We also examine their applications in sustained, pulsatile, and stimuli-responsive release, targeted therapy, theranostics, and regenerative medicine. Finally, we discuss unresolved issues such as biocompatibility, scalability, and translational barriers, emphasizing the transformative potential of metamaterial-enabled DDSs in advancing precision medicine and healthcare innovation.

Keywords: Bioprinting; Drug delivery; Metamaterials

***Corresponding authors:**
Wanchong He
(hewanchong@gmail.com)

Qinghua Zeng
(zengqinghua@lcu.edu.cn)

Citation: He W, Zeng Q. Beyond structure: A review of intelligent, bioresponsive, and sustainable design paradigms for three-dimensional-printed metamaterials in drug delivery. *Int J Bioprint*. 2026;12(1):38-70. doi: 10.36922/IJB025420422

Received: September 11, 2025
Revised: October 14, 2025
Accepted: October 23, 2025
Published online: November 18, 2025

Copyright: © 2025 Author(s). This is an Open Access article distributed under the terms of the Creative Commons Attribution License, permitting distribution, and reproduction in any medium, provided the original work is properly cited.

Publisher's Note: AccScience Publishing remains neutral with regard to jurisdictional claims in published maps and institutional affiliations.

1. Introduction

Drug administration plays a crucial role in directing therapeutic compounds precisely to diseased tissues, thereby enhancing their pharmacological effectiveness while minimizing systemic harm. This goal is often achieved through drug delivery systems

(DDSs), which are engineered constructs designed to transport active molecules selectively to pathological regions, ensuring minimal impact on adjacent healthy cells, tissues, and organs.[1–3] Their functionality arises from the controlled encapsulation,[4] storage,[5] and release dynamics of the therapeutic agents.[6] Historically, DDSs were relatively rudimentary, involving the incorporation of medicines into natural matrices such as carbohydrates,[7] lipids,[8] or proteins for oral administration.[9] Modern biomedical innovations, however, have catalyzed rapid expansion in pharmaceutical strategies to achieve targeted release with fewer adverse effects by employing a wide spectrum of advanced natural and synthetic carriers. Examples include membrane-cloaked nanostructures,[10] extracellular vesicles,[11] liposomal formulations,[12] aerosolized nanosprays,[13] biodegradable scaffolds,[14] polymer-based nanocarriers,[15] monoclonal antibodies and antibody–drug conjugates,[16,17] and multifunctional hydrogels.[18] Moreover, hybrid DDSs exhibiting multiple modes of responsiveness have been engineered to achieve superior precision, often by integrating hydrogels with nanoscale or macroscale delivery modules.[19–21] Despite their diversity, many of these platforms are unified by shared physicochemical traits, including porosity,[22] biodegradability,[23] injectability,[24] adaptability,[25] and self-repairing capacity.[26] Beyond these intrinsic features, several can be designed to respond to external or endogenous stimuli, such as changes in temperature,[27] pH,[28] enzymatic activity,[29] or light exposure,[30] thereby enabling modulation of their release kinetics. Nonetheless, persistent barriers remain, particularly in attaining high loading efficiency,[31] achieving precise site selectivity,[32] minimizing chronic toxicity,[33] and realizing extended release profiles,[34] all of which pose considerable challenges for their clinical translation.

Recent scientific progress has increasingly emphasized the engineering of artificial materials that exhibit behaviors absent in nature. Among the most striking outcomes of this effort is the creation of metamaterials, sometimes referred to as architected materials, whose unique characteristics are derived from carefully arranged geometries and microstructural designs rather than their chemical composition.[35,36] Originally introduced in 1968 within the context of materials science, the concept of metamaterials has since extended to biomedical domains, including drug delivery, where their unusual physical features are being explored for therapeutic benefit. At dimensions smaller than the wavelength of incoming stimuli, metamaterials exhibit extraordinary interactions with electromagnetic radiation and acoustic waves. Such subwavelength control enables these materials to serve as "intelligent" carriers that respond selectively to environmental or externally applied triggers, ranging from pH fluctuations and thermal changes to magnetic fields, ultrasound, and microwaves, thereby releasing their therapeutic payload only at the intended pathological site while reducing off-target toxicity.[37–41] Through controlled interactions with electromagnetic radiation, metamaterials can generate localized thermal effects or photonic activation, enabling externally regulated drug release triggered by infrared or microwave energy.[42] Moreover, many exhibit negative refractive indices, which enhance optical manipulation and facilitate the precise stimulation of delivery systems through targeted light exposure, a capability particularly advantageous for oncology, where spatial accuracy is critical. In addition, their inherent flexibility and design adaptability permit adjustment to complex physiological environments, improving penetration and distribution within tissues. Despite these advantages, manufacturing metamaterials with reproducible precision remains a substantial challenge. To achieve their intricate architectures, researchers increasingly employ additive manufacturing strategies,[43] such as advanced three-dimensional (3D) printing, which builds carriers layer by layer with programmable geometries capable of adapting dynamically to biological conditions, including pH shifts or temperature variations.[36,44–47]

Certain classes of materials possess the intrinsic ability to undergo self-assembly as a result of their chemical and molecular characteristics. Nevertheless, to broaden or optimize these self-assembling behaviors, researchers have introduced a variety of complementary fabrication approaches. Among them, 3D printing has emerged as a particularly powerful tool in biomaterials and bioengineering research. Using extrusion-based strategies, materials with distinct mechanical and physicochemical properties can be deposited through specialized nozzles to create hierarchical composites with tailored architectures. The ability to achieve finely tuned spatial and temporal control during the printing process enables the engineering of metamaterials that better emulate the structural and functional intricacies of natural biological tissues, thereby enhancing the effectiveness of therapeutic DDSs.[48,49] A further advantage of 3D bioprinting lies in its ability to incorporate functional biomolecules, including growth factors,[50] enzymes,[51] or active pharmaceutical agents,[52] directly into scaffold matrices, which facilitates controlled and localized release while simultaneously promoting tissue repair and regeneration.[53] By engineering concentration gradients of these bioactive substances within a scaffold, researchers can create biomimetic environments highly beneficial for regenerative medicine. In addition, these printed constructs can be designed to degrade at tunable rates, allowing for programmed therapeutic release over clinically relevant time scales. The

versatility of bioprinting also enables the integration of multiple materials with distinct physical and mechanical properties within a single construct, providing structural robustness alongside efficient delivery performance.[54,55] Collectively, these advances underscore the unique capabilities of 3D printing in producing metamaterials with sophisticated, customizable geometries that are ideally suited for biomedical applications. 3D-printed metamaterials have recently emerged as a transformative class of engineered architectures with extraordinary structural, mechanical, and functional tunability, enabling sophisticated control over drug transport and release. While prior reviews, including Singh *et al*.,[56] have systematically summarized the physical properties and fabrication strategies of these systems, the field is rapidly shifting toward a new era emphasizing biological intelligence, adaptive responsiveness, and sustainability. These emerging paradigms extend beyond structural optimization, incorporating living components, real-time feedback mechanisms, and eco-conscious design philosophies. In this context, the present review redefines the landscape by exploring intelligent, biohybrid, and sustainable metamaterial-based DDSs, addressing how advanced computation, responsive bioprinting, and circular manufacturing approaches can together accelerate the translation of metamaterials from structural novelty to clinical reality.

This review critically examines the most recent progress in the development and application of printed metamaterials for drug delivery, offering a comprehensive overview of their distinctive attributes—encompassing structural, mechanical, electromagnetic, and functional properties—as well as key considerations in design, material selection, fabrication methodologies, and optimization approaches. In doing so, we highlight how these engineered systems are being integrated into drug delivery platforms to achieve higher therapeutic efficiency with reduced adverse effects. By integrating the core principles of metamaterials with recent progress in 3D printing, this review seeks to offer both conceptual understanding and practical guidance that are critical for the development of next-generation DDSs. It is our view that such an overview not only summarizes the current state of the art in this field but also sparks continued exploration into this rapidly evolving discipline. In particular, by outlining the challenges and opportunities related to biocompatibility, scalability, and translational hurdles, we emphasize how the convergence of metamaterials and additive manufacturing holds the potential to drive transformative advances in precision medicine and next-generation therapeutic delivery systems.

2. Physical properties of metamaterials

The growing attention to metamaterials in recent years stems from their extraordinary ability to display electromagnetic, acoustic, and mechanical behaviors that are seldom observed in natural substances, a property rooted in their distinct structural configurations and engineered 3D architectures.[57,58] Typically, these materials are constructed from periodic or quasi-periodic arrangements, whose structural organization dictates how they interact with incident electromagnetic radiation. By being engineered at dimensions significantly smaller than the wavelength of the applied electromagnetic field, metamaterials can be characterized in terms of their permittivity (ε; describing the response to electric fields) and permeability (μ; describing the response to magnetic fields). Under specific conditions, the effective electric permittivity and magnetic permeability can attain negative values, resulting in negative-index or left-handed materials in which wave propagation obeys the left-hand rule of electromagnetism. Such optical and electromagnetic metamaterials enable an unprecedented degree of control over the guidance and transmission of light and electromagnetic waves. In parallel, mechanical metamaterials are deliberately engineered to regulate responses across elastic, nonlinear elastic, plastic, and fracture domains, allowing precise tuning of properties such as isotropy, auxeticity, and fracture resistance. These tailored characteristics hold critical significance not only for biomedical innovations, including drug delivery platforms and implantable systems, but also for aerospace technologies and the advancement of next-generation composite materials.[59,60] Collectively, these innovations overcome the constraints imposed by naturally available material properties, thereby reshaping the landscape of functional material design and establishing metamaterials as a central focus of modern materials science.

Within the domain of additive manufacturing, and particularly in bioprinting, one of the most persistent hurdles is the commercial-scale fabrication of intricate micro- and nanoscale metamaterial architectures.[61] While microscale constructs have been successfully realized in research environments, the reliable production of large, fully functional metamaterial assemblies remains challenging, continuing to limit broader applications. Consequently, the field increasingly demands advanced 3D and emerging four-dimensional (4D) printing technologies that combine exceptional precision with high throughput and scalability, thereby enabling the fabrication of complex structures at commercially relevant volumes.[62] Achieving such progress necessitates not only technical innovations in printing methodologies but also a comprehensive

understanding of the mechanical, electromagnetic, structural, and functional characteristics that govern the behavior of metamaterials. Only by bridging these aspects can their immense potential be unlocked across a wide spectrum of applications, particularly in healthcare, where tailored metamaterial-based solutions could address pressing clinical and therapeutic challenges.[63]

The following discussion highlights the fundamental properties of metamaterials that are essential to their successful integration into biomedical and healthcare technologies.

2.1. Structural properties and transport control strategies in metamaterial-based drug delivery

The structural features of metamaterials—especially those emerging from microgeometry-based design approaches—greatly expand the opportunities for tuning material behavior and enhancing their functionality in the contexts of cell–material interactions and DDSs.[64] In this framework, factors such as unit cell topology, pore size, and overall porosity are recognized as key regulators of scaffold mechanics, permeability, and biological performance. Consequently, there is a growing demand for materials whose microscopic morphology can be precisely engineered and controlled. Features including porosity,[65] permeability,[66] and surface-to-volume ratio exert a significant influence on the mechanical response of metamaterial constructs.[67,68] Porosity plays a particularly decisive role in modulating cellular behavior as well as in facilitating the transport of nutrients and therapeutic agents. Recent studies have demonstrated that mesenchymal stem cells grown on diamond-derived scaffolds with graded density exhibited markedly elevated alkaline phosphatase activity, a well-established indicator of osteogenic differentiation and lineage specification.[69] These scaffolds were intentionally designed with lower porosity in the inner regions, which enhanced initial cell adhesion, while higher porosity in the outer layers promoted cell proliferation and reduced the risk of pore blockage. Complementary computational models of gyroid lattice structures further confirmed that greater porosity, together with the resulting increase in permeability, primarily stimulated cellular proliferation. Although scaffolds with larger pore sizes initially displayed diminished adhesion, their superior ability to support oxygen and nutrient transport ultimately led to more rapid cell growth and expansion.

It is worth emphasizing that achieving an appropriate cellular density within scaffolds relies on a delicate balance between available surface area and material permeability, parameters that are particularly important in biomedical contexts such as bone tissue engineering. While high porosity can facilitate fluid penetration and nutrient diffusion, it typically compromises overall strength, thereby limiting structural stability. Consequently, the design of porous scaffolds requires careful optimization to maintain adequate transport of metabolites while preserving compatibility with native tissue. Moreover, the kinetics of drug release from porous carriers are governed by a variety of factors beyond pore architecture alone, including physicochemical properties of the surrounding fluid, interfacial tension, and molecular interactions between the therapeutic payload and the carrier matrix. Thus, modifications in porosity alone are insufficient to guarantee predictable drug release, especially when exposed to dynamic physiological environments.[70]

Hydrodynamic metamaterials represent a class of engineered structures whose internal architectures are deliberately designed to manipulate fluid transport in controlled and predictable ways.[71] By introducing anisotropy into their microstructural organization, these systems can exhibit unconventional flow behaviors that are not typically achievable in natural porous materials. Such fine-tuned regulation of fluid motion across micro- and macroscales offers opportunities to enhance transport processes and improve the performance of biomedical devices. In the context of drug delivery, porous hydrodynamic metamaterials are particularly attractive for implantable systems, as they can facilitate site-specific administration of therapeutics while reducing systemic exposure and collateral tissue damage. One of their remarkable features lies in their ability to function as "hydrodynamic cloaks," generating protected zones of minimal fluid velocity that serve as local drug reservoirs. Upon demand, these structures can be reconfigured into "concentrators" or intermediate states, effectively boosting local flow intensity and drug dosage at the target region. This dynamic switching capability offers precise spatiotemporal control over release kinetics, making it adaptable to individual therapeutic requirements. Importantly, unlike conventional scaffold strategies, where release is primarily dictated by pore size and diffusion pathways, hydrodynamic metamaterials achieve regulation through direct modulation of fluid flow patterns.[72] This distinctive mechanism underscores their promise as a next-generation platform for highly responsive and personalized drug delivery.

The surface-to-volume ratio is also a critical microgeometric parameter that exerts a profound influence on both the loading capacity and the release kinetics of a metamaterial-based DDS, as well as on cell fate. A high surface-to-volume ratio, achievable through intricate nanoscale architectures or highly porous micro-lattices, provides an extensive interface for drug adsorption and cell attachment. In the context of drug delivery, a

large interfacial area can significantly enhance the initial loading efficiency of therapeutic agents, particularly those with high molecular weight or with strong affinity for the scaffold material. Subsequently, during the release phase, a high surface-to-volume ratio facilitates a more rapid initial release (burst release) due to the greater number of drug molecules situated near the interface, while also sustaining a more effective long-term release profile by maintaining a high concentration gradient between the carrier's interior and the surrounding medium.[73] From a biological perspective, the surface-to-volume ratio directly modulates cell–material interactions. A higher surface-to-volume ratio presents more anchoring sites for cell adhesion proteins (e.g., fibronectin, vitronectin), thereby potentiating stronger cell adhesion and spreading.[74,75] This is particularly crucial for guiding stem cell differentiation, as specific lineages are sensitive to adhesion density. For instance, osteogenic differentiation of mesenchymal stem cells is often promoted on surfaces that support robust adhesion and spreading, a condition favored by a high surface-to-volume ratio.[76] Furthermore, in highly convoluted architectures with a massive surface-to-volume ratio, the local micro-environment—including protein adsorption, ion exchange, and the presentation of biochemical cues—can be finely controlled, making the scaffold itself a potent, active signaling entity rather than a passive physical support. A compelling illustration of this principle is found in nanoscale metamaterials, such as those fabricated via two-photon lithography. These structures can achieve surface-to-volume ratios that are orders of magnitude higher than those of conventional scaffolds. Studies have shown that such nano-architected surfaces can induce significant lipid peroxidation and cytoplasmic membrane blebbing in cancer cells, leading to potent, mechanics-driven cell death—a therapeutic effect that is intrinsically tied to the extreme surface-to-volume ratio and its direct physical interaction with the cellular membrane, offering a novel mechanism to overcome drug resistance.[77]

Overall, metamaterials provide distinct benefits through their capacity to finely tune key structural features, including porosity, permeability, surface-to-volume ratio, and fluid transport behavior, that are fundamental to the optimization of DDSs.[22,78,79] Such controllable characteristics not only enable the efficient regulation of molecular diffusion and convective flow but also create a favorable microenvironment for nutrient exchange, cellular adhesion, and metabolic waste clearance. These integrated effects collectively enhance cell viability and functionality while accelerating processes of tissue repair and regeneration, underscoring the potential of metamaterials as versatile platforms for advanced therapeutic delivery. We present the stel nanoscale archeta materials and their corresponding drug delivery functions in Table 1.

2.2. Mechanical properties of metamaterials for improving drug delivery efficiency

The continuous drive to expand the functional limits of materials has fostered the emergence of mechanical metamaterials, a class of architected structures with unconventional elastic responses.[80–82] A hallmark feature of these systems is their anisotropic elasticity, which governs how they deform under defined loading conditions. Their mechanical responses are generally described by constitutive relationships valid at low strain levels and under near-isothermal environments. Classical elastic constants, including Young's modulus, bulk modulus, shear modulus, and Poisson's ratio, are central in characterizing stiffness, compressibility, and rigidity, thereby providing benchmarks for assessing the performance of structural

Table 1. Structural properties of metamaterials and their drug delivery functions

Structural properties	Mechanism/key physical feature	Relevant drug delivery system scenario	Advantages vs. conventional carriers
Auxetic (negative Poisson's ratio)	Expands laterally under tension; strain redistribution	Expandable stents, wound dressings, adaptive scaffolds	Tunable pore opening under load, improved tissue integration
Gyroid/Triply periodic minimal surface structures	Interconnected continuous pores, high surface area	Oral controlled-release printlets, tissue scaffolds	Geometry-dependent diffusion; enhanced mass transport
Pentamode metamaterials	High bulk modulus but near-zero shear modulus (liquid-like)	Pressure-responsive release systems	Fluid-like stress response for mechanically triggered release
Hydrodynamic metamaterials	Microstructural anisotropy controls local flow	Implantable local infusion devices	Direct regulation of convection-driven release
Acoustic metamaterials	Induce microstreaming and enhance penetration	Transdermal rapid delivery (e.g., epinephrine patch)	On-demand multi-burst dosing, faster systemic uptake
Electromagnetic/ terahertz biodegradable metamaterials	Resonance shifts and localized heating/monitoring	Smart patches with real-time theranostics	Simultaneous drug release + monitoring; biodegradable

systems subjected to elastic strain. Unlike conventional materials, mechanical metamaterials utilize rationally designed microarchitectures to tune these constants, resulting in behaviors that would otherwise be inaccessible in natural systems.[83] For instance, structures exhibiting negative stiffness can facilitate rather than resist deformation, producing dramatic volume changes under stress. Particularly significant in this context is Poisson's ratio, which quantifies lateral contraction or expansion relative to longitudinal strain under uniaxial loading. While typical materials display positive Poisson's ratios, recent innovations have broadened this design space to include highly negative values. Gao *et al.*[84] verified this concept by engineering a metamaterial characterized by highly adjustable negative Poisson's ratios (NPRs) together with reduced localized stress accumulation. The architecture, constructed from cylindrical shell–beam modules, was realized through a combination of finite element simulations and stereolithography-based 3D printing, which enabled both fabrication and experimental validation of the system. Experimental validation under tensile and compressive loading confirmed numerical predictions, with NPRs as low as −1.618 in tension and −1.657 in compression. Such architectures offer potential for minimally invasive medical applications, including controlled percutaneous delivery and personalized therapies.[84]

Babaee *et al.*[85] developed kirigami-inspired stents, designed as auxetic mechanical metamaterials with patterned architectures that allow adjustable stiffness, controlled directional expansion, and enhanced compliance. These systems incorporate a kirigami-patterned sheath resembling snake skin in combination with a compliant actuator, enabling controlled distribution of drug reservoirs along both the circumferential and longitudinal orientations of tubular tissues, including the gastrointestinal tract, blood vessels, and respiratory passages. Verification in living porcine models with budesonide confirmed that temporary stent deployment facilitated localized submucosal drug storage, providing a sustained release profile that lasted for approximately 1 week.[85] However, one limitation of auxetic designs is their inability to maintain structural integrity under significant compressive deformation, where symmetry loss can suppress auxetic effects. Because chirality-induced rotation largely determines this behavior, introducing soft hinges, stiffer cores, or hybrid cell architectures can stabilize deformation. Jiang *et al.*[86] advanced this concept by embedding re-entrant units within chiral cores, yielding hybrid auxetic lattices capable of sequential cell opening under strains ranging from 2.91% to 52.6%. This hierarchical deformation pathway enabled the controlled release of particles under mechanical stimuli. Both simulations and experimental analyses revealed that the ratio of cell dimensions (c/b_0) together with the re-entrant angle (θ) serve as key determinants governing stiffness, the magnitude of the NPR, and the kinetics of release behavior.[86] Reducing c/b_0 or increasing θ shifted the strain threshold for release without markedly affecting other parameters. Collectively, these strategies demonstrate how mechanical metamaterials, through engineered auxetic responses and programmable deformation modes, can be harnessed to create advanced DDSs and multifunctional biomedical devices.[86]

In addition to exhibiting NPR behavior, mechanical metamaterials can display atypical mechanical responses, such as achieving a near-zero shear modulus while maintaining a relatively high bulk modulus. This unusual combination allows the material to withstand compressive forces while exhibiting fluid-like flow characteristics, thereby offering precise opportunities for regulating drug release. A prominent example is the pentamode metamaterial, which retains a solid framework but mechanically mimics a liquid by selectively supporting compression while minimizing resistance to shear deformation.[87] Such properties make pentamode architectures highly attractive for engineering drug release platforms that respond dynamically to applied mechanical stimuli, enabling sustained and site-specific therapeutic delivery. Applications of pentamode-inspired systems have been proposed for diverse biomedical contexts, including oncology, chronic disease management, and regenerative medicine, where localized and prolonged administration is required. When combined with auxetic designs, these structures further improve spatial targeting, proving especially advantageous for addressing tumor microenvironments or localized infections.

Mechanical metamaterials have also shown particular promise in the gastrointestinal tract, where controlled retention and release are crucial for effective treatment. For instance, a soft, gastric-resident metamaterial was specifically designed for oral drug delivery.[85] The device was specifically designed with high compressibility and elasticity, permitting its secure transit through the esophagus in a minimized cylindrical configuration. Upon entering the stomach, it reconfigured into an enlarged, porous, spherical shape—a structure that allows for extended retention within the gastric cavity. Fabricated with thermos-responsive materials, the device gradually released encapsulated therapeutics over a 2-week timeframe. Importantly, exposure to an endoscopically applied warm fluid (55°C) triggered disassembly of the structure, ensuring safe elimination without obstruction. This innovative design highlights the potential of mechanical metamaterials to function as minimally

invasive, thermally activated drug delivery vehicles that provide sustained release while maintaining patient safety and comfort.[85]

A deeper understanding of metamaterial-based systems requires first examining their underlying mechanical performance, where achieving an optimal balance between strength and toughness is central to maintaining structural reliability and functionality during drug delivery.[88] Material strength refers to the ability of a structure to resist external loads without structural collapse, whereas toughness denotes its capacity to dissipate energy and undergo considerable deformation prior to breaking. To optimize these mechanical features, researchers have employed multilayered arrangements and diverse topological designs to reinforce strength, while toughness has been advanced through mechanisms that redistribute strain, including auxetic lattice patterns, tensegrity-inspired networks, and hybrid systems integrating both stiff and flexible elements.[89] Despite these advances, strength and toughness remain inherently competing attributes, as reinforcing one often diminishes the other.[90] Consequently, an overarching goal in metamaterial design is to integrate both high strength and toughness, producing materials that remain resilient under stress yet capable of bending without fracturing—an essential property in demanding biomedical environments.

An active acoustic metamaterial patch for minimally invasive, transdermal drug delivery has recently been developed.[91] This compact therapeutic platform enhanced skin permeability by creating micron-scale transport channels and facilitating drug delivery into the dermis and deeper tissue layers through localized acoustic streaming. Additionally, the platform enabled programmable and patient-tailored modulation of drug release kinetics through digital control. When tested in a murine model of anaphylaxis, the transdermal patch successfully administered epinephrine in a multi-pulsatile manner, yielding enhanced therapeutic outcomes relative to traditional self-injection methods. Such acoustic metamaterial systems highlight the potential of combining mechanical robustness with adaptability to create advanced platforms for percutaneous drug administration and real-time pharmacokinetic management.

Overall, by enabling precise adjustment of parameters such as Poisson's ratio, bulk and shear moduli, strength, and toughness, mechanical metamaterials provide versatile platforms for biomedical use.[92–94] Their unique ability to withstand compression while simultaneously permitting fluid-like behavior makes them particularly promising for advanced DDSs requiring accurate and tunable release profiles.

2.3. Electrical properties

Precise regulation of electromagnetic wave behavior underpins progress in fields such as wireless communication, high-resolution imaging, and advanced sensing.[95] Yet, the intrinsic atomic-scale characteristics of naturally occurring materials impose inherent limitations, preventing fine-tuned control over wave transmission and propagation. To overcome this limitation, engineered metamaterials are designed with tunable unit cell geometries, sizes, and arrangements, enabling tailored responses such as controlled radiation, scattering, and propagation.[96] Biodegradable metamaterial platforms have been developed that allow simultaneous control of drug release and real-time monitoring through resonance shifts in reflected terahertz (THz) signals. Antibiotic-loaded silk patches function as resorbable antibacterial systems that do not require retrieval after implantation, making them highly attractive for site-specific therapies.[97]

In addition to programmable degradation and release behaviors, the ability to tailor structural features provides access to unconventional electromagnetic characteristics, including the emergence of a negative refractive index.[98] Such phenomena occur when both the electric permittivity and magnetic permeability exhibit negative values, producing wave–matter interactions that are absent in naturally existing substances. For example, novel ferrite-based metamaterials composed of permanent magnetic ferrite rods and metal wires have been developed that achieve negative and near-zero refraction without the need for an external magnetic field.[99] Numerical and experimental analyses confirmed their effectiveness, demonstrating strong potential for waveguiding, imaging, and precise delivery of electromagnetic energy. Such effects could be harnessed to direct electromagnetic waves to targeted tissues, enabling controlled, noninvasive drug release.[100]

Overall, electromagnetic metamaterials expand the ability to manipulate radiation in unprecedented ways, unlocking biomedical applications in high-resolution imaging,[101] *in vivo* sensing, and implantable or wearable antennas that improve medical device communication.[102]

2.4. Functional properties

Beyond their mechanical, structural, and electrical properties, the functional attributes of metamaterials are increasingly recognized for their pivotal role in drug delivery, as they enable controlled release kinetics, site-specific targeting, and responsiveness to external stimuli. By incorporating therapeutic molecules into their internal frameworks, these platforms enable precise and sustained administration, maintaining therapeutically relevant concentrations over time and enhancing treatment efficacy.

Nano-metamaterials, in particular, leverage multilevel nanoscale architectures to directly influence drug release and therapeutic efficacy at the single-cell level. In tumor models, multilevel nanoscale architectures induced the accumulation of lipid, cytoplasmic, and mitochondrial ROS, driving uncontrolled cell death via severe membrane damage and blebbing, thereby overcoming drug resistance. Such precisely engineered nano-architectures demonstrate how drug delivery can be tuned at the cellular level to modulate biochemical responses and death pathways.[103] In a related development, Sun *et al.*[104] developed silk-derived THz metamaterial patches loaded with antibiotics, demonstrating their potential for targeted antibacterial treatment. When applied to *Staphylococcus aureus*-infected wounds in rats, these flexible patches adhered firmly to the skin, facilitating both drug delivery and real-time monitoring. Within 48 h, visible wound healing was evident, and colony-forming unit assays confirmed efficient eradication of the infection. Together, these studies highlight the versatility of functional metamaterials in creating intelligent therapeutic platforms that combine controlled kinetics, responsiveness, and diagnostic capabilities for next-generation drug delivery.

In summary, the combined influence of metamaterials' structural, mechanical, electrical, and functional attributes forms the foundation for engineering sophisticated systems optimized for therapeutic use. Features such as negative refraction permit precise control of electromagnetic waves, supporting targeted drug delivery while minimizing off-target interactions, whereas near-zero refractive indices enhance signal transmission, ensuring accurate *in vivo* delivery. Collectively, these integrated properties allow the development of therapeutic platforms that are both highly efficient and dependable. Beyond their mechanical robustness and sensing or actuation capabilities, additional physical attributes, such as optical, acoustic, and electromagnetic responses, together with biocompatibility, remain essential for driving the continuous innovation and clinical translation of these emerging artificial materials. We summarize the above stimuli-responsive metamaterial systems in Table 2.

3. Beyond static structures: toward intelligent, responsive, and programmable systems

Traditional metamaterial research has focused on harnessing fixed geometries to yield static, predictable mechanical or electromagnetic properties, such as an NPR or negative refractive index. While foundational, this paradigm treats DDSs as passive entities. The inherent complexity and dynamism of biological systems, however, demand a new generation of DDSs capable of active dialogue with their microenvironment. This section moves beyond a mere recitation of these static properties to focus on a more advanced frontier: how the convergence of material selection, architectural design, and manufacturing processes can bestow dynamic, programmable intelligence upon metamaterials. We systematically dissect three core capabilities that define this next generation: (i) responsiveness, the ability to perceive and react to physiological cues; (ii) multifunctional integration, the fusion of delivery, sensing, and actuation within a single architecture, and (iii) shape programmability, the capacity for prescribed morphological evolution post-fabrication. Finally, we highlight how artificial intelligence (AI) and generative design are emerging as central driving forces, fundamentally revolutionizing the way we conceive and realize these sophisticated systems.

3.1. Responsive strategies: from passive diffusion to active targeting

Responsive metamaterials enable DDSs to react to physiological cues rather than relying solely on passive diffusion. For instance, a pH-sensitive hydrogel arranged

Table 2. Stimuli-responsive metamaterial systems in drug delivery

Stimulus	Responsive materials/strategies	Triggered-release mechanism
Temperature	Shape-memory polymers (polylactic acid/ polycaprolactone blends), thermosensitive hydrogels	Pore size/volume change, triggered disassembly
pH	Eudragit®, alginate, chitosan	pH-induced swelling/degradation
Enzyme	Natural polymers (chitosan, collagen, extracellular matrix)	Enzyme-mediated degradation
Light (visible/near-infrared)	Photothermal agents, photo-crosslinkable groups	Local heating or bond cleavage
Magnetic field	Magnetic nanoparticles, composites	Magnetic hyperthermia or field-induced release
Ultrasound/acoustic	Acoustic metamaterials, cavitation-enhanced hydrogels	Enhanced penetration, fast burst release
Electric field	Conductive polymers, embedded heating wires	Joule heating or electrochemical release

in an auxetic lattice configuration can transform a minor swelling event induced by an environmental pH shift into a dramatic pore opening.[105] This structural amplification facilitates a rapid, burst-like drug release profile not readily achievable with conventional hydrogel spheres, enabling swift therapeutic action in response to specific pathological zones (e.g., acidic tumor microenvironments or inflamed tissues).[106]

Metamaterials can be engineered to transduce intrinsic mechanical forces—such as vascular pulsation, muscle contraction, or tumor tissue pressure—into a trigger for drug release. A compressible, helicallt structured scaffold, for instance, can function as a micro-pump, expelling drug payloads from its internal reservoir upon exposure to cyclic compressive strains.[107] This facilitates pulsatile drug administration synchronized with physiological rhythms, enhancing therapeutic efficacy and reducing off-target effects.

Metamaterials can act as "energy lenses," concentrating and enhancing the effects of external physical fields (e.g., ultrasound, light, magnetic fields) at precise locations. Acoustic metamaterials, for example, can focus planar ultrasound waves into micron-scale "hotspots" of pressure or microstreaming. This focused energy can transiently permeabilize cell membranes or disrupt the carrier's internal structure, enabling the release of drugs with exceptional spatial accuracy. This approach minimizes the required energy dose systemically, thereby augmenting safety.

3.2. Multifunctional integration: from single delivery to theranostic platforms

The inherently structured nature of metamaterials provides an ideal platform for integrating diverse functional components at the microscale, elevating them from mere "carriers" to autonomous "therapeutic platforms." A pivotal advancement involves integrating conductive nano-networks (e.g., graphene, MXene) within the metamaterial scaffold to serve as embedded sensors.[108] These sensors can continuously monitor local biochemical markers (e.g., glucose, hydrogen peroxide, cytokines). The acquired data are then processed by an integrated microfluidic circuit or a wireless module, which in turn commands an actuator (e.g., a microscale heater that triggers a phase-change material, or an electroactive polymer valve) to modulate drug release. This creates a self-regulated, closed-loop therapeutic system that autonomously maintains homeostasis. The concept of theranostics is elevated by pre-programming imaging contrast agents (e.g., superparamagnetic iron oxide nanoparticles for magnetic resonance imaging,[109] gold nanorods for photoacoustic imaging[110]) directly into the metamaterial's lattice. This design ensures that the carrier itself acts as a high-fidelity imaging probe, allowing for real-time and precise tracking of its biodistribution and localization. Subsequently, the same physical properties can be harnessed to initiate on-demand therapy (e.g., magneto-thermal or photo-thermal ablation) alongside controlled chemical release, enabling simultaneous diagnosis, treatment, and monitoring. A frontier in autonomous implants is the integration of energy-harvesting mechanisms. Metamaterials can incorporate triboelectric nanogenerators or piezoelectric elements that convert endogenous mechanical energy (e.g., from heartbeats, respiration, or body movement) into electricity.[111–116] This harvested power can directly drive drug release mechanisms (e.g., electroosmotic pumps) or sustain the operation of sensing and communication modules. This paradigm paves the way for self-sustaining, battery-free implantable DDSs capable of long-term operation.

3.3. Shape programmability: four-dimensional printing for spatiotemporal control

Four-dimensional printing enables the fabrication of constructs with anisotropic material distribution or internal stresses, allowing them to undergo a predefined, multi-stage morphological transformation sequence *in vivo*.[117] A single oral capsule, for example, could be designed to first swell gradually for sustained release, then twist open at a specific intestinal pH for a second pulse of drug, and finally unfold completely to facilitate rapid clearance. This allows for complex, time-dependent release profiles from a single, simple-to-administer dosage form.[118,119]

3.4. The artificial intelligence-driven paradigm: generative and inverse design

Artificial intelligence excels at managing competing design objectives. A single model can be tasked with simultaneously maximizing drug loading capacity, minimizing initial burst release, ensuring mechanical resilience under physiological loads, and matching a target biodegradation timeline. Through high-throughput virtual screening, AI can evaluate millions of candidate designs *in silico*, identifying the optimal trade-offs and drastically accelerating the research and development cycle from years to days.[120] Machine learning algorithms can analyze real-time sensor data during 3D printing (e.g., melt pool monitoring in selective laser sintering [SLS]) to predict and correct defects. Furthermore, computer vision can analyze post-fabrication micro-computed tomography scans of a printed metamaterial to non-destructively predict its *in vivo* release performance, creating a robust design–manufacture–verification intelligent loop.[121]

4. The convergence of digital manufacturing and biofabrication: toward hybrid and four-dimensional-printed metamaterials

The integration of metamaterials with 3D printing technologies significantly enhances fabrication precision and expands structural versatility, enabling the creation of dynamic and stimulus-responsive platforms for biomedical applications.[122–124] This synergy enables the production of intricate, patient-specific architectures that can alter their form or function in response to environmental cues, thereby supporting the development of more personalized therapeutic strategies. In contrast to traditional materials, metamaterials derive their distinctive behaviors from carefully designed periodic architectures rather than their chemical composition, endowing them with highly adjustable properties that can be programmed to reshape or deform under specific conditions. However, achieving features such as auxetic behavior (NPR), superelasticity, or tunable stiffness is challenging with traditional fabrication methods, which lack the resolution and adaptability required at the microscale. Incorporating 3D and 4D printing overcomes these limitations by offering precise control over geometry and spatial arrangement. While 3D bioprinting enables the construction of complex biomedical scaffolds using cellularized biomaterials and bioactive factors,[125,126] 4D printing introduces a temporal dimension, allowing fabricated systems to dynamically reconfigure in response to physiological or external stimuli.[127] This convergence of metamaterials with advanced bioprinting technologies paves the way for multifunctional platforms tailored to next-generation biomedical applications. While existing literature has meticulously catalogued conventional 3D printing modalities such as extrusion, stereolithography, and SLS, the current frontier lies in hybrid biofabrication and 4D printing, where materials can evolve, heal, and reconfigure over time. This section examines how multimaterial bioprinting, cell-laden constructs, and stimuli-responsive inks are being integrated to produce living or adaptive metamaterials. Furthermore, AI- and data-assisted design frameworks now enable predictive optimization of printing parameters, offering unprecedented precision in fabricating hierarchical architectures. We also discuss how additive manufacturing interfaces with microfluidics, nanorobotics, and organ-on-chip systems, illustrating how dynamic and biocompatible metamaterial platforms are enabling programmable drug release and regenerative functionalities previously unattainable by static designs.

4.1. Raw materials for three-dimensional-printed metamaterials

Native tissues are inherently complex heterogeneous structures composed of hierarchically organized building blocks across multiple length scales, a feature that imparts multifunctionality.[128] Inspired by this principle, 3D printing, particularly bioprinting, has become a powerful strategy for constructing biomimetic scaffolds that emulate both the architecture and functions of living tissues.[129] Central to this approach is the development of bioinks—carefully engineered formulations that allow precise spatial positioning of cells, biomolecules, and scaffold materials into organized 3D constructs. In the fabrication of metamaterials for biomedical applications, including drug delivery, optimizing bioink composition is particularly crucial.[128] Their design must strike a careful balance between printability, biocompatibility, and mechanical integrity to ensure that the resulting structures fulfill both functional and therapeutic objectives.[130]

Bioinks are typically formulated from a mixture of biomaterials, living cells, and bioactive agents, enabling the fabrication of constructs that closely mimic native tissue.[131] Their successful integration with 3D printing platforms is crucial for advancing toward clinical translation. Nonetheless, several barriers remain, including insufficient biocompatibility, inadequate mechanical strength, and poor structural fidelity during fabrication.[131] Furthermore, exposure to harsh processing parameters, including high temperatures or organic solvents, can negatively impact both cell survival and functional integrity of embedded biomolecules. Constructing high-resolution, multilayered architectures that faithfully mimic native physiological behavior remains a significant challenge in this area of research.[132]

Bioink formulations typically utilize two primary categories of polymers: synthetic materials such as polycaprolactone (PCL), polylactic acid (PLA), poly(lactic-co-glycolic acid) (PLGA),[133–135] and polyethylene oxide terephthalate–co–butylene terephthalate (PEO/PBT), as well as natural polymers including alginate, hyaluronic acid, gelatin, decellularized extracellular matrix, agarose, and nanocellulose.[136–138] Incorporating cells and biomolecules tailored to the target tissue further enhances the functional capabilities of the engineered metamaterials. For successful bioprinting, bioinks must possess appropriate rheological characteristics, crosslinking capacity, and biological activity. Through precise adjustment of these characteristics via polymer blending and sophisticated fabrication techniques, bioengineered metamaterials can be customized for diverse tissue-specific applications, increasingly serving as programmable, localized DDSs with promise in regenerative medicine and individualized therapeutic strategies.

While the microarchitectural design of metamaterials critically shapes their performance and functional

behavior, the choice of constituent bulk materials remains a key determinant of the properties that can ultimately be realized.[131] Although the designed geometries of metamaterials dictate numerous distinctive properties, the inherent traits of the base materials impose essential limitations. Metamaterials are commonly fabricated from metals,[139] polymers,[140] and ceramics,[141] and the advancement of additive manufacturing has significantly expanded opportunities for producing materials with unprecedented functionalities.[142] In some cases, bulk material properties are indispensable for enabling specific behaviors. For instance, shape-morphing systems, including self-folding origami constructs,[143] exploit the shape-memory properties of specialized polymers or engineered alloys to enable programmable deformation.[144,145] In biomedical contexts, metallic metamaterials must meet stringent criteria for biocompatibility, bioactivity, and controlled biodegradability. Biocompatibility and bioactivity are comparatively easier to address, as metals like tantalum inherently exhibit compatibility with biological tissues,[146] and standard surface modification techniques—like anodizing and plasma electrolytic oxidation—can further improve cell–material interactions.[147,148] In comparison, the emphasis on biodegradability within metallic metamaterials has emerged only recently as a research priority. Investigations have largely centered on magnesium,[149] zinc,[150] iron, and their alloys. However, efforts to fabricate biodegradable metallic metamaterials remain limited, mainly due to processing challenges in additive manufacturing.

In drug delivery contexts, auxetic metamaterials can be designed in diverse structural configurations—including rigid frameworks, chiral lattices, honeycomb networks, aerogels, and hydrogels—tailored to meet particular biomedical requirements. Selecting appropriate base materials is crucial for achieving biocompatibility, responsiveness to external stimuli, and effective release kinetics. Biodegradable polymers such as PLGA, polyethylene glycol (PEG), and PCL are particularly advantageous, as they allow controlled degradation and enable environment-triggered release, for instance, in response to changes in pH or temperature.[151] Auxetic hydrogels, owing to their NPR, represent promising candidates for biomedical use.[152] Their swelling and release behaviors can dynamically adjust to environmental stimuli.[93] Likewise, mechanical metamaterials coated with polymers combine auxetic properties with lightweight construction, adjustable stiffness, and enhanced mechanical durability, rendering them ideal candidates for drug-releasing bone implants. These implants are capable of supporting physiological loads while providing excellent shear resistance, energy absorption, and indentation tolerance, thereby improving their potential for clinical implementation.[153] The adaptable nature of metamaterials further enhances their applicability, especially in devices such as vascular stents. These stents can be delivered in a compact, compressed form during minimally invasive procedures and subsequently expanded at the target location, where structural modifications enable controlled, localized drug release. Materials with shape-memory properties—including specific polymers, metals, and alloys—can revert from a deformed "frozen" state back to their original configuration upon exposure to external triggers such as heat, light, magnetic fields, or electrical stimulation. This reversible transformation supports both structural adaptability and on-demand drug release.[154] However, it is worth noting that not all metamaterials are suitable for stent fabrication. Beyond vascular applications, smart wound dressings based on metamaterials are also emerging. For instance, auxetic filament-based bandages can autonomously respond to wound swelling by opening to release therapeutic agents and closing again as the wound heals.[155] Despite these advancements, comprehensive assessments of auxetic hydrogels—such as those based on polyvinyl alcohol and polytetrafluoroethylene—within biological settings remain scarce, underscoring the need for further research.

Looking forward, material selection for metamaterial design is expected to increasingly emphasize the integration of electronics into structural frameworks, coupling physicochemical properties with advanced functions such as sensing, actuation, signal processing, and drug release modulation. A consistent theme across metamaterial research is the synergistic integration of multiple material responses within a single substrate. Many of the most innovative features rely on the coexistence of components with contrasting properties. For instance, electronic systems demand combinations of conductive, semiconductive, and insulating elements, while magnetic functionalities depend on the integration of magnetic and non-magnetic phases.[156] Similarly, achieving mechanical robustness and adaptability often requires combining soft and rigid components,[157] or designing composites that exhibit instantaneous, delayed, or restrained shape transformations depending on application needs. Recent studies have demonstrated the feasibility of such approaches in biomedical systems. For example, Jang *et al.* engineered a polymer-based hydrogel composite incorporating a deployable radio-frequency antenna alongside an integrated Joule-heating component.[158] Upon remote activation, localized heating induced the hydrogel to cross its lower critical solution temperature, causing it to transition from a solid to a liquid state and thereby triggering on-demand drug release. Likewise, auxetic

chiral polymeric combinations have proven effective in drug delivery constructs as well as skin-mounted electrophysiological sensors, due to their flexibility and conformability. Building on this concept, auxetic chiral hybrid metamaterials function as multifunctional platforms for sensing, actuation, and programmable drug delivery.[159] Despite these advancements, a major challenge in additive manufacturing-enabled metamaterials lies in achieving differential material responses within a single construct. Central to this limitation is material selection, as many biomedical applications demand polymers that are simultaneously auxetic, biocompatible, and biodegradable. However, identifying materials that m*eet all* three criteria remains difficult, representing a critical barrier to the broader clinical translation of such systems.

4.2. Design principles of three-dimensional-printed metamaterials

The primary objective in metamaterial design is to engineer microscale architectures that elicit targeted properties at the macroscale. This methodology, often referred to as rational design, combines core physical principles with analytical and computational modeling to identify microstructural configurations that maximize overall performance.[160] In the context of biomedical applications, particularly for 3D-printed DDSs, this approach highlights the importance of aligning structural architecture with material composition. The success of such systems depends not only on selecting biocompatible and responsive bulk materials but also on designing interconnected microstructures that can translate these properties into predictable, large-scale therapeutic performance.

Control over geometry lies at the core of metamaterial engineering, with internal architectures—such as gyroid, cubic, or honeycomb lattices—designed to modulate porosity and surface-area-to-volume ratios. Structures with low infill densities accelerate release by maximizing surface exposure, whereas high-density architectures slow release due to reduced permeability.[161] Core–shell architectures provide an additional layer of regulation; for instance, pH-responsive shells can protect encapsulated drugs until they encounter the alkaline conditions of the intestinal tract.[162] Layered architectures, such as bilayer systems with segregated drug compartments, also enable the execution of sequential or combined therapeutic strategies. Different additive manufacturing techniques provide unique yet complementary advantages. Fused deposition modeling is widely employed to produce drug-loaded filaments, allowing the fabrication of tablets with controlled-release properties using matrices such as hydroxypropyl cellulose or ethyl cellulose.[163] Digital light processing (DLP) enables high-resolution hydrogel architectures that incorporate stimuli-responsive functionalities, while SLS generates mechanically robust gyroid-lattice "printlets" with tunable release kinetics across various polymer blends.[164] Multi-material printing further expands these capabilities by combining structural polymers with functional hydrogels in a single construct, facilitating advanced, personalized, and programmable drug delivery strategies.

Another key consideration is the choice of material, which directly influences functional performance. Synthetic polymers like PLA and PCL provide mechanical robustness and tunable degradation rates, making them essential for long-term implant applications.[165] Thermo-responsive shape-memory polymers, including PCL/PLA blends, undergo deformation at physiological temperatures, modulating pore dimensions and controlling drug release kinetics. Ion-responsive platforms, fabricated from synthetic polyelectrolytes such as [2-(acryloyloxy) ethyl]trimethylammonium–PEG diacrylate (PEGDA), release drugs in response to local ionic fluctuations within target tissues.[166] Natural polymers, such as chitosan and alginate, offer intrinsic bioactivity, enabling enzyme-mediated drug release in the colon through microbial degradation. Dynamic metamaterials can further detect physiological cues to enable on-demand delivery; for example, pH-sensitive hydrogels, such as alginate, swell in the intestinal environment to release encapsulated therapeutics, like simvastatin. Enzyme-responsive systems leverage chitosan's susceptibility to microbial lysozymes in the colon to achieve localized release.[167] Hybrid constructs, including alginate–PEGDA composites, combine printability with stimulus responsiveness, while Eudragit® polymers (e.g., L100-55) enable pH-triggered, site-specific delivery in the upper gastrointestinal tract.[168]

The majority of metamaterial research starts with a design concept rooted in fundamental physical principles, which is then honed through parametric analyses and computational simulations to correlate microscale architectures with their resulting macroscopic properties. A key consideration in this workflow is defining what qualifies as a microarchitectural design. Initial studies concentrated mainly on geometric configuration, largely because additive manufacturing techniques capable of producing complex free-form structures were not yet widely accessible. These early designs typically consisted of a single material interspersed with voids, forming simple material–void composite systems. The key challenge was to identify microstructural geometries that could impart the desired large-scale properties. In the past decade, however, the emergence and growing accessibility of multi-material 3D printing have transformed the design landscape. These advances allow for the fabrication of intricate architectures with precise spatial arrangements, where individual

layers may possess distinct features and functions.[169] This advancement has greatly broadened the design landscape, allowing for the tailored specification of not only unit cell topology and overall geometry but also the mechanical and physical properties of individual voxels (3D pixels) throughout the structure.[170]

In recent years, the integration of machine learning and AI has opened up novel avenues for designing metamaterials. Two primary approaches have emerged: (i) deep learning and other AI techniques that facilitate the resolution of inverse design challenges,[171] and (ii) generative models, such as generative adversarial networks and variational autoencoders,[172] that are capable of creating candidate designs tailored to specific target properties, thereby extending the scope of rational design.[173] Simultaneously, mathematical approaches such as topology optimization have demonstrated efficacy in determining the micro- and nanoscale architectures of both single-material and multi-material systems.[174] Despite this progress, several challenges remain. These include reliable quality prediction, development of robust AI models for optical or mechanical properties, data handling and standardization, automation of design processes, and safety assurance in biomedical contexts. Moreover, specifying clear objective functions for gradient-based topology optimization is not always feasible, which limits the efficiency of these methods.[175] Addressing these issues will require the integration of theoretical and experimental approaches to establish unbiased and scalable design methodologies. Such efforts could accelerate the discovery of novel metamaterial concepts beyond those attainable through intuition or traditional physical reasoning.

4.3. Fabrication strategies of three-dimensional-printed metamaterials

As outlined in the previous sections, several fabrication strategies can be employed to produce metamaterials; however, additive manufacturing has emerged as the most transformative approach. Additive manufacturing, widely referred to as 3D printing, allows for the fabrication of intricate and customizable structures spanning macro-, micro-, and nanoscale dimensions.[176] The typical workflow entails creating designs using computer-aided design software, translating them into printer-compatible formats, and producing the structures through precise, layer-by-layer fabrication. The broader adoption of additive manufacturing has been driven by decreasing costs of 3D printers, along with ongoing improvements in both hardware and software platforms that support the technology.[177] A wide spectrum of additive manufacturing techniques is now available, including extrusion-based printing, fused deposition, SLS, and melt electro-writing, each offering distinct advantages for tailoring metamaterial architectures.

Three-dimensional-printed mechanical metamaterials enable precise, layer-by-layer construction and offer advantages including improved strength-to-weight ratios, tunable stiffness, customizable mechanical properties, and shape-transforming capabilities, rendering them especially suitable for biomedical applications.[178] Masoumi *et al.*[179] examined the compressive performance of 3D-printed bone scaffolds composed of metamaterial architectures with discrete porosities organized in cubic unit cells. Their results indicated that, although the metamaterial bone scaffolds exhibited a 5.97 % reduction in weight compared to solid bone samples, the compressive strength of vertically oriented solid standard samples remained superior to that of horizontally oriented counterparts.[179]

Fina *et al.*[164] introduced a novel hybrid multi-material 3D printing platform that integrates top-down DLP with direct ink writing to fabricate composite structures and multifunctional devices within a single printing workflow. The vat photopolymerization-based DLP module enabled high-speed, high-resolution printing of complex material matrices, while the material extrusion-based direct ink writing module allows deposition of functional materials, including liquid crystal elastomers and conductive silver inks. This hybrid system offered a broad selection of inks and resins, facilitating the fabrication of functional composites with tunable mechanical properties, enhanced interfacial bonding, and multifunctional capabilities. This platform provided a versatile and robust strategy for the 3D printing of multifunctional devices applicable to soft robotics, electronics, active metamaterials, and biomedical applications. Mohammadi *et al.*[180] investigated soft robotic hands inspired by the biomechanics of human finger joints, constructed from auxetic metamaterials. These architectures offer increased flexibility and an extensive bending range, enabling the precise handling of delicate components, such as wires and cables. These characteristics indicate significant potential for the advancement of site-specific, minimally invasive DDSs.[180] Flamourakis *et al.*[181] fabricated 3D auxetic scaffolds for tissue engineering applications, employing a re-entrant hexagonal geometry constructed from the organic–inorganic photopolymer SZ2080, which supported mouse fibroblast proliferation and guided directional cellular growth.[181]

Unlike traditional 3D printing, 4D printing enables materials to undergo predetermined shape and structural transformations in response to external stimuli, such as electric or magnetic fields, temperature fluctuations, pH shifts, or other environmental triggers.[182] Conceptually, 4D printing represents a spatiotemporal extension of additive

manufacturing, where the added dimension is time, allowing dynamic adaptation of the printed construct.[183] This emerging area of 3D printing exploits materials possessing intrinsic shape-memory or energy-responsive behaviors. Hydrogels, polymers, and scaffold materials are commonly utilized in 4D printing within biomedical engineering,[184] facilitating the creation of stimulus-responsive smart DDSs. In a specialized layered Carbopol supporting bath with different water concentrations, Gungor-Ozkerim *et al.*[133] printed zein gel in an ethanol–water mixture, where modulation of hydrophobic and hydrogen bonding induced temporal changes in functions. The part of the construct printed in a supporting bath with higher water content exhibits higher drug loading, faster drug release, and a higher degradation rate than those printed in the supporting bath with lower water content. Che *et al.*[185] used hydroxybutyl methacrylated chitosan, which possesses dual temperature- and photo-sensitive properties, to create microneedles. The DLP approach enabled a quick generation of hydroxybutyl methacrylate-based microneedles with high resolution. The microneedles exhibited 4D properties, changing in needle dimensions upon exposure to temperature, which enhances resolution, sharpens the needles, and improves mechanical strength. These microneedles exhibited high mechanical strength, efficient tissue penetration, and the capability to deliver small-molecule drugs with sustained release profiles.[185]

The integration of 4D printing with metamaterials enables the fabrication of highly dynamic, programmable, and stimuli-responsive structures that can undergo controlled deformation or shape transformation in response to external environmental cues. This integration significantly expands the scope of biomedical applications, offering new possibilities for the development of adaptive and intelligent drug delivery platforms, tissue engineering scaffolds, and responsive implantable devices. As shown in Table 3, we summarized common 3D/4D printing techniques for metamaterial-based drug delivery strategies.

4.4. Optimization and development strategies of three-dimensional-printed metamaterials

The production of polymer-based auxetic metamaterials for biomedical purposes presents both notable challenges and opportunities for refinement. A key difficulty arises from the intricate geometries of auxetic architectures, which require precise multi-scale control—from macro- to micro- to nanoscale—to consistently achieve the intended NPR. Conventional manufacturing techniques often fall short in producing such intricate re-entrant or chiral architectures with sufficient fidelity. Another major limitation involves material selection, as these constructs

Table 3. Comparison of common three- and four-dimensional printing techniques for metamaterial-based drug delivery

Printing technique	Typical resolution/ feature size	Common materials (examples)	Advantages (relevance to drug delivery systems/metamaterials)	Limitations/considerations
Fused deposition modeling	~100–500 μm	Polylactic acid, polycaprolactone, polyvinyl alcohol, thermoplastic polymers	Low-cost, widely available, suitable for large porous constructs and drug-loaded filaments, enabling controlled-release tablets	Heat may damage thermosensitive drugs; limited resolution
Digital light processing/ stereolithography	~10–100 μm	Photopolymer resins, modified hydrogels	High resolution, capable of fabricating complex microstructures (microneedles, micro-reservoirs)	Biocompatibility concerns with photo-initiators; material options are limited
Selective laser sintering	~50–200 μm	Polymer–drug powder blends	Single-step fabrication of porous drug carriers (e.g., gyroid printlets), tunable release profiles	High equipment cost, complex processing parameters
Direct ink writing/ extrusion-based bioprinting	~50–500 μm (ink/ nozzle dependent)	Hydrogels, bioinks, drug suspensions	Direct printing of cell-laden or drug-loaded hydrogels, versatile formulation design, and bioresponsive scaffolds	Requires rheological optimization and post-crosslinking
Melt electro-writing/ multi-photon lithography (high-resolution techniques)	<10 μm (multi-photon lithography: nanoscale)	Biodegradable polymers, functional inks	Ultra-high resolution, ideal for micro- and nanoscale metamaterial units	High cost, low throughput, limited material compatibility
Four-dimensional printing (stimuli-responsive materials)	Method-dependent	Shape-memory polymers, smart hydrogels, responsive composites	Adds temporal dimension; programmable transformation and stimuli-responsive drug release	Requires precise design of response speed and biodegradability

must simultaneously exhibit auxetic behavior and biocompatibility.[186] Identifying polymers that fulfill both requirements, particularly in biodegradable forms, remains a considerable hurdle.[187] Process-related constraints further complicate fabrication; for instance, techniques such as SLS or conventional 3D printing frequently encounter problems with resolution, interlayer adhesion, and material degradation during production. Finally, maintaining the mechanical performance of auxetic metamaterials under physiological conditions presents an additional layer of complexity, demanding careful optimization to balance durability, flexibility, and biofunctionality.

Two major challenges in additive manufacturing must be overcome to further advance metamaterial development. One key limitation stems from the inherently layer-by-layer nature of 3D printing, which results in extended fabrication times for structures that are significantly larger than the printer's resolution. To mitigate this issue, advanced additive manufacturing techniques—such as melt electro-writing and multi-photon lithography—provide promising solutions.[188] These techniques enable precise control over both geometric features and material properties, allowing the fabrication of auxetic architectures with high fidelity. Moreover, additive manufacturing can be used to create molds,[189] lithography masks,[190] or imprinting stamps, facilitating scalable fabrication in both size and quantity by shortening production times. An emerging strategy involves self-assembly methods, such as spinodal decomposition, to create nano-architected metamaterials.[191] Despite limitations imposed by the intrinsic dynamics of the fabrication process, recent research has shown that spinodal-inspired metamaterials possess exceptional mechanical and biomechanical properties.[192] A further challenge is the limited ability to process a wide range of materials using high-resolution additive manufacturing techniques. Although indirect additive manufacturing approaches can partially overcome this restriction, they inherently constrain design flexibility relative to direct fabrication methods. Addressing this challenge will require the development of specialized additive manufacturing systems capable of handling multiple material classes with ultrahigh resolution. Examples include machines with multiple laser sources that can accommodate different material chemistries within a single build process. In parallel, computational design and simulation tools will play a vital role in predicting the structure–property relationships of candidate architectures, enabling rational optimization tailored to specific biomedical applications. Moreover, future research should focus on developing innovative material systems specifically designed for compatibility with next-generation, ultrahigh-resolution additive manufacturing platforms.

Progress in material engineering—such as designing novel polymer blends and composites that merge auxetic properties with biocompatibility—can substantially enhance the performance of biomedical metamaterials. At the same time, fine-tuning fabrication parameters, including laser intensity, scanning speed, and layer thickness, is essential to achieve high structural accuracy and reproducibility. Moving forward, research should prioritize the co-development of advanced additive manufacturing techniques and tailored materials to ensure exceptional quality, scalability, and multifunctionality in the fabrication of metamaterials, meta-structures, and meta-devices.

4.5. Toward living and adaptive metamaterials via artificial intelligence-guided biofabrication

Moving beyond conventional lattice-based designs, AI-assisted topology optimization (TO) represents a paradigm shift toward creating highly efficient, functionally graded metamaterial architectures tailored for specific biological outcomes. Unlike parametric studies of unit cells, TO algorithms iteratively distribute material within a defined design domain to meet a set of performance objectives and constraints. When augmented with machine learning, this process is drastically accelerated and can handle highly complex, multi-objective problems inherent to biology. For instance, TO can be employed to design a bone scaffold that simultaneously maximizes permeability for nutrient diffusion and cell migration while maintaining mechanical stiffness to match the native tissue and guiding osteogenic differentiation through controlled local strain fields.[193] Deep learning models, particularly generative adversarial networks, can learn from TO-generated data to produce novel, non-intuitive architectures that optimally balance these competing demands.[194] Furthermore, TO can design fluidic metamaterial channels that generate specific shear stress profiles to direct endothelial cell organization for pre-vascularization, or create chemical concentration gradients by optimizing the spatial arrangement of diffusion barriers. This computational approach enables the a priori design of metamaterials that are not merely biocompatible but are proactively instructive, actively recruiting and guiding host cells or encapsulated cells towards a desired therapeutic endpoint.

The realization of computationally optimized, biologically active architectures necessitates advanced fabrication strategies that can orchestrate multiple materials and cell types with high spatial precision. Multi-material bioprinting fulfills this role, enabling the fabrication of "living metamaterials"—constructs where the engineered microarchitecture and the living cellular component are inseparable and co-manufactured.

Techniques such as extrusion-based printing with switching nozzles and DLP with dynamic photomasks allow for the deposition of distinct bioinks within a single construct. This capability is pivotal for creating complex, biomimetic tissue microenvironments. For example, a single print can combine a soft, cell-laden gelatin methacryloyl bioink to mimic the parenchyma of an organ with a stiffer, PEGDA bioink patterned into a reinforcing auxetic lattice, providing mechanical support while supporting tissue maturation.[195] Crucially, this allows for the precise spatial patterning of different cell types (e.g., hepatocytes & endothelial cells) and biochemical cues (e.g., growth factors tethered to specific regions of the scaffold) in accordance with the topological design. The resulting living metamaterials are therefore not passive implants but dynamic, metabolically active tissues engineered from the ground up, with their global mechanical behavior and mass transport properties dictated by the synergism between the living cells and the rationally designed, non-living metamatrix.

5. Drug delivery applications of three-dimensional-printed metamaterials and bioresponsive, self-regulated, and personalized drug delivery systems

Owing to their exceptional structural, spatial, and temporal characteristics, metamaterials hold considerable promise for advancing precision and personalized strategies in drug delivery. In the following sections, we highlight the key design aspects and material strategies that can be integrated into additive manufacturing processes to establish their role as next-generation platforms for controlled and patient-specific therapeutic applications. The next generation of metamaterial-based DDSs transcends traditional controlled-release paradigms, entering the realm of autonomous, self-regulated, and patient-specific therapy. Instead of acting as passive carriers, these smart systems integrate real-time sensing, feedback control, and actuation to achieve precise temporal and spatial regulation of drug kinetics. This section examines cutting-edge applications in closed-loop drug delivery, implantable and wearable bioresponsive devices, and 4D metamaterial scaffolds that can adapt to pathological microenvironments. Special attention is given to personalized metamaterial platforms, where computational modeling, patient-derived bioinks, and AI-guided fabrication jointly enable tailored drug dosing and on-demand release strategies. Such innovations bridge the gap between digital healthcare and advanced materials engineering, marking a decisive step toward precision medicine.

5.1. Controlled drug release

The application of metamaterials fabricated through 3D printing presents significant promise for advancing DDSs, capitalizing on the adaptability and exactitude of this manufacturing approach to improve treatment outcomes. Illustratively, auxetic structures, characterized by an NPR, have been integrated into therapeutic dressings that mechanically react to edema, thus permitting the regulated administration of medicinal compounds. The treatment of critical medical events, including anaphylactic shock, remains particularly difficult due to the necessity for both swift intervention and exact control over drug behavior in the body. In response to this challenge, recent scientific inquiry has investigated the use of sonically activated metamaterials, which employ acoustic energy to facilitate the passage of pharmaceuticals through physiological obstructions, such as the dermal layer. Through the deliberate design of their resonant properties, such platforms achieve improved tissue penetration and accurate tuning of the drug release profile, substantially augmenting the performance of cutaneous delivery methodologies. Azithromycin-loaded contact lenses were fabricated using PEGDA as the cross-linking reagent, PEG-400 as a solvent, and a photoinitiator to enable polymerization, with azithromycin incorporated as the therapeutic agent.[196] The resulting lenses demonstrated sustained antimicrobial activity *in vitro* against both Gram-positive and Gram-negative bacteria. These findings highlight the potential of 3D-printed drug-loaded contact lenses as a platform for effective localized ocular drug delivery. By enabling controlled and prolonged release of antibiotics directly at the infection site, this approach provides a promising strategy for treating bacterial eye infections while reducing systemic side effects and improving patient compliance.[196]

A 3D-printed bento box model was fabricated by Kraisit *et al.*[197] with either one chamber or two chambers to achieve controlled drug release of propranolol hydrochloride at varying time intervals, following the United States Pharmacopeia dissolution guidelines.[197] Commercially available extruded polyvinyl alcohol filament was employed as the polymeric printing material. As shown in Figure 1, the structure of the printed bento boxes (Figure 1B) closely matched the digital design generated by the modeling software (Figure 1A). The final models appeared yellowish brown in color, slightly darker than the original filament, likely due to the thermal effects of the printing process. The printed surfaces exhibited minor roughness, arranged in the programmed rectilinear pattern.

The one-chamber design contained both propranolol hydrochloride powder and matrix tablets in a single chamber, whereas the two-chamber design separated the two forms of the drug, with powders occupying one

compartment and the tablet in the adjacent compartment (Figure 1C). For comparison, Figure 1D shows that the size of the 3D-printed bento box was similar to that of a commercial capsule, though the bento boxes exhibited greater width, while the capsule was slightly longer. These results demonstrate that 3D-printed bento boxes can be tailored for multi-modal drug loading, presenting a versatile strategy for controlled and sequential drug

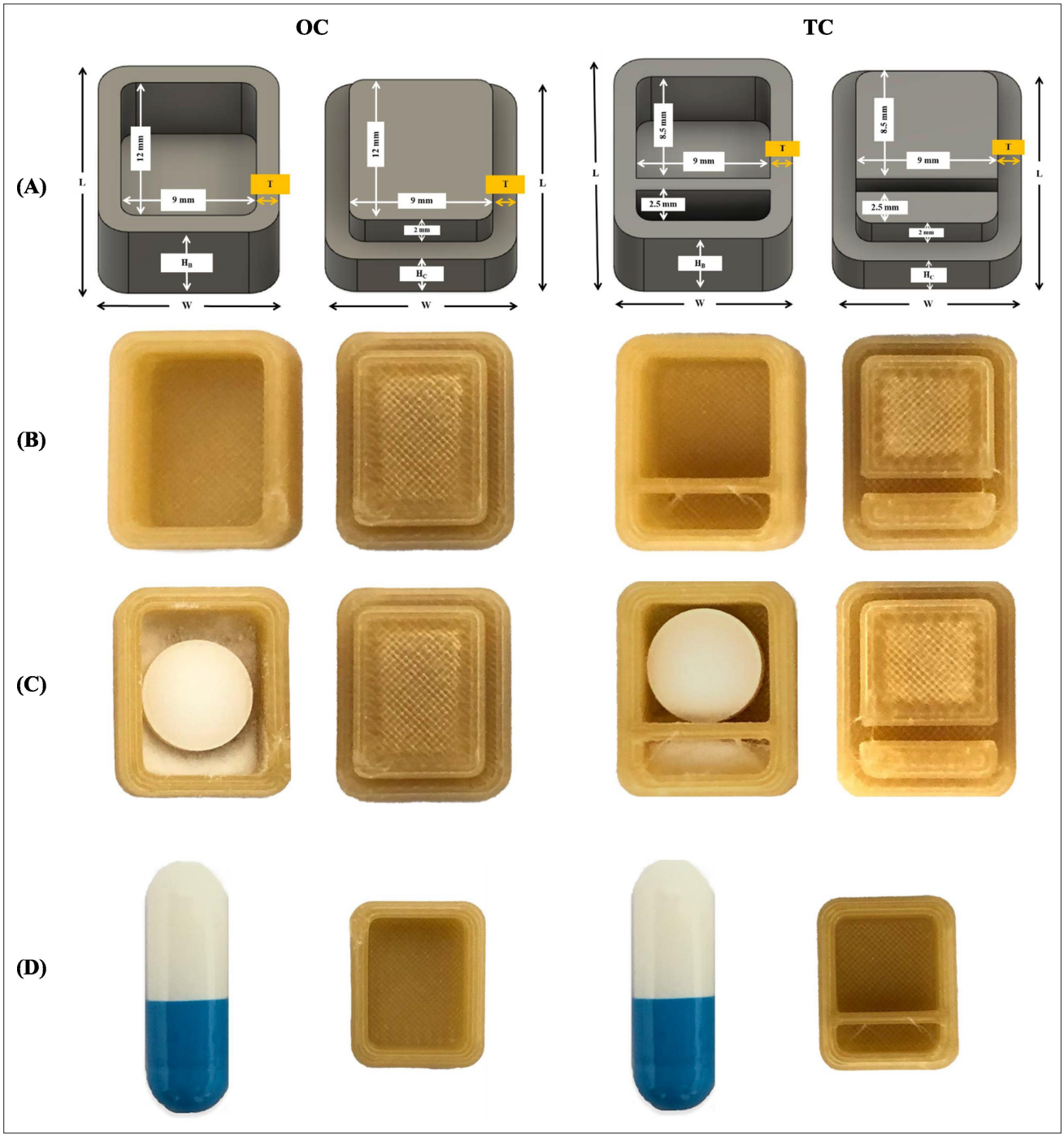


Figure 1. Schematic representations and images of a three-dimensional (3D)-printed bento box for controlled drug release. (A) Images of the 3D-printed bento box model. (B) A fabricated bento box produced by 3D printing. (C) Bento box loaded with propranolol hydrochloride powder and matrix tablets. (D) Comparison of the size between a commercial capsule No. 0 and the 3D-printed bento box.[197] Adapted with permission from Kraisit *et al.*[197] Copyright © 2022, Elsevier.

delivery. The similarity in size to conventional capsules further supports their feasibility as a future dosage form for patient-specific therapies.[197]

Sun *et al.*[104] designed a biodegradable antibacterial skin patch using a silk-derived, antibiotic-loaded flexible THz metamaterial platform. By incorporating THz metamaterial resonators, the silk fibroin construct was engineered for programmable disintegration, adhering to a pre-established timeline and velocity. The liberation of the pharmaceutical agent was intrinsically coupled to this structural breakdown, a relationship that was quantitatively monitored through shifts in the metamaterial's resonant signature. Validation in a rodent model of dermal infection confirmed that this antibacterial silk-based patch possesses considerable promise for enabling synchronized drug administration and ongoing surveillance of treatment efficacy.[104]

In another study, Jiang *et al.*[86] engineered a novel class of chiral mechanical metamaterials with a hybrid architecture. This was accomplished through the strategic incorporation of re-entrant unit cells into a matrix composed of conventional chiral cellular structures.[86] This novel design enabled sequential particle release, suggesting its applicability in DDSs requiring multi-stage delivery. Moreover, the structural adaptability of these metamaterials points toward broader applications in multifunctional composites, sensors, and actuators responsive to environmental cues.[86] Together, these examples illustrate how metamaterial-enabled DDSs can be engineered to achieve spatiotemporal control, multifunctionality, and responsiveness, offering promising pathways toward next-generation precision therapeutics.

Metamaterials provide a highly tunable and large surface area, making them excellent candidates for biofunctionalization via coatings and surface modifications to support drug delivery applications. Such strategies have been applied to enhance osseointegration and reduce bacterial colonization on implants.[198,199] Common approaches include electrochemical modification,[200] chemical surface treatments,[201] and advanced coating techniques.[202] In orthopedic surgery, where unmet clinical needs often involve both infection control and bone regeneration, surface-engineered metamaterials hold particular promise. For instance, Yavari *et al.*[203] developed additively-manufactured porous metallic scaffolds that were sequentially coated with multiple functional layers, specifically designed to simultaneously suppress implant-associated microbial colonization and stimulate bone regeneration. The layered surfaces served as reservoirs for controlled delivery of vancomycin together with bone morphogenetic protein 2, releasing these agents gradually over a period of approximately 2–3 weeks. This strategy produced strong antibacterial effects, eliminating planktonic organisms and adherent bacteria on the implant by nearly eight orders of magnitude and preventing biofilm establishment. In parallel, the modified coatings enhanced the osteogenic potential of mesenchymal stem cells, as indicated by a two-fold elevation in alkaline phosphatase activity and mineral deposition levels reaching up to four times those observed in controls. *In vivo* subcutaneous implantation for 8 weeks revealed no signs of foreign body response, while the coatings facilitated connective tissue ingrowth. Collectively, these results highlight the potential of surface-functionalized metamaterials to address dual challenges in orthopedic applications by enabling both localized drug delivery and enhanced tissue integration.[203]

These developments suggest that integrating additive manufacturing with metamaterial design may open avenues for constructing customizable drug delivery platforms that can finely tune the timing and localization of therapeutic release to enhance overall treatment outcomes. By harnessing the structural adaptability of metamaterials alongside the versatile fabrication capabilities of additive manufacturing, these platforms can be customized to individual patient requirements, supporting applications that include infection-resistant implants, wound-healing scaffolds, and stimuli-responsive oral or transdermal delivery devices. The integration of design flexibility, functional materials, and advanced fabrication techniques points toward a promising route for next-generation precision medicine. Metamaterials produced through additive manufacturing offer significant promise for pharmaceutical applications, enabling the design of smart nanoscale architectures that facilitate advanced diagnostic strategies and next-generation treatment modalities. By combining programmable architectures with responsive materials, these systems can support highly personalized treatment approaches, ultimately bridging the gap between next-generation drug delivery platforms and precision medicine. We summarize representative studies in Table 4.

5.2. Targeted delivery for cells and tissues

A key goal in tissue engineering is to develop metamaterials that not only facilitate cell homing but also direct specific cellular activities. Mechanical metamaterials offer a versatile platform for modulating mechanical cues, making them attractive for scaffolds that precisely control tissue and cell behaviors.[204] Cellular responses to high-aspect-ratio nanostructured surfaces are heavily dependent on features such as spacing, sharpness, and height, which govern membrane–material interactions and subsequent intracellular signaling pathways.[205] Importantly, the Poisson's ratio of metamaterials has been shown to affect

Table 4. Representative case studies of metamaterial-based drug delivery systems

Study	Architecture/material	Fabrication method	Application	Key findings
Fina *et al.*[212]	Gyroid-lattice printlets	Selective laser sintering	Oral controlled-release tablets	Tunable dissolution via geometry; versatile dosage design
Xu *et al.*[91]	Acoustic metamaterial patch	Microstructured acoustic units + electronics	Transdermal epinephrine for anaphylaxis	Multi-burst, on-demand dosing; superior to injections in mice
Sun *et al.*[104]	Silk-based terahertz resonator patch + antibiotics	Printable degradable metamaterial	Antibacterial wound patch	Combined drug release and real-time monitoring; accelerated healing
Babaee *et al.*[85]	Gastric-resident structures	Multi-material three-dimensional printing	Long-term gastric devices	Safe retention in the stomach; foundation for a prolonged oral drug delivery system
Yarali *et al.*[210]	Auxetic bone scaffolds	Stereolithography/ bioinspired design	Orthopedic implants	Tunable porosity and mechanical modulus; enhanced osteogenic activity

cellular characteristics.[206] Among these, auxetic constructs have gained particular attention in tissue engineering, as their NPR imparts unique mechanical cues that can direct cellular responses and promote functional tissue development.[69]

As shown in Figure 2, Jia *et al.*[207] utilized the potential of a generative computational framework to regulate stress distributions across multiple predefined values, measurement parameters, control zones, and loading scenarios. As an illustration, a femoral support structure was optimized with tailored, irregularly architected materials designed to enhance orthopedic healing following a fracture (Figure 2A–D). The customized femur support was shown to accurately reproduce the intended stress distribution (Figure 2B), thereby reducing the risks of aseptic loosening and peri-prosthetic fractures, while simultaneously preserving an adequate level of shear stress on the fractured site to promote bone regeneration. This design was fabricated using a commercial masked stereolithography 3D printer (Figure 2D), which required fewer fabrication steps compared with other multi-scale structural design methodologies. This advantage arises because the generated material architectures consist of self-supporting assemblies of building blocks that inherently comply with the minimum feature size required for manufacturability.[207] Due to their ability to redistribute mechanical loads while simultaneously

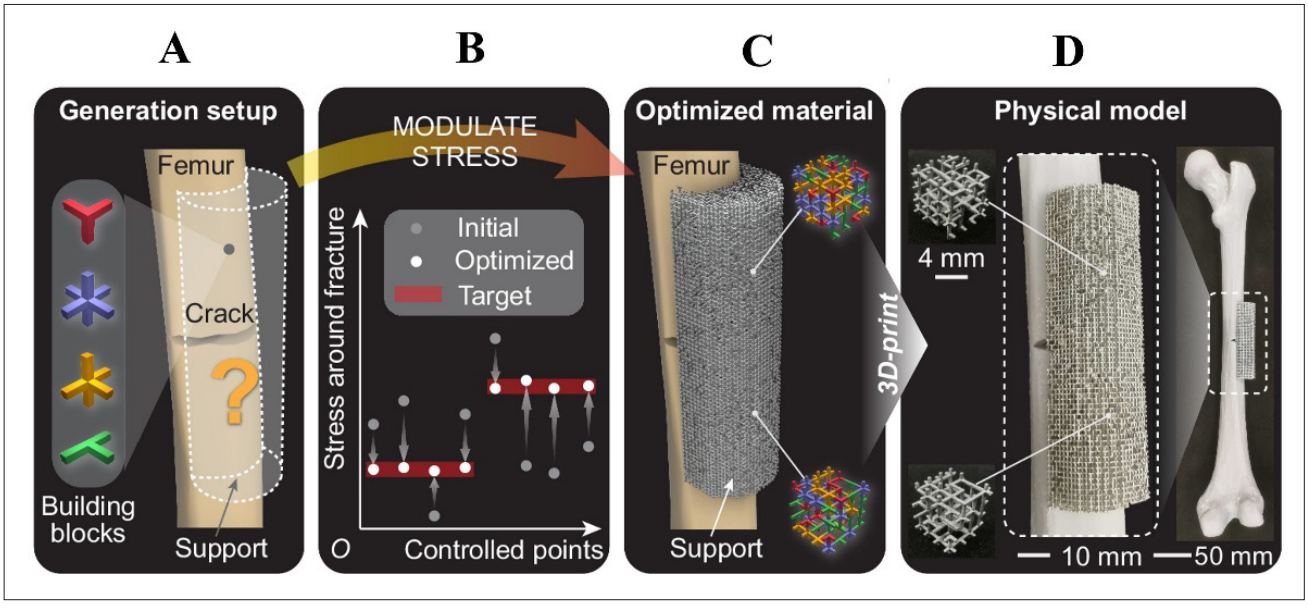


Figure 2. Generation and application of irregular architected materials with optimization-enabled stress modulation. (A) Schematic representation of the construction setup, consisting of a fractured femur stabilized by a support designed from four fundamental unit types. (B) Comparison of the stress distribution in the control region adjacent to the fracture, showing the homogeneous state at the start, the computationally optimized profile, and the desired target stress. (C) Resulting support structure composed of irregularly optimized materials, with disordered microarchitectures highlighted in the two magnified insets. (D) Additively manufactured samples produced at multiple length scales. Reprinted from Jia *et al.*[207]

maintaining an appropriate level of stress that targets bone regeneration, Jia *et al.*[207] highlighted the prospective use of stress-programmable architected materials as supportive structures in femoral orthopedic repair.

Despite progress in nucleic acid therapeutics, achieving precise delivery to specific tissues remains a significant challenge, often hindered by low transfection rates and difficulties in scaling that vary with both cellular phenotype and anatomical environment. To address this, a recent study reported a controllable, vertically aligned configuration of biodegradable porous silicon nanoneedles, which could directly access the cytoplasm and simultaneously introduce small interfering RNA and DNA with efficiencies exceeding 90%.[208] Using this strategy, the nanoneedle system successfully transferred the *VEGF*-165 gene in animal models, promoting persistent angiogenesis and resulting in nearly a sixfold increase in blood flow within the affected muscle region. Additionally, the nanoneedles promoted the organized development of new vasculature, indicating potential for precise, site-specific regulation of both physiological function and structural organization in selected tissue regions.

The convergence of bioprinting with metamaterials research in DDSs has driven significant progress in engineering intricate and functional architectures. These emerging technologies enable the realization of geometries that were previously unattainable through conventional means, thereby unlocking novel metamaterial applications with exceptional and unconventional properties.

5.3. Regenerative medicine

A distinguishing merit of metamaterials lies in their inherently large interfacial area, a property that lends itself well to chemical or biological modification. Implementing such surface engineering strategies can substantially augment the functional capacity of these materials, with particular promise for promoting cell growth and tissue restoration in regenerative medicine applications.[207,209]

To overcome persistent clinical limitations in orthopedic surgery, the use of metamaterials requires the incorporation of additional surface functionalities, which can be achieved through the application of purpose-engineered coating strategies. Yarali *et al.*[210] developed a bone-regenerative system employing metamaterials, drawing inspiration from the influence of Poisson's ratio on osteogenic cell behavior, as illustrated in the fabrication scheme shown in Figure 3A. They defined pore size as the diameter of the largest sphere that can fit within a unit cell of the meta-biomaterials (the yellow sphere in Figure 3B & C). The resulting metamaterial-based implant exhibited mechanical features aligned with clinical requirements, including controlled porosity and elastic modulus, while also supporting favorable osteogenic activity of pre-osteoblasts within the micro-structured scaffold (Figure 3D–F).[210] Such engineered constructs are anticipated to accelerate tissue repair and improve regenerative outcomes.

Barri *et al.*[211] reported a novel approach to constructing self-powered metamaterials. Their work revealed that cage-shaped implants with built-in contact-electrification capability can generate internal voltage signals that reflect the progress of bone regeneration. When subjected to axial compressive loading in spinal models, these devices delivered a voltage of 9.2 V and a current of 4.9 nA. Acting as triboelectric nanogenerators, such metamaterial implants have the potential to energize low-power electronics, thereby advancing surgical outcomes for spinal cord injury patients and reshaping implantable device technologies.[211]

Auxetic porous materials can improve the delivery of nutrients and therapeutic agents, as well as the removal of metabolic waste, and have been identified as candidates for the development of adaptable scaffolds for tissue engineering applications. Flamourakis *et al.*[181] demonstrated that 3D auxetic structures constructed through multi-photon lithography can serve as scaffolds for cell cultures. Even though SZ2080 is fundamentally a stiff material with a positive Poisson's ratio, the bowtie structures fabricated with it exhibit auxetic behavior and high elasticity due to their architected design. In addition, Flamourakis *et al.*[181] showed that mouse fibroblasts can readily penetrate and proliferate in these scaffolds, adapting the scaffold shape to their needs, increasing their proliferation, and promoting aligned, directional growth.

5.4. Autonomous and adaptive therapeutic systems

The ultimate goal of smart drug delivery is a system that self-regulates in real-time based on physiological feedback. Metamaterials are uniquely suited to form the physical core of such closed-loop systems. Their structured nature allows for the seamless integration of sensing and actuating modalities. For instance, a metamaterial scaffold can incorporate microfluidic channels functionalized with biosensing hydrogels that swell in the presence of a specific biomarker (e.g., glucose, tumor necrosis factor alpha). This swelling can mechanically modulate the flow through adjacent drug-loaded microchannels, creating a purely mechanical feedback loop. More advanced systems leverage embedded conductive networks (e.g., based on graphene or liquid metal) within the metamatrix to act as electrochemical sensors. The detected signal is processed by a miniaturized circuit, which then triggers an actuation mechanism—such as the Joule heating of a thermally responsive polymer nanogel reservoir within the metamaterial, causing it to collapse and release a therapeutic dose. This creates a self-correcting, bio-

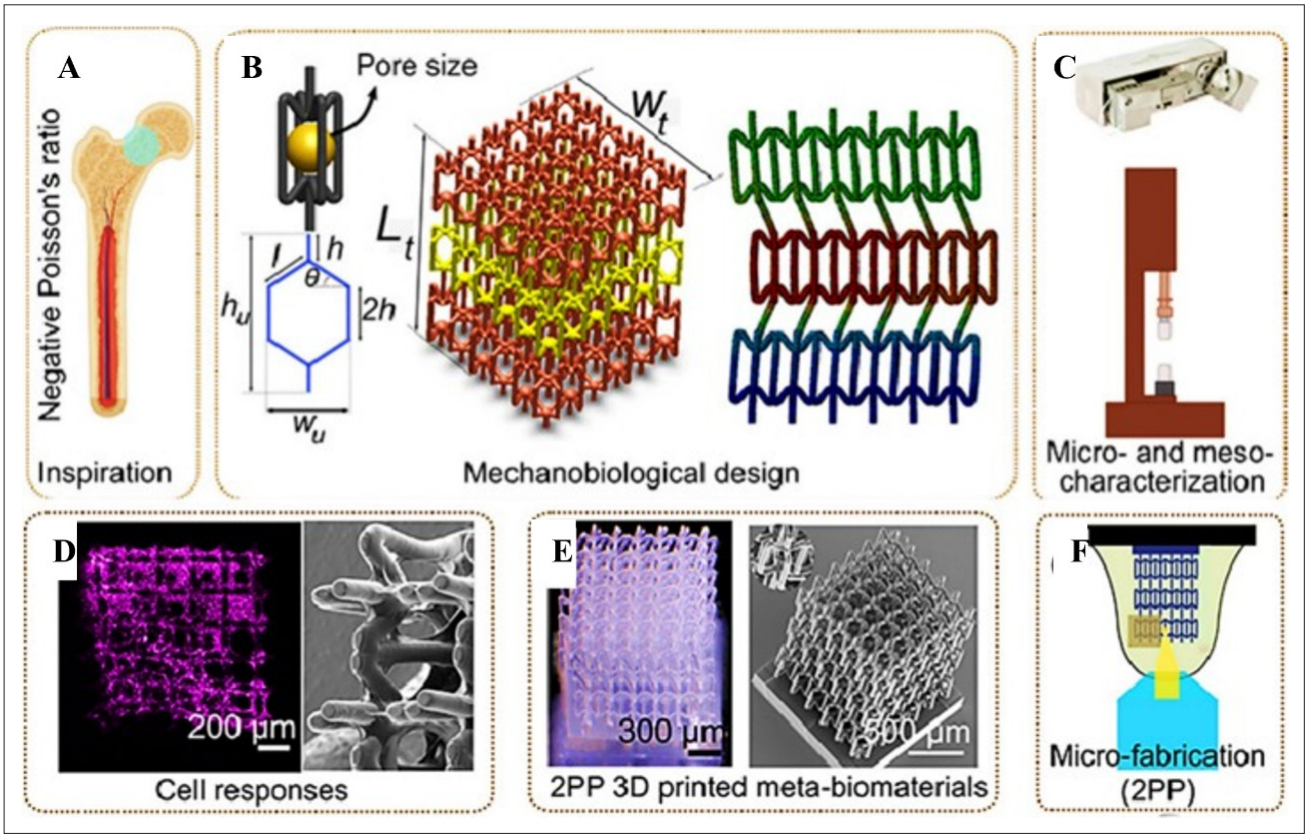


Figure 3. Metamaterial-enabled platforms for therapeutic and diagnostic use. (A) Conceptual inspiration derived from the negative Poisson's ratio of bone. (B) Schematic workflow for metamaterial fabrication. (C) Structural and property characterization. (D) Osteogenic activity of pre-osteoblasts cultured within the metamaterial framework. Scale bar: 200 μm; magnification: 10×. (E) Macroscopic view of the printed scaffolds. Scale bars: 300 μm, 500 μm; magnifications: 10×. (F) Example of microfabricated constructs generated via three-dimensional printing.[210] Adapted with permission from Yarali *et al.*[210] Copyright © 2024, Elsevier.

electronic interface that maintains homeostasis without external intervention, representing a monumental leap beyond simple, pre-programmed release kinetics.

Unlike featureless hydrogels, 3D-printed metamaterials can be designed to replicate the mechanical anisotropy and complex porosity of native tissue extracellular matrix. When integrated into a microfluidic chip, these architectures provide a more realistic microenvironment for cultured cells, guiding tissue-level organization and function. A prime application is a "vascularized tumor metamaterial model" for oncology drug screening. A sacrificial metamaterial can be printed to create a perfusable, hierarchical vascular network, which is then seeded with endothelial cells. Tumor cells encapsulated within a surrounding, tissue-specific metamaterial scaffold can be positioned at a defined distance from the vasculature. This setup allows for high-fidelity assessment of drug penetration, efficacy, and toxicity in a human-relevant system that captures key aspects of the tumor microenvironment, including nutrient gradients and interstitial fluid pressure. This moves drug testing from a static two-dimensional culture to a dynamic, human-specific, and predictive platform.

By precisely controlling the topography, stiffness, and ligand presentation at the cellular level, metamaterials can be designed to direct the fate and function of immune cells. For example, a scaffold with a specific range of pore sizes and surface chemistry can be designed to preferentially recruit M2 macrophages over the M1 phenotype, promoting a healing and regenerative environment instead of a pro-inflammatory one. Furthermore, these scaffolds can serve as localized depots for immunomodulatory agents (e.g., cytokines, checkpoint inhibitors). The release kinetics can be spatially and temporally controlled by the architecture; for instance, an outer layer with fast-release kinetics could deliver an initial signal to recruit specific immune cells, while an inner core with slow-release kinetics provides a sustained polarizing signal. This approach could be transformative for cancer immunotherapy (as an *in*

situ cancer vaccine) and regenerative medicine, where controlled inflammation is crucial for tissue repair.

6. Translational roadmap: from lab-scale design to regulatory and sustainable production

Despite significant progress in functionality and performance, the large-scale translation of metamaterial-based DDSs faces emerging challenges in sustainability, manufacturability, and regulatory compliance. Current research often overlooks the environmental and ethical implications of material selection, energy-intensive printing processes, and post-use biodegradability. This section provides a sustainability-oriented perspective, discussing the use of bio-based inks, low-carbon fabrication strategies, and circular economy principles in the context of metamaterial production. In parallel, it outlines a regulatory roadmap for next-generation biofabricated metamaterials, encompassing safety validation, quality control, and digital traceability frameworks. By integrating green engineering and regulatory governance into material innovation, this section advocates for a holistic approach that aligns scientific advancement with global sustainability and compliance goals.

The intricate and often multi-material nature of 3D-printed metamaterials presents a paradigm shift for regulatory bodies such as the United States Food and Drug Administration and the European Medicines Agency. A primary challenge is the "device–drug combination product" classification. A metamaterial implant that releases a therapeutic agent blurs the traditional lines between a medical device and a pharmaceutical, requiring a hybrid and often complex regulatory submission process. Regulators will require proof that the critical quality attributes of the drug product—such as release kinetics, stability, and sterility—are intrinsically linked to the print fidelity, architectural parameters (e.g., pore size, strut thickness), and material composition of the metamaterial. This necessitates a robust quality-by-design approach, where the design space for the microstructure is rigorously defined and controlled. Standard ISO 10993 biocompatibility testing must be re-evaluated for metamaterials. The high surface-area-to-volume ratio and potential for novel degradation products arising from complex material combinations (e.g., polymer–ceramic–metal composites) pose unique risks. Assessments must go beyond cytotoxicity to evaluate long-term foreign body response, immunogenicity, and the fate of degradation byproducts from the architected matrix itself. The layer-by-layer additive manufacturing process introduces variability. Regulatory approval will hinge on validating that every printed batch is equivalent. This requires the development of new in-process analytics and non-destructive testing methods (e.g., micro-computed tomography) to verify internal architecture and ensure the absence of critical defects that could compromise performance or safety.

The environmental footprint of advanced manufacturing cannot be ignored. A cradle-to-grave life cycle assessment is crucial for evaluating the true ecological cost of metamaterial-based DDSs. High-resolution 3D printing techniques (e.g., two-photon polymerization) and post-processing (e.g., SLS powder recycling) are energy-intensive. Comparisons with conventional manufacturing are needed. The environmental impact of sourcing synthetic polymers and metals must be weighed against the use of biodegradable alternatives derived from natural sources. Furthermore, support materials and failed prints contribute to plastic waste, necessitating the use of closed-loop recycling systems or water-soluble supports. The ideal scenario for single-use, implantable DDSs is complete, non-toxic biodegradation into metabolizable byproducts. Research must therefore prioritize green material strategies, including developing architectures from polymers such as PLGA and PCL with tunable degradation profiles, and utilizing chitosan, alginate, silk fibroin, and decellularized extracellular matrix to create metamaterials with inherent biocompatibility and reduced environmental impact.

The complexity of metamaterials demands a paradigm shift in quality control, moving from statistical sampling of final products to a comprehensive, data-driven assurance of every single unit. This can be achieved through the implementation of a digital twin framework. A digital twin is a virtual replica of the physical manufacturing process and the product itself. It begins with the computational design file and is fed by real-time data from printers (e.g., thermal cameras, laser power monitoring). This creates an unbroken "digital thread" linking design to production. Machine learning algorithms analyze the manufacturing data in real-time against the digital twin to predict critical quality attributes. For instance, a minor fluctuation in laser power during SLS could be flagged as potentially leading to a region of insufficient sintering that would alter drug release, allowing for the part to be rejected automatically.[212] The digital twin, informed by the precise internal architecture from micro-computed tomography scans, can run finite element analysis and computational fluid dynamics simulations to predict *in vivo* performance.[213,214] This includes forecasting drug release profiles,[215] predicting mechanical stability under load,[216] and estimating cell–scaffold interactions, providing a powerful tool for de-risking clinical translation and supporting regulatory submissions.

7. Conclusion

This review has outlined how the convergence of metamaterial science with additive manufacturing holds strong potential to reshape modern DDSs by enabling unprecedented precision in both therapeutic targeting and release regulation. Unlike conventional carriers, metamaterials with engineered microarchitectures can interact with biological tissues and electromagnetic fields in ways that confer higher levels of selectivity and functionality. These interactions open avenues for improving drug loading capacity and stability, increasing bioavailability, refining spatial and temporal release patterns, and thereby minimizing adverse reactions while enhancing overall therapeutic performance. By leveraging adjustable properties—such as pore structure, molecular transport capacity, and sensitivity to external stimuli including heat, acidity, and illumination—metamaterial-derived platforms provide a foundation for creating highly individualized therapeutic strategies. Their structural programmability also permits coupling with electromagnetic waves to direct or modulate drug transport, and carefully engineered configurations can be optimized to target specific cell populations or organ systems. Moreover, integrating responsive elements into these platforms enables finely tuned, externally triggered release profiles, thereby reducing systemic exposure and enhancing efficacy. Photoresponsive hydrogels, for example, maintain mechanical stability while undergoing light-induced volumetric changes, enabling controlled activation and long-term dosing. Importantly, biodegradable constructs circumvent the need for surgical removal and are preferable to non-degradable counterparts in clinical scenarios. Recent advances demonstrate that 3D-printed metamaterials, such as antibacterial wound patches, deliver tightly regulated drug release with minimal off-target effects, highlighting their advantages in safety and efficiency. The capacity to adapt to diverse stimuli further enhances therapeutic customization and supports precision medicine strategies. Taken together, these structural, mechanical, and electromagnetic characteristics highlight that bio- or 3D-printed architected metamaterials represent a compelling substitute for conventional DDSs, providing distinctive opportunities for tunable shape-memory functions and next-generation therapeutic release strategies.

Despite these encouraging developments, several critical challenges remain. First, the translation of complex laboratory-scale constructs into clinically viable products requires the establishment of reproducible, regulatory-compliant, and scalable manufacturing processes. Second, the biocompatibility, long-term safety, and biodegradability of emerging metamaterial-based carriers must be rigorously assessed through systematic preclinical and clinical studies. Third, the integration of smart, stimuli-responsive functionalities with real-time sensing and theranostic capabilities is still in its early stages, necessitating the convergence of materials science, engineering, and biomedical research. Moreover, the field would benefit from the development of standardized evaluation metrics to compare different architectures and from computational modeling approaches that can more accurately predict drug transport and tissue responses.

Looking ahead, the future of 3D-printed metamaterials for drug delivery will likely be defined by three major directions. The first is personalized medicine, where patient-specific anatomical data and pharmacokinetic requirements can be directly translated into bespoke metamaterial-based devices. The second is the incorporation of multifunctional hybrid platforms, which combine structural programmability with biochemical cues, biosensing modules, and digital health interfaces for remote monitoring and control. The third is the establishment of manufacturing workflows that prioritize sustainability and compliance with regulatory standards will be crucial for translating laboratory breakthroughs into broad clinical implementation. The convergence of AI, bioresponsive design, and sustainable manufacturing is poised to redefine the trajectory of 3D-printed metamaterials in biomedical applications. The future will likely witness the emergence of intelligent metamaterials that self-learn from physiological feedback, adapt their microstructure autonomously, and coordinate with other therapeutic platforms in real time. To achieve this vision, interdisciplinary collaboration among material scientists, bioengineers, data scientists, and regulatory experts will be essential.

In conclusion, while metamaterial-inspired DDSs are still in their infancy, their potential to transform therapeutic strategies is evident. Continued interdisciplinary collaboration, coupled with advances in materials engineering and translational research, will be key to realizing their promise in personalized, efficient, and intelligent drug delivery.

Acknowledgments

None

Funding

This work was supported by the Key R&D Program of Shandong Province, China (2022TZXD0033), the Science and Technology SMEs Innovation Ability Improvement Project of Shandong Province (2023TSGC0386, 2023TSGC0362), the Doctoral Research Startup Foundation

of Liaocheng University (318052315, 318052366), and the Collaborative Innovation Project of "Vice General Manager of Technology" of Liaocheng (2024XT02).

Conflict of interest

The authors declare that they have no conflict of interest.

Author contributions

Conceptualization: Wanchong He
Funding acquisition: Qinghua Zeng
Writing–original draft: Wanchong He
Writing–review & editing: Qinghua Zeng

Ethics approval and consent to participate

Not applicable.

Consent for publication

Not applicable.

Availability of data

Not applicable.

References

1. Nazir F, Tabish TA, Tariq F, Iftikhar S, Wasim R, Shahnaz G. Stimuli-sensitive drug delivery systems for site-specific antibiotic release. *Drug Discov Today*. 2022;27(6):1698-1705. doi: 10.1016/j.drudis.2022.02.014

2. Bahadur S, Sharma M. Liposome based drug delivery for the management of psoriasis - a comprehensive review. *Curr Pharm Biotechnol*. 2023;24(11):1383-1396. doi: 10.2174/1389201024666221213144228

3. Adepu S, Ramakrishna S. Controlled drug delivery systems: current status and future directions. *Molecules*. 2021;26(19):5905. doi: 10.3390/molecules26195905

4. He C, He X, Zhang Y, *et al*. Development of a microfluidic formatted ultrasound-controlled monodisperse lipid vesicles' hydrogel dressing combined with ultrasound for transdermal drug delivery system. *Macromol Biosci*. 2023;23(9):e2300049. doi: 10.1002/mabi.202300049

5. Xu X, Kwong CHT, Li J, Wei J, Wang R. "Zombie" macrophages for targeted drug delivery to treat acute pneumonia. *ACS Appl Mater Interfaces*. 2023;15(24):29012-29022. doi: 10.1021/acsami.3c06025

6. Guo S-H, Yu X-K, Zhu Y-L, Zhang L-L, Huang Y-N. Controlled release mechanism of drugs from onion-like dendrimersomes: insight from dissipative particle dynamics simulations. *Phys Chem Chem Phys*. 2025;27(17):9087-9094. doi: 10.1039/d4cp04780j

7. Di XJ, Liang X, Shen C, Pei YW, Wu B, He ZY. Carbohydrates used in polymeric systems for drug delivery: from structures to applications. *Pharmaceutics*. 2022; 14(4):739. doi: 10.3390/pharmaceutics14040739

8. Nishida K. Recent advances in lipid-based drug delivery. *Pharmaceutics*. 2021;13(7):926. doi: 10.3390/pharmaceutics13070926

9. Eid AH. Drugging dancing protein clouds: a close look at disorder-based drug design. Editorial. *Pharmacol Rev*. 2025;77(2):100010. doi: 10.1016/j.pharmr.2024.100010

10. Li J, Tang W, Yang Y, *et al*. A programmed cell-mimicking nanoparticle driven by potato alkaloid for targeted cancer chemoimmunotherapy. *Adv Healthc Mater*. 2021;10(13):2100311. doi: 10.1002/adhm.202100311

11. Lin S-W, Tsai J-C, Shyong Y-J. Drug delivery of extracellular vesicles: Preparation, delivery strategies and applications. *Int J Pharm*. 2023;642:123185. doi: 10.1016/j.ijpharm.2023.123185

12. Matalqah S, Lafi Z, Mhaidat Q, Asha N, Yousef Asha S. Applications of machine learning in liposomal formulation and development. *Pharm Dev Technol*. 2025;30(1):126-136. doi: 10.1080/10837450.2024.2448777

13. Li R, Hu X, Li W, *et al*. Nebulized pH-responsive nanospray combined with pentoxifylline and edaravone to lungs for efficient treatments of acute respiratory distress syndrome. *ACS Appl Mater Interfaces*. 2024;16(7):8310-8320. doi: 10.1021/acsami.3c15691

14. Malek-Khatabi A, Tabandeh Z, Nouri A, *et al*. Long-term vaccine delivery and immunological responses using biodegradable polymer-based carriers. *ACS Appl Bio Mater*. 2022;5(11):5015-5040. doi: 10.1021/acsabm.2c00638

15. Jan N, Shah H, Khan S, *et al*. Old drug, new tricks: polymer-based nanoscale systems for effective cytarabine delivery. *Naunyn-Schmiedeberg's Arch Pharmacol*. 2024;397(6):3565-3584. doi: 10.1007/s00210-023-02865-z

16. Arslan FB, Ozturk K, Calis S. Antibody-mediated drug delivery. *Int J Pharm*. 2021;596:120268. doi: 10.1016/j.ijpharm.2021.120268

17. Hong J, Li K, He J, Liang M. A new age of drug delivery: a comparative perspective of ferritin-drug conjugates (FDCs) and antibody-drug conjugates (ADCs). *Bioconjug Chem*. 2024;35(8):1142-1147. doi: 10.1021/acs.bioconjchem.4c00254

18. Taokaew S, Kaewkong W, Kriangkrai W. Recent development of functional chitosan-based hydrogels for pharmaceutical and biomedical applications. *Gels*. 2023;9(4):277. doi: 10.3390/gels9040277

19. Lin S-H, Hsu S-H. Smart hydrogels for in situ tissue drug delivery. *J Biomed Sci*. 2025;32(1):70. doi: 10.1186/s12929-025-01166-2

20. Bordbar-Khiabani A, Gasik M. Smart hydrogels for advanced drug delivery systems. *Int J Mol Sci*. 2022;23(7):3665. doi: 10.3390/ijms23073665

21. Yu YB, Cheng Y, Tong JY, Zhang L, Wei Y, Tian M. Recent advances in thermo-sensitive hydrogels for drug delivery. *J Mater Chem B*. 2021;9(13):2979-2992. doi: 10.1039/d0tb02877k

22. Orbay S, Sanyal R, Sanyal A. Porous microgels for delivery of curcumin: Microfluidics-based fabrication and cytotoxicity evaluation. *Micromachines*. 2023;14(10):1969. doi: 10.3390/mi14101969

23. Sepe F, Valentino A, Marcolongo L, *et al*. Polysaccharide hydrogels as delivery platforms for natural bioactive molecules: from tissue regeneration to infection control. *Gels*. 2025;11(3):198. doi: 10.3390/gels11030198

24. Sarmadi M, Behrens AM, McHugh KJ, *et al*. Modeling, design, and machine learning-based framework for optimal injectability of microparticle-based drug formulations. *Sci Adv*. 2020;6(28):eabb6594. doi: 10.1126/sciadv.abb6594

25. Zhu S, Cui H, Pan Y, *et al*. Responsive-hydrogel aquabots. *Adv Sci*. 2024;11(36):e2401215. doi: 10.1002/advs.202401215

26. Ouyang JL, Hong XZ, Gao Y. Retardation and self-repair of erosion pits by a two-stage barrier on bioactive-glass/layered double hydroxide coating of biomedical magnesium alloys. *Surf Coat Technol*. 2021;405:126562. doi: 10.1016/j.surfcoat.2020.126562

27. Sam R, Divanbeigi Kermani M, Ohadi M, Salarpour S, Dehghannoudeh G. Different applications of temperature responsive nanogels as a new drug delivery system mini review. *Pharm Dev Technol*. 2023;28(5):492-500. doi: 10.1080/10837450.2023.2209796

28. Gvozdeva Y, Staynova R. pH-dependent drug delivery systems for ulcerative colitis treatment. *Pharmaceutics*. 2025;17(2):226. doi: 10.3390/pharmaceutics17020226

29. Rathi R, Sanshita, Kumar A, *et al*. Advancements in rectal drug delivery systems: clinical trials, and patents perspective. *Pharmaceutics*. 2022;14(10):2210. doi: 10.3390/pharmaceutics14102210

30. Abdelmohsen HAM, Copeland NA, Hardy JG. Light-responsive biomaterials for ocular drug delivery. *Drug Deliv Transl Res*. 2023;13(8):2159-2182. doi: 10.1007/s13346-022-01196-5

31. Singh G, Nenavathu BP. Development of rGO encapsulated polymeric beads as drug delivery system for improved loading and controlled release of doxycycline drug. *Drug Dev Ind Pharm*. 2020;46(3):462-470. doi: 10.1080/03639045.2020.1724137

32. Chen Z, Ren Z, Coluccini C, Coghi P. From micro to marvel: unleashing the full potential of click chemistry with micromachine integration. *Micromachines*. 2025;16(6):712. doi: 10.3390/mi16060712

33. Patil V, Patil PS, Kulkarni MV, Pattekari SN, Khan ZG. Advanced microneedle arrays for transdermal antibiotic delivery. *Curr Opin Pharmacol*. 2025;83:102542. doi: 10.1016/j.coph.2025.102542

34. Wang JT, Xie BJ, Zhu ZC, Xie GJ, Luo B. 3D-printed construct from hybrid suspension as spatially and temporally controlled protein delivery system. *J Biomater Appl*. 2021;36(2):264-275. doi: 10.1177/08853282211023257

35. Yang YJ, Liu X, Kan C. Point cloud based online detection of geometric defects for the certification of additively manufactured mechanical metamaterials. *J Manuf Syst*. 2022;65:591-604. doi: 10.1016/j.jmsy.2022.09.011

36. He H, Peng W, Le Ferrand H. Thermal rectification in modularly designed bulk metamaterials. *Adv Mater*. 2024;36(8):e2307071. doi: 10.1002/adma.202307071

37. Wang Q, Chen Q, Lin Y, He D, Ji H, Tan CSH. Spike-in proteome enhances data-independent acquisition for thermal proteome profiling. *Anal Chem*. 2024;96(49):19695-19705. doi: 10.1021/acs.analchem.4c04837

38. Yang CT, Korangath P, Stewart J, *et al*. Systemically delivered antibody-labeled magnetic iron oxide nanoparticles are less toxic than plain nanoparticles when activated by alternating magnetic fields. *Int J Hyperthermia*. 2020;37(3):59-75. doi: 10.1080/02656736.2020.1776901

39. Ahamad N, Prabhakar A, Mehta S, *et al*. Trigger-responsive engineered-nanocarriers and image-guided theranostics for rheumatoid arthritis. *Nanoscale*. 2020;12(24):12673-12697. doi: 10.1039/d0nr01648a

40. Panikkanvalappil SR, Bhagavatula SK, Deans K, Jonas O, Rashidian M, Mishra S. Enhanced tumor accumulation of multimodal magneto-plasmonic nanoparticles via an implanted micromagnet-assisted delivery strategy. *Adv Healthc Mater*. 2023;12(2):e2201585. doi: 10.1002/adhm.202201585

41. Guan GQ, Zhang C, Liu HY, *et al*. Ternary alloy PtWMn as a Mn nanoreservoir for high-field MRI monitoring and highly selective ferroptosis therapy. *Angew Chem Int Ed*. 2022;61(31):e202117229. doi: 10.1002/anie.202117229

42. Thakkar A, Ma JC, Braun JE, Horton WT, Arrieta AF. Energy-efficient defrosting of heat exchanger fins with embedded negative stiffness structures. *Appl Therm Eng*. 2023;222:119850.
doi: 10.1016/j.applthermaleng.2022.119850

43. Renjith SC, Park K, Kremer GEO. A design framework for additive manufacturing: Integration of additive manufacturing capabilities in the early design process. *Int J Precis Eng Manuf*. 2020;21(2):329-345.
doi: 10.1007/s12541-019-00253-3

44. Gong P, Yue S, Wang J, *et al*. Effect of ultrasound synergistic pH shift modification treatment on Hericium erinaceus protein structure and its application in 3D printing. *Int J Biol Macromol*. 2025;295:139562.
doi: 10.1016/j.ijbiomac.2025.139562

45. Yatmaz E. Growth control agent for filamentous fungi: FDM based 3D printed cubes for suspended *Aspergillus sojae* fermentation. *Enzyme Microb Technol*. 2021;150:109867.
doi: 10.1016/j.enzmictec.2021.109867

46. Zhao F, Liu J, Zhao J, Ge X, Ding C, Zhuang X. The mechanism of 3D-printed high internal phase Pickering emulsion gels improved by soybean protein isolate/bacterial cellulose co-assemblies. *Int J Biol Macromol*. 2025;302:140435.
doi: 10.1016/j.ijbiomac.2025.140435

47. Mao Y, Chen WH, Lee MH. On the simulation of 3D printing process by a novel meshless analysis procedure. *J Mech*. 2020;36(3):285-294. Pii: s1727719119000285.
doi: 10.1017/jmech.2019.28

48. Lamprou DA, Douroumis D, Andrews GP, Jones DS. 3D printing in pharmacological and pharmaceutical sciences. *J Pharm Pharmacol*. 2022;74(10):1365-1366.
doi: 10.1093/jpp/rgac049

49. S Algahtani M, Ahmad J. 3D printing technique in the development of self-nanoemulsifying drug delivery system: scope and future prospects. *Ther Deliv*. 2022;13(3):135-139.
doi: 10.4155/tde-2021-0082

50. Zhan L, Zhou Y, Liu R, *et al*. Advances in growth factor-containing 3D printed scaffolds in orthopedics. *Biomed Eng Online*. 2025;24(1):14-14.
doi: 10.1186/s12938-025-01346-z

51. Eugster R, Ganguin AA, Seidi A, Aleandri S, Luciani P. 3D printing injectable microbeads using a composite liposomal ink for local treatment of peritoneal diseases. *Drug Deliv Transl Res*. 2024;14(6):1567-1581.
doi: 10.1007/s13346-023-01472-y

52. Cesur S. Combination techniques towards novel drug delivery systems manufacturing: 3D PCL scaffolds enriched with tetracycline-loaded PVP nanoparticles. *Eur J Pharm Biopharm*. 2024;194:36-48.
doi: 10.1016/j.ejpb.2023.11.022

53. Zhang P, He R. 3D-printed silicon nitride ceramic implants for clinical applications: the state of the art and prospects. *RSC Adv*. 2025;15(1):406-419.
doi: 10.1039/d4ra07970a

54. Huang W, Zhang JH, Singh V, *et al*. Digital light 3D printing of a polymer composite featuring robustness, self-healing, recyclability and tailorable mechanical properties. *Addit Manuf*. 2023;61:103343.
doi: 10.1016/j.addma.2022.103343

55. Zou L, Hu L, Pan PP, *et al*. Icariin-releasing 3D printed scaffold for bone regeneration. *Compos B Eng*. 2022;232:109625.
doi: 10.1016/j.compositesb.2022.109625

56. Singh H, Tuffaha M, Tripathi S, *et al*. 3D printed metamaterials: properties, fabrication, and drug delivery applications. *Adv Drug Del Rev*. 2025;224:115636.
doi: 10.1016/j.addr.2025.115636

57. Usta F, Scarpa F, Türkmen HS, Johnson P, Perriman AW, Chen YY. Multiphase lattice metamaterials with enhanced mechanical performance. *Smart Mater Struct*. 2021;30(2):025014.
doi: 10.1088/1361-665X/abd15d

58. Jin SM, Hwang JH, Wang K, *et al*. Symmetry breaking of Au nanospheres confined in 1D nanocylinders: exploring helical assembly by 3D transmission electron microscopy. *Mater Chem Front*. 2020;4(10):3032-3039.
doi: 10.1039/d0qm00374c

59. Chen YX, Ai B, Wong ZJ. Soft optical metamaterials. *Nano Converg* 2020;7(1):18.
doi: 10.1186/s40580-020-00226-7

60. Xie PT, Shi ZC, Feng M, *et al*. Recent advances in radio-frequency negative dielectric metamaterials by designing heterogeneous composites. *Adv Compos Hybrid Mater*. 2022;5(2):679-695.
doi: 10.1007/s42114-022-00479-2

61. Yusoff NHM, Teo LRI, Phang SJ, Wong VL, Cheah KH, Lim SS. Recent advances in polymer-based 3D printing for wastewater treatment application: an overview. *Chem Eng J*. 2022;429:132311.
doi: 10.1016/j.cej.2021.132311

62. Münchinger A, Hsu LY, Fürniss F, Blasco E, Wegener M. 3D optomechanical metamaterials. *Mater Today*. 2022;59:9-17.
doi: 10.1016/j.mattod.2022.08.020

63. Ren ZH, Chang YH, Ma YM, Shih KL, Dong BW, Lee C. Leveraging of MEMS technologies for optical metamaterials applications. *Adv Optic Mater*. 2020;8(3):1900653.
doi: 10.1002/adom.201900653

64. Tsushima N, Higuchi R. Stiffness and strength evaluation of lattice-based mechanical metamaterials by decoupled two-scale analysis. *Mater Today Commun*. 2022;31:103598.
doi: 10.1016/j.mtcomm.2022.103598

65. Tian XY, Chen WJ, Gao RJ, Liu ST, Wang JX. Design of pore layout for perforated auxetic metamaterials with low-frequency band gaps. *Appl Phys Express*. 2020;13(4): 045503.
doi: 10.35848/1882-0786/ab7f5b

66. Davidovich MV. Can isotropic negative permittivity ε and permeability μ metamaterials exist? *JETP*. 2021;132(2):159-176.
doi: 10.1134/S1063776121020102

67. Lin IM, Yang C-Y, Wang Y-M, *et al*. Flexible block copolymer metamaterials featuring hollow ordered nanonetworks with ultra-high porosity and surface-to-volume ratio. *Small*. 2024;20(14):e2307487.
doi: 10.1002/smll.202307487

68. Cai J, Shahryari B, Seyedkanani A, Sasmito AP, Akbarzadeh A. Topology-dependent enhancement of pyroelectric property in nanoarchitected GaN metamaterials. *Nano Lett*. 2025;25(18):7603-7610.
doi: 10.1021/acs.nanolett.5c01586

69. Wang C, Vangelatos Z, Grigoropoulos CP, Ma Z. Micro-engineered architected metamaterials for cell and tissue engineering. *Mater Today Adv*. 2022;13:100206.
doi: 10.1016/j.mtadv.2022.100206

70. Siboro SAP, Anugrah DSB, Ramesh K, Park SH, Kim HR, Lim KT. Tunable porosity of covalently crosslinked alginate-based hydrogels and its significance in drug release behavior. *Carbohydr Polym*. 2021;260:117779.
doi: 10.1016/j.carbpol.2021.117779

71. Xu G, Zhou X, Chen W, *et al*. Hydrodynamic moire superlattice. *Science*. 2024;386(6728):1377-1383.
doi: 10.1126/science.adq2329

72. Kharbedia M, Caselli N, Herráez-Aguilar D, *et al*. Moulding hydrodynamic 2D-crystals upon parametric Faraday waves in shear-functionalized water surfaces. *Nat Commun*. 2021;12(1):1130.
doi: 10.1038/s41467-021-21403-0

73. Wang X, Roy M, Wang R, *et al*. Towards in vitro - in vivo correlation models for in situ forming drug implants. *J Control Release*. 2024;372:648-660.
doi: 10.1016/j.jconrel.2024.06.058

74. Skrzypek K, Nibbelink MG, Liefers-Visser J, *et al*. A high cell-bearing capacity multibore hollow fiber device for macroencapsulation of islets of langerhans. *Macromol Biosci*. 2020;20(8):2000021.
doi: 10.1002/mabi.202000021

75. Rauer SB, Stuwe L, Steinbeck L, *et al*. Cell adhesion and local cytokine control on protein-functionalized PNIPAM-co-AAc hydrogel microcarriers. *Small*. 2025;21(2): e2404183.
doi: 10.1002/smll.202404183

76. Priyadarsini SS, Saxena S, Pradhan JR, Dasgupta S. Inkjet-printed transparent micro-supercapacitors with morphology tailored co-continuous mesoporous Mn3O4. *J Mater Chem A*. 2022;10(40):21551-21564.
doi: 10.1039/d2ta04901e

77. Morales Ovalle MA, Raineri M, Vasquez Mansilla M, *et al*. Cytotoxic impact of catalytic activity and heating efficiency of manganese ferrite nanoparticles with different particle sizes for magnetic fluid hyperthermia. *J Biomed Mater Res B Appl Biomater*. 2025;113(9):e35638.
doi: 10.1002/jbm.b.35638

78. Omata D, Munakata L, Maruyama K, Suzuki R. Enhanced vascular permeability by microbubbles and ultrasound in drug delivery. *Biol Pharm Bull*. 2021;44(10):1391-1398.
doi: 10.1248/bpb.b21-00453

79. Bhandari A. Ocular fluid mechanics and drug delivery: a review of mathematical and computational models. *Pharmacol Res*. 2021;38(12):2003-2033.
doi: 10.1007/s11095-021-03141-6

80. Kwakernaak LJ, van Hecke M. Counting and sequential information processing in mechanical metamaterials. *Phys Rev Lett*. 2023;130(26):268204.
doi: 10.1103/PhysRevLett.130.268204

81. Jiao P, Mueller J, Raney JR, Zheng XR, Alavi AH. Mechanical metamaterials and beyond. *Nat Commun*. 2023;14(1):6004.
doi: 10.1038/s41467-023-41679-8

82. Su R, Chen J, Zhang X, *et al*. 3D-printed micro/nano-scaled mechanical metamaterials: fundamentals, technologies, progress, applications, and challenges. *Small*. 2023;19(29):e2206391.
doi: 10.1002/smll.202206391

83. Sinha P, Mukhopadhyay T. Programmable multi-physical mechanics of mechanical metamaterials. *Mater Sci Eng R Rep*. 2023;155:100745.
doi: 10.1016/j.mser.2023.100745

84. Gao S, Liu W, Zhang L, Gain AK. A new polymer-based mechanical metamaterial with tailorable large negative Poisson's ratios. *Polymers*. 2020;12(7):1492.
doi: 10.3390/polym12071492

85. Babaee S, Pajovic S, Kirtane AR, *et al*. Temperature-responsive biometamaterials for gastrointestinal applications. *Sci Transl Med*. 2019;11(488):eaau8581.
doi: 10.1126/scitranslmed.aau8581

86. Jiang Y, Li Y. 3D printed auxetic mechanical metamaterial with chiral cells and re-entrant cores. *Sci Rep*. 2018; 8(1):2397.
doi: 10.1038/s41598-018-20795-2

87. Huang Y, Zhang XZ, Zhang LL, Cai CX. Theoretical verification of three-dimensional manufacturable pentamode metamaterial microstructure. *J Phys Condens Matter*. 2021;33(48):485702.
doi: 10.1088/1361-648X/ac244c

88. Xiao R, Feng XB, Liu WG, *et al*. Direct 3D printing of thin-walled cardiovascular stents with negative Poisson's ratio

(NPR) structure and functional metallic coating. *Compos Struct*. 2023;306:116572.
doi: 10.1016/j.compstruct.2022.116572

89. Biswas D, Gupta S. Effect of adaptation functions and multilayer topology on synchronization. *Phys Rev E*. 2024;109(2-1):024221.
doi: 10.1103/PhysRevE.109.024221

90. Li Y. A multiscale framework for designing high-toughness composite materials. *Int J Comput Methods*. 2020;17(5):1940008.
doi: 10.1142/S0219876219400085

91. Xu J, Cai H, Wu Z, *et al*. Acoustic metamaterials-driven transdermal drug delivery for rapid and on-demand management of acute disease. *Nat Commun*. 2023;14(1):869.
doi: 10.1038/s41467-023-36581-2

92. Veerabagu U, Palza H, Quero F. Review: auxetic polymer-based mechanical metamaterials for biomedical applications. *ACS Biomater Sci Eng*. 2022;8(7):2798-2824.
doi: 10.1021/acsbiomaterials.2c00109

93. Pruksawan S, Teo RLJ, Cheang YH, Chong YT, Ng ELL, Wang F. Structurally transformable and reconfigurable hydrogel-based mechanical metamaterials and their application in biomedical stents. *ACS Appl Mater Interfaces*. 2025;17(2):4055-4066.
doi: 10.1021/acsami.4c20599

94. Li T, Li Y. 3D tiled auxetic metamaterial: a new family of mechanical metamaterial with high resilience and mechanical hysteresis. *Adv Mater*. 2024;36(15):e2309604.
doi: 10.1002/adma.202309604

95. Vakalis S, Colon-Berrios JR, Chen D, Nanzer JA. Non-destructive imaging of defects using non-cooperative 5G millimeter-wave signals. *Sensors*. 2023;23(14):6421.
doi: 10.3390/s23146421

96. Fan Y, Chen J, Mou C. Pattern-reconfigurable integrated array antenna based on a coding metasurface. *Opt Express*. 2024;32(6):8816-8827.
doi: 10.1364/OE.515878

97. Sun L, Zhou ZT, Zhong JJ, *et al*. Implantable, degradable, therapeutic terahertz metamaterial devices. *Small*. 2020;16(17):2000294.
doi: 10.1002/smll.202000294

98. Galleani G, Abou Khalil A, Canioni L, *et al*. Fluorine and sodium depletion followed by refractive index modification imprinted on fluorophosphate glass surface by thermal poling. *J Non-Cryst Solids*. 2023;601:122054.
doi: 10.1016/j.jnoncrysol.2022.122054

99. Bi K, Guo Y, Zhou J, *et al*. Negative and near zero refraction metamaterials based on permanent magnetic ferrites. *Sci Rep*. 2014;4(1):4139.
doi: 10.1038/srep04139

100. Sukonthachat J, Bubpamala T, Poo-Arporn RP, Pholpabu P. Validation of electrochemical device setup for detection of dual antibiotic drug release from hydrogel. *J Pharm Biomed Anal*. 2024;245:116165.
doi: 10.1016/j.jpba.2024.116165

101. Huang MT, Tan AJ, Büttner F, *et al*. Voltage-gated optics and plasmonics enabled by solid-state proton pumping. *Nat Commun*. 2019;10:5030.
doi: 10.1038/s41467-019-13131-3

102. Royo I, Fernandez-Garcia R, Gil I. Microwave resonators for wearable sensors design: a systematic review. *Sensors*. 2023;23(22):9103.
doi: 10.3390/s23229103

103. Yu HP, Zhu YJ, Xiong ZC, Lu BQ. Bioinspired fiberboard-and-mortar structural nanocomposite based on ultralong hydroxyapatite nanowires with high mechanical performance. *Chem Eng J*. 2020;399:125666.
doi: 10.1016/j.cej.2020.125666

104. Sun L, Gu C, Tao TH, Zhou Z. A degradable antibacterial skin patch of flexible terahertz metamaterials made from silk proteins. 2020:13-15.
doi: 10.1109/MEMS46641.2020.9056132

105. Ayazi H, Akhavan O, Raoufi M, Varshochian R, Motlagh NSH, Atyabi F. Graphene aerogel nanoparticles for in-situ loading/pH sensitive releasing anticancer drugs. *Colloids Surf B Biointerfaces*. 2020;186:110712.
doi: 10.1016/j.colsurfb.2019.110712

106. Wu M, Liu Y, Zhu X, *et al*. Advances in i-motif structures: Stability, gene expression, and therapeutic applications. *Int J Biol Macromol*. 2025;311(Pt 4):143555.
doi: 10.1016/j.ijbiomac.2025.143555

107. Meng ZJ, He JK, Li DC. Additive manufacturing and large deformation responses of highly-porous polycaprolactone scaffolds with helical architectures for breast tissue engineering. *Virtual Phys Prototyp*. 2021;16(3):291-305.
doi: 10.1080/17452759.2021.1930069

108. Wu W, Ren MX, Pi B, Wu Y, Cai W, Xu JJ. Scaffold metamaterial and its application as strain sensor. *Appl Phys Lett*. 2015;107(9):091104.
doi: 10.1063/1.4929887

109. Sikorski J, Matczuk M, Stepien M, Ogorek K, Ruzik L, Jarosz M. Fe_3O_4 SPIONs in cancer theranostics-structure versus interactions with proteins and methods of their investigation. *Nanotechnology*. 2024;35(21)
doi: 10.1088/1361-6528/ad2c54

110. Salah D, Moghanm FS, Arshad M, *et al*. Polymer-peptide modified gold nanorods to improve cell conjugation and cell labelling for stem cells photoacoustic imaging. *Diagnostics*. 2021;11(7):1196.
doi: 10.3390/diagnostics11071196

111. Tao HC, Gibert J. Multifunctional mechanical metamaterials with embedded triboelectric nanogenerators. *Adv Funct Mater*. 2020;30(23):2001720.
doi: 10.1002/adfm.202001720

112. Imani IM, Kim HS, Shin J, *et al*. Advanced ultrasound energy transfer technologies using metamaterial structures. *Adv Sci*. 2024;11(31):e2401494. doi: 10.1002/advs.202401494

113. Barri K, Jiao PC, Zhang QY, Chen J, Wang ZL, Alavi AH. Multifunctional meta-tribomaterial nanogenerators for energy harvesting and active sensing. *Nano Energy*. 2021;86:106074. doi: 10.1016/j.nanoen.2021.106074

114. Hao Y, Niu Z, Yang J, *et al*. Self-powered terahertz modulators based on metamaterials, liquid crystals, and triboelectric nanogenerators. *ACS Appl Mater Interfaces*. 2024;16(25):32249-32258. doi: 10.1021/acsami.4c04251

115. Xu XC, Wu Q, Pang YK, *et al*. Multifunctional metamaterials for energy harvesting and vibration control. *Adv Funct Mater*. 2022;32(7):2107896. doi: 10.1002/adfm.202107896

116. Jiao P, Zhang H, Li W. Origami tribo-metamaterials with mechanoelectrical multistability. *ACS Appl Mater Interfaces*. 2023;15(2):2873-2880. doi: 10.1021/acsami.2c16681

117. Goo B, Hong CH, Park K. 4D printing using anisotropic thermal deformation of 3D-printed thermoplastic parts. *Mater Des*. 2020;188:108485. doi: 10.1016/j.matdes.2020.108485

118. Patdiya J, Kandasubramanian B. Progress in 4D printing of stimuli responsive materials. *Polym Plast Technol Mater*. 2021;60(17):1845-1883. doi: 10.1080/25740881.2021.1934016

119. Chen M, Gao M, Bai L, Zheng H, Qi HJ, Zhou K. Recent advances in 4D printing of liquid crystal elastomers. *Adv Mater*. 2023;35(23):e2209566. doi: 10.1002/adma.202209566

120. Kumar R, Sharma A, Alexiou A, Ashraf GM. Artificial intelligence in de novo drug design: are we still there? *Curr Top Med Chem*. 2022;22(30):2483-2492. doi: 10.2174/1568026623666221017143244

121. Yu CL, Jiang JC. A perspective on using machine learning in 3D bioprinting. *Int J Bioprint*. 2020;6(1):253. doi: 10.18063/ijb.v6i1.253

122. Chang X-Z, Liu J-S, Lu J-Q. Digital light processing 3D printing technology in biomedical engineering: a review. *Macromol Biosci*. 2025;25(8):e2500101. doi: 10.1002/mabi.202500101

123. Chattopadhyay J, Srivastava N, Pathak TS. Comprehensive review of 3D printing techniques emphasizing thermal characterization in biomedical prototyping. *J Biomater Appl*. 2025;39(9):971-995. doi: 10.1177/08853282251314672

124. Lai JH, Wang C, Wang M. 3D printing in biomedical engineering: processes, materials, and applications. *Appl Phys Rev*. 2021;8(2):021322. doi: 10.1063/5.0024177

125. Ünlüer Ö, Diltemiz SE, Say MG, Hür D, Say R, Ersöz A. A powerful combination in designing polymeric scaffolds: 3D bioprinting and cryogelation. *Int J Polym Mater Polym Biomater*. 2022;71(4):278-290. doi: 10.1080/00914037.2020.1825083

126. Choi YJ, Cho DW, Lee H. Development of silk fibroin scaffolds by using indirect 3D-bioprinting technology. *Micromachines*. 2022;13(1):43. doi: 10.3390/mi13010043

127. Ma J, Bharambe VT, Persson KA, *et al*. Metallophobic coatings to enable shape reconfigurable liquid metal inside 3D printed plastics. *ACS Appl Mater Interfaces*. 2021;13(11):12709-12718. doi: 10.1021/acsami.0c17283

128. Brassard JA, Nikolaev M, Hübscher T, Hofer M, Lutolf MP. Recapitulating macro-scale tissue self-organization through organoid bioprinting. *Nat Mater*. 2021;20(1):22-29. doi: 10.1038/s41563-020-00803-5

129. Koffler J, Zhu W, Qu X, *et al*. Biomimetic 3D-printed scaffolds for spinal cord injury repair. *Nat Med*. 2019;25(2):263. doi: 10.1038/s41591-018-0296-z

130. Schwab A, Levato R, D'Este M, Piluso S, Eglin D, Malda J. Printability and shape fidelity of bioinks in 3D bioprinting. *Chem Rev*. 2020;120(19):10850-10877. doi: 10.1021/acs.chemrev.0c00084

131. Daly AC, Riley L, Segura T, Burdick JA. Hydrogel microparticles for biomedical applications. *Nat Rev Mater*. 2020;5(1):20-43. doi: 10.1038/s41578-019-0148-6

132. Cui HT, Nowicki M, Fisher JP, Zhang LG. 3D bioprinting for organ regeneration. *Adv Healthc Mater*. 2017;6(1): 1601118. doi: 10.1002/adhm.201601118

133. Gungor-Ozkerim PS, Inci I, Zhang YS, Khademhosseini A, Dokmeci MR. Bioinks for 3D bioprinting: an overview. *Biomater Sci*. 2018;6(5):915-946. doi: 10.1039/c7bm00765e

134. Li JH, Wu CT, Chu PK, Gelinsky M. 3D printing of hydrogels: rational design strategies and emerging biomedical applications. *Mater Sci Eng R Rep*. 2020;140:100543. doi: 10.1016/j.mser.2020.100543

135. Ashammakhi N, Ahadian S, Xu C, *et al*. Bioinks and bioprinting technologies to make heterogeneous and biomimetic tissue constructs. *Mater Today Bio*. 2019;1:100008. doi: 10.1016/j.mtbio.2019.100008

136. Rutz AL, Hyland KE, Jakus AE, Burghardt WR, Shah RN. A multimaterial bioink method for 3D printing tunable, cell-compatible hydrogels. *Adv Mater*. 2015;27(9):1607-1614. doi: 10.1002/adma.201405076

137. Lim KS, Galarraga JH, Cui XL, Lindberg GCJ, Burdick JA, Woodfield TBF. Fundamentals and applications of photo-cross-linking in bioprinting. *Chem Rev*. 2020;120(19):10637-10669.
doi: 10.1021/acs.chemrev.9b00812

138. Cui XL, Li J, Hartanto Y, *et al*. Advances in extrusion 3D bioprinting: a focus on multicomponent hydrogel-based bioinks. *Adv Healthc Mater*. 2020;9(15):1901648.
doi: 10.1002/adhm.201901648

139. Grigorenko AN, Polini M, Novoselov KS. Graphene plasmonics. *Nat Photon*. 2012;6(11):749-758.
doi: 10.1038/NPHOTON.2012.262

140. Zheng XY, Lee H, Weisgraber TH, *et al*. Ultralight, ultrastiff mechanical metamaterials. *Science*. 2014;344(6190):1373-1377.
doi: 10.1126/science.1252291

141. Lee HE, Ahn HY, Mun J, *et al*. Amino-acid- and peptide-directed synthesis of chiral plasmonic gold nanoparticles. *Nature*. 2018;556(7701):360.
doi: 10.1038/s41586-018-0034-1

142. Geyer R, Jambeck JR, Law KL. Production, use, and fate of all plastics ever made. *Sci Adv*. 2017;3(7):e1700782.
doi: 10.1126/sciadv.1700782

143. Coulais C, Sabbadini A, Vink F, van Hecke M. Multi-step self-guided pathways for shape-changing metamaterials. *Nature*. 2018;561(7724):512.
doi: 10.1038/s41586-018-0541-0

144. Yang C, Boorugu M, Dopp A, *et al*. 4D printing reconfigurable, deployable and mechanically tunable metamaterials. *Mater Horiz*. 2019;6(6):1244-1250.
doi: 10.1039/c9mh00302a

145. Yao QF, Chen TK, Yuan X, Xie JP. Toward total synthesis of thiolate-protected metal nanoclusters. *Acc Chem Res*. 2018;51(6):1338-1348.
doi: 10.1021/acs.accounts.8b00065

146. Wauthle R, van der Stok J, Amin Yavari S, *et al*. Additively manufactured porous tantalum implants. *Acta Biomater*. 2015;14:217-225.
doi: 10.1016/j.actbio.2014.12.003

147. Rupp F, Liang L, Geis-Gerstorfer J, Scheideler L, Hüttig F. Surface characteristics of dental implants: a review. *Dent Mater*. 2018;34(1):40-57.
doi: 10.1016/j.dental.2017.09.007

148. Bakhsheshi-Rad HR, Hamzah E, Ismail AF, Aziz M, Najafinezhad A, Daroonparvar M. Synthesis and in-vitro performance of nanostructured monticellite coating on magnesium alloy for biomedical applications. *J Alloys Compd*. 2019;773:180-193.
doi: 10.1016/j.jallcom.2018.08.310

149. Zhi PX, Liu LX, Chang JK, *et al*. Advances in the study of magnesium alloys and their use in bone implant material. *Metals*. 2022;12(9):1500.
doi: 10.3390/met12091500

150. Mohammed N, Palaniandy P, Shaik F. Optimization of solar photocatalytic biodegradability of seawater using statistical modelling. *J Indian Chem Soc*. 2021;98(12):100240.
doi: 10.1016/j.jics.2021.100240

151. Shamsuri AA, Jamil S, Abdan K. A brief review on the influence of ionic liquids on the mechanical, thermal, and chemical properties of biodegradable polymer composites. *Polymers*. 2021;13(16):2597.
doi: 10.3390/polym13162597

152. Pruksawan S, Chee HL, Wang ZZ, *et al*. Toughened hydrogels for 3D printing of soft auxetic structures. *Chem Asian J*. 2022;17(19):e202200677.
doi: 10.1002/asia.202200677

153. Gerasimov RA, Eremeyev VA, Petrova TO, Egorov VI, Maksimova OG, Maksimov AV. Study of mechanical properties of ferroelectrics metamaterials using computer simulation. *Ferroelectrics*. 2017;508(1):151-160.
doi: 10.1080/00150193.2017.1289767

154. Hu YQ, Jia F, Fu ZJ, Liu YJ, Leng JS. A constitutive model and its numerical implementation for reversible behavior of shape memory hydrogels. *Smart Mater Struct*. 2022;31(9):095032.
doi: 10.1088/1361-665X/ac8257

155. Dong RN, Guo BL. Smart wound dressings for wound healing. *Nano Today*. 2021;41:101290.
doi: 10.1016/j.nantod.2021.101290

156. Calder S, Baral R, Buchanan CC, *et al*. Low-dimensional metal-organic frameworks: a pathway to design, explore and tune magnetic structures. *Acta Crystallogr B Struct Sci Cryst Eng Mater*. 2024;80(Pt 5):430-442.
doi: 10.1107/S2052520624008023

157. Wang C. A plug-and-play interface technology: Boosting simple but robust stretchable device assembly. *Sci Bull*. 2023;68(7):661-663.
doi: 10.1016/j.scib.2023.03.014

158. Jang KI, Chung HU, Xu S, *et al*. Soft network composite materials with deterministic and bio-inspired designs. *Nat Commun*. 2015;6:6566.
doi: 10.1038/ncomms7566

159. Jiang YY, Li YN. Novel 3D-printed hybrid auxetic mechanical metamaterial with chirality-induced sequential cell opening mechanisms. *Adv Eng Mater*. 2018;20(2):1700744.
doi: 10.1002/adem.201700744

160. Chen B, Wang J, Xu Z, *et al*. Controllable configuration of constitutional units in vanadium/iron-based polyanionic compounds for sodium-ion storage. *Adv Mater*. 2025;37(43):e09966-e09966.
doi: 10.1002/adma.202509966

161. Nashed N, Lam M, Ghafourian T, *et al*. An insight into the impact of thermal process on dissolution profile and physical

characteristics of theophylline tablets made through 3D printing compared to conventional methods. *Biomedicines*. 2022;10(6):1335.
doi: 10.3390/biomedicines10061335

162. Zohreh N, Rastegaran Z, Hosseini SH, Akhlaghi M, Istrate C, Busuioc C. pH-triggered intracellular release of doxorubicin by a poly(glycidyl methacrylate)-based double-shell magnetic nanocarrier. *Mater Sci Eng C Mater Biol Appl*. 2021;118:111498.
doi: 10.1016/j.msec.2020.111498

163. Shi KJ, Salvage JP, Maniruzzaman M, Nokhodchi A. Role of release modifiers to modulate drug release from fused deposition modelling (FDM) 3D printed tablets. *Int J Pharm*. 2021;597:120315.
doi: 10.1016/j.ijpharm.2021.120315

164. Fina F, Goyanes A, Madla CM, *et al*. 3D printing of drug-loaded gyroid lattices using selective laser sintering. *Int J Pharm*. 2018;547(1-2):44-52.
doi: 10.1016/j.ijpharm.2018.05.044

165. Dhayer M, Barral V, Cleret D, *et al*. Material and biological characterization of 3D knitted bioresorbable poly (D,L-lactide) (PLA) and polycaprolactone (PCL) scaffolds for soft tissue regeneration: From fabrication to in vivo performance. *J Biol Eng*. 2025;19(1):53-53.
doi: 10.1186/s13036-025-00504-0

166. Vaupel S, Mau R, Kara S, Seitz H, Kragl U, Meyer J. 3D printed and stimulus responsive drug delivery systems based on synthetic polyelectrolyte hydrogels manufactured viadigital light processing. *J Mater Chem B*. 2023;11(28):6547-6559.
doi: 10.1039/d3tb00285c

167. Li H, Cheng S, Zhou K, Zang J, Wang Z, Du M. Carboxymethyl-beta-cyclodextrin grafted chitosan embedded oyster (*Crassostrea gigas*) ferritin can alleviate lead-induced liver injury by oral administration. *Food Res Int*. 2025;212:116417.
doi: 10.1016/j.foodres.2025.116417

168. Zhou WD, Zhang H, Liu YF, *et al*. Preparation of calcium alginate/polyethylene glycol acrylate double network fiber with excellent properties by dynamic molding method. *Carbohydr Polym*. 2019;226:115277.
doi: 10.1016/j.carbpol.2019.115277

169. Rafiee M, Farahani RD, Therriault D. Multi-material 3D and 4D printing: a survey. *Adv Sci*. 2020;7(12):1902307.
doi: 10.1002/advs.201902307

170. Egan PF, Shea KA, Ferguson SJ. Simulated tissue growth for 3D printed scaffolds. *Biomech Model Mechanobiol*. 2018;17(5):1481-1495.
doi: 10.1007/s10237-018-1040-9

171. Khatib O, Ren SM, Malof J, Padilla WJ. Deep learning the electromagnetic properties of metamaterials—a comprehensive review. *Adv Funct Mater*. 2021;31(31):2101748.
doi: 10.1002/adfm.202101748

172. Mohammadjafari S, Ozyegen O, Cevik M, Kavurmacioglu E, Ethier J, Basar A. Designing mm-wave electromagnetic engineered surfaces using generative adversarial networks. *Neural Comput Appl*. 2021;33(17):11309-11323.
doi: 10.1007/s00521-020-05656-2

173. Hsu YC, Yang ZZ, Buehler MJ. Generative design, manufacturing, and molecular modeling of 3D architected materials based on natural language input. *APL Mater*. 2022;10(4):041107.
doi: 10.1063/5.0082338

174. Christiansen RE, Vester-Petersen J, Madsen SP, Sigmund O. A non-linear material interpolation for design of metallic nano-particles using topology optimization. *CMAME*. 2019;343:23-39.
doi: 10.1016/j.cma.2018.08.034

175. Tezsezen E, Yigci D, Ahmadpour A, Tasoglu S. AI-based metamaterial design. *ACS Appl Mater Interfaces*. 2024;16(23):29547-29569.
doi: 10.1021/acsami.4c04486

176. Han D, Ren X, Zhang Y, *et al*. Lightweight auxetic metamaterials: Design and characteristic study. *Compos Struct*. 2022;293:115706.
doi: 10.1016/j.compstruct.2022.115706

177. Pantelidakis M, Mykoniatis K, Liu J, Harris G. A digital twin ecosystem for additive manufacturing using a real-time development platform. *Int J Adv Manuf Technol*. 2022;120(9-10):6547-6563.
doi: 10.1007/s00170-022-09164-6

178. Mora S, Pugno NM, Misseroni D. 3D printed architected lattice structures by material jetting. *Mater Today*. 2022;59:107-132.
doi: 10.1016/j.mattod.2022.05.008

179. Masoumi Ravandi MR, Dezianian S, Ahmad MT, Ghoddosian A, Azadi M. Compressive strength of metamaterial bones fabricated by 3D printing with different porosities in cubic cells. *Mater Chem Phys*. 2023; 299:127515.
doi: 10.1016/j.matchemphys.2023.127515

180. Mohammadi A, Hajizadeh E, Tan Y, Choong P, Oetomo D. A bioinspired 3D-printable flexure joint with cellular mechanical metamaterial architecture for soft robotic hands. *Int J Bioprint*. 2023;9(3):696.
doi: 10.18063/ijb.696

181. Flamourakis G, Spanos I, Vangelatos Z, *et al*. Laser-made 3D auxetic metamaterial scaffolds for tissue engineering applications. *Macromol Mater Eng*. 2020;305(7):2000238.
doi: 10.1002/mame.202000238

182. Manshor MR, Alli YA, Anuar H, Ejeromedoghene O, Omotola EO, Suhr J. 4D printing: historical evolution, computational insights and emerging applications. *Mater Sci Eng B*. 2023;295:116567.
doi: 10.1016/j.mseb.2023.116567

183. Rezvani Ghomi E, Khosravi F, Neisiany RE, Singh S, Ramakrishna S. Future of additive manufacturing in healthcare. *Curr Opin Biomed Eng*. 2021;17:100255. doi: 10.1016/j.cobme.2020.100255

184. Fu P, Li H, Gong J, *et al*. 4D printing of polymers: techniques, materials, and prospects. *Prog Polym Sci*. 2022;126:101506. doi: 10.1016/j.progpolymsci.2022.101506

185. Che QT, Seo JW, Charoensri K, Nguyen MH, Park HJ, Bae H. 4D-printed microneedles from dual-sensitive chitosan for non-transdermal drug delivery. *Int J Biol Macromol*. 2024;261(Pt 2):129638. doi: 10.1016/j.ijbiomac.2024.129638

186. Wang XH. Biodegradable polymers, history tells polymer science's fortune. *Chin J Polym Sci*. 2022;40(5):431-432. doi: 10.1007/s10118-022-2737-x

187. Shamsuri AA, Abdan K, Jamil S. Preparations and properties of ionic liquid-assisted electrospun biodegradable polymer fibers. *Polymers*. 2022;14(12):2308. doi: 10.3390/polym14122308

188. Wang X, Cao C, Shen X, *et al*. Universal intermolecular energy transfer strategy for extending initiator libraries of photoinhibited multiphoton lithography. *ACS Appl Mater Interfaces*. 2025;17(16):24327-24338. doi: 10.1021/acsami.5c00344

189. Marazzi D, Trovalusci F, Vesco S, Di Nardo P. Manufacturing process of prostheses using semirigid molds by additive technologies. *Methods Mol Biol*. 2024;2835:317-323. doi: 10.1007/978-1-0716-3995-5_27

190. Li T, Wang S, Weng Z, *et al*. Laser interference additive manufacturing: Mask bundle shape bionic shark skin structure. *ACS Appl Mater Interfaces*. 2024;16(28):37183-37196. doi: 10.1021/acsami.4c04916

191. Salvalaglio M, Bouabdellaoui M, Bollani M, *et al*. Hyperuniform monocrystalline structures by spinodal solid-state dewetting. *Phys Rev Lett*. 2020;125(12):126101. doi: 10.1103/PhysRevLett.125.126101

192. Kumar S, Tan SH, Zheng L, Kochmann DM. Inverse-designed spinodoid metamaterials. *NPJ Comput Mater*. 2020;6(1):73. doi: 10.1038/s41524-020-0341-6

193. Smit T, Koppen S, Ferguson SJ, Helgason B. Conceptual design of compliant bone scaffolds by full-scale topology optimization. *J Mech Behav Biomed Mater*. 2023;143:105886. doi: 10.1016/j.jmbbm.2023.105886

194. Sim EA, Lee S, Oh J, Lee J. GANs and DCGANs for generation of topology optimization validation curve through clustering analysis. *Adv Eng Softw*. 2021;152:102957. doi: 10.1016/j.advengsoft.2020.102957

195. Wang T, Migliori B, Miccoli B, Shin SR. Bioinspired soft robot with incorporated microelectrodes. *J Vis Exp*. 2020;(156):e60717. doi: 10.3791/60717

196. Goto E, Tagami T, Ogawa K, Ozeki T. Fabrication of 3D-printed contact lens composed of polyethylene glycol diacrylate for controlled release of azithromycin. *Biol Pharm Bull*. 2023;46(10):1461-1467. doi: 10.1248/bpb.b23-00443

197. Kraisit P, Limpamanoch P, Hirun N, Limmatvapirat S. Design and development of 3D-printed bento box model for controlled drug release of propranolol HCl following pharmacopeia dissolution guidelines. *Int J Pharm*. 2022;628:122272. doi: 10.1016/j.ijpharm.2022.122272

198. Guan S, Xu W, Tan J, *et al*. Metainterface heterostructure enhances sonodynamic therapy for disrupting secondary biofilms. *ACS Nano*. 2024;18(23):15114-15129. doi: 10.1021/acsnano.4c02605

199. van Hengel IAJ, Riool M, Fratila-Apachitei LE, *et al*. Selective laser melting porous metallic implants with immobilized silver nanoparticles kill and prevent biofilm formation by methicillin-resistant *Staphylococcus aureus*. *Biomaterials*. 2017;140:1-15. doi: 10.1016/j.biomaterials.2017.02.030

200. Gupta R, Singh B. Chemical modification of carboxylated MWCNTs for enhanced electrical conducting and magnetic properties. *Mater Sci Eng B Adv Funct Solid State Mater*. 2020;262:114730. doi: 10.1016/j.mseb.2020.114730

201. Nguyen DD, Kim I. Vibrational circular dichroism unveils hidden clues. *Light Sci Appl*. 2023;12(1):210-210. doi: 10.1038/s41377-023-01239-7

202. Parsa A, Wang D, O'Hern CS, Shattuck MD, Kramer-Bottiglio R, Bongard J. Evolving programmable computational metamaterials. GECCO '22: Proceedings of the Genetic and Evolutionary Computation Conference Companion; 2022: 122-129. doi: 10.1145/3512290.3528861

203. Yavari SA, Croes M, Akhavan B, *et al*. Layer by layer coating for bio-functionalization of additively manufactured meta-biomaterials. *Addit Manuf*. 2020;32:100991. doi: 10.1016/j.addma.2019.100991

204. Kalogeropoulou M, Kracher A, Fucile P, Mihaila SM, Moroni L. Blueprints of architected materials: a guide to metamaterial design for tissue engineering. *Adv Mater*. 2024;36(47):e2408082. doi: 10.1002/adma.202408082

205. Cooper DA, DePaolo-Boisvert J, Nicholson SA, Gad B, Minh DDL. Intracellular pocket conformations determine signaling efficacy through the μ opioid receptor. *J Chem Inf Model*. 2025;65(3):1465-1475. doi: 10.1021/acs.jcim.4c01437

206. Lyu SN, Qin B, Deng HC, Ding XL. Origami-based cellular mechanical metamaterials with tunable Poisson's ratio: construction and analysis. *IJMS*. 2021;212:106791. doi: 10.1016/j.ijmecsci.2021.106791

207. Jia Y, Liu K, Zhang XS. Modulate stress distribution with bio-inspired irregular architected materials towards optimal tissue support. *Nat Commun*. 2024;15(1):4072. doi: 10.1038/s41467-024-47831-2

208. Chiappini C, De Rosa E, Martinez JO, *et al*. Biodegradable silicon nanoneedles delivering nucleic acids intracellularly induce localized in vivo neovascularization. *Nat Mater*. 2015;14(5):532-539. doi: 10.1038/NMAT4249

209. Li SN, Zhang LY, Chen XF. 3D-printed terahertz metamaterial absorber based on vertical split-ring resonator. *J Appl Phys*. 2021;130(3):034504. doi: 10.1063/5.0056276

210. Yarali E, Klimopoulou M, David K, *et al*. Bone cell response to additively manufactured 3D micro-architectures with controlled Poisson's ratio: auxetic vs. non-auxetic meta-biomaterials. *Acta Biomater*. 2024;177: 228-242. doi: 10.1016/j.actbio.2024.01.045

211. Barri K, Zhang QY, Swink I, *et al*. Patient-specific self-powered metamaterial implants for detecting bone healing progress. *Adv Funct Mater*. 2022;32(32):2203533. doi: 10.1002/adfm.202203533

212. Fina F, Madla CM, Goyanes A, Zhang JX, Gaisford S, Basit AW. Fabricating 3D printed orally disintegrating printlets using selective laser sintering. *Int J Pharm*. 2018;541(1-2):101-107. doi: 10.1016/j.ijpharm.2018.02.015

213. Fogsgaard MB, Iannuzzo F. FEM-aided damage model calibration method for experimental results. *MiRe*. 2020;114:113915. doi: 10.1016/j.microrel.2020.113915

214. Catsoulis S, Singh JS, Narayanan C, Lakehal D. Integrating supervised learning and applied computational multi-fluid dynamics. *Int J Multiph Flow*. 2022;157:104221. doi: 10.1016/j.ijmultiphaseflow.2022.104221

215. Schuett M, Stamatopoulos K, Batchelor HK, Simmons MJH, Alexiadis A. Development of a digital twin of a tablet that mimics a real solid dosage form: differences in the dissolution profile in conventional mini-USP II and a biorelevant colon model. *Eur J Pharm Sci*. 2022;179:106310. doi: 10.1016/j.ejps.2022.106310

216. Islavath SR, Deb D, Kumar H. Life cycle analysis and damage prediction of a longwall powered support using 3D numerical modelling techniques. *Arab J Geosci*. 2019;12(14):441. doi: 10.1007/s12517-019-4574-y

ACCSCIENCE PUBLISHING

International Journal of Bioprinting

REVIEW ARTICLE

Acoustic lithography: Field-directed cell patterning for bio-systems engineering

Yuyang Li[1,2*], Dengjie Sun[1], Chenglin Miao[1], Yuqi Gao[1], Bin Zhao[1], Xu Du[1], Xiaoming Liu[2], Tatsuo Arai[2,3], and Zhongqiang Zhang[1*]

[1]Key Laboratory of Intelligent Flexible Actuation and Control in Universities of Jiangsu Province and School of Mechanical Engineering, Jiangsu University, Zhenjiang, Jiangsu, China

[2]Key Laboratory of Biomimetic Robots and Systems, Ministry of Education, State Key Laboratory of Intelligent Control and Decision of Complex System, School of Mechatronical Engineering, Beijing Institute of Technology, Beijing, China

[3]Center for Neuroscience and Biomedical Engineering, The University of Electro-Communications, Tokyo, Japan

(This article belongs to the *Special Issue*: *Intelligent 3D Bioprinting Strategies for Future Regenerative Medicine*)

Abstract

The precise spatial patterning of living cells represents a foundational capability in bio-systems engineering, enabling the systematic study of collective cellular behaviors and the fabrication of increasingly complex functional tissues. Conventional methods for achieving this control, while numerous, are often constrained by static pattern formation, the need for biochemical labels that can alter cell function, or requirements for non-physiological media. In this context, acoustic-field-based manipulation has emerged as a uniquely powerful and biocompatible alternative. This review synthesizes these advancements under the unifying concept of "acoustic lithography," a framework that captures the technology's capacity for rapid, parallel, and label-free cellular organization. The discussion covers the core physical principles of acoustic radiation force and acoustic streaming before surveying the diverse technological landscape, from bulk and surface acoustic waves to advanced acoustic holography. It further highlights the impact of these tools across a spectrum of applications, including high-throughput analysis, biomimetic co-culture engineering, advanced biofabrication, and clinical sorting. Collectively, these applications demonstrate the field's trajectory as it moves beyond static patterning to encompass the integrated control of structure, environment, and function. Viewing the technology through this broader engineering lens underscores its significance as a vital platform, charting a course for the next generation of dynamically engineered living systems.

Keywords: Acoustic lithography; Acoustofluidics; Biofabrication; Bio-systems engineering; Cell patterning

***Corresponding authors:**
Yuyang Li
(leeyunth@bit.edu.cn)

Zhongqiang Zhang
(zhangzq@ujs.edu.cn)

Citation: Li Y, Sun D, Miao C, *et al*. Acoustic lithography: Field-directed cell patterning for bio-systems engineering. *Int J Bioprint*. 2026;12(1):71-101. doi: 10.36922/IJB025410420

Received: October 12, 2025
Revised: November 7, 2025
Accepted: November 11, 2025
Published online: November 17, 2025

Copyright: © 2025 Author(s). This is an Open Access article distributed under the terms of the Creative Commons Attribution License, permitting distribution, and reproduction in any medium, provided the original work is properly cited.

Publisher's Note: AccScience Publishing remains neutral with regard to jurisdictional claims in published maps and institutional affiliations.

1. Introduction

The ability to actively engineer the spatial distribution of cells is pivotal for advancing biological discovery and regenerative medicine.[1,2] While modern microscopy has unlocked unprecedented vistas of the microscopic realm, the capacity to move beyond

passive observation and actively pattern cells into defined structures is essential for understanding and directing collective biological functions.[3,4] This technique, known as cell patterning, is fundamental for decoding processes such as tissue morphogenesis, directed migration, and intercellular signaling.[5–7] Such processes underpin transformative applications in drug screening, disease modeling, and the engineering of functional tissues, laying the groundwork for advanced biofabrication and tissue engineering strategies.[8–11] Critically, conventional two-dimensional (2D) cell cultures fail to recapitulate the complex microenvironment and cell–cell interactions of native tissues, and animal models present challenges in throughput and species-specific differences, limiting their predictive power for human physiology.[12–14] Cell patterning emerges as an essential strategy to bridge this gap, providing geometrically controlled microenvironments that enable the systematic investigation of cellular physiology in a manner that reflects *in vivo* complexity.[15–18]

The drive to engineer increasingly complex cellular constructs has fueled the evolution of diverse patterning methodologies, each presenting distinct advantages and limitations.[4,5,19] Template-based techniques, such as those using elastomeric stencils, offer simplicity and high throughput by physically confining cells within predefined apertures.[20,21] However, this static approach affords limited flexibility for dynamic studies, and stencil removal requires careful consideration to maintain pattern integrity.[22] In contrast, field-directed strategies provide dynamic, reconfigurable control.[23,24] Magnetic manipulation, for instance, uses functionalized nanoparticles to guide cells with high specificity,[25,26] though this reliance on pre-labeling necessitates careful optimization to avoid influencing the cells' native state. For ultimate precision, optical tweezers employ focused laser beams to achieve subcellular resolution.[27] The highly focused energy, however, requires careful power management to mitigate potential photothermal effects, and scaling this high-precision method for high-throughput applications remains a challenge.[6,28] Another label-free alternative, dielectrophoresis (DEP), separates cells based on their intrinsic dielectric properties.[22,29] For optimal performance, DEP is typically conducted in low-conductivity buffers, which may require careful formulation to ensure long-term compatibility with cell health.[30] In contrast, acoustic field-directed patterning operates effectively in standard physiological buffers, as it relies on intrinsic mechanical properties rather than electrical polarizability.[31–36] This key advantage, combined with its tag-free and minimally invasive nature, positions acoustic manipulation as a uniquely versatile approach.[37–39]

To capture these collective advancements and emphasize their potential for creating user-defined, complex biological structures, this review frames the field under the concept of "acoustic lithography," by analogy with optical lithography in microfabrication. It is important to differentiate this concept from the broader, well-established field of acoustofluidics. Acoustofluidics encompasses a wide range of dynamic operations like separation, mixing, and transport. We propose acoustic lithography, much like optical lithography, to define its specific role in fabrication. The essence of this concept is the use of acoustic fields to construct preset and complex cellular structures.[40,41] The method's exceptional biocompatibility is well-documented, with studies showing preserved viability in erythrocytes and unaltered development in zebrafish embryos after prolonged exposure. This advantage stems from the fundamental nature of acoustic energy transfer: as mechanical waves, acoustic waves can propagate deep into optically opaque tissues with minimal absorption and negligible thermal loading, a significant benefit over light-based methods.[42,43] Furthermore, because acoustic forces are generated based on intrinsic mechanical properties (density and compressibility), the technology functions effectively in standard physiological buffers, whose high ionic strength would otherwise screen the electric fields required for dielectrophoretic. This reliance on inherent acoustic contrast obviates the need for the chemical labels required for magnetic approaches, thus preserving the native state of the cells.[44]

The rapid evolution of this field has created a need for an updated, cohesive synthesis of its principles and applications. While several excellent reviews cover the fundamentals of acoustofluidics and key applications in tissue engineering,[31,32,45–49] the technological landscape has expanded dramatically. Breakthroughs now extend beyond static patterning to include the integration of acoustics with smart, stimuli-responsive biomaterials for 4D biofabrication, pioneering *in vivo* applications such as targeted drug delivery and the remote assembly of tissue constructs within living organisms.[50–52] These emerging areas, alongside novel techniques like acoustical holography, sonogenetics, and single-molecule force spectroscopy,[53–59] are often dispersed across various disciplines. This fragmentation creates a pressing need for an updated synthesis to bridge the gap between fundamental acoustofluidic principles and their translational potential. This review synthesizes these advancements through the framework of acoustic lithography, providing a strong control-oriented perspective. This perspective is highlighted in our discussion on broader engineering principles, which illuminates the field's trajectory through a clear engineering logic arc—progressing from first,

controlling cellular structure, to second, engineering the dynamic microenvironment, and ultimately to third, regulating biological function. We believe this broader engineering perspective, which focuses on unifying design goals rather than disparate methodologies, provides a fresh vantage point that is critical for guiding future innovation in the field. Indeed, the expanding body of research reveals an increasingly sophisticated and diverse technological ecosystem, integrating novel materials, computational design, and multi-physics approaches to achieve unprecedented levels of control.[56–63]

This review is structured to build a comprehensive understanding of acoustic lithography from the ground up (Figure 1). We first elucidate the fundamental physics that form the toolkit for acoustic manipulation. Following this, we systematically survey the key methodologies, showcasing how these tools are engineered into increasingly sophisticated machines for cell patterning. We then explore the diverse applications of these machines in solving critical problems in bio-systems engineering. Finally, to fully appreciate the field's trajectory and potential, we step back from the technical details to introduce a cross-disciplinary perspective. This synthesis highlights the field's key advantages: its excellent biocompatibility in native media, its capacity for true three-dimensional (3D) precision, and its unique potential for dynamic, reconfigurable control, which together chart a course for future innovation.

2. Physical principles of acoustic cell manipulation

The ability of acoustic waves to manipulate cells and other microparticles in a fluid stems from nonlinear effects that generate time-averaged forces and bulk fluid motion.[39,64,65] Even at small scales relevant to cell patterning, these acoustic effects dominate, easily overcoming gravitational forces, which are negligible for individual cells in suspension. This manipulation is primarily achieved through two distinct yet interconnected physical phenomena: the acoustic radiation force (ARF) and acoustic streaming (a steady, time-averaged fluid motion generated by the acoustic field).[66] The ARF is directly exerted on a particle due to the scattering of the incident acoustic wave.[67] This force effectively creates a potential energy landscape, pushing or pulling the particle toward stable trapping positions. Simultaneously, acoustic streaming is an indirect effect,[68] in which the absorption of acoustic energy within the fluid generates steady, often vortical, flows that induce a gentle drag on suspended particles.[69] The interplay and relative dominance of these two forces—determined by factors

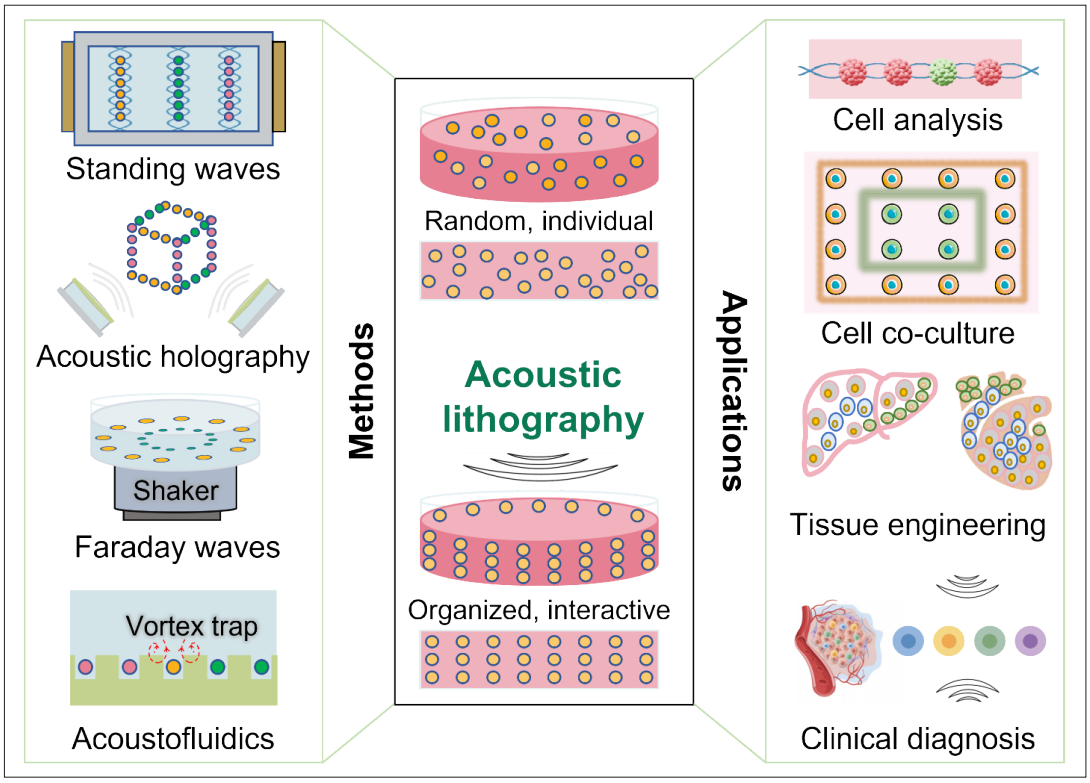


Figure 1. The overarching framework of this review.

such as the acoustic frequency, particle properties, and fluid environment—form the cornerstone of all acoustic lithography techniques.[70]

2.1. Acoustic radiation force

The ARF arises from the transfer of momentum from the acoustic wave to the particle. A complete description of this force requires considering the time-averaged momentum flux tensor, $\langle \prod \rangle$, integrated over a surface S enclosing the particle.[71,72] The brackets $\langle\ \rangle$ denote the time-average.

$$F = -\oint_s \langle \prod \rangle \cdot dS \tag{1}$$

This general formulation is comprehensive but complex. Gor'kov derived a simplified and powerful expression for a specific and highly relevant case: when particles are much smaller than the acoustic wavelength. This condition defines the Rayleigh regime, where the product of the wavenumber k and particle radius R is $kR \ll 1$ —a condition that most cells satisfy. He achieved this by treating the interaction as an effective potential energy field, U. The resulting force is then simply the negative gradient of this potential[73]:

$$F_{ARF} = -\nabla U \tag{2}$$

The Gor'kov potential U is a function of the time-averaged squares of the acoustic pressure $\langle p^2 \rangle$ and fluid velocit $\langle v^2 \rangle$ at the particle's location, and is given by:

$$U = V_p \left(\frac{1}{2} f_1 \kappa_f \langle p^2 \rangle - \frac{3}{4} f_2 \rho_f \langle v^2 \rangle \right) \tag{3}$$

Here, V_p is the particle volume, while ρ_f and κ_f are the fluid density and compressibility, respectively. The particle's response to the acoustic field is captured by two dimensionless acoustic contrast factors, f_1 and f_2, which depend on the particle's compressibility (κ_p) and density (ρ_p) relative to the surrounding fluid:

$$f_1 = 1 - \frac{\kappa_p}{\kappa_f} \tag{4}$$

$$f_2 = \frac{2\left(\rho_p - \rho_f\right)}{2\rho_p + \rho_f} \tag{5}$$

The first term in the potential, proportional to f_1, represents the force contribution from the particle's compressibility (a monopole scattering term), while the second term, proportional to f_2, represents the contribution from its density (a dipole scattering term). In a standing wave, which is the most common configuration for cell patterning, the pressure and velocity fields are spatially modulated, creating a periodic potential landscape. In a simple one-dimensional standing wave, this results in a force that can be expressed as:

$$F_{ARF} = -\left(\frac{\pi p_0^2 V_p \kappa_f}{2\lambda} \right) \Phi(\kappa, \rho) \sin(2kx) \tag{6}$$

where p_0 is the pressure amplitude, V_p is the particle volume, λ is the wavelength, x is the position, and Φ is the overall acoustic contrast factor,[74] which combines the effects of compressibility and density differences between the particle and the medium:

$$\Phi(\kappa, \rho) = \frac{5\rho_p - 2\rho_f}{2\rho_p + \rho_f} - \frac{\kappa_p}{\kappa_f} \tag{7}$$

The sign of this contrast factor determines the particle's destination.[39] For most mammalian cells in aqueous media, $\Phi > 0$, causing them to migrate to the pressure nodes (regions of minimum pressure amplitude). Conversely, for less dense and more compressible objects like lipid droplets or gas bubbles, $\Phi < 0$, driving them to the pressure antinodes.

When multiple particles are brought into close proximity by the primary radiation force, inter-particle forces, known as secondary radiation forces or Bjerknes forces, become significant. These forces arise from the acoustic field scattered by one particle acting upon its neighbors. For two pulsating bubbles in an acoustic field, for instance, this interaction force can be attractive or repulsive depending on their relative phase of oscillation, and it scales with the inverse square of the distance between them.[75,76] For cells, these secondary forces are generally attractive and are crucial for promoting the formation of tight, compact multicellular clusters and spheroids.[77] Thus, in most cell patterning applications, it is the dominant role of the ARF that drives cells toward designated positions, establishing it as the primary power source for acoustic actuation.

2.2. Acoustic streaming

In any real fluid, acoustic energy is dissipated through viscosity, leading to a transfer of momentum from the wave to the fluid.[78] This process generates the steady, time-averaged fluid motion known as acoustic streaming.[79] The force exerted by this flow on a particle is a drag force, which

can be harnessed for transport, mixing, and pumping. The general source term for acoustic streaming, F_S, is given by the negative divergence of the Reynolds stress tensor:

$$F_S = -\rho_0 \nabla \cdot \langle \tilde{v} \otimes \tilde{v} \rangle \quad (8)$$

where $\tilde{v}$ is the first-order acoustic velocity field and ρ_0 is the density of the fluid at rest. The specific nature and utility of the resulting flow depend critically on where the acoustic energy is dissipated. For clarity, it is useful to distinguish between different types of streaming phenomena arising from this principle. Theoretically, Eckart streaming arises from thermoviscous dissipation in the bulk of the fluid, far from any boundaries. This typically results in a large-scale, unidirectional flow.

While fundamental, this type of streaming is not the dominant effect in microfluidic devices, where the system size is small and boundary interactions are ubiquitous. In such micro-scale systems, dissipation at solid boundaries is the primary driver of streaming. This gives rise to Schlichting streaming, a flow confined within the thin oscillatory viscous boundary layer adjacent to any surface.[80] This layer has a thickness given by $\delta_v = \sqrt{2\nu / \omega}$, where ν is the kinematic viscosity and ω is the angular frequency. This boundary-layer flow acts as the fundamental engine for the most useful streaming patterns. The shear generated by this engine, in turn, drives a larger-scale, stable flow in the bulk fluid known as Rayleigh streaming.[81]

It is this Rayleigh streaming, often manifesting as stable, counter-rotating vortices, that is most important for practical applications in microfluidics. By precisely engineering the geometry of the channel walls, such as by incorporating sharp edges or trapping microbubbles, researchers can control the location and intensity of the underlying Schlichting streaming.[82] This allows the creation of highly localized and predictable Rayleigh streaming vortices, which serve as powerful micro-tools for trapping, concentrating, and manipulating cells. The drag force exerted by these engineered streaming flows on a small spherical particle is well-described by Stokes' law:

$$F_{drag} = 6\pi\rho_f \nu R v_s \quad (9)$$

where v_s is the relative velocity between the particle and the fluid. The linear dependence of this force on particle radius makes acoustic streaming particularly effective for manipulating larger objects or for size-based sorting applications. This clear distinction between the "engine" (Schlichting) and the "tool" (Rayleigh) provides the physical basis for designing sophisticated acoustofluidic devices. Excellent reviews on detailed mathematical models and acoustic streaming mechanisms are provided by Wiklund *et al.*[79] and Sadhal, respectively.[83]

2.3. Interplay and synergy of forces

ARF and acoustic streaming invariably coexist, and their interplay determines the ultimate trajectory and final position of the target cells. The relative importance of the two forces is strongly dependent on particle size. The ARF scales as R^3 because it is a volume-dependent effect, whereas the streaming-induced drag force scales linearly with the radius R. Consequently, there exists a critical particle size below which streaming effects dominate and above which the radiation force dictates the motion. For a typical 2 MHz system in water, this transition has been shown to occur at a diameter of approximately 2 μm. Most biological cells are larger than this, so the radiation force is often the dominant positioning mechanism, dictated by their intrinsic mechanical properties.[84,85]

However, this is not a universal rule, and the two forces can be synergistically combined to achieve manipulation capabilities that neither could accomplish alone. A prominent strategy involves using large-scale streaming flows to transport cells over long distances into a region of interest, where finely tuned radiation forces then perform precise, short-range patterning. Another powerful synergistic approach has been demonstrated for the assembly of larger biological structures. In these systems, acoustic streaming is engineered to create stable microvortices that gently capture and confine a cellular spheroid, while a carefully configured radiation force field acts as a soft potential well, preventing the spheroid from escaping. This dual-force mechanism enables complex, programmable 3D assembly.[86,87] A clear understanding and deliberate control of the balance between these forces is therefore crucial for designing effective and versatile acoustic lithography systems.

These physical principles map directly onto the application scenarios discussed later. For instance, high-throughput bulk acoustic wave (BAW) cell sorting typically employs the ARF at frequencies in the 1–10 MHz range.[88] High-resolution surface acoustic wave (SAW) patterning also relies on ARF, but at much higher frequencies, often in the sub-gigaHertz range, to achieve finer spatial control.[89] In contrast, localized streaming, which dominates precision trapping and rotation, is often generated at lower frequencies, from the kiloHertz range to a few megaHertz.[90] Volumetric assembly via holography also operates in the 0.5–5 MHz range to balance penetration and resolution,[91,92] while large-area Faraday-wave patterning operates at the very low hydrodynamic frequencies of 10–100 Hz.[93,94]

This section has outlined the fundamental physical principles governing the interaction between acoustic fields and microparticles. The primary mechanisms—ARF and acoustic streaming—provide the foundational toolkit for acoustic lithography. While the diverse patterning methodologies discussed in the subsequent sections may involve more complex, geometry-specific phenomena, their underlying actuation mechanisms are invariably rooted in the interplay of these two principal forces. A clear understanding of these core principles is therefore essential for the rational design and optimization of any acoustic cell manipulation system.

3. Acoustic patterning methodologies

A variety of techniques have been developed to harness acoustic forces for cell patterning, many of which rely on the generation of acoustic standing waves to create force potential landscapes. This section surveys key methodologies based on the complexity of this wave engineering. We begin with foundational techniques like BAW and SAW, which create simple, periodic standing waves. The discussion then progresses to acoustic holography as a powerful extension of this principle, capable of generating complex, arbitrary standing wave fields for user-defined 3D assembly. Finally, we cover two distinct approaches: Faraday waves, which leverage fluid–surface instabilities for large-area patterning, and the novel and flexible approach of localized acoustofluidics, which employs engineered microstreaming for precise, dynamic manipulation.

3.1. Bulk acoustic waves

In acoustofluidic technology, BAW represents a core method with tremendous potential for cell patterning. Its primary working principle involves generating a standing wave field within a fluid-filled cavity: a piezoelectric transducer converts an electrical signal into mechanical vibrations, launching acoustic waves into the fluid. These waves interfere with reflected waves or waves from an opposing transducer, forming a stable standing wave with stationary pressure nodes and antinodes.[95] Cells, driven by the ARF, aggregate at the pressure nodes.[96] The final pattern is dictated by experimental parameters such as wave frequency, device dimensions, and fluid properties, allowing for precise control over cell arrangement.[60]

With the rapid development of cell patterning in biomedical applications, research on BAW technology has produced a series of innovative methods that expand its scope and practicality. For example, a common design for 2D patterning employs two orthogonal pairs of piezoelectric transducers (Figure 2A).[41] By independently controlling the standing waves in each direction, this design allows flexible adjustment of both the orientation and spacing of cellular grid patterns. To achieve more complex arrangements, devices with more intricate transducer configurations have been developed. The heptagonal acoustic tweezer (Figure 2B)[97] is a notable example, using seven transducers whose frequencies and phases can be independently controlled. By activating different combinations, cells can be organized into complex grid-like patterns that meet the requirements for simulating sophisticated biological structures.

To better integrate BAW technology with biomaterial fabrication, methods combining BAW transducers with microfluidic conduits have also been developed. One such approach (Figure 2C)[98] uses a transducer coupled to a glass capillary. The acoustic standing wave pattern cells within a liquid hydrogel precursor, which is then fixed by photopolymerization. This enables the continuous extrusion of hydrogel fibers with embedded, organized cells, providing an effective means for constructing anisotropic tissues such as muscle. Similar research (Figure 2D)[99] has explored how capillary shape influences the acoustic pressure field, enabling the formation of unique radial cell patterns. These patterns can also be fixed within hydrogel fibers or tubules, further enriching the application of BAW technology in biomaterial preparation.

In principle, BAW-based devices are foundational and robust. Their core strength lies in generating acoustic waves that propagate through the entire volume of a fluid-filled chamber, enabling true 3D force fields.[56,100] The versatility of BAW systems has been significantly expanded through these innovative device configurations, making them invaluable tools for both fundamental patterning and applied biofabrication.[101] While BAW systems are robust for 3D patterning, SAW systems, which we discuss next, offer a pathway to higher-resolution, planar manipulation by confining energy to a substrate.

3.2. Surface acoustic waves

SAWs are generated by applying an alternating electrical signal to an interdigital transducer (IDT) fabricated on a piezoelectric substrate. This process creates mechanical waves confined to and propagating along the substrate's surface. The most common type of fluid manipulation is the Rayleigh waves, as its vertical displacement component efficiently leaks acoustic energy into an overlying fluid, whereas other types like shear-horizontal SAWs cannot effectively couple with liquids and are mainly used for sensing applications. When these surface waves leak into a microchannel, they create pressure fields capable of manipulating particles. By precisely adjusting the frequency, phase, and power, and by optimizing the geometry of the IDTs, whose finger width and spacing directly define the

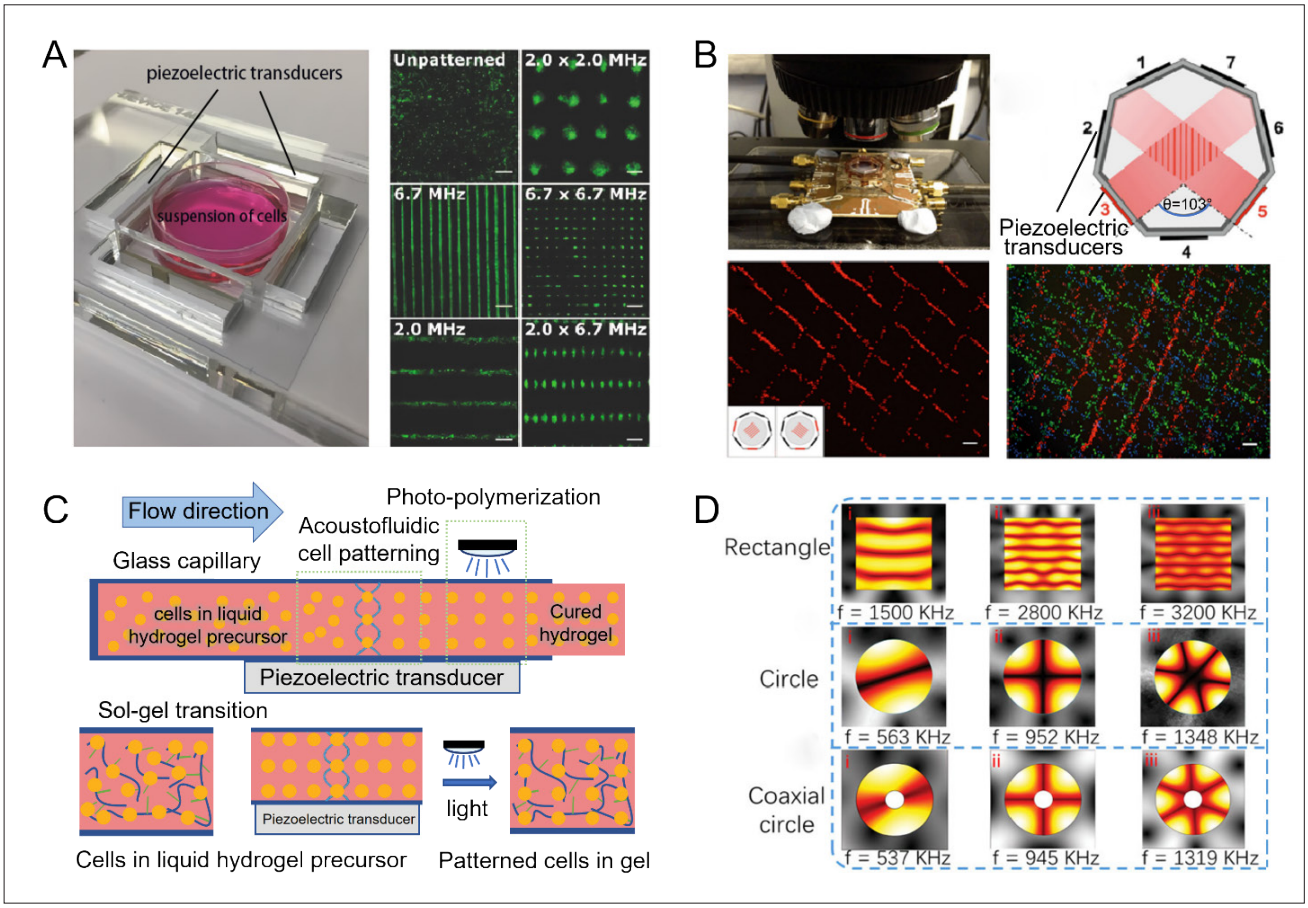


Figure 2. Methodologies for cell patterning using the BAW technology. (A) A 2D patterning device employing orthogonal pairs of piezoelectric transducers to dynamically control the orientation and spacing of cellular grids. Scale: 200 μm. Reprinted from Ref.[41] (B) A heptagonal acoustic tweezer that generates complex, reconfigurable patterns by selectively activating different transducer combinations. Scale: 100 μm. Reprinted from Ref.[97] (C) Integration of BAW with biomaterial fabrication, where a transducer coupled to a glass capillary enables the continuous production of hydrogel fibers with embedded cellular structures. Adapted from Ref.[98] (D) Influence of capillary geometry on the acoustic pressure field, demonstrated through simulations and experimental results of tunable radial cell patterning. Reprinted from Ref.[99] Abbreviations: f, frequency; 2D, two dimensional; BAW, bulk acoustic wave.

acoustic wavelength, acoustic energy can be focused to generate nodes and antinodes for non-invasive trapping, transport, and rotation of cells. A key breakthrough of SAW technology is the miniaturization of acoustic field control: the micron-scale period of lithographically defined IDTs allows for the formation of subwavelength-scale pressure nodes, supporting nanoscale positioning accuracy.[102,103] Furthermore, SAW devices can operate at much higher frequencies (up to ~1 GHz) than typical BAW systems, making them exceptionally well-suited for the high-resolution manipulation of sub-micrometer particles.

The versatility of SAW technology enables diverse device configurations and manipulation strategies. When interdigital IDTs are fabricated on the surface of a piezoelectric substrate and bonded with a microfluidic channel layer made of polydimethylsiloxane, the SAWs excited by a pair of IDTs propagate to the polydimethylsiloxane–piezoelectric interface, where acoustic energy leakage occurs, generating leaky waves. These waves couple upward into the liquid region within the channel, exciting longitudinal acoustic waves in the fluid. When two pairs of IDTs are positioned in the medium, they generate counter-propagating SAWs. The interference of these waves establishes a standing acoustic wave field in the fluid, enabling precise manipulation of microparticles. The ARF induced by this periodic pressure distribution serves as the key physical mechanism for separating particles or cells (Figure 3A).[103] For nanoscale bioparticle separation, a tilted-angle standing SAW system can be configured for continuous, two-stage processing to achieve complex separations. In a representative application for blood component isolation, the first stage removes components larger than 1 μm, such as red blood

cells, white blood cells, and platelets, while the second stage fractionates vesicle subsets. This system has demonstrated the capability to directly isolate exosomes from whole blood at a flow rate of 4 μL/min. A key advantage of this technology is its operational flexibility: the separation process can be actively controlled by switching the acoustic field on or off (Figure 3B).[104]

In cell patterning, when a standing SAW is generated through the interference of counter-propagating waves from opposing IDTs, a 2D grid-like acoustic field composed of multiple pressure nodes is established within the fluid. When the wavelength of the high-frequency SAW is on the same order of magnitude as the cell size (λ ~ D), the intersecting waves form a 2D array of potential wells. This configuration enables highly precise single-cell-per-well patterning (Figure 3C).[30] A significant advancement in SAW-based platforms is the wavenumber-spiral acoustic tweezers, designed for dynamic and reconfigurable cell manipulation. This system employs multiple pairs of centrosymmetrically arranged IDTs that are simultaneously and independently controlled by a single multi-frequency signal. By modulating the signal's frequency, phase, and amplitude, the interference of the resulting multidirectional waves reshapes the acoustic field in real time, overcoming the static limitations of conventional tweezers. This capability enables a suite of powerful functions, including transforming entire cell patterns from one lattice configuration to another and

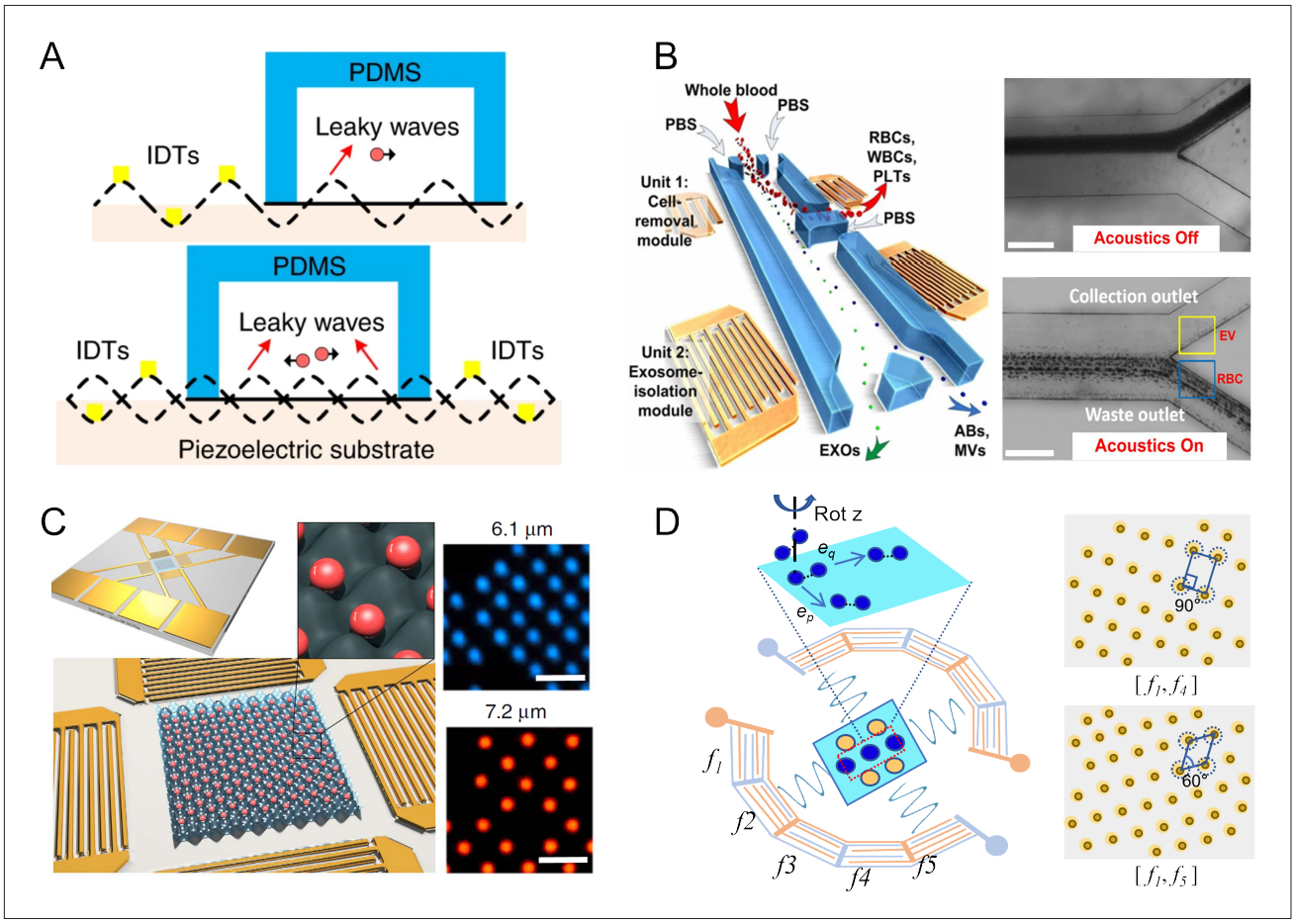


Figure 3. Key methodologies for cell and particle patterning using SAWs. (A) An integrated, two-module acoustofluidic chip for complex separations, where tilted-angle standing SAWs are applied sequentially to remove cells and then isolate nanoscale exosomes from whole blood. Scale: 500 μm. Reprinted from Ref. [103] (B) Massively multiplexed, high-density submicron particle patterning using an array of acoustically oscillating nanocavities as individual trapping sites. Reprinted from Ref. [104] (C) A single-cell patterning method using intersecting high-frequency SAWs with wavelengths comparable to cell diameters to form a 2D grid of single-cell traps. Scale: 30 μm. Reprinted from Ref. [30] (D) Dynamic, reconfigurable manipulation using wave-number spiral acoustic tweezers. Modulation of a multitone excitation signal enables real-time reshaping of acoustic fields to translate patterns or move particles along complex trajectories. Adapted from Ref. [105] Abbreviations: Abs, antibodies; EXOs, exosomes; IDTs, interdigital transducer; MVs, microvesicles; PBS, phosphate-buffered saline; PDMS, polydimethylsiloxane; PLTs, platelets; RBC, red blood cell; WBCs, white blood cells; 2D, two dimensional; SAWs, surface acoustic waves.

precisely guiding individual particles along complex, user-defined trajectories (Figure 3D).[105]

Collectively, these attributes position SAW as a high-precision toolkit within acoustic lithography.[104] Its defining characteristic is the confinement of acoustic energy to the substrate surface, which fundamentally distinguishes it from the volume-based actuation of BAW. This provides higher spatial resolution and facilitates seamless integration with planar microfluidic platforms, making SAW a powerful tool for both precise cell manipulation and integrated sensing.[106–108] While BAW and SAW methods excel at creating periodic or simple geometries, acoustic holography constitutes a significant leap forward, enabling arbitrarily complex, user-defined fields.

3.3 Acoustic holography

Acoustic holography represents a major advance in patterning technology, enabling the creation of arbitrarily complex 3D acoustic fields to engineer cell patterns that mimic natural biological structures. The core principle involves using 3D-printed acoustic holograms or phased-array transducers to precisely control the phase and amplitude of acoustic waves.[109,110] This produces a user-defined complex acoustic field in which cells are guided by radiation forces and acoustic streaming into a preset pattern.[111–113]

Implementation of this principle has evolved through several innovative strategies that progressively enhance spatial and temporal control. The foundational approach utilizes a static, 3D-printed acoustic hologram as a passive phase mask driven by a simple plane-wave transducer (Figure 4A).[54] The hologram's topography encodes phase information, which shapes the wavefront to assemble cells into a 2D pattern. To overcome the "one hologram, one pattern" limitation, a programmable method was developed that uses a single plate to achieve switchable patterning by altering the sound speed of the fluid medium, thus changing the effective wavelength and resulting diffraction pattern (Figure 4B).[114]

Building on these concepts, acoustic holography has been extended into the third dimension to achieve one-step volumetric 3D cell assembly (Figure 4C).[91] This is accomplished by using multiple holograms to collaboratively form a complex pressure field that matches a target 3D shape, enabling the simultaneous aggregation of cells throughout the entire volume and offering a significant advantage over slower, layer-by-layer fabrication methods. For the ultimate level of control, the passive hologram is replaced by a dynamic phased array transducer, which functions as a fully electronic, reconfigurable hologram (Figure 4D).[92] By electronically regulating each array element, complex acoustic fields such as focused vortex beams can be generated and morphed in real-time, enabling sophisticated tasks including the precise positioning and orientation of organoids.

Acoustic holography provides an unparalleled level of control for cell patterning. Its defining advantage is the ability to generate arbitrarily complex, user-defined acoustic energy landscapes,[91] moving far beyond the simple periodic patterns of BAW and SAW. The capacity for one-step volumetric assembly and the transition to fully dynamic phased arrays position acoustic holography as a key enabling technology for advanced applications in organoid construction, complex tissue engineering, and targeted *in vivo* therapies.[53,92] The methods discussed so far—BAW, SAW, and holograms—rely on engineered transducers to shape the sound field. In contrast, the following sections explore two alternative approaches: fluid–surface instabilities, known as Faraday waves, and localized microstreaming.

3.4. Faraday waves

Faraday waves offer a unique method for large-area patterning based on fluid-surface instabilities.[115] These are nonlinear standing waves that spontaneously form on the surface of a fluid subjected to vertical vibration when the driving intensity exceeds a critical threshold.[116] The initially flat surface transforms into a regular pattern of crests and troughs. The core principle for cell patterning lies in harnessing the hydrodynamic forces generated by these waves, such as acoustic streaming and pressure gradients, to drive the directional migration and aggregation of suspended cells into patterns that mirror the underlying wave structure.[117,118]

The practical application of this phenomenon has been demonstrated through several key strategies. A typical setup involves a chamber containing the cell suspension mounted on a vertical shaker (Figure 5A).[93] As the chamber vibrates, periodic standing waves form, and suspended particles migrate to the nodal regions, producing a large-area, periodic pattern. This platform has been used to investigate the differential assembly of cells based on their intrinsic physical properties (Figure 5B).[119] By leveraging subtle differences in size and density, various cell types can be spatially segregated, enabling structured co-culture arrangements. To extend this inherently 2D technique into the third dimension, a layer-by-layer assembly method has been explored (Figure 5C).[94] In this approach, a thin layer of cell-laden hydrogel is patterned and then rapidly polymerized, and by repeating this process, complex 3D cellular constructs with defined geometries can be fabricated.

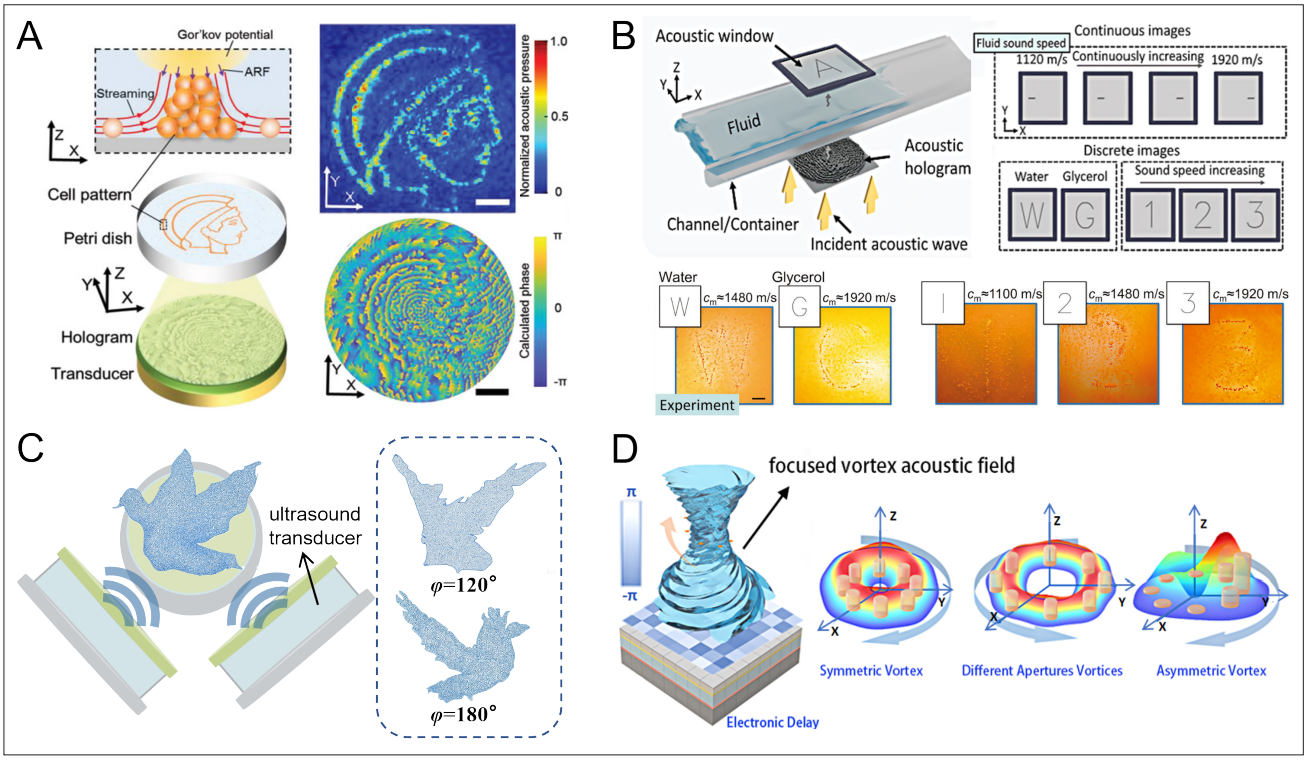


Figure 4. Strategies for cell patterning using acoustic holography. (A) Static 2D patterning using a 3D-printed hologram as a passive phase mask for planar wavefront shaping. Scale: 5 mm. Reprinted from Ref.[54] (B) Reconfigurable patterning from a single hologram achieved by modulating the sound speed of the intervening medium, thereby altering the resulting diffraction pattern. Reprinted from Ref.[114] (C) One-step volumetric assembly of 3D structures using multiple holograms to collaboratively shape a complex acoustic field. Adapted from Ref.[91] (D) Dynamic patterning and manipulation using an ultrasonic phased array acting as an electronic, reconfigurable hologram capable of generating complex acoustic fields in real time. Reprinted from Ref.[92] Abbreviation: ARF, acoustic radiation force.

Faraday-wave-driven patterning stands apart from other acoustic methods because it reliance on a macroscopic fluid instability rather than direct acoustic–particle interactions within the bulk fluid. Its primary advantages are the simplicity of the setup and its intrinsic capacity to generate highly ordered, large-area periodic patterns without complex transducers.[120] Although its resolution may not match that of high-frequency techniques, its scalability makes it a valuable tool for applications requiring large, uniform cellular arrays and for fundamental studies of pattern formation.[38]

3.5. Acoustofluidics using localized phenomena

While many methods rely on global, chamber-scale acoustic fields, a significant branch of acoustofluidics leverages highly localized phenomena for precision manipulation.[121] Instead of creating large-scale standing waves, these devices use micro-machined features such as sharp edges or oscillating microbubbles that act as active acoustic actuators. When a global acoustic field is applied, these microstructures become sites of intense energy dissipation, generating stable and highly localized microvortices via acoustic streaming.[39,45] These well-defined vortices serve as non-contact micro-tools for trapping, concentrating, and rotating individual cells or small clusters with exceptional precision.[5,122]

This approach is particularly powerful for single-cell analysis and precision fluid control. For instance, one method for single-cell extraction uses a spiral array of micropillars. When subjected to circular vibration, this array generates a global whirling flow that transports cells toward a central trapping mechanism made of a thermo-responsive gel, which can then capture and release a single cell through temperature modulation (Figure 6A).[123] Another powerful technique achieves highly localized manipulation using 3D-printed, subwavelength micro-resonators. These mass-spring structures are driven into resonance by a global BAW, generating intense, localized acoustic fields that trap nearby particles. Because these resonators can be arranged into arbitrary patterns, this method enables the coordinated assembly of particles into complex, user-defined shapes, such as letters and logos (Figure 6B).[124] A versatile platform for dynamic control is the reconfigurable acoustofluidic metasurface, a passive

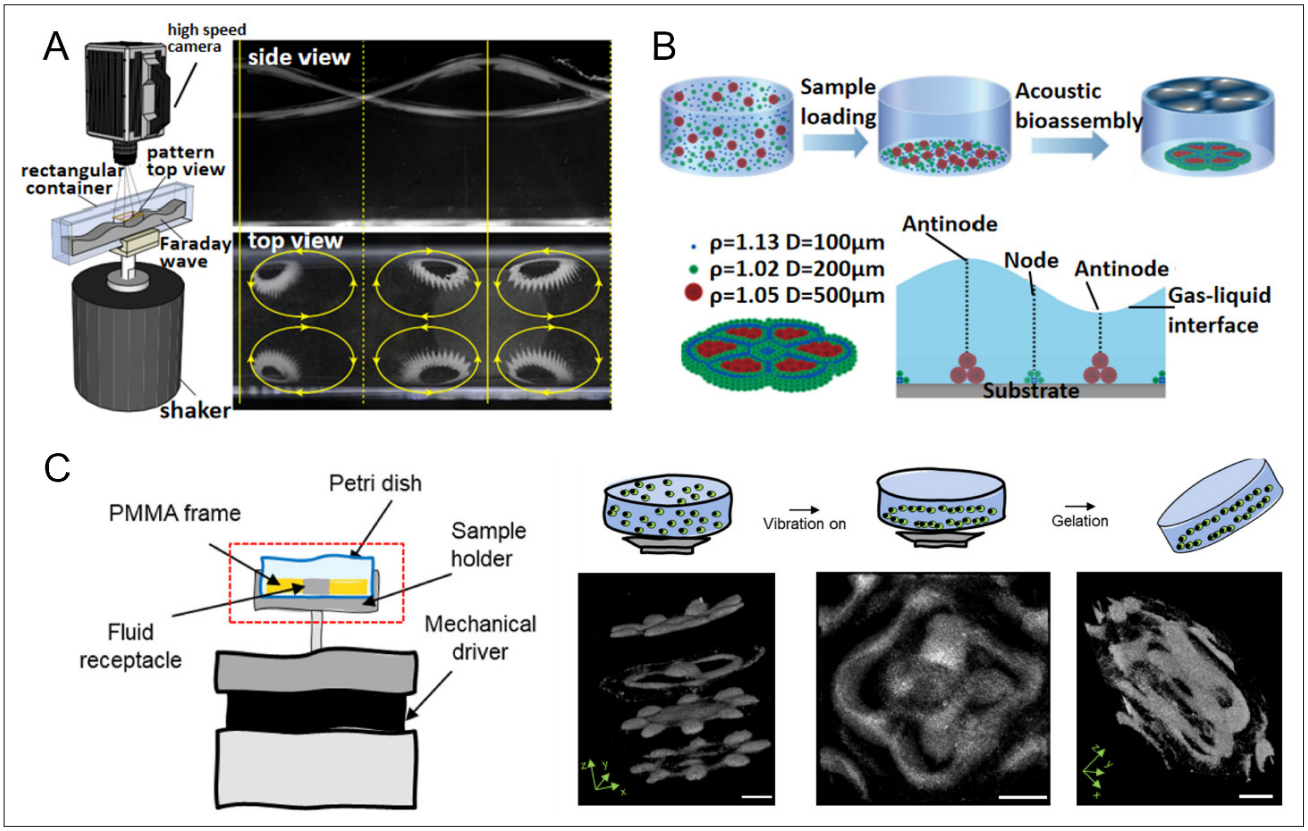


Figure 5. Principles and applications of cell patterning using Faraday waves. (A) Fundamental mechanism: vertical vibration of a fluid interface generates periodic standing waves. Reprinted from Ref. [93] The Faraday wave setup consists of a rectangular acrylic container (26.5 × 280 × 55 mm) connected to a vertical electromechanical shaker. (B) Differential bioassembly showing spatial segregation of heterogeneous cell populations based on intrinsic physical properties. Reprinted from Ref. [119] (C) Layer-by-layer fabrication strategy of 3D cellular constructs, shown with a computed tomography reconstruction of a multi-layered assembly. Scale: 3mm. Reprinted from Ref. [94] Abbreviation: PMMA, polymethyl methacrylate.

array of membrane resonators that generates localized, subwavelength standing waves. By tuning the frequency and phase of an external far-field acoustic source, the trapping field can be reshaped in real-time to enable not only collective patterning but also the precise translation and rotation of individual particles (Figure 6C).[125] Acoustic streaming can also be engineered for complex, multi-degree-of-freedom manipulations in 3D space, rooted in the precise control of 3D fluid phenomena.[126] By oscillating a single bubble trapped at a micropipette tip, a highly controllable 3D vortex is formed, which can serve as an acoustic "hand" for non-contact trapping, rotation, and cross-planar transport of objects ranging from single cells to spheroids (Figure 6D).[90]

Acoustofluidics based on localized phenomena provides a complementary toolkit to global-field techniques.[127] The primary advantage of this streaming-dominated approach is the unparalleled control it offers at the single-cell and small-volume scale. By engineering microfeatures to act as local actuators,[128–130] researchers can create dynamic, on-demand fluidic operations using simple external acoustic fields, making this an indispensable technology for single-cell genomics, rare-cell isolation, and point-of-care diagnostics.[131]

The diverse methodologies surveyed in this section—each leveraging acoustic phenomena in a unique manner—collectively form the versatile toolkit of acoustic lithography. To provide a clear comparative overview, the distinct characteristics and operational trade-offs of these principal techniques are summarized in Table 1. This synthesis highlights a clear progression in the field, moving from the generation of simple, periodic patterns using global resonance phenomena (BAW and Faraday waves) toward increasingly sophisticated and reconfigurable control over cellular organization. SAW technology represents a pivotal step in this evolution, offering higher resolution and seamless integration with microfluidic systems by confining energy to a substrate surface. This

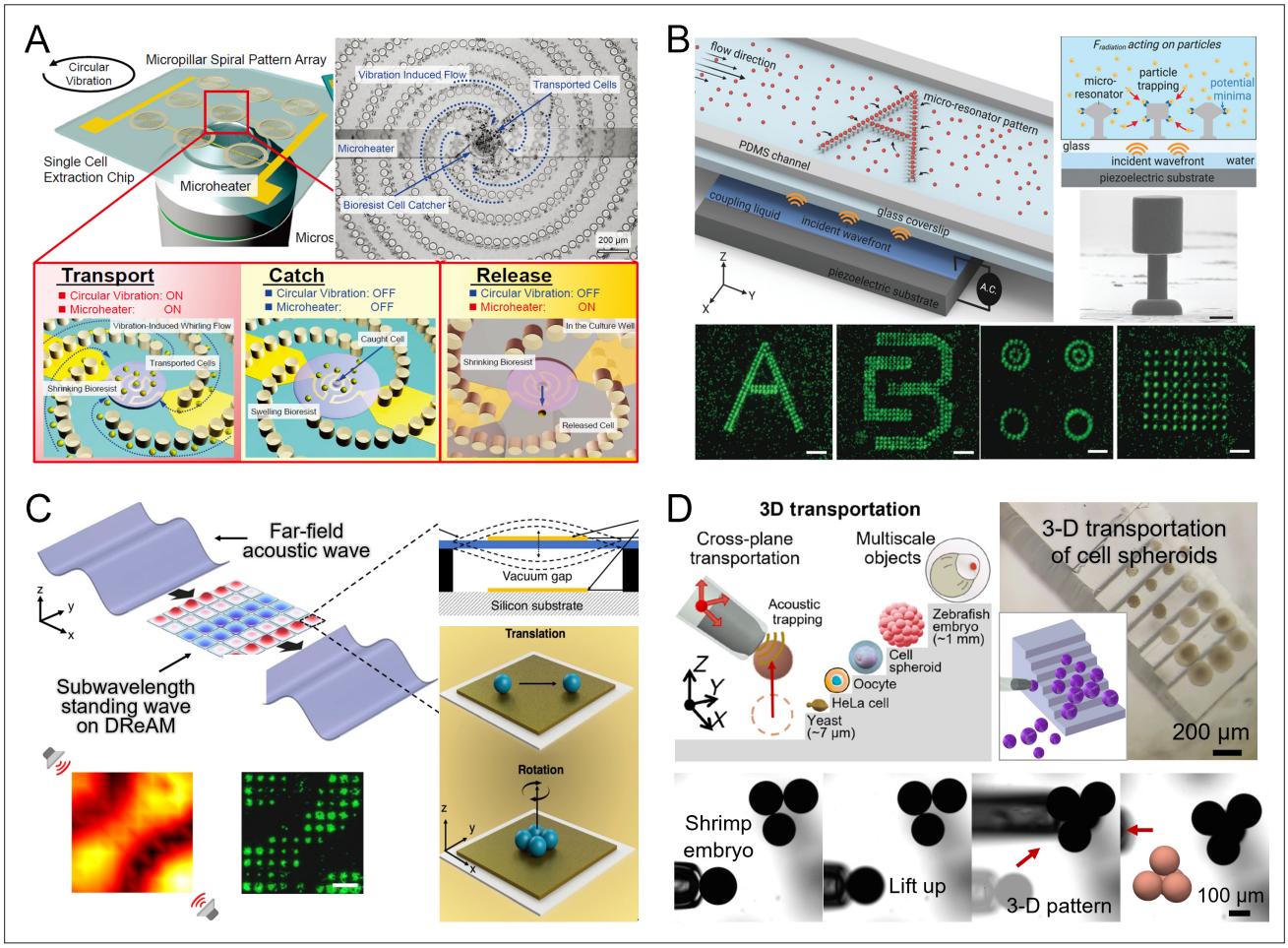


Figure 6. Precision microscale manipulation using localized acoustofluidic phenomena. (A) A single-cell extraction chip employing vibration-induced whirling flow from a spiral micropillar array for cell transport, combined with a thermo-responsive gel for capture and release. Reprinted from Ref. [123] (B) 3D acoustofluidics using sub-wavelength micro-resonators, where a global acoustic wave drives 3D-printed structures into resonance to create highly localized fields for trapping and assembling particles into arbitrary, user-defined patterns. Scale: 100 μm. Reprinted from Ref. [124] (C) A dynamically reconfigurable acoustofluidic metasurface that generates localized standing waves. Frequency and phase tuning reshape trapping patterns in real-time to enable particle translation and rotation. Scale: 200 μm. Reprinted from Ref. [125] (D) The μSonic-hand technique, in which an oscillating bubble at a pipette tip generates a controllable 3D vortex for complex manipulations including cross-planar cell transport. Reprinted with permission from Ref. [90] Copyright © 2025, American Association for the Advancement of Science. Abbreviations: DReAM, dynamically reconfigurable acoustofluidic metasurface; *F*, frequency; PDMS, polydimethylsiloxane.

enables more complex, yet still largely 2D, patterning capabilities. Acoustic holography offers a fundamentally new approach, moving beyond the constraints of device geometry to generate arbitrarily complex and, through phased arrays, fully dynamic 3D acoustic fields, providing unparalleled control over volumetric cell assembly.

Complementing these radiation-force-dominant methods, acoustofluidics based on localized streaming phenomena capitalizes on engineered microstructures to convert global acoustic fields into precise microscale fluidic operations. This approach excels in high-precision single-cell manipulation rather than large-scale patterning. The choice among these methods is therefore dictated by a balance of required resolution, desired pattern complexity, throughput, and the scale of the intended biological construct—reflecting a trade-off between the large-area patterning capabilities of simpler systems and the high-precision, dynamic control offered by more advanced technologies. Having established this diverse technological toolkit, researchers are now positioned to address key challenges across bio-systems engineering, as explored in the following section.

Table 1. Comparison of acoustic patterning methodologies

Methods	Characteristics	Resolution	Reconfigurability	Throughput	Typical applications
BAW	Generates strong volumetric force fields; pattern complexity limited by device resonance	Moderate (typically >100 μm)	Low: Produces simple, periodic 1D or 2D patterns (lines, grids); limited tuning via frequency changes	High	High-throughput cell alignment, patterned hydrogel fiber fabrication, cell washing
SAW	High resolution and microfluidic-compatible; energy confined near the surface	High (micron to sub-micron)	Moderate: Enables complex 2D patterns; dynamically reconfigurable with multiple IDTs	Scalable	Single-cell tweezers, dynamic pattern generation, biosensing
Acoustic holography	Allows arbitrary, user-defined 3D field shaping; complex dynamic control	High (wavelength-dependent)	High: Supports arbitrary 2D and 3D patterns; fully reconfigurable with phased arrays	Moderate to high	Complex tissue engineering, organoid assembly, targeted cell therapy delivery
Faraday waves	Simple, scalable, large-area patterning; limited to low-resolution periodic patterns	Low (mm to cm scale)	Low: produces large-area periodic patterns (squares, hexagons) with limited reconfigurability	High	Fundamental fluid physics studies, periodic cellular array creation, materials assembly
Acousto-fluidics	Enables high-precision single-cell manipulation; unsuited for large-scale patterning	Very high (single-cell level)	N/A	Low to moderate	Cell/particle sorting, focusing, single-cell analysis, rare-cell isolation

Abbreviations: BAW, bulk acoustic wave; IDTs, interdigital transducers; N/A, not available; SAW, surface acoustic wave.

4. Applications in bio-systems engineering

The fundamental physical principles of acoustic lithography, namely, its ability to exert gentle forces in a tag-free manner, make it an exceptionally versatile tool for bio-systems engineering. By preserving cell viability and native physiological states, this technology directly addresses the core limitations of many conventional manipulation techniques, propelling its adoption across a wide spectrum of applications. This section reviews the remarkable impact of acoustic lithography, tracing its evolution from foundational research tools to complex, multi-component systems with direct translational relevance. We survey its applications in foundational cell analysis, the engineering of biomimetic co-culture systems, advanced biofabrication, and its pivotal role in high-throughput sorting for clinical diagnostics, thereby illustrating how precise physical control can be translated into sophisticated biological function. The section concludes with an engineering perspective that synthesizes these applications, illustrating the conceptual progression from simple structural patterning to the sophisticated regulation of biological function.

4.1. Cell manipulation and analysis

As the fundamental units of life, the structure, function, and behavior of cells are directly linked to key biomedical questions concerning physiological regulation, disease mechanisms, and drug responses. Precise and efficient cellular analysis is therefore essential. It not only advances our understanding of fundamental life processes but is also critical to evaluating novel therapeutics, elucidating complex systemic interactions, and improving clinical prognostics in precision and regenerative medicine.[132–135] While traditional methods are often limited in precision, throughput, or biomimetic capabilities, acoustic techniques offer innovative solutions by leveraging their non-invasive, label-free, and dynamically controllable characteristics.[136] For instance, acoustic tweezers have become powerful tools for probing biophysical properties at a fundamental level through applications like force spectroscopy.[137] By trapping and applying piconewton-level forces to microbeads attached to a single molecule, these systems enable high-throughput measurements of molecular interactions.[138] Furthermore, localized acoustic streaming can precisely rotate single cells, facilitating multi-angle 3D imaging or detailed studies of cellular mechanics.

These foundational capabilities are increasingly integrated into sophisticated microfluidic platforms to achieve complex analytical tasks. A prominent application is sheathless particle separation, which addresses a key limitation of many flow-based sorting systems.[139] One such device employs a two-stage microfluidic design: standing SAWs first focus a mixed population of particles into a single stream without requiring sheath flow, thereby avoiding sample dilution and system complexity.[140,141]

In the second stage, the aligned particles are exposed to a different acoustic field that drives them toward off-center pressure nodes, enabling size-based separation into multiple collection outlets (Figure 7A).[142] This integrated approach provides a basis for high-throughput, contact-free sorting of cells and exosomes. Beyond sorting, acoustic energy has been incorporated into culture platforms for biofabrication.[143] Standing SAWs have been used to rapidly form cell spheroids for applications such as bioinks. This method has been shown to be highly biocompatible: cells patterned using both low-frequency (10.4 MHz) and high-frequency (23.8 MHz) excitation maintained viability above 90% for up to 7 days, with no statistical difference from the unmanipulated control groups, confirming the safety of the patterning process (Figure 7B).[140]

Furthermore, acoustic levitation has been developed into a robust, scaffold-free method for long-term 3D cell culture. Multi-trap acoustic levitation platforms can produce and maintain hundreds of uniform mesenchymal stem cell spheroids in parallel for over 24 hours (Figure 7C).[144] Cells in these levitated spheroids remain viable, maintain their characteristic surface markers, and exhibit a higher differentiation capacity compared to standard 2D cultures, highlighting the technology's potential for creating highly biomimetic models for drug screening and tissue engineering. To quantify this enhanced potential, Guo *et al.* applied programmable acoustic stimulation at varying power levels (300, 400, and 500 mW) to mesenchymal stem cell spheroids (Figure 7D).[145] Fluorescence images of the stimulated cells and analysis of molecular uptake, such as doxorubicin, showed a clear power-dependent effect. Their results confirm that precisely manipulating mechanical forces and inducing cell deformation via acoustic streaming enables controlled modulation of cell membrane permeability. This provides a promising new tool for drug delivery and cell therapy.

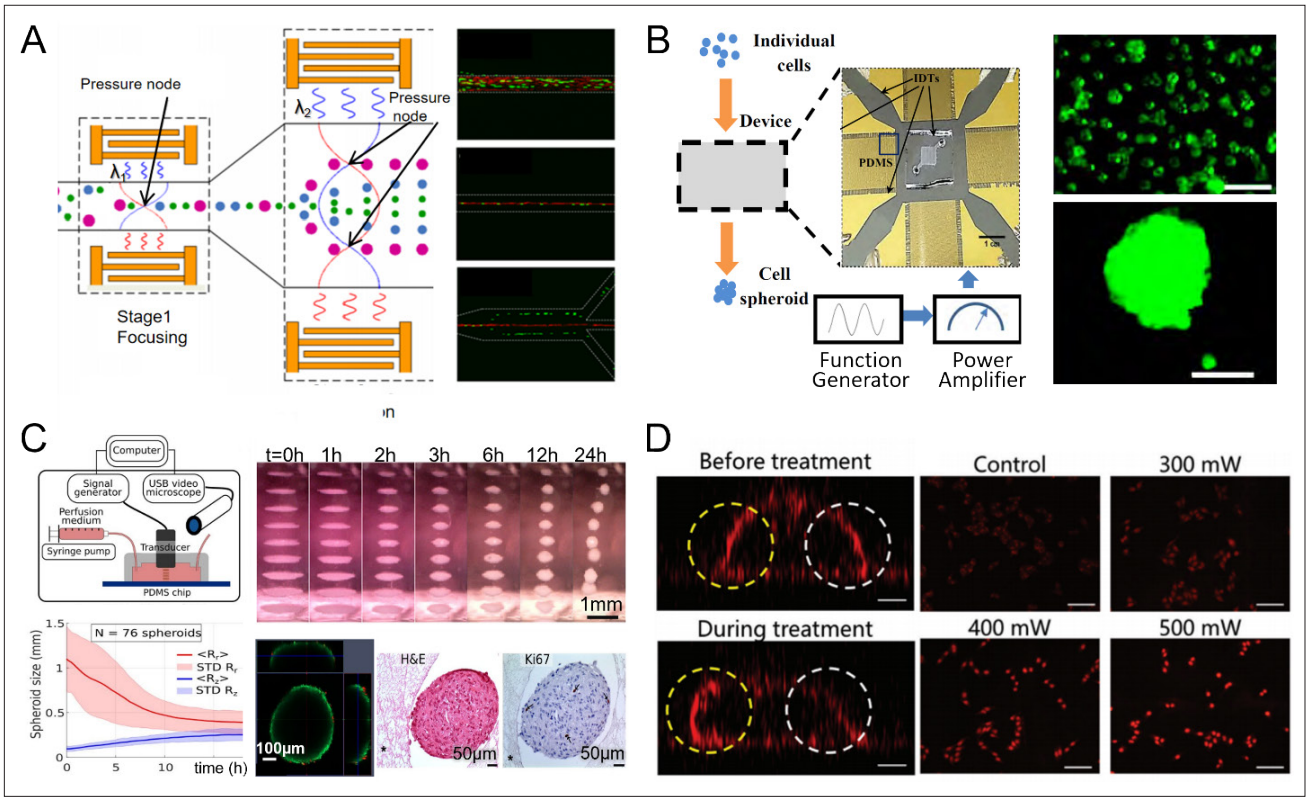


Figure 7. Acoustofluidic cell sorting and spheroid culture. (A) A two-stage surface acoustic wave (SAW) sorting strategy using wavelength switching for size-based separation. Fluorescent images show the distribution of 10 μm (green) and 3 μm (red) particles. Reprinted from Ref.[142] (B) Demonstration of high biocompatibility during spheroid formation with standing SAWs; viability remains above 90% at both low and high frequencies, comparable to controls. Scale: 20 μm. Reprinted from Ref.[140] (C) On-chip formation and functional characterization of viable, proliferative spheroids, including quantitative growth curves and histological analysis. Scale: 1 mm, 100 μm, and 50 μm, respectively. Reprinted from Ref.[144] (D) Programmable acoustic streaming applied to cells at varying power levels to modulate membrane permeability. Representative fluorescence images show power-dependent uptake of doxorubicin, demonstrating that acoustic stimulation can control intracellular transport. Scale: 5 μm. Reprinted from Ref.[145] Abbreviation: PDMS, polydimethylsiloxane.

4.2. Engineering co-culture systems

In vitro cell culture is essential for applications such as drug screening and the study of cell–cell interactions.[146] However, traditional monocultures fail to replicate the complex *in vivo* environment, where cells interact with neighboring cells, the extracellular matrix, and soluble biochemical factors. Co-culture systems, which incorporate two or more distinct cell types, partially address this limitation and are crucial for studying heterotypic interactions.[147]

Nevertheless, conventional co-culture methods often lack sufficient spatial control and microenvironmental regulation, making it difficult to replicate the dynamic interplay found in tissues such as the tumor microenvironment. Acoustic technology offers a novel solution to these challenges.[148] Its non-contact, biocompatible, and highly adjustable nature enables the precise spatial arrangement of multiple cell types and the dynamic regulation of the microenvironment,[149] providing a technical foundation for constructing highly biomimetic co-culture systems.[150] This engineering capability allows for the creation of specific 3D configurations, such as core–shell structures that mimic vascularized tissues, by sequentially patterning different cell types.[151,152]

Recent advancements have demonstrated the power of acoustics in constructing sophisticated co-culture models that more faithfully recapitulate physiological and pathological conditions.[153,154] In one approach to simulate tumor–immune interactions, tumor cells are first mixed with an acoustic virtual 3D scaffold hydrogel to promote self-assembly into tumor-like tissues, which are then co-cultured with T cells (Figure 8A).[155] Further, acoustic trapping technology can overcome the spatial limitations of traditional methods by precisely assembling tumor, immune, and stromal cells into 3D multicellular clusters (Figure 8B).[156] This system facilitates direct drug treatment within a biomimetic microenvironment and allows real-time monitoring of tumor cell survival, creating an efficient platform for rapidly screening personalized drug regimens.

Acoustic streaming effects can also be harnessed to dynamically regulate the culture environment by enhancing convective transport. For example, in a vascular co-culture model, the application of acoustic streaming improved barrier function—as evidenced by a 50% reduction in macromolecular leakage (Figure 8C)[157]—by promoting the diffusion of paracrine factors that strengthen cell junctions. Moreover, standing SAWs have been applied to fabricate functional therapeutic tissues that mimic the structure of natural vasculature. In this application, endothelial cells and adipose stem cells are co-aligned into 3D collateral cylindroids within a biocompatible hydrogel. This precise acoustophoretic patterning enhances cell–cell contacts and the secretion of angiogenic and anti-inflammatory factors, which, when tested in an *in vivo* ischemia model, lead to remarkable recovery of damaged tissue (Figure 8D).[89] This enhanced function arises because the acoustic field can act as a surrogate for the *in vivo* mechanical microenvironment: by physically condensing cells, the acoustic force promotes the critical cell–cell interactions and paracrine signaling essential for tissue maturation and function.

4.3. Biofabrication and tissue engineering

The construction of functional tissues and organs is a critical goal in biomedicine,[158] aimed at addressing organ transplant shortages and advancing disease modeling.[159] Tissue engineering combines biomaterials, cells, and growth factors to repair or replace damaged tissues. However, traditional methods often struggle to create complex structures, facing issues like uneven cell distribution and inefficient nutrient delivery.[160]

Acoustic technology, with its non-invasive and tunable properties, offers new methodologies to overcome these limitations. It enables the precise, contactless assembly of cells and biomaterials into organized structures, facilitating the fabrication of tissues that better mimic native complexity.[161,162] This has been demonstrated in the creation of functional tissues such as anisotropic muscle fibers and aligned cardiac tissue, where cellular organization is critical for function.[163] A key challenge in engineered tissues is vascularization; acoustic patterning has proven highly effective at organizing endothelial cells into predefined networks within scaffolds, significantly enhancing their integration with host vasculature upon implantation.[164]

The versatility of acoustic biofabrication is highlighted by its diverse applications across tissue types and fabrication strategies. A significant innovation is the integration of acoustics with volumetric 3D printing, a method termed SonoPrint. This technique first employs an acoustic standing wave field to organize reinforcement particles into complex, user-defined patterns—such as parallel lines, hexagons, or polygons—within a photosensitive liquid resin. A volumetric printer then solidifies the entire 3D structure simultaneously by projecting a series of patterned light images onto the rotating vial. This approach fabricates a complete composite object within minutes, embedding the preformed acoustic pattern throughout the volume and enhancing the final structure's mechanical properties (Figure 9A).[165]

Subsequent polymerization of the surrounding gel fixes the configuration, allowing the cells to proliferate and form hollow tubular structures that mimic blood vessels or nerve bundles. In another application, ultrasonic standing waves

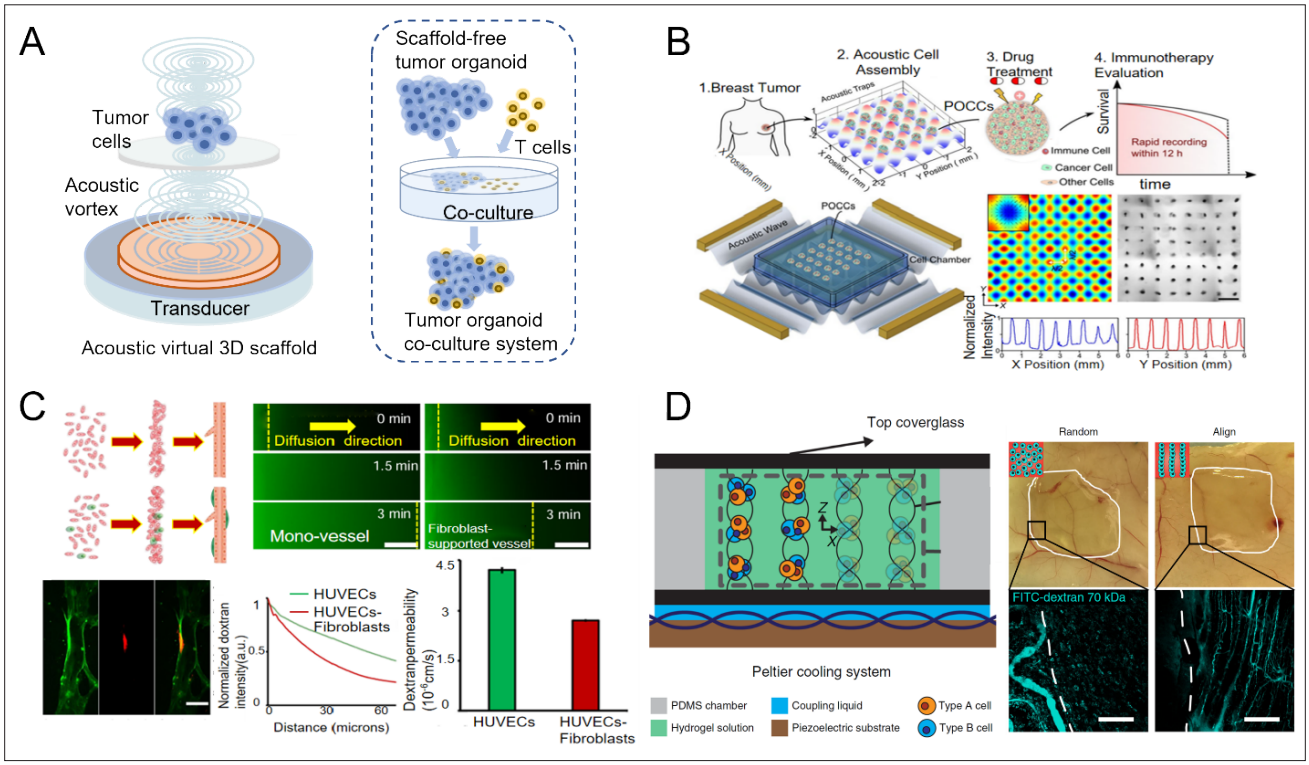


Figure 8. Acoustically engineered biomimetic co-culture models for advanced tissue microenvironment studies. (A) Tumor organoid formation via acoustic-assisted self-assembly in AV-Scaf hydrogel. Adapted from Ref. [155] (B) High-throughput tumor-immune droplet platform for real-time cytotoxicity screening and drug testing. Reprinted from Ref. [156] (C) Acoustic streaming enhances vascular barrier function in an endothelial–fibroblast co-culture model, demonstrated by reduced macromolecular leakage. Scale: 1 mm. Reprinted from Ref. [157] (D) High-resolution 3D cell patterning to construct functional vascular tissue: standing surface acoustic waves co-align endothelial and stem cells into therapeutic cylindroids within a hydrogel, restoring function in a mouse ischemia model. Scale: 200 μm. Reprinted from Ref. [89] Abbreviations: AV-Scaf, acoustic virtual 3D scaffold; FITC, fluorescein isothiocyanate; PDMS, polydimethylsiloxane; POCCs, primary tumor-derived organotypic cell clusters.

have been used to manipulate chondrocytes in an agarose solution, guiding them into a radially layered structure that recapitulates the zoned structure of natural cartilage (Figure 9B).[166] After thermal gelation and *in vitro* culture, this process yields engineered cartilage with a distinct, biomimetic organization. ARF also provides a flexible strategy for patterning cells suspended in a photosensitive hydrogel precursor into complex arrangements like stripes or arrays, which are subsequently fixed through UV-induced polymerization (Figure 9C).[98]

Significant advances in precision patterning are also being made through analytically driven holographic methods. A prime example is acoustography, which uses analytically designed IDTs to generate intricate, configurable 3D acoustic fields based on orbital angular momentum beams (Figure 9D).[167] This platform achieves enhanced resolution with a pixel size of ~25 μm and has been used to pattern microparticles into complex 3D structures, such as a triple helix, and to manipulate DNA carriers. This approach represents a move toward high-fidelity, configurable patterning for advanced biofabrication. Another distinct concept in acoustic additive manufacturing is holographic direct sound printing, in which acoustic holograms induce sonochemical polymerization for rapid, remote fabrication through barriers.[168]

4.4. Sorting for clinical applications

Cell separation and sorting are indispensable processes in biomedical applications, including diagnostics and therapeutics.[169–171] This is particularly crucial in oncology, where the isolation of rare circulating tumor cells (CTCs) from blood provides invaluable insight into a patient's disease status.[172–174] The extreme rarity of CTCs necessitates separation methods that are not only highly efficient and pure but also gentle enough to preserve cell viability for downstream analyses such as drug sensitivity testing and *in vitro* expansion. In this context, acoustic patterning has emerged as a robust, label-free strategy for CTC isolation that maintains high cell viability and supports high-throughput processing.

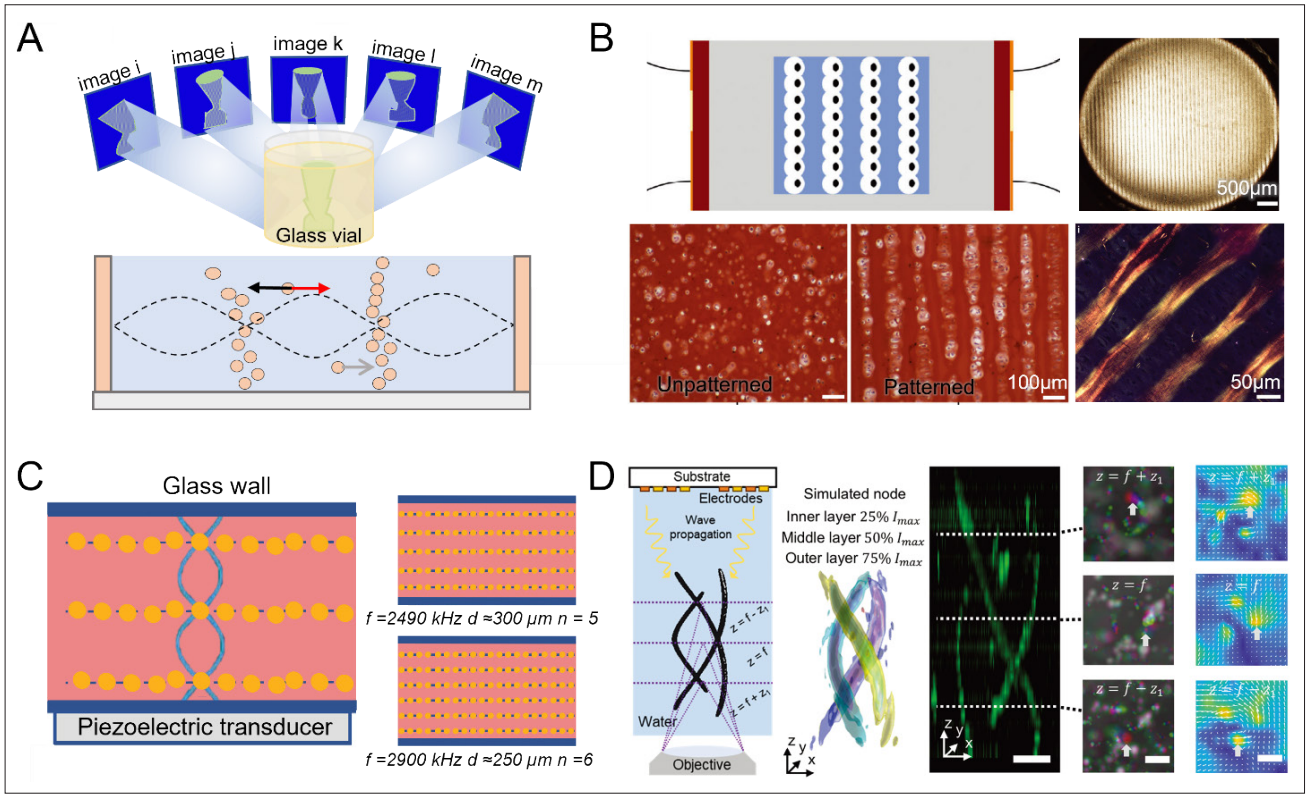


Figure 9. Advanced biofabrication strategies for tissue engineering using physical fields. (A) SonoPrint: an acoustically assisted volumetric 3D-printing method in which an acoustic field first patterns reinforcement particles within a photosensitive resin before simultaneous polymerization to produce mechanically enhanced composites. Adapted from Ref. [165] (B) Ultrasound standing-wave patterning of chondrocytes in agarose followed by thermal gelation to create structured cartilage. Reprinted from Ref. [166] (C) Patterned cell organization within a phase-changeable hydrogel for constructing 2D and 3D tissue models. Adapted from Ref. [98] (D) Advanced 3D acoustography using the BEACON platform, demonstrating correspondence between a simulated 3D triple-helix acoustic trap and experimentally patterned microparticles (captured using confocal microscopy). The technology uses an analytically designed interdigital transducer to generate complex, reconfigurable acoustic fields. Scale: 100 μm. Reprinted from Ref. [167] Abbreviations: BEACON, beam engineering and acoustic control node; *d*, diameter; *f*, frequency.

A variety of acoustic platforms have been developed to meet this clinical need, each leveraging a distinct strategy to isolate CTCs from the much more numerous blood cells. One prominent BAW-based approach utilizes a two-stage acoustic process within a microfluidic chip. First, a high-frequency pre-focusing wave aligns all cells into a single band. Subsequently, a lower-frequency separation field exploits intrinsic differences in cell size, density, and compressibility; the larger CTCs migrate more rapidly toward the central pressure node for collection, while smaller blood cells are carried away. This method has successfully enriched CTCs from whole blood with higher sensitivity than commercial platforms, providing a new liquid biopsy tool (Figure 10A).[175]

Another strategy employs a two-step acoustophoretic method designed for processing whole blood after red blood cell lysis. An initial acoustophoresis step enriches a population of CTCs based on their acoustic properties, followed by a secondary purification step that uses antibody-functionalized particles to deplete residual leukocytes via negative selection. This gentle, contact-free approach delivers viable cancer cells suitable for *in vitro* culture, paving the way for personalized therapeutic strategies (Figure 10B).[176]

Innovation has also come from hybridizing acoustic forces with other physical principles. One multistage platform combines inertial and acoustic forces: a helical microchannel first uses inertial forces to pre-focus the cells, after which the cells enter a straight segment where a SAW field generates multiple pressure nodal lines. Cells are then captured and aligned on these lines according to their diameter, achieving rapid separation of CTCs, leukocytes, and erythrocytes (Figure 10C).[88] To further enhance capture efficiency, other platforms have applied an alternating-frequency acoustic field to a piezoceramic microfluidic chip. This approach has successfully isolated cancer cells from various tumor origins with a capture efficiency exceeding 94% and has been validated on patient

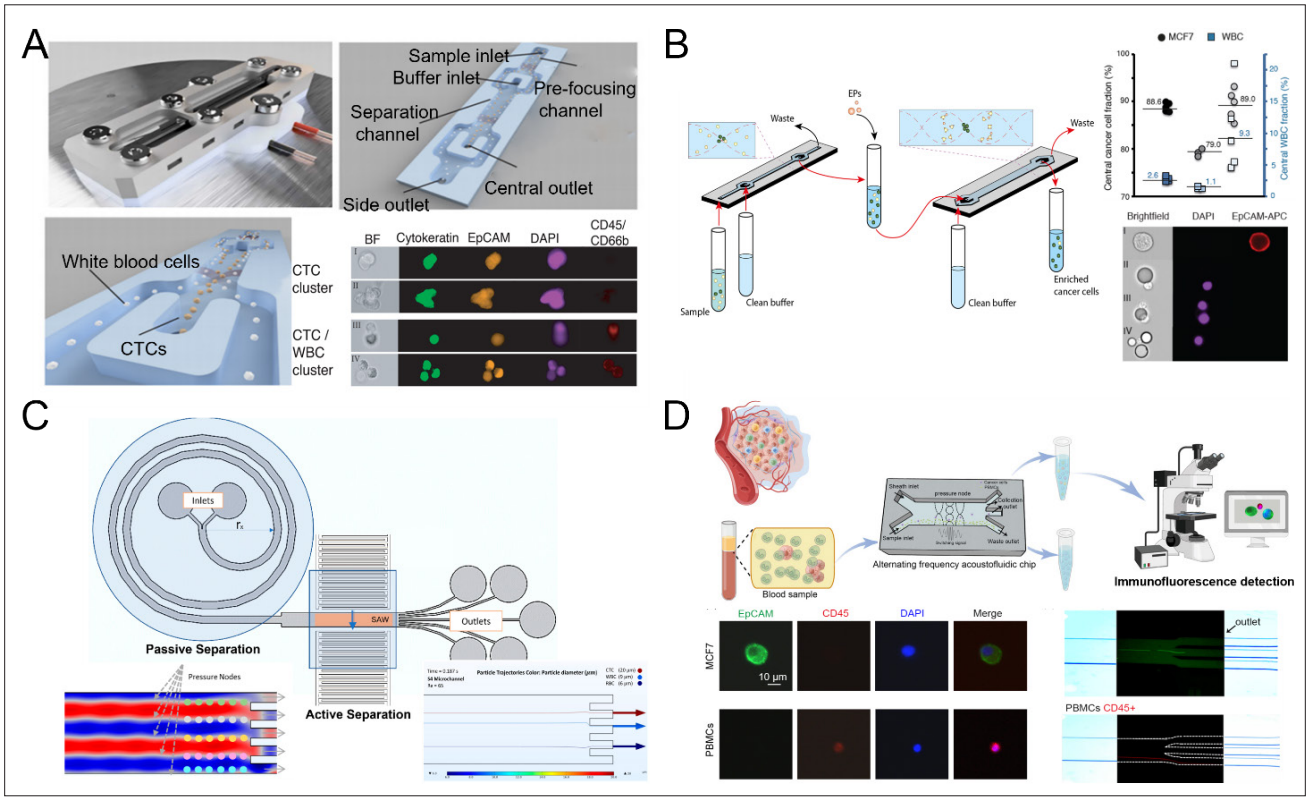


Figure 10. Acoustofluidic platforms for clinical cell sorting. (A) Illustration of the acoustofluidic microchip and the cell separation principle. The device features an initial prefocusing channel (20 mm × 300 μm × 150 μm) for cell aggregation. Reprinted from Ref. [175] (B) A two-step acoustophoresis method for separating live tumor cells from whole blood, utilizing a microchannel with dimensions of 30 mm × 380 μm × 150 μm. Reprinted from Ref. [176] (C) Schematic of a hybrid spiral microfluidic platform combining passive and active IDT components for cell focusing and separation. Reprinted from Ref. [88] (D) Schematic diagram of the separation process in an alternating frequency acoustofluidic chip. Scale: 10 μm. Reprinted from Ref. [177] Abbreviations: APC, allophycocyanin; BF, bright field; CD, cluster of differentiation; CTCs, circulating tumor cells; DAPI, 4',6-diamidino-2-phenylindole; EpCAM, epithelial cell adhesion molecule; PBMCs, peripheral blood mononuclear cells; WBC, white blood cell; n.s., no significance

samples spanning different cancer types. A key advantage of this method is that effective separation is achieved even when CTCs and other blood cells exhibit similar sizes. These examples collectively underscore the significant clinical potential of acoustic lithography as a robust and versatile liquid-biopsy tool for oncology and, more broadly, for applications such as non-invasive prenatal diagnostics and stem cell therapies (Figure 10D).[177] The high viability preserved in these sorting applications is a key advantage, stemming directly from the technology's mechanism: acoustic forces are inherently gentle, label-free, and operate in native physiological media, avoiding the high shear stresses or harsh chemical treatments of many other sorting methods.

4.5. Considerations for bio-systems engineering

A critical challenge for bio-systems engineering is translating these dynamic patterning methods into stable, functional constructs without compromising cell viability. Because acoustic forces merely hold cells in place, the transient pattern must be fixed via a rapid crosslinking step. This introduces the main engineering constraint: the fixation process itself must be both rapid and cytocompatible, whether through photopolymerization of materials such as gelatin methacrylate,[93] thermal gelation of hydrogels like agarose,[166] or chemical crosslinking of materials such as hyaluronic acid–catechol.[89] A successful workflow must precisely tune the acoustic patterning time, which may be only seconds, to match the material's gelation kinetics, ensuring both high pattern fidelity and high cell viability.

The preceding sections have detailed a wide range of applications, from high-throughput sorting to high-precision 3D assembly. To provide researchers with a clear, implementation-level quantitative reference, Table 2 summarizes the typical performance metrics, resolution, and compatible fixation methods for these applications. This quantitative summary leads into the following discussion, which steps back from these specific

applications to synthesize the unifying engineering logic underlying the field's trajectory.

4.6. Broader perspectives: from patterning to function

The applications detailed above showcase the current capabilities of acoustic lithography. To chart its future trajectory, however, it is instructive to step back and recognize that these specific successes are manifestations of a universal engineering principle: the precise command of acoustic and other physical fields to organize matter and orchestrate function.[57] By placing acoustic lithography within this broader context, we can identify shared principles with other advanced scientific domains and draw inspiration for future innovation.[51,56] This perspective reveals a common, multi-scale engineering logic for acoustic control that progresses from manipulating foundational structure to dynamically shaping the environment and, ultimately, regulating emergent biological function.

The principle of controlling structure to dictate function is fundamental across engineering disciplines. Its importance is well-established in materials science, where creating hierarchical structures from base materials is a core strategy for achieving desired macroscopic properties, as seen in the fabrication of advanced functional materials.[38,41,178–182] This same principle is evident in food science, where preserving the integrity of the cellular matrix is the primary determinant of food texture and quality.[183–185] The innovation of acoustic lithography lies in providing the acoustic tools needed to apply this established principle to living systems, building upon seminal works that demonstrated the ability to create arbitrary, complex structures using acoustic holography.[91,109,110] By consciously borrowing concepts of hierarchical assembly validated in materials science, future acoustic control strategies could be designed not only to position cells but also to guide their multi-scale self-organization, moving beyond simple patterning[186–191] toward more sophisticated forms of acoustic structural bio-control.

Beyond static structure, truly functional systems require the active engineering of their operational environment. To understand how to achieve this, we can draw valuable insights from parallel fields. In antimicrobial technology, for instance, the goal is to create microenvironments hostile to pathogens, using either natural compounds or targeted physical energy.[192–202] Similarly, advanced nano-

Table 2. Performance metrics for typical acoustic lithography applications

Application/ goal	Methods	Scale/ throughput	Patterning time	Post-patterning viability	Key outcome/ metric	Compatible fixation/ crosslinking	Ref.
Spheroid formation	BAW levitation	High (parallel, >100/run)	~15–30 min	High (no necrosis)	High uniformity in size & shape	Scaffold-free	[144]
Anisotropic tissue patterning	BAW adhesion/ SAW in gel	Medium (cm-scale)	~10 s–30 min	~90%	High cell alignment (>80% oriented)	Oxidative (HA–CA) or adhesion	[98,89]
Zoned cartilage engineering	Standing waves	Low-medium	~10 min	High (n.s. vs control)	Zoned matrix deposition	Thermal (agarose)	[166]
Complex volumetric 3D assembly	Acoustic holography	Low-medium (volumetric)	~1 min	High (n.s. vs control)	Arbitrary 3D complexity	Chemical (hydrogel) or culture	[91,92]
Large-area periodic patterning	Faraday waves	Very high (wafer-scale)	< 5 min	>95%	Large-scale order; simplicity	Photopolymerization	[93,94]
Complex co-culture assembly	Acoustic trapping	Low (cluster-by-cluster)	~10–20 min	N/A	Heterogeneous 3D clusters	Culture	[156]
Clinical sorting	Acoustophoresis	~75 µL/min	Continuous	N/A (fixed cells)	CTC & cluster detection	N/A	[88]
High-precision single-cell analysis	Localized streaming	Very low (single-cell)	Continuous/< 1 min	>90%	Precise 3D rotation & positioning	N/A	[90]

Abbreviations: BAW, bulk acoustic wave; CA, catechol; CTC, circulating tumor cell; HA, hyaluronic acid; n.s., no significance; N/A, not available; SAW, surface acoustic wave.

delivery systems are engineered to transport and release bioactive compounds in a controlled manner.[160] This vision of environmental engineering is directly achievable in acoustofluidics, a concept articulated in extensive reviews on the applications of acoustic streaming.[79] By integrating these ideas, we can envision the next generation of acoustic platforms in which the dynamic fluid control provided by acoustic streaming is combined with acoustically triggered release from nanocarriers. Such systems would transform acoustic devices from simple cell patterning tools into microenvironment regulators capable of creating truly biomimetic *in vitro* systems.

The pinnacle of this engineering logic is the direct regulation of function. This goal is exemplified in biotechnology, where microbial consortia in bioreactors are precisely controlled to optimize the production of therapeutics or chemicals, and physical fields such as ultrasound are used to enhance reaction efficiency. The key lesson here is the shift from merely providing an environment to using sound to actively direct a system's dynamic behavior and functional output.[92,157,203–210] This represents the ultimate frontier for acoustic lithography. The concept is rooted in the broader field of ultrasound-responsive systems, where acoustic energy is already used to trigger drug release or modulate biological barriers.[38] By learning from the control strategies used in bioreactors, acoustic fields could be programmed to guide stem cell differentiation *in situ* through targeted mechanotransduction or to enhance the efficacy of immunomodulatory drugs.[150,154,211–213] This approach would establish a new class of "acousto-ceuticals," in which acoustic energy becomes an active, programmable regulator of biological processes.

5. Bottlenecks and challenges

While the near-term outlook detailed in the following section is promising, the widespread adoption of acoustic lithography in clinical settings hinges on addressing several fundamental challenges. One of the most significant hurdles is the persistent trade-off between manipulation resolution and throughput. Although techniques like acoustic holography offer unprecedented pattern complexity, achieving true single-cell or even subcellular precision in dense, 3D environments remains a formidable challenge. Future research must focus on developing novel acoustic field-generation methods, potentially leveraging acoustic metamaterials or phononic crystals, to overcome the diffraction limit without sacrificing the ability to process biologically relevant sample volumes.

Another critical area requiring systematic investigation is the biological impact of acoustic exposure. Although acoustic methods are generally considered highly biocompatible, a comprehensive understanding of the dose–response relationship between specific acoustic parameters (frequency, intensity, duration) and long-term cellular fate is still lacking.[214] Standardized protocols and reporting metrics are urgently needed to enable cross-platform comparisons. Future studies must move beyond simple viability assays to explore how acoustic forces influence complex cellular processes such as mechanotransduction pathways, gene expression, and epigenetic modifications. Understanding these mechanisms is critical not only for ensuring the safety and efficacy of therapeutic applications but also for establishing the biosafety and ethical guidelines required for responsible *in vivo* translation.[215]

Furthermore, translating these technologies for *in vivo* applications presents a unique set of obstacles. These include the miniaturization of acoustic devices for implantation, integration with real-time imaging, and efficient transmission of acoustic energy through heterogeneous biological tissues. Moreover, the inherent system complexity and cost of advanced platforms, such as multi-transducer phased arrays or holographic setups, may limit their practical adoption outside specialized centers. The development of intelligent, biocompatible micro-robots powered and controlled by ultrasound represents an exciting frontier, but achieving this vision will require significant advances in materials science, robotics, and control theory before clinical deployment becomes feasible.[216]

6. Conclusion and outlook

Acoustic lithography has matured from a promising set of techniques into a versatile and powerful platform for bio-systems engineering, bridging the gap between high-throughput assembly and single-cell precision.[217] By leveraging the gentle, non-contact forces of acoustic radiation and streaming, it overcomes various limitations of conventional methods, offering unparalleled biocompatibility in native physiological media. This review has surveyed the fundamental physical principles, diverse methodologies—from BAW and SAW to advanced acoustic holography—and the broad applications of these tools in orchestrating cellular structures.[218] The preceding discussion on broader engineering principles places these achievements in context. It crystallizes the review's control-oriented perspective and highlights the field's clear engineering logic: a progression from controlling structure, to engineering the environment, and finally to regulating biological function. By drawing inspiration from established approaches in other engineering domains, the field can accelerate its transition from a manipulation tool to a functional control system.

Looking forward, the field is poised for transformative growth, likely to be driven by deeper integration with other cutting-edge technologies. Synergy with artificial intelligence and machine learning, for instance, could automate the design of highly complex, bespoke acoustic fields, accelerating research in developmental biology and regenerative medicine.[219–223] Combining acoustic patterning with 3D bioprinting and smart, acoustically responsive materials will unlock possibilities for creating four-dimensional constructs that change their shape or function over time in response to acoustic stimuli.[224,225] These near-term advancements will push the boundaries of what is possible in fabricating dynamic, life-like systems *in vitro*.

Ultimately, acoustic lithography is catalyzing a transformation in bio-systems engineering. As the technology matures and becomes more accessible, its translation from the research laboratory to clinical settings, for applications ranging from point-of-care diagnostics to *in situ* tissue repair, will become increasingly viable. By addressing the fundamental challenges of precision, control, and standardization, the field is well-positioned to unlock new therapeutic strategies and usher in a new era of engineered biology and regenerative medicine.

Acknowledgments

The authors would like to thank the Acoustic Robotics Systems Laboratory at ETH Zurich for sharing relevant and cutting-edge research papers.

Funding

This work was supported in part by the National Natural Science Foundation of China under grants 62273052 and W2431050; the Jiangsu Natural Science Foundation Grant under grants BK20240856 and BK20250842; the China Postdoctoral Science Foundation under grant 2024M764123; and the Talent Research Initiation Funding of Jiangsu University under grant 5501110024.

Conflict of interest

The authors declare that they have no competing interests.

Author contributions

Conceptualization: Yuyang Li, Xu Du, Xiaoming Liu, Zhongqiang Zhang
Visualization: Yuyang Li
Writing–original draft: All authors
Writing–review & editing: Yuyang Li, Dengjie Sun, Zhongqiang Zhang

Ethics approval and consent to participate

Not applicable.

Consent for publication

Not applicable.

Availability of data

Not applicable.

References

1. Bishop ES, Mostafa S, Pakvasa M, *et al*. 3-D bioprinting technologies in tissue engineering and regenerative medicine: current and future trends. *Genes Dis*. 2017;4(4):185-195. doi: 10.1016/j.gendis.2017.10.002

2. Derakhshanfar S, Mbeleck R, Xu K, Zhang X, Zhong W, Xing M. 3D bioprinting for biomedical devices and tissue engineering: a review of recent trends and advances. *Bioact Mater*. 2018;3(2):144-156. doi: 10.1016/j.bioactmat.2017.11.008

3. Martinez-Rivas A, González-Quijano GK, Proa-Coronado S, Séverac C, Dague E. Methods of micropatterning and manipulation of cells for biomedical applications. *Micromachines (Basel)*. 2017;8(12):347. doi: 10.3390/mi8120347

4. Che H, Selig M, Rolauffs B. Micro-patterned cell populations as advanced pharmaceutical drugs with precise functional control. *Adv Drug Deliv Rev*. 2022;184:114169. doi: 10.1016/j.addr.2022.114169

5. Yang W, Wang Z, Yu T, Chen Y, Ge, Z. Recent advance in cell patterning techniques: approaches, applications and future prospects. *Sens Actuators A Phys*. 2022;333:113229. doi: 10.1016/j.sna.2021.113229

6. Wang Z, Lang B, Qu Y, Li L, Song Z, Wang Z. Single-cell patterning technology for biological applications. *Biomicrofluidics*. 2019;13(6):061502. doi: 10.1063/1.5123518

7. Deinum EE. The systems and interactions underpinning complex cell wall patterning. *Biochem Soc Trans*. 2024;52(6):2385-2398. doi: 10.1042/BST20230642

8. Vijayavenkataraman S, Yan WC, Lu WF, Wang CH, Fuh JYH. 3D bioprinting of tissues and organs for regenerative medicine. *Adv Drug Deliv Rev*. 2018;132:296-332. doi: 10.1016/j.addr.2018.07.004

9. Gu Z, Fu J, Lin H, He Y. Development of 3D bioprinting: from printing methods to biomedical applications. *Asian J Pharm Sci*. 2020;15(5):529-557. doi: 10.1016/j.ajps.2019.11.003

10. Dare SC, Bajaj PS, Wankhede AN, Tawade SU, Manik KN. Three-dimensional bioprinting as a tool for tissue

engineering: a review. *J Pharm Bioallied Sci*. 2024;16(Suppl 4):S3027-S3030.
doi: 10.4103/jpbs.jpbs_678_24

11. Vidler C, Halwes M, Kolesnik K, *et al*. Dynamic interface printing. *Nature*. 2024;634(8036):1096-1102.
doi: 10.1038/s41586-024-08077-6

12. Laschke MW, Menger MD. Life is 3D: boosting spheroid function for tissue engineering. *Trends Biotechnol*. 2017;35(2):133-144.
doi: 10.1016/j.tibtech.2016.08.004

13. Yoo J, Jung Y, Char K, Jang Y. Advances in cell coculture membranes recapitulating in vivo microenvironments. *Trends Biotechnol*. 2023;41(2):214-227.
doi: 10.1016/j.tibtech.2022.07.014

14. Wang H, Brown PC, Chow ECY, *et al*. 3D cell culture models: drug pharmacokinetics, safety assessment, and regulatory consideration. *Clin Transl Sci*. 2021;14(5):1659-1680.
doi: 10.1111/cts.13066

15. Lembong J, Lerman MJ, Kingsbury TJ, Civin CI, Fisher JP. A fluidic culture platform for spatially patterned cell growth, differentiation, and cocultures. *Tissue Eng Part A*. 2018;24(23-24):1715-1732.
doi: 10.1089/ten.TEA.2018.0020

16. Ning J, Sah RK, Wang J. Coculture of mesenchymal stem cells and macrophage: a narrative review. *J Pharmacol Exp Ther*. 2025;392(4):103531.
doi: 10.1016/j.jpet.2025.103531

17. Al-Qadami G, Raposo A, Chien CC, *et al*. Intestinal organoid coculture systems: current approaches, challenges, and future directions. *Am J Physiol Gastrointest Liver Physiol*. 2025;328(3):G252-G276.
doi: 10.1152/ajpgi.00203.2024

18. Turunen S, Haaparanta AM, Aänismaa R, Kellomäki M. Chemical and topographical patterning of hydrogels for neural cell guidance in vitro. *J Tissue Eng Regen Med*. 2013;7(4):253-270.
doi: 10.1002/term.520

19. Funano SI, Tanaka N, Tanaka Y. User-friendly cell patterning methods using a polydimethylsiloxane mold with microchannels. *Dev Growth Differ*. 2020;62(3):167-176.
doi: 10.1111/dgd.12637

20. Wu H, Wu L, Zhou X, Liu B, Zheng B. Patterning hydrophobic surfaces by negative microcontact printing and its applications. *Small*. 2018;14(38):e1802128.
doi: 10.1002/smll.201802128

21. Slavík J, Skopalík J, Provazník I, Hubálek J. Multi-electrode array with a planar surface for cell patterning by microprinting. *Sensors (Basel)*. 2019;19(24):5379.
doi: 10.3390/s19245379

22. Soffe R, Tang SY, Baratchi S, *et al*. Controlled rotation and vibration of patterned cell clusters using dielectrophoresis. *Anal Chem*. 2015;87(4):2389-2395.
doi: 10.1021/ac5043335

23. Mohanty S, Khalil ISM, Misra S. Contactless acoustic micro/nano manipulation: a paradigm for next generation applications in life sciences. *Proc Math Phys Eng Sci*. 2020;476(2243):20200621.
doi: 10.1098/rspa.2020.0621

24. Mölder A, Czanner S, Costen N, Hartshorne G. Automatic detection of embryo location in medical imaging using trigonometric rotation for noise reduction. IEEE. 2014; 3239-3244.
doi: 10.1109/ICPR.2014.558

25. Lin Z, Fan X, Sun M, Gao C, He Q, Xie H. Magnetically actuated peanut colloid motors for cell manipulation and patterning. *ACS Nano*. 2018;12(3):2539-2545.
doi: 10.1021/acsnano.7b08344

26. Rong N, He S, Li B, *et al*. Coupled magnetic nanoparticle-mediated isolation and single-cell image recognition to detect *Bacillus*' cell size in soil. *Eur J Soil Sci*. 2022;73(3):e13236.
doi: 10.1111/ejss.13236

27. Liang S, Cao Y, Dai Y, *et al*. A versatile optoelectronic tweezer system for micro-objects manipulation: transportation, patterning, sorting, rotating and storage. *Micromachines (Basel)*. 2021;12(3):271.
doi: 10.3390/mi12030271

28. Zhang S, Li W, Elsayed M, *et al*. Integrated assembly and photopreservation of topographical micropatterns. *Small*. 2021;17(37):e2103702.
doi: 10.1002/smll.202103702

29. Chu HK, Huan Z, Mills JK, Yang J, Sun D. Three-dimensional cell manipulation and patterning using dielectrophoresis via a multi-layer scaffold structure. *Lab Chip*. 2015;15(3):920-930.
doi: 10.1039/c4lc01247j

30. Collins DJ, Morahan B, Garcia-Bustos J, Doerig C, Plebanski M, Neild A. Two-dimensional single-cell patterning with one cell per well driven by surface acoustic waves. *Nat Commun*. 2015;6:8686.
doi: 10.1038/ncomms9686

31. Wu Z, Pan M, Wang J, Wen B, Lu L, Ren H. Acoustofluidics for cell patterning and tissue engineering. *Eng Regen*. 2022;3(4):397-406.
doi: 10.1016/j.engreg.2022.08.005

32. Rasouli R, Villegas KM, Tabrizian M. Acoustofluidics - changing paradigm in tissue engineering, therapeutics development, and biosensing. *Lab Chip*. 2023;23(5):1300-1338.
doi: 10.1039/d2lc00439a

33. Yang S, Rufo J, Chen Y, *et al*. Acoustic tweezers for advancing precision biology and medicine. *Nat Rev Methods Primers*. 2025;5(1):49.

doi: 10.1038/s43586-025-00415-w

34. Baudoin M, Thomas JL. Acoustic tweezers for particle and fluid micromanipulation. *Annu Rev Fluid Mech*. 2020;52(1):205-234. doi: 10.1146/annurev-fluid-010719-060154.

35. Zhou Y, Ma Z, Ai Y. Submicron particle concentration and patterning with ultralow frequency acoustic vibration. *Anal Chem*. 2020;92(19):12795-12800. doi: 10.1021/acs.analchem.0c02765

36. Tayebi M, O'Rorke R, Wong HC, *et al*. Massively multiplexed submicron particle patterning in acoustically driven oscillating nanocavities. *Small*. 2020;16(17):e2000462. doi: 10.1002/smll.202000462

37. Yang Y, Ma T, Zhang Q, *et al*. 3D acoustic manipulation of living cells and organisms based on 2D array. *IEEE Trans Biomed Eng*. 2022;69(7):2342-2352. doi: 10.1109/TBME.2022.3142774

38. Athanassiadis AG, Ma Z, Moreno-Gomez N, *et al*. Ultrasound-responsive systems as components for smart materials. *Chem Rev*. 2022;122(5):5165-5208. doi: 10.1021/acs.chemrev.1c00622

39. Liu Y, Yin Q, Luo Y, *et al*. Manipulation with sound and vibration: a review on the micromanipulation system based on sub-MHz acoustic waves. *Ultrason Sonochem*. 2023;96:106441. doi: 10.1016/j.ultsonch.2023.106441

40. Li K, Huang W, Guo H, *et al*. Advancements in robotic arm-based 3D bioprinting for biomedical applications. *Life Med*. 2023;2(6):lnad046. doi: 10.1093/lifemedi/lnad046

41. Armstrong JPK, Puetzer JL, Serio A, *et al*. Engineering anisotropic muscle tissue using acoustic cell patterning. *Adv Mater*. 2018;30(43):e1802649. doi: 10.1002/adma.201802649

42. Yoo J, Ahn J, Ha H, Claud Jonas J, Kim C, Ham Kim H. Single-beam acoustic tweezers for cell biology: molecular to in vivo level. *IEEE Trans Ultrason Ferroelectr Freq Control*. 2024;71(10):1269-1288. doi: 10.1109/TUFFC.2024.3456083

43. Mehmood M, Khan UF, Maka AOM, *et al*. A review of thermal impact of surface acoustic waves on microlitre droplets in medical applications. *Adv Mech Eng*. 2022;14(8):16878132221116481. doi: 10.1177/16878132221116481

44. Barani A, Paktinat H, Janmaleki M, *et al*. Microfluidic integrated acoustic waving for manipulation of cells and molecules. *Biosens Bioelectron*. 2016;85:714-725. doi: 10.1016/j.bios.2016.05.059

45. Leong T, Johansson L, Juliano P, McArthur SL, Manasseh R. Ultrasonic separation of particulate fluids in small and large scale systems: a review. *Ind Eng Chem Res*. 2013;52(47):16555-16576. doi: 10.1021/ie402295r

46. Stringer M, Zeng Z, Zhang X, *et al*. Methodologies, technologies, and strategies for acoustic streaming-based acoustofluidics. *Appl Phys Rev*. 2023;10(1):011315. doi: 10.1063/5.0134646

47. Chen H, Hardwick J, Gao L, Plasencia DM, Subramanian S, Hirayama R. Acoustics in additive manufacturing: a path toward contactless, scalable, and high-precision manufacturing. *Appl Phys Rev*. 2025;12(3):031305. doi: 10.1063/5.0271688

48. Rufo J, Zhang P, Zhong R, Lee LP, Huang TJ. A sound approach to advancing healthcare systems: the future of biomedical acoustics. *Nat Commun*. 2022;13(1):3459. doi: 10.1038/s41467-022-31014-y

49. Wang J, Shang X, Zhou X, Chen H. Research advances of acoustic particle manipulation techniques in field-assisted manufacturing. *Nanoscale*. 2025;17(10):5654-5671. doi: 10.1039/d4nr04891a

50. Stroganov V, Pant J, Stoychev G, *et al*. 4D biofabrication: 3D cell patterning using shape-changing films. *Adv Funct Mater*. 2018;28(11):1706248. doi: 10.1002/adfm.201706248

51. Schrage M, Medany M, Ahmed D. Ultrasound microrobots with reinforcement learning. *Adv Mater Technol*. 2023;8(10):2201702. doi: 10.1002/admt.202201702

52. Zhang Z, Sukhov A, Harting J, Malgaretti P, Ahmed D. Rolling microswarms along acoustic virtual walls. *Nat Commun*. 2022;13(1):7347. doi: 10.1038/s41467-022-35078-8

53. Burstow R, Andrés D, Jiménez N, Camarena F, Thanou M, Pouliopoulos AN. Acoustic holography in biomedical applications. *Phys Med Biol*. 2025;70(6): 06TR01. doi: 10.1088/1361-6560/adb89a

54. Ma Z, Holle AW, Melde K, *et al*. Acoustic holographic cell patterning in a biocompatible hydrogel. *Adv Mater*. 2020;32(4):e1904181. doi: 10.1002/adma.201904181

55. Yang S, Tian Z, Wang Z, *et al*. Harmonic acoustics for dynamic and selective particle manipulation. *Nat Mater*. 2022;21(5):540-546. doi: 10.1038/s41563-022-01210-8

56. Guex AG, Di Marzio N, Eglin D, Alini M, Serra T. The waves that make the pattern: a review on acoustic manipulation in biomedical research. *Mater Today Bio*. 2021;10:100110. doi: 10.1016/j.mtbio.2021.100110

57. Zhang C, Brunet P, Liu S, *et al*. Acoustofluidics at audible frequencies—a review. *Eng*. 2025;44:51-72. doi: 10.1016/j.eng.2024.03.020

58. Qian J , Huang W , Yang R , Lam RHW , Lee JE . Low-cost laser-cut patterned chips for acoustic concentration of

micro- to nanoparticles and cells by operating over a wide frequency range. *Analyst*. 2021;146(10):3280-3288. doi: 10.1039/d1an00197c

59. Maramizonouz S, Tao X, Rahmati M, *et al*. Flexible and bendable acoustofluidics for particle and cell patterning. *Int J Mech Sci*. 2021;202-203:106536. doi: 10.1016/j.ijmecsci.2021.106536

60. Armstrong JPK, Maynard SA, Pence IJ, Franklin AC, Drinkwater BW, Stevens MM. Spatiotemporal quantification of acoustic cell patterning using Voronoï tessellation. *Lab Chip*. 2019;19(4):562-573. doi: 10.1039/c8lc01108g

61. Raymond SJ, Collins DJ, O'Rorke R, Tayebi M, Ai Y, Williams J. A deep learning approach for designed diffraction-based acoustic patterning in microchannels. *Sci Rep*. 2020;10(1):8745. doi: 10.1038/s41598-020-65453-8

62. Zhu Z, Chen T, Huang F, *et al*. Free-boundary microfluidic platform for advanced materials manufacturing and applications. *Adv Mater*. 2024;36(7):e2304840. doi: 10.1002/adma.202304840

63. Liu S, Li Y, Liu Q, *et al*. Thermal manipulation in multi-layered anisotropic materials via computed thermal patterning. *Adv Funct Mater*. 2022;32(13):2109674. doi: 10.1002/adfm.202109674

64. Ma Z, Fischer P. Acoustic micro-manipulation and its biomedical applications. *Eng*. 2023;24:13-16. doi: 10.1016/j.eng.2022.06.006

65. Rudenko OV, Sarvazyan AP, Emelianov SY. Acoustic radiation force and streaming induced by focused nonlinear ultrasound in a dissipative medium. *J Acoust Soc Am*. 1996;99(5):2791-2798. doi: 10.1121/1.414805

66. Bruus H. Acoustofluidics 7: the acoustic radiation force on small particles. *Lab Chip*. 2012;12(6):1014-1021. doi: 10.1039/c2lc21068a

67. Sarvazyan AP, Rudenko OV, Fatemi M. Acoustic radiation force: a review of four mechanisms for biomedical applications. *IEEE Trans Ultrason Ferroelectr Freq Control*. 2021;68(11):3261-3269. doi: 10.1109/TUFFC.2021.3112505

68. Yin Q, Li X, Ma Z, Zhang W. Acoustically activated nozzle for microdroplet generation and dispensing. *Phys Rev Appl*. 2023;20(2):024067. doi: 10.1103/PhysRevApplied.20.024067

69. Maramizonouz S, Rahmati M, Link A, Franke T, Fu Y. Numerical and experimental studies of acoustic streaming effects on microparticles/droplets in microchannel flow. *Int J Eng Sci*. 2021;169:103563. doi: 10.1016/j.ijengsci.2021.103563

70. Huang Z, Su M, Yang Q, *et al*. A general patterning approach by manipulating the evolution of two-dimensional liquid foams. *Nat Commun*. 2017;8:14110. doi: 10.1038/ncomms14110

71. Sarvazyan AP, Rudenko OV, Nyborg WL. Biomedical applications of radiation force of ultrasound: historical roots and physical basis. *Ultrasound Med Biol*. 2010;36(9):1379-1394. doi: 10.1016/j.ultrasmedbio.2010.05.015

72. Beyer RT. Radiation pressure—the history of a mislabeled tensor. *J Acoust Soc Am*. 1978;63(4):1025-1030. doi: 10.1121/1.381833

73. Gor'kov LP. On the forces acting on a small particle in an acoustical field in an ideal fluid. In: *Selected Papers of Lev P. Gor'kov*. 2014;315-317. doi: 10.1142/9789814366960_0008

74. Laurell T, Petersson F, Nilsson A. Chip integrated strategies for acoustic separation and manipulation of cells and particles. *Chem Soc Rev*. 2007;36(3):492-506. doi: 10.1039/b601326k

75. Doinikov AA, Regnault G, Mauger C, Blanc-Benon P, Inserra C. Acoustic microstreaming produced by two interacting gas bubbles undergoing axisymmetric shape oscillations. *J Fluid Mech*. 2021;931:A19. doi: 10.1017/jfm.2021.926

76. Rabaud D, Thibault P, Mathieu M, Marmottant P. Acoustically bound microfluidic bubble crystals. *Phys Rev Lett*. 2011;106(13):134501. doi: 10.1103/PhysRevLett.106.134501

77. Saeidi D, Saghafian M, Haghjooy Javanmard S, Wiklund M. A Quantitative study of the secondary acoustic radiation force on biological cells during acoustophoresis. *Micromachines (Basel)*. 2020;11(2):152. doi: 10.3390/mi11020152

78. Zhang P, Bachman H, Ozcelik A, Huang TJ. Acoustic microfluidics. *Annu Rev Anal Chem (Palo Alto Calif)*. 2020;13(1):17-43. doi: 10.1146/annurev-anchem-090919-102205

79. Wiklund M, Green R, Ohlin M. Acoustofluidics 14: applications of acoustic streaming in microfluidic devices. *Lab Chip*. 2012;12(14):2438-2451. doi: 10.1039/c2lc40203c

80. Lighthill J. Acoustic streaming. *J Sound Vib*. 1978;61(3):391-418. doi: 10.1016/0022-460x(78)90388-7

81. Červenka M, Bednařík M. Effect of inhomogeneous temperature fields on acoustic streaming structures in resonators. *J Acoust Soc Am*. 2017;141(6):4418. doi: 10.1121/1.4985386

82. Doinikov AA, Gerlt MS, Pavlic A, Dual J. Acoustic streaming produced by sharp-edge structures in microfluidic devices. *Microfluid Nanofluid*. 2020;24(5):32. doi: 10.1007/s10404-020-02335-5

83. Sadhal SS. Acoustofluidics 13: analysis of acoustic streaming by perturbation methods. *Lab Chip*. 2012;12(13):2292-2300. doi: 10.1039/c2lc40202e

84. Liu S, Yang Y, Ni Z, *et al*. Investigation into the effect of acoustic radiation force and acoustic streaming on particle patterning in acoustic standing wave fields. *Sensors (Basel)*. 2017;17(7):1664. doi: 10.3390/s17071664

85. Shi Q, Wang B, Mao H, Liu Y. Calibration and measurement of micrometre-scale pollen particles for discrete element method parameters based on the Johnson-Kendal-Roberts model. *Biosyst Eng*. 2024;237:83-91. doi: 10.1016/j.biosystemseng.2023.11.013

86. Comeau ES, Vander Horst MA, Raeman CH, Child SZ, Hocking DC, Dalecki D. In vivo acoustic patterning of endothelial cells for tissue vascularization. *Sci Rep*. 2023;13(1):16082. doi: 10.1038/s41598-023-43299-0

87. Yin Q, Chen K, Zhou C, *et al*. Acoustofluidic pick-and-place operation for label-free spatial assembly of cellular spheroid. *Int J Extrem Manuf*. 2025;7(4):045501. doi: 10.1088/2631-7990/adbb34

88. Altay R, Yapici MK, Koşar A. A hybrid spiral microfluidic platform coupled with surface acoustic waves for circulating tumor cell sorting and separation: a numerical study. *Biosensors (Basel)*. 2022;12(3):171. doi: 10.3390/bios12030171

89. Kang B, Shin J, Park HJ, *et al*. High-resolution acoustophoretic 3D cell patterning to construct functional collateral cylindroids for ischemia therapy. *Nat Commun*. 2018;9(1):5402. doi: 10.1038/s41467-018-07823-5

90. Liu X, Li Y, Liu F, *et al*. μSonic-hand: biomedical micromanipulation driven by acoustic gas-liquid-solid interactions. *Sci Adv*. 2025;11(13):eads8167. doi: 10.1126/sciadv.ads8167

91. Melde K, Kremer H, Shi M, *et al*. Compact holographic sound fields enable rapid one-step assembly of matter in 3D. *Sci Adv*. 2023;9(6):eadf6182. doi: 10.1126/sciadv.adf6182

92. Gao Z, Wang S, Sui Y, *et al*. A multifunctional acoustic tweezer for heterogenous assembloids patterning. *Small Struct*. 2023;4(5):2370012. doi: 10.1002/sstr.202370012

93. Alarcón H, Herrera-Muñoz M, Périnet N, Mujica N, Gutiérrez P, Gordillo L. Faraday-wave contact-line shear gradient induces streaming and tracer self-organization: from vortical to hedgehoglike patterns. *Phys Rev Lett*. 2020;125(25):254505. doi: 10.1103/PhysRevLett.125.254505

94. Tognato R, Parolini R, Jahangir S, *et al*. Sound-based assembly of three-dimensional cellularized and acellularized constructs. *Mater Today Bio*. 2023;22:100775. doi: 10.1016/j.mtbio.2023.100775

95. Chansoria P, Narayanan LK, Schuchard K, Shirwaiker R. Ultrasound-assisted biofabrication and bioprinting of preferentially aligned three-dimensional cellular constructs. *Biofabrication*. 2019;11(3):035015. doi: 10.1088/1758-5090/ab15cf

96. Lei J, Cheng F, Liu G, Li K, Guo Z. Dexterous formation of unconventional Chladni patterns using standing bulk acoustic waves. *Appl Phys Lett*. 2020;117(18). doi: 10.1063/5.0032304

97. Gesellchen F, Bernassau AL, Déjardin T, Cumming DR, Riehle MO. Cell patterning with a heptagon acoustic tweezer—application in neurite guidance. *Lab Chip*. 2014;14(13):2266-2275. doi: 10.1039/c4lc00436a

98. Deshmukh DV, Reichert P, Zvick J, *et al*. Continuous production of acoustically patterned cells within hydrogel fibers for musculoskeletal tissue engineering. *Adv Funct Mater*. 2022;32(30):2113038. doi: 10.1002/adfm.202113038

99. Yin Q, Luo Y, Yu X, *et al*. Acoustic cell patterning for structured cell-laden hydrogel fibers/tubules. *Adv Sci (Weinh)*. 2024;11(14):e2308396. doi: 10.1002/advs.202308396

100. Comeau ES, Hocking DC, Dalecki D. Ultrasound patterning technologies for studying vascular morphogenesis in 3D. *J Cell Sci*. 2017;130(1):232-242. doi: 10.1242/jcs.188151

101. Ozcelik A, Rufo J, Guo F, *et al*. Acoustic tweezers for the life sciences. *Nat Methods*. 2018;15(12):1021-1028. doi: 10.1038/s41592-018-0222-9

102. Nguyen TD, Tran VT, Pudasaini S, *et al*. Large-scale fabrication of 3D scaffold-based patterns of microparticles and breast cancer cells using reusable acoustofluidic device. *Adv Eng Mater*. 2021;23(6):2001377. doi: 10.1002/adem.202001377

103. Wu M, Ozcelik A, Rufo J, Wang Z, Fang R, Jun Huang T. Acoustofluidic separation of cells and particles. *Microsyst Nanoeng*. 2019;5(1):32. doi: 10.1038/s41378-019-0064-3

104. Wu M, Ouyang Y, Wang Z, *et al*. Isolation of exosomes from whole blood by integrating acoustics and microfluidics. *Proc Natl Acad Sci U S A*. 2017;114(40):10584-10589. doi: 10.1073/pnas.1709210114

105. Tian Z, Yang S, Huang PH, *et al*. Wave number-spiral acoustic tweezers for dynamic and reconfigurable manipulation of particles and cells. *Sci Adv*. 2019;5(5):eaau6062. doi: 10.1126/sciadv.aau6062

106. Shi J, Ahmed D, Mao X, Lin SC, Lawit A, Huang TJ. Acoustic tweezers: patterning cells and microparticles using standing surface acoustic waves (SSAW). *Lab Chip*.

2009;9(20):2890-2895.
doi: 10.1039/b910595f

107. Jiang D, Liu J, Pan Y, Zhuang L, Wang P. Surface acoustic wave (SAW) techniques in tissue engineering. *Cell Tissue Res*. 2021;386(2):215-226.
doi: 10.1007/s00441-020-03397-1

108. Xu M, Lee PVS, Collins DJ. Microfluidic acoustic sawtooth metasurfaces for patterning and separation using traveling surface acoustic waves. *Lab Chip*. 2021;22(1):90-99.
doi: 10.1039/d1lc00711d

109. Melde K, Mark AG, Qiu T, Fischer P. Holograms for acoustics. *Nature*. 2016;537(7621):518-522.
doi: 10.1038/nature19755

110. Melde K, Choi E, Wu Z, Palagi S, Qiu T, Fischer P. Acoustic fabrication via the assembly and fusion of particles. *Adv Mater*. 2018;30(3):1704507.
doi: 10.1002/adma.201704507

111. Brown MD. Phase and amplitude modulation with acoustic holograms. *Appl Phys Lett*. 2019;115(5):053701.
doi: 10.1063/1.5110673

112. Marzo A, Seah SA, Drinkwater BW, Sahoo DR, Long B, Subramanian S. Holographic acoustic elements for manipulation of levitated objects. *Nat Commun*. 2015;6:8661.
doi: 10.1038/ncomms9661

113. Marzo A, Drinkwater BW. Holographic acoustic tweezers. *Proc Natl Acad Sci U S A*. 2019;116(1):84-89.
doi: 10.1073/pnas.1813047115

114. Xu M, Wang J, Harley WS, Lee PVS, Collins DJ. Programmable acoustic holography using medium-sound-speed modulation. *Adv Sci (Weinh)*. 2023;10(23):e2301489.
doi: 10.1002/advs.202301489

115. Kucher S, Wesfreid JE, Cobelli PJ. Discovery of propagating trains of oscillons over Faraday waves in a 1D experiment. *Europhys Lett*. 2025,150(3):33003.
doi: 10.1209/0295-5075/add180

116. Chen P, Viñals J. Amplitude equation and pattern selection in Faraday waves. *Phys Rev E Stat Phys Plasmas Fluids Relat Interdiscip Topics*. 1999;60(1):559-570.
doi: 10.1103/physreve.60.559

117. Lu HF, Tien WH. Comparison of acoustic streaming flow patterns induced by solid, liquid and gas obstructions. *Micromachines (Basel)*. 2020;11(10):891.
doi: 10.3390/mi11100891

118. Chen P, Luo Z, Güven S, *et al*. Microscale assembly directed by liquid-based template. *Adv Mater*. 2014;26(34):5936-5941.
doi: 10.1002/adma.201402079

119. Gu L, Jiang S, Xu X, *et al*. Size- and density-dependent acoustic differential bioassembly of spatially-defined heterocellular architecture. *Biofabrication*. 2022;15(1):015019.
doi: 10.1088/1758-5090/aca79c

120. Bush JWM, Oza AU. Hydrodynamic quantum analogs. *Rep Prog Phys*. 2020;84(1):017001.
doi: 10.1088/1361-6633/abc22c

121. Xu F, Celli J, Rizvi I, Moon S, Hasan T, Demirci U. A three-dimensional in vitro ovarian cancer coculture model using a high-throughput cell patterning platform. *Biotechnol J*. 2011;6(2):204-212.
doi: 10.1002/biot.201000340

122. Foresti D, Kroll KT, Amissah R, *et al*. Acoustophoretic printing. *Sci Adv*. 2018;4(8):eaat1659.
doi: 10.1126/sciadv.aat1659

123. Hayakawa T, Sakuma S, Fukuhara T, Yokoyama Y, Arai F. A single cell extraction chip using vibration-induced whirling flow and a thermo-responsive gel pattern. *Micromachines*. 2014; 5(3):681-696.
doi: 10.3390/mi5030681

124. Harley W S, Kolesnik K, Xu M, *et al*. 3D Acoustofluidics via sub-wavelength micro-resonators. *Adv Funct Mater*. 2023;33(9):10.
doi: 10.1016/j.biosystemseng.2020.03.003

125. Surappa S, Pavagada S, Soto F, *et al*. Dynamically reconfigurable acoustofluidic metasurface for subwavelength particle manipulation and assembly. *Nat Commun*. 2025;16(1):494.
doi: 10.1038/s41467-024-55337-0

126. Jiang Y, Li H, Hua L, *et al*. Three-dimensional flow breakup characteristics of a circular jet with different nozzle geometries. *Biosyst Eng*. 2020;193:216-231.
doi: 10.1016/j.biosystemseng.2020.03.003

127. Bai X, Bin S, Yuguo D, *et al*. Parallel trapping, patterning, separating and rotating of micro-objects with various sizes and shapes using acoustic microstreaming. *Sens Actuators A Phys*. 2020;315:112340.
doi: 10.1016/j.sna.2020.112340

128. Hayakawa T, Sakuma S, Arai F. On-chip 3D rotation of oocyte based on a vibration-induced local whirling flow. *Microsyst Nanoeng*. 2015;1(1):1-9.
doi: 10.1038/micronano.2015.1

129. Collins DJ, O'Rorke R, Neild A, Han J, Ai Y. Acoustic fields and microfluidic patterning around embedded micro-structures subject to surface acoustic waves. *Soft Matter*. 2019;15(43):8691-8705.
doi: 10.1039/c9sm00946a

130. Huo J, Bai X, Yong J, *et al*. How to adjust bubble's adhesion on solid in aqueous media: Femtosecond laser-ablated patterned shape-memory polymer surfaces to achieve bubble multi-manipulation. *Chem Eng J*. 2021;414:128694.
doi: 10.1016/j.cej.2021.128694

131. Yang Y, Jin K, Qi H, *et al*. Acoustic streaming microgripper for programmable three-dimensional manipulation of single cells. *npj Acoust*. 2025;1(1):19.
doi: 10.1038/s44384-025-00022-9

132. Wang L, Zhang C, Ma J, *et al*. Mammalian Ste20-like

kinase 1 regulates AMPK to mitigate the progression of non-alcoholic fatty liver disease. *Eur J Med Res*. 2025; 30(1):296.
doi: 10.1186/s40001-025-02557-9

133. Zhou Y, Xu Q, Dong Y, Zhu S, Song S, Sun S. Supplementation of mussel peptides reduces aging phenotype, lipid deposition and oxidative stress in D-galactose-induce aging mice. *J Nutr Health Aging*. 2017;21(10):1314-1320.
doi: 10.1007/s12603-016-0862-3

134. Cassotta M, Forbes-Hernández TY, Calderón Iglesias R, *et al*. Links between nutrition, infectious diseases, and microbiota: emerging technologies and opportunities for human-focused research. *Nutrients*. 2020;12(6):1827.
doi: 10.3390/nu12061827

135. Zhang J, Qiu Y, Zhang H, Fan Y. Impact of frailty on adverse outcomes in patients with abdominal aortic aneurysm undergoing surgery: a systematic review and meta-analysis. *J Nutr Health Aging*. 2024;28(5):100213.
doi: 10.1016/j.jnha.2024.100213

136. Cushing K, Undvall E, Ceder Y, Lilja H, Laurell T. Reducing WBC background in cancer cell separation products by negative acoustic contrast particle immuno-acoustophoresis. *Anal Chim Acta*. 2018;1000:256-264.
doi: 10.1016/j.aca.2017.11.064

137. Li J, Li H. New insights into the folding-unfolding mechanism and conformations of cytochrome C. *Chem Sci*. 2022;13(25):7498-7508.
doi: 10.1039/d2sc01126c

138. Abraham Punnoose J, Thomas KJ, Chandrasekaran AR, *et al*. High-throughput single-molecule quantification of individual base stacking energies in nucleic acids. *Nat Commun*. 2023;14(1):631.
doi: 10.1038/s41467-023-36373-8

139. Woolf MS, Dignan LM, Karas SM, *et al*. Characterization of a centrifugal microfluidic orthogonal flow platform. *Micromachines (Basel)*. 2022;13(3):487.
doi: 10.3390/mi13030487

140. Sriphutkiat Y, Kasetsirikul S, Zhou Y. Formation of cell spheroids using standing surface acoustic wave (SSAW). *Int J Bioprint*. 2017;4(1):130.
doi: 10.18063/IJB.v4i1.130

141. Zheng W, Jiang X. Synthesizing living tissues with microfluidics. *Acc Chem Res*. 2018;51(12):3166-3173.
doi: 10.1021/acs.accounts.8b00417

142. Guldiken R, Jo MC, Gallant ND, Demirci U, Zhe J. Sheathless size-based acoustic particle separation. *Sensors (Basel)*. 2012;12(1):905-922.
doi: 10.3390/s120100905

143. Brugger MS, Baumgartner K, Mauritz SCF, *et al*. Vibration enhanced cell growth induced by surface acoustic waves as in vitro wound-healing model. *Proc Natl Acad Sci U S A*. 2020;117(50):31603-31613.
doi: 10.1073/pnas.2005203117

144. Jeger-Madiot N, Arakelian L, Setterblad N, *et al*. Self-organization and culture of mesenchymal stem cell spheroids in acoustic levitation. *Sci Rep*. 2021;11(1):8355.
doi: 10.1038/s41598-021-87459-6

145. Guo X, Sun M, Yang Y, *et al*. Controllable cell deformation using acoustic streaming for membrane permeability modulation. *Adv Sci (Weinh)*. 2020;8(3):2002489.
doi: 10.1002/advs.202002489

146. Chiang HJ, Yeh SL, Peng CC, Liao WH, Tung YC. Polydimethylsiloxane-polycarbonate microfluidic devices for cell migration studies under perpendicular chemical and oxygen gradients. *J Vis Exp*. 2017;(120): 55292.
doi: 10.3791/55292

147. Hadady H, Alam A, Khurana I, *et al*. Optimizing alkaline hydrothermal treatment for biomimetic smart metallic orthopedic and dental implants. *J Mater Sci Mater Med*. 2024;35(1):31.
doi: 10.1007/s10856-024-06794-y

148. Sugiura S, Cha JM, Yanagawa F, Zorlutuna P, Bae H, Khademhosseini A. Dynamic three-dimensional micropatterned cell co-cultures within photocurable and chemically degradable hydrogels. *J Tissue Eng Regen Med*. 2016;10(8):690-699.
doi: 10.1002/term.1843

149. Fan L, Luo T, Guan Z, *et al*. Gravitational sedimentation-based approach for ultra-simple and flexible cell patterning coculture on microfluidic device. *Biofabrication*. 2020;12(3):035005.
doi: 10.1088/1758-5090/ab80b5

150. Wei J, Sun Y, Wang H, *et al*. Designer cellular spheroids with DNA origami for drug screening. *Sci Adv*. 2024;10(29):eado9880.
doi: 10.1126/sciadv.ado9880

151. Soto J, Linsley C, Song Y, *et al*. Engineering materials and devices for the prevention, diagnosis, and treatment of COVID-19 and infectious diseases. *Nanomaterials (Basel)*. 2023;13(17):2455.
doi: 10.3390/nano13172455

152. Oliveira NM, Martins-Cruz C, Oliveira MB, Reis RL, Mano JF. Coculture of spheroids/2D cell layers using a miniaturized patterned platform as a versatile method to produce scaffold-free tissue engineering building blocks. *Adv Biosyst*. 2017;2(1):1700069.
doi: 10.1002/adbi.201700069

153. Chen J, Zhang X, Cross R Jr, *et al*. Atherosclerotic three-layer nanomatrix vascular sheets for high-throughput therapeutic evaluation. *Biomaterials*. 2024;305:122450.
doi: 10.1016/j.biomaterials.2023.122450

154. Liu X, Cheng J, Zhao Y. Tumor microenvironment based on extracellular matrix hydrogels for on-chip drug

screening. *Biosensors (Basel)*. 2024;14(9):429.
doi: 10.3390/bios14090429

155. Shan H, Chen M, Zhao S, *et al*. Acoustic virtual 3D scaffold for direct-interacting tumor organoid-immune cell coculture systems. *Sci Adv*. 2024;10(47):eadr4831.
doi: 10.1126/sciadv.adr4831

156. Wu Z, Ao Z, Cai H, *et al*. Acoustofluidic assembly of primary tumor-derived organotypic cell clusters for rapid evaluation of cancer immunotherapy. *J Nanobiotechnology*. 2023;21(1):40.
doi: 10.1186/s12951-023-01786-6

157. Wu Y, Zhao Y, Islam K, *et al*. Acoustofluidic engineering functional vessel-on-a-chip. Preprint. *ArXiv*. 2023;arXiv:2308.06219v2

158. He Z, Wang J, Fike BJ, *et al*. A portable droplet generation system for ultra-wide dynamic range digital PCR based on a vibrating sharp-tip capillary. *Biosens Bioelectron*. 2021;191:113458.
doi: 10.1016/j.bios.2021.113458

159. Ji S, Guvendiren M. Complex 3D bioprinting methods. *APL Bioeng*. 2021;5(1):011508.
doi: 10.1063/5.0034901

160. Ginghină O, Hudiță A, Zaharia C, *et al*. Current landscape in organic nanosized materials advances for improved management of colorectal cancer patients. *Materials (Basel)*. 2021;14(9):2440.
doi: 10.3390/ma14092440

161. Ricci G, Gibelli F, Sirignano A. Three-dimensional bioprinting of human organs and tissues: bioethical and medico-legal implications examined through a scoping review. *Bioengineering (Basel)*. 2023;10(9):1052.
doi: 10.3390/bioengineering10091052

162. Ao Z, Cai H, Wu Z, *et al*. Controllable fusion of human brain organoids using acoustofluidics. *Lab Chip*. 2021;21(4):688-699.
doi: 10.1039/d0lc01141j

163. Son J, Bang MS, Park JK. Hand-maneuverable collagen sheet with micropatterns for 3D modular tissue engineering. *ACS Biomater Sci Eng*. 2019;5(1):339-345.
doi: 10.1021/acsbiomaterials.8b01066

164. Seguret M, Vermersch E, Jouve C, Hulot JS. Cardiac organoids to model and heal heart failure and cardiomyopathies. *Biomedicines*. 2021;9(5):563.
doi: 10.3390/biomedicines9050563

165. Agrawal P, Zhuang S, Dreher S, Mitter S, Ahmed D. SonoPrint: acoustically assisted volumetric 3D printing for composites. *Adv Mater*. 2024;36(40):e2408374.
doi: 10.1002/adma.202408374

166. Armstrong JPK, Pchelintseva E, Treumuth S, *et al*. Tissue engineering cartilage with deep zone cytoarchitecture by high-resolution acoustic cell patterning. *Adv Healthc Mater*. 2022;11(24):e2200481.
doi: 10.1002/adhm.202200481

167. Yu W, Zhu H, Upreti N, *et al*. Acoustography by beam engineering and acoustic control node: BEACON. *Adv Sci (Weinh)*. 2024;11(46):e2403742.
doi: 10.1002/advs.202403742

168. Derayatifar M, Habibi M, Bhat R, Packirisamy M. Holographic direct sound printing. *Nat Commun*. 2024;15(1):6691.
doi: 10.1038/s41467-024-50923-8

169. Song K, Li G, Zu X, Du Z, Liu L, Hu Z. The fabrication and application mechanism of microfluidic systems for high throughput biomedical screening: a review. *Micromachines (Basel)*. 2020;11(3):297.
doi: 10.3390/mi11030297

170. Weaver WM, Tseng P, Kunze A, *et al*. Advances in high-throughput single-cell microtechnologies. *Curr Opin Biotechnol*. 2014;25:114-123.
doi: 10.1016/j.copbio.2013.09.005

171. Zhang YS, Yue K, Aleman J, *et al*. 3D bioprinting for tissue and organ fabrication. *Ann Biomed Eng*. 2017;45(1):148-163.
doi: 10.1007/s10439-016-1612-8

172. Schneck H, Blassl C, Meier-Stiegen F, *et al*. Analysing the mutational status of PIK3CA in circulating tumor cells from metastatic breast cancer patients. *Mol Oncol*. 2013;7(5):976-986.
doi: 10.1016/j.molonc.2013.07.007

173. Ge MJ, Wu QC, Wang M, *et al*. Detection of circulating tumor cells (CTCs) in patients with lung carcinoma by real-time fluorescent quantitative-PCR approach before and after chemotherapy. *Health*. 2009;01(03):231-238.
doi: 10.4236/health.2009.13038

174. Song D, Wang Z, Li X, *et al*. Application of circulating tumor cells in peripheral blood in judging the prognosis of patients with renal cancer and related indexes of blood coagulation. *Open J Urol*. 2022;12(1):1-6.
doi: 10.4236/oju.2022.121001

175. Magnusson C, Augustsson P, Undvall Anand E, *et al*. Acoustic enrichment of heterogeneous circulating tumor cells and clusters from metastatic prostate cancer patients. *Anal Chem*. 2024;96(18):6914-6921.
doi: 10.1021/acs.analchem.3c05371

176. Undvall Anand E, Magnusson C, Lenshof A, Ceder Y, Lilja H, Laurell T. Two-step acoustophoresis separation of live tumor cells from whole blood. *Anal Chem*. 2021;93(51):17076-17085.
doi: 10.1021/acs.analchem.1c04050

177. Zhang Y, Zhang Z, Zheng D, Huang T, Fu Q, Liu Y. Label-free separation of circulating tumor cells and clusters by alternating frequency acoustic field in a microfluidic

chip. *Int J Mol Sci*. 2023;24(4):3338.
doi: 10.3390/ijms24043338

178. Wu H, Chen H, Shao X, *et al*. All-wood-based hybrid membrane derived from waste sawdust for efficient emulsion separation. *Food Bioprod Process*. 2024;149:92-99.
doi: 10.1016/j.fbp.2024.11.017

179. Ahmad K, Din Z, Ullah H, *et al*. Preparation and characterization of bio-based nanocomposites packaging films reinforced with cellulose nanofibers from unripe banana peels. *Starch-Stärke*. 2022;74(5-6):2100283.
doi: 10.1002/star.202100283

180. Liu Y, Jing ZF, Zhang T, et al. Fabrication of functional biomass carbon aerogels derived from sisal fibers for application in selenium extraction. Food Bioprod Process. 2018;111:93-103.
doi: 10.1016/j.fbp.2018.07.004

181. Zhang T, Yuan D, Guo Q, *et al*. Preparation of a renewable biomass carbon aerogel reinforced with sisal for oil spillage clean-up: inspired by green leaves to green tofu. *Food Bioprod Process*. 2019;114:154-162.
doi: 10.1016/j.fbp.2018.12.007

182. Jing Z, Ding J, Zhang T, *et al*. Flexible, versatility and superhydrophobic biomass carbon aerogels derived from corn bracts for efficient oil/water separation. *Food Bioprod Process*. 2019;115:134-142.
doi: 10.1016/j.fbp.2019.03.010

183. Liu C, Xue Y, Guo J, *et al*. Citric acid and sucrose pretreatment improves the crispness of puffed peach chips by regulating cell structure and mechanical properties. *LWT-Food Sci Technol*. 2021;142:111036.
doi: 10.1016/j.lwt.2021.111036

184. Chen Z, Huang Q, Xia Q, *et al*. Intact endosperm cells in buckwheat flour limit starch gelatinization and digestibility in vitro. *Food Chem*. 2020;330:127318.
doi: 10.1016/j.foodchem.2020.127318

185. Li HT, Chen SQ, Bui AT, Xu B, Dhital S. Natural 'capsule'in food plants: cell wall porosity controls starch digestion and fermentation. *Food Hydrocoll*. 2021;117:106657.
doi: 10.1016/j.foodhyd.2021.106657

186. Sun L, Han J, Wu J, *et al*. Cellulose pretreatment with inorganic salt hydrate: Dissolution, regeneration, structure and morphology. *Ind Crops Prod*. 2022;180:114722.
doi: 10.1016/j.indcrop.2022.114722

187. Yang X, Ma L, Zheng J, Qiao Y, Bai J, Cai J. Effects of atmospheric pressure plasma treatment on the quality and cellulose modification of brown rice. *Innov Food Sci Emerg Technol*. 2024;96:103744.
doi: 10.1016/j.ifset.2024.103744

188. Pu Y, Zhou Q, Yu L, *et al*. Longitudinal analyses of lignin deposition in green asparagus by microscopy during high oxygen modified atmosphere packaging. *Food Packag Shelf Life*. 2020;25:100536.
doi: 10.1016/j.fpsl.2020.100536

189. Liu Y, Sun W, Li B, *et al*. Dehydration characteristics and evolution of physicochemical properties of *Platycodon grandiflorum* (Jacq. A. DC.) roots (PGR) during pulse-spouted microwave vacuum drying (PSMVD). *Ind Crops Prod*. 2022;177:114449.
doi: 10.1016/j.indcrop.2021.114449

190. Khin MN, Easdani M, Aziz T, *et al*. Schiff's base crosslinked gelatin-dialdehyde cellulose film with gallic acid for improved water resistance and antimicrobial properties. *Food Hydrocoll*. 2025;166:111331.
doi: 10.1016/j.foodhyd.2025.111331

191. Li Y, Kong W, Li M, *et al*. *Litsea cubeba* essential oil as the potential natural fumigant: Inhibition of *Aspergillus flavus* and AFB1 production in licorice. *Ind Crops Prod*. 2015;80:186-193.
doi: 10.1016/j.indcrop.2015.11.008

192. Su M, Liu F, Luo Z, *et al*. The antibacterial activity and mechanism of chlorogenic acid against foodborne pathogen *Pseudomonas aeruginosa*. *Foodborne Pathog Dis*. 2019;16(12):823-830.
doi: 10.1089/fpd.2019.2678

193. Dai J, Bai M, Li C, Cheang WS, Cui H, Lin L. Antibacterial properties of citral against Staphylococcus aureus: from membrane damage to metabolic inhibition. *Food Biosci*. 2023;53:102770.
doi: 10.1016/j.fbio.2023.102770

194. Song L, Yang H, Cheng S, *et al*. Combination effects of ultrasound and citral nanoemulsion against Shigella flexneri and the preservation effect on fresh-cut carrots. *Food Control*. 2024;155:110069.
doi: 10.1016/j.foodcont.2023.110069

195. Kang L, Liang Q, Liu Y, *et al*. Preparation technology and preservation mechanism of novel Ag NPs-loaded ZIF-67 packaging film. *Food Packag Shelf Life*. 2024;45:101338.
doi: 10.1016/j.fpsl.2024.101338

196. Jayan H, Yin L, Xue S, Zou X, Guo Z. Raman spectroscopy-based microfluidic platforms: a promising tool for detection of foodborne pathogens in food products. *Food Res Int*. 2024;180:114052.
doi: 10.1016/j.foodres.2024.114052

197. Xia JJ, Zou B, Liu F, Wang PY, Yan Y. Sensitive glucose biosensor based on cyclodextrin modified carbon nanotubes for detecting glucose in honey. J Food Compos Anal. 2022;105: 104221.
doi: 10.1016/j.jfca.2021.104221

198. Hashim SBH, Tahir HE, Lui L, *et al*. Smart films of carbohydrate-based/sunflower wax/purple Chinese cabbage anthocyanins: a biomarker of chicken freshness. *Food Chem*. 2023;399:133824.
doi: 10.1016/j.foodchem.2022.133824

199. Hussain M, Xu J, Ahmad I, *et al*. Efficacy of nano-based

strategies on the safe delivery and bioavailability of vitamin D: review. *Food Rev Int*. 2024;40(6):1581-1599.
doi: 10.1080/87559129.2023.2225591

200. Luo S, Yu L, Song J, Wu C, Li Y, Zhang C. Hybridization of glucosyl stevioside and hydroxypropyl methylcellulose to improve the solubility of lutein. *Food Chem*. 2022; 394:133490.
doi: 10.1016/j.foodchem.2022.133490

201. Xiao X, Bai J, Zhang J, Wu J, Dong Y. Inhibitory effect of fermented selected barley extracts with Lactobacillus plantarum dy-1 on the proliferation of human HT-29 cells. *J Food Biochem*. 2019;43(11):e12989.
doi: 10.1111/jfbc.12989

202. Farid W, Masud T, Sohail A, *et al*. Gastrointestinal transit tolerance, cell surface hydrophobicity, and functional attributes of *Lactobacillus acidophilus* strains isolated from indigenous dahi. *Food Sci Nutr*. 2021;9(9):5092-5102.
doi: 10.1002/fsn3.2468

203. Chen Q, Fang Z, Yang Z, *et al*. *Lactobacillus plantarum*-derived extracellular vesicles modulate macrophage polarization and gut homeostasis for alleviating ulcerative colitis. *J Agric Food Chem*. 2024;72(26):14713-14726.
doi: 10.1021/acs.jafc.4c01758

204. Geng A, Li N, Zayas-Garriga A, Xie R, Zhu D, Sun J. Direct conversion of minimally pretreated corncob by enzyme-intensified microbial consortia. Agric. 2024;14 (9):1610.
doi: 10.3390/agriculture14091610

205. Pan S, Zabed HM, Wei Y, Qi X. Technoeconomic and environmental perspectives of biofuel production from sugarcane bagasse: current status, challenges and future outlook. *Ind Crops Prod*. 2022;188:115684.
doi: 10.1016/j.indcrop.2022.115684

206. Huang W, He X, Wu J, *et al*. The evaluation of deep eutectic solvents and ionic liquids as cosolvents system for improving cellulase properties. *Ind Crops Prod*. 2023;197:116555.
doi: 10.1016/j.indcrop.2023.116555

207. Ji QH, Yu XJ, Yagoub AEG, Chen L, Zhou CS. Efficient removal of lignin from vegetable wastes by ultrasonic and microwave-assisted treatment with ternary deep eutectic solvent. *Ind Crops Prod*. 2020;149:112357.
doi: 10.1016/j.indcrop.2020.112357

208. Qian J, Zhou C, Ma H, Li S, Yagoub AEA, Abdualrahman MAY. Biological effect and inactivation mechanism of bacillus subtilis exposed to pulsed magnetic field: morphology, membrane permeability and intracellular contents. *Food Biophys*. 2016;11(4):429-435.
doi: 10.1007/s11483-016-9442-7

209. Qian J, Zhou C, Ma H, Li S, Yagoub AEA, Abdualrahman MAY. Proteomics analyses and morphological structure of bacillus subtilis inactivated by pulsed magnetic field. *Food Biophys*. 2016;11(4):436-445.
doi: 10.1007/s11483-016-9444-5

210. Ijinu TP, De Lellis LF, Shanmugarama S, *et al*. Anthocyanins as immunomodulatory dietary supplements: a nutraceutical perspective and micro-/nano-strategies for enhanced bioavailability. *Nutrients*. 2023;15(19):4152.
doi: 10.3390/nu15194152

211. Miao T, Chen K, Wei X, *et al*. High-throughput fabrication of cell spheroids with 3D acoustic assembly devices. *Int J Bioprint*. 2023;9(4):733.
doi: 10.18063/ijb.733

212. Xu D, Pei Y, Qiu W. Continuous and tunable droplet splitting using standing-wave acoustofluidics. *Lab Chip*. 2025.
doi: 10.1039/d5lc00592b

213. Sun J, Yao K, An J, Jing L, Huang K, Huang D. Machine learning and 3D bioprinting. *Int J Bioprint*. 2023;9(4):717.
doi: 10.18063/ijb.717

214. Komosa ER, Lin WH, Ogle BM. Toward robust and reproducible pluripotent stem cell expansion in bioprinted GelMA constructs. *Int J Bioprint*. 2025;11(1):363-381.
doi: 10.36922/ijb.4633

215. Yang Z, Liu S, Li L, *et al*. From nano robotic manipulation to nano manipulation robot. *SmartBot*. 2025;1(3):e12021.
doi: 10.1002/smb2.12021

216. Ates G, Bartolo P. Computational fluid dynamics for the optimization of internal bioprinting parameters and mixing conditions. *Int J Bioprinting*. 2023;9(6):0219.
doi: 10.36922/ijb.0219

217. Ng WL, Tan JS. Application of machine learning in 3D bioprinting of cultivated meat. *Int J AI Mater Des*. 2024;1(1):3.
doi: 10.36922/ijamd.2279

218. Nama N, Huang PH, Huang TJ, Costanzo F. Investigation of acoustic streaming patterns around oscillating sharp edges. *Lab Chip*. 2014;14(15):2824-2836.
doi: 10.1039/c4lc00191e

219. Li C, Mendis BL, Holland L, Li P. Investigation of the impact of liquid presence on the acoustic streaming generated by a vibrating sharp tip capillary. *Microfluid Nanofluid*. 2024;28(4):17
doi: 10.1007/s10404-024-02713-3

220. Martinez-De-Anda AA, Rodriguez-Salvador M, Castillo-Valdez PF. The attractiveness of 4D printing in the medical field: revealing scientific and technological advances in design factors and applications. *Int J Bioprinting*. 2023;9(6):1112.
doi: 10.36922/ijb.1112

221. Ma W, Lu H, Xiao Y, *et al*. Advancing organoid development with 3D bioprinting. *Organoid Res*. 2025;1(1):025040004.
doi: 10.36922/or025040004

222. He Y, Xia J, Mai JDH, Upreti N, Lee LP, Huang TJ. Acoustic technologies for the orchestration of cellular functions for therapeutic applications. *Sci Adv*. 2025;11(29):eadu4759.

doi: 10.1126/sciadv.adu4759

223. Zhu W, Ma L, Shi Z, *et al*. Early-stage fertilised egg viability detection based on machine vision. *Br Poult Sci*. 2025;66(5):613-624.
doi: 10.1080/00071668.2025.2470275

224. Sup Yoon M, Min Lee J, Jeong Jo M, *et al*. Advancements in 3D bioprinting for nanoparticle evaluation: Techniques, models, and biological applications. *Int J Bioprinting*. 2024;10(5):4273.
doi: 10.36922/ijb.4273

225. Zhang Z, Shi Z, Ahmed D. SonoTransformers: transformable acoustically activated wireless microscale machines. *Proc Natl Acad Sci U S A*. 2024;121(6):e2314661121.
doi: 10.1073/pnas.2314661121

ACCSCIENCE PUBLISHING

International Journal of Bioprinting

REVIEW ARTICLE

Application and prospects of chitosan-based 3D-printed scaffolds in the repair of osteochondral defects

Jiahui Liang[1,2†], Jiyang Zou[1†], Yuqing He[1†], Jiyuan Qi[1], Yihan Wang[1], Zhaoyang Liu[1], Weiguo Zhang[1], Duo Zhang[3], Xiaolin Cui[3*], Xing Wang[2*] and Kang Tian[1*]

[1] Department of Joint and Sports Medicine, First Affiliated Hospital of Dalian Medical University, Dalian, Liaoning, China

[2] Beijing National Laboratory for Molecular Sciences, Institute of Chemistry, Chinese Academy of Sciences, Beijing, China

[3] School of Medicine, the Chinese University of Hong Kong, Shenzhen, Guangdong, China

(This article belongs to the *Special Issue*: *Biofabrication Breakthroughs: Innovation and Application in Bioprinting, Biomaterials, and Organoid*)

†These authors have contributed equally to this work.

***Corresponding authors:**
Kang Tian
(tiankang@dmu.edu.cn)

Xing Wang
(wangxing@iccas.ac.cn)

Xiaolin Cui
(Stevencui@cuhk.edu.cn)

Citation: Liang J, Zou J, He Y, *et al.* Application and prospects of chitosan-based 3D-printed scaffolds in the repair of osteochondral defects. *Int J Bioprint.* 2026;12(1):102-124. doi: 10.36922/IJB025430430

Received: October 20, 2025
1st revised: November 17, 2025
2nd revised: November 26, 2025
Accepted: November 26, 2025
Published online: December 1, 2025

Copyright: © 2025 Author(s). This is an Open Access article distributed under the terms of the Creative Commons Attribution License, permitting distribution, and reproduction in any medium, provided the original work is properly cited.

Publisher's Note: AccScience Publishing remains neutral with regard to jurisdictional claims in published maps and institutional affiliations.

Abstract

Osteochondral defects, which involve injury to both the articular cartilage and the underlying subchondral bone, present a considerable therapeutic challenge due to cartilage's poor intrinsic capacity for regeneration and the intricate, gradient structure of the osteochondral junction. Tissue engineering offers a promising strategy for regenerating this biphasic tissue. Chitosan has attracted significant research interest due to its favorable biocompatibility, controlled degradability, natural antibacterial activity, and structural resemblance to endogenous glycosaminoglycans. Integrating chitosan with 3D printing allows the production of scaffolds with customizable structures, porosity, and mechanical properties tailored to patient needs. Moreover, chitosan can easily be blended with various natural polymers to develop composite bioinks that improve osteogenic and chondrogenic potential, thereby enhancing the functional performance of scaffolds. This review examines research literature spanning January 2020 to October 2025. Recent advances include the development of functionalized chitosan derivatives for improved printability and crosslinking, as well as the incorporation of cells and growth factors to create bioactive, cell-laden constructs. This review provides an extensive overview of the physicochemical and biological characteristics of chitosan pertinent to osteochondral regeneration, discusses diverse 3D printing strategies utilized to construct chitosan-based composite scaffolds, and emphasizes their demonstrated potential in improving cellular responses, stimulating bone and cartilage formation, supporting biomineralization, and achieving controlled delivery of bioactive agents. Finally, we discuss current challenges, such as optimizing scaffold degradation kinetics and vascularization, and future perspectives on the clinical translation of these innovative constructs for effective osteochondral regeneration.

Keywords: 3D-printed; Chitosan; Osteochondral defect; Scaffold.

1. Introduction

Osteochondral defects, a common challenge in orthopedics, are often difficult to repair completely due to the considerable heterogeneity in the structure, composition, and mechanical properties of cartilage and subchondral bone tissue.[1,2] Once osteochondral injuries occur, failure to intervene promptly can easily lead to joint dysfunction and even the onset and progression of osteoarthritis.[3,4] Traditional clinical treatments can alleviate symptoms and promote tissue repair to some extent; however, they generally suffer from limitations such as inadequate mechanical properties of the repaired tissues and a tendency for regenerated tissues to consist predominantly of fibrocartilage. This makes it difficult to achieve long-term, stable functional reconstruction.[5,6] The inherent heterogeneity of cartilage and subchondral bone in their composition, mechanical properties, and biological requirements makes designing a single scaffold that supports the regeneration of both tissues highly complicated.[7,8]

In recent years, promising alternatives in tissue engineering and regenerative medicine have emerged through the integration of scaffolds, cells, and bioactive molecules to replicate natural tissue environments.[9-11] Among various scaffold materials, chitosan stands out as an ideal osteochondral scaffold material due to its excellent biocompatibility, degradability, and antimicrobial properties.[12] More importantly, its molecular structure is highly similar to the glycosaminoglycans (GAGs) in the extracellular matrix (ECM) of cartilage, facilitating chondrocyte adhesion, proliferation, and cartilage-specific matrix secretion.[13] Meanwhile, with the rapid advancement of 3D printing technologies, chitosan-based tissue engineering scaffolds can now be fabricated with enhanced precision and tailored to meet patient-specific requirements.[7,14,15] 3D printing not only enables the construction of complex porous structures but also allows the optimization of microenvironmental conditions such as cell migration, nutrient transport, and angiogenesis by adjusting pore size, interconnectivity, and hierarchical distribution.[16] Additionally, 3D printing can be combined with bioactive factor loading to achieve spatially controlled, multi-factor delivery, thereby regulating chondrogenic and osteogenic differentiation simultaneously. This approach more closely mimics the natural repair pattern of the osteochondral interface.[17] Based on these advantages, 3D-printed chitosan-based composite scaffolds exhibit significant promise for osteochondral defect repair and provide new insights and technical support for future clinical translation.

Research on chitosan-based 3D-printed scaffolds demonstrates substantial diversity in material formulations, reflecting the various strategies researchers adopt to address repair requirements across different levels of osteochondral tissue. Regarding printing techniques, distinct 3D printing processes have been selected based on the intended application. In addition, performance evaluation approaches differ markedly. While most studies include fundamental physicochemical characterization alongside biological assessment, the scope of evaluation varies considerably. Some investigations focus solely on *in vitro* cell experiments, whereas others extend to *in vivo* animal studies. Overall, the application of chitosan 3D-printed scaffolds in osteochondral tissue engineering is rapidly advancing, characterized by multiple technical developments, diverse application fields, and varying evaluation criteria. However, this rapid development has also led to notable fragmentation and inconsistencies within the field. Differences in material formulations, printing processes, crosslinking methods, structural designs, and performance assessments create challenges in directly comparing results and hinder the establishment of consensus on optimal strategies. Therefore, a comprehensive and systematic review is urgently needed to help researchers more readily identify the strengths and limitations of chitosan-based 3D-printed scaffolds. In this context, we also discuss current challenges and future directions for translating these innovative scaffold designs from laboratory research to clinical applications.

This review followed a predefined search strategy applied to PubMed and Web of Science. Searches spanned January 1, 2020, to October 1, 2025, and were limited to English-language publications. Keywords included "chitosan," "3D printing," and "cartilage/osteochondral defect." After de-duplication, two authors independently screened titles and abstracts against prespecified inclusion and exclusion criteria, followed by full-text assessment to ensure accuracy. In total, 116 studies were included. Inclusion criteria encompassed studies investigating chitosan-based 3D-printed scaffolds for osteochondral repair, cartilage defect repair, or bone regeneration, using either pure chitosan or chitosan-based composites. Exclusion criteria were studies that did not involve 3D-printed chitosan scaffolds, were unrelated to the topic, or addressed non-osteochondral tissue engineering without reporting cartilage or bone repair outcomes.

2. Advantages of 3D printing technology in osteochondral tissue engineering

2.1. The complexity of osteochondral repair and its traditional limitations

The osteochondral tissue structure exhibits a unique gradient arrangement, progressing from superficial hyaline cartilage to intermediate calcified cartilage and finally to deep subchondral bone. Each layer of osteochondral tissue demonstrates a continuous gradient change in cellular morphology, ECM composition, and mechanical properties (e.g., stiffness, compressive strength) (Figure 1A).[18,19] This complex anatomical structure severely limits the self-repair capacity of osteochondral tissue following injury. Traditional treatment methods such as microfracture, autologous chondrocyte transplantation, or osteochondral grafting, though widely used clinically (Figure 1B), have significant limitations. First, the repaired tissue is predominantly fibrocartilage rather than hyaline cartilage, resulting in inadequate mechanical properties. Additionally, these approaches face challenges, including limited donor availability, secondary injury, and poor interface integration.[20,21] More importantly, the bonding strength at the osteochondral interface is often insufficient, leading to suboptimal repair outcomes.[22] Consequently, designing comprehensive repair strategies that replicate the hierarchical architecture and functional gradients of native osteochondral tissue has become a major challenge in osteochondral tissue engineering.

2.2. High-precision bionic manufacturing using 3D printing technology

2.2.1. Precise construction of gradient structures

Three-dimensional printing techniques allow accurate regulation of scaffold pore dimensions, overall porosity, and spatial organization at both micro- and nanoscale levels. This capability enables the precise fabrication of architectures that replicate the mechanical and biological gradient transitions between cartilage and subchondral bone at the osteochondral interface (Figure 2A and C).[23,24] Specifically, 3D printing not only enables the compartmentalized deposition of multiple materials within a single scaffold but also supports the construction of pore size, density, and composition gradients through adjustable printing parameters. This facilitates the formation of biomimetic structures that combine mechanical stability with biological activity.[25] Moreover, this technology can integrate bioactive factors or cells to achieve spatially targeted, multi-factor release, thereby inducing bone marrow-derived mesenchymal stem cells (BMSCs) to undergo region-specific differentiation and promoting synergistic repair at the osteochondral interface (Figure 2B).[20,26] For example, one study utilized hydroxypropyl chitosan and oxidized chondroitin sulfate as base materials to fabricate a dual-layer scaffold via 3D printing technology for osteochondral defect repair.[27] The upper layer of chitosan and chondroitin sulfate supports chondrocyte proliferation, while the lower layer incorporates calcium phosphate to facilitate osteogenesis and angiogenesis. This 3D-printed scaffold achieves a compositional gradient between the bone and cartilage layers, effectively promoting osteochondral repair. 3D-printed chitosan composite scaffolds combine the printability, modifiability, and bioactivity of chitosan with dual-layer and gradient structural designs. The upper layer provides a cartilage-like hydrogel microenvironment, while the lower layer incorporates composite materials enriched with osteogenic factors to enhance osseointegration.[7,28,29] Through 3D printing, continuous interlayer transitions and personalized pore size and shape control are achieved,

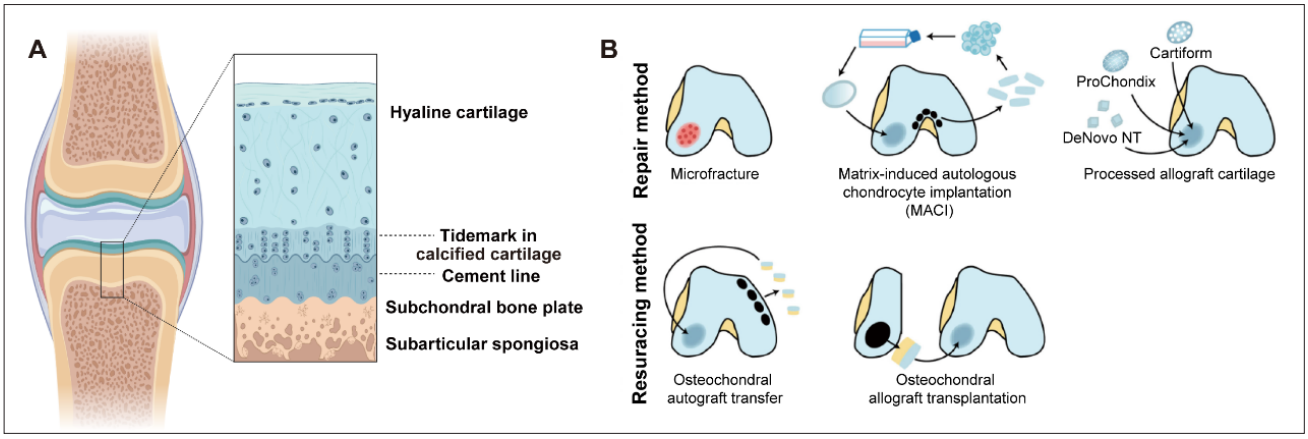


Figure 1. The structure of osteochondral tissue and treatment of osteochondral defects. (A) Schematic diagram of the structure of osteochondral tissue (Created in BioRender. der, b. (2025) https://BioRender.com/qfyzeqi). (B) Clinical treatment strategies for osteochondral defects. Reprinted with permission from Ref. [21] Copyright © 2019, Springer Nature Limited.

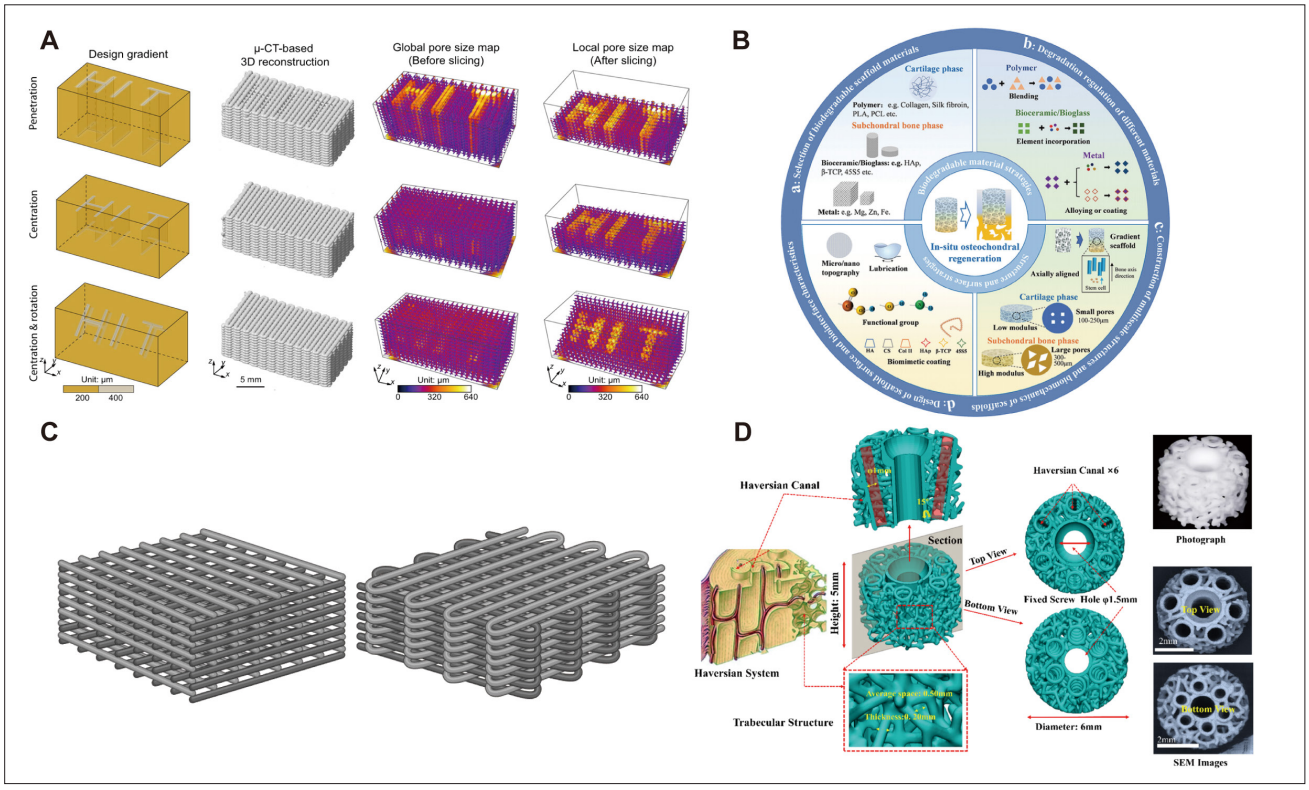


Figure 2. Structure, components, and parameters of 3D-printed osteochondral scaffolds. (A) Gradient structures with highly tunable pore size. Reprinted from Ref.[24] Copyright © 2024, The Authors. (B) Schematic diagram of key components for tissue engineering of osteochondral scaffolds. Reprinted with permission from Ref.[20] Copyright © 2024, Wiley-VCH GmbH. (C) Schematic diagram of the structure of a 3D-printed porous scaffold. Reprinted with permission from Ref.[20] Copyright © 2024, Wiley-VCH GmbH. (D) 3D design drawing of a bone scaffold incorporating Haversian canals and a trabecular porous structure. Reprinted from Ref.[30] Copyright © 2025, The Authors. Abbreviations: Col II: Collagen type II; CS: Chitosan; Fe: Iron; HAp: Hydroxyapatite; Mg: Magnesium; PCL: Polycaprolactone; PLA: Polylactic acid; SEM: Scanning electron microscopy; Zn: Zinc; β-TCP: Beta tricalcium phosphate; μ-CT: Micro-computed tomography.

ultimately delivering simultaneous benefits in three key aspects: interfacial integration, mechanical matching, and tissue-specific regeneration.

2.2.2. Precise regulation of surface microstructure

In osteochondral tissue engineering, scaffolds must not only possess overall mechanical stability and a macro-gradient structure but also provide a surface-level microenvironment that mimics the natural ECM. Such microstructural precision allows for effective modulation of cellular behaviors, including adhesion, migration, proliferation, and differentiation. Previous research has shown that the pore size, surface roughness, surface topology, and the spatial arrangement of scaffolds can significantly influence cellular morphological characteristics and signaling pathways, thereby determining the functional state of osteoblasts and chondrocytes.[31,32] Wang *et al.*[30] fabricated a dual-bionic ceramic scaffold combining Haversian canals and trabeculae via DLP 3D printing, incorporating surface microstructure modifications. The core mechanisms—structural orientation guidance, mechanical space maintenance, and bioactive microcrystals—offer a novel solution for precise shaping and efficient osteogenesis in maxillofacial bone defect repair (Figure 2D). Tang *et al.*[33] designed a 3D chitosan scaffold loaded with zinc oxide nanoparticles. Nanoparticle decoration enhanced the nanoscale topography and increased pore-wall roughness, thereby improving osteogenic potential. For chitosan-based 3D-printed scaffolds, pore-wall roughness, micro- and nanoparticle distribution, surface roughness, and overall topography can be regulated by adjusting printing parameters (such as filament diameter, layer thickness, and nozzle speed), applying post-processing techniques (including crosslinking, mineralization, and nanofiller modification), and incorporating composite materials. Integrating these design elements can significantly enhance the scaffold's potential for functional repair in osteochondral defects.

2.2.3. Personalized adaptation and surgical innovation

Three-dimensional printing technology offers personalized solutions for osteochondral repair by customizing scaffolds to match patient-specific shape, size, and internal structure based on computed tomography/magnetic resonance imaging data. This is particularly beneficial for irregular articular surface reconstruction. Robotic-assisted *in situ* printing systems can deposit bioink directly onto defect sites, using intraoperative 3D scanning to dynamically adjust printing paths for minimally invasive, precision repair.[34] The integration of 3D bioprinting with robot-assisted minimally invasive surgery provides a promising approach for accurately repairing localized cartilage lesions in the knee joint.[35] 3D-printed chitosan composite scaffolds achieve tailored mechanical properties and degradation profiles suitable for osteochondral defects through material compositing and modification. Their biomimetic structural designs ensure both anatomical conformity and compatibility with the cellular microenvironment, while optimized functional loading supports the sequential demands of osteochondral repair. This approach represents an ideal strategy for personalized treatment of osteochondral defects. With ongoing advancements in smart materials, artificial intelligence-assisted design, and 3D printing technology, 3D-printed chitosan-based composite scaffolds are expected to play an increasingly important role in precision and minimally invasive osteochondral tissue engineering.

3. Overview of chitosan

3.1. Structure

Chitosan is the only naturally occurring cationic polysaccharide and is widely found in the cells of lower plants, the cell walls of higher plants, and the shells of crustaceans. Its structure consists of randomly distributed N-acetylglucosamine and D-glucosamine units. The molecular structure of chitosan resembles certain polysaccharide repeating units found in articular cartilage, giving it properties similar to hyaluronic acid and GAGs within the ECM.[5] Therefore, chitosan can partially mimic the ECM of articular cartilage and promote cartilage tissue formation. Furthermore, the numerous hydroxyl and amino groups distributed along the chitosan molecular chain confer excellent hydrophilicity, biocompatibility, and chemical reactivity.[16,36,37] These functional groups also facilitate chemical modification, making chitosan readily compatible with composite applications with other materials. For example, Chen *et al.*[38] grafted the chondrogenic-promoting small-molecule drug kartogenin (KGN) onto chitosan to construct a cartilage repair hydrogel. *In vitro* and *in vivo* experiments confirmed that the KGN-functionalized chitosan hydrogel effectively promotes cartilage regeneration. In addition, the positive charges inherent to chitosan support its interaction with negatively charged cells and proteins. In summary, chitosan is a promising natural biomaterial for repairing cartilage defects.

3.2. Physicochemical properties

Chitosan exhibits poor solubility in water and alkaline media but readily dissolves in dilute acidic environments. Under acidic conditions, the amino groups in chitosan bind with hydrogen ions from the acid, forming positively charged ions that allow the chitosan molecules to dissolve.[39] This pH-dependent solubility enables its processing under mild conditions, creating opportunities for various 3D printing techniques.[40] Chitosan solutions display pronounced viscosity, a rheological property that offers unique advantages during 3D printing.[41] Compared with commonly used natural polymers such as sodium alginate and hyaluronic acid, hydrogen bonding and electrostatic interactions between chitosan molecules generate stronger cohesive forces. This enables chitosan to form continuous, uniform, and stable filaments during extrusion printing, reducing filament breakage and spreading. As a result, printing precision and repeatability are significantly enhanced.[42] Meanwhile, chitosan solutions maintain their designed morphology for a short period after deposition, providing a sufficient operational window for subsequent physical or chemical crosslinking. This characteristic is particularly crucial for achieving regionalized printing of cartilage and bone tissues.[43]

During 3D printing, the printability of the material is a crucial factor determining dimensional accuracy and structural stability.[18] An ideal bioink should possess suitable rheological properties to ensure smooth flow through the nozzle while rapidly maintaining its designed shape after deposition.[41,44] Due to its distinctive molecular configuration and favorable rheological behavior in solution, chitosan demonstrates excellent suitability for printing applications. On the one hand, chitosan solutions exhibit moderate viscoelasticity within a specific concentration range, enabling smooth extrusion under shear forces and ensuring continuity and consistency during the printing process.[42,45] On the other hand, their excellent interlayer adhesion significantly enhances the overall stability of printed structures, supporting the successful construction of complex 3D porous and gradient structures without collapse or deformation.[11]

3.3. Biological function

3.3.1. Excellent biocompatibility

Chitosan-based composite scaffolds play a crucial role in promoting cellular bioactivity due to their similarity to the natural ECM, supporting cell adhesion, proliferation, and differentiation.[12] They also demonstrate excellent biocompatibility and biodegradability in osteochondral tissue engineering.[13] Chitosan can be gradually degraded by ECM enzymes after implantation and ultimately absorbed or eliminated by the body, thus avoiding immune or toxic reactions associated with long-term implantation.[46] The incorporation of graphene into chitosan scaffolds enhances both mechanical integrity and biocompatibility. Studies have shown that 3D-bioprinted composite scaffolds composed of chitosan, gelatin, hyaluronic acid, and graphene effectively support the adhesion, proliferation, and growth of BMSCs.[15] Chang *et al.*[46] prepared a methyl acrylate–glycol chitosan bioink loaded with MG-63 cells and fabricated scaffolds using a photopolymerization-based 3D printing system. As shown in Figure 3A, *in vitro* experiments demonstrated that cell viability exceeded 92%, while the proliferation rate remained above 96%. These findings confirm the scaffold's excellent biocompatibility and highlight its strong potential for bone tissue regeneration.

3.3.2. Antibacterial activity

Osteochondral tissue engineering often involves trauma repair and implant surgery, where surgical sites are susceptible to bacterial infection, potentially leading to repair failure or delayed recovery.[47] Chitosan, as a natural antimicrobial material, therefore offers significant advantages for osteochondral repair. Its antibacterial activity mainly originates from its protonated amino groups ($-NH_2$), which interact electrostatically with negatively charged bacterial membranes, disrupting membrane integrity and function.[48] Modifying chitosan's molecular structure or combining it with other antimicrobial agents can further enhance its activity, especially against Gram-negative bacteria.[11,49] One study fabricated chitosan scaffolds via 3D printing and incorporated chitosan microspheres loaded with vancomycin and diflunisal to achieve coordinated control of bacterial infection for treating osteomyelitis (Figure 3B).[47] To further improve antibacterial efficacy, chitosan has been modified into quaternized chitosan (QCS) and combined with tricalcium phosphate (TCP) for 3D printing. When loaded with iron-doped barium titanate, tricobalt oxide, curcumin, and engineered cell membranes, this approach yields 3D-printed chitosan-based scaffolds containing magneto-ultrasonic dual-responsive nanoparticles (Figure 3C).[11] Both *in vitro* and *in vivo* studies have shown that these scaffolds effectively eradicate biofilms, exhibit immunoregulatory properties, and promote bone regeneration, offering a promising strategy for treating infected bone defects.

3.3.3. Cell proliferation and differentiation promotion

Chitosan facilitates the proliferation of osteoblasts and chondrocytes while inducing the differentiation of BMSCs, processes that are essential for effective osteochondral tissue regeneration.[50] Chitosan can bind to receptors on cell membranes, enhancing the affinity between cells and scaffolds.[51] It can also trigger various cellular signaling cascades by interacting with cell membrane receptors, including pathways like mitogen-activated protein kinase (MAPK) and phosphoinositide 3-kinase (PI3K)/protein kinase B (Akt). These signaling pathways are essential for regulating cellular processes such as proliferation, survival, and growth.[52] Polyethylene glycol diacrylate (PEGDA), a commonly used 3D printing material, lacks biocompatibility and osteogenic activity. However, by incorporating chitosan into the bioink, the scaffold's biocompatibility was significantly enhanced, indicating that it has the potential to promote cell proliferation.[14] Nguyen and colleagues[7] developed a 3D-printed bilayer scaffold specifically engineered to meet the distinct functional needs of cartilage and bone tissues. The cartilage component consisted of N, O-carboxymethyl chitosan combined with oxidized xanthan gum (OXG), designed to replicate the characteristics of the native ECM. The subchondral bone layer incorporated biphasic calcium phosphate (BCP) to enhance osteoconductivity. This bilayer printing approach achieved structural biomimicry, mechanical matching, and synergistic bioactivity, thereby improving the efficiency of osteochondral defect repair (Figure 3D).[7] Studies have demonstrated that chitosan-based materials stimulate the proliferation of bone marrow-derived osteoprogenitor cells and promote their maturation into functional osteoblasts through the upregulation of osteogenic gene expression.[53] Furthermore, chitosan significantly promotes bone formation by upregulating the expression of key genes, including *RUNX2*, *ALP*, and osteocalcin, in osteoblasts.[54] Chitosan also enhances the activity of the cartilage-inducing growth factor transforming growth factor-beta (TGF-β), thereby promoting cartilage formation.[55]

3.3.4. Loading of bioactive molecules

In osteochondral tissue engineering, scaffolds must not only provide structural support but also facilitate cellular proliferation, differentiation, and tissue regeneration. In recent years, bioactive agents—including metal ions, growth factors, and pharmacological compounds—have attracted considerable research interest due to their pivotal functions in regulating cell behavior and promoting tissue repair and regeneration. Incorporating these bioactive

components into scaffold systems can significantly enhance cellular activity, thereby expediting the processes of osteochondral healing and regeneration.[56] Chitosan scaffolds, known for their superior biocompatibility, degradability, and adjustable structure, serve as an ideal platform for delivering bioactive factors. Additionally, 3D printing technology provides innovative solutions for the precise incorporation of these factors into the scaffolds. A 3D-printed hydrogel was constructed using recombinant collagen, chitosan, nano-clay, and KGN-loaded nanoparticles through electrostatic interactions and photopolymerization (Figure 3E). The controlled release of KGN from the scaffold promoted the chondrogenic differentiation of BMSCs, markedly increasing the expression of collagen type II and GAGs.[17] In a related study, a cartilage regeneration platform was developed using a chitosan hydrogel combined with a 3D-printed polycaprolactone (PCL) scaffold incorporating tetrahedral framework nucleic acids (TFNAs) and mesenchymal stem cells (MSCs). TFNAs, a class of DNA nanomaterials capable of optimizing the regenerative microenvironment, were introduced into MSCs to stimulate their proliferation and chondrogenic differentiation, thereby enhancing cartilage formation and improving the repair of cartilage lesions.[57]

3.4. Advantages compared with other 3D printing materials

In the field of osteochondral tissue engineering, 3D printing has emerged as a versatile platform for fabricating scaffolds or bioinks with customized architecture, controlled porosity, and spatial distribution of cells and biomolecules. The selection of the printing material is a critical determinant of the scaffold's mechanical properties, degradation profile, biocompatibility, cell-adhesive behavior, and ultimately regenerative outcome. Here, we compare major classes of materials used in 3D printing for osteochondral regeneration and then highlight the specific advantages of chitosan-based systems.

Natural polymers include collagen, gelatin, alginates, hyaluronic acid, chitosan, and others.[58] Their advantages lie in excellent biocompatibility, similarity to ECM components, and typically good cell adhesion and bioactivity.[59] However, they also share significant limitations, such as generally low mechanical strength, rapid degradation, poor printability, and insufficient mechanical stability for load-bearing bone applications. Synthetic polymers include PCL, poly (lactic-co-glycolic acid), polyethylene glycol (PEG), and polyetheretherketone.[60] These materials typically offer good mechanical property tunability, high structural strength, slower and controllable degradation characteristics, and are widely used in 3D printing.[59] However, they generally lack inherent bioactivity, produce acidic degradation products that hinder tissue repair, fail to mimic ECM signaling, and exhibit poor cell infiltration or vascular integration.[61] Bioceramic composites include hydroxyapatite, β-TCP, and bioactive glass. They exhibit excellent osteogenic properties, superior bioactivity, suitability for bone regeneration, and typically high mechanical strength.[20] However, they are relatively brittle with poor flexibility, which poses challenges when printing complex geometries or gradient structures, especially in softer cartilage regions.[62] Additionally, they may degrade too slowly or fail to match the mechanical modulus of cartilage.[63]

Recent studies indicate that chitosan-based 3D printed composite scaffolds demonstrate significant potential in osteochondral tissue engineering compared to other 3D printing materials, primarily due to the following aspects. First, chitosan can be readily modified or blended with other polymers to form bioinks with tunable rheological properties.[7,33] Second, chitosan exerts beneficial effects on both osteogenesis and chondrogenesis, making it highly suitable for osteochondral scaffold design, particularly under the regenerative demands of these dual tissue types.[64,65] Chitosan readily forms covalent bonds with other bioactive molecules and can be combined with other materials to enhance its mechanical and biological properties.[38] Unlike certain synthetic polymers that may degrade into acidic byproducts, chitosan undergoes a mild degradation process, yielding harmless products.[58] This is particularly important for tissue engineering. In cartilage regeneration, chitosan's ability to mimic the ECM and support GAG and type II collagen production is paramount. Finally, due to structural and functional differences between cartilage and subchondral bone, osteochondral repair scaffolds often require gradient compositions or zoned architectures.[7,16] Chitosan's flexibility and compatibility with blending other materials make it well-suited for such designs. Therefore, compared to existing biomaterials, chitosan emerges as a highly promising 3D-printable material for osteochondral regeneration strategies due to its biofunctionality, adaptability, and suitability for gradient designs.

4. Mechanism of chitosan in promoting osteochondral repair

Chitosan has been widely investigated for its potential in promoting cartilage repair and bone tissue regeneration. Its biological activity is not only reflected in its excellent biocompatibility and degradability but also in its regulatory effects on cells. Particularly during osteochondral repair, chitosan can promote cartilage and bone regeneration through multiple molecular mechanisms (Figure 4).

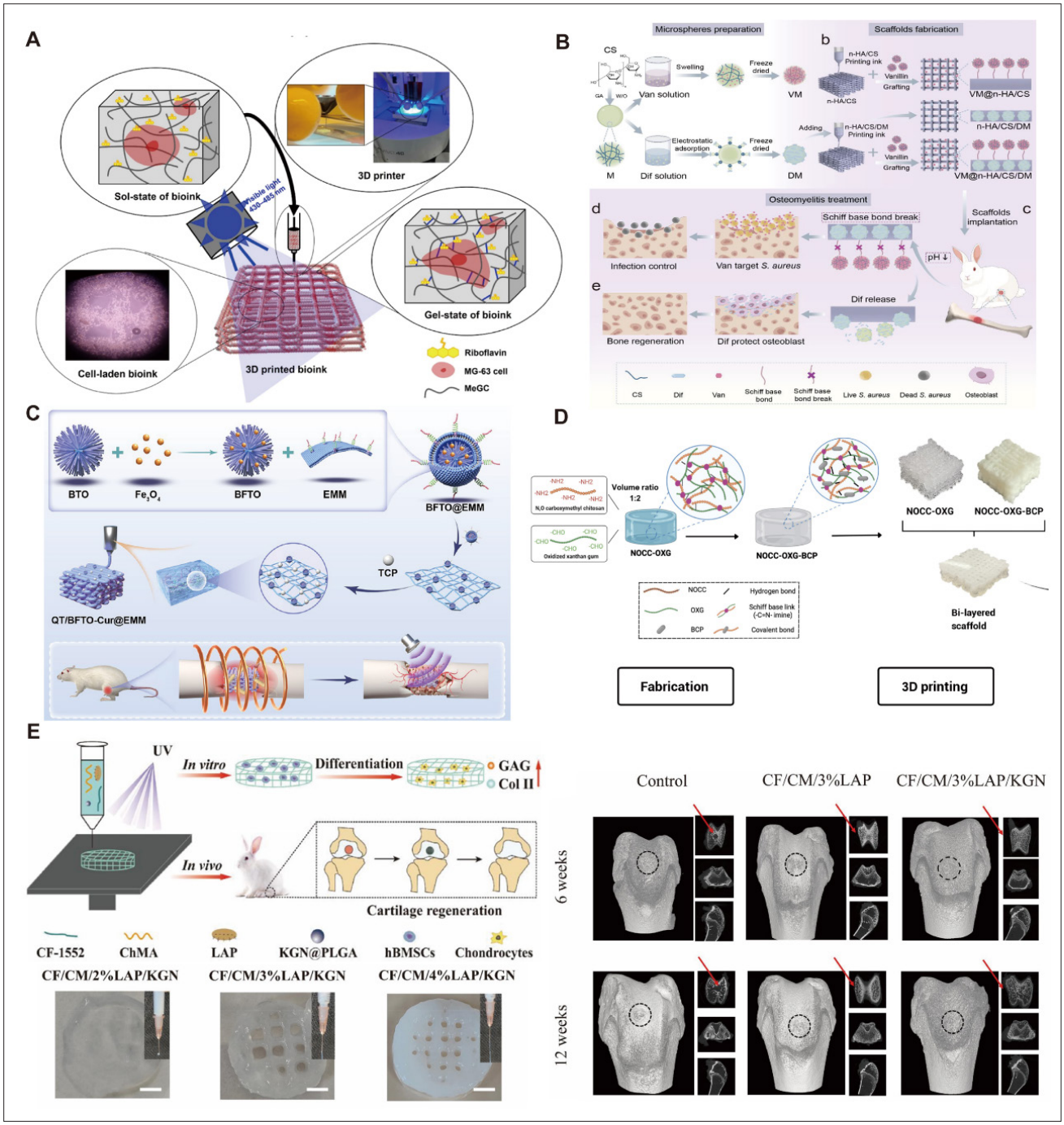


Figure 3. Utilization of 3D-printed chitosan-based composite scaffolds in the field of osteochondral tissue engineering. (A) Schematic representation of the fabrication process for 3D bioprinting using methyl acrylate-glycol chitosan (MeGC)-based bioink. Reprinted with permission from Ref. [46]. Copyright © 2025, Elsevier. (B) The 3D-printed chitosan scaffold loaded with vancomycin-chitosan microspheres (VM) is used for the treatment of osteomyelitis. Reprinted with permission from Ref. [47]. Copyright © 2025, Elsevier. (C) Quaternized chitosan combined with dual-responsive nanoparticles for the treatment of infected bone defects. Reprinted with permission from Ref. [11]. Copyright © 2024, American Chemical Society. (D) 3D-printed chitosan bilayer scaffolds for osteochondral defects. Reprinted from Ref. [7]. Copyright © 2025, Elsevier. (E) Chitosan hydrogels loaded with kartogenin (KGN) at different nanoclay concentrations promote cartilage repair. Reprinted from Ref. [17]. Copyright © 2024, The Authors. Abbreviations: BCP: Biphasic calcium phosphate; BFTO: Iron-doped barium titanate; BTO: Barium titanate; CF: Recombinant collagen CF-1552; Col II: Collagen type II; CM: chitosan methacrylate (ChMA); CS: Chitosan; Cur: Curcumin; DM: Diflunisal-loaded chitosan microsphere; EMM: Engineered mesenchymal stem cell membranes; GA: Glutaraldehyde; GAG: Glycosaminoglycans; hBMSCs: Human bone marrow-derived mesenchymal stem cells; LAP: Lithium phenyl-2,4,6-trimethylbenzoylphosphinate; NOCC: N, O-carboxymethyl chitosan; n-HA: Nano-hydroxyapatite; OXG: Oxidized xanthan gum; PLGA: Poly (lactic-co-glycolic acid); QT: quaternized chitosan (QCS); *S. aureus*: *Staphylococcus aureus*; TCP: Tricalcium phosphate; UV: Ultraviolet.

4.1. Molecular mechanisms promoting cartilage repair

Chitosan enhances the adhesion of MSCs by facilitating electrostatic interactions between its NH_2 groups and the negatively charged components of the MSC membrane, thereby improving the scaffold's overall cell-binding efficiency.[66] By interacting with specific receptors on the chondrocyte surface, chitosan can trigger various signaling cascades, such as the PI3K/Akt and MAPK pathways, thereby enhancing chondrocyte proliferation and differentiation and promoting the regeneration of injured cartilage tissue.[64]

Chitosan facilitates cellular adhesion and proliferation through electrostatic interactions between its positively charged functional groups and the GAGs present in the ECM.[5] The Wnt/β-catenin signaling pathway is pivotal in regulating the lineage commitment of MSCs. When Wnt/β-catenin activity is moderately stimulated, MSCs exhibit elevated expression of pluripotency-associated genes such as *Oct4*, *Sox2*, and *Nanog*, thereby enhancing their capacity for chondrogenic differentiation.[66] In addition, chitosan influences the Notch signaling cascade, which is essential for preserving MSC stemness and preventing premature differentiation.[67] Chitosan can also modulate the hypoxia-inducible factor-1 alpha pathway, which enables MSCs to maintain their stemness under hypoxic conditions and enhances the chondrogenic differentiation capacity of BMSCs.[68] The structure of chitosan resembles that of natural GAGs in cartilage tissue, providing chondrocytes with a favorable microenvironment that helps maintain the cartilage phenotype.[65]

Chitosan is also instrumental in regulating macrophage polarization, a key process in tissue repair. Chitosan facilitates the transition of macrophages from the pro-inflammatory M1 state to the regenerative M2 phenotype by modulating receptor-mediated signaling and cytokine secretion.[69] Interleukin (IL)-10, TGF-β, and insulin-like growth factor 1 (IGF-1) released by M2 macrophages can suppress excessive inflammatory responses and promote the proliferation and differentiation of chondrocytes, thereby contributing to cartilage regeneration.[70] Additionally, chitosan can promote chondrocyte proliferation and the chondrogenic differentiation of MSCs by modulating the M2 macrophage phenotype and activating the TGF-β receptor signaling pathway.[4]

4.2. Molecular mechanisms promoting osteogenesis

Chitosan not only promotes cartilage repair by regulating BMSCs and chondrocytes but also exerts regulatory effects on bone-formation-related cells such as osteoblasts and osteoclasts. These cells play crucial roles in osteochondral regeneration, and chitosan can influence their functions through multiple mechanisms.

4.2.1. Regulation of osteoblasts

Osteoblasts serve as the principal cells responsible for bone formation and mineral deposition. Chitosan influences osteoblast behavior by modulating their proliferation, differentiation, and mineralization processes. It enhances osteogenic differentiation by upregulating key transcription factors, including *Runx2* and *Osterix*, which are essential for osteoblast maturation and function.[71] The activation of these genes promotes osteoblast maturation and enhances bone matrix synthesis. Chitosan can also promote osteoblast differentiation through the Wnt/β-catenin signaling pathway. This pathway is essential for osteoblast development, and chitosan enhances the mineralization capacity of osteoblasts via its activation.[72] Chitosan enhances the expression of alkaline phosphatase (ALP) and osteocalcin, which are hallmark molecules involved in osteoblast mineralization.[54] Furthermore, when combined with bone-inducing materials such as hydroxyapatite and calcium phosphate, chitosan can further enhance bone mineralization.[7,14]

4.2.2. Regulation of osteoclasts

Osteoclasts are essential for bone remodeling and resorption. Chitosan modulates osteoclast function through several mechanisms. It can inhibit osteoclast differentiation and activity by promoting osteoblast secretion of osteoprotegerin, which competitively binds receptor activator of NF-kappaB ligand (RANKL) and prevents its interaction with the RANK receptor on osteoclast precursor cells.[73] Because RANKL is a critical regulator of osteoclast differentiation, its inhibition reduces bone resorption and supports bone regeneration. A composite scaffold integrating cerium-doped nano-hydroxyapatite with chitosan demonstrates superior osteoinductive potential. This hybrid structure enhances MSC adhesion and proliferation, elevates the expression of osteogenic markers such as *Runx2* and osteopontin, and concurrently suppresses osteoclast differentiation.[73,74] Chitosan also reduces osteoclast activity and bone resorption by inhibiting the secretion of inflammatory cytokines. Inflammatory cytokines such as tumor necrosis factor alpha and IL-6 typically activate osteoclasts by enhancing RANKL expression, making chitosan's anti-inflammatory effects beneficial for bone repair.[75]

Chitosan promotes osteochondral regeneration through multiple mechanisms, encompassing cartilage repair, osteoblast differentiation, bone mineralization, and immune regulation. In cartilage repair, chitosan is essential for stimulating chondrocyte proliferation and differentiation while enhancing cartilage matrix

synthesis. Regarding the molecular mechanisms involving osteoblasts, osteoclasts, and macrophages, chitosan promotes bone tissue repair by regulating relevant gene expression, inhibiting bone resorption, and modulating immune responses. Future optimization of chitosan's biological activity, particularly through composite use with other biomaterials, holds promising prospects for its application in osteochondral tissue engineering.

5. Applications of modified chitosan materials in 3D printing technology

To further optimize the performance of chitosan-based 3D-printed scaffolds in osteochondral tissue engineering, various modification techniques are commonly employed to enhance their mechanical properties, degradation characteristics, and bioactivity. Modified chitosan materials can better meet clinical demands, demonstrating particular advantages in osteochondral tissue repair. The following sections detail the applications of several commonly used modified chitosan 3D-printed materials in osteochondral tissue engineering.

5.1. Carboxymethyl chitosan

Carboxymethyl chitosan (CMCS) is synthesized through the chemical modification of hydroxyl and amino functional groups on the chitosan backbone using carboxymethylation reagents. This material degrades during tissue regeneration with low toxicity and minimal inflammatory response, making it widely used in tissue engineering.[36] A study employed 3D printing to construct a bilayer scaffold, incorporating a CMCS–OXG hydrogel as the cartilage layer and BCP as the underlying bone layer. This structure mimics natural osteochondral tissue and promotes osteochondral regeneration (Figure 5A and 5B).[7] Wang *et al.*[12] enhanced hydrogel cross-linking, mineralization, and degradation rates tailored to the osteogenic cycle by adjusting the CMCS concentration in the hydrogel scaffold. This adjustment imparted a bioactive, microscale porous architecture to the material. *In vitro* experiments confirmed the scaffold's osteogenic potential, revealing that CMCS effectively enhances BMSC adhesion, proliferation, and differentiation.[12]

5.2. Quaternized chitosan

Quaternized chitosan inhibits bacterial metabolic activity by interfering with the tricarboxylic acid cycle, which disrupts cell wall formation and increases cell membrane permeability, thereby exerting strong antibacterial effects.[16,37] Additionally, QCS stimulates macrophages to secrete pro-inflammatory factors, inducing M1 polarization and enhancing antibacterial efficacy, with notable advantages in promoting bone regeneration in infected bone defects.[37] In one study, biologically active iron-doped barium titanate nanoparticles were synthesized and integrated into a composite of QCS and TCP, resulting in a bioink designed for 3D printing of antibacterial bone regeneration scaffolds. *In vivo* experiments demonstrated that these scaffolds markedly improved the repair of infected bone defects and highlighted macrophage-targeted modulation as an effective approach for simultaneously combating infection and enhancing bone regeneration.[11] Kang *et al.*[29] developed a composite scaffold (dGQH) consisting of a decellularized ECM, gelatin, QCS, and nano-hydroxyapatite. The dGQH20 scaffold exhibited excellent antibacterial properties (94.90 ± 2.44% inhibition of *Escherichia coli* and 95.41 ± 2.65% inhibition of

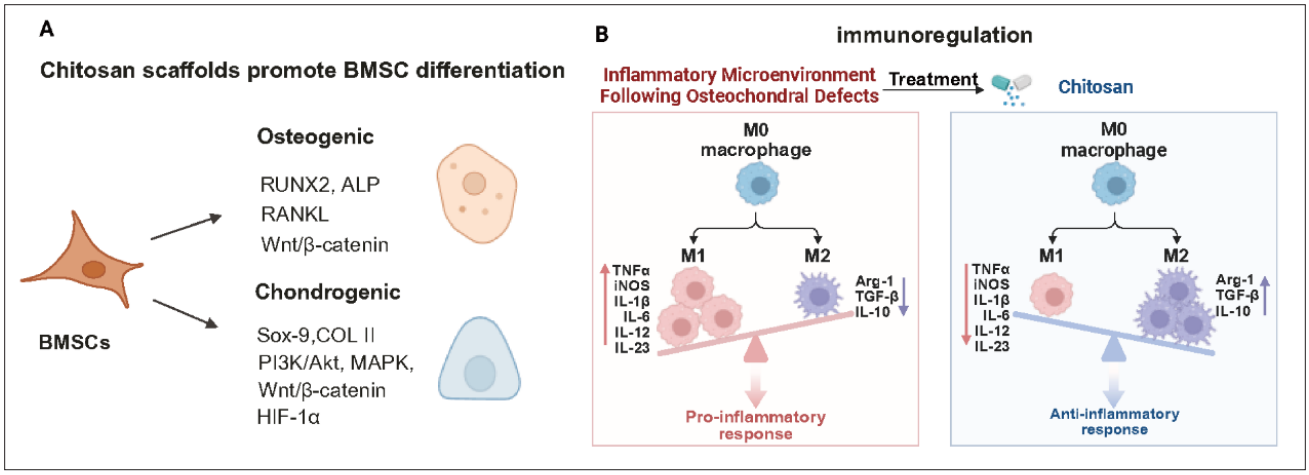


Figure 4. The mechanisms through which chitosan biomaterials influence the function of mesenchymal stem cells and macrophages (*Created in BioRender. der, b. (2025) https://BioRender.com/qfyzeqi*). Abbreviations: Arg-1: Arginase-1; BMSCs: Bone marrow-derived mesenchymal stem cells; IL: Interleukin; iNOS: Inducible nitric oxide synthase; TGF-β: Transforming growth factor-beta; TNFα: Tumor necrosis factor alpha

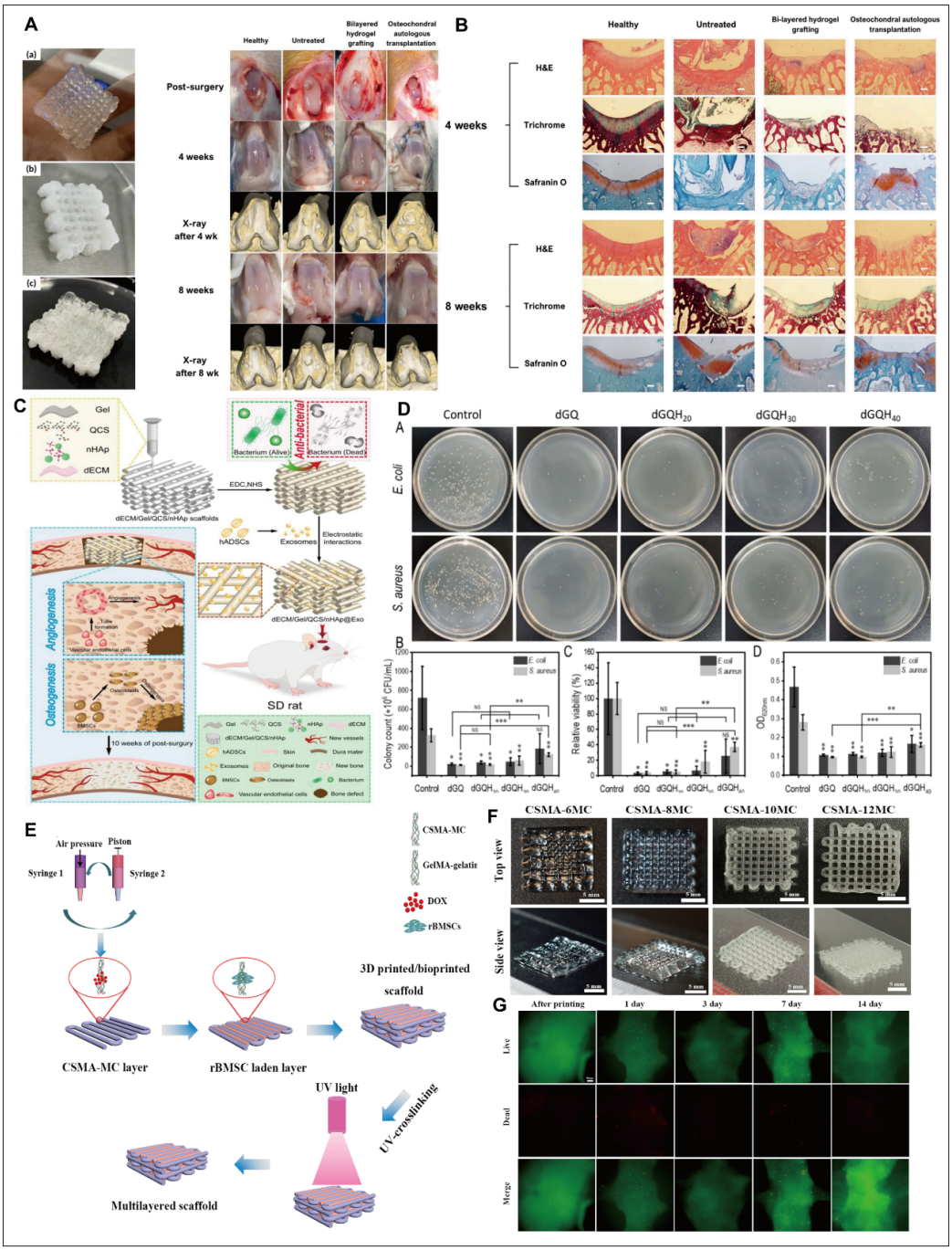


Figure 5. Application of modified chitosan 3D-printed scaffolds in osteochondral defects. (A) Schematic diagram of the bilayer printed scaffold and analysis of its efficacy in repairing osteochondral defects. Reprinted from Ref. [7]. Copyright © 2025, The Authors. (B) Histological analysis of repaired osteochondral tissue. Reprinted from Ref. [7]. Copyright © 2025, The Authors. (C) Schematic illustration of the fabrication process for the decellularized extracellular matrix (dECM)/gelatin (Gel)/quaternized chitosan (QCS)/nano-hydroxyapatite (nHAp) composite scaffold. Reprinted with permission from Ref. [29]. Copyright © 2023, IOP Publishing Ltd. (D) Antibacterial properties of QCS scaffolds. Reprinted with permission from Ref. [29]. Copyright © 2023, IOP Publishing Ltd. (E) Schematic depicting the construction of a stratified hydrogel scaffold incorporating both therapeutic agents and living cells. Reprinted from Ref. [77]. Copyright © 2024, The Authors. (F) Physical images of 3D-printed hydrogels containing different components. Reprinted from Ref. [77]. Copyright © 2025, The Authors. (G) Biocompatibility of bioprinted cell-loaded scaffolds. Reprinted from Ref. [77]. Copyright © 2025, The Authors. Abbreviations: CSMA: Chitosan methacrylate; dGQ: 3D hybrid scaffold composed of dECM, Gel, and QCS; dGQH: 3D hybrid scaffold composed of dECM, Gel, QCS, and nHAp; DOX: Doxorubicin; EDC: Ethyldimethylaminopropyl Carbodiimide; *E. coli*: *Escherichia coli*; GelMA: Gelatin methacrylate; hADSCs: Human adipose derived stem cells; MC: Methylcellulose; NHS: N-Hydroxysuccinimide; rBMSC: Rat bone marrow mesenchymal stem cell; SD: Sprague–Dawley; *S. aureus*: *Staphylococcus aureus*; UV: Ultraviolet.

Staphylococcus aureus), while also significantly promoting osteogenesis and angiogenesis at bone defect sites (Figure 5C and 5D).

5.3. Chitosan methacrylate

Chitosan methacrylate (CSMA) enhances crosslinking and structural stability by introducing methacrylate groups into the chitosan backbone. During 3D printing, CSMA exhibits superior shape retention and mechanical stability, making it suitable for fabricating osteochondral repair scaffolds that require high strength and durability.[76] Customized mechanical properties can be achieved by adjusting the methacrylation degree, solution concentration, and crosslinking conditions to meet the mechanical demands of osteochondral structures.[46] A study employed 3D printing to fabricate hydrogel scaffolds composed of CSMA and methylcellulose. The photopolymerized porous scaffolds exhibited excellent biocompatibility and mechanical properties, along with controllable drug release capabilities (Figure 5E–5G).[77] Researchers have also modified CSMA by grafting KGN to functionalize it. Hydrolysis of the amide bonds in the hydrogel enables continuous KGN release, promoting cartilage repair.[78] Additional components can also be incorporated into bioinks to achieve bone and cartilage regeneration. Zhang *et al.*[17] prepared photopolymerizable bioink using CSMA loaded with KGN nanoparticles to promote cartilage tissue regeneration. Additionally, cells can be incorporated into 3D-printed hydrogels to construct osteochondral scaffolds. Liu *et al.*[79] prepared a bioink by blending gelatin methacrylate with CSMA and encapsulating BMSCs to print a cartilage scaffold. Cell viability within the scaffold reached 91.1%, and the construct supported cartilage differentiation. Transplantation of the bioprinted hydrogel loaded with BMSCs into cartilage defects resulted in effective hyaline cartilage repair.[79]

Modified chitosan scaffolds demonstrate significant advantages in 3D printing technology. By introducing specific functional groups, the water solubility, antibacterial properties, and mechanical strength of chitosan are enhanced. Overall, these functional modifications improve the comprehensive performance of the scaffolds, offering a superior solution for osteochondral tissue engineering.

6. Limitations of chitosan composite scaffolds

Although the properties of chitosan and its derivatives have been described in detail, inherent limitations still exist that impact clinical translation. First, chitosan possesses several limitations in its physicochemical properties. Native chitosan is virtually insoluble under neutral and alkaline conditions, with its solubility and protonation strongly dependent on pH.[80] This results in restricted swelling, stability, and gelation windows under physiological conditions. Additionally, variations in source, degree of deacetylation, and molecular weight distribution lead to batch-to-batch inconsistencies and reproducibility issues.

Second, pure chitosan hydrogel scaffolds exhibit insufficient compressive strength, fatigue resistance, and shear resistance. Ionic crosslinking of chitosan provides weak structural stability under mechanical load, whereas photo-crosslinked derivatives such as CSMA require photoinitiators and ultraviolet or visible light exposure, which may introduce cytotoxic effects depending on dose and exposure duration.[78] Consequently, achieving a balance between printability, stability, and cytocompatibility remains a major technical bottleneck.

Furthermore, chitosan is degraded primarily via lysozyme-mediated enzymolysis and dissolution, resulting in unpredictable degradation kinetics.[81] Excessively rapid degradation may lead to scaffold collapse before tissue regeneration, whereas slow degradation can hinder new matrix deposition. The degradation rate is highly sensitive to the degree of deacetylation and polymer sequence, which are difficult to precisely regulate during synthesis. Chitosan is also highly susceptible to molecular degradation during sterilization. γ- or β-irradiation significantly reduces its molecular weight, altering viscosity, color, and mechanical strength, whereas ethylene oxide sterilization may leave cytotoxic residues.[82] These sensitivities complicate large-scale manufacturing, quality assurance, and regulatory compliance for clinical applications. Although layered or gradient scaffolds have shown encouraging results *in vitro* and in preclinical studies, complete integration between bone and cartilage compartments remains a key challenge.[51] Current constructs often exhibit inadequate interfacial strength, insufficient lubrication, and suboptimal fatigue resistance under cyclic joint loading. Long-term performance comparable to native osteochondral tissue has yet to be demonstrated.

Functional derivatives such as CMCS or QCS improve solubility, processability, and antibacterial activity; however, these modifications may reduce stiffness, alter charge density, or induce undesired cellular stress responses.[81] Similarly, photopolymerizable derivatives rely on external initiators, raising potential concerns regarding biocompatibility and reproducibility.

The current limitations and corresponding solutions are summarized in Table 1.

7. 3D printing technology based on chitosan-based composite scaffolds

In the field of osteochondral repair, various 3D printing technologies are employed to prepare scaffold materials, each with its own advantages and disadvantages. This section provides a comprehensive overview of the advantages, disadvantages, and future directions of different 3D printing methods combined with chitosan-based composite bioinks (Table 2; Figure 6). Furthermore, bioinks are crucial for the successful printing of tissue structures. Different 3D printing technologies impose distinct requirements on bioinks based on their underlying principles. Therefore, we also summarize the application scenarios for chitosan-based 3D bioinks.

7.1. Extrusion bioprinting

Extrusion-based bioprinting (EBP) employs a highly regulated dispensing mechanism to sequentially deposit bioinks, enabling the construction of complex 3D architectures (Figure 6A and 6B). The key to this technology lies in material extrusion, typically achieved by heating or applying mechanical pressure to force the bioink—usually composed of cells and biopolymers—through a nozzle, depositing it at predetermined locations.[91] Compared to other bioprinting techniques, EBP offers higher material compatibility, a larger printing range, and lower costs. Nguyen *et al.*[7] prepared hydrogels of CMCS and OXG using 3D printing technology to fabricate a bilayer osteochondral hydrogel scaffold. A BCP layer was added to the lower layer to induce osteogenesis. The cartilage layer was printed at a thickness of 1 mm, while the subchondral bone layer was printed at 2 mm. A porosity of 30% was set, which was demonstrated to be conducive to cell ingrowth and proliferation.[7] By modifying chitosan with double bonds and combining it with recombinant collagen and nano-clay to prepare a photopolymerizable bioink, a small-molecule drug (KGN) was loaded to promote cartilage differentiation. *In vivo* assessment revealed that scaffolds engineered via EBP successfully supported the regeneration of native cartilage tissues.[17]

However, EBP suffers from a narrow rheological window, leading to shear-induced cell damage, nozzle clogging, and limited resolution.[84] The ionic crosslinking typically used in chitosan systems provides poor long-term stability and nonuniform gelation, while weak interlayer bonding and low wear resistance restrict mechanical performance under joint loading.[92] Additionally, native chitosan exhibits pH-dependent solubility and limited cell adhesion, necessitating blending or modification.[93] Future progress will rely on multimodal crosslinking, microgel-reinforced formulations, and nanofiller incorporation to enhance mechanical integrity and bioactivity. Coaxial or microfluidic extrusion and 4D-printing strategies are expected to improve structural gradients, nutrient diffusion, and dynamic tissue integration, advancing chitosan-based bioinks toward functional osteochondral regeneration.

7.2. Stereolithography

Stereolithography (SLA) uses laser or ultraviolet light to cure photopolymer resin layer by layer, forming 3D

Table 1. Summary of major limitations of chitosan-based composite scaffolds and derivatives for osteochondral repair and common improvement strategies

Limitation	Manifestations	Improvement strategy	Ref.
pH-dependent solubility; batch variability	Difficult gelation/stability at physiological pH; inconsistent printability and biological outcomes	Use of water-soluble derivatives (CMCS, QCS); buffer optimization; control of MW	80
Insufficient mechanical properties	Low load-bearing capacity and poor boundary lubrication on cartilage surfaces	Composite or double-network designs; layered structures	83,84
Narrow crosslinking; photoinitiator cytotoxicity	Ionically crosslinked CS weak under load; photoinitiators may induce cell stress/toxicity	Visible-light initiators; optimized irradiation; hybrid chemical–physical crosslinking	85,86
Degradation-rate incompatibility	Rapid dissolution or enzyme-mediated degradation outpaces new tissue formation	Tuning MW; enzyme-responsive systems; mineral-reinforced composites for bone layers	87
Sterilization sensitivity	γ-/β-irradiation lowers molecular weight (MW), altering viscosity and mechanical stability	Validated irradiation doses; non-EtO sterilization; post-sterilization quality control	82,88
Poor interface integration	Weaker interface bonding; limited fatigue/lubrication matching under long-term cyclic loading	Gradient or bilayered scaffolds; tribological validation under simulated joint	51,89
Trade-offs of charged/soluble derivatives	QCS or carboxymethyl CS improves solubility but reduces stiffness or alters cell behavior	Control charge density; combine with inorganic fillers; low-toxicity initiator systems	81,90

Abbreviations: CMCS: Carboxymethyl chitosan; CS: Chitosan; EtO: Ethylene oxide; QCS: Quaternized chitosan.

objects. Compared to other 3D printing methods, SLA offers significant advantages in resolution and precision, enabling the creation of finer structures suitable for biomedical applications.[96] In osteochondral tissue engineering, the high-precision forming capability of SLA aids in reconstructing complex osteochondral structures and intricate microenvironments, providing an ideal scaffold for cell growth and differentiation. In this context, SLA printing combined with chitosan-based composite bioinks demonstrates distinct advantages in applications requiring microscale precision and surface fidelity rather than bulk mechanical strength. Its superior resolution makes it particularly suitable for fabricating cartilage-like zones, interfacial gradient layers, and microstructured templates that replicate the hierarchical organization of native cartilage. Conversely, SLA remains less suited for load-bearing subchondral scaffolds, where EBP or fused deposition modeling (FDM) techniques provide better mechanical stability. One study utilized SLA technology to construct a bilayer biomimetic periosteum. The upper layer consisted of a high-mechanical-property fiber layer made of PEGDA/chitosan/TCP, which prevented muscle compression and soft tissue invasion. The lower layer comprised a gelatin methacrylate/PEGDA/ammonium molybdate cambium layer. When combined with 808 nm near-infrared photothermal effects, this layer promoted MC3T3-E1 cell proliferation and osteogenic differentiation. This approach offers a novel strategy for bone defect repair through the synergistic effects of physical barriers, chemical induction, and physical stimulation.[97] Risangud developed a self-healing hydrogel fabricated through SLA technology, composed of CMCS and oxidized dextran (ODex). By tuning the concentration of CMCS and the oxidation level

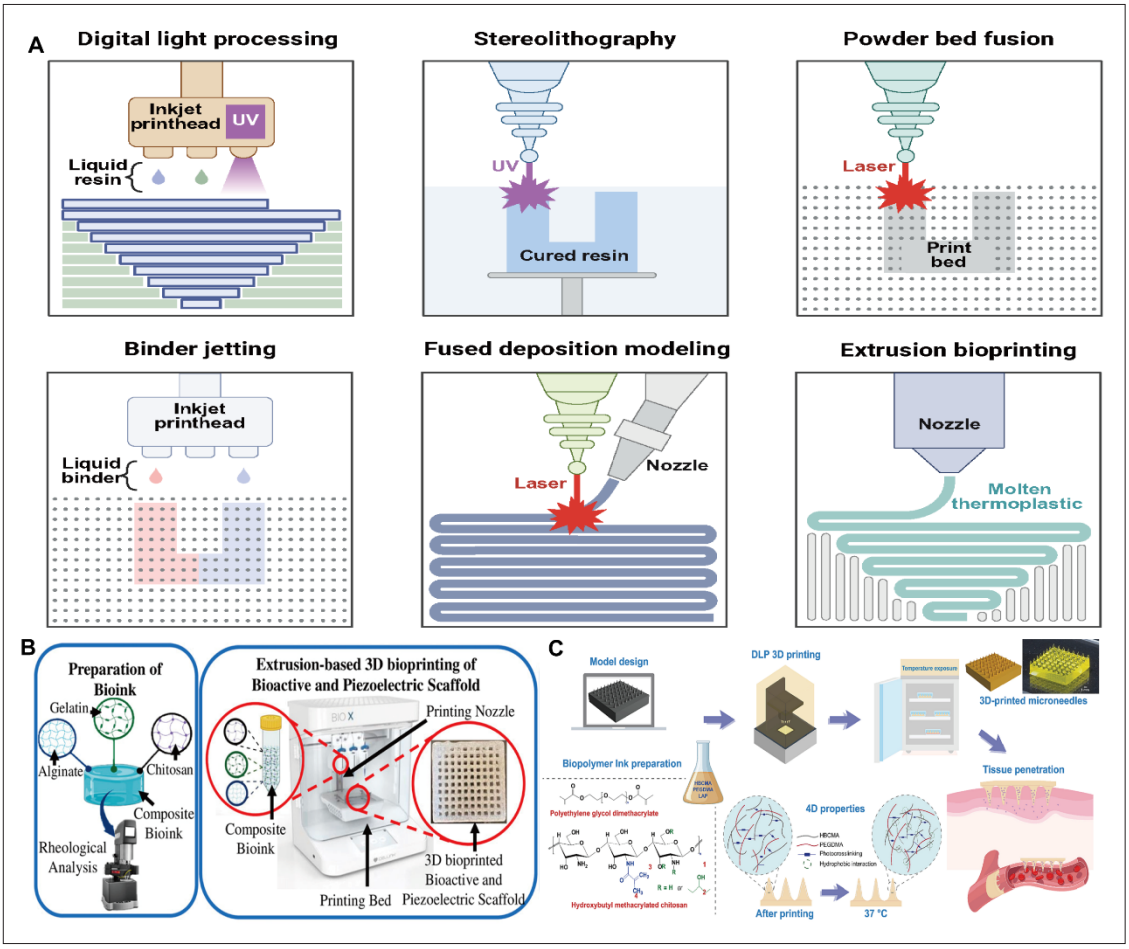


Figure 6. 3D Printing technology based on chitosan hydrogels. (A) Schematic diagram of the most common 3D printing techniques (created in https://BioRender.com). (B) Extrusion-based 3D printing technology. Reprinted with permission from Ref. [94]. Copyright © 2025, Mary Ann Liebert, Inc. (C) Fabrication of hydroxybutyl methacrylate chitosan microneedles using digital light processing (DLP) 3D printing. Reprinted with permission from Ref. [95]. Copyright © 2025, Elsevier. Abbreviations: HBCMA: Hydroxybutyl methacrylated chitosan; LAP: Lithium phenyl-2,4,6-trimethylbenzoylphosphinate; PEGDMA: Polyethylene glycol dimethacrylate; UV: Ultraviolet.

of ODex, the mechanical characteristics and biological performance of the hydrogel could be effectively tailored.[98]

However, SLA processing requires low-viscosity bioinks, which limits cell encapsulation and filler incorporation. Light scattering, shallow penetration depth, and photoinitiator-induced cytotoxicity often compromise curing uniformity and biocompatibility.[99] Moreover, methacrylation may alter chitosan degradation and reduce mechanical strength, making SLA less suitable for load-bearing or high-cell-density constructs.[76] Future efforts should focus on visible-light or enzyme-initiated crosslinking, dual-network and nanocomposite formulations, and hybrid SLA–extrusion systems to enhance mechanical robustness and biological functionality. SLA's precision and reproducibility make it particularly advantageous for fabricating cartilage-layer architectures and microstructured osteochondral interfaces where fine resolution outweighs load-bearing requirements.

7.3. Fused deposition modeling

With FDM technology, thermoplastic materials are heated to a molten state and then deposited layer by layer through a nozzle onto the build platform, ultimately forming a 3D scaffold. FDM offers a cost-effective, scalable, and structurally stable platform for fabricating osteochondral scaffolds. When integrated with chitosan-based composites such as polylactic acid (PLA), PCL, or surface-modified chitosan filaments, FDM enables precise construction of load-bearing subchondral frameworks with tunable porosity and mechanical strength. Its high shape fidelity and design flexibility make it particularly suitable for bone-side scaffolds requiring mechanical support and anatomical conformity. In one study, chitosan was incorporated to reinforce the mechanical performance of PLA scaffolds fabricated via FDM technology.[100] Findings revealed that the mechanical strength of PLA/chitosan composites is strongly influenced by the chitosan loading content and packing density. Because FDM is restricted to thermoplastic materials, chitosan is often employed as a surface-modification agent to enhance the biocompatibility and bioactivity of printed polymers. One study utilized chitosan to enhance the mechanical properties of PLA scaffolds, with the material printed using an FDM setup.[101] Singh *et al.*[100] fabricated PLA/PEG 3D-printed scaffolds coated with chitosan–PEG nanofibers loaded with vancomycin and IGF-1, achieving mechanical support, antibacterial properties, and enhanced osteointegration for bone repair. Some researchers directly coated scaffolds with chitosan solution. For instance, Ye and colleagues[102] fabricated 3D printed poly (3-hydroxybutyrate-co-3-hydroxyvalerate) (PHBV) scaffolds and subsequently coated them with chitosan. Compared to uncoated PHBV constructs, the chitosan-coated scaffolds significantly enhanced the adhesion and proliferation of BMSCs and promoted osteogenic differentiation by upregulating osteogenesis-related gene expression.[102] With ongoing innovations in materials science and manufacturing precision, FDM demonstrates strong potential for osteochondral tissue engineering applications. Continued optimization of the mechanical strength, structural accuracy, and biodegradability of chitosan-based composite scaffolds is expected to further facilitate their translation into clinical therapies.

However, the non-meltable and hydrophilic nature of native chitosan limits its direct processability and compatibility with hydrophobic thermoplastics. High chitosan content can reduce filament printability and mechanical integrity, while poor interfacial adhesion between the printed polymer framework and subsequent hydrogel layers impairs overall integration.[103,104] Consequently, FDM is best applied as a supportive structural framework, combined with extrusion or hydrogel-based deposition to create hybrid osteochondral constructs that couple strength with bioactivity.[105] Future research should focus on surface grafting and compatibilizer modification to improve polymer–biopolymer bonding, gradient co-printing to achieve continuous transitions across bone–cartilage regions, and bioactive filler incorporation to enhance osteoconductivity. Integration of multi-material and hybrid FDM–bioprinting systems will further enable the fabrication of patient-specific, mechanically functional, and biologically responsive osteochondral scaffolds.

7.4. Digital light processing

Digital light processing (DLP) technology utilizes a digital light source (such as ultraviolet light) to project light onto the surface of photosensitive resin, causing it to cure layer by layer in the illuminated areas and rapidly form intricate 3D structures.[106] DLP technology is capable of achieving submicron-level printing precision, making it suitable for manufacturing complex osteochondral scaffolds, particularly those requiring intricate pore structures and smooth surface finishes. However, DLP technology imposes stringent material requirements. In osteochondral scaffold design, chitosan often requires integration with complementary materials to improve its mechanical performance and augment its biological functionality.[107] A study utilized PEGDA as the base material, combined with chitosan, to fabricate a multi-channel nerve-guiding conduit via DLP printing. This approach achieved structural guidance and bio-induced synergistic repair of peripheral nerve injuries.[60] Furthermore, chitosan microneedles produced by DLP technology have been employed for the controlled administration of small-

molecule pharmaceuticals, exhibiting outstanding soft tissue penetration (Figure 6C).

Additionally, DLP requires low-viscosity bioinks, limiting cell density and the inclusion of reinforcing fillers.[108] Light scattering and restricted penetration depth can result in incomplete curing in thick constructs, while cytotoxicity of photoinitiators and potential photothermal stress remain challenges for biocompatibility.[99] Moreover, the mechanical strength of DLP-printed chitosan hydrogels is typically insufficient for load-bearing applications, restricting their use to cartilage or interface regions rather than the subchondral bone zone. In practice, DLP excels in engineering high-fidelity cartilage-like zones, zonal gradient architectures, and bioactive coatings that demand precision rather than bulk strength. Its combination with extrusion-based deposition or FDM frameworks enables multi-material osteochondral constructs with both structural integrity and biological functionality. Future development will focus on visible-light and enzyme-initiated photopolymerization to enhance cytocompatibility, nanocomposite reinforcement to improve modulus, and dual-network hydrogel systems to achieve balanced strength and elasticity. Integration of multi-photon and grayscale DLP techniques will further expand its potential for biomimetic gradient and multilayer cartilage–bone interfaces.

8. Conclusions and future perspectives

Chitosan-based 3D-printed scaffolds exhibit significant potential in osteochondral repair. These scaffolds, fabricated using technologies like FDM, low-temperature deposition, and photopolymerization SLA, offer controllable porous structures that enhance cell migration, adhesion, and nutrient delivery. Compared with other printing methods, EBP has the broadest adaptability to ink viscosity and is particularly suitable for chitosan-based inks. The extrusion method enables stable deposition of high-viscosity polymer hydrogel precursor materials, even those with high cell density, a characteristic demonstrated in previous studies.[112,113] Several studies have identified high viscosity, shear thinning, and rapid shape recovery as key rheological characteristics that facilitate high-conformal printing with chitosan-based inks.[2,114,115] Correspondingly, the extrusion method can satisfy the combined requirements of extrudability, continuity, interlayer support, and conformability within a broad process window. In recent years, researchers have further expanded the printability and mechanical limits of chitosan through strategies such as freeze-dried/rehydrated inks composed of chitosan nanofibers/hyaluronic acid blends or direct printing of high-strength chitosan hydrogels. These systems have achieved high printing resolution and excellent cell compatibility on extrusion platforms, highlighting the extrusion method's adaptability advantages for chitosan.[116] The integration of chitosan with synthetic polymers and bio-ceramics improves mechanical strength, enabling the scaffolds to withstand joint loading. In terms of bioactivity, chitosan-based composite scaffolds support osteoblast and chondrocyte growth, with modifications such as methacrylation and composite bioinks enhancing printability and cellular compatibility. Incorporating

Table 2. Summary of limitations, disadvantages, and applications of different 3D printing techniques combined with chitosan-based biomaterials for osteochondral repair

Printing Method	Limitations	Disadvantages	Future directions	Application scenarios	Ref.
EBP	Nozzle clogging; limited stability; low resolution	Difficulty balancing elasticity and stiffness; weak layer adhesion under cyclic load	Dual crosslinking; coaxial printing; microgel reinforcement; nanoparticle fillers	Cell-laden bioinks; bilayer and gradient structure construction	84,92,93
Extrusion + photocuring	Cytotoxic; light scattering; poor mechanical properties	Nonuniform curing in thick constructs; limited wear/lubrication; poor fatigue strength	Visible-light, low-tox initiators (e.g., LAP); two-step curing; nanoparticle reinforcement	Moderate-resolution bioprinting; multilayer constructs; fast gelation; tunable stiffness	109-111
DLP/SLA	Poor cell loading; phototoxicity; incomplete deep curing; complex setup	Poor wear resistance; poor fatigue resistance	Visible-light initiators; filler reinforcement; gradient structures via DLP	High-precision fabrication; mimicking native cartilage	76,99,108
FDM	Non-meltable; poor adhesion; low mechanical strength	Poor interface bonding	Surface modification; coupling agents; gradient co-printing	Cost-efficient fabrication; subchondral bone scaffolds; mechanical support	103-105

Abbreviations: DLP: Digital light processing; EBP: Extrusion-based bioprinting; FDM: Fused deposition modeling; LAP: Lithium phenyl-2,4,6-trimethylbenzoylphosphinate; SLA: Stereolithography.

bioactive factors such as bone morphogenetic protein 2 and TGF-β facilitates controlled release, promoting osteogenesis and chondrogenesis at specific defect sites. In cell delivery and tissue integration, 3D bioprinting enables the precise placement of MSCs, chondrocytes, or osteoblasts within chitosan hydrogels. Dual- or triple-nozzle systems allow for the creation of biphasic or triphasic scaffolds that mimic the osteochondral structure. Combined with exosome-based acellular therapies, these approaches improve cell viability, maintain stem cell potency, and modulate the immune microenvironment, offering new strategies for tissue regeneration.

Although significant advancements have been achieved in the development of chitosan-based 3D printed scaffolds, numerous obstacles still hinder their translation from experimental research to routine clinical use, highlighting key areas for future investigation. Future research should focus on developing novel chitosan derivatives and composite materials. For example, chemical modifications such as phosphorylation, carboxymethylation, and quaternization can not only improve solubility but also introduce new biological functions. Additionally, exploring the incorporation of nanomaterials, novel synthetic hydrogels, or high-toughness polymers can help achieve mechanical properties that match native tissues, or even feature gradient variations, while maintaining biological activity. The current resolution, speed, and multi-material capabilities of 3D printing technologies still leave room for improvement. Future printing technologies with higher precision will enable the creation of finer microstructures that better replicate the nanoscale topology of the ECM. 4D bioprinting, introducing time as the fourth dimension, will allow printed scaffolds to undergo pre-programmed shape or functional transformations in response to external stimuli after implantation, opening new pathways for minimally invasive surgery and dynamic tissue remodeling. Furthermore, *in situ* 3D printing technology, which allows direct printing at the defect site, will significantly reduce surgical time and improve the fitting of implants to irregular defects, making it an attractive frontier.

Future scaffolds should not only provide physical support but also act as intelligent systems that dynamically respond to and guide the regeneration process. This includes: precise delivery of bioactive factors, requiring the development of more advanced controlled-release systems capable of sequential, spatiotemporal delivery of multiple growth factors to accurately simulate the natural healing cascade; immune modulation, through scaffolds with active immunoregulatory functions—such as integrating anti-inflammatory drugs or using chitosan and its composites to induce macrophage polarization toward the M2 anti-inflammatory phenotype—to create a favorable immune microenvironment for regeneration. It is also necessary to optimize bioink formulations, printing parameters, and crosslinking methods to maximize cell viability. For large-scale bone regeneration, promoting rapid vascularization within the scaffold is a key factor for success. Future designs may incorporate specific angiogenic factors or pre-constructed microchannel networks. Finally, establishing standardized quality control and safety evaluation systems, followed by large-scale, long-term preclinical and clinical studies, is an essential step toward transitioning chitosan-based 3D printed scaffolds from the laboratory to the market.

In conclusion, chitosan-based 3D printed scaffolds have demonstrated great potential and vitality in the field of osteochondral repair. Through interdisciplinary collaboration—integrating the latest advancements in materials science, bioengineering, mechanical manufacturing, and clinical medicine—and by continuously overcoming existing challenges, we are optimistic about achieving truly personalized and functional osteochondral regeneration in the near future, bringing hope to countless patients.

Acknowledgments

None.

Funding

This work is supported by the Beijing Natural Science Foundation (L244037), National Natural Science Foundation of China (No.81601901), the Natural Science Foundation of Liaoning, China (No.2019-MS-079), the Peak Climbing Program, Dalian (No.2022DF012), and the Dalian Science and Technology Innovation Fund (No.2023JJ13SN051). Xiaolin Cui would like to acknowledge the support from The Chinese University of Hong Kong (CUHK)-Practical Biotech Joint Laboratory Fund, the University Development Fund (UDF01002532) of The CUHK, Shenzhen, the CUHK Shenzhen start-up funding (K10120220254), the Shenzhen Natural Science Foundation, the Shenzhen-Hong Kong Cooperation Zone for Technology and Innovation (HZQB-KCZYB-2020056), the Shenzhen Peacock Talent Program, the key project at central government level: The Ability Establishment of Sustainable Use for Valuable Chinese Medicine Resources (2060302), the Ministry of Science and Technology of China's International Young Scholar Grant (QN2023032004L), and the CUHK, Shenzhen University, and Affiliated Hospital Collaboration Fund (HUUF-ZD-202305).

Conflict of interest

The author declares no conflict of interest, financial or otherwise.

Author contributions

Conceptualization: Jiahui Liang, Xiaolin Cui
Visualization: Jiyuan Qi, Yihan Wang, Zhaoyang Liu
Supervision: Weiguo Zhang, Duo Zhang
Writing–original draft: Jiahui Liang, Jiyang Zou, Yuqing He
Writing–review & editing: Xiaolin Cui, Xing Wang, Kang Tian

Ethics approval and consent to participate

Not applicable.

Consent for publication

Not applicable.

Availability of data

Not applicable.

References

1. Lu J, Gao Y, Cao C, *et al*. 3D bioprinted scaffolds for osteochondral regeneration: advancements and applications. *Mater Today Bio*. 2025;32:101834. doi: 10.1016/j.mtbio.2025.101834
2. Taghizadeh M, Taghizadeh A, Yazdi MK, *et al*. Chitosan-based inks for 3D printing and bioprinting. *Green Chem*. 2022; 24(1), 62-101. doi: 10.1039/D1GC01799C
3. Lin X, Zhang Y, Li J, *et al*. Biomimetic multizonal scaffolds for the reconstruction of zonal articular cartilage in chondral and osteochondral defects. *Bioact Mater*. 2025;43: 510-549. doi: 10.1016/j.bioactmat.2024.10.001
4. Zhang G, He S, He X, *et al*. Local Recruitment of Autologous Stem Cells via a Targeting Microgel for Precise Cartilage Repair without Surgery. *Adv Mater*. 2025;37(33):e2505544. doi: 10.1002/adma.202505544
5. Zhang B, Zhang M, Jiang C, Yan W, Pan Y, Meng F. Engineered polysaccharide scaffolds for cartilage regeneration: Mechanisms, functionalization, and clinical prospects. *Colloids Surf B Biointerfaces*. 2025;257:115134. doi: 10.1016/j.colsurfb.2025.115134
6. Kunze KN, Persaud S, Briano J, *et al*. Outcomes of Revision Cartilage Restoration Surgery for Failed Primary Treatment of Chondral or Osteochondral Defects of the Knee: A Systematic Review. *Am J Sports Med*. 2025;53(6): 1515-1523. doi: 10.1177/03635465241260271
7. Nguyen MN, Vu BT, Truong DM, *et al*. Fabrication of 3-Dimensional-Printed Bilayered Scaffold Carboxymethyl Chitosan/Oxidized Xanthan Gum, Biphasic Calcium Phosphate for Osteochondral Regeneration. *Biomater Res*. 2025;29:0186. doi: 10.34133/bmr.0186
8. Wang X, Wu S, Li R, *et al*. ROS-Activated Nanohydrogel Scaffolds with Multi-Factors Controlled Release for Targeted Dual-Lineage Repair of Osteochondral Defects. *Adv Sci (Weinh)*. 2025;12(20):e2412410. doi: 10.1002/advs.202412410
9. Koh RH, Kim J, Kim JU, *et al*. Bioceramic-mediated chondrocyte hypertrophy promotes calcified cartilage formation for rabbit osteochondral defect repair. *Bioact Mater*. 2024;40:306-317. doi: 10.1016/j.bioactmat.2024.06.018
10. Wu Z, Yao H, Sun H, *et al*. Enhanced hyaline cartilage formation and continuous osteochondral regeneration via 3D-Printed heterogeneous hydrogel with multi-crosslinking inks. *Mater Today Bio*. 2024;26:101080. doi: 10.1016/j.mtbio.2024.101080
11. Wu H, Chen C, Li J, *et al*. Engineered Magneto-Piezoelectric Nanoparticles-Enhanced Scaffolds Disrupt Biofilms and Activate Oxidative Phosphorylation in Icam1(+) Macrophages for Infectious Bone Defect Regeneration. *ACS Nano*. 2024;18(52):35575-35594. doi: 10.1021/acsnano.4c13562
12. Wang Y, Zhou X, Jiang J, *et al*. Carboxymethyl chitosan-enhanced multi-level microstructured composite hydrogel scaffolds for bone defect repair. *Carbohydr Polym*. 2025;348(Pt B):122847. doi: 10.1016/j.carbpol.2024.122847
13. Wei P, Zhou J, Xiong S, *et al*. Chestnut-Inspired Hollow Hydroxyapatite 3D Printing Scaffolds Accelerate Bone Regeneration by Recruiting Calcium Ions and Regulating Inflammation. *ACS Appl Mater Interfaces*. 2024;16(8):9768-9786. doi: 10.1021/acsami.3c17087
14. Ngau SM, Cheah KH, Wong VL, Khiew PS, Lim SS. 3D-printed poly(ethylene) glycol diacrylate (PEGDA)-chitosan-nanohydroxyapatite scaffolds: Structural characterization and cellular response. *Int J Biol Macromol*. 2025;296:139652. doi: 10.1016/j.ijbiomac.2025.139652
15. Hu X, Man Y, Li W, *et al*. 3D Bio-Printing of CS/Gel/HA/Gr Hybrid Osteochondral Scaffolds. *Polymers (Basel)*. 2019;11(10). doi: 10.3390/polym11101601
16. Xu J, Su Y, Yang J, *et al*. A 3D bioprinted gelatin/quaternized chitosan/decellularized extracellular matrix based hybrid bionic scaffold with multifunctionality for infected full-

thickness skin wound healing. *Int J Biol Macromol*. 2025;309(Pt 1):142816.
doi: 10.1016/j.ijbiomac.2025.142816

17. Zhang W, Shi K, Yang J, *et al*. 3D printing of recombinant collagen/chitosan methacrylate/nanoclay hydrogels loaded with Kartogenin nanoparticles for cartilage regeneration. *Regen Biomater*. 2024;11:rbae097.
doi: 10.1093/rb/rbae097

18. Corrado F, Di Maio L, Palmero P, *et al*. Vat photo-polymerization 3D printing of gradient scaffolds for osteochondral tissue regeneration. *Acta Biomater*. 2025;200:67-86.
doi: 10.1016/j.actbio.2025.05.042

19. Jacob G, Shimomura K, Nakamura N. Osteochondral Injury, Management and Tissue Engineering Approaches. *Front Cell Dev Biol*. 2020;8:580868.
doi: 10.3389/fcell.2020.580868

20. Wu H, Wang X, Wang G, *et al*. Advancing Scaffold-Assisted Modality for In Situ Osteochondral Regeneration: A Shift From Biodegradable to Bioadaptable. *Adv Mater*. 2024;36(47):e2407040.
doi: 10.1002/adma.202407040

21. Kwon H, Brown WE, Lee CA, *et al*. Surgical and tissue engineering strategies for articular cartilage and meniscus repair. *Nat Rev Rheumatol*. 2019;15(9):550-570.
doi: 10.1038/s41584-019-0255-1

22. Gao F, Xu Z, Liang Q, *et al*. Direct 3D Printing of High Strength Biohybrid Gradient Hydrogel Scaffolds for Efficient Repair of Osteochondral Defect. *Adv Funct Mater*. 2018;28(13):1706644.
doi: 10.1002/adfm.201706644

23. Gu Y, Zou Y, Huang Y, *et al*. 3D-printed biomimetic scaffolds with precisely controlled and tunable structures guide cell migration and promote regeneration of osteochondral defect. *Biofabrication*. 2023;16(1):015003.
doi: 10.1088/1758-5090/ad0071

24. Qu H, Gao C, Liu K, *et al*. Gradient matters via filament diameter-adjustable 3D printing. *Nat Commun*. 2024;15(1):2930.
doi: 10.1038/s41467-024-47360-y

25. Li CJ, Park JH, Jin GS, *et al*. Strontium/Silicon/Calcium-Releasing Hierarchically Structured 3D-Printed Scaffolds Accelerate Osteochondral Defect Repair. *Adv Healthc Mater*. 2024;13(20):e2400154.
doi: 10.1002/adhm.202400154

26. Li Q, Yu H, Zhao F, *et al*. 3D Printing of Microenvironment-Specific Bioinspired and Exosome-Reinforced Hydrogel Scaffolds for Efficient Cartilage and Subchondral Bone Regeneration. *Adv Sci (Weinh)*. 2023;10(26):e2303650.
doi: 10.1002/advs.202303650

27. Li C, Wang K, Li T, *et al*. Patient-specific Scaffolds with a Biomimetic Gradient Environment for Articular Cartilage-Subchondral Bone Regeneration. *ACS Appl Bio Mater*. 2020;3(8):4820-4831.
doi: 10.1021/acsabm.0c00334

28. Jahani A, Nourbakhsh MS, Moradi A, Mohammadi M, Tayebi L. Incorporating insulin into alginate-chitosan 3D-printed scaffolds: A comprehensive study on structure, mechanics, and biocompatibility for cartilage tissue engineering. *Carbohydr Polym Technol Appl*. 2025;9:100696.
doi: 10.1016/j.carpta.2025.100696

29. Kang Y, Xu J, Meng L, *et al*. 3D bioprinting of dECM/Gel/QCS/nHAp hybrid scaffolds laden with mesenchymal stem cell-derived exosomes to improve angiogenesis and osteogenesis. *Biofabrication*. 2023;15(2):024103.
doi: 10.1088/1758-5090/acb6b8

30. Wang W, Zheng L, Liu W, *et al*. Enhanced efficacy of 3D architectural glass–ceramic scaffolds in vertical bone augmentation compared with conventional bone-block grafts of different origins. *Mater Des*. 2025;253,113989.
doi: 10.1016/j.matdes.2025.113989

31. Sun Q, Qiu T, Liu X, Wei Q. Cellular Spatial Sensing Determines Cell Mechanotransduction Activity on the Aligned Nanofibers. *Small*. 2025;21(13):e2410351.
doi: 10.1002/smll.202410351

32. Cho S, Lee KS, Lee K, *et al*. Surface Crystal and Degradability of Shape Memory Scaffold Essentialize Osteochondral Regeneration. *Small*. 2024;20(40):e2401989.
doi: 10.1002/smll.202401989

33. Tang W, Pan P, Chen T, *et al*. 3D chitosan scaffolds loaded with ZnO nanoparticles for bone tissue engineering. *Colloids Surf B Biointerfaces*. 2025;245:114199.
doi: 10.1016/j.colsurfb.2024.114199

34. Zhao W, Chen H, Zhang Y, *et al*. Adaptive multi-degree-of-freedom in situ bioprinting robot for hair-follicle-inclusive skin repair: A preliminary study conducted in mice. *Bioeng Transl Med*. 2022;7(3):e10303.
doi: 10.1002/btm2.10303

35. Lipskas J, Deep K, Yao W. Robotic-Assisted 3D Bio-printing for Repairing Bone and Cartilage Defects through a Minimally Invasive Approach. *Sci Rep*. 2019;9(1):3746.
doi: 10.1038/s41598-019-38972-2

36. Shariatinia Z. Carboxymethyl chitosan: Properties and biomedical applications. *Int J Biol Macromol*. 2018;120(Pt B):1406-1419.
doi: 10.1016/j.ijbiomac.2018.09.131

37. Liu Y, Yuan K, Lin Y, *et al*. Directional Freeze-Casting Cryogel Loaded with Quaternized Chitosan Modified Gallium Metal-Organic Frameworks to Capture and Eradicate the Resistant Bacteria for Guided Regeneration in Infected Bone Defects. *Adv Mater*. 2025;37(9):e2414437.
doi: 10.1002/adma.202414437

38. Chen YR, Yan X, Yuan FZ, *et al*. Kartogenin-Conjugated Double-Network Hydrogel Combined with Stem Cell

Transplantation and Tracing for Cartilage Repair. *Adv Sci (Weinh)*. 2022;9(35):e2105571.
doi: 10.1002/advs.202105571

39. Islam MM, Shahruzzaman M, Biswas S, Nurus Sakib M, Rashid TU. Chitosan based bioactive materials in tissue engineering applications-A review. *Bioact Mater*. 2020;5(1):164-183.
doi: 10.1016/j.bioactmat.2020.01.012

40. Furuike T, Komoto D, Hashimoto H, Tamura H. Preparation of chitosan hydrogel and its solubility in organic acids. *Int J Biol Macromol*. 2017;104(Pt B):1620-1625.
doi: 10.1016/j.ijbiomac.2017.02.099

41. Jirofti N, Hashemi M, Moradi A, Kalalinia F. Fabrication and characterization of 3D printing biocompatible crocin-loaded chitosan/collagen/hydroxyapatite-based scaffolds for bone tissue engineering applications. *Int J Biol Macromol*. 2023;252:126279.
doi: 10.1016/j.ijbiomac.2023.126279

42. Kumi M, Wang T, Ejeromedoghene O, Wang J, Li P, Huang W. Exploring the Potentials of Chitin and Chitosan-Based Bioinks for 3D-Printing of Flexible Electronics: The Future of Sustainable Bioelectronics. *Small Methods*. 2024;8(9):e2301341.
doi: 10.1002/smtd.202301341

43. Jiang T, Yang Y, Lin Z, Hong Y, Luo Z. Modified Polysaccharides: Potential Biomaterials for Bioprinting. *J Funct Biomater*. 2025;16(9):338.
doi: 10.3390/jfb16090338

44. Qin S, Wang W, Chen L, *et al*. 3D printed osteochondral lineage-specific biphasic scaffolds for functional repair of full-thickness articular cartilage defects in weight-bearing area. *Biofabrication*. 2025;17(3):035025.
doi: 10.1088/1758-5090/ade8a9

45. Liu K, Zhang Y, Huang L, *et al*. Enhanced printability of high-viscosity chitosan/acrylamide inks via aluminum ions coordination for precision 3D bioprinting of scaffolds. *Carbohydr Polym*. 2025;355:123359.
doi: 10.1016/j.carbpol.2025.123359

46. Chang HK, Yang DH, Ha MY, *et al*. 3D printing of cell-laden visible light curable glycol chitosan bioink for bone tissue engineering. *Carbohydr Polym*. 2022;287:119328.
doi: 10.1016/j.carbpol.2022.119328

47. Lin M, Stehle Y, Chen L, *et al*. A 3D-printed chitosan-based pH-responsive dual functional scaffold for osteomyelitis: synergistic antibacterial and osteogenic treatment. *Carbohydr Polym*. 2025;366:123866.
doi: 10.1016/j.carbpol.2025.123866

48. Liu X, Wang Y, Zhang W, *et al*. Caffeic acid and adenine modified chitosan dual-network hydrogel with antioxidant and pro-proliferative properties for diabetic wound healing. *Carbohydr Polym*. 2025;369:124290.
doi: 10.1016/j.carbpol.2025.124290

49. Wang X, Zhang J, Shan J, *et al*. Polypyrrole-Modified Triple-Responsive Hydrogel Dressing Based on Bacterial Cellulose and Quaternary Ammonium Chitosan and Its Synergistic Antibacterial Mechanism. *ACS Appl Mater Interfaces*. 2025;17(36):50417-50431.
doi: 10.1021/acsami.5c12061

50. Liu Y, Zhou C, Zhang X, Liu W. Chirality Hydroxyapatite Gradient Scaffold Drives Osteochondral Regeneration via YAP/TAZ-Mediated Mechanotransduction. *Adv Healthc Mater*. 2025;14(22):e2501668.
doi: 10.1002/adhm.202501668

51. Pitrolino KA, Felfel RM, Pellizzeri LM, *et al*. Development and in vitro assessment of a bi-layered chitosan-nano-hydroxyapatite osteochondral scaffold. *Carbohydr Polym*. 2022;282:119126.
doi: 10.1016/j.carbpol.2022.119126

52. Cui R, Lu Q, Teng Y, Li K, Li N. Chitosan Promoted the Corneal Epithelial Wound Healing via Activation of ERK Pathway. *Curr Eye Res*. 2017;42(1):21-27.
doi: 10.3109/02713683.2016.1145235

53. Hoemann CD, Rodríguez González J, Guzmán-Morales J, Chen G, Jalali Dil E, Favis BD. Chitosan coatings with distinct innate immune bioactivities differentially stimulate angiogenesis, osteogenesis and chondrogenesis in poly-caprolactone scaffolds with controlled interconnecting pore size. *Bioact Mater*. 2022;10:430-442.
doi: 10.1016/j.bioactmat.2021.09.012

54. Olza S, Hadj Bouzidi NM, Rubatat L, *et al*. Mineralized chitin nanocrystals enhance osteoinductive ability of chitosan 3D porous biohybrid scaffolds for bone tissue regeneration. *Carbohydr Polym*. 2025;366:123911.
doi: 10.1016/j.carbpol.2025.123911

55. Tu C, Gao X, Zheng H, *et al*. Innovative injectable, self-healing, exosome cross-linked biomimetic hydrogel for cartilage regeneration. *J Control Release*. 2025;381:113608.
doi: 10.1016/j.jconrel.2025.113608

56. Tikakosol P, Topham PD, Derry MJ, *et al*. Kartogenin-encapsulated self-healing injectable hydrogel based on hyaluronic acid and chitosan derivative for use as viscosupplementation in knee osteoarthritis. *Int J Biol Macromol*. 2025;328(Pt 1):147304.
doi: 10.1016/j.ijbiomac.2025.147304

57. Li P, Fu L, Liao Z, *et al*. Chitosan hydrogel/3D-printed poly(ε-caprolactone) hybrid scaffold containing synovial mesenchymal stem cells for cartilage regeneration based on tetrahedral framework nucleic acid recruitment. *Biomaterials*. 2021;278:121131.
doi: 10.1016/j.biomaterials.2021.121131

58. Xu J, Ji J, Jiao J, *et al*. 3D Printing for Bone-Cartilage Interface Regeneration. *Front Bioeng Biotechnol*. 2022;10:828921.
doi: 10.3389/fbioe.2022.828921

59. Fan D, Liu Y, Wang Y, *et al*. 3D printing of bone and cartilage with polymer materials. *Front Pharmacol*. 2022;13:1044726.

doi: 10.3389/fphar.2022.1044726

60. Pourfaraj A, Najmoddin N, Behzadnasab M, Pedram MS, Pezeshki-Modaress M. Rapid continuous 3D printed multi-channel poly(ethylene glycol) diacrylate/chitosan nerve guidance conduit: In vivo study. *Int J Biol Macromol*. 2025;321(Pt 4):146491.
doi: 10.1016/j.ijbiomac.2025.146491

61. Wang Z, Sun Y, Li C. Advances in 3D printing technology for preparing bone tissue engineering scaffolds from biodegradable materials. *Front Bioeng Biotechnol*. 2024;12:1483547.
doi: 10.3389/fbioe.2024.1483547

62. Liu G, Wei X, Zhai Y, *et al*. 3D printed osteochondral scaffolds: design strategies, present applications and future perspectives. *Front Bioeng Biotechnol*. 2024;12:1339916.
doi: 10.3389/fbioe.2024.1339916

63. Novotná R, Franková J. Materials Suitable for Osteochondral Regeneration. *ACS Omega*. 2024;9(28):30097-30108.
doi: 10.1021/acsomega.4c04789

64. Li S, Liu J, Liu S, Jiao W, Wang X. Chitosan oligosaccharides packaged into rat adipose mesenchymal stem cells-derived extracellular vesicles facilitating cartilage injury repair and alleviating osteoarthritis. *J Nanobiotechnology*. 2021;19(1):343.
doi: 10.1186/s12951-021-01086-x

65. Chen Y, Mehmood K, Chang YF, Tang Z, Li Y, Zhang H. The molecular mechanisms of glycosaminoglycan biosynthesis regulating chondrogenesis and endochondral ossification. *Life Sci*. 2023;335:122243.
doi: 10.1016/j.lfs.2023.122243

66. Mochizuki M, Yamagata N, Philp D, *et al*. Integrin-dependent cell behavior on ECM peptide-conjugated chitosan membranes. *Biopolymers*. 2007;88(2):122-30.
doi: 10.1002/bip.20684

67. Yeh HY, Liu BH, Sieber M, Hsu SH. Substrate-dependent gene regulation of self-assembled human MSC spheroids on chitosan membranes. *BMC Genomics*. 2014;15(1):10.
doi: 10.1186/1471-2164-15-10

68. Xu B, Ye J, Song S, *et al*. Inherently bioactive iron-chelating Poly (N-acryloyl 2-glycine)/chitosan hydrogel scaffolds orchestrating dual hypoxic-immune microenvironment for functional meniscus regeneration. *Bioact Mater*. 2025;54:492-508.
doi: 10.1016/j.bioactmat.2025.08.028

69. Liu H, Liu S, Liao L, Liao H, Pan W, Hu J. Dual stimulus-responsive dECM cryogel sequentially regulate bone microenvironment for one-step surgical therapy of chronic osteomyelitis. *Mater Today Bio*. 2025;34:102243.
doi: 10.1016/j.mtbio.2025.102243

70. He S, Lin B, Zhang C, *et al*. Injectable chitosan-based thermosensitive hydrogel loaded with adipose-derived mesenchymal stem cells promotes pressure ulcer healing. *Colloids Surf B Biointerfaces*. 2025;256(Pt 2):115089.
doi: 10.1016/j.colsurfb.2025.115089

71. Hia EM, Park J, Suh IW, Park CH. Synergistic effects of modified zinc oxide nanoparticle in a hybrid chitosan-gelatin hydrogel for bone regeneration. *Int J Biol Macromol*. 2025;315(Pt 2):144490.
doi: 10.1016/j.ijbiomac.2025.144490

72. Mokhtari H, Bahari M, Yeganeh F. Chitosan-based Biomaterials in Regenerative Medicine: Optimizing Mesenchymal Stem Cell Viability and Function. *Stem Cell Rev Rep*. 2025;21(7):2010-2030.
doi: 10.1007/s12015-025-10901-z

73. Liu XL, Zhang CJ, Shi JJ, *et al*. Nacre-mimetic cerium-doped nano-hydroxyapatite/chitosan layered composite scaffolds regulate bone regeneration via OPG/RANKL signaling pathway. *J Nanobiotechnology*. 2023;21(1):259.
doi: 10.1186/s12951-023-01988-y

74. Pahlevanzadeh F, Emadi R, Kharaziha M, *et al*. Amorphous magnesium phosphate-graphene oxide nano particles laden 3D-printed chitosan scaffolds with enhanced osteogenic potential and antibacterial properties. *Biomater Adv*. 2024;158:213760.
doi: 10.1016/j.bioadv.2024.213760

75. Duan X, Hu K, Wang J, *et al*. Core-shell engineered Col/Cs@ECM microspheres for macrophage-targeted intracellular drug release in RA therapy. *Bioact Mater*. 2025;54:715-729.
doi: 10.1016/j.bioactmat.2025.08.043

76. Klak M, Kosowska K, Czajka M, *et al*. The Impact of the Methacrylation Process on the Usefulness of Chitosan as a Biomaterial Component for 3D Printing. *J Funct Biomater*. 2024;15(9):251.
doi: 10.3390/jfb15090251

77. Chen XD, Zhang XY, Zhu HQ, Lu HH, Wang M. Three-Dimensional Printing of Hydrogel Blend Tissue Engineering Scaffolds with In Situ Delivery of Anticancer Drug for Treating Melanoma Resection-Induced Tissue Defects. *J Funct Biomater*. 2024;15(12).
doi: 10.3390/jfb15120381

78. Ding Y, Zhu J, Guan X, *et al*. Photocrosslinkable hydrogel of kartogenin functionalized chitosan methacrylate preserves chondrogenesis. *Int J Biol Macromol*. 2025;321(Pt 3):146378.
doi: 10.1016/j.ijbiomac.2025.146378

79. Liu Y, Du L, Zhang H, *et al*. Bioprinted biomimetic hydrogel matrices guiding stem cell aggregates for enhanced chondrogenesis and cartilage regeneration. *J Mater Chem B*. 2024;12(22):5360-5376.
doi: 10.1039/d4tb00323c

80. Lingait D, Rahagude R, Gaharwar SS, *et al*. A review on versatile applications of biomaterial/polycationic chitosan: An insight into the structure-property relationship. *Int J Biol Macromol*. 2024;257(Pt 2):128676.
doi: 10.1016/j.ijbiomac.2023.128676

81. Tomal W, Ortyl J. Water-Soluble Photoinitiators in Biomedical Applications. *Polymers (Basel)*. 2020;12(5). doi: 10.3390/polym12051073

82. Wang L, Huang P, Huang J, *et al*. Modeling of molecular weight changes of polysaccharides subjected to irradiation. *Carbohydr Polym Technol Appl*. 2025;10(000):100815. doi: 10.1016/j.carpta.2025.100815

83. Torgal S, Subramani G, Manian R. Comprehensive insights into chitosan hydrogels: from crosslinking and characterization to immunomodulation, microbiome interactions and biomedical uses. *Biomass Convers Biorefin*. 2025;(9):15. doi: 10.1007/s13399-024-06350-2

84. Taghizadeh M, Taghizadeh A, Yazdi MK, *et al*. Chitosan-based inks for 3D printing and bioprinting (vol 24, pg 62, 2022). *Green Chem*. 2025;(18):27. doi: 10.1039/d5gc90073e

85. Afra S, Samadi A, Asadi P, *et al*. Chitosan crosslinkers and their functionality in 3D bioprinting to produce chitosan-based bioinks. *Inorg Chem Commun*. 2024;168(000):12. doi: 10.1016/j.inoche.2024.112842

86. Williams CG, Malik AN, Kim TK, Manson PN, Elisseeff JH. Variable cytocompatibility of six cell lines with photoinitiators used for polymerizing hydrogels and cell encapsulation. *Biomaterials*. 2005;26(11):1211-8. doi: 10.1016/j.biomaterials.2004.04.024

87. Pitrolino K, Felfel R, Roberts G, Scotchford C, Grant D, Sottile V. In vitrodegradation of a chitosan-based osteochondral construct points to a transient effect on cellular viability. *Biomed Mater*. 2024;19(5):055025. doi: 10.1088/1748-605X/ad6547

88. Rahayu DP, Yunus AL, Yunus MY, *et al*. Study the effect of gamma-irradiation on the physical properties of Chitosan powder with the presence of water. *AIP Conf Proc*. 2024;3074(1):5. doi: 10.1063/5.0211274

89. Cowie RM, Macri-Pellizzeri L, Mclaren J, *et al*. Functional performance of a bi-layered chitosan-nano-hydroxyapatite osteochondral scaffold: a pre-clinical in vitro tribological study. *R Soc Open Sci*. 2024;11(1):13. doi: 10.1098/rsos.230431

90. Andreica BI, Cheng X, Marin L. Quaternary ammonium salts of chitosan. A critical overview on the synthesis and properties generated by quaternization. *Eur Polym J*. 2022;(164-):164. doi: 10.1016/j.eurpolymj.2020.110016

91. Jergitsch M, Mateos-Timoneda MA. 3D extrusion bioprinting: rational bioink design and advanced fabrication techniques. *Trends Biotechnol*. 2025; S0167-7799(25)00223-9. doi: 10.1016/j.tibtech.2025.06.008

92. Agarwal T, Chiesa I, Costantini M, *et al*. Chitosan and its derivatives in 3D/4D (bio) printing for tissue engineering and drug delivery applications. *Int J Biol Macromol*. 2023;246:125669. doi: 10.1016/j.ijbiomac.2023.125669

93. Chen XB, Fazel Anvari-Yazdi A, Duan X, *et al*. Biomaterials / bioinks and extrusion bioprinting. *Bioact Mater*. 2023;28:511-536. doi: 10.1016/j.bioactmat.2023.06.006

94. Sonaye SY, Bohara S, Welsh BL, *et al*. Extrusion-Based 3D Bioprinting of Bioactive and Piezoelectric Scaffolds as Potential Therapy for Treating Critical Soft Tissue Wounds. *Adv Wound Care (New Rochelle)*. 2025;14(3):143-158. doi: 10.1089/wound.2024.0073

95. Che QT, Seo JW, Charoensri K, Nguyen MH, Park HJ, Bae H. 4D-printed microneedles from dual-sensitive chitosan for non-transdermal drug delivery. *Int J Biol Macromol*. 2024;261(Pt 2):129638. doi: 10.1016/j.ijbiomac.2024.129638

96. Li W, Wang M, Ma H, Chapa-Villarreal FA, Lobo AO, Zhang YS. Stereolithography apparatus and digital light processing-based 3D bioprinting for tissue fabrication. *iScience*. 2023;26(2):106039. doi: 10.1016/j.isci.2023.106039

97. Zhou X, Zou B, Chen Q, Yang G, Lai Q, Wang X. Construction of bilayer biomimetic periosteum based on SLA-3D printing for bone regeneration. *Colloids Surf B Biointerfaces*. 2025;246:114368. doi: 10.1016/j.colsurfb.2024.114368

98. Risangud N, Lertwimol T, Sitthisang S, Wongvitvichot W, Uppanan P, Tanodekaew S. The preparation of 3D-printed self-healing hydrogels composed of carboxymethyl chitosan and oxidized dextran via stereolithography for biomedical applications. *Int J Biol Macromol*. 2025;292:139251. doi: 10.1016/j.ijbiomac.2024.139251

99. Zhang X, Cheng F, Islam MR, Li H. The fabrication of the chitosan-based bioink for in vitro tissue repair and regeneration: A review. *Int J Biol Macromol*. 2024;257(Pt 2):128504. doi: 10.1016/j.ijbiomac.2023.128504

100. Singh S, GurminderPrakash, ChanderRamakrishna, SeeramLamberti, LucianoPruncu, Catalin, I. 3D printed biodegradable composites: An insight into mechanical properties of PLA/chitosan scaffold. *Polym Test*. 2020;89(1):106722. doi: 10.1016/j.polymertesting.2020.106722

101. Guo W, Peng Z, Ning D, *et al*. Chitosan microporous foam filled 3D printed polylactic acid-pearl macroporous scaffold: Dual-scale porous structure, biological and mechanical properties. *Int J Biol Macromol*. 2025;303:140508. doi: 10.1016/j.ijbiomac.2025.140508

102. Ye X, Li L, Lin Z, *et al*. Integrating 3D-printed PHBV/Calcium sulfate hemihydrate scaffold and chitosan hydrogel for enhanced osteogenic property. *Carbohydr Polym*. 2018;202:106-114.

doi: 10.1016/j.carbpol.2018.08.117

103. Hui I, Pasquier E, Solberg A, Agrenius K, Håkansson J, Chinga-Carrasco G. Biocomposites containing poly(lactic acid) and chitosan for 3D printing - Assessment of mechanical, antibacterial and in vitro biodegradability properties. *J Mech Behav Biomed Mater*. 2023;147:106136. doi: 10.1016/j.jmbbm.2023.106136

104. Bera T, Vincent S, Mohanty S. Mechanical Properties of Polylactic Acid/Chitosan Composites by Fused Deposition Modeling. *J Mater Eng Perform*. 2025;34(16):17106-17120. doi: 10.1007/s11665-024-10506-6

105. Blanzeanu E, Marin M, Verziu MN, *et al*. Chitosan-polylactic acid composites: from seafood waste to advanced functional materials for 3D printing. *Adv Compos Hybrid Mater*. 2025;8(1). doi: 10.1007/s42114-024-01131-x

106. Alparslan C, Bayraktar Ş. Advances in Digital Light Processing (DLP) Bioprinting: A Review of Biomaterials and Its Applications, Innovations, Challenges, and Future Perspectives. *Polymers (Basel)*. 2025;17(9). doi: 10.3390/polym17091287

107. Shen Y, Tang H, Huang X, *et al*. DLP printing photocurable chitosan to build bio-constructs for tissue engineering. *Carbohydr Polym*. 2020;235:115970. doi: 10.1016/j.carbpol.2020.115970

108. Zanon M, Cue-López R, Martínez-Campo E, *et al*. Bioderived dyes-mediated vat photopolymerization 3D printing of chitosan hydrogels for tissue engineering. *Addit Manuf*. 2023;69(c):103553. doi: 10.1016/j.addma.2023.103553

109. He Y, Wang F, Wang X, Zhang J, Wang D, Huang X. A photocurable hybrid chitosan/acrylamide bioink for DLP based 3D bioprinting. *Mater Des*. 2021;202(1):109588. doi: 10.1016/j.matdes.2021.109588

110. García-García A, Pérez-Álvarez L, Ruiz-Rubio L, Larrea-Sebal A, Martin C, Vilas-Vilela JL. Extrusion-Based 3D Printing of Photocrosslinkable Chitosan Inks. *Gels*. 2024;10(2):126. doi: 10.3390/gels10020126

111. Banigo AT, Nauta L, Zoetebier B, Karperien M. Hydrogel-Based Bioinks for Coaxial and Triaxial Bioprinting: A Review of Material Properties, Printing Techniques, and Applications. *Polymers (Basel)*. 2025;17(7):917. doi: 10.3390/polym17070917

112. Mccauley PJ, Fromen CA, Bayles AV. Cell viability in extrusion bioprinting: the impact of process parameters, bioink rheology, and cell mechanics. *Rheol Acta*. 2025; 64(9-10):497-515. doi: 10.1007/s00397-025-01504-z

113. Rossi A, Pescara T, Gambelli AM, *et al*. Biomaterials for extrusion-based bioprinting and biomedical applications. *Front Bioeng Biotechnol*. 2024;12:1393641. doi: 10.3389/fbioe.2024.1393641

114. Rajabi M, McConnell M, Cabral J, Ali MA. Chitosan hydrogels in 3D printing for biomedical applications. *Carbohydr Polym*. 2021;260:117768. doi: 10.1016/j.carbpol.2021.117768

115. Elango J, Zamora-Ledezma C. Rheological, Structural, and Biological Trade-Offs in Bioink Design for 3D Bioprinting. *Gels*. 2025;11(8):659. doi: 10.3390/gels11080659

116. Hirami R, Sakai S. Freeze-dryable inks combining chitosan nanofibers and hyaluronic acid for extrusion bioprinting. *Int J Biol Macromol*. 2025;322(Pt 1):146679. doi: 10.1016/j.ijbiomac.2025.146679

ACCSCIENCE PUBLISHING

International Journal of Bioprinting

REVIEW ARTICLE

AI-driven integration of multimodal CT/MRI imaging and 3D printing in medicine: Advances, clinical applications, and future directions

Weipeng Zhou, Lihua Gao, Meng Wu, and Jianhua Liu*

Department of Radiology, The Second Hospital of Jilin University, Changchun, Jilin, China

(This article belongs to the *Special Issue*: *3D-Printed Biomedical Devices*)

Abstract

The integration of artificial intelligence (AI)-enabled multimodal computed tomography (CT)/magnetic resonance imaging (MRI) medical imaging and three-dimensional (3D) printing technology represents a pivotal direction in medical engineering for advancing precision diagnosis and therapy. Multimodal data fusion serves as the primary strategy to enhance the accuracy of 3D-printed models; however, cross-modal data fusion is hindered by inherent technical challenges, including failures in feature alignment and discrepancies in the physical properties of imaging datasets. In recent years, the advancement and seamless integration of AI technology have emerged as the core link bridging the entire workflow, from multimodal CT/MRI imaging acquisition to 3D printing, offering novel paradigms for the development of high-precision 3D printing technology in clinical settings. This review systematically elaborates on AI's core technical underpinnings for multimodal imaging and 3D printing: AI effectively mitigates integration and adaptation hurdles arising from intrinsic discrepancies in data source characteristics through three key pathways—artifact reduction and optimization of raw imaging data, precise cross-modal registration, and fine-grained segmentation of anatomical structures. Furthermore, AI-driven optimization of 3D rendering effects, combined with four-view projection, significantly enhances the fidelity of anatomical detail reproduction, thereby minimizing the matching error between 3D-printed models and *in vivo* physical entities. Subsequently, the review details the clinical application value of multimodal 3D printing technology across key medical specialties, including orthopedics, oncological surgery, dentistry, and vascular surgery, while concomitantly highlighting prevailing challenges in technical translation and clinical adoption. Finally, it outlines future development directions from three critical dimensions: technological synergy (among AI, imaging, and 3D printing), material advancement (targeting durability and functional adaptability), and application expansion (to underserved clinical scenarios such as rehabilitation). This work aims to provide a comprehensive reference for accelerating the clinical translation of this interdisciplinary technology.

Keywords: 3D printing technology; AI-enabled image preprocessing; Cross-modal data alignment; Multimodal CT/MRI imaging

***Corresponding author:**
Jianhua Liu
(Jian_hua@jlu.edu.cn)

Citation: Zhou W, Gao L, Wu M, Liu J. AI-driven integration of multimodal CT/MRI imaging and 3D printing in medicine: Advances, clinical applications, and future directions *Int J Bioprint*. 2026;12(1):125-144. doi: 10.36922/IJB025390404

Received: September 28, 2025
Revised: November 2, 2025
Accepted: November 3, 2025
Published online: November 7, 2025

Copyright: © 2025 Author(s). This is an Open Access article distributed under the terms of the Creative Commons Attribution License, permitting distribution, and reproduction in any medium, provided the original work is properly cited.

Publisher's Note: AccScience Publishing remains neutral with regard to jurisdictional claims in published maps and institutional affiliations.

1. Introduction

In the current era of precision medicine's deep evolution toward "personalized diagnosis and treatment," the convergence of medical imaging technology and advanced manufacturing technology has emerged as a core strategy for addressing complex clinical diagnostic and therapeutic challenges.[1,2] Multimodal computed tomography (CT) and magnetic resonance imaging (MRI) stand as primary modalities for clinical diagnosis and preoperative assessment, each exhibiting distinct technical strengths. CT, with its high spatial resolution and rapid imaging capabilities, enables clear visualization of hard-tissue details (e.g., bone structures, calcifications), providing precise osseous landmarks for anatomical localization. MRI, by contrast, excels in delineating tumor margins, neurovascular trajectories, and the extent of tissue edema due to its superior soft-tissue contrast resolution, addressing the gap in functional and soft-tissue assessment that persists with hard-tissue-dominant imaging.[3–5]

However, both modalities have inherent technical limitations. CT imaging relies on ionizing X-ray radiation, and repeated or high-dose scans increase radiation exposure risks for patients. Additionally, its inherently low soft-tissue contrast constrains the visualization of small lesions and soft-tissue tumors, and it is highly prone to metal-induced artifacts that obscure the observation of adjacent structures.[6,7] While MRI avoids radiation hazards, it suffers from high equipment costs and limited accessibility; further, examination durations are prolonged, rendering it less suitable for patients with intravascular or implanted metallic devices, critically ill individuals, and those unable to maintain prolonged immobilization (e.g., infants, agitated patients). Concurrently, its imaging performance for air-filled organs (e.g., lungs, gastrointestinal tract) and osseous structures remains suboptimal.[8–10]

The isolated application of single-modal CT or MRI images cannot accurately reconstruct the detailed information of various anatomical structures in the human body.[11] Moreover, their simple superposition leads to issues such as data misalignment and artifact interference due to differences in their imaging principles, which restrict the fidelity of digital models. Therefore, the precise fusion of multimodal CT/MRI imaging data constitutes a critical bottleneck in achieving the transformation from "virtual images to physical models" during the interdisciplinary integration of medical imaging technology and advanced manufacturing technology.

Three-dimensional (3D) printing technology is one of the most rapidly advancing manufacturing methods in recent years and is categorized under rapid prototyping. Medical imaging-based 3D printing begins with acquiring raw anatomical data using medical imaging scanners, followed by generating 3D-printable stereolithography (STL)-format models through sequential steps: 3D reconstruction, model segmentation, and optimization. Controlled by the 3D printing system, filamentous, liquid, or powdered feedstocks are deposited and layered with precise spatial positioning, ultimately producing physical anatomical models that closely replicate *in vivo* structures.[12]

The selection of 3D printing technologies in medical applications must primarily balance precision, cost, and biocompatibility. Each mainstream technology possesses unique adaptive characteristics. SLA/digital light processing achieves a precision of 20–50 μm, is compatible with biocompatible photosensitive resins, and is suitable for scenarios requiring high precision, such as dental implant guides. Binder jetting (BJ) utilizes titanium alloy and hydroxyapatite as raw materials, offers excellent biocompatibility, and is well-suited for orthopedic implant manufacturing. Material extrusion (fused deposition modeling [FDM]) is cost-effective, can print materials such as poly(lactic acid), and is mostly used for educational phantoms. Bioprinting specifically refers to the precise deposition of living cells, biomaterials (e.g., hydrogels), and bioactive molecules through layer-by-layer deposition to construct functional biological structures such as tissues, organs, or organoids. Matching the performance requirements of different technologies provides key guidance for clinical selection.[13]

The advent and advancement of 3D printing have established a critical technical platform for translating medical imaging data into physical constructs. Medical imaging-based 3D printing transforms digital imaging data into scaled, clinically actionable physical anatomical models, providing tangible tools for preoperative planning (e.g., tumor resection simulation), surgical rehearsal, and personalized implant design.[14] The accuracy and clinical applicability of 3D printing essentially depend on the quality of the digital model generated from upstream imaging data. If the precise fusion and optimization of CT/MRI multimodal images are not achieved, 3D printed models will struggle to balance the anatomical fidelity of hard and soft tissues, thereby losing their clinical guiding value. Therefore, constructing multimodal imaging data into a digital model with high accuracy and compatibility with 3D printing processes is the core challenge in achieving clinical translation.

The concept of artificial intelligence (AI) first emerged several decades ago. However, recent breakthrough advancements in machine learning (ML) and neural

network (NN)-based algorithms have sparked a profound revolution in the field.[15] The integration of AI with 3D printing, particularly when combined with multimodal imaging, has become a prominent research focus in recent years. The historical stages and progress of this integration are summarized in Table 1.

Against this backdrop, the integration of AI technology has become the core link connecting the entire workflow of "multimodal CT/MRI imaging–3D printing".[16] In recent years, AI-assisted multimodal CT/MRI–3D printing interdisciplinary technology has been applied in fields such as orthopedics, oncological surgery, dentistry, and vascular surgery.[17–19] However, current research still faces numerous issues that hinder the technology's transition from the "laboratory" to "clinical application." Therefore, this paper aims to systematically summarize the research progress and clinical practice outcomes of the interdisciplinary application of multimodal CT/MRI imaging and 3D printing technology, analyze the current technical and clinical challenges, and propose future breakthrough directions. It provides a reference for promoting the development of this interdisciplinary field toward "high fidelity, high adaptability, and standardization," and facilitates the in-depth integration of precision medicine with the diagnosis and treatment of complex diseases.

2. Core technology support for multimodal CT/MRI and 3D printing

Within the integrative framework of multimodal CT/MRI and 3D printing technologies, AI assumes a central role, with its technical interventions encompassing the entire workflow of their integration. On one hand, by addressing the inherent data heterogeneity of multimodal imaging, AI mitigates compatibility challenges across different modalities. Through a sequence of operations—including preprocessing optimization (e.g., denoising, contrast enhancement), high-precision cross-modal registration, and fine-grained anatomical segmentation—AI converts raw imaging data into high-fidelity anatomical digital templates that meet the stringent requirements of 3D printing. On the other hand, AI facilitates the critical interface stage between multimodal imaging and 3D printing: it enhances the reproduction fidelity of micro-anatomical details via advanced 3D rendering techniques while providing data-driven guidance for subsequent adjustments of 3D printing parameters (e.g., layer height, infill density). This dual functionality minimizes precision discrepancies caused by workflow fragmentation between technical stages. Figure 1 illustrates the complete technical roadmap for the integration of AI-driven multimodal CT/MRI and 3D printing.

2.1. Artificial intelligence-assisted preprocessing techniques for multimodal imaging

Multimodal imaging, by integrating imaging data from diverse modalities (e.g., CT and MRI), underpins the establishment of digital models with more holistic information. However, during data acquisition, multimodal imaging data are prone to degradation caused by factors such as variations in equipment parameters, patient positional shifts, tissue motion artifacts, and noise interference. Such perturbations contribute to spatial misregistration, inhomogeneous gray-level intensity, and disparate feature scales across different modalities—severely compromising the accuracy of digital model construction.[20–22] As a

Table 1. Development history of artificial intelligence (AI) in medical image segmentation and 3D printing

Development stage	Core AI technology type	Representative algorithm/model	3D printing applicable scenario	Key progress
Early exploration stage (2010–2015)	Traditional machine learning	Support vector machine, random forest	Simple osseous structures (e.g., femur, skull)	Enabled semi-automatic segmentation of medical images; model error exceeded 1 mm, and was applicable only to non-weight-bearing bone models
Rapid development stage (2016–2020)	Basic deep learning	U-Net, ResNet, FCN	Soft tissue tumors (e.g., liver cancer), large blood vessels	Achieved breakthroughs in end-to-end segmentation; Dice coefficient increased to 0.85–0.90, and model error was reduced to 0.5–1.0 mm
Precision optimization stage (2021–present)	Optimized deep learning	ECR-UNet, dual U-Net, CTGANs, Res-UNet	Calcified tumors, small blood vessels, repair of bone defects	Introduced attention mechanism and cross-modal fusion; Dice coefficient exceeded 0.91, supporting naked-eye 3D visualization and personalized implant printing with an error of less than 0.5 mm

Abbreviations: CTGANs, conditional tabular generative adversarial networks; ECR, express connect router; FCN, fully convolutional network; Res, residual.

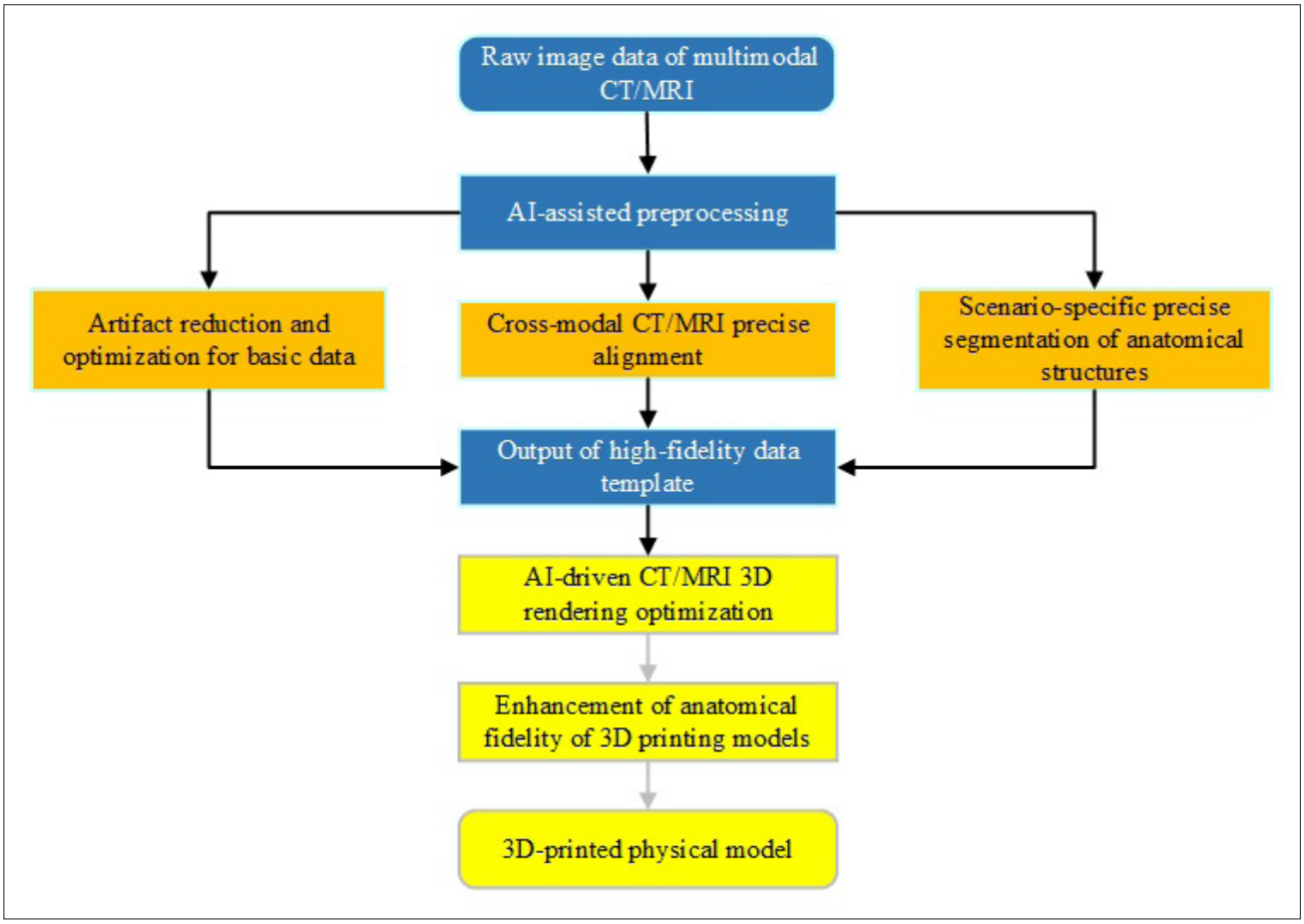


Figure 1. Artificial intelligence-driven flowchart of multimodal computed tomography (CT)/magnetic resonance imaging (MRI)–3D printing fusion.

pivotal component of the multimodal imaging analysis workflow, the core objective of preprocessing is to refine data quality through procedures such as noise reduction, normalization, spatial registration, modality alignment, and weak data adaptation.[20] Traditional preprocessing methods rely on manual expertise for parameter tuning, leading to cumbersome workflows, low efficiency, and poor generalizability—limitations that render them inadequate for processing large-scale multimodal imaging datasets. In contrast, AI technology models the inherent correlations and feature patterns of multimodal data via deep learning and related algorithms. It enables intelligent processing capabilities, including adaptive noise suppression, precise cross-modal spatial registration, and dynamic gray-level normalization, thereby substantially enhancing the efficiency, accuracy, and robustness of preprocessing.[23] Consequently, it delivers high-quality data support for subsequent 3D printing.

2.1.1. Classification of machine learning models and data foundations for multimodal fusion

In multimodal imaging preprocessing workflows, ML models are categorized into the following three groups based on their alignment with clinical demand scenarios.

(a) Supervised learning models for multimodal fusion

One of the primary objectives of multimodal imaging preprocessing is to achieve precise alignment of CT and MRI data, as well as accurate segmentation of anatomical structures (e.g., tumor boundary extraction, bone structure localization). Using annotated data such as segmentation masks and alignment labels, these models learn the mapping between inputs (raw imaging data) and outputs (segmentation and alignment results), thereby fulfilling the requirements for precise segmentation and alignment.

In terms of performance, these models demonstrate significant accuracy advantages. For instance, the dual U-Net network achieves a Dice similarity coefficient of

0.864 for cross-modal alignment,[24] while the ECA CBAM Res (ECR)–U-Net attains an 89.13% Dice similarity coefficient for segmenting tumor calcification regions.[25] Additionally, they can visualize key regions, such as tumor boundaries, through feature maps. However, certain limitations must be acknowledged: these models require large-scale annotated datasets (e.g., the training of ECR-UNet relies on 153 whole-slide pathological sections from 39 tumor patients[25]), and varying quality of labeled data may affect model performance. To mitigate the impact of device variability, targeted optimization of data quality during training is essential. For example, improved 3D deep convolutional neural network (iDCNN) processes brain MRI data from 46 patients with Wilson's disease (WD) using "four-fold rotation and grayscale normalization",[26] whereas dual U-Net addresses device bias in CT/MRI data from 12 patients undergoing anterior cruciate ligament (ACL) reconstruction through " deformation field and the non-rigid registration fusion module".[24]

These models directly provide high-fidelity multimodal fused data for clinical scenarios such as tumor preoperative planning and orthopedic implant design. Even when constrained by factors such as limited data scale and device variability, these models can still satisfy the multimodal integration requirements of most routine cases through optimization techniques like data normalization, thereby establishing a robust data foundation for subsequent precision medical procedures.

One recent study[27] demonstrates that Residual (Res)–U-Net transfer learning offers significant advantages in cerebrovascular segmentation: it addresses the gradient vanishing problem in deep networks through residual connections, achieving a segmentation Dice coefficient of 0.914. Furthermore, its segmentation results can be directly exported as STL files (without additional format optimization), reducing 3D printing preparation time.

(b) Generative models for small-sample scenarios

In clinical practice, the volume of imaging data for rare diseases (e.g., mandibular tumors) or specific postoperative cases is often insufficient to support model training, necessitating the use of "data generation" to supplement samples. Generative models, such as conditional tabular generative adversarial networks (CTGANs), employ an adversarial training mechanism involving a generator and discriminator to produce anatomically consistent synthetic data based on a limited amount of real data. This approach makes them well-suited for scenarios involving data completion or small-sample augmentation.

The core value of these models lies in overcoming limitations related to data volume. For example, Ref. 28 utilized only 27 cases of postoperative CT data of mandibular tumors to generate virtually complete samples of defect regions, effectively repairing incomplete images such as mandibular defects. During training, "defect region masks" were used as inputs and "completed mandibular models" as outputs. Data quality was evaluated using mean squared error (MSE = 2411.9 ± 833.6) to ensure the anatomical plausibility of the generated data. However, the training process is unstable and prone to "mode collapse" (producing repetitive structures); thus, the generated results must be validated clinically.

Although clinical validation of generated results is necessary, incorporating anatomical rationality evaluations (e.g., the MSE metric) effectively broadens the scope of medical applications for multimodal imaging, enabling more patients with unique cases to benefit from AI-assisted precision diagnosis and treatment.

(c) Object detection models for real-time localization in intraoperative navigation

Intraoperative navigation demands the rapid identification of key anatomical structures, such as lumbar pedicles, and places extremely high requirements on model processing speed. Object detection models, exemplified by You Only Look Once version 5x (YOLOv5x), utilize an "end-to-end detection" mechanism that directly outputs the locations of target regions, making them well-suited for real-time localization scenarios.

The primary advantage of these models is their high processing efficiency (>20 frames per second), which enables real-time intraoperative navigation. However, due to inherent limitations in their detection principles, their accuracy in identifying small targets (e.g., tiny calcifications) remains relatively low.[25,29] During the training phase, maintaining consistency in data annotation is essential. For example, using over 100 cases of lumbar CT data, pedicle centers are annotated, and annotation quality is assessed using the Kappa coefficient to minimize annotation bias and ensure accurate model localization.[30]

From the perspective of clinical translation needs, these models transform preoperative multimodal imaging data (CT/MRI) into intraoperative real-time navigation information, directly supporting precision surgical procedures such as orthopedic pedicle screw implantation. Although their accuracy in detecting small targets is limited, they can still satisfy the clinical requirements for most intraoperative real-time localization tasks through targeted annotation optimization (e.g., precise annotation of pedicle centers).

2.1.2. Basic data optimization

As a foundational component of data optimization, the preprocessing stage poses distinct challenges to

AI in processing multimodal imaging data. These challenges primarily manifest in three core issues: weak signal detection challenges, incomplete lesion region modeling, and interference from modality-specific structural artifacts. Regarding weak signal detection, low-contrast features arising from the intrinsic limitations of imaging modalities (e.g., subtle infiltration signals of early tumors or slight density changes in cerebral white matter rarefaction) impede AI models from capturing their statistical patterns through a single feature channel. Furthermore, rare diseases—characterized by low incidence rates—lack sufficient high-quality annotated MRI samples, compromising the model's capacity to fully acquire disease-specific features.[26] The complexity of lesion region modeling also represents a major bottleneck restricting the precise development of 3D-printed digital models. This stems from the morphological heterogeneity of lesion tissues, their ill-defined boundaries, and disrupted topological associations with normal anatomical structures. For instance, pathological changes such as tissue boundary erosion due to tumor invasion, discrete distribution of bone fragments post-fracture, surgical tissue defects, and infection-induced soft tissue swelling render traditional threshold-based segmentation or morphology-driven modeling approaches incapable of accurately delineating lesion extents. Over-segmentation may erroneously incorporate normal tissues into the lesion area, causing volume distortion in 3D-printed models, while under-segmentation may omit small lesions or critical structures—leading to misjudgments regarding the extent of lesion invasion during surgical planning.[23,31] Interference from modality-specific structural artifacts is even more technically intricate. For example, star-burst artifacts induced by metal implants in CT and chemical shift artifacts resulting from magnetic field inhomogeneity in MRI not only exhibit modality-specific, morphologically diverse features but also frequently induce signal ambiguity with adjacent anatomical structures (e.g., cortical bone surrounding orthopedic implants or gray matter near intracranial metal foreign bodies). This requires AI algorithms to preserve structural fidelity while suppressing artifacts, avoiding the loss of anatomical details caused by over-processing.[32]

To mitigate these challenges, AI technology has employed multi-faceted strategies to achieve targeted breakthroughs. For weak signal detection, it leverages multi-scale feature fusion networks integrated with attention mechanisms to enhance the hierarchical representation of low-contrast features, and it utilizes cross-modal associative learning to explore potential mapping patterns between signals.[33] For deficiencies in lesion region modeling, it incorporates a transfer learning framework to transfer general anatomical knowledge to small-sample scenarios and employs generative adversarial networks to generate anatomically consistent virtual lesion samples for training set expansion.[31,28] For modality-specific artifacts, it develops physics-constrained adversarial denoising networks that suppress CT metal artifacts and MRI motion artifacts while preserving key anatomical details via a structural fidelity loss function.[31,32] Collectively, these strategies enhance data quality through end-to-end optimization, laying a highly consistent foundation for subsequent multimodal registration and 3D reconstruction. The following examples demonstrate how AI techniques have been applied to resolve key preprocessing challenges in multimodal imaging.

(a) 3D AI enhancement for weak MRI data

To address the issue of "weak training data" in cerebral WD of the brain—characterized by small MRI sample sizes and lesion identification biases caused by white matter hyperintensities—Agarwal *et al.*[26] proposed an iDCNN for WD diagnosing. This training dataset comprised 50 cases of brain MRI data from patients with WD, including T1 and T2 sequences. The input consisted of raw MRI scans, while the output consisted of artifact-free, enhanced MRI images. By modifying the rectified linear unit activation function, optimizing the number of convolutional NN layers, and applying data augmentation (2–5 times) to increase the number of training images, the accuracy of brain tissue classification was ultimately improved to 98.28%, representing a 15.35% increase compared with the traditional support vector machine model. This technology enables multimodal preprocessing of brain tumors: prior to fusing CT bone structures with tiny MRI metastases, it enhances MRI lesion signals via 3D AI, and quantifies lesion feature intensity using bispectrum analysis, thereby providing clear anatomical and functional boundaries for 3D-printed "tumor-bone structure" combined models.[26]

(b) AI-based completion of lesion CT images

To address the difficulty in 3D printing modeling caused by CT image defects after mandibular tumor resection, Liang *et al.*[28] developed a CTGAN. The training dataset comprised 27 cases of postoperative CT scans of mandibular tumors. The input consisted of raw CT images of defective mandibles (including metal artifacts), while the output consisted of completed mandibular models. The discriminator accurately distinguished the mandible from other structures. The completed images were combined with the second-generation combined osteotomy and reconstruction pre-shaped plate position method to design 3D-printed guides, resulting in postoperative deviations of only −1.32±0.72 mm (negative deviation) and 1.90±1.05 mm (positive deviation) among 27 patients undergoing

mandibular reconstruction. This approach successfully adapted to cases with trans-midline defects, resolving the anatomical distortion issue associated with traditional mirroring-based completion methods.[28]

(c) Removal of artifact fiber overlap in CT images

To address the issue of anatomical distortion in 3D-printed models caused by fiber structure artifacts in CT images, such as those in orthopedics and maxillofacial surgery, Zhou *et al.*[34] proposed an artifact fiber overlap removal algorithm based on radial basis functions. This algorithm was developed to eliminate artifactual fiber overlaps within fiber structures extracted from micro-CT images of fiber-reinforced polymer matrix composites. Precise artifact elimination was achieved through gradient adjustment, while the introduction of graphics processing unit acceleration enhances efficiency by 29% compared with traditional methods in scenarios with high fiber volume fractions. This technology can be applied to the preprocessing of CT images of orthopedic implants and maxillofacial bones, providing artifact-free and precise structural data for 3D-printed "bone–fiber" composite structure models (e.g., knee joint models containing ligament fibers).[34]

2.1.3. Cross-modal data alignment in multimodal synergistic fusion

With multimodal imaging data meeting quality benchmarks, AI further facilitates the synergistic integration of structural and functional multimodal imaging. The core challenge lies in overcoming the inherent modality barriers between CT and MRI, as well as enabling precise cross-modal spatial registration and comprehensive information complementarity. CT excels at visualizing the anatomical details of hard tissues (e.g., bone), whereas MRI offers superior soft-tissue contrast resolution and functional imaging capabilities; their synergistic integration enables a comprehensive "structure–function" analytical framework.[35] However, gray-level inhomogeneity inherent to differing imaging principles, along with organ motion-induced spatial misalignment, poses significant challenges to achieving high-precision registration with traditional methods. Additionally, manually uncovering the latent inter-modal correlations remains impractical.

AI optimizes the multimodal integration process through a multi-tiered strategy. At the spatial registration tier, it leverages deep learning-based non-rigid registration models that can rectify positional discrepancies by learning modality-specific deformation fields, while safeguarding structural consistency by integrating mutual information loss with anatomical priors. At the information complementarity tier, a multimodal feature-fusion framework (early concatenation, mid-interaction, late decision-making) adaptively assigns weights to the structural features derived from CT and the functional signals extracted from MRI. It explores cross-modal associations to augment information richness, thereby addressing the core challenges of cross-modal spatial registration and information complementarity between CT and MRI.

Building on these strategies, several representative approaches have been developed to achieve precise cross-modal alignment and synergistic fusion in clinical multimodal imaging workflows.

(a) Preoperative CT/MRI multimodal synergistic fusion and cross-modal data AI alignment for ACL reconstruction

To address the differences in modal characteristics between CT (clear bone structure but weak ligament visualization) and MRI (excellent soft-tissue imaging but blurred bone boundaries) in preoperative planning for ACL reconstruction, and to achieve accurate cross-modal data alignment during their multimodal collaborative fusion, Yu *et al.*[24] developed a dual U-Net network architecture. This architecture established a cross-modal data alignment mechanism for CT and MRI through a deformation field module and a non-rigid registration fusion module. The training dataset comprised paired CT and MRI data from 12 patients undergoing ACL reconstruction. The CT scans included annotations of femoral and tibial osseous structures, while the MRI scans contained annotations of ACL signals. The input consisted of unaligned CT images (slice thickness = 0.625 mm; HU values = 800–1000), and the output was a spatially aligned, fused CT–MRI image. The results demonstrated that the alignment accuracy—measured by a Dice coefficient of 0.864—was significantly superior to that of conventional Affine (Dice = 0.678) and Symmetric Normalization (SyN); Dice = 0.794) algorithms. Based on the accurately aligned cross-modal data, key sites of the femoral/tibial bone tunnels (critical positions for drilling) could be automatically extracted with an error of only 2 pixels. Validation using 3D-printed phantom bone models demonstrated no statistically significant difference (p=0.952) between the planned femoral tunnel length derived from the aligned data (37.61±1.28 mm) and the measured value (37.58±1.06 mm). This confirms the effectiveness of CT/MRI multimodal collaborative fusion and accurate cross-modal data alignment, providing data support for the precise design of 3D-printed orthopedic guides.[24]

(b) "Standardization–adaptation–fusion" three-stage synergistic fusion and AI-assisted cross-modal data alignment for multimodal imaging

To address the challenge of cross-modal data heterogeneity in multimodal imaging, Ogbuanya *et al.*[35] designed a three-tier "standardization–adaptation–fusion" technical framework to achieve precise cross-modal data alignment under multimodal collaborative fusion. The primary input consisted of CT and MRI images of the same organ, while the auxiliary input included intermediate data generated from these primary images during the fusion process. The final output was a fused multimodal image. At the dataset level, a standardized dataset was created using the Harvard Medical Image Database, containing 14 pairs of pre-registered CT–MRI images—each pair comprising one CT image and one MRI image of the same organ—with a spatial resolution of 256×256 pixels. To ensure semantic consistency, the study standardized the MATLAB simulation environment and experimental parameters. At the model level (Figure 2), edge features were retrieved via the Sobel gradient compass to create detail-oriented images, thereby accomplishing initial feature calibration. Following this, a variable-order fractional operator was utilized to enhance the multi-objective Darwinian particle swarm optimization algorithm. The weight matrix was then optimized with dual objectives—reducing fusion time to a minimum and maximizing fusion quality—to accommodate variations in cross-modal features. During the fusion phase, leveraging the optimized weight matrix, non-adaptive pixel-level fusion was implemented; this approach not only reinforced the modal strengths of distinct regions but also required only 0.085 seconds for processing. The performance of the framework was verified using various evaluation metrics such as inverted generational distance and hypervolume, combined with classification evaluation based on support vector machines (accuracy = 0.895; F1 score = 0.677). In clinical scenarios like skull base tumor operations, the framework was capable of precisely retaining anatomical correlations—confirming both its efficacy in cross-modal alignment and its suitability for clinical application.[35]

2.1.4. Scenario-specific precise image segmentation

To address the precise diagnostic and therapeutic requirements of specific clinical contexts (e.g., oncology, spinal disorders), AI has advanced its multimodal image segmentation capabilities—enabling accurate extraction of key anatomical structures and pathological tissues, and providing core technical support for the high-fidelity reproduction of 3D-printed models. In these contexts, the infiltrative margins of tumors, heterogeneous tissue signal properties, and topological complexity of fine spinal structures pose significant challenges for traditional threshold-based or morphology-driven segmentation methods in balancing accuracy and comprehensiveness. This frequently results in the misrepresentation of critical information in 3D-printed models.[31]

AI overcomes these limitations through targeted optimization of deep learning architectures—for instance, by integrating dual-attention mechanism networks to enable fine-grained segmentation of specific regions and structures, or by incorporating anatomical prior constraints to suppress noise and artifact-related interference as well

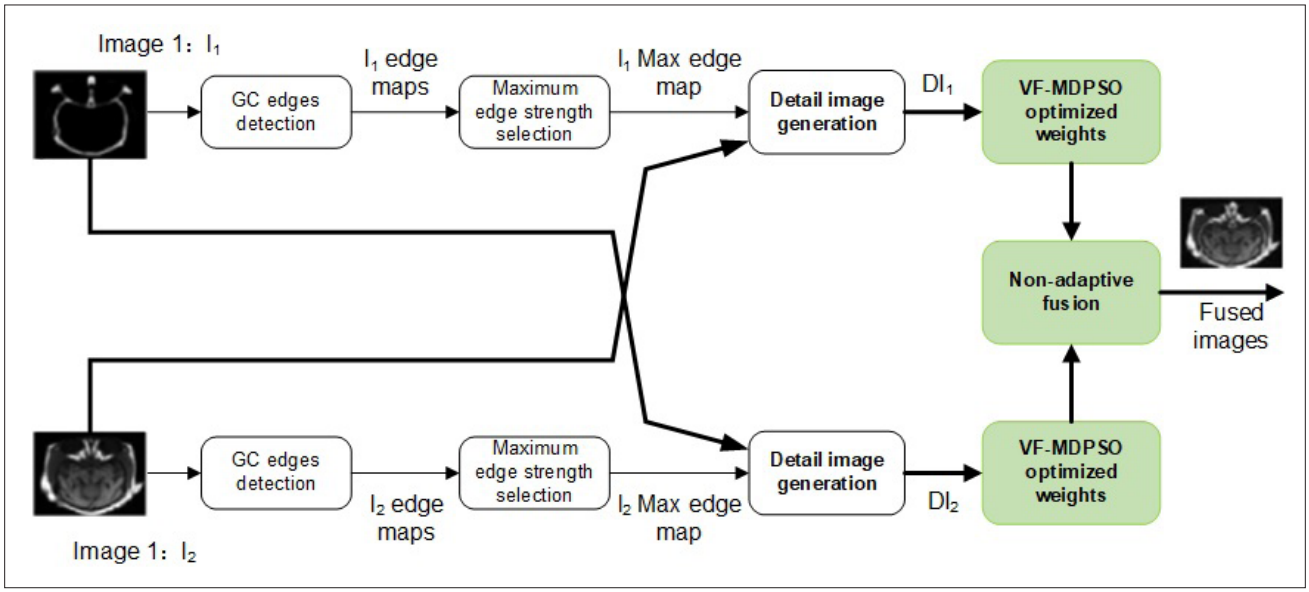


Figure 2. Schematic diagram of the three-stage synergistic fusion and artificial intelligence-assisted cross-modal data alignment. Adapted from Ref. 35. Copyright © 2025, The authors. Abbreviations: DI, Detailed Image; GC, Gradient Compass; VF-MDPSO, Variable-order Fractional-order-Multi-objective darwinian particle swarm optimization.

as constrain segmentation errors. It also integrates semi-supervised learning strategies to improve generalization performance for rare or complex cases.[25,36]

Building upon these advancements, several representative AI-driven approaches have been developed to achieve precise, scenario-specific image segmentation for clinical and 3D printing applications.

(a) Intelligent segmentation of tumor calcification

To address the insufficient segmentation accuracy of CT calcified lesions and MRI tumor parenchyma in calcified tumors (e.g., hepatocellular carcinoma), Wan *et al.*[25] proposed the ECR-U-Net segmentation network. Built on U-Net, it integrated the ResNet34 module (to enhance deep feature extraction) and a dual-attention mechanism—convolutional block attention module for capturing spatial features and efficient channel attention for optimizing channel weights—to improve segmentation precision. The training dataset comprised 1687 pieces of image data from 39 patients with calcified tumors. The inputs included image data augmented via multiple data augmentation methods, while the output was segmentation masks identifying tumor calcified regions. Using this method, the Dice coefficient for calcified region segmentation improved to 89.13%, accuracy reached 98.94%, and external contour extraction accuracy attained 99.05%. This technology can accurately extract the boundaries of CT calcified lesions and MRI tumor blood supply areas, while solving the problem of computational overload in large-scale imaging through the combined strategy of block cutting and overall stitching. It provides guidance for the highlighted marking of calcified lesions in 3D-printed transparent phantoms, thereby avoiding accidental injury during surgery.[25]

(b) AI-based 3D visual medical image segmentation

Jia *et al.*[27] presented their research team's novel AI-Enabled 3D Printing and Naked-Eye 3D Visual Medical Image Segmentation System. By integrating AI into medical image analysis, this platform facilitates automatic contour extraction of target organs/tumors, while supporting 3D visualization and 3D printing workflows. Primarily developed using the Interactive Data Language, the platform encompasses core functionalities including multimodal image registration, AI-driven automatic segmentation, and support for naked-eye 3D visualization and 3D printing.

The platform's core AI algorithms are as follows:

- Accurate localization of prostate organs from T2-weighted MRI images using the YOLOv3 algorithm.
- Segmentation of prostate cancer and bladder cancer tumor regions from MRI images via U-Net/Global Context(GC)-U-Net architectures.
- Fine-grained segmentation of cerebral blood vessels from multimodal MRI images through model-driven transfer learning combined with the U-Net network.
- Notably, the platform has been clinically validated across multiple disease scenarios:
- Prostate cancer: 17 clinically confirmed positive patients from the I2CVB dataset, achieving a Dice coefficient of 0.91 for combined three-parameter map-based segmentation.
- Bladder cancer: 2000 annotated images from the ISICDM2019 dataset, with a Dice coefficient of 0.875 for GC-U-Net-based tumor segmentation.
- Osteosarcoma: 3D printing-facilitated surgical planning following preoperative CT image segmentation of tumor and surrounding bone structures.
- Breast cancer: Customized 3D-printed chest supports to minimize tissue displacement during radiotherapy.
- Cerebrovascular diseases: High-resolution 3T MRI images of six patients with intracranial atherosclerosis, yielding a Dice coefficient of 0.914 for Res-U-Net-based cerebral vessel segmentation.

Additionally, the platform is equipped with user-friendly naked-eye 3D visualization (featuring four-view projection that eliminates the need for virtual reality glasses) and gesture- and voice-based control functionalities. Future plans include expanding its segmentation capabilities to more imaging modalities (e.g., positron emission tomography–CT) and disease types (e.g., liver cancer).[27]

2.2. Three-dimensional rendering optimization of multimodal imaging and integration with 3D printing

3D rendering of multimodal imaging serves as a crucial bridge between multimodal imaging data and 3D-printed physical models, facilitating the transition from basic anatomical structure visualization to AI-driven precision refinement. Such 3D rendering provides robust, high-fidelity data support specifically tailored to the requirements of 3D printing.

2.2.1. Fundamentals of compatibility between CT/MRI data and 3D printing

To clarify the technical integration between CT/MRI data and 3D printing, this section elaborates on compatibility from three perspectives—file format conversion, data precision adaptation, and modality matching—to ensure

that imaging data effectively supports 3D printing requirements. The key aspects are discussed as follows:

a File format compatibility

Raw CT/MRI data (in DICOM and Neuroimaging Informatics Technology Initiative [NIfTI] formats) must be converted to standard 3D printing formats (STL/OBJ) using professional software such as Mimics and Geomagic. During conversion, simultaneous surface mesh optimization—maintaining the number of faces between 500,000 and 800,000—and topological structure repair are required to prevent the loss of anatomical detail caused by model lightweighting.[12,14,25]

b Data precision compatibility

CT defines tissue density using HU values—hard tissues range from 800 to 1000 HU, while soft tissues range from 20 to 40 HU. These values must be mapped to 3D printing parameters such as material type and infill density. For example, HU values above 800 correspond to hydroxyapatite composite materials, whereas HU values between 20 and 40 correspond to silicone rubber. MRI differentiates soft tissues based on T1/T2-weighted signals, and AI is required to convert signal intensity into the structural thickness of printed models. For instance, signal intensity in tumor regions is positively correlated with the wall thickness of the printed models.

c Modality adaptation compatibility

CT requires optimization of inter-slice resolution to prevent printing distortions of hard tissues; for example, a 128-slice spiral CT typically uses a slice thickness of 0.625 mm. For MRI, algorithms such as dual U-Net are necessary to achieve cross-modal alignment with CT, compensating for MRI's insufficient spatial resolution and ensuring that printed models accurately reproduce the anatomical relationships between hard and soft tissues.[24]

Notably, within the aforementioned framework of modality adaptation compatibility between MRI and 3D printing, the targeted selection of MRI pulse sequences is a crucial step to further ensure data quality and achieve precise alignment between printing objectives and imaging data.[27]

The following MRI pulse sequences are commonly utilized to enhance data compatibility with 3D printing and to ensure accurate visualization of diverse tissue and lesion characteristics:

- T1-weighted sequence (T1WI): This sequence provides high soft tissue contrast and clearly delineates the boundaries between tumors (e.g., gliomas) and normal tissues, serving as the core sequence for tumor-related 3D printing.
- T2-weighted sequence (T2WI): This sequence is sensitive to edema and cystic lesions, making it suitable for 3D printing of fractures complicated by soft tissue injuries or spinal cord lesions, and for assisting in the delineation of lesion scope.
- Three-dimensional time-of-flight sequence (3D TOF): This enables vascular imaging without contrast agents and offers a high signal-to-noise ratio, making it the preferred sequence for 3D printing of cerebral blood vessels and coronary arteries (e.g., Circle of Willis models).
- 3D fluid attenuated inversion recovery sequence: This suppresses cerebrospinal fluid signals and highlights small white matter lesions, suitable for localizing small lesions (e.g., brain metastases) in 3D printing.
- Dynamic contrast-enhanced MRI: This technique quantifies tissue perfusion and extracts information about tumor blood supply areas. During 3D printing, high-perfusion regions can be labeled via color coding to guide surgical resection.

2.2.2. Progressive optimization of rendering techniques

To address challenges such as inadequate segmentation precision of multimodal medical images, disjointed workflow between 3D rendering and 3D printing—which result in low preoperative planning efficiency—and suboptimal adaptability of clinical physical models, this study aims to meet clinical demands for accurate extraction of pathological structures, glasses-free 3D visualization, and end-to-end automation.

The U-Net convolutional NN is commonly used to automatically segment CT/MRI multimodal images, accurately extracting tumor, organ, and vascular structures, thus addressing the issue of insufficient rendering data precision. Subsequently, single-view training is replaced by multi-view constrained learning, and the 3D Gaussian properties are jointly optimized through the structure and appearance of multiple views to avoid overfitting. For example, four-view projection is adopted to achieve naked-eye 3D visualization; meanwhile, "model lightweighting" is used to optimize rendering fluency, balancing the relationship between "detail preservation" and "real-time interaction" and avoiding process lag caused by data overload. Finally, STL files are directly output to drive 3D printing. Through cross-modal registration algorithms, printing errors can be controlled within the precision range, enabling the full-process automation of "image

segmentation → 3D rendering → physical printing" and addressing the precision gap in the conversion from "virtual images to physical models" in medical scenarios.

2.2.3. Empirical validation of multimodal technology and 3D printing in typical medical application scenarios

The empirically validated 3D-printed physical models—derived from optimized multimodal rendering data and tested across diverse medical contexts—span applications ranging from affordable foundational teaching tools to specialized clinical regenerative interventions. These models effectively translate the intrinsic value of multimodal imaging, encompassing multidimensional anatomical and pathological insights, into tangible clinical utility.[38] The translational potential of the proposed multimodal imaging and 3D printing approach is exemplified in the following key application domains.

(a) Educational applications

To address the high cost and limited functionality of commercial MRI teaching phantoms, Yusuff *et al.*[39] developed a modular cylindrical MRI teaching phantom using optimized MRI data. FDM was used to fabricate the low-cost polyethylene terephthalate glycol shell, while STL enabled high-resolution printing of functional components—integrating five core teaching modules, including spatial resolution, geometric accuracy, and slice thickness accuracy. The phantom can be filled with DOTA-Gd^{3+} solution to mimic MRI signals of various tissues and accurately assess geometric distortion differences in MRI systems operating at 1.5T and 0.31T magnetic fields. Furthermore, its open-source STL files are compatible with consumer-grade 3D printers, and the total cost per phantom is under 50 euros. These results confirm the feasibility of 3D-printed phantoms for mitigating the shortage of multimodal imaging teaching equipment in primary healthcare facilities.

(b) Clinical regenerative applications

To address the clinical need for craniofacial bone regeneration, Hindi *et al.*[40] developed an alginate–hydroxyapatite bioink compatible with 3D bioprinting, using segmented and optimized craniofacial defect data derived from CT/MRI. The team identified 8% hydroxyapatite as the optimal concentration, with a loading density of 5×10^6 autologous adipose-derived stem cells per milliliter. Using a standard 3D bioprinter, they directly printed the bioink *in situ* onto the calvarial defects in live rabbits, achieving precise geometric congruence with the defects. This approach established a closed, integrated pathway of "image rendering → 3D bioprinting → bone regeneration," offering a novel paradigm for clinical repair of craniofacial bone defects, underscoring the synergistic value of multimodal imaging (CT/MRI) and 3D bioprinting in regenerative medicine.[40]

(c) Validation of porous media micro-models

To address the challenge of inadequate structural and functional congruence between 3D-printed phantoms and native tissues, Lee *et al.*[41] developed 3D porous media micro-models using a random reconstruction method based on multimodal imaging data. Material jetting technology was employed to fabricate the micro-models at a resolution of 16 μm—enabling high-fidelity reproduction of microstructural features. The porosity and permeability of the fabricated micro-models were validated against natural sandstone (the target material for simulation) using X-ray micro-CT and microfluidic assays, exhibiting deviations of < 10–41% for both parameters. Furthermore, the results were consistent with theoretical predictions of the Kozeny–Carman equation (where the constant k_0=6.6, when $\varphi\geq0.2$). This work establishes a validation framework for the 3D fabrication of orthopedic porous implants and tumor drug-loaded phantoms, ensuring that the physical properties of fabricated constructs align with clinical specifications.[41]

2.3. Limitations of artificial intelligence and machine learning in supporting multimodal imaging and 3D printing technology

Although AI/ML models play a central role in multimodal preprocessing, they still face significant limitations regarding reliability and interpretability. These challenges represent major barriers to the clinical translation of the technology and manifest in the following specific ways:

(i) Reliability challenges

In real-world clinical scenarios, model stability is influenced by data characteristics and application environments.

- Limited adaptability to niche modalities: For specialized imaging modalities such as low-dose CT (characterized by high noise) and functional MRI (fMRI), the model's processing accuracy declines significantly. For instance, the segmentation error of models trained on low-dose CT data increases by 0.55 mm,[26] which fails to meet the diagnostic and therapeutic requirements for rare diseases (e.g., WD, where sample availability is limited).
- Poor cross-center generalization: Variations in imaging parameters between devices (e.g., GE vs. Siemens CT scanners) reduce model adaptability.[36] For example, the public liver CT dataset (ISBI LiTS 2017), derived from 6 centers with different scanners

and protocols, exhibits significant resolution variations (0.55–1.0 mm), which may affect model generalization

- Small-sample dependency: When the volume of training data is fewer than 20 cases (e.g., rare tumors), models are prone to overfitting.[26] For instance, given only 9 WD training samples (37 control samples), iDCNN was trained with 4-fold data augmentation, achieving an accuracy of 98.28±1.55%—an improvement of more than 10% compared with the model trained without data augmentation.
- Susceptibility to overfitting and sensitivity to noise: Deep learning models often overfit when addressing complex tasks, leading to distortions in 3D reconstruction and 3D printing outcomes.

(ii) Deficiencies in interpretability

Due to the technical characteristics of the models, their decision-making logic is often difficult to intuitively understand in clinical practice.

- Black-box decision-making issue: The outputs of deep learning models (e.g., CTGANs and ECR-UNet) do not reveal the key driving features behind their predictions.[34,36] For example, when ECR-UNet identifies a region as a calcified lesion, it cannot specify whether HU values, texture features, or shape features are the dominant factors, making it difficult to gain clinicians' trust.
- Lack of quantitative confidence: The system outputs only segmentation and alignment results without providing a measure of result reliability, such as a confidence probability. For example, after alignment using a dual U-Net, it does not indicate a "95% confidence level for alignment in this region," which limits its utility in supporting risk assessment during high-risk surgeries, such as cardiovascular procedures.

These limitations constitute major bottlenecks in the clinical translation of AI-assisted multimodal imaging technology. The underlying mechanisms and potential breakthrough strategies will be further analyzed and discussed in the following sections.

3. Clinical applications of multimodal fusion and 3D printing

3.1. Orthopedic scenario

Orthopedic surgery demands a high degree of congruence between bony anatomical structures and soft-tissue interfaces; the complementary strengths of different imaging modalities effectively address this clinical requirement.[14] Accordingly, the integration of multimodal imaging fusion with 3D printing has been increasingly incorporated into key orthopedic workflows, including preoperative planning, intraoperative navigation, robotic surgical assistance, and imaging system calibration. By leveraging the synergistic strengths of multimodal imaging and 3D printing, orthopedic surgeons have achieved significant improvements in surgical planning accuracy and intraoperative guidance, as illustrated in the following representative cases:

(i) Precise operation assistance for ACL reconstruction

To address the challenge of positional deviations in bone tunnel placement caused by the isolated reliance on CT for bony structures and MRI for ligamentous signals in traditional surgery (with a malposition rate of 73.5%), Yu *et al.*[24] employed a dual U-N*et al*gorithm to enable automated CT–MRI imaging fusion (Dice similarity coefficient=0.864). They fabricated 3D-printed knee joint bony models incorporating preoperatively planned bone tunnel trajectories. Intraoperatively, bone tunnels were drilled in accordance with the model's trajectory guidance. The planned and measured intra-articular distances showed no statistically significant difference (27.49±1.01 mm vs. 26.95±0.67 mm, p=0.085). The rate of bone tunnel malposition was reduced to <5%, and preoperative planning time was reduced to 3.0±0.5 min. This approach addresses the longstanding challenge of poor coordination between soft-tissue and bony structures in traditional surgery.

(ii) Robot-assisted enhancement for lumbar disc herniation diagnosis and treatment

To address the challenges of pedicle screw placement—including heavy reliance on surgeon experience (traditional placement accuracy of ~85%) and high intraoperative radiation exposure— Researchers[42] employed the YOLOv5x model (achieving > 90% diagnostic accuracy) to analyze lumbar CT/MRI images, and subsequently fabricated 3D-printed personalized reduction guides based on these imaging analyses. When integrated with the "Tianji" surgical robot, this approach increased pedicle screw placement accuracy to 100% and reduced intraoperative radiation exposure by 23.8%. This integrated strategy enables comprehensive precision control over imaging analysis, reduction guide fabrication, and robotic assistance in pedicle screw placement.

3.2. Oncological surgery scenario

Oncological diagnosis and treatment demand spatial precision in lesion localization and the preservation of normal tissue function. To address these clinical requirements, the multimodal imaging-integrated 3D printing approach has been applied across the entire

process of oncological diagnosis and treatment. The following representative applications illustrate the use of this technology in enhancing surgical accuracy and treatment outcomes:

(i) Precise resection of calcified tumors

For calcified tumors—such as liver cancer or lung cancers with calcifications, where the spatial relationship between CT-detected calcifications and MRI-visualized tumor parenchyma is clinically ambiguous—a multimodal imaging-based workflow is utilized. First, calcifications are segmented from CT images (HU range: 100–3000), while tumor vascular supply regions are extracted via MRI dynamic contrast enhancement. Subsequently, integrated segmentation of these targets is performed using the ECR-UN*et al*gorithm (Dice similarity coefficient: 89.13%). Finally, a 3D-printed anatomical model with three-color coding is fabricated, displaying calcifications in white, tumor parenchyma in pink, and blood vessels in blue. This workflow reduces surgeons' preoperative rehearsal time by 35% and lowers the rate of calcification-related tissue injury from 18% to 2%.[27] This technology is particularly suitable for complex cases involving discrete calcification distributions.

(ii) ^{125}I seed implantation for tumors

To address the issues of insufficient integration between traditional 3D-printed non-coplanar templates (3DPNCT) and CT multimodal imaging workflows, as well as the difficulty of fixed puncture angles adapting to complex tumor anatomies, Wang *et al.*[43] optimized the clinical application of multimodal fusion and 3D printing in ^{125}I seed implantation for malignant tumors. The study adopted CT as the core multimodal foundation. Preoperatively, lesions were localized via CT with 2-mm slice thickness, and the data were imported into the Treatment Planning System (TPS) for target volume planning. In accordance with the TPS design protocol, the 3DPNCT was fabricated using 3D rapid prototyping technology and photopolymer resin. The treatment process of radioactive ^{125}I radioactive iodine seed (RIS) implantation combined with 3DPNCT is shown in Figure 3. Sixty-six patients with locally recurrent rectal cancer underwent CT-guided ^{125}I RIS implantation combined with 3DPNCT. No severe perioperative complications occurred, and only 9.1% of patients experienced grade ≥3 adverse events. Postoperative dosimetric evaluation showed that the median D90 (the dose received by 90% of the gross tumor volume [GTV]) was 140.7±33.1 Gy, and the median V100 (the proportion of GTV receiving 100% of the prescribed dose) was 91.0±13.3%. Good consistency was observed between the preoperative plan and the actual postoperative dose. At three months after surgery, the complete response ratereached 18.2% (12/66), and the objective response rate reached 84.9%, confirming that this regimen effectively enhances clinical outcomes.

(iii) Application of fMRI in 3D printing for brain tumors

To address the critical requirement in brain tumor surgery—"protecting functional areas while achieving complete tumor resection"—the blood oxygen level-dependent (BOLD) sequence of fMRI can precisely localize functional areas (e.g., motor, language, and visual regions) surrounding the tumor, thereby endowing 3D-printed models with both anatomical and functional information.[44,31] The specific application workflow is as follows:

- Data acquisition: Synchronously acquire T1-weighted contrast-enhanced MRI (to delineate tumor boundaries), fMRI (BOLD sequence, to localize functional areas), and CT scans (to extract bony landmarks) from brain tumor patients;
- AI-based fusion: Utilize an AI algorithm to achieve cross-modal alignment of fMRI functional areas with CT/MRI anatomical data, ensuring accurate spatial mapping of the relationships between functional areas and the tumor;
- 3D printing optimization: Apply color-coded labeling in the digital model (tumor: pink; motor area: green; language area: yellow; skull: white), and employ STL technology for printing to preserve millimetric spatial relationships between functional areas and the tumor;
- Clinical application: In glioma surgery, surgeons use the model to simulate resection pathways preoperatively to avoid functional areas. Two clinical cases showed that the tumor resection rates reached over 95% and over 90% respectively
- This approach has reduced the incidence of postoperative dysfunction by 25% (validated in 15 clinical cases).

3.3. Dental scenario

To address the limitations of traditional dental implant planning—such as reliance on 2D software, time-consuming manual segmentation of multimodal data, and operator-dependent accuracy—Mangano *et al.*[45] developed a multimodal fusion solution integrating AI, mixed reality (MR), and 3D-printed surgical guides to enable precise dental implant placement. Figure 4 demonstrates the AI algorithm-based automatic segmentation and co-registration of intraoral scanner data (dental crowns) and cone-beam CT data (dental roots, jawbone, and inferior alveolar nerve). The multimodal images achieve

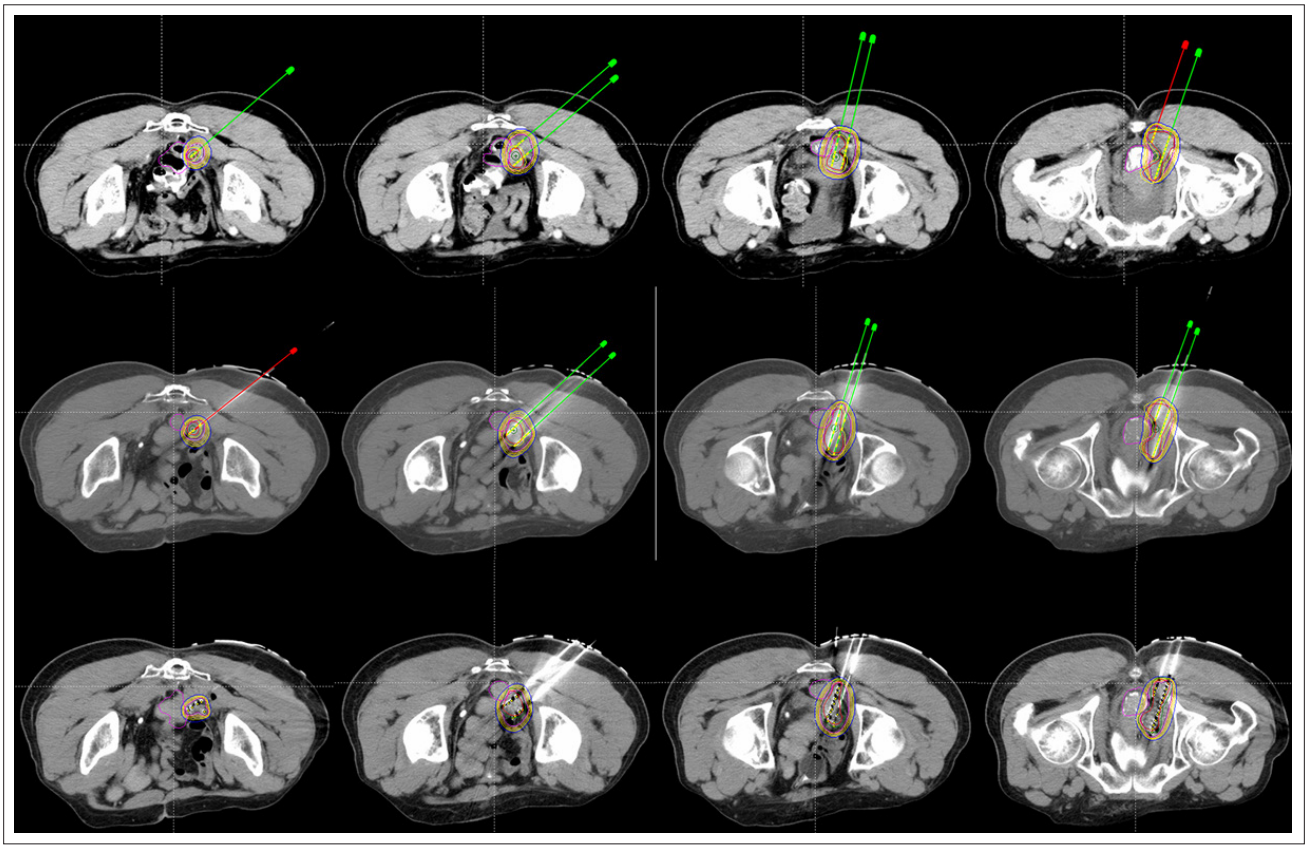


Figure 3. Treatment Process of ^{125}I radioactive iodine seed implantation combined with 3D-printed navigation template. The first row depicts the preoperative plan. The second row shows the actual positions of the needles before seed implantation during surgery. The third line presents the actual distribution of the seeds after implantation. Adapted from Ref. 43. Copyright © 2023, The authors.

precise superimposition, featuring seamless integration of dental crowns and roots, as well as clear visualization and labeling of nerve structures. The entire modeling process is completed in 15 min without manual adjustments, providing a high-precision foundation for subsequent implant planning. The 3D-printed surgical guide, visible from both the occlusal surface and the basal view, is designed based on STL files exported from multimodal planning and equipped with zirconia sleeves compatible with different drill bits, ensuring consistency between the intraoperative and planned implant paths. Validation results indicated that implants placed at dental positions #36 and #46 had coronal deviations of only 0.16–0.31 mm and apical deviations of 0.44–0.55 mm, confirming that multimodal fusion integrated with 3D printing significantly improves the accuracy and efficiency of dental implant placement.

3.4. Vascular surgery

The diagnosis and treatment of vascular diseases (e.g., aortic aneurysms, vascular malformations) rely on precise assessment of vascular anatomy and hemodynamics. The integration of multimodal imaging (computed tomography angiography [CTA]/magnetic resonance angiography [MRA]/ultrasound) and 3D printing enables intuitive visualization of vascular spatial relationships, supporting surgical planning and implant selection. The following representative applications highlight the clinical utility of this approach in vascular surgery:

(i) Surgical planning and stent adaptation verification for thoracic aortic aneurysm

Winkel *et al.*[46] reported a case involving a patient with a thoracic aortic aneurysm eroding the spine. Data of the aortic aneurysm and spinal bony structures were extracted via CTA, and the elasticity of the aneurysm neck vessel wall was evaluated by MRA. After alignment using the ML algorithm, a 1:1 3D-printed model was constructed using BJ technology with white composite as the primary material (PXL VisiJet). The model clearly demonstrated the extent of aneurysmal erosion involving the sixth to seventh thoracic vertebrae. Based on this model, the surgical team simulated the stent deployment path, ruled out conventional straight stents (which were prone to

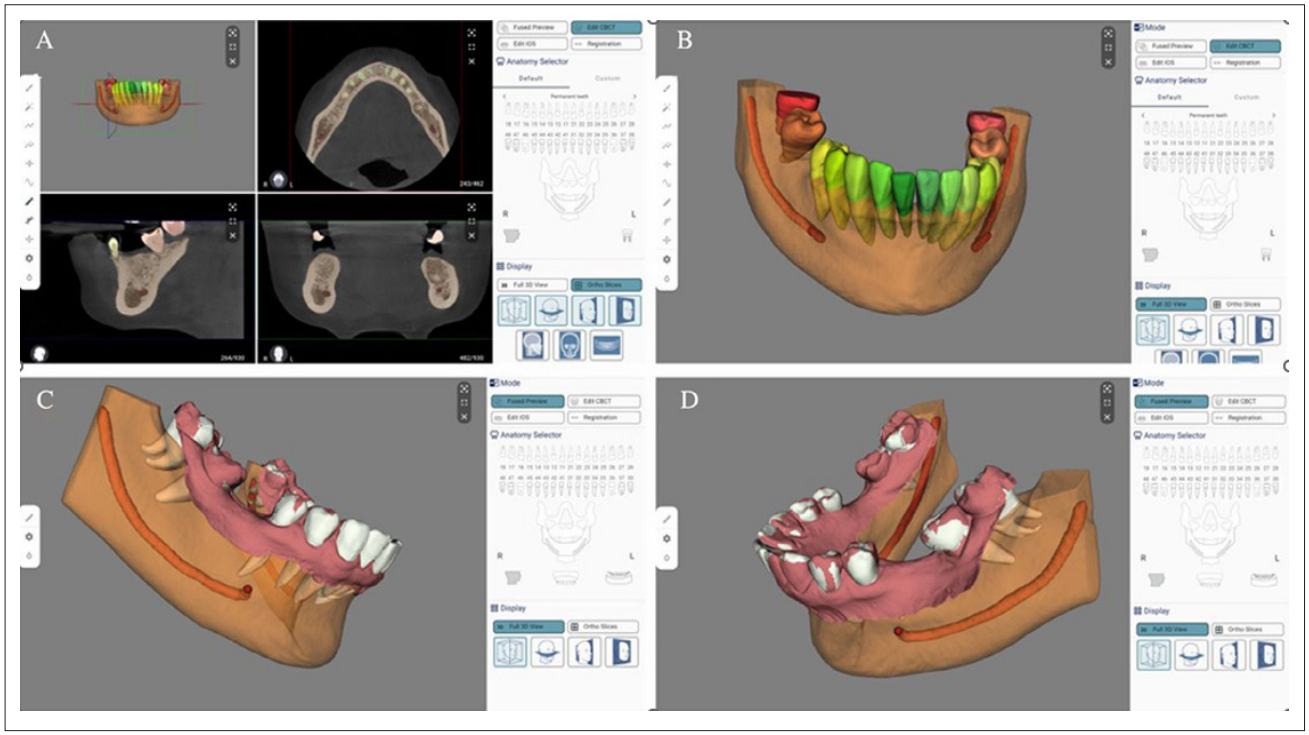


Figure 4. An artificial intelligence (AI) algorithm-based automatic segmentation and registration process of multimodal data. (A) Automatic segmentation from cone-beam computed tomography (CBCT). (B) Details of the 3D model automatically segmented by AI. (C) Overlay of 3D models from the intraoral scan on the CBCT-based segmentation, right lateral view. (D) Overlay of 3D models from the intraoral scan on the CBCT-based segmentation, left lateral view. Reprinted with permission from Ref. 45. Copyright © 2024, Wiley Periodicals LLC.

compressing the spinal cord), and selected a customized curved stent that matched the aneurysm neck angle of 15°. Postoperative CTA verification showed accurate stent positioning, absence of endoleak, and preservation of spinal cord blood supply.

(ii) Interventional training and surgical simulation for cerebral vascular malformations

Illi *et al.*,[14] Minkenberg *et al.*,[47] and Fogarasi *et al.*[59] utilized 3D TOF-MRA data (slice thickness=1 mm, interslice spacing=0.5 mm) from patients with Circle of Willis saccular aneurysms to fabricate 3D-printed vascular models using FDM technology. These models, made from acrylonitrile styrene acrylate for the vascular structure and water-soluble butenediol vinyl alcohol co-polymer (BVOH) as support material, accurately replicate the saccular aneurysms and their branching connections within the Circle of Willis.

The models were integrated into a blood flow simulation system (flow rate=15 mL/s; pressure=120/80 mmHg) for embolization training of neurointerventionalists. Results showed that the embolization operation time for novice physicians decreased from 45±5 min to 22±3 min, while the simulated complication rate (e.g., vascular perforation) dropped from 32% to 8%. These findings confirm the practical value of 3D-printed models in vascular interventional training.

3.5. Imaging-device exploration scenario

Performance calibration and quality control of multimodal imaging equipment depend on the use of standardized phantoms. 3D printing technology allows the fabrication of customized phantoms derived from multimodal data, addressing the limitations of traditional commercial phantoms—such as insufficient anatomical specificity and limited functionality. The following examples demonstrate the role of 3D printing in advancing imaging-device calibration and validation:

(i) Precision verification phantoms for medical imaging equipment

Zhang *et al.*[37] integrated CT (HU values=800–1000) and MRI (T1-weighted signal intensity= 1500–2000) data to fabricate multimodal verification phantoms using FDM 3D printing. The phantom contained five spherical cavities with diameter gradients (2–10 mm), simulating lesions. These cavities were filled with Gadolinium-labeled

diethylenetriaminepentaacetic acid solutions of varying concentrations (0.1–0.5 mmol/L) to mimic MRI signal intensities of different tissues. The phantoms were used for precision testing of 64-slice CT and 3.0T MRI systems. The detection rate of 2-mm cavities by CT reached 92% (compared to 75% for traditional phantoms), and the MRI signal uniformity error (3.2%) was lower than that of commercial phantoms (5.8%), providing a more accurate evaluation tool for routine imaging quality control.

(ii) Phantom support for emerging imaging technologies

To meet the verification needs for the material separation function of photon-counting CT (PCCT), Holmes *et al.*[48] fabricated rigid phantoms using 3D printing technology. SLA-printed inserts were embedded with simulated calcified plaques and iohexol (simulating contrast agents, HU=267.7–4119). PCCT scanning showed that the phantom could clearly distinguish between calcium salts and iodine (material separation $P<0.05$), providing phantom support for the validation and optimization of PCCT in vascular calcification and plaque assessment.

4. Key challenges and future trends

4.1. Actual challenges

While multimodal imaging and 3D printing technologies have demonstrated significant promise across diverse clinical domains, several key challenges continue to limit their large-scale clinical adoption. These challenges can be broadly categorized into technical, material, and standardization issues, as outlined below:

(i) Technical bottlenecks: Limited AI generalization and multimodal compatibility

AI models often exhibit poor cross-center generalization. For instance, a dual U-Net model trained on CT data from Center A showed a decrease in alignment accuracy when applied to data from Center B.[37,45] Furthermore, these models demonstrate limited adaptability to niche modalities, such as low-dose CT and fMRI, with segmentation errors in low-dose CT increasing by 0.55 mm. Additionally, inconsistencies in multimodal data formats—such as metadata discrepancies between DICOM 3.0 and NIfTI—lead to reduced fusion efficiency. This issue necessitates the development of additional format conversion plug-ins, thereby increasing technical translation costs for clinical implementation.[49]

(ii) Material limitations: Insufficient functional adaptability and durability

Current 3D printing materials face challenges in balancing "anatomical fidelity" with "clinical functional requirements." For example, although STL resin models provide high precision (0.02 mm), their low mechanical strength (compressive strength=50 MPa) limits their ability to simulate the load-bearing function of bone.[50,53,55] Additionally, the degradation cycle of bioinks (e.g., alginate–hydroxyapatite, 4–8 weeks) does not align with the bone regeneration cycle (3–6 months), resulting in premature scaffold failure during craniofacial bone defect repair.

(iii) Standardization gaps: Lack of unified precision verification and clinical protocols

Precision evaluation metrics for 3D-printed models are inconsistent; for example, some studies use Dice coefficients, while others rely on distance errors. Additionally, standardized clinical application guidelines are lacking. Acceptable printing error thresholds for orthopedic implant models vary widely.[38,45] Furthermore, sterilization procedures for these models—such as the effects of high-temperature sterilization on resin model deformation—remain unstandardized, posing potential risks of cross-infection.

4.2. Future directions

To achieve substantial breakthroughs in multimodal imaging–integrated 3D printing, future research should focus on three key dimensions: technological integration, material upgrading, and scenario expansion. The following directions outline the main development pathways for enhancing this technological ecosystem[51–52]:

(i) Technological synergy: End-to-end integration of AI and 3D printing

Building on the framework of "AI segmentation → naked-eye 3D visualization → 3D printing" proposed by Jia *et al.*,[27] a future end-to-end system could evolve into a fully automated workflow of "multimodal data input → AI-driven modeling → direct 3D printer output." Virtual samples generated by CTGANs will be used to augment training datasets, while federated learning will aggregate multi-center data (e.g., orthopedic data from 10 hospitals) to enhance the generalization capability of AI models. Additionally, an AI-driven adaptive adjustment module for printing parameters could be developed to optimize print quality dynamically; for instance, automatically adjusting infill density based on signal intensity in tumor vascular supply areas (80% infill for high-supply areas and 50% for low-supply areas).

(ii) Material innovation: Development of functionally graded materials and smart-responsive materials

Future efforts should emphasize the development of "mechanical–biological" functionally graded materials. For example, BJ technology may be employed to fabricate

titanium alloy–hydroxyapatite composite scaffolds, with hydroxyapatite content gradually varying from 10% to 30% to simulate the mechanical transition from cortical to cancellous bone (elastic modulus=4.86–58.02MPa).[53,54,56] In addition, smart-responsive composite scaffolds designed for gradual degradation over 3–6 months will be developed to match the bone regeneration process, thereby meeting clinical repair requirements.[53,57]

(iii) Scenario expansion: Extension to rehabilitation medicine and preventive medicine

In rehabilitation medicine, personalized rehabilitation aids can be 3D-printed based on patients' CT/MRI data. For instance, in stroke patients with foot drop, ankle-foot orthoses equipped with pressure sensors may be fabricated to monitor gait pressure in real time. Data collected from these devices can be transmitted via Bluetooth to rehabilitation applications, establishing a closed-loop system of "assessment–assistive device customization–efficacy monitoring".[53,55] In preventive medicine, 3D-printed multimodal phantoms can be used to calibrate the sensitivity of early disease screening devices. By simulating hepatic nodules of varying sizes and densities, the accuracy of low-dose CT for liver malignant tumors screening can be significantly improved.[7]

5. Conclusion

This review systematically synthesizes advancements in the interdisciplinary integration of AI-assisted multimodal CT/MRI imaging and 3D printing technologies. Through three core approaches—basic data optimization (e.g., iDCNN-driven artifact removal), cross-modal alignment (e.g., dual UNet-based registration), and scenario-specific segmentation (e.g., ECR–UNet-based calcification segmentation)—AI has effectively addressed challenges related to multimodal data heterogeneity and limited compatibility with 3D printing.[27,53] In clinical applications, this technology has demonstrated significant value across multiple domains, such as orthopedics (ACL bone tunnel malalignment rate < 5%),[53,54] oncologic surgery (objective response rate of 84.9% for implantation in locally recurrent rectal cancer[53]), and dentistry (dental implant axial deviation < 0.5 mm). Additionally, it has improved imaging equipment quality control and enhanced interventional training through 3D-printed phantoms.[7,27]

However, existing technologies still face three major challenges: limited AI generalization capabilities, insufficient material functionality, and the absence of standardized clinical protocols. Future breakthroughs must therefore focus on achieving end-to-end technological integration, developing functionally graded materials, and establishing robust clinical standards.[53,54,56,57] The interdisciplinary convergence represents not only a critical enabler of precision medicine but also a transformative shift in medical engineering, from "passive adaptation to clinical needs" toward "proactive leadership in diagnostic and therapeutic innovation".[55,58–60] Such progress will provide a new paradigm for the personalized diagnosis and treatment of complex diseases.

Acknowledgments

The author expresses sincere gratitude to all team members, as this work was completed through their collective efforts. Special thanks are extended to the corresponding author, Professor Jianhua Liu, for their significant contributions to the writing of this article.

Funding

This work was supported by the Innovation and Entrepreneurship Talent Funding Program of Jilin Province,china and the Health Special Project of the Finance Department of Jilin Province,china.

Conflict of interest

The authors declare that they have no competing interests.

Author contributions

Conceptualization: Jianhua Liu, Lihua Gao
Writing–original draft: Weipeng Zhou
Writing–review & editing: Jianhua Liu, Weipeng Zhou, Meng Wu

Ethics approval and consent to participate

Not applicable.

Consent for publication

Not applicable.

Availability of data

Not applicable.

References

1. Farid AR, Comtesse S, Sagi HC, *et al*. Enabling technology in fracture surgery: state of the art. *J Bone Joint Surg*. 2025;107(14):1636-1647. doi:10.2106/JBJS.24.00938

2. Streckenbach A, Schubert N, Streckenbach F, *et al*. Current state and outlook in medical 3D printing and the role of radiology. *RofoFortschrRontg*. 2025;197(7):770-780. doi:10.1055/a2436-7185

3. Santiago FR, Ramos-Bossini AJL, Wáng YXJ, Barbero JPM, Espinosa JG, Martínez AM. The value of magnetic resonance imaging and computed tomography in the study of spinal disorders. *Quant Imaging Med Surg*. 2022;12(7):3947. doi:10.21037/qims-2022-04

4. Cejvanovic S, Sheikh Z, Hamann S, Subramanian PS. Imaging the brain: diagnosis aided by structural features on neuroimaging studies. *Eye*. 2024;38(12):2380-2391. doi:10.1038/s41433-024-03142-w

5. Martucci M, Russo R, Schimperna F, *et al*. Magnetic resonance imaging of primary adult brain tumors: state of the art and future perspectives. *Biomedicines*. 2023;11(2):364. doi:10.3390/biomedicines11020364

6. Schultz CH, Fairley R, Murphy LSL, Doss M. The risk of cancer from CT scans and other sources of low-dose radiation: a critical appraisal of methodologic quality. *Prehosp Disaster Med*. 2020;35(1):3-16. doi:10.1017/S1049023X1900520X

7. Lyu P, Li Z, Chen Y, *et al*. Deep learning reconstruction CT for liver metastases: low-dose dual-energy vs standard-dose single-energy. *Eur Radiol*. 2024;34(1):28-38. doi:10.1007/s00330-023-10033-3

8. Usman M, Latif S, Asim M, Lee BD, Qadir J. Retrospective motion correction in multishot MRI using generative adversarial network. *Sci Rep*. 2020;10(1):4786. doi:10.1038/s41598-020-61705-9

9. Wu L, Gao C, Wu T, *et al*. Magnetic resonance imaging in the clinical evaluation of lung disorders: current status and future prospects. *J Magn Reson Imaging*. 2025;62(5): 1260-1279. doi:10.1002/jmri.29802

10. Kuiper RJA, Colaris JW, Stockmans F, *et al*. Impact of bone and cartilage segmentation from CT and MRI on both bone forearm osteotomy planning. *Int J Comput Assist Radiol Surgery*. 2023;18(12):2307-2318. doi:10.1007/s11548-023-02929-8

11. Jacobson N, Carerra E, Smith L, *et al*. Defining soft tissue: bitmap printing of soft tissue for surgical planning. *3D Print Addit Manuf*. 2022;9(6):461-472. doi:10.1089/3dp.2021.0141

12. Marro A, Bandukwala T, Mak W, Three-dimensional printing and medical imaging: a review of the methods and applications. *Curr Probl Diagn Radiol*. 2016;45(1):2-9. doi: 10.1067/j.cpradiol.2015.07.009

13. Ng WL, An J, Chua CK. Process, material, and regulatory considerations for 3D printed medical devices and tissue constructs. *Engineering*. 2024;36(1):146-166. doi:10.1016/j.eng.2024.01.028

14. Illi J, Bernhard B, Nguyen C, *et al*. Translating imaging into 3D printed cardiovascular phantoms: a systematic review of applications, technologies, and validation. JACC *Basic Transl Sci*. 2022;7(10):1050-1062. doi:10.1016/j.jacbts.2022.01.002

15. Qin Y, Xu Z, Wang X, Skare M. Artificial intelligence and economic development: an evolutionary investigation and systematic review. *J Knowl Econ*. 2024;15:1736-1770. doi:10.1007/s13132-023-01183-2

16. Mendoza-Cerezo L, Jesús MRR, Macías-García A, Marcos-Romero AC, Díaz-Parralejo A. Evolution of bioprinting and current applications. *Int J Bioprint*. 2023;9(4):367-382. doi:10.18063/ijb.742

17. Tappa K, Bird JE, Arribas EM, Santiago L. Multimodality imaging for 3D printing and surgical rehearsal in complex spine surgery. *RadioGraphics*. 2024;44(3):e230116. doi:10.1148/rg.230116

18. Albertini JN, Derycke L, Millon A, Soler R. Digital twin and artificial intelligence technologies for predictive planning of endovascular procedures. *Semin Vasc Surg*. 2024;37(3):306-313. doi:10.1053/j.semvascsurg.2024.07.002

19. Dai Y, Wang P, Mishra A, *et al*. 3D bioprinting and artificial intelligence-assisted biofabrication of personalized oral soft tissue constructs. *Adv Healthc Mater*. 2025;14(13):2402727. doi:10.1002/adhm.202402727

20. Jeon K, Park WY, Kahn CE Jr, Nagy P, You SC, Yoon SH. Advancing medical imaging research through standardization: The path to rapid development, rigorous validation, and robust reproducibility. *Invest Radiol*. 2025;60(1):1-10. doi:10.1097/RLI.0000000000001106

21. Huang H, Liu B, Xu Y, Zhou W. Synthetic-to-real domain adaptation with deep learning for fitting the intravoxel incoherent motion model of diffusion-weighted imaging. *Med Phys*. 2023;50(3):1614-1622. doi:10.1002/mp.16031

22. Chau RCW, Hsung RTC, McGrath C, Pow EHN, Lam WYH. Accuracy of artificial intelligence-designed single-molar dental prostheses: a feasibility study. *J Prosthet Dent*. 2024;131(6):1111-1117. doi:10.1016/j.prosdent.2022.12.004

23. Chen Z, Pawar K, Ekanayake M, Pain C, Zhong S, Egan GF. Deep learning for image enhancement and correction in magnetic resonance imaging—state-of-the-art and challenges. *J Digit Imaging*. 2023;36(1):204-230. doi:10.1007/s10278-022-00721-9

24. Yu H, Dong X, Li H, *et al*. Application of artificial intelligence deep learning-based multimodal CT-MRI images automatic fusion and segmentation in preoperative planning for anterior cruciate ligament reconstruction. *Chin J Bone Joint Surg*. 2025;18(1):27-35. doi:10.3969/j.issn.2095-9958.2025.01.05

25. Wan Z, Li H, Shi N, Liu Y, Liu F. Intelligent evaluation of tumor calcification areas based on whole slide images. *Laser Optoelectron Prog*. 2024;61(22):2217001.

doi:10.3788/LOP240787

26. Agarwal M, Saba L, Gupta SK, *et al*. Wilson disease tissue classification and characterization using seven artificial intelligence models embedded with 3D optimization paradigm on a weak training brain magnetic resonance imaging datasets: a supercomputer application. *Med Biol Eng Comput*. 2021;59(3):511-533. doi:10.1007/s11517-021-02322-0

27. Jia G, Huang X, Tao S, *et al*. Artificial intelligence-based medical image segmentation for 3D printing and naked eye 3D visualization. *Intell Med*. 2022;2(1):48-53. doi:10.1016/j.imed.2021.04.001

28. Liang Y, Wang Q, Zhang YW, *et al*. A pilot study on clinical application of three-dimensional morphological completion of lesioned mandibles assisted by generative adversarial networks. *Chin J Stomatol*. 2024;59(12):1213-1220. doi:10.3760/cma.j.cn112144-20240930-00367.

29. Wenran HU, Rong FU. Trans-YOLOv5: a YOLOv5-based prior transformer network model for automated detection of abnormal cells or clumps in cervical cytology images. *J South Med Univ*. 2024;44(7):1217-1226. doi:10.12122/j.issn.1673-4254.2024.07.01

30. Xiaoyun Z, Shuxiong B, Shuai H. CT multiple-level reconstruction for preoperational estimation of facet joint violation in lumbar percutaneous pedicle screw placement. *Chin J Tissue Eng Res*. 2020;24(21):3347-3352. doi:10.3969/j.issn.2095-4344.2683

31. Bhardwaj N, Sood M, Gill SS. 3D-bioprinting and AI-empowered anatomical structure designing: a review. *Curr Med Imaging*. 2024;20(1):e15734056259274. doi:10.2174/0115734056259274231019061329

32. Luo M, Zhou N, Wang T, *et al*. Bi-constraints diffusion: a conditional diffusion model with degradation guidance for metal artifact reduction. *IEEE Trans Med Imaging*. 2025;44(9):3552-3562. doi:10.1109/TMI.2024.3442950

33. Liu Z, Zhu Z, Zheng S, Liu Y, Zhou J, Zhao Y. Margin preserving self-paced contrastive learning towards domain adaptation for medical image segmentation. *IEEE J Biomed Health Inform*. 2022;26(2):638-647. doi:10.1109/JBHI.2022.3140853

34. Zhou Y, Yan Z, Hubert P. An artifactual fibre overlap removal algorithm for micro-computed tomography image post-processing and 3D microstructure generation with graphics processing unit acceleration. *Mater Des*. 2024;247:113376. doi:10.1016/j.matdes.2024.113376

35. Ogbuanya CE, Obayi A, Larabi-Marie-Sainte S, Saad AO, Berriche L. A hybrid optimization approach for accelerated multimodal medical image fusion. *PLoS One*. 2025;20(7):e0324973. doi:10.1371/journal.pone.0324973

36. Huang H, Zheng H, Lin L, *et al*. Medical image segmentation with deep atlas prior. *IEEE Trans Med Imaging*. 2021;40(12):3519-3530. doi:10.1109/TMI.2021.3089661

37. Zhang J, Zhang N, Li Y, Zhou J, Cao D, He K. Research progress of 3D printing-based construction of experimental physical models for medical imaging devices. *Chin Med Equip J*. 2022;43(8):1-6. doi:10.19745/j.1003-8868.2022173

38. Yang H, Yang R, Zhu H, *et al*. Design of multi-modal vertebral phantom based on tissue equivalence and 3D printing technology. *Chin J Med Phys*. 2016;33(9):6. doi:10.3969/j.issn.1005-202X.2016.09.011

39. Yusuff H, Zorn PE, Giraudeau C, *et al*. Development of a cost-effective 3D-printed MRI phantom to enhance teaching of system performance and image quality concepts. *Magn Reson Mater Phys Biol Med*. 2025;38(3):561-574. doi:10.1007/s10334-024-01217-z

40. Hindi OA, Pinarbasi B, Bakici M, *et al*. In situ bioprinting enhances bone regeneration in a live animal model of craniofacial defects. *ACS Biomater Sci & Eng*. 2025;11(12):5027-5037. doi:10.1021/acsbiomaterials.5c00780

41. Lee D, Ruf M, Karadimitriou N, *et al*. Development of stochastically reconstructed 3D porous media micromodels using additive manufacturing: numerical and experimental validation. *Sci Rep*. 2024;14(1):9375. doi:10.1038/s41598-024-60075-w

42. Zhang Z, Chen L, Sheng W, *et al*. Application of artificial intelligence in the diagnosis and treatment of lumbar disc herniation: evolution towards standardization, efficiency, and precision of diagnosis and treatment methods. *Chin J Tissue Eng Res*. 2025;29(29):6269-6276. doi:10.12307/2025.759

43. Wang L, Wang H, Jiang Y, *et al*. The efficacy and dosimetry analysis of CT-guided ^{125}I seed implantation assisted with 3D-printing non-co-planar template in locally recurrent rectal cancer. *Radiat Oncol*. 2020;15(1):179-183. doi:10.1186/s13014-020-01607-2

44. Gomez-Feria J, Narros J L, Go´ mez Ciriza G, *et al*. 3D printing of diffuse low-grade gliomas involving eloquent cortical areas and subcortical functional pathways: technical note. *World Neurosurg*. 2021;147:164-171. doi:10.1016/j.wneu.2020.12.082

45. Mangano FG, Yang KR, Lerner H, Admakin O, Mangano C. Artificial intelligence and mixed reality for dental implant planning: a technical note. *Clin Implant Dent Relat Res*. 2024;26(5):942-953. doi:10.1111/cid.13357

46. Winkel DJ, Mujagic E, Staub D, Harder D, Bremerich J, Obmann MM. Multimodal imaging and 3D printing of a thoracoabdominal aortic aneurysm eroding the spine. *Radiol Case Rep*. 2023;18(2):657-660. doi:10.1016/j.radcr.2022.11.020.

47. Minkenberg JG, Bender L, Franz C, *et al*. Accurate full-scale patient-specific Circle of Willis models including aneurysms: a novel manufacturing approach. *PLoS One*. 2025;20(7):e0328300. doi:10.1371/journal.pone.0328300

48. Holmes T W, Yin Z, Bujila R, *et al*. Ultrahigh-resolution K-edge imaging of coronary arteries with prototype deep-silicon photon-counting CT: initial results in phantoms. *Radiology*. 2024;311(3):e231598. doi:10.1148/radiol.231598.

49. Sato K, Yamashiro A, Koyama T. Material investigation for the development of non-rigid phantoms for CT-MRI image registration. *Nihon Hoshasen Gijutsu Gakkai Zasshi*. 2022;78(6):615-624. doi:10.6009/jjrt.2022-1241

50. Wang X, Zhao F, Zhen P. Physicochemical properties of 3D printed bioactive glass/hydroxyapatite bone repair materials. *J Ningxia Med Univ*. 2022;44(5):511-516. doi:10.16050/j.cnki.issn1674-6309.2022.05.013

51. Lichtenstein J, Heinzel S, Kurz B, *et al*. Are we ready for virtual planning and 3D-printed titanium plates in zygomatic fractures? A feasibility study based on 16 post-mortem fractures. *J Craniomaxillofac Surg*. 2025;53(3):325-331. doi:10.1016/j.jcms.2024.11.004

52. Jin Z, Zhang Z, Shao X, Gu GX. Monitoring anomalies in 3D bioprinting with deep neural networks. *ACS Biomater Sci Eng*. 2023;9(7):3945-3952. doi:10.1021/acsbiomaterials.0c01761

53. Zang XL, Sun J, Li YL, *et al*. 3D-bioprinting manufacturing polylactic-co-glycolic acid/nano-hydroxyapatite scaffold/bone morphogenetic protein-2 sustained release composite. *Chin J Tissue Eng Res*. 2016;20(16):2405-2411. doi:10.3969/j.issn.2095-4344.2016.16.017

54. Wu BY, Ye K, Chen JH, *et al*. Biocompatibility of 3D printed polyetheretherketone/hydroxyapatite composites. *Chin J Tissue Eng Res*. 2023;27(12):1932-1937. doi:10.12307/2023.079

55. Li P, Cheng W, Wang JQ, *et al*. Osteogenesis effect of bone marrow mesenchymal stem cells combined with bionic bone scaffold. *Henan Med Res*. 2022;31(7):1153-1158. doi:10.3969/j.issn.1004-437X.2022.07.001

56. Hu CR, Qiu B, Zhou ZX, Yang Y, Li J. In vitro biocompatibility of 3D printed polycaprolactone/nano-hydroxyapatite composite scaffold with bone marrow mesenchymal stem cells. *Chin J Tissue Eng Res*. 2020;24(4):589-595. doi:10.3969/j.issn.2095-4344.1880

57. Liu D, Qin H, Wang YX, *et al*. 3D-printed hydroxyapatite/polylactic acid network composites for skull defects. *Chin J Tissue Eng Res*. 2019;23(6):833-837. doi:10.3969/j.issn.2095-4344.0676

58. Silva G, Ashford R. Using artificial intelligence to predict outcomes of operatively managed neck of femur fractures. *Br J Hosp Med*. 2024;85(6):1-12. doi:10.12968/hmed.2024.0034

59. Fogarasi M, Coburn J C, Ripley B. Algorithms used in medical image segmentation for 3D printing and how to understand and quantify their performance. *3D Print Med*. 2022;8(1):18. doi:10.1186/s41205-022-00145-9

60. Yang B, Gong K, Liu H, Li Q, Zhu W. Anatomically guided pet image reconstruction using conditional weakly-supervised multi-task learning integrating self-attention. *IEEE Trans Med Imaging*. 2024;43(6):2098-2112. doi:10.1109/TMI.2024.3356189

ACCSCIENCE PUBLISHING

International Journal of Bioprinting

REVIEW ARTICLE

Precision hydrogel environments for advanced microbial culture and patterning

Jeremy Elias[1], Catherine Klein[2], Benjamin Wu[1], Xuesong He[3], and Jirun Sun[1]*

[1] Department of Mineralized Tissue Biology, ADA Forsyth Institute, Somerville, Massachusetts, USA

[2] Center for Regenerative Medicine, Institute of Science and Innovation in Medicine, Faculty of Medicine, Clínica Alemana CAS–UDD, University of Development, Santiago, Chile

[3] Department of Microbiology, ADA Forsyth Institute, Somerville, Massachusetts, USA

Abstract

Hydrogel materials and scaffolds have emerged as transformative tools in biological research by offering precise control over cell viability, metabolism, and productivity. Their compatibility with three-dimensional (3D) bioprinting and patterning technologies enables the precise and reproducible organization of living components, facilitating novel experimental paradigms across diverse disciplines. Although most 3D hydrogel research has emphasized mammalian cell applications, particularly in tissue engineering, there is a growing body of research applying these technologies to study, manipulate, and harness a variety of microorganisms, such as bacteria. This review explores the latest advances in microbial hydrogel encapsulation, focusing on material selection and patterning methods designed to preserve microbial viability and function. We compare the distinct requirements and challenges of culturing microorganisms in hydrogels versus mammalian systems and highlight recent breakthroughs in bacterial bioprinting that are advancing microbiological research, paving the way for current and emerging applications in various areas, including oral health. By synthesizing current knowledge and identifying promising future directions, this review underscores the potential of microbial hydrogel culture as a versatile platform for investigating microbial communities, probing bacterial–material interactions, and engineering living materials with applications in human health and environmental systems.

Keywords: Bacteria–material interaction; Bacterial bioprinting; Microbial hydrogel culture; Microbial living materials; Three-dimensional bioprinting

***Corresponding author:**
Jirun Sun
(jsun@forsyth.org)

Citation: Elias J, Klein C, Wu B, He X, Sun J. Precision hydrogel environments for advanced microbial culture and patterning. *Int J Bioprint*. 2026;12(1):145-172. doi: 10.36922/IJB025420426

Received: October 16, 2025
Revised: November 18, 2025
Accepted: November 20, 2025
Published online: November 26, 2025

Copyright: © 2025 Author(s). This is an Open Access article distributed under the terms of the Creative Commons Attribution License, permitting distribution, and reproduction in any medium, provided the original work is properly cited.

Publisher's Note: AccScience Publishing remains neutral with regard to jurisdictional claims in published maps and institutional affiliations.

1. Introduction

Bacteria and biofilms have been extensively studied due to their omnipresence in nature, critical roles in human health, and potential for both beneficial applications and harmful effects across diverse industries and ecosystems.[1,2] Microbial culture systems are fundamental tools that facilitate the study of microbial behavior under controlled experimental conditions, enabling investigations into interspecies interactions and antimicrobial resistance.[3] These systems are also utilized to harness microbial

metabolism for the production of valuable bioproducts, or for bioremediation applications that address environmental contamination.[4,5] Advances in synthetic biology are further expanding the frontiers of engineered microbial systems, enabling tailored applications in therapeutic and industrial contexts.[6]

Traditional microbial culture methods, generally consisting of planktonic growth in liquid media and two-dimensional (2D) surface cultivation, remain widely adopted throughout the research community due to their simplicity and ease of use. However, these methods fall short in replicating the complex, three-dimensional (3D) microenvironments that organisms naturally inhabit, such as porous biofilm structures or tissue-like matrices.[7] In contrast, 3D culture techniques, including microbial immobilization within hydrogels and other 3D matrices, offer significant advantages.

Hydrogels are 3D, cross-linked polymer networks that absorb and retain large volumes of aqueous fluid while preserving structural integrity. Their mechanical behavior—including tunable stiffness and viscoelasticity (i.e., the time-dependent response under stress)—can be precisely engineered, enabling these materials to mimic the microenvironments of native tissues and microbial biofilms.[8,9] Recent studies show that embedding bacterial populations within hydrogel-based 3D matrices enhances the physiological relevance of *in vitro* models, better replicating natural environments and facilitating more accurate behaviors, such as regulated growth, intercellular signaling, metabolic activity, and functional outcomes.[10,11] Moreover, 3D biofilm models, particularly those generated via bioprinting, exhibit markedly greater antimicrobial resistance compared with traditional 2D cultures, thereby better recapitulating *in vivo* conditions.[12] Figure 1 illustrates the applications and associated drawbacks of planktonic and 2D plate-based microbial cultures, contrasting these methods with the potential advantages of 3D and hydrogel-based cultures and biofilms.

Moreover, growing evidence shows that bacterial behavior is fundamentally altered by physical confinement within 3D matrices.[7] These environments introduce diffusion limitations and structural constraints that cannot be replicated in homogeneous liquid or surface cultures. By embedding microbes within tailored scaffolds—particularly hydrogels—researchers not only create environments that reflect biological reality more accurately but also protect microbial cells from environmental stresses. This physiologically relevant protection is crucial in a

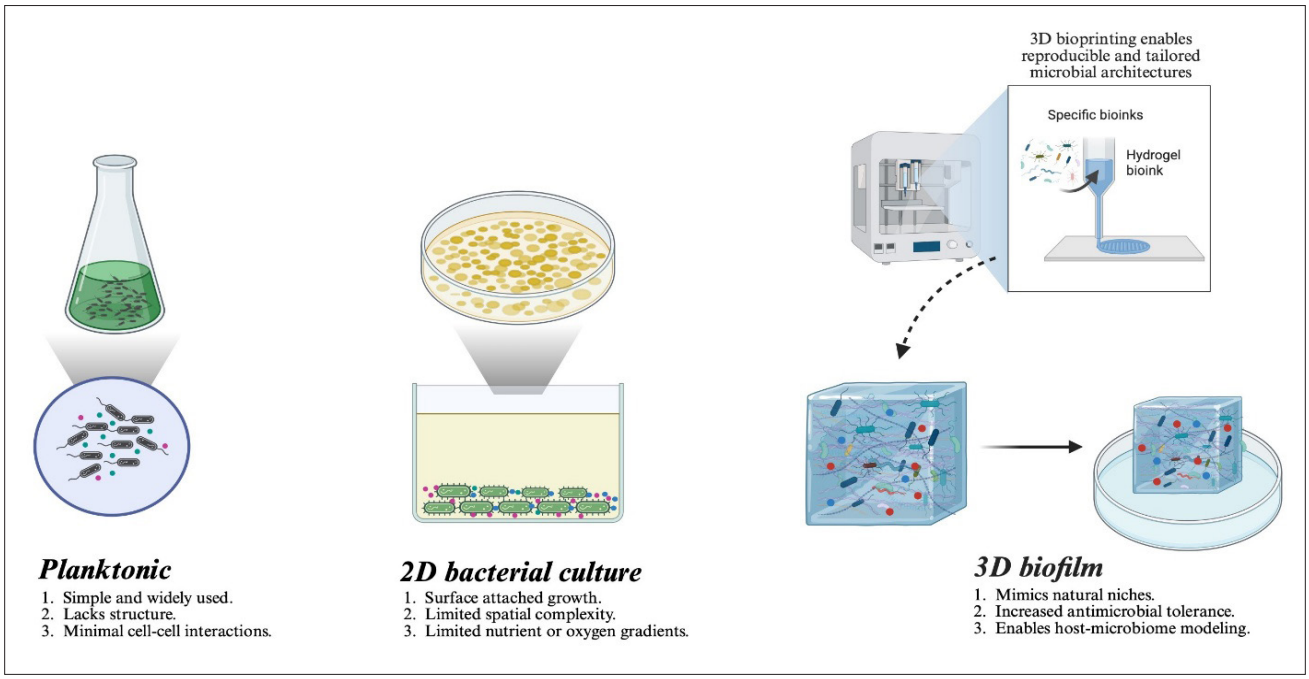


Figure 1. Comparison of microbial culture methods. Planktonic cultures are simple and widely used but lack structure and cell–cell interactions. 2D surface-attached cultures allow microbial growth on agar or plastic but oversimplify natural biofilms as they lack spatial complexity and nutrient or oxygen gradients. In contrast, 3D hydrogel-based biofilms mimic natural niches by providing structural confinement, nutrient and oxygen gradients, and enhanced microbial interactions, resulting in increased antimicrobial tolerance and enabling host–microbe modeling. Created in BioRender. Klein, C. (2025) https://BioRender.com/0y4ljkp. Abbreviations: 2D, Two-dimensional; 3D, Three-dimensional.

variety of applications, including fundamental microbial studies and antimicrobial evaluation, providing superior relevance to biofilms, a predominant form of microbial existence in which bacterial cells can exhibit up to a 1,000-fold greater antibiotic tolerance than their planktonic counterparts.[13] The precision and reproducibility of 3D bioprinting also support the construction of functional microbial architectures optimized for research, industrial, or environmental applications.

This review aims to examine the evolution of hydrogel-based bacterial culture systems, assessing how material selection, fabrication techniques, and bioprinting strategies provide tailored levels of spatial and metabolic control over microbial communities. We synthesize advances in 3D bacterial culture methodologies, highlighting how precision, from macroscale encapsulation for bioproduction to microscale patterning for single-cell analysis, enables applications ranging from scalable bioremediation and engineered living materials (ELMs) to advanced models for studying biofilm dynamics and host–microbe interactions. Finally, we discuss current limitations and future directions, with a focus on opportunities for innovation in microbiology applications, such as oral research, where hydrogel-based systems offer unique potential to mimic complex natural biogeography.

2. Literature methodology

We adopted a narrative-review framework[14] to explore recent advances in 3D hydrogel platforms for microbial culture and manipulation. A narrative review was deemed most appropriate because the heterogeneity of study designs, materials, and microbial targets rendered a formal systematic review unsuitable. This approach provides the flexibility needed to integrate diverse methodologies and conceptual developments in a coherent, interpretive synthesis.

A comprehensive literature search was conducted for English-language, peer-reviewed articles published from January 2010 to July 2025. We utilized PubMed, Web of Science, and Google Scholar, incorporating both controlled vocabulary and free-text terms, such as "microbial hydrogel culture," "bacterial bioprinting," and "microbial living materials." This strategy balanced sensitivity and specificity, ensuring coverage of key publications while aligning with best practices in narrative review methodology.

Studies were considered eligible if they met all of the following criteria: (i) reported original empirical data; (ii) developed, characterized, or applied hydrogel-based constructs for microbial culture; and (iii) employed 3D bioprinting or comparable spatial patterning techniques. The scope of analysis regarding printed constructs was limited to 3D bioprinting applications utilizing cell-laden bioinks designed to support microbial viability and function. Studies describing 3D printing with acellular materials ("biomaterial printing") were excluded, although the term "3D printing" is sometimes used in the literature to refer to both approaches. Two reviewers independently screened titles and abstracts, resolving conflicts through discussion before proceeding to full-text review. This dual-review process, though within a narrative context, reinforces transparency and rigor.

For each included study, we extracted the following key details: microbial species, hydrogel composition (e.g., natural vs. synthetic), immobilization or patterning technique, 3D bioprinting modality used, intended function, and application domain (e.g., biosensing, bioproduction, or bioremediation). These data were organized thematically to enable comparative analysis of natural versus synthetic hydrogels, crosslinking chemistries, and printing strategies, with a particular focus on how material and architectural choices influence microbial viability, spatial distribution, and functional output. Given the narrative nature of this review, we did not conduct a meta-analysis. Instead, we synthesized methodological innovations and persistent challenges, structured by application domains to guide future research directions.

3. Materials and techniques for increased microbial culture precision

Advancements in hydrogel fabrication and processing have enhanced our ability to encapsulate and culture diverse microorganisms with control over their microenvironment and behavior. The selection of hydrogel materials and additional chemical groups, as well as material modifications and patterning techniques, play a critical role in determining bioactivity and microbial compatibility, making material choice and tailoring critical for the development of precision 3D microbial materials.[15,16]

While hydrogel-based culture and bioprinting are more established for mammalian cells, primarily for tissue engineering, their application to microbes presents a distinct set of requirements and challenges. Mammalian cell systems demand tailored conditions to mimic physiological environments, including strict temperature control and high biocompatibility to support delicate cell membranes and behaviors like cell binding.[17] In some cases, to encapsulate mammalian cells, biomaterial systems must also exhibit degradation kinetics to facilitate cell growth[18] and extracellular matrix (ECM) production, as well as sophisticated porosity for nutrient diffusion and eventual vascularization.[17,19,20] The properties, requirements, and

challenges of specific mammalian cell patterning methods and the materials they utilize are also extensively discussed in recent reviews.[20–24]

In contrast, microbial encapsulation leverages the inherent robustness conferred by bacterial cell walls and protective behaviors, such as spore formation,[25] which allows for a wider range of processing parameters, such as higher extrusion temperatures or freeze-drying.[26,27] However, this robustness introduces unique design constraints. The rapid growth rate of bacteria necessitates bioinks and containment strategies that prevent overgrowth and structural degradation, while also addressing the challenge of ensuring effective physical containment to prevent environmental contamination or unintended pathogenesis.[28,29] Interestingly, despite these divergent requirements, the base hydrogel materials (e.g., alginate, gelatin methacryloyl [GelMA]) are often similar; the key differences lie in the processing methods and the exploitation of microbial attributes, such as integrating self-secreted extracellular polymeric substances to enhance printability and the biomimicry of natural biofilms.[30,31]

Both naturally derived and synthetic hydrogel materials can be modified through crosslinking, pore generation, and 3D patterning on different length scales. These modifications affect nutrient and bioproduct transport, microbial architecture, and potential interspecies interactions, which must be tailored to optimize microbial viability, metabolic activity, and functional output.[27] The foundation of material choice and advantages of microstructural control and spatial patterning in increasing the precision of microbial cultures are illustrated in Figure 2.

3.1. Hydrogel materials

A variety of hydrogel materials and precursors are available for integrating microbial species for applications in culture or for harnessing different microbial functions. Hydrogels can be derived from natural or synthetic sources and subsequently modified by the addition of different functional groups to support microbial growth and function within the matrices. A summary of the most commonly used hydrogel materials for cellular encapsulation and bioinks is provided in Table 1.

Natural hydrogels such as collagen, gelatin,[32,33] alginate,[34] hyaluronic acid, and bacterial cellulose[35] are advantageous for microbial culture and bioprinting applications due to their ability to emulate the conditions of ECM and tissue environments, supporting microbial growth, and function. Alginate- and gelatin-based hydrogel materials comprise the most studied and utilized natural hydrogels for bioprinting applications. Alginate is widely used in extrusion-based bioprinting systems due to its ability to quickly crosslink and stabilize printed filaments upon contact with calcium compounds, such as calcium chloride. This rapid gelation mechanism allows for excellent shape

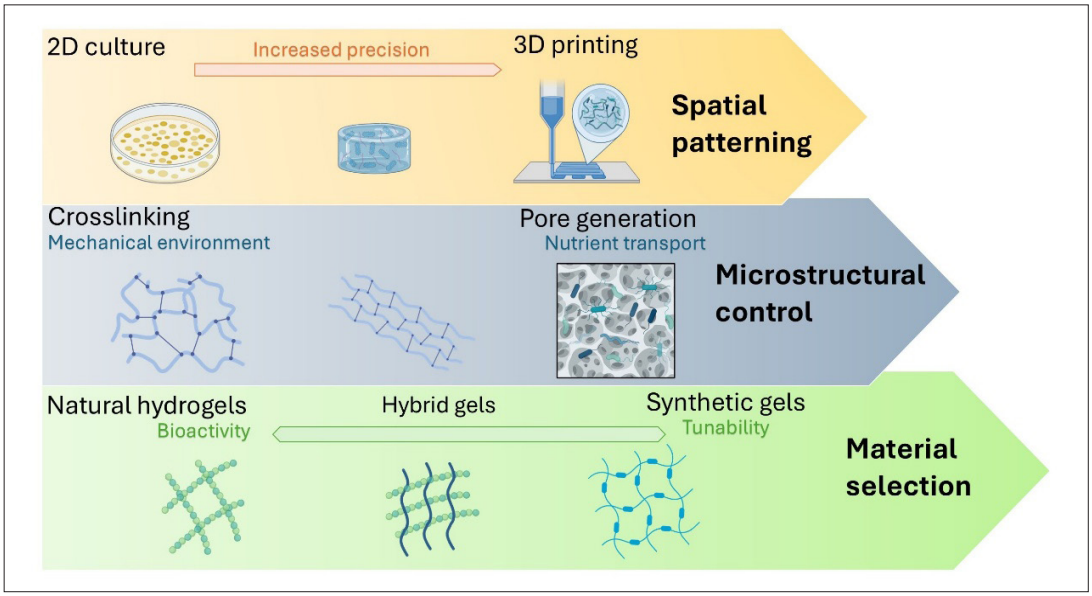


Figure 2. Schematic illustration of material modifications and their impact on microbial culture effects. Material selection forms the foundation, balancing overall tunability and biocompatibility of hydrogels for culture, whereas crosslinking and pore generation methods provide versatility in microbial microenvironments and nutrient transport. These features enable precise hydrogel culture and 3D patterning, offering advantages in microbial study and manipulation compared to 2D and planktonic cultures. Created in BioRender. Elias, J. (2025) https://BioRender.com/2qe2f6y. Abbreviations: 2D, Two-dimensional; 3D, Three-dimensional.

fidelity during printing processes. One of the alginate's most valuable contributions to the bioprinting field is its effectiveness for mammalian cell encapsulation. The mild gelation conditions required for alginate crosslinking can maintain cell viability and long-term cell survival, allowing cells to be mixed with the alginate solution prior to printing and subsequently encapsulated within the hydrogel matrix after crosslinking. The alginate matrix can also be utilized for the delivery of growth factors and other bioactive components, creating microenvironments that can direct and enhance specific cellular responses.[36,37] However, unlike other natural bioink materials, such as collagen, fibrin, or gelatin, which contain integrin-binding sites, alginate lacks the functional groups and recognition sites that allow for direct cell attachment, requiring chemical modifications, or combinations with other natural polymers to supplement its bioactive capabilities.

Gelatin represents a versatile biomaterial derived from the denatured form of collagen, obtained through partial hydrolysis. Like collagen, gelatin can be readily obtained from animal tissues, typically bovine or porcine sources, providing advantages for its biomaterial uses. Despite undergoing denaturation, gelatin maintains similar advantages to its parent molecule, most notably the presence of the Arg-Gly-Asp (RGD) peptide sequence, which promotes robust cell interactions.[32,33] The most distinctive characteristic of gelatin for bioprinting applications is its unique thermo-responsive behavior—existing in gel form at low temperatures and undergoing a transition to a liquid state at higher temperatures above 37 °C. When cooled below approximately 25 °C, gelatin molecules create a physically crosslinked network that imparts gel-like properties. This temperature-dependent phase transition offers significant advantages for bioprinting workflows, as at reduced temperatures, it exhibits suitable viscosity and structural stability for extrusion and shape maintenance during the printing process. This allows for the creation of complex structures with good resolution and fidelity.

The thermo-responsive nature of gelatin also presents challenges. Due to its dissolution into a liquid state at physiological temperatures (37 °C), modification through crosslinking or combination with other biomaterials is needed for gelatin to be utilized effectively in bioprinting applications requiring long-term structural stability. Chemical crosslinkers such as glutaraldehyde, genipin, or carbodiimides (e.g., *N*-ethyl-*N*'-(3-dimethylaminopropyl) carbodiimide and *N*-hydroxysuccinimide) are used to stabilize gelatin structures through the formation of covalent bonds between amino groups on adjacent gelatin chains.[38] Photocrosslinking represents another widely employed approach for gelatin stabilization. This typically involves the modification of gelatin with photosensitive groups, such as in GelMA, which contains methacryloyl groups grafted onto the gelatin backbone. This approach enables precise spatial and temporal control over the crosslinking process through exposure to ultraviolet (UV) or visible light, allowing for complex structuring of the material during bioprinting.

Materials such as collagen, a major component of many mammalian tissues,[39] or bacterial cellulose, which is secreted and can be isolated from natural microbial sources,[40] provide advantages of emulating physical properties, nutrient transport conditions, and functional groups experienced by microbes in their natural environments of growth and function. While naturally derived hydrogel materials carry many advantages, they may suffer drawbacks such as poorer reproducibility[41] and lower mechanical properties compared to their synthetic counterparts,[21,42] thereby requiring chemical modifications to improve their properties for ideal microbial interactions.

Synthetic hydrogels, such as polyethylene glycol (PEG), polyacrylamide, polyvinyl alcohol (PVA),[43,44] and poloxamers (also known by the trade name Pluronic) are less widely used than natural-based hydrogels in many studies,[21] but continue to provide advantages such as tunability, batch-to-batch consistency, and the ability to functionalize with a wide variety of chemical groups to customize bioactive properties and microbial interactions.

Polyethylene glycol has emerged as one of the most widely used synthetic polymers in biomedical devices and applications, establishing itself as a versatile platform technology in tissue engineering, drug delivery, and bioprinting. The use of PEG stems from its unique combination of chemical simplicity, biocompatibility, and versatility for functionalization. One unique advantage of PEG is its ability to be highly customized with a variety of proteins and bioactive polymers to create tailored biomaterials with specific functionalities. The terminal hydroxyl groups of PEG molecules serve as reactive sites that can be readily modified, enabling the attachment of bioactive molecules, including growth factors, cell adhesion peptides, enzymes, and other functional proteins that can direct cellular behavior within engineered tissues.[45] PEG can be tailored for different protein adsorption and bioactive properties through conjugation or variation of chemistry, providing exceptional control over cell–material interactions. A significant benefit of PEG in bioprinting applications is its ability to be modified with groups such as diacrylate and methacrylate to crosslink and modify mechanical properties. These functional end groups transform PEG into photocrosslinkable macromers, such as poly(ethylene glycol) diacrylate (PEGDA) or poly(ethylene glycol) dimethacrylate.[46] These modified PEG molecules

can undergo rapid polymerization with photocrosslinking, forming covalently crosslinked hydrogel networks with tunable mechanical properties.

Pluronic is a triblock copolymer with a central hydrophobic poly(propylene oxide) block flanked by two hydrophilic poly(ethylene oxide) blocks. This amphiphilic structure enables unique phase behavior and self-assembly properties that have been utilized across a spectrum of biomedical applications, from drug delivery systems to tissue engineering scaffolds and, more recently, bacterial culture platforms. The versatility of Pluronic stems from the ability to precisely control the molecular weight and ratio of the hydrophilic to hydrophobic blocks during synthesis. This control allows for the creation of numerous Pluronic variants, each offering distinct properties optimized for specific applications. Pluronic is often used in combination with other hydrogels, such as PEG for drug delivery[47] or natural materials like collagen or hyaluronic acid for cell culture,[48] creating hybrid systems that leverage the complementary advantages of each component. These composite approaches address some of the limitations of pure Pluronic systems, such as their relatively weak mechanical properties and rapid dissolution under dilute conditions. Pluronic possesses thermoreversible gelation properties that provide initial structural stability, but these physical hydrogels can dissolve over time under physiological conditions, thereby limiting their application in longer-term implants or sustained delivery systems. To address this limitation, Pluronic can be modified through enzymatic crosslinking[49] or photocrosslinking methods[50] to enhance mechanical strength, creating more stable networks with prolonged persistence *in vivo*.

One overall drawback of these synthetic hydrogel materials is the lack of inherent biocompatibility and bioactive groups possessed by natural ECM materials,[24,51] thereby requiring modification to influence and enhance the behavior of microbial cells in certain circumstances.[21] The integration of multiple material types into hybrid hydrogels presents a powerful strategy to overcome the limitations of single-component systems, enhancing control over the microbial microenvironment. By synergistically combining natural and synthetic polymers, these hybrids merge the biofunctionality and biocompatibility of natural materials with the tunable mechanical properties and enhanced structural fidelity of synthetic networks.[11] This approach enables the creation of scaffolds that present the chemical cues of native tissue while offering independent adjustment of mechanical stiffness and degradation kinetics, which are critical for directing microbial growth and biofilm formation. For example, Denton *et al.*[11] utilized a gelatin–PEGDA hybrid hydrogel to model tonsillitis biofilms, leveraging gelatin's biocompatibility and cell-adhesive motifs while utilizing the PEGDA network to compensate for gelatin's characteristically low mechanical strength to achieve a stable and biomimetic 3D culture environment. Hybrid hydrogel formation also presents the opportunity for direct incorporation of microbial-derived components, such as secreted polysaccharides[52] or curli fibers, into synthetic or natural hydrogel backbones. This leverages the enhanced functionality of natural biofilm matrices while retaining the versatility and precision offered by tailored polymer chemistry for microbial manipulation and culture.[52]

3.2. Hydrogel modifications for increased precision

In addition to material choice, hydrogels can be engineered to better support and manipulate microbial growth and behavior. Microbial behavior, biogeography, and function are linked to characteristics such as local architecture and confinement, chemical signals, and nutrient transport, many of which are dictated by the natural hydrogels and substrates in *in vivo* environments of microbial growth. In *in vitro* microbial culture models, these characteristics can be manipulated by varying the hydrogel's chemical composition, porosity, and pore architecture, as well as by patterning at micro- and macroscales, thereby achieving additional advantages for hydrogel-based cultures.

3.2.1. Crosslinking strategies

Crosslinking is a fundamental strategy for tailoring the mechanical and functional properties of hydrogels, particularly in bioinks and microbial encapsulation systems, where structural integrity and stability are critical. Crosslinking is essential for the gelation and robustness of hydrogels, enabling the increased precision and tunability of physical and chemical properties that allow for more precise microbial manipulation.[62] Modulating hydrogel crosslinking density provides a fundamental mechanism for tailoring the network mesh size, or spaces within the crosslinked hydrogel network, which dictates scaffold permeability.[63,64] This permeability is critical for microbial applications, as it regulates the inward diffusion of nutrients, the outward diffusion of microbial metabolites, and the physical confinement or controlled release of bacterial cells within the engineered matrix.

The selection of a hydrogel crosslinking strategy is critical for the precision, stability, and biocompatibility of microbial culture platforms. Physical crosslinking, driven by hydrogen bonding, ionic interactions, or hydrophobic forces, offers significant advantages for sensitive microbes, primarily due to its mild, reagent-free gelation conditions that preserve biocompatibility. Methods such as ionic crosslinking of alginate with calcium ions are widely adopted for microbial encapsulation due to their rapid, gentle, and effective stabilization.[65] However, these methods

Table 1. Summary of hydrogel materials used for cellular encapsulation

Hydrogel material	Concentration range	Primary advantages	Primary limitations	References
Alginate	1–3% w/v	• Easy ionic crosslinking with divalent cations. • Excellent biocompatibility. • Biodegradable and tunable mechanical properties. • Inexpensive and readily available. • Versatile in composite formulations.	• Lacks bioactive components. • Requires surface modification (RGD peptide conjugation) for cell adhesion promotion. • Moderate mechanical properties when used alone.	[51,54]
Collagen	0.8–4 mg/mL	• Predominant structural protein in mammalian ECM. • Superior *in vitro* and *in vivo* biocompatibility. • Tissue-matching physicochemical properties. • Promotes cell attachment and tissue-specific differentiation. • Supports intercellular communication.	• Variable printability across different crosslinking methods. • Mechanical properties highly dependent on formulation. • Requires careful crosslinking strategy to avoid cell toxicity. • Batch-to-batch variability from natural sources.	[42,51,55]
Gelatin (modified GelMA)	2–10% w/v	• Biodegradable with low antigenicity. • Contains intrinsic RGD cell adhesion motifs. • Low cost and ease of processing. • Thermosensitive gelation at physiological temperatures. • Accessible active groups for chemical modification.	• Low mechanical properties without reinforcement. • Limited structural rigidity in standalone application. • Mechanical strength decreases during the culture period. • Requires dual crosslinking procedures (physical + ionic/chemical).	[42,56]
HA	0.5–2% w/v	• Naturally occurs in mammalian ECM. • Excellent biocompatibility and biodegradability. • Bioresorbable in physiological environments. • High porosity facilitates nutrient diffusion. • Maintains hydrated microenvironment for wound healing.	• Poor cell adhesion without functionalization. • Low water solubility stability leads to degradation. • Requires a combination with other polymers for functional applications.	[51]
Chitosan	0.5–2% w/v	• Biodegradable *in vivo*. • Antibacterial and wound healing properties. • Positively charged (promotes cell adhesion). • Versatile gel-forming capability.	• Poor mechanical properties when used alone. • Limited standalone applications. • Requires a combination formulations. • Variable bioactivity depending on the deacetylation degree.	[42,57]
Gellan gum	0.5–2% w/v (in composites: 0.5–1.5% combined)	• FDA-approved food additive (low toxicity profile). • Fine processability and tunable mechanical properties. • Improved rheological properties in composite bioinks. • Promotes cell proliferation (higher concentrations benefit cells). • Rheology tunable via ionic interactions.	• Limited mechanical properties when used alone. • Requires a combination with other polymers (GelMA, alginate). • Ionic crosslinking may affect cell viability if not optimized. • Concentration-dependent behavior.	[42]
Fibrin	2–10 mg/mL	• Natural ECM component. • Excellent biocompatibility. • Supports cell attachment and differentiation. • Biodegradable through enzymatic pathways.	• High mechanical variability between batches. • Rapid degradation in physiological conditions. • Difficult to standardize for clinical translation. • Limited printability without modification.	[42,58]

Table 1. Summary of hydrogel materials used for cellular encapsulation

Hydrogel material	Concentration range	Primary advantages	Primary limitations	References
Matrigel	0.5–30 μg/mL	• Contains laminin, collagen, and entactin proteins. • Includes endogenous peptides and growth factors. • Promotes cell growth and adhesion.	• Poor mechanical strength. • Potential immunogenicity concerns. • Decreasing scaffold degradability with increased Matrigel concentration.	[42]
Silk fibroin	1–5% w/v	• Abundant natural polymer (silkworm/spider sources). • Excellent mechanical properties and biocompatibility. • Controllable degradability. • Shear thinning properties ideal for extrusion printing. • Physical crosslinking possible.	• Low viscosity (limited printability alone). • Frequent clogging during extrusion printing. • Requires bulking agents or composite formulation. • Requires crosslinking support in most applications.	[42,59]
Dextran (with HA)	Variable (1–3% combined with HA)	• Nontoxic polysaccharide. • Hydrophilic nature. • Biodegradable in mammalian tissues (via dextranase). • Tunable viscoelastic properties. • Useful for semi- interpenetrating polymer network structures.	• Limited mechanical properties when used alone. • Requires a combination with other biomaterials (e.g., HA). • Dextranase-mediated degradation may be unpredictable *in vivo*.	[42,60]
PEG	10–20 wt%	• Mechanical and biochemical properties can be precisely tailored through chemical modification. • Can be rapidly crosslinked via light-based methods • Can be formulated to achieve robust, stable, and elastic networks	• Lacks inherent cell-adhesive motifs and biological cues • Cell viability is highly dependent on crosslinking parameters • Unmodified PEG is often unsuitable for bioprinting, requiring chemical derivatization	[51,61]
Poly(vinyl alcohol)	10–40 wt% (optimal 30–35 wt%)	• Synthetic, nontoxic, and biocompatible. • Low cost and easy production. • Excellent water solubility and hydrophilicity. • Good thermal stability. • Autonomous self-healing capability (freezing/thaw method). • Highly tunable mechanical and physical properties. • Low immunogenicity.	• Limited mechanical properties at lower concentrations. • Crystallinity-dependent behavior affects chain mobility. • Concentration-dependent self- healing efficiency. • Lower fracture stress compared to the original hydrogel (72% recovery at 48 h) • Air bubble formation in solution preparation.	[43]

Abbreviations: ECM, Extracellular matrix; FDA, Food and Drug Administration; GelMA, Gelatin methacryloyl; HA, Hyaluronic acid; PEG, Polyethylene glycol.

suffer from inherent limitations for high-precision applications: they yield networks with weak mechanical strength, exhibit instability under physiological conditions, and offer minimal spatial control over gelation. While the responsive nature of these gels (e.g., to temperature[66] or pH) allows for dynamic tunability, the formation of crosslinks is diffusion-limited, which prevents high-resolution patterning without advanced techniques like light-directed ion release.[67]

In contrast, chemical crosslinking strategies provide the robust, tunable, and mechanically stable networks required for advanced microbial manipulation.[68] Among these, photopolymerization is particularly favored due to its exceptional spatiotemporal precision, enabling the fabrication of constructs with defined architectures and controlled gelation kinetics through photopatterning. This capability is especially important for programming microbial biogeography and creating complex cocultures. However, this enhanced control introduces new biocompatibility challenges. UV light can be antimicrobial or cytotoxic,[69] thereby necessitating the use of visible light systems and compatible photoinitiators like riboflavin[70] to preserve microbial viability. Furthermore, conventional free-radical polymerization is susceptible to oxygen inhibition and network heterogeneity, which can compromise structural fidelity and reproducibility.[71] These drawbacks can be mitigated through additives such as

oxygen scavengers[72] or next-generation chemistries, such as thiol-ene click reactions[71,73] and mixed-mode systems,[45] which offer improved reaction uniformity, reduced oxygen sensitivity, and greater cytocompatibility. The evolution of chemical crosslinking, in addition to physical methods, can expand precision techniques in microbial hydrogel culture, enabling the fabrication of complex living materials with defined functions.

These emerging advanced chemistries also offer tunable mechanical properties and stimuli-responsive behavior for controlled microbial release, nutrient diffusion, metabolite transport, and drug delivery.[74] To further optimize hydrogel performance, hybrid crosslinking strategies[75,76] can be leveraged for increased customization in microbial cocultures and tissue engineering applications. Versatile hybrid crosslinking techniques go hand in hand with material choice as well, for example, the combination of weaker physical crosslinks of alginate gels and the stronger covalent crosslinks of acrylamide gels explored by Sun *et al*.,[77] creating tough hydrogels with tailored mechanical properties that mitigate drawbacks of poor mechanical stability, such as microbial release from matrices and cell death.

3.2.2. Pore generation techniques

The manipulation of hydrogel porosity—specifically pore size, distribution, and interconnectivity—serves as a critical design parameter for directing microbial behavior and function within ELMs. Precisely tuned pore architectures govern essential dynamics, such as nutrient diffusion, metabolic waste removal, microbial motility, and cell–cell communication,[78] each of which directly influences the efficacy of applications ranging from bioproduction to biofilm modeling. Creating and modifying microstructures in hydrogels is also essential for mimicking the complexity of native ECM or biofilms, where mechanical properties and nutrient transport affect cell behavior.[79]

Several established techniques enable the creation of porous hydrogel structures, each offering distinct advantages and limitations for microbial culture applications.[80] Salt templating is a widely adopted approach in which polymer or hydrogel precursors undergo crosslinking around a salt template, followed by salt leaching from the matrix to generate defined pore structures.[81] Alternative porogens, including hydrogel microbeads[82] and other sacrificial materials, can substitute for traditional salts in this process. This method provides control over pore size and offers good compatibility with cells and microorganisms. However, salt templating faces challenges in achieving complete porogen removal and generally produces discontinuous pore structures that may limit efficient nutrient transport throughout the scaffold.

Gas foaming involves the bubbling or generation of gas bubbles within polymer precursors during polymerization. Various agents facilitate this process, including carbonates, nitrates, or solid foaming agents such as carbon dioxide (CO_2).[80] This technique is a rapid and inexpensive method with minimal dependence on porogen extraction procedures; however, gas foaming provides limited control over pore size and distribution, potentially resulting in inconsistent pore architectures.[83] This lack of precision makes it less suitable for applications requiring predictable microbial infiltration or structured community formation.

Emulsion templating employs emulsions composed of two or more immiscible liquids, where a pore-generating internal phase becomes dispersed within an external or continuous phase that subsequently undergoes crosslinking.[84] This approach is effective in generating high porosity levels and good pore interconnectivity, creating well-connected pore networks favorable for cellular communication and nutrient transport.[85] However, emulsion templating suffers from inadequate control over pore size parameters and complications arising when organic solvents interfere with living biological components, potentially compromising cell viability and function. Similar mechanisms exploiting liquid–liquid phase separation have been utilized for hybrids of resilin-like polypeptide and PEG in hydrogels, in which phase separation combined with photocrosslinking enables more precise control of microstructure and polymer domain size based on timing.[86] This control enhances properties such as cell viability and can be used to localize cells and microbes preferentially around specific domains.[86]

The selection of a pore generation strategy is therefore a trade-off between architectural control, biocompatibility, and practicality,[87] and additional techniques such as combinations of methods or leveraging additive manufacturing[80] can pave the way for next-generation scaffolds with hierarchically structured porosity, offering spatial command over microbial microenvironments. Dong *et al*.[88] utilized tailorable hydrogel networks in this fashion to extend expansion microscopy analyses and evaluate microbial interactions at a single-cell level, providing increased precision and control for endpoint microbial analyses. Additionally, previous studies have exploited swelling of an acrylamide-based hydrogel network due to electrostatic interactions to expand aggregated cells in biofilm communities, increasing resolution of individual microbial components,[88] and enabling quantification of adhesive interactions between cells.[88,89] These techniques reveal the importance of hydrogel microstructural control in evaluating interactions within and between microbes in communities.

3.3. 3D patterning methods

In addition to parameters of hydrogel material selection, crosslinking and chemical modification, and pore customization, hydrogel patterning can also be manipulated to precisely modify and assess microbial positioning, proximity, and metabolic behavior. Traditional 2D and planktonic methods offer limited to no control over bacterial positioning and biofilm architectures; however, encapsulation and immobilization in hydrogel matrices allow for both precision in spatial patterning and tunability in chemical and physical properties to manipulate and enhance microbial behavior.[90] The use of conventional molds and hydrogel patterning remains prominent for the integration of living cells with hydrogel matrices due to their cost-effectiveness, high throughput, and material versatility. Simple molding, utilizing basic geometries like cylindrical,[19,91] is particularly valuable for high-throughput *in vitro* studies where reproducibility and scalability are critical. For more sophisticated applications, micromolding techniques bridge the gap between simplicity and precision; by leveraging templates fabricated via photolithography, they enable the creation of hydrogel structures with microscale features that more accurately emulate complex physiological environments while maintaining compatibility with a wide range of polymers and allowing gentle crosslinking conditions to ensure cell viability.[92,93]

Moreover, additive manufacturing and 3D bioprinting methods have emerged to provide additional capabilities for microbial patterning and customization, each with its own associated benefits and drawbacks. Prominent 3D bioprinting techniques of vat polymerization, inkjet, and extrusion-based printing are illustrated in Figure 3, and a list of selected hydrogel patterning methods for structural control and corresponding potential applications based on precision is provided in Table 2.

Extrusion-based printing serves as a versatile workhorse for patterning microbial communities within hydrogels,[20] extending spatial control and precision from simple encapsulation to defined macroscale structures. It is one of the most widely used methods for bioprinting[34] and among the first to be harnessed for biological applications.[94] Extrusion-based printing can be carried out through a variety of approaches and is generally executed by the extrusion of viscous hydrogel materials with air pressure, known as pneumatic printing, or by mechanical force with

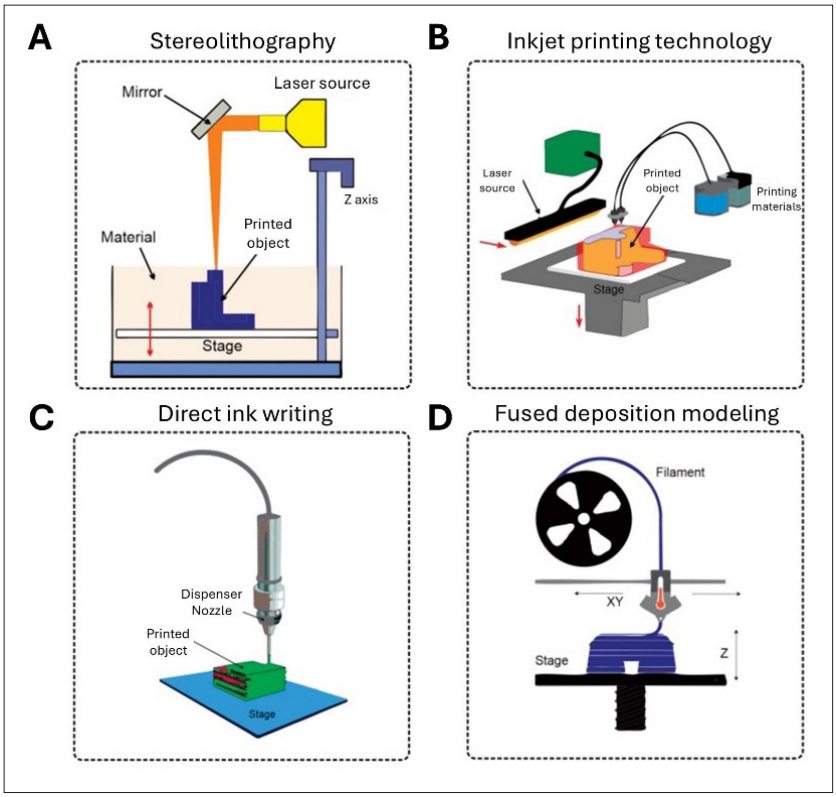


Figure 3. Schematic illustration of various 3D printing techniques, including light-based methods, such as (A) stereolithography and (B) inkjet printing technology, as well as extrusion methods, such as (C) direct ink writing and (D) fused deposition modeling. Reprinted with permission.[19]

Table 2. Examples of hydrogel patterning techniques and applications based on the precision level

Precision level	Macroscale encapsulation (>1 mm)	Mesoscale patterning (100 μm)	Microscale patterning (100 nm–1 μm)
Techniques	Hydrogel molding, simple gel casting.	Extrusion bioprinting, inkjet printing, spin coating.	Digital light processing, stereolithography, multiphoton lithography.
Applications	• Bulk bioproduction (e.g., biofuels, bioplastics). • Whole-cell biosensing and diagnostics. • Therapeutic probiotic delivery. • Bioremediation.	• Structured biofilm and antimicrobial resistance studies. • Synthetic microbial ecology and coculture. • Engineered living materials with logic functions.	• Single-cell analysis and confinement. • High-resolution quorum-sensing studies. • Decoding interspecies communication. • Precision biomolecule gradient formation.

pistons or screws.[95] Modifications through sacrificial and freeform printing, which use support baths[96,97] or "fugitive" inks to form stable complex networks,[98–102] or coaxial printing, where multiple streams of bioink are deposited in concentric rings, allow materials and components to be deposited within or enveloping one another in printed filaments.[103]

A major challenge in extrusion bioprinting lies in the inherent trade-off between structural printability and cell viability. While high viscosity bioinks are essential for achieving construct stability and shape fidelity, the shear forces and extrusion pressures required to deposit them can compromise the integrity of encapsulated cells. Methods and modifications, such as in situ crosslinking during bioprinting, serve to address these challenges and strike a balance between spatial precision and material versatility, preserving suitable printability while providing tunable, biocompatible environments for microorganisms.[104] In situ crosslinking methods, which stabilize hydrogels through photocrosslinking during the printing process and prior to deposition, enable precise patterning of nonviscous inks, mitigating shear forces on cells to preserve viability while also maintaining compatibility with a wider range of materials to support and influence cell and microbe microenvironments. These methods and techniques enable the patterning of hydrogels and the printing of bioinks that are traditionally outside of the criteria for cell and microbe support, expanding the range of possibilities for the study and manipulation of microbial species.[105] One main disadvantage of extrusion processes for some applications is the relatively low resolution (approximately 100 μm) of extruded filaments,[95] thereby limiting the resolution and size of components that can be patterned for applications at various length scales.

While extrusion printing is effective at creating robust structures, achieving higher-resolution patterning requires alternative methods; inkjet bioprinting addresses this need by employing precise droplet deposition to control microbial placement at a finer scale.[106] The resolution of inkjet bioprinting, characterized by droplet diameters in the tens of microns and volumes under 100 pL, is most commonly achieved through either thermal or piezoelectric actuation to deposit bioinks in precise, predefined patterns.[22,23] The precision in droplet patterning enables control over properties, such as porosity and pore distribution, and it allows for the embedding of various biological factors for additional material tailoring. Although its droplet-based approach allows for greater spatial patterning than extrusion, inkjet printing suffers from poor structural stability in the resulting constructs and presents challenges for maintaining cell viability due to shear stresses and the small volumes involved.[107] Jet-based bioprinting generally demands low-viscosity, low-cell-density bioinks that can rapidly solidify after printing to ensure structural integrity. This requirement for fast gelation also limits the selection of suitable hydrogels and necessitates strategies to mitigate challenges like cell sedimentation prior to fixation.

For applications demanding a higher degree of spatial fidelity, light-based printing techniques transcend the resolution limits of droplet-based methods to pattern microbes with up to single-cell precision.[108] Stereolithography and digital light processing printing achieve superior spatial resolution, down to approximately 10 μm,[109,110] by using focused light to photopolymerize hydrogels with micrometer-scale precision, enabling increased control over the patterning of various microenvironments. While light-based printing methods offer the advantage of high resolutions, they have limited use in some other areas of bioprinting. The need for photocurable inks limits material versatility for constructs, and vat polymerization methods have limited capabilities for creating cocultured environments with spatial specificity. To mitigate the drawbacks of some bioprinting methods, combinations of approaches can be used to take advantage of the benefits of multiple processes, such

as the combination of digital light processing and direct ink writing.[111]

This progression in patterning technologies, from the community-level architecture of extrusion-based methods to the droplet-level control of inkjet, and to the near-cellular resolution of light-based printing, provides a toolkit for researchers to select the appropriate level of precision required to interrogate and manipulate the microbial world.

4. 3D hydrogel culture applications and advancements

Applications and advancements in the field of microbial hydrogel culture and encapsulation, including hybrid microbial–hydrogel materials, can be categorized into four main areas of study: bioproduction, bioremediation, responsive and sensing materials, and fundamental microbial study, with different levels of spatial precision and microbial manipulation tailored to enhance each application beyond planktonic and 2D culture methods. Within this review, applications are categorized based on the characteristic scale of microbial manipulation: macroscale (>1 mm), mesoscale (100 μm–1 mm), and microscale (<100 μm). Techniques within the four main application categories are presented to correlate their achievable resolution with the level of control required for specific microbial studies. An overview of hydrogel microbial culture applications, based on technique and precision, is shown in Table 3.

4.1. Bioproduction applications from the macroscale

Microbial biosynthesis has long been harnessed for producing high-value compounds, including antimicrobials,[133] bioplastics,[134] and biofuels.[135] While traditional bioreactors remain the standard for industrial-scale fermentation due to their high volumetric productivity,[136] hydrogel-based culture systems are increasingly recognized for their ability to enhance and control microbial metabolism through tailored material environments. These systems offer superior regulation of nutrient diffusion, product retention, and cell viability, enabling more efficient and stable bioproduction processes. Although scalability often prioritizes lower-resolution methods like extrusion bioprinting, precision in material design—from polymer selection to spatial patterning—is critical for optimizing microbial function and coculture synergies in ELMs.

Smith and Francis[137] highlighted the strategic use of hydrogels to manipulate microbial metabolism and interspecies interactions. They developed a hydrogel-based coculture system using the *Synechococcus elongatus* cscB strain, a cyanobacterium engineered to secrete sucrose under osmotic stress, providing an alternative sucrose source for other organisms. By tailoring the swelling of poly(sodium acrylate) hydrogels encapsulating *S. elongatus* cscB, they controlled osmotic stress and subsequent sucrose production. This system was applied in a coculture with *Azotobacter vinelandii* AV3, an ammonia-secreting bacterium capable of producing biopolymers like polyhydroxybutyrate. The bulk hydrogel encapsulation enhanced the bioproduction of *A. vinelandii* AV3, demonstrating the advantages of this approach for mutually dependent cocultures. Their results highlight how hydrogel encapsulation allows metabolic conditions of one species to be modified and optimized without disrupting the other, offering a promising strategy for engineered microbial systems and sustained multispecies bioproduction.

Beyond metabolic tuning in bulk hydrogels and constructs, hydrogels provide physical protection that stabilizes microbial biocatalysts. Johnston *et al.*[90] demonstrated these advantages of hydrogel preservation with increased spatial precision by printing programmed *Escherichia coli* and yeast cells in F127 dimethacrylate and inducing the production of "high-value" products, such as 2,3-butanediol, levodopa, and antibiotics. These printed cell-laden hydrogels maintained similar levels of production even after lyophilization and rehydration, demonstrating increased stability due to microbial incorporation into bioink matrices. Integrating ECM material produced by microbes into hydrogel matrices can provide additional reinforcement to biofilm-inspired environments, enhancing resistance to both antibiotics and chemical dissolution of the hydrogels.[30] This reinforcement was harnessed and demonstrated by Schmieden *et al.*,[31] in which extrusion printing of *E. coli* in alginate-based gels provided space and conditions for biofilm-forming CsgA protein secretion. The patterned biofilms with microbial secretion exhibited increased protection and linkage of the microbial cells even under conditions where the alginate matrix was later dissolved. This spatial control, patterning, and induction of natural microbial biofilms, though limited in resolution, demonstrates promise in scalability for living structured materials for a variety of applications harnessing natural bioproducts. This approach was advanced by Duraj-Thatte *et al.*,[138] who printed *E. coli* through extrusion-based methods using their own ECM as a bioink. Secreted CsgA nanofibers were collected and printed into predefined structures, and incorporated *E. coli* were programmed for various applications, including secretion of an anticancer drug or sequestration of bisphenol A,[138] highlighting how precision in material sourcing and printing can enable multifunctional living systems.

Table 3. Comparative overview of microbial immobilization in hydrogel architectures

Application	Microorganism	Immobilization technique	Material	Purpose	Refs..
Study of microbial dynamics and biocatalysis	*Pseudomonas aeruginosa*	Photolithography (micro-3D printing)	Photocrosslinked gelatin	Real-time study of quorum-sensing communication	[113]
	Escherichia coli	Extrusion-based bioprinting	2% agarose and 2% alginate	Spatially organize bacteria for controlled growth, communication, and guided chemotaxis	[114]
	Escherichia coli, Lactobacillus rhamnosus GG.	Extrusion-based bioprinting (continuous chaotic bioprinting)	Alginate	Build microenvironments to study interface-driven competition and cooperation	[115]
	Soil microparticles	Laser bioprinting	Hyaluronic acid-based gel	Use laser engineering of microbial systems to recover rare uncultivable soil microbes with minimal habitat disruption	[116]
Bioremediation and biosensing	*Synechococcus sp.* PCC 7002	Extrusion-based bioprinting with ionic crosslinking	Alginate–methylcellulose hydrogel with sea sand	Bioprinted scaffolds incorporating cyanobacteria to induce calcium carbonate formation for sustainable construction	[117]
	Escherichia coli, *Photobacterium kishitanii*	Digital light processing and volumetric printing	Photopolymerizable methacrylated hyaluronic acid and Pluronic F-127	Light-based printing of bacteria for autonomous chemical sensing	[118]
	Geobacillus stearothermophilus, *Bacillus atrophaeus*	Thermal inkjet printing	Guar gum	Colorimetric temperature indicator	[119]
	Escherichia coli, *Caulobacter crescentus*	Projection microstereolithography (SLAM bioprinting)	PEGDA	Enhance the sequestration and sensing of rare earth elements and uranium	[120]
	Escherichia coli	Extrusion-based bioprinting	Alginate	Determine how biofilm matrix composition enhances bioremediation resilience	[121]
	Chlorella zofingiensis	Extrusion-based bioprinting + tannic acid coating	Alginate and PEGDA	Confine microalgae in retrievable 3D-printed hydrogels to enable antibiotic degradation with leakage control	[122]
	Chlorella vulgaris, *Bacillus subtilis*	Extrusion-based bioprinting	Hyaluronic acid with methacrylate groups and cysteine–phenylalanine dipeptides	Create reusable, printable dual-network bioinks that sustain bioremediation	[123]
	Pseudomonas aeruginosa	Electro-assisted bioprinting of hydrogel beads	Alginate, silk fibroin methacryloyl	Create an interwoven-network bioink for stable cell immobilization and pollutant removal	[124]
	Synechococcus elongatus	Extrusion-based bioprinting (direct ink writing)	Alginate	Enable stimulus-responsive dye degradation with adjustable cell death	[125]
	Escherichia coli	Hydrogel encapsulation (alginate core–shell capsules)	Alginate	Biosensing platform for diagnosing dextran–sodium sulfate-induced colitis	[28]

Table 3. Comparative overview of microbial immobilization in hydrogel architectures

Application	Microorganism	Immobilization technique	Material	Purpose	Refs..
Bioproduction	*Saccharomyces cerevisiae*	Extrusion-based bioprinting (direct ink writing)	PEGDA	Enhance ethanol catalysis by boosting glucose and carbon dioxide production through engineered porous 3D geometries	[26]
	Escherichia coli	Extrusion-based bioprinting	Alginate	Demonstrate a proof-of-concept for low-cost, sustainable bacterial material fabrication using simple 3D printing	[126]
	Escherichia coli, Saccharomyces cerevisiae (mono- and cocultures)	Extrusion-based bioprinting	F127–bisurethane methacrylate	Enable freeze-dried, extrusion-printed compartments to preserve and reactivate microbes for on-demand biosynthesis of levodopa or 2,3-butanediol	[90]
	Lactobacillus reuteri	Encapsulation of bacteria in microspheres, + photocrosslinking	Methacrylate-modified hyaluronic acid bulk hydrogel incorporating methacrylated gelatin microspheres	Living hydrogel scaffold enhances wound healing via bacterial secretion of antibacterial agents	[127]
Living materials	*Bacillus subtilis*	Extrusion Bioprinting and microencapsulation	TasA amyloid biofilms	Programmable, self-renewing living materials that merge catalytic functionality with structural integrity	[128]
	Pseudomonas putida, *Acetobacter xylinum*	Extrusion-based bioprinting (direct ink writing)	Hyaluronic acid, κ-carrageenan, and fumed silica (Flink).	Enhance bacterial metabolism and growth to enable cellulose production for biomedical applications or phenol degradation for bioremediation	[129]
	Caulobacter crescentus	Hydrogel culture with self-assembled protein matrix	Engineered BUD fusion displayed via RsaA	Engineer bacteria to display and secrete a self-assembling protein matrix for tunable living materials	[130]
	Escherichia coli	Autonomous secretion and surface-guided assembly of engineered curli fibrils.	Amyloid curli fibrils (engineered CsgA variants) forming a hierarchical protein matrix	Integration of bacteria into multiscale assemblies for functional composite materials	[131]
	Bacillus subtilis	Extrusion-based bioprinting	Agarose hydrogel	Embed spores in printed hydrogel to enable long-term storage and on-demand germination for sensing/actuation	[132]
	Escherichia coli	Extrusion-based bioprinting	Alginate	Combine 3D printing and inducible curli expression to create stable, spatially patterned biofilm-inspired materials	[31]
	Shewanella oneidensis MR-1	Extrusion-based bioprinting (direct ink writing)	Alginate and cellulose	Create a functional living anode with improved bioelectrochemical performance	[133]

Abbreviations: 3D, Three-dimensional; PEGDA, Polyethylene glycol dimethacrylate.

The scope of microbial bioproduction extends beyond *E. coli*, a popular model organism for analysis and manipulation of ECM production, to include specialized species whose innate biosynthetic capabilities are enhanced by 3D patterning. *Streptococcus zooepidemicus* was encapsulated in GelMA-based gels and induced to produce hyaluronic acid (HA).[139] Previous research described this production as an example of a "3D-printed bioreactor," noting that scaffold orientation and geometry could also be manipulated to affect HA yield. *Bacillus subtilis* is also utilized for living materials in addition to its study as a model of biofilm formation. These bacteria are attractive due to being "generally regarded as safe," and the amyloid fibers that form biofilms of *B. subtilis* can be harnessed for adhesion to host tissues and antibiotic resistance.[126] The versatility of printed biofilms containing these amyloid fibers was demonstrated by Huang *et al.*,[127] where *B. subtilis* was programmed to secrete biofilm-forming proteins with varied functional properties based on customized domains. These tunable patterned biofilms represent an added advantage over planktonic or free microbial cells in applications, such as drug delivery, where greater precision in protein and biomolecule release is needed. Qian *et al.*[26] utilized freeze-dried and printed cells of Baker's yeast (*Saccharomyces cerevisiae*) with nanocellulose to act as a biocatalyst for the metabolism of glucose. The 3D-printed lattice structures showed improved efficiency over bulk structures, demonstrating the advantages of combining 3D patterning with biofilm technologies.

Hydrogel culture and bioprinting have significantly advanced microbial bioproduction by enabling the precise spatial organization of microbial cells and cocultures. This controlled physical placement, achieved through methods ranging from bulk encapsulation to extrusion-based patterning, creates tailored microenvironments that enhance metabolic efficiency and the yield of target bioproducts and biopolymers. A primary limitation, however, is the inherent trade-off between precision and scalability; in some cases, the specialized materials and fabrication processes required for these tailored environments incur high costs and material usage that are not yet practical for large-scale, low-value commodity production. Future progress hinges on developing more biomaterial-efficient and cost-effective fabrication strategies, which would dramatically expand the economic viability of these platforms, particularly for the synthesis of high-value compounds. Overall, these advances highlight a shift in microbial bioproduction from large-scale, unstructured fermentation toward spatially and materially optimized systems where hydrogel design dictates microbial output.

4.2. Multiscale microbial control for bioremediation

Engineered living materials are redefining decontamination by embedding pollutant-degrading microorganisms in 3D-printed hydrogels that capture metals, detoxify organics, and even mineralize CO_2. A persistent bottleneck, however, is achieving the dual requirement of mechanical strength and biocompatibility, without which the resident biocatalysts cannot function effectively. 3D-printed, engineered biofilms offer a versatile platform for environmental remediation: they can support bioremediation, selectively capture rare-earth elements (REE) and heavy metals, strip assimilable organic carbon from water, and be incorporated into wastewater-treatment systems.[30]

Balasubramanian *et al.*[120] 3D-printed four-layer stripes (approximately 550 μm) of curli$^+$/cellulose$^+$ *E. coli* encapsulated in a calcium alginate hydrogel bioink. After 1 week, the constructs developed approximately 300–400 μm anoxic cores, withstood 1% Virkon S—a broad-spectrum disinfectant—with only a two-log viability loss, and fully recovered their geometry after manual folding or twisting, offering the mechanical resilience demanded by in-situ bioremediation reactors and turbulent wastewater streams.[120] In contrast to native *E. coli*, which successfully mineralizes aromatic acids, genetically engineered derivatives can degrade complex hydrocarbons and immobilize Cu^{2+}, Ni^{2+}, Hg^{2+}, Pb^{2+}, and atrazine.[141] Incorporating these genetically engineered strains within the printed scaffold would thus broaden its catalytic repertoire, accelerate pollutant turnover, and sustain performance even under high shear, continuous-flow treatment regimens.[120]

Using projection microstereolithography (SLAM), Dubbin *et al.*[119] photopolymerized a 15% PEGDA bioresin layer by layer; the projected light polymerizes the resin into a hydrogel, providing a supportive matrix for the immobilized bacteria and achieving 10 μm z-resolution. Grid-printed films expressing lanthanide-binding peptides halve soluble neodymium in 5 min ($T_{1/2}$), whereas cube controls required 120 min—a kinetic edge that accelerates REE recovery, which is vital for clean energy supply chains.[119] A companion Pphyt-GFP *Caulobacter crescentus* biosensor emitted strong fluorescence, providing a cost-effective in situ biosensor for environmental uranium levels that are otherwise challenging to detect.[119] Together, SLAM-printed, cell-laden hydrogel films fuse rapid REE capture with responsive uranium sensing for next-generation bioremediation materials.[119]

Jiang *et al.*[122] extrusion-bioprinted microalgae hydrogel networks (MHN@TA) by photocrosslinking a PEGDA/sodium alginate bioink laden with *Chlorella zofingiensis*

and then coating the lattice with tannic acid, which generates a semipermeable membrane that prevents cells from escaping. This tannic acid layer limited algal leakage to ≤0.7% over 7 days and allowed the construct to be recovered and reused without loss of integrity.[121] In batch tests, MHN@TA removed 99.3% of 100 mg/L tetracycline within 72 h and maintained >95% efficiency even at 400 mg/L, outperforming suspended cultures.[121] By coupling high-performance antibiotic degradation with robust containment and recyclability, this matrix offers a durable and sustainable solution for treating pharmaceutical wastewater.[121]

Additive manufacturing yielded a dual-network hydrogel from methacrylated, cysteine–phenylalanine-modified HA; UV photopolymerization further stiffened the self-supportive lattice architecture.[122] Compartmentalized *B. subtilis* and *Chlorella vulgaris* synergistically degraded 70% methyl orange and 40% acrylamide (textile dye pollutants) within 12 h, converting CO_2 that algae photosynthetically returned to O_2, thereby sustaining bacterial respiration.[122] The living material therefore fast-tracks pollutant mineralization while maintaining biosafety and recyclability.[122] Wang *et al.*[123] developed an interpenetrating 1.5% sodium alginate/20% silk-methacryloyl hydrogel beads (1.5SA/20SilMA-S-Ca) that withstand 300 mg/L sodium and preserve porosity after prolonged use. They selected this formulation to assess pollutant control. Beads entrapped *Pseudomonas aeruginosa* PAO1—an aerobic denitrifier capable of using nitrate or nitrite as terminal electron acceptors.[123] In synthetic wastewater, they outperformed free bacteria, cutting total nitrogen by 74.4% in 12 h with negligible nitrate accumulation and delivering faster COD decline.[123] The mechanically robust matrix thus couples efficient aerobic denitrification with bacterial immobilization, offering a reusable platform for high-salinity wastewater treatment.[123]

With construction generating 39% of global CO_2 emissions, Reinhardt *et al.*[116] bioprinted *Synechococcus* PCC 7002 into ELMs by extrusion of alginate–methylcellulose hydrogels. Besides photosynthetic uptake, the cyanobacteria fix carbon through microbially induced carbonate precipitation, depositing calcium carbonate that acts as a biocement within the printed lattice.[116] Extrusion-based bioprinting yields self-supporting scaffolds with sustained cell viability while enhancing compressive strength as mineralization proceeds.[117] This demonstrates a scalable living biomaterial that sequesters atmospheric CO_2 while forming environmentally friendly construction components.[116]

In line with cyanobacterial research, Datta *et al.*[124] modified an ELM by 3D-printing an alginate hydrogel scaffold with *Synechococcus elongatus* genetically engineered to overexpress CotA laccase for chemical decontamination. Encapsulated bacteria stayed viable, photosynthetically active, and released laccase that oxidized and removed the textile dye indigo carmine, showing efficient bioremediation.[124] The printed construct also integrated a theophylline-triggered "kill switch" for biocontainment.[124] This research shows how additive manufacturing can program responsive, self-sustaining ELMs for practical pollutant management. Together, these next-generation materials illustrate how judicious bioink design and microbial engineering can convert environmental liabilities into self-sustaining detoxification platforms. Continued advances in scaffold chemistry, genetic safeguards, and reactor integration should soon translate their laboratory innovations into solid, ready-to-use solutions for the most stubborn water-quality challenges.[140]

4.3. Programmable living materials: High-resolution responses from macro- to microscale

Microbial 3D bioprinting methods have enabled the creation of improved living materials, or combinations of cells and biologically engineered matrices.[90] Some notable advances include the incorporation of bacteria into soft robotic devices, as demonstrated by Justus *et al.*,[141] where engineered bacteria are incorporated for the detection of environmental signals or chemicals, and the bacterial responses are converted into electronic signals for robotic gripping abilities.[141] Methods that utilize 2D bacterial culture on different substrates, or the patterning of planktonic bacteria in molds or channels, have proved transformative for the secretion of products or the execution of functions in response to tailored conditions.[142] Embedding these microbes and systems in man-made or natural hydrogels provides additional versatility in 3D patterning and precision for the detection of environmental factors or the display of chemical or mechanical signals.

For systemic therapeutic delivery and diagnostics, macroscale encapsulation strategies prioritize functional precision over spatial resolution. This approach has proved significant for therapeutic applications, providing protection from environmental factors while enabling precision in the detection and treatment of physiological issues. Aghlara-Fotovat *et al.*[28] demonstrated the diagnostic potential of hydrogel-encapsulated bacteria for detecting inflammatory conditions, specifically colitis. They encapsulated engineered *E. coli*—designed to sense thiosulfate, a biomarker of gut inflammation—within ionically crosslinked alginate hydrogel capsules, which

maintained structural integrity and bacterial viability. Upon oral delivery to rat models, the encapsulated bacteria successfully detected colitis, as evidenced by the activation of fluorescent reporters upon exposure to inflammatory conditions. Notably, the hydrogel system enabled higher bacterial retrieval and detection rates compared to free-floating bacteria, enhancing diagnostic reliability. This hydrogel platform provides an advantage for microbial diagnostics by offering a stable, targeted approach to monitor inflammation, potentially extending to other diseases that are difficult to assess through conventional methods.[28]

Similarly, Ming *et al.*[126] developed an innovative probiotic-loaded hydrogel system to enhance wound healing. They encapsulated *Lactobacillus reuteri* within gelatin hydrogel microparticles, which were then incorporated into a photopolymerizable methacrylated HA precursor, forming an injectable living wound dressing. The hydrogels were stabilized via photocrosslinking to ensure microbial growth, viability, and retention within the wound site. The hydrogel matrix provided a dual function: protecting *L. reuteri* from environmental stresses and challenges from the immune system while also facilitating its antibacterial function through sustained lactic acid and antimicrobial secretion, combating pathogenic bacteria. Hydrogel encapsulation also prevented bacterial escape into surrounding tissues, thereby mitigating potential risks. Their study highlights the promise of probiotic–hydrogel hybrid therapies for tissue regeneration and infection control in wound care applications.

Notable studies involving the manipulation of *E. coli* include its printing in various patterns through extrusion-based methods and its induction to form curli fibers, a natural component of *E. coli* biofilm in ECM.[31,125] Biofilm components, such as curli, play significant roles in bacterial adhesion and pathogenesis[143]; therefore, studying these factors in reproducible environments is of critical importance. 3D bioprinting and hydrogel culture methods enhance control over biofilm characteristics, such as composition and microbial density, which are essential for tunable responses and induction of diverse behaviors, such as biomolecule production.[31] Liu *et al.*[144] developed a Pluronic F127 diacrylate-based material system containing programmed *E. coli* bacteria. This system combined chemicals and chemical signals that act as inputs, with cells, which act as outputs for logic gate functions. These materials and microbial systems have also demonstrated potential for decision-making functions, spatiotemporal patterning, and wearable devices that can exhibit fluorescence in response to various stimuli.[144]

At the highest level of integration, microscale synthesis techniques harness microbial activity to directly constitute or modify the material itself. Reinhardt *et al.*[116] also utilized cyanobacteria to modify and strengthen hydrogel matrices. *Synechococcus sp.* bacteria were incorporated into alginate–methylcellulose gels containing sea sand, and the bacteria were induced to mineralize the matrices with calcium carbonate mineral. The bacteria-incorporated matrices displayed maintained viability and higher compressive strength than normal matrices, showing potential for "living building materials" that can be used for construction purposes. Schaffner *et al.*[128] demonstrated the utility of bioprinted living materials for both bioremediation and biomedical resource production. They encapsulated *Pseudomonas putida,* which can degrade harmful environmental products, or *Acetobacter xylinum,* which can fabricate bacterial cellulose for a variety of biomedical applications, into HA-based hydrogels via extrusion-based printing. The hydrogel encapsulation provided distinct advantages over free or planktonic bacteria in each application, as immobilization of bacteria in biocompatible gel matrices preserved the microbes for sustained, programmable bioconversion while preventing bacterial overgrowth.[128]

Engineered living materials exemplify the transformative potential of hydrogel-based microbial culture, leveraging spatial patterning and encapsulation to create sophisticated biosensing and responsive systems. The protective hydrogel matrix enables precise processing of environmental inputs and microbial outputs at customizable resolutions, while simultaneously safeguarding the encapsulated microbes. A central challenge is achieving simultaneous control over two critical material properties: the tailored diffusion of molecular signals to ensure rapid sensor response, and robust containment of microbial cells to prevent environmental release. Promisingly, recent advances in material design and advanced crosslinking strategies demonstrate that these competing requirements can be reconciled through meticulous system engineering. Overcoming this hurdle will be pivotal for unlocking the full potential of hydrogel-based living materials in real-world applications, from environmental monitoring to smart therapeutic devices.

4.4. High-precision methods for fundamental microbial study

Hydrogel materials have become valuable tools in fundamental microbial research, providing the reproducibility, customizability, and biomimetic properties necessary to reconstruct and probe complex microbial behaviors from community-level interactions to single-cell functions.[145] By offering increased tunable control over

the physical and chemical microenvironment, hydrogel-based platforms enable researchers to tailor experimental systems with varying levels of precision to address specific biological questions, moving beyond the limitations of traditional planktonic or agar-based cultures.

Extrusion-based bioprinting has emerged as a versatile method for investigating clinically relevant microbial community behaviors, such as biofilm formation and antibiotic resistance. Ning *et al.*[12] compared 2D and 3D microbial cultures using extrusion-based hydrogel printing methods, noting that antibiotic treatments developed for planktonic cultures can become ineffective once the bacteria form biofilms. They employed alginate hydrogels to maintain long-term cultures of clinically relevant pathogens, including *E. coli*, *P. aeruginosa*, and *Staphylococcus aureus*. Antimicrobial susceptibility testing revealed significantly enhanced resistance in 3D-printed *S. aureus* and *E. coli* biofilms compared to their 2D counterparts, better mirroring the resilience observed in clinical infections. This highlights crucial advantages of hydrogels and 3D bioprinting for microbial study, emphasizing that biofilm properties can be altered when embedded in the host ECM.[12]

Multispecies evaluations using advanced hydrogel formulation techniques have also enabled recapitulation of more complex environments and conditions relevant to natural tissues. Zheng *et al.*[146] developed an engineered microbiota culture platform using multilayered PEGDA-based hydrogels fabricated via spin coating—a technique that deposits uniform polymer films by spinning precursor solutions at high speeds—to isolate and culture gut bacteria. This system maintained microbial diversity and composition comparable to natural gut microbiota, offering improved reproducibility over conventional liquid cultures. Additionally, the hydrogel-based platform supported coculture with host cells, enabling a more physiologically relevant *in vitro* model. They leveraged this system to evaluate the efficacy of chemotherapeutic drugs, with results closely mirroring *in vivo* outcomes. Furthermore, the platform allowed for the assessment of patient-derived gut microbiome influences on drug response, facilitating tailored therapeutic adjustments, including dose optimization or combination with cytokines like granulocyte–macrophage colony-stimulating factor to enhance treatment efficacy.[146]

Aliyazdi *et al.*[147] also demonstrated the use of combined microbial hydrogel cultures and host cells by creating a controlled, bioprinted model to investigate host–pathogen interactions. They engineered *E. coli* MG1655 into custom lattice-patterned biofilms (Figure 4B), recapitulating the large-scale architecture (sometimes exceeding ≈1,000 μm) observed in natural environments. They successfully cultured these printed biofilms on monolayers of human bronchial epithelial cells while preserving host cell viability and function.[147] Such approaches, which simultaneously meet the stringent biocompatibility requirements of mammalian cells and the structural demands of microbial bioprinting, represent a significant step forward. Establishing design principles for using 3D bioprinting to achieve increased control and reproducibility in *in vitro* infection models enables the direct investigation of the interplay between living host tissues and structured bacterial communities, providing a valuable tool for personalized medicine and drug development.

The ability to control microbial arrangement within hydrogels enables direct investigation of social behaviors and biogeographical effects. Ceballos-Gonzalez *et al.*[115] utilized extrusion-based microbial printing with modifications to bioink flow and bacterial spatial arrangements to evaluate the social behavior of bacteria with respect to biogeography and local environments. Their use of a "continuous chaotic bacterial bioprinting" method (Figure 4A) enabled the creation of various patterns and organizations incorporating different *E. coli* strains within extruded filaments. The bacterial communities were analyzed with fluorescent microscopy and scanning electron microscopy, and they highlighted that increased physical intimacy and interfacial contact between strains disrupted bacterial community stability.

Three-dimensional bioprinting and patterning methods, such as photolithography, allow for the highest spatial precision for microbial spatial manipulation, which provides a key advantage for analyzing bacterial communities and gaining insight into fundamental single-cell level properties, such as quorum sensing[148] and antibacterial resistance.[149] The multiphoton lithography-based "micro-3D printing" methods utilized by Connell *et al.*[149,150] further enhance the benefits of high resolution in creating 3D structures and enable the entrapment of single bacterial cells to probe properties of bacterial communities in response to community size (Figure 4). They noted that the behavior of small bacterial clusters in confinement is crucial for assessing the social behaviors of bacteria and their potential roles in infections.[150] These high-resolution micro-3D printing methods were shown to be effective in combination with analytical methods such as scanning electrochemical microscopy to map chemical signals and evaluate quorum-sensing relationships with respect to microbial colony size and spatial arrangements.[112]

Lithography-based micro-3D printing methods were utilized for multispecies analysis, exploiting the ability to confine multiple bacterial populations in arrangements

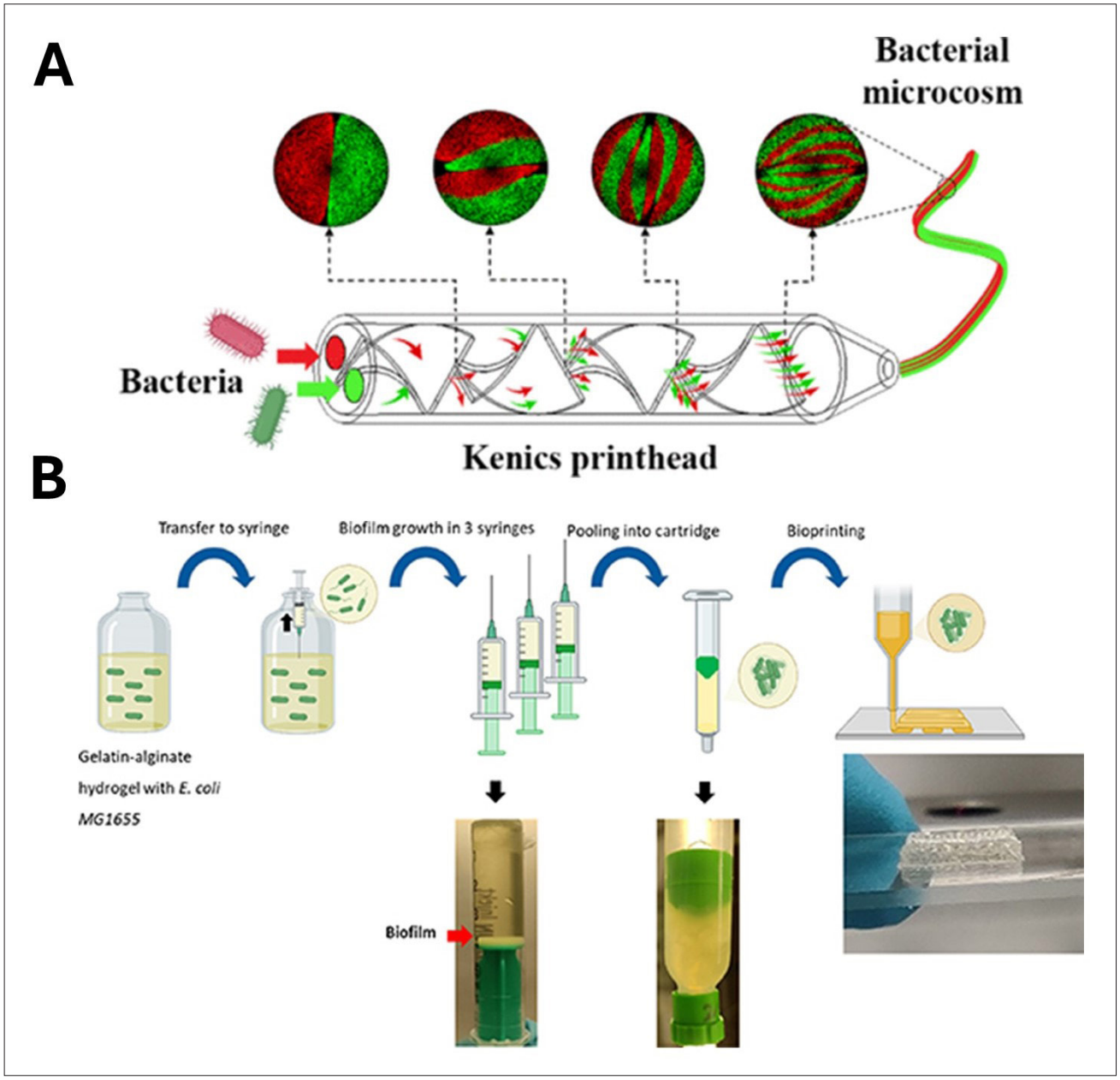


Figure 4. Illustrations of microbial bioprinting and encapsulation strategies at different precision levels. (A) Multilamellar bacterial patterns generated via continuous chaotic bacterial bioprinting to analyze interactions between *Escherichia coli* strains (image adapted with permission from Ceballos-González *et al.*[114] Copyright © 2021, American Chemical Society). (B) Schematic workflow of bioink preparation and bioprinting process of *E. coli* MG1655 biofilms for printing on mammalian cell monolayers. Inoculated gelatin–alginate-based hydrogels are loaded into syringes for growth, pooled, and printed with the capability for postprinting crosslinking. Reprinted from.[147] Copyright.

that are physically separated but can chemically communicate for analysis.[149] These methods revealed that the presence of *P. aeruginosa* in localized shells was able to lower *S. aureus* susceptibility to antibiotic agents, demonstrating how precision hydrogel patterning can decode complex interspecies interactions and their role in infection resilience.[149]

Hydrogel-based platforms provide a critical advancement for microbial and biomedical studies by recapitulating tissue-like mechanical and transport properties, enabling the investigation of host–microbe interactions and phenotypes—such as antimicrobial resistance—that are poorly represented in traditional 2D or planktonic cultures. This capacity to tailor 3D

microenvironments offers a more physiologically relevant context for analyzing dynamic microbial behaviors. A primary limitation hindering the full potential of these systems is the current lack of standardized bioink formulations and fabrication parameters, which compromises reproducibility and cross-study comparisons. Establishing such standards is a crucial step, as it would significantly enhance the translational relevance of these models for both fundamental research into single-cell microbial dynamics and applied biomedical screening.

The studies encompassing these main applications highlight a central theme: the level of spatial and material control offered by hydrogel systems can be strategically matched to the biological or mechanistic question at hand. As shown in Figure 5, advancements in microbial research enabled by hydrogel-based culture and 3D patterning are categorized by fabrication technique and associated levels of spatial precision. Whether using extrusion printing for community-level biofilm models or lithography for single-cell signaling dynamics, hydrogel-based design provides a versatile and powerful framework for advancing microbial science.

5. Limitations and future perspectives

The advancement of microbial bioprinting and hydrogel encapsulation holds significant promise for biomedical research, sustainable bioproduction, and environmental applications. However, its development and adoption currently lag behind that of mammalian cell bioprinting and hydrogel culture due to distinct technical and conceptual challenges. A primary limitation is the perceived lack of clinical urgency; unlike mammalian tissues, microbial cultures often do not require complex ECM-mimetic hydrogels for basic survival, given their inherent robustness. This reduces incentives to develop sophisticated bioinks for microbes outside specialized applications in which replicating native biofilm microenvironments with precise chemical gradients, spatial organization, and host interactions is essential.

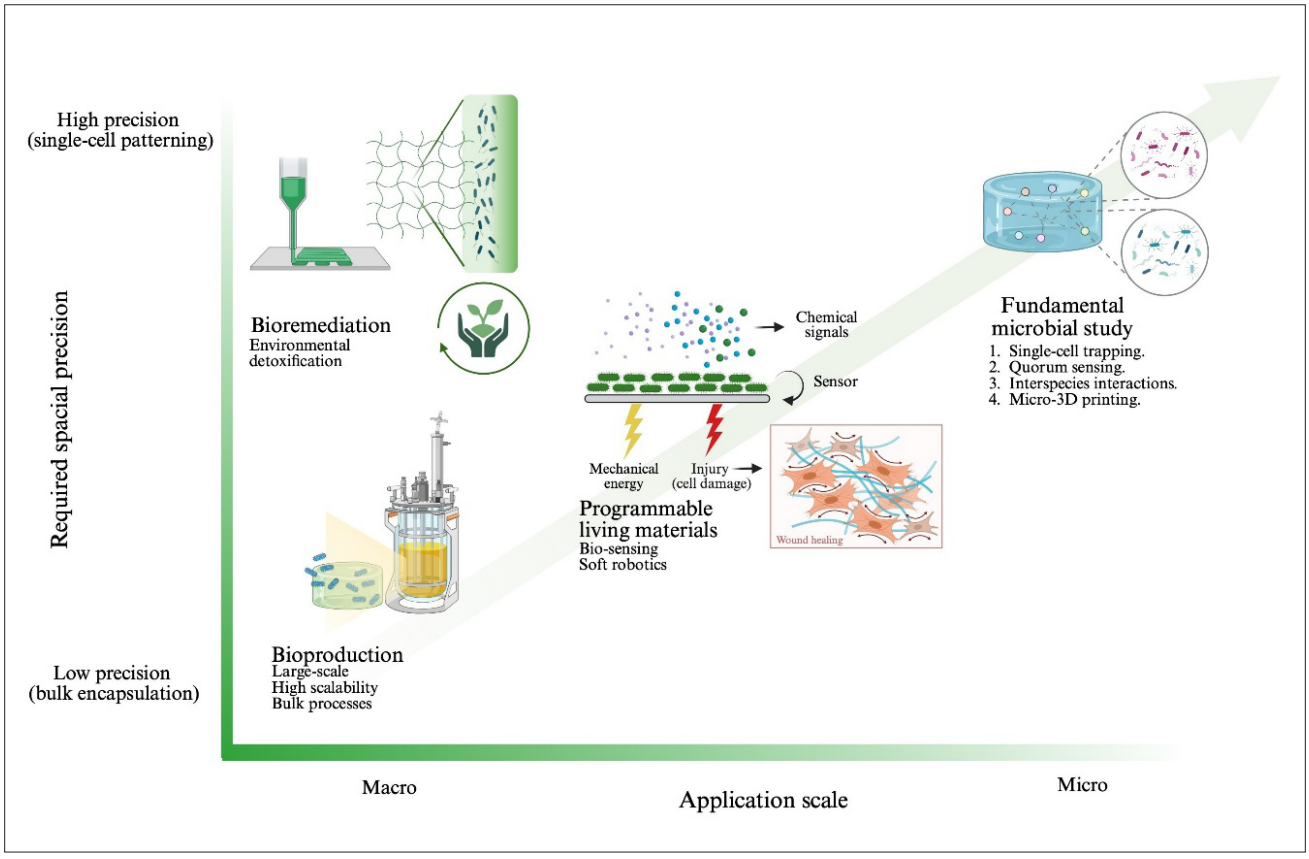


Figure 5. Conceptual applications map showing how spatial precision requirements correspond to application scale in microbial bioprinting. The figure highlights that the required level of precision should be matched to the intended application: macroscale bulk encapsulation for bioproduction and bioremediation, and microscale single-cell patterning for programmable living materials and fundamental microbial studies. Created in BioRender. Klein, C. UDD, D. (2025) https://BioRender.com/y6mmky5. Abbreviation: 3D, Three-dimensional.

Nevertheless, the unique benefits of increased spatial and metabolic control continue to drive innovation in the field. Hydrogel-based systems enable precise manipulation of microbial ecosystems, allowing researchers to dictate cell positioning, control nutrient diffusion, engineer chemical gradients, and stabilize cocultures—capabilities largely unattainable with traditional liquid cultures or growth on 2D substrates. These advantages are critical for applications, such as synthetic ecology, advanced bioremediation, and personalized medicine, where community structure and function directly determine system performance.

With the four main microbial culture applications—bioproduction, bioremediation, responsive programmable materials, and fundamental microbial study—in mind, there are crucial future developments that can be pursued to overcome current limitations and broaden applicability. Current and next-generation hydrogels can be engineered to respond to microbial activity and environmental changes, such as pH conditions and metabolite secretion. Such materials could adapt to their physical properties or release antimicrobials/nutrients in real-time, enabling closed-loop control of microbial growth and function. This is particularly relevant for oral or gut microbiome applications, where dynamic conditions require biomimetic adaptability.

While high-resolution techniques, such as lithography offer single-cell precision, scaling these methods for industrial or clinical use remains a challenge. Future work must bridge the gap between resolution and scalability, potentially through hybrid printing (e.g., combining extrusion for structure with light-based or inkjet patterning for surface functionalization) or the development of rapid, continuous fabrication processes. With respect to tissue engineering applications, hybrid bioprinting that combines multiple techniques and material types has demonstrated the potential to incorporate complex, multifunctional tissue models into single constructs.[151,152] These strategies may also enable the creation of hierarchically structured microbial constructs where critical functions, such as nutrient transport, waste removal, and product secretion, are engineered directly into the architecture. This approach provides a pathway to scale functional complexity[152] beyond increasing size, thereby enhancing the production capabilities and practical viability of ELMs.

Establishing standardized bioink formulations and printing parameters for microbial systems remains an essential priority in the field. Establishing benchmarks for viability, function, and stability postprinting is essential for reproducibility and comparison across studies. Versatility in hydrogel materials and fabrication methods also allows for advanced in situ monitoring techniques, such as embedded sensors for metabolic tracking or compatibility with advanced imaging, which are needed to validate microbial activity within 3D constructs over time.

For biomedical applications, future platforms must also improve the integration between printed microbial communities and host tissues, such as oral or gut microbiome components within dynamic and interconnected physical and chemical conditions. A critical design parameter will be replicating the microscale architecture of native tissues. For instance, successful integration in the oral cavity requires recapitulating the precise pore sizes (often in the low micrometer range[153]), as well as chemical gradients of pH, oxygen, and nutrients, and topographical features that dictate microbial colonization and host–microbe interactions. By engineering hydrogels with enhanced detail and precision, we can create more predictive models for oral biofilm formation and develop effective antimicrobial or probiotic delivery systems that function within the complex *in vivo* landscape.

Emerging technologies, such as stimulus-responsive materials that adapt to oral pH changes or microbial secretion, exemplify the potential for intelligent hydrogel systems to operate in dynamic environments. By focusing on these future directions, microbial hydrogel culture can transition from a niche tool to a robust platform for programming microbial communities with precision, enabling breakthroughs in medicine, biotechnology, and beyond.

6. Conclusion

The encapsulation and culture of microbes within hydrogels have emerged as a powerful platform in microbial research, offering precise control over 3D spatial organization, nutrient transport, and coculture conditions. This review highlights the advantages of 3D microbial culture that stem from key hydrogel properties, including material composition, crosslinking methods, porosity, and 3D architecture. These characteristics collectively enhance microbial metabolism, provide protective immobilization, and enable the creation of tailored microenvironments. By tuning these parameters, hydrogel–microbial systems have found use in a diverse range of applications, from advanced studies of microbial behavior and programmable responsive materials to optimized bioproduction and bioremediation strategies. Looking ahead, continued improvements in hydrogel fabrication, such as improved 3D bioprinting strategies and dynamic crosslinking, will further expand these capabilities, enabling more accurate replication of complex microbial niches, such as oral microbiomes, and accelerating translational research in medicine, biotechnology, and environmental science.

Acknowledgments

None

Funding

This work was funded by the National Institute of Dental and Craniofacial Research (Nos. R01DE029479A and DE029479S). Financial support was also provided through the ADA Forsyth Institute (Grant No. AFISU105).

Conflict of interest

The authors declare they have no competing interests.

Author contributions

Conceptualization: All authors
Formal analysis: Jeremy Elias, Catherine Klein
Funding acquisition: Jirun Sun, Xuesong He, Benjamin Wu
Investigation: Jeremy Elias, Catherine Klein, Jirun Sun
Methodology: Jeremy Elias, Catherine Klein, Jirun Sun
Supervision: Jirun Sun, Xuesong He, Benjamin Wu
Visualization: Jeremy Elias, Catherine Klein, Jirun Sun
Writing–original draft: Jeremy Elias, Catherine Klein, Jirun Sun
Writing–review & editing: All authors

Ethics approval and consent to participate

Not applicable.

Consent for publication

Not applicable.

Availability of data

Not applicable.

References

1. Pascalie J, Potier M, Kowaliw T, *et al*. Developmental design of synthetic bacterial architectures by morphogenetic engineering. *ACS Synth Biol*. 2016;5(8):842-861. doi:10.1021/acssynbio.5b00246
2. Brenner K, You L, Arnold FH. Engineering microbial consortia: a new frontier in synthetic biology. *Trends Biotechnol*. 2008;26(9):483-489. doi:10.1016/j.tibtech.2008.05.004
3. Gajic I, Kabic J, Kekic D, *et al*. Antimicrobial susceptibility testing: a comprehensive review of currently used methods. *Antibiotics*. 2022;11(4):427. doi:10.3390/antibiotics11040427
4. Prindle A, Selimkhanov J, Li H, Razinkov I, Tsimring LS, Hasty J. Rapid and tunable post-translational coupling of genetic circuits. *Nature*. 2014;508(7496):387-391. doi:10.1038/nature13238
5. Sulaeva I, Henniges U, Rosenau T, Potthast A. Bacterial cellulose as a material for wound treatment: properties and modifications. A review. *Biotechnol Adv*. 2015;33(8):1547-1571. doi:10.1016/j.biotechadv.2015.07.009
6. McCarty NS, Ledesma-Amaro R. Synthetic biology tools to engineer microbial communities for biotechnology. *Trends Biotechnol*. 2019;37(2):181-197. doi:10.1016/j.tibtech.2018.11.002
7. Sreepadmanabh M, Ganesh M, Sanjenbam P, Kurzthaler C, Agashe D, Bhattacharjee T. Cell shape affects bacterial colony growth under physical confinement. *Nat Commun*. 2024;15(1):9561. doi:10.1038/s41467-024-53989-6
8. Wells M, Schneider R, Bhattarai B, *et al*. Perspective: the viscoelastic properties of biofilm infections and mechanical interactions with phagocytic immune cells. *Front Cell Infect Microbiol*. 2023;13. doi:10.3389/fcimb.2023.1102199
9. Storm C, Pastore JJ, MacKintosh FC, Lubensky TC, Janmey PA. Nonlinear elasticity in biological gels. *Nature*. 2005;435(7039):191-194. doi:10.1038/nature03521
10. Lazarus E, Meyer AS, Ikuma K, Rivero IV. Three dimensional printed biofilms: fabrication, design and future biomedical and environmental applications. *Microb Biotechnol*. 2024;17(1):e14360. doi:10.1111/1751-7915.14360
11. Denton O, Wan Y, Beattie L, *et al*. Understanding the role of biofilms in acute recurrent tonsillitis through 3D bioprinting of a novel gelatin-PEGDA hydrogel. *Bioengineering*. 2024;11(3):202. doi:10.3390/bioengineering11030202
12. Ning E, Turnbull G, Clarke J, *et al*. 3D bioprinting of mature bacterial biofilms for antimicrobial resistance drug testing. *Biofabrication*. 2019;11(4):045018. doi:10.1088/1758-5090/ab37a0
13. Stewart PS, Costerton JW. Antibiotic resistance of bacteria in biofilms. *Lancet Lond Engl*. 2001;358(9276):135-138. doi:10.1016/s0140-6736(01)05321-1
14. Paré G, Kitsiou S. Chapter 9 methods for literature reviews. In: *Handbook of eHealth Evaluation: An Evidence-Based Approach [Internet]*. Victoria (BC): University of Victoria; 2017. https://www.ncbi.nlm.nih.gov/books/NBK481583/. Accessed August 22, 2025.
15. Mobaraki M, Ghaffari M, Yazdanpanah A, Luo Y, Mills DK. Bioinks and bioprinting: a focused review. *Bioprinting*. 2020;18:e00080. doi:10.1016/j.bprint.2020.e00080

16. Farasati Far B, Safaei M, Nahavandi R, *et al*. Hydrogel encapsulation techniques and its clinical applications in drug delivery and regenerative medicine: a systematic review. *ACS Omega*. 2024;9(27):29139-29158. doi:10.1021/acsomega.3c10102

17. Theus AS, Ning L, Hwang B, *et al*. Bioprintability: physiomechanical and biological requirements of materials for 3D bioprinting processes. *Polymers*. 2020; 12(10):2262. doi:10.3390/polym12102262

18. Zhang Y, Zhou D, Chen J, *et al*. Biomaterials based on marine resources for 3D bioprinting applications. *Mar Drugs*. 2019;17(10):555. doi:10.3390/md17100555

19. Hwang CM, Sant S, Masaeli M, *et al*. Fabrication of three-dimensional porous cell-laden hydrogel for tissue engineering. *Biofabrication*. 2010;2(3):035003. doi:10.1088/1758-5082/2/3/035003

20. Ng WL, Vyas C, Huang B, Yeong WY, Bartolo P. Advanced bioprinting strategies for fabrication of biomimetic tissues and organs. *Int J Extreme Manuf*. 2025;7(6):062006. doi:10.1088/2631-7990/adeee0

21. Mancha Sánchez E, Gómez-Blanco JC, López Nieto E, *et al*. Hydrogels for bioprinting: a systematic review of hydrogels synthesis, bioprinting parameters, and bioprinted structures behavior. *Front Bioeng Biotechnol*. 2020;8. doi:10.3389/fbioe.2020.00776

22. Hospodiuk M, Dey M, Sosnoski D, Ozbolat IT. The bioink: a comprehensive review on bioprintable materials. *Biotechnol Adv*. 2017;35(2):217-239. doi:10.1016/j.biotechadv.2016.12.006

23. Hölzl K, Lin S, Tytgat L, Van Vlierberghe S, Gu L, Ovsianikov A. Bioink properties before, during and after 3D bioprinting. *Biofabrication*. 2016;8(3):032002. doi:10.1088/1758-5090/8/3/032002

24. Khoeini R, Nosrati H, Akbarzadeh A, *et al*. Natural and synthetic bioinks for 3D bioprinting. *Adv NanoBiomed Res*. 2021;1(8):2000097. doi:10.1002/anbr.202000097

25. González LM, Mukhitov N, Voigt CA. Resilient living materials built by printing bacterial spores. *Nat Chem Biol*. 2020;16(2):126-133. doi:10.1038/s41589-019-0412-5

26. Qian F, Zhu C, Knipe JM, *et al*. Direct writing of tunable living inks for bioprocess intensification. *Nano Lett*. 2019;19(9):5829-5835. doi:10.1021/acs.nanolett.9b00066

27. Herzog J, Franke L, Lai Y, Gomez Rossi P, Sachtleben J, Weuster-Botz D. 3D bioprinting of microorganisms: principles and applications. *Bioprocess Biosyst Eng*. 2024;47(4):443-461. doi:10.1007/s00449-023-02965-3

28. Aghlara-Fotovat S, Musteata E, Doerfert MD, *et al*. Hydrogel-encapsulation to enhance bacterial diagnosis of colon inflammation. *Biomaterials*. 2023;301:122246. doi:10.1016/j.biomaterials.2023.122246

29. Barreiros dos Santos M, Azevedo S, Agusil JP, *et al*. Label-free ITO-based immunosensor for the detection of very low concentrations of pathogenic bacteria. *Bioelectrochemistry*. 2015;101:146-152. doi:10.1016/j.bioelechem.2014.09.002

30. Balasubramanian S, Aubin-Tam ME, Meyer AS. 3D printing for the fabrication of biofilm-based functional living materials. *ACS Synth Biol*. 2019;8(7):1564-1567. doi:10.1021/acssynbio.9b00192

31. Schmieden DT, Basalo Vázquez SJ, Sangüesa H, van der Does M, Idema T, Meyer AS. Printing of patterned, engineered E. coli biofilms with a low-cost 3D Printer. *ACS Synth Biol*. 2018;7(5):1328-1337. doi:10.1021/acssynbio.7b00424

32. Sakai S, Hirose K, Taguchi K, Ogushi Y, Kawakami K. An injectable, *in situ* enzymatically gellable, gelatin derivative for drug delivery and tissue engineering. *Biomaterials*. 2009;30(20):3371-3377. doi:10.1016/j.biomaterials.2009.03.030

33. Yeh M kung, Liang Y ming, Cheng K ming, Dai NT, Liu C che, Young J jong. A novel cell support membrane for skin tissue engineering: gelatin film cross-linked with 2-chloro-1-methylpyridinium iodide. *Polymer*. 2011;52(4): 996-1003. doi:10.1016/j.polymer.2010.10.060

34. Ozbolat IT, Hospodiuk M. Current advances and future perspectives in extrusion-based bioprinting. *Biomaterials*. 2016;76:321-343. doi:10.1016/j.biomaterials.2015.10.076

35. Utoiu E, Manoiu VS, Oprita EI, Craciunescu O. Bacterial cellulose: a sustainable source for hydrogels and 3D-printed scaffolds for tissue engineering. *Gels*. 2024;10(6):387. doi:10.3390/gels10060387

36. Purcell EK, Singh A, Kipke DR. Alginate composition effects on a neural stem cell–seeded scaffold. *Tissue Eng Part C Methods*. 2009;15(4):541-550. doi:10.1089/ten.tec.2008.0302

37. Augst AD, Kong HJ, Mooney DJ. Alginate hydrogels as biomaterials. *Macromol Biosci*. 2006;6(8):623-633. doi:10.1002/mabi.200600069

38. Hellio D, Djabourov M. Physically and chemically crosslinked gelatin gels. *Macromol Symp*. 2006;241(1): 23-27. doi:10.1002/masy.200650904

39. Parenteau-Bareil R, Gauvin R, Berthod F. Collagen-based biomaterials for tissue engineering applications. *Materials*. 2010;3(3):1863-1887. doi:10.3390/ma3031863

40. Yin N, Santos TMA, Auer GK, Crooks JA, Oliver PM, Weibel DB. Bacterial cellulose as a substrate for microbial cell culture. *Appl Environ Microbiol*. 2014;80(6):1926-1932. doi:10.1128/AEM.03452-13

41. Pu X, Wu Y, Liu J, Wu B. 3D bioprinting of microbial-based living materials for advanced energy and environmental applications. *Chem Bio Eng*. 2024;1(7):568-592. doi:10.1021/cbe.4c00024

42. Benwood C, Chrenek J, Kirsch RL, *et al*. Natural biomaterials and their use as bioinks for printing tissues. *Bioengineering*. 2021;8(2):27. doi:10.3390/bioengineering8020027

43. Zhang H, Xia H, Zhao Y. Poly(vinyl alcohol) hydrogel can autonomously self-heal. *ACS Macro Lett*. 2012;1(11):1233-1236. doi:10.1021/mz300451r

44. Rovetta R, Pallavicini A, Ginestra PS. Bioprinting process optimization: case study on PVA (polyvinyl alcohol) and graphene oxide biocompatible hydrogels. *Procedia CIRP*. 2022;110:145-149. doi:10.1016/j.procir.2022.06.027

45. Lin CC, Anseth KS. PEG hydrogels for the controlled release of biomolecules in regenerative medicine. *Pharm Res*. 2009;26(3):631-643. doi:10.1007/s11095-008-9801-2

46. Kadilak AL, Rehaag JC, Harrington CA, Shor LM. A 3D-printed microbial cell culture platform with in situ PEGDA hydrogel barriers for differential substrate delivery. *Biomicrofluidics*. 2017;11(5):054109. doi:10.1063/1.5003477

47. Gong CY, Shi S, Dong PW, *et al*. In vitro drug release behavior from a novel thermosensitive composite hydrogel based on Pluronic f127 and poly(ethylene glycol)-poly(ε-caprolactone)-poly(ethylene glycol) copolymer. *BMC Biotechnol*. 2009;9:8. doi:10.1186/1472-6750-9-8

48. Vashi AV, Keramidaris E, Abberton KM, *et al*. Adipose differentiation of bone marrow-derived mesenchymal stem cells using Pluronic F-127 hydrogel in vitro. *Biomaterials*. 2008;29(5):573-579. doi:10.1016/j.biomaterials.2007.10.017

49. Lee SH, Lee Y, Lee SW, *et al*. Enzyme-mediated cross-linking of Pluronic copolymer micelles for injectable and in situ forming hydrogels. *Acta Biomater*. 2011;7(4):1468-1476. doi:10.1016/j.actbio.2010.11.029

50. Vandenhaute M, Schelfhout J, Van Vlierberghe S, Mendes E, Dubruel P. Cross-linkable, thermo-responsive Pluronic® building blocks for biomedical applications: synthesis and physico-chemical evaluation. *Eur Polym J*. 2014;53:126-138. doi:10.1016/j.eurpolymj.2014.01.016

51. Gungor-Ozkerim PS, Inci I, Zhang YS, Khademhosseini A, Dokmeci MR. Bioinks for 3D bioprinting: an overview. *Biomater Sci*. 2018;6(5):915-946. doi:10.1039/C7BM00765E

52. Qamar SA, Riasat A, Jahangeer M, *et al*. Prospects of microbial polysaccharides-based hybrid constructs for biomimicking applications. *J Basic Microbiol*. 2022;62(11):1319-1336. doi:10.1002/jobm.202100596

53. Zarrintaj P, Manouchehri S, Ahmadi Z, *et al*. Agarose-based biomaterials for tissue engineering. *Carbohydr Polym*. 2018;187:66-84. doi:10.1016/j.carbpol.2018.01.060

54. Tomić SL, Babić Radić MM, Vuković JS, Filipović VV, Nikodinovic-Runic J, Vukomanović M. Alginate-based hydrogels and scaffolds for biomedical applications. *Mar Drugs*. 2023;21(3):177. doi:10.3390/md21030177

55. Osidak EO, Kozhukhov VI, Osidak MS, Domogatsky SP. Collagen as bioink for bioprinting: a comprehensive review. *Int J Bioprinting*. 2020;6(3):270. doi:10.18063/ijb.v6i3.270

56. Sharifi S, Sharifi H, Akbari A, Chodosh J. Systematic optimization of visible light-induced crosslinking conditions of gelatin methacryloyl (GelMA). *Sci Rep*. 2021;11(1):23276. doi:10.1038/s41598-021-02830-x

57. Lazaridou M, Bikiaris DN, Lamprou DA. 3D bioprinted chitosan-based hydrogel scaffolds in tissue engineering and localised drug delivery. *Pharmaceutics*. 2022;14(9):1978. doi:10.3390/pharmaceutics14091978

58. Sanz-Horta R, Matesanz A, Gallardo A, *et al*. Technological advances in fibrin for tissue engineering. *J Tissue Eng*. 2023;14:20417314231190288. doi:10.1177/20417314231190288

59. Trucco D, Sharma A, Manferdini C, *et al*. Modeling and fabrication of silk fibroin–gelatin-based constructs using extrusion-based three-dimensional bioprinting. *ACS Biomater Sci Eng*. 2021;7(7):3306-3320. doi:10.1021/acsbiomaterials.1c00410

60. Pescosolido L, Schuurman W, Malda J, *et al*. Hyaluronic acid and dextran-based semi-IPN hydrogels as biomaterials for bioprinting. *Biomacromolecules*. 2011;12(5):1831-1838. doi:10.1021/bm200178w

61. Ashammakhi N, Ahadian S, Xu C, *et al*. Bioinks and bioprinting technologies to make heterogeneous and biomimetic tissue constructs. *Mater Today Bio*. 2019;1:100008. doi:10.1016/j.mtbio.2019.100008

62. Kandemir N, Vollmer W, Jakubovics NS, Chen J. Mechanical interactions between bacteria and hydrogels. *Sci Rep*. 2018;8(1):10893. doi:10.1038/s41598-018-29269-x

63. Burczak K, Fujisato T, Hatada M, Ikada Y. Protein permeation through poly(vinyl alcohol) hydrogel membranes. *Biomaterials*. 1994;15(3):231-238. doi:10.1016/0142-9612(94)90072-8

64. Cai MH, Chen XY, Fu LQ, *et al*. Design and development of hybrid hydrogels for biomedical applications: recent trends in anticancer drug delivery and tissue engineering. *Front Bioeng Biotechnol*. 2021;9. doi:10.3389/fbioe.2021.630943

65. Lee KY, Mooney DJ. Alginate: Properties and biomedical applications. *Prog Polym Sci*. 2012;37(1):106-126. doi:10.1016/j.progpolymsci.2011.06.003

66. Haq MA, Su Y, Wang D. Mechanical properties of PNIPAM based hydrogels: a review. *Mater Sci Eng C*. 2017;70: 842-855. doi:10.1016/j.msec.2016.09.081

67. Chueh B han, Zheng Y, Torisawa Y Suke, *et al*. Patterning alginate hydrogels using light-directed release of caged calcium in a microfluidic device. *Biomed Microdevices*. 2010;12(1):145-151. doi:10.1007/s10544-009-9369-6

68. Fisch P, Broguiere N, Finkielsztein S, Linder T, Zenobi-Wong M. Bioprinting of cartilaginous auricular constructs utilizing an enzymatically crosslinkable bioink. *Adv Funct Mater*. 2021;31(16):2008261. doi:10.1002/adfm.202008261

69. Gupta A, Avci P, Dai T, Huang YY, Hamblin MR. Ultraviolet radiation in wound care: sterilization and stimulation. *Adv Wound Care*. 2013;2(8):422-437. doi:10.1089/wound.2012.0366

70. Hu J, Hou Y, Park H, *et al*. Visible light crosslinkable chitosan hydrogels for tissue engineering. *Acta Biomater*. 2012;8(5):1730-1738. doi:10.1016/j.actbio.2012.01.029

71. Pereira RF, Bártolo PJ. 3D bioprinting of photocrosslinkable hydrogel constructs. *J Appl Polym Sci*. 2015;132(48). doi:10.1002/app.42458

72. Elkhoury K, Zuazola J, Vijayavenkataraman S. Bioprinting the future using light: a review on photocrosslinking reactions, photoreactive groups, and photoinitiators. *SLAS Technol*. 2023;28(3):142-151. doi:10.1016/j.slast.2023.02.003

73. Nair DP, Podgórski M, Chatani S, *et al*. The thiol-Michael addition click reaction: a powerful and widely used tool in materials chemistry. *Chem Mater*. 2014;26(1):724-744. doi:10.1021/cm402180t

74. Baldwin AD, Kiick KL. Tunable degradation of maleimide-thiol adducts in reducing environments. *Bioconjug Chem*. 2011;22(10):1946-1953. doi:10.1021/bc200148v

75. Yang X, Lu Z, Wu H, Li W, Zheng L, Zhao J. Collagen-alginate as bioink for three-dimensional (3D) cell printing based cartilage tissue engineering. *Mater Sci Eng C*. 2018;83:195-201. doi:10.1016/j.msec.2017.09.002

76. Gao T, Gillispie GJ, Copus JS, *et al*. Optimization of gelatin–alginate composite bioink printability using rheological parameters: a systematic approach. *Biofabrication*. 2018;10(3):034106. doi:10.1088/1758-5090/aacdc7

77. Sun JY, Zhao X, Illeperuma WRK, *et al*. Highly stretchable and tough hydrogels. *Nature*. 2012;489(7414):133-136. doi:10.1038/nature11409

78. Hernandez JL, Woodrow KA. Medical applications of porous biomaterials: features of porosity and tissue-specific implications for biocompatibility. *Adv Healthc Mater*. 2022;11(9):e2102087. doi:10.1002/adhm.202102087

79. Dvir T, Timko BP, Kohane DS, Langer R. Nanotechnological strategies for engineering complex tissues. *Nat Nanotechnol*. 2011;6(1):13-22. doi:10.1038/nnano.2010.246

80. De France KJ, Xu F, Hoare T. Structured macroporous hydrogels: progress, challenges, and opportunities. *Adv Healthc Mater*. 2018;7(1). doi:10.1002/adhm.201700927

81. Loh QL, Choong C. Three-dimensional scaffolds for tissue engineering applications: role of porosity and pore size. *Tissue Eng Part B Rev*. 2013;19(6):485-502. doi:10.1089/ten.teb.2012.0437

82. Kim J, Yaszemski MJ, Lu L. Three-dimensional porous biodegradable polymeric scaffolds fabricated with biodegradable hydrogel porogens. *Tissue Eng Part C Methods*. 2009;15(4):583-594. doi:10.1089/ten.tec.2008.0642

83. Dehghani F, Annabi N. Engineering porous scaffolds using gas-based techniques. *Curr Opin Biotechnol*. 2011;22(5):661-666. doi:10.1016/j.copbio.2011.04.005

84. Aldemir Dikici B, Claeyssens F. Basic principles of emulsion templating and its use as an emerging manufacturing method of tissue engineering scaffolds. *Front Bioeng Biotechnol*. 2020;8. doi:10.3389/fbioe.2020.00875

85. Annabi N, Nichol JW, Zhong X, *et al*. Controlling the porosity and microarchitecture of hydrogels for tissue engineering. *Tissue Eng Part B Rev*. 2010;16(4): 371-383. doi:10.1089/ten.teb.2009.0639

86. Lau HK, Paul A, Sidhu I, *et al*. Microstructured elastomer-PEG hydrogels via kinetic capture of aqueous liquid–liquid phase separation. *Adv Sci*. 2018;5(6): 1701010. doi:10.1002/advs.201701010

87. Foudazi R, Zowada R, Manas-Zloczower I, Feke DL. Porous hydrogels: present challenges and future opportunities. *Langmuir*. 2023;39(6):2092-2111. doi:10.1021/acs.langmuir.2c02253

88. Dong PT, Shi W, He X, Borisy GG. Adhesive interactions within microbial consortia can be differentiated at the single-cell level through expansion microscopy. *Proc Natl Acad Sci USA*. 2024;121(48):e2411617121. doi:10.1073/pnas.2411617121

89. Lim Y, Shiver AL, Khariton M, *et al*. Mechanically resolved imaging of bacteria using expansion microscopy. *PLOS Biol*. 2019;17(10):e3000268. doi:10.1371/journal.pbio.3000268

90. Johnston TG, Yuan SF, Wagner JM, *et al*. Compartmentalized microbes and co-cultures in hydrogels for on-demand bioproduction and preservation. *Nat Commun*. 2020;11(1):563. doi:10.1038/s41467-020-14371-4

91. Jin GZ, Kim HW. Effects of type I collagen concentration in hydrogel on the growth and phenotypic expression of rat chondrocytes. *Tissue Eng Regen Med*. 2017;14(4): 383-391. doi:10.1007/s13770-017-0060-3

92. Yeh J, Ling Y, Karp JM, *et al*. Micromolding of shape-controlled, harvestable cell-laden hydrogels. *Biomaterials*. 2006;27(31):5391-5398. doi:10.1016/j.biomaterials.2006.06.005

93. Occhetta P, Sadr N, Piraino F, Redaelli A, Moretti M, Rasponi M. Fabrication of 3D cell-laden hydrogel microstructures through photo-mold patterning. *Biofabrication*. 2013;5(3):035002. doi:10.1088/1758-5082/5/3/035002

94. Landers R, Hübner U, Schmelzeisen R, Mülhaupt R. Rapid prototyping of scaffolds derived from thermoreversible hydrogels and tailored for applications in tissue engineering. *Biomaterials*. 2002;23(23):4437-4447. doi:10.1016/S0142-9612(02)00139-4

95. Zhang YS, Haghiashtiani G, Hübscher T, *et al*. 3D extrusion bioprinting. *Nat Rev Methods Primer*. 2021;1(1):1-20. doi:10.1038/s43586-021-00073-8

96. Hinton TJ, Jallerat Q, Palchesko RN, *et al*. Three-dimensional printing of complex biological structures by freeform reversible embedding of suspended hydrogels. *Sci Adv*. 2015;1(9):e1500758. doi:10.1126/sciadv.1500758

97. Bhattacharjee T, Zehnder SM, Rowe KG, *et al*. Writing in the granular gel medium. *Sci Adv*. 2015;1(8):e1500655. doi:10.1126/sciadv.1500655

98. Bertassoni LE, Cecconi M, Manoharan V, *et al*. Hydrogel bioprinted microchannel networks for vascularization of tissue engineering constructs. *Lab Chip*. 2014;14(13):2202-2211. doi:10.1039/C4LC00030G

99. Homan KA, Kolesky DB, Skylar-Scott MA, *et al*. Bioprinting of 3D convoluted renal proximal tubules on perfusable chips. *Sci Rep*. 2016;6(1):34845. doi:10.1038/srep34845

100. Liu T, Liu Q, Anaya I, *et al*. Investigating lymphangiogenesis in a sacrificially bioprinted volumetric model of breast tumor tissue. *Methods*. 2021;190:72-79. doi:10.1016/j.ymeth.2020.04.003

101. Miller JS, Stevens KR, Yang MT, *et al*. Rapid casting of patterned vascular networks for perfusable engineered three-dimensional tissues. *Nat Mater*. 2012;11(9):768-774. doi:10.1038/nmat3357

102. Wu W, DeConinck A, Lewis JA. Omnidirectional printing of 3D microvascular networks. *Adv Mater*. 2011;23(24):H178-H183. doi:10.1002/adma.201004625

103. Liu W, Zhong Z, Hu N, *et al*. Coaxial extrusion bioprinting of 3D microfibrous constructs with cell-favorable gelatin methacryloyl microenvironments. *Biofabrication*. 2018;10(2):024102. doi:10.1088/1758-5090/aa9d44

104. Ouyang L, Highley CB, Sun W, Burdick JA. A generalizable strategy for the 3D bioprinting of hydrogels from nonviscous photo-crosslinkable Inks. *Adv Mater*. 2017;29(8): 1604983. doi:10.1002/adma.201604983

105. Galarraga JH, Kwon MY, Burdick JA. 3D bioprinting via an in situ crosslinking technique towards engineering cartilage tissue. *Sci Rep*. 2019;9(1):19987. doi:10.1038/s41598-019-56117-3

106. Barui S. 3D inkjet printing of biomaterials: principles and applications. *Med Devices Sens*. 2021;4(1):e10143. doi:10.1002/mds3.10143

107. Li X, Liu B, Pei B, *et al*. Inkjet bioprinting of biomaterials. *Chem Rev*. 2020;120(19):10793-10833. doi:10.1021/acs.chemrev.0c00008

108. Nieto D, Marchal Corrales JA, Jorge de Mora A, Moroni L. Fundamentals of light-cell–polymer interactions in photo-cross-linking based bioprinting. *APL Bioeng*. 2020;4(4):041502. doi:10.1063/5.0022693

109. Manapat JZ, Chen Q, Ye P, Advincula RC. 3D printing of polymer nanocomposites via stereolithography. *Macromol Mater Eng*. 2017;302(9):1600553. doi:10.1002/mame.201600553

110. Stampfl J, Baudis S, Heller C, *et al*. Photopolymers with tunable mechanical properties processed by laser-based high-resolution stereolithography. *J Micromech Microeng*. 2008;18(12):125014. doi:10.1088/0960-1317/18/12/125014

111. Peng X, Kuang X, Roach DJ, *et al*. Integrating digital light processing with direct ink writing for hybrid 3D printing of functional structures and devices. *Addit Manuf*. 2021;40:101911. doi:10.1016/j.addma.2021.101911

112. Connell JL, Kim J, Shear JB, Bard AJ, Whiteley M. Real-time monitoring of quorum sensing in 3D-printed bacterial aggregates using scanning electrochemical microscopy. *Proc Natl Acad Sci USA*. 2014;111(51):18255-18260. doi:10.1073/pnas.1421211111

113. Müller J, Jäkel AC, Richter J, Eder M, Falgenhauer E, Simmel FC. Bacterial growth, communication, and guided chemotaxis in 3D-bioprinted hydrogel environments. *ACS Appl Mater Interfaces*. 2022;14(14):15871-15880. doi:10.1021/acsami.1c20836

114. Ceballos-González CF, Bolívar-Monsalve EJ, Quevedo-Moreno DA, *et al*. High-throughput and continuous chaotic bioprinting of spatially controlled bacterial microcosms. *ACS Biomater Sci Eng*. 2021;7(6):2408-2419. doi:10.1021/acsbiomaterials.0c01646

115. Yusupov VI, Gorlenko MV, Cheptsov VS, *et al*. Laser engineering of microbial systems. *Laser Phys Lett*. 2018;15(6):065604. doi:10.1088/1612-202X/aab5ef

116. Reinhardt O, Ihmann S, Ahlhelm M, Gelinsky M. 3D bioprinting of mineralizing cyanobacteria as novel approach for the fabrication of living building materials. *Front Bioeng Biotechnol*. 2023;11. doi:10.3389/fbioe.2023.1145177

117. Binelli MR, Kan A, Rozas LEA, Pisaturo G, Prakash N, Studart AR. Complex living materials made by light-based printing of genetically programmed bacteria. *Adv Mater*. 2023;35(6):2207483. doi:10.1002/adma.202207483

118. Mohammadi Z, Rabbani M. Bacterial bioprinting on a flexible substrate for fabrication of a colorimetric temperature indicator by using a commercial inkjet printer. *J Med Signals Sens*. 2018;8(3):170-174. doi:10.4103/jmss.JMSS_41_17

119. Dubbin K, Dong Z, Park DM, *et al*. Projection microstereolithographic microbial bioprinting for engineered biofilms. *Nano Lett*. 2021;21(3):1352-1359. doi:10.1021/acs.nanolett.0c04100

120. Balasubramanian S, Yu K, Cardenas DV, Aubin-Tam ME, Meyer AS. Emergent biological endurance depends on extracellular matrix composition of three-dimensionally printed *Escherichia coli* biofilms. *ACS Synth Biol*. 2021;10(11):2997-3008. doi:10.1021/acssynbio.1c00290

121. Jiang M, Zheng J, Tang Y, *et al*. Retrievable hydrogel networks with confined microalgae for efficient antibiotic degradation and enhanced stress tolerance. *Nat Commun*. 2025;16(1). doi:10.1038/s41467-025-58415-z

122. He F, Ou Y, Liu J, *et al*. 3D Printed biocatalytic living materials with dual-network reinforced bioinks. *Small*. 2022;18(6). doi:10.1002/smll.202104820

123. Wang D, Li X yan, Li A. Natural bioink of interpenetrating network hydrogels mimicking extracellular polymeric substances for microbial immobilization in water pollution control. *Environ Res*. 2024;262:119856. doi:10.1016/j.envres.2024.119856

124. Datta D, Weiss EL, Wangpraseurt D, *et al*. Phenotypically complex living materials containing engineered cyanobacteria. *Nat Commun*. 2023;14(1). doi:10.1038/s41467-023-40265-2

125. Lehner BAE, Schmieden DT, Meyer AS. A straightforward approach for 3D bacterial printing. *ACS Synth Biol*. 2017;6(7):1124-1130. doi:10.1021/acssynbio.6b00395

126. Ming Z, Han L, Bao M, *et al*. Living bacterial hydrogels for accelerated infected wound healing. *Adv Sci*. 2021;8(24):2102545. doi:10.1002/advs.202102545

127. Huang J, Liu S, Zhang C, *et al*. Programmable and printable Bacillus subtilis biofilms as engineered living materials. *Nat Chem Biol*. 2019;15(1):34-41. doi:10.1038/s41589-018-0169-2

128. Schaffner M, Rühs PA, Coulter F, Kilcher S, Studart AR. 3D printing of bacteria into functional complex materials. *Sci Adv*. 2017;3(12):eaao6804. doi:10.1126/sciadv.aao6804

129. Molinari S, Tesoriero RF, Li D, *et al*. A de novo matrix for macroscopic living materials from bacteria. *Nat Commun*. 2022;13(1):5544. doi:10.1038/s41467-022-33191-2

130. Chen AY, Deng Z, Billings AN, *et al*. Synthesis and patterning of tunable multiscale materials with engineered cells. *Nat Mater*. 2014;13(5):515-523. doi:10.1038/nmat3912

131. Freyman MC, Kou T, Wang S, Li Y. 3D printing of living bacteria electrode. *Nano Res*. 2020;13(5):1318-1323. doi:10.1007/s12274-019-2534-1

132. Pham JV, Yilma MA, Feliz A, *et al*. A review of the microbial production of bioactive natural products and biologics. *Front Microbiol*. 2019;10. doi:10.3389/fmicb.2019.01404

133. Sun M, Gao AX, Liu X, Bai Z, Wang P, Ledesma-Amaro R. Microbial conversion of ethanol to high-value products: progress and challenges. *Biotechnol Biofuels Bioprod*. 2024;17(1):115. doi:10.1186/s13068-024-02546-w

134. da Silva TL, Gouveia L, Reis A. Integrated microbial processes for biofuels and high value-added products: the

way to improve the cost effectiveness of biofuel production. *Appl Microbiol Biotechnol*. 2014;98(3):1043-1053. doi:10.1007/s00253-013-5389-5

135. Nikita S, Mishra S, Gupta K, Runkana V, Gomes J, Rathore AS. Advances in bioreactor control for production of biotherapeutic products. *Biotechnol Bioeng*. 2023;120(5):1189-1214. doi:10.1002/bit.28346

136. Smith MJ, Francis MB. Improving metabolite production in microbial co-cultures using a spatially constrained hydrogel. *Biotechnol Bioeng*. 2017;114(6):1195-1200. doi:10.1002/bit.26235

137. Duraj-Thatte AM, Manjula-Basavanna A, Rutledge J, *et al*. Programmable microbial ink for 3D printing of living materials produced from genetically engineered protein nanofibers. *Nat Commun*. 2021;12(1):6600. doi:10.1038/s41467-021-26791-x

138. Cui Z, Feng Y, Liu F, Jiang L, Yue J. 3D bioprinting of living materials for structure-dependent production of hyaluronic acid. *ACS Macro Lett*. 2022;11(4):452-459. doi:10.1021/acsmacrolett.2c00037

139. Sharma S, Pathania S, Bhagta S, *et al*. Microbial remediation of polluted environment by using recombinant E. coli: a review. *Biotechnol Environ*. 2024;1(1). doi:10.1186/s44314-024-00008-z

140. Zhang Y, Hsu HH, Wheeler JJ, Tang S, Jiang X. Emerging investigator series: emerging biotechnologies in wastewater treatment: from biomolecular engineering to multiscale integration. *Environ Sci Water Res Technol*. 2020;6(8):1967-1985. doi:10.1039/D0EW00393J

141. Justus KB, Hellebrekers T, Lewis DD, *et al*. A biosensing soft robot: autonomous parsing of chemical signals through integrated organic and inorganic interfaces. *Sci Robot*. 2019;4(31):eaax0765. doi:10.1126/scirobotics.aax0765

142. Gilbert C, Tang TC, Ott W, *et al*. Living materials with programmable functionalities grown from engineered microbial co-cultures. *Nat Mater*. 2021;20(5):691-700. doi:10.1038/s41563-020-00857-5

143. Barnhart MM, Chapman MR. Curli biogenesis and function. *Annu Rev Microbiol*. 2006;60:131-147. doi:10.1146/annurev.micro.60.080805.142106

144. Liu X, Yuk H, Lin S, *et al*. 3D printing of living responsive materials and devices. *Adv Mater*. 2018;30(4):1704821. doi:10.1002/adma.201704821

145. Majerle A, Schmieden DT, Jerala R, Meyer AS. Synthetic biology for multiscale designed biomimetic assemblies: from designed self-assembling biopolymers to bacterial bioprinting. *Biochemistry*. 2019;58(16):2095-2104. doi:10.1021/acs.biochem.8b00922

146. Zheng DW, Qiao JY, Ma JC, *et al*. A microbial community cultured in gradient hydrogel for investigating gut microbiome-drug interaction and guiding therapeutic decisions. *Adv Mater*. 2023;35(22):2300977. doi:10.1002/adma.202300977

147. Aliyazdi S, Frisch S, Hidalgo A, *et al*. 3D bioprinting of E. coli MG1655 biofilms on human lung epithelial cells for building complex in vitro infection models. *Biofabrication*. 2023;15(3):035019. doi:10.1088/1758-5090/acd95e

148. Darch SE, Simoska O, Fitzpatrick M, *et al*. Spatial determinants of quorum signaling in a pseudomonas aeruginosa infection model. *Proc Natl Acad Sci USA*. 2018;115(18):4779-4784. doi:10.1073/pnas.1719317115

149. Connell JL, Ritschdorff ET, Whiteley M, Shear JB. 3D printing of microscopic bacterial communities. *Proc Natl Acad Sci USA*. 2013;110(46):18380-18385. doi:10.1073/pnas.1309729110

150. Connell JL, Wessel AK, Parsek MR, Ellington AD, Whiteley M, Shear JB. Probing prokaryotic social behaviors with bacterial "Lobster Traps." *mBio*. 2010;1(4):e00202-10. doi:10.1128/mBio.00202-10

151. Aftab M, Ikram S, Ullah M, *et al*. Recent trends and future directions in 3D printing of biocompatible polymers. *J Manuf Mater Process*. 2025;9(4). doi:10.3390/jmmp9040129

152. Ma X, Xu M, Cui X, Yin J, Wu Q. Hybrid 3D bioprinting of sustainable biomaterials for advanced multiscale tissue engineering. *Small Weinh Bergstr Ger*. Published online March 27, 2025:e2408947. doi:10.1002/smll.202408947

153. Zhang TC, Bishop PL. Density, porosity, and pore structure of biofilms. *Water Res*. 1994;28(11):2267-2277. doi:10.1016/0043-1354(94)90042-6

ACCSCIENCE PUBLISHING

International Journal of Bioprinting

REVIEW ARTICLE

3D bioprinting-driven strategies for tissue regeneration and controlled immune modulation

Jianfeng Zhang[1†], Fujia Ren[2†], Fangtian Bu[3], Yao Yao[4*], and Mengmeng Li[1*]

[1] Department of Pharmacy, Tongde Hospital of Zhejiang Province Affiliated to Zhejiang Chinese Medical University, Hangzhou, Zhejiang, China

[2] Department of Pharmacy, Hangzhou Women's Hospital, Hangzhou, Zhejiang, China

[3] College of Pharmacy, School of Medicine, Hangzhou Normal University, Hangzhou, Zhejiang, China

[4] Department of Pharmacy, Women's Hospital School of Medicine, Zhejiang University, Hangzhou, Zhejiang, China

Abstract

Tissue loss, fibrosis-prone repair, and immune-mediated graft failure remain persistent obstacles in regenerative medicine. Within this context, 3D bioprinting is shifting from structure-centric fabrication to a platform for programmed immune modulation. This review synthesizes evidence across materials, architecture, and living components to delineate how bioprinted constructs can steer host responses toward resolution and durable function. We first examine events at the blood–biomaterial interface, including protein corona formation, complement–coagulation crosstalk, and leukocyte recruitment, and map them to tunable parameters, such as chemistry, stiffness, degradability, topography, and pore geometry that direct macrophage and dendritic-cell programs. We compare natural and synthetic bioinks, emphasizing printability windows, batch control, and impurity management as prerequisites for interpretable immunological readouts. We survey stimuli-responsive inks triggered by pH, reactive oxygen species, enzymes, light, or magnetic fields to deliver cytokines, chemokines, and metabolites with temporal precision, and highlight architected lattices and gradients that guide cell trafficking, vascular and lymphatic integration, and mechano-immune conditioning. Cell- and signal-centric strategies include immune–stromal coprinting, extracellular vesicle embedding, membrane cloaking for immune stealth or targeting, and synthetic circuits that sense inflammation and secrete immunoregulatory payloads. Finally, we identify translational bottlenecks and outline opportunities in 4D bioprinting, AI-assisted design, digital twins, and *in situ* printing. Treating immunity as a primary design variable is essential for predictable, durable, and clinically credible bioprinted therapies.

Keywords: 3D bioprinting; Bioinks; Foreign body response; Immunomodulation; Macrophage polarization; Regenerative medicine

†These authors contributed equally to this work.

***Corresponding authors:**
Yao Yao (yaoyaofb@zju.edu.cn)

Mengmeng Li (limengmeng920911@163.com)

Citation: Zhang J, Ren F, Bu F, Yao Y, Li M. 3D bioprinting-driven strategies for tissue regeneration and controlled immune modulation. *Int J Bioprint*. 2026;12(1):173-198. doi: 10.36922/IJB025460474

Received: November 13, 2025
Revised: December 4, 2025
Accepted: December 12, 2025
Published online: December 18, 2025

Copyright: © 2025 Author(s). This is an Open Access article distributed under the terms of the Creative Commons Attribution License, permitting distribution, and reproduction in any medium, provided the original work is properly cited.

Publisher's Note: AccScience Publishing remains neutral with regard to jurisdictional claims in published maps and institutional affiliations.

1. Introduction

Clinical translation of tissue engineering remains constrained by recurrent regenerative failure, chronic inflammation leading to fibrotic encapsulation (foreign body reaction, FBR), and graft rejection with immune-related complications that impair function and necessitate re-interventions.[1-3] Upon implantation or blood contact, adsorbed protein layers rapidly form on material surfaces and trigger complement–coagulation–contact pathway crosstalk, amplifying leukocyte recruitment, thrombosis, and fibrosis that undermine long-term performance.[4,5] These realities highlight that structural reconstruction alone does not guarantee durable functional recovery without parallel control of host immunity.[3]

Three-dimensional (3D) bioprinting—defined as digitally guided, layer-by-layer deposition of living cells, bioactive matrices ("bioinks"), and signaling cues to build tissue-like architectures—has matured from proof-of-concept to versatile biofabrication for preclinical modeling and regenerative therapy.[6,7] Contemporary reviews catalog technique families (extrusion, inkjet, light-based), material classes, and cross-scale design rules that enable spatial control of mechanics, porosity, and cell distribution.[8] Beyond geometry, emerging work positions bioprinting as a platform to encode immunological functions into constructs, aligning scaffold architecture with immune-instructive chemistry and controlled release to steer healing trajectories.[6,7]

Converging evidence shows that biomaterial physicochemical cues—stiffness, topography, wettability, and pore architecture—direct macrophage polarization and dendritic-cell priming, thereby dictating downstream angiogenesis, matrix remodeling, and scarring.[9,10] Immunomodulatory strategies now integrate cytokines (e.g., IL-4/IL-10), chemokine gradients, and pro-resolving mediators within bioinks to achieve spatiotemporal control of innate and adaptive responses.[11,12] In parallel, delivery materials are being engineered to recruit and reprogram immune and stromal cells (macrophages, T cells, MSCs), enabling "materials-as-medicine" concepts that couple regeneration with immune homeostasis.[13] Together, these advances motivate the design of immune-competent constructs—printed tissues capable not only of providing structure but also of sensing, modulating, and stabilizing host immune signaling for durable repair.[9,12]

This review therefore addresses the central question: how can 3D bioprinting move beyond structural replacement to enable immune-controlled regeneration? We analyze early events at the blood/material and tissue interfaces—including complement activation and protein corona formation—as programmable targets, and we map how construct architecture, surface chemistry, and payload release can de-escalate acute inflammation, prevent chronic FBR, and promote functional integration.[1,5,14,15]

Scope and search strategy. We surveyed peer-reviewed literature across PubMed, Scopus, and Web of Science from January 1, 2015 to November 5, 2025, using combinations of keywords ("3D bioprinting/bioprinted," "bioink," "immunomodulation/immunoengineering," "macrophage polarization," "complement activation," "foreign body reaction," "immune-competent constructs," "organoids/organ-on-chip"). Inclusion criteria were: (i) English-language original experimental or clinical studies, or reviews, that involved 3D bioprinting or bioprinted constructs and (ii) reported at least one immune-related outcome (e.g., immune-cell phenotype, cytokine/chemokine profiles, complement/coagulation activation, or histological inflammation or fibrosis). We excluded duplicate records, conference abstracts, nonpeer-reviewed theses or preprints, purely manufacturing or process-optimization papers lacking any biological or immunological validation, purely computational articles without experimental confirmation, and additive-manufacturing reports unrelated to immunity. Within this narrative synthesis, we applied an a priori hierarchy of evidence adapted from evidence-based medicine levels-of-evidence, classifying key studies as Level 1 (systematic reviews or randomized clinical trials of bioprinted constructs), Level 2 (prospective nonrandomized clinical studies or controlled *in vivo* animal studies with predefined endpoints), Level 3 (exploratory *in vivo* animal studies and *ex vivo* organoid/organ-on-chip models), Level 4 (mechanistic *in vitro* cell–material interface investigations), and Level 5 (methodological, conceptual, or commentary articles). Within each level, we qualitatively considered methodological signals of quality (e.g., explicit randomization or allocation concealment, blinding of outcome assessment, justification of sample size, and reproducible reporting of dosing/printing parameters) when deciding which studies to feature in detail, whereas small, single-arm or incompletely reported experiments were treated as hypothesis-generating. Reporting of the search and selection approach follows PRISMA 2020 guidance for transparency.[16,17] Evidence was graded using a simplified scheme adapted from the 2011 Oxford Center for Evidence-Based Medicine (OCEBM) levels of evidence.[16] Briefly, Level 1 denotes randomized or prospective clinical studies, Level 2 other human observational studies or systematic reviews, Level 3 controlled *in vivo* animal experiments, Level 4 *in vitro* or *ex vivo* mechanistic studies, and Level 5 methodological or conceptual papers. For each group of findings, we explicitly indicate in the text and tables whether the supporting data are clinical (Levels

1–2), preclinical *in vivo* (Level 3), or *in vitro*/mechanistic only (Levels 4–5). Reporting of the search approach follows PRISMA 2020 guidance for transparency.[17,18]

2. Conceptual framework of immuno-modulated regeneration

After tissue injury, the host response can be parsed into overlapping hemostasis, acute inflammation, proliferative tissue formation, and remodeling phases orchestrated by innate immune and stromal cells. Rather than detailing every cytokine and cell subset, for 3D bioprinting it is most important that (i) early danger sensing and neutrophil/monocyte recruitment clear contaminants but also condition the matrix, (ii) resolution programs reprogram macrophages and fibroblasts from proinflammatory to proregenerative phenotypes, and (iii) vascular and lymphatic ingrowth restore perfusion and immune surveillance. These process-level concepts, synthesized in canonical wound-healing reviews, provide the background for understanding how printed constructs can either accelerate resolution or lock tissues into chronic foreign-body fibrosis.[19-21]

In 3D-bioprinted constructs, the blood–material interface is the first decision point for immune compatibility. Protein adsorption, complement activation, and contact coagulation occur within seconds of implantation and are strongly influenced by surface chemistry, topography, and degradation products. Here, we therefore focus on two practical axes: control of the adsorbed protein corona, which shapes downstream leukocyte recruitment and macrophage polarization, and modulation of complement–coagulation crosstalk, which can be harnessed for hemostasis and vascularization but, if excessive, drives thromboinflammation and fibrotic encapsulation. Mechanistic work on biomaterial–complement interactions now provides concrete design rules—such as hydrophilic or zwitterionic coatings and immobilized complement regulators—that are directly transferable to bioink and scaffold optimization.[4,14,22]

A third pillar of our framework is innate–adaptive crosstalk and immune memory. Rather than exhaustively cataloging T-cell and antigen-presenting-cell subsets, we emphasize that macrophage–dendritic-cell–T-cell loops and stromal niches together determine whether implanted constructs induce acute rejection, immune tolerance, or "trained" hyper-responsiveness. Recent work on trained immunity highlights how prior exposures imprint long-lived metabolic and epigenetic programs in innate cells; in the context of bioprinting, this implies that the same scaffold can elicit very different responses in naïve versus pre-inflamed tissues, and that dynamic control of danger signals, antigen load, and metabolic cues is essential to maintain a regenerative rather than pathologic memory state.[23,24]

Finally, immune outcomes—tolerance versus trained immunity—link early programming to long-term graft performance. Inappropriately engaged trained innate responses can perpetuate chronic inflammation around implants, whereas antigen-specific tolerance mediated by Tregs and tolerogenic DCs supports durable integration; designing 3D-printed constructs that avoid maladaptive "training" while locally favoring context-appropriate tolerance is therefore central to achieving immune-competent regeneration.

To connect materials, printing parameters, and immune outcomes in a more systematic fashion, we treat "immune-competency" as a quantifiable design objective rather than a binary pass/fail property.[25-27] At the materials/printing level, each construct can be described by a shared set of physicochemical and architectural descriptors, including surface chemistry and charge, crosslink density and stiffness, degradation kinetics, pore size and interconnectivity, and the spatial–temporal presentation of ligands, cytokines, and other bioactive cues. At the biology level, we advocate a tiered immune readout panel that captures (i) early protein corona and complement–coagulation activation, (ii) innate-cell phenotypes and secretomes (e.g., macrophage and dendritic-cell states), (iii) adaptive immune activation versus tolerance (T-cell activation, exhaustion and regulatory markers, and antigen-specific responses), and (iv) tissue-level endpoints such as vascularization, fibrotic capsule thickness, and integration with host parenchyma across *in vitro*, *ex vivo*, and *in vivo* models. Aggregating these variables into indication-specific composite indices—provisionally conceptualized here as an "immune-competency score"—would allow comparison of bioprinted constructs across materials and printing modalities and provide a bridge between mechanistic immunology, pharmacology, and regulatory evaluation.

3. Bioinks and smart biomaterials

To keep the focus on immune design, we now summarize base bioink classes only briefly. Natural matrices such as collagen/gelatin, alginate, and tissue-specific decellularized extracellular matrix (dECM) provide native ligands and cytokine reservoirs but show batch-to-batch variability and potential residual immunostimulatory contaminants, whereas synthetic platforms including poly(ethylene glycol) (PEG) and degradable polyesters poly(lactic-co-glycolic acid) (PLGA) polycaprolactone (PCL) offer more predictable mechanics and degradation at the expense of

intrinsic bioactivity; detailed pros and cons are consolidated in Table 1 rather than described extensively in the main text. To avoid conflating mechanistic and translational findings, in this and subsequent technical sections we specify whether cited studies are based on *in vitro* experiments (Level 4–5), preclinical *in vivo* models (Level 3), or human data (Levels 1–2), according to the OCEBM-derived evidence scheme outlined in the Introduction.[16]

Printability and the "4S" properties define engineering constraints and clinical readiness. Strength and shape fidelity arise from rheology (shear-thinning/yield stress) and crosslinking kinetics that maintain filament integrity and pore geometry postdeposition.[28] Signaling capacity depends on retained ECM motifs, tethered cytokines, and degradation-controlled release.[29] Safety requires validated processes to remove cells/DNA from dECM (commonly <50 ng DNA/mg dry ECM; fragments <200 bp) and to eliminate endotoxin or residual photoinitiators that confound immune readouts.[30,31] Harmonized biocompatibility testing for cell-laden inks is essential to link material variables with host immune outcomes.[28]

Immunofunctionalization strategies fall on a spectrum from "immune-silent" to "pro-immunomodulatory." PEG or zwitterionic coatings can minimize protein opsonization and complement activation, reducing foreign-body responses.[32] Conversely, proactive designs harness topography, degradability, and ligands (e.g., CSF-1/IL-4-mimetic cues or arginyl-glycyl-aspartic acid motifs) to steer macrophage polarization, angiogenesis, and resolution of inflammation within printed constructs.[33] With natural polymers, purification and tailored chemistry (e.g., ultralow-endotoxin alginate; selective oxidation of ECM) help avoid unintended TLR-driven activation while preserving prohealing signaling.[34,35] Key base materials and their immune footprints are summarized in Table 1.

Stimuli-responsive ("smart") bioinks enable on-demand, spatiotemporal immune control.[39] A highly self-supporting, rapidly reversible chitosan-based hydrogel network—driven by weak electrostatic interactions and hydrogen bonding—enables high-fidelity prints (e.g., microtubes, multicomponent structures). Incorporation of AgNPs and a HIF-1α stabilizer (VH298) confers antimicrobial activity and prohealing efficacy *in vivo* (Figure 1). pH-responsive networks release anti-inflammatory agents preferentially in acidic, inflamed niches.[40] Reactive-oxygen-species (ROS)-responsive hydrogels scavenge oxidative stress and couple this with timed delivery of immunoreparative payloads in wounds and bone defects.[41,42] Enzyme-cleavable (e.g., MMP-responsive) linkers align drug release with matrix-remodeling phases to coordinate macrophage transition and vascularization.[43] Light-responsive, photocrosslinkable systems provide surgical-time activation with attention to initiator dose to protect resident immune cells.[44] Magnetic cues can remotely modulate macrophage infiltration and phenotype within printed gels, adding a noninvasive control layer for immune-competent constructs.[45] Representative smart bioinks and triggers are summarized in Table 2.

Table 1. Immunomodulatory bioinks and base materials: composition, immune footprint, printability, and evidence.

Bioink/material (type)	Immune-facing features	Printing suitability/notes	Key immune outcomes/readouts	Model/context	Refs.
Tissue-specific dECM (natural)	Native ligands/cytokine reservoirs; tissue-matched cues	Extrusion/DLP compatible; batch-to-batch bioactivity variance	Guides macrophage and T-cell behavior to pro-regenerative states	dECM bioinks overview & tissue-matched immunocues	29,35,36
PEG-based hydrogels (synthetic)	Inert backbone for precise ligand/peptide display; reduced opsonization	Broad modality compatibility; tunable crosslinking	Minimizes protein adsorption/complement activation; modular immunoregulation	Immuno-inert coatings & hydrogel platforms	32
PLGA / PCL (polyesters)	Structural robustness; degradable	Good filament fidelity; acidic PLGA by-products to buffer	Acidic degradation biases M1-like macrophage programs unless neutralized	Immunological effects of polyester degradation	37
Alginate (natural)	Widely used hydrogel; ionic crosslinking	Extrusion-friendly; viscosity adjustable	Impurities/endotoxin can activate innate immunity—need ultralow-endotoxin grades	Innate activation by unpurified alginate	34
Heparin-affinity hydrogels	Affinity capture & sustained release of cytokines (e.g., IL-4)	Photocrosslinkable or enzyme-set matrices	Sustained IL-4 polarizes macrophages and accelerates bone repair	Bone immuno-regeneration with IL-4 retention	38
Decellularization quality controls	DNA/endotoxin removal	GMP relevance; QC thresholds	Prevents confounded immune readouts	dECM safety and process validation	30,31

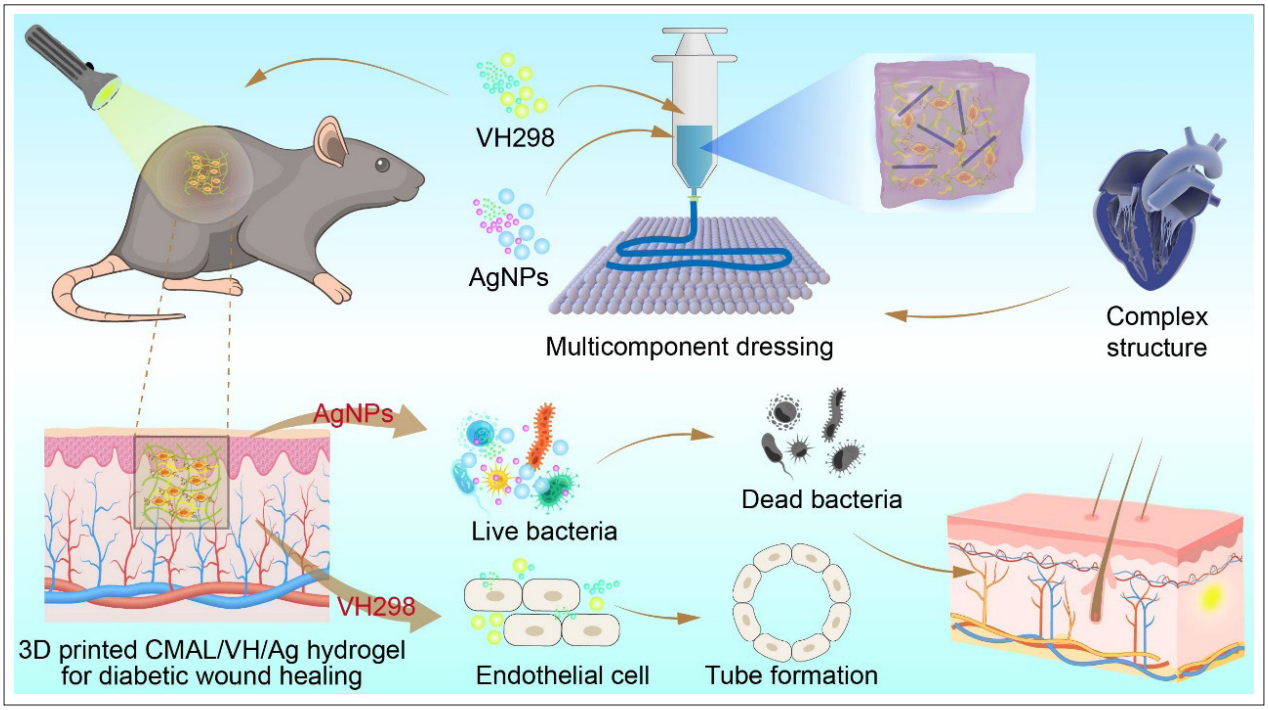


Figure 1. *In vivo* application of highly self-supporting chitosan-based hydrogel ink. The highly self-supporting chitosan-based hydrogel ink possesses a strong and rapidly reversible physical crosslinking network driven by dense weak electrostatic interactions and hydrogen bonds. This network facilitates a variety of high-fidelity direct 3D-printing processes, such as microtube fabrication and multicomponent or complex structure printing. Incorporating silver nanoparticles (AgNPs) and a hypoxia-inducible factor-1α (HIF-1α, VH298) stabilizer into the CMAL ink results in excellent therapeutic efficacy *in vivo*.

4. Printing modalities and architectures

Modality comparison. Extrusion bioprinting remains the workhorse for building centimeter-scale tissue constructs because it tolerates viscous, cell-dense bioinks, and supports multimaterial codeposition, though shear exposure during nozzle transit is a key limitation for delicate immune and stromal cells.[57] Inkjet (jetting) enables noncontact, high-throughput patterning with fine droplets but typically requires low-viscosity inks and offers limited cell loading.[58] Digital light processing (DLP/SLA) projects entire layers with rapid, high-resolution curing and is well-suited to architected microstructures, with attention to photoinitiator choice and dose to minimize phototoxicity.[59] Two-photon polymerization (TPP) pushes resolution into the submicrometer regime for microvasculature-like and lymphatic-scale features, at the cost of slower build rates.[60] Across platforms, coordinated multimaterial printing (e.g., structural ink + immune-modulatory ink) is increasingly used to spatially segregate mechanical support and immunological functions.[61] Immune-relevant trade-offs across printing modalities are compared in Table 3.

Architectural parameters and immune guidance. Porosity and pore size strongly condition innate immune set-points: precision-templated scaffolds with uniform ~40 μm pores reduce foreign-body reaction and increase vascular density relative to smaller or larger pores,[62] and large-pore additively manufactured PEEK implants used as nonbioprinted load-bearing scaffolds bias macrophages toward prohealing M2 polarization at the bone–implant interface, improving osteogenesis and angiogenesis.[63] In this context, PEEK is processed as a high-temperature, rigid implant material rather than as a cell-laden bioink, and the Yang *et al.* study is cited to illustrate how precisely controlled pore architecture in a structural frame can be leveraged in future hybrid systems where a soft, bioprinted hydrogel is integrated with a PEEK cage to decouple mechanical and immunological design spaces.[63-65] Anisotropy and surface alignment further steer leukocyte trafficking; aligned conductive polyurethane conduits enhance macrophage recruitment and M2 polarization, supporting peripheral nerve repair.[66] At the cell scale, shape/topography cues modulate macrophage phenotype independent of soluble cytokines, enabling "mechanotype-aware" immuno-instruction via ridge, pit, or fiber geometries.[67] Gradients of stiffness or ligand density (mechanical and biochemical) can serve as "immune taxis" to bias dendritic/macrophage migration and localization within printed tissues.[68] Architecture-level cues and immune effects are compiled in Table 4.

Table 2. Summary of reported bioinks.

Bioink (material)	Representative composition/variant	Crosslinking/curing	Key printability/biological notes & typical use	Refs.
Alginate	Alginate (various MW; M/G ratios)	Ionic (Ca^{2+}) ± secondary	Printability strongly depends on MW and M/G; tunable mechanics for extrusion	46
Gelatin methacryloyl (GelMA)	GelMA (various % solids)	Photopolymerization (UV/visible)	Cell-adhesive (RGD); widely used; supports neurogenesis/neuronal models	47
Hyaluronic acid (HAMA)	HAMA ± tissue-specific ECM blends	Photopolymerization	HA derivatives printable; HAMA+pECM supports islet applications	48
Collagen	Type I/II/III collagen inks; FRESH-compatible	pH/thermal; embedded (FRESH)	Native ECM protein; improved fidelity via embedded printing; broad TE use	49
Fibrin/Fibrinogen	Fibrinogen→Fibrin (± blends)	Enzymatic (thrombin); *in situ*	Biocompatible but soft; strategies include blends/support baths to boost fidelity	50
Decellularized ECM (dECM)	Organ-specific dECM inks	Thermal/enzymatic/photocuring (formulation-dependent)	High biomimicry; often low mechanics—blend/modify to improve printability	36
Chitosan (derivatives)	Methacrylated/phenol-modified chitosan	Visible–light radical (e.g., SPS/$Ru(bpy)_3$)	Works for extrusion & vat printing; antimicrobial/biodegradable hydrogels	51
Nanocellulose (NFC/CNF)	Nanocellulose–alginate blends	Ionic (Ca^{2+})	Good shape fidelity; supported chondrocytes and complex ear/meniscus prints	52
Gellan gum	Gellan gum ± laminin-peptide tethering	Ionic (Ca^{2+}) ± peptide tethering	Shear-thinning; peptide-tethered variants improve adhesion & mechanics	53
κ-Carrageenan	κ-Carrageenan (pristine or MA-modified)	Ionic/dual crosslinking or photo	Printable scaffolds with high water content; tunable 24–100 kPa modulus	54
Agarose (incl. carboxylated)	Carboxylated agarose (CA)	Thermal/photochemical (variant-dependent)	Free-standing, high-stiffness structures via microextrusion; good fidelity	55
PEG-based (synthetic)	PEGDA/PEGNB ± RGD/gelatin fragments	Photo-crosslinking (thiol-ene/MA)	Chemically defined; mechanics & bioactivity tunable; broad TE models	56

From an engineering standpoint, the spatial patterning of immune cues is ultimately constrained by the lateral and axial resolution of multimaterial bioprinting. Comparative analyses of bioprinting modalities indicate that continuous inkjet typically generates droplets on the order of ~100 μm, whereas drop-on-demand (DOD) inkjet can reproducibly form much smaller droplets (~20–50 μm), allowing different cell- or cytokine-laden inks to be placed side-by-side at tens-of-micrometer spacing.[69] Microfluidics-enabled maskless stereolithography (MMSLA) further improves discretization in light-based systems: by digitally switching between multiple photocurable bioinks, Miri *et al*. demonstrated voxel-wise patterning of several hydrogel compositions with inter-material interfaces registered within a single projected pixel (tens of micrometers in the x–y plane) while maintaining cell viability.[70] At the single-cell scale, Kim *et al*. used a 30-μm DOD inkjet nozzle to achieve "cell-level" deposition, with ~1–3 mammalian cells per droplet in 20 × 20 arrays, illustrating that immune cells, such as macrophages could in principle be patterned with ~30–60 μm center-to-center accuracy.[71] In contrast, extrusion-based multimaterial printheads remain limited by nozzle diameters and filament spreading, so that adjacent immune-modulatory strands typically have effective feature sizes in the 100–300 μm range for cell-laden hydrogels.[69] Collectively, these data suggest that current high-definition inkjet and light-assisted systems can already pattern distinct immune bioinks at length scales comparable to small clusters of immune cells (tens of micrometers), whereas replicating the full 3D hierarchy of larger immune niches (hundreds of micrometers) still requires combining printed architectures with subsequent cell self-organization and remodeling.

Vascular and lymphatic microstructures. Functional immunity in engineered tissues requires rapid perfusion and drainage. Extrusion with coaxial nozzles yields perfusable, branching channels that support endothelialization and flow,[72] while light-based μCOB/DLP prints prevascularized microarchitectures at high speed and fidelity.[73] Prevascularization strategies integrated into bioprinting improve inosculation and immunocompetence by shortening hypoxic/inflammatory windows postimplantation.[74] Beyond blood vessels, "lymph-mimetic" features are emerging: tumor-on-a-chip models with a bioprinted blood–lymphatic vessel pair recapitulate interstitial transport and drug

clearance, highlighting the role of blind-ended lymphatic channels in solute drainage.[75] New lymphatics-on-a-chip platforms demonstrate engineered lymphatic vessels capable of draining nanoparticles and modeling immune cell trafficking, offering templates for lymph-inclusive printed constructs.[76]

Inline quality control and print-path–immune coupling. Real-time, *in situ* monitoring is moving from aspiration to practice: embedded bioprinting systems with on-board imaging quantify strand fidelity and defects as they occur[77]; *in situ* photorheology reveals crosslinking kinetics and viscoelastic evolution during light-based printing, enabling dose-to-property control.[78] Frameworks that connect rheology/flow to viability now span experiments, analytics, and machine learning to predict printability and cell survival.[79,80] Crucially, nozzle shear and postdeposition flows are not only cytotoxic risks—they can shift macrophage programs toward inflammatory states, linking print path and extrusion conditions to downstream immune outcomes.[81,82] As such, interpretable models that map toolpath, speed, pressure, and exposure to cytokine readouts will be essential for designing "immune-competent" prints with reproducible host responses. To give these relationships quantitative context, microvalve-based extrusion studies that explicitly controlled nozzle wall shear report that maintaining average wall shear stresses below ~5 kPa preserves >90% stem cell viability, whereas stresses in the 5–10 kPa range cause modest losses and ≥10–20 kPa are associated with a steep decline in viability and proliferation.[83]

Table 3. Printing modalities: process constraints and immune considerations.

Modality	Typical ink properties	Cell viability (immune/stromal)	Immune-specific concerns	Typical feature resolution	Representative outcomes/notes	Refs.
Extrusion	Viscous, shear-thinning, cell-dense	Good for immune/stromal coprinting; shear stress is key	Nozzle shear & postflow can bias macrophages proinflammatory	≈ 50–500 μm (strand diameter / nozzle-limited)	Map toolpath/pressure to cytokine readouts	[57,81,82]
Inkjet (drop-on-demand)	Low-viscosity, low cell density	High patterning throughput; gentler shear	Limited cell loading; droplet impact on cells	≈ 20–100 μm (droplet-limited)	Useful for gradiented immunocues	[58]
DLP/SLA (light-based)	Photocurable, moderate viscosity	Layer-wide curing, high resolution	Photoinitiator dose–immune cell compatibility	≈ 10–50 μm (projected pixel-limited)	Architected microstructures for immune guidance	[59]
Two-photon polymerization (TPP)	Specialized resins; submicron	High precision; limited throughput	Long exposure; potential photostress	≈ 0.1–1 μm (hundreds of nm; sub-100 nm demonstrable)	Microvasculature/lymphatic-scale features	[60]
Multimaterial coordinated printing	Orthogonal inks in one build	Spatially segregate mechanical vs. immuno-functional inks	Cross-talk between inks; curing compatibility	Set by underlying modality (typically ≈ 10–500 μm; can reach sub-μm if TPP integrated)	Immune "hotspots" encoded in specific regions	[61]

Table 4. Architecture-guided immune modulation in printed constructs.

Architectural cue	Design parameter	Immune effect	Tissue/functional outcome	Notes	Refs.
Precision-templated porosity	Uniform ~40 μm pores	Reduced FBR; balanced myeloid influx	↑Vascular density; less fibrotic encapsulation	Size-dependent immune set-points	[62]
Large-pore PEEK scaffolds	Increased pore size/porosity	Bias toward M2-like macrophages	Improved osteogenesis & angiogenesis	Osteoimmunology link	[63]
Anisotropy/alignment	Aligned conduits/surfaces	Enhanced recruitment + M2 polarization	Better nerve repair outcomes	Conductive PU example	[66]
Micro/nano-topography	Ridges/pits/fibers	Mechanotype-dependent macrophage programming	Cytokine profile shift without soluble cues	Geometry as immune "language"	[67]
Stiffness/ligand gradients	Mechanical/biochemical gradients	"Immune taxis" of DCs/macrophages	Region-specific localization/function	Gradiented guidance in lattices	[68]

5. Engineering the immune microenvironment

Innate immune modulation. Sterile inflammation from DAMPs often converges on the NLRP3 inflammasome and complement—the two systems also intersect with coagulation at blood–material interfaces, amplifying thromboinflammation.[4,84,85] Surface strategies that recruit or present complement regulators (e.g., factor H–binding peptides) or use nanoscale topographies can curb alternative-pathway C3 activation and C5a generation, reducing leukocyte recruitment and clotting on implants.[4,85] Lactate signaling via the GPR81 axis can directly suppress TLR-primed NLRP3 activation and IL-1β release, suggesting a metabolite-based route to dampen early sterile inflammation in printed constructs.[84]

Adaptive immune modulation. Biomaterial delivery of tolerogenic cues can steer effector–regulatory balance. IL-10–functionalized PEG hydrogels support dendritic cells that drive $CD25^{+}FoxP3^{+}$ Treg induction, offering a materials handle to tilt responses away from Th1/Th17-dominant inflammation.[86] Localized release of TGF-β1 from microporous scaffolds reduces peri-implant cytokines and leukocyte infiltration and improves graft function, illustrating that protolerogenic cytokines can be embedded without blunting tissue integration.[87] Nanoparticles codelivering IL-2 and TGF-β to $CD4^{+}$ T cells expand functional Tregs *in vivo*, a concept readily translatable to bioink-compatible depot systems for printed grafts.[88]

Spatiotemporal "signal-release" modules. Sequential or gradiented cytokine delivery can choreograph the innate–adaptive handoff. IL-4–programmed release (alone or in IFN-γ→IL-4 sequences) polarizes macrophages toward pro-regenerative phenotypes that favor constructive remodeling around scaffolds.[89] Heparin-affinity hydrogels tuned for IL-4 sustain bioactivity and accelerate bone repair, underscoring the value of affinity-based temporal control.[38] Embedding TGF-β1 or IL-10 in defined depots within lattice architectures enables local tolerance while preserving peripheral immunity, a design principle for immune-competent bioprinted tissues.[86,87]

Immunometabolic targeting within constructs. Immune cell fate is metabolically gated; leveraging this in 3D bioprints adds a powerful, orthogonal control layer. Lactate accumulation can epigenetically reprogram macrophages via histone lysine lactylation to induce wound-healing gene programs, providing a rationale for lactate-releasing matrices in late repair phases.[90] Conversely, succinate stabilizes HIF-1α to boost IL-1β, so buffering or scavenging succinate around grafts may limit necroinflammatory loops.[91] Short-chain fatty acids (SCFAs), such as butyrate and propionate promote extrathymic Treg differentiation through histone deacetylase (HDAC) inhibition and G protein–coupled receptor (GPCR) signaling; incorporating SCFA reservoirs or SCFA-releasing promaterials into bioinks could couple metabolic and epigenetic tolerance at the host–graft interface.[92] Finally, material chemistry that modulates complement opsonization on particles/scaffolds can secondarily shape humoral immunity, offering routes to avoid unwanted B-cell activation and antibodies against the graft.[93]

Key takeaways for 3D bioprinting. Combining surface complement-control, Treg-skewing cytokine depots, and metabolite-guided reprogramming (lactate/SCFAs) yields immune-competent, yet quiet, niches that support integration and long-term function of printed tissues.[86,87,90,92]

6. Cells and immune-smart constructs

Immune-smart bioprinted constructs aim to actively shape host responses by coprinting or sequentially seeding immune cells and by embedding programmable cues that steer inflammation toward resolution and regeneration.[94] Coprinting macrophages, dendritic cells, NK, Treg, or B cells—together with stromal populations—enables spatiotemporal "training" of innate and adaptive immunity; in bone repair models, 3D-printed scaffolds that bias macrophages toward an M2-like phenotype enhance angiogenesis and tissue integration.[95,96]

Designing staged delivery (e.g., early CSF-1R inhibition to curb M1 activation, followed by proresolving cues) within printed architectures exemplifies how immune education can be scripted into the build plan.[95] Mesenchymal stromal cells (MSCs) are central "conductors" of this dialogue: they suppress antigen-presenting cell activity and induce IL-10–dominant programs via PGE2/IDO/TGF-β, thereby expanding Tregs and tempering Th1/Th17 responses.[97] Crucially, much of the MSC effect is paracrine; MSC-derived extracellular vesicles (MSC-EVs) reproduce immunomodulation with lower immunogenicity and are increasingly integrated into bioinks for cell-free yet immune-active constructs.[98] Recent analyses detail EV dosing, release kinetics, and cargo engineering (miRNAs, TGF-β/IL-10) compatible with extrusion and light-based printing workflows, supporting scalable incorporation into printed scaffolds.[98] Membrane cloaking offers another layer of immune stealth and targeting. Cell-membrane-coated nanoparticles and microgels—leveraging red blood cell, platelet, or leukocyte membranes—inherit "self" proteins (e.g., CD47) to reduce opsonization, complement activation, and phagocytic clearance, while enabling homotypic adhesion to inflamed or tumor endothelium.[99] Within regenerative settings, platelet-membrane coatings confer lesion homing via P-selectin/ICAM interactions and can be adapted to hemostatic or prorepair payloads,

a concept extensible to printable hydrogel carriers.[100] Broader overviews emphasize that membrane sources (RBC, platelet, neutrophil, macrophage) and hybrid coatings can be matched to indication-specific immune barriers, informing design libraries for "immunity-aware" bioinks.[101]

Finally, synthetic biology endows living components with on-demand immunoregulatory outputs. Engineered living materials equipped with CRISPRa/i or sensor-actuator circuits can sense inflammatory mediators or damage-associated signals and secrete immunomodulators (e.g., IL-10, TGF-β, CXCL12) accordingly, closing the loop between sensing and response *in situ*.[102] Programmable synthetic receptors—including synNotch and next-generation context-sensing designs—allow cells within printed constructs to decode microenvironmental cues and trigger tailored cytokine release or differentiation programs, improving safety and precision.[103] Cell- and signal-centric strategies for immune-competent constructs are outlined in Table 5. At the same time, these synthetic-biology–driven circuits generally depend on stable genome editing or vector integration in therapeutic cells, which introduces risks of off-target edits, large structural variants and insertional mutagenesis that require rigorous mapping and long-term follow-up before clinical use.[104] Recent work on engineered living materials further highlights the importance of controlling mutation, horizontal gene transfer, and ecological containment when living cells are embedded in macroscopic constructs.[105] Beyond technical issues, biomedical synthetic biology raises participant-safety, biosafety, and biosecurity concerns that demand dedicated governance frameworks extending beyond conventional biomaterials regulation.[106]

In sum, immune-smart constructs integrate (i) immune-cell coprinting and temporal "training," (ii) MSC/EV paracrine orchestration, (iii) membrane cloaking for immune evasion and targeting, and (iv) gene-circuit logic for closed-loop cytokine delivery—collectively advancing bioprinted tissues from passive grafts to active, immune-competent therapeutics.[94,97,99,102]

7. Applications and disease contexts

Skin and mucosa. Bioprinted, vascularized skin substitutes now integrate keratinocytes, fibroblasts and endothelium to accelerate re-epithelialization while supporting immune surveillance and angiogenesis.[107] Clinical priorities include infection control (e.g., antimicrobial bioinks) and scar immunobiology—shifting macrophage phenotypes and

Table 5. Cell- and signal-centric strategies to build immune-competent constructs.

Strategy	Implementation in bioprints	Primary immune target	Key result/readout	Application context	Refs.
Staged macrophage programming	Early CSF-1R inhibition → later IL-4 (or IFN-γ→IL-4 sequence) depots	M1→M2 transition; resolution	Reduced pro-inflammatory cytokines; pro-healing remodeling; early IFN-γ priming induces a transient M1 phase (debris clearance, angiogenic cue release), followed by IL-4-driven M2 transition that supports constructive tissue remodeling	Bone/soft-tissue repair	[89,95]
Treg-skewing cytokine depots	IL-10–functionalized PEG gels; localized TGF-β1 release	Tolerogenic DCs, $CD25^{+}FoxP3^{+}$ Tregs	↑Tregs, ↓Th1/Th17; improved graft function	Local immune tolerance near graft	[86,87]
MSC coprinting / paracrine orchestration	MSC-laden inks or postseeding	APC suppression; Treg expansion	IL-10/IDO/PGE2-mediated dampening	Broad regenerative contexts	[97]
MSC-EV–integrated bioinks	EVs embedded with controlled release	Low-immunogenic immunoregulation	Dose/release-controlled IL-10/TGF-β cargo effects	Cell-free immune-active constructs	[98]
Membrane cloaking (RBC/platelet/leukocyte)	Membrane-coated microgels/particles within constructs	Reduced opsonization/ complement; lesion homing	↓Complement activation; improved "self" signaling	Immune stealth & targeting	[99-101]
Synthetic biology circuits	Sensor–actuator cells (e.g., synNotch; engineered living materials) coprinted or embedded	On-demand cytokine secretion (IL-10/ TGF-β/CXCL12)	Closed-loop immunomodulation *in situ*	Adaptive, programmable grafts	[102,103]

TGF-β signaling to reduce hypertrophic scarring and fibrosis.[108]

Bone and cartilage. Inflammatory milieus (e.g., rheumatoid arthritis) uncouple osteoblast–osteoclast crosstalk, driving erosions, and systemic bone loss; osteoimmunology highlights TNF/IL-17–enhanced osteoclastogenesis as a dominant axis.[109] Bioprinted immunomodulatory scaffolds that cue macrophage polarization (spatiotemporal M1→M2 or pro-osteogenic subtypes) restore osteogenesis/chondrogenesis under inflammation and improve integration at the bone–implant interface.[110] Xingge Yu and colleagues developed a bioink based on a 10% gelatin methacryloyl (GelMA)/5% strontium-doped calcium silicate (Sr-CSH) nanocomposite hydrogel to encapsulate bone marrow mesenchymal stem cells (BMSCs), and used extrusion-based 3D bioprinting to fabricate biomimetic bone tissue for bone defect repair and regeneration[111] (Figure 2). In addition to sterile inflammatory conditions, infection-associated bone and periodontal defects require scaffolds that integrate antibacterial activity with immune modulation. For example, Guo *et al.* designed infection-sensitive 3D-printed PLGA scaffolds coated with superparamagnetic iron oxide nanoparticles (SPIONs), which resist bacterial adhesion, shift macrophages toward IL-10–producing M2 phenotypes, and enhance periodontal regeneration in a Porphyromonas gingivalis infection model.[112] Recent work by Qiao and colleagues reported composite poly(L-lactic acid) (PLLA)/Pearl scaffolds loaded with rifampicin- and moxifloxacin-PLGA microspheres; these 3D-printed constructs achieved local bacterial eradication and simultaneous bone defect repair in a rabbit infected bone defect model of the radius, illustrating how antibiotic delivery can be integrated into architected scaffolds for orthopedic infections.[113] Related studies on PLGA/Cu(I)@ZIF-8 nanocomposite scaffolds and broader reviews of antimicrobial, biodegradable 3D-printed scaffolds for orthopedic infections further highlight how scaffold chemistry, porosity, and degradation products can be tuned to couple anti-infective function with proregenerative immunological conditioning.[114,115]

Myocardium and vasculature. Postischemic repair demands time-staged control of immune clearance, neovascularization, and scar remodeling. Bioprinted

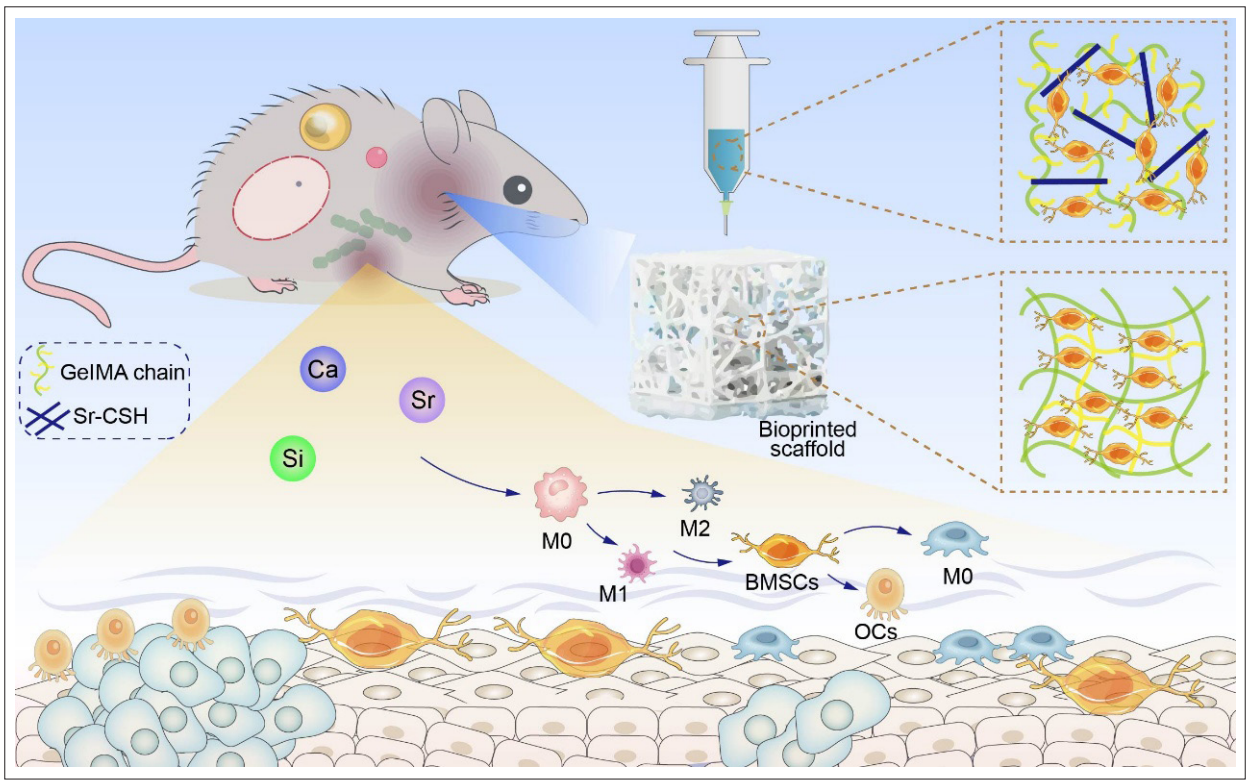


Figure 2. 3D bioprinting for constructing biomimetic bone tissue. A novel GelMA-Sr-CSH nanocomposite bioink improves printing precision and mechanical performance while exhibiting excellent biocompatibility. Sr-CSH induces macrophage M2 polarization: by releasing active ions, Sr-CSH modulates the inflammatory microenvironment and promotes the osteogenic differentiation of BMSCs. 3D-bioprinted scaffolds achieve complete bone repair: in a rat model, GelMA-Sr-CSH bioink scaffolds loaded with BMSCs demonstrated superior bone regeneration capacity.

cardiac patches combining aligned cardiomyocytes with conductive/vasculogenic architectures improve perfusion and electromechanical coupling.[116] Parallel work maps innate/adaptive responses to bioprinting biomaterials, guiding choices that limit FBR, fibrosis, and thrombosis after epicardial implantation.[117]

Liver/kidney/gut models for pharma–toxicology and immune safety. Humanized 3D liver models (e.g., hiHep-based or xeno-free hepatocyte cocultures) improve CYP activity, bile acid handling, and detection of drug-induced liver injury (DILI)phenotypes relevant to cholestasis and idiosyncrasy.[118,119] Bioprinted proximal tubule tissues with endothelial–interstitial compartments capture transporter-dependent nephrotoxicity and fibrotic responses for hazard identification.[120] Immunocompetent intestine-on-chip and bioprinted intestinal tissues enable mucosal barrier, microbiota interaction, and cytokine readouts for complement/inflammation risk assessment.[121,122]

Obstetrics and gynecology. For endometrial injury and Asherman's syndrome, bioactive, cell-laden scaffolds (e.g., hMSC-printed constructs) enhance vascularization and immunomodulation, supporting glandular regeneration, and antifibrotic remodeling.[123] Pelvic floor/perineal reconstruction leverages mechanically robust, biocompatible meshes, and emerging bioprinted muscle/tendon constructs, with attention to chronic inflammation and foreign-body responses.[124] Bioprinted placental organoids and maternal–fetal interface models incorporate trophoblasts, endothelial and immune cells to probe tolerance, complement activation, and drug safety in a physiologic context.[125]

Tumor-margin regeneration. After oncologic resection, multifunctional 3D scaffolds can couple tissue regeneration with local chemo-/immunotherapy to suppress recurrence while supporting prohealing immunity.[126] In parallel, bioprinted tumor microenvironments with stromal and immune compartments serve as prescreening platforms for surveillance, checkpoint response, and relapse biology at the resection edge.[127] Schematic of an implantable 3D-printed hydrogel that delivers local chemotherapy and self-amplifying immunomodulation at the resection bed, illustrating immune-cell recruitment, controlled drug release, and suppression of postsurgical tumor recurrence *in vivo* (Figure 3).

Together, these scenarios position 3D bioprinting not only as "structure reconstruction," but as a platform for **immune-competent** regeneration and drug testing across dermatologic, musculoskeletal, cardiovascular, hepatic–renal–intestinal, reproductive, and oncologic indications.

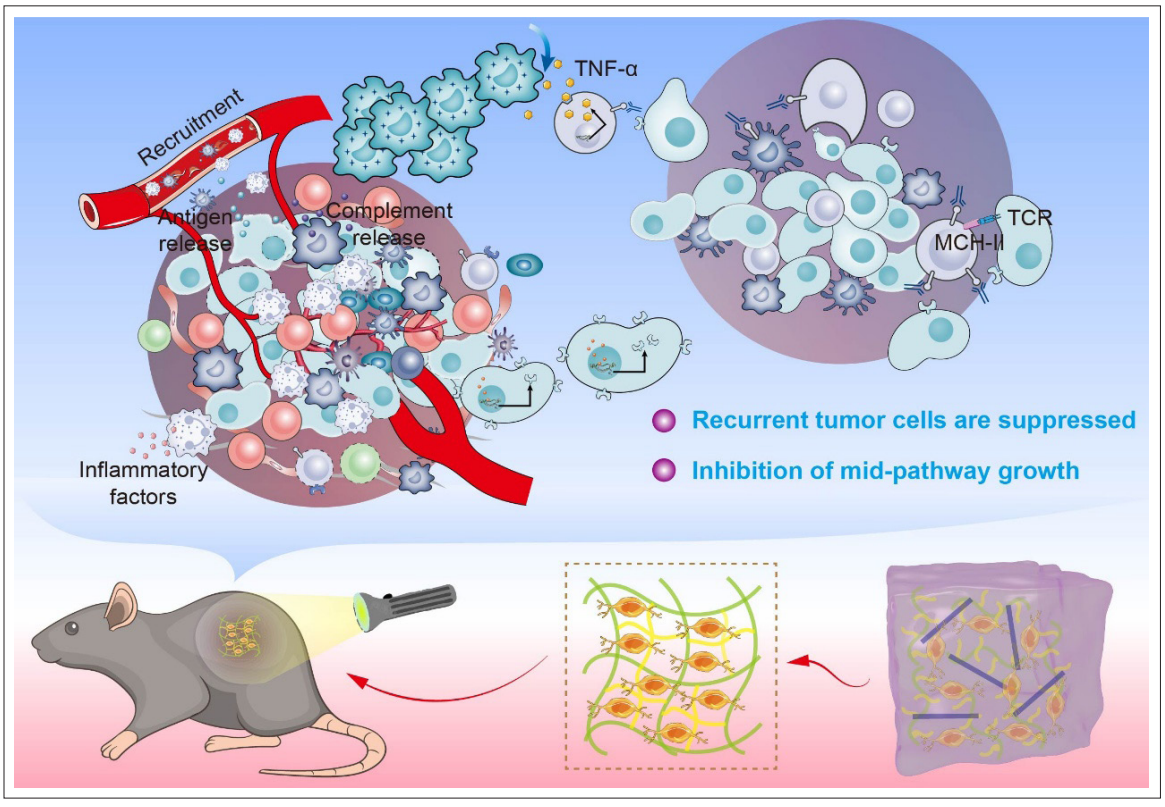


Figure 3. *In vivo* antitumor application of 3D-printed hydrogels.

8. Pharmacology, efficacy, and immunotoxicity

Immunocompetent organoids and microtissues now enable mechanism-aware pharmacology for immunotherapies by preserving native lymphoid components and physical barriers that dictate drug penetration and cell–cell interactions.[128] Patient-derived, T-cell–retaining tumor organoids capture antigen-specific cytotoxicity and allow assessment of small-molecule and biologic combinations in the context of endogenous T cells, offering a more faithful readout than cytotoxicity assays alone.[129] Notably, patient-derived glioblastoma organoids cotreated with autologous CAR-T cells mirrored clinical pharmacodynamics, including target loss, cytolysis, and cytokine signatures that correlated with patient cerebrospinal fluid profiles, supporting their utility for efficacy ranking and cytokine-release–related risk evaluation.[130] Across the evidence map synthesized in this review, only a minority of bioprinting-based immune-modulation strategies are currently supported by human clinical data (Levels 1–2), such as early trials of bioprinted skin substitutes and tumor resection guides. By contrast, most examples remain at the stage of controlled animal models (Level 3) or *in vitro*/*ex vivo* mechanistic work (Levels 4–5). We therefore report the highest OCEBM-derived evidence level supporting each key conclusion and treat lower-level data as mechanistic reinforcement rather than definitive proof.[16]

Conceptual view of 3D-printed organoids in which living cells and bioinks are assembled layer-by-layer to create perfusable, physiologically relevant mini-organs that retain immune components for efficacy and immunotoxicity testing (Figure 4). Multimodal analytics strengthen these platforms. High-content, live 3D imaging frameworks such as BEHAV3D classify engineered T-cell behaviors and link them to tumor organoid death dynamics, enabling quantitative mode-of-action mapping and early detection of inefficient infiltration or synapse formation.[131] A standardized protocol further operationalizes this approach for reproducible screening across donors and products.[132] Single-cell and spatial transcriptomics reveal how cellular composition and spatial organization steer immunotherapy response, supplying biomarkers for pharmacodynamic (PD) stratification and resistance mapping.[133] Complementarily, immunometabolomics exposes metabolic bottlenecks in CAR-T and tumor-infiltrating T cells—such as nutrient competition and inhibitory metabolites—that blunt efficacy and can be leveraged to guide combination strategies.[134,135] Together,

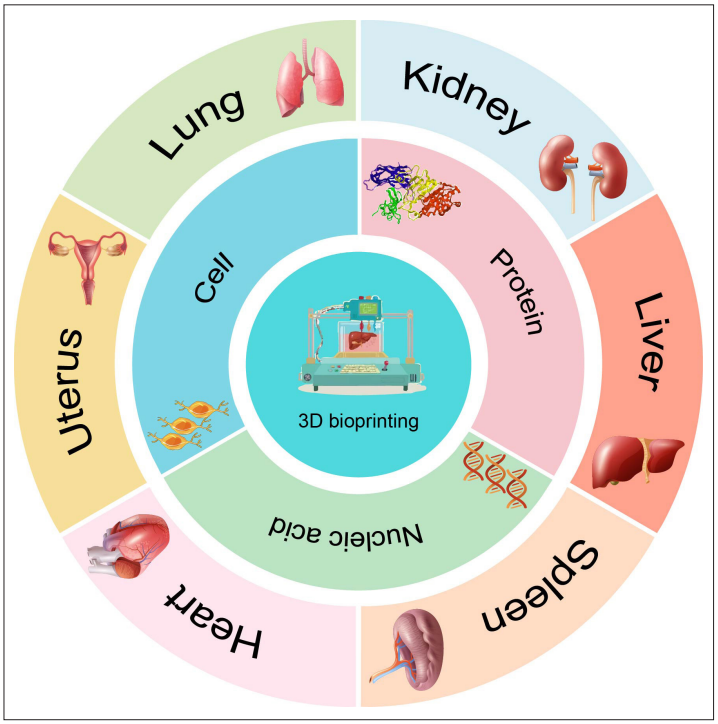


Figure 4. 3D-printed organoids. Biological 3D printing is a technology that uses 3D printing to construct biologically active tissues or organs. Through bio-3D printing, living cells (such as stem cells or primary cells) and biocompatible materials (bioinks) are assembled layer by layer to form miniature organ models with 3D structures and physiological functions. The core of this technology lies in seeding living cells into scaffolds, allowing them to grow *in vitro* and ultimately form functional tissues.

these readouts create an integrated pharmacology stack that couples behavior, transcriptional state, spatial context, and metabolism to actionable PD endpoints.

To reduce animal use while improving human predictivity, organ-on-chip (OoC) and organoid-on-chip (OrgOC) systems provide controlled perfusion, immune–stromal crosstalk, and multiorgan coupling for absorption, distribution, metabolism, and excretion (ADME)-tox, efficacy, and immunotoxicity testing.[136] OrgOC frameworks fuse organoids with microfluidics to maintain tissue fidelity under flow and support patient-specific testing; they are increasingly positioned for precision medicine applications and cross-donor "bioequivalence-like" comparisons.[137,138] Crucially, coupling OoC outputs to physiologically based pharmacokinetic (PBPK) models enables PK/PD translation, scenario testing (dose, schedule, route), and in silico sensitivity analyses that anticipate off-target exposure and cytokine-storm liabilities.[139] In practice, an integrated print–organoid–chip pipeline can expose 3D constructs (including immune-competent tissues) to candidate therapies under human-relevant flow and barrier conditions, while multiomics and imaging deliver PD fingerprints aligned to modeled exposure, supporting go/no-go and combination design with improved external validity.[136,137]

Organoids and organoids-on-chip are increasingly adopted in traditional Chinese medicine (TCM) research to dissect efficacy, mechanisms, and toxicity of multicomponent formulations while preserving human-relevant tissue architecture and immune context.[140] Hepatic organoid-based high-content imaging has differentiated stereoisomer-dependent hepatotoxicity of stilbene glucosides from Polygonum multiflorum (He Shou Wu), offering a predictive platform for herb-induced liver injury and early de-risking of candidate preparations.[141] Complementarily, recent studies show raw versus processed P. multiflorum exhibit distinct hepatotoxicity with a ferroptosis signature, underscoring how processing alters safety profiles that can be quantified on organoid/OoC pipelines.[142] On the immunopharmacology side, flavonoids from Scutellaria, such as baicalin and baicalein attenuate inflammasome-driven inflammation—baicalin inhibits NLRP3 activation in macrophages, and baicalein suppresses NLRP3/AIM2 assembly and pyroptosis—providing tractable readouts for cytokine kinetics and myeloid programming in immunocompetent organoids,[143,144] Astragaloside IV modulates tumor-associated macrophage polarization and suppresses protumor M2 programs, a mechanism that can be ranked in patient-derived tumor organoids retaining endogenous T cells and myeloid cells to couple efficacy with immunotoxicity screening.[145] Together, integrating TCM compound libraries with printed organoids/OoCs and single-cell/spatial analytics can rationalize multitarget actions while flagging herb-specific immunotoxic liabilities for translation.[140,141]

Building on these platforms, we propose a unified "immune-competency" readout panel for preclinical testing of 3D-bioprinted grafts.[25,26,146] As a minimal set, studies should report (i) acute innate activation, including complement split products and, where appropriate, neutrophil recruitment, and NETosis markers; (ii) quantitative spectra of macrophage and dendritic-cell phenotypes (e.g., M1/M2-like indices, antigen-presenting capacity, and secretion of IL-1β, TNF-α, IL-10, and TGF-β); (iii) adaptive immune activation versus tolerance, including effector/Treg ratios, exhaustion markers, and antigen-specific responses; and (iv) histological or imaging-based features of vascularization, matrix remodeling, and fibrotic encapsulation. Normalizing these measurements to application-appropriate controls and combining them into organ- or indication-specific immune-competency indices would facilitate cross-study comparison and benchmarking of printed constructs. Importantly, such scorecards can be harmonized with established osteoimmunomodulatory and foreign-body-response assessment frameworks, providing a practical path to standardizing how constructive versus pathological host responses to biomaterials are quantified.

9. Limitations and challenges

A central, practical barrier is unrecognized immunogenic impurities and batch variability in commonly used bioinks and scaffolds. Endotoxin contamination of polymers and metals is frequent and can confound *in vitro* readouts and *in vivo* host responses unless rigorously quantified and removed, yet many studies do not report limulus amebocyte lysate testing or surface-bound endotoxin controls.[31] For dECM inks, incomplete cell removal and altered matrix composition vary with tissue source and protocol, driving heterogeneous immune activation and remodeling outcomes across lots.[30] Batch-to-batch biochemical differences in dECM bioinks remain a nontrivial source of experimental variability and translational risk that is often underappreciated at the design stage.[147]

Processing steps that enable printing can themselves prime inflammation. Terminal sterilization alters mechanics, swelling, and even printability of hydrogels: ethylene oxide or autoclaving can reduce stiffness or cell viability in GelMA constructs, whereas γ-irradiation may increase stiffness but impair sol–gel transition and degrade print performance.[148-150] Photopolymerization adds another layer of risk: commonly used photoinitiators

and UV/visible light doses exhibit cell-type-dependent cytotoxicity and can generate residual radicals if conversion is incomplete, with Irgacure 2959 generally more toxic than LAP at equivalent concentrations [151,152]. In practical terms, shorter-wavelength UV systems (~365–405 nm) support high theoretical feature resolution but often yield relatively shallow penetration in cell-dense, scattering hydrogels, so that achieving full-depth cure may require higher doses that increase phototoxic and immunotoxic risk. By contrast, visible–light initiation (~405–450 nm) combined with appropriately tuned initiator chemistry can provide deeper, more homogeneous curing at lower photon energy, which is advantageous for preserving viability and function of professional immune cells in thick constructs, albeit sometimes at a modest cost in achievable voxel resolution. Without reporting of light spectrum, dose, initiator concentration, and postcure washing, reproducibility and immune safety are difficult to evaluate across studies.[151]

Beyond impurities and processing-induced epitopes, a fundamental constraint in immune-instructive 3D bioprinting is the "printability window" in which sufficient viscosity, yield stress and crosslinking are achieved for strand stability and shape fidelity, without imposing excessive shear stress or over-stiffening that compromise cell viability and ECM-encoded bioactivity. Increasing polymer content and crosslinking density improves filament stability but typically requires higher extrusion pressures and produces stiffer networks, which can damage cells, denature growth factors, and alter mechano-immunological signaling, whereas overly dilute inks preserve native ligands yet collapse under their own weight.[79,153,154] For ECM- and especially dECM-based bioinks, recent design strategies aim to decouple printability from biochemical content by blending dECM with rheology-modifying but relatively inert carriers (e.g., gelatin, alginate, gellan gum, silk), optimizing the degree of enzymatic digestion, and using interpenetrating or double-network architectures so that mechanical support is provided by a secondary network while dECM concentration remains high enough to retain glycosaminoglycans and matricellular proteins.[36,155,156] In parallel, embedded and granular printing approaches—including support-bath/FRESH methods and jammed microgel or microparticle bioinks—allow very soft, highly bioactive matrices to be printed within a mechanically supporting phase, thereby achieving high shape fidelity while keeping local stiffness and shear stresses low.[157,158] Finally, fragile immunomodulatory signals such as cytokines, chemokines, or exosomes can be protected during printing by affinity-based hydrogels (e.g., heparin-containing matrices) or nano/microparticle carriers, which shield bioactive factors from thermal, photochemical, and shear damage and enable controlled release that favors proregenerative macrophage and lymphocyte responses.[38,159] Together, these strategies illustrate how rheological tuning, printing mode, and factor-delivery design can be combined to balance printability with preservation of native ECM bioactivity and immunocompatibility in dECM-rich bioinks.

Printing physics also modulate immunity in ways that are still being systematized. Extrusion shear and nozzle geometry can push macrophages toward a proinflammatory phenotype, with downstream effects on endothelial barriers and fibrosis, implying that shear history is an immunomodulatory variable—not just a fabrication parameter.[160] Fluid-dynamics modeling and controlled bioprinting experiments indicate that, under typical nozzle diameters of 200–400 μm and shear-thinning hydrogel bioinks, calculated wall shear stresses commonly fall in the low-to-mid-kPa range, and conditions that exceed ~10 kPa coincide with marked drops in cell viability and function.[83] Beyond cell stress, architecture matters: precision-templated scaffolds with ~40-μm interconnected pores reduce chronic inflammation/foreign-body reaction compared with larger or smaller pores, highlighting a narrow structural "safe window" for host integration.[62] Relatedly, appropriately sized pores in 3D-printed PEEK implants fabricated by high-temperature additive manufacturing (nonbioprinted) promote macrophage M1→M2 transition and better osseointegration at load-bearing interfaces, but effects are material- and context-dependent, complicating generalization across platforms.[63] These rigid PEEK devices are widely used as structural spinal and orthopedic implants rather than as bioinks, yet they provide a useful paradigm for how pore metrics in a supporting frame could be codesigned with bioprinted, cell-laden hydrogels to program peri-implant immune responses.[63,64] These data argue for reporting shear rates, dwell times, and pore metrics alongside standard biological endpoints to interpret immune outcomes credibly.[62]

For constructs that contact blood, complement–coagulation crosstalk and the adsorbed protein corona remain under-tested liabilities. Surfaces and nanoparticles can activate complement via classical or alternative pathways (e.g., through C1q-mediated binding), recruiting platelets and leukocytes and amplifying thromboinflammation under flow.[4,161,162] Even when tested, complement analytics are prone to preanalytical and assay pitfalls that yield false activation signals or mask true ones, confounding risk assessment and comparability across labs[163] Routine hemocompatibility testing under physiologic shear, with pathway-specific complement readouts and anticoagulant controls, is still not standard in many bioprinting studies.[162]

Finally, preclinical translation is constrained by model choice and manufacturing control. Rodent inflammatory programs frequently diverge from humans, while humanized mice correct only part of the gap; contradictory meta-analyses mean that immune findings in small animals demand careful human validation before clinical claims.[164,165] On the manufacturing side, regulators continue to grapple with how to classify and control living, patient-specific printed products as advanced therapy medicinal products and to define robust release criteria and comparability requirements for multicomponent constructs.[166,167] Translating immunomodulatory bioprinted grafts from bench to bedside will therefore likely require adopting pharmaceutical Quality-by-Design (QbD) and process analytical technology (PAT) principles to explicitly link critical material attributes (e.g., bioink rheology, crosslink density, encapsulated-cell dose) and critical process parameters (e.g., extrusion pressure and temperature, light dose, culture duration) to immunological critical quality attributes, such as defined cytokine set-points, macrophage polarization profiles, or antigen-specific tolerance markers.[168,169] Recent work in regenerative medicine manufacturing illustrates how sensor technologies and robotics-driven production lines can be combined into closed, automated workflows with in-line imaging, electrical, or optical readouts to support nondestructive, real-time assessment of constructs and enable scalable, GMP-compatible bioprocessing for living implants.[170,171] In parallel, standardized biocompatibility and immunotoxicity test batteries inspired by ISO 10993 "Big Three" panels (cytotoxicity, sensitization, and irritation) are being refined for medical devices and provide a starting point for developing dedicated assays tailored to bioprinted, cell-laden constructs.[172] Although *in-situ* monitoring (e.g., ultrasound- or fluorescence-based process analytics) is emerging to detect defects and heterogeneity in real time,[138,139], such tools are not yet widely integrated into bioprinting platforms operating under full GMP control, and harmonized reporting of process and quality-control metrics will be essential for cross-study comparability and regulatory approval.[166,170] Collectively, these practical hurdles—contaminants, processing-induced bioeffects, architecture–immunity coupling, hemocompatibility pitfalls, model limitations, and immature process controls—define the near-term bottlenecks for immune-competent bioprinting and should be addressed explicitly in study design and reporting.[166]

Engineered cell reinfusion, immunogenicity, and genetic drift. For immune-programmed bioprinted constructs that incorporate gene-edited immune or stromal cells (e.g., CAR-T/Treg or sensor–effector mesenchymal stromal cells), reinfusion, or transplantation of long-lived engineered cells introduces specific safety and regulatory challenges beyond those of degradable scaffolds.[173] Genome editing and integrating viral vectors can generate off-target mutations, chromosomal rearrangements and high-copy insertions that favor clonal outgrowth, as illustrated by case reports and integration-site analyses in CAR-T trials.[104,174,175] Regulators therefore require extensive release testing (vector copy number, karyotyping, insertion-site mapping), GMP-compliant manufacturing and long-term pharmacovigilance registries for cell and gene therapies, and similar requirements are likely to apply to synthetic-biology-enhanced bioprinted products.[173] Immunogenicity is an additional bottleneck: patients may mount antibody and T-cell responses against nonhuman gene-editing components, CAR constructs or synthetic receptors, which can drive cytokine release, loss of persistence, or loss of efficacy upon repeat dosing.[104,176] Mitigation strategies under active investigation include humanized or fully human receptor designs, hypoimmunogenic Cas variants and reducing the exposure window by using mRNA or ribonucleoprotein delivery rather than integrating vectors.[104,176] Finally, engineered cells residing within 3D-printed tissues may undergo phenotypic drift and accumulate genetic or epigenetic changes under chronic inflammatory or regenerative selection, making serial sampling, single-cell multiomics and functional assays essential to monitor genetic drift and to define stopping rules for long-term follow-up.[173,177] Taken together, these considerations suggest that early synthetic-biology-enabled bioprinted constructs should follow stepwise implementation pathways aligned with existing advanced-therapy medicinal product and cell/gene-therapy guidance, rather than entirely novel regulatory routes.[173]

In addition to these practical constraints, the literature underpinning this review is inherently heterogeneous. The included studies span diverse bioprinting modalities, scaffold chemistries, cell sources and species, implantation sites, and immune readouts, with inconsistent reporting of effect sizes and variance. As a result, we did not attempt formal meta-analysis, statistical heterogeneity metrics, or funnel-plot-based publication-bias tests; instead, we synthesized evidence qualitatively, emphasizing convergent trends across independent platforms and explicitly noting where findings are supported by single studies or remain contradictory. Moreover, the preclinical field is likely affected by selective reporting and a bias toward positive immune outcomes, which should be taken into account when extrapolating to clinical translation. Future evidence-based biomaterials and bioprinting reviews with pre-registered protocols, standardized immune outcome sets, and sufficient homogeneity within narrowly defined

questions will be needed to support rigorous quantitative heterogeneity and publication-bias assessment.

10. Outlooks

Four-dimensional (4D) bioprinting adds the time dimension to 3D constructs by combining stimuli-responsive biomaterials, cell-generated forces, and programmed degradation so that shape, stiffness, and factor release evolve *in vivo*. Recent reviews highlight classes of 4D architectures highly relevant to immune modulation: shape-morphing scaffolds that can be delivered minimally invasively and then deploy to restore anatomical defects; hydrogels that stiffen or soften in response to enzymes, pH, or reactive oxygen species characteristic of inflamed tissue; and constructs whose porosity and ligand display change over time to gradually shift macrophage and T-cell phenotypes from inflammatory to regulatory states.[178-180] For programmed immune modulation, these systems enable temporal separation of functions—for example, early burst release of anti-inflammatory or tolerogenic cues to dampen acute damage, followed by slower presentation of proregenerative growth factors and, finally, late-stage signals that promote tissue-resident memory without chronic activation. Translationally, 4D bioprinting raises specific regulatory questions on how to characterize time-dependent deformation and release under clinically relevant stimuli, how to guarantee long-term predictability of actuation, and how to integrate mechanical and immune endpoints into good-laboratory-practice test batteries. Current regulatory science is beginning to address these issues, suggesting that the most realistic near-term path will be relatively simple, mechanically robust 4D functions with clearly demonstrable clinical benefits, such as reduced re-operation rates or improved graft integration.[178,179] In practice, 4D immune-instructive constructs are designed by first specifying the target initial and final configurations of the scaffold, then mapping the stimulus type and dose (e.g., temperature, pH, enzymatic activity, magnetic field) to spatiotemporal changes in modulus, crosslink density, and ligand exposure that can be predicted by finite-element and multiphysics models.[178,181] For immunomodulatory applications, design variables, such as stimulus threshold, actuation kinetics, and sequence of epitope/ligand unveiling can be explicitly linked to quantitative readouts including macrophage M1/M2 ratios, dendritic-cell maturation markers, and cytokine trajectories, allowing 4D printing to be framed as an optimization problem over dynamic immune responses rather than static morphology alone.[178,181]

AI-assisted design and digital twins provide a complementary layer for de-risking complex immunomodulatory constructs before they enter the clinic (Figure 5). At the preclinical stage, supervised and reinforcement-learning models can link bioink composition, rheology, and toolpath parameters to print fidelity, cell viability, and early immune readouts, thereby

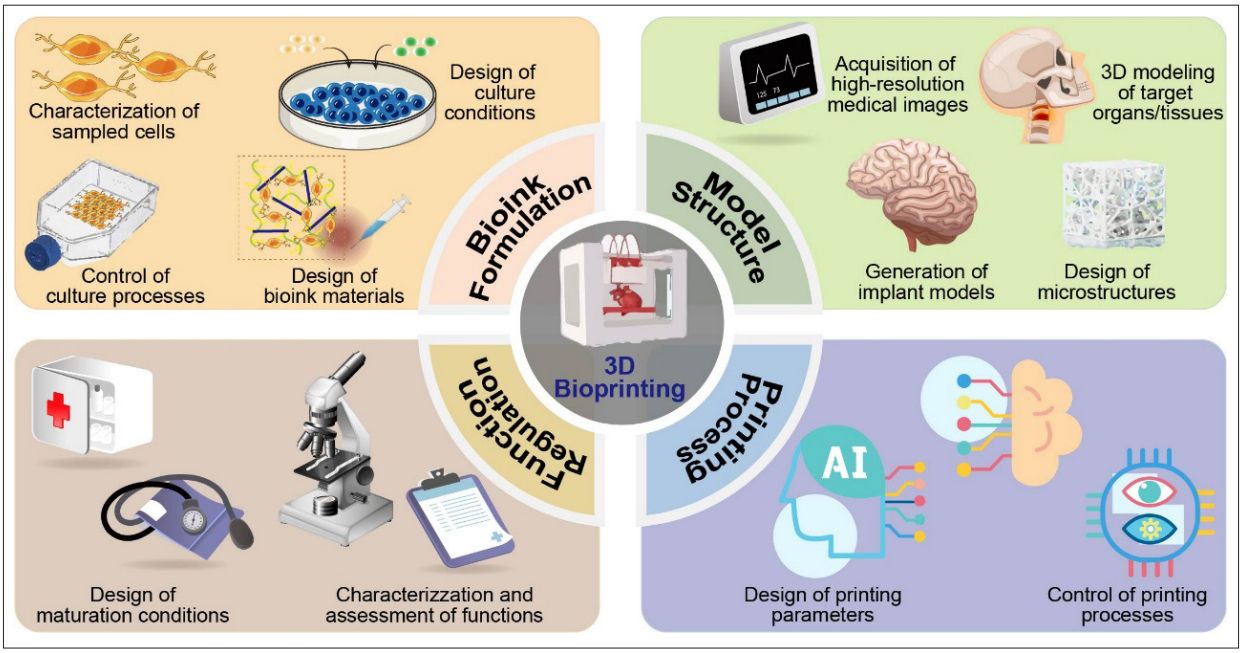


Figure 5. Schematic illustration of the integration between 3D bioprinting and artificial intelligence (AI) technologies.

shrinking the design space and enabling quality-by-design workflows for 3D and 4D bioprinting.[182,183] More recent frameworks couple patient-specific imaging, multiomics, and biomechanical simulations into "bioprinting digital twins" that simulate how a printed graft will deform, vascularize, and interact with the host immune system over months, allowing virtual testing of multiple designs and dosing schedules before first-in-human trials.[183,184] In our conceptual roadmap, such AI-guided and model-based tools are not merely add-ons but core components of the clinical translation pathway: they support automated in-line quality control during manufacturing, stratify patients according to predicted benefit–risk profiles, and generate the quantitative evidence needed for regulators to evaluate long-term safety and performance of immune-programmed bioprinted products.[182,184] Recent work has shown that machine-learning models can map topographical and physicochemical descriptors of biomaterial surfaces—such as multiscale roughness, skewness, contact angle, and surface energy—to quantitative macrophage polarization indices and cytokine ratios (e.g., IL-10/TNF-α), offering a concrete example of how high-dimensional design variables can be linked to immune readouts.[185] Analogously, AI-guided design of hydrogels and other soft biomaterials increasingly encodes polymer chemistry, crosslinker content, mesh size, and degradation constants as model inputs and predicts cell viability, inflammatory mediator release, and tissue-integration scores as outputs, providing a template for multiobjective optimization of "materials–structure–immune" performance in 3D/4D bioprinted constructs.[185]

In-body and on-body bioprinting will shorten the distance from CAD to care, with handheld or robotic systems depositing cell-laden bioinks directly onto wounds or organ surfaces to better match native curvature and mechanics.[186] After implantation, closed-loop constructs that sense local biomarkers (e.g., IL-6, TNF-α, pH) and trigger on-demand drug release can maintain immune homeostasis and prevent flares.[187] Experience from glucose-sensing, implantable biosensors underscores materials challenges (biofouling, drift, stability) and control algorithms needed for safe, autonomous immunotherapy—knowledge that can be ported to immune-responsive implants.[188]

Microbe–metabolite coengineering offers a powerful axis for immunometabolic reprogramming of printed grafts. Short-chain fatty acids (SCFAs) modulate barrier integrity, Treg induction, and inflammasome activity; embedding SCFA-releasing depots or prebiotic niches into bioinks could bias local immunity toward tolerance and repair.[189,190] Bile-acid signaling via FXR and TGR5 shapes innate and adaptive responses and is perturbed by dysbiosis; printing scaffolds that tune bile-acid gradients or present BAR-targeted ligands may rebalance Th17/Treg and macrophage states at tissue-device interfaces.[191] Together, metabolite-aware bioinks move beyond passive scaffolding toward active, immune-smart microenvironments.[191]

Finally, synthetic-immunology-enabled living constructs point to "programmable biologic drugs" embedded within printed tissues. Engineered immune cells with sensor–effector circuits (e.g., synNotch) can detect pathological cues and secrete IL-10, GM-CSF, or checkpoint modulators on demand, enabling local, titratable therapy with reduced systemic exposure.[192] In parallel, engineered-living-materials strategies use hydrogel containment to host therapeutic microbes with defined sensing-secretion programs, offering manufacturable, biocontained "living dressings" for chronic wounds or mucosal repair.[193] Integrating these cells with 4D, AI-optimized architectures could deliver self-tuning grafts that learn and adapt to patient-specific immune dynamics.[192,193]

Realizing these visions will require dedicated industry–academia–regulator consortia that treat immuno-active bioprinted products as a distinct class of advanced therapies rather than isolated case-by-case prototypes. Building on public–private partnership models already established for additive manufacturing and biomanufacturing (e.g., BioFabUSA/ARMI and NIIMBL), such alliances can align academic centers (mechanistic immunology, bioink discovery, *in vitro*/*in vivo* immune modeling), industrial partners (GMP bioink and printer platforms, scalable workflows, process analytical technologies), and regulatory agencies (definition of reference materials, immune potency assays, and critical quality attributes for batch release and change control) around shared translational roadmaps.[194] Within these consortia, regulatory-science innovations could include Quality-by-Design-based "platform" approvals for families of related scaffold architectures, regulatory sandboxes for AI-assisted design tools and immune digital twins, and the structured use of in silico virtual patient cohorts to complement preclinical and clinical data in benefit–risk assessment, thereby accelerating safe bench-to-bedside translation while maintaining rigorous oversight.[194-196]

11. Conclusion

3D bioprinting is reshaping regenerative medicine by coupling architectural precision with intentional immune modulation. The central lesson emerging across applications is that structure alone rarely ensures function; durable regeneration depends on orchestrating the early inflammatory cascade, guiding innate–adaptive crosstalk, and fostering tissue-specific tolerance. A "structure +

immunity" dual objective reframes design criteria: bioinks, architectures, and embedded payloads must be selected not only for mechanical fidelity and cell viability, but also for their capacity to dampen foreign body reactions, polarize macrophages toward proregenerative states, calibrate complement/coagulation interfaces, and ultimately support vascular and lymphatic integration.

This dual objective also changes how success is measured. Beyond histology and biomechanics, critical quality attributes should include immune kinetics (cytokine dynamics, complement activity), spatial phenotypes (myeloid and T cell distributions), and durability of immune homeostasis. Platforms that are "immune-competent by design"—whether through dECM-based inks, responsive release of immunoregulatory cues, or coprinted immune cells—offer realistic paths to reduce chronic fibrosis, improve graft take, and accelerate functional recovery.

Translationally, the roadmaps are clearer: quality-by-design frameworks, standardized immune assays, and modular release testing can align manufacturing with clinical endpoints. Digital design loops—AI-assisted material selection, multiphysics printing simulators, and data-driven immune prediction—will shorten iteration cycles and improve reproducibility. In parallel, 4D bioprinting, *in situ* printing, and closed-loop constructs that sense inflammatory mediators and respond with on-demand payloads can move the field from static implants to adaptive therapies. From a translational standpoint, embedding QbD- and PAT-informed control strategies together with robotics-assisted, closed bioprocessing platforms into bioprinting workflows will be as critical as innovations in bioink chemistry for delivering reproducible, regulator-ready immune-modulating constructs at clinical scale.[168,169,171]

Key challenges remain—long-term immune surveillance, patient-to-patient immune heterogeneity, scale-up under GMP, and cost/access—but they are tractable with coordinated standards, shared datasets, and early engagement with regulators. Ethically, longitudinal monitoring and transparent risk–benefit communication are essential as constructs become "living medicines."

In sum, the decisive gains in clinical translation will come from designs that treat immunity as a primary design variable rather than a downstream constraint. Achieving this requires tight collaboration among immunologists, bioengineers, clinicians, and regulators. When structure and immunity are co-optimized from the outset, 3D bioprinting can deliver not just repaired tissues, but resilient, self-maintaining organ function.

Acknowledgments

None.

Funding

None.

Conflict of interest

The authors declare they have no competing interests.

Author contributions

Conceptualization: Yao Yao, Fujia Ren, Fangtian Bu
Writing–original draft: Jianfeng Zhang, Mengmeng Li, Yao Yao, Fujia Ren
Writing–review & editing: Jianfeng Zhang, Mengmeng Li, Yao Yao, Fujia Ren

Ethics approval and consent to participate

Not applicable.

Consent for publication

Not applicable.

Availability of data

Not applicable.

References

1 Anderson JM, Rodriguez A, Chang DT. Foreign body reaction to biomaterials. *Semin Immunol.* 2008;20(2):86-100. doi: 10.1016/j.smim.2007.11.004

2 Carnicer-Lombarte A, Chen ST, Malliaras GG, Barone DG. Foreign body reaction to implanted biomaterials and its impact in nerve neuroprosthetics. *Front Bioeng Biotechnol.* 2021;9:622524. doi: 10.3389/fbioe.2021.622524

3 Gomes YVR, Tavares AA, Barbosa RC, *et al*. Biological responses to biomaterials: a review. *Braz J Med Biol Res.* 2025;58:e14599. doi: 10.1590/1414-431X2025e14599

4 Nilsson B, Ekdahl KN, Mollnes TE, Lambris JD. The role of complement in biomaterial-induced inflammation. *Mol Immunol.* 2007;44(1-3):82-94. doi: 10.1016/j.molimm.2006.06.020

5 Chenoweth DE. Complement activation produced by biomaterials. *Artif Organs.* 1988;12(6):508-510. doi: 10.1111/j.1525-1594.1988.tb02815.x

6 Thakur KK, Lekurwale R, Bansode S, Pansare R. 3D bioprinting: a systematic review for future research direction. *Indian J Orthop.* 2023;57(12):1949-1967.

doi: 10.1007/s43465-023-01000-7

7 Agarwal T, Onesto V, Banerjee D, *et al*. 3D bioprinting in tissue engineering: current state-of-the-art and challenges towards system standardization and clinical translation. *Biofabrication*. 2025;17:4.
doi: 10.1088/1758-5090/ade47a

8 Raees S, Ullah F, Javed F, *et al*. Classification, processing, and applications of bioink and 3D bioprinting: a detailed review. *Int J Biol Macromol.* 2023;232:123476.
doi: 10.1016/j.ijbiomac.2023.123476

9 Lee J, Byun H, Madhurakkat Perikamana SK, Lee S, Shin H. Current advances in immunomodulatory biomaterials for bone regeneration. *Adv Healthc Mater.* 2019;8(4): e1801106.
doi: 10.1002/adhm.201801106

10 Yang T, Fang Z, Zhang J, Zheng S. Physical cues in biomaterials modulate macrophage polarization for bone regeneration: a review. *Front Bioeng Biotechnol.* 2025;13:1640560.
doi: 10.3389/fbioe.2025.1640560

11 Yang HC, Park HC, Quan H, Kim Y. Immunomodulation of biomaterials by controlling macrophage polarization. *Adv Exp Med Biol.* 2018;1064:197-206.
doi: 10.1007/978-981-13-0445-3_12

12 Zarubova J, Hasani-Sadrabadi MM, Ardehali R, Li S. Immunoengineering strategies to enhance vascularization and tissue regeneration. *Adv Drug Deliv Rev.* 2022;184:114233.
doi: 10.1016/j.addr.2022.114233

13 Est-Witte S, Jain M, Ben-Akiva E, *et al*. Immunomodulatory delivery materials for tissue repair. *Adv Healthc Mater.* 2025;14(23):e2501400.
doi: 10.1002/adhm.202501400

14 Modinger Y, Teixeira GQ, Neidlinger-Wilke C, Ignatius A. Role of the complement system in the response to orthopedic biomaterials. *Int J Mol Sci.* 2018;19:11.
doi: 10.3390/ijms19113367

15 Trindade R, Albrektsson T, Tengvall P, Wennerberg A. Foreign body reaction to biomaterials: on mechanisms for buildup and breakdown of osseointegration. *Clin Implant Dent Relat Res.* 2016;18(1):192-203.
doi: 10.1111/cid.12274

16 Durieux N, Vandenput S, Pasleau F. OCEBM levels of evidence system. *Rev Med Liege.* 2013;68(12):644-649.

17 Page MJ, McKenzie JE, Bossuyt PM, *et al*. The PRISMA 2020 statement: an updated guideline for reporting systematic reviews. *BMJ.* 2021;372:n71.
doi: 10.1136/bmj.n71

18 Page MJ, McKenzie JE, Bossuyt PM, *et al*. The PRISMA 2020 statement: an updated guideline for reporting systematic reviews. *PLoS Med.* 2021;18(3):e1003583.
doi: 10.1371/journal.pmed.1003583

19 Gurtner GC, Werner S, Barrandon Y, Longaker MT. Wound repair and regeneration. *Nature.* 2008;453(7193):314-321.
doi: 10.1038/nature07039

20 Landen NX, Li D, Stahle M. Transition from inflammation to proliferation: a critical step during wound healing. *Cell Mol Life Sci.* 2016;73(20):3861-3885.
doi: 10.1007/s00018-016-2268-0

21 Reinke JM, Sorg H. Wound repair and regeneration. *Eur Surg Res.* 2012;49(1):35-43.
doi: 10.1159/000339613

22 Ekdahl KN, Huang S, Nilsson B, Teramura Y. Complement inhibition in biomaterial- and biosurface-induced thromboinflammation. *Semin Immunol.* 2016;28(3):268-277.
doi: 10.1016/j.smim.2016.04.006

23 Netea MG, Dominguez-Andres J, Barreiro LB, *et al*. Defining trained immunity and its role in health and disease. *Nat Rev Immunol.* 2020;20(6):375-388.
doi: 10.1038/s41577-020-0285-6

24 Dagenais A, Villalba-Guerrero C, Olivier M. Trained immunity: a "new" weapon in the fight against infectious diseases. *Front Immunol.* 2023;14:1147476.
doi: 10.3389/fimmu.2023.1147476

25 Mestres G, Carter SD, Hailer NP, Diez-Escudero A. A practical guide for evaluating the osteoimmunomodulatory properties of biomaterials. *Acta Biomater.* 2021;130:115-137.
doi: 10.1016/j.actbio.2021.05.038

26 Martin KE, Garcia AJ. Macrophage phenotypes in tissue repair and the foreign body response: implications for biomaterial-based regenerative medicine strategies. *Acta Biomater.* 2021;133:4-16.
doi: 10.1016/j.actbio.2021.03.038

27 Piatnitskaia S, Rafikova G, Bilyalov A, *et al*. Modelling of macrophage responses to biomaterials in vitro: state-of-the-art and the need for the improvement. *Front Immunol.* 2024;15:1349461.
doi: 10.3389/fimmu.2024.1349461

28 Holzl K, Lin S, Tytgat L, Van Vlierberghe S, Gu L, Ovsianikov A. Bioink properties before, during and after 3D bioprinting. *Biofabrication*. 2016;8(3):032002.
doi: 10.1088/1758-5090/8/3/032002

29 Gungor-Ozkerim PS, Inci I, Zhang YS, Khademhosseini A, Dokmeci MR. Bioinks for 3D bioprinting: an overview. *Biomater Sci.* 2018;6(5):915-946.
doi: 10.1039/c7bm00765e

30 Crapo PM, Gilbert TW, Badylak SF. An overview of tissue and whole organ decellularization processes. *Biomaterials.* 2011;32(12):3233-3243.
doi: 10.1016/j.biomaterials.2011.01.057

31 Lieder R, Petersen PH, Sigurjonsson OE. Endotoxins-the invisible companion in biomaterials research. *Tissue Eng Part B Rev.* 2013;19(5):391-402.
doi: 10.1089/ten.TEB.2012.0636

32 Lin CC, Anseth KS. PEG hydrogels for the controlled release of biomolecules in regenerative medicine. *Pharm Res.* 2009;26(3):631-643.
doi: 10.1007/s11095-008-9801-2

33 Fernandez-Yague MA, Hymel LA, Olingy CE, *et al*. Analyzing immune response to engineered hydrogels by hierarchical clustering of inflammatory cell subsets. *Sci Adv.* 2022;8(8):eabd8056.
doi: 10.1126/sciadv.abd8056

34 Yang D, Jones KS. Effect of alginate on innate immune activation of macrophages. *J Biomed Mater Res A.* 2009;90(2):411-418.
doi: 10.1002/jbm.a.32096

35 Choudhury D, Tun HW, Wang T, Naing MW. Organ-derived decellularized extracellular matrix: a game changer for bioink manufacturing? *Trends Biotechnol.* 2018;36(8):787-805.
doi: 10.1016/j.tibtech.2018.03.003

36 Abaci A, Guvendiren M. Designing decellularized extracellular matrix-based bioinks for 3D bioprinting. *Adv Healthc Mater.* 2020;9(24):e2000734.
doi: 10.1002/adhm.202000734

37 Ma S, Feng X, Liu F, Wang B, Zhang H, Niu X. The pro-inflammatory response of macrophages regulated by acid degradation products of poly(lactide-co-glycolide) nanoparticles. *Eng Life Sci.* 2021;21(10):709-720.
doi: 10.1002/elsc.202100040

38 Zhao Y, Feng X, Zhao Z, Song Z, Wang W, Zhao H. Interleukin-4-loaded heparin hydrogel regulates macrophage polarization to promote osteogenic differentiation. *ACS Biomater Sci Eng.* 2024;10(9):5774-5783.
doi: 10.1021/acsbiomaterials.4c00589

39 Pacifici N, Bolandparvaz A, Lewis JS. Stimuli-responsive biomaterials for vaccines and immunotherapeutic applications. *Adv Ther (Weinh).* 2020;3(11):2000129.
doi: 10.1002/adtp.202000129

40 Yu H, Gao R, Liu Y, Fu L, Zhou J, Li L. Stimulus-responsive hydrogels as drug delivery systems for inflammation targeted therapy. *Adv Sci (Weinh).* 2024;11(1):e2306152.
doi: 10.1002/advs.202306152

41 Pranantyo D, Yeo CK, Wu Y, *et al*. Hydrogel dressings with intrinsic antibiofilm and antioxidative dual functionalities accelerate infected diabetic wound healing. *Nat Commun.* 2024;15(1):954.
doi: 10.1038/s41467-024-44968-y

42 Huang Q, Qu Y, Tang M, *et al*. ROS-responsive hydrogel for bone regeneration: controlled dimethyl fumarate release to reduce inflammation and enhance osteogenesis. *Acta Biomater.* 2025;195:183-200.
doi: 10.1016/j.actbio.2025.02.026

43 Chen H, Wang W, Yang Y, *et al*. A sequential stimuli-responsive hydrogel promotes structural and functional recovery of severe spinal cord injury. *Biomaterials.* 2025;316:122995.
doi: 10.1016/j.biomaterials.2024.122995

44 Lai Y, Xiao X, Huang Z, *et al*. Photocrosslinkable biomaterials for 3D bioprinting: mechanisms, recent advances, and future prospects. *Int J Mol Sci.* 2024;25:23.
doi: 10.3390/ijms252312567

45 Li L, Alsema E, Beijer NRM, Gumuscu B. Magnetically driven hydrogel surfaces for modulating macrophage behavior. *ACS Biomater Sci Eng.* 2024;10(11):6974-6983.
doi: 10.1021/acsbiomaterials.4c01624

46 Gorronogoitia I, Urtaza U, Zubiarrain-Laserna A, Alonso-Varona A, Zaldua AM. A study of the printability of alginate-based bioinks by 3D bioprinting for articular cartilage tissue engineering. *Polymers (Basel).* 2022;14:2.
doi: 10.3390/polym14020354

47 Cruz EM, Machado LS, Zamproni LN, *et al*. A gelatin methacrylate-based hydrogel as a potential bioink for 3D bioprinting and neuronal differentiation. *Pharmaceutics.* 2023;15:2.
doi: 10.3390/pharmaceutics15020627

48 Wang D, Guo Y, Zhu J, *et al*. Hyaluronic acid methacrylate/pancreatic extracellular matrix as a potential 3D printing bioink for constructing islet organoids. *Acta Biomater.* 2023;165:86-101.
doi: 10.1016/j.actbio.2022.06.036

49 Osidak EO, Kozhukhov VI, Osidak MS, Domogatsky SP. Collagen as bioink for bioprinting: a comprehensive review. *Int J Bioprint.* 2020;6(3):270.
doi: 10.18063/ijb.v6i3.270

50 de Melo BAG, Jodat YA, Cruz EM, Benincasa JC, Shin SR, Porcionatto MA. Strategies to use fibrinogen as bioink for 3D bioprinting fibrin-based soft and hard tissues. *Acta Biomater.* 2020;117:60-76.
doi: 10.1016/j.actbio.2020.09.024

51 Hidaka M, Kojima M, Nakahata M, Sakai S. Visible light-curable chitosan ink for extrusion-based and vat polymerization-based 3D bioprintings. *Polymers (Basel).* 2021;13:9.
doi: 10.3390/polym13091382

52 Markstedt K, Mantas A, Tournier I, Martinez Avila H, Hagg D, Gatenholm P. 3D bioprinting human chondrocytes with nanocellulose-alginate bioink for cartilage tissue engineering applications. *Biomacromolecules.* 2015;16(5):1489-1496.
doi: 10.1021/acs.biomac.5b00188

53 Alheib O, da Silva LP, Youn YH, Kwon IK, Reis RL, Correlo VM. 3D bioprinting of gellan gum-based hydrogels tethered with laminin-derived peptides for improved cellular behavior. *J Biomed Mater Res A.* 2022;110(10):1655-1668.
doi: 10.1002/jbm.a.37415

54 Marques DMC, Silva JC, Serro AP, Cabral JMS, Sanjuan-Alberte P, Ferreira FC. 3D bioprinting of novel kappa-

carrageenan bioinks: an algae-derived polysaccharide. *Bioengineering (Basel).* 2022;9:3.
doi: 10.3390/bioengineering9030109

55 Gu Y, Schwarz B, Forget A, Barbero A, Martin I, Shastri VP. Advanced bioink for 3D bioprinting of complex free-standing structures with high stiffness. *Bioengineering (Basel).* 2020;7:4.
doi: 10.3390/bioengineering7040141

56 Piluso S, Skvortsov GA, Altunbek M, *et al*. 3D bioprinting of molecularly engineered PEG-based hydrogels utilizing gelatin fragments. *Biofabrication.* 2021;13:4.
doi: 10.1088/1758-5090/ac0ff0

57 Rossi A, Pescara T, Gambelli AM, *et al*. Biomaterials for extrusion-based bioprinting and biomedical applications. *Front Bioeng Biotechnol.* 2024;12:1393641.
doi: 10.3389/fbioe.2024.1393641

58 Li X, Liu B, Pei B, *et al*. Inkjet bioprinting of biomaterials. *Chem Rev.* 2020;120(19):10793-10833.
doi: 10.1021/acs.chemrev.0c00008

59 Jeong YG, Yoo JJ, Lee SJ, Kim MS. 3D digital light process bioprinting: cutting-edge platforms for resolution of organ fabrication. *Mater Today Bio.* 2024;29:101284.
doi: 10.1016/j.mtbio.2024.101284

60 Jing X, Fu H, Yu B, Sun M, Wang L. Two-photon polymerization for 3D biomedical scaffolds: overview and updates. *Front Bioeng Biotechnol.* 2022;10:994355.
doi: 10.3389/fbioe.2022.994355

61 Lee SJ, Jeong W, Atala A. 3D bioprinting for engineered tissue constructs and patient-specific models: current progress and prospects in clinical applications. *Adv Mater.* 2024;36(49):e2408032.
doi: 10.1002/adma.202408032

62 Hady TF, Hwang B, Pusic AD, *et al*. Uniform 40-micrompore diameter precision templated scaffolds promote a pro-healing host response by extracellular vesicle immune communication. *J Tissue Eng Regen Med.* 2021;15(1):24-36.
doi: 10.1002/term.3160

63 Yang X, Gao J, Yang S, *et al*. Pore size-mediated macrophage M1 to M2 transition affects osseointegration of 3D-printed PEEK scaffolds. *Int J Bioprint.* 2023;9(5):755.
doi: 10.18063/ijb.755

64 Liao C, Li Y, Tjong SC. Polyetheretherketone and its composites for bone replacement and regeneration. *Polymers (Basel).* 2020;12:12.
doi: 10.3390/polym12122858

65 Adamson M, Eslami B. Post-processing PEEK 3D-printed parts: experimental investigation of annealing on microscale and macroscale properties. *Polymers (Basel).* 2025;17:6.
doi: 10.3390/polym17060744

66 Sun Y, Zhang Y, Guo Y, *et al*. Electrical aligned polyurethane nerve guidance conduit modulates macrophage polarization and facilitates immunoregulatory peripheral nerve regeneration. *J Nanobiotechnol.* 2024;22(1):244.
doi: 10.1186/s12951-024-02507-3

67 McWhorter FY, Wang T, Nguyen P, Chung T, Liu WF. Modulation of macrophage phenotype by cell shape. *Proc Natl Acad Sci USA.* 2013;110(43):17253-17258.
doi: 10.1073/pnas.1308887110

68 Wu J, Mao Z, Tan H, Han L, Ren T, Gao C. Gradient biomaterials and their influences on cell migration. *Interface Focus.* 2012;2(3):337-355.
doi: 10.1098/rsfs.2011.0124

69 Miri AK, Mirzaee I, Hassan S, *et al*. Effective bioprinting resolution in tissue model fabrication. *Lab Chip.* 2019;19(11):2019-2037.
doi: 10.1039/c8lc01037d

70 Miri AK, Nieto D, Iglesias L, *et al*. Microfluidics-enabled multimaterial maskless stereolithographic bioprinting. *Adv Mater.* 2018;30(27):e1800242.
doi: 10.1002/adma.201800242

71 Kim YK, Park JA, Yoon WH, Kim J, Jung S. Drop-on-demand inkjet-based cell printing with 30-mum nozzle diameter for cell-level accuracy. *Biomicrofluidics.* 2016;10(6):064110.
doi: 10.1063/1.4968845

72 Jia W, Gungor-Ozkerim PS, Zhang YS, *et al*. Direct 3D bioprinting of perfusable vascular constructs using a blend bioink. *Biomaterials.* 2016;106:58-68.
doi: 10.1016/j.biomaterials.2016.07.038

73 Zhu W, Qu X, Zhu J, *et al*. Direct 3D bioprinting of prevascularized tissue constructs with complex microarchitecture. *Biomaterials.* 2017;124:106-115.
doi: 10.1016/j.biomaterials.2017.01.042

74 Dellaquila A, Le Bao C, Letourneur D, Simon-Yarza T. In vitro strategies to vascularize 3D physiologically relevant models. *Adv Sci (Weinh).* 2021;8(19):e2100798.
doi: 10.1002/advs.202100798

75 Cao X, Ashfaq R, Cheng F, *et al*. A tumor-on-a-chip system with bioprinted blood and lymphatic vessel pair. *Adv Funct Mater.* 2019;29:31.
doi: 10.1002/adfm.201807173

76 Lu R, Lee BJ, Lee E. Three-dimensional lymphatics-on-a-chip reveals distinct, size-dependent nanoparticle transport mechanisms in lymphatic drug delivery. *ACS Biomater Sci Eng.* 2024;10(9):5752-5763.
doi: 10.1021/acsbiomaterials.4c01005

77 Sergis V, Kelly D, Pramanick A, Britchfield G, Mason K, Daly AC. In-situquality monitoring during embedded bioprinting using integrated microscopy and classical computer vision. *Biofabrication.* 2025;17:2.
doi: 10.1088/1758-5090/adaa22

78 Quirk EL, Burroughs MC, Mai DJ. In situ photo-rheology monitors viscoelastic changes in photo-responsive polymer networks. *J Vis Exp.* 2025:220.

doi: 10.3791/68394

79 Malekpour A, Chen X. Printability and cell viability in extrusion-based bioprinting from experimental, computational, and machine learning views. *J Funct Biomater.* 2022;13:2.
doi: 10.3390/jfb13020040

80 Nair K, Gandhi M, Khalil S, *et al*. Characterization of cell viability during bioprinting processes. *Biotechnol J.* 2009;4(8):1168-1177.
doi: 10.1002/biot.200900004

81 Jui E, Kingsley G, Phan HKT, *et al*. Shear stress induces a time-dependent inflammatory response in human monocyte-derived macrophages. *Ann Biomed Eng.* 2024;52(11):2932-2947.
doi: 10.1007/s10439-024-03546-5

82 Son H, Choi HS, Baek SE, *et al*. Shear stress induces monocyte/macrophage-mediated inflammation by upregulating cell-surface expression of heat shock proteins. *Biomed Pharmacother.* 2023;161:114566.
doi: 10.1016/j.biopha.2023.114566

83 Blaeser A, Duarte Campos DF, Puster U, Richtering W, Stevens MM, Fischer H. Controlling shear stress in 3D bioprinting is a key factor to balance printing resolution and stem cell integrity. *Adv Healthc Mater.* 2016;5(3):326-333.
doi: 10.1002/adhm.201500677

84 Hoque R, Farooq A, Ghani A, Gorelick F, Mehal WZ. Lactate reduces liver and pancreatic injury in toll-like receptor- and inflammasome-mediated inflammation via GPR81-mediated suppression of innate immunity. *Gastroenterology.* 2014;146(7):1763-1774.
doi: 10.1053/j.gastro.2014.03.014

85 Ekdahl KN, Lambris JD, Elwing H, *et al*. Innate immunity activation on biomaterial surfaces: a mechanistic model and coping strategies. *Adv Drug Deliv Rev.* 2011;63(12):1042-1050.
doi: 10.1016/j.addr.2011.06.012

86 Beskid NM, Kolawole EM, Coronel MM, *et al*. IL-10-functionalized hydrogels support immunosuppressive dendritic cell phenotype and function. *ACS Biomater Sci Eng.* 2022;8(10):4341-4353.
doi: 10.1021/acsbiomaterials.2c00465

87 Liu JMH, Zhang J, Zhang X, *et al*. Transforming growth factor-beta 1 delivery from microporous scaffolds decreases inflammation post-implant and enhances function of transplanted islets. *Biomaterials.* 2016;80:11-19.
doi: 10.1016/j.biomaterials.2015.11.065

88 McHugh MD, Park J, Uhrich R, Gao W, Horwitz DA, Fahmy TM. Paracrine co-delivery of TGF-beta and IL-2 using CD4-targeted nanoparticles for induction and maintenance of regulatory T cells. *Biomaterials.* 2015;59:172-181.
doi: 10.1016/j.biomaterials.2015.04.003

89 Spiller KL, Nassiri S, Witherel CE, *et al*. Sequential delivery of immunomodulatory cytokines to facilitate the M1-to-M2 transition of macrophages and enhance vascularization of bone scaffolds. *Biomaterials.* 2015;37:194-207.
doi: 10.1016/j.biomaterials.2014.10.017

90 Zhang D, Tang Z, Huang H, *et al*. Metabolic regulation of gene expression by histone lactylation. *Nature.* 2019;574(7779):575-580.
doi: 10.1038/s41586-019-1678-1

91 Tannahill GM, Curtis AM, Adamik J, *et al*. Succinate is an inflammatory signal that induces IL-1beta through HIF-1alpha. *Nature.* 2013;496(7444):238-242.
doi: 10.1038/nature11986

92 Furusawa Y, Obata Y, Fukuda S, *et al*. Commensal microbe-derived butyrate induces the differentiation of colonic regulatory T cells. *Nature.* 2013;504(7480):446-450.
doi: 10.1038/nature12721

93 Vauthier C, Persson B, Lindner P, Cabane B. Protein adsorption and complement activation for di-block copolymer nanoparticles. *Biomaterials.* 2011;32(6):1646-1656.
doi: 10.1016/j.biomaterials.2010.10.026

94 Debnath S, Latiyan S, Jain N, *et al*. 3D Bioprinted Immunomodulation horizontal line the advancing landscape of next-generation immuno-oncology. *Biomacromolecules.* 2025;26(6):3255-3280.
doi: 10.1021/acs.biomac.4c01816

95 Li C, Li C, Ma Z, *et al*. Regulated macrophage immune microenvironment in 3D printed scaffolds for bone tumor postoperative treatment. *Bioact Mater.* 2023;19:474-485.
doi: 10.1016/j.bioactmat.2022.04.028

96 Xuan Y, Guo Y, Li L, *et al*. 3D-printed bredigite scaffolds with ordered arrangement structures promote bone regeneration by inducing macrophage polarization in onlay grafts. *J Nanobiotechnology.* 2024;22(1):102.
doi: 10.1186/s12951-024-02362-2

97 Muller L, Tunger A, Wobus M, *et al*. Immunomodulatory properties of mesenchymal stromal cells: an update. *Front Cell Dev Biol.* 2021;9:637725.
doi: 10.3389/fcell.2021.637725

98 Kou M, Huang L, Yang J, *et al*. Mesenchymal stem cell-derived extracellular vesicles for immunomodulation and regeneration: a next generation therapeutic tool? *Cell Death Dis.* 2022;13(7):580.
doi: 10.1038/s41419-022-05034-x

99 Fang RH, Gao W, Zhang L. Targeting drugs to tumours using cell membrane-coated nanoparticles. *Nat Rev Clin Oncol.* 2023;20(1):33-48.
doi: 10.1038/s41571-022-00699-x

100 Han H, Bartolo R, Li J, Shahbazi MA, Santos HA. Biomimetic platelet membrane-coated nanoparticles for targeted therapy. *Eur J Pharm Biopharm.* 2022;172:1-15.

doi: 10.1016/j.ejpb.2022.01.004

101 Liu H, Su YY, Jiang XC, Gao JQ. Cell membrane-coated nanoparticles: a novel multifunctional biomimetic drug delivery system. *Drug Deliv Transl Res.* 2023;13(3):716-737. doi: 10.1007/s13346-022-01252-0

102 Cai Y, Wang Y, Hu S. Synthetic Gene circuits enable sensing in engineered living materials. *Biosensors (Basel).* 2025;15:9. doi: 10.3390/bios15090556

103 Teng F, Cui T, Zhou L, Gao Q, Zhou Q, Li W. Programmable synthetic receptors: the next-generation of cell and gene therapies. *Signal Transduct Target Ther.* 2024;9(1):7. doi: 10.1038/s41392-023-01680-5

104 Guo C, Ma X, Gao F, Guo Y. Off-target effects in CRISPR/Cas9 gene editing. *Front Bioeng Biotechnol.* 2023;11:1143157. doi: 10.3389/fbioe.2023.1143157

105 Luo J, Chen J, Huang Y, You L, Dai Z. Engineering living materials by synthetic biology. *Biophys Rev (Melville).* 2023;4(1):011305. doi: 10.1063/5.0115645

106 Ou Y, Guo S. Safety risks and ethical governance of biomedical applications of synthetic biology. *Front Bioeng Biotechnol.* 2023;11:1292029. doi: 10.3389/fbioe.2023.1292029

107 Baltazar T, Merola J, Catarino C, *et al*. Three dimensional bioprinting of a vascularized and perfusable skin graft using human keratinocytes, fibroblasts, pericytes, and endothelial cells. *Tissue Eng Part A.* 2020;26(5-6):227-238. doi: 10.1089/ten.TEA.2019.0201

108 Pasierb A, Jezierska M, Karpuk A, Czuwara J, Rudnicka L. 3D skin bioprinting: future potential for skin regeneration. *Postepy Dermatol Alergol.* 2022;39(5):845-851. doi: 10.5114/ada.2021.109692

109 Aureal M, Machuca-Gayet I, Coury F. Rheumatoid arthritis in the view of osteoimmunology. *Biomolecules.* 2020;11:1. doi: 10.3390/biom11010048

110 Dutta SD, Ganguly K, Patil TV, Randhawa A, Lim KT. Unraveling the potential of 3D bioprinted immunomodulatory materials for regulating macrophage polarization: state-of-the-art in bone and associated tissue regeneration. *Bioact Mater.* 2023;28:284-310. doi: 10.1016/j.bioactmat.2023.05.014

111 Yao Y, Cai X, Chen Y, Zhang M, Zheng C. Estrogen deficiency-mediated osteoimmunity in postmenopausal osteoporosis. *Med Res Rev.* 2025;45(2):561-575. doi: 10.1002/med.22081

112 Guo Y, Shi Z, Han L, *et al*. Infection-sensitive SPION/PLGA scaffolds promote periodontal regeneration via antibacterial activity and macrophage-phenotype modulation. *ACS Appl Mater Interfaces.* 2024;16(32):41855-41868. doi: 10.1021/acsami.4c06430

113 Qiao Z, Zhang W, Jiang H, Li X, An W, Yang H. 3D-printed composite scaffold with anti-infection and osteogenesis potential against infected bone defects. *RSC Adv.* 2022;12(18):11008-11020. doi: 10.1039/d2ra00214k

114 Zou F, Jiang J, Lv F, Xia X, Ma X. Preparation of antibacterial and osteoconductive 3D-printed PLGA/Cu(I)@ZIF-8 nanocomposite scaffolds for infected bone repair. *J Nanobiotechnology.* 2020;18(1):39. doi: 10.1186/s12951-020-00594-6

115 Dubey A, Vahabi H, Kumaravel V. Antimicrobial and biodegradable 3D printed scaffolds for orthopedic infections. *ACS Biomater Sci Eng.* 2023;9(7):4020-4044. doi: 10.1021/acsbiomaterials.3c00115

116 Wang Z, Wang L, Li T, *et al*. 3D bioprinting in cardiac tissue engineering. *Theranostics.* 2021;11(16):7948-7969. doi: 10.7150/thno.61621

117 Elalouf A. Immune response against the biomaterials used in 3D bioprinting of organs. *Transpl Immunol.* 2021;69:101446. doi: 10.1016/j.trim.2021.101446

118 Ma Y, He R, Deng B, *et al*. Advanced 3D bioprinted liver models with human-induced hepatocytes for personalized toxicity screening. *J Tissue Eng.* 2025;16:20417314241313341. doi: 10.1177/20417314241313341

119 Ali ASM, Berg J, Roehrs V, *et al*. Xeno-free 3D bioprinted liver model for hepatotoxicity assessment. *Int J Mol Sci.* 2024;25:3. doi: 10.3390/ijms25031811

120 King SM, Higgins JW, Nino CR, *et al*. 3D proximal tubule tissues recapitulate key aspects of renal physiology to enable nephrotoxicity testing. *Front Physiol.* 2017;8:123. doi: 10.3389/fphys.2017.00123

121 Andreev AL, Andreeva TB, Kompanets IN, Zalyapin NV. Space-inhomogeneous phase modulation of laser radiation in an electro-optical ferroelectric liquid crystal cell for suppressing speckle noise. *Appl Opt.* 2018;57(6):1331-1337. doi: 10.1364/AO.57.001331

122 Feile A, Wegner VD, Raasch M, Mosig AS. Immunocompetent intestine-on-chip model for analyzing gut mucosal immune responses. *J Vis Exp.* 2024:207. doi: 10.3791/66603

123 Ji W, Hou B, Lin W, *et al*. 3D bioprinting a human iPSC-derived MSC-loaded scaffold for repair of the uterine endometrium. *Acta Biomater.* 2020;116:268-284. doi: 10.1016/j.actbio.2020.09.012

124 Tinggaard Pedersen N, Cohn J. Intact megakaryocytes in the venous blood as a marker for thrombopoiesis. *Scand J Haematol.* 1981;27(1):57-63. doi: 10.1111/j.1600-0609.1981.tb00452.x

125 Richards C, Chen H, O'Rourke M, *et al*. Matrix directs trophoblast differentiation in a bioprinted organoid model of

early placental development. *Nat Commun.* 2025;16(1):8267. doi: 10.1038/s41467-025-62996-0

126 Luo X, Liu Z, Fang S, *et al*. Implantable hydrogel-based scaffold integrating cascaded chemotherapy and self-amplified immunotherapy to suppress postsurgical tumor recurrence. *J Colloid Interface Sci.* 2025;700(Pt 2):138475. doi: 10.1016/j.jcis.2025.138475

127 Fang L, Liu Y, Qiu J, Wan W. Bioprinting and its use in tumor-on-a-chip technology for cancer drug screening: a review. *Int J Bioprint.* 2022;8(4):603. doi: 10.18063/ijb.v8i4.603

128 Neal JT, Li X, Zhu J, *et al*. Organoid modeling of the tumor immune microenvironment. *Cell.* 2018;175(7):1972-1988 e1916. doi: 10.1016/j.cell.2018.11.021

129 Zhao Z, Zhang S, Jiang N, *et al*. Patient-derived Immunocompetent tumor organoids: a platform for chemotherapy evaluation in the context of t-cell recognition. *Angew Chem Int Ed Engl.* 2024;63(9):e202317613. doi: 10.1002/anie.202317613

130 Logun M, Wang X, Sun Y, *et al*. Patient-derived glioblastoma organoids as real-time avatars for assessing responses to clinical CAR-T cell therapy. *Cell Stem Cell.* 2025;32(2):181-190 e184. doi: 10.1016/j.stem.2024.11.010

131 Dekkers JF, Alieva M, Cleven A, *et al*. Uncovering the mode of action of engineered T cells in patient cancer organoids. *Nat Biotechnol.* 2023;41(1):60-69. doi: 10.1038/s41587-022-01397-w

132 Alieva M, Barrera Roman M, de Blank S, *et al*. BEHAV3D: a 3D live imaging platform for comprehensive analysis of engineered T cell behavior and tumor response. *Nat Protoc.* 2024;19(7):2052-2084. doi: 10.1038/s41596-024-00972-6

133 Abdulrahman Z, Slieker RC, McGuire D, Welters MJP, van Poelgeest MIE, van der Burg SH. Single-cell spatial transcriptomics unravels cell states and ecosystems associated with clinical response to immunotherapy. *J Immunother Cancer.* 2025;13:3. doi: 10.1136/jitc-2024-011308

134 Renauer P, Park JJ, Bai M, *et al*. Immunogenetic metabolomics reveals key enzymes that modulate CAR T-cell metabolism and function. *Cancer Immunol Res.* 2023;11(8):1068-1084. doi: 10.1158/2326-6066.CIR-22-0565

135 Shi H, Chen S, Chi H. Immunometabolism of CD8(+) T cell differentiation in cancer. *Trends Cancer.* 2024;10(7):610-626. doi: 10.1016/j.trecan.2024.03.010

136 Ingber DE. Human organs-on-chips for disease modelling, drug development and personalized medicine. *Nat Rev Genet.* 2022;23(8):467-491. doi: 10.1038/s41576-022-00466-9

137 Wang H, Ning X, Zhao F, Zhao H, Li D. Human organoids-on-chips for biomedical research and applications. *Theranostics.* 2024;14(2):788-818. doi: 10.7150/thno.90492

138 Man Y, Liu Y, Chen Q, *et al*. Organoids-on-a-chip for personalized precision medicine. *Adv Healthc Mater.* 2024;13(30):e2401843. doi: 10.1002/adhm.202401843

139 Yang Y, Chen Y, Wang L, *et al*. PBPK modeling on organs-on-chips: an overview of recent advancements. *Front Bioeng Biotechnol.* 2022;10:900481. doi: 10.3389/fbioe.2022.900481

140 Li T, Yang Y, Yang F, *et al*. Organoids and organoids-on-chip in traditional chinese medicine research: applications, advantages, and future prospects. *Cell Biol Int.* 2025;49(10):1233-1244. doi: 10.1002/cbin.70067

141 Liu J, Li T, Li R, *et al*. Hepatic organoid-based high-content imaging boosts evaluation of stereoisomerism-dependent hepatotoxicity of stilbenes in herbal medicines. *Front Pharmacol.* 2022;13:862830. doi: 10.3389/fphar.2022.862830

142 Huang C, Jiang Y, Bao Q, *et al*. Study on the differential hepatotoxicity of raw polygonum multiflorum and polygonum multiflorum praeparata and its mechanism. *BMC Complement Med Ther.* 2024;24(1):161. doi: 10.1186/s12906-024-04463-9

143 Li CG, Yan L, Mai FY, *et al*. Baicalin inhibits NOD-like receptor family, pyrin containing domain 3 inflammasome activation in murine macrophages by augmenting protein kinase A signaling. *Front Immunol.* 2017;8:1409. doi: 10.3389/fimmu.2017.01409

144 Ning B, Shen J, Liu F, Zhang H, Jiang X. Baicalein suppresses NLRP3 and AIM2 inflammasome-mediated pyroptosis in macrophages infected by mycobacterium tuberculosis via induced autophagy. *Microbiol Spectr.* 2023;11(3):e0471122. doi: 10.1128/spectrum.04711-22

145 Xu F, Cui WQ, Wei Y, *et al*. Astragaloside IV inhibits lung cancer progression and metastasis by modulating macrophage polarization through AMPK signaling. *J Exp Clin Cancer Res.* 2018;37(1):207. doi: 10.1186/s13046-018-0878-0

146 Kim A, Downer MA, Berry CE, Valencia C, Fazilat AZ, Griffin M. Investigating immunomodulatory biomaterials for preventing the foreign body response. *Bioengineering (Basel).* 2023;10:12. doi: 10.3390/bioengineering10121411

147 Dzobo K, Motaung K, Adesida A. Recent trends in decellularized extracellular matrix bioinks for 3d printing: an updated review. *Int J Mol Sci.* 2019;20:18. doi: 10.3390/ijms20184628

148 Rizwan M, Chan SW, Comeau PA, Willett TL, Yim EKF. Effect of sterilization treatment on mechanical properties, biodegradation, bioactivity and printability of GelMA hydrogels. *Biomed Mater.* 2020;15(6):065017. doi: 10.1088/1748-605X/aba40c

149 Pohan G, Mattiassi S, Yao Y, *et al*. Effect of ethylene oxide sterilization on polyvinyl alcohol hydrogel compared with gamma radiation. *Tissue Eng Part A*. 2020;26(19-20):1077-1090. doi: 10.1089/ten.TEA.2020.0002

150 Zhang F, Scull G, Gluck JM, Brown AC, King MW. Effects of sterilization methods on gelatin methacryloyl hydrogel properties and macrophage gene expressionin vitro. *Biomed Mater.* 2022;18:1. doi: 10.1088/1748-605X/aca4b2

151 Xu H, Casillas J, Krishnamoorthy S, Xu C. Effects of Irgacure 2959 and lithium phenyl-2,4,6-trimethylbenzoylphosphinate on cell viability, physical properties, and microstructure in 3D bioprinting of vascular-like constructs. *Biomed Mater.* 2020;15(5):055021. doi: 10.1088/1748-605X/ab954e

152 Godar DE, Gurunathan C, Ilev I. 3D Bioprinting with UVA1 radiation and photoinitiator Irgacure 2959: can the ASTM Standard L929 cells predict human stem cell cytotoxicity? *Photochem Photobiol.* 2019;95(2):581-586. doi: 10.1111/php.13028

153 Schwab A, Levato R, D'Este M, Piluso S, Eglin D, Malda J. Printability and shape fidelity of bioinks in 3D bioprinting. *Chem Rev.* 2020;120(19):11028-11055. doi: 10.1021/acs.chemrev.0c00084

154 Chaudhuri O, Cooper-White J, Janmey PA, Mooney DJ, Shenoy VB. Effects of extracellular matrix viscoelasticity on cellular behaviour. *Nature.* 2020;584(7822):535-546. doi: 10.1038/s41586-020-2612-2

155 Wang H, Yu H, Zhou X, *et al*. An overview of extracellular matrix-based bioinks for 3D bioprinting. *Front Bioeng Biotechnol.* 2022;10:905438. doi: 10.3389/fbioe.2022.905438

156 Zhe M, Wu X, Yu P, *et al*. Recent advances in decellularized extracellular matrix-based bioinks for 3D bioprinting in tissue engineering. *Materials (Basel).* 2023;16:8. doi: 10.3390/ma16083197

157 Zhang H, Wang Y, Zheng Z, *et al*. Strategies for improving the 3D printability of decellularized extracellular matrix bioink. *Theranostics.* 2023;13(8):2562-2587. doi: 10.7150/thno.81785

158 Xin S, Deo KA, Dai J, *et al*. Generalizing hydrogel microparticles into a new class of bioinks for extrusion bioprinting. *Sci Adv.* 2021;7(42):eabk3087. doi: 10.1126/sciadv.abk3087

159 Schirmer L, Atallah P, Werner C, Freudenberg U. StarPEG-Heparin hydrogels to protect and sustainably deliver IL-4. *Adv Healthc Mater.* 2016;5(24):3157-3164. doi: 10.1002/adhm.201600797

160 Jui E, Kingsley G, Jimenez S, Birla RK, Keswani SG, Grande-Allen KJ. Shear-induced macrophage secretome promotes endothelial permeability. *bioRxiv.* 2025;660831. doi: 10.1101/2025.06.20.660831

161 Ding T, Sun J. Formation of protein corona on nanoparticle affects different complement activation pathways mediated by C1q. *Pharm Res.* 2019;37(1):10. doi: 10.1007/s11095-019-2747-8

162 Wiegner R, Chakraborty S, Huber-Lang M. Complement-coagulation crosstalk on cellular and artificial surfaces. *Immunobiology.* 2016;221(10):1073-1079. doi: 10.1016/j.imbio.2016.06.005

163 Brandwijk R, Michels M, van Rossum M, *et al*. Pitfalls in complement analysis: a systematic literature review of assessing complement activation. *Front Immunol.* 2022;13:1007102. doi: 10.3389/fimmu.2022.1007102

164 Seok J, Warren HS, Cuenca AG, *et al*. Genomic responses in mouse models poorly mimic human inflammatory diseases. *Proc Natl Acad Sci USA*. 2013;110(9):3507-3512. doi: 10.1073/pnas.1222878110

165 Takao K, Miyakawa T. Genomic responses in mouse models greatly mimic human inflammatory diseases. *Proc Natl Acad Sci USA*. 2015;112(4):1167-1172. doi: 10.1073/pnas.1401965111

166 Mladenovska T, Choong PF, Wallace GG, O'Connell CD. The regulatory challenge of 3D bioprinting. *Regen Med.* 2023;18(8):659-674. doi: 10.2217/rme-2022-0194

167 Taylor S, Mueller E, Jones LR, Makela AV, Ashammakhi N. Translational aspects of 3D and 4D printing and bioprinting. *Adv Healthc Mater.* 2024;13(27): e2400463. doi: 10.1002/adhm.202400463

168 Yu LX, Amidon G, Khan MA, *et al*. Understanding pharmaceutical quality by design. *AAPS J.* 2014;16(4):771-783. doi: 10.1208/s12248-014-9598-3

169 Kim EJ, Kim JH, Kim MS, Jeong SH, Choi DH. Process analytical technology tools for monitoring pharmaceutical unit operations: a control strategy for continuous process verification. *Pharmaceutics.* 2021;13:6. doi: 10.3390/pharmaceutics13060919

170 McCorry MC, Reardon KF, Black M, *et al*. Sensor technologies for quality control in engineered tissue manufacturing. *Biofabrication.* 2022;15:1. doi: 10.1088/1758-5090/ac94a1

171 Decoene I, Nasello G, Madeiro de Costa RF, *et al*. Robotics-driven manufacturing of cartilaginous microtissues for skeletal tissue engineering applications. *Stem Cells Transl Med.* 2024;13(3):278-292.

doi: 10.1093/stcltm/szad091

172 Kandarova H, Pobis P. The "Big Three" in biocompatibility testing of medical devices: implementation of alternatives to animal experimentation-are we there yet? *Front Toxicol.* 2023;5:1337468.
doi: 10.3389/ftox.2023.1337468

173 Lee NK, Chang JW. Manufacturing cell and gene therapies: challenges in clinical translation. *Ann Lab Med.* 2024;44(4):314-323.
doi: 10.3343/alm.2023.0382

174 Shah NN, Qin H, Yates B, *et al*. Clonal expansion of CAR T cells harboring lentivector integration in the CBL gene following anti-CD22 CAR T-cell therapy. *Blood Adv.* 2019;3(15):2317-2322.
doi: 10.1182/bloodadvances.2019000219

175 Nobles CL, Sherrill-Mix S, Everett JK, *et al*. CD19-targeting CAR T cell immunotherapy outcomes correlate with genomic modification by vector integration. *J Clin Invest.* 2020;130(2):673-685.
doi: 10.1172/JCI130144

176 Wagner DL, Fritsche E, Pulsipher MA, *et al*. Immunogenicity of CAR T cells in cancer therapy. *Nat Rev Clin Oncol.* 2021;18(6):379-393.
doi: 10.1038/s41571-021-00476-2

177 Wielscher M, Mandaviya PR, Kuehnel B, *et al*. DNA methylation signature of chronic low-grade inflammation and its role in cardio-respiratory diseases. *Nat Commun.* 2022;13(1):2408.
doi: 10.1038/s41467-022-29792-6

178 Ashammakhi N, Ahadian S, Zengjie F, *et al*. Advances and future perspectives in 4D bioprinting. *Biotechnol J.* 2018;13(12):e1800148.
doi: 10.1002/biot.201800148

179 Noroozi R, Arif ZU, Taghvaei H, *et al*. 3D and 4D bioprinting Technologies: a game changer for the biomedical sector? *Ann Biomed Eng.* 2023;51(8):1683-1712.
doi: 10.1007/s10439-023-03243-9

180 Lai J, Liu Y, Lu G, *et al*. 4D bioprinting of programmed dynamic tissues. *Bioact Mater.* 2024;37:348-377.
doi: 10.1016/j.bioactmat.2024.03.033

181 Rahimnejad M, Jahangiri S, Zirak Hassan Kiadeh S, *et al*. Stimuli-responsive biomaterials: smart avenue toward 4D bioprinting. *Crit Rev Biotechnol.* 2024;44(5):860-891.
doi: 10.1080/07388551.2023.2213398

182 Freeman S, Calabro S, Williams R, Jin S, Ye K. Bioink formulation and machine learning-empowered bioprinting optimization. *Front Bioeng Biotechnol.* 2022;10:913579.
doi: 10.3389/fbioe.2022.913579

183 An J, Chua CK, Mironov V. Application of machine learning in 3d bioprinting: focus on development of big data and digital twin. *Int J Bioprint.* 2021;7(1):342.
doi: 10.18063/ijb.v7i1.342

184 Zhang Z, Zhou X, Fang Y, Xiong Z, Zhang T. AI-driven 3D bioprinting for regenerative medicine: from bench to bedside. *Bioact Mater.* 2025;45:201-230.
doi: 10.1016/j.bioactmat.2024.11.021

185 Chen C, Xie Z, Yang S, *et al*. Machine learning approach to investigating macrophage polarization on various titanium surface characteristics. *BME Front.* 2025;6:0100.
doi: 10.34133/bmef.0100

186 Samandari M, Mostafavi A, Quint J, Memic A, Tamayol A. In situ bioprinting: intraoperative implementation of regenerative medicine. *Trends Biotechnol.* 2022;40(10):1229-1247.
doi: 10.1016/j.tibtech.2022.03.009

187 Cicha I, Priefer R, Severino P, Souto EB, Jain S. Biosensor-integrated drug delivery systems as new materials for biomedical applications. *Biomolecules.* 2022;12:9.
doi: 10.3390/biom12091198

188 Scholten K, Meng E. A review of implantable biosensors for closed-loop glucose control and other drug delivery applications. *Int J Pharm.* 2018;544(2):319-334.
doi: 10.1016/j.ijpharm.2018.02.022

189 Correa-Oliveira R, Fachi JL, Vieira A, Sato FT, Vinolo MA. Regulation of immune cell function by short-chain fatty acids. *Clin Transl Immunol.* 2016;5(4):e73.
doi: 10.1038/cti.2016.17

190 Nogal A, Valdes AM, Menni C. The role of short-chain fatty acids in the interplay between gut microbiota and diet in cardio-metabolic health. *Gut Microbes.* 2021;13(1):1-24.
doi: 10.1080/19490976.2021.1897212

191 Biagioli M, Marchiano S, Carino A, *et al*. Bile acids activated receptors in inflammatory bowel disease. *Cells.* 2021;10:6.
doi: 10.3390/cells10061281

192 Roybal KT, Lim WA. Synthetic immunology: hacking immune cells to expand their therapeutic capabilities. *Annu Rev Immunol.* 2017;35:229-253.
doi: 10.1146/annurev-immunol-051116-052302

193 Yu S, Sun H, Li Y, Wei S, Xu J, Liu J. Hydrogels as promising platforms for engineered living bacteria-mediated therapeutic systems. *Mater Today Bio.* 2022;16:100435.
doi: 10.1016/j.mtbio.2022.100435

194 Adamo JE, Grayson WL, Hatcher H *et al*. Regulatory interfaces surrounding the growing field of additive manufacturing of medical devices and biologic products. *J Clin Transl Sci.* 2018;2(5):301-304.
doi: 10.1017/cts.2018.331

195 Laubenbacher R, Mehrad B, Shmulevich I, Trayanova N. Digital twins in medicine. *Nat Comput Sci.* 2024;4(3):184-191.
doi: 10.1038/s43588-024-00607-6

196 Niarakis A, Laubenbacher R, An G, *et al*. Immune digital twins for complex human pathologies: applications, limitations, and challenges. *NPJ Syst Biol Appl.* 2024;10(1):141.
doi: 10.1038/s41540-024-00450-5

ACCSCIENCE PUBLISHING

International Journal of Bioprinting

REVIEW ARTICLE

Advances in three-dimensional bioprinted tumor organoids: From model construction to clinical translation

Yuwen Wang[1†], Jiaqi Shi[2†], Yali Wang[3†], Sihan Zhao[4], Hui Ren[5], Huanhuan Huang[6], Wenyue Lv[2], Huiheng Feng[2], Yunxiang Zhou[7*], Kun Ji[8*], and Wei Wu[9*]

[1]Department of Medical Oncology, Sir Run Run Shaw Hospital, Zhejiang University School of Medicine, Hangzhou, Zhejiang, China

[2]State Key Laboratory of Advanced Drug Delivery and Release Systems, Liangzhu Laboratory, College of Pharmaceutical Sciences, Zhejiang University, Hangzhou, Zhejiang, China

[3]Department of Breast Surgery, Fujian Medical University Union Hospital, Fuzhou, Fujian, China

[4]Department of Health Management, School of Humanities and Management School, Zhejiang Chinese Medical University, Hangzhou, Zhejiang, China

[5]Department of Medical Oncology, The First Affiliated Hospital, Zhejiang University School of Medicine, Hangzhou, Zhejiang, China

[6]Department of Thoracic Oncology, Postgraduate Training Base Alliance of Wenzhou Medical University (Zhejiang Cancer Hospital), Hangzhou, Zhejiang, China

[7]Department of Breast Surgery and Oncology, The Second Affiliated Hospital, Zhejiang University School of Medicine, Hangzhou, Zhejiang, China

[8]Division of Hepatobiliary and Pancreatic Surgery, Hepatobiliary and Pancreatic Interventional Treatment Center, the First Affiliated Hospital, Zhejiang University School of Medicine, Hangzhou, Zhejiang, China

[9]Department of Hepato-Pancreato-Biliary & Gastric Medical Oncology, Zhejiang Cancer Hospital, Hangzhou Institute of Medicine, Chinese Academy of Sciences, Hangzhou, Zhejiang, China

[†]These authors contributed equally to this work.

***Corresponding authors:**
Yunxiang Zhou
(yxzhou@zju.edu.cn)

Kun Ji
(jikun@zju.edu.cn)

Wei Wu
(onco_wuwei@zju.edu.cn)

Citation: Wang Y, Shi J, Wang Y, *et al*. Advances in three-dimensional bioprinted tumor organoids: From model construction to clinical translation. *Int J Bioprint*. 2026;12(1):199-224. doi: 10.36922/IJB025390393

Received: September 22, 2025
Revised: November 30, 2025
Accepted: December 4, 2025
Published online: December 23, 2025

Copyright: © 2025 Author(s). This is an Open Access article distributed under the terms of the Creative Commons Attribution License, permitting distribution, and reproduction in any medium, provided the original work is properly cited.

Publisher's Note: AccScience Publishing remains neutral with regard to jurisdictional claims in published maps and institutional affiliations.

Abstract

Traditional cancer research models face inherent limitations, as two-dimensional cell cultures fail to capture the complexity of tumor biology, while animal models are confounded by species-specific discrepancies. The integration of tumor organoids with three-dimensional (3D) bioprinting has recently emerged as a transformative strategy. This approach combines the histological and genetic fidelity of organoids with the spatial precision and structural controllability of 3D bioprinting, thereby enabling the fabrication of biomimetic tumor models. Such models more faithfully recapitulate critical features of the tumor microenvironment (TME), addressing major gaps in conventional experimental systems. This review systematically examines the principles, recent advances, and translational applications of 3D bioprinting-enabled tumor organoids, including the biological basis of organoids, key bioprinting strategies, and technical considerations. Major applications include constructing heterogeneous TMEs with immune interactions, engineering vascularized tumor structures, enabling high-throughput drug screening, validating bioprinted organoids using clinical samples, and advancing clinical translation, regulatory frameworks, and Good Manufacturing Practice-compliant manufacturing of tumor organoids. Despite substantial progress, several challenges remain, including limited printing resolution, bioink instability, difficulties in sustaining long-term cultures,

and gaps in standardization. Nevertheless, integration with emerging technologies, such as microfluidics, artificial intelligence, big data analytics, and standardized biomanufacturing platforms, is anticipated to bridge the gap between basic tumor research and clinical translation. Ultimately, these synergistic advances may accelerate the development of personalized cancer therapies and improve patient outcomes.

Keywords: Clinical translation; Drug screening; Three-dimensional bioprinting; Tumor microenvironment; Tumor organoids

1. Introduction

Cancer is among the leading causes of morbidity and mortality worldwide. Its complex pathogenesis and pronounced interpatient and intratumoral heterogeneity have long posed major challenges in both clinical treatment and basic research.[1] To address the challenges of cancer treatment, establishing research models that can accurately simulate the biological characteristics of human tumors has become crucial. An ideal tumor model must meet three core requirements: structural mimicry, functional relevance, and clinical translatability. However, traditional research models have insurmountable limitations.[2]

Although two-dimensional (2D) cell culture systems enable high-throughput experimentation, they lack three-dimensional (3D) structure and interactions with the extracellular matrix (ECM).[3] This limitation makes it impossible to reproduce the polar organization, nutrient gradient distribution, and heterogeneous phenotypes of tumor cells.[4,5] Animal models can partially simulate the *in vivo* microenvironment; however, due to species differences, significant deviations exist in metabolic pathways and immune responses. For instance, the rate of drug metabolism in rodents often differs significantly from that in humans, and the activation patterns of immune cells, such as T lymphocytes, show notable species-specific variations. This discrepancy contributes to the extremely high failure rate of candidate drugs that are effective in animal models during clinical trials.[6,7] These dilemmas highlight the urgency of developing new tumor models, and the cross-integration of organoid technology with 3D bioprinting is providing a revolutionary solution to this problem.[6,8]

Organoid technology enables the formation of self-organizing, miniaturized organ structures through *in vitro* 3D culture of stem cells or primary tumor cells, which closely resemble the source tumors in terms of gene expression profiles, histopathological features, and drug response patterns.[5,6,9–11] The foundational development of organoid technology can be traced back to the establishment of intestinal organoids by Sato *et al.*[12] in 2009, which demonstrated that single $Lgr5^+$ stem cells could self-organize into crypt–villus structures *in vitro* without a mesenchymal niche—a breakthrough that laid the groundwork for subsequent tumor organoid models. Subsequently, tumor organoid technology rapidly expanded to multiple cancer types, such as breast cancer[13] and colorectal cancer,[14] providing a "patient avatar" model for personalized medical research. However, because organoids form spontaneously, it is difficult to precisely control the spatial distribution of cells and microenvironmental components, especially when simulating complex biological processes such as tumor–stroma interactions and vascular infiltration.[6,10,15]

The emergence of 3D bioprinting technology has addressed these limitations. Through computer-aided design and the precise deposition of biological materials, this technology enables the spatial positioning and assembly of cells and matrices, allowing the construction of complex tissue models with biomimetic structures.[6] When combined with tumor organoids, 3D bioprinting not only preserves tumor-derived characteristics of organoids but also endows models with a precise structural hierarchy and functional compartmentalization through controlled printing, forming a "bioengineered tumor microenvironment (TME)".[9] This innovative approach can simulate dynamic processes such as tumor invasion and metastasis and facilitate the construction of multicellular interaction networks involving blood vessels, immune cells, and fibroblasts. Consequently, it provides an unprecedented research platform for investigating TME regulatory mechanisms and developing novel targeted therapies.[4,15]

This review systematically examines the integrated application of tumor organoids and 3D bioprinting technology, comprehensively analyzing technical advances and existing challenges, from model construction principles to clinical translation potential, with the aim of

providing theoretical insights and practical guidance to advance precision oncology research.

2. Overview of tumor organoids

2.1. Definition and biological characteristics of tumor organoids

Tumor organoids are miniature tumor structures formed through the self-renewal and differentiation of stem cells/progenitor cells isolated from tumor tissues or cancer cell lines in a 3D culture system that simulates the *in vivo* microenvironment.[6,15,16] Their core characteristics include: histological fidelity (retention of the glandular structure and cellular heterogeneity of the original tumor), genetic stability (maintenance of gene mutation profiles during long-term culture), and functional relevance (exhibition of tumor biological behaviors such as proliferation, invasion, and drug response).[15,17]

Tumor organoids can be divided into three categories based on their origin: patient-derived organoids (PDOs),[17] cell line-derived organoids,[18–20] and genetically engineered organoids[21] (Figure 1). Among these, PDOs are directly derived from clinical samples and most accurately reflect individual tumor characteristics, making them the gold standard model for personalized medical research.[22]

2.2. Comparison of tumor organoids with conventional tumor models

2D cell culture systems form monolayers of cells through adherent growth. Although they enable large-scale expansion, they often disrupt the native spatial organization of cell–cell junctions and reduce interaction with the ECM, resulting in significant differences in gene expression profiles compared with *in vivo* tumors.[15,16,23]

Patient-derived xenograft (PDX) models, a branch of animal models, transplant patient tumor tissues into immunodeficient mice, and can better preserve aspects of the TME.[24] However, these models present several limitations. For example, their construction success rate is relatively low, and human stromal cells are gradually replaced by murine cells during serial passaging.[19,25] This replacement distorts the original TME, leading to inaccurate experimental outcomes, especially in studies focusing on stromal–tumor cell interactions. As a result, the application of PDX models in personalized precision medicine is severely restricted, limiting their ability to effectively guide clinical treatment decisions.

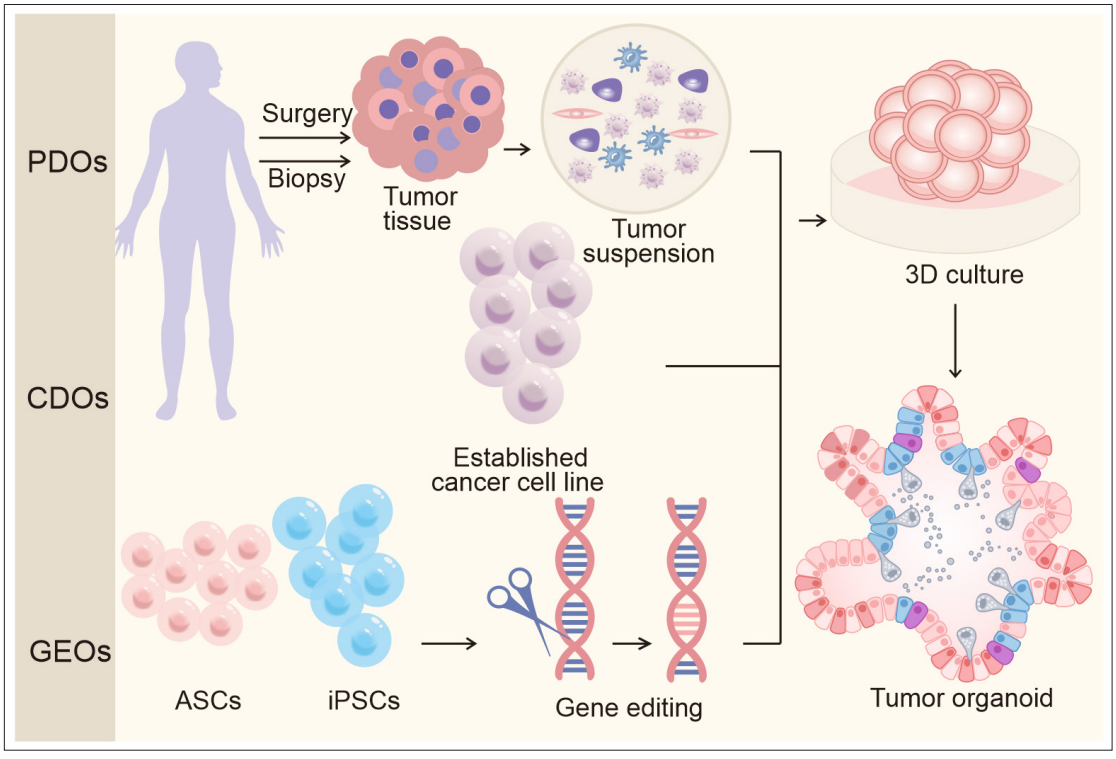


Figure 1. Generation of tumor organoids. Tumor organoids are categorized into PDOs, CDOs, and GEOs. All types are cultured in 3D systems to form tumor organoids, with PDOs being the most effective at capturing individual tumor characteristics. Created using CorelDRAW 2021 (Corel Corporation, Ottawa, Canada). Abbreviations: ASCs, adult stem cells; iPSCs, induced pluripotent stem cells; PDOs, patient-derived organoids; CDOs, cell line-derived organoids; GEOs, genetically engineered organoids.

Another branch of animal models is the cell line-derived xenograft (CDX) model, which involves inoculating *in vitro*-passaged tumor cell lines into immunodeficient mice to induce tumor formation.[26] Compared with PDX models, CDX models exhibit a higher construction success rate and shorter experimental cycles. They are widely used for preliminary *in vivo* drug efficacy evaluation because standardized cell lines yield relatively consistent experimental results.[27] However, prolonged *in vitro* passaging leads to the loss of certain *in vivo* characteristics, and the resulting TME is relatively simplistic, lacking the diverse cellular interactions and stromal components present in patient tumors.[28]

Tumor organoids represent a balance between 2D cell cultures and animal models (Table 1). They simulate ECM interactions through matrices such as Matrigel, thereby maintaining cell polarity and signaling pathway activity.[19] Moreover, long-term stable passaging can be achieved by optimizing culture conditions, such as supplementing epidermal growth factor.[17,22] To consolidate these advantages within a unified theoretical framework, the 2014 perspective by Lancaster and Knoblich[29] provided a formal definition of organoids as self-organizing 3D structures that recapitulate organ-specific cell types and tissue-level functions, thereby establishing benchmark criteria against which tumor organoids are now evaluated.

While tumor organoids already provide an intermediate platform between 2D cultures and animal models, 3D bioprinted tumor organoids further distinguish themselves from other 3D systems, such as multicellular spheroids and organ-on-a-chip devices. Unlike spheroids, which self-assemble without spatial control, bioprinted organoids enable precise, layer-by-layer deposition of patient-derived cancer cells, stromal components, and ECM mimetics, thereby preserving intratumoral heterogeneity and spatial architecture.[30] A representative example of spheroids is neurospheres, a non-bioprinted 3D model used to support neural progenitor cell expansion and investigate early neural development; however, neurospheres exhibit inherent limitations, including batch-to-batch variability, limited clonality, and lack of complex tissue architecture.[31] Furthermore, compared with microfluidic tumor-on-a-chip models—which often require cleanroom fabrication and are limited to 6–10 parallel replicates per run—3D bioprinted tumor organoids can be produced at 96- to 384-well throughput in a standard biosafety cabinet and are already integrated with automated high-content imaging platforms.[32–34]

2.3. Application advantages and challenges of tumor organoids

In basic research, tumor organoids provide an ideal tool for analyzing mechanisms of carcinogenesis. Through clustered regularly interspaced short palindromic repeats (CRISPR)–CRISPR-associated protein 9-mediated gene editing in PDOs, the functions of driver genes can be accurately verified.[16] Using organoid-on-a-chip technology, the invasion trajectories of tumor cells can be observed in real-time, revealing the spatiotemporal dynamics of the epithelial–mesenchymal transition (EMT) process.[17,35]

In clinical settings, PDOs have been applied to individualized drug sensitivity testing. For instance, they have been used to screen the efficacy of aurovertin B in patients with triple-negative breast cancer (TNBC).[19] They also play a role in elucidating drug resistance mechanisms, such as investigating how Hedgehog signaling mediates sorafenib resistance in hepatocellular carcinoma PDOs.[35] Additionally, PDOs contribute to new drug development,

Table 1. Comparison of tumor research models

Model type	Physiologic fidelity	Reproducibility	Cost	Application scenarios	Limitations	References
Two-dimensional cell lines	Low	High	Low	High-throughput drug screening	Lack of 3D structure; simple microenvironment; significant genetic drift	[15,16,23]
PDX models	High	Low	High	Individualized treatment	Long construction cycle (8–12 weeks); species differences; ethical restrictions	[19,25]
CDX models	Medium	High	Medium	Preliminary *in vivo* drug efficacy verification; potential drug screening	Lack of patient tumor stromal components/cell interactions; reduced sub-clonality; not suitable for immunotherapy	[26–28]
Organoids	Medium-high	Medium-high	Medium	Drug screening; mechanism research	Insufficient vascularization; lack of immune components; structural randomness	[17,19,22]

Abbreviations: CDX: cell line-derived xenograft; PDX: patient-derived xenograft.

exemplified by the verification of the efficacy of the bispecific antibody MCLA-158 (an anti-B7-H3 humanized monoclonal antibody) using colorectal cancer PDOs.[35]

To strengthen translational relevance, a milestone for clinical translation was achieved in 2015, when van de Wetering *et al.*[36] established a living biobank of 55 colorectal cancer PDOs and demonstrated >80% concordance between organoid drug responses and patient outcomes, thereby consolidating the "patient avatar" concept. Moreover, Vlachogiannis *et al.*[37] conducted a large-scale clinical trial involving patients with metastatic gastrointestinal cancers and reported that PDOs predicted patient responses to targeted therapies and chemotherapy with over 80% accuracy. Together, these studies provide robust evidence supporting the clinical utility of PDOs in guiding personalized treatment decisions.

In July 2022, the United States Food and Drug Administration (FDA) for the first time allowed organoid-on-a-chip data to support the initiation of a clinical trial for a new drug (Sutimlimab) without requiring traditional animal data, marking a regulatory milestone for organoid applications in drug development.[35,38]

More recently, a translational study further validated the clinical predictive power of PDOs. In a cohort of 128 patients with locally advanced rectal cancer, organoid responses to combined chemoradiotherapy achieved 93.75% accuracy and 96.3% sensitivity in predicting patient outcomes, with synergistic and antagonistic treatment effects faithfully recapitulated *in vitro*.[39]

Despite these advances, tumor organoids continue to face multiple interconnected challenges. Organoids derived from the same patient sample often exhibit structural heterogeneity, including variations in size and morphology, which undermine experimental reproducibility.[35] In addition, their microenvironment remains oversimplified, lacking key components like blood vessels, nerves, and immune cells; thereby limiting the simulation of dynamic tumor–host interactions.[17] Long-term culture stability is another concern; organoids from certain cancer types, such as pancreatic cancer, are prone to phenotypic drift during passaging, resulting in the loss of original tumoral characteristics.[35]

These overlapping limitations have collectively driven the need for innovation, particularly the integration of organoid technology with advanced engineering approaches capable of addressing inherent drawbacks.[18,40] Tumor organoids excel at recapitulating intrinsic tumor biology but lack structural uniformity and precise spatiotemporal control over microenvironmental components.[41] In contrast, 3D bioprinting offers unparalleled capabilities for engineering complex, spatially defined constructs with tailored microenvironments.[41] This complementary relationship creates a powerful synergy: 3D bioprinting can "upgrade" tumor organoids by reducing structural heterogeneity and microenvironmental oversimplification, while tumor organoids provide 3D bioprinting with biologically relevant building blocks to generate more clinically translatable models.[42] This synergy motivates the in-depth exploration of 3D bioprinting principles, technologies, and materials in the following section.

3. Core aspects of three-dimensional bioprinting: from technology classification to bioinks

3.1. Classification and working mechanisms of three-dimensional bioprinting technologies

3D bioprinting technology constructs 3D scaffolds through the layer-by-layer deposition of biological materials and living cells.[43] This process involves the precise positioning and assembly of materials and cells under computer control, enabling the fabrication of complex structures that mimic the architecture and function of native tissues. Based on their forming principles, mainstream 3D bioprinting technologies can be categorized into three primary types (Table 2), each with distinct mechanisms and applications in tumor model construction (Figure 2; Table 3).

Table 2. Comparison of three mainstream three-dimensional bioprinting technologies

Printing technology	Precision	Speed	Cell damage	Suitable materials	Typical application scenarios	References
Extrusion-based	Medium	Medium	Low	Alginate–gelatin; GelMA; collagen	Tumor–stroma co-culture models; breast tumor spheroid construction	[44,45]
Inkjet-based	High	High	Medium	PEG-4MAL; low-viscosity hydrogels	High-throughput drug screening arrays; real-time cell movement monitoring	[44]
Photocurable	High	High	High	GelMA; PEGDA; methacrylated hyaluronic acid	High-precision vascular networks; micro-patterned TME	[44,46]

Abbreviations: GelMA: gelatin methacryloyl; PEGDA: polyethylene glycol diacrylate; PEG-4MAL: 4-arm polyethylene glycol maleimide; TME: tumor microenvironment.

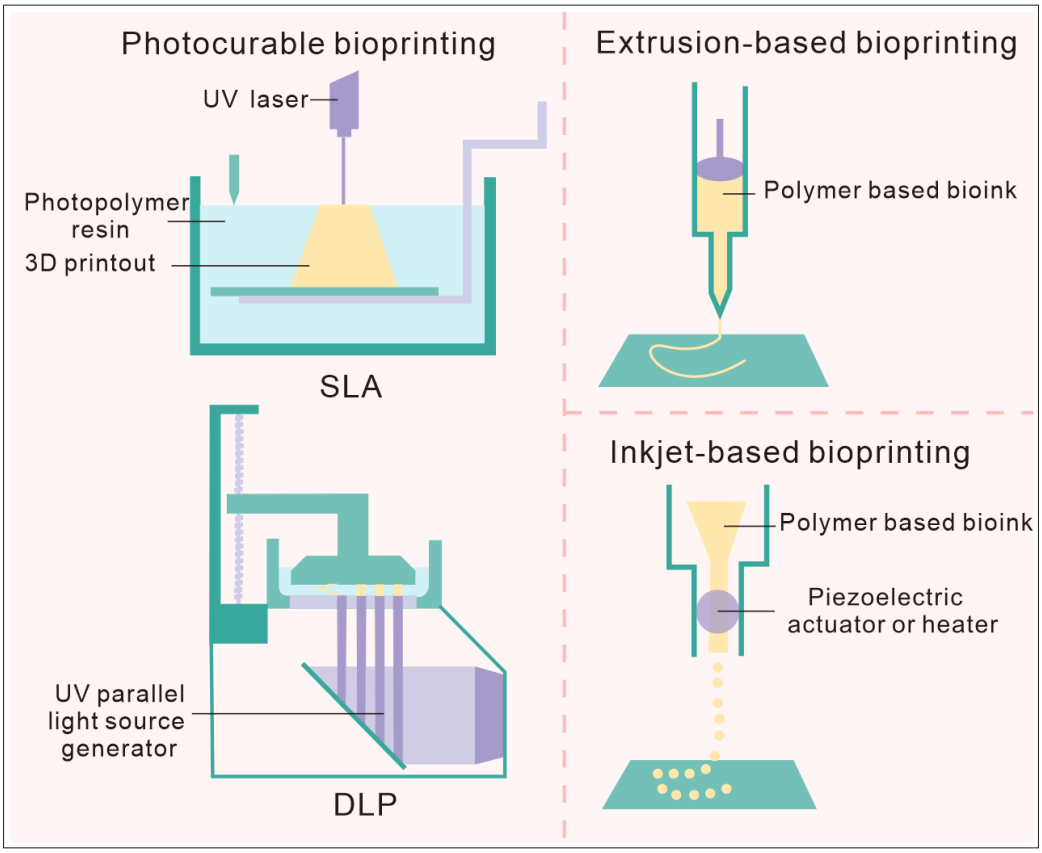


Figure 2. 3D bioprinting technologies applied in tumor model construction. Photocurable bioprinting (SLA and DLP) utilizes light to solidify bioinks, whereas extrusion-based bioprinting deposits bioinks through pressure, and inkjet-based bioprinting dispenses microdroplets of bioinks. Each approach exhibits unique mechanisms and applications for constructing tumor-relevant structures. Created using CorelDRAW 2021 (Corel Corporation, Ottawa, Canada). Abbreviations: UV: ultraviolet; 3D: three core three-dimensional; SLA: stereolithography; DLP: digital light processing.

Table 3. A comparison of three-dimensional bioprinting technologies in tumor organoid engineering

Technology	Typical spatial resolution	Cell survival after printing	Strengths for tumor modeling	Major limitations	References
Extrusion-based	100–300 μm	85–95%	Multi-cell/type & ECM deposition; scalable to several mm^3; compatible with high-viscosity composite hydrogels	Comparatively low resolution; risk of nozzle clogging; axial heterogeneity when printing branched vascular trees	[47–51]
Inkjet-based	50–100 μm	75–90%	High speed, low reagent volume; 96-well plate-compatible mini-tumor arrays for high-throughput screening; real-time live-cell imaging after dispensing	Limited to low-viscosity bioinks (<10 mPa·s); difficulty in maintaining vertical orientation; 3D architecture; possible heat damage to cells	[52–55]
Photocurable	10–50 μm	90–98%	Ultra-high resolution for micro-vessels & hypoxic niches; rapid layerless curing; compatible with stimuli-responsive or multi-material resins	Requires photo-initiator (cytotoxicity risk); shallow construct height (mm scale) without z-stage translation; post-print stiffness may hinder cell spreading	[56,57]

Abbreviations: 3D: three-dimensional; ECM: extracellular matrix.

Extrusion-based bioprinting operates by applying mechanical or pneumatic pressure to extrude bioink through a nozzle, which is then deposited onto a platform following a preprogrammed path to build structures layer-by-layer.[6] It employs sacrificial (temporary, dissolvable frameworks), support (temporary rigid supports for sag-prone parts), and embedded (printing in soft protective gels) strategies to facilitate the fabrication of large-scale constructs and complex organ models,[58] making it particularly suitable for constructing multicellular structures,[59] such as heterogeneous TMEs composed of tumor cells, stromal cells, and immune cells.[6,60] This technology is compatible with a wide range of hydrogels and has been used to generate tumor–stroma coculture models using cell-laden bioinks, such as collagen.[60] Quantitative benchmarks indicate that filament diameters of 100–300 μm can be routinely achieved while maintaining 85–95% cell viability when nozzle diameters of ≥200 μm and extrusion pressures of ≤200 kPa are used. Moreover, extrusion-based bioprinting tolerates high-viscosity composite hydrogels and can be scaled to construct several mm^3 in size, offering the highest throughput among current bioprinting modalities.[50,51,61] However, its comparatively low resolution and susceptibility to nozzle clogging may introduce axial heterogeneity, particularly when printing branched vascular structures.[62,63]

Inkjet-based bioprinting is inspired by conventional inkjet printing and generates microdroplets of bioink through thermal bubble or piezoelectric actuation.[64] These droplets are precisely deposited at designated locations.[6] This technology features non-contact, nozzle-less operation with minimal cellular damage.[58] Drop-on-demand systems routinely achieve lateral resolutions of 50–100 μm and maintain 75–90% cell viability, provided the bioink viscosity remains <10 mPa·s and cell density $<10^6$ cells/mL.[55,65] These characteristics allow for the rapid production (in minutes) of 96-well-plate–compatible mini-tumor arrays for high-throughput drug screening, with real-time live-cell imaging performed immediately after dispensing.[52,66] Nevertheless, requirements for low-viscosity bioinks, challenges in maintaining vertical 3D architecture, and potential heat-induced damage in thermal modes restrict its application to relatively thin tumor models.[53,54]

Photocurable bioprinting employs ultraviolet or visible light[67] to initiate photocrosslinking reactions in photosensitive bioinks, rapidly solidifying the material to form the desired structures. Representative technologies include stereolithography and digital light processing.[68] This technique enables computer-assisted patterning of 3D, cell-laden constructs using photoactivatable bioresins, offering significantly enhanced resolution compared with extrusion-based methods.[48,58] Layer-free projection methods achieve the highest spatial resolution among the three modalities (10–50 μm) while maintaining 90–98% cell viability when photoinitiator concentrations are kept <0.25% (w/v) and irradiance <20 mW/cm^2.[69,70] These capabilities support the fabrication of ultra-high-resolution micro-vessels and hypoxic niches that closely mimic tumor neovasculature, and the rapid curing speed is compatible with stimuli-responsive or multimaterial resins.[71–73] However, the mandatory use of photoinitiators poses potential cytotoxicity risks, and limited light-penetration restricts construct height to the millimeter scale unless z-stage translation is employed.[57,74]

3.2. Component selection, cutting-edge designs, and printing parameter optimization of bioinks

3.2.1. Core constituents of bioinks

Bioinks are the core materials in 3D bioprinting and play a pivotal role in determining printing success and the functionality of the resulting constructs.[75] It must simultaneously meet the dual requirements of printability and biocompatibility. The careful selection and design of bioinks are therefore essential for achieving optimal printing results and biological performance.

The cellular component of bioinks is tailored to the specific requirements of the model. For example, liver organoid bioinks are supplemented with hepatocytes, hepatic stellate cells, and Kupffer cells to restore liver physiology,[76] whereas tumor bioinks ideally contain patient-derived cancer cells to preserve intrinsic heterogeneity, as demonstrated in colorectal cancer organoid arrays.[77] Once the appropriate cell population is selected, single-cell viability must remain ≥80% throughout printing and subsequent culture, because this fraction determines the physiological relevance of the final construct.[47] At the pipeline level, Schütte *et al.*[78] increased the overall success rate of establishing patient-derived colorectal organoid lines to above 70% by adding amphotericin B and a Rho-associated coiled-coil containing kinase II inhibitor during the first week—an optimization now widely adopted by academic biobanks. Ultimately, the precise combination of cell types determines how accurately the model can replicate tumor biology and its microenvironment.

Scaffold materials form the structural framework of the bioink and can be divided into natural and synthetic materials. Natural materials, such as collagen, gelatin,[79], and sodium alginate, offer excellent biocompatibility, as they are derived from biological sources and possess chemical compositions similar to the natural ECM. For instance, gelatin methacryloyl (GelMA), a photo-crosslinkable derivative of gelatin, retains cell-adhesive RGD motifs and

enzymatic degradation sites, promoting cell adhesion and proliferation.[80] However, pure GelMA hydrogels exhibit low mechanical strength, with compressive strengths as low as 2.98 kPa at 5% concentration, limiting their use in load-bearing applications.[76,81] Synthetic materials provide superior mechanical stability and controllable degradation rates.[82] Polyethylene glycol (PEG), for example, is FDA-approved and degrades into non-toxic, water-soluble byproducts, making it highly biocompatible.[83] However, PEG lacks cell-adhesive motifs, which may reduce cell attachment and tissue integration.[84] To overcome these limitations, composite scaffolds have been developed. For example, gelatin–PEG blends combine the biocompatibility of gelatin with the mechanical strength of PEG, resulting in hydrogels with tunable mechanical properties and improved cell compatibility.[85] Specifically, GelMA–PEG composite hydrogels have been shown to balance stiffness and remodeling, supporting both mechanical integrity and ECM deposition.[86] Thus, composite scaffolds such as gelatin–PEG blends represent the mainstream choice in current bioink design, offering balanced performance in biocompatibility, mechanical strength, and degradation kinetics.[76,82] For instance, Yue *et al.*[87] demonstrated that incorporating 5% (w/v) PEG diacrylate into GelMA hydrogels increased the compressive modulus from 3 to 12 kPa while maintaining over 85% cell viability.

Functional factors and physical cues are integrated into bioinks to simulate the TME. For example, hydrogel stiffness can mimic the mechanical properties of colorectal cancer stroma and thereby regulate carcinoembryonic antigen-related cell adhesion molecule 5 expression.[77] Geometric constraints can also guide neural axon sprouting or liver organoid polarization.[88] Soluble factors, such as growth factors, can also be added to modulate cell behavior.

3.2.2. Advanced bioink designs

Beyond static composite hydrogels, the last 5 years have seen three converging directions that transform bioinks into "active" biomaterials: multi-material patterning, dynamic self-healing networks, and stimulus-responsive systems.

(i) Multi-material patterning enables voxel-specific mechanical or biochemical gradients that single polymer inks cannot achieve. For example, an alginate–gelatin–nano-hydroxyapatite ink was co-printed with an RGD-functionalized alginate to generate a 250 μm mineralized shell around a soft, cell-rich core, driving site-specific osteogenesis of patient-derived bone marrow stromal cells without the need for exogenous osteogenic media.[89] Similarly, coaxial deposition of a GelMA core containing colorectal cancer organoids and an alginate–fibrin shell loaded with cancer-associated fibroblasts yielded a 500 μm-thick pseudocapsule that upregulated α-smooth muscle actin and interleukin (IL) 6 within 72 h.[90]

(ii) Dynamic, self-healing hydrogels replace permanent covalent networks with reversible supramolecular interactions. Host–guest hydrogels based on cyclodextrin–adamantane-modified hyaluronic acid shear-thin during extrusion yet instantly self-heal after deposition, producing ≤50 μm filaments with >95% post-printing viability of human induced pluripotent stem cell-derived hepatocytes.[91]

(iii) Stimulus-responsive bioinks undergo preprogrammed shape or functional changes after printing. For instance, Kirillova *et al.*[92] demonstrated that methacrylated alginate and hyaluronic acid hydrogels self-fold into perfusable tubular structures upon green-light illumination, enabling the formation of vascular-like conduits with high spatial resolution and cell compatibility. Similarly, Cao *et al.*[93] developed bilayer hydrogels composed of polycaprolactone and sodium alginate that undergo temperature-triggered shape transformation, rolling into tubular constructs mimicking native blood vessels, with tunable diameter and wall thickness controlled by layer composition and external stimuli.

3.2.3. Critical printing parameters for optimizing bioink performance

Optimizing the physical printing window is equally critical to the rational design of bioinks, as suboptimal printing conditions can significantly compromise the performance of bioinks. Extrusion pressure, nozzle speed, temperature, and crosslinking kinetics all play a role in determining post-printing cell viability, structural fidelity, and long-term culture stability. Excessive shear stress (>25 kPa) or high nozzle translation speeds (>15 mm/s) can reduce patient-derived tumor-cell survival to <70% within 24 h, whereas 15–20 kPa and 5–10 mm/s preserve ≥85% viability without sacrificing resolution.[49] Maintaining the bioink at 4–10°C delays premature gelation, and brief ultraviolet exposure (5–10 mW/cm^2, <10 s) ensures uniform crosslinking with minimal photoinitiator toxicity.[68] Using layer thickness ≤100 μm helps mitigate the effects of limited light penetration (1.5–2.0 mm at 405 nm in GelMA), thereby reducing the risk of hypoxic cores during extended culture.[57] Thus, parameter optimization is as critical as bioink composition for generating clinically relevant tumor organoids.

4. Applications of three-dimensional bioprinting in tumor organoids

4.1. Three-dimensional bioprinting for the construction of heterogeneous tumor microenvironments with immune interactions

4.1.1. Precise construction of heterogeneous tumor microenvironments

The heterogeneity of the TME is a key factor leading to treatment resistance.[94] The TME has a complex composition, encompassing a variety of cell types and ECM components (Figure 3). 3D bioprinting technology enables the precise arrangement of various TME components through spatial positioning techniques, overcoming the structural randomness inherent in organoid formation. This precision is reflected not only in the spatial distribution of different cell types but also in the simulation of physicochemical microenvironments analogous to those *in vivo*, thereby providing a more authentic model for in-depth investigations into tumor occurrence and progression[95] (Table 4).

The heterogeneous TMEs precisely constructed using 3D bioprinting technology have been extensively applied in the research of various tumor types, including lung cancer, glioblastoma (GBM), liver cancer, colorectal cancer, gastric cancer, and pancreatic cancer.

In lung cancer model construction (Figure 4A), researchers have optimized GelMA scaffolds by incorporating hyaluronic acid methacrylate, a strategy that enables the model to house multiple cell types, including lung epithelial cells, vascular endothelial cells, and mesenchymal cells.[99] This 3D bioengineered model effectively simulates cell–matrix interactions and matches the microenvironmental characteristics of lung tissues by regulating the scaffold composition,[100,101] highlighting the advantages of 3D bioengineering in constructing physiologically relevant TMEs.

In GBM models (Figure 4B), 3D bioprinting has been employed to reconstruct complex TMEs containing glioma cells, macrophages, and endothelial cells, with the printing of co-culture models featuring spatial zoning.[102,103] GBM is characterized by high invasiveness and drug resistance,[104] which are closely associated with interactions between tumor cells and immune cells in the TME. Utilizing GelMA-based bioink, researchers developed a "tumor–macrophage" co-culture model in which macrophages are polarized into a pro-tumor phenotype under the induction of glioma cells, secreting cytokines such as transforming

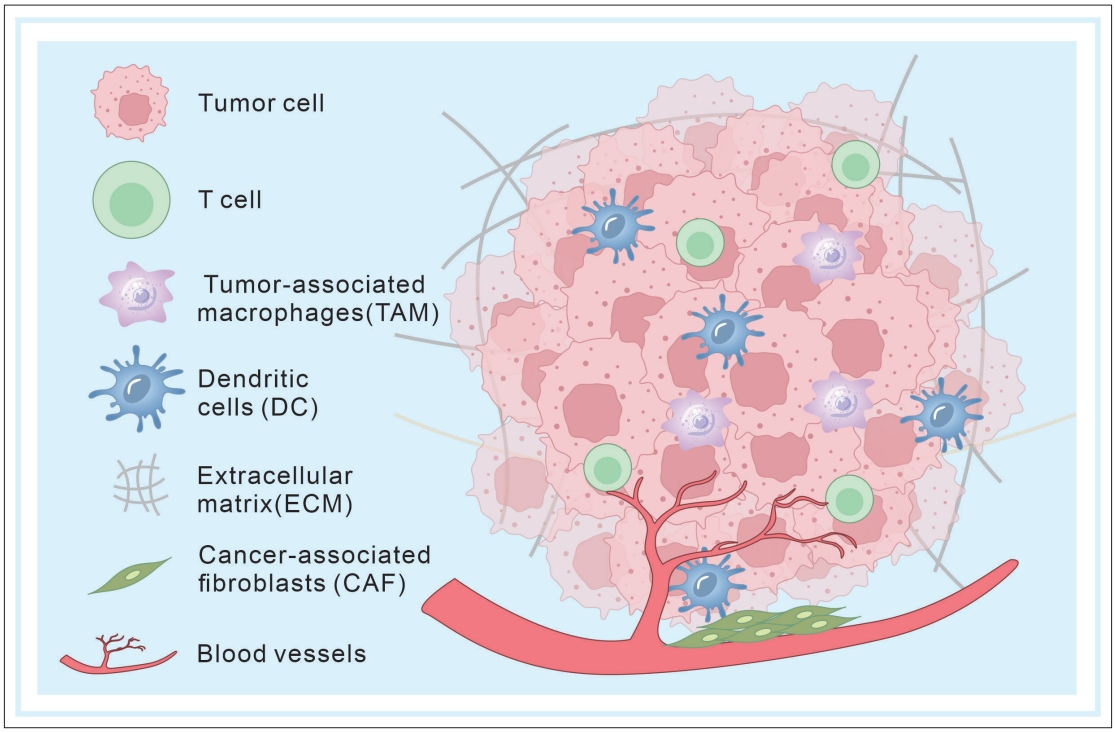


Figure 3. Components of the tumor microenvironment (TME), including tumor cells, immune cells (T cells, tumor-associated macrophages, dendritic cells), extracellular matrix, cancer-associated fibroblasts, and blood vessels, organized by 3D bioprinting to represent heterogeneous TMEs for cancer research. Created using CorelDRAW 2021 (Corel Corporation, Ottawa, Canada).

Table 4. Selected three-dimensional bioprinted tumor microenvironment models

Tumor type	Construction strategies	Key outcomes	References
Colorectal cancer	Build PDOs; recapitulate tumor structure and composition	Retain genetic heterogeneity; mimic TME; support tumor and drug study	[14,36,96–98]
Lung cancer	Optimize GelMA scaffolds with hyaluronic acid; house multiple cells	Simulate cell–matrix interactions; match lung microenvironment	[99–101]
GBM	Reconstruct TME with glioma, macrophage, and endothelial cells; print co-culture model	Simulate pro-tumor macrophages; reflect drug resistance with 25% higher survival than 2D culture	[102–105]
Liver cancer	Construct TME with hepatoma cells, hepatic stellate cells, and ECM; control stiffness to 4–10 kPa	Activate stellate cells for collagen secretion; enhance migration and invasion with 30% higher EMT	[106–109]
Gastric cancer	Build 3D model with GelMA via extrusion; design grid; optimize bioink mechanics	Mimic TME; provide biomimetic ECM for cell adhesion and proliferation	[110]
Pancreatic cancer	Control stroma proportion; simulate fibrotic TME	Represent proliferation and drug resistance; aid drug screening and mechanism study	[111,112]

Abbreviations: 3D: three-dimensional; ECM: extracellular matrix; EMT: epithelial–mesenchymal transition; GBM: glioblastoma; GelMA: gelatin methacryloyl; PDOs: patient-derived organoids; TME: tumor microenvironment.

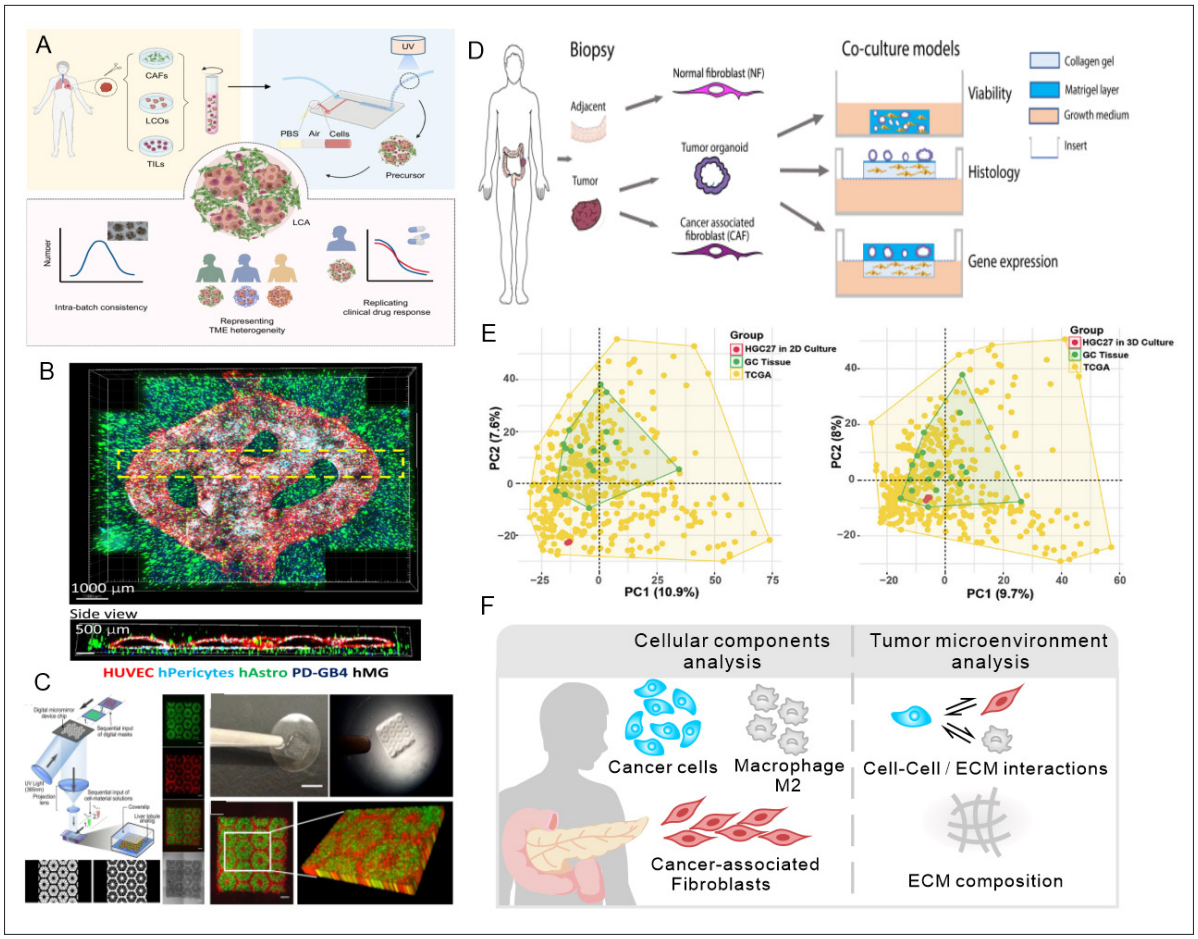


Figure 4. Applications of precisely engineered heterogeneous tumor microenvironment (TME) in three-dimensional bioprinted and organoid cancer models. Representative examples include (A) lung cancer (reprinted from Zhang *et al.*[113]); (B) glioblastoma (reprinted from Neufeld *et al.*[103]), scale bar: 500, 1000 μm; (C) liver cancer (reprinted from Datta *et al.*[114]); (D) colorectal cancer (reprinted from Atanasova *et al.*[115]); (E) gastric cancer (reprinted with permission from Ju *et al.*[110]; copyright © 2025, Wiley-VCH GmbH); and (F) pancreatic cancer (The image was created by the authors using CorelDRAW 2021 (Corel Corporation, Ottawa, Canada).

growth factor-β to promote glioma cell invasion.[105] When treated with temozolomide, the survival rate of glioma cells in this 3D bioprinted model was approximately 25% higher than that in 2D culture models, a result consistent with the *in vivo* drug resistance characteristics of GBM.[106,116]

In liver cancer models (Figure 4C), 3D bioprinting technology has been applied to construct a microenvironment containing hepatocellular carcinoma (HCC) cells, hepatic stellate cells, and liver decellularized ECM (dECM).[76] Liver cancer is often accompanied by cirrhosis, and the stiffness of the liver matrix is an important factor affecting tumor progression.[108] By adjusting the ratio of GelMA and dECM in the bioink, the stiffness of the model was controlled to 4–10 kPa, which is similar to the stiffness of cirrhotic liver tissues.[109] Experimental results showed that in this stiffness environment, hepatic stellate cells were activated to secrete a large amount of collagen. Meanwhile, the migration and invasion ability of HCC cells was significantly enhanced, with the expression of EMT-related markers increased by about 30% compared with the low-stiffness model.[106,107]

In colorectal cancer research (Figure 4D), the PDO construction strategy facilitates the precise establishment of heterogeneous TMEs by recapitulating the structural features and cellular composition of the original tumor tissue.[96] These organoids retain the genetic heterogeneity of the primary tumor, including somatic mutations, copy number variations, and gene expression profiles that are consistent with clinical colorectal cancer tissues.[14] For example, the "cystic versus solid" epithelial organization observed in primary colorectal tumors is generally preserved in these organoids.[36] Marker expression analysis reveals both inter-patient heterogeneity and heterogeneity among individual organoids within each culture, which accurately reflect the heterogeneous characteristics of the *in vivo* TME.[97] Such precise recapitulation enables organoids to better mimic the *in vivo* biological behavior of tumors, offering a reliable model for studying tumor progression and drug responses that traditional models, which often fail to preserve tissue-specific heterogeneity, cannot provide.[36,98]

In gastric cancer models (Figure 4E), researchers used GelMA hydrogel as bioink to construct a 3D bioprinted model via extrusion-based printing. This model accurately mimics the heterogeneous TME of gastric cancer. It is designed with a grid-like structure to simulate the spatial arrangement of tumor cells *in vivo*. The bioink formulation is optimized to match the mechanical properties of gastric cancer tissues, providing a biomimetic ECM microenvironment for cell adhesion and proliferation.[110]

In addition, in pancreatic cancer models (Figure 4F), 3D bioprinting precisely constructs a heterogeneous TME. Pancreatic cancer is known for rich stromal fibrosis, which is an important reason for treatment difficulty.[111] Researchers simulate its fibrotic microenvironment by controlling the proportion and distribution of stromal components via 3D bioprinting. These models represent cancer cell proliferation and drug resistance, aiding drug screening and mechanism research.[112]

In summary, this section provides foundational model support for the subsequent simulation of tumor–immune crosstalk (**Section 4.1.2**).

4.1.2. Spatial simulation of tumor–immune crosstalk

Beyond integrating immune cells into tumor-specific models, 3D bioprinting enables targeted replication of spatially dependent tumor–immune interactions—a critical feature lacking in 2D co-culture systems and traditional organoids.[117–119] By controlling the spatial arrangement of multiple cell types, bioprinted models more accurately reproduce the structure of the TME, allowing for the investigation of how spatial organization affects immune responses.

In breast cancer models, the integration of bioprinting with magnetic levitation technology enables the positioning of tumor cells, immune cells, and stromal cells in distinct scaffold regions, mimicking the layered structure of the breast tumor TME. This spatial arrangement recreates key TME crosstalk, such as macrophage secretion of IL-10 and the subsequent inhibition of $CD8^+$ T-cell activity, providing insights into how spatial separation of immune and tumor cells influences immune suppression.[120]

Composite bioinks are critical for maintaining the survival and functionality of both tumor and immune cells.[114] Unlike single-component bioinks, which may compromise either tumor organoid formation or immune cell viability, these blends ensure that immune cells retain their ability to migrate, activate, and interact with tumor cells, thereby replicating the functional dynamics of the *in vivo* TME.[121]

These integrated models overcome a core limitation of traditional organoids by recapitulating tumor–immune crosstalk events, such as immune checkpoint activation, macrophage-mediated immune suppression, and T-cell exhaustion.[98,122] Consequently, they serve as valuable tools for exploring immune escape mechanisms and screening immunotherapies. Ongoing optimization of bioink materials and printing precision is expected to further enhance their utility in guiding clinical precision treatments.[114]

4.2. Strategies for building vascularized tumor organoids

Tumor vascularization is crucial for nutrient supply and the development of distant metastasis. Traditional organoids often suffer from central necrosis due to the lack of a functional vascular network and cannot simulate hematogenous metastasis.[123–126] (Figure 5A). 3D bioprinting addresses this limitation through two strategies, each with distinct advantages that can be selected and optimized according to specific research needs.

Direct printing of vascular channels is one key approach. Photocurable technologies are used to fabricate vascular scaffolds with branched structures.[126] After seeding endothelial cells, a connected vascular network is formed. In GBM models, this vascularized structure recreates physiological interstitial fluid flow and provides

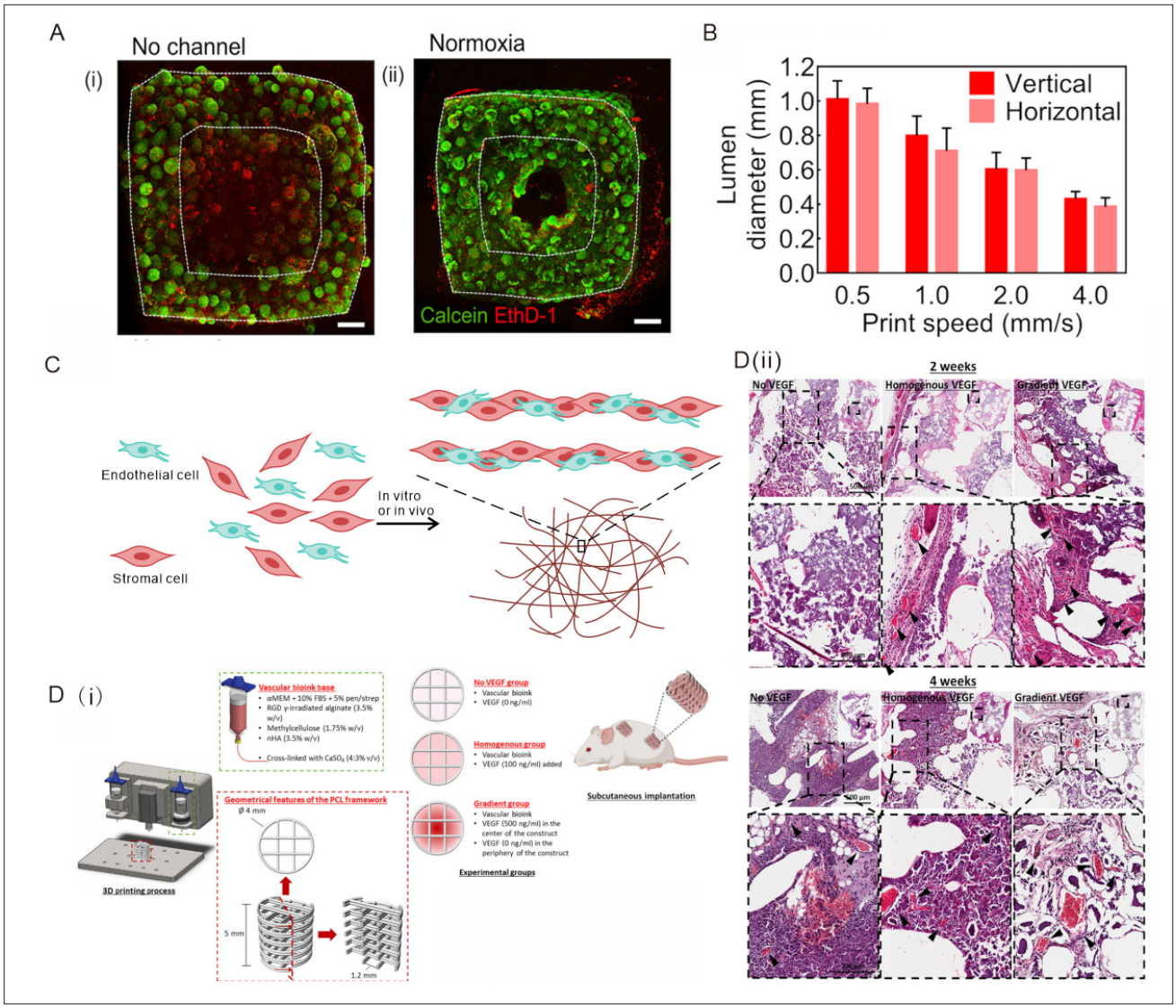


Figure 5. Strategies for engineering vascularized tumor organoids and their impact on angiogenesis and drug delivery. (A) (i) Vascularized perfusion abolishes central necrosis and sustains viability across 4 mm, whereas (ii) avascular organoids develop a necrotic core, demonstrating that functional vasculature is essential for nutrient delivery and metastasis modeling. Scale bar: 500 μm. (B) By adjusting the print speed, channel diameters can be precisely controlled between 400 and 1000 μm. Reprinted from Skylar-Scott *et al.*[126] (C) Endothelial cells form tubular structures in response to vascular endothelial growth factor (VEGF) gradients. Reprinted with permission from O'Connor *et al.*[132] Copyright © 2022, Springer Nature Limited. (D) Spatially controlled VEGF gradients within three-dimensional (3D)-printed constructs direct angiogenesis. (i) Schematic of 3D-printed scaffolds with varying VEGF gradients and (ii) Quantification of vessel density *in vivo* at 2- and 4-weeks post-implantation, demonstrating the influence of VEGF gradients on angiogenic guidance and density. Scale bar: 500 μm; magnification: 200 μm. Reprinted from Freeman *et al.*[127]

a microenvironment that supports tumor cell survival and phenotypic differentiation.[128] The diameter of the vascular scaffold can be precisely controlled to mimic *in vivo* tumor microvessels, which is essential for reconstructing the tumor vascular microenvironment (Figure 5B). Oxygen and nutrient transport efficiency can be further optimized by adjusting scaffold porosity.[129] In such vascularized models, tumor cells located in the perivascular regions exhibit higher viability and drug resistance compared to those in peripheral regions, reflecting the supportive role of vascular structures in tumor survival.[130]

To enhance endothelial cell adhesion and proliferation on scaffolds, researchers grafted GRGDSP peptides containing RGD sequences onto polycarbonate urethane (PCU) surfaces using photoactive 4-benzoylbenzoic acid under ultraviolet irradiation. Higher peptide concentrations significantly improved cell adhesion and spreading. For example, PCU200 (200 μg peptides/cm^2) exhibited increased cell adhesion and larger cell spreading areas. It also promoted proliferation and retained approximately 92% of cells under flow shear stress, whereas unmodified PCU retained only about 1% of cells. These results show its potential for use in small-diameter vascular grafts.[131]

Induction of angiogenesis represents the second major strategy. Sustained-release systems loaded with growth factors can be embedded within bioinks. Following bioprinting, endothelial cells migrate along stromal-derived vascular endothelial growth factor (VEGF) gradients and self-assemble into perfusable microvessels that anastomose with the surrounding environment[132] (Figure 5C). In lung cancer models, vascular networks constructed by this approach effectively support drug delivery, with distribution patterns highly consistent with those observed in clinical tumor tissue sections.[133] Additionally, the loading dose and release rate of growth factor sustained-release systems can be precisely regulated. Studies have shown that when the initial VEGF release rate is maintained within an optimal range, endothelial cell migration is significantly accelerated, enabling the formation of a preliminary vascular network within 7 days.[132]

Adjusting the composition and structure of bioinks enables control over VEGF gradient distribution, thereby guiding the directionality and density of angiogenesis[127,132] (Figure 5D). In lung cancer models, VEGF concentrations within the tumor area are approximately 2–3 times higher than in surrounding areas. This gradient promotes preferential endothelial cell migration toward the tumor, forming a tumor-centered vascular network.[134] Hemodynamic characteristics of the network, including blood flow velocity and flow rate, can be monitored using laser Doppler flowmetry, revealing similarities to vascular parameters observed in clinical lung cancer tissues.[132] In paclitaxel delivery experiments, these vascular networks effectively transport drugs into tumors, achieving drug concentrations approximately twice those of traditional models and a more uniform intratumoral distribution.[133]

Finally, vascularized organoids not only realistically simulate the delivery of chemotherapeutic drugs but also provide an ideal platform for evaluating anti-angiogenic therapies. Their drug response curves show high consistency with PDX models.[134,135] In evaluations of bevacizumab efficacy, tumor vascular density in vascularized organoid models decreases by ~40% following treatment, closely matching results observed in PDX models.[136] In contrast, traditional organoid models fail to accurately reflect anti-angiogenic effects due to the absence of vascular structures.[132]

4.3. High-throughput drug screening using three-dimensional bioprinted organoids

The integration of 3D bioprinting and microfluidic technologies enables the construction of miniaturized, perfusable platforms for drug screening.[137] These platforms recapitulate vascular network topology and hemodynamic cues, offering high throughput, high sensitivity, and low reagent consumption. Moreover, they enable the rapid screening of effective antitumor drugs to support clinical decision-making.[112,132,138]

Standardized tumor organoid arrays can be generated in 96-well plates using 3D bioprinting.[52] These arrays are subsequently integrated with microfluidic chips to achieve precise drug delivery under perfusable conditions, as well as real-time monitoring of vascular perfusion and organoid responses.[132,138] The bioprinted organoid arrays exhibit high consistency, characterized by uniform morphology and spatial distribution, which ensures the reliability of subsequent quantitative analysis.[138,139] Through microchannel design, the microfluidic chips enable precise control of drug concentration gradients and administration timing, with a minimum administration volume of 10 nL. When combined with perfusable, vascular-like networks that mimic *in vivo* drug transport, this approach substantially reduces drug consumption. Moreover, sensors and imaging modules integrated into the chips allow real-time monitoring of organoid viability, metabolic activity, and morphological changes, providing multi-parameter evaluation metrics for drug screening.[132]

In clinical studies of breast cancer[13] and colorectal cancer,[36] 3D bioprinting platforms constructed using GelMA/adipose dECM composite bioinks have been employed to assess the sensitivity of patient-derived cancer

organoids to chemotherapeutic drugs. These assays can be completed within a short culture period, and the resulting organoids cultured exhibit drug response profiles consistent with the biological behavior of patient tumor tissues.[138] Organoid cell viability is commonly evaluated using adenosine triphosphate (ATP) release assays, which serve as an endpoint validation method consistent with label-free biomass monitoring results.[139] When drug concentrations reach specific thresholds, ATP levels decrease significantly, enabling the determination of drug sensitivity.[140] For each drug, concentration gradients are established, and therapeutic efficacy is compared by calculating half-maximal inhibitory concentration values.[141]

In addition, by bioprinting heterogeneous models that incorporate tumor cells, immune cells, and vascular networks, the cytotoxic effects of drugs on different cell subpopulations can be evaluated simultaneously, providing a rational basis for designing combination therapies.[132,142] In these mixed models, the proportions of cellular subpopulations can be adjusted according to the genetic and morphological characteristics of clinical samples, thereby preserving the intrinsic heterogeneity of original tumors. Through selective labeling of tumor and immune cells, drug-induced cytotoxic effects can be clearly distinguished. For example, in one study evaluating the combined use of colony-stimulating factor 1 receptor inhibitors and signal transducer and activator of transcription 6 inhibitors, a synergistic effect was observed in regulating macrophage polarization and suppressing tumor cell growth, with combination therapy demonstrating significantly greater efficacy than monotherapy.[142]

This high-throughput platform offers several advantages. It minimizes tissue requirements, typically requiring only 5–10 mm of tumor tissue, which is particularly important given the limited availability of clinical samples.[143] It also shortens experimental timelines: PDOs can be established within hydrogels in 1–2 weeks, and drug screening assays can be completed within a few days, enabling rapid feedback for clinical treatment decisions[144,145] (Figure 6A). Additionally, the platform supports multi-parameter analysis, allowing simultaneous assessment of cell viability, immune cell activation, and cytokine secretion to comprehensively evaluate drug efficacy.[146] Beyond viability measurements, immunofluorescence can be used to detect tumor-infiltrating T cells[147] (Figure 6B), while quantitative reverse transcription polymerase chain

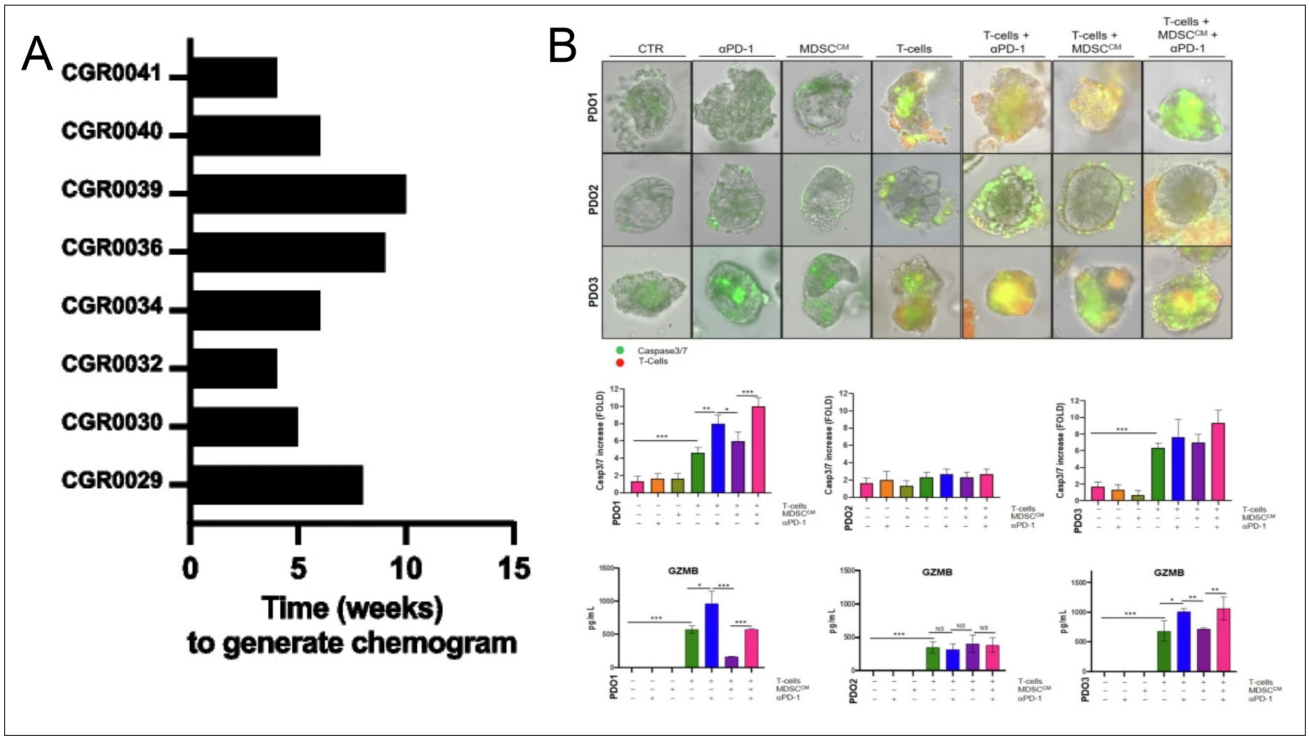


Figure 6. Integrated evidence supporting the high-throughput patient-derived organoid (PDO) platform. (A) Core needle biopsy-derived PDOs enable completion of chemograms within 6 weeks. Reprinted from Cartry *et al.*[145] (B) A patient-derived immuno-organoid platform simultaneously evaluates apoptosis (caspase 3/7), T-cell activation (granzyme B), and responses to immunotherapy. Reprinted from Esposito *et al.*[147] Together, these results demonstrate that PDO-based platforms require minimal tissue input, operate on clinically relevant timelines, and enable the multi-parametric evaluation of both tumor cell fate and immune engagement, highlighting their potential for precision oncology and studies of resistance mechanisms.

reaction enables analysis of tumor-killing factor expression, providing deeper insights into drug-induced modulation of tumor–immune interactions[142,147] (Figure 6B).

Finally, this platform serves as a powerful tool for investigating mechanisms of drug resistance. Following drug treatment, organoids can be subjected to gene sequencing and proteomic analyses to identify genes and proteins associated with resistance. These findings facilitate the discovery of novel therapeutic targets for overcoming resistance phenotypes.[142]

4.4. Validation of bioprinted organoids in clinical samples

To validate 3D bioprinted tumor organoids against clinical samples, multidimensional, multimodal approaches have been implemented across different cancer types to ensure that these models faithfully recapitulate the biological characteristics of patient-derived tumors.

In breast cancer studies, bioprinted organoids generated using patient-derived TNBC cells and GelMA scaffolds are validated by comparing their gene expression profiles with those of clinical TNBC tissue samples and PDX models using RNA sequencing. Key cancer hallmarks, such as cell proliferation, invasion, and drug response, are assessed in bioprinted organoids and correlated with clinical treatment outcomes.[148] For instance, organoid resistance to doxorubicin shows high consistency with both PDX models and patient response data. Furthermore, one study confirms that bioprinted scaffolds encapsulating *Citrus limon* L.-derived extracellular vesicles retain the anticancer efficacy observed in clinical TNBC samples, as evidenced by inhibited phosphorylation of phosphoinositide 3-kinase/protein kinase B and mitogen-activated protein kinase/extracellular signal-regulated kinase pathway proteins, consistent with molecular changes detected in patient tumors.[148]

In liver cancer research, bioprinted organoids constructed from patient-derived HCC cells, hepatic stellate cells, and dECM are validated through the assessment of liver-specific functions, including albumin secretion, urea synthesis, and cytochrome P450 enzyme activity, and are compared with primary human hepatocytes obtained from clinical samples.[77] Moreover, gene expression of HCC-related markers in the organoids aligns with RNA sequencing data from clinical HCC tissues. Their responses to hepatotoxic drugs, such as acetaminophen, also correspond to clinical cases of drug-induced liver injury, confirming their predictive accuracy. Patient-derived liver organoids have additionally been shown to replicate genetic defects associated with hereditary liver diseases, such as α-1 antitrypsin deficiency, further demonstrating their ability to model *in vivo* pathological conditions.[77]

For gastric cancer, bioprinted GelMA-based organoids incorporating patient-derived gastric cancer cells are validated through histopathological staining and immunofluorescence analyses, which demonstrate close resemblance to the morphological and phenotypic features of clinical gastric cancer tissues.[110] Transcriptomic analysis reveals that these organoids retain gastric cancer-specific genetic alterations, such as *TP53* mutations and *MET* amplification, as well as gene expression signatures such as activation of the transforming growth factor-β signaling pathway. Furthermore, their sensitivity to chemotherapeutic agents, including oxaliplatin and 5-fluorouracil, is consistent with responses observed in PDX models and patient clinical records.[110] These organoids also exhibit metabolic features characteristic of clinical gastric cancer tissues, such as the Warburg effect, as confirmed by extracellular acidification rate measurements, further validating their physiological relevance.[110]

In pancreatic ductal adenocarcinoma (PDAC) studies, bioprinted organoids that simulate the dense fibrotic TME using patient-derived PDAC cells and cancer-associated fibroblasts are validated by comparing the expression of stromal markers, such as α-smooth muscle actin and collagen I, with those observed in clinical PDAC tissue sections.[111] Drug responses to gemcitabine and nab-paclitaxel were evaluated and correlated with patient treatment outcomes. Notably, the high drug resistance observed in these organoids, attributed to stromal barrier effects, closely mirrors the poor clinical response of PDAC patients to standard chemotherapy.[111] Proteomic analysis further revealed similar expression patterns of drug resistance-related proteins, such as ATP-binding cassette transporters, in both bioprinted organoids and clinical PDAC samples. Additionally, patient-derived PDAC organoids recapitulate the immunosuppressive TME of clinical tumors, including high infiltration of M2-type macrophages, which aligns with immune profiling data from patient biopsies.[111]

In summary, the validation of bioprinted organoids across multiple cancer types has been achieved through comprehensive, multi-faceted approaches, including gene expression profiling, functional assays, histopathological assessments, and drug response evaluations against clinical samples and PDX models. Collectively, these validation strategies demonstrate the biological fidelity and clinical relevance of bioprinted organoids, supporting their use as robust preclinical platforms for cancer research and personalized medicine.

4.5. Clinical translation, regulatory frameworks, and Good Manufacturing Practice compliance of tumor organoids

Tumor organoids, especially patient-derived tumor organoids (PDTOs), have emerged as a crucial link between preclinical research and clinical practice. In rectal cancer, a biobank of 142 rectal cancer organoids has been established with an optimized success rate of 90.2%, accurately predicting clinical responses to neoadjuvant chemoradiotherapy, with predictive accuracies of 92.5% and 93.75% in discovery and validation cohorts, respectively.[39] These organoids have also been used to identify synergistic and antagonistic interactions among therapeutic agents. In gastrointestinal cancers, PDTOs have been used in clinical trials to guide personalized treatments.[149] In pancreatic cancer, PDTO-guided therapies improved the 6-month disease control rate by 23%. Similarly, in colorectal cancer, PDTOs predicted the efficacy of cetuximab and regorafenib with 78% consistency.[149] PDTOs have also enhanced the efficacy of adoptive cell therapies, and in breast cancer, they have supported preclinical evaluation of chimeric antigen receptor–macrophage therapies, demonstrating significant anti-tumor activity.[150]

Regulatory pathways governing the clinical translation of tumor organoids are progressively being standardized, with laboratory-developed tests serving as the primary regulatory framework for early clinical applications. As outlined in organoid-based clinical laboratory development testing, PDTO-based drug sensitivity assays must undergo rigorous analytical validation and clinical validation prior to clinical implementation.[151] In the United States, the FDA has recognized the potential of organoid models to reduce reliance on animal testing and has collaborated with biotechnology companies to validate gastrointestinal organoid-on-a-chip platforms for evaluating drug safety. In the European Union, PDTOs have been integrated into Innovative Medicines Initiative projects aimed at harmonizing technical standards for their application in clinical trials.[152]

Compliance with Good Manufacturing Practice (GMP) standards constitutes a core prerequisite for the large-scale clinical translation of tumor organoids. GMP regulations encompass the entire production workflow. Raw materials such as Matrigel and culture media must have traceable batch records and meet sterility and stability requirements,[149] while tissue sample processing requires standardized operating procedures. For example, digestion of rectal cancer tissue is strictly controlled to 15–20 min with intermittent agitation to maintain cell viability and minimize genetic damage.[39] During manufacturing, automated systems are increasingly employed to minimize batch-to-batch variation. A microfluidic-based PDTO culture system has been developed to enable automated drug administration and real-time imaging, reducing manual operation errors by 35%.[152] Quality control represents another critical GMP component, requiring microbial testing, short tandem repeat authentication to verify donor identity, and genetic validation.[151] In the establishment of a gastric cancer PDTO biobank, GMP-compliant cryopreservation protocols ensured that thawed PDTOs retained >50% viability and stable histological features, thereby supporting long-term storage and multi-center clinical collaboration.[149] Collectively, these GMP-compliant practices provide a solid foundation for the reliable application of tumor organoids in precision oncology.

5. Advantages and current challenges

3D bioprinting-based tumor organoids offer precise spatial control,[6,30,153] personalized modeling capabilities,[154] improved standardization,[155] and high-throughput potential.[156,157] These advantages address key limitations of traditional organoid systems, like random architecture and uneven cell distribution,[158] while enabling more accurate studies of TME interactions.[156]

Despite significant progress, 3D bioprinting of tumor organoids still faces several challenges that limit its broader application:

Limited printing resolution: Extrusion-based systems typically achieve resolutions of 100–300 μm, which is insufficient for accurately recreating microvessels or tumor–stroma interfaces.[159] Although stereolithography-based approaches can reach resolutions of 10–50 μm and have been used to fabricate perfusable microvessels in GBM organoids, construct height is often restricted to <2 mm due to limitations in light penetration and potential photoinitiator cytotoxicity.[68] In bioprinted gastric cancer models, the inability of extrusion-based methods to generate microvessels has been shown to weaken the therapeutic effects of trastuzumab/ramucirumab, leading to discrepancies with clinical monoclonal antibody responses.[160]

Bioink instability: Bioinks exhibit multiple forms of instability arising from their chemical and physical properties. Natural hydrogels like Matrigel possess undefined chemical compositions that result in batch-to-batch variability, while weak crosslinking leads to mechanical instability.[161] Synthetic hydrogels may undergo uncontrolled degradation over extended culture periods, compromising structural integrity, and some bioinks exhibit photoinstability, with batch-to-batch optical drift reducing light transmittance.[162] Collectively, these issues can lead to structural collapse, cell death, or failure to

meet clinical performance standards. To address these limitations, composite hydrogels, e.g., GelMA blended with dECM, have been formulated, achieving storage moduli of 4–10 kPa while maintaining cell viability >90% for up to 14 days.[76,77] However, Yoon *et al.*[163] reported that batch-to-batch optical drift in electron beam-sterilized collagen-derived dECM bioinks significantly reduced light transmittance, falling below graft transparency thresholds and ultimately hindering clinical translation of bioprinted corneal patches.

Long-term culture viability: Sustaining long-term viability remains a major bottleneck in 3D bioprinted constructs, primarily due to inadequate nutrient and oxygen diffusion. Under static culture conditions, this limitation becomes more pronounced as constructs exceed the oxygen diffusion limit of approximately 100–200 μm in diameter. Consequently, cells within the core experience nutrient deprivation and impaired metabolic waste removal, leading to necrotic core formation, typically within 2–3 weeks.[158] The integration of microfluidic perfusion systems, operating at a flow rate of 20–50 μL/min, has been shown to double viable tissue thickness and preserve drug response fidelity for up to 6 weeks.[132]

Standardization gaps: Variability in bioink composition, printer parameters, and analytical readouts continues to hinder interlaboratory reproducibility.[154] For example, natural bioinks, such as Matrigel, exhibit undefined compositions and batch-to-batch differences, whereas synthetic hydrogels often lack standardized formulations tailored to specific cancer models, resulting in inconsistent cell behavior across studies. Printer parameters, such as extrusion pressure and crosslinking conditions, further affect reproducibility, as demonstrated in breast cancer spheroid studies, where variations in printing conditions altered cell viability and sensitivity to paclitaxel. In addition, inconsistent readout metrics complicate data comparison across laboratories.[154] To address these challenges, a recently developed modular bioprinting platform standardized GelMA/dECM ratios, nozzle height, and post-print crosslinking dose, yielding intra-batch coefficients of variation <5% while preserving patient-specific drug responses.[77] Furthermore, a newly reported aspiration-assisted bioprinting protocol provides unified guidelines for hardware assembly, software parameter configuration, and post-bioprinting validation. This approach enables consistent fabrication of tumor organoids with positional errors <50 μm across experimental batches, effectively mitigating interlaboratory reproducibility issues.[164] Yang *et al.*[61] similarly emphasize that only rigorously standardized formulations, protocols, and artificial intelligence (AI)-monitored perfusion platforms can maintain both precision and predictive power in routine bioprinting workflows.

6. Future perspectives

To realize the full potential of 3D bioprinted tumor organoids, deeper integration with AI, big data analytics, and microfluidics is rapidly evolving from a conceptual vision to a quantitative reality.

Artificial intelligence can be employed to optimize bioprinting parameters by learning from large datasets of printing outcomes, thereby improving reproducibility and structural fidelity. For instance, machine learning algorithms have been used to predict post-printing cell viability based on real-time imaging and bioink composition, significantly reducing trial-and-error during protocol development.[165] More specifically, AI models trained on live microscopy images can automatically adjust printing speed and extrusion pressure in real time to maintain uniform strand diameters and minimize shear-induced cell death.[166,167] Additionally, AI has been applied to the design and performance prediction of tissue engineering materials, optimizing mechanical properties and enhancing structural design.[168] In the context of bioprinting, AI-driven approaches such as GRACE (generative, adaptive, context-aware 3D printing) enable the creation of complex, adaptive geometries that respond to the spatial distribution of cells or organoids, facilitating the fabrication of biomimetic scaffolds with highly controlled architectures.[169] Such levels of automation and adaptability would be impractical with manual design, substantially streamlining fabrication workflows while expanding the complexity and functionality of achievable structures.

Beyond optimizing printing parameters, material design, and performance prediction, AI is increasingly integrated into post-printing analysis and the clinical translation of bioprinted tumor models. Recently, Han *et al.*[77] developed an embedded bioprinting-enabled arrayed PDO platform that combines 3D bioprinting with supervised learning-based morphometric analysis. This platform achieved 98–99% accuracy in classifying colorectal cancer patients into high- and low-carcinoembryonic antigen-related cell adhesion molecule 5 expression subgroups using a majority voting algorithm and demonstrated significantly higher gene expression similarity to primary tumor tissues compared with conventional PDO models. Importantly, it successfully replicated individual patient responses to 5-fluorouracil chemotherapy, highlighting the potential of AI-enhanced platforms for personalized treatment planning.[77]

Big data, particularly multi-omics datasets from patient tumors, can further guide the design of personalized bioinks and organoid architectures that more accurately recapitulate individual tumor phenotypes. This approach has been demonstrated in integrated platforms where

genomic and proteomic information informs the selection of matrix stiffness and growth factor composition in bioprinted models.[170]

Microfluidics complements bioprinting by enabling dynamic culture environments that simulate physiological gradients of oxygen, nutrients, and drugs. For example, perfusable microfluidic chips integrated with bioprinted vascularized tumor organoids have been used to investigate hypoxia-driven drug resistance in non-small cell lung cancer, offering a more clinically relevant model than static culture systems.[106] Notably, microfluidic chips embedded with real-time oxygen sensors can generate hypoxic niches within printed tumors, allowing precise investigation of hypoxia-inducible factor 1 alpha-mediated drug resistance under defined oxygen gradients.[171,172] Although challenges remain in terms of throughput and long-term perfusion stability, addressing these engineering limitations is expected to unlock the full potential of chip-integrated bioprinted tumors for high-content, patient-specific drug screening.[173,174]

Together, these technologies form a feedback-augmented loop in which omics data train AI algorithms, AI governs bioprinting processes, and microfluidic readout feedback to refine both the biological models and computational frameworks. This closed-loop system enables the transformation of multi-modal biological information into quantitative precision oncology assays.

7. Conclusion

The integration of 3D bioprinting with tumor organoid technology marks a pivotal advancement in cancer research. By combining the histological and genetic fidelity of organoids with the spatial precision and structural controllability of 3D bioprinting, these hybrid models effectively overcome many limitations of traditional *in vitro* systems. They accurately recapitulate key features of the TME, including cellular heterogeneity, vascular networks, and tumor–immune crosstalk. Consequently, bioprinted tumor organoids show strong potential for modeling tumor progression, engineering vascularized tissues, enabling high-throughput drug screening, and investigating immunotherapy mechanisms. Despite these advances, several challenges remain, including limited printing resolution for fine microstructures, bioink instability, difficulties in maintaining long-term cultures, and ethical and regulatory considerations. Looking ahead, continued convergence with microfluidics, AI, and big data analytics, alongside the development of universally standardized platforms, is expected to drive further innovation. These advances will strengthen the translational bridge between basic research and clinical application, ultimately accelerating the development of personalized cancer therapies and improving patient outcomes.

Acknowledgments

None.

Funding

This work is supported by the Zhejiang Medical and Health Science and Technology Program (Grant No. 2025KY032), the Young Scientists Fund of the National Natural Science Foundation of China (Grant No. 82503786), and the National Natural Science Foundation of China for Young Student Basic Research Projects (Grant No. T24B2014).

Conflict of interest

The authors declare that they have no competing interests.

Author contributions

Conceptualization: Wei Wu, Kun Ji, Yunxiang Zhou
Writing–original draft: Yuwen Wang, Jiaqi Shi, Wei Wu
Writing–review & editing: Yali Wang, Sihan Zhao, Hui Ren, Huanhuan Huang, Wenyue Lv, Huiheng Feng, Yunxiang Zhou, Kun Ji

Ethics approval and consent to participate

Not applicable.

Consent for publication

Not applicable.

Availability of data

Not applicable.

References

1. Kvåle G, Heuch I, Nilssen S. Parity in relation to mortality and cancer incidence: a prospective study of Norwegian women. *Int J Epidemiol*. 1994;23(4):691-699. doi: 10.1093/ije/23.4.691.
2. Martin DB, Nelson PS. From genomics to proteomics: techniques and applications in cancer research. *Trends Cell Biol*. 2001;11(11):S60-S65. doi: 10.1016/s0962-8924(01)02123-7.
3. Tang XY, Wu S, Wang D, *et al*. Human organoids in basic research and clinical applications. *Signal Transduct Target Ther*. 2022;7(1):168. doi: 10.1038/s41392-022-01024-9.
4. Wang G, Mao X, Wang W, Wang X, Li S, Wang Z. Bioprinted research models of urological malignancy. *Exploration*. 2024;4(4):20230126.

doi: 10.1002/EXP.20230126.

5. Hwangbo H, Chae S, Kim W, Jo S, Kim GH. Tumor-on-a-chip models combined with mini-tissues or organoids for engineering tumor tissues. *Theranostics*. 2024;14(1):33-55. doi: 10.7150/thno.90093.

6. Zhou Z, Pang Y, Ji J, *et al*. Harnessing 3D in vitro systems to model immune responses to solid tumours: a step towards improving and creating personalized immunotherapies. *Nat Rev Immunol*. 2024;24(1):18-32. doi: 10.1038/s41577-023-00896-4.

7. Lv J, Du X, Wang M, Su J, Wei Y, Xu C. Construction of tumor organoids and their application to cancer research and therapy. *Theranostics*. 2024;14(3):1101-1125. doi: 10.7150/thno.91362.

8. Ma W, Lu H, Xiao Y, Wu C. Advancing organoid development with 3D bioprinting. *Organoid Res*. 2025;1(1):025040004. doi: 10.36922/or025040004.

9. Xu X, Li H, Chen J, *et al*. A universal strategy to construct high-performance homo- and heterogeneous microgel assembly bioinks. *Small Methods*. 2024;8(12):e2400223. doi: 10.1002/smtd.202400223.

10. Wang X, Luo Y, Ma Y, Wang P, Yao R. Converging bioprinting and organoids to better recapitulate the tumor microenvironment. *Trends Biotechnol*. 2024;42(5):648-663. doi: 10.1016/j.tibtech.2023.11.006.

11. An Y, He Y, Ge N, Guo J, Yang F, Sun S. Organoids to remodel SARS-CoV-2 research: updates, limitations and perspectives. *Aging Dis*. 2023;14(5):1677-1699. doi: 10.14336/ad.2023.0209.

12. Sato T, Vries RG, Snippert HJ, *et al*. Single Lgr5 stem cells build crypt-villus structures in vitro without a mesenchymal niche. *Nature*. 2009;459(7244):262-265. doi: 10.1038/nature07935.

13. Sachs N, de Ligt J, Kopper O, *et al*. A living biobank of breast cancer organoids captures disease heterogeneity. *Cell*. 2018;172(1-2):373-386.e310. doi: 10.1016/j.cell.2017.11.010.

14. Drost J, van Jaarsveld RH, Ponsioen B, *et al*. Sequential cancer mutations in cultured human intestinal stem cells. *Nature*. 2015;521(7550):43-47. doi: 10.1038/nature14415.

15. Viegas J, Sarmento B. Bridging the gap between testing and clinics exploring alternative pre-clinical models in melanoma research. *Adv Drug Deliv Rev*. 2024;208:115295. doi: 10.1016/j.addr.2024.115295.

16. Mierke CT. Bioprinting of cells, organoids and organs-on-a-chip together with hydrogels improves structural and mechanical cues. *Cells*. 2024;13(19):1638. doi: 10.3390/cells13191638.

17. Blandino G, Satchi-Fainaro R, Tinhofer I, *et al*. Cancer organoids as reliable disease models to drive clinical development of novel therapies. *J Exp Clin Cancer Res*. 2024;43(1):334. doi: 10.1186/s13046-024-03258-7.

18. Fredrikson JP, Roth DM, Cosgrove JA, *et al*. Engineering neuronal networks in granular microgels to innervate bioprinted cancer organoids on-a-chip. *Lab Chip*. 2025;25(14):3467-3481. doi: 10.1039/d5lc00134j.

19. Gu WJ, Liu XX, Shen YW, *et al*. TRIM4 enhances small-molecule-induced neddylated-degradation of CORO1A for triple negative breast cancer therapy. *Theranostics*. 2024;14(18):7023-7041. doi: 10.7150/thno.97662.

20. Barretina J, Caponigro G, Stransky N, *et al*. The Cancer Cell Line Encyclopedia enables predictive modelling of anticancer drug sensitivity. *Nature*. 2012;483(7391):603-607. doi: 10.1038/nature11003.

21. Dietlein F, Weghorn D, Taylor-Weiner A, *et al*. Identification of cancer driver genes based on nucleotide context. *Nat Genet*. 2020;52(2):208-218. doi: 10.1038/s41588-019-0572-y.

22. Yu M, Ni M, Xu F, *et al*. NSUN6-mediated 5-methylcytosine modification of NDRG1 mRNA promotes radioresistance in cervical cancer. *Mol Cancer*. 2024;23(1):139. doi: 10.1186/s12943-024-02055-2.

23. Lencioni G, Gregori A, Toledo B, *et al*. Unravelling the complexities of resistance mechanism in pancreatic cancer: insights from in vitro and ex-vivo model systems. *Semin Cancer Biol*. 2024;106-107:217-233. doi: 10.1016/j.semcancer.2024.09.002.

24. Liu Y, Wu W, Cai C, *et al*. Patient-derived xenograft models in cancer therapy: technologies and applications. *Signal Transduct Target Ther*. 2023;8(1):160. doi: 10.1038/s41392-023-01419-2.

25. Dogan E, Galifi CA, Cecen B, Shukla R, Wood TL, Miri AK. Extracellular matrix regulation of cell spheroid invasion in a 3D bioprinted solid tumor-on-a-chip. *Acta Biomater*. 2024;186:156-166. doi: 10.1016/j.actbio.2024.07.040.

26. Kuwata T, Yanagihara K, Iino Y, *et al*. Establishment of novel gastric cancer patient-derived xenografts and cell lines: pathological comparison between primary tumor, patient-derived, and cell-line derived xenografts. *Cells*. 2019;8(6):585. doi: 10.3390/cells8060585.

27. Lang Y, Lyu Y, Tan Y, Hu Z. Progress in construction of mouse models to investigate the pathogenesis and immune therapy of human hematological malignancy. *Front Immunol*. 2023;14:1195194. doi: 10.3389/fimmu.2023.1195194.

28. Lallo A, Schenk MW, Frese KK, Blackhall F, Dive C. Circulating tumor cells and CDX models as a tool for

preclinical drug development. *Transl Lung Cancer Res*. 2017;6(4):397-408.
doi: 10.21037/tlcr.2017.08.01.

29. Lancaster MA, Knoblich JA. Organogenesis in a dish: modeling development and disease using organoid technologies. *Science*. 2014;345(6194):1247125.
doi: 10.1126/science.1247125.

30. Huang MS, Christakopoulos F, Roth JG, Heilshorn SC. Organoid bioprinting: from cells to functional tissues. *Nat Rev Bioeng*. 2024;3(2):126-142.
doi: 10.1038/s44222-024-00268-0.

31. D'Antoni C, Mautone L, Sanchini C, *et al*. Unlocking neural function with 3D in vitro models: a technical review of self-assembled, guided, and bioprinted brain organoids and their applications in the study of neurodevelopmental and neurodegenerative disorders. *Int J Mol Sci*. 2023;24(13):10762.
doi: 10.3390/ijms241310762.

32. Puls TJ, Tan X, Husain M, Whittington CF, Fishel ML, Voytik-Harbin SL. Development of a novel 3D tumor-tissue invasion model for high-throughput, high-content phenotypic drug screening. *Sci Rep*. 2018;8(1):13039.
doi: 10.1038/s41598-018-31138-6.

33. Cao R, Li NT, Shing CB, Kutulakos Z, Tan CM, McGuigan AP. Reproducible manufacturing of SPOT as a high-throughput scaffold-based culture platform. *J Vis Exp*. 2025;221:e68405.
doi: 10.3791/68405.

34. Maloney E, Clark C, Sivakumar H, *et al*. Immersion bioprinting of tumor organoids in multi-well plates for increasing chemotherapy screening throughput. *Micromachines*. 2020;11(2):208.
doi: 10.3390/mi11020208.

35. Yang Q, Li M, Yang X, *et al*. Flourishing tumor organoids: history, emerging technology, and application. *Bioeng Transl Med*. 2023;8(5):e10559.
doi: 10.1002/btm2.10559.

36. van de Wetering M, Francies HE, Francis JM, *et al*. Prospective derivation of a living organoid biobank of colorectal cancer patients. *Cell*. 2015;161(4):933-945.
doi: 10.1016/j.cell.2015.03.053.

37. Vlachogiannis G, Hedayat S, Vatsiou A, *et al*. Patient-derived organoids model treatment response of metastatic gastrointestinal cancers. *Science*. 2018;359(6378):920-926.
doi: 10.1126/science.aao2774.

38. Xiang D, He A, Zhou R, *et al*. Building consensus on the application of organoid-based drug sensitivity testing in cancer precision medicine and drug development. *Theranostics*. 2024;14(8):3300-3316.
doi: 10.7150/thno.96027.

39. Xu X, Lv T, Yao Y, *et al*. Comprehensive dissection of rectal cancer organoids in responses to chemoradiation. *Cell Rep Med*. 2025;6(10):102397.
doi: 10.1016/j.xcrm.2025.102397.

40. Zhou Z, He J, Pang Y, Sun W. Reconstruction of tumor microenvironment via in vitro three-dimensional models. *Biofabrication*. 2023;15(3):032002.
doi: 10.1088/1758-5090/acd1b8.

41. Liu Q, Mille LS, Villalobos C, *et al*. 3D-bioprinted cholangiocarcinoma-on-a-chip model for evaluating drug responses. *Bio-des Manuf*. 2023;6(4):373-389.
doi: 10.1007/s42242-022-00229-9.

42. Yang J, Chen Z, Gao C, *et al*. A mechanical-assisted post-bioprinting strategy for challenging bone defects repair. *Nat Commun*. 2024;15(1):3565.
doi: 10.1038/s41467-024-48023-8.

43. Latimer JM, Maekawa S, Yao Y, Wu DT, Chen M, Giannobile WV. Regenerative medicine technologies to treat dental, oral, and craniofacial defects. *Front Bioeng Biotechnol*. 2021;9:704048.
doi: 10.3389/fbioe.2021.704048.

44. Cui X, Jiao J, Yang L, *et al*. Advanced tumor organoid bioprinting strategy for oncology research. *Mater Today Bio*. 2024;28:101198.
doi: 10.1016/j.mtbio.2024.101198.

45. Shi W, Mirza S, Kuss M, *et al*. Embedded bioprinting of breast tumor cells and organoids using low-concentration collagen-based bioinks. *Adv Healthc Mater*. 2023;12(26):e2300905.
doi: 10.1002/adhm.202300905.

46. Murphy JF, Lavelle M, Asciak L, *et al*. Biofabrication and biomanufacturing in Ireland and the UK. *Biodes Manuf*. 2024;7(6):825-856.
doi: 10.1007/s42242-024-00316-z.

47. Budharaju H, Sundaramurthi D, Sethuraman S. Embedded 3D bioprinting – an emerging strategy to fabricate biomimetic & large vascularized tissue constructs. *Bioact Mater*. 2024;32:356-384.
doi: 10.1016/j.bioactmat.2023.10.012.

48. Zhang X, Zhang X, Li Y, Zhang Y. Applications of light-based 3D bioprinting and photoactive biomaterials for tissue engineering. *Materials*. 2023;16(23):7461.
doi: 10.3390/ma16237461.

49. Zhao Y, Li Y, Mao S, Sun W, Yao R. The influence of printing parameters on cell survival rate and printability in microextrusion-based 3D cell printing technology. *Biofabrication*. 2015;7(4):045002.
doi: 10.1088/1758-5090/7/4/045002.

50. Blaeser A, Duarte Campos DF, Puster U, Richtering W, Stevens MM, Fischer H. Controlling shear stress in 3D bioprinting is a key factor to balance printing resolution and stem cell integrity. *Adv Healthc Mater*. 2016;5(3):326-333.
doi: 10.1002/adhm.201500677.

51. You S, Xiang Y, Hwang HH, *et al*. High cell density and high-resolution 3D bioprinting for fabricating vascularized tissues. *Sci Adv*. 2023;9(8):eade7923.

doi: 10.1126/sciadv.ade7923.

52. Utama RH, Atapattu L, O'Mahony AP, *et al*. A 3D bioprinter specifically designed for the high-throughput production of matrix-embedded multicellular spheroids. *iScience*. 2020;23(10):101621. doi: 10.1016/j.isci.2020.101621.

53. Xu T, Jin J, Gregory C, Hickman JJ, Boland T. Inkjet printing of viable mammalian cells. *Biomaterials*. 2005;26(1):93-99. doi: 10.1016/j.biomaterials.2004.04.011.

54. Mandrycky C, Wang Z, Kim K, Kim DH. 3D bioprinting for engineering complex tissues. *Biotechnol Adv*. 2016;34(4):422-434. doi: 10.1016/j.biotechadv.2015.12.011.

55. Parodi I, Di Lisa D, Pastorino L, Scaglione S, Fato MM. 3D bioprinting as a powerful technique for recreating the tumor microenvironment. *Gels*. 2023;9(6):482. doi: 10.3390/gels9060482.

56. Ma X, Qu X, Zhu W, *et al*. Deterministically patterned biomimetic human iPSC-derived hepatic model via rapid 3D bioprinting. *Proc Natl Acad Sci U S A*. 2016;113(8): 2206-2211. doi: 10.1073/pnas.1524510113.

57. Melchels FP, Feijen J, Grijpma DW. A review on stereolithography and its applications in biomedical engineering. *Biomaterials*. 2010;31(24):6121-6130. doi: 10.1016/j.biomaterials.2010.04.050.

58. Huang S, Wu Y, Zhao H, *et al*. Advancements in bone organoids: perspectives on construction methodologies and application strategies. *J Adv Res*. 2025;S2090-1232(25):00397-2. doi: 10.1016/j.jare.2025.06.011.

59. Burns N, Rajesh A, Manjula-Basavanna A, Duraj-Thatte A. 3D extrusion bioprinting of microbial inks for biomedical applications. *Adv Drug Deliv Rev*. 2025;217:115505. doi: 10.1016/j.addr.2024.115505.

60. Lee Y, Min J, Kim S, Park W, Ko J, Jeon NL. Recapitulating the cancer-immunity cycle on a chip. *Adv Healthc Mater*. 2025;14(1):e2401927. doi: 10.1002/adhm.202401927.

61. Yang Q, Li M, Xiao Z, Feng Y, Lei L, Li S. A new perspective on precision medicine: the power of digital organoids. *Biomater Res*. 2025;29:0171. doi: 10.34133/bmr.0171.

62. Daskalakis P, Kanakousaki E, Ntoulias C, *et al*. 3D bioprinting with high-viscosity bioinks: a custom-designed extrusion head for high-resolution cellulose acetate scaffolds. *Int J Bioprinting*. 2025;11(3):337-357. doi: 10.36922/ijb025060047.

63. Barjuei ES, Shin J, Kim K, Lee J. Precision improvement of robotic bioprinting via vision-based tool path compensation. *Sci Rep*. 2024;14(1):17764. doi: 10.1038/s41598-024-68597-z.

64. Cui X, Boland T, D'Lima DD, Lotz MK. Thermal inkjet printing in tissue engineering and regenerative medicine. *Recent Pat Drug Deliv Formul*. 2012;6(2):149-155. doi: 10.2174/187221112800672949.

65. Ng WL, Yeong WY, Naing MW. Polyvinylpyrrolidone-based bio-ink improves cell viability and homogeneity during drop-on-demand printing. *Materials*. 2017;10(2):190. doi: 10.3390/ma10020190.

66. Stepanov I, Gottshall NR, Ahmadianyazdi A, *et al*. Low-cost robotic manipulation of live microtissues for cancer drug testing. *Sci Adv*. 2025;11(20):eads1631. doi: 10.1126/sciadv.ads1631.

67. Lee SY, Phuc HD, Um SH, Mongrain R, Yoon J-K, Bhang SH. Photocuring 3D printing technology as an advanced tool for promoting angiogenesis in hypoxia-related diseases. *J Tissue Eng*. 2024;15:1-21. doi: 10.1177/20417314241282476.

68. Li Z, Chen L, Wu J, *et al*. A review of 3D bioprinting for organoids. *Med Rev*. 2025;5(4):318-338. doi: 10.1515/mr-2024-0089.

69. Chansoria P, Rizzo R, Rütsche D Liu H, Delrot P, Zenobi-Wong M. Light from afield: fast, high-resolution, and layer-free deep vat 3D printing. *Chem Rev*. 2024;124(14): 8787-8822. doi: 10.1021/acs.chemrev.4c00134.

70. Sabnis A, Rahimi M, Chapman C, Nguyen KT. Cytocompatibility studies of an in situ photopolymerized thermoresponsive hydrogel nanoparticle system using human aortic smooth muscle cells. *J Biomed Mater Res A*. 2009;91(1):52-59. doi: 10.1002/jbm.a.32194.

71. Bhusal A, Dogan E, Nguyen HA, *et al*. Multi-material digital light processing bioprinting of hydrogel-based microfluidic chips. *Biofabrication*. 2021;14(1):014103. doi: 10.1088/1758-5090/ac2d78.

72. Son J, Li S, Jeong W. Bioprinting vascularized constructs for clinical relevance: engineering hydrogel systems for biological maturity. *Gels*. 2025;11(8):636. doi: 10.3390/gels11080636.

73. Paulsen SJ, Mitcham TM, Pan CS, *et al*. Projection-based stereolithography for direct 3D printing of heterogeneous ultrasound phantoms. *PLoS One*. 2021;16(12):e0260737. doi: 10.1371/journal.pone.0260737.

74. Kim GT, Go HB, Yu JH, *et al*. Cytotoxicity, colour stability and dimensional accuracy of 3D printing resin with three different photoinitiators. *Polymers*. 2022;14(5):979. doi: 10.3390/polym14050979.

75. Banigo AT, Nauta L, Zoetebier B, Karperien M. Hydrogel-based bioinks for coaxial and triaxial bioprinting: a review of material properties, printing techniques, and applications. *Polymers*. 2025;17(7):917. doi: 10.3390/polym17070917.

76. Bhatt SS, Krishna Kumar J, Laya S, Thakur G, Nune M. Scaffold-mediated liver regeneration: a comprehensive exploration of current advances. *J Tissue Eng*. 2024;15:1-31. doi: 10.1177/20417314241286092.

77. Han J, Jeong HJ, Choi J, *et al*. Bioprinted patient-derived organoid arrays capture intrinsic and extrinsic tumor features for advanced personalized medicine. *Adv Sci*. 2025;12(20):e2407871. doi: 10.1002/advs.202407871.

78. Schütte M, Risch T, Abdavi-Azar N, *et al*. Molecular dissection of colorectal cancer in pre-clinical models identifies biomarkers predicting sensitivity to EGFR inhibitors. *Nat Commun*. 2017;8:14262. doi: 10.1038/ncomms14262.

79. Wierzbicka A, Bartniak M, Waśko J, Kolesińska B, Grabarczyk J, Bociaga D. The impact of gelatin and fish collagen on alginate hydrogel properties: a comparative study. *Gels*. 2024;10(8):491. doi: 10.3390/gels10080491.

80. Yuan W, Sun Y, Du B, *et al*. Double network hydrogel based on curdlan and gelatin methacryloyl (GelMA) with enhanced mechanical and tissue adhesive properties. *nt J Biol Macromol*. 2025;320(Pt 3):146080. doi: 10.1016/j.ijbiomac.2025.146080.

81. Tanadchangsaeng N, Pasanaphong K, Tawonsawatruk T, *et al*. 3D bioprinting of fish skin-based gelatin methacryloyl (GelMA) bio-ink for use as a potential skin substitute. *Sci Rep*. 2024;14(1):23240. doi: 10.1038/s41598-024-73774-1.

82. Janmohammadi M, Nazemi Z, Salehi AOM, *et al*. Cellulose-based composite scaffolds for bone tissue engineering and localized drug delivery. *Bioact Mater*. 2023;20:137-163. doi: 10.1016/j.bioactmat.2022.05.018.

83. Paneer Selvam S, Ayyappan S, I Jamir S, Sellappan LK, Manoharan S. Recent advancements of hydroxyapatite and polyethylene glycol (PEG) composites for tissue engineering applications – a comprehensive review. *Eur Polym J*. 2024;215:113226. doi: 10.1016/j.eurpolymj.2024.113226.

84. Wang M, Lin S, Liu M, *et al*. An injectable and rapidly degraded carboxymethyl chitosan/polyethylene glycol hydrogel for postoperative antiadhesion. *Chem Eng J*. 2023;463:142283. doi: 10.1016/j.cej.2023.142283.

85. Li X, Ren J, Huang Y, Cheng L, Gu Z. Applications and recent advances in 3D bioprinting sustainable scaffolding techniques. *Molecules*. 2025;30(14):3027. doi: 10.3390/molecules30143027.

86. Perry AC, Lan X, Ma Z, *et al*. Gelatin methacryloyl bioinks for bioprinting nasal cartilage: Balancing mechanical integrity and extracellular matrix formation. *Int J Biol Macromol*. 2025;311(Pt 1):143559. doi: 10.1016/j.ijbiomac.2025.143559.

87. Yue K, Trujillo-de Santiago G, Alvarez MM, Tamayol A, Annabi N, Khademhosseini A. Synthesis, properties, and biomedical applications of gelatin methacryloyl (GelMA) hydrogels. *Biomaterials*. 2015;73:254-271. doi: 10.1016/j.biomaterials.2015.08.045.

88. Urciuolo A, Giobbe GG, Dong Y, *et al*. Hydrogel-in-hydrogel live bioprinting for guidance and control of organoids and organotypic cultures. *Nat Commun*. 2023;14(1):3128. doi: 10.1038/s41467-023-37953-4.

89. Korkeamäki JT, Rashad A, Ojansivu M, *et al*. Systematic development and bioprinting of novel nanostructured multi-material bioinks for bone tissue engineering. *Biofabrication*. 2025;17(2):025005. doi: 10.1088/1758-5090/ada63b.

90. Ravanbakhsh H, Karamzadeh V, Bao G, Mongeau L, Juncker D, Zhang YS. Emerging technologies in multi-material bioprinting. *Adv Mater*. 2021;33(49):e2104730. doi: 10.1002/adma.202104730.

91. Loebel C, Rodell CB, Chen MH, Burdick JA. Shear-thinning and self-healing hydrogels as injectable therapeutics and for 3D-printing. *Nat Protoc*. 2017;12(8):1521-1541. doi: 10.1038/nprot.2017.053.

92. Kirillova A, Maxson R, Stoychev G, Gomillion CT, Ionov L. 4D biofabrication using shape-morphing hydrogels. *Adv Mater*. 2017;29(46):1703443. doi: 10.1002/adma.201703443.

93. Cao P, Yang J, Gong J, *et al*. 4D printing of bilayer tubular structure with dual-stimuli responsive based on self-rolling behavior. *J Appl Polym Sci*. 2023;140(1):e53241. doi: 10.1002/app.53241.

94. Jia Q, Wang A, Yuan Y, Zhu B, Long H. Heterogeneity of the tumor immune microenvironment and its clinical relevance. *Exp Hematol Oncol*. 2022;11(1):24. doi: 10.1186/s40164-022-00277-y.

95. Meng F, Meyer CM, Joung D, Vallera DA, McAlpine MC, Panoskaltsis-Mortari A. 3D bioprinted in vitro metastatic models via reconstruction of tumor microenvironments. *Adv Mater*. 2019;31(10):e1806899. doi: 10.1002/adma.201806899.

96. Yang H, Sun L, Liu M, Mao Y. Patient-derived organoids: a promising model for personalized cancer treatment. *Gastroenterol Rep*. 2018;6(4):243-245. doi: 10.1093/gastro/goy040.

97. Alsaed B, Lin L, Son J, *et al*. Intratumor heterogeneity of EGFR expression mediates targeted therapy resistance and formation of drug tolerant microenvironment. *Nat Commun*. 2025;16(1):28. doi: 10.1038/s41467-024-55378-5.

98. Wang J, Tao X, Zhu J, *et al*. Tumor organoid-immune co-culture models: exploring a new perspective of tumor immunity. *Cell Death Discov*. 2025;11(1):195. doi: 10.1038/s41420-025-02407-x.

99. Zhang L, Liao W, Chen S, *et al*. Towards a new 3Rs era in the construction of 3D cell culture models simulating tumor microenvironment. *Front Oncol*. 2023;13:1146477. doi: 10.3389/fonc.2023.1146477.

100. Miao Y, Pek NM, Tan C, *et al*. Co-development of mesoderm and endoderm enables organotypic vascularization in lung and gut organoids. *Cell*. 2025;188(16):4295-4313. doi: 10.1016/j.cell.2025.05.041.

101. Velasco-Rodriguez B, Diaz-Vidal T, Rosales-Rivera LC, *et al*. Hybrid methacrylated gelatin and hyaluronic acid hydrogel scaffolds. Preparation and systematic characterization for prospective tissue engineering applications. *Int J Mol Sci*. 2021;22(13):6758. doi: 10.3390/ijms22136758.

102. Tang M, Xie Q, Gimple RC, *et al*. Three-dimensional bioprinted glioblastoma microenvironments model cellular dependencies and immune interactions. *Cell Res*. 2020;30(10):833-853. doi: 10.1038/s41422-020-0338-1.

103. Neufeld L, Yeini E, Reisman N, *et al*. Microengineered perfusable 3D-bioprinted glioblastoma model for in vivo mimicry of tumor microenvironment. *Sci Adv*. 2021;7(34):eabi9119. doi: 10.1126/sciadv.abi9119.

104. Dymova MA, Kuligina EV, Richter VA. Molecular mechanisms of drug resistance in glioblastoma. *Int J Mol Sci*. 2021;22(1):351. doi: 10.3390/ijms22126385.

105. Zhao W, Zhang Z, Xie M, *et al*. Exploring tumor-associated macrophages in glioblastoma: from diversity to therapy. *NPJ Precis Oncol*. 2025;9(1):126. doi: 10.1038/s41698-025-00920-x.

106. Shukla P, Yeleswarapu S, Heinrich MA, Prakash J, Pati F. Mimicking tumor microenvironment by 3D bioprinting: 3D cancer modeling. *Biofabrication*. 2022;14:032002. doi: 10.1088/1758-5090/ac6d11.

107. Lachowski D, Cortes E, Rice A, Pinato D, Rombouts K, Del Rio Hernandez A. Matrix stiffness modulates the activity of MMP-9 and TIMP-1 in hepatic stellate cells to perpetuate fibrosis. *Sci Rep*. 2019;9(1):7299. doi: 10.1038/s41598-019-43759-6.

108. Schrader J, Gordon-Walker TT, Aucott RL, *et al*. Matrix stiffness modulates proliferation, chemotherapeutic response, and dormancy in hepatocellular carcinoma cells. *Hepatology*. 2011;53(4):1192-1205. doi: 10.1002/hep.24108.

109. Zhang H, Wang Y, Zheng Z, *et al*. Strategies for improving the 3D printability of decellularized extracellular matrix bioink. *Theranostics*. 2023;13(8):2562-2587. doi: 10.7150/thno.81785.

110. Ju M, Jin Z, Yu X, *et al*. Gastric cancer models developed via GelMA 3D bioprinting accurately mimic cancer hallmarks, tumor microenvironment features, and drug responses. *Small*. 2025;21(8):e2409321. doi: 10.1002/smll.202409321.

111. Heinrich MA, Mostafa A, Morton JP, Hawinkels L, Prakash J. Translating complexity and heterogeneity of pancreatic tumor: 3D in vitro to in vivo models. *Adv Drug Deliv Rev*. 2021;174:265-293. doi: 10.1016/j.addr.2021.04.018.

112. Monteiro MV, Ferreira LP, Rocha M, Gaspar VM, Mano JF. Advances in bioengineering pancreatic tumor-stroma physiomimetic biomodels. *Biomaterials*. 2022; 287:121653. doi: 10.1016/j.biomaterials.2022.121653.

113. Zhang Y, Hu Q, Pei Y, *et al*. A patient-specific lung cancer assembloid model with heterogeneous tumor microenvironments. *Nat Commun*. 2024;15(1):3382. doi: 10.1038/s41467-024-47737-z.

114. Datta P, Dey M, Ataie Z, Unutmaz D, Ozbolat IT. 3D bioprinting for reconstituting the cancer microenvironment. *NPJ Precis Oncol*. 2020;4:18. doi: 10.1038/s41698-020-0121-2.

115. Atanasova VS, de Jesus Cardona C, Hejret V, *et al*. Mimicking tumor cell heterogeneity of colorectal cancer in a patient-derived organoid-fibroblast model. *Cell Mol Gastroenterol Hepatol*. 2023;15(6):1391-1419. doi: 10.1016/j.jcmgh.2023.02.014.

116. Sabetta S, Vecchiotti D, Clementi L, Di Vito Nolfi M, Zazzeroni F, Angelucci A. Comparative analysis of dasatinib effect between 2D and 3D tumor cell cultures. *Pharmaceutics*. 2023;15(2):372. doi: 10.3390/pharmaceutics15020372.

117. Yang R, Wang S, Li Z, Yin C, Huang W, Huang W. Patient-derived organoid co-culture systems as next-generation models for bladder cancer stem cell research. *Cancer Lett*. 2025;625:217793. doi: 10.1016/j.canlet.2025.217793.

118. Kraja FP, Jurisic VB, Hromić-Jahjefendić A, *et al*. Tumor-infiltrating lymphocytes in cancer immunotherapy: from chemotactic recruitment to translational modeling. *Front Immunol*. 2025;16:1601773. doi: 10.3389/fimmu.2025.1601773.

119. Mu P, Zhou S, Lv T, *et al*. Newly developed 3D in vitro models to study tumor-immune interaction. *J Exp Clin Cancer Res*. 2023;42(1):81. doi: 10.1186/s13046-023-02653-w.

120. Ringquist R, Ghoshal D, Jain R, Roy K. Understanding and improving cellular immunotherapies against cancer: from cell-manufacturing to tumor-immune models. *Adv Drug Deliv Rev*. 2021;179:114003. doi: 10.1016/j.addr.2021.114003.

121. Li P, Huang M, Ma Y, Zhang Y, Shi C. Novel research model for in vitro immunotherapy: co-culturing tumor organoids

with peripheral blood mononuclear cells. *Cancer Cell Int*. 2024;24(1):438.
doi: 10.1186/s12935-024-03628-3.

122. Zhang Z, Chen X, Gao S, Fang X, Ren S. 3D bioprinted tumor model: a prompt and convenient platform for overcoming immunotherapy resistance by recapitulating the tumor microenvironment. *Cell Oncol*. 2024;47(4):1113-1126.
doi: 10.1007/s13402-024-00935-9.

123. Maishi N, Hida K. Tumor endothelial cells accelerate tumor metastasis. *Cancer Sci*. 2017;108(10):1921-1926.
doi: 10.1111/cas.13336.

124. Nwokoye PN, Abilez OJ. Bioengineering methods for vascularizing organoids. *Cell Rep Methods*. 2024;4(6):100779.
doi: 10.1016/j.crmeth.2024.100779.

125. Liu J, Zhao Y, Ren B, *et al*. Multi-scale vascularized tumor-on-a-chip via bioprinting for drug research. *Int J Bioprinting*. 2025;11(4):378–391.
doi: 10.36922/ijb025180180.

126. Skylar-Scott MA, Uzel SGM, Nam LL, *et al*. Biomanufacturing of organ-specific tissues with high cellular density and embedded vascular channels. *Sci Adv*. 2019;5(9): eaaw2459.
doi: 10.1126/sciadv.aaw2459.

127. Freeman FE, Pitacco P, van Dommelen LHA, *et al*. 3D bioprinting spatiotemporally defined patterns of growth factors to tightly control tissue regeneration. *Sci Adv*. 2020;6(33).
doi: 10.1126/sciadv.abb5093

128. DePalma TJ, Sivakumar H, Skardal A. Strategies for developing complex multi-component in vitro tumor models: highlights in glioblastoma. *Adv Drug Deliv Rev*. 2022;180:114067.
doi: 10.1016/j.addr.2021.114067.

129. Mukasheva F, Adilova L, Dyussenbinov A, Yernaimanova B, Abilev M, Akilbekova D. Optimizing scaffold pore size for tissue engineering: insights across various tissue types. *Front Bioeng Biotechnol*. 2024;12:1444986.
doi: 10.3389/fbioe.2024.1444986.

130. Pun S, Prakash A, Demaree D, *et al*. Rapid biofabrication of an advanced microphysiological system mimicking phenotypical heterogeneity and drug resistance in glioblastoma. *Adv Healthc Mater*. 2024;13(30):e2401876.
doi: 10.1002/adhm.202401876.

131. Li J, Ding M, Fu Q, Tan H, Xie X, Zhong Y. A novel strategy to graft RGD peptide on biomaterials surfaces for endothelization of small-diamater vascular grafts and tissue engineering blood vessel. *J Mater Sci Mater Med*. 2008;19(7):2595-2603.
doi: 10.1007/s10856-007-3354-5.

132. O'Connor C, Brady E, Zheng Y, Moore E, Stevens KR. Engineering the multiscale complexity of vascular networks. *Nat Rev Mater*. 2022;7(9):702-716.
doi: 10.1038/s41578-022-00447-8.

133. Palikuqi B, Nguyen DT, Li G, *et al*. Adaptable haemodynamic endothelial cells for organogenesis and tumorigenesis. *Nature*. 2020;585(7825):426-432.
doi: 10.1038/s41586-020-2712-z.

134. Bertassoni LE. Bioprinting of complex multicellular organs with advanced functionality-recent progress and challenges ahead. *Adv Mater*. 2022;34(3):e2101321.
doi: 10.1002/adma.202101321.

135. Thorel L, Perréard M, Florent R, *et al*. Patient-derived tumor organoids: a new avenue for preclinical research and precision medicine in oncology. *Exp Mol Med*. 2024;56(7):1531-1551.
doi: 10.1038/s12276-024-01272-5.

136. Lê H, Deforges J, Hua G, *et al*. In vitro vascularized immunocompetent patient-derived model to test cancer therapies. *iScience*. 2023;26(10):108094.
doi: 10.1016/j.isci.2023.108094.

137. Riester O, Laufer S, Deigner HP. Direct 3D printed biocompatible microfluidics: assessment of human mesenchymal stem cell differentiation and cytotoxic drug screening in a dynamic culture system. *J Nanobiotechnology*. 2022;20(1):540.
doi: 10.1186/s12951-022-01737-7.

138. Dai R, Chen W, Chen Y, *et al*. 3D bioprinting platform development for high-throughput cancer organoid models construction and drug evaluation. *Biofabrication*. 2024;16(3):035026.
doi: 10.1088/1758-5090/ad51a6.

139. Tebon PJ, Wang B, Markowitz AL, *et al*. Drug screening at single-organoid resolution via bioprinting and interferometry. *Nat Commun*. 2023;14(1):3168.
doi: 10.1038/s41467-023-38832-8.

140. Fäs L, Chen M, Tong W, *et al*. Physiological liver microtissue 384-well microplate system for preclinical hepatotoxicity assessment of therapeutic small molecule drugs. *Toxicol Sci*. 2025;203(1):79-87.
doi: 10.1093/toxsci/kfae123.

141. Sánchez-Díez M, Romero-Jiménez P, Alegría-Aravena N, *et al*. Assessment of cell viability in drug therapy: IC50 and other new time-independent indices for evaluating chemotherapy efficacy. *Pharmaceutics*. 2025;17(2):247.
doi: 10.3390/pharmaceutics17020247.

142. Zhou X, Qu M, Tebon P, *et al*. Screening cancer immunotherapy: when engineering approaches meet artificial intelligence. *Adv Sci*. 2020;7(19):2001447.
doi: 10.1002/advs.202001447.

143. Chen H, Wu Z, Gong Z, *et al*. Acoustic bioprinting of patient-derived organoids for predicting cancer therapy responses. *Adv Healthc Mater*. 2022;11(13):e2102784.
doi: 10.1002/adhm.202102784.

144. Tayler IM, Stowers RS. Engineering hydrogels for personalized disease modeling and regenerative medicine. *Acta Biomater*. 2021;132:4-22.

doi: 10.1016/j.actbio.2021.04.020.

145. Cartry J, Bedja S, Boilève A, *et al*. Implementing patient derived organoids in functional precision medicine for patients with advanced colorectal cancer. *J Exp Clin Cancer Res*. 2023;42(1):281.
doi: 10.1186/s13046-023-02853-4.

146. Paran Y, Liron Y, Batsir S, Mabjeesh N, Geiger B, Kam Z. Multi-parametric characterization of drug effects on cells. *F1000Res*. 2020;9:1199.
doi: 10.12688/f1000research.26254.2.

147. Esposito A, Agostini A, Quero G, *et al*. Colorectal cancer patients-derived immunity-organoid platform unveils cancer-specific tissue markers associated with immunotherapy resistance. *Cell Death Dis*. 2024;15(12):878.
doi: 10.1038/s41419-024-07266-5.

148. Cui L, Perini G, Minopoli A, *et al*. Plant-derived extracellular vesicles release combined with systemic DOX exhibits synergistic effects in 3D bioprinted triple-negative breast cancer. *Biomed Pharmacother*. 2024;181:117637.
doi: 10.1016/j.biopha.2024.117637.

149. Song SL, Li B, Carvalho MR, *et al*. Complex in vitro 3D models of digestive system tumors to advance precision medicine and drug testing: progress, challenges, and trends. *Pharmacol Ther*. 2022;239:108276.
doi: 10.1016/j.pharmthera.2022.108276.

150. Mei J, Liu X, Tian HX, *et al*. Tumour organoids and assembloids: Patient-derived cancer avatars for immunotherapy. *Clin Transl Med*. 2024;14(4):e1656.
doi: 10.1002/ctm2.1656.

151. Kim SY, van de Wetering M, Clevers H, Sanders K. The future of tumor organoids in precision therapy. *Trends Cancer*. 2025;11(7):665-675.
doi: 10.1016/j.trecan.2025.03.005.

152. Carvalho MR, Yan LP, Li B, *et al*. Gastrointestinal organs and organoids-on-a-chip: advances and translation into the clinics. *Biofabrication*. 2023;15(4):042004.
doi: 10.1088/1758-5090/acf8fb.

153. Maharjan S, Ma C, Singh B, *et al*. Advanced 3D imaging and organoid bioprinting for biomedical research and therapeutic applications. *Adv Drug Deliv Rev*. 2024;208:115237.
doi: 10.1016/j.addr.2024.115237.

154. Hockney S, Parker J, Turner JE, *et al*. Next generation organoid engineering to replace animals in cancer drug testing. *Biochem Pharmacol*. 2023;213:115586.
doi: 10.1016/j.bcp.2023.115586.

155. Ho YH, Liao Y, Liao L, Mao T, Guan Y, Xu R. Advances of cell printing technology in organoid engineering. *Tissue Eng Part B Rev*. 2025.
doi: 10.1089/ten.teb.2025.0048.

156. Jubelin C, Muñoz-Garcia J, Griscom L, *et al*. Three-dimensional in vitro culture models in oncology research. *Cell Biosci*. 2022;12(1):155.
doi: 10.1186/s13578-022-00887-3.

157. Qu J, Kalyani FS, Liu L, Cheng T, Chen L. Tumor organoids: synergistic applications, current challenges, and future prospects in cancer therapy. *Cancer Commun*. 2021;41(12):1331-1353.
doi: 10.1002/cac2.12224.

158. Revokatova D, Bikmulina P, Heydari Z, *et al*. Getting blood out of a stone: vascularization via spheroids and organoids in 3D bioprinting. *Cells*. 2025;14(9):665.
doi: 10.3390/cells14090665.

159. Liu S, Jin P. Advances and challenges in 3D bioprinted cancer models: opportunities for personalized medicine and tissue engineering. *Polymers*. 2025;17(7):948.
doi: 10.3390/polym17070948.

160. Du L, Zheng Z, Zhang K, *et al*. Exploring personalized prediction of clinical chemotherapy efficacy and revealing tumor heterogeneity using patient-derived 3D bioprinting gastric cancer models. *Mol Cancer*. 2025;24(1):259.
doi: 10.1186/s12943-025-02466-9.

161. Ullah MW, Ul-Islam M, Shehzad A, *et al*. From bioinks to functional tissues and organs: advances, challenges, and the promise of 3D bioprinting. *Macromol Mater Eng*. 2025;310(12):e00251.
doi: 10.1002/mame.202500251.

162. Song K, Compaan AM, Chai W, Huang Y. Injectable gelatin microgel-based composite ink for 3D bioprinting in air. *ACS Appl Mater Interfaces*. 2020;12(20):22453-22466.
doi: 10.1021/acsami.0c01497.

163. Yoon J, Lee Yj, Kim M, Park JY, Jang J. Enhanced bioprinting of 3D corneal stroma patches with reliability, assessing product consistency and quality through optimized electron beam sterilization. *Adv Healthc Mater*. 2025;14(9):e2403118.
doi: 10.1002/adhm.202403118.

164. Kim MH, Ozbolat IT. Aspiration-assisted bioprinting of spheroids. *Nat Protoc*. 2025.
doi: 10.1038/s41596-025-01240-x.

165. Chen H, Du L, Li J, *et al*. Modeling cancer metastasis using acoustically bio-printed patient-derived 3D tumor microtissues. *J Mater Chem B*. 2022;10(11):1843-1852.
doi: 10.1039/d1tb02789a.

166. Zhang Z, Zhou X, Fang Y, Xiong Z, Zhang T. AI-driven 3D bioprinting for regenerative medicine: from bench to bedside. *Bioact Mater*. 2025;45:201-230.
doi: 10.1016/j.bioactmat.2024.11.021.

167. Li M, Freeman S, Franco-Barraza J, *et al*. A bioprinted sea-and-island multicellular model for dissecting human pancreatic tumor-stroma reciprocity and adaptive metabolism. *Biomaterials*. 2024;310:122631.
doi: 10.1016/j.biomaterials.2024.122631.

168. Kong M, Zeng Y, Wu Z, *et al*. Artificial intelligence for design strategies of tissue engineering materials. *Fundam Res*. 2025.
doi: 10.1016/j.fmre.2025.09.010.

169. Florczak S, Größbacher G, Ribezzi D, *et al*. Adaptive and context-aware volumetric printing. *Nature*. 2025;645(8079):108-114.
doi: 10.1038/s41586-025-09436-7.

170. Rodrigues J, Heinrich MA, Teixeira LM, Prakash J. 3D in vitro model (r)evolution: unveiling tumor-stroma interactions. *Trends Cancer*. 2021;7(3):249-264.
doi: 10.1016/j.trecan.2020.10.009.

171. Xiang H, Chen F, Dong Z, *et al*. A microfluidic tumor-on-chip platform deciphers hypoxia-driven FOXO3a/PD-L1 signaling in gastric cancer immunotherapy resistance. *Mater Today Bio*. 2025;33:101925.
doi: 10.1016/j.mtbio.2025.101925.

172. Oh JM, Begum HM, Liu YL, Ren Y, Shen K. Recapitulating tumor hypoxia in a cleanroom-free, liquid-pinning-based microfluidic tumor model. *ACS Biomater Sci Eng*. 2022;8(7):3107-3121.
doi: 10.1021/acsbiomaterials.2c00207.

173. Fang L, Liu Y, Qiu J, Wan W. Bioprinting and its use in tumor-on-a-chip technology for cancer drug screening: a review. *Int J Bioprint*. 2022;8(4):603.
doi: 10.18063/ijb.v8i4.603.

174. Gaebler D, Hachey SJ, Hughes CCW. Improving tumor microenvironment assessment in chip systems through next-generation technology integration. *Front Bioeng Biotechnol*. 2024;12:1462293.
doi: 10.3389/fbioe.2024.1462293.

ACCSCIENCE PUBLISHING

International Journal of Bioprinting

REVIEW ARTICLE

Extracellular matrix-inspired 4D SMART biomaterials for bioprinting in tissue engineering

Ryan Martin[1], Haiwei Zhai[2], Daehoon Han[3], Fanben Meng[2,4]*, and Daeha Joung[1,5]*

[1]Department of Physics, College of Humanities and Sciences, Virginia Commonwealth University, Richmond, Virginia, United States

[2]Department of Mechanical and Materials Engineering, College of Engineering, University of Nebraska-Lincoln, Lincoln, Nebraska, United States

[3]School of Chemical Engineering, Chonnam National University, Gwangju, Republic of Korea

[4]Nebraska Center for Integrated Biomolecular Communication, University of Nebraska-Lincoln, Lincoln, Nebraska, United States

[5]Massey Comprehensive Cancer Center, Virginia Commonwealth University, Richmond, Virginia, United States

(This article belongs to the *Special Issue*: *Multidisciplinary Efforts in Bioprinting*)

Abstract

Tissue development and regeneration arise from a dynamic interplay among cells, the extracellular matrix (ECM), and surrounding biophysical and biochemical cues. These interactions form the basis for stimuli-responsive materials for advanced regenerative technologies (SMART) that drive innovation in four-dimensional (4D) bioprinting for tissue engineering. This review discusses the biophysical foundations of SMART materials, emphasizing native ECM components, their interactions, and organ-specific properties that inform biomimetic material design. We highlight recent advances in 4D SMART systems, including ionic self-healing, pH-, thermal-, hydration-, and magneto-responsive materials, and their roles in mimicking developmental and regenerative processes. This is followed by a comparative overview of these stimuli-responsive material classes, benchmarked against one another, native ECM performance, and clinical translation requirements, revealing persistent gaps in long-term stability, multi-stimuli integration, and regulatory feasibility. Together, these insights provide an interdisciplinary framework for designing adaptive, responsive biomaterials that guide tissue morphogenesis and advance the future of regenerative medicine.

Keywords: Biomaterials; Extracellular matrix; Four-dimensional bioprinting; Four-dimensional tissue engineering; Regenerative medicine; Stimuli-responsive materials

***Corresponding authors:**
Fanben Meng
(fmeng5@unl.edu)

Daeha Joung
(joungd2@vcu.edu)

Citation: Martin R, Zhai H, Han D, Meng F, Joung D. Extracellular matrix-inspired 4D SMART biomaterials for bioprinting in tissue engineering. *Int J Bioprint*. 2026;12(1):225-261. doi: 10.36922/IJB025440447

Received: October 29, 2025
1st revised: December 6, 2025
2nd revised: December 17, 2025
Accepted: December 26, 2025
Published online: January 12, 2026

Copyright: © 2026 Author(s). This is an Open Access article distributed under the terms of the Creative Commons Attribution License, permitting distribution, and reproduction in any medium, provided the original work is properly cited.

Publisher's Note: AccScience Publishing remains neutral with regard to jurisdictional claims in published maps and institutional affiliations.

1. Introduction

Extracellular matrix (ECM) has reigned as biology's unrivaled, living four-dimensional (4D) engine—continuously self-remodeling over seconds to decades, reversibly

stiffening and softening via closed-loop signaling with cells, thereby directing multicellular organization and scarless regeneration.[1] In an effort to recapitulate ECM dynamics, researchers have developed stimuli-responsive materials for advanced regenerative technologies (SMART), which represent a multidisciplinary convergence of chemistry, physics, engineering, and biomedicine aimed at addressing complex challenges in tissue regeneration, disease modeling, and therapeutic innovation. By integrating time (temporal dynamics) as the fourth dimension, these developments have paved the way for 4D bioprinting and 4D tissue engineering. When combined with SMART materials, these emerging approaches show strong promise for enabling safer and less invasive clinical interventions.[2,3]

However, current 4D SMART materials still rely on abiotic, one-shot triggers that bear no resemblance to the ECM's biotic, reversible, and multi-cycle dynamics driven by cell-secreted enzymes, traction forces, and redox state.[4–6] Because current materials cannot continuously turn over, expose fresh ligands, or reversibly re-crosslink in response to ongoing cellular cues—the very mechanisms that keep native ECM recognized as intrinsic to the body and fibrosis-free—they remain mechanically incompetent, immunologically provocative, and biologically obsolete long before any clinically meaningful regeneration can occur.[7] Consequently, the field has reached an inflection point, where establishing yet another single-trick material or platform is no longer defensible as "progress." Instead, absolute ECM fidelity must now be adopted as the non-negotiable standard and primary metric of success, requiring that next-generation 4D platforms exhibit continuous molecular turnover, cell-controlled reversible crosslinking, release of anti-fibrotic matrikines, strain-rate-matched viscoelasticity, and sustained immunological silence before they can be considered candidates for clinical translation.[8]

To bridge this gap, contemporary SMART material development integrates interdisciplinary advances to recapitulate seven key hallmarks of living tissues: biomimetic composition, multi-stimuli responsiveness, spatiotemporal heterogeneity, mechano-reciprocity, bioactive signaling, immunomodulation, and vascularization.[7,9,10] Biological insight—particularly into cellular mechanotransduction, self-organization, and differentiation—guides this effort, while chemical innovation enables dynamic bioinks and cross-linkers capable of programmed, time-evolving mechanics and biochemical responses. Physics provides precise control over internal and external cues (e.g., mechanical constraints, optical triggers, and acoustic fields) that orchestrate shape morphing, cell–matrix dialog, and biomechanical fidelity.[9–11] Finally, engineering optimizes bioreactor platforms and stimulus-delivery systems to ensure scalability and clinical translatability.[12–15] This convergent framework for achieving ECM fidelity through these seven key hallmarks aims to transform SMART materials into truly biomimetic 4D constructs poised for regenerative medicine.

Before delving into the critical assessment of the field, it is essential—given the inherently interdisciplinary nature of 4D bioprinting and 4D tissue engineering—to clarify foundational concepts and terminology that enable effective collaboration across specialties. 4D bioprinting extends conventional three-dimensional (3D) bioprinting, including extrusion-, inkjet-, stereolithography-, laser-assisted, or volumetric techniques—in which living cells are precisely deposited within biocompatible hydrogels or bioinks—by incorporating stimuli-responsive materials (SRMs) that confer time-dependent structural and functional evolution to the printed construct.[16] Following fabrication, these SMART materials undergo programmed or stimuli-triggered transformations (e.g., shape change, stiffness modulation, or matrix remodeling) in response to physiological, biochemical, or external cues, more faithfully recapitulating the spatiotemporal complexity of the native ECM and its active role in directing cell fate, tissue morphogenesis, and organ-level function.[15,17,18]

In contrast, 4D tissue engineering represents a broader paradigm that encompasses all time-dependent strategies for creating dynamically evolving constructs, irrespective of fabrication method. While this includes bioprinting-based approaches, the term is used in this review to also encompass non-bioprinting techniques—such as scaffold-free cellular self-assembly, constructs incorporating embedded responsive molecules, or the direct application of external physical stimuli (e.g., acoustic fields, mechanical vibration, magnetic forces, or fluid shear). In every instance, programmed temporal transformations are driven by endogenous biochemical cues or externally applied stimuli. These changes facilitate mechanotransduction, structural remodeling, functional maturation, and phenotypic specification, as reflected by alterations in cell morphology, behavior, or biochemical profiles.[11,19]

The SMART materials are advanced, multifunctional composites designed to actively sense and transduce environmental cues into programmable physicochemical changes, thereby establishing bidirectional, dynamic reciprocity with embedded cells and tissues. At the molecular level, these materials incorporate responsive motifs—such as thermoresponsive poly(*N*-isopropylacrylamide) (PNIPAAm) chains, photo-cleavable o-nitrobenzyl groups, pH-sensitive ionizable moieties, enzyme-cleavable peptide linkers, or mechanotransductive

crosslinkers—whose conformational transitions or bond scission events trigger macroscopic property shifts.[5,6] These shifts include reversible or irreversible modulation of storage and loss moduli (often spanning 10 Pa to over 100 kPa), viscoelastic creep compliance, hydraulic permeability, mesh size, ligand tether mobility, and cryptic domain exposure.[20] By coupling such biophysical outputs to cellular force generation (typically 10–10,000 nN per cell), SMART materials recapitulate key ECM feedback loops: force-dependent stiffening/softening, stress–relaxation-driven lineage commitment, durotaxis, and matrix metalloproteinase (MMP)-mediated remodeling.[9,15,20–22]

Within 4D bioprinting for tissue engineering, these materials enable precise spatiotemporal orchestration of morphogenesis, such as sequential unfolding or folding, gradient stiffening mimicking embryonic condensation, or on-demand release of growth factors and signaling molecules. Emerging electroactive subclasses—such as piezoelectric polyvinylidene fluoride (PVDF) composites, conducting polymers, including poly(3,4-ethylenedioxythiophene):polystyrene sulfonate (PEDOT:PSS) and polyaniline (PANI), and carbon-nanotube-reinforced hydrogels—enable the transduction or application of electric fields (0.1–100 mV mm^{-1}), supporting electromechanical coupling critical for cardiac, neural, and musculoskeletal tissues.[23,24] This convergence of mechanical, chemical, and electrical responsiveness positions SMART materials as essential platforms for interrogating developmental mechanobiology, engineering load-bearing tissues, and constructing organoids that faithfully recapitulate in vivo patterning dynamics.[15,25]

Native ECMs serve as the principal inspiration for SMART biomaterial design in 4D tissue engineering through two interconnected mechanisms. First, the core biophysical and biochemical principles of the ECM—such as dynamic stiffness modulation, viscoelasticity, spatially patterned ligand presentation, force-dependent cryptic site exposure, and protease-mediated remodeling—directly

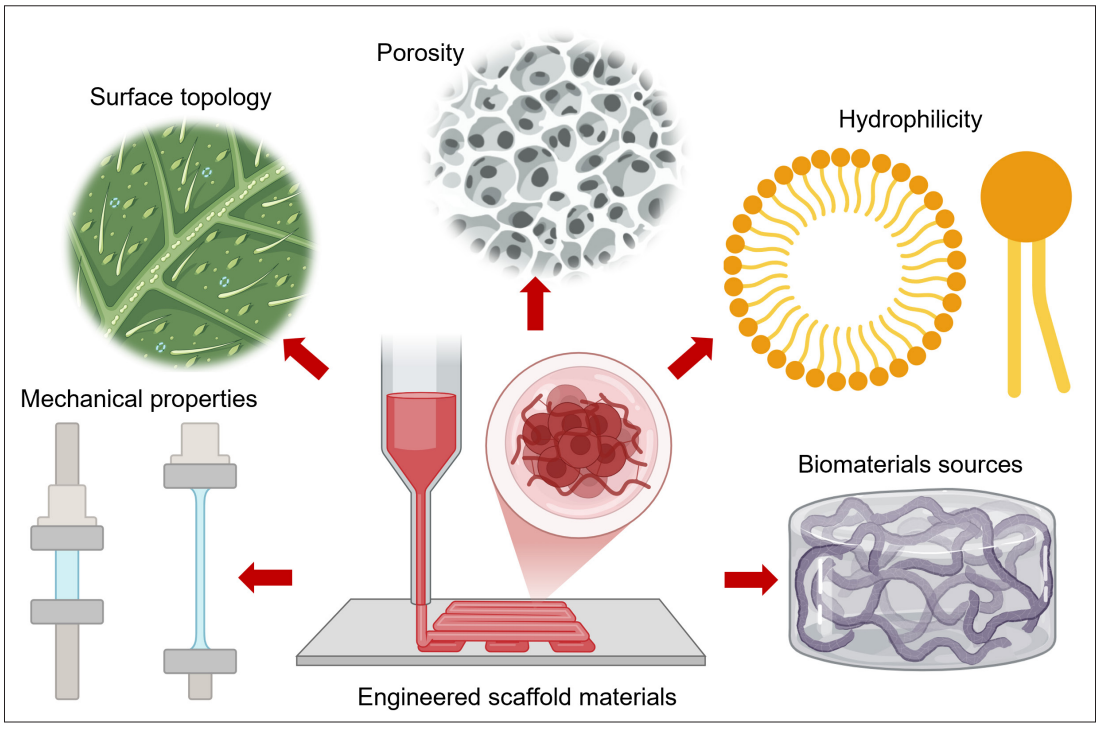


Figure 1. Biophysical traits of stimuli-responsive materials for advanced regenerative technologies (SMART) materials in tissue engineering and bioprinting. This schematic illustration highlights the core properties of stimuli-responsive biomaterials that dynamically emulate the native extracellular matrix (ECM). Five key attributes branch from the central SMART scaffold: (i) surface topology: micro- and nanoscale patterns, roughness, and fibrous structures that replicate ECM textures; (ii) mechanical properties: tunable stiffness (0.1–1 kPa for soft tissues like brain; 10–100 kPa for rigid tissues like bone), elasticity, viscoelasticity, and tensile strength; (iii) porosity and architecture: 50–90% interconnected porosity forming three-dimensional frameworks analogous to the hydrated, porous ECM gel; (iv) hydrophilicity: wettability and water retention that mimic the glycosaminoglycan-rich ECM environment; (v) biomaterial source: natural (e.g., collagen, chitosan) providing bioactivity and RGD (arginine–glycine–aspartic acid) signaling motifs; synthetic (e.g., polycaprolactone, polylactic acid) enabling precise customization and controlled degradation; or hybrid (e.g., decellularized ECM combined with polyethylene glycol), balancing biodegradability, bioactivity, and reduced immunogenicity. Created in BioRender. Joung, D. (2025). https://BioRender.com/bt3s7z1.

inform the engineering of stimuli-responsive "SMART" materials.[26] These principles are translated into synthetic or hybrid composites that recapitulate tunable mechanics, degradability, and bioactivity, thereby enabling precise regulation of cell traction forces, mechanotransduction pathways, and cell fate decisions.[26,27]

Second, the ECM's inherent spatiotemporal dynamism actively guides the development of SMART materials by providing a blueprint for their programmed evolution over time. The ECM undergoes continuous maturation, stiffening, and topographic reconfiguration during development and repair. Replicating these time-dependent transitions has driven the incorporation of stimuli-responsive polymers, shape-memory components, and cell-mediated remodeling cues into 4D platforms. This ensures that printed or assembled constructs do not remain static but instead mature, fold, stiffen, or functionally specialize in synchrony with resident cells—mirroring morphogenetic and homeostatic processes observed *in vivo*.[22,28] Thus, ECM-derived design rules elevate SMART biomaterials from passive structural supports to active, instructive participants in tissue morphogenesis.

By orchestrating tissue development, homeostasis, and regeneration through a suite of interdependent biophysical traits: the ECM possesses organ-specific biochemical composition, tunable stiffness and viscoelasticity, hierarchical surface topography, interconnected porosity and 3D architecture, and finely regulated hydrophilicity (Figure 1).[29–31] Each of these features defines tissue functionality from early development through maturation and regeneration.

Surface topology defines the microstructural interface of materials, ranging from aligned collagen fibrils and basement-membrane nanoridges that provide contact guidance, to microscale roughness that governs initial protein adsorption and cell spreading.[28,32] Mechanical properties, such as stiffness and viscoelasticity, allow biomaterials to approximate physiological moduli (1–100 kPa for soft tissues) and thereby transmit forces to cells and drive mechanotransduction via integrin clustering and Yes-associated protein (YAP)/transcriptional coactivator with PDZ-binding motif (TAZ) nuclear shuttling.[33–36] Interconnected porosity (typically 50–500 μm pores) and 4D architecture establish diffusion gradients for oxygen, nutrients, and waste while permitting cell migration and vascular ingrowth.[37] Hydrophilicity reflects a material's water-attracting capacity, conferred by hydroxyl, carboxyl, and sulfate groups, and maintains hydration, stabilizes adsorbed protein conformation, and facilitates integrin-mediated adhesion.[28] Collectively, these biophysical cues, along with the biomaterial source (natural, synthetic, or hybrid), render the ECM a dynamic, instructive microenvironment that actively regulates cell fate, tissue morphogenesis, and functional restoration.[28,38]

Current ECM-derived and ECM-inspired biomaterials for bioprinting and tissue engineering encompass native structural and adhesive proteins (e.g., collagen type I/IV, fibrin), glycosaminoglycans (GAGs; e.g., hyaluronic acid [HA], heparan sulfate [HS]), decellularized ECM (dECM) from various tissues, semi-synthetic hybrids (e.g., gelatin-methacryloyl [GelMA], methacrylated HA [HAMA], thiolated/norbornene-modified HA), and fully synthetic mimics (e.g., polyethylene glycol [PEG]-based peptide conjugates, polycaprolactone [PCL]/PEG block copolymers).[39–41] Although these materials recapitulate baseline ECM features—including ligand identity (e.g., RGD, isoleucine–lysine–valine–alanine–valine [IKVAV], tyrosine–isoleucine–glycine–serine–arginine [YIGSR]), fibrillar topography, initial viscoelasticity, and protease-dependent degradability—their storage moduli (G'), loss moduli (G"), stress–relaxation timescales, mesh size, and ligand presentation remain essentially fixed post-fabrication, thereby failing to capture the profound temporal evolution observed *in vivo*.[42]

In contrast, ECM-derived SMART materials engineer true dynamic reciprocity by building directly upon native or bio-orthogonal ECM chemistries, actively emulating the physiologically relevant viscoelastic spectrum, force-dependent ligand uncaging, traction-mediated remodeling, and spatiotemporal bioactive epitope gradients of developing and healing tissues, thereby transforming conventional ECM mimics into temporally evolving, instructive matrices that orchestrate morphogenesis in 4D bioprinted and bioassembled constructs.[43]

While previous review articles have provided overviews of 4D printing with SMART materials, focusing on applications in wearable devices, soft robotics, and tissue engineering, they typically survey established technologies and highlight niche challenges.[44,45] In contrast, this review uniquely integrates ECM-derived insights across subfields to establish a new biomimetic framework for future 4D SMART material development in bioprinting, emphasizing the inherent dynamic properties of ECM components that the field implicitly seeks to replicate. We first explore the core biophysical, biochemical, and organ-specific mechanisms of the ECM that should now serve as the uncompromising blueprint for all future biomaterial design. Then, we examine the activation mechanisms in current SMART materials, their applications in mechanistic research, and potential for clinical translation, followed by a comparative review of each stimulus approach. We conclude by outlining emerging directions and remaining

challenges in developing adaptive, next-generation materials for regenerative medicine.

2. Biophysical foundation of SMART materials

2.1. Extracellular matrix components and their cellular interactions

The ECM serves as a dynamic blueprint for engineering 4D SMART materials, offering explicit, translatable design rules derived from native biophysical and biochemical cues that profoundly shape cellular attributes such as orientation, stiffness, contractility, and polarity through topographic features, substrate rigidity, and ligand density.[46,47] Topographic alignment can be replicated using electrospun fibers (200–800 nm diameter) or microgrooved polydimethylsiloxane substrates (2–10 μm groove width), inducing over 80% cell alignment along the principal axis.[21,48–50] Similarly, substrate stiffness can be tuned from 0.5 kPa (brain-like) to 50 kPa (pre-calcified bone) using polyacrylamide or PEG-based hydrogels, directly modulating YAP/TAZ nuclear localization and contractility.[9]

Beyond structural support, the ECM regulates cell signaling through sequestered growth factors or cytokines, mechanotransduction pathways (the conversion of mechanical signals to biochemical responses), and dynamic remodeling mediated by enzymes such as lysyl oxidase and MMPs.[31,46,51] In 4D tissue engineering, growth factor presentation is engineered via heparin-mimetic domains or MMP-degradable cross-linkers (e.g., VPMSMRGG peptide sequences), enabling on-demand release of vascular endothelial growth factor (VEGF) or transforming growth factor (TGF)-β1, with a release half-life of 3–14 days.[52] Acting as a modulator of cell–ECM adhesion, growth factor availability, and chemotactic (chemokine gradients)/haptotactic (directional migration) guidance cues, the ECM orchestrates differentiation, maturation, and directed migration of both resident and recruited cells.[47,51,53]

Serving as a non-cellular, 3D scaffold, the ECM integrates mechanical and biochemical cues to regulate cell fate. Its biophysical properties arise from four core classes of macromolecules that directly inform biomaterial design: structural proteins, elastic fibers, adhesive proteins, and amorphous proteoglycans (Figure 2).[54,55] These native components are increasingly preserved in dECM derived from tissues or organs, which retains organ-specific architecture, ligand presentation, and mechanical gradients. When combined with 3D or 4D bioprinting, dECM provides a direct, customized template that translates complex biophysical hierarchies into programmable, evolving scaffolds.[56,57]

Among the ECM's molecular constituents, structural proteins—including fibrillar collagens (types I–III, V; hydrated Young's modulus of 0.5–100 kPa), network-forming collagen IV (approximately 400 nm wire sheets, 10–50 kPa), fibril-associated collagen VI (beaded microfilaments), elastin (entropic recoil, 0.1–1.5 MPa), and fibrillin-rich microfibrils—constitute the hierarchical, load-bearing backbone that generates anisotropic stiffness gradients, pronounced strain-stiffening, and viscoelastic dissipation (Figure 2A and B).[54,58] Secreted by fibroblasts, chondrocytes, and osteoblasts, collagens self-assemble into fibrils, primarily influenced by hydrophobic and electrostatic interactions between collagen molecules; the resulting fibrillar architecture influences cell polarity and supports morphogenesis. In contrast, elastin governs tissue elastic modulus for recoil while guiding cell alignment and differentiation via integrin-mediated signaling.[59]

These native biophysical signatures are recapitulated in engineered scaffolds through 200 nm electrospun fibers (produced via rotating mandrels or parallel electrodes) for contact guidance and durotaxis, tunable cross-linking density with genipin (0.05–0.5 wt%) or ruthenium/sodium persulfate photo-cross-linking to replicate physiological strain-stiffening and relaxation timescales, and incorporation of recombinant tropoelastin or elastin-like polypeptides for recoverable entropic elasticity.[49,60,61]

Nevertheless, current structural protein-derived and protein-informed materials still fall short of native fatigue resistance (>10^7 cycles at 10–20% strain), long-term *in vivo* stability (elastin half-life >70 years versus months-to-years for most constructs), batch-to-batch reproducibility, and regulatory approval due to residual cross-linker toxicity and telopeptide immunogenicity.[62,63] In 4D tissue engineering, these deficiencies have become critical bottlenecks, as the materials typically lack the robust creep resistance and reversible viscoelasticity needed to sustain programmed, time-evolving shape changes and adaptive remodeling under decades-long physiological loading, resulting in premature loss of dynamic function well before full tissue maturation.[63] This has led to commercial collagen gels often being blended with synthetic polymers like PEG to improve long-term stability.[64]

While structural proteins provide mechanical robustness, adhesive proteins (e.g., fibronectin, laminin, and thrombospondins [TSPs]) act as molecular bridges between cells and the ECM by presenting integrin-binding domains (e.g., RGD, IKVAV, YIGSR) at precise densities and nanometer-scale spacings (optimal 10–150 nm; Figure 2C).[54] These parameters directly control focal

adhesion maturation, cytoskeletal tension, and downstream cell polarity, thereby dictating the required grafting chemistry, peptide concentration (0.1–10 mM), and patterning method (microcontact printing, nanopatterned surfaces) for material design.[65,66]

Fibronectin is a mechanosensitive glycoprotein that serves as a master organizer of the ECM, enabling integrin-mediated cell adhesion, fibril assembly, and exposure of cryptic binding sites under mechanical load to regulate matrix remodeling, stability, and downstream focal adhesion kinase/extracellular signal-regulated kinase signaling, which are critical for polarization, collective migration, morphogenesis, and gastrulation.[67,68] In 4D tissue engineering, precise spatial presentation of its RGD and PHSRN synergy sites at 10–70 nm spacing is essential to trigger maturation of focal adhesions, generate cytoskeletal tension, and drive time-dependent cell polarity and shape changes in dynamic matrices.[55,69–71] Current examples include adsorbed full fibronectin or linear/cyclic RGD-grafted PEG, HA, or polyacrylamide hydrogels and poly(lactic-co-glycolic acid) (PLGA) scaffolds, which significantly improve initial cell attachment and viability.[4,72,73] However, adsorbed protein may denature or orient randomly, xenogeneic sources show batch variability, and short linear RGD peptides exhibit 100–1000-fold lower affinity than native fibronectin, requiring non-physiological densities that fail to recapitulate synergy-dependent mechanotransduction or maintain long-term stemness.[74]

Laminin, the primary adhesive glycoprotein of basement membranes, provides essential IKVAV, YIGSR, and isoform-specific RGD motifs that direct cell polarization, axon guidance, epithelial, muscular, or vascular differentiation, and tissue barrier formation through integrin and dystroglycan binding and synergistic interactions with collagen type IV and nidogen (Figure 2C).[47,54,59,75] In polarized tissue engineering (e.g., vessels, neural tubes, kidney organoids), 4D systems require precise nanoscale clustering and orientation of adhesive peptides to drive apico-basal polarity and sustained lineage commitment within stimuli-responsive matrices.[55,75] Currently, laminin-derived materials such as Matrigel, Cultrex, or Geltrex, laminin-111/521 coatings, and PEG/HA hydrogels functionalized with IKVAV or YIGSR, have been observed to promote vascularization and neural regeneration in preclinical models.[76–78] However, tumor-derived Matrigel has an undefined composition, high batch variability, residual mitogens, and tumorigenic risk.[79] Similarly, purified full-length laminin remains prohibitively expensive and unstable. At the same time, short peptides mimic its activity only partially and show markedly weaker polarization, axon extension, and organoid morphogenesis compared to the native protein.[80]

In addition, TSPs are context-dependent matricellular proteins. TSP-5, also known as cartilage oligomeric matrix protein (COMP), and TSP-1–4 modulate angiogenesis, inflammation, collagen fibrillogenesis, and mechanotransduction via RGD (TSP-1/2), cysteine–serine–valine–threonine–cysteine–glycine (TSP-1), and valine–valine–methionine (TSP-5) motifs, with TSP-1/2 typically anti-angiogenic through VEGF sequestration and TGF-β activation, whereas TSP-5/COMP supports high-load tissue assembly in cartilage and tendons (Figure 2D).[81–83] Their mechano-responsive incorporation enables time-controlled switching between pro- and anti-angiogenic states and stiffness reinforcement during load-bearing tissue maturation. Current applications include COMP-supplemented collagen scaffolds for tendon/ligament repair and TSP-1/2 peptide-doped fibrin or collagen gels to fine-tune vascular ingrowth.[83–85] However, limitations remain significant due to high context- and concentration-dependence (excess TSP-1/2 strongly inhibits vascularization and delays healing),[86] often resulting in the uneven incorporation and rapid *in vivo* degradation of multimeric proteins, restricting predictable 4D control over angiogenesis and mechanical evolution.

Beyond structural and adhesive proteins, proteoglycans and their GAG chains—HA, HS, and chondroitin/dermatan sulfate (CS/DS)—are primary regulators of ECM hydration, compressive resistance, viscoelasticity, and morphogen presentation. Their high negative charge density generates substantial osmotic swelling pressures (200–1000% volume increase), while specific binding pockets for fibroblast growth factors (FGFs), VEGF, bone morphogenetic proteins (BMPs), and TGF-β establish gradients, amplify signaling, and protect growth factors from degradation. Together, these functions modulate collagen assembly and mechanotransduction across cartilage, basement membranes, and other load-bearing tissues (Figure 2E and F).[55,87–90] These gradients are essential for processes such as angiogenesis, chondrogenesis, and neural development. For example, perlecan facilitates BMP-2 signaling and TGF-β activity during bone formation, and aggrecan supports cartilage zonal organization.[76,90,91]

Proteoglycans are used in tissue engineering for their extreme swelling capacity, shear-thinning injectability, enzyme-triggered degradability (hyaluronidase, heparanase, chondroitinase), and growth-factor sequestration/release kinetics,[88,90] thereby promoting highly dynamic, cell-mediated remodeling systems that evolve stiffness, porosity, and bioactive gradients over time for vascularization, chondrogenesis, organoid patterning,

and load-adaptive maturation.[56,90] Nevertheless, substantial limitations remain due to native GAG sulfation patterns and molecular weight-dependent bioactivities being nearly impossible to replicate synthetically, and animal-derived GAGs exhibiting batch variability and immunogenicity.[92]

Extending beyond classical ECM molecules, growth factors (e.g., VEGF, FGF, platelet-derived growth factor, BMPs, TGF-β), cytokines (e.g., interleukin-6, tumor necrosis factor α, interferons), and cell–cell adhesion molecules (e.g., cadherins, selectins, connexins, and non-RGD-binding integrin heterodimers) collectively orchestrate proliferation, migration, differentiation, inflammation, immune cell trafficking, junction formation, and tissue-level morphogenesis through highly transient, gradient-dependent, and switchable signaling that classical ECM proteins alone cannot provide.[54,93] These molecules enable temporal control of signaling via affinity-regulated, enzyme-, plasmin-, light-, or shear-triggered release systems, dynamic morphogen gradients, reversible cell

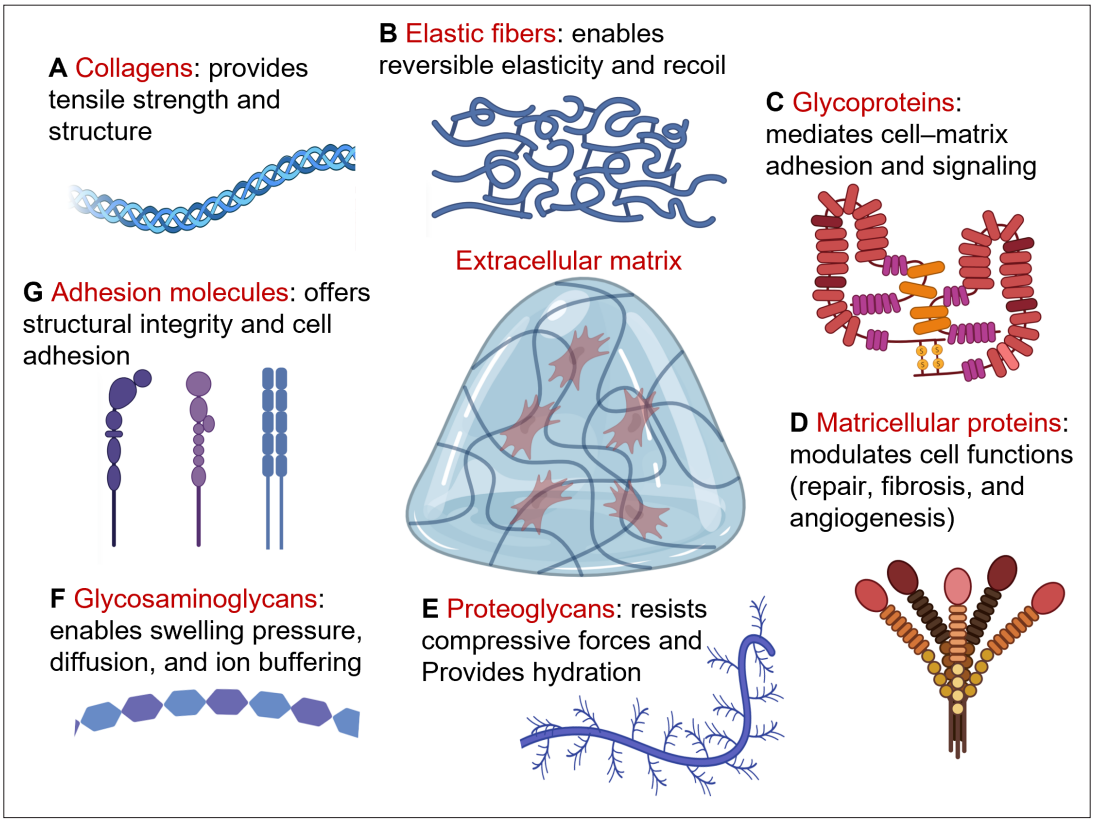


Figure 2. Key extracellular matrix (ECM) components and their functional roles. (A) Collagens (fibrillar collagens types I–III and V; network-forming collagen type IV): Providing tensile strength and structural scaffolding in ECMs, forming fibrils (types I–III and V) for resistance to traction and networks (type IV) in basement membranes for tissue organization. (B) Elastic fibers (e.g., elastin, microfibrils): Permitting reversible elasticity and recoil to tissues such as arteries, lungs, and skin, enabling repetitive deformation. Elastin provides long-range extensibility via cross-linked tropoelastin, while microfibrils (fibrillins) act as scaffolds. (C) Glycoproteins (e.g., laminins, fibronectin, thrombospondins): Mediating cell–matrix adhesion and signaling. Laminins form basement membrane networks for tissue morphogenesis, cell differentiation, migration, and homeostasis. Fibronectin organizes ECM assembly, promotes cell adhesion via integrins, and regulates migration, proliferation, and wound healing. (D) Matricellular proteins (e.g., thrombospondins (TSP)-5/cartilage oligomeric matrix protein and TSP 1–4): Temporarily modulate cell functions without structural roles. TSP-5/cartilage oligomeric matrix protein regulates cartilage organization, collagen fibrillogenesis, and chondrocyte proliferation. TSP 1–4 control angiogenesis, fibrosis, wound healing, and cell–matrix interactions, with anti-angiogenic and pro-fibrotic activities in disease contexts. (E) Proteoglycans (e.g., aggrecan, versican, brevican): Provide hydration, compression resistance, and signaling modulation. Aggrecan aggregates with hyaluronan in cartilage for shock absorption. Versican regulates cell motility, proliferation, and tissue morphogenesis. Brevican supports neuronal adhesion and the formation of the brain ECM. (F) Glycosaminoglycans (e.g., chondroitin sulfate, heparan sulfate, heparin, and hyaluronic acid): Provide hydration, create negative charge, and space-filling properties. Chondroitin sulfate enables swelling and compression resistance. Heparan sulfate/heparin binds growth factors for signaling and angiogenesis. Hyaluronic acid maintains tissue hydration, facilitates cell migration, and regulates inflammation and wound healing. (G) Adhesion molecules (e.g., cadherins, selectins, connexins): Facilitate cell–cell and cell–matrix interactions. Cadherins mediate calcium-dependent cell adhesion to maintain tissue integrity and support morphogenesis. Selectins enable leukocyte rolling and adhesion during inflammation. Connexins form gap junctions for intercellular communication and signaling in tissues like the heart and the nervous system. Created in BioRender. Joung, D. (2025). https://BioRender.com/hbg6tqr.

clustering, epithelial–mesenchymal transitions, and inflammation-to-resolution switching, all essential for vascular sprouting, organoid self-organization, immune-evasive implants, and tissue fusion.[55,93]

Current platforms include heparin/star-shaped PEG (starPEG) or MMP-degradable PEG hydrogels for sustained/sequential VEGF–platelet-derived growth factor–BMP-2 delivery in bone and vascular models, and cadherin-11 or N-cadherin peptide-functionalized modular HA/PEG assemblies for cardiac and neural spheroid fusion.[94,95] Even so, cadherin/connexin peptides achieve only 1–10% of native affinity and cannot replicate inside-out signaling or catch bonds.[96] Above all, the lack of true ON/OFF switchable systems forces 4D constructs into irreversible, one-time-release approaches, failing to mimic the oscillatory, feedback-regulated signaling of native development and healing.[97]

Together, these ECM and microenvironmental components form a spatiotemporally orchestrated system that cohesively regulates tissue mechanics, hydration, adhesion, polarity, morphogen gradients, inflammation, and remodeling via nanoscale ligand display, force-dependent unfolding, enzyme-triggered release, and feedback signaling. These elements directly guide 4D SMART biomaterial design by providing blueprints for dynamic stiffness evolution, on-demand ligand clustering, switchable growth-factor gradients, reversible cell polarity, inflammation resolution, and load-adaptive remodeling, thereby converting static scaffolds into regenerative microenvironments that drive vascularization, organoid patterning, zonal maturation, and host integration.

Current platforms integrate multi-domain peptides, injectable GAG hydrogels, heparin/HS affinity modules, MMP-degradable linkers, and cadherin/RGD assemblies to mimic physiological dynamics in bone, cartilage, vascular, neural, and cardiac models. However, clinical translation is constrained by incomplete replication of native complexity (e.g., sulfation codes, synergy sites, catch bonds, oscillatory signaling), batch variability and immunogenicity of biological sources, loss of responsiveness from over-stabilization, and the absence of truly reversible, multi-modal triggers. Synthetic ECMs, therefore, remain partial mimics of natural developmental and homeostatic fidelity. Table 1 summarizes the functions of major ECM and microenvironment components used in 4D SMART materials, as described above.

2.2. Tissue-specific extracellular matrix compositions

Now that we have explored the ECM components, the next step is to examine how their integration at varying

Table 1. Extracellular matrix and microenvironment components and their roles in 4D SMART materials

Component	Role in 4D SMART materials	Materials available	Ref.
Collagens	Enables tunable stiffness and degradation	Collagen gels, collagen–polyethylene glycol bioinks, electrospun nanofibers.	15,48,55
Elastin	Provides elasticity and recoil for dynamic tissues	Tropoelastin hydrogels, ELP additives	98–101
Elastic microfibrils	Enables tension-responsive unfolding and growth factor release	Fibrillin composites, microfibril-GelMA	55,70
Fibronectin	Improves adhesion and signaling via RGD	Fibronectin-based hybrids, PNIPAAm gels	102–105
Laminin	Supports BM formation and cell polarity	Laminin-enriched, laminin peptide-hybrids	77,106,107
Glycoproteins/TSPs	Modulate angiogenesis, stabilize cartilage, and control growth factor release	TSP-based hybrids, glycoprotein additives.	85
Proteoglycans	Provide hydration and growth factor reservoirs	Aggrecan–HA, perlecan–HS, syndecan–polyethylene glycol scaffolds	108–110
Glycosaminoglycans	Enable turgor-based shape changes and bind growth factors for controlled release	HA hydrogels, heparin-functionalized gels	73,99
Growth factors	Drive cell differentiation and patterning	VEGF, EGF, FGF-2, BMP-2, TGF-β	109,111–113
Cytokines	Modulate inflammation and tissue integration	IL-4, G-CSF, SDF-1α	114,115
Adhesion molecules	Enhance force-responsive adhesion and self-organization	RGD/LDV-polymers, cadherin/integrin/selectin-additives	72,116,117

Abbreviations: 4D: four-dimensional; BM: basement membrane; BMP: bone morphogenetic protein; EGF: epidermal growth factor; ELP: elastin-like polypeptide; FGF: fibroblast growth factor; G-CSF: granulocyte colony-stimulating factor; GelMA: gelatin methacryloyl; HA: hyaluronic acid; HS: heparan sulfate; IL: interleukin; LDV: leucine–aspartic acid–valine; SDF-1α: stromal cell–derived factor 1α; SMART: stimuli-responsive materials for advanced regenerative technologies; RGD: arginine–glycine–aspartic acid; TGF: transforming growth factor; TSP: thrombospondin; PNIPAAm: poly(N-isopropylacrylamide); VEGF: vascular endothelial growth factor.

ratios generates tissue-specific functionality—ultimately informing future experimental design. Tissue-specific ECM compositions emerge from organ-unique ratios and spatiotemporal assembly of structural proteins (e.g., collagen types I–V, elastin), adhesive glycoproteins (e.g., fibronectin, laminin, TSPs), amorphous proteoglycans/GAGs (e.g., HA, HS, CS/DS), and transient cues (e.g., growth factors, cytokines, cadherins), yielding either collagen/proteoglycan-dominant interstitial matrices for load-bearing tissues (e.g., cartilage, bone, tendon, dermis) or laminin/collagen type IV/perlecan-rich basement membranes for polarized tissues (e.g., epithelium, endothelium, neural).[26] These signatures define organ-specific mechanics (0.1–1000 kPa), viscoelasticity, ligand spacing, hydration, and morphogen kinetics, serving as the foundational template for 4D SMART biomaterials.

Successful clinical application requires precise replication of these ratios using translatable modules (e.g., Matrigel, Cultrex, HAMA, starPEG–heparin, recombinant collagens, RGD/cadherin peptides) combined with degradable linkers and affinity systems. This would enable authentic dynamic evolution of stiffness, ligand presentation, gradients, and remodeling, thereby driving proper lineage commitment, polarity, vascularization, and zonal maturation while preventing fibrosis or aberrant differentiation from generic matrices.

Starting with general epithelial tissues, these tissues primarily possess a thin, basement membrane-dominated ECM with characteristic compositional ratios (collagen type IV: ~30–40%, laminins: ~10–15%, HS proteoglycans [e.g., perlecan]: ~5–10%, minor interstitial collagens type I/III: ~20–25%, fibronectin: ~10–15%, and HA: ~5–10% for hydration), which set low initial stiffness (0.1–5 kPa), strong apico-basal polarity cues, and selective permeability for nutrient/waste transport.[26,54,118] In polarized epithelia located in glands, intestines, or kidneys, these precise starting ratios must be faithfully reproduced in dynamic hydrogels to initiate authentic stem cell symmetry breaking, lumenogenesis, and barrier maturation.[119,120] Deviation from these tissue-specific ratios can disrupt lumen formation, invert polarity, or trigger unwanted epithelial–mesenchymal transition.[120,121]

Similar to general epithelia, skin ECM exhibits a hierarchical composition, with the dermal interstitial matrix dominated by collagens (~70–80%, primarily type I [~60–70%] and type III [~10–15%]), elastin (~2–5%), fibronectin (~5–10%), and proteoglycans such as decorin/biglycan (~5–10%), with chondroitin/dermatan sulfate-rich GAGs (~5–10%), capped by a thin epidermal basement membrane enriched in collagen type IV, laminin-332, and perlecan. This arrangement collectively establishes high tensile strength (10–100 kPa), viscoelastic recoil, rapid hydration/swelling, and layered polarity essential for barrier integrity, wound contraction, and sensory function.[54,122] This multi-layered matrix supports keratinocytes in the epidermis (basement membrane) and fibroblasts in the dermis, facilitating barrier function, providing elasticity and hydration, supporting wound healing (driven by fibronectin and HA), and serving sensory roles that the protective skin layer needs to continuously maintain.[26,76,122]

In contrast to the skin's compact matrix, lung ECM is distinctly compartmentalized into thin basement membranes and loose interstitial matrices, with defined compositional ratios (collagens: ~40–50%, primarily types I/III [~30–40%] and type IV [~10–15%]; elastin: ~15–20%; versican proteoglycans: ~20–25%; and heparan/chondroitin sulfate GAGs: ~10–15%) that collectively confer ultra-low stiffness (0.1–5 kPa), extreme viscoelastic recoil, and high hydration, supporting efficient gas diffusion, alveolar expansion, and lung compliance.[123–125] In 4D bioengineering of alveolar or bronchial constructs, these ratios can be recapitulated in ultra-soft, poroelastic hydrogels as an initial instructive template to drive authentic type I/II pneumocyte barrier formation, endothelial capillarization, and cyclic mechanical breathing-like actuation.[26,124,126,127] Additionally, abundant elastin and versican enable passive recoil and matrix swelling, ensuring ventilation fidelity, while tightly regulated collagen content limits premature fibrotic deposition yet permits stretch-induced remodeling. HS domains preserve VEGF/FGF gradients required for vascular parity, with subsequent MMP- and heparanase-triggered matrix evolution facilitating inflammation resolution and physiological stiffening only in response to injury cues.[124,126,128–130] Deviations from these compositional ratios trigger irreversible scarring, alveolar collapse, or stiff, non-compliant constructs, which likely underlie the widespread failure of generic matrices to produce functional, gas-exchanging lung organoids or regenerative implants.

Skeletal muscle ECM displays hierarchically organized compositional ratios (~5–10% collagen, primarily types IV/VI in the endomysium and I/III in the perimysium, together with decorin/biglycan proteoglycans, elastin, and heparan/chondroitin sulfate GAGs) that generate aligned anisotropy, viscoelastic compliance (0.1–10 MPa), and specialized pericellular niches supporting myofiber force transmission, contraction, and satellite cell-mediated repair.[46,131–133] This matrix forms a flexible pericellular network that anchors or aligns myofibers, facilitating force transmission, muscle contraction, and satellite cell-driven regeneration, thereby supporting functional mobility and tissue repair.[26,46,51,133] In bioprinting and tissue engineering of volumetric muscle constructs, these defined ratios

should be recapitulated in aligned fibrillar hydrogels as an instructive template to drive authentic myoblast fusion, sarcomerogenesis, and load-responsive maturation.[134] Collagen type IV/VI and HS-rich domains preserve early soft niches for satellite cell activation and migration. In contrast, collagen type I/III, elastin, and decorin enable subsequent stretch-induced fibril alignment and stiffening, supporting mature contractile bundle formation and vascular integration.[14,46,133,134]

Moving from soft to semi-rigid tissues, the cartilage ECM exemplifies a matrix specialized for compressive load bearing and hydration retention. Found in articulating surfaces, tracheal rings, and the embryonic skeleton, hyaline cartilage consists of collagen type II (~40–50%), aggrecan proteoglycans (~25–35%), GAGs (chondroitin and keratan sulfates; ~20–30%), and fibronectin (~5–10%).[26,54,135] The aggrecan–hyaluronan aggregates generate high osmotic swelling pressure, imparting viscoelastic resistance and smooth, low-friction surfaces essential for joint articulation.[135,136] These compositional principles have been leveraged in bioprinting and tissue-engineering approaches, where dECM scaffolds and stem cell-laden constructs recapitulate cartilage structure for osteoarthritis repair and joint resurfacing.[32,137] Deviations from these ratios have been shown to induce fibrous tissue formation, superficial delamination, or ectopic ossification.[99,136,138]

Building upon this progressive increase in rigidity, bone ECM is predominantly composed of collagen type I (~85–90%), with hydroxyapatite minerals (inorganic phase), biglycan/decorin proteoglycans (~1–5%), and GAGs such as chondroitin/dermatan sulfate (~1–5%).[54,139] This ratio confers extreme stiffness (100–200 MPa), fracture toughness, and nanostructured porosity through aligned mineralized fibrils, supporting compressive and tensile strength, impact absorption, and osteocyte mechanotransduction.[137,139–141] Accordingly, material composites such as calcium phosphate–collagen hydrogels, HA–PCL, and tricalcium phosphate–CS blends mimic the mineralized ECM for osteoporosis models, enhance load-bearing, and improve antimicrobial properties.[91,140–142]

Closely related yet functionally distinct, the ECM in cardiac muscle is a dynamic network primarily composed of collagen types I/III (~5–15%) and IV (~5–10%), syndecan-4 proteoglycans (~5–10%), elastin (~5–10%), and GAGs (~5–10%).[125,143] It serves as a reservoir for growth factors, cytokines, and proteases.[125] Structurally divided into the basement membrane/pericellular matrix (around cardiomyocytes, rich in laminin and collagen type IV) and the interstitial matrix (providing structural support via collagen type I/III), cardiac fibroblasts are the main producers of cardiac ECM, with contributions from endothelial cells and cardiomyocytes.[54,125,143] This organization yields a compliant scaffold for rhythmic function, cardiomyocyte adhesion, and electrical conduction, essential for heartbeat regulation.[144,145]

Soft, dynamic hydrogels serve as the optimal starting template to drive authentic human induced pluripotent stem cell–cardiomyocyte alignment, synchronous beating, and fibroblast co-maturation.[145] Elevated pericellular laminin, collagen type IV, and syndecan-4 preserve early compliant niches for calcium transient initiation, whereas controlled interstitial collagen type I/III and elastin enable cyclic strain amplification and elastic recoil, ultimately permitting cell-driven, lysyl oxidase-mediated matrix stiffening and VEGF gradient formation that yield vascularized, contractile cardiac tissue.[143]

Extending this structural hierarchy, vascular ECM in arteries is formed through a layered structure beginning with the tunica intima (an endothelial basement membrane rich in collagen type IV and laminin), tunica media (smooth muscle cells embedded in elastic lamellae of elastin and fibrillin), and tunica adventitia (rich in collagen types I and III, conferring tensile strength).[123,144] Generalized vascular ECM includes elastin (~20–30%), collagen types I/III (~30–40%) and IV (~10–15%), syndecan/perlecan proteoglycans (~10–15%), and GAGs like HS (~10–15%).[123,125,146] This matrix creates a distensible conduit for circulation, supports endothelial barrier function, anticoagulation, and hemodynamic adaptation, and promotes nutrient transport and inflammatory regulation.[123,144,147] Biomaterials used to emulate the biophysical dynamics of this tissue range from decellularized aorta hydrogels to composites that integrate elastin-like peptides with collagen or PCL, supporting vascular grafts and 3D vascular network formation in bioprinting constructs.[22,146,148–150] Disruptions of these vascular-specific ratios can result in thrombosis, intimal hyperplasia, or rupture.

Lastly, the central nervous system ECM, which occupies approximately 10–20% of brain volume, exhibits compositional ratios (aggrecan/brevican/neurocan proteoglycans ~20–30% with chondroitin sulfate GAGs ~20–30%, collagen type IV ~5–10%, and laminins ~10–15%) that form ultra-soft (0.1–1 kPa) diffuse perisynaptic gels and condensed perineuronal nets for neuroprotection against oxidative stress and excitotoxicity, while constraining molecular diffusion to enable synaptic stabilization, activity-dependent plasticity, and long-term potentiation.[151–156] Decellularized brain ECM coatings and scaffolds created with HA-dominant chondroitin sulfate proteoglycans-rich hydrogels enhance neuronal viability, neurite outgrowth, and network formation in neuron–glia co-cultures.[157] Failure to preserve these neural-specific

ratios can lead to hyperexcitability, gliosis, or failed synaptogenesis.

Taken together, these examples illustrate how tissue-specific ECM composition and architecture dictate distinct mechanical, biochemical, and signaling landscapes across organ systems. Understanding these nuances provides the foundation for designing 4D SMART materials that can dynamically replicate, remodel, and respond to native tissue microenvironments—bridging the gap between static biomaterials and living, adaptive tissue constructs.

3. 4D SMART materials

3.1. Applications of stimuli-responsive materials

Characterized by their stimuli-responsive adaptivity, SMART materials build off first-generation ECM-mimicked biomaterials which provide baseline localized biochemical and biophysical cues to influence cell behavior, and advance toward a next-generation transformative class of biomaterials that evolve over time in response to external triggers such as temperature, humidity, pH, light, or magnetic fields, thereby enabling dynamic shape-shifting, self-assembly, and conformational changes akin to living systems (Table 2).[12,22,76,158]

Specifically engineered to mimic key properties of the ECM, many current materials are multi-adaptive, integrating two or more response mechanisms to support cell encapsulation and enable stimuli-triggered behaviors, such as self-folding in 4D bioprinting.[18,91,145] Replicating the biophysical dynamics of the ECM introduces inherent biomaterial toxicity risks, typically arising from material composition (e.g., residual monomers, oxidative groups), dose/concentration, exposure duration, and processing conditions (e.g., crosslinking agents), thereby affecting cell viability. Cell viability is further influenced by material biocompatibility, porosity, stiffness, and nutrient and reagent diffusion capacity, and is often assessed via assays such as the 3-(4,5-dimethylthiazol-2-yl)-2,5-diphenyltetrazolium bromide (MTT) assay (metabolic activity) and live/dead staining.[3,159,160] With this context, we next organize SMART materials by primary stimulus class and highlight representative systems, followed by multi-trigger integrations that exemplify 4D behavior.

3.1.1. Thermo-responsive polymers for four-dimensional actuation and tissue engineering

Thermo-responsive (temperature-sensitive) materials are primarily found as polymers, such as PNIPAAm, PNIPAAm derivatives, or Pluronic, which undergo reversible physicochemical changes in response to temperature shifts.[184,185] These materials mimic the temperature-driven conformational shifts of collagen and elastin during wound healing and development, enabling printed constructs to soften or stiffen in situ, mimicking maturing tissues.[5] These polymers are classified into two types: lower critical solution temperature (LCST) and upper critical solution temperature (UCST).[5,186] LCST types involve a phase transition (~32–34°C) in which, below LCST, solubility is maintained through hydrogen bonding with water, and above LCST, intramolecular hydrophobic collapse results in dehydration, gelation, or aggregation.[6,184] In UCST polymers (sulfobetaine-based), activation below UCST causes insolubility through strong hydrogen bonding or ion pairing, and above UCST, dissolution is promoted by thermal energy, hydrogen bonding, or electrostatic disruption.[5,6,184,187]

These polymers have been used in tissue engineering to facilitate cell sheet harvesting, where cooling triggers hydrophilic swelling, detaching intact cell sheets without enzymes, and preserving cell junctions for layered tissues such as the cornea or myocardium.[5,145,188] While PNIPAAm is praised for enabling enzyme-free cell harvesting in

Table 2. Activation of stimuli-responsive materials for advanced regenerative technologies

Stimulus type	Mechanism of activation	Ref.
Temperature	Triggers phase transitions in polymers, leading to shape recovery or transformation	161–166
pH	Triggers protonation/deprotonation in polymers, causing swelling/shrinking and shape changes in acidic or basic environments	164,167,168
Hydration	Induces swelling or deswelling in hydrophilic polymer networks, leading to volume expansion, shape deformation, or actuation	164,169–171
Light	Photothermal, photochemical, or photoisomerization processes (NIR, IR, UV), enabling localized deformation, recovery, or actuation	162,168,172–174
Ionic strength	Crosslinking or gelation enabling shape fixation, actuation, or stiffness changes	175–177
Magnetic	External B-field, inducing actuation, alignment, or deformation	178–180
Electrical	External E-field, generating bending, contraction, or expansion	25,181–183

Abbreviations: NIR: near-infrared; IR: infrared; UV: ultraviolet.

cell sheet engineering and preserving cell junctions, its biocompatibility has been a key limitation, with issues including delayed re-solubilization upon cooling, potential cytotoxicity from monomers (*N*-isopropylacrylamide), and inflammatory responses *in vivo* at higher concentrations.[184] Generally, thermo-responsive hydrogels (e.g., PNIPAAm, PNIPAAm derivatives, Pluronic) are biocompatible with minimal effects on cell viability in short-term studies; however, long-term cytotoxicity and material degradation need to be further evaluated.[5,184,185]

3.1.2. pH-responsive polymers for four-dimensional dynamic biomaterials

pH-responsive materials, such as polymers and peptides, undergo reversible physicochemical transitions triggered by anionic interactions, which swell above a pKa via deprotonation (e.g., carboxylic acids), and cationic interactions, which swell below a pKa through protonation (e.g., amines).[189,190] These materials replicate the charge-dependent swelling and matrix remodeling observed in acidic inflammatory or tumor microenvironments, enabling localized volume changes akin to ECM acidification-driven fibrosis.[191]

Anionic polymers, such as poly(acrylic acid) or carboxymethyl cellulose (CMC), activate through deprotonation. When responses exceed the pKa thresholds, COO^- groups repel one another, leading to chain expansion and swelling. Conversely, below these thresholds, protonation neutralizes charges, leading to collapse.[189,190] Cationic polymers, such as chitosan (CS), protonate below pKa thresholds, where NH_3^+ repulsion induces swelling, while deprotonation above pKa thresholds promotes contraction.[189,191–193] CS is commonly used in dual-responsive bilayers, such as CS/CMC, which exhibit bidirectional actuation. CS swells at acidic pH due to NH_3^+ formation, whereas CMC swells at basic pH via COO^- ionization, with a structural equilibrium at neutral pH.[167] Mimicking pH shifts that occur during wound healing (inflammation), pH-responsive materials have been shown to facilitate the development of various programmable dynamic scaffolds and drug delivery systems.[189,190,194] These materials are generally considered biocompatible, and their toxicity and impact on cell viability depend on factors such as concentration, molecular weight, degree of modification, exposure duration, and pH.[189,190]

High doses or prolonged exposure can lead to cytotoxicity through mechanisms such as membrane disruption, oxidative stress, or apoptosis, and toxicity may vary as the material's conformation changes.[167,195] In recent studies, poly(acrylic acid) exhibits low to moderate cytotoxicity at typical biomedical concentrations, CMC shows excellent cell viability (>90%) at concentrations up to 5 mg/mL, and CS nanoparticles show dose-dependent toxicity, with >80% viability in lung carcinoma (A549) cells at <0.006% w/v, but <50% at higher doses due to reactive oxygen species (ROS) and membrane damage.[192,195–198]

3.1.3. Hydration-responsive materials for four-dimensional morphing scaffolds

Hydration-responsive, water-responsive, or humidity-sensitive materials (e.g., hydrogels, silk-based fibers, cellulose nanofibrils [CNF]) have been designed to mimic biological systems, where water plays a pivotal role in structural dynamics, and undergo reversible physical changes such as swelling, contraction, folding, or shape transformation through osmotic forces, molecular interactions with water, or changes in environmental relative humidity.[169,199,200] These behaviors are often observed in cartilage hydration during joint loading or in the maintenance of corneal transparency, enabling printed constructs to autonomously adjust stiffness and nutrient permeability in aqueous physiological environments.[201] These materials have been shown to be among the most biocompatible due to their organic sourcing, with more than 80% viability in alginate/HA scaffolding, 85–95% in CS/silk fibroin, and more than 90% in CNF composites.[196,197,202,203]

Integrating hydration- and thermo-responsive properties, Liu *et al.*[161] designed an amphiphilic dynamic thermoset polyurethane (DTPU) material for 4D printing to enable scaffolds with multidimensional morphing capabilities (1D–3D) for minimally invasive implantation, as shown in Figure 3A. These dual-responsive materials replicate the coupled moisture- and temperature-dependent viscoelasticity of articular cartilage and skin dermis, where combined humidity absorption and body-heat triggers produce synergistic softening or stiffening that mimics diurnal tissue compliance changes and thermoregulatory matrix remodeling.[204] DTPU—composed of PCL-triol as a thermo-responsive soft segment, PEG for hydrophilicity modulation, isophorone diisocyanate for pre-polymerization, and Diels–Alder (DA)-diol as a dynamic chain extender—forms a covalently crosslinked network with thermally reversible DA bonds, allowing extrusion-based fused deposition modeling printing at high temperatures.[161] Scaffolds were shown to exhibit body-temperature–triggered shape memory for initial recovery (1D–2D), which relies on PCL-triol's low melting point, enabling reversible transitions between glassy and rubbery states (Figure 3B).[161]

Followed by programmable deformation (2D–3D) through water absorption at 37°C, swelling induces a mismatch in bilayer structures, where high-swelling layers (DTPU-0.5-4k, swelling ratio: 118.1%) expand more than low-swelling ones (DTPU-0.25-4k, swelling ratio: 41.3%),

thereby generating internal stress for bending/folding into 3D shapes within 10 minutes (Figure 3C).[161] Stiffening also occurs in variants of PEG (molecular weight ≥2000), where hydration drives microphase separation, causing hydrophilic PEG aggregates to separate from hydrophobic PCL/DA segments, forming domains that increase the Young's modulus (*E*) up to 2.9-fold (0.7 MPa [dry] to 2.0 MPa [hydrated]; Figure 3D).[161] DTPU showed low toxicity, consistent with its PCL/PEG-based composition, with reported cell viabilities >90%.[4] Initial mild inflammation (cell infiltration) occurred at week 1, which eventually resolved by weeks 2–4 with tissue integration, with no significant toxicity or viability reduction *in vitro*.[161]

3.1.4. Photoactive polymers and nanomaterials in four-dimensional bioprinting

Light or photo-responsive (near-infrared [NIR], infrared [IR], ultraviolet [UV]) materials encompass polymers, peptides, and nanomaterials that undergo reversible or irreversible physicochemical changes upon exposure, enabling precise spatiotemporal control.[174,205–207] These systems emulate light-regulated cellular processes (e.g., phytochrome-like signaling in plants or UV-induced dermal remodeling), thereby providing precise, on-demand control over local stiffness and topography that mimics scar formation or angiogenic sprouting.[208] These materials are commonly observed as GelMA hydrogels, azobenzene-based polymers/peptides, carbon nanomaterials, and other functionalized nanoparticles.[148,205,207,209] Activation wavelengths are used to classify these materials. UV is used for high-energy reactions, where activation is enabled via photoisomerization (azobenzene trans-cis switching, altering hydrophobicity for self-assembly) or photocleavage (o-nitrobenzyl esters uncaging RGD peptides, exposing adhesive sites).[174,205,210,211] UV activation is associated with higher toxicity due to its high energy, limited tissue penetration, and potential to cause DNA damage or ROS production in the cellular environment.[209,210,212]

However, viability assays (e.g., MTT) have shown more than 80% cell survival for short exposures, whereas prolonged UV exposure can disrupt the cytoskeleton and reduce viability by 20–30%.[174] NIR/IR mechanisms involve up-conversion, triggering downstream reactions such as bond cleavage or photothermal heating, which converts light into heat via absorbers such as carbon nanotubes, causing hyperthermia for shape-memory transitions, drug/growth factor release, or cell modulation.[173,205,206,211] Due to overlapping thermal effects, NIR and IR are considered the safest options, with lower phototoxicity and deeper tissue penetration than UV or visible light.[205] Research shows that viability decreases by <20%, and neuronal cell viability remains >85% post-NIR exposure.[173,205,206,211]

Photo-responsive SMART materials have also been used to recapitulate angiogenesis by inducing growth factor release. For example, Meng *et al.*[213] engineered photothermal-responsive microcapsules composed of a GelMA core loaded with epidermal growth factor (EGF) or VEGF, encased within a PLGA shell functionalized with gold nanorods.[113,214] Upon NIR laser irradiation, localized heating ruptured the shell without compromising cell viability (>93% post-irradiation) or molecular functionality (Figure 4A).[213] Sequential activation every two days generated sustained VEGF gradients over a two-week period—mirroring physiological timescales of proliferation, migration, and angiogenic sprouting. This system overcame limitations of conventional 2D cultures and static 3D models by combining precise spatial organization of tumor cells, stromal fibroblasts, and endothelial cells with dynamic chemical signaling through programmable growth-factor release (Figure 4B). Using A549 lung carcinoma and M4A4 melanoma cells, they recapitulated key stages of metastatic progression—including tumor-driven VEGF secretion, endothelial activation, vessel sprouting, intravasation, and angiogenic expansion—closely mimicking how solid tumors stimulate neovascularization under hypoxic stress (Figure 4C–G). Collectively, these case studies demonstrate how light-responsive SMART materials translate developmental physics—including cell division, folding, lumen formation, and vascularization—into programmable, time-evolving constructs that more faithfully reproduce the dynamic behaviors of living tissues.

3.1.5. Multi-stimuli–responsive and reconfigurable four-dimensional biomaterial assemblies

To exploit multiple cues simultaneously, researchers are building reconfigurable assemblies with photocontrolled adhesion layered atop pH- and thermal-responsive components. For example, by incorporating pH, light, and temperature responsivity, multi-design reconfigurable hydrogel assemblies have been fabricated using a photocontrolled metallopolymer adhesive composed of ruthenium-containing (P-Ru) and thioether-containing (P-S) polymers, where reversible gluing of individual hydrogel units is used to form four distinct constructs (Figure 5).[168] This approach directly translates the multifaceted, orthogonal remodeling of ECM observed in dynamic niches such as the wound bed or tumor stroma, where simultaneous acidification, local heating, and optical signaling (e.g., from inflammatory ROS or photothermal events) orchestrate sequential deswelling, stiffening, and topographical reconfiguration akin to scar maturation and angiogenic invasion fronts.[5,9,21,208] The adhesive forms strong bonds via metal–ligand

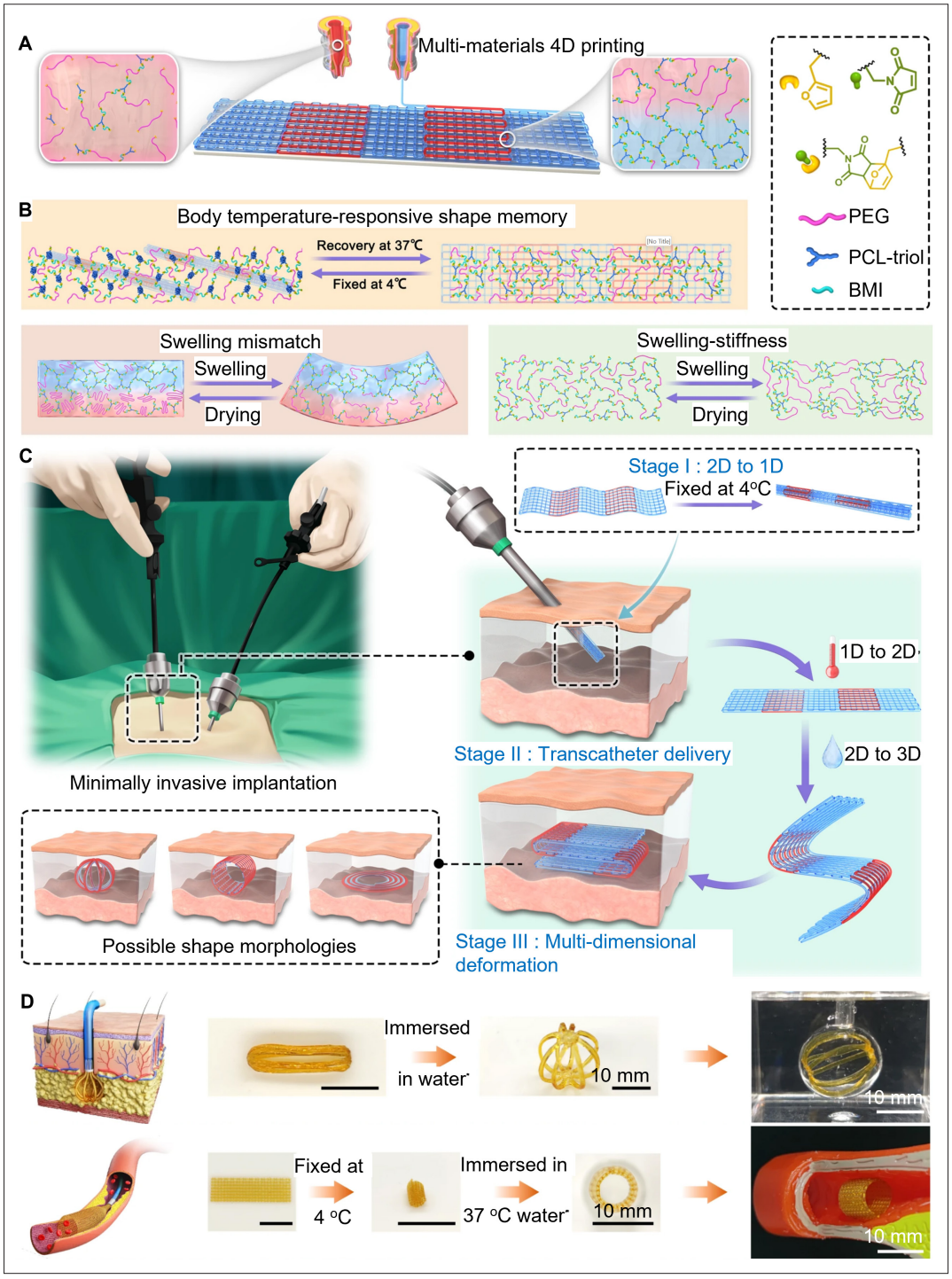


Figure 3. Hydration- and thermo-responsive stimuli-responsive materials for advanced regenerative technologies. (A) Fabrication of scaffolds via multi-material 4D printing, in which amphiphilic dynamic thermoset polyurethane is extruded through nozzles heated above the retro-Diels–Alder reaction threshold and layered onto a base to generate structures with differential swelling. (B) Fabricated scaffold demonstrating responsive shape memory activated by body temperature, with hydration-induced shape formation and increased rigidity upon water absorption. (C) Shape-shifting progression of the scaffold from 1D to 3D configurations in response to thermal and aqueous stimuli, enabling potential minimally invasive surgical deployment. (D) Diagrams and images of fabricated constructs illustrating multi-dimensional shape transformations, highlighting potential applications in soft tissue repair and vascular scaffolding. Shape changes are driven by water-activated programmable morphing and thermo-responsive recovery coupled with water-mediated reconfiguration. Adapted from Ref. [161] Abbreviations: 1D: one-dimensional; 2D: two-dimensional; 3D: three-dimensional; 4D: four-dimensional; BMI: bismaleimide; PCL: polycaprolactone; PEG: polyethylene glycol.

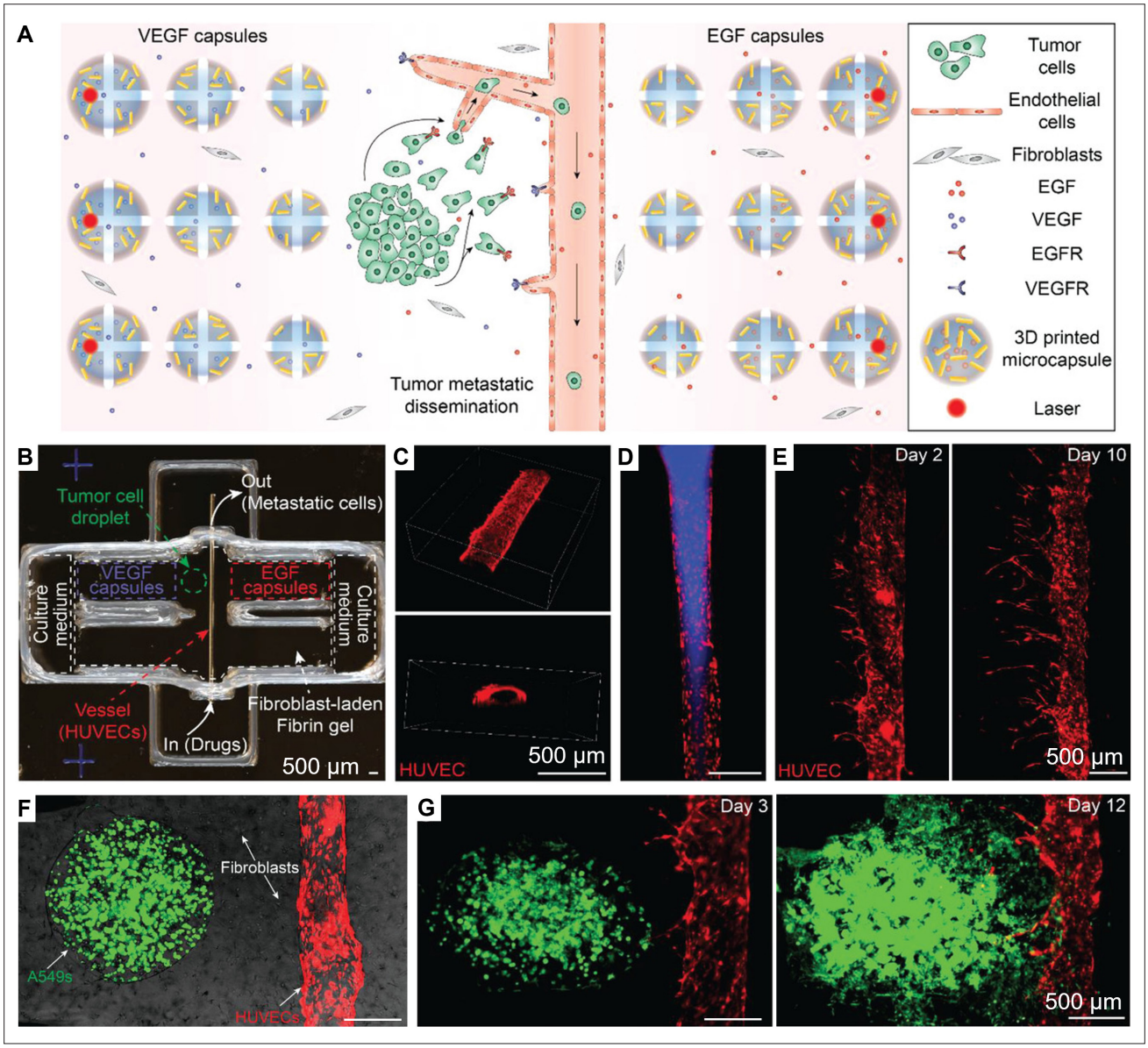


Figure 4. Tumor-induced neovascularization mimicking cancer metastasis. (A) Schematic of 3D bioprinted *in vitro* tumor models integrating tumor cells, endothelial-lined vascular conduits, and biochemical signals within a fibroblast-laden fibrin gel to recapitulate the tumor microenvironments. EGF and VEGF gradients are dynamically generated via programmable release capsules targeting EGFR and VEGFR. (B) Image of a 3D-printed culture chamber designed to guide tumor cell dissemination (scale bar: 500 μm). (C) Confocal images showing top (upper) and cross-sectional (lower) views of HUVEC-lined microchannels in fibrin gel, highlighting the vessel lumen (scale bar: 500 μm). (D) Fluorescence image of a vessel perfused with blue fluorescent fluid (derived from poly(fluorescein isothiocyanate allylamine hydrochloride)) (scale bar: 500 μm). (E) Panoramic fluorescence images showing directional vessel sprouts over time (days 2 and 10) guided by VEGF capsules (scale bar: 500 μm). (F) Composite image of a representative tumor model prior to laser-triggered EGF and VEGF capsule rupture (green: GFP-A549 cells; red: RFP-HUVECs; bright-field: fibroblasts) (scale bar: 500 μm). (G) Time-lapse fluorescence images (days 3 and 12) showing GFP-A549 tumor cells invading the fibroblast-laden fibrin gel and entering the vasculature (green: GFP-A549; red: RFP-HUVECs) (scale bar: 500 μm). Reprinted with permission from Ref. [213] Copyright © 2019, John Wiley & Sons. Abbreviations: 3D: three-dimensional; EGF: epidermal growth factor; EGFR: epidermal growth factor receptor; HUVEC: human umbilical vein endothelial cell; RFP: red fluorescent protein; VEGF: vascular endothelial growth factor; VEGFR: vascular endothelial growth factor receptor.

coordination and polymer chain entanglement, using blue light irradiation (470 nm) to trigger photochemical hydrolysis and dissociation of Ru-S to Ru-H_2O, thereby inducing a gel-to-liquid transition and detachment, as shown in Figure 5A. This enables constructs that respond to temperature and pH stimuli, where non-responsive P1 gels (cross-linked *N*-hydroxyethyl acrylamide) are combined with thermo-responsive P2 gels (zwitterionic 3-dimethyl[methacryloyloxyethyl] ammonium propane sulfonate/2-hydroxyethyl acrylate [HEA]) and pH-responsive P3 gels (HEA/acrylic acid) (Figure 5B–D).[168] Each design exhibits programmable shape changes, such as bending or folding, and can be disassembled with light for reconfiguration.

In the temperature-responsive P2 gel, LCST behavior causes swelling at low temperatures (25°C) due to the zwitterionic moiety, whereas heating (70°C) drives dehydration via enhanced hydrophobic interactions, resulting in shrinkage and deswelling. Within the pH-responsive P3 gel, activation occurs through ionization of carboxylic acid groups from acrylic acid. At high pH (e.g., pH 10), swelling occurs due to deprotonation, generating negatively charged carboxylate ions that increase electrostatic repulsion and osmotic pressure (Figure 5C). At low pH (e.g., pH 4), protonation neutralizes the groups, reducing repulsion and inducing shrinkage.[168] Due to significant variations in swelling ratios, stable pH-triggered motions are sustained over multiple cycles. While no cytotoxicity or viability assessments were explicitly stated, photoactive Ru(II) polypyridyl complexes, often used in photodynamic therapy for cancer, can be cytotoxic in non-targeted contexts; however, polymer encapsulation reduces leaching.[215–217] Although direct analyses of P1, P2, and P3 gel toxicity or cell viability were not performed, composite derivatives similar to these formulations have shown low cytotoxicity and cell viability exceeding 80%.[218–221]

3.1.6. Ionic-responsive materials for extracellular matrix-mimetic remodeling

Ionic-responsive materials—such as polyelectrolyte hydrogels (CS, alginate, or HA with tunable ionizable groups) and ionogels (polymer matrices infused with ionic liquids)—undergo physical or chemical changes, including swelling, contraction, gelation, or phase transitions, in response to ionic stimuli such as salt concentration, specific ions (e.g., Fe^{3+}, citrate), or environmental ionic strength.[222,223] These materials emulate the charge-screening and Donnan osmotic behaviors of native ECM GAGs (e.g., aggrecan and hyaluronan in cartilage or intervertebral disc), where physiological shifts in Na^+, Ca^{2+}, or K^+ concentration rapidly induce reversible swelling/deswelling and stiffness modulation, enabling printed constructs to mimic load-dependent hydration, fixed-charge density changes during skeletal growth, and ionic homeostasis-driven tissue remodeling in electrically active environments such as cardiac or neural niches.[224]

Ionic activation relies on ion–polymer interactions that alter network structure, solubility, or crosslinking, through Donnan equilibrium/osmotic swelling, Hofmeister effect (salting in/out), metal–ion coordination/redox switching, and electrochemical/iontronic effects.[223,225–227] In polyelectrolyte gels like ionized PNIPAAm, fixed charges create ion imbalances, facilitating osmotic swelling in low-ionic-strength solutions, whereas at high ionic strength, charge screening reduces repulsion, causing deswelling.[223,228] Ionic-responsive materials generally exhibit high cell viability and low toxicity due to their natural origin; however, as with any other SMART material, viability and toxicity can be affected by crosslinking concentrations when cells are present.[176,222,223]

In poly(vinyl alcohol) (PVA)/CNF hydrogels, kosmotropic ions ($citrate^{3-}$) polarize water, promoting polymer dehydration and crystallization. Citrate induces gradient densification via hydrogen-bond enhancement, while chaotropic ions (Cl^-) hydrate chains to maintain solubility (Figure 6A–C).[229–231] These properties have been used to create self-healing ionogels that are tunable by ion type and concentration for controlled stiffness gradients.[223,232,233]

This hierarchically heterogeneous PVA/CNF hydrogel—composed of PVA and CNFs—is fabricated via a sequential self-assembly process using directional freezing to align polymer chains and CNFs into honeycomb-like structures, followed by prestretch-assisted salting out in sodium citrate solution.[232] This yields a heterogeneous core–sheath architecture with a compact, highly crosslinked sheath (~23.2 wt% swollen) encasing an aligned porous core featuring belt-like bundles that mimic hierarchical micro- and nanofibrils (Figure 6D and E).[232] This hydrogel surpasses most hydrogels, elastomers, and natural materials by exhibiting exceptional mechanical properties, including tensile strength (55.3 MPa), stiffness (9.5 MPa), stretchability (3300%), toughness (1031 $MJ{\cdot}m^{-3}$), fracture energy (552.7 $kJ{\cdot}m^{-2}$), and fatigue threshold (40.9 $kJ{\cdot}m^{-2}$) (Figure 6F).[232]

The hydrogel also supports regeneration via swelling–resalting, enhances toughness to 1898 $MJ{\cdot}m^{-3}$ over 10 cycles, and exhibits rapid adhesion, making it suitable for cartilage, tendons, or artificial muscle applications (Figure 6G and H). Although no cell viability assessment was performed, the toxicity profile of this hydrogel can be inferred as very low, given that PVA is inherently non-toxic and that CNF (from cellulose) is also biocompatible.[223,230,231]

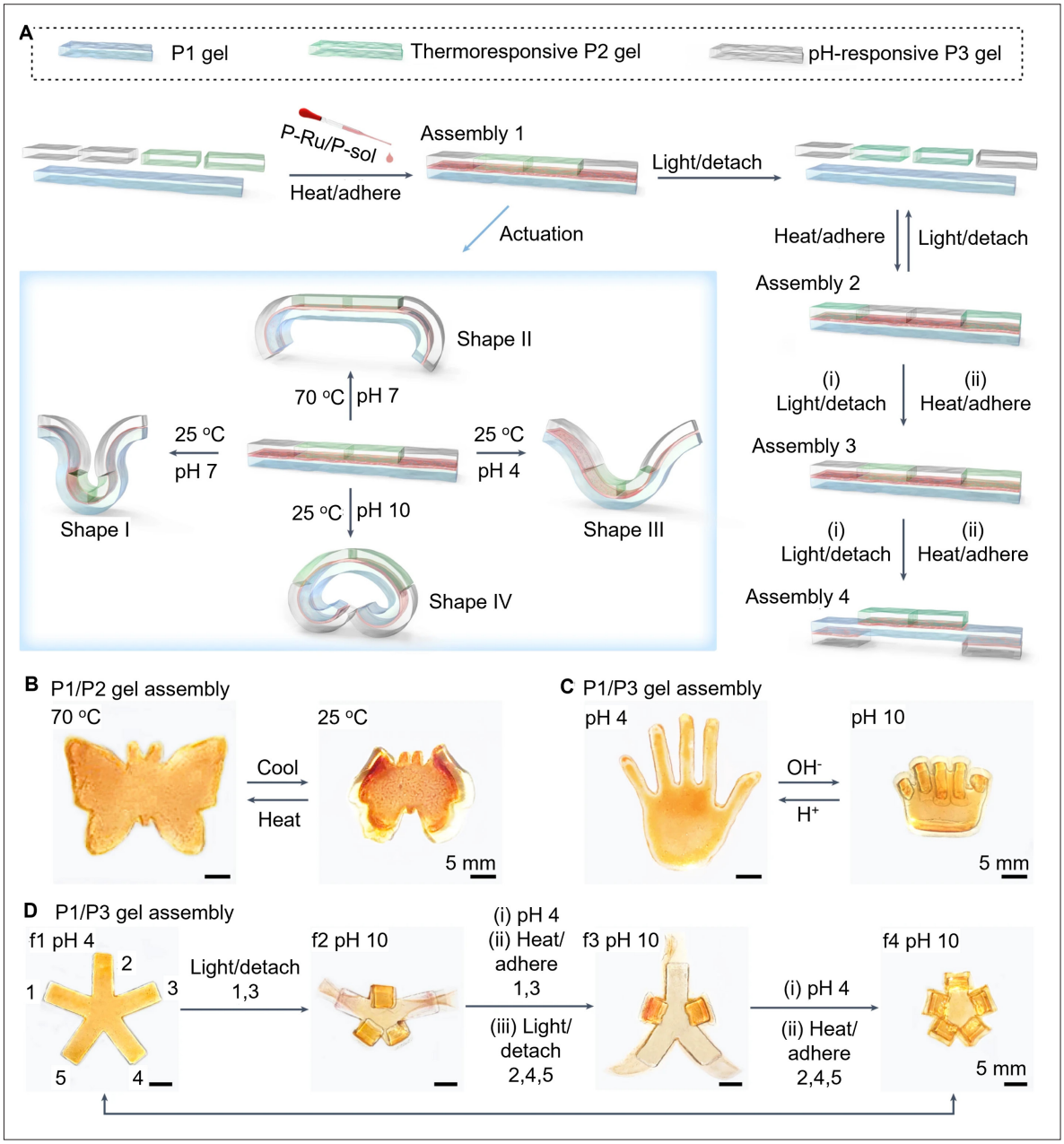


Figure 5. Multi-responsive stimuli-responsive materials for advanced regenerative technologies (pH, light, and temperature). (A) Schematic of hydrogel constructs with complex architectures, illustrating their morphing behavior under varying thermal and pH conditions. Five hydrogel components are linked via the P-Ru/P-S binder to form Construct 1, which can be reorganized into Constructs 2–4. Each construct is capable of transforming into four distinct configurations depending on its design. (B) Actuation of a butterfly-like P1/P2 hydrogel construct in response to different temperatures. (C) Images showing pH-induced actuation of a hand-like P1/P3 hydrogel construct. (D) Selective reversible uncoupling and recoupling of limbs in a five-limbed P1/P3 hydrogel construct, with corresponding actuation under varying pH conditions. Adapted from Ref. [168]

3.1.7. Magnetic-responsive materials for dynamic microenvironment

Magnetic-responsive materials incorporating magnetic nanoparticles (MNPs) such as iron oxide (Fe_3O_4) undergo magnetostriction (shape change) and torque alignment (particles aligning along field lines) through the movement of magnetic domains within the material when subjected to an external magnetic field.[179,234] These materials reproduce the rapid mechanical perturbations transmitted through the ECM during muscle contraction or hemodynamic shear, facilitating cyclic loading that mimics physiological compressive and tensile cues guiding

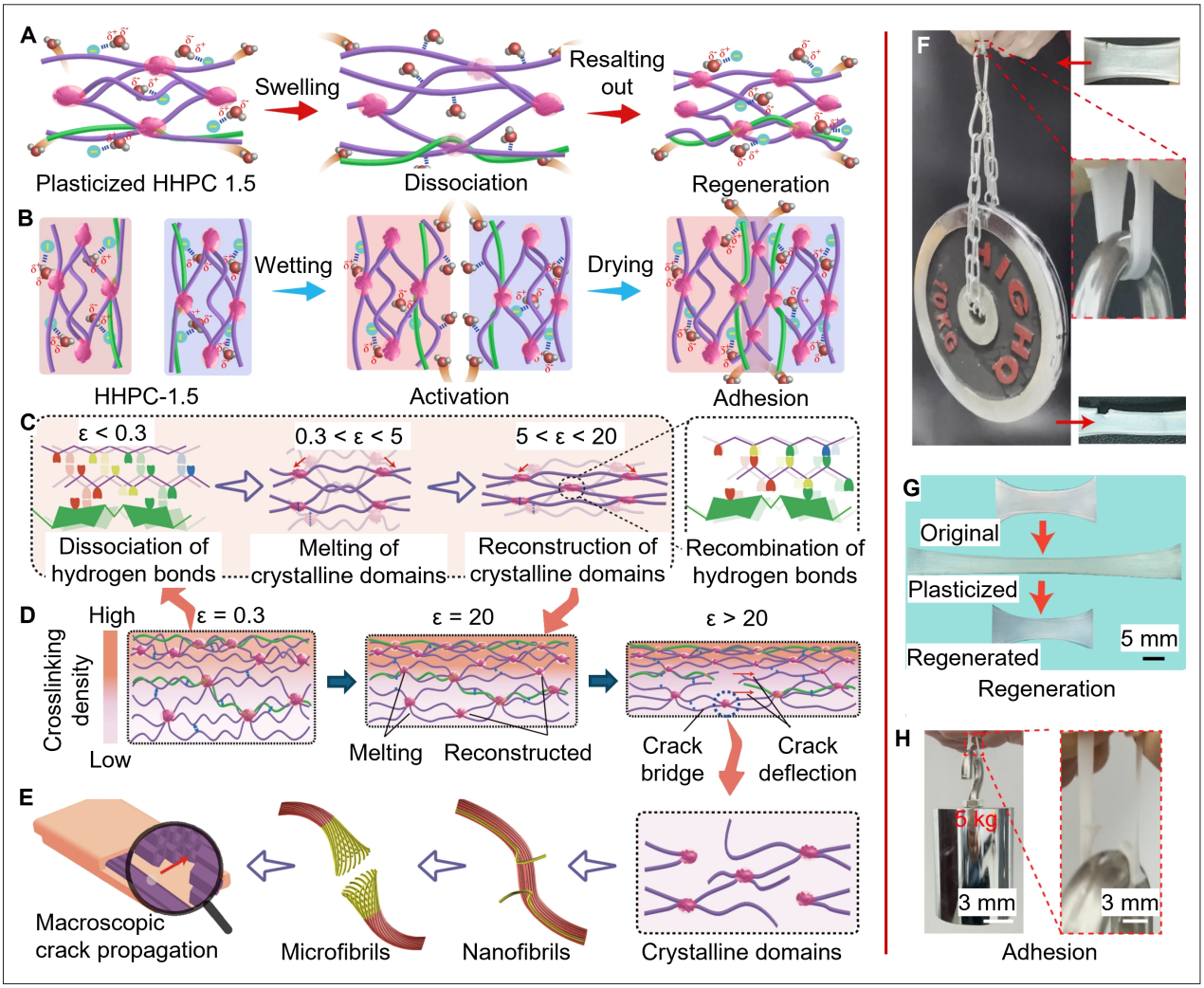


Figure 6. Ionic self-healing hierarchically heterogenous poly(vinyl alcohol)/cellulose nanofibrils (HHPC) hydrogel for regenerative applications. (A) Schematic illustration of the hydrogel regeneration process via breakdown and reconstruction of crystalline structures, driven by interactions between water molecules and kosmotropic ions. (B) Polymer strand mobilization on the densely packed exterior facilitates bonding through hydrogen-bond interactions between water and polymer chains. (C) Synergistic toughening via sheath-led energy absorption, achieved through dissolution and reformation of crystalline regions. (D) Core-led crack-tip passivation through bridging and redirection of fractures. (E) Multi-level energy dissipation via sequential disruption of crystalline regions, nanofibrils, and microfibrils prior to large-scale fracture. (F) HHPC-1.5 hydrogel (~0.4 mm thick) with a 20% pre-cut notch supporting a 10 kg load without crack propagation. (G) Restoration of a deformed HHPC-1.5 hydrogel from a 2 mm clamp spacing via the regeneration procedure. (H) Three HHPC-1.5 hydrogel segments bonded over a 50 mm^2 contact area, sustaining a 5 kg load. Reprinted with permission from Ref. [232] Copyright © 2025, Xu *et al.*

osteogenesis and myogenesis.[235,236] Embedded MNPs are generally nontoxic when encapsulated (PEGylation); however, uncoated MNPs can reduce cell viability and induce lysosomal damage.[237] Another class of magnetic-responsive materials, superparamagnetic nanoparticles, enables pulsatile responses through alternating magnetic fields (100–500 kHz), generating heat via Néel or Brownian relaxation to trigger drug release or hyperthermia.[238,239] These materials support dynamic functionality for guided cell assembly and controlled drug delivery, addressing the common limitations of static tissue-engineering scaffolds.

As shown in Figure 7A, Daul *et al.*[179] used magnetic origami scaffolds with embedded Fe_3O_4 MNPs to integrate bioprinting with ferromagnetism, providing a versatile platform for mimicking dynamic 3D microenvironments. This magnetostriction, activated by exposure to an external field, alters scaffold geometry, creating tapered channels and generating subsequent gravitational cues from folding, which facilitate mechanotransduction and heterogeneous

cell interactions between NIH/3T3 fibroblasts and A549 cancer cells (Figure 7B).[179] An intermediate ECM hydrogel layer modulated cell interactions and proliferation, reduced shear, and enhanced nutrient gradients and media flow for cell guidance between scaffold layers. In these origami scaffolds, iron ion leaching—common with embedded Fe_3O_4 MNPs—remained below toxic levels (100 ppm), maintaining cell viability above 94% over seven days.[179,240]

3.1.8. Electroactive materials for dynamic tissue interfaces

Electro-responsive (electroactive) materials convert electrical energy into mechanical work or vice versa, enabling dynamic interactions with biological systems.[241] These materials emulate the electromechanical coupling and charge-propagation properties of native ECM in excitable tissues (e.g., collagen-mediated piezoelectricity in bone, pericardium, and tendons, or GAG/perlecan-mediated ion channeling in myocardium and nerve), enabling printed constructs to undergo rapid stiffness modulation, directional alignment, or shape change in response to physiological-range electric fields (~1–100 mV/mm).[241–244] They are generally classified into types such as conducting polymers, piezoelectric polymers, and electroactive hydrogels/composites.[242,243,245,246] Conducting

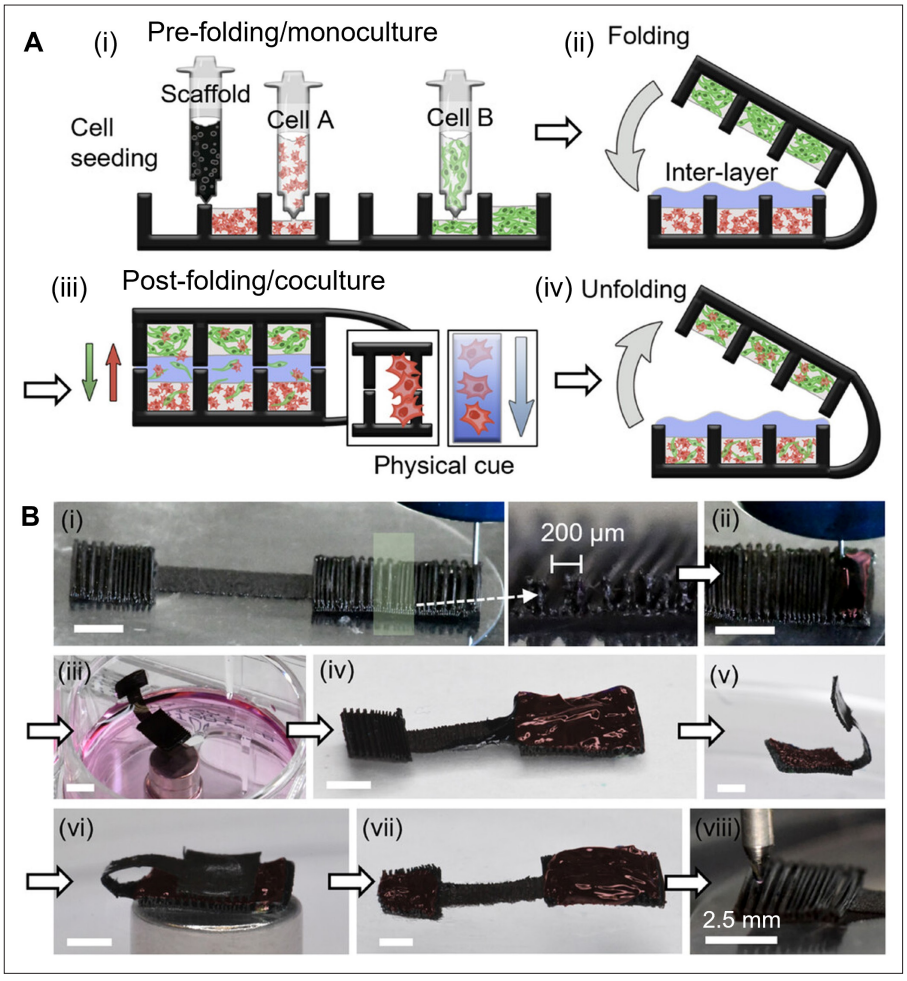


Figure 7. Magnetic-responsive origami platform for guided tissue assembly. (A) Schematic illustration of the experimental workflow for the magnetic-responsive platform: (i) sequential three-dimensional (3D) printing of the scaffold followed by monoculture seeding with cancer cells (red) and fibroblasts (green) prior to folding; (ii) application of hydrogel to form an intermediate extracellular layer between scaffold segments; (iii) formation of a post-folding coculture system, allowing cell clusters to migrate through the intermediate extracellular layer between scaffold sections, guided by scaffold geometry and gravity; and (iv) unfolding of the platform upon magnet removal to assess cell proliferation. (B) Experimental images illustrating each step: (i) 3D printing of the platform with 200 μm channel widths; (ii) cell seeding within microchannels; (iii) pre-folding culture of the seeded scaffold; (iv) application of the intermediate extracellular layer to the bottom scaffold section; (v) magnetic folding of the platform; (vi) post-folding cell culture; (vii) platform unfolding via magnet removal; and (viii) bioindentation analysis of the constructs. Reprinted from Ref. [179]

polymers—including polypyrrole (PPy), PANi, and polythiophene derivatives such as PEDOT:PSS—conduct electricity through conjugated π-electron systems (delocalized electrons due to overlapping p-orbitals) and can be doped to enhance conductivity.[242,247]

Conductive variants (e.g., PEDOT:PSS, MXene, or carbon-nanotube composites) simultaneously mimic the low-resistance extracellular pathways that facilitate synchronous cardiomyocyte contraction, axonal action-potential guidance, and piezo-stimulated osteogenesis observed in load-bearing and neural tissues.[23,25,248] Common conducting polymer composites (e.g., PEDOT:PSS/PPy composites) have enabled stimuli-responsive constructs capable of voltage-triggered swelling or drug release while enhancing mechanical flexibility and biocompatibility.

Piezoelectric polymers, including PVDF and its copolymers (e.g., PVDF-trifluoroethylene, polyhydroxyalkanoates, and poly(L-lactic acid)), generate electric charges under mechanical stress or undergo deformation in response to electric fields, mimicking bioelectricity observed in tissues such as bone and providing piezoelectricity cues for tissue remodeling.[24,242,243] A key advantage of piezoelectric polymers is their ability to transduce mechanical signals into electrical cues, influencing mechanosensitive cellular components, such as ion channels and integrins. This promotes osteogenesis, chondrogenesis, or neural repair without requiring external power sources.[24,181,249] No significant immune responses have been reported in piezoelectric materials, with cell viability maintained above 95% in nerve repair applications.[24]

These materials mimic the hydrated, charged environment of the ECM, which influences biophysical components such as gap junctions for synchronized cell signaling. Electroactive hydrogels and composites integrate responsive elements (conductive fillers like graphene, metallic nanoparticles, or carbon nanotubes) into hydrated networks (e.g., alginate, HA) to enable tunable conductivity and swelling.[243,245] Electroactive materials excel in soft tissue applications due to their material properties, which can be precisely tuned via composite design.[243,245] Similar to MNPs, the toxicity of hydrogels and composites depends on material leaching and the concentration and type of conductive filler used to enable electroactive/electroresponsive properties.[241,242]

Together, these stimulus classes—and their deliberate integration—provide a framework for 4D bioprinting, where material responsiveness is matched to biological timescales and microenvironmental cues, enabling on-demand morphing, signal delivery, and cell-instructive remodeling while maintaining the strict biocompatibility and stability required for translational applications.

3.2. Comparative overview of stimuli-responsive materials

With these foundational insights into native ECM dynamics and the evolving portfolio of ECM-inspired 4D SMART materials, we now present a comparative analysis of the principal stimulus-responsive classes, along with a critical assessment of their readiness and remaining barriers to clinical translation. As noted earlier, conventional 3D bioprinting yields static constructs whose geometry, stiffness, porosity, and bioactivity are fixed upon deposition, with any subsequent evolution limited to passive degradation or non-programmed cell-mediated remodeling.[16] In contrast, 4D bioprinting harnesses stimuli-responsive bioinks engineered for precise, triggerable actuation—manifesting as controlled folding, twisting, swelling/deswelling, stiffening/softening transitions, anisotropic alignment, or spatially resolved porosity changes—in direct response to biophysical and biochemical cues (e.g., temperature, pH, ionic strength, light, electric/magnetic fields, enzymes, or metabolites).[12]

These engineered actuation mechanisms enable 4D SMART systems to emulate previously inaccessible ECM dynamics, including on-demand curvature-driven morphogenesis, cyclic strain-induced fiber alignment, hydration-gated permeability transitions, localized enzyme-triggered remodeling, and cell-force–amplified shape evolution.[250] In doing so, they deliver autonomous, self-organizing tissue behaviors that remain unattainable with static 3D bioprinted scaffolds. Direct comparison of these 4D approaches (Table 3) provides further insight into their current ECM fidelity, clinical translation progress, representative applications where dynamic responsiveness consistently outperforms static 3D bioprinting, and the critical limitations that remain the principal barriers to widespread clinical adoption.

Thermo-responsive hydrogels (predominantly PNIPAAm copolymers) remain the most widely adopted class due to printing compatibility and decades of safety data from non-printed devices. They reliably mimic temperature-driven collagen remodeling and wound-stiffening trajectories (1–100 kPa over days), driving robust chondrogenic and corneal epithelial differentiation in organoids.[251] Nevertheless, their slow response kinetics (>5 min), hysteresis, and persistent concerns over residual NIPAAm monomer cytotoxicity continue to restrict them to preclinical cartilage and ocular trials.[252,253]

Table 3. Cross-comparison of stimuli-responsive SMART materials in 4D bioprinting

Stimulus class	**Closest native ECM behavior mimicked**	**Spatio-temporal control vs. ECM**	**Reversibility and speed vs. ECM**	**Long-term *in vivo* stability**	**Multi-stimuli integration capability**	**Regulatory feasibility**	**Clinical translation stage**	**Near-term *ex vivo* application**	**Ref**
Thermo-responsive	Collagen remodeling, wound maturation	Medium (whole-construct)/poor match	Good/100–1000 times slower than ECM	4–8 weeks (monomer leaching)	Moderate (thermo+pH common)	Moderate (PNIPAAm history in devices)	Preclinical	Stiffness-maturation models (cartilage, cornea)	[5,7,184,185,251–253]
pH-responsive	Inflammation-driven fibrosis	Regional/reasonable match	Poor reversibility	<4 weeks (pH drift, degradation)	High	Low (cell damage risk)	Preclinical only	Tumor microenvironment platforms	[7,189–191,254,255]
Light-responsive	Ultraviolet-dermal remodeling, reactive oxygen species signaling	Highest precision/ excellent local match	High or irreversible	2–6 weeks (photoproduct accumulation)	High (light+thermo widespread)	Low (phototoxicity data scarce)	Preclinical	Vascular branching and perfusion models	[205,207,208,256–261]
Magnetic-responsive	Hemodynamic shear, muscle loading	Whole-construct/ good mechanical match	Excellent/near-ECM speed	6–12 weeks (iron oxidation)	Moderate	Very low (metal particles)	Preclinical	Dynamic soft robotics	[179,235,236,262,263]
Ionic-responsive	Cartilage GAG fixed-charge swelling	Diffusion-limited/ very close chemically	Excellent/Near-ECM	4–8 weeks (ion leaching)	High	Moderate	Early preclinical	Osteoarthritis and disc degeneration models	[222–225,264–266]
Electro-/ conductive	Myocardial conduction, bone piezoelectricity	Directional/closest functional match	Excellent/ECM-like mechanical response	3–12 months (best in class)	High	Highest (ongoing phase I)	Phase I human trials (cardiac patches)	Cardiac patches and *ex vivo* heart-on-chip	[24,241–248,267–269]
Hydration-responsive	Interstitial fluid shifts, corneal swelling	Passive/good osmotic match	Slow but reversible	>12 weeks (inert polymers)	Very high (bilayer combinations)	High (no exogenous energy)	Preclinical (bilayer tubular grafts)	Barrier tissues and simple tubular grafts	[199–203,270–272]
Multi-responsive	Developmental folding, wound progression	Highest complexity/ closest to real ECM	Variable, often reduced	Worst (compounded degradation)	Intrinsic	Lowest (combination product)	Furthest from clinical translation	Complex disease and developmental models	[5,7,9,21,208]

Abbreviations: ECM: extracellular matrix; GAG: glycosaminoglycan; PNIPAAm: poly(*N*-isopropylacrylamide).

pH-responsive polymers effectively model pathological acidification (e.g., tumor stroma, chronic wounds), producing localized stiffening and drug-release zones that drive realistic cancer cell invasion.[254] Nonetheless, their narrow safe triggering window and irreversible drift in physiological buffers severely limit in vivo utility and keep them in preclinical drug-delivery rather than structural 4D applications.[255]

Hydration/water-responsive bilayers represent the simplest and safest route to 4D behavior. By exploiting differential swelling of hydrophilic polymers (e.g., poly(ethylene glycol)) diacrylate versus poly(hydroxyethyl methacrylate)), they passively self-fold into tubes or open porous networks upon immersion in aqueous media, closely imitating diurnal hydration shifts in skin and cornea.[270,271] Applications directed toward urethral and small-vessel models can roll into perfusable conduits within hours without exogenous energy, offering a clear advantage over manual suturing or sacrificial templating required in 3D bioprinting.[272] However, actuation remains slow (hours–days) and difficult to program precisely, but the absence of toxic triggers provides this class with one of the highest regulatory feasibility scores.

Light-responsive systems provide unparalleled spatiotemporal precision (sub-100 μm) through photo-isomerization (e.g., azobenzene) or photocleavage (e.g., o-nitrobenzyl) mechanisms,[256] enabling on-demand vascular branching and topographical reconfiguration that mimics angiogenic sprouting and dermal remodeling.[257,258] A striking *ex vivo* demonstration used visible-light-triggered spiropyran-containing hydrogels to create self-bending cardiac microtissues.[259,260] Upon blue-light patterning, localized softening induced anisotropic curvature, directing cardiomyocyte alignment and producing spontaneously beating helical bundles within five days. This outcome remains unattainable in rigid 3D GelMA constructs, which yield only isotropic monolayers.[261] Despite this precision, limited penetration depth (less than 1 mm for visible light, approximately 1 cm for NIR), phototoxicity from prolonged exposure, and NIR-induced hyperthermia continue to confine clinical applications to thin tissues or *ex vivo* platforms.[205,256]

Ionic-responsive systems exhibit the closest chemical mimicry of GAG-rich matrices such as articular cartilage and intervertebral disc. Alginate- and hyaluronan-based inks crosslinked by physiological Ca^{2+} or Mg^{2+} concentrations reproduce the fixed-charge density and Donnan osmotic pressure with near-native accuracy, producing reversible 50–300% volume changes under load.[264] *Ex vivo* intervertebral disc models subjected to diurnal ionic cycles maintain height and modulus for over eight weeks, whereas static 3D alginate collapses within days.[265,266]

Magnetic-responsive ferrogels excel at delivering remote, penetration-unlimited mechanical stimulation with sub-second response times, effectively replicating physiological cyclic compression in bone and cartilage or hemodynamic shear in vascular niches.[262] A representative *ex vivo* application employed magnetic-field-guided crawling constructs seeded with mesenchymal stem cells to create self-navigating soft robots that actively compact and remodel printed collagen matrices, achieving 5.3 times higher alkaline phosphatase activity and mineralized nodule formation within 14 days compared with identical but non-actuated 3D controls.[263,273] Despite these capabilities, long-term oxidative release of iron ions, particle aggregation, chronic inflammation, and magnetic resonance imaging incompatibilities remain insurmountable barriers to clinical translation.

Electro-conductive materials currently deliver the highest functional ECM fidelity for excitable tissues. By restoring low-resistance pathways (10^{-3}–10^{1} S/cm) and true electromechanical coupling, they enable synchronous cardiomyocyte contraction, action-potential propagation in neuronal networks, and piezoelectric-like signaling in bone—capabilities entirely absent in insulating 3D-printed scaffolds.[267,268] This has translated directly into the most advanced clinical status, with multiple phase I human trials for conductive cardiac patches ongoing, and 3-to-12-month electrode stability already demonstrated in large-animal models.[269] The dominant remaining limitations are delamination at the bioelectronic interface and chronic inflammation triggered by conductive polymer degradation. These remain significant but are actively being addressed with biodegradable alternatives (e.g., PEDOT–lignin).[268]

This proposed hierarchy provides a realistic translational roadmap for 4D bioprinting. Looking forward, the years 2026–2030 will likely yield the first regulatory-approved 4D products, namely electro-conductive cardiac and nerve patches, together with hydration- and thermo-responsive self-assembling tubular grafts. From 2030 to 2035, hybrid ionic–electronic constructs suitable for joints and myocardium are expected to reach clinical application. Multi-responsive, fully vascularized tissues capable of true organ replacement are the furthest from realization and will likely not emerge until after 2035, once robust, orthogonal, and degradation-resistant chemistries become available. Until then, the primary clinical value of 4D bioprinting will lie in its capacity to generate dynamic, human-relevant models and minimally complex dynamic implants rather than in whole-organ reconstruction.

4. Conclusion, technical challenges, and outlook

Looking forward, the unification of each respective domain (physics, biology, chemistry, engineering, and medicine) has become central to the evolution of future research in 4D bioprinting and 4D tissue engineering. These emerging outcomes facilitate 4D SMART materials to advance from proof-of-concept demonstrations toward tangible applications across the translational spectrum. *In vitro*, multi-responsive (pH, thermo, and light) tumor models that sequentially stiffen and fold over 7–14 days predict metastasis 2–3 times more accurately than static 3D cultures.[3,214,219,274] *Ex vivo*, bone and cartilage scaffolds change shape or stiffness in response to physiological conditions, while electro-conductive cardiac patches enable high-fidelity arrhythmogenic studies.[8,91,138]

Clinically, electro-conductive cardiac patches (PEDOT:PSS/GelMA) are in phase I human trials for post-infarction conduction restoration, while large-animal preclinical studies show 8–12-week survival of thermo-responsive, self-folding tracheal tubes, and hydration-driven self-rolling vascular grafts.[8,145,169,268,275] Although no 4D-printed solid organ has reached human transplantation, the technology already delivers its greatest near-term impact through advanced human disease models for precision medicine and through restoration of dynamic electrical and mechanical function in thin, excitable tissues.

Using this shift in perspective, radical breakthroughs, such as the development of bioreactors for functional, human-scale tissues and organ transplantation, could potentially be realized.[13,276] These advances will realign scientific incentives for bolder experimentation to address the stagnation of specialization approaches.[255,277] However, radical developments can only come after we address current challenges and limitations in each respective domain. 4D bioprinting and tissue engineering processes are inherently more complex than 3D methods due to the requirements for precise spatiotemporal control over dynamic transformations of the SMART materials used. Having previously covered SMART material mechanical properties that fail to fully mimic the multi-responsive *in vivo* environment and their poor cytocompatibility, we will conclude this review by addressing the constraints of the printing process and how printability, scaling, and regulatory considerations have brought the field to its current state.[2,140,277,278]

From a technological standpoint, one of the most persistent challenges lies in print resolution and fidelity. Existing extrusion-based bioprinters typically achieve feature sizes of 100–200 μm, which remain too coarse to reproduce the intricate microvascular networks required for nutrient diffusion in tissues such as skin, myocardium, or vasculature.[279] This limitation often results in hypoxic cores and reduced construct viability beyond 1–2 mm thickness.[250] While extrusion-based methods continue to dominate, they also struggle to achieve high throughput and scalability for human-scale tissues.

In contrast, laser-guided or coaxial printing offers precision but at higher costs and even lower throughput.[280] In 4D contexts, maintaining fidelity during dynamic changes is difficult, as materials may warp unpredictably post-print. This limits the formation of heterogeneous skin structures with adaptive porosity and cardiac patches that mimic curvature.[145,281] Emerging multi-nozzle systems and 6D robotic bioprinting systems significantly mitigate these limitations by incorporating multi-material deposition, three rotational axes (pitch, yaw, roll) alongside translational ones, and enabling unprecedented flexibility in orientation and path planning.[282,283] Automation of these systems aims to synchronize extrusion with robotic motion, potentially boosting speed and reproducibility while maintaining cell viability and functionality, thereby advancing toward clinical translation.[250,283]

However, technological progress alone is insufficient without a parallel evolution in regulatory and ethical frameworks. At present, regulatory systems for 4D bioprinting remain underdeveloped, relying heavily on precedents set for 3D bioprinting and traditional medical devices. This mismatch leads to ambiguous product classifications, delayed approvals, and uncertainties in clinical translation.[284–286] In the United States, the Food and Drug Administration classifies bioprinted constructs as combination products—integrating biologics, devices, and drugs—subjecting them to rigorous premarket approval under 21 CFR Parts 1270–1271 for human cells, tissues, and products (HCT/Ps).[287,288] However, it currently lacks specific guidelines for 4D dynamic materials, leaving uncertainty around long-term safety and performance in applications.[289]

In the European Union, the Medical Device Regulation 2017/745 governs custom-made devices under Article 2(3) and Annex XIII 277, which categorize high-risk bioprinted implants as Class III, but struggle to address customized 4D products, raising legal challenges, including risk assessment and conformity.[290] The European Medicines Agency regulates 4D bioprinted tissues under Regulation EC No 1394/2007 on advanced therapy medicinal products,[291] requiring rigorous clinical trials and safety or efficacy data.[292] However, it overlooks SRMs, and globally, these gaps contribute to slow commercialization, resulting

in only one bioprinted ear in trials as of 2025.[293] The World Health Organization has called for harmonized standards; however, disparities persist,[294] with stricter European Union regulations contrasting with more flexible approaches in the United States.[284,286] This lack of international consensus on standards for stimuli-responsive devices poses a risk of unintended *in vivo* transformations, potentially violating safety protocols under national laws such as the United Kingdom's Human Tissue Act (2004).[8,290,295]

Given these substantial obstacles, the translation of 4D bioprinting from bench to bedside continues to lag by 5–10 years behind laboratory advances. Technical limitations constrain scalability and reproducibility, while regulatory uncertainty prolongs validation and licensing, forming a bottleneck that stifles clinical innovation.[8,255] To overcome these challenges, the field requires coordinated global reform—including updated Food and Drug Administration/European Medicines Agency joint guidelines tailored to 4D systems, interdisciplinary regulatory boards that integrate material scientists and clinicians, and international standardization efforts led by the World Health Organization and the International Organization for Standardization.[284,292,294] Only through such harmonization can researchers and policymakers ensure the safe and accelerated translation of adaptive, living biomaterials into the clinic. By aligning technological readiness with ethical and legal accountability, 4D bioprinting may finally progress from conceptual promise to a practical platform for regenerative medicine and human-scale tissue replacement.

Acknowledgments

None.

Funding

This research was supported by the Commonwealth Health Research Board (236-08-21); the National Institutes of Health, under the National Institute of General Medical Sciences grant (P20GM113126); the American Cancer Society (IRG-22-146-07-IRG); National Institutes of Health, under the National Cancer Institute grant (CA036727), the Nexus of Virology, Immunology, and Bioengineering; the Nebraska Tobacco Settlement Biomedical Research Development Funds; the "Regional Innovation System & Education (RISE)" program, through the Gwangju RISE Center, funded by the Ministry of Education and the Gwangju Metropolitan Government, Republic of Korea (2025-RISE-05-011).

Conflict of interest

Fanben Meng and Daeha Joung serve as the guest editors of this Special Issue, but did not in any way involve in the editorial and peer-review process conducted for this paper, directly or indirectly. Other authors declare they have no competing interests.

Author contributions

Conceptualization: Ryan Martin, Daeha Joung
Writing–original draft: Ryan Martin, Haiwei Zhai, Fanben Meng, Daehoon Han,
Writing–review & editing: Ryan Martin, Fanben Meng, Daeha Joung

Ethics approval and consent to participate

Not applicable.

Consent for publication

Not applicable.

Availability of data

Not applicable.

References

1. Crossley RM, Johnson S, Tsingos E, *et al*. Modeling the extracellular matrix in cell migration and morphogenesis: a guide for the curious biologist. *Front Cell Dev Biol*. 2024;12:1354132.
doi: 10.3389/fcell.2024.1354132

2. Martin R, Joung D. The promise and challenges of bioprinting in tissue engineering. *Micromachines*. 2024;15(12):1529.
doi: 10.3390/mi15121529

3. Lu P, Ruan D, Huang M, *et al*. Harnessing the potential of hydrogels for advanced therapeutic applications: current achievements and future directions. *Signal Transduct Target Ther*. 2024;9(1):166.
doi: 10.1038/s41392-024-01852-x

4. Dethe MR, Prabakaran A, Ahmed H, Agrawal M, Roy U, Alexander A. PCL-PEG copolymer based injectable thermosensitive hydrogels. *J Control Release*. 2022;343:217-236.
doi: 10.1016/j.jconrel.2022.01.035

5. Doberenz F, Zeng K, Willems C, Zhang K, Groth T. Thermoresponsive polymers and their biomedical application in tissue engineering – a review. *J Mater Chem B*. 2020;8(4):607-628.
doi: 10.1039/C9TB02052G

6. Pei Y, Chen J, Yang L, *et al*. The effect of pH on the LCST of poly(N-isopropylacrylamide) and poly(N-isopropylacrylamide-co-acrylic acid). *J Biomat Sci Polymer Edn*. 2004;15(5):585-594. doi: 10.1163/156856204323046852

7. Correa S, Grosskopf AK, Lopez Hernandez H, *et al*. Translational applications of hydrogels. *Chem Rev*. 2021;121(18):11385-11457. doi: 10.1021/acs.chemrev.0c01177

8. Taylor S, Mueller E, Jones LR, Makela AV, Ashammakhi N. Translational aspects of 3D and 4D printing and bioprinting. *Adv Healthc Mater.* 2024;13(27):2400463. doi: 10.1002/adhm.202400463

9. Cao H, Duan L, Zhang Y, Cao J, Zhang K. Current hydrogel advances in physicochemical and biological response-driven biomedical application diversity. *Signal Transduct Target Ther*. 2021;6(1):426. doi: 10.1038/s41392-021-00830-x

10. Di X, Gao X, Peng L, *et al*. Cellular mechanotransduction in health and diseases: from molecular mechanism to therapeutic targets. *Signal Transduct Target Ther*. 2023;8(1):282. doi: 10.1038/s41392-023-01501-9

11. Ambattu LA, Yeo LY. Sonomechanobiology: vibrational stimulation of cells and its therapeutic implications. *Biophys Rev.* 2023;4(2):021301. doi: 10.1063/5.0127122

12. Arif ZU, Khalid MY, Ahmed W, Arshad H. A review on four-dimensional (4D) bioprinting in pursuit of advanced tissue engineering applications. *Bioprinting*. 2022;27:e00203. doi: 10.1016/j.bprint.2022.e00203

13. Zhou W, Chen Y, Roh T, *et al*. Multifunctional bioreactor system for human intestine tissues. *ACS Biomater Sci Eng*. 2018;4(1):231-239. doi: 10.1021/acsbiomaterials.7b00794

14. Williamson A, Khoshmanesh K, Pirogova E, *et al*. Bioreactors: a regenerative approach to skeletal muscle engineering for repair and replacement. *Adv Nanobiomed Res*. 2024;4(10):2400030. doi: 10.1002/anbr.202400030

15. Yarali E, Mirzaali MJ, Ghalayaniesfahani A, Accardo A, Diaz-Payno PJ, Zadpoor AA. 4D printing for biomedical applications. *Adv Mater.* 2024;36(31):2402301. doi: 10.1002/adma.202402301

16. Wang J, Wang Y, Wang R, *et al*. A review on 3D printing processes in pharmaceutical engineering and tissue engineering: applications, trends and challenges. *Adv Mater Technol.* 2025;10(2):2400620. doi: 10.1002/admt.202400620

17. Joung D, Lavoie NS, Guo S, Park SH, Parr AM, McAlpine MC. 3D printed neural regeneration devices. *Adv Funct Mater.* 2020;30(1):1906237. doi: 10.1002/adfm.201906237

18. Li YC, Zhang YS, Akpek A, Shin SR, Khademhosseini A. 4D bioprinting: the next-generation technology for biofabrication enabled by stimuli-responsive materials. *Biofabrication*. 2016;9(1):012001. doi: 10.1088/1758-5090/9/1/012001

19. Michael PL, Lam YT, Mitchell TC, *et al*. Harnessing physiological shear stress in a perfusion bioreactor for enhanced endothelialization of small-diameter vascular grafts. *Adv Nanobiomed Res*. 2025;5:2500025. doi: 10.1002/anbr.202500025

20. Mierke CT. Viscoelasticity, like forces, plays a role in mechanotransduction. *Front Cell Dev Biol*. 2022;10:789841. doi: 10.3389/fcell.2022.789841

21. Asadi Tokmedash M, Kim C, Chavda AP, Li A, Robins J, Min J. Engineering multifunctional surface topography to regulate multiple biological responses. *Biomaterials*. 2025;319:123136. doi: 10.1016/j.biomaterials.2025.123136

22. Özkale B, Sakar MS, Mooney DJ. Active biomaterials for mechanobiology. *Biomaterials*. 2021;267:120497. doi: 10.1016/j.biomaterials.2020.120497

23. Kayser LV, Lipomi DJ. Stretchable conductive polymers and composites based on PEDOT and PEDOT:PSS. *Adv Mater.* 2019;31(10):1806133. doi: 10.1002/adma.201806133

24. Bryan AE, Krutko M, Rebholz S, *et al*. Development of a bioactive, piezoelectric PVDF-TrFE scaffold with evaluation of tissue reaction for potential in nerve repair. *Biomater Sci*. 2025;13(20):5769-5785. doi: 10.1039/D5BM01054C

25. Mariano A, Lubrano C, Bruno U, Ausilio C, Dinger NB, Santoro F. Advances in cell-conductive polymer biointerfaces and role of the plasma membrane. *Chem Rev*. 2022;122(4):4552-4580. doi: 10.1021/acs.chemrev.1c00363

26. Tonti OR, Larson H, Lipp SN, *et al*. Tissue-specific parameters for the design of ECM-mimetic biomaterials. *Acta Biomater.* 2021;132:83-102. doi: 10.1016/j.actbio.2021.04.017

27. Valdoz JC, Johnson BC, Jacobs DJ, *et al*. The ECM: to scaffold, or not to scaffold, that is the question. *Int J Mol Sci*. 2021;22(23):12690. doi: 10.3390/ijms222312690

28. Rahmati M, Silva EA, Reseland JE, A. Heyward C, Haugen HJ. Biological responses to physicochemical properties of biomaterial surface. *Chem Soc Rev*. 2020;49(15):5178-5224. doi: 10.1039/D0CS00103A

29. Yamada KM, Doyle AD, Lu J. Cell–3D matrix interactions: recent advances and opportunities. *Trends Cell Biol.* 2022;32(10):883-895.

doi: 10.1016/j.tcb.2022.03.002

30. Hervé S, Miroshnikova YA. Biophysical determinants of nuclear shape and mechanics and their implications for genome integrity. *Curr Opin Biomed Eng*. 2024;30:100521. doi: 10.1016/j.cobme.2024.100521

31. Miroshnikova YA, Wickström SA. Mechanical forces in nuclear organization. *Cold Spring Harb Perspect Biol*. 2022;14(1):a039685. doi: 10.1101/cshperspect.a039685

32. Vermeulen S, Honig F, Vasilevich A, *et al*. Expanding biomaterial surface topographical design space through natural surface reproduction. *Adv Mater*. 2021;33(31):2102084. doi: 10.1002/adma.202102084

33. Comelles J, Fernández-Majada V, Acevedo V, Rebollo-Calderon B, Martínez E. Soft topographical patterns trigger a stiffness-dependent cellular response to contact guidance. *Mater Today Bio*. 2023;19:100593. doi: 10.1016/j.mtbio.2023.100593

34. Min K, Karuppannan SK, Tae G. The impact of matrix stiffness on hepatic cell function, liver fibrosis, and hepatocellular carcinoma-based on quantitative data. *Biophys Rev*. 2024;5(2):021306. doi: 10.1063/5.0197875

35. Elosegui-Artola A, Gupta A, Najibi AJ, *et al*. Matrix viscoelasticity controls spatiotemporal tissue organization. *Nat Mater*. 2023;22(1):117-127. doi: 10.1038/s41563-022-01400-4

36. Wu Y, Song Y, Soto J, *et al*. Viscoelastic extracellular matrix enhances epigenetic remodeling and cellular plasticity. *Nat Commun*. 2025;16(1):4054. doi: 10.1038/s41467-025-59190-7

37. Wan S, Chen Y, Huang C, *et al*. Scalable ultrastrong MXene films with superior osteogenesis. *Nature*. 2024;634(8036):1103-1110. doi: 10.1038/s41586-024-08067-8

38. Cheng Y, Wang Y, Wang Y, *et al*. Microenvironment-feedback regulated hydrogels as living wound healing materials. *Nat Commun*. 2025;16(1):6050. doi: 10.1038/s41467-025-60858-3

39. Zhang C, Cai D, Liao P, *et al*. 4D printing of shape-memory polymeric scaffolds for adaptive biomedical implantation. *Acta Biomater*. 2021;122:101-110. doi: 10.1016/j.actbio.2020.12.042

40. Benwood C, Chrenek J, Kirsch RL, *et al*. Natural biomaterials and their use as bioinks for printing tissues. *Bioengineering*. 2021;8(2):27. doi: 10.3390/bioengineering8020027

41. Chen XB, Fazel Anvari-Yazdi A, Duan X, *et al*. Biomaterials/bioinks and extrusion bioprinting. *Bioact Mater*. 2023;28:511-536. doi: 10.1016/j.bioactmat.2023.06.006

42. Carvalho EM, Kumar S. Lose the stress: viscoelastic materials for cell engineering. *Acta Biomater*. 2023;163:146-157. doi: 10.1016/j.actbio.2022.03.058

43. Fonseca AC, Melchels FP, Ferreira MJ, *et al*. Emulating human tissues and organs: a bioprinting perspective toward personalized medicine. *Chem Rev*. 2020;120(19):11093-11139. doi: 10.1021/acs.chemrev.0c00342

44. Khalid MY, Otabil A, Mamoun OS, Askar K, Bodaghi M. Transformative 4D printed SMPs into soft electronics and adaptive structures: innovations and practical insights. *Adv Mater Technol*. 2025;10(19):e00309. doi: 10.1002/admt.202500309

45. Mirasadi K, Yousefi MA, Jin L, *et al*. 4D printing of magnetically responsive shape memory polymers: toward sustainable solutions in soft robotics, wearables, and biomedical devices. *Adv Sci*. 2025:e13091. doi: 10.1002/advs.202513091

46. Zhang W, Liu Y, Zhang H. Extracellular matrix: an important regulator of cell functions and skeletal muscle development. *Cell Biosci*. 2021;11(1):65. doi: 10.1186/s13578-021-00579-4

47. Hynes RO. The extracellular matrix: not just pretty fibrils. *Science*. 2009;326(5957):1216-1219. doi: 10.1126/science.1176009

48. Zhang S-y, Li X-y, Yang N, *et al*. Electrospun collagen nanofibers reduce inflammation, inhibit fibrosis, and promote wound healing on the ocular surface. *ACS Appl Nano Mater*. 2024;7(17):20267-20278. doi: 10.1021/acsanm.4c03180

49. Orr SB, Chainani A, Hippensteel KJ, *et al*. Aligned multilayered electrospun scaffolds for rotator cuff tendon tissue engineering. *Acta Biomater*. 2015;24:117-126. doi: 10.1016/j.actbio.2015.06.010

50. Kim HN, Jiao A, Hwang NS, *et al*. Nanotopography-guided tissue engineering and regenerative medicine. *Adv Drug Deliv Rev*. 2013;65(4):536-558. doi: 10.1016/j.addr.2012.07.014

51. Putra VDL, Kilian KA, Knothe Tate ML. Biomechanical, biophysical and biochemical modulators of cytoskeletal remodelling and emergent stem cell lineage commitment. *Commun Biol*. 2023;6(1):75. doi: 10.1038/s42003-022-04320-w

52. Pike DB, Cai S, Pomraning KR, *et al*. Heparin-regulated release of growth factors in vitro and angiogenic response in vivo to implanted hyaluronan hydrogels containing VEGF and bFGF. *Biomaterials*. 2006;27(30):5242-5251. doi: 10.1016/j.biomaterials.2006.05.018

53. Zhao T, Huang Y, Zhu J, *et al*. Extracellular matrix signaling cues: biological functions, diseases, and therapeutic targets. *MedComm*. 2025;6(8):e70281. doi: 10.1002/mco2.70281

54. Karamanos NK, Theocharis AD, Piperigkou Z, *et al*. A guide to the composition and functions of the extracellular matrix. *FEBS J*. 2021;288(24):6850-6912. doi: 10.1111/febs.15776

55. Nicolas J, Magli S, Rabbachin L, Sampaolesi S, Nicotra F, Russo L. 3D extracellular matrix mimics: fundamental concepts and role of materials chemistry to influence stem cell fate. *Biomacromolecules*. 2020;21(6):1968-1994. doi: 10.1021/acs.biomac.0c00045

56. Liu C, Pei M, Li Q, Zhang Y. Decellularized extracellular matrix mediates tissue construction and regeneration. *Front Med*. 2022;16(1):56-82. doi: 10.1007/s11684-021-0900-3

57. Zhang X, Chen X, Hong H, Hu R, Liu J, Liu C. Decellularized extracellular matrix scaffolds: Recent trends and emerging strategies in tissue engineering. *Bioact Mater*. 2022;10:15-31. doi: 10.1016/j.bioactmat.2021.09.014

58. Xie R, Yu X, Cao T, *et al*. Fibrous viscoelastic extracellular matrix assists precise neuronal connectivity. *Adv Funct Mater*. 2023;33(36):2301926. doi: 10.1002/adfm.202301926

59. Karsdal MA, ed. *Biochemistry of Collagens, Laminins and Elastin: Structure, Function and Biomarkers*. 3rd ed. London. United Kingdom: Academic Press. An imprint of Elsevier; 2024.

60. Wang Z, Liu H, Luo W, *et al*. Regeneration of skeletal system with genipin crosslinked biomaterials. *J Tissue Eng*. 2020;11:2041731420974861. doi: 10.1177/2041731420974861

61. Despanie J, Dhandhukia JP, Hamm-Alvarez SF, MacKay JA. Elastin-like polypeptides: Therapeutic applications for an emerging class of nanomedicines. *J Control Release* 2016;240:93-108. doi: 10.1016/j.jconrel.2015.11.010

62. Wang K, Meng X, Guo Z. Elastin structure, synthesis, regulatory mechanism and relationship with cardiovascular Diseases. *Front Cell Dev Biol*. 2021;9:596702. doi: 10.3389/fcell.2021.596702

63. Dai X, Wu D, Xu K, Ming P, Cao S, Yu L. Viscoelastic mechanics: from pathology and cell fate to tissue regeneration biomaterial development. *ACS Appl Mater Interfaces*. 2025;17(6):8751-8770. doi: 10.1021/acsami.4c18174

64. Tillman BW, Yazdani SK, Lee SJ, Geary RL, Atala A, Yoo JJ. The in vivo stability of electrospun polycaprolactone-collagen scaffolds in vascular reconstruction. *Biomaterials*. 2009;30(4):583-588. doi: 10.1016/j.biomaterials.2008.10.006

65. Shao Y, Fu J. Integrated micro/nanoengineered functional biomaterials for cell mechanics and mechanobiology: a materials perspective. *Adv Mater*. 2014;26(10):1494-1533. doi: 10.1002/adma.201304431

66. Cavalcanti-Adam EA, Aydin D, Hirschfeld-Warneken VC, Spatz JP. Cell adhesion and response to synthetic nanopatterned environments by steering receptor clustering and spatial location. *HFSP J*. 2008;2(5):276-285. doi: 10.2976/1.2976662

67. Longstreth JH, Wang K. The role of fibronectin in mediating cell migration. *Am J Physiol Cell Physiol*. 2024;326(4):C1212-C1225. doi: 10.1152/ajpcell.00633.2023

68. Parisi L, Toffoli A, Ghezzi B, Mozzoni B, Lumetti S, Macaluso GM. A glance on the role of fibronectin in controlling cell response at biomaterial interface. *J Dent Sci Rev*. 2020;56(1):50-55. doi: 10.1016/j.jdsr.2019.11.002

69. Kupfer ME, Lin WH, Ravikumar V, *et al*. In situ expansion, differentiation, and electromechanical coupling of human cardiac muscle in a 3D bioprinted, chambered organoid. *Circ Res*. 2020;127(2):207-224. doi: 10.1161/CIRCRESAHA.119.316155

70. Ahn S, Jain A, Kasuba KC, *et al*. Engineering fibronectin-templated multi-component fibrillar extracellular matrices to modulate tissue-specific cell response. *Biomaterials*. 2024;308:122560. doi: 10.1016/j.biomaterials.2024.122560

71. Oliver-Cervelló L, Martin-Gómez H, Mas-Moruno C. New trends in the development of multifunctional peptides to functionalize biomaterials. *J Pept Sci*. 2022;28(1):e3335. doi: 10.1002/psc.3335

72. Hersel U, Dahmen C, Kessler H. RGD modified polymers: biomaterials for stimulated cell adhesion and beyond. *Biomaterials*. 2003;24(24):4385-4415. doi: 10.1016/S0142-9612(03)00343-0

73. Xu X, Jha AK, Harrington DA, Farach-Carson MC, Jia X. Hyaluronic acid-based hydrogels: from a natural polysaccharide to complex networks. *Soft Matter*. 2012;8(12):3280. doi: 10.1039/c2sm06463d

74. Bellis SL. Advantages of RGD peptides for directing cell association with biomaterials. *Biomaterials*. 2011;32(18):4205-4210. doi: 10.1016/j.biomaterials.2011.02.029

75. Miner JH, Yurchenco PD. Laminin functions in tissue morphogenesis. *Annu Rev Cell Dev Biol*. 2004;20(1):255-284. doi: 10.1146/annurev.cellbio.20.010403.094555

76. Mota C, Camarero-Espinosa S, Baker MB, Wieringa P, Moroni L. Bioprinting: from tissue and organ development to *in vitro* models. *Chem Rev*. 2020;120(19):10547-10607. doi: 10.1021/acs.chemrev.9b00789

77. He L, Liao S, Quan D, *et al*. The influence of laminin-derived peptides conjugated to Lys-capped PLLA on neonatal mouse cerebellum C17.2 stem cells. *Biomaterials*. 2009;30(8):1578-1586.

doi: 10.1016/j.biomaterials.2008.12.020

78. Penton CM, Badarinarayana V, Prisco J, *et al*. Laminin 521 maintains differentiation potential of mouse and human satellite cell-derived myoblasts during long-term culture expansion. *Skelet Muscle*. 2016;6(1):44. doi: 10.1186/s13395-016-0116-4

79. Aisenbrey EA, Murphy WL. Synthetic alternatives to matrigel. *Nat Rev Mater*. 2020;5(7):539-551. doi: 10.1038/s41578-020-0199-8

80. Speer JE, Barcellona MN, Lu MY, *et al*. Development of a library of laminin-mimetic peptide hydrogels for control of nucleus pulposus cell behaviors. *J Tissue Eng*. 2021;12:20417314211021220. doi: 10.1177/20417314211021220

81. Adams JC. Thrombospondins: conserved mediators and modulators of metazoan extracellular matrix. *Int J Exp Pathol*. 2024;105(5):136-169. doi: 10.1111/iep.12517

82. Calabro NE, Kristofik NJ, Kyriakides TR. Thrombospondin-2 and extracellular matrix assembly. *Biochim Biophys Acta*. 2014;1840(8):2396-2402. doi: 10.1016/j.bbagen.2014.01.013

83. Calabro NE, Barrett A, Chamorro-Jorganes A, *et al*. Thrombospondin-2 regulates extracellular matrix production, LOX levels, and cross-linking via downregulation of miR-29. *Matrix Biol*. 2019;82:71-85. doi: 10.1016/j.matbio.2019.03.002

84. Bornstein P, Kyriakides TR, Yang Z, Armstrong LC, Birk DE. Thrombospondin 2 modulates collagen fibrillogenesis and angiogenesis. *J Investig Dermatol Symp Proc*. 2000;5(1):61-66. doi: 10.1046/j.1087-0024.2000.00005.x

85. Xu ZY, Wang M, Shi JY, *et al*. Engineering a dynamic extracellular matrix using thrombospondin-1 to propel hepatocyte organoids reprogramming and improve mouse liver regeneration post-transplantation. *Mater Today Bio*. 2025;32:101700. doi: 10.1016/j.mtbio.2025.101700

86. Kyriakides TR, MacLauchlan S. The role of thrombospondins in wound healing, ischemia, and the foreign body reaction. *J Cell Commun Signal*. 2009;3(3-4):215-225. doi: 10.1007/s12079-009-0077-z

87. Chen D, Smith LR, Khandekar G, *et al*. Distinct effects of different matrix proteoglycans on collagen fibrillogenesis and cell-mediated collagen reorganization. *Sci Rep*. 2020;10(1):19065. doi: 10.1038/s41598-020-76107-0

88. Iozzo RV, Schaefer L. Proteoglycan form and function: a comprehensive nomenclature of proteoglycans. *Matrix Biol*. 2015;42:11-55. doi: 10.1016/j.matbio.2015.02.003

89. Schönherr E, Hausser HJ. Extracellular matrix and cytokines: a functional unit. *J Immunol Res*. 2000;7(2-4):89-101. doi: 10.1155/2000/31748

90. Nguyen M, Panitch A. Proteoglycans and proteoglycan mimetics for tissue engineering. *Am J Physiol Cell Physiol*. 2022;322(4):C754-C761. doi: 10.1152/ajpcell.00442.2021

91. Wei H, Cui J, Lin K, Xie J, Wang X. Recent advances in smart stimuli-responsive biomaterials for bone therapeutics and regeneration. *Bone Res*. 2022;10(1):17. doi: 10.1038/s41413-021-00180-y

92. Perez S, Makshakova O, Angulo J, *et al*. Glycosaminoglycans: what remains to be deciphered? *JACS Au*. 2023;3(3):628-656. doi: 10.1021/jacsau.2c00569

93. Wang Z, Wang Z, Lu WW, Zhen W, Yang D, Peng S. Novel biomaterial strategies for controlled growth factor delivery for biomedical applications. *NPG Asia Mater*. 2017;9(10):e435-e435. doi: 10.1038/am.2017.171

94. Kempen DHR, Lu L, Heijink A, *et al*. Effect of local sequential VEGF and BMP-2 delivery on ectopic and orthotopic bone regeneration. *Biomaterials*. 2009;30(14):2816-2825. doi: 10.1016/j.biomaterials.2009.01.031

95. Riley LA, Merryman WD. Cadherin-11 and cardiac fibrosis: a common target for a common pathology. *Cell Signal*. 2021;78:109876. doi: 10.1016/j.cellsig.2020.109876

96. Koirala R, Priest AV, Yen CF, *et al*. Inside-out regulation of E-cadherin conformation and adhesion. *Proc Natl Acad Sci U S A*. 2021;118(30):e2104090118. doi: 10.1073/pnas.2104090118

97. Hassan M, Mohanty AK, Wang T, Dhakal HN, Misra M. Current status and future outlook of 4D printing of polymers and composites—a prospective. *Compos Part C Open Access*. 2025;17:100602. doi: 10.1016/j.jcomc.2025.100602

98. Daamen W, Veerkamp J, Vanhest J, Vankuppevelt T. Elastin as a biomaterial for tissue engineering. *Biomaterials*. 2007;28(30):4378-4398. doi: 10.1016/j.biomaterials.2007.06.025

99. Zhu D, Wang H, Trinh P, Heilshorn SC, Yang F. Elastin-like protein-hyaluronic acid (ELP-HA) hydrogels with decoupled mechanical and biochemical cues for cartilage regeneration. *Biomaterials*. 2017;127:132-140. doi: 10.1016/j.biomaterials.2017.02.010

100. Wang H, Zhu D, Paul A, *et al*. Covalently adaptable elastin-like protein–hyaluronic acid (ELP–HA) hybrid hydrogels with secondary thermoresponsive crosslinking for injectable stem cell delivery. *Adv Funct Mater*. 2017;27(28):1605609. doi: 10.1002/adfm.201605609

101. Sugawara-Narutaki A, Nakamura J, Ohtsuki C. Elastin-like hydrogels as tissue regeneration scaffolds. In: *Hydrogels for Tissue Engineering and Regenerative Medicine*. Amsterdam, Netherlands: Elsevier; 2024:65-77.

doi: 10.1016/B978-0-12-823948-3.00018-X

102. Nguyen LT, Odeleye AO, Chui C, Baudequin T, Cui Z, Ye H. Development of thermo-responsive polycaprolactone macrocarriers conjugated with poly(N-isopropyl acrylamide) for cell culture. *Sci Rep*. 2019;9(1):3477. doi: 10.1038/s41598-019-40242-0

103. Trujillo S, Gonzalez-Garcia C, Rico P, *et al*. Engineered 3D hydrogels with full-length fibronectin that sequester and present growth factors. *Biomaterials*. 2020;252:120104. doi: 10.1016/j.biomaterials.2020.120104

104. Namgung S, Kim T, Baik KY, Lee M, Nam J, Hong S. Fibronectin–carbon-nanotube hybrid nanostructures for controlled cell growth. *Small*. 2011;7(1):56-61. doi: 10.1002/smll.201001513

105. Shiwarski DJ, Tashman JW, Tsamis A, *et al*. Fibronectin-based nanomechanical biosensors to map 3D surface strains in live cells and tissue. *Nat Commun*. 2020;11(1):5883. doi: 10.1038/s41467-020-19659-z

106. Silva GA, Czeisler C, Niece KL, *et al*. Selective differentiation of neural progenitor cells by high-epitope density nanofibers. *Science*. 2004;303(5662):1352-1355. doi: 10.1126/science.1093783

107. Ishihara J, Ishihara A, Fukunaga K, *et al*. Laminin heparin-binding peptides bind to several growth factors and enhance diabetic wound healing. *Nat Commun*. 2018;9(1):2163. doi: 10.1038/s41467-018-04525-w

108. Hayes AJ, Farrugia BL, Biose IJ, Bix GJ, Melrose J. Perlecan, a multi-functional, cell-instructive, matrix-stabilizing proteoglycan with roles in tissue development has relevance to connective tissue repair and regeneration. *Front Cell Dev Biol*. 2022;10:856261. doi: 10.3389/fcell.2022.856261

109. Jha AK, Yang W, Kirn-Safran CB, Farach-Carson MC, Jia X. Perlecan domain I-conjugated, hyaluronic acid-based hydrogel particles for enhanced chondrogenic differentiation via BMP-2 release. *Biomaterials*. 2009;30(36):6964-6975. doi: 10.1016/j.biomaterials.2009.09.009

110. Kiani C, Chen L, Wu YJ, Yee AJ, Yang BB. Structure and function of aggrecan. *Cell Res*. 2002;12(1):19-32. doi: 10.1038/sj.cr.7290106

111. Deng Z, Fan T, Xiao C, *et al*. TGF-β signaling in health, disease and therapeutics. *Signal Transduct Target Ther*. 2024;9(1):61. doi: 10.1038/s41392-024-01764-w

112. Rahman MS, Akhtar N, Jamil HM, Banik RS, Asaduzzaman SM. TGF-β/BMP signaling and other molecular events: regulation of osteoblastogenesis and bone formation. *Bone Res*. 2015;3(1):15005. doi: 10.1038/boneres.2015.5

113. Li Y, Liu Y, Bai H, *et al*. Sustained release of VEGF to promote angiogenesis and osteointegration of three-dimensional printed biomimetic titanium alloy implants. *Front Bioeng Biotechnol*. 2021;9:757767. doi: 10.3389/fbioe.2021.757767

114. Schutte RJ, Xie L, Klitzman B, Reichert WM. In vivo cytokine-associated responses to biomaterials. *Biomaterials*. 2009;30(2):160-168. doi: 10.1016/j.biomaterials.2008.09.026

115. Tu Z, Zhong Y, Hu H, *et al*. Design of therapeutic biomaterials to control inflammation. *Nat Rev Mater*. 2022;7(7):557-574. doi: 10.1038/s41578-022-00426-z

116. Barthel SR, Gavino JD, Descheny L, Dimitroff CJ. Targeting selectins and selectin ligands in inflammation and cancer. *Expert Opin Ther Targets*. 2007;11(11):1473-1491. doi: 10.1517/14728222.11.11.1473

117. Pang X, He X, Qiu Z, *et al*. Targeting integrin pathways: mechanisms and advances in therapy. *Signal Transduct Target Ther*. 2023;8(1):1. doi: 10.1038/s41392-022-01259-6

118. Hu M, Ling Z, Ren X. Extracellular matrix dynamics: tracking in biological systems and their implications. *J Biol Eng*. 2022;16(1):13. doi: 10.1186/s13036-022-00292-x

119. Lu P, Weaver VM, Werb Z. The extracellular matrix: a dynamic niche in cancer progression. *J Cell Biol*. 2012;196(4):395-406. doi: 10.1083/jcb.201102147

120. Estrach S, Vivier CM, Féral CC. ECM and epithelial stem cells: the scaffold of destiny. *Front Cell Dev Biol*. 2024;12:1359585. doi: 10.3389/fcell.2024.1359585

121. Kozyrina AN, Piskova T, Di Russo J. Mechanobiology of epithelia from the perspective of extracellular matrix heterogeneity. *Front Bioeng Biotechnol*. 2020;8:596599. doi: 10.3389/fbioe.2020.596599

122. Pfisterer K, Shaw LE, Symmank D, Weninger W. The extracellular matrix in skin inflammation and infection. *Front Cell Dev Biol*. 2021;9:682414. doi: 10.3389/fcell.2021.682414

123. Wagenseil JE, Mecham RP. Vascular extracellular matrix and arterial mechanics. *Physiol Rev*. 2009;89(3):957-989. doi: 10.1152/physrev.00041.2008

124. Burgess JK, Weiss DJ, Westergren-Thorsson G, *et al*. Extracellular matrix as a driver of chronic lung diseases. *Am J Respir Cell Mol Biol*. 2024;70(4):239-246. doi: 10.1165/rcmb.2023-0176PS

125. Del Monte-Nieto G, Fischer JW, Gorski DJ, Harvey RP, Kovacic JC. Basic biology of extracellular matrix in the cardiovascular system, part 1/4. *J Am Coll Cardiol*. 2020;75(17):2169-2188. doi: 10.1016/j.jacc.2020.03.024

126. Luo Y, Li N, Chen H, *et al*. Spatial and temporal changes in extracellular elastin and laminin distribution during lung alveolar development. *Sci Rep*. 2018;8(1):8334. doi: 10.1038/s41598-018-26673-1

127. Mura M, Binnie M, Han B, *et al*. Functions of type II pneumocyte-derived vascular endothelial growth factor in alveolar structure, acute inflammation, and vascular permeability. *Am J Pathol.* 2010;176(4):1725-1734. doi: 10.2353/ajpath.2010.090209

128. Ahmed DW, Tan ML, Liu Y, *et al*. Local photocrosslinking of native tissue matrix regulates lung epithelial cell mechanosensing and function. *Nat Mater*. 2025;24:1812–1825. doi: 10.1038/s41563-025-02329-0

129. Merrilees MJ, Ching PS, Beaumont B, Hinek A, Wight TN, Black PN. Changes in elastin, elastin binding protein and versican in alveoli in chronic obstructive pulmonary disease. *Respir Res*. 2008;9(1):41. doi: 10.1186/1465-9921-9-41

130. Ye X, Gaucher JF, Vidal M, Broussy S. A structural overview of vascular endothelial growth factors pharmacological ligands: from macromolecules to designed peptidomimetics. *Molecules.* 2021;26(22):6759. doi: 10.3390/molecules26226759

131. Csapo R, Gumpenberger M, Wessner B. Skeletal muscle extracellular matrix – what do we know about its composition, regulation, and physiological roles? A narrative review. *Front Physiol*. 2020;11:253. doi: 10.3389/fphys.2020.00253

132. Takala TE, Virtanen P. Biochemical composition of muscle extracellular matrix: the effect of loading. *Scand Med Sci Sports.* 2000;10(6):321-325. doi: 10.1034/j.1600-0838.2000.010006321.x

133. Gillies AR, Lieber RL. Structure and function of the skeletal muscle extracellular matrix. *Muscle Nerve.* 2011;44(3):318-331. doi: 10.1002/mus.22094

134. Stern MM, Myers RL, Hammam N, *et al*. The influence of extracellular matrix derived from skeletal muscle tissue on the proliferation and differentiation of myogenic progenitor cells ex vivo. *Biomaterials.* 2009;30(12):2393-2399. doi: 10.1016/j.biomaterials.2008.12.069

135. Wachsmuth L, Söder S, Fan Z, Finger F, Aigner T. Immunolocalization of matrix proteins in different human cartilage subtypes. *Histol Histopathol*. 2006;(21):477-485. doi: 10.14670/HH-21.477

136. Han B, Li Q, Wang C, *et al*. Decorin regulates the aggrecan network integrity and biomechanical functions of cartilage extracellular matrix. *ACS Nano.* 2019;13(10):11320-11333. doi: 10.1021/acsnano.9b04477

137. McKee TJ, Perlman G, Morris M, Komarova SV. Extracellular matrix composition of connective tissues: a systematic review and meta-analysis. *Sci Rep*. 2019;9(1):10542. doi: 10.1038/s41598-019-46896-0

138. Vainieri ML, Lolli A, Kops N, *et al*. Evaluation of biomimetic hyaluronic-based hydrogels with enhanced endogenous cell recruitment and cartilage matrix formation. *Acta Biomater*. 2020;101:293-303. doi: 10.1016/j.actbio.2019.11.015

139. Fontcuberta-Rigo M, Nakamura M, Puigbò P. Phylobone: a comprehensive database of bone extracellular matrix proteins in human and model organisms. *Bone Res*. 2023;11(1):44. doi: 10.1038/s41413-023-00281-w

140. Qin L, Yang S, Zhao C, *et al*. Prospects and challenges for the application of tissue engineering technologies in the treatment of bone infections. *Bone Res*. 2024;12(1):28. doi: 10.1038/s41413-024-00332-w

141. Hua R, Ni Q, Eliason TD, *et al*. Biglycan and chondroitin sulfate play pivotal roles in bone toughness via retaining bound water in bone mineral matrix. *Matrix Biol.* 2020;94:95-109. doi: 10.1016/j.matbio.2020.09.002

142. Lewns FK, Tsigkou O, Cox LR, Wildman RD, Grover LM, Poologasundarampillai G. Hydrogels and bioprinting in bone tissue engineering: creating artificial stem-cell niches for in vitro models. *Adv Mater*. 2023;35(52):2301670. doi: 10.1002/adma.202301670

143. Silva AC, Pereira C, Fonseca ACRG, Pinto-do-Ó P, Nascimento DS. Bearing my heart: the role of extracellular matrix on cardiac development, homeostasis, and injury response. *Front Cell Dev Biol*. 2021;8:621644. doi: 10.3389/fcell.2020.621644

144. Barallobre-Barreiro J, Loeys B, Mayr M, Rienks M, Verstraeten A, Kovacic JC. Extracellular matrix in vascular disease, part 2/4. *J Am Coll Cardiol.* 2020;75(17): 2189-2203. doi: 10.1016/j.jacc.2020.03.018

145. El-Husseiny HM, Mady EA, El-Dakroury WA, Doghish AS, Tanaka R. Stimuli-responsive hydrogels: smart state of-the-art platforms for cardiac tissue engineering. *Front Bioeng Biotechnol*. 2023;11:1174075. doi: 10.3389/fbioe.2023.1174075

146. Pohl U. Connexins: key players in the control of vascular plasticity and function. *Physiol Rev.* 2020;100(2): 525-572. doi: 10.1152/physrev.00010.2019

147. Davis MJ, Earley S, Li YS, Chien S. Vascular mechanotransduction. *Physiol Rev.* 2023;103(2):1247-1421. doi: 10.1152/physrev.00053.2021

148. Lee TT, García JR, Paez JI, *et al*. Light-triggered in vivo activation of adhesive peptides regulates cell adhesion, inflammation and vascularization of biomaterials. *Nat Mater*. 2015;14(3):352-360. doi: 10.1038/nmat4157

149. Amelung CD, Gerecht S. Cell–material interactions in vascular tissue engineering. *Acc Mater Res*. 2025;6(5):577-588.
doi: 10.1021/accountsmr.4c00390

150. Grigoryan B, Paulsen SJ, Corbett DC, *et al*. Multivascular networks and functional intravascular topologies within biocompatible hydrogels. *Science*. 2019;364(6439):458-464.
doi: 10.1126/science.aav9750

151. Suttkus A, Morawski M, Arendt T. Protective properties of neural extracellular matrix. *Mol Neurobiol*. 2016; 53(1):73-82.
doi: 10.1007/s12035-014-8990-4

152. Chelyshev YA, Kabdesh IM, Mukhamedshina YO. Extracellular matrix in neural plasticity and regeneration. *Cell Mol Neurobiol*. 2022;42(3):647-664.
doi: 10.1007/s10571-020-00986-0

153. Wareham LK, Baratta RO, Del Buono BJ, Schlumpf E, Calkins DJ. Collagen in the central nervous system: contributions to neurodegeneration and promise as a therapeutic target. *Mol Neurodegener*. 2024;19(1):11.
doi: 10.1186/s13024-024-00704-0

154. Weickenmeier J, De Rooij R, Budday S, Steinmann P, Ovaert TC, Kuhl E. Brain stiffness increases with myelin content. *Acta Biomater*. 2016;42:265-272.
doi: 10.1016/j.actbio.2016.07.040

155. Moshayedi P, Ng G, Kwok JC, *et al*. The relationship between glial cell mechanosensitivity and foreign body reactions in the central nervous system. *Biomaterials*. 2014;35(13):3919-3925.
doi: 10.1016/j.biomaterials.2014.01.038

156. Dityatev A, Schachner M, Sonderegger P. The dual role of the extracellular matrix in synaptic plasticity and homeostasis. *Nat Rev Neurosci*. 2010;11(11):735-746.
doi: 10.1038/nrn2898

157. Lam D, Enright HA, Cadena J, *et al*. Tissue-specific extracellular matrix accelerates the formation of neural networks and communities in a neuron-glia co-culture on a multi-electrode array. *Sci Rep*. 2019;9(1):4159.
doi: 10.1038/s41598-019-40128-1

158. Rozario T, DeSimone DW. The extracellular matrix in development and morphogenesis: a dynamic view. *Dev Biol*. 2010;341(1):126-140.
doi: 10.1016/j.ydbio.2009.10.026

159. Muir VG, Burdick JA. Chemically modified biopolymers for the formation of biomedical hydrogels. *Chem Rev*. 2021;121(18):10908-10949.
doi: 10.1021/acs.chemrev.0c00923

160. Joyce K, Fabra GT, Bozkurt Y, Pandit A. Bioactive potential of natural biomaterials: identification, retention and assessment of biological properties. *Signal Transduct Target Ther*. 2021;6(1):122.
doi: 10.1038/s41392-021-00512-8

161. Liu B, Li H, Meng F, *et al*. 4D printed hydrogel scaffold with swelling-stiffening properties and programmable deformation for minimally invasive implantation. *Nat Commun*. 2024;15(1):1587.
doi: 10.1038/s41467-024-45938-0

162. Ni C, Chen D, Yin Y, *et al*. Shape memory polymer with programmable recovery onset. *Nature*. 2023;622(7984):748-753.
doi: 10.1038/s41586-023-06520-8

163. Wang XQ, Chan KH, Lu W, *et al*. Macromolecule conformational shaping for extreme mechanical programming of polymorphic hydrogel fibers. *Nat Commun*. 2022;13(1):3369.
doi: 10.1038/s41467-022-31047-3

164. Yao X, Chen H, Qin H, Wu QH, Cong HP, Yu SH. Solvent-adaptive hydrogels with lamellar confinement cellular structure for programmable multimodal locomotion. *Nat Commun*. 2024;15(1):9254.
doi: 10.1038/s41467-024-53549-y

165. Wang M, Zhang P, Shamsi M, *et al*. Tough and stretchable ionogels by in situ phase separation. *Nat Mater*. 2022;21(3):359-365.
doi: 10.1038/s41563-022-01195-4

166. Kim J, Choi H, Kim Y, Song S. Thermo-responsive nanocomposite bioink with growth-factor holding and its application to bone regeneration. *Small*. 2023;19(9): 2203464.
doi: 10.1002/smll.202203464

167. Parimita S, Kumar A, Krishnaswamy H, Ghosh P. 4D printing of pH-responsive bilayer with programmable shape-shifting behaviour. *Eur Polym J*. 2025;222:113581.
doi: 10.1016/j.eurpolymj.2024.113581

168. Liu J, Huang YS, Liu Y, *et al*. Reconfiguring hydrogel assemblies using a photocontrolled metallopolymer adhesive for multiple customized functions. *Nat Chem*. 2024;16(6):1024-1033.
doi: 10.1038/s41557-024-01476-2

169. Chiesa I, Esposito A, Vozzi G, Gottardi R, De Maria C. 4D bioprinted self-folding scaffolds enhance cartilage formation in the engineering of trachea. *Adv Mater Technol*. 2025;10(6):2401210.
doi: 10.1002/admt.202401210

170. Zhou B, Zou Y, You H, Zhang B, Lu X. Preparation and evaluation of 4D-printed poly(L-lactic) acid/silk fibroin polymer blends with enhanced mechanical properties and water-induced shape memory effects. *Adv Eng Mater*. 2025;27(7):2402496.
doi: 10.1002/adem.202402496

171. Lai J, Xiong T, Chen S, *et al*. Facile single-nanocomposite 4D bioprinting of dynamic hydrogel constructs with thickness-controlled gradient. *Adv Sci*. 2025;12:e09449.
doi: 10.1002/advs.202509449

172. Miao W, Zou W, Jin B, *et al*. On demand shape memory polymer via light regulated topological defects in a dynamic covalent network. *Nat Commun*. 2020;11(1):4257. doi: 10.1038/s41467-020-18116-1

173. Zhang L, Huang X, Cole T, *et al*. 3D-printed liquid metal polymer composites as NIR-responsive 4D printing soft robot. *Nat Commun*. 2023;14(1):7815. doi: 10.1038/s41467-023-43667-4

174. Matsuura K, Inaba H. Photoresponsive peptide materials: spatiotemporal control of self-assembly and biological functions. *Biophys Rev*. 2023;4(4):041303. doi: 10.1063/5.0179171

175. Butenko S, Nagalla RR, Guerrero-Juarez CF, *et al*. Hydrogel crosslinking modulates macrophages, fibroblasts, and their communication, during wound healing. *Nat Commun*. 2024;15(1):6820. doi: 10.1038/s41467-024-50072-y

176. McCracken JM, Rauzan BM, Kjellman JCE, Su H, Rogers SA, Nuzzo RG. Ionic hydrogels with biomimetic 4D-printed mechanical gradients: models for soft-bodied aquatic organisms. *Adv Funct Mater*. 2019;29(28):1806723. doi: 10.1002/adfm.201806723

177. Díaz-Payno PJ, Kalogeropoulou M, Muntz I, *et al*. Swelling-dependent shape-based transformation of a human mesenchymal stromal cells-laden 4D bioprinted construct for cartilage tissue engineering. *Adv Healthc Mater*. 2023;12(2):2201891. doi: 10.1002/adhm.202201891

178. Araújo-Custódio S, Gomez-Florit M, Tomás AR, *et al*. Injectable and magnetic responsive hydrogels with bioinspired ordered structures. *ACS Biomater Sci Eng*. 2019;5(3):1392-1404. doi: 10.1021/acsbiomaterials.8b01179

179. Daul B, Martin R, Glass P, *et al*. 3D printed magnetic origami scaffolds for guided tissue assembly. *Adv Mater Interfaces*. 2025;12:2400903. doi: 10.1002/admi.202400903

180. Zhang H, Hua S, He C, *et al*. Application of 4D-printed magnetoresponsive fogs hydrogel scaffolds in auricular cartilage regeneration. *Adv Healthc Mater*. 2025;14(9):2404488. doi: 10.1002/adhm.202404488

181. Rajan Unnithan A, Krishnamoorthi Kaliannagounder V, Rao Alluri N, Park CH, Veluswamy P, Ramachandra Kurup Sasikala A. Design and application of piezoelectric conductive smart scaffold for noninvasive neural tissue regeneration via custom-made in vitro mechano-stimulator. *Adv Nanobiomed Res*. 2025;5:2500058. doi: 10.1002/anbr.202500058

182. Ebrahimi S, Khoomortezaei S, Fan J, *et al*. Conducting polymer coatings for bioelectronic arthroscopy probes. *Adv Healthc Mater*. 2025;27:e02269. doi: 10.1002/adhm.202502269

183. Liu W, Zhao H, Zhang C, *et al*. In situ activation of flexible magnetoelectric membrane enhances bone defect repair. *Nat Commun*. 2023;14(1):4091. doi: 10.1038/s41467-023-39744-3

184. Yuan Y, Raheja K, Milbrandt NB, *et al*. Thermoresponsive polymers with LCST transition: synthesis, characterization, and their impact on biomedical frontiers. *RSC Appl Polym*. 2023;1(2):158-189. doi: 10.1039/D3LP00114H

185. Qiao SL, Mamuti M, An HW, Wang H. Thermoresponsive polymer assemblies: from molecular design to theranostics application. *Prog Polym Sci*. 2022;131:101578. doi: 10.1016/j.progpolymsci.2022.101578

186. Frazar EM, Shah RA, Dziubla TD, Hilt JZ. Multifunctional temperature-responsive polymers as advanced biomaterials and beyond. *J Appl Polym Sci*. 2020;137(25):48770. doi: 10.1002/app.48770

187. Heskins M, Guillet JE. Solution properties of poly(N-isopropylacrylamide). *J Macromol Sci Part A*. 1968;2(8):1441-1455. doi: 10.1080/10601326808051910

188. Tang Z, Okano T. Recent development of temperature-responsive surfaces and their application for cell sheet engineering. *Regen Biomater*. 2014;1(1):91-102. doi: 10.1093/rb/rbu011

189. Li Z, Zhu Y, Matson JB. pH-responsive self-assembling peptide-based biomaterials: designs and applications. *ACS Appl Bio Mater*. 2022;5(10):4635-4651. doi: 10.1021/acsabm.2c00188

190. Vegad U, Patel M, Khunt D, Zupančič O, Chauhan S, Paudel A. pH stimuli-responsive hydrogels from non-cellulosic biopolymers for drug delivery. *Front Bioeng Biotechnol*. 2023;11:1270364. doi: 10.3389/fbioe.2023.1270364

191. Qu X, Wirsén A, Albertsson AC. Novel pH-sensitive chitosan hydrogels: swelling behavior and states of water. *Polymer*. 2000;41(12):4589-4598. doi: 10.1016/S0032-3861(99)00685-0

192. Zhu L, Bratlie KM. pH sensitive methacrylated chitosan hydrogels with tunable physical and chemical properties. *Biochem Eng J*. 2018;132:38-46. doi: 10.1016/j.bej.2017.12.012

193. Ollier RC, Webber MJ. Mechanoresponsive hydrogels emerging from dynamic and non-covalent interactions. *Adv Mater*. 2025;37(40):2507397. doi: 10.1002/adma.202507397

194. Yang EC, Divine R, Miranda MC, *et al*. Computational design of non-porous pH-responsive antibody nanoparticles. *Nat Struct Mol Biol*. 2024;31(9):1404-1412. doi: 10.1038/s41594-024-01288-5

195. Mintis DG, Mavrantzas VG. Effect of pH and molecular length on the structure and dynamics of short poly(acrylic

acid) in dilute solution: detailed molecular dynamics study. *J Phys Chem B.* 2019;123(19):4204-4219. doi: 10.1021/acs.jpcb.9b01696

196. Farasati Far B, Omrani M, Naimi Jamal MR, Javanshir S. Multi-responsive chitosan-based hydrogels for controlled release of vincristine. *Commun Chem*. 2023;6(1):28. doi: 10.1038/s42004-023-00829-1

197. Zoe LH, David SR, Rajabalaya R. Chitosan nanoparticle toxicity: a comprehensive literature review of in vivo and in vitro assessments for medical applications. *Toxicol Rep.* 2023;11:83-106. doi: 10.1016/j.toxrep.2023.06.012

198. Shin Y, Kim D, Hu Y, *et al*. pH-responsive succinoglycan-carboxymethyl cellulose hydrogels with highly improved mechanical strength for controlled drug delivery systems. *Polymers.* 2021;13(18):3197. doi: 10.3390/polym13183197

199. Héraly F, Zhang M, Åhl A, Cao W, Bergström L, Yuan J. Nanodancing with moisture: humidity-sensitive bilayer actuator derived from cellulose nanofibrils and reduced graphene oxide. *Adv Intell Syst*. 2022;4(1):2100084. doi: 10.1002/aisy.202100084

200. Guo F, Kim F, Han TH, Shenoy VB, Huang J, Hurt RH. Hydration-responsive folding and unfolding in graphene oxide liquid crystal phases. *ACS Nano.* 2011;5(10):8019-8025. doi: 10.1021/nn2025644

201. Formisano N, Van Der Putten C, Grant R, *et al*. Mechanical properties of bioengineered corneal stroma. *Adv Healthc Mater*. 2021;10(20):2100972. doi: 10.1002/adhm.202100972

202. Pérez-Madrigal MM, Shaw JE, Arno MC, Hoyland JA, Richardson SM, Dove AP. Robust alginate/hyaluronic acid thiol-yne click-hydrogel scaffolds with superior mechanical performance and stability for load-bearing soft tissue engineering. *Biomater Sci.* 2020;8(1):405-412. doi: 10.1039/C9BM01494B

203. Jamilludin MA, Dinatha IKH, Supii AI, Partini J, Kusindarta DL, Yusuf Y. Functionalized cellulose nanofibrils in carbonate-substituted hydroxyapatite nanorod-based scaffold from long-spined sea urchin (*Diadema setosum*) shells reinforced with polyvinyl alcohol for alveolar bone tissue engineering. *RSC Adv*. 2023;13(46):32444-32456. doi: 10.1039/D3RA06165E

204. Lawless BM, Sadeghi H, Temple DK, Dhaliwal H, Espino DM, Hukins DWL. Viscoelasticity of articular cartilage: analysing the effect of induced stress and the restraint of bone in a dynamic environment. *J Mech Behav Biomed Mater.* 2017;75:293-301. doi: 10.1016/j.jmbbm.2017.07.040

205. Lee HP, Gaharwar AK. Light-responsive inorganic biomaterials for biomedical applications. *Adv Sci*. 2020;7(17):2000863. doi: 10.1002/advs.202000863

206. Chen G, Cao Y, Tang Y, *et al*. Advanced near-infrared light for monitoring and modulating the spatiotemporal dynamics of cell functions in living systems. *Adv Sci*. 2020;7(8):1903783. doi: 10.1002/advs.201903783

207. Lu Y, Chen C, Li H, *et al*. Visible light-responsive hydrogels for cellular dynamics and spatiotemporal viscoelastic regulation. *Nat Commun*. 2025;16(1):1365. doi: 10.1038/s41467-024-54880-0

208. Guo P, Dong L, Xue B, Cao Y, Yang J. From light to life: molecular mechanisms and macroscopic transformations in photoresponsive hydrogels. *Polym Sci Technol.* 2025;1:812−831. doi: 10.1021/polymscitech.5c00102

209. Overchuk M, Weersink RA, Wilson BC, Zheng G. Photodynamic and photothermal therapies: synergy opportunities for nanomedicine. *ACS Nano.* 2023;17(9):7979-8003. doi: 10.1021/acsnano.3c00891

210. Jayakumar MKG, Idris NM, Zhang Y. Remote activation of biomolecules in deep tissues using near-infrared-to-UV upconversion nanotransducers. *Proc Natl Acad Sci U S A.* 2012;109(22):8483-8488. doi: 10.1073/pnas.1114551109

211. Liu TM, Conde J, Lipiński T, Bednarkiewicz A, Huang CC. Revisiting the classification of nir-absorbing/emitting nanomaterials for in vivo bioapplications. *NPG Asia Mater*. 2016;8(8):e295-e295. doi: 10.1038/am.2016.106

212. Lee CH, Wu SB, Hong CH, Yu HS, Wei YH. Molecular mechanisms of UV-induced apoptosis and its effects on skin residential cells: the implication in UV-Based Phototherapy. *Int J Mol Sci.* 2013;14(3):6414-6435. doi: 10.3390/ijms14036414

213. Meng F, Meyer CM, Joung D, Vallera DA, McAlpine MC, Panoskaltsis-Mortari A. 3D bioprinted in vitro metastatic models via reconstruction of tumor microenvironments. *Adv Mater*. 2019;31(10):1806899. doi: 10.1002/adma.201806899

214. He D, Zhao A, Su H, *et al*. An injectable scaffold based on temperature-responsive hydrogel and factor-loaded nanoparticles for application in vascularization in tissue engineering. *J Biomed Mater Res.* 2019;107(10): 2123-2134. doi: 10.1002/jbm.a.36723

215. Bonnet S. Ruthenium-based photoactivated chemotherapy. *J Am Chem Soc*. 2023;145(43):23397-23415. doi: 10.1021/jacs.3c01135

216. Munteanu AC, Notaro A, Jakubaszek M, *et al*. Synthesis, characterization, cytotoxic activity, and metabolic studies of ruthenium(II) polypyridyl complexes containing flavonoid ligands. *Inorg Chem*. 2020;59(7):4424-4434. doi: 10.1021/acs.inorgchem.9b03562

217. António JPM, Gandioso A, Nemati F, *et al*. Polymeric encapsulation of a ruthenium(II) polypyridyl complex: from synthesis to *in vivo* studies against high-grade epithelial ovarian cancer. *Chem Sci*. 2023;14(2):362-371. doi: 10.1039/D2SC05693C

218. Bolanta SO, Malijauskaite S, McGourty K, O'Reilly EJ. Synthesis of poly(acrylic acid)-cysteine-based hydrogels with highly customizable mechanical properties for advanced cell culture applications. *ACS Omega*. 2022;7(11):9108-9117. doi: 10.1021/acsomega.1c03408

219. Suhail M, Liu JY, Hung MC, Chiu IH, Minhas MU, Wu PC. Preparation, in vitro characterization, and cytotoxicity evaluation of polymeric pH-responsive hydrogels for controlled drug release. *Pharmaceutics*. 2022;14(9):1864. doi: 10.3390/pharmaceutics14091864

220. Leigh BL, Cheng E, Xu L, Derk A, Hansen MR, Guymon CA. Antifouling photograftable zwitterionic coatings on PDMS substrates. *Langmuir*. 2019;35(5):1100-1110. doi: 10.1021/acs.langmuir.8b00838

221. Zhao C, Zheng J. Synthesis and characterization of poly(*N*-hydroxyethylacrylamide) for long-term antifouling ability. *Biomacromolecules*. 2011;12(11):4071-4079. doi: 10.1021/bm2011455

222. Fernandes LC, Correia DM, Costa CM, Lanceros-Mendez S. Recent advances in ionic liquid-based hybrid materials for electroactive soft actuator applications. *Macromol Mater Eng*. 2025;310(2):2400279. doi: 10.1002/mame.202400279

223. Datta D, Colaco V, Bandi SP, *et al*. Stimuli-responsive self-healing ionic gels: a promising approach for dermal and tissue engineering applications. *ACS Biomater Sci Eng*. 2025;11(3):1338-1372. doi: 10.1021/acsbiomaterials.4c02264

224. Plaas AHK, Moran MM, Sandy JD, Hascall VC. Aggrecan and hyaluronan: the infamous cartilage polyelectrolytes – then and now. In: Connizzo BK, Han L, Sah RL, eds. *Electromechanobiology of Cartilage and Osteoarthritis*. Vol. 1402. Advances in Experimental Medicine and Biology. Cham, Switzerland: Springer International Publishing; 2023:3-29. doi: 10.1007/978-3-031-25588-5_1

225. Ricka J, Tanaka T. Swelling of ionic gels: quantitative performance of the Donnan theory. *Macromolecules*. 1984;17(12):2916-2921. doi: 10.1021/ma00142a081

226. Wei W. Hofmeister effects shine in nanoscience. *Adv Sci*. 2023;10(22):2302057. doi: 10.1002/advs.202302057

227. Huang S, Zhao Z, Feng C, Mayes E, Yang J. Nanocellulose reinforced P(AAm-co-AAc) hydrogels with improved mechanical properties and biocompatibility. *Compos A Appl Sci Manuf*. 2018;112:395-404. doi: 10.1016/j.compositesa.2018.06.028

228. Echeverria C, Fernandes SN, Godinho MH, Borges JP, Soares PIP. Functional stimuli-responsive gels: hydrogels and microgels. *Gels*. 2018;4(2):54. doi: 10.3390/gels4020054

229. Chen H, Wei P, Qi Y, Xie Y, Huang X. Water-induced cellulose nanofibers/poly(vinyl alcohol) hydrogels regulated by hydrogen bonding for in situ water shutoff. *ACS Appl Mater Interfaces*. 2023;15(33):39883-39895. doi: 10.1021/acsami.3c07989

230. Xu W, Newton MAA, Chen Z, Xin B. Design, characterization, and performance evaluation of novel PVA/CS/CNF/MOP TN ionic conductive hydrogels for flexible sensors. *J Polym Sci*. 2024;62(12):2744-2761. doi: 10.1002/pol.20240043

231. Zhang H, Fu C, Yong LC, Sun N, Liu FG. Flexible and transparent PVA/CNF hydrogel with ultrahigh dielectric constant. *ACS Appl Polym Mater*. 2024;6(10):5706-5713. doi: 10.1021/acsapm.4c00302

232. Xu Z, Chen H, Yang HB, *et al*. Hierarchically aligned heterogeneous core-sheath hydrogels. *Nat Commun*. 2025;16(1):400. doi: 10.1038/s41467-024-55677-x

233. Zhang A, Yue Z, Grove B, *et al*. Highly-soft, scalable, personalizable skin-interfaced systems via self-healing gels. *Adv Funct Mater*. 2025;35(50):e07821. doi: 10.1002/adfm.202507821

234. Mistral J, Ve Koon KT, Fernando Cotica L, *et al*. Chitosan-coated superparamagnetic Fe_3O_4 nanoparticles for magnetic resonance imaging, magnetic hyperthermia, and drug delivery. *ACS Appl Nano Mater*. 2024;7(7):7097-7110. doi: 10.1021/acsanm.3c06118

235. Mammoto A, Mammoto T, Ingber DE. Mechanosensitive mechanisms in transcriptional regulation. *J Cell Sci*. 2012:125 (13): 3061–3073. doi: 10.1242/jcs.093005

236. Lucariello M, Valicenti ML, Giannoni S, *et al*. Mechanobiology in action: biomaterials, devices, and the cellular machinery of force sensing. *Biomolecules*. 2025;15(6):848. doi: 10.3390/biom15060848

237. Estelrich J, Busquets MA, Del Carmen Morán M. Effect of PEGylation on ligand-targeted magnetoliposomes: a missed goal. *ACS Omega*. 2017;2(10):6544-6555. doi: 10.1021/acsomega.7b00778

238. Masoumi Godgaz S, Asefnejad A, Bahrami SH. Fabrication of PEGylated SPIONs-loaded niosome for codelivery of paclitaxel and trastuzumab for breast cancer treatment: in vivo study. *ACS Appl Bio Mater*. 2024;7(5):2951-2965. doi: 10.1021/acsabm.4c00027

239. Carter TJ, Agliardi G, Lin F, *et al*. Potential of magnetic hyperthermia to stimulate localized immune activation. *Small*. 2021;17(14):2005241.

doi: 10.1002/smll.202005241

240. Moonesi Rad R, Daul B, Glass P, *et al*. 3D printed magnet-infused origami platform for 3D cell culture assessments. *Adv Mater Technol*. 2023;8(8):2202204. doi: 10.1002/admt.202202204

241. Yang D, Hu Y, Liu S, *et al*. Synthesis and assembly strategy of electroactive biomaterials and systems for soft tissue engineering applications. *Chem*. 2025;11(9):102596. doi: 10.1016/j.chempr.2025.102596

242. Ning C, Zhou Z, Tan G, Zhu Y, Mao C. Electroactive polymers for tissue regeneration: Developments and perspectives. *Prog Polym Sci*. 2018;81:144-162. doi: 10.1016/j.progpolymsci.2018.01.001

243. Chen AY, Pegg E, Chen A, Jin Z, Gu GX. 4D printing of electroactive materials. *Adv Intell Syst*. 2021;3(12):2100019. doi: 10.1002/aisy.202100019

244. Grodzinsky AJ. Electromechanical and physicochemical properties of connective tissue. *Crit Rev Biomed Eng*. 1983;9(2):133-199. doi: 10.1016/0021-9290(87)90282-x.

245. Pillay V, Tsai T, Choonara YE, *et al*. A review of integrating electroactive polymers as responsive systems for specialized drug delivery applications. *J Biomed Mater Res*. 2014;102(6):2039-2054. doi: 10.1002/jbm.a.34869

246. Acharya R, Dutta SD, Patil TV, Ganguly K, Randhawa A, Lim KT. A review on electroactive polymer–metal composites: development and applications for tissue regeneration. *J Funct Biomater*. 2023;14(10):523. doi: 10.3390/jfb14100523

247. Rivnay J, Inal S, Collins BA, *et al*. Structural control of mixed ionic and electronic transport in conducting polymers. *Nat Commun*. 2016;7(1):11287. doi: 10.1038/ncomms11287

248. Deng X, Zhuang Y, Cui J, *et al*. Open challenges and opportunities in piezoelectricity for tissue regeneration. *Adv Sci*. 2025;12(38):e10349. doi: 10.1002/advs.202510349

249. Filippi M, Badolato A, Georgopoulou A, *et al*. Bioprinting of piezoresistive organohydrogel networks for advanced real-time mechanosensing in engineered tissue models. *Trends Biotechnol*. 2025;43(10):2509-2538. doi: 10.1016/j.tibtech.2025.05.026

250. Faber L, Yau A, Chen Y. Translational biomaterials of four-dimensional bioprinting for tissue regeneration. *Biofabrication*. 2024;16(1):012001. doi: 10.1088/1758-5090/acfdd0

251. Narayana S, Gowda BHJ, Hani U, Ahmed MG, Asiri ZA, Paul K. Smart poly(N-isopropylacrylamide)-based hydrogels: a tour d'horizon of biomedical applications. *Gels*. 2025;11(3):207. doi: 10.3390/gels11030207

252. Cui Z, Lee BH, Pauken C, Vernon BL. Degradation, cytotoxicity, and biocompatibility of NIPAAm-based thermosensitive, injectable, and bioresorbable polymer hydrogels. *J Biomed Mater Res*. 2011;98A(2):159-166. doi: 10.1002/jbm.a.33093

253. Allyn MM, Luo RH, Hellwarth EB, Swindle-Reilly KE. Considerations for polymers used in ocular drug delivery. *Front Med*. 2022;8:787644. doi: 10.3389/fmed.2021.787644

254. Chu S, Shi X, Tian Y, Gao F. pH-responsive polymer nanomaterials for tumor therapy. *Front Oncol*. 2022;12:855019. doi: 10.3389/fonc.2022.855019

255. Gao W, Chan JM, Farokhzad OC. pH-responsive nanoparticles for drug delivery. *Mol Pharm*. 2010;7(6):1913-1920. doi: 10.1021/mp100253e

256. Linsley CS, Wu BM. Recent advances in light-responsive on-demand drug-delivery systems. *Ther Deliv*. 2017;8(2):89-107. doi: 10.4155/tde-2016-0060

257. Verbroekken RMC, Savchak OK, Alofs TFJ, Schenning APHJ, Gumuscu B. Light-responsive liquid crystal surface topographies for dynamic stimulation of cells. *ACS Appl Mater Interfaces*. 2025;17(19):27871-27881. doi: 10.1021/acsami.5c02526

258. Lungu CN, Gurau G, Mehedinti MC. Pro-angiogenic bioactive molecules in vascular morphogenesis: integrating endothelial cell dynamics. *Curr Issues Mol Biol*. 2025;47(10):851. doi: 10.3390/cimb47100851

259. Bril M, Saberi A, Jorba I, *et al*. Shape-morphing photoresponsive hydrogels reveal dynamic topographical conditioning of fibroblasts. *Adv Sci*. 2023;10(31):2303136. doi: 10.1002/advs.202303136

260. Li C, Iscen A, Palmer LC, Schatz GC, Stupp SI. Light-driven expansion of spiropyran hydrogels. *J Am Chem Soc*. 2020;142(18):8447-8453. doi: 10.1021/jacs.0c02201

261. Yue K, Trujillo-de Santiago G, Alvarez MM, Tamayol A, Annabi N, Khademhosseini A. Synthesis, properties, and biomedical applications of gelatin methacryloyl (GelMA) hydrogels. *Biomaterials*. 2015;73:254-271. doi: 10.1016/j.biomaterials.2015.08.045

262. Nowak BP, Niehues M, Ravoo BJ. Magneto-responsive hydrogels by self-assembly of low molecular weight peptides and crosslinking with iron oxide nanoparticles. *Soft Matter*. 2021;17(10):2857-2864. doi: 10.1039/D0SM02049D

263. Hu K, Yu T, Tang S, *et al*. Dual anisotropicity comprising 3D printed structures and magnetic nanoparticle assemblies: towards the promotion of mesenchymal stem cell osteogenic differentiation. *NPG Asia Mater*. 2021;13(1):19. doi: 10.1038/s41427-021-00288-x

264. Malektaj H, Drozdov AD, deClaville Christiansen J. Mechanical properties of alginate hydrogels cross-linked with multivalent cations. *Polymers.* 2023;15(14):3012. doi: 10.3390/polym15143012

265. Salari P, Easson GWD, Broz KS, Kelly MP, Tang SY. Effects of sustained tensile distraction on vertebrae and intervertebral disc growth: an in vivo study using a mouse tail model. *J Bone Joint Surg Am*. 2025;107(10):1107-1115. doi: 10.2106/JBJS.24.00224

266. Freeman FE, Kelly DJ. Tuning alginate bioink stiffness and composition for controlled growth factor delivery and to spatially direct MSC fate within bioprinted tissues. *Sci Rep*. 2017;7(1):17042. doi: 10.1038/s41598-017-17286-1

267. Meyers K, Lee BP, Rajachar RM. Electroactive polymeric composites to mimic the electromechanical properties of myocardium in cardiac tissue repair. *Gels*. 2021;7(2):53. doi: 10.3390/gels7020053

268. Roshanbinfar K, Schiffer M, Carls E, *et al*. Electrically conductive collagen-PEDOT:PSS hydrogel prevents post-infarct cardiac arrhythmia and supports hiPSC-cardiomyocyte function. *Adv Mater*. 2024;36(28):2403642. doi: 10.1002/adma.202403642

269. Jebran AF, Seidler T, Tiburcy M, *et al*. Engineered heart muscle allografts for heart repair in primates and humans. *Nature*. 2025;639(8054):503-511. doi: 10.1038/s41586-024-08463-0

270. Zhu J. Bioactive modification of poly(ethylene glycol) hydrogels for tissue engineering. *Biomaterials*. 2010;31(17):4639-4656. doi: 10.1016/j.biomaterials.2010.02.044

271. Patel DK, Jung E, Priya S, Won SY, Han SS. Recent advances in biopolymer-based hydrogels and their potential biomedical applications. *Carbohydr Polym*. 2024;323:121408. doi: 10.1016/j.carbpol.2023.121408

272. Sexton ZA, Rütsche D, Herrmann JE, *et al*. Rapid model-guided design of organ-scale synthetic vasculature for biomanufacturing. *Science*. 2025;388(6752):1198-1204. doi: 10.1126/science.adj6152

273. Chen Z, Wang Y, Chen H, *et al*. A magnetic multi-layer soft robot for on-demand targeted adhesion. *Nat Commun*. 2024;15(1):644. doi: 10.1038/s41467-024-44995-9

274. Pang X, Liang S, Wang T, *et al*. Engineering thermo-pH dual responsive hydrogel for enhanced tumor accumulation, penetration, and chemo-protein combination therapy. *Int J Nanomed*. 2020;15:4739-4752. doi: 10.2147/IJN.S253990

275. Kumar K, Nain A. Emerging 4D fabrication of tubular structures and clinical challenges: critical perspective. *ACS Mater Au*. 2025;5(6):886-895. doi: 10.1021/acsmaterialsau.5c00101

276. Huang G, Zhao Y, Chen D, *et al*. Applications, advancements, and challenges of 3D bioprinting in organ transplantation. *Biomater Sci*. 2024;12(6):1425-1448. doi: 10.1039/D3BM01934A

277. Osouli-Bostanabad K, Masalehdan T, Kapsa RM, *et al*. Traction of 3D and 4D printing in the healthcare industry: from drug delivery and analysis to regenerative medicine. *ACS Biomater Sci Eng*. 2022;8(7):2764-2797. doi: 10.1021/acsbiomaterials.2c00094

278. Ramesh S, Harrysson OLA, Rao PK, *et al*. Extrusion bioprinting: recent progress, challenges, and future opportunities. *Bioprinting*. 2021;21:e00116. doi: 10.1016/j.bprint.2020.e00116

279. Li MX, Wei QQ, Mo HL, *et al*. Challenges and advances in materials and fabrication technologies of small-diameter vascular grafts. *Biomater Res*. 2023;27(1):58. doi: 10.1186/s40824-023-00399-2

280. Sun J, Gong Y, Xu M, Chen H, Shao H, Zhou R. Coaxial 3D bioprinting process research and performance tests on vascular scaffolds. *Micromachines*. 2024;15(4):463. doi: 10.3390/mi15040463

281. Damiati LA, Alsudir SA, Mohammed RY, *et al*. 4D printing in skin tissue engineering: a revolutionary approach to enhance wound healing and combat infections. *Bioprinting*. 2025;45:e00386. doi: 10.1016/j.bprint.2025.e00386

282. Bonatti AF, Batoni E, Fortunato GM, Vitale-Brovarone C, Vozzi G, De Maria C. Robust design methodologies to engineer multimaterial and multiscale bioprinters. *Bioprinting*. 2024;44:e00372. doi: 10.1016/j.bprint.2024.e00372

283. Albrecht FB, Schmidt FF, Schmidt C, Börret R, Kluger PJ. Robot-based 6D bioprinting for soft tissue biomedical applications. *Eng Life Sci*. 2024;24(7):e2300226. doi: 10.1002/elsc.202300226

284. Pettersson ABV, Ballardini RM, Mimler M, *et al*. Core legal challenges for medical 3D printing in the EU. *Healthcare*. 2024;12(11):1114. doi: 10.3390/healthcare12111114

285. Gilbert F, O'Connell CD, Mladenovska T, Dodds S. Print me an organ? Ethical and regulatory issues emerging from 3D bioprinting in medicine. *Sci Eng Ethics*. 2018;24(1):73-91. doi: 10.1007/s11948-017-9874-6

286. Ricles LM, Coburn JC, Di Prima M, Oh SS. Regulating 3D-printed medical products. *Sci Transl Med*. 2018;10(461):eaan6521. doi: 10.1126/scitranslmed.aan6521

287. U.S. Food and Drug Administration. 21 CFR Part 1271—Human cells, tissues, and cellular and tissue-based products. Code of Federal Regulations; 2024. https://www.ecfr.gov/current/title-21/chapter-I/subchapter-L/part-1271

288. U.S. Food and Drug Administration. Classification of products as drugs and devices and additional product classification issues: Guidance for industry and FDA staff (Footnote 12); 2017
https://www.fda.gov/regulatory-information/search-fda-guidance-documents/classification-products-drugs-and-devices-and-additional-product-classification-issues

289. Vijayavenkataraman S, Lu WF, Fuh JYH. 3D bioprinting – an ethical, legal and social aspects (ELSA) framework. *Bioprinting*. 2016;1-2:11-21.
doi: 10.1016/j.bprint.2016.08.001

290. Melvin T. The European medical device regulation–what biomedical engineers need to know. *IEEE J Transl Eng Health Med*. 2022;10:1-5.
doi: 10.1109/JTEHM.2022.3194415

291. European Parliament & Council. Regulation (EC) No 1394/2007 on advanced therapy medicinal products, OJ L. 2007;324:121–137.
https://eur-lex.europa.eu/eli/reg/2007/1394/oj/eng

292. Dwenger A, Straßburger J, Schwerdtfeger W. Regulation (EC) No. 1394/2007 on advanced therapy medicinal products: incorporation into national law. *Bundesgesundheitsblatt Gesundheitsforschung Gesundheitsschutz*. 2010;53(1):14-19.
doi: 10.1007/s00103-009-0985-3

293. Kim M, Kim YJ, Kim YS, *et al*. One-year results of ear reconstruction with 3d printed implants. *Yonsei Med J*. 2024;65(8):456.
doi: 10.3349/ymj.2023.0444

294. World Health Organization. Considerations in developing a regulatory framework for human cells and tissues and for advanced therapy medicinal products (TRS 1048, Annex 3); 2023.
https://www.who.int/publications/m/item/considerations-in-developing-a-regulatory-framework-for-human-cells-and-tissues-and-for-advanced-therapy-medicinal-products

295. Human Tissue Act 2004, c. 30. (2004). UK Public General Acts.
https://www.legislation.gov.uk/ukpga/2004/30/contents

ACCSCIENCE PUBLISHING

International Journal of Bioprinting

RESEARCH ARTICLE

Converging *Pvt1* signaling and 3D bioprinting technology for next-generation biodegradable tracheal replacement constructs

Wei Zuo[1], Shao-Xiao Qiu[2], Jian Cui[1], Wen-Jian Liao[1], Jun-Tao Zou[1], Qing Jie Chen[3]*, and Fei Xu[2]*

[1]Department of Respiratory and Critical Care Medicine, the First Affiliated Hospital of Nanchang University, Nanchang, Jiangxi, China

[2]Department of Respiratory and Critical Care Medicine, Shenzhen Bao'an People's Hospital, Shenzhen, Guangdong, China

[3]Department of Nuclear Medicine, the First Affiliated Hospital of Nanchang University, Nanchang, Jiangxi, China

Abstract

Tracheal reconstruction remains a major clinical challenge due to persistent limitations in graft vascularization, epithelialization, and long-term mechanical compatibility. Conventional synthetic scaffolds and autologous grafts often fail to achieve durable integration, underscoring the need for innovative biofabrication strategies. In the present study, we elucidate the mechanoregulatory role of the long non-coding (lnc) RNA *Pvt1* in controlling endothelial cell proliferation and focal adhesion dynamics during tracheal regeneration. Patient-specific tracheal stents were fabricated using extrusion-based three-dimensional bioprinting with hierarchically optimized architectures that combined polycaprolactone (PCL) copolymers with endothelial progenitor cell (EPC)-recruiting motifs. Computational fluid dynamics-guided nozzle path planning and *in situ* piezoelectric characterization enabled sub-200 μm resolution in replicating native tracheal microtopography while maintaining 94% EPC viability after printing. *Pvt1*-enriched bioinks significantly enhanced vascularization, yielding a 2.3-fold increase in neovascularization compared with controls in rat tracheal defect models, alongside a 38% reduction in fibrotic markers. The constructs exhibited a dual-stage biodegradation profile (30% mass loss at eight weeks), providing mechanical compatibility with tissue ingrowth patterns as confirmed by micro-computed tomography-based strain mapping. Collectively, these findings demonstrate the convergence of lncRNA biology and precision bioprinting, delivering an off-the-shelf solution for complex tracheal reconstruction that addresses current barriers in graft epithelialization and immunomodulatory response. The study advances the translational potential of bioengineered airway substitutes through molecularly informed design principles.

Keywords: Biodegradable materials; Endothelial cells; Personalized treatment; *Pvt1*; Tracheal repair; Three-dimensional printing

***Corresponding authors:**
Qing Jie Chen
(17770879369@163.com)

Fei Xu
(drFeiXuuue@163.com)

Citation: Zuo W, Qiu SX, Cui J, *et al.* Converging *Pvt1* signaling and 3D bioprinting technology for next-generation biodegradable tracheal replacement constructs. *Int J Bioprint.* 2026;12(1):262-282. doi: 10.36922/IJB025160146

Received: April 14, 2025
1st revised: June 26, 2025
2nd revised: August 30, 2025
Accepted: August 9, 2025
Published Online: August 9, 2025

Copyright: © 2025 Author(s). This is an Open Access article distributed under the terms of the Creative Commons Attribution License, permitting distribution, and reproduction in any medium, provided the original work is properly cited.

Publisher's Note: AccScience Publishing remains neutral with regard to jurisdictional claims in published maps and institutional affiliations.

1. Introduction

Tracheal defects represent a life-threatening condition that can arise from surgical trauma, burns, and infections.[1] Clinical manifestations include breathing difficulties, sore throat, coughing, fever, and other severe manifestations.[2] Without timely intervention, tracheal defects pose a serious threat to patient survival and quality of life.[3] Current therapeutic strategies primarily involve tracheal reconstruction surgery or tracheal transplantation.[4] Tracheoplasty employs autologous cartilage or synthetic materials to repair tracheal defects,[5] whereas tracheal transplantation utilizes donor trachea to restore airway continuity.[6] Despite clinical utility, both approaches remain limited. Tracheal reconstruction may result in complications such as cartilage displacement and recurrent laryngeal nerve injury,[7] while transplantation is hindered by immune rejection and a lack of inherent regenerative capacity.[8] These shortcomings underscore the urgent need for more effective and durable treatment strategies.[9]

This study aims to investigate a biotechnology-based therapeutic approach for tracheal defects.[10] Stem cell technology was employed to cultivate tracheal replacement stents with optimized material properties, enhancing biocompatibility and regenerative potential.[11] Additionally, gene editing technology was used to enhance the self-healing ability of tracheal replacement stents and improve their therapeutic efficacy.[12] Such advances hold considerable significance, as the development of an effective biological treatment is expected to transform tracheal defect management by providing safer, more effective, and sustainable options for patients.[13–15]

In recent years, the application of degradable materials in tracheal replacement stents has garnered substantial attention, particularly with the integration of three-dimensional (3D) printing technology into tracheal defect repair.[16,17] Presently, degradable materials mainly encompass polylactic acid, polyhydroxybutyrate, and polycaprolactone (PCL), all degrade *in vivo* without causing adverse effects.[18] Furthermore, 3D printing technology enables precise fabrication of tracheal replacement stents with optimal shape, size, structure, and physical attributes, offering a short production cycle and significant production advantages.[19] Based on these advances, researchers have focused on designing and fabricating biodegradable tracheal replacement stents.[17] Collectively, biodegradable stents represent a promising repair strategy for tracheal defects,[20] and the emergence of 3D printing technology provides a powerful platform for their rational design and scalable production.[21]

Pvt1, a long non-coding RNA located on human chromosome 8q24,[22] spans approximately 1.4 Mb and constitutes a large transcriptional unit comprising 18 exons and 17 introns, with an average exon length of 96 kb.[23] *Pvt1* shows elevated expression across multiple tissues, with particularly high levels in tumor cells.[24] It is also expressed in normal human cells, where its transcription is regulated by diverse signaling pathways, implicating it in a broad range of physiological and pathological processes.[25] Evidence indicates that *Pvt1* exerts critical regulatory functions in cell proliferation, metabolism, and apoptosis.[26] In tumor cells, its overexpression promotes proliferation, invasion, and metastasis.[27] *Pvt1* also plays multifaceted roles in other diseases, such as insulin secretion regulation in diabetes and endothelial function modulation in cardiovascular diseases.[28] Notably, *Pvt1* aggravates airway inflammation and epithelial barrier dysfunction in asthma by regulating miR-149.[29] In addition, *Pvt1* is also involved in interleukin (IL)-1β-induced chondrocyte injury.[30] Given its central roles in diverse disease contexts and its consistently high expression in tumor cells, *Pvt1* is strongly implicated as a key regulator in tracheal defect repair.[26] In the context of tracheal defect repair, *Pvt1* is likely to influence cell proliferation, apoptosis, and differentiation, thereby facilitating the growth and regeneration of tracheal tissue.[26]

In summary, the present study investigates the regulatory role of *Pvt1* in endothelial cell proliferation and adhesion on the luminal surface of a 3D-printed biodegradable tracheal replacement stent. It aims to discern *Pvt1*'s involvement in the tracheal defect repair mechanism mediated by the tracheal replacement stent and explore its scientific and clinical significance. This study offers novel insights and directions for tracheal defect treatment by elucidating the role of endothelial cells. The anticipated findings may drive continued advances in treatment strategies and technological refinement, ultimately improving patient recovery and long-term outcomes.

2. Materials and methods

2.1. Experimental animals

Ten-week-old male F344 rats (n = 112) were purchased from Beijing Vital River Laboratory Animal Technology Co., Ltd. (Beijing, China). All animal experiments were reviewed and approved by the Ethics Committee of the First Affiliated Hospital of Nanchang University. Experimental procedures were conducted strictly in accordance with the Experimental Animal Ethics Committee guidelines, ensuring adherence to principles of animal protection, welfare, and ethics. All protocols complied with national regulations on laboratory animal welfare and ethical use in China.

2.2. Design and three-dimensional printing of polycaprolactone tracheal replacement stent

Polycaprolactone, a widely used biodegradable material, was utilized for the 3D printing of tracheal replacement stents. The stent design was modeled after the native trachea of 10-week-old F344 rats. Printing was performed using the Biomaker system (Beijing Shangpu Bio, China). The printing parameters were as follows: nozzle temperature, 21°C; platform temperature, ambient; printing speed, 5 mm^3/s; initial layer speed, 5 mm^3/s; idle speed, 20 mm^3/s; extrusion speed, 1 mm^3/s; and layer height, 0.2 mm. Continuous blue light illumination was applied throughout the printing process. Immediately after fabrication, the stents were immersed in 2% calcium chloride solution for ionic cross-linking, followed by three washes with phosphate-buffered saline (PBS). To assess the material properties of PCL before and after printing, Fourier-transform infrared spectroscopy (Thermo Fisher, USA) and differential scanning calorimetry (DSC-500T, Shanghai INESA, China) were performed.[31]

The degradation behavior and surface morphology of PCL scaffolds were analyzed at defined time points. Chondrocytes were harvested and resuspended in Dulbecco's Modified Eagle Medium (DMEM; Gibco, USA) supplemented with 10% fetal bovine serum (FBS; Hyclone, USA) at a final concentration of 5.0×10^7 cells/mL. Prior to cell seeding, scaffolds were pre-wetted by immersion in culture medium. Each scaffold was incubated with 2 mL of cell suspension in a 15 mL centrifuge tube under 5% carbon dioxide at 37°C for 30 min, with gentle inversion every 10 min to ensure uniform cell attachment across scaffold surfaces. Scaffolds were then transferred into a six-well culture plate (Becton Dickinson, USA), and 7.5 mL of DMEM containing 10% FBS, 50 μg/mL vitamin C (Sigma-Aldrich, USA), 100 U/mL penicillin, 100 mg/mL streptomycin, and 0.1 mM non-essential amino acids (Invitrogen, USA) was added. After 3 days of static culture, constructs were placed on a shaker at 100 rpm under 5% carbon dioxide at 37°C and cultured for 2–4 weeks. At each time point, scaffolds were vacuum freeze-dried, sputter-coated with gold, and analyzed using scanning electron microscopy (SEM; Quanta 250, FEI, USA).[32]

2.3. Three-point bending test

The mechanical properties of three tracheal replacement stents were evaluated using electronic universal testing machines (INSTRON 3345 and INSTRON 5584; Instron, USA) equipped with Bluehill 3 software. For the three-point bending test, each rectangular or circular cross-sectional specimen was positioned on a bending fixture, the span was adjusted, and the sample was loaded until either the specified bending displacement was reached or the specimen fractured. For rectangular samples, height and width were measured at both ends and at the midpoint of the span. The mean values of the three measurements for width and height were used for analysis. The testing software recorded displacement/load curves, compressive strength,[33] force distribution, and rotation angle.[34]

2.4. Radial compression force measurement

Radial compression tests were performed on three tracheal replacement stents using the HY-940FS computerized tensile and compression testing machine (Shanghai Hengyu, China). The compression rate was set at 2 mm/min, and the radial compression force and percentage of deformation were continuously recorded. Radial compression force–deformation curves were generated for each specimen. All tests were conducted under controlled environmental conditions (temperature 20 ± 1 °C, relative humidity 65 ± 2%).

2.5. Construction of an artificial trachea using *in vitro* cell-alginate hydrogel-polycaprolactone stent structure

The PCL tracheal replacement stent was designed with a longitudinal length of 10 mm and a diameter of 5 mm, corresponding to the average tracheal size of 10-week-old F344 rats. Each stent consisted of five layers. The innermost and outermost layers were constructed from porous PCL mesh to facilitate cell adhesion, proliferation, and neovascularization, whereas the central PCL layer formed a non-porous cylindrical structure to provide mechanical reinforcement. Alginate hydrogel layers were interposed between the PCL layers to spatially separate endothelial and chondrocyte populations. Endothelial cells were isolated from rat pulmonary arteries using a trypsin-collagenase digestion method combined with differential adhesion and cultured in an endothelial cell medium (A0020, Shanghai Yuchun Biotech, China). Chondrocytes were isolated from rat cartilage using type II collagenase digestion and cultured in chondrocyte medium (4651, Shanghai Zhongqiao Xinzhou Biotech, China). Syngeneic cells were used to minimize immune rejection and ensure optimal biocompatibility. Cell morphology was observed daily, and the artificial trachea was imaged using SEM.

2.6. Cell distribution in the three-dimensional-printed artificial trachea

Cell distribution in agarose gels containing alginates was identified using CellTracker™ fluorescent probes (C2925, C2927, Thermo Fisher Scientific Inc., USA). The fluorescent dye was dissolved in DMSO at a final concentration of 10 mM, and serum-free medium was added before heating the solution to 37 °C. Endothelial cells were resuspended in the pre-warmed red dye solution, while chondrocytes

were resuspended in the green dye solution. Both cell suspensions were incubated at 37 °C in a carbon dioxide incubator for 30 min. Following incubation, the cells were centrifuged, the supernatant was removed, and the cell pellets were collected for 3D bioprinting as previously described.[35] Finally, the cells in the artificial trachea were observed under the BX50 optical microscope (Olympus Corporation, Japan) using appropriate optical filters based on the dye color.

2.7. Live/dead assay

Artificial tracheal constructs were cultured in DMEM (PM150210, Wuhan Nuosi Life Science Technology Co., Ltd., China) enriched with 10% FBS, 1% penicillin-streptomycin, 10 μg/mL amphotericin B, and 50 μg/mL gentamicin. Cell viability was assessed on Days 1, 3, 7, and 14 using the Live/Dead Cytotoxicity Kit (L3224; Thermo Fisher Scientific, USA). Staining was performed at 37°C for an hour with Calcium Green-1 AM (1:500) and tetramethylrhodamine ethyl ester (TMRE; 1:100). Images were acquired using confocal laser scanning microscopy (FV3000, Olympus, Japan). For quantitative analysis, the number of live and dead cells in each image was determined using ImageJ software (version 1.53k, NIH, USA). The percentage of viable cells was calculated as the ratio of live cell nuclei (green fluorescence) to the total number of nuclei per image field.

2.8. Construction of rat models with tracheal defects and artificial trachea transplantation

A rat tracheal resection model was established to evaluate the *in vivo* transplantation efficacy of the artificial trachea. Forty-eight rats with normal respiration were randomly assigned into the following four groups ($n = 12$ per group): control group (artificial tracheal implantation without epithelial cell coverage), experimental group (artificial tracheal implantation with epithelial cell coverage), short hairpin (sh)-negative control (NC) group (artificial tracheal implantation with sh-NC-transfected epithelial cells), and sh-*Pvt1* group (artificial tracheal implantation with sh-*Pvt1*-transfected epithelial cells).

Rats were anesthetized and placed in the prone position. A longitudinal midline incision was made along the ventral neck, followed by exposure and incision of the anterior tracheal wall to create the defect. The artificial trachea corresponding to each group was implanted into the defect, and proximal and distal ends of the native trachea were anastomosed using absorbable polydioxanone II sutures (Johnson & Johnson, USA). The surgical site was closed in layers, and rats were allowed to recover spontaneous breathing postoperatively.[32,36,37]

Postoperative tracheal diameter was monitored monthly using X-ray imaging (VXR-9 M, DRGEM, South Korea). Before sacrifice, tracheal morphology was assessed using computed tomography (Brivo 385, GE Healthcare, South Korea) and endoluminal evaluation with a bronchoscope (CV 260 S, Olympus, Japan). Vascular remodeling at the proximal and distal ends of the stent was examined using a Volcano intravascular ultrasound system (s5 Imaging System, Philips Volcano, USA). Measurements were obtained at 1 mm intervals within a 5 mm range, and plaque composition between the stent inner edge and lumen outer boundary was quantified with a virtual histology software (IVUSLab version 3.2, Philips Volcano, USA). Fibrous tissue was classified as green, fibro-fatty tissue as yellow-green, calcified components as white, and necrotic tissue as red. Incomplete stent expansion was defined as a minimum area of <5 mm^2.

2.9. Histopathological examination

To assess tracheal lumen narrowing and epithelialization, the trachea, including adjacent native segments, was dissected from surrounding tissue in rats. Each tracheal ring was sectioned, and the native trachea served as a normal control for gross and histological comparisons.

Samples were fixed in 10% phosphate-buffered formalin, embedded in paraffin, and dried at 65°C for 3 h. After routine deparaffinization and dehydration, tissues were treated sequentially with 10% trichloroacetic acid and 10% potassium dichromate for 40 min each, followed by rinsing in tap water. Sections were then stained with hematoxylin (PT001; Shanghai Bogu Biotechnology Co., Ltd., China) for 8 min and rinsed again. Counterstaining was performed using a mixture of 1% rhodamine B (R21983; Shangbao Biotechnology, China) and 1% eosin (R23166; Shangbao Biotechnology, China) for 40 min. The reaction was terminated with a solution containing 1% acetic acid and 1% ammonium molybdate. Subsequently, a mixture of 1% bright green dye and 1% phosphoric acid was applied to terminate residual staining. Sections were dehydrated through graded ethanol, cleared with xylene, and mounted with neutral resin. Histological changes were observed under an optical microscope (BX50; Olympus Corporation, Japan).[36]

2.10. Immunohistochemical analysis

Formalin-fixed, paraffin-embedded sections were prepared from rat tracheal tissue, including adjacent native segments. Antigen retrieval was performed in 10 mM sodium citrate buffer (pH 6.0) at 95°C for 20 min to expose target proteins. After cooling, sections were blocked with 3% bovine serum albumin (10×; diluted in PBS; Thermo Fisher, USA) for 30 min at room temperature, followed by overnight incubation at 4°C with primary antibodies:

rabbit anti-CD34 (1 μg/mL, Catalog No. PA5-78978, Thermo Fisher, USA) or anti-CD326 (EpCAM; 10 μg/mL, 14-9326-82, Thermo Fisher, USA). After washing with Triton X-100 Surfact-Amps detergent solution (Thermo Fisher, USA), endogenous peroxidase activity was blocked with a peroxidase inhibitor (Thermo Fisher, USA) for 30 min at room temperature. Detection was performed using biotinylated goat anti-rabbit IgG (H+L) horseradish peroxidase secondary antibody (1:500; Biotinylated goat anti-rabbit IgG (H+L), HRP, Catalog No. 65-6140 Invitrogen, USA), followed by streptavidin–biotin complex and colorimetric visualization with 3,3-diaminobenzidine substrate (Thermo Scientific Metal Enhanced DAB Kit; Thermo Fisher, USA). Slides were counterstained with hematoxylin, dehydrated, and mounted for analysis. Imaging was performed under a 40× optical microscope (BX50, Olympus, Japan).[38]

2.11. Masson staining analysis

Paraffin-embedded sections were dewaxed, rehydrated, and rinsed with distilled water. Nuclei were stained with Weigert's hematoxylin for 5–10 min, followed by rinsing. Sections were then stained with Masson's Ponceau acid red solution for 5–10 min, briefly immersed in 2% glacial acetic acid, and differentiated in 1% phosphomolybdic acid solution for 3–5 min. Without rinsing, the sections were stained with aniline blue for 5 min and immersed in 0.2% glacial acetic acid for 1 min. Finally, sections were dehydrated with absolute ethanol, cleared in xylene, and mounted with neutral resin for histological analysis.

2.12. Immunofluorescence analysis

Tracheal sections were cut transversely at a 7–14 μm thickness and mounted on chrome-alum gelatin-coated glass slides for drying. After washing with PBS, the slides were incubated at room temperature with 1% normal serum in PBS containing 0.5% Triton X-100 (pH 7.4) for 30 min. Endothelial cells were labeled with CD202b (TIE2) antibody (1:200; #PA5-116042, Thermo Fisher, USA), and epithelial cells were labeled with 5-hydroxytryptamine rabbit polyclonal antibody (1:10,000; AB_572263, ABClonal, USA) at 37°C for 1 h. Secondary antibodies included mouse anti-β-tubulin and goat anti-rabbit IgG conjugated to Alexa Fluor 594 (red, 1:200; A-11012, Invitrogen, USA) and Alexa Fluor 488 (green, 1:200; A-11008, Invitrogen, USA). Sections were counterstained with 4',6-diamidino-2-phenylindole (blue; No. D1306, Thermo Fisher Scientific, USA) at 37°C for an hour and imaged under a fluorescence microscope (BX53, Olympus, Japan).

2.13. RNA extraction and sequencing

Three rats were randomly selected from the control group and the experimental group, respectively, for the study. Tracheal tissues from the tracheal transplantation site were collected, and total RNA was extracted using Trizol reagent (Invitrogen, USA). Sample concentration and purity were measured using a Nanodrop 2000 spectrophotometer (Nanodrop, USA). Only samples with RNA integrity number ≥7.0 and 28S:18S ratio ≥1.5 were used for sequencing. Library construction and sequencing were performed by CapitalBio Technology (China). A total of 5 μg RNA per sample was processed, and ribosomal RNA was depleted using the Ribo-Zero™ Magnetic Kit (Epicentre Technologies, USA). Library preparation was performed using the NEB Next Ultra RNA Library Prep Kit (NEB, USA). RNA was fragmented into ~300 bp in the NEB Next First Strand Synthesis Reaction Buffer (5×). First-strand complementary DNA (cDNA) was synthesized using reverse transcriptase and random primers, followed by second-strand cDNA synthesis with dUTP-containing buffer (10×). Ends of cDNA fragments were repaired, poly(A) tails were added, and Illumina sequencing adapters were ligated. USER Enzyme (NEB, USA) was used to digest the second strand of cDNA, generating strand-specific libraries. The DNA libraries were amplified, purified, and enriched by polymerase chain reaction (PCR). Library quality was assessed using Agilent 2100 Bioanalyzer (Agilent Technologies, USA), and concentration was determined using the KAPA Library Quantification Kit (KAPA Biosystems, USA). Paired-end sequencing was performed on the Illumina NextSeq CN500 system (Illumina, USA).

2.14. Quality control of sequencing data and alignment to the reference genome

Raw paired-end reads were evaluated using FastQC v0.11.8 (www.bioinformatics.babraham.ac.uk). Illumina sequencing adapters and poly(A) tails were removed with Cutadapt v1.18. Reads containing more than 5% ambiguous bases (N) were excluded using Perl scripts, and those with ≥70% of bases having a quality score >20 were retained using FASTX Toolkit v0.0.13 (http://hannonlab.cshl.edu/fastx_toolkit/). Sequence correction was performed using BBMap (https://sourceforge.net/projects/bbmap/). High-quality reads were then aligned to the rat reference genome using HISAT2 v0.7.12.

2.15. Bioinformatics analysis

Differential gene expression analysis of transcriptome sequencing data was performed using the limma package in R (version 4.2.2). False discovery rate correction was applied to *p*-values, and significantly differentially expressed genes were defined by the thresholds $|\log_2(\text{fold change})| > 1$ and false discovery rate <0.05. The proteins encoded by the top 50 differentially expressed genes were imported into the STRING database (https://cn.string-db.org/) to construct a protein–protein interaction (PPI) network. Key

genes were identified by ranking adjacent nodes within the network. In addition, the distribution of CpG islands within the *Dlk1* promoter region was predicted using the MethPrimer online tool (http://www.urogene.org/cgi-bin/methprimer/methprimer.cgi).

2.16. Lentiviral vector construction and cell grouping

The interference vector pSIH1-H1-copGFP (SI501A-1, System Biosciences, USA) was used to construct lentivirus-based silencing vectors targeting *Pvt1* and *Dlk1*. Lentiviral particles were packaged in HEK-293T cells using a lentivirus packaging kit (Invitrogen, USA). Viral supernatants were collected 48 h after transfection, and the viral titer was determined to be 1×10^8 TU/mL.

The sh-NC sequence was CTGACTGG GATCAATCGAACT, the sh-*Pvt1*-1 sequence was CAAGAAGATGTGGAGAGAGTT, the sh-*Pvt1*-2 sequence was CAAAGGCTGTCCACAAGAAGA, the sh-*Dlk1*-1 sequence was GACGGGAAATTCT GCGAAATA, and the sh-*Dlk1*-2 sequence was CCATCGTCTTTCTCAACAAGT.

Rat endothelial cells were divided into four groups according to the experimental design: sh-NC, sh-*Pvt1*+sh-NC, sh-*Pvt1*+sh-*Dlk1*, and sh-*Pvt1*. Each group was infected with 1 mL of the corresponding lentivirus, and transduction efficiency was assessed 48 h after infection.

2.17. Cell counting Kit-8 assay

Cell proliferation was assessed using a cell counting Kit-8 (CCK-8) assay (Beijing Solarbio Science & Technology Co., Ltd., China). Endothelial cells in the logarithmic growth phase were seeded into 96-well plates at a density of 1×10^4 cells/well and pre-cultured for 24 h. Cells were then transfected according to experimental groupings. At 0, 24, 48, and 72 h post-transfection, 10 μL of CCK-8 reagent was added to each well, followed by incubation at 37 °C for 3 h. Absorbance was measured at 450 nm using a microplate reader (Synergy H1, BioTek, USA), with values reflecting cell proliferation. Growth curves were plotted based on absorbance data. Each experiment was repeated three times.

2.18. Flow cytometry

Endothelial cells were harvested 48 h after transfection for apoptosis analysis. Cells were digested with 0.25% trypsin (Shanghai Yubo Biotechnology Co., Ltd., China), centrifuged, and washed three times with cold PBS. Apoptosis was evaluated using the annexin-V-fluorescein isothiocyanate (FITC) apoptosis detection kit (Biovision, USA). The annexin-V-FITC/propidium iodide staining solution was prepared at a ratio of 1:2:50 (Annexin-V-FITC: propidium iodide: HEPES buffer). A total of 1×10^6 cells were resuspended in 100 μL staining buffer, gently vortexed, and incubated at room temperature for 15 min, followed by the addition of 1 mL HEPES buffer (Wuhan Promega Life Sciences Co., Ltd., China). FITC and propidium iodide fluorescence were excited at 488 nm, and emission was detected using 525 and 620 nm bandpass filters, respectively. Each experiment was repeated three times.

2.19. Quantitative real-time polymerase chain reaction

Total RNA was extracted from rat endothelial cells using TRIzol (ThermoFisher, USA), and the concentration and purity were measured using a NanoDrop2000 spectrophotometer (ThermoFisher, USA). cDNA was synthesized from RNA using the PrimeScript RT reagent kit (Takara, Japan). Gene-specific primers were synthesized by Takara (**Table S1, Supporting Information**). Quantitative real-time PCR was performed using the 7500 Fast Real-Time PCR System (Thermo Fisher Scientific, USA). The thermal cycling conditions were as follows: initial denaturation at 95°C for 10 min, followed by 40 cycles of denaturation at 95°C for 10 s, annealing at 60°C for 20 s, and extension at 72°C for 34 s. *Gapdh* served as an internal reference gene. Relative gene expression levels were calculated using the $2^{-\Delta\Delta Ct}$ method. Each experiment was independently repeated three times.

2.20. Western blot

Total proteins were extracted from cells using radioimmunoprecipitation assay buffer (Beyotime, China). Cells were incubated on ice for 30 min, followed by centrifugation at 8000 × *g* for 10 min at 4°C, and the supernatant was collected. The total protein concentration was determined using a bicinchoninic acid assay kit (ThermoFisher, USA). A total of 50 μg of protein was mixed with 2× sodium dodecyl sulfate sample buffer, heated at 100°C for 5 min, and subjected to sodium dodecyl sulfate–polyacrylamide gel electrophoresis. The separated proteins were transferred onto a polyvinylidene fluoride membrane and blocked with 5% skimmed milk at room temperature for an hour. The membrane was then incubated overnight at 4°C with primary antibodies diluted in buffer: rabbit anti-cyclin-dependent kinase 2 (1:1500; ab32147, Abcam, United Kingdom), anti-proliferating cell nuclear antigen (1:2500; ab92552, Abcam), anti-B-cell lymphoma 2 (1:2000; ab182858, Abcam), anti-Bcl-2-associated protein X (1:1000; ab32503, Abcam), and anti-glyceraldehyde-3-phosphate dehydrogenase (1:10,000; ab181602, Abcam) as an internal reference. After incubation, the membrane was washed thrice using Tris-buffered saline with Tween 20 (10 min each). Subsequently, the membrane was incubated for an hour with horseradish peroxidase-

conjugated goat anti-rabbit IgG H&L secondary antibody (1:2000; ab97051, Abcam) and additional Tris-buffered saline with Tween 20 washes. Equal volumes of solution A and solution B from the enhanced chemiluminescence kit (ABclonal Technology Co., LTD, China) were mixed in the dark and applied to the membrane. Protein bands were visualized using the Bio-Rad image analysis system (Bio-Rad, USA), and band intensities were quantified with Quantity One software (v4.6.2). The relative expression levels of target proteins were normalized to the intensity of the glyceraldehyde-3-phosphate dehydrogenase band. Each experiment was repeated three times, and the average value was calculated.

2.21. Enzyme-linked immunosorbent assay

Cell culture supernatants were collected, and the concentrations of adhesion factors intercellular adhesion molecule 1 (ICAM-1) and vascular cell adhesion protein 1 (VCAM-1) were determined by enzyme-linked immunosorbent assay (ELISA). The ELISA kit for ICAM-1 was purchased from Abcam (United Kingdom), and the kit for VCAM-1 was obtained from Shanghai Jialai Biotech Co., Ltd. (China).

2.22. Methylation-specific polymerase chain reaction

The enrichment of DNA methyltransferases (DNMT1, DNMT3a, and DNMT3b) at the *Dlk1* gene promoter region was examined using a chromatin immunoprecipitation (ChIP) assay kit (Sino Biological Inc., China). When cell confluence reached 70–80%, 1% formaldehyde was added to cross-link proteins and DNA at room temperature for 10 min. DNA was fragmented by sonication (10 s on/10 s off, 15 cycles), followed by centrifugation at 13,000 rpm at 4°C. The supernatant was divided into three tubes and incubated overnight at 4°C with different antibodies: RNA polymerase II rabbit polyclonal antibody (positive control, 1:100; ab238146; Abcam, United Kingdom); rabbit IgG (negative control, 1:100; ab172730; Abcam, United Kingdom); rabbit anti-DNMT1 (1:100; NBP3-15856, Novus Biological, USA); rabbit anti-DNMT3a (1:100; NB100-265, Novus Biological, USA); and rabbit anti-DNMT3b (1:100; NB300-516, Novus Biological, USA). Protein–DNA complexes were precipitated with protein agarose/sepharose beads, centrifuged, and washed to remove nonspecific binding. Cross-links were reversed overnight at 65 °C, and DNA fragments were purified using phenol-chloroform extraction. The promoter region of *Dlk1* was amplified by quantitative PCR using the following primers: forward 5'-AACTCCACAATGGCAAGGCT-3' and reverse 5'-AACGCACACCACGAAGATGT-3'. Methylation-specific primer sequences are provided in **Table S2, Supporting Information**.

2.23. Chromatin immunoprecipitation assay

A ChIP assay was performed using the ChIP kit (Sino Biological Inc., China) to assess the enrichment of DNA methyltransferases (DNMT1, DNMT3a, DNMT3b) in the *Dlk1* gene promoter region. Cells at 70–80% confluence were cross-linked with 1% formaldehyde at room temperature for 10 min. DNA was then fragmented by sonication into appropriate sizes (10-s bursts with 10-s pauses, 15 cycles). The lysates were centrifuged, and the supernatants were divided into three tubes at 4 °C. Each tube was incubated overnight with either a positive control antibody (RNA polymerase II rabbit polyclonal antibody [1:100; ab238146, Abcam, United Kingdom]), a negative control antibody (rabbit IgG [1:100; ab172730, Abcam, United Kingdom]), or antibodies against DNMT1 (1:100; NBP3-15856, Novus Biological, USA), DNMT3a (1:100; NB100-265, Novus Biological, USA), and DNMT3b (1:100; NB300-516, Novus Biological, USA). Immune complexes were precipitated using protein agarose/sepharose beads, centrifuged, and washed to remove nonspecific binding. Cross-links were reversed by overnight incubation at 65°C, followed by phenol-chloroform extraction and DNA purification. Enrichment of the *Dlk1* promoter region was quantified using quantitative PCR with the following primers: forward 5'-AACTCCACAATGGCAAGGCT-3' and reverse 5'-AACGCACACCACGAAGATGT-3'.

2.24. RNA immunoprecipitation assay

The interaction between *Pvt1* and DNMT1, DNMT3a, and DNMT3b proteins was detected using the RNA immunoprecipitation (RIP) Kit (Sai Cheng Biotechnology Co., Ltd., China). Cells were washed with pre-cooled PBS, lysed on ice with radioimmunoprecipitation assay buffer (Beyotime, China), and centrifuged at 12,000 × g for 10 min at 4°C. The supernatant was collected for immunoprecipitation.

Magnetic beads (50 μL) were washed with 100 μL RIP wash buffer, conjugated with 5 μg antibody, and incubated to allow binding. After resuspension in 900 μL RIP wash buffer, 100 μL of cell extract was added and incubated overnight at 4°C. The bead–antibody–protein–RNA complexes were isolated with a magnetic stand, digested with proteinase K, and the RNA was extracted for PCR detection. Antibodies used included rabbit anti-DNMT1 (1:100; NBP3-15856, Novus Biological, USA), rabbit anti-DNMT3a (1:100; NB100-265, Novus Biological, USA), and rabbit anti-DNMT3b (1:100; NB300-516, Novus Biological, USA). Rabbit anti-IgG (1:100; ab172730, Abcam, United Kingdom) was used as the negative control.

2.25. Statistical analysis

All statistical analyses were conducted using the Statistical Package for Social Sciences software version 21.0 (IBM,

USA). Data are presented as mean ± standard deviation (SD). Comparisons between two normally distributed groups were performed using an unpaired Student's *t*-test. Multiple group comparisons were analyzed by one-way analysis of variance, followed by Tukey's post hoc test. A p-value < 0.05 was considered statistically significant.

3. Results

3.1. Three-dimensionally printed biodegradable polycaprolactone tracheal stents

Polycaprolactone is a synthetic biodegradable polymer with potential applications in tissue engineering and is compatible with 3D bioprinting without requiring toxic solvents.[39] In this study, we constructed a 3D-printed tracheal replacement stent using PCL material (Figure 1A). The scaffold was designed with a longitudinal length of 10 mm and a diameter of 5 mm, dimensions based on the average native tracheal size of 10-week-old F344 rats. The construct consisted of five layers, with the innermost and outermost layers formed by porous PCL mesh to enhance cell adhesion, proliferation, and neovascularization. Additionally, a schematic of the three-layer PCL-constructed 3D-printed trachea is shown in **Figure 1B**. To determine the stability of the PCL chemical structure during the 3D printing process of the tracheal replacement stent, we conducted a Fourier-transform infrared spectroscopy analysis. The absorption spectra of raw PCL, 3D-printed scaffolds, and sterilized scaffolds displayed no detectable differences (**Figure 1C**), indicating that neither 3D printing nor sterilization altered the chemical structure of PCL. Thermal performance was further evaluated by differential scanning calorimetry. All three groups demonstrated endothermic peaks at approximately 60°C, consistent with the melting point of PCL (Figure 1D). During the 3D printing process of PCL, the chamber and nozzle were maintained at 90 and 110 °C, respectively. No significant thermal decomposition phenomenon was observed within this temperature range among the three groups. The crystal structure of PCL remained unchanged before and after the 3D printing and sterilization processes. These findings confirm that the adopted 3D printing method reliably preserves the chemical and thermal stability of PCL.

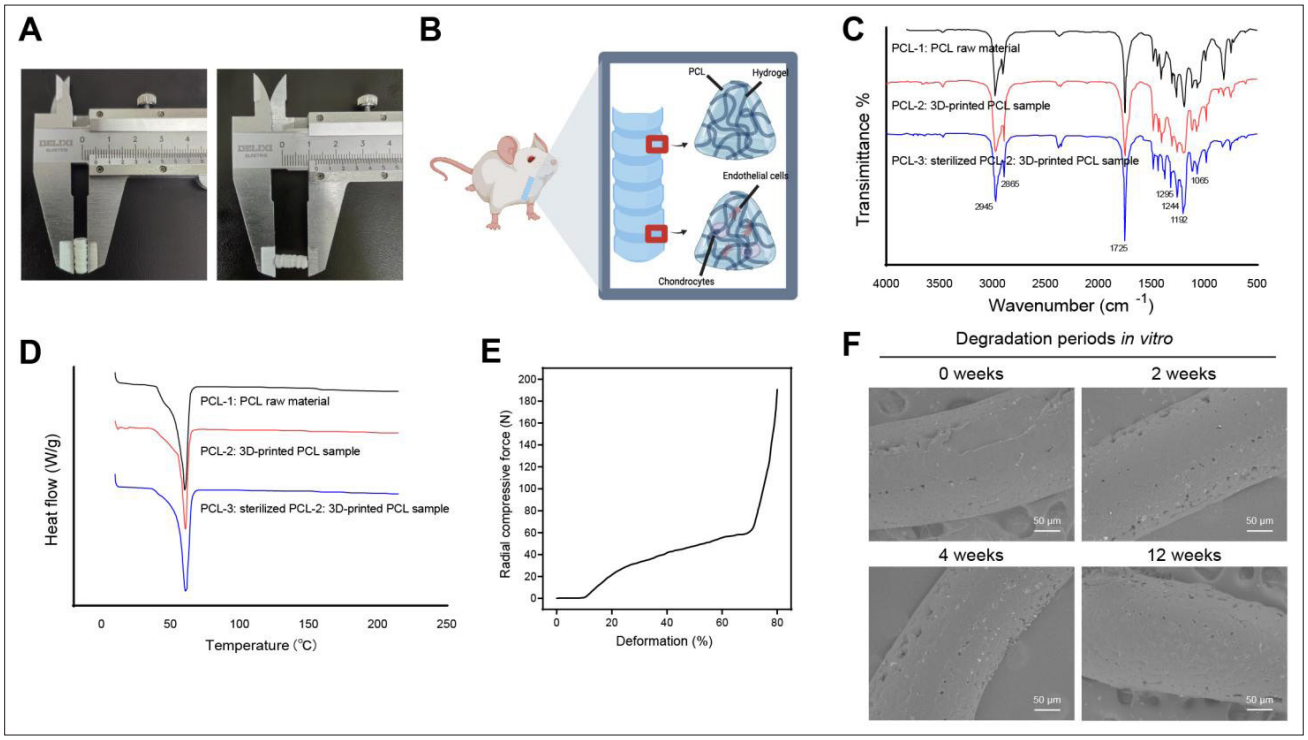


Figure 1. Constructing a degradable PCL tracheal replacement stent using 3D printing. (A) Overview of an artificial tracheal replacement stent fabricated by a 3D bioprinter. (B) Schematic of the three-layer structure of the PCL-constructed 3D-printed trachea. (C) Representative FT-IR spectra of PCL raw materials, 3D-printed PCL samples, and sterilized 3D-printed PCL samples. (D) Differential scanning calorimetry analysis of PCL raw materials, 3D-printed PCL samples, and sterilized 3D-printed PCL samples. (E) Representative radial compression force–deformation curve of the tracheal replacement stent. (F) Scanning electron microscopy observation of PCL tracheal replacement stent after *in vitro* degradation for 2, 4, and 12 weeks. Scale bar: 50 μm; magnification: XX×. All experiments were performed in triplicate. Abbreviations: 3D, three-dimensional; FT-IR, Fourier-transform infrared spectroscopy; PCL, polycaprolactone.

Mechanical properties were evaluated through radial compressive force–deformation testing. Deformation of 10–20% occurred under a compressive force of 20 N, while 70% deformation was observed under 60 N (Figure 1E). The compressive forces corresponding to 10%, 40%, and 70% deformation were 14.52 ± 9.95, 43.20 ± 10.17, and 58.55 ± 11.60 N, respectively. These results demonstrate that the 3D-printed scaffold provides sufficient radial support for *in vivo* transplantation. The three-point bending test confirmed that the scaffold maintained substantial compressive strength (Table S3, Supporting Information).

Scanning electron microscopy (Figure 1F) revealed that the surface morphology of PCL scaffolds remained largely unchanged after *in vitro* degradation for 2, 4, and 12 weeks (Figure 1F). Weight loss analysis showed gradual degradation, with values of 1.1 ± 0.1% at 2 weeks, 2.5 ± 0.2% at 4 weeks, and 5.5 ± 0.2% at 12 weeks. These results indicate that the scaffold degrades slowly while maintaining luminal patency during the early postoperative period.

In summary, a 3D-printed degradable PCL tracheal replacement stent with stable structure, favorable mechanical strength, and controlled degradation was successfully fabricated, establishing a solid foundation for tracheal transplantation.

3.2. Construction of an *in vitro* cell-alginate gel-polycaprolactone tracheal stent

Alginate is a biocompatible and biodegradable material widely applied in tracheal regeneration.[40] In this study, alginate hydrogel was selected as the supporting matrix for cell printing, and both endothelial cells and chondrocytes were incorporated into the scaffold.

Endothelial cells and chondrocytes were successfully isolated from rat tissues (Figure 2A and B). The PCL tracheal replacement stent was designed based on the average tracheal size of 10-week-old F344 rats, with a length of 10 mm, a diameter of 5 mm, and a five-layer structure (Figure 2C). The innermost and outermost PCL layers were fabricated as porous mesh to promote cell adhesion, proliferation, and neovascularization, while the middle layer was a non-porous cylinder providing mechanical strength and separating endothelial cells from chondrocytes. Between each PCL layer, alginate hydrogel was used to embed distinct cell populations (Figure 2D). CellTracker™ staining demonstrated that endothelial cells (red) localized to the inner layer and chondrocytes (green) to the outer layer, with uniform cell distribution throughout the alginate hydrogel (Figure 2E). Cell viability assessed by Live/Dead assay confirmed robust survival: approximately 70% of cells remained viable on Day 1, and viability exceeded 80% from Day 3 onward (Figure 2F). These results indicate the feasibility of constructing an artificial trachea using an extracellular matrix-alginate hydrogel-PCL tracheal replacement stent structure.

3.3. Three-dimensionally printed degradable polycaprolactone tracheal stents with endothelial cell coverage on the inner diameter enhance tracheal defect repair

The re-epithelialization of the long-segment tracheal substitutes depends on the implantation of epithelial cells on the substitutes. In this study, rat endothelial cells were used. To investigate the repair effect of endothelial cells covered on the inner diameter of the degradable PCL tracheal replacement stent fabricated by 3D printing on tracheal defects, a rat tracheal defect model was established, and artificial trachea were implanted at the defect sites. The experimental group received stents with endothelial cells seeded on the inner lumen, whereas the control group received stents without endothelial cell coverage (Figure 3A).

Computed tomography imaging demonstrated that the luminal diameter at the transplantation site was significantly narrowed in the control group, whereas no reduction in luminal diameter was detected in the experimental group (Figure 3B). Bronchoscopic examination confirmed marked stenosis in the control group, with granulomatous tissue partially obstructing the airway, while the experimental group maintained a near-normal luminal diameter and internal morphology (Figure 3C). Histological analysis further supported these findings. Masson's trichrome staining revealed the absence of epithelial regeneration in the control group, accompanied by severe luminal narrowing, whereas the experimental group exhibited consistent *in vivo* regeneration of ciliated epithelial cells covering the inner surface of the stent, closely resembling the structure of a native trachea (Figure 3D). Functional outcomes were further validated by vascular repair analysis. Post-transplantation follow-up (Table S4, Supporting Information) indicated favorable epithelial and vascular regeneration in the experimental group, with no airway obstruction. Ultrasonographic and histological assessment confirmed segmental repair and lumen patency. Immunohistochemical staining reinforced these results: CD34 staining revealed a significant endothelial cell presence in the graft group, consistent with the transplanted vascular endothelial cells, whereas neither normal nor injured trachea exhibited positive staining (Figure 3E). CD326 (EpCAM) staining demonstrated robust regeneration in the graft group, in contrast to minimal epithelial coverage in the injured trachea and normal staining patterns in uninjured tissue. These findings suggest that grafted endothelial cells contributed

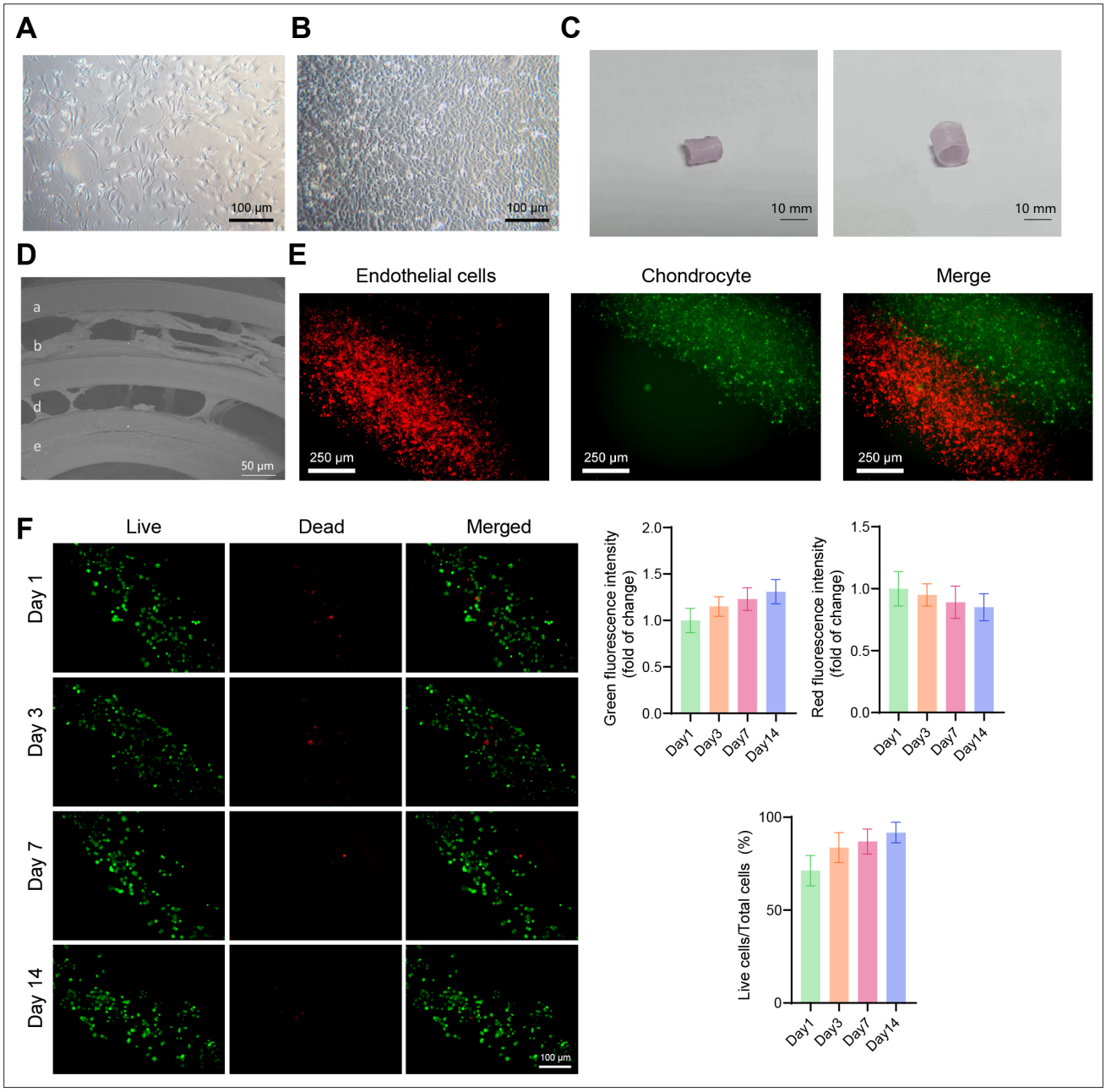


Figure 2. Construction of an *ex vivo* cell-alginate hydrogel-PCL tracheal replacement stent structure. (A) Light microscope morphology of endothelial cells. Scale bar: 100 μm; magnification: 100×. (B) Light microscope morphology of chondrocytes. Scale bar: 100 μm; magnification: 100×. (C) Longitudinal and vertical views of the artificial trachea, with a scaffold length of 10 mm, a five-layer structure, and a diameter of 5 mm. (D) Scanning electron microscopy image showing the enlarged scaffold structure, with layers a, c, and e composed of PCL; layer b composed of alginate gel and chondrocytes; and layer d composed of alginate gel and endothelial cells. Scale bar: 50 μm; magnification: 200x. (E) Observation of the artificial trachea under an optical microscope, with red representing the inner layer of endothelial cells and green representing the outer layer of chondrocytes. Scale bar: 10 μm; magnification: 40x. (F) *In vitro* Live/Dead assay, green and red represent live and dead cells, respectively. Scale bar: 250μm; magnification: 100×. All cellular experiments were repeated three times. Abbreviation: PCL, polycaprolactone.

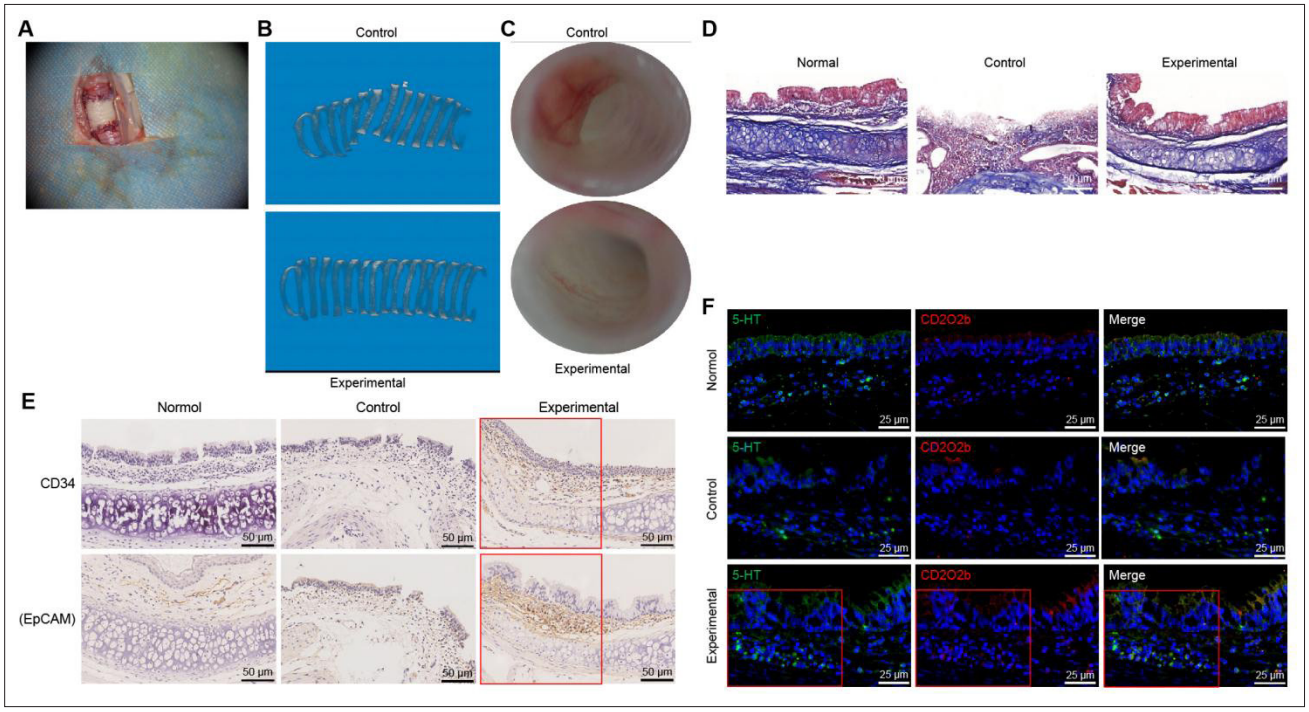


Figure 3. The reparative effect of a 3D-printed degradable PCL tracheal replacement stent with an inner diameter covering endothelial cells on the tracheal injury. (A) Schematic diagram of the artificial tracheal transplantation model. (B) Computed tomography images of rats in the control and experimental groups. (C) Bronchoscope images of rats in the control and experimental groups. Scale bar: 50 μm; magnification: 200×. (D) Masson staining to detect regeneration of epithelial cells in rats in the control and experimental groups, with the native trachea used as a normal control. Scale bar: 50 μm; magnification: 200×. (E) Immunohistochemical staining of CD34 and CD326 (EpCAM) in epithelial and endothelial cells in rats in the control and experimental groups, with the native trachea as a normal control. Scale bar: 50 μm; magnification: 200×. (F) Immunofluorescent staining of 5-hydroxytryptamine (5-HT) in epithelial cells and CD202b in endothelial cells in rats in the control and experimental groups, with the native trachea as a normal control. Scale bar: 25 μm; magnification: 400×. Red boxes highlight the graft scaffold area. 12 rats per group. All cellular experiments were repeated three times.

to epithelial lining repair, potentially through endothelial–epithelial transition (Figure 3E). Immunofluorescence analysis confirmed enhanced epithelial regeneration in the graft group compared to normal and injured trachea, with evidence of endothelial cells differentiating into epithelial cells (Figure 3F).

These results demonstrate that 3D printing of a degradable PCL tracheal replacement stent with an inner diameter covered by endothelial cells can effectively enhance the repair of tracheal defects by the tracheal replacement stent.

3.4. *Pvt1* may affect endothelial cell mesenchymal transition through negative regulation of *Dlk1*

Re-epithelialization of endothelial cells is critical for repairing tracheal injury, and this process is closely associated with cell proliferation and adhesion functions.[41] To investigate the molecular mechanisms underlying endothelial cell transdifferentiation into epithelial cells, transcriptome sequencing was performed on tracheal tissues collected from three rats in both the control and experimental groups. Differential expression analysis identified 267 differentially expressed genes, including 151 downregulated and 116 upregulated genes, with the lncRNA *Pvt1* exhibiting the highest fold change upregulation (Figure 4A and B). Consistent with previous reports, *Pvt1* has been shown to promote endothelial cell proliferation.[42] PPI network analysis of the top 50 differentially expressed genes using the STRING database revealed *Dlk1* as a central node (Figure 4C and D). *Dlk1* expression was significantly downregulated in the experimental group (Figure 4E). Given that *Dlk1* is reported to suppress endothelial cell proliferation,[43] its downregulation suggests a potential role in promoting endothelial–mesenchymal transition during re-epithelialization.

Previous studies have reported that DNA methylation is essential in regulating gene expression in endothelial cells.[44] In the present study, we identified multiple CpG islands within the promoter region of *Dlk1* (Figure 4F), suggesting that its transcriptional activity may be modulated through epigenetic modification. Moreover, evidence indicates that lncRNAs can recruit DNA

methyltransferases (DNMT1, DNMT3a, DNMT3b) to specific promoter regions, thereby modulating DNA methylation and transcriptional activity.[45] Based on these findings, we propose a mechanistic model in which *Pvt1* recruits DNMTs to the *Dlk1* promoter, enhances DNA methylation, and negatively regulates *Dlk1* expression, ultimately facilitating the epithelialization of endothelial cells and contributing to tracheal repair.

3.5. *Pvt1* silencing can downregulate the methylation level of *Dlk1* by reducing the enrichment of DNA methyltransferase in the promoter region of *Dlk1*

We first detected the methylation level of the *Dlk1* promoter CPG island in endothelial cells through Methylation-Specific Polymerase Chain Reaction (MSP) experiments. As shown in Figure 5A, the methylation level of the CpG island in the *Dlk1* promoter region was down-regulated after silencing *Pvt1*. Consistently, ChIP assays revealed that the enrichment of DNMT1, DNMT3a, and DNMT3b at the *Dlk1* promoter was significantly diminished upon *Pvt1* knockdown (Figure 5B). Furthermore, RIP analysis confirmed that *Pvt1* directly interacts with DNA methyltransferases (Figure 5C): after *Pvt1* silencing, the amount of *Pvt1* immunoprecipitated with DNMT1, DNMT3a, and DNMT3b antibodies was markedly reduced. These findings indicate that silencing *Pvt1* may downregulate the methylation level of *Dlk1* by reducing the enrichment of DNA methyltransferases in the *Dlk1* promoter region.

3.6. *Pvt1* silencing can inhibit endothelial cell proliferation and adhesion by upregulating *Dlk1* expression

To investigate whether *Pvt1* regulates endothelial cell proliferation and adhesion via *Dlk1*, endothelial cells were grouped for knockdown experiments. Real-time quantitative PCR analysis confirmed (Figure 6A) that *Pvt1*

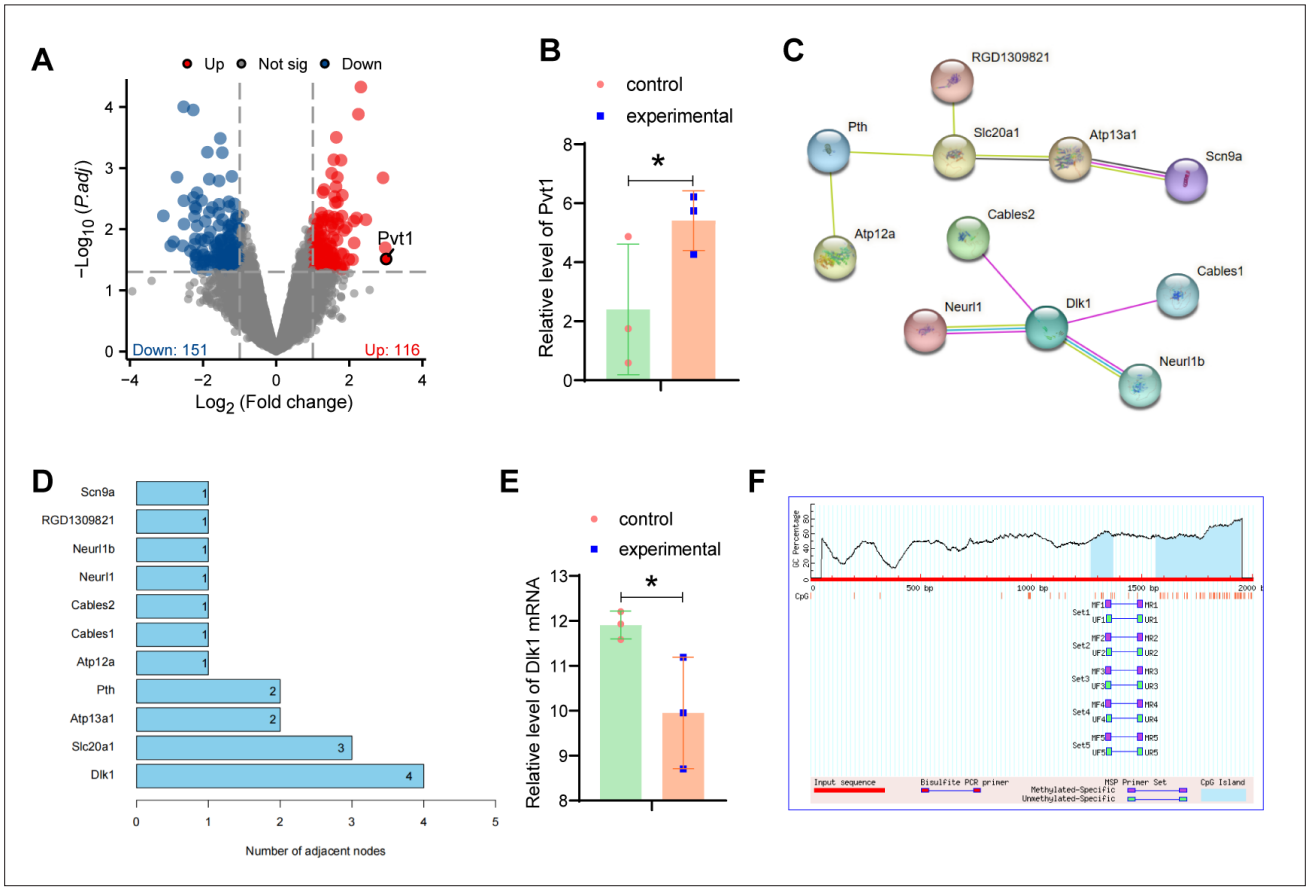


Figure 4. Gene screening through bioinformatics analysis. (A) Volcano plot for differentially expressed genes in the dataset, gray dots represent genes with no differential expression, red dots represent significantly upregulated genes, and blue dots represent significantly down-regulated genes. *Pvt1*, indicated by the plot, represents the gene with the highest upregulation factor. (B) Differential expression of *Pvt1* in tracheal tissues of rats in the control and experimental groups. (C) PPI protein interaction network. (D) Protein interaction adjacent node ranking in the PPI protein interaction network. (E) Differential expression of *Dlk1* in tracheal tissues of rats in the control and experimental groups. (F) Methprimer online website predicts CpG island distribution in the *Dlk1* promoter region. Abbreviation: PPI, protein–protein interaction.

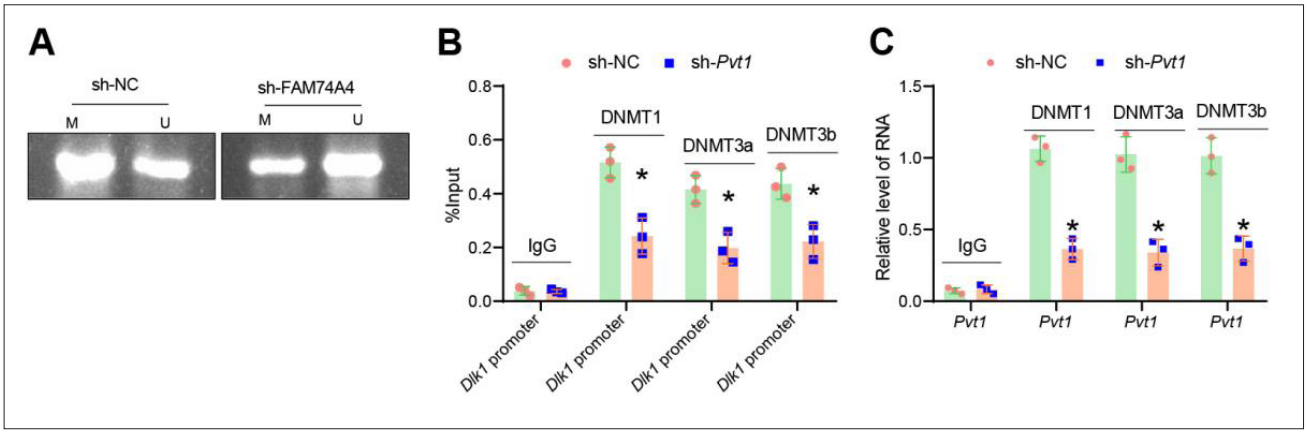


Figure 5. Study on the mechanism of *Pvt1* regulating *Dlk1*. (A) Methylation level detection of CpG island in the *Dlk1* promoter region in endothelial cells using Methylation-Specific Polymerase Chain Reaction (MSP) experiment, with M representing methylated and U representing unmethylated. (B) DNA methyltransferase enrichment detection in the *Dlk1* promoter region using chromatin immunoprecipitation experiment. (C) Binding of *Pvt1* with DNA methyltransferase detection using RNA immunoprecipitation experiment. * indicates a significant difference between the two groups with a *p*-value of less than 0.05. All cell experiments were performed in triplicate. Abbreviations: DNMT, DNA methyltransferase; NC, negative control; sh, short hairpin.

and *Dlk1* were efficiently silenced, with sh-*Pvt1*-2 and sh-*Dlk1*-2 showing the highest knockdown efficiency and therefore selected for further assays. Compared with the sh-NC group, *Pvt1* knockdown significantly reduced *Pvt1* expression and concomitantly increased *Dlk1* expression. In contrast, co-silencing *Dlk1* abrogated this effect, reducing *Dlk1* expression without altering *Pvt1* levels, indicating that *Pvt1* silencing upregulates *Dlk1* expression.

Functional assays further demonstrated the consequences of this regulatory relationship. CCK-8 and flow cytometry analyses showed (Figure 6B and C) that *Pvt1* knockdown significantly inhibited endothelial cell proliferation and promoted apoptosis, while simultaneous silencing of *Dlk1* reversed these effects. Western blotting supported these findings: *Pvt1* silencing decreased cyclin-dependent kinase 2, proliferating cell nuclear antigen, and B-cell lymphoma 2 expression and increased Bcl-2-associated protein X expression, whereas *Dlk1* silencing restored their levels (Figure 6D). Moreover, ELISA revealed that secretion of adhesion molecules ICAM-1 and VCAM-1 was markedly reduced after *Pvt1* knockdown but recovered upon *Dlk1* silencing (Figure 6E). These results indicate that silencing *Pvt1* can inhibit the proliferation and adhesion of endothelial cells by upregulating the expression of *Dlk1*.

3.7. *Pvt1* silencing impairs repair by endothelial-lined three-dimensionally printed tracheal stents

Our *in vitro* findings demonstrated that silencing *Pvt1* reduces endothelial cell proliferation and adhesion. To further examine the *in vivo* consequences of *Pvt1* silencing on tracheal defect repair, endothelial cells with *Pvt1* knockdown were seeded onto the inner diameter of 3D-printed biodegradable PCL tracheal stents and transplanted into tracheal defect sites in rats. Computed tomography imaging revealed (Figure 7A) that the tracheal lumen in the sh-*Pvt1* group was markedly reduced compared with the sh-NC group. Bronchoscopic evaluation (Figure 7B) confirmed severe tracheal narrowing in the sh-*Pvt1* group, accompanied by granulation tissue proliferation and partial airway obstruction. Regarding epithelial regeneration within the artificial trachea, Masson staining (Figure 7C) demonstrated that, compared with the sh-NC group, the regenerated epithelium in the sh-*Pvt1* group was irregular and poorly organized, accompanied by significant narrowing of the tracheal lumen. In addition, analysis of inflammation-related factors revealed that the levels of *Il6* and *Tnfa* were markedly elevated in the sh-*Pvt1* group compared with the sh-NC group (Figure 7D), indicating the occurrence of a pronounced inflammatory response in the newly formed epithelium.

In summary, 3D printing a degradable PCL tracheal replacement stent with an inner diameter covering silencing *Pvt1* in endothelial cells can inhibit the stent's repairing effect on tracheal defects.

4. Discussion

Tracheal defects are rare but potentially life-threatening conditions that can arise from trauma, tracheal malignancies, surgical injuries, or other causes.[1,46] These defects can lead to airway obstruction and, in severe cases, pose a significant risk to the patient's life.[47] Current clinical management strategies mainly include tracheoplasty and tracheal transplantation. Tracheoplasty is generally effective for repairing short-segment tracheal defects, yet

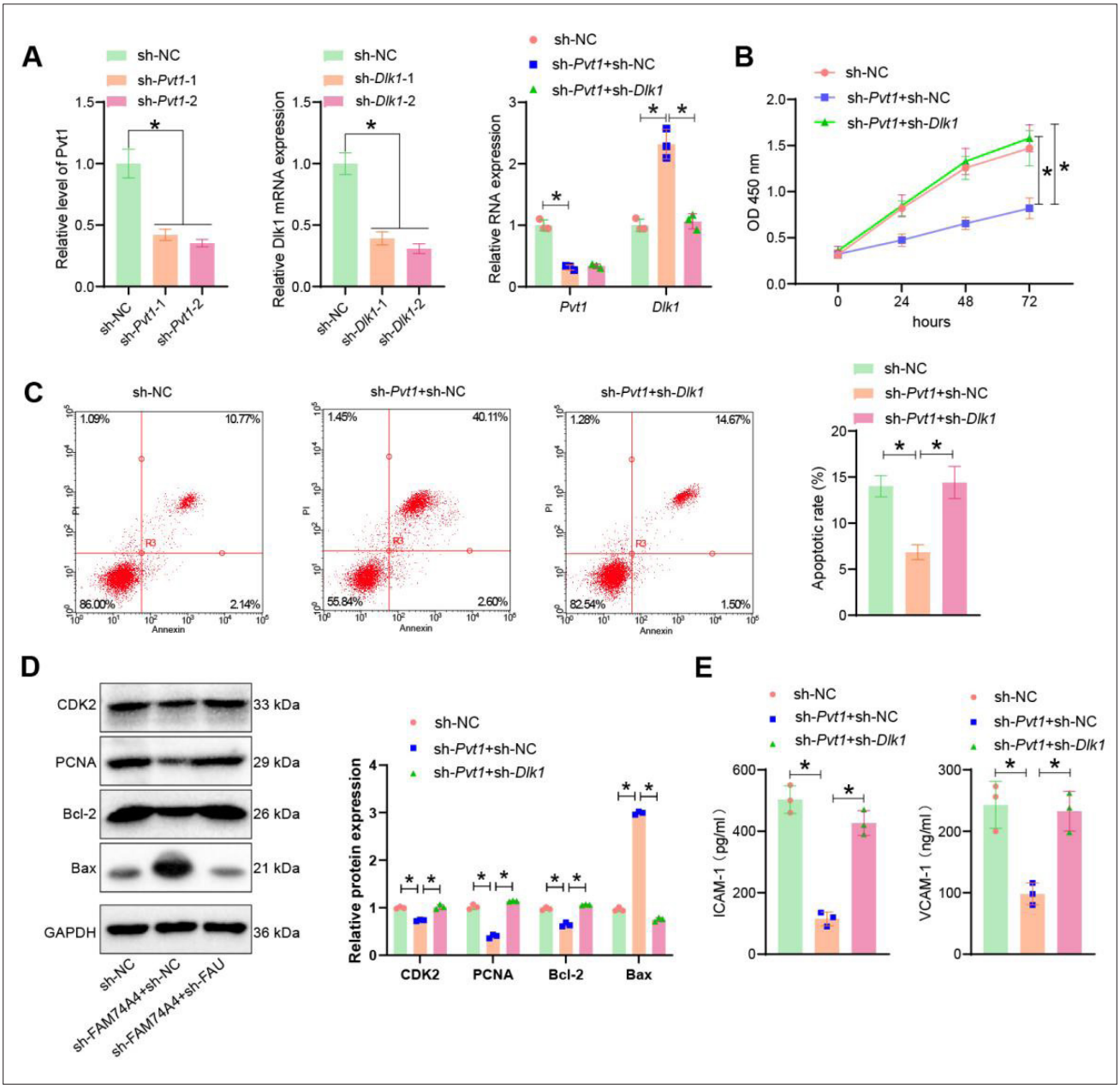


Figure 6. The impact of *Pvt1* on endothelial cell proliferation and adhesion function through regulation of *Dlk1*. (A) Detection of *Pvt1* and *Dlk1* expression levels in cells of each group using real-time quantitative polymerase chain reaction. (B) Assessment of cell proliferation ability in each group using the Cell Counting Kit-8 assay. (C) Measurement of cell apoptosis rate in each group using flow cytometry. (D) Analysis of expression levels of proliferation and apoptosis-related proteins in cells of each group using Western blot. (E) Determination of levels of adhesion factors ICAM-1 and VCAM-1 in the supernatant of cells in each group using enzyme-linked immunosorbent assay. * indicates a significant difference between the two groups with a *p*-value of less than 0.05. All cell experiments were performed in triplicate. Abbreviations: Bax, Bcl-2-associated X protein; Bcl-2, B-cell lymphoma 2; CDK2, cyclin-dependent kinase 2; NC, negative control; PCNA, proliferating cell nuclear antigen; sh, short hairpin.

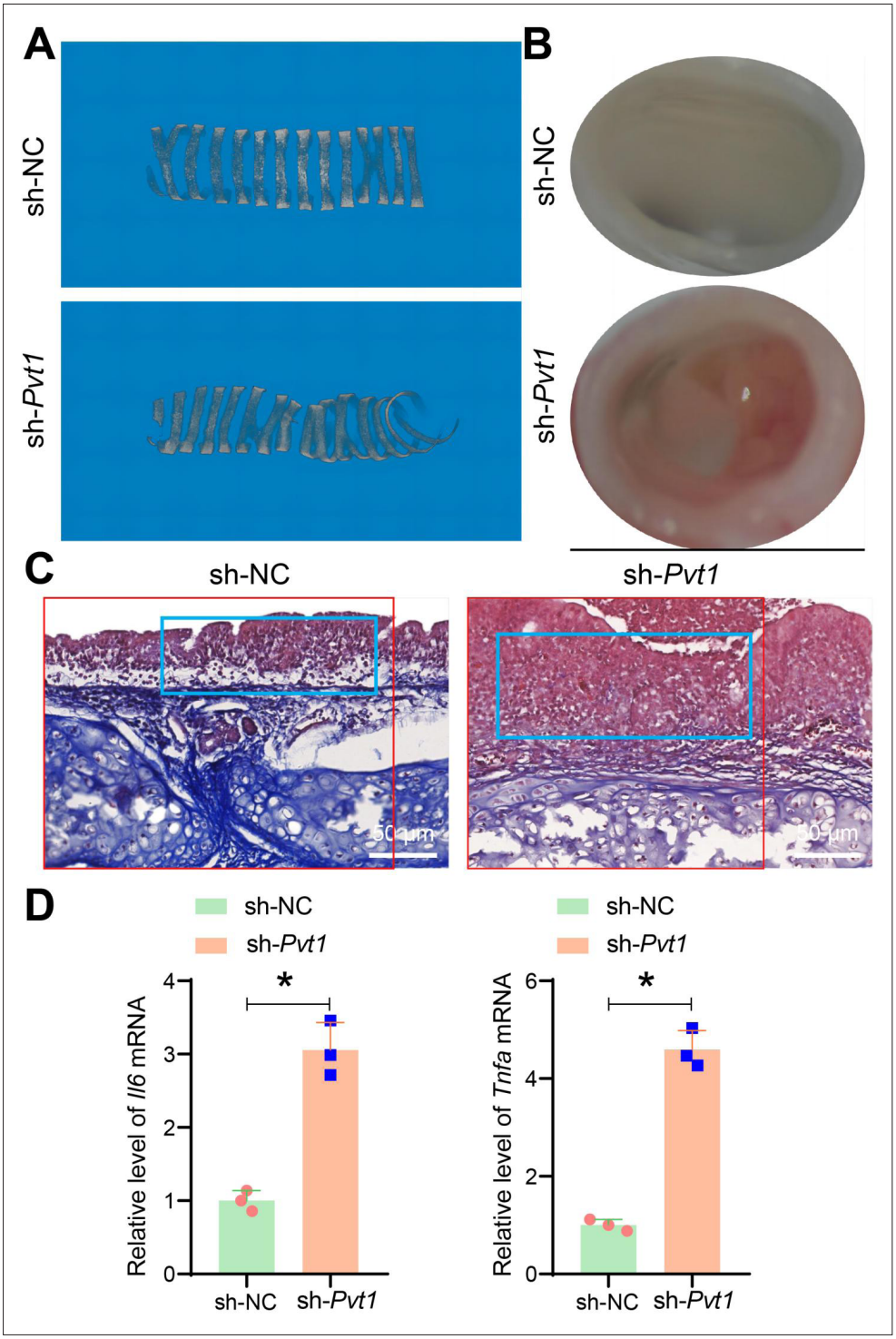


Figure 7. The impact of silencing *Pvt1* on tracheal injury repair in endothelial cells. (A) Computed tomography images of sh-NC and sh-*Pvt1* group rats. (B) Bronchoscopy images of sh-NC and sh-*Pvt1* group rats. (C) Masson staining was used to detect epithelial cell regeneration in the sh-NC and sh-*Pvt1* group rats, with the native trachea serving as a normal control. Scale bar: 50 μm; magnification: 200×. Red boxes highlight the graft scaffold area; (D) Real-time quantitative polymerase chain reaction analysis of *Il6* and levels in cells from sh-NC and sh-*Pvt1* groups, with three independent experiments, * indicates *Tnfas* $p < 0.05$, 12 rats per group. Abbreviations: NC, negative control; sh, short hairpin.

its clinical application is restricted by the complexity of the procedure and the risk of postoperative complications, including tracheomalacia and injury to the recurrent laryngeal nerve.[48] Although progress has been made in tracheal transplantation, major obstacles such as immune rejection and the absence of intrinsic regenerative capacity continue to hinder its widespread clinical adoption.[49–51]

Compared to these traditional treatments, 3D printing provides new solutions for tracheal repair. This method enables precise customization of tracheal replacement stents tailored to a patient's anatomical characteristics, thereby overcoming the limitations of individual variability often encountered with conventional procedures.[52–54] Among the materials available, PCL, a biodegradable polymer, has been widely adopted. PCL-based 3D-printed stents gradually degrade *in vivo* while simultaneously providing mechanical support and facilitating tissue ingrowth, ultimately enhancing repair of tracheal defects. Compared to traditional treatments, 3D-printed tracheal replacement stents have several distinct advantages. First, their porous architecture promotes cell adhesion and proliferation, accelerating tissue reconstruction and regeneration. Second, the structural morphology closely mimics the native trachea, ensuring accurate anatomical fit and physiological functionality. Third, 3D printing enables patient-specific customization, allowing truly personalized treatment. Fourth, as a biodegradable and biocompatible material, PCL provides adequate mechanical strength during the critical repair phase while supporting cell colonization and tissue integration. The long-term goal is that controlled PCL degradation facilitates anastomosis formation and promotes epithelialization through host cell participation.[32,55] Moreover, 3D-printed PCL stents reduce the risk of immune rejection and donor-site complications, while promoting tissue regeneration, further underscoring their clinical promise.[56] Despite these advantages, challenges remain. A significant issue is achieving a balance between the mechanical stability of the scaffold and its biodegradation rate, as premature degradation may compromise airway patency, whereas delayed degradation may impede natural tissue integration. Furthermore, robust clinical evidence is still required to confirm the long-term safety and efficacy of these implants in humans.[32]

In contrast, traditional methods such as tracheoplasty and tracheal transplantation have the following advantages. Tracheoplasty has been shown to achieve satisfactory long-term functional recovery and is supported by a substantial body of clinical data, while tracheal transplantation benefits from a more extended clinical history with relatively well-defined procedures and outcomes. However, these approaches are also limited by notable drawbacks. Tracheoplasty carries inherent risks, including donor site complications and immune rejection, and its technical complexity further restricts its applicability.[57,58] Similarly, tracheal transplantation faces significant challenges related to immune rejection, donor availability, and long-term graft sustainability, which hinder its broader clinical adoption.

This study investigated the role of *Pvt1* in endothelial cell proliferation and adhesion and revealed its potential in repairing tracheal defects using 3D-printed biodegradable PCL tracheal replacement stents. The results demonstrated that 3D-printed biodegradable PCL tracheal stents played a significant role in the repair of tracheal defects, especially when the inner lumen was covered with endothelial cells. It is well established that biological tissues comprise more than one cell type. When tracheal substitute scaffolds are seeded with two or more cell types, they become more similar to native biological tissues, functioning more effectively *in vivo*. In the context of long-segment tracheal defect repair and reconstruction, three critical challenges remain to be addressed: re-epithelialization, revascularization, and neo-cartilage formation.[59] Therefore, endothelial cells and chondrocytes were applied to the tracheal substitute scaffold. Notably, the slow degradation rate of PCL was sufficient to maintain airway patency during the critical early stages of implantation, ensuring structural stability and long-term repair efficacy. Previous studies have shown that the aliphatic ester bonds in PCL are susceptible to hydrolysis, enabling resorption within approximately 24–36 months, coinciding with new tissue growth phases during childhood development.[60] These properties support the suitability of PCL as an ideal material for tracheal replacement. Mechanistically, we further found that *Pvt1* regulates endothelial–mesenchymal transition through modulation of *Dlk1* expression,[43] thereby facilitating tracheal epithelialization and repair. In contrast, silencing *Pvt1* in endothelial cells markedly impaired repair efficacy, underscoring its promotive role in tracheal regeneration.

Moreover, bioinformatics analysis revealed that *Pvt1* negatively regulates endothelial cell mesenchymal transition by modulating *Dlk1*, thereby impacting the effectiveness of tracheal repair. Consistent with earlier studies, *Pvt1* is highly expressed in various tumors and plays a significant role in cell proliferation, invasion, and metastasis.[61] However, despite its significant role in tracheal repair, therapeutic strategies targeting *Pvt1* may pose certain risks by potentially stimulating tumor cell proliferation. Therefore, future research should further explore the dual role of *Pvt1* in different diseases and treatment contexts to develop more refined therapeutic strategies. Given that *Pvt1* is also expressed in normal tissues, molecular markers such as miR-150-5p, octamer-binding transcription factor 4, and c-myc may be valuable indicators for monitoring *Pvt1* activity in cancer-related

contexts.[62,63] Future studies should also explore targeted delivery strategies as a research direction.

Despite the significant advantages of 3D-printed tracheal replacement stents in repairing tracheal defects, several challenges remain. One of the most critical issues is balancing the biodegradation rate and long-term mechanical stability. Excessively rapid degradation may compromise structural integrity, whereas overly slow degradation may hinder tissue remodeling and integration. In our study, degradation assessment at 2, 4, and 12 weeks revealed that PCL tracheal stents underwent relatively rapid degradation during the initial 2 weeks, followed by a more gradual decline. Importantly, even at 12 weeks, the stents retained sufficient mechanical strength and luminal stability to maintain airway patency. To further validate the long-term *in vivo* stability of the material, future investigations should extend the evaluation period to 6 months or even 1 year, if conditions allow. Supplementary indicators such as weight change should also be incorporated to provide a more comprehensive assessment of the degradation profile and mechanical durability. Another key challenge lies in enhancing vascularization of the stent, which is essential for promoting neovascular growth and ensuring long-term survival of the repair site. Ongoing work has begun to explore accelerated aging experiments and long-term follow-up studies to generate more complete data on biodegradation and biocompatibility. Collectively, these findings strengthen the evidence supporting the potential of 3D-printed degradable PCL tracheal replacement stents for tracheal repair and offer new insights and strategies for addressing tracheal defects.

To address these challenges, future research should prioritize several directions. First, the degradation rate and mechanical strength of PCL tracheal replacement stents should be optimized to achieve long-term stability. Second, other biodegradable or composite materials should be explored to enhance the performance of tracheal stents. Third, gene editing and surface modification technologies should be applied to improve immune compatibility and reduce rejection. Fourth, novel therapeutic strategies targeting key molecules such as *Pvt1* and *Dlk1* should be developed to optimize tracheal repair while minimizing potential tumor risks.[26] Additionally, future studies should focus on extending the follow-up time in animal models and conducting more extensive preclinical research to validate the effectiveness of 3D-printed tracheal replacement stents in different clinical scenarios.

This study provides new insights into the role of *Pvt1* in endothelial cell proliferation and adhesion, revealing its potential in tracheal defect repair. By offering new perspectives on tracheal replacement stent design and identifying new therapeutic targets, this study contributes to advancing tracheal repair technologies. Although significant challenges remain, continued technological innovation and a deeper understanding of molecular mechanisms offer strong potential for 3D-printed degradable PCL tracheal replacement stents to emerge as an essential therapeutic option for tracheal defects. Future research should further validate these findings and promote the clinical translation of tracheal repair technologies.[64,59]

5. Conclusion

The present study provides an in-depth evaluation of the potential of 3D-printed degradable PCL tracheal replacement stents for tracheal defect repair and elucidates the role of *Pvt1* in regulating endothelial cell proliferation and adhesion. Through advanced 3D printing technology, personalized tracheal replacement stents were fabricated to closely replicate the anatomical features of the native trachea (**Figure 8**). The use of biodegradable PCL ensured both biocompatibility and predictable degradation. The findings demonstrated that *Pvt1*, a long non-coding RNA, may facilitate tracheal repair by regulating *Dlk1* expression and modulating the endothelial–mesenchymal transition. The interaction between *Pvt1* and *Dlk1* highlights a promising direction for future molecularly targeted interventions. Despite these advantages, challenges remain in balancing long-term mechanical stability with degradation rate, requiring further material optimization and validation. Future research should focus on enhancing stent properties, investigating the therapeutic potential of *Pvt1* and related pathways, and improving the long-term safety and efficacy of tracheal repair. Collectively, these results provide new mechanistic insights and strong technical support for advancing clinical applications in tracheal defect treatment.

Acknowledgments

The authors would like to thank all the colleagues in the Comprehensive Laboratory of the First Affiliated Hospital of Nanchang University for their significant contributions to this research.

Funding

This study was supported by the National Natural Science Foundation of China (82260015), Jiangxi Key Research and Development Plan (No.20243BBI91018), the Jiangxi Provincial Health Commission Science and Technology Project (No.202410200), the Jiangxi Province Traditional Chinese Medicine Science and Technology Project (No.2023A0302), the Shenzhen Baoan People's Hospital academic leader research start-up fund (No.202400120201),

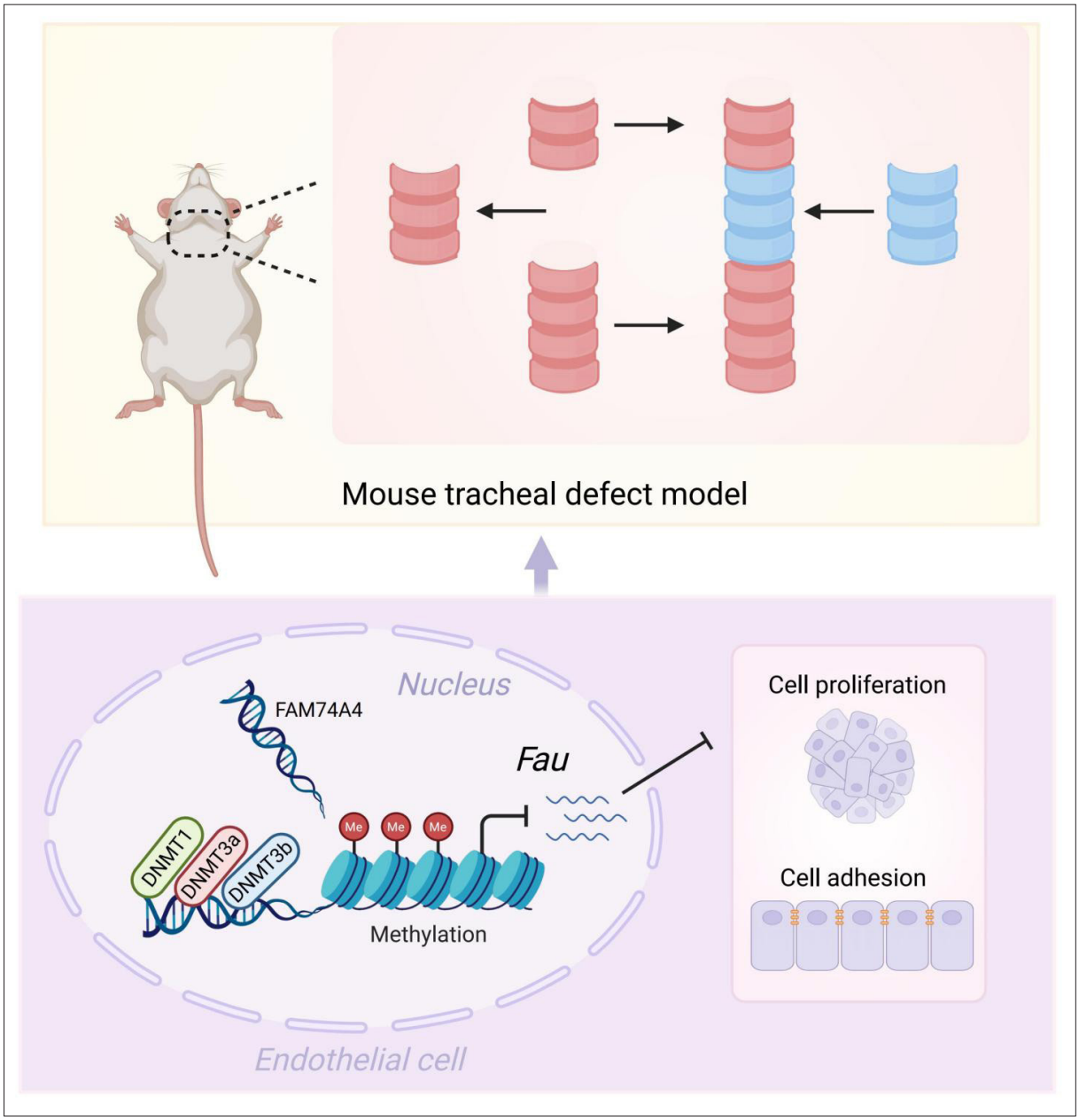


Figure 8. Schematic diagram of the molecular mechanism of three-dimensionally printed biodegradable tracheal replacement stents for repairing tracheal defects. Abbreviation: DNMT, DNA methyltransferase.

and the Shenzhen Baoan District Medical Health Research Project (No.BAGZL2024036).

Conflict of interest

The author(s) declared no potential conflicts of interest concerning the research, authorship, and/or publication of this article.

Author contributions

Conceptualization: W.Z., S.-X.Q., and J.C.
Formal analysis: Q.J.C.
Investigation: J.-L.W. and J.-T.Z.
Methodology: W.Z., S.-X.Q., and J.C.
Supervision: F.X.
Writing–original draft: All authors
Writing–review & editing: All authors

Ethics approval and consent to participate

The experimental and animal study protocols have been approved by the Ethics Committee of the First Affiliated Hospital of Nanchang University.

Consent for publication

Not applicable.

Availability of data

The data supporting this study's findings are available on request from the corresponding author.

References

1. Aydin S, Oz G, Dumanli A, Dongel I, Camas HE. Management of life-threatening tracheal emergencies. *Ann Ital Chir*. 2022;93:626-632.
2. Wang H. Chronic adenoiditis. *J Int Med Res*. 2020;48(11):300060520971458. doi: 10.1177/0300060520971458
3. Filip C, Socolov DG, Albu E, Filip C, Serban R, Popa RF. Serological parameters and vascular investigation for a better assessment in DVT during pregnancy—a systematic review. *Medicina (Kaunas)*. 2021;57(2):160. doi: 10.3390/medicina57020160
4. Sawamoto K, Alvarez Gonzalez J, Piechnik M, *et al*. Mucopolysaccharidosis IVA: diagnosis, treatment, and management. *Int J Mol Sci*. 2020;21(4):1517. doi: 10.3390/ijms21041517
5. Cetrano E, Trezzi M, Secinaro A, *et al*. Bronchial mismatch as a predictor of respiratory failure after congenital tracheal stenosis repair. *Ann Thorac Surg*. 2018;105(4):1264-1271. doi: 10.1016/j.athoracsur.2017.10.046
6. Ren J, Xu Y, Zhiyi G, *et al*. Reconstruction of the trachea and carina: surgical reconstruction, autologous tissue transplantation, allograft transplantation, and bioengineering. *Thorac Cancer*. 2022;13(3):284-295. doi: 10.1111/1759-7714.14315
7. Richardson CM, Hart CK, Johnson KE, Gerber ME. Slide tracheoplasty. *Otolaryngol Clin North Am*. 2022;55(6):1253-1270. doi: 10.1016/j.otc.2022.07.014
8. Zhang S, Xiao G, Peng R, Zhang P, Hong J. Clinical consequences of herpes simplex virus DNA in donor corneas: different prognosis and management of endothelial keratoplasty and deep anterior lamellar keratoplasty. *J Clin Virol*. 2020;129:104508. doi: 10.1016/j.jcv.2020.104508
9. Broersen LHA, Andela CD, Dekkers OM, Pereira AM, Biermasz NR. Improvement but no normalization of quality of life and cognitive functioning after treatment for Cushing's syndrome. *J Clin Endocrinol Metab*. 2019;104(10):4501-4512. doi: 10.1210/jc.2019-01054
10. Wei G, Wang Y, Yang G, Wang Y, Ju R. Recent progress in nanomedicine for enhanced cancer chemotherapy. *Theranostics*. 2021;11(13):6370-6392. doi: 10.7150/thno.57828
11. Shai SE, Lai YL, Hung YW, *et al*. De novo cartilage growth after implantation of a 3-D-printed tracheal graft in a porcine model. *Am J Transl Res*. 2020;12(7):3728-3740.
12. Raguram A, Banskota S, Liu DR. Therapeutic in vivo delivery of gene editing agents. *Cell*. 2022;185(15):2806-2827. doi: 10.1016/j.cell.2022.03.045
13. Perez RE, Santiago JC, Lopez MC, *et al*. Behavior of calcium, phosphorus, and parathormone before transplantation and in months 1, 3, 6, 9, and 12 after transplantation. *Transplant Proc*. 2020;52(4):1152-1156. doi: 10.1016/j.transproceed.2020.01.065
14. Bertolin J, Sanchez V, Ribera A, *et al*. Treatment of skeletal and non-skeletal alterations of mucopolysaccharidosis type IVA by AAV-mediated gene therapy. *Nat Commun*. 2021;12(1):4944. doi: 10.1038/s41467-021-25697-y
15. Chang NW, Dai HJ, Shih YY, *et al*. Biomarker identification of hepatocellular carcinoma using a methodical literature mining strategy. *Database (Oxford)*. 2017;2017:bax082. doi: 10.1093/database/bax082
16. Wu J, Lee B, Saha P, Kumta PN. A feasibility study of biodegradable magnesium–aluminum–zinc–calcium–manganese (AZXM) alloys for tracheal stent application. *J Biomater Appl*. 2019;33(8):1080-1093. doi: 10.1177/0885328218824775
17. Luffy SA, Wu J, Kumta PN, Gilbert TW. Evaluation of magnesium alloys for use as an intraluminal tracheal for pediatric applications in a rat tracheal bypass model. *J Biomed Mater Res B Appl Biomater*. 2019;107(6):1844-1853. doi: 10.1002/jbm.b.34277
18. Wu DT, Munguia-Lopez JG, Cho YW, *et al*. Polymeric scaffolds for dental, oral, and craniofacial regenerative medicine. *Molecules*. 2021;26(22):7043. doi: 10.3390/molecules26227043
19. Gao C, Lu C, Jian Z, *et al*. 3D bioprinting for fabricating artificial skin tissue. *Colloids Surf B Biointerfaces*. 2021;208:112041. doi: 10.1016/j.colsurfb.2021.112041
20. Stramiello JA, Mohammadzadeh A, Ryan J, Brigger MT. The role of bioresorbable intraluminal airway stents in pediatric tracheobronchial obstruction: a systematic review. *Int J Pediatr Otorhinolaryngol*. 2020;139:110405. doi: 10.1016/j.ijporl.2020.110405
21. Feuerbach T, Kock S, Thommes M. Slicing parameter optimization for 3D printing of biodegradable drug-eluting tracheal stents. *Pharm Dev Technol*. 2020;25(6):650-658. doi: 10.1080/10837450.2020.1727921

22. Yao W, Li S, Liu R, *et al*. Long non-coding RNA PVT1: a promising chemotherapy and radiotherapy sensitizer. *Front Oncol*. 2022;12:959208.
doi: 10.3389/fonc.2022.959208

23. Dvorak P, Leupen S, Soucek P. Functionally significant features in the 5′ untranslated region of the ABCA1 gene and their comparison in vertebrates. *Cells*. 2019; 8(6):623.
doi: 10.3390/cells8060623

24. Shi Y, Yang F, Wei S, Xu G. Identification of key genes affecting results of hyperthermia in osteosarcoma based on integrative ChIP-seq/TargetScan analysis. *Med Sci Monit*. 2017;23:2042-2048.
doi: 10.12659/msm.901191

25. Zhou C, Yi C, Yi Y, *et al*. LncRNA PVT1 promotes gemcitabine resistance of pancreatic cancer via activating Wnt/β-catenin and autophagy pathway through modulating the miR-619-5p/Pygo2 and miR-619-5p/ATG14 axes. *Mol Cancer*. 2020;19(1):118.
doi: 10.1186/s12943-020-01237-y

26. Chen S, Shen X. Long noncoding RNAs: functions and mechanisms in colon cancer. *Mol Cancer*. 2020;19(1):167.
doi: 10.1186/s12943-020-01287-2

27. Zhang M, Zhang L, Fu L, *et al*. Positive feedback regulation of lncRNA PVT1 and HIF2α contributes to clear cell renal cell carcinoma tumorigenesis and metastasis. *Oncogene*. 2021;40(37):5639-5650.
doi: 10.1038/s41388-021-01971-7

28. Shang R, Lal N, Lee CS, *et al*. Cardiac-specific VEGFB overexpression reduces lipoprotein lipase activity and improves insulin action in rat heart. *Am J Physiol Endocrinol Metab*. 2021;321(6):E753-E765.
doi: 10.1152/ajpendo.00219.2021

29. Ma L, Zhang Q, Hao J, Wang J, Wang C. LncRNA PVT1 exacerbates the inflammation and cell-barrier injury during asthma by regulating miR-149. *J Biochem Mol Toxicol*. 2020;34(11):e22563.
doi: 10.1002/jbt.22563

30. Lu X, Yu Y, Yin F, *et al*. Knockdown of PVT1 inhibits IL-1β-induced injury in chondrocytes by regulating miR-27b-3p/TRAF3 axis. *Int Immunopharmacol*. 2020;79:106052.
doi: 10.1016/j.intimp.2019.106052

31. Gao B, Jing H, Gao M, *et al*. Long-segmental tracheal reconstruction in rabbits with pedicled tissue-engineered trachea based on a 3D-printed scaffold. *Acta Biomater*. 2019;97:177-186.
doi: 10.1016/j.actbio.2019.07.043

32. Gao M, Zhang H, Dong W, *et al*. Tissue-engineered trachea from a 3D-printed scaffold enhances whole-segment tracheal repair. Sci Rep. 2017;7(1):5246.
doi: 10.1038/s41598-017-05518-3

33. Park HS, Lee JS, Jung H, *et al*. An omentum-cultured 3D-printed artificial trachea: in vivo bioreactor. *Artif Cells Nanomed Biotechnol*. 2018;46(suppl 3):1131-1140.
doi: 10.1080/21691401.2018.1533844

34. Ahn CB, Son KH, Yu YS, Kim TH, Lee JI, Lee JW. Development of a flexible 3D printed scaffold with a cell-adhesive surface for artificial trachea. *Biomed Mater*. 2019;14(5):055001.
doi: 10.1088/1748-605X/ab2a6c

35. Bae SW, Lee KW, Park JH, *et al*. 3D bioprinted artificial trachea with epithelial cells and chondrogenic-differentiated bone marrow-derived mesenchymal stem cells. *Int J Mol Sci*. 2018;19(6):1624.
doi: 10.3390/ijms19061624

36. Park JH, Yoon JK, Lee JB, *et al*. Experimental tracheal replacement using 3-dimensional bioprinted artificial trachea with autologous epithelial cells and chondrocytes. *Sci Rep*. 2019;9(1):2103.
doi: 10.1038/s41598-019-38565-z

37. Taniguchi D, Matsumoto K, Tsuchiya T, *et al*. Scaffold-free trachea regeneration by tissue engineering with bio-3D printing. *Interact Cardiovasc Thorac Surg*. 2018;26(5):745-752.
doi: 10.1093/icvts/ivx444

38. Jensen EC. Quantitative analysis of histological staining and fluorescence using ImageJ. *Anat Rec (Hoboken)*. 2013;296(3):378-381.
doi: 10.1002/ar.22641

39. Kaye R, Goldstein T, Grande DA, Zeltsman D, Smith LP. A 3-dimensional bioprinted tracheal segment implant pilot study: rabbit tracheal resection with graft implantation. *Int J Pediatr Otorhinolaryngol*. 2019;117: 175-178.
doi: 10.1016/j.ijporl.2018.11.010

40. Lee KY, Mooney DJ. Alginate: properties and biomedical applications. *Prog Polym Sci*. 2012;37(1):106-126.
doi: 10.1016/j.progpolymsci.2011.06.003

41. Liu M, Liu Z, Chen Y, *et al*. Dendritic epidermal T cells secreting exosomes promote the proliferation of epidermal stem cells to enhance wound re-epithelialization. *Stem Cell Res Ther*. 2022;13(1):438.
doi: 10.1186/s13287-022-02783-6

42. Zheng J, Hu L, Cheng J, *et al*. lncRNA PVT1 promotes the angiogenesis of vascular endothelial cell by targeting miR-26b to activate CTGF/ANGPT2. *Int J Mol Med*. 2018;41(3):1742-1752.
doi: 10.3892/ijmm.2018.3595

43. Schober A, Nazari-Jahantigh M, Wei Y, *et al*. MicroRNA-126-5p promotes endothelial proliferation and limits atherosclerosis by suppressing Dlk1. *Nat Med*. 2014;20(4):368-376.
doi: 10.1038/nm.3487

44. Shirodkar AV, St Bernard R, Gavryushova A, *et al*. A mechanistic role for DNA methylation in endothelial cell-enriched gene expression: relationship with DNA replication timing. *Blood*. 2013;121(17): 3531-3540.
doi: 10.1182/blood-2013-01-479170

45. Herman AB, Tsitsipatis D, Gorospe M. Integrated lncRNA function upon genomic and epigenomic regulation. *Mol Cell*. 2022;82(12):2252-2266.
doi: 10.1016/j.molcel.2022.05.027

46. Welter S, Essaleh W. Management of tracheobronchial injuries. *J Thorac Dis*. 2020;12(10):6143-6151.
doi: 10.21037/jtd-2019-as-05

47. Frauenfelder C, Maughan E, Kenth J, *et al*. Tracheal resection for critical airway obstruction in Morquio A syndrome. *Case Rep Pediatr*. 2023;2023:7976780.
doi: 10.1155/2023/7976780

48. Leivaditis V, Skevis K, Mulita F, *et al*. Advancements in the management of postoperative air leak following thoracic surgery: from traditional practices to innovative therapies. *Medicina (Kaunas)*. 2024;60(5):802.
doi: 10.3390/medicina60050802

49. Genden EM, Laitman BM. Human tracheal transplantation. *Transplantation*. 2023;107(8):1698-1705.
doi: 10.1097/TP.0000000000004509

50. Delaere P, Meulemans J, Vranckx J, Vos R, Poorten VV. Tracheal transplantation. *Thorac Surg Clin*. 2025;35(1):131-141.
doi: 10.1016/j.thorsurg.2024.07.002

51. Samat AA, Hamid ZAA, Yahaya BH. Tissue engineering for tracheal replacement: strategies and challenges. *Adv Exp Med Biol*. 2022;137:137-163.
doi: 10.1007/5584_2022_707

52. Tracy T, Wu L, Liu X, Cheng S, Li X. 3D printing: Innovative solutions for patients and pharmaceutical industry. *Int J Pharm*. 2023;631:122480.
doi: 10.1016/j.ijpharm.2022.122480

53. Uchida DT, Bruschi ML. 3D printing as a technological strategy for the personalized treatment of wound healing. *AAPS PharmSciTech*. 2023;24(1):25.
doi: 10.1208/s12249-023-02503-0

54. Serrano DR, Kara A, Yuste I, *et al*. 3D printing technologies in personalized medicine, nanomedicines, and biopharmaceuticals. *Pharmaceutics*. 2023;15(2):313.
doi: 10.3390/pharmaceutics15020313

55. Wang P, Sun Y, Shi X, Shen H, Ning H, Liu H. 3D printing of tissue engineering scaffolds: a focus on vascular regeneration. *Bio-Des Manuf*. 2021;4(2):344-378.
doi: 10.1007/s42242-020-00109-0

56. Guerra AJ, Cano P, Rabionet M, Puig T, Ciurana J. 3D-printed PCL/PLA composite stents: towards a new solution to cardiovascular problems. *Materials (Basel)*. 2018;11(9):1679.
doi: 10.3390/ma11091679

57. Townsend JM, Hukill ME, Fung KM, *et al*. Biodegradable electrospun patch containing cell adhesion or antimicrobial compounds for trachea repair in vivo. *Biomed Mater*. 2020;15(2):025003.
doi: 10.1088/1748-605X/ab5e1b

58. Genden EM, Miles BA, Harkin TJ, *et al*. Single-stage long-segment tracheal transplantation. *Am J Transplant*. 2021;21(10):3421-3427.
doi: 10.1111/ajt.16752

59. Park JH, Ahn M, Park SH, *et al*. 3D bioprinting of a trachea-mimetic cellular construct of a clinically relevant size. *Biomaterials*. 2021;279:121246.
doi: 10.1016/j.biomaterials.2021.121246

60. Wahbeh JM, Lama J, Park S, Ebramzadeh E, Hollister SJ, Sangiorgio SN. Degradation and fatigue behavior of 3D-printed bioresorbable tracheal splints. *J Biomed Mater Res B Appl Biomater*. 2024;112(12):e35501.
doi: 10.1002/jbm.b.35501

61. Ji K, Zhang Q, Song W, *et al*. LncRNA PVT1 promotes cell proliferation, invasion, and migration and inhibits cell apoptosis by phosphorylating YAP. *Can J Gastroenterol Hepatol*. 2022;2022:5332129.
doi: 10.1155/2022/5332129

62. Li X, Ren H. Long noncoding RNA PVT1 promotes tumor cell proliferation, invasion, migration and inhibits apoptosis in oral squamous cell carcinoma by regulating miR-150-5p/GLUT-1. *Oncol Rep*. 2020;44(3):1101-1112.
doi: 10.3892/or.2020.7706

63. Cui M, Chang Y, Fang QG, *et al*. Non-coding RNA Pvt1 promotes cancer stem cell–like traits in nasopharyngeal cancer via inhibiting miR-1207. *Pathol Oncol Res*. 2019;25(4):1411-1422.
doi: 10.1007/s12253-018-0453-1

64. Du J, Zheng L, Gao P, *et al*. A small-molecule cocktail promotes mammalian cardiomyocyte proliferation and heart regeneration. *Cell Stem Cell*. 2022;29(4):545-558.e13.
doi: 10.1016/j.stem.2022.03.009

ACCSCIENCE PUBLISHING

International Journal of Bioprinting

RESEARCH ARTICLE

Hydroxyapatite/BMP-2–mineralized decellularized amniotic membrane scaffolds for orbital defect repair

Bing Qin[1†], Yi Wang[2,3†], Yiyi Chen[4], Yabo Shi[1], and Wei Liu[1*]

[1]Department of Ophthalmology, The Affiliated Suqian First People's Hospital of Nanjing Medical University, Suqian, Jiangsu, China

[2]Department of Ophthalmology, Peking University Third Hospital, Beijing, China

[3]Beijing Key Laboratory of Restoration of Damaged Ocular Nerve, Peking University Third Hospital, Beijing, China

[4]Department of Ophthalmology, The People's Hospital of Yangzhong City, Affiliated Hospital of Yangzhou University, Zhenjiang 212200, Jiangsu, China

Abstract

Orbital wall fractures often result in midfacial deformities characterized by herniation of orbital adipose and soft tissues into the maxillary sinus, potentially causing endophthalmitis or subbulbar inflammation. However, current orbital reconstruction materials face critical limitations, including inadequate osteogenic capacity and poor osseointegration, predisposing implants to displacement, immune rejection, and infection. To overcome these challenges, we fabricated a three-dimensional (3D)-printed scaffold based on hydroxyapatite/bone morphogenetic protein-2–mineralized decellularized amniotic membrane for orbital defect repair. By precisely modulating the material composition and leveraging advanced 3D printing techniques, we achieved simultaneous control over the scaffold's physicochemical properties and biological activity. The resulting constructs feature optimized macro- and micro-architectures. This study establishes a novel strategy for orbital reconstruction, addressing both bone volume restoration and functional regeneration, offering a transformative approach for personalized craniofacial repair.

Keywords: 3D printing; Acellular matrix; BMP-2; Composite scaffolds; Orbital reconstruction

†The authors contributed equally to this work.

***Corresponding author:**
Wei Liu (m13813182298@163.com)

Citation: Qin B, Wang Y, Chen Y, Shi Y, Liu W. Hydroxyapatite/BMP-2–mineralized decellularized amniotic membrane scaffolds for orbital defect repair. *Int J Bioprint*. 2026;12(1):283-301. doi: 10.36922/IJB025330336

Received: August 17, 2025
Revised: September 27, 2025
Accepted: October 11, 2025
Published online: October 14, 2025

Copyright: © 2025 Author(s). This is an Open Access article distributed under the terms of the Creative Commons Attribution License, permitting distribution and reproduction in any medium, provided the original work is properly cited.

Publisher's Note: AccScience Publishing remains neutral with regard to jurisdictional claims in published maps and institutional affiliations.

1. Introduction

The orbital bone structure is particularly susceptible to fracture under external impact due to its thin structure, especially along the infraorbital wall. With the accelerated advancement of contemporary transportation and increased activities, the incidence of orbital fractures has demonstrated a discernible upward trajectory on an annual basis. Orbital fractures can lead to herniation and entrapment of orbital contents through the bone defect. In severe cases, prompt surgical intervention is necessary to achieve morphological repair and functional reconstruction. Clinically, the surgical approach of filling the orbital bone defect to support the infraorbital tissues and maintain the

normal position of the eyeball has been identified as an effective means of management.[1] However, the orbital wall is adjacent to the paranasal sinuses and has a relatively poor blood supply, with the defect area often covered by fibromucosal tissue, posing challenges for bone regeneration.[2] Therefore, bone graft materials should possess excellent osteoinductive activity to overcome the unfavorable conditions of local osteoblast deficiency, as well as good biodegradability and integration to guide new bone ingrowth rather than being isolated by fibrous tissue.

At present, the materials used in clinical orbital bone defect repair include traditional titanium mesh, high-density polyethylene, and autologous bone fragments. However, these materials have shortcomings in orbital bone defect repair.[3–7] First, non-resorbable materials are incapable of degrading *in vivo*, and their long-term presence as foreign bodies increases the risk of complications, such as displacement, rejection, and infection. Second, fibrous tissue is biologically inert and tends to become entangled, often leading to cyst formation. Third, the absence of osteoinductivity properties delays the regeneration of native bone, resulting in unsatisfactory repair of orbital bone defects. Moreover, existing materials prove inadequate for effective orbital bone reconstruction, as their biological and mechanical properties frequently fall short of clinical demands. Therefore, there is a pressing clinical need to develop novel materials and repair strategies to overcome the challenges associated with orbital bone defect repair and reconstruction, and to reduce the risks posed by traditional implant materials.

Human acellular amniotic membrane matrix (HAM) is a natural scaffold material derived from the collagenous extracellular matrix of the human placenta. It serves as a cost-effective and biocompatible alternative to other biomaterials. HAM expresses various growth factors and promotes neovascularization by stimulating epithelial cell proliferation and migration.[8,9] Although HAM exhibits inherent mechanical limitations, these can be effectively mitigated by forming composite materials, thereby improving its biomechanical properties. Studies have reported the application of HAM in reconstructing oral and maxillofacial defects, with evidence supporting its role in bone differentiation, repair, and regeneration.[10] To enhance both biological and mechanical performance, researchers have employed different strategies, including hydrogel fabrication, integration with electrospun layers, and surface coating.[11,12]

Hydroxyapatite (HAP), a pioneering material in porous orbital implants, received rapid approval from the United States (US) Food and Drug Administration and has been commercialized as the Bio-Eye sphere.[13] Composites of HAP with organic polymers not only mimic the composition of natural bone but also significantly improve the mechanical properties of scaffold materials.[14] Incorporating HAP into gel-based and pure HAM systems offers a promising approach to combine their advantages and develop biomaterials with superior mechanical performance.[15,16] However, simply mixing the two components cannot replicate the nanoscale architecture of mineralized collagen found in natural bone. In contrast, molecular template-mediated biomimetic mineralization allows controlled deposition of HAP crystals within and between collagen fibers, emulating the biological features of native bone and thus improving bone regeneration. Bone morphogenetic protein 2 (BMP-2) is recognized as one of the most potent osteoinductive factors, capable of recruiting bone marrow mesenchymal stem cells to sites of bone injury and promoting their proliferation and osteogenic differentiation.[17] Therefore, developing bioactive scaffold materials tailored to the local orbital microenvironment is of great significance for the repair of orbital bone defects.

To overcome the limitations of current orbital implant materials, this study developed a methacrylate-functionalized HAM (HAMMA), achieved by grafting methacrylic anhydride (MA) onto HAM. Decellularized HAM was mineralized with a HAP/BMP-2 coating via immersion in 10× simulated body fluid (SBF) supplemented with BMP-2. The composite scaffold (HAMMA/HAP/BMP-2) was fabricated using HAP particles, BMP-2, and HAMMA via three-dimensional (3D) printing combined with UV curing. The mechanical properties, swelling behavior, and degradation profile of the composite scaffolds were comprehensively evaluated. Furthermore, the potential of HAMMA/HAP/BMP-2 for orbital bone repair was assessed through *in vitro* cell studies and *in vivo* animal experiments.

2. Materials and methods

2.1. Preparation of HAMMA

The HAM was prepared from amniotic membranes obtained within 24 h following natural delivery and stored at 4°C. The study protocol was approved by the institutional review board. Briefly, the amniotic membrane was separated from the chorion via blunt dissection and washed three times with phosphate-buffered saline (PBS) to eliminate blood and cellular debris. Subsequently, the amniotic membrane was treated with a 0.1% ethylenediaminetetraacetic acid solution for 2 h at 37°C, followed by gentle scraping using a cell scraper to remove the epithelial layer. Following these treatments, the acellular amniotic membrane matrix was spread on a smooth and flat glass slab and air-dried overnight. The acellular amniotic membrane matrix was dissolved in 0.5 M acetic acid at a concentration of 10 mg/mL, and the pH was adjusted to a range of 8–9 using

NaOH. The mixture was then reacted with MA for 24 h. The resulting product was loaded into a dialysis bag with a molecular weight cutoff of 3500 Da and dialyzed for 2 days, followed by lyophilization to obtain spongy HAMMA.

2.2. Fabrication of HAMMA composite scaffolds

Kokubo's protocol was used to prepare 10× SBF. Recombinant human BMP-2 (10426-H01H, SinoBiological, China), at a concentration of 1% (w/v) of the total SBF volume, was added to the 10× SBF and gently vortexed to ensure thorough mixing while preventing aggregation. The 10% (w/v) spongy HAM was immersed in 10× SBF supplemented with 1% BMP-2 and incubated at 37°C under gentle agitation (50 rpm) for 7 days. The solution was replaced every 48 h to maintain ion saturation. The mineralized HAMA/HAP/BMP-2 was centrifuged, precipitated, and formed into a sol at 4°C. Then, 0.1% (w/v) lithium phenyl phosphate photoinitiator (LAP; L0290, TCI Shanghai, China) was added to the aforementioned mixture, and three scaffolds were constructed separately using 3D printing technology (SunP BioMaker 2, MilliporeSigma, US). Due to the physical filling and hydrogen bonding of HAP, the structure might be compromised once the printing process is complete. The scaffolds were subjected to photo-crosslinking under a UVLED point light source (395–480 nm, 10.5 mm curing tip; Ultradent Products, US) for 30 s—a step that could enhance the long-term stability of the composite scaffold.

2.3. Characterization of HAMMA composite scaffolds

The morphology and elemental distribution of the HAMMA composite scaffolds were characterized using scanning electron microscopy (SEM; Nova NanoSEM 450, Thermo Fisher Scientific, US). The crystalline phases were analyzed with an X-ray diffractometer (XRD; SmartLab-SE, Rigaku Corporation, Japan). The tensile properties of the scaffolds were measured on a universal testing machine (INSTRON 5943, Instron, US). The chemical composition of the HAP/BMP-2–mineralized scaffolds was examined using Fourier transform infrared spectroscopy (FTIR; IN10, Thermo Fisher Scientific, US) over the wavenumber range of 400–4000 cm^{-1}.

2.4. Degradation of HAMMA composite scaffolds

The HAMMA composite scaffolds were immersed in a PBS solution (10 mL, 9 mg/L, 37°C). After centrifugation at 7000 rpm for 10 min, the supernatant was collected and re-immersed in a fresh PBS solution (10 mL, 9 mg/L, 37°C). The experiment was continued for 28 days. Subsequently, the concentrations of BMP-2 in the supernatant were quantified using the human BMP-2 ELISA kit (E-EL-H0011, Elabscience, China). The degraded samples were centrifuged weekly, and the supernatant was discarded and replaced with fresh PBS. The mass loss of the composite scaffolds was calculated by deriving the mass difference, and the weight loss percentages of each sample were calculated based on Equation (1).

$$\text{Weight loss (\%)} = (W_1 - W_2)/W_1 \times 100\% \quad (1)$$

where W_2 is the mass of dry scaffolds at a specific time point, and W_1 is the initial weight of the dry scaffolds.

2.5. Swelling experiment of HAMMA composite scaffolds

The weight of HAMMA composite scaffolds was recorded as W_0. The scaffolds were then immersed in ultra-pure water for 0, 1, 2, 4, 6, 8, 12, or 24 h. Following the removal of the scaffolds, any surface moisture was removed by blotting with filter paper. The weight was subsequently recorded as W_1. The swelling ratio was calculated as follows:

$$\text{Swelling ratio (\%)} = (W_1 - W_0)/W_0 \times 100\% \quad (2)$$

where W_1 denotes the weight of the water-swollen gel at various time points and W_0 represents its final weight after the gelation process is complete.

2.6. Cell culture

The murine preosteoblast cell line MC3T3-E1 was obtained from the BeNa Culture Collection (China). The cells were cultured in alpha Eagle's minimal essential medium (Gibco, US) supplemented with 10% fetal bovine serum (Gibco, US) and 1% penicillin–streptomycin (Gibco, US), with the medium replaced every 3 days. For osteogenic differentiation induction, confluent MC3T3-E1 cells were stimulated with 10 nM dexamethasone (Sigma-Aldrich, US), 0.2 mM ascorbic acid (Sigma-Aldrich, US), and 10 mM β-glycerophosphate (Sigma-Aldrich, US). The induction medium was also refreshed every 3 days.

2.7. Cell compatibility

MC3T3-E1 cells were cultured with the HAMMA composite scaffolds for different time intervals (1, 3, or 5 d). Subsequently, cell counting kit 8 solution was added, followed by incubation in the dark at 37°C for 30 min. Absorbance was measured at 450 nm using the microplate reader to calculate cell viability. Meanwhile, the Calcein/PI Kit (Beyotime Biotechnology Institute, China) was prepared 30 min in advance and placed at room temperature. The staining working solution was prepared according to the instructions. After incubation at room temperature in the dark for 30 min, the samples were gently washed three times with PBS. Green fluorescence was imaged at the same location using a fluorescence microscope and documented. To examine cell morphology and spreading,

MC3T3-E1 cells were stained with TRITC phalloidin and 4',6-diamidino-2-phenylindole (DAPI) for cytoskeletal and nuclear visualization, respectively, and examined under an inverted fluorescence microscope (IX71, Olympus, Japan). A cell-free "scratch wound" was created on a monolayer of adherent cells, and cell migration ability was quantitatively assessed by monitoring cell movement into the scratched area over time using the same microscope system.

2.8. Alkaline phosphatase activity assay

After 7 days of differentiation and cultured with HAMMA composite scaffolds, MC3T3-E1 cells were washed three times with PBS and fixed with 4% paraformaldehyde for 30 min at room temperature, followed by washing with PBS. The fixed cells were treated with a 5-bromo-4-chloro-3-indolyl phosphate/nitroblue tetrazolium substrate kit (Beyotime Biotechnology Institute, China) for chromogenic detection of alkaline phosphatase (ALP) activity. The procedure was carried out in strict compliance with the manufacturer's protocol, and images were captured using an inverted microscope (Olympus IX71, Japan).

2.9. Alizarin red S staining

After 21 days of differentiation and culture with HAMMA composite scaffolds, MC3T3-E1 cells were washed three times with PBS and fixed in 4% paraformaldehyde for 30 min at room temperature. Following fixation, the cells were rinsed again with PBS. Subsequently, they were stained with 1% (w/v) alizarin red S solution for 15 min, followed by two additional PBS washes. Images were captured using an inverted microscope.

2.10. Western blot analysis

Cell lysates were prepared for Western blot analysis. Total protein was separated through sodium dodecyl sulfate–polyacrylamide gel electrophoresis. Following electrophoresis, the proteins were transferred onto polyvinylidene fluoride membranes. For immunodetection, the membranes were blocked with 5% non-fat dry milk for 12–16 h at 25°C. Primary antibodies (all purchased from Proteintech, US) against glyceraldehyde-3-phosphate dehydrogenase (GAPDH; 10494-1-AP), osteopontin (OPN; 25715-1-AP), Runx2 (20700-1-AP), and collagen type I (COL I; 14695-1-AP) were diluted at 1:1000. Detection was performed using horseradish peroxidase (HRP)-conjugated anti-mouse secondary antibodies (HRP-60004, Proteintech, US) diluted at 1:3000 in 5% non-fat dry milk prepared in Tris-buffered saline with Tween 20. Blots were visualized using enhanced chemiluminescence and a protein blot detection system.

2.11. RNA sequencing

MC3T3-E1 cells (3×10^6) cultivated with the composite scaffolds were treated with TRIzol reagent (Invitrogen, US) at 8 h after ultrasound treatment. The experiments were independently conducted three times for each group. RNA sequencing was performed at the Beijing Genomics Institute (China). A heatmap illustrating gene expression levels across various samples was generated using the Heatmap software (v1.0.8). Briefly, differential expression analysis was conducted with DESeq2 (v1.4.5), applying a significance threshold of Q value ≤ 0.05. To further explore phenotypic alterations, gene ontology and Kyoto Encyclopedia of Genes and Genomes (KEGG) enrichment analyses were carried out on the differentially expressed genes (DEGs) using the Phyper software, which employs hypergeometric tests. The significance levels of the enriched terms and pathways were adjusted using the Bonferroni correction method, with a stringent cutoff of Q value ≤ 0.05.

2.12. Quantitative real-time PCR analysis

Total RNA was isolated from MC3T3-E1 cells or bone tissues using TRIzol reagent. Complementary DNA was synthesized with a reverse transcription kit (Invitrogen, US) following the manufacturer's protocol. Gene expression levels were quantified through real-time quantitative polymerase chain reaction (RT-PCR). The mRNA expression in each sample was normalized to the expression of the *GAPDH* gene. All experiments were conducted in triplicate. The specific primer sequences used for both cells and tissues are listed in Table S1 of the Supporting information.

2.13. Model of rat skull defect and canine orbital wall bone defect

The animals used in the experiments were obtained from the Hubei Provincial Center for Disease Control and Prevention (China). All procedures involving animals were carried out in compliance with protocols approved by the Chinese National Committee for the Protection and Utilization of Institutional Animals (QR-ADM-G004-4.0). Prior to the procedure, the animals were anesthetized through intraperitoneal injection of pentobarbital (3.5 mg/100 g). An area of approximately 2 cm^2 on the scalp was disinfected with alcohol to define the anatomical site.

A total of thirty 7-week-old, male Sprague-Dawley rats weighing approximately 250 g were selected for skull defects. Skull defects were induced with an orthopedic ring drill with a diameter of 5 mm. Subsequently, all rats were randomly assigned to one of three groups: Control group (n=10), HAMMA/HAP group (n=10), and HAMMA/HAP/BMP-2 group (n=10).

Three 12-month-old, male beagle dogs of similar weight were used. Incisions were made along the inner canthus and lower orbital margins of the left and right eyes to separate the periosteum. Following the separation of the periosteum, the inner wall of the orbit was exposed without

performing enucleation of the eyeball. A ring drill was employed to create an orbital wall defect with a diameter of 10 mm, and approximately 5 mm of surrounding periosteum and ethmoid mucosa were removed. Animal bone defects on the eyes were then implanted with the following composite scaffolds: Control group (left eye; n=3) and HAMMA/HAP/BMP-2 (right eye; n=3) group.

2.14. Micro-computed tomography

The rats and canines were sacrificed at a specified time point after the operation and fixed for 24 h. Subsequently, the samples were scanned using a SkyScan 1176 micro-computed tomography (micro-CT) system (Bruker, Belgium), utilizing a monochromatic beam with 30 keV energy and a resolution of 18 μm. The images and data obtained were processed using CTVox and CTAn software, respectively, and voxels were extracted with a gray value of 130.

2.15. Histological analysis

After micro-CT scanning, the specimens were embedded in paraffin and sectioned at a thickness of 7 μm. All sections were subsequently stained with hematoxylin and eosin (H&E; Sigma-Aldrich, US) and Masson's trichrome (Sigma-Aldrich, US). H&E staining was employed to evaluate the overall tissue architecture and morphology, including cellular distribution and organization.

2.16. Immunofluorescence staining

The immunofluorescence staining protocol involved dewaxing of paraffin-embedded sections, retrieving antigen using an appropriate solution, heating at 95–100°C, and blocking with 5% goat serum for 30 min. Sections were then incubated with the following primary antibodies (all purchased from Proteintech, US) diluted in blocking buffer: OPN polyclonal antibody (1:50; 22952-1-AP), osteocalcin (OCN) polyclonal antibody (1:200; 23418-1-AP), and cluster of differentiation (CD)31 antibody (1:800, 11265-1-AP). Subsequently, samples were incubated with secondary antibodies Cy3-conjugated AffiniPure goat anti-rabbit IgG (H+L; SA00009-2, Proteintech, US) and FITC-conjugated AffiniPure goat anti-rabbit IgG (H+L; SA00003-2, Proteintech, US) diluted in 1% bovine serum albumin/PBS, at 4°C for 24 h. After three washes, fixed cell samples were counterstained with DAPI.

2.17. Statistical analysis

Statistical analyses were conducted using SPSS 18 (IBM, US). All data are presented as mean ± standard deviation. For multiple comparisons in the *in vivo* studies, a one-way analysis of variance was used. Comparisons between two groups were performed using paired t-tests. A p-value of less than 0.05 was considered statistically significant.

3. Results

3.1. Characterization of HAMMA composite scaffolds

The hydrogel scaffold possessed a solid structure at room temperature (Figure 1A). The XRD spectra (Figure 1B) showed that the nano-apatite exhibited characteristic diffraction peaks at 2θ=25°, 31.4°, 32.1°, 32.7°, 39.4°, 46.2°, 53.1°, and 64.1°—a result in accordance with the standard card of HAP (JCPDS-09-0432). However, the characteristic peak of HAP was evident in the hydrogel scaffold, with peak positions similar to those of the standard card of HAP, suggesting that the double crosslinking method did not disrupt the crystalline structure of HAP. The FTIR spectra (Figure 1C) revealed characteristic absorption peaks corresponding to gelatin, specifically the amide I band (C=O stretching vibration) at 1627 cm^{-1}, the amide II band (N–H bending vibration) at 1521 cm^{-1}, and the amide III band (C–N stretching vibration) at 1234 cm^{-1}. The characteristic absorption peaks of (HAP) included the stretching vibration peak of PO_4^{3-} at 1024 and 965 cm^{-1}, the deformation vibration peaks of PO_4^{3-} at 603 and 555 cm^{-1}, the OH stretching vibration peak at 3600 cm^{-1}, and the bending vibration peak at 633 cm^{-1}. Following the addition of HAP to the hydrogel scaffold, the characteristic peaks of HAP appeared at 603 and 555 cm^{-1}, while the O–H peak shifted to 3277 cm^{-1} with a notable increase in width. The peak at 1627 cm^{-1} (amide I band) exhibited a significant broadening, and the peak at 1521 cm^{-1} (amide II band) shifted to 1550 cm^{-1}, confirming the interaction and formation of hydrogen bonds. The SEM morphology of the composite hydrogel is illustrated in Figure 1D. The incorporation of HAP particles did not change the porous network structure of the hydrogel, and the pore size ranged from 500 to 800 μM. The energy spectrum analysis revealed that the HAP particles were uniformly distributed and dispersed (Figure 1E).

The compressive modulus of the hydrogel was determined from the linear region (0–10% strain) of the stress–strain curve. As illustrated in Figure 1F, the elastic modulus of the pure hydrogel without HAP was 3.18 ± 0.09 kPa. The incorporation of HAP particles as reinforcing fillers led to a notable enhancement in the mechanical strength of the hydrogel, accompanied by a considerable increase in the elastic modulus. Moreover, the hydrogel exhibited favorable tensile and bending resistance. In a dry state, the hydrogel could withstand 50 g of weight (Figure 1G). Figure 1H illustrates the water absorption rate of the hydrogels at various time points. All hydrogels exhibited rapid water absorption during the initial hour, with swelling curves demonstrating a gradual increase over time. The addition of HAP particles resulted in a reduction in both the swelling rate and the ultimate water absorption

capacity of the scaffolds, consequently improving their dimensional stability (Figure 1I). In addition, the degradation rates of different composite hydrogels indicated that the pure hydrogel group exhibited the highest weight loss rate, reaching 100% on day 5, indicative of complete degradation (Figure 1J). The incorporation of HAP particles resulted in a notable reduction in the degradation rate of hydrogel scaffolds. The *in vitro* drug release profiles demonstrated that the hydrogel scaffolds were capable of releasing BMP-2 in a continuous manner. On day 7, BMP-2 was released explosively, followed by a gradual flattening of the release profile (Figure 1K). These results demonstrate that the hydrogel scaffolds possess the capacity to load and release drugs.

3.2. *In vitro* biocompatibility and osteogenesis evaluation

As shown in Figure 2A, CCK-8 assay results indicated that HAMMA/HAP/BMP-2 consistently enhanced cellular activity over time. After 1 and 5 days of incubation, cells in each group were stained using a Calcein/PI kit and examined under an inverted fluorescence microscope. The green fluorescence revealed that the cells in each group were evenly distributed and exhibited a polygonal morphology (Figure 2B). In the scratch experiment, the migration speed of cells in HAMMA/HAP/BMP-2 was obviously accelerated, and the scratch area was completely closed within 48 h (Figure 2C). The results of nuclear membrane staining showed that the cells also exhibited a fully extended polygonal structure with no discernible alteration in morphology, which is consistent with the results of the cell viability test, indicating that the hydrogel scaffolds have no obvious cytotoxicity (Figure 2D).

The results of ALP staining (Figure 2E) showed that HAMMA/HAP/BMP-2–treated cells showed a strong blue–purple color compared with the control, indicating that HAMMA/HAP/BMP-2 composite scaffolds result in enhanced ALP activity. Alizarin red staining (Figure 2F) results showed that compared with the control group, HAMMA/HAP composite scaffolds-treated cells had more obvious mineralized nodules and were densely arranged. With the introduction of BMP-2, the extent of red deposition was enhanced, accompanied by more pronounced mineralization nodule formation. COL I, an extracellular matrix protein, promotes osteoblast adhesion and differentiation. OPN, a non-collagenous protein abundantly present in the bone matrix and secreted by osteoblasts, stimulates osteoclast formation and enhances the resorptive activity of mature osteoclasts. Runx2 regulates the phenotype of osteoblasts and the expression of osteoblast-specific matrix proteins, including ALP, COL I, and OPN, ultimately stimulating bone nodule mineralization. Compared to the control group, the expression of osteogenesis-related proteins and factors, such as COL I, OPN, and Runx2, was significantly higher in the group treated with the HAMMA/HAP hydrogel scaffold (Figure 3G & 3H). When the cells were treated with the HAMMA/HAP/BMP-2 hydrogel scaffold, these expressions were further increased.

3.3. *In vitro* osteogenesis mechanism

Following *in vitro* analyses, the molecular mechanisms underlying the effects of HAMMA composite scaffold treatment on MC3T3-E1 cells were determined through RNA sequencing. A total of 2387 DEGs, including 2003 upregulated and 984 downregulated genes, were identified between the HAMMA/HAP composite scaffolds and control groups (Figure S1A & S1C). A total of 2413 DEGs, including 1501 upregulated and 912 downregulated genes, were identified between the HAMMA/HAP/BMP-2 composite scaffolds and control groups (Figure S1B & S1D).

The KEGG pathway analysis was performed to identify signaling pathways that showed significant enrichment among the DEGs when comparing the HAMMA/HAP or HAMMA/HAP/BMP-2 groups with the control group (Figure 3A & 3B). The results demonstrated that osteogenesis-related signaling pathways, such as the mitogen-activated protein kinase (MAPK) signaling pathway, phosphatidylinositol 3-kinase–protein kinase B signaling pathway, calcium signaling pathway, Ras-related protein 1 signaling pathway, and cGMP–protein kinase G signaling pathway, were enriched. The DEGs between the HAMMA/HAP/BMP-2 group and the control group had two additional signaling pathways—the FoxO signaling pathway and the ATP-binding cassette transporters. The protein–protein interaction network analysis of DEGs between the HAMMA/HAP or HAMMA/HAP/BMP-2 group and the control group (Figure 3C & 3D) was performed. The results demonstrated that the osteogenesis-related gene network center included *Fgfr2*, *Fgfr3*, *Fgf18*, *Pik3r3*, *Egf*, *Igf1*, and *Irs1*. To further explore the osteogenesis mechanism, the KEGG pathway results between the HAMMA/HAP group and the HAMMA/HAP/BMP-2 group (Figure 3E) revealed interleukin-17, MAPK, and vascular endothelial growth factor (VEGF) signaling pathways. The protein–protein interaction network analysis of DEGs between the HAMMA/HAP group and HAMMA/HAP/BMP-2 group (Figure 3F) was further performed, demonstrating that the osteogenesis-related gene network center comprised *Fgfr2*, *Fgfr3*, *Pik3r3*, *Egf*, *Igf1*, *Irs1*, *Tgfbr1*, *Smad9*, and *Bmpr1a*.

The differentially expressed proteins and genes in interaction networks were further validated through molecular biology techniques. The RT-PCR analysis

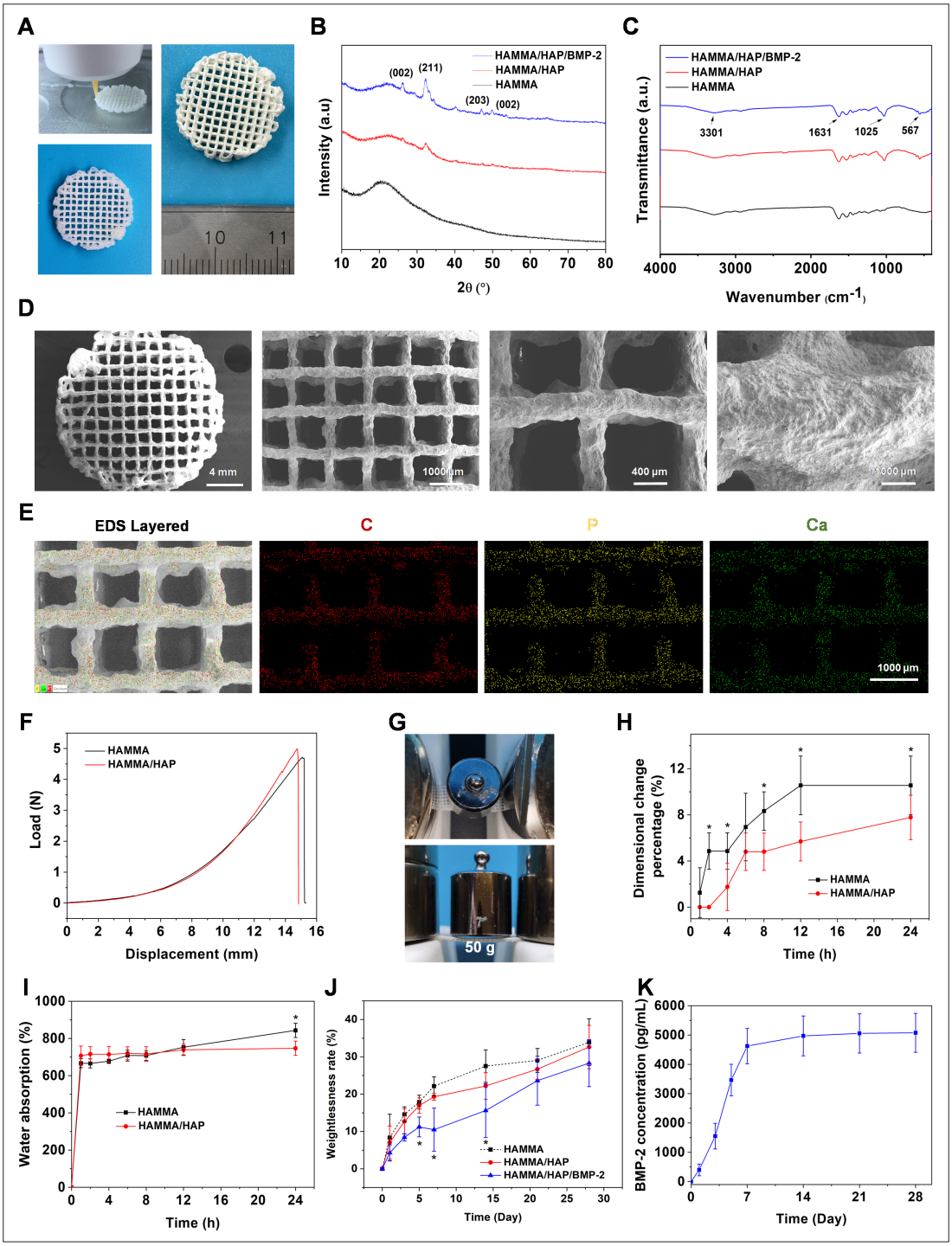


Figure 1. Characterization of HAMMA composite scaffolds. (A) The optical photographs of HAMMA/HAP/BMP-2. The (B) X-ray diffractometry spectra and (C) Fourier transform infrared spectra of HAMMA, HAMMA/HAP, and HAMMA/HAP/BMP-2. (D) The microstructure of HAMMA/HAP/BMP-2. Scale bars (from left to right): 4 mm, 1000, 400, and 1000 μm; magnifications (from left to right): × 6, × 20, × 50, × 200. (E) The element distribution of C, P, and Ca in HAMMA/HAP/BMP-2. Scale bar: 1000 μm; magnification: × 30. The element distribution of HAMMA, HAMMA/HAP, and HAMMA/HAP/BMP-2. (F) The tensile mechanical properties of HAMMA and HAMMA/HAP. (G) Bending performance test of HAMMA (or HAMMA/HAP). The (H) morphological diagram and (I) water absorption rates of materials immersed in water over different durations. (J) The weightlessness rate of HAMMA, HAMMA/HAP, and HAMMA/HAP/BMP-2. (K) The release kinetics of BMP-2 from HAMMA/HAP/BMP-2 composite scaffolds. Notes: n=3; *$p < 0.05$ compared to HAMMA. Abbreviations: BMP-2, bone morphogenetic protein 2; HAMMA, methacrylate-functionalized human acellular amniotic membrane matrix; HAP, hydroxyapatite.

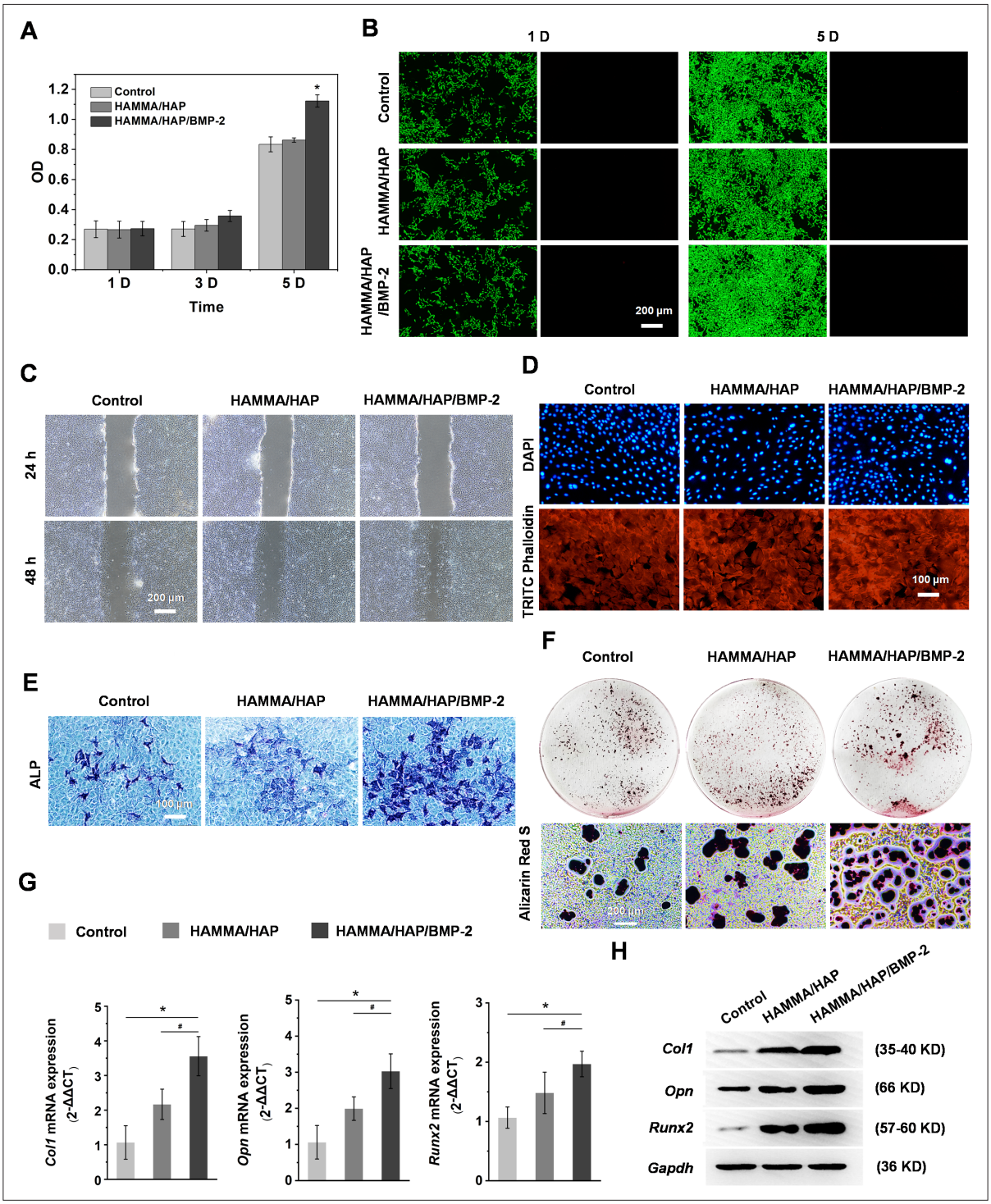


Figure 2. Effect of HAMMA composite scaffolds on biocompatibility and osteogenic differentiation. (A) CCK-8 is used for cell viability determination. (B) The viability of MC3T3-E1 cells *in vitro* was assessed via the Calcein/PI Kit. Scale bar: 200 μm; magnification: ×40. (C) The migration speed of cells in HAMMA/HAP and HAMMA/HAP/BMP-2. Scale bar: 200 μm; magnification: ×40 . (D) The morphology staining of the MC3T3-E1 cells was assessed via nuclear membrane staining. 100 μm; magnification: ×100. (E) The ALP staining of the MC3T3-E1 on day 7. Scale bar: 100 μm; magnification: × 100. (F) Alizarin red S staining of MC3T3-E1 cells on day 14. Scale bar: 200 μm; magnification: × 40. (G & H) Real-time quantitative polymerase chain reaction and Western blotting analysis to assess the expression of osteogenic proteins, including Runx-2, collagen type I, and OPN. Notes: n=3; $^{*}p < 0.05$ compared to controls; $^{\#}p < 0.05$ compared to HAMMA/HAP. Abbreviations: ALP, alkaline phosphatase; BMP-2, bone morphogenetic protein 2; HAMMA, methacrylate-functionalized human acellular amniotic membrane matrix; HAP, hydroxyapatite; OPN, osteopontin.

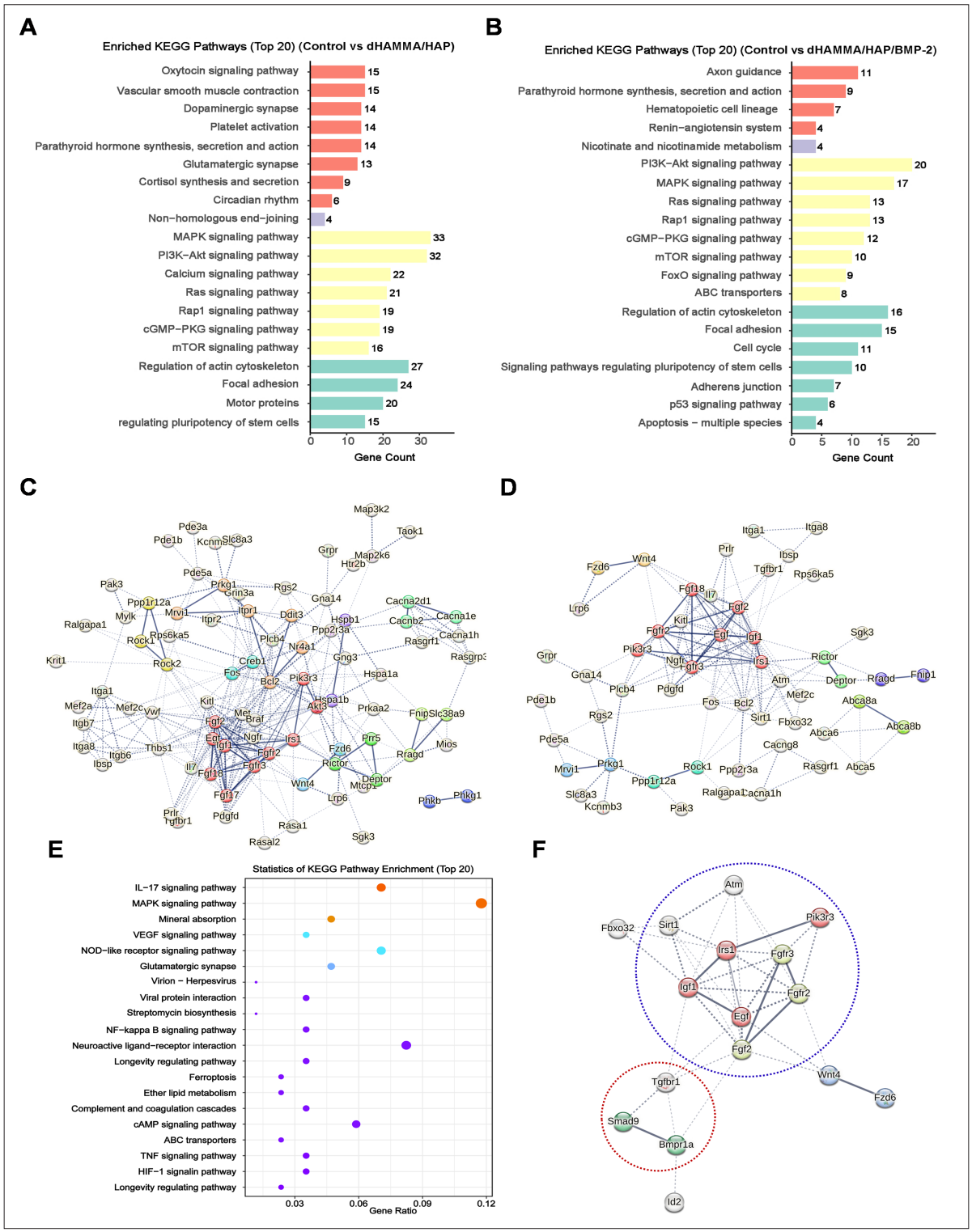


Figure 3. Potential osteogenesis mechanisms of HAMMA composite scaffolds. KEGG pathway enrichment analysis of DEGs (A) between the control and HAMMA/HAP groups; and (B) between the control and HAMMA/HAP/BMP-2 groups. Protein–protein interaction network of DEGs (C) between the control and HAMMA/HAP groups; and (D) between the control and HAMMA/HAP/BMP-2 groups. (E) KEGG pathway enrichment analysis and (F) protein–protein interaction network of DEGs between the HAMMA/HAP and HAMMA/HAP/BMP-2 groups. Abbreviations: BMP-2, bone morphogenetic protein 2; DEG, differentially expressed gene; HAMMA, methacrylate-functionalized human acellular amniotic membrane matrix; HAP, hydroxyapatite; KEGG, Kyoto Encyclopedia of Genes and Genomes.

showed that the DEGs *Fgfr2* (Figure 4A), *Fgfr3* (Figure 4B), *Bmpr1a* (Figure 4C), *Smad9* (**Figure 4D**), and *Wnt4* (**Figure S3A**) were upregulated in the HAMMA/HAP/BMP-2 group. These genes were mainly involved in BMP-2 signaling pathways. Meanwhile, the DEGs *Irs1* (Figure 4E), *Tgfbr1* (Figure 4F), *Fbox32* (Figure 4G), *Sirt1* (Figure 4H), and *Atm* (Figure S3B) were upregulated in the HAMMA/HAP and HAMMA/HAP/BMP-2 groups. These genes were mainly involved in the VEGF signaling pathway. The Western blotting analysis also showed that the expression of proteins insulin receptor substrate 1 (IRS1), fibroblast growth factor receptor 2 (FGFR2), FGFR3, and bone morphogenetic protein receptor type 1A (BMPR1A) were upregulated in HAMMA/HAP/BMP-2 group, while the expression of protein transforming growth factor beta receptor type 1 (TGFBR1) were upregulated in the HAMMA/HAP and HAMMA/HAP/BMP-2 groups. These results indicate that the HAMMA/HAP/BMP-2 composite promotes the differentiation and proliferation of undifferentiated mesenchymal stem cells into osteoblasts, enhances the differentiation and maturation of osteoblasts, and participates in bone growth and remodeling processes, thereby accelerating the repair of bone defects.

3.4. *In vivo* osteogenesis evaluation

To assess their capacity to stimulate osteogenesis and angiogenesis *in vivo*, HAMMA composite scaffolds were implanted into a 5-mm rat calvarial defect model. Samples were obtained and analyzed at 20 and 60 days after surgery (Figure 5A). Immunofluorescence evaluation of the expression of differential protein (Figure 5B) showed that FGFR3 and BMPR1A were upregulated in the HAMMA/HAP/BMP-2 group, and FGFR2 was upregulated in the HAMMA/HAP and HAMMA/HAP/BMP-2 groups (Figure 5C–E). These *in vivo* results were similar to those of the *in vitro*.

The degradation of the HAMMA composite scaffolds was accompanied by the ingrowth of new bone tissues, as revealed in 3D images reconstructed using micro-CT software. Furthermore, bone formation was detected to be higher in the HAMMA/HAP/BMP-2 group than in the control group at 60 days after implantation (Figure 6A). The regenerated bone volumes at the implantation sites of the three samples were also calculated separately to evaluate bone regeneration more accurately (Figures 6B & S4B). The control group exhibited a mean value of 6.21 ± 2.1%, while the HAMMA/HAP group demonstrated a mean value of 13.7 ± 6.33%. In contrast, the HAMMA/HAP/BMP-2 group exhibited the highest mean value of 24.64 ± 9.30%. Histological analysis was applied to provide detailed observations of osteogenesis and angiogenesis in the HAMMA/HAP and HAMMA/HAP/BMP-2 groups at 60 days (Figure 6C). H&E staining and Masson trichrome staining further revealed that all HAMMA composite scaffolds were absorbed gradually after implantation into the bone defect. In contrast, new bone tissues and blood vessels containing murine erythrocytes were formed around HAMMA/HAP and HAMMA/HAP/BMP-2. Obviously, more trabecular bones and blood vessels were observed in the HAMMA/HAP/BMP-2–treated implant than others.

The immunohistochemical analysis revealed that the expression levels of CD31, OPN, and OCN surrounding the HAMMA/HAP/BMP-2 implants at 60 days were significantly higher compared to those in the HAMMA/HAP and control groups (Figure 7), suggesting that VEGF produced by cells in bone could stimulate the formation of new blood vessels. Additionally, the staining results for OPN and OCN revealed significantly higher bone formation activity in the HAMMA/HAP/BMP-2 group compared to both the HAMMA/HAP and control groups at weeks 4 and 8.

3.5. *In vivo* therapeutic efficacy of orbital bone defects

Our results have shown that HAMMA/HAP/BMP-2 could induce faster bone formation and maturation in a rat full-thickness skull defect. However, the size and location of the defect were the main determinants of the innate ability of bone healing. In particular, the bone of the orbital wall was thin, the adjacent bone contained fewer mesenchymal stem cells, and its proximity to the paranasal sinuses resulted in a poor blood supply. Therefore, we conducted a second *in vivo* study to evaluate the potential application of HAMMA/HAP/BMP-2 in canine orbital wall bone defect, which is considered a severe test for bone implantation (Figures 8A, 8B, & S5).

The entire canine cranium, including the orbital bone defects, was scanned and reconstructed in 3D via micro-CT post-treatment. As depicted in **Figure 8C**, 90 days after implantation, the blank control group showed significant bone defects at the infraorbital margin of the orbital bone fractures, with the implanted material having completely degraded. Conversely, an increase in bone mineral density was observed, indicative of neoplastic bone tissue growth. A quantitative analysis was performed on the reconstructed 3D models derived from micro-CT imaging, and the bone volume/total volume (BV/TV) values were calculated for each group of samples. The results in Figure S6 depict a significant increase in the BV/TV value of the HAMMA/HAP/BMP-2 group (11.37 ± 2.93%) after 90 days of implantation compared to the control group (32.06 ± 3.76%).

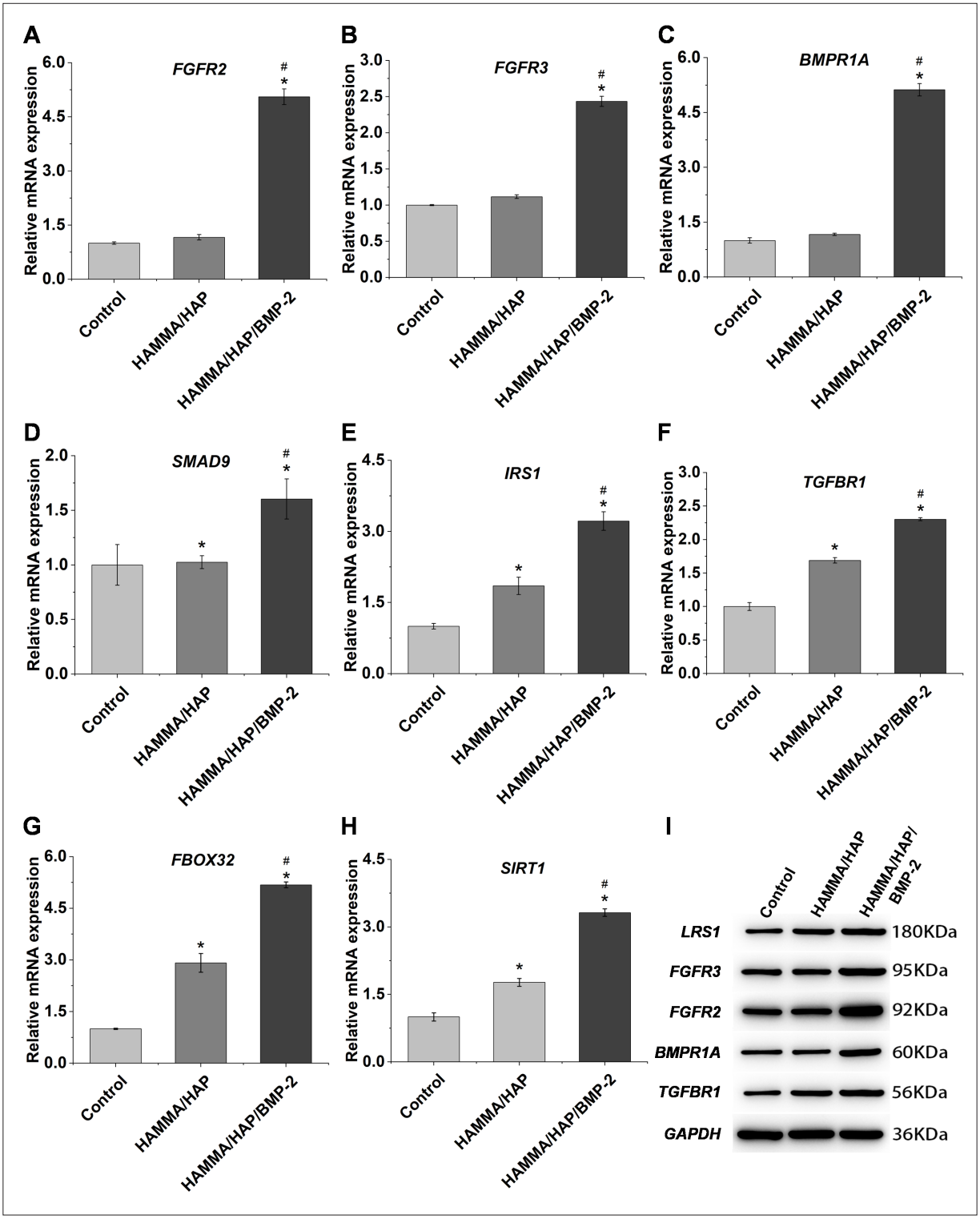


Figure 4. Verification of differentially expressed genes and proteins in interaction networks. RT-PCR analysis to assess the expression of differentially expressed genes: (A) *FgFr2*, (B) *FgFr3*, (C) *Bmpr1a*, (D) *Smad9*, (E) *Irs1*, (F) *Tgfbr1*, (G) *Fbox32*, and (H) *Sirt1*. (I) Western blotting analysis to assess the expression of differentially expressed proteins, IRS1, FGFR2, FGFR3, BMPR1A, and TGFBR1. Notes: n=3; *$p < 0.05$ compared to control; #$p < 0.05$ compared to HAMMA/HAP. Abbreviations: BMP-2, bone morphogenetic protein 2; BMPR1A, bone morphogenetic protein receptor type 1A; FGFR2/3, fibroblast growth factor receptor 2/3; GAPDH, glyceraldehyde-3-phosphate dehydrogenase; HAMMA, methacrylate-functionalized human acellular amniotic membrane matrix; HAP, hydroxyapatite; IRS1, insulin receptor substrate 1; TGFBR1, transforming growth factor beta receptor type 1.

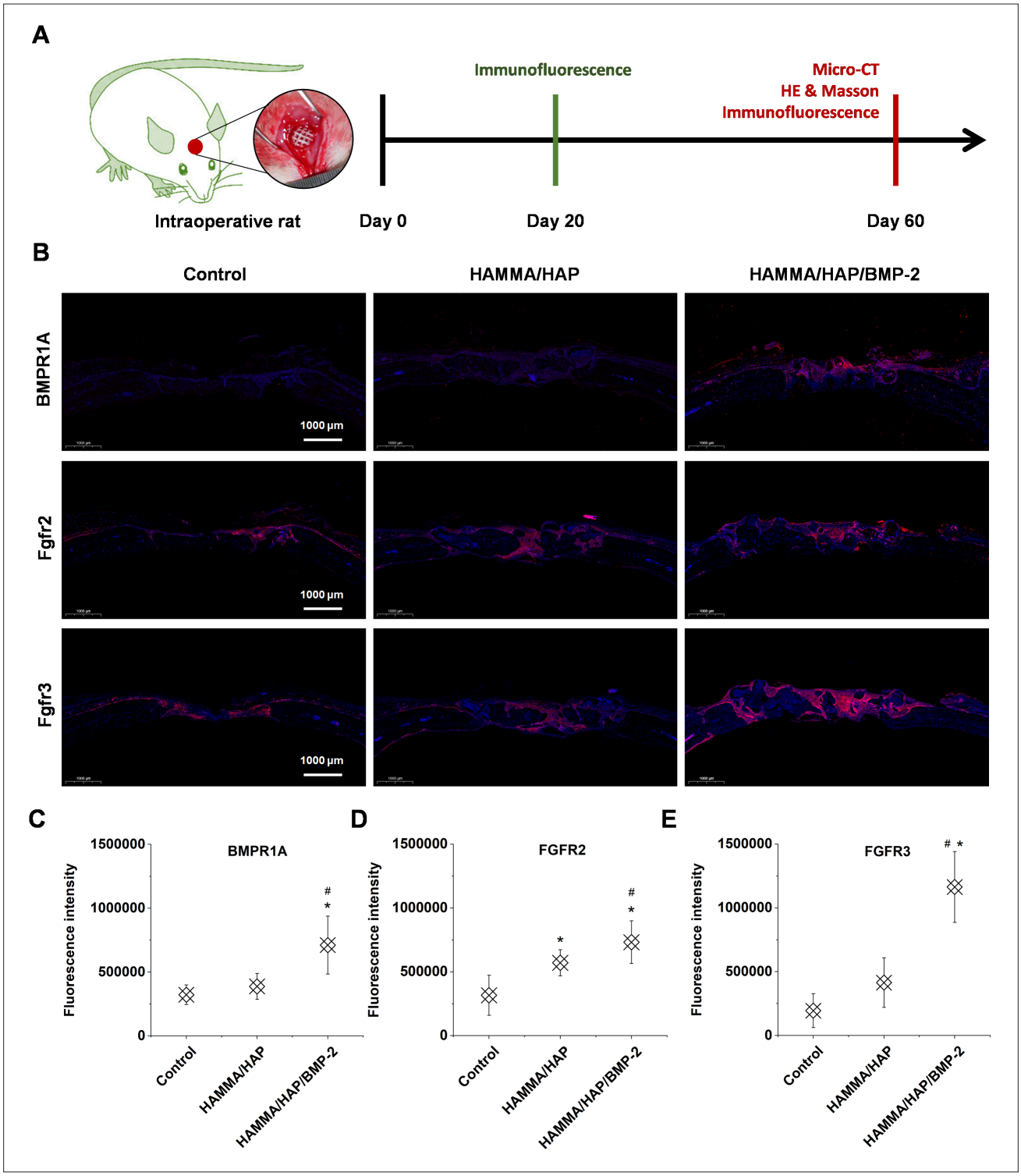


Figure 5. *In vivo* study of HAMMA composite scaffolds in the treatment of rat calvarial defect. (A) Establishment of rat calvarial defect and implantation of scaffolds. (B) Immunofluorescence evaluation of the expression of proteins under different treatments after 20 days. Scale bars: 1000 μm; magnifications: × 4. (C–E) Statistics of immunofluorescence intensity from differentially expressed proteins. Notes: n=3; *$p < 0.05$ compared to control; #$p < 0.05$ compared to HAMMA/HAP. Abbreviations: BMP-2, bone morphogenetic protein 2; BMPR1A, bone morphogenetic protein receptor type 1A; FGFR2/3, fibroblast growth factor receptor 2/3; HAMMA, methacrylate-functionalized human acellular amniotic membrane matrix; HAP, hydroxyapatite; HE, hematoxylin and eosin.

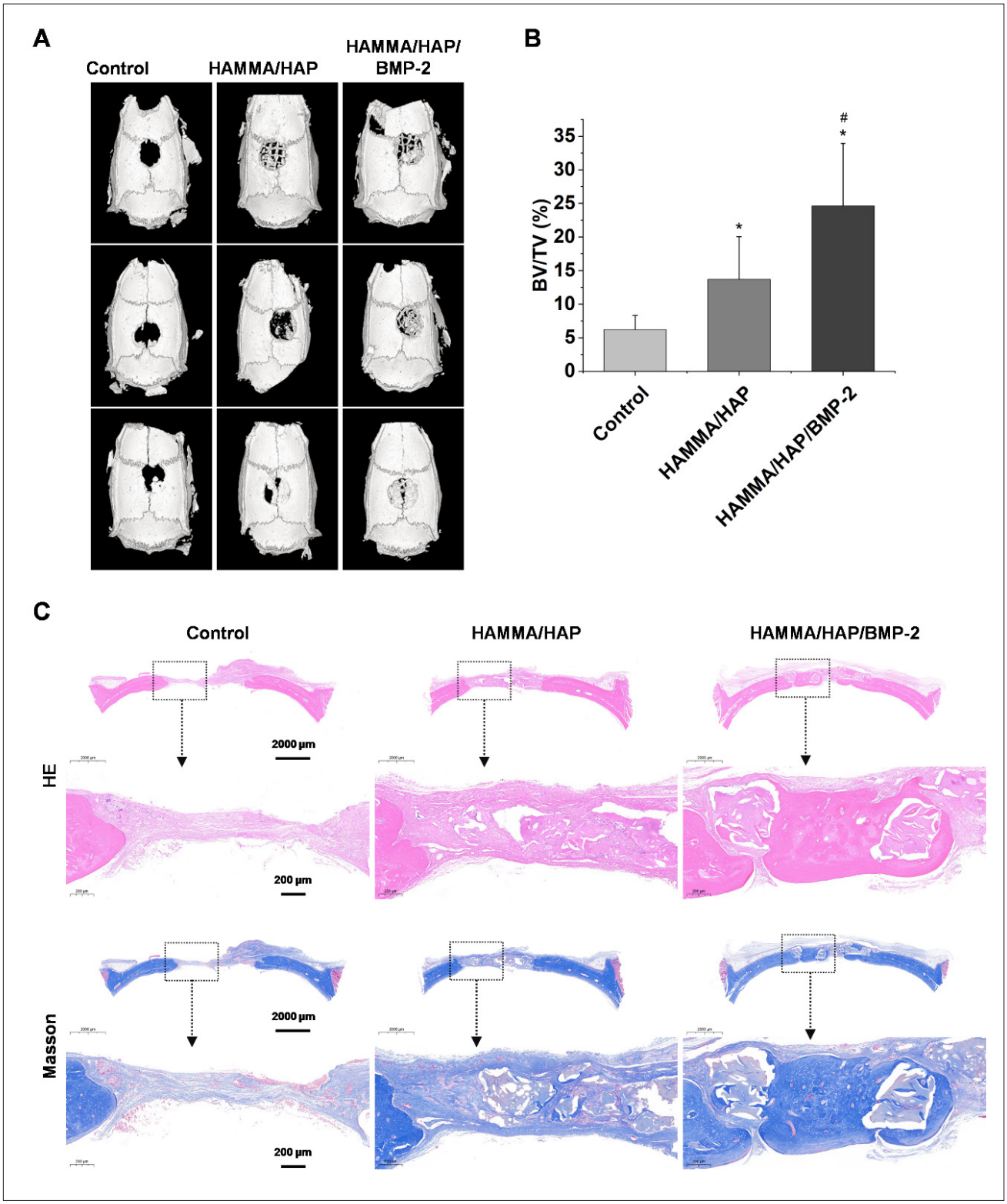


Figure 6. Regeneration of bone defects in rats. (A) Representative micro-CT reconstruction images in coronal and sagittal views in different groups at 60 days post-surgery. (B) Micro-CT quantification of the calvarial defects. (C) HE and MT staining of the calvarial defects. Scale bars: 2000 μm (top), 200 μm (bottom); magnifications: × 4 (top), ×40 (bottom). Notes: n=3; *$p < 0.05$ compared to control; #$p < 0.05$ compared to HAMMA/HAP. Abbreviations: BMP-2, bone morphogenetic protein 2; BV/TV, bone volume/total volume; CT, computed tomography; HAMMA, methacrylate-functionalized human acellular amniotic membrane matrix; HAP, hydroxyapatite; HE, hematoxylin and eosin; MT, Masson's trichrome.

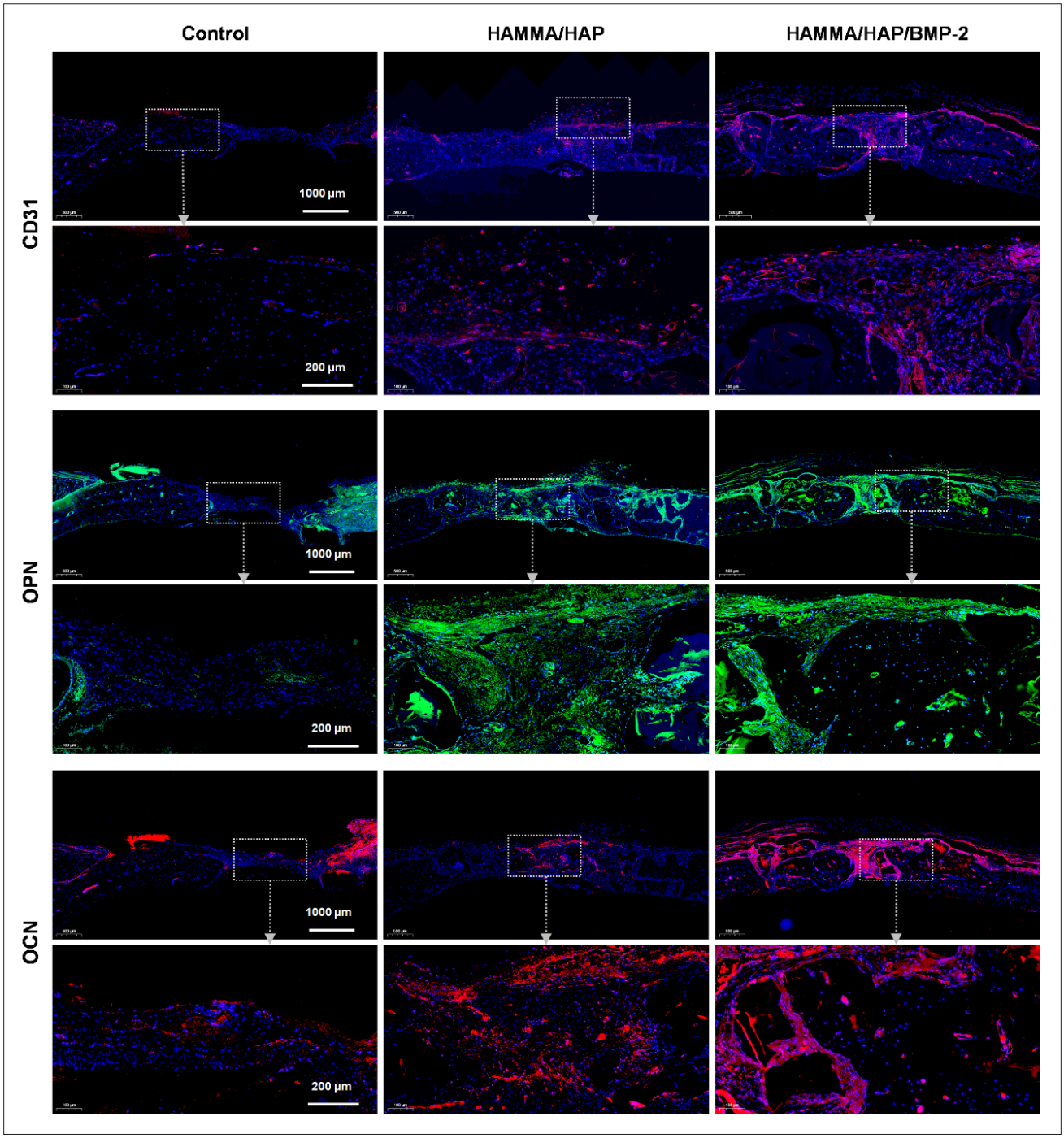


Figure 7. Co-staining of CD31 (red), OPN (green), OCN (red), and DAPI (nucleus, blue) in specimens from the calvarial defects. Scale bars: 1000 μm (top), 200 μm (bottom); magnifications: ×4 (top), ×40 (bottom). Abbreviations: BMP-2, bone morphogenetic protein 2; CD31, cluster of differentiation 31; DAPI, 4',6-Diamidino-2-phenylindole; HAMMA, methacrylate-functionalized human acellular amniotic membrane matrix; HAP, hydroxyapatite; OCN, osteocalcin; OPN, osteopontin.

After 90 days of implantation, histological sections of the samples were subjected to H&E and Masson's trichrome staining, with the results presented in Figure 8D. In the control group, only a little orbital bone tissue growth was observed in the area of the orbital bone defect. However, part of the mucosa of the ethmoid sinus was completely repaired, and a small amount of paperboard bone fragments of ethmoid bone were observed to be growing towards the central area. In the scaffold groups, the scaffolds were fully degraded. New bone tissues appeared light red and light blue, while mature bone tissues were stained red and blue. Immunofluorescence staining for OCN (red) and OPN (green) in different scaffold groups is presented in Figure 8E. The OCN and OPN fluorescence intensity in the HAMMA/HAP/BMP-2 group was significantly enhanced than the control groups, demonstrating that the bone formation activity of the HAMMA/HAP/BMP-2 group was stronger than the control groups.

4. Discussion

The bone of the orbital wall is structurally fragile and susceptible to fracture and collapse in the presence of external force. Most of the bone defect areas after fracture are typically covered by fibrous mucosal tissues, which are often ineffective in restoring the mechanical properties of the original bony orbital wall. Consequently, enophthalmos or displacement, diplopia, and eye movement disorders may arise, as well as potential visual loss or decline. The current surgical treatment strategies primarily entail the repair of orbital soft tissues and subsequent bridging of the bone wall defects with artificial materials.[17] However, the complex geometry of the orbital bones, their limited thickness, and the intricate interface between bone and biomaterials pose considerable challenges in the development of porous bioactive scaffolds for repairing orbital bone defects. Research on the application of porous biological scaffolds in thin-walled bone tissue is still limited. In recent years, 3D printing technology has been employed to fabricate bone implants with internal pores and external geometry conforming to the specific requirements of personalized orbital fractures.[18] In this study, HAMMA composite scaffolds featuring controlled micromorphological and microstructural parameters were successfully fabricated via 3D printing technology and subsequently applied in the reconstruction of orbital bone defects.

The FTIR results indicate that the hydrogel scaffolds are formed through a combination of physical (hydrogen bonding) and chemical crosslinking (photocrosslinking), ensuring both material uniformity and strong adhesion. XRD results indicate that the double crosslinking approach does not disrupt the crystalline structure of HAP, which could be attributed to the elevated surface energy of HAP. In order to maintain the structural stability of porous scaffolds during bone growth repair, it is necessary to provide mechanical support to the defect area. Our results showed that the HAMMA/HAP scaffold exhibited a higher tensile strength than the pure HAMMA scaffold. In addition, the final water absorption of the scaffold was observed to be lower than that of the pure HAMMA scaffold. These findings suggest that HAP-doped scaffolds are superior to pure HAMMA scaffolds in terms of mechanical strength and dimensional stability.

Although the incorporation of HAP reduces the internal space of the hydrogel, it significantly influences the crosslinking density, which was observed to be closely associated with the swelling ratio. A higher crosslinking degree results in reduced swelling capacity and improved dimensional stability. The relatively low swelling ability of these hydrogels may promote the exchange of nutrients and metabolic waste within the hydrogel matrix, as well as cell encapsulation and cell survival, by reducing the likelihood of water molecules entering the hydrogels.[19] In contrast, biodegradation represents another important factor of biological scaffolds. HAP can act as a noncovalent cross-linker between polymer chains, effectively increasing the overall molecular weight of the polymer network and thereby significantly improving the cohesive strength of the adhesive. Consequently, the degradation rate is found to decrease significantly with an increase in HAP particle content.[20]

The physical properties of hydrogel scaffolds, including stability, capacity to transport nutrients, drug release time, and their biological properties that promote cell adhesion, metabolism, and new bone regeneration, are significantly affected by their swelling and degradation properties.[21–23] An acellular scaffold exhibiting superior hydrophilic properties was employed as a carrier for the incorporation of BMP-2. BMP-2 and the hydrogel were combined through hydrogen bonding, which prolonged the drug release time. Studies have shown that the initial burst release of BMP-2 can activate downstream signaling pathways, such as BMP/mothers against decapentaplegic homolog (SMAD) and MAPK pathways, more strongly, thus significantly promoting early osteogenic differentiation.[24] Furthermore, the addition of inorganic nanoHAP particles with reduced hydrophilicity leads to the formation of mutual bonding between the raw materials and nanoHAP, resulting in a reduction in the internal pore size of the hydrogel scaffold, an increase in the density of internal structure, and an enlargement of the pore wall thickness. Thereafter, this reduction in the free passage space available to water molecules leads to decreased equilibrium swelling and slower degradation rates. As a result, the release of BMP-2

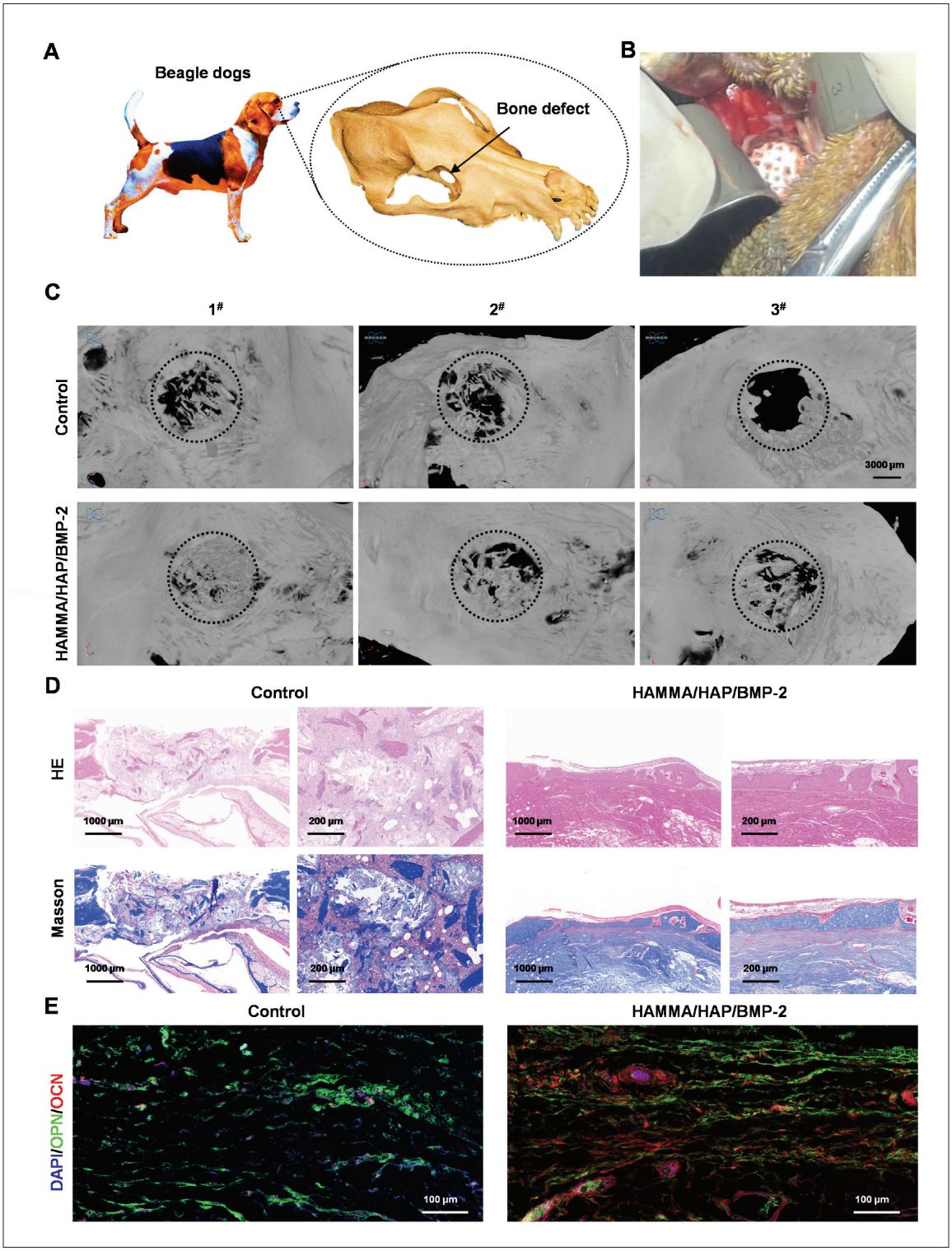


Figure 8. *In vivo* study of HAMMA composite scaffolds in the treatment of orbital bone defects. (A, B) Establishment of orbital bone defects and the implantation of scaffolds. (C) Representative micro-CT reconstruction images in the control and scaffolds groups at 90 days post-surgery. Scale bar: 500 μm; magnification: ×4 . (D) HE and MT staining of orbital bone defects. Scale bars: 1000 or 200 μm; magnifications:×4 or × 40. (E) Immunofluorescence of the osteogenic proteins. Scale bars: 100 μm; magnifications: × 100. Abbreviations: BMP-2, bone morphogenetic protein 2; CD31, cluster of differentiation 31; DAPI, 4',6-diamidino-2-phenylindole; HAMMA, methacrylate-functionalized human acellular amniotic membrane matrix; HAP, hydroxyapatite; HE, hematoxylin and eosin; OCN, osteocalcin; OPN, osteopontin.

can be effectively regulated, maintaining a therapeutically effective drug concentration within the bone defect area. This controlled release helps modulate the immune microenvironment during the early stages of bone repair, promotes the recruitment of osteoblasts, and accelerates the healing of bone defects.[25,26]

The BMP-2 protein can regulate bone metabolism through the classical BMP/SMAD pathway and non-classical MAPK pathway.[27] In a non-canonical mechanism, BMP-2 rapidly activates the transforming growth factor-beta activated kinase (TAK)1/2–mitogen-activated protein kinase (MAPK)1/2–extracellular signal-regulated kinase (ERK)1/2 signaling pathway by recruiting the TAK1-binding protein 1–TAK1 complex via BMPR1A. This activation modulates the expression of target genes and influences osteogenic differentiation.[28] Meanwhile, Wnt signaling upregulates the expression of Runx transcription factor family genes, promotes early differentiation of mesenchymal stem cells, and suppresses their late apoptosis, thereby facilitating osteogenic differentiation.[29] Cell signal pathways are interconnected to form a complex network to accurately regulate the differentiation process. *Jag1*, one of the target genes of the Wnt classical pathway in osteoblasts, encodes a protein that is an important ligand of the Notch signaling pathway, thus becoming an important node associated with Notch and Wnt pathways, whereas the Wnt pathway is also regulated by other signaling pathways. During the activation process of the Wnt pathway, calcium channels need to be opened, protein kinase C (PKC)/ERK needs to be involved, and calcium channel proteins need to be sulfhydrylated at specific cysteine sites to play a biological role.[30] As the enhanced activity of a calcium peak initiated by HAP nanorods leads to the activation of c-Jun and thus suppresses the expression of gamma-aminobutyric acid (GABA)ergic/glutamatergic selection gene *TLX3*, HAP may activate calcium channels during the activation process of the Wnt pathway.[31]

The HAM is a natural, acellular extracellular matrix material enriched with a variety of bioactive factors. It has been extensively utilized in skin and ocular surface tissue engineering to promote tissue regeneration. However, its application in bone tissue engineering remains relatively unexplored, mainly owing to the need for further research into its mechanical properties, compatibility with the cellular growth microenvironment, and potential to support bone regeneration. Studies have shown that HAMs, which exhibit excellent biocompatibility, facilitate the proliferation and osteogenic differentiation of bone marrow mesenchymal stem cells. Moreover, they can upregulate the expression of genes related to cell recruitment and bone remodeling, such as *CXCR4*, *MCP1*, *OC*, and *Catk*.[32] Additionally, BMP-2 has been shown to promote the differentiation and proliferation of undifferentiated mesenchymal stem cells into chondrocytes and osteoblasts, enhance the differentiation and maturation of osteoblasts, play a crucial role in the growth, development, and remodeling of bone and cartilage, and accelerate the repair of bone defects. In this work, BMP-2 was introduced to increase the biological activity of the HAM. *The in vivo* and *in vitro* osteogenesis experiments suggest that BMP-2 has a significant impact on bone regeneration.

Given the unique anatomical location and bone tissue structure of the orbital wall, tissue-engineered bone constructs were used to repair circular, full-thickness bone defects measuring 10 mm in diameter in the medial orbital wall of dogs. This study also explored the feasibility of employing a hydrogel for the reconstruction of orbital wall bone defects. CT imaging revealed that the implanted HAP composite material degraded gradually, and the surrounding bone wall was repaired. In the control group, the degradation was accompanied by only a small amount of new bone formation, thereby maintaining obvious defects. The histological examination clearly revealed the morphology of new bone tissues, which is significant for assessing bone remodeling and new bone metabolism. The strategy employed in this study is not only applicable to orbital bone repair but also provides a transferable research paradigm for tissue engineering of other thin-walled bones, such as cranial vault and jawbones, and even load-bearing bones. HAMMA, as a functionally versatile matrix material, holds promise for application in the regeneration of other tissues such as cartilage and skin through combination with different bioactive factors or inorganic components. It also plays an important theoretical and practical foundation for future research directions in bone tissue engineering, such as personalized treatment, composite biomaterial design, and optimization of vertical bone augmentation.[33]

5. Conclusion

In conclusion, a HAP/BMP-2–mineralized decellularized amniotic membrane scaffold was developed for bone tissue engineering applications. In this study, 10× SBF was used as a simple and easy strategy to modify the amniotic membrane with HAP and BMP-2. The physicochemical properties and biological activity of acellular amniotic membrane matrix composite scaffolds (HAMMA/HAP/BMP-2) were modulated through chemical composition changes combined with advanced 3D printing technology, thus optimizing the macro- and microstructural design of materials. A novel porous scaffold with multiple functions, such as effectively inducing and guiding tissue growth, was successfully prepared, providing an innovative research perspective for the design and preparation of orbital

repair materials. This work addresses the limitations of current clinical orbital repair materials, including those used for repairing orbital bone wall defects and filling orbital prosthesis.

Acknowledgments

None.

Funding

This work was supported by grants from the National Natural Science Foundation of China (32201109), the New Clinical Diagnosis and Treatment Technology and Public Health of Suqian First Hospital (SY202205), and the Basic and Applied Basic Research Foundation of Guangdong Province (2021A1515110557).

Conflict of interest

The authors declare no conflict of interest.

Author contributions

Conceptualization: Bing Qin, Wei Liu
Formal analysis: Yabo Shi, Yi Wang
Investigation: Bing Qin, Yiyi Chen
Methodology: Bing Qin, Yabo Shi
Writing–original draft: Bing Qin, Yi Wang
Writing–review & editing: Wei Liu

Ethics approval and consent to participate

The animals used in the experiments were obtained from the Hubei Provincial Center for Disease Control and Prevention (Wuhan, China). All procedures involving animals were carried out in compliance with protocols approved by the Chinese National Committee for the Protection and Utilization of Institutional Animals (QR-ADM-G004-4.0).

Consent for publication

Not applicable.

Availability of data

Data will be made available upon reasonable request to the corresponding author.

References

1 Sachs ME. Orbital floor fractures: the maxillary approach. *Adv Ophthalmic Plast Reconstr Surg*. 1987;6(1):387-391.

2. Ni X, Feng J, Liang M, *et al*. Enhancing bone repair with β-TCP-based composite scaffolds: a review of design strategies and biological mechanisms. *Orthop Res Rev*. 2025;17:313-340.
doi: 10.2147/ORR.S525959

3. Al-Khdhairi OBH, Abdulrazaq SS. Is orbital floor reconstruction with titanium mesh safe?. *J Craniofac Surg*. 2017;28(7):e692-e694.
doi: 10.1097/SCS.0000000000003896

4. Shah HA, Shipchandler T, Vernon D, *et al*. Extra-ocular movement restriction and diplopia following orbital fracture repair. *Am J Otolaryngol*. 2018;39(1):34-36.
doi: 10.1016/j.amjoto.2017.08.008

5. Kwon H, Kim HJ, Seo BF, Jeong YJ, Jung SN, Shim HS. The role of resorbable plate and artificial bone substitute in reconstruction of large orbital floor defect. *Biomed Res Int*. 2016;2016:1358312.
doi: 10.1155/2016/1358312

6. Song X, Li L, Sun Y, Fan X, Li Z. Long-term infectious complications of using porous polyethylene mesh for orbital fracture reconstruction. *Medicine (Baltimore)*. 2016;95(25):e3819.
doi: 10.1097/MD.0000000000003819

7. Zheng YX, Zhao HY, Jing XB, *et al*. Reconstruction of orbital floor defect with polylacticglycolide acid/recombinant human bone morphogenetic protein 2 compound implanted material in sheep. [in Chinese] *Zhonghua Yan Ke Za Zhi*. 2006;42(6):535-539.

8. Samadikuchaksaraei A, Mehdipour A, Habibi Roudkenar M, *et al*. A dermal equivalent engineered with TGF-β3 expressing bone marrow stromal cells and amniotic membrane: cosmetic healing of full-thickness skin wounds in rats. *Artif Organs*. 2016;40(12):266-279.
doi: 10.1111/aor.12807

9. Zheng Y, Ji S, Wu H, *et al*. Topical administration of cryopreserved living micronized amnion accelerates wound healing in diabetic mice by modulating local microenvironment. *Biomaterials*. 2017;113:56-67.
doi: 10.1016/j.biomaterials.2016.10.031

10. Etchebarne M, Fricain JC, Kerdjoudj H, *et al*. Use of amniotic membrane and its derived products for bone regeneration: a systematic review. *Front Bioeng Biotechnol*. 2021;9:661332.
doi: 10.3389/fbioe.2021.661332

11. Leal-Marin S, Kern T, Hofmann N, *et al*. Human amniotic membrane: a review on tissue engineering, application, and storage. *J Biomed Mater Res B Appl Biomater*. 2021;109(8):1198-1215.
doi: 10.1002/jbm.b.34782

12. Dadkhah Tehrani F, Firouzeh A, Shabani I, Shabani A. A review on modifications of amniotic membrane for biomedical applications. *Front Bioeng Biotechnol*. 2021;8:606982.
doi: 10.3389/fbioe.2020.606982

13. Suter AJ, Molteno AC, Bevin TH, *et al*. Long term follows up of bone derived hydroxyapatite orbital implants. *Br J Ophthalmol*. 2002;86(11):1287-1292.
doi: 10.1136/bjo.86.11.1287

14. Yan S, Feng L, Zhu Q, *et al*. Controlled release of BMP-2 from a Heparin-conjugated strontium-substituted nanohydroxyapatite/silk fibroin scaffold for bone regeneration. *ACS Biomater Sci Eng*. 2018;4(9):3291-3303.
doi: 10.1021/acsbiomaterials.8b00549

15. Dewey MJ, Johnson EM, Slater ST, Milner DJ, Wheeler MB, Harley BAC. Mineralized collagen scaffolds fabricated with amniotic membrane matrix increase osteogenesis under inflammatory conditions. *Regen Biomater*. 2020;7(3):247-258.
doi: 10.1093/rb/rbaa005

16. Jia Z, Ma H, Liu J, *et al*. Preparation and characterization of polylactic acid/nano hydroxyapatite/nano hydroxyapatite/human acellular amniotic membrane (PLA/nHAp/HAAM) hybrid scaffold for bone tissue defect repair. *Materials (Basel)*. 2023;16(5):1937.
doi: 10.3390/ma16051937.

17. Cole P, Boyd V, Banerji S, Hollier LH. Comprehensive management of orbital fractures. *Plast Reconstr Surg*. 2007;120(7 Suppl 2):57S-63S.
doi: 10.1097/01.prs.0000260752.20481.b4

18. Wallace J, Wang M, Thompson P, *et al*. Validating continuous digital light processing (cDLP) additive manufacturing accuracy and tissue engineering utility of a dye-initiator package. *Biofabrication*. 2014;6(1):015003.
doi: 10.1088/1758-5082/6/1/015003

19. Zhong M, Sun J, Wei D, *et al*. Establishing a cell-affinitive interface and spreading space in a 3D hydrogel by introduction of microcarriers and an enzyme. *J Mater Chem B*. 2014;2(38):6601-6610.
doi: 10.1039/c4tb00887a

20. Yang R, Chen B, Zhang X, Bao Z, Yan Q, Luan S. Degradable nanohydroxyapatite-reinforced superglue for rapid bone fixation and promoted osteogenesis. *ACS Nano*. 2024;18(11):8517-8530.
doi: 10.1021/acsnano.4c01214

21. Jamnezhad S, Asefnejad A, Motififard M, *et al*. Development and investigation of novel alginate-hyaluronic acid bone fillers using freeze drying technique for orthopedic field. *Nanomed Res J*. 2020;5(4):306-315.
doi: 10.22034/nmrj.2020.04.001

22. Lakkireddy C, Vishwakarma SK, Bardia A, *et al*. Biofabrication of allogenic bone grafts using cellularized amniotic scaffolds for application in efficient bone healing. *Tissue Cell*. 2021;73:101631.
doi: 10.1016/j.tice.2021.101631

23. Dawiec G, Niemczyk W, Wiench R, Niemczyk S, Skaba D. Introduction to amniotic membranes in maxillofacial surgery-a scoping review. *Medicina (Kaunas)*. 2024;60(4):663.
doi: 10.3390/medicina60040663

24. Han S, Paeng KW, Park S, Jung UW, Cha JK, Hong J. Programmed BMP-2 release from biphasic calcium phosphates for optimal bone regeneration. *Biomaterials*. 2021;272:120785.
doi: 10.1016/j.biomaterials.2021.120785

25. Bölgen N, Plieva F, Galaev I, Mattiasson B, Pişkin E. Cryogelation for preparation of novel biodegradable tissue-engineering scaffolds. *J Biomater Sci Polym Ed*. 2007;18(9):1165-1179.
doi: 10.1163/156856207781554046

26. Xu M, Qin M, Zhang X, *et al*. Porous PVA/SA/HA hydrogels fabricated by dual-crosslinking method for bone tissue engineering. *J Biomater Sci Polym Ed*. 2020;31(6):816-831.
doi: 10.1080/09205063.2020.1720155

27. Dorman LJ, Tucci M, Benghuzzi H. In vitro effects of bmp-2, bmp-7, and bmp-13 on proliferation and differentation of mouse mesenchymal stem cells. *Biomed Sci Instrum*. 2012;48:81-87.

28. Kua HY, Liu H, Leong WF, *et al*. c-Abl promotes osteoblast expansion by differentially regulating canonical and non-canonical BMP pathways and p16INK4a expression. *Nat Cell Biol*. 2012;14(7):727-737.
doi: 10.1038/ncb2528

29. Grassi F, Tyagi AM, Calvert JW, *et al*. Hydrogen sulfide is a novel regulator of bone formation implicated in the bone loss induced by estrogen deficiency. *J Bone Miner Res*. 2016;31(5):949-963.
doi: 10.1002/jbmr.2757

30. Matsumoto Y, Otsuka F, Takano-Narazaki M, *et al*. Estrogen facilitates osteoblast differentiation by upregulating bone morphogenetic protein-4 signaling. *Steroids*. 2013;78(5):513-520.
doi: 10.1016/j.steroids.2013.02.011

31. Shen Y, Liu F, Duan J, *et al*. Biomaterial cues regulated differentiation of neural stem cells into GABAergic neurons through Ca2+/c-Jun/TLX3 signaling promoted by hydroxyapatite nanorods. *Nano Lett*. 2021;21(17):7371-7378.
doi: 10.1021/acs.nanolett.1c02708

32. Tang K, Wu J, Xiong Z, Ji Y, Sun T, Guo X. Human acellular amniotic membrane: a potential osteoinductive biomaterial for bone regeneration. *J Biomater Appl*. 2018;32(6):754-764.
doi: 10.1177/0885328217739753

33. Akhlaghi F, Hesami N, Rad MR, Nazeman P, Fahimipour F, Khojasteh A. Improved bone regeneration through amniotic membrane loaded with buccal fat pad-derived MSCs as an adjuvant in maxillomandibular reconstruction. *J Craniomaxillofac Surg*. 2019;47(8):1266-1273.
doi: 10.1016/j.jcms.2019.03.030

ACCSCIENCE PUBLISHING

International Journal of Bioprinting

RESEARCH ARTICLE

Electrohydrodynamically printed microfibrous scaffolds with different pore sizes modulate macrophage polarization and foreign body reaction to enhance bone regeneration

Junzheng Liu[1,2†], Zijie Meng[2,3,4,5†], Jiaming Yu[6], Qin Guo[1], Jiahao Zhang[1], Yulin Wang[1], Le Jia[1], Jiankang He[2,4,5*], and Wei Wang[1*]

[1]Comprehensive Orthopedics Department, The Second Affiliated Hospital of Xi'an Jiaotong University, Xi'an, Shaanxi, China

[2]State Key Laboratory for Manufacturing Systems Engineering, Xi'an Jiaotong University, Xi'an, Shaanxi, China.

[3]Frontier Institute of Science and Technology, Xi'an Jiaotong University, Xi'an, Shaanxi, China

[4]National Medical Products Administration Key Laboratory for Research and Evaluation of Additive Manufacturing Medical Devices, Xi'an Jiaotong University, Xi'an, Shaanxi, China

[5]State Industry–Education Integration Center for Medical Innovations, Xi'an Jiaotong University, Xi'an, Shaanxi, China

[6]Department of Integrated Traditional Chinese and Western Medicine, Faculty of The First Clinical Medical College, Shaanxi University of Chinese Medicine, Xi'an, Shaanxi, China

[†]These authors contributed equally to this work.

***Corresponding authors:**
Jiankang He
(jiankanghe@mail.xjtu.edu.cn)

Wei Wang
(dr.wangwei@xjtu.edu.cn)

Citation: Liu J, Meng Z, Yu J, *et al*. Electrohydrodynamically printed microfibrous scaffolds with different pore sizes modulate macrophage polarization and foreign body reaction to enhance bone regeneration. *Int J Bioprint*. 2026;12(1):302-322. doi: 10.36922/IJB025410415

Received: October 9, 2025
1st revised: November 7, 2025
2nd revised: November 19, 2025
Accepted: November 19, 2025
Published online: November 19, 2025

Copyright: © 2025 Author(s). This is an Open Access article distributed under the terms of the Creative Commons Attribution License, permitting distribution and reproduction in any medium, provided the original work is properly cited.

Publisher's Note: AccScience Publishing remains neutral with regard to jurisdictional claims in published maps and institutional affiliations.

Abstract

Foreign body reaction (FBR) is a major obstacle to effective osseointegration in bone defect repair. The pore size of scaffolds is a key determinant of FBR; however, its impact on FBR remains controversial, with limited *in vivo* evidence available. In this study, electrohydrodynamically printed polycaprolactone scaffolds with pore sizes of 100 μm, 200 μm, and 300 μm were fabricated to investigate their effects on macrophage polarization, FBR, and bone regeneration. *In vitro* experiments showed that the 300 μm group promoted M2 polarization of macrophages, reduced tumor necrosis factor-alpha expression (0.71-fold and 0.81-fold relative to the 100 μm and 200 μm groups, respectively), and increased transforming growth factor-beta 1 expression (1.39-fold and 1.19-fold, respectively), thereby enhancing osteogenic gene expression in MC3T3-E1 cells (*Runx2*, *Col1*, and *Ocn*). Finite element analysis and transcriptomics sequencing revealed that pore size-dependent changes in scaffold stiffness modulate Piezo1 activation, influencing macrophage polarization. *In vivo* experiments showed that the 300 μm group exhibited the thinnest fibrous capsule (0.78-fold and 0.79-fold relative to the 100 μm and 200 μm groups, respectively), demonstrated enhanced angiogenesis, and achieved better bone regeneration, with increased bone volume/total volume and bone mineral density. These findings indicate that 300 μm pore-sized scaffolds promote bone regeneration by modulating macrophage polarization and attenuating FBR, providing a basis for optimized scaffold design and clinical translation in bone defect repair.

Keyword: Bone regeneration; Electrohydrodynamic printing; Foreign body reaction; Polarization; Pore size

1. Introduction

Bone defects caused by trauma, infection, inflammation, and tumor resection often exceed the critical size for self-repair.[1–3] These defects often require the implantation of tissue-engineered bone to facilitate bone tissue repair and functional reconstruction.[4,5] Although tissue-engineered bone has significant advantages in treating such defects, its clinical application still faces challenges, among which foreign body reaction (FBR) is the key issue.[6–8] FBR refers to a cascade of complex immune responses initiated by the interaction between an implanted material and host tissue. These responses typically include acute and chronic inflammation, macrophage activation, the formation of multinucleated giant cells, and fibrous capsule development.[9] These reactions hinder bone tissue growth into the implant, which not only reduces the implant's repair capacity but may also ultimately lead to osseointegration failure.[10,11]

Currently, to mitigate FBRs and improve the biocompatibility of implants, researchers are focusing on modifying implants through biological, chemical, and physical means.[12] Biological means focus on loading anti-inflammatory factors (e.g., interleukin [IL]-10 and transforming growth factor-beta [TGF-β]) on the surface of the implants or promoting tissue repair and integration through bioactive coatings (e.g., angiogenic factors and osteogenic coatings).[13,14] Chemical modification, on the other hand, involves adjusting the surface functional groups, hydrophilicity, and degradability of the implants, or releasing drugs or biokines through the degradation process of the implants to precisely modulate the intensity and duration of the immune response.[15,16] Physical means are mainly used to optimize the pore size,[17] shape,[18] and surface morphology of the implants to regulate the adhesion and activation of immune cells, thus reducing the inflammatory response.[19] Notably, physical modifications are intrinsic to the implants and can be seamlessly combined with biological and chemical strategies without introducing toxicity.

Among the physical properties, pore size is a hot topic that has been studied extensively.[20] However, the immune response induced by implants with different pore sizes remains controversial. For example, Jiang *et al.*[21] used a cryoprotectant-assisted freeze-drying method to prepare scaffolds with large (80 μm) and small (30 μm) pore sizes. The experimental results revealed that mouse bone marrow-derived macrophages exhibited a preference for M2 polarization in scaffolds with large pores (80 μm), whereas they were more likely to adopt an M1 phenotype in materials with smaller pores (30 μm). Similarly, Li *et al.*[11] found that scaffolds with a 600 μm pore size more effectively promoted M2 polarization compared to those with a 200 μm pore size. On the other hand, Hady *et al.*[22] fabricated scaffolds with pore sizes of 100 μm and 40 μm using a precise template-based method. Their experimental results demonstrated that the 40 μm scaffold elicited a lower inflammatory response compared to the 100 μm scaffold. The occurrence of two opposite results may be due to the difficulty in establishing a stable immune microenvironment, as it is challenging to achieve precise and controllable dimensions for each pore using these methods.

Emerging additive manufacturing technologies, such as electrohydrodynamic (EHD) printing, have recently provided new solutions for the precise control of pore size.[23,24] EHD printing enables precise control of pore size and fiber arrangement to create a stable immune microenvironment.[25–27] However, there are limited studies on the effect of EHD-printed scaffolds with varying pore sizes on macrophage polarization and their modulation of bone regeneration. To the best of our knowledge, only Tylek *et al.*[28] found that EHD-printed scaffolds with small pore sizes (40 μm) significantly promoted macrophage M2 polarization compared with large pore scaffolds (100 μm), but this study was limited to *in vitro* experiments and did not further explore how macrophage polarization regulates osteogenic differentiation or validate it in an *in vivo* model. Moreover, the underlying mechanisms by which pore size modulates macrophage polarization have yet to be fully elucidated. Notably, *in vivo* studies have indicated that excessively small pores (<100 μm) favor fibroblast differentiation and the infiltration of non-mineralized soft tissue,[29] whereas excessively large pores (>300 μm) may impair cell adhesion, infiltration, and mechanical stability, ultimately compromising bone repair.[30,31]

To address these research gaps, this study utilized EHD printing technology to fabricate polycaprolactone (PCL) scaffolds with pore sizes of 100 μm, 200 μm, and 300 μm, aiming to systematically evaluate their effects on macrophage polarization, FBR, and bone regeneration. The scaffolds were co-cultured with macrophages to assess their impact on macrophage polarization, and the conditioned media from each group were subsequently applied to osteoblast cultures to examine their osteogenic differentiation capacity. Additionally, finite element analysis was conducted to evaluate changes in scaffold stiffness associated with different pore sizes, and transcriptomic sequencing was performed to explore the molecular mechanisms regulating macrophage polarization. A rat subcutaneous implantation model was employed to evaluate scaffold-induced inflammation and FBR. Finally, the effect of pore size on bone regeneration

in vivo was evaluated using a critical-sized cranial defect model (Figure 1).

2.Materials and methods

2.1. Preparation and characterization of polycaprolactone scaffolds

Medical-grade PCL (molecular weight = 80,000 g/mol, Jinan Daigang Biomaterial Co., Ltd., China) scaffolds were printed using a commercial EHD printing device (Shaanxi Baipusheng Medical Technologies Co., Ltd., China). Three groups of scaffolds were designed, each with a fiber crossing angle of 90° and fiber spacing of 100 μm, 200 μm, and 300 μm, respectively. Specifically, PCL particles were loaded into a glass syringe and maintained at 90°C until a uniform molten phase was formed. During the printing process, a 20-gauge nozzle was used, with a feed rate of 20 μL/h, an applied voltage of 2.4 kV, and a carrier stage speed of 50 mm/s. Throughout the printing process, the

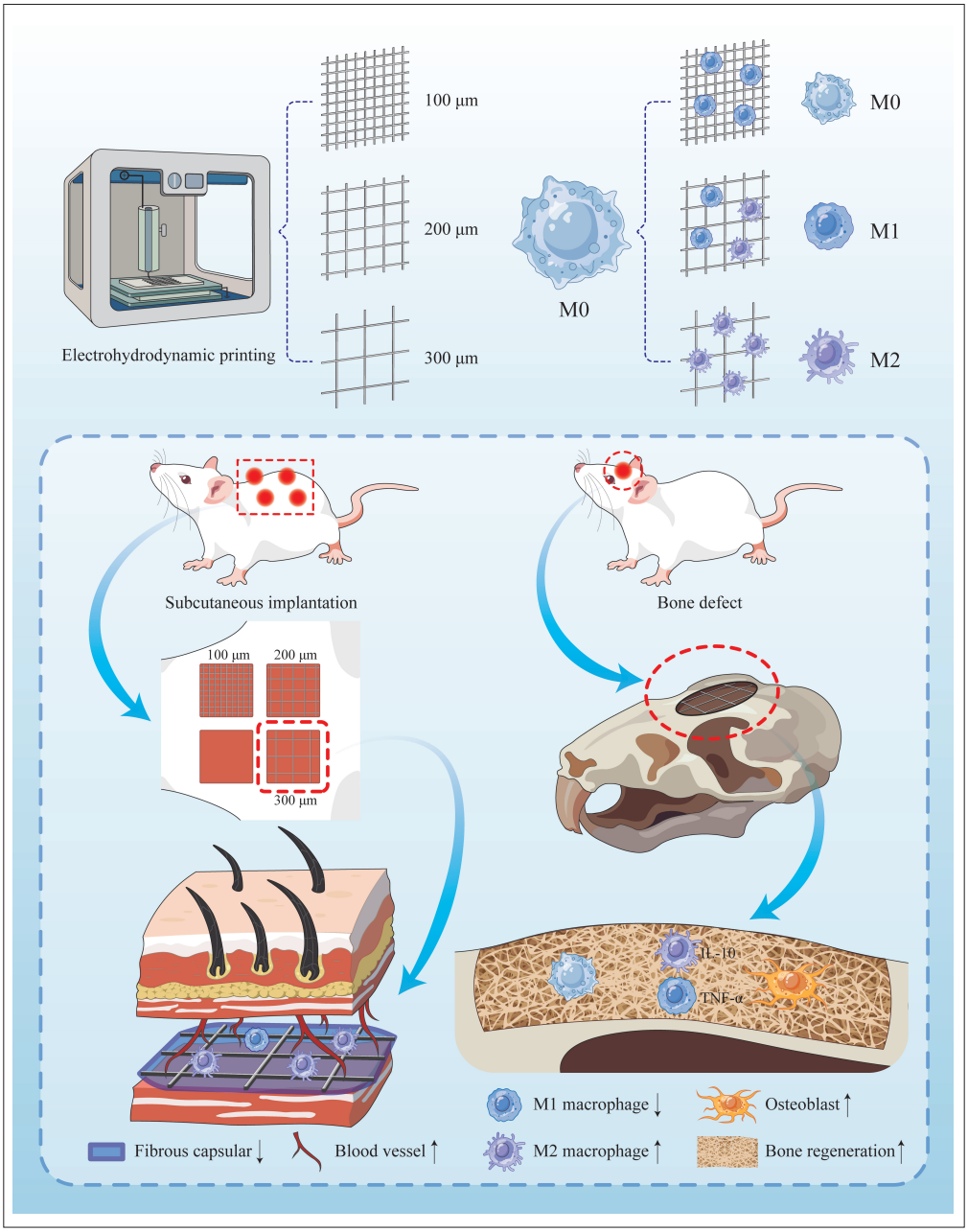


Figure 1. Schematic illustration of electrohydrodynamically printed scaffolds with different pore sizes modulating macrophage polarization and foreign body reaction to promote osteogenesis *in vitro* and *in vivo*. Abbreviations: IL-10, interleukin-10; TNF-α, tumor necrosis factor-alpha.

distance between the nozzle and the collection substrate (indium–tin oxide, glass plate) was maintained at a constant level of 1 mm.[32] The surface morphology and pore architecture of the printed scaffolds were examined using a scanning electron microscope (SEM; SU8010, Hitachi, Japan). The pore sizes of the scaffolds were quantified from SEM micrographs using the ImageJ software (v 1.54h, National Institutes of Health, United States of America [USA]). Tensile tests were then carried out on a universal testing machine (ETM 103A, Jilin Guanteng Automation Technology Co., Ltd.,China) to determine the mechanical performance of the scaffolds.

2.2. Macrophage culture and polarization analysis

RAW264.7 macrophages were maintained in high-glucose Dulbecco's modified medium (DMEM; Gibco, USA) supplemented with 10% fetal bovine serum (Biological Industries, Israel) and 1% penicillin–streptomycin (Gibco, USA). Printed PCL scaffolds were placed in 24-well plates under sterile conditions. After disinfecting the scaffolds by immersing them in 75% ethanol, they were washed three times with sterile phosphate-buffered saline and equilibrated in DMEM medium for 1 h. Subsequently, 1×10^5 RAW264.7 cells were seeded onto the scaffold surface and incubated at 37°C in a humidified environment with 5% CO_2.

The effect of different pore-sized scaffolds on macrophage polarization was detected by immunofluorescence staining. Following fixation with 4% paraformaldehyde for 20 min, samples were permeabilized using 0.1% Triton X-100 for 15 min and then blocked with 5% bovine serum albumin for 1 h. Subsequently, primary antibodies, including anti-inducible nitric oxide synthase (iNOS; 1:200, Affinity, Biosciences, USA) and anti-cluster of differentiation 206 (CD206; 1:200, Affinity, Biosciences, USA), were added and incubated overnight at 4°C. After washing, the samples were treated with Alexa Fluor 488- or 594-conjugated secondary antibodies (1:200, Thermo Fisher Scientific, USA) for 1 h at room temperature. Nuclei were then counterstained with 4',6-diamidino-2-phenylindole (DAPI), and images were captured using a confocal laser scanning microscope (A1, Nikon, Japan).

The levels of pro-inflammatory cytokines, including tumor necrosis factor-alpha (TNF-α) and IL-6, as well as anti-inflammatory cytokines, such as IL-4 and IL-10, were quantified using enzyme-linked immunosorbent assay (ELISA) kits (Servicebio, China) following the manufacturer's protocol. Nitric oxide (NO) concentration was measured using the Griess reagent (Beyotime, China). Quantitative real-time polymerase chain reaction (qRT-PCR) was employed to quantify the messenger RNA (mRNA) expression of inflammation-related genes, including *iNos*, *Il1b*, *Tnfa*, *Cd206*, *Tgfb1*, and *Arg1*, in macrophages. Total RNA was isolated from cells using TRIzol reagent (Invitrogen, USA). Complementary DNA was synthesized with a reverse transcription kit (Takara Biotechnology, China). Quantitative amplification was carried out using the SYBR Premix Taq kit (Takara Biotechnology, China), with *Gapdh* as the internal control. The primer sequences used in this study are listed in **Table S1**.

2.3. Osteogenic differentiation assay

To investigate the role of macrophage polarization in regulating osteogenic differentiation, RAW264.7 cells were co-cultured with scaffolds of different pore sizes for 2 days. The collected supernatant was centrifuged at 60 rcf for 5 min and filtered through a 0.22 μm filter to remove any residual cells (Figure S1). The resulting supernatant was mixed with fresh Minimum Essential Medium in a 1:1 ratio to obtain a macrophage-conditioned medium (MCM). MC3T3-E1 osteoblast precursor cells were seeded into 24-well plates at a density of 2×10^4 cells per well and cultured in MCM for 14 days.

The marker of early osteogenic differentiation, collagen type I (COL-I), was detected by immunofluorescence staining using anti-COL-I antibody (1:200, Affinity, USA), following the same steps described above. Alkaline phosphatase (ALP) activity and Alizarin Red S (ARS) staining, followed by quantification, were used to assess mid- to late-stage osteogenesis. ALP activity in MC3T3-E1 cells was evaluated using the BCIP/NBT Alkaline Phosphatase Chromogenic Kit (Beyotime, China) on days 7 and 14 of culture. Cells were stained using the ARS kit (Beyotime, China), and a 0.5 N HCl solution containing 5% sodium dodecyl sulfate was added and incubated for 1 h on days 14 and 21 of culture. Absorbance at 405 nm was measured using a microplate reader (Multiskan GO, Thermo Fisher Scientific, USA). Additionally, qRT-PCR was performed to evaluate the expression of genes associated with osteogenesis, including *Col1*, *Alp*, *Runx2*, and *Ocn*. Primer sequences are provided in **Table S1**.

2.4. Simulation analysis model

The relative stiffness of scaffolds with varying pore sizes was assessed using a finite element simulation model based on the simplified beam bending theory.[33] This model calculated the theoretical deflection resulting from a cellular contractile force applied to scaffold fibers at a defined distance from the fiber junction. Based on SEM and fluorescence imaging of cell-seeded scaffolds, the contractile force was assumed to act 30 μm from the fiber intersection. For simplification, it was assumed that each fiber spanned the underlying scaffold layer without deflection or mechanical interference from adjacent fibers.

The total deflection of each group was normalized to the maximum deflection observed in the 300 μm group to allow for relative comparison. To ensure consistency, the applied cellular force was assumed to be constant across all scaffold groups. In addition, since all scaffolds were fabricated using the same material and fiber diameter, both the elastic modulus (E) and the second moment of area (I)—key determinants of bending stiffness—were held constant across groups.

2.5. Transcriptomic sequencing

After 2 days of culture, RAW 264.7 cells were lysed with TRIzol reagent on different scaffold substrates. Total RNA was extracted and sequenced using the Illumina NovaSeq 6000 platform (USA). Differentially expressed genes (DEGs) were identified with criteria of $|\log_2\text{FoldChange}| > 1$ and $p < 0.05$. Kyoto Encyclopedia of Genes and Genomes (KEGG) pathway enrichment analysis was performed using the online tool at https://www.bioinformatics.com.cn. Key signaling pathways were subsequently validated through immunofluorescence staining and qRT-PCR.[34]

2.6. Subcutaneous implantation in rats

All animal procedures were approved by the Animal Research Committee of Xi'an Jiaotong University and performed in accordance with its guidelines. A total of 24 male Sprague–Dawley (SD) rats, weighing 200 g, were used in this study.

Eight SD rats were used to establish the subcutaneous implantation model. Specifically, the night before the operation, all animals were fasted and were administered 1% pentobarbital (30 mg/kg) for anesthesia in a sterile and clean environment. After satisfactory anesthesia, four longitudinal incisions were made on the back of the rats. After blunt separation, sterile scaffolds were placed in three of the incisions, with the fourth serving as the control. Subsequently, a 4-0 suture was used for suturing. All the animals were in good condition after the operation. To prevent infection, 80,000 units of penicillin were administered within 3 days after surgery. The rats were divided into two groups ($n = 4$ per group) and sacrificed on days 7 (group 1) and 28 (group 2) after implantation. Scaffolds and skin tissues from the incision sites were collected for further study.

2.7. Bone defect model of rats

For the bone defect model, 16 male SD rats were randomly assigned to four groups ($n = 4$ per group). Before the experiment, all animals were acclimatized in the experimental environment for 2 weeks. Food and water were fasted the night before surgery. On the day of surgery, anesthesia was administered with 1% sodium pentobarbital (30 mg/kg) in a sterile and clean environment. After sufficient anesthesia, the rats were shaved at the top of the skull and immobilized. An incision was made along the midline of the head to expose the skull. The defect area was localized according to the anatomical landmarks of the medial canthus and the middle cranial suture. A circular bone defect was precisely induced using an 8 mm-diameter ring drill, taking care to avoid thermal damage. In the experimental groups, an 8 mm-diameter, 0.5 mm-high circular scaffold was placed on the defect area, while the control group received no treatment. The surgical incisions of all animals were subsequently closed layer by layer. Postoperatively, 80,000 units of penicillin were administered intramuscularly daily for 3 days to prevent infection. Rats were euthanized 12 weeks later, and cranial specimens were collected for analysis.

2.8. Micro-computed tomography analysis

The cranial specimens were cleaned and fixed in 10% formalin solution after collection. Subsequently, the samples were analyzed with micro-computed tomography (CT), with an 8 mm-diameter, 2 mm-high cylinder defined as the region of interest (ROI). The scanning parameters were set to a tube voltage of 80 kV and a tube current of 0.06 mA, and a 3D reconstruction analysis was performed. New bone formation was evaluated by calculating the bone volume-to-tissue volume ratio (BV/TV) and bone mineral density (BMD).

2.9. Histological analysis

Subcutaneously implanted animal models were analyzed using hematoxylin–eosin (HE) and toluidine blue (TB) staining. At day 7 post-operation, relative inflammatory cell counts were calculated using the same threshold range in ImageJ. The same statistical analysis was performed for the mast cell counts. The area of two adjacent fibers surrounded by a fibrous capsule was chosen as the ROI, and the cell count was recorded under high magnification. Four ROIs were randomly selected per sample to calculate the density of inflammatory cells. At day 28 post-operation, neovascularization, thickness of the fibrous capsule, and inflammatory cell density were measured from the HE-stained images. The fibrous capsular thickness was calculated using the following equation:

$$\text{Capsular thickness} = \frac{\text{Area enclosed by the blue line} - \text{Area enclosed by the red line}}{\text{Length of the red line}} \quad (1)$$

After micro-CT scanning, all samples were decalcified, followed by paraffin embedding and section preparation. These sections were analyzed by HE and Masson staining to observe new bone formation and collagen fiber distribution. Additionally, immunohistochemical staining was used to

measure the expression levels of TNF-α, IL-10, COL-I, and osteocalcin (OCN) at 12 weeks post-surgery to evaluate inflammatory regulation and bone formation. Meanwhile, the M1/M2 phenotypic distribution of macrophages in the defect area was quantified by immunofluorescence staining to further explore the influence of the inflammatory microenvironment on bone repair.

2.10. Statistical analysis

All data are presented as mean ± standard deviation. Prism 9.5.0 (GraphPad Software, USA) was used for statistical analysis. Group differences were analyzed using a two-tailed Student's *t*-test for two groups, and one-way ANOVA followed by Tukey's post-hoc test for comparisons among three or more groups. A $p < 0.05$ was considered statistically significant.

3. Results

3.1. Material characteristics

As shown in Figure 2A, SEM images of PCL scaffolds fabricated by EHD printing showed that the fibers were deposited according to a predetermined trajectory, forming an orthogonal structure with uniform spacing. The measured scaffold pore diameters were 99.83 ± 1.22 μm, 201.40 ± 1.69 μm, and 301.80 ± 1.92 μm, which were very close to the designed target pore diameters of 100 μm, 200 μm, and 300 μm, respectively (Figure 2B).

A universal mechanical tester was used to assess the mechanical properties of the scaffolds. The mechanical properties of the scaffolds showed a decreasing trend with increasing pore diameter (Figure 2C). Specifically, the maximum tensile strength of the 100 μm group was 1.87-fold higher than the 200 μm group and 3.06-fold higher than the 300 μm group (Figure 2D). Although the mechanical properties of the 300 μm groups were lower compared to the other two groups, the mechanical demands of implants for cranial defect repair are relatively low. Previous studies, such as those by Shi *et al.*,[34] have demonstrated that PCL scaffolds with a tensile strength as low as 1 N are sufficient for successful cranial defect repair in rats. Accordingly, the 300 μm group fabricated in this study met the mechanical requirements for cranial defect

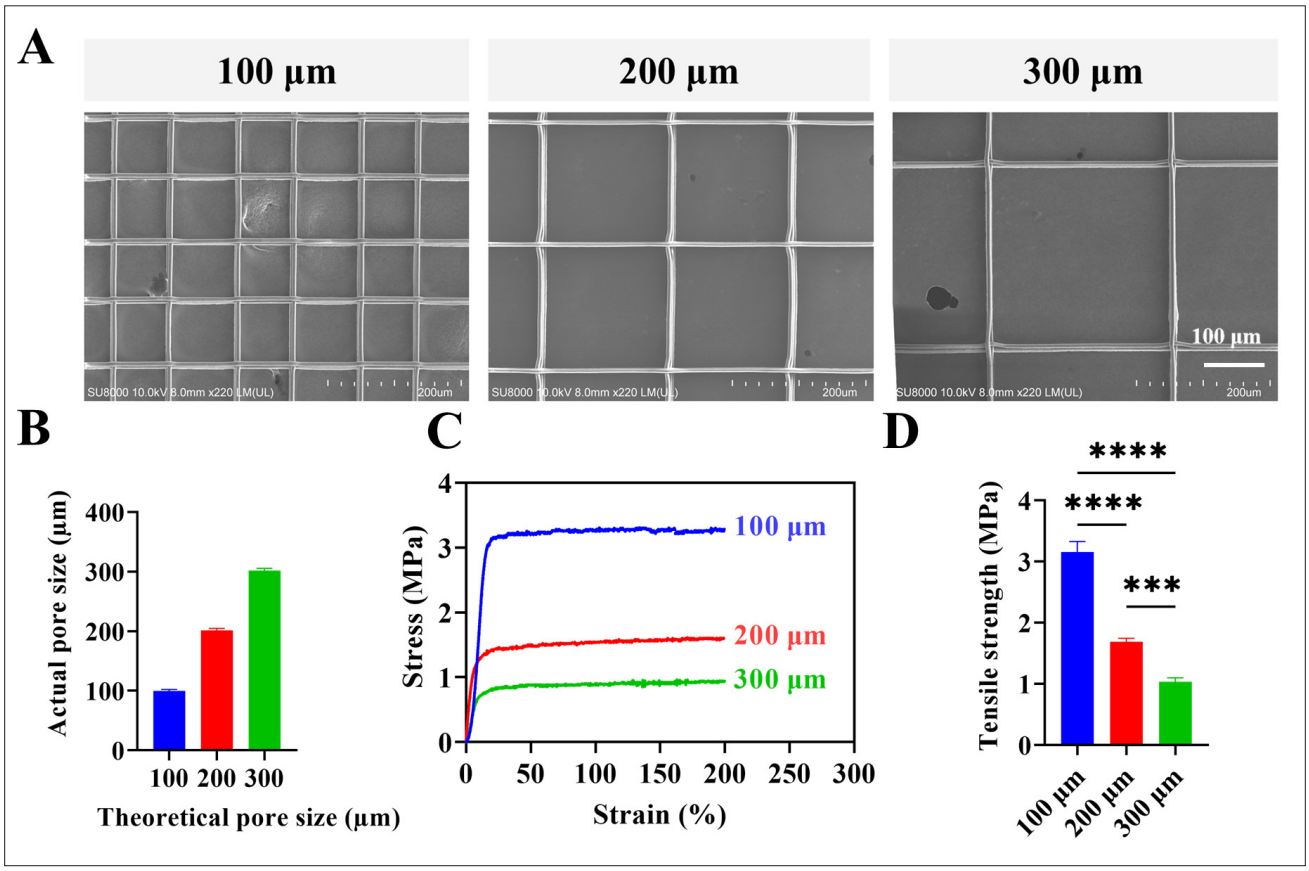


Figure 2. Characterization of microscale fibrous scaffolds with varying pore sizes. (A) Scanning electron microscopy images. Scale bars: 100 μm; magnifications: ×220. (B) Actual pore size measurements. (C) Tensile stress–strain curves. (D) Maximum fracture tensile strength. Notes: $n = 3$; ***$p < 0.001$, ****$p < 0.0001$.

repair. Altogether, PCL scaffolds with pore sizes of 100 μm, 200 μm, and 300 μm were successfully fabricated in accordance with the intended design specifications.

3.2. Modulation of macrophage polarization by scaffolds with different pore sizes

To evaluate the effects of scaffolds with different pore sizes on macrophage polarization, RAW264.7 macrophages were co-cultured with scaffolds of 100 μm, 200 μm, and 300 μm pore sizes for 2 days. Immunofluorescence staining was used to quantify M1 (iNOS, red) and M2 (CD206, green) marker expression. The intensity of CD206-positive staining was greatest in the 300 μm scaffold group (Figure 3A), with fluorescence intensities that were 1.91-fold and 1.71-fold higher than those observed in the 100 μm and 200 μm groups, respectively (Figure 3C). Conversely, the iNOS-positive fluorescence intensity of the 300 μm scaffold group was the lowest (Figure 3B & D).

To further investigate the effects of different pore sizes on macrophages, the levels of cytokine profiles of RAW264.7 cells were measured by ELISA. The 300 μm group demonstrated the most favorable immunomodulatory profile, characterized by minimal TNF-α/IL-6 and maximal IL-4/IL-10 (Figure 3E & F). Additionally, qRT-PCR analysis confirmed that the 300 μm scaffolds promoted an M2-polarized phenotype, showing downregulated M1 markers (*iNos*, *Il1b*, and *Tnfa*) and upregulated M2 markers (*Cd206*, *Tgfb1*, and *Arg1*) (Figure 3G & H).

Meanwhile, NO is an important effector molecule in macrophages, and differences in its concentration regulate the functional state of macrophages through multiple signaling pathways.[35] The NO concentrations in the 100 μm and 200 μm groups were 2.22-fold and 2.14-fold higher than those in the 300 μm group, respectively (Figure 3I).

3.3. Modulation of the immune microenvironment by scaffolds with different pore sizes to alter osteogenic differentiation

After scaffold implantation *in vivo*, osteoblasts and immune cells were simultaneously recruited to the scaffold surface.[36,37] To mimic the *in vivo* environment and explore the impact of scaffolds with varying pore sizes on immune regulation of osteogenic differentiation, MCM was used to culture MC3T3-E1 pre-osteoblast cells, and osteogenic differentiation markers were assessed at different time points (Figure S1).

In the bone matrix, COL-I, a major component, is secreted by osteoblasts during the early stage and serves as an early indicator of osteogenic differentiation.[38] As shown in Figure 4A, immunofluorescence images showed that the 300 μm group had the highest COL-I deposition, with semi-quantitative analysis revealing levels that were 2.04-fold and 1.90-fold higher than those of the 100 μm and 200 μm groups, respectively (Figure 4D). This trend was confirmed by qRT-PCR results (Figure 4E).

To assess the mid- and late-stage markers of osteogenic differentiation, ALP and ARS staining were conducted.[39] ALP staining is an indicator of early- to mid-stage osteogenic differentiation. At days 7 and 14, the staining image of the 300 μm group showed the highest staining intensity (Figure 4B). Quantitative analysis of ALP activity also confirmed that the 300 μm group had the highest ALP activity (Figure 4F). Similarly, ARS staining reflects calcium deposition, which is considered a marker of late osteogenesis. Compared with other groups, calcium deposition was more extensive and staining intensity was higher in the 300 μm group (Figure 4C). Quantitative analysis of ARS staining supported this finding (Figure 4G).

Additionally, the expression of key osteogenic genes, including *Alp*, *Runx2*, and *Ocn*, was analyzed. The results demonstrated that the expression levels of these genes were consistently highest in the 300 μm group, both at day 7 and day 14 (Figure 4H & I). Notably, after 14 days of culture, these gene expression levels in the 300 μm group were more than double those in the 100 μm group. These results indicate that pore size can alter the immune microenvironment, thereby affecting osteogenesis, with the 300 μm group showing the largest osteogenic effect.

3.4. Simulation and transcriptomic analysis of scaffolds with different pore sizes

To elucidate the potential mechanisms underlying the regulation of macrophage polarization by different pore sizes, simulation analysis and transcriptomic sequencing were performed to examine gene expression differences between groups.

Previous studies, including that by Xu *et al.*,[40] have demonstrated that high scaffold stiffness promotes M1 polarization of macrophages and enhances the secretion of pro-inflammatory cytokines. Accordingly, we constructed a simulation model to investigate how the pore size affects the local stiffness at the cell–scaffold interface. As shown in Figure 5A and B, the scaffold with a 100 μm pore size exhibited markedly increased local fiber bending stiffness. At the microstructural level, fibers spanned the gaps between the underlying support fibers, and the effective span length depended on the interlayer pore size, directly influencing fiber bending behavior. In scaffolds with a 100 μm pore size, the shortest support distance between fiber joints under a given unit load resulted in the smallest maximum deflection, indicating higher local structural

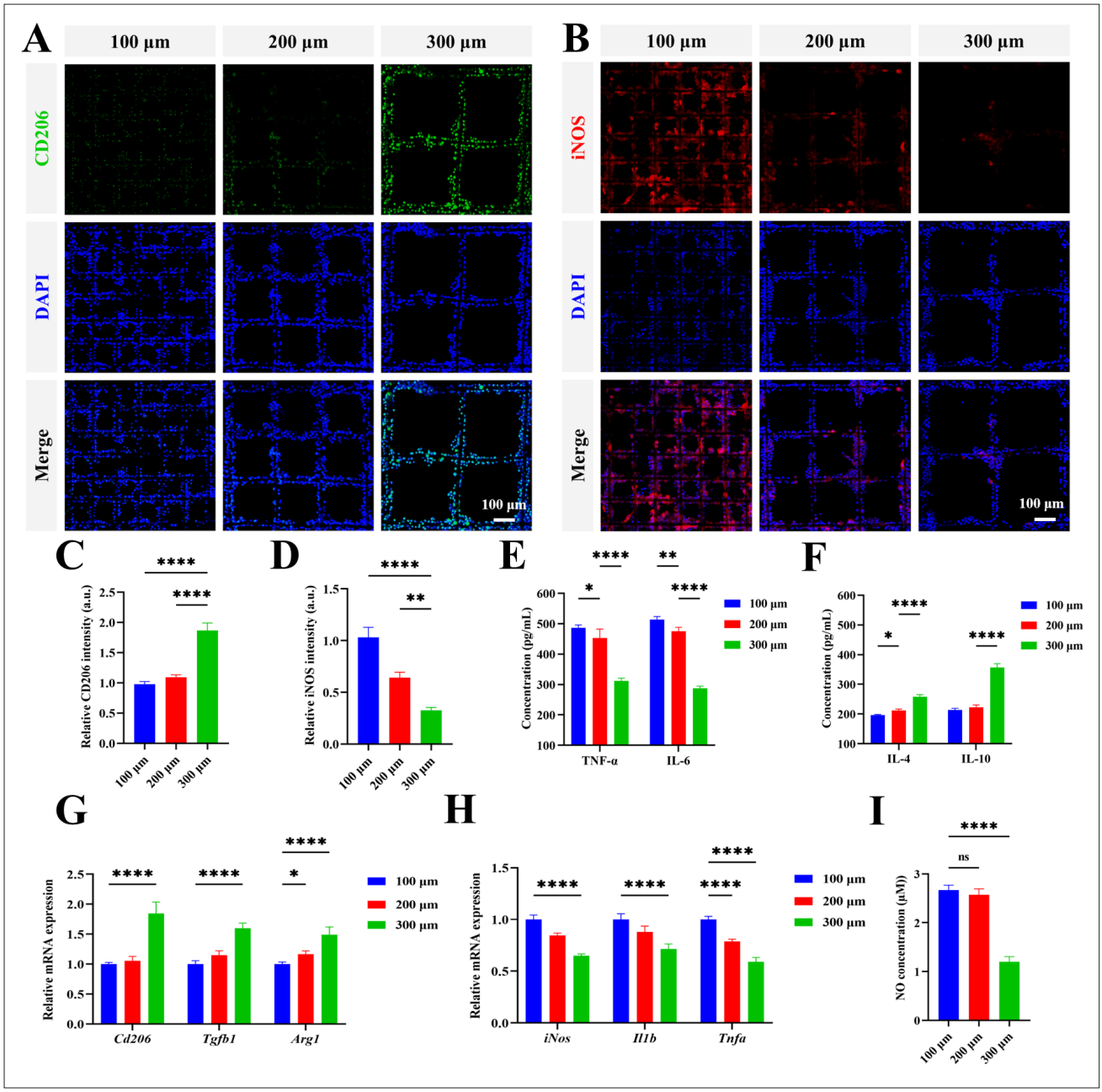


Figure 3. Modulation of macrophage polarization by scaffolds with different pore sizes. Immunofluorescence staining of (A) CD206 and (B) iNOS. Scale bars: 100 μm; magnifications: ×30. Semi-quantitative analysis of (C) CD206 and (D) iNOS. (E) Concentrations of TNF-α and IL-6. (F) Concentrations of IL-4 and IL-10. (G) Gene expression levels of *Cd206*, *Tgfb1*, and *Arg1*. (H) Gene expression levels of *iNos*, *Il1b*, and *Tnfa*. (I) Concentrations of NO. Notes: $n = 3$; $^{*}p < 0.05$, $^{**}p < 0.01$, $^{****}p < 0.0001$. Abbreviations: NO: CD206, cluster of differentiation 206; IL, interleukin; iNOS, inducible nitric oxide synthase; mRNA, messenger RNA, nitric oxide; TNF-α, tumor necrosis factor-alpha; ns, non-significant.

stiffness. For example, at a point 15 μm away from the fiber junction, simulation results showed that the local bending stiffness of the 100 μm group was approximately 4.10-fold higher than that of the 200 μm group, and 9.28-fold higher than that of the 300 μm group. Moreover, as the distance from the fiber intersection increased, the difference in local stiffness became more pronounced.

To further investigate the impact of local stiffness on macrophage polarization, transcriptomic sequencing analysis was performed. Compared with the 100 μm

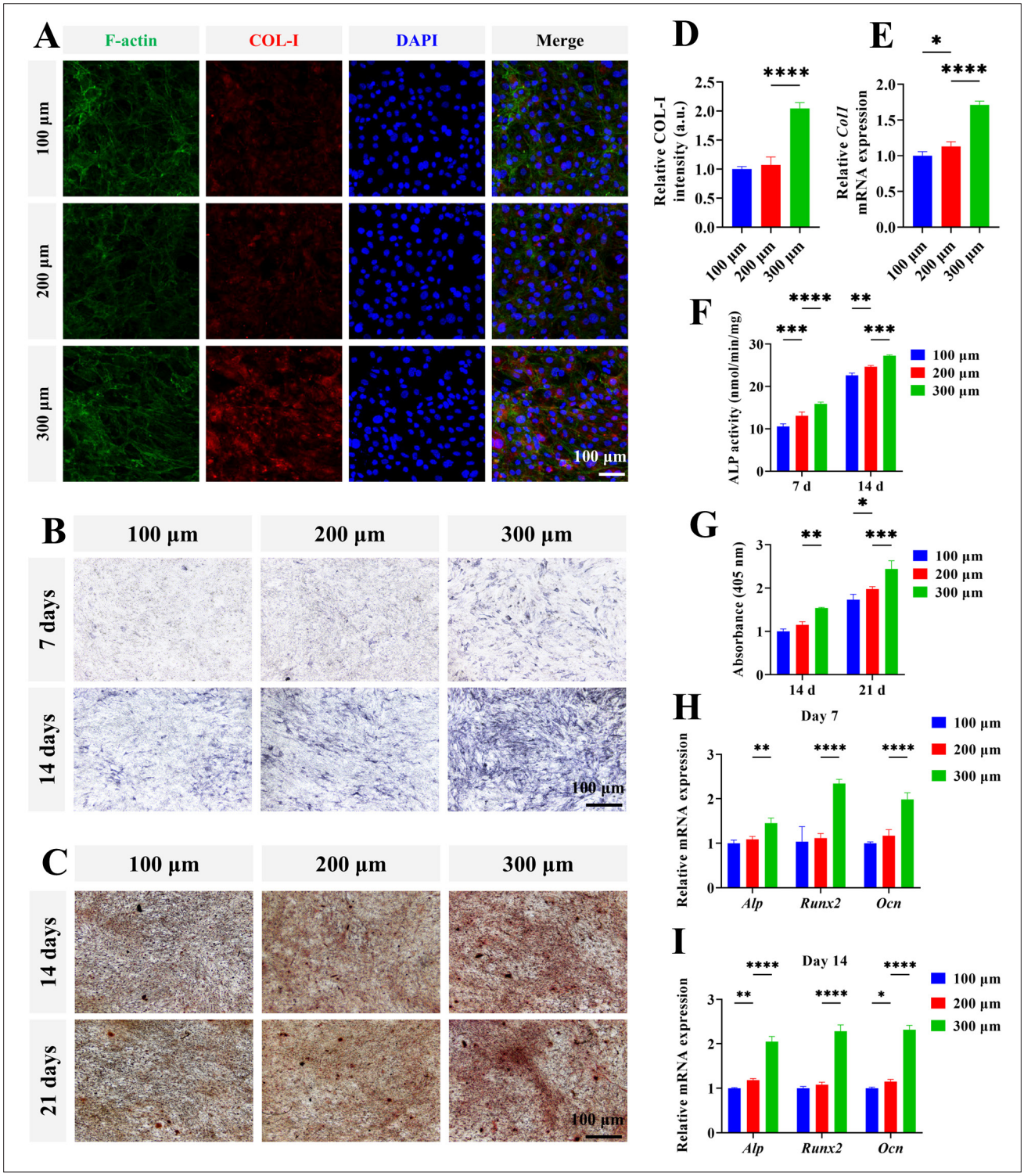


Figure 4. Scaffolds with different pore sizes modulate the immune microenvironment to affect osteogenic differentiation. (A) Immunofluorescence staining of COL-I. Scale bars: 100 μm; magnifications: ×40 . (B) ALP staining images at 7 days and 14 days. Scale bars: 100 μm; magnifications: ×60. (C) ARS staining images at 14 days and 21 days. Scale bars: 100 μm; magnifications: ×60 . (D) Semi-quantitative analysis of COL-I. (E) Gene expression levels of *Col1*. (F) Determination of ALP activity. (G) Quantitative analysis of the ARS. Gene expression levels of *Alp*, *Runx2*, and *Ocn* at (H) day 7 and (I) day 14. Notes: $n = 3$; *$p < 0.05$, **$p < 0.01$, ***$P < 0.001$, ****$p < 0.0001$. Abbreviations: ALP, alkaline phosphatase; ARS, alizarin Red S; COL-I, collagen type I; DAPI, 4',6-diamidino-2-phenylindole; mRNA, messenger RNA.

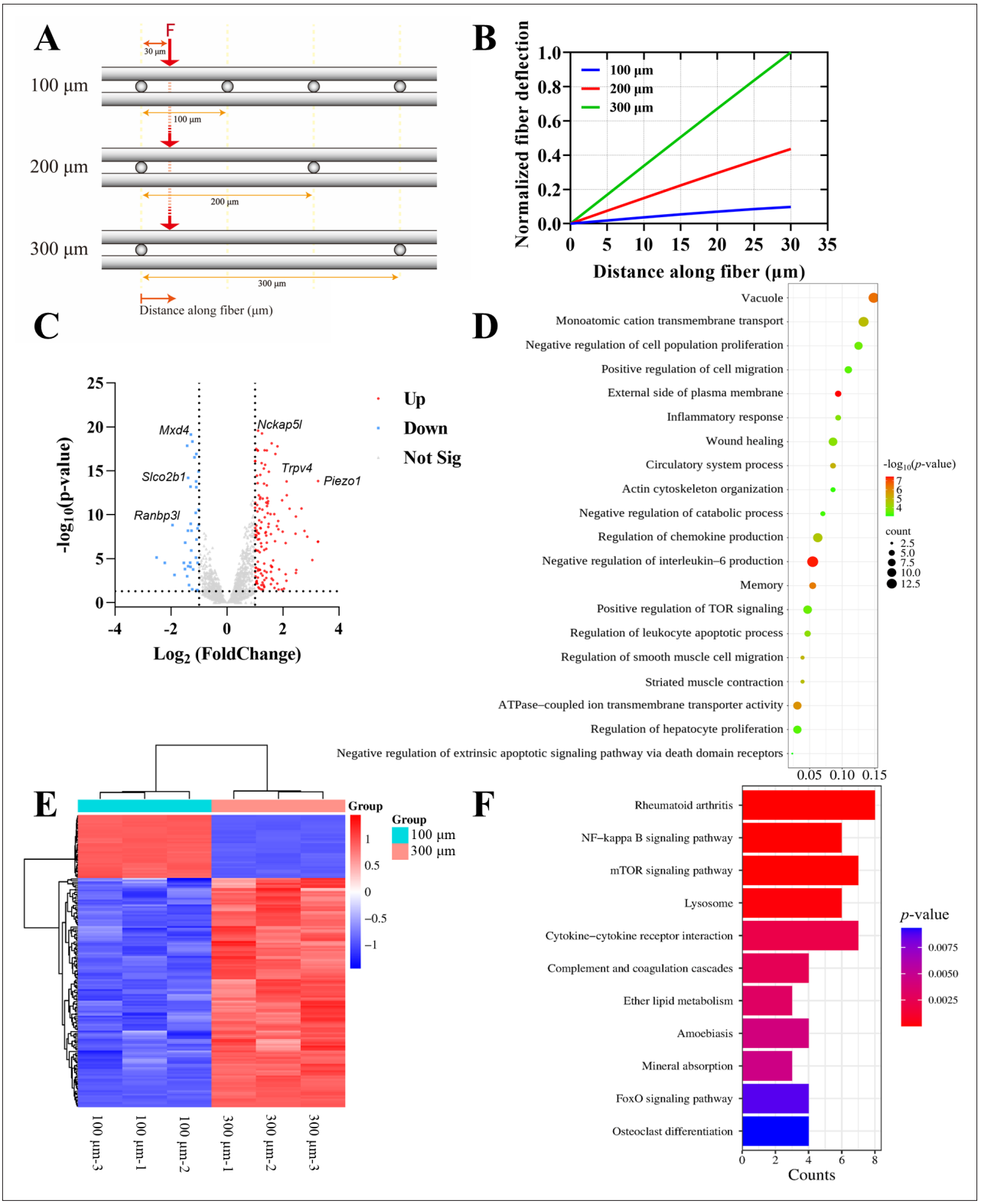


Figure 5. Simulation and transcriptomic analysis of scaffolds with different pore sizes. (A) Analysis model of relative stiffness. (B) Relative deflection. (C) Volcano plot, (D) gene ontology enrichment analysis, (E) heatmap, and (F) KEGG pathway enrichment analysis of differentially expressed genes between the 100 μm and 300 μm groups. Abbreviations: KEGG: Kyoto Encyclopedia of Genes and Genomes; mTOR, mammalian target of rapamycin; TOR, target of rapamycin.

group, the 300 μm group exhibited 138 upregulated and 38 downregulated DEGs (Figure 5C & E). These DEGs were subsequently subjected to gene ontology enrichment analysis, which identifies overrepresented functional categories among a set of genes. As shown in Figure 5D, these DEGs were predominantly enriched in pathways related to the cytoskeleton and ATP-dependent ion transmembrane transporter activity. Additionally, KEGG pathway analysis was conducted to investigate the potential functional implications of these DEGs (Figure 5F). The results indicated that these DEGs may be involved in signaling pathways such as mammalian target of rapamycin and nuclear factor-kappa B, both of which are known downstream targets of the mechanosensitive ion channel Piezo1, which plays a crucial role in converting mechanical stimuli into biochemical signals.[41]

3.5. Modulation of Piezo1 expression and macrophage polarization by scaffolds with varying pore sizes

To verify whether scaffolds with different pore sizes regulate macrophage polarization through Piezo1 activation, immunofluorescence staining and qRT-PCR were conducted. The immunofluorescence results revealed that macrophages cultured on the 300 μm group exhibited significantly higher Piezo1 fluorescence intensity compared to those on the 100 μm and 200 μm groups (Figure 6A & B). Consistently, semi-quantitative fluorescence analysis and qRT-PCR collectively demonstrated the most pronounced Piezo1 expression in the 300 μm group (Figure 6C).

To further validate the role of Piezo1, macrophages cultured on the 300 μm group were treated with small interfering RNA (siRNA)-mediated knockdown and the Piezo1-specific inhibitor GsMTx4 to suppress Piezo1 expression. Both siRNA transfection and GsMTx4 treatment significantly reduced Piezo1 protein expression compared to the untreated control group (Figure 6D).

Subsequently, the polarization status of macrophages was assessed following Piezo1 inhibition. As shown in Figure 6E, the expression of M2 macrophage polarization markers was markedly decreased in the Piezo1-suppressed groups relative to the controls. These findings suggest that Piezo1 may regulate macrophage polarization by modulating the cellular response to mechanical cues, particularly affecting the transition toward the anti-inflammatory M2 phenotype.

Collectively, these results demonstrate that scaffold pore size can influence macrophage polarization by altering the mechanical stiffness of the material. Further mechanistic investigation revealed that the upregulation of the mechanosensitive ion channel Piezo1 underlies this process. Through Piezo1 activation, macrophages are able to detect variations in scaffold stiffness, thereby modulating their polarization states accordingly.

3.6. Assessment of the foreign body reaction in a rat subcutaneous implantation model

The results of *in vitro* experiments showed that a 300 μm pore size could further promote macrophage M2 polarization, improving the osteogenic immune microenvironment. To further evaluate the immune responses of scaffolds with different pore sizes *in vivo*, we implanted the scaffolds subcutaneously in rats and assessed the acute and chronic inflammatory responses. After 7 days of implantation *in vivo*, histological evaluation employing HE and TB staining was performed to detect acute inflammation. The HE staining demonstrated a significant reduction in inflammatory cells on the surfaces of the 300 μm scaffolds compared to the other two groups (Figure 7A & F). Notably, dense clusters of foreign body giant cells (FBGCs), indicative of FBR, were observed at the interface between scaffolds and host tissues in the 100 μm group. The TB staining further demonstrated that the number of mast cells, which are markers of acute inflammation, was significantly higher in the 100 μm and 200 μm groups than in the 300 μm group (Figure 7C & G). These findings indicate that the acute inflammatory response was considerably milder in the 300 μm group.

To assess the chronic inflammatory response, the HE staining was performed at 28 days post-implantation. The 300 μm group exhibited significant neovascularization within the scaffold (Figure 7B), suggesting enhanced tissue integration and remodeling. Furthermore, the number of inflammatory cells was markedly lower in the 300 μm group compared to the 100 μm and 200 μm groups (Figure 7E). The thickness of the fibrous capsule at the scaffold–host tissue interface, an indicator of chronic inflammation and biocompatibility, was also evaluated. Compared with other groups, the 300 μm group showed the thinnest fibrous capsule (Figure 7D & H), further indicating a more favorable immune response and reduced FBR.

3.7. Effect of scaffolds with different pore sizes on macrophage phenotypic switching in a bone defect model

Macrophages play a pivotal role in bone repair and reconstruction by mediating the initial inflammatory response and secreting various factors that regulate osteogenesis and osteoblastogenesis.[42] They are essential for the process of osseointegration following foreign body implantation.[43] Our results have demonstrated that a 300 μm pore size effectively promotes macrophage M2 polarization *in vitro*.

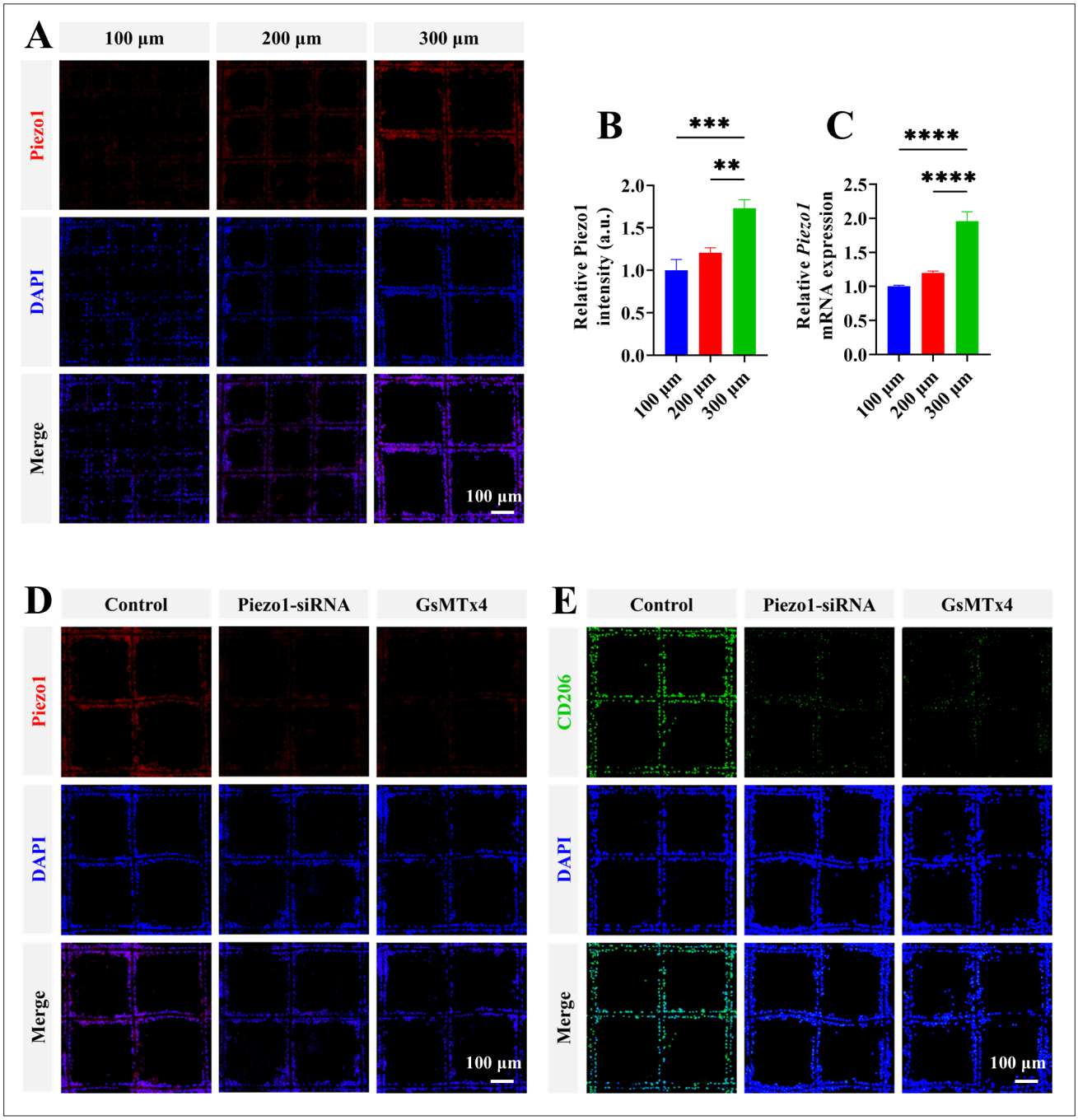


Figure 6. Scaffold pore size modulates Piezo1 expression and regulates macrophage polarization. (A) Immunofluorescence staining (scale bars: 100 μm; magnifications: ×30) and (B) semi-quantitative analysis of Piezo1 in the three groups of scaffolds. (C) Gene expression level of *Piezo1*. Immunofluorescence images of (D) Piezo1 and (F) CD206 expressions in macrophages in the 300 μm group after siRNA knockdown and GsMTx4 treatment. Scale bars: 100 μm; magnifications: ×30. Notes: $n = 3$; $^{**}p < 0.01$, $^{***}p < 0.001$, $^{****}p < 0.0001$. Abbreviations: DAPI, 4',6-diamidino-2-phenylindole; siRNA, small interfering RNA.

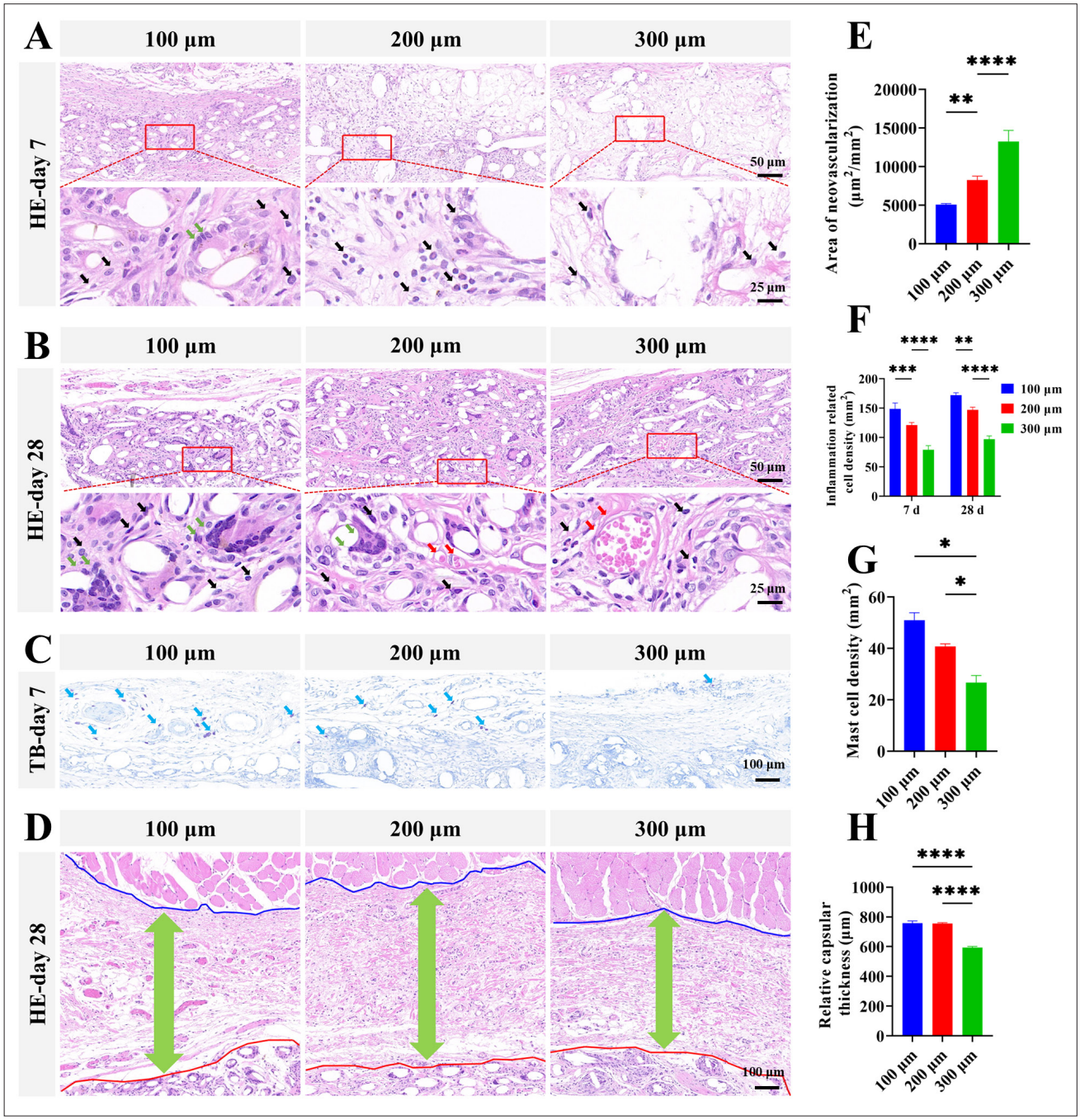


Figure 7. Assessment of the effects of scaffolds with varying pore sizes on foreign body reaction in the rat subcutaneous implantation model *in vivo*. HE staining images at (A) day 7 and (B) day 28. Scale bars: (top) 50 μm, (bottom) 25 μm; magnifications: (top) ×80, (bottom) ×160. (C) TB staining images at day 7. Scale bars: 100 μm; magnifications: ×40. (D) Fibrous capsule measurements at day 28. Scale bars: 100 μm; magnifications: ×40. Statistical analyses of the (E) neovascularization, (F) inflammatory cell density, (G) mast cell density, and (H) Fibrous capsule thickness measurements. Notes: Black arrows indicate inflammatory cells; green arrows indicate FBGC; red arrows indicate neovascularization; blue arrows indicate mast cells; $n = 4$; $^{*}p < 0.05$, $^{**}p < 0.01$, $^{***}p < 0.001$, $^{****}p < 0.0001$. Abbreviations: FBGC, foreign body giant cells; HE, hematoxylin–eosin; TB, toluidine blue.

To further investigate this phenomenon, we conducted *in vivo* experiments using a rat cranial bone defect model to examine the influence of scaffold pore size on macrophage phenotypic transition. Immunofluorescence analysis was performed to evaluate macrophage phenotypes following implantation of scaffolds with three different pore sizes (100 μm, 200 μm, and 300 μm) into the bone defect site. CD163 was used as a marker for M2 macrophages, while iNOS was used to label M1 macrophages. The results showed that the 300 μm group had the highest green fluorescence intensity, indicating that it had the highest number of M2 macrophages (Figure 8A). In contrast, the 100 μm group showed the strongest red fluorescence intensity, indicating the highest M1 macrophage density, whereas the 300 μm group showed the weakest. Further analysis of the M2/M1 macrophage ratio revealed that the 300 μm group achieved a ratio of 1.64, which was 2.52-fold and 1.51-fold higher than that of the 100 μm and 200 μm groups, respectively (Figure 8C).

Additionally, immunohistochemical staining was employed to assess the deposition of the pro-inflammatory cytokine TNF-α and the anti-inflammatory cytokine IL-10 in each group. Compared with the 100 μm and 200 μm groups, the 300 μm group showed a significant decrease in TNF-α deposition and a significant increase in IL-10 deposition (Figure 8B, D, & E).

3.8. Bone regeneration in a rat cranial defect model treated with scaffolds of varying pore sizes

To investigate the effects of scaffolds with different pore sizes on osteogenesis after modulating the immune microenvironment, we conducted a series of *in vivo* experiments using a cranial defect model. Micro-CT analysis was first performed on skull specimens implanted with scaffolds of varying pore sizes. The osteogenic capacity, as determined by 3D reconstruction, was markedly superior in all scaffold groups relative to the scaffold-free control. Among them, the 300 μm group exhibited the highest volume of newly formed bone, although the difference was not visually striking (Figure 9A). Quantitative confirmation was provided by 2D sagittal CT images, which identified the least residual bone defect in the 300 μm group (Figure 9B).

To quantify bone formation, histomorphometric parameters, including BV/TV and BMD, were measured within the bone defect region. Micro-CT analysis showed that the 300 μm group had significantly higher BV/TV and BMD compared to the other groups. This aligns with the quantitative nature of these measurements, despite the relatively subtle visual differences among the reconstructed images (Figure 9C & D).

Histological analyses were conducted using the HE staining and Masson's trichrome staining to assess new bone formation and maturation.[44] The HE staining results revealed that the control group exhibited minimal new bone formation, whereas the 300 μm group had the largest area of newly formed bone and the smallest residual defect length (Figure 9G). The Masson's trichrome staining results showed that the 300 μm group had the highest bone tissue maturity, characterized by dense collagen deposition and regular bone plate structure (Figure 9H).

Additionally, the deposition of COL-I and OCN, key markers of bone formation and maturation, was assessed. Compared to the control group, the 100 μm group, and the 200 μm group, the 300 μm group showed significantly more COL-I and OCN deposition (Figure 9E, F, & I). These findings suggest that scaffolds with a 300 μm pore size provide an optimal microenvironment for promoting osteogenesis and bone maturation *in vivo*. This is likely achieved through enhanced modulation of the immune microenvironment, highlighting the potential of 300 μm pore-sized scaffolds for improved bone regeneration and repair.

4. Discussion

In this study, PCL scaffolds with specific pore sizes (100 μm, 200 μm, and 300 μm) were fabricated via EHD printing, and the effects of the pore sizes on macrophage polarization, FBR, immune microenvironment, and bone regeneration were comprehensively evaluated. The results showed that the 300 μm pore-sized scaffolds significantly promoted macrophage M2 polarization, decreased the expression of M1-related pro-inflammatory factors, improved the immune microenvironment at the bone defect site, and enhanced the generation and maturation of new bone under both *in vivo* and *in vitro* conditions. These findings underscore the potential of a 300 μm pore size as an optimal parameter in scaffold design for bone tissue regeneration.

There are inconsistent results in the literature regarding how different pore size materials regulate macrophage polarization.[21,22,45] Such differences may arise from variations in material fabrication methods, pore size designs, and scaffold geometrical characteristics. Specifically, the freeze-drying method used by Jiang *et al.*[21] yielded materials with irregular pore size distributions and limited control over pore uniformity, whereas the precision template–based approach used by Hady *et al.*[22] may also have been affected by slight deviations in pore size distribution. In the present study, the precise control of pore size was achieved using EHD printing technology, which significantly reduced the variable interference

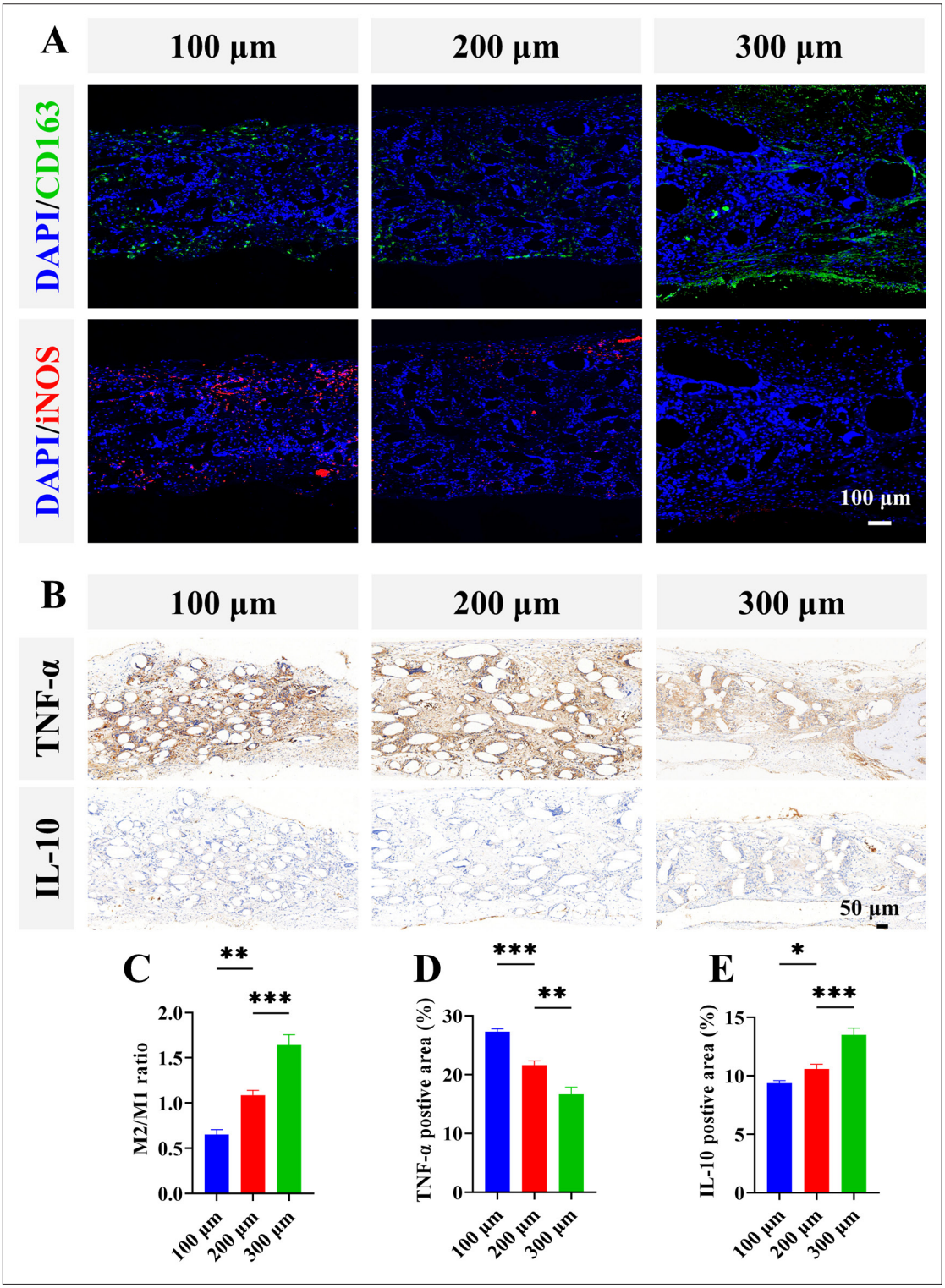


Figure 8. Effect of scaffolds with different pore sizes on macrophage phenotypic switching in a bone defect model. (A) Immunofluorescence staining images. Green indicates CD163 (M2 marker) and red indicates iNOS (M1 marker). Scale bars: 100 μm; magnifications: ×40. (B) Immunochemical staining images of TNF-α and IL-10. Scale bars: 50 μm; magnifications: ×40. (C) M2/M1 ratio and percentages of positive areas of (D) TNF-α and (E) IL-10 in the three groups of scaffolds. Notes: $n = 4$; $^{*}p < 0.05$, $^{**}p < 0.01$, $^{***}p < 0.001$. Abbreviations: CD163, cluster of differentiation 163; IL-10, interleukin-10; iNOS, inducible nitric oxide synthase; TNF-α, tumor necrosis factor-alpha.

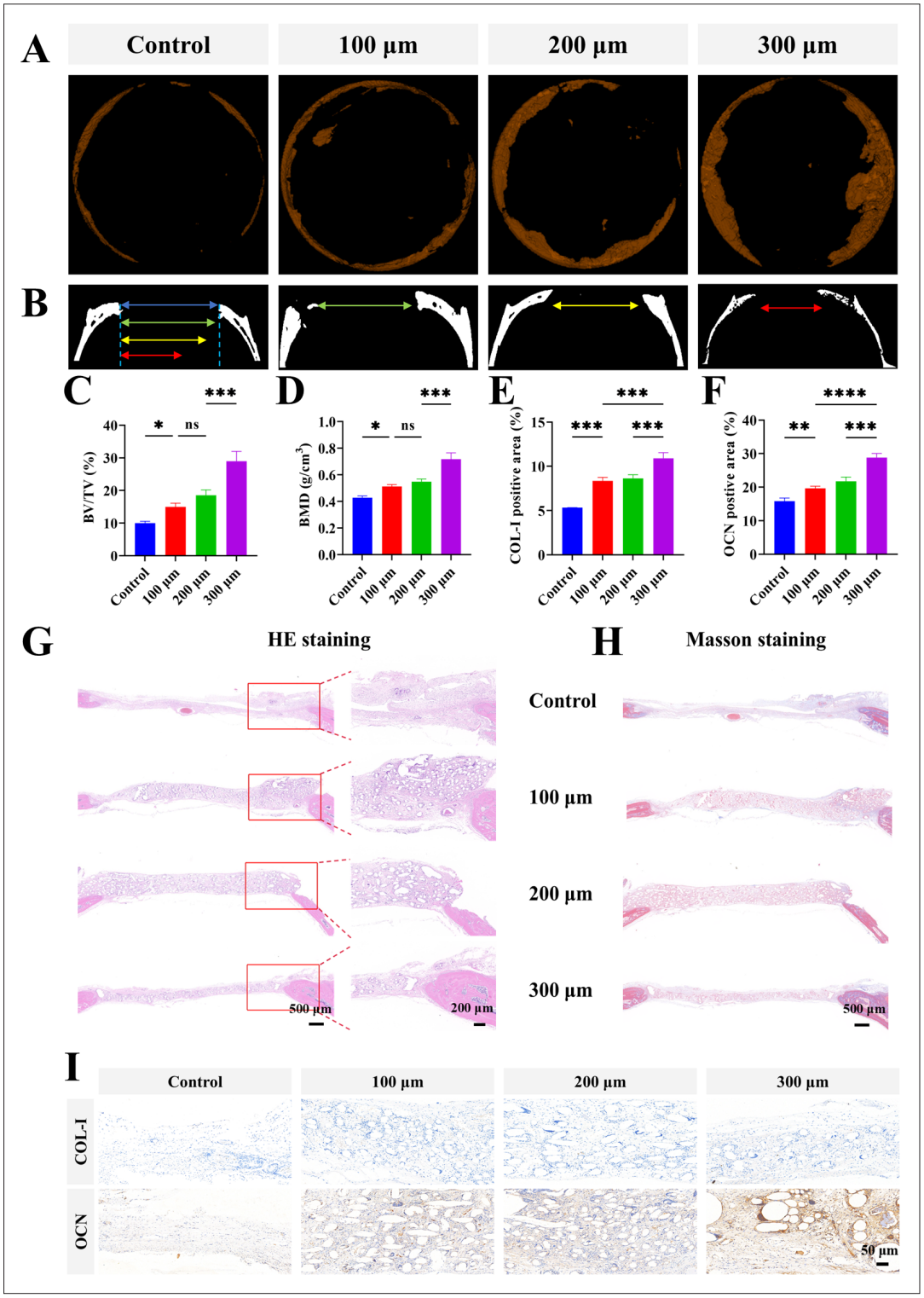


Figure 9. Bone regeneration in a rat cranial defect model treated with scaffolds of different pore sizes. (A) 3D reconstructed images of scaffolds in the four groups. (B) Sagittal positional images. Quantitative analysis results of (C) BV/TV, (D) BMD, and positive areas of (E) COL-I and (F) OCN in the four groups. (G) HE staining. Scale bars: (left) 500 μm, (right) 200 μm; magnifications: (left) ×4 , (right) ×10 . (H) Masson staining. Scale bars: 500 μm; magnifications: ×4. (I) Immunochemical staining of COL-I and OCN. Scale bars: 50 μm; magnifications: ×40. Notes: $n = 4$; *$p < 0.05$, **$p < 0.01$, ***$p < 0.001$, ****$p < 0.0001$. Abbreviations: BMD, bone mineral density; BV/TV, bone volume-to-tissue volume ratio; COL-I, collagen type-I; HE, hematoxylin–eosin; OCN, olsteocalcin.

due to uneven pore size. This enabled a more reliable demonstration of the promoting effect of the 300 μm pore size on macrophage M2 polarization and helped clarify, to a certain extent, the controversy regarding the relationship between scaffold pore size and macrophage polarization.

Additionally, compared with 100 μm and 200 μm pore sizes, the 300 μm pore size not only improved the spatial fitness of macrophages but also reduced the pro-inflammatory response triggered by high-density cell aggregation. Previous studies have shown that a larger pore size can provide a softer mechanical environment for macrophages by reducing the stiffness of the scaffold, thereby promoting their transition to the M2 phenotype.[40,46] In this study, simulation analysis and transcriptomic sequencing revealed that scaffold stiffness can regulate the direction of macrophage polarization by modulating the activation of the Piezo1 protein. In addition, scaffolds with larger pore sizes typically have improved breathability and nutrient supply, providing a more favorable growth environment for macrophages. This promotes their polarization toward the M2 type in relatively mild environments, thereby enhancing anti-inflammatory and tissue repair effects.[17] Moreover, the 300 μm pore-sized scaffolds promoted an M1-to-M2 phenotypic shift, as evidenced by a distinct cytokine profile (TNF-α, IL-6, IL-10, and TGF-β), fostering a pro-regenerative immune microenvironment. In *in vivo* experiments, the open structure of the 300 μm pore-sized scaffold enhanced angiogenesis, which is critical for immune modulation and bone regeneration. Neovascularization provided increased oxygen and nutrients, mitigating the detrimental effects of the hypoxic environment on macrophage phenotype and supporting their dynamic shift toward an anti-inflammatory phenotype. Furthermore, angiogenesis provided a favorable circulatory environment for osteoblast recruitment and differentiation, further enhancing local bone repair.

Previous studies have indicated that scaffolds with smaller pore sizes are more prone to eliciting an FBR.[47–50] This is attributed to the limited porosity of the scaffold surface, which leads to the sustained accumulation of pro-inflammatory macrophages and multinucleated giant cells. For example, Ivanova *et al.*[51] found that scaffolds with pore sizes less than 56 μm were more likely to induce fibrous capsule formation. Consistently, the results of this study showed that a 300 μm pore size significantly reduced the occurrence of FBR. In the *in vivo* implantation experiments, a large number of multinucleated FBGCs and thick fibrous capsule formation were observed on the surface of the scaffolds in the 100 μm and 200 μm groups. In contrast, the 300 μm group not only significantly reduced the aggregation of FBGCs but also suppressed the chronic inflammatory response by upregulating the expression of the anti-inflammatory factor IL-10. Further analysis revealed that the fibrous capsule thickness in the 300 μm group was significantly lower than that in the other two groups, accompanied by increased neovascularization and reduced inflammatory cell infiltration. These results suggest that the 300 μm pore-sized scaffold can significantly reduce the FBR by regulating macrophage phenotype switching and reducing pro-inflammatory signaling, thereby enhancing the biocompatibility of the material.

Macrophage phenotype plays a key role in bone regeneration.[52–55] In this study, we achieved precise control of pore size through EHD printing and established a causal link between macrophage phenotype, scaffold pore size, and osteogenic differentiation. The 300 μm group not only increased the M2/M1 ratio of macrophages but also potently activated the expression of osteogenic markers (*Runx2*, *Col1*, and *Ocn*), highlighting pore size as a critical parameter orchestrating the coupling between immunomodulation and osteogenesis. In *in vivo* experiments, the 300 μm group showed significant increases in BV/TV and BMD, even though the magnitude of the increase was not pronounced. Such moderate yet significant enhancement is reasonable for a cell-free scaffold without any osteoinductive factors, where substantial bone formation is generally limited. Moreover, histological and morphological analyses revealed clearer pore size-dependent differences in tissue infiltration, vascular-like structures, and osteoid deposition. These results indicate that macrophage polarization synergizes with osteogenesis temporally and spatially, and the 300 μm scaffold optimizes the dynamic balance in this process.

Despite the remarkable results of this study, some limitations exist. First, only PCL was selected as the matrix material, and its biocompatibility and degradation behavior may limit the broad applicability of the results. Future studies should incorporate multicomponent composites, such as hydroxyapatite and collagen, to verify the generalizable effect of pore size on different materials. Second, the experiments were primarily based on a rat model, which, despite providing important *in vivo* data, has an immune system that differs from that of humans. Therefore, further validation using large animal models or clinical trials is necessary to enhance translational potential. Future research could also focus on the development of personalized scaffold design solutions using artificial intelligence techniques to comprehensively optimize the pore size, shape, and mechanical properties of scaffolds, thereby providing more precise solutions for bone regeneration. Furthermore, research should explore the effects of scaffold structure on other immune cells, such as T cells, B cells, and dendritic cells, to gain a more

comprehensive understanding of immune responses in tissue regeneration.

5. Conclusion

In this study, PCL scaffolds with varying pore sizes (100 μm, 200 μm, and 300 μm) were fabricated using EHD printing, and their modulatory effects on macrophage polarization, the immune microenvironment, and bone regeneration were systematically elucidated. Scaffolds with a 300 μm pore size significantly improved the local immune microenvironment by driving macrophage polarization toward the M2 phenotype, enhancing anti-inflammatory factor expression, suppressing pro-inflammatory mediators, and promoting angiogenesis. Furthermore, simulation analysis and transcriptomics sequencing indicated that pore size regulates macrophage Piezo1 activation by influencing scaffold stiffness, thereby affecting the polarization process. Moreover, scaffolds with a 300 μm pore size significantly alleviated the FBR, enhanced the expression of osteogenic genes and mineralized matrix deposition, and promoted new bone formation and tissue maturation both *in vitro* and *in vivo*. This study clarifies the superiority of 300 μm pore size in PCL scaffold design, provides an important basis for promoting bone regeneration through immunomodulation, and offers scientific evidence to support the development and clinical translation of high-performance tissue engineering scaffolds.

Acknowledgments

None.

Funding

This work was financially supported by the National Key R&D Program of China (No. 2024YFB4607800), the National Natural Science Foundation of China (52125501, 52405325, 82072522), the Cross training Support Project for Doctoral Students at Xi'an Jiaotong University (IDT2315), the Key Research Project of Shaanxi Province (2021LLRH-08), the Program for Innovation Team of Shaanxi Province (2023-CX-TD-17), the Postdoctoral Fellowship Program of CPSF (GZB20230573), the Postdoctoral Project of Shaanxi Province (2023BSHYDZZ30), and the Fundamental Research Funds for the Central Universities (xzy012023022).

Conflict of interest

Jiankang He serves as the Editorial Board Member of the journal, but did not in any way involve in the editorial and peer-review process conducted for this paper, directly or indirectly. Other authors declare they have no competing interests.

Author contributions

Funding acquisition: Wei Wang, Jiankang He
Investigation: Junzheng Liu, Jiahao Zhang
Methodology: Junzheng Liu, Jiaming Yu, Qin Guo, Yulin Wang, Jiahao Zhang
Resources: Jiankang He
Software: Junzheng Liu, Jiaming Yu, Le Jia
Validation: Zijie Meng, Qin Guo, Wei Wang
Writing–original draft: Junzheng Liu, Zijie Meng
Writing–review and editing: Wei Wang, Jiankang He

Ethics approval and consent to participate

The animal study was approved by the Ethics Committees of Xi'an Jiaotong University (2020-752).

Consent for publication

Not applicable.

Availability of data

The raw data underlying this study are available from the corresponding author upon reasonable request.

References

1. Liu L, Chen H, Zhao X, *et al*. Advances in the application and research of biomaterials in promoting bone repair and regeneration through immune modulation. *Mater Today Bio*. 2024;30:101410.
doi: 10.1016/j.mtbio.2024.101410

2. Szczodra A, Houaoui A, Agniel R, *et al*. Boron substitution in silicate bioactive glass scaffolds to enhance bone differentiation and regeneration. *Acta Biomater*. 2024;186:489-506.
doi: 10.1016/j.actbio.2024.07.053

3. He X, Liu Y, Dai Z *et al*. Yoda1 pretreated BMSC derived exosomes accelerate osteogenesis by activating phospho-ErK signaling via Yoda1-mediated signal transmission. *J Nanobiotechnol*. 2024;22(1):407.
doi: 10.1186/s12951-024-02669-0

4. Dang Y, Zhang Y, Luo G, *et al*. The decisive early phase of biomaterial-induced bone regeneration. *Appl Mater Today*. 2024;38:102236.
doi: 10.1016/j.apmt.2024.102236

5. Jin S, Wen J, Zhang Y, *et al*. M2 macrophage-derived exosome-functionalized topological scaffolds regulate the foreign body response and the coupling of angio/osteoclasto/osteogenesis. *Acta Biomater*. 2024;177:91-106.
doi: 10.1016/j.actbio.2024.01.043

6. Qiu D, Cao C, Prasopthum A, *et al*. Elucidating osseointegration in vivo in 3D printed scaffolds eliciting different foreign body responses. *Mater Today Bio*. 2023;22:100771. doi: 10.1016/j.mtbio.2023.100771

7. Mesa-Restrepo A, Byers E, Brown JL, Ramirez J, Allain JP, Posada VM. Osteointegration of Ti bone implants: a study on how surface parameters control the foreign body response. *ACS Biomater Sci Eng*. 2024;10(8):4662-4681. doi: 10.1021/acsbiomaterials.4c00114

8. Dondossola E, Holzapfel BM, Alexander S, Filippini S, Hutmacher DW, Friedl P. Examination of the foreign body response to biomaterials by nonlinear intravital microscopy. *Nat Biomed Eng*. 2016;1:0007. doi: 10.1038/s41551-016-0007

9. Anderson JM, Rodriguez A, Chang DT. Foreign body reaction to biomaterials. *Semin Immunol*. 2008;20(2):86-100. doi: 10.1016/j.smim.2007.11.004

10. Fu M, Yang C, Sun G. Recent advances in immunomodulatory hydrogels biomaterials for bone tissue regeneration. *Mol Immunol*. 2023;163:48-62. doi: 10.1016/j.molimm.2023.09.010

11. Li W, Dai F, Zhang S, *et al*. Pore size of 3D-printed polycaprolactone/polyethylene glycol/hydroxyapatite scaffolds affects bone regeneration by modulating macrophage polarization and the foreign body response. *ACS Appl Mater Interfaces*. 2022;14(18):20693-20707. doi: 10.1021/acsami.2c02001.

12. Franz S, Rammelt S, Scharnweber D, Simon JC. Immune responses to implants - a review of the implications for the design of immunomodulatory biomaterials. *Biomaterials*. 2011;32(28):6692-6709. doi: 10.1016/j.biomaterials.2011.05.078.

13. Kastellorizios M, Papadimitrakopoulos F, Burgess DJ. Multiple tissue response modifiers to promote angiogenesis and prevent the foreign body reaction around subcutaneous implants. *J Control Release*. 2015;214:103-111. doi: 10.1016/j.jconrel.2015.07.021.

14. Spiller KL, Nassiri S, Witherel CE, *et al*. Sequential delivery of immunomodulatory cytokines to facilitate the M1-to-M2 transition of macrophages and enhance vascularization of bone scaffolds. *Biomaterials*. 2015;37:194-207. doi: 10.1016/j.biomaterials.2014.10.017.

15. Li R, Zhang K, Dong C, Wang K, Gu X, Qin Y. Osteoinductivity enhancement by tailoring the surface chemical bond status: a strategy to mobilize host bone growth factors for in situ bone regeneration. *Mater Today Bio*. 2024;29:101256. doi: 10.1016/j.mtbio.2024.101256.

16. Vegas AJ, Veiseh O, Doloff JC, *et al*. Combinatorial hydrogel library enables identification of materials that mitigate the foreign body response in primates. *Nat Biotechnol*. 2016;34(6):345-352. doi: 10.1038/nbt0616-666e.

17. Xiong S, Zhang Y, Zeng J, *et al*. DLP fabrication of HA scaffold with customized porous structures to regulate immune microenvironment and macrophage polarization for enhancing bone regeneration. *Mater Today Bio*. 2024;24:100929. doi: 10.1016/j.mtbio.2023.100929.

18. Veiseh O, Doloff JC, Ma M, *et al*. Size- and shape-dependent foreign body immune response to materials implanted in rodents and non-human primates. *Nat Mater*. 2015;14(6):643–651. doi: 10.1038/nmat4290.

19. Sridharan R, Cavanagh B, Cameron AR, Kelly DJ, O'Brien FJ. Material stiffness influences the polarization state, function and migration mode of macrophages. *Acta Biomater*. 2019;89:47-59. doi: 10.1016/j.actbio.2019.02.048.

20. Xia D, Wang Y, Wu R, *et al*. The effect of pore size on cell behavior in mesoporous bioglass scaffolds for bone regeneration. *Appl Mater Today*. 2022;29:101607. doi: 10.1016/j.apmt.2022.101607

21. Jiang S, Lyu C, Zhao P, *et al*. Cryoprotectant enables structural control of porous scaffolds for exploration of cellular mechano-responsiveness in 3D. *Nat Commun*. 2019;10(1):3491. doi: 10.1038/s41467-019-11397-1.

22. Hady TF, Hwang B, Pusic AD, *et al*. Uniform 40-μm-pore diameter precision templated scaffolds promote a pro-healing host response by extracellular vesicle immune communication. *J Tissue Eng Regen Med*. 2020; 15(1):24-36. doi: 10.1002/term.3160.

23. Meng Z, Yang S, Yin F, *et al*. 3D-printed biodegradable polycaprolactone rib implants with tissue-specific mechanical properties promote chest wall recovery by stimulating tissue fibrosis. *Virtual Phys Prototyp*. 2024;19(1):2346816. doi: 10.1080/17452759.2024.2346816.

24. He J, Xia P, Li D. Development of melt electrohydrodynamic 3D printing for complex microscale poly (ε-caprolactone) scaffolds. *Biofabrication*. 2016;8(3):035008. doi: 10.1088/1758-5090/8/3/035008.

25. Han K, He J, Fu L, Mao M, Kang Y, Li D. Engineering highly-aligned three-dimensional (3D) cardiac constructs for enhanced myocardial infarction repair. *Biofabrication*. 2022;15(1):015003. doi: 10.1088/1758-5090/ac94f9.

26. Shi Y, Wang L, Sun L, *et al*. Melt electrospinning writing PCL scaffolds after alkaline modification with outstanding cytocompatibility and osteoinduction. *Int J Bioprint*. 2023;9(6):1071. doi: 10.36922/ijb.1071.

27. Yao C, Qiu Z, Li X, Zhu H, Li D, He J. Electrohydrodynamic printing of microfibrous architectures with cell-scale spacing

for improved cellular migration and neurite outgrowth. *Small.* 2023;19(19):2207331.
doi: 10.1002/smll.202207331.

28. Tylek T, Blum C, Hrynevich A, *et al*. Precisely defined fiber scaffolds with 40 μm porosity induce elongation driven M2-like polarization of human macrophages. *Biofabrication.* 2020;12(2):025007.
doi: 10.1088/1758-5090/ab5f4e.

29. Bružauskaitė I, Bironaitė D, Bagdonas E, Bernotienė E. Scaffolds and cells for tissue regeneration: different scaffold pore sizes—different cell effects. *Cytotechnology.* 2016;68(3):355-369.
doi: 10.1007/s10616-015-9895-4.

30. Zhang Y, Li R, Wu W, *et al*. Adhesion and proliferation of osteoblast-like cells on porous polyetherimide scaffolds. *Biomed Res Int.* 2018;2018:1491028.
doi: 10.1155/2018/1491028.

31. Lai Y, Cao H, Wang X, *et al*. Porous composite scaffold incorporating osteogenic phytomolecule icariin for promoting skeletal regeneration in challenging osteonecrotic bone in rabbits. *Biomaterials.* 2017;153:1-13.
doi: 10.1016/j.biomaterials.2017.10.025.

32. Hu S, Meng Z, Zhou J, *et al*. Enhanced attachment and collagen type I deposition of MC3T3-E1 cells via electrohydrodynamic printed sub-microscale fibrous architectures. *Int J Bioprint.* 2022;8(2):514.
doi: 10.18063/ijb.v8i2.514.

33. Brennan CM, Eichholz KF, Hoey DA. The effect of pore size within fibrous scaffolds fabricated using melt electrowriting on human bone marrow stem cell osteogenesis. *Biomed Mater.* 2019;14(6):065016.
doi: 10.1088/1748-605x/ab49f2.

34. Shi Y, Tao W, Yang W, *et al*. Calcium phosphate coating enhances osteointegration of melt electrowritten scaffold by regulating macrophage polarization. *J Nanobiotechnol.* 2024;22(1):47.
doi: 10.1186/s12951-024-02310-0.

35. Palmieri EM, McGinity C, Wink DA, McVicar DW. Nitric oxide in macrophage immunometabolism: hiding in plain sight. *Metabolites.* 2020;10(11):429.
doi: 10.3390/metabo10110429.

36. Zhao DW, Liu C, Zuo KQ, *et al*. Strontium-zinc phosphate chemical conversion coating improves the osseointegration of titanium implants by regulating macrophage polarization. *Chem Eng J.* 2020;408:127362.
doi: 10.1016/j.cej.2020.127362.

37. Lv L, Xie Y, Li K, *et al*. Unveiling the mechanism of surface hydrophilicity-modulated macrophage polarization. *Adv Healthc Mater.* 2018;7(19):1800675.
doi: 10.1002/adhm.201800675.

38. Abedin E, Lari R, Mahdavi Shahri N, Fereidoni M. Development of a demineralized and decellularized human epiphyseal bone scaffold for tissue engineering: a histological study. *Tissue Cell.* 2018;55:46-52.
doi: 10.1016/j.tice.2018.09.003.

39. Wei X, Zhou W, Tang Z, *et al*. Magnesium surface-activated 3D printed porous PEEK scaffolds for in vivo osseointegration by promoting angiogenesis and osteogenesis. *Bioact Mater.* 2023;20:16-28.
doi: 10.1016/j.bioactmat.2022.05.011.

40. Xu J, Guan W, Kong Y, *et al*. Regulation of macrophage behavior by chitosan scaffolds with different elastic modulus. *Coatings.* 2022;12(11):1742.
doi: 10.3390/coatings12111742.

41. Du Y, Xu B, Li Q, Peng C, Yang K. The role of mechanically sensitive ion channel Piezo1 in bone remodeling. *Front Bioeng Biotechnol.* 2024;12:1342149.
doi: 10.3389/fbioe.2024.1342149.

42. Li W, Xu F, Dai F, *et al*. Hydrophilic surface-modified 3D printed flexible scaffolds with high ceramic particle concentrations for immunopolarization-regulation and bone regeneration. *Biomater Sci.* 2023;11:3976-3997.
doi: 10.1039/d3bm00362k.

43. Mahon OR, Browe DC, Gonzalez-Fernandez T, *et al*. Nano-particle mediated M2 macrophage polarization enhances bone formation and MSC osteogenesis in an IL-10 dependent manner. *Biomaterials.* 2020;239:119833.
doi: 10.1016/j.biomaterials.2020.119833.

44. Li Y, He J, Zhou J, *et al*. A conductive photothermal non-swelling nanocomposite hydrogel patch accelerating bone defect repair. *Biomater Sci.* 2022;10:1326-1341.
doi: 10.1039/d1bm01937f.

45. Garg K, Pullen NA, Oskeritzian CA, Ryan JJ, Bowlin GL. Macrophage functional polarization (M1/M2) in response to varying fiber and pore dimensions of electrospun scaffolds. *Biomaterials.* 2013;34(18):4439-4451.
doi: 10.1016/j.biomaterials.2013.02.065.

46. Yin Y, He XT, Wang J, *et al*. Pore size-mediated macrophage M1-to-M2 transition influences new vessel formation within the compartment of a scaffold. *Appl Mater Today.* 2019;18:100466.
doi: 10.1016/j.apmt.2019.100466.

47. Sridharan R, Cameron AR, Kelly DJ, Kearney CJ, O'Brien FJ. Biomaterial based modulation of macrophage polarization: a review and suggested design principles. *Mater Today.* 2015;18(6):313-325.
doi: 10.1016/j.mattod.2015.01.019.

48. Zhang D, Chen Q, Shi C, *et al*. Dealing with the foreign-body response to implanted biomaterials: strategies and applications of new materials. *Adv Funct Mater.* 2021;31(6):2007226.

doi: 10.1002/adfm.202007226.

49. Liu Y, Suarez-Arnedo A, Riley L, Miley T, Xia J, Segura T. Spatial confinement modulates macrophage response in microporous annealed particle (MAP) scaffolds. *Adv Healthcare Mater.* 2023;12(26):2300823. doi: 10.1002/adhm.202300823.

50. Sheikh Z, Brooks P, Barzilay O, Fine N, Glogauer M. Macrophages, foreign body giant cells and their response to implantable biomaterials. *Materials.* 2015;8(9):5671-5701. doi: 10.3390/ma8095269

51. Ivanova E, Fayzullin A, Minaev N, *et al*. Surface topography of PLA implants defines the outcome of foreign body reaction: an in vivo study. *Polymers*. 2023;15(20):4119. doi: 10.3390/polym15204119.

52. Zhao SJ, Kong FQ, Jie J, *et al*. Macrophage MSR1 promotes BMSC osteogenic differentiation and M2-like polarization by activating PI3K/AKT/GSK3β/β-catenin pathway. *Theranostics*. 2020;10(1):17-35. doi: 10.7150/thno.36930.

53. Fan S, Zhang C, Sun X, *et al*. Metformin enhances osteogenic differentiation of BMSC by modulating macrophage M2 polarization. *Sci Rep*. 2024;14(1):20267. doi: 10.1038/s41598-024-71318-1.

54. Feito MJ, Casarrubios L, Oñaderra M, *et al*. Response of RAW 264.7 and J774A.1 macrophages to particles and nanoparticles of a mesoporous bioactive glass: a comparative study. *Colloids Surf B Biointerfaces.* 2021;208:112110. doi: 10.1016/j.colsurfb.2021.112110

55. Trentini M, D'Amora U, Ronca A, *et al*. Bone regeneration revolution: pulsed electromagnetic field modulates macrophage-derived exosomes to attenuate osteoclastogenesis. *Int J Nanomed*. 2024;19:8695-8707. doi: 10.2147/ijn.s470901.

ACCSCIENCE PUBLISHING

International Journal of Bioprinting

RESEARCH ARTICLE

Fibrous bioinks for bioprinting anisotropic micro- and nanoscale scaffolds: A novel strategy for *in vitro* skeletal muscle engineering

Gerardina Ruocco[1,2,3†], Elena Marcello[1,2,3†*], Camilla Paoletti[1,2,3], Massimo Salvi[2,4], Alice Zoso[1,2,3], Mattia Spedicati[1,2,3], Irene Carmagnola[1,2,3‡], and Valeria Chiono[1,2,3‡]

[1]Department of Mechanical and Aerospace Engineering, Politecnico di Torino, Turin, Italy

[2]PolitoBIOMed Lab, Politecnico di Torino, Turin, Italy

[3]Interuniversity Center for the Promotion of 3Rs Principles in Teaching and Research, Pisa, Italy

[4]Department of Electronics and Telecommunications, Politecnico di Torino, Turin, Italy

(This article belongs to the *Special Issue*: *Biofabrication Breakthroughs: Innovation and Application in Bioprinting, Biomaterials, and Organoid*)

Abstract

Replicating skeletal muscle architecture remains challenging in 3D bioprinting, as conventional bioinks lack multiscale directional cues. Herein, we propose a next-generation fibrous bioink composed of fragmented electrospun gelatin fibers (f-GFs), uniformly embedded in an alginate/gelatin hydrogel matrix (f-ALG/Gel). Upon microextrusion bioprinting, shear-induced f-GF alignment enabled the fabrication of microfilament-based scaffolds with intrinsic anisotropy. The resulting constructs exhibited high shape fidelity, favorable viscoelastic properties, and physiologically relevant stiffness (Young's modulus: 16.1 ± 1.7 kPa). *In vitro* studies using C2C12 murine myoblasts demonstrated that the embedded f-GFs provided strong topographical guidance, enhancing cell alignment and myogenesis. After 14 days of culture, the f-ALG/Gel scaffolds supported a 2.5-fold increase in myotube fusion index and length, alongside reduced angular dispersion. These effects were achieved without the need for biochemical induction with a differentiation medium, underscoring the key role of structural cues at the micro- and nanoscale in C2C12 differentiation and maturation. In conclusion, this work proposes a scalable, cell-compatible strategy to recapitulate the hierarchical organization of skeletal muscle tissue within 3D-printed constructs. The platform holds broad potential for applications in regenerative medicine, skeletal muscle tissue modeling, and the engineering of cultured meat.

Keywords: anisotropy; 3D bioprinting; fibrous bioinks; skeletal muscle; topographical cue

†These authors contributed equally to this work

‡These authors contributed equally as senior authors

***Corresponding author:**
Gerardina Ruocco
(gerardina.ruocco@polito.it)

Citation: Ruocco G, Marcello E, Paoletti C, *et al*. Fibrous bioinks for bioprinting anisotropic micro- and nanoscale scaffolds: A novel strategy for *in vitro* skeletal muscle engineering.
Int J Bioprint. 2026;12(1):323-347.
doi: 10.36922/IJB025440455

Received: July 2, 2025
Revised: October 30, 2025
Accepted: November 10, 2025
Published Online: November 10, 2025

Copyright: © 2025 Author(s). This is an Open Access article distributed under the terms of the Creative Commons Attribution License, permitting distribution and reproduction in any medium, provided the original work is properly cited.

Publisher's Note: AccScience Publishing remains neutral with regard to jurisdictional claims in published maps and institutional affiliations.

1. Introduction

Skeletal muscle tissue (SMT) accounts for 40–45% of body mass and is essential for movement, metabolism, and homeostasis.[1,2] While minor damage can be repaired by resident stem cells,[3,4] volumetric muscle loss (VML) exceeds this capacity.[5] Traditional

reconstructive surgery, based on autologous tissue transfer (free tissue flaps) and bracing, is limited by insufficient tissue regeneration and functional recovery owing to implant mismatch and donor site morbidity.[6–9] SMT engineering strategies hold promise to restore muscle function and architecture to pre-injury levels, offering therapeutic potential for VML and muscle diseases, such as muscular dystrophies.

Beyond therapeutic applications, engineered SMT is increasingly pursued for disease modeling and preclinical drug testing to better understand muscle-related diseases and/or to explore new therapeutic solutions, overcoming the limitations of traditional drug discovery-to-clinic pipelines.[10] More recently, SMT engineering is gaining attention for cultured meat production, offering an ethical alternative to animal-derived meat, while tackling concerns related to environmental impact and public health.[6,7] Key to SMT engineering is the design of biomimetic scaffolds, mimicking the native-like extracellular matrix (ECM) of SMT, thereby regulating biological functions, facilitating cell–cell communication, and providing the mechanical, topographical, and biochemical cues essential for myoblast alignment, fusion, and myogenesis.[11]

In vivo, SMT is a highly organized and hierarchical tissue predominantly consisting of long multinucleated muscle fibers (i.e., myofibers) filled with contractile proteins organized into sarcomeres. Guided by the anisotropic biophysical microenvironment (e.g., ECM architecture and elasticity), myoblasts undergo differentiation and fusion, forming bundles of parallelly aligned myofibers able to contract unidirectionally.[12] To promote cell orientation and myogenic development *in vitro*, engineered anisotropic scaffolds, replicating the SMT structure, are highly sought.

Several tissue engineering methods have been proposed to induce *in vitro* cell alignment through grooved or ridged micro/nanopatterned substrates,[13] nanofibers,[14] hydrogels,[5] chemical surface patterning,[13] mechanical stimulation,[15] and exposure to electrical or magnetic fields.[16] Among them, electrospinning has emerged as a simple and versatile technique for the preparation of aligned nanofibrous structures from a wide variety of biomaterials, with the potential to operate under mild processing conditions.[11] Although electrospun fibers effectively provide directional cues for cell anisotropy and myogenesis, they are unable to replicate the 3D SMT structure.

On the other hand, 3D microextrusion bioprinting enables precise deposition of cells and biomaterials, resulting in 3D constructs with biomimetic composition and mechanical properties. Strand-like bioprinted microstructures may reproduce the architectural bundle-like structure of SMTs. Indeed, bioprinting shear stresses may unfold and orient bioink polymeric chains and align embedded fillers and/or cells, producing hierarchical anisotropic constructs.[8,9,17,18]

Recently, innovative fibrous bioinks, based on hydrogels with embedded micro- and nanofibers, have been proposed for the engineering of *in vivo*-like anisotropic tissues, such as cardiac tissue and tendon.[19] Fibrous bioinks may overcome the lack of 3D topographical cues of conventional hydrogel bioinks and have demonstrated tunable mechanical stiffness, viscoelastic properties, stability, and printability. Prendergast *et al.*[19] developed anisotropic gelatin (Gel) methacryloyl (GelMA)-based hydrogels by bioprinting constructs with embedded norbornene-modified hyaluronic acid microfibers. Although the method supported cell alignment and viability across multiple cell types, the fiber fragmentation process was poorly scalable, as it involves manual extrusion through syringes and filtration. Additionally, the fibrous bioink with the maximum GelMA concentration (5%), which allows for preserving cell viability, showed a limited stiffness (< 3 kPa), which is suboptimal for the engineering of cardiac tissue[20] and SMT.[21] Meanwhile, Choi *et al.*[22] developed a microfiber-infused ink by embedding fragmented fibronectin-coated Gel fibers (GFs) into pre-crosslinked alginate/Gel (ALG/Gel) hydrogels for cardiac tissue engineering. Although postprinted scaffolds supported the formation of anisotropic, functional cardiac tissue, the need for pre-crosslinking required high extrusion pressures, making the approach unsuitable for cytocompatible bioprinting.

To the best of our knowledge, only a few studies have investigated the use of fibrous bioinks for SMT applications. Kamaraj *et al.*[23] proposed a silk microfiber-reinforced silk fibroin hydrogel for *in situ* 3D handheld bioprinting for VML treatment. Although the engineered scaffolds provided structural support and fiber alignment, silk fibroin fibers were fragmented via NaOH-based hydrolysis, a method that may leave cytotoxic residues, reduce molecular weight, and mechanical integrity, and is poorly suited for large-scale production due to environmental impact and morphological variability. Li *et al.*[24] developed a fibrin/GelMA bioink that supports myotube formation through the combined effect of the hydrogel's viscoelastic properties and the fibrillar structure of fibrin. Although these scaffolds showed potential for repairing VML *in vivo*, the approach is restricted to fibril-forming biomaterials (e.g., fibrin or collagen) and does not employ electrospinning.

Currently, fibrous bioinks have not been optimized for SMT bioprinting, despite their potential to impart biophysical directional cues at the nano- and microscales that are crucial for SMT maturation. In this study, we

addressed this gap by developing a novel 3D-bioprinted fibrous scaffold specifically designed to replicate the hierarchical anisotropy of native SMT. A novel fibrous bioink was designed with the ability to acquire an oriented micro-/nanostructure upon microextrusion printing of fibrous hydrogel precursors under mild processing conditions. The bioink was able to undergo rapid crosslinking postprinting under cytocompatible conditions to stabilize scaffold anisotropy, preventing swelling and spreading at the nozzle exit.[25] Electrospun GFs were mechanically fragmented (f-GFs) for the first time in SMT engineering. Unlike chemical dissolution, mechanical fragmentation provides a simple, solvent-free, and highly scalable method to generate short, cell-adhesive fiber fragments. This process preserves native fiber diameter and surface morphology, allows precise control over fragment length, and achieves sufficient yields for bioink formulation. Incorporated into a hydrogel, f-GFs can be aligned through extrusion shear, imparting multiscale anisotropy that closely mimics the hierarchical organization of SMT. By introducing this strategy, our work establishes a new design principle for fiber-reinforced bioinks, advancing beyond classical electrospinning or chemical modification approaches.

Specifically, f-GFs were homogeneously dispersed onto the ALG/Gel prehydrogel matrix (f-ALG/Gel), and, during microextrusion bioprinting, provided anisotropic architectural cues. The printed structures were rapidly stabilized by dual crosslinking with calcium ions and microbial transglutaminase (mTG), yielding constructs with mechanical properties comparable to native muscle tissue. Parallel microfilaments embedded with oriented f-GFs and C2C12 cells replicated the hierarchical anisotropy of SMT, with cells forming aligned, multinucleated myofibers within 14 days of culture. Myotube maturation (area, length, alignment, and fusion index) was quantitatively assessed using a fully automated image analysis pipeline, confirming that bioprinted f-ALG/Gel constructs promote the formation of mature myofibers with biomimetic organization. This strategy paves the way for next-generation SMT therapies and *in vitro* models, replacing C2C12 cells with human primary or human-induced pluripotent stem cell (hiPSC)-derived myoblasts. Beyond healthcare, these fibrous bioinks could also be harnessed to bioprint cultured meat by embedding primary animal myoblasts.

2. Materials and methods

2.1. Materials

Gelatin (300 g bloom, Type A, porcine skin, suitable for cell culture), phosphate-buffered saline (PBS) tablets, 3-glycidyloxypropyl trimethoxysilane (GPTMS, ≥ 98%), bovine serum albumin (BSA), and Hank's balanced salt solution (HBSS) were obtained from Sigma-Aldrich (United States [US]). mTG from *Streptoverticillium mobaraense* (ACTIVA WM, 85–135 U/g) was supplied by Ajinomoto Co., Inc. (Japan). Sodium alginate (ALG, alginic acid sodium salt, medium viscosity) was purchased from MP Biomedicals (US). Glacial acetic acid (AA, $C_2H_4O_2$, molecular weight: 60.05 g/mol), 10% fetal bovine serum (FBS), 1% penicillin/streptomycin, 2% *L*-glutamine, and Dulbecco's modified Eagle medium (DMEM) were acquired from Thermo Fisher Scientific (US), while absolute anhydrous ethanol was obtained from Carlo Erba (Italy). Calcium chloride ($CaCl_2$, ≥ 95%) was obtained from Fluka Analytical (Switzerland).

2.2. Gelatin fiber fabrication and fragmentation

The Gel was electrospun using the NovaSpider instrument (NovaSpider v5, Nadatech Innovations, US). Gel powder was dissolved in a mixture of AA and ultrapure water (AA:water, 75:25 v/v) under constant magnetic stirring to obtain a 20% w/v homogeneous solution. GFs were covalently stabilized using GPTMS, a silane coupling agent selected based on preliminary optimization and literature reports to ensure effective crosslinking while preserving cytocompatibility.[26,27] To enable Gel crosslinking, GPTMS (1.84% v/v) was added and stirred for 40 min at room temperature (RT; 25°C).[28] Then, the Gel–GPTMS solution was loaded into a 5 mL syringe, coupled to a Teflon capillary, and connected to a metal needle (21G) and driven by a high-voltage power supply. Aligned nanofibers (A-Gels) were produced onto an aluminum-covered rotating mandrel (250 mm length × 70 mm diameter; (NovaSpider v5, Nadatech Innovations, US), using the following process parameters: 4,000 rpm mandrel rotation, 28 kV voltage, 1,500 µL/h flow rate, 10 cm needle-collector distance at RT. The electrospun mats were placed under a chemical hood for 48 h to allow complete solvent evaporation and crosslinking. The f-GFs were then obtained via mechanical fragmentation of A-Gel membranes, according to a previously reported protocol.[29] In detail, A-Gel mats were cut into 1 × 1 cm specimens, weighed, and immersed in cold ethanol to a final concentration of 1 mg/mL. A-Gel mats were fragmented using a PT 1200E homogenizer (Polytron, Indonesia) for 10 cycles of 30 s at 25,000 rpm, with the solution kept ice-cooled throughout. The obtained f-GFs were centrifuged at 8,000 rpm for 8 min to remove ethanol. The resulting pellets were collected, and any residual ethanol was evaporated under a laminar-flow hood. Subsequently, the pellets were promptly resuspended in sterile PBS or DMEM for further use.

2.3. Gelatin fiber characterization

A-Gel surface morphology was examined by scanning electron microscopy (SEM; TESCAN VEGA SEM platform, TESCAN Orsay Holdings, Czech Republic). Before the analysis, scaffold specimens were sputter-coated with gold using the AGB7234 high-resolution sputter coater (Agar Scientific Ltd, UK). The acquired images were processed through ImageJ/FIJI software (National Institutes of Health, US), and the average fiber diameter was calculated ($n \geq 50$, from three different images). The ImageJ/FIJI directionality tool (Fourier-transform-based analysis) was exploited to measure the fiber anisotropy degree. A-Gel surface wettability was evaluated by static water contact angle (WCA) measurements with the Krüss Drop Shape Analyzer-DSA25 device (Krüss GmbH, Germany). WCA analysis was performed by selecting the Sessile Drop tool, and data were processed using Krüss Drop Shape Analysis software (Krüss GmbH, Germany). Specifically, three drops of deionized water (2 µL) were carefully deposited on the surface of each sample ($n = 3$), and 100 frames per second were acquired using the high-frame-rate camera. Tangent fitting for the drop shape was implemented to calculate both right and left angles.

To investigate fiber chemistry after fragmentation, attenuated total reflectance (ATR)-FTIR spectroscopy was performed. Specifically, 100 µL of f-GF suspension (5 mg/mL in PBS) was dried for 48 h. Spectra were recorded on a Thermo Scientific Nicolet iS50 FTIR Spectrometer (US) equipped with a diamond crystal ATR accessory, with a wavelength range of 4,000–600 cm^{-1} and a resolution of 4 cm^{-1} using 32 scans per sample. A Gel powder was used as the control. f-GF morphology and length distribution were evaluated through brightfield microscopy (A1 HD25, Nikon, Japan). A suspension of f-GFs was pipetted onto a microscope slide for imaging: 40 images were captured, and 150 single f-GFs were analyzed using the Line tool provided by the ImageJ/FIJI program.

2.4. Hydrogel formulation and optimization

A stock ALG solution (8% w/v, 5 mL) was prepared by dissolving ALG powder in PBS under mild magnetic stirring overnight at RT. The solution was then transferred into a 5 mL syringe and centrifuged at 4,000 rpm for 5 min to remove air. Similarly, an 8% w/v Gel stock solution (5 mL) was prepared by dissolving Gel powder in PBS with magnetic stirring overnight at 50°C. The stock solutions were subsequently combined using an appropriate volume of PBS diluent to produce homogeneous ALG/Gel solutions at final polymer concentrations of 6, 8, and 10% w/v (ALG:Gel, 30:70% w/w). ALG/Gel or f-ALG/Gel hydrogel precursors were cast and incubated for 10 min at RT before undergoing dual crosslinking via ionic and enzymatic mechanisms. Crosslinking solutions containing 0.1 M $CaCl_2$ and different concentrations of mTG (2.5%, 5%, and 10% w/v) were prepared following an optimized protocol,[18] vortexed until fully dissolved, and stored in the dark. All solutions were sterilized using 0.22 µm filters. Each sample (120 µL) was immersed in 500 µL of the mTG+Ca^{2+} solution for 15 min at RT, after which the crosslinked scaffolds were rinsed twice with HBSS to remove any unreacted residues.

For biological experiments, ALG powder was washed three times in absolute ethanol for 10 min and exposed to UV light for 1 h prior to solubilization. The Gel stock solution was sterilized by filtering through 0.22 µm filters. To formulate fibrous hydrogels (f-ALG/Gel), f-GFs were diluted in PBS and subsequently mixed with ALG and Gel stock solutions, as described above, to achieve final fiber concentrations of 1% and 2% w/v (f-ALG/Gel [1%] and f-ALG/Gel [2%]). F-ALG/Gel hydrogels were dual-crosslinked as described above.

2.5. Fibrous hydrogel characterization

2.5.1. Rheology

Rheological experiments were carried out using an MCR 302 rheometer (Anton Paar, Austria), equipped with a parallel plate geometry (25 mm diameter and 0.15 mm fixed gap). All rheological experiments were performed in triplicate to ensure reproducibility. Before fiber embedding, the printability of the bioink was evaluated as a function of ALG/Gel total polymer concentration (6, 8, and 10% w/v). A temperature sweep test was performed to assess printing performance by gradually increasing the temperature from 20 to 40°C at a rate of 1.5°C/min (frequency: 1 Hz; strain: 1%) while monitoring the viscoelastic properties (i.e., storage modulus, loss modulus, and complex viscosity). To determine shear-thinning properties, viscosity profiles of hydrogel precursor solutions were obtained using a continuously ramped shear rate (0.01–1,000 s^{-1}). To quantitatively assess shear-thinning behavior, a power-law model was applied

$$\eta(\dot{g}) = K \times \dot{g}^{(n-1)} \quad (1)$$

where η is the viscosity, $\dot{g}$ is the shear rate, K is the consistency index (viscosity at the shear rate of 1 s^{-1}), and n is the shear-thinning index. The analysis was conducted on ALG/Gel as well as fibrous formulations containing 1% and 2% w/v f-GFs (f-ALG/Gel [1%] and f-ALG/Gel [2%]). The n index was derived from the slope (angular coefficient [m]) of the viscosity-shear rate plot. Specifically, a linear fitting function was used, and n was calculated ($n = m + 1$) while K was defined from the intercept (c) as $K = 10^c$. Before analysis, samples (2 mm height) were soaked in PBS at 37°C for 180 s to ensure thermal equilibration. A solvent

trap filled with ultrapure water was used during the tests to prevent hydrogel drying. For this analysis, an angular frequency range of 0.1–100 rad/s was used, along with a constant nondestructive strain of 1.0%, as determined from the preliminary assessment of the sample's linear viscoelastic region. The effect of dual crosslinking ($CaCl_2$ + mTG) and fiber concentration (1% and 2%) was evaluated through frequency sweep tests performed on 2 mm-height samples at a constant strain of 1%, varying the frequency from 0.1 to 100 rad/s.

2.5.2. Wet weight ratio under physiological conditions

To investigate the effects of dual crosslinking on wet weight under physiological conditions, ALG/Gel and f-ALG/Gel hydrogels (120 µL each) were immersed in 500 µL of PBS containing 0.1% $CaCl_2$. Samples ($n = 4$ for each formulation) were incubated at 37°C, and the solution was refreshed every 2–3 days to mimic cell culture conditions and prevent the accumulation of released materials. At specific time points (0, 1, 3, 5, 7, 14, 21, and 28 days), the wet weight was recorded, ensuring precise measurement by carefully removing the supernatant solution. The hydrogel wet weight ratio percentage was calculated using the following equation

$$Percentage\,wet\,weight\,ratio\left(\%\right)=\frac{wf}{wi}\times 100 \qquad (2)$$

where w_f and w_i are the weight of the wet hydrogel on the 5th day and day 0, respectively.

2.5.3. Mechanical characterization

Compression tests were carried out on crosslinked hydrogels to determine the mTG concentration (2.5%, 5%, and 10% w/v) and fiber density (0%, 1%, and 2% w/v) that best reproduced SMT mechanical properties. Uniaxial compressive tests were then performed on optimized hydrogel compositions (polymer final concentration, fiber density, and mTG percentage) immediately after sample production and following a 24-h incubation in PBS at 37°C. Cylindrical samples ($n = 4$) with a regular geometry were prepared by casting 200 µL of hydrogel into a 48-well plate. The compression tests were conducted using the MTS QTest/10 system (MTS Systems S.r.l., Italy) equipped with the Testwork 4 software (MTS Systems S.r.l., Italy). A 10 N load cell and a test speed of 1 mm/min were used for all measurements. Each test was automatically stopped by the Testwork 4 software when the applied load reached the load cell's maximum limit of 10 N. The engineering compressive stress (σ) was calculated using the following equation

$$\sigma=\frac{F}{\pi\times r^2} \qquad (3)$$

where r represents the original radius of the specimen. The engineering strain (ε) under compression was defined as the percentage change in the specimen's thickness relative to its original thickness. Stress and strain values between 0% and 10% of ε were used to determine the initial compressive modulus (E).

Unless otherwise specified, the term f-ALG/Gel will hereafter refer to the optimized formulation consisting of 6% w/v ALG/Gel (30:70 w/w),[25] supplemented with 2% w/v f-GFs and crosslinked using 2.5% w/v mTG.

2.6. 3D printing of fibrous microfilaments

The precursors ALG/Gel and f-ALG/Gel were microextruded using the R-GEN 200 printing station (REGENHU, 3D Discovery, Switzerland). ALG/Gel and f-ALG/Gel inks were loaded into a 3 mL bioprinting cartridge using a Luer-lock coupler and kept at 34°C before printing. The loaded cartridges were fitted with a 250 µm (34 Gauge, inner diameter) conical nozzle, and the whole setting was placed in the printing head. The layer height was set at 80% of the needle diameter (0.20 mm). Pressure was kept within the range of 25–30 kPa, and the feed rate was varied from 16 to 27 mm/s.[25] After constructs were printed, crosslinking was carried out by incubating them in mTG + Ca^{2+} solution as described above. A specific aligned pattern, based on consecutive layers of long parallel microfilaments, was created using BioCAD software (REGENHU, Switzerland), to reproduce the arrangement of muscle bundles *in vivo*. To evaluate f-GF alignment, one layer with aligned patterns was printed on a glass slide at different feed rates (16, 20, and 27 mm/s), and samples were imaged in brightfield (Spinning Disk Nikon Crest Optics Ti2-E_X-Light V3, Nikon, Japan) at high magnifications (60× or 100×) to detect fiber distribution.

2.7. 3D printing of model square grid-shaped scaffolds to assess shape fidelity

To evaluate shape fidelity after printing, square grids (15 mm side, 3 mm spacing) were designed and printed at three different feed rates: 16, 20, and 27 mm/s. The printability index (PI) was used as a quantitative measure to assess printing at increasing speeds. For each experimental group, three pores from one-layer grid structures were imaged using a brightfield microscope (4× magnification; A1 HD25, Nikon, Japan). The resulting images were analyzed using a custom-made MATLAB script to calculate the PI according to the following equation

$$PI=\frac{L^2}{16\times A} \qquad (4)$$

where L is the pore perimeter and A is the pore area.

2.8. C2C12 cell maintenance

The C2C12 murine myoblasts (derived from satellite cells) were expanded in cell culture flasks using a growth medium composed of DMEM, 10% FBS, 1% penicillin/streptomycin, and 2% *L*-glutamine. Cells were maintained at 37°C in a humid atmosphere with 5% CO_2. To generate cell pellets for *in vitro* experiments, C2C12 cells were washed with PBS and removed from the culture flasks using 0.25% trypsin–EDTA (Thermo Fisher Scientific, US). The cell number was determined using a Neubauer hemocytometer. Next, the C2C12 cells were diluted to the desired amount and centrifuged at 900 rpm for 5 min.

2.9. Biological validation

Before cell culture, GFs were sterilized through immersion in 70% (v/v) ethanol for 1 h, PBS rinsing (two times), and UV treatment (30 min). To preliminarily study the interaction with GFs, C2C12 cells were seeded (5×10^3 cells/cm^2) onto GFs and control tissue culture-treated polystyrene 24-well plates (control) and cultured for 7 days in growth medium. Prior to bioprinting, to assess hydrogel suitability for 3D cell encapsulation, 3D cell cultures were carried out by embedding C2C12 cells into 120 µL of ALG/Gel and f-ALG/Gel hydrogels (5×10^6 cells/mL). Specifically, the cell pellet was first resuspended in the available volume of diluent (DMEM), then Gel volume was added, and the appropriate volume of ALG was measured using a precision syringe. The entire system (bioink) was gently mixed with a gel pipette, avoiding excessive stress on the cells and promoting their homogeneous dispersion within the final system. After constructs were cast, they were dual-crosslinked as explained in **Section 2.4.**, and washed three times with HBSS prior to the addition of cell culture media. Cells were cultured for 7 days in growth medium.

After 7 days of culture, C2C12 cells were washed with HBSS and fixed for 15 min in 4% paraformaldehyde (PFA) in PBS. Subsequently, the samples were washed three times in PBS and incubated in the dark in a PBS solution containing 4′,6-diamidino-2-phenylindole (DAPI; 1:1000 in PBS; Invitrogen, US) and phalloidin (rhodamine phalloidin F-actin, 1:1000 in PBS; Thermo Fisher Scientific, US). 3D-printed anisotropic constructs were prepared by loading ALG/Gel or f-ALG/Gel bioinks into a 5 mL cartridge, which was then placed in the printing head preheated to 33–35°C for 15 min. Typically, the printing head temperature was maintained at 33–35°C during the whole printing process. All prints were completed at RT under aseptic conditions.

The conical nozzle was calibrated on 3-(trimethoxysilyl) propyl methacrylate (TMSPMA)-coated glass slides prior to positioning a 24-well plate on the printing sample holder. Following computer-aided design (CAD; BioCAD software) and microextrusion parameter optimization, 3D-aligned C2C12 cell-laden structures were printed at a speed of 27 mm/s and a pressure of 25–30 kPa. At least six replicates for each composition ($n \geq 6$) were extruded through a 34-gauge nozzle. After the constructs were printed, they were dual crosslinked as explained in **Section 2.4.** and were washed three times with HBSS prior to the addition of cell culture media.

The 3D-printed cellular scaffolds were cultured for 14 days. Cell culture medium was replaced with fresh medium every 2–3 days. In detail, after 7 days in growth medium, the medium was replaced with a myoblast differentiation medium composed of DMEM, 2% horse serum (HS; Gibco, US), 1% penicillin/streptomycin, and 2% *L*-glutamine to promote musculoskeletal differentiation.[24] After 14 days of culture, C2C12 cells were washed with HBSS and fixed for 15 min in 4% PFA in PBS. Subsequently, three washes in PBS were performed, and cells were permeabilized with 0.1% Triton X-100 (Qiagen, Germany) solution. To block the nonspecific binding sites of antibodies, a solution of 1% w/v BSA was added and incubated for 1 h. Subsequently, cells were incubated overnight at 4°C in PBS–BSA (3:1 v/v) containing primary antibodies against skeletal fast myosin (1:200 in PBS; M1570, Sigma-Aldrich, US). After washing three times in PBS, samples were incubated in the dark with a PBS solution containing DAPI (1:1,000), phalloidin (1:1,000), and Alexa Fluor 647 anti-mouse secondary antibody (1:500, Invitrogen, US).

Samples were mounted on microscopy slides and observed under a fluorescence microscope (Nikon Eclipse Ti2 inverted microscope, Nikon, Japan). The quantification of myofiber organization was performed using a custom pipeline developed in MATLAB (R2024b, MathWorks, US). Immunofluorescence images were preprocessed through Gaussian filtering and adaptive contrast enhancement (CLAHE) to reduce noise while preserving edge information. Initial segmentation was performed using global thresholding, followed by morphological operations to clean and refine the detected structures. A watershed-based separation algorithm was applied to accurately identify individual instances of nuclei and fibers. Then, the segmented structures underwent morphological validation based on shape criteria (eccentricity, axial ratio, and area).

Quantitative analysis was performed to extract parameters characterizing tissue organization. The average fiber area was calculated from the segmented myosin-positive regions, providing a measure of muscle fiber size. Fiber length was computed through major axis analysis of the segmented regions, quantifying the longitudinal extension of myotubes. Fiber orientation was measured as

the angle between each fiber's major axis and the horizontal axis. The fusion index was determined as the ratio of nuclei within multinucleated myosin-positive myotubes (≥2 nuclei) to total nuclei.

Myogenic transcription factors were analyzed through droplet digital polymerase chain reaction (ddPCR) after 14 days of culture. Bioink-encapsulated cells (ALG/Gel and f-ALG/Gel) were extracted for RNA isolation through treatment with type 2 collagenase (255 U/mL; Worthington Biochemical Corporation, USA) for 45 min at 37°C, followed by trypsin–EDTA (0.25%, Gibco, US) for 5 min at 37°C to dissolve the gel. After treatment, samples were centrifuged at 400 × g for 10 min to collect the cells. Total RNA was isolated with TRIzol reagent (Invitrogen, US) following the manufacturer's instructions. RNA concentration and quality were assessed using the NanoQuant plate (Tecan Group Ltd, Switzerland). cDNA (200 ng) was obtained using the High-Capacity cDNA Reverse Transcription Kit (Applied Biosystems, US) following the manufacturer's protocol. ddPCR was performed to quantify the expression of myoblast determination protein 1 (*Myod1*; ID assay: dHsaCPE5052344) and myogenin (*Myog*; ID assay: qHsaCEP0050426) using ddPCR Supermix for probes without dUTP. Droplet generation was performed according to the manufacturer's instructions. Thermal-cycling conditions were 95°C for 10 min (1 cycle), 94°C for 30 s and 55°C for 30 s (40 cycles), 98°C for 10 min (1 cycle), and a 4°C infinite hold. Glyceraldehyde-3-phosphate dehydrogenase (*Gapdh*; ID assay: dHsaC-PE5031597) was used as a housekeeping gene for normalization. PCR plates were read on the Bio-Rad QX100 droplet reader (Bio-Rad Laboratories, US), and data were analyzed using the QuantaSoft analysis software (QX Manager v1.0 Standard Edition, Bio-Rad Laboratories, US). Results were reported as the concentration (cDNA copies per µL) of the gene of interest relative to *Gapdh*. No-template controls with water were included in each assay. Experiments were performed in triplicate and repeated twice. RNA samples of low quality were excluded from analysis.

2.10. Statistical analysis

Unless otherwise specified, all measurements were made in triplicate, and data are reported as mean values ± standard deviation (SD). Data were analyzed using one-way ANOVA when comparing multiple groups, and pairwise comparisons between two experimental groups were assessed using *t*-tests, all implemented in GraphPad Prism 9 (GraphPad Software, Inc., US). Tukey post hoc test was applied following ANOVA to identify significant differences between two or more groups. In particular, $*p < 0.05$, $**p < 0.01$, $***p < 0.001$, and $****p < 0.0001$ were considered statistically significant.

3. Results

3.1. Gelatin fiber production, fragmentation, and characterization

Using the electrospinning technique, GPTMS-crosslinked GFs were successfully fabricated. The morphology of the fibers was examined using SEM (Figure 1A). SEM images analyzed using the ImageJ software revealed an average fiber diameter of 425 ± 60nm. Fiber surface wettability was assessed via static contact angle measurements (Figure S1A), showing an average contact angle of 39° ± 2°. The angular speed of the collecting mandrel (3,800 rpm) promoted fiber alignment, as demonstrated by directionality histograms (ImageJ/FIJI), which exhibited a narrow, single-peak distribution (Figure S1B). GF biocompatibility was evaluated *in vitro* using C2C12 murine skeletal muscle cells cultured on GFs versus standard tissue culture plates. After 7 days, C2C12 cells were fixed and immunoassayed for myosin heavy chain (myosin), a key protein involved in myotube formation and SMT development (Figure 1B). GFs were found to promote C2C12 cell adhesion and structural organization compared to control, attributed to their ordered fibrous structure, supporting cell orientation, cell–cell interaction, and myoblast fusion. Furthermore, GFs induced a myogenic-like behavior in C2C12 cells, resulting in a pronounced expression of myosin compared to the control and promoting their organization into long, parallelly aligned myotubes with striated structures.

The GF mats were fragmented into separate short fibers (f-GFs) through mechanical homogenization, avoiding the use of chemical agents, and performed under ice cooling to minimize ductile fracture and prevent fiber aggregation. The method allowed accurate control over fiber length and morphology. Moreover, f-GFs were easily suspended in water without clustering. The fiber chemical composition before and after fragmentation was investigated through ATR-FTIR. In Figure 2C, the ATR-FTIR spectra of Gel powder, GFs, and f-GFs are presented. All spectra showed the characteristic bands of amide I at 1,633 cm^{-1} (C=O stretching vibrations)[30] and amide II at 1,525 cm^{-1} (N–H bending vibrations). Additionally, at 1,110 cm^{-1}, GFs and f-GFs spectra showed the characteristic band of Si–O–Si bonds,[31] confirming successful GPTMS-mediated crosslinking.[32] Furthermore, the peaks at 1,456 and 1,200 cm^{-1} were due to CH_2 bending and CH_3 rocking vibrations of the siloxyalkyl group (Si–O–CH_3) in GPTMS, respectively.

3.2. Hydrogel characterization

The rheological behavior of the hydrogel precursors was initially assessed via temperature sweep and flow tests to evaluate their printability. As shown in Figure 3A and B, increasing the total polymer concentration from 6% to

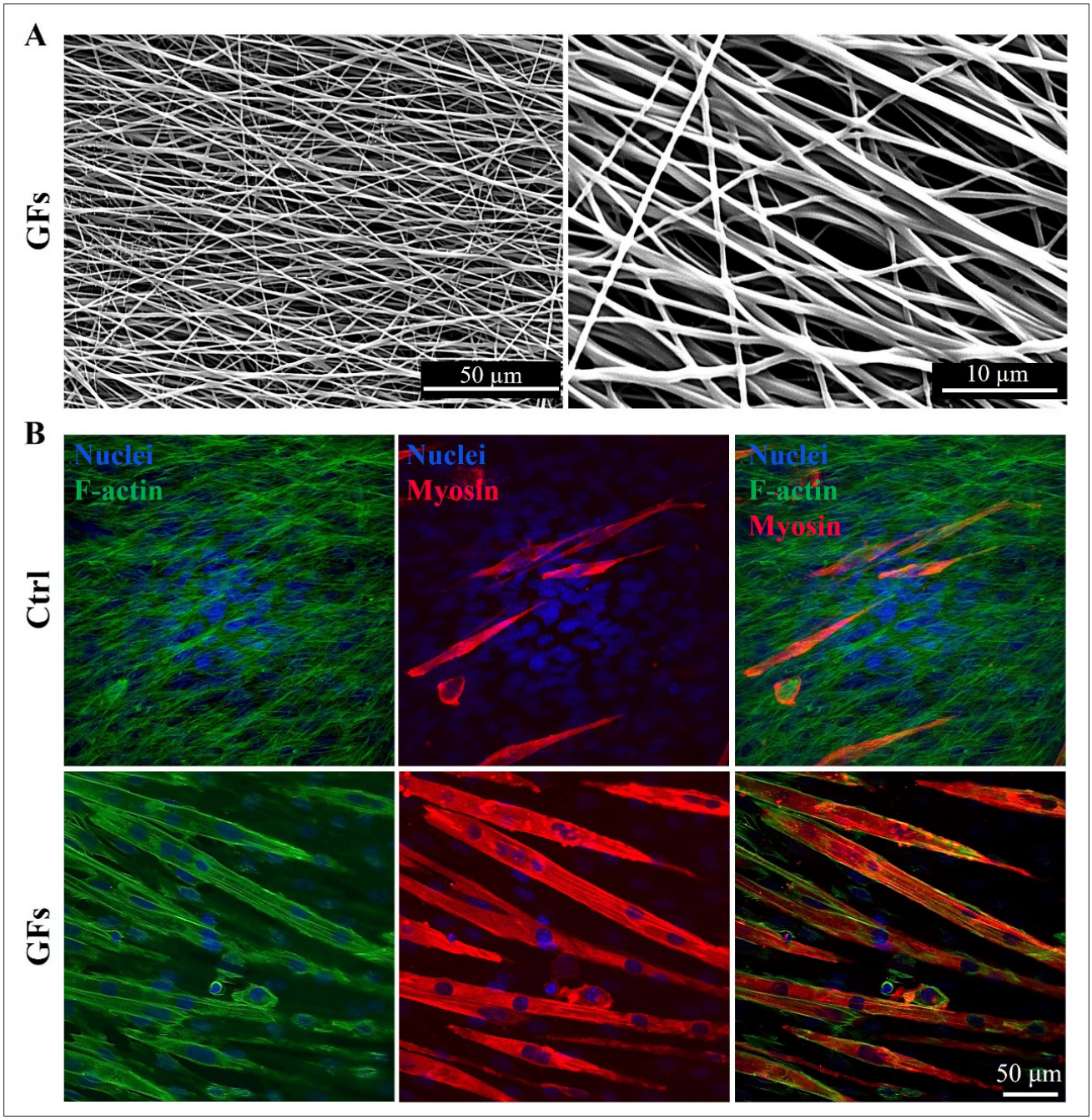


Figure 1. Gelatin fiber (GF) characterization and biological validation. (A) Scanning electron microscopy images of GFs at different magnifications. Scale bars: 10 μm; magnifications: 5000× (left), 10,000× (right). (B) Immunofluorescence images after 7 days of C2C12 cell culture on controls and GFs. Myosin in red, nuclei in blue, and F-actin in green. Scale bars: 50 μm; magnifications: 60×.

10% w/v led to higher viscosity and viscoelastic moduli across the tested temperature range (20–40°C). However, formulations with 8% and 10% polymer content exhibited excessively high viscosities and rapid loss of structural integrity near physiological temperature (~33°C), resulting in unstable flow and impaired extrusion performance. Due to these limitations, the 6% ALG/Gel formulation, exhibiting more favorable viscosity and thermal response, was selected as the bulk ink for further incorporation of f-GFs and subsequent characterization.

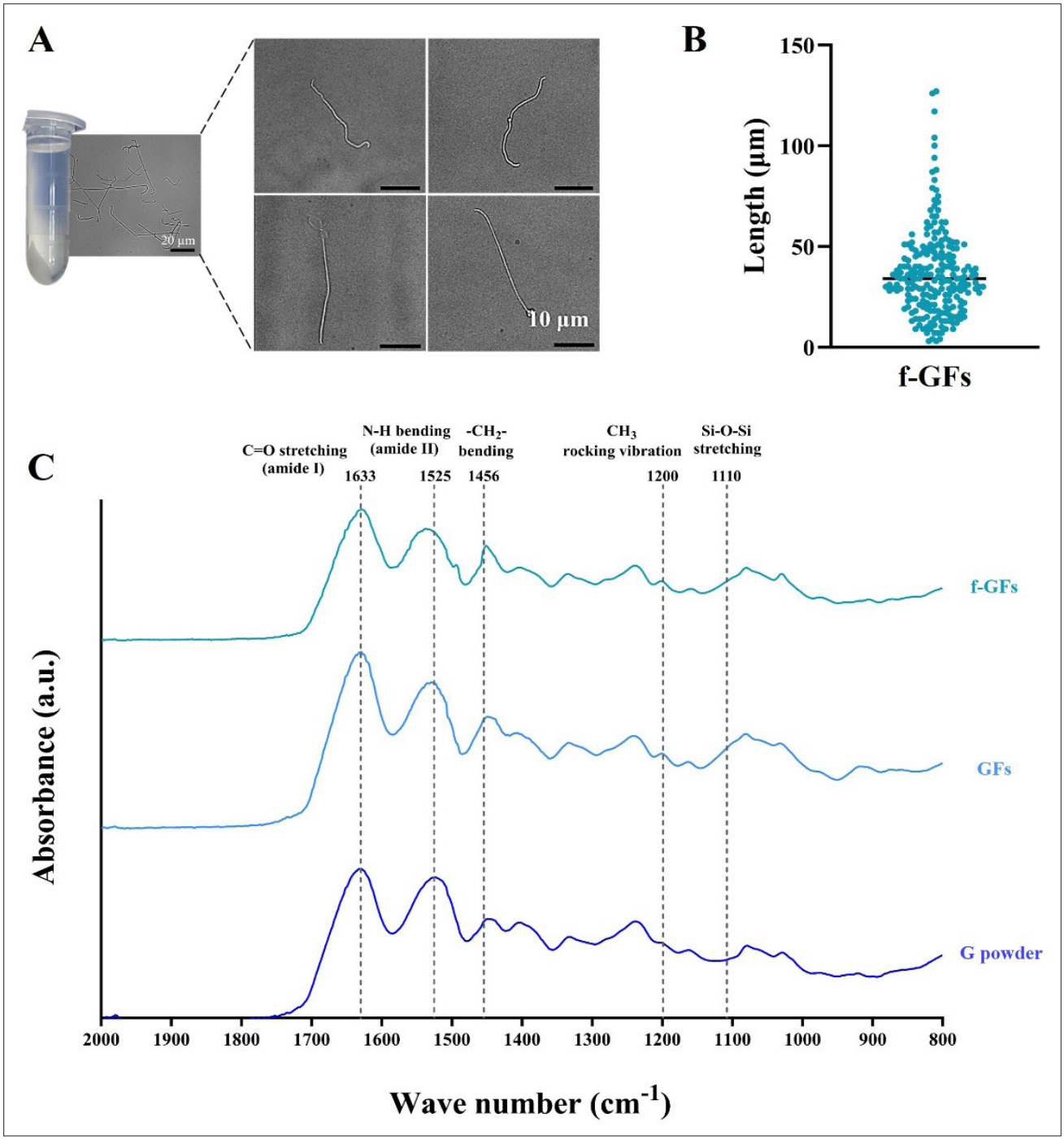


Figure 2. Characterization of fragmented gelatin fibers (f-GFs). (A) Pellet collecting and brightfield microscope images of f-GFs. Scale bar: 20 µm (left panel), 10 µm (right panel); magnifications: 20× (left panel), 60× (right panel). (B) Length distribution analysis, plotting individual values and their median. Range: 0–130 µm. (C) Attenuated total reflectance-Fourier transform infrared spectroscopy (ATR-FTIR) spectra of gelatin powder (G powder), GFs, and f-GFs, showing gelatin-related absorption bands for all samples and GPTMS-related absorption bands for GFs and f-GFs.

To evaluate the influence of fiber density on shear-thinning behavior, viscosity profiles were recorded at 33°C under a continuously ramped shear rate (0.01–1,000 s^{-1}) for ALG/Gel and f-ALG/Gel precursors containing 1% and 2% f-GFs (Figure 3C). All formulations exhibited non-Newtonian, shear-thinning behavior. Notably, f-ALG/Gel samples displayed higher viscosity at low shear rates (<10 s^{-1}), potentially due to the presence of fibrous elements contributing to a more entangled network, while viscosity values converged across all groups at higher shear rates (10–1,000 s^{-1}).

Shear-thinning indices (n) were derived from the slope of the log–log viscosity vs. shear rate curve using the power-law model (Figure 3D). All n values were <1, confirming shear-thinning behavior. f-ALG/Gel inks presented significantly lower n values (0.31 ± 0.03 for 2% f-GFs; 0.68 ± 0.05 for 1% f-GFs) compared to ALG/Gel (0.81 ± 0.02), indicating a more pronounced shear-thinning effect that enhances shape fidelity during printing. F-GFs (0%, 1%, and 2% w/v) were incorporated into ALG/Gel hydrogel precursors and subjected to dual crosslinking. ALG was crosslinked through $CaCl_2$ addition (0.1 M), leading to calcium ion complexation of glucuronic acid units. Enzymatic crosslinking was carried out using mTG (2.5%, 5%, or 10% w/v), promoting the formation of isopeptide bonds between the side-chain amide groups of glutamine residues and ε-amino groups of lysine residues.

To optimize the crosslinking conditions of ALG/Gel hydrogels, we evaluated the effects of varying the duration of ionic crosslinking with 0.1 M $CaCl_2$ (15 vs. 30 min) and the concentration of enzymatic crosslinking with mTG at 2.5%, 5%, or 10% w/v. Mechanical testing revealed that higher mTG concentrations (5% and 10% w/v) resulted in excessive stiffening, compromising the biomimetic compliance of the hydrogels. Consequently, the combination of 0.1 M $CaCl_2$ for 15 min and 2.5% mTG was selected as the optimal crosslinking condition for subsequent experiments (Figure S2A–D).

To further assess fiber density influence on viscoelastic properties, frequency sweep tests were performed on dual crosslinked hydrogels (Ca^{2+} = 0.1 M-15 min + mTG = 2.5% w/v; Figure 3E). All groups exhibited $G'>G''$ across the frequency range (0.1–100 rad/s), consistent with a predominantly elastic behavior. The addition of f-GFs reinforced the hydrogel network, as evidenced by the increased G' values. At 1 rad/s, G' was significantly higher for f-ALG/Gel (2%; 11,900 ± 436 Pa) compared to f-ALG/Gel (1%; 9,180 ± 670 Pa) and ALG/Gel (9,960 ± 240 Pa) (Figure 3F). No statistical difference was observed between f-ALG/Gel (1%) and ALG/Gel.

Next, uniaxial compression tests were conducted to evaluate the mechanical performance of the hydrogels after fiber embedding (Figure 3G and H). The stress–strain profiles showed greater resistance to deformation with increasing fiber content. Young's modulus, derived from the linear region of the curve (Figure 3H), confirmed enhanced stiffness with f-GFs incorporation: 8.1 ± 1.3 kPa for ALG/Gel, 11.5 ± 3.8 kPa for f-ALG/Gel (1%), and 18.3 ± 2.9 kPa for f-ALG/Gel (2%). No statistical difference was observed between f-ALG/Gel (1%) and ALG/Gel.

These findings support the ability of embedded fibers to reinforce the matrix and confer more biomimetic mechanical properties suitable for SMT engineering. Based on these results, the f-ALG/Gel formulation containing 2% w/v fibers was selected for subsequent experiments. For all cell-based assays, the nonfibrous ALG/Gel hydrogel was used as the experimental control. From this point forward, f-ALG/Gel was used to indicate the selected formulation composed of 6% w/v ALG/Gel (30:70 w/w), containing 2% w/v f-GFs and crosslinked with 2.5% w/v mTG, unless stated otherwise.

The SEM analysis of freeze-dried crosslinked ALG/Gel and f-ALG/Gel samples, fractured in liquid nitrogen, showed a similar porous structure. However, in f-ALG/Gel samples (Figure 4A), the pore walls exhibited fibrous features attributable to the embedded f-GFs. The percentage wet weight ratio of crosslinked ALG/Gel and f-ALG/Gel hydrogel samples in PBS at 37°C was investigated to provide information on their long-term stability in physiological conditions (Figure 4B). The temporal trend of wet weight percentage was similar for both hydrogels: an initial weight loss of around 25% was observed after 1–3 days, followed by a weight increase from 3 to 5 days, reaching 100% and settling at this value up to 10 days, then progressively decreasing from 15 to 28 days. At 28 days, f-ALG/Gel and ALG/Gel hydrogels were found to retain 83% and 73% of their initial wet weight, respectively.

Uniaxial compressive tests were performed on freshly prepared hydrogels and after 24 h of incubation in PBS at 37°C (Figure 4C and D). Compressive moduli were calculated as the slopes of the stress–strain curves in the initial linear zone (0–10%) (Figure 4C). The average moduli of f-ALG/Gel were significantly higher than those of ALG/Gel, both for freshly prepared hydrogels (18.3 ± 2.9 vs. 8.1 ± 1.3 kPa; $^{***}p < 0.001$) and samples incubated in PBS for 24 h (16.1 ± 1.7 vs. 6.4 ± 1.1 kPa; $^{****}p < 0.0001$). Notably, the mechanical properties of both ALG/Gel and f-ALG/Gel decreased after 24 h of incubation in PBS at 37°C (Figure 4D), attributed to their wet weight loss (Figure 4B).

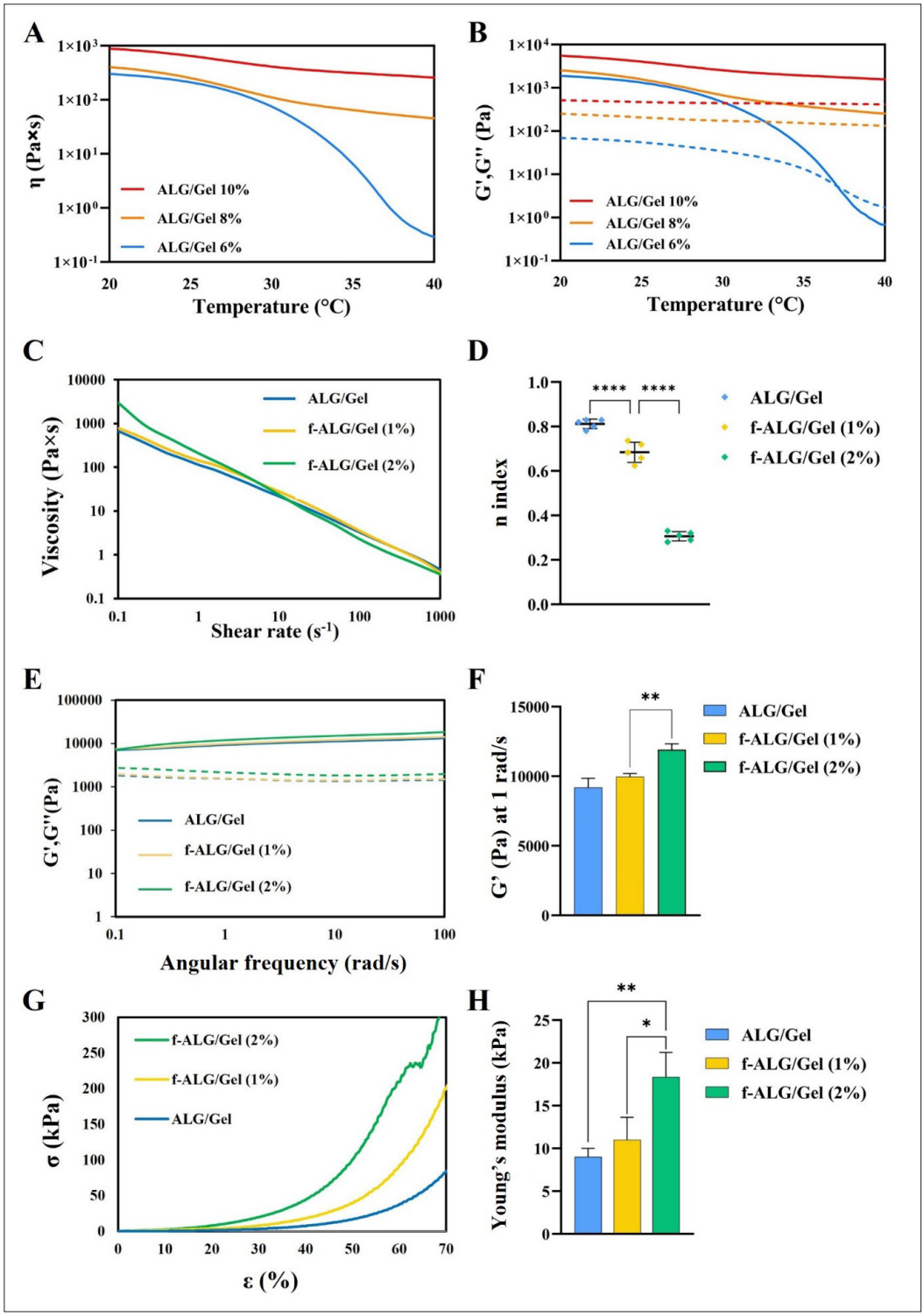


Figure 3. Rheological and mechanical characterization of ALG/Gel and f-ALG/Gel hydrogels. (A) Complex viscosity. (B) Storage (*G′*, solid lines) and loss (*G″*, dashed lines) moduli as a function of temperature (20–40°C, 1.5°C/min) of ALG/Gel formulations at 6%, 8%, and 10% w/v polymer concentration (ALG:Gel, 30:70 w/w; $n = 3$). (C) Viscosity profiles as a function of shear rate (0.01–1,000 s^{-1}) for optimized 6% w/v ALG/Gel and f-ALG/Gel bioinks with 1% and 2% w/v fiber content ($n = 3$). (D) Shear-thinning index (n) derived from power-law model fitting. (E) *G′* (solid lines) and *G″* (dashed lines) moduli as a function of frequency (0.1–100 rad/s) for dual-crosslinked hydrogels (Ca^{2+}/mTG; $n = 3$). (F) *G′* values obtained from frequency sweep tests at 1 rad/s ($n = 3$). (G) Representative stress–strain curves obtained from uniaxial compression tests. (H) Young's modulus derived from the linear region of the stress–strain curves ($n = 4$). Notes: $^{*}p < 0.05$, $^{**}p < 0.01$, $^{****}p < 0.0001$. Abbreviations: ALG, Alginate; f-ALG/Gel, alginate/gelatin with fibers; Gel, Gelatin.

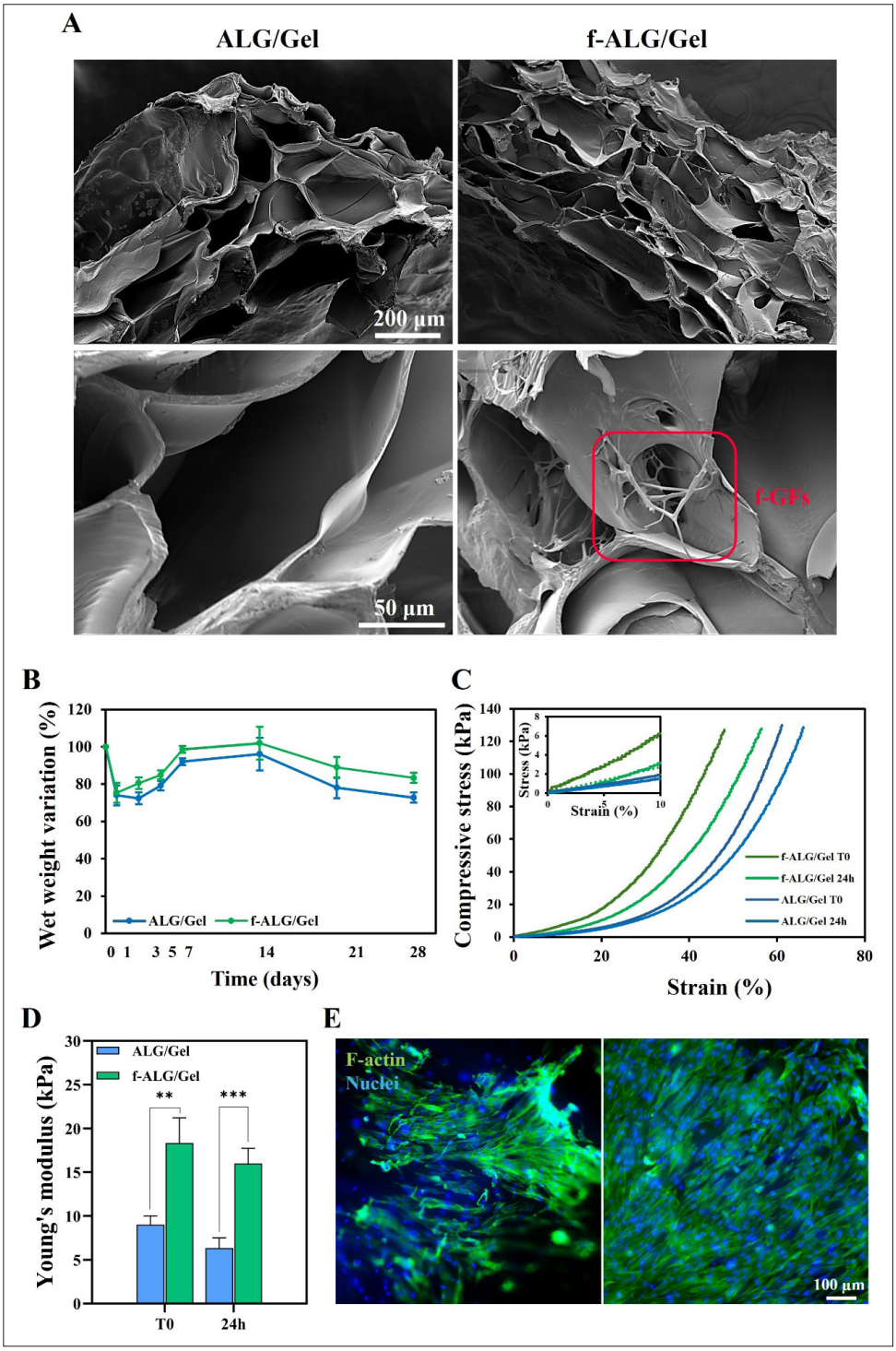


Figure 4. Characterization of optimized fibrous hydrogel. (A) Scanning electron microscopy images of ALG/Gel and f-ALG/Gel hydrogels after freeze-drying and brittle fracture in liquid nitrogen. Scale bars: 200 μm (upper panels), 50 μm (lower panels); magnifications: 300× (upper panels), 1500× (lower panels). (B) Wet weight variations of ALG/Gel and f-ALG/Gel hydrogels at 0, 1, 3, 5, 7, 14, 21, and 28 days of incubation in PBS at 37°C ($n = 4$). (C) Stress–strain (σ–ε%) curves from uniaxial compression tests for ALG/Gel and f-ALG/Gel hydrogels, performed after 0 day (freshly prepared) and after 1 day of incubation in PBS, and (D) corresponding Young's modulus values ($n = 6$). (E) Fluorescence images of C2C12 cells embedded into nonprinted ALG/Gel and f-ALG/Gel hydrogels and maintained in culture for 7 days, showing phalloidin staining of F-actin (green) and DAPI staining of nuclei (blue). Scale bars: 100 μm; magnifications: 20×. Notes: $^{**}p < 0.01$, $^{***}p < 0.001$ Abbreviations: ALG, Alginate; f-ALG/Gel, alginate/gelatin with fibers; Gel, Gelatin; PBS, Phosphate-buffered saline

Then, ALG/Gel and f-ALG/Gel hydrogels were characterized for their ability to support 3D cell culture. ALG/Gel and f-ALG/Gel hydrogels with embedded C2C12 cells were cultured in 24-well plates. After 7 days of culture, samples were stained for phalloidin/DAPI and analyzed under a confocal microscope (Figure 4E). Samples were analyzed at different z-planes (z-stack acquisition, 5 μm steps), showing a high density of cells with an elongated shape. These findings suggest that both hydrogels provided a suitable microenvironment for C2C12 cell culture.

3.3. 3D microextrusion printing optimization

The development of biomimetic 3D-printed anisotropic structures requires accurate control of scaffold geometry. To optimize microextrusion printing, model square grid-shaped structures of ALG/Gel and f-ALG/Gel were printed using a conical needle (inner diameter: 250 μm), at a pressure of 15–20 kPa, and three different printing speeds (16, 20, and 27 mm/s). The shape fidelity of the printed structures was assessed using the PI, calculated by analyzing pore geometry in brightfield microscopy images (4× magnification, $n = 5$; Figure 5A). The PI was determined by measuring the diameter and area of the grid pores, while pore circularity was evaluated using MATLAB software.

As shown in Figure 5B, PI < 1 indicates excessive filament spreading (poor printability), PI = 1 represents ideal printability with well-defined grid structures, and PI > 1 signifies filament gaps or breaks. For ALG/Gel, PI ranged from 0.93 to 0.96, indicating slight spreading of printed filaments. In contrast, f-ALG/Gel achieved PI values closer to 1.00, particularly at 20 and 27 mm/s, reflecting ideal printability and consistent grid formation. Based on these results, a printing speed of 27 mm/s was selected for 3D bioprinting.

To demonstrate the ability to extrude 3D structures with good shape retention, seven-layer grids were fabricated at the highest printing speed of 27 mm/s. As shown in Figure 5A (7 layers - 27 mm/s), the ALG/Gel system failed to maintain structural integrity, as the low viscosity causes the structure to collapse after the deposition of consecutive layers. In contrast, the f-ALG/Gel system supports the fabrication of stable 3D scaffolds, maintaining excellent geometric fidelity before crosslinking, aligning with the rheological data.

Next, to replicate the macro- and microarchitecture of SMT, characterized by bundles of muscle fibers, parallel hydrogel filaments were printed (Figure 5C). Optical microscopy images confirmed the printing of a uniform filament with an aligned structure. Additionally, embedded f-GFs showed a high degree of alignment along the filaments due to the applied shear stresses and filament postprinting crosslinking.

3.4. 3D fiber-embedded microextrusion bioprinting

Following printing parameter optimization, C2C12 cell-laden ALG/Gel and f-ALG/Gel bioinks were extruded into aligned 3D structures (Figure 6A) and maintained in culture for 14 days to promote cell spreading and organization within the engineered 3D microenvironments. *In vitro* cell culture was performed with/without HS addition to study the influence of combined biochemical and biophysical cues in inducing C2C12 cell differentiation and myotube maturation by assessing myofibrillar protein expression. As shown in Figure 6A, no detached cells with a round shape were detected upon F-actin staining. In contrast, in all conditions, C2C12 cells exhibited elongated shapes, suggesting successful cell adhesion and confirming the cytocompatibility of the bioprinting parameters.

To thoroughly investigate the effect of 3D topography on myoblast differentiation, immunofluorescence analysis of myosin heavy chain expression was performed after culturing the cells in contact with a proliferation or differentiation medium (HS supplemented) for 14 days. Limited myosin expression was observed for ALG/Gel constructs, with poorly aligned and scattered myotubes. Nuclei appeared dispersed, without clear alignment or clustering, indicating inefficient myoblast fusion. The addition of HS enhanced myosin expression, with some improvement in alignment and elongation of myotubes. However, the degree of myotube formation remained suboptimal. In contrast, f-ALG/Gel constructs showed unidirectional C2C12 cell growth along embedded GFs, with cells displaying elongated shape and cytoskeleton structure, significantly enhanced myosin expression, as well as well-aligned, elongated, and mature myotubes, as evidenced by the intense myosin staining and organized nuclei. The nuclei exhibited a more clustered and aligned organization, consistent with successful myoblast fusion and early-stage myotube formation under the 3D anisotropic stimulus without the need for further HS supplementation. *In vitro* C2C12 cell culture in 3D f-ALG/Gel constructs in the presence of HS led to a further significant increase in the formation of multinucleated myotubes with fiber-like morphologies.

Myogenic gene expression was quantified by ddPCR after 14 days of culture in ALG/Gel and f-ALG/Gel constructs (Figure 6B and C). A significant upregulation of *Myod1* mRNA expression was detected in f-ALG/Gel compared to ALG/Gel (**$p < 0.01$; Figure 6B), indicating increased activation of early myogenic pathways. Likewise, *Myog* expression was significantly higher in f-ALG/Gel (*p

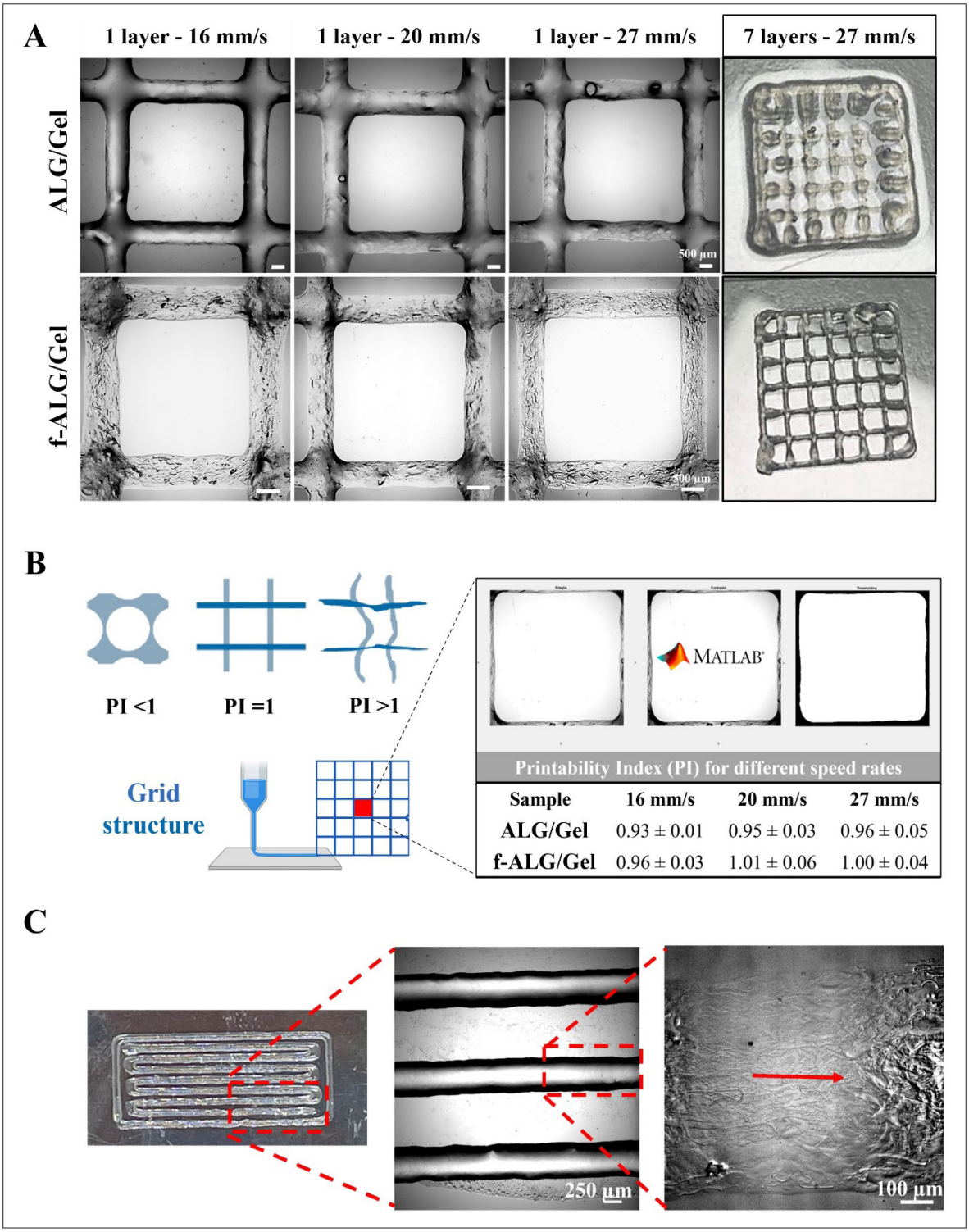


Figure 5. Microextrusion printing optimization. (A) Brightfield images of ALG/Gel and f-ALG/Gel square-grid structures, printed at a pressure of 25–30 kPa and increasing speed rates (16, 20, and 27 mm/s; $n = 4$; scale bars: 500 µm; magnifications: 4× [top panels], 4× [bottom panels]), and the macroscopic view of seven-layer printed constructs at 27 mm/s. (B) Schematic representation of printed grid-shaped structures with different PI values (left) and quantification of ALG/Gel and f-ALG/Gel hydrogel printability through PI at different speed rates (right). (C) Optical microscopy images at varying magnifications of the 3D-printed structures mimicking SMT architecture. The red arrow indicates the printing direction and fiber main orientation. Scale bars: 250 µm (middle panel), 100 µm (right panel); magnifications: 20× (middle panel), 60× (right panel). Abbreviations: ALG, Alginate; f-ALG/Gel, alginate/gelatin with fibers ; Gel, Gelatin; PI, Printability index; SMT, Skeletal muscle tissue.

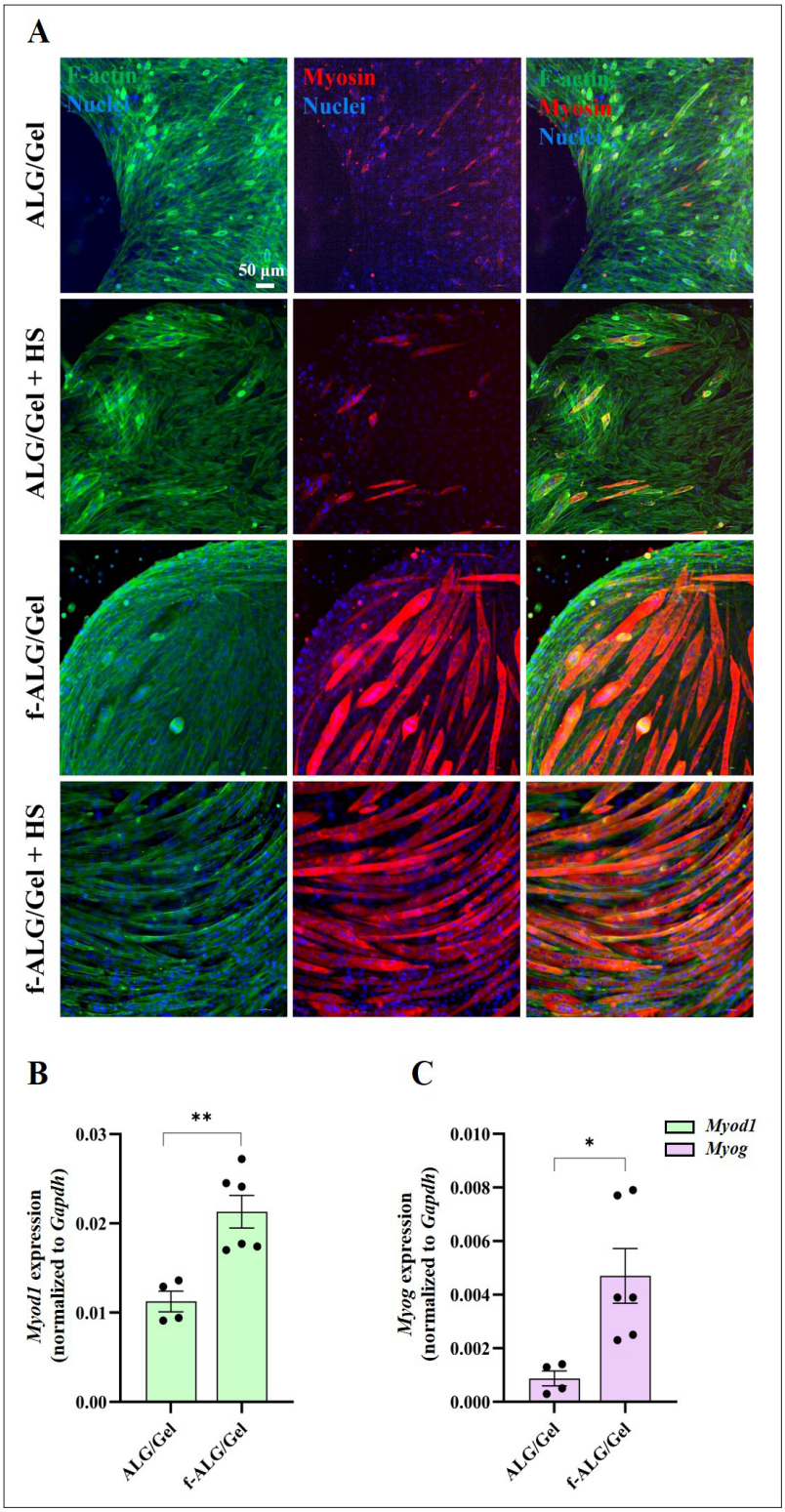


Figure 6. Characterization of C2C12 myogenic differentiation within ALG/Gel and f-ALG/Gel constructs. (A) Fluorescence microscopy images of myosin protein expression after 14 days of culture in the bioprinted scaffolds. Scale bars: 50 μm; magnifications: 40×. (B–C) ddPCR quantification of (B) *Myod* and (C) *Myog* mRNA expression normalized to *Gapdh*, showing enhanced activation of myogenic pathways in f-ALG/Gel. Notes: Data are presented as mean ± SEM ($n \geq 4$); *$p < 0.05$, **$p < 0.01$; unpaired *t*-test. Abbreviations: ALG, Alginate; ddPCR, Droplet digital polymerase chain reaction; f-ALG/Gel, alginate/gelatin with fibers; Gel, Gelatin; HS, Horse serum.

< 0.05; Figure 6C), confirming enhanced transcriptional activity of late myogenic markers.

Fluorescence microscopy images (Figure 7A) were analyzed using MATLAB software to derive four key metrics for the quantification of myotube organization and maturation: muscle fiber area, length, fusion index, and orientation variability (Figure 7B–E). In detail, the average values of myotube area, length, and fusion index, weighted by the total number of muscle fibers ($58 \leq n \leq 320$), were measured for each bioprinted construct from ≥5 independent images. 3D cell culture in bioprinted f-ALG/Gel scaffolds significantly enhanced muscle fiber properties compared to ALG/Gel scaffolds, including increased muscle fiber area (8,238 ± 2,848 vs. 3,317 ± 605 μm^2; Figure 7B), fiber length (306 ± 78 vs. 129 ± 22 μm; Figure 7C), and fusion index (27.8 ± 8.6% vs. 9.7 ± 0.9%; Figure 7D), while reducing muscle fiber orientation variability (Figure 7E).

By contrast, muscle fiber length did not change by 3D cell culture in bioprinted f-ALG/Gel scaffolds with additional HS stimulation (287 ± 41 μm), while HS increased muscle fiber length in cells cultured in bioprinted ALG/Gel scaffolds (153 ± 65 μm). Overall, these results suggest that biophysical cues through longitudinally oriented and cell-adhesive GFs embedded into f-ALG/Gel scaffolds significantly enhanced C2C12 cell spreading, differentiation, and fusion, leading to myotube formation, alignment, and maturation, compared to ALG/Gel scaffolds with/without further HS stimulation. The effect of the topographical biophysical cues was more pronounced than that of HS biochemical stimulation, demonstrating the key role of bioprinted fibrous scaffolds with anisotropic micro- and nanoscale organization in SMT engineering. The combination of biophysical cues with biochemical HS stimulation provided a synergistic effect in enhancing myotube differentiation, fusion, alignment, elongation, and maturation.

4. Discussion

The engineering of SMT aims to design functional tissue substitutes for regenerative medicine applications, such as replacement therapies and *in vitro* SMT models, and has recently gained attention as a promising strategy for cultured meat production.[6,7,33] To be effective, engineered scaffolds should closely replicate key biophysical features of native SMT, including its multiscale hierarchy,[34,35] mechanics, and contact guidance cues.[36] In this context, anisotropic substrates that mimic the nanoscale organization of collagen fibrils hold great potential.[37,38] While longitudinally oriented electrospun membranes can reproduce fibril morphology (260–410 nm in diameter),[16] they fail to capture the full 3D complexity of native SMT architecture, which plays a critical role in tissue functionality. This limitation highlights the need for advanced fabrication strategies capable of creating scaffolds that better emulate the structural and functional intricacies of native tissue. Developing 3D scaffolds that combine biomimetic anisotropy, appropriate mechanical properties, and cell-supportive environments remains a major challenge in the field. To address this gap, we designed a novel fibrous bioink for the bioprinting of 3D structures that replicate SMT anisotropy at both the nano- and microscale. This bioink consists of cell-adhesive GFs with nanometric dimensions embedded within a soft, cell-adhesive, shear-thinning hydrogel.

Regarding the fibrous component, electrospun GFs were prepared and mechanically fragmented via cryogenic milling to enable uniform dispersion within the hydrogel matrix. A-GFs with an average diameter of 425 ± 60 nm were prepared through electrospinning, closely matching the nanostructural characteristics of the native SMT ECM[16] (Figure 1A). Gel, a Food and Drug Administration-approved and cost-effective material derived from collagen,[39] was selected for its biocompatibility, biodegradability, and processability. Furthermore, Gel promotes cell adhesion due to the Arg–Gly–Asp (RGD) peptide motifs along its chains, which are fundamental for supporting the growth and differentiation of skeletal myoblasts.[40,41]

To enhance the mechanical stability of electrospun GFs, GPTMS was selected as a crosslinking agent owing to its well-established biocompatibility and proven efficacy in Gel-based systems.[42] GPTMS mediates covalent stabilization through epoxide–amine reactions and subsequent Si–O–Si condensation, thus improving aqueous resistance while preserving fibrous morphology. Unlike conventional postprocessing approaches,[22] GPTMS-mediated crosslinking occurs *in situ* during electrospinning and is completed after solvent evaporation, thereby preventing fiber swelling or partial dissolution and ensuring structural integrity.[26,27] This method avoids disruptive postprocessing steps and preserves fiber morphology. In addition, GPTMS does not alter the viscosity of the spinning solution, representing a further advantage compared with alternative crosslinkers, such as genipin. In this work, GPTMS was used at 1.84% v/v based on previous studies, showing excellent fiber stability and cytocompatibility with human fibroblasts. While higher concentrations (3–6% v/v) are commonly reported with proven cytocompatibility, our results suggest that effective crosslinking can be achieved at a lower dosage, reducing potential cytotoxicity and enhancing the translational relevance of the bioink under mild, cytocompatible conditions.

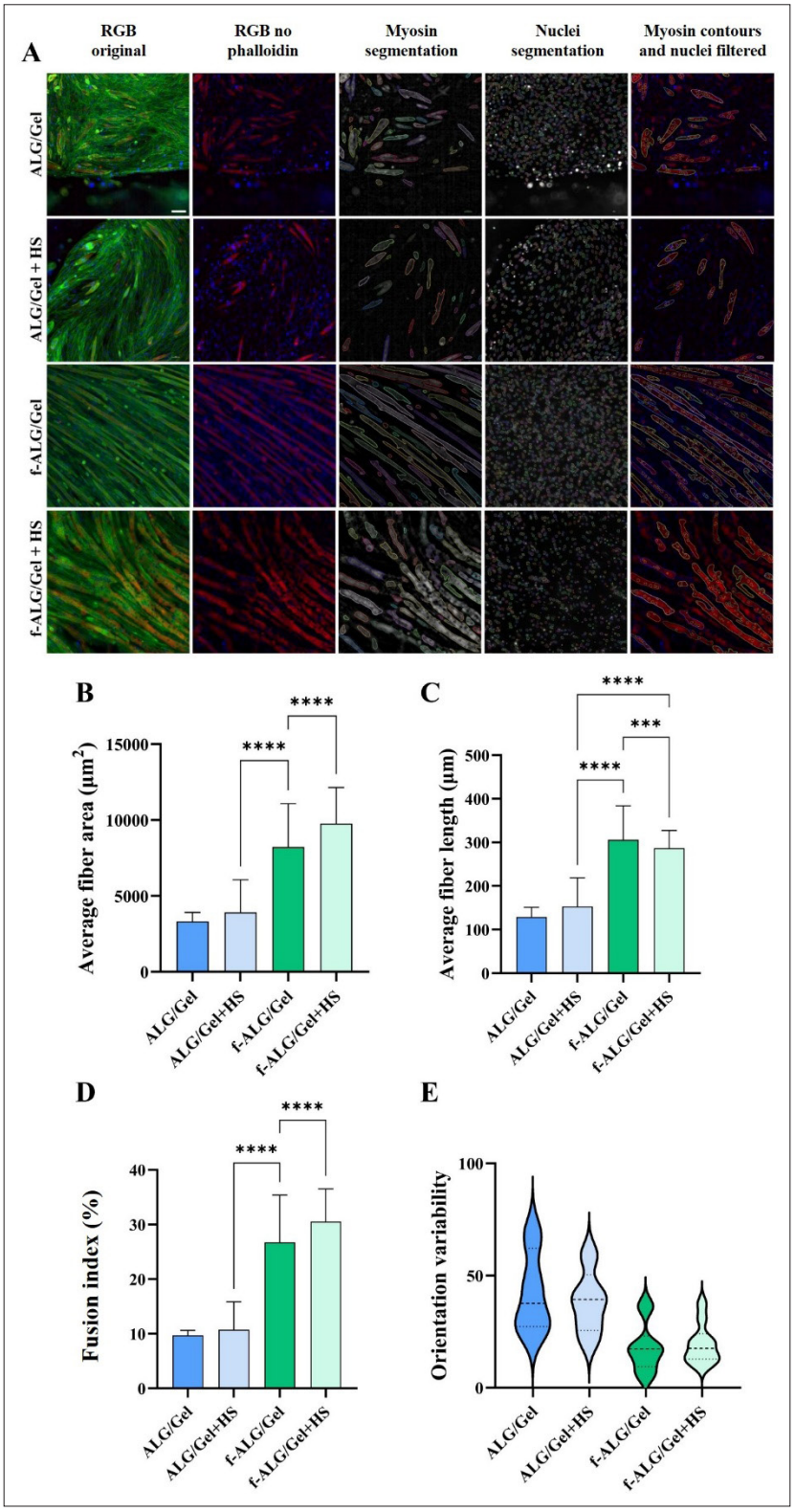


Figure 7. Image elaboration through Gaussian filtering and adaptive contrast enhancement (CLAHE). (A) Representative images from the custom pipeline developed in MATLAB. Scale bars: 50 μm; magnifications: 40×. (B) Average muscle fiber area. (C) Average fiber length. (D) Fusion index. (E) Orientation variability of myotubes, presented as violin plots. Notes: 58≤ *n* muscle fibers ≤320 from more than five independent images; Data are presented as mean ± standard deviation; ***$p < 0.001$; ****$p < 0.0001$. Abbreviations: ALG, Alginate; f-ALG/Gel, alginate/gelatin with fibers; Gel, Gelatin; HS, Horse

In this work, GPTMS-crosslinked GFs exhibited an intermediate wettability (Figure S1A), which preserved their ability to interact with the natural polymer components of the hydrogels while reducing inter-fiber interactions. Additionally, the electrospun membranes (GFs) with unidirectionally oriented morphology (directionality histograms; Figure S1B) showed the ability to impart contact guidance to C2C12 cells after 7 days of culture (Figure 1B). Compared to the control condition, cells cultured on GFs acquired an anisotropic organization, with parallel and elongated myotubes (showing high myosin expression). These findings are in agreement with previous reports suggesting that the orientation, size, and density of the substrate topographical cues play a significant role in skeletal muscle cell behavior. Specifically, previous reports have shown that cell attachment and alignment can be achieved by culturing cells on fibers with a diameter of approximately 500 nm,[43–45] confirming the morphological biomimicry of the herein obtained GFs, which had an average diameter of 425 ± 60 nm.

To favor brittle fracture and avoid heating during the process, GF fragmentation was performed by mechanical homogenization under ice cooling.[46,47] This method offers several advantages, including ease of application, short processing times, high yield, control over fragmented fiber size, and preservation of fiber diameter and surface morphology, as confirmed by brightfield microscopy images (Figure 2A and B). The topography of GFs (Figure S1B) reduced entanglements between adjacent fibers and facilitated their separation after milling. f-GFs showed an average length of <100 µm (Figure 2A and B), allowing their extrusion through the printing nozzle with a 250 µm diameter when embedded into a hydrogel bioink.

The ATR-FTIR spectra of GFs before and after fragmentation (Figure 2C) were similar, suggesting no alterations in their chemical composition during fragmentation. ALG/Gel (30:70 w/w) with 6% w/v total polymer content was selected based on previous experiments[25] and further validated through temperature sweep test analysis (Figure 3A and B) to meet printability requirements. Although 8% and 10% w/v compositions exhibited higher viscosity, their rapid gelation near physiological temperatures and excessively high resistance to flow impaired extrusion performance, making them unsuitable for bioprinting applications.

Gelatin was chosen as the primary hydrogel component for its cell-adhesive properties and its ability to interact with embedded f-GFs due to their similar composition.[46] ALG was introduced for its shear-thinning behavior and fast calcium-mediated gelation, making it a suitable component in bioinks for tissue engineering applications.[47] Notably, bioinks should support cell survival during and postprinting, ensure printability, and produce high-resolution, shape-stable 3D structures.[48] In this regard, polymer concentration plays a crucial role. Higher bioink concentrations enhance printing resolution and fidelity, but also increase shear stresses, potentially affecting cell viability.[49,50] Additionally, excessive polymer concentration and/or crosslinking density can limit nutrient diffusion and waste removal, restrict cell spreading postgelation, and hinder hydrogel remodeling by encapsulated cells, crucial for tissue maturation.[51] To address these challenges, shear-thinning bioinks with optimized viscosity and low polymer content have been proposed by incorporating small amounts of micro- or nanofillers (0.5–10% w/v),[52–54] thereby promoting cell viability and spreading in 3D microenvironments.

In this study, compared with previously published ALG/Gel bioinks,[55] the presence of a small amount (2% w/v) of f-GFs enabled precise printing of self-standing, cell-laden, 3D-aligned filaments, without the need for sacrificial layers, support baths, or high polymer concentration.[56,57] Herein, we demonstrated that the incorporation of f-GFs (2% w/v) into ALG/Gel hydrogels (6% w/v) significantly improved the ink's rheological properties (Figure 3C–F), potentially due to the formation of additional secondary interactions between ALG and Gel chains. At 33°C, f-ALG/Gel precursors (1% and 2% w/v) exhibited higher viscosity than ALG/Gel, particularly at low shear rates (<10 s^{-1}),[58] as shown in Figure 3C. Although all formulations exhibited shear-thinning behavior, this increase was more pronounced in the formulation containing 2% w/v f-GFs. The enhanced shear-thinning properties of f-ALG/Gel hydrogel precursors are critical not only for facilitating the printing process but also for promoting the alignment of embedded fibers within the printed filaments.[22,59] Additionally, f-ALG/Gel (2%) exhibited the lowest n value (0.31 ± 0.03), indicating a stronger shear-thinning effect than the 1% formulation (0.68 ± 0.05), and a significantly improved performance compared to ALG/Gel (0.81 ± 0.02) (Figure 3D). These results suggest that increasing fiber content leads to a more entangled microstructure, enhancing printability by reducing viscosity more effectively under shear. f-ALG/Gel (1%) showed intermediate behavior, providing partial enhancement but less pronounced compared to f-ALG/Gel (2%), supporting the choice of the latter for optimal print fidelity and fiber organization during extrusion.

The enhancement in rheological properties observed in the f-ALG/Gel (2%) hydrogel precursors was retained following ionic and enzymatic crosslinking with calcium chloride and transglutaminase, respectively. Frequency-sweep tests (Figure 3E) revealed that G' was consistently

higher than *G*" across the 1–100 Hz range, reflecting the solid-like behavior of both hydrogel formulations. Notably, both *G*' and *G*" values were higher for f-ALG/Gel formulations, indicating matrix reinforcement due to the incorporation of f-GFs. Particularly, at 1 rad/s, *G*' was significantly higher for f-ALG/Gel (2%) compared to f-ALG/Gel (1%) and ALG/Gel (Figure 3F), suggesting improved mechanical integrity. Similar results were reported by Kamaraj *et al*.,[23] who observed an increase in *G*'/*G*" at higher fiber concentrations compared to those used in this study. Compressive tests demonstrated that f-ALG/Gel (2%) effectively matched SMT mechanical properties (Figure 3G and H).

Overall, 2% w/v f-GFs showed the lowest shear-thinning index (0.31 ± 0.03), higher storage modulus, and a physiologically relevant Young's modulus (16.1 ± 1.7 kPa). Therefore, it was selected for the engineering of hierarchically aligned fibrous structures by microextrusion printing (Figure 4A). Unless otherwise specified, the term f-ALG/Gel will hereafter refer to the optimized formulation consisting of 6% w/v ALG/Gel (30:70 w/w), supplemented with 2% w/v f-GFs and crosslinked using 2.5% w/v mTG.

Traditional 2D cultures of C2C12 cells are generally unsuitable for long-term studies, as differentiated myotubes tend to detach from tissue culture polystyrene plates.[60,61] This limitation highlights the need for encapsulating cells within a 3D microenvironment to support their adhesion, maturation, and functional stability over time. To this end, the crosslinked f-ALG/Gel hydrogels were investigated for their stability under physiological conditions. The developed hydrogels exhibited an initial weight loss of approximately 20% during the first 24 h of incubation in PBS at 37°C (Figure 4B), potentially due to the release of unreacted materials. Additionally, they demonstrated excellent stability over a period of 28 days, enabling long-term cell culture supporting myotube formation and maturation.[62]

In vitro myogenic differentiation is markedly affected by the mechanical properties of the engineered biomaterial substrates. Therefore, the stiffness of freshly prepared f-ALG/Gel and ALG/Gel hydrogels was studied after 24 h of incubation in PBS to assess potential changes in mechanical behavior due to polymer release (Figure 3C and D). The incorporation of f-GFs significantly enhanced the compressive strength of hydrogels, in agreement with findings from frequency sweep tests. After 24 h of incubation in PBS, the Young's modulus was 6.3 ± 1.2 and 16.1 ± 1.7 kPa for ALG/Gel and f-ALG/Gel hydrogels, respectively, confirming that the stiffness of f-ALG/Gel falls within the physiological range of SMT (10–60 kPa).[63] Based on the literature, f-ALG/Gel stiffness results are optimal for promoting myotube formation. Consistently, Engler *et al*.[64] previously demonstrated that the maturation of myotubes is enhanced on hydrogels with a physiological Young's modulus of approximately 12 kPa. Overall, f-ALG/Gel hydrogels reproduced key biophysical features of SMT, including a fibrous structure that promotes contact guidance and tissue-like mechanical stiffness. ALG/Gel and f-ALG/Gel bulk hydrogels were initially investigated for their suitability for 3D C2C12 cell encapsulation (Figure 3E). Following 7 days of culture, phalloidin/DAPI staining demonstrated excellent 3D cell colonization, spreading, and organization for both formulations, confirming hydrogel bioactivity. Qualitatively, higher cell proliferation was observed in the f-ALG/Gel system. Next, the printability of f-ALG/Gel was evaluated, with a focus on exploiting shear stresses to promote f-GF alignment. Importantly, the selected f-GF concentration did not cause needle clogging during microextrusion. Recent studies have shown that the introduction of homogeneously dispersed short silk or nanocellulose fibers into hydrogels can strongly enhance their printability. As previously underlined, fibrous fillers increase the bioink viscosity at low shear rates through the establishment of physical interactions with hydrogel polymer components,[52,65,66] improving printability and shape fidelity postprinting. Shape fidelity indicates that the printed geometries closely match the original CAD design and preserve their structure postprinting.[67] In this work, the nonlinear rheological properties and enhanced stiffness of f-ALG/Gel inks (Figure 3) accounted for their continuous extrusion with minimal postextrusion swelling and spreading (Figure 5A). Shape fidelity was enhanced for f-ALG/Gel vs. ALG/Gel hydrogels (Figure 5B) across all tested printing speed rates (16, 20, and 27 mm/s), resulting in well-defined grid structures, particularly at 27 mm/s. This facilitated the formation of aligned-fiber-embedded 3D constructs, which were used to direct myoblast alignment, myogenesis, and myotube maturation, as shown in Figure 5C.

The optimized properties of f-ALG/Gel inks enabled the printing of self-supporting structures with a thickness ranging from 250 to 500 μm without the need for sacrificial materials or baths (Figure 5C). Postprinting, the rapid external crosslinking of the hydrogel precursors by calcium ions and mTG minimized die-swelling and preserving the shear-induced anisotropic structure. Following shear application, f-GF orientation was successfully achieved across the entire printed filaments within 3D aligned structures, as reported in Figures 5C and S3C. Shear stresses effectively aligned the embedded f-GFs along the printing direction, with the effect being particularly pronounced at a printing speed of 27 mm/s (Figure S3C). Fast gelation post-printing allowed the prompt stabilization of the

printed structures, including shear-induced alignment of embedded f-GFs. The dual crosslinking of ALG/Gel hydrogels was achieved upon 15 min of immersion in a solution containing Ca^{2+} ions and mTG.[56]

Transglutaminase is an enzyme that catalyzes the formation of covalent bonds between protein chains, including Gel, and is widely used in regenerative medicine as well as in the food industry for improving the texture of processed meat products.[68] In this work, mTG was preferred over animal-derived enzymes due to its cost-effective production.[69] Postprinting crosslinking ensured that the viscosity and physicochemical properties of the system were preserved.

Cell-laden scaffolds with anisotropic micro- and nanoscale SMT organization can be obtained by printing parallel microfilaments, embedding aligned nanosized f-GFs. Following microextrusion and cell encapsulation optimization, 3D bioprinting was carried out to design cellular structures that capture the complexity of SMT *in vivo*, as shown in Figure 6A.

The degree of myogenesis and maturation in response to substrate biophysical cues was investigated by marking myosin, a key protein involved in SMT development. ALG/Gel and f-ALG/Gel 3D-printed aligned scaffolds successfully supported C2C12 cell growth. In ALG/Gel hydrogels, C2C12 cells exhibited isotropic spreading, with F-actin filaments extending in all directions, consistent with the absence of topographical cues. The lack of preferential orientation decreased cell differentiation and myotube maturation, as suggested by the weak expression of myosin protein. These results demonstrate that the bioprinting process alone was insufficient to induce cell anisotropy and efficient differentiation.

In contrast, immunofluorescence analysis of 3D-bioprinted f-ALG/Gel constructs (Figure 6A) showed the formation of packed and elongated myotubes with a mature structure, oriented along the microfilaments. The upregulation of *Myod1* (Figure 6B) and *Myog* (Figure 6C) in f-ALG/Gel hydrogels confirms the enhanced activation of the myogenic pathway promoted through the fibrous reinforcement. *Myod1* is a master regulator of myogenesis, whose expression is initiated upon myoblast activation and sustained during proliferation and early differentiation phases, promoting withdrawal from the cell cycle and commitment toward the myogenic lineage.[70] Conversely, *Myog* is specifically associated with late-stage differentiation and myotube maturation.[71] A similar sequential upregulation of *Myod1* and *Myog* has been observed in other biomimetic hydrogel systems supporting myoblast alignment and fusion,[72] reflecting the physiological transition of activated progenitors toward terminal differentiation. These findings are consistent with the enhanced myosin expression observed using immunofluorescence, suggesting that the anisotropic fibrous microarchitecture provides topographical and mechanical cues that promote full myogenic maturation of encapsulated cells.

The effect of anisotropic microenvironmental cues on C2C12 cell morphology, phenotype, and directional growth was quantified by immunofluorescence image analysis (Figure 7). The pipeline for image analysis employed Gaussian filtering and CLAHE to enhance contrast and reduce noise while preserving edge information. In this study, initial segmentation was performed using global thresholding, followed by morphological operations to refine detected structures. A watershed-based algorithm was then applied to separate overlapping features, ensuring accurate identification of nuclei and fibers. Morphological validation using shape parameters (eccentricity, axial ratio, and area) further ensured segmentation accuracy. Such approaches, inspired by advanced contrast enhancement and segmentation techniques, emphasize robustness in biomedical image processing, balancing noise reduction with detail preservation for precise analysis.

The 3D-bioprinted f-ALG/Gel scaffolds significantly improved C2C12 cell fusion (fusion index) and 3D myogenic differentiation (myotube length and spreading area). Particularly, previous publications[73] reported an F-actin coverage per cell of up to 615 μm^2; in this work, we demonstrated the formation of more elongated myotubes with an average area of 8,498 μm^2 for ALG/Gel and 10,014 μm^2 for f-ALG/Gel. These results confirmed the ability of 3D topographical cues to regulate C2C12 cell spatial arrangement and myotube organization without the need for mechanical or electrical stimulation. Similar results were achieved in the literature exploiting fiber-reinforced systems; however, they required longer culture times (≥ 21 days) to achieve an adequate degree of myogenesis and maturation.[74] Indeed, regarding the recently proposed silk fiber-reinforced bioinks for SMT engineering,[23] the currently proposed f-ALG/Gel hydrogels showed superior biomimicry due to the presence of GFs, resembling tissue-like collagen fibers. Recent literature has already shown that Gel-based fibers efficiently support C2C12 viability during *in vitro* culture and stimulate their differentiation, as suggested by the expression of myogenic regulatory factors.[40,41]

Overall, the bioprinted f-ALG/Gel scaffolds were found to provide an optimal microenvironment for C2C12 cell culture, differentiation, and myotube maturation, attributed to their biomimetic fibrous micro-/nanostructure, mechanical stiffness, and stability in

physiological conditions. Bioprinted f-ALG/Gel-based constructs showed great promise for SMT engineering because they guided the uniaxial arrangement of C2C12 cells, which is critical for achieving cell maturation.

The developed platform demonstrates high versatility and holds significant potential for a range of future applications, including *in vivo* tissue regeneration, *in vitro* models, and the engineering of cultured meat, all of which require further investigation. In future studies, the currently employed C2C12 murine myoblast cells can be replaced with hiPSC-derived skeletal muscle cells for regenerative medicine and *in vitro* SMT modeling, or with animal-derived skeletal muscle cells for cultured meat production. By incorporating f-GFs, the approach can be extended to a variety of natural and synthetic polymers, making it suitable not only for skeletal muscle but also for other aligned tissues. These fibers can also be tailored to specific cell types by including cell-interactive proteins (e.g., laminin) to enhance tissue-specific functionality. In terms of *in vivo* degradation, the system contains a high proportion of Gel, a component readily susceptible to enzymatic degradation, and its rate can be tailored through controlled crosslinking. As ALG is not inherently degradable, it could be replaced with ALG dialdehyde, where the degree of oxidation and molecular weight can be modulated to achieve tunable biodegradability.[25] Finally, the platform is also well-suited for strategies to promote vascularization, either through the incorporation of growth factors, such as vascular endothelial growth factor, into the bioink to stimulate *in situ* vessel formation, or by directly introducing vascularization through the printing of tubular vessel-like structures within the 3D constructs, exploiting the fibrous bioink to promote radial alignment of vascular smooth muscle cells.[24,75]

5. Conclusion

Innovative f-ALG/Gel bioinks were developed for the 3D bioprinting of anisotropic scaffolds that replicate the hierarchical micro- and nanoscale fibrous architecture, mechanical stiffness, and cell-supportive properties of SMT ECM. GF fragments served as hydrogel fillers, significantly enhancing bioink printability, the shape fidelity of printed constructs, and their mechanical stiffness. Such bioinks enabled the fabrication of self-supporting, cell-laden constructs without the need for sacrificial materials or supporting baths. Notably, the shear stress-induced anisotropic alignment of embedded fibers provided biomimetic biophysical cues that facilitated C2C12 cell adhesion, alignment, and differentiation into mature, parallelly aligned myotubes, closely mimicking the native structure of SMT. Furthermore, during bioink production, the preparation of GF fragments through cryogenic milling ensures scalability, while the avoidance of any potentially toxic agents and solvents provides an environmentally sustainable process. In the future, the substitution of C2C12 cells with primary human myoblasts or myogenic cells derived from hiPSCs will allow the engineering of human-relevant SMT. Human bioprinted constructs will be cultured for different durations, and functional SMT will be validated through contractility tests and calcium imaging assays. In parallel, the use of animal myoblasts will enable the application of this process to cultured meat engineering. In conclusion, a new class of structurally instructive bioinks has been designed by integrating advanced bioengineering strategies, showing significant promise for the bioprinting of next-generation SMT constructs with broad applications in regenerative medicine, *in vitro* SMT modeling, and the engineering of cultured meat.

Acknowledgments

The authors thank Beatrice Francesca Massel and Francesca Sanna for their contributions to the *in vitro* modeling experiments as part of their Master's thesis research at the Politecnico di Torino.

Funding

This work was supported by the European Research Council (ERC) under the European Union's Horizon 2020 Research and Innovation Programme (Grant Agreement No. 772168), through the BIORECAR ERC Consolidator project (www.biorecar.polito.it); and under the European Union's Research and Innovation Programme (Grant Agreement No. 101158332) for the ERC-2023-POC EMPATIC project.

Conflict of interest

Elena Marcello serves as the Editorial Board Member of the journal, but did not in any way involve in the editorial and peer-review process conducted for this paper, directly or indirectly. Other authors declare they have no competing interests.

Author contributions

Conceptualization: Gerardina Ruocco, Elena Marcello, Irene Carmagnola

Data curation: Gerardina Ruocco, Mattia Spedicati

Formal analysis: Gerardina Ruocco, Mattia Spedicati

Funding acquisition: Valeria Chiono

Investigation: Gerardina Ruocco, Elena Marcello, Irene Carmagnola, Valeria Chiono

Methodology: Gerardina Ruocco, Elena Marcello, Camilla Paoletti, Irene Carmagnola

Project administration: Irene Carmagnola, Valeria Chiono
Resources: Valeria Chiono
Software: Gerardina Ruocco, Massimo Salvi
Supervision: Elena Marcello, Camilla Paoletti, Alice Zoso, Irene Carmagnola, Valeria Chiono
Validation: Elena Marcello, Camilla Paoletti, Alice Zoso
Writing–original draft: Gerardina Ruocco, Massimo Salvi
Writing–review & editing: Elena Marcello, Irene Carmagnola, Valeria Chiono

Ethics approval and consent to participate

Not applicable.

Consent for publication

Not applicable.

Availability of data

Data will be made available upon reasonable request to the corresponding author.

Further disclosure

Part of the findings have been presented at the ESB2025 and Biofabrication conferences.

References

1. Hulett NA, Scalzo RL, Reusch JEB. Glucose uptake by skeletal muscle within the contexts of type 2 diabetes and exercise: An integrated approach. *Nutrients*. 2022;14(3):647. doi: 10.3390/nu14030647
2. Kim J, Kim IU, Lee ZF, Sim G, Jeon JS. Strategic approaches in generation of robust microphysiological 3D musculoskeletal tissue system. *Adv Funct Mater*. 2024;34(52). doi: 10.1002/adfm.202410872
3. García-Lizarribar A, Villasante A, Lopez-Martin JA, *et al*. 3D bioprinted functional skeletal muscle models have potential applications for studies of muscle wasting in cancer cachexia. *Biomater Adv*. 2023;150:213426. doi: 10.1016/j.bioadv.2023.213426
4. Zhuang P, An J, Chua CK, Tan LP. Bioprinting of 3D in vitro skeletal muscle models: A review. *Mater Des*. 2020;193:108794. doi: 10.1016/j.matdes.2020.108794
5. Volpi M, Paradiso A, Costantini M, Święszkowski W. Hydrogel-based fiber biofabrication techniques for skeletal muscle tissue engineering. *ACS Biomater Sci Eng*. 2022;8(2):379-405. doi: 10.1021/acsbiomaterials.1c01145
6. Lou H, Lu H, Zhang S, *et al*. Highly aligned myotubes formation of piscine satellite cells in 3D fibrin hydrogels of cultured meat. *Int J Biol Macromol*. 2024;282:136879. doi: 10.1016/j.ijbiomac.2024.136879
7. Li X, Sim D, Wang Y, *et al*. Fiber-based biomaterial scaffolds for cell support towards the production of cultivated meat. *Acta Biomater*. 2025;191:292-307. doi: 10.1016/j.actbio.2024.11.006
8. Sabetkish S, Currie P, Meagher L. Recent trends in 3D bioprinting technology for skeletal muscle regeneration. *Acta Biomater*. 2024;181:46-66. doi: 10.1016/j.actbio.2024.04.038
9. Schwab A, Hélary C, Richards RG, Alini M, Eglin D, D'Este M. Tissue mimetic hyaluronan bioink containing collagen fibers with controlled orientation modulating cell migration and alignment. *Mater Today Bio*. 2020;7:100058. doi: 10.1016/j.mtbio.2020.100058
10. Mehmood H, Kasher PR, Barrett-Jolley R, Walmsley GL. Aligning with the 3Rs: Alternative models for research into muscle development and inherited myopathies. *BMC Vet Res*. 2024;20(1):477. doi: 10.1186/s12917-024-04309-z
11. Kang MS, Lee SH, Park WJ, Lee JE, Kim B, Han DW. Advanced techniques for skeletal muscle tissue engineering and regeneration. *Bioengineering*. 2020;7(3):99. doi: 10.3390/bioengineering7030099
12. Trovato F, Imbesi R, Conway N, Castrogiovanni P. Morphological and functional aspects of human skeletal muscle. *J Funct Morphol Kinesiol*. 2016;1(3):289-302. doi: 10.3390/jfmk1030289
13. Nikkhah M, Edalat F, Manoucheri S, Khademhosseini A. Engineering microscale topographies to control the cell–substrate interface. *Biomaterials*. 2012;33(21):5230-5246. doi: 10.1016/j.biomaterials.2012.03.079
14. Wang L, Wu Y, Guo B, Ma PX. Nanofiber yarn/hydrogel core–shell scaffolds mimicking native skeletal muscle tissue for guiding 3D myoblast alignment, elongation, and differentiation. *ACS Nano*. 2015;9(9):9167-9179. doi: 10.1021/acsnano.5b03644
15. Mueller C, Trujillo-Miranda M, Maier M, Heath DE, O'Connor AJ, Salehi S. Effects of external stimulators on engineered skeletal muscle tissue maturation. *Adv Mater Interfaces*. 2021;8(1). doi: 10.1002/admi.202001167
16. Ostrovidov S, Hosseini V, Ahadian S, *et al*. Skeletal muscle tissue engineering: Methods to form skeletal myotubes and their applications. *Tissue Eng Part B Rev*. 2014;20(5):403-436. doi: 10.1089/ten.teb.2013.0534
17. Kim H, Jang J, Park J, *et al*. Shear-induced alignment of collagen fibrils using 3D cell printing for corneal stroma tissue engineering. *Biofabrication*. 2019;11(3):035017. doi: 10.1088/1758-5090/ab1a8b
18. Moncal KK, Ozbolat V, Datta P, Heo DN, Ozbolat IT. Thermally-controlled extrusion-based bioprinting of collagen. *J Mater Sci Mater Med*. 2019;30(5):55.

doi: 10.1007/s10856-019-6258-2

19. Prendergast ME, Davidson MD, Burdick JA. A biofabrication method to align cells within bioprinted photocrosslinkable and cell-degradable hydrogel constructs via embedded fibers. *Biofabrication*. 2021;13(4). doi: 10.1088/1758-5090/AC25CC

20. Chaudhuri O, Cooper-White J, Janmey PA, Mooney DJ, Shenoy VB. Effects of extracellular matrix viscoelasticity on cellular behaviour. *Nature*. 2020;584(7822):535-546. doi: 10.1038/s41586-020-2612-2

21. Lloyd EM, Hepburn MS, Li J, *et al*. Multimodal three-dimensional characterization of murine skeletal muscle micro-scale elasticity, structure, and composition: Impact of dysferlinopathy, duchenne muscular dystrophy, and age on three hind-limb muscles. *J Mech Behav Biomed Mater*. 2024;160:106751. doi: 10.1016/j.jmbbm.2024.106751

22. Choi S, Lee KY, Kim SL, *et al*. Fibre-infused gel scaffolds guide cardiomyocyte alignment in 3d-printed ventricles. *Nat Mater*. 2023;22(8):1039-1046. doi: 10.1038/s41563-023-01611-3

23. Kamaraj M, Rezayof O, Barer A, *et al*. Development of silk microfiber-reinforced bioink for muscle tissue engineering and in situ printing by a handheld 3d printer. *Biomater Adv*. 2025;166:214057. doi: 10.1016/j.bioadv.2024.214057

24. Li T, Hou J, Wang L, *et al*. Bioprinted anisotropic scaffolds with fast stress relaxation bioink for engineering 3D skeletal muscle and repairing volumetric muscle loss. *Acta Biomater*. 2023;156:21-36. doi: 10.1016/j.actbio.2022.08.037

25. Stola GP, Paoletti C, Nicoletti L, *et al*. Internally-crosslinked alginate dialdehyde/alginate/gelatin-based hydrogels as bioinks for prospective cardiac tissue engineering applications. *Int J Bioprint*. 2024;10(6):544-566. doi: 10.36922/ijb.4014

26. Tonda-Turo C, Gentile P, Saracino S, *et al*. Comparative analysis of gelatin scaffolds crosslinked by genipin and silane coupling agent. *Int J Biol Macromol*. 2011;49(4):700-706. doi: 10.1016/j.ijbiomac.2011.07.002

27. Tonda-Turo C, Cipriani E, Gnavi S, *et al*. Crosslinked gelatin nanofibres: Preparation, characterisation and in vitro studies using glial-like cells. *Mater Sci Eng: C*. 2013;33(5):2723-2735. doi: 10.1016/j.msec.2013.02.039

28. Giuntoli G, Muzio G, Actis C, *et al*. In-vitro characterization of a hernia mesh featuring a nanostructured coating. *Front Bioeng Biotechnol*. 2021;8. doi: 10.3389/fbioe.2020.589223

29. John JV., McCarthy A, Wang H, *et al*. Engineering biomimetic nanofiber microspheres with tailored size, predesigned structure, and desired composition via gas bubble–mediated coaxial electrospray. *Small*. 2020;16(19). doi: 10.1002/smll.201907393

30. Carmagnola I, Chiono V, Ruocco G, *et al*. PLGA membranes functionalized with gelatin through biomimetic mussel-inspired strategy. *Nanomaterials*. 2020;10(11):2184. doi: 10.3390/nano10112184

31. Salgado-Delgado AM, González-Mondragón EG, Hernández-Pérez R, Salgado-Delgado R, Santana-Camilo JA, Olarte-Paredes A. Obtention and characterization of GO/Epoxy and GO-GPTMS/epoxy nanocompounds with different oxidation degrees and ultrasound methods. *C (Basel)*. 2023;9(1):28. doi: 10.3390/c9010028

32. Sitthiracha M, Kilmartin PA, Edmonds NR. Novel organic–inorganic hybrid materials based on epoxy-functionalized silanes. *J Solgel Sci Technol*. 2015;76(3):542-551. doi: 10.1007/s10971-015-3804-3

33. Wang X, Wang M, Xu Y, Yin J, Hu J. A 3D-printable gelatin/alginate/ε-poly-l-lysine hydrogel scaffold to enable porcine muscle stem cells expansion and differentiation for cultured meat development. *Int J Biol Macromol*. 2024; 271:131980. doi: 10.1016/j.ijbiomac.2024.131980

34. Yeong WY, Yu H, Lim KP, *et al*. Multiscale topological guidance for cell alignment via direct laser writing on biodegradable polymer. *Tissue Eng Part C Methods*. 2010;16(5):1011-1021. doi: 10.1089/ten.tec.2009.0604

35. Guven S, Chen P, Inci F, Tasoglu S, Erkmen B, Demirci U. Multiscale assembly for tissue engineering and regenerative medicine. *Trends Biotechnol*. 2015;33(5):269-279. doi: 10.1016/j.tibtech.2015.02.003

36. Kerativitayanan P, Carrow JK, Gaharwar AK. Nanomaterials for engineering stem cell responses. *Adv Healthc Mater*. 2015;4(11):1600-1627. doi: 10.1002/adhm.201500272

37. Rizzi R, Bearzi C, Mauretti A, Bernardini S, Cannata S, Gargioli C. Tissue engineering for skeletal muscle regeneration. *Muscles Ligaments Tendons J*. 2012;2(3):230-234.

38. Griffith LG, Swartz MA. Capturing complex 3D tissue physiology in vitro. *Nat Rev Mol Cell Biol*. 2006;7(3):211-224. doi: 10.1038/NRM1858

39. Dutta SD, Ganguly K, Jeong MS, *et al*. Bioengineered lab-grown meat-like constructs through 3D bioprinting of antioxidative protein hydrolysates. *ACS Appl Mater Interfaces*. 2022;14(30):34513-34526. doi: 10.1021/acsami.2c10620

40. Yi H, Forsythe S, He Y, *et al*. Tissue-specific extracellular matrix promotes myogenic differentiation of human muscle progenitor cells on gelatin and heparin conjugated alginate hydrogels. *Acta Biomater*. 2017;62:222-233. doi: 10.1016/j.actbio.2017.08.022

41. Rao KM, Kim HJ, Won S, Choi SM, Han SS. Effect of grape seed extract on gelatin-based edible 3D-hydrogels for cultured meat application. *Gels*. 2023;9(1):65.

doi: 10.3390/gels9010065

42. Valliant EM, Romer F, Wang D, *et al*. Bioactivity in silica/poly(γ-glutamic acid) sol–gel hybrids through calcium chelation. *Acta Biomater*. 2013;9(8):7662-7671. doi: 10.1016/j.actbio.2013.04.037

43. Li X, Wang X, Yao D, *et al*. Effects of aligned and random fibers with different diameter on cell behaviors. *Colloids Surf B Biointerfaces*. 2018;171:461-467. doi: 10.1016/j.colsurfb.2018.07.045

44. Tian F, Hosseinkhani H, Hosseinkhani M, *et al*. Quantitative analysis of cell adhesion on aligned micro- and nanofibers. *J Biomed Mater Res A*. 2008;84(2):291-299. doi: 10.1002/jbm.a.31304

45. Martino F, Perestrelo AR, Vinarský V, Pagliari S, Forte G. Cellular mechanotransduction: From tension to function. *Front Physiol*. 2018;9. doi: 10.3389/fphys.2018.00824

46. Davidenko N, Schuster CF, Bax D V., *et al*. Evaluation of cell binding to collagen and gelatin: A study of the effect of 2D and 3D architecture and surface chemistry. *J Mater Sci Mater Med*. 2016;27(10):148. doi: 10.1007/s10856-016-5763-9

47. Abdin M, Salama MA, Riaz A, Akhtar HMS, Elsanat SY. Enhanced the entrapment and controlled release of syzygium cumini seeds polyphenols by modifying the surface and internal organization of alginate-based microcapsules. *J Food Process Preserv*. 2021;45(1). doi: 10.1111/jfpp.15100

48. Levato R, Jungst T, Scheuring RG, Blunk T, Groll J, Malda J. From shape to function: The next step in bioprinting. *Adv Mater*. 2020;32(12). doi: 10.1002/adma.201906423

49. Tirella A, Orsini A, Vozzi G, Ahluwalia A. A phase diagram for microfabrication of geometrically controlled hydrogel scaffolds. *Biofabrication*. 2009;1(4):045002. doi: 10.1088/1758-5082/1/4/045002

50. Nam SY, Park SH. ECM based bioink for tissue mimetic 3d bioprinting. *Adv Exp Med Biol.* 2018; 1064:335-353. doi: 10.1007/978-981-13-0445-3_20

51. Malda J, Visser J, Melchels FP, *et al*. 25th anniversary article: Engineering hydrogels for biofabrication. *Adv Mater*. 2013;25(36):5011-5028. doi: 10.1002/adma.201302042

52. Sakai S, Yoshii A, Sakurai S, Horii K, Nagasuna O. Silk fibroin nanofibers: A promising ink additive for extrusion three-dimensional bioprinting. *Mater Today Bio*. 2020;8:100078. doi: 10.1016/j.mtbio.2020.100078

53. Jessop ZM, Al-Sabah A, Gao N, *et al*. Printability of pulp derived crystal, fibril and blend nanocellulose-alginate bioinks for extrusion 3D bioprinting. *Biofabrication*. 2019;11(4):045006. doi: 10.1088/1758-5090/ab0631

54. Markstedt K, Mantas A, Tournier I, Martínez Ávila H, Hägg D, Gatenholm P. 3D bioprinting human chondrocytes with nanocellulose–alginate bioink for cartilage tissue engineering applications. *Biomacromolecules*. 2015;16(5):1489-1496. doi: 10.1021/acs.biomac.5b00188

55. Seiti M, Mazzoldi EL, Pandini S, *et al*. FRESH 3D bioprinting of alginate – cellulose – gelatin constructs for soft tissue biofabrication. *Procedia CIRP*. 2024;125:42-47. doi: 10.1016/j.procir.2024.08.008

56. Distler T, McDonald K, Heid S, Karakaya E, Detsch R, Boccaccini AR. Ionically and enzymatically dual cross-linked oxidized alginate gelatin hydrogels with tunable stiffness and degradation behavior for tissue engineering. *ACS Biomater Sci Eng*. 2020;6(7):3899-3914. doi: 10.1021/acsbiomaterials.0c00677

57. Sonaye SY, Ertugral EG, Kothapalli CR, Sikder P. Extrusion 3D (bio)printing of alginate-gelatin-based composite scaffolds for skeletal muscle tissue engineering. *Materials*. 2022;15(22):7945. doi: 10.3390/ma15227945

58. Sonnleitner D, Schrüfer S, Berglund L, Schubert DW, Lang G. Correlating rheology and printing performance of fiber-reinforced bioinks to assess predictive modelling for biofabrication. *J Mater Res*. 2021;36(19):3821-3832. doi: 10.1557/s43578-021-00276-5

59. Hausmann MK, Rühs PA, Siqueira G, *et al*. Dynamics of cellulose nanocrystal alignment during 3D printing. *ACS Nano*. 2018;12(7):6926-6937. doi: 10.1021/acsnano.8b02366

60. Chaturvedi V, Dye DE, Kinnear BF, van Kuppevelt TH, Grounds MD, Coombe DR. Interactions between skeletal muscle myoblasts and their extracellular matrix revealed by a serum free culture system. *PLoS One*. 2015;10(6):e0127675. doi: 10.1371/journal.pone.0127675

61. Denes LT, Riley LA, Mijares JR, *et al*. Culturing C2C12 myotubes on micromolded gelatin hydrogels accelerates myotube maturation. *Skelet Muscle*. 2019;9(1):17. doi: 10.1186/s13395-019-0203-4

62. Jensen JH, Cakal SD, Li J, *et al*. Large-scale spontaneous self-organization and maturation of skeletal muscle tissues on ultra-compliant gelatin hydrogel substrates. *Sci Rep*. 2020;10(1):13305. doi: 10.1038/s41598-020-69936-6

63. Spedicati M, Zoso A, Mortati L, Chiono V, Marcello E, Carmagnola I. Three-dimensional microfibrous scaffold with aligned topography produced via a combination of melt-extrusion additive manufacturing and porogen leaching for in vitro skeletal muscle modeling. *Bioengineering*. 2024;11(4):332. doi: 10.3390/bioengineering11040332

64. Engler AJ, Sen S, Sweeney HL, Discher DE. Matrix elasticity directs stem cell lineage specification. *Cell*. 2006;126(4):677-689.

doi: 10.1016/j.cell.2006.06.044

65. Cui W, Huang Y, Chen L, *et al*. Tiny yet tough: Maximizing the toughness of fiber-reinforced soft composites in the absence of a fiber-fracture mechanism. *Matter*. 2021;4(11):3646-3661.
doi: 10.1016/j.matt.2021.08.013

66. Heher P, Maleiner B, Prüller J, *et al*. A novel bioreactor for the generation of highly aligned 3D skeletal muscle-like constructs through orientation of fibrin via application of static strain. *Acta Biomater*. 2015;24:251-265.
doi: 10.1016/j.actbio.2015.06.033

67. Schwab A, Levato R, D'Este M, Piluso S, Eglin D, Malda J. Printability and shape fidelity of bioinks in 3D bioprinting. *Chem Rev Am Chem Soc*. 2020;120(19):11028-11055.
doi: 10.1021/acs.chemrev.0c00084

68. Heck T, Faccio G, Richter M, Thöny-Meyer L. Enzyme-catalyzed protein crosslinking. *Appl Microbiol Biotechnol*. 2013;97(2):461-475.
doi: 10.1007/s00253-012-4569-z

69. Kashiwagi T, Yokoyama K ichi, Ishikawa K, *et al*. Crystal Structure Of Microbial Transglutaminase From Streptoverticillium mobaraense. *J Biol Chem*. 2002;277(46):44252-44260.
doi: 10.1074/jbc.M203933200

70. Kitzmann M, Carnac G, Vandromme M, Primig M, Lamb NJC, Fernandez A. The muscle regulatory factors MyoD and Myf-5 undergo distinct cell cycle–specific expression in muscle cells. *J Cell Biol*. 1998;142(6):1447-1459.
doi: 10.1083/jcb.142.6.1447

71. Yang HS, Lee B, Tsui JH, *et al*. Electroconductive nanopatterned substrates for enhanced myogenic differentiation and maturation. *Adv Healthc Mater*. 2016;5(1):137-145.
doi: 10.1002/adhm.201500003

72. Niknezhad SV, Mehrali M, Khorasgani FR, *et al*. Enhancing volumetric muscle loss (VML) recovery in a rat model using super durable hydrogels derived from bacteria. *Bioact Mater*. 2024;38:540-558.
doi: 10.1016/j.bioactmat.2024.04.006

73. Kim K, Jin S, Shin M. Effect of 3D-printable anisotropic fibrous hydrogels on fabricating artificial skeletal muscle constructs. *Adv Ther (Weinh)*. 2024;7(1).
doi: 10.1002/adtp.202300170

74. Lee S, Kim W, Kim G. Efficient myogenic activities achieved through blade-casting-assisted bioprinting of aligned myoblasts laden in collagen bioink. *Biomacromolecules*. 2023;24(11):5219-5229.
doi: 10.1021/acs.biomac.3c00749

75. Li Q, Yu S, Wang Y, *et al*. Programmable embedded bioprinting for one-step manufacturing of arterial models with customized contractile and metabolic functions. *Trends Biotechnol*. 2025;43(4):918-945.
doi: 10.1016/j.tibtech.2024.11.019

ACCSCIENCE PUBLISHING

International Journal of Bioprinting

RESEARCH ARTICLE

Three-dimensional-printed bionic dual crosslinked drug-loaded hydrogel composite scaffolds for large bone defect repair

Xulin Hu[1,2†*], Zhen Zhang[3†], Lijin Ning[4†], Yixuan Lan[1], Wang Gong[1], Jiayu Liu[1], Shuhao Yang[5], Haoming Wu[1], Weiming Zhao[1], Jian He[6], Kainan Li[1*], and Weizong Weng[7,8*]

[1] Department of Orthopedics, Clinical Medical College and Affiliated Hospital of Chengdu University, Chengdu University, Chengdu, Sichuan, China

[2] Department of Biotherapy, Cancer Center and State Key Laboratory of Biotherapy, West China Hospital, Sichuan University, Chengdu, Sichuan, China

[3] Department of Chemistry, Chengdu Institute of Organic Chemistry, Chinese Academy of Sciences, Chengdu, Sichuan, China

[4] Department of Dentistry, School of Jinzhou Medical University, Jinzhou Medical University, Jinzhou, Liaoning, China.

[5] Department of Orthopedics, The First Affiliated Hospital of Chongqing Medical University, Chongqing, China

[6] Department of Basic Medicine, Faculty of Medicine, Henan University of Science and Technology, Luoyang, Henan, China

[7] Department of Orthopaedics, Chenggong Hospital, Xiamen University, Xiamen, Fujian, China

[8] Department of Orthopedics, Institute of Translational Medicine, Shanghai University, Shanghai, China

[†]These authors contributed equally to this work.

***Corresponding authors:**
Xulin Hu
(huxulin1993@163.com)

Kainan Li
(likainan1961cdfy@126.com)

Weizong Weng
(drwengweizong@163.com)

Citation: Hu X, Zhang Z, Ning L, *et al.* Three-dimensional-printed bionic dual crosslinked drug-loaded hydrogel composite scaffolds for large bone defect repair. *Int J Bioprint.* 2026;12(1):348-370. doi: 10.36922/IJB025380391

Received: September 21, 2025
1st revised: October 20, 2025
2nd revised: November 5, 2025
Accepted: November 12, 2025
Published online: November 12, 2025

Copyright: © 2025 Author(s). This is an Open Access article distributed under the terms of the Creative Commons Attribution License, permitting distribution, and reproduction in any medium, provided the original work is properly cited.

Publisher's Note: AccScience Publishing remains neutral with regard to jurisdictional claims in published maps and institutional affiliations.

Abstract

The structure, composition, and function of natural bone have long been the focus of bone tissue engineering. However, existing organic–inorganic three-dimensional (3D) printing systems are limited by the stability of hydrogels and the content of inorganic salts, hindering the fabrication of robust 3D scaffolds. In this study, we developed a hydrogel–inorganic particle bioink and implemented a multi-step crosslinking strategy. The organic phase, composed of sodium alginate, gelatin, and chitosan, was combined with β-tricalcium phosphate and crosslinked via ionic pre-crosslinking followed by a Schiff base reaction to form a dual-crosslinked network. The resulting scaffolds exhibited excellent mechanical properties and biomimetic microarchitecture while maintaining shape stability under physiological conditions. Furthermore, the tunable swelling behavior of the hydrogel enabled efficient loading and controlled release of the small molecule epigallocatechin gallate. This composite scaffold demonstrated adjustable swelling, controllable degradation, and significantly enhanced cellular compatibility, providing a novel, efficient, and scalable strategy for repairing complex bone defects and offering new insights for the design and application of 3D-printed bone scaffolds.

***Keywords*:** β-tricalcium phosphate; Bionic tissue structure; Hydrogel base; Three-dimensional printing

1. Introduction

Bone loss, instigated by severe trauma and infectious diseases, is a pressing concern affecting millions globally. Recent studies indicate that approximately three million cases annually are related to significant bone loss due to these causes.[1] Depending on the extent of the damage, bone loss can be categorized into two types: minor bone loss (less than 2 cm of bone length affected) and major bone loss (more than 2 cm of bone length affected).[2–5] When comparing the two, bones with a minor loss have a 70% self-healing rate, whereas those with major bone loss exhibit a self-healing capability of only 30%. Current traditional treatments for major bone loss, such as bone grafting, have only a 50% success rate, highlighting the difficulty in addressing substantial clinical needs. In this regard, researchers have proposed the employment of artificial bones to solve the current clinical problem of large bone loss.[6,7]

Artificial bone is a synthetic or biological material engineered to emulate the structure and function of natural bone, intended for the treatment of fractures or the repair of bone defects.[8] Bone is a complex structural tissue primarily composed of cortical bone and cancellous bone.[9–11] Cortical bone, also known as compact bone, predominantly forms the external layer of bones, providing them with strength and support.[12] In contrast, cancellous bone, often referred to as trabecular or spongy bone, is primarily found within the interior regions of bones, such as the ends of long bones and in flat bones. Its unique porous structure, characterized by an intricate network of trabeculae interspersed with marrow-filled spaces, plays a pivotal role in the biological processes of bone, especially in bone repair and remodeling. The extensive surface area of cancellous bone, coupled with the marrow it houses, offers a rich reservoir of cells and growth factors vital for bone regeneration. Therefore, cancellous bone is often considered the primary component of repair in research.[13–16] During the bone healing process, multiple types of cells are involved, including osteoblasts, osteoclasts, osteocytes, and chondrocytes. These cells are primarily responsible for forming bone and cartilage in bone tissue. Osteoclasts are mainly responsible for the absorption of bone cells.[17] The average bone balance is achieved by regulating the relationship between osteoblasts and osteoclasts. The repair process of bone injury requires the coordination of multiple histological processes and different biochemical stages. It can be divided into three stages: the inflammatory stage, the stage of granulation tissue formation, and the remodeling stage of the tissue.[18,19] Studies have shown that bionic tissue structures can imitate the micro- and macrostructures of bone tissue, provide cells with a growth environment similar to their natural environment,[20] and offer cells similar physical and chemical signals, thereby promoting their natural proliferation and growth (Figure 1).[21–23]

In the field of biomaterials science, hydrogels are engineered to possess a three-dimensional, porous

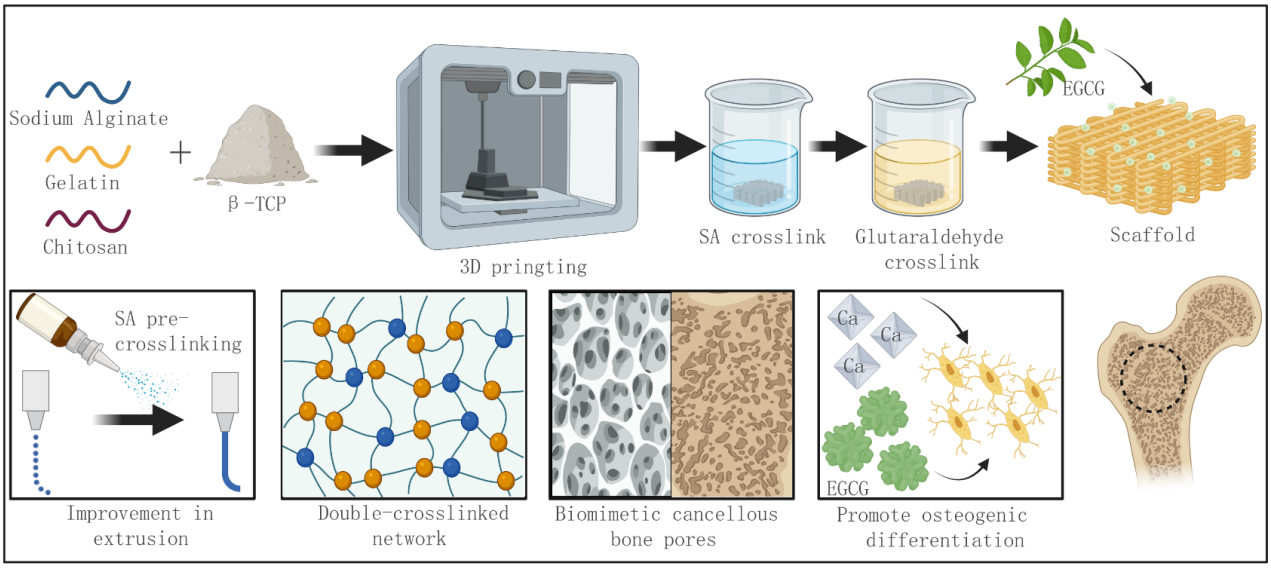


Figure 1. Schematic illustration of a biomimetically multilevel three-dimensional (3D) printing scaffold for repairing large bone defects. Different materials are physically blended to form a bioink suitable for 3D printing. A dual-crosslinking strategy endows the scaffold with stable, comprehensive properties and a biomimetic tissue structure, and the scaffold is loaded with drugs to promote the repair of large bone defects. Abbreviations: β-TCP, β-tricalcium phosphate; EGCG, epigallocatechin gallate; H&E, hematoxylin & eosin; CT, computed tomography.

structure that closely mimics the nanofibrous architecture of native extracellular matrices (ECM). This biomimicry is achieved through the careful design of hydrogel networks to replicate ECM components such as collagen and glycosaminoglycans, facilitating cellular attachment, proliferation, and differentiation.[24–25] While hydrogels with such intrinsically biomimetic structures have found applications in wound dressings, ophthalmic devices, and other biomedically relevant areas, their deployment in bone tissue engineering remains limited.[26–28] One primary limitation is their poor stability, especially in the dynamic and multifaceted environment of physiological fluids. Additionally, the inherent mechanical properties of hydrogels often fall short of the rigorous biomechanical demands expected of bone scaffolds. These challenges necessitate further research and innovation to harness the potential of hydrogels in bone tissue regeneration.[26,29] In recent research, Nie et al. compounded hydrogels with inorganic ceramic materials to prepare scaffolds through 3D printing technology and achieved a bionic tissue structure inside the scaffold. However, after testing the mechanical properties of the scaffold, they found that the compressive modulus of the scaffold was significantly lower.[30] According to our analysis, the lower the compressive modulus is, the larger the pore structure of the three-dimensional network formed. This is due to the polymer formed by a single cross-linked hydrogel. Adhesion between the polymer networks will occur during the freeze-drying process (when water molecules are removed, the interactions between polymer chains may become more closely connected, such as van der Waals forces and hydrogen bonds). This will cause adhesion between polymer chains.). In this regard, we found that as early as 2005, some researchers proposed a double network structure.[31] The so-called double network refers to a polymer network formed by cross-linking two different polymers. When freeze drying, due to its unique combination during the process, the dual network structure can better cope with the stress generated, thereby reducing the damage of ice crystals to the network structure, ensuring a relatively stable network structure and enabling the scaffold to have a more penetrating and tight interpenetrating network connection. It can improve the compression modulus of the stent and maintain the application accuracy of the scaffold.[32–34]

This study aims to use 3D printing technology to prepare a hydrogel-based composite scaffold with a bionic tissue structure and stable mechanical properties (Figure 1). Sodium alginate, a linear anionic polysaccharide with excellent cross-linking properties, is selected as the base, and calcium ions are selected for cross-linking,[35–37] together with the crosslinking molding of gelatin, a double crosslinked double network system is formed to enhance the stability of the hydrogel and. In the dual-crosslinking system, chemical crosslinking provides the composite system with a certain degree of strength and mechanical stability, while physical crosslinking not only maintains the drug-loading capacity of the hydrogel components but also contributes to energy dissipation. Considering the reduction of cell-binding sites in gelatin after crosslinking, chitosan with strong cell adhesion was introduced.[38–41] At the same time, To enhance the osteogenic differentiation capability of the hydrogel system and maintain the shape stability of the hydrogel-based scaffold during the degradation process, add a certain proportion of β-tricalcium phosphate to the hydrogel, which can release calcium ions during the degradation process.[42] After compounding with hydrogel, prepare bioink and use an extrusion Bio-3D printer with precross-linking Strategies for printing composite scaffolds. After analyzing a series of properties of the composite scaffold, we found that the prepared composite scaffold has a bionic tissue structure and can effectively promote cell proliferation and differentiation. It also has certain mechanical properties to meet the mechanical properties of the implanted scaffold in the early stage of bone healing requirements. At the same time, the hydrogel component was used to realize the payload of the drug EGCG. Animal experiment results show that the prepared scaffold has excellent in vivo osteogenic properties.

2. Materials and methodology

2.1. Materials

Sodium alginate (SA; 216.126 kDa), chitosan (degree of deacetylation ≥ 95%), anhydrous calcium chloride, and gelatin (Gel) were obtained from Shanghai Aladdin Bio (China), while β-tricalcium phosphate (β-TCP) was purchased from Kunshan Chinese Technology New Materials (China). Epigallocatechin gallate (EGCG) was provided by the Tea Research Institute of the Chinese Academy of Agricultural Sciences (China). Glutaraldehyde was provided by the West China Hospital of Sichuan University (China).

2.2. Preparation of bioink

In the initial phase of the experiment, without altering the chitosan content, we screened various hydrogel compositions (comprising SA and Gel in different ratios). Our evaluation criteria were based on simple mechanical properties and porosity (Figure S1), as well as the subsequent printability of the biological ink. Ultimately, we selected a hydrogel composition consisting of 3% SA, 2% chitosan, and 10% Gel. The preparation process of the bioink can be divided into two stages. For the preparation of the hydrogel precursor solution, SA powder was weighed

Table 1. Distribution ratio of each group of bioink

Group	Sodium alginate (w/v%)	Chitosan (w/v%)	Gelatin (w/v%)	β-tricalcium phosphate (w/v%)
SCG	3%	2%	10%	0
SCG-30%	3%	2%	10%	30%
SCG-40%	3%	2%	10%	40%
SCG-50%	3%	2%	10%	50%

according to the ratios shown in Table 1. The measured amount was then placed in a beaker, and deionized water was added to it. The mixture was stirred at 300 rpm using a magnetic stirrer for 2 h to ensure complete dissolution of SA, yielding a 3% SA solution. Subsequently, a measured quantity of chitosan powder was added directly to the SA solution, and the mixture was stirred at 200 rpm for 3 h to achieve uniform dispersion of chitosan in the SA precursor, resulting in a 3% SA + 2% chitosan hydrogel precursor solution.

Next, the Gel was weighed according to the proportions shown in Table 1 and stirred mechanically to disperse the Gel evenly. The sealed beaker was placed in a water bath at 60°C until the Gel completely dissolved. During this process, periodic replenishment of water was performed to maintain constant concentrations of the bioink components. After complete Gel dissolution, the precursor solution was transferred to a 60°C oven and subjected to intermittent heating (30 min each time) until most of the bubbles were removed. At this point, the preparation of the hydrogel components was concluded. The formulated hydrogel precursor solution was stored at 4°C for subsequent use.

After preparing the hydrogel precursor solution, different proportions of β-TCP were added to create a bioink. The specific procedure involved initial grinding and sieving of the β-TCP powder to ensure printability. The β-TCP powder was placed in a mortar and mechanically ground for 1 h, followed by sieving through a 200-mesh sieve to control the particle size of β-TCP to less than 80 μm. Subsequently, the previously prepared hydrogel precursor solution was dissolved in a water bath at 60°C. A specific volume of the hydrogel precursor solution was then extracted according to preestablished ratios and mixed with the sieved β-TCP. This completed the preparation of the bioink, ensuring its printability for subsequent applications. The pure hydrogel component was designated SCG, while the addition of various β-TCP components was named SCG-30%, SCG-40%, and SCG-50%.

2.3. Selection and characterization of crosslinking strategies for bioink

The specific operational steps were as follows: a specific amount of anhydrous calcium chloride was weighed and dissolved in deionized water to prepare a 0.6% (w/v) calcium ion solution. To ensure a good dissolution of chitosan, a specific amount of glacial acetic acid was added dropwise to the prepared calcium ion solution, adjusting the solution to a weakly acidic condition with a pH of 4.8. The scaffold was immersed in an acidic calcium ion solution for 3 h to ensure complete crosslinking of SA in the composition. The crosslinking of Gel is crucial for maintaining the stability of the hydrogel structure. Previous studies have shown that the degree of Gel crosslinking affects both cell compatibility and structural stability. A commonly used Gel crosslinking agent is glutaraldehyde, and a concentration of 0.6% (v/v) glutaraldehyde was chosen. The crosslinking of Gel in the hydrogel was carried out at 50°C for 3 h to achieve optimal crosslinking effects. This choice aimed to utilize the lowest concentration of glutaraldehyde to achieve the best crosslinking results. After crosslinking, the hydrogel was washed thoroughly at least three times to remove residual crosslinking agents from the hydrogel surface. Through this two-step crosslinking process, a dual-crosslinked interpenetrating network system consisting of both physical and chemical crosslinks was established, significantly enhancing the stability and mechanical properties of the hydrogel system.

2.4. Analysis of gelation ability and relevant physicochemical characterization of bioink

The calcium ion-crosslinked hydrogel component used in this study was SA. Studies have shown that higher calcium ion concentrations form a dense surface film on the hydrogel, reducing calcium ion entry and thus crosslinking. Choosing a lower calcium ion concentration will result in better crosslinking. In this study, a calcium ion concentration of 0.6% was used. Since the concentration was low, we first evaluated the gel-forming effect of the bioink to determine the crosslinking effect of calcium ions on SA. The gelation effect of calcium ion crosslinking on the hydrogel was determined using an inclined and inverted method. Specifically, the prepared hydrogel precursor solution was dissolved in a 60°C water bath. After dissolution, 2.5 mL of the hydrogel precursor solution was extracted and placed in a bottle. Subsequently, 1 mL of a preprepared 0.6% w/v acidic calcium chloride solution was added. To exclude the influence of the temperature-sensitive characteristics of Gel, the bottle was consistently

heated in a 37°C water bath. Five time points (1 min, 5 min, 10 min, 30 min, and 60 min) were selected, and the calcium ions were poured out of the bottle at each time point.

2.4.1. Fourier transform infrared spectra analysis

To analyze the changes in groups between the components of the scaffold after preparation and crosslinking, a Fourier transform infrared (EQUINX55, Brücher Crop, Germany) analysis was conducted. Data were scanned and collected across the spectral range of 500–4000/cm. The obtained spectral data underwent in-depth analysis and graphical representation using the ORIGIN software (OriginPro 2023).

2.4.2. Hydrophilicity evaluation

Hydrophilicity was assessed using a contact angle measurement instrument (CA200, Ysenmed, China). Composite hydrogel films with varying components were prepared and polished to achieve uniform surfaces. The films were subjected to deionized water droplets dispensed at a rate of 5 μL/s. After a 10-s equilibrium, images were captured and analyzed for contact angle using dedicated software (ImageJ 1.53). This process was repeated three times for each composite hydrogel, ensuring reliability in evaluating the hydrophilic characteristics of the films in contact with water.

2.4.3. Equilibrium swelling test

To assess the equilibrium swelling properties of the hydrogel, the following steps were employed. The bioink was placed within a cylindrical mold (10 × 5 mm) to form cylindrical hydrogel samples. After crosslinking and freeze-drying, the dried composite hydrogel was obtained. Three samples per group were weighed to determine the dry weight (*Wd*). These samples were then immersed in phosphate-buffered saline at 37°C. At various time intervals, the scaffolds were removed, excess surface water was gently absorbed using absorbent paper, and the samples were reweighed (*Ww*) at each time point. The swelling ratio (*SR*) was calculated using **Equation (1)**:

$$SR = (Ww - Wd)/Wd \quad (1)$$

This process was repeated for each time point, providing insights into the hydrogel's capacity to absorb water over time.

2.5. Scaffold fabrication and characterization

2.5.1. Pre-crosslinking strategy

Since we chose a higher proportion of hydrogel to ensure the formation of a bionic structure inside the hydrogel, it is difficult to guarantee the molding accuracy of the scaffold. To ensure improved layer-to-layer structural integrity, a pre-crosslinking approach was employed. The specific steps for pre-crosslinking were as follows. The prepared bioink was placed in a constant-temperature water bath at 60°C until it was completely dissolved. Different ratios of calcium ion solution (0.2%, 0.4%, 0.6%, 0.8% w/v) were extracted using a syringe and then added to the bioink in a fixed proportion of 2:0.1 (v/v) of bioink to calcium ions. After the addition of the calcium ion solution, vigorous mechanical stirring was immediately initiated to continuously disrupt the gel state, thereby increasing the viscosity of the bioink. This process lasted for 5 min to ensure thorough mixing. Following mixing, scaffold printing commenced. Utilizing a biological three-dimensional (3D) printer (EFL-BP-6601, Yongqinquan Intelligent Equipment Co., Ltd., China) under the conditions of a selected 22-gauge printing needle (internal aperture 420 μm), printing speed of 10 mm/min, and pressure set at 100 kPa, scaffolds of different compositions were printed. The extrudability of the ink and the formation state of the printed scaffold were used as criteria for evaluating the pre-crosslinking concentration. The concentration of calcium ions used for scaffold pre-crosslinking was determined based on the ability of the ink to extrude into threads and the overall print quality of the scaffold.

2.5.2. Scaffold volume shrinkage analysis

Using a caliper, the dimensions were recorded, and the initial volume (*V*1) was calculated after crosslinking. After freeze-drying, measurements were taken, and the final volume (*V*2) was calculated. The volume shrinkage (P_s) was determined using **Equation (2)**:

$$Ps = \frac{V1 - V2}{V1} \times 100\% \quad (2)$$

This analysis informed the accuracy of the scaffold in scenarios involving bone defects.

2.5.3. Scaffold porosity analysis

The porosity of the composite scaffold was determined using Archimedes' principle of displacement. Initially, the volume of the freeze-dried scaffold, denoted as *V*1, was calculated using a Vernier caliper. Subsequently, 10 mL of anhydrous ethanol was placed in a test tube, with the liquid level marked at this point (ensuring it covered the scaffold). The scaffold was then placed into the test tube, sealed with sealing glue, and left undisturbed for 24 h. During this period, the test tube was gently tapped to allow any trapped air bubbles to escape. Upon complete infiltration of anhydrous ethanol into the interior of the scaffold, the height of the liquid level, *h*, was recorded. The inner diameter of the test tube, denoted as *d*, was measured using a Vernier caliper, and the volume change was

denoted as $V2$. The porosity (P) of the composite scaffold was calculated using **Equation (3)**:

$$P = \frac{V1 - V2}{V1} \times 100\% \quad V2 = \frac{\pi d^2}{4} \circ h \tag{3}$$

2.5.4. Microscopic characterization of the surface and cross-section of scaffolds

The freeze-dried scaffold was cryogenically fractured in liquid nitrogen. Subsequently, the microstructures of the surface and cross-sections of different scaffold components were observed under various magnifications using scanning electron microscopy (SEM; ZEISS Sigma 300, ZEISS, Germany). Additionally, the Nano Measurer software (version 1.2) was utilized to analyze the pore size distribution across the cross-sections.

2.5.5. Characterization of mechanical properties

The mechanical properties of different components of the freeze-dried scaffolds were analyzed using a universal testing machine (Instron 5967, China). The dimensions of the scaffolds were maintained at 10 × 10 × 5 mm, with three parallel samples for each group. Compression testing was conducted in accordance with the national standard GB/T 1041-2008. The testing parameters included a loading rate of 1 mm/min and a 5 kN load cell. The obtained stress–strain curves were used to calculate the compressive modulus, determined by the slope of the curve.

2.5.6. In vitro degradation performance evaluation of composite scaffolds

The Wd of the freeze-dried scaffold was denoted as $W1$. The scaffold was immersed in 15 mL of phosphate-buffered saline (pH 7.4) and continuously incubated at 37°C for 2, 4, and 8 weeks. At each time point, the scaffold was retrieved and thoroughly rinsed with deionized water to remove surface phosphate-buffered saline and mineralization. The weight of the scaffold measured after degradation was denoted as $W2$. Simultaneously, a pH meter was used to measure the pH of the degradation solution at various time points, documenting the changes in pH that occurred during the degradation process. The degradation rate (Pd) of the scaffold was evaluated using **Equation (4)**:

$$Pd = \frac{W1 - W2}{W1} \times 100\% \tag{4}$$

2.5.7. Characterization of in vitro mineralization capacity

Simultaneously, the degraded scaffold at the 8th week underwent compression testing using a universal testing machine after being rinsed and freeze-dried. The variation in compressive modulus between the degraded scaffold at the 8th week and the original composition was measured, and the percentage loss of compressive modulus was calculated.

2.5.8. In vitro mineralization

Under 37°C conditions, the scaffold was placed in a simulated body fluid, which facilitated the formation of hydroxyapatite on the material surface, predicting its *in vitro* bone bioactivity. The development of bone-like hydroxyapatite on the scaffold surface was observed using SEM at different time intervals, specifically at the 3rd, 7th, and 14th days. XRD (ARL Equinox 1000, Thermo Fisher Scientific, USA) was employed to analyze their crystalline structures.

2.5.9. Drug-loaded scaffold fabrication

Drug loading into the scaffold was achieved through the swelling principle of hydrogels. The loaded drug was EGCG, which possesses antibacterial and anti-inflammatory properties.[43–45] and a certain ability to promote osteogenic differentiation.[46,47] Based on prior investigations, the SCG-50% scaffold exhibited superior overall performance. Therefore, only the SCG-50% component was selected for drug loading. Furthermore, two drug concentration gradients were established: one with a high drug concentration (25 μM) component, denoted as SCG-50%-H, and the other with a low drug concentration (12.5 μM) component, denoted as SCG-50%-L. Taking high-concentration EGCG loading as an example, the specific steps were as follows. After considering previous swelling rate assessments (indicating equilibrium after 4 h of water absorption), the scaffolds of different compositions were immersed in EGCG solutions of varying concentrations. The scaffolds were sealed and left to stand for 4 h to ensure thorough absorption of EGCG. After 4 h, the scaffold was extracted with forceps, and the surface EGCG solution was rinsed away with deionized water. Drug loading was completed following the freeze-drying process.

2.6. Cell biocompatibility and proliferation

Samples of different components were prepared into 5 × 1 mm scaffolds, dried for 12 h, and then sterilized using ultraviolet irradiation for 24 h. Rat embryonic osteoblasts (MC3T3-E1; Beyotime, China) were cultured in high-glucose Dulbecco's Modified Eagle Medium in a carbon dioxide incubator until the third passage. Subsequently, the scaffolds were immersed in a cell suspension, removed after 2 h, and placed in a 96-well plate, where they were seeded with MC3T3-E1 cells at a density of 1×10^4 cells per well. The plate was incubated at 37°C for 1, 3, and 7 days. At each time point, a live/dead cell staining kit (Beyotime,China) was used on the scaffold surface (live cells appear green, dead cells appear red). After staining,

the cells were rinsed with phosphate-buffered saline, and scaffold surface cell adhesion was observed using an inverted fluorescence microscope (Axio Observer 7, ZEISS, Germany). Simultaneously, after ethanol dehydration, electron microscopy was used to observe the morphology of dead cells on the scaffold surface.

2.7. Cell counting kit-8 assay

Samples of different components were prepared into square scaffolds measuring 5 mm × 1 mm. The samples were dried in a vacuum oven for 12 h and then sterilized using ultraviolet irradiation for 24 h. The sterilized square scaffolds were submerged in the cell culture medium for 2 h. Subsequently, the cells were placed in a 24-well plate, and osteoblasts were seeded at a density of 5×10^4 cells per well. The plate was incubated in a carbon dioxide incubator for 1, 3, and 5 days, with media changes every 2 days. At each time point, a 10% cell counting kit-8 (Merck Millipore, Germany) solution was added to each well using a pipette, with care taken to avoid introducing bubbles into the wells, as these may interfere with the optical density readings. The plate was incubated in a carbon dioxide incubator for 1 h. The absorbance was measured at 450 nm using a microplate reader. Cell viability was calculated using **Equation (5)**. GraphPad statistical software (Graphpad Prism 9.5) was used for data analysis, plotting cell proliferation and cell viability graphs.

$$\text{Cell viability (\%)} = (a-c)/(b-c) \times 100 \quad (5)$$

where a is the absorbance of the wells of the microsphere scaffolds of different components of the experimental group, b is the absorbance of the control wells, and c is the absorbance of the blank.

2.8. *In vitro* osteogenic differentiation tests

Furthermore, in order to more accurately describe the osteogenic performance of the scaffold in vitro, we conducted co-culture of cells with the scaffold and performed alizarin red staining and ALP staining. The results are shown in Figures S8 and S9.

The supplementary section in the methodology is as follows:

The alkaline phosphatase (ALP) activity of the cells was assayed using an ALP kit (Beyotime, China). Rat embryonic osteoblasts (MC3T3-E1; Beyotime, China) were inoculated in 24-well plates with samples at a density of 5×10^4 cells/well. The cells were cultured for 1 day and then replaced with an osteoinductive solution to continue incubation for 3 and 7 days. ALP was then quantitatively characterized.

The calcium deposition on the scaffolds was evaluated using Alizarin Red S (ARS) staining (Beyotime, China). MC3T3-E1 were seeded in 24-well plates containing the scaffolds at a density of 5×10^4 cells/well. After 21 days of culture in an osteoinductive medium, the samples were washed twice with PBS, fixed in 4% paraformaldehyde for 30 minutes, and rinsed with distilled water. The fixed cells were then stained with 1% Alizarin Red S solution (pH 4.2) at room temperature for 30 minutes. After washing off excess dye with deionized water, the stained calcium nodules were imaged under a light microscope.

To assess the inhibitory or promotional effects of β-TCP and EGCG on the expression of osteogenic-related genes, SCG-50% and SCG-50%-L scaffolds were co-cultured with MC3T3-E1 for 7 days.

Relative expression of BMP2, RUNX2, COL1A1, OPN, and SP7 in SCG-50% and SCG 50%-L scaffolds after co-culture with MC3T3-E1 for 7 days.

2.9. Real-time quantitative polymerase chain reaction analysis

To assess the inhibitory or promotional effects of β-TCP and EGCG on the expression of osteogenic-related genes, SCG-50% and SCG-50%-L scaffolds were co-cultured with MC3T3-E1 for 7 days. Subsequently, the scaffolds were frozen in liquid nitrogen and ground, and Nucleo-ZOL (Macherey-Nagel, Germany) was employed to extract total cellular RNA. The Super-Mix reagent kit (Macherey-Nagel, Germany) was used to synthesize complementary DNA from total RNA through reverse transcription. A real-time polymerase chain reaction was conducted using the SYBR Green Master Mix reagent kit (Macherey-Nagel, Germany) to detect gene expression levels in the samples. To standardize the results, the $2^{-\Delta\Delta CT}$ method was applied to quantify gene expression levels. The primers used are detailed in **Table 2**.

2.10. *In vivo* tests

Rat cranial defects were used as models for large bone defects because they share similar bone healing mechanisms and challenges with large bone defects, and can be accurately replicated and observed in experimental animals.[48] Animal care and use procedures were approved by the Animal Ethics Committee of West China Hospital of Stomatology, Sichuan University, and followed all applicable institutional and governmental regulations regarding the ethical use of animals. The experimental manipulations were performed as follows. 12-week-old male Sprague–Dawley rats (n = 24, Dashuo, China) were anesthetized and shaved. Following that, a circular 5 mm defect was created in the rat skull using a dental ring drill, and the wound was sutured after implantation of

Table 2. Primer sequences

Gene	Forward primer	Reverse primer
Gapdh	5'-AATGTGTTCCGTCGTGGATCTG-3'	5'-CAACCTGGTCCTCAGTGTAGC -3'
Bmp2	5'-GGGACCCGCTGTCTTCTAGT-3'	5'-TCAACTCAAATTCGCTGAGGAC-3
Runx2	5'- GACTGTGGTTACCGTCATGGC -3'	5'ACTTGGTTTTTCATAACAGCGGA -3'
Col1a1	5'-TCGTGCCTAGCAACATGCC-3'	5'-ATTGGGGACCCTTAGGCCAT-3'
Sp7	5'-TCCCTGGATATGACTCATCCCT-3'	5'-CCAAGGAGTAGGTGTGTTGCC-3'

the sample. Postoperative antibiotics and cephalosporin antibiotics were injected daily for 3 consecutive days to prevent postoperative infection. The experiment was divided into five groups: Blank, SCG, SCG-50%, SCG-50%-L, and SCG-50%-H. Cranial samples were removed at 6 weeks and 12 weeks postoperatively, and the tissue was fixed with 4% paraformaldehyde. *In vivo* bone formation was scanned and analyzed using a computed tomography scanner (45 μCT; SCANCO Medical, Switzerland) with an X-ray voltage of 60 kV, a current of 500 μA, and an effective pixel size of 200 μm. Bone volume fraction (BV/TV) and bone mineral density (BMD) were calculated in the area of the bone defect using the Viscal software (version 2.1). The rat skull cap was subsequently decalcified for one month, embedded in paraffin, and sectioned at a thickness of 5 μm. The sections were fixed in xylene and stained with hematoxylin and eosin (H&E) and Masson's trichrome to visualize the tissue and bone structure.

2.11. Statistical analysis

The data were statistically and graphically analyzed using GraphPad Prism 8.0, and data analysis was performed using one-way analysis of variance. A p-value < 0.05 was considered significant (*p<0.05, **p<0.01, ***p<0.001, and ****p<0.0001).

2.12. Routine blood analysis.

At 12 weeks post-implantation, blood samples were collected from the retro-orbital venous plexus of the anesthetized rats into EDTA-anticoagulant tubes. The samples were immediately analyzed using an automatic hematology analyzer (Mindray BC-5000, Mindray, China) to evaluate systemic inflammation and biocompatibility. Key parameters, including white blood cell (WBC), red blood cell (RBC), and platelet (PLT) counts, were recorded to assess the host response.

3. Results and discussion

3.1. Characterization of the materialization properties of bioink

The gelation capability of hydrogels was assessed using the inversion method. The gelation capacity of different bioink components at various time intervals is depicted in Figure 2**A**. Following the addition of a fixed quantity of acidic 0.6% calcium chloride solution, the gel formation ability of the composite hydrogels gradually increased with prolonged crosslinking time. At 60 min of crosslinking time, hydrogels from all components were fully formed, showing no structural collapse even when tilted or inverted. Both the internal and external portions of the hydrogels were thoroughly crosslinked. This suggests that the use of acidic 0.6% calcium ions for crosslinking SA can lead to the formation of stable and uniform crosslinked hydrogels. Subsequently, the hydrogels crosslinked with acidic calcium ions were further crosslinked with 0.6% glutaraldehyde at 50°C for 3 h, followed by freeze-drying for 24 h, resulting in the fabrication of composite hydrogel materials.

To assess the emergence of new chemical groups and evaluate changes in group migration and bonding strength during the crosslinking and post-treatment processes of composite hydrogels, various samples were subjected to infrared spectroscopy analysis. The infrared spectra of the raw materials constituting the composite hydrogel are shown in Figure 2B. The vibrational absorption peaks of phosphate ions for β-TCP were observed at 551 cm^{-1} and 606 cm^{-1}, the asymmetric stretching vibration peak for P=O was observed at 1045 cm^{-1}, Gel showed characteristic peaks at 1651 cm^{-1} (C=O stretching vibration) and 1490 cm^{-1} (C–N stretching vibration), chitosan exhibited peaks at 2881 cm^{-1} (C–H stretching vibration) and 840 cm^{-1} (out-of-plane bending vibration of C–H), and SA had a symmetric stretching vibration peak for COO– group at 1414 cm^{-1}.

As depicted in Figure 2C, after composite formation and crosslinking between the materials, the characteristic peaks of each material remained, indicating that no new substances were generated during the crosslinking and post-treatment processes of the various component bioinks. However, changes in peak intensity and position were observed. Notably, after crosslinking with calcium ions, the carboxyl groups of SA were replaced by oxygen atoms closer to calcium ions, resulting in a noticeably weakened symmetric stretching vibration peak of the COO– group at 1414 cm^{-1}. This was a consequence of

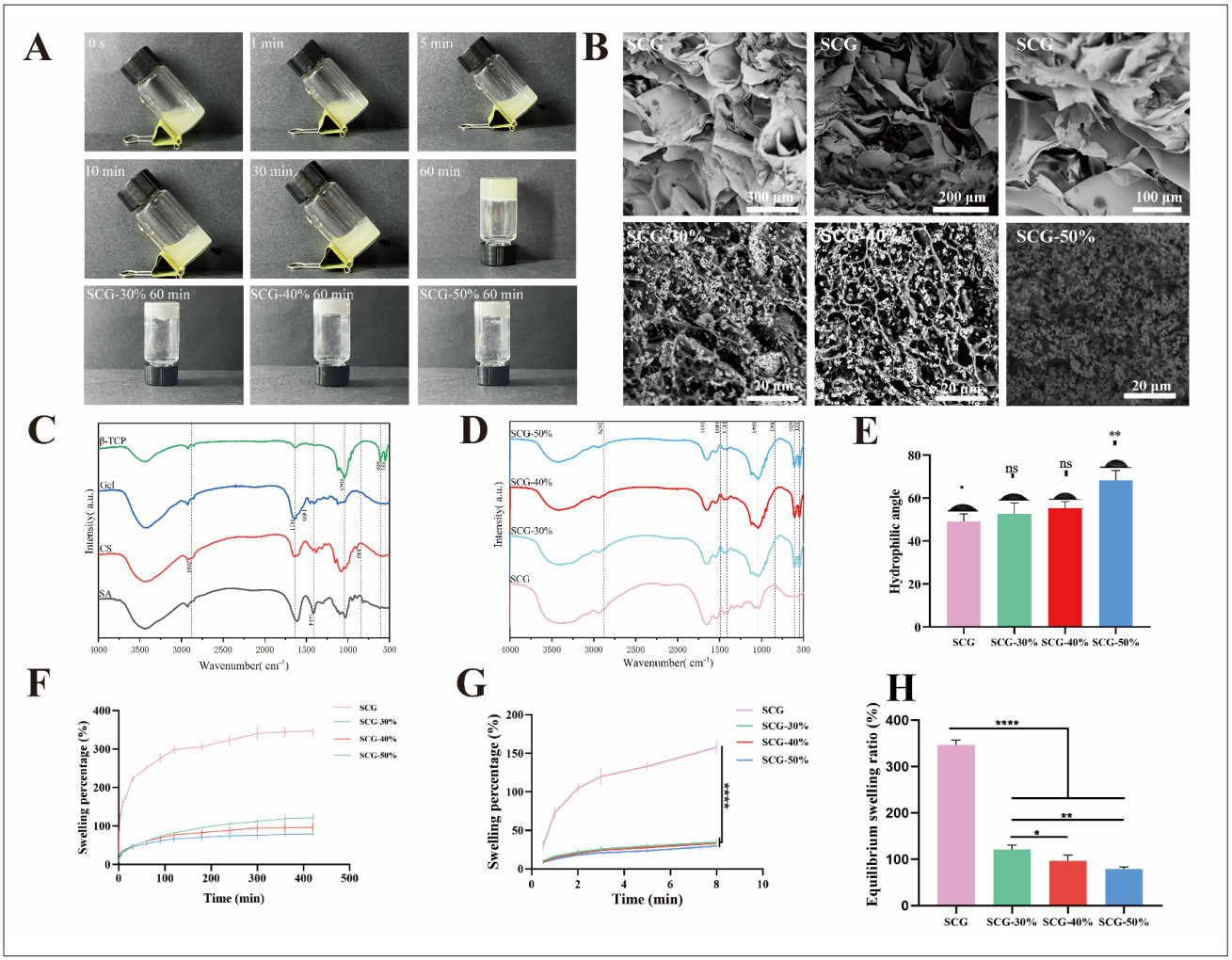


Figure 2. Basic characterization of bioink properties. (A) Schematic diagram of bioink gel capability. (B) Representative SEM images of SCG, SCG-30%, SCG-40%, and SCG-50%. (C) FTIR of sodium alginate (SA), chitosan (CS), gelatin (Gel), and β-tricalcium phosphate (β-TCP). (D) FTIR of SCG, SCG-30%, SCG-40%, SCG-50%, SCG-50%-L (low), and SCG-50%-H (high). (E) Hydrophilic angles of SCG, SCG-30%, SCG-40%, SCG-50%, SCG-50%-L, and SCG-50%-H films. (F) Change in swelling ratio of SCG, SCG-30%, SCG-40%, SCG-50%, SCG-50%-L, and SCG-50%-H composite hydrogels. (G) Change in swelling rate in each component for 8 min. (H) Comparison of equilibrium swelling ratio. Statistical significance determined at $^{*}p < 0.05$, $^{**}p < 0.01$, $^{***}p < 0.001$, and $^{****}p < 0.0001$; ns refers to not significant; n=3.

the formation of complexes between the carboxyl groups of polysaccharides, amino groups, and calcium ions. It was also notable that a new characteristic peak appeared at 1545 cm^{-1}. This was due to the vibration of the imine bond formed by the crosslinking of chitosan and Gel with glutaraldehyde, which manifested as a characteristic peak at approximately 1545 cm^{-1}. Additionally, the use of a crosslinking agent stabilized the crystal structure of β-TCP, leading to an increase in the intensity of the characteristic peak for phosphate ions. After crosslinking with glutaraldehyde, the intensity of the C=O group at 1651 cm^{-1} in the Gel decreased due to the reaction between the amino groups in the Gel and the aldehyde groups in glutaraldehyde, resulting in the formation of carboxylic acid condensation products. Consequently, the absorption peak of the C=O bond in Gel shifted to lower wavenumbers in the infrared spectrum. Moreover, changes in the absorption peak position of the C–N bond at 1490 cm^{-1} also occurred due to reactions between the amino groups in Gel and the aldehyde groups in glutaraldehyde. These changes robustly demonstrate the molecular interactions and good molecular compatibility between SA, chitosan, and Gel.

Hydrophilicity refers to the affinity of materials with hydrophilic groups for water molecules. Materials with strong hydrophilicity exhibit robust cell adhesion, and high hydrophilicity is advantageous for cell growth, reproduction, and fluid exchange. A smaller contact angle

indicates better hydrophilicity. After measuring the contact angle of the materials, the results, as shown in Figure 2D, reveal that the SCG pure hydrogel component exhibited strong hydrophilicity with an average contact angle of 49°. This is attributed to the presence of hydrophilic groups (hydroxyl & carboxyl groups) in the materials constituting the hydrogel. β-TCP is an inorganic material with relatively poor hydrophilicity compared to natural polymer materials. Consequently, with the addition of β-TCP, the contact angle gradually increased, indicating a decrease in hydrophilicity. When β-TCP was added up to 50%, the average contact angle was 68.33°. Although there was a trend of decreasing hydrophilicity with the addition of β-TCP, the contact angle remained below the hydrophilic–hydrophobic threshold of 90°, indicating that this inorganic salt–gel system exhibited good hydrophilicity, which may facilitate cell adhesion and proliferation.

The swelling rate calculation was employed to assess the water absorption and swelling properties of composite hydrogel materials over a specified duration. Composite hydrogel materials exhibiting a higher swelling rate demonstrate enhanced fluid exchange capabilities, facilitating cellular interactions and substance transport. Nevertheless, research indicates that when applied in bone tissue repair, especially in the restoration of spinal and cranial injuries, excessive swelling can lead to deformation and expansion of the hydrogel, exerting pressure on nerves. Moreover, a higher swelling rate significantly compromises the mechanical properties. Therefore, it is crucial to control the swelling characteristics of hydrogel substrates. The results of swelling rate measurements, as depicted in Figure 2E, reveal the outstanding swelling properties of the SCG group, reaching equilibrium at approximately 300 min with a swelling rate of 340.52%. Upon the addition of β-TCP, there was a notable reduction in the equilibrium swelling rate, accompanied by an extended time to reach equilibrium. Specifically, the SCG-50% sample took approximately 360 min to achieve equilibrium swelling, and the equilibrium swelling rate decreased to 73.99%.

Figure 2F illustrates the variations in short-term swelling rates for samples with different compositions. The SCG group exhibited rapid swelling, while samples containing β-TCP showed diminished but still rapid swelling capabilities, reaching approximately 40% swelling within 8 min. In Figure 2G, a statistical analysis of the equilibrium swelling rates of composite hydrogels for each component demonstrates that the inclusion of β-TCP significantly inhibited the swelling behavior of the hydrogel. As the quantity of β-TCP increased, the equilibrium swelling rate consistently decreased. Therefore, the addition of β-TCP allowed for the regulation of the swelling rate of SCG hydrogels, effectively suppressing excessive swelling behavior.

3.2. Scaffold fabrication and characterization

To enhance the high-level formability of the scaffold, a pre-crosslinking approach was employed to augment the viscosity of the bioink. Throughout this process, varying concentrations of calcium ions were employed at 0.2%, 0.4%, 0.6%, and 0.8% w/v, following a bioink-to-calcium ion ratio of 2:0.1 (v/w). The evaluation criteria encompassed the extrusion behavior of the bioink and the formability of the scaffold. As depicted in Figure 3A, the results indicate that the scaffold exhibited optimal formability when the pre-crosslinking calcium ion concentration was 0.6%. This superiority was attributed to the synergistic interplay of multiple factors. Primarily, pre-crosslinking, by elevating the viscosity of the scaffold, ensured the accuracy of filamentous shape retention during the extrusion process of the bioink. Simultaneously, rapid solidification of the thermosensitive Gel was facilitated by the use of a cold plate, enabling better shaping of the bottom layer of the scaffold. Conversely, in the absence of pre-crosslinking treatment, the lower viscosity of the bioink resulted in poor continuity of extrusion, leading to structural collapse and deformation issues during the printing process. Through pre-crosslinking, we successfully heightened the viscosity of the bioink, ensuring a more uniform and stable extrusion. Furthermore, due to the enhanced viscosity, the formability of the scaffold was significantly augmented, mitigating issues of collapse. This experimental outcome unequivocally underscores the necessity and efficacy of the pre-crosslinking strategy. Furthermore, we verified the printing performance of the ink through rheological analysis. Through oscillation experiments, it was observed that SCG and SCG-50% exhibited higher moduli at low strains, while the ink modulus decreased under high strain application, accompanied by a recovery of the strain recovery modulus, indicating that the printed ink can be extruded and reformed under the shear thinning effect (Figure S2).

Following the completion of pre-crosslinking, scaffolds with varying β-TCP content were fabricated using an extrusion-based 3D bioprinting system. Subsequently, after crosslinking with acidic calcium ions and glutaraldehyde, the scaffolds underwent freeze-drying to achieve the final form. Figure 3B illustrates the states of the scaffolds at different stages. After acidic calcium ion crosslinking, the morphology of the scaffolds remained unchanged, while an increase in hardness was observed. However, following glutaraldehyde crosslinking, the color of the scaffold changed to pale yellow. This phenomenon resulted from the Schiff base reaction between Gel and

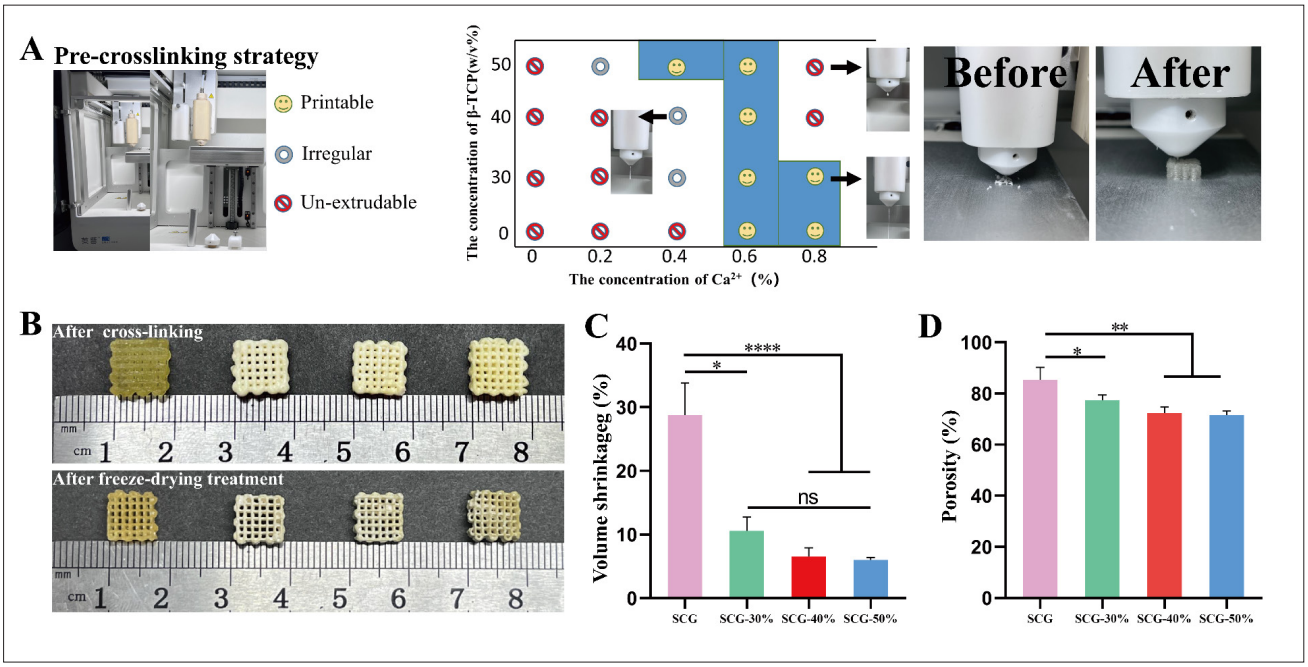


Figure 3. Printing and characterization of scaffolds. (A) Determination of pre-crosslinking effect and concentration. (B) Changes in macroscopic morphology of scaffolds during post-treatment. (C) Volume shrinkage of SCG, SCG-30%, SCG-40%, and SCG-50% scaffolds before and after freeze-drying. (D) Porosity of SCG, SCG-30%, SCG-40%, and SCG-50% scaffolds. Statistical significance determined at $^{*}p < 0.05$, $^{**}p < 0.01$, $^{***}p < 0.001$, and $^{****}p < 0.0001$; $n=3$. Abbreviation: β-TCP, β-tricalcium phosphate; ns, not significant.

glutaraldehyde, leading to the formation of a crosslinked structure that altered the conformation and charge state of Gel molecules, influencing light absorption and scattering characteristics and thus causing a change in the scaffold color. Simultaneously, the crosslinking action further increased the scaffold's hardness and induced the formation of a double network structure with interpenetrating crosslinks within the interior. Finally, after freeze-drying, the removal of internal ice crystals significantly improved the varying degrees of contraction in the scaffold, resulting in a roughened surface. Concomitantly, the mechanical properties of the scaffold significantly improved. The outcomes of these sequential preparation steps reflected changes in the structure and performance of the scaffold at different stages, providing crucial information about its effectiveness in biomedical applications.

Upon conducting statistical analyses on the volume shrinkage rates of scaffolds with different β-TCP contents before and after freeze-drying, as depicted in Figure 3C, the volume shrinkage rate of the pure water gel scaffold was found to be 28.79%. Undoubtedly, this would adversely affect the precision of scaffold applications. However, with the addition of β-TCP, the volume shrinkage rates of the scaffolds decreased to 10.57%, 6.55%, and 6.01%, respectively. There was a significant difference in the volume shrinkage rates between the pure water gel scaffold and those incorporating β-TCP. This observation underscores that the inclusion of β-TCP markedly enhances the shape stability and fidelity of the scaffold before and after freeze-drying.

This improvement is attributed to the uniform attachment of β-TCP to the network structure of the water gel scaffold. This attachment effectively impeded the volume shrinkage of the water gel during freeze-drying, maintaining the stability of the scaffold shape. The incorporation of β-TCP has been proven instrumental in preserving the structural integrity of scaffolds during the freeze-drying process.

The results of the application of the Archimedes drainage method for measuring scaffold porosity are presented in Figure 3D. The porosity of the pure water gel scaffold reached a high value of 85.33%. However, upon the addition of β-TCP, the scaffold porosity significantly decreased to 77.37%, 72.33%, and 71.64%, respectively. It is noteworthy that the porosity of trabecular bone in the human body typically ranges between 70% and 90%. Thus, the porosity of the prepared scaffolds met the requirements for trabecular bone. Importantly, the pure water gel composition exhibited a significant difference in porosity compared to the other groups. This further underscores

that the addition of β-TCP significantly enhances the shape fidelity of the scaffold during post-processing. This has crucial implications for the biocompatibility and performance of the scaffold, especially in bone tissue engineering and medical applications, where scaffold porosity can influence cell adhesion and bone tissue growth. Therefore, these results highlight the advantages of incorporating β-TCP, with the potential to improve scaffold performance, making it more suitable for bone tissue repair and biomedical applications.

3.3. Microscopic morphological characterization of scaffold cross-sectional surface

Figure 4A shows the SEM images of the surfaces of the SCG, SCG-30%, SCG-40%, and SCG-50% scaffolds. The SEM results reveal that the surface of the SCG pure hydrogel scaffold was smooth and devoid of micropores, a result of the crosslinking process, underscoring the thoroughness of scaffold crosslinking. Conversely, upon the introduction of β-TCP, the scaffold surface undergoes a transformation due to the incorporation of β-TCP into the hydrogel, resulting in a roughened texture and a porous state. This morphological alteration, characterized by a rough surface, proves advantageous for cell adhesion and growth on the scaffold surface. The presence of surface micropores further facilitates the transport of nutrients and the exchange of substances within bodily fluids. The integration of β-TCP not only altered the surface topography but also enhanced the scaffold's biocompatibility, rendering it conducive to cellular activities and promoting efficient material exchange at the interface of the scaffold and the biological milieu. These findings underscore the pivotal role of β-TCP in modulating the structural and functional characteristics of the scaffold surface, thereby influencing its performance in tissue engineering applications.

Figure 4B presents the SEM images of the cross-sections of SCG, SCG-30%, SCG-40%, and SCG-50% scaffolds. The SEM images distinctly reveal that the cross-sections of all scaffold components exhibited a continuous network of porous structures after freeze-drying. Upon closer examination of the cross-sectional SEM results of the SCG pure hydrogel scaffold, it was evident that the polymer network of the pure hydrogel underwent contraction and adhesion between polymer strands after the freeze-drying process. This resulted in a decrease in the shape fidelity of the scaffold, accompanied by an enlargement of pores compared to other components. This microscopic

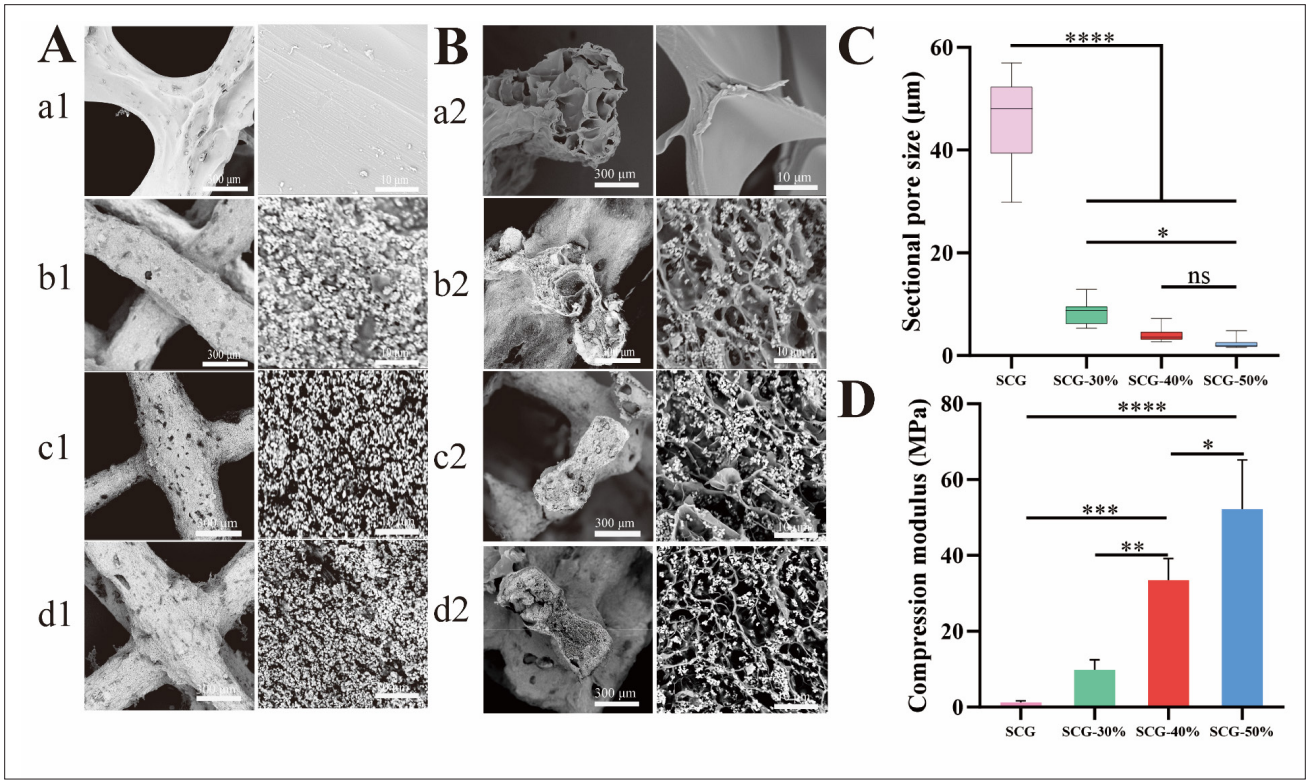


Figure 4. Microstructure morphology and related performance characterization of scaffolds with different components. (A) Surface morphology of scaffolds. Scale bars: 10 μm, 300 μm; magnifications: 15×. (B) Cross-sectional morphology of scaffolds. Scale bars: 10 μm, 300 μm; magnifications: 15×. (C) Analysis of the cross-sectional aperture of the scaffold. (D) Compression modulus of scaffolds. Statistical significance determined at $^{*}p < 0.05$, $^{**}p < 0.01$, $^{***}p < 0.001$, and $^{****}p < 0.0001$; ns refers to not significant; n=3.

observation elucidates the reasons for the volume shrinkage of the scaffold before and after post-processing. With the addition of β-TCP, it adhered uniformly to the 3D crosslinked network structure. This uniform adhesion, combined with the hydration process of ceramic materials, ensured that a high degree of fidelity is maintained within the 3D structure of the composite scaffold. Moreover, the close integration of β-TCP with the hydrogel network enhanced the mechanical properties of the scaffold. At the same time, we also printed scaffolds SCG-60% and SCG-70% with higher β-TCP content. The electron microscopy results are shown in Figure S3. The inside of the scaffold was filled with β-TCP, resulting in the loss of its bionic structural organization.

Subsequently, the Nano Measurer software was employed to statistically analyze the micropore sizes on the cross-sections of the scaffolds. The statistical results revealed that the micropore diameter of the cross-sections of the SCG pure hydrogel scaffold was approximately 50 μm, displaying a significant difference compared to other components. The micropore sizes on the scaffold cross-sections exhibited a decreasing trend with the gradual addition of β-TCP. The analysis in Figure 4C further explores the distribution of micropore sizes on the cross-sections of various components, indicating that the micropores in the scaffold with added β-TCP were distributed in the range of 1–20 μm. This size range was comparable to the pore sizes between trabeculae in cancellous bone, suggesting that the scaffold possesses a biomimetic internal structure.

Following compression modulus testing of the scaffolds using a universal testing machine, the results depicted in the graph (Figures 4D and S4) indicate that the average compression modulus of the SCG pure hydrogel scaffold was 1.25 MPa. In contrast, the SCG-30% scaffold exhibited an average compression modulus of 9.80 MPa, SCG-40% had an average compression modulus of 33.50 MPa, and SCG-50% demonstrated an average compression modulus of 52.22 MPa. Furthermore, we also conducted compression tests on the scaffolds in a humid environment. The test results showed that the compression modulus of the SCG scaffold was only 111.5 ± 5.24 kPa. However, after adding β-TCP, the compression modulus of the SCG-50% scaffold increased to 1080.75 ± 62.30 kPa (Figure S5). The inclusion of β-TCP in the scaffolds aligns with the compressive modulus requirements of cancellous bone. Significant differences were observed between the SCG pure hydrogel component and the components with added β-TCP, suggesting a substantial enhancement in the mechanical strength of the scaffold upon the addition of β-TCP. Moreover, the compression modulus showed an increasing trend with increasing β-TCP content. The primary reason for this change is the uniform attachment of β-TCP to the hydrogel network, reinforcing the hydrogel scaffold's ability to resist deformation.

3.4. *In vitro* degradation performance analysis

After subjecting the scaffolds to degradation for 2, 4, and 8 weeks, we conducted a comprehensive analysis of the degradation rates, changes in the degradation fluid pH, variations in the scaffold's compressive modulus, and morphological characteristics of scaffolds with different components. First, as shown in Figure 5A, after a period of degradation, the surface of each scaffold showed apparent changes. The SCG pure hydrogel component scaffold exhibited the most significant change, and fractures were observed on its surface. This was due to the instability of SA during the degradation process, resulting in uncrosslinking and leading to phase separation between polymers. This phenomenon was more evident after 8 weeks of degradation. For scaffolds with β-TCP added, the scaffold surface rarely broke, but instead formed smooth, crater-like depressions due to the continuous release of calcium ions from β-TCP during the degradation process, which can enhance inter-tissue communication. The adhesive was continuously crosslinked with SA to ensure the stability of the scaffold. As depicted in Figure 5B, we observed variations in the degradation rate (mass loss rate) of the scaffolds at different time points. The results revealed that in the 2nd week, all scaffold components exhibited noticeable degradation behavior. Notably, scaffolds composed of SCG pure hydrogels displayed the most rapid degradation, with a mass loss rate of up to 10%. By week 4, the degradation rate of these scaffolds further increased to 15%. Concerningly, by the 8-week mark, structural collapse of the scaffolds occurred, resulting in degradation rates reaching approximately 25%.

In contrast, scaffolds doped with β-TCP maintained morphological stability throughout the degradation process and effectively reduced the degradation rate. At the 8-week time point, the degradation rate of these scaffolds did not exceed 20%. Importantly, it was observed that the degradation rates of scaffolds with different components were significantly influenced by the β-TCP content. This observation indicates that the addition of β-TCP distinctly modulates the degradation behavior of the scaffolds. This effect can be attributed to the hydration reaction of β-TCP bioceramics during degradation, which led to the gradual release of calcium ions, thereby preserving the structural stability of the hydrogel components.

The variation in pH levels of the degradation fluid during the scaffold degradation process plays a pivotal role in determining whether an inflammatory response occurs within the organism. Consequently, we conducted a comprehensive assessment of the pH levels in the

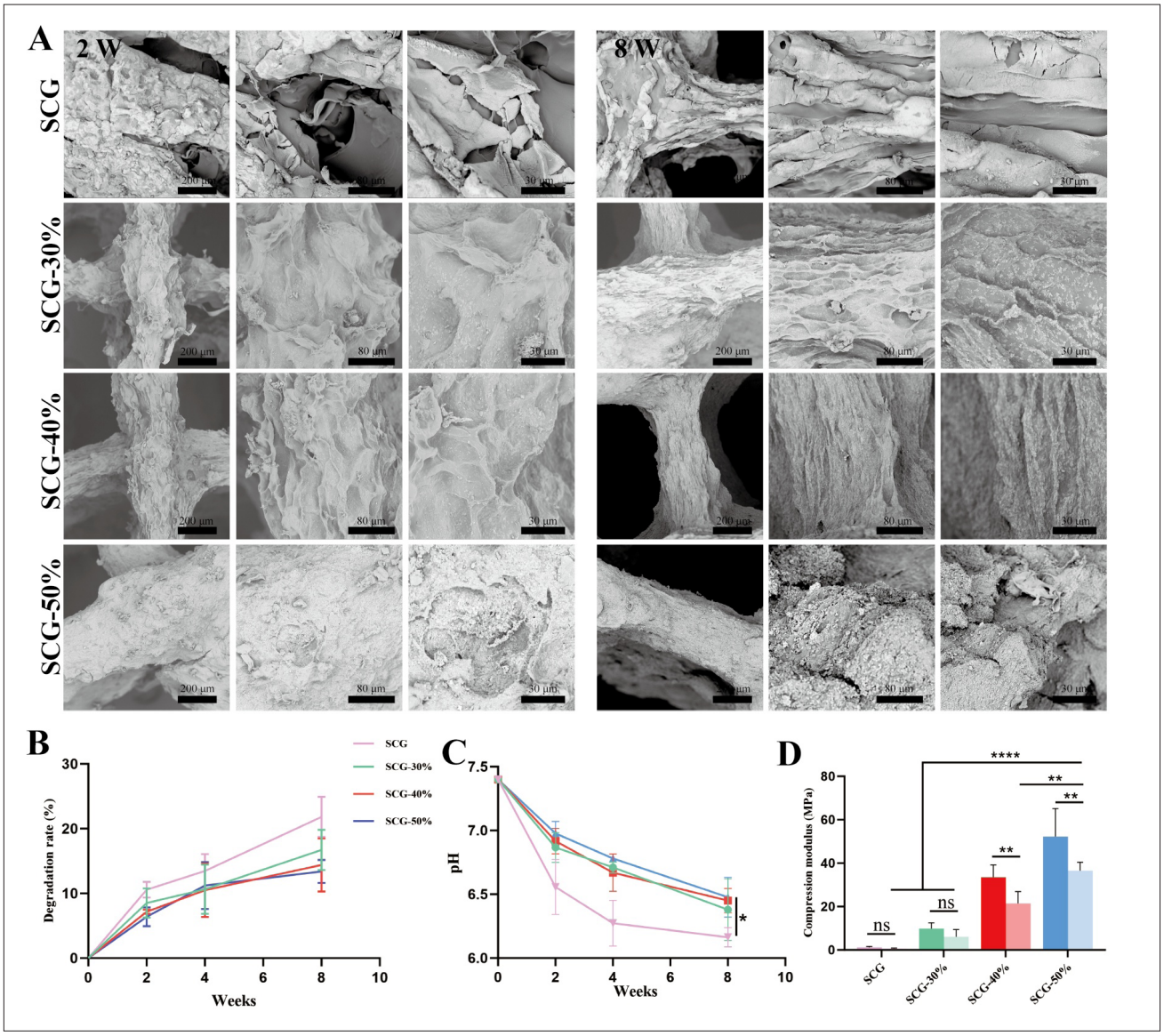


Figure 5. Performance changes of scaffolds with different components during *in vitro* degradation. (A) The micromorphology of the SCG, SCG-30%, SCG-40%, and SCG-50% scaffolds changed after 2 and 8 weeks of degradation. Scale bars: 30 μm, 80 μm, 200 μm; magnifications: 20×. (B) Degradation rate of different components of scaffolds. (C) Changes in degradation cycle pH. (D) Compression modulus changes of scaffolds after 8 weeks of degradation of SCG, SCG-30%, SCG-40%, and SCG-50% scaffolds. (E) Compression modulus loss rate of each component scaffold after 8 weeks of degradation, Statistical significance determined at $^{*}p < 0.05$, $^{**}p < 0.01$, $^{***}p < 0.001$, and $^{****}p < 0.0001$; ns refers to not significant; n=3.

degradation fluid. As illustrated in Figure 5C, we observed pH variations at different time points for various β-TCP scaffolds. The results revealed a discernible declining trend in pH values during the scaffold degradation process. Notably, the pH value of the pure hydrogel scaffolds had already plummeted to below 6.5 by week 4. This decline can be attributed to the hydrolysis process of the Gel, wherein peptide chains progressively unfold, break apart, and ultimately degrade into smaller peptide chains, such as collagen. Typically, the pH of collagen falls within the range of 6.0 to 7.5, and pH values within this range generally do not adversely affect the acid-base balance of an animal's body, nor do they impact the adhesion properties of human cells or cellular metabolism. Conversely, the pH values of scaffolds incorporating β-TCP remained relatively stable, hovering at approximately 6.5 after 8 weeks of degradation. This outcome signifies that the addition of β-TCP markedly ameliorated the declining pH trend during the degradation process, aligning with the degradation behavior trend. Consequently, it can be inferred that β-TCP scaffolds contribute to the maintenance of an acid-base equilibrium in the surrounding scaffold environment during

degradation. This holds promising prospects for mitigating the risk of unnecessary inflammatory responses within the organism, thereby bearing significant positive implications for the biomedical application of such scaffolds.

The loss of the scaffold's compressive modulus due to degradation is inevitable. The compressive modulus of the scaffold, both before and after degradation, is presented in Figure 5D. This figure compares the compressive modulus of the scaffold after 8 weeks of degradation with its initial compressive modulus. From the results, it is evident that scaffolds with different components all exhibited a significant decline in their compressive modulus after degradation, with notable differences among them. As shown in Figure 5E, after a period of degradation, the compressive modulus attenuation rate for the SCG-50% component scaffold was 30.12%, 35.64% for the SCG-40% component scaffold, 37.76% for the SCG-30% component scaffold, and 48.8% for the SCG component scaffold. Thus, the addition of β-TCP significantly reduced the attenuation of the compressive modulus of the scaffold during the degradation process, thereby enhancing the stability of the scaffold's structure and mechanical properties.

In summary, these findings underscore the significant enhancement of structural stability and effective regulation of degradation behavior in scaffolds achieved through the incorporation of β-TCP. These results hold crucial implications for the long-term stability and performance of scaffolds in biomedical applications.

3.5. *In vitro* mineralization capability analysis

In the realm of bone tissue engineering scaffolds, materials endowed with robust *in vitro* mineralization capabilities can facilitate the formation of stable inorganic compound layers on their surfaces. This distinctive attribute enhances the biocompatibility and mechanical performance of the materials, thereby promoting the scaffold's integration with the surrounding tissue. Consequently, it expedites the rehabilitation and growth of compromised bone tissue.

As depicted in Figure 6, SEM images showed the formation of hydroxyapatite-like layers on the surfaces of scaffolds SCG, SCG-30%, SCG-40%, and SCG-50% during cultivation periods of 3, 7, and 14 days in a simulated body fluid, firmly adhering to the scaffold surfaces. Moreover, an explicit trend emerged with prolonged incubation time, where the hydroxyapatite-like layer particles exhibited gradual enlargement, accompanied by an outward expansion tendency. These *in vitro* mineralization experiments unequivocally underscore the remarkable *in vitro* mineralization capacity inherent to these scaffold materials. Furthermore, we conducted X-ray diffraction analysis on the mineralized scaffolds, and the results revealed characteristic peaks of hydroxyapatite, confirming the success of the mineralization process (Figure S6).

3.6. *In vitro* biocompatibility

Good biocompatibility is a crucial condition for implantable stents. At the same time, the addition of active factors is required to accelerate the bone regeneration cycle. EGCG was loaded through the swelling effect of the stent. We measured the drug release rate of EGCG. The results showed that the release rate of EGCG was slow over the first 14 days, thereby achieving a good sustained-release effect (Figure S7).

Figure 7 presents the experimental results of the scaffold *in vitro* cell culture. The outcomes, depicted in Figure 7A, reveal that during the initial phase, on the 1st day of cultivation, minimal attachment of MC3T3-E1 cells was observed on the scaffold surfaces, indicating relatively low cell adhesion. However, as the cultivation period extended, the cell population on the scaffold surfaces rapidly increased. By day 7, the scaffold surfaces were completely covered by cells, signifying an optimal cellular growth environment provided by the scaffold. Notably, the results of live/dead cell staining distinctly indicated an abundance of viable cells on the scaffold surfaces, underscoring the scaffold's compatibility with cells. This observation underscores the scaffold's ability to support cell viability, a crucial attribute in evaluating its biocompatibility for potential applications in tissue engineering and regenerative medicine.

For a more in-depth understanding of the cellular status on scaffold surfaces, scaffolds cultivated for 7 days were subjected to ethanol dehydration treatment and subsequently observed under SEM at various magnifications. Figure 7B represents the surface morphology of scaffolds SCG, SCG-30%, SCG-40%, SCG-50%, SCG-50%-L, and SCG-50%-H, respectively, with different compositions. Through electron microscopy images, a clear depiction of the morphology and structure of cells on the scaffold surfaces was discernible.

In comparison to the scaffold composed of pure water gel, the surfaces of scaffolds incorporating β-TCP exhibited a rougher and more porous microstructure. This microscopic structural characteristic facilitated better adhesion of cell pseudopodia onto the micropores on the scaffold surface. This feature provided increased surface area and opportunities, aiding in cell attachment and growth on the scaffold surface. Importantly, this observation adds supplementary support and explanation for the enhanced cell compatibility of the scaffold, as it offers additional surface features conducive to cell adhesion and growth.

According to the data presented in Figure 7C, absorbance measurements were conducted to assess cell

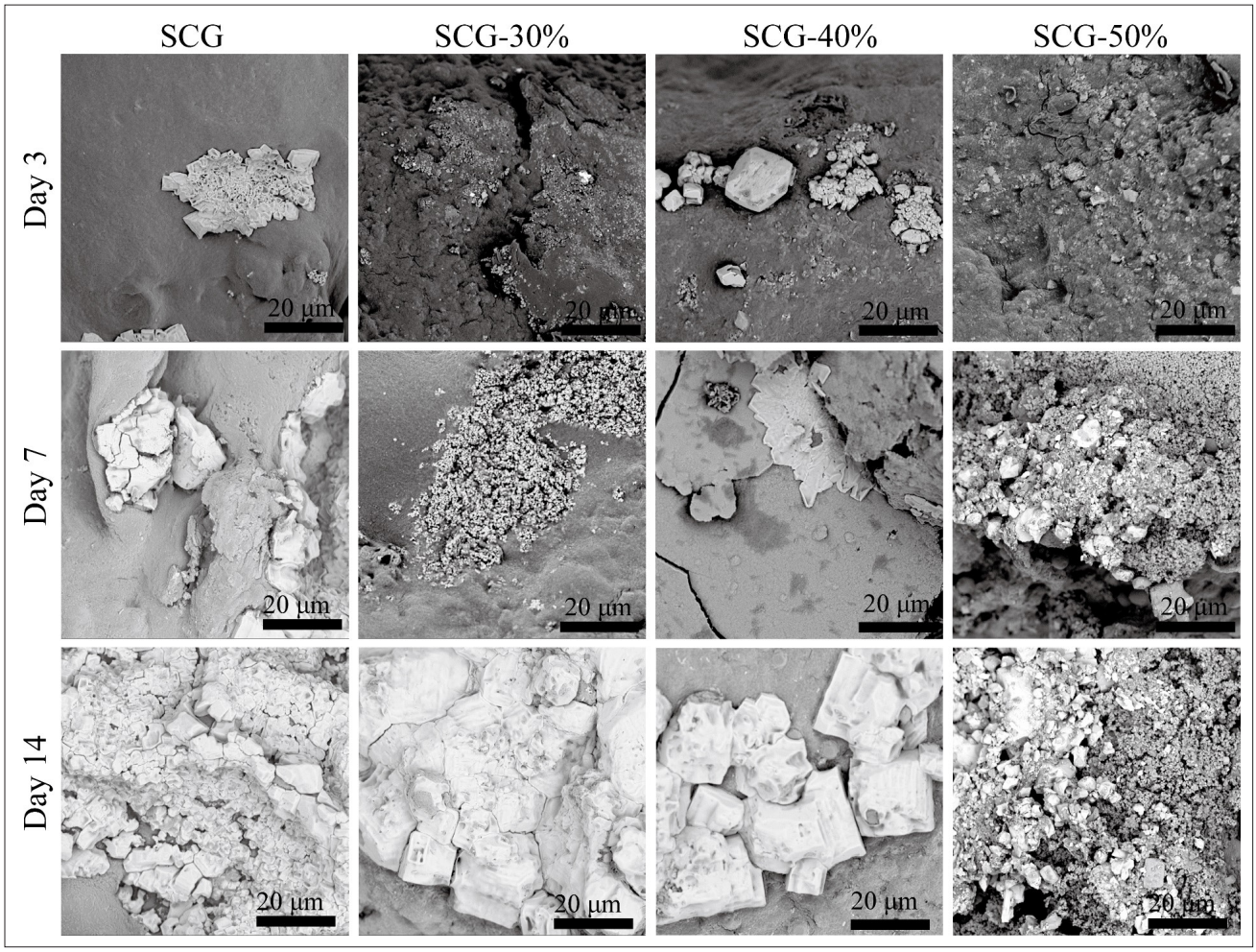


Figure 6. The formation of a hydroxyapatite-like layer on the scaffold surface after days 3, 7, and 14 of mineralization in the simulated body fluid. Scale bar: 20 μm; magnification: 40×.

proliferation on scaffolds with different compositions. Initially, on the 1st day, the absorbance values (optical density values) for each group were similar, indicating a relatively consistent impact of the scaffolds on cells at the initial stage. However, as the cultivation time extended to the 3rd day and 5th day, we observed that the absorbance values for the experimental groups were significantly higher than those of the control group. Scaffolds incorporating β-TCP exhibited notable differences, indicating a significant enhancement of cell proliferation due to the addition of β-TCP. Furthermore, the absorbance of scaffolds loaded with EGCG was markedly higher than that of other compositions, indicating that the addition of EGCG contributes to a more effective promotion of cell proliferation. The SCG-50%-L composition demonstrated particularly outstanding promotion effects, while the effects of the SCG-50%-H composition were relatively weaker, possibly due to the cytotoxicity associated with the higher concentration of EGCG. The calculated cell viability rates were further illustrated, showing that the cell viability rates for all scaffold compositions exceeded 100%. This outcome aligns with the absorbance trends, indicating that scaffolds from all compositions were nontoxic to cells. Moreover, scaffolds containing β-TCP components exhibited superior cell viability rates, with scaffolds loaded with a low concentration of EGCG exerting the most significant impact on cell viability.

The addition of β-TCP significantly promoted cell proliferation, and the incorporation of EGCG had a positive influence on cell proliferation. These findings provide robust scientific evidence for the biocompatibility and cell adhesion of the scaffolds.

As depicted in Figure 7D, we conducted a study on ALP activity, a characteristic enzyme within osteoblasts. On day 7 of cultivation, the ALP activities for scaffolds

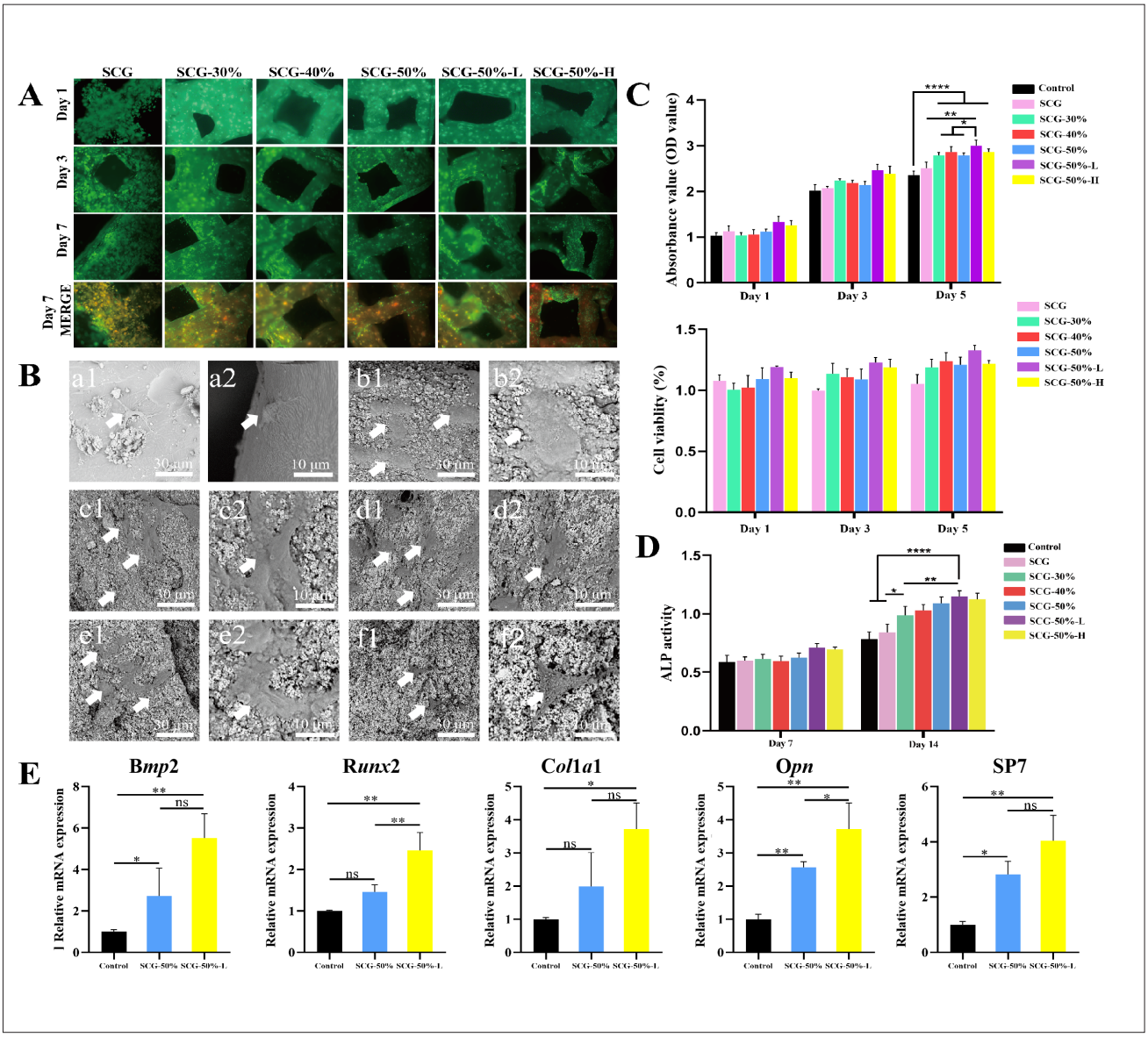


Figure 7. Cell compatibility and expression of osteogenic-related genes in scaffolds with different compositions. (A) Staining of SCG, SCG-30%, SCG-40%, SCG-50%, SCG-50%-L (low), and SCG-50%-H (high) scaffolds on the surface of scaffolds co-cultured with rat embryonic osteoblasts for 7 days. (B) Morphology of dead cells on the surface of SCG (a1 & a2), SCG-30% (b1 & b2), SCG-40% (c1 & c2), SCG-50% (d1 & d2), SCG-50%-L (e1 & e2), and SCG-50%-H (f1 & f2) scaffolds after co-culture for 7 days. Scale bars: 10 μm, 30 μm; magnifications: 40×. (C) Optical density (OD) values of cell proliferation and cell survival rate of SCG, SCG-30%, SCG-40%, SCG-50%, SCG-50%-L, and SCG-50%-H scaffolds at days 1, 3, and 5. (D) Alkaline phosphatase (ALP) activity of different components of scaffolds at days 7 and 14. (E) Relative expression of *BMP2*, *RUNX2*, *COL1A1*, *OPN*, and *SP7* in SCG-50% and SCG-50%-L scaffolds after co-culture with mesenchymal stem cells for 7 days. Statistical significance determined at $^{*}p < 0.05$, $^{**}p < 0.01$, $^{***}p < 0.001$, and $^{****}p < 0.0001$; ns refers to not significant; n=3.

from different compositions were relatively similar, indicating a comparable impact of the scaffolds on osteoblast activity at the initial stage. However, as the cultivation period extended to day 14, the difference in ALP activity between scaffolds loaded with β-TCP and the SCG pure water gel scaffold significantly increased. This result unequivocally indicates that the addition of β-TCP significantly influences and enhances the activity of ALP, providing clear support for the osteogenic function of bone cells. Moreover, compared to other compositions, the SCG-50%-L scaffold exhibited significantly higher ALP activity, suggesting that low concentrations of EGCG have a more potent promoting effect on ALP activity. This finding reveals the crucial role of EGCG in enhancing the osteogenic function of bone cells within the scaffold. Therefore, this research not only underscores the benefits

of β-TCP but also highlights the potential application prospects of low-concentration EGCG, bearing significant scientific implications for the advancement of bone tissue engineering and regenerative medicine.

The primary focus of this experiment was to examine the gene expression of SCG-50% and SCG-50%-L scaffolds, with the aim of exploring the corresponding gene expression in scaffolds containing β-TCP and EGCG. The expression of five genes was analyzed after day 7 of cultivation. These genes include recombinant human bone morphogenetic protein-2 (*BMP2*), runt-related transcription factor 2 (*RUNX2*), alpha-1 type I collagen (*COL1A1*), which promotes the formation of connective tissue, osteopontin (*OPN*), which is closely associated with bone formation and development, and zinc finger transcription factor (*SP7*), which promotes the differentiation of osteoblasts into mature osteoblasts and bone cells. The results, as depicted in Figure 7E, reveal significant expression of the detected genes, indicating that the composite scaffolds can better promote the expression of genes related to osteogenesis. Moreover, the relative gene expression levels of the scaffolds loaded with EGCG were higher than those without EGCG, demonstrating the osteogenic-promoting function of EGCG.

At the same time, to better characterize the *in vitro* osteogenic performance of the scaffold, we examined calcium deposition and cytoskeletal morphology, and performed alizarin staining and cytoskeletal staining. The results are shown in Figures S8 and S9.

3.7. The *in vivo* osteogenic effects of the scaffolds

All rats survived after scaffold implantation, and no rejection or inflammation was found in subsequent feedings. The weight changes of the rats are shown in Figure S10**.** At the same time, we conducted a routine blood assessment and found that all rats in all groups exhibited an increase in inflammatory indicators (Figures S11 & S12). The scaffold was removed at different time points, as shown in Figure S13**.** The 3D reconstructions of micro-computed tomography scans at different time points (6 weeks and 12 weeks) depicting the bone defect sites are illustrated in Figure 8A. It is evident from the images that at week 6, the blank control group exhibited minimal new bone formation, whereas the macroscopic osteogenic efficiency of the SCG-50%, SCG-50%-L, and SCG-50%-H groups surpassed that of the pure hydrogel and blank control groups. To further elucidate the observed outcomes, quantitative analysis was conducted. As shown in Figure 8B, at the 6th week, the BV/TV ratio for the blank control group was only 5.18%, whereas the SCG group presented a BV/TV value of 8.03%. At the same time, we found that in complex humoral environments, SCG scaffolds have undergone structural collapse and dispersion. SCG-50% demonstrated a BV/TV value of 13.03%, and the SCG-50%-L scaffold, incorporating EGCG, exhibited optimal osteogenic performance with a BV/TV value of 18.59%. The scaffold loaded with a high concentration of drug, SCG-50%-H, achieved a BV/TV value of 17.48%. By the 12th week, the BV/TV values for all scaffold components showed a significant increase. Notably, the SCG-50%-L component displayed the most favorable reparative effects, attaining a BV/TV value of 23.40%, surpassing both the SCG group (9.10%) and the SCG-50% group (15.73%). The BV/TV values at different time points suggest that the addition of β-TCP effectively promoted new bone formation, and EGCG demonstrates a pronounced enhancement in osteogenesis.

As depicted in Figure 8C, the BMD values of various scaffold components at different time intervals are illustrated. At week 6, the BMD for the blank control component was 73.89 mg HA/ccm, the SCG component exhibited a BMD value of 160.52 mg HA/ccm, and the SCG-50% component had a BMD value of 201.17 mg HA/ccm. Notably, the SCG-50%-L component, featuring a low drug concentration, achieved the highest bone density with a BMD value of 247.99 mg HA/ccm, while the high drug concentration SCG-50%-H component showed a relatively lower BMD value of 224.18 mg HA/ccm compared to the low drug concentration counterpart. By the 12th week, a noticeable increase in bone density was observed for all scaffold components. Remarkably, the SCG-50%-L component exhibited the highest bone density, with a BMD value soaring to 290.86 mg HA/ccm, and the other components also demonstrated substantial growth. The BMD values mirror the trends observed in BV/TV values, indicating that the addition of β-TCP significantly promotes new bone formation, and EGCG exhibits a marked enhancement in osteogenesis.

In the 12th week, tissue histological analysis was conducted on decalcified tissues to further assess the bone formation process (Figure 9A). According to the H&E staining results at week 12, a significant amount of fibrous tissue was observed in the bone defect area, indicating the presence of a self-repair mechanism. Simultaneously, scaffolds loaded with β-TCP exhibited a stronger new bone-inducing effect. The newly formed bone tissue exhibited a bridging interface with the original bone, and drug-loaded scaffolds demonstrated enhanced bone-inducing and bone-integrating capabilities.

Masson staining stains dense collagen fibers, muscle fibers, and red blood cells red, while loose collagen fibers and cellulose are stained blue. As shown in Figure 9B, bone tissue appeared blue, indicating that the rat cranial

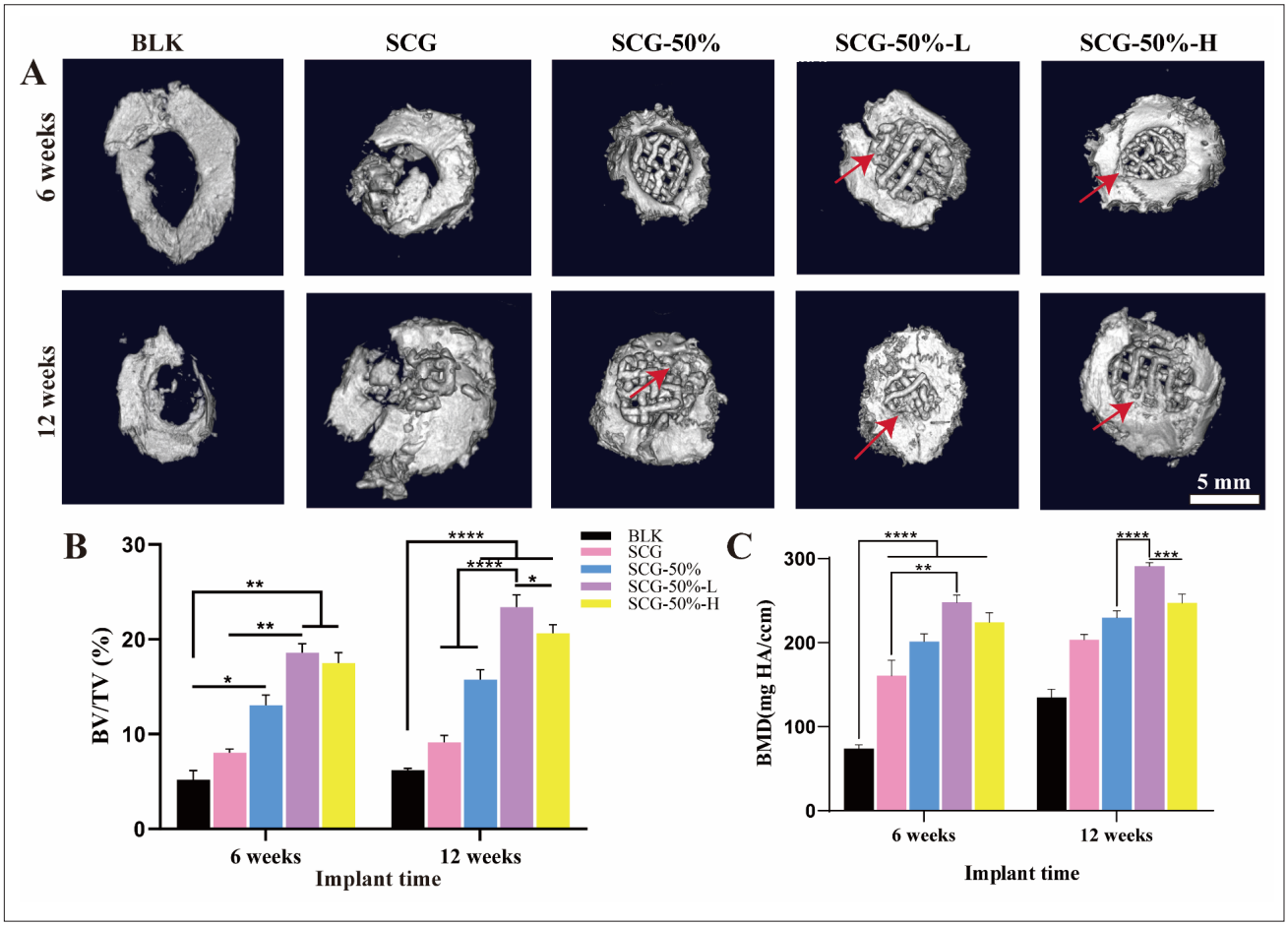


Figure 8. The *in vivo* development of large bone defects and the bone-healing effect. (A) Micro-computed tomography images of cranial defects in rats (red represents new bone tissue). Scale bar: 5 mm ; magnification: 2×. (B–C) Quantitative analysis of micro-computed tomography data: BV/TV (%) and BMD (mg HA/ccm). Statistical significance determined at $^{*}p < 0.05$, $^{**}p < 0.01$, $^{***}p < 0.001$, and $^{****}p < 0.0001$; $n=3$. Abbreviations: BLK, blank control; BMD, bone mineral density; BV/TV, bone volume/total volume; ns, not significant.

bone defect was primarily composed of loose collagen fibers. After 12 weeks of implantation, the control group exhibited minimal new bone formation, with the defect site predominantly filled with abundant muscle or fibrous tissue. The SCG and SCG-50% groups without drug loading showed a small amount of new bone at the interface with host bone tissue; however, the scaffold degraded and accumulated severely at the defect site, resulting in a lack of tissue ingrowth. In the drug-loaded groups, SCG-50%-L and SCG-50%-H, a substantial amount of new bone tissue was observed. These results collectively suggest that drug-loaded groups significantly promote bone regeneration. This finding is consistent with the H&E staining results.

Further analysis of this study indicates that the dual-crosslinked network scaffold significantly enhanced the mechanical properties and *in vivo* stability of the material. The incorporation of β-TCP not only provides additional mechanical support but also releases calcium ions and phosphate ions, promoting osteoblast adhesion and mineralization. EGCG may regulate anti-inflammatory signaling pathways such as nuclear factor kappa B, thereby creating a favorable immune microenvironment for bone regeneration. Compared with previous studies, our scaffold design achieved an optimized dual-network structure, whereas most earlier studies employed single-crosslinked systems and lacked biomimetic designs for the hierarchical porosity of cancellous bone, making it difficult to achieve effective bone regeneration through hydrogel networks. Although additional mechanistic experiments were not conducted in this study, existing literature sufficiently supports our explanations regarding the functions of dual-network hydrogels, β-TCP, and EGCG. Future work will further combine molecular-level experiments to provide a deeper understanding of these mechanisms and a more comprehensive understanding of the bone regeneration process.

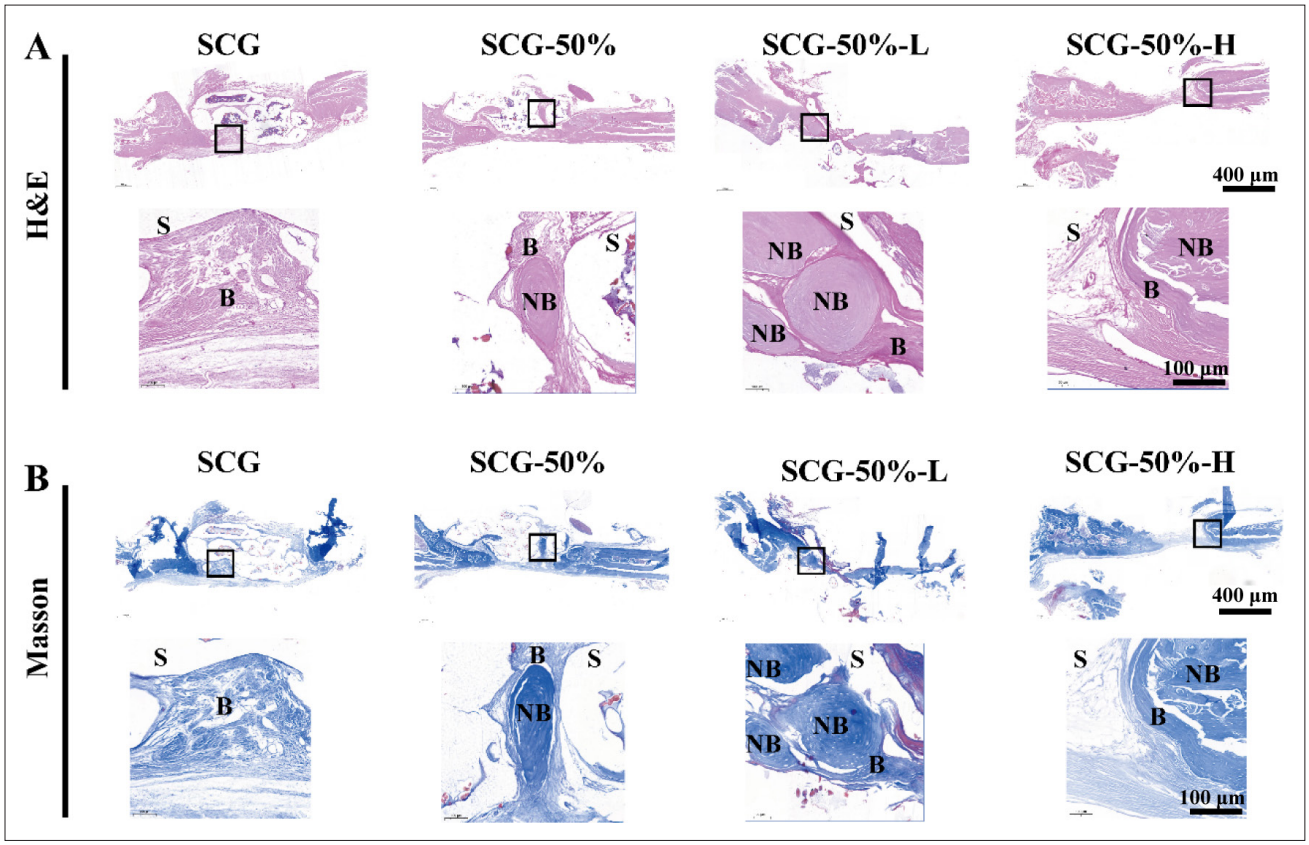


Figure 9. Histological analysis of calvaria 12 weeks after implantation. (A) Hematoxylin and eosin (H&E) staining results after 12 weeks of scaffold implantation, where B indicates host bone, NB indicates new bone, and S indicates scaffold. Scale bar: 400 μm; magnification: 4×. (B) Masson's trichrome (Masson) staining. Scale bar: 100 μm; magnification: 16×.

4. Conclusion

This study integrated the biomimetic tissue structure of hydrogels with the excellent bone-inducing capability and mechanical reinforcement ability of β-TCP. By combining these factors, a bioink was prepared. Through a pre-crosslinking strategy and regulation of printing parameters, personalized hydrogel-based composite scaffolds were 3D printed using extrusion-based bioprinting technology. By examining scaffold materials and relevant properties, we found that the scaffold exhibited excellent biomimetic structure, mechanical performance, drug-loading capacity, outstanding biocompatibility, and the ability to promote the expression of osteogenesis-related genes. *In vivo* experiments further demonstrated the scaffold's potent bone-inducing and bone-integrating capabilities. In summary, the artificially engineered bone scaffold developed in this study holds promise for clinical applications in addressing significant challenges related to bone loss.

Acknowledgments

None.

Funding

This study was supported by the National Science Foundation of China (NSFC, #82402822, 82202674), the Central Government of Sichuan through the Special Project of Local Science and Technology Development (#2024ZYD0155), the Health Commission of Sichuan Province Medical Science and Technology Program (#24QNMP036), and the Natural Science Foundation of Xiamen, China (3502Z20227124).

Conflict of interest

Xulin Hu serves as the Editorial Board Member of the journal, but did not in any way involve in the editorial and peer-review process conducted for this paper, directly or indirectly. Other authors declare they have no competing interests.

Author contributions

Conceptualization: Weizong Weng, Kainan Li
Formal analysis: Xulin Hu, Yixuan Lan, Wang Gong, Jiayu Liu
Investigation: Jian He, Weiming Zhao
Methodology: Zhen Zhang, Lijin Ning
Writing–original draft: Xulin Hu
Writing–review & editing: Shuhao Yang, Haoming Wu

Ethics approval and consent to participate

All animal experiments were conducted with the approval of the Ethics Committee of West China Hospital of Stomatology, Sichuan University (Approval number: WCHSIRB-D-2021-240).

Consent for publication

Not applicable

Availability of data

Data will be made available upon request to the corresponding author.

Reference

1. Wang Y, Zhang H, Hu Y, Jing Y, Geng Z, Su J. Bone repair biomaterials: a perspective from immunomodulation. *Adv Funct Mater.* 2022;32(51):2208639. doi: 10.1002/adfm.202208639
2. Batra P, Das S, Jain S. Correlation of radiovisuographic analysis of interdental and interradicular bone loss in furcation involvement of mandibular first molars: a retrospective study. *Indian J Dent Res*. 2018;29(3):329-332. doi: 10.4103/ijdr.IJDR_52_16. PMID: 29900917
3. Chang HY, Park SY, Kim JA, Kim YK, Lee HJ. Early radiographic diagnosis of peri-implantitis enhances the outcome of peri-implantitis treatment: a 5-year retrospective study after non-surgical treatment. *J Periodontal Implant Sci*. 2015;45(3):82-93. doi: 10.5051/jpis.2015.45.3.82
4. Kironde E, Sekimpi P, Kajja I, Mubiri P. Prevalence and patterns of traumatic bone loss following open long bone fractures at Mulago Hospital. *OTA Int*. 2019.2(1): e015-e015. doi: 10.1097/OI9.0000000000000015
5. Puisys A, Auzbikaviciute V, Minkauskaite A, et al. Early crestal bone loss: is it really loss? *Clin Case Rep*. 2019;7(10):1913-1915. doi: 10.1002/ccr3.2376
6. Zhou H, Liang B, Jiang H, Deng Z, Yu K. Magnesium-based biomaterials as emerging agents for bone repair and regeneration: from mechanism to application. *J Magnes Alloy*. 2021;9(3):779-804. doi: 10.1016/j.jma.2021.03.004
7. Du M, Chen J, Liu K, Xing H, Song C. Recent advances in biomedical engineering of nano-hydroxyapatite including dentistry, cancer treatment and bone repair. *Compos Part B Eng*. 2021;215:108790. doi: 10.1016/j.compositesb.2021.108790
8. Feng P, Zhao R Y, Tang W M, et al. Structural and functional adaptive artificial bone: materials, fabrications, and properties. *Adv Funct Mater*. 2023;33(23):2214726. doi: 10.1002/adfm.202214726
9. Nissen FI, Andreasen C, Borgen TT, Bjørnerem Å, Hansen AK. Cortical bone structure of the proximal femur and incident fractures. *Bone*. 2022;155:116284. doi: 10.1016/j.bone.2021.116284
10. Rodriguez-Palomo A, Ostergaard M, Birkedal H. Bone hierarchical structure: heterogeneity and uniformity. *Adv Funct Mater*. 2023;34(35):2307026. doi: 10.1002/adfm.202307026
11. Zhou C, Zhang XL, Ai J, et al. Chiral hierarchical structure of bone minerals. *Nano Res*. 2022;15(2):1295-1302. doi: 10.1007/s12274-021-3653-z
12. Yusof F, Sha'ban M, Azhim A. Decellularization strategies to engineer fibrocartilage bioscaffolds: a review. *J Biomater Tissue Eng*. 2021;11(8):1435-1451. doi: 10.1166/jbt.2021.2740
13. He J, Fang J, Wei P, *et al.* Cancellous bone-like porous Fe@Zn scaffolds with core-shell-structured skeletons for biodegradable bone implants. *Acta Biomater*. 2021;121:665-681. doi: 10.1016/j.actbio.2020.11.032
14. Yoon SJ, Kim SH, Choi JW, Chun HJ, Yang DH. Guided cortical and cancellous bone formation using a minimally invasive technique of BMSC- and BMP-2-laden visible light-cured carboxymethyl chitosan hydrogels. *Int J Biol Macromol*. 2023;227:641-653. doi: 10.1016/j.ijbiomac.2022.12.13
15. Zhao ZY, Li G, Ruan HT, et al. Capturing magnesium ions via microfluidic hydrogel microspheres for promoting cancellous bone regeneration. *ACS Nano*. 2021;15(8):13041-130540. doi: 10.1021/acsnano.1c02147
16. Hu X, Lin Z, He J, et al. Recent progress in 3D printing degradable polylactic acid-based bone repair scaffold for the application of cancellous bone defect. *MedComm Biomater Appl*. 2022;1(1):e14. doi: 10.1002/mba2.14
17. Riggs C, Goodship A. Bone structure and function. *Fractures in the Horse*. 2022:11-27. doi: 10.1002/9781119431749.ch2

18. Li C, Du YW, Zhang TT, et al. "Genetic scissors" CRISPR/Cas9 genome editing cutting-edge biocarrier technology for bone and cartilage repair. *Bioact Mater*. 2023;22:254-273. doi: 10.1016/j.bioactmat.2022.09.026

19. Salhotra A, Shah HN, Levi B, Longaker MT. Mechanisms of bone development and repair. *Nat Rev Mol Cell Biol*. 2020;21(11):696-711. doi: 10.1038/s41580-020-00279-w

20. Seidi A, Ramalingam M. Engineering of gradient biomaterials as biomimetic systems for tissue engineering. *J Biomater Tissue Eng*. 2011;1(2):139-148. doi: 10.1166/jbt.2011.1020

21. Li J, Chen Q, Zhang Q, et al. Improving mechanical properties and biocompatibilities by highly oriented long chain branching poly(lactic acid) with bionic surface structures. *ACS Appl Mater Interfaces*. 2020;12(12):14365-14375. doi: 10.1021/acsami.9b20264

22. Qi T, Zhang X, Gu X, Cui S. Experimental study on repairing peripheral nerve defects with novel bionic tissue engineering. *Adv Healthc Mater*. 2023;12(17):e2203199. doi: 10.1002/adhm.202203199

23. Wang Y, Jiang X, Li X, et al. Bionic ordered structured hydrogels: structure types, design strategies, optimization mechanism of mechanical properties and applications. *Mater Horiz*. 2023;10(10):4033-4058. doi: 10.1039/d3mh00326d

24. Wang L, Li AF, Zhang D, et al. Injectable double-network hydrogel for corneal repair. *Chem Eng J*. 2023;455:140698. doi: 10.1016/j.cej.2022.140698.

25. Zhu WX, Zhou Z, Huang YT, et al. A versatile 3D-printable hydrogel for antichondrosarcoma, antibacterial, and tissue repair. *J Mater Sci Technol*. 2023;136:200-211. doi: 10.1016/j.jmst.2022.07.010

26. Ahmed EM. Hydrogel: preparation, characterization, and applications: a review. *J Adv Res*. 2015;6(2):105-121. doi: 10.1016/j.jare.2013.07.006

27. Lee KY, Mooney DJ. Alginate: properties and biomedical applications. *Prog Polym Sci*. 2012;37(1):106-126. doi: 10.1016/j.progpolymsci.2011.06.003

28. Liang YP, He JH, Guo BL. Functional hydrogels as wound dressing to enhance wound healing. *ACS Nano*. 2021;15(8):12687-12722. doi: 10.1021/acsnano.1c04206

29. Correa CS, Grosskopf AK, Hernandez HL, Chan D, Appel EA. Translational applications of hydrogels. *Chem Rev*. 2021;121(18):11385-11457. doi: 10.1021/acs.chemrev.0c01177

30. Nie R, Sun Y, Lv H, et al. 3D printing of MXene composite hydrogel scaffolds for photothermal antibacterial activity and bone regeneration in infected bone defect models. *Nanoscale*. 2022;14(22):8112-8129. doi: 10.1039/D2NR02176E

31. Gong JP, Katsuyama Y, Kurokawa T, Osada Y. Double-network hydrogels with extremely high mechanical strength. *Adv Mater*. 2003;15(14):1155-1158. doi: 10.1002/adma.200304907

32. Aldana AA, Houben S, Moroni L, Baker MB, Pitet LM. Trends in double networks as bioprintable and injectable hydrogel scaffolds for tissue regeneration. *ACS Biomater Sci Eng*. 2021;7(9):4077-4101. doi: 10.1021/acsbiomaterials.0c01749

33. Xu X, Jerca VV, Hoogenboom R. Bioinspired double network hydrogels: from covalent double network hydrogels via hybrid double network hydrogels to physical double network hydrogels. *Mater Horiz*. 2021;8(4):1173-1188. doi: 10.1039/d0mh01514h

34. Yang J, Li K, Tang C, et al. Recent progress in double network elastomers: one plus one is greater than two. *Adv Funct Mater*. 2022;32(19):2110244. doi: 10.1002/adfm.202110244

35. Gao N, Zhang Y, Yang Z, et al. Ba2+/Ca2+ co-crosslinked alginate hydrogel filtration membrane with high strength, high flux and stability for dye/salt separation. *Chin Chem Lett*. 2023;35(5):108820. doi: 10.1016/j.cclet.2023.108820

36. Zhang A, Wang F, Chen L, et al. 3D printing hydrogels for actuators: a review. *Chin Chem Lett*. 2021;32(10):2923-2932. doi: 10.1016/j.cclet.2021.03.073

37. Wang Y, Jiao Y, Zeng Z, Chang J, Yang C, Dong Z. Three-dimensional printed Zn2SiO4/sodium alginate composite scaffold with multiple biological functions for tendon-to-bone repair. *MedComm Biomater Appl*. 2023;2(4):e61. doi: 10.1002/mba2.61

38. Kankariya Y, Chatterjee B. Biomedical application of chitosan and chitosan derivatives: a comprehensive review. *Curr Pharm Des*. 2023;29(17):1311-1325. doi: 10.2174/1381612829666230524153002

39. Manna S, Seth A, Gupta P, et al. Chitosan derivatives as carriers for drug delivery and biomedical applications. ACS *Biomater Sci Eng*. 2023;9(5):2181-2202. doi: 10.1007/978-981-15-0263-7

40. Sacco P, Pedroso-Santana S, Kumar Y, Joly N, Martin P, Bocchetta P. Ionotropic gelation of chitosan flat structures and potential applications. *Molecules*. 2021;26(3):660. doi: 10.3390/molecules26030660

41. Yan D, Li Y, Liu Y, Li N, Zhang X, Yan C. Antimicrobial properties of chitosan and chitosan derivatives in the treatment of enteric infections. *Molecules*. 2021;26(23):7136. doi: 10.3390/molecules26237136

42. Xulin H, Hu L, Liang Q, et al. 369Fabrication of 3D gel-printed β-tricalcium phosphate/titanium dioxide porous

scaffolds for cancellous bone tissue engineering. *Int J Bioprint*. 2023;9(2):673. Published 2023 Jan 19. doi: 10.18063/ijb.v9i2.673

43. Peres I, Rocha S, do Carmo Pereira M, Coelho M, Rangel M, Ivanova G. NMR structural analysis of epigallocatechin gallate loaded polysaccharide nanoparticles. *Carbohydr Polym*. 2010;82(3):861-866. doi: 10.1016/j.carbpol.2010.06.007

44. Zhang S, Mao B, Cui S, et al. Absorption, metabolism, bioactivity, and biotransformation of epigallocatechin gallate. *Crit Rev Food Sci Nutr.* 2024;64(19):6546-6566. doi: 10.1080/10408398.2023.2170972

45. Guo Z, Liu W, Liu T, et al. Engineered exosome hybrid copper nanoscale antibiotics facilitate simultaneous self-assembly imaging and elimination of intracellular multidrug-resistant superbugs. *Chin Chem Lett.* 2023;35(7):109060. doi: 10.1016/j.cclet.2023.109060

46. Baranwal A, Aggarwal P, Rai A, Kumar N. Pharmacological actions and underlying mechanisms of catechin: a review. *Mini Rev Med Chem.* 2022;22(5):821-833. doi: 10.2174/1389557521666210902162120

47. Cabezas Perez RJ, Ávila Rodríguez MF, Rosero Salazar DH. Exogenous antioxidants in remyelination and skeletal muscle recovery. *Biomedicines.* 2022;10(10):2557. doi: 10.3390/biomedicines10102557

48. Spicer PP, Kretlow JD, Young S, Jansen JA, Kasper FK, Mikos AG. Evaluation of bone regeneration using the rat critical size calvarial defect. *Nat Protoc.* 2012;7(10):1918-1929. doi: 10.1038/nprot.2012.113

ACCSCIENCE PUBLISHING

International Journal of Bioprinting

RESEARCH ARTICLE

Integrated 3D printing of cementless CoCrMo femoral condyles optimizes trabecular surfaces and material performance

Jiawei Wu[1†], Zhiwei Zhou[1†], Tianbai Yu[1,2], Wei Wang[1], and Brian Y. Chang[3,4*]

[1]Suzhou Microport Orthorecon Co., Ltd., Suzhou, Jiangsu, China

[2]School of Health Science and Engineering, University of Shanghai for Science & Technology, Shanghai, China

[3]Institute for Medical Engineering and Science, Massachusetts Institute of Technology, Cambridge, MA, United States of America

[4]Miracle Point Global LLC, Irvine, CA, United States of America

(This article belongs to the *Special Issue*: *3D-Printed Biomedical Devices*)

Abstract

Conventional cementless femoral condyles in artificial knee systems are commonly manufactured by casting followed by a surface treatment using plasma spraying or metallic sintering. However, both techniques suffer from weak coating-substrate interfaces that contribute to early loosening and higher revision rates. To overcome this limitation, we employed integrated 3D printing (I3P), an additive manufacturing strategy based on laser powder bed fusion, to fabricate monolithic cobalt-chromium-molybdenum femoral condyles with trabecular-inspired porous architectures. Compared with cast-sintered counterparts, I3P substrates exhibited refined microstructures and superior mechanical performance after hot isostatic pressing, reaching a yield strength of 637.33 MPa, ultimate tensile strength of 1140.00 MPa, and elongation of 27.33%. The I3P femoral condyles also showed enhanced fatigue resistance, withstanding 10 million cycles under a 3000 N load, and demonstrated improved wear behavior against ultrahigh-molecular-weight polyethylene liners. Furthermore, the trabecular-inspired lattice achieved stronger integration with the substrate than sintered coatings, with tensile and shear strengths of 56.09 and 49.97 MPa, respectively. Together, these findings establish I3P as a robust manufacturing strategy that integrates substrate and surface in a single step, enabling the production of durable, osteointegrative femoral condyles with significant potential to improve implant longevity and clinical outcomes in knee joint reconstruction.

Keywords: Additive manufacturing; Cementless femoral condyles; Cobalt-chromium-molybdenum alloys; Fatigue and wear resistance; Integrated 3D printing; Osteointegration; Total knee arthroplasty; Trabecular surface architecture

†These authors contributed equally to this work.

***Corresponding author:**
Brian Y. Chang
(bychang@mit.edu)

Citation: Wu J, Zhou Z, Yu T, Wang W, Chang BY. Integrated 3D printing of cementless CoCrMo femoral condyles optimizes trabecular surfaces and material performance. *Int J Bioprint*. 2026;12(1):371-384. doi: 10.36922/IJB025380389

Received: September 19, 2025
Revised: November 1, 2025
Accepted: November 3, 2025
Published online: November 11, 2025

Copyright: © 2025 Author(s). This is an Open Access article distributed under the terms of the Creative Commons Attribution License, permitting distribution, and reproduction in any medium, provided the original work is properly cited.

Publisher's Note: AccScience Publishing remains neutral with regard to jurisdictional claims in published maps and institutional affiliations.

1. Introduction

Total knee arthroplasty (TKA) is one of the most effective surgical treatments for end-stage knee disorders, such as osteoarthritis, rheumatoid arthritis, and post-traumatic arthritis,

aiming to relieve pain, correct deformities, and restore joint function.[1–3] The procedure involves the implantation of artificial joint components, primarily a femoral condyle implant that replaces the load-bearing surface of the distal femur. As TKAs are increasingly performed in younger and active patients with higher expectations for postoperative mobility, long-term prosthesis durability and stability have become crucial.[4] The clinical success of cementless femoral condyle implants hinges on osseointegration, where host bone forms a strong biomechanical interface with the implant to ensure durable fixation and mechanical stability.

To facilitate this, standardized femoral condyle implants are traditionally manufactured in a two-step process. First, cobalt-chromium-molybdenum (CoCrMo) alloy is cast to form the bulk geometry of the femoral condyle. The resulting surface is smooth and biologically inert, limiting osseointegration. Therefore, a secondary surface treatment is applied to create a trabecula-inspired porous structure that is conducive to osseointegration. The trabecular structure promotes bone in-growth that forms the strong biomechanical interface that ensures durable fixation.[5,6] Modern surface modification treatments can be done by plasma-spraying coatings or, more commonly, sintering coatings.[7,8]

Plasma-spraying is a widely used surface modification technique for cementless implants, in which metallic or bioactive ceramic particles, such as hydroxyapatite (HA), are propelled onto the implant surface to create the porous, textured coating. However, plasma-sprayed coatings rely primarily on mechanical interlocking rather than metallurgical bonding, which results in relatively low interfacial strength and increases the risk of delamination under cyclic loading. In addition, HA coatings, while bioactive, are susceptible to long-term degradation, which can further compromise mechanical stability over time.[9–11] Examples of current commercial designs include cementless femoral condyles with a cast CoCrMo substrate and dual plasma-sprayed coatings of HA and pure titanium (Chunli Medical, China), as well as designs featuring a single-layer plasma-sprayed titanium coating (JUST Medical, China).

Sintering is a more common surface modification technique used to enhance osseointegration in cementless implants. Metallic beads or particles are bonded to the implant surface at high temperatures, promoting atomic diffusion between the coating and the substrate. This metallurgical bonding results in stronger and more stable interfaces compared to plasma-sprayed coatings. However, the high-temperature sintering process can lead to grain coarsening in the underlying metallic substrate, potentially reducing its mechanical properties. Additionally, sintering requires longer production cycles, limiting manufacturing efficiency.[12,13] Commercial examples include femoral condyles with cast CoCrMo substrates and dual-layer surfaces composed of sintered CoCrMo beads combined with a HA solution-deposited coating (Triathlon Tritanium, Stryker, USA). Another design features a dual plasma-sprayed coating of pure titanium and calcium phosphate (e.motion, B. Braun, Germany).

The compromises of traditional manufacturing TKA implants stem from requiring two steps to manufacture a mechanically stable bulk geometry via casting with a biocompatible surface that promotes osseointegration via a subsequent surface treatment. In contrast, additive manufacturing techniques, such as 3D printing may pose a solution without these compromises. CoCrMo alloys produced by 3D printing are widely used in dental prosthetics, but their application in cementless knee implants remains limited. Laser powder bed fusion (LPBF) is among the most established technologies in metal additive manufacturing.[14,15] The process begins with a computer-aided design CAD model which is then segmented into a sequence of thin two-dimensional layers. On the build platform, a recoater blade or roller spreads a fine layer of metal powder (typically 20–60 μm). A high-power fiber laser selectively scans the powder bed according to the sliced geometry, fully melting the particles to form dense metallurgical bonds. After each layer is consolidated, the platform lowers by one layer thickness, new powder is deposited, and the next layer is fused to the previous one. This cycle is repeated until the entire part is completed.[16–18] Upon completion, the component is removed from the powder bed, excess powder and support structures are eliminated, and postprocessing such as heat treatment, wire cutting, or finishing may be performed. A unique advantage of LPBF is the ability to precisely control porosity, pore size, strut thickness, therefore allowing it to produce dense substrates as well as precise trabecula-inspired lattices.[19–21]

Consequently, LPBF can be adapted to replace the traditional two-step casting and surface treatment by manufacturing a stable bulk geometry and a porous trabecula-inspired surface layer in a single step known as integrated 3D printing (I3P). Unlike traditional LPBF, I3P simultaneously prints the CoCrMo substrate and trabecular lattice with the same process. I3P reduces manufacturing steps and achieves stronger bonding between the porous lattice and the metallic base when compared with traditional sintering or plasma spraying.[22] To date, I3P has been primarily applied in complex anatomical reconstructions and revision TKA procedures where patient-specific customization is essential.[23] However, with the maturation of additive manufacturing, standardized I3P manufactured cementless femoral

condyle implants are expected to achieve broader clinical adoption in primary TKA procedures.[24–26]

In this study, we employed I3P techniques to fabricate the design of a standardized commercially available femoral condyle implant (EVOLUTION, MicroPort Orthopedics, USA). Comparative analyses were performed against the conventionally manufactured implant that uses a sintered surface treatment. The evaluation focused on raw material characteristics, as well as the fatigue and wear performance of the implants. In addition, the tensile and shear tests were conducted specifically to quantify the interfacial bonding strength between the trabecular-inspired lattice layer and the CoCrMo substrate. These assessments collectively confirmed the advantages and feasibility of standardized I3P-fabricated cementless femoral condyles, offering a novel solution for future primary TKAs.

2. Materials and methods

To enable direct comparison with conventional commercially available implants, femoral condyles of identical geometric design were fabricated using I3P. Experimental evaluation was divided into two components: (i) the substrate material, representing the traditionally cast bulk CoCrMo alloy; and (ii) the surface material, representing the porous layer typically applied via plasma spraying or sintering in conventional manufacturing. This approach allowed for independent assessment of the intrinsic material properties and interfacial performance associated with each manufacturing strategy.

2.1. Materials

ASTM F75 compliant CoCr02 cobalt-chromium-molybdenum alloy powder (AVIC Maite Additive Manufacturing Technology, Beijing, China) was used as the raw I3P material. The powder was produced using gas atomization via nonvacuum induction melting (Table 1).

Table 1. Chemical composition and physical properties of CoCr02 cobalt-chromium-molybdenum alloy powder used as the raw material for manufacturing by integrated 3D printing

Properties		Results
Chemical composition	C	0.161%
	N	0.12%
	Si	0.63%
	Mn	0.44%
	Ni	0.24%
	Fe	0.49%
	Cr	27.10%
	Mo	5.60%
	B	0.004%
	Co	Balance
Physical properties	Particle size	D10: 17.01 μm D50: 28.94 μm D90: 48.51 μm
	Apparent density	4.7 g/cm³
	Tap density	5.4 g/cm³
	Hall flowmeter	13.6 s/50g

Notes: The powder was produced by gas atomization through nonvacuum induction melting (AVIC Maite Additive Manufacturing Technology, Beijing, China). These baseline characteristics establish material compliance and quality for subsequent femoral condyle fabrication.

2.2. Sample preparation

2.2.1. Integrated 3D printing process

The specimens were produced using a BLT S310 LPBF system (Xi'an Bright Laser Technologies, China) with 30 μm layer thickness, 160 W laser power, a scanning speed of 800 mm/s, and a laser spot size of 100 μm. During fabrication, the build chamber was purged with argon to maintain an oxygen concentration below 0.1%. The external geometry of the I3P-fabricated products was identical to that of a commercially available cast and sintered femoral condyle (*EVOLUTION,* MicroPort Orthopedics, USA). The trabecular-inspired porous structures were designed using Autodesk Within (Autodesk Inc., USA), with target pore size pf 0.75 mm, trabecular topology, and a 0.2 mm uniform strut thickness. The model was exported in STL format and subsequently sliced using BLT BP software (BLT, China), where parameters such as layer thickness, laser power, and scanning speed were defined and controlled. The total thickness of trabecular-inspired porous structures was 700–1000 μm, which is similar to that of the traditionally manufactured counterparts.

After I3P, the samples were separated from the build plate by wire electrical discharge machining. Postprocessing included hot isostatic pressing (HIP), carried out at 1167°C and 135 MPa for 4 h in an argon atmosphere, followed by vacuum quenching (WuXi Falcon Advanced Materials Technology, China). This process mirrors the process-processing performed on commercially available traditionally manufactured implants. The HIP-treated products were then finish-machined for testing. The parameters adopted in this study represent a relatively optimized scheme based on comprehensive considerations. Specimen for tensile and trabecular interfacial bonding tests were prepared under the same design and processing conditions as the implant. For comparative purposes, additional tensile specimens were fabricated using the identical I3P parameters but without HIP treatment.

2.2.2. Traditional casting-sintering

The cast and sintered cementless femoral condyles (EVOLUTION, MicroPort Orthopedics, USA) were directly obtained from commercial sources. According to the manufacturer, the implant is manufactured using a CoCrMo bead-sintering surface treatment. Following sintering, the components underwent the same HIP treatment as the I3P specimens. Specimens for tensile and trabecular interfacial bonding tests were prepared under identical design and processing parameters as the commercial implants.

2.3. Substrate material testing

2.3.1. Tensile testing

Tensile testing was conducted in accordance with ASTM E8/E8M using a SUNS UTM 5205X universal testing machine. The specimens had a total length of 92 mm, with a gauge diameter of 6 mm and a gauge length of 36 mm, and were prepared in the form of cylindrical round bars. For each group, five specimens were tested from the cast substrate, the I3P substrate before HIP, and the I3P substrate after HIP. The tests were performed under displacement control at a crosshead separation rate of 2.54 mm/min, and continued until specimen failure. The following mechanical properties were recorded: 0.2% offset yield strength (Rp0.2), ultimate tensile strength, and elongation at fracture. From the recorded data, means and sample standard deviations were computed. Statistical significance was evaluated using two-sample, two-tailed Student's *t*-tests.

2.3.2. Microstructure evaluation

Microstructural observations were performed in accordance with ISO 643 using a NIKON LV150N upright metallographic microscope. The specimens were sectioned from the tensile bars. Electrical discharge machining was employed to cut sections both parallel and perpendicular to the build direction, which were then prepared for microstructural examination. The specimens were mounted using hot compression mounting, followed by sequential grinding with SiC abrasive papers ranging from 180# to 2000# grit, progressing from coarse to fine. Polishing was then carried out on a metallographic polishing machine until the surfaces were free of visible scratches, after which the samples were rinsed and air-dried. To clearly reveal the grain boundaries, carbide phases, and matrix microstructure of the CoCrMo alloy, the polished surfaces were etched with a mixed acid solution consisting of 20 mL of 37% hydrochloric acid and 1 mL of 30% hydrogen peroxide. In addition, a scanning electron microscope (Prisma E with Xflash Detector 630M, Thermo Fisher Scientific, USA) was employed for further magnified analyses of the black spots observed in the microstructure

2.3.3. Wear testing

Femoral condyle accelerated wear testing was conducted in accordance with ISO 14243-3 using a Jointwear-K4301 knee wear simulator (Shanghai Aose Inspection Technology Co., Ltd, China). For each group (I3P and CS), three femoral condyles were tested. During testing, the femoral condyles were articulated with compatible commercially available tibial tray and tibial insert (MicroPort Orthopedics, USA). Prior to testing, all specimens were cleaned and dried according to the standard procedure. Calf serum was used as the lubricant during the wear simulation. Specimens were removed, weighed using an electronic balance, and the lubricant was replaced every 500,000 cycles before resuming the test. At each 500,000-cycle interval, for each group (I3P and CS), the mean and sample standard deviation of the measurements were calculated. The wear simulation was continued until either 5 million cycles were completed or surface failure occurred, whichever came first.

2.3.4. Fatigue testing

Fatigue testing was conducted in accordance with ASTM F3210 and carried out using an Instron fatigue testing machine (Instron Corporation, USA). Prior to testing, following ASTM F3161, finite element analysis (FEA) located the maximum principal-stress point within the condyle bisection-plane region. The embedding position was set 4.5 mm below this point, as shown in Figure 1. Embedded femoral condyle assemblies were then mounted on the testing machine for fatigue evaluation. The loading head of the tester was positioned on the highest point of the posterior femoral condyle. A sinusoidal cyclic load starting from 2300 N was applied with a load ratio of R = 0.1 and a frequency of 15 Hz. A step-loading method was employed to test a series of femoral components. The test was terminated when either 10 million cycles were reached or specimen failure occurred. At each loading stage, three specimens per group (CS and I3P) were tested. For each group, the mean and sample standard deviation were computed, and results were plotted on a logarithmic scale. Error bars correspond to the logarithm of the mean plus or minus one standard deviation (*i.e.*, log(mean ± SD)).

2.4. Methods for surface material testing

2.4.1. Porosity evaluation

The morphology of the trabecula-inspired lattice structures was characterized using an industrial CT scanner (Nikon XTH225) with a scanning resolution of 8 μm. During testing, the X-ray source voltage and current were adjusted to generate beams of appropriate energy to penetrate the

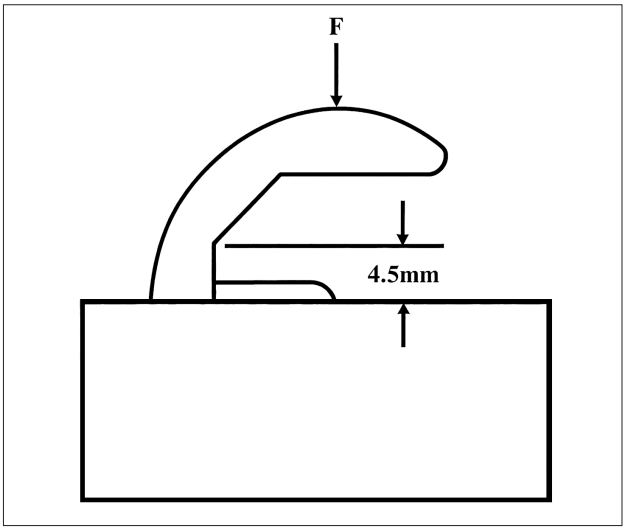


Figure 1. Schematic for fatigue testing of cementless femoral condyles. Specimens were embedded in dental stone and mounted in an Instron fatigue testing machine with cyclic loading applied to the posterior condyle. This preparation enabled controlled evaluation of long-term mechanical performance under simulated gait conditions.

porous metallic specimens. The transmitted signals were collected by the detector, converted into digital data, and reconstructed into computed tomography (CT) images through computational projection algorithms.

Subsequently, image segmentation, 3D reconstruction, region growing, and quantitative statistical analysis using a Gaussian model were performed to determine morphological parameters, including porosity, pore size, and strut thickness of the tested structures.

2.4.2. Tensile testing

Tensile testing of the trabecula-inspired porous structures was conducted in accordance with ASTM F1147 using a SUNS UTM 5205X universal testing machine. Ten specimens were prepared each for the sintered substrate bars and the I3P substrate bars. Prior to testing, the porous surface of each specimen was bonded to a flat substrate of the same base material using an adhesive with a tensile strength of not less than 34.5 MPa.

Both the porous-coated substrate bars and the flat substrate bars had a cross-sectional area of 5.07 cm^2. During testing, the tensile load was applied perpendicular to the plane of the trabecula-inspired porous structures at a constant crosshead speed of 0.25 cm/min, and was continued until failure occurred at the bonded interface. Strength data for each group were summarized and analyzed using box-and-whisker plots. Statistical significance was evaluated using two-sample, two-tailed Student's *t*-tests.

2.4.3. Shear testing

Shear testing of the trabecula-inspired porous structures was conducted in accordance with ASTM F1147 using a SUNS UTM 5205X universal testing machine. Ten specimens were prepared each for the CS substrate bars and the I3P substrate bars. Prior to testing, the porous surface of each specimen was bonded to a flat substrate of the same base material using an adhesive with a tensile strength of not less than 34.5 MPa.

Both the porous-coated substrate bars and the flat substrate bars had a cross-sectional area of 2.84 cm^2. During testing, the shear load was applied parallel to the plane of the trabecula-inspired porous structures at a constant crosshead speed of 0.25 cm/min, and loading continued until failure occurred at the bonded interface. Strength data for each group were summarized and analyzed using box-and-whisker plots. Statistical significance was evaluated using two-sample, two-tailed Student's *t*-tests.

3. Results

3.1. Substrate material

For a femoral condyle, the mechanical properties of the substrate material determine its resistance to failure during service and critically influence its overall performance. Tensile properties are the most representative indicators of comprehensive mechanical behavior and are strongly correlated with the underlying microstructure of the raw material. Thus, the tensile properties and microstructures of CoCrMo alloys from I3P (pre- and post-HIP) and conventionally cast femoral condyles were directly compared (Figure 2).

Conventionally cast CoCrMo substrate tensile testing result in a yield strength of 523.33 ± 12.92 MPa, a tensile strength of 786.00 ± 41.67 MPa, and an elongation at fracture of 14.33 ± 0.24%. I3P-manufactured CoCrMo substrate yielded mixed material characteristics prior to HIP with a yield strength of 508.38 ± 9.88 MPa, an ultimate tensile strength of 922 ± 9.57 MPa, and an elongation at fracture of 8.83 ± 2.25%. However, I3P substrate characteristics were superior to casting following HIP with a yield strength of 637.33 ± 1.70 MPa, a tensile strength of 1140.00 ± 31.82 MPa, and an elongation at fracture of 27.33 ± 4.99%.

This phenomenon corresponds with microscopic findings (Figure 2). Prior to HIP, the I3P substrate contained numerous micropores (Figure 2F). Pores were less pronounced on the planes perpendicular to the laser direction than on those parallel to it, suggesting they may originate from incomplete interlayer fusion during the additive manufacturing process (Figure 2A and 2B). The presence of these micropores may result in

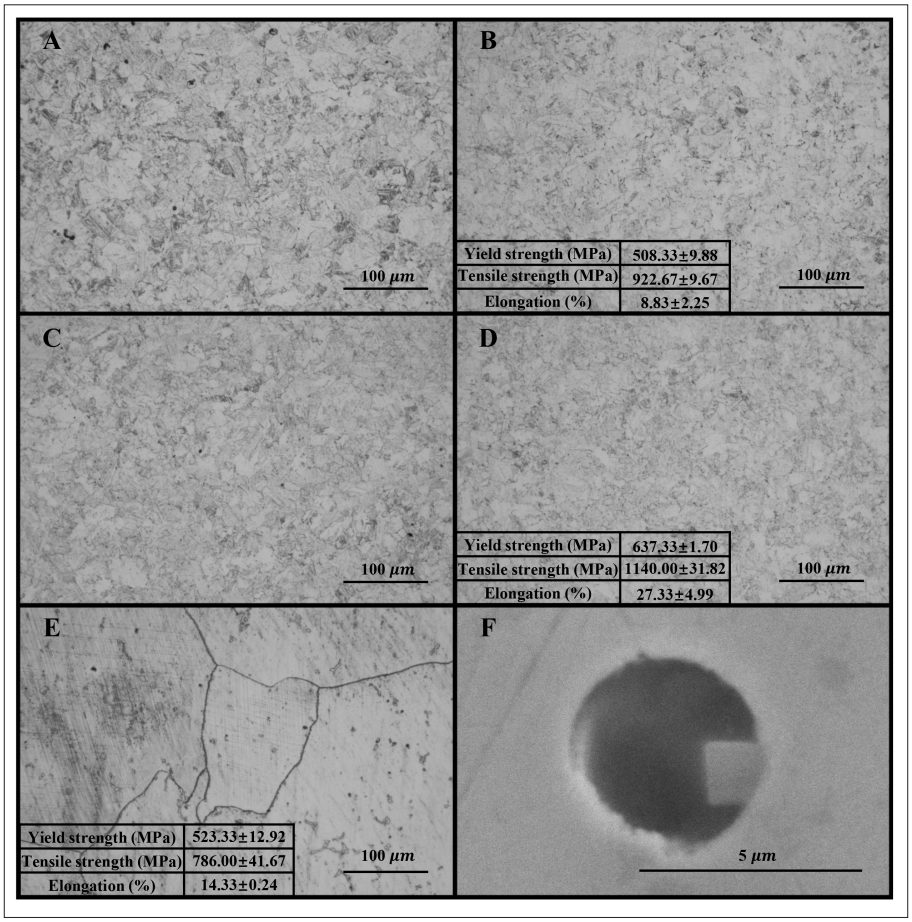


Figure 2. Microstructure and tensile properties of CoCrMo substrates manufactured by I3P and CS. (A,B) I3P substrate before HIP showing numerous micropores, more pronounced parallel to the laser direction (A) than perpendicular to it (B), which corresponded with reduced ductility (elongation: 8.8 ± 2.3%). (C,D) I3P substrate after HIP showing substantial pore elimination in both orientations, resulting in markedly improved mechanical performance (yield strength: 637 ± 1.7 MPa; UTS: 1140 ± 31.8 MPa; elongation: 27.3 ± 5.0%). (E) CS substrate after HIP exhibiting coarser grains and lower overall strength (yield strength: 523 ± 12.9 MPa; UTS: 786 ± 41.7 MPa; elongation: 14.3 ± 0.2%) compared with I3P after HIP. *HIP-treated I3P specimens demonstrated significantly superior properties compared with CS specimens, with two-sample Student's *t*-test *p*-values of 1.16×10^{-7}, 8.67×10^{-7}, and 8.19×10^{-4} for yield strength, tensile strength, and elongation, respectively. (F) Enlarged SEM micrograph highlighting residual micropores (black spots) prior to HIP. Abbreviations: HIP: Hot isostatic pressing; I3P: integrated 3D printing; SEM: Scanning electron microscopy; UTS: Ultimate tensile strength; CS: cast-sintered.

tensile properties inferior to those of the HIP-treated cast substrate. After HIP, however, such defects were largely eliminated in both orientations (Figure 2C and 2D), and combined with the refined microstructure, led to the post-HIP I3P substrate outperforming the cast substrate.

In summary, HIP not only improves the mechanical performance but also the structural stability of I3P materials, enabling I3P femoral condyles to exhibit superior properties compared with their conventionally cast counterparts.

3.2. Implant performance

During *in vivo* service, the implant is subject to long-term wear and cyclic fatigue stresses, which are a consequence of substrate material characteristics. Each gait cycle imposes frictional wear stress on the articulating surface and fatigue stresses on the entire femoral condyle. Wear and fatigue resistance are consequently two critical determinants of the prosthesis's long-term functionality and revision rate.

Wear resistance was quantified by measuring mass loss every 500,000 cycles, up to 5,000,000 cycles, during articulated wear testing of three samples each from the post-HIP I3P manufactured and cast substrates. The I3P-manufactured femoral condyle demonstrated superior wear resistance with reduced change in mass (Figure 3) and superior hardness (31 Rockwell Hardness C scale (HRC) vs. 23 HRC). This advantage can be attributed to

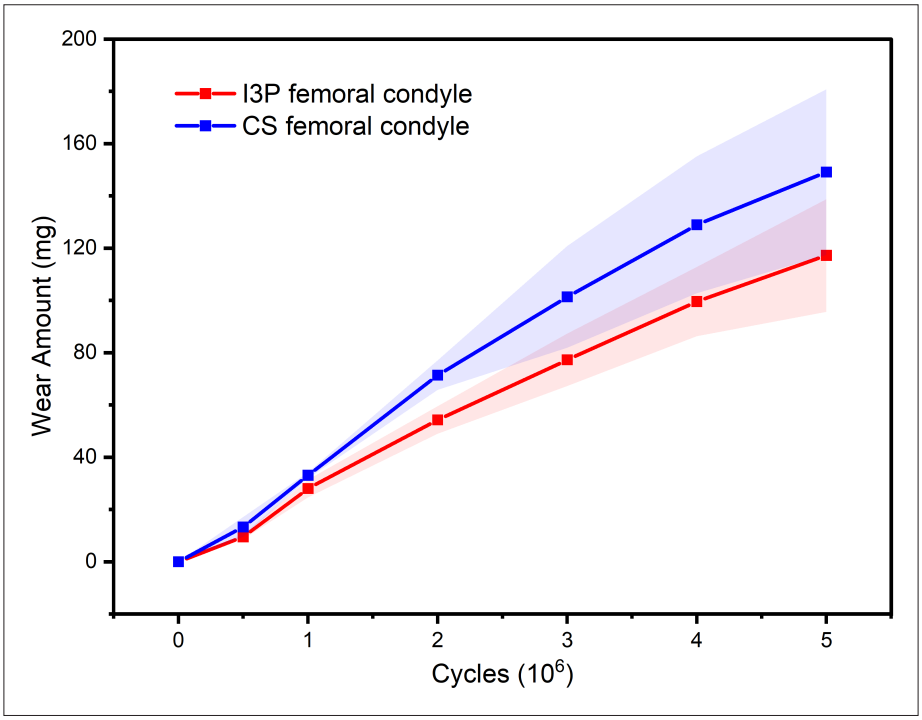


Figure 3. Wear resistance of I3P and CS cementless CoCrMo femoral condyles. Wear testing was performed for three specimens per group, with mass measured every 500,000 cycles up to 5,000,000 cycles of articulated motion. I3P femoral condyles demonstrated reduced mass loss compared with cast counterparts, consistent with their higher hardness (31 vs. 23 HRC) and finer, more homogeneous microstructure. These characteristics enabled smoother polishing and less counterface wear, resulting in superior overall wear performance of the coupled system. Abbreviations: CS, Cast-sintered; I3P, Integrated 3D printing.

the finer and more homogeneous grain structure of the I3P material, which provides higher hardness.

Fatigue resistance was evaluated by applying increasing sinusoidal cyclic loads in a step-loading method starting from 2300 N until implant failure or until a maximum of 10,000,000 cycles in seven groups of each manufacturing type. The I3P femoral condyle demonstrated superior fatigue resistance by surviving to the maximum load cycle up to 3000 N compared to 2900 N for the cast femoral condyle (Figure 4). Furthermore, the I3P femoral condyle maintained a trend of surviving a higher number of cycles for each subsequent increase in cyclic load (Figure 4). This superior performance can also be attributed to the homogeneity of the I3P substrate and its refined microstructural morphology, which enable more uniform distribution and transmission of applied stresses, thereby enhancing overall fatigue resistance.

The I3P femoral condyle demonstrated superior wear performance and fatigue resistance potentially due to finer and more homogeneous microstructure, an outcome that is consistent with the inherent material benefits of the I3P manufacturing approach.

3.3. Trabecular surface material

An essential feature of a cementless femoral condyle implant is its bone-contacting surface, which interfaces with host bone through a trabecula-inspired porous structure. The evaluation concerns two aspects: (i) connectivity and pore size distribution, which influence osteointegration, and (ii) bonding strength with the substrate, which influences durability and mechanical stability. In this comparison, the trabecular layer thickness of I3P products was controlled within the same range as sintered counterparts (700–1000 μm).

The connectivity and pore size of I3P-produced trabeculations was directly compared with that generated in a traditional sintering process through CT imaging. Connectivity was quantified by evaluating the lattice structure, I3P produced thinner struts (mean diameter 190.7 ± 44.3 vs. 247.6 ± 27.2 μm) with higher porosity (67.6% vs. 40.5%) (Figure 5A and 5C), characteristics conducive to promote osteointegration. The pore characteristics themselves were also measured with I3P yielding a mean pore size of 317.2 ± 124.4 μm and sintering yielding a mean pore size of 141.6 ± 49.2 μm (Figure 5B and 5D). Although the optimal pore

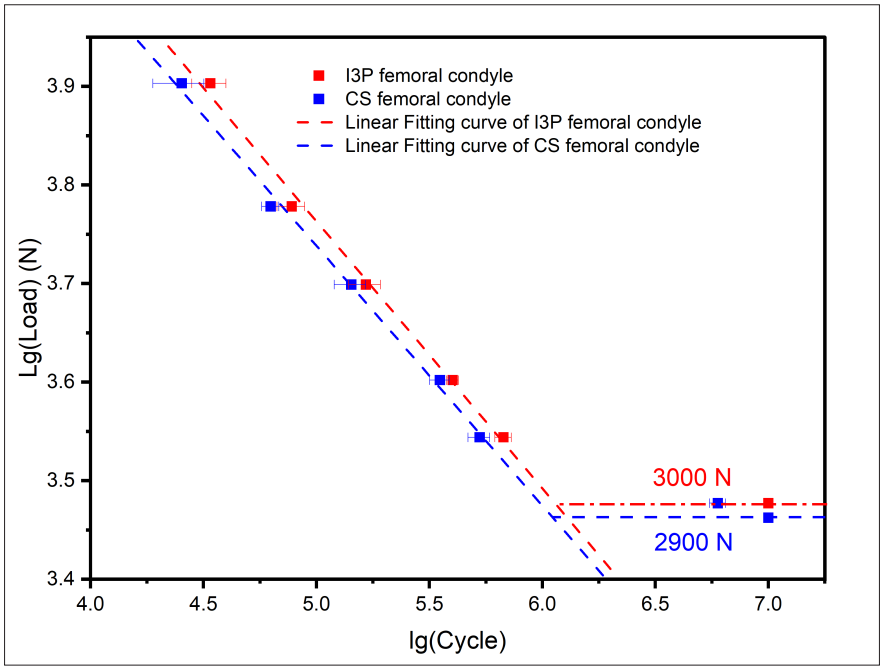


Figure 4. Fatigue performance of I3P and CS cementless CoCrMo femoral condyles. Seven specimens per group were tested using a step-loading protocol with sinusoidal cyclic loading (R = 0.1, 15 Hz), beginning at 2300 N and continuing until failure or 10 million cycles. I3P femoral condyles consistently survived more cycles at each load step and reached a maximum endurance of 3000 N, compared with 2900 N for cast counterparts. Superior performance is attributed to the finer grain structure and more homogeneous microstructure of I3P, which enable more uniform stress distribution and enhanced fatigue resistance. Abbreviations: CS, Cast-sintered; I3P, integrated 3D printing.

size for bone ingrowth is generally considered to be within 100–500 μm,[27] a broader pore size distribution is more favorable for accommodating different stages of osteointegration.[28–31]

Bond strength between the substrate and trabeculated surface layer was evaluated using a universal testing machine with 10 specimens each of I3P-produced and traditional sintered parts. I3P parts exhibited superior tensile strength (56.1 MPa) and shear strength (50.0 MPa) exceeding that of the sintered components (Figure 6), suggesting the superiority of producing the implant in a single step. Consequently, I3P provides a more durable and reliable bonding interface, establishing a level of structural stability that is difficult to achieve with conventional sintering techniques.

In summary, compared to conventional sintering, I3P yields a trabecular layer with higher porosity, more favorable pore size distribution, and stronger bonding to the substrate. These combined characteristics support more effective osteointegration while also providing superior mechanical stability, underscoring the advantages of I3P as a next-generation approach for cementless femoral condyle implants.

4. Discussion

As an emerging manufacturing technology, additive manufacturing provides remarkable advantages for fabrication of cementless femoral condyles. Yet most current implementations adopt a hybrid architecture in which a trabecular lattice is printed and then welded or brazed to a cast substrate (Longility, Abonisi Medical Technology). Compared with conventional sintered coating, 3D printing enables precise control of porosity, pore size, and 3D interconnectivity, thereby creating a microenvironment closer to human cancellous bone. However, the welded or brazed interface constitutes a mechanical weak link and a likely site for fatigue-crack initiation under the cyclic loads of daily walking and running, and the cast substrate is not readily patient-specific. In addition, a nonbiomimetic femoral condyle has been manufactured using additive manufacturing for complex clinical cases (Beijing Naton Medical Technology), but this approach does not fully exploit the advantages of 3D-printed trabecular architectures.

In contrast, the I3P strategy investigated in this study leverages the distinctive strengths of additive manufacturing to realize a truly monolithic, biomimetic design. The critical difference is I3P produces the

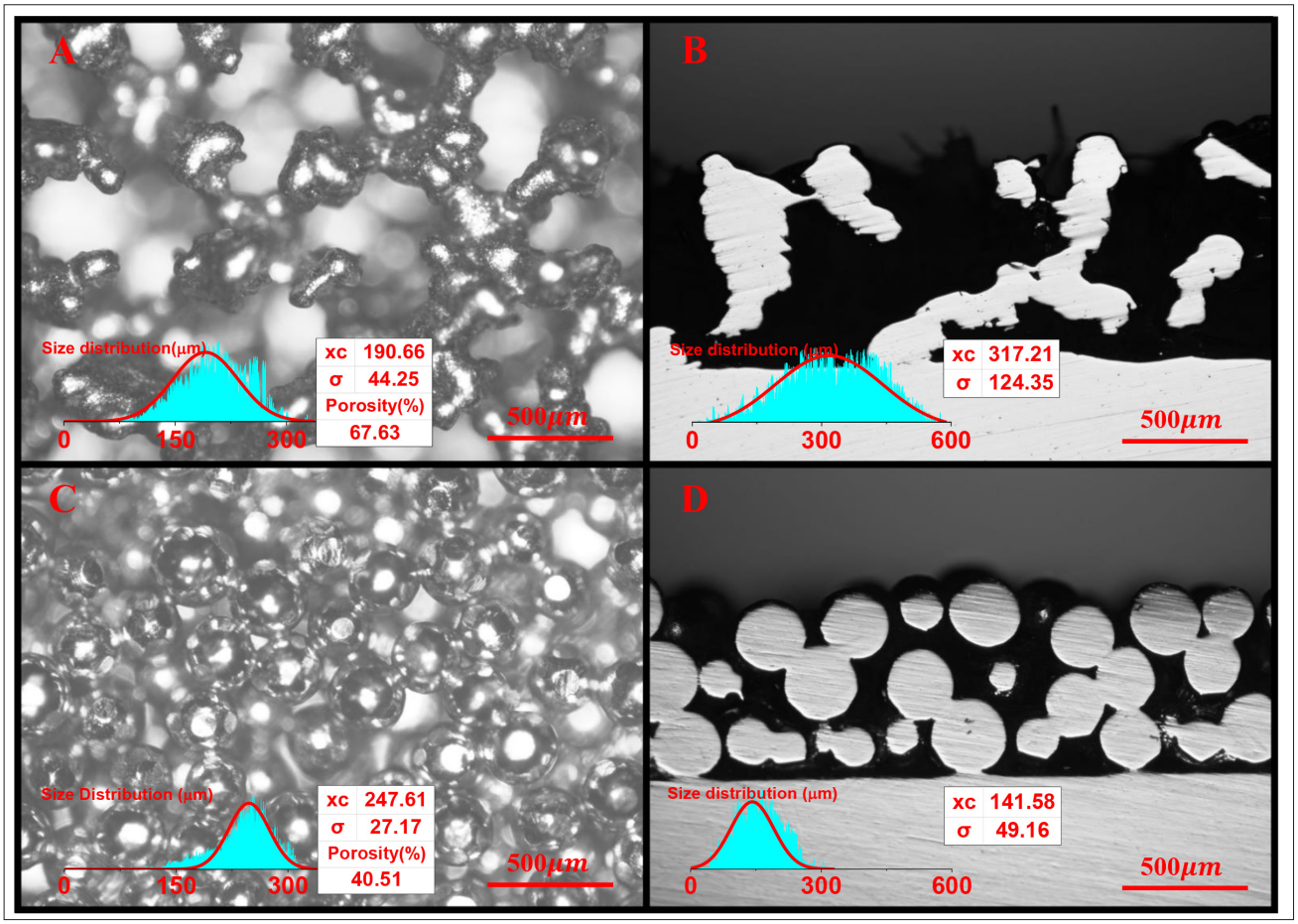


Figure 5. Trabecula-inspired lattice and pore characteristics of I3P and CS femoral condyles. (A) I3P lattice morphology with strut size distribution and Gaussian fitting. I3P struts were thinner (mean diameter: 190.7 ± 44.3 μm) and exhibited a broader size distribution, closely mimicking the heterogeneity of natural trabeculae. (B) I3P pore morphology with pore size distribution and Gaussian fitting. I3P generated larger pores (mean: 317.2 ± 124.4 μm) with a wider distribution, favorable for staged bone ingrowth. (C) CS lattice morphology with size distribution and Gaussian fitting. CS struts were thicker (mean: 247.6 ± 27.2 μm), less variable, and yielded lower overall porosity (40.5% vs. 67.6% in I3P), limiting osteointegration potential. (D) CS pore morphology with pore size distribution and Gaussian fitting. CS pores were smaller (mean: 141.6 ± 49.2 μm) and more narrowly distributed, reflecting limited controllability from bead-packing and sintering. All Gaussian fittings were performed without normalization and with the baseline parameter fixed at 0. Collectively, I3P produced trabecular layers with higher porosity, broader pore distributions, and more biomimetic architecture compared to the conventional sintering approach, highlighting the superior osteointegration potential in constructs made by I3P. Abbreviations: CS, Cast-sintered; I3P, integrated 3D printing.

trabecular and laminar structures in a single process. With I3P, the production workflow is unified and streamlined, eliminating uncertainties associated with multistep processes, such as sintering or plasma spraying, as well as the conventional additive manufacturing methods, which is particularly beneficial for industrial-scale production. I3P also offers unmatched controllability over product properties and allows patient-specific customization, a key advantage in the context of future clinical practice that increasingly emphasizes individualized implants.

4.1. Substrate characteristics

From a substrate perspective, I3P substrates exhibit refined and homogeneous grain structures that conventional casting cannot achieve. Although forging can partly compensate for the deficiencies of cast alloys, the brittleness of CoCrMo and irregular casting porosity make such improvements technically challenging and costly. I3P using LPBF may display anisotropy due to directional grain growth (Figure 2). However, this study showed that optimized processing, such as HIP, minimized such anisotropy, resulting in no pronounced texture in the grain structures (Figure 2). This translated to improved material characteristics such as yield strength and ultimate tensile strength that surpassed the corresponding conventional cast implants (Figure 2). This microstructural refinement was directly linked to superior mechanical properties.

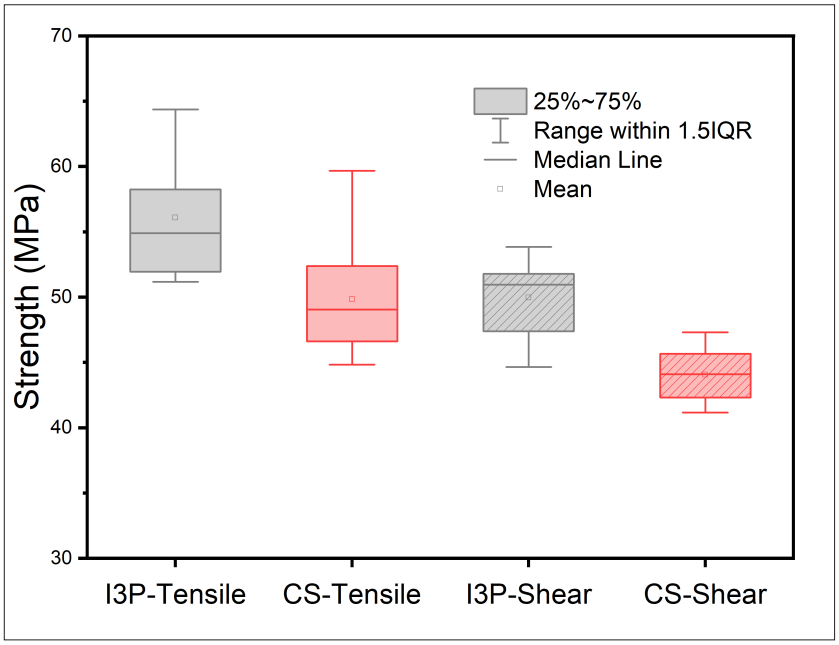


Figure 6. Interfacial bonding strength between trabecula-inspired porous layers and substrates fabricated by I3P and CS. Tensile and shear bond strength were measured using a universal testing machine with 10 specimens per group. I3P structures demonstrated significantly higher values (tensile: 56.1 MPa; shear: 50.0 MPa) compared with sintered counterparts, reflecting the advantage of forming the porous layer and substrate in a single integrated step. In contrast, sintered structures are prone to incomplete melting and nonuniform particle necking, which weakens the interface. The superior bonding performance of I3P establishes a more durable and reliable substrate–porous junction, reducing risks of delamination and enhancing long-term implant stability. *Compared with the CS specimens, the I3P specimens showed two-sample Student's *t*-test *p*-values of 7.41×10^{-3} for tensile strength. **Compared with the CS specimens, the I3P specimens showed two-sample Student's *t*-test *p*-values of 4.67×10^{-5} for shear strength. Abbreviations: CS: Cast-sintered; I3P: integrated 3D printing.

The improvement in mechanical properties and its connection with microstructural refinement is clearly highlighted by the quantitative tensile testing. Prior to HIP, I3P substrates showed mixed performance when compared with cast substrates. However, after HIP the I3P substrates significantly outperformed the cast counterparts in yield strength, tensile strength, and ductility (Figure 3). This demonstrates the central importance of eliminating micropores and residual interlayer defects from LPBF (Figure 2) through an optimized HIP process.

This microstructure refinement also improves wear and fatigue resistance. The finer microstructure of I3P alloys translated into superior hardness (31 HRC vs. 23 HRC for cast), enabling smoother polishing and reduced counterface wear. In long-term wear testing up to 5 million cycles, I3P femoral condyles consistently showed lower mass loss compared to cast controls (Figure 3). This performance reflects both higher intrinsic hardness and the reduced local hardness variability afforded by the uniform I3P microstructure. Cast alloys, by contrast, contain microstructural inhomogeneities that limit surface smoothness and accelerate tibial insert wear.

Finally, in terms of fatigue resistance, I3P femoral condyles demonstrated superior performance, surviving at least 10 million cycles at 3000 N, compared with 2900 N for cast femoral condyles (Figure 4). At each step increase in load, I3P specimens maintained a higher survival rate and endured more cycles before failure. This improved fatigue performance is attributed to the homogeneity of the I3P substrate, which distributes applied stresses more uniformly, thereby reducing stress concentrations that typically initiate cracks in coarser cast alloys.

Taken together, I3P substrates feature a refined grain structure, higher tensile strength and ductility after HIP, greater hardness and wear resistance, and improved fatigue life, as compared with conventionally cast substrates. These attributes confer superior durability and risk resistance, supporting I3P as a promising manufacturing route for cementless femoral condyles.

Trabecular surface characteristics

The bone-contacting surface of a cementless femoral condyle implant is central to its clinical performance, as both the pore architecture and the integrity of the substrate–porous interface determines osteointegration

and long-term mechanical stability. I3P can outperform conventional additive manufacturing methods in terms of interfacial bonding strength, and has demonstrated clear advantages over traditional sintering in both respects.

CT-based characterization revealed that I3P trabeculations were formed with thinner mean struts and substantially higher porosity (67.6% vs. 40.5%) (Figure 5). These characteristics are directly favorable for osteointegration, since increased porosity and reduced strut thickness enhance surface area for bone apposition while providing more open channels for vascular and cellular infiltration. The mean pore size of I3P trabeculae (317.2 ± 124.4 μm) was more than twice that of sintered layers (141.6 ± 49.2 μm), placing it firmly within the widely recognized 100–500 μm window for bone ingrowth (Figure 5).[27] Importantly, the broader pore size distribution produced by I3P offers additional biological advantages: smaller pores can facilitate early osteoid deposition and cell adhesion, while larger pores accommodate neovascularization and subsequent bone remodeling.[28–31] By contrast, the narrower pore size distribution of sintered coatings are constrained by bead diameter and stacking behavior. This limits biological adaptability and does not recapitulate the morphological heterogeneity of native trabecular bone. Together, these findings underscore I3P's capacity to produce pore architectures that are not only within the optimal osteoconductive range but also more biomimetic and adaptable across different phases of bone healing.

The integrity of the interface between the porous layer and the dense substrate is equally critical to implant performance, as failures often occur by delamination or particle shedding. Mechanical testing confirmed that I3P generated a stronger and more reliable interface compared to those of sintered counterparts (Figure 6). This difference arises from fundamental differences in process physics. In sintering, discrete beads fuse through neck formation that is often incomplete or nonuniform, leaving weak links at both bead–bead junctions and at the porous–substrate boundary. This random packing and limited metallurgical continuity elevate the risk of interface separation under cyclic load. By contrast, I3P builds the porous trabeculae and solid substrate in a single integrated step, ensuring full material continuity and densification across the transition zone. Even though the average I3P struts are thinner than sintered beads, the absence of incomplete melting or weak necks produces a far stronger and more stable bond. This continuity translates into lower delamination risk, higher structural reliability, and longer-term stability of the implant surface *in vivo*.

Structurally, the trabecula-inspired porous layers generated by I3P not only provide superior control over porosity and interconnectivity but also enable precise tailoring of these parameters to match biological and mechanical requirements. The ability to adjust pore size distribution, strut thickness, and layer thickness within a controlled design framework opens opportunities for patient-specific implants optimized for anatomical site, bone quality, or activity level. Moreover, the integration of porous and dense regions in a single build eliminates the delamination and particle shedding risks inherent in sintered or mechanically bonded coatings. These combined features support more effective osteointegration and more durable long-term fixation, underscoring the clinical potential of I3P as a next-generation manufacturing approach for cementless femoral condyle implants.

4.3. Clinical significance and future directions

Taken together, I3P femoral condyles unite three essential performance attributes: a substrate with refined microstructure and superior mechanical strength to withstand abnormal stresses, enhanced hardness and fatigue resistance to extend service life, and a trabecula-inspired porous layer optimized for osteointegration. This unique triad positions I3P as a superior alternative to conventional additive manufacturing and to casting-and-sintering approaches, particularly for cementless fixation where both mechanical integrity and biological integration are critical.[32]

At the same time, product-level outcomes remain influenced by implant geometry and patient-specific variables such as anatomy, activity level, and bone quality. The present study addressed this variability by employing the worst-case model by a head-to-head using a particular commercial implant geometry, thereby ensuring that the comparative results are both stringent and representative. With its structural precision and flexibility, I3P is expected to deliver even greater adaptability and performance across a wider spectrum of implant geometries and patient conditions.

Although the present study focused on mechanical and structural performance of I3P, the biological response to I3P surfaces is an important direction of future work. *In vitro* and *in vivo* studies examining osteoblast adhesion, bone ingrowth, and interfacial remodeling complement the mechanical findings reported here. Prior investigations of lattice architectures with comparable pore size and interconnectivity have demonstrated favorable osteoconductive behavior, suggesting similar potential for the I3P trabecular surfaces described in this study. Future work will address detailed evaluation of these biological aspects.

Beyond the knee, the intrinsic versatility of I3P supports translation of this approach to other load-bearing and articulating systems, including hip, shoulder, and wrist implants, as well as spinal devices. Based on the advantages demonstrated here, I3P holds promise to improve fixation, durability, and long-term stability across multiple orthopedic applications, reinforcing its potential as a scalable platform technology for next-generation implant design.

5. Conclusion

This study demonstrates the advantages of I3P in the fabrication of cementless femoral condyles through a comprehensive evaluation of its substrate- and product-level performance compared with conventional manufacturing routes. I3P substrates exhibited finer and more homogeneous microstructures than cast or sintered alloys, resulting in superior tensile properties, improved fatigue resistance, and greater hardness that allowed smoother polishing and reduced counterface wear. At the surface level, I3P outperformed sintering by producing trabecula-inspired structures with controllable pore size distribution, enhanced interconnectivity, and stronger bonding to the substrate. Together, these attributes highlight I3P as a robust platform for extending implant longevity and improving biological integration.

The intrinsic flexibility and precision of additive manufacturing further positions I3P as a versatile tool for optimizing implant design according to patient-specific anatomy and *in vivo* loading conditions, enabling iterative advances toward personalized solutions for even primary procedures. The integrated nature of the process also ensures product stability, underscoring its scalability for industrial production and clinical translation. While this work focused on femoral condyles, the same principles can be extended to hip, shoulder, and wrist implants, as well as spinal systems. Collectively, these findings establish a foundation for the broader application of I3P in cementless arthroplasty and support its potential as a next-generation strategy in orthopedic implant manufacturing.

Acknowledgments

None.

Funding

All materials, products, equipment, and funding for this study were provided by Suzhou Microport Orthorecon Co., Ltd.

Conflict of interest

J.W., Z.Z., T.Y., and W.W. are employees of Suzhou Microport Orthorecon, a subsidiary of MicroPort Orthopedics which produces and markets the commercial EVOLUTION femoral condyle implant examined in this study. B.Y.C. is an employee of MicroPort at the time of publication of this work.

Author contributions

Conceptualization: Tianbai Yu, Jiawei Wu, Zhiwei Zhou, Brian Chang
Formal analysis: Jiawei Wu, Zhiwei Zhou
Investigation: Zhiwei Zhou, Jiawei Wu
Methodology: Zhiwei Zhou, Jiawei Wu, Wei Wang
Writing–original draft: Jiawei Wu, Zhiwei Zhou
Writing–review & editing: Zhiwei Zhou, Jiawei Wu, Brian Chang

Ethics approval and consent to participate

Not applicable.

Consent for publication

Not applicable.

Availability of data

The datasets generated and/or analyzed during the current study are partially available from the corresponding author upon reasonable request. Certain data are subject to corporate confidentiality restrictions and therefore cannot be made publicly available.

References

1. Batailler C, Swan J, Sappey Marinier E, Servien E, Lustig S. New technologies in knee arthroplasty: Current concepts. *J Clin Med*. 2020;10(1):47. doi: 10.3390/jcm10010047
2. Mukartihal R, Das R, Chandan S, *et al*. Technologies in total knee arthroplasty. *J Karnataka Orth Assc*. 2023; 11(1):5-12. doi: 10.13107/jkoa.2023.v11i01.057
3. Prakash R, Agrawal Y. Robotic technology in total knee arthroplasty. *Br J Hosp Med*. 2023;84(6):1-9. doi: 10.12968/hmed.2022.0491
4. Haslhofer DJ, Kraml N, Stadler C, Gotterbarm T, Klotz MC, Klasan A. Cementless fixation in total knee arthroplasty: Current evidence and future perspective. *Arch Orthop Trauma Surg*. 2024;145(1):101. doi: 10.1007/s00402-024-05670-2

5. Lohberger B, Eck N, Glaenzer D, Lichtenegger H, Ploszczanski L, Leithner A. Cobalt chromium molybdenum surface modifications alter the osteogenic differentiation potential of human mesenchymal stem cells. *Materials (Basel)*. 2020;13(19):4292.
doi: 10.3390/ma13194292

6. Anselme K, Linez P, Bigerelle M, *et al*. The relative influence of the topography and chemistry of TiAl6V4 surfaces on osteoblastic cell behaviour. *Biomaterials*. 2000;21(15):1567-1577.
doi: 10.1016/S0142-9612(00)00042-9

7. Logan N, Sherif A, Cross AJ, *et al*. TiO_2-coated CoCrMo: Improving the osteogenic differentiation and adhesion of mesenchymal stem cells *in vitro*. *J Biomed Mater Res*. 2015;103(3):1208-1217.
doi: 10.1002/jbm.a.35264

8. Saroya M, Singh N, Singh A. Thermal spray coating technology – A review. *Int J Multidiscip Res*. 2023;5(3):2990.
doi: 10.36948/ijfmr.2023.v05i03.2990

9. Heimann RB. Thermal spraying of biomaterials. *Surf Coat Technol*. 2006;201(5):2012-2019.
doi: 10.1016/j.surfcoat.2006.04.052

10. Kumari R, Majumdar JD. Microstructure and surface mechanical properties of plasma spray deposited and post spray heat treated hydroxyapatite (HA) based composite coating on titanium alloy (Ti-6Al-4V) substrate. *Mater Charact*. 2017;131:12-20.
doi: 10.1016/j.matchar.2017.06.011

11. Mittal M, Nath S, Prakash S. Splat formation and degradation of hydroxyapatite during plasma spraying process. *Adv Mater Sci*. 2011;11(2).
doi: 10.2478/v10077-011-0008-6

12. Patel B, Inam F, Reece M, *et al*. A novel route for processing cobalt–chromium–molybdenum orthopaedic alloys. *J R Soc Interface*. 2010;7(52):1641-1645.
doi: 10.1098/rsif.2010.0036

13. Minouei H, Fathi M, Meratin M, Ghazvinizadeh H. Heat treatment of cobalt-base alloy surgical implants with hydroxyapatite-bioglass for surface bioactivation. *Iran J Mater Sci Eng*. 2012;9(3):33-39.

14. Das A, Rajkumar P. Metal 3D printing of biometals for prostheses and implants: A review. *Explor BioMat X*. 2025;2:101338.
doi: 10.37349/ebmx.2025.101338

15. Chowdhury S, Yadaiah N, Prakash C, *et al*. Laser powder bed fusion: A state-of-the-art review of the technology, materials, properties & defects, and numerical modelling. *J Mater Res Technol*. 2022;20:2109-2172.
doi: 10.1016/j.jmrt.2022.07.121

16. Archaryagie KCS, Tang Y. Enhancing powder bed quality in laser powder bed fusion: A review of monitoring, data processing, and adaptive control strategies. *J Manuf Process*. 2025;149:276-304.
doi: 10.1016/j.jmapro.2025.05.058

17. Walker J, Middendorf JR, Lesko CCC, Gockel J. Multi-material laser powder bed fusion additive manufacturing in 3-dimensions. *Manuf Lett*. 2022;31:74-77.
doi: 10.1016/j.mfglet.2021.07.011

18. Hasan N, Habibor Rahman M, Wessman A, Smith T, Shafae M. Process defects knowledge modeling in laser powder bed fusion additive manufacturing: An ontological framework. *Manuf Lett*. 2023;35:822-833.
doi: 10.1016/j.mfglet.2023.08.132

19. Sandu AV, Baltatu MS, Nabialek M, Savin A, Vizureanu P. Characterization and mechanical proprieties of new TiMo alloys used for medical applications. *Materials (Basel)*. 2019;12(18):2973.
doi: 10.3390/ma12182973

20. Baltatu MS, Tugui CA, Perju MC, *et al*. Biocompatible titanium alloys used in medical applications. *Rev Chim*. 2019;70(4):1302-1306.
doi: 10.37358/RC.19.4.7114

21. Jiao J, Hong Q, Zhang D, *et al*. Influence of porosity on osteogenesis, bone growth and osteointegration in trabecular tantalum scaffolds fabricated by additive manufacturing. *Front Bioeng Biotechnol*. 2023;11:1117954.
doi: 10.3389/fbioe.2023.1117954

22. Zhou Y, Ning F, Zhang P, Sharma A. Geometrical, microstructural, and mechanical properties of curved-surface AlSi10Mg parts fabricated by powder bed fusion additive manufacturing. *Mater Des*. 2021;198:109360.
doi: 10.1016/j.matdes.2020.109360

23. Ramavath D, Yeole SN, Kode JP, Pothula N, Devana SR. Development of patient-specific 3D printed implants for total knee arthroplasty. *Explor Med*. Published online December 28, 2023:1033-1047.
doi: 10.37349/emed.2023.00193

24. Velásquez-García LF, Kornbluth Y. Biomedical applications of metal 3D printing. *Annu Rev Biomed Eng*. 2021;23(1):307-338.
doi: 10.1146/annurev-bioeng-082020-032402

25. Chowdhury MS, Oliullah MS, Hossen MZ, *et al*. Additive manufacturing in bone science: A cutting-edge review of its potential and progress. *Med Nov Technol Devices*. 2025;27:100379.
doi: 10.1016/j.medntd.2025.100379

26. Li Y, Jiang D, Zhu R, Yang C, Wang L, Zhang LC. Revolutionizing medical implant fabrication: Advances in additive manufacturing of biomedical metals. *Int J Extrem Manuf*. 2025;7(2):022002.
doi: 10.1088/2631-7990/ad92cc

27. Li G, Wang L, Pan W, *et al*. In vitro and in vivo study of additive manufactured porous Ti6Al4V scaffolds for repairing bone defects. *Sci Rep*. 2016;6(1):34072. doi: 10.1038/srep34072

28. Otsuki B, Takemoto M, Fujibayashi S, Neo M, Kokubo T, Nakamura T. Pore throat size and connectivity determine bone and tissue ingrowth into porous implants: Three-dimensional micro-CT based structural analyses of porous bioactive titanium implants. *Biomaterials*. 2006;27(35):5892-5900. doi: 10.1016/j.biomaterials.2006.08.013

29. Wang X, Zhang D, Peng H, Yang J, Li Y, Xu J. Optimize the pore size-pore distribution-pore geometry-porosity of 3D-printed porous tantalum to obtain optimal critical bone defect repair capability. *Biomater Adv*. 2023;154:213638. doi: 10.1016/j.bioadv.2023.213638

30. Jones A, Arns C, Sheppard A, Hutmacher D, Milthorpe B, Knackstedt M. Assessment of bone ingrowth into porous biomaterials using MICRO-CT. *Biomaterials*. 2007;28(15):2491-2504. doi: 10.1016/j.biomaterials.2007.01.046

31. Li J, Yang Y, Sun Z, *et al*. Integrated evaluation of biomechanical and biological properties of the biomimetic structural bone scaffold: Biomechanics, simulation analysis, and osteogenesis. *Materials Today Bio*. 2024;24:100934. doi: 10.1016/j.mtbio.2023.100934

32. Qu Z, Yue J, Song N, Li S. Innovations in three-dimensional-printed individualized bone prosthesis materials: Revolutionizing orthopedic surgery: A review. *Int J Surg*. 2024;110(10):6748-6762. doi: 10.1097/JS9.0000000000001842

ACCSCIENCE PUBLISHING

International Journal of Bioprinting

RESEARCH ARTICLE

3D-printed biodegradable hydrogel microrobots for controlled therapeutic delivery

Pan Liao[1,2,3]*, Junyang Li[2], Shuxun Chen[2], Yi Hou[4]*, Guangda Zhu[3]*, and Dong Sun[2]

[1] Laoshan Laboratory, Qingdao, Shandong, China

[2] Department of Biomedical Engineering, City University of Hong Kong, Hong Kong, China

[3] Research Center for Materials, Architectures, and Integration of Nanomembranes, TU Chemnitz, Chemnitz, Germany

[4] Centre for Translational Bone, Joint and Soft Tissue Research, TU Dresden, Dresden, Germany

Abstract

Precise delivery of therapeutic agents to targeted sites within the body is a significant challenge, especially in complex and confined physiological environments. Magnetically actuated microrobots offer a promising solution by enabling remote, controllable, and minimally invasive navigation; however, most existing microrobotic systems are fabricated from nondegradable materials and lack controlled drug release capability, which significantly limits their clinical translation. Here, we report 3D-printed biodegradable magnetic microrobots based on gelatin methacryloyl (GelMA) hydrogel capable of controlled therapeutic delivery. Using high-resolution direct laser writing, dual-layer GelMA microrobots with distinct crosslinking degrees were fabricated, enabling tunable degradation and controlled release of encapsulated drugs. The low-crosslinked outer shell functions as a protective barrier that prevents premature drug diffusion, while the highly crosslinked inner core enables sustained drug release during enzymatic degradation. The microrobots demonstrate excellent biocompatibility and controllable degradation in cellular environments. In addition, the integration of a biocompatible magnetic skeleton within the GelMA body enhances mechanical stability and enables precise magnetic actuation. This study presents a versatile strategy for developing biodegradable, magnetically actuated microrobots with controlled therapeutic release, offering strong potential for targeted drug delivery, tissue regeneration, and minimally invasive biomedical applications.

Keywords: Biodegradable microrobots; Controlled drug release; Direct laser writing; Magnetic actuation; Targeted therapy

***Corresponding authors:**
Pan Liao (pliao@lsnl.cn)

Yi Hou (houyicool@iccas.ac.cn)

Guangda Zhu (zhuguangda@iccas.ac.cn)

Citation: Liao P, Li J, Chen S, Hou Y, Zhu G, Sun D. 3D-printed biodegradable hydrogel microrobots for controlled therapeutic delivery. *Int J Bioprint*. 2026;12(1):385-397. doi: 10.36922/IJB025460475

Received: November 14, 2025
Revised: November 30, 2025
Accepted: December 2, 2025
Published online: December 2, 2025

Copyright: © 2025 Author(s). This is an Open Access article distributed under the terms of the Creative Commons Attribution License, permitting distribution, and reproduction in any medium, provided the original work is properly cited.

Publisher's Note: AccScience Publishing remains neutral with regard to jurisdictional claims in published maps and institutional affiliations.

1. Introduction

The active transport and precise delivery of drugs, genes, and vaccines to specific sites within the body hold great potential for a wide range of biomedical applications, including targeted therapy, tissue repair and regeneration, and effective vaccination.[1-5] However, achieving accurate delivery of these therapeutics to diseased sites, particularly

within complex and confined regions of the body such as the gastrointestinal tract, brain, and spinal cord, remains a major challenge.[6–8] Microrobots, with characteristic sizes ranging from several to hundreds of micrometers, offer a promising solution by enabling active navigation and targeted transport of therapeutic agents into these inaccessible regions of the human body.[9–15] In particular, magnetically actuated microrobots have attracted increasing attention in the biomedical field due to their wireless controllability, high positioning precision, and noninvasive therapeutic potential,[16–21] with significant progress demonstrated in applications such as thrombus ablation and biofilm removal from tympanostomy tubes and biliary stents.[22–27]

Targeted therapeutic agents are typically incorporated into biocompatible magnetic microrobots through either surface functionalization or encapsulation within the microrobot body.[28–33] Surface-functionalized microrobots loaded with various drugs can achieve stimulus-responsive release[33–37]; however, most of these systems are fabricated from nonbiodegradable materials, which may induce inflammatory responses or other adverse biological effects. In contrast, biocompatible and biodegradable microrobots allow therapeutic payloads to be directly encapsulated within their structural matrix, thereby enhancing loading efficiency and enabling controlled, sustained release through gradual degradation under physiological conditions.[38–41] Among biodegradable materials, gelatin methacryloyl (GelMA) stands out as a particularly promising candidate due to its excellent cytocompatibility, intrinsic bioactivity, and enzymatic degradability.[42–44] GelMA-based magnetic microrobots, including enzymatically degradable microswimmers, have demonstrated remarkable potential for targeted drug or cell transport and localized therapy.[38,45–47] Recent advances in gelatin-based magnetic microrobots have enabled the integration of electromagnetic navigation, release catheters, and dissolvable drug-loaded capsules, demonstrating effective navigation in human vasculature models and successful tracking in large-animal studies.[48] Moreover, the therapeutic efficacy depends on both delivery precision and release kinetics.[1,49–52] Premature or uncontrolled release of encapsulated agents caused by early degradation of the microrobots before reaching the target site can severely compromise therapeutic performance. Therefore, achieving spatiotemporally controlled drug release is essential to ensure on-demand therapeutic action while minimizing premature drug leakage during navigation. However, the development of magnetic microrobots that combine precise actuation, tunable biodegradation, and controlled drug release remains a challenge.

Herein, we present 3D-printed biocompatible and biodegradable GelMA-based magnetic microrobots with controllable delivery capability. The microrobots are fabricated using high-resolution direct laser writing (DLW) based on two-photon polymerization and feature a dual-layer architecture with distinct crosslinking degrees (Figure 1A), enabling tunable degradation behavior for controlled drug release. The low-crosslinked outer GelMA shell serves as a protective barrier that prevents premature drug loss, while the highly crosslinked GelMA inner core allows sustained, on-demand release of therapeutic agents, thereby improving overall delivery efficiency. The microrobots exhibit excellent biocompatibility, undergoing gradual degradation during co-culture with MC3T3 cells and complete degradation in a trypsin–EDTA enzymatic medium. Furthermore, a biocompatible magnetic skeleton is embedded within the GelMA body to enable magnetic actuation (Figure 1B). The incorporation of this magnetic skeleton enhances mechanical integrity and provides precise, responsive magnetic control, allowing reliable detachment of printed microrobots from the printing substrate and stable operation under an external magnetic field. Overall, this design strategy establishes a versatile platform for developing next-generation biodegradable microrobots that integrate magnetic navigation, tunable biodegradation, and controlled therapeutic release, offering new opportunities for targeted drug delivery, tissue regeneration, and precision medicine.

2. Materials and methods

2.1. Preparation of biodegradable hydrogel precursor

The biodegradable hydrogel precursor was prepared by dissolving 100 mg of gelatin methacryloyl (GelMA), 25 mg of lithium phenyl-2,4,6-trimethylbenzoylphosphinate (LAP), and 50 mg of polyethylene glycol (PEG, 50% in H_2O, M_W = 4000) in 950 μL of phosphate-buffered saline (PBS). The resulting solution was stored at 4°C prior to use. For fluorescence imaging, 1 mg of Rhodamine B-PEG-Thiol (RB-PEG-SH) was added when required.

2.2. Preparation of magnetic precursor

The magnetic precursor used for fabricating the magnetic skeleton was prepared by dissolving 50 mg of photoinitiator Easepi EDB, 10 mg of photosensitizer 2-isopropyl-9H-thioxanthen-9-one (Easepi ITX), and 20 μL of Fe_3O_4 magnetic nanoparticles (MNPs; 100 nm, 260 mg/mL in γ-butyrolactone) in a mixture of 0.5 mL poly(ethylene glycol) diacrylate (PEGDA, M_n = 575) and 0.5 mL pentaerythritol tetraacrylate (PETA). The mixture was vortexed and shaken at 300 rpm for at least 30 min until a uniform dispersion was obtained.

2.3. 3D printing of dual-layer GelMA microstructures and magnetic microrobots

Before printing, the GelMA precursor was liquefied by incubation in a 37°C deionized water bath for 10 min and then deposited onto a glass substrate for DLW. The GelMA microstructures were fabricated using a commercial DLW system (Photonic Professional GT, Nanoscribe GmbH) equipped with a 63× oil-immersion objective (NA = 1.4) and a 780 nm femtosecond laser. After printing, the samples were developed in deionized water at 40°C for 10 min to remove unpolymerized precursor. Dual-layer GelMA microstructures were fabricated by repeating the GelMA printing process. The alignment of different layers was achieved using the built-in interface finder along the Z-axis and marker-based positioning along the XY-axis. The magnetic microrobots, consisting of a magnetic skeleton (see Figure S1) and a GelMA body, were produced following the same procedure. After fabrication, all microrobots were stored in PBS at 4°C until further use. For the dual-layer GelMA microstructures, we trimmed a small portion from the bottom of each sphere to create a flat contact area to enhance adhesion between the spherical microrobots and the substrate during fabrication (see Figure S2). For the magnetic microrobots with a magnetic skeleton, the printed skeleton already adheres well to the substrate, and thus no additional design modifications are required.

2.4. Cell culture and cytocompatibility evaluation

In this experiment, MC3T3-E1 cells (ATCC CRL-2594) obtained from American Type Culture Collection (ATCC) were used. The cells were cultured in Dulbecco's Modified Eagle Medium (DMEM) supplemented with 10% fetal bovine serum (FBS) and 1% penicillin–streptomycin, and maintained at 37°C in a humidified 5% CO_2 incubator. For cytocompatibility evaluation, GelMA microstructures were co-cultured with MC3T3-E1 cells in standard growth medium, and the morphology of both cells and microstructures was monitored at predetermined time points using phase-contrast microscopy. Upon reaching confluency, cells were treated with 125 μg/mL trypsin–EDTA to induce GelMA degradation and promote cargo release. All images were acquired using an inverted fluorescence microscope (Ts2R-FL, Nikon).

2.5. Drug loading

GelMA microstructures were lyophilized overnight using a freeze dryer (FD-10-ME, Labfreez). DNA plasmid (2 μg) was mixed with 10 μL of transfection reagent (Lipofectamine™ 2000) and diluted in 100 μL PBS. The resulting DNA–lipoplex solution was added to the dried microstructures and incubated overnight. After incubation, the microstructures were washed three times with PBS and subsequently co-cultured with MC3T3-E1 cells for gene transfection and protein expression. Fluorescence images were obtained using an inverted fluorescence microscope (Ts2R-FL, Nikon).

2.6. Enzymatic degradation

Dual-layer GelMA microstructures with different crosslinking degrees were fabricated to investigate their enzymatic degradation behavior. The samples were incubated in PBS containing 12.5 mg/mL trypsin–EDTA, and the degradation process was monitored using a confocal laser scanning microscope (TCS SP8, Leica Microsystems). Fluorescent images were captured at defined time intervals and analyzed using Fiji–ImageJ software (National Institutes of Health, USA).

2.7. Magnetic actuation of microrobots

The magnetic microrobots were actuated using a permanent magnet. A cubic neodymium iron boron (NdFeB) magnet with dimensions of 50 mm × 30 mm × 5 mm and a field strength of approximately 70 mT was used, and the working distance was kept below 50 mm. The locomotion behavior under magnetic stimulation was observed and recorded using an optical microscope.

2.8. Statistical analysis

All experiments were performed in triplicate. Statistical and graphical analyses were conducted in Excel using data, including fluorescence intensity measurements, exported from the Fiji–ImageJ software (National Institutes of Health, USA). All data are presented as mean ± standard deviation.

3. Results and discussion

3.1. Design of biodegradable hydrogel microrobots

To achieve controlled therapeutic delivery, we designed biodegradable dual-layer GelMA microstructures and magnetically actuated microrobots with precise structural and functional tunability (Figure 1A and 1B). The microrobots were constructed with a spherical geometry to ensure isotropic homogeneity during fabrication and operation. For the dual-layer GelMA microstructures, the diameters of each layer can be precisely tuned to achieve different drug release profiles. In this study, the diameters of the inner core and the outer shell were set to 30 μm and 50 μm, respectively (Figure 1A). The dual-layer GelMA microstructures were fabricated using DLW based on two-photon polymerization, a high-resolution 3D printing technique that provides submicron precision and accurate spatial control of polymerization, allowing multi-material integration through sequential printing.[53–57] Using this approach, dual-layer GelMA microstructures with distinct crosslinking degrees and magnetic microrobots

composed of different materials were fabricated. GelMA hydrogel precursors (Figure 1C) were employed as the printing material for the microrobot body because of their excellent biocompatibility, intrinsic bioactivity, and enzymatic degradability.[42–44] As a proteolytically degradable biomaterial, GelMA has been widely used for controlled drug delivery, cell encapsulation, and tissue engineering applications, serving as a versatile scaffold for supporting cell proliferation and differentiation.[58–60] In parallel, the magnetic skeleton (Figure 1B) was fabricated from a magnetic precursor containing poly(ethylene glycol) diacrylate (PEGDA), pentaerythritol tetraacrylate (PETA), and Fe_3O_4 MNPs (Figure 1C), consistent with our previous work.[5,24] The PEGDA–PETA matrix provides both mechanical robustness and degradability, while the incorporation of Fe_3O_4 MNPs imparts magnetic responsiveness, enabling remote and precise actuation of the microrobots.

Figure 1D schematically illustrates the sequential fabrication process of the dual-layer GelMA microstructures using direct laser writing (DLW). The GelMA core with a high crosslinking degree was first printed within a droplet of hydrogel precursor solution at a high laser power (Figure 1D (i)) and then developed in a 37°C deionized water bath for 5 minutes to remove unpolymerized residues. The cleaned and dried microstructures were then coated with a second droplet of hydrogel precursor and realigned with the original coordinates for the subsequent printing step (Figure 1D (ii)). The outer shell was printed at a lower laser power to achieve a lower crosslinking density, forming a degradable layer that serves as a protective barrier to prevent premature drug loss. This sequential process allows the precise fabrication of dual-layer GelMA microstructures with well-defined interfaces and accurately controlled structural dimensions, as illustrated in Figure 1D (iii). Figure 1E schematically presents the fabrication workflow of the magnetically actuated microrobots composed of a magnetic skeleton (see Figure S1 for detailed structural parameters) and a GelMA body. The magnetic skeleton, composed of PEGDA, PETA, and Fe_3O_4 MNPs, was first printed, followed by printing the GelMA body using the same sequential fabrication approach as for printing the dual-layer GelMA microstructures. This dual-material 3D printing strategy provides a flexible and efficient route to integrate biodegradability, biocompatibility, and magnetic actuation within a single microrobotic platform. The resulting fabrication methodology establishes a robust foundation for creating functional microrobots with tunable degradation, controlled drug release, and precise magnetic responsiveness, offering significant potential for targeted therapeutic delivery and minimally invasive biomedical applications.

3.2. Fabrication and tunable degradability of dual-layer GelMA microstructures

First, the controlled degradability of the 3D-printed dual-layer GelMA structures with varying crosslinking degrees was investigated. Figure 2A schematically illustrates the designed structure of the dual-layer GelMA microstructures, accompanied by bright-field and fluorescence microscopy images confirming successful fabrication. The inner core and outer shell have diameters of 30 μm and 50 μm, respectively. The core, containing rhodamine B, exhibits red fluorescence, whereas the outer shell, containing FITC, emits green fluorescence (Figure 2A). To achieve sustained and programmable release, GelMA microstructures were designed with two layers exhibiting distinct crosslinking degrees (Figure 2B). Such structures can be fabricated by tuning the DLW parameters, particularly the laser power, which determines the crosslinking density and thereby controls the degradation kinetics and release behavior of the encapsulated cargo. Highly crosslinked GelMA networks contain fewer water molecules and exhibit lower permeability to surrounding aqueous media, effectively minimizing premature drug diffusion. As enzymatic degradation proceeds, the polymer network gradually loosens, leading to an increase in mesh size that facilitates drug diffusion and release. In contrast, low-crosslinked GelMA hydrogels possess larger initial mesh sizes, resulting in faster degradation and more rapid cargo release. Therefore, constructing microrobots with layers of varying crosslinking degrees enables stepwise degradation and controlled, sustained drug release. We selected laser powers of 30, 45, and 60 mW because these values produced GelMA microstructures with good mechanical stability while offering distinct crosslinking levels. At lower laser powers, insufficiently crosslinked structures were too soft to maintain their spherical geometry in air. Conversely, excessively high laser powers easily induced cavitation bubbles during scanning, leading to deformation of the printed GelMA microstructures. The combination of 30, 45, and 60 mW laser powers with a scanning speed of 5 mm/s was therefore optimal for fabricating stable GelMA microstructures with controlled crosslinking gradients. Figure 2C and 2D show the degradation and release behavior of the printed dual-layer GelMA microstructures in PBS containing 12.5 μg/mL trypsin–EDTA. The inner core was fabricated at a laser power of 60 mW and exhibited red fluorescence, while the outer shells were printed at 45 mW and 30 mW, respectively. Bright-field (Figure 2C) and fluorescence (Figure 2D) microscopy images recorded at different time intervals clearly reveal the gradual degradation of the outer shell, which serves as a sacrificial barrier protecting the encapsulated drugs in the inner core from premature release. The outer shell printed at 30 mW (Figure 2C(i)) degraded first within 60

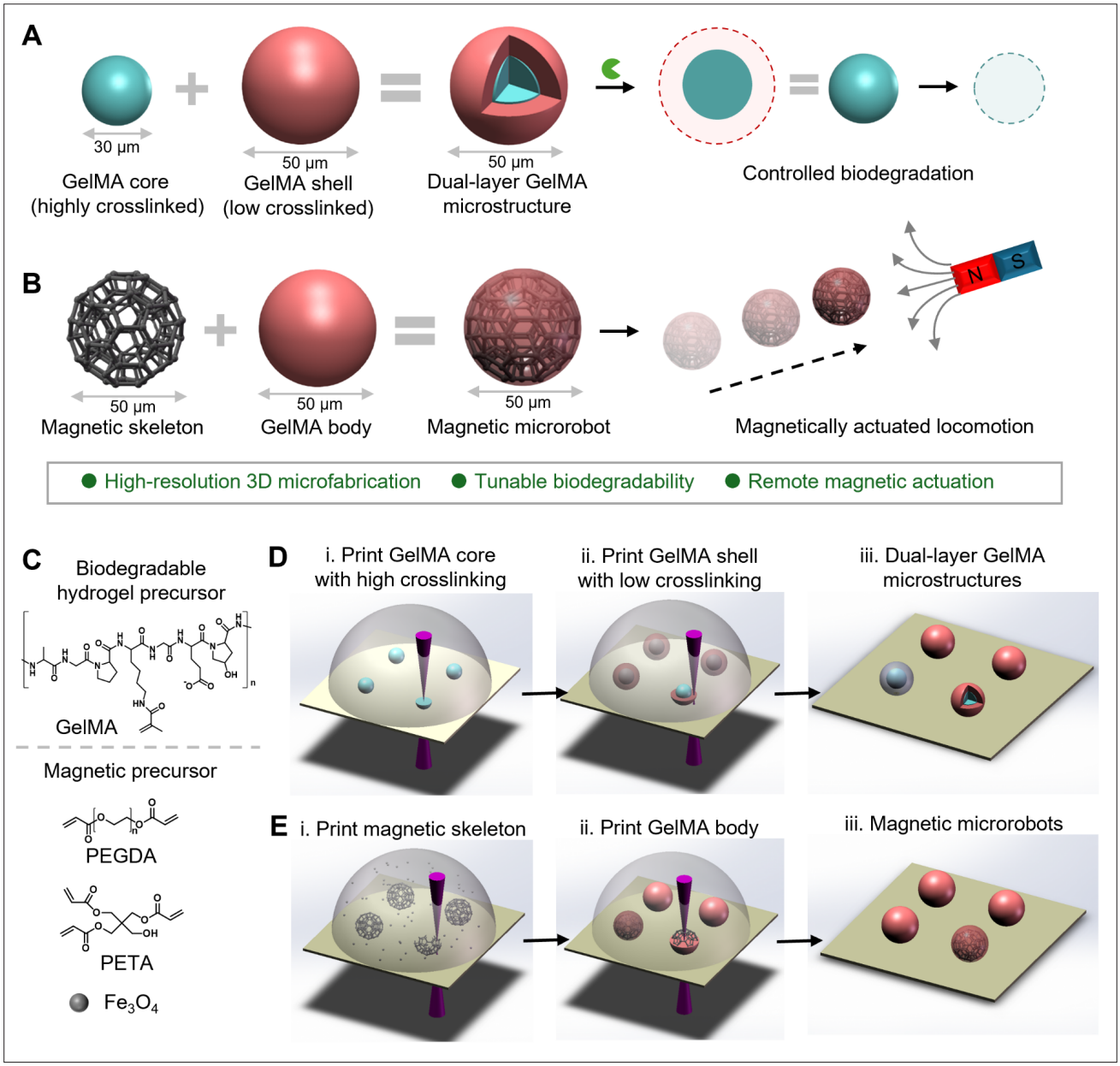


Figure 1. Schematic illustration of the design and fabrication of the biodegradable hydrogel microrobots. (A) Structural design of the dual-layer GelMA microstructures with tunable crosslinking degrees for controlled biodegradation. (B) Structural design of the magnetic microrobots composed of a magnetic skeleton and a GelMA body. (C) Chemical composition of the developed precursors used for 3D printing of dual-layer GelMA microstructures and magnetic microrobots. (D) Schematic representation of the sequential 3D printing process for fabricating dual-layer GelMA microstructures. (E) Schematic representation of the 3D printing process for fabricating magnetically actuated microrobots. Abbreviations: GelMA: Gelatin methacryloyl; PEGDA: Poly(ethylene glycol) diacrylate; PETA: Pentaerythritol tetraacrylate.

minutes (Figure 2C(ii)), delaying the release of fluorescent nanoparticles from the inner core printed at 60 mW until approximately 120 minutes (Figure 2C(iii) and 2D(iii)). In contrast, GelMA microstructures without an outer shell, printed solely at 60 mW, underwent complete degradation and released their fluorescent nanoparticles within the same period (Figure 2C(iii) and 2D(iii)). Notably, GelMA microstructures with an outer shell printed at 45 mW maintained their integrity for a longer duration (Figure 2C(iv)), postponing the onset of release to over 150 minutes (Figure 2D(iv)). As shown in the degradation profiles generated by calculating the average fluorescence intensity per cross-sectional area of the rhodamine-loaded GelMA microstructures (Figure 2E), dual-layer GelMA

microstructures with an outer shell exhibited significantly prolonged degradation compared to those without, confirming the effectiveness of the outer protective layer in delaying degradation and achieving controlled drug release. In addition to laser power, scanning speed can also be used to modulate the crosslinking density. In this study, we maintained a constant scanning speed of 5 mm/s and focused on varying the laser power to achieve different crosslinking levels. Nonetheless, scanning speed represents another viable parameter for adjusting crosslinking density,[61–63] further highlighting the design flexibility of our fabrication process. Compared with previously reported GelMA-based magnetic microrobots,[45–47] our printed dual-layer GelMA microstructures not only exhibit comparable biodegradability and achieve drug release within hours, but also provide an additional advantage: degradability can be further regulated by introducing an outer sacrificial barrier. This design minimizes the risk of early or uncontrolled cargo leakage before the microrobots reach the target site, which would otherwise severely compromise therapeutic efficacy.

3.3. Drug-loading capability and biodegradation of GelMA microstructures

After investigating the controlled degradability of the printed GelMA microstructures, we next evaluated their drug-loading capability and degradation behavior in cellular environments. *In vitro* experiments were conducted to assess the drug-loading capability (using DNA as a model molecule) and biodegradability of the fabricated GelMA microstructures under cell culture conditions. The GelMA microstructures were first dehydrated by freeze drying and subsequently incubated in PBS containing 2 μg of DNA lipoplex overnight. After incubation, the microstructures were rinsed three times with PBS to remove unbound DNA and subsequently co-cultured with cells. After 48 hours, enhanced green fluorescent protein (EGFP) expressing cells were observed under fluorescence microscopy, showing merged images of the GelMA microstructures and EGFP cells (Figure 3A). Figure S3 presents the control group without GelMA microstructures, confirming that green fluorescence signals originated from the DNA-loaded GelMA microstructures shown in Figure 3A. To quantify the DNA loading capacity, 10 μL of trypsin-EDTA was added to samples containing 50 GelMA microstructures (50 μm in diameter) or 100 GelMA microstructures (20 μm in diameter) to induce rapid degradation. The DNA concentration in the degraded solution was then measured using a NanoDrop spectrophotometer (Figure 3B). As expected, the larger 50 μm GelMA microstructures exhibited higher DNA loading than the smaller 20 μm ones due to their greater internal volume and surface area available for adsorption.

The cytocompatibility of the GelMA microstructures was further evaluated by co-culturing them with MC3T3 E1 fibroblasts. The dual-layer microstructures consisted of two GelMA layers fabricated at different laser powers: an inner rhodamine-containing core (30 μm, 45 mW) and an outer shell (50 μm, 30 mW) without rhodamine. The MC3T3 cells were cultured with the GelMA microstructures for one week, and time-lapse microscopy images were recorded to monitor cellular growth and interaction with the GelMA microstructures (Figure 3C). As shown in the figure, MC3T3 cells proliferate rapidly and typically begin adhering and spreading within approximately 3 hours. At 18 hours, most MC3T3 cells exhibit the expected spreading morphology, and only a few early apoptotic events are observed, clearly demonstrating that the rounded morphology at later stages is primarily due to overconfluence rather than poor adhesion or cytotoxic effects. By 42 hours, the cell density in the imaged region had become sufficiently high that individual cells could no longer maintain distinct spreading morphologies. The results indicate that cells adhered to the surface of the GelMA microstructures and continued to proliferate across the culture substrate, demonstrating good cytocompatibility and cell affinity. During culture, partial deformation and degradation of the outer shell were observed in some GelMA microstructures, suggesting gradual enzymatic degradation of GelMA by cell-secreted proteases. Figure 3D compares the shape changes of GelMA microstructures incubated in PBS and cell culture medium. In PBS at 37°C, the GelMA microstructure exhibited minor and uniform expansion, whereas those cultured with cells displayed irregular deformation, likely caused by localized enzymatic activity. Figure 3E further shows the degradation behavior of GelMA microstructures exposed to trypsin–EDTA (125 μg/mL) enzymatic medium. GelMA microstructures without the outer protective layer degraded rapidly and disappeared from their initial positions within 10 minutes, while those with an outer layer, which had already undergone partial degradation during cell culture, were completely degraded at a later stage. These findings confirm that the dual-layer GelMA microstructures possess tunable biodegradation and excellent biocompatibility. Their ability to gradually degrade under enzymatic or cellular conditions, while maintaining structural integrity for controlled cargo release, highlights their strong potential for use in biologically relevant environments for targeted and sustained therapeutic delivery.

3.4. Fabrication and magnetic actuation of GelMA-based microrobots

To fabricate the magnetic microrobots, we designed a magnetic skeleton that could be effectively embedded within the GelMA matrix to enable remote magnetic

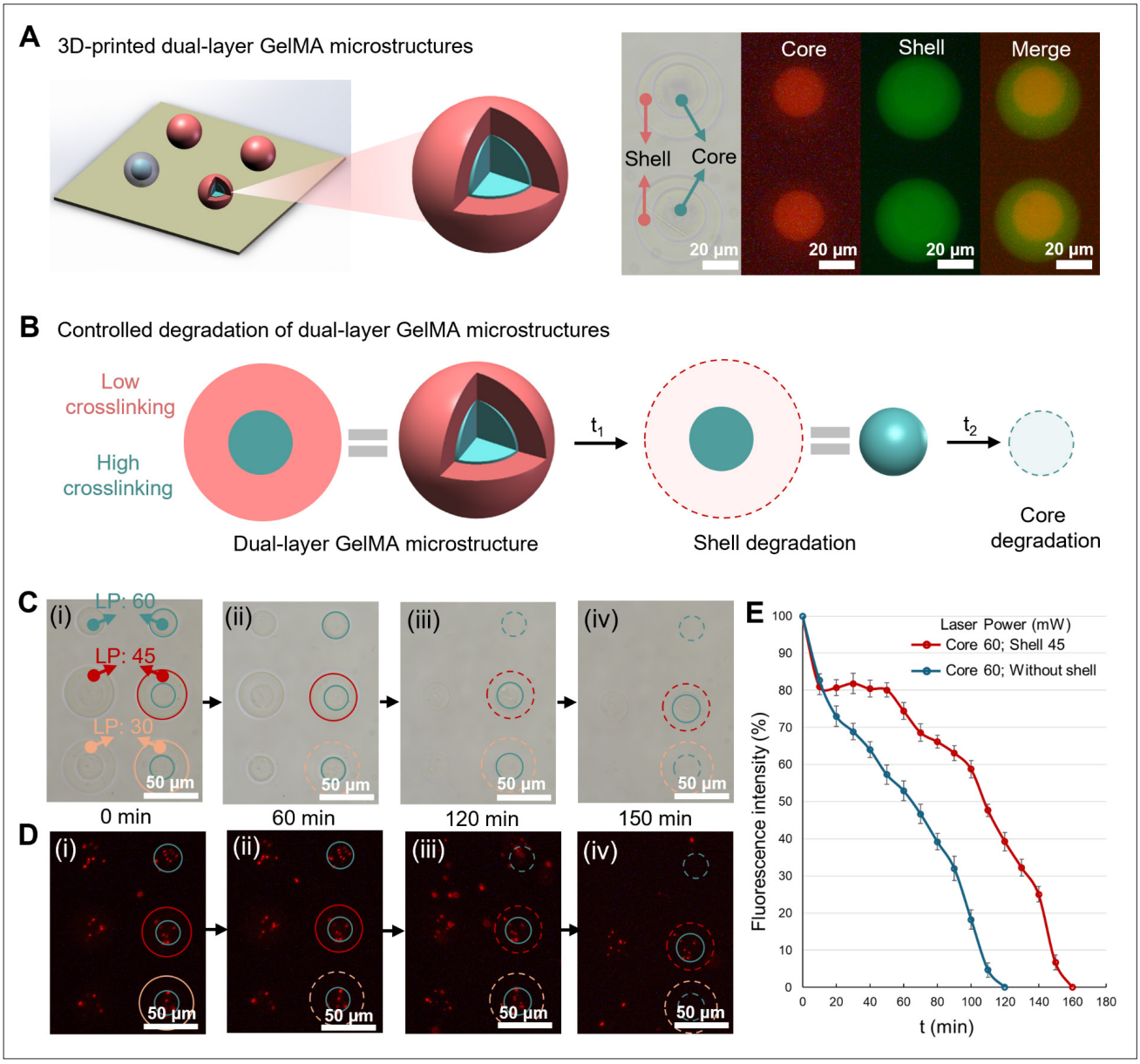


Figure 2. Tunable degradability of printed dual-layer GelMA microstructures. (A) Schematic illustration and microscopy images of the 3D-printed dual-layer GelMA microstructures. (B) Schematic representation of the controlled degradation of GelMA microstructures. (C) Bright-field microscopy images showing the degradation of GelMA microstructures in trypsin–EDTA enzymatic solution. (D) Fluorescence microscopy images showing the controlled release of rhodamine from the GelMA microstructures. (E) Degradation profiles of the 3D-printed GelMA microstructures with and without an outer shell. Data are presented as mean ± standard deviation (SD). Abbreviation: GelMA: Gelatin methacryloyl.

actuation. Figure 4A schematically illustrates the structural design of the magnetic microrobots, together with bright-field and fluorescence microscopy images confirming their successful fabrication. The microrobots consist of an internal magnetic skeleton and a GelMA body, both with a diameter of 50 μm. The magnetic skeleton, composed of PEGDA and PETA integrated with Fe_3O_4 MNPs, exhibits distinct red and blue fluorescence, verifying its successful incorporation within the GelMA body. Figure 4B shows the detachment process of the magnetic microrobots from the glass substrate, as demonstrated in Video S1. The microrobots containing the magnetic skeleton could be easily detached, indicating that the embedded magnetic framework effectively enhances their mechanical stability. In contrast, microstructures fabricated solely from GelMA without the magnetic skeleton appeared soft and adhesive, making them difficult to detach from the glass substrate (Video S2). This comparison clearly demonstrates that

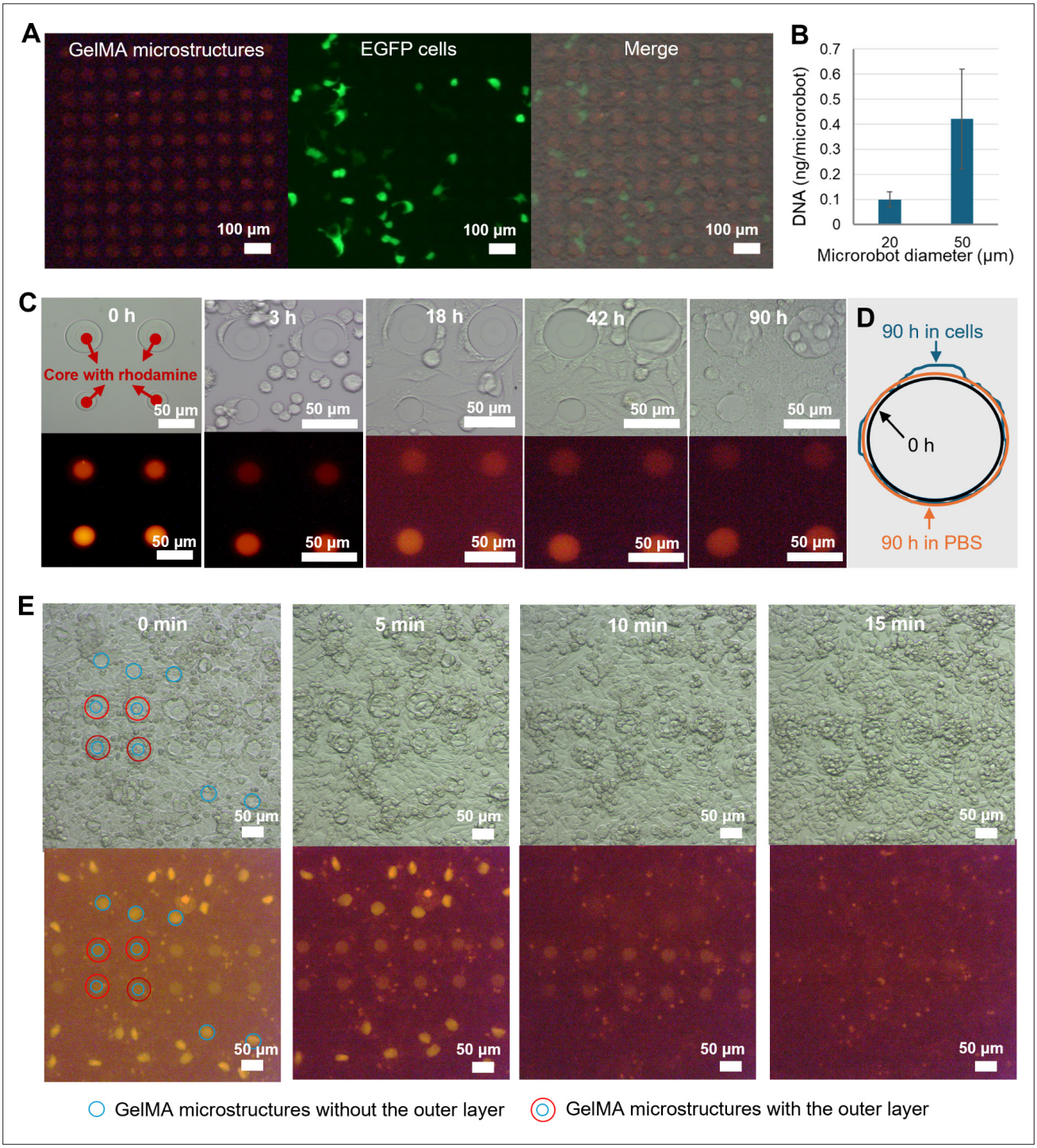


Figure 3. Drug-loading capability and biodegradation of GelMA microstructures. (A) Fluorescence microscopy images showing GelMA microstructures containing rhodamine, EGFP-expressing cells after 48 h co-culture, and merged images of microstructures and EGFP cells. (B) Quantitative analysis of DNA loading capacity on GelMA microstructures of different sizes. Data are presented as mean ± standard deviation (SD). (C) Time lapse images showing microstructures' behavior and cell proliferation during MC3T3 culture. (D) Comparison of GelMA microstructure outlines in PBS and cell culture after 90 h. The black line represents the original outline, while orange and blue lines indicate deformation in PBS and cell culture, respectively. (E) Degradation process of the GelMA microstructures in trypsin–EDTA enzymatic solution. Abbreviations: EGFP: Enhanced green fluorescent protein; GelMA: Gelatin methacryloyl; PBS: Phosphate-buffered saline.

the incorporation of the magnetic skeleton improves the microrobots' structural robustness and handling reliability.

The embedded Fe_3O_4 MNPs within the magnetic skeleton impart strong magnetic responsiveness, as demonstrated in our previous studies,[5,24] enabling precise and remote control of microrobot motion under an external magnetic field (Figure 4C). The locomotion behavior of the microrobots was evaluated under a permanent magnetic field to assess their controllability. As shown in Figure 4D and Video S3, the microrobot exhibited directional locomotion toward the target position in response to the applied magnetic field, demonstrating stable and controlled actuation. Although only linear motion driven by a permanent magnet was demonstrated in this study, more complex trajectories could be achieved under rotating magnetic fields generated by previously reported electromagnetic systems.[24,26,35,64] Such magnetic control strategies could further enable precise navigation of the microrobots through biological fluids and intricate physiological environments.[29,34,64–66] Overall, these results indicate that the developed GelMA-based magnetic microrobots possess excellent controllability, mechanical robustness, and biocompatibility, providing a promising foundation for future *in vivo* applications, including targeted drug delivery, minimally invasive surgery, and localized diagnostic interventions.

4. Conclusion

In summary, we developed 3D-printed biodegradable GelMA-based hydrogel microrobots capable of controlled therapeutic delivery. Using high-resolution direct laser writing, dual-layer GelMA architectures with distinct

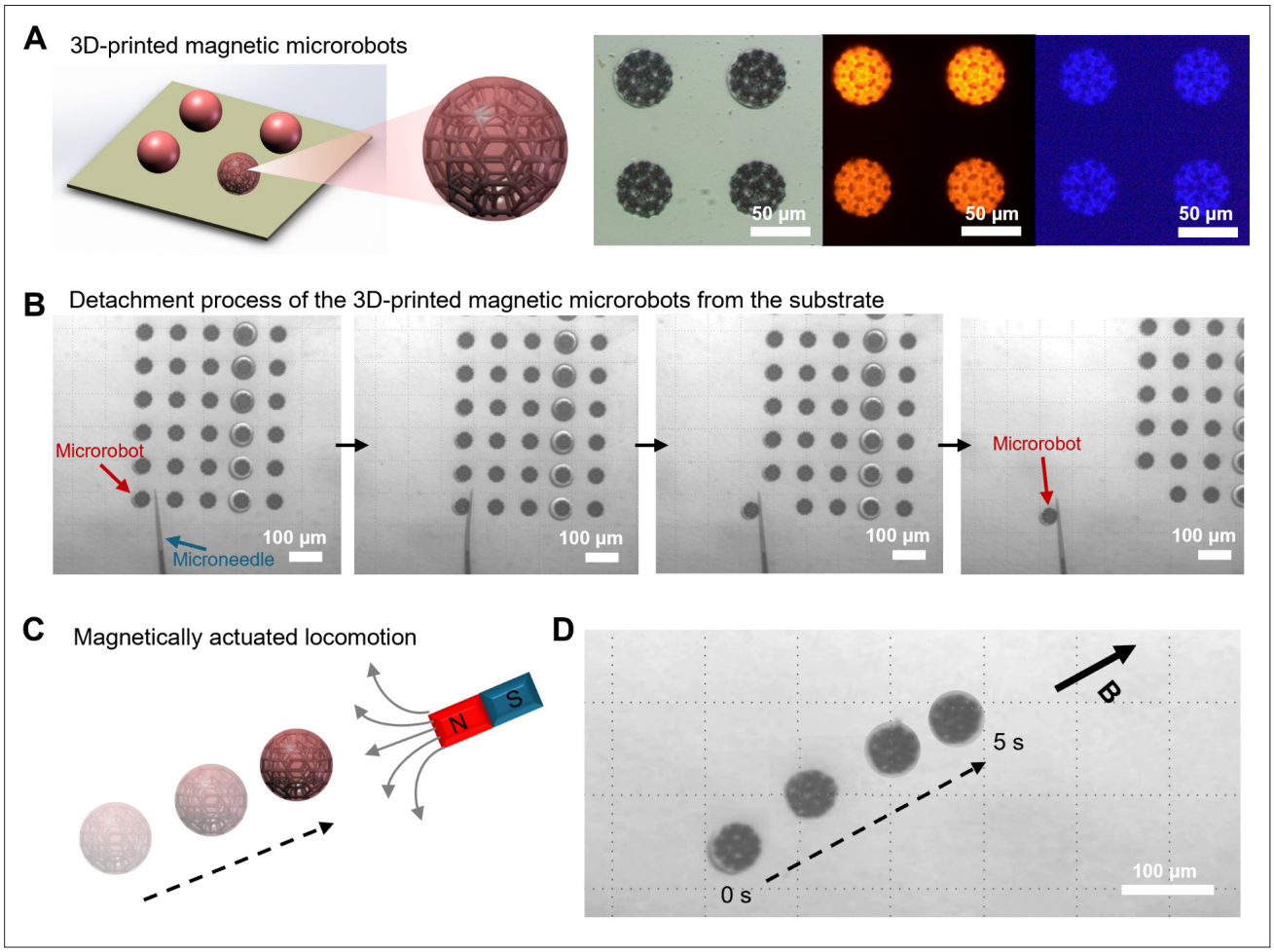


Figure 4. Magnetic actuation of printed GelMA-based microrobots. (A) Schematic illustration along with bright-field, and fluorescence microscopy images of the 3D-printed magnetic microrobots. (B) Microscopy images showing the detachment process of the 3D-printed microrobots from the substrate. (C) Schematic illustration of the magnetic actuation of the 3D-printed microrobots under an external magnetic field. (D) Time-lapse microscopy images showing the magnetically actuated locomotion of the microrobot. Abbreviation: GelMA: Gelatin methacryloyl.

crosslinking degrees were fabricated, enabling tunable degradation and programmable release of encapsulated drugs. The low-crosslinked outer shell serves as a protective barrier, preventing premature release of encapsulated drugs, while the highly crosslinked inner core allows sustained and controllable release upon degradation. The integration of a biocompatible magnetic skeleton composed of PEGDA, PETA, and Fe_3O_4 MNPs provides the microrobots with enhanced mechanical strength and precise magnetic responsiveness, facilitating controlled locomotion under an external magnetic field. These microrobots exhibit excellent biocompatibility and gradual enzymatic degradability, demonstrating their potential as safe and efficient platforms for therapeutic delivery. Overall, this work establishes a versatile strategy for fabricating biodegradable magnetically actuated microrobots, offering new opportunities for targeted drug delivery, tissue engineering, and minimally invasive biomedical interventions.

Although the current system is promising, it still has several limitations. Achieving real-time tracking of microrobot motion and *in situ* monitoring of drug release within deep or dynamic physiological environments remains challenging, yet is crucial for clinical translation. Furthermore, the present study focuses on a single model drug and the delivery of multiple drugs with programmable release profiles at specific times and locations has yet to be realized. Therefore, future research should focus on integrating real-time imaging or sensing modalities to monitor microrobot trajectories and drug release dynamics *in vivo*. The platform should also be expanded to enable the spatiotemporal release of multiple therapeutic agents. Such advancements would further expand the range of applications of biodegradable, magnetically actuated microrobots in targeted drug delivery, tissue engineering, and minimally invasive biomedical interventions.

Acknowledgments

None.

Funding

This work was supported by the Shandong Provincial Natural Science Foundation (Grant No. ZR2025QC1530) and the Taishan Scholars Program.

Conflict of interest

The authors declare they have no competing interests.

Author contributions

Conceptualization: Pan Liao
Formal analysis: Pan Liao, Junyang Li, Shuxun Chen, Yi Hou, Guangda Zhu
Investigation: Pan Liao
Methodology: Pan Liao, Junyang Li, Shuxun Chen
Writing–original draft: Pan Liao, Yi Hou, Guangda Zhu
Writing–review & editing: Pan Liao, Yi Hou, Guangda Zhu, Dong Sun

Ethics approval and consent to participate

Not applicable

Consent for publication

Not applicable

Availability of data

All data are available in the main text or the supplementary materials. Additional data are available from the corresponding author upon request.

References

1. Manzari MT, Shamay Y, Kiguchi H, *et al*. Targeted drug delivery strategies for precision medicines. *Nat Rev Mater.* 2021;6(4):351-370.
doi: 10.1038/s41578-020-00269-6.

2. Huang S, Zhu Y, Zhang L, *et al*. Recent advances in delivery systems for genetic and other novel vaccines. *Adv Mater.* 2022;34(46):2107946.
doi: 10.1002/adma.202107946.

3. Bian X, Zhou L, Luo Z, *et al*. Emerging delivery systems for enabling precision nucleic acid therapeutics. *ACS Nano.* 2025;19(4):4039-4083.
doi: 10.1021/acsnano.4c11858.

4. Yang Z, Xu C, Lee JX, *et al*. Magnetic miniature soft robot with reprogrammable drug-dispensing functionalities: toward advanced targeted combination therapy. *Adv Mater.* 2024;36(48):2408750.
doi: 10.1002/adma.202408750.

5. Wei T, Liu J, Li D, *et al*. Development of magnet-driven and image-guided degradable microrobots for the precise delivery of engineered stem cells for cancer therapy. *Small.* 2020;16(41):1906908.
doi: 10.1002/smll.201906908.

6. Gao J, Xia Z, Gunasekar S, *et al*. Precision drug delivery to the central nervous system using engineered nanoparticles. *Nat Rev Mater.* 2024;9(8):567-588.
doi: 10.1038/s41578-024-00695-w.

7. Tambuyzer E, Vandendriessche B, Austin CP, *et al*. Therapies for rare diseases: therapeutic modalities, progress and challenges ahead. *Nat Rev Drug Discov.* 2020;19(2):93-111.
doi: 10.1038/s41573-019-0049-9.

8. Akhtar A, Andleeb A, Waris TS, *et al*. Neurodegenerative diseases and effective drug delivery: A review of challenges and novel therapeutics. *J Controlled Release.* 2021;330:1152-1167. doi: 10.1016/j.jconrel.2020.11.021.

9. Chen Z, Sánchez MM. Microrobots in gynaecological care and reproductive medicine. *Nat Rev Electr Eng.* 2024;1(12):759-761. doi: 10.1038/s44287-024-00102-0.

10. Nelson BJ, Pané S. Delivering drugs with microrobots. *Science*. 2023;382(6675):1120-1122. doi: 10.1126/science.adh3073.

11. Magdanz V, Khalil ISM, Simmchen J, *et al*. IRONSperm: Sperm-templated soft magnetic microrobots. *Sci Adv.* 2020;6(28):eaba5855. doi: 10.1126/sciadv.aba5855.

12. Wang X, Chen X, Alcântara CCJ, *et al*. MOFBOTS: metal-organic-framework-based biomedical microrobots. *Adv Mater.* 2019;31(27):1901592. doi: 10.1002/adma.201901592.

13. Ju X, Chen C, Oral CM, *et al*. Technology roadmap of micro/nanorobots. *ACS Nano.* 2025;19(27):24174-24334. doi: 10.1021/acsnano.5c03911.

14. Liu D, Wang T, Lu Y. Untethered microrobots for active drug delivery: from rational design to clinical settings. *Adv Healthc Mater.* 2022;11(3):2102253. doi: 10.1002/adhm.202102253.

15. Wang B, Kostarelos K, Nelson BJ, *et al*. Trends in micro-/nanorobotics: materials development, actuation, localization, and system integration for biomedical applications. *Adv Mater.* 2021;33(4):2002047. doi: 10.1002/adma.202002047.

16. Sun M, Wu Y, Zhang J, *et al*. Versatile, modular, and customizable magnetic solid-droplet systems. *Proc Natl Acad Sci.* 2024;121(32):e2405095121. doi: 10.1073/pnas.2405095121.

17. Sun M, Sun B, Park M, *et al*. Individual and collective manipulation of multifunctional bimodal droplets in three dimensions. *Sci Adv.* 2024; 10(29): eadp1439. doi: 10.1126/sciadv.adp1439.

18. Sun M, Yang S, Jiang J, *et al*. Bioinspired self-assembled colloidal collectives drifting in three dimensions underwater. *Sci Adv.* 2023;9(45):eadj4201. doi: 10.1126/sciadv.adj4201.

19. Sun M, Hao B, Yang S, *et al*. Exploiting ferrofluidic wetting for miniature soft machines. *Nat Commun.* 2022;13(1):7919. doi: 10.1038/s41467-022-35646-y.

20. Xia N, Jin D, Yang Z, *et al*. Inverse programming of ferromagnetic domains for 3D curved surfaces of soft materials. *Nat Synth.* 2025;4(5):642-654. doi: 10.1038/s44160-025-00746-2.

21. Yang C, Liu X, Song X, *et al*. Design and batch fabrication of anisotropic microparticles toward small-scale robots using microfluidics: recent advances. *Lab Chip.* 2024;24(19):4514-4535. doi: 10.1039/D4LC00566J.

22. Dong Y, Wang L, Iacovacci V, *et al*. Magnetic helical micro-/nanomachines: Recent progress and perspective. *Matter.* 2022;5(1):77-109. doi: 10.1016/j.matt.2021.10.010.

23. Zhang L, Wang S, Hou Y. Magnetic micro/nanorobots in cancer theranostics: from designed fabrication to diverse applications. *ACS Nano.* 2025;19(8):7444-7481. doi: 10.1021/acsnano.4c10382.

24. Li J, Li X, Luo T, *et al*. Development of a magnetic microrobot for carrying and delivering targeted cells. *Sci Robot.* 2018;3(19):eaat8829. doi: 10.1126/scirobotics.aat8829.

25. Wang Q, Du X, Jin D, *et al*. Real-time ultrasound doppler tracking and autonomous navigation of a miniature helical robot for accelerating thrombolysis in dynamic blood flow. *ACS Nano.* 2022;16(1):604-616. doi: 10.1021/acsnano.1c07830.

26. Dong Y, Wang L, Zhang Z, *et al*. Endoscope-assisted magnetic helical micromachine delivery for biofilm eradication in tympanostomy tube. *Sci Adv.* 2022;8(40):eabq8573. doi: 10.1126/sciadv.abq8573.

27. Sun M, Chan KF, Zhang Z, *et al*. Magnetic microswarm and fluoroscopy-guided platform for biofilm eradication in biliary stents. *Adv Mater.* 2022;34(34):2201888. doi: 10.1002/adma.202201888.

28. Choi J, Hwang J, Kim J, *et al*. Recent progress in magnetically actuated microrobots for targeted delivery of therapeutic agents. *Adv Healthc Mater.* 2021;10(6):2001596. doi: 10.1002/adhm.202001596.

29. Jin D, Yuan K, Du X, *et al*. Domino reaction encoded heterogeneous colloidal microswarm with on-demand morphological adaptability. *Adv Mater.* 2021;33(37): 2100070. doi: 10.1002/adma.202100070.

30. Dong M, Wang X, Chen X, *et al*. 3D-printed soft magnetoelectric microswimmers for delivery and differentiation of neuron-like cells. *Adv Funct Mater.* 2020;30(17):1910323. doi: 10.1002/adfm.201910323.

31. Sun B, Sun M, Zhang Z, *et al*. Magnetic hydrogel micromachines with active release of antibacterial agent for biofilm eradication. *Adv Intell Syst.* 2024;6(2):2300092. doi: 10.1002/aisy.202300092.

32. Terzopoulou A, Wang X, Chen X, *et al*. Biodegradable metal-organic framework-based microrobots (MOFBOTs). *Adv Healthc Mater.* 2020;9(20):2001031. doi: 10.1002/adhm.202001031.

33. Wang B, Chan KF, Yuan K, *et al*. Endoscopy-assisted magnetic navigation of biohybrid soft microrobots with rapid endoluminal delivery and imaging. *Sci Robot.* 2021;6(52):eabd2813. doi: 10.1126/scirobotics.abd2813.

34. Rajabasadi F, Moreno S, Fichna K, *et al*. Multifunctional 4D-printed sperm-hybrid microcarriers for assisted reproduction. *Adv Mater.* 2022;34(50):2204257. doi: 10.1002/adma.202204257.

35. Alapan Y, Bozuyuk U, Erkoc P, *et al*. Multifunctional surface microrollers for targeted cargo delivery in physiological blood flow. *Sci Robot.* 2020;5(42): eaba5726. doi: 10.1126/scirobotics.aba5726.

36. Su L, Jin D, Wang Y, *et al*. Modularized microrobot with lock-and-detachable modules for targeted cell delivery in bile duct. *Sci Adv.* 2023;9(50):eadj0883. doi: 10.1126/sciadv.adj0883.

37. Xin C, Jin D, Hu Y, *et al*. Environmentally adaptive shape-morphing microrobots for localized cancer cell treatment. *ACS Nano.* 2021;15(11):18048-18059. doi: 10.1021/acsnano.1c06651.

38. Chen S, Tan Z, Liao P, *et al*. Biodegradable microrobots for DNA vaccine delivery. *Adv Healthc Mater*. 2023;12(21):2202921. doi: 10.1002/adhm.202202921.

39. Zhang F, Guo Z, Li Z, *et al*. Biohybrid microrobots locally and actively deliver drug-loaded nanoparticles to inhibit the progression of lung metastasis. *Sci Adv.* 2024;10(24):eadn6157. doi: 10.1126/sciadv.adn6157.

40. Llacer-Wintle J, Rivas-Dapena A, Chen X-Z, *et al*. Biodegradable small-scale swimmers for biomedical applications. *Adv Mater.* 2021;22:2102049. doi: 10.1002/adma.202102049.

41. Li J, Yu J. Biodegradable microrobots and their biomedical applications: a review. *Nanomaterials*. 2023;13(10): 1590. doi: 10.3390/nano13101590.

42. He J, Sun Y, Gao Q, *et al*. Gelatin methacryloyl hydrogel, from standardization, performance, to biomedical application. *Adv Healthc Mater.* 2023;12(23):2300395. doi: 10.1002/adhm.202300395.

43. Das S, Jegadeesan JT, Basu B. Gelatin methacryloyl (GelMA)-based biomaterial inks: process science for 3D/4D printing and current status. *Biomacromolecules*. 2024;25(4):2156-2221. doi: 10.1021/acs.biomac.3c01271.

44. Xia B, Liu Y, Xing Y, *et al*. Biodegradable medical implants: reshaping future medical practice. *Adv Sci*. 2025;12(35):e08014. doi: 10.1002/advs.202508014.

45. Wang X, Qin X-H, Hu C, *et al*. 3D printed enzymatically biodegradable soft helical microswimmers. *Adv Funct Mater.* 2018;28(45):1804107. doi: 10.1002/adfm.201804107.

46. Ceylan H, Yasa IC, Yasa O, *et al*. 3D-printed biodegradable microswimmer for theranostic cargo delivery and release. *ACS Nano.* 2019;13(3):3353-3362. doi: 10.1021/acsnano.8b09233.

47. Noh S, Jeon S, Kim E, *et al*. A biodegradable magnetic microrobot based on gelatin methacrylate for precise delivery of stem cells with mass production capability. *Small.* 2022;18(25):2107888. doi: 10.1002/smll.202107888.

48. Landers FC, Hertle L, Pustovalov V, *et al*. Clinically ready magnetic microrobots for targeted therapies. *Science.* 2025;390:6774. doi: 10.1126/science.adx1708.

49. Wong PT, Choi SK. Mechanisms of drug release in nanotherapeutic delivery systems. *Chem Rev.* 2015;115(9):3388-3432. doi: 10.1021/cr5004634.

50. Mitchell MJ, Billingsley MM, Haley RM, *et al*. Engineering precision nanoparticles for drug delivery. *Nat Rev Drug Discov.* 2021;20(2):101-124. doi: 10.1038/s41573-020-0090-8.

51. Paarakh MP, Jose PA, Setty C, *et al*. Release kinetics-concepts and applications. *Int J Pharm Res Technol.* 2023;8(1):12-20. doi: 10.31838/ijprt/08.01.02.

52. Tibbitt MW, Dahlman JE, Langer R. Emerging frontiers in drug delivery. *J Am Chem Soc.* 2016;138(3):704-717. doi: 10.1021/jacs.5b09974.

53. Pinheiro T, Morais M, Silvestre S, *et al*. Direct laser writing: from materials synthesis and conversion to electronic device processing. *Adv Mater.* 2024;36(26):2402014. doi: 10.1002/adma.202402014.

54. Balena A, Bianco M, Pisanello F, *et al*. Recent advances on high-speed and holographic two-photon direct laser writing. *Adv Funct Mater.* 2023;33(39):2211773. doi: 10.1002/adfm.202211773.

55. Jaiswal A, Rastogi CK, Rani S, *et al*. Two decades of two-photon lithography: Materials science perspective for additive manufacturing of 2D/3D nano-microstructures. *iScience*. 2023;26(4):106374. doi: 10.1016/j.isci.2023.106374.

56. O'Halloran S, Pandit A, Heise A, *et al*. Two-photon polymerization: fundamentals, materials, and chemical modification strategies. *Adv Sci.* 2023;10(7):2204072. doi: 10.1002/advs.202204072.

57. Wang H, Zhang W, Ladika D, *et al*. Two-photon polymerization lithography for optics and photonics: fundamentals, materials, technologies, and applications. *Adv Funct Mater.* 2023;2214211.

doi: 10.1002/adfm.202214211.

58. Jia X, Fan X, Chen C, *et al*. Chemical and structural engineering of gelatin-based delivery systems for therapeutic applications: a review. *Biomacromolecules*. 2024;25(2):564-589. doi: 10.1021/acs.biomac.3c01021.

59. Mamidi N, Ijadi F, Norahan MH. Leveraging the recent advancements in GelMA scaffolds for bone tissue engineering: an assessment of challenges and opportunities. *Biomacromolecules*. 2024;25(4):2075-2113. doi: 10.1021/acs.biomac.3c00279.

60. Jiao W, Shan J, Gong X, *et al*. GelMA hydrogel: A game-changer in 3D tumor modeling. *Mater Today Chem*. 2024;38:102111. doi: 10.1016/j.mtchem.2024.102111.

61. Drobecq I, Bigot C, Soppera O, *et al*. Optimizing dimensional accuracy in two-photon polymerization: Influence of energy dose and proximity effects on sub-micrometric fiber structures. *Addit Manuf.* 2025;103:104735. doi: 10.1016/j.addma.2025.104735.

62. Bornillo K, Sorgato M, Lucchetta G. Optimizing two-photon polymerization for rapid and high-resolution prototyping of low-friction microtextured surfaces. *Prog Addit Manuf.* 2025;10(9):5977-5992. doi: 10.1007/s40964-025-00947-3.

63. Fu H, Yu B. 3D micro/nano hydrogel structures fabricated by two-photon polymerization for biomedical applications. *Front Bioeng Biotechnol.* 2024;12:1339450. doi: 10.3389/fbioe.2024.1339450.

64. Dong Y, Wang L, Yuan K, *et al*. Magnetic microswarm composed of porous nanocatalysts for targeted elimination of biofilm occlusion. *ACS Nano.* 2021;15(3):5056-5067. doi: 10.1021/acsnano.0c10010.

65. Xu H, Medina-Sánchez M, Schmidt OG. Magnetic micromotors for multiple motile sperm cells capture, transport, and enzymatic release. *Angew Chem Int Ed.* 2020;59(35):15029-15037. doi: 10.1002/anie.202005657.

66. Liu D, Guo R, Wang B, *et al*. Magnetic micro/nanorobots: a new age in biomedicines. *Adv Intell Syst*. 2022;4(12):2200208. doi: 10.1002/aisy.202200208.

ACCSCIENCE PUBLISHING

International Journal of Bioprinting

RESEARCH ARTICLE

3D-bioprinted active gingival hydrogel for periodontal soft tissue regeneration via TGF-β/Smad and Wnt/β-Catenin-mediated extracellular matrix remodeling

Han Hu[1†], Yue Liao[1†], Jiachen Dong[1], Mengjun Sun[1], Xin Sun[2], Guodong Zhou[3*], and Zhongchen Song[1*]

[1] Department of Periodontology, Shanghai Ninth People's Hospital, Shanghai Jiao Tong University School of Medicine; College of Stomatology, Shanghai Jiao Tong University; National Center for Stomatology; National Clinical Research Center for Oral Diseases; Shanghai Key Laboratory of Stomatology; Shanghai Research Institute of Stomatology, Shanghai, China

[2] Shanghai Key Laboratory of Orthopedic Implants, Department of Orthopedic Surgery, Shanghai Ninth People's Hospital, Shanghai Jiao Tong University School of Medicine, Shanghai, China

[3] Department of Stomatology, Shanghai Yangpu District Kongjiang Hospital, Shanghai, China

[†]These authors contributed equally to this work.

***Corresponding authors:**
Zhongchen Song
(szhongchen@sina.com)

Guodong Zhou
(18321801391@163.com)

Citation: Hu H, Liao Y, Dong J, *et al.* 3D-bioprinted active gingival hydrogel for periodontal soft tissue regeneration via TGF-β/Smad and Wnt/β-catenin-mediated extracellular matrix remodeling. *Int J Bioprint.* 2026;12(1):398-412. doi: 10.36922/IJB025430444

Received: October 26, 2025
Revised: November 28, 2025
Accepted: December 4, 2025
Published online: December 4, 2025

Copyright: © 2025 Author(s). This is an Open Access article distributed under the terms of the Creative Commons Attribution License, permitting distribution, and reproduction in any medium, provided the original work is properly cited.

Publisher's Note: AccScience Publishing remains neutral with regard to jurisdictional claims in published maps and institutional affiliations.

Abstract

Soft tissue management is essential in periodontal, orthodontic, and implant therapies, yet autologous grafts remain limited by donor-site morbidity, inconsistent tissue quality, and restricted availability. To address these challenges, we developed an active gingival hydrogel (AGH) composed of gelatin methacrylate, chondroitin sulfate methacrylate, and gingival fibroblasts, which was fabricated into cell-laden hydrogels using extrusion-based 3D bioprinting. The AGH exhibited excellent rheological performance, print fidelity, and interconnected porous microstructures that supported nutrient diffusion and cell migration. Gingival fibroblasts cocultured with the AGH showed robust adhesion, proliferation, and collagen matrix deposition, accompanied by significant upregulation of fibronectin and type I collagen. Mechanistic studies revealed that these effects were mediated through activation of the Wnt/β-catenin and transforming growth factor-β/Smad signaling pathways, which synergistically regulate extracellular matrix remodeling and epithelial keratinization. *In vivo* experiments demonstrated that AGH implantation significantly enhanced gingival thickness, collagen density, and neovascularization while reducing inflammatory infiltration, as verified by magnetic resonance imaging as well as histological and immunohistochemical analyses. Furthermore, coculture with gingival epithelial cells promoted upregulation of *Krt10* and *Krt14*, indicating improved epithelial differentiation. Collectively, this study establishes a 3D-bioprinted active gingival hydrogel as a biomimetic and functional substitute for autologous grafts, offering a promising strategy for periodontal and peri-implant soft tissue regeneration.

Keywords: Bioprinting; Gingival fibroblast; Gingival phenotype; Soft tissue augmentation; Tissue engineering

1. Introduction

Periodontal and peri-implant soft-tissue augmentation frequently relies on autologous connective tissue grafts, which remain the clinical gold standard for increasing gingival thickness and improving long-term stability.[1-3] However, their application is fundamentally limited by donor-site morbidity, restricted tissue availability, and postoperative discomfort.[4-6]

Beyond autologous free gingival grafts and connective tissue grafts, a variety of xenogeneic and allogeneic soft-tissue substitutes—such as acellular dermal matrices and porcine collagen matrices—have been introduced to reduce donor-site morbidity and surgical time while improving patient comfort.[7-9] These materials can increase keratinized tissue width and soft-tissue thickness around teeth and implants compared with flap procedures alone, and they are now widely used in daily practice. However, recent clinical trials and systematic reviews[3,10,11] consistently indicate that most soft-tissue substitutes still fall short of autologous grafts in the magnitude and long-term stability of keratinized tissue gain and mucosal thickening, particularly when a stable ≥2-mm band of keratinized tissue is desired. In addition, currently available substitutes are largely acellular and function as passive scaffolds, with limited ability to actively modulate extracellular matrix (ECM) remodeling or epithelial phenotype.

In this context, there is a clear need for next-generation, biology-informed constructs that combine the surgical advantages of soft-tissue substitutes with the biological performance of autologous connective tissue.

Gingival fibroblasts (GFs) play a central role in gingival phenotype maintenance and wound healing.[12] Compared with fibroblasts in nonkeratinized oral mucosa, GFs exhibit stronger ECM synthetic capacity and higher expression of collagen (COL)1, COL3, and fibronectin (FN)—molecules essential for collagen remodeling, mechanical resistance, and epithelial–mesenchymal crosstalk.[12-15] Recent studies on oral mucosal repair also highlight the importance of the Wnt/β-catenin and transforming growth factor (TGF)-β/Smad pathways in regulating fibroblast activation, ECM deposition, and keratinocyte differentiation. Wnt/β-catenin signaling promotes fibroblast migration and fibronectin transcription, whereas TGF-β/Smad is the key driver of COL1/COL3 synthesis during connective tissue maturation.[16,17] Together, these pathways contribute to the rapid, scar-resistant healing characteristic of the gingiva and provide a mechanistic basis for designing biomaterials that can actively modulate cellular behavior.

To functionally mimic the ECM microenvironment of gingival connective tissue, gelatin methacrylate (GelMA) and chondroitin sulfate methacrylate (ChsMA) are particularly suitable candidates. GelMA provides arginine-glycine-asparagine (RGD) adhesion motifs and an adjustable stiffness that resembles that of the lamina propria, supporting fibroblast attachment and elongation. ChsMA, a glycosaminoglycan-derived component, enhances hydration, viscoelasticity, and collagen synthesis while modulating inflammation.[18,19] Together, these materials can create a microenvironment favorable for fibroblast proliferation, ECM remodeling, and subsequent epithelial keratinization.

Three-dimensional (3D) bioprinting further enables the fabrication of cell-laden constructs with controlled architecture, interconnected porosity, and reproducible mechanical properties—features that conventional scaffolds cannot achieve.[20,21] By precisely arranging bioinks containing viable fibroblasts within a biomimetic matrix, bioprinting provides a promising platform for engineering living gingival-like tissue that more closely recapitulates the hierarchical structure and function of native connective tissue.

In this study, guided by single-cell transcriptomic profiling of gingival and oral mucosal fibroblasts, we designed an "active gingival hydrogel" (AGH) based on a photocrosslinkable GelMA/ChsMA matrix laden with GFs. This construct was designed to recreate a gingiva-like extracellular microenvironment, promote FN/COL1-mediated matrix remodeling, and engage Wnt/β-catenin and TGF-β/Smad signaling to support soft-tissue thickening and epithelial keratinization. The present study evaluates the printability, mechanical behavior, and biocompatibility of this construct, elucidates its underlying molecular mechanisms *in vitro*, and tests its capacity to augment gingival thickness in a rat incisor model.

This work seeks to provide a biologically active alternative to autologous grafts and to offer new insights into the design of functional substitutes for periodontal soft-tissue augmentation.

2. Materials and methods

2.1. Cell isolation and primary culture

Gingival tissue specimens containing both epithelial and connective layers were aseptically harvested from the hard palate of Sprague–Dawley rats ($n = 3$).

For GFs, fresh tissues were immediately immersed in sterile phosphate-buffered saline (PBS; Gibco, USA) supplemented with 1% penicillin–streptomycin (Gibco). Sequential enzymatic digestion was performed using collagenase IV and 0.25% trypsin–ethylenediaminetetraacetic acid (EDTA) for 60 min at 37°C. Cell suspensions were centrifuged and resuspended in Dulbecco's Modified Eagle Medium (DMEM; Gibco)

containing 10% fetal bovine serum (FBS; Gibco) and 1% antibiotics. Primary cells (P0) were expanded until reaching 80–90% confluence and subsequently passaged. Cells at passages 3–4 were used for experiments.

For gingival epithelial cells (GECs), tissues were subjected to cold enzymatic digestion with 0.4% collagenase IV for 24 h at 4°C. Epithelial sheets were mechanically separated and further digested with 0.25% trypsin–EDTA for 15 min. Cells were cultured in defined keratinocyte-serum-free medium (Gibco).

2.2. Bioprinting of scaffolds

The bioink formulations employed were: (i) 5 wt% GelMA; (ii) 5 wt% GelMA + 1 wt% ChsMA; and (iii) 5 wt% GelMA + 3 wt% ChsMA. GelMA and ChsMA were purchased from Engineering For Life Bioscience, China.

For the cell-laden constructs (AGH), passage 3–4 GFs were harvested with 0.25% trypsin–EDTA, centrifuged, and resuspended in the prewarmed bioink at a final density of 2×10^6 cells/mL. The acellular hydrogel (GC) used the same polymer formulations without cells. All printing procedures were performed using a pneumatic extrusion bioprinter equipped with a 25G stainless-steel nozzle. The printing pressure and speed were kept constant for all groups (pressure: 15–20 kPa; speed: 5 mm/s) to ensure dimensional consistency.

Immediately after printing, the constructs were crosslinked under 405 nm visible light (10 mW/cm^2) for 60 s to obtain stable hydrogels. For *in vitro* experiments, hydrogels were printed and cultured in complete DMEM. For *in vivo* implantation, GC and AGH constructs were printed using the same protocol and then trimmed into slabs of identical length, width, and thickness to fit the buccal gingival flap area.

In this study, GC used in cell and animal experiments refers to 5 wt% GelMA + 3 wt% ChsMA, and AGH refers to cell-laden GC.

2.3. Physicochemical characterization

For morphological analysis, lyophilized scaffolds were gold-sputtered (10 nm) and imaged using scanning electron microscopy (SEM; Zeiss SIGMA HD, Germany; 5 kV).

Rheological properties were evaluated through dynamic oscillatory measurements performed on a rotational rheometer (AR-G2, TA Instruments, USA) with a 20 mm cone–plate geometry. Measurements were conducted at 37°C under 1% strain and 1 Hz frequency, and the storage modulus (*G*') and loss modulus (*G*") were recorded over a 10-min period.

Mechanical testing was performed using a universal testing machine (Instron 5567, USA) equipped with a 0.1 N load cell, and the compressive modulus was determined at a strain rate of 1 mm/min.

2.4. Water contact angle measurement

Contact angles were measured at room temperature using a contact angle goniometer (OCA 20, DataPhysics Instruments, Germany). A 2–3 μL droplet of deionized water was gently deposited onto the hydrogel surface using a microsyringe, and images were captured within 5 s of droplet placement. The left and right contact angles were automatically calculated by the instrument software, and their mean value was recorded as the contact angle for each droplet.

2.5. Biocompatibility assessment

Biocompatibility was assessed using the Cell Counting Kit-8 (CCK-8) assay, viability staining, and cytoskeletal analysis: Sterile hydrogel discs of each formulation (5% GelMA, 5% GelMA + 1% ChsMA, and 5% GelMA + 3% ChsMA) were prepared as described above, and cells cultured on tissue culture plates without hydrogels served as the control group. Relative cell numbers were quantified by measuring optical density at 450 nm using a microplate reader (Multiskan FC, Thermo Fisher Scientific, USA).

Cell viability was further examined using acridine orange/ethidium bromide dual staining (Beyotime Biotechnology, China) on days 1, 3, 5, and 7, and live/dead cell ratios were analyzed by fluorescence microscopy (Zeiss Axio Observer).

For cytoskeletal organization, AGH constructs were fixed with 4% paraformaldehyde for 30 min and permeabilized with 0.5% Triton X-100 for 10 min. F-actin was stained with rhodamine phalloidin (1:200; Cytoskeleton, USA), and nuclei were labeled with 4',6-diamidino-2-phenylindole (DAPI; 1:1000; Thermo Fisher, USA). 3D morphology was reconstructed using confocal laser scanning microscopy (Zeiss LSM 880).

2.6. Scratch wound assay

Confluent monolayers of GFs and GECs in six-well plates were scratched with a sterile 200 μL pipette tip. Detached cells were removed by washing with PBS, and the cultures were then maintained in low-serum medium (2% FBS). Cell migration was monitored over a 24-h period. Experimental groups included GFs (tissue-culture-plastic–grown fibroblasts), GC (hydrogel-only material control), and AGH.

2.7. Single-cell RNA sequencing data analysis

Publicly available single-cell RNA-sequencing data were obtained from the Gene Expression Omnibus dataset

GSE164241, which contains transcriptional profiles of human gingival mucosa and oral buccal mucosa. Raw data were processed using Seurat v4.1.1 (Satija Lab USA). Quality control included removal of genes expressed in fewer than three cells and exclusion of cells with >20% mitochondrial gene content. Data were normalized by SCTransform with 3,000 variable features. Clustering was performed using Uniform Manifold Approximation and Projection (resolution = 0.6), and differentially expressed genes were identified using the FindMarkers function.

2.8. Quantitative reverse transcription polymerase chain reaction analysis

Complementary DNA (cDNA) was synthesized from total RNA using a reverse transcription kit (Takara, Japan) and subsequently amplified with SYBR Green Master Mix (Roche, Switzerland). Relative gene expression was calculated using the 2^−ΔΔCt method. The primer sequences used for each target gene are listed in Table 1.

2.9. Western blotting

Proteins were extracted, separated by sodium dodecyl sulfate–polyacrylamide gel electrophoresis, and transferred onto polyvinylidene fluoride membranes. After blocking with 5% BSA, membranes were incubated with primary antibodies (β-catenin, N-cadherin, COL-I, SMAD2/3/4) overnight at 4°C, followed by incubation with horseradish peroxidase-conjugated secondary antibodies. Chemiluminescent signals were detected using ECL Prime (GE Healthcare, USA) and quantified with Image-Pro Plus 6.0 (Media Cybernetics, USA).

2.10. Immunofluorescence

Cells or tissue sections were incubated with primary antibodies overnight at 4°C, followed by rhodamine-conjugated anti-rabbit IgG (1:200; Invitrogen, USA). Nuclei were counterstained with DAPI (5 μg/mL). Images were acquired using a Zeiss Axio Imager M2 microscope.

2.11. Animal models and groupings

Eight-week-old Sprague–Dawley rats (n = 3) were used. A partial-thickness flap was raised on the buccal side of the maxillary incisors by a mesiodistal incision. The control group received direct suturing, whereas the experimental groups received implantation of GC or AGH under the flap before suturing. Animals were randomly assigned to the control, GC, or AGH groups. This study was carried out following the recommendations of the Animal Care and Experiment Committee of Shanghai Ninth People's Hospital, Shanghai Jiao Tong University School of Medicine. The protocol was approved by the Animal Care and Experiment Committee of Shanghai Ninth People's Hospital, Shanghai Jiao Tong University School of Medicine (SH9H-2024-A1046-SB), and conducted in accordance with institutional guidelines for the care and use of laboratory animals and the Animal Research: Reporting of *In Vivo* Experiments recommendations.

2.12. Magnetic resonance imaging

At 6 weeks after surgery, gingival thickness was evaluated using a small-animal magnetic resonance imaging (MRI) system (Bruker BioSpin MRI GmbH, Germany). Rats were anesthetized and placed in a prone position in a dedicated animal cradle, with the maxillary incisors aligned along a predefined reference line to standardize head orientation. T2-weighted coronal images of the maxillary incisor region were acquired using a rapid acquisition with relaxation enhancement sequence.

To minimize spatial variability, coronal slices were obtained perpendicular to the long axis of the maxillary incisors. Gingival thickness was measured at the mid-buccal aspect of the incisors using the cemento–enamel junction and incisal edge as anatomical landmarks. For each animal, measurements were taken on three consecutive slices centered on the mid-buccal site; the distances from the outer gingival surface to the underlying hard-tissue reference plane were recorded and averaged to obtain a single gingival thickness value per site. Image analysis was performed in ImageJ (Developer, Country) by a single examiner blinded to group allocation. Repeated measurements on a randomly selected subset of scans confirmed good intra-observer reproducibility.

After MRI acquisition, animals were euthanized, and the maxillary anterior segments were harvested for subsequent histological and immunohistochemical analyses.

Table 1. Primer sequences used for quantitative reverse transcription polymerase chain reaction

Gene name	Forward	Reverse
Col1a1	5'-CCTGGTAAAGATGGTGCC-3'	5'-CACCAGGTTCACCTTTCG-3'
Fn	5'-GACCTGACAGTCGGAGAAG-3'	5'-TGACACGGAGTAACGGTTC-3'
Krt10	5'-GAGGAGCTGCTGAAGAAGG-3'	5'-CTGGTGGTGTTGTTGATGG-3'
Krt14	5'-CCAGACCTACAGCAACAGC-3'	5'-GGTCCAGGTTCTCTTGGTG-3'
Gapdh	5'-GATGCCTGCTTCACCACCT-3'	5'-GTGGTGCAGGATGCATTGCT-3'

2.13. Histological staining

Samples were fixed in formalin, dehydrated through a graded ethanol series, and embedded in paraffin. Sections (5 μm) were stained with hematoxylin and eosin (H&E) and Masson's trichrome and examined under an optical microscope.

For immunohistochemistry, sections were rehydrated, subjected to antigen retrieval, and incubated overnight at 4°C with a cluster of differentiation (CD)34 antibody (1:100; Abcam, Country). A biotinylated secondary antibody and avidin–biotin–peroxidase complex were applied, and staining was visualized with 3,3'-diaminobenzidine substrate. Sections were counterstained with hematoxylin, mounted, and examined microscopically.

2.14. Statistical analysis

All data are presented as mean ± standard deviation. Comparisons between two groups were performed using independent-samples *t*-tests. One-way analysis of variance was used for multiple group comparisons in GraphPad Prism 9.0 (Developer, Country). A p-value < 0.05 was considered statistically significant.

3. Results

3.1. Physicochemical properties of 3D-bioprinted scaffolds

Figure 1A shows that rheological experiments confirmed the normal photocuring behavior of GelMA and GelMA–ChsMA hydrogels. Prior to 405 nm light irradiation, all groups exhibited a *G*" higher than the *G*', indicating that the inks remained in a liquid state and underwent viscous deformation. After 30 s of irradiation, *G*' exceeded *G*", confirming the transition into a hydrogel. Among all formulations, the 5% GelMA + 3% ChsMA displayed a significantly higher *G*' (approximately 3.7 kPa) compared with the other groups (Figure 1B).

As shown in Figure 1C, the stress–strain curves of all three groups exhibited nonlinear elastic behavior within the 40% strain range. Furthermore, Figure 1D demonstrates that the compressive strength of the 5% GelMA + 3% ChsMA group reached 6.4 kPa, which was significantly greater than that of the other formulations.

Figure 1E illustrates that the printed constructs in all groups maintained intact, interconnected grid structures without evidence of pore collapse. SEM images corroborated the presence of open, porous architectures with uniformly distributed macropores. As the ChsMA concentration increased, well-aligned microfilaments with distinct boundaries were observed (Figure 1F). The 5% GelMA + 3% ChsMA group exhibited smaller and more uniformly distributed pores compared with the 5% GelMA + 1% ChsMA group.

Surface wettability of the hydrogels was evaluated by static water contact angle measurements (Figure 1). Pure 5% GelMA exhibited a moderate contact angle of

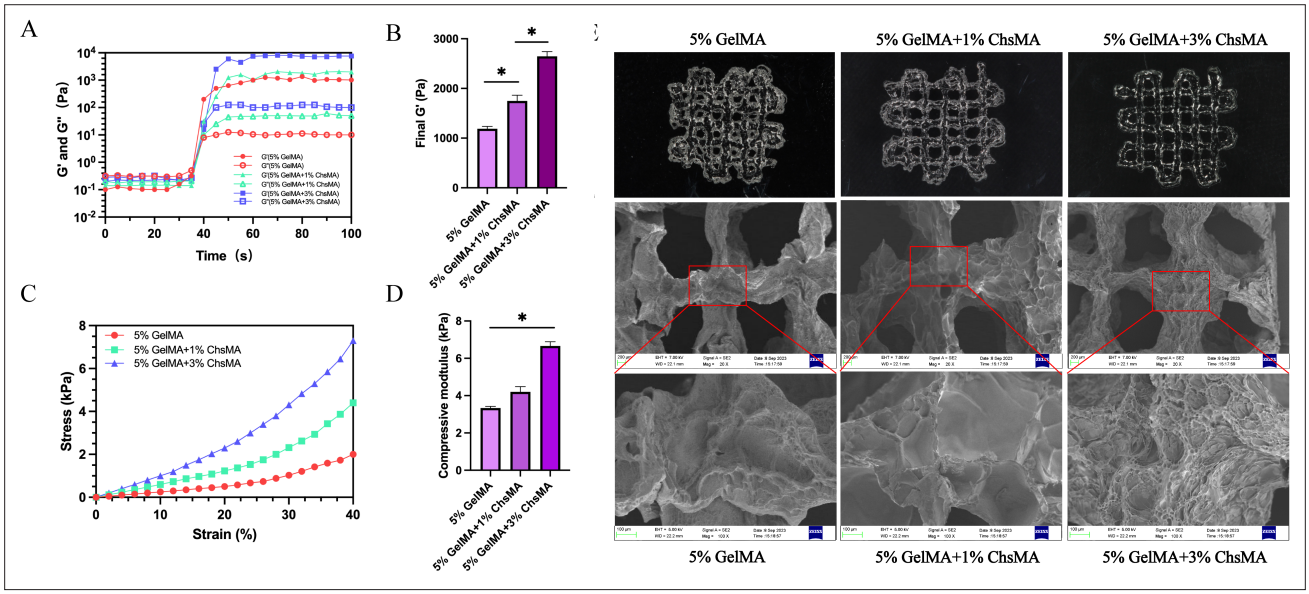


Figure 1. Rheological and physicochemical properties and morphology of 3D-bioprinted scaffolds. (A) Light-curing process of scaffolds with different groups. (B) Final storage modulus (*G*') after curing. (C) Stress–strain curves of different groups. (D) Compressive modulus of different groups. (E) Morphology of printed constructs captured using digital camera. (F) Scanning electron microscopy images of different groups (magnifications = 20× [top panels], 100× [bottom panels]; scales = 200 μm [top panels], 100 μm [bottom panels]). Notes: *p < 0.05, **p < 0.01, ***p < 0.001; n = 3. Abbreviations: ChsMA, Chondroitin sulfate methacrylate; GelMA, Gelatin methacrylate.

approximately 77.5°, whereas the incorporation of ChsMA markedly increased surface hydrophilicity, decreasing the contact angle to about 57.5° for 5% GelMA + 1% ChsMA and 46.0° for 5% GelMA + 3% ChsMA. Thus, higher ChsMA content resulted in a progressively more hydrophilic hydrogel surface.

The effects of different hydrogel compositions on GF viability and proliferation were further evaluated by CCK-8 assay over 7 days (Figure S2). In all groups, including the plate-cultured control as well as the 5% GelMA, 5% GelMA + 1% ChsMA, and 5% GelMA + 3% ChsMA hydrogels, OD450 values increased continuously from day 1 to day 7, indicating sustained cell growth without detectable cytotoxicity. At each time point, no statistically significant differences in cell proliferation were observed among the hydrogel formulations or between the hydrogel groups and the control.

Collectively, these characterization results demonstrate that the 5% GelMA + 3% ChsMA bioink possesses favorable rheological and mechanical properties suitable for extrusion-based bioprinting. Therefore, 5% GelMA + 3% ChsMA was selected as the working composition for all subsequent cell culture and *in vivo* experiments.

3.2. Identification of gingiva-specific extracellular matrix-remodeling signatures by single-cell transcriptomic profiling

To investigate the intrinsic molecular characteristics of GFs, we reanalyzed the public single-cell RNA-sequencing dataset GSE164241, which includes gingival and oral mucosal tissues. Unsupervised clustering revealed four major cell compartments—epithelial (*KRT14*, *KRT5*, *S100A2*, *CTSA*, *SPRR1B*), fibroblast (*LUM*, *COL3A1*, *DCN*, *COL1A1*, *CFD*), endothelial (*ACKR1*, *RAMP2*, *SELE*, *VWF*, *PECAM1*), and immune populations (*CD69*, *CD52*, *CXCR4*, *PTPRC*, *HCST*)—each expressing canonical markers (Figure 2A and B).

Comparison of tissue composition showed similar proportions of major cell types between the gingiva and oral mucosa (Figure 2C). Reclustering of fibroblasts further identified four transcriptionally distinct subpopulations

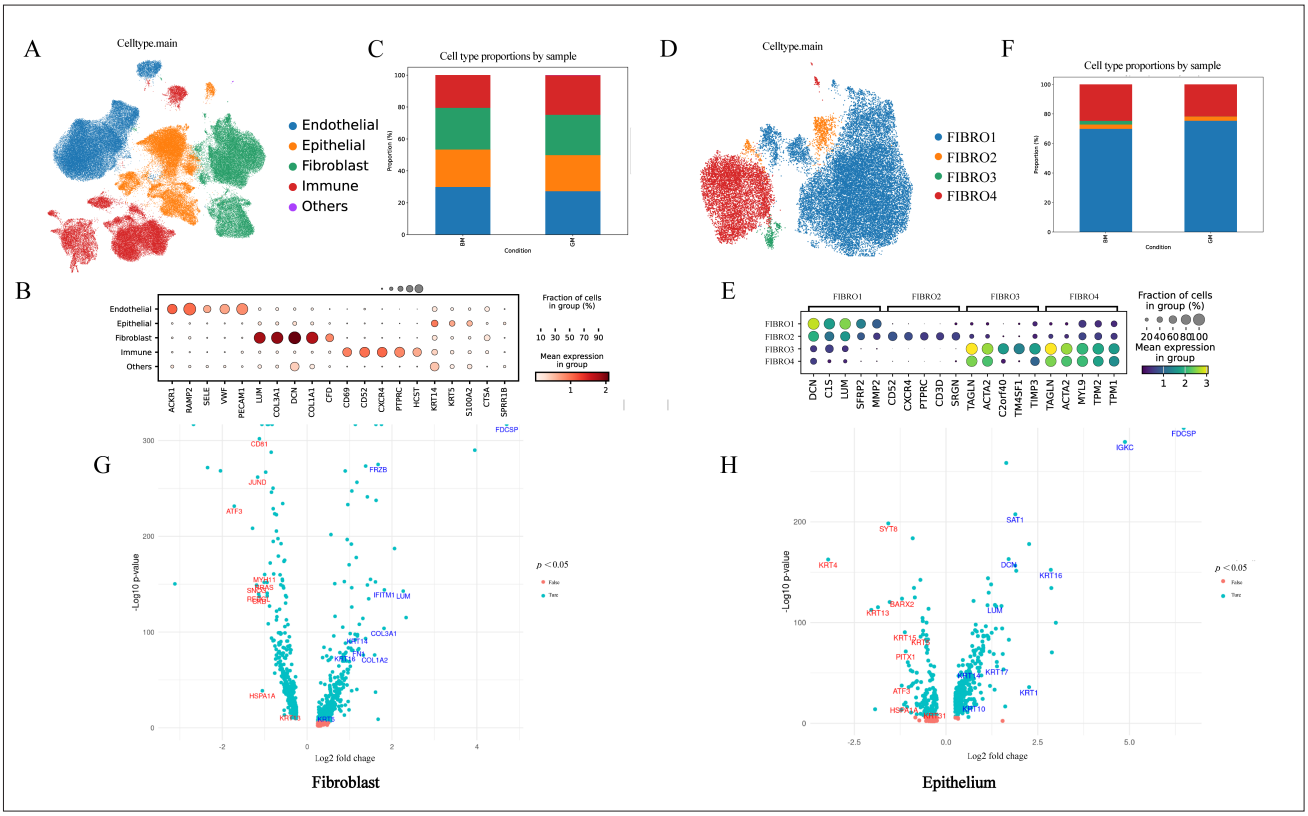


Figure 2. Differential gene expression between fibroblasts and epithelial cells in oral mucosa and gingiva. (A) After dimensionality reduction and clustering, five cell subpopulations were identified. (B) Bubble plots displaying signature gene expression in each cell type. (C) Proportion of different cell subpopulations in the gingiva and oral mucosa. (D) Reclustering of fibroblasts identified four subtypes. (E) Bubble plots showing signature gene expression in each fibroblast subtype. (F) Proportion of fibroblast subpopulations in the gingiva and oral mucosa. (G) Volcano plot exhibiting differential gene expression in gingival and oral mucosal tissue fibroblasts. (H) Volcano plots displaying differential gene expression in gingival and oral mucosal tissue epithelial cells. Note: Red, downregulated genes; blue, upregulated genes.

(Figure 2D). Among these, FIBRO1 displayed a matrix-remodeling phenotype characterized by high expression of *DCN*, *LUM*, *COL3A1*, and other ECM-associated genes (Figure 2E). This population was enriched in gingival tissue (Figure 2F), suggesting the presence of a gingiva-specific fibroblast subset with enhanced regenerative potential.

Differential gene expression analysis further demonstrated that GFs exhibited significantly elevated expression of key ECM components, including *COL1A1* and *FN1*, compared with oral mucosal fibroblasts (Figure 2G and H). These two genes are central regulators of collagen organization, cell adhesion, and tissue remodeling. In contrast, epithelial cells showed higher levels of keratinization-related genes *KRT10* and *KRT14*.

Collectively, the single-cell analysis highlights that GFs possess a distinct ECM-remodeling signature dominated by *COL1* and *FN*, providing a strong biological rationale for selecting these genes as downstream molecular readouts in our hydrogel-based experiments.

3.3. Biocompatibility of active gingival hydrogel and upregulation of extracellular matrix-related genes in gingival fibroblasts

Live/dead staining showed that GFs maintained high viability within the hydrogel throughout the 1-, 3-, 5-, and 7-day culture period, with only a few nonviable cells appearing at later time points (Figure 3A). These findings indicate that the GelMA/ChsMA matrix provides a permissive environment for cell survival. Cytoskeleton staining further revealed progressive morphological changes: fibroblasts initially appeared rounded but

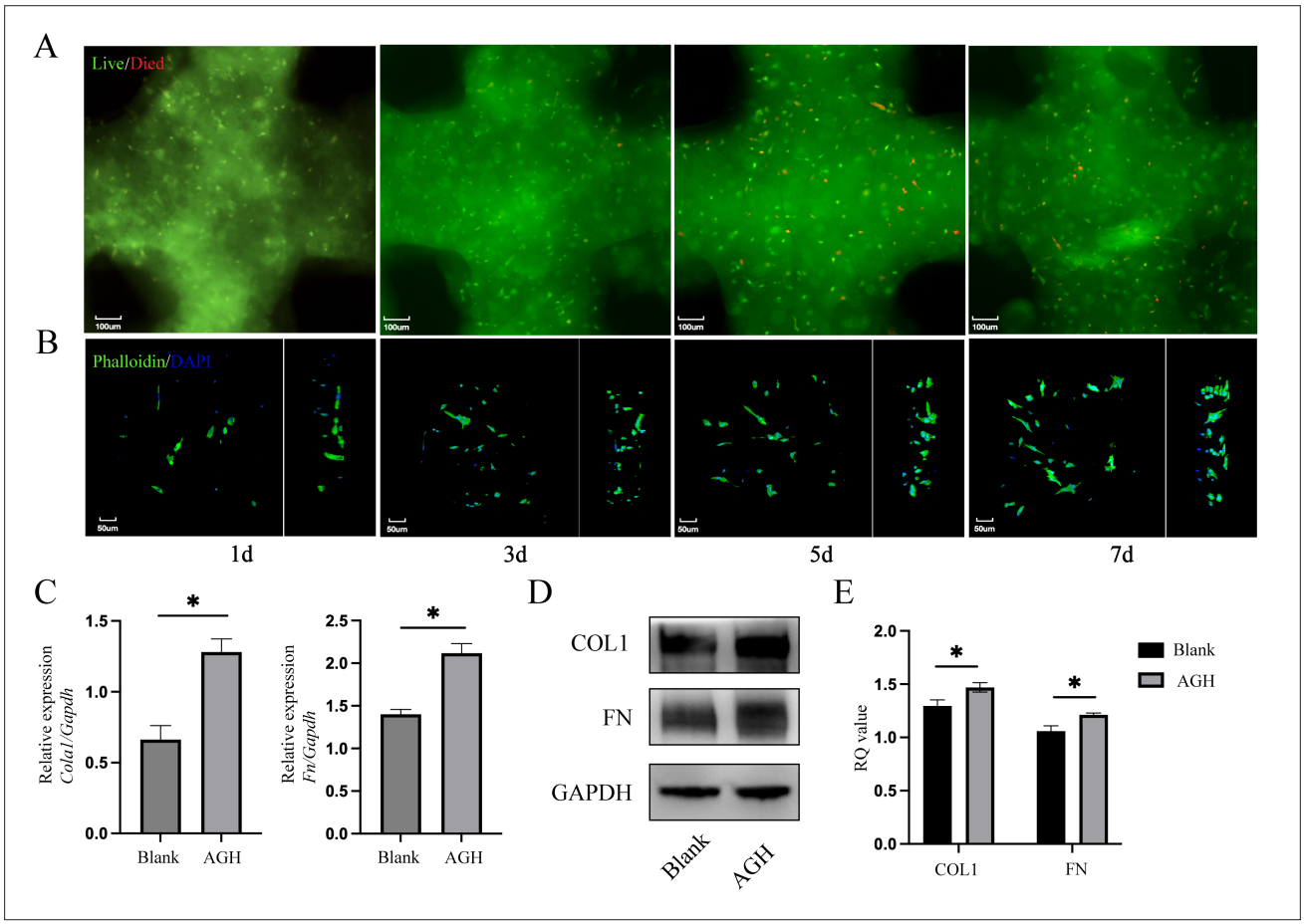


Figure 3. Biocompatibility and promotion of extracellular matrix synthesis by the bioink. (A) Live-dead staining of gingival fibroblasts in bioprinted scaffolds (magnification = 200×; scale = 100 μm). (B) Cytoskeletal staining of gingival fibroblasts in bioprinted scaffolds (magnification = 400×; scale = 50 μm). (C) Relative gene expression of *Col1a1* and *Fn* in bioprinted gingival fibroblast scaffolds. (D) Protein expression levels of COL1 and FN in bioprinted gingival fibroblast scaffolds. (E) Quantification of COL1 and FN expression. Notes: Blank: Tissue culture control. $^{*}p < 0.05$, $^{**}p < 0.01$, $^{***}p < 0.001$; $n = 3$. Abbreviations: AGH, Active gingival hydrogel; COL1, Collagen type 1; d, Day(s); FN, Fibronectin; GAPDH, Glyceraldehyde 3-phosphate dehydrogenase.

gradually expanded along the hydrogel network, displaying polygonal cell bodies and distinct pseudopodia by day 7 (Figure 3B). Such cytoskeletal organization is consistent with enhanced adhesion and early migratory activity within the 3D microenvironment.

At the molecular level, cells cultured in AGH showed significantly elevated transcription of *Col1a1* and *Fn* compared with cells cultured on standard tissue culture plastic (Figure 3C). Western blot analysis confirmed the corresponding increase in protein levels (Figure 3D), and quantification of band intensities further supported this trend (Figure 3E). Immunofluorescence staining also demonstrated more abundant and organized deposition of COL1 and FN within the AGH constructs, reflecting active matrix remodeling by the embedded fibroblasts.

Together, these observations show that the AGH not only supports fibroblast survival but also promotes their adhesion, spreading, and ECM production. The coordinated upregulation of COL1 and FN—two key structural proteins essential for matrix remodeling and cell–matrix interactions—indicates that GFs actively engage with and remodel the printed hydrogel, providing a biological foundation for subsequent tissue regeneration.

3.4. Effects of active gingival hydrogel on fibroblast activity and epithelial keratinization

Gingival fibroblasts were cultured under three conditions: tissue culture plastic (GFs), acellular hydrogel (GC), and AGH, respectively. Cytoskeletal staining (Figure 4A) revealed that fibroblasts in the AGH group exhibited superior spreading morphology compared with those in the GFs and GC groups. Specifically, AGH-treated cells displayed a pronounced polygonal shape, broader spreading, more uniform cytoskeletal distribution, thicker actin fibers, and enhanced structural integrity.

Scratch assay results (Figure 4B) showed that the AGH group achieved the fastest wound closure, with the smallest residual scratch area at 24 hours. Consistently, Western blotting (Figure 4C and D) and immunofluorescence staining (Figure 4E and F) demonstrated that *Col1a1* and *Fn* expression in fibroblasts was significantly elevated in the AGH group. Furthermore, when AGH was cocultured with GECs, transcription levels of *Krt10* and *Krt14* were upregulated (Figure 4G and H), suggesting a potential role for AGH in promoting epithelial differentiation and keratinization.

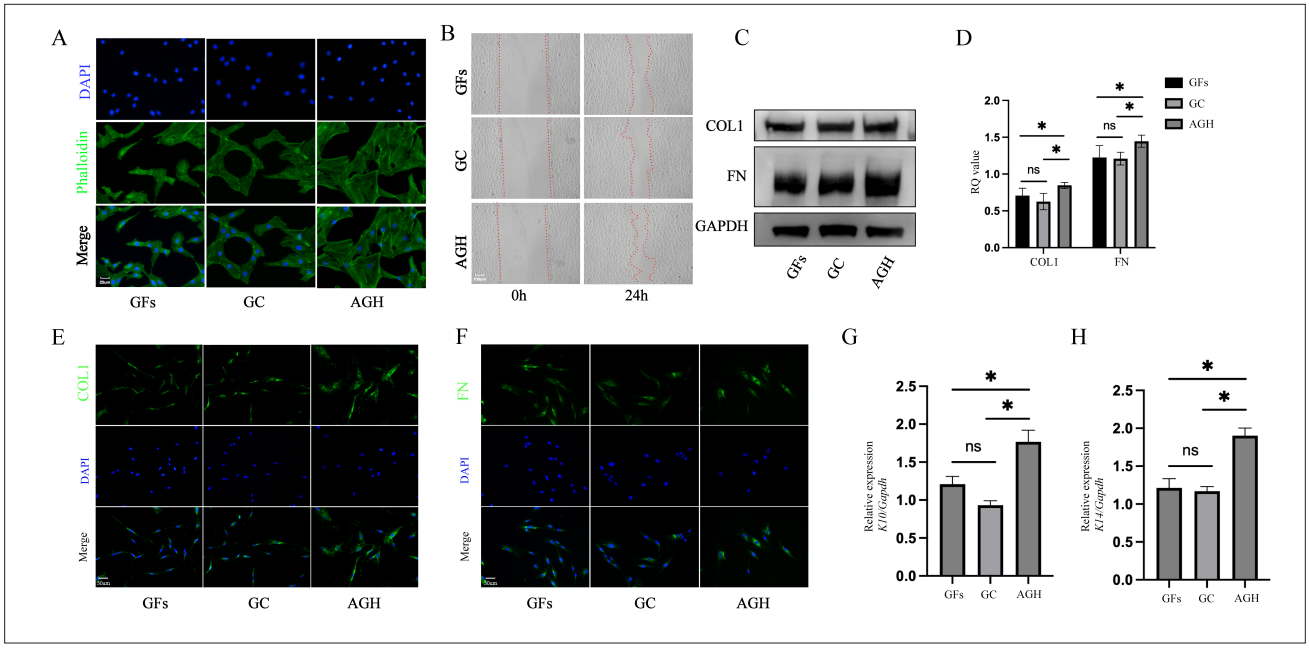


Figure 4. The impact of bioprinted scaffolds on gingival fibroblasts and epithelial cells. (A) Gingival fibroblast adhesion (magnification = 800×; scale = 25 μm). (B) Gingival fibroblast migration (magnification = 200×; scale = 100 μm). (C) Protein expression of COL1 and FN in gingival fibroblasts. (D) Quantification of COL1 and FN proteins in WB. (E,F) Immunofluorescence staining of COL1 and FN in gingival fibroblasts treated with GFs, GC, and AGH for 24 h (magnifications = 400× [E], 400× [F]; scales = 50 μm [E], 50 μm [F]). (G,H) Relative gene expression of K10 and K14 in epithelial cells. Note: $^{*}p < 0.05$, $^{**}p < 0.01$, $^{***}p < 0.001$; $n = 3$. Abbreviations: AGH, Active gingival hydrogel; COL, Collagen type 1; DAPI, 4',6-diamidino-2-phenylindole; FN, Fibronectin; GAPDH, Glyceraldehyde 3-phosphate dehydrogenase; GC, Acellular hydrogel; GFs, Gingival fibroblasts; ns, Not significant.

3.5. Activation of Wnt/β-catenin and transforming growth factor-β/Smad signaling pathways by active gingival hydrogel

COL1 and FN are well-recognized ECM components that can activate Wnt/β-catenin and TGF-β/Smad signaling pathways, both of which play critical roles in fibroblast-mediated tissue remodeling and keratinization. These findings suggest that the FIBRO1 subpopulation may contribute to postgrafting keratinization in nonkeratinized epithelium through ECM–signaling interactions.

To further investigate the underlying mechanisms, we examined the involvement of the Wnt/β-catenin and TGF-β/Smad pathways. Western blotting and immunofluorescence revealed that AGH markedly upregulated the expression of β-catenin and N-cadherin compared with the other groups, and this effect was reversed by the Wnt/β-catenin pathway inhibitor methyl-sulfonyl AB (Figure 5A–C). In parallel, analysis of SMAD signaling showed that the levels of phosphorylated SMAD2, SMAD3, and SMAD4 were significantly increased in the AGH group (Figure 5D–G).

3.6. *In vivo* gingival thickening, collagen deposition, and angiogenesis with active gingival hydrogel

As shown in Figure 6A, GC and AGH constructs were implanted beneath partial-thickness flaps of rat incisor gingiva. Six weeks after implantation, T2-weighted small animal MRI scans enabled a clear distinction between hard tissue (dark signal) and soft tissue (bright signal). Quantitative measurements at multiple sites demonstrated that gingival thickness in the AGH group was significantly greater than that in the GC and blank groups (Figure 6B and F). Importantly, MRI provided a noninvasive and dynamic approach to monitor gingival soft tissue augmentation, highlighting its value as a translational tool.

Histological evaluation further supported these findings. H&E and Masson's trichrome staining (Figure 6C and D) showed well-preserved tissue boundaries and

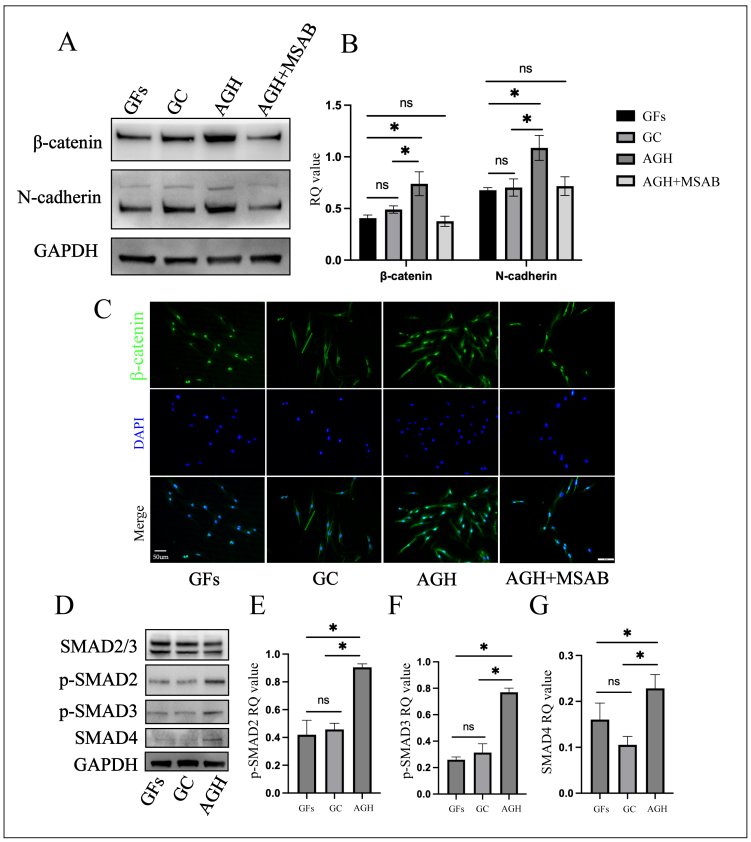


Figure 5. Activation of Wnt/β-catenin and SMAD signaling in gingival fibroblasts. (A) Western blot analysis of β-catenin and N-cadherin in gingival fibroblasts. (B) Quantification of β-catenin and N-cadherin expression. (C) Immunofluorescence of β-catenin (green) in gingival fibroblasts (magnification = 400×; scale = 50 μm). (D) Western blot analysis of SMAD pathway proteins: SMAD2/3, p-SMAD2, p-SMAD3, and SMAD4. (E–G) Quantification of SMAD pathway proteins. Notes: $^{*}p < 0.05$, $^{**}p < 0.01$, $^{***}p < 0.001$; $n = 3$. Abbreviations: AGH, Active gingival hydrogel; DAPI, 4',6-diamidino-2-phenylindole; GAPDH, Glyceraldehyde 3-phosphate dehydrogenase; GC, Acellular hydrogel; GFs, gingival fibroblasts; MSAB, Methyl-sulfonyl AB; ns, Not significant.

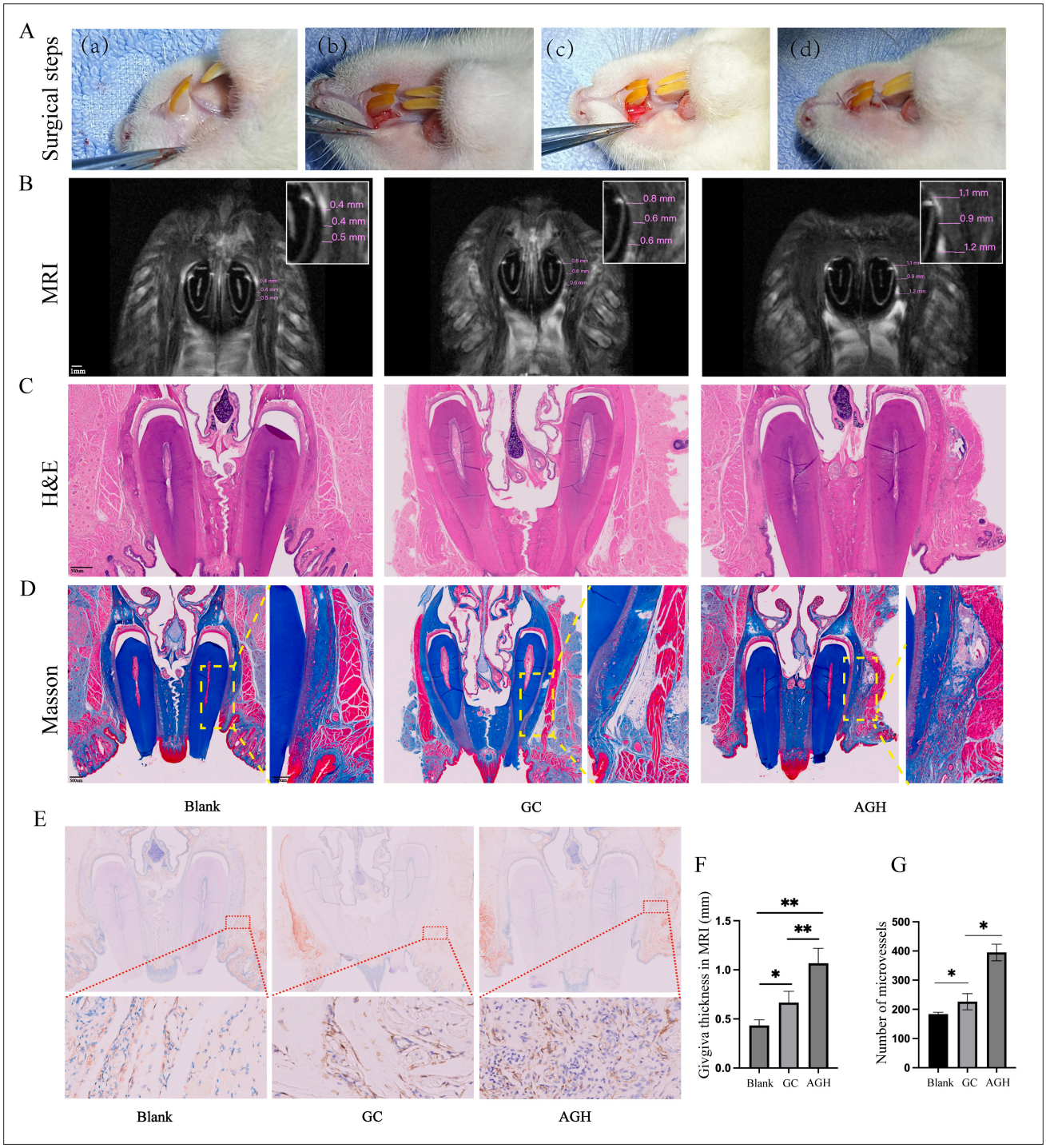


Figure 6. *In vivo* gingival augmentation using bioprinted scaffolds. (A) Surgical procedure: (a) preoperative view, (b) elevation of partial-thickness flap, (c) scaffold implantation, (d) suturing. (B) T2-weighted magnetic resonance imaging (MRI) images of the gingiva. (C) Hematoxylin and eosin (H&E)-stained gingival sections (magnifications = 4×; scales = 500 μm). (D) Masson's trichrome-stained sections (magnifications = 4×, 8×; scales =500 μm ,250 μm). (E) Immunohistochemical staining of CD34 (magnifications = 4×, 40×; scales =500 μm ,50 μm). (F) Quantification of gingival thickness from MRI. (G) Quantification of microvessel density in immunohistochemistry. Notes: Blank, Sham operation; GC, Hydrogel-only control. $^{*}p < 0.05$, $^{**}p < 0.01$, $^{***}p < 0.001$; $n = 3$. Abbreviations: AGH, Active gingival hydrogel; CD34, Cluster of differentiation 34.

intact layer structures without tearing or damage. The gingival epithelium consisted of multiple cell layers, while the lamina propria contained abundant vasculature and crisscrossed collagen fibers supporting epithelial attachment. After 6 weeks, the hydrogel was fully degraded. In the AGH group, newly formed connective tissue was evident, accompanied by mild infiltration of inflammatory cells. Masson's staining revealed substantial new collagen deposition, consistent with enhanced ECM remodeling.

Immunohistochemical staining of CD34 confirmed a markedly higher density of neovascularization in the AGH group compared with the other groups (Figure 6E and G). Collectively, these results indicate that AGH promotes gingival thickening, collagen deposition, and angiogenesis, while MRI provides a novel, noninvasive strategy for evaluating periodontal soft tissue regeneration *in vivo*.

4. Discussion

We prepared a new photocrosslinkable polymer ink composed of ChsMA and GelMA. The combination of GelMA and ChsMA addresses the three major challenges faced by traditional biomaterials in gingival augmentation—insufficient structural precision, lack of bioactivity, and poor mechanical adaptability—through biomimetic ECM components, tunable mechanical properties, and multifunctional synergistic effects.

Single-cell transcriptomic analysis was incorporated into this study to clarify the intrinsic biological features of GFs that are directly relevant to soft-tissue regeneration. Reanalysis of the GSE164241 dataset revealed that GFs—compared with oral mucosal fibroblasts—displayed markedly higher expression of ECM-associated genes, such as *COL1A1* and *FN1*, as well as members of the small leucine-rich proteoglycan family (e.g., *LUM*, *DCN*), which are known regulators of collagen fibrillogenesis and matrix organization. These findings are consistent with prior oral wound-healing studies showing that gingival connective tissue possesses a unique molecular profile characterized by faster matrix turnover, reduced fibrosis, and more efficient remodeling.[16] Importantly, the transcriptomic analyses of GFs and epithelial cells were not conceived as a separate exploratory block but rather as the biological foundation for our bioink design. The enrichment of Fn and COL1 in GFs, together with higher KRT10 and KRT14 expression in gingival epithelium compared with oral mucosa, highlighted gingiva-derived fibroblasts as a cell source intrinsically geared toward ECM remodeling and keratinization. These observations directly informed our decision to use GFs in the GelMA/ChsMA bioink and to focus on FN/COL1 and KRT10/KRT14 as functional readouts of the 3D-bioprinted constructs. The subsequent *in vitro* and *in vivo* results—showing FN/COL1 upregulation, activation of Wnt/β-catenin and TGF-β/Smad signaling, and increased KRT10/KRT14 expression—therefore represent a mechanistic realization of the transcriptomic profile identified at the beginning of the study.

Rheological characteristics of hydrogels and bioinks play a crucial role in extrusion-based bioprinting.[22] Successful printing relies on the formation of a stable flow filament during extrusion and sufficient mechanical strength to maintain the structural integrity of the printed constructs afterward.[23] The compressive strength of GC reached 6.4 kPa, a level that not only imparts adequate mechanical strength to the hydrogel but also matches the biomechanical properties of natural gingiva.[24] Its relatively soft texture and high water content enable GFs to continue growing, proliferating, and secreting/depositing collagen fibers after printing. The gradual decrease in contact angle with increasing ChsMA content indicates that GelMA/ChsMA hydrogels become progressively more hydrophilic. This trend is consistent with the highly polar, anionic nature of chondroitin sulfate, which introduces additional carboxyl and sulfate groups into the network and enhances water–polymer interactions.

Gelatin methacrylate, with its RGD motifs and tunable stiffness, replicates the gingival lamina propria's biomechanics while supporting fibroblast adhesion.[25] ChsMA complements this by emulating glycosaminoglycan-rich ECMs and enhancing COL1/COL3 synthesis. This material strategy not only offers a promising new solution for soft-tissue regeneration but also lays the foundation for personalized medicine and precision dental treatment.[26-28] The GC hydrogel possesses an appropriate pore size and porosity, which enable cells to stretch and migrate freely. This suitable pore structure provides sufficient space for cells and facilitates nutrient and waste exchange, maintaining normal physiological function and promoting cell adhesion and migration.

Animal experiments and clinical studies have shown that the connective tissue beneath the epithelium of keratinized gingiva can induce surface epithelial cells to differentiate into keratinized gingival epithelium.[14,15] Fibroblasts, as the main cellular component of the connective tissue, play a significant role in this transformation process. They primarily originate from mesenchyme, and their main function is to synthesize ECM, providing a physical scaffold for cellular activity and promoting rapid tissue repair following tissue injury.[29] Anatomically, fibroblasts can be categorized into reticular-layer and papillary-layer fibroblasts.[30] However, fibroblasts may also exhibit functional diversity within the same anatomical location,

indicating that simple anatomical stratification is no longer sufficient to understand fibroblast heterogeneity.

Fibroblasts proliferate within the hydrogel and form a unique microenvironment that promotes FN secretion by GFs. FN binds to integrin receptors on the cell surface and activates intracellular signaling pathways, such as the focal adhesion kinase/Src kinase pathway, thereby regulating focal adhesion formation and actin cytoskeleton reorganization, which together facilitate cell migration. COL1 increases adhesion between cells and the hydrogel, and its fibrous structure also provides directional cues for cell migration.[31]

In the classic Wnt/β-catenin signaling pathway, binding of the Wnt ligands to the Frizzled receptor and the low-density lipoprotein receptor-related protein 5/6 coreceptor inhibits glycogen synthase kinase-3β activity, preventing β-catenin degradation. Accumulated β-catenin in the cytoplasm translocates to the nucleus, binds to the T-cell factor (TCF)/lymphoid enhancer factor transcription factors, and regulates downstream gene expression.[32] FN has been identified as a target gene regulated by β-catenin/TCF transcription. TGF-β, an important cytokine, activates receptor-regulated SMADS, such as SMAD2 and SMAD3. These activated SMADS form heteromultimers with SMAD4 and are transported into the nucleus to regulate the expression of various target genes, including *COL1* and *FN*. In many cell types, such as fibroblasts, TGF-β stimulation significantly upregulates *COL1* and *FN* expression via the SMAD pathway, promoting ECM synthesis and deposition. The SMAD pathway can also interact with other signaling cascades, such as phosphoinositide 3-kinase/protein kinase B and mitogen-activated protein kinase, to jointly regulate *COL1* and *FN* expression.[33]

Current approaches to assessing gingival thickness include direct and imaging-based methods, each with specific advantages and limitations. Direct techniques include probe estimation, which is simple but subjective, and surgical flap measurement, which is accurate but invasive and carries a risk of tissue damage.[34,35] Imaging modalities offer noninvasive alternatives: cone-beam computed tomography provides 3D visualization but suffers from limited soft-tissue resolution and radiation exposure, while ultrasound is operator-dependent and less reliable in thick tissues. MRI has emerged as an optimal preclinical tool due to its superior soft-tissue contrast (<0.5 mm resolution), absence of radiation, and ability to visualize multilayered gingival structures—features that are critical for longitudinal studies in rodent models.[36,37] In our current study, MRI was used for the first time to evaluate gingival thickness in living rats. Its high soft-tissue resolution enabled direct visualization of gingival thickness changes following AGH implantation. Another important consideration is the degradation behavior of the GC/AGH hydrogels. In the present study, we did not perform a dedicated quantitative analysis of *in vivo* mass loss. Instead, gingival thickness was assessed using MRI as the distance between the soft-tissue surface and the underlying hard-tissue reference plane. At the 6-week endpoint, histological sections did not reveal clearly demarcated remnants of dense, acellular hydrogel; instead, the implantation sites were replaced by vascularized connective tissue rich in collagen fibers, suggesting substantial substitution of the initial matrix by host tissue. Nevertheless, we cannot completely rule out the presence of small residual hydrogel fragments that may still contribute to the soft-tissue volume signal on MRI. Future studies will therefore incorporate labeled or otherwise trackable hydrogels, along with earlier and extended observation time points, to more precisely correlate *in vivo* degradation kinetics with dynamic changes in gingival thickness and collagen remodeling.

3D bioprinting emerges as a transformative strategy by enabling the precise fabrication of vascularized, anatomically tailored constructs.[38] Unlike conventional substitutes, this technology allows layer-specific deposition of cells and biomaterials, thereby reconstructing the epithelial–stromal interface and microvascular networks that are essential for graft integration and long-term stability. Liu *et al.*[39] printed acellular dermal matrix scaffolds encapsulating GFs to increase keratinized gingival width, demonstrating that cell-laden scaffolds promoted soft-tissue regeneration more effectively than cell-free scaffolds, findings that are consistent with our results. However, their research had several limitations, including a small animal sample size, a lack of histological assessments, and the absence of mechanistic analyses. In contrast, our study focused on the equally important phenotype of gingival thickness, not only verifying its efficacy and stability in an animal model but also providing a more in-depth investigation into the mechanisms of regeneration and rekeratinization. These advances highlight the advantages of our material system. Dai *et al.*[40] utilized artificial intelligence to design bioprinted *in vitro* free-gingival substitutes with precise dimensions; however, the lack of animal experiments leaves the *in vivo* regenerative potential of their constructs unresolved.

Although gingival tissue exhibits a remarkable intrinsic healing capacity, this regenerative ability is largely limited to re-epithelialization and defect closure rather than *de novo* thickening of the underlying connective tissue. In the partial-thickness flap model used in this study, untreated sites healed predictably through epithelial coverage, yet connective-tissue volume remained essentially unchanged, as confirmed by MRI and histological results in the control groups. This outcome aligns with clinical observations that

natural healing rarely increases gingival thickness without surgical grafting. In contrast, AGH implantation produced a clear and quantifiable enhancement of soft-tissue volume and collagen deposition, demonstrating a biological effect that exceeds the capacity of spontaneous healing. Therefore, this model well well-suited for evaluating a material's ability to modulate connective-tissue remodeling—a biological outcome not achieved through natural repair alone. This distinction underscores the regenerative advantage of AGH and supports its clinical relevance for soft-tissue augmentation.

In summary, we constructed a bioprintable ink for GFs that forms a hydrogel with good biocompatibility and stable mechanical properties following photocuring. Bioprinting enhances gingival thickness through precise structural replication of the lamina propria, biomimetic bioinks that guide fibroblast proliferation and collagen synthesis, and vascular integration facilitated by embedded angiogenic factors. GFs can proliferate, migrate, and adhere within the construct, and they continue to synthesize ECM components. As a substitute for gingival connective tissue, AGH activates the Wnt/β-catenin and SMAD signaling pathways in GFs and promotes keratinization in GECs. After transplantation *in vivo*, AGH achieved a stable and measurable thickening of the gingiva. Nonetheless, although this study demonstrates clear efficacy in increasing gingival thickness, it lacks sufficient depth regarding the widening of keratinized gingiva and its underlying mechanisms. Future work will therefore focus on material refinement to address these aspects.

5. Conclusion

In conclusion, we developed an active gingival hydrogel with favorable mechanical properties and excellent biocompatibility that effectively remodels the gingival phenotype in a rat model. AGH holds substantial promise for periodontal/peri-implant soft-tissue augmentation.

Acknowledgments

None.

Funding

This work was supported by the Biomaterials and Regenerative Medicine Institute Cooperative Research Project, Shanghai Jiao Tong University School of Medicine (Project No. 2022LHB04), and the Fundamental Research Program Funding of Ninth People's Hospital Affiliated to Shanghai Jiao Tong University School of Medicine (Project No. JYZZ210). The National Key Research and Development Program of China (2023YFC2413600).

Conflict of interest

The authors declare that they have no competing interests.

Author contributions

Conceptualization: Zhongchen Song, Guodong Zhou
Formal analysis: Han Hu, Yue Liao, Jiachen Dong
Investigation: Han Hu, Zhongchen Song
Methodology: Han Hu, Xin Sun
Writing–original draft: Han Hu
Writing–review & editing: Han Hu, Yue Liao, Jiachen Dong, Mengjun Sun, Zhongchen Song

Ethics approval and consent to participate

This study was carried out following the recommendations of the Animal Care and Experiment Committee of Shanghai Ninth People's Hospital, Shanghai Jiao Tong University School of Medicine. The protocol was approved by the Animal Care and Experiment Committee of Shanghai Ninth People's Hospital, Shanghai Jiao Tong University School of Medicine (SH9H-2024-A1046-SB).

Consent for publication

Not applicable.

Availability of data

The data generated and analyzed in this study are available from the corresponding author upon reasonable request.

References

1. Malpartida-Carrillo V, Tinedo-Lopez PL, Guerrero ME, Amaya-Pajares SP, Özcan M, Rösing CK. Periodontal phenotype: a review of historical and current classifications evaluating different methods and characteristics. *J Esthet Restor Dent*. 2021;33(3):432-445.
doi: 10.1111/jerd.12661

2. Ramanauskaite A, Sader R. Esthetic complications in implant dentistry. *Periodontol 2000*. 2022;88(1): 73-85.
doi: 10.1111/prd.12412

3. Stefanini M, Barootchi S, Sangiorgi M, *et al*. Do soft tissue augmentation techniques provide stable and favorable peri-implant conditions in the medium and long term? A systematic review. *Clin Oral Implants Res*. 2023;34 Suppl 26:28-42.
doi: 10.1111/clr.14150

4. Thoma DS, Benić GI, Zwahlen M, Hämmerle CH, Jung RE. A systematic review assessing soft tissue augmentation techniques. *Clin Oral Implants Res*. 2009;20 Suppl 4: 146-165.
doi: 10.1111/j.1600-0501.2009.01784.x

5. Edel A. Clinical evaluation of free connective tissue grafts used to increase the width of keratinised gingiva. *J Clin Periodontol*. 1974;1(4):185-196.
doi: 10.1111/j.1600-051x.1974.tb01257.x

6. Hürzeler MB, Weng D. A single-incision technique to harvest subepithelial connective tissue grafts from the palate. *Int J Periodontics Restorative Dent*. 1999;19(3): 279-287.

7. Bertl K, Melchard M, Pandis N, Müller-Kern M, Stavropoulos A. Soft tissue substitutes in non-root coverage procedures: a systematic review and meta-analysis. *Clin Oral Investig*. 2017;21(2):505-518.
doi: 10.1007/s00784-016-2044-4

8. Song YW, Kim S, Waller T, *et al*. Soft tissue substitutes to increase gingival thickness: histologic and volumetric analyses in dogs. *J Clin Periodontol*. 2019;46(1):96-104.
doi: 10.1111/jcpe.13034

9. Valles C, Vilarrasa J, Barallat L, Pascual A, Nart J. Efficacy of soft tissue augmentation procedures on tissue thickening around dental implants: a systematic review and meta-analysis. *Clin Oral Implants Res*. 2022;33 Suppl 23:72-99.
doi: 10.1111/clr.13920

10. Montero E, Molina A, Matesanz P, Monje A, Sanz-Sánchez I, Herrera D. Efficacy of soft tissue substitutes, in comparison with autogenous grafts, in surgical procedures aiming to increase the peri-implant keratinized mucosa: a systematic review. *Clin Oral Implants Res*. 2022;33 Suppl 23:32-46.
doi: 10.1111/clr.13751

11. Rotundo R, Pancrazi GL, Grassi A, Ceresoli L, Di Domenico GL, Bonafede V. Soft tissue substitutes in periodontal and peri-implant soft tissue augmentation: a systematic review. *Materials (Basel)*. 2024;17(5)
doi: 10.3390/ma17051221

12. Alfonso García SL, Parada-Sanchez MT, Arboleda Toro D. The phenotype of gingival fibroblasts and their potential use in advanced therapies. *Eur J Cell Biol*. 2020;99(7): 151123.
doi: 10.1016/j.ejcb.2020.151123

13. Chiquet M, Katsaros C, Kletsas D. Multiple functions of gingival and mucoperiosteal fibroblasts in oral wound healing and repair. *Periodontol 2000*. 2015;68(1):21-40.
doi: 10.1111/prd.12076

14. Squier CA, Kammeyer GA. The role of connective tissue in the maintenance of epithelial differentiation in the adult. *Cell Tissue Res*. 1983;230(3):615-630.
doi: 10.1007/bf00216205

15. Hsieh PC, Jin YT, Chang CW, Huang CC, Liao SC, Yuan K. Elastin in oral connective tissue modulates the keratinization of overlying epithelium. *J Clin Periodontol*. 2010;37(8):705-711.
doi: 10.1111/j.1600-051X.2010.01542.x

16. Chuhuaicura P, Rodríguez-Niklitschek C, Oporto GH, Salazar LA. Distinct molecular mechanisms in oral mucosal wound healing: translational insights and future directions. *Int J Mol Sci*. 2025;26(21)
doi: 10.3390/ijms262110660

17. Gumede DB, Abrahamse H, Houreld NN. Targeting Wnt/β-catenin signaling and its interplay with TGF-β and Notch signaling pathways for the treatment of chronic wounds. *Cell Commun Signal*. 2024;22(1):244.
doi: 10.1186/s12964-024-01623-9

18. Das S, Jegadeesan JT, Basu B. Gelatin methacryloyl (GelMA)-based biomaterial inks: process science for 3D/4D printing and current status. *Biomacromolecules*. 2024;25(4):2156-2221.
doi: 10.1021/acs.biomac.3c01271

19. Zhang X, Huang C, Huang K, *et al*. Living and injectable porous hydrogel microspheres promoting inflammation modulation and extracellular matrix remodeling for intervertebral disc regeneration. *ACS Appl Mater Interfaces*. 2025;17(42):57953-57966.
doi: 10.1021/acsami.5c13982

20. Wei Long N, Cian V, Boyang H, Wai Yee Y, Paulo B. Advanced bioprinting strategies for fabrication of biomimetic tissues and organs. *Int J Extreme Manuf*. 2025;7(6):062006.
doi: 10.1088/2631-7990/adeee0

21. Kim JJ, Cho D-W. Advanced strategies in 3D bioprinting for vascular tissue engineering and disease modelling using smart bioinks. *Virtual Phys Prototyping*. 2024;19(1):e2395470.
doi: 10.1080/17452759.2024.2395470

22. Schwab A, Levato R, D'Este M, Piluso S, Eglin D, Malda J. Printability and shape fidelity of bioinks in 3D bioprinting. *Chem Rev*. 2020;120(19):11028-11055.
doi: 10.1021/acs.chemrev.0c00084

23. Osi AR, Zhang H, Chen J, *et al*. Three- dimensional-printable thermo/photo-cross-linked methacrylated chitosan-gelatin hydrogel composites for tissue engineering. *ACS Appl Mater Interfaces*. 2021;13(19):22902-22913.
doi: 10.1021/acsami.1c01321

24. Choi JJE, Zwirner J, Ramani RS, *et al*. Mechanical properties of human oral mucosa tissues are site dependent: a combined biomechanical, histological and ultrastructural approach. *Clin Exp Dent Res*. 2020;6(6):602-611.
doi: 10.1002/cre2.305

25. Yue K, Trujillo-de Santiago G, Alvarez MM, Tamayol A, Annabi N, Khademhosseini A. Synthesis, properties, and biomedical applications of gelatin methacryloyl (GelMA) hydrogels. *Biomaterials*. 2015;73:254-271.
doi: 10.1016/j.biomaterials.2015.08.045

26. Guan S, Zhang XL, Lin XM, Liu TQ, Ma XH, Cui ZF. Chitosan/gelatin porous scaffolds containing hyaluronic acid and heparan sulfate for neural tissue engineering. *J Biomater Sci Polym Ed*. 2013;24(8):999-1014.

doi: 10.1080/09205063.2012.731374

27. Gong H, Agustin J, Wootton D, Zhou JG. Biomimetic design and fabrication of porous chitosan–gelatin liver scaffolds with hierarchical channel network. *J Mater Sci Mater Med*. 2014;25(1):113-120.
doi: 10.1007/s10856-013-5061-8

28. Yin J, Yan M, Wang Y, Fu J, Suo H. 3D Bioprinting of low-concentration cell-laden gelatin methacrylate (GelMA) bioinks with a two-step cross-linking strategy. *ACS Appl Mater Interfaces*. 2018;10(8):6849-6857.
doi: 10.1021/acsami.7b16059

29. Peña OA, Martin P. Cellular and molecular mechanisms of skin wound healing. *Nat Rev Mol Cell Biol*. 2024;25(8):599-616.
doi: 10.1038/s41580-024-00715-1

30. Wei K, Nguyen HN, Brenner MB. Fibroblast pathology in inflammatory diseases. *J Clin Invest*. 2021;131(20).
doi: 10.1172/jci149538

31. Hu J, Li J, Jiang J, *et al*. Design of synthetic collagens that assemble into supramolecular banded fibers as a functional biomaterial testbed. *Nat Commun*. 2022;13(1):6761.
doi: 10.1038/s41467-022-34127-6

32. Mascharak S, Talbott HE, Januszyk M, *et al*. Multi-omic analysis reveals divergent molecular events in scarring and regenerative wound healing. *Cell Stem Cell*. 2022;29(2):315-327.e6.
doi: 10.1016/j.stem.2021.12.011

33. Zeng Y, Wang T, Liu Y, *et al*. Wnt and Smad signaling pathways synergistically regulated the osteogenic differentiation of fibroblasts in ankylosing spondylitis. *Tissue Cell*. 2022;77:101852.
doi: 10.1016/j.tice.2022.101852

34. Sharma S, Thakur SL, Joshi SK, Kulkarni SS. Measurement of gingival thickness using digital vernier caliper and ultrasonographic method: a comparative study. *J Investig Clin Dent*. 2014;5(2):138-143.
doi: 10.1111/jicd.12026

35. Wang J, Cha S, Zhao Q, Bai D. Methods to assess tooth gingival thickness and diagnose gingival phenotypes: a systematic review. *J Esthet Restor Dent*. 2022;34(4):620-632.
doi: 10.1111/jerd.12900

36. Heil A, Schwindling FS, Jelinek C, *et al*. Determination of the palatal masticatory mucosa thickness by dental MRI: a prospective study analysing age and gender effects. *Dentomaxillofac Radiol*. 2018;47(2):20170282.
doi: 10.1259/dmfr.20170282

37. Schwarz L, Unger E, Gahleitner A, Rausch-Fan X, Jonke E. A novel approach for gingiva thickness measurements around lower anterior teeth by means of dental magnetic resonance imaging. *Clin Oral Investig*. 2023;28(1):18.
doi: 10.1007/s00784-023-05459-4

38. Wang Z, Wang L, Li T, *et al*. 3D bioprinting in cardiac tissue engineering. *Theranostics*. 2021;11(16):7948-7969.
doi: 10.7150/thno.61621

39. Liu P, Li Q, Yang Q, *et al*. Evaluation of the effect of 3D-bioprinted gingival fibroblast-encapsulated ADM scaffolds on keratinized gingival augmentation. *J Periodontal Res*. 2023;58(3):564-574.
doi: 10.1111/jre.13126

40. Dai Y, Wang P, Mishra A, *et al*. 3D bioprinting and artificial intelligence-assisted biofabrication of personalized oral soft tissue constructs. *Adv Healthc Mater*. 2024:e2402727.
doi: 10.1002/adhm.202402727

ACCSCIENCE PUBLISHING

International Journal of Bioprinting

RESEARCH ARTICLE

3D-printed PETG/BC scaffolds for bone tissue repair

Evangelos Daskalakis[1,2†*], Mohamed H. Hassan[2†*], Abdalla M. Omar[2†], Maria Kapousidou[3], Dino Freitas[1], Mehmet Cagirici[1], Cian Vyas[1], Hussein Mishbak[4], Alexandra Lanot[5], Niel C. Bruce[5], Prasad Potluri[3,6], Wajira Mirihanage[3], and Paulo J.D.S. Bartolo[1*]

[1]Singapore Centre for 3D Printing, School of Mechanical and Aerospace Engineering, Nanyang Technological University, Singapore, Singapore

[2]Department of Mechanical, Aerospace, and Civil Engineering, University of Manchester, Manchester, United Kingdom

[3]Department of Materials, The University of Manchester, Manchester, United Kingdom

[4]Department of Biomedical Engineering, School of Engineering, University of Thi Qar, Nasiriyah, Iraq

[5]Centre for Novel Agricultural Products, Department of Biology, University of York, York, United Kingdom

[6]Northwest Composites Centre and Aerospace Research Institute, Department of Materials, Faculty of Science and Engineering, The University of Manchester, Manchester, United Kingdom

[†]These authors contributed equally to this work.

***Corresponding authors:**
Evangelos Daskalakis (daskalakis.evangelos@ntu.edu.sg)

Mohamed H. Hassan (Mohamed.hassan@manchester.ac.uk)

Paulo J.D.S. Barrtolo (pbartolo@ntu.edu.sg)

Citation: Daskalakis E, Hassan MH, Omar AM, *et al.* 3D-printed PETG/BC scaffolds for bone tissue repair. *Int J Bioprint*. 2026;12(1):413-431. doi: 10.36922/IJB025210212

Received: May 21, 2025
Revised: July 10, 2025
Accepted: July 15, 2025
Published online: July 16, 2025

Copyright: © 2025 Author(s). This is an Open Access article distributed under the terms of the Creative Commons Attribution License, permitting distribution and reproduction in any medium, provided the original work is properly cited.

Publisher's Note: AccScience Publishing remains neutral with regard to jurisdictional claims in published maps and institutional affiliations.

Abstract

Bone tissue supports the body, enables movement, protects organs, produces blood cells, and stores minerals. In regenerative medicine, bone's natural healing ability drives the need for engineered solutions to treat fractures, defects, and support implants. This study explores the development of polyethylene terephthalate glycol (PETG) and PETG/bacterial cellulose (BC) composite scaffolds with varying BC contents (10, 15, and 20 wt%) for bone tissue engineering (TE). Scanning electron microscopy and atomic force microscopy revealed porous structures with increasing surface roughness as BC content increased. Water contact angle analysis revealed enhanced hydrophilicity in PETG/BC composites, particularly at higher BC levels. Fourier transform infrared spectroscopy, X-ray diffraction, and differential scanning calorimetry confirmed successful BC integration and interactions with PETG, along with increased crystallinity. Mechanical testing indicated that compressive strength improved with higher BC content, with 20 wt% BC achieving optimal performance. Biological tests using human adipose-derived stem cells displayed enhanced proliferation, differentiation, and mineralization on PETG/BC scaffolds. Among the tested BC scaffolds, the 20 wt% BC scaffold demonstrated the most favorable physical, mechanical, and biological properties. Overall, PETG/BC scaffolds, especially those with 20 wt% BC, display strong potential for future bone TE applications.

Keywords: Additive manufacturing; Bacterial cellulose; Biomaterial; Polyethylene terephthalate glycol; Stem cells; Tissue engineering

1. Introduction

Tissue engineering (TE) integrates biological sciences with engineering strategies to create solutions that restore, support, or enhance tissue or organ function. It involves two principal strategies: the scaffold-based method and the cell-laden approach.[1,2] The scaffold-based approach, commonly applied in bone TE, utilizes 3D, biodegradable, and biocompatible porous structures that support cell adhesion, differentiation, and proliferation within a suitable biomechanical environment.[3,4] For successful applications, the scaffold degradation rate must match the tissue regeneration rate, and the scaffolds should exhibit high porosity and pore interconnectivity. These scaffolds should promote cellular function while ensuring adequate mechanical strength and rigidity to endure the stresses present in the host tissue environment. Moreover, they must exhibit appropriate surface properties (*e.g.*, chemistry, hardness, roughness, stiffness) to promote cell adhesion and adequate biomechanical coupling between the scaffolds and host tissue.[5,6]

Various biodegradable materials have been utilized for scaffold fabrication, including inorganic, organic, and composite materials.[7] A commonly used material in TE is polycaprolactone (PCL), which is an aliphatic polyester and has demonstrated promising results in bone applications. Scaffolds made from PCL with different porosities have been reported to support osteoblast and mesenchymal stem cell adhesion, contributing to osteogenesis and bone development.[8,9] Additionally, several studies demonstrated the effective application of PCL scaffolds in repairing critical-sized calvaria defects in rats, facilitating new tissue formation.[10] Despite its advantages, PCL presents weak bioactivity, low strength, and slow degradation, limiting its use in load-bearing bone repair.[2] To address these challenges, our group explored polyethylene terephthalate glycol (PETG), an aliphatic polyester, and demonstrated its effectiveness in bone applications.[11] PETG is a glycol-modified derivative of polyethylene terephthalate (PET), engineered to reduce the melting temperature and enhance printability. In comparison to PCL, PETG has higher mechanical properties and bioactivity.[11] However, the mechanical properties of PETG are still lower than those of cortical bone ; as a consequence, PETG scaffolds may not provide the necessary structural integrity for load-bearing applications, such as cortical bone regeneration.[12] Additionally, PETG lacks controlled degradation, which can hinder the natural healing process and integration of the scaffold.[13]

Bacterial cellulose (BC), produced by specific bacteria such as *Acetobacter xylinum*, is among the most abundant and renewable natural polymers found on the planet, with an estimated 100 –150 billion tons of cellulose produced globally each year.[14,15] BC has been widely used in various applications, including structural reinforcement, paper making, textiles, and biomedicine, owing to its fibrous morphology, low production costs, abundance, and biocompatibility.[16,17] These characteristics make BC a potential ideal reinforcement material for PETG scaffolds, overcoming the limitations previously mentioned.[18] Moreover, the natural hydrophilicity of BC could have a potential positive impact on cell attachment.[19] Additionally, the faster degradation of BC can compensate for the slow degradation rate of PETG, allowing the design of scaffolds with tunable degradation profiles.[20] Although no direct studies on BC/PETG composites are currently available, related work has demonstrated that incorporating BC into polylactic acid (PLA) matrices results in significantly enhanced degradation behavior. For example, PLA/BC scaffolds displayed approximately 18.75% mass loss in simulated body fluid over 6 weeks, compared to 14.38% for pure BC, while maintaining suitable mechanical stability for TE applications.[21,22] Similarly, BC has been used in composites with hydroxyapatite, chitosan, and polyvinyl alcohol, demonstrating improved biodegradability and mechanical performance tailored to bone tissue regeneration.[23,24] BC has also been reported to enhance osteoblast adhesion and proliferation, particularly when used in composites with bioceramics like hydroxyapatite, promoting osteoinduction and bone regeneration.[25] Furthermore, modification techniques, such as nanoparticle incorporation or surface patterning, have been successfully used to improve BC's mechanical and bio-functional properties for bone tissue applications.[26] The combination of PETG and BC can potentially produce scaffolds with better mechanical properties, degradation profiles, and biocompatibility.

This work investigates the use of BC as a potential reinforcement for PETG scaffolds. Various percentages of BC were mixed with PETG and analyzed using different techniques to assess the impact of BC on the physicochemical and biological properties of PETG scaffolds.

2. Materials and methods

2.1. Materials

PETG filament, with a diameter of 1.75 mm, was purchased from RS Components Ltd. (UK). *Gluconacetobacter xylinus* bacterial strain American Type Culture Collection (ATCC) 53524 was purchased from the bioresource center of the ATCC (USA). MesenPRO RSTM basal medium, growth supplement, glutamine, penicillin, the STEMPRO osteogenesis differentiation kit, bicinchoninic acid (BCA) Protein Assay Kit (Micro BCA), Alexa Fluor 594-conjugated phalloidin, 4′,6-diamidino-2-phenylindole

(DAPI), and Dulbecco's phosphate-buffered saline (PBS) were sourced from Thermo Fisher Scientific (UK). Bacterial peptone, yeast extract, disodium phosphate, citric acid monohydrate (with 2% glucose), Triton X-100, hexamethyldisilane (HMDS), and formaldehyde were purchased from Sigma-Aldrich (UK). The MTT Cell Proliferation Assay Kit was provided by Abcam (UK), and the SensoLyte® NPP Alkaline Phosphatase (ALP) Assay Kit was supplied by AnaSpec (Eurogentec, Belgium).

2.2. Bacterial cellulose production

BC was produced using *Komagataeibacter xylinus* ATCC 53524 (ATCC, USA). The strain was cultured in Hestrin–Schramm medium that contains 50 g/L bacterial peptone, 50 g/L yeast extract, 27 g/L disodium phosphate, and 15 g/L citric acid monohydrate in the presence of 2% glucose.[27] The bacteria were cultured at 30 °C under static conditions. After 6 days, the cellulose pellicles were harvested, incubated at 80 °C for 4 h in 0.1 M sodium hydroxide, and then air-dried after extensive washing with deionized water. Finally, dried cellulose pellicles were milled using a ball mill at a frequency of 30 s^{-1} for 1 min (TissueLyserII, Qiagen, Germany).

2.3. Filament production

The PETG filaments were pelletized (4 mm) using the Process 16 Pelletizer (Thermo Fisher Scientific, UK). Simultaneously, BC powder and PETG pellets were fed, in a controlled manner, into two different Twin Screw Brabender feeders (Kubota Brabender Technologie GmbH, Germany), and then passed through the Haake Polylab Rheomex Twin Screw Extruder (Thermo Fisher Scientific, UK), heated at 190 °C, to melt the polymers and extrude them into a strand. The mixed PETG/BC strand was pulled through a water bath to reduce the temperature of the material. The cooled strand was then fed into the pelletizer, producing 4 × 1.75 mm (length × diameter) pellets. The procedure was repeated for the production of three different concentrations of PETG/BC (90/10, 85/15, and 80/20 wt%). In order to achieve an accurate mixing between BC and PETG, it was important to determine the volumetric flow rate (**Equation I**) and gravimetric flow rate (**Equation II**):

$$VF = \frac{Q}{\rho} \quad \text{(I)}$$

$$GF = \frac{m}{t} \quad \text{(II)}$$

where VF is the volumetric flow rate, Q is the feed rate, ρ is the density of the polymer, GF is the gravimetric flow rate, m is the mass of the polymer, and t is the duration of the flow. Table S1 presents the VF and GF results for the different material concentrations. After the mixing process, the pellets were left to dry inside an oven at 50 °C for 48 h. The dried pellets were extruded using the 3Devo filament maker (3Devo, Netherlands) at 190 °C, producing 1.75 mm filaments.

2.4. Fabrication process

Scaffolds were fabricated using Prusa i3 MK3S (Prusa Research, Czech Republic) at 210 °C. Scaffolds of different material concentrations were fabricated with dimensions of 30 × 30 × 5 mm (length × width × height) and subsequently cut into smaller pieces for compression tests, according to the ASTM D695-15 standard.

2.5. Morphological characterization

The morphology of the 3D-printed scaffolds was examined using scanning electron microscopy (SEM) (FEI Quanta 650, FEI Company, USA). Prior to imaging, a 10-nm layer of platinum/palladium (80:20) was applied using an EMITECH K550X sputter coater (Quorum Technologies, UK). ImageJ was used for the analysis of top and cross-sectional images of the 3D-printed scaffolds. The gravimetric method was used to calculate scaffold porosity ($n = 4$) as follows:

$$Porosity\,(\%) = \left(1 - \frac{\rho_s}{\rho_m}\right) \times 100 \quad \text{(III)}$$

with

$$\rho_s = \frac{m_s}{v_s} \quad \text{(IV)}$$

where ρ_s is the apparent density of the scaffold, ρ_m is the density of the PETG/BC scaffold, m_s is the measured mass of the scaffold, and v_s is the volume of the scaffold. The theoretical densities of PETG and BC are 1.27 and 1.6 g/cm^3, respectively.[28,29]

2.6. Surface morphology

Atomic force microscopy (AFM) characterization was performed using the ScanAsyst mode (Bruker Optik GmbH, UK), with ScanAsyst Air silicon nitride probes, 70 KHz nominal frequency, 0.4 N/m spring constant, and 2 nm nominal tip radius. Using Bruker data analysis software (Bruker Optik GmbH, UK), all images were flattened, and the background was subtracted.

2.7. Wettability

Water contact angle (WCA) measurements were carried out using a CAM 200 Optical Contact Angle Meter with an integrated goniometer (KSV CAM 200, Leuven,

Finland). Deionized water droplets were dispensed onto the scaffold surface, and contact angle images were recorded immediately (0 s) and after 1 min to assess temporal changes.

2.8. Rheology

Rotational and oscillation tests were conducted using the Discovery HR-3 Rheometer (TA Instruments, USA). A steel parallel plate (diameter = 20 mm) with a gap of 450 μm was used for testing the different material blends (n = 3). The printing temperature of pure PETG filaments is typically between 190 and 210 °C; therefore, three temperatures were selected for rheological evaluation (190, 200, and 210 °C). A constant strain of 1% and a frequency of 10 –0.01 Hz were used for the logarithmic sweep in the oscillation test, while a shear rate of 0.01– 100 s^{-1} was applied for the logarithmic sweep in the rotational test. The viscoelastic properties of the blends were evaluated by measuring the storage modulus (G′) and loss modulus (G″), representing the elastic and viscous responses, respectively. Storage and loss moduli were calculated using the following equations:

$$G' = \left(\frac{\sigma_o}{\gamma_o}\right) \times cos\delta \quad \text{(V)}$$

$$G'' = \left(\frac{\sigma_o}{\gamma_o}\right) \times sin\delta \quad \text{(VI)}$$

where σ_o is stress amplitude, γ_o is strain amplitude, and δ is the phase angle between 0° and 90°. The loss factor (tanδ) was calculated as follows:

$$tan\delta = \frac{G'}{G''} \quad \text{(VII)}$$

Rotational tests evaluated the blend's structural and compositional behavior. Newton's law was used to describe the viscous behavior of the blends:

$$\tau = \eta\dot{\gamma}^n \quad \text{(VIII)}$$

where τ denotes the shear stress (Pa), η represents the flow consistency index (Pa·s^n), $\dot{\gamma}$ is the shear rate (s^{-1}), and n is the power-law exponent characterizing the material's flow behavior.

2.9. Fourier- transform infrared spectroscopy

Fourier- transform infrared (FTIR) spectroscopy, operated in attenuated total reflection (ATR) mode using a Vertex 70 spectrometer (Bruker Optik GmbH, Germany) equipped with a platinum ATR accessory and diamond crystal, was employed to verify the incorporation of BC in the printed filaments. Spectral data were collected over the 400–4000 cm^{-1} range at a resolution of 1 cm^{-1} for material characterization.

2.10. X- ray diffraction

The X-ray diffractometer (XRD) X'Pert Pro PANalytical (Malvern Panalytical, UK), equipped with Cu/Kα radiation (wavelength: 0.154 nm), was used to confirm the crystalline structure by scanning in the 2θ range of 0–50° at a scanning speed of 0.1 °/min . The average crystallite size (D) was determined using the Scherrer equation:

$$D = \frac{K\lambda}{Bcoscos\,\theta} \quad \text{(IX)}$$

where λ is the wavelength (1.54 Å), B is the full width at half maximum, θ is the Bragg's diffraction angle, and K is a constant of 0.94.

2.11. Differential scanning calorimetry

Differential scanning calorimetry (DSC) tests were performed using a TA Q100 instrument (TA Instruments, USA) under a nitrogen atmosphere with a flow rate of 50 mL/min and a heat –cool –heat procedure. The samples (n = 3) were initially heated from −90 to 280 °C at a rate of 20 °C/min, then rapidly cooled back to −90 °C at the same rate, followed by a second heating cycle to 280 °C at a reduced rate of 10 °C/min. The melting temperature (T_m), crystallization temperature (T_c), melting enthalpy (ΔH_m), crystallization enthalpy (ΔH_{mc}), and glass transition temperature (T_g) were analyzed from the DSC graphs using Universal Analysis Software (TA Instruments, USA). Crystallinity (χ_c) was calculated using the following equation:

$$\chi_c(\%) = \left(\frac{\Delta H_m - \Delta H_p}{\Delta H_m}\right) \times 100 \quad \text{(X)}$$

where ΔH_m is the melting enthalpy and ΔH_p = 8 J/g is the melting enthalpy of PETG with complete crystallization.[30]

2.12. Mechanical analysis

Uniaxial static compression testing was performed using an Instron 3344 system (Instron, USA). The scaffolds were sectioned into small cubic samples with approximate dimensions of 4.5 × 4.5 × 5 mm (length × width × height). For each material concentration, samples (n = 4) were tested using a 500 N load cell and a strain rate of 0.5 mm/min. Compressive modulus was obtained from the linear region

of the stress–strain curve, while the yield strength was determined by the intersection of the 0.2% strain offset line with the stress–strain curve .

2.13. *In vitro* studies

2.13.1. Cell culture

Scaffolds ($n = 5$) were cut into small cubes of approximately 6.5 × 6.5 × 2.5 mm (length × width × height), sterilized using ethanol/deionized water (80:20) for 4 h, and washed twice with PBS. The scaffolds were placed into 24-well plates and left to dry under a cell culture hood for 24 h. Human adipose-derived stem cells (hADSCs) (ThermoFisher Scientific, UK) (passage 6) were cultured in T-75 cell culture flasks using MesenPRO RS cell culture medium containing 2 vol% growth supplement, 1 vol% penicillin/streptomycin, and 1 vol% glutamine. The flasks were placed inside an incubator (37 °C, 5% CO_2, and 95% humidity) for 2 days to achieve 92 –95% cell confluency. Cells were then seeded onto each scaffold (in dry state) at a density of approximately 62,500 cells/μL, using 0.8 μL cell suspension (approximately 50,000 cells). The culture medium was replaced every 2 days.

2.13.2. Cell metabolic activity

On days 1, 3, 7, and 14, the Resazurin assay (Alamar Blue) was used to assess metabolic activity and seeding of the cells. Samples were incubated for 4 h by adding 0.01% (v/v) of Alamar Blue (70 μL) in cell culture media (0.7 mL). The absorbance of the sample solution (0.2 mL) was read using the Infinite 200 microplate reader (Tecan, Switzerland) at a wavelength of 570 nm.

2.13.3. Cell proliferation analysis

The MTT (3-(4,5-dimethylthiazol-2-yl)-2, 5-diphenyltetrazolium bromide) assay kit was used to evaluate cell proliferation on different materials over a 14-day culture period. A 50 wt% MTT reagent solution was mixed with an equal volume of 50 wt% DMEM (Dulbecco's Modified Eagle Medium) and applied to each sample (0.5 mL). The samples were incubated in the dark, covered with aluminum foil, for 3 h . After incubation, the reagent was removed without washing with PBS, and 0.75 mL of a 1:1:3 MTT solvent was added to each sample, which was again covered with aluminum foil. The plates were then gently stirred for 15 min at room temperature (25 °C). The absorbance of the scaffold solutions (0.2 mL) was measured at 590 nm using the Infinite 200 microplate reader (Tecan, Switzerland).

2.13.4. Cell differentiation analysis

The ALP Assay Kit was employed to assess the differentiation potential of the materials over a 14-day differentiation period. Cells were seeded on the scaffolds and allowed to proliferate for 7 days. Thereafter, the proliferation medium was replaced with the osteogenesis differentiation medium. Scaffolds were washed twice with 1×ALP assay buffer, followed by the addition of 1×ALP assay buffer containing 0.2 vol% Triton X-100. Following this, the samples were agitated using a vortex mixer for 1 min, ultrasonicated for 3 min, and subsequently subjected to repeated freez e–thawing at −80 °C. Samples underwent centrifugation at 2500 × g for 10 min at 4 °C. The collected supernatant was combined with a para-nitrophenyl phosphate substrate solution and incubated at room temperature (25 °C) for 1 h. The absorbance of the scaffold solution (0.2 mL) was measured at 405 nm using the Infinite 200 microplate reader (Tecan, Switzerland). ALP activity was normalized to the total protein concentration determined by the BCA assay, with results calculated based on a standard curve.

2.13.5. Immunofluorescence analysis

Confocal immunofluorescence microscopy was used to evaluate cell proliferation, bridging, and morphology. Confocal images were taken using a Leica TCS SP8 Confocal Microscope (Leica Company, Germany). Cells on day 14 were fixed on the scaffolds using formaldehyde (37%) for 30 min and rinsed thoroughly three times with PBS . Cells were permeabilized with Triton-X 100 (0.1% in PBS) solution for 3 min and blocked with 0.5% fetal bovine serum for 1 h. Scaffolds were incubated with 1:400 Alexa Fluor 594 Phalloidin solution for 45 min and subsequently with 300 nM DAPI solution for 5 min. After each step, the scaffolds were rinsed three times with PBS. Confocal images were analyzed using Image J.

2.13.6. Scanning electron microscopy

SEM was used to assess cell proliferation and expansion on the top and cross-section of the scaffolds using the dry-freezing technique. Scaffolds on day 14 were fixed using formaldehyde (37%) for 30 min and rinsed thoroughly three times. Thereafter, ethanol and deionized water mixtures (v/v) at different ratios (50:50, 60:40, 70:30, 80:20, 90:10, 100:0) were used, followed by a 50:50 (v/v) solution of HMDS and ethanol; e ach step lasted 15 min. Finally, 100% HMDS was applied and left to evaporate overnight under the cell culture hood . The scaffolds were then coated with a 10 nm-thick layer of platinum/palladium (80:20).

2.14. Statistical analysis

Each methodology section includes the number of scaffolds and materials (n) used for the tests. The results were presented as mean ± standard deviation . Statistical analysis was conducted using one-way analysis of variance with Tukey post hoc test using Prism 10 software (GraphPad Software Inc., USA). Significant differences

were considered at $^{*}p < 0.05$, $^{**}p < 0.01$, $^{***}p < 0.001$, and $^{****}p < 0.0001$. Data analysis was conducted using Prism 10 software and Origin 2021 (Origin Lab Corporation, USA).

3. Results

3.1. Morphological and surface characterization properties of fabricated filaments and 3D-printed scaffolds

Filaments composed of PETG and PETG/BC, with a constant diameter of 1.75 mm, were successfully produced. PETG-based scaffolds with a uniform structure were then fabricated using material extrusion 3D printing (Figure 1a and b). The 3D-printed scaffolds exhibit similar morphological properties (pore size, filament width, layer thickness, and porosity) to the designed parameters (Table S2). For all material compositions, the scaffolds present uniform circular filaments during the extrusion process, indicating a constant printing procedure. Top and cross-sectional analyses revealed that PETG/BC filaments have a rougher surface with visible surface micro-pores, and the roughness increases with increasing BC concentration. In contrast, PETG-only scaffolds exhibit a smooth surface (Figure 1a and b; Table S3).

The WCA of the scaffolds at 0 s ranges from ~106° to ~97°, indicating that all scaffolds are hydrophobic. However, the increase of BC concentration decreases the hydrophobicity of the scaffolds (Figure 2a and b; Table 1). After 1 min, the hydrophobicity of the scaffolds significantly decreases (94.1° for PETG/BC [90/10 wt%], 90.77° for PETG/BC [85/15 wt%], and 84° for PETG/BC [80/20 wt%]) (Figure 2a; Table 1). In contrast, PETG-scaffolds maintain a slightly higher hydrophobicity (~95°). As observed for both time points, the highest WCA values were obtained for PETG/BC (80/20 wt%) scaffolds, while the lowest values were observed for PETG-only scaffolds.

Figure 2d–g displays the AFM topographical maps taken over a 1 μm scan area for all scaffolds, while Figure 2h–k features the corresponding maps taken over a 10 μm area. Figure 2c presents the Root Mean Square (RMS) Roughness (Rq) values, which indicate the deviation from the average roughness (Ra). The topographical maps and roughness measurements indicate that PETG scaffolds exhibit higher roughness at increasing BC concentration, as evidenced by the increase in amplitude between peaks and valleys . BC content up to 10 wt% appears to have minimal impact on surface characteristics, whereas concentrations of 10 –15 wt% and 15–20 wt% result in notable changes in surface texture and roughness.

3.2. Rheological analysis

Rheology tests were conducted to investigate the printability of the materials fabricated using fused deposition modeling (FDM) at three different temperatures (190, 200, and 210 °C) (Figure 3a–c). Oscillation results revealed that the incorporation of BC enhances storage and loss moduli, indicating increased energy stored within the polymer (Figure 3a). However, at 200 °C, PETG/BC (85/15 wt %) and PETG/BC (80/20 wt%) exhibited a decrease in both moduli compared to pure PETG. Moreover, results indicated that both moduli decreased with increas ing temperature, reflecting a reduction in melt stiffness due to increased thermal energy that promotes polymer chain mobility and reduces resistance to deformation. Conversely, the increase in frequency increases both storage and loss moduli for all material blends, indicating enhanced viscoelasticity and a transition from liquid-like (viscous) to more solid-like (elastic) behavior under faster deformation . However, the storage modulus remains lower compared to the loss modulus, confirming the viscoelastic behavior of the blends. The loss factor (tanδ) decreases as the frequency increases beyond 0.1 Hz. Similarly, at frequencies above 0.1 Hz, an increase in temperature displays a similar pattern. This suggests that the materials behave more elastically, making them easier to print (Figure 3b). The incorporation of BC did not significantly impact tanδ, suggesting that BC does not significantly alter the balance between elastic and viscous responses during deformation. The rotational results revealed that viscosity increases with higher BC content at low shear rates (Figure 3c). However, as the shear rate increases, the viscosity decreases, indicating a shear-thinning behavior for all material blends. This can be explained by the high melting point of BC (> 330 °C) and the interconnection between the BC particles and the polymer. Moreover, the increase in temperature results in a decrease in dynamic viscosity, likely due to increased polymer chain mobility, thereby enhancing flow behavior and the printability of the materials.

3.3. Physical properties of the 3D-printed scaffolds

The PETG and PETG/BC scaffolds exhibit a stress–strain curve characterized by an initial elastic region followed by plastic deformation, where the stress surpasses the yield point (Figure 4a). Results indicate an increase in plastic deformation with the incorporation of BC particles, with yield stress values increasing from 7.8 MPa for pure PETG to 9.3 MPa for PETG/BC (90/10 wt%), 11.7 MPa for PETG/BC (85/15 wt%), and 12.5 MPa for PETG/BC (80/20 wt%), reflecting an increase in stiffness (Figure 4a). For all materials, the plastic region features a smooth curve, indicating that PETG and PETG/BC are ductile materials. In addition, the 0.2 offset yield strength and compression increase with increasing BC concentration from ~9.5 to ~12 MPa and ~205 to ~230 MPa, respectively (Figure 4b and c). Overall, PETG/BC (80/20 wt%) exhibited the

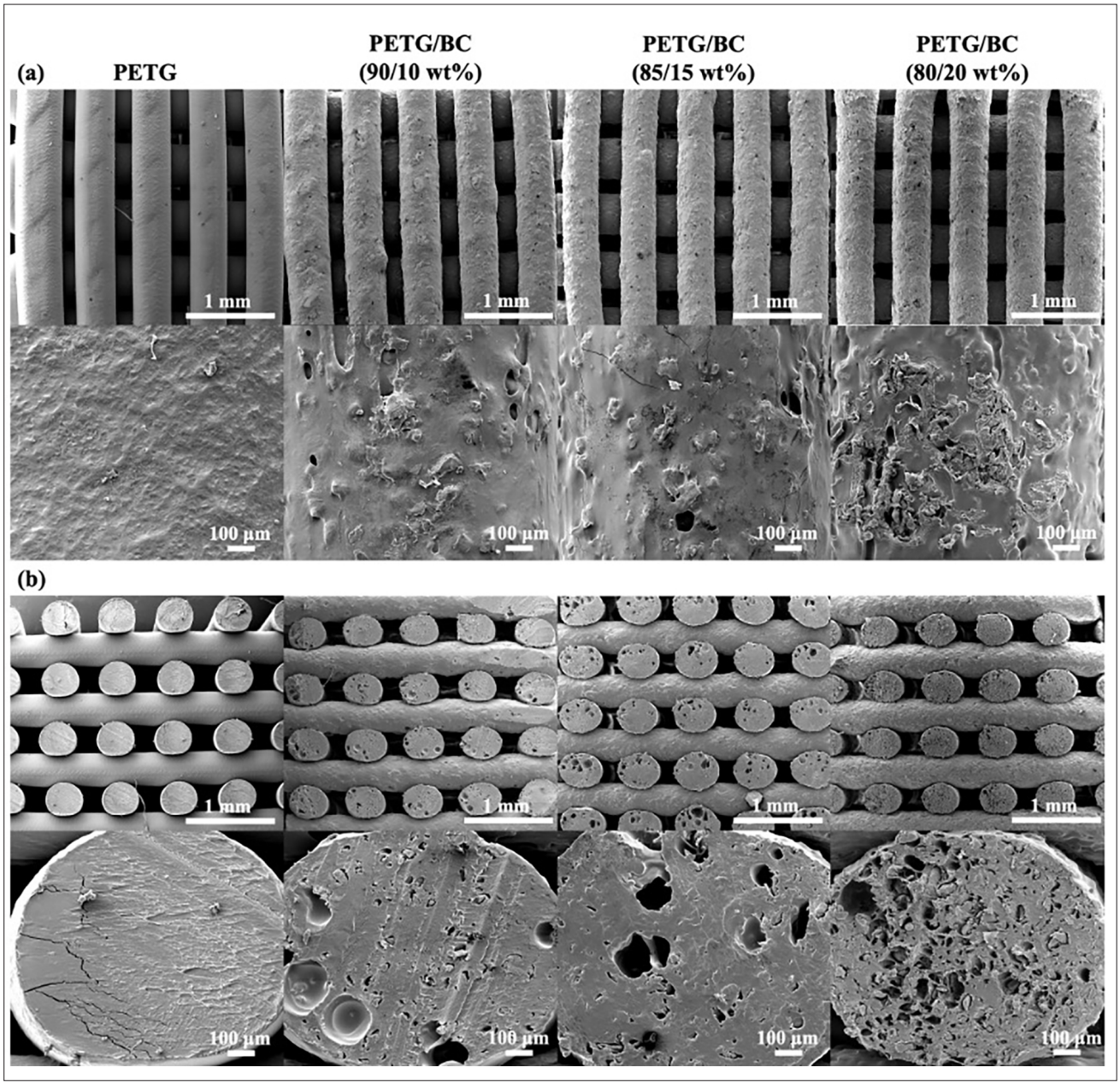


Figure 1. Scanning electron microscopy images of (a) top view and (b) cross-sectional view of PETG, PETG /BC (90/10 wt%), PETG/BC (85/15 wt%), and PETG/BC (80/20 wt%). Scale bars: 1 mm (a and b, top); 100 µm (a and b, bottom). Abbreviations: BC: bacterial cellulose; PETG: polyethylene terephthalate glycol.

highest compression (~230 MPa) properties compared to the other material blends.

3.4. Chemical properties of the 3D-printed scaffolds

The effect of BC as a potential nucleation agent for crystallization was investigated using DSC to identif y the thermal cycling effect on the materials' properties.[30] The results (Figure 5a–e; Table 2) indicate that during the first heating cycle, the incorporation of BC increases the glass transition temperature (T_g), melting temperature (T_m), enthalpy (ΔH), and crystallinity (χ_c). In contrast, an opposite

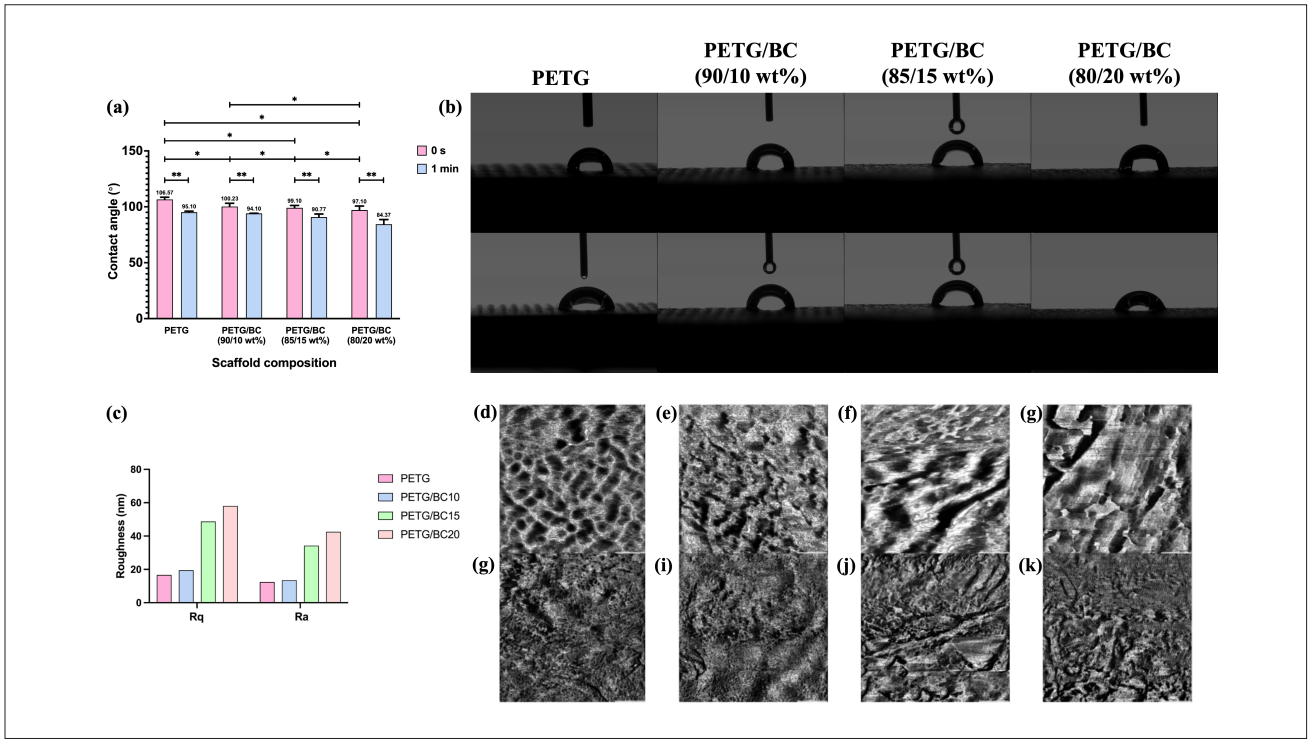


Figure 2. Scaffold morphology and roughness. (a) Water contact angle (WCA) results at 0 s and 1 min. (b) WCA images of PETG and PETG/BC scaffolds. (c) Rq and Ra roughness values measured using atomic force microscopy (AFM) images. (d–k) AFM images taken at 1 μ m scale for PETG (d), PETG/BC (90/10 wt%) (e), PETG/BC15 (85/15 wt%) (f), and PETG/ BC (80/20 wt%) (g), as well as at 10 (m scale for PETG (h), PETG/ BC (90/10 wt%) (i), PETG/ BC (85/15 wt%) (j), and PETG/ BC (80/20 wt%) (k). *$p < 0.05$; **$p < 0.01$; $n = 4$. Scale bars: 1 μm (d–g); 1 μm (h–k). Abbreviations: BC: bacterial cellulose; PETG: polyethylene terephthalate glycol.

Table 1. Water contact angle results of printed scaffolds at 0 s and 1 min

Materials	Water contact angle (°)	
	0 s	1 min
PETG	106.57 ± 1.99	95.1 ± 1.03
PETG/BC (90/10 wt%)	100.23 ± 2.96	94.1 ± 0.1
PETG/BC (85/15 wt%)	99.1 ± 2.1	90.77 ± 2.78
PETG/BC (80/20 wt%)	97.1 ± 3.6	84.37 ± 4.24

Abbreviations: BC: bacterial cellulose; PETG: polyethylene terephthalate glycol.

effect was observed during the second heating cycle (Figure 5a and b). During the heat –cool –heat process, the ΔH initially increased from 17.02 J/g for pure PETG to 17.92 J/g for PETG/BC (90/10 wt%), 18.49 J/g for PETG/BC (85/15 wt%), and 20.91 J/g for PETG/BC (80/20 wt %) in the first heating cycle; decreased to 15.26 J/g for pure PETG, 11.32 J/g for PETG/BC (90/10 wt%), 12.48 J/g for PETG/ BC (85/15 wt%), and 13.11 J/g for PETG/BC (80/20 wt%) during the cooling phase; and increased again to 16.98 J/g for pure PETG, 16.46 J/g for PETG/BC (90/10 wt%), 15.22 J/g for PETG/BC (85/15 wt%), and 13.72 J/g for PETG/ BC (80/20 wt%) in the second heating phase (Table 2). Moreover, χ_c significantly decreases from the first heating phase (52.92% for pure PETG, 53.09% for PETG/BC [90/10 wt%], 54.86% J/g for PETG/BC [85/15 wt%], and 59.48% for PETG/BC [80/20 wt%]) to the second heating phase (50.35% for pure PETG, 48.67% for PETG/BC [90/10 wt%], 45.08% J/g for PETG/BC [85/15 wt%], and 40.69% for PETG/BC [80/20 wt%]), suggesting limited rearrangement of the polymeric chains. However, during the second heating phase, BC has a negative effect on the crystallinity, indicating poor interconnectivity between BC and PETG after the recrystallisation process. The T_m results did not display significant differences with the incorporation of BC for both the first heating cycle (~76–78 °C) and second heating cycle (~76–78 °C), indicating that the incorporation

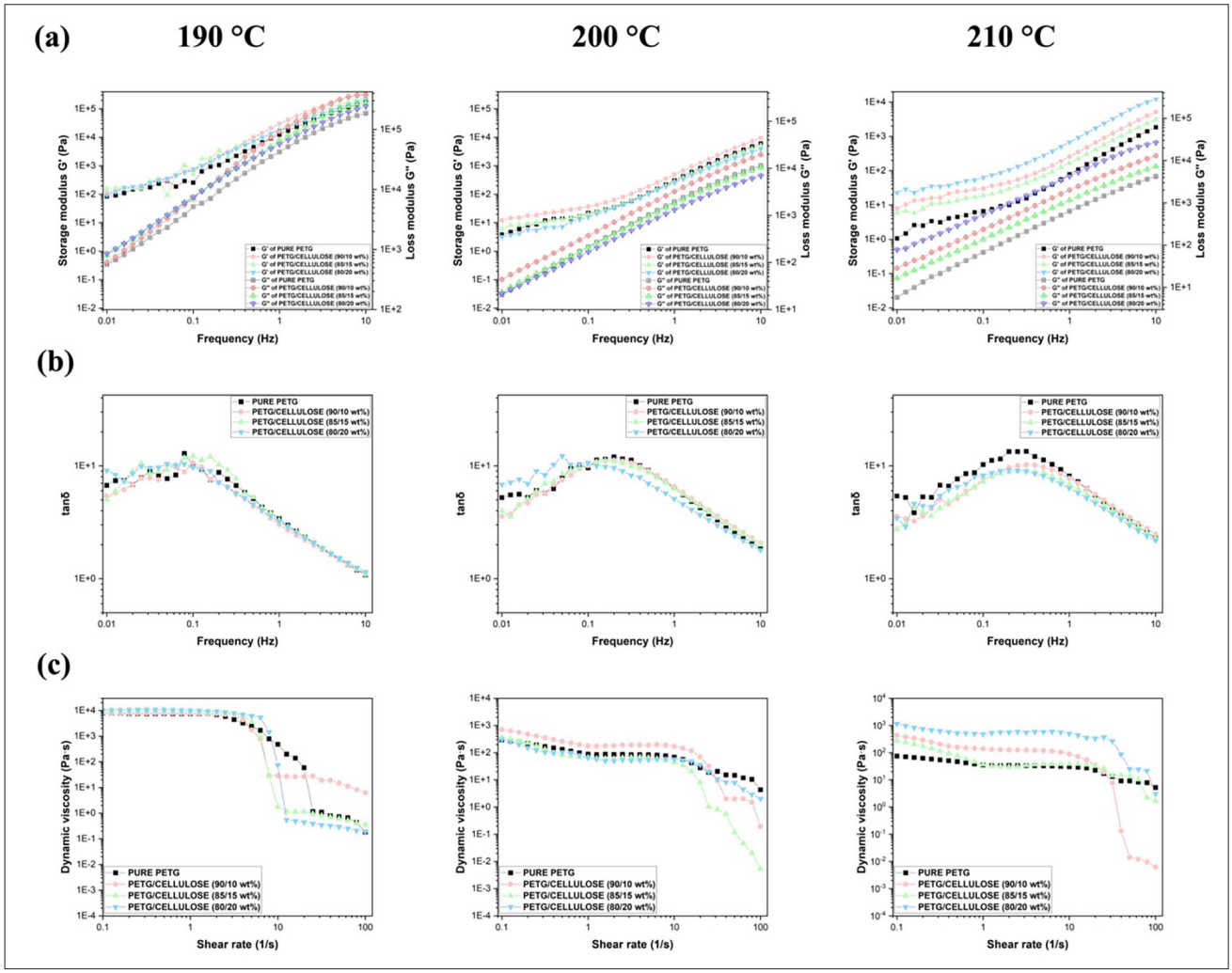


Figure 3. Rheological properties of material blends at different temperatures (190, 200, and 210 °C). (a) Storage and loss moduli results. (b) Loss factor (tanδ) results. (c) Dynamic viscosity results. Abbreviations: BC: bacterial cellulose; PETG: polyethylene terephthalate glycol.

of BC does not affect the energy required for the system to break down the crystal microstructure. The incorporation of BC did not affect the T_c of the polymer (~76–79 °C), indicating that the recrystallisation process and polymer chain mobility are not affected during the transition from the molten to solid state . Similarly, the T_m of the materials remained nearly constant (Figure 5c). For all material blends, the T_g results did not present any differences with the increase of BC content for both the first heating cycle (~68 °C) and the second heating cycle (~65 °C). However, the slight decrease in T_g during the second heating cycle suggests that neither the incorporation of BC, the printing process, nor reheating the materials affects the amorphous region of PETG (Figure 5d and e).

The FTIR analysis verified the successful incorporation of both PETG and BC in the scaffold matrix (Figure 6a). The similarity in the peaks confirms that the thermal blending method is a physical phenomenon that does not change the PETG chemical structure. However, there are some minor shifts with the incorporation of BC, which can be attributed to the interactions between the chemical groups. PETG peaks at 725 and 958 cm^{-1} represent the out-of-plane C –H and cyclohexylene ring, respectively.[31] Peaks at 1240, 1451, and 1712 cm^{-1} are attributed to the C(O)–O stretching of the ester group, $–CH_2–$deformation band, and C=O ester groups.[32] Moreover, peaks found at 2850 and 2924 cm^{-1} are the asymmetric and symmetric aliphatic C–H stretching vibrations.[33] Additionally, BC peaks are found at 847 and 3347 cm^{-1}, depicting the β-1, 4-glycosidic bond vibration and the –OH stretching vibration. With the incorporation of BC, the 2924 cm^{-1} peak shifts to a lower wavenumber by 5 cm^{-1}.

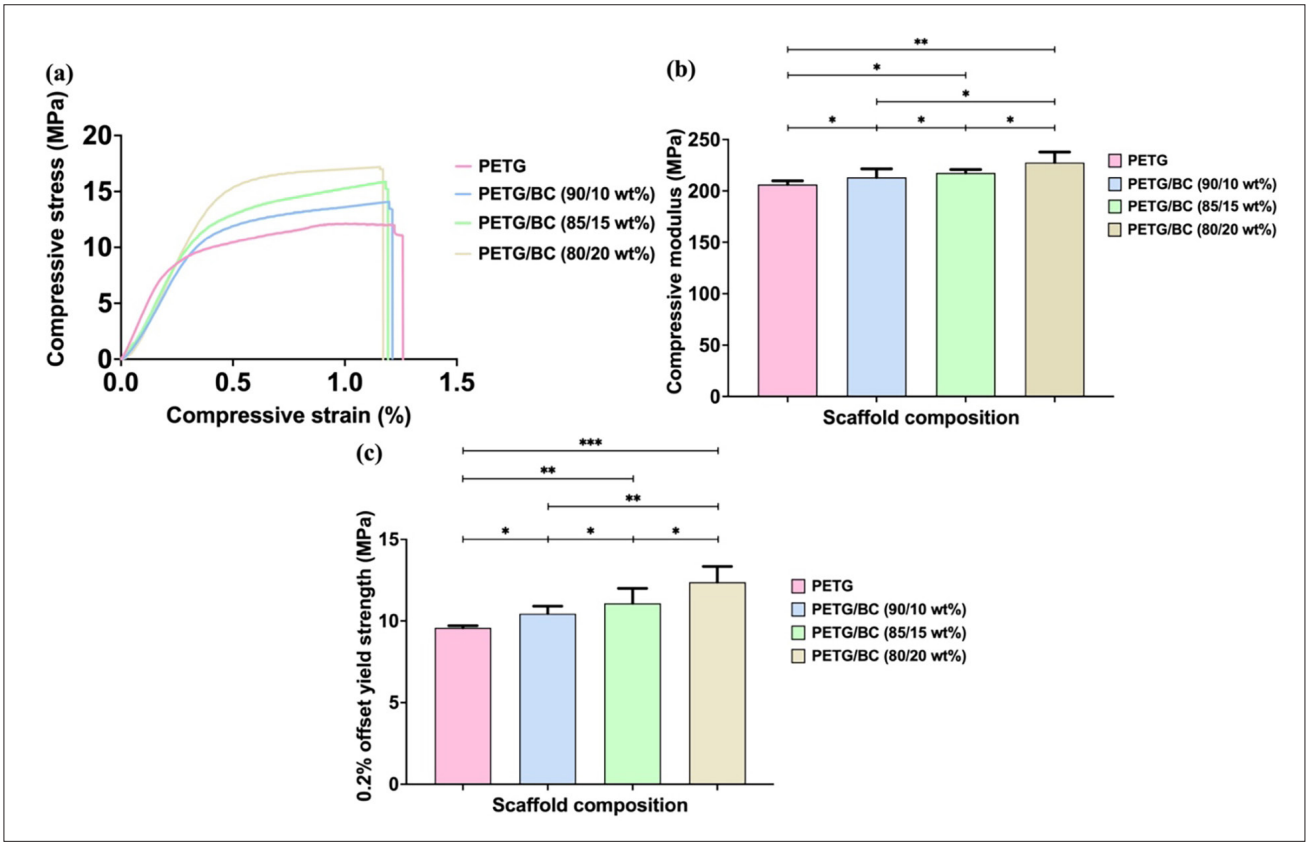


Figure 4. Mechanical properties of printed scaffolds: (a) compressive stress–strain curves, (b) compressive modulus results, and (c) 0.2% offset yield strength results . $^{*}p < 0.05$, $^{**}p < 0.01$, $^{***}p < 0.001$; $n = 4$. Abbreviations: BC: bacterial cellulose; PETG: polyethylene terephthalate glycol.

Figure 6b presents four spectra of PETG, PETG/ BC (90/10 wt%), PETG/ BC (85/15 wt%), and PETG/ BC (80/20 wt%). The spectra have the constituent peaks for PETG at 27.56°, 36.16°, 39.29°, 41.38°, and 44.16°.[34] With the incorporation of BC, three different phenomena can be identified: (i) broadening of the primary peak at 19.11°, (ii) the appearance of a new peak at 22.33°, and (iii) a shift of several peaks to ward lower angles.[35] These observations highlight the chemical and physical changes in the material due to BC incorporation. Additionally, the scaffolds' crystallinity and crystallite size were analyzed using the Scherrer method to study the effect of BC on the nucleation behavior. As displayed in Figure 6b and c, the increase in crystallinity and crystallite sizes can be attributed to the increase in BC content. Crystallinity increased by 10%, and the crystallite size increased from 29.48 to 32.64 nm as the BC content increased from 10 to 20 wt%.

These findings align with the thermal analysis, where DSC results displayed increased crystallinity and enthalpy with higher BC content (Table 2). Taken together, the FTIR, XRD, and DSC results confirm that BC acts as a physical reinforcement and nucleating agent within the PETG matrix, improving both the structural order and thermal behavior of the composite scaffolds.

3.5. *In vitro* properties of the 3D-printed scaffolds

hADSCs were seeded on the different scaffolds to assess cell attachment, proliferation, and differentiation. Cellular metabolic activity was assessed using the Alamar Blue assay. From day 3 to day 14, a progressive increase in cell metabolic activity was observed, suggesting active proliferation and spreading on the scaffolds. This activity may be linked to the minerals released during material degradation (Figure 7a). Moreover, BC incorporation increased cell metabolic activity, with the highest value (~16,000 AU) observed for PETG/BC (80/20 wt%) on day 14, implying that cell proliferation is positively affected by the presence of BC. In contrast, PETG-only scaffolds exhibited the lowest metabolic activity (~12,000 AU).

The MTT assay was used to quantify cell attachment and proliferation on the scaffolds (Figure 7b). The results were consistent with those from the Alamar Blue assay . On day 3, a high number of cells was observed across all the different material concentrations, with PETG/BC (90/10

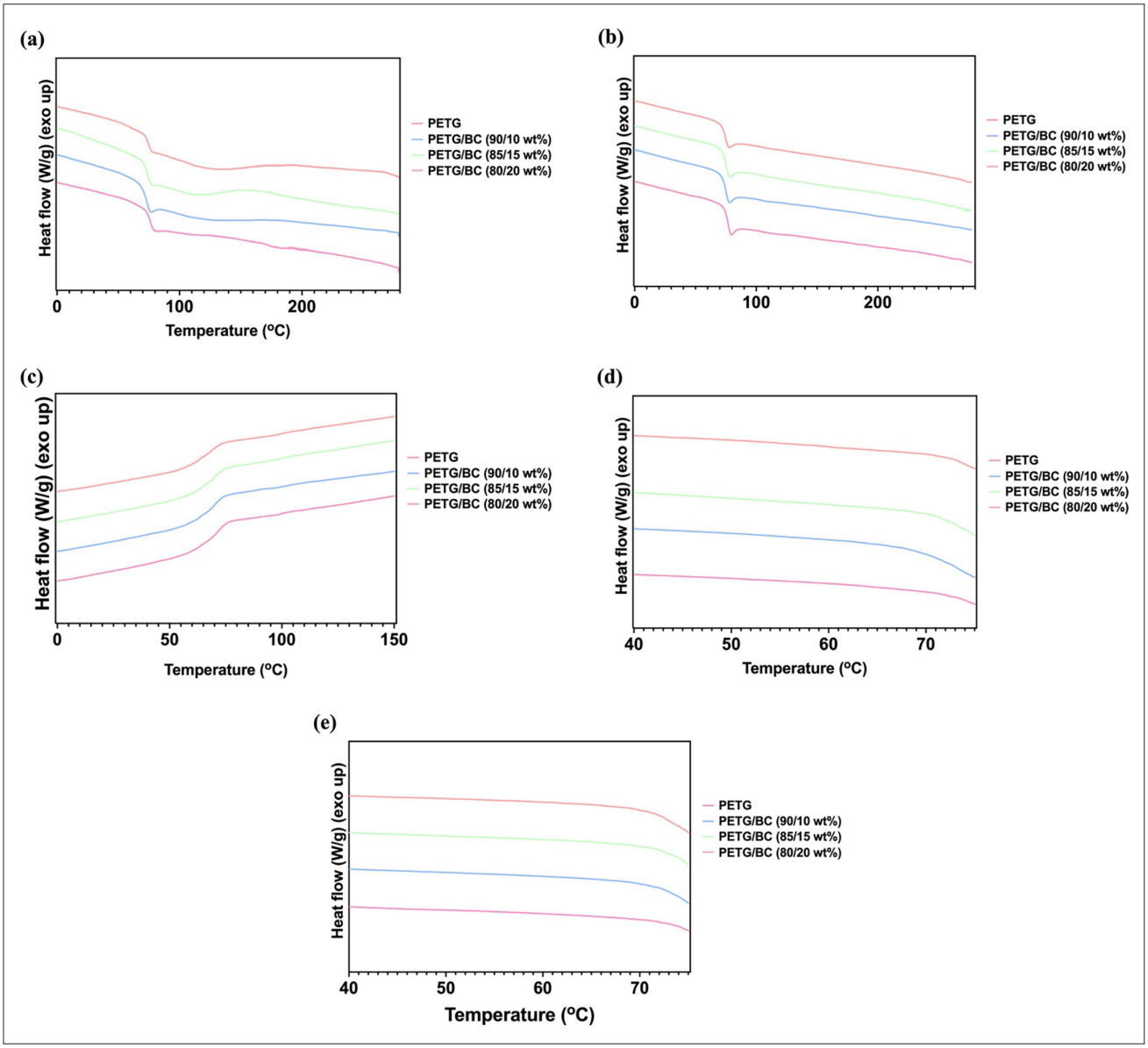


Figure 5. Differential scanning calorimetry (DSC) analysis: (a) first heating cycle; (b) second heating cycle; (c) cooling cycle; (d) glass transition temperature during the first heating cycle; and (e) glass transition temperature during the second heating cycle. Abbreviations: BC: bacterial cellulose; PETG: polyethylene terephthalate glycol.

wt%) presenting the highest number of cells (~53,000 cells) and PETG/BC (80/20 wt%) reporting the lowest number of cells (~43,000 cells). The lower number of cells in PETG/BC (80/20 wt%) is attributed to the smaller pore size and limited available space for cell growth and proliferation. On day 7, cell numbers increased but displayed a similar trend to day 3, ranging from ~132,000 cells for the PETG/BC (80/20 wt%) scaffold to ~142,000 cells for the PETG/BC (90/10 wt%) scaffold. By day 14, cell numbers continued to increase, with the PETG/BC (80/20 wt%) scaffold presenting the highest cell count (~204,000 cells), followed by the PETG/BC (85/15 wt%) scaffold (~179,000 cells) and the PETG/BC (90/10 wt%) scaffold (~177,000 cells). Pure PETG exhibited the lowest cell count (~164,000 cells). This trend is ascribed to the increased surface roughness of PETG/BC (80/20 wt%) scaffolds, which may facilitate better cell adhesion and growth.

The ALP assay was used to evaluate the osteogenic differentiation of cells across different BC concentrations

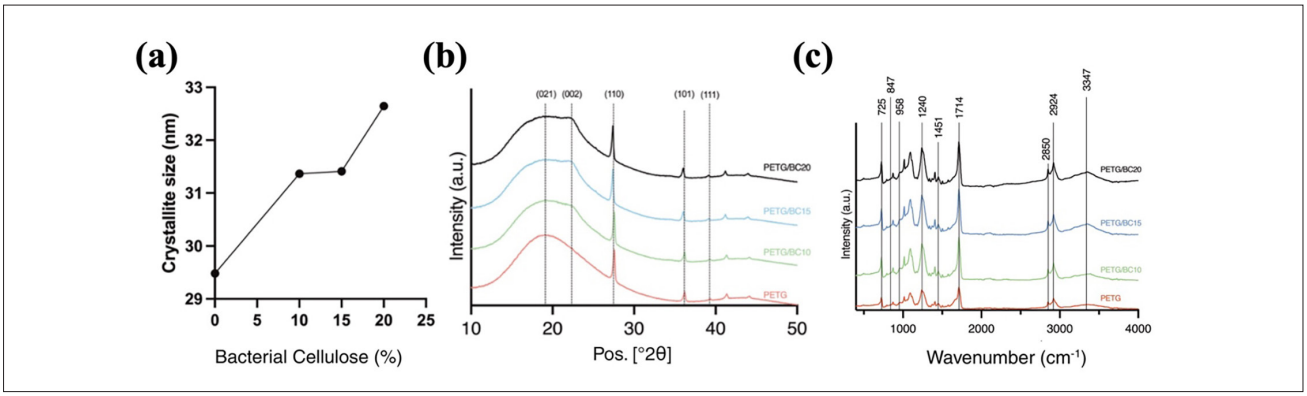


Figure 6. Physical characteristics of the printed scaffolds: (a) FTIR analysis; (b) XRD analysis of PETG and PETG/BC scaffolds; and (c) analysis of crystallite size. Abbreviations: BC, bacterial cellulose; PETG, polyethylene terephthalate glycol; FTIR, Fourier transform infrared spectroscopy; XRD, X-ray diffraction.

Table 2. Differential scanning calorimetry (DSC) results of the printed scaffolds

Cycle	Material	T_g (°C)	T_m (°C)	T_c (°C)	χ_c (%)
First heating	PETG	68.66 ± 0.07	78.86 ± 0.15	17.02 ± 0.1	52.91 ± 0.77
	PETG/BC (90/10 wt%)	68.45 ± 0.04	76.34 ± 0.08	17.92 ± 0.03	53.09 ± 0.95
	PETG/BC (85/15 wt%)	68.27 ± 0.01	76.46 ± 0.07	18.49 ± 0.05	54.86 ± 1.68
	PETG/ BC (80/20 wt%)	68.19 ± 0.08	77.39 ± 0.12	20.91 ± 0.09	59.48 ± 2.63
Cooling	PETG	–	75.72 ± 0.03	15.26 ± 0.06	45.15 ± 1.81
	PETG/BC (90/10 wt%)	–	73.95 ± 0.33	11.32 ± 0.03	35.55 ± 0.86
	PETG/BC (85/15 wt%)	–	74.01 ± 0.09	12.48 ± 0.01	36.98 ± 0.3
	PETG/BC (80/20 wt%)	–	73.08 ± 0.07	13.11 ± 0.07	39.12 ± 2.62
Second heating	PETG	66.23 ± 0.02	78.45 ± 0.21	16.98 ± 0.04	50.35 ± 1.46
	PETG/BC (90/10 wt%)	65.94 ± 0.02	76.72 ± 0.14	16.46 ± 0.07	48.67 ±2.16
	PETG/BC (85/15 wt%)	64.74 ± 0.03	76.44 ± 0.17	15.22 ± 0.01	45.08 ± 1.3
	PETG/BC (80/20 wt%)	64.44 ± 0.06	76.43 ± 0.22	13.72 ± 0.05	40.69 ± 1.7

Abbreviations: BC: bacterial cellulose; PETG: polyethylene terephthalate glycol.

(Figure 7c). A significant increase in ALP activity was observed from day 3 to day 14, indicating enhanced osteogenic differentiation of the hADSCs. On day 3, BC-containing scaffolds presented higher ALP activity compared to pure PETG scaffolds, though not statistically significant . By days 7 and 14, ALP activity increased with BC content, again without significant differences . Among the different scaffolds, PETG/BC (80/20 wt%) displayed the highest ALP activity, likely due to its high surface roughness, which better mimics natural bone.

SEM and confocal images confirmed that cells spread and filled the porous areas of the scaffolds, indicating no cytotoxicity (Figure 8a and b). Cell numbers and surface coverage increased with higher BC concentrations . Due to the dense cell population, DAPI staining produced overly bright signals, limiting confocal image clarity (Figure S1). Therefore, bright -field imaging was applied in Figure S1, highlighting cell bridging and proliferation between the porous areas, with an increased number of cells being observed at increas ing BC concentration.

4. Discussion

In this research, 3D-printed scaffolds were successfully fabricated using FDM, and their characteristics were studied. A twin-screw extruder was used to produce a homogeneous mixture of PETG and BC. In order to achieve a well-defined 3D printed structure, the influence of printing parameters and filler concentration on material properties was investigated. Among those parameters, the most critical are the extruding parameters and rheology characteristics of the materials.

The incorporation of BC increas ed the printing temperature and viscosity, corresponding to a decrease in

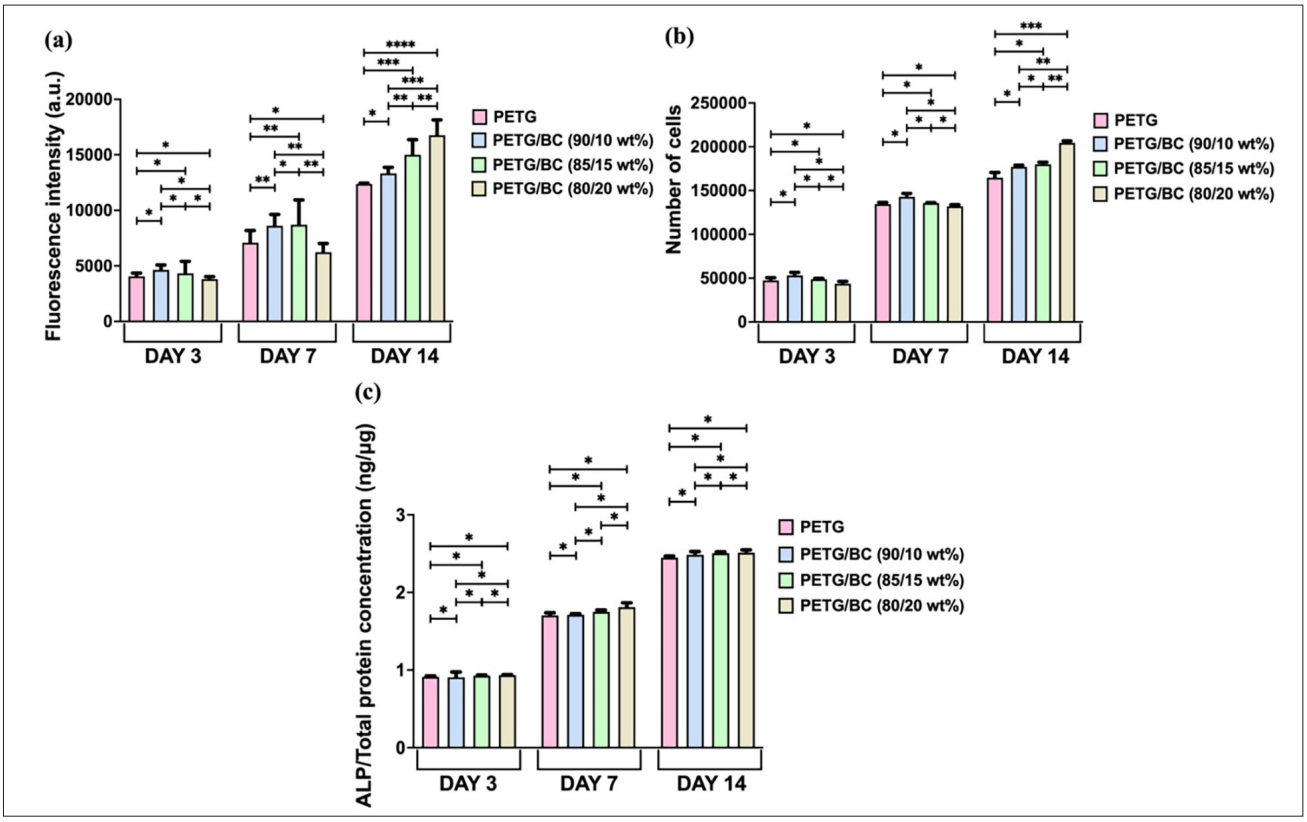


Figure 7. Biological characteristics of the printed scaffolds. (a) Metabolic activity of hADSCs assessed by Alamar Blue assay on days 3, 7, and 14. (b) Cell proliferation measured by MTT assay on days 3, 7, and 14. (c) Normalized ALP activity indicating osteogenic differentiation of hADSCs across different scaffold compositions on days 3, 7, and 14. $^{*}p < 0.05$, $^{**}p < 0.01$, $^{***}p < 0.001$, $^{****}p < 0.0001$; $n = 5$. Abbreviations: BC: bacterial cellulose; PETG: polyethylene terephthalate glycol.

polymer chain movement and flowability. Techawinyutham *et al.*[36] fabricated PETG with recycled high-density polyethylene and low-density polyethylene at various concentrations (0–100 wt%) using a compression molding process, and revealed that decreas ing the PETG content led to decreases in storage modulus, loss modulus, and viscosity. A similar trend was observed by Bhandari *et al.*,[37] who observed that increasing carbon fiber concentration in PETG, using an extrusion-based 3D printing process, led to reductions in storage modulus, loss modulus, and viscosity. Therefore, the results reported in this paper are consistent with previous studies, indicating that BC incorporation in the blend enhances viscosity.

The FDM 3D-printed scaffolds exhibited pore sizes and filament widths consistent with the design specifications, with no direct effect from BC incorporation. Morphological analysis confirmed the presence of micro por es and increased surface roughness, both of which were intensified with higher BC content. The formation of micro por es and increased surface roughness can be attributed to the high temperatures used during filament fabrication (>190 °C) and rapid solidification.[38] Based on *in vitro* and *in vivo* assessments, the formation of intrafiber pores on scaffolds promoted better cell adhesion, proliferation, growth, and differentiation compared to scaffolds with smooth surfaces and no intrafiber pores.[39] This was confirmed by the biological results in this study, where increased fiber microporosity, and thus surface area, promoted greater cell adhesion, proliferation, and growth. While microporosity is associated with reduced mechanical properties due to crack formation and structure failure,[40] the scaffolds in this study maintained mechanical integrity, likely due to increase d crystallinity.[41]

Wettability analysis revealed that increas ing BC content reduced WCA, enhancing scaffold hydrophilicity due to the hydrophilicity of BC.[42] Scaffold morphology—governed by surface roughness and microporosity—played a key role in this behavior . Higher BC concentration led to rougher surfaces and more micro pores, which improved water absorption and further decreased WCA.[43] According

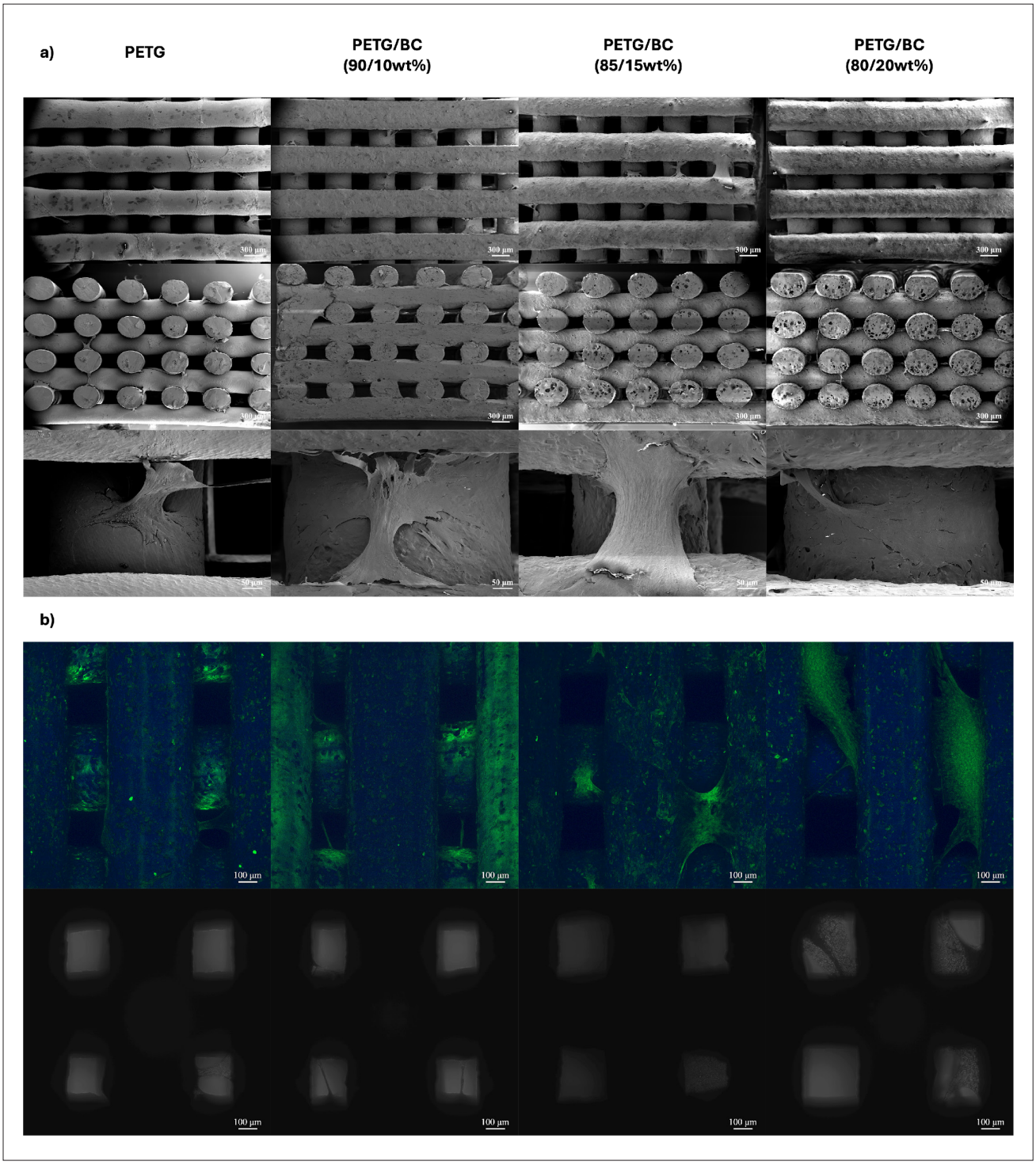


Figure 8. Cell attachment and proliferation on scaffold surfaces on day 14. (a) SEM images of the top and cross-sectional views of cell-seeded scaffolds . (b) Confocal and bright-field images (top and cross-sectional views) of cell-seeded scaffolds . Scale bars: 300 µm (a, top and middle); 100 µm (b); 50 µm (a, bottom). Abbreviations: BC: bacterial cellulose; PETG: polyethylene terephthalate glycol; SEM: scanning electron microscopy.

to previous studies, increased wettability, surface roughness, and microporosity correlate with improved cell adhesion and tissue repair, indicating enhanced bioactivity with BC incorporation.[44]

The AFM topographical maps of PETG-based scaffolds highlight significant changes in surface morphology and roughness with increasing BC content. Pure PETG exhibited a relatively smooth surface with minor variations between peaks and valleys. At 10 wt% BC, a slight increase in overall roughness is observed, while 15 wt % BC exhibited more defined valleys and peaks, reflected in elevated Rq and Ra values (Figure 1g and k). At 20 wt% BC, the surface transitions to larger, planar peaks, indicating a significant morphological shift. These changes mimic the natural roughness of bone tissue, enhancing surface area and promoting cell attachment and growth, as supported by the biological results .

The DSC analysis revealed an increase in crystallinity and enthalpy with the incorporation of BC, while the T_g remained largely unchanged. These parameters are critical for influencing the mechanical and biological properties of the materials.[45] As PETG is predominantly amorphous (35–40% crystallinity), the incorporation of crystalline BC (60–80% crystallinity) serves as a nucleating agent, enhancing crystallinity through increased nucleation site formation and increased chain mobility.[46] The observed rise in enthalpy corresponds with increased crystallinity, reflecting the greater energy exchange during thermal cycling.[47] The unchanged T_g indicates that the amorphous nature of the blend remains dominant.[48]

The XRD analysis was used to evaluate the structure of PETG/BC scaffolds and the effect of BC concentration on crystallite sizes, which is key in improving the mechanical properties of bone tissue scaffolds to match bone tissue. As BC concentration increased, crystallite size generally grew, aligning with improvements in tensile strength. However, between 10–15 wt% BC, crystallite size remained relatively constant despite a marked increase in compressive strength. This suggests that crystallite growth primarily supports tensile properties, while compressive strength may be more affected by factors like voids or microstructural defects.

The FTIR results displayed a pronounced –OH peak at 3347 cm^{-1}, resembling the characteristic fingerprint of collagen in the 2750–3500 cm^{-1} range.[49] This is attributed to the hydrogen bonds present in both collagen and cellulose structures. Incorporating cellulose into synthetic polyesters like PETG enables the formation of strong hydrogen bonds akin to those in bone collagen,[50] which likely contributes to the enhanced mechanobiological performance observed with increasing BC content. FTIR analysis suggests that the optimal composition is PETG/BC at 80/20 wt%.

The chemical and morphological characteristics of the scaffolds significantly influence their mechanical properties. Compression tests revealed that increas ing BC concentration enhanced mechanical properties. Key parameters, such as porosity, pore size, and filament deposition, strongly impact the mechanical properties of the scaffolds.[3] Studies have reported that increas ing the porosity and pore size decreases the compressive modulus.[11] The 0/90° filament deposition has demonstrated much higher compression properties compared to 0/30° and 0/45° due to better connectivity between the pores and reduced surface density.[51] Yao and Chen[52] observed that the increased surface roughness also contributed to better mechanical properties by enlarging the contact area between fibers and matrix. Additionally, crystallinity and crystallite size directly impact the mechanical behavior of materials. Shuai *et al.*[53] produced scaffolds using poly(3-hydroxybutyrate-co-3-hydroxyvalerate) (PHBV) reinforced with zinc oxide (1, 3, and 5 wt%), which enhanced the mechanical properties of PHBV due to ordered stacking of polymer chains. The same trend was observed for poly-L- lactic acid (PLLA) scaffolds reinforced with carbon nanotubes (CNTs) (0.25, 0.5, and 1 wt%), where CNTs increase the crystallization of PLLA, leading to enhanced compressive modulus.[54] Huang *et al.*[55] also reported enhanced mechanical properties and increased crystallite size using PCL and β-tricalcium phosphate (20 and 40 wt%), validating the correlation between crystallite size and mechanical characteristics .

For bone tissue applications, scaffold biocompatibility and bioactivity are critical, alongside morphology, crystallinity, crystallite size, and mechanical properties of the scaffolds. Increas ing BC concentration enhanced cell attachment, proliferation, and differentiation, likely due to the release of bioactive elements, minerals, and increased oxygen availability.[56] The rougher surfaces and micropores introduced by BC enhanced scaffold hydrophilicity, supporting better cell interactions.[39] BC also increased crystallinity and crystallite size, enhancing mechanical properties and roughness of the scaffolds, which promote cell attachment and proliferation.[57] Scaffolds should be able to withstand high loads and provide mechanical properties similar to bone. Cell adhesion, proliferation, and differentiation rely on the cell's ability to sense and respond to mechanical cues at the nanoscale and microscale. Cells detect the density and stiffness of the material they attach to (mechanosensitivity) and convert this information into biochemical signals, leading to changes inside the cell.[58] Moreover, studies have reported that cell adhesion is

strongly dependent on the cytoskeleton, which is affected by the nanotopographical features of the material's surface, leading to the cell differentiation into bone or muscle tissue. Therefore, the incorporation of BC (and higher BC concentrations) significantly enhances the mechanical characteristics of the scaffolds, comparable to or exceeding those of trabecular bones (14–1 100 MPa), indicating an increase in bioactivity.[59,60]

This study focused on the effect of BC incorporation on the mechanical and biological behavior of PETG for bone tissue applications. While pure PETG demonstrated substantial mechanical and biological properties suitable for load-bearing applications and cell attachment and proliferation, the incorporation of BC significantly enhanced these properties . Among all blends, PETG/BC (80/20 wt%) exhibited the most favorable mechanical and biological properties .

5. Conclusion

In this study, PETG and PETG/BC scaffolds (0, 15, and 20 wt% BC) were successfully fabricated using the FDM additive manufacturing process. The incorporation of BC resulted in the formation of micro porous regions and increased surface roughness, enhancing scaffold morphology while maintaining consistent geometry and printability. Moreover, the presence of BC improved scaffold wettability, with WCA measurements indicating increased hydrophilicity at higher BC content. These morphological and surface modifications contributed to improved biological responses.

Chemical and thermal analyses confirmed the successful integration of BC into the PETG matrix. Higher BC content led to increased crystallinity and crystallite size, which positively influenced the scaffold's mechanical properties. All material blends exhibited shear-thinning behavior, making them suitable for FDM processing. Mechanical testing revealed that compressive modulus and yield strength increased with BC incorporation, with PETG/BC (80/20 wt%) demonstrating the highest mechanical performance.

Biological assays indicated that the PETG/BC scaffolds supported hADSCs attachment, proliferation, and osteogenic differentiation without signs of cytotoxicity. Increased BC content correlated with higher metabolic activity and ALP expression, suggesting improved bioactivity. Among all tested compositions, the PETG/BC (80/20 wt%) scaffold exhibited the most favorable combination of morphological, mechanical, and biological properties, indicating its strong potential for bone TE applications.

Acknowledgments

The authors would like to thank the University of Manchester, UK Research and Innovation (UKRI), Engineering and Physical Sciences Research Council (EPSRC), Henry Royce Institute for Advanced Materials, Nanyang Technological University (NTU), and Singapore Centre for 3D Printing (SC3DP) for their support and facilities.

Funding

This project was partially supported by the University of Manchester and UKRI through EPSRC (grant number: EP/V011766/1). Additionally, this work was also supported by the Henry Royce Institute for Advanced Materials (grant number: EP/S019367/1).

Conflict of interest

Paulo J.D.S. Bartolo is an Editorial Board Member of the journal, but was not in any way involved in the editorial and peer-review process conducted for this paper, directly or indirectly. Other authors declare they have no competing interests.

Author contributions

Conceptualization: Evangelos Daskalakis, Mohamed H. Hassan, Abdalla M. Omar, Paulo J.D.S. Bartolo

Data curation: Evangelos Daskalakis, Mohamed H. Hassan, Abdalla M. Omar, Maria Kapousidou, Dino Freitas, Mehmet Cagirici, Alexandra Lanot

Formal analysis: Evangelos Daskalakis, Mohamed H. Hassan, Abdalla M. Omar

Funding acquisition: Paulo J.D.S. Bartolo

Investigation: Evangelos Daskalakis, Mohamed H. Hassan, Abdalla M. Omar

Methodology: Evangelos Daskalakis, Mohamed H. Hassan, Abdalla M. Omar, Maria Kapousidou, Alexandra Lanot

Project administration: Evangelos Daskalakis, Mohamed, H. Hassan, Abdalla M. Omar, Paulo J.D.S. Bartolo

Resources: Evangelos Daskalakis, Mohamed H. Hassan, Abdalla M. Omar, Maria Kapousidou, Dino Freitas, Mehmet Cagirici

Software: Evangelos Daskalakis, Mohamed H. Hassan, Abdalla M. Omar, Maria Kapousidou, Alexandra Lanot

Supervision: Evangelos Daskalakis, Mohamed H. Hassan, Abdalla M. Omar, Paulo J.D.S. Bartolo

Validation: Evangelos Daskalakis, Mohamed H. Hassan, Abdalla M. Omar, Maria Kapousidou, Dino Freitas, Mehmet Cagirici, Alexandra Lanot, Paulo J.D.S. Bartolo

Visualization: Evangelos Daskalakis, Mohamed H. Hassan, Abdalla M. Omar
Writing – original draft: Evangelos Daskalakis, Mohamed H. Hassan, Abdalla M. Omar
Writing – review & editing: All authors

Ethics approval and consent to participate

Not applicable.

Consent for publication

Not applicable.

Availability of data

Data is available from the corresponding author upon reasonable request

References

1. Wang Y, Pereira FR, Peach C, Huang B, Vyas C, Bartolo P. Robotic *in situ* bioprinting for cartilage tissue engineering. *Int J Extreme Manuf.* 2023;5(3):032004. doi: 10.1088/2631-7990/acda67
2. Dwivedi R, Mehrotra D. 3D bioprinting and craniofacial regeneration. *J Oral Biol Craniofac Res*. 2020;10(4): 650-659. doi: 10.1016/j.jobcr.2020.08.011
3. Baptista R, Guedes M. Morphological and mechanical characterization of 3D printed PLA scaffolds with controlled porosity for trabecular bone tissue replacement. *Mater Sci Eng C*. 2021;118:111528. doi: 10.1016/j.msec.2020.111528
4. Loh QL, Choong C. Three-dimensional scaffolds for tissue engineering applications: role of porosity and pore size. *Tissue Eng Part B Rev*. 2013;19(6):485-502. doi: 10.1089/ten.teb.2012.0437
5. Rahmati M, Silva EA, Reseland JE, Heyward CA, Haugen HJ. Biological responses to physicochemical properties of biomaterial surface. *Chem Soc Rev*. 2020;49(15): 5178–5224. doi: 10.1039/D0CS00103A
6. Wang C, Huang W, Zhou Y, *et al.* 3D printing of bone tissue engineering scaffolds. *Bioact Mater*. 2020;5(1): 82-91. doi: 10.1016/j.bioactmat.2020.01.004
7. Ribas RG, Schatkoski VM, Montanheiro TLA, *et al.* Current advances in bone tissue engineering concerning ceramic and bioglass scaffolds: a review. *Ceram Int*. 2019;45(17):21051-21061. doi: 10.1016/j.ceramint.2019.07.096
8. Vyas C, Ates G, Aslan E, Hart J, Huang B, Bartolo B. Three-dimensional printing and electrospinning dual-scale polycaprolactone scaffolds with low-density and oriented fibers to promote cell alignment. *3D Print Addit Manuf*. 2020;7(3):105-113. doi: 10.1089/3dp.2019.0091
9. Huang B, Aslan E, Jiang Z, et al. Engineered dual-scale poly(ε-caprolactone) scaffolds using 3D printing and rotational electrospinning for bone tissue regeneration. *Addit Manuf.* 2020;36:101452. doi: 10.1016/j.addma.2020.101452
10. Caetano G, Violante R, Sant'Ana AB, *et al.* Cellularized versus decellularized scaffolds for bone regeneration. *Mater Lett*. 2016;182:318-322. doi: 10.1016/j.matlet.2016.05.152
11. Hassan MH, Omar AM, Daskalakis E, *et al.* The potential of polyethylene terephthalate glycol as biomaterial for bone tissue engineering. *Polymers*. 2020;12(12):3045. doi: 10.3390/polym12123045
12. Martins RF, Branco R, Martins M, *et al.* Mechanical properties of additively manufactured polymeric materials—PLA and PETG—for biomechanical applications. *Polymers*. 2024;16(13):1868. doi: 10.3390/polym16131868
13. Moreno Nieto D, Alonso-García M, Pardo-Vicente MA, Rodríguez-Parada L. Product design by additive manufacturing for water environments: study of degradation and absorption behavior of PLA and PETG. *Polymers*. 2021;13(7):1036. doi: 10.3390/polym13071036
14. Habibi Y, Lucia LA, Rojas OJ. Cellulose nanocrystals: chemistry, self-assembly, and applications. *Chem Rev*. 2010;110(6):3479-3500. doi: 10.1021/cr900339w
15. Saxena IM, Brown RM. Cellulose biosynthesis: current views and evolving concepts. *Ann Bot*. 2005;96(1):9–21. doi: 10.1093/aob/mci155
16. Bhatnagar A, Sain M. Processing of cellulose nanofiber-reinforced composites. *J Reinf Plast Compos*. 2005;24(12):1259-1268. doi: 10.1177/0731684405049864
17. Wu Q, Henriksson M, Liu X, Berglund LA. A high strength nanocomposite based on microcrystalline cellulose and polyurethane. *Biomacromolecules*. 2007;8(12):3687-3692. doi: 10.1021/bm701061t
18. Utoiu E, Manoiu VS, Oprita EI, Craciunescu O. Bacterial cellulose: a sustainable source for hydrogels and 3D-printed scaffolds for tissue engineering. *Gels*. 2024;10(6):387. doi: 10.3390/gels10060387
19. Shrivastav P, Pramanik S, Vaidya G, *et al.* Bacterial cellulose as a potential biopolymer in biomedical applications: a state-of-the-art review. *J Mater Chem B*. 2022;10(17): 3199-3241. doi: 10.1039/d1tb02709c

20. Torgbo S, Sukyai P. Biodegradation and thermal stability of bacterial cellulose as biomaterial: the relevance in biomedical applications. *Polym Degrad Stabil*. 2020;179:109232. doi: 10.1016/j.polymdegradstab.2020.109232

21. Wu Y, Wang Y, Wang F, Huang Y, He J. Preparation of 3D printed polylactic acid/bacterial cellulose composite scaffolds for tissue engineering applications. *Polymers*. 2022;14(21):4756. doi: 10.3390/polym14214756

22. Panaitescu MD, Frone NA, Chiulan I, Gabor RA, Spataru IC, Căşărică A. Biocomposites from polylactic acid and bacterial cellulose nanofibers obtained by mechanical treatment. *Bioresources*. 2017;12(1):662-672. doi: 10.15376/biores.12.1.662-672

23. Yodsanga S, Poeaim S, Chantarangsu S, Swasdison S. Investigation of biodegradation and biocompatibility of chitosan–bacterial cellulose composite scaffold for bone tissue engineering applications. *Cells*. 2025;14(10):723. doi: 10.3390/cells14100723

24. Saska S, Barud SH, Gaspar MMA, Marchetto R, Ribeiro SJL, Messaddeq Y. Bacterial cellulose-hydroxyapatite nanocomposites for bone regeneration. *Int J Biomater*. 2011;2011:1-8. doi: 10.1155/2011/175362

25. Boyetey BM, Torgbo S, Sukyai P. Bio-scaffold for bone tissue engineering with focus on bacterial cellulose, biological materials for hydroxyapatite synthesis and growth factors. *Eur Polym J*. 2023;194:112168. doi: 10.1016/j.eurpolymj.2023.112168

26. Wang X, Zhang Y, Luo J, *et al.* Printability of hybridized composite from maleic acid-treated bacterial cellulose with gelatin for bone tissue regeneration. *Adv Compos Hybrid Mater*. 2023;6:134. doi: 10.1007/s42114-023-00711-7

27. Lee CM, Gu J, Kafle K, Catchmark J, Kim SH. Cellulose produced by *Gluconacetobacter xylinus* strains ATCC 53524 and ATCC 23768: pellicle formation, post-synthesis aggregation and fiber density. *Carbohydr Polym*. 2015;133:270-276. doi: 10.1016/j.carbpol.2015.06.091

28. Yan C, Kleiner C, Tabigue A, *et al.* PETG: applications in modern medicine. *Eng Regen*. 2024;5(1):45-55. doi: 10.1016/j.engreg.2023.11.001

29. Daicho K, Kobayashi K, Fujisawa S, Saito T. Crystallinity-independent yet modification-dependent true density of nanocellulose. *Biomacromolecules*. 2019;21(2):939-945. doi: 10.1021/acs.biomac.9b01584

30. Saxena P, Shukla P, Gaur M. Thermal analysis of polymer blends and double layer by DSC. *Polym Polym Compos*. 2020;29(9):S11-S18. doi: 10.1177/0967391120984606

31. Martínez Cortizas A, López-Costas O. Linking structural and compositional changes in archaeological human bone collagen: an FTIR-ATR approach. *Sci. Rep.* 2020;10(1): 17888. doi: 10.1038/s41598-020-74993-y

32. Figueiredo M, Fernando A, Martins G, Freitas J, Judas F, Figueiredo H. Effect of the calcination temperature on the composition and microstructure of hydroxyapatite derived from human and animal bone. *Ceram Int*. 2010;36(8):2383–2393. doi: 10.1016/j.ceramint.2010.07.016

33. Zhu X, Chen T, Feng B, *et al.* Biomimetic bacterial cellulose-enhanced double-network hydrogel with excellent mechanical properties applied for the osteochondral defect repair. *ACS Biomater Sci Eng.* 2018;4(10):3534-3544. doi: 10.1021/acsbiomaterials.8b00682

34. Loskot J, Jezbera D, Loskot R, *et al.* Influence of print speed on the microstructure, morphology, and mechanical properties of 3D-printed PETG products. *Polym Test*. 2023;123:108055. doi: 10.1016/j.polymertesting.2023.108055

35. Aguayo MG, Fernández Pérez A, Reyes G, *et al.* Isolation and characterization of cellulose nanocrystals from rejected fibers originated in the Kraft pulping process. *Polymers*. 2018;10(10):1145. doi: 10.3390/polym10101145

36. Techawinyutham L, Tengsuthiwat J, Srisuk R, Techawinyutham W, Rangappa SM, Siengchin S. Recycled LDPE/PETG blends and HDPE/PETG blends: mechanical, thermal, and rheological properties. *J Mater Res Technol*. 2021;15:2445-2458. doi: 10.1016/j.jmrt.2021.09.052

37. Bhandari S, Lopez-Anido RA, Gardner DJ. Enhancing the interlayer tensile strength of 3D printed short carbon fiber reinforced PETG and PLA composites via annealing. *Addit Manuf*. 2019;30:100922. doi: 10.1016/j.addma.2019.100922

38. Rand B, Robinson R. Surface characteristics of carbon fibres from PAN. *Carbon*. 1977;15(4):257-263. doi: 10.1016/0008-6223(77)90011-2

39. Calore AR, Srinivas V, Groenendijk L, *et al.* Manufacturing of scaffolds with interconnected internal open porosity and surface roughness. *Acta Biomater*. 2023;156:158-176. doi: 10.1016/j.actbio.2022.07.017

40. Ahn J-H, Kim J, Han G, *et al.* 3D-printed biodegradable composite scaffolds with significantly enhanced mechanical properties via the combination of binder jetting and capillary rise infiltration process. *Addit Manuf*. 2021;41:101988. doi: 10.1016/j.addma.2021.101988

41. McAdam B, Fournet MB, McDonald P, Mojicevic M. Production of polyhydroxybutyrate (PHB) and factors impacting its chemical and mechanical characteristics. *Polymers*. 2020;12(12):2908. doi: 10.3390/polym12122908

42. Oh JE, Park N-M. Hydrophilic, transparent, and stretchable film using unmodified cellulose fibers. *Mater Lett.* 2022;309:131385. doi: 10.1016/j.matlet.2021.131385

43. Huang K, Zhu T, Nie J, *et al.* Microporous spongy scaffolds based on biodegradable elastic polyurethanes for the migration and growth of host cells. *ACS Appl Polym Mater.* 2022;4(5):3942-3951. doi: 10.1021/acsapm.2c00398

44. Zou M, Zhao X, Zhang X, Zhao Y, Zhang C, Shi K. Bio-inspired multiple composite film with anisotropic surface wettability and adhesion for tissue repair. *Chem Eng J.* 2020;398:125563. doi: 10.1016/j.cej.2020.125563

45. Conrad TL, Jaekel DJ, Kurtz SM, Roeder RK. Effects of the mold temperature on the mechanical properties and crystallinity of hydroxyapatite whisker-reinforced polyetheretherketone scaffolds. *J Biomed Mater Res B.* 2013;101(4):576-583. doi: 10.1002/jbm.b.32859

46. Bhattarai N, Li Z, Edmondson D, Zhang M. Alginate-based nanofibrous scaffolds: structural, mechanical, and biological properties. *Adv Mater.* 2006;18(11):1463-1467. doi: 10.1002/adma.200502537

47. Hassan MH, Omar AM, Daskalakis E, Liu F, Bartolo P. Preliminary studies on the suitability of PETG for 4D printing applications. MATEC Web Conf. 2020;318:01010. doi: 10.1051/matecconf/202031801010

48. Lanyi FJ, Wenzke N, Kaschta J, Schubert DW. On the determination of the enthalpy of fusion of α-crystalline isotactic polypropylene using differential scanning calorimetry, X-ray diffraction, and Fourier-transform infrared spectroscopy: an old story revisited. *Adv Eng Mater.* 2019;22(9):1900796. doi: 10.1002/adem.201900796

49. Paszkiewicz S, Szymczyk A, Pawlikowska D, *et al.* Synthesis and characterization of poly(ethylene terephthalate-co-1,4-cyclohexanedimethylene terephthalate)-block-poly(tetramethylene oxide) copolymers. *RSC Adv.* 2017;7(66):41745-41754. doi: 10.1039/c7ra07172h

50. Atykyan N, Revin V, Shutova V. Raman and FT-IR spectroscopy investigation of the cellulose structural differences from bacteria gluconacetobacter sucrofermentans during different regimes of cultivation on a molasses media. *AMB Express.* 2020;10(1):84. doi: 10.1186/s13568-020-01020-8

51. Bagwan JK, Ahuja BB, Mulay AV, Jawale KJ. Geometrical analysis of extrusion-based (additively manufactured) 3D designed scaffold for bone tissue engineering: a finite element approach, *Mater Today Proc.* 2022;50(5):1465-1471. doi: 10.1016/j.matpr.2021.09.049

52. Yao Y, Chen S. The effects of fiber's surface roughness on the mechanical properties of fiber-reinforced polymer composites. *J. Compos. Mater.* 2012;47(23):2909-2923. doi: 10.1177/0021998312459871

53. Shuai C, Wang C, Qi F, *et al.* Enhanced crystallinity and antibacterial of PHBV scaffolds incorporated with zinc oxide. *J Nanomater.* 2020:1-12. doi: 10.1155/2020/6014816

54. Wang G, Qi F, Yang W, *et al.* Crystallinity and reinforcement in poly-L-lactic acid scaffold induced by carbon nanotubes. *Adv Polym Technol.* 2019:1-10. doi: 10.1155/2019/8625325

55. Huang B, Wang Y, Vyas C, Bartolo B. Crystal growth of 3D poly(ε-caprolactone) based bone scaffolds and its effects on the physical properties and cellular interactions. *Adv Sci.* 2020;10(1):2203183. doi: 10.1002/advs.202203183

56. Ustunel S, Prévôt ME, Webb G, *et al.* Mechanically tunable elastomer and cellulose nanocrystal composites as scaffolds for in vitro cell studies. *Mater Adv.* 2021;2(1):464-476. doi: 10.1039/d0ma00676a

57. Lužanin O, Gudurić V, Bernhardt A, *et al.* Impact of in-process crystallinity of biodegradable scaffolds fabricated by material extrusion on the micro- and nanosurface topography, viability, proliferation, and differentiation of human mesenchymal stromal cells. *Polymers.* 2023;15(6):1468. doi: 10.3390/polym15061468

58. Wen JH, Vincent LG, Fuhrmann A, *et al.* Interplay of matrix stiffness and protein tethering in stem cell differentiation. *Nat Mater.* 2014;13(10):979-987. doi: 10.1038/nmat4051

59. Morgan EF, Unnikrisnan GU, Hussein AI. Bone mechanical properties in healthy and diseased states. *Annu Rev Biomed Eng.* 2018;20:119-143. doi: 10.1146/annurev-bioeng-062117-121139

60. Öhman-Mägi C, Holub O, Wu D, Hall RM, Persson C. Density and mechanical properties of vertebral trabecular bone—a review. *JOR Spine.* 2021;4(4):e1176. doi: 10.1002/jsp2.1176

ACCSCIENCE PUBLISHING

International Journal of Bioprinting

RESEARCH ARTICLE

A visible light-crosslinkable decellularized kidney matrix bioink for 3D bioprinting of organoids and drug testing

Wenqi Hu[1,2†], Guohua Wu[3], Mengjiao Xia[6], Di Wu[4,5], Qijun Du[1,2,6], Qinrui Lu[1,2], Jiashu Wang[1,2], Ao Xie[1,2], Chenwei Sun[1,2], Haijie Hu[7], Litian Zhao[1,2], Zipeng Yao[1,2,6†*], and Shuqi Wang[1,2,6,8]

[1]College of Biomedical Engineering, Sichuan University, Chengdu, Sichuan, China

[2]National Engineering Research Center for Biomaterials, Sichuan University, Chengdu, Sichuan, China

[3]Luoyang Key Laboratory of Clinical Multiomics and Translational Medicine, Henan Key Laboratory of Rare Diseases, Endocrinology and Metabolism Center, The First Affiliated Hospital and College of Clinical Medicine, Henan University of Science and Technology, Luoyang, Henan, China

[4]Henan Key Laboratory of Rare Diseases, Endocrinology and Metabolism Center, The First Affiliated Hospital and College of Clinical Medicine, Henan University of Science and Technology, Luoyang, Henan, China

[5]Department of Respiratory and Critical Care Medicine, West China Hospital, Sichuan University, Chengdu, Sichuan, China

[6]State Key Laboratory of Respiratory Health and Multimorbidity, West China Hospital, Sichuan University, Chengdu, Sichuan, China

[7]Division of Biliary Surgery, Department of General Surgery, West China Hospital, Sichuan University, Chengdu, Sichuan, China

[8]Clinical Research Center for Respiratory Disease, West China Hospital, Sichuan University, Chengdu, Sichuan, China

[†]These authors contributed equally to this work.

***Corresponding author:**
Zipeng Yao
(yetiman@163.com)

Citation: Hu W, Wu G, Xia M, *et al*. A visible light-crosslinkable decellularized kidney matrix bioink for 3D bioprinting of organoids and drug testing. *Int J Bioprint*. 2026;12(1):432-447. doi: 10.36922/IJB025480497

Received: November 27, 2025
Revised: December 11, 2025
Accepted: December 15, 2025
Published online: December 19, 2025

Copyright: © 2025 Author(s). This is an Open Access article distributed under the terms of the Creative Commons Attribution License, permitting distribution, and reproduction in any medium, provided the original work is properly cited.

Publisher's Note: AccScience Publishing remains neutral with regard to jurisdictional claims in published maps and institutional affiliations.

Abstract

Decellularized kidney extracellular matrix (DKM) is an acellular scaffold rich in structural proteins and glycosaminoglycans that can promote tissue regeneration and support organoid culture. Porcine-derived DKM contains abundant extracellular matrix (ECM) components, such as collagen, laminin, and fibronectin, and offers native biochemical cues. However, conventional decellularized ECM hydrogels often exhibit weak mechanical properties, poor printability, and slow gelation, limiting their use in high-throughput applications. Here, we report a visible-light-mediated crosslinking strategy for rapid gelation of DKM based on a tris(2,2′-bipyridyl) ruthenium (II) chloride hexahydrate/sodium persulfate (Ru/SPS) photoinitiator system. Illumination at 405 nm (30 mW/cm^2) in the presence of Ru/SPS achieves gelation in about 40 s, yielding a composite DKM–Ru/SPS bioink with tunable modulus by adjusting DKM, Ru, and SPS concentrations. High-fidelity 3D constructs were produced by extrusion bioprinting using a representative formulation (15 mg/mL DKM, 0.25 mM Ru, 2.5 mM SPS). As proof of concept, organoids encapsulated in the DKM–Ru/SPS bioink exhibited viability, proliferation, and lineage marker expression during culture. This work demonstrates a rapid, cell-compatible photocrosslinking approach for DKM–Ru/SPS that integrates organoid culture with 3D bioprinting and drug testing, supporting its potential use as a standardized bioink in tissue engineering and functional screening.

Keywords: 3D bioprinting; Decellularized kidney matrix; Drug screening; Organoid culture; Visible-light-crosslinkable

1. Introduction

Out of every 10 drug candidates undergoing clinical trials, only one typically receives Food and Drug Administration (FDA) approval, primarily due to unforeseen toxicity. Traditional methodologies, such as two-dimensional (2D) cell cultures and animal models, are insufficient in this regard: 2D cultures fail to replicate the complexity of human biology, while animal models are hindered by interspecies differences, low throughput, high costs, lengthy processes, and ethical concerns, all of which diminish their predictive accuracy for human outcomes.[1] In response to this challenge, three-dimensional (3D) organoid models have been established. Organoids derived from various stem cell sources harness the intrinsic self-organizing capacity of stem cells to form multicellular structures that closely mimic the architecture, functionality, and cellular heterogeneity of human organs.[2–4] Because organoids retain the morphology and genetic features of the source tissues, their reactions to external stimuli, including pharmacological agents, closely resemble those of native tissues, thereby improving the reliability of drug evaluation.[5–7]

The establishment and growth of these 3D structures critically depend on an embedding hydrogel matrix, which provides indispensable structural support and biochemical cues. Matrigel, derived from Engelbreth–Holm–Swarm mouse sarcoma, is widely recognized as the standard substrate for organoid culture.[8] However, its inherent limitations hinder advancements in precision oncology. Additionally, its origin from a nonhuman species poses challenges for clinical application. The low Young's modulus of Matrigel (<2 kPa) inadequately mimics the rigid, fibrotic stroma typical of advanced cancers, which plays a critical role in tumor progression and drug resistance.[9] Furthermore, Matrigel lacks the high collagen fiber content found in tumor tissues, potentially failing to accurately replicate the tumor microenvironment.[10–12]

Decellularized extracellular matrix (dECM) hydrogels offer a natural microenvironment for cell attachment and organoid development due to the absence of immunogenic cells and the presence of essential extracellular matrix (ECM) components.[13–17] Unlike synthetic hydrogels, tissue-specific dECM can increase the physiological relevance of organoids and improve translational fidelity. For example, decellularized kidney matrix (DKM) is rich in collagen IV and laminin, providing vital niche signals. However, DKM hydrogels often rely on thermoresponsive crosslinking, resulting in slow gelation (over 30 min) and temperature-dependent mechanical properties, making them unsuitable for automated high-throughput applications like 3D bioprinting, which is essential for addressing variability and standardization challenges in manual organoid culture.[13,18] Therefore, it is essential to develop methods for producing dECM-based hydrogels with rapid gelation. Various ultraviolet-responsive hydrogels, such as methylcellulose–norbornene gelatin,[19] methacrylated gelatin,[20,21] and polyethylene glycol-based hydrogels,[22,23] can harm cells. In contrast, a visible light-activated tris(2,2'-bipyridyl) ruthenium (II) chloride hexahydrate/sodium persulfate (Ru/SPS) system enables dityrosine crosslinking in ECM proteins (e.g., collagen) without prior chemical modification, thereby allowing efficient visible-light crosslinking of DKM. Traditional organoid cultures struggle with high-throughput drug testing due to labor demands, scalability limitations, and standardization issues, leading to bias and variability.[24–26] In contrast, 3D bioprinting offers precise and reproducible organoid formation, overcoming drawbacks of manual methods, such as heterogeneity and labor intensity. It supports the generation of automated organoid arrays, which are ideal for high-throughput screening.[27–29] To date, no studies have explored DKM–Ru/SPS hydrogels for 3D bioprinted organoids or systematically examined dECM-derived photocrosslinkable bioinks, despite their potential to maintain bioactivity and customizable properties for cell and drug delivery.

In this study, we utilized visible light-mediated crosslinking to create a DKM–Ru/SPS hydrogel bioink. We analyzed the decellularized matrix and its light-crosslinking materials at various concentrations, focusing on properties like ECM preservation, endotoxin levels, microstructure, and rheological behavior. We assessed cytocompatibility and organoid growth in DKM–Ru/SPS compared with Matrigel, demonstrating its suitability for printed organoid arrays and drug treatment workflows. The bioink's viability for organoid culture was evaluated to determine the optimal formulation. Additionally, the DKM–Ru/SPS bioink was combined with organoids and processed using a 3D bioprinter for drug sensitivity testing. This study presents a workflow that integrates rapid photogelation with 3D bioprinting to overcome challenges associated with dECM hydrogels, such as slow gelation and poor printability, while preserving bioactivity. It lays

the foundation for standardized, scalable, and automated organoid culture and drug testing.

2. Materials and methods

2.1. Porcine tissue decellularization and DKM–Ru/SPS solution preparation

Porcine kidneys were collected from a local market and preserved at −80°C. Tissues underwent three freeze–thaw cycles, were thawed to room temperature, and were cut into 5 × 5 × 5 mm pieces to increase the surface contact area. The cut tissue pieces were flushed three times (30 min each) with sterile water containing 100 U/mL penicillin and 100 μg/mL streptomycin (P/S) until all visible blood traces were removed. The rinse steps were as follows: (i) 1% sodium dodecyl sulfate (SDS; ≥ 99.9%; Sigma-Aldrich, St Louis, MO) in sterile water for 24 h (exchanged at 12 h), (ii) sterile water for 6 h, (iii) 1% Triton X-100 (Sigma-Aldrich) in sterile water for 48–72 h (exchanged daily), (iv) sterile water for 12 h until no foam was observed, and (v) 60 U/mL DNase I for 2 h. Finally, the tissue pieces were rinsed with sterile water containing P/S. All steps were performed on a magnetic stirrer (200 rpm, 25°C), and all solutions were filtered. The decellularized pieces were lyophilized for 72 h, milled into powder (<1 mm), and preserved at −80°C.

Dry DKM powder (10 mg) was dissolved in 1 mL of 1 mg/mL pepsin (Sigma-Aldrich) in hydrochloric acid solution (0.1 M) and digested at 25°C for 72 h with constant stirring (200 rpm). Digestion was terminated by neutralizing the solution to pH 7.4 with 1 N NaOH in 10× phosphate-buffered saline (PBS) on ice. Subsequently, Ru/SPS powder was dissolved in the DKM solution (1 mL) under stirring to obtain the DKM–Ru/SPS bioink, which was stored at 4°C in the dark. To observe thermogelation, the DKM solution and Matrigel were placed at 37°C for varying durations. To validate photocrosslinking, the DKM–Ru/SPS bioink was exposed to 405 nm visible light for 40 s, and gelation was confirmed using the Eppendorf tilting method.

2.2. Characterization of decellularized tissues

To evaluate cellular removal, native and decellularized tissues were fixed with 4% paraformaldehyde overnight, embedded in optimal cutting temperature compound, frozen, and sectioned (4 μm). Tissue slides were stained with hematoxylin and eosin (H&E) and Masson's trichrome and observed under a Zeiss microscope (Oberkochen, Germany). DNA content was quantified to assess decellularization. DNA was extracted from 100 mg samples using a TIANAmp DNA kit (Tiangen, China) according to the manufacturer's protocol, and total DNA content was quantified using a Nanodrop spectrophotometer (NanoDrop Lite, Thermo Fisher Scientific, USA).

Sulfated glycosaminoglycan (GAG) and collagen contents in native and decellularized tissues were quantified using Blyscan GAGs and collagen assay kits (Biocolor, UK) following the manufacturer's instructions to assess ECM preservation. Endotoxin levels in dECM hydrogels were measured using a Limulus Amebocyte Lysate chromogenic quantitation kit (Meimian, China). Residual SDS was quantified using a detection kit (Sangon Biotech, China) according to the manufacturer's guidelines. Transforming growth factor-beta (TGF-β), insulin-like growth factor 1 (IGF-1), and epidermal growth factor (EGF) concentrations in the DKM solution were measured using enzyme-linked immunosorbent assay kits (Meimian, China), and optical density values (n = 3) were read at 450 nm. The microstructure of the dECM hydrogel was examined by scanning electron microscopy (SEM; SU5000, Hitachi, Japan). Hydrogels were fixed in 2% osmium tetroxide, washed, dehydrated through an ascending ethanol gradient, vacuum dried, and sputter-coated with gold.

2.3. Evaluation of rheological properties of DKM–Ru/SPS bioink

Rheological characteristics were evaluated using a rheometer (TA Instruments, USA) with a 15 mm plate. Storage (G') and loss (G'') moduli of DKM (10, 15, and 20 mg/mL) mixed with varying Ru/SPS concentrations (0.125, 0.25, and 0.5 mM) were determined via strain sweep (0.01–10% strain). Steady shear sweep analyses were conducted at 25°C to investigate shear-thinning properties. For stability analysis, DKM–Ru/SPS bioink droplets (5 mm diameter) were dispensed, submerged in PBS, and cultured at 37°C, while gel morphology, diameter, and area were monitored. All rheological measurements were performed in triplicate.

To characterize various DKM hydrogels and Matrigel, Young's modulus was assessed as an indicator of stiffness. The hydrogels were shaped into cylinders with a height of 3 mm and a diameter of 7 mm and cured in an incubator at 37°C or under 405 nm visible light. A mechanical analyzer (EFL-MT5600, Suzhou, China) was used to measure the Young's modulus of the hydrogels at a rate of 1 mm/min at room temperature. The maximum load was set to 1 N.

2.4. Compatibility of the DKM–Ru/SPS bioink material

L929 cells were cultured in medium supplemented with 15% fetal bovine serum and 0.5% P/S. Cells were maintained at 37°C and 5% carbon dioxide (CO_2), passaged at a 1:3 ratio at 90% confluence, and the medium was refreshed

every 2 days. For 3D culture, L929 cells were mixed into the ice-cold DKM–Ru/SPS bioink (10,000 cells/25 μL) and plated in a 48-well plate. After gelation, 500 μL of culture media was added to each well, and the encapsulated cells were incubated. Cell viability was assessed using a live/dead assay kit (Invitrogen, USA). A staining solution (3 μL calcein-acetoxymethyl ester and 2 μL PI in 1 mL PBS) was added (500 μL/well) and incubated for 30 min at 37°C. Cells were imaged at distinct time points using fluorescence microscopy (Propidium iodide, Zeiss). All experiments were performed in triplicate.

2.5. Organoid establishment and passage

Mouse lung and liver tissues were harvested according to protocols approved by the Institutional Animal Care and Use Committee of West China Hospital, Sichuan University (Approval No. 108, 2023). Adipose tissue was dissected, and tissues were rinsed with Dulbecco's PBS, minced, and enzymatically digested with type IV collagenase (1 mg/mL) and DNase I (0.1 mg/mL) in Dulbecco's Modified Eagle Medium (DMEM) GlutaMAX (Gibco, USA) at 37°C for 30 min. Digestion was stopped by adding DMEM GlutaMAX. The suspension was filtered through a 100 μm strainer, centrifuged (299 g, 5 min), and the pellet was treated with 1 mL red blood cell lysis buffer (Servicebio, China) for 15 min. After washing, the cell pellet was counted and embedded (5×10^4 cells/well) in 30 μL of Matrigel or DKM–Ru/SPS in a 24-well plate. Matrigel was cured for 30 min (37°C), while the DKM–Ru/SPS bioink was cured using 405 nm light. Organoid medium (Aimingtmed, China) supplemented with 0.1% Y-27632 was added. Organoid formation efficiency and size were quantified.

For passaging, Matrigel was degraded with TrypLE (37°C, 5 min), and the DKM–Ru/SPS bioink was degraded with 5 mg/mL collagenase I (37 °C, 10 min). Harvested organoids were rinsed and re-encapsulated. Organoids were passaged every 5–10 days. Viability was assessed using a live/dead assay kit (Invitrogen, USA) and imaged by fluorescence microscopy (Zeiss). For cryopreservation, collected organoids were centrifuged (299 g, 5 min) and resuspended in cryopreservation solution (Gibco). For immunohistochemistry, lung organoids were fixed with paraformaldehyde, permeabilized with 1% Triton X-100, and sections were incubated overnight with antibodies against thyroid transcription factor-1 (TTF-1, a marker of lung progenitor and alveolar epithelial cells) and p63 (a basal cell marker), or subjected to H&E staining.

2.6. Drug assay

After 7 days of culture, the culture medium was replaced with medium containing varying doses of sorafenib, cisplatin, and acetaminophen (1, 10, 25, and 50 μM) for cytotoxicity assessment in liver organoids. After drug treatment, representative images of live/dead staining cells were acquired at 72 h utilizing an inverted fluorescent microscope (Zeiss, Oberkochen, Germany) to examine morphological alterations.

2.7. 3D bioprinting

A 3D bioprinter was utilized to fabricate a droplet microarray, resulting in a homogeneously dispersed bioink array. By modulating the printing nozzle inner diameter, platform temperature, and extrusion pressure, the consistency of the printed droplet sphere diameters was evaluated. By validating the outcomes of various parameters, optimization of the printing conditions was achieved.

The bioprinter was further employed to fabricate organoid arrays. Using software programming, dispense positions for a 12 × 8 array were designed as coordinates. The bioprinter nozzle was installed on the platform, and bioink was extruded at a specified pressure. This printing method was utilized to fabricate organoid arrays. Once printing and curing were completed, organoid medium was introduced, and the constructs were maintained in an incubator at 37 °C with 5% CO_2. The bioink was printed using a 3D bioprinter in a 96-well plate to obtain designed patterns to evaluate the consistency and reliability of the 3D system.

Organoid models were generated using the designed 3D bioprinting system. A syringe was loaded with DKM–Ru/SPS bioink and cooled at 4 °C. The bioink was then extruded through an 18-G nozzle under different pneumatic pressures to generate a droplet array in a 96-well plate. The printed constructs were cured for 40 s under 405 nm. Subsequently, the organoid medium was added to the 96-well plate and incubated at 37°C (Table 1).

Table 1. 3D bioprinting parameters for DKM–Ru/SPS bioink.

Parameter	Value/range
Bioink temperature in the syringe	4°C
Nozzle gauge (inner diameter)	18 G
Extrusion mode	Pneumatic
Extrusion pressure	3 kPa (tested range: 3–10 kPa)
Printing speed	3–5 mm s^{-1}
Photocrosslinking wavelength	405 nm
Light intensity	30 mW cm^{-2}
Exposure time	40 s
Array format	12 × 8 (96-well plate compatible)

Abbreviations: DKM: Decellularized kidney extracellular matrix; Ru/SPS: Tris(2,2'-bipyridyl) ruthenium (II) chloride hexahydrate/sodium persulfate.

2.8. Statistical analysis

All data are reported as the mean ± standard error of the mean and were derived from at least three biological replicates. Statistical analyses were performed using GraphPad Prism 10.4.3 (San Diego, CA, USA, employing Student's *t*-tests for paired comparisons and one-way or two-way ANOVA for multiple-group assessments. Statistical significance was defined as $^{*}p < 0.05$, $^{**}p < 0.01$, $^{***}p < 0.001$, and $^{****}p < 0.0001$.

3. Results and discussion

3.1. Preparation and characterization of DKM bioink

Decellularized extracellular matrix hydrogels face numerous challenges, including poor mechanical properties, limited printability, and extended gelation duration, which have restricted their application in organoid culture and pharmacological testing. To address these limitations, a tyramine-rich DKM bioink was developed.[30,31] This advanced system integrates a Ru/SPS photoinitiator to enable rapid tyrosine crosslinking, thereby providing an efficient and rapid solution for research. Separately, mouse liver and lung were expanded into organoids and subsequently combined with the DKM–Ru/SPS bioink formulation. Using 3D bioprinting, the organoid-embedded bioink was precisely deposited into 96-well plates (Figure 1).

In addition, the high biocompatibility of the DKM bioink, coupled with its rapid light-triggered crosslinking capability (~40 s with Ru/SPS), was demonstrated to effectively minimize cell stress during printing while maintaining organoid viability. This innovative light-triggered crosslinking strategy, combined with 3D bioprinting, is thus established as a promising platform for fabricating complex hydrogel-based tissues and advancing organoid culture systems for diverse therapeutic and diagnostic applications.

Decellularized tissues have been regarded as promising biomaterials for replicating the complex native ECM microenvironment, given their similarity to native tissues. This similarity is primarily attributed to the preservation of organ-specific biochemical composition (e.g., collagens, laminin), native 3D architecture, and critical mechanical properties.[32] Kidney tissue was harvested and analyzed for its microstructural features and compositional characteristics. To achieve this, the tissue was sectioned into small fragments, subjected to detergent-based decellularization, and subsequently lyophilized. Upon temperature equilibration under physiological conditions (37°C), decellularized DKM solutions exhibited temperature-dependent solution–gel transitions, ultimately yielding robust and well-defined hydrogels (Figure 2A).

Decellularization efficacy was verified through SEM, H&E, and immunofluorescence staining. SEM confirmed that the kidney tissue exhibited a fibrous, mesh-like morphology following decellularization, indicative of successful cellular removal while preserving structural integrity (Figure 2B). H&E staining for cellular components and 4',6-diamidino-2-phenylindole fluorescence staining for nuclear material detection were performed. Prior to decellularization, stained sections showed collagen (blue) alongside extensive red staining, indicating the presence of muscle fibers. After decellularization, tissue sections primarily exhibited blue coloration with no visible red fibers, demonstrating effective removal of cellular muscle components while retaining the collagen matrix, thereby confirming the efficacy of the decellularization process (Figure 2C). Moreover, immunohistochemical analysis confirmed the preservation and structural integrity of key ECM components, including collagen I, collagen IV, laminin, and fibronectin after decellularization (Figure 2D).

Quantitative analysis of DNA content was conducted to evaluate the efficiency of cellular component removal, demonstrating a statistically significant reduction in decellularized tissue relative to native tissue ($p < 0.001$), corresponding to a 95.1% decrease in residual DNA content. To assess ECM preservation, quantitative analyses demonstrated that collagen content in decellularized tissue increased to 1,431 μg mg^{-1} compared with 314 μg mg^{-1} in native tissue, representing an approximately 4.6-fold increase in relative abundance, attributable to the efficient removal of cellular materials. Meanwhile, GAG content was retained at 65.55% relative to native tissue. Collectively, these results show that the protocol effectively removed cellular remnants while preserving critical ECM components (Figure 2E).

The presence of growth factors in the DKM solution was confirmed following the decellularization process. After treatment, the concentrations were measured as follows: IGF-1, 130.00 ± 17.21 ng/mL; EGF, 0.8007 ± 0.0299 ng/mL; and TGF-β, 1.6693 ± 0.04833 ng/mL. These values were comparable to those measured before decellularization: IGF-1, 130.08 ± 5.57 ng/mL; EGF, 0.7851 ± 0.0648 ng/mL; and TGF-β, 1.4550 ± 0.3073 ng/mL (Figure S1A). Previous studies have indicated that IGF-1 and EGF promote development and inhibit apoptosis, while TGF-β has been implicated in regulating cell formation and inhibiting differentiation.[33-34] These results indicate that growth factors were effectively retained throughout the decellularization process. The elevated concentrations of IGF-1, EGF, and TGF-β in DKM may provide an optimal environment and underlie the successful culture of organoids.

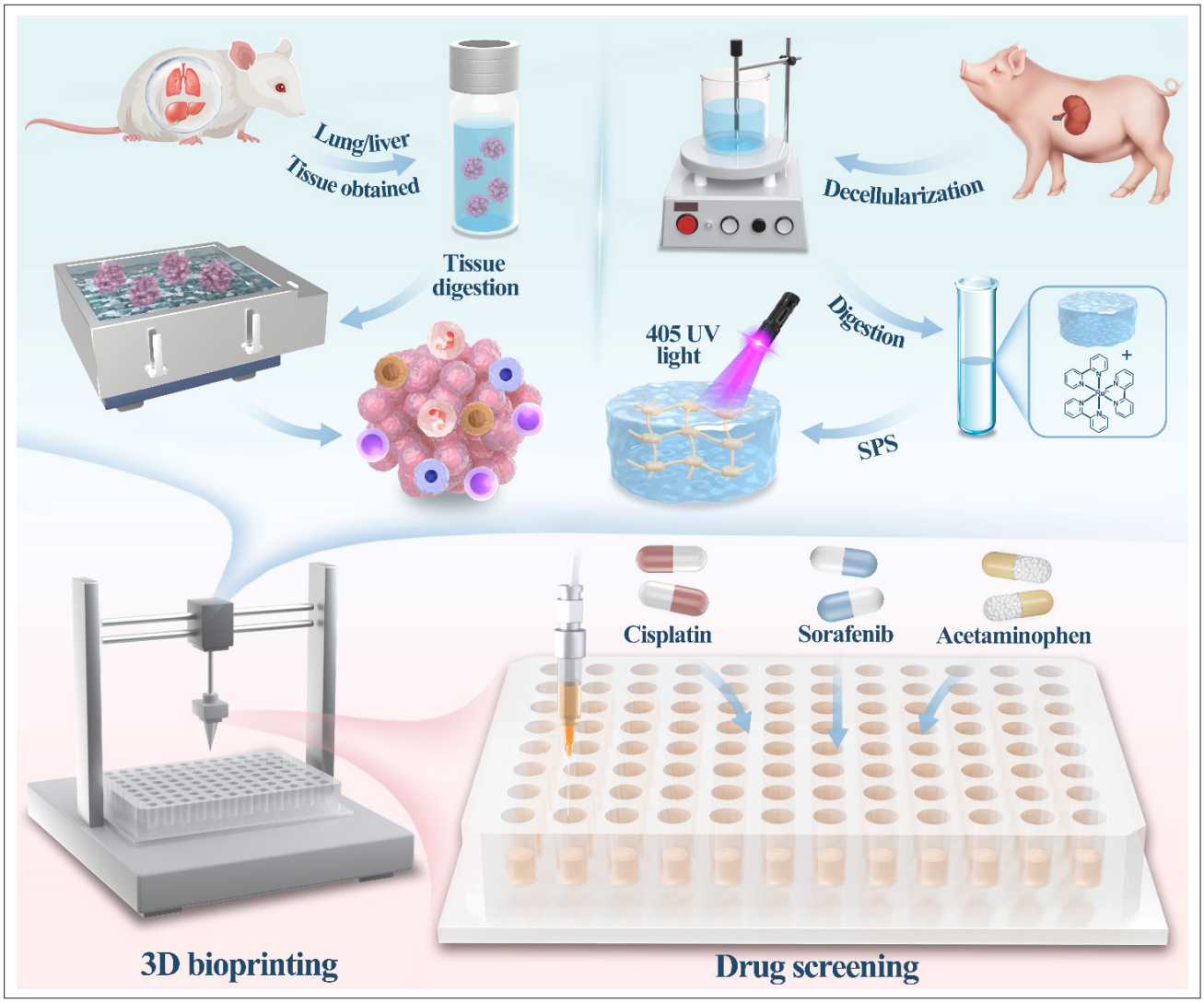


Figure 1. Schematic illustrating the DKM–Ru/SPS bioink preparation and 3D bioprinting procedures. Porcine kidney tissue was decellularized to produce the DKM solution. The DKM solution was mixed with Ru/SPS to initiate the photocrosslinking process. Mouse-derived cells (digested and isolated) were embedded within the DKM–Ru/SPS bioink, followed by photocrosslinking. Using a 3D bioprinter, the cell-laden bioink was deposited into a 96-well plate to form bioprinted organoids, which were subsequently subjected to drug screening. Abbreviations: DKM: Decellularized kidney extracellular matrix; Ru: Tris(2,2'-bipyridyl) ruthenium (II) chloride hexahydrate; SPS; Sodium persulfate UV: Ultraviolet.

To assess the biocompatibility of the DKM, potential residual contaminants were also quantified. Endotoxin levels were measured at 0.08,245 ± 0.01,288 EU/mL for lot 1, 0.03,601 ± 0.00,255 EU/mL for lot 2, and 0.04,708 ± 0.02,985 EU/mL for lot 3. Endotoxin analysis across three DKM lots revealed levels below the FDA limit of 0.5 EU/mL (Figure S1B).[35] Furthermore, residual SDS concentrations were measured as 0.000,597 ± 0.000,524 mg/mL for lot 1, 0.002,598 ± 0.001,637 mg/mL for lot 2, and 0.001,565 ± 0.001,003 mg/mL for lot 3. The residual SDS content was determined to be below 0.005 mg/mL (Figure S1C). Collectively, these results demonstrate that our protocol yielded a safe, biocompatible, and ECM-rich material suitable for bioink formulation.

3.2. Rheological characterization of DKM–Ru/SPS bioink

Numerous prior studies have indicated that a Ru-to-SPS ratio of 1:10 is optimal for efficient crosslinking. Guided by this, we designed a series of concentration proportions. The physical characterization of light-crosslinked bioink was assessed as a function of both DKM bioink concentration (10, 15, 20 mg/mL) and Ru/SPS photoinitiator concentration (0.125, 0.25, 0.5 mM). The morphological integrity of the DKM–Ru/SPS bioinks was evaluated over

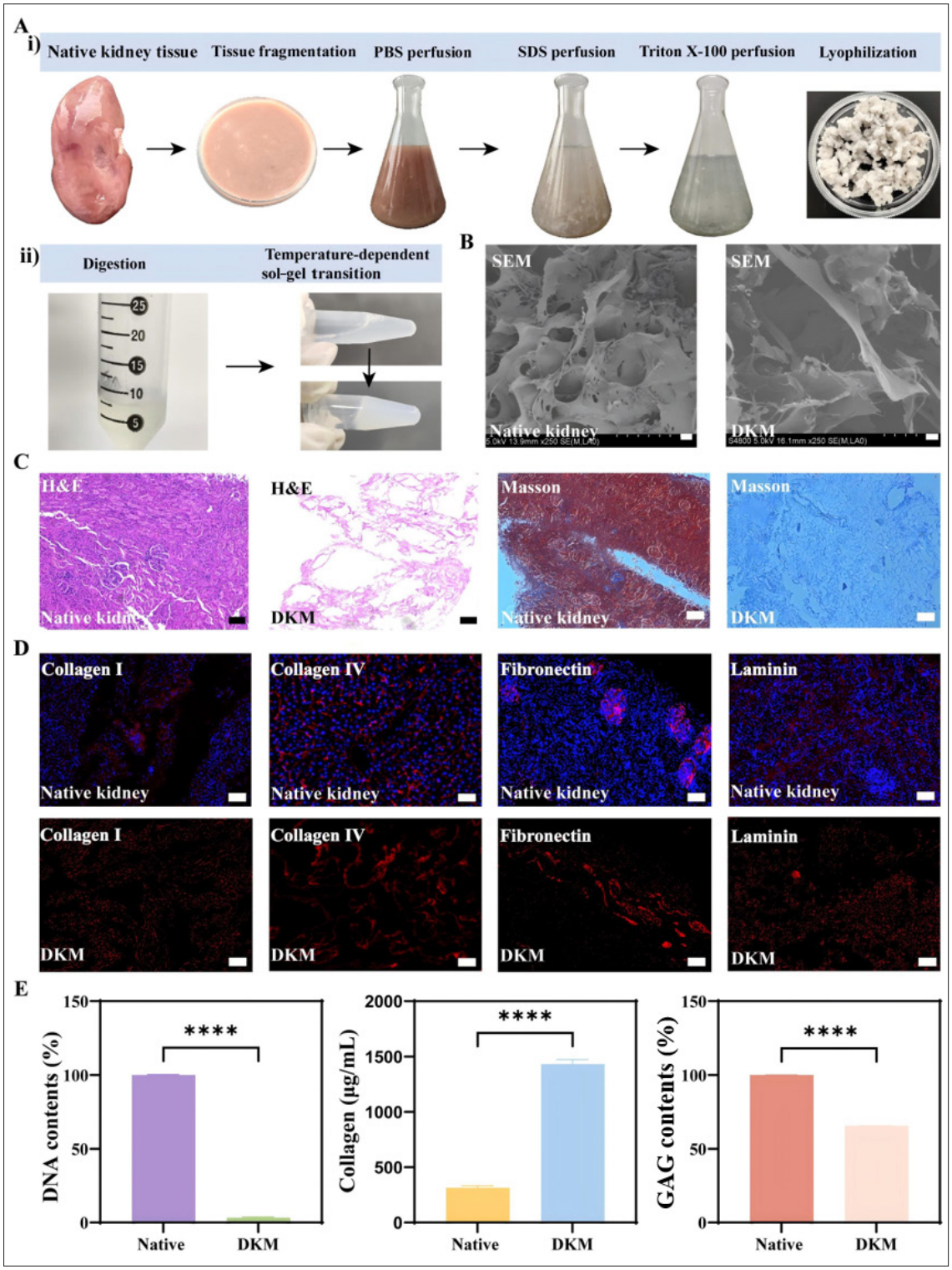


Figure 2. Structural and compositional analysis of the kidney scaffold before and after decellularization. (A) Schematic illustration of DKM (i) bioink fabrication and (ii) gel transition process. (B) Scanning electron microscopy (SEM), (C) hematoxylin and eosin (H&E) and Masson's trichrome staining, and (D) immunofluorescence staining of extracellular matrix components (laminin, fibronectin, and collagen) before and after decellularization. All sections were counterstained with 4',6-diamidino-2-phenylindole (blue). Scale bar: 200 μm; magnification: 4×. (E) Quantitative analysis of DNA, collagen, and glycosaminoglycan (GAG) content before and after the decellularization process. Notes: $n = 3$; mean ± standard error of the mean; ****$p < 0.0001$. Abbreviations: DKM, Decellularized kidney extracellular matrix; PBS, Phosphate-buffered saline; SDS, Sodium dodecyl sulfate.

a 20-day period in well plates. Representative images (Figure 3Ai) show that all bioink formulations maintained their original, well-defined circular morphology without noticeable disintegration. Quantitative analysis of diameter (Figure 3Aii) and area (Figure 3Aiii) confirmed these observations, revealing no statistically significant changes in bioink dimensions during culture. This long-term stability under physiological conditions is a critical attribute for bioinks, as it ensures that the printed constructs can serve as durable and reliable scaffolds throughout the crucial phases of cell proliferation and tissue maturation. The preserved integrity of the bioinks provided a consistent 3D architecture for potential cellular ingrowth and organization.

We then characterized the bioink's rheological properties. As illustrated in Figure 3B, visual inspection revealed a progressive reduction in droplet size with increasing concentrations of either DKM or Ru/SPS, indicating the formation of a denser and more compact crosslinked network. This observation was further substantiated by mechanical analysis (Figure 3C), which confirmed the formation of a solid-like hydrogel, as the storage modulus (*G*') consistently exceeded the loss modulus (*G*") across all tested frequencies. Importantly, the stiffness was tunable and increased significantly with higher DKM concentrations (e.g., 20 > 15 > 10 mg/mL).

A higher concentration of DKM provides more available crosslinking sites, while a higher concentration of the Ru/SPS system generates a greater number of free radicals upon illumination. Visible-light Ru/SPS systems have been widely applied for the rapid photocrosslinking of gelatin-based and dECM-derived hydrogels with improved print fidelity and cell compatibility.[36–37] Our DKM–Ru/SPS formulation extends these approaches to a kidney-specific dECM, providing a fast and mild crosslinking strategy while preserving native ECM composition. These factors act synergistically to promote rapid and extensive radical polymerization, resulting

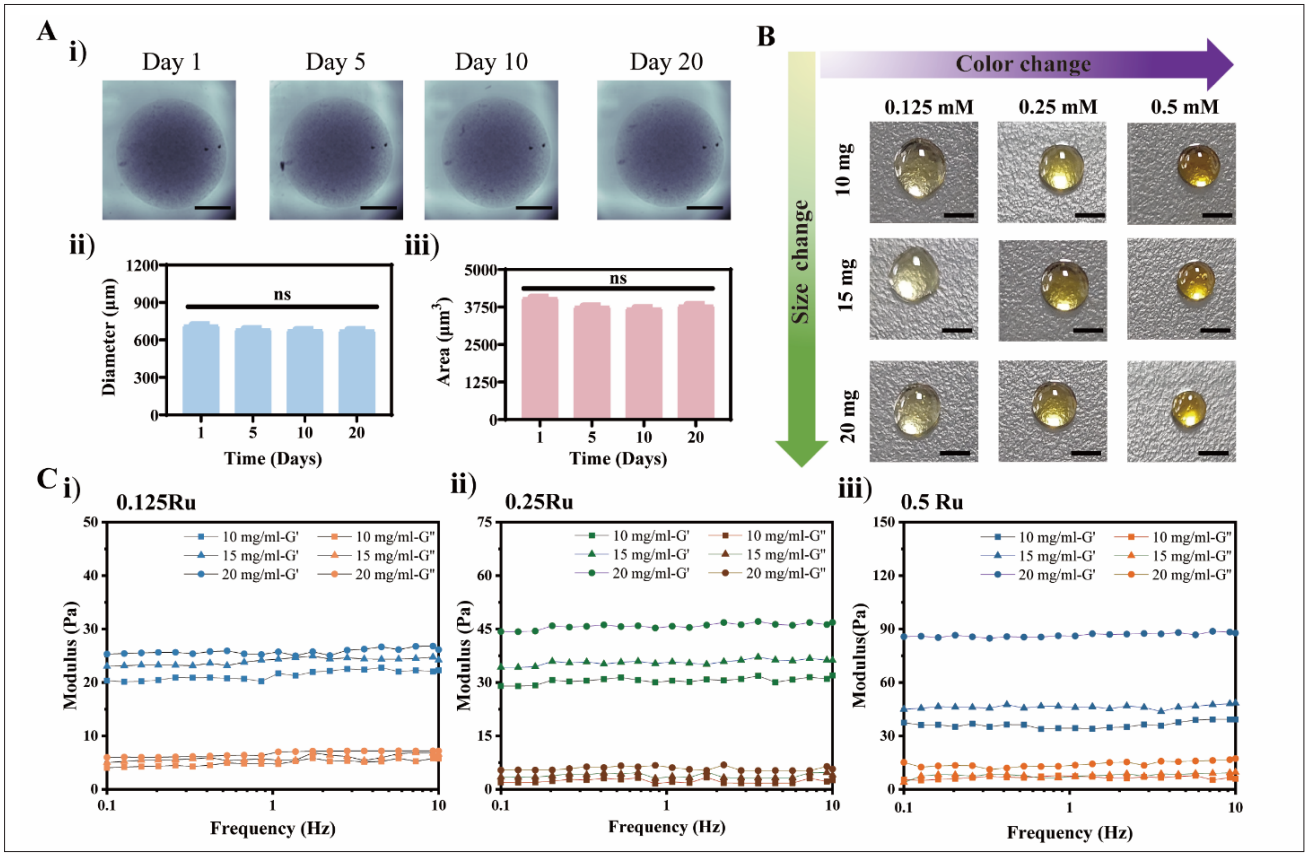


Figure 3. Microstructural, physical, and chemical analysis of DKM–Ru/SPS bioinks. (A) (i) Morphological characterization of bioinks immersed in a 24-well plate for 20 days and analysis of (ii) diameter and (iii) area of bioinks. Scale bar = 2 mm. Data are representative of three independent experiments (n = 3). (B) Photographic images of DKM– Ru/SPS bioink (10, 15, 20 mg/mL) with varying Ru/SPS concentrations (0.125, 0.25, 0.5 mM). Scale bar = 5 mm. (C) Rheological assessment of DKM–Ru/SPS bioinks at different concentrations: (i–iii) shear-thinning characteristics. Abbreviations: DKM; Decellularized kidney extracellular matrix; *G*', Storage modulus; *G*", Loss modulus; ns: Not statistically significant; Ru/SPS; Tris(2,2'-bipyridyl) ruthenium (II) chloride hexahydrate/sodium persulfate.

in a tighter polymer network that undergoes greater contraction upon gelation. This tunability enables precise control over scaffold properties through simple adjustment of the initial composition, thereby allowing the customization of the bioink to support specific tissue microenvironments.

A bioink must possess appropriate physical properties to ensure successful bioprinting and long-term culture. We therefore examined the gelation kinetics of the DKM–Ru/SPS bioink (Figure S2). While pure DKM and Matrigel exhibited slow, temperature-dependent gelation (~30 min at 37°C), the DKM–Ru/SPS bioink, in addition to this thermoresponsive behavior, could be rapidly light-crosslinked into a stable hydrogel within ~40 s using 405 nm light. This rapid light-crosslinking capability is critical for stabilizing printed structures while maintaining cell viability. The DKM–Ru/SPS bioink exhibited significantly enhanced mechanical properties through optimized visible light-mediated crosslinking. As illustrated in Figure S3, direct crosslinking resulted in a Young's modulus of 22.76 ± 1.91 kPa, representing an approximately fourfold increase compared with thermal gelation alone. Notably, this stiffness exceeds the typical modulus range of widely used commercial hydrogels, such as Matrigel, thereby providing a mechanically superior alternative for 3D bioprinting applications.

3.3. Printability and biocompatibility optimization of DKM–Ru/SPS bioink

To identify the optimal formulation, mechanical performance was balanced against cytocompatibility. As illustrated in Figure S4, cell viability exceeded 98%, demonstrating the good biocompatibility of the DKM bioink. L929 cells were cultured in bioinks with graded crosslinker concentrations. At a fixed Ru/SPS ratio of 0.125:1.25 mM, cell viabilities in bioinks containing 10, 15, and 20 mg/mL DKM were 98.04 ± 2.23%, 98.61 ± 1.01%, and 98.62 ± 0.84% on Day 7, respectively. When the Ru/SPS ratio was increased to 0.25:2.5 mM, viabilities improved to 99.21 ± 0.68%, 99.316 ± 0.212%, and 99.363 ± 0.283%. In contrast, at a Ru/SPS ratio of 0.5:5 mM, cell viability decreased substantially to 64.79 ± 1.03%, 82.37 ± 2.17%, and 95.22 ± 2.15% across the same DKM concentrations. While Ru/SPS ratios of 0.125 and 0.25 mM supported excellent cellular survival (>98%), the 0.5 mM ratio induced significant dose-dependent cytotoxicity (Figure 4A–C).

Further evaluation of cell encapsulation within the composite DKM–Ru/SPS bioink revealed that increasing Ru/SPS concentration correlated with reduced cell viability. Conversely, higher DKM concentrations partially mitigated this cytotoxic effect, likely due to their cytoprotective properties and increased availability of crosslinking sites, which may shield cells from excessive free radical exposure. A Ru/SPS ratio above a 0.25:2.5 mM was therefore detrimental to cell survival, irrespective of DKM concentration.

Following cytocompatibility assessment, printing parameters for cell-laden bioinks were optimized. The rheological behavior of the DKM–Ru/SPS bioink, which is essential for 3D bioprinting, was highly dependent on composition. In particular, the 0.25 Ru/SPS formulation demonstrated pronounced shear-thinning behavior, facilitating smooth extrusion, as well as temperature-dependent gelation. Furthermore, viscosity increased proportionally with DKM concentration (10, 15, and 20 mg/mL) (Figure 4D), a trend attributed to the dense macromolecular network of the dECM. This inherent viscosity and tunable viscosity, even at relatively low concentrations, are advantageous for achieving high structural fidelity in printed constructs.[38] Collectively, these rheological characteristics enhance the broader applicability of the DKM-based biomaterial for biomedical use. Based on these findings, the 0.25 mM Ru/2.5 mM SPS ratio was selected as the optimal formulation, providing rapid gelation and robust mechanics without compromising cell viability.

Printability analysis under varying extrusion pressures (3, 5, and 10 kPa) demonstrated precise control over droplet dimensions: at a fixed bioink concentration, droplet size increased with higher pressure, while at constant pressure, droplet size decreased with increasing bioink concentration (Figure 4E). Through optimization of extrusion pressure (3 kPa) and DKM concentration, multiple replicas with precise dimensions were fabricated. The DKM bioink maintained sufficient viscosity during *in situ* printing, ensuring accurate deposition and structural fidelity. Consequently, the 0.25 mM Ru/SPS DKM bioink, with its favorable biofunctional characteristics and adaptable rheological properties, represents a promising material for advanced 3D bioprinting applications. In comparison, manually dispensed droplets exhibited irregular shapes and significant size variability, whereas 3D-printed droplets were uniform in both morphology and diameter (Figure S5). This result demonstrates that 3D bioprinting offers significantly enhanced stability and control over droplet size compared with manual dispensing. Such reproducibility is critical for ensuring consistent cell encapsulation and deposition, thereby supporting high cell viability and the formation of predictable, functional tissue constructs.

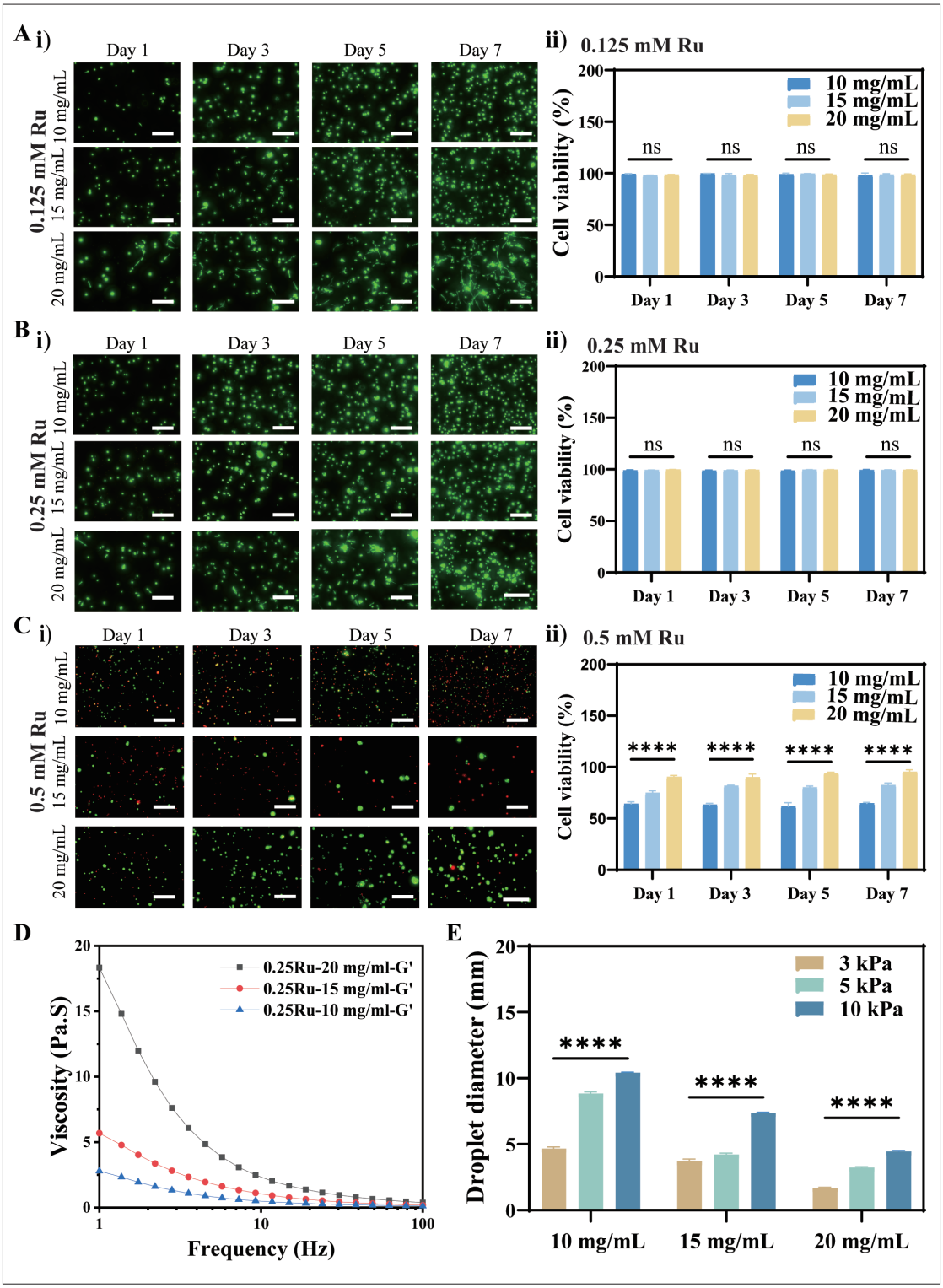


Figure 4. Biocompatibility and printability assessment of DKM–Ru/SPS bioink with varying crosslinker concentrations. (A–C) (i) Representative fluorescence images and (ii) quantitative assessment of live/dead cell viability in L929 cells over 7 days with Ru/SPS concentrations of 0.125, 0.25, and 0.5 mM. Scale bar: 300 μm; magnification: 4×. (D) Viscosity profiles of bioinks at different concentrations under shear strain. (E) Analysis of droplet dimensions at extrusion pressures of (i) 3 kPa, (ii) 5 kPa, and (iii) 10 kPa across different bioink concentrations. Notes: Data are presented as mean ± standard error of the mean; ****$p < 0.0001$; $n = 3$. Abbreviations: DKM, Decellularized kidney extracellular matrix; *G'*, Storage modulus; ns, Not statistically significant; Ru/SPS, Tris(2,2'-bipyridyl) ruthenium (II) chloride hexahydrate/sodium persulfate.

3.4. Assessment of DKM–Ru/SPS bioink for 3D lung organoid culture and bioprinting

To evaluate the performance of our developed DKM–Ru/SPS bioink for 3D culture, we systematically applied it to lung organoid cultivation and compared its efficacy with that of Matrigel. We first investigated the effect of DKM–Ru/SPS bioink concentration on organoid formation. Mouse lung organoids were embedded in bioinks with varying concentrations (10, 15, and 20 mg/mL). Although organoids formed under all tested conditions, quantitative analysis revealed that the 15 mg/mL formulation yielded the highest formation efficiency and optimal organoid diameter, establishing it as the optimal concentration for subsequent experiments (Figure 5Ai–ii). We next compared organoid growth in the DKM–Ru/SPS bioink with that in Matrigel. Organoids cultured in the base DKM–Ru/SPS bioink grew effectively but exhibited lower formation efficiency than those cultured in Matrigel. Notably, supplementation of the DKM–Ru/SPS bioink with 0.1 mg/mL laminin resulted in a significant improvement. The diameter of organoids grown in DKM–Ru/SPS–laminin were comparable to those cultured in Matrigel, and their formation efficiency showed no statistically significant difference relative to the Matrigel control, indicating that laminin is a crucial component for maximizing bioink performance (Figure 5Bi–ii). The superior organoid formation observed at 15 mg/mL indicates that this concentration provides optimal biophysical support for lung organoid development. Furthermore, marked enhancement achieved through laminin supplementation confirms that specific ECM components are essential for maximizing bioink functionality. Collectively, the comparable performance between the optimized DKM–Ru/SPS–laminin formulation and Matrigel validates its effectiveness for lung organoid culture. Beyond supporting organoid growth, Matrigel has been widely used to mimic the tumor microenvironment for *in vitro* disease modeling.[39–40] Considering the demonstrated ability of our DKM–Ru/SPS bioink to support both liver and lung organoid culture, this dECM-based visible-light-crosslinkable bioink may serve as a versatile platform for mimicking disease-associated microenvironments and for investigating how ECM conditions regulate organoid behavior.

The viability of organoids cultured in the DKM–Ru/SPS bioink was further assessed using live/dead staining (Figure S6). Although viability in the DKM–Ru/SPS was slightly lower than that in Matrigel on Day 1, by Day 5, the bioink supported organoids with viability exceeding 95%, with no statistically significantly different compared to Matrigel, demonstrating excellent biocompatibility (Figure 5C). To assess long-term culture capacity, lung organoids embedded in the DKM–Ru/SPS bioink were serially passaged. Representative bright-field images confirmed successful formation and robust growth of organoids over multiple passages, up to passage 8, indicating that the bioink supports stable and sustained development without compromising growth potential (Figure 5D). To further demonstrate the versatility and practical applicability of the DKM–Ru/SPS bioink, we employed 3D bioprinting to fabricate lung organoid constructs with defined architectures. As shown in Figure S7A, lung organoid-laden bioink was successfully printed into a predefined array within a 96-well plate. After 10 days of culture, bright-field imaging revealed that the printed organoids maintained structural integrity and exhibited robust growth and development, confirming the excellent printability and printing compatibility of the bioink.

Subsequent histological and immunohistochemical analyses were performed to further characterize organoids cultured within the printed bioink constructs. H&E staining revealed the formation of complex cyst-like structures containing multiple lumens, a hallmark of well-developed organoids. Immunohistochemical analysis further confirmed positive expression of key lung lineage markers, including TTF-1 and P63. The presence of these distinct cell populations (Figure S7B) conclusively demonstrates effective differentiation and maturation of lung organoids within the 3D-printed DKM–Ru/SPS bioink, underscoring its utility as a biomimetic platform for engineering physiologically relevant tissue models.

3.5. Evaluation of DKM–Ru/SPS bioink for liver organoid culture and drug screening

After demonstrating its efficacy in lung organoid cultures, we next assessed the broader applicability of the DKM–Ru/SPS bioink for the culture and pharmacological testing of mouse primary liver organoids. Figure 6A presents a schematic overview of the integrated workflow, illustrating the progression from organoid fabrication using a 3D bioprinter to high-throughput drug screening. Liver organoids cultured in the DKM–Ru/SPS bioink exhibited substantial growth and characteristic morphological development from Days 1 to 7, comparable to organoids cultured in Matrigel (Figure 6B). Quantitative analysis demonstrated that both organoid diameter and formation efficiency in the DKM–Ru/SPS bioink were not significantly different from those observed in Matrigel throughout the culture period (Figure 6C), highlighting the bioink's strong support for liver organoid proliferation and development. Additionally, viability assessment via live/dead staining after 7 days of culture further revealed that liver organoids maintained high cell viability (>95%) within the DKM–Ru/SPS bioink (Figure S8), comparable to Matrigel controls.

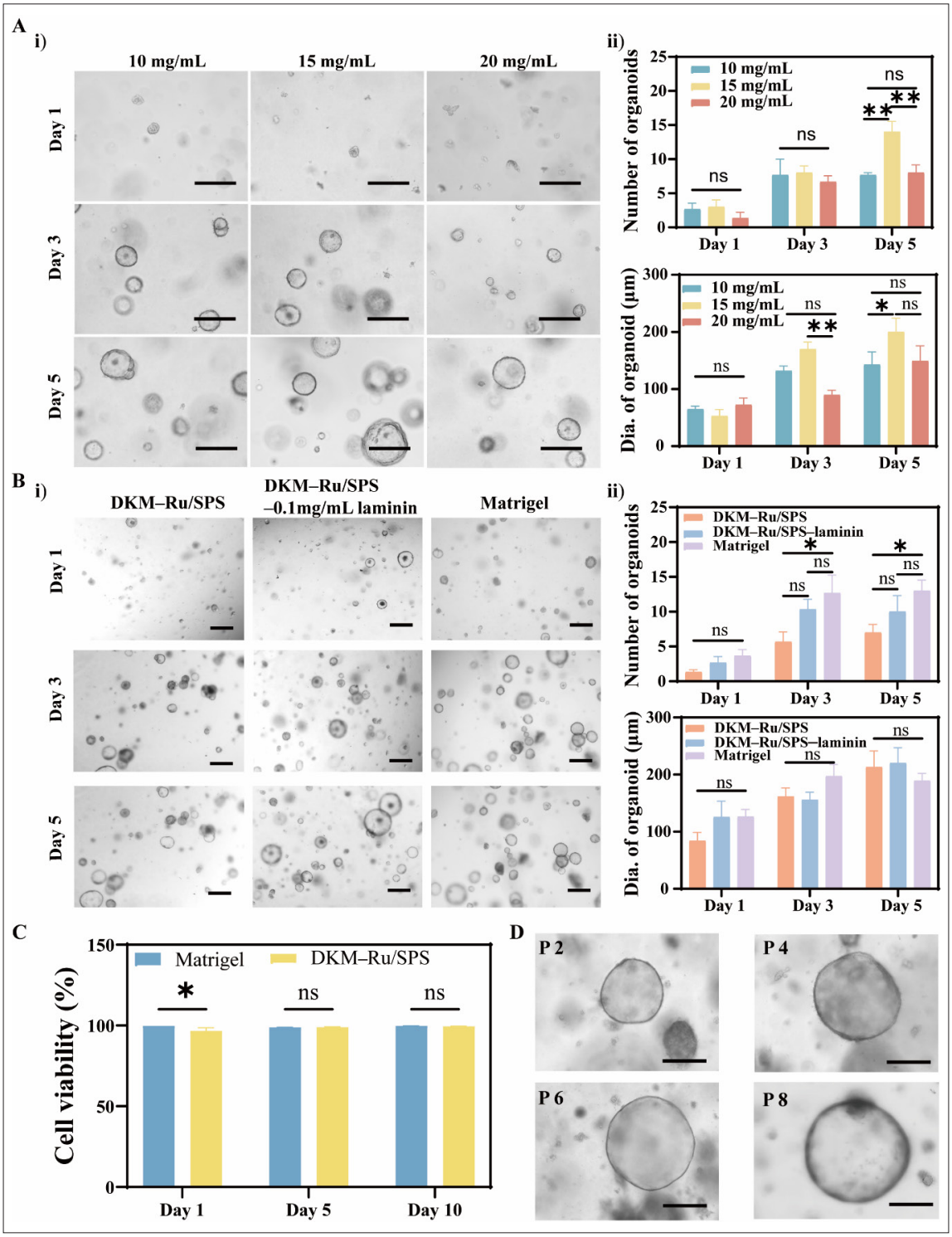


Figure 5. Characterization of lung organoid growth, viability, and development in DKM–Ru/SPS bioink. (A) (i) Bright-field images of lung organoids cultured in various concentrations of DKM–Ru/SPS bioink at Day 5 and (ii) quantitative analysis of organoid size and formation efficiency. Scale bar = 300 μm; magnification: 4×. (B) (i) Organoids seeded in DKM–Ru/SPS, DKMRu/SPS –laminin, and Matrigel for 5 days with (ii) corresponding quantitative measurements. Scale bar = 300 μm; magnification: 4×. (C) Live/dead viability analysis of organoids cultured in DKM–Ru/SPS bioinks and Matrigel. (D) Representative bright-field images of lung organoids formation at passage 2, 4, 6, and 8. Scale bar: 300 μm; magnification: 40×. Notes: $n = 3$; mean ± standard error of the mean; one-way analysis of variance; $^{*}p < 0.05$, $^{**}p < 0.01$. Abbreviations: Dia, Diameter; DKM: Decellularized kidney extracellular matrix; ns: Not statistically significant; Ru/SPS; Tris(2,2'-bipyridyl) ruthenium (II) chloride hexahydrate/sodium persulfate.

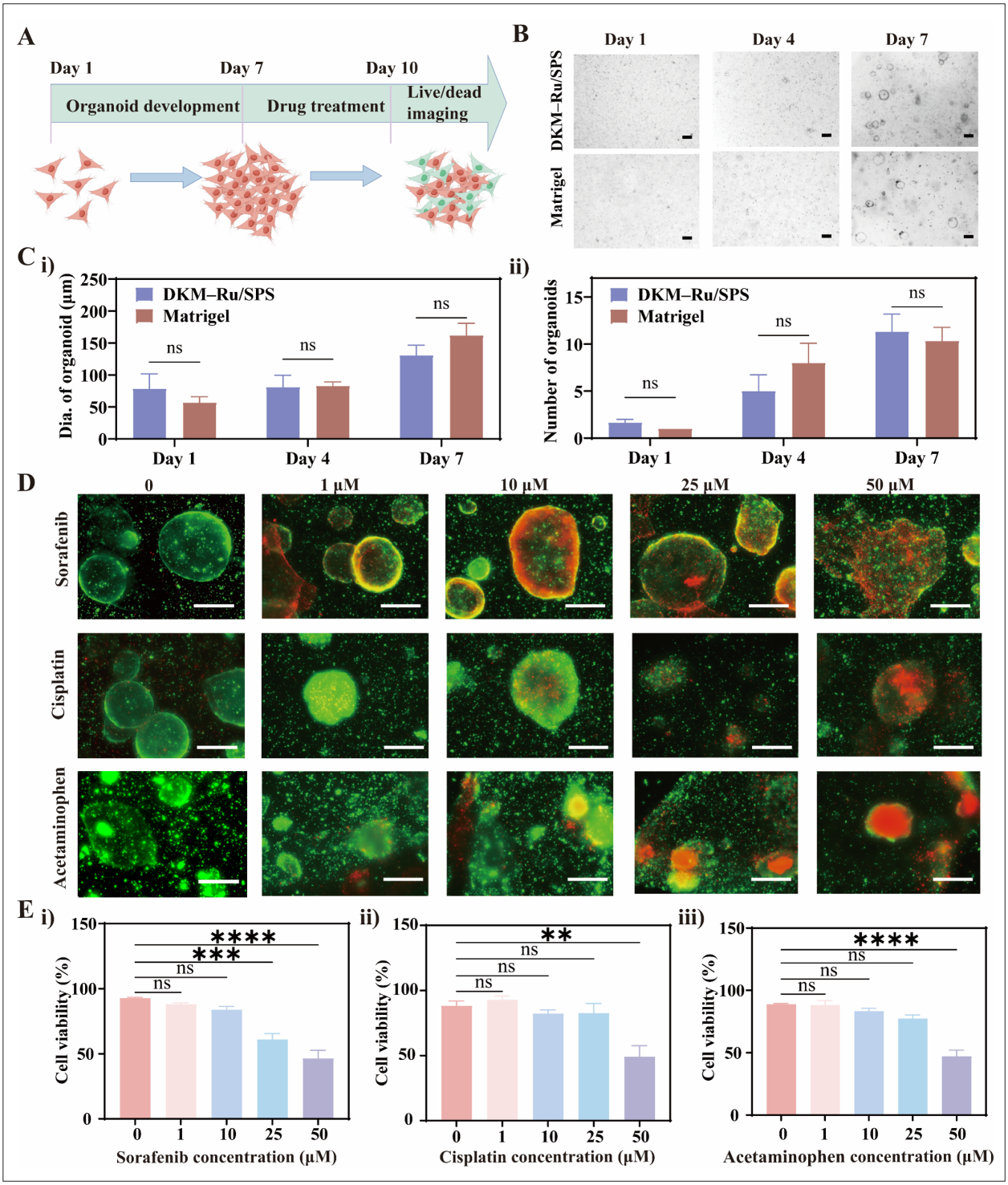


Figure 6. Application of DKM–Ru/SPS bioink for liver organoid culture and drug screening. (A) Schematic illustration of organoid fabrication and drug screening using a 3D bioprinter. (B) Culture of mouse primary liver organoids (P0) in DKM–Ru/SPS bioink and Matrigel, with representative bright-field images captured at 4× magnification from Days 1 to 7. Scale bar = 300 μm. (C) Quantification of (i) organoid size and (ii) formation efficiency from panel B. (D) Live/dead staining of liver organoids treated with increasing doses (1–50 μM) of sorafenib, cisplatin, and acetaminophen. Scale bar = 300 μm; magnification: 40×. (E) Quantitative analysis of live/dead staining for (i) sorafenib, (ii) cisplatin, and (iii) acetaminophen. Notes: Data are representative of three independent experiments (n = 3); mean ± standard error of the mean, one-way analysis of variance; ****p < 0.0001, ***p < 0.001, **p < 0.01. Abbreviations: Dia, Diameter; DKM: Decellularized kidney extracellular matrix; ns: Not statistically significant; Ru/SPS; Tris(2,2'-bipyridyl) ruthenium (II) chloride hexahydrate/sodium persulfate.

This robust growth was also confirmed in the context of 3D bioprinting, as representative bright-field images obtained after 7 days showed well-developed and healthy liver organoids embedded within printed DKM–Ru/SPS bioink structures arranged in a 96-well plate (Figure S9). These observations confirm both the structural integrity of the printed constructs and the functional viability of the organoids.

As a proof of concept for drug screening, sorafenib, cisplatin, and acetaminophen were selected as representative hepatotoxic compounds. Quantitative analysis of live/dead staining (Figure 6D and E) revealed a dose-dependent decrease in cell viability for all three compounds. Following treatment, liver organoid viability after exposure to sorafenib at 0, 1, 10, 25, and 50 μM was 92.73 ± 1.09%, 88.12 ± 1.73%, 83.84 ± 4.31%, 61.06 ± 7.62%, and 46.23 ± 11.10%, respectively. For cisplatin at the same concentrations, viability was 88.27 ± 6.42%, 92.84 ± 5.20%, 82.24 ± 4.89%, 82.61 ± 13.02%, and 49.08 ± 14.72%. Similarly, acetaminophen treatment resulted in viabilities of 90.26 ± 0.3%, 88.23 ± 6.36%, 83.42 ± 3.90%, 77.43 ± 5.03%, and 47.04 ± 8.71%. In all experiments, viability in untreated control groups (0 μM) remained above 90%. Statistically significant toxicity ($p < 0.05$) was observed at 25 and 50 μM for sorafenib and at 50 μM for both cisplatin and acetaminophen, confirming the platform's sensitivity for drug toxicity screening.

The effective implementation of drug testing in this study serves two critical objectives. It confirms that the DKM–Ru/SPS bioink creates a universally applicable and physiologically responsive microenvironment that not only promotes the growth of various organoid types, including lung and liver organoids, but also facilitates their maturation for pharmacological investigations. Furthermore, liver organoids exhibited significant dose-dependent responses to both hepatocyte-specific drugs (acetaminophen) and broad-spectrum chemotherapeutic agents (cisplatin), indicating that this platform has strong potential for diverse toxicity screening applications.

The present work establishes DKM–Ru/SPS as a visible-light-crosslinkable bioink with broad potential applications. In future studies, this dECM-based bioink could be combined with patient-derived organoids to enable personalized drug sensitivity testing within a tissue-mimetic ECM. Integration with microfluidic organ-on-a-chip platforms may further enable incorporation of perfusion, mechanical cues, and multiorgan interactions, as advocated for next-generation functional hydrogels and microphysiological systems.[37] Additionally, systematic tuning of DKM content and Ru/SPS concentration could facilitate modeling of progressive fibrosis or desmoplastic tumor stroma, enabling investigation of how such matrices, in combination with tumor microenvironment-responsive nanomedicines, regulate immune responses and therapeutic resistance.[39,40]

4. Conclusion

In conclusion, this study establishes a visible-light-crosslinkable DKM bioink integrated with the Ru/SPS photoinitiator system as a robust and versatile platform for 3D bioprinting and organoid culture. The key innovation lies in its ability to achieve rapid photocrosslinking within 40 s, representing a significant advancement over conventional thermosensitive dECM hydrogels. This system enables high-fidelity bioprinting of organoid-laden constructs and effectively supports the growth and maturation of lung and liver organoids, with performance comparable to that of Matrigel. Furthermore, its successful application in hepatoxicity assessment demonstrates its potential for drug testing using an *in vitro* biomimetic platform. By addressing critical limitations related to gelation kinetics and printability, the DKM–Ru/SPS bioink not only broadens the biomedical applications of dECM-derived biomaterials but also paves the way for standardized, automated, and high-throughput organoid-based models for drug discovery and regenerative medicine.

Acknowledgments

None.

Funding

The authors acknowledge the financial support from the National Key Research and Development Program of China (Nos. 2022YFA1105200 and 2022YFB3804700), the Central Government Guiding Local Science and Technology Development Special Fund Projects in Sichuan Province (No. 2023ZYD0166), the Chengdu City Science and Technology Project of "Unveiling and Commanding" (No. 2024-JB00-00018-GX), and the Eastern New District of Chengdu for the Implementation of Technological Innovation Projects (No. 2024-DBXQ-KJYF002).

Conflict of interest

The authors declare no conflicts of interest.

Author contributions

Conceptualization: Wenqi Hu, Chengwei Sun, Haijie Hu, Litian Zhao, Zipeng Yao, Shuqi Wang
Formal analysis: Guohua Wu, Mengjiao Xia, Di Wu
Investigation: Wenqi Hu, Guohua Wu, Mengjiao Xia, Di Wu
Methodology: Wenqi Hu

Writing–original draft: Qijun Du, Qinrui Lu, Jiashu Wang
Writing–review & editing: Ao Xie, Chengwei Sun, Haijie Hu, Litian Zhao, Zipeng Yao, Shuqi Wang

Ethics approval and consent to participate

All animal experiments were approved by the West China Hospital Animal Care Ethics Committee (Approval No. 108, 2023).

Consent for publication

Not applicable.

Availability of data

The raw data supporting the findings of this study are available from the corresponding author upon reasonable request.

References

1. Frankell AM, Dietzen M, Al Bakir M, *et al*. The evolution of lung cancer and impact of subclonal selection in TRACERx. *Nature*. 2023;616(7957):525-533. doi: 10.1038/s41586-023-05783-5
2. Lian L, Xie M, Luo Z, *et al*. Rapid volumetric bioprinting of decellularized extracellular matrix bioinks. *Adv Mater*. 2024;36(34):2304846. doi: 10.1002/adma.202304846
3. Kratochvil MJ, Seymour AJ, Li TL, Paşca SP, Kuo CJ, Heilshorn SC. Engineered materials for organoid systems. *Nat Rev Mater*. 2019;4(9):606-622. doi: 10.1038/s41578-019-0129-9
4. Xie M, Sun Y, Wang J, *et al*. Thermo-sensitive sacrificial microsphere-based bioink for centimeter-scale tissue with angiogenesis. *IJB*. 2022;8(4):599. doi: 10.18063/ijb.v8i4.599
5. Liu J, Wu G, Wu D, *et al*. Microfluidic organoid-slice-on-a-chip system for studying anti-cholangiocarcinoma drug efficacy and hepatorenal toxicity. *Lab Chip*. 2025;25(12): 2839-2850. doi: 10.1039/D4LC00902A
6. Wu G, Wu D, Hu W, *et al*. A novel microfluidic self-perfusion chip (MSPC) for pumpless 3D cell, microtissue and organoid culture. *Lab Chip*. 2025;25(15):3694-3706. doi: 10.1039/D5LC00030K
7. Hu W, Bei HP, Jiang H, *et al*. DLM–GelMA/tumor slice sandwich structured tumor on a chip for drug efficacy testing. *Lab Chip*. 2024;24(15):3718-3727. doi: 10.1039/D4LC00278D
8. Wu M, Huang K, Long C, Yang C, Tong Y. In vitro extracellular matrix model to evaluate stroma cell response to transvaginal mesh. *Neurourol Urodyn*. 2013;33(4):449-454. doi: 10.1002/nau.22425
9. Song H, Jiang H, Hu W, *et al*. Cervical extracellular matrix hydrogel optimizes tumor heterogeneity of cervical squamous cell carcinoma organoids. *Sci Adv*. 2024;10(20):eadl3511. doi: 10.1126/sciadv.adl3511
10. Kim J, Kim J, Gao G, *et al*. Bioprinted organoids platform with tumor vasculature for implementing precision personalized medicine targeted towards gastric cancer. *Adv Funct Mater*. 2023;34(11):2306676. doi: 10.1002/adfm.202306676
11. Treacy NJ, Clerkin S, Davis JL, *et al*. Growth and differentiation of human induced pluripotent stem cell (hiPSC)-derived kidney organoids using fully synthetic peptide hydrogels. *Bioact Mater*. 2023;21:142-156. doi: 10.1016/j.bioactmat.2022.08.003
12. Lin L, Jiang S, Yang J, *et al*. Application of 3D-bioprinted nanocellulose and cellulose derivative-based bio-inks in bone and cartilage tissue engineering. *IJB*. 2022;9(1):637. doi: 10.18063/ijb.v9i1.637
13. Garreta E, Moya-Rull D, Marco A, *et al*. Natural hydrogels support kidney organoid generation and promote in vitro angiogenesis. *Adv Mater*. 2024;36(34):2400306. doi: 10.1002/adma.202400306
14. Jin Y, Zhang J, Xu Y, *et al*. Stem cell-derived hepatocyte therapy using versatile biomimetic nanozyme incorporated nanofiber-reinforced decellularized extracellular matrix hydrogels for the treatment of acute liver failure. *Bioact Mater*. 2023;28:112-131. doi: 10.1016/j.bioactmat.2023.05.001
15. Wei Q, Liu D, Chu G, *et al*. TGF-β1-supplemented decellularized annulus fibrosus matrix hydrogels promote annulus fibrosus repair. *Bioact Mater*. 2023;19:581-593. doi: j.bioactmat.2022.04.025
16. Zhang X, Chen X, Hong H, Hu R, Liu J, Liu C. Decellularized extracellular matrix scaffolds: Recent trends and emerging strategies in tissue engineering. *Bioact Mater*. 2022; 10:15-31. doi: j.bioactmat.2021.09.014
17. Lu J, Huang J, Jin J, Xie C, Xue B, Lai J. The design and characterization of a strong Bio-Ink for meniscus regeneration. *IJB*. 2022;8(4):600. doi: 10.18063/ijb.v8i4.600
18. Nerger BA, Sinha S, Lee NN, *et al*. 3D hydrogel encapsulation regulates nephrogenesis in kidney organoids. *Adv Mater*. 2024;36(14):2308325. doi: 10.1002/adma.202308325
19. Lee J, Hong J, Kim W, Kim GH. Bone-derived dECM/alginate bioink for fabricating a 3D cell-laden mesh structure for bone tissue engineering. *Carbohydr Polym*. 2020;250:116914. doi: j.carbpol.2020.116914

20. Rizzo R, Ruetsche D, Liu H, Zenobi-Wong M. Optimized photoclick (bio)resins for fast volumetric bioprinting. *Adv Mater*. 2021;33(49):2102900. doi: 10.1002/adma.202102900

21. Chen S, Wu C, Zhou T, *et al*. Aldehyde-methacrylate-hyaluronan profited hydrogel system integrating aligned and viscoelastic cues for neurogenesis. *Carbohydr Polym*. 2022;278:118961. doi: 10.1016/j.carbpol.2021.118961

22. Milton LA, Davern JW, Hipwood L, *et al*. Liver click dECM hydrogels for engineering hepatic microenvironments. *Acta Biomater*. 2024;185:144-160. doi: 10.1016/j.actbio.2024.06.037

23. Elvitigala KCML, Mohan L, Mubarok W, Sakai S. Phototuning of hyaluronic-acid-based hydrogel properties to control network formation in human vascular endothelial cells. *Adv Healthc Mater*. 2024;13(17):2303787. doi: 10.1002/adhm.202303787

24. Lim KS, Schon BS, Mekhileri NV, *et al*. New visible-light photoinitiating system for improved print fidelity in gelatin-based bioinks. *ACS Biomater Sci Eng*. 2016;2(10):1752-1762. doi: 10.1021/acsbiomaterials.6b00149

25. Kim H, Kang B, Cui X, *et al*. Light-activated decellularized extracellular matrix-based bioinks for volumetric tissue analogs at the centimeter scale. *Adv Funct Mater*. 2021;31(32):2011252. doi: 10.1002/adfm.202011252

26. Wang L, Riediger L, Rao Q, *et al*. Tunable synthetic hydrogel modulates hepatic lineage specification of human liver organoid. *Adv Funct Mater*. 2025;19(8):e08430. doi: 10.1002/adfm.202508430

27. Fang W, Yang M, Wang L, *et al*. Hydrogels for 3D bioprinting in tissue engineering and regenerative medicine: current progress and challenges. *IJB*. 2023;9(5):759. doi: 10.18063/ijb.759

28. Wang Z, Boretto M, Millen R, *et al*. Rapid tissue prototyping with micro-organospheres. *Stem Cell Rep*. 2022;17(9):1959-1975. doi: 10.1016/j.stemcr.2022.07.016

29. Liu F, Liu C, Chen Q, *et al*. Progress in organ 3D bioprinting. *IJB*. 2024;4(1):128. doi: 10.18063/ijb.v4i1.128

30. Hu Y, Zhu T, Cui H, Cui H. Integrating 3D bioprinting and organoids to better recapitulate the complexity of cellular microenvironments for tissue engineering. *Adv Healthc Mater*. 2024;14(3):2403762. doi: 10.1002/adhm.202403762

31. Choi Y mi, Lee H, Ann M, Song M, Rheey J, Jang J. 3D bioprinted vascularized lung cancer organoid models with underlying disease capable of more precise drug evaluation. *Biofabrication*. 2023;15(3):034104. doi: 10.1088/1758-5090/acd95f

32. Han Y, Yang J, Zhao W, *et al*. Biomimetic injectable hydrogel microspheres with enhanced lubrication and controllable drug release for the treatment of osteoarthritis. *Bioact. Mater*. 2021;6(10):3596-3607. doi: 10.1016/j.bioactmat.2021.03.022

33. Rawal P, Tripathi DM, Ramakrishna S, Kaur S. Prospects for 3D bioprinting of organoids. *Bio-Des Manuf*. 2021;4(3):627-640. doi: 10.1007/s42242-020-00124-1

34. Alam K, Nair L, Mukherjee S, *et al*. Cellular interplay to 3D in vitro microphysiological disease model: cell patterning microbiota–gut–brain axis. *Bio-Des Manuf*. 2024;7(3):320-357. doi: 10.1007/s42242-024-00282-6

35. Keselowsky BG, Bridges AW, Burns KL, *et al*. Role of plasma fibronectin in the foreign body response to biomaterials. *Biomaterials*. 2007;28(25):3626-3631. doi: j.biomaterials.2007.04.035

36. Xie M, Lian L, Mu X, *et al*. Volumetric additive manufacturing of pristine silk-based (bio)inks. *Nat Commun*. 2023;14(1):210. doi: 10.1038/s41467-023-35807-7

37. Yang H, Zeng T, Jiang T, *et al*. Recent progress on functional hydrogels as biomaterial for biomedicine. *Results Chem*. 2025;16:102464. doi: 10.1016/j.rechem.2025.102464

38. Datta P, Barui A, Wu Y, Ozbolat V, Moncal KK, Ozbolat IT. Essential steps in bioprinting: from pre- to post-bioprinting. *Biotechnol Adv*. 2018;36(5):1481-1504. doi: 10.1016/j.biotechadv.2018.06.003

39. Luo Y, He X, Du Q, *et al*. Metal-based smart nanosystems in cancer immunotherapy. *Exploration*. 2024;4(6):20230134. doi: 10.1002/EXP.20230134

40. Chen B, Guo K, Zhao X, *et al*. Tumor microenvironment-responsive delivery nanosystems reverse immunosuppression for enhanced CO gas/immunotherapy. *Exploration*. 2023;3(6):20220140. doi: 10.1002/EXP.20220140

ACCSCIENCE PUBLISHING

International Journal of Bioprinting

RESEARCH ARTICLE

Fabrication of biomimetic corneas featuring epithelial, stromal, and endothelial layers via bioprinting

Tong Zhu[1,2†], Renhao Ni[1†], Haowen Sun[1,3], Shengkai Yu[1], Xu Cao[1,4], Shang Chen[1], Jingyu Shi[4], Cuicui Su[1], Yang Luo[1,4*], Lu Yang[2*], and Hua Zhang[1*]

[1]Research Institute of Smart Medicine and Biological Engineering, Health Science Center, Ningbo University, Ningbo, Zhejiang, China

[2]Department of Ophthalmology, The First Affiliated Hospital of Ningbo University, Ningbo, Zhejiang, China

[3]College of Pharmacy, Guizhou University of Traditional Chinese Medicine, Guiyang, Guizhou, China

[4]Department of Urology, The First Affiliated Hospital of Ningbo University, Ningbo, Zhejiang, China

[†]These authors contributed equally to this work.

***Corresponding authors:**
Yang Luo
(2101140092@nbu.edu.cn)

Lu Yang
(yanglu@nbu.edu.cn)

Hua Zhang
(zhanghua@nbu.edu.cn)

Citation: Zhu T, Ni R, Sun H, *et al.* Fabrication of biomimetic corneas featuring epithelial, stromal, and endothelial layers via bioprinting. *Int J Bioprint*. 2026;12(1):448-466. doi: 10.36922/IJB025380380

Received: September 15, 2025
1st revised: November 1, 2025
2nd revised date: November 28, 2025
3rd revised date: December 10, 2025
Accepted: December 12, 2025
Published online: December 18, 2025

Copyright: © 2025 Author(s). This is an Open Access article distributed under the terms of the Creative Commons Attribution License, permitting distribution and reproduction in any medium, provided the original work is properly cited.

Publisher's Note: AccScience Publishing remains neutral with regard to jurisdictional claims in published maps and institutional affiliations.

Abstract

The bioengineering of full-thickness corneal substitutes presents significant challenges, primarily due to the complex stratified structure of the cornea, which consists of the epithelium, stroma, and endothelium, as well as its critical functional requirements, including optical transparency, mechanical stability, and biocompatibility. Herein, we present an integrated fabrication strategy that combines embedded hydrogel bioprinting with subsequent two-dimensional endothelial cell seeding to create biomimetic corneal structures using a gelatin methacryloyl (GelMA)/hyaluronic acid methacryloyl (HAMA) composite hydrogel. The engineered scaffold successfully recapitulates the native cornea's trilaminar architecture (epithelium, stroma, and endothelium) and exhibits 30–80% optical transparency across the visible spectrum. The hybrid hydrogel exhibits optimal wettability (a contact angle of approximately 50° and minimal swelling of less than 10%) and controlled degradation kinetics, effectively addressing the limitations of single-component hydrogels. The scaffold maintains structural integrity during suturing and supports robust cellular proliferation and migration. Gene expression analysis revealed the phenotypic orientation of seeded cells toward key corneal lineages, with upregulation of epithelial (*Klf4* and *Pax6*), stromal (*Col1a1* and *Col4a4*), and endothelial (*Zeb1* and *Foxc1*) markers. Overall, the bioprinted GelMA/HAMA biomimetic cornea presents a promising proof of concept for a trilayered tissue-engineered corneal construct.

Keywords: Biomimetic cornea; Hydrogel; Multi-cell types; Three-dimensional bioprinting; Tissue engineering

1. Introduction

The cornea is the transparent tissue at the front of the eye, primarily responsible for refracting light and protecting the internal structures of the eye.[1] It is vulnerable to infections caused by bacteria, viruses, and fungi, as well as to physical injuries and chemical damage, leading to corneal blindness in approximately 10 million people worldwide.[2] Although allogeneic corneal transplantation remains the gold-standard therapeutic intervention, its widespread application is constrained by severe donor shortages and inherent risks of immune rejection.[3] Moreover, despite donor screening, allografts carry additional risks of transmissible infections (e.g., hepatitis and human immunodeficiency viruses), prion diseases, and microbial keratitis.[4] Beyond the risks associated with allografts, conditions such as dystrophies, keratoconus, and other noninfectious opacities further underscore the need for safer, standardized bioengineered substitutes.[5] Thus, there is a pressing clinical need to develop bioengineered corneal substitutes.[6]

Anatomically, the cornea comprises five principal layers: the epithelium, Bowman's layer, stroma, Descemet's membrane, and endothelium. Each layer has distinct barrier, biomechanical, and optical functions, which impose stringent design requirements on engineered substitutes. Current tissue-engineering approaches have yielded various corneal substitutes utilizing natural polymers, synthetic materials, or their hybrid composites.[7] Although these constructs successfully replicate corneal components and biochemical cues, limitations such as the difficulty in reconstructing the stratified corneal structure (epithelium–stroma–endothelium), the lack of precise spatial organization of multiple cell types, inadequate mechanical stability for suturing, and low optical transparency restrict their application.[8] Among these challenges, the development of multilayered biomimetic constructs with precise spatial cell distributions remains the most formidable obstacle, due to the native cornea's complex asphericity and gradient thickness (ranging from 500 to 700 μm).[9]

Hydrogels are playing an increasingly transformative role in advancing ocular tissue engineering. For instance, Vijayaraghavan et al.[10] created three-dimensional (3D)-bioprinted corneal mimics using gelatin methacryloyl (GelMA)-methylcellulose blends that support keratocyte phenotype and display favorable transparency. Cai et al.[11] reported an injectable, self-healing zwitterionic hydrogel with stable intraocular performance in vitrectomy models. Kim et al.[12] further engineered a retina-on-a-chip with functional blood–retina barriers using multinozzle bioprinting of decellularized extracellular matrix bioinks, enabling pathological modeling of retinal vein occlusion. These studies collectively highlight the potential of advanced hydrogels and bioprinting to address the global shortage of donor corneas.[7] Among various bioprinting technologies, digital light processing (DLP) excels at fabricating corneal stromal layers with precise microarchitecture due to its high resolution (10–50 μm) and rapid fabrication speed.[13] Utilizing photopolymerization principles, this noncontact approach achieves exceptional control over corneal curvature gradients and surface topography.[14] However, the application of DLP in cell-laden, full-thickness constructs is constrained by light-path attenuation and scattering caused by cellular components and photoinitiators. This phenomenon necessitates higher light doses, which can induce phototoxicity and compromise transparency.[15] In contrast, microextrusion bioprinting excels at constructing complex, multilayered corneal architectures by enabling synchronous deposition of multiple bioinks and cell types.[16] This capability facilitates the 3D heterotypic organization of epithelium–stroma–endothelium structures, which is essential for functional corneal regeneration.[17] Nevertheless, this approach presents a resolution–viability trade-off, as maintaining > 85% viability typically requires filament diameters of 100–250 μm.[18] This limitation hinders the fabrication of ultrathin, curved constructs featuring cellular layers as narrow as 3–5 cells, while preserving structural and functional integrity.[14]

The microextrusion printability of cell-laden hydrogels, particularly in terms of cell viability and the structural integrity of the printed constructs, is closely related to the flow properties of the hydrogel inks, the sol–gel transition, and the stiffness of the gels.[19] Shear thinning of the hydrogel inks enhances extrusion fluidity and reduces shear stress that can harm cells.[20] Rapid gelation is crucial and must occur within seconds after extrusion, with the hydrogel's elastic modulus postgelation required to exceed 50 kPa to ensure shape fidelity and effectively support the printed structure.[21] For instance, Puistola et al.[22] developed a hyaluronic acid hydrogel ink exhibiting shear-thinning characteristics and an elastic modulus of 112.2 kPa via the dynamic crosslinking of aldehyde-functionalized hyaluronic acid and dopamine-carbodihydrazide-modified hyaluronic acid. Utilizing microextrusion printing technology, they successfully fabricated a bilayer hydrogel corneal structure with a 12 mm diameter, comprising a 320 μm-thick stromal layer and a 240 μm-thick epithelial layer. Similarly, Xu et al.[14] constructed a convex corneal implant using 3D printing of GelMA and collagen type I as composite inks. By regulating the temperature of the printing ink and optimizing photocuring conditions, a biomimetic cornea with a curved architecture and thicknesses ranging from 186 to 625 μm was produced. To provide adequate

structural support for the thin, curved construct, the hydrogel's compressive modulus was increased to 130 kPa, rendering the scaffold effective for surface cell seeding but incompatible with 3D cell-laden printing.[23] Despite these advancements in structural biomimicry, achieving a multilayered and multicellular construct that accurately replicates the functional equivalence of native corneas remains a considerable challenge. These difficulties primarily arise from the complexities involved in achieving the printability of multicellular biomimetic hydrogels.

To address the challenge of printing thin, curved corneas using microextrusion printing hydrogel, we developed an integrated "3D-3D-two-dimensional (2D)" fabrication strategy that combines embedded bioprinting of a stromal/epithelial cell-laden hydrogel with subsequent

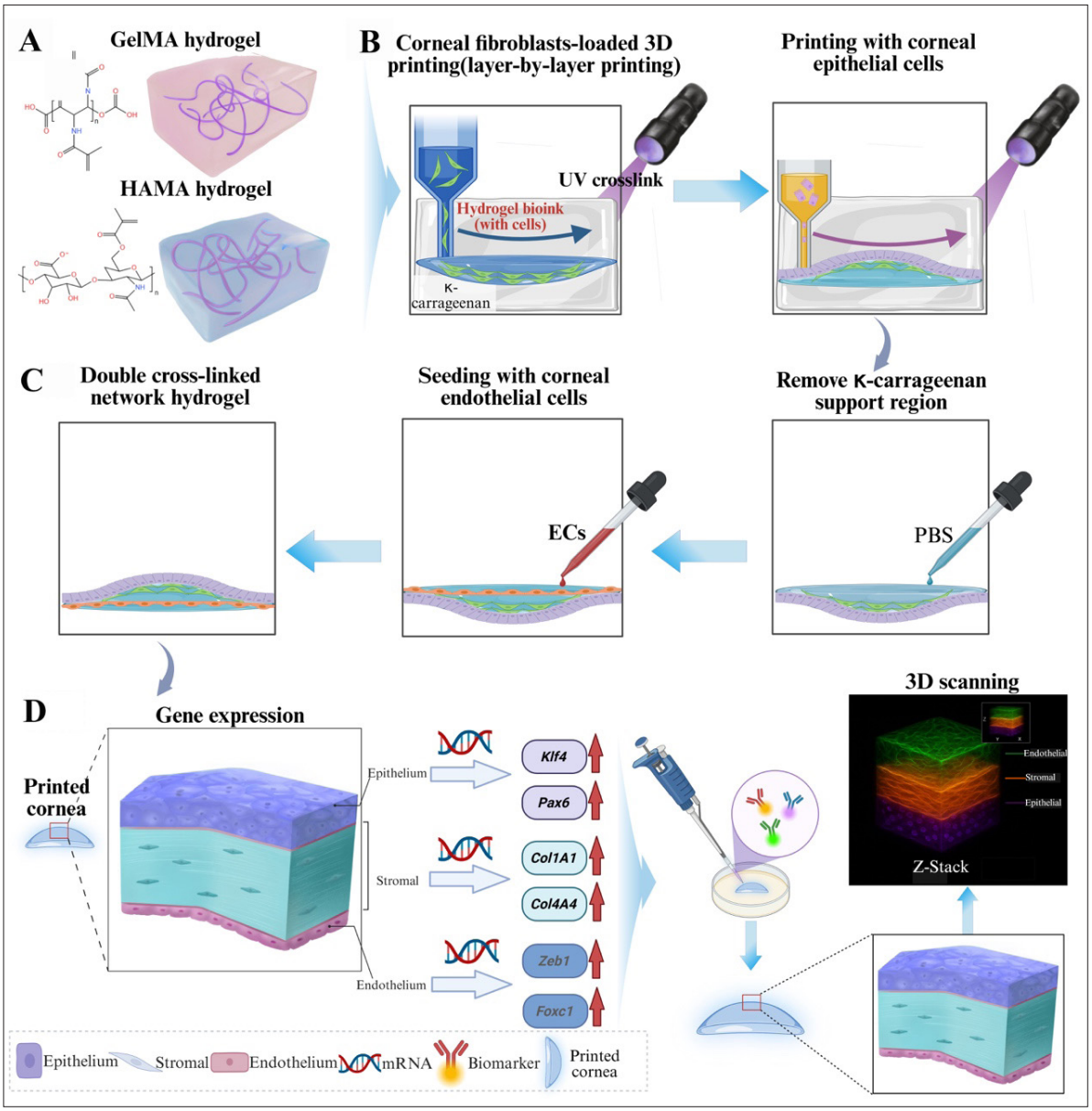


Figure 1. Schematic illustration of the construction and analysis of a trilayered 3D bioengineered cornea. (A) Molecular structures of GelMA/HAMA hydrogel bioinks. (B,C) Embedded 3D printing of the stromal (B) and epithelial (C) layers in a κ-carrageenan support bath. (D) Removal of the κ-carrageenan support bath. (E) Seeding of endothelial cells to form the trilayered construct. (F) Depiction of the resulting trilayer construct within a dual-crosslinked network. (G,H) Characterization by layer-specific quantitative polymerase chain reaction (G) and 3D confocal imaging (H) of architecture and interfaces. Abbreviations: 3D: Three-dimensional; Ecs: Endothelial cells; GelMA: Gelatin methacryloyl; HAMA: Hyaluronic acid methacryloyl; PBS: Phosphate-buffered saline; UV: Ultraviolet.

endothelial cell seeding to create a trilayered, biomimetic corneal equivalent (Figure 1). We designed a thermally and photocrosslinkable composite hydrogel of GelMA and hyaluronic acid methacrylate (HAMA) to encapsulate corneal epithelial and stromal cells (Figure 1A). The GelMA/HAMA composite exhibited temperature-sensitive physical gelation, allowing for immediate shape retention during embedded printing, followed by photopolymerization to form a stable covalent network that maintained the delicate curved structure (Figure 1B). The incorporation of HAMA into the GelMA network was optimized to achieve greater transparency and wettability compared to GelMA alone. Comprehensive rheological characterization confirmed optimal shear-thinning behavior and tunable sol–gel transitions responsive to both thermal and photochemical stimuli, facilitating the effective printing of biomimetic corneal hydrogel scaffolds. Cellular assays, including 2D surface seeding and coculturing, confirmed the biocompatibility and migratory capabilities of the GelMA/HAMA biomimetic corneal hydrogel. We successfully engineered a biomimetic corneal structure with distributed epithelial, stromal, and endothelial cells (Figure 1C). This construct significantly facilitated the 3D survival and growth of epithelial and stromal cells, alongside elevated expression of relevant genes (Figure 1D). This study lays the foundation for the future engineering of functional corneal tissue.

2. Materials and methods

2.1. Synthesis of gelatin methacryloyl

Porcine skin gelatin (100 g; Sigma-Aldrich, USA) was dissolved in phosphate-buffered saline (PBS, 1 L, pH 7.4; VivaCell, China) at 50°C with constant stirring. Methacrylic anhydride (MA, 20 mL; Sigma-Aldrich, USA) was added dropwise, and the reaction was maintained at 50°C for 3 h. The reaction mixture was then transferred to dialysis tubing (molecular weight cutoff [MWCO] 8–10 kDa) and dialyzed against deionized water at 37°C for 4 days, with the water being changed twice daily. Finally, the retentate was lyophilized to obtain GelMA as a white porous foam.

2.2. Synthesis of hyaluronic acid methacryloyl

Sodium hyaluronate (3 g) was dissolved in ice-cold deionized water (300 mL) with stirring at 4°C. After complete dissolution, MA (5.5 mL) was added slowly, and the pH of the reaction mixture was maintained at approximately 8.0 by dropwise addition of 10 mol L^{-1} sodium bicarbonate. The resulting mixture was then transferred to dialysis tubing (MWCO 8–10 kDa) and dialyzed against deionized water for 7 days, with the water being changed daily. Finally, the retentate was freeze-dried to yield HAMA.

2.3. Nuclear magnetic resonance spectroscopy analysis

Samples of gelatin, GelMA, hyaluronic acid, and HAMA (≈50 mg each) were dissolved in 600 µL deuterium oxide. ^{1}H nuclear magnetic resonance (NMR) spectra were recorded at 400 MHz using an NMR spectrometer (AVANCE III 400 Bruker, Germany) at 25°C. For GelMA, the methacrylate vinyl protons were integrated over the range of 5.3–6.1 ppm (I_{vinyl}) and normalized to the gelatin α-CH region at 3.9–4.5 ppm ($I_{\alpha\text{-CH}}$). The degree of methacrylation (DoM) was calculated using **Equation (1).**

$$DoM\,(\%) = \left(1 - \frac{\frac{I_{vinyl}}{3}}{\frac{I_{\alpha-CH}}{1}}\right) \times 100\% \quad (1)$$

For HAMA, I_{vinyl} (5.3–6.1 ppm) was normalized to the invariant N-acetyl–CH_3 signal at 1.90 ppm ($I_{Ac\text{-}CH3}$), resulting in **Equation (2).**

$$DoM\,(\%) = \left(1 - \frac{\frac{I_{vinyl}}{3}}{\frac{I_{Ac-CH3}}{3}}\right) \times 100\% = \frac{I_{vinyl}}{I_{Ac-CH3}} \times 100\% \quad (2)$$

All integrations were performed using MestReNova software (Version 14.0, Mestrelab Research S.L., Spain) with automatic phase and baseline correction. For each material, ^{1}H NMR spectra were recorded from independently synthesized batches (n = 3). The DoM was calculated for each batch as described above, and the results are reported as mean ± standard deviation (SD).

2.4. Preparation of gelatin methacryloyl/hyaluronic acid methacryloyl mixed solution and hydrogel

Separate stock solutions of GelMA (10 g) and HAMA (1 g) were prepared in PBS at concentrations of 20% (w/v) and 2% (w/v), respectively. These stock solutions were then mixed at a 1:1 volume ratio, and lithium phenyl-2,4,6-trimethylbenzoylphosphinate (LAP, 0.03 g) was added to a final concentration of 0.3% (w/v), yielding the final precursor solution (10% GelMA + 1% HAMA). Control precursors of 10% GelMA and 1% HAMA were prepared identically. All solutions were photopolymerized under 405 nm near-ultraviolet (UV) light (10 mW cm^{-2}) for 60 s.

2.5. Contact angle and hydrophilicity

Hydrogel disks (≈2 mm thick) were prepared in silicone molds via UV-curing. Static water contact angles were measured at 25°C and 50–60% relative humidity using a goniometer (DSA100, Kruss, Germany). A 2 μL droplet of ultrapure water was deposited on the hydrogel surface, and the contact angle was measured within 5 s of droplet settlement. For each hydrogel disk (sample), three random locations were measured, and the values were averaged to represent the sample's contact angle. For each hydrogel formulation, three independently prepared disks (n = 3) were analyzed. Data are reported as mean ± SD.

2.6. Transmittance

The optical transparency of each hydrogel formulation was quantified using a UV–visible (UV–vis) spectrophotometer (UV-2600, Shimadzu, Japan). Square films (~1 mm thick) were equilibrated in PBS for 24 h, blotted to remove surface moisture, and mounted in quartz cuvettes. Transmittance spectra were collected from 380 to 780 nm at a scan rate of 1 nm s^{-1}, using deionized water as the baseline. For each formulation, three independently prepared hydrogels were measured (n = 3), and the spectra are reported as mean ± SD. The transmittance (T, %) was calculated using **Equation (3)**

$$T(\%) = \frac{I}{I_0} \times 100\% \quad (3)$$

where I is the transmitted light intensity of the sample, and I_0 is the background transmitted light intensity.

2.7. Rheological properties of hydrogels and *κ*-carrageenan

The rheological properties were characterized using a rheometer (Discovery HR-20, TA Instruments, USA) equipped with a 60 mm diameter parallel plate geometry and a Peltier temperature control system. All measurements were performed with a fixed gap of 500 μm. A temperature sweep was conducted from 20 to 40°C at a heating rate of 5°C min^{-1} to characterize the thermoresponsive behavior. Steady-state flow measurements were performed by recording the viscosity over a shear rate range of 0.001–1,000 s^{-1} after equilibrating the sample at 37°C for 5 min. To monitor photocrosslinking kinetics, time-sweep measurements were initiated, and the sample was immediately exposed to continuous 405 nm irradiation at 10 mW cm^{-2}. The flow curves of κ-carrageenan precursor solutions (0.2–0.5% w/v) were obtained in shear ramp mode by applying a logarithmic shear rate ramp from 0.01 to 1,000 s^{-1} at 37°C. The κ-carrageenan solutions were subjected to a test that alternated between a high-shear destruction phase (100 s^{-1} for 60 s) and a low-shear recovery phase (0.01 s^{-1} for 60 s) to quantify the time-dependent recovery of viscosity.

2.8. 3D bioprinting of biomimetic corneal constructs

A biomimetic corneal template was designed in Rhino (Version 7, Robert McNeel & Associates, USA) and processed in Pango (Version 2.1.1, Panowin, China) with the following parameters: 160 μm layer height, filament width matching the nozzle inner diameter, 100% concentric infill to mimic the lamellar architecture, 60 mm s^{-1} printing speed, and 80 mm s^{-1} travel speed, all optimized to maximize geometric fidelity. The bioink was prepared by dissolving 10% GelMA and 1% HAMA in sterile PBS (pH 7.4) containing 0.30% (w/v) LAP as a photoinitiator. The mixture was gently blended at 37°C and degassed by centrifugation (2,000 rpm, 5 min), then maintained at 37°C until printing. A granular 0.4% κ-carrageenan support bath (8–10 mm depth) was pre-equilibrated to 15°C to facilitate rapid physical gelation upon ink deposition. The prepared bioink was loaded into a 5 mL syringe equipped with a 160 μm inner-diameter steel nozzle and mounted onto an extrusion bioprinter. After calibrating the build plate and Z-offset, a 10–15 mm filament purge was performed to ensure stable flow, followed by printing at a constant extrusion rate of 0.06 mL min^{-1}. Constructs were immediately photocrosslinked after deposition using 405 nm light (10 mW cm^{-2}, 60 s) to establish covalent networks. The κ-carrageenan support was then gently rinsed away with PBS. To mimic the lamellar structure of the native cornea, a core GelMA/HAMA layer was first printed and crosslinked, followed by an outer layer with infill orientation rotated by 180° relative to the core. The second layer was subsequently photocured to form a full-thickness, stratified corneal analog. Final printed grafts were rinsed with PBS and stored fully hydrated to maintain structural geometry until further use.

2.9. Suturing ability

The surgical handling potential of the bioengineered cornea was evaluated qualitatively. A cornea-shaped construct was 3D-printed from the GelMA/HAMA precursor and photocrosslinked (405 nm, 10 mW cm^{-2}, 60 s). After equilibration in PBS at 37°C for 24 h, a 9-0 polypropylene suture was passed through the full thickness of the construct, 3 mm from its edge, using a standard curved needle. The suture track was then visually examined for any gross tearing or crack propagation. The absence of such damage was documented as an indicator of the construct's basic robustness and surgical handleability. This test was designed as a qualitative assessment of handling characteristics during a simulated suturing procedure, not

as a quantitative measure of suture retention strength or a direct comparison to native human corneal tissue.

2.10. Swelling and degradation

The hydration capacity and network stability of the printed corneal constructs were evaluated through swelling and degradation studies. For swelling tests, constructs were photopolymerized under 405 nm light and then lyophilized to a constant weight to determine the dry mass (W_d). The samples were immersed in PBS (pH 7.4, 37°C) and weighed (W_s) at predefined intervals until mass equilibrium was reached. The swelling ratio was calculated as shown in **Equation (4).**

$$Swelling\ ratio(\%) = \frac{W_s + W_d}{W_d} \times 100\% \quad (4)$$

The optical transmittance of the fully hydrated constructs was measured after swelling equilibrium across 380–800 nm using a UV–vis spectrophotometer and reported as percent transmission. The dimensional stability of the swelled constructs was assessed using a corneal topographer to measure the anterior corneal curvature and diameter.

For degradation studies, identical hydrogel discs were weighed (W_0) after preparation and incubation in PBS or PBS supplemented with 10 U mL^{-1} collagenase II at 37°C. At scheduled time points, the samples were rinsed, blotted dry, and weighed (W_t). The degradation rate (D) was calculated as shown in **Equation (5).**

$$D(\%) = \frac{W_0 - W_t}{W_0} \times 100\% \quad (5)$$

Data from both swelling and degradation studies are presented as mean ± SD, obtained from three independent samples per condition.

2.11. Tensile and suture retention characterization

Precursor solutions of GelMA, HAMA, and GelMA/HAMA hydrogels were sterile-filtered (0.22 μm), mixed with LAP (0.3% w/v), and cast into silicone strip molds (25 mm × 4 mm × 1.0 mm). The samples were photocrosslinked under 405 nm light (10 mW cm^{-2}, 60 s) and equilibrated in PBS (pH 7.4) at 37°C for 24 h. Before testing, the width and thickness of each sample were measured at three locations and averaged.

For uniaxial tensile testing, hydrated specimens were tested in a temperature-controlled chamber (37°C) using a universal testing machine with a 100 N load cell and pneumatic grips with rubber-faced jaws. Samples were secured at an initial gauge length of 10 mm. Tensile extension was performed at 10 mm min^{-1}. Engineering stress (σ) and strain (ε) were calculated as in **Equations (6)** and **(7).**

$$\sigma = \frac{F}{A_0} \quad (6)$$

$$\varepsilon = \frac{\Delta L}{L_0} \quad (7)$$

where F is the instantaneous force, A_0 is the original cross-sectional area, ΔL is the change in length, and L_0 is the initial length. Young's modulus (E) was then determined from the linear region of the stress–strain curve (0–10% strain). The ultimate tensile strength and failure strain were defined as the peak stress and corresponding strain at rupture, respectively.

For the suture retention test, equilibrated hydrogels were sutured with a 9-0 nylon monofilament using a single stitch placed 2.0 mm from the edge with a 1.0 mm bite. A square knot was tied, leaving 5 mm tails. The suture loop was attached to the upper grip, and the sample was secured in the lower grip, ensuring the pulling direction was perpendicular to the suture line. Specimens were pulled at a constant rate of 5 mm min^{-1} until failure. The peak load was recorded as the suture retention strength and was normalized by sample thickness (N mm^{-1}). For each hydrogel formulation, five strips were tested in uniaxial tension (n = 5), and five independent sutured constructs were evaluated for suture retention (n = 5).

2.12. Burst pressure testing

Disc-shaped samples of GelMA/HAMA composite hydrogels (diameter: 12–14 mm; hydrated thickness 0.50 ± 0.02 mm) were prepared by photocuring and equilibrated in PBS at 37°C for at least 2 h. Each disc was mounted in a two-piece circular fixture with a silicone O-ring, defining a circular test area with an inner diameter of 10 mm. The outlet of the fixture was connected via tubing to a digital pressure sensor (MD-S260, Moekon Sensor Technology Co., Ltd., China) with 0–100 ± 0.1 kPa accuracy, with a syringe serving as the hydraulic pressure source and the entire system filled with PBS. After zeroing the sensor and purging air, the pressure was increased steadily at 1–2 kPa s^{-1}. The burst pressure was recorded as the peak value preceding the first abrupt drop or sustained leak,

preventing further pressurization. Results are expressed as mean ± standard deviation (n = 5). Any tests showing clamp slippage, sample edge tearing, or seal failure were excluded from the analysis.

2.13. Cellular viability assay

The three hydrogel formulations were cast into the bottom of 24-well plates under aseptic conditions and photocrosslinked under 405 nm blue light. The resulting hydrogels were rinsed with sterile PBS to remove unreacted components, then equilibrated in their respective culture media for 24 h. Corneal epithelial cells, stromal fibroblasts, and endothelial cells were seeded onto the hydrogel surfaces at a density of 5×10^4 cells cm^{-2} and incubated at 37°C with 5% carbon dioxide (CO_2). At predetermined time points (Days 1, 3, 5, and 7), the culture medium was replaced with a fresh medium containing 10% (v/v) cell counting kit (CCK)-8 solution. After incubation for 1 h, the absorbance of the CCK-8 solution was measured at 450 nm using a microplate reader (YP-96-1, U-Unip, China) to quantify cellular viability and proliferation. Each condition was tested in three independent wells per time point. Absorbance values are presented as mean ± SD.

To investigate the chemoattractive potential of the biomimetic hydrogel, a Transwell-based coculture assay was established. Sterilized GelMA/HAMA hydrogel precursor was cast into the upper chamber of Transwell inserts (8 μm pore size) to form a thin barrier layer and photocrosslinked. The hydrogel-coated inserts were then equilibrated for 24 h in Dulbecco's Modified Eagle Medium (DMEM)/F-12 medium (VivaCell, China) supplemented with 10% fetal bovine serum (FBS) and 1% penicillin–streptomycin. A chemoattractant gradient was established by adding DMEM/F-12 medium with 10% FBS to the lower chamber. Corneal epithelial cells, stromal fibroblasts, or endothelial cells, suspended in a low-serum medium (DMEM/F-12 with 1% FBS), were seeded onto the surface of the hydrogel in the upper chamber at a density of 5×10^4 cells cm^{-2}. The plates were incubated for 5 days at 37°C under 5% CO_2. After incubation, noninvading cells remaining on the top surface of the hydrogel were carefully removed using a cotton swab. The cells that had invaded into and through the hydrogel layer were then fixed with 4% paraformaldehyde, stained with 0.1% (w/v) crystal violet, and imaged under a bright-field microscope (MSD-S820, Murzider, China). Quantitative analysis was performed by calculating the percentage of the total area occupied by the stained, invaded cells across multiple predefined fields of view. Three independent inserts were analyzed per condition.

2.14. Cell-laden bioprinting and fluorescent imaging

Primary mouse corneal stromal cells (P3–P4; iCell Bioscience, China) were harvested, counted, and resuspended in a sterile GelMA/HAMA prepolymer solution containing 0.30% (w/v) LAP at a density of 5×10^6 cells mL^{-1}. The cell–bioink mixture was gently mixed at 37°C and maintained at this temperature. A granular κ-carrageenan support bath (8–10 mm depth) was autoclave-sterilized and equilibrated to 15°C. The stromal cell-laden bioink was loaded into a sterile 5 mL syringe equipped with a 160 μm nozzle, mounted on an extrusion bioprinter, and purged (10–15 mm) to stabilize flow. Following the protocol in **Section 2.8**, the stromal core was printed directly into the support bath using a layer height of 160 μm and a 100% concentric infill pattern under constant volumetric extrusion (0.06 mL min^{-1}; print and travel speeds of 60 and 80 mm s^{-1}, respectively). Constructs were immediately photocrosslinked (405 nm, 10 mW cm^{-2}, 60 s), after which the κ-carrageenan support was dissolved and carefully rinsed away with PBS.

For the epithelial layer, primary mouse corneal epithelial cells (P3–P4) were suspended in fresh GelMA/HAMA/LAP prepolymer at 3×10^6 cells mL^{-1} and processed identically. The printed stromal graft was rotated 180°, and the epithelial bioink was deposited onto its outer surface and photocured (405 nm, 10 mW cm^{-2}, 60 s). Finally, primary mouse corneal endothelial cells (P3–P4) were seeded onto the inner (posterior) surface via repeated pipette dripping (2–3 passes at 4×10^5 cells cm^{-2}) onto the pre-equilibrated hydrogel surface. After a 20–30-min attachment period at 37°C, the graft was gently rinsed with PBS. The bioprinted corneal equivalents were maintained in DMEM/F-12 medium and incubated at 37°C in a humidified 5% CO_2 atmosphere.

After 2 days of culture, constructs were rinsed with PBS and incubated in a solution containing 2 μM calcein-acetoxymethyl ester and 4 μM ethidium homodimer-1 for 40 min at 37°C to assess cell viability. The stained constructs were then imaged using a confocal microscope (STELLARIS 5, Leica, Germany). After 7 days of culture, samples were fixed in 4% paraformaldehyde and permeabilized with 0.1% Triton X-100. They were then stained with fluorescein isothiocyanate (FITC)-phalloidin for 60 min to visualize F-actin, washed three times with PBS, counterstained with 4',6-diamidino-2-phenylindole (DAPI) to label nuclei, and imaged by confocal microscopy to assess cell distribution and structural integrity.

2.15. 3D confocal imaging of the bioprinted cornea

The spatial organization of cells within the 3D-bioprinted corneal constructs was visualized using multiplex immunofluorescence staining and confocal microscopy.

The constructs, comprising epithelial, stromal, and endothelial layers, were fixed, stained, and imaged as follows: The 3D-bioprinted corneal constructs were washed with PBS and immobilized in a 24-well plate for processing. They were then fixed with a 4% paraformaldehyde and 0.25% glutaraldehyde solution at room temperature for 45 min, followed by three 5-min washes with PBS. We then permeabilized the constructs with 0.5% Triton X-100 in PBS for 30 min and subsequently blocked with 3% BSA in PBS for 1 h at room temperature. For multiplex immunofluorescence staining, the constructs were incubated overnight at 4°C with a mixture of the following primary antibodies diluted in 3% BSA/PBS: anticytokeratin 18 (647-conjugated, 1:200 dilution; 10830-1-AP, Proteintech, China) to label epithelial cells and anti-ATP1A1 (FITC-conjugated, 1:200 dilution; 14418-1-AP, Proteintech, China) to label endothelial cells. After incubation, the constructs were washed three times with PBS for 5 min each. Following the primary antibody staining, the constructs were incubated with CoraLite-labeled Phalloidin (1:500 dilution; PF0003, Proteintech, China) for 30 min at room temperature to label F-actin in stromal cells. Finally, all samples were counterstained with DAPI for 10 min to visualize nuclei and washed thoroughly with PBS. The stained constructs were imaged using a confocal microscope. The following excitation/emission settings were used: cytokeratin 18 (647 nm/pink), phalloidin (594 nm/red), ATP1A1 (488 nm/green), and DAPI (405 nm/blue). Z-stacks were acquired to capture the full 3D structure of the constructs. All staining and imaging procedures were performed on three independently fabricated constructs ($n = 3$). For each construct, at least three nonoverlapping fields of view were imaged per channel.

2.16. Gene expression analysis in corneal cells by quantitative polymerase chain reaction

To evaluate the gene expression profiles of corneal cells cultured on different hydrogel substrates, corneal epithelial, stromal, and endothelial cells were seeded at a density of 5×10^5 cells mL^{-1} within GelMA, HAMA, and GelMA/HAMA hydrogels. After the culture period, total RNA was extracted directly from the cell-laden hydrogels using the High Purity RNA Extraction Kit (Q20802, TransGen Biotech, China). Genomic DNA was removed, and first-strand cDNA was synthesized from the purified RNA using the TransScript One-Step gDNA Removal and cDNA Synthesis SuperMix kit (AT311, TransGen Biotech, China) according to the manufacturer's instructions. Quantitative PCR (qPCR) was performed using the PerfectStart Green qPCR SuperMix (AQ601, TransGen Biotech, China) on a real-time qPCR system. *Actb* (β-actin) was used as the reference gene for normalization, and reactions were performed using gene-specific primers (sequences listed in **Table S1**). Relative gene expression levels were calculated using the $2^{-\Delta\Delta Ct}$ method. For each cell type and hydrogel condition, RNA was isolated from three independent biological replicates ($n = 3$), with each sample assayed in technical triplicate. Gene expression data are presented as mean ± SD.

2.17. Statistical analysis

All statistical analyses were performed using Statistical Package for Social Sciences (SPSS 20.0, IBM, USA) and GraphPad Prism (version 9.5.1, Dotmatics, UK). Data are presented as mean ± SD. Group comparisons were carried out using one-way analysis of variance, followed, where appropriate, by Tukey's honestly significant difference post hoc test. Homogeneity of variances was assessed with Levene's test. Unless otherwise stated, all tests were two-sided with a significance level of $\alpha = 0.05$. Statistical significance is indicated as $^*p < 0.05$, $^{**}p < 0.01$, and $^{***}p < 0.001$. For analyses involving multiple hypotheses, p-values were adjusted using the Benjamini–Hochberg procedure to control the false discovery rate. Sample sizes (n) for each experiment are reported in the corresponding figure legends.

3. Results

3.1. Synthesis and characterization of the gelatin methacryloyl/hyaluronic acid methacryloyl hydrogel

The UV-curable, temperature-sensitive GelMA/HAMA composite hydrogel, consisting of 10% (w/v) GelMA, 1% (w/v) HAMA, and 0.3% (w/v) LAP, was designed as a corneal scaffold to enable embedded bioprinting, as detailed in our previous reports.[24] GelMA and HAMA were synthesized by reacting gelatin and hyaluronic acid with MA, with methacrylation degrees of 73.6 ± 0.3% and 13.7 ± 0.1%, respectively (Figure S1). While GelMA provides a supportive scaffold for corneal cell growth, the incorporation of HAMA aims to modulate key physical characteristics relevant to corneal function. Contact angle measurements revealed that GelMA hydrogel exhibited a high contact angle (>84°), indicating a relatively hydrophobic surface (Figure 2A and B). In contrast, the HAMA hydrogel showed a markedly lower contact angle (< 25°), attributable to its abundance of hydroxyl and carboxyl groups that enhance water affinity. The GelMA/HAMA hydrogel presented an intermediate contact angle (~50°) closer to the wettability range of the native cornea (55–65°).[25] Optical characterization across the visible spectrum (380–780 nm) demonstrated that the GelMA/HAMA composite hydrogel achieved moderate optical clarity, with transmittance increasing

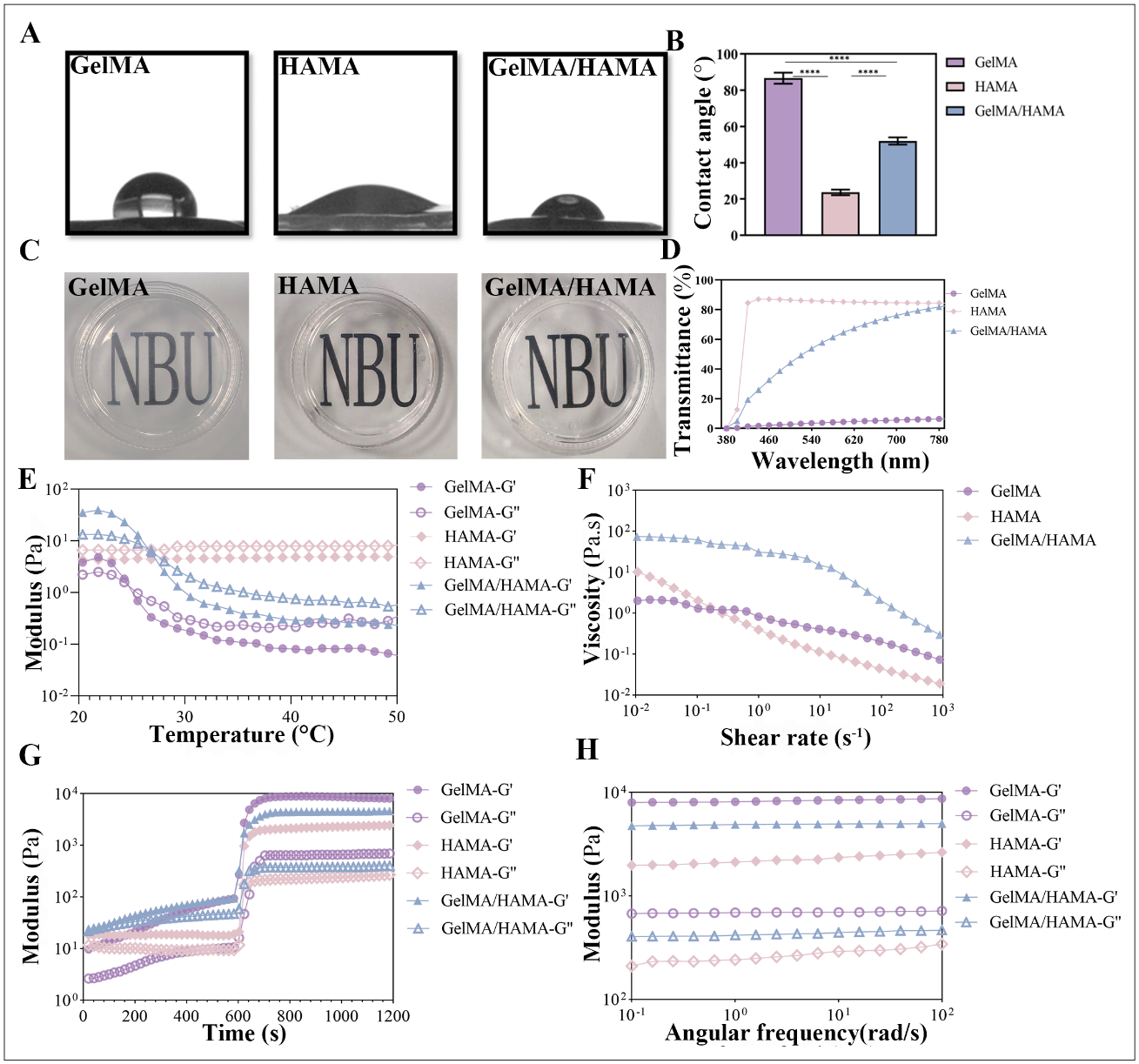


Figure 2. Rheological and physicochemical characterization of GelMA, HAMA, and GelMA/HAMA hydrogels. (A) Representative sessile-drop contact-angle images on hydrogel surfaces. (B) Contact angle (°; $n = 3$). (C) Macroscopic appearance of hydrated samples at identical thickness. (D) Ultraviolet–visible transmittance spectra across 380–780 nm; $n = 3$). (E) Temperature sweep (20–50°C) monitoring the gel–sol transition. (F) Shear-flow ramp at 37°C (0.01–100 s^{-1}) revealing zero-shear viscosity and shear-thinning behavior. (G) Time-sweep monitoring of storage (*G'*) and loss (*G"*) moduli during photocrosslinking (405 nm irradiation initiated at 600 s). (H) Frequency sweep of photocrosslinked hydrogels. For panel (B), statistical comparisons among hydrogels were performed using one-way analysis of variance. Note: ****$p < 0.0001$. Abbreviations: GelMA: Gelatin methacryloyl; HAMA: Hyaluronic acid methacryloyl.

from approximately 30% at 400 nm to around 80% at longer wavelengths (Figure 2C and D). This performance represents a substantial improvement over GelMA alone (<20% transmittance), though it remains lower than that of the highly transparent HAMA hydrogel (> 90%). Collectively, the transmittance spectrum of 30–80% positions the composite as an optically promising, yet not native-equivalent, material for corneal scaffold applications, effectively balancing transparency with other essential properties.

The temperature sensitivity and UV-curable gelation of GelMA/HAMA composites used as bioprinting inks were analyzed through rheological measurements. As shown in Figure 2E, both GelMA and GelMA/HAMA precursors

underwent gel–sol transitions at 24 and 27°C, respectively, while HAMA maintained a relatively stable modulus across the entire temperature range. The stiffness of the GelMA/HAMA gels formed below 27°C was found to be greater than that of both GelMA and HAMA, whereas the modulus of the sol state above 27°C fell between the values of GelMA and HAMA. This reversible, temperature-mediated sol–gel transition facilitates smooth flow extrusion during printing. Moreover, the rapid formation of high-modulus gels ensures the stability and fidelity of the printed structures. Additionally, the GelMA/HAMA precursors at 37°C exhibited shear-thinning behavior (Figure 2F), improving the printability of the inks under lower shear stress, thereby protecting cell viability during cell-laden bioprinting.

Upon UV initiation, the GelMA/HAMA composite rapidly transformed from a thermosensitive soft gel into a covalently crosslinked hydrogel with a storage modulus of 4,497 Pa, exceeding that of the HAMA hydrogel but remaining lower than that of the GelMA (Figure 2G). Moreover, frequency-sweep analyses showed that the loss modulus of the GelMA/HAMA hydrogel increased slightly with frequency, while the storage modulus remained nearly constant (Figure 2H). These results indicate that incorporating HAMA into GelMA yields a mechanically robust yet compliant network, which is advantageous for maintaining shape fidelity in curved corneal bioprinting. Tensile tests demonstrated that GelMA, HAMA, and GelMA/HAMA hydrogels all exhibited failure stresses of 250–300 kPa (Figure S2), with the composite showing performance comparable to GelMA. In *ex vivo* suturing tests, the constructs maintained mechanical integrity, exhibiting only localized softening around the suture site without macroscopic tearing. These results support good handling characteristics and resistance to suture-induced damage under experimental conditions. Consistently, burst-pressure tests yielded a mean failure pressure of 11.4 ± 0.31 kPa (Figure S3), which is several times the physiological intraocular pressure and falls within the lower range of experimental corneal sealants. These results suggest that the GelMA/HAMA hydrogel provides sufficient short-term pressure retention, though further improvements are needed to achieve more stringent mechanical performance requirements.

3.2. Embedded printing of the 3D corneal constructs

To fabricate curved corneal constructs with high geometric fidelity via embedded micro-extrusion printing, we employed a sacrificial support bath composed of a κ-carrageenan microgel suspension, optimized based on our previous work.[26,27] A 0.4% κ-carrageenan suspension was selected, as it demonstrated suitable yield stress, pronounced shear-thinning, and rapid self-healing properties at the printing temperature (Figure 3B and C). These rheological characteristics are essential for supporting the deposition and shape retention of fine, curved filaments without causing structural collapse. A 3D corneal model was designed in Rhino with the following dimensions: an outer radius of curvature of 7.8 mm, an inner radius of curvature of 6.8 mm, a transverse diameter of 11.0 mm, a longitudinal diameter of 10.0 mm, and a central thickness of 0.5 mm (Figure 3C). When the GelMA/HAMA ink was extruded through a 160 μm inner-diameter nozzle into this support bath, the deposited filaments rapidly underwent physical gelation upon cooling to the ambient temperature of the bath (Figure 3D). After printing, the entire structure was photocrosslinked under UV light and then gently extracted from the κ-carrageenan support. The obtained hydrogel corneal scaffold accurately replicated the curvature and dimensions of the original digital model.

Suturing is a fundamental procedure in corneal surgery. To assess the handling characteristics and structural robustness of the GelMA/HAMA corneal scaffold in a simulated surgical context, we performed a qualitative suturing test. Eight evenly spaced stitches were placed circumferentially using ophthalmic-grade 9-0 polypropylene sutures. As shown in Figure 3E, the scaffold maintained its structural integrity throughout the procedure, resisting macroscopic tearing or significant deformation at the suture sites. This result demonstrates the scaffold's ability to withstand basic surgical manipulation *in vitro*, indicating favorable handling characteristics for potential use in ophthalmic tissue engineering research. This excellent suture retention property can be linked to the balanced mechanical stability and flexibility inherent to the GelMA/HAMA composite hydrogels.

3.3. *In vitro* swelling and degradation of gelatin methacryloyl/hyaluronic acid methacryloyl corneal constructs

The controlled swelling behavior and degradation of scaffolds are crucial for surgical success and postoperative recovery. An ideal corneal scaffold must exhibit minimal swelling (<10%) to maintain optical clarity and structural stability, while demonstrating controlled degradation kinetics synchronized with corneal regeneration (4–8 weeks). The swelling and degradation properties of the GelMA/HAMA corneal scaffolds were systematically evaluated to assess their suitability for corneal applications. As shown in Figure 3F, the scaffolds demonstrated optimal water absorption characteristics in PBS (pH 7.4), reaching an equilibrium swelling ratio of 9.11 ± 0.48% within 360 min. This relatively low swelling was consistent with preservation of moderate optical transmittance across the visible spectrum before and after hydration (Figure 3G).

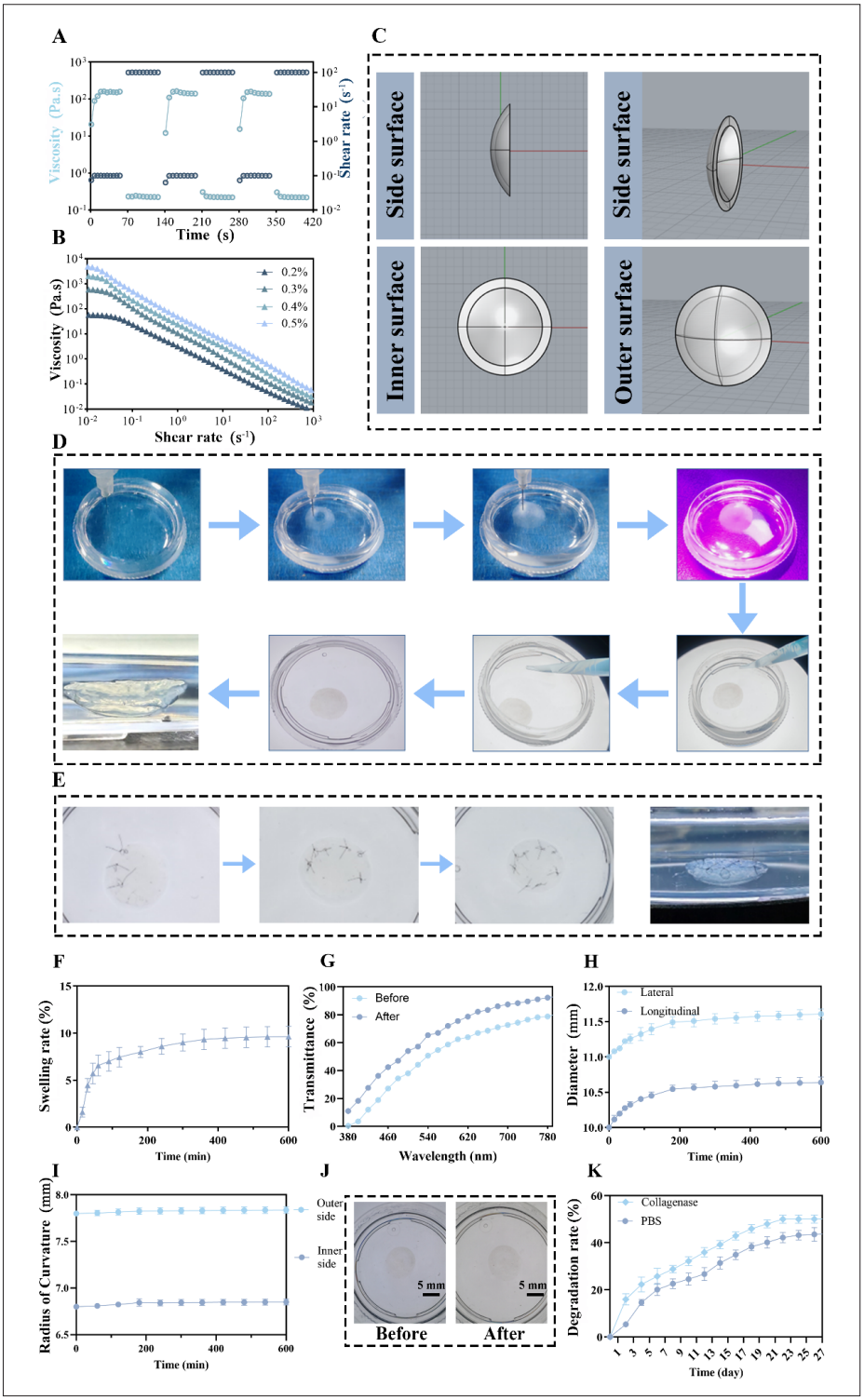


Figure 3. Rheological properties, fabrication process, and structural stability of the bioengineered corneal scaffold. (A) Self-healing behavior of the κ-carrageenan support bath under alternating shear. (B) Shear-thinning flow behavior of κ-carrageenan at varying concentrations. (C) Computer-aided design model illustrating corneal geometry and curvature. (D) Sequential bioprinting process for scaffold fabrication. (E) Suture retention test demonstrating surgical feasibility. (F) *In vitro* degradation profiles in phosphate-buffered saline (PBS) and collagenase environments. (G) Optical transmittance before and after swelling (mean ± standard deviation [SD], $n = 3$). (H) Temporal changes in lateral and longitudinal dimensions during hydration (mean ± SD, $n = 3$). (I) Evolution of outer and inner curvature radii during hydration (mean ± SD, $n = 3$). (J) Macroscopic view of scaffolds before and after hydration. Scale bar: 5 mm. (K) Enzymatic degradation in collagenase compared to PBS control (mean ± SD, $n = 3$).

The hydrated constructs also maintained dimensional stability, with the outer curvature radius remaining below 7.9 mm, the inner curvature radius below 6.9 mm, the transverse diameter below 11.59 mm, and the longitudinal diameter below 10.6 mm (Figure 3H and I).

Degradation studies were performed under both passive (PBS only) and enzymatic (collagenase II, 10 U mL^{-1}) conditions to model different aspects of *in vivo* breakdown. In PBS at 37°C, the GelMA/HAMA scaffolds showed a gradual degradation profile with 44.22 ± 0.37% mass retention after 28 days, following near-linear kinetics. In collagenase solution, the scaffolds exhibited bioresponsive degradation behavior. They maintained structural integrity during the critical initial 2-week epithelialization period (≤ 39.55% mass loss) and subsequently accelerated degradation (50.46 ± 0.17% total mass loss at the 4th week). This enzyme-responsive degradation profile suggests that the scaffold's stability could be modulated by local proteolytic activity. Overall, the observed minimal swelling supports the scaffold's potential to maintain dimensional and optical consistency in an aqueous environment, while the tunable degradation kinetics in collagenase indicate a capacity for cell- or enzyme-mediated remodeling. These *in vitro* properties are consistent with initial requirements for a corneal stromal scaffold, though their functional relevance must be further evaluated in biological systems.

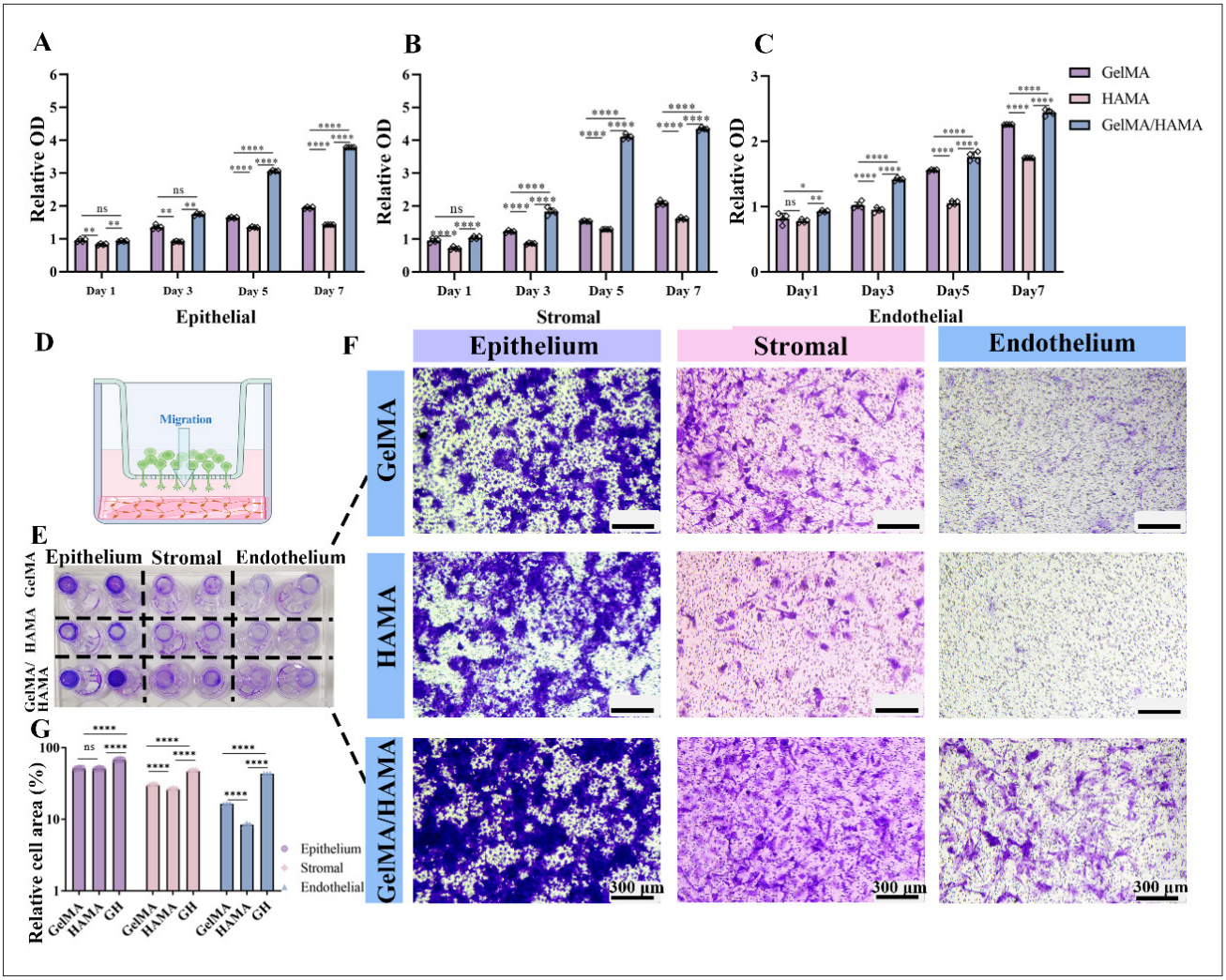


Figure 4. Cell viability and migration of corneal cells on hydrogel substrates. (A–C) Viability of corneal epithelial (A), stromal (B), and endothelial (C) cells on GelMA, HAMA, and GelMA/HAMA hydrogels measured by Cell Counting Kit-8 assay at designated time points (mean ± standard deviation [SD], $n = 3$). (D) Schematic illustration of the Transwell migration assay. (E) Representative images of the Transwell assay setup. (F) Micrographs of migrated cells on the underside of the membranes. 20×. (G) Quantification analysis of cell migration, presented as the percentage of area covered by migrated cells (%, mean ± SD, $n = 3$). For panels (A–C, G), group differences were analyzed by one-way analysis of variance with Tukey's honestly significant difference post hoc test. Notes: ns, not significant; $^{*}p < 0.05$; $^{**}p < 0.01$; $^{****}p < 0.0001$.

3.4. Proliferation and migration of corneal cells on gelatin methacryloyl/hyaluronic acid methacryloyl hydrogels

The cytocompatibility of GelMA/HAMA hydrogels was evaluated by culturing corneal epithelial, stromal, and endothelial cells on their surfaces, using single-component GelMA and HAMA hydrogels as controls. Cell viability and proliferation were assessed via CCK-8 assay at Days 1, 3, 5, and 7. As illustrated in Figure 4A, the optical density (OD) values of corneal epithelial cells on Days 1 and 3 were comparable across all hydrogel groups. However, by Days 5 and 7, corneal epithelial cells demonstrated a significantly higher proliferation rate on the GelMA/HAMA composite hydrogels compared to those on the GelMA and HAMA hydrogels. For corneal stromal and endothelial cells, the OD value on the composite hydrogels was significantly greater than on HAMA hydrogels as early as Day 1. This trend continued through Days 3–7, with marked increases in proliferation observed by Day 5 relative to both HAMA and GelMA hydrogels (Figure 4B and C). These results showed that corneal epithelial cells exhibited a lower proliferation rate on the composite hydrogel substrate relative to stromal and endothelial cells. Notably, the relative OD values for all three cell types on the composite hydrogels on Days 5 and 7 were similar, suggesting the onset of contact inhibition, a characteristic of normal cell growth behavior. Collectively, these findings demonstrate that the GelMA/HAMA composite hydrogel provides a highly cytocompatible substrate that supports robust, coordinated proliferation of key corneal cell types.

To assess the chemotactic response of corneal cells to the printed scaffolds, we performed a Transwell-based migration assay (Figure 4D). Hydrogel samples were placed in the lower chamber, and cells were seeded in the upper chamber. After 24 h, cells that had migrated to the underside of the membrane were stained and quantified. As illustrated in Figure 4G, the GelMA/HAMA hydrogel supported the most pronounced directional migration toward the hydrogel-containing lower compartment, followed by GelMA and then HAMA, demonstrating that cell migration is guided by material-specific biochemical cues. Quantitative analysis further revealed that the GelMA/HAMA composite hydrogel significantly enhanced cell spreading area compared to single-component hydrogels. Notably, endothelial cells exhibited the strongest response, with a 5.17 ± 0.29-fold increase compared to HAMA. These results suggest that the GelMA/HAMA composite presents biochemical or physical cues that promote corneal cell migration in this *in vitro* assay.

3.5. 3D bioprinted multilayered cell-laden corneal constructs

The favorable rheological properties, biocompatibility, and ability to support corneal cell proliferation and migration make GelMA/HAMA a suitable bioink for fabricating cell-laden constructs. To create a trilaminar biomimetic structure, we printed a stromal layer by extruding GelMA/HAMA bioink laden with corneal stromal cells. After 24 h of culture, live/dead cell staining revealed that the stromal cells maintained robust viability of 93% (Figure 5A). Furthermore, after 48 h, 80% of the cells had spread and formed pseudopodia within the 3D culture matrix (Figure 5B). These observations confirm that the GelMA/HAMA hydrogel provides a conducive 3D microenvironment for stromal cell survival and early integration.

Given the differential proliferation rates observed for epithelial and endothelial cells on the hydrogel surface, we adopted a sequential bioprinting and seeding strategy to assemble the full-thickness construct (Figure 5C). Corneal epithelial cell-laden hydrogels were first printed onto the anterior surface of the printed stromal layer. After 24 h of culture to allow for initial epithelial growth, corneal endothelial cells were seeded onto the posterior surface. Following an additional 48 h of culture, the constructs were immunostained for cytokeratin 18 (epithelium), ATP1A1 (endothelium), F-actin (stromal cytoskeleton), and nuclei. Confocal imaging revealed that epithelial, stromal, and endothelial cells were distributed in spatially distinct layers, recapitulating the trilaminar organization of the cornea (Figure 5D).

To evaluate the structural stability of the layered architecture, we extended the culture period and conducted layer-resolved confocal imaging of the same trilayer constructs on Days 7 and 14 (Figure S4). Whole-mount and high-magnification images confirmed the maintenance of distinct cellular strata throughout the culture period. The epithelial layer formed a dense, continuous covering on the anterior surface; the stromal region developed a highly organized, fibrillar extracellular matrix; and the endothelial layer remained as a confluent, polygonal monolayer on the posterior side. Importantly, this stratified epithelial–stromal–endothelial organization remained intact throughout the 14-day culture, with no signs of delamination or substantial loss of coverage. These results demonstrate that the printed corneal equivalents maintain their layer-specific architecture over relevant timeframes. The sustained structural fidelity of the constructs underscores the capability of the GelMA/HAMA hydrogel scaffold in replicating the native, multilayered organization of the cornea.

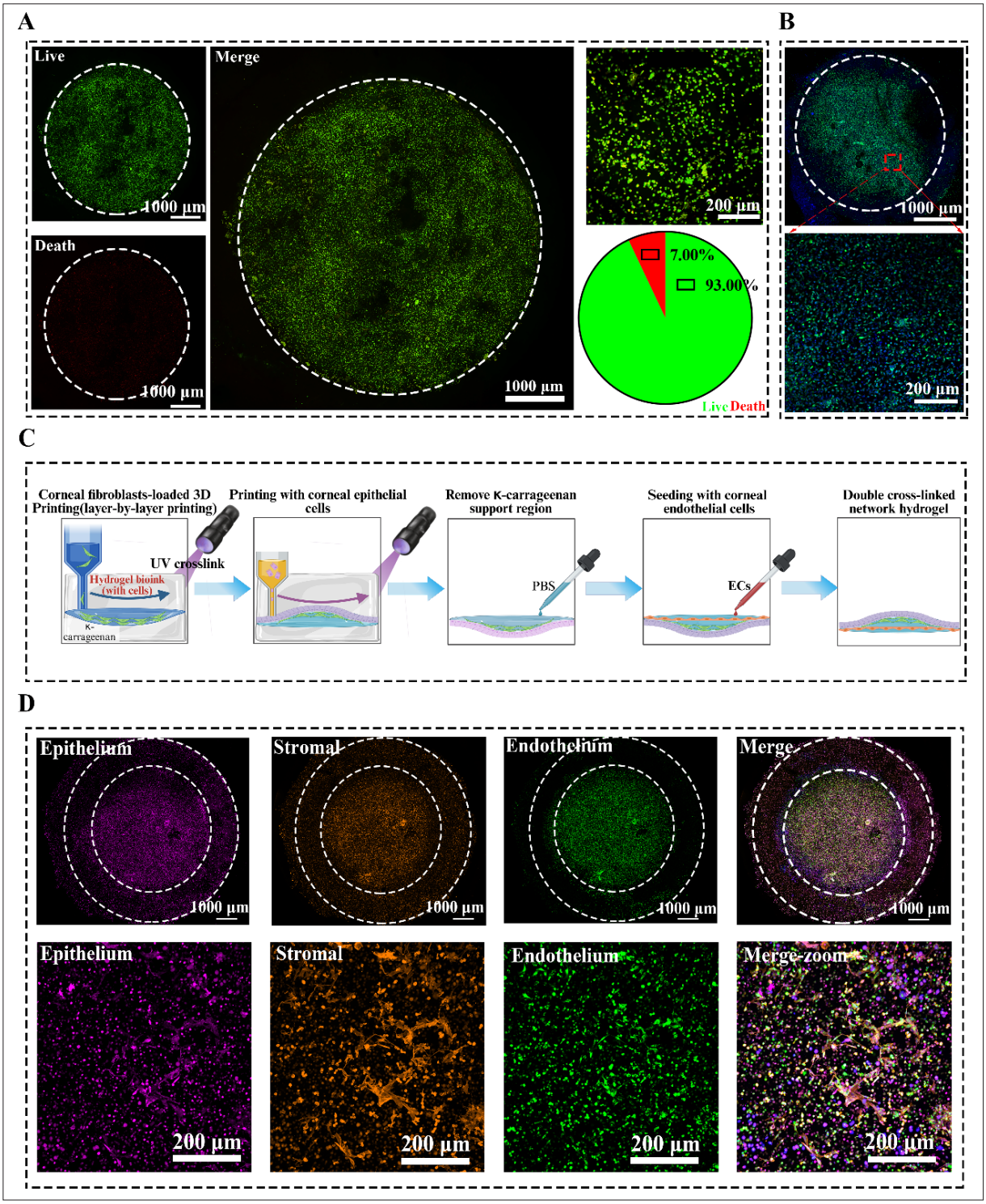


Figure 5. Cell viability and morphology of a trilaminar, cell-laden bioengineered cornea. (A) Confocal live/dead micrographs of the printed construct showing high cell viability. Scale bars: whole-mount (X-Y tiled): 10×, 1,000 μm; representative field of view (FOV): 10×, 200 μm. (B) Confocal visualization of the cytoskeletal architecture within the cell-laden corneal construct, with whole-mount and region-of-interest zooms. Scale bar: whole-mount (X-Y tiled): 1,000 μm, representative FOV: 10×, 200 μm. (C) Schematic diagram of the biofabrication process: embedded printing of a keratocyte-laden stromal layer; UV crosslinking; deposition of epithelial cells; removal of the κ-carrageenan support bath; seeding of ECs, and formation of the final composite hydrogel construct. (D) Confocal micrographs of the multilayered construct showing epithelial, stromal, and endothelial layers with a merged view and high-magnification insets; the outer circle indicates the construct boundary. Scale bars: whole-mount (X-Y tiled): 10×, 1,000 μm, representative FOV: 10×, 200 μm. Abbreviations: Ecs: Endothelial cells; PBS: Phosphate-buffered saline; UV: Ultraviolet.

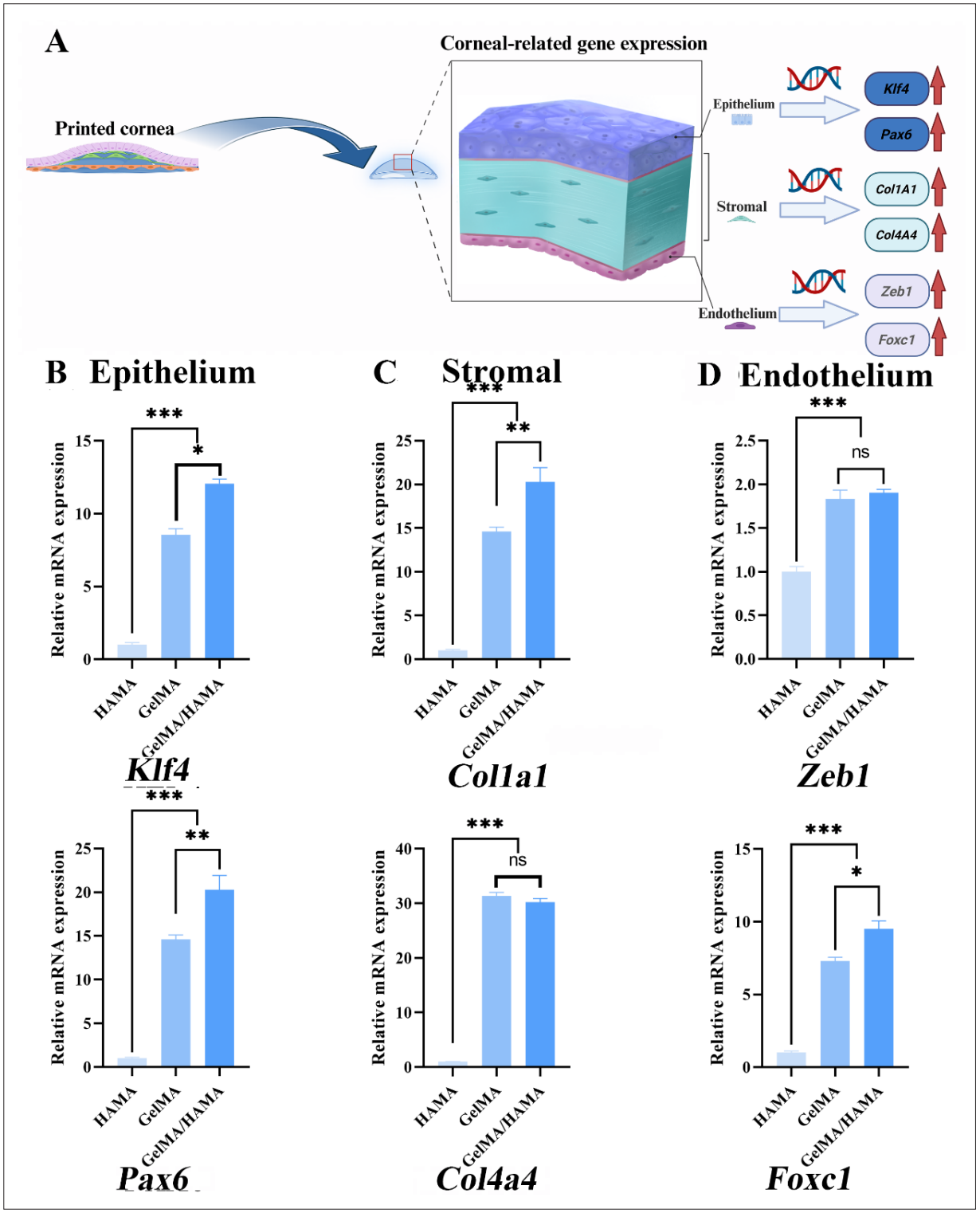


Figure 6. Layer-specific expression of corneal lineage markers in a 3D bioengineered cornea. (A) Schematic of postculture sampling and qPCR workflow for the printed construct. (B,D) Relative mRNA expression of (B) epithelial identity genes (*Klf4*, *Pax6*), (C) stromal extracellular matrix genes (*Col1a1*, *Col4a4*), and (D) endothelial-associated markers (*Zeb1*, *Foxc1*) on hyaluronic acid methacryloyl (HAMA), gelatin methacryloyl (GelMA), and GelMA/HAMA hydrogels. Data are shown as mean ± standard deviation (SD) from $n = 3$ biological replicates. Group differences were assessed by one-way analysis of variance with Tukey's honestly significant difference post hoc test. The p-values were adjusted for multiple testing using the false discovery rate. Notes: ns, not significant; *$p < 0.05$; **$p < 0.01$; ***$p < 0.001$.

3.6. Gene expression analysis in the 3D-bioprinted biomimetic cornea

To evaluate the phenotypic development of cells within the bioprinted construct, real-time qPCR was performed on distinct cell layers after 72 h of culture (Figure 6A). Gene expression levels were normalized to the housekeeping gene *Actb* (β-actin). In the epithelial layer, we observed pronounced upregulation of *Klf4*, which is a barrier-maintenance factor that preserves epithelial homeostasis and restrains epithelial–mesenchymal transition, and *Pax6*, the master regulator of ocular-surface lineage commitment (Figure 6B). Both genes were maximally expressed on the GelMA/HAMA composite (GelMA/HAMA > GelMA >> HAMA), indicating that the hybrid matrix most effectively promotes epithelial differentiation and barrier maturation. Within the stromal compartment, *Col1a1* (fibrillar collagen I) and *Col4a4* (basement membrane–associated collagen IV) were robustly expressed (Figure 6C), following the pattern GelMA/HAMA ≥ GelMA >> HAMA, consistent with active extracellular-matrix production and coordinated collagen I/IV assembly that underpins optical clarity and mechanical cohesion.

In the endothelial layer, transcriptional regulators *Zeb1* and *Foxc1*, which are associated with endothelial identity and junctional organization, were both upregulated compared to the HAMA control (Figure 6D), providing evidence of phenotypic orientation toward an endothelial-like state rather than demonstrating fully mature, functionally equivalent human corneal endothelium. Specifically, *Foxc1* expression was significantly higher in the GelMA/HAMA group than in the GelMA group, while *Zeb1* levels showed no significant difference between these two conditions. These findings indicate that the composite hydrogel promotes an endothelial-like, junction-forming phenotype. Broader temporal qPCR analysis over 3, 7, and 14 days (Figure S5) further indicated that the GelMA/HAMA environment consistently suppressed markers of myofibroblast transition (*Acta2* [α-smooth muscle actin], *Tagln* [transgelin], and *Myl9*) relative to single-component controls, while maintaining or enhancing expression of genes associated with transport and barrier formation (*Aqp1*, *Atp1a1* [Na^+/K^+-ATPase α1], and *Slc4a4* [sodium bicarbonate cotransporter 1]). Furthermore, elevated expression of *Col1a1*, *Mmp2*, and the chemokine receptor *Cxcr4* was observed, suggesting the establishment of a microenvironment conducive to controlled extracellular matrix remodeling and cellular migration. Overall, these results demonstrate that our 3D-bioprinted corneal construct recapitulates key molecular features of the native cornea within 72 h and sustains a pro-regenerative microenvironment over time. This microenvironment coordinately supports epithelial and stromal gene expression programs, promotes an endothelial-like transcriptional profile, and attenuates pathways linked to fibrosis.

4. Discussion

This study presents a proof-of-concept for fabricating a biomimetic corneal scaffold using embedded microextrusion 3D bioprinting of a GelMA/HAMA composite hydrogel. The scaffold partially replicates key structural features of the native cornea, exhibiting moderate yet promising optical transparency in the visible spectrum, experimentally assessed mechanical robustness suitable for *in vitro* handling and suturing, and excellent *in vitro* biocompatibility. The hybrid GelMA/HAMA network established through photopolymerization offers an improved balance among printability, transparency, and support for corneal cell growth compared to reports on single-component hydrogels.[28-30] The tailored rheological properties of the bioink, featuring shear-thinning at 37°C and a reversible sol–gel transition near 27°C, enable high-fidelity printing and cell viability during the "extrude–stabilize–cure" sequence. Subsequent photocrosslinking (405 nm) yields a covalently crosslinked network with a plateau modulus of ~4.5 kPa, which provides sufficient structural integrity for multilayer fabrication while remaining compliant enough to preserve curvature and withstand basic surgical manipulation *in vitro*.

We employed a sequential "epithelial printing–matrix printing–endothelial seeding" strategy to assemble a trilaminar, cell-populated structure. Biologically, the 3D-printed hydrogel matrix supported high cell viability and promoted the expression of molecular characteristics of corneal lineages. Layer-specific qPCR analysis confirmed phenotype-specific maturation across all layers. In the epithelial compartment, coordinated upregulation of *Klf4* and *Pax6* promoted stratified differentiation and cornea-specific keratin expression, consistent with barrier-associated differentiation and a smoother epithelial coverage. Within the stroma, elevated expression of *Col1a1* and *Col4a4* indicates active extracellular matrix synthesis. In the endothelial layer, upregulation of *Zeb1* and *Foxc1*, along with sustained expression of transporters, such as *Aqp1* and *Atp1a1*, suggests the development of an endothelial-like, junction-associated transcriptional profile under these culture conditions.

Taken together, this work establishes an early-stage proof-of-concept for a trilayered GelMA/HAMA-based corneal construct. We have demonstrated controlled structural organization, cytocompatibility with the three principal corneal lineages, and preliminary phenotypic and transcriptional markers indicative of epithelial-, stromal-,

and endothelial-like identities. However, functional performance remains incompletely characterized, and our current evidence is restricted to short-term *in vitro* assays without direct validation of barrier or pump function, or long-term behavior under physiologically relevant ocular surface conditions. Future work should therefore systematically evaluate the material's long-term optical stability in tear film environments, including its behavior under dynamic conditions, such as hydration cycling, protein/lipid adsorption, blink-induced shear stress, and surface wetting energetics. In parallel, establishing a comprehensive immunocompatibility profile will be essential to control potential postimplantation neovascularization and fibrosis, while ensuring durable biocompatibility with both corneal epithelial and endothelial tissues. Finally, 6- to 12-month rabbit corneal injury models can be employed to comprehensively assess postimplantation outcomes, including immune rejection, tissue regeneration capacity, reinnervation efficiency, and tear film dynamics (assessed through tear break-up time, interferometry, and contact angle hysteresis), with benchmarking against current state-of-the-art corneal substitutes. These systematic investigations will be required before this engineered platform can be credibly considered as a candidate to help address the clinical challenges of donor shortage and graft rejection.

5. Conclusion

In summary, this study demonstrates the feasibility of fabricating a trilaminar, cell-laden corneal construct using embedded microextrusion 3D bioprinting with a GelMA/HAMA composite hydrogel. The engineered scaffold recapitulates key structural features of the native cornea and exhibits promising *in vitro* properties, including moderate optical transparency (30–80% across the visible spectrum), a wettability profile suitable for epithelial attachment (contact angle ~50°), minimal swelling (<10%), and controlled degradation kinetics. The scaffold exhibited mechanical robustness sufficient for basic experimental handling, with a burst pressure (~11.4 kPa) exceeding typical physiological intraocular pressure, indicating short-term *in vitro* stability rather than clinical readiness. Furthermore, the printed GelMA/HAMA scaffold supported robust cellular proliferation of corneal epithelial, stromal, and endothelial cells. Gene expression analysis confirmed the phenotypic orientation of these cells toward their respective lineages, evidenced by the upregulation of *Klf4* and *Pax6* in the epithelium, *Col1a1* and *Col4a4* in the stroma, and *Zeb1* and *Foxc1* in the endothelium. Collectively, these results establish this bioprinted, trilayered construct as a solid proof-of-concept model for corneal tissue engineering. This work provides a foundational platform for further *in vitro* studies and sets the stage for subsequent investigations into long-term functional performance.

Acknowledgments

We thank the Core Facilities, Health Science Center of Ningbo University, for their technical support.

Funding

This research was supported by the Science and Technology Innovation 2035 Major Project of Ningbo (No. 2024Z212), the Ningbo Natural Science Foundation (No. 2022J121), Zhejiang Provincial Disease Prevention and Control Science and Technology Program (Grant No. 2025JK276) and the Key Laboratory of Polymeric Composite & Functional Materials of the Ministry of Education (No. PCFM-2025A02).

Conflict of interest

The authors declare that they have no known competing financial interests or personal relationships that could have influenced the work reported in this paper.

Author contributions

Conceptualization: Yang Luo, Hua Zhang, Tong Zhu
Formal analysis: Tong Zhu, Cuicui Su, Lu Yang
Investigation: Tong Zhu, Shengkai Yu, Jingyu Shi
Methodology: Tong Zhu, Renhao Ni, Haowen Sun, Xu Cao, Shang Chen
Writing–original draft: Tong Zhu, Renhao Ni
Writing–review & editing: Hua Zhang, Yang Luo, Lu Yang

Ethics approval and consent to participate

Not applicable.

Consent for publication

Not applicable.

Availability of data

The datasets generated and/or analyzed during the current study are not publicly available due to ongoing studies, but are available from the corresponding author upon reasonable request.

References

1. Meek KM, Knupp C, Lewis PN, Morgan SR, Hayes S. Structural control of corneal transparency, refractive power and dynamics. *Eye*. 2025;39(4):644-650. doi: 10.1038/s41433-024-02969-7.

2. Brown L, Leck AK, Gichangi M, Burton MJ, Denning DW. The global incidence and diagnosis of fungal keratitis. *Lancet Infect Dis.* 2021:21(3):e49-e57. doi: 10.1016/s1473-3099(20)30448-5.

3. Gain P, Jullienne R, He Z, *et al*. Global survey of corneal transplantation and eye banking. *JAMA Ophthalmol.* 2016:134(2):167-173. doi: 10.1001/jamaophthalmol.2015.4776.

4. Deogaonkar K, Roy A. Donor related corneal graft infection: a review of literature and preventive strategies. *Semin Ophthalmol.* 2023:38(3):219-225. doi: 10.1080/08820538.2022.2095873.

5. Weiss JS, Rapuano CJ, Seitz B, *et al*. IC3D classification of corneal dystrophies-Edition 3. *Cornea.* 2024:43(4): 466-527. doi: 10.1097/ico.0000000000003420.

6. Rafat M, Jabbarvand M, Sharma N, *et al*. Bioengineered corneal tissue for minimally invasive vision restoration in advanced keratoconus in two clinical cohorts. *Nat Biotechnol.* 2023;41(1):70-81. doi: 10.1038/s41587-022-01408-w.

7. Li Y, Wang Z. Biomaterials for corneal regeneration. *Adv Sci.* 2025;12(6):e2408021. doi: 10.1002/advs.202408021.

8. Maher C, Chen Z, Zhou Y, *et al*. Innervation in corneal bioengineering. *Acta Biomater.* 2024;189:73-87. doi: 10.1016/j.actbio.2024.10.009.

9. Camburu G, Zemba M, Tătaru CP, Purcărea VL. The measurement of central corneal thickness. *Rom J Ophthalmol.* 2023;67(2):168-174. doi: 10.22336/rjo.2023.29.

10. Vijayaraghavan R, Loganathan S, Valapa RB. 3D bioprinted photo crosslinkable GelMA/methylcellulose hydrogel mimicking native corneal model with enhanced in vitro cytocompatibility and sustained keratocyte phenotype for stromal regeneration. *Int J Biol Macromol.* 2024;264(Pt 1):130472. doi: 10.1016/j.ijbiomac.2024.130472.

11. Cai Y, Tan Y, Cao J, *et al*. Dual-crosslinked betaine-based amphiphilic hydrogel as a promising vitreous substitute: anti-adhesion, anti-fouling, and anti-cell proliferation. *Adv Sci.* 2025;12(36):e13455. doi: 10.1002/advs.202413455.

12. Kim JJ, Bae M, Kim J, *et al*. Development of a 3D cell-printed RVO model by advancing a retina-on-a-chip with hybrid retinal dECM bioink and an integrated 3D bioprinting system. *Adv Compos Hybrid Mater* 2025; 8(5):364. doi: 10.1007/s42114-025-01455-2.

13. Chand R, Janarthanan G, Elkhoury K, Vijayavenkataraman S. Digital light processing 3D bioprinting of biomimetic corneal stroma equivalent using gelatin methacryloyl and oxidized carboxymethylcellulose interpenetrating network hydrogel. *Biofabrication*. 2025;17(2). doi: 10.1088/1758-5090/adab27.

14. Xu Y, Liu J, Song W, *et al*. Biomimetic convex implant for xorneal regeneration through 3D printing. *Adv Sci.* 2023;10(11):e2205878. doi: 10.1002/advs.202205878.

15. Goodarzi Hosseinabadi H, Dogan E, Miri AK, Ionov L. Digital Light processing bioprinting advances for microtissue models. *ACS Biomater Sci Eng.* 2022;8(4):1381-1395. doi: 10.1021/acsbiomaterials.1c01509.

16. Chen A, Wang W, Mao Z, *et al*. Multimaterial 3D and 4D bioprinting of heterogenous constructs for tissue engineering. *Adv Mater.* 2024;36(34):e2307686. doi: 10.1002/adma.202307686.

17. Grönroos P, Mörö A, Puistola P, *et al*. Bioprinting of human pluripotent stem cell derived corneal endothelial cells with hydrazone crosslinked hyaluronic acid bioink. *Stem Cell Res Ther.* 2024;15(1):81. doi: 10.1186/s13287-024-03672-w.

18. Ouyang L, Yao R, Mao S, *et al*. Three-dimensional bioprinting of embryonic stem cells directs highly uniform embryoid body formation. *Biofabrication*. 2015; 7(4):044101. doi: 10.1088/1758-5090/7/4/044101.

19. Shi B, Zhu T, Luo Y, *et al*. Three-dimensional bioprinted cell-adaptive hydrogel with anisotropic micropores for enhancing skin wound healing. *Int J Biol Macromol.* 2024;280(Pt 4):136106. doi: 10.1016/j.ijbiomac.2024.136106.

20. Guo K, Li G, Yu Q, *et al*. Injectable hyaluronate-based hydrogel with a dynamic/covalent dual-crosslinked architecture for bone tissue engineering: enhancing osteogenesis and immune regulation. *Int J Biol Macromol.* 2024;282(Pt 5):137249. doi: 10.1016/j.ijbiomac.2024.137249.

21. Asim S, Tuftee C, Qureshi AT, *et al*. Multi-functional gelatin-dithiolane hydrogels for tissue engineering. *Adv Funct Mater.* 2025;35(3):2407522. doi: 10.1002/adfm.202407522.

22. Puistola P, Miettinen S, Skottman H, Mörö A. Novel strategy for multi-material 3D bioprinting of human stem cell based corneal stroma with heterogenous design. *Mater Today Bio.* 2024;24:100924. doi: 10.1016/j.mtbio.2023.100924.

23. Ahn M, Park GT, Shukla AK, *et al*. 3D Bioprinting-assisted engineering of stem cell-laden hybrid biopatches with distinct geometric patterns considering the mechanical characteristics of regular and irregular connective tissues. *Adv Healthc Mater.* 2025;14(25):e2502763. doi: 10.1002/adhm.202502763.

24. Xu R, Zhang H, Luo Y, *et al*. Magnetically bioprinted anisotropic hydrogels promote BMSC osteogenic differentiation for bone defect repair. *Mater. Today Bio.* 2025;32:101885.
doi: 10.1016/j.mtbio.2025.101885.

25. Sang S, Yan Y, Shen Z, *et al*. Photo-crosslinked hydrogels for tissue engineering of corneal epithelium. *Exp Eye Res.* 2022;218:109027.
doi: 10.1016/j.exer.2022.109027.

26. Zhang H, Luo Y, Hu Z, *et al*. Cation-crosslinkedκ-carrageenan sub-microgel medium for high-quality embedded bioprinting. *Biofabrication*. 2024;16(2).
doi: 10.1088/1758-5090/ad1cf3.

27. Zhang H, Luo Y, Li G, *et al*. Micelle-facilitated gelation kinetics and viscoelasticity of dynamic hyaluronan hydrogels for bioprinting of mimetic constructs and tissue repair. *Composites, Part B: Eng.* 2025;294:112151.
doi: 10.1016/j.compositesb.2025.112151.

28. Larrañeta E, Henry M, Irwin NJ, *et al*. Synthesis and characterization of hyaluronic acid hydrogels crosslinked using a solvent-free process for potential biomedical applications. *Carbohydr Polym.* 2018;181:1194-1205.
doi: 10.1016/j.carbpol.2017.12.015.

29. Velasco-Rodriguez B, Diaz-Vidal T, Rosales-Rivera LC, *et al*. Hybrid methacrylated gelatin and hyaluronic acid hydrogel scaffolds. preparation and systematic characterization for prospective tissue engineering applications. *Int J Mol Sci.* 2021;22(13).
doi: 10.3390/ijms22136758.

30. Zhou M, Yue K, Zhao J, *et al*. Optimizing GBM organoid construction with hydrogel-based models: GelMA-HAMA scaffold supports GBM organoids with clonal growth for drug screening. *Cell Transplant.* 2025;34:9636897251347537.
doi: 10.1177/09636897251347537.

ACCSCIENCE PUBLISHING

International Journal of Bioprinting

RESEARCH ARTICLE

Three-dimensional-printed hydroxyapatite/zirconium dioxide composite scaffold incorporating bone morphogenetic protein-2 for lumbar vertebral bone defect repair in rhesus macaques

Rui Qiu[1], Hua-Teng Zhou[2], Ren-Fu Quan[2]*, Can-Da Xu[2], Tuo Wang[2], Wei-Bin Du[2], Huan-Huan Gao[2], Xiao-Long Huang[2], Cai-Yin Xu[3], Long-Bao Lv[3], Xi-Cheng Wei[4], and Jin-Fu Wang[5]

[1] Department of Orthopedic Surgery, Huang Jia Si Hospital of Yushan County (Yushan People's Hospital), Shangrao, Jiangxi, China

[2] Department of Orthopedics, Affiliated Jiangnan Hospital of Zhejiang Chinese Medical University, Hangzhou, Zhejiang, China

[3] Kunming Institute of Zoology, Chinese Academy of Sciences, Kunming, Yunnan, China

[4] Department of Polymer Materials, School of Materials Science and Engineering, Shanghai University, Shanghai, China

[5] Institute of Cell and Development, College of Life Sciences, Zhejiang University, Hangzhou, Zhejiang, China

***Corresponding author:**
Ren-Fu Quan
(quanrenfu@126.com)

Citation: Qiu R, Zhou HT, Quan RF, *et al.* Three-dimensional-printed hydroxyapatite/zirconium dioxide composite scaffold incorporating bone morphogenetic protein-2 for lumbar vertebral bone defect repair in rhesus macaques. *Int J Bioprint*. 2026;12(1):467-484. doi: 10.36922/IJB025390400

Received: September 26, 2025
Revised: November 30, 2025
Accepted: December 9, 2025
Published online: December 18, 2025

Copyright: © 2025 Author(s). This is an Open Access article distributed under the terms of the Creative Commons Attribution License, permitting distribution, and reproduction in any medium, provided the original work is properly cited.

Publisher's Note: AccScience Publishing remains neutral with regard to jurisdictional claims in published maps and institutional affiliations.

Abstract

Bone defects caused by various factors have become a persistent challenge in orthopedic clinics, and traditional treatment methods mainly involve the use of artificial bone or autologous bone transplantation. However, these methods have considerable limitations, such as donor site bone loss, immune rejection, and the risk of secondary infection at the donor site. Therefore, considering these limitations and the rapid development of the field of bone tissue engineering, this study adopted light-curing stereolithography three-dimensional (3D) printing technology to design bone scaffold materials. The technology was used to prepare hydroxyapatite (HA)/zirconium dioxide (ZrO_2) porous composites with satisfactory mechanical properties as tissue-engineering bone scaffolds. A bone morphogenetic protein-2-loaded gelatin/chitosan hydrogel sustained-release system was prepared via an emulsification and cross-linking process. Subsequently, rhesus macaque bone marrow mesenchymal stem cells, acting as osteogenic progenitors, were seeded into the system. Novel HA/ZrO2 scaffolds were fabricated using stereolithography 3D printing technology to serve as bone graft substitutes. The resulting scaffold exhibited a 3D interconnected porous structure and showed good biocompatibility and osteoinductive ability in a rhesus macaque lumbar vertebral bone defect model. The results confirmed that the scaffold achieved osteogenic efficiency comparable to that of autologous bone grafting in rhesus macaques. Therefore, the developed scaffold material has promising potential in bone defect repair.

Keywords: Hydroxyapatite; Nanomaterials; Three-dimensional printing; Tissue-engineered bone; Vertebral defect; Zirconium dioxide

1. Introduction

As an important branch of regenerative medicine, bone tissue engineering aims to construct functional bone tissue by combining biomaterials, cells, and growth factors to repair large-scale bone defects and to overcome the limitations of traditional transplantation techniques. Remarkable progress has been made in this field in terms of osteogenic mechanisms, material innovation, and clinical translation.[1,2] The application of three-dimensional (3D) printing technology in bone tissue engineering has also shown considerable potential and diverse advancements. By precisely manipulating the macroscopic and microscopic structures of the scaffold, this technology can be used to fabricate a bone defect repair scaffold with biomimetic pore size, porosity, and connectivity similar to that of natural bone, which can effectively promote cell adhesion, proliferation, and new bone generation.[3,4] Various biomaterials have been widely researched and developed as bone substitutes.

In the present study, a hydroxyapatite (HA)/zirconium dioxide (ZrO_2) composite scaffold material with a favorable surface morphology and a unique 3D interconnected porous structure was prepared using light-curing stereolithography (SLA) 3D-printing technology. The hydroxyapatite component is similar to natural apatite mineral and is the main inorganic component of vertebrate bone and teeth. After implantation, it partially degrades, releasing calcium and phosphorus ions that are reabsorbed and utilized by the body, thereby promoting effective integration with the host bone.[5] The ZrO_2 component improves the mechanical strength of the material and provides resistance to biodegradation, thereby conferring long-term biostability. The inclusion of ZrO_2 substantially improves the fracture toughness of the material and establishes a strong biological connection at the bone interface.[6] Bone morphogenetic protein 2 (BMP-2) is one of the most potent known osteogenic inducers and directly induces osteoblast (OB) differentiation and bone formation. Moreover, BMP-2 upregulates the expression of vascular endothelial growth factor (VEGF) in a concentration- and time-dependent manner during the induction of osteogenic precursor cell differentiation, thereby promoting vascularization and angiogenesis.[7] VEGF not only enhances the recruitment and survival of mesenchymal stem cells by promoting the formation of vascular networks but also enhances the osteogenic response of mesenchymal stem cells to BMP-2, thus forming a positive osteogenesis–angiogenesis feedback loop.[8,9] However, endogenous BMP-2 has shortcomings, such as a short half-life and low biological concentration. Moreover, the sustainable release of exogenous BMP-2 to maintain effective local concentrations and ensure its biological potency during initial repair is difficult to achieve. Accordingly, a BMP-2 gelatin/chitosan hydrogel sustained-release system was prepared via re-emulsification cross-linking, and effective bone defect repair was facilitated by its slow and continuous release.[10] Bone marrow mesenchymal stem cells (BMSCs) can be cultured, isolated, and expanded *in vitro* and have the potential for multidirectional differentiation. Additionally, BMSCs can transform into OBs under induction conditions. Consequently, BMSCs are considered to be ideal seed cells for tissue engineering and regenerative medicine owing to their wide range of sources, easy availability, strong multidirectional differentiation potential, low immunogenicity, and strong tissue repair ability.[11,12] Therefore, this study aimed to develop HA/ZrO_2 composites with satisfactory mechanical properties using SLA 3D-printing technology. The porosity and pore diameter of the materials were designed to overcome the abovementioned shortcomings. BMSCs were used as seed cells, and BMP-2 was used as an osteogenic inducer. The BMP-2 gelatin/chitosan hydrogel sustained-release system was prepared using the complex emulsion cross-linking method. After *in vitro* culture, the system was implanted into a 3D-printed gradient composite HA/ZrO_2 scaffold material to construct novel tissue-engineered bone. The engineered bone was then implanted into a rhesus macaque lumbar vertebral bone defect model. 16 weeks postoperatively, the osteogenic effect of the tissue-engineered bone in rhesus macaques was assessed by observing postoperative X-ray and microcomputed tomography (CT) images, performing hard-tissue sectioning and histological observation, and detecting the expression of osteogenic-related proteins (OGPs).

2. Materials and methods

2.1. Experimental animals and grouping

The experimental animals comprised 26 healthy rhesus macaque monkeys (14 male and 12 female, aged 4–6 years), each with a body weight of 6–10 kg (obtained from Kunming Animal Research Institute of the Chinese Academy of Sciences; Production License Number: SCXK(Dian)K2013-0005, Use License Number: SYXK(Dian)K2013-0012). The breeding operations were strictly carried out in accordance with the Breeding Requirements for Experimental Animals of the Kunming Animal Research Institute, Chinese Academy of Sciences. During the experiment, the 3R principles were followed to provide humane care and treatment of animals according to the Guiding Opinions on the Humane Treatment of Experimental Animals.

The 26 rhesus macaque monkeys were randomly assigned to four groups: tissue-engineered bone group A

(n = 10), which received the new gradient composite HA/ZrO_2 scaffold prepared via 3D printing, loaded with the BMP-2 gelatin/chitosan hydrogel sustained-release system and third-passage BMSCs2 (Rhesus monkeys (Macaca mulatta); blank material group B (n = 10), which received the blank gradient composite HA/ZrO_2 nanoscaffold; group C, the autologous iliac bone group (n = 4); and group D, the lumbar vertebral defect model group (n = 2).

2.2. Creation of lumbar vertebral defect model

Two rhesus macaque monkeys were selected to establish the lumbar vertebral defect model (n = 2). Anesthesia was induced via intramuscular injection of ketamine hydrochloride (Fujian Gutian Pharmaceutical Co., Ltd., Fujian, China (Batch No. 20161106). at a dose of 10 mg/kg, followed by intravenous anesthesia with pentobarbital sodium (Beijing Chemical Reagent Co., Ltd., Beijing, China (Batch No. 20160922) at a dose of 30 mg/kg. The rhesus macaque monkeys were secured in a right lateral recumbent position on the operating table, shaved, cleaned, and disinfected, and the surgical area was draped. An anterolateral approach was applied to the lumbar spine, and an oblique incision along the edge of the external oblique muscle from the lower end of the 12th rib downward to the midpoint of the pubic symphysis and navel was made, measuring 8–12 cm on the right side. The skin, subcutaneous tissue, and deep fascia were sequentially incised layer by layer. Hemostasis was achieved, and the lateral abdominal tendon was exposed and bluntly separated along the muscle fibers. The internal oblique muscle was incised, and the retroperitoneal space was bluntly dissected to expose the surgical segment (L4 or L5) of the vertebral body. The L4 vertebral body and the adjacent upper and lower vertebrae were exposed, and the accompanying lumbar arteries and veins were ligated. Thereafter, using the transverse process as a boundary, the anterior two-thirds of the vertebral body parallel to the coronal plane were completely chiseled off, and the upper and lower intervertebral discs and the cartilage endplates on both sides were scraped off to create a vertebral body defect model (Figure 1A–1B).

2.3. Fabrication of scaffolds, hydrogel system, and tissue-engineered bone

2.3.1. Photopolymerization 3D printing of ZrO_2 ceramics

The lumbar vertebral defect model was then scanned with micro-CT (SKYSCAN, Bruker Corporation, Belgium) to obtain plain images along with two-dimensional (2D) and 3D reconstruction images. The data were copied, and the resulting output was in DICOM format. The porosity of the composite scaffold material was set to 25 pores per inch, and the obtained STL format file was further processed. Finally, a hollow semicylindrical body with uniform pores and a pore diameter of approximately 500 μm that penetrated the inner and outer wall was obtained and exported in STL format. The obtained STL file was further

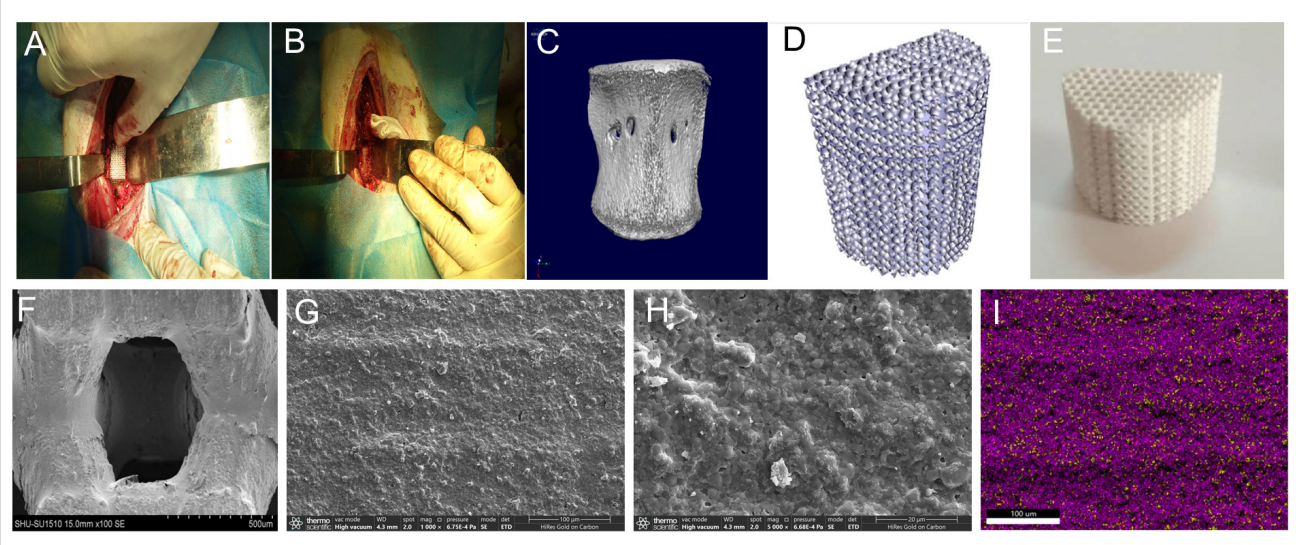


Figure 1. Preparation of tissue-engineered bone. (A,B) Establishment of the lumbar vertebral defect model and implantation of the tissue-engineered bone in animal experiments. (C) Placement of the excised L4 vertebral defect models into a microcomputed tomography system for plain scan imaging and 2D and 3D reconstructions. (D) 3D structure of the material formed after postprocessing the data. (E) HA/ZrO_2 gradient composite material prepared by photocuring and subsequent defatting and sintering. (F–H) Scanning electron microscope images of the HA/ZrO_2 gradient composite material. Scale bars: (F) 500 μm, (G) 100 μm, (H) 20 μm; magnifications: (F) 100×, (G) 1,000×, (H) 1,000×. (I) Elemental scanning analysis of hydroxyapatite/zirconia gradient composite materials.

processed and imported into a CeraFab 7500 photopolymer 3D printer. The planar resolution was set to 40 μm (635 dpi), pixel (X,Y) 1920 × 1080, stage size (X,Y,Z) 76 mm × 43 mm × 150 mm, layer thickness 25 μm, exposure time 1 s, and the initial printing layer thickness parameter was set to 10 μm. Nanograde ZrO_2 slurry was prepared, and photosensitive resin was added to achieve a ZrO_2-to-resin mass ratio of 15%, which was then poured into the material tank. The printing program was started according to the set parameters. The integrated UV-LED light source of the CeraFab 7500 (Lithoz GmbH, Vienna, Austria) induced a polymerization reaction in the resin, and the material solidified layer by layer to form a composite photosensitive resin preform. After the preform was formed, it underwent further debinding and sintering treatment, which was carried out simultaneously. The specific steps were as follows:

(i) Drying and evaporation stage: The temperature was increased from 25 to 75°C over 4 h, the heating rate was 0.208 K/min, and the holding time was 6 h to allow the excess water to evaporate. The temperature was then raised to 500°C with specific heating rates and holding times adjusted for each stage.

(ii) Degreasing and high-temperature sintering stage: From 500 to 1,250°C, the heating time was controlled at 7.5 h, the rate was 1.677 K/min, and no holding was required after the temperature reached 1,250°C. The temperature continued to rise to 1,450°C, with the heating rate set at 3.333 K/min, taking 1 h and holding for 2 h.

(iii) Cooling stage: After reaching the highest sintering temperature of 1,450°C, it was held for 2 h and then cooled at −0.660 K/min for 36 h to 25°C. The entire degreasing and sintering process lasted 120.5 h (Figure 1C–1E).

2.3.2. Preparation of HA/ZrO_2 gradient composite scaffolds (dip-coating method)

The HA/ZrO_2 gradient composite material was prepared via a dip-coating method. The slurry for the first layer consisted of 31.1% nanosized ZrO_2 powder (prepared by the School of Materials Science and Engineering, Shanghai University, Shanghai, China), 13.3% nanosized HA powder (prepared by the School of Materials Science and Engineering, Shanghai University, Shanghai, China), 53% double-distilled water, 1.4% ethyl phosphate (prepared by the School of Materials Science and Engineering, Shanghai University, Shanghai, China), and 0.2% ethyl cellulose (prepared by the School of Materials Science and Engineering, Shanghai University, Shanghai, China). HA was heated to 800°C and held for 2 h. The double-distilled water was heated to 50°C, and the above materials were mixed and added to the double-distilled water, stirring thoroughly. The photocured pure ZrO_2 ceramic was immersed in the slurry to ensure full penetration, then removed, and the excess slurry was discarded. It was dried in a 100°C electric furnace for 2 h, then heated to 900°C and held for 5 h, and finally heated to 1,250°C and held for 1 h. The second-layer slurry composition was 3.9% nanosized ZrO_2 powder, 35.5% nanosized HA powder, and 58% double-distilled water. The ratio of ethyl phosphate to ethyl cellulose remained unchanged. The above steps were repeated. After cooling, the HA/ZrO2 gradient composite material was obtained. The 3D-printed HA/ZrO_2 gradient composite scaffold material was placed on the sample stage and fixed with conductive adhesive. Thereafter, the 3D surface structure was observed, and elemental scans were performed using a scanning electron microscope (SU-1510, Hitachi, Tokyo, Japan) (Figure 1F–1I).

2.3.3. Preparation of gelatin microspheres and chitosan hydrogel system

One gram of gelatin powder (Shanghai Zhuojing Electronic Technology Co., Ltd., Shanghai, China) was weighed using an electronic balance (Sigma-Aldrich, St. Louis, MO) and dissolved in 10 mL of 50°C deionized water. Under magnetic stirring (500 rpm), the dissolved gelatin solution was added dropwise to 60 mL of preheated 50°C olive oil (Shanghai Nuochen Biotechnology Co., Ltd., Shanghai, China) under magnetic stirring (500 rpm; Shanghai Boxun Medical Biological Instrument Corp., Shanghai, China). Stirring was maintained to form a stable emulsion, and subsequently continued until the mixture gradually cooled to 4°C to form solid microspheres. The microspheres were rinsed three times each with acetone (Sinopharm Chemical Reagent Co., Ltd., Shanghai, China) and ethanol (Sinopharm Chemical Reagent Co., Ltd., Shanghai, China) at 4°C. Finally, the resulting microspheres were freeze-dried. An appropriate amount of ethanol solution containing 50 mM glyoxal (Sinopharm Chemical Reagent Co., Ltd., Shanghai, China) was taken, and the prepared gelatin microspheres were placed into the ethanol solution. The mixture was stirred at 25°C for 10 h and allowed to stand until the microspheres precipitated. The supernatant was discarded, and the microspheres were washed twice with ethanol, filtered, and freeze-dried.

To prepare the gelatin microsphere-encapsulated chitosan hydrogel, chitosan powder (Sigma-Aldrich, St. Louis, MO) was dissolved in aqueous acetic acid (Sinopharm Chemical Reagent Co., Ltd., Shanghai, China) to obtain a 1.5% (w/v) solution under sterile conditions. Separately, sodium β-glycerophosphate (Sinopharm Chemical Reagent Co., Ltd., Shanghai, China) was

dissolved in deionized water to obtain a 50% (w/v) solution, which was filtered and stored at 4°C. The dissolved BMP-2 (Sigma-Aldrich, St. Louis, MO) and the prepared gelatin microspheres were added to 50 mL of 1.5% (w/v) chitosan solution. The pH was adjusted to 6.3 using precision pH paper. A 50% (w/v) sodium β-glycerophosphate solution was added dropwise to the chitosan solution under magnetic stirring until the final solution contained 88 mM sodium β-glycerophosphate and had a pH of approximately 7.2. The resulting hydrogel was incubated at 37°C for 3 h. The specimen was then removed and fixed to a sample holder with cryo-glue (Sigma-Aldrich, St. Louis, MO). Scanning electron microscopy (SEM; SU-1510, Hitachi, Tokyo, Japan) was performed on the gelatin/chitosan microspheres and the gelatin/chitosan microsphere-encapsulated BMP-2 hydrogel to observe their surface morphology and internal structure (Figure 2A–2C).

2.3.4. Encapsulation efficiency, drug loading, and in vitro sustained-release evaluation

The amount of residual BMP-2 in the supernatant was detected using an enzyme-linked immunosorbent assay (ELISA) kit (Abcam, Cambridge, MA (Catalog No. ab11985) to infer the drug loading and encapsulation efficiency of the chitosan-encapsulated gelatin microsphere BMP-2 hydrogel. The absorbance (optical density [OD]) at A450 and calibrated A570 wavelengths was measured using a spectrophotometer (Beijing Persee General Instrument Co., Ltd., Beijing, China) according to the ELISA kit instructions. The BMP-2 concentration in the sample was calculated using the standard equation of the standard curve, thus determining the BMP-2 content in the washing supernatant and the sample. The relevant curves were plotted according to the relationship between BMP-2 concentration and OD values over time.

Three test tubes (5 mL each) were prepared, and 150 mg of BMP-2 gelatin/chitosan hydrogel was added to each tube. 2 mL of PBS (pH 7.2) were added to each, and the tubes were incubated in a 37°C water bath with shaking. At different time points (6, 16 h, 1 d, 2, 3, 6, 9, 12, and 15 d), 100 μL of supernatant from each test tube was taken, and BMP-2 was measured using an ELISA detection kit, following the abovementioned procedures. The average was calculated, and based on ELISA measurements, the

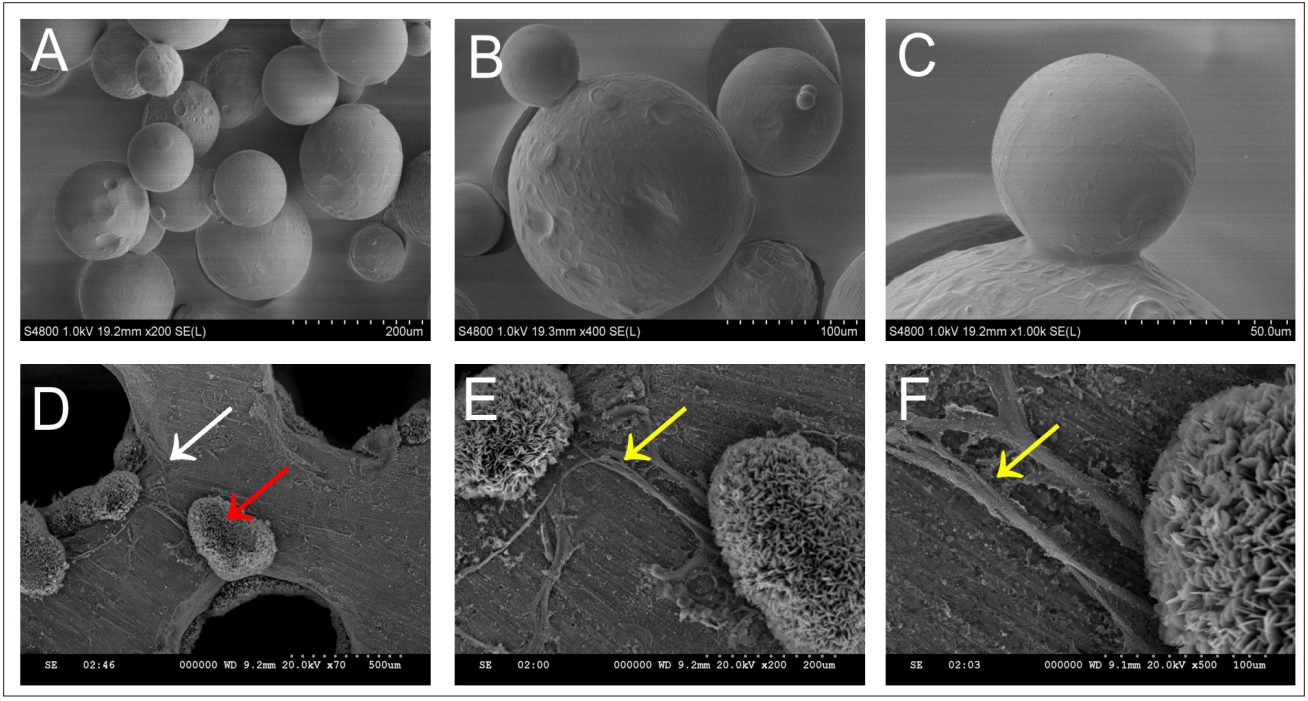


Figure 2. Morphological characterization of the gelatin/chitosan hydrogel system and the novel tissue-engineered bone. (A–C) Surface morphology of gelatin microspheres coated with chitosan hydrogel at different time points, observed by scanning electron microscope. Scale bars: (A) 200 μm, (B) 100 μm, (C) 50 μm; magnifications: (A) 200×, (B) 400×, (C) 1,000×. (D–F) Scanning electron microscopy images of the composite of HA/ZrO_2 gradient composite scaffold material, bone morphogenetic protein (BMP)-2 gelatin/chitosan sustained-release hydrogel system, and bone marrow mesenchymal stem cells (BMSCs). Scale bars: (D) 500 μm, (E) 200 μm, (F) 100 μm; magnifications: (D) 70×, (E) 200×, (F) 500×. The white arrow indicates the scaffold material, the yellow arrow indicates the BMSCs, and the red arrow indicates the BMP-2 gelatin/chitosan sustained-release hydrogel system. Both cells and hydrogel adhered to the nanoscaffold material, with favorable cell viability and morphology.

cumulative release curve of BMP-2 from the gelatin/chitosan hydrogel was plotted.

2.3.5. Construction of novel tissue-engineered bone

The prepared HA/ZrO_2 material was shaped into 5 mm × 5 mm × 5 mm cubic bodies. After high-temperature sterilization, the bodies were soaked overnight in a 0.01% (w/v) poly-L-lysine solution and then allowed to dry under aseptic conditions. The sterilized material was then placed in a culture dish and covered with culture medium. The prepared BMP-2 gelatin/chitosan hydrogel sustained-release system and third-passage BMSCs were made into a suspension and then slowly added dropwise to the cubic blocks of the composite scaffold material. The third-passage BMSCs were seeded on the material at a density of $5\times10^3/cm^2$. An induction solution (containing 100 nM dexamethasone, 50 mg/mL vitamin C, and 10 mM β-glycerophosphate) was added. The specimen was then cultured at 37°C for 48 h in a 5% CO_2 incubator. The culture medium and particles were washed away with PBS to obtain novel tissue-engineered bone. The specimen was removed, fixed to a sample holder with cryo-glue, and scanned by SEM to observe its surface morphology and internal structure (Figure 2D–2F).

2.3.6. Calculation of encapsulation efficiency and drug loading

The amount of remaining BMP-2 in the supernatant and the total amount of BMP-2 added were detected using ELISA. The drug loading and encapsulation efficiency of the gelatin/chitosan microsphere hydrogel encapsulating BMP-2 were then calculated using the following formulas:

(i) Drug loading efficiency calculation:

Drug loading efficiency = (Total amount of BMP-2 added - Amount of BMP-2 measured in the supernatant)/ Total mass of microspheres × 100% (1)

(ii) Encapsulation efficiency calculation:

Encapsulation efficiency = (Total amount of BMP-2 added - Amount of BMP-2 measured in the supernatant)/ Total amount of BMP-2 added × 100% (2)

2.4. Implantation procedures and postoperative animal management

All experimental animals were confirmed to have no lumbar deformities before surgery via X-ray. Following the established protocol, vertebral defect models were successfully created in 24 of the rhesus macaques. The tissue-engineered bone group (n = 10) was implanted with the new gradient composite HA/ZrO_2 tissue-engineered bone material prepared using 3D printing, which was loaded with the BMP-2 gelatin/chitosan hydrogel sustained-release system and passage 3 BMSCs. The blank material group (n = 10) was implanted with blank gradient composite HA/ZrO_2 nanoscaffold material, and the autologous iliac bone group (n = 4) was implanted with autologous iliac bone. During the surgery, X-ray positioning was used to confirm satisfactory implant placement, followed by fixation with a specially made contact steel plate of appropriate length (75 mm). The surgical site was thoroughly irrigated with saline, and after ensuring no instruments or gauze were left behind, the incision was closed layer by layer. Postoperatively, the experimental rhesus macaque monkeys were housed individually, with daily cleaning and disinfection of the wound, and were administered penicillin sodium (1.6 million U; (North China Pharmaceutical Co., Ltd., Shijiazhuang, China) intramuscularly once daily for 3 d to prevent infection.

2.5. Postoperative gross observation and X-ray imaging

The basic conditions of the rhesus macaque monkeys, such as activity and food intake, were checked daily. Any redness, swelling, discharge, abscess, infection, or ulceration at the surgical incision was recorded, and the walking activity of the lower limbs was noted.

At 8 and 16 weeks postoperatively, animals in each experimental group were anesthetized via intramuscular injection of ketamine hydrochloride (10 mg/kg). Anteroposterior and lateral radiographs of the lumbar spine were then taken using an X-ray device (HF100HA, Mikasa X-Ray, Japan) for each group to assess integration with the host bone and to observe whether the implanted biomaterials showed any fractures, degradation, or callus growth around the material. At 16 weeks, gross specimens were collected by euthanizing the animals via intramuscular injection of ketamine hydrochloride combined with bloodletting, followed by careful dissection to expose the experimental lumbar segments of the rhesus macaque monkeys. The fixation steel plates and screws were removed, and the surrounding soft tissues were rinsed and cleaned. The condition of the implanted biomaterials and the surrounding bone in the removed specimens was then evaluated.

2.6. Biomechanical testing and hard-tissue sectioning

Twelve animals (four per group) were euthanized with a ketamine and potassium chloride overdose at 16 weeks postsurgery to harvest bone samples. All residual musculature was carefully removed from the specimens to preserve all ligamentous structures. The specimens were trimmed, creating two parallel planes, and fixed on a testing machine (MTS 858, MiniBionix) along a plane that

was parallel to the long axis of the implants. Compression testing was performed at a speed of 20 mm/min, and the load was increased from zero until the specimens were destroyed. The maximal load, energy to maximal load, stiffness, and maximum compressive strength were then recorded.

After the bone tissue samples were collected, they were fixed with 10% neutral formalin (a volume 20 times that of the tissue; (Kunming Chemical Reagent Co., Ltd., Kunming, China) for 48 h, followed by tissue dehydration with a gradient of 70%, 80%, 85%, 90%, 95%, 100%, and 100% alcohol for 3 h each. Next, the samples were treated with xylene I (Sinopharm Chemical Reagent Co., Ltd., Shanghai, China) for 3 h, xylene II (Sinopharm Chemical Reagent Co., Ltd., Shanghai, China) for 3 h, methyl methacrylate infiltration solution I (Sinopharm Chemical Reagent Co., Ltd., Shanghai, China) for 3 d, and infiltration solution II (Sinopharm Chemical Reagent Co., Ltd., Shanghai, China) for 5 d. They were then embedded into a gel to form a resin block. Slow saw cutting was used to create 300-μm thick slices for sticking and grinding using a EXAKT 310 CP (EXAKT Technologies, Inc., Oklahoma City, OK). The slices were then ground to below 50-μm thickness and polished until scratch-free. Transverse and sagittal sections were then used to evaluate the formation of new bone.

2.7. Microcomputed tomography analysis and histological evaluation

At 8 and 16 weeks postsurgery, four animals (n = 2 from both groups A and B) were sacrificed as described previously to evaluate new bone formation via micro-CT (SkyScan, Bruker micro-CT, Belgium). Soft tissue was removed from the surface of the specimens from each rhesus macaque monkey. The specimens were then removed, wrapped, and fixed with plastic wrap, and then scanned using micro-CT under the following conditions: 80 kV, 80 μA, 2,000 ms, frame averaging of 4, and a pixel combination of 1 × 1. A 180° X-ray scan was used to locate the entire material area as the region of interest, and the CT signal selection function was used to suppress the ultrahigh signal area of the material itself to form a 2D image of the new bone. Micro-CT was then used to calculate the amount of new bone (bone volume [BV]) in the material area. Considering the different lengths of the modeled bone in each group, the amount of new bone per unit area was calculated according to this ratio. The built-in Microview ABA analysis software CTAn (CT Analyser), developed by Bruker, Kontich, Belgium was used for BV analysis.

Following micro-CT observation, the specimens were dehydrated with 70%, 80%, 95%, and 100% alcohol in a gradient manner, made transparent with xylene, and then infiltrated with a resin gradient. They were then embedded and solidified into embedding blocks. The embedding blocks were initially trimmed to the corresponding position using the EXAKT cutting and grinding system (EXAKT Apparatus GmbH & Co., Germany). Subsequently, the tissue within the embedding blocks was ground to the maximum surface using a grinding blade and adhered to a slide. The side with the adhered slide was cut to approximately 200 μm thickness, and the sections were further ground to a thickness of 50 μm on an EXAKT microgrinder, polished to a traceless finish, and subjected to hematoxylin and eosin (HE), toluidine blue, and immunofluorescence staining. The stained sections were observed under an optical microscope. HE staining showed cytoplasm and connective tissue as red or purple-red and nuclei as blue, while toluidine blue staining revealed bone cell nuclei in blue, cartilage in purple, osteoid in light blue, newly mineralized bone in dark blue, and mature bone in light blue.

2.7.1. Section treatment and antigen retrieval

The sections were soaked sequentially in xylene I for 15 min, xylene II for 15 min, anhydrous ethanol I for 5 min, anhydrous ethanol II for 5 min, 85% alcohol for 5 min, and 75% alcohol for 5 min, and then rinsed in distilled water. The tissue sections were then placed in a retrieval box filled with ethylenediaminetetraacetic acid antigen retrieval buffer (pH 8.0). Antigen retrieval was performed in a microwave oven at medium heat for 8 min; heating was then halted for 8 min before switching to medium-low heat for 7 min, which prevented excessive evaporation of the buffer and dehydration of the sections. After cooling naturally, the slides were soaked in phosphate-buffered saline (PBS; pH 7.4) and then shaken and washed on a decolorizing shaker three times for 5 min each.

2.7.2. Autofluorescence quenching and serum blocking

After lightly shaking off the sections, a circle was drawn around the tissue with a histology pen to prevent antibody diffusion. Autofluorescence quencher was then added to the circle for 5 min and rinsed with running water for 10 min. For serum blocking, bovine serum albumin was added to the circle and incubated for 30 min.

The blocking solution was gently shaken off, and the primary antibody diluted in PBS was added to the sections. The slides were then placed flat in a humid box and incubated at 4°C overnight. The slides were then soaked in PBS (pH 7.4), shaken, and washed on a decolorizing shaker three times for 5 min each. After gently shaking off excess liquid, the secondary antibody corresponding to the primary antibody was added to cover the tissue, followed by a 50-min incubation at approximately 24°C in the dark.

2.7.3. Nuclear staining and mounting

The slides in PBS (pH 7.4) were shaken and washed on a decolorizing shaker three times for 5 min each. After gently shaking off excess liquid, 4',6-diamidino-2-phenylindole (DAPI) staining solution was added to the circle and incubated at approximately 24°C in the dark for 10 min. For mounting, the slides in PBS (pH 7.4) were shaken and washed on a decolorizing shaker three times for 5 min each. After gently shaking off excess liquid, the slides were mounted with an antifluorescence quenching mounting medium.

2.7.4. Microscopy and image acquisition

Images were observed and collected using a fluorescence microscope. The DAPI ultraviolet excitation wavelength was 330–380 nm, the emission wavelength was 420 nm, and it emitted blue light. The fluorescein excitation wavelength was 465–495 nm, the emission wavelength was 515–555 nm, and it emitted green light. The Cyanine3 excitation wavelength was 510–560 nm, the emission wavelength was 590 nm, and it emitted red light.

2.8. Postoperative osteogenic protein analysis

16 weeks postoperatively, two rhesus macaque monkeys from each of the lumbar tissue-engineered bone group, the blank material group, and the autologous iliac bone group were selected. The animals were euthanized under anesthesia via intramuscular injection of ketamine hydrochloride combined with bloodletting. Under sterile conditions, the surgical segment of the vertebrae was removed, and the implanted materials were separated and cut into pieces. They were then placed in a tube containing lysis solution. Reverse transcription polymerase chain reaction (RT-PCR) and western blot analysis of alkaline phosphatase (ALP), osteocalcin (OCN), osteoprotegerin (OPG), VEGF, basic fibroblast growth factor (bFGF), osteopontin (OPN), and type I collagen were then performed.

2.9. Statistical analysis

Data were analyzed using SPSS 22.0 software (SPSS Inc., USA), and the results are presented as the mean ± standard deviation, with statistical significance set at $p < 0.05$. Differences between the experimental groups were compared and validated via one-way analysis of variance using the Fisher protected least significant difference method.

3. Results

3.1. Morphological characteristics of the novel tissue-engineered bone

The drug loading and encapsulation efficiency of BMP-2 in gelatin/chitosan microsphere hydrogels at different time points were calculated using the above formulas: In the first 2 d, both drug loading and encapsulation efficiency remained at relatively high levels (62.1% and 53.5%, respectively). Starting from Day 3, they decreased rapidly, reaching 36.3% ± 0.7% and 54.5% ± 0.5% by Day 6. From Days 6 to 12, the decline slowed, with drug loading and encapsulation efficiency decreasing to 36.3% ± 0.7% and 45.9%±0.7% by Day 12. From Days 12 to 15, these parameters entered a stable phase, and by Day 15, drug loading and encapsulation efficiency remained above 30% and 45%, respectively (Table 1). The drug loading and encapsulation efficiency profiles over time are illustrated in Figure 3A.

The A450 and calibrated A570 wavelength absorbance (OD) values were determined according to the ELISA method. The concentration and OD value of BMP-2 gradually increased over time, rising slowly on the first day, and reaching 627.62 ± 5.41 (pg/mL) and 0.365 ± 0.004, respectively. From Days 2 to 6, they increased rapidly, reaching 2274.76 ± 10.91 (pg/mL) and 1.518 ± 0.008 on Day 6. After Day 6, they continued to increase slowly, reaching 3021±12.9 (pg/mL) and 2.042±0.009 on Day 15 (Table 2). A corresponding curve illustrating the relationship between BMP-2 concentration and OD values over time was then plotted (Figure 3B–3C).

The recombinant protein BMP-2 exhibited a phased release pattern. Within the first 24 h, the release rate was slow, corresponding to the adaptation phase. From Days 1 to 6, BMP-2 showed a burst release phase, with the cumulative release rate reaching 45.5% ± 0.25% on Day 6. Thereafter, it gradually entered a slow-release phase (Days 6–12), with the cumulative release rate reaching 54.1% ± 0.5% on Day 12, and finally entered a stable phase (Days 12–15), with the BMP-2 release rate at 55% ± 0.16% on Day 15. The BMP-2 concentration in the samples was calculated according to the standard curve formula, thereby determining the BMP-2 content in the washing supernatant and the samples and plotting the BMP-2 release curve and the standard curve (Figure 3D–3E).

Table 1. Bone morphogenetic protein-2 drug loading and encapsulation efficiency.

Time	6 h	16 h	1 d	2 d	3 d	6 d	9 d	12 d	15 d
Drug loading (%)	62.1 ± 0.9	59.4 ± 0.8	58.2 ± 0.5	53.5 ± 0.9	43.4 ± 0.6	36.3 ± 0.7	33.3 ± 0.8	30.6 ± 0.5	30.1 ± 0.4
Encapsulation efficiency (%)	93.7 ± 0.8	89.1 ± 0.5	87.4 ± 0.9	80.3 ± 1.0	65.1 ± 0.9	54.5 ± 0.5	50.0 ± 0.9	45.9 ± 0.7	45.2 ± 0.6

Abbreviations: d, Day; h, Hour.

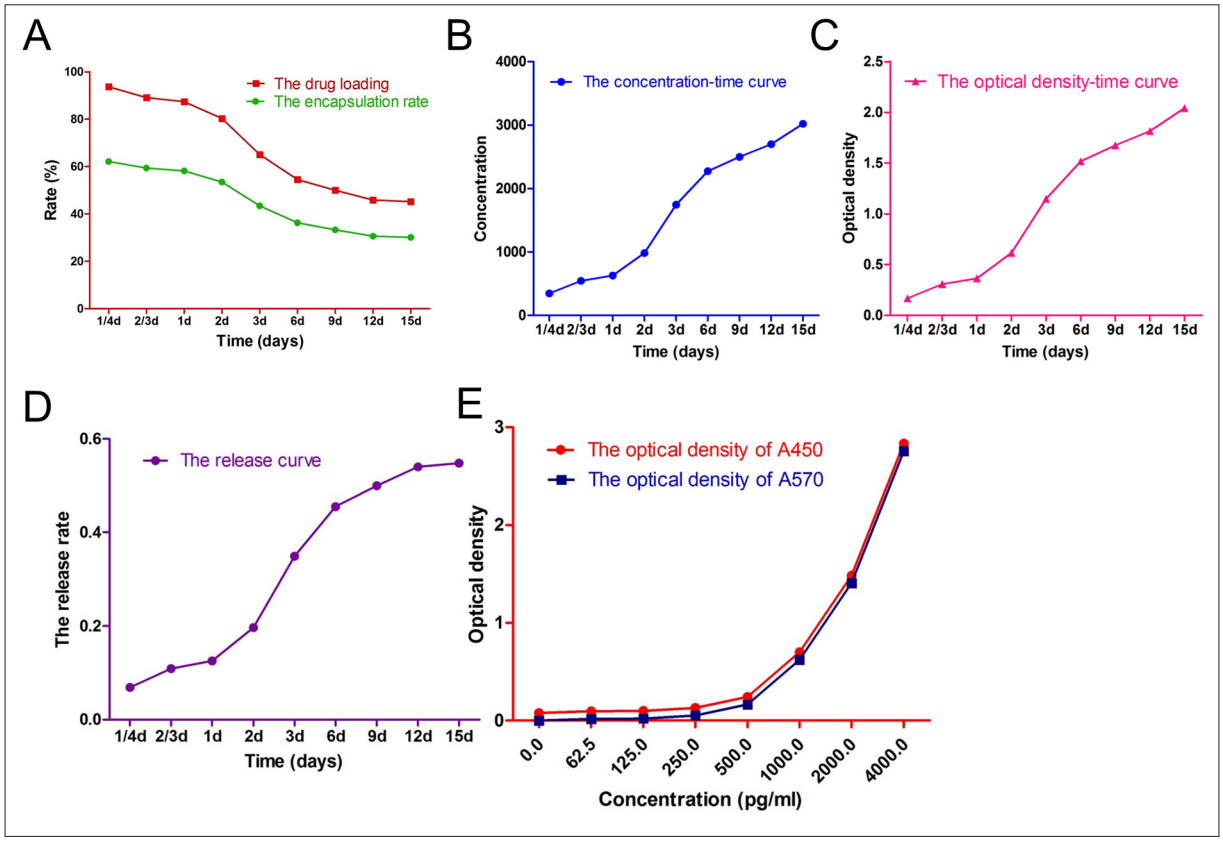


Figure 3. Drug loading, encapsulation efficiency, and *in vitro* release kinetics of the BMP-2 gelatin/chitosan hydrogel system. (A) Drug loading and encapsulation efficiency of the gelatin/chitosan sustained-release hydrogel loaded with bone morphogenetic protein (BMP)-2 at different time points. (B,C) Concentration–time curve and optical density–time curve for BMP-2. (D,E) Cumulative release curve of BMP-2 from the gelatin/chitosan sustained-release hydrogel and the standard curve of BMP-2.

Table 2. Bone morphogenetic protein-2 concentration and OD value.

Time	6 h	16 h	1 d	2 d	3 d	6 d	9 d	12 d	15 d
Concentration (pg/mL)	346.19 ± 0.82	545.24 ± 0.82	627.62 ± 5.41	983.81 ± 11.89	1745.24 ± 25.65	2274.76 ± 10.91	2498.1 ± 16.5	2700.5 ± 29.3	3021 ± 12.9
OD Value	0.168 ± 0.001	0.308 ± 0.001	0.365 ± 0.004	0.615 ± 0.008	1.148 ± 0.018	1.518 ± 0.008	1.675 ± 0.012	1.816 ± 00.021	2.042 ± 0.009

Abbreviations: d, Day; h, Hour; OD, Optical density.

Scanning electron microscopy observations at various magnifications revealed that the HA/ZrO_2 gradient composite scaffold material had a smooth surface and uniform structure. The fracture surfaces were tightly bonded to each other without distinct boundaries, and the uniform porosity of the material could provide a framework and channels for the ingrowth of new bone tissue, effectively ensuring uniform stress distribution in the composite scaffold material. The scaffold material possessed a 3D reticular structure, with chitosan microspheres evenly distributed on the material surface and within the pores. The material surface was uniformly coated with BMSCs, with cells adhering and dispersing without forming clumps. The gelatin/chitosan sustained-release hydrogel containing BMP-2 and BMSCs was evenly encapsulated on the material and within the pores.

3.2. Lumbar defect repair effects and histological analysis

All experimental rhesus macaques survived and remained healthy until the end of the experiment and were able to stand, walk, and eat independently after surgery. However, their appetite decreased owing to postoperative pain. Defecation and urination remained normal, and the monkeys demonstrated good activity levels and responsiveness to the external environment. 2

weeks postoperatively, all experimental rhesus macaques showed primary healing of the incision with good soft tissue coverage. 1 month postoperatively, the limbs of the experimental rhesus macaques moved freely.

Immediately after the operation, X-ray imaging in anteroposterior and lateral views of the lumbar spine showed that the lumbar bone defect model was well-established, the scaffold material was implanted, and the internal fixation in the lumbar group was satisfactory. 8 weeks postoperatively, the scaffold materials in groups A and B were not displaced or fractured; no spinal deformity was observed at the surgical segment, the bone defect ends were absorbed, and callus formation gradually increased, which was more pronounced in group A. In the autologous bone group, there was continuous callus formation between the implanted bone ends and the bone defect ends. 16 weeks postoperatively, X-ray images showed that the scaffold material in group A was slightly degraded, the material density was comparable with that of the host bone, and the surrounding new bone was closely connected to the host bone. In group B, the scaffold material was partially degraded, the density was lower than before, the gap between the scaffold material and the break ends was gradually filled with new bone, and the boundary was more blurred than before. In the autologous bone group, the implanted bone and the host bone cut line disappeared, and the two had completely fused (Figure 4).

Immediate postoperative imaging revealed well-formed lumbar spinal bone defect models, with satisfactory implant positioning and internal fixation. 8 weeks postoperatively, the density of the scaffold materials in groups A and B was slightly reduced, with no displacement or protrusion of the material, no spinal deformity at the surgical segment, and no protrusion or fracture of the internal fixation within the lumbar group (Figure 4A–4B). Moreover, the boundaries between the biomaterials and the fracture ends were slightly blurred, with external callus formation at the bone defect ends, which was more pronounced in group A (Figure 4A–4B). In the autologous iliac bone group, obvious bone hyperplasia and external callus formation were observed at the osteotomy site, with the boundary between the implanted bone and the defect site becoming blurred and continuous callus bridging the defect (Figure 4C). 16 weeks postoperatively, in group A, the material was gradually degraded, surrounded by new bone callus, and the density of the transplanted material was close to that of the host bone (Figure 4A). Furthermore, the boundary and internal structure of the bone defect were blurred, with ground-glass opacity indicating new bone formation inside, and the boundary between the biomaterial and the fracture end disappeared (Figure 4A). In group B, the density of the scaffold material was reduced, and the material was partially degraded, with callus formation at the bone defect end (Figure 4B). In addition, the boundary between the biomaterial and the fracture end was more blurred (Figure 4B). In the autologous bone group, the transplanted bone and the host bone completely fused, and the osteotomy line disappeared (Figure 4C).

16 weeks postoperatively, eight animals were euthanized (four each from groups A and B). Macroscopic examination showed that the scaffold materials were well integrated with the host bone. In group A, substantial new bone tissue covered and enveloped the internal fixation, with new bone callus growing into the internal pores of the material, thereby demonstrating continuity. In addition, some material degradation was observed, with the newly formed bone tightly connected to the remaining scaffold material. In group B, the amount of new bone was less than that in group A, the connection between the scaffold material and the host bone was sparser, and some parts of the scaffold material remained exposed (Figure 5A). The specimens were placed in the micro-CT for scanning, reconstruction, and calculation of the total amount of new bone in each group. In group A, partial degradation of the scaffold material was observed during 3D scanning, with material density higher than that of the host bone. Moreover, trabecular bone formed inside the material, with a large amount of new bone formation at the contact end between the material and the host bone, and the two were tightly connected. In group B, partial degradation of the material was observed, with new bone growing into the material; however, this was considerably less than that in group A, and the connection between the two was looser (Figure 5B). According to the Microview ABA software analysis results, the BV in group A was consistently higher than that in group B (Table 3).

Hard-tissue sectioning was performed on the excised specimens. The hard-tissue sections showed that both the tissue-engineered bone group and the blank material group achieved integration between the scaffold material and the host bone. The tissue-engineered bone group exhibited a large amount of new bone tissue that had grown into the internal pores of the material, thereby showing continuity. Moreover, some material degradation was observed, with the newly formed bone tightly connected to the undegraded material. In contrast, the blank material group had less new bone, and the connection between the scaffold material and the host bone was sparser, indicating that the tissue-engineered bone group had better osteogenic efficacy than the blank material group (Figure 5C).

12 animals (n = 4 per experimental group) were euthanized 16 weeks after surgery to harvest bone samples

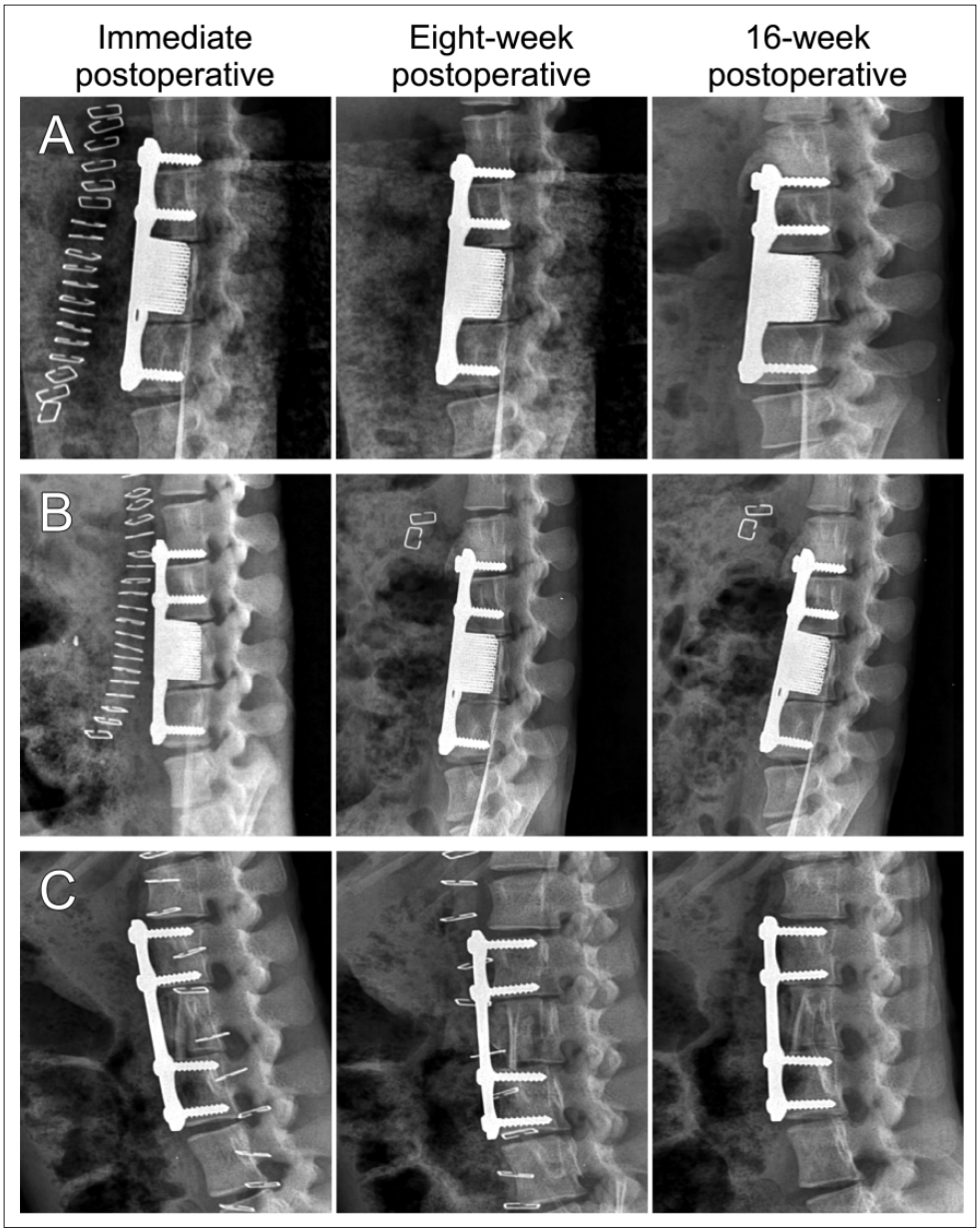


Figure 4. X-ray results. (A–C) Immediately postoperative, 8-week postoperative, and 16-week postoperative lumbar X-ray results for groups A, B, and C, respectively.

for biomechanical testing. The maximal load, stiffness, and maximal pressure in group B were significantly lower than those of the other two experimental groups and the nonoperated healthy group ($p < 0.05$), whereas the energy to maximal load in groups A and C was significantly higher than that in group B ($p < 0.05$) (Table 4).

Specimens were subjected to HE and toluidine blue staining as well as immunofluorescence processing. Both groups showed new trabecular bone that gradually crept into the pores of the scaffold material and increased in mass over time. 16 weeks postoperatively, at the connection between the implanted material and the host bone in group A, new lamellar bone was interwoven and fused with the host bone. Inward observations revealed that the new bone plate longitudinal ligament was surrounded by new woven bone, with elongated vertical grooves in the lamellar bone, which contained microvessels and osteogenic-related cells. Inside the pores of the implanted material, new bone tissue was distributed in a trabecular-woven bone pattern, with denser osteogenic-related cells visible within the trabecular

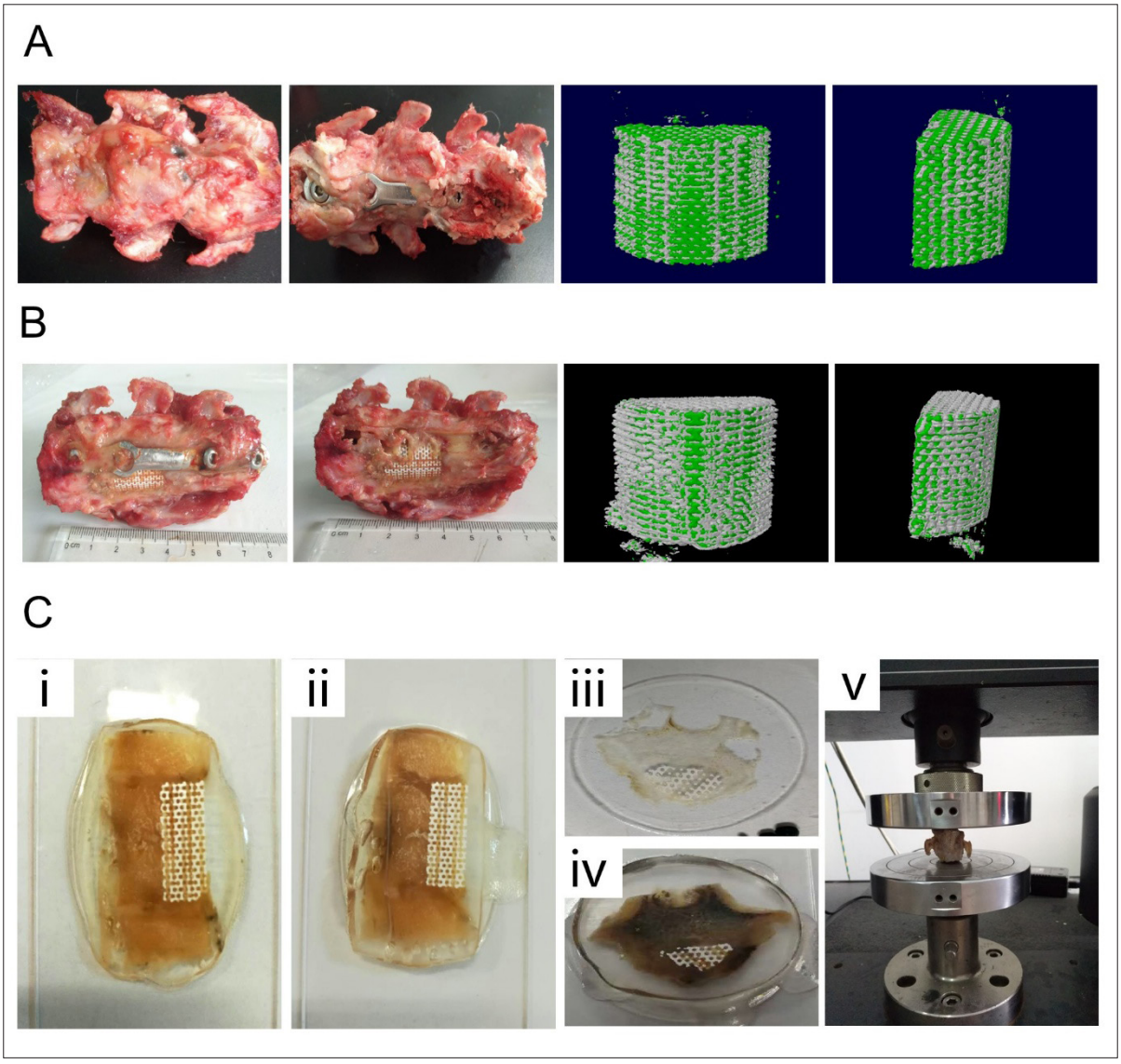


Figure 5. Evaluation of osteogenic efficacy and scaffold integration in rhesus macaques at 16 weeks postimplantation. (A,B) Macroscopic appearance and 3D microcomputed tomography (CT) images of specimens from groups A and B 16 weeks postoperatively. In group A, the scaffold material is completely covered by new bone tissue, with callus enveloping the internal fixation. In contrast, group B shows less callus formation, with parts of the scaffold material remaining exposed. In the micro-CT images, white represents the scaffold material and green represents new bone tissue; group A demonstrates significantly more new bone formation than group B. (C [i–ii]) Sagittal section of the hard-tissue slices of specimens from groups A and B 16 weeks postoperatively. (C [iii–iv]) Transverse sections of hard-tissue slices of specimens from groups A and B 16 weeks postoperatively. In the sagittal view, the scaffold materials of both groups are tightly connected to the host bone, with group A showing more yellow-brown bone tissue growing into the scaffold pores than group B. In the transverse view, new bone envelopes the scaffold material in both groups, with more degradation of the scaffold material in group A than in group B. (C [v]) Trimmed specimens from each group subjected to biomechanical testing.

Table 3. Microcomputed tomography new bone volume (BV) in the defect region.

Group	BV (mm^3), individual values			BV (mm3), mean ± standard deviation
Lumbar spine A (n = 3)	467.89	476.46	498.25	487.33 ± 11.62
Lumbar spine B (n = 3)	372.14	365.27	388.46	375.38 ± 10.51

Table 4. Biomechanical results at 16 weeks postoperative.

Item	Group A	Group B	Group C
Maximal load (N)	2,525.3 ± 298.8	1,373.5 ± 101.6*	2,920.6 ± 282.8
Maximal pressure (MPa)	3.2 ± 1.0	2.4 ± 0.7*	3.8 ± 1.1
Stiffness (N/mm)	1,779.5 ± 177.6	1,130.4 ± 119.4*	1,988.6 ± 221.7
Energy to maximal load (J)	3.2 ± 0.4	1.4 ± 0.2	7.1 ± 1.3*

Notes: Results are expressed as mean ± standard deviation. An asterisk (*) indicates a statistically significant difference compared with the normal group.

pores. In group B, partial degradation of the biomaterial was observed, with fewer newly formed trabecular bones that did not form an interconnected pattern with the scaffold, leaving clear gaps between them (Figure 6). Immunofluorescence showed OPG in red within the cytoplasm and nuclei in blue. The expression levels of ALP, OCN, OPG, VEGF, bFGF, OPN, and type I collagen were higher in group A than in group B (Figure 7).

3.3 Expression analysis of osteogenic proteins

16 weeks postoperatively, four animals were euthanized (two each from groups A and B). The expression of ALP, OCN, OPG, VEGF, bFGF, OPN, and type I collagen was detected using RT-PCR and western blotting. RT-PCR revealed that gene expression levels in group A were significantly higher than those in group B (Figure 8A). The western blot results were consistent with the RT-PCR findings, indicating that the expression levels of OGPs in

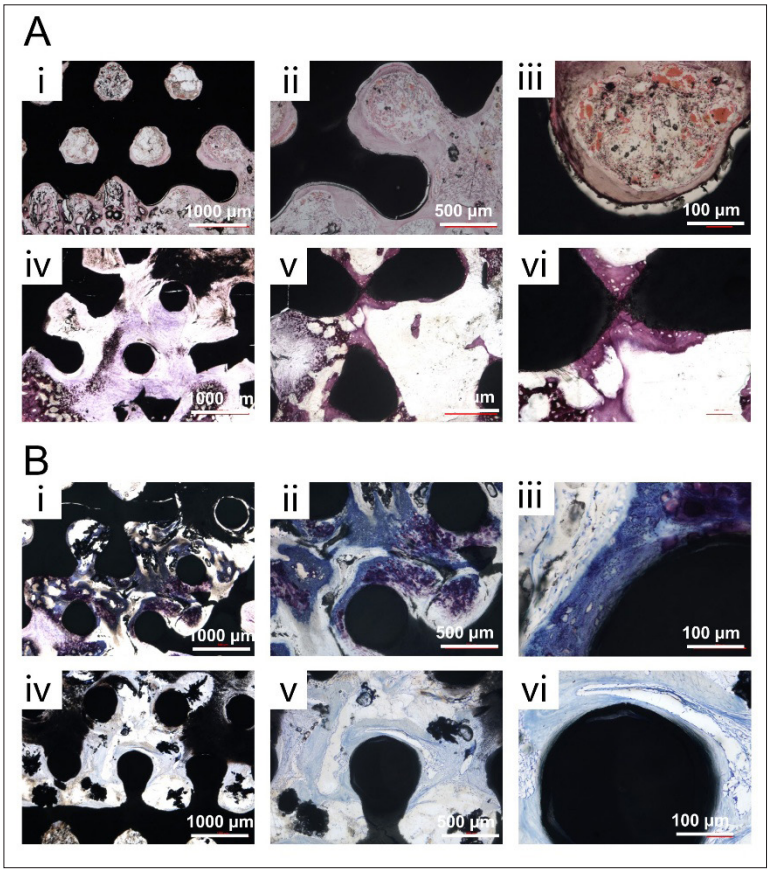


Figure 6. Hematoxylin and eosin (HE) and toluidine blue staining of groups A and B. (A-i–ii, A-iii–iv, A-v–vi) HE staining at different magnifications shows new bone callus infiltrating the scaffold pores, along with partial scaffold degradation. (B-i–ii, B-iii–iv, B-v–vi) Toluidine blue staining of groups A and B at different magnifications: purple areas (red arrows) indicate new cartilage, light blue areas (yellow arrows) denote osteoid, and lighter blue areas (white arrows) correspond to mature bone. Scale bars: B-i (1000 μm) B-ii (500 μm) B-iii (100 μm) B-iv (1000 μm) B-v (500 μm) B-vi (100 μm). Both HE and toluidine blue staining reveal more extensive and continuous bone callus formation in group A compared with group B, where scaffold pores remain incompletely filled by new bone tissue.

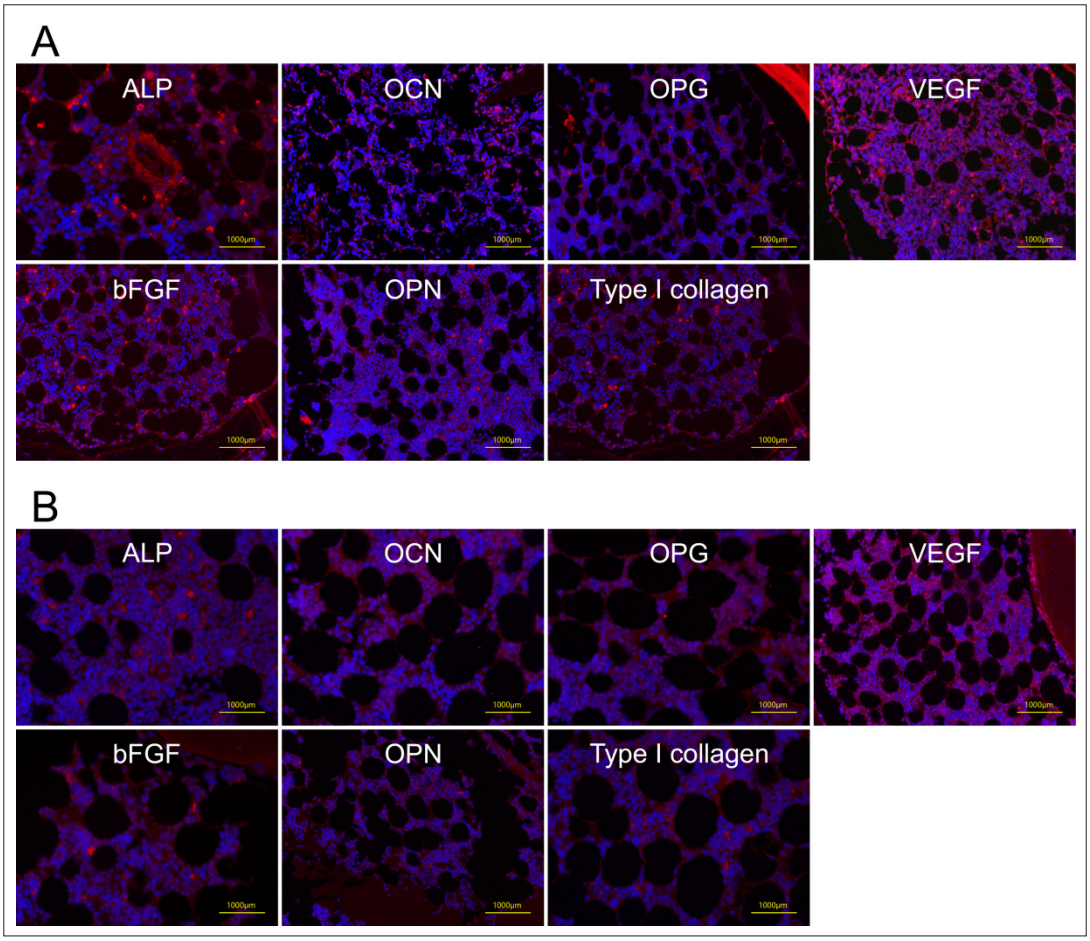


Figure 7. Immunofluorescence of osteogenic-related proteins (OGPs) (A,B). Immunofluorescence of alkaline phosphatase (ALP), osteocalcin (OCN), osteoprotegerin (OPG), vascular endothelial growth factor (VEGF), basic fibroblast growth factor (bFGF), osteopontin (OPN), and type I collagen in specimens from groups A and B 16 weeks postoperatively. Expression levels in group A were higher than those in group B.

group A were higher than those in group B (Figure 8B; raw western blot images are shown in Figure S1).

4. Discussion

In this study, a novel bone scaffold material was designed and prepared. The material consisted of a porous gradient HA/ZrO_2 composite and a gelatin/chitosan sustained-release hydrogel. The HA/ZrO_2 composite was prepared using SLA 3D-printing technology, and the hydrogel contained BMP-2 and BMSCs. Ultimately, the scaffold material was used to repair lumbar vertebral bone defects in rhesus macaques, and its efficacy in bone defect repair was evaluated. With the rapid development of 3D printing in the medical field, light-curing SLA printing technology has been increasingly applied in the preparation of biomedical materials.[13,14] SLA printing technology adjusts the porosity (70%–90%), pore size (100–500 μm), and connectivity of the material according to the different characteristics of the bone defect site. This allows for the preparation of personalized scaffold material that matches the morphology of the bone defect.[15] Personalized design of scaffolds, including porous structures, nanoscale channels, and gradient material distributions, helps promote cell growth, vascularization, and bone regeneration. The porous structure is designed to provide sufficient surface area for cell attachment and proliferation, while its internal structure mimics the microscopic environment of native bone tissue. This promotes osteogenic development and mineralization and provides a framework for the differentiation, expansion, and migration of OBs, chondrocytes, and vascular endothelial cells.[16] Additionally, this 3D interconnected structure facilitates the transport of nutrients and metabolites and provides a site for the continuous deposition and accumulation of extracellular matrix.[17] Moreover, the scaffold material exhibits excellent biocompatibility, and the porous

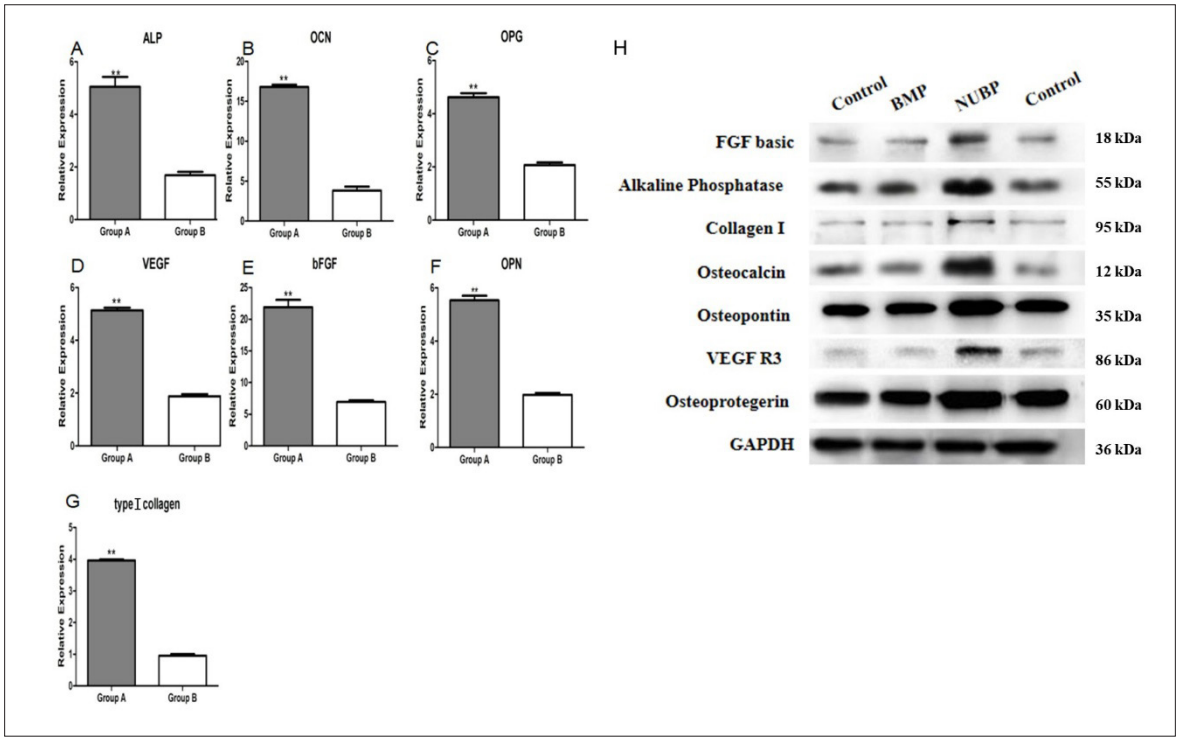


Figure 8. Reverse transcription polymerase chain reaction (RT-PCR) and immunoblotting analysis of osteogenic-related genes and proteins (OPGs). (A) RT-PCR results for alkaline phosphatase (ALP), osteocalcin (OCN), osteoprotegerin (OPG), vascular endothelial growth factor (VEGF), basic fibroblast growth factor (bFGF), osteopontin (OPN), and type I collagen in groups A and B. Gene expression levels in group A were significantly higher than those in group B. (B) Immunoblotting analysis showing higher expression levels of OPGs in group A than in group B. Raw western blot images are available in **Figure S1**.

structure markedly increases the surface area of the connection between the graft material and the new bone, which allows the material to form a strong connection to the host bone.[18] Histological analysis showed that over time after surgery, the trabeculae and amount of new bone in the composite scaffold material gradually increased, and the progressive formation of new bone and its reconstruction in the scaffold pores were clearly evident. Postoperative micro-CT scans revealed that the internal pores of the composite scaffold maintained a cross-linked 3D structure, which was covered internally by new bone tissue components. Some of these components were degraded and replaced by new bone, while undegraded material was tightly wrapped by newly formed trabecular bone, creating a cross-linked and integrated structure. Bone regeneration relies not only on intramembranous and endochondral ossification but also on the synergistic effects of angiogenesis and neurogenesis. Toluidine blue staining showed new cartilage in purple, osteoid in light blue, newly mineralized bone in dark blue, and mature bone in light blue, suggesting that bone formation within the scaffold was related to both endochondral and intramembranous osteogenesis.[19] Zirconia, being an inert material, possesses strong mechanical properties and low toxicity. It is nondegradable after implantation and does not accumulate in body tissues, muscles, or bones.[20,21] In this study, the use of zirconia resulted in a scaffold material with reliable mechanical strength and good mechanical properties. The mechanical testing showed that the mechanical strength and elastic modulus of the scaffold material group were higher than those of the blank group. As this study primarily focused on *in vivo* osteogenesis and biomechanical outcomes, the specific mechanical parameters of the scaffolds before implantation were not quantified. However, the rigorous sintering process at 1,450°C ensures the densification and intrinsic mechanical stability of the zirconia matrix. Moreover, the high compressive strength observed 16 weeks postimplantation provides strong indirect evidence that the initial scaffolds possessed sufficient load-bearing capacity to support spinal stability during the critical early healing phase. Hence, the material could be used for implantation in load-bearing areas of the body.

Osteoblasts can secrete osteogenic proteins, such as ALP, type I collagen, and OCN. In the matrix secreted by

OBs, the main structural component is type I collagen, and the amorphous components are OPN, OCN, and various growth factors, such as bFGF and VEGF.[22,23] Type I collagen, an early marker secreted by OBs, constitutes the main component of bone organic matrix and the primary extracellular matrix.[24–26] ALP is a recognized differentiation and histological marker for OBs; its activity reflects the degree of OB differentiation, with higher ALP activity indicating stronger osteogenic activity. OCN is a bone-specific noncollagenous protein synthesized by mature OBs that plays an important role in maintaining normal bone calcification. OCN promotes bone mineralization and is a specific marker of mature OBs.[27] Moreover, bFGF maintains the osteogenic properties of BMSCs, stimulates DNA synthesis, increases OCN levels in differentiated OBs, accelerates bone calcification, and promotes new bone formation. Additionally, bFGF induces chemotaxis of various cells in the vascular intima, promotes their migration and growth, and promotes neovascularization *in vivo* and *in vitro*. Therefore, bFGF is an important angiogenic factor.[28–30] Moreover, VEGF promotes neovascularization in the implant material and stimulates the migration and growth of vascular endothelial cells, thereby playing an important role in the regeneration and reconstruction of bone defects. Furthermore, VEGF promotes the migration of bone progenitor cells and stimulates the differentiation of primary OBs, which also play critical roles in the repair and reconstruction of bone defects.[31,33] Therefore, VEGF plays an important role in both neovascularization and bone regeneration. In this study, the expression levels of OGPs were detected using RT-PCR and western blotting. The relative expression levels of ALP, OCN, OPG, VEGF, bFGF, OPN, and type I collagen were markedly higher in group A than in group B. This suggests that osteogenic activity was greater in group A than in group B.

Although 3D printing technology has shown great potential in bone tissue engineering, there are still limitations in printing accuracy and in the complexity of structures that can be fabricated, and printing equipment and process parameters require further optimization. BMSCs often require additional surgical procedures for harvesting and are constrained by time, anatomical location, and tissue source. In contrast, induced pluripotent stem cells (iPSCs) possess pluripotent and multilineage differentiation capabilities similar to embryonic stem cells but without the ethical concerns or risk of immune rejection associated with these cells.[32] At present, iPSCs can be obtained through somatic reprogramming from autologous hosts, offering the possibility of obtaining mesenchymal stem cells via *in vitro* differentiation of iPSCs, thereby overcoming the limitations associated with traditional BMSCs.

5. Conclusion

In this study, a novel HA/ZrO_2 composite scaffold material was created using light-curing printing technology. The scaffold material exhibits nanoscale characteristics and an interconnected 3D structure, which are conducive to the growth of bone and blood vessels. Therefore, the material may effectively address the challenge of personalized bone defect repair. A key innovation of this study lies in the ability to customize the scaffold morphology to precisely match individual bone defects using 3D-printing technology. This approach enables the fabrication of highly biomimetic 3D porous structures with adjustable pore size, porosity, and connectivity, significantly enhancing OB adhesion, proliferation, and differentiation. Notably, BMP-2 is integrated into the composite scaffold material as an osteogenic inductive factor, which further enhances the osteogenic differentiation capacity of BMSCs. Overall, the composite scaffold material showed good cellular biocompatibility, excellent osteogenic efficacy, and satisfactory biomechanical strength, indicating its promising potential as a bone tissue repair material.

Acknowledgments

We thank the School of Materials Science and Engineering (Shanghai University) for preparing the novel porous gradient HA/ZrO2 scaffold material and providing information on its structure.

Funding

This work was supported by the Medical and Health Science and Technology Project in Zhejiang Province [2024KY261] and Zhejiang Natural Science Foundation Project (LQN25H270017).

Conflict of interest

The authors declare no conflict of interest.

Author contributions

Conceptualization: Tuo Wang and Huan-Huan Gao
Formal analysis: Can-Da Xu, Xiao-Long Huang
Investigation: Rui Qiu, Hua-Teng Zhou, Wei-Bin Du, Xi-Cheng Wei, Long-Bao Lv, Cai-Yin Xu
Methodology: Ren-Fu Quan, Rui Qiu
Supervision: Ren-Fu Quan, Rui Qiu
Writing–original draft: Rui Qiu
Writing–review & editing: Ren-Fu Quan, Jin-Fu Wang
All authors have read and approved the final manuscript.

Ethics approval and consent to participate

All animal procedures described were approved by the Committee of Kunming Institute of Zoology (KIZ) (production license number: SCXK-K2013-0005, research use license number: SYXK-K2013-0012). The animal experiment protocol was approved by the Institutional Animal Care and Use Committee of KIZ, Chinese Academy of Sciences, and was performed strictly following Chinese laws on animal experimentation. The feeding conformed to the standards of the animal feeding requirements set by KIZ.

Consent for publication

Not applicable.

Availability of data

The datasets generated during and/or analyzed during the current study are available from the corresponding author on reasonable request.

References

1. Dec P, Modrzejewski A, Pawlik A, Existing and novel biomaterials for bone tissue engineering. *Int J Mol Sci*. 2022:24:529. doi: 10.3390/ijms24010529
2. Jagadale S, Damle M, Joshi MG. Bone tissue engineering: from biomaterials to clinical trials. *Adv Exp Med Biol*. 2025;1479:73-115. doi: 10.1007/5584_2024_841
3. Brachet A, Bełżek A, Furtak D. *et al*. Application of 3D printing in bone grafts. *Cells*. 2023;12:859. doi: 10.3390/cells12060859
4. Maresca JA, DeMel DC, Wagner GA, *et al*. Three-dimensional bioprinting applications for bone tissue engineering. *Cells*. 2023;12:1230.
5. Chatzipetros E, Damaskos S, Tosios KI, *et al*. The effect of nano-hydroxyapatite/chitosan scaffolds on rat calvarial defects for bone regeneration. *Int J Implant Dent*. 2021;7:40. doi: 10.1186/s40729-021-00327-w
6. Quan RF, Tang YH, Huang ZM, *et al*. Difference of adherence, proliferation and osteogenesis of mesenchymal stem cells cultured on different HA/ZrO2 composites. *Chin J Traumatol*. 2012;15:131-139.
7. Ingwersen LC, Frank M, Naujokat H, *et al*. BMP-2 long-term stimulation of human pre-osteoblasts induces osteogenic differentiation and promotes transdifferentiation and bone remodeling processes. *Int J Mol Sci*. 2022;23:3077. doi: 10.3390/ijms23063077
8. Grosso A, Lunger A, Burger MG, *et al*. VEGF dose controls the coupling of angiogenesis and osteogenesis in engineered bone. *NPJ Regen Med*. 2023;8:15. doi: 10.1038/s41536-023-00288-1
9. Gorskaya YF, Danilova TA, Karyagina AS, *et al*. Effects of combined treatment with complex S. typhimurium antigens and factors stimulating osteogenesis (curettage, BMP-2) on multipotent bone marrow stromal cells and serum concentration of cytokines in CBA mice. *Bull Exp Biol Med*. 2015;158:465-470. doi: 10.1007/s10517-015-2786-z
10. Kong D, Shi Y, Gao Y, *et al*. Preparation of BMP-2 loaded MPEG-PCL microspheres and evaluation of their bone repair properties. *Biomed Pharmacother.* 2020;130: 110516. doi: 10.1016/j.biopha.2020.110516
11. Arthur A, Gronthos S. Clinical application of bone marrow mesenchymal stem/stromal cells to repair skeletal tissue. *Int J Mol Sci*. 2020;21:9759. doi: 10.3390/ijms21249759
12. Gholami Farashah MS, Javadi M, Mohammadi A, *et al*. Bone marrow mesenchymal stem cell's exosomes as key nanoparticles in osteogenesis and bone regeneration: specific capacity based on cell type. *Mol Biol Rep*. 2022;49:12203-12218. doi: 10.1007/s11033-022-07807-1
13. Yazdanpanah Z, Sharma NK, Raquin A, *et al*. Printing tissue-engineered scaffolds made of polycaprolactone and nano-hydroxyapatite with mechanical properties appropriate for trabecular bone substitutes. *Biomed Eng Online*. 2023; 22:73. doi: 10.1186/s12938-023-01135-6
14. Rajabi M, Cabral JD, Saunderson S, *et al*. Development and optimisation of hydroxyapatite-polyethylene glycol diacrylate hydrogel inks for 3D printing of bone tissue engineered scaffolds. *Biomed Mater*. 2023;18(6). doi: 10.1088/1748-605X/acf90a
15. Bahraminasab M, Talebi A, Doostmohammadi N, *et al*. The healing of bone defects by cell-free and stem cell-seeded 3D-printed PLA tissue-engineered scaffolds. *J Orthop Surg Res*. 2022;17:320. doi: 10.1186/s13018-022-03213-2
16. Zalewska J, Przekora A, Pałka K, *et al*. Gypsum-related compensation of ions uptake by highly porous hydroxyapatite ceramics: – consequences for osteoblasts growth and proliferation. *Biomater Adv.* 2022;133:112665. doi: 10.1016/j.msec.2022.112665
17. Ostrowska B, Di Luca A, Szlazak K, *et al*. Influence of internal pore architecture on biological and mechanical properties of three-dimensional fiber deposited scaffolds for bone regeneration. *J Biomed Mater Res A*. 2016;104:991-1001. doi: 10.1002/jbm.a.35637

18. Shao RX, Quan RF, Huang XL, *et al*. Evaluation of porous gradient hydroxyapatite/zirconia composites for repair of lumbar vertebra defect in dogs. *J Biomater Appl*. 2016;30:1312-1321.
doi: 10.1177/0885328215627616

19. Julien A, Perrin S, Martínez-Sarrà E, *et al*. Skeletal stem/progenitor cells in periosteum and skeletal muscle share a common molecular response to bone injury. *J Bone Miner Res*. 2022;37:1545-1561.
doi: 10.1002/jbmr.4616

20. Salamanca E, Wu YF, Aung LM, *et al*. Allylamine coating on zirconia dental implant surface promotes osteogenic differentiation *in vitro* and accelerates osseointegration *in vivo*. *Clin Oral Implants Res*. 2024;35:1101-1113.
doi: 10.1111/clr.14300

21. Kim J, Kang IG, Cheon KH, *et al*. Stable sol-gel hydroxyapatite coating on zirconia dental implant for improved osseointegration. *J Mater Sci Mater Med*. 2021;32:81.
doi: 10.1007/s10856-021-06550-6

22. Kusuyama J, Amir MS, Albertson BG, *et al*. JNK inactivation suppresses osteogenic differentiation, but robustly induces osteopontin expression in osteoblasts through the induction of inhibitor of DNA binding 4 (Id4). *FASEB J*. 2019;33:7331-7347.
doi: 10.1096/fj.201802465R

23. Mardiyantoro F, Chiba N, Seong CH, *et al*. Two-sided function of osteopontin during osteoblast differentiation. *J Biochem*. 2025;177:121-131.
doi: 10.1093/jb/mvae080

24. Selvaraj V, Sekaran S, Dhanasekaran A, *et al*. Type 1 collagen: synthesis, structure and key functions in bone mineralization. *Differentiation*. 2024;136:100757.
doi: 10.1016/j.diff.2024.100757

25. Asakura T, Diep TTT, Ueda Y, *et al*. Analysis of the effect of human type I collagen-derived peptide on bone regenerative capacity and comparison with various collagen materials *in vivo*. *Medicina (Kaunas)*. 2025;61:57.
doi: 10.3390/medicina61010057

26. Tateno A, Asano M, Akita D, *et al*. Transplantation of dedifferentiated fat cells combined with a biodegradable type I collagen-recombinant peptide scaffold for critical-size bone defects in rats. *J Oral Sci*. 2019;61:534-538.
doi: 10.2334/josnusd.18-0458

27. Vimalraj S. Alkaline phosphatase: structure, expression and its function in bone mineralization. *Gene*. 2020;754:144855.

28. Wu H, Yin G, Pu X, *et al*. Inhibitory effects of combined bone morphogenetic protein 2, vascular endothelial growth factor, and basic fibroblast growth factor on osteoclast differentiation and activity. *Tissue Eng Part A*. 2021;27:1387-1398.
doi: 10.1089/ten.TEA.2020.0325

29. Nakamichi M, Akishima-Fukasawa Y, Fujisawa C, *et al*. Basic fibroblast growth factor induces angiogenic properties of fibrocytes to stimulate vascular formation during wound healing. *Am J Pathol*. 2016;186:3203-3216.
doi: 10.1016/j.ajpath.2016.08.015

30. Pasanen S, Mootha A, Hirata I, *et al*. Enhanced growth of bone marrow-derived mesenchymal stem cells on the microcarriers tethered with engineered basic fibroblast growth factor. *Biotechnol J*. 2025;20:e70057.
doi: 10.1002/biot.70057

31. Hu K, Olsen BR. Osteoblast-derived VEGF regulates osteoblast differentiation and bone formation during bone repair. *J Clin Invest*. 2016;126:509-526.
doi: 10.1172/JCI82585

32. Veraitch O, Mabuchi Y, Matsuzaki Y, *et al*. Induction of hair follicle dermal papilla cell properties in human induced pluripotent stem cell-derived multipotent LNGFR(+)THY-1(+) mesenchymal cells. *Sci Rep*. 2017;7:42777.
doi: 10.1038/srep42777

ACCSCIENCE PUBLISHING

International Journal of Bioprinting

RESEARCH ARTICLE

Optimization of 3D bioprinting of mouse preosteoblasts using nanofibrillated cellulose hydrogels

Na Li[1], LinGe Wang[2], Roxana Guillen De La Cruz[1]*, and Zhenyu Jason Zhang[1]*

[1] School of Chemical Engineering, University of Birmingham, Birmingham, UK

[2] South China Advanced Institute for Soft Matter Science and Technology, School of Emergent Soft Matter, Guangdong Provincial Key Laboratory of Functional and Intelligent Hybrid Materials and Devices, Guangdong Basic Research Centre of Excellence for Energy and Information Polymer Materials, South China University of Technology, Guangzhou, Guangdong, China

Abstract

Development and optimization of advanced bioink formulations for living tissue-engineered scaffolds remain a challenging task. Herein, a nanofibrillated cellulose (NFC)-composited gelatin methacryloyl (G)/alginate (A) formulation (G/A/NFC100) was prepared for 3D bioprinting of mouse preosteoblasts MC3T3-E1, whereby the G/A formulations with a mixed NFC/microfibrillated cellulose and without NFC were included for comparison. The rheological properties of G/A formulation were enhanced by the addition of NFC, as evidenced by a decreased viscosity index characterizing shear thinning behavior from 0.52 (G/A) to 0.19 (G/A/NFC100). To construct 3D scaffolds with excellent shape fidelity while minimizing shear damage to cells during extrusion, the bioprinting conditions of the formulations were optimized based on the parameter optimization index. The G/A/NFC100 scaffold printed at a printing speed of 2 mm/s and a dispensing pressure of 30 kPa from a 27-gauge nozzle displayed a high shape fidelity (printability index of 0.883). The mechanical stability of the crosslinked 20-layered G/A/NFC100 structures were demonstrated by three consecutive press-relax cycles. The successful bioprinting of mouse preosteoblasts using the G/A/NFC100 formulation translated into an increased cell viability (above 97.64%) up to 21 days post-bioprinting. These results emphasize the exceptional potential of NFC-composited G/A formulation for bioprinting of bone tissue analogues for biomedical applications. In addition, the long-term controlled release of ampicillin (67.42% after 72 h) by G/A/NFC100 scaffolds demonstrates the feasibility of utilizing porous cellulose fibers as drug-delivery carriers to enable multifunctionality in bone tissue repair.

Keywords: 3D bioprinting; Bioink formulation; Cell viability; Hydrogel; Nanofibrillated cellulose; Printability

***Corresponding authors:**
Roxana Guillen De La Cruz (rxg011@alumni.bham.ac.uk)

Zhenyu Jason Zhang (Z.J.Zhang@bham.ac.uk)

Citation: Li N, Wang L, De La Cruz RG, Zhang ZJ. Optimization of 3D bioprinting of mouse preosteoblasts using nanofibrillated cellulose hydrogels. *Int J Bioprint*. 2026;12(1):485-499. doi: 10.36922/IJB025420428

Received: October 18, 2025
1st revised: November 20, 2025
2nd revised: December 4, 2025
Accepted: December 8, 2025
Published online: December 16, 2025

Copyright: © 2025 Author(s). This is an Open Access article distributed under the terms of the Creative Commons Attribution License, permitting distribution, and reproduction in any medium, provided the original work is properly cited.

Publisher's Note: AccScience Publishing remains neutral with regard to jurisdictional claims in published maps and institutional affiliations.

1. Introduction

Three-dimensional (3D) bioprinting technology has emerged as a novel approach for fabricating biologically active 3D constructs in tissue engineering.[1-5] This cutting-edge

technique empowers the layer-by-layer deposition of diverse cell types, biomaterials, and biomolecules (collectively known as bioinks), facilitating the construction of predesigned, biologically functional 3D architectures.[6] By meticulously arranging the bioink in a sequential manner, 3D bioprinting overcomes the limitations of conventional scaffold fabrication methods, such as hydrogelation, freeze-drying, and electrospinning, thereby opening up new vistas in the realm of tissue-engineered substitute development.[7,8] Numerous 3D bioprinting technologies have emerged in the past decade,[9,10] among which extrusion-based bioprinting has gained the most popularity due to its operational practicality, high cell-encapsulation densities, and no exposure to high temperature or laser radiation.[11]

For extrusion bioprinting, the design of bioink formulation has been the focus of research due to the diverse performance requirements of 3D scaffolds for different tissues.[12] Natural polymer-based hydrogels, such as gelatin, collagen, fibroin, chitosan, sodium alginate, silk, and hyaluronic acid, can mimic the microenvironment of natural tissue and regulate cell fate at a high degree of hydration, making them the preferred materials for extrusion-based 3D bioprinting.[13,14] Traditional bioink formulations composed of gelatin (or gelatin methacryloyl) and alginate have been extensively studied due to their inherent biocompatibility and the complementary combination of photocrosslinkable and ionically crosslinkable networks.[15,16] However, this binary system still suffers from several intrinsic limitations, including insufficient rheological integrity for stable extrusion, inadequate mechanical robustness under highly hydrated conditions.[17,18] Cellulose, the most abundant natural polymers on the Earth,[19] has been shown to be suitable for a range of tissue engineering applications, e.g., wound healing, artificial blood vessels, soft tissue engineering, and bone engineering, due to its exceptional hydrophilicity, biocompatibility, and tunable physicochemical properties.[20,21] It is worth highlighting that nanocellulose, such as nanofibrillated cellulose (NFC) and cellulose nanocrystals (CNC), has been extensively used to address the shortcomings of conventional bioink formulations, such as poor processability, low gel strength, and rapid degradation after printing.[21-23] For example, NFC, as a reinforcing agent, was composited with a fucose-rich polysaccharide FucoPol to formulate a bioink with excellent rheological, mechanical, and biological characteristics for extrusion bioprinting of keratinocytes (HaCaT) and melanoma (A375) cells.[24] High cell viabilities (above 88%) up to 21 days post-bioprinting demonstrated the potential of such cellulose-composited formulation for the development of *in vitro* skin tissue analogues.

In our previous study, both NFC and microfibrillated cellulose (MFC), were introduced to gelatin methacryloyl (G)/alginate (A) system as mechanical strengthening agents.[25] By characterizing the multiscale mechanical properties of cellulose-composited ion–covalent entanglement (ICE) G/A hydrogels, new mechanical reinforcement mechanisms were demonstrated. Controlling the ratio of MFC to NFC can modulate Young's modulus of the hydrogel system to broaden its application range. We also found that adjusting the incorporation concentration of pure MFC in the G/A formulation can balance the rheological properties, mechanical properties, and a range of biological behaviors of the formulation.[26] Building up the capability to control the mechanical properties of cellulose-composited hydrogel, the optimization of extrusion-based 3D bioprinting of mouse preosteoblasts-encapsulated NFC-composited G/A formulations was investigated in this work according to the workflow for the bioink development proposed by Gatenholm *et al.*[27] We sequentially evaluated the rheology, printability, crosslinking stability, sterility, bioprinting, and cell proliferation of the cellulose-composited hydrogel, with a particular emphasis on its potential as a drug delivery vehicle.

2. Materials and methods

2.1. Materials

Gelatin from porcine skin (gel strength 300, type A), methacrylic anhydride (MA, 94%), sodium alginate from *Macrocystis pyrifera* (A, mannuronate/guluronate ratio of 2.03, M_v of 478.44 kDa), 2-hydroxy-4′-(2-hydroxyethoxy)-2-methylpropiophenone (Irgacure 2959), ampicillin sodium salt (AMP), Miller Luria–Bertani (LB) broth, and tryptic soy broth (TSB) were purchased from Sigma-Aldrich (Somerset, UK). Microfibrillated cellulose (MFC) suspension (0.7 wt%, purity of 99.9% cellulose, negative surface zeta-potential of −24.0 ± 0.5 mV at pH 5.7, cellulose fibrils with an average diameter of 0.3–2 μm[25]), prepared by mechanical grinding of softwood bleached Kraft pine pulp, was kindly donated by FiberLean Technologies Ltd (Par, UK). Nanofibrillated cellulose (NFC) suspension (3 wt%, purity of 85% cellulose, 12% hemicellulose, and 3% lignin, negative surface zeta-potential of −15.0 ± 0.4 mV at pH 4.2, cellulose fibrils with an average diameter of 30–100 nm[25]), prepared by high pressure homogenization of bleached softwood Kraft pulp, was purchased from Cellulose Lab (Canada) and diluted to 1 wt% for use. Calcium chloride ($CaCl_2$), sodium hydroxide (NaOH), phosphate-buffered saline (PBS) tablets, and nutrient agar were purchased from Fisher Scientific (Loughborough, UK). Calcium chloride was prepared as a 2% solution and NaOH was prepared as a 1 M solution for use.

Mouse preosteoblasts MC3T3-E1 Subclone 4 cells (ATCC-2593) were purchased from LGC standards (Middlesex, UK). Alpha Minimum Essential Medium (αMEM) with *L*-glutamine, fetal bovine serum (FBS), penicillin–streptomycin (10,000 U/mL), trypsin–EDTA (0.05%), trypan blue (0.4%), Dulbecco's phosphate-buffered saline (dPBS, 1×) with and without calcium and magnesium, and collagenase type II were purchased from Gibco, Thermo Fisher Scientific (Loughborough, UK). LIVE/DEAD Viability/Cytotoxicity Kit for mammalian cells was obtained from Invitrogen, Thermo Fisher Scientific (Loughborough, UK). Basal culture media of MC3T3-E1 cells comprised αMEM, 10% FBS, and 1% penicillin–streptomycin. Collagenase type II was dissolved in 1× dPBS to prepare a stock solution (50,000 U/mL), followed by sterilization using 0.2 μm PES syringe filter. The stock solution of collagenase type II was stored at −18°C until use.

Strains of *Escherichia coli* (*E. coli*; MG1655, ATCC 47076) and *Staphylococcus aureus* (*S. aureus*; ATCC 29213) were obtained from the School of Biochemical Engineering, University of Birmingham, UK. Nutrient agar, PBS tablets, LB broth, and TSB broth were all dissolved in deionized water with appropriate concentrations and autoclaved at 121°C for 20 min following the manufacturer's protocol.

2.2. Preparation of cell-free bioink formulations

Gelatin methacryloyl (G, 80% methacrylated) was synthesized by gelatin and MA, as described in our previous study.[25] MFC and NFC in PBS were mixed and homogenized at five different volume ratios of 0:100, 25:75, 50:50, 75:25, and 100:0, separately. The corresponding cellulose suspensions were named NFC100, MFC25/NFC75, MFC50/NFC50, MFC75/NFC25, and MFC100. Cell-free cellulose-composited G/A bioink was formulated by adding 7.5 w/v% G, 2 w/v% A, and 0.35 w/v% Irgacure 2959 to the above five types of cellulose suspensions, followed by homogenization at room temperature (19°C) and then heating in a 50°C water bath for 12 h until sample G and A reached a dissolution equilibrium. The resulting product was centrifuged at 500 rpm for 1 min to remove air bubbles and stored at room temperature for use. The five different bioink formulations were named G/A/NFC100, G/A/MFC25/NFC75, G/A/MFC50/NFC50, G/A/MFC75/NFC25, and G/A/MFC100, respectively.

2.3. Rheological characterization

Rheological measurement of bioink formulations was carried out using a rheometer (Discovery HR-1, TA Instrument, UK), with a Peltier cone-plate measurement geometry (diameter of 40 mm, cone angle of 4°, truncation gap of 112 μm). Samples were subjected to a shear rate (γ) sweep ranging from 0.01 to 100 s^{-1} while the shear stress (σ) was recorded. Power-law flow model was used to analyze the flow behavior of samples:

$$\sigma = k_{PL}\gamma^{n_f} \quad \text{(I)}$$

where k_{PL} and n_f are flow consistency index and viscosity index, respectively. The rapid recoverability of viscosity for bioink formulations postextrusion was assessed by a dedicated peak hold program, with which the shear rate was set to 1 s^{-1} for 60 s initially, increased to 300 s^{-1} for 5 s to replicate the extrusion process, and finally reduced to 0.1 s^{-1} for 235 s. Furthermore, a strain cycle program was applied to track the recoverability of storage modulus (*G'*) and loss modulus (*G"*) upon four cycles of high strain (100%) for 150 s and low strain (1%) for 150 s at a frequency of 1 Hz. The sample was allowed to stabilize for 5 s at each transition between high and low strain. The testing temperature was set at 25°C. The sample was placed on the geometry plate for 3 min before each test to ensure a uniform temperature. Every type of measurement was repeated in triplicate.

2.4. 3D printing

The printability of cell-free bioink formulations was assessed by a nozzle-based pneumatic extrusion bioprinter (RegenHU, 3D Discovery, Switzerland). The effects of printing parameters, including dispensing pressure (P), printing speed, and nozzle gauge (G_N), on printing accuracy and shear stress were investigated by measuring the width of extruded filament line (W_L). Parameter optimization index (POI) was introduced to determine the optimal printing conditions of formulations and is expressed as follows:

$$POI_i = \frac{1}{W_L \cdot P \cdot G_N} \quad \text{(II)}$$

$$POI = \frac{POI_i}{POI_{MAX,n}} \quad \text{(III)}$$

where POI_i stands for POI in an individual set of parameters and $POI_{MAX,n}$ denotes the maximum POI_i over the total range of parameter combinations n. Therefore, the value of POI is between 0 (the worst) and 1 (the best).[28,29] The dispensing pressure was adjusted in the range of 20–60 kPa and printing speed was chosen from 2 to 74 mm/s. The predicted widths of the filament provided by the bioprinting software are 0.47 and 0.23 mm when being extruded from 22- (22G) and 27-gauge (27G) nozzles, respectively. Images of filaments at different printing parameters were captured

and analyzed using Image J software (National Institutes of Health, USA). At least ten different positions on the filament were selected to calculate the averaged width of the filament.

The formulated bioinks were subsequently printed to two-dimensional (2D) lattices (side of 20 mm, line space of 4 mm, grids of 5 × 5) at the optimal printing conditions to investigate 2D printability using printability index (*Pr*):

$$Pr = \frac{L^2}{16A} \quad \text{(IV)}$$

where L and A are the perimeter and area of one grid constructed, respectively. Bioink formulations that produced square grids in the printed lattice have the optimum *Pr* of 1, while samples with circular grids due to interlayer fusion showed the worst *Pr* of $\pi/4$.[30]

Stability of the crosslinked scaffolds was evaluated by constructing a 20-layered structure with three different shapes: an 8 mm square, a 9 mm pentagram, and a 10 mm-diameter tube. Formulated G/A/NFC100 was dispensed by a 22G nozzle at a printing speed of 22 mm/s and dispensing pressure of 25 kPa. These structures were subsequently crosslinked by exposing to a ultraviolet (UV) source (OmniCure S2000 Spot UV Curing System, wavelength of 365 nm, iris setting of 70%, working distance of 2 cm) for 3 min, followed by immersion in a 2% $CaCl_2$ solution for 3 min. These hollow structures were pressed manually, of which the shape recovery process was recorded.

2.5. Swelling

The formulated bioinks were placed in a customized elastomer mould, followed by UV irradiating for 3 min and submerging in 2% $CaCl_2$ for 12 h at room temperature to allow double crosslinking. Cellulose-composited ICE G/A hydrogel discs with a thickness of 4 mm and a diameter of 12 mm were immersed in PBS solution for 24 h to remove unreacted Irgacure 2959 and Ca^{2+}. Such hydrogel discs were freeze-dried to measure their initial dry mass (W_{dry}), and subsequently immersed in deionized water for 48 h at room temperature. Equilibrium hydration degree (EHD) of the hydrogel disc was estimated using the wet mass after 48 h swelling ($W_{wet,48\,h}$) based on the following equation:

$$EHD(\%) = \frac{W_{wet,48h} - W_{dry}}{W_{wet,48h}} \times 100 \quad \text{(V)}$$

2.6. Biodegradation characterization

Each dried hydrogel disc was immersed in 1 mL of 1× dPBS containing 5 U/mL collagenase type II and kept at 37°C. The enzymatic biodegradation solution was replaced every 2 days. After 1, 3, 7, and 10 days, the remaining hydrogel disc was lyophilized and weighed, based on which the biodegradation rate (*BDR*) was calculated according to the equation below:

$$BDR(\%) = \frac{W_{dry} - W_n}{W_{dry}} \times 100 \quad \text{(VI)}$$

where W_n is the remaining dry mass of the samples after biodegradation of n day.

2.7. Morphological characterization

Changes in the morphology of the hydrogel during biodegradation were recorded by scanning electron microscopy (SEM; XL-30 field emission, Philips, USA). Freeze-dried hydrogel discs were coated with a gold layer with a thickness of approximately 20 nm prior to the SEM measurement. Micro-computed tomography (μCT; SkyScan 1172, Bruker, Germany) was used to investigate the structural characteristics of the freeze-dried hydrogel discs in 360° at a rotation step of 0.4°. The resulting 2D projection images of specimens were reconstructed by NRecon and organized to 3D images in CT Analyzer (CTAn; Bruker, Germany) software program to obtain the porosity and pore size distribution of the sample.

2.8. Bioprinting

Formulation component G, A, and Irgacure 2959 were dissolved in an autoclaved NFC suspension under the sterile environment, followed by homogenization, water bath, and degassing. The resulting sterile G/A/NFC100 formulation was gently mixed with mouse preosteoblasts MC3T3-E1 Subclone 4 (passages 6–9). The cell-containing bioink formulation with a density of 1.56×10^6 cells/mL was loaded into the bioprinter and extruded with a 27G nozzle at a print speed of 2 mm/s and a dispensing pressure of 25 kPa. The resulting scaffolds with side length of 10 mm and layer numbers of 4–6 were exposed to UV radiation for 10 and 15 s, respectively, and immersed in 2% $CaCl_2$ subsequently for 5 min. Cell-encapsulated scaffolds were cultured in a humidified incubator at 37°C with 5% CO_2, and cell culture medium was changed every 2 days.

2.9. Live/dead assay

Cell viability in 4- and 6-layered scaffolds was measured using the Live/Dead assay following the manufacturer's protocol. Calcein-AM and ethidium homodimer-1 were diluted in sterile dPBS and mixed thoroughly. At each time point, the scaffold sample was incubated in 1 mL of staining solution containing 1 μL/mL calcein-AM and 4 μL/mL ethidium homodimer-1 at 37°C with 5% CO_2 for 20 min. Once the staining reagent was gently aspirated, the scaffold was washed once with dPBS to minimize any

potential background signal. The cell-loaded scaffolds were imaged using a confocal laser scanning microscope (Zeiss LSM780, Carl Zeiss Microscopy, US). ImageJ was then used to process the Z-stack images of the cells and to perform live/dead cell counts.

2.10. Drug loading

Ampicillin was used as a model drug to study the controlled drug release profile of hydrogels in this work. Preweighted dried hydrogel discs were immersed in 50 mL standard solution of ampicillin (100 μg/mL), followed by incubation at 20°C with a continuous agitation at 100 rpm. At scheduled time intervals, free ampicillin of 1 mL was aspirated, and the absorbance was read at 220 nm immediately using a UV/Vis spectrometer (BiochromLibraS12, Cambridge, UK). The standard calibration curve of ampicillin was obtained before the test. The withdrawn liquid was replaced with an equal volume of fresh sterile PBS. The drug loading capacity (*LC*, measured as mg/g) after 24 h was determined following the equation below[31]:

$$LC\left(\frac{mg}{g}\right)=\frac{W_{\mathrm{Amp,T}}-W_{\mathrm{Amp,F}}}{W_{\mathrm{dry}}} \quad \text{(VII)}$$

where $W_{\mathrm{Amp,T}}$ (mg) is the total ampicillin mass, while $W_{\mathrm{Amp,F}}$ (mg) represents the free mass of ampicillin after 24 h. In this work, the ampicillin-loaded hydrogel specimens were named as G/A-AMP and G/A/NFC100-AMP.

2.11. Drug release

Ampicillin-loaded hydrogels were immersed in 50 mL of sterile PBS at 20°C, shaken continuously at 80 rpm. At predetermined time intervals, 1 mL release medium was pipetted and replaced with same amount of fresh PBS solution. The amount of cumulative released ampicillin ($W_{\mathrm{Amp,R}}$) was recorded using a spectrometer. The cumulative release (*CR*) of ampicillin was estimated by the following equation:

$$CR(\%)=\frac{W_{\mathrm{Amp,R}}}{W_{\mathrm{Amp,T}}-W_{\mathrm{Amp,F}}}\times 100 \quad \text{(VIII)}$$

The measurement was terminated when the absorbance of the release medium reached equilibrium. The first 60% release of ampicillin was logarithmically fitted based on the power-law model:

$$\frac{M_t}{M_\infty}=kt^{n_r} \quad \text{(IX)}$$

where M_t and M_∞ are the cumulative release amount of the drug at time t and the total amount of drug that can be released, respectively; k is the release rate constant.[32] More importantly, the release index (n_r) is used to characterize the drug release mechanism. For cylindrical polymer release system applicable to this work, $n_r \leq 0.45$ indicates a Fickian diffusion-controlled release (case I transport), while n_r of 0.89 (case II transport) means that the drug is released at a constant rate and independent of drug concentration and time. In most cases reported in the literature, n_r lies between 0.45 and 0.89, suggesting that the drug release is governed by a combination of diffusion and other complex factors where the release mechanism is anomalous transport. Only in rare cases, such as when the polymer matrix is severely modified, the release index is greater than 0.89 and a super case II diffusion occurs.[33,34]

2.11. Agar disc diffusion assay

E. coli was incubated in LB broth while *S. aureus* in TSB medium overnight at 37°C with a constant shaking at 150 rpm. The overnight grown bacterial cultures were pelleted, washed twice, and resuspended in the corresponding growth media to achieve an optical density (OD) at 600 nm of 0.5 AU. G/A-AMP and G/A/NFC100-AMP hydrogel discs were filled into agar plate wells. Bacterial cultures of 150 μL were distributed uniformly across the agar plate and statically incubated at 30°C for *E. coli* and 37°C for *S. aureus* for 24 h, respectively. The inhibitory zones for bacterial growth were subsequently measured. All samples were transferred from the day-1 plates into freshly inoculated agar plates and subsequently incubated for an additional 24 h followed by the same measurements. This procedure was repeated, and the inhibitory results were recorded after a total incubation period of 3 days. Both positive (100 μg/mL ampicillin-loaded filter paper discs with 13 mm diameter) and negative control (G/A and G/A/NFC100) procedures were carried out in accordance with the same protocol. Every sample against bacterial strains was subjected to three independent replicates.

2.12. Statistical analysis

The results from quantitative experiments were analyzed in OriginPro 2022 (OriginLab, USA) and expressed as mean ± standard deviation ($n \geq 3$). Significant differences were determined using one-way analysis of variance (ANOVA) followed by Tukey's post hoc test for pairwise comparisons. Statistical significance was determined at the 0.05 level. The p-values labeled in all figures are $^{*}p \leq 0.05$, $^{**}p \leq 0.01$, and $^{***}p \leq 0.001$, respectively.

3. Results and discussion

3.1. Rheological properties

Viscosity of the bioink plays a pivotal role in 3D bioprinting. Because the viscoelastic behavior of each formulation is influenced by the intrinsic properties of the components applied, suitable viscosity range of bioink formulations

for extrusion bioprinters covers a broad range from 30 to 6 × 10^7 mPa s^{-1}.[35] For a given formulation, it is crucial to consider the upper limit of viscosity (principle of not clogging the nozzle), the lower limit (criterion for forming connected filaments rather than droplets), and the change in viscosity during the extrusion process for a successful printing execution while minimizing the impact of the shear on the encapsulated cells.[36] In this work, flow behaviors of the mixed cellulose suspensions were characterized (Figure 1A) prior to investigating the change in viscosity of formulated bioinks as a function of the shear rate. With an increased shear rate from 10^{-2} to 10^2 s^{-1}, viscosity of cellulose suspensions was found to decrease by five orders of magnitude within above viscosity range of 30–6 × 10^7 mPa s^{-1}, exhibiting an excellent shear-thinning behavior. Our previous study shows that the viscosity of the G/A formulation decreases from 40.4 to 2.1 Pa·s in the same shear rate range and the corresponding viscosity index is 0.52.[26] However, once the cellulose fibres were introduced to the G/A formulation, the viscosity range of the bioink formulations is expanded significantly to three orders of magnitude (about 8,000 to 7 Pa·s) under the same shear rate range (Figure 1B). The rheological behavior of all five samples was found to follow power law model (R^2 of greater than 0.99) with n_f numbers of approximately 0.2 (Figure 1C), which is in a good agreement with the shear thinning properties previously observed for nanocellulose system by other research groups.[37,38] The shear-thinning behavior of the cellulose-composited G/A formulations confirms that the polymeric constituents of the bioink formulation could be aligned in the direction of the shear-induced flow since the interactions between them were readily disrupted by the shear forces. It is worth noting that neither the differences in cellulose fiber size nor the NFC/MFC ratios in bioink formulations has a notable impact on the shear-thinning behavior of the cellulose composited G/A bioink.

The fast self-healing or recovery properties of the bioink post extrusion were characterized by peak hold (Figure 1D) and dynamic low-high strain tests (Figure 1E). The viscosity of all cellulose-composited G/A formulations

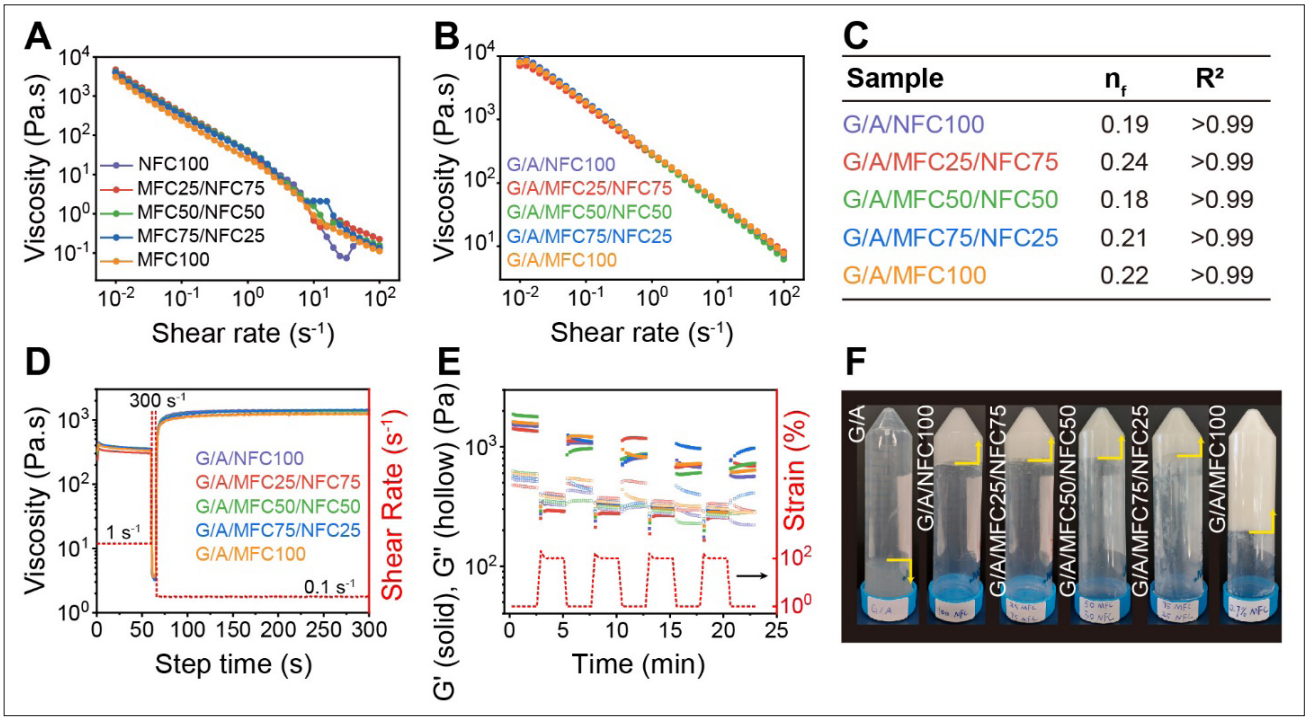


Figure 1. Rheological properties of G/A formulation enhanced by fibrillated cellulose. (A) Viscosity of cellulose suspension NFC100, MFC25/NFC75, MFC50/NFC50, MFC75/NFC25, and MFC100 as a function of shear rate. (B) Viscosity of bioink formulation G/A/NFC100, G/A/MFC25/NFC75, G/A/MFC50/NFC50, G/A/MFC75/NFC25, and G/A/MFC100 as a function of shear rate. (C) Power law viscosity index (n_f) of cellulose incorporated G/A formulations. Both MFC and NFC can improve the shear-thinning behavior of G/A formulation. (D) The viscosity response of cellulose-composited G/A bioinks to sudden increase in shear rate to 300 s^{-1} at 60 s and decrease to 0.1 s^{-1} at 65 s, respectively. (E) Changes of storage modulus (*G'* in solid points) and loss modulus (*G"* in hollow points) for formulations in dynamic strain cycle alternating 1% for 150 s and 100% strain for 150 s. (F) Cellulose-composited G/A formulations and the benchmark are inverted for 1 h. The benchmark G/A flows to the top of the sample tube, while cellulose-composited G/A formulations remain in the initial position, indicating the gel state of the formulations. Abbreviations: G/A, Gelatin methacryloyl/alginate; MFC, Microfibrillated cellulose; NFC, Nanofibrillated cellulose.

immediately decrease to approximately 4 Pa·s when the shear rate rises from 1 to 300 s^{-1} but increase to nearly 1050 Pa·s in just 8 s responding to the sudden drop of shear rate to 0.1 s^{-1} (Figure 1D). Moreover, the formulations display the characteristic rheological behavior of a gel ($G' > G''$) at low strains (1%). However, G' drastically decreases, suggesting a sol state is formed ($G'' > G'$), once a high strain (100%) is applied, following which a gel-like behavior is observed upon the introduction of low strain. Such recovery behavior can be observed after four high-low strain repeated cycles (Figure 1E). The results align with our previous work concerning MFC-composited G/A formulation,[26] and further evidence the high recovery properties of pure NFC-composited and hybrid cellulose-composited G/A formulations.

Figure 1F and Figure S1 show the macroscopic gel or sol behavior with visual evidence by inverting the centrifuge tubes containing the bioink formulation after 1 h. In both the single-component and binary systems, all samples migrated to the opposite end of the tube, exhibiting a freely flowing, sol-like behavior. This observation indicates that the physical entanglement among the components in these one- and two-component formulations is too weak to achieve the minimum viscosity required for maintaining continuous filaments after extrusion. In contrast, any ternary formulation of G/A containing cellulose remained in place, demonstrating that all three components are indispensable; the mutual entanglement among them yields a sufficiently high viscosity that drives the system into a gel-like state. Such gel-like behavior not only helps maintain a stable and homogeneous formulation prior to printing but also enables the extruded filaments to retain their shape after deposition.

3.2. Printability analysis of formulations

To determine the optimal printing conditions for the bioink formulations, the effects of dispensing pressure, print speed, and nozzle size on the precision of extruded filaments were studied. Figure S2 shows the acquired images and corresponding line widths of filaments formed by G/A/MFC100 formulation using a 27G nozzle as a function of dispensing pressures and print speeds. The gray area is the printable area. Both Figure S2 and Figure 2A show that the line width decreases exponentially as the printing speed increases under a constant dispensing pressure. Figure 2B reveals that the line width increases linearly with the rise of dispensing pressure at a constant printing speed. It is worth highlighting that the filament exhibits the thinnest line width of 0.49 mm when the print speed is 24 mm/s and the dispensing pressure is 55 kPa. Taking consideration of the damage to the encapsulated cells by shear stress during the extrusion process and the accuracy of printing, Figure 2C shows that *POI* has a maximum value with a line width of 0.5 mm when the print speed is 2 mm/s and the dispensing pressure is 30 kPa, which is the optimal printing condition for such formulation when using a 27G nozzle.

The continuity of the filament is observed to be seriously damaged, so-called under-extrusion, when the dispensing pressure is less than 30 kPa (pink area), or the print speed is too fast (yellow zone), as shown outside the gray printable area of Figure S2. If the bioink formulation is extruded at a print speed of less than 2 mm/s at a dispensing pressure of 30–40 kPa, especially when constructing larger-sized scaffolds, long printing time would naturally cause water evaporation in the scaffold, resulting in a failed construction (orange region). When the print speed is less than 2 mm/s and the distribution pressure is greater than 45 kPa, the resolution of the filament drops sharply, resulting in over-extrusion (blue area). In addition, distribution pressure should be adjusted by taking serious consideration of the impact of shear force on cell viability (green zone).

When a 22G nozzle was used to extrude G/A/MFC100 formulation, the printable area (gray region) was found to be greater than that when using a 27G nozzle (Figure S3). It is clear that the increased nozzle inner diameter (200–410 μm) allows the 3D printer to dispense filament at an increased print speeds for high resolution. The influence of print speed and dispensing pressure on filament line width (Figure 2D and E) is consistent with the findings when using a 27G nozzle. Although the thinnest line width (0.67 mm) was produced at a print speed of 60 mm/s and a dispensing pressure of 40 kPa (Figure S3), the optimal printing condition was identified as 22 mm/s and 25 kPa, resulting in a line width of 0.85 mm, once taking consideration of the maximum *POI* value (Figure 2F).

It can be concluded that the printing resolution and printability index (0.892) of G/A/MFC100 are the highest and the degree of interlayer fusion of G/A/MFC100 is the lowest among all three samples studied (Figure 3A) when bioink formulation G/A, G/A/NFC100, and G/A/MFC100 were printed to 2D lattice under the optimal printing condition of G/A/MFC100. The internal lattice of G/A/NFC100 scaffold also tends to be square, as quantified by *Pr* of 0.883, confirming that G/A/MFC100 and G/A/NFC100 show a very similar printability.

The shape fidelity of NFC-composited G/A bioink formulation G/A/NFC100 was evaluated by building a 20-layered construct with different shapes. Since the difference in *Pr* between G/A/NFC100 and G/A/MFC100 is not significant ($p > 0.05$), the optimal printing condition of G/A/MFC100 (printing speed of 22 mm/s, dispensing pressure of 25 kPa, 22G nozzle) was used to extrude

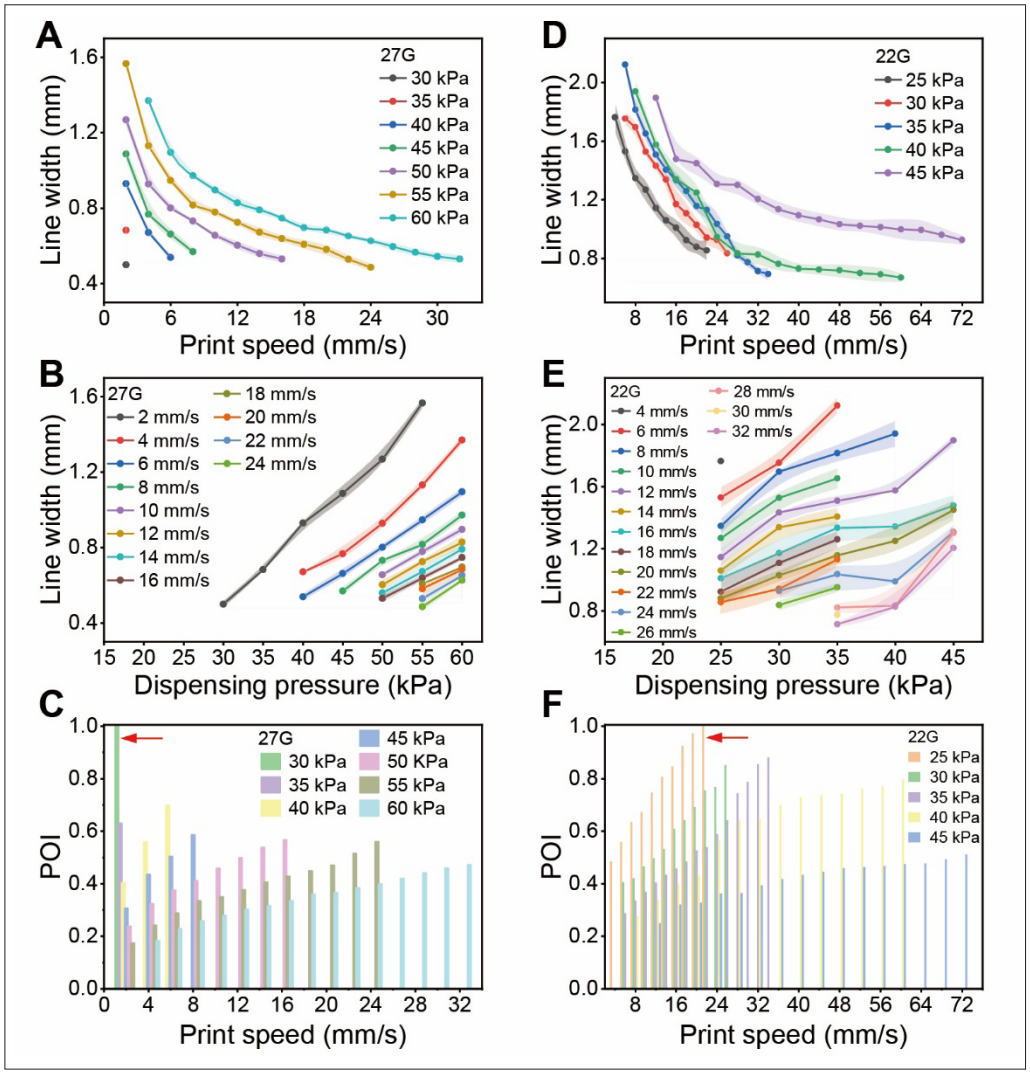


Figure 2. The effects of dispensing pressure, print speed, and nozzle size on the precision of extruded filaments. (A,B) Line width of G/A/MFC100 filament extruded from 27G nozzle as a function of print speed at constant dispensing pressures (A) and dispensing pressure at constant print speeds (B). (C) Comparison of *POI* when G/A/MFC100 was extruded from 27G nozzle, displaying that the optimal printing condition is at 2 mm/s print speed and 30 kPa dispensing pressure. (D,E) Line width of G/A/MFC100 filament extruded from 22G nozzle as a function of print speed at constant dispensing pressures (D) and dispensing pressure at constant print speeds (E). (F) Comparison of *POI* when G/A/MFC100 was extruded from 22G nozzle, demonstrating the optimal printing condition at 22 mm/s print speed and 25 kPa dispensing pressure. Abbreviations: G/A, Gelatin methacryloyl/alginate; MFC, Microfibrillated cellulose; POI, Parameter optimization index.

G/A/NFC100 layer by layer. Figure 3B and C displays the 3D model design and top views of the corresponding constructs, respectively. It is obvious that the side length of the square structure (8 mm) and the length between the two nonadjacent vertices of the five-pointed star (9 mm) are consistent with their corresponding lengths in the design, demonstrating the excellent shape fidelity of NFC-composited ICE hydrogel scaffolds. However, when the tubular structure was constructed, the diameter of the structure is slightly greater than the designed length (10 mm) by approximately 1 mm, indicating that the printing resolution of the G/A/NFC100 formulation needs further improvement. It is worth noting that the G/A/MFC100 formulation was selected as the representative system in determining the optimal printing conditions. Although G/A/MFC100 and G/A/NFC100 exhibit no significant differences in rheological behavior, the latter is intended for printing more complex scaffold geometries in the subsequent stages. Therefore, the current printing parameters serve as a baseline, and the established relationships between filament resolution, printing speed, and dispensing pressure will guide the refinement of the

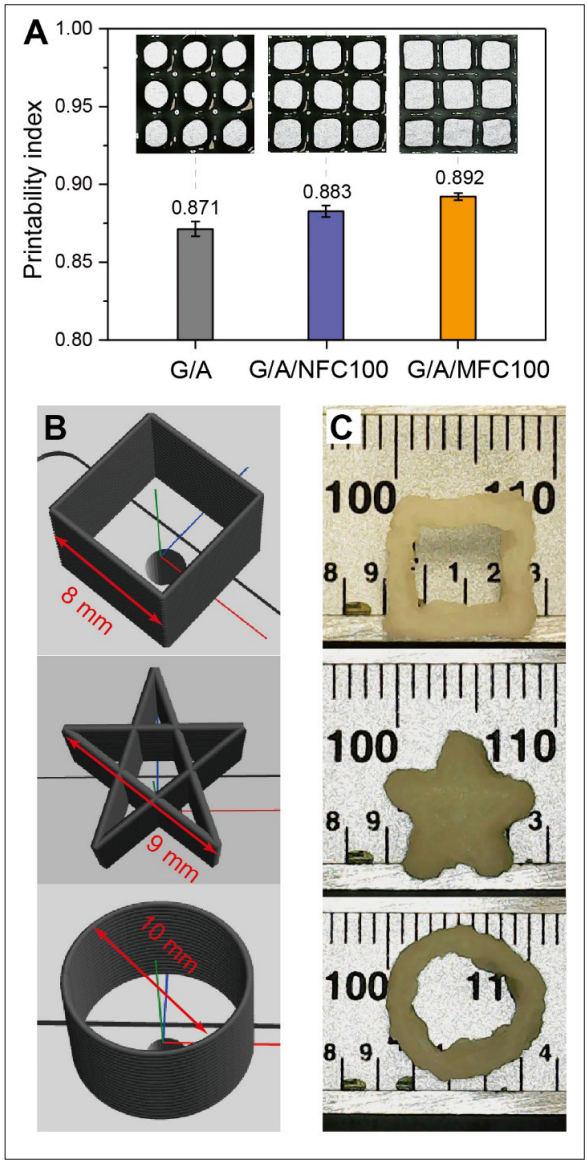


Figure 3. The printability of G/A/NFC100 formulation and the shape fidelity of corresponding constructs. (A) Printability indices and images of scaffolds extruded with G/A, G/A/NFC100, and G/A/MFC100 under the same printing condition (print speed of 2 mm/s, dispensing pressure of 30 kPa, and 27G nozzle). (B) Models and (C) corresponding 20-layered printed structures of G/A/NFC100 at a printing speed of 22 mm/s and a dispensing pressure of 25 kPa using a 22G nozzle. Abbreviations: G/A, Gelatin methacryloyl/alginate; MFC, Microfibrillated cellulose; NFC, Nanofibrillated cellulose.

optimal printing window for G/A/NFC100 to enable the fabrication of high-resolution constructs.

In addition, by performing three consecutive press-relax cycles from the sides of these three constructs using a tweezer (Videos S1, S2, and S3), we showed that the shape of the constructs changed accordingly, but returned to the initial state after the last relax fully, proving the mechanical stability of crosslinked interlayers and excellent elasticity of the crosslinked body. As demonstrated in our previous work,[25] this mechanical stability arises from the synergistic interactions within the ion–covalent interpenetrating dual network formed by gelatin methacryloyl and sodium alginate, further reinforced by the additional cooperation of NFC with this dual-network structure.

3.3. The effect of cellulose on equilibrium hydration degree and enzymatic biodegradation behavior of G/A ICE hydrogel

Previous experiments by the authors show that the swelling ratio of the dried hydrogel G/A/MFC100 reaches equilibrium after 1 day of immersion in water and remains

constant for 10 days.[26] In this work, the effects of NFC and hybrid cellulose on the *EHD* of G/A ICE hydrogels were evaluated based on the same protocol, of which the results are shown in Figure 4A**.** G/A/NFC100 and hybrid cellulose-composited G/A ICE hydrogels (G/A/MFC25/NFC75, G/A/MFC50/NFC50, G/A/MFC75/NFC25) have no significant differences in *EHD* with G/A/MFC100 ($p > 0.05$) and all remain around 87%, indicating that the size of fibrillated fiber does not have a noticeable effect on the water content of the hydrogel.

The effect of NFC on the enzymatic biodegradation profile of G/A ICE hydrogel in dPBS containing 5 U/mL collagenase type II was investigated. As shown in Figure 4B and Figure S4, *BDRs* of G/A/NFC100 after 3, 7, and 12 days are 5.56%, 37.08%, and 50.99%, respectively, slightly faster than that of G/A/MFC100 (3.21%, 31.77%, and 45.52% after 3, 7, and 12 days, respectively). In contrast, *BDR* of G/A reaches 62.55% after 7 days, and the G/A sample fully biodegrades over 12 days.[26] Hence, the incorporation of fibrillated cellulose can significantly slow down the chain breakage of gelatin methacryloyl and consequently prolong the biodegradation process of G/A ICE hydrogel. This result is supported by the porosity data of the materials (60.85% of G/A, 41.9% of G/A/MFC, and 43.19% G/A/NFC100) reported in our previous studies.[25] The entanglement between fibrillated cellulose and the ICE network enhances the crosslinking density and reduces the porosity of the system, and thus increases the diffusion resistance of collagenase type II. In addition, the morphology and pore size distribution of the G/A/NFC100 hydrogel were captured by SEM (Figure 4C, D, and E) and μCT (Figure 4F) before biodegradation, after 3 and 7 days upon initiation of the biodegradation. Although the biodegradation behavior of G/A/NFC100 results in an increased pore size and an expanded pore size distribution, G/A/NFC100 retains an internally connected pore structure after 7 days of biodegradation, which is consistent with the morphological changes of G/A/MFC100 during the biodegradation process, but is in obvious contrast to those of G/A (characterized by pore wall cracking and nonconnectivity).[26] Connected pore structure of G/A/fibrillated cellulose hydrogel during *in vivo* and *in vitro* culturing process is important for the ordered transportation of nutrients and metabolic wastes of cells within the scaffold.

3.4. Bioprinting of cell-laden scaffolds and cell viability after bioprinting

The biocompatibility of G/A/NFC100 was studied by printing cell-encapsulated scaffolds and culturing them continuously for 21 days. As shown in Figure 4G–H and Figure S5, MC3T3-E1 are evenly distributed in the scaffold, and the cell viabilities in the 4- and 6-layered scaffolds gradually increase from 67.89% to 96.25% and from 79.83% to 97.64%, respectively, within the first 10 days. After 14 days in culture, cells started elongating along the inner structure of the scaffold. Furthermore, cells proliferated significantly after 21 days, confirming the cytocompatibility of G/A/NFC100. Moreover, it was found that the growth profiles of MC3T3-E1 within G/A/NFC100 and G/A/MFC100[26] scaffolds are consistent, indicating that despite the size differences between NFC and MFC, both types of fibrillated cellulose can protect cells from shear damage during extrusion printing and do not affect the growth kinetics of encapsulated MC3T3-E1 over the 21-day *in vitro* culture period. On the other hand, the cell-attachment properties of gelatin have been widely reported[39] and our experimental results further illustrate that the growth process of cells in the scaffold was relatively slow before adhesion occurred, but the life activities of the cells can be significantly accelerated after adhesion to gelatin. Furthermore, changes in the pore structure of the cell-encapsulated G/A/NFC100 scaffolds were captured over 21 days of culture (Figure 4I). Compared with the samples cultured for 7 days, the pore sizes of the 4- and 6-layered scaffolds cultured for 21 days were found to increase, which can be attributed to the natural degradation caused by the decreased crosslinking density of the scaffold and the biodegradation associated with cellular activities. It is believed that the increasing pore size of the scaffold and the growth of cells can offer complementary advantages, forming a favorable environment for tissue remodeling.

3.5. Drug release profile and effects of NFC on functions of ampicillin in hydrogels

According to **Equation (VII)**, the saturated loading capacities of the dried hydrogel disc G/A and G/A/NFC100 after 24 h of immersion in standard ampicillin solution are 7.34 and 8.12 mg/g, respectively, demonstrating the ability of NFC to increase the drug loading of G/A. Additionally, NFC incorporation was found to significantly alter the drug release profile of G/A-AMP when ampicillin was released from hydrogel samples, as shown in Figure 5A. Based on the 50% cumulative release of ampicillin, we found that NFC could prolong the drug release from G/A-AMP from 4.92 h to 24–48 h. Moreover, the cumulative release of ampicillin from G/A/NFC100-AMP was 67.42% until 72 h, higher than that of G/A/MFC100-AMP (43.75%) due to the difference in porosities (Figure S6A). Yet, both G/A/NFC100-AMP and G/A/MFC100-AMP displayed an initial mild release in the first 6 h followed by a prolonged release phase (Figure S6A).[26] When analyzing the cumulative release of ampicillin with the power-law model (**Equation IX**), it was found that the release kinetics of ampicillin changes from Fickian diffusion control (release

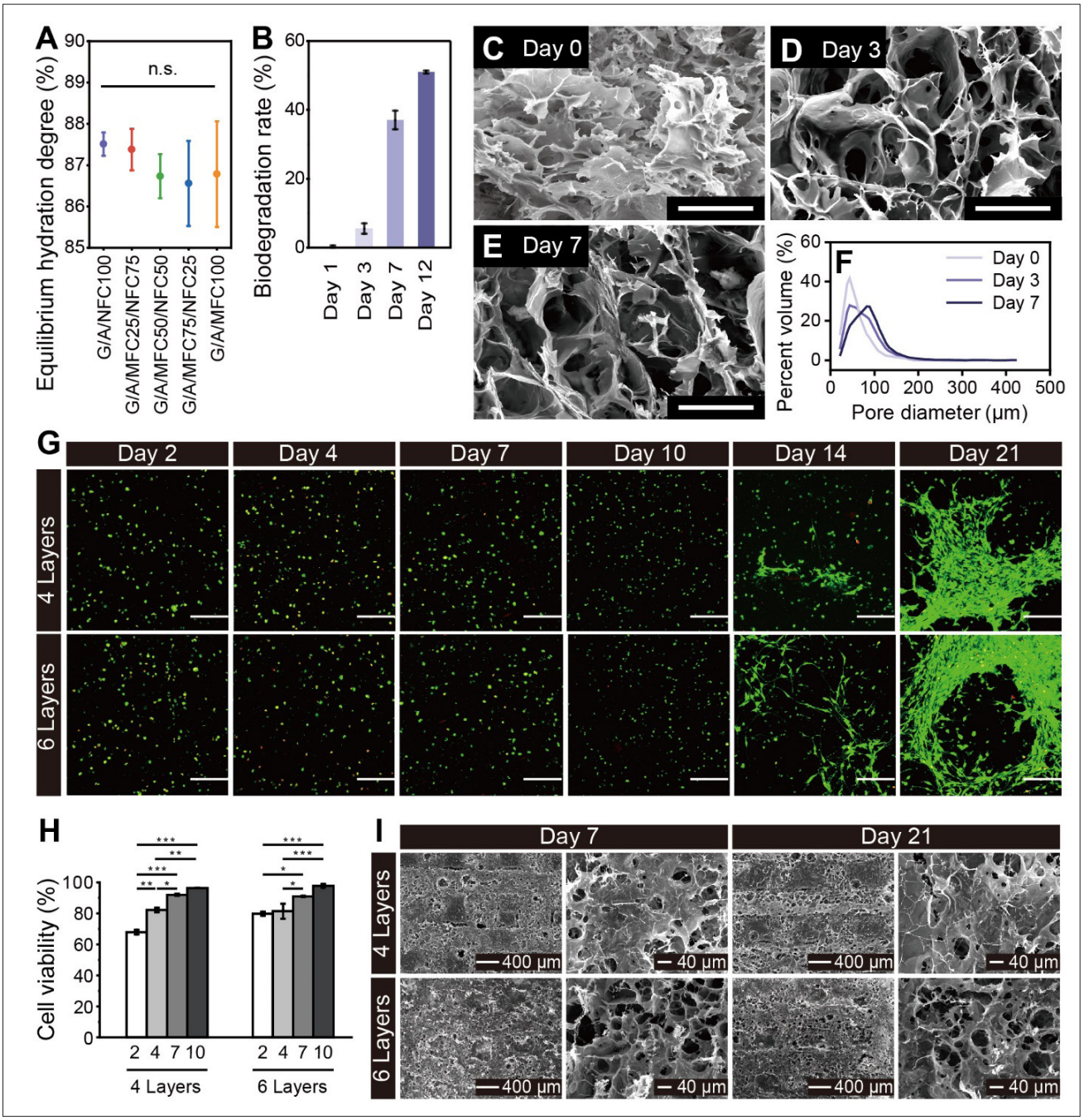


Figure 4. Prolonged biodegradation of G/A/NFC100 hydrogel and cytocompatibility of G/A/NFC100 scaffolds. (A) Equilibrium hydration degree of cellulose-composited G/A ICE hydrogels after 48 h of swelling in deionized water. The size of fibrillated fiber does not have much effect on the water content of the hydrogel. (B) Biodegradation rates of G/A/NFC100 after 1, 3, 7, and 12 days of immersion in 1× dPBS with 5 U/mL collagenase type II. (C–E) Morphologies of G/A/NFC100 hydrogel before biodegradation (C), after 3 days (D), and 7 days of biodegradation (E) by SEM. Scale bar = 100 μm. (F) The pore size distribution of G/A/NFC100 after 0, 3, and 7 days of biodegradation by μCT. (G) Confocal Z-stack images of merged dead and live cells in 4- and 6-layered G/A/NFC100 scaffolds over 21 days. Scale bar = 200 μm. (H) Cell viability in bioprinted G/A/NFC100 scaffolds with 4 and 6 layers after incubation of 2, 4, 7, and 10 days. (I) SEM images of cell-loaded 4- and 6-layered G/A/NFC100 scaffolds after incubation of 7 and 21 days at different magnifications. Abbreviations: dPBS, Dulbecco's phosphate-buffered saline; G/A, Gelatin methacryloyl/alginate; ICE, Ion–covalent entanglement; MFC, Microfibrillated cellulose; μCT, Micro-computed tomography; NFC, Nanofibrillated cellulose; SEM, Scanning electron microscopy.

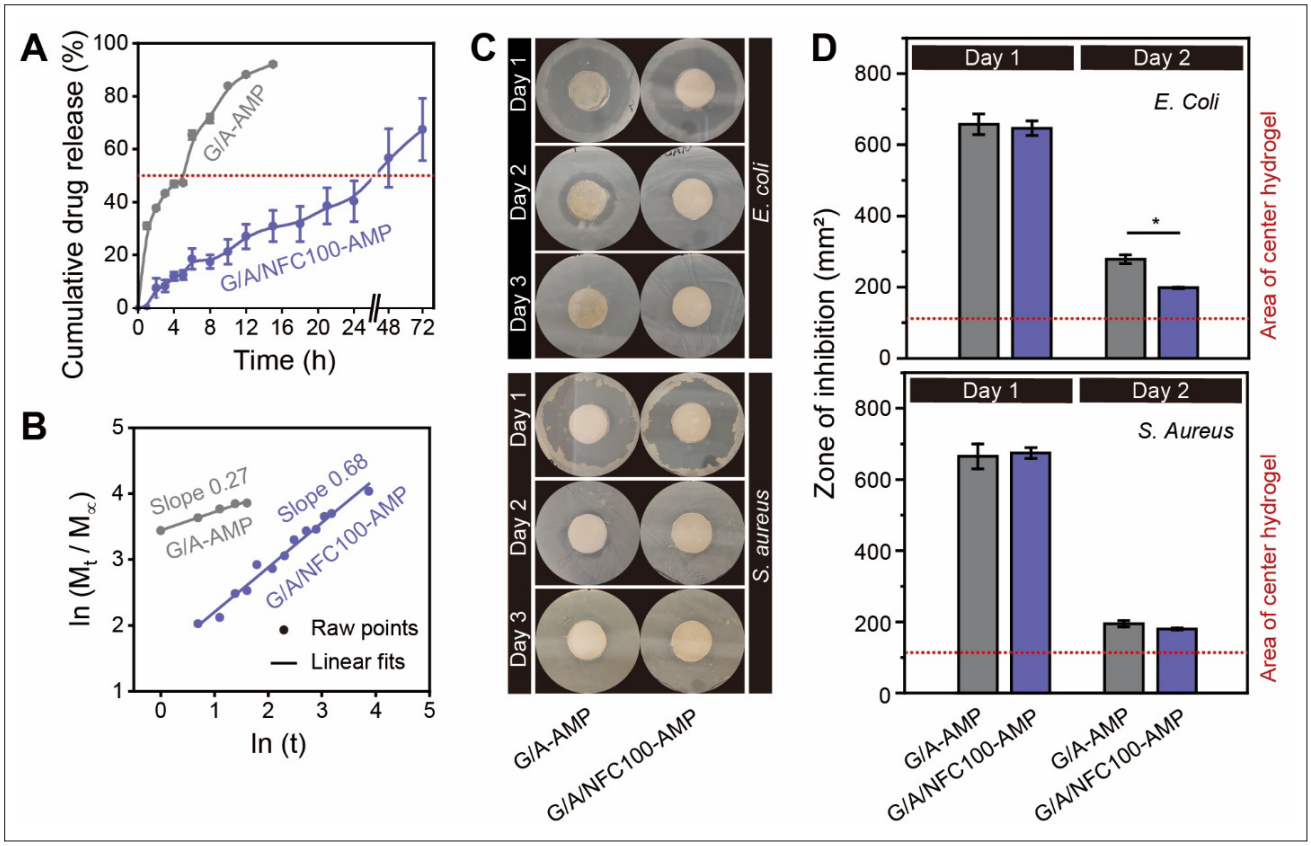


Figure 5. Controlled drug release and antibacterial properties of G/A/NFC100-AMP hydrogels. (A) Representative curves of cumulative drug released from G/A-AMP and G/A/NFC100-AMP hydrogel discs over time. NFC slows down the process of ampicillin release from the hydrogel discs. (B) Linear fits of the first 60% cumulative drug release according to **Equation IX**. The slope of the linear fits represents the release index (n_r), characterizing the drug release mechanism. The addition of NFC changes the ampicillin release mechanism of G/A hydrogel from Fickian diffusion-controlled release to anomalous transport. (C) Antibacterial activities of ampicillin-loaded hydrogels against *E. coli* and *S. aureus* on agar plates after incubating 1, 2, and 3 days. (D) Areas of the inhibition zone for sample G/A-AMP and G/A/NFC100-AMP against *E. coli* and *S. aureus*. Abbreviations: AMP, Ampicillin sodium salt; G/A, Gelatin methacryloyl/alginate; NFC, Nanofibrillated cellulose.

index n_r of 0.27) in G/A-AMP to anomalous transport (n_r of 0.68) in G/A/NFC100-AMP, as demonstrated in Figure 5B. Moreover, the size differences between NFC and MFC do not significantly affect the release kinetics of ampicillin since n_r all fall within the range of 0.45–0.89 (Figure S6B). The above results indicate that the large specific surface area and porous nature of NFC could promote the physical adsorption of ampicillin on NFC,[40] which not only increases drug loading capacity of G/A/NFC100, but also facilitates the long-term slow release of ampicillin in the sample.

Finally, the impact of NFC incorporation on the capacity of ampicillin to execute its own antimicrobial function within the hydrogel was investigated. In Figure 5C and Figure S7, both G/A-AMP and G/A/NFC100-AMP exhibit clear zones of inhibition against *E. coli* and *S. aureus* on the first day. The inhibition zone is significantly reduced on the second day, while only G/A/NFC100-AMP shows a slight zone of inhibition on the third day. When the area of the inhibitory zone was quantified (Figure 5D), no difference in inhibition against *E. coli* and *S. aureus* was observed between the two samples on the first day. However, the inhibition against *E. coli* by G/A-AMP was superior to that of G/A/NFC100-AMP on the second day, which may be related to the rapid release of ampicillin in G/A-AMP. The above results indicate that NFC does not hinder the antimicrobial properties of ampicillin in hydrogels although AMP physically adsorbs on the NFC network.

4. Conclusion

In this work, nanofibrillated cellulose (NFC)-composited G/A formulation (G/A/NFC100) was developed for 3D bioprinting of mouse preosteoblasts MC3T3-E1. The

excellent shear thinning property, recoverability in viscosity and modulus, and gel-like macro fluidity of G/A/NFC100 evidence that it can be successfully extruded to develop 3D scaffolds suitable for tissue reconstruction. Furthermore, the effects of dispensing pressure, print speed, and nozzle size on the accuracy of extruded filaments were investigated, based on which the optimal printing conditions were confirmed. 20-layered crosslinked scaffolds with different geometries were constructed, which showed an excellent mechanical stability. Moreover, MC3T3-E1 encapsulated in printed G/A/NFC100 scaffolds remained consistently high viability throughout the 21 days of incubation, demonstrating the cytocompatibility of G/A/NFC100 scaffolds. The nanofibrillated cellulose was also able to promote the drug loading capacity of G/A hydrogel and the long-term controlled release of ampicillin. Thus, such active and drug-loaded 3D scaffolds are expected to play a role in multifunctional biomedical applications such as tissue regeneration and drug development.

Acknowledgments

The first author would like to thank Dr. David Bassett and Dr. Miruna Chipara in the Healthcare Technologies Institute for their support on her research.

Funding

We thank the financial support provided by the UKRI (Horizon Europe Guarantee scheme, 10066793), and FiberLean Technologies for kindly providing microfibrillated cellulose samples. Z.J.Z. thanks the financial support given by the Engineering and Physical Science Research Council (EP/V029762/1). N.L. acknowledges the Chinese Scholarship Council for the awarded scholarship (CSC201906950042).

Conflict of interest

The authors declare they have no competing interests.

Author contributions

Conceptualization: Na Li, Zhenyu Jason Zhang
Formal analysis: Na Li, Roxana Guillen De La Cruz, Zhenyu Jason Zhang
Investigation: Na Li, LinGe Wang, Zhenyu Jason Zhang
Methodology: Na Li, Roxana Guillen De La Cruz, Zhenyu Jason Zhang
Writing–original draft: Na Li, LinGe Wang, Zhenyu Jason Zhang
Writing–review & editing: All authors

Ethics approval and consent to participate

Not applicable.

Consent for publication

Not applicable.

Availability of data

Data will be made available upon request to the corresponding author.

References

1 Fang Y, Guo Y, Liu T, *et al*. Advances in 3D bioprinting. *Chin J Mech Eng Addit Manuf Front*. 2022;1(1): 100011.
doi: 10.1016/j.cjmeam.2022.100011

2 Zhang B, Gao L, Ma L, Luo Y, Yang H, Cui Z. 3D bioprinting: a novel avenue for manufacturing tissues and organs. *Engineering*. 2019;5(4):777-794.
doi: 10.1016/j.eng.2019.03.009

3 Sharma C, Raza MA, Purohit SD, *et al*. Cellulose-based 3D printing bio-inks for biomedical applications: a review. *Int J Biol Macromol*. 2025;305:141174.
doi: 10.1016/j.ijbiomac.2025.141174

4 Mo Q, Huang L, Sheng Y, *et al*. Crosslinking strategy and promotion role of cellulose as a composite hydrogel component for three-dimensional printing – a review. *Food Hydrocoll*. 2024;154:110079.
doi: 10.1016/j.foodhyd.2024.110079

5 You P, Sun H, Chen H, *et al*. Composite bioink incorporating cell-laden liver decellularized extracellular matrix for bioprinting of scaffolds for bone tissue engineering. *Biomater Adv*. 2024;165:214017.
doi: 10.1016/j.bioadv.2024.214017

6 Ouiyangkul P, Hirun N, Suknuntha K, Tantishaiyakul V. Development and characterization of 3D bioprintable and mechanically reinforced hydrogel based on gellan gum/methylcellulose/cellulose nanocrystals. *Polym Adv Technol*. 2024;35(1):e6206.
doi: 10.1002/pat.6206

7 Suamte L, Tirkey A, Barman J, Jayasekhar Babu P. Various manufacturing methods and ideal properties of scaffolds for tissue engineering applications. *Smart Mater Manuf*. 2023;1:100011.
doi: 10.1016/j.smmf.2022.100011

8 Mohammed A, Jiménez A, Bidare P, *et al*. Review on engineering of bone scaffolds using conventional and additive manufacturing technologies. *3D Print Addit Manuf*. 2023;11(4):1418-1440.

doi: 10.1089/3dp.2022.0360

9 Li N, Guo R, Zhang ZJ. Bioink formulations for bone tissue regeneration. *Front Bioeng Biotechnol*. 2021;9. doi: 10.3389/fbioe.2021.630488

10 Yang J, Wang J, Yang Y, *et al*. 3D-printed bioactive scaffolds: an emerging strategy for the regeneration of infectious bone defects. *Int J Bioprint*. 2024;11(2):79-138. doi: 10.36922/ijb.4986

11 Zhao T, Liu Y, Wu Y, Zhao M, Zhao Y. Controllable and biocompatible 3D bioprinting technology for microorganisms: fundamental, environmental applications and challenges. *Biotechnol Adv*. 2023;69:108243. doi: 10.1016/j.biotechadv.2023.108243

12 Chen A, Wang W, Mao Z, *et al*. Multimaterial 3D and 4D bioprinting of heterogenous constructs for tissue engineering. *Adv Mater*. 2024;36(34):2307686. doi: 10.1002/adma.202307686

13 Liu S, Yu J-M, Gan Y-C, *et al*. Biomimetic natural biomaterials for tissue engineering and regenerative medicine: new biosynthesis methods, recent advances, and emerging applications. *Mil Med Res*. 2023;10(1):16. doi: 10.1186/s40779-023-00448-w

14 Tarsitano M, Ming CLC, Idais D, *et al*. Sericin improves alginate-gelatin hydrogels' mechanical properties, porosity, durability, and viability of fibroblasts in cardiac spheroids. *Int J Bioprint*. 2024;11(1):327-346. doi: doi: 10.36922/ijb.5678

15 Jahani A, Nourbakhsh MS, Ebrahimzadeh MH, Mohammadi M, Yari D, Moradi A. Biomolecules- loading of 3D-printed alginate-based scaffolds for cartilage tissue engineering applications: a review on current status and future prospective. *Arch Bone Jt Surg*. 2024;12(2):92-101. doi: 10.22038/abjs.2023.73275.3396

16 Liu F, Jiang J, Zhe M, Yu P, Xing F, Xiang Z. Alginate-based 3D bioprinting strategies for structure–function integrated tissue regeneration. *J Mater Chem B*. 2025;13(40):12765-12811. doi: 10.1039/D5TB01489A

17 de Souza JR, Rahimnejad M, Mendes Soares IP, *et al*. 3D printing β-TCP-laden GelMA/alginate interpenetrating-polymer-network biomaterial inks for bone tissue engineering. *Bioprinting*. 2025;49:e00413. doi: 10.1016/j.bprint.2025.e00413

18 Aldana AA, Valente F, Dilley R, Doyle B. Development of 3D bioprinted GelMA-alginate hydrogels with tunable mechanical properties. *Bioprinting*. 2021;21:e00105. doi: 10.1016/j.bprint.2020.e00105

19 Seddiqi H, Oliaei E, Honarkar H, *et al*. Cellulose and its derivatives: towards biomedical applications. *Cellulose*. 2021;28(4):1893-1931. doi: 10.1007/s10570-020-03674-w

20 Tabatabaei Hosseini BS, Meadows K, Gabriel V, Hu J, Kim K. Biofabrication of cellulose-based hydrogels for advanced wound healing: a special emphasis on 3D bioprinting. *Macromol Biosci*. 2024;24(5):2300376. doi: 10.1002/mabi.202300376

21 Singh P, Baniasadi H, Gupta S, *et al*. 3D-printed cellulose nanocrystals and gelatin scaffolds with bioactive cues for regenerative medicine: advancing biomedical applications. *Int J Biol Macromol*. 2024;278:134402. doi: 10.1016/j.ijbiomac.2024.134402

22 Jiao H, Shi Y, Sun J, *et al*. Sawdust-derived cellulose nanofibrils with high biosafety for potential bioprinting. *Ind Crops Prod*. 2024;209:118025. doi: 10.1016/j.indcrop.2024.118025

23 Carvalho JPF, Lameirinhas NS, Teixeira MC, *et al*. All-cellulose hydrogel-based bioinks for the versatile 3D bioprinting of different cell lines. *Biomacromolecules*. 2025;26(3):1761-1770. doi: 10.1021/acs.biomac.4c01546

24 Lameirinhas NS, Carvalho JPF, Teixeira MC, *et al*. Nanocomposite hydrogel-based bioinks composed of a fucose-rich polysaccharide and nanocellulose fibers for 3D-bioprinting applications. *Bioprinting*. 2025;45: e00382. doi: 10.1016/j.bprint.2024.e00382

25 Li N, Qi S, Buccoli L, *et al*. Multiscale mechanical properties and enhancement mechanism of cellulose-composited hydrogels. *Carbohydr Polym*. 2025;357:123421. doi: 10.1016/j.carbpol.2025.123421

26 Li N, Bassett DC, Zhang ZJ. Microfibrillated cellulose (MFC)-composite formulations for 3D bioprinting with excellent printability, mechanical strength, and biological functionality. *Chem Eng J*. 2025:169037. doi: 10.1016/j.cej.2025.169037

27 Gatenholm P, Martinez H, Karabulut E, *et al*. Development of nanocellulose-based bioinks for 3D bioprinting of soft tissue. In: Ovsianikov A, Yoo J, Mironov V, eds. *3D Printing and Biofabrication*. New York, NY: Springer International Publishing; 2016:1-23. doi: 10.1007/978-3-319-45444-3_14

28 Webb B, Doyle BJ. Parameter optimization for 3D bioprinting of hydrogels. *Bioprinting*. 2017;8:8-12. doi: 10.1016/j.bprint.2017.09.001

29 Lewicki J, Bergman J, Kerins C, Hermanson O. Optimization of 3D bioprinting of human neuroblastoma cells using sodium alginate hydrogel. *Bioprinting*. 2019;16:e00053. doi: 10.1016/j.bprint.2019.e00053

30 Ouyang L, Yao R, Zhao Y, Sun W. Effect of bioink properties on printability and cell viability for 3D bioplotting of embryonic stem cells. *Biofabrication*. 2016;8(3):035020. doi: 10.1088/1758-5090/8/3/035020

31 Thakur B, Sharma G, Kumar A, *et al*. Designing of bentonite based nanocomposite hydrogel for the adsorptive removal and controlled release of ampicillin. *J Mol Liq*. 2020;319:114166.
doi: 10.1016/j.molliq.2020.114166

32 Ignacio M, Slater GW. Using fitting functions to estimate the diffusion coefficient of drug molecules in diffusion-controlled release systems. *Phys A* 2021;567:125681.
doi: 10.1016/j.physa.2020.125681

33 Ritger PL, Peppas NA. A simple equation for description of solute release I. Fickian and non-fickian release from non-swellable devices in the form of slabs, spheres, cylinders or discs. *J Controlled Release*. 1987;5(1):23-36.
doi: 10.1016/0168-3659(87)90034-4

34 Llabot JM, Manzo RH, Allemandi DA. Drug release from carbomer:carbomer sodium salt matrices with potential use as mucoadhesive drug delivery system. *Int J Pharm*. 2004;276(1):59-66.
doi: 10.1016/j.ijpharm.2004.02.006

35 Karvinen J, Kellomäki M. Design aspects and characterization of hydrogel-based bioinks for extrusion-based bioprinting. *Bioprinting*. 2023;32:e00274.
doi: 10.1016/j.bprint.2023.e00274

36 Hernández-Sosa A, Ramírez-Jiménez RA, Rojo L, *et al*. Optimization of the rheological properties of self-assembled tripeptide/alginate/cellulose hydrogels for 3D printing. *Polymers*. 2022;14(11).
doi: 10.3390/polym14112229

37 Nechyporchuk O, Belgacem MN, Pignon F. Rheological properties of micro-/nanofibrillated cellulose suspensions: wall-slip and shear banding phenomena. *Carbohydr Polym*. 2014;112:432-439.
doi: 10.1016/j.carbpol.2014.05.092

38 Markstedt K, Mantas A, Tournier I, Martínez Ávila H, Hägg D, Gatenholm P. 3D Bioprinting human chondrocytes with nanocellulose–alginate bioink for cartilage tissue engineering applications. *Biomacromolecules*. 2015;16(5):1489-1496.
doi: 10.1021/acs.biomac.5b00188

39 Mogha P, Iyer S, Majumder A. Extracellular matrix protein gelatin provides higher expansion, reduces size heterogeneity, and maintains cell stiffness in a long-term culture of mesenchymal stem cells. *Tissue Cell*. 2023;80:101969.
doi: 10.1016/j.tice.2022.101969

40 El-Samaligy MS, El-Mahrouk GM, El-Kirsh TA. Adsorption—desorption effect of microcrystalline cellulose on ampicillin and amoxycillin. *Int J Pharm*. 1986;31(1):137-144.
doi: 10.1016/0378-5173(86)90223-1

ACCSCIENCE PUBLISHING

International Journal of Bioprinting

RESEARCH ARTICLE

Effect of seed distribution characteristics on mechanical properties, degradation behavior, and osteogenic differentiation of additively manufactured Voronoi-based biomimetic scaffolds

Boxun Liu[1,2], Yunhui Wang[1,2], Yushan Huang[2], Zhi Dong[2], Yi Zhang[1], Zhengbo Wen[1], QiXin Liang[1], and Changjun Han[2]*

[1] Huamei (Shenzhen) BioTech Co., Ltd, Shenzhen, Guangdong, China

[2] School of Mechanical and Automotive Engineering, South China University of Technology, Guangzhou, Guangdong, China

Abstract

The application of bionic porous structures based on Voronoi diagrams in bone defect repair has been extensively studied, with seed distribution characteristics recognized as key parameters affecting the performance of Voronoi scaffolds. In this study, a controllable parametric design method for Voronoi scaffolds was employed to experimentally and numerically investigate the effects of seed count and porosity on the mechanical properties, degradation behavior, mass transfer efficiency, and cell activity of laser powder bed fusion–printed degradable zinc-based Voronoi bone scaffolds. The results revealed the influence mechanisms of seed distribution characteristics on the mechanical properties and deformation modes of Voronoi scaffolds, achieving a 26.9% enhancement in failure stress. Moreover, by adjusting seed distribution, the degradation rate was precisely regulated within the range of 0.027–0.157 mm/year, enabling a 5.8-fold control over the release of zinc ion. Additionally, the effect of seed density on the osteogenic performance and gene expression of mouse pre-osteoblast cells were examined, demonstrating that higher seed densities predominantly upregulated *COL1* and *ALP* expression to promote osteogenic differentiation. Increasing the seed count density elevated *COL1* expression to 4.5 times that of the control group. These findings provide a theoretical basis for the clinical application and performance optimization of degradable zinc-based Voronoi bionic bone scaffolds.

Keywords: Additive manufacturing; Cell activity; Degradation behavior; Laser powder bed fusion; Seed density; Voronoi scaffold

***Corresponding author:**
Changjun Han
(cjhan@scut.edu.cn)

Citation: Liu B, Wang Y, Huang Y, *et al*. Effect of seed distribution characteristics on mechanical properties, degradation behavior, and osteogenic differentiation of additively manufactured Voronoi-based biomimetic scaffolds. *Int J Bioprint*. 2026;12(1):500-522. doi: 10.36922/IJB025450466

Received: November 4, 2025
Revised: December 7, 2025
Accepted: December 9, 2025
Published online: December 18, 2025

Copyright: © 2025 Author(s). This is an Open Access article distributed under the terms of the Creative Commons Attribution License, permitting distribution, and reproduction in any medium, provided the original work is properly cited.

Publisher's Note: AccScience Publishing remains neutral with regard to jurisdictional claims in published maps and institutional affiliations.

1. Introduction

Metal bionic bone scaffolds manufactured via laser powder bed fusion (LPBF) technology feature complex and fine internal bionic architectures,[1,2] with highly interconnected pores that closely mimic the natural morphology of human bone tissue.[3-5] These porous

scaffolds not only provide mechanical support but also offer design flexibility to regulate structural parameters for enhancing cell adhesion, proliferation, and differentiation.[6] During the design phase, various biocompatible metal materials, such as titanium alloys, 316L stainless steel, cobalt-chromium alloys, and zinc alloy, can be selected to meet the specific performance requirements of different anatomical sites.[7-9] In addition, computer-aided design tools enable patient-specific customization of metal bone scaffolds, facilitating clinical applications, such as craniofacial defect repair and interbody fusion cage implantation.[10-12] Despite significant progress in repairing site-specific bone defects, the biological and structural complexity of cancellous bone poses a major challenge in developing truly biomimetic implants. As an essential internal scaffold within the skeletal system, cancellous bone provides critical mechanical support and energy absorption, contributing to bone tissue development and overall biomechanical functionality.[13-14] However, its complex three-dimensional (3D) porous architecture makes it difficult to replicate using conventional manufacturing techniques.[15] Therefore, there is an urgent need with high structural fidelity to native cancellous bone and matched biomechanical performance.

To achieve LPBF-printed scaffolds with structural and mechanical properties closely matching those of cancellous bone, it is necessary to investigate and design based on elemental structural characteristics. Traditional designs employ periodic lattice porous configurations,[16] such as body-centered cubic (BCC) and face-centered cubic (FCC), which are constructed through uniform struts connected at regular nodes. These lattice configurations, often inspired by atomic crystal arrangements, offer advantages in weight reduction and enhanced energy absorption while maintaining mechanical strength.[17] However, their inherent regularity limits the ability to replicate the stochastic pore architecture of cancellous bone. To address this limitation, biomimetic approaches have gained increasing attention in bone implant design.[18-19] Among these, Voronoi diagrams, which are computational geometric segmentation based on seed point distribution,[20] applied in materials science, biology, and medicine.[21] Fantini and Curto[22] introduced a bioinspired structural generation method utilizing Voronoi tessellation, demonstrating that Voronoi-based porous architectures can effectively mimic the morphological features of natural trabecular bone. Moreover, such scaffolds exhibited excellent geometric adaptability to complex bone defect contours and ensured mechanical continuity, making them highly promising for medical implant applications.[23-24] Zhao *et al.*[25] further developed an optimized Voronoi-based design approach, showing that irregular porous structures derived from Voronoi segmentation exhibited superior structural stability compared to traditional regular lattices. Additionally, they achieved gradient scaffolds with tunable mechanical properties that closely matched the Young's modulus of natural bone, providing a theoretical basis for designing functionally graded irregular porous scaffolds. Gómez *et al.*[26] employed Voronoi segmentation to construct a porous model with virtual isotropy, which demonstrated highly consistency with key bi-morphological parameters of trabecular bone and enabled precise regulation of structural properties during the preliminary stages of microstructural design and histomorphometric analysis. In summary, biomimetic bone implant designs based on the Voronoi principle can accurately replicate the irregular microarchitecture of natural bone,[27] achieve close alignment with trabecular morphometric parameters through parametric control,[28] and thus show significant potential for application in bone tissue engineering and biomedical implants.[29-33]

Currently, numerous studies have integrated Voronoi-based biomimetic bone implants with LPBF. However, research on LPBF-printed Voronoi metallic bone scaffolds primarily focuses on the influences of process parameters, such as laser power, scanning speed, scanning strategy, and porosity, on the printing quality and mechanical properties of these scaffolds.[34-38] For example, Hou *et al.*[39] studied how different laser parameters and scanning strategies affected the geometric accuracy and internal defect formation in Ti6Al4V Voronoi scaffolds printed by LPBF. Their findings demonstrated that optimizing LPBF process parameters could significantly enhance the structural fidelity of Voronoi architectures. He *et al.*[40] developed a biomimetic scaffold featurin1g a Voronoi-graded pore distribution, achieving favorable mechanical performance by regional porosity control. The resulting Young's modulus and ultimate strength range ranged from 1.50 to 7.12 GPa and 38.55 to 268.03 MPa, respectively. Despite these advances, limited attention has been paid to the seed configuration in Voronoi scaffolds. As a critical design parameter, seeds directly determine the average pore size and the stochastic strut distribution morphology of Voronoi scaffolds,[41-46] which are crucial for tailoring bionic bone scaffolds to meet site-specific clinical requirements. Furthermore, recent work has demonstrated the fabrication of Voronoi metamaterials with lattice-inspired topologies using LPBF, showing that such design strategy based on modified seed distributions can generate periodically arranged architectures with improved mechanical properties.[47] Therefore, the seeds play an important role in determining the performance of Voronoi scaffolds printed by LPBF.[48-50] There remain gaps in the research on the degradation and biological performance of LPBF-printed Voronoi scaffolds with the variation of seed control. Moreover, the combined effects of seed distribution and porosity on the structural

properties (i.e., mechanical properties, degradation behavior, mass transfer efficiency, and cell viability) of Voronoi scaffolds have not been systematically investigated.

Therefore, the work primarily studied the effects of seed distribution characteristics on the mechanical properties, degradation ability, mass transfer efficiency, and osteogenic differentiation of zinc-based Voronoi bone scaffolds printed by LPBF. Specifically, Voronoi scaffold models with varying seed counts and densities as well as porosities were designed. The mechanical properties, deformation mechanisms, and failure modes of these scaffolds were analyzed through a combination of experimental testing and finite element simulations. The degradation behavior, mass transfer efficiency, and cell responses of the LPBF-printed zinc-based Voronoi scaffolds were evaluated by adjusting porosity and seed distributions. The findings can provide a valuable insight to the biomimetic design of biodegradable Voronoi-based scaffolds for trabecular bone implant applications.

2. Materials and methods

2.1. Design of Voronoi-based biomimetic scaffolds

The Voronoi diagram is defined as follows, given a set of discrete seeds of number k ($k > 1$) in an m-dimensional Euclidean space[51]:

$$P = \{p_1, \ldots, p_k\} \in R^m \quad \text{(I)}$$

where m represents the dimensionality of the space, R denotes the m-dimensional Euclidean space, p_k is the ith seed ($i = 1, \ldots, k$); and P denotes the set of all seeds. In the 2D plane, the boundaries of the Voronoi diagram consist of vertical bisectors between adjacent seeds. In 3D space, the separating surfaces of Voronoi cells are formed by the intersection of spheres centered at neighboring seeds. For each seed p_i, the corresponding Voronoi cell $V(P_i)$ consists of all points in space whose distance to p_i is less than or equal to the distance to any other seed p_j ($j \neq i$). The Voronoi cell can be formally defined by the following mathematical expression

$$V(p_i) = \{p | d(p, p_i) \leq d(p, p_j), j \neq i, j = 1, \ldots, n\}. \quad \text{(II)}$$

Here, p_i-p_n denotes a finite set of seeds located in the geometric domain, and $d(p, p_i)$ represents the Euclidean distance between a point p and the seed p_i.

The design procedure of the Voronoi biomimetic scaffolds is illustrated in Figure 1. In 3D space, the boundaries of the Voronoi cells were formed through the expansion and mutual contact of spheres centered at the

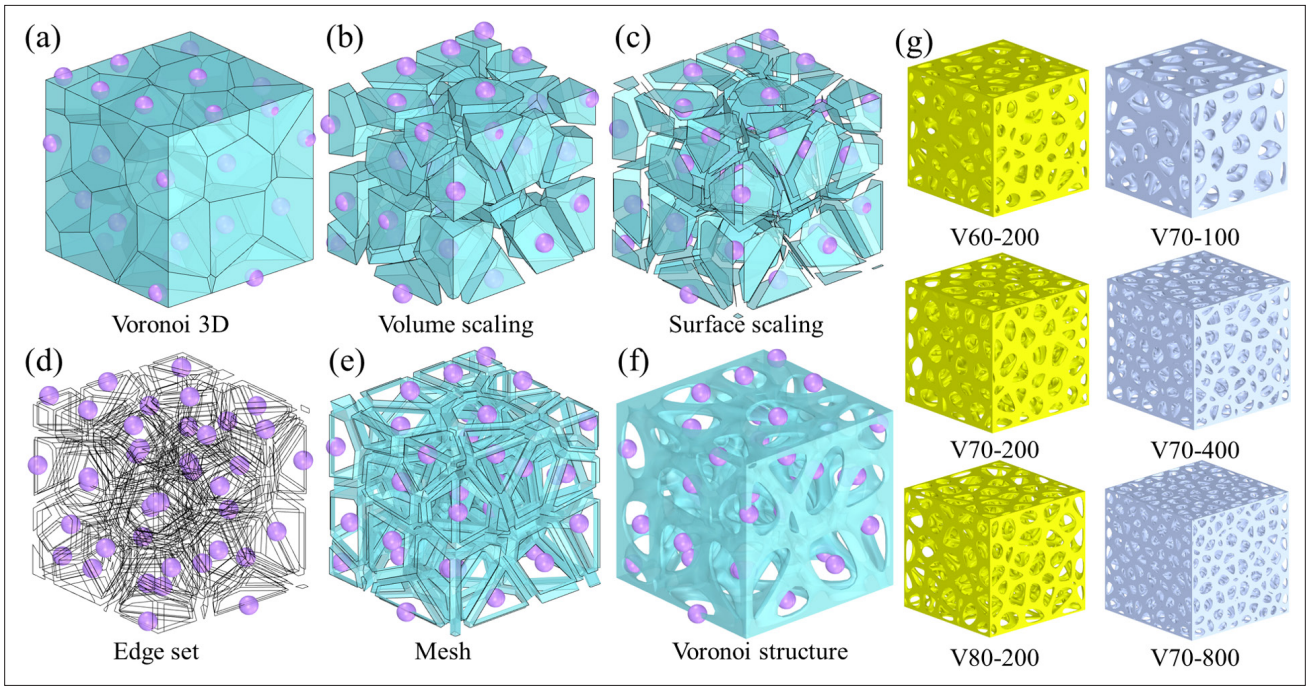


Figure 1. Design procedures of Voronoi biomimetic scaffolds. (a) Voronoi 3D. (b) Cell face scaling. (c) Cell body scaling, (d) Edge line extraction. (e) Mesh extraction. (f) Voronoi biomimetic scaffold construction. (g) 3D models with different seed counts and porosities.

seeds; the Voronoi cells were defined by the perpendicular bisecting surfaces connecting adjacent seeds. To achieve strut morphologies with high connectivity, large specific surface area, and structural similarity to bone trabeculae, the pore volume of the bionic structure was generated by hollowing out the Voronoi cells and enabling inter-pore penetration through shared faces. First, Voronoi cells were constructed via Delaunay triangulation based on the seed set P and boundary constrains. Each resulting Voronoi cell served as a pore precursor in the porous structure. Subsequently, volumetric and facial elements of the Voronoi polygons were uniformly scaled using scaling coefficients *Sv* and *Sf* (Figure 1b and c), yielding the edge network of the Voronoi bionic scaffold (Figure 1d). A mesh was then generated based on the mapping relationship of these edges, defining the solid–pore interface of the structure (Figure 1e). Finally, postprocessing of the boundary surface mesh produced the completed Voronoi scaffold (Figure 1f).

To achieve parametric control in the design of Voronoi scaffolds, the mathematical relationships among structural porosity u, seed count n, average pore diameter d_m, and the design parameters *Sv* and *Sf* were established. The internal pores of the scaffold were approximated by scaled Voronoi cells. The volume of the ith pore ($i = 1, ..., n$) in the Voronoi-based trabecular bone scaffold was approximated by the volume $V(P_i)$ of the corresponding scaled Voronoi cell. An approximately proportional relationship existed between the porosity u of the Voronoi scaffold and the scaling factor *Sv*, expressed as

$$u \approx S_v. \tag{III}$$

The derivation of the formula proceeded as follows: $V(C_i)$ denotes the volume of the ith ($i = 1, ..., n$) unscaled Voronoi cell, and n represents both the spatial seed count and the number of corresponding Voronoi polygons. The total spatial volume within the geometric boundary is then given by

$$V_{box} = \sum_{i=1}^{n} V(C_i). \tag{IV}$$

The volume of the porous part, scaling factor, and porosity can be respectively expressed by

$$V_P \approx \sum_{i=1}^{n} V(P_i), \tag{V}$$

$$S_v = \frac{\sum_{i=1}^{n} V(P_i)}{\sum_{i=1}^{n} V(C_i)} = \frac{V_P}{V_{\text{box}}}, \tag{VI}$$

$$u \approx \frac{V_P}{V_{\text{box}}} = S_v. \tag{VII}$$

Based on this, the pore volume $V(P_i)$ in the Voronoi scaffold is approximated as a sphere for calculation. Consequently, under constant porosity, a relationship between the number of spatial seeds n and the average pore diameter d_m can be established as follows

$$n = \frac{u * V_{\text{box}}}{\frac{4}{3}\pi(\frac{d_m}{2})^3} = \frac{6u * V_{\text{box}}}{\pi d_m^{\ 3}}. \tag{VIII}$$

The higher porosity of cancellous bone endows it with characteristics, such as low density, a reduced Young's modulus, and a large surface area. These properties not only facilitate mechanical load transmission while providing sufficient space for bone tissue attachment and growth, but also enhance the diffusion of nutrients and metabolic waste. Cancellous bone typically exhibits porosity exceeding 50%. To ensure compatibility between implant porosity and native bone, square Voronoi models ($10 \times 10 \times 10$ mm^3) with porosities of 60%, 70%, and 80%—generated using 200 seeds (hereafter referred to as V60-200, V70-200, and V80-200, respectively)—were used to study the influence of porosity on the performance of Voronoi biomimetic scaffolds. These models exhibited average pore diameters of 2.37, 1.49, and 1.18 mm, respectively. In addition, to examine the effect of seed density—and consequently average pore diameter—on structural performance at a constant material volume fraction, Voronoi scaffold models incorporating 100, 400, and 800 seeds were analyzed. These models yielded average pore diameters of 1.97, 1.88, and 1.79 mm, respectively, within a consistent $10 \times 10 \times 10$ mm^3 cubic dimensions and a fixed porosity of 70% (hereafter denoted as V70-100, V70-400, and V70-800). All scaffold models are presented in Figure 1g.

2.2. Material and LPBF process

The LPBF process used atomized zinc powder exhibiting a smooth surface and high sphericity, with only a minor presence of satellite particles, as observed using scanning electron microscopy (SEM; FEI Nova nano 430, Netherlands) (Figure 2a). Particle size distribution was analyzed using a laser particle size analyzer (LPSA;

Microtrac S3500), revealing an average particle diameter of 10.9 μm and an overall normal distribution pattern (Figure 2b). The processing parameters included a laser spot diameter of 70 μm, a laser power of 80 W, a scanning speed of 600 mm/s, a hatch spacing of 55 μm, a layer thickness of 30 μm, and a scanning direction rotated by 45° between consecutive layers. The LPBF-printed Voronoi-based zinc scaffolds with different seed distributions and porosities are shown in Figure 2c. The sample porosity was determined based on the Archimedes displacement method.

2.3. Quasistatic compressive testing and FEM simulation

The compressive performance of LPBF-printed Voronoi scaffolds was evaluated using a CMT5105 universal testing machine (SANS Experimental Equipment Co., Ltd, China). Prior to testing, the scaffold samples were subjected to ultrasonical cleaning to remove residual powder and cutting fluid adhering inside the structural pores. The compression termination displacement was set at 60% of the sample height. The compressive stress–strain curve was derived by converting the recorded force–displacement curve data. Three replicate samples were tested for each parameter and configuration of the Voronoi scaffolds, and the average response was taken to represent the compressive performance under the given condition. The energy absorption (*EA*) of the printed Voronoi scaffolds was calculated by integrating the area under the force–displacement curve, as described by

$$EA(d) = \int_0^d F(x)\,dx, \tag{IX}$$

where d represents the compression displacement. To comprehensively evaluate the energy absorption capacity of the samples under different porosities, specific energy

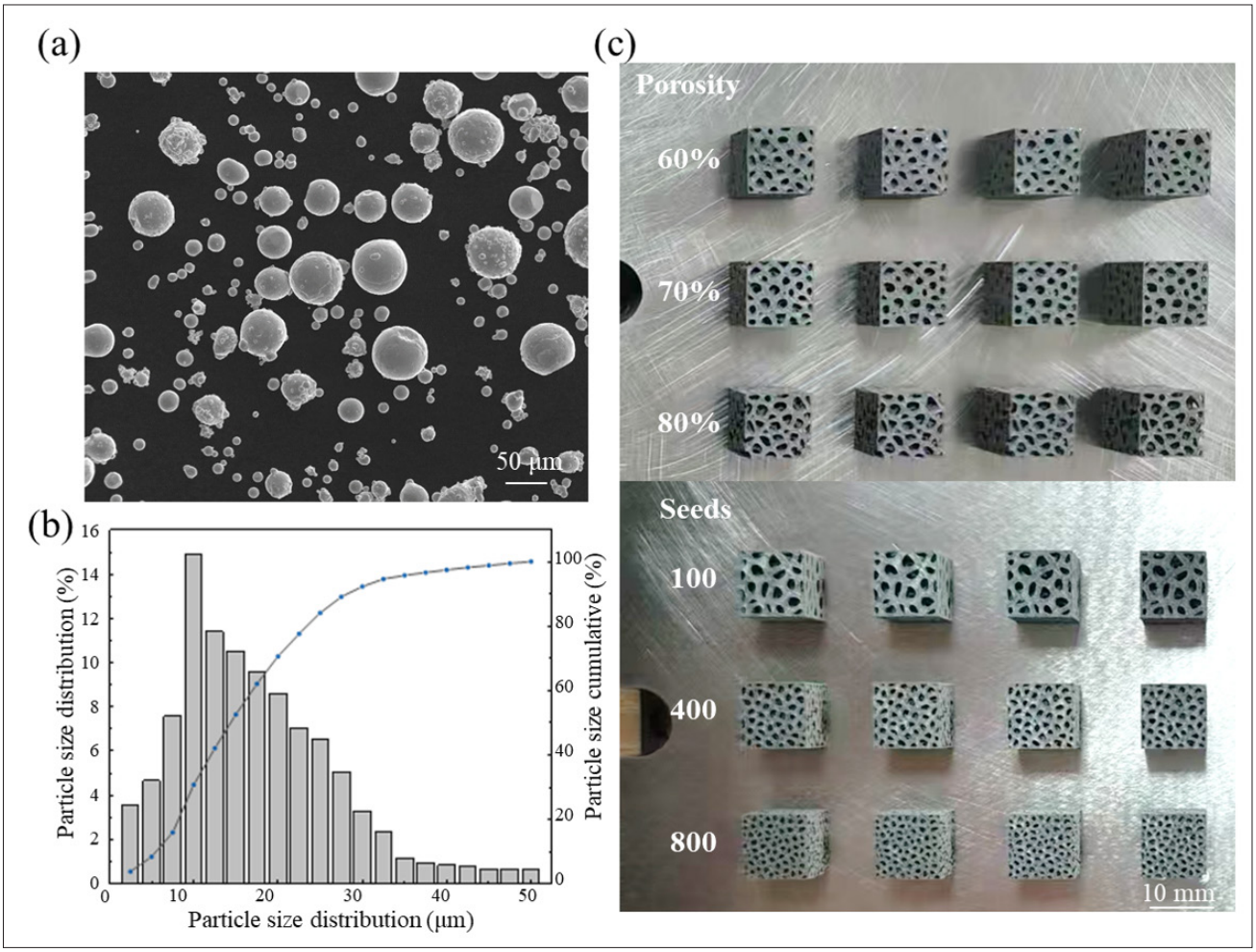


Figure 2. Characteristics of zinc powder and the zinc-based Voronoi scaffolds printed via LPBF (a) Morphology of zinc powder. (b) Particle size distribution of zinc powder. (c) LPBF-printed Voronoi scaffolds with different porosities and seed counts. Abbreviation: LPBF, Laser powder bed fusion.

absorption (*SEA*) is used to quantify the energy absorption performance per unit mass. The calculation method is as follows

$$SEA(d) = \frac{EA(d)}{m}, \quad \text{(X)}$$

where m represents the mass of the scaffold. The finite element method (FEM) simulation model consisted of a compression plate, a fixed plate, and a Voronoi scaffold. The Voronoi scaffold was positioned on the fixed plate and subjected to loading from the compression plate. Both the compression and fixed plates were assigned reference points and defined as rigid bodies. A surface-to-surface contact interaction was established between each plate and the Voronoi scaffold to accurately capture interfacial behavior. An explicit dynamic solver was employed, along with an elastoplastic hardening material model. The Voronoi scaffold was discretized using C3D10M (modified 10-node quadratic tetrahedral elements) with a mesh feature size of 0.3 mm. Material properties were derived from the tensile stress–strain response of LPBF-printed zinc,[52-53] with the following parameters: density of 7.16×10^{-9} t/mm^3, Young's modulus of 93.16 GPa, yield strength of 93.71 MPa, and tensile fracture strain of 11.17%. To ensure the accuracy of the results, the ratio of kinetic energy to internal energy was maintained below 5%.

2.4. Computational fluid dynamics simulation

The permeability of the biomimetic bone scaffold plays a critical role in facilitating the transport of nutrients and metabolic products, as well as influencing cell adhesion and proliferation. To evaluate its capability of effective mass transport, a computational fluid dynamics (CFD) model was developed based on continuum mechanics and mass transfer principles using COMSOL Multiphysics (COMSOL Inc., Sweden), enabling the simulation of fluid flow under laminar conditions. By applying the conservation of momentum, the Navier–Stokes equations were used to describe the mass transport behavior of viscous, incompressible fluids within the continuous fluid domain, as expressed by

$$\rho \frac{DV}{Dt} = \rho f - \nabla p + \mu \nabla^2 V \quad \text{(XI)}$$

where ρ represents the fluid density; $\frac{DV}{Dt}$ denotes the guiding number; V is the velocity vector of the fluid; f represents the noncontact volumetric force applied to the fluid; ∇, p, and μ represent the Hamiltonian operator, pressure, and dynamic viscosity, respectively. Based on this, the permeability of the Voronoi scaffold and its relationship with the pressure gradient are determined using Darcy's law

$$k = Q\mu L / A\Delta P, \quad \text{(XII)}$$

where k represents the permeability; Q represents the volumetric flow rate; L represents the length of the Voronoi scaffold along the fluid flow direction; A represents the cross-sectional area of the model; and ΔP is the pressure drop between the inlet surface and the outlet surface. A square region with a cross-sectional area of 10×10 mm^2 and a height of 15 mm was defined to perform Boolean cutting on the Voronoi model, thereby constructing the fluid domain for CFD simulation. The fluid entered though the top surface inlet in the negative Z direction at a constant velocity of 1.0 mm/s, simulating typical human body fluid flow rates.[54] During the simulation of the pressure drop and velocity distribution, the inlet speed was maintained constant, the outlet pressure was set to zero, and the four lateral surfaces perpendicular to the xy-plane were designated as wall boundary planes. The working fluid was deionized water, with a density of 1,000 kg/m^3 and a viscosity of 1.01×10^{-3} Pa·s. To balance computational accuracy and efficiency, the fluid domain was discretized into tetrahedral elements with a nominal edge length of 0.3 mm.

Finally, the Reynolds number was calculated to determine whether the flow regime was laminar, thus evaluating the applicability of Darcy's law. The formula is given as

$$Re = \rho v l / \mu \quad \text{(XIII)}$$

where v represents the velocity of the inlet surface, and l represents the characteristic length. The simulation results indicated that all computed Reynolds numbers were below 10, verifying the validity of Darcy's law under the studied conditions.

2.5. Degradation behavior

This degradation experiment simulates the human physiological environment by conducting an *in vitro* degradation test of the zinc-based Voronoi scaffold in accordance with the ASTM-G31-72 standard.[55] The degradation process was carried out in simulated body fluid (SBF) with an initial pH of 7.4. Before weighing, the samples were ultrasonically cleaned and then dried in an oven at 50 °C for 1 h. After drying, the initial mass

of each sample was measured using an electronic balance and recorded as M_0 (g). The SBF volume was determined based on a ratio of 10 mL/1 mm^2 of sample surface area (mm^2: mL = 10:1). All samples were placed in test tubes containing the SBF solution and immersed in a constant-temperature water bath maintained at 37 °C. Following 28 days of *in vitro* degradation, the samples were removed and slowly rinsed with deionized water to remove surface residues, and dried again at 50 °C for 1 h. The morphology of degradation products, including the corrosion layer formed on the sample surfaces, was analyzed using SEM. Subsequently, a corrosion solution was used to remove residual degradation products for accurate weight loss measurement. The corrosion solution was prepared by mixing 10 g of CrO_3, 16 mL of $AgNO_3$, and 34 mL of deionized water. After thorough cleaning, the samples were dried at 50 °C for 1 h, and their final mass M_1 (g) was recorded. Each sample group was tested in triplicate to ensure reproducibility. The degradation rate of the zinc-based Voronoi scaffold can be calculated according to the following formula

$$D_v = 8.76\times10^4 * \frac{M_0 - M_1}{\rho * \mathrm{A} * t}, \quad \text{(XIV)}$$

where D_v represents the degradation rate (mm/year), ρ is the density of Zn, A indicates the initial surface area of the sample (cm^2), and t represents the degradation time (hours).

2.6. Osteogenic performance and gene expression testing

The osteogenic performance and gene expression of the scaffolds were evaluated using mouse osteogenic precursor cells (MC3T3-E1). The Voronoi scaffolds were sterilized by ultraviolet irradiation and then immersed in Dulbecco's Modified Eagle Medium (DMEM) supplemented with 10% fetal bovine serum. Following incubation at 37°C for 72 h, the supernatant was collected to prepare a 100% extract, which was then diluted to 10% extract for experiments. The osteoinductive potential of the scaffolds was assessed by measuring alkaline phosphatase (ALP) activity and calcium nodule formation. MC3T3-E1 cells were seeded at a density of 4×10^4 cells per well in 24-well plates and cultured in medium containing 10% extract from different scaffold groups. After 7 and 14 days of culture, ALP activity was determined using an alkaline phosphatase assay kit (Beyotime, China), while calcium deposition was visualized using Alizarin red staining (ARS) (200 μL, Beyotime, China). Stained samples were imaged under a microscope (IX73, Olympus, Japan) to assess *in vitro* osteogenic differentiation. For quantitative real-time polymerase chain reaction (qRT-PCR) analysis, MC3T3-E1 cells were cultured under identical conditions for 7 and 14 days. Total RNA was extracted using Trizol reagent (Thermo Fisher Scientific, USA), and RNA concentration was quantified using a Nanodrop microplate spectrophotometer (Colibri, Titertek, USA) to evaluate gene expression levels. Sequences of primers used are shown in Table S1.

3. Results and discussion

3.1. LPBF printability

Table 1 presents the designed and experimental porosity values of the LPBF-printed Voronoi scaffolds. The experimental porosity was slightly lower than the designed value, primarily due to powder bonding during the LPBF process, which increased the thickness of struts. When seed count increased and seed density rose, the deviation between experimental and designed porosity became more pronounced. This trend could be attributed to the higher specific surface area associated with denser pore number, which intensified powder adhesion and fusion. Figure 3 displays the SEM images of the upper surfaces of Voronoi scaffolds with varying porosities and seed densities. These images revealed pores resulting from evaporation and unmelted powder particles.[56-57] Given that zinc is a low-boiling-point material, the rapid heating from the Gaussian laser beam and the uneven energy distribution led to swift evaporation of zinc within the molten pool. This generated turbulent vapor flow that

Table 1. Porosity of LPBF-printed Voronoi scaffolds with different seed density and porosity values.

Structural type	Design porosity (%)	Actual porosity (%)	Deviation (%)
V60-200	60	55.8 ± 0.5	−4.2
V70-200	70	65.6 ± 0.7	−4.4
V80-200	80	75.3 ± 0.3	−4.7
V70-100	70	65.1 ± 0.4	−4.9
V70-400	70	63.4 ± 0.4	−6.6
V70-800	70	63.3 ± 0.1	−6.7

Abbreviation: LPBF, Laser powder bed fusion.

disrupted the molten pool dynamics and causes spattering. As the porosity increased, the strut volume decreased, reducing local heat dissipation efficiency and making the surface more susceptible to slagging. Moreover, as the seed density increased, the strut size decreased. Due to the thin arc features at strut boundaries, localized thermal stress accumulation caused slight warping of strut contours. Both higher porosity and greater seed counts reduced local strut sizes, thereby compromising the structural integrity and overall printing quality.

3.2. Simulation and experimental mechanical responses

Quasistatic uniaxial compression tests and finite element simulations were conducted to investigate the mechanical response characteristics of Voronoi scaffolds with different seed counts and porosities (Figure 4). The simulated stress–strain curves agreed with the experimental results, except for the V80-200 sample, where the simulation slightly overestimated the stress. This discrepancy may be attributed to the amplification of the LPBF-produced defects at the microscale. The mechanical response during the stress plateau stage varied significantly with the seed count used to generate the scaffolds. As depicted in Figure 4a, the stress–strain curve of the V70-100 sample showed large fluctuations and a low plateau stress value. In contrast, the V70-400 sample exhibited reduced fluctuation and maintained a relatively stable flow stress up to 50% compressive strain. Beyond this point, the scaffold entered the densification phase. The mechanical response of the V70-800 sample was similar to that of V70-400 (Figure 4c), with the minor difference that its plateau stress was slightly lower than the failure stress, and it transitioned into the densification stage earlier. Increasing seed density resulted in a smoother stress plateau during the plastic flow stage and enhanced structural resistance to compression during densification, thereby improving yield strength. Moreover, higher seed density caused the Voronoi scaffold to reach the failure stress at lower engineering strains. These mechanical response characteristics were directly governed by the internal pore distribution, which was determined by the seed generation process. Figure 4d–f shows the compressive stress–strain behavior of V60-200, V70-200 and V80-200 samples. During compression, the Voronoi scaffolds with 60% porosity initially underwent elastic deformation, transitioned into plastic deformation, and reached the peak stress at 10% strain, with certain struts entering the strain hardening stage. The flow stress then increased gradually, and upon reaching 20% strain,

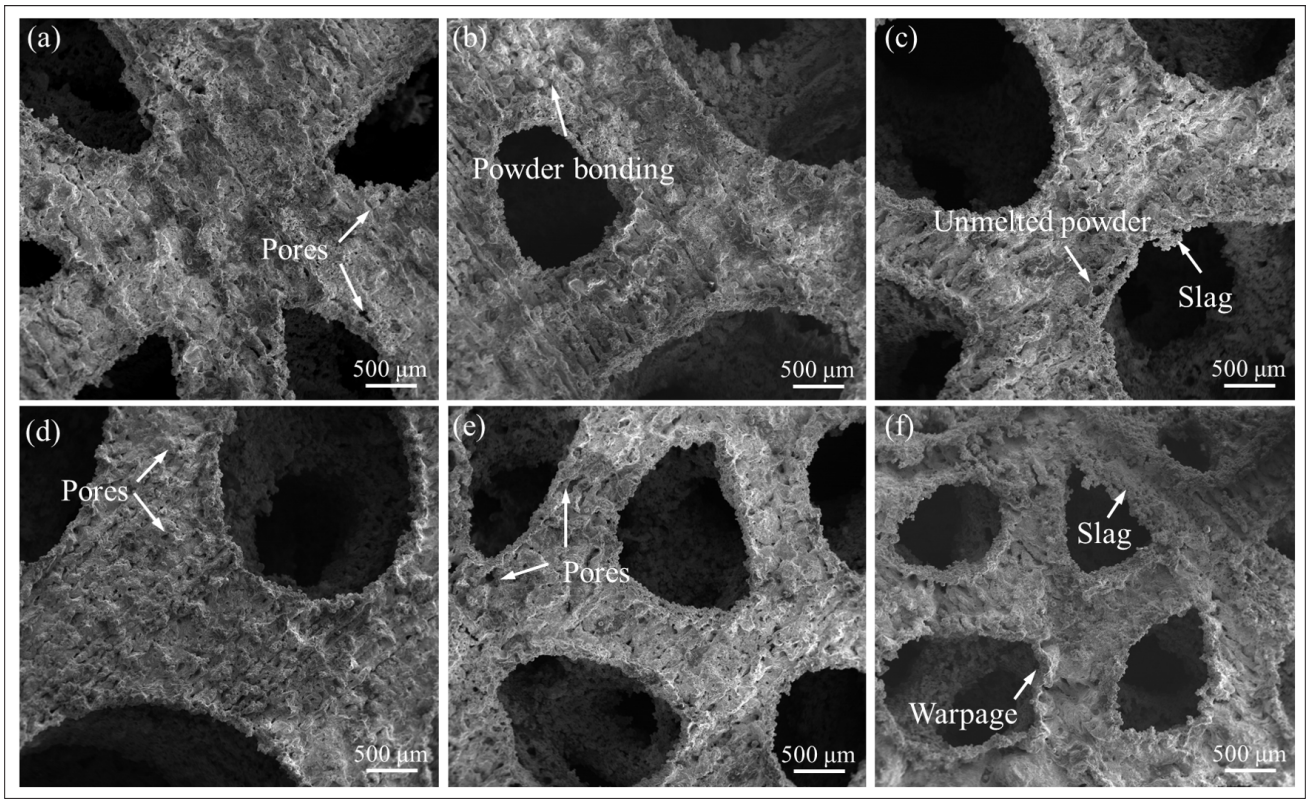


Figure 3. Surface morphology of Voronoi scaffold samples with different seed counts and porosities. (a) V60-200; (b) V70-200; (c) V70-200; (d) V70-100; (e) V70-400; (f) V70-800.

strut-to-strut contact and mutual compression-initiated densification, leading to an overall strain-hardening-typed response, and the stress–strain curve continued to rise (Figure 4d). The Voronoi scaffolds with 70% porosity exhibited a similar initial deformation behavior to the 60% counterpart. However, after attaining the stress peak, the stress–strain curve entered a sustained plateau stage with minor fluctuations (Figure 4e). The stress–strain curve of the Voronoi scaffold with 80% porosity exhibited a rapid decline after reaching the peak stress (Figure 4f). The V80-200 sample displayed a steep stress plateau, indicating extensive regions of severe and alternating strut fracture, which resulted in an unstable mechanical response. These results suggested that increasing porosity promoted a more unstable deformation behavior in the LPBF-printed Voronoi scaffolds.

The mechanical properties of the LPBF-printed Voronoi scaffolds are shown in Figure 5. The yield strength values of the Voronoi structure with 100 and 400 seeds were similar (Figure 5a), which were 10.35 and 10.12 MPa, respectively. Both were higher than that of the Voronoi scaffold with 800 seeds (8.96 MPa). Similarly, all three Voronoi scaffolds reached the failure at the initial stage of plastic deformation, and the effect of seed density on failure stress mirrored its effect on yield strength. The failure stress of the V70-100 sample (15.03 MPa) was slightly higher than that of the V70-400 sample (14.67 MPa), and both were greater than that of the V70-800 sample (11.84 MPa). These results indicated that higher seed density tended to reduce both yield strength and failure stress. The plateau stress of the V70-100 sample was 10.58 MPa. Due to pronounced fluctuations and a low stress trough during the plateau stage, this value was considerably lower than the corresponding failure stress. In contrast, the V70-400 sample exhibited a higher plateau stress (12.67 MPa) owing to a more stable stress-strain response with reduced fluctuation compared to the V70-100 sample. Similarly, the V70-800 sample achieved a higher plateau stress (11.37 MPa) than V70-100, despite having a much lower yield strength, benefiting from a smoother and more sustained stress plateau stage. This suggested that increased seed density contributed to a relatively higher plateau stress. During the printing process of Voronoi scaffolds by LPBF, formation defects such as those caused by evaporation, adhesion, and unmelted particles occur. An increase in seed density leads to a reduction in the diameter of the struts. The size effect magnifies the influence of these defects on the mechanical properties of the Voronoi scaffold, resulting in a more fluctuating stress plateau for Voronoi scaffolds at high seed densities. The Young's modulus of zinc-based Voronoi scaffolds printed by LPBF across three porosity levels ranged from 0.26 to 0.81 GPa.

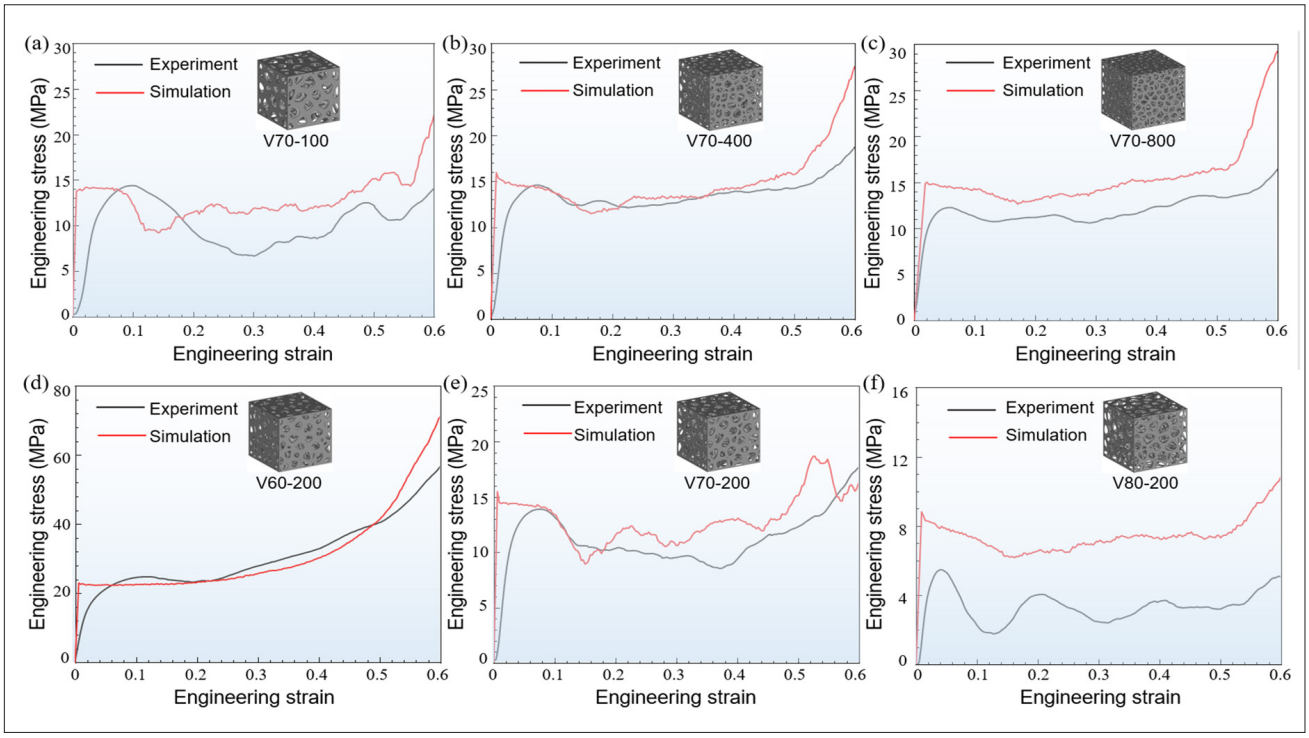


Figure 4. Compressive stress–strain curves of Voronoi scaffolds from simulation and experimentation with different seed counts and porosities. (a) V70-100; (b) V70-400; (c) V70-800; (d) V60-200; (e) V70-200; (f) V80-200.

Seed density had minimal impact on the Young's modulus, as values for the different seed configurations remained close (0.53–0.59 GPa). All measured modulus fell within or near the range of trabecular bone (0.462–1.181 GPa),[58-59] indicating potential to mitigate stress shielding after implantation, facilitate stress transfer, and promote bone cell growth. Figure 5b demonstrates the specific energy absorption of Voronoi scaffolds with different seed counts under compression loading. The values were 2.88 J/g for V70-100, 3.06 J/g for V70-400, and 2.67 J/g for V70-800, respectively. Among the three scaffolds, the V70-400 sample achieved the highest energy absorption, due to its yield strength being comparable to that of V70-100 and its higher plateau stress.

The yield strength of the Voronoi scaffold with 60% porosity was 15.87 MPa (Figure 5c), which was higher than those with 70% and 80% porosity. The normalized yield strengths followed the trend: V60-200 (39.69 MPa) > V70-200 (31.23 MPa) > V80-200 (19.2 MPa), indicating that the normalized yield strength increased as the porosity decreased. The three Voronoi scaffolds reached failure at the onset of plastic deformation, with failure stresses of V60-200 (26.35 MPa), V70-200 (13.46 MPa), V80-200 (5.15 MPa), respectively, followed by a transition into the stress plateau stage after the first stress peak. The mechanical properties of the Voronoi scaffolds under different seed densities were normalized to evaluate the influence of the systematic deviation of the actual porosity on the mechanical properties (Figure S1). The results showed that the V70-100 sample with the strongest yield strength exhibited stronger mechanical properties after strength normalization due to its relatively larger actual porosity. The trends of the yield strength and failure stress of the structures under different seed densities remained unchanged. As shown in Figure 5c, the plateau stress for V60-200 was 26.3 MPa, nearly equal to its failure stress due to the minimal stress drop. In contrast, the plateau stress of V70-200 was 10.08 MPa, approximately 25% lower than its failure stress, owing to a more pronounced

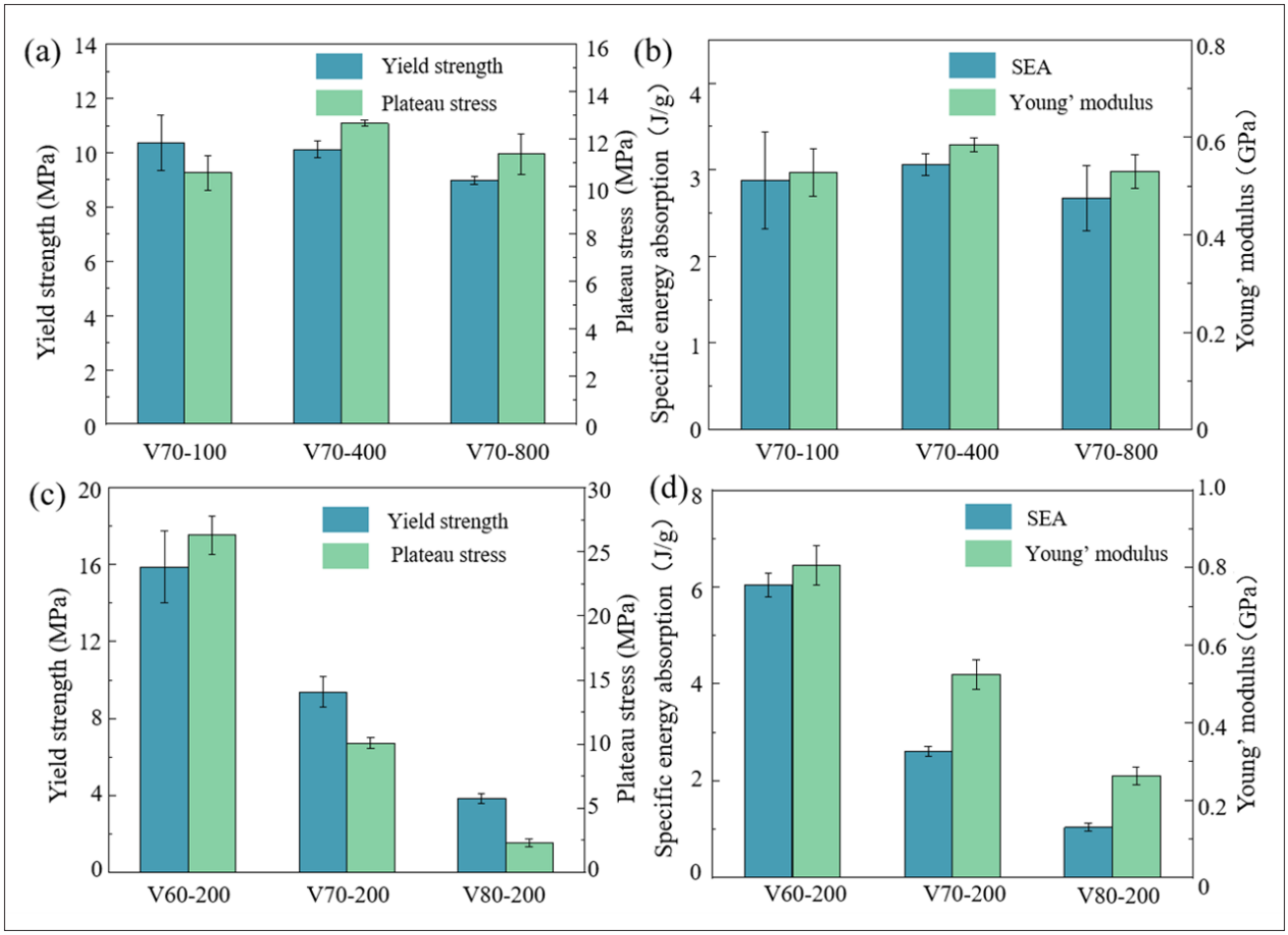


Figure 5. Mechanical properties of Voronoi scaffolds printed by LPBF with different seed counts and porosities. (a,c) Yield strength and plateau stress. (b,d) Specific energy absorption and Young's modulus. Abbreviation: LPBF, Laser powder bed fusion.

stress drop. For the 80% porosity scaffold (V80-200), the plateau stress was only 2.29 MPa, significantly lower than its failure stress, attributed to a large-amplitude fluctuation in the stress–strain curve. These results demonstrated that porosity directly affected the plateau stress behavior, with lower porosity scaffolds exhibiting superior plateau stress performance. For energy absorption capacity, the specific energy absorption values of V60-200, V70-200, and V80-200 samples were 6.04, 2.6, and 1.04 J/g, respectively (Figure 5d). Since a stable stress plateau enhanced energy absorption, the higher failure stress and more gradual plateau stage contributed to the significant improved energy absorption and specific energy absorption observed in the V60-200 scaffold.

3.3. Deformation behaviors and mechanisms

To analyze the compressive deformation behavior and underlying mechanisms of Voronoi scaffolds with different seed counts and porosities, the stress distribution under small deformations was examined. As shown in Figure 6a, at a constant material volume fraction, a lower seed counts led to fewer struts and a large strut diameter in the V70-100 sample. During loading, each strut consequently bore a higher load compared to those in the V70-400 and V70-800 scaffolds. Therefore, when the load reached a critical threshold, the fracture of any single strut resulted in a more significant reduction in overall structural load-bearing capacity, leading to pronounced fluctuations in the platform stress of the V70-100 sample. Additionally, the large pore diameter reduced strut connectivity, hindering full densification throughout the compression process. In contrast, scaffolds with a higher seed density, such as V70-800, exhibited smaller pores and a denser strut network. Here, fractured struts were more likely to fill adjacent pores and continue contributing to load bearing and transfer, promoting a gradual densification process during compression and a corresponding rise in compressive stress. The V70-800 sample, with its higher seed density, entered the densification stage earlier. In addition, due to its dense strut network and randomly distributed stress concentrations, the V70-800 sample experienced local strut failure at an earlier strain level compared to others. This localized failure initiated a cascading effect, ultimately leading to a lower macroscopic yield strength and an earlier onset of structural failure.

The random distribution of struts in the Voronoi scaffold resulted in nonuniform load transfer during loading, leading to an uneven stress distribution among the struts and causing random occurrences of stress concentration. This uneven stress distribution promoted batch fracture of internal struts as strain increased under compression. Such a failure mode induced fluctuation in the stress plateau, with the extent of deformation directly affecting the amplitude of the stress–strain curve. As shown in Figure 6b, the Voronoi scaffold with 60% porosity exhibited no distinct low-stress regions, with stress predominantly localized on a few struts. In the 70% porosity scaffold, the stress concentration areas expanded, and some low-stress areas appeared at the bottom of the structure. When the porosity increased to 80%, numerous high-stress regions developed within the internal struts. At this stage, significant stress concentration was observed along the upper right boundary of the scaffold, accompanied by bending deformation. The inherent randomness of the Voronoi scaffold led to nonuniform stress distribution, resulting in uncontrolled strut deformation, increased susceptibility to local damage, and thus degraded mechanical performance of the overall scaffold.

The simulation and experimental results of compression deformation characteristics for Voronoi scaffolds with different seed counts under 10%, 30%, and 50% strain are presented in Figure 7. In the V70-100 sample, pores with powder bonding could be observed on the side. At 10% compressive strain, the boundary strut underwent slight bending (Figure 7a), accompanied by a minor rightward tilt of the overall structure. As the strain increased to 30%, the strut in the lower-left corner of the boundary experienced compressive and shear-induced fracture during bending, leading to localized collapse of the pore structure in that region. In addition, surface cracks emerged and the structure exhibited progressive rightward tilting and deformation. The larger strut sizes in the V70-100 sample caused batch failure due to uneven stress distribution, resulting in a significant drop in load-bearing capacity and severe structural deformation. When the strain reached 50%, the internal load imbalance and strut failure triggered global structural instability, manifesting as a ~60° rightward deformation.

In contrast, the higher seed count in the V70-400 sample led to significantly smaller strut diameters compared to V70-100, resulting in lower printing quality. At 30% strain, the bending deformation intensified in the right-side struts, accompanied by the initiation of small surface cracks. The left-side struts experienced shear-induced compression, but the load-bearing capacity remained relatively stable due to limited damage and recontact among struts. Consequently, the deformation process of the V70-400 sample was smoother, which primarily accounted for its more stable stress plateau. When the strain increased to 50%, the bending deformation in the right portion of the scaffold intensified and expanded laterally in combination with crack propagation. On the left side, a local collapse phenomenon was observed due to extensive cracking. At this stage, certain pores were compressed and closed, initiating structural densification. Figure 7c illustrates the compressive deformation process

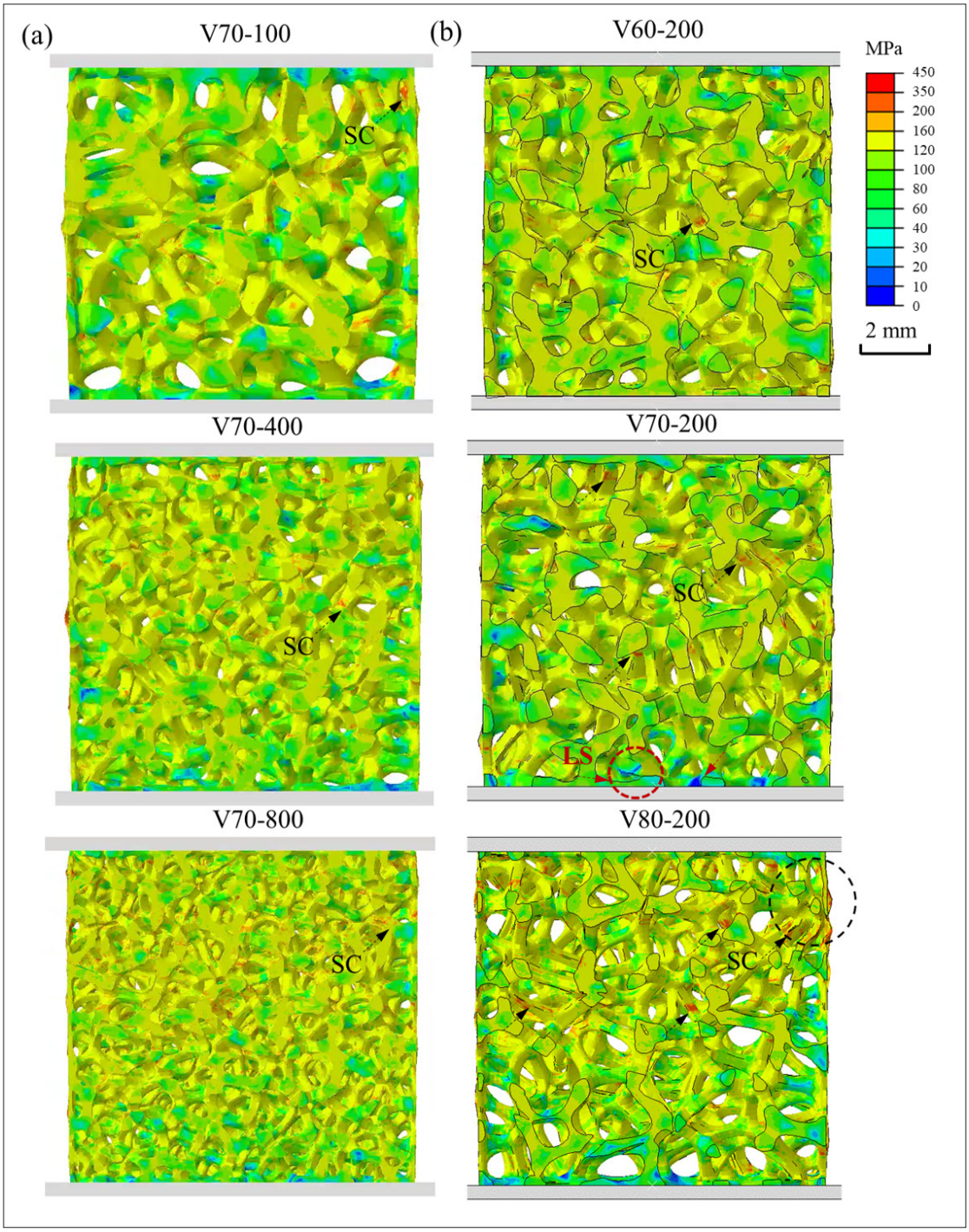


Figure 6. Stress distribution of Voronoi scaffolds with different structural parameters under 5% strain. (a) Different seed counts. (b) Different porosity values.

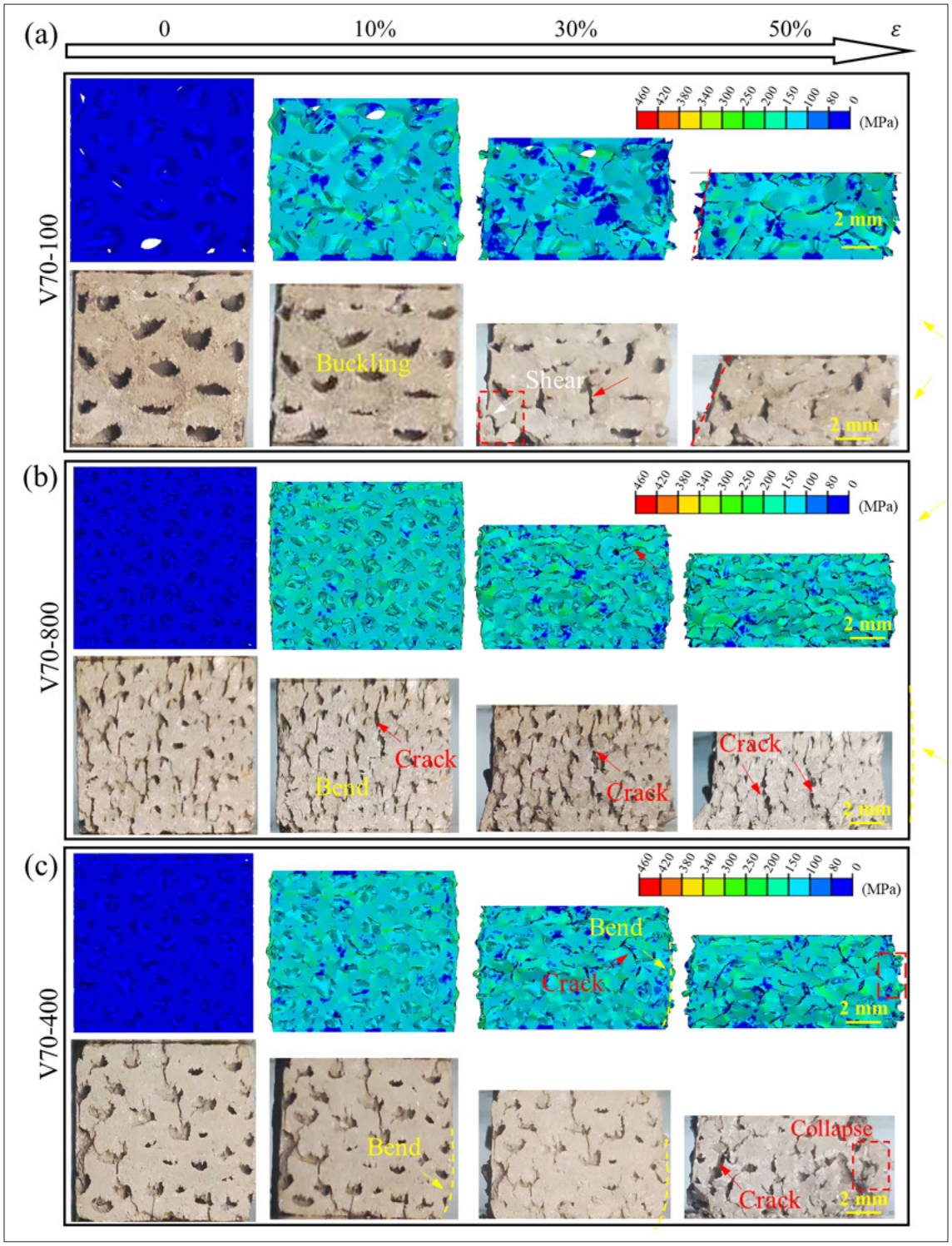


Figure 7. Compressive deformation behaviors of Voronoi scaffolds with different seed counts under 10%, 30%, and 50% strain from simulation and experimentation. (a) V70-100; (b) V70-400; (c) V70-800.

of the V70-800 sample. At 10% strain, asymmetric bending deformation occurred on both sides, and the strut fractures led to pore interconnection and the formation of elongated cracks. As the strain increased, bending deformation was aggravated, and crack connectivity extended progressively, forming distinct crack bands that affected the lower layers of the scaffold.

In summary, with the increase in seed density, the number of struts in the Voronoi scaffold also increased. The resulting high-density, randomly distributed struts were more prone to damage, leading to an increase in localized deformation regions with distinct characteristics. The interaction among these regions gave rise to complex deformation modes and reduced the structural load-bearing capacity. However, the dense and random strut distribution mitigated the influence of localized strut failure on the overall mechanical properties, thereby enhancing structural stability during deformation and resulting in higher and more gradual stress plateaus. When the porosity varied, the Voronoi scaffolds with higher porosity exhibited a greater strut length-to-diameter ratio, making them more prone to buckling and fracture under compression. Consequently, at both 70% and 80% porosity levels, the Voronoi scaffolds displayed more pronounced crack band propagation and intensified deformation behavior compared to those at 60% porosity (Figure S2). These differences in deformation directly affected the mechanical response of the scaffolds.

3.4. Mass transfer performance

Figure 8 shows the simulation results of pressure drop and permeability fluid dynamics in Voronoi scaffolds. At the same inlet flow rate, the pressure drops for the V70-100, V70-400, and V70-800 scaffolds are 0.381, 0.941, and 1.48 Pa, respectively. As the number of seeds increased, the internal fluid channels in the Voronoi scaffold became more irregularly distributed and geometrically complex, leading to higher flow resistance and reduced permeability. The permeability was inversely correlated with the pressure drop, with a higher seed number guiding lower permeability. Specifically, the permeability of the V70-100 sample (26.5×10^{-9} m^2) was 3.9 times greater than that of the V70-800 sample (6.81×10^{-9} m^2). Under different porosity levels, the permeability of the V60-200, V70-200, V80-200 scaffolds increased from 10.2×10^{-9} to 17.2×10^{-9} m^2, and finally to 26.1×10^{-9} m^2. The larger pore volume reduced the fluid flow resistance, thereby enhancing permeability. Due to their trabecular architecture, Voronoi scaffolds with different parameters exhibited permeability values within the reported range for human trabecular bone (0.75×10^{-9} to 7.43×10^{-8} m^2).[60-61] This similarity supported effective transport of nutrients and metabolic waste in Voronoi-based bone implants during physiological service.

Figure 9 presents the fluid flow pressure and velocity distribution contours of Voronoi scaffolds under different seed counts using CFD simulation. The pressure contour maps revealed a trend that the farther the location from the outlet, the higher the pressure. Comparing the three scaffolds, it is evident that the high connectivity and randomness of fluid channels in these scaffolds resulted in minimal fluctuations in pressure isosurfaces. Within the same height range, Voronoi scaffolds with greater seed counts exhibited higher pressure distributions. Specifically, the overall pressure levels in the V70-100 sample remained below 0.4 Pa, whereas those in the V70-800 sample were significantly higher. This difference arose from the increased internal surface area in the V70-800 sample,

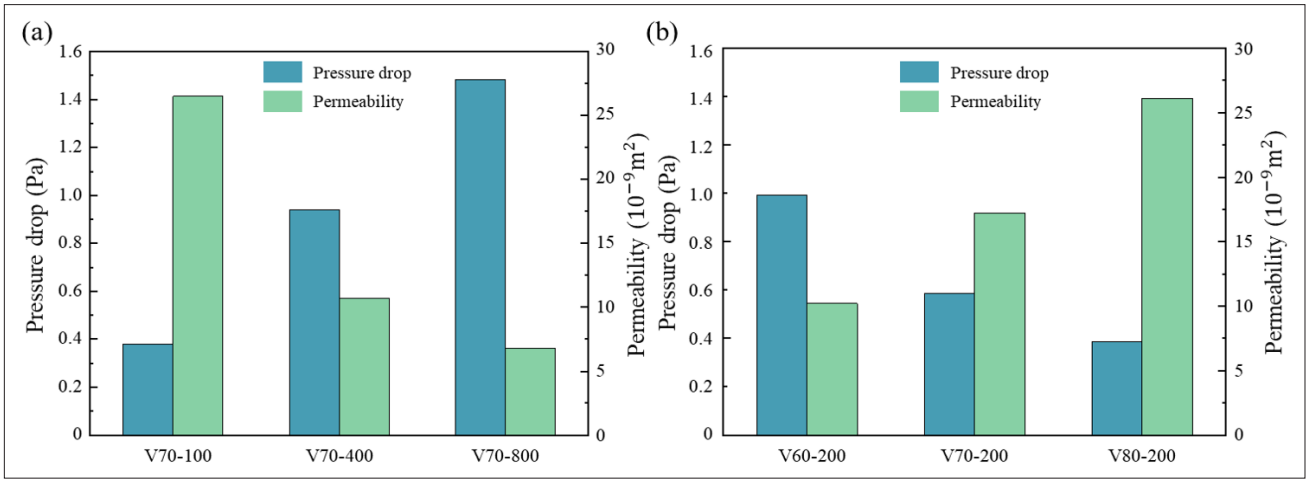


Figure 8. Pressure drops and permeability of Voronoi scaffolds from fluid dynamics simulation results. (a) Varying seed counts. (b) Different porosity levels.

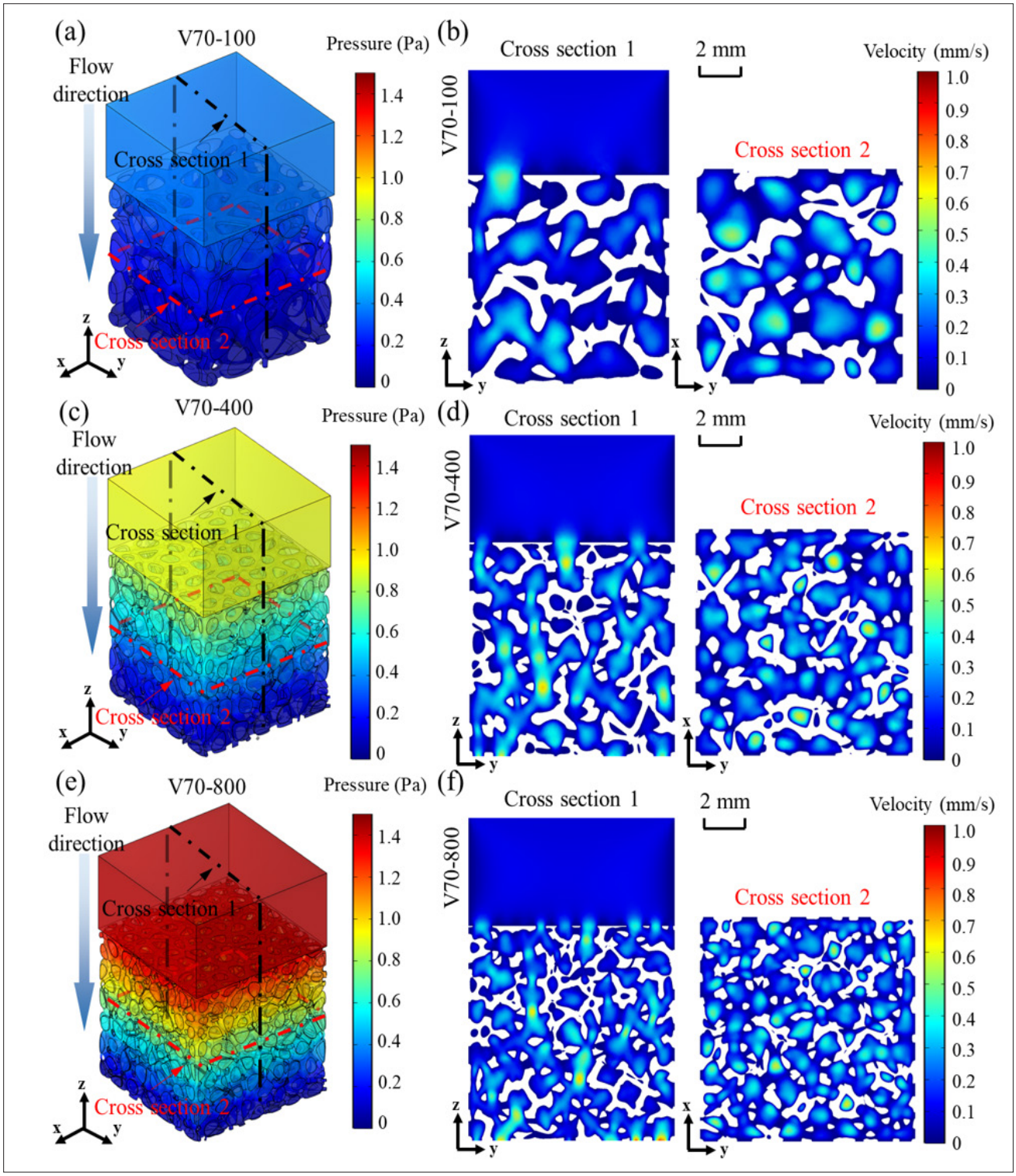


Figure 9. Fluid flow analysis of Voronoi scaffolds with different seed counts. (a,c,e) Pressure distribution. (b,d,f) Flow velocity distribution.

which enhanced viscous friction resistance both between the fluid and the solid matrix and among adjacent flow layers within the channels. In addition, the more intricate and staggered flow channels in the V70-800 sample contributed to greater energy dissipation during fluid transport. These factors collectively led to substantial flow energy loss in the V70-800 sample due to its complex fluid channel architecture, thus reducing permeability. Under different porosity levels, reduced pore volume restricted the fluid channels in the Voronoi scaffolds, leading to larger pressure drops and the emergence of localized regions with high flow velocity, which further diminished permeability (Figure S3). Taken together, an increase in both the number and volume of heterogeneous pore channels leads to a greater loss in fluid flow energy.

The mechanical properties and permeability values of the Voronoi scaffolds with different parameters within the reported range of human trabecular bone are similar. Particularly, when compared to the performance of other topological scaffolds (Table S2), the Voronoi scaffolds exhibit properties that are more similar to those of natural cancellous bone. This similarity facilitates the effective transportation of nutrients and metabolic waste by bone implants based on the Voronoi scaffold during biomedical applications and reduces the possibility of stress shielding.

3.5. Degradation behaviors

The degradation behavior of zinc-based Voronoi scaffolds not only affects the service life of degradable implants but also influences bone cell growth due to the release of zinc ions during degradation. In this study, *in vitro* degradation experiments were conducted to investigate the degradation behavior of zinc-based Voronoi scaffolds with different structural parameters after 28 days of immersion. To quantitatively compare the degradation rate differences among structures with different seed counts, the weight losses of the V70-100, V70-400, and V70-800 scaffolds after 28 days were measured as 0.153, 0.082, and 0.043 g, respectively. The corresponding degradation rates were calculated as 0.157, 0.056, and 0.027 mm/year, respectively, with the degradation rate of the V70-100 sample being 5.8 times higher than that of the V70-800 sample (Figure 10a). As shown in Figure 10b, zinc-based Voronoi scaffolds with higher porosity exhibited faster degradation rates. Specifically, the degradation rate of the V80-200 sample (0.133 mm/year) was 1.47 times greater than that of the V60-200 sample (0.090 mm/year). These experimental results indicated that increasing the number of seeds significantly reduced the degradation rate of zinc-based Voronoi scaffolds.

To further analyze the degradation behavior of the zinc-based Voronoi scaffolds, SEM imaging was conducted on theirs surfaces after 28 days of immersion in SBF. As zinc ions reacted chemically with inorganic salts and other components in the SBF solution, the elemental composition of the degradation products (such as zinc, oxygen, phosphorus, chlorine, calcium, and carbon elements) was analyzed (Figure 11). A uniform, shell-like corrosion layer formed on the surface of the Voronoi scaffold. At higher magnification, isolated white degradation products were observed on both the surface and edges of this layer (Figure 11a). Around the sample surface and within the surrounding areas, degradation products accumulated in various morphologies, including needle-like, sheet-like, snowflake-like, and shell-like structures. These formations

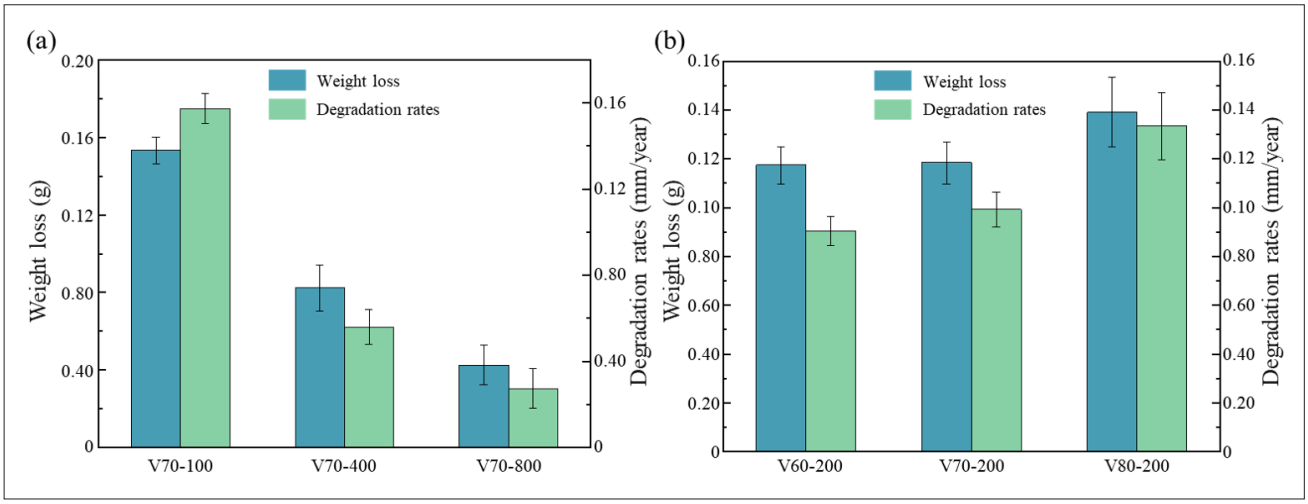


Figure 10. Weight loss and permeability of the LPBF-printed zinc-based Voronoi scaffolds: (a) Different seed counts. (b) Different porosity levels. Abbreviation: LPBF, Laser powder bed fusion.

resulted from a series of chemical reactions occurring between zinc and the SBF solution

$$Zn \rightarrow Zn^{2+} + 2e^{-}, \quad (XV)$$

$$O_2 + 2H_2O + 4e^{-} \rightarrow 4OH^{-}, \quad (XVI)$$

$$Zn^{2+} + 2OH^{-} \rightarrow Zn(OH)_2. \quad (XVII)$$

The reduction of H_2O and oxygen produced OH^- ions. As the initial reaction progressed, the accumulation of OH^- ions caused an increase in the pH value. Zinc is more susceptible to passivation, forming $Zn(OH)_2$.[62-63] The Zn^{2+} ions generated at the anode subsequently reacted with other ions and species present in the solution

$$Zn^{2+} + 2Cl^{-} \rightarrow ZnCl_2, \quad (XVIII)$$

$$4Zn(OH)_2 + ZnCl_2 + H_2O \rightarrow Zn_5(OH)_8Cl_2 \cdot H_2O. \quad (XIX)$$

The detection of chlorine element in the Voronoi scaffolds after 28 days of degradation was nearly negligible, whereas chlorine distribution was still observable in certain samples after 14 days (Figure S4). This observation might be attributed to the inherent instability of basic zinc chloride ($Zn_5(OH)_8Cl_2 \cdot H_2O$), which tended to decompose into zinc oxide (ZnO) under alkaline conditions and release Zn^{2+} ions under acidic conditions

$$Zn_5(OH)_8Cl_2 + 2OH^{-} \rightarrow 5ZnO + 2Cl^{-} + 5H_2O, \quad (XX)$$

$$Zn_5(OH)_8Cl_2 + 8H^{+} \rightarrow 5Zn^{+} + 8H_2O + 2Cl^{-}. \quad (XXI)$$

This led to the predominant presence of chlorine as chloride ions in the solution.[64] Moreover, since SBF contained buffering systems, such as bicarbonate and hydrogen phosphate, dissolved carbon dioxide reacted with OH^- to form HCO_3^-, contributing to the formation of a small amount of basic zinc carbonate precipitation

$$5Zn(OH)_2 + 2HCO_3^{-} + 2H^{+} \rightarrow Zn_5(CO_3)_2(OH)_6 + 4H_2O, \quad (XXII)$$

$$2HPO_4^{2-} + 3Zn(OH)_2 + 4H^{+} \rightarrow Zn_3(PO_4)^{2+} + 6H_2O \quad (XXIII)$$

Therefore, the zinc-based Voronoi scaffolds degraded in the SBF solution to form major degradation products, such as ZnO, basic carbonate zinc ($Zn_5(CO_3)_2(OH)_6$), and $Zn_5(OH)_8Cl_2 \cdot H_2O$. The extensive distribution of P further suggested the potential formation of phosphorous compounds within the degradation layer. The cross-sectional energy-dispersive X-ray spectroscopy (EDS) analysis revealed that the degradation products adhering to the strut surface were rich in zinc and oxygen, while calcium was mainly present in the outer regions of the degradation layer, farther from the strut surface.[65] This indicated that calcium-containing compounds precipitated during the later stages of degradation. Additionally, with prolonged degradation time, these products progressively accumulated and spread outward, leading to the blockage and coverage of pores within the Voronoi scaffold (Figure 10e). As the seed count increased, the interconnected pore channels became increasingly narrower. Under the influence of low permeability, this facilitated further degradation and blockage of internal pores, hindering the diffusion of Zn^{2+} ions and their interaction with SBF, thereby inhibiting the overall degradation process. This mechanism may account for the significant reduction in the degradation rate observed in the V70-800 sample.

3.5. Biological activity

Alkaline phosphatase (ALP) is synthesized by osteoblasts and secreted into both the bone matrix and the bloodstream, where it serves as a key enzyme in bone matrix synthesis and mineralization. As shown in Figure S5, ALP staining was employed to evaluate the osteogenic differentiation potential of zinc-based Voronoi scaffolds. ALP expression levels increased over time across all scaffold groups. While variations in porosity had minimal impact on ALP secretion, the seed count significantly affected enzymatic activity. Notably, the V70-800 group exhibited the most intense blue staining and significantly higher ALP activity compared to other groups. Alizarin red staining (ARS) results corroborated these findings: the V70-800 group displayed a substantially greater number of mineralized nodules and the largest ARS-positive area (Figure 12), indicating enhanced extracellular matrix mineralization and calcium deposition. Concurrent cell proliferation assays demonstrated that the zinc-based

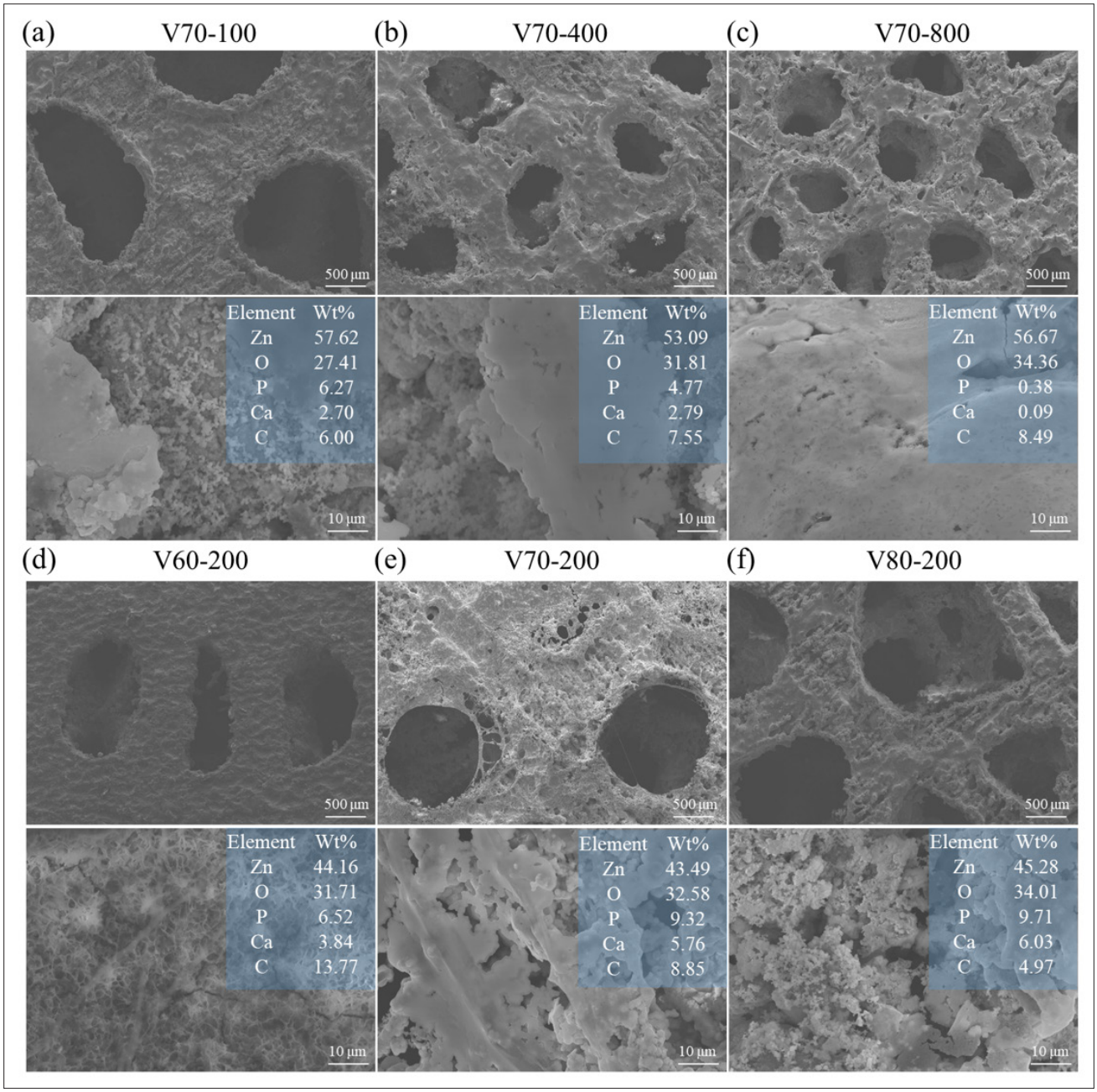


Figure 11. Morphology and elemental analysis of LPBF-printed zinc-based Voronoi scaffolds after immersion for 28 days. (a–d) Different seed counts. (e,f) Different porosity levels. Abbreviation: LPBF, Laser powder bed fusion.

Voronoi scaffolds exhibited excellent biocompatibility without obvious cytotoxicity. In the experimental groups with high seed density, increased cell density was observed, along with more favorable cell morphological characteristics (Figure S6). Furthermore, the V70-800 group demonstrated a significant slower degradation rate than other experimental groups. The sustained release of low concentrations of Zn^{2+} from this scaffold promoted osteogenic activity by improving enzyme function without disrupting intracellular metal ion homeostasis or inducing cytotoxicity.

To further investigate the underlying mechanism of the osteogenic differentiation–promoting effect of the zinc-based Voronoi scaffolds, the V70-800 group that exhibited superior osteogenic activity, along with the control

group and two additional experimental groups, showed moderately different outcomes. The mRNA expression levels of osteogenic-related key genes, such as type I collagen α1 chain (*COL1*), *ALP*, and osteocalcin (*OCN*), were quantified by means of qRT-PCR to verify and assess the osteoinductive capacity of the scaffolds. As illustrated in Figure 13, all experimental groups exhibited upregulated expression of *COL1* and *ALP* at the mRNA level, with the V70-800 group demonstrating the most robust enhancement. On the day 7, the V70-800 group showed significantly higher expression of both *COL1* and *ALP* compared to the control group, and this difference became more pronounced by the day 14. Notably, *COL1* expression in the V70-800 group reached 4.5-fold that of the control group on the day 14. COL1 facilitated osteoblast adhesion and signaling through specific peptide sequences such as the RGD integrin-binding site and the GFOGER collagen-binding motif, thereby activating downstream pathways that promoted osteogenic differentiation. The zinc-based Voronoi scaffolds effectively stimulated MC3T3-E1 cells to synthesize and secret osteogenic-related proteins. At lower concentrations, Zn^{2+} preferentially enhanced the expression of type I collagen α1 chain, suggesting a targeted regulatory role in early-stage osteogenic differentiation. In summary, adjusting the seed density is a critical determinant for endowing zinc-based Voronoi scaffolds with proliferative and osteoinductive functionalities.

4. Conclusion

In this study, the effects of seed count and porosity on the mechanical properties, mass transfer properties, degradation behavior, and osteogenic differentiation of zinc-based Voronoi scaffolds fabricated by LPBF were studied. The main findings are concluded as follows:

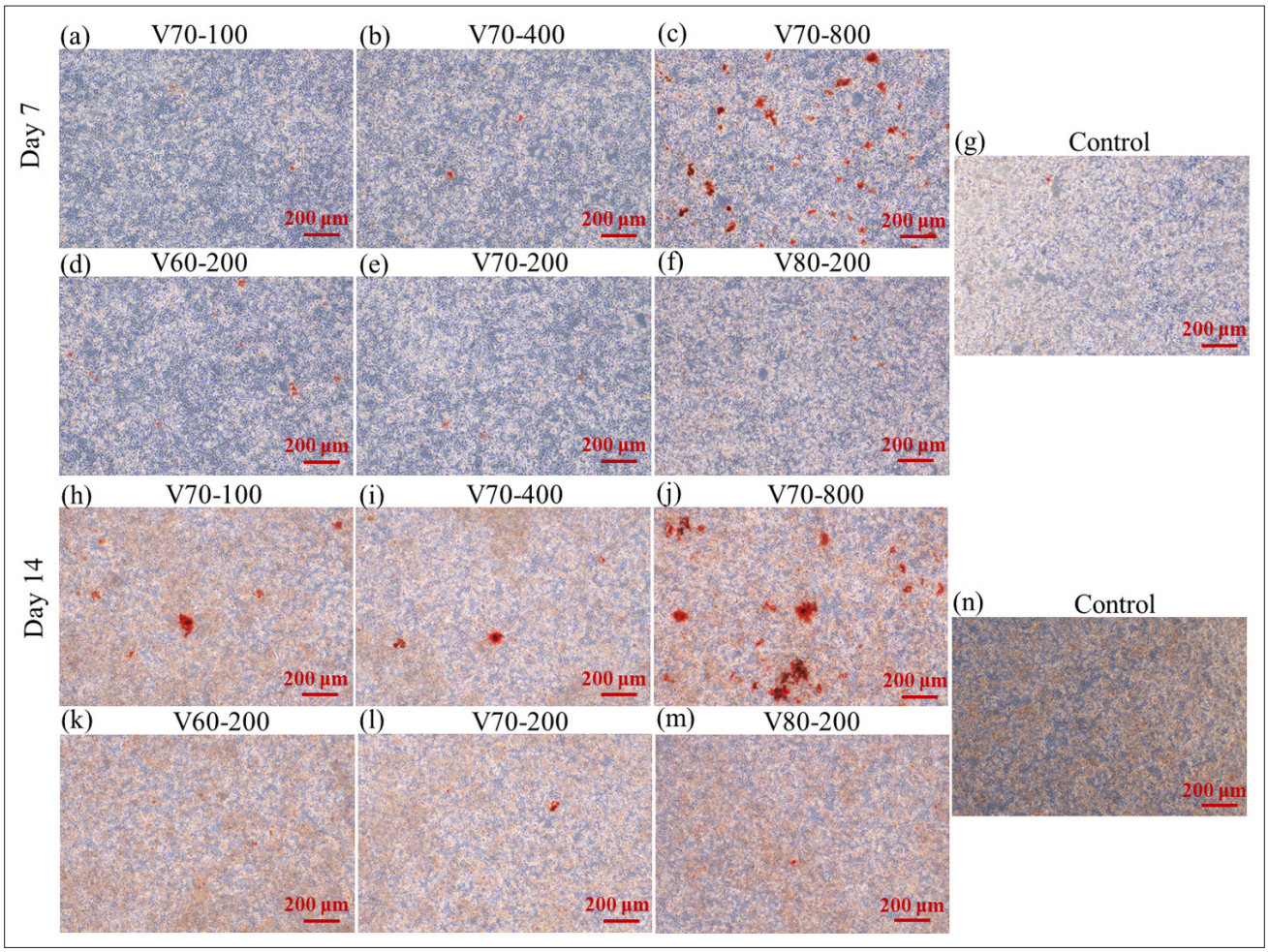


Figure 12. Osteogenic differentiation visualized with Alizarin red staining using the 10% extract of the LPBF-printed zinc-based Voronoi scaffolds: (a–g) On day 7. (h–n) On day 14. Abbreviation: LPBF, Laser powder bed fusion.

The influence law of porosity and seed density on Voronoi mechanical properties and deformation mechanism was revealed. The failure and fracture of struts caused by the increase of aspect ratio was the main reason for the decrease of mechanical properties of Voronoi scaffold at a high porosity. The increase of seed density caused more random local strut damage, reduced the structural strength, and reduced the influence of local strut failure on the overall performance of the structure, so as to obtain higher platform stress. Reducing seed counts from 800 to 100 increased the Voronoi scaffold failure stress by 26.9% and decreased the plateau stress by 6.9%.

The permeability of 70% porosity Voronoi scaffolds with different seed counts was in the range of 6.81×10^{-9} – 26.5×10^{-9} m^2. The permeability of the V70-100 sample (26.5×10^{-9} m^2) was 3.9 times higher than that of the V70-800 sample (6.81×10^{-9} m^2). Increasing the seed counts boosted the irregular fluid channel inside the Voronoi scaffold, allowing the fluid flow resistance to increase, leading to lower permeability.

The degradation rate of zinc-based Voronoi scaffold decreased with the increase of seed counts, and the degradation rate of V70-100 sample (0.157 mm/year) was 5.8 times that of V70-800 sample (0.027 mm/year). The high number of seeds reduced the connected pore size inside the Voronoi scaffold, and the high pore density and low permeability caused degradation products to deposit more readily and block internal pores, thereby inhibiting Zn^{2+}release.

The seed counts in the zinc-based Voronoi structure significantly affected ALP secretion, and the high number of seeds Voronoi scaffold positively regulates extracellular matrix mineralization and calcification by reducing Zn^{2+} release rate. It mainly increased the expression of COL1 and ALP to promote osteogenic differentiation. The expression level of COL1 in the V70-800 group was 4.5 times that of the control group. This work provides a basis for the clinical application of Voronoi scaffolds. However, there are still certain limitations, such as the lack of *in vivo* degradation experiments and long-term degradation research results.

Acknowledgments

None.

Funding

This study was supported by the following funds: the Fundamental Research Funds for the Central Universities (No. 2024ZYGXZR079), the National Natural Science Foundation of China (Nos. 52305358 and W2421079), the Young Elite Scientists Sponsorship Program by CAST (No. 2023QNRC001), and the Science and Technology Project of Guangzhou (No. 2025A04J5196).

Conflict of interest

The authors declare they have no competing interests.

Author contributions

Conceptualization: Boxun Liu, Yunhui Wang, Changjun Han

Formal analysis: Boxun Liu, Yunhui Wang, Yi Zhang, Zhengbo Wen, QiXin Liang

Investigation: Boxun Liu, Yunhui Wang, Zhi Dong

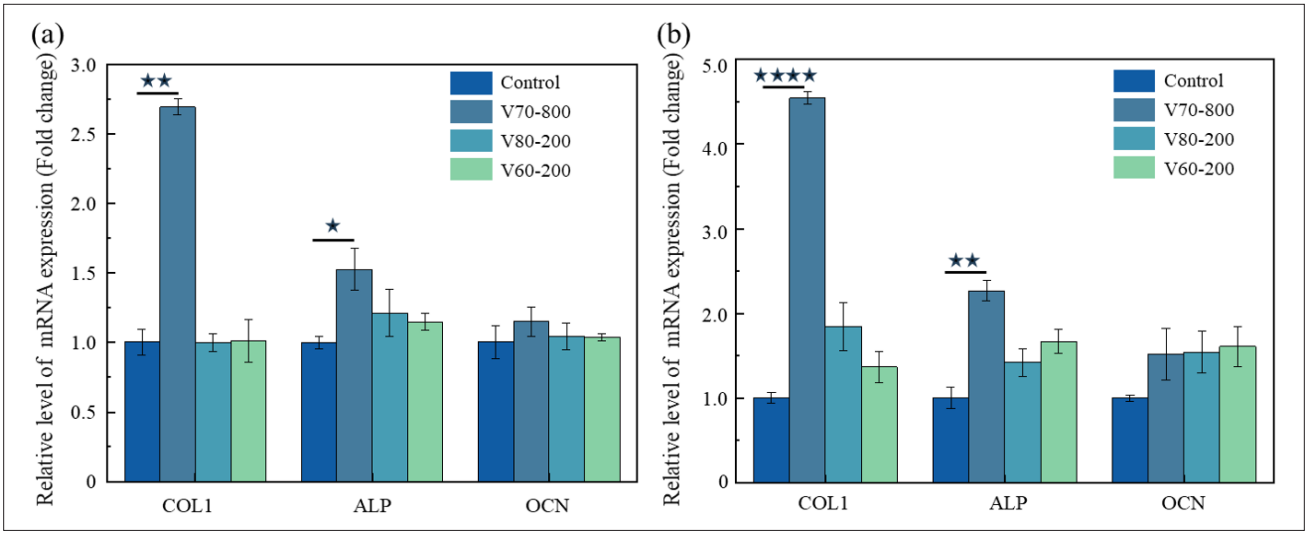


Figure 13. Influence of zinc-based Voronoi scaffolds on the relative expression levels of key osteogenic genes COL1, ALP and OCN. (a) On day 7. (b) On day 14.

Methodology: Yi Zhang, Zhengbo Wen, QiXin Liang
Writing–original draft: Boxun Liu, Yunhui Wang, Yushan Huang
Writing–review & editing: Changjun Han, Yunhui Wang, Yushan Huang

Ethics approval and consent to participate

Not applicable.

Consent for publication

Not applicable.

Availability of data

Data are available from the corresponding author upon reasonable request

References

1. Ling C, Li Q, Zhang Z, *et al*. Influence of heat treatment on microstructure, mechanical and corrosion behavior of WE43 alloy fabricated by laser-beam powder bed fusion. *Int J Extreme Manuf.* 2023;6(1):015001. doi: 10.1088/2631-7990/acfad5
2. Wu X, Liu J, Yang Y, *et al*. Laser powder bed fusion of biodegradable magnesium alloys: process, microstructure and properties. *Int J Extreme Manuf.* 2024;7(2):022007. doi: 10.1088/2631-7990/ad967e
3. Tan C, Zou J, Li S, *et al*. Additive manufacturing of bio-inspired multi-scale hierarchically strengthened lattice structures. *Int J Mach Tools Manuf.* 2021;167:103764. doi: 10.1016/j.ijmachtools.2021.103764
4. Wei S, Ma J, Xu L, *et al*. Biodegradable materials for bone defect repair. *Mil Med Res.* 2020;7(1):54. doi: 10.1186/s40779-020-00280-6
5. Yang Y, Jiang R, Han C, *et al*. Frontiers in laser additive manufacturing technology. *Addit Manuf Front.* 2024;3(4):200160. doi: 10.1016/j.amf.2024.200160
6. Lu Y, Chen G, Long Z, *et al*. Novel 3D-printed prosthetic composite for reconstruction of massive bone defects in lower extremities after malignant tumor resection. *J Bone Oncol.* 2019;16:100220. doi: 10.1016/j.jbo.2019.100220
7. Ran Q, Yang W, Hu Y, *et al*. Osteogenesis of 3D printed porous Ti6Al4V implants with different pore sizes. *J Mech Behav Biomed Mater.* 2018;84:1-11. doi: 10.1016/j.jmbbm.2018.04.010
8. Zhang W, Wang L, Feng Z, *et al*. Research progress on selective laser melting (SLM) of magnesium alloys: a review. *Optik.* 2020;207:163842. doi: 10.1016/j.ijleo.2019.163842
9. Yang M, Yang L, Peng S, *et al*. Laser additive manufacturing of zinc: formation quality, texture, and cell behavior. *Bio-Des Manuf.* 2023;6(2):103-120. doi: 10.1007/s42242-022-00216-0
10. Bandyopadhyay A, Mitra I, Avila JD, *et al*. Porous metal implants: processing, properties, and challenges. *Int J Extreme Manuf.* 2023;5(3):032014. doi: 10.1088/2631-7990/acdd35
11. Gao Z, Ren P, Wang H, *et al*. Additive manufacture of ultrasoft bioinspired metamaterials. *Int J Mach Tools Manuf.* 2024;195:104101. doi: 10.1016/j.ijmachtools.2023.104101
12. Jin J, Wu S, Yang L, *et al*. Ni–Ti multicell interlacing Gyroid lattice structures with ultra-high hyperelastic response fabricated by laser powder bed fusion. *Int J Mach Tools Manuf.* 2024;195:104099. doi: 10.1016/j.ijmachtools.2023.104099
13. Gibson L. The mechanical behaviour of cancellous bone. *J Biomech.* 1985;18(5):317-328. doi: 10.1016/0021-9290(85)90287-8
14. Yang Y, Ling C, Li Y, *et al*. Microstructure development and biodegradation behavior of additively manufactured Mg-Zn-Gd alloy with LPSO structure. *J Mater Sci Technol.* 2023;144:1-14. doi: 10.1016/j.jmst.2022.09.059
15. Gatto ML, Cerqueni G, Groppo R, *et al*. Improved biomechanical behavior of 316L graded scaffolds for bone tissue regeneration produced by laser powder bed fusion. *J Mech Behav Biomed Mater.* 2023;144:105989. doi: 10.1016/j.jmbbm.2023.105989
16. Tyagi SA, Manjaiah M. Additive manufacturing of titanium-based lattice structures for medical applications–a review. *Bioprinting.* 2023;30:e00267. doi: 10.1016/j.bprint.2023.e00267
17. Wang D, Liu L, Tang J, *et al*. Recent advances on additive manufacturing of heterogeneous/gradient metallic materials via laser powder bed fusion. *Int J Extreme Manuf.* 2025;7(6):062007. doi: 10.1088/2631-7990/adf69e
18. Ma S, Tang Q, Han X, *et al*. Manufacturability, mechanical properties, mass-transport properties and biocompatibility of triply periodic minimal surface (TPMS) porous scaffolds fabricated by selective laser melting. *Mater Des.* 2020;195:109034. doi: 10.1016/j.matdes.2020.109034
19. Zhang L, Wang B, Song B, *et al*. 3D printed biomimetic metamaterials with graded porosity and tapering topology for improved cell seeding and bone regeneration. *Bioact Mater.* 2023;25:677-688. doi: 10.1016/j.bioactmat.2022.07.009
20. Fortune S. A sweepline algorithm for Voronoi diagrams. *Proc Second Annu Symp Comput Geom.* 1986:313-322.

doi: 10.1145/10515.10549

21. Du Q, Faber V, Gunzburger M. Centroidal Voronoi tessellations: applications and algorithms. *SIAM Rev.* 1999;41(4):637-676.
doi: 10.1137/S0036144599352836

22. Fantini M, Curto M. Interactive design and manufacturing of a Voronoi-based biomimetic bone scaffold for morphological characterization. *Int J Interact Des Manuf.* 2018;12:585-596.
doi: 10.1007/s12008-017-0416-x

23. Dong Z, Du H, Xu S, *et al*. Achieving near-isotropic strength and ductility in laser additively manufactured zinc via columnar-to-equiaxed grain transition under thermoelectric magnetic effect. *J Mater Sci Technol.* 2025;258:107-120.
doi: 10.1016/j.jmst.2025.09.023

24. Li D, Xie H, Gao C, *et al*. Harmonic heterostructured pure Ti fabricated by laser powder bed fusion for excellent wear resistance via strength-plasticity synergy. *Opto-Electron Adv.* 2025;8(9):250043-1-250043-21.
doi: 10.29026/oea.2025.250043

25. Zhao H, Han Y, Pan C, *et al*. Design and mechanical properties verification of gradient Voronoi scaffold for bone tissue engineering. *Micromachines.* 2021;12(6):664.
doi: 10.3390/mi12060664

26. Gómez S, Vlad M D, López J, *et al*. Design and properties of 3D scaffolds for bone tissue engineering. *Acta Biomater.* 2016;42:341-350.
doi: 10.1016/j.actbio.2016.06.032

27. Herath B, Suresh S, Downing D, *et al*. Mechanical and geometrical study of 3D printed Voronoi scaffold design for large bone defects. *Mater Des.* 2021;212:110224.
doi: 10.1021/acsbiomaterials.1c01482

28. Zou S, Gong H, Gao J. Additively Manufactured Multilevel Voronoi-Lattice Scaffolds with Bonelike Mechanical Properties [J]. *ACS Biomater Sci Eng*. 2022;8(7): 3022-3037
doi: 10.1007/s12008-017-0416-x

29. Guaglione F, Caprio L, Previtali B, *et al*. Single point exposure LPBF for the production of biodegradable Zn-alloy lattice structures. *Addit Manuf.* 2021;48:102426.
doi: 10.1016/j.addma.2021.102426

30. Xu S, Xue Y, Hu X, *et al*. Relation between materials, process, structure and property of metallic porous bone scaffolds fabricated by laser powder bed fusion (LPBF): a review. *Opt Laser Technol.* 2025;191:113377.
doi: 10.1016/j.optlastec.2025.113377

31. Wang H, Shu Z, Chen P, *et al*. Laser powder bed fusion printed poly-ether-ether-ketone/bioactive glass composite scaffolds with dual-scale pores for enhanced osseointegration and bone ingrowth. *Acta Biomater.* 2024;189:605-620.
doi: 10.1016/j.actbio.2024.09.055

32. Yang J, Jin X, Gao H, *et al*. Additive manufacturing of trabecular tantalum scaffolds by laser powder bed fusion: mechanical property evaluation and porous structure characterization. *Mater Character.* 2020;170:110694.
doi: 10.1016/j.matchar.2020.110694

33. Zhou X, Feng Y, Zhang J, *et al*. Recent advances in additive manufacturing technology for bone tissue engineering scaffolds. *Int J Adv Manuf Technol.* 2020;108(11):3591-606.
doi: 10.1007/s00170-020-05444-1

34. Deering J, Dowling KI, Dicecco LA, *et al*. Selective Voronoi tessellation as a method to design anisotropic and biomimetic implants. *J Mech Behav Biomed Mater.* 2021;116:104361.
doi: 10.1016/j.jmbbm.2021.104361

35. Duan Y, Du B, Zhao X, *et al*. The cell regularity effects on the compressive responses of additively manufactured Voronoi foams. *Int J Mech Sci.* 2019;164:105151.
doi: 10.1016/j.ijmecsci.2019.105151

36. Jiao C, Xie D, He Z, *et al*. Additive manufacturing of Bio-inspired ceramic bone Scaffolds: structural design, mechanical properties and biocompatibility. *Mater Des.* 2022;217:110610.
doi: 10.1016/j.matdes.2022.110610

37. Sotomayor OE, Tippur HV. Role of cell regularity and relative density on elastoplastic compression response of 3-D open-cell foam core sandwich structure generated using Voronoi diagrams. *Acta Mater.* 2014;78:301-313.
doi: 10.1016/j.actamat.2014.06.051

38. Tang L, Shi X, Zhang L, *et al*. Effects of statistics of cell's size and shape irregularity on mechanical properties of 2D and 3D Voronoi foams. *Acta Mech.* 2014;225(4):1361-1372.
doi: 10.1007/s00707-013-1054-4

39. Hou C, Sinico M, Vrancken B, *et al*. Investigation of the laser powder bed fusion manufacturing process and quasi-static behaviour of Ti6Al4V Voronoi structures. *J Mater Process Technol.* 2024;328:118410.
doi: 10.1016/j.jmatprotec.2024.118410

40. Wu T, Yu S, Chen D, *et al*. Bionic design, materials and performance of bone tissue scaffolds. *Materials.* 2017;10(10):1187.
doi: 10.3390/ma10101187

41. Edelsbrunner H, Seidel R. Voronoi diagrams and arrangements. *Proc First Annu Symp Comput Geom.* 1985:251-262.
doi: 10.1145/323233.323266

42. Canny J, Donald B. Simplified Voronoi diagrams. *Proc Third Annu Symp Comput Geom, F.* 1987:153-161.
doi: 10.1145/41958.41974

43. Erwig M. The graph Voronoi diagram with applications. *Netw: Int J.* 2000;36(3):156-163.
doi: 10.1002/1097-0037(200010)36:3<156::AID-NET2>3.0.CO;2-L

44. Goharian A, Daneshjoo K, Mahdavinejad M, *et al*. Voronoi geometry for building facade to manage direct sunbeams. *J Sustain Archit Civil Eng.* 2022;31(2):109-124. doi: 10.5755/j01.sace.31.2.30800

45. Lazar EA, Lu J, Rycroft CH. Voronoi cell analysis: the shapes of particle systems. *Am J Phys.* 2022;90(6):469-480. doi: 10.1119/5.0087591

46. Sugihara K. Approximation of generalized Voronoi diagrams by ordinary Voronoi diagrams. *CVGIP: Graph Models Image Process.* 1993;55(6):522-531. doi: 10.1006/cgip.1993.1039

47. Han C, Wang Y, Wang Z, *et al*. Enhancing mechanical properties of additively manufactured Voronoi-based architected metamaterials via a lattice-inspired design strategy. *Int J Mach Tools Manuf.* 2024;202:104199. doi: 10.1016/j.ijmachtools.2024.104199

48. Soro N, Attar H, Wu X, *et al*. Investigation of the structure and mechanical properties of additively manufactured Ti-6Al-4V biomedical scaffolds designed with a Schwartz primitive unit-cell. *Mater Sci Eng: A.* 2019;745:195-202. doi: 10.1016/j.msea.2018.12.104

49. Xiao L, Xu X, Feng G, *et al*. Compressive performance and energy absorption of additively manufactured metallic hybrid lattice structures. *Int J Mech Sci.* 2022;219:107093. doi: 10.1016/j.ijmecsci.2022.107093

50. Zhong H, Das R, Gu J, *et al*. Low-density, high-strength metal mechanical metamaterials beyond the Gibson-Ashby model. *Mater Today.* 2023;68:96-107. doi: 10.1016/j.mattod.2023.07.018

51. Fantini M, Curto M, De Crescenzio F. A method to design biomimetic scaffolds for bone tissue engineering based on Voronoi lattices. *Virt Phys Prototyp.* 2016;11(2):77-90. doi: 10.1080/17452759.2016.1172301

52. Dong Z, Han C, Zhao Y, *et al*. Role of heterogenous microstructure and deformation behavior in achieving superior strength-ductility synergy in zinc fabricated via laser powder bed fusion. *Int J Extreme Manuf.* 2024;6(4):045003. doi: 10.1088/2631-7990/ad3929

53. Dong Z, Han C, Liu G, *et al*. Revealing anisotropic mechanisms in mechanical and degradation properties of zinc fabricated by laser powder bed fusion additive manufacturing. *J Mater Sci Technol.* 2025;214:87-104. doi: 10.1016/j.jmst.2024.06.045

54. Syahrom A, Abdul KMR, Abdullah J, *et al*. Permeability studies of artificial and natural cancellous bone structures. *Med Eng Phys.* 2013;35(6):792-799. doi: 10.1016/j.medengphy.2012.08.011

55. Yang Y, Lu C, Shen L, *et al*. In-situ deposition of apatite layer to protect Mg-based composite fabricated via laser additive manufacturing. *J Magnesium Alloys.* 2023;11(2):629-640. doi: 10.1016/j.jma.2021.04.009

56. Wang C, Hu Y, Zhong C, *et al*. Microstructural evolution and mechanical properties of pure Zn fabricated by selective laser melting. *Mater Sci Eng: A.* 2022;846:143276. doi: 10.1016/j.msea.2022.143276

57. Gu D, Zhang H, Dai D, *et al*. Laser additive manufacturing of nano-TiC reinforced Ni-based nanocomposites with tailored microstructure and performance. *Composites, Part B.* 2019;163:585-597. doi: 10.1016/j.compositesb.2018.12.146

58. Maconachie T, Leary M, Lozanovski B, *et al*. SLM lattice structures: properties, performance, applications and challenges. *Mater Des.* 2019;183:108137. doi: 10.1016/j.matdes.2019.108137

59. Gu XN, Zheng YF. A review on magnesium alloys as biodegradable materials. *Front Mater Sci China.* 2010;4(2):111-115. doi: 10.1007/s11706-010-0024-1

60. Grimm MJ, Williams JL. Measurements of permeability in human calcaneal trabecular bone. *J Biomech.* 1997;30(7):743-745. doi: 10.1016/S0021-9290(97)00016-X

61. Zhang L, Wang B, Song B, *et al*. 3D printed biomimetic metamaterials with graded porosity and tapering topology for improved cell seeding and bone regeneration. *Bioact Mater.* 2023;25:677-688. doi: 10.1016/j.bioactmat.2022.07.009

62. Liu L, Meng Y, Volinsky AA, *et al*. Influences of albumin on in vitro corrosion of pure Zn in artificial plasma. *Corros Sci.* 2019;153:341-356. doi: 10.1016/j.corsci.2019.04.003

63. Thomas S, Cole IS, Sridhar M, *et al*. Revisiting zinc passivation in alkaline solutions. *Electrochim Acta.* 2013;97:192-201. doi: 10.1016/j.electacta.2013.03.008

64. Mouanga M, Berçot P, Rauch JY. Comparison of corrosion behaviour of zinc in NaCl and in NaOH solutions. Part I: corrosion layer characterization. *Corros Sci.* 2010;52(12):3984-3992. doi: 10.1016/j.corsci.2010.08.003

65. Qin Y, Liu A, Guo H, *et al*. Additive manufacturing of Zn-Mg alloy porous scaffolds with enhanced osseointegration: in vitro and in vivo studies. *Acta Biomater.* 2022;145:403-415. doi: 10.1016/j.actbio.2022.03.055

ACCSCIENCE PUBLISHING

International Journal of Bioprinting

RESEARCH ARTICLE

Multimaterial vat photopolymerization: Computational optimization of slicing workflow for complex tissue geometries

Alejandro González-Santos[1], Adrian García[2], Nadina Usseglio[2], Julián Flores[1], and Daniel Nieto[2,3]*

[1]Department of Electronics and Computing, University of Santiago de Compostela. Santiago de Compostela, Galicia, Spain.

[2]Advanced Biofabrication Laboratory (DNIETO Lab), Interdisciplinary Center for Chemical and Biology, Universidade da Coruña, A Coruña, Galicia, Spain.

[3]Oportunius Program, Axencia Galega de Innovación, Santiago de Compostela, Galicia, Spain

Abstract

Multimaterial printing using digital light processing (DLP) has progressed from a niche laboratory method to a scalable technology capable of fabricating complex and functional tissue constructs. However, current multimaterial DLP workflows face significant limitations. Material changes typically require repeated washing and reloading steps, which increase print time, raise the risk of cross-contamination or layer misalignment, and ultimately constrain scaffold design complexity and biological relevance. To address these challenges, we present a computational pipeline that significantly improves the efficiency, precision, and usability of DLP for multimaterial bioprinting. Our system includes three key innovations: (i) a high-resolution segmentation and material-labeling method using computer graphics techniques for accurate material assignment in Standard Tessellation Language (STL) models; (ii) a computer vision-based algorithm for real-time detection and correction of material interference or contamination; and (iii) a GPU-accelerated layer sequencing method that supports rapid, precise material switching within single-layer projections. Experimental validation demonstrates improved print fidelity, reduced processing time, and higher material resolution. We further showcase the practical utility of our system by bioprinting a multimaterial tissue construct composed of a poly(ethylene glycol) diacrylate-based scaffold integrated with a gelatin methacryloyl-based cell-laden microenvironment. This work represents a significant step toward enabling scalable, high-resolution, and biologically functional scaffold fabrication for advanced tissue engineering applications.

Keywords: 3D printing protocol; Multimaterial digital light processing printer; Process planning algorithm; Slicing

***Corresponding author:**
Daniel Nieto
(daniel.nieto@udc.es)

Citation: González-Santos A, García A, Usseglio N, Flores J, Nieto D. Multimaterial vat photopolymerization: Computational optimization of slicing workflow for complex tissue geometries. *Int J Bioprint*. 2026;12(1):523-539. doi: 10.36922/IJB025470480

Received: November 18, 2025
Revised: December 12, 2025
Accepted: December 16, 2025
Published online: December 19, 2025

Copyright: © 2025 Author(s). This is an Open Access article distributed under the terms of the Creative Commons Attribution License, permitting distribution and reproduction in any medium, provided the original work is properly cited.

Publisher's Note: AccScience Publishing remains neutral with regard to jurisdictional claims in published maps and institutional affiliations.

1. Introduction

Three-dimensional (3D) bioprinting has emerged as a transformative technology for fabricating biological structures. This field leverages additive manufacturing principles to create complex, cell-laden tissues with precise spatial arrangements.[1] Recent advances

in bioprinting techniques and biomaterials have opened new possibilities for developing transplantable tissues, including vascular grafts, bone, cartilage, and cardiac structures.[2,3] However, the fabrication of fully functional organs remains an ongoing challenge, as current bioprinting methods struggle to replicate the intricate microstructures and physiological complexity of human tissues.[4]

Light-based bioprinting technologies are a subset of 3D bioprinting methods that utilize light to precisely pattern and solidify bioinks containing living cells and biomaterials. Among them, vat photopolymerization (VPP) is an additive manufacturing technology in which a liquid photosensitive resin is selectively solidified layer by layer using a controlled light source. The primary techniques include stereolithography (SLA)[5] and digital light processing (DLP).[6] In SLA, a focused UV laser scans the surface of the resin, curing the material point by point to build each layer with very high precision and smooth surface quality. In DLP, an entire layer is cured at once by exposing the bioink to light patterns using a digital micromirror device, allowing for faster fabrication while maintaining precision. Both techniques enable the production of detailed, accurate parts. However, SLA excels in surface finish and fine features, whereas DLP stands out for its ability to produce high-resolution tissue structures with scalable fabrication capabilities using photosensitive bioinks. While the DLP process can be highly precise, it requires careful control of factors such as ink surface levels, material purity, and biomaterial management.[6]

While early applications typically relied on monomaterial printing due to its simplicity, the limitations of this approach became apparent as the need arose to recreate structures containing different cell types and structural matrices. The transition to multimaterial manufacturing represents a significant advance, focusing on optimizing not only the performance of the printing process but also the morphological and functional qualities of the resulting structure.[7]

The slicing strategies used in DLP bioprinting remain largely planar and uniform, which limits the ability to fabricate anatomically accurate or functionally graded tissues. Although adaptive and non-planar slicing algorithms have been proposed, their integration into DLP systems is challenging due to hardware constraints and a lack of standardized, user-friendly software.[8] In addition, most DLP platforms operate in an open-loop mode, meaning they cannot compensate for dynamic changes during printing—such as thermal expansion and the settling of bioinks—which can lead to geometric distortions or layer delamination. While real-time imaging techniques (e.g., optical coherence tomography and fluorescence monitoring) have been explored for feedback control,[9] incorporating these into DLP systems remains technically complex and cost-prohibitive for most laboratories. This is particularly important when manufacturing objects composed of multiple materials, as efficient material management becomes crucial for success. For example, Kim *et al.*[10] proposed an algorithm to optimize material transitions in DLP bioprinting, reducing the need for frequent cleaning and leveling during material changes. Segmenting and converting this data into printable models without introducing artifacts or compromising resolution is non-trivial, and current slicing tools often lack the sophistication to preserve biologically relevant features.

Some researchers have previously reported multimaterial VPP strategies for 3D printing. Shaukat *et al.*[11] categorized the principal strategies into: (i) sequential resin–vat exchange, (ii) in-vat selective activation via dual-wavelength or graded doses, and (iii) dual-curing or multi-reaction systems. A recent experimental example is the dual-vat DLP implementation for vitrimers, described by Shaukat *et al.*,[12] which achieves high functional integration by physically exchanging vats during the build process. Another notable advance is the dual-wavelength VPP method reported by Chin *et al.*,[13] which enables the production of multimaterial or multi-color prints from a single resin vat by modulating photoreactions with different wavelengths. In addition, Ghaderi *et al.*[14] have demonstrated a multimaterial VPP platform based on dual vats combined with an intermediate ultrasonic cleaning station and automated vat switching, enabling efficient fabrication of complex structures such as scaffolds for bone regeneration while mitigating resin cross-contamination.

The primary objective of this study is to enhance the precision and efficiency of top–down DLP bioprinting for multimaterial, cell-laden constructs by algorithmically optimizing the slicing workflow and material change sequence, independent of major hardware modifications. By minimizing the number of material-switch events and aligning layer sequences to reduce idle or cleaning times, we directly address efficiency bottlenecks inherent in prior methods. The algorithm operates directly on a voxelized 3D model, enabling accurate layer control and reducing the number of material transitions during printing. Following theoretical validation and acellular printing tests, the system was applied to the fabrication of living tissue constructs, demonstrating high structural fidelity and good cell viability, confirming its potential for advanced biofabrication applications. The methodology is presented in **Section 2**, followed by results and discussion in **Section 3** and a conclusion in **Section 4**.

2. Materials and methods

2.1. Bioprinting system and methodology

For the work presented in this study, we utilized a custom-built DLP-based stereolithographic "top–down" 3D bioprinter designed for multimaterial bioprinting applications (Figure 1A). The system integrates several key components: a high-resolution DLP projector (Wintech PRO6600, Wintech Digital Systems Technology Corp., United States [US]) with 4K resolution (3840 × 2160 pixels), a 385 nm wavelength, and over 3000 mW power output to initiate photopolymerization; a *Z*-axis-controlled printing platform driven by a stepper motor for precise vertical positioning; a 4K-capable webcam (ELP USB4KHDR01-KL100, Shenzhen Ailipu Technology Co., Ltd., China) for real-time process monitoring and video recording; and a control computer equipped with custom software that allows coordinated operation of all components through an integrated touchscreen interface (Figure 1A).

To demonstrate the multimaterial capabilities of the developed algorithm, we designed two initial printing models: (i) a two-material lateral intersection, where distinct materials meet side by side (Figure 1Bi); and (ii) a two-material embedded configuration, where one material is printed within another (Figure 1Bii). As a more complex demonstration, we further introduced a multimaterial bioprinting model consisting of a gelatin methacryloyl (GelMA)-based, cell-laden bioink embedded within a poly(ethylene glycol) diacrylate (PEGDA)-based structural scaffold (Figure 1C).

2.2. Bioprinting workflow

2.2.1. Single material slicing

The workflow from a computer-aided design (CAD) single-material model to a real object printed with an SLA or DLP printer begins with designing the object using CAD software, followed by optimization by engineers or designers to ensure its correct manufacturability. After the model is finalized, it is exported to a file format compatible with 3D printing. The most commonly used format is STL. STL files represent the surface of the 3D model as a mesh of interconnected triangles. This file format captures the geometry but does not include color, texture, and material properties. Then, the STL file is loaded into slicing software tailored for SLA/DLP printers. The slicer generates a layer-by-layer representation of the object, along with other process parameters, such as exposure time and the

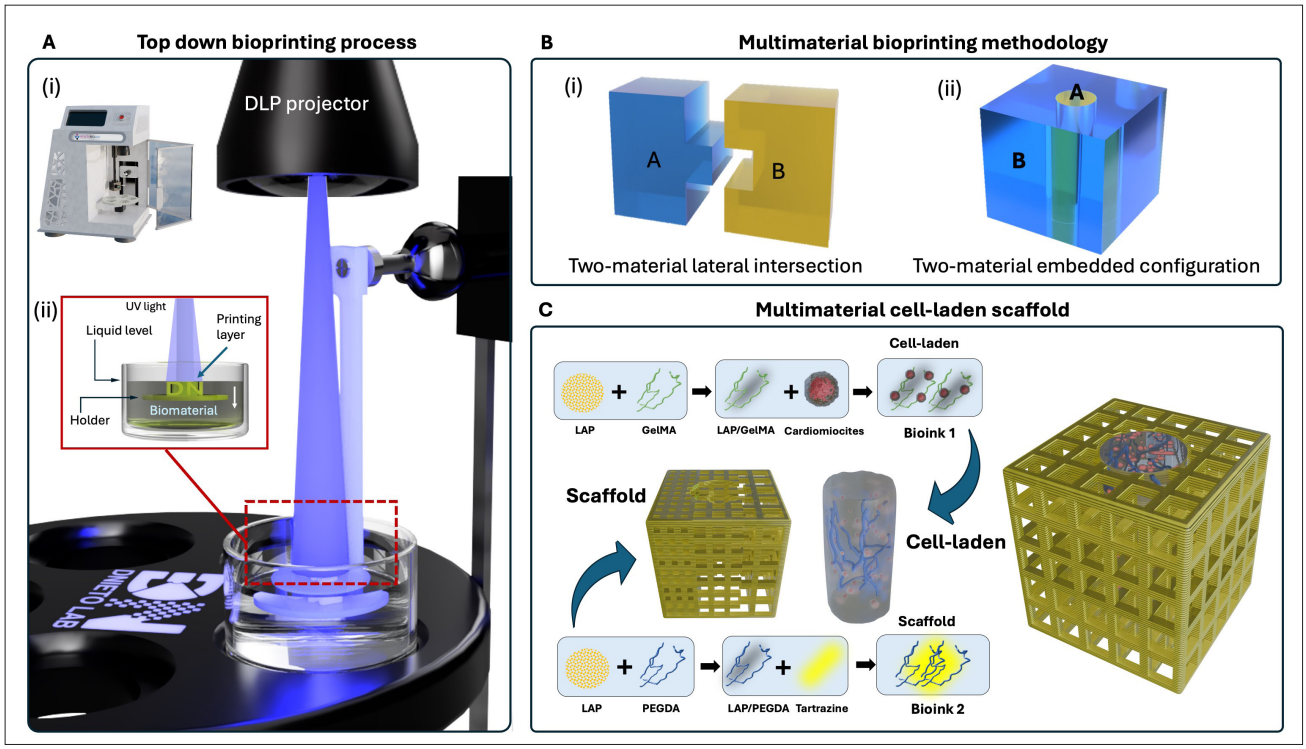


Figure 1. Overview of the top–down multimaterial DLP bioprinting platform and workflow enabled by the proposed algorithm. (A) Top–down bioprinting process: (i) the bioprinter and (ii) schematic of the working chamber. (B) Multimaterial bioprinting configurations used to demonstrate the capabilities of the proposed algorithm: (i) a two-material lateral intersection and (ii) a two-material embedded configuration. (C) Multimaterial cell-laden scaffold bioprinting workflow. Abbreviations: DLP: digital light processing; GelMA; gelatin methacryloyl; LAP: lithium phenyl-2,4,6-trimethylbenzoylphosphinate; PEGDA: poly(ethylene glycol) diacrylate.

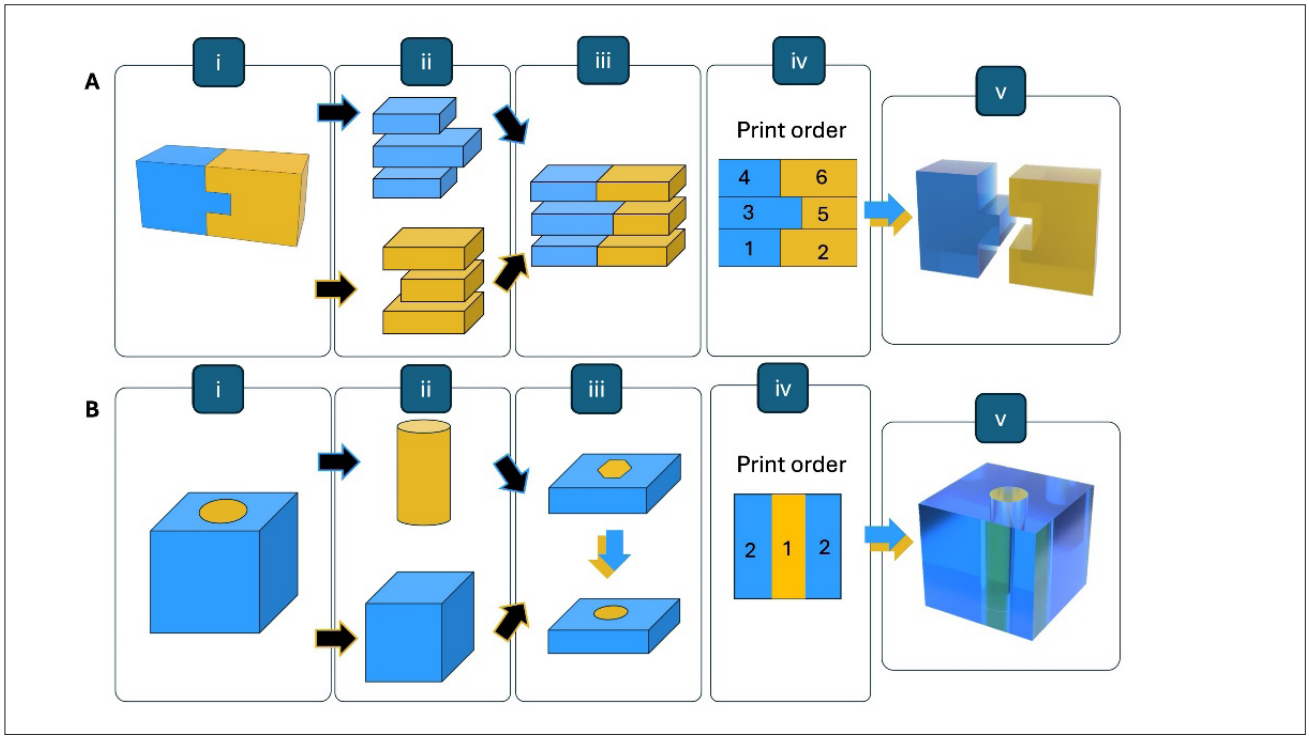


Figure 2. Overview of the digital light processing printing workflow for multimaterial objects using the (A) intersection and (B) enclosed configurations: (i) virtual object, (ii) conversion of the virtual object to a standard tessellation language (STL) model, (iii) generation and verification of sliced images from the STL model, (iv) determination of printing order, and (v) projection of the images to fabricate the physical objects.

intensity of the laser or DLP projector. The slicing software provides a layer-by-layer preview to inspect the object for errors, such as missing supports or incomplete layers. It must inform the user of any problems or potential artifacts that may occur. This step must ensure the file is ready for printing (Figure 2).

Once the printer is prepared, the printing process is initiated. The printer creates the object layer by layer, image by image, by curing the ink using a DLP projector that displays a full slice of the layer simultaneously. Each image is a single layer, whose thickness is determined by the user, and its combination will be the final physical object.

2.2.2. Multimaterial slicing

The manufacturing of a multimaterial object using a DLP 3D printer differs from that of a single-material object, as it involves solving several challenges. The first of these challenges is directly associated with the use of STL files for representation, as the STL format represents the surface of an object as a mesh of triangles and does not include material properties; it only defines the geometry. Therefore, the primary issue is how to identify and differentiate each material within an STL file. Since the format lacks the capability to encode material information, alternative approaches must be developed, such as using multiple STL files (one for each material) or adopting more advanced file formats like OBJ, 3MF, or AMF, which support multimaterial representation. Some printers use custom software to identify materials within a model; however, the most widely adopted solution for fused deposition modeling printers is dividing the model into several STL files and assigning each material to a separate file. This approach does not pose any issues for end users, as most CAD software allows for splitting models, selecting independent parts, and exporting them as separate STL files.

Another challenge in the tessellation of multimaterial 3D objects into triangular meshes is the introduction of approximation errors. This issue is particularly pronounced in organic shapes, which are defined by complex curvatures rather than planar surfaces. These problems arise during the triangulation process, when two closely spaced curved elements are discretized or even within a single object featuring proximate surfaces, the resulting facets may intersect, despite the original geometries being non-intersecting (Figure 3). In these cases, the boundaries between different materials are often spatially coincident or separated by a negligible distance. The subsequent mesh intersections represent a critical failure mode for 3D printing, as they lead to ambiguous material boundaries

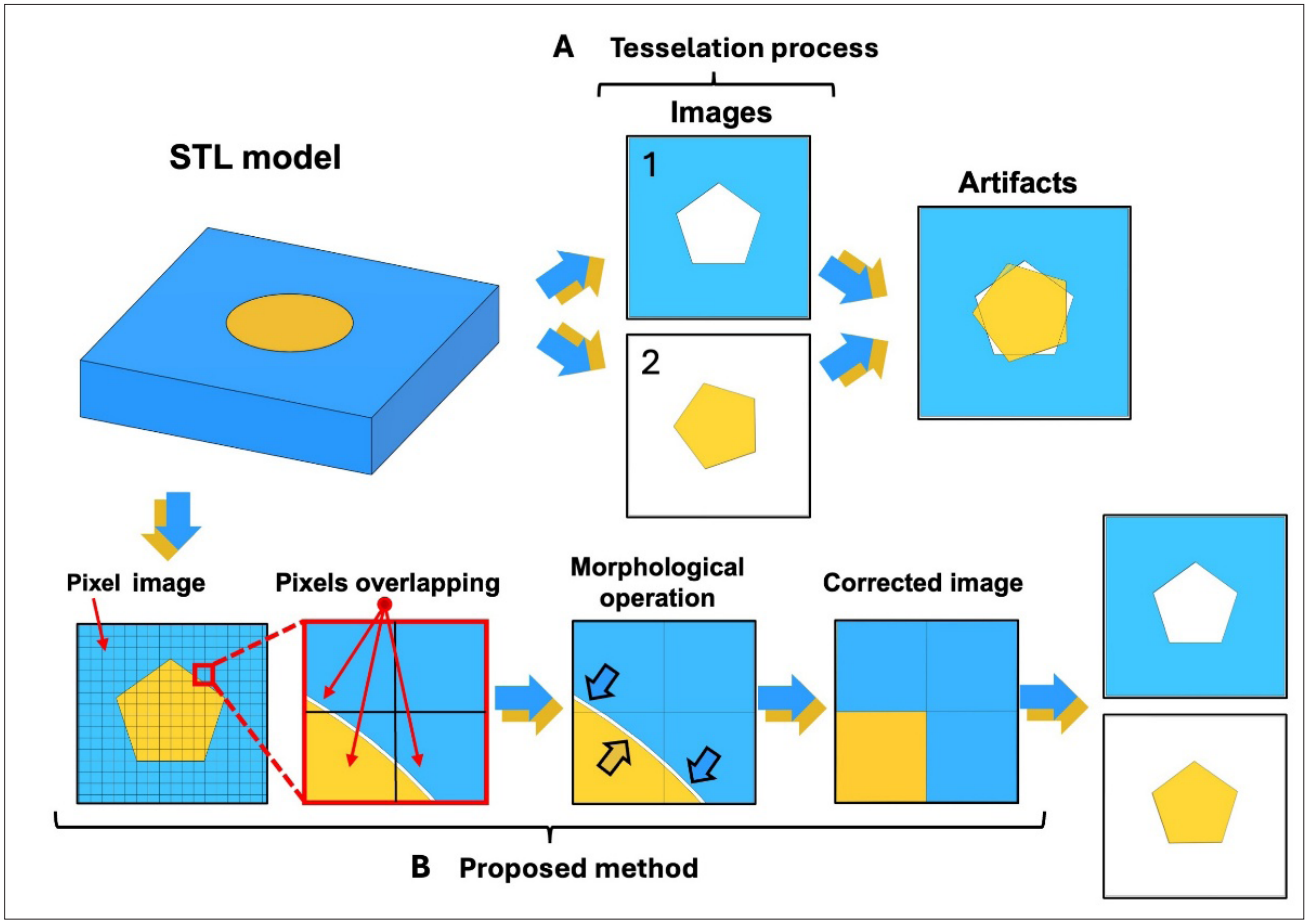


Figure 3. Identification and correction of tessellation-induced artifacts in multimaterial STL representations. (A) Two-material object tessellations showing artifacts introduced during triangulation and their superposition in the final image representation. (B) Standard tessellation approximation (top) and corresponding morphological correction (bottom). Abbreviation: STL: Standard Tessellation Language.

and processing errors. Consequently, the fabrication of multimaterial objects is complicated, necessitating meticulous mesh repair, stringent alignment tolerances, or the use of specialized file formats and software tools to ensure non-interfering material geometries.[15]

2.3. Slicing algorithm and workflow

The process workflow, illustrated in Figure 2, comprises four key stages: first, the multimaterial STL model is decomposed into distinct single-material sub-models; second, the printing layers for each sub-model are generated; third, a geometric analysis is performed to identify and resolve inter-layer intersections arising from tessellation; and finally, a topological optimization of the layer sequence is conducted to consolidate printing phases, thereby preventing bioink accumulation and minimizing washing cycles. The initial step involves separating the multimaterial object into its constituent parts, with each component exported as an individual STL file. Although our custom-developed software was used for this separation procedure, conventional slicing platforms such as Chitubox, Lychee Slicer, and NanoDLP, as well as standard CAD software, are equally suitable. Subsequently, these files are sliced independently, generating a distinct set of images for each material (Figure 3, Step 2). Once separated, each STL file undergoes the slicing process, generating the set of images required to print each material part of the objects. The number of images depends on the object's size and the layer height selected for the print.

For the slicing, we used the computer graphics algorithm described by Keeter.[16] The slicing process begins by dividing the input STL model into layers of a user-defined thickness. The core challenge is then to determine which regions of each layer constitute the solid object. To solve this, each layer is discretized into a grid of voxels, where each voxel corresponds to a pixel in the image of each layer. For each voxel/pixel, a ray is cast from outside the object's bounding volume until the height of the layer that is to be printed. The number of intersections of a ray with the model's triangles

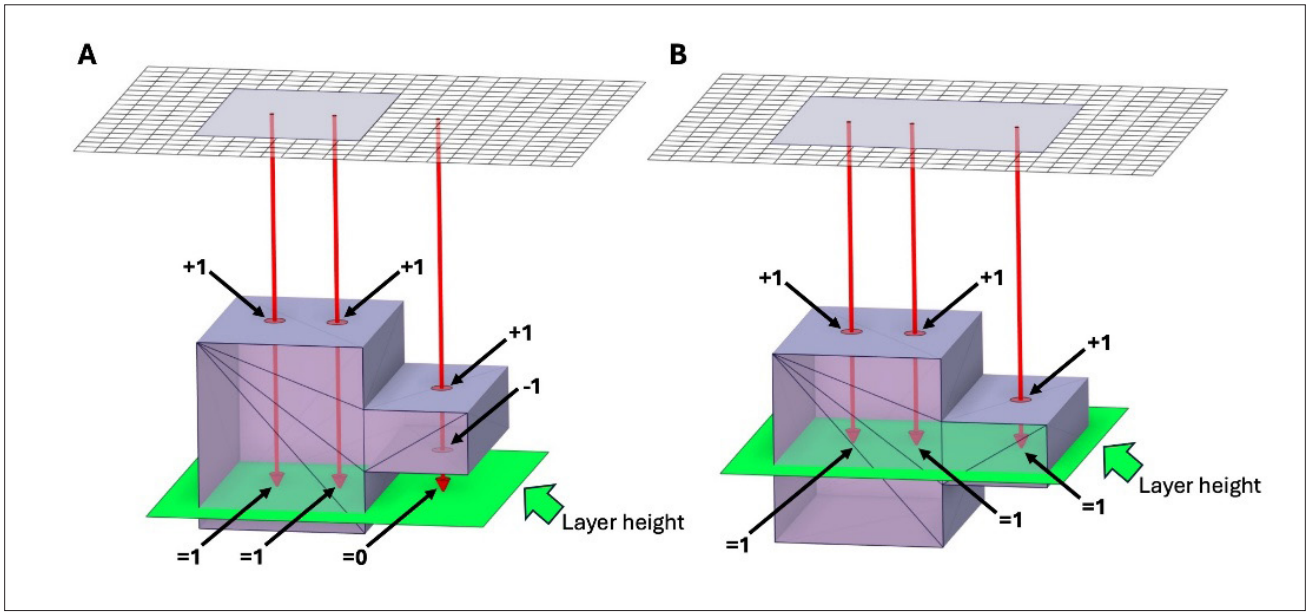


Figure 4. Ray-casting algorithm.[16] (A) Four rays cast from the screen pass through the object once, up to the layer height, corresponding to filled pixels in the image. (B) The third ray enters the object (+1) and exits (−1), resulting in a net value of 0, which corresponds to an empty pixel in the image for that layer.

is counted using a winding-order rule: an intersection with a front-facing triangle increments a counter, while an intersection with a back-facing triangle decrements it. A final count greater than zero indicates the voxel is inside the solid, and therefore the pixel must be set to on (Figure 4). This logic is efficiently implemented on the GPU via a stencil buffer[17] technique in three rendering passes: the buffer is first incremented on front-facing fragments, then decremented on back-facing ones, and finally, only pixels with a positive value are preserved. This approach executes the insideness test in a massively parallel manner, effectively offloading the complex computational burden of intersection detection from the Central Processing Unit (CPU) to the Graphics Processing Unit (GPU).

Once the object is divided into material-specific layers, the previously mentioned approximation errors (intralayer errors) from triangulation can be analyzed (Figure 3, Steps 3 & 4; and Figure 5). In our case, since the models were sliced into independent sets of images, these approximation errors manifested as image overlapping issues. These problems were easy to detect, as we only needed to perform a Boolean operation to assess whether the same pixel was assigned to more than one layer of one material. These phantom overlaps were removed using a morphological erosion operation on the images (Figure 3B).[18] The radius for this operation is derived from a user-defined tolerance parameter, and a new validation check ensures that each pixel contains at most one material. In other words, it is guaranteed that a pixel will never be occupied by more than one material. If the overlap cannot be corrected, the process is aborted, and the user is notified of the issue. The software then allows the user to either increase the tolerance parameter or review the STL models before proceeding with the printing process. This method aligns more closely with the intrinsic operation of the DLP projection device by working at the pixel level, thereby avoiding purely geometric operations. Consequently, in the event of modifications to the device, such as an increase in its resolution, the adjustment process would be significantly more straightforward. With this step, we obtained the final set of images and arranged them correctly for projection.

2.4. Problem statement

Once the models were processed into sets of slices, we determined the order in which those slices would be printed. As mentioned in the introduction, the order significantly impacts the efficiency of the printing process. The platform must then be aligned with the surface of the previously printed slice of the same material, taking into account the ink's surface and the offset between layers.

Therefore, the ideal approach would be to print each layer of material sequentially, starting from the bottom and moving to the top, followed by all layers of the second material, and so on, until all layers of every material are printed. However, certain physical constraints in the printing process make this optimal plan unfeasible for some 3D shapes:

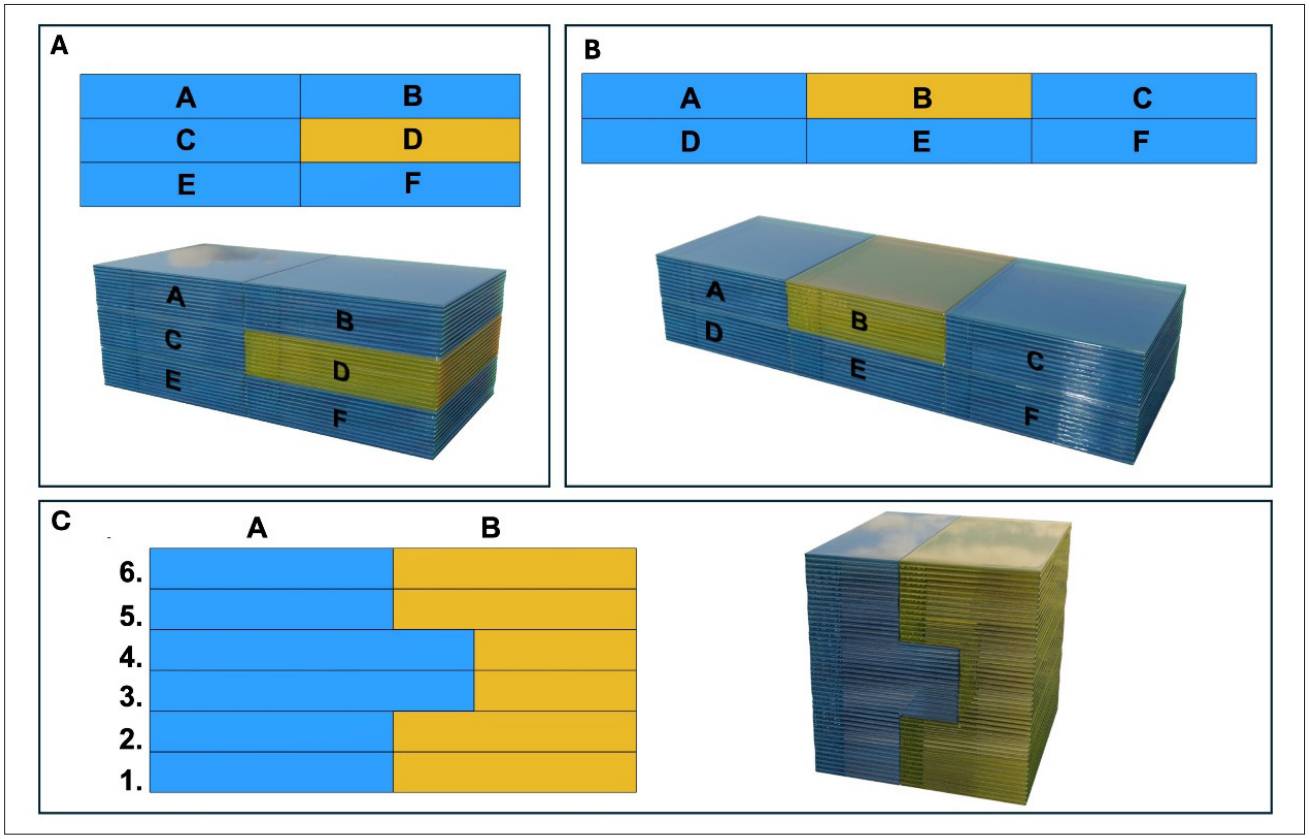


Figure 5. Examples of objects in which the identified constraints apply (side view): (A) Overlapping materials: segment B cannot be printed before segment D, requiring a material change after segment C is printed; (B) Trapped ink: segment B must be printed before segments A and C; otherwise, uncured ink of the orange material would be trapped inside B; (C) Additional example of overlapping materials: material B of layer 2 must be printed before material A of layer 3, and material A of layer 4 must be printed before material B of layer 5.

- If a layer of one material is placed directly on top of another layer of a different material (Figure 5A), the bottom layer must be printed first. Otherwise, the upper layer would block the light from reaching the lower one, making printing impossible.
- If a layer of one material completely encloses a layer of a different material at the same height, the inner layer must be printed first. Otherwise, the outer layer would trap the ink inside (Figure 5B), preventing it from being replaced by the new material's ink. A more aggressive cleaning process could remove the trapped ink, but this would be wasteful if a large volume of uncured material is involved.

2.5. Algorithm

The core principle of the algorithm is to trace a ray in a given direction and divide it into smaller segments, analyzing how each segment interacts with its surrounding environment. In our most basic case, we cast a ray downward from a point in a material layer. This ray advances in steps equal to the layer's thickness, checking at each step whether it intersects or encounters a different material in another layer.

This technique offers two key advantages. First, it allows for easy topological inclusion analysis. For example, in the case of a completely enclosed material, tracing rays in multiple directions around the voxel under study is sufficient to determine whether it encounters different materials. Second, since the algorithm is efficiently implemented on a GPU, voxel evaluations can be performed in parallel, significantly accelerating the process.

It is not necessary to perform this operation for every pixel of the image. Instead, the image can be voxelized with a voxel size determined by the projector's resolution as the base and the layer height. If the image resolution is provided by the slicer, it matches the resolution of the projector, meaning that pixels and voxels have the same dimensions. However, larger images are typically used to enhance precision and reduce aliasing issues. Using this approach, we developed the following algorithm: Two 3D Boolean arrays of size $m \times n \times z$ are created, where $m \times$

n represents the number of voxels/pixels in the projected image and z corresponds to the number of slices. Every element was initialized to zero. The first array (printed pixels) stores information about voxels that have already been printed, regardless of the material. The second array (pending) contains the voxels that belong to the model but have not yet been printed, irrespective of the material. The steps of the algorithm are as follows:

1 Select the first slice of the first material and print it.

2 Pick the next unprinted layer of the currently selected material (layers of the same material are always printed sequentially, from bottom to top):

   a Apply the ray marching technique by tracing a ray from each voxel in the layer down to the bottom edge of the model. Record the index of the highest intersected layer for each material.

   b Check material dependencies:

      (i) If the highest intersected layer of a given material is above its highest printed layer, that layer must be printed first.

      (ii) Switch to that material and return to Step 2, repeating these checks for the next pending layer of the newly selected material.

   c Check for trapped uncured ink:

      (i) Extract the contour of the layer image, fill it (removing any holes), and perform a Boolean AND operation with the pending voxels of that layer.

      (ii) If the holes overlap any pending voxels, switch to the material with the most pending trapped voxels and return to Step 2.

3 Update the printing sequence:

   a Add the selected layer-material combination to the printing sequence.

   b Mark its voxels as printed in the Printed array and remove them from the Pending array.

4 Repeat until completion:

   a If there are still pending layers, return to Step 2.

   b Otherwise, the printing process is complete.

This layer-sorting algorithm aligns with the printing process by operating directly on the images to be projected, bypassing traditional geometric relationships. Furthermore, it can be fully implemented on the GPU, significantly accelerating processing speed. The ray tracing Step 2a of this algorithm requires that for each voxel in each layer under consideration, all voxels beneath it must be checked. This leads to a total of $(n-1)(n-2)$ checks per x, y position, where n is the number of layers. As a result, the algorithm has an $O(n^2)$ complexity with respect to the number of layers. This issue was addressed by introducing an auxiliary integer-valued 3D texture for each material. Each voxel in this texture stores the layer index (Z position) of the highest pending voxel below it. Therefore, to obtain the index of the highest pending voxel intersecting the ray between the voxel and the bottom of the 3D model, we only needed to read a single value from the auxiliary texture, reducing the complexity to $O(n)$ with respect to the number of layers. However, the memory usage of the required auxiliary array scales with the total number of voxels. Therefore, if the number of layers is small, the original approach might be preferable, as the performance benefits may not outweigh the increased memory consumption.

2.6. 3D printing

2.6.1. 3D design

All digital models were designed using Autodesk Fusion 2025 (Autodesk Inc., US; educational license) and exported as STL files. Three model families were created to address distinct objectives within this study: (i) PEGDA-only test structures used to assess DLP resolution/capability and to exercise the multimaterial planning logic; (ii) solid cylinders (radius 4 mm, height 6 mm) for subsequent physical characterization; and (iii) multimaterial scaffolds consisting of a square PEGDA lattice (5 × 5 × 5 mm) with gap sizes of 200, 400, or 600 μm and a concentric GelMA interior cylinder (radius 1 mm, height 5 mm). All schematic figures were created in Blender 4.5 LTS (Blender Foundation, The Netherlands), using a consistent scale across figures to maintain consistent metric dimensions.

2.6.2. 3D printing process

To evaluate the algorithm's performance in 3D printing, two bicomponent models were fabricated using a PEGDA solution with two different dyes (yellow and red). The printing parameters were set as follows: LED intensity of 21.5 mW/cm^2, exposure time of 5 s, and layer thickness of 100 μm. After each print, images of the models were captured using a magnifying lens.

2.6.3. Printing resolution assessment

To evaluate optical resolution and layer fidelity, three PEGDA lattice scaffolds (5 × 5 × 5 mm) were printed with nominal gap sizes of 200, 400, and 600 μm. The printing parameters were set as follows: LED intensity of 15.14 mW/cm^2, exposure time of 5 s, and layer thickness of 100 μm. Printed scaffolds were imaged using a Leica MATEO FL fluorescence microscope (Leica Microsystems, Germany).

2.6.4. Relationship between light exposure and material crosslinking

(a)Stiffness characterization
Cylindrical specimens (4 mm diameter, 6 mm height) were printed from 5% w/v PEGDA (molecular weight [MW] = 575 Da) containing 0.1% w/v lithium phenyl-2,4,6-trimethylbenzoylphosphinate (LAP) and 0.025% w/v tartrazine, using a layer height of 0.10 mm and the same layer exposure as above. Immediately after printing, samples were either tested as printed or subjected to a post-cure consisting of a 60 s exposure at the projector's maximum irradiance (95.83 mW/cm^2; cumulative dose 5.75 J/cm^2) while keeping the constructs hydrated. Unconfined compression tests were performed on a Mach-1 system (Biomomentum, Canada) in stress–relaxation mode at 37°C with samples submerged in phosphate-buffered saline (PBS); constructs were compressed to 40% strain at 20% speed. The apparent elastic modulus was calculated from the initial linear region of the stress–strain curve and reported as mean ± SD ($n \geq 3$ per condition).

(b) Swelling ratio
The swelling ratio (Q_M) of PEGDA constructs was evaluated to estimate crosslinking density and water uptake capacity, parameters that influence nutrient diffusion and mechanical behavior in hydrogels.[19] Disk-shaped samples were printed using the same formulation and dimensions described above. After printing and post-curing, specimens were immersed in PBS at 37°C for 24 h to reach equilibrium swelling, blotted to remove surface liquid, and weighed to obtain the swollen mass (W_s). The samples were then dried at 60°C for 48 h to obtain the dry mass (W_d). The Q_M was calculated as[20,21]:

$$Q_M = (W_s - W_d)/W_d \quad (1)$$

Measurements were performed in triplicate.

2.7. Cell bioprinting

2.7.1. Cell sourcing

Cardiomyoblasts (H9c2) were used in this study. The cells were cultured in Dulbecco's modified Eagle medium (DMEM; Gibco, US), supplemented with 10% fetal bovine serum (Capricorn Scientific, Germany) and 1% penicillin/streptomycin (Sigma-Aldrich, US), under standard culture conditions (37°C, 5% CO_2). Upon reaching approximately 80% confluence, cells were subcultured using 0.25% trypsin-ethylenediaminetetraacetic acid (Sigma-Aldrich, US).

2.7.2. Preparation of bioinks

Two bioinks were formulated: a 5% w/v PEGDA (MW = 575 Da) solution containing 0.1% w/v LAP as a photoinitiator, and 0.025% w/v tartrazine as a photoabsorber; and a 5% w/v GelMA solution with 0.1% w/v LAP. The GelMA solution was combined with an H9c2 suspension to achieve 0.7 × 10^6 cells/mL, mixing slowly at 37°C. Both solutions were prepared using DMEM as a solvent.

2.7.3. Bioprinting procedure

A multimaterial scaffold consisting of a square PEGDA lattice (5 × 5 × 5 mm) with a gap size of 200 μm and a concentric GelMA interior cylinder (radius 1 mm, height 5 mm) was designed with a layer thickness of 100 μm. The structure was divided into two by the materials that composed it. The printing parameters were set to 5 s of exposure per layer and a light intensity of 15.14 mW/cm^2. First, the PEGDA structure was printed. After printing, the structure was cleaned with Hank's Balanced Salt Solution (HBSS, Sigma Aldrich, US) to remove excess non-crosslinking material and then exposed for 60 s at 95.83 mW/cm^2 to ensure complete crosslinking of the material.

Subsequently, the printing process was continued with the GelMA cylinder containing the cell-laden bioink, and another cleaning step was performed to remove excess material. Immediately, the constructs were covered with culture medium and incubated under standard conditions (37°C, 5% CO_2) for up to 5 days. All the samples were prepared in triplicate.

2.7.4. Cell viability assay

Cell viability within the bioprinted constructs was assessed at days 1, 3, and 5 post-printing using the Live/Dead Cell Imaging Kit (Sigma-Aldrich, US). Briefly, samples were washed twice with HBSS and stained with calcein-AM, propidium iodide, and Hoechst 33342, following the manufacturer's instructions. Samples were incubated for 60 min in the dark, and fluorescence images were acquired using a fluorescence microscope (MATEO FL, Leica, Germany). Image analysis was performed using FIJI (ImageJ) software.[22]

2.8. Statistical analysis

The data collected in this work are presented as mean ± SD, and were statistically analyzed using one-way analysis of variance with GraphPad Prism (8.0.1, GraphPad Software, Inc., US). The differences were considered significant if p-values were less than 0.05.

3. Results and discussion

To validate the capabilities of the proposed algorithm, we first performed a theoretical comparison of the number of material changes and, therefore, the cleaning sequences required for three example objects using our approach compared to a naïve sequencing method. Then, we experimentally validated the method by printing

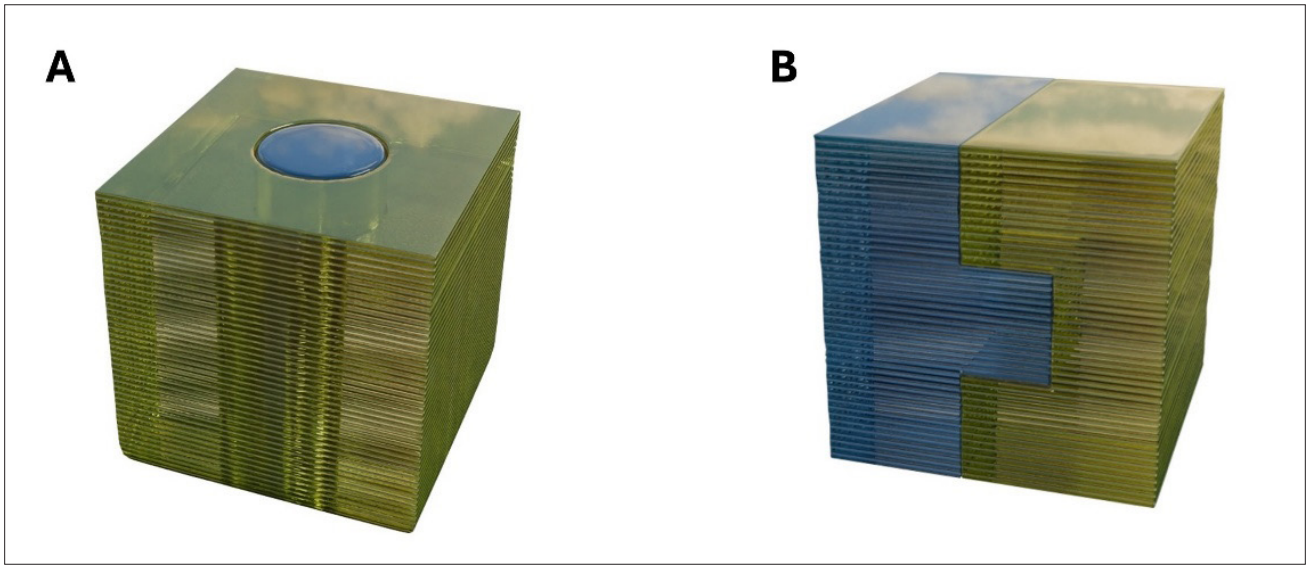


Figure 6. Models used for theoretical validation. (A) Cube with an enclosed cylinder. (B) Cube composed of two interlocking pieces.

two objects, each showcasing the previously identified challenges, and conducting a biocompatibility assessment on one of the printed structures.

3.1. Theoretical validation

The algorithm was executed on two models selected to showcase its capabilities, specifically, those with layer overlapping and ink trapping constraints described in the problem statement. The chosen models are:

(i) A cube with a cylinder of a different material enclosed in it (Figure 6A). This is an example of the trapping constraint: if the cylinder is printed before the cube, the ink will be trapped in the hole, preventing the cylinder material from being introduced. It also showcases the interference caused by tessellation between layers of different materials, resolved by morphological erosion.

(ii) A cube composed of two interlocking pieces made of different materials (Figure 6B). The protruding part of piece A is overlapped by the top of piece B, which is an example of the overlapping constraint.

Three approaches to layer sequencing are:

(i) Naïve sequencing: The layers are printed in order. In the worst case, if each layer has two materials, the process ensures that the material A of each layer is always printed before material B. Therefore, for a three-layer and two-material model, the sequence is A–B–A–B–A–B. The number of material changes required is $L \times M - 1$, where L is the number of layers, and M is the number of materials.

(ii) Alternating naïve sequencing: The layers are printed in order, and the order of materials is inverted in each subsequent layer. Therefore, for a three-layer and two-material model, the sequence is A–A–B–B–A–A. This saves one material change with respect to the previous naïve method, as the first material fabricated in a new layer is the same as the last material in the previous layer. The number of changes required for a two-material object is equal to the total number of layers, approximately half that of naïve sequencing.

(iii) Our method: The algorithm described in **Section 2.4** minimizes the number of changes while satisfying the overlapping and trapping constraints (Table 1).

Table 1. Comparison of the material changes required for our method

Model	Number of material changes		
	Naïve sequence (A–B–A–B–A–B)	Alternating naïve sequence (A–A–B–B–A–A)	Our method
Interlocked cube	99	50	2
Cube with cylinder	99	50	1

3.2. Printing validation

The first test involved printing the interlocked cube. Figure 7A illustrates a section of the part where the overlapping layers are easily identifiable, corresponding to the referenced issue. The planned process proceeds as follows: it begins with material B, printing layers 1–34 in sequence. After that, a cleaning step with Milli-Q water starts to remove excess non-crosslinking material and prevent cross-contamination between the materials. Then, it switches to material A, printing all layers (1–50) without interruption, followed by another cleaning step. Finally, it returns to material B to print the remaining layers (35–50). In this case, using the developed algorithm optimized the material change, requiring only two material switches instead of 50. Figure 7A shows the structure printed using the proposed algorithm in a continuous printing process, alongside the same structure printed by fabricating each material separately and then manually assembling them. As can be seen, the resulting model exhibited perfect integration between the two materials, as they were printed *in situ*. In contrast, the manually assembled structure showed clear separations between the materials, as indicated by the arrows. The sub-part, composed of either material B or material A, was completed according to the sequence determined by the algorithm.

The second object that was printed was a cube with an internal cylinder (Figure 7B). This object encompasses the two issues discussed above: interference caused by tessellation between layers of different materials and trapped ink. The first issue was effectively resolved using growth and shrinkage techniques. The printing process began with layers of the blue material, spreading around the base of the cylinder. Once finished, the ink was washed, and the vat was changed to print the entire second material. In this case, the developed algorithm optimized the material change to only one instead of 50 changes. Figure 7B compares structures printed via the continuous process and those manually assembled. Once again, the manually assembled structures displayed noticeable gaps (highlighted by arrows), whereas the continuous printing process produced a homogeneous structure with superior integration.

As an additional qualitative validation, a yin–yang model composed of two materials was printed to verify the accuracy of material boundary definition and the effectiveness of the cleaning process between consecutive material changes (Figure 7C). This simple yet illustrative geometry demonstrated a clear separation between materials, confirming the proper functioning of the multimaterial workflow.

To further quantitatively assess the efficiency of the proposed printing algorithm, additional structures with more than two materials were fabricated and analyzed. In these tests, the number of material changes required using the optimized algorithm was compared against a conventional layer-by-layer multimaterial printing method. Structures such as those presented in Figure 7D & E were printed and evaluated to quantify the optimization achieved in material switching.

The results, as summarized in Table 2, showed a substantial reduction in the total number of material changes when using the proposed algorithm, confirming its scalability and effectiveness for multimaterial printing beyond two-material configurations.

Additionally, the printing method was validated using a DNA-like helix structure to demonstrate its applicability for geometries that cannot be printed separately and later assembled. Figure 7F shows the printed structure from lateral and top views, where the material transitions and the perfect integration between them are clearly visible.

To optimize the fabrication of PEGDA-based scaffolds via photopolymerization, we systematically tuned printing parameters, with a particular focus on pore architecture and optical resolution (Figure 8). Scaffolds with gap sizes of 200 μm (Figure 8A), 400 μm (Figure 8B), and 600 μm (Figure 8C) were printed to evaluate the impact of feature dimensions on resolution fidelity and structural integrity. To mitigate light scattering and reduce *out-of-focus* crosslinking, 0.025% w/v tartrazine was incorporated as a photoabsorber.[23] This incorporation effectively quenched excess light penetration beyond the intended voxel boundary, improving *z*-axis resolution and enabling sharper feature definition. The combined optimization of gap size and photopolymer composition allowed for enhanced control over scaffold geometry, which is critical for tissue engineering applications.[24]

Table 2. Reduction in the total number of material changes when using the proposed algorithm

Model	Number of materials	Layers	Material switches (conventional layer-by-layer)	Material switches (optimized algorithm)
"Traffic light"	4	50	81	4
"Yin–yang"	2	20	40	2
"Yin Yan Yun"	3	20	60	3

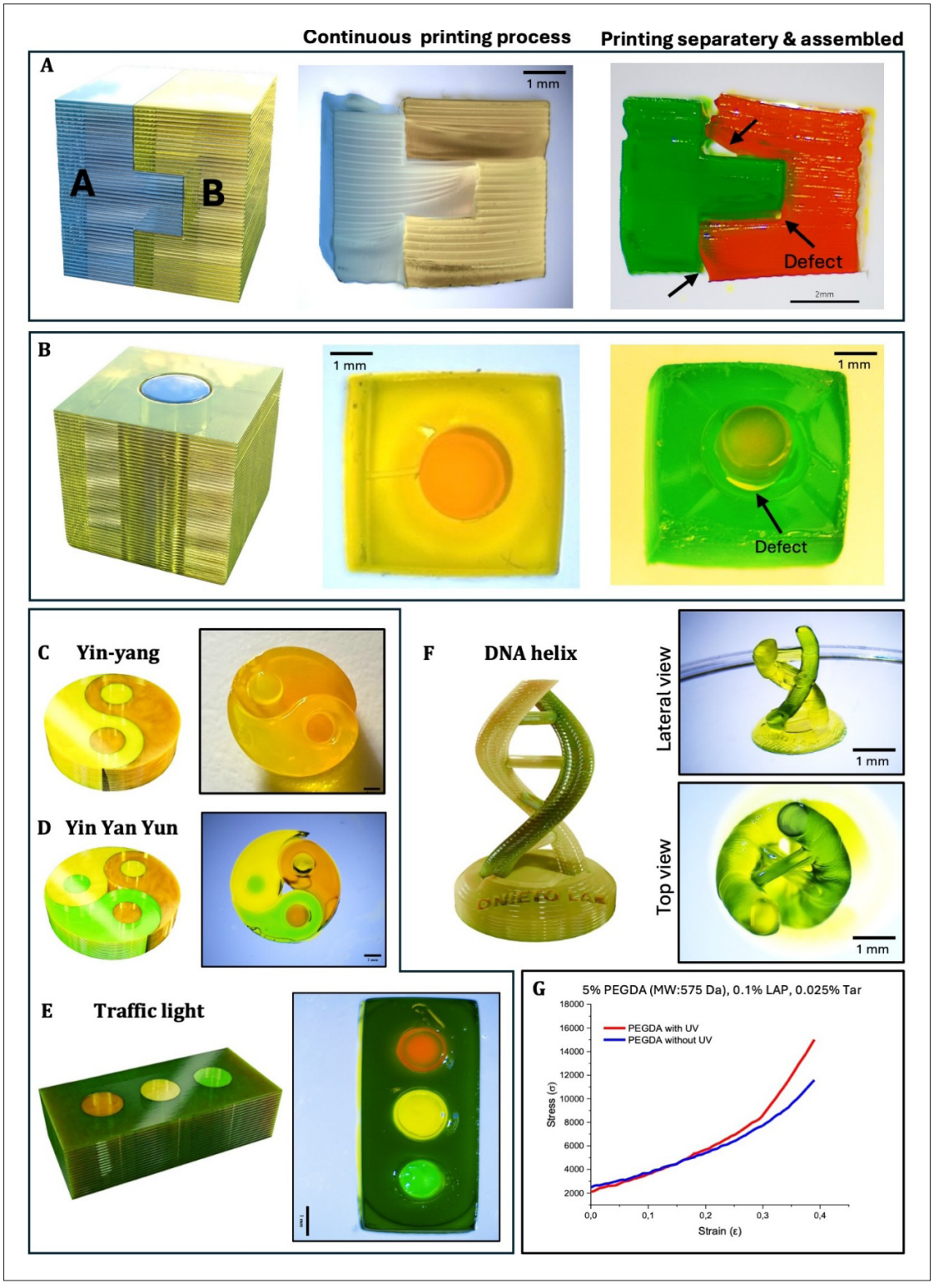


Figure 7. Multimaterial DLP bioprinting of complex structures and mechanical characterization. (A & B) Objects composed of subcomponents with shared layers, illustrating the contrast between a continuous multimaterial printing process and printing the components separately, followed by manual assembly. (C–F) Examples of multimaterial printed objects highlighting the capabilities of the bioprinter: (C) yin–yang design, (D) Yin Yan Yun variation, (E) traffic light model, and (F) DNA-like helix structure. (G) Stiffness measurements of printed objects before and after post-printing UV exposure. Abbreviations: LAP: lithium phenyl-2,4,6-trimethylbenzoylphosphinate; MW: molecular weight; PEGDA: poly(ethylene glycol) diacrylate; Tar: tartrazine.

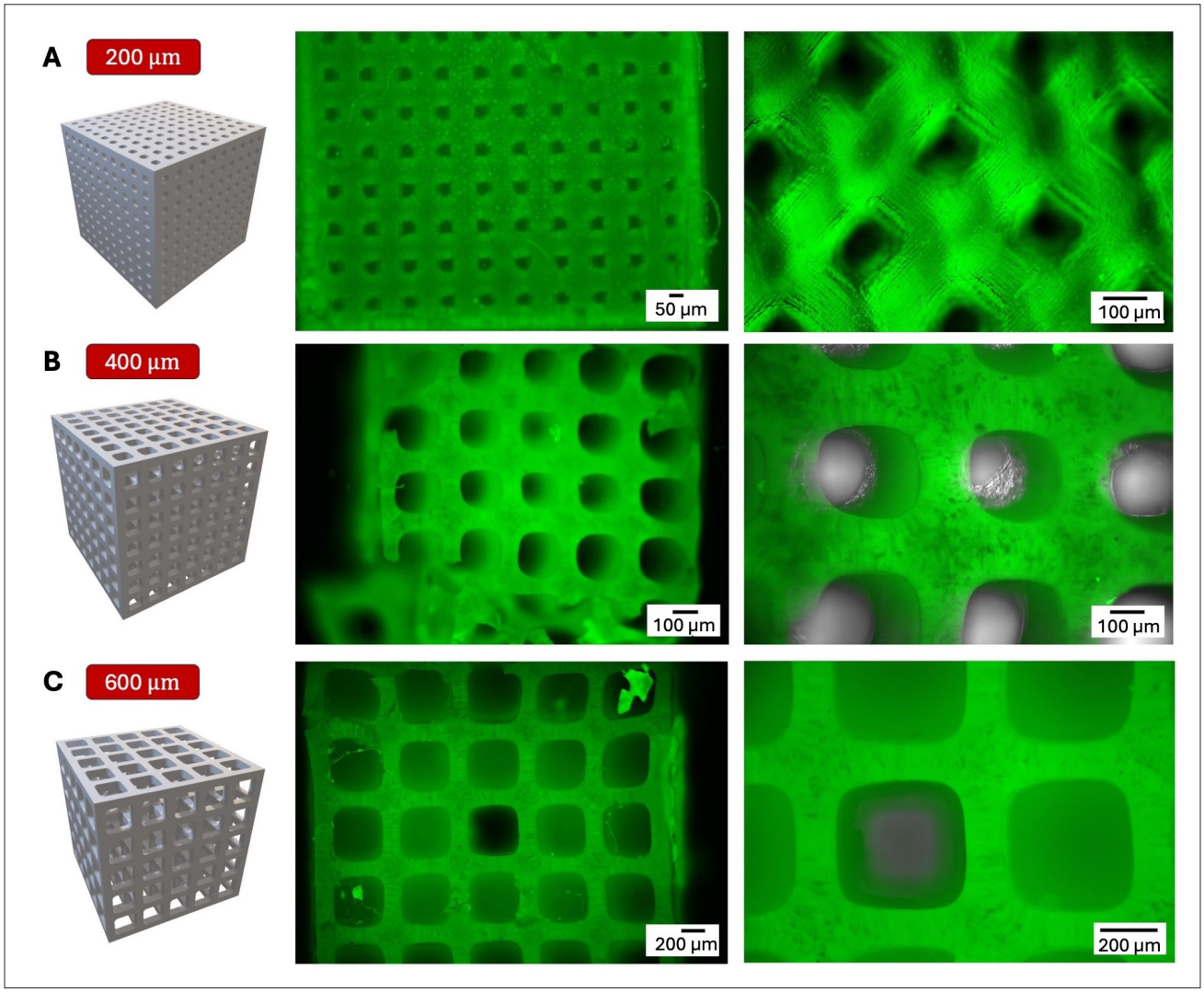


Figure 8. Microscopy images of the bioprinted scaffolds with various dimensions: (A) 200 µm (scale bars: 50 µm [left], 100 µm [right]; magnifications: 4× [left], 10× [right]), (B) 400 µm (scale bar: 100 µm; magnifications: 4× [left], 10× [right]), and (C) 600 µm (scale bar: 200 µm; magnifications: 4× [left], 10× [right]).

To enhance the mechanical properties of PEGDA hydrogels, we applied a high-irradiance post-curing step intended to increase the strain tolerance of the material. This additional curing phase promotes further crosslinking within the polymer network, potentially leading to improved structural integrity.[25] Apparent compressive modulus and equilibrium Q_M were measured on PEGDA disks with and without the 60-s high-irradiance post-cure to evaluate the impact of post-curing on both mechanical stiffness and swelling behavior (Figure 7D).

In addition to material optimization, the structural fidelity of these lattice scaffolds is not solely dependent on material composition, but is also intrinsically linked to the slicing strategy. Unlike standard geometric slicing, which can introduce artifacts or erroneous overlaps at fine strut intersections, our voxel-based approach employs morphological erosion to eliminate these interferences prior to projection. This computational correction ensures that pore geometries remain open and well-defined, effectively translating the digital design into the physical object without the pore closure often observed in conventional workflows.

3.3. Relationship between light exposure and material crosslinking

Apparent compressive modulus and equilibrium Q_M were measured on PEGDA disks with and without the 60-s high-irradiance post-cure (Table 3).

Swelling tests provide an estimate of the crosslink density of the materials: a lower crosslink density generally

Table 3. Apparent compressive modulus and equilibrium swelling ratio (Q_M)

Material	Post-cure	Apparent elastic modulus (kPa)	Q_M
PEGDA (5% w/v, MW = 575 Da)	No	12.36 ± 0.66	14.45 ± 3.10
PEGDA (5% w/v, MW = 575 Da)	Yes	14.34 ± 1.40	13.05 ± 2.18

Abbreviations: MW: molecular weight; PEGDA: poly(ethylene glycol) diacrylate.

allows for greater swelling (a higher Q_M), while a highly crosslinked network produces less swelling.[26] In our PEGDA builds, post-curing modestly reduced the Q_M, while the apparent elastic modulus increased slightly (Figure 7D). These trends indicate a slight densification of the network; however, the similarity of the moduli before and after post-curing suggests that the layer exposures used during printing already produced a highly converted PEGDA network.

3.4. Cell viability

To assess the bioprinting capabilities, a multimaterial cube scaffold loaded with H9c2 cardiomyoblasts was successfully fabricated (Figure 9). Live/Dead staining revealed consistently high levels of cell survival across all evaluated time points. The quantitative analysis of viability (Figure 9E) at days 1, 3, and 5 showed no significant differences among groups, indicating that cell viability remained stable throughout the culture period, as expected due to the cell adhesion properties and excellent biocompatibility of GelMA.[27,28]

3.5. Comparison of theoretical vs. printing process

This work presents a novel algorithm to address the aforementioned challenges by generating an optimized set of printing layers that minimizes the number of required cleaning cycles. Theoretical predictions from the sequencing algorithm were validated through multimaterial printing of the two test models: the interlocked cube and the cube containing an internal cylinder. In both cases, the algorithm successfully minimized material changes while satisfying critical constraints, including layer overlapping and ink trapping. For the interlocked cube, the theoretical sequence (printing layers 1–34 of material B, followed by all layers of material A, and then returning to material B for layers 35–50) was implemented experimentally, resulting in only two material changes compared to 50 required by alternating naïve sequencing. The printed structure (Figure 7A) closely matched the intended design, with clear resolution of overlapping features. Similarly, the internal cylinder model demonstrated the algorithm's effectiveness in avoiding ink trapping by printing the cylinder (material B) entirely before enclosing it with the cube (material A), requiring only a single material change instead of 50. The experimental print (Figure 7B) confirmed the theoretical model's accuracy, with successful resolution of tessellation artifacts through morphological operations and correct material sequencing. Together, these results confirm that the theoretical sequencing model translates reliably to physical prints, optimizing both process efficiency and structural fidelity. Three approaches to layer sequencing are compared in Table 1.

4. Conclusion

This work presents a novel slicing system for optimizing multimaterial bioprinting using a top–down DLP printer. The proposed algorithm addresses key challenges such as layer overlapping and tessellation artifacts that arise when multiple materials are present within the same layer. Our approach operates at a hardware-oriented level by applying morphological operations directly to the bitmap images sent to the digital micromirror device. This low-level image processing strategy aligns natively with the projector's pixel-level functioning, ensuring high geometric fidelity throughout the print.

To optimize printing performance, the algorithm is designed to minimize the number of material changes during fabrication. This reduces the risk of cross-material interference in subsequent layers and shortens overall printing time without compromising print quality or resolution. Importantly, the system also mitigates ink retention issues that occur during the lamination process, especially in scenarios where one material is fully enclosed by another.

We validated the system both theoretically and experimentally using test models and a complex multimaterial, cell-laden microenvironment. The implementation of morphological and advanced image processing operations enables high parallelization on modern GPUs, making the computational pipeline highly efficient and scalable. This allows for the rapid handling of complex models with numerous layers or intricate morphologies.

Experimental results demonstrated improved print fidelity, reduced processing time, and enhanced material resolution. We further highlighted the practical utility of our system by fabricating a multimaterial tissue construct consisting of a PEGDA-based structural scaffold integrated with a GelMA-based, cell-laden microenvironment.

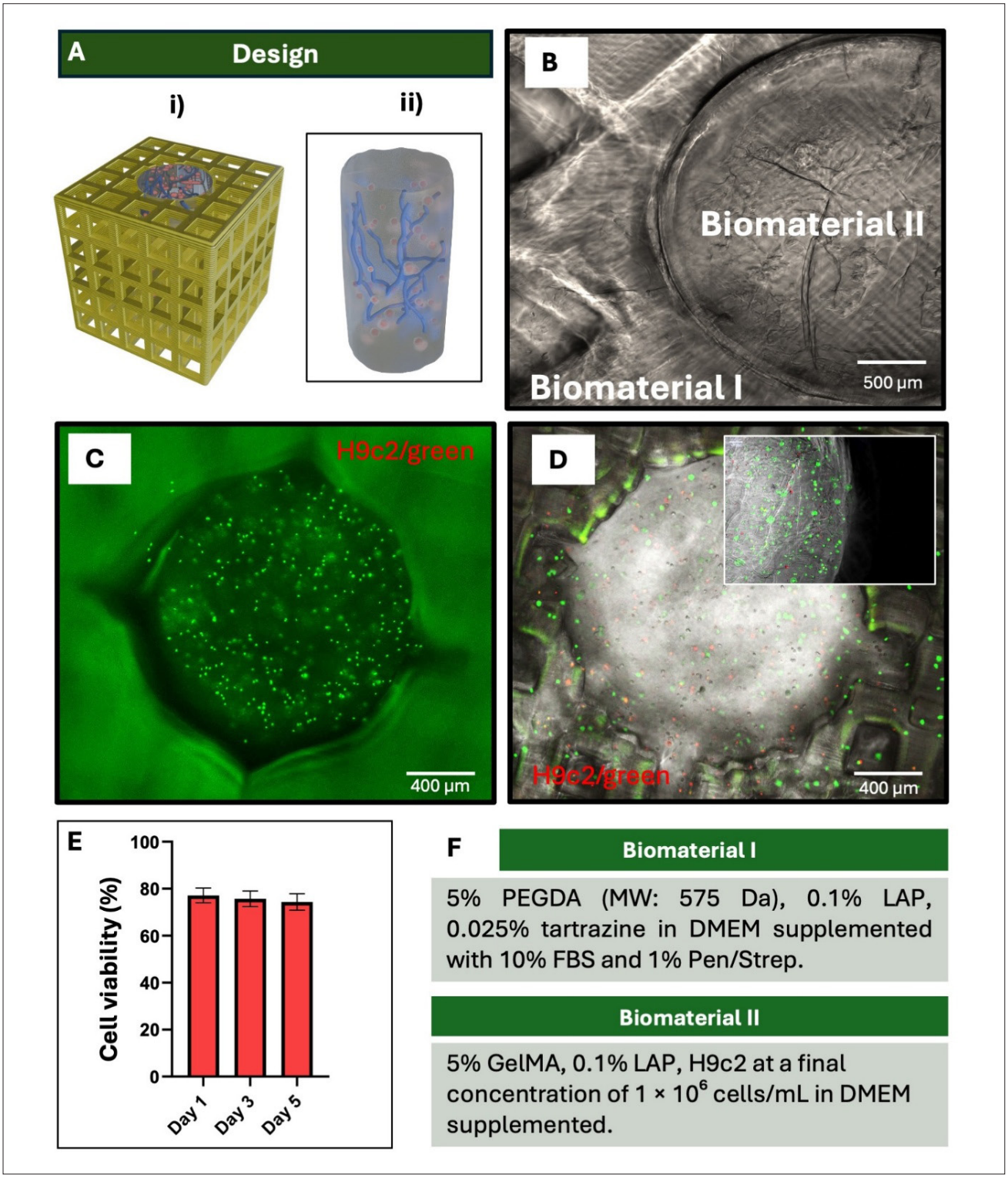


Figure 9. Multimaterial cell-laden scaffold bioprinting and in vitro cell viability assessment. (A) Design of the two-material cell-laden scaffolds. (B) Microscope image of a two-material printed scaffold (scale bar: 500 µm; magnification: 20×). (C) Microscope image of a multimaterial scaffold embedded with H9c2 cells (scale bar: 400 µm; magnification: 10×). (D) Image of live/dead assay results. The inset shows H9c2 cells seeded on the scaffolds after 24 h of culture (scale bars: 400 µm, magnifications: 10X µm [inset]; magnifications: YYY, YYY [inset]). (E) Cell viability. (F) Composition of the two materials used. Abbreviations: DMEM: Dulbecco's modified Eagle medium; FBS: fetal bovine serum; GelMA: gelatin methacryloyl; LAP: lithium phenyl-2,4,6-trimethylbenzoylphosphinate; MW: molecular weight; PEGDA: poly(ethylene glycol) diacrylate; Pen/Strep: penicillin/streptomycin.

Acknowledgments

None

Funding

Alejandro González-Santos was supported by a predoctoral research grant from the Xunta de Galicia (Consellería de Cultura, Educación, Formación Profesional e Universidades). This grant was co-funded by the European Union (FSE+ Galicia 2021-2027). Daniel Nieto was funded by the European Research Council Consolidator Grant (101125172 HOT-BIOPRINTING- HE-ERC-2023COG) and was supported by the Oportunius Programme (Xunta de Galicia) since 2024.

Conflict of interest

The authors declare that they have no conflict of interest.

Author contributions

Conceptualization: Julián Flores, Daniel Nieto
Formal analysis: Alejandro González-Santos, Nadina Usseglio
Investigation: Alejandro González-Santos, Adrian García, Nadina Usseglio
Methodology: Alejandro González-Santos, Adrian García, Julián Flores, Daniel Nieto
Supervision: Julián Flores, Daniel Nieto
Writing – original draft: Julián Flores, Daniel Nieto
Writing – review & editing: Alejandro González-Santos, Nadina Usseglio, Julián Flores, Daniel Nieto

Ethics approval and consent to participate

Not applicable.

Consent for publication

Not applicable.

Availability of data

The authors declare that the data supporting the findings of this study are available within the paper. Should any raw data files be needed in another format, they are available from the corresponding author upon reasonable request.

References

1. Deo KA, Singh KA, Peak CW, Alge DL, Gaharwar AK. Bioprinting 101: design, fabrication, and evaluation of cell-laden 3D bioprinted scaffolds. *Tissue Eng Part A*. 2020;26(5-6):318-338. doi: 10.1089/ten.tea.2019.0298
2. Tripathi S, Mandal SS, Bauri S, Maiti P. 3D bioprinting and its innovative approach for biomedical applications. *MedComm (2020)*. 2023;4(1):e194. doi: 10.1002/mco2.194
3. Mirshafiei M, Rashedi H, Yazdian F, Rahdar A, Baino F. Advancements in tissue and organ 3D bioprinting: current techniques, applications, and future perspectives. *Mater Des*. 2024;240:112853. doi: 10.1016/j.matdes.2024.112853
4. Leberfinger AN, Dinda S, Wu Y, *et al*. Bioprinting functional tissues. *Acta Biomater*. 2019;95:32-49. doi: 10.1016/j.actbio.2019.01.009
5. Li W, Wang M, Ma H, Chapa-Villarreal FA, Lobo AO, Zhang YS. Stereolithography apparatus and digital light processing-based 3D bioprinting for tissue fabrication. *iScience*. 2023;26(2):106039. doi: 10.1016/j.isci.2023.106039
6. Alparslan C, Bayraktar Ş. Advances in digital light processing (DLP) bioprinting: a review of biomaterials and its applications, innovations, challenges, and future perspectives. *Polymers (Basel)*. 2025;17(9):1287. doi: 10.3390/polym17091287
7. Nazir A, Gokcekaya O, Md Masum Billah K, *et al*. Multi-material additive manufacturing: a systematic review of design, properties, applications, challenges, and 3D printing of materials and cellular metamaterials. *Mater Des*. 2023;226:111661. doi: 10.1016/j.matdes.2023.111661
8. Kwok TH. Comparing slicing technologies for digital light processing printing. *J Comput Inf Sci Eng*. 2019;19(4):044502. doi: 10.1115/1.4043672
9. Yang S, Wang L, Chen Q, Xu M. In situ process monitoring and automated multi-parameter evaluation using optical coherence tomography during extrusion-based bioprinting. *Addit Manuf*. 2021;47:102251. doi: 10.1016/j.addma.2021.102251
10. Kim H, Choi J, Wicker R. Scheduling and process planning for multiple material stereolithography. *Rapid Prototyp J*. 2010;16(4):232-240. doi: 10.1108/13552541011049243
11. Shaukat U, Rossegger E, Schlögl S. A review of multi-material 3D printing of functional materials via vat photopolymerization. *Polymers (Basel)*. 2022;14(12):2449. doi: 10.3390/polym14122449
12. Shaukat U, Thalhamer A, Rossegger E, Schlögl S. Dual-vat photopolymerization 3D printing of vitrimers. *Addit Manuf*. 2024;79:103930. doi: 10.1016/j.addma.2023.103930
13. Chin KCH, Ovsepyan G, Boydston AJ. Multi-color dual wavelength vat photopolymerization 3D printing via spatially controlled acidity. *Nat Commun*. 2024;15(1):3867. doi: 10.1038/s41467-024-48159-7

14. Ghaderi I, Behravesh AH, Hedayati SK, *et al*. Multimaterial additive manufacturing of poly-L-lactic acid–hydroxylapatite/graphene oxide scaffold fabricated via vat photopolymerization: experimental investigation, analysis and cell study. *Rapid Prototyp J*. 2024;30(9): 1789-1802.
doi: 10.1108/RPJ-02-2024-0085

15. Preparata FP, Shamos MI. *Computational Geometry*. New York: Springer; 1985.
doi: 10.1007/978-1-4612-1098-6

16. Keeter M. DLP Slicer. https://www.mattkeeter.com/projects/dlp

17. Shreiner D, Sellers G, Kessenich JM, Licea-Kane BM. *OpenGL Programming Guide: The Official Guide to Learning OpenGL, Version 4.3*. Massachusetts, United States: Addison Wesley; 2013:984.

18. Gonzalez RC, Woods RE. *Digital Image Processing*. Harlow Essex, England: Pearson Education; 2018.

19. Choi YJ, Park H, Ha DH, Yun HS, Yi HG, Lee H. 3D bioprinting of in vitro models using hydrogel-based bioinks. *Polymers (Basel)*. 2021;13(3):366.
doi: 10.3390/polym13030366

20. Gao J, Li M, Cheng J, *et al*. 3D-printed GelMA/PEGDA/F127DA scaffolds for bone regeneration. *J Funct Biomater*. 2023;14(2):96.
doi: 10.3390/jfb14020096

21. Mancha Sánchez E, Gómez-Blanco JC, López Nieto E, *et al*. Hydrogels for bioprinting: a systematic review of hydrogels synthesis, bioprinting parameters, and bioprinted structures behavior. *Front Bioeng Biotechnol*. 2020;8:776.
doi: 10.3389/fbioe.2020.00776

22. Schneider CA, Rasband WS, Eliceiri KW. NIH Image to ImageJ: 25 years of image analysis. *Nat Methods*. 2012;9(7):671-675.
doi: 10.1038/nmeth.2089

23. Yang Y, Zhou Y, Lin X, Yang Q, Yang G. Printability of external and internal structures based on digital light processing 3D printing technique. *Pharmaceutics*. 2020;12(3):207.
doi: 10.3390/pharmaceutics12030207

24. Flores-Jiménez MS, Garcia-Gonzalez A, Fuentes-Aguilar RQ. Review on porous scaffolds generation process: a tissue engineering approach. *ACS Appl Bio Mater*. 2023; 6(1):1-23.
doi: 10.1021/acsabm.2c00740

25. Şener Raman T, Kuehnert M, Daikos O, *et al*. A study on the material properties of novel PEGDA/gelatin hybrid hydrogels polymerized by electron beam irradiation. *Front Chem*. 2023;10:1094981.
doi: 10.3389/fchem.2022.1094981

26. Metz J, Gonnerman K, Chu A, Chu TMG. Effect of crosslinking density on swelling and mechanical properties of PEGDA400/PCLTMA900 hydrogels. *Biomed Sci Instrum*. 2006;42:389-394.

27. Bupphathong S, Quiroz C, Huang W, Chung PF, Tao HY, Lin CH. Gelatin methacrylate hydrogel for tissue engineering applications—a review on material modifications. *Pharmaceuticals*. 2022;15(2):171.
doi: 10.3390/ph15020171

28. Fowler M, Moreno Lozano A, Krause J, *et al*. Guiding vascular infiltration through architected GelMA/PEGDA hydrogels: an *in vivo* study of channel diameter, length, and complexity. *Biomater Sci*. 2025;13(11):2951-2960.
doi: 10.1039/D5BM00193E

ACCSCIENCE PUBLISHING

International Journal of Bioprinting

RESEARCH ARTICLE

Psoralen immunomodulation: *In vitro* macrophage reprogramming to enhance osseointegration of 3D-printed porous titanium scaffolds in osteoporosis

Jian Ji[1†], Jijie Peng[2,3†], Yilong Wu[4†], Yue Meng[5], Di Che[6], Siyan Chen[6], Jingyang Chen[6], Xingmao Zhou[6], Junzhe Wu[6*], Yufeng He[2,3*], and Yuzhu Wang[6*]

[1]Department of Breast Surgery, The Fifth Affiliated Hospital, Southern Medical University, Guangzhou, Guangdong, China

[2]State Key Laboratory of Mechanism and Quality of Chinese Medicine, Faculty of Chinese Medicine, Macau University of Science and Technology, Macao, Macao SAR, China

[3]Department of Traditional Treatment Center, Zhongshan Hospital of Traditional Chinese Medicine Affiliated to Guangzhou University of Traditional Chinese Medicine, Zhongshan, Guangdong, China

[4]Department of Orthopaedic Surgery, Faculty of Medicine, University of Miyazaki, Miyazaki, Miyazaki, Japan

[5]Department of Orthopaedic Surgery, The Fifth Affiliated Hospital, Southern Medical University, Guangzhou, Guangdong, China

[6]Department of Orthopaedic Surgery, Zhongshan Hospital of Traditional Chinese Medicine Affiliated to Guangzhou University of Traditional Chinese Medicine, Zhongshan, Guangdong, China

[†]These authors contributed equally to this work.

***Corresponding authors:**
Junzhe Wu (wujunzhe@zsszyy.net)

Yufeng He (heyufeng@zsszyy.net)

Yuzhu Wang (wangyuzhu@zsszyy.net)

Citation: Ji J, Peng J, Wu Y, *et al.* Psoralen immunomodulation: *In vitro* macrophage reprogramming to enhance osseointegration of 3D-printed porous titanium scaffolds in osteoporosis *Int J Bioprint*. 2026;12(1):540-558. doi: 10.36922/IJB025480495

Received: November 25, 2025
1st revised: December 15, 2025
2nd revised: December 22, 2025
Accepted: December 24, 2025
Published online: January 8, 2026

Copyright: © 2026 Author(s). This is an Open Access article distributed under the terms of the Creative Commons Attribution License, permitting distribution, and reproduction in any medium, provided the original work is properly cited.

Publisher's Note: AccScience Publishing remains neutral with regard to jurisdictional claims in published maps and institutional affiliations.

Abstract

Psoralen inhibits osteoclast activity and bone resorption while enhancing osteoblast activity and bone formation. However, its role in modulating macrophage polarization to enhance osteoblast function and scaffold osseointegration under osteoporotic conditions remains underexplored. We fabricated Voronoi-structured metal scaffolds by 3D printing and evaluated psoralen *in vitro* in a macrophage–bone marrow mesenchymal stem cell co-culture system using serum from psoralen-treated rats, and *in vivo* in an osteoporotic bone-defect model with oral psoralen administration. The results demonstrated that psoralen treatment promoted M2 macrophage polarization, increased the M2/M1 ratio, and upregulated osteogenic gene expression *in vitro*. Improved bone formation parameters—including bone volume fraction, trabecular thickness, and trabecular number—around the implanted scaffolds were observed *in vivo*. The findings suggest a synergistic effect between gradient scaffold structures and psoralen in enhancing M2-mediated osteogenesis. Taken together, these findings may provide novel strategies for improving bone repair and prosthesis integration in osteoporosis.

Keywords: Macrophage polarization; Osseointegration; Osteoporosis; Psoralen

1. Introduction

In osteoporosis, bone remodeling homeostasis is disrupted, and bone resorption exceeds bone formation.[1] Psoralen may help restore bone remodeling balance through bidirectional regulation: on the one hand, it promotes bone formation; on the other hand, it inhibits bone resorption.[2] Psoralen can promote the osteogenic differentiation of bone marrow mesenchymal cells.[3] It initiates and accelerates the formation of new bone by activating key osteogenic signaling pathways such as Wnt/β-catenin and upregulating the expression of key transcription factors such as Runx2 (the main regulatory factor of osteoblast differentiation) and Osterix.[4] In terms of bone resorption inhibition, psoralen mainly exerts its effect by interfering with the canonical pathway of receptor activator of nuclear factor-κB ligand/receptor activator of nuclear factor-κB/nuclear factor-κB (NF-κB). This pathway is the central signaling axis in the generation and activation of osteoclasts. By inhibiting this pathway, psoralen can effectively reduce the formation of osteoclasts and lower their bone resorption activity.[5]

Psoralen may promote tissue repair by modulating macrophage polarization. Psoralen has been reported to inhibit nitric oxide (NO) production and 15-lipoxygenase activity and reduced pro-inflammatory Th1 cytokines (e.g., interferon [IFN]-γ, tumor necrosis factor [TNF]-α, and interleukin [IL]-2) while increasing the secretion of anti-inflammatory cytokines (e.g., IL-4, IL-6, and IL-10) in activated RAW 264.7 macrophage cells.[6] Further studies showed that psoralen inhibited the phosphorylation of Fyn and protein kinase Cδ, thereby inhibiting the activation of the mitogen-activated protein kinase and NF-κB pathways and suppressing the expression of pro-inflammatory cytokines in microglia.

Furthermore, psoralen reduced oxidative stress, neuronal damage, and apoptosis by inhibiting neuroinflammation. It decreased the expression of inducible NO synthase, cluster of differentiation (CD)-86, and TNF-α, and increased the expression of arginase-1, CD206, and IL-10. This indicates that psoralen inhibited the M1 microglial phenotype and promoted the M2 microglial phenotype.[7] However, osseointegration of titanium alloy scaffolds is often compromised in osteoporosis because of a dysregulated inflammatory microenvironment. Few studies have investigated whether psoralen can enhance titanium scaffold bone ingrowth by modulating macrophage polarization.

This study examined whether psoralen promotes osseointegration in osteoporotic bone defects by modulating macrophage polarization. We designed Voronoi-based scaffolds by metal three-dimensional (3D) printing, evaluated osteogenesis in a scaffold–macrophage–bone marrow-derived mesenchymal stem cell (BMSC) co-culture system, and validated scaffold osseointegration in an ovariectomy (OVX)-induced osteoporotic rat model.

2. Materials and methods

2.1. Design of the porous scaffolds

Using a multi-modal approach (Figure 1A), we systematically assessed how psoralen affects the immuno-osteogenic properties of Voronoi-based scaffolds. These scaffolds feature irregular pores created computationally using Voronoi tessellation theory. Each Voronoi cell follows the geometric principle described in **Equation (1)**, where points inside it are closer to its own seed point than to any other seed.[8] We designed two types of these Voronoi structures, namely, uniform irregular (UI; Figure S1) and graded irregular (GI; Figure S2), using Rhino 7's Grasshopper interface (McNeel & Associates, USA). By controlling seed distribution and strut thickness (Figure 1B and C; Table 1), the GI and UI structures were designded.[9]

$$V(P_i) = \{P/d(P, P_i) \leq d(P, P_j), j \neq i, j = 1, \ldots \ldots, n\} \quad (1)$$

where:

P_i is the core seed point of a sub-region space;

P is any point within the sub-region space other than P_i;

P_j is the core seed point in another sub-region space;

d is the distance between two points;

V represents the sub-region space.

This platform uses advanced algorithms to precisely control key design features, including seed density (N) and strut thickness. These parameters directly affect the scaffold's effective elastic modulus and porosity (P). The relationship between porosity and seed count is given by the following equations:

$$P = \frac{V_{total} - V_s}{V_{total}} \times 100\% \quad (2)$$

$$N \approx \frac{V_{total} \times P_1}{\frac{4 \times \pi}{3} \times r_1^3} \quad (3)$$

where V_{total} is the volume of the specific design space, V_s is the solid volume of the structure, P is the porosity of the porous structure, P_1 is the target porosity, r_1 is the target

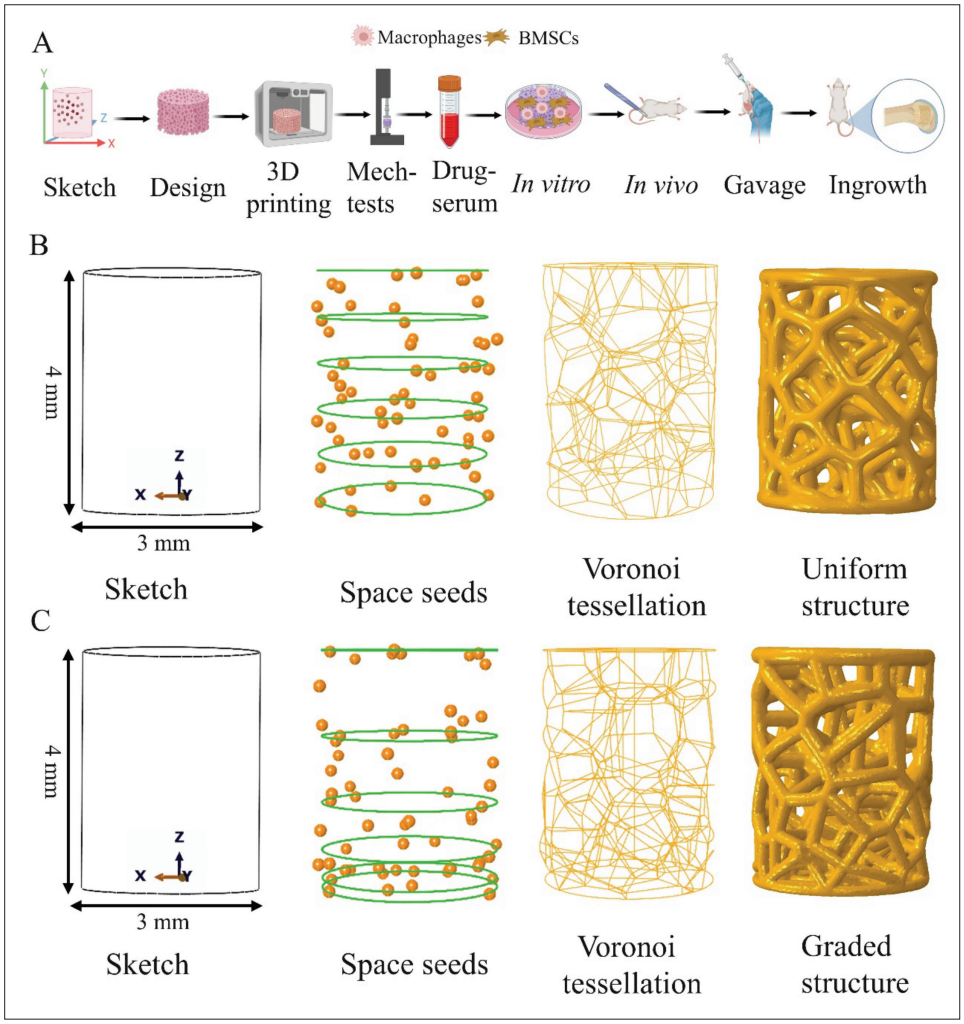


Figure 1. Bio-psoralen intervention for osteoporotic scaffold osseointegration: (A) Schematic illustration of bio-psoralen intervention on scaffold osseointegration under osteoporotic conditions, (B) design of the uniform scaffold, and (C) design of the graded scaffold. Abbreviations: 3D, three-dimensional; BMSC, bone marrow-derived mesenchymal stem cell.

Table 1. Construction of Voronoi-based scaffolds

Porosity (%)	UI structure[a]			GI structure[a]		
	Seeds (*N*)	Scale factors	Effective Volumes (mm^3)	Seeds (*N*)	Scale factors	Effective Volumes (mm^3)
44	60	0.17	15.57	60	0.09–0.234	15.57
52		0.155	13.46		0.09–0.208	13.46
59		0.141	11.41		0.09–0.182	11.41
66		0.126	9.44		0.09–0.155	9.44
73		0.112	7.61		0.09–0.129	7.61

Note:[a]The volumes of bulk Ti-64 alloy are 28.26 mm^3 (3(Ø) × 4(h) mm^3). Abbreviations: GI: graded irregular; UI: uniform irregular.

average pore radius of the structure, and N is the number of seeds.

2.2. Three-dimensional printing of the metal scaffolds

The computer-aided design models were fabricated via selective laser sintering (Farsoon FS273M, Farsoon Technologies, China) using Ti6Al4V powder under specified conditions (Table 2). A total of 12 scaffolds ($n = 6$ per group) were printed at 59% porosity (reported to promote bone ingrowth when exceeding 50%) for both UI and GI types (Figure 2A).

After printing, scaffolds were removed, and the surfaces were polished using zirconia sandblasting. They were then ultrasonically cleaned sequentially in acetone, anhydrous ethanol, and deionized water (15 min each), followed by disinfection and high-temperature drying.[10]

Scaffold architecture was verified using micro-computed tomography (micro-CT) (Bruker SkyScan1276, Bruker, USA) with DataViewer (Bruker, USA) and CTvox software (Bruker, USA) (Figure 2B). SEM imaging revealed smooth surfaces on both UI (Figure 2C) and GI (Figure 2D) scaffolds, with no significant cracks or powder residue.[11]

2.3. Experimental mechanical tests of the scaffolds

We tested UI and GI scaffolds (Figure 2E) under quasi-static compression along the z-axis with a QX-W600 universal testing machine (Qixiang Corp., China). The stiffness was calculated from the stress–strain curves using **Equation (4)**:

$$E_{effective} = \frac{\sigma}{\varepsilon} = \frac{F_R / A}{\Delta h / h} \quad (4)$$

where F_R, A, Δh, and h represent the reaction force, cross-sectional area, change in length, and original length of the porous structure, respectively. The GI scaffolds showed a significantly lower effective elastic modulus (1539.5 ± 180.01 MPa) than the UI structures (2163.3 ± 138.42 MPa), as observed in the stress–strain curves (Figure 2F) and modulus comparison (Figure 2G).[12]

2.4. Immuno-osteogenic differentiation testing *in vitro*

2.4.1. Preparation of osteoporosis and bio-psoralen containing serum

The study protocol was approved by the Ethics Committee of Zhongshan Hospital of Traditional Chinese Medicine, Guangzhou University of Chinese Medicine (AEWC-2023008; SYXK 2020–0109). Figure 3A illustrates the intervention of bio-psoralen on scaffold-mediated macrophage regulation under osteoporotic conditions *in vitro* and its effects on bone ingrowth *in vivo*.

A total of 30 female 2-month-old Sprague–Dawley rats—obtained from the Guangdong Medical Animal Laboratory Center (approval no.: SCXK 2022-0002)—were randomly divided into three groups: normal (N; $n = 10$), OVX-induced osteoporosis (OP; $n = 10$), and OVX + bio-psoralen (BP; $n = 10$) groups.

All rats were housed under specific pathogen-free conditions with *ad libitum* access to food. After 2 weeks of acclimation, OP and BP groups underwent bilateral OVX under isoflurane anesthesia (3% induction, 2% maintenance; 1.2 L/min O_2), while the N group received sham surgery (skin incision only).

To confirm successful model establishment, one randomly selected surviving rat from the N group and one from the OP group were subjected to dual-energy X-ray absorptiometry of the lumbar vertebrae after 10 weeks of observation.

Following confirmation of osteoporosis induction in the OP and BP groups, bio-psoralen (Jule Pharmaceutical Co., China) was administered orally to the BP group at a dose of 14 mg/kg/day, dissolved in 0.9% sodium chloride solution. After 4 weeks, all rats were anesthetized, and blood was collected via abdominal aorta puncture. The samples were centrifuged, and the serum was stored at −80°C for subsequent *in vitro* experiments.[13]

Table 2. Parameter settings of three-dimensional metal printing by selective laser sintering

Materials	Technical type	Layer thickness (mm; range)	Fill laser power (W; range)	Fill speed (mm/s; range)	Support laser power (W; range)	Support speed (mm/s; range)	Hatch spacing (mm; range)	Atmosphere (O_2 level) (%)	Powder specs (mm)	Build orientation
Ti-6Al-4V	Selective laser sintering	0.035 (0.03–0.04)	200 (150–250)	1,000 (950–1,250)	100 (50–170)	500 (400–700)	0.1 (0.08–0.12)	0.06	$D_{10} = 0.02$, $D_{50} = 0.034$	90° (z-axis)

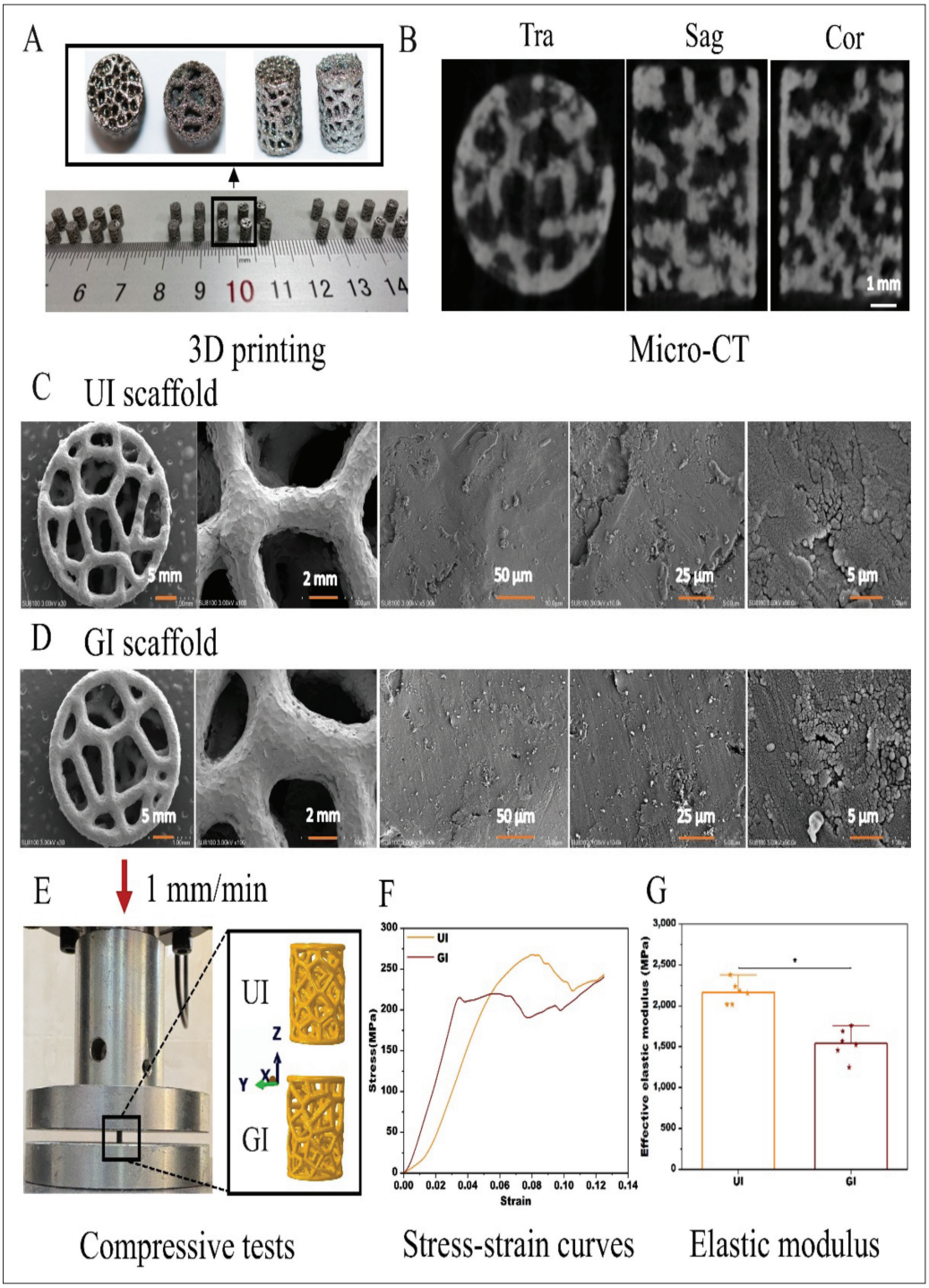


Figure 2. Biomechanical properties and 3D printing of porous metal scaffolds: (A) 3D printing of the porous metal scaffolds, (B) micro-CT images of the porous specimens (scale bar: 1 mm; magnification: 50×), (C) surface morphology of uniform scaffolds observed using scanning electron microscope (scale bar: 5 mm, magnification: 10×; scale bar: 2 mm, magnification: 20×; scale bar: 50 μM, magnification: 100×; scale bar: 25 μM, magnification: 200×; scale bar: 5 μM, magnification: 1000×), (D) surface morphology of the graded scaffolds observed using scanning electron microscope (scale bar: 5 mm, magnification: 10×; scale bar: 2 mm, magnification: 20×; scale bar: 50 μM, magnification: 100×; scale bar: 25 μM, magnification: 200×; scale bar: 5 μM, magnification: 1000×), (E) mechanical testing of the porous scaffolds, (F) representative stress–strain curves of the scaffolds, and (G) effective elastic modulus of the scaffolds ($n = 6$). Data are expressed as the mean ± standard deviation. $^{*}p < 0.05$ and $^{**}p < 0.01$ indicate statistical significance. Abbreviations: 3D: three-dimensional; Cor: coronal section; CT: computed tomography; GI: graded irregular; UI: uniform irregular; Sag: sagittal section; Tra: transverse section.

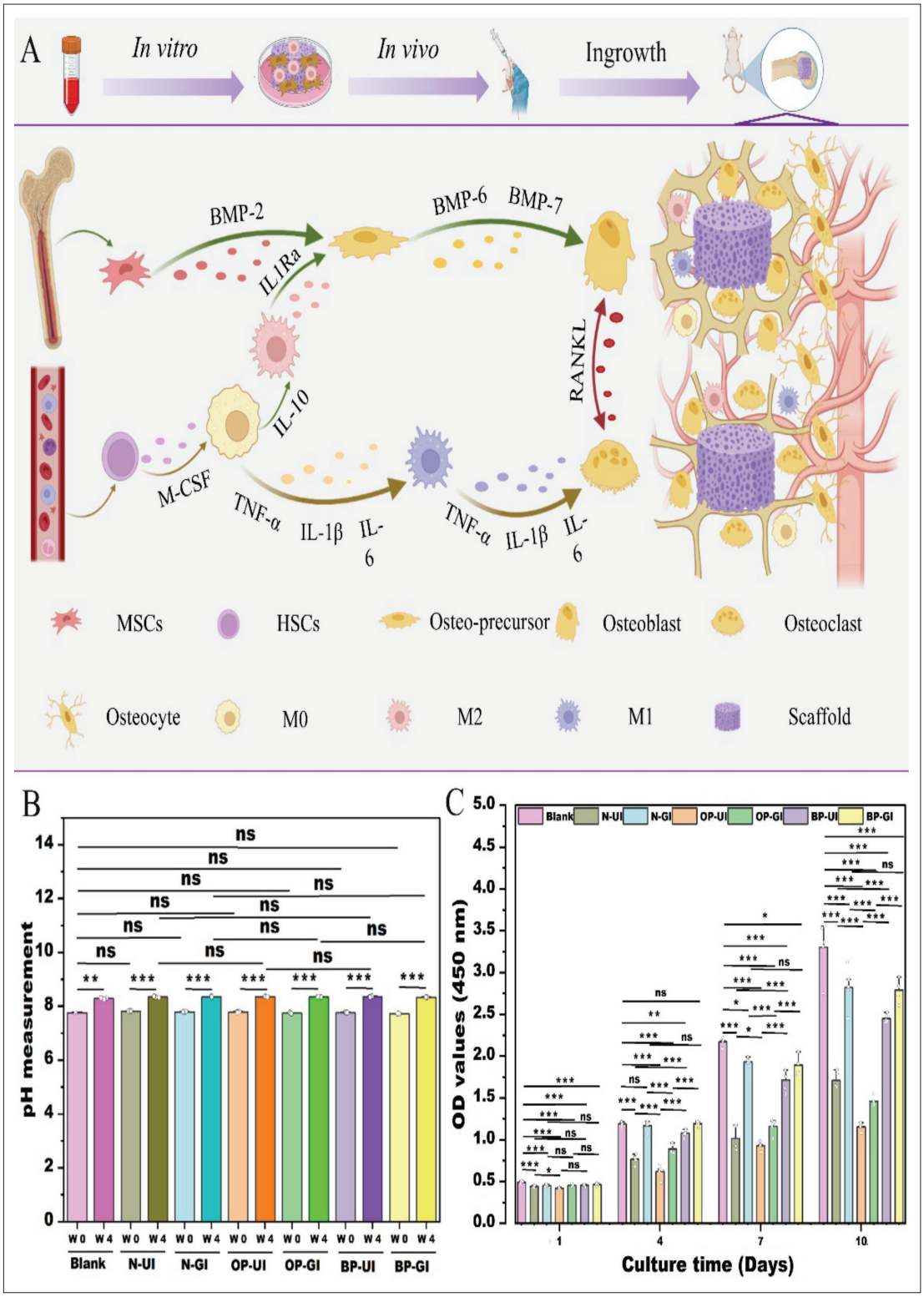


Figure 3. Effect of BP on cell proliferation. (A) Schematic illustration of macrophage polarization-mediated bone remodeling around implants regulated by BP; (B) pH measurement of scaffold-conditioned culture media at different time points (n = 3); and (C) cell proliferation assessed at different time points (n = 5). Data are expressed as mean ± standard deviation. $^{*}p < 0.05$, $^{**}p < 0.01$, and $^{***}p < 0.001$ indicate statistical significance. Abbreviations: ns: no statistical significance; BP: bio-psoralen; GI: graded irregular; HSC: hematopoietic stem cell; MSC: mesenchymal stem cell; N: normal; OD: optical density; OP: osteoporosis; UI: uniform irregular.

2.4.2. Preparation of scaffold-conditioned medium

After ultrasonic cleaning in acetone, ethanol, and deionized water (15 min each), scaffolds were air-dried and autoclaved. UI and GI scaffolds were then immersed for 4 weeks in three types of serum: the N, OP, and BP group sera. For the blank control, scaffolds were incubated in α-Minimum Essential Medium supplemented with 10% fetal bovine serum (Gibco, USA), 100 μg/mL streptomycin (Gibco, USA), and 100 U/mL penicillin (Gibco, USA). The pH of the scaffold-conditioned media was measured before and after the 4 weeks of immersion in the serum (n = 3). Scaffold surfaces were examined post-immersion using high-resolution SEM to assess structural changes.

2.4.3. Culture of bone mesenchymal stem cells

Rat BMSCs (rBMSCs) were isolated from the femoral bone marrow of 4-week-old Sprague–Dawley rats (n = 10). Cells were cultured in α-Minimum Essential Medium at 37°C with 5% CO_2, passaged at a 1:3 ratio, and used at passage 3.

2.4.4. Culture of macrophage cells

The RAW264.7 murine macrophage cell line (Shanghai Institutes for Biological Sciences, China) was cultured in growth medium containing 10% fetal bovine serum, 100 U/mL penicillin, and 100 μg/mL streptomycin at 37°C with 5% CO_2. Cells were passaged at a 1:3 ratio and used between passages 3 and 5.

2.4.5. Cell proliferation testing

Rat BMSCs were seeded in 24-well plates and cultured in scaffold-conditioned medium. Cell proliferation was assessed at days 1, 4, 7, and 10 using the cell counting kit (CCK)-8 assay following the manufacturer's instructions, and the absorbance was measured at 450 nm (n = 3).

2.4.6. Macrophage phenotypic characterization

RAW264.7 macrophages were seeded in 12-well plates and stimulated with 100 ng/mL lipopolysaccharide (LPS) in serum-free medium for 6 h at approximately 80% confluency to model acute inflammation. Cells were then cultured in scaffold-conditioned medium for 3 days. Immunostaining was performed using fluorescein isothiocyanate-conjugated anti-CD11c (M1 macrophage marker; 1:400; 11-0114-82, Thermo Fisher Scientific, USA) and allophycocyanin-conjugated anti-CD206 (M2 macrophage marker; 1:300; 17-2061-82, Thermo Fisher Scientific, USA) in phosphate-buffered saline/1% bovine serum albumin for 1 h.

Flow cytometric analysis was conducted using a sequential gating strategy with debris and doublet exclusion, starting from the total cell population. Debris was excluded first, followed by sequential gating to identify the target macrophage subpopulations. Data were acquired using a CytoFLEX LX (Beckman Coulter, USA) and analyzed with CytExpert 2.4 software (Beckman Coulter, USA) using standardized gating parameters.

2.4.7. Detection of gene expression related to macrophage polarization and inflammation

RAW264.7 cells in 24-well plates underwent RNA extraction and reverse transcription to cDNA. Gene expression of TNF-α, IL-1β, IL-6, IL-1Ra, IL-10, and arginase-1 was analyzed by real-time quantitative polymerase chain reaction.

2.4.8. Preparation of scaffold-modulated macrophage conditioned media

To assess how scaffold-conditioned macrophage secretions affect rBMSC osteogenic differentiation, we collected conditioned medium from polarized RAW264.7 cells. Macrophages in T75 flasks (approximately 80% confluency) were primed with 100 ng/mL LPS for 6 h and then cultured in scaffold-conditioned serum medium. After incubation, the culture media were centrifuged, and the supernatants were mixed at a 1:2 ratio with fresh growth medium. Conditioned medium from macrophages cultured without scaffold exposure served as the control.

2.4.9. Alkaline phosphatase activity assay

Alkaline phosphatase (ALP) activity in rBMSCs was measured spectrophotometrically (405 nm) after 4 and 7 days using a commercial ALP activity kit (EEA002, Thermo Fisher Scientific, USA) to assess early osteogenic differentiation. Mineralization was evaluated at day 14 via alizarin red staining (quantified at 630 nm). Osteogenic gene expression (*Alp*, *Col1*, *Ocn*, *Runx2*, *Opn*) was analyzed using real-time quantitative reverse transcription polymerase chain reaction.

2.5. *In vivo* evaluation of scaffolds

2.5.1. Preparation of osteoporotic animals

A total of 72 female 2-month-old Sprague–Dawley rats—obtained from the Guangdong Medical Animal Laboratory Center—were randomly divided into three treatment groups: normal (N; sham surgery), OP (OVX-induced osteoporosis), and BP (OVX + bio-psoralen). Each treatment group was further subdivided according to scaffold type (UI or GI) and implantation time point, resulting in 12 experimental groups (n = 6 per group).

Samples were collected at 4 and 8 weeks to evaluate osseointegration, with six groups assessed at each time point (4 weeks: N-UI 4W, N-GI 4W, OP-UI 4W, OP-GI 4W, BP-UI 4W, and BP-GI 4W; 8 weeks: N-UI 8W, N-GI 8W, OP-UI 8W, OP-GI 8W, BP-UI 8W, and BP-GI 8W).

All rats were housed under specific pathogen-free conditions with *ad libitum* access to food. After 2 weeks of acclimation, the OP and BP groups underwent bilateral OVX under isoflurane anesthesia (3% induction, 2% maintenance), while the N group received sham surgery (skin incision only). To confirm successful osteoporosis induction, one randomly selected surviving rat from the N group and one from the OP group were subjected to dual-energy X-ray absorptiometry of the lumbar vertebrae after 10 weeks of observation.

2.5.2. Scaffold implantation and bio-psoralen intervention

Following confirmation of osteoporosis induction, the right femoral condyle of rats in the relevant groups received pre-sterilized UI or GI single scaffold (59% porosity) under isoflurane anesthesia.

After prone positioning and skin disinfection, a 3-cm longitudinal incision was made to expose the right femoral condyle. Scaffolds were implanted into drilled sites and irrigated with saline solution. After 1 week, ovariectomized rats received an oral bio-psoralen suspension, prepared by dissolving bio-psoralen in 0.9% sodium chloride solution, and administered via gavage at a dose of 14 mg/kg per day.

After 4 and 8 weeks of bio-psoralen intervention, rats were euthanized by cervical dislocation. The right femurs were dissected, soft tissue removed, fixed in 4% paraformaldehyde, and stored at 25°C for micro-CT analysis.

2.5.3. Micro-computed tomography images and analysis

Bone–scaffold complexes were scanned via micro-CT (SkyScan1276, Bruker) at 10 μm isotropic resolution (80 kV, 100 μA). Reconstructed images were analyzed using CTAn software (Bruker, USA) to quantify new bone parameters: bone volume fraction (BV/TV; %), trabecular thickness (Tb.Th; mm), and trabecular number (Tb.N; mm^{-1}).

2.5.4. Histological staining evaluation

New bone regeneration was assessed histologically. Bone–scaffold complexes were fixed in 10% formaldehyde for 7 days at 4°C, rinsed overnight, dehydrated through graded ethanol, cleared in xylene, and embedded in polymethyl methacrylate. Sections (800 μm thick) were cut perpendicular to the implant axis using a Leica 1600 microtome (Leica Microsystems, Germany), stained with Toluidine Blue and Van Gieson's (VG), and examined under a Leica DMLA microscope (Leica Microsystems, Germany) at 40× and 100× magnification.

2.6. Statistical analysis

Data were analyzed using SPSS 17.0 (IBM, USA) and visualized in Origin Pro 2021b (Northampton, USA). Group comparisons were conducted using one-way ANOVA with Tukey's post hoc correction. Results are presented as mean ± standard deviation. $^{*}p < 0.05$, $^{**}p < 0.01$, $^{***}p < 0.001$, and $^{****}p < 0.0001$ were considered statistically significant.

3. Results

3.1. Proliferation of bone mesenchymal stem cells in scaffold-conditioned media

The findings revealed that the pH of all scaffold-conditioned media increased after 4 weeks of immersion, with no significant differences between groups at the endpoint (Figure 3B), indicating minimal influence of scaffolds on medium chemistry. BMSC proliferation, assessed by the CCK-8 assay, increased over 10 days, with the BP group showing higher activity than the OP group but lower than the N group and blank controls (Figure 3C). SEM revealed no structural defects or degradation after 4 weeks of media immersion (Figure 4).

Live/dead staining showed decreasing BMSC viability in the OP-scaffold groups over 7 days, with dead cells visible at days 4 and 7. In contrast, N- and BP-scaffolds maintained high cellular viability throughout the observation period, showing no discernible signs of cell death (Figure 5). The proliferation trend indicated by CCK-8 correlated well with the cell viability patterns observed via live/dead staining.

3.2. Macrophage phenotype and marker expression in different culture media

Flow cytometry showed a higher M2/M1 ratio in BP-scaffolds than in OP-scaffolds, although both were lower than the N group. The N- and BP-scaffolds favored M2 polarization, whereas OP-scaffolds skewed toward M1 (Figure 6A).

Pro-inflammatory cytokines (e.g., TNF-α, IL-1β, and IL-6) were elevated in OP vs. BP scaffolds, and in UI vs. GI scaffolds (Figure 6B–D), while anti-inflammatory markers (IL-1Ra, IL-10, arginase-1) were higher in BP vs. OP scaffolds and in GI vs. UI scaffolds, but remained below normal levels (Figure 6E–G).

3.3. Osteogenic differentiation of bone mesenchymal stem cells in different culture media

Osteogenic induction assessed by alizarin red staining and ALP activity revealed that ALP activity and osteogenic nodule formation in BP-scaffold groups were higher than in OP groups, and in GI groups were higher than in UI groups (Figure 7A–C). RT-PCR analysis indicated that the gene expression of *Alp*, *Opn*, *Ocn*, *Col1*, and *Runx2* (week 4: Figure 7D–H; week 8: Figure 7I–M) in BP-scaffold

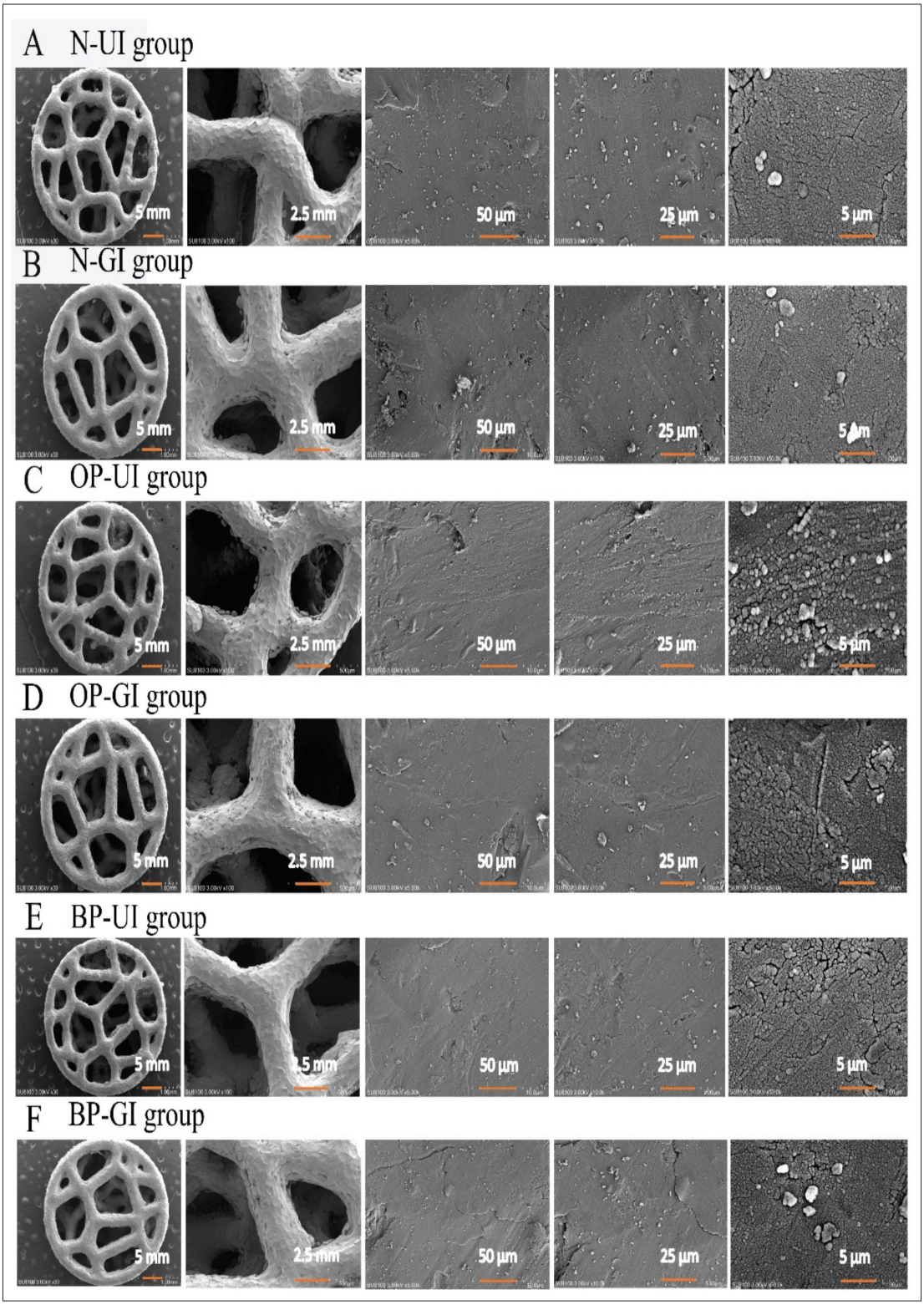


Figure 4. Surface morphology of the specimens after 4 weeks of immersion in different media: (A) N-UI, (B) N-GI, (C) OP-UI, (D) OP-GI, (E) BP-UI, and (F) BP-GI (scale bar: 5 mm, magnification: 10×; scale bar: 2.5 mm, magnification: 20×; scale bar: 50 μM, magnification: 100×; scale bar: 25 μM, magnification: 200×; scale bar: 5 μM, magnification: 1000×). Abbreviations: BP: bio-psoralen; GI: graded irregular; N: normal; OP: osteoporosis; UI: uniform irregular.

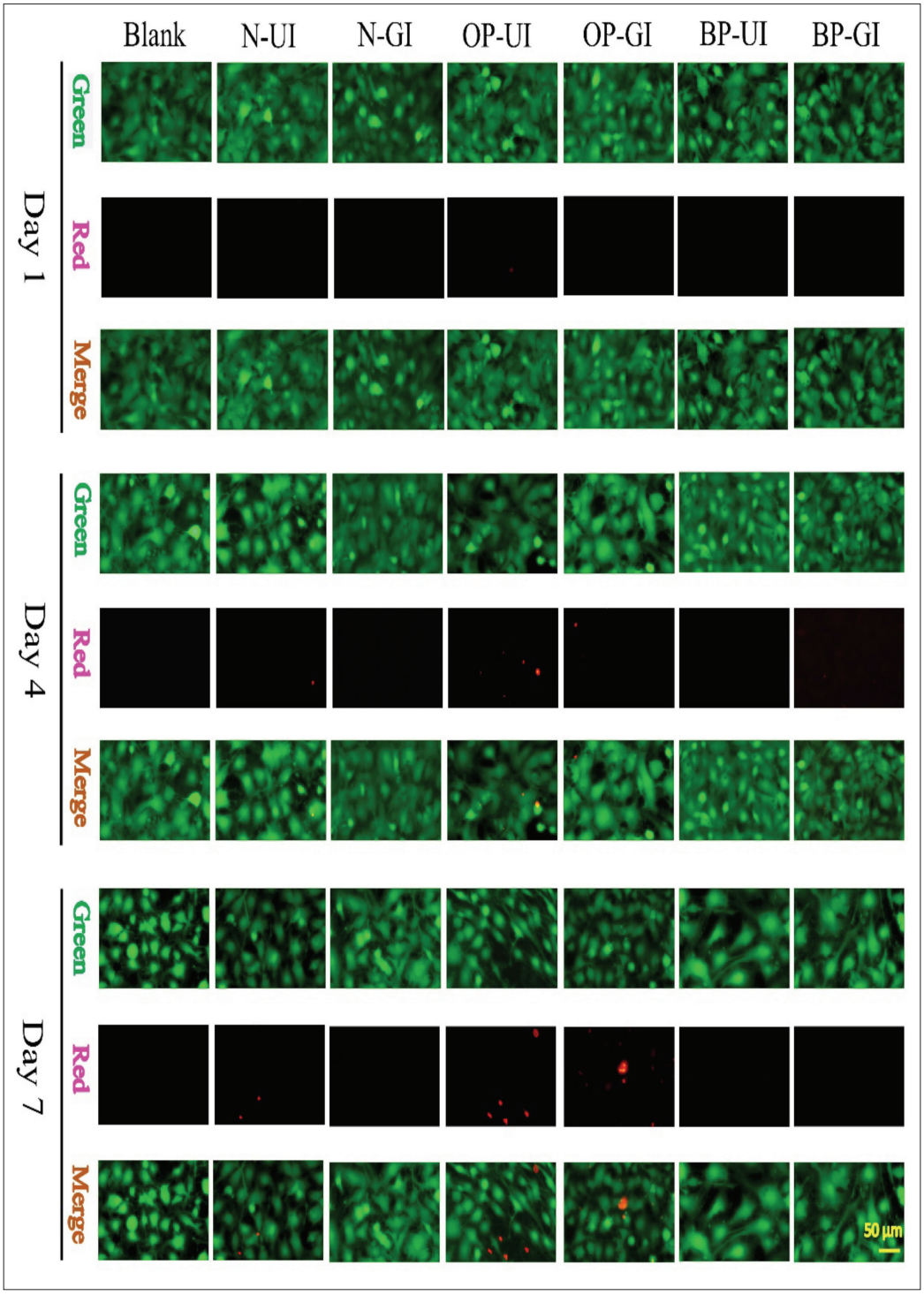


Figure 5. Cell morphology assessed using immunofluorescence double staining at different time points. Green indicates live cells, and red indicates dead cells (scale bar: 50 μm; magnification: 100×). Abbreviations: BP: bio-psoralen; GI: graded irregular; N: normal; OP: osteoporosis; UI: uniform irregular.

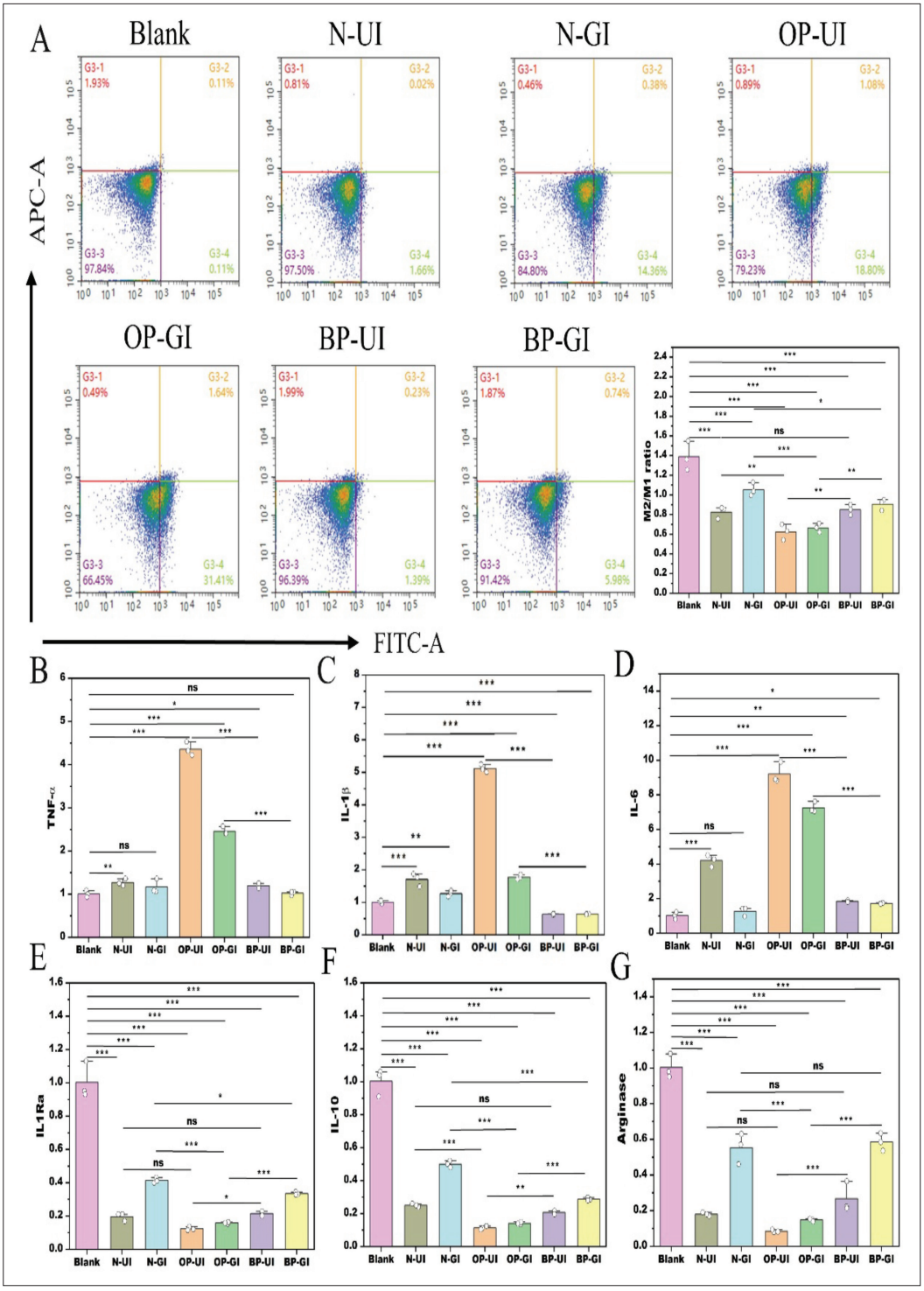


Figure 6. Macrophage expression in different culture media. (A) M2/M1 macrophage ratio determined by dual-labeling flow cytometry. (B–G) Expression of cytokines and markers: (B) TNF-α, (C) IL-1β, (D) IL-6, (E) IL-1Ra, (F) IL-10, and (G) arginase. Data are expressed as mean ± standard deviation ($n = 3$). $^{*}p < 0.05$, $^{**}p < 0.01$, $^{***}p < 0.001$, and $^{****}p < 0.0001$ indicate statistical significance. Abbreviations: ns: no statistical significance; APC: allophycocyanin; BP: bio-psoralen; FITC: fluorescein isothiocyanate; GI: graded irregular; IL: interleukin; N; normal; OP: osteoporosis; TNF: tumor necrosis factor; UI: uniform irregular.

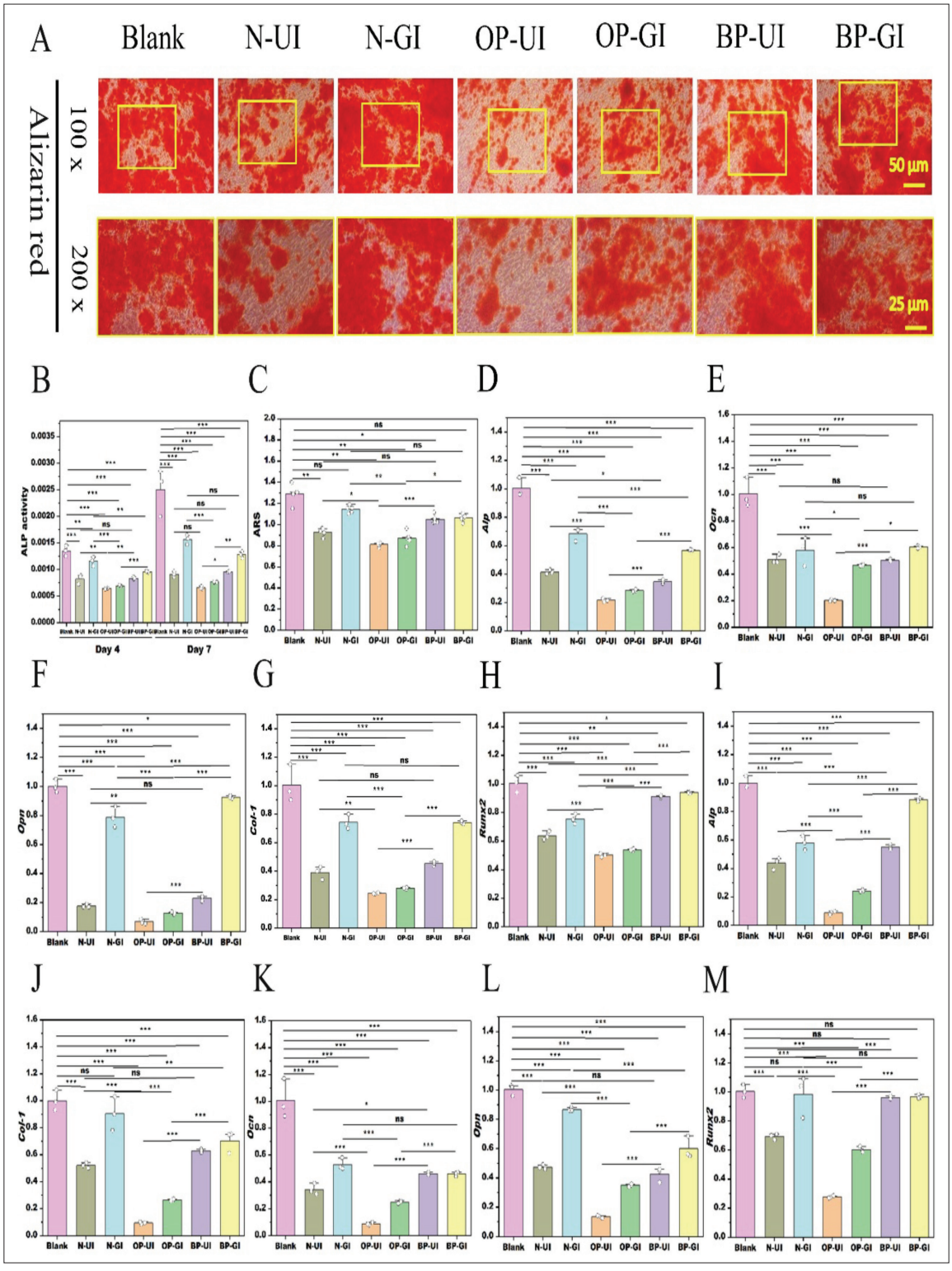


Figure 7. *In vitro* osteogenic differentiation of cells. (A) Extracellular matrix mineralization assessed by ARS (scale bar: 50 μm, magnification: 100×; scale bar: 25 μm, magnification: 200×). (B) ALP activity of cells at different time points ($n = 3$). (C) ARS quantification of extracellular matrix mineralization ($n = 5$). (D–H) Gene expression at week 4 ($n = 3$): (D) *Alp*, (E) *Ocn*, (F) *Opn*, (G) *Col1*, and (H) *Runx2*. (I–M) Gene expression at week 8 ($n = 3$): (I) *Alp*, (J) *Ocn*, (K) *Opn*, (L) *Col1*, and (M) *Runx2*. Data are expressed as the mean ± standard deviation. $^{*}p < 0.05$, $^{**}p < 0.01$, $^{***}p < 0.001$, and $^{****}p < 0.0001$ indicate statistical significance. Abbreviations: ns: no statistical significance; ALP: alkaline phosphatase; ARS: alizarin red staining; BP: bio-psoralen; GI: graded irregular; N: normal; OP: osteoporosis; UI: uniform irregular.

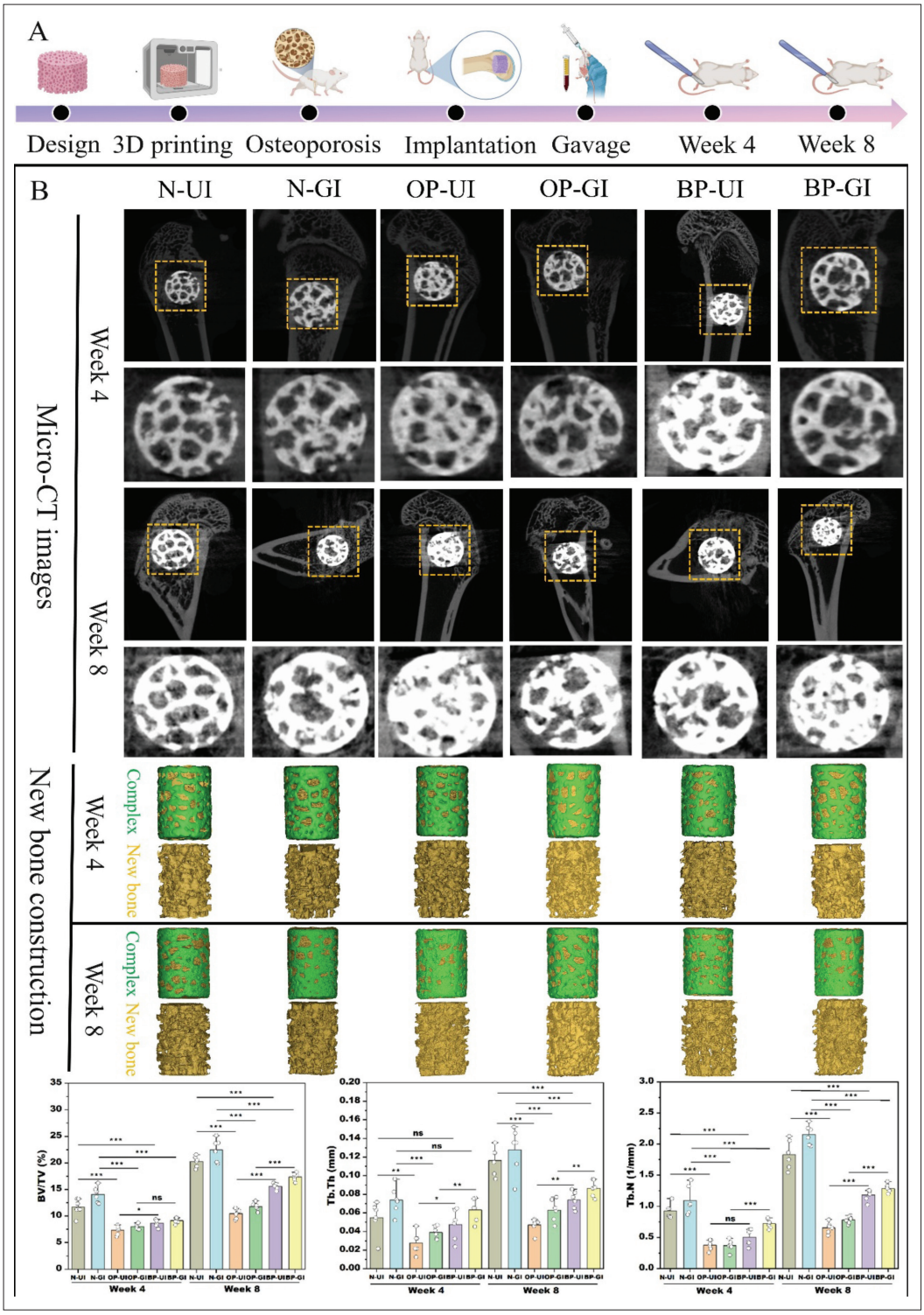


Figure 8. *In vivo* osseointegration analysis. (A) Schematic illustration of scaffold implantation for osseointegration. (B) Quantification of new bone from micro-CT images of bone–scaffold complexes, including reconstruction and measurement of BV/TV, Tb.Th, and Tb.N of new bone (n = 6). Data are expressed as the mean ± standard deviation. *p < 0.05, **p < 0.01, ***p < 0.001, and ****p < 0.0001 indicate statistical significance. Abbreviations: ns: no statistical significance; 3D: three-dimensional; BP: bio-psoralen; BV/TV: bone volume fraction; CT: computed tomography; GI: graded irregular; N: normal; OP: osteoporosis; Tb.N: trabecular number; Tb.Th: trabecular thickness; UI: uniform irregular.

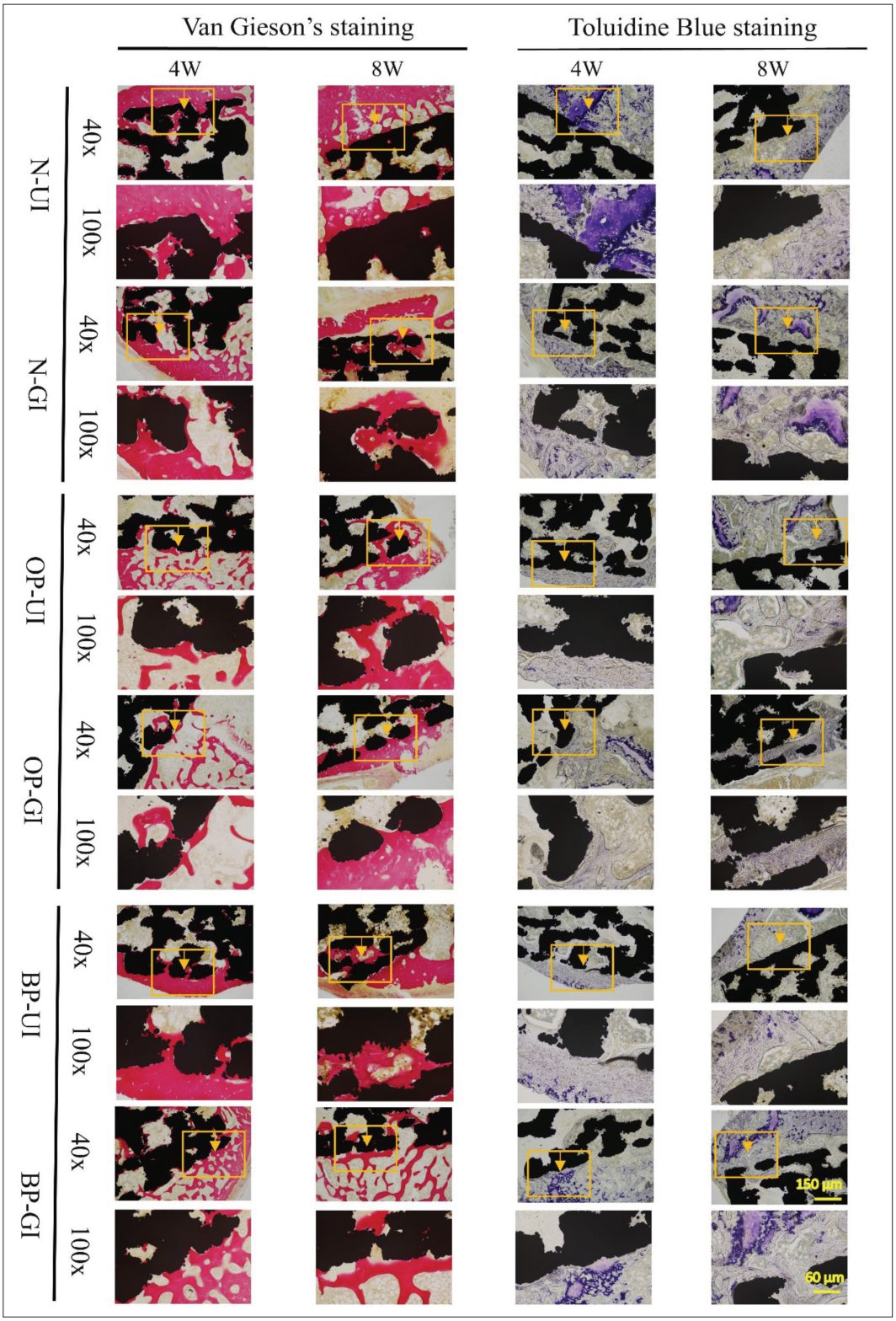


Figure 9. Histological analysis of new bone using Van Gieson's and Toluidine Blue staining (scale bar: 150 μm, magnification: 40×; scale bar: 60 μm, magnification: 100×). Abbreviations: BP: bio-psoralen; GI: graded irregular; N: normal; OP: osteoporosis; UI: uniform irregular.

groups was higher than in OP-scaffold groups, and in GI groups was higher than in UI groups.

3.4. Micro-computed tomography reconstruction and quantitative analysis

All implants were confirmed to be infection-free and stable before harvest. Osseointegration was assessed in Sprague–Dawley rats (Figure 8A). Micro-CT two-dimensional reconstructions visualized new bone ingrowth at weeks 4 and 8. Quantitative 3D analysis showed significantly higher BV/TV (%), Tb.Th, and Tb.N in BP-scaffolds vs. OP-scaffolds, and in GI vs. UI scaffolds (Figure 8B).

3.5. Histological analysis

Histological analysis showed new bone formation progressing from scaffold edges toward the inner pores, as confirmed by both VG and Toluidine Blue staining (Figure 9). Toluidine Blue specifically highlighted new osteoid and mineralized bone in deeper regions. These spatial patterns corresponded to the micro-CT reconstructions, validating osseointegration.

4. Discussion

This study explored the role of psoralen in promoting osseointegration of titanium alloy scaffolds in an osteoporotic environment by regulating macrophage polarization via oral administration. The findings revealed that psoralen promotes macrophage polarization toward the M2 anti-inflammatory phenotype, thereby inducing the osteogenic differentiation of mesenchymal stem cells *in vitro*. Compared with psoralen-coated tissue-engineering scaffolds, oral administration enables long-term delivery, maintains a more stable systemic drug concentration, and achieves long-term efficacy.

Due to the excellent biocompatibility and low cytotoxicity of titanium alloy,[14] it exerts minimal influence on scaffold-conditioned media under different conditions. Conversely, the culture media under varying conditions do not cause significant erosion or structural changes to the titanium alloy surface.[15,16] Therefore, the effects of osteoporotic serum and psoralen-containing serum on the viability and osteogenic differentiation of mesenchymal stem cells cultured within 3D scaffolds can be accurately assessed.

Based on the findings, the stable pH profiles across all groups (Figure 3B) and preserved scaffold integrity after 4 weeks of immersion (Figure 4) confirmed material stability.[17] Critically, BP-scaffolds significantly enhanced BMSC viability compared with scaffolds exposed to osteoporotic serum. Live/dead staining revealed progressive cell death in OP groups at days 4 and 7, whereas BP groups maintained viability comparable to normal scaffolds (Figure 5). Furthermore, CCK-8 results indicated that treatment with psoralen-containing serum partially rescued the impaired proliferation capacity of BMSCs under osteoporotic conditions,[18] exhibiting intermediate activity between normal and OP groups (Figure 3C).

Evidence suggests that in osteoporosis, serum levels of Th17 cytokines (e.g., IL-17) are elevated, whereas regulatory T cell (Treg) cytokines (e.g., IL-10) are reduced, leading to a pro-inflammatory state.[19–21] However, psoralen-containing serum from treated individuals shows a significant decrease in Th17 secretion and an increase in Treg secretion.[22] This is accompanied by downregulation of the transcription factor retinoic acid-related orphan receptor γt and upregulation of forkhead box P3, thereby correcting the immune imbalance.[23]

Osteoporosis deteriorates the bone microenvironment, leading to the release of inflammatory factors and consequently increasing serum cytokine levels. Intervention with psoralen can improve the bone microenvironment, reducing the release of inflammatory factors.[24,25] Specifically, psoralen reduces pro-inflammatory Th1/M1 cytokines (e.g., TNF-α, IL-1β, IFN-γ, IL-2) and increases anti-inflammatory/M2 cytokines (e.g., IL-4, IL-6, IL-10). The reduction in TNF-α and IL-1β removes a major stimulus for osteoclast formation and activity, whereas the increase in IL-4 and IL-10 directly inhibits osteoclastogenesis and supports bone formation.[2,26]

Flow cytometry analysis revealed a notable polarization shift: BP-scaffolds significantly increased the M2/M1 macrophage ratio compared with OP-scaffolds (Figure 6A), indicating effective immunomodulation.[27,28] This finding was further supported by cytokine profiles, which showed that BP-scaffolds suppressed pro-inflammatory mediators (e.g., TNF-α, IL-1β, IL-6; Figure 6B–D) while promoting anti-inflammatory factors (e.g., IL-1Ra, IL-10, arginase; Figure 6E–G). Importantly, the cytokine levels in the BP group remained below those of normal controls, suggesting only partial reversal of OP-associated inflammation.

The impact of macrophage polarization on osteogenic differentiation is central to bone immune regulation.[29] M1 macrophages primarily inhibit osteogenic differentiation and disrupt the osteogenic microenvironment through the secretion of pro-inflammatory factors. In contrast, M2 macrophages strongly promote osteogenic differentiation both directly and indirectly by releasing anti-inflammatory, growth-promoting, and angiogenic factors.[30] BP-scaffolds exhibited significantly superior performance over OP-scaffolds in terms of ALP activity and mineralized nodule

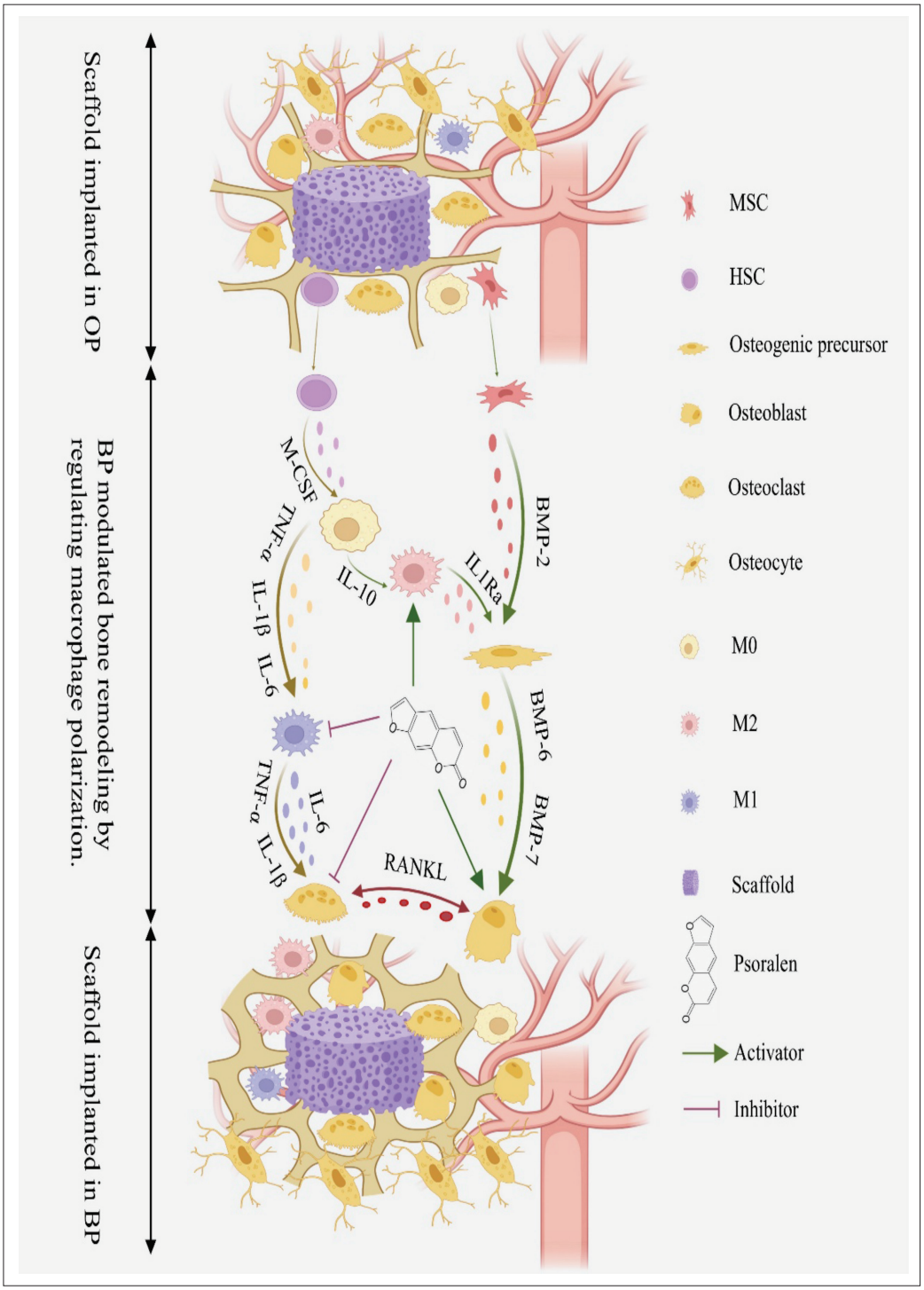


Figure 10. Mechanism of macrophage polarization-mediated bone remodeling around osteoporotic implants regulated by BP. Abbreviations: BP, biopsoralen; HSC, hematopoietic stem cell; MSC, mesenchymal stem cell; OP, osteoporosis.

formation (Figure 7A–C), along with enhanced expression of osteogenic genes (e.g., *Alp*, *Opn*, *Ocn*, *Col1*, *Runx2*; Figure 7D–M). The coordinated upregulation of early markers (e.g., *Runx2*, *Alp*) alongside late markers (*Ocn* and mineralization) indicates that BP-scaffolds effectively support the complete cascade of osteogenic differentiation (Figure 10).[31,32] Additionally, the GI structure showed significant advantages over the UI structure in regulating the polarization of M2 macrophages, enhancing *in vitro* osteogenic differentiation, and promoting *in vivo* bone integration.

However, several limitations remain in this study. First, although Sprague-Dawley rats and their derived mesenchymal stem cells serve as a valid model for osteoporosis research, they may differ from human postmenopausal osteoporosis in bone metabolic characteristics, potentially limiting clinical translation.[33] Second, with the advancement of organoid and organ-on-a-chip technologies, future studies utilizing 3D culture systems may provide greater potential for dynamically investigating the effects of biomaterials on osteoporosis and psoralen interventions.[34–36] Third, the molecular pathways governing psoralen-mediated macrophage polarization (e.g., NF-κB/STAT signaling) remain uncharacterized, requiring validation through knockout studies.[37] Fourth, the 8-week experimental period is insufficient to evaluate the long-term impact of psoralen on bone remodeling in the context of chronic osteoporosis.[38] Finally, this study employed oral administration. Individual differences in serum drug concentrations may affect therapeutic outcomes. Recently, drug-coated scaffolds with local delivery have been proposed as an alternative, but ensuring stability and sustained release of the drug coating remains a challenge.[39]

5. Conclusion

The findings demonstrate that psoralen may promote osteogenic differentiation and scaffold osseointegration in osteoporotic bone by regulating macrophage polarization toward the M2 phenotype *in vitro*. Furthermore, the gradient scaffold structure may synergize with psoralen to enhance M2 macrophage-mediated osteogenic effects *in vitro*. This study provides novel intervention strategies for osteoporotic bone repair and the osseointegration of osteoporotic prostheses, and offers a new perspective for mechanistic investigations of psoralen treatment of osteoporosis.

Acknowledgments

We would like to thank the professors of the Pharmacological Medical Research Center at Zhongshan Hospital of Traditional Chinese Medicine, affiliated with Guangzhou University of Chinese Medicine, for their guidance and for providing experimental facilities and equipment for this study.

Funding

This work was supported by the Traditional Chinese Medicine Inheritance Innovation Development Research Project of Zhongshan City (No. 2024B3019) and China Postdoctoral Science Foundation (No. 2024M750668). The funders had no role in the design of the study, the collection, analysis, and interpretation of the data, or in writing the manuscript.

Conflict of interest

The authors declare that they have no competing interests.

Author contributions

Conceptualization: Jijie Peng
Data curation: Jingyang Chen
Formal analysis: Di Che
Funding acquisition: Yuzhu Wang
Investigation: Siyan Chen
Methodology: Jian Ji
Project administration: Junzhe Wu
Resources: Yuzhu Wang
Software: Yilong Wu
Supervision: Yuzhu Wang
Validation: Yue Meng
Visualization: Xingmao Zhou
Writing–original draft preparation: Jian Ji
Writing–review and editing: Yufeng He
All authors have read and agreed to the published version of the manuscript.

Ethics approval and consent to participate

The animal research protocol was approved by the Ethics Committee of Zhongshan Hospital of Traditional Chinese Medicine Affiliated to Guangzhou University of Chinese Medicine (No. AEWC-2023008). The animals were obtained from Guangdong Medical Animal Laboratory Center for medical research purposes (approval no. SCXK 2022-0002).

Consent for publication

Not applicable.

Availability of data

The data are available from the corresponding authors upon reasonable request.

References

1. Johnston CB, Dagar M. Osteoporosis in older adults. *Med Clin North Am*. 2020;104(5):873-884. doi: 10.1016/j.mcna.2020.06.004
2. Ren Y, Song X, Tan L, *et al*. A review of the pharmacological properties of psoralen. *Front Pharmacol*. 2020;11:571535. doi: 10.3389/fphar.2020.571535
3. An J, Yang H, Zhang Q, *et al*. Natural products for treatment of osteoporosis: the effects and mechanisms on promoting osteoblast-mediated bone formation. *Life Sci*. 2016;147:46-58. doi: 10.1016/j.lfs.2016.01.024
4. Li F, Li Q, Huang X, *et al*. Psoralen stimulates osteoblast proliferation through the activation of nuclear factor-κB-mitogen-activated protein kinase signaling. *Exp Ther Med*. 2017;14(3):2385-2391. doi: 10.3892/etm.2017.4771
5. Li JP, Xie BP, Zhang WJ, *et al*. Psoralen inhibits RAW264.7 differentiation into osteoclasts and bone resorption by regulating CD4+T cell differentiation. *Zhongguo Zhong Yao Za Zhi*. 2018;43(6):1228-1234. Chinese. doi: 10.19540/j.cnki.cjcmm.20180104.017
6. Isa AI, Fouotsa H, Mohammed OA, *et al*. Psoralen isolated from the roots of *Dorstenia psilurus* Welw. Modulate Th1/Th2 cytokines and inflammatory enzymes in LPS-stimulated RAW 264.7 macrophages. *Mediators Inflamm*. 2024;2024:8233689. doi: 10.1155/2024/8233689
7. Guo Y, Xu S, Pan X, *et al*. Psoralen protects neurons and alleviates neuroinflammation by regulating microglial M1/M2 polarization via inhibition of the Fyn-PKCδ pathway. *Int Immunopharmacol*. 2024;137:112493. doi: 10.1016/j.intimp.2024.112493
8. Luo L, Zheng W, Li J, *et al*. 3D-printed titanium trabecular scaffolds with sustained release of hypoxia-induced exosomes for dual-mimetic bone regeneration. *Adv Sci (Weinheim)*. 2025;12(23):e2500599. doi: 10.1002/advs.202500599
9. Pirogova Y, Tashkinov M, Vindokurov I, *et al*. Design of lattice structures for trabecular-bone scaffolds: comparative analysis of morphology and compressive mechanical behaviour. *Biomech Model Mechanobiol*. 2025;24(5):1535-1564. doi: 10.1007/s10237-025-01980-5
10. Walczak M, Okuniewski W, Nowak WJ, Chocyk D, Pasierbiewicz K. Corrosion behavior of shot peened Ti6Al4V alloy fabricated by conventional and additive manufacturing. *Materials (Basel)*. 2025;18(10):2274. doi: 10.3390/ma18102274
11. Xu M, Lin Y, Lin Z, Cheng H. Elastic and fatigue properties of additively manufactured and milled Ti-6Al-4V removable partial denture clasps. *J Prosthet Dent*. 2025;133(1):230.e1-230.e8. doi: 10.1016/j.prosdent.2024.09.017
12. Wang Y, Ma C, Wu Y, Gao D, Meng Y, Wang H. Comprehensive evaluation of biomechanical and biological properties of the porous irregular scaffolds based on voronoi-tessellation. *J Bionic Eng*. 2025;22:322-340. doi: 10.1007/s42235-024-00630-3
13. Wang Y, Wu Z, Li C, *et al*. Effect of bisphosphonate on bone microstructure, mechanical strength in osteoporotic rats by ovariectomy. *BMC Musculoskelet Disord*. 2024;25(1):725. doi: 10.1186/s12891-024-07846-8
14. Sartori M, Bregoli C, Carniato M, *et al*. Biological characterization of Ti6Al4V additively manufactured surfaces: comparison between ultrashort laser texturing and conventional post-processing. *Adv Healthc Mater*. 2025;14(4):e2402873. doi: 10.1002/adhm.202402873
15. Yan K, Ngadiman NHA, Saman MZM, Mustafa NS. Advancements in selective laser melting (SLM) of titanium alloy scaffolds for bone tissue engineering. *Biofabrication*. 2025;17(2):022016. doi: 10.1088/1758-5090/adc6c0
16. Habijan T, Haberland C, Meier H, *et al*. The biocompatibility of dense and porous nickel-titanium produced by selective laser melting. *Mater Sci Eng C Mater Biol Appl*. 2013;33(1):419-426. doi: 10.1016/j.msec.2012.09.008
17. Sevcikova J, Pavkova Goldbergova M. Biocompatibility of NiTi alloys in the cell behaviour. *Biometals*. 2017;30(2):163-169. doi: 10.1007/s10534-017-0002-5
18. Si Y, Dong S, Li M, *et al*. Curcumin-encapsulated exosomes in bisphosphonate-modified hydrogel microspheres promote bone repair through macrophage polarization and DNA damage mitigation. *Mater Today. Bio*. 2025;32:101874. doi: 10.1016/j.mtbio.2025.101874
19. Peng P, Wong P, Lv Z, *et al*. Tectorigenin ameliorates glucocorticoid-induced osteoporosis by inhibiting the NF-κB signal pathway and modulating Treg-Th17 cell balance. *J Cell Mol Med*. 2025;29(13):e70705. doi: 10.1111/jcmm.70705
20. Shen X, Zhang Q, Ding J, *et al*. Licochalcone D inhibits osteoclast differentiation and postmenopausal osteoporosis by inactivating the NF-κB signaling pathway. *J Orthop Surg Res*. 2025;20(1):713. doi: 10.1186/s13018-025-06132-0
21. Ma Z, Liu Y, Shen W, *et al*. Osteoporosis in postmenopausal women is associated with disturbances in gut microbiota and migration of peripheral immune cells. *BMC musculoskeletal disorders*, 2024;25(1):791. doi: 10.1186/s12891-024-07904-1

22. Talaat RM, Sidek A, Mosalem A, Kholief A. Effect of bisphosphonates treatment on cytokine imbalance between TH17 and Treg in osteoporosis. *Inflammopharmacology.* 2015;23(2–3):119-125.
doi: 10.1007/s10787-015-0233-4

23. Chen Z, Lin F, Gao Y, *et al.* FOXP3 and RORγt: transcriptional regulation of Treg and Th17. *Int Immunopharmacol.* 2011;11(5):536-542.
doi: 10.1016/j.intimp.2010.11.008

24. Weng Z, Ye J, Cai C, *et al.* Inflammatory microenvironment regulation and osteogenesis promotion by bone-targeting calcium and magnesium repletion nanoplatform for osteoporosis therapy. *J Nanobiotechnol.* 2024:22(1):314.
doi: 10.1186/s12951-024-02581-7

25. Xu W, Zhang Y, Huang X, *et al.* Alendronate carbon dots targeting bone immune microenvironment for the treatment of osteoporosis. *Chem Eng J*. 2024;494:152209.
doi: 10.1016/j.cej.2024.152209

26. Maruthamuthu V, Henry LJK, Ramar MK, Kandasamy R. Myxopyrum serratulum ameliorates airway inflammation in LPS-stimulated RAW 264.7 macrophages and OVA-induced murine model of allergic asthma. *J Ethnopharmacol.* 2020;255:112369.
doi: 10.1016/j.jep.2019.112369

27. Wu S, Ma J, Liu J, *et al.* Immunomodulation of telmisartan-loaded PCL/PVP scaffolds on macrophages promotes endogenous bone regeneration. *ACS Appl Mater Interfaces.* 2022;14(14):15942-15955.
doi: 10.1021/acsami.1c24748

28. Abedi N, Sadeghian A, Kouhi M, *et al.* Immunomodulation in bone tissue engineering: recent advancements in scaffold design and biological modifications for enhanced regeneration. *ACS Biomater Sci Eng.* 2025; 11(3): 1269-1290.
doi: 10.1021/acsbiomaterials.4c01613

29. Ji X, Yuan X, Ma L, *et al.* Mesenchymal stem cell-loaded thermosensitive hydroxypropyl chitin hydrogel combined with a three-dimensional-printed poly(ε-caprolactone) / nano-hydroxyapatite scaffold to repair bone defects via osteogenesis, angiogenesis and immunomodulation. *Theranostics.* 2020;10(2):725-740.
doi: 10.7150/thno.39167

30. Zhang F, Lv M, Wang S, *et al.* Ultrasound-triggered biomimetic ultrashort peptide nanofiber hydrogels promote bone regeneration by modulating macrophage and the osteogenic immune microenvironment. *Bioact Mater.* 2023;31:231-246.
doi: 10.1016/j.bioactmat.2023.08.008

31. Song Q, Zhang Y, Hu H, *et al.* Multifunctional hydrogel with synergistic reactive oxygen species scavenging and macrophage polarization-induced osteo-immunomodulation for enhanced bone regeneration. *ACS Appl Mater Interfaces.* 2025;17(27):38985-39001.
doi: 10.1021/acsami.5c08737

32. Wu M, Liu H, Li D, *et al.* Smart-responsive multifunctional therapeutic system for improved regenerative microenvironment and accelerated bone regeneration via mild photothermal therapy. *Adv Sci (Weinh).* 2024;11(2):e2304641.
doi: 10.1002/advs.202304641

33. Xu L, Zhu J, Rong L, *et al.* Osteoblast-specific down-regulation of NLRP3 inflammasome by aptamer-functionalized liposome nanoparticles improves bone quality in postmenopausal osteoporosis rats. *Theranostics.* 2024;14(10):3945-3962.
doi: 10.7150/thno.95423

34. Hu Y, Zhang H, Wang S, *et al.* Bone/cartilage organoid on-chip: construction strategy and application. *Bioact Mater.* 2023;25:29-41.
doi: 10.1016/j.bioactmat.2023.01.016

35. Kong Y, Yang Y, Hou Y, Wang Y, Li W, Song Y. Advance in the application of organoids in bone diseases. *Front Cell Dev Biol.* 2024;12:1459891.
doi: 10.3389/fcell.2024.1459891

36. Bai L, Zhou D, Li G, Liu J, Chen X, Su J. Engineering bone/cartilage organoids: strategy, progress, and application. *Bone Res.* 2024;12(1):66.
doi: 10.1038/s41413-024-00376-y

37. Rogers TL, Holen I. Tumour macrophages as potential targets of bisphosphonates. *J Transl Med.* 2011;9:177.
doi: 10.1186/1479-5876-9-177

38. Brown JP. Long-term treatment of postmenopausal osteoporosis. *Endocrinol Metab (Seoul)*. 2021;36(3):544-552.
doi: 10.3803/EnM.2021.301

39. Su N, Villicana C, Zhang C, *et al.* Aspirin synergizes with mineral particle-coated macroporous scaffolds for bone regeneration through immunomodulation. *Theranostics.* 2023;13(13):4512-4525.
doi: 10.7150/thno.85946

ACCSCIENCE PUBLISHING

International Journal of Bioprinting

RESEARCH ARTICLE

Generative design of patient-specific bone plates for Schatzker type VI tibial plateau fractures

Weiting Xu[1], Xiaoqiang Zheng[2], Yan Xu[1], Rixiang Quan[1], Yi Huang[1], Weiqiang Li[3], Cian Vyas[4], Paulo Bartolo[4,5], Di Wang[2], and Fengyuan Liu[1]*

[1]School of Electrical, Electronic, and Mechanical Engineering, University of Bristol, Bristol, United Kingdom

[2]School of Mechanical & Automotive Engineering, South China University of Technology, Guangzhou, Guangdong, China

[3]Shenzhen Jinshi 3D Printing Technology Co., Ltd., Shenzhen, Guangdong, China

[4]Singapore Centre for 3D Printing, Nanyang Technological University, Singapore

[5]School of Mechanical and Aerospace Engineering, Nanyang Technological University, Singapore

Abstract

Schatzker type VI fractures are complex tibial plateau injuries characterized by multiple fracture lines and complete separation between the plateau and the shaft. These features reduce the effectiveness of standard commercial fixation plates, which often fail to conform to the irregular anatomy. Patient-specific plates, tailored to individual bone geometry, offer improved anatomical fit and fixation. This study aims to compare two patient-specific designs, based on 3D reconstruction (3DP) and generative design (GDP), with a conventional commercial plate (CP). To enable rapid and cost-effective evaluation, all designs were first prototyped in poly(lactic acid) using fused deposition modeling. In bending tests, both 3DP and GDP were significantly stiffer than CP, with stiffness increases of 23.8% and 10.0%, respectively. In biomechanical compression tests, both patient-specific designs exhibited approximately 15% lower displacement than CP under a 750 N load. Based on these results, the GDP design was selected for metal additive manufacturing using laser powder bed fusion. The metal-printed GDP was tested under a compressive load of 750 N and showed a mean displacement of 2.11 ± 0.01 mm, remaining below the commonly accepted clinical threshold of 3 mm. This work highlights the potential of combining PLA-based prototyping with targeted metal validation to support surgical decision-making and streamline implant development.

***Keywords*:** 3D printing; generative design; patient-specific bone plate; Schatzker type VI fractures

***Corresponding author:**
Fengyuan Liu
(fengyuan.liu@bristol.ac.uk)

Citation: Xu W, Zheng X, Xu Y, *et al.* Generative design of patient-specific bone plate for Schatzker type VI tibial plateau fractures. *Int J Bioprint.* 2026;12(1):559-575. doi: 10.36922/IJB025400410

Received: October 2, 2025
Revised: October 29, 2025
Accepted: November 4, 2025
Published online: November 4, 2025

Copyright: © 2025 Author(s). This is an Open Access article distributed under the terms of the Creative Commons Attribution License, permitting distribution, and reproduction in any medium, provided the original work is properly cited.

Publisher's Note: AccScience Publishing remains neutral with regard to jurisdictional claims in published maps and institutional affiliations.

1. Introduction

Schatzker type VI tibial fractures, also classified as *Arbeitsgemeinschaft für Osteosynthesefragen*/Orthopedic Trauma Association 41-C fractures, are among the most severe and complex types of tibial plateau fractures.[1,2] These fractures account for 23% of complex tibial plateau injuries and occur in 1–2% of all fractures, with an overall incidence of 51.7 per 100,000 individuals each year, based on a 10-year epidemiological

study from the Swedish Fracture Register.[3–6] They involve multiple parts of the tibia, including the lateral and medial tibial plateaus, the metaphysis, and the diaphysis. This damage results in a complete separation between the joint surface and the tibial shaft, causing significant instability,[7] as illustrated in Figure 1A.

The primary cause of these fractures is high-energy trauma, such as motor vehicle accidents or falls from significant heights.[8] In addition to bone damage, these injuries are often associated with soft tissue injuries and ligament tears due to the force of impact. Because the fracture lines extend into the joint, treatment must address both joint stability and load-bearing capacity. Furthermore, the complex anatomical geometry of these fractures poses significant challenges to effective treatment and healing. Without timely and appropriate intervention, patients face a high risk of complications, including infection, malunion, nonunion, and post-traumatic osteoarthritis.[9]

Surgical intervention is crucial for managing Schatzker type VI fractures, with the primary goals of stabilizing the fracture, restoring joint function, and minimizing long-term complications. Treating these complex fractures often involves a variety of tools. External devices, such as external fixators, are frequently used for initial stabilization, while circular wire fixators can provide additional support to the diaphyseal region when necessary. Internal tools, including intramedullary nailing, K-wires for provisional alignment, and bone grafts for filling bone defects, are commonly employed to address specific fracture components.[10,11] Considering the high biomechanical load conditions of the knee joint, open reduction and internal fixation with bone

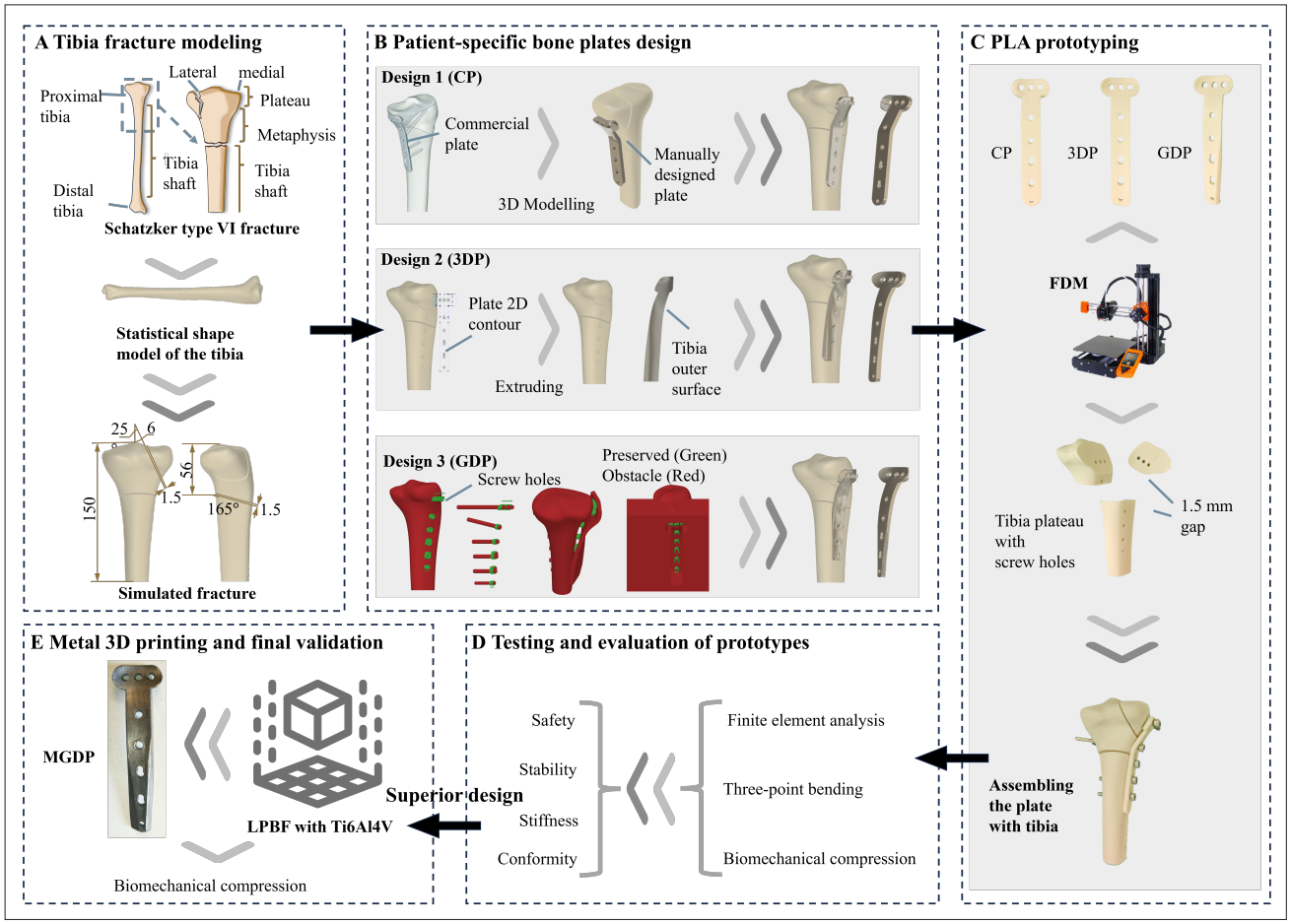


Figure 1. Workflow of the study: (A) Simulation of a Schatzker type VI fracture with a 1.5 mm gap; (B) Design of the baseline plate (CP) and patient-specific bone plates 3DP and GDP; (C) Fabrication of PLA prototypes using FDM; (D) Mechanical and biomechanical testing of the prototypes; (E) Metal additive manufacturing of the GDP using LPBF followed by biomechanical testing. Abbreviations: CP, commercial plate; FDM, fused deposition modeling; GDP, generatively designed patient-specific bone plate; LPBF, laser powder bed fusion; MGDP, metal generatively designed bone plate; PLA, poly(lactic acid); 3DP, 3D reconstruction design plate.

plates and screw systems remains the most common and widely adopted approach.[12]

Bone plates, typically made of biomedical metal materials such as 316L stainless steel or titanium alloys due to their superior mechanical properties, play a critical role in restoring joint alignment and stability while bearing the load required for early mobilization.[13] Despite their critical role, standard bone plates have limitations. They may not precisely conform to the unique anatomical structure of each patient, potentially leading to improper fixation or loosening of the plate or screws, which may require revision surgery.[14,15] Additionally, standard plates carry the risk of stress shielding, in which the plate bears too much load, reducing stress on the bone and increasing the risk of healing complications or deformities.[16,17] These limitations highlight the need for improved designs tailored to individual patients to optimize outcomes in the treatment of Schatzker type VI fractures.

Recently, the development of patient-specific bone plates has become increasingly common, driven by advancements in metal additive manufacturing (AM).[18] These plates are primarily created using 3D reconstruction methods, which enable precise customization for individual fracture sites by integrating advanced scanning technologies and collaborative designs between engineers and surgeons.[19] For instance, Teo *et al.*[20] designed a patient-specific bone plate for lateral tibial plateau fractures that was produced using selective laser melting with 316L stainless steel in 24–29 hours. This turnaround time enabled implantation before the onset of bone healing, thereby reducing the risk of complications associated with prolonged immobility. Similarly, Tilton *et al.*[21] demonstrated that AM-centric fixation designs for patient-specific plates reduced average varus collapse (medial fracture gap displacement) by 47.2% and the risk of screw cut-out by 14.6% compared to conventional plate designs. However, applying metal AM in biomedical implant design presents several challenges. Most patient-specific plates are produced using laser powder bed fusion (LPBF), a technique that involves high equipment and material costs.[22] In addition, extensive post-processing—such as support removal, machining, polishing, and heat treatment—is often required to ensure surface quality, dimensional accuracy, and biocompatibility.[23] These steps are time-consuming and add significant complexity, especially in the early design phase when multiple iterations are typically needed.

Alternatively, generative design (GD) has emerged as a transformative approach for patient-specific bone plate design, attracting growing research attention. This artificial intelligence (AI)-assisted methodology iteratively generates diverse design solutions based on predefined constraints and objectives, enabling precise and optimized outcomes.[24] Baumgartner *et al.*[25] applied GD to develop bridging plates for mandibular bone defects in dogs, achieving superior mechanical performance compared to traditional designs. Kanagalingam *et al.*[26] further demonstrated the potential of GD for high tibial osteotomy plates, designing and fabricating plates using electron beam melting. The success of this study demonstrates that GD, when combined with AM, offers a promising approach for patient-specific implant development. By leveraging AI to generate personalized and biomechanically optimized solutions, this method has the potential to significantly reduce design time and eliminate the iterative communication between surgeons and engineers during the design cycle. Recent work has begun to extend GD from planar parts to anatomically complex implants and fixation devices. Cheng *et al.*[27] proposed a semi-automated GD workflow in Fusion 360 for orthognathic plates, reporting shorter hands-on design time and acceptable stress levels for titanium hardware. Dewey *et al.*[28] combined GD-architected Voronoi meshes with mineralized collagen to produce trim-to-fit craniofacial composites that conform to irregular defects while maintaining predictable stiffness. Alvarado-Moreno *et al.*[29] used GD to reconstruct mandibular continuity after tumor resection, balancing mass and rigidity and verifying mechanical response with finite element analysis for polymer implants secured by titanium or stainless-steel hardware. However, most existing studies focus on implants subjected to limited or simplified loading conditions rather than realistic load-bearing scenarios. This indicates that the full potential of GD has yet to be realized, particularly for bone plates that experience complex, multi-directional forces, such as those in proximal tibia fixation. Further research is required to enhance GD's capability to model and optimize designs under physiological load conditions for clinically relevant and load-bearing applications.

This study focuses on designing patient-specific bone plates for Schatzker type VI fractures using 3D reconstruction and GD and comparing their performance with commercial plates (CPs) through biomechanical experimental tests. To facilitate rapid design validation, the patient-specific plates are initially fabricated using fused deposition modeling (FDM) with poly(lactic acid) (PLA), allowing cost-effective prototyping and experimental verification of mechanical property trends. Based on these evaluations, selected designs are further manufactured in Ti6Al4V using LPBF for definitive biomechanical testing. The findings from this study aim to provide a thorough assessment of patient-specific plate designs and contribute to the optimization of treatment strategies for managing complex tibial fractures.

2. Materials and methods

2.1. Base tibia model and Schatzker type VI tibial fracture simulation

In this study, the open-access statistical shape models (SSMs) of the tibia developed by Keast *et al.*[30] were utilized as the foundation for design (Figure 1A). These models were generated from computed tomography scans of 30 cadavers (20 male, 10 female) sourced from the New Mexico Decedent Image Database. Keast *et al.*[30] employed segmentation and reconstruction of both cortical and trabecular structures of the tibia and fibula. Principal component analysis was applied to capture 95% of the geometric variation present within the dataset, resulting in anatomically accurate and statistically robust tibial representations. Although an SSM is generated from a population dataset, it can still support patient-specific design by statistically representing anatomical variations across individuals.[31,32] By fitting or sampling the model to approximate a given morphology, it provides a realistic surrogate of a patient's tibia when direct imaging data are unavailable.[33] This allows the design workflow, optimization, and validation processes to be developed and tested under anatomically credible conditions consistent with patient-specific design principles. For this study, the mean tibia shape model was exported in Standard Tessellation Language (STL) format and imported into Autodesk Fusion 360 v2.0 (Autodesk Inc., United States of America). This workflow ensured precise control over tibial shape and geometry during the design process. The design focused on a plate for proximal tibia fixation, particularly addressing lateral tibial plateau involvement.

The fracture simulation, crucial for evaluating the designed bone plate, was conducted in Autodesk Fusion 360 v2.0 (Autodesk Inc., United States of America) using the imported tibia model, as shown in Figure 1A. According to the Schatzker classification, type VI fractures are characterized by complete dissociation between the metaphysis and diaphysis of the tibia, often with significant articular involvement and extensive comminution of the lateral tibial plateau. To replicate this fracture pattern, the proximal 150 mm of the tibia was segmented to simulate articular-diaphyseal separation.

In fracture fragment reduction, a 0 mm gap is ideal, as it ensures absolute stability and direct bone healing. However, in complex fractures such as Schatzker type VI, achieving complete fragment contact is often impractical due to comminution and anatomical constraints. Clinically, fracture gaps during surgery typically range from 0 to 3 mm, with gaps exceeding 2 mm being associated with delayed union and increased nonunion risk. Studies indicate that a controlled 1.5 mm gap provides a balance between mechanical stability and biological stimulation, allowing sufficient micromotion for callus formation while avoiding excessive strain.[34–38]

In this study, the fracture gaps were carefully designed to simulate a clinically relevant Schatzker type VI fracture while ensuring accurate analysis of the mechanical behavior of the fixation. A 1.5 mm gap was introduced 56 mm from the proximal end of the tibia, extending through the shaft and separating the plateau from the tibial body at an angle of 15°. Furthermore, a 25° inclined gap, offset 6 mm from the central axis of the lateral tibial plateau, was created to replicate the typical lateral disruption observed in type VI fractures, as illustrated in Figure 1A. These fracture configurations were modeled in Fusion 360 v2.0 (Autodesk Inc., United States of America), ensuring an anatomically accurate representation of the injury.

2.2. Bone plate design

2.2.1. Commercial plate design (baseline)

The design for the comparison group was created to align with the simulated fracture's position and size, ensuring consistency with the anatomical and mechanical requirements of the study. Using Autodesk Fusion 360 v2.0 (Autodesk Inc., United States of America), the implant geometry was replicated from the DePuy Synthes Locking Compression Plate (LCP) Periarticular Plating System, specifically the 4.5 mm thickness LCP Medial Proximal Tibia Plate (DePuy Synthes, United States of America).[39] This plate, designed for the right tibia, features four main holes and measures 106 mm in length. The resulting design, referred to as the comparison CP, was modeled to match the geometry and specifications of the original plate as accurately as possible, ensuring it could serve as a reference for evaluating the patient-specific design. The final design of the CP is shown in Figure 1B, illustrating its structure and alignment with the original implant specifications.

2.2.2. Patient-specific plate design based on 3D reconstruction

In this study, the 3D reconstructed patient-specific plate (3DP) was developed using Autodesk Fusion 360 v2.0 (Autodesk Inc., United States of America), ensuring it accurately conformed to the outer surface contours of the reconstructed tibia model. The 3DP approach followed the standard workflow commonly used in patient-specific bone plate studies, involving surface reconstruction from computed tomography data, contour fitting to the anatomical model, and screw position design.[40,41] Its purpose was to establish a representative and reproducible patient-specific design reference for comparison with the GD method. The design process began with sketching the outer boundary of the plate from a posterior view,

positioned 18 mm below the top of the tibial plateau. The plate measured 106 mm in length, with a width of 32 mm proximally and 16 mm distally in the T-shaped section. This sketch was extruded toward the tibia to capture the natural surface geometry of the bone, forming the external profile of the insertion area. The surface was then thickened to 4.5 mm, completing the geometric design of the plate. The screw hole configuration was replicated from the CP to maintain consistency in evaluations. The final design of the 3DP is shown in Figure 1B, illustrating its alignment with the tibia's natural contours and its suitability for addressing the simulated fracture.

2.2.3. Patient-specific plate design via generative design

The GD-designed patient-specific bone plate (GDP) was also developed using Fusion 360 v2.0 (Autodesk Inc., United States of America). The process began by creating screw holes with a thickness of 4.5 mm and specific configurations on the plate. These holes were extruded outward by 2 mm to form preserved geometry, serving as fixed features during the GD process. To achieve the final plate design, GD iteratively connected these features under predefined constraints.

To ensure a precise fit and effective biomechanics, geometric and mechanical constraints were carefully defined. The proximal tibial surface was designated as obstacle geometry to prevent implant penetration into the cortical surface. A boundary constraint zone was designed to represent the plate's outer contour, ensuring appropriate shape and thickness. Additionally, a curved thickness constraint layer adjacent to the tibia, with a thickness of 4.5 mm, was set as an obstacle to maintain the plate's anatomical accuracy and ensure it did not exceed the design thickness of 4.5 mm. Cylindrical geometries were also added to simulate screws passing through the plate and into the bone, ensuring proper alignment of the screw holes. These geometric settings are shown in Figure 2. A 750 N compressive load, defined as described in **Section 2.3**, represented the typical biomechanical loading experienced by the tibia during normal gait. A wall thickness of 1.5 mm was preserved around the screw holes to maintain structural integrity while enabling lightweight optimization. The maximum overhang angle of 65° and a layer thickness of 0.8 mm reflected the buildability limits of metal powder-bed fusion, preventing the generation of geometries that would require extensive support or risk printing defects. The design objective of minimizing mass further promoted a lightweight yet mechanically robust plate suitable for load-bearing and long-term implantation. All mechanical constraints, including load-bearing capacity, objectives, and manufacturing methods, were specified to meet biomechanical requirements, as summarized in Table 1. This approach generated a set of patient-specific plates tailored to the individual's anatomy and structural requirements. Specifically, three design variants were produced, each incorporating minor differences in geometry that led to variations in predicted mechanical performance. Among the three variants, the design with the highest safety factor was identified as the most reliable option and was therefore selected as the generative GDP for subsequent fabrication and experimental testing.

2.3. Finite element analysis for early design evaluation

To rapidly evaluate the design outcomes at the early stage, finite element analysis (FEA) was applied prior to manufacturing the physical prototypes for experimental testing. The FEA served as a concept-screening tool to qualitatively compare stress distribution and displacement patterns among the plate designs.

The models were developed from the parametric computer-aided design model of the SSM tibia and the three patient-specific bone plates in Fusion 360 v2.0 (Autodesk Inc., United States of America). The bone fragments and implants were assembled to replicate the implantation configuration before FEA modeling. The screws were represented as cylinders with a diameter of 5 mm and merged with the plate to approximate the threaded connection between the screw head and the plate.

For the boundary and loading conditions, the distal section of the tibia was fixed to ensure stability. A total knee joint reaction force of approximately three times bodyweight during single-leg stance was considered, and the load was distributed between the medial plateau (55%) and the lateral plateau (45%).[42,43] A vertical compressive point load of 750 N was applied to the lateral region of the tibial plateau, representing the lateral share of the total reaction force. This condition simulated the single-leg stance of a 55 kg individual, which is clinically relevant for assessing fixation stability.

The bone plates were assigned Ti6Al4V material properties, a titanium alloy widely used in orthopedic implants due to its high strength-to-weight ratio and biocompatibility. The simulations were conducted in the Fusion 360 v2.0 (Autodesk Inc., United States of America) using the Autodesk Nastran solver. A tetrahedral mesh was generated in Fusion 360 using the default adaptive settings, with a model-based average element size of 10%, parabolic element order, and a maximum turn angle on curves of 60°. Under these identical settings, the element counts were approximately 4 million for the CP, 50 million for the 3DP, and 60 million for the GDP. The lower element number in the CP model was due to its relatively simple

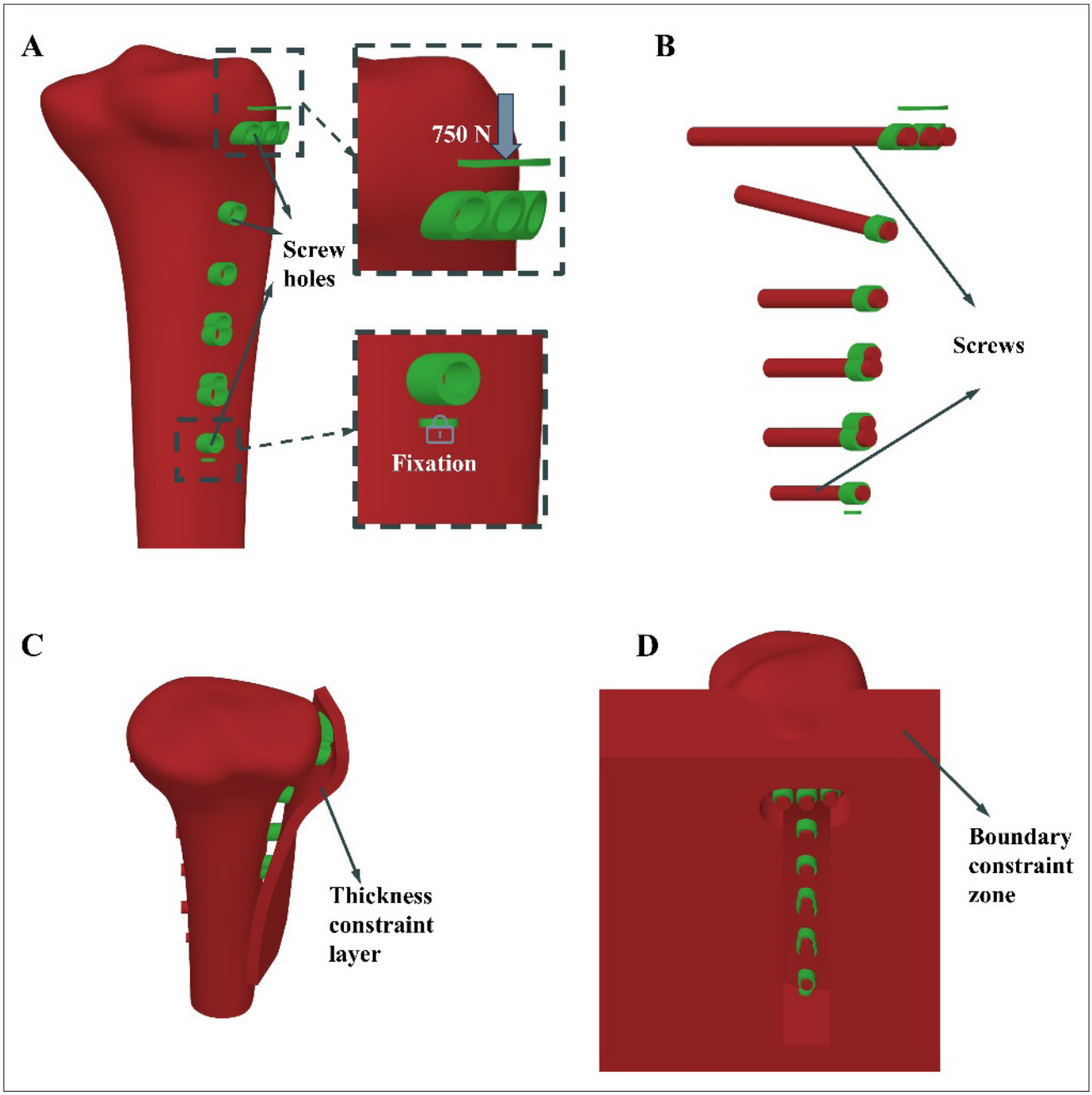


Figure 2. Design constraints and boundary conditions for the patient-specific bone plate. (A) The preserved geometry includes screw holes and fixation regions with an applied load of 750 N. The obstacle geometries are (B) screws, (C) a thickness constraint layer that defines the allowable plate thickness by maintaining a gap above the bone surface, and (D) a boundary constraint zone that limits the plate width and length during generative design.

Table 1. Parameter settings for generative design in patient-specific bone plate design

Parameter	Setting value
Preserved hole thickness	1.5 mm
Material	Ti6Al4V
Load	750 N
Design objective	Minimize mass
Manufacturing method	AM
Maximum overhang angle	65.0°
Minimum layer thickness	0.8 mm

and flat geometry, which required less mesh refinement to capture surface details. The higher element numbers in the 3DP and GDP models resulted from their more complex geometries, which led the software's model-based meshing algorithm to refine elements locally to maintain geometric accuracy and mesh quality.

2.4. Prototypes and tests

In this study, PLA prototypes were fabricated to experimentally validate the relative mechanical performance of the designed plates at the concept stage. PLA was selected for its cost-effectiveness, ease of printing, and suitability for comparative evaluation before metal fabrication. The mechanical assessment focused on two key aspects: plate quality and fixation stability. These are essential for ensuring that the bone plate provides sufficient structural strength to withstand physiological loading while maintaining stable fixation to support effective fracture healing. Three-point bending tests were performed in accordance with ASTM F382-17 to assess bending strength and stiffness.[44] Biomechanical compression tests were conducted to evaluate fixation stability under physiological conditions, as stable load transfer and minimal displacement at the fracture site are vital for promoting proper bone healing and preventing implant failure.[42,45]

2.4.1. Additive manufacturing of the tibia model and bone plates

The STL files of the tibia, including the fracture region from the virtual 3D model, were prototyped using FDM on a Prusa MINI+ 3D printer (Prusa Research a.s., Czech Republic). The skeletal model was printed in PLA + white filament with a layer resolution of 0.20 mm and a density of 100%. The finalized patient-specific bone plate designs were also converted to STL format and prepared for 3D printing using the PrusaSlicer v2.8 (Prusa Research a.s., Czech Republic). These designs were printed on the same Prusa FDM printer in PLA + white filament (Raise3D, United States of America) with a layer resolution of 0.15 mm and a density of 100%.

2.4.2. Three-point bending tests

The 3D printed PLA bone plates were subjected to three-point bending tests using a Shimadzu universal AGS-X testing machine (Shimadzu Corporation, Japan) with a 1 kN sensor. The test setup included two support rollers spaced 104 mm apart to provide stable support for the plates. A third roller applied the load at the midpoint of each plate, perpendicular to its surface, ensuring consistent loading conditions, as illustrated in Figure 3A.

The tests were conducted under displacement control at a constant rate of 1 mm/s to simulate progressive loading conditions. The load and axial displacement were continuously recorded throughout the test. Each test was terminated once the reaction force began to decrease after reaching the maximum load. Data recorded beyond the point of maximum load were excluded from the analysis to focus on the plate's peak performance and structural integrity under loading. The stiffness of each plate was determined as the slope of the linear elastic region of the load–displacement curve.

2.4.3. Biomechanical tests

The 3D-printed PLA bone plate was first fixed onto the corresponding 3D-printed fractured tibia model using stainless steel screws. Specifically, three M5 screws (40 mm in length) were inserted through the distal screw holes of the plate, and four M5 screws (80 mm in length) were inserted proximally to secure fixation. To examine the mechanical stability of the different plate designs under physiologically relevant loading, compression was primarily evaluated at 750 N, representing the typical tibial load during single-leg stance. The assembled plate–tibia construct was then mounted on a Shimadzu universal testing machine equipped with a 1 kN load cell for compression testing.

To ensure consistent alignment and test repeatability, the model was positioned on a custom-designed support base. A stainless steel load applicator, contoured to replicate the distal femur anatomy derived from the SSM, was custom-fabricated using LPBF in stainless steel (Shenzhen WeNext Technology Co., Ltd, China). This applicator was placed on the tibial plateau to simulate physiological loading representative of a standing human. The overall experimental setup is illustrated in Figure 3B.

Compression was applied under displacement control at a constant rate of 1 mm/s to simulate progressive axial loading. The load and displacement were continuously recorded throughout each test. Testing was terminated when the applied load reached the maximum sensor capacity of 1 kN. Displacement values at 500 N, 750 N, and 1000 N were recorded for comparison against the 3 mm threshold under a broader loading range, as excessive fragment displacement greater than 3 mm is

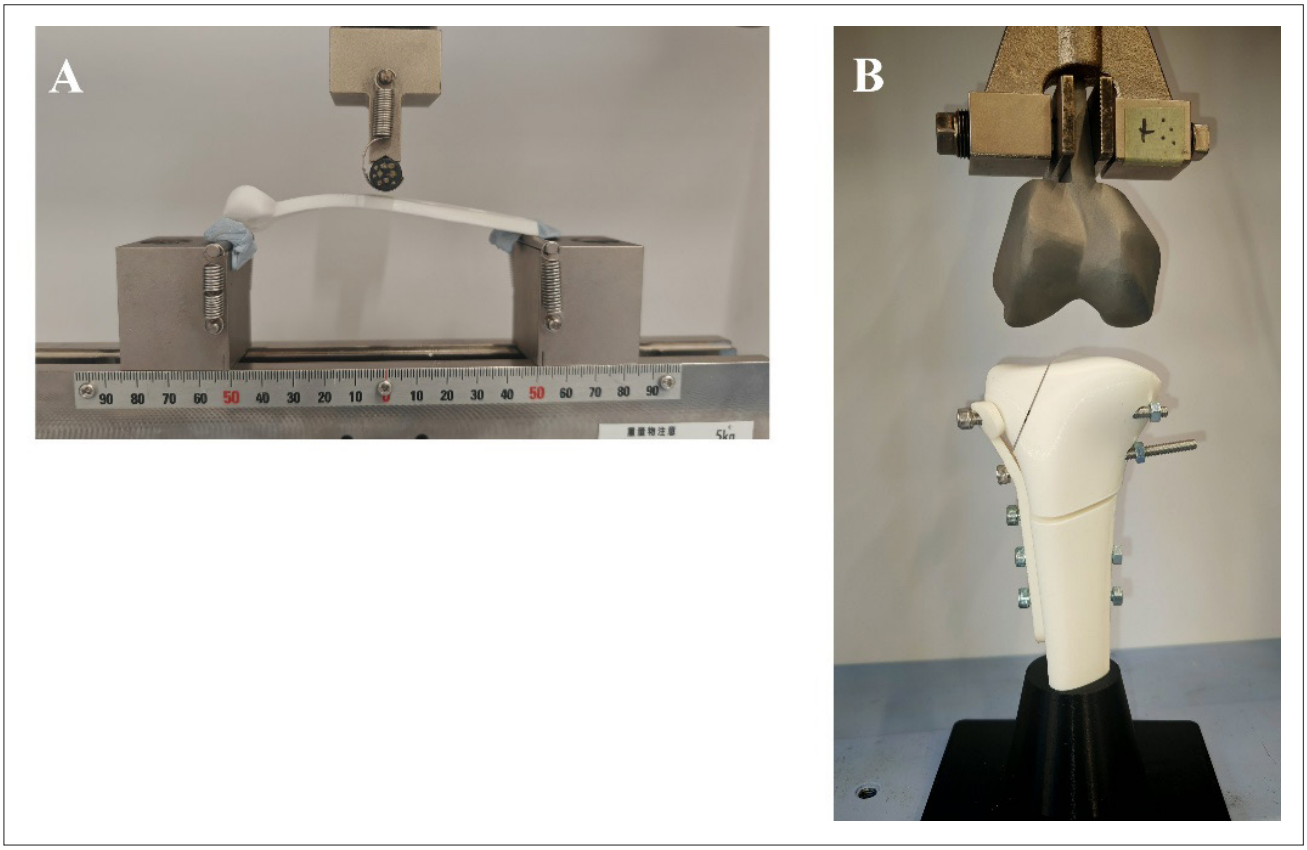


Figure 3. Experimental setup for biomechanical testing of bone plates: (A) three-point bending test and (B) biomechanical compression test.

widely recognized as a critical indicator of poor fracture healing and severe complications.[42,45–47]

2.5. Metal 3D printing for the generatively designed patient-specific bone plate

To further evaluate its mechanical performance, the final GDP was fabricated using the LPBF process on a DiMetal-280 metal AM machine (Shenzhen Jinshi 3D Printing Technology Co., Ltd., China). Ti6Al4V powder (Zhongyuan Advanced Material Co., Ltd., China) with a particle size range of 15–53 μm (D_{10} = 20 μm, D_{50} = 30 μm, D_{90} = 50 μm) was used for manufacturing the patient-specific bone plate. The printing parameters included a slicing layer thickness of 0.03 mm, laser power of 190 W, scanning spacing of 0.09 mm, and scanning speed of 1000 mm/s, with a 67° interlayer spiral filling strategy and 8 mm-wide stripe partitioning. The plate was positioned at a 45° inclination relative to the *X*-axis to enhance forming efficiency and surface quality on the downward-facing surface, with non-solid intelligent supports applied to overhangs below 30° and additional block supports placed at the lowest points. Post-processing was conducted in sequence, beginning with heat treatment (annealing) to relieve residual stress and stabilize the microstructure, followed by wire-cutting separation to remove the plate from the build substrate. The printed supports were then mechanically removed, after which the plate was precision-ground and polished to achieve the required dimensional tolerances and smoothness. Finally, surface shot peening was performed to improve surface integrity and enhance fatigue resistance. These steps ensured that the plate met the necessary dimensional accuracy, surface quality, and mechanical reliability for subsequent testing. Figure 4A presents the finalized metal generatively designed bone plate (MGDP).

Subsequently, the MGDP was subjected to biomechanical compression testing using the same setup as described for the PLA prototypes. The plate was fixed to the 3D printed tibia model with identical screw configurations, and a 750 N axial load was applied to record the corresponding displacement. This allowed a direct comparison between the PLA prototype and the metal version of the GDP under equivalent testing conditions.



Figure 4. Fabricated generatively designed plates: (A) the metal generatively designed bone plate manufactured from Ti6Al4V via laser powder bed fusion after post-processing; (B) the corresponding poly(lactic acid) prototype fabricated by fused deposition modeling for early-stage biomechanical validation.

2.6. Statistical analysis

A one-way analysis of variance (ANOVA) was performed to determine whether there were significant differences in stiffness and maximum load from the three-point bending tests, as well as displacement from the biomechanical compression tests, among the three plate designs. Post hoc analyses were performed using the Tukey honestly significant difference (HSD) test when variances were equal and the Games–Howell test when variances were unequal, based on the results of Levene's test. A significance level of 0.05 was used for all statistical tests. Statistical analysis was conducted using SPSS Statistics v27.0 (IBM Corp., United States of America).

3.Results

The final designs of the CP, 3DP, and GDP plates are presented in Figure 5, providing a visual comparison of the three design approaches prior to mechanical and biomechanical evaluation.

3.1. Finite element analysis

The FEA results, shown in Figure 6, illustrate the stress and displacement distributions of the plate–bone system for the three plate designs under a 750 N load. All designs remained within the material's ultimate strength and the 3 mm displacement threshold for bone fragments. In all cases, the maximum von Mises stress was localized in the central region of the plate. Implantation of the plates reduced stress concentrations in the tibia, helping to avoid excessive loading in the bone. All three designs met the basic structural and fixation requirements for a bone plate under the simulated loading condition.

3.2. Three-point bending test results of poly(lactic acid) prototypes

The three-point bending test results for the three plate designs are shown in Figure 7, which presents the mean load–displacement curves for the 3DP, CP, and GDP plates ($n = 5$) with error bars representing one standard deviation. The numerical values for stiffness and maximum load are summarized in Table 2. Both patient-specific designs (3DP and GDP) outperformed the CP plate. The 3DP plate demonstrated approximately 24% higher stiffness and 15% higher maximum load compared with CP, while the GDP plate achieved about 10% higher stiffness and 13% higher maximum load. Statistical analysis confirmed significant differences among groups ($p < 0.05$). Post hoc tests further indicated that both 3DP and GDP were superior to CP, while no significant difference was observed between GDP

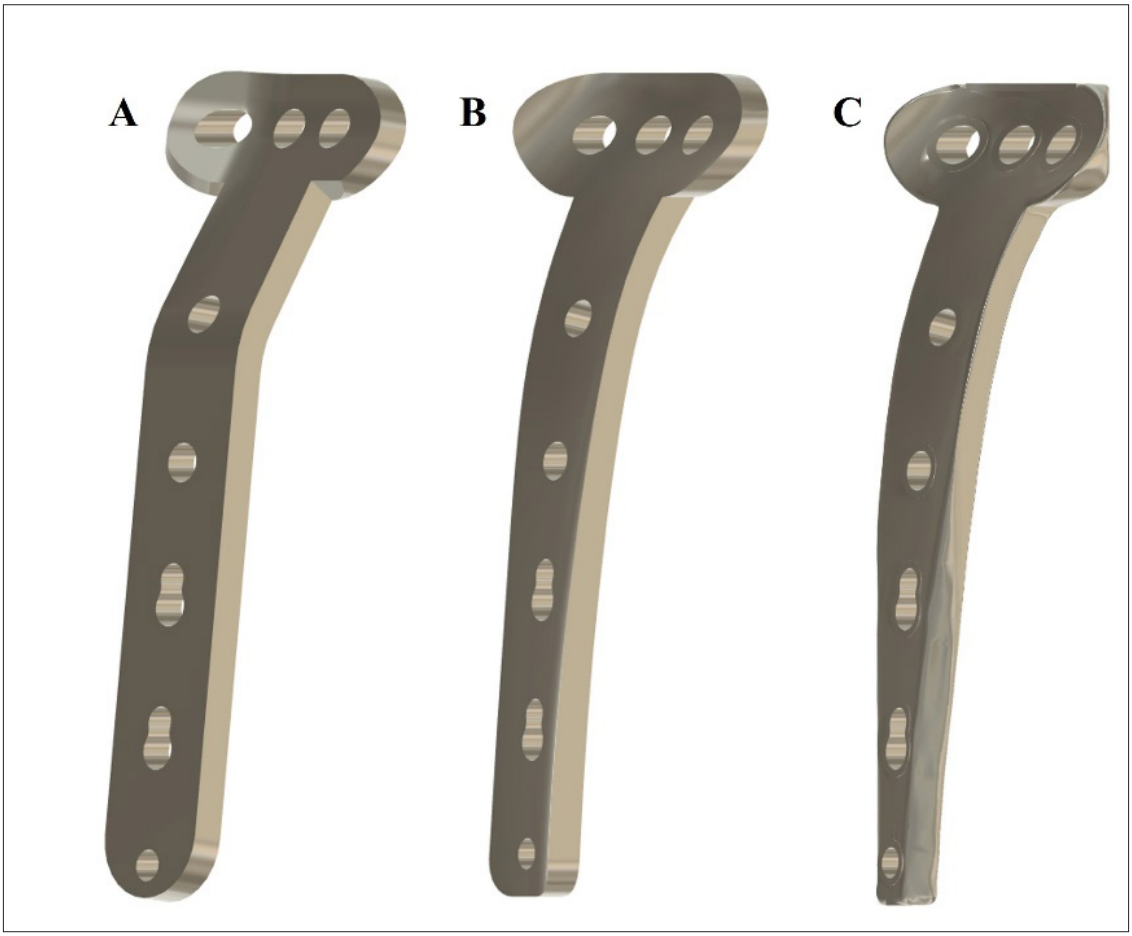


Figure 5. Final designs of the three plate types: (A) baseline plate (commercial plate), (B) patient-specific plate 3D reconstruction design plate, and (C) generatively designed patient-specific bone plate.

and 3DP ($p > 0.05$), supporting the non-inferiority of GDP relative to the established 3DP approach.

3.3. Biomechanical compression results of poly(lactic acid) and metal plates

The biomechanical compression test results are summarized in Table 3, showing the vertical displacement of the three PLA plate designs (CP, 3DP, GDP) and the metallic MGDP plate under loads of 500 N, 750 N, and 1000 N. At each load level, one-way ANOVA followed by

Tukey HSD post hoc testing revealed significant differences among the PLA designs ($p < 0.05$). Across all conditions, both GDP and 3DP provided significantly more stable fixation than CP ($p < 0.05$), with no significant difference between GDP and 3DP ($p > 0.05$). Specifically, mean displacements for the CP, 3DP, and GDP were 2.36 ± 0.16, 2.00 ± 0.08, and 1.96 ± 0.13 mm at 500 N; 2.87 ± 0.11, 2.45 ± 0.06, and 2.43 ± 0.20 mm at 750 N; and 3.09 ± 0.11, 2.65 ± 0.07, and 2.65 ± 0.22 mm at 1000 N, respectively. The MGDP demonstrated the smallest displacement across all loads, with values of 1.53 ± 0.09, 2.11 ± 0.01, and 2.39 ± 0.04 mm, remaining well below the commonly accepted clinical threshold of 3 mm.

4. Discussion

In the early stage of this study, the FEA indicated that all designed plates met the basic requirements for fixation stability and structural safety, supporting their progression to the prototype fabrication and manufacturing stages. This analysis functioned as a preliminary screening step within the overall workflow, allowing rapid, qualitative assessment of stress distribution and displacement patterns before committing resources to physical testing. Such a preliminary evaluation is valuable for identifying potential mechanical concerns and confirming that each design concept is fundamentally viable. However, the FEA modeling assumed isotropic Ti6Al4V material properties and did not incorporate the anisotropy or process-specific

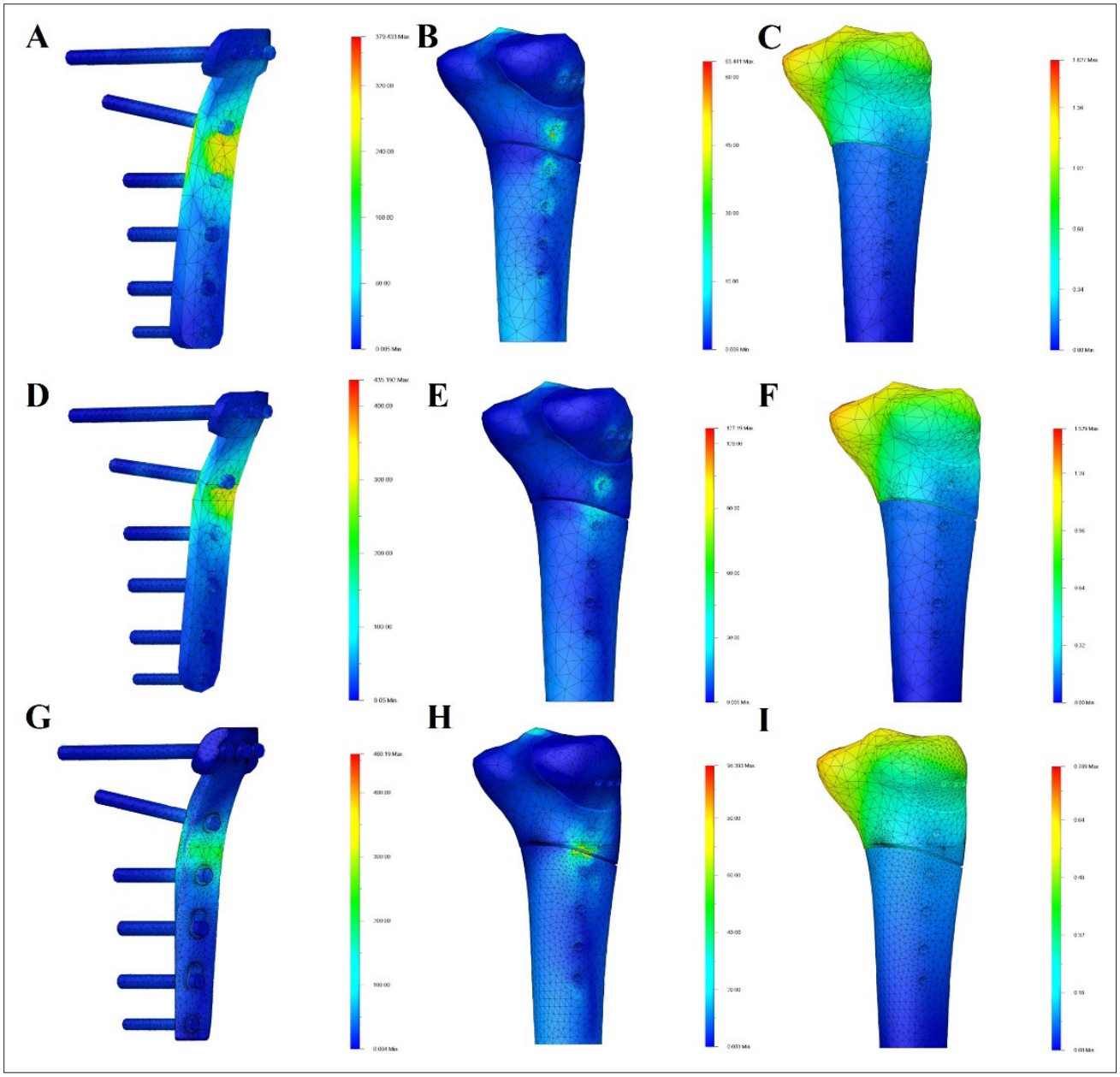


Figure 6. Biomechanical finite element analysis results of the three bone plate designs under a 750 N load. Stress distribution on (A) the CP only, (B) the tibia with the CP, and (C) displacement distribution of the tibial fragment with the CP. Stress distribution on (D) the 3DP only, (E) the tibia with the 3DP, and (F) displacement distribution of the tibial fragment with the 3DP. Stress distribution on (G) the GDP only, (H) the tibia with the GDP, and (I) displacement distribution of the tibial fragment with the GDP. Abbreviations: CP, commercial plate; GDP, generatively designed patient-specific bone plate; 3DP, 3D reconstruction design plate.

behavior associated with FDM or LPBF manufacturing, meaning the results are not directly representative of real-world performance.[48,49] Consequently, experimental testing was essential to obtain accurate and clinically relevant data, enabling a more reliable comparison of designs and validation of their suitability for practical application.

The three-point bending test results demonstrated that both patient-specific plate designs outperformed the conventional CP in terms of stiffness and maximum load capacity, as shown in Figure 7. Table 2 indicates that both patient-specific designs (3DP and GDP) were significantly stiffer and withstood higher maximum loads than the CP plate ($p < 0.05$), while no significant difference was

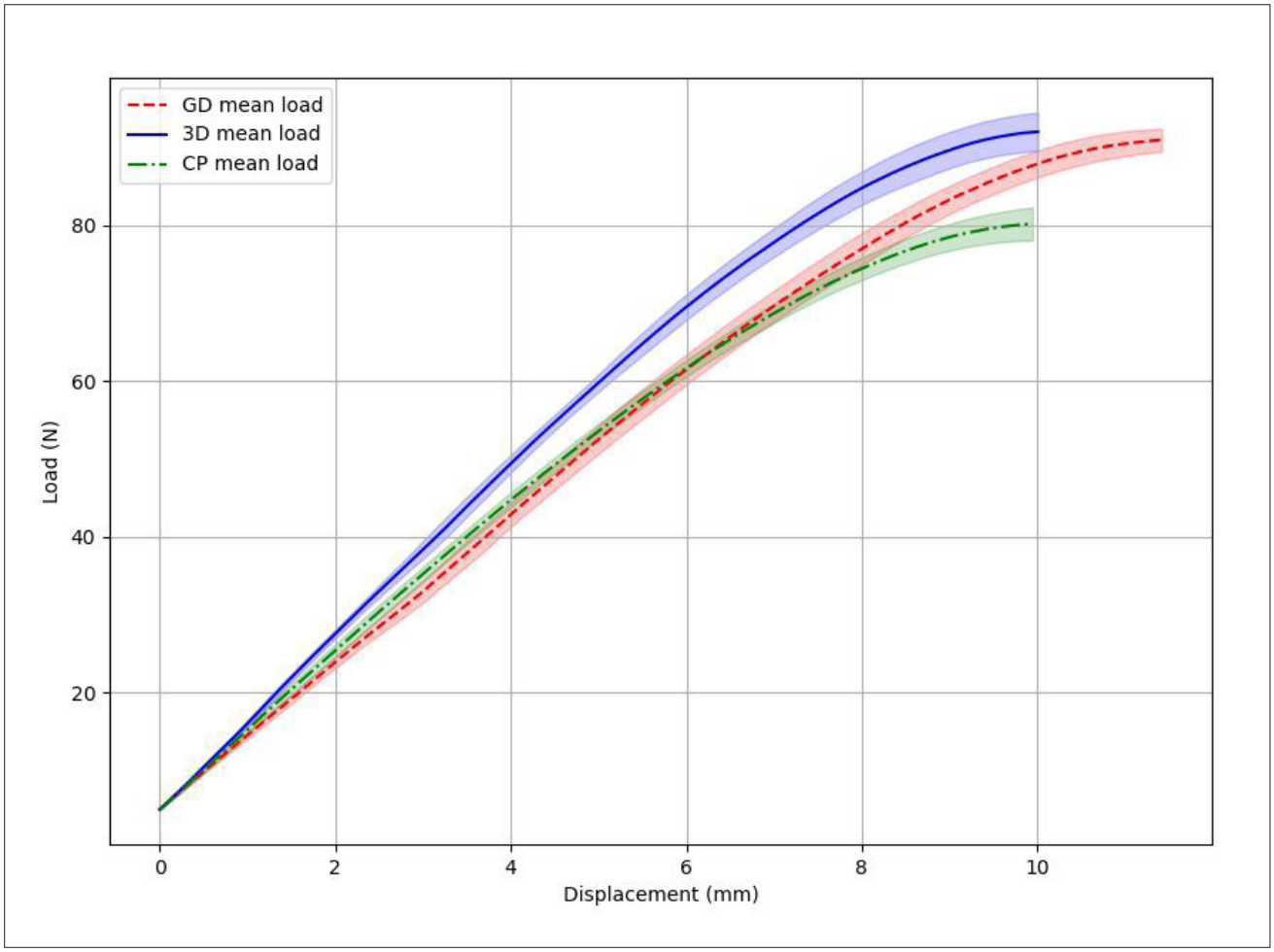


Figure 7. Load–displacement curves from three-point bending tests for the three bone plate designs (CP, 3DP, and GDP). The solid lines represent mean load values, while the shaded regions indicate one standard deviation. Abbreviations: CP, commercial plate; GDP, generatively designed patient-specific bone plate; 3DP, 3D reconstruction design plate.

Table 2. Stiffness and maximum load of CP, 3DP, and GDP designs from bending tests

Groups	Stiffness (N/mm)	Maximum load (N; $n = 5$)
CP	8.18 ± 0.25	80.45 ± 2.51
3DP	10.13 ± 0.90	92.16 ± 2.49
GDP	9.00 ± 0.45	91.21 ± 1.19

Abbreviations: CP, commercial plate; GDP, generatively designed patient-specific bone plate; 3DP, 3D reconstruction design plate.

Table 3. Vertical displacement of PLA and Ti6Al4V plates under compression loads of 500 N, 750 N, and 1000 N, tested using the same experimental setup ($n = 3$)

Design	Material/process	500 N (mm)	750 N (mm)	1000 N (mm)
CP	PLA (FDM)	2.36 ± 0.16	2.87 ± 0.11	3.09 ± 0.11
3DP	PLA (FDM)	2.00 ± 0.08	2.45 ± 0.06	2.65 ± 0.07
GDP	PLA (FDM)	1.96 ± 0.13	2.43 ± 0.20	2.65 ± 0.22
MGDP	Ti6Al4V (LPBF)	1.53 ± 0.09	2.11 ± 0.01	2.39 ± 0.04

Abbreviations: CP, commercial plate; FDM, fused deposition modeling; GDP, generatively designed patient-specific bone plate; LPBF, laser powder bed fusion; MGDP, metal generatively designed bone plate; PLA, poly(lactic acid); 3DP, 3D reconstruction design plate.

observed between 3DP and GDP. These differences may be attributed to the design characteristics of the plates. The CP features sharp transitions between its proximal and distal segments, which can create stress concentrations during bending and reduce structural stiffness. In contrast, the 3DP and GDP were designed to match the anatomical curvature of the tibia, resulting in smoother and more natural transitions that help distribute stress more evenly. This likely contributes to their superior bending performance. Between the two patient-specific designs, the 3DP performed slightly better, which may be due to its near-rectangular cross-section that offers greater resistance to bending. The GDP, although optimized for material efficiency, features a tapered, trapezoidal cross-section in the distal region. This geometry may have slightly reduced its stiffness compared with the 3DP, despite still achieving a significant improvement over the CP. The biomechanical compression test results showed that both patient-specific plate designs (GDP and 3DP) provided significantly better fixation stability compared with the conventional CP. As presented in **Table 3**, the mean displacement values under a 750 N compressive load were 2.87 mm for CP, 2.45 mm for 3DP, and 2.43 mm for GDP. Statistical analysis confirmed significant differences among the three groups ($p < 0.05$), with post hoc tests indicating that both GDP and 3DP achieved significantly lower displacement than the CP. These results suggest that anatomically conforming, patient-specific plates provide more stable fixation upon implantation by improving load transfer and minimizing micromotion at the fracture site. The enhanced stability can be attributed to the improved contact between the plate and bone surface, reducing stress concentration and promoting more uniform force distribution.[22,40,50] At 500 N and 1000 N, a similar trend was observed, with both patient-specific designs showing smaller displacements than the CP and no significant difference between GDP and 3DP. Notably, at 1000 N, the CP displacement exceeded 3 mm, indicating fixation instability, whereas both patient-specific designs remained within the clinically acceptable range, further supporting their superior mechanical reliability under higher loading conditions.

The experimental results from the bending and compression tests showed similar performance trends, with the CP consistently identified as the weakest performer. Both GDP and 3DP demonstrated improved mechanical stability compared with the CP, with GDP consistently exhibiting the lowest displacement in compression tests and 3DP achieving the highest stiffness in the three-point bending tests. Although PLA does not replicate the mechanical properties of metallic implants, it provides a rapid, low-cost, and accessible solution for comparative evaluation during the design phase.[17,25] PLA-based prototyping enables efficient screening of design alternatives, particularly in research and development settings where metal AM is costly and time-consuming. This approach also allows for safe, repeatable testing without requiring a clinical-grade environment, making it well-suited for iteration and optimization prior to final metal fabrication. Overall, the use of PLA supports design verification while reducing lead time and resource consumption.

GD is a computational approach in which designers define high-level constraints and performance goals, allowing algorithms to automatically generate and refine design solutions through iterative evaluation.[51–53] Unlike traditional modeling methods, which require manual adjustment of predefined geometry, GD enables broad exploration of design possibilities and can optimize multiple objectives, including mechanical strength, weight reduction, and manufacturability.[54–56] In this study, 3DP was used as a conventional method for designing patient-specific bone plates and achieved the highest stiffness and bending strength among the tested designs. The GDP, although a newer method, showed comparable fixation stability and achieved the lowest displacement in the biomechanical compression tests. These results demonstrate that GD can produce clinically acceptable outcomes while reducing material use and implant weight. Based on its high performance and design efficiency, the GDP was selected for further validation using metal AM. The MGDP was tested under a 750 N load and showed a mean displacement of 2.11 ± 0.01 mm. This value is well below the commonly accepted clinical threshold of 3 mm, confirming that GD is suitable not only for early-stage design but also for producing patient-specific implants that meet clinical standards.[22,40,50]

However, this study has several limitations. The biomechanical evaluation was simplified and did not include soft tissue structures such as ligaments and muscles, which are important for accurately simulating joint stability.[57–63] Future research could address this limitation by integrating soft-tissue constraints and healing-related biological processes into computational models. For instance, Tits and Ruffoni[58] demonstrated how tendon-to-bone interfaces can be represented using graded material transitions to capture load transfer through soft tissues, while Roland *et al.*[59] incorporated progressive callus formation and multiple healing phases in finite element simulations to mimic the mechanical environment throughout recovery. Similarly, Xu *et al.*[60] linked mechanical regulation models with fracture-healing theory to optimize plate stiffness, offering a framework to couple implant mechanics with tissue differentiation. Building

on these approaches, future modeling of patient-specific plates could incorporate ligament and muscle forces, as well as temporal changes in callus stiffness, using imaging-based anatomical data and validated mechanobiological parameters. Such models would enable a more realistic evaluation of fixation stability and healing outcomes under physiological loading conditions. In addition, the applied load was static and limited to simulating a standing condition, without accounting for dynamic or multi-axial loading scenarios encountered during activities such as walking, stair climbing, or twisting motions.[61,62] Although metal 3D printing was used to validate the GD under clinically relevant material conditions, the other plate designs were tested only in PLA, which may limit the direct comparison across designs due to differences in material properties and mechanical behavior. Furthermore, the study did not account for manufacturing constraints such as overhangs, thermal distortion, or anisotropy, which may affect printability and structural integrity.[63] Future work should include metal testing for all designs and incorporate manufacturing constraints into the design and manufacturing process.

5. Conclusion

In conclusion, this study compared the mechanical and biomechanical performance of patient-specific bone plates with a conventional commercial design. The results showed that patient-specific plates provide better anatomical fit and greater stiffness. They also offer improved stability for fracture fixation. These advantages suggest strong potential to enhance surgical outcomes and support faster, more reliable healing. Among the customized designs, the GD approach showed non-inferior fixation stability compared with the commonly used patient-specific bone plate design method, highlighting its potential to achieve biomechanically stable and clinically reliable outcomes. Although the GDP showed slightly lower stiffness, it achieved a more efficient balance between mechanical strength and overall weight. The GD process also offers a promising way to streamline the design workflow, potentially reducing dependence on engineers and shortening the time between diagnosis and surgery. In addition, FDM-printed PLA prototypes were used to evaluate the plate designs in the early development stage. While they do not fully replicate the properties of metal implants, the PLA models showed consistent trends with the FEA results, supporting their use as a practical, low-cost method for rapid design screening. This study focused on a Schatzker type VI tibial plateau fracture, one of the most complex and unstable fracture patterns. Demonstrating the effectiveness of GD-based patient-specific bone plates in such a demanding case indicates that the approach is not confined to a single fracture type. Instead, it has the potential to be adapted for a broader range of fractures and anatomical regions. With further validation, the GD workflow could provide a flexible and scalable framework for customized implant design, thereby broadening the clinical application of patient-specific solutions in orthopedic surgery.

Acknowledgments

None

Funding

This work was supported by the China Scholarship Council (Project No. 202208060391) and by the United Kingdom Research and Innovation Oversea Travel Grant (UKRI2858).

Conflict of interest

Paulo Bartolo and Fengyuan Liu are members of the Editorial Board of this journal but were not involved, directly or indirectly, in the editorial or peer-review process for this article. The other authors declare that they have no competing interests.

Author contributions

Conceptualization: Weiting Xu, Fengyuan Liu
Formal analysis: Weiting Xu
Investigation: Weiting Xu
Methodology: Weiting Xu, Fengyuan Liu
Resources: Xiaoqiang Zheng, Weiqiang Li, Di Wang
Supervision: Fengyuan Liu
Writing–original draft: Weiting Xu
Writing–review & editing: All authors

Ethics approval and consent to participate

Not applicable.

Consent for publication

Not applicable.

Availability of data

The data analyzed in this study are available from the corresponding author upon reasonable request.

References

1. Schatzker J, McBroom R, Bruce D. The tibial plateau fracture. The Toronto experience 1968–1975. *Clin Orthop Relat Res.* 1979;(138):94-104.

2. Meinberg EG, Agel J, Roberts CS, Karam MD, Kellam JF. Fracture and dislocation classification compendium—2018. *J Orthop Trauma*. 2018;32:S1. doi: 10.1097/BOT.0000000000001063

3. Wennergren D, Bergdahl C, Ekelund J, Juto H, Sundfeldt M, Möller M. Epidemiology and incidence of tibia fractures in the Swedish Fracture Register. *Injury*. 2018;49(11):2068-2074. doi: 10.1016/j.injury.2018.09.008

4. Tarazona D, Karadsheh M. Tibial Plateau Fractures - Trauma - Orthobullets. May 2024. https://www.orthobullets.com/trauma/1044/tibial-plateau-fractures?hideLeftMenu=true. Accessed October 22, 2024.

5. Reátiga Aguilar J, Rios X, González Edery E, De La Rosa A, Arzuza Ortega L. Epidemiological characterization of tibial plateau fractures. *J Orthop Surg Res*. 2022;17(1):106. doi: 10.1186/s13018-022-02988-8

6. Bormann M, Neidlein C, Gassner C, *et al*. Changing patterns in the epidemiology of tibial plateau fractures: a 10-year review at a level-I trauma center. *Eur J Trauma Emerg Surg*. 2023;49(1):401-409. doi: 10.1007/s00068-022-02076-w

7. Lowe J. Tibia (Shinbone) Shaft Fractures - OrthoInfo - AAOS. 2018. https://www.orthoinfo.org/en/diseases--conditions/tibia-shinbone-shaft-fractures/. Accessed November 5, 2023.

8. Kommuru D, Singh S, Shetty S, Kale S, Srivastava A. Treatment of proximal tibia fractures with locking compression plate: a prospective study. *Int J Res Orthop*. 2022;9(1):47-52. doi: 10.18203/issn.2455-4510.IntJResOrthop20223438

9. Egol KA, Tejwani NC, Capla EL, Wolinsky PL, Koval KJ. Staged management of high-energy proximal tibia fractures (OTA Types 41): the results of a prospective, standardized protocol. *J Orthop Trauma*. 2005;19(7):448. doi: 10.1097/01.bot.0000171881.11205.80

10. Wheeless CR. Type IV (Medial) Tibial Plateau Fractures. Wheeless' Textbook of Orthopaedics. July 22, 2020. https://www.wheelessonline.com/bones/type-iv-medial-tibial-plateau-fractures/. Accessed June 20, 2024

11. Hansen M, Pesántez R. Treatment of Complete Articular Fracture, Simple Articular, Simple Metaphyseal. 2024. https://surgeryreference.aofoundation.org/orthopedic-trauma/adult-trauma/proximal-tibia/complete-articular-fracture-simple-articular-simple-metaphyseal. Accessed November 21, 2024.

12. Hansen M, Pesántez R. ORIF - Plates Without Angular Stability for Complete Articular Fracture, Simple Articular, Simple Metaphyseal. 2024. https://surgeryreference.aofoundation.org/orthopedic-trauma/adult-trauma/proximal-tibia/complete-articular-fracture-simple-articular-simple-metaphyseal/orif-plates-without-angular-stability. Accessed June 20, 2024.

13. Giannoudis PV, Einhorn TA, Marsh D. Fracture healing: the diamond concept. *Injury*. 2007;38:S3-S6. doi: 10.1016/S0020-1383(08)70003-2

14. Brouwer de Koning SG, de Winter N, Moosabeiki V, *et al*. Design considerations for patient-specific bone fixation plates: a literature review. *Med Biol Eng Comput*. 2023;61(12):3233-3252. doi: 10.1007/s11517-023-02900-4

15. Dobbe JGG, Peymani A, Roos HAL, Beerens M, Streekstra GJ, Strackee SD. Patient-specific plate for navigation and fixation of the distal radius: a case series. *Int J CARS*. 2021;16(3):515-524. doi: 10.1007/s11548-021-02320-5

16. Huiskes R, Weinans H, van Rietbergen B. The relationship between stress shielding and bone resorption around total hip stems and the effects of flexible materials. *Clin Orthop Relat Res*. 1992;(274):124-134.

17. Al-Tamimi AA. Topology optimization of patient-specific custom-fit distal tibia plate: a spiral distal tibia bone fracture. *Appl Sci*. 2022;12(20):10569. doi: 10.3390/app122010569

18. Xu W, Nassehi A, Liu F. Metal additive manufacturing of orthopedic bone plates: an overview. *MSAM*. 2023;2(4):2113. doi: 10.36922/msam.2113

19. Javaid M, Haleem A. Current status and challenges of additive manufacturing in orthopaedics: an overview. *J Clin Orthop Trauma*. 2019;10(2):380-386. doi: 10.1016/j.jcot.2018.05.008

20. Teo AQA, Ng DQK, Lee P, O'Neill GK. Point-of-care 3D printing: a feasibility study of using 3D printing for orthopaedic trauma. *Injury*. 2021;52(11):3286-3292. doi: 10.1016/j.injury.2021.02.041

21. Tilton M, Lewis GS, Bok Wee H, Armstrong A, Hast MW, Manogharan G. Additive manufacturing of fracture fixation implants: design, material characterization, biomechanical modeling and experimentation. *Addit Manuf*. 2020;33:101137. doi: 10.1016/j.addma.2020.101137

22. Jo WL, Chung YG, Shin SH, Lim J hak, Kim MS, Yoon DK. Structural analysis of customized 3D printed plate for pelvic bone by comparison with conventional plate based on bending process. *Sci Rep*. 2023;13(1):10542. doi: 10.1038/s41598-023-37433-1

23. Wang C, Chen Y, Wang L, *et al*. Three-dimensional printing of patient-specific plates for the treatment of acetabular fractures involving quadrilateral plate disruption. *BMC Musculoskelet Disord*. 2020;21(1):451. doi: 10.1186/s12891-020-03370-7

24. Briard T, Segonds F, Zamariola N. G-DfAM: a methodological proposal of generative design for additive manufacturing in the automotive industry. *Int J Interact Des Manuf*. 2020;14(3):875-886.

doi: 10.1007/s12008-020-00669-6

25. Baumgartner D, Schramel JP, Kau S, *et al*. 3D printed plates based on generative design biomechanically outperform manual digital fitting and conventional systems printed in photopolymers in bridging mandibular bone defects of critical size in dogs. *Front Vet Sci*. 2023;10:1165689. https://www.frontiersin.org/articles/10.3389/fvets.2023.1165689. Accessed November 30, 2023

26. Kanagalingam S, Dalton C, Champneys P, *et al*. Detailed design for additive manufacturing and post processing of generatively designed high tibial osteotomy fixation plates. *Prog Addit Manuf*. 2023;8(3):409-426. doi: 10.1007/s40964-022-00342-2

27. Cheng M, Nayak A, Leung YY. A semi-automated design workflow for patient-specific implants in orthognathic surgery using generative design. *Int J Oral Maxillofac Surg*. 2025;54(12):1195-1200. doi: 10.1016/j.ijom.2025.03.011

28. Dewey MJ, Chang RSH, Nosatov AV, *et al*. Generative design approach to combine architected Voronoi foams with porous collagen scaffolds to create a tunable composite biomaterial. *Acta Biomater*. 2023;172:249-259. doi: 10.1016/j.actbio.2023.10.005

29. Alvarado-Moreno C, Beltrán-Fernández JA, González Rebattú M, Hermida Ochoa JC. Generative design for a case of tumoral resection, reconstruction of the mandibular continuity. In: Öchsner A, Altenbach H, eds. *Engineering Design Applications VII*. Switzerland: Springer Nature; 2025:235-241. doi: 10.1007/978-3-031-84346-4_17

30. Keast M, Bonacci J, Fox A. Geometric variation of the human tibia-fibula: a public dataset of tibia-fibula surface meshes and statistical shape model. *PeerJ*. 2023;11:e14708. doi: 10.7717/peerj.14708

31. Kote V, Pant A, Templin T, Frazer L, Eliason T, Nicolella DP. Personalized tibial strain prediction: feasibility of a novel approach using markerless motion capture and statistical shape models. *J Biomech Eng*. 2025;147(12):121005. doi: 10.1115/1.4069774

32. Cai X, Wu Y, Huang J, Wang L, Xu Y, Lu S. Application of statistical shape models in orthopedics: a narrative review. *Intell Med*. 2024;4(4):249-255. doi: 10.1016/j.imed.2024.05.001

33. van Veldhuizen WA, van der Wel H, Kuipers HY, *et al*. Development of a statistical shape model and assessment of anatomical shape variations in the hemipelvis. *J Clin Med*. 2023;12(11):3767. doi: 10.3390/jcm12113767

34. Thiart M, Ikram A, Lamberts RP. How well can step-off and gap distances be reduced when treating intra-articular distal radius fractures with fragment specific fixation when using fluoroscopy. *Orthop Traumatol Surg Res*. 2016;102(8):1001-1004. doi: 10.1016/j.otsr.2016.09.005

35. Albayrak K, Misir A, Alpay Y, Buyuk AF, Akpinar E, Gursu SS. Effect of fracture level on the residual fracture gap during tibial intramedullary nailing for tibial shaft fractures. *SICOT J*. 2023;9:26. doi: 10.1051/sicotj/2023023

36. Meeson R, Moazen M, Sanghani-Kerai A, Osagie-Clouard L, Coathup M, Blunn G. The influence of gap size on the development of fracture union with a micro external fixator. *J Mech Behav Biomed Mater*. 2019;99:161-168. doi: 10.1016/j.jmbbm.2019.07.015

37. Kim TH, Heo YM, Kim KK, *et al*. Fracture gap and working length are important actionable factors affecting bone union after minimally invasive plate osteosynthesis for the treatment of simple diaphyseal or distal metaphyseal tibia fractures. *Orthop Traumatol Surg Res*. 2024;110(2):103770. doi: 10.1016/j.otsr.2023.103770

38. Liao B, Sun J, Xu C, *et al*. A mechanical study of personalised Ti6Al4V tibial fracture fixation plates with grooved surface by finite element analysis. *Biosurf Biotribol*. 2021;7(3):142-153. doi: 10.1049/bsb2.12019

39. DePuy Synthes. LCP™ Proximal Tibia Plate (3.5 and 4.5 mm) | DePuy Synthes. J&J MedTech. 2025. https://www.jnjmedtech.com/en-US/product/lcp-proximal-tibia-plate. Accessed March 12, 2025.

40. Assink N, Oldhoff MGE, Ten Duis K, *et al*. Development of patient-specific osteosynthesis including 3D-printed drilling guides for medial tibial plateau fracture surgery. *Eur J Trauma Emerg Surg*. 2024;50(1):11-19. doi: 10.1007/s00068-023-02313-w

41. Steffen C, Sellenschloh K, Willsch M, *et al*. Patient-specific miniplates versus patient-specific reconstruction plate: a biomechanical comparison with 3D-printed plates in mandibular reconstruction. *J Mech Behav Biomed Mater*. 2023;140:105742. doi: 10.1016/j.jmbbm.2023.105742

42. Ren W, Zhang W, Jiang S, *et al*. The study of biomechanics and clinical anatomy on a novel plate designed for posterolateral tibial plateau fractures via anterolateral approach. *Front Bioeng Biotechnol*. 2022;10. doi: 10.3389/fbioe.2022.818610

43. Le Quang H, Schmoelz W, Lindtner RA, Schwendinger P, Blauth M, Krappinger D. Biomechanical comparison of fixation techniques for transverse acetabular fractures – single-leg stance vs. sit-to-stand loading. *Injury*. 2020;51(10):2158-2164. doi: 10.1016/j.injury.2020.07.008

44. ASTM International. *ASTM F382-17. Standard specification and test method for metallic bone plates*. West Conshohocken, PA: ASTM International; 2017 doi: 10.1520/F0382-17

45. Feng W, Fu L, Liu J, Qi X, Li D, Yang C. Biomechanical evaluation of various fixation methods for proximal extra-articular tibial fractures. *J Surg Res*. 2012;178(2):722-727. doi: 10.1016/j.jss.2012.04.014

46. Teo AQA, Ng DQK, Ramruttun AK, O'Neill GK. Standard versus customised locking plates for fixation of Schatzker II tibial plateau fractures. *Injury*. 2022;53(2):676-682. doi: 10.1016/j.injury.2021.11.051

47. Samsami S, Pätzold R, Neuy T, *et al*. Biomechanical comparison of 2 double plating methods in a coronal fracture model of bicondylar tibial plateau fractures. *J Orthop Trauma*. 2022;36(4):e129. doi: 10.1097/BOT.0000000000002257

48. Ngo TD, Kashani A, Imbalzano G, Nguyen KTQ, Hui D. Additive manufacturing (3D printing): a review of materials, methods, applications and challenges. *Compos B Eng*. 2018;143:172-196. doi: 10.1016/j.compositesb.2018.02.012

49. Liu S, Shin YC. Additive manufacturing of Ti6Al4V alloy: a review. *Mater Des*. 2019;164:107552. doi: 10.1016/j.matdes.2018.107552

50. Vancleef S, Wesseling M, Duflou JR, Nijs S, Jonkers I, Vander Sloten J. Thin patient-specific clavicle fracture fixation plates can mechanically outperform commercial plates: an in silico approach. *J Orthop Res*. 2022;40(7):1695-1706. doi: 10.1002/jor.25178

51. Barbieri L, Muzzupappa M. Performance-driven engineering design approaches based on generative design and topology optimization tools: a comparative study. *Appl Sci*. 2022;12(4):2106. doi: 10.3390/app12042106

52. Frazer J. Creative design and the generative evolutionary paradigm. In: Bentley PJ, Corne DW, eds. *Creative Evolutionary Systems*. San Francisco, CA: Morgan Kaufmann; 2002:253-274 doi: 10.1016/B978-155860673-9/50047-1

53. Tel A, Kornfellner E, Moscato F, *et al*. Optimizing efficiency in the creation of patient-specific plates through field-driven generative design in maxillofacial surgery. *Sci Rep*. 2023;13(1):12082. doi: 10.1038/s41598-023-39327-8

54. Krish S. A practical generative design method. *Comput Aided Des*. 2011;43(1):88-100. doi: 10.1016/j.cad.2010.09.009

55. Watson M, Leary M, Brandt M. Generative design of truss systems by the integration of topology and shape optimisation. *Int J Adv Manuf Technol*. 2022;118(3):1165-1182. doi: 10.1007/s00170-021-07943-1

56. Wang Z, Zhang Y, Bernard A. A constructive solid geometry-based generative design method for additive manufacturing. *Addit Manuf*. 2021;41:101952. doi: 10.1016/j.addma.2021.101952

57. Mehboob A, Barsoum I, Mehboob H, Abu Al-Rub RK, Ouldyerou A. Topology optimization and biomechanical evaluation of bone plates for tibial bone fractures considering bone healing. *Virtual Phys Prototyp*. 2024;19(1):e2391475. doi: 10.1080/17452759.2024.2391475

58. Tits A, Ruffoni D. Joining soft tissues to bone: insights from modeling and simulations. *Bone Rep*. 2020;14:100742. doi: 10.1016/j.bonr.2020.100742

59. Roland M, Diebels S, Wickert K, Pohlemann T, Ganse B. Finite element simulations of smart fracture plates capable of cyclic shortening and lengthening: which stroke for which fracture? *Front Bioeng Biotechnol*. 2024;12:1420047. doi: 10.3389/fbioe.2024.1420047

60. Xu S, Ding X, Xiong M, Duan P, Zhang H, Li Z. The optimal design of 3D-printed lattice bone plate by considering fracture healing mechanism. *Int J Numer Methods Biomed Eng*. 2023;39(3):e3682. doi: 10.1002/cnm.3682

61. Moosabeiki V, de Winter N, Cruz Saldivar M, *et al*. 3D printed patient-specific fixation plates for the treatment of slipped capital femoral epiphysis: topology optimization *vs.* conventional design. *J Mech Behav Biomed Mater*. 2023;148:106173. doi: 10.1016/j.jmbbm.2023.106173

62. Zong H, Lou B, Yuan H, *et al*. Integrating kinematic and dynamic factors with generative design for high-performance additive manufacturing structures. *Virtual Phys Prototyp*. 2025;20(1):e2501383. doi: 10.1080/17452759.2025.2501383

63. Attar H, Ehtemam-Haghighi S, Kent D, Dargusch MS. Recent developments and opportunities in additive manufacturing of titanium-based matrix composites: a review. *Int J Mach Tools Manuf*. 2018;133:85-102. doi: 10.1016/j.ijmachtools.2018.06.003

ACCSCIENCE PUBLISHING

International Journal of Bioprinting

RESEARCH ARTICLE

Design and performance evaluation of a 3D-printed transoral tracheal intubation fixation device

Guihua Hao[1,2†], Dinghao Luo[3†], Yayuan Tian[1†], Yu Guo[3], Tian Xie[4], Lili Hou[1*], Yongqiang Hao[3*], and Jingjing Dai[1*]

[1] Department of Nursing, Shanghai Ninth People's Hospital, Shanghai Jiao Tong University School of Medicine, Shanghai, China

[2] School of Nursing, Shanghai Jiao Tong University, Shanghai, China

[3] Clinical and Translational Research Center for 3D Printing Technology, Shanghai Ninth People's Hospital, Shanghai Jiao Tong University School of Medicine, Shanghai, China.

[4] Department of General Surgery, Shanghai Ninth People's Hospital, Shanghai Jiao Tong University School of Medicine, Shanghai, China

Abstract

Effective fixation of the endotracheal tube is essential to prevent displacement, unplanned extubation, and pressure injuries (PIs), which remain common complications with traditional fixation methods. Advances in three-dimensional (3D) printing technology offer opportunities to design personalized devices that may improve airway security and patient outcomes. However, no prior study has evaluated the use of 3D-printed fixation devices as an alternative to traditional methods. We aim to design and evaluate the effectiveness of an endotracheal tube fixation device produced using 3D printing technology in patients receiving mechanical ventilation. In a single-center, prospective, non-concurrent, controlled cohort trial, patients with an expected duration of mechanical ventilation exceeding 24 hours were stratified into an observation group (using a 3D-printed device; n = 51) and a control group (using a traditional device; n = 97). The primary endpoints were tracheal tube displacement and unplanned endotracheal extubation (UEE). The incidence of endotracheal tube displacement was 1/51 (1.9%) in the observation group vs. 12/97 (12.4%) in the control group (odds ratio [OR]: 6.28, 95% confidence interval [CI]: 1.91–21.05), yielding a 99% probability of benefit (POB). UEE incidence was 0/51 in the observation group, whereas it was 4/97 (4.1%) in the control group (OR: 5.26, 95% CI: 1.08–26.31), yielding a 98% POB. Lip PI occurred in 0/51 patients in the observation group vs. 10/97 (10.3%) patients in the control group (OR: 8.72, 95% CI: 2.11–35.98), yielding a 99% POB. The observation group exhibited significantly higher nurse satisfaction scores compared to the control group (p = 0.015). There were no significant differences in facial PI between the two groups. These findings suggest that the 3D-printed device reduced the incidence of tracheal tube displacement, UEE, and lip PI, while improving nurse satisfaction.

Keywords: Endotracheal tube; Fixation; Pressure injury; Three-dimensional printing; Tracheal tube displacement

[†]These authors contributed equally to this work.

***Corresponding authors:**
Lili Hou (pisces_liz@163.com)

Yongqiang Hao (hao_yongqiang@hotmail.com)

Jingjing Dai (daijingjing8011@163.com)

Citation: Hao G, Luo D, Tian Y, *et al.* Design and performance evaluation of a 3D-printed transoral tracheal intubation fixation device. *Int J Bioprint*. 2026;12(1):576-585. doi: 10.36922/IJB025430439

Received: October 24, 2025
Revised: December 6, 2025
Accepted: December 8, 2025
Published online: December 17, 2025

Copyright: © 2025 Author(s). This is an Open Access article distributed under the terms of the Creative Commons Attribution License, permitting distribution, and reproduction in any medium, provided the original work is properly cited.

Publisher's Note: AccScience Publishing remains neutral with regard to jurisdictional claims in published maps and institutional affiliations.

1. Introduction

Endotracheal intubation is the primary method of establishing an artificial airway in critically ill patients, providing optimal conditions for suctioning the airway and preventing aspiration.[1] Secure fixation of the orotracheal tube is critical for maintaining adequate respiratory function. Common clinical methods for securing endotracheal tubes include the use of adhesive tape, cotton straps, and commercially available fixation devices. Despite their widespread use, these methods are prone to inducing complications, such as displacement of the endotracheal tube, lip pressure injury (PI), and facial PI.[2] Displacement of the endotracheal tube by only 2 cm can result in insufficient ventilation.[3] The transportation of critically ill patients and the implementation of other intensive care technologies also pose significant threats to airway stability, requiring greater effort to maintain the correct position of the endotracheal tube.[4] In addition to endotracheal tube displacement, unplanned endotracheal extubation (UEE) frequently occurs in intensive care units (ICUs), with a reported incidence ranging from 1% to 43%.[4,5] UEE can result in a series of adverse complications, such as laryngeal injury, bronchospasm, arrhythmia, hypoxic brain injury, and death.[6] Skin injuries of the lips, head, and face are common nursing complications.[7] These complications not only increase pain in patients but also reduce their tolerance to tracheal intubation, prolong the length of hospital stay, and increase healthcare expenses.[8] With the development of three-dimensional (3D) printing technology, its application in the medical industry has expanded, enabling personalized customization.[9,10] To our knowledge, this study represents the first attempt to develop a 3D-printed tracheal tube fixator and conduct a comparative analysis with conventional methods.

Therefore, we developed a novel device using 3D printing technology, which has been authorized by the China National Intellectual Property Administration (patent No.: ZL202222274621.1). The present study evaluated the performance of this 3D-printed device in patients undergoing mechanical ventilation. We hypothesized that the 3D-printed fixation device would reduce tube displacement, UEE, and lip PI while improving nurse satisfaction.

2. Materials and methods

2.1. Study design

This single-center, prospective, non-concurrent, controlled cohort study was designed to compare the efficacy of a novel 3D-printed device (Figure 1A) with that of a traditional counterpart (Figure 1B) in critically ill adult patients requiring intubation and mechanical ventilation for a minimum duration of 24 hours. It is important to note that the fixation device used in this study serves solely as an external stabilizer for the intraoral segment of the endotracheal tube. The device has minimal contact with the mucosal surface and does not enter or interact with deeper tissues. All endotracheal tubes used in this study were standard commercially available products (Wellead, China) approved by the National Medical Products Administration and inserted via the oropharyngeal route. This study was approved by the Institutional Review Board of the Shanghai Ninth People's Hospital, School of Medicine, Shanghai Jiaotong University (No. SH9H-2023-T119-2). The trial was registered in the Research Registry (ID: 11697).

2.2. Study participants

Patients admitted to the ICU of the participating hospital between January 2023 and June 2023, who needed endotracheal intubation and met all predefined inclusion criteria, were enrolled in the present study. The enrolled patients were allocated to two groups according to their admission time. Patients admitted between January and March 2023 were included in the control group and treated using traditional fixation methods (Figure 1D), while those admitted between April and June 2023 were included in the experimental group and fitted with the 3D-printed fixation device (Figure 1C). Both groups of patients had their fixation devices replaced routinely, with each operation performed by nurses who had worked in the department for more than 2 years. Suctioning of sputum and oral secretions was performed as needed for patients in both groups.

Inclusion criteria included (i) patients aged 18 years and above; (ii) patients who underwent tracheal intubation; and (iii) patients who signed informed consent forms, either personally or via their family members.

The exclusion criteria were (i) patients who had undergone endotracheal intubation for more than 12 hours prior to ICU admission; (ii) patients with a history of skin or oral mucosal diseases; (iii) patients who had undergone nasotracheal intubation; (iv) patients who were allergic to adhesive tape; and (v) patients with a history of mental disorders who were unable to cooperate.

The withdrawal criteria were (i) patients who underwent mechanical ventilation for <24 hours; (ii) patients who abandoned the treatment during the trial; and (iii) patients or family members who voluntarily requested withdrawal during the trial.

2.3. Finite element analysis

The 3D structural design file of the tracheal tube fixation device was first exported in X-T format, then imported

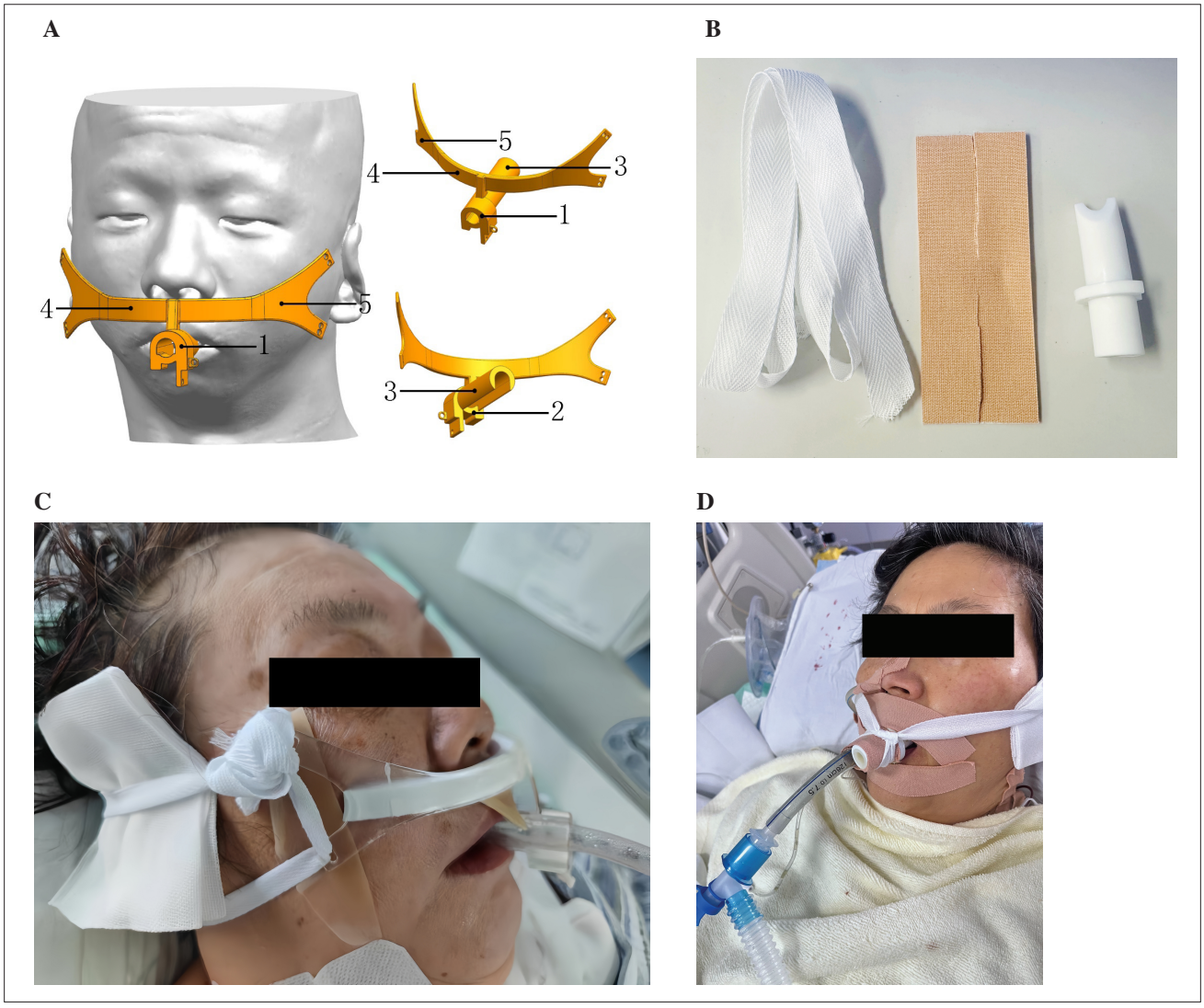


Figure 1. Design and application examples of the 3D-printed fixator and traditional fixation method. (A) Schematic diagram of the 3D-printed endotracheal tube fixation device. The number 1 refers to the upper limit stop; 2 refers to the lower limit stop; 3 refers to the tooth pad; 4 refers to the curved bend section; and 5 refers to the branch section. (B) Schematic diagram of the traditional endotracheal tube fixation device. (C) Patient wearing the 3D-printed endotracheal tube fixation device. (D) Patient wearing the conventional endotracheal tube fixation device.

into ANSYS Workbench 19.2 software for subsequent simulations. The material was defined as Clear 10, a photosensitive resin, with the parameters summarized in Table 1.

Automatic meshing was applied to generate the finite element mesh. In the boundary condition settings, the strap holes at both ends of the bracket were defined as "fixed supports," while loads were applied upward, downward, and laterally to the inner walls of the circular holes to simulate stresses exerted by the human body. For mesh-independence testing, a load of 2 N was used. For mechanical performance evaluation, a clinically relevant load of 5 N was applied.

2.4. Facial parameters data collection

The patients' facial parameters were measured, including the distance from the philtrum to the bottom of the chin (H), the distance between the left and right wisdom teeth (D), and the acute angle of the face in the supine position (a) to establish the curve of the retainer. One-third of the distance from the incisors to the mandibular angle was measured to determine the mouthpiece length. The collected facial parameter data were provided to a 3D printing technician for digital modeling of the fixation device.

2.5. Three-dimensional modeling

The patients' computed tomography scan DICOM images were imported into Mimics Research 19.0 (Materialise,

Table 1. Finite element mechanical analysis parameters for tracheal tube fixation devices

Category	Value	Unit
Young's modulus	2880	MPa
Poisson ratio	0.4	-
Bending strength	84	MPa
Tensile strength	56	MPa

Belgium) software to reconstruct a 3D model of the patients' lips and cheeks. The model was then calculated and exported in STL format for modeling.

2.6. Three-dimensional printing

Clear 10 resin (Uniontech, China) was selected as the printing material, and the splint thickness was set to 3.5 mm. Magics 24.0 (Materialise, Belgium) was used for slicing, with a layer thickness of 0.1 mm. Finally, the file was imported into a 3D printer (Uniontech, China), and the device was printed. Auxiliary materials, such as pads and straps, were then added to complete the production.

2.7. Device usage

After completing the endotracheal intubation, the tube was slid into the U-shaped groove of the fixator until it reached the space between the upper and lower incisors. The lower limit stop was inserted to secure the endotracheal tube in place. The securing strap was passed through a small opening at the other end of the fixator, wrapped around the patient's occipital region and neck, and tied securely in place (Figure 2A & B).

2.8. Patients' data collection

A comprehensive dataset was collected, including the following variables: age, sex, height, weight, Acute Physiology and Chronic Health Evaluation II score, ethnicity, duration of mechanical ventilation, patient complications, and clinical recovery status. The aforementioned data were retrieved from the hospital's electronic case management system. The research procedure is illustrated in Figure 3.

2.9. Study outcomes

The primary outcomes were tracheal tube displacement and UEE. Tracheal tube displacement was defined as tube dislodgement or a positional change exceeding 1.5 cm[11];

The secondary outcomes were (i) the incidence of endotracheal intubation-related PI, which was assessed by evaluating the integrity of the oral mucosa, tongue, and facial/cranial skin and confirmed by members of the hospital's PI prevention team; (ii) mechanical ventilation duration; and (iii) the satisfaction of the nursing staff. Based on a literature review and expert consultations, a questionnaire was designed to assess nurses' satisfaction with the two fixation methods. The Cronbach's α coefficient of the questionnaire was 0.942, and the overall content validity index was 0.979. The questionnaire encompassed six dimensions: fixation stability, operational convenience, hygiene condition, aesthetic appearance,

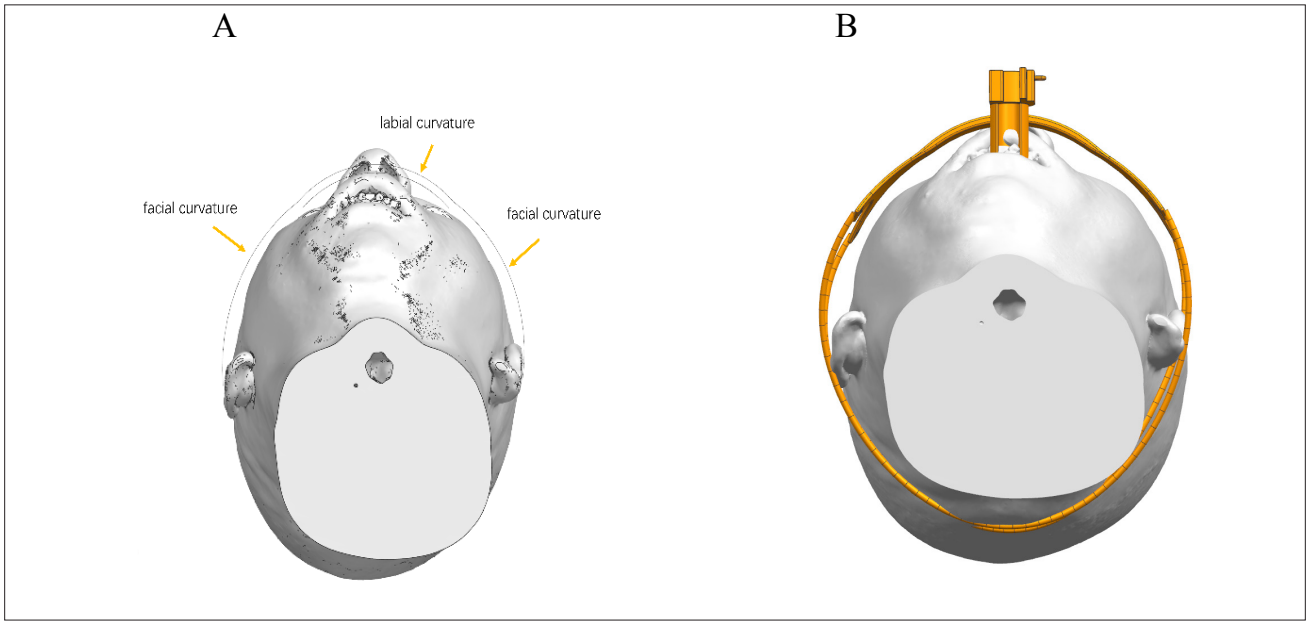


Figure 2. Curvature characteristics and design scheme of the wearable 3D-printed tracheal tube fixation device. (A) Wearable device curvature. (B) Design scheme.

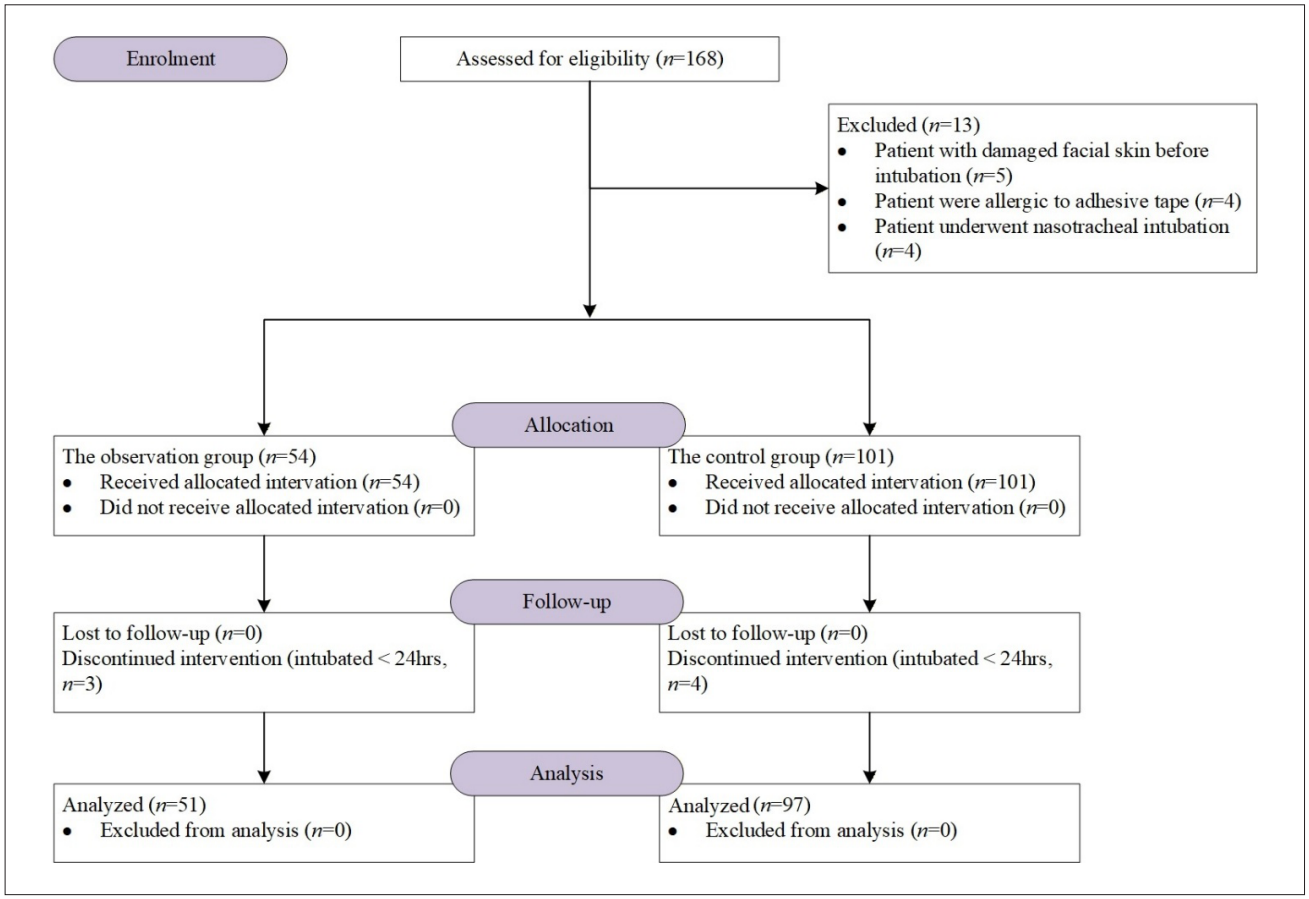


Figure 3. Flow diagram of enrolment and randomization of patients

adjustment frequency, and degree of interference with other operations. A five-point Likert scale was adopted for satisfaction scoring, where "Strongly Satisfied" was scored 5, "Satisfied" as 4, "Neutral" as 3, "Dissatisfied" as 2, and "Strongly Dissatisfied" as 1. Higher scores indicate greater satisfaction (Table S1).

2.10. Statistical analysis

Continuous variables were first tested for normality using the Shapiro–Wilk test. Variables following a normal distribution were presented as mean ± standard deviation (SD), whereas those with a non-normal distribution were expressed as median (interquartile range). Between-group comparisons of continuous variables were performed using an independent sample *t*-test for normally distributed data or a Mann–Whitney *U* test for non-normally distributed data. Categorical variables were summarized as counts (percentages). The Pearson's χ^2 test was used for intergroup comparisons when the expected frequency of all cells in the contingency table was ≥5; otherwise, Fisher's exact test was applied to avoid statistical bias caused by sparse data.

Bayesian logistic regression models were constructed to analyze the primary outcomes (tracheal tube displacement & UEE) and secondary categorical outcomes (lip/facial PIs). A non-informative prior distribution (normal distribution: mean=0, SD = 1.645) was adopted to minimize prior influence on the results. Posterior odds ratios (ORs) and their corresponding 95% confidence intervals (CIs) were estimated to quantify the effect size. The posterior probability of benefit (POB) was defined as the percentage of posterior samples where the OR (control group vs. observation group) exceeded 1. For the continuous secondary outcome (nurse satisfaction score), between-group comparison was conducted using the independent sample *t*-test, and the results were presented as mean ± SD. All statistical analyses were performed using R software (version 4.3.1; R Foundation for Statistical Computing, Austria). Bayesian inference was implemented using the Stan software (version 2.32.2). For frequentist statistics, statistical significance was set at a two-sided p-value < 0.05; for Bayesian statistics, a 95% CI was used.

3. Results

3.1. Basic characteristics of the study participants

A total of 51 patients were allocated to the observation group and 97 to the control group after applying the inclusion, exclusion, and withdrawal criteria. The two groups were well-matched in terms of baseline characteristics, with no significant between-group disparities (Table 2).

3.2. Finite element analysis

Under upward, lateral, and downward loading, the maximum local stresses of the fixation device were 1.258, 2.496, and 1.258 MPa, respectively, with corresponding maximum displacements of 49.6, 239.3, and 49.6 μm. Stress concentration was most pronounced under lateral loading, whereas upward and downward loading produced the lowest stress concentrations (Figure 4). In all directions, the local stresses remained below both the fracture and yield strengths, confirming the safety and reliability of the device. The maximum local deformation was 239.3 μm, which is within clinically acceptable limits and lower than the material's fracture elongation threshold (7.5%).

3.3. Clinical outcomes

The incidence of endotracheal tube displacement was 1.9% (1/51) in the observation group, as compared with 12.4% (12/97) in the control group. Utilizing a neutral prior probability, the OR was 6.28 (95% CI: 1.91–21.05), and the corresponding probability of clinical benefit was determined to be 99%. UEE incidence was 0% (0/51) in the observation group, whereas it was 4.1% (4/97) in the control group. The OR was estimated to be 5.26 (95% CI: 1.08–26.31), yielding a POB of 98% (Table 3).

No lip PI occurred in the observation group, whereas 10 out of 97 patients (10.3%) in the control group developed this complication. The OR was estimated to be 8.72 (95% CI: 2.11–35.98), yielding a POB of 99%. The nurse satisfaction scores in the observation group were significantly higher than those in the control group, with respective values of 28.29 ± 1.49 and 22.29 ± 4.79 (p = 0.015). There were no

Table 2. Comparison of general clinical information between the two patient groups

Characteristic	Observation group (n = 51)	Control group (n = 97)	t/χ^2	p-value
Age, years (mean ± SD)	60.73 ± 17.91	61.48 ± 21.38	0.17	0.87
Male sex	33 (64.7)	67 (69.1)	0.29	0.59
Body mass index, kg/m^2 (mean ± SD)	23.39 ± 4.78	22.55 ± 6.42	−0.82	0.42
APACHE II (mean ± SD)	13.91 ± 6.55	14.39 ± 4.99	0.46	0.64
Braden score (mean ± SD)	12.08 ± 3.59	11.26 ± 1.56	0.35	0.93
RASS score (mean ± SD)	1.06 ± 0.66	−0.57 ± 0.26	1.80	0.07
Physical restraint	50 (98)	89 (91.7)	2.31	0.13
Duration of mechanical ventilation, hours (mean ± SD)	44.57 ± 28.12	40.46 ± 34.19	−0.74	0.46
Indication for intubation			0.23	0.89
Postoperative transfer	40 (78.4)	77 (79.4)		
Hemodynamic instability	3 (5.8)	4 (4.1)		
Respiratory failure	8 (15.7)	16 (16.5)		
Comorbidities				
Smoking	15 (29.4)	25 (25.7)	0.07	0.78
Alcohol addiction	11 (21.5)	16 (16.5)	0.28	0.59
Heart disease	9 (17.6)	17 (17.5)	0.00	1.00
Diabetes mellitus	8 (18.6)	18 (18.5)	0.04	0.83
End-stage renal disease	2 (3.9)	3 (3.1)	0.00	1.00
Cancer	7 (12.3)	12 (12.4)	0.00	1.00
Admission type			0.00	1.00
Medical	5 (9.8)	9 (9.3)		
Surgical	46 (90.2)	88 (90.7)		

Note: Data presented as n (%), unless stated otherwise.
Abbreviations: APACHE: Acute Physiology and Chronic Health Evaluation; RASS: Richmond Agitation-Sedation Scale; SD: standard deviation.

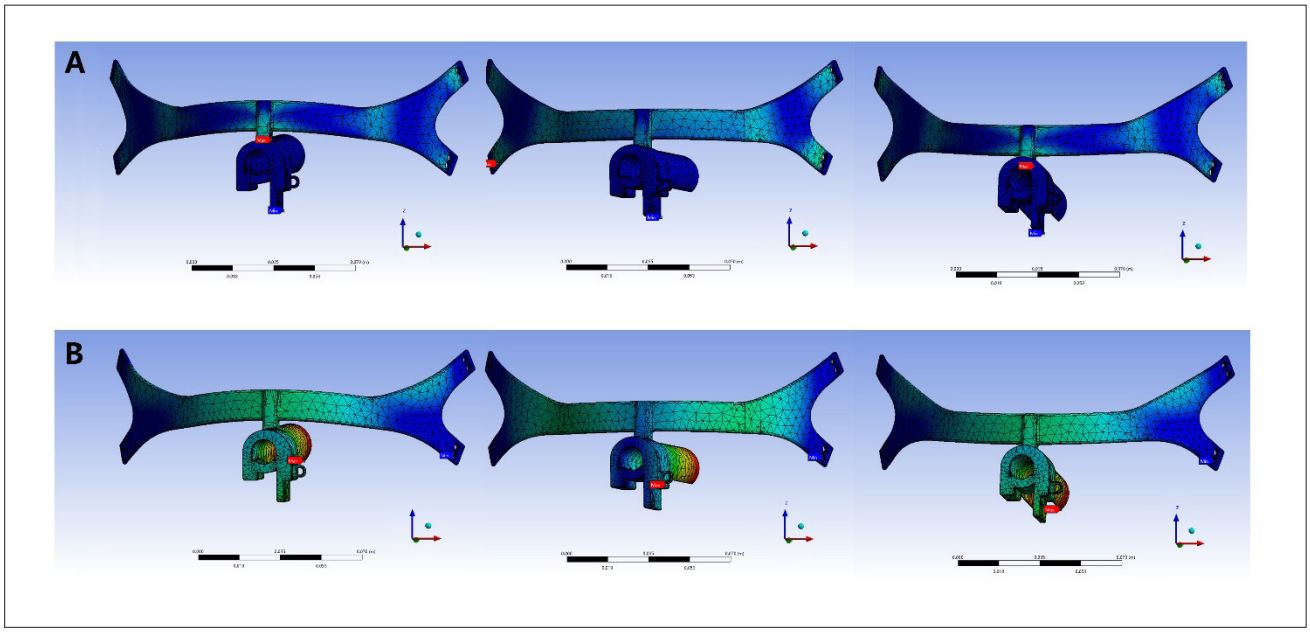


Figure 4. Finite element simulation verification of the mechanical properties of the suspended tracheal tube fixator. (A) Local stress distributions. (B) Local displacement distributions.

Table 3. Clinical outcomes of the two groups

Outcomes	No./total no. (%)	No./total no. (%)	Posterior probability of benefit (%)	Posterior OR (95% CI)
	Group 1 (*n*=97)	Group 2 (*n*=51)		
Endotracheal tube displacement	12/97 (12.4)	1/51 (1.9)	99	6.28 (1.91–21.05)
UEE	4/97 (4.1)	0/51 (0.0)	98	5.26 (1.08–26.31)
Lip pressure injuries	10/97 (10.3)	0/51 (0.0)	99	8.72 (2.11–35.98)
Facial pressure injuries	6/97 (6.2)	2/51 (3.9)	68	1.58 (0.54–4.59)

Abbreviations: CI: confidence interval; OR: odds ratio; UEE: unplanned endotracheal extubation.

significant between-group differences in the occurrence of facial PIs (**Table 3**).

4. Discussion

This study is the first to utilize 3D printing technology in the design and manufacture of tracheal intubation fixators. Our findings revealed that the observation group exhibited a significantly lower incidence of endotracheal tube displacement, UEE, and a marked reduction in lip PI incidence relative to the control group. In contrast, the incidences of facial PI did not differ significantly between the two groups. Furthermore, nurse satisfaction scores were significantly higher in the observation group.

The present study emphasizes the significance of structural strength in maintaining the functional stability and safety of tracheal tube fixation devices.[12] The proposed adjustable retaining clip, incorporating an indentation to fully encircle the tube, was shown to effectively redistribute mechanical loads and mitigate stress concentrations arising from multidirectional displacement. This structural optimization substantially reduced the risk of severe local deformation or fracture of adjacent components, thereby enhancing overall device safety. Finite element mechanical simulation further confirmed that, even under tensile forces equivalent to a 500 g weight, the U-shaped fixation groove exhibited a maximum displacement of only 0.13 mm. This minimal deformation is well within clinically acceptable thresholds, underscoring the device's ability to provide secure and reliable tracheal tube fixation. Collectively, these findings suggest that the optimized design not only meets clinical performance requirements but also offers a practical solution to improving fixation stability and reducing complications associated with tracheal intubation.

Biomechanical analysis provides evidence supporting the optimization of fixation methods for endotracheal intubation. The force required for endotracheal tube displacement and UEE varies with changes in fixation methods and the angle at which the force is applied. Previous studies compared the extubation force required during UEE across seven common fixation methods and found that an integrated system offered the best overall performance in terms of fixation.[4,13] This study focused on an integrated endotracheal tube fixation system that combined a perioral fixation device with a bite block. This increases the force required for extubation and ensures optimal fixation performance. Additionally, its design effectively reduces pressure on the patient's lips, minimizes the risk of pressure ulcers, and enhances patient comfort. It also facilitates oral care procedures for critically ill patients performed by clinical nurses, thereby improving nurse satisfaction ($p = 0.015$).

3D-printed tracheal tube fixation devices are more effective than traditional methods in preventing tube displacement. Incorrect tracheal tube positioning, whether too long or too short, can impair ventilation.[14] If the tube is too long, its tip may enter the right main bronchus, leading to hyperventilation of the right lung, pneumothorax, and other complications. Conversely, if the tube is too short, unplanned extubation may occur, resulting in prolonged mechanical ventilation, airway mucosa damage, increased care requirements for chronic conditions, higher medical costs, and potential complications such as bronchospasm, aspiration pneumonia, arrhythmia, or death.[15] Reducing the incidence of unplanned extubation has become an urgent issue in clinical practice and has been designated as a nursing-sensitive quality indicator.[16] In this study, the bite portion of the 3D-printed tracheal tube retainer enveloped the tracheal tube, reducing the pressure on the lips, gums, and tongue surface. This design effectively prevented patients from dislodging the tube with their tongues, and edentulous patients did not experience movement of the tracheal tube as the dental pad moved up and down. Furthermore, wide fixation straps were wrapped around the occipital and cervical regions to provide stable fixation. The results of this study indicate that the 3D-printed tracheal tube fixation device effectively reduced the incidence of tracheal tube displacement. The device demonstrated superior fixation efficacy compared with the control group.

Compared with traditional methods, 3D-printed tracheal tube fixation devices resulted in fewer lip PIs. From a mechanical standpoint, patients receiving ventilation are at high risk of developing lip PI.[17] In clinical practice, inappropriate fixation methods can subject the lips and surrounding skin to pressure, friction, and shear forces from the tube and adhesive tape. Additionally, because tracheal tubes are inserted through the mouth, patients often have their mouths continuously open, leading to increased oral secretions.[18] The lip mucosa and surrounding areas are frequently exposed to moisture, impaired blood circulation, prolonged ischemia, hypoxia, and malnutrition, which can result in lip PI. Furthermore, dental pads are often used to assist with fixation after tracheal intubation.[19] Lip pressure ulcers are easily overlooked, regardless of the medical procedure in which dental pads are used. The occurrence of lip pressure ulcers increases patient discomfort and reduces tolerance to tracheal intubation, which is detrimental to the recovery process. Our device has a suspended design that effectively reduces the contact pressure between the lips and the surrounding area. Its integrated design facilitates oral care and suction of oral secretions. In this study, none of the 51 patients in the observation group developed lip pressure ulcers, demonstrating a statistically significant advantage over the control group in preventing them.

The personalized advantages of the 3D-printed fixation device may offer specific benefits for patient populations at higher risk of inadequate tube stabilization or device-related PIs when using conventional fixation methods. Edentulous patients represent a notable subgroup in whom traditional adhesive or bite–block-based devices often fail to achieve secure anchorage due to reduced oral structural support and altered perioral tissue tension. In this population, the absence of dentition increases the likelihood of tube malposition and focal soft-tissue compression. The ability of our device to conform precisely to the patient's maxillofacial contour, as derived from computed tomography imaging, ensures a stable and evenly distributed contact surface, thereby potentially lowering displacement risk while minimizing mucosal loading. Similarly, patients with congenital or acquired facial deformities—such as mandibular defects, maxillofacial asymmetry, post-traumatic abnormalities, or postoperative reconstructive changes—pose a challenge for standardized fixation systems designed for typical craniofacial geometries. Poor fit in these individuals may not only compromise fixation security but also predispose them to high-pressure points and ulceration. Our results support that personalized design can overcome these anatomical limitations by enabling device geometry to mirror patient-specific surface morphology. This tailored fit likely contributed to the observed reduction in lip PIs in the present study and may be even more impactful among patients with distorted soft-tissue contours. Furthermore,

critically ill populations with fragile skin, severe cachexia, or long-term mechanical ventilation may also benefit from the improved pressure distribution enabled by individualized support structures. Although our cohort did not specifically stratify these subgroups due to sample size limitations, future studies with targeted enrolment of edentulous patients, those with facial deformities, or patients with impaired tissue integrity are warranted to further clarify the magnitude of benefit. Overall, the personalized nature of the 3D-printed fixation device represents a promising approach to addressing anatomical variability, which has long limited the performance of conventional fixation techniques.

This study had some limitations, including its non-randomized controlled design, single-center nature, and relatively small sample size—factors that may introduce potential bias into the findings. First, selection bias is inherently associated with the non-randomized design, and unmeasured or residual confounding factors cannot be completely mitigated. Second, the non-random assignment precludes the establishment of definitive causal relationships between the intervention (a personalized transoral endotracheal tube fixation device) and primary outcomes. Our findings therefore reflect associative rather than causal links, and their generalizability to broader clinical populations may be constrained. Notably, because the proposed personalized transoral endotracheal tube fixation device represents a novel concept, no comparable customized fixation devices have been reported in the literature to date, rendering the establishment of a parallel control group for direct comparison infeasible. Accordingly, our mechanical simulation experiments primarily evaluated deformation characteristics to demonstrate the device's clinical safety under external mechanical perturbations and its efficacy in preventing deformation-induced tube displacement. Multicenter prospective studies are warranted to further advance the understanding of 3D-printed devices for mechanically ventilated patients. Future research should explore the integration of sensors into 3D-printed fixation devices, which would facilitate real-time monitoring of skin integrity and blood perfusion, with the potential to reduce the incidence of endotracheal intubation-related PIs.

5. Conclusion

This study incorporated 3D printing technology into the development of a tracheal intubation fixation device, enabling precise, personalized design to enhance patient safety in artificial airways and reduce the incidence of adverse complications, especially lip PI, thereby demonstrating the effective integration of medicine and 3D printing technology.

Acknowledgments

We would like to thank the medical staff in the ICU and the 3D Printing Center Engineer Team for their assistance with the trial.

Funding

This study was supported by grants from the Nursing Development Program (SJTUHLXK2024) and the Excellent Nursing Talent Training Program of the Ninth People's Hospital of Shanghai Jiaotong University School of Medicine (JYHRC22-L02), and the Nursing Research Project of Shanghai Jiao Tong University School of Medicine (Jyhl2519).

Conflict of interest

Yongqiang Hao serves as the Editorial Board Member of the journal, but did not in any way involve in the editorial and peer-review process conducted for this paper, directly or indirectly. Other authors declare they have no competing interests.

Author contributions

Conceptualization: Guihua Hao, Yongqiang Hao
Formal analysis: Tian Xie
Investigation: Yu Guo, Yayuan Tian
Methodology: Dinghao Luo, Yu Guo
Visualization: Dinghao Luo, Yongqiang Hao
Writing – original draft: Guihua Hao
Writing – review & editing: Yu Guo, Jingjing Dai, Dinghao Luo, Lili Hou, Yongqiang Hao
All authors read and approved the final version of the manuscript.

Ethics approval and consent to participate

The study was conducted in accordance with the Declaration of Helsinki and was approved by the Medical Ethics Committee of the Ninth People's Hospital, Shanghai Jiao Tong University School of Medicine (No. SH9H-2023-T119-2). All patients have signed the written informed consent form.

Consent for publication

Patients provided informed consent for the publication of the image.

Availability of data

All data analyzed have been presented in the paper.

References

1. Long B, Gottlieb M. Emergency medicine updates: endotracheal intubation. *Am J Emerg Med*. 2024;85:108-116. doi: 10.1016/j.ajem.2024.08.042.
2. Amrani G, Gefen A. Which endotracheal tube location minimises the device-related pressure ulcer risk: the centre or a corner of the mouth. *Int Wound J*. 2020;17(2):268-276. doi: 10.1111/iwj.13267.
3. Kaplow R, Bookbinder M. A comparison of four endotracheal tube holders. *Heart Lung*. 1994;23(1):59-66.
4. Wagner JL, Shandas R, Lanning CJ. Extubation force depends upon angle of force application and fixation technique: a study of 7 methods. *BMC Anesthesiol*. 2014;14:74. doi: 10.1186/1471-2253-14-74.
5. Anis A, Patel R, Tanios MA. Analytical review of unplanned extubation in intensive care units and recommendation on multidisciplinary preventive approaches. *J Intensive Care Med*. 2024;39(6):507-513. doi: 10.1177/08850666231199055.
6. Zhang P, Liu LP. Design of assessment tool for unplanned endotracheal extubation of artificial airway patients. *Nurs Open*. 2021;8(4):1696-1703. doi: 10.1002/nop2.807.
7. Zuo M, Chu H, Qian X. Protective restraint nursing interventions in ICU patients: assessing their influence on unplanned extubation and skin injury incidence. *Altern Ther Health Med*. 2024;30(5):264-269.
8. Li P, Sun Z, Xu J. Unplanned extubation among critically ill adults: a systematic review and meta-analysis. *Intensive Crit Care Nurs*. 2022;70:103219. doi: 10.1016/j.iccn.2022.103219.
9. Kantaros A. 3D printing in regenerative medicine: technologies and resources utilized. *Int J Mol Sci*. 2022;23(23):14621. doi: 10.3390/ijms232314621.
10. Shim KW. Medical applications of 3D printing and standardization issues. *Brain Tumor Res Treat*. 2023;11(3):159-165. doi: 10.14791/btrt.2023.0001.
11. Lee K, Park JS, Kim MS, Tae N, Lee D, Oh YJ. Impact of obesity on double-lumen endobronchial tube displacement after lateral decubitus positioning. *Korean J Anesthesiol*. 2023;76(3):227-234. doi: 10.4097/kja.22493.
12. Sturgess DJ, Greenland KB, Senthuran S, Ajvadi FA, van Zundert A, Irwin MG. Tracheal extubation of the adult intensive care patient with a predicted difficult airway — a narrative review. *Anaesthesia*. 2017;72(2): 248-261. doi: 10.1111/anae.13668.
13. Torrini F, Gendreau S, Morel J, *et al*. Prediction of extubation outcome in critically ill patients: a systematic review and meta-analysis. *Crit Care*. 2021;25(1):391. doi: 10.1186/s13054-021-03802-3.
14. Herway ST, Benumof JL. The tracheal accordion and the position of the endotracheal tube. *Anaesth Intensive Care*. 2017;45(2):177-188. doi: 10.1177/0310057X1704500207.
15. Minda Z, Samuel H, Aweke S, Mekete G, Seid A, Eshetie D. Magnitude and associated factors of unplanned extubation in intensive care unit: a multi-center prospective observational study. *Ann Med Surg (Lond)*. 2022;79:103936. doi: 10.1016/j.amsu.2022.103936.
16. Zhang Y, Liu L, Hu J, *et al*. Assessing nursing quality in paediatric intensive care units: a cross-sectional study in China. *Nurs Crit Care*. 2017;22(6):355-361. doi: 10.1111/nicc.12246.
17. Zhang Q, Zhang X, Han C, *et al*. Successful treatment of endotracheal intubation-related lip pressure injury using a self-developed fixation device. *Crit Care*. 2023; 27(1):298. doi: 10.1186/s13054-023-04577-5.
18. Hajhosseini B, Longaker MT, Gurtner GC. Pressure injury. *Ann Surg*. 2020;271(4):671-679. doi: 10.1097/SLA.0000000000003567.
19. Arundel L, Irani E, Barkema G. Reducing the incidence of medical device-related pressure injuries from use of CPAP/BiPAP masks: a quality improvement project. *J Wound Ostomy Continence Nurs*. 2021;48(2): 108-114. doi: 10.1097/WON.0000000000000742.

ACCSCIENCE PUBLISHING

International Journal of Bioprinting

RESEARCH ARTICLE

Black phosphorus scaffolds for efficient bone defect repair via anti-inflammatory, osteogenic, and photothermal therapeutic effects

Peng Xue[1†*], Hongzhong Xi[2†], Wei Zhang[1], Anlong Liu[1], Aoyun Hu[1], Chenjian Peng[1], Jianning Zhao[1*], and Jun Wang[1*]

[1]Department of Orthopedics, Nanjing Hospital of Chinese Medicine Affiliated to Nanjing University of Chinese Medicine, Jiangsu, China

[2]Department of Orthopedics, The Affiliated Hospital of Nanjing University of Chinese Medicine, Nanjing, Jiangsu, China

(This article belongs to the *Special Issue*: *3D Printing for Advancing Orthopedic Applications*)

Abstract

Bone defects pose a high risk of non-union and permanent disability, making effective bone regeneration a critical focus in the development of bone repair materials. Current research primarily emphasizes enhancing the single osteogenic function of bone repair materials, while neglecting the impact of the complex microenvironment in bone defect areas. This has resulted in the failure of many developed bone repair materials to achieve effective *in vivo* bone regeneration. In this study, a multifunctional near-infrared light-responsive black phosphorus (BP) bone repair scaffold was fabricated via low-temperature deposition 3D printing. *In vitro* characterization demonstrated that the scaffold possesses a cancellous bone-like structure, moderate compressive strength, and cytocompatibility, with the ability to promote osteogenesis under inflammatory conditions. *In vivo* studies further confirmed its favorable photothermal responsiveness, enabling photothermal therapy (PTT) to accelerate bone regeneration while reducing inflammation in the defect area. These findings indicate that the multifunctional BP scaffold achieves superior bone repair outcomes through synergistic effects of anti-inflammation, promotion of osteogenic differentiation, and PTT, thereby improving the success rate of defect repair. Moreover, the simple fabrication process and satisfactory therapeutic efficacy of this multifunctional BP scaffold highlight its high potential for clinical translation.

Keywords: Anti-inflammation; Black phosphorus; Bone repair scaffold; Osteogenic differentiation; Photothermal therapy

1. Introduction

Bone defects can result from a variety of factors, including trauma, tumors, and osteonecrosis.[1–3] Failure to adequately repair such defects may lead to persistent pain, pathological fractures, and functional impairment.[4,5] Epidemiological studies have shown that over six million people in China suffer from bone defects or functional disorders

†These authors contributed equally to this work.

***Corresponding authors:**
Peng Xue (aiwellme@163.com)

Jianning Zhao (zhaojianning.0207@163.com)

Jun Wang (wangjun198607@163.com)

Citation: Xue P, Xi H, Zhang W, *et al*. Black phosphorus scaffolds for efficient bone defect repair via anti-inflammatory, osteogenic, and photothermal therapeutic effects. *Int J Bioprint*. 2026;12(1):586-606. doi: 10.36922/IJB025310310

Received: July 31, 2025
1st revised: August 28, 2025
2nd revised: December 17, 2025
Accepted: December 22, 2025
Published online: December 24, 2025

Copyright: © 2025 Author(s). This is an Open Access article distributed under the terms of the Creative Commons Attribution License, permitting distribution, and reproduction in any medium, provided the original work is properly cited.

Publisher's Note: AccScience Publishing remains neutral with regard to jurisdictional claims in published maps and institutional affiliations.

each year, among whom approximately two-thirds require bone grafting treatment. It is projected that by 2050, the costs associated with the treatment of bone defects will exceed 600 billion yuan, imposing a significant burden on patients and society.[6] Autologous bone transplantation, as the gold standard for repairing bone defects, is restricted in its clinical application due to issues such as limited sources and donor site complications.[7] Therefore, the development of artificial bone repair materials has long been a research hotspot in the field of bone tissue engineering.[8] Despite extensive efforts, there is still no widely accepted bone repair material that has successfully transitioned from laboratory research to routine clinical application.

Currently, promoting the proliferation and osteogenic differentiation of bone marrow mesenchymal stem cells (BMSCs) within bone defect areas remains the primary research focus for most bone repair materials. For instance, strategies include incorporating bone repair factors into these materials,[9] loading BMSCs onto them,[10] or engineering material interfaces that are more conducive to BMSC adhesion and proliferation.[11] Despite the promising osteogenic efficacy demonstrated *in vitro*, such scaffolds still fail to achieve satisfactory bone repair outcomes *in vivo*. This discrepancy arises from the intricate microenvironment within *in vivo* bone defects. Under the influence of the complex physiological environment *in vivo*, the robust osteogenic capacity of bone repair materials observed *in vitro* does not guarantee their ability to achieve effective bone repair outcomes *in vivo*. Furthermore, previous research has revealed that under identical intervention conditions, scaffold–host bone integration fails in some experimental animals, compromising the overall success rate of bone repair materials.[12–14] This observation suggests the existence of inter-individual heterogeneity in bone repair responses. These challenges have emerged as significant barriers hindering the translation of bone repair materials from laboratory research to clinical application.

Studies have demonstrated that upon the occurrence of bone defects, the microenvironment at the injured site undergoes significant alterations, primarily characterized by elevated concentrations of hydrogen peroxide and pro-inflammatory factors.[15] These changes impede the expression of osteogenic differentiation transcription factors, thereby inhibiting the differentiation of BMSCs into osteoblasts. Concurrently, the heightened metabolic activity of inflammatory cells (e.g., neutrophils and macrophages) leads to the release of substantial amounts of acidic substances such as lactic acid and carbon dioxide, resulting in a local pH reduction (typically ranging from 5.5 to 6.8, in contrast to the physiological pH of approximately 7.3–7.4 in normal bone tissue).[16] This acidic microenvironment not only hinders normal bone regeneration but may even induce osteolysis. Therefore, excessive levels of pro-inflammatory factors in the bone defect area compromise bone repair through multiple mechanisms. Furthermore, previous clinical studies have revealed inter-individual heterogeneity in bone repair, which is influenced by various risk factors, including age, bone quality, and the use of hormonal medications.[17–19] For patients with delayed bone repair, additional interventions are often required to mitigate the risk of repair failure induced by these factors. Hence, in addition to osteogenesis-promoting properties, bone repair materials need to possess multiple functionalities, including regulating local inflammation in the bone defect area and balancing inter-individual repair heterogeneity through targeted regulatory measures. Such multifunctional materials are more conducive to bone defect healing and enhance the success rate of repair.

Phosphorus is one of the essential elements for bone regeneration, contributing to the maintenance of bone growth and mechanical strength.[20] Black phosphorus (BP), a two-dimensional nanomaterial composed of single phosphorus atoms, exhibits broad-band absorption in the near-infrared (NIR) region and possesses excellent photothermal conversion efficiency.[21] This unique property renders BP a promising photothermal agent, enabling its application in the construction of photothermal nanomaterials for photothermal therapy (PTT). Literature has reported that BP simultaneously exerts both favorable osteogenic and anti-inflammatory effects, thereby facilitating effective bone repair in the bone defect microenvironment.[22] Notably, mild PTT induced by NIR excitation of BP not only promotes osteogenesis and anti-inflammation but also accelerates the release of BP, which in turn enhances its osteogenic and anti-inflammatory efficacy, thereby achieving a synergistic effect.[23] Furthermore, PTT allows for additional regulatory intervention based on individual bone repair status after scaffold implantation, which can accelerate bone healing, balance repair discrepancies caused by inter-individual heterogeneity in bone repair, and prevent repair failure due to delayed bone regeneration. Based on these findings, we intend to develop BP bone repair materials, aiming to fully utilize their multiple functionalities and synergize with PTT to promote bone repair in defect areas, ultimately improving the success rate of bone regeneration.

In the present study, based on our previously developed poly(lactic-co-glycolic acid) (PLGA)/β-tricalcium phosphate (β-TCP) printing paste (composed of β-TCP and PLGA) and low-temperature deposition 3D printing technology,[13] BP/PLGA/β-TCP scaffolds (BP scaffolds) were constructed. The scaffolds were characterized, and their photothermal response properties were examined. Meanwhile, an inflammatory microenvironment was

simulated *in vitro* to assess the osteogenic efficacy of the scaffolds under such conditions. Subsequently, the scaffolds were implanted into a rat model of distal femoral bone defects to investigate their *in vivo* bone repair efficacy under PTT regulation. This study confirmed that BP scaffolds can achieve favorable bone repair outcomes in defect areas through multiple mechanisms, including promoting osteogenic differentiation of BMSCs, regulating local inflammation, and enabling efficient osteogenesis via PTT modulation, thereby exhibiting potential for clinical application.

2. Materials and methods

2.1. Materials

BP nanosheets (Φ100–200 nm) were provided by the College of Engineering, China Pharmaceutical University (Nanjing, China). PLGA and β-TCP powder were purchased from Regenovo Co. (China). Lipopolysaccharides (LPS) were purchased from Yuanye Bio-Technology Co., Ltd. (China). Minimal essential medium Eagle–alpha modification (α-MEM) was purchased from Biological Industries (Israel). Fetal bovine serum, penicillin–streptomycin solution, Live/Dead staining kit, 4',6-diamidino-2-phenylindole (DAPI) staining kit, Alizarin red S (ARS) staining kit, and alkaline phosphatase (ALP) staining kit were purchased from Beyotime Biotechnology (China). Enzyme-linked immunosorbent assay (ELISA) kits (bone morphogenetic protein 2 [BMP-2], ALP, runt-related transcription factor 2 [RUNX2], osteocalcin [OCN]) were purchased from Jingren Medical Research (China). BMP-2 (66383-1-Ig), tumor necrosis factor-alpha (TNF-α; [17590-1-AP, and cluster of differentiation 86 (CD86; 26903-1-AP)]) antibodies were purchased from Proteintech Biotechnology Co., Ltd. (China). ALP (sc-365765), RUNX2 (sc-101145), OCN(sc-73464), and β-actin (sc-517582) antibodies were purchased from Santa Cruz Biotechnology (United States of America [USA]). Hematoxylin and eosin (H&E) and Masson staining kits were purchased from Ai Fang Bio Co. (China).

2.2. Preparation of black phosphorus scaffold

According to a published research protocol,[13] a mixture was prepared by dispersing 10 g of PLGA granules and 2.5 g of β-TCP in 42 mL of a 1,4-dioxane solution using vortex shaking for 1 min, followed by magnetic stirring until a homogeneous solution was obtained. Various ratios of BP (0%, 0.5%, 1%, and 2%) were added to the solution and stirred again. The resulting BP-doped slurry was then transferred to a printing cylinder equipped with a piston and a needle of appropriate size (Φ0.25 mm) and loaded onto a biological 3D printer (Regenovo Co.). After printing, the scaffolds were pre-cooled in a refrigerator at −80°C for 2 h, freeze-dried for 24 h, and stored at −20°C for future use. The resulting scaffolds were named BP scaffolds and classified as 0BP, 0.5BP, 1BP, and 2BP according to the BP doping amount.

2.3. Characterization of black phosphorus scaffold

The characterization of the scaffolds was based on a previously reported research protocol. Specifically, scanning electron microscopy (SEM; Apreo 2, Thermo Fisher Scientific, USA), atomic force microscopy (Hyperion II System, Thermo Fisher Scientific, USA), and energy-dispersive X-ray spectroscopy (EDS; Dual-X Super-X EDS System, Thermo Fisher Scientific, USA), Fourier transform infrared spectroscopy (FTIR; Nicolet iS50, Thermo Fisher Scientific, USA), X-ray photoelectron spectroscopy (XPS; Escalab 250Xi, Thermo Fisher Scientific, USA), and X-ray diffraction (D8 VENTURE, Bruker, Germany). The compressive strength was measured using a universal mechanical tester (Shenzhen SUNS, China). The porosity and pore diameter of the scaffolds were calculated using the software (Bio Architect) provided by the printing company (Regenovo Co.).

2.4. Analysis of the photothermal performance of the scaffolds

An 808 nm NIR laser (New Industries Optoelectronics Technology Co., Ltd., China) with a power of 0.8 W/cm^2 was used to irradiate different scaffolds for 300 s, and the temperature was recorded. Infrared images were captured using an infrared thermal camera (Model: H23, Hikmicrotech Co., Ltd., China), and the temperatures were quantified to plot temperature rise curves. The temperature trends of different scaffolds under 808 nm NIR laser irradiation at 0.8 W/cm^2 were obtained.

The 2BP scaffolds were irradiated with an 808 nm NIR laser at different power densities (0.6, 0.7, 0.8, 0.9, and 1.0 W/cm^2), and the temperature changes were recorded and plotted.

An 808 nm NIR laser at 0.8 W/cm^2 was used to irradiate the BP scaffolds for 300 s, and the endpoint temperatures were recorded. The process was repeated 10 times.

2.5. Cytotoxicity analysis

2.5.1. Cell culture

Rat BMSCs and RAW 264.7 cells were purchased from the Shanghai Cell Bank of the Chinese Academy of Sciences (China) and cultured in α-MEM complete medium containing 10% fetal bovine serum and 1% penicillin–streptomycin. Cells were maintained at 37°C in a humidified atmosphere with 5% carbon dioxide. The medium was changed every 2 days. Cells were passaged under an inverted microscope (Model, Olympus, Japan)

at 80%–90% confluence, and passage 3 cells were used for subsequent experiments. Unless otherwise specified, the NIR irradiation conditions were as follows: 808 nm, 0.8 W/cm^2, 5 min per day.

2.5.2. Cytotoxicity

Leaching solutions were prepared according to previously reported methods. Briefly, the scaffolds were rinsed with phosphate-buffered saline (PBS), sterilized with ethylene oxide, and placed in extraction vessels. The leaching solutions were prepared at a concentration of 0.2 g/mL in complete medium and incubated at 37°C for 72 h.

For the Cell Counting Kit-8 (CCK-8) assay, BMSCs were seeded into 96-well plates at a density of 1000 cells/well. Subsequently, 100 μL of the different leaching solutions was added to each well, and the medium was refreshed every 24 h. After incubation for 1, 3, and 5 days, the medium was discarded, and 100 μL of α-MEM containing 10% CCK-8 solution was added to each well, followed by an additional 2 h of incubation. The absorbance at 450 nm (A450) was measured using a microplate reader (BioTek, USA).

For Live/Dead staining, cells were cultured under the same conditions as described above, with 2000 cells seeded per well. Live/Dead staining was performed according to the instructions of the calcein acetoxymethyl and propidium iodide staining kit. Images were captured using an inverted fluorescence microscope (Olympus, Japan), where green fluorescence represents live cells and red fluorescence indicates dead cells.

2.5.3. Co-culture of cells and scaffolds

Cell growth on different scaffolds was observed by nuclear staining. Cells were seeded on the scaffolds at a density of 1×10^4 cells/well, and the medium was removed after 24 h of co-culture. Cells were then fixed with paraformaldehyde for 5 min and rinsed with PBS for 10 min. Subsequently, 0.5% TritonX-100 was added and incubated for 20 min. The nuclei were stained with the DAPI (blue) staining kit according to the manufacturer's instructions. Images were captured using an inverted fluorescence microscope (Olympus, Japan).

2.6. Osteogenic induction under an inflammation-free microenvironment

BMSCs were inoculated into 12-well plates at a density of 3×10^4 cells/well and incubated. When cell confluence reached 80%–90%, scaffolds that had been immersed in complete medium for 30 min were placed into the 12-well plates. Subsequently, osteogenic induction medium was added (50 mg/L ascorbic acid, 10 mmol/L β-glycerophosphate, and 100 nmol/L dexamethasone) and changed every 2 days. ALP and ARS staining was performed according to the manufacturer's instructions after 6 days and 14 days of incubation, respectively. After termination of the reactions, the staining results were observed under an inverted microscope (Olympus, Japan). Six regions of interest were randomly selected for quantitative analysis of positive staining areas using ImageJ (version 1.54r, Developer: Wayne Rasband, National Institutes of Health, USA).

2.7. Photothermal therapy-enhanced bone repair efficacy of scaffolds

The 0BP scaffolds were used as the control group, and the 2BP scaffolds were used as the experimental group. The groups were further subdivided into PTT and non-PTT groups according to whether NIR irradiation (808 nm, 0.8 W/cm^2) was applied at a frequency of 5 min/day. To observe more pronounced *in vitro* osteogenic effects, ALP and ARS staining were performed on days 9 and 21 of osteogenic induction, respectively. All other cell culture procedures, data collection, and analysis steps were conducted as described above.

2.8. Molecular mechanisms underlying scaffold-promoted bone repair

2.8.1. Western blotting

Scaffolds were co-cultured with the cells for 5 days to analyze the expression of osteogenesis-related proteins in BMSCs. Cells on the scaffold and in the culture dishes were lysed by adding 200 μL of lysis buffer and incubated for 20 min. After centrifugation at 12,000 rpm for 20 min, the precipitate was discarded, and the protein concentration in the supernatant was determined using a bicinchoninic acid protein assay kit. Protein samples were separated by sodium dodecyl sulfate–polyacrylamide gel electrophoresis and transferred onto polyvinylidene fluoride membranes. The membranes were blocked with 5% skimmed milk for 2 h and then incubated overnight at 4°C with BMP-2 (1:500), RUNX2 (1:800), ALP (1:500), OCN (1:1000), and β-actin (1:5000). Subsequently, the membranes were incubated with secondary antibodies (1:3000) for 1 h at room temperature. Target protein bands were detected using a chemiluminescent imaging system (Bio-Rad, USA).

2.8.2. Enzyme-linked immunosorbent assay

Cellular proteins were extracted using the same method as described above. The levels of BMP-2, RUNX2, ALP, and OCN in the protein samples were quantified and statistically analyzed according to the ELISA instructions.

2.9. Osteogenic induction under an inflammatory microenvironment

The osteogenic induction medium was prepared under an inflammatory microenvironment according to previously reported methods. RAW 264.7 cells were seeded in 12-well

plates at a density of 5×10^5/well, and the culture medium was collected after 24 h of co-culture. After centrifugation, the supernatant was mixed with osteogenic induction medium at a volume ratio of 1:2 to obtain inflammatory osteogenic induction medium. According to the experimental groups (control, LPS, LPS+0BP, LPS+2BP, and LPS+2BP+NIR), BP scaffolds (0BP or 2BP) pre-immersed in complete medium for 30 min were placed into 12-well plates for co-culture with BMSCs. NIR irradiation frequency and other experimental procedures were performed as described above. After 14 days of osteogenic induction, ALP staining was conducted to evaluate osteogenic differentiation.

2.10. Anti-inflammatory mechanism of black phosphorus scaffolds

RAW 264.7 cells were seeded in 12-well plates at a density of 5×10^5/well. After LPS induction, the cells were co-cultured with different BP scaffolds for 48 h and subjected to NIR irradiation according to the group design (LPS+0BP, LPS+2BP, and LPS+2BP+NIR). CD86 immunofluorescence staining was performed following the cytotoxicity assay. The culture medium was discarded, and the cells were washed with PBS for 5 min. Cells were fixed with 4% paraformaldehyde for 15 min and washed three times with PBS for 5 min each. Subsequently, cells were permeabilized with 2 mL of 0.5% Triton X-100 for 10 min and washed with PBS. Blocking was performed using 2% goat serum for 30 min. Cells were then incubated with fluorescent primary antibodies against CD86 for 1 h at room temperature, washed with PBS, and incubated with fluorescent secondary antibodies for 40 min. After washing three times with PBS, DAPI was added for 5 min to stain the nuclei. After final washing (three times), images were captured using an inverted fluorescence microscope (Olympus, Japan). Western blotting was conducted as described in **Section 2.8.1**.

Total RNA was extracted and sequenced on an Illumina NovaSeq 6000 platform (PE150; Illumina, USA). Clean reads were aligned to the rat reference genome (mRatBN7.2) using HISAT2 (v2.0.4). Transcript assembly and fragments per kilobase million quantification were performed using StringTie (v1.3.0). Differentially expressed genes (DEGs) between the 0BP and 2BP groups were identified using edgeR, with thresholds of $|\log_2 FC| \geq 1$ and Q-value ≤ 0.05. Functional enrichment analysis of DEGs was conducted using DAVID. Selected DEGs were validated by quantitative polymerase chain reaction (qPCR) using gene-specific primers (**Table S1**). Complementary DNA was synthesized from total RNA, and qPCR reactions were performed using SYBR Green (Bio-Rad Laboratories, USA). Gene expression levels were normalized to *Gapdh* and calculated using the $2^{-\Delta\Delta Ct}$ method, with six biological replicates ($n = 6$). Statistical significance was assessed using Student's t-test ($p < 0.05$).

2.11. Animal feeding and modeling

2.11.1. Animal husbandry

This study was approved by the Ethics Committee of the Affiliated Hospital of Nanjing University (Approval No. 2025 DW-002-01). Thirty Sprague–Dawley male rats (200 ± 10 g; Jiangsu Qinglongshan Biotechnology Co., Ltd., China) were housed at 24–26°C. All animals were humanely cared for in accordance with the Guide for the Care and Use of Laboratory Animals.

2.11.2. Bone defect modeling and scaffold implantation

After anesthesia, the surgical area was prepared with the lateral femoral condyle as the center. A 1 cm incision was made to expose the femoral shaft, centered on the lateral femoral condyle. The skin, fascia, and muscle were incised layer by layer to expose the lateral side of the knee joint. A bone tunnel with a diameter of 3 mm was drilled in the center of the lateral femoral condyle using a handheld electric drill. The scaffold was then implanted into the bone defect area, and the incision was closed in layers and sterilized with iodine. 3 days postoperatively, 200,000 units of penicillin were administered intramuscularly daily to prevent infection, and incision healing and the animals' condition were monitored.

2.12. Evaluation of the near-infrared response of the scaffold *in vivo*

After surgery, anesthetized rats were irradiated with NIR light (808 nm, 1.2 W/cm^2, 10 min) once per week. An infrared thermal camera was utilized to capture photothermal images, and the corresponding temperature variations were monitored.

2.13. Evaluation of scaffolds for bone repair *in vivo*

2.13.1. Specimen collection

Animals were euthanized at 6 weeks postoperatively to collect the distal femur on the operated side for evaluation of bone repair. Major organs, including the heart, liver, spleen, lungs, and kidneys, were also collected for safety analysis.

2.13.2. Radiological evaluation

Bone regeneration within the defect area was assessed using high-resolution micro-computed tomography (Siemens, Germany) with the following parameters: 80 kV voltage, tube current of 500 μA, and a pixel resolution of 40.5 μm. Reconstructed images in sagittal, coronal, and horizontal planes were acquired, and bone quality within the defect area was quantified using trabecular thickness,

trabecular number, bone mineral density, and bone volume/total volume.

2.13.3. Histological evaluation

After fixation in 4% paraformaldehyde, bone tissue specimens were completely decalcified in 10% ethylenediaminetetraacetic acid and dehydrated in ethanol. The samples were then embedded in paraffin, and 6 μm-thick sections were prepared for histological and immunohistochemical analysis. H&E, Masson's trichrome, BMP-2, and CD86 staining were performed according to the manufacturers' instructions. The stained sections were examined using a light microscope (Model, Nikon, Japan). Image J software was used to evaluate positively stained areas for semi-quantitative analysis.

2.14. *In vivo* biocompatibility analysis

H&E staining of major organs was performed to assess the presence of pathological changes.

2.15. Statistical analysis

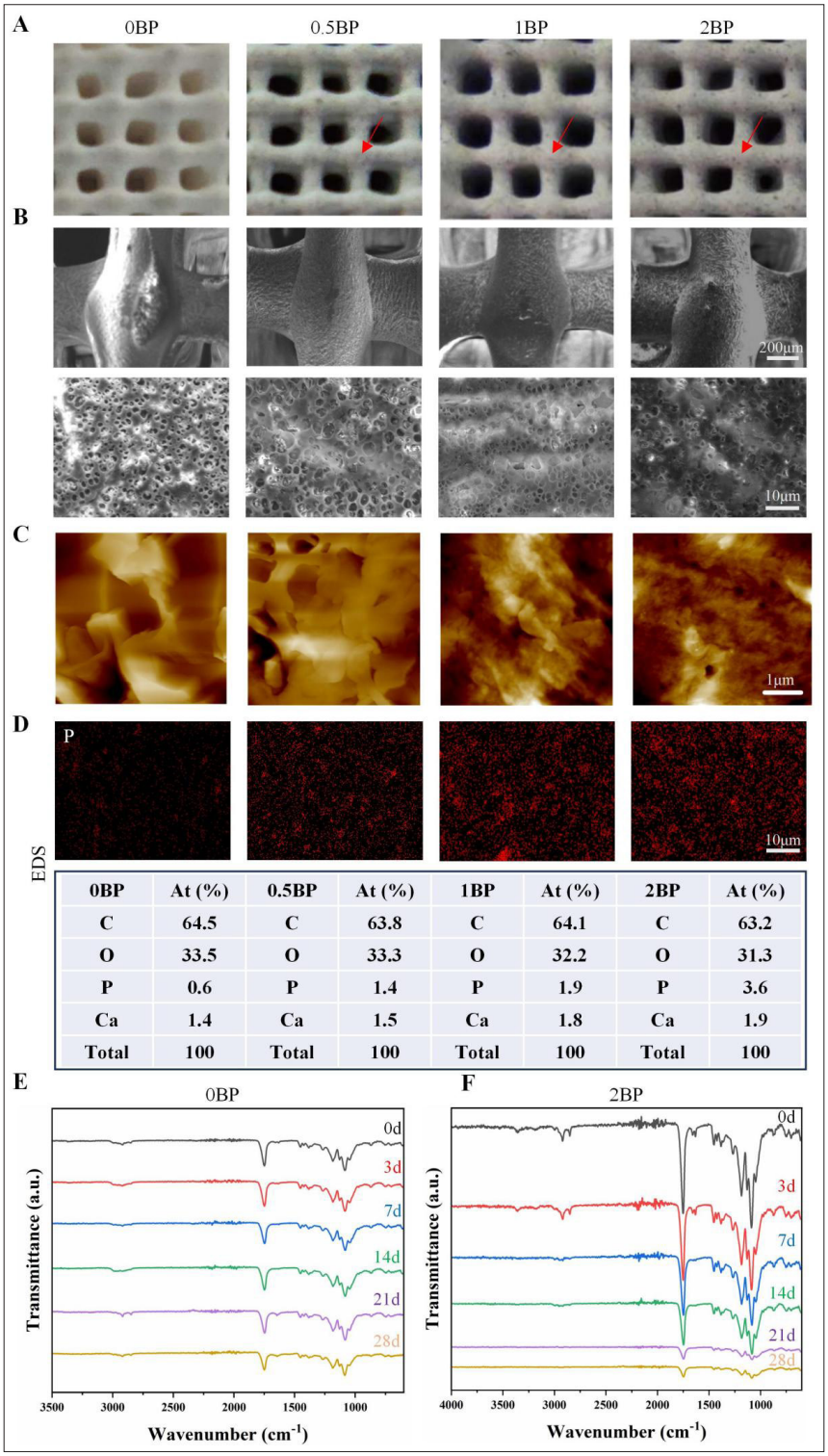
All data are expressed as the mean ± standard deviation. Statistical analyses were performed using analysis of variance followed by Tukey's post hoc test unless otherwise stated. A value of $p < 0.05$ was considered statistically significant ($^{*}p < 0.05$, $^{**}p < 0.01$, $^{***}p < 0.001$) while $p > 0.05$ was considered non-different (ns). Statistical analyses were performed using SPSS 22.0 software (IBM, USA).

3. Results and discussion

3.1. Morphological and chemical characteristics of black phosphorus scaffolds

Figure 1A presents digital images of BP scaffolds with varying mass ratios of BP, all of which exhibit regular, permeable, and porous structures. Given that BP is a black powder, the scaffold without BP incorporation appears milky white, while BP-containing scaffolds generally display a darker color, with uniformly distributed BP visible throughout the scaffolds (indicated by red arrows). The color intensity of the scaffolds gradually deepens with increasing BP content. Notably, excessive BP incorporation leads to clogging of the printing nozzle, hindering scaffold fabrication. After multiple optimizations, a BP mass ratio of 2% was determined to be the maximum feasible concentration. SEM images (Figure 1B) reveal that the scaffold struts are regularly shaped with slight surface curvature. High-magnification SEM images further demonstrate the complex, hierarchical porous structures characteristic of low-temperature deposition technology, which facilitate substance metabolism and exchange, as well as cellular infiltration into the scaffold interior, enabling creeping substitution. Importantly, these porous structures are consistently observed across all scaffolds, indicating that BP incorporation does not alter the scaffold microstructure. Atomic force microscopy further confirms the porous structure morphology and verifies that BP incorporation does not affect the scaffold microstructure (Figure 1C). EDS was employed to analyze phosphorus elemental variations in BP scaffolds. As BP consists solely of phosphorus, changes among the scaffolds were primarily reflected in the phosphorus content. With increasing BP ratio, phosphorus content exhibited a positive correlation with BP incorporation, while the proportions of other elements showed only minor, non-significant fluctuations (Figure 1D).

Figure 1E displays the FTIR spectra of the blank scaffold (0BP), and Figure 1F presents the spectra of the scaffold containing 2% BP (2BP). The primary components of the 0BP scaffold are β-TCP and PLGA. Characteristic absorption peaks at 1750 cm^{-1} and 1080 cm^{-1} correspond to the C=O and C–O bonds of PLGA, respectively. Peaks at 1453 cm^{-1}, 1381 cm^{-1}, 1266 cm^{-1}, and 1190 cm^{-1} are associated with the rocking and bending vibrations of CH_2 and CH_3 groups in PLGA.[24] Absorption peaks in the range of 543–605 cm^{-1} are attributed to the bending vibrations of PO_4^{3-} groups in β-TCP (Figure 1D, black curve).[25,26] Due to the extremely low BP content and overlapping FTIR bands of β-TCP and BP, no distinct spectral differences were observed after BP addition (Figure 1F, black curve).[27] Additionally, Figure 1E and F presents the FTIR spectra of scaffolds immersed in simulated body fluid for 3 days (red curve), 7 days (blue curve), 14 days (green curve), 21 days (purple curve), and 28 days (yellow curve). No significant spectral changes were observed for either 0BP or 2BP over time, indicating minimal chemical alteration or degradation of the scaffolds. These results suggest that the scaffolds possess excellent stability and can maintain their structural and physical properties over the examined period. Figure S1A shows the X-ray diffraction patterns of 0BP and 2BP scaffolds. No obvious differences were observed between the two groups, and the diffraction peaks correspond well with those of tricalcium phosphate ($Ca_3(PO_4)_2$, PDF#86-1585), with characteristic peaks at $2\theta = 30.94°$ and 34.14°. To further confirm the presence of BP in the scaffolds, XPS was conducted to analyze the surface chemical composition. As shown in the XPS survey spectrum (Figure S1B), the phosphorus (P2p) signal is detectable, although relatively weak due to low BP content. High-resolution P2p spectra clearly confirm the presence of phosphorus in the 0.5BP, 1BP, and 2BP scaffolds (Figure S1C), consistent with the EDS results. Collectively, these findings confirm the successful fabrication of BP scaffolds.



0BP	At (%)	0.5BP	At (%)	1BP	At (%)	2BP	At (%)
C	64.5	C	63.8	C	64.1	C	63.2
O	33.5	O	33.3	O	32.2	O	31.3
P	0.6	P	1.4	P	1.9	P	3.6
Ca	1.4	Ca	1.5	Ca	1.8	Ca	1.9
Total	100	Total	100	Total	100	Total	100

Figure 1. Morphology and characterization of BP scaffolds. (A) Top views of scaffolds with different BP contents captured using a digital camera. (B) Scanning electron microscopy images of the scaffolds at different magnifications (scale bars: 200 μm [top row] and 10 μm [bottom row]; magnifications: 60× [top row] and 1000× [bottom row]). (C) Atomic force microscopy images of scaffolds (scale bar: 1 μm; magnification: 2000×). (D) Elemental surface analysis of different scaffolds (scale bar: 10 μm; magnification: 1000×). Fourier transform infrared spectra of (E) 0BP and (F) 2BP scaffolds after immersion in simulated body fluid for 0, 3, 7, 14, 21, and 28 days (d). 0BP, 0.5BP, 1BP, and 2BP represent scaffolds containing 0%, 0.5%, 1%, and 2% BP by mass, respectively. Abbreviations: BP, black phosphorus; EDS, energy-dispersive X-ray spectroscopy.v

3.2. Physical characteristics and *in vitro* photothermal performance of black phosphorus scaffolds

As scaffolds for bone tissue engineering, appropriate porosity and compressive strength are crucial for supporting bone regeneration. Figure 2A and B demonstrates that the fabricated scaffolds exhibited a porosity of 75 ± 3% and a compressive strength of 2.5±0.2 MPa. These parameters fall within the commonly accepted range in bone tissue engineering for mimicking the mechanical and structural properties of cancellous bone.[13] These architectural features are critical for facilitating nutrient exchange, cellular infiltration, and ultimately, the formation of new bone tissue within the defect site. In addition to structural suitability, adequate mechanical strength is pivotal for maintaining stability at the defect area during the early stages of bone healing. Figure 2C shows that scaffolds initially exhibited compressive strength comparable to that of cancellous bone, enabling effective mechanical support immediately after implantation. Although a gradual decrease in compressive strength was observed during degradation, the scaffolds retained most of their mechanical integrity within 4 weeks, ensuring sufficient support during the critical early phase of bone regeneration. Subsequently, the *in vitro* photothermal performance of BP scaffolds was evaluated. Figure 2D illustrates the temperature changes of different scaffolds under NIR irradiation at a constant power. All BP scaffolds exhibited excellent photothermal responsiveness, characterized by a rapid temperature increase within 5 s, followed by a stable plateau. This rapid and stable heating profile is advantageous for achieving controlled thermal stimulation in a timely manner.

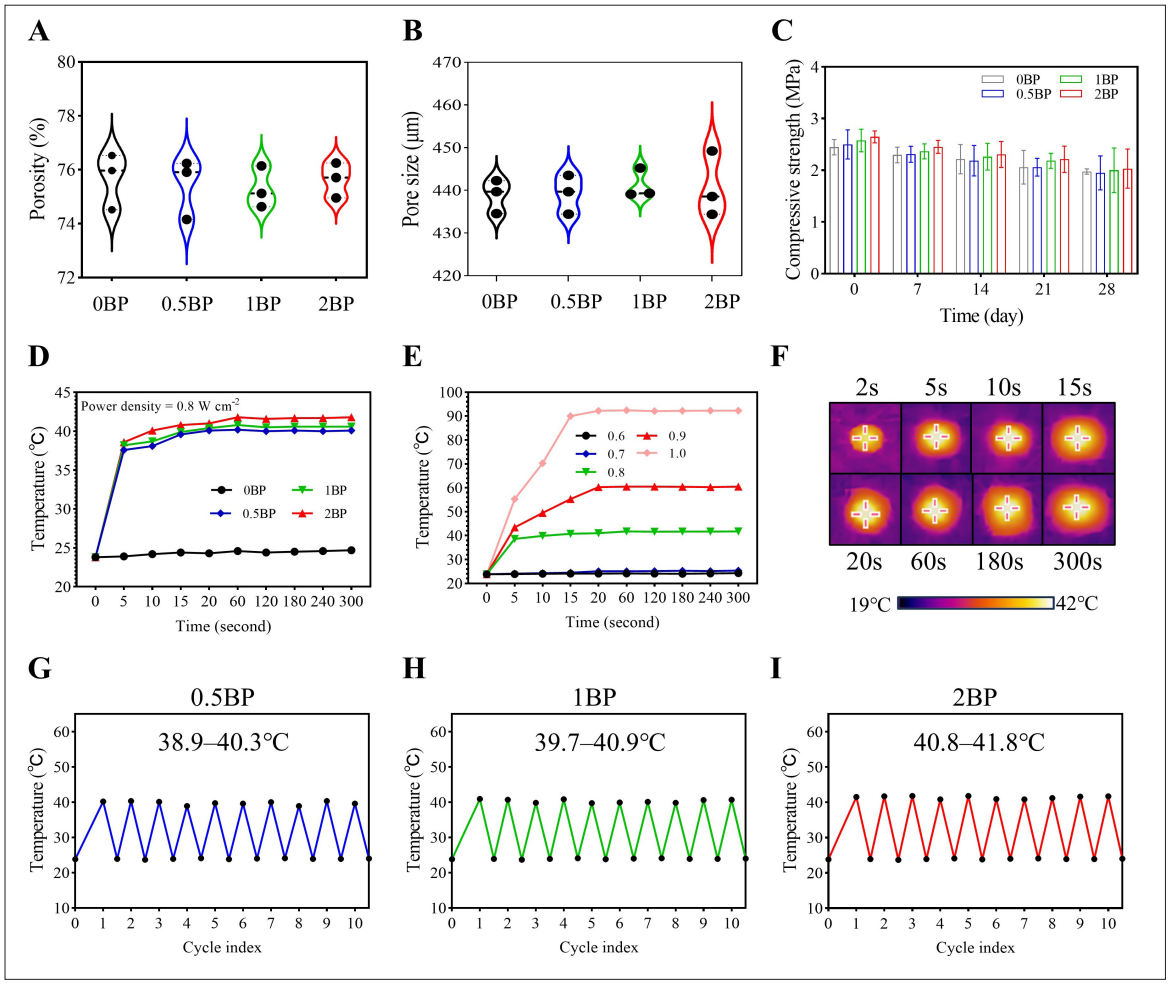


Figure 2. Characterization and photothermal response of black phosphorus (BP) scaffolds. (A) Porosity, (B) pore size, and (C) compressive strength of the scaffolds over time. (D) Temperature rise curves of different scaffolds under near-infrared (NIR) irradiation (808 nm, 0.8 W/cm^2). (E) Temperature rise curves of 2BP under NIR irradiation at different power densities (808 nm, 0.6–1.0 W/cm^2). (F) Infrared thermal images of 2BP under NIR irradiation (808 nm, 0.8 W/cm^2). (G–I) Cyclic photothermal performance of different scaffolds. 0BP, 0.5BP, 1BP, and 2BP represent scaffolds containing 0%, 0.5%, 1%, and 2% BP by mass, respectively.

To optimize the NIR power density, the temperature response of the 2BP under varying NIR power densities was further investigated (Figure 2E). At 0.6 W/cm^2, negligible temperature changes were observed, indicating that a threshold power density is required to trigger effective photothermal conversion. As the power density increased, both photothermal response efficiency and scaffold temperature rose accordingly, with irradiation at 1.0 W/cm^2 resulting in a stable high temperature exceeding 90°C. However, such extreme temperatures pose a risk of thermal damage to surrounding cells and tissues, underscoring the need to identify an optimal power density that balances therapeutic efficacy and biocompatibility. Notably, numerous studies have reported that PTT induced by mild thermal stimulation (40–42°C) promotes BMSC proliferation and osteogenic differentiation, enhances ALP activity, and accelerates mineralization—key processes in effective bone regeneration.[28] Under 0.8 W/cm NIR irradiation, the 2BP scaffold demonstrated efficient photothermal conversion, with the temperature stabilizing within the optimal range (40–42°C) within 5 s (Figure 2E). This observation was further corroborated by infrared thermal images acquired at different time points, which confirmed stable maintenance of mild hyperthermia (Figure 2F). For *in vivo* applications, repeated NIR-irradiation is often required to sustain therapeutic effects, necessitating stable photothermal performance over multiple cycles. Figure 2G–I shows that the 2BP maintained consistent photothermal conversion efficiency over 10 NIR irradiation cycles, ensuring its suitability for repeated therapeutic interventions.

Collectively, these results demonstrate that the BP scaffolds possess favorable physical properties, including appropriate porosity, pore size, and mechanical strength, as well as efficient photothermal conversion capability. Under the optimized NIR power density (0.8 W/cm^2), the scaffolds can generate controlled mild thermal stimulation (40–42°C), which is expected to synergistically enhance bone regeneration by modulating cellular activities while providing structural support. This combination of structural and functional attributes establishes a solid foundation for potential applications in bone defect repair.

3.3. Cytotoxicity and osteogenic induction under an inflammation-free microenvironment *in vitro*

For scaffolds intended for *in vivo* implantation, non-cytotoxicity is a fundamental prerequisite to ensure biocompatibility and avoid adverse host responses. Rat BMSCs were selected as the model cells to evaluate the cytocompatibility of BP scaffolds (Figure 3). Live/Dead staining after co-culture (Figure 3A) revealed minimal red-stained dead cells at all-time points, with extensive green-stained viable cells uniformly distributed, confirming the non-cytotoxic nature of the scaffolds. Consistent with these observations, CCK-8 assays (Figure 3E) demonstrated robust proliferation of BMSCs in all groups over time, further validating the excellent cytocompatibility of the scaffolds. Additionally, nuclear staining of cells co-cultured with scaffolds for 24 h revealed abundant cell adhesion on the scaffold surfaces (Figure 3B), indicating that the scaffolds provide a favorable microenvironment for initial cell attachment. This initial adhesion is a critical step for subsequent cellular processes such as proliferation and differentiation. To determine the optimal BP mass ratio for enhancing osteogenesis, osteogenic induction assays were performed. BMSCs were co-cultured with scaffolds in osteogenic induction medium, and ALP staining was conducted to assess early osteogenic differentiation, as ALP is a key marker enzyme of mature osteoblasts and directly reflects the extent of BMSC osteogenic commitment.[29] The ALP staining results (Figure 3C) showed that the positively stained area increased with increasing BP mass ratios, with statistically significant differences observed among groups (Figure 3F). These results indicate that BP scaffolds promote BMSC osteogenic differentiation in a dose-dependent manner within the tested range, with the 2BP exhibiting the strongest effect. ARS staining was further employed to evaluate late-stage osteogenic mineralization, as calcium nodule formation by osteoblasts represents a terminal marker of mineral deposition. As shown in Figure 3D and **G**, BP scaffolds significantly enhanced mineralization compared to the control, and a higher BP content was associated with increased mineral nodule formation. Collectively, these findings demonstrate that BP scaffolds exhibit excellent biocompatibility (non-cytotoxicity) and significantly promote BMSC osteogenic differentiation and mineralization under inflammation-free conditions. Among the tested formulations, the 2BP scaffold showed the most pronounced osteogenic effect, supporting its selection for subsequent *in vitro* and *in vivo* studies.

3.4. The promotional effect and mechanism of photothermal therapy on osteogenesis of black phosphorus scaffolds

Building upon the above preliminary screening, 2BP was identified as the optimal formulation and was therefore selected for subsequent investigations into the effect of mild PTT (40–42°C) induced by NIR irradiation on osteogenesis. The study design included a control group (0BP) and an experimental group (2BP), with additional NIR-irradiated subgroups to evaluate photothermal-mediated effects. In the absence of NIR stimulation, 2BP already exhibited superior osteogenic potential compared with 0BP, as evidenced by more intense ALP staining and larger areas of mineralized nodules in ARS staining

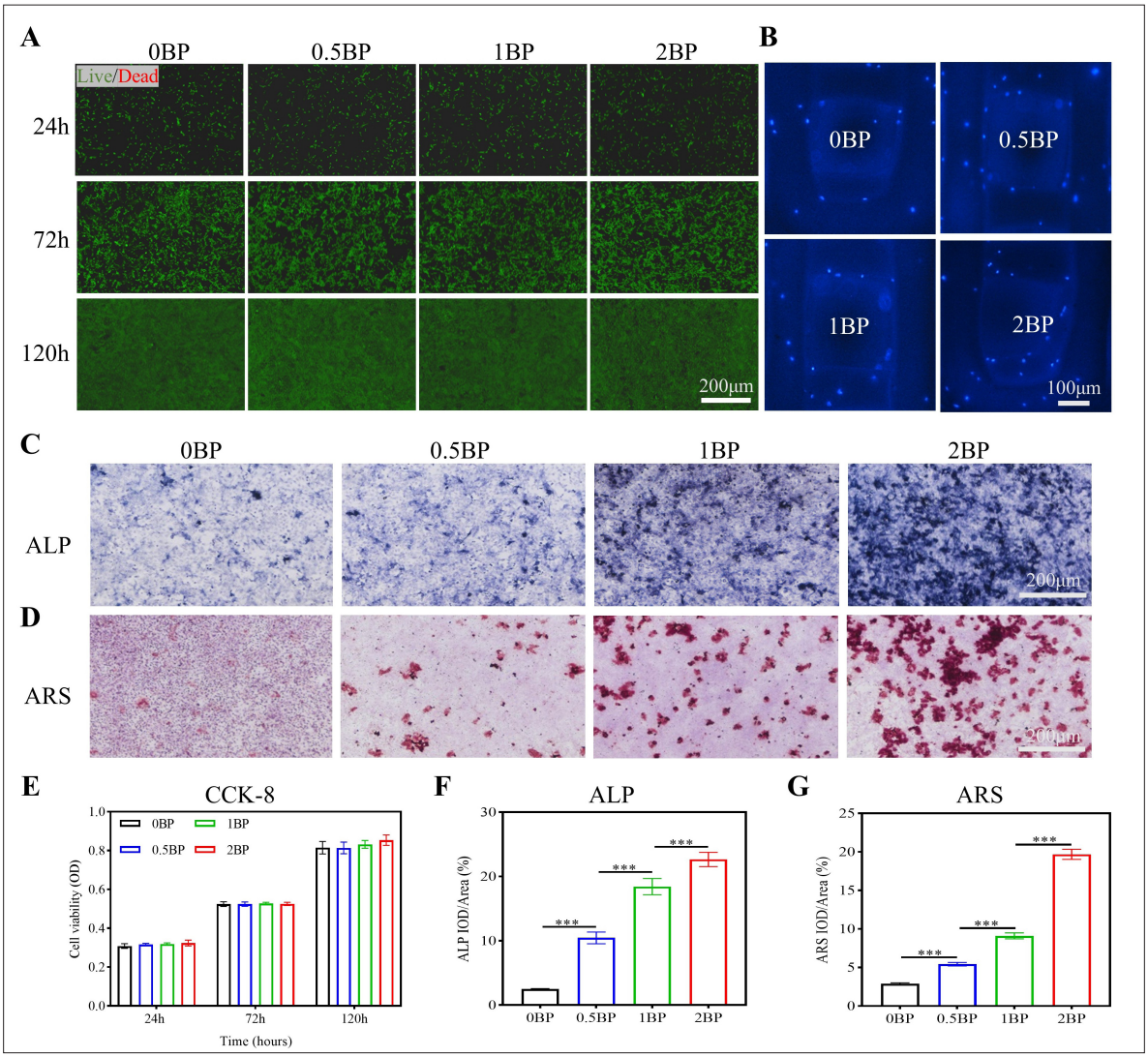


Figure 3. Biocompatibility and osteogenic capacity of black phosphorus (BP) scaffolds. (A) Live/Dead staining of bone marrow mesenchymal stem cells (BMSCs) cultured in scaffold leaching solutions (scale bar: 200 μm; magnification: 40×). (B) Nuclear staining of BMSCs on scaffold surfaces (scale bar: 100 μm; magnification: 40×). (C) alkaline phosphatase (ALP) staining after 6 days of co-culture and (D) Alizarin red S (ARS) staining after 14 days of co-culture (scale bar: 200 μm; magnification: 40×). (E) Cell Counting Kit-8 (CCK-8) assay of BMSCs cultured in scaffold leaching solutions. (F) Semi-quantitative analysis of ALP staining. (G) Semi-quantitative analysis of ARS staining. $n = 6$; ns = $p > 0.05$, *** $p < 0.001$. 0BP, 0.5BP, 1BP, and 2BP represent scaffolds containing 0%, 0.5%, 1%, and 2% BP by mass, respectively.

(Figure 4A & B). Upon NIR irradiation, the 2BP+NIR group showed the most robust osteogenic induction among all groups, with maximal positive expression in both ALP and ARS staining under the same induction period. In contrast, NIR irradiation failed to enhance osteogenesis in the 0BP group, which can be attributed to the lack of BP—a critical photothermal converter—resulting in the inability to generate the requisite mild hyperthermia for PTT.

To explore the underlying mechanism by which 2BP promotes BMSC osteogenic differentiation, an ELISA was performed. The results revealed that the 2BP upregulated the expression of key osteogenic proteins, including BMP-2, RUNX2, ALP, and OCN, with further enhancement observed upon NIR irradiation (Figure 4C). These proteins play pivotal roles in orchestrating osteogenic differentiation and bone maturation: BMP-2 initiates the osteogenic cascade, RUNX2 acts as a master transcription factor regulating osteoblast commitment, ALP mediates early mineralization, and OCN is a late marker of osteoblast maturation, collectively contributing to bone regeneration. The synergistic effect of NIR irradiation is likely dual-faceted: NIR not only accelerates BP degradation to release bioactive phosphorus ions but also provides mild

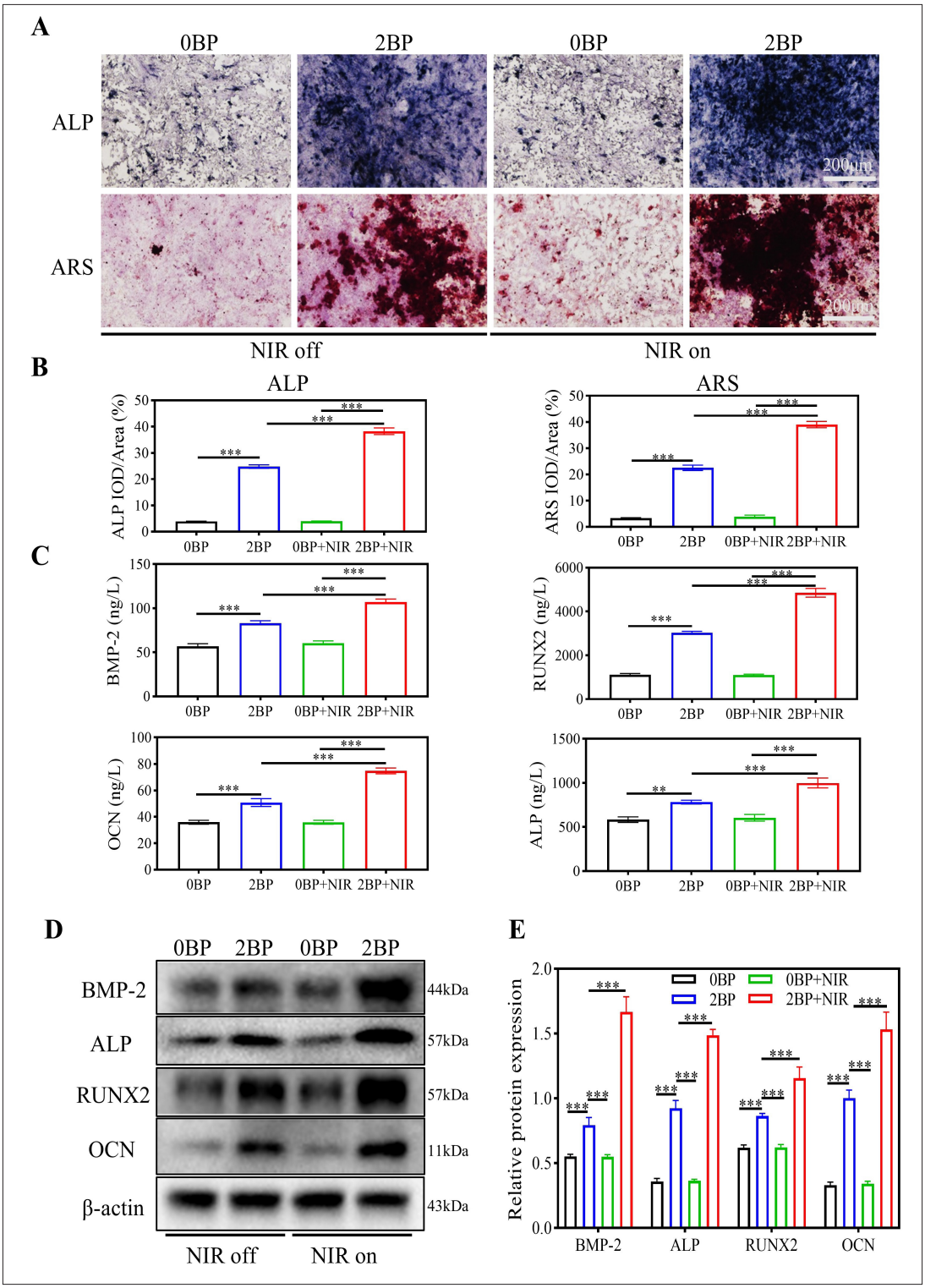


Figure 4. Evaluation of PTT-promoted scaffolds for *in vitro* osteogenesis. (A) ALP staining after cells were co-cultured with scaffolds for 9 days and ARS staining at 21 days (scale bar: 200 μm; magnification: 40×). (B) Semi-quantitative analysis of ALP and ARS staining. (C) Enzyme-linked immunosorbent assay after co-culture of scaffolds with BMSCs. (D) WB after co-culture of scaffolds with BMSCs. (E) Semi-quantitative analysis of WB. Notes: NIR parameters: 808 nm, 0.8 W/cm^2, 5 min per day. $n = 6$, $^*p < 0.05$, $^{**}p < 0.01$, $^{***}p < 0.001$. 0BP and 2BP represent scaffolds containing 0% and 2% BP by mass, respectively. Abbreviations: ALP, alkaline phosphatase; ARS, Alizarin red S; BMP-2, bone morphogenetic protein 2; BMSCs, bone marrow mesenchymal stem cells; NIR, near-infrared; OCN, osteocalcin; PTT, photothermal therapy; RUNX2, runt-related transcription factor 2; WB, Western blot.

thermal stimulation to amplify osteogenic signaling. This mechanism was further validated by Western blot analysis, in which the expression trends of BMP-2, RUNX2, ALP, and OCN were consistent with the ELISA results, with statistically significant upregulation in the 2BP+NIR group (Figure 4D and E). Taken together, these findings demonstrate that 2BP inherently possesses favorable osteogenic capacity and that its combination with NIR-induced mild PTT synergistically enhances osteogenesis through the upregulation of critical osteogenic proteins. This NIR-responsive osteogenic amplification effect highlights 2BP as a promising smart platform for controlled bone regeneration.

3.5. Osteogenic induction under an *in vitro* inflammatory microenvironment

The acute phase of bone injury is typically accompanied by a massive accumulation of pro-inflammatory factors, among which TNF-α and CD86 exert detrimental effects on bone regeneration by disrupting osteoblast differentiation, promoting osteoclast activation, and impairing matrix mineralization. Therefore, modulating the levels of these pro-inflammatory mediators represents a crucial yet often underappreciated strategy to facilitate early-stage bone healing. To address this issue, an *in vitro* model was established to mimic the early inflammatory microenvironment following bone defects, using LPS to induce post-traumatic inflammation, and to evaluate the osteogenic potential of 2BP under pathological conditions (Figure 5).

ALP staining (Figure 5A) and quantitative analysis (Figure 5D) revealed that LPS treatment significantly suppressed BMSC osteogenic differentiation, highlighting the inhibitory effect of excessive inflammation on bone formation. In contrast, 2BP partially reversed this LPS-induced impairment, as evidenced by increased ALP activity compared with the LPS-treated control group. Notably, NIR irradiation further potentiated the osteogenic capacity of 2BP, resulting in the highest ALP expression among all experimental groups and indicating a synergistic interaction between BP and mild photothermal stimulation in counteracting inflammatory inhibition. To elucidate the anti-inflammatory mechanisms underlying these observations, immunofluorescence staining was performed to assess the expression of CD86, a key marker of pro-inflammatory M1 macrophage polarization and a critical mediator of sustained inflammatory cascades.[30] To further analyze the anti-inflammatory mechanism of BP scaffolds and NIR irradiation, the scaffolds were co-cultured with RAW 264.7 cells induced by LPS. As shown in Figure 5B and F, CD86 expression was markedly downregulated in both the 2BP and 2BP+NIR groups, with the latter exhibiting the most pronounced reduction. This suggests that 2BP, particularly when combined with NIR irradiation, exerts robust anti-inflammatory effects by suppressing the expression of pro-inflammatory mediators. These findings were further validated by Western blot analysis (Figure 5C & E), which demonstrated decreased protein levels of both CD86 and TNF-α in the 2BP groups compared with the LPS-treated control. The 2BP+NIR group showed the lowest expression of these pro-inflammatory factors, confirming that NIR-induced mild PTT synergizes with BP to enhance anti-inflammatory efficacy. This synergism may arise from two complementary mechanisms: (i) accelerated BP degradation under NIR irradiation, releasing bioactive phosphorus species with inherent immunomodulatory properties; and (ii) mild thermal stimulation directly suppressing pro-inflammatory signaling pathways in BMSCs and infiltrating immune cells.

Collectively, these results indicate that 2BP possesses intrinsic anti-inflammatory properties, enabling it to partially reverse inflammation-mediated osteogenic inhibition. Under NIR irradiation, this dual functionality—attenuating excessive inflammation while promoting osteogenesis—is significantly enhanced, making 2BP a promising therapeutic platform for bone defect repair under pathological inflammatory conditions. This capacity to simultaneously modulate the inflammatory microenvironment and enhance osteogenic activity addresses a critical unmet need in bone tissue engineering scaffolds.

To further investigate the underlying mechanisms, RNA sequencing analysis was performed on cells from the 0BP and 2BP groups (Figure 6). As shown in Figure 6A, compared with the 0BP group, a total of 4775 genes were significantly upregulated and 2372 genes were significantly downregulated in the 2BP group. Among these DEGs, key regulators including *Hmox1*, *Grem1*, Sqstm1, *Egr1*, and *Irf9* were markedly upregulated (Figure 6B & E). *Hmox1* is a central gene in anti-inflammatory and antioxidant responses, exerting broad cytoprotective, anti-inflammatory, and immunomodulatory effects by degrading heme to produce carbon monoxide, biliverdin, and bilirubin. Furthermore, *Hmox1* promotes osteoblast differentiation, inhibits osteoclastogenesis, and facilitates bone repair.[31,32] *Grem1*, acting as a BMP antagonist, plays a pivotal role in skeletal development and homeostasis by precisely regulating the balance between osteogenesis and chondrogenesis.[33] *Sqstm1* is involved in autophagy and the nuclear factor erythroid 2-related factor 2–Kelch-like ECH-associated protein 1 signaling pathway and is crucial for maintaining osteoblast function; its deficiency

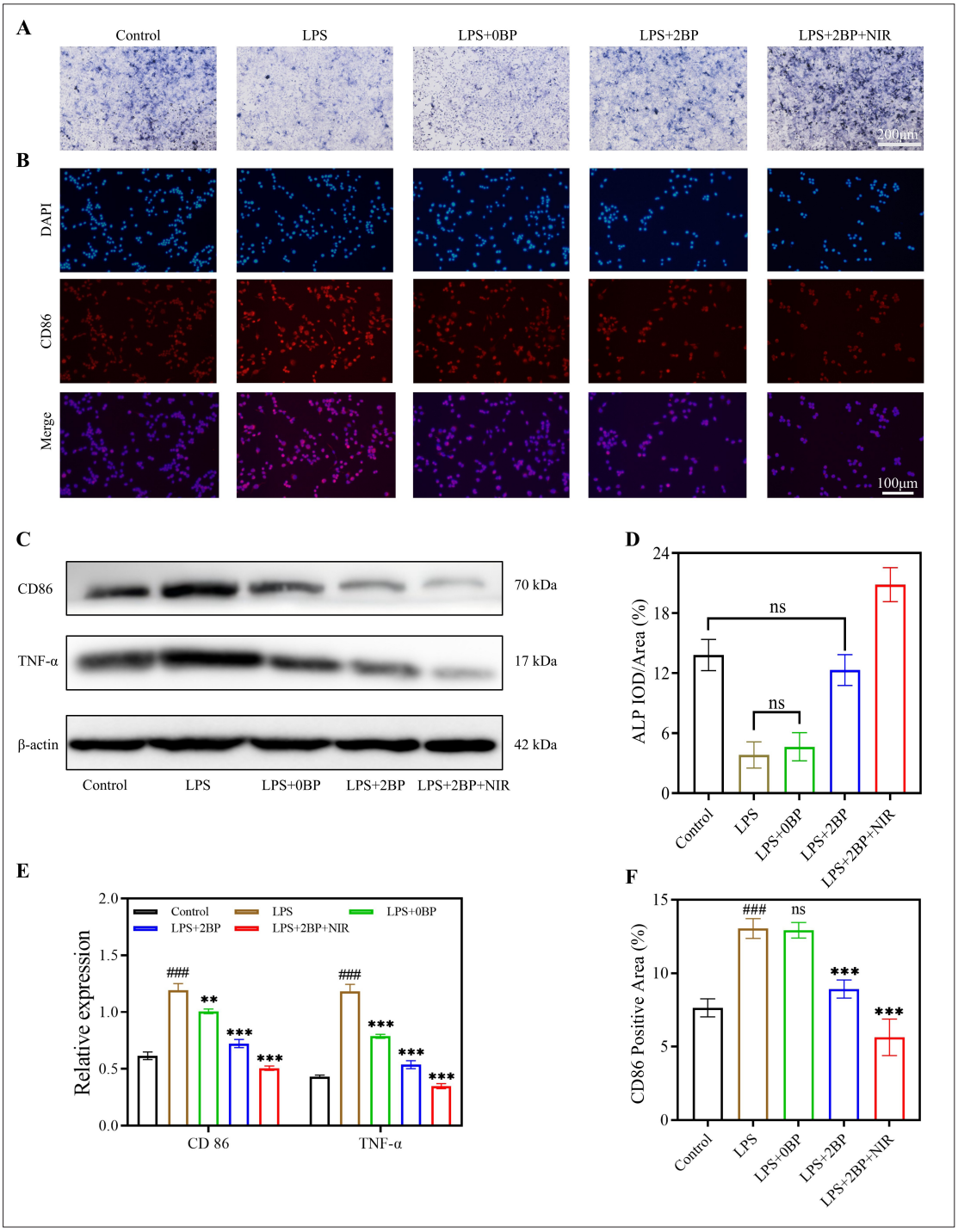


Figure 5. Osteogenic differentiation of BMSCs in an inflammatory microenvironment induced by macrophage-conditioned medium and secretion of inflammatory factors by RAW 264.7 cells under different culture conditions. (A) Alkaline phosphatase staining of BMSCs cultured in conditioned medium for 14 days. The osteogenic induction medium under inflammatory conditions for the control group was prepared by mixing RAW 264.7 culture medium (without additional intervention) and regular osteogenic induction medium at a 1:2 volume ratio (scale bar: 100 μm; magnification: 40×). (B) CD86 staining of LPS-incubated RAW 264.7 cells treated with different BP scaffolds for 48 h. (C) Pro-inflammatory protein expression (CD86, TNF-α) in LPS-incubated RAW 264.7 cells after co-culture with different BP scaffolds for 48 h. (D) Quantitative analysis of BMSCs cultured in conditioned medium for 14 days. (E) Relative protein expression levels. (F) Percentage of CD86-positive cells in different groups. Notes: NIR parameters: 808 nm, 0.8 W/cm^2, 5 min per day. $n = 6$, ns = $p > 0.05$, $^{###}p < 0.001$ vs. control group; $^{**}p < 0.01$ and $^{***}p < 0.001$ vs. LPS group. 0BP and 2BP represent scaffolds containing 0% and 2% BP by mass, respectively. Abbreviation: BMSCs, bone marrow mesenchymal stem cells; CD86, cluster of differentiation 86; DAPI, 4',6-diamidino-2-phenylindole; LPS, lipopolysaccharide; NIR, near-infrared; TNF-α, tumor necrosis factor α.

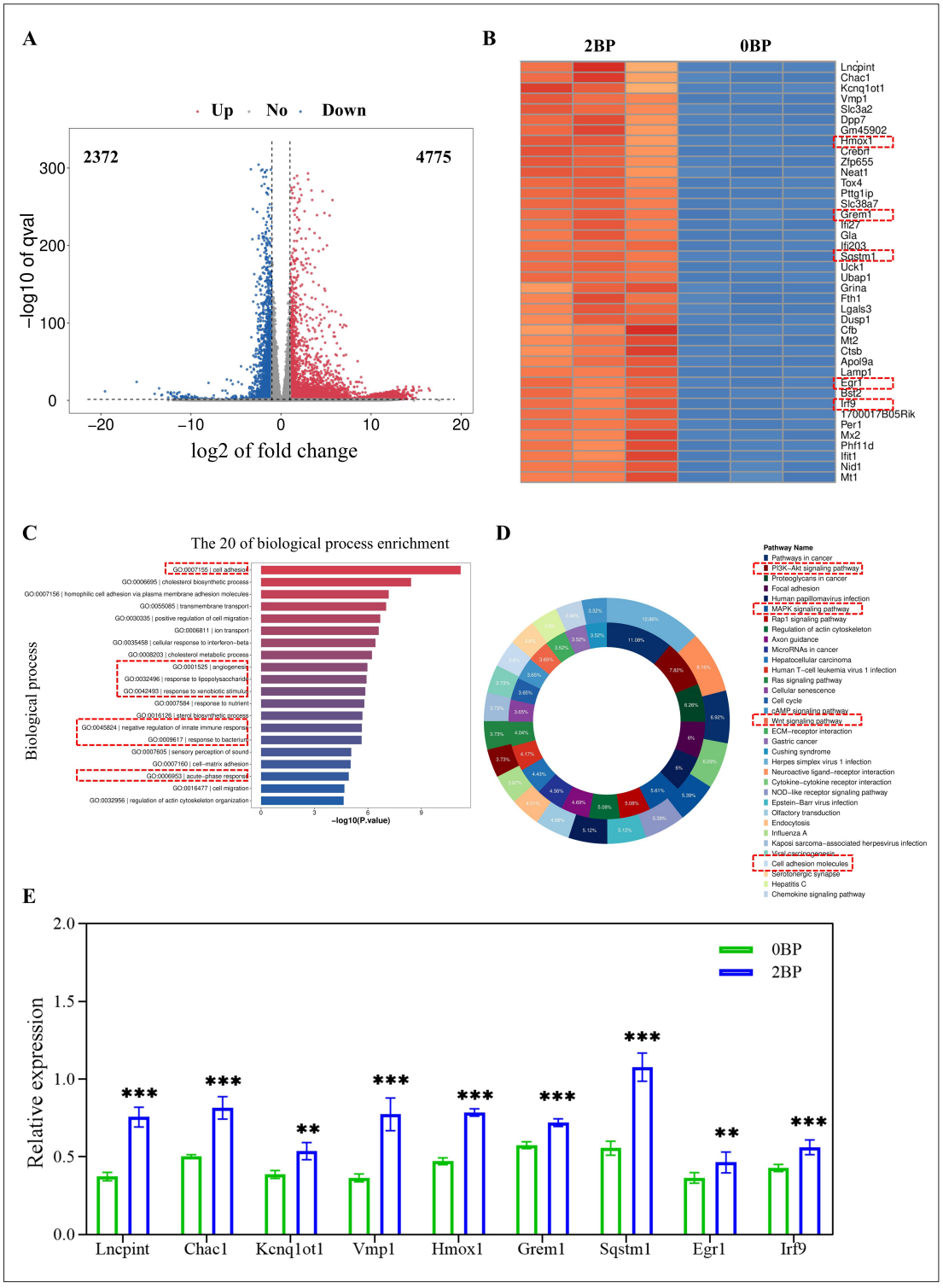


Figure 6. Sequencing results of cells from the 0BP and 2BP groups. (A) Volcano plot of DEGs; downregulated and upregulated genes are shown in blue and red, respectively. (B) Hierarchical clustering heatmap of DEGs. (C) Gene Ontology functional analysis and (D) Kyoto Encyclopedia of Genes and Genomes enrichment analysis of DEGs. (E) Relative expression levels of selected DEGs. $n = 6$; $^{**}p < 0.01$, $^{***}p < 0.001$. 0BP and 2BP represent scaffolds containing 0% and 2% BP by mass, respectively. Abbreviations: AKT, protein kinase B; cAMP, cyclic adenosine monophosphate; DEGs, differentially expressed genes; ECM, extracellular matrix; MAPK, mitogen-activated protein kinase; NOD, nucleotide-binding oligomerization domain-like; PI3K, phosphoinositide 3-kinase; Rap1, ras-proximate-1.

can lead to disrupted bone metabolism. Studies also indicate that *Sqstm1* can induce the expression of various anti-inflammatory genes, including *Hmox1*.[34–36] *Egr1* is a key transcription factor in mechanotransduction-induced osteogenesis, directly promoting the expression of osteogenic genes.[37] *Irf9*, a core component of the interferon signaling pathway, plays a dual role in immune regulation.[38] Collectively, the upregulation of these genes suggests that 2BP can promote the expression of genes associated with both osteogenesis and anti-inflammation. Gene Ontology enrichment analysis of the DEGs revealed several biological processes potentially linked to these effects (Figure 6C), including responses to xenobiotic stimulus, LPS, bacteria, and acute-phase response, all of which are closely associated with anti-inflammatory mechanisms. Conversely, processes such as angiogenesis, cell migration, positive regulation of cell migration, cell–matrix adhesion, and regulation of actin cytoskeleton organization are critically relevant to the proliferation, adhesion, and function of osteogenic cells. Kyoto Encyclopedia of Genes and Genomes pathway analysis further highlighted several signaling pathways that may mediate the osteogenic and anti-inflammatory properties of 2BP, including the phosphoinositide 3-kinase/protein kinase B, mitogen-activated protein kinase, and Wnt signaling pathways, which are well-established regulators of bone formation and inflammatory responses.[38–40] In summary, these transcriptomic findings indicate that the 2BP scaffold may exert its beneficial effects by activating key biological pathways related to osteogenesis and anti-inflammation.

3.6. Radiological evaluation of bone regeneration *in vivo* promoted by black phosphorus scaffolds

A rat model of distal femoral bone defect was established, and scaffolds were implanted into the defect area to evaluate their *in vivo* bone regeneration efficacy (Figure 7A). Figure 7B shows the scaffold (indicated by red arrows) implanted into the bone defect region (marked by green arrows). Infrared thermometry monitoring revealed that the femoral defect area of rats implanted with 2BP exhibited a gradual temperature increase under NIR irradiation, confirming that 2BP can mediate photothermal effects *in vivo* (Figure 7C and D). Specifically, 2BP generated moderate photothermal feedback *in vivo*: under 808 nm NIR irradiation at 1.2 W/cm^2, the local temperature increased significantly within 20 s and reached 41.1°C after 60 s, which falls within the optimal range for promoting osteogenesis without inducing thermal damage. These results further validate that a photothermal converter (i.e., BP) is an essential component for fabricating NIR-responsive scaffolds, as 0BP failed to exhibit measurable temperature elevation under identical conditions. Collectively, these data demonstrate that 2BP can generate mild photothermal effects *in vivo* upon external NIR stimulation, a property hypothesized to accelerate bone repair through thermally modulated cellular activities and enhanced tissue perfusion.

At 6 weeks post-implantation, micro-computed tomography was performed to assess bone regeneration in the defect area. As shown in Figure 7E, all scaffold groups exhibited new bone formation around the implant, with the formation of a regenerative bone bridge connecting the host bone and scaffold. Notably, the BP scaffold group showed a significantly thicker and denser bone bridge compared with the 0BP group, indicating that BP incorporation enhances bone repair. Among all groups, the 2BP+NIR group achieved the most extensive bone regeneration, with visible trabecular ingrowth into the scaffold pores, consistent with the *in vitro* findings of synergistic osteogenesis under photothermal stimulation. Interestingly, the 0BP+NIR group exhibited slightly improved bone repair compared with the 0BP group, despite the lack of significant differences in osteogenic markers observed *in vitro*. This *in vivo–in vitro* discrepancy may be attributed to the following: although 0BP cannot generate BP-mediated photothermal conversion, NIR irradiation may induce mild hyperthermia in the surrounding tissues through non-specific absorption, thereby improving local blood circulation and nutrient exchange—factors that play a more prominent role *in vivo* than in static *in vitro* cultures. However, this effect was relatively modest and did not reach statistical significance, reinforcing the necessity of BP as a specific photothermal agent for robust therapeutic efficacy. Quantitative analysis of new bone formation (Figure 7F) included trabecular thickness (μm), trabecular number (1/mm), bone mineral density (g/cm^2), and bone volume fraction (%). All parameters, which are well-recognized indicators of bone quality and regeneration extent, positively correlated with the qualitative repair outcomes: the 2BP+NIR group achieved the highest values, followed by the 2BP group, while the 0BP+NIR group showed a non-significant trend toward improved outcomes compared with the 0BP group.

In summary, 2BP exhibits excellent NIR responsiveness *in vivo*, and NIR irradiation significantly accelerates bone repair. Clinically, such efficient bone regeneration could mitigate repair failure caused by inter-individual heterogeneity, which remains a major challenge in current bone defect treatments. Furthermore, accelerated bone healing aligns with the principles of Enhanced Recovery After Surgery, which emphasize minimizing surgical trauma and promoting rapid functional recovery.[41] By

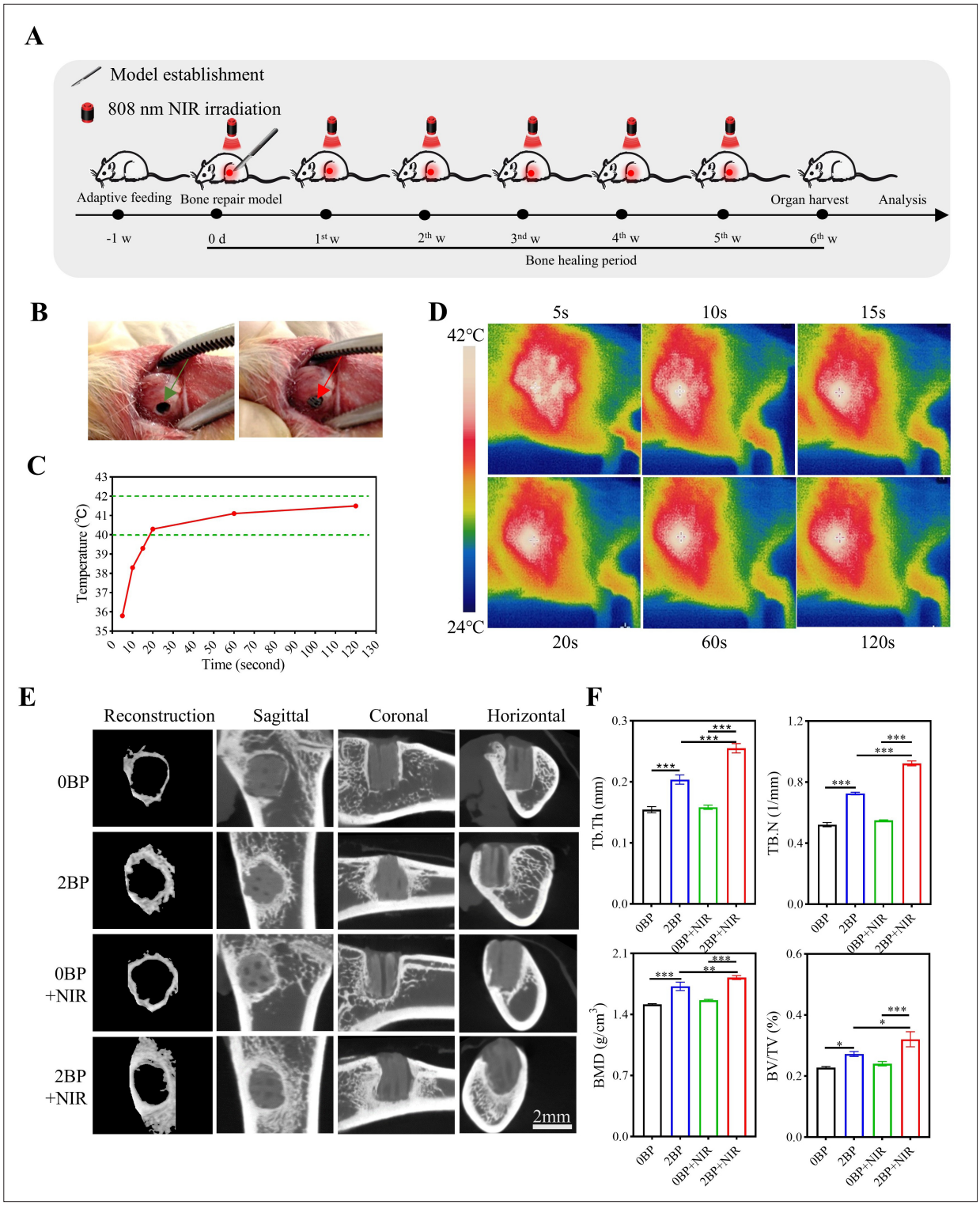


Figure 7. *In vivo* photothermal response properties of scaffolds and radiological evaluation of bone repair. (A) Flow chart of the animal experiment. (B) Scaffolds implantation process. Green arrow: bone defect area; red arrow: scaffold. (C) Temperature rise curves at different time points and (D) *in vivo* photothermal effect of 2BP at corresponding time points. (E) Qualitative micro-computed tomography images of bone repair in the distal femur of rats 6 weeks after surgery. (F) Quantitative analysis of bone repair. Notes: NIR parameters: 808 nm, 1.2 W/cm^2, 10 min per week. $n = 3$, $^*p < 0.05$, $^{**}p < 0.01$, $^{***}p < 0.001$. 0BP and 2BP represent scaffolds containing 0% and 2% BP by mass, respectively. Abbreviations: BMD, bone mineral density; BV/TV, bone volume/total volume; NIR, near-infrared; TB.N, trabecular number; Tb.Th, trabecular thickness.

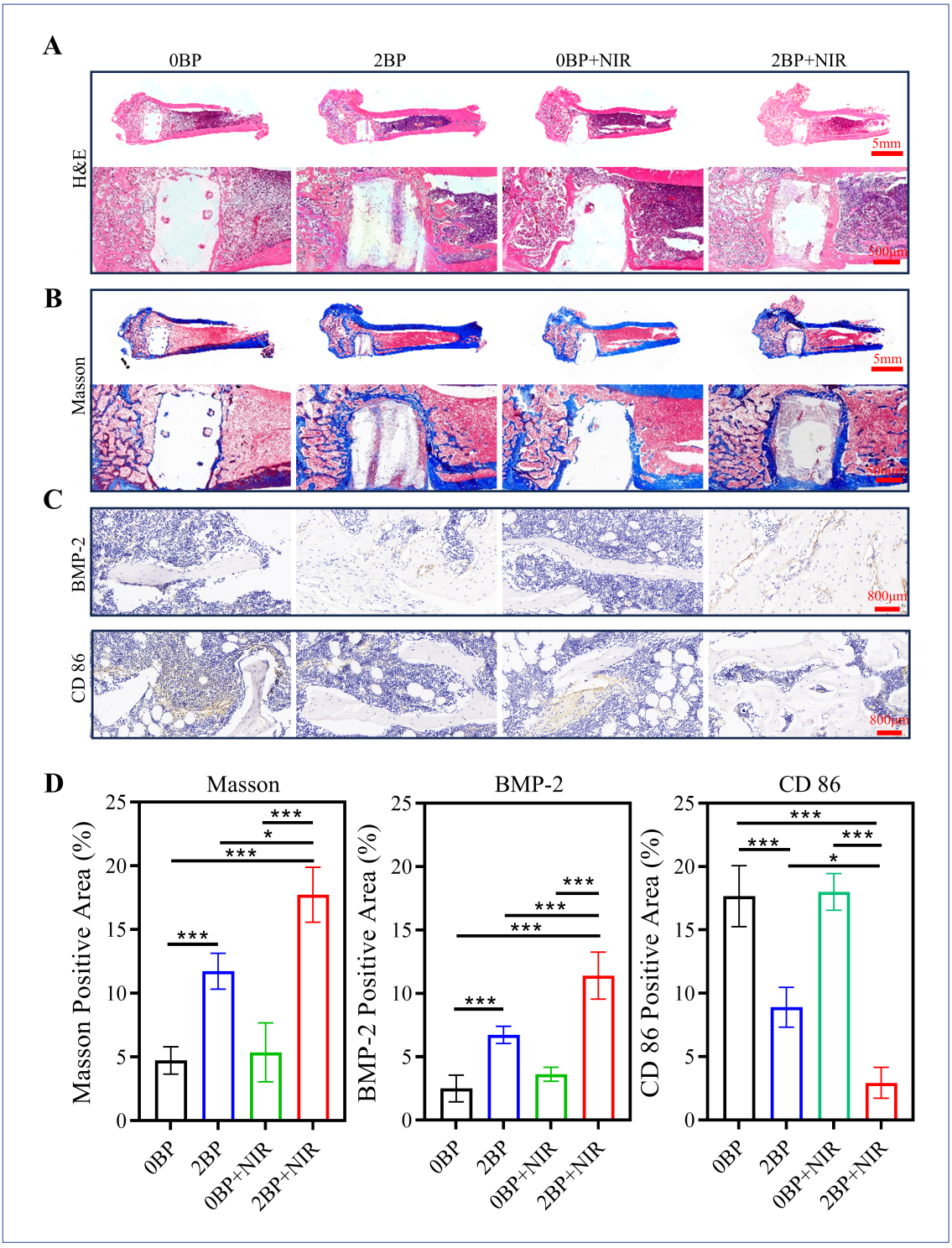


Figure 8. Bone tissue analysis for the bone defects of animals. (A) Hematoxylin and eosin (H&E) staining and (B) Masson's trichrome staining (scale bars: 5 mm [top row] and 500 μm [bottom row]; magnifications: 4× [top row] and 40×[bottom row]). (C) bone morphogenetic protein 2 (BMP-2) and cluster of differentiation 86 (CD86) staining (scale bar: 800 μm). (D) Corresponding relative positive area for Masson's trichrome, BMP-2, and CD86 staining. Notes: Near infrared (NIR) parameters: 808 nm, 1.2 W/cm^2, 10 min per week. $n = 3$, $^*p < 0.05$, $^{**}p < 0.01$, $^{***}p < 0.001$. 0BP and 2BP represent scaffolds containing 0% and 2% BP by mass, respectively.

enabling controlled photothermal stimulation to enhance regeneration, the 2BP holds promise for addressing unmet clinical needs in personalized bone defect therapy.

3.7. Histological evaluation of black phosphorus scaffolds for promoting bone regeneration *in vivo*

To further validate the bone repair efficacy of the scaffolds in defect areas, histological evaluations of peri-scaffold bone regeneration were performed. H&E staining and Masson's trichrome staining (Figure 8A & B) consistently demonstrated varying degrees of bone repair across all groups at 6 weeks post-implantation, with the 2BP+NIR group exhibiting the most robust regenerative outcomes. Specifically, this group showed dense trabecular bone formation, a thick and well-integrated bone repair bridge, and substantial new bone tissue within the defect area, indicating successful scaffold–host bone integration and progressive defect filling. BMP-2 is a key cytokine that directs BMSC differentiation into osteoblasts, promotes osteoblast maturation, and orchestrates bone remodeling, making it a critical mediator of *in vivo* bone repair. Immunohistochemical staining for BMP-2 and subsequent quantitative analysis (Figure 8C & D) were consistent with the histological repair patterns: the 2BP+NIR group displayed the highest BMP-2 expression, with statistically significant differences compared with other groups, confirming enhanced osteogenic signaling. In parallel, CD86 staining (Figure 8C & D) revealed that 2BP significantly suppressed local CD86 expression, with NIR irradiation further amplifying this anti-inflammatory effect to a statistically significant extent. These findings corroborate earlier *in vitro* observations, highlighting the scaffold's ability to modulate the inflammatory microenvironment *in vivo*, which is pivotal for establishing a favorable milieu for bone regeneration.

Collectively, these results confirm that 2BP outperforms conventional scaffolds (0BP) in promoting bone repair, likely through the dual mechanisms of upregulating pro-osteogenic factors and downregulating pro-inflammatory markers. Importantly, NIR irradiation synergistically enhances these effects, leading to significantly accelerated and more robust bone regeneration. Notably, sporadic cases of repair failure—characterized by scaffold loosening and lack of host bone integration—were observed in all groups except the 2BP+NIR group. This observation underscores a critical advantage of NIR-mediated photothermal stimulation: by enabling highly efficient bone regeneration, it mitigates the inter-individual heterogeneity in repair outcomes that often compromises conventional bone grafting strategies. Consequently, the 2BP+NIR approach holds promise for improving the overall success rate of bone defect repair, particularly in patient populations with limited regenerative capacity.

3.8. Biosafety evaluation of black phosphorus scaffolds *in vivo*

H&E staining (Figure S2) of major organs, including heart, liver, spleen, lungs, and kidneys, harvested from rats at week 6, revealed no pathological abnormalities. These results indicate that the BP scaffolds exhibit good biocompatibility and can be safely applied *in vivo*.

4. Conclusion

In this study, BP—a photothermal agent with excellent photothermal conversion efficiency—was incorporated into previously developed PLGA/β-TCP slurry to fabricate NIR-responsive BP scaffolds. These scaffolds were designed for bone defect repair by leveraging exogenous mild photothermal stimulation to enable PTT for accelerated bone regeneration. Structurally, the BP scaffolds mimicked cancellous bone architecture and were characterized by interconnected pores that facilitate nutrient exchange and cellular infiltration. Biologically, they exhibited superior biomineralization capacity, excellent biocompatibility, and non-cytotoxicity, as validated by *in vitro* cellular assays. The incorporation of BP endowed the scaffolds with robust NIR responsiveness, enabling on-demand, repeated, and controllable PTT interventions—a critical feature for personalized therapeutic regimens. Among the formulations tested, 2BP demonstrated optimal osteogenic and anti-inflammatory properties, making it particularly suitable for *in vivo* bone defect repair. These intrinsic functionalities were significantly potentiated under NIR irradiation, likely through synergistic mechanisms: (i) BP-mediated photothermal conversion generating mild hyperthermia (40–42°C) to enhance osteogenic signaling and modulate immune responses; (ii) accelerated BP degradation under NIR irradiation, leading to the release of bioactive phosphorus species that further promote mineralization and dampen inflammation. Notably, NIR-triggered PTT using 2BP represents a minimally invasive, spatiotemporally controllable intervention strategy that aligns with clinical needs for safe and efficient acceleration of bone repair. *In vivo* studies confirmed that the 2BP+NIR group achieved the highest bone repair success rate, with a reduced incidence of repair failure caused by inter-individual heterogeneity. This advantage is attributed to the scaffold's ability to override suboptimal regenerative microenvironments through controlled photothermal stimulation. Collectively, the NIR-responsive BP scaffold integrates multiple complementary functionalities, including structural mimicry, biocompatibility, osteogenesis promotion, anti-inflammatory effects, and controllable photothermal stimulation, to drive rapid bone defect repair. Its versatility and therapeutic efficacy position it as a promising candidate for clinical translation,

particularly in challenging scenarios such as large bone defects or bone repair in inflamed microenvironments.

Acknowledgments

None

Funding

This research was funded by the Eaglet Take-off Project of Jiangsu Provincial Association of Chinese Medicine (No. CYTF2024022) and the Feihong Plan of Nanjing TCM Hospital Affiliated to Nanjing University of Chinese Medicine (No. FHJH202405).

Conflict of interest

The authors declare that they have no known competing financial interests or personal relationships that could have influenced the work reported in this article.

Author contributions

Conceptualization: Chenjian Peng
Formal analysis: Peng Xue
Funding acquisition: Peng Xue
Investigation: Wei Zhang
Methodology: Anlong Liu, Chenjian Peng, Jun Wang
Project administration: Hongzhong Xi, Anlong Liu
Resources: Jianning Zhao
Software: Aoyun Hu
Supervision: Jianning Zhao
Validation: Hongzhong Xi, Wei Zhang, Jun Wang
Visualization: Aoyun Hu
Writing–original draft: Peng Xue
Writing–review & editing: Peng Xue, Hongzhong Xi

Ethics approval and consent to participate

This study was approved by the Ethics Committee of The Affiliated Hospital of Nanjing University (approval number: 2025 DW-002-01).

Consent for publication

Not applicable.

Availability of data

The data that support the findings of this study are available from the corresponding author upon reasonable request.

References

1. Wang J, Wu Y, Li G, *et al*. Engineering large-scale self-mineralizing bone organoids with bone matrix-inspired hydroxyapatite hybrid bioinks. *Adv Mater*. 2024;36(30):e2309875.
doi: 10.1002/adma.202309875

2. Chen H, Xi H, Guo M, *et al*. PLGA/β-TCP/ICT composite scaffold incorporating MXene (Ti3C2Tx) promotes osteogenesis through near-infrared-mediated mild photothermal therapy. *Mater Des*. 2024;244:113083.
doi: 10.1016/j.matdes.2024.113083

3. Chen H, Tan X, Fu J, *et al*. γ-Fe2O3/polydopamine/TiO2 nano-porous array composite coating (FPTCC) to modulate antibacterial, osteogenesis, and osseointegration through photothermal-magnetic response. *Mater Des*. 2024;248:113516.
doi: 10.1016/j.matdes.2024.113516

4. Hu X, Chen J, Yang S, *et al*. 3D printed multifunctional biomimetic bone scaffold combined with TP-Mg nanoparticles for the infectious bone defects repair. *Small*. 2024;20(40):e2403681.
doi: 10.1002/smll.202403681

5. Xie C, Ye J, Liang R, *et al*. Advanced strategies of biomimetic tissue-engineered grafts for bone regeneration. *Adv Healthc Mater*. 2021;10(14):e2100408.
doi: 10.1002/adhm.202100408

6. Huang Y, Wan X, Su Q, *et al*. Ultrasound-activated piezo-hot carriers trigger tandem catalysis coordinating cuproptosis-like bacterial death against implant infections. *Nat Commun*. 2024;15(1):1643.
doi: 10.1038/s41467-024-45619-y

7. Robin M, Mouloungui E, Castillo Dali G, *et al*. Mineralized collagen plywood contributes to bone autograft performance. *Nature*. 2024;636(8041):100-107.
doi: 10.1038/s41586-024-08208-z

8. Shen X, Zhang Z, Cheng C, *et al*. Bone regeneration and antibacterial properties of calcium-phosphorus coatings induced by gentamicin-loaded polydopamine on magnesium alloys. *Biomed Technol*. 2024;5:87-101.
doi: 10.1515/bmt-2023-0104

9. Liu X, Zhou J, Chen M, *et al*. 3D-printed biomimetic bone scaffold loaded with lyophilized concentrated growth factors promotes bone defect repair by regulation the VEGFR2/PI3K/AKT signaling pathway. *Int J Biol Macromol*. 2024;282(Pt 2):136938.
doi: 10.1016/j.ijbiomac.2024.136938

10. Liang W, Zhou C, Liu X, Pan B, Qian Y, Yang W. Current status of nano-embedded growth factors and stem cells delivery to bone for targeted repair and regeneration. *J Orthop Transl*. 2025;50:257-273.
doi: 10.1016/j.jot.2024.12.003

11. Zhao R, Han F, Yu Q, *et al*. A multifunctional scaffold that promotes the scaffold-tissue interface integration and rescues the ROS microenvironment for repair of annulus fibrosus defects. *Bioact Mater*. 2024;41:257-270.

doi: 10.1016/j.bioactmat.2024.06.025

12. Sun X, Gao Y, Li Z, He J, Wu Y. Magnetic responsive hydroxyapatite scaffold modulated macrophage polarization through PPAR/JAK-STAT signaling and enhanced fatty acid metabolism. *Biomaterials*. 2023;295: 122051.
doi: 10.1016/j.biomaterials.2023.122051

13. Xue P, Tan X, Xi H, *et al*. Low-temperature deposition 3D printing biotin-doped PLGA/β-TCP scaffold for repair of bone defects in osteonecrosis of femoral head. *IJB*. 2023;10(1):1152.
doi: 10.36922/ijb.1152

14. Xue P, Chen H, Xi H, *et al*. Magnesium dopped calcium-fluoride/icaritin composite multi-layer coating functionalized 3D printed β-TCP scaffold induces sustained bone regeneration in a rabbit model. *Mater Des*. 2022;223:111156.
doi: 10.1016/j.matdes.2022.111156

15. Sun H, Xu J, Wang Y, *et al*. Bone microenvironment regulative hydrogels with ROS scavenging and prolonged oxygen-generating for enhancing bone repair. *Bioact Mater*. 2023;24:477-496.
doi: 10.1016/j.bioactmat.2022.12.021

16. Yang X, Yang X, Luo P, *et al*. Novel one-pot strategy for fabrication of a pH-responsive bone-targeted drug self-frame delivery system for treatment of osteoporosis. *Mater Today Bio*. 2023;20:100688.
doi: 10.1016/j.mtbio.2023.100688

17. Xue P, Xi H, Chen H, He S, Liu X, Du B. Predictive value of clinical features and CT radiomics in the efficacy of hip preservation surgery with fibula allograft. *J Orthop Surg Res*. 2023;18(1):940.
doi: 10.1186/s13018-023-04431-y

18. Chen H, Xue P, Xi H, *et al*. A deep-learning model for predicting the efficacy of non-vascularized fibular grafting using digital radiography. *Acad Radiol*. 2024;31(4):1501-1507.
doi: 10.1016/j.acra.2023.10.023

19. Chen H, Xue P, Xi H, *et al*. Predicting efficacy and guiding procedure choice in non-vascularized bone grafting: a CT radiomics and clinical predictor approach. *BMC Musculoskelet Disord*. 2023;24(1):959.
doi: 10.1186/s12891-023-07095-1

20. Couce ML, Saenz de Pipaon M. Bone mineralization and calcium phosphorus metabolism. *Nutrients*. 2021;13(11):3692.
doi: 10.3390/nu13113692

21. Hou J, Yin S, Jiao R, *et al*. The combination of hydrogels and rutin-loaded black phosphorus nanosheets treats rheumatoid arthritis. *Mater Today Bio*. 2024;29:101264.
doi: 10.1016/j.mtbio.2024.101264

22. Huang S, Xu S, Hu Y, *et al*. Preparation of NIR-responsive, ROS-generating and antibacterial black phosphorus quantum dots for promoting the MRSA-infected wound healing in diabetic rats. *Acta Biomater*. 2022;137:199-217.
doi: 10.1016/j.actbio.2021.10.008

23. Wang W, Zhang G, Wang Y, *et al*. An injectable and thermosensitive hydrogel with nano-aided NIR-II phototherapeutic and chemical effects for periodontal antibacteria and bone regeneration. *J Nanobiotechnology*. 2023;21(1):367.
doi: 10.1186/s12951-023-02124-6

24. Wang M, Lu X, Yin X, *et al*. Synchrotron radiation-based Fourier-transform infrared spectromicroscopy for characterization of the protein/peptide distribution in single microspheres. *Acta Pharm Sin B*. 2015;5(3):270-276.
doi: 10.1016/j.apsb.2015.03.008

25. Zairani NAS, Jaafar M, Ahmad N, Abdul Razak K. Fabrication and characterization of porous β-tricalcium phosphate scaffolds coated with alginate. *Ceram Int*. 2016;42(4):5141-5147.
doi: 10.1016/j.ceramint.2015.12.034

26. Kang KR, Piao ZG, Kim JS, *et al*. Synthesis and characterization of β-tricalcium phosphate derived from *Haliotis* sp. shells. *Implant Dent*. 2017;26(3):378-387.
doi: 10.1097/ID.0000000000000559

27. Ma S, Wei Y, Sun R, *et al*. Calcium phosphate bone cements incorporated with black phosphorus nanosheets enhanced osteogenesis. *ACS Biomater Sci Eng*. 2023;9(1):292-302.
doi: 10.1021/acsbiomaterials.2c00742

28. Xue P, Chang Z, Chen H, *et al*. Macrophage membrane (MMs) camouflaged near-infrared (NIR) responsive bone defect area targeting nanocarrier delivery system (BTNDS) for rapid repair: promoting osteogenesis via phototherapy and modulating immunity. *J Nanobiotechnology*. 2024;22(1):87.
doi: 10.1186/s12951-024-02351-5

29. Shen G, Ren H, Shang Q, *et al*. Foxf1 knockdown promotes BMSC osteogenesis in part by activating the Wnt/β-catenin signalling pathway and prevents ovariectomy-induced bone loss. *EBioMedicine*. 2020;52:102626.
doi: 10.1016/j.ebiom.2020.102626

30. Kennedy A, Waters E, Rowshanravan B, *et al*. Differences in CD80 and CD86 transendocytosis reveal CD86 as a key target for CTLA-4 immune regulation. *Nat Immunol*. 2022;23(9):1365-1378.
doi: 10.1038/s41590-022-01289-w

31. He R, Wang Z, Cui M, *et al*. HIF1A alleviates compression-induced apoptosis of nucleus pulposus derived stem cells via upregulating autophagy. *Autophagy*. 2021;17(11): 3338-3360.
doi: 10.1080/15548627.2021.1872227

32. Hu L, Yu Y, Shen Y, *et al*. Ythdf2 promotes pulmonary hypertension by suppressing Hmox1-dependent anti-inflammatory and antioxidant function in alveolar macrophages. *Redox Biol*. 2023;61:102638.

doi: 10.1016/j.redox.2023.102638

33. Ng JQ, Jafarov TH, Little CB, *et al*. Loss of Grem1-lineage chondrogenic progenitor cells causes osteoarthritis. *Nat Commun*. 2023;14(1):6909. doi: 10.1038/s41467-023-42199-1

34. Agas D, Gabai V, Sufianov AA, Shneider A, Sabbieti MG. P62/SQSTM1 enhances osteogenesis and attenuates inflammatory signals in bone marrow microenvironment. *Gen Comp Endocrinol*. 2022;320:114009. doi: 10.1016/j.ygcen.2022.114009

35. Tang D, Kang R. SQSTM1 is a therapeutic target for infection and sterile inflammation. *Cytokine*. 2023;169: 156317. doi: 10.1016/j.cytokine.2023.156317

36. Lingli Z, Xing H, Liqiu W, *et al*. Palmitoylation restricts SQSTM1/p62-mediated autophagic degradation of NOD2 to modulate inflammation. *Cell Death Differ*. 2022;29(8):1541-1551. doi: 10.1038/s41418-022-00942-z

37. Li Y, Lu D, Xu F, *et al*. EGR1 promotes craniofacial bone regeneration via activation of ALPL^{+}PDGFD^{+} periosteal stem cells. *Adv Sci (Weinh)*. 2025;12(30):e10243. doi: 10.1002/advs.202410243

38. Zhang H, Cai D, Bai X. Macrophages regulate the progression of osteoarthritis. *Osteoarthritis Cartilage*. 2020;28(5):555-561. doi: 10.1016/j.joca.2020.01.007

39. Wang J, Zhang Y, Cao J, *et al*. The role of autophagy in bone metabolism and clinical significance. *Autophagy*. 2023;19(9):2409-2427. doi: 10.1080/15548627.2023.2186112

40. Katz JN, Arant KR, Loeser RF. Diagnosis and treatment of hip and knee osteoarthritis: a review. *JAMA*. 2021;325(6):568-578. doi: 10.1001/jama.2020.22171

41. Xie C, Liang R, Ye J, *et al*. High-efficient engineering of osteo-callus organoids for rapid bone regeneration within one month. *Biomaterials*. 2022;288:121741. doi: 10.1016/j.biomaterials.2022.121741

ACCSCIENCE PUBLISHING

International Journal of Bioprinting

RESEARCH ARTICLE

Antibacterial photocurable resin loaded with cetylpyridinium chloride for vat photopolymerization 3D printing in dental applications

Tomoe Nishikawa[1,2], Yuki Nagamatsu[1], Yusaku Nishizawa[1,2], Yasuhiko Akama[1,2], Jun J. Miyamoto[2], Kaori Gunjigake-Kometani[2], Tatsuo Kawamoto[2], and Hiroshi Ikeda[1]*

[1] Division of Biomaterials, Department of Oral Functions, Kyushu Dental University, Fukuoka, Japan

[2] Division of Orofacial Functions and Orthodontics, Department of Health Improvement, Kyushu Dental University, Fukuoka, Japan

Abstract

Bacterial adhesion and biofilm formation are critical issues for 3D-printed dental resin. This study aims to develop a novel cetylpyridinium chloride (CPC)-based antibacterial photocurable resin for vat photopolymerization (VPP) 3D printing and evaluate its printability, mechanical properties, antibacterial activities, and CPC-release behavior for potential use in dental prostheses and orthodontic devices. Photocurable resins containing 0–3 wt.% CPC were formulated from methacrylate and acrylate monomers. Printability of the photocurable resins was assessed by measuring viscosity, cure depth, over-curing, and the degree of conversion. The photocurable resins were printed using a VPP 3D printer, and the resulting specimens were evaluated for mechanical properties using three-point bending and Vickers hardness tests. Antibacterial activity against *Streptococcus mutans* was examined by bacterial viability and plaque-formation assays. CPC-release behavior was analyzed by UV–visible spectroscopy. CPC incorporation up to 3% slightly increased resin viscosity, cure depth, and over-curing while maintaining adequate printability. The degree of conversion was not significantly affected by CPC content. The 1% CPC-loaded printed resin exhibited mechanical properties comparable to the CPC-free control, whereas 3% CPC markedly reduced them. The 1% CPC-loaded resin showed strong antibacterial activity, achieving an antibacterial activity value of 5.6 (>99.99% bacterial reduction), and demonstrated sustained plaque inhibition. Sustained CPC release from the printed resins was confirmed throughout the 14-day evaluation period. These results demonstrate that 1% CPC-loading provides an optimal balance among printability, mechanical properties, and antibacterial performance. The developed material shows potential for application in 3D-printed dental polymer-based prostheses and orthodontic devices.

Keywords: 3D printing; Additive manufacturing; Antibacterials; Biomaterials; Cetylpyridinium chloride; Dental materials; Dental resin

***Corresponding author:**
Hiroshi Ikeda
(r16ikeda@fa.kyu-dent.ac.jp)

Citation: Nishikawa T, Nagamatsu Y, Nishizawa Y, *et al.* Antibacterial photocurable resin loaded with cetylpyridinium chloride for vat photopolymerization 3D printing in dental applications. *Int J Bioprint.* 2026;12(1):607-621. doi: 10.36922/IJB025470484

Received: November 20, 2025
Revised: December 26, 2025
Accepted: January 7, 2026
Published online: January 12, 2026

Copyright: © 2026 Author(s). This is an Open Access article distributed under the terms of the Creative Commons Attribution License, permitting distribution and reproduction in any medium, provided the original work is properly cited.

Publisher's Note: AccScience Publishing remains neutral with regard to jurisdictional claims in published maps and institutional affiliations.

1. Introduction

Vat photopolymerization (VPP) 3D printing has emerged as a widely adopted additive manufacturing technique for resin-based materials due to its high printing accuracy, excellent surface quality, and cost-effectiveness. In dentistry, VPP systems—including liquid crystal display (LCD), digital light processing, and stereolithography—are increasingly incorporated into digital workflows alongside intraoral optical scanning, computer-aided design (CAD), and computer-aided manufacturing technologies.[1] This comprehensive digital approach enables the precise fabrication of a wide range of dental prostheses and appliances. In particular, VPP-based resin materials have gained notable attention for producing removable orthodontic and prosthodontic devices, such as aligners, retainers, and dentures.[2,3]

Despite these advantages, a major clinical concern associated with VPP-printed resin materials is their high susceptibility to bacterial adhesion and biofilm formation.[4–7] The layer-by-layer fabrication process generates characteristic micro-grooved surface textures, which facilitate microbial retention and biofilm development, thereby increasing the risk of oral diseases such as dental caries and periodontitis.[8] Accordingly, establishing effective strategies to inhibit bacterial colonization on 3D-printed dental resins is essential for improving their long-term clinical performance.

Incorporating antimicrobial agents into dental polymeric materials has been investigated as a promising approach to reduce bacterial adhesion and biofilm formation on prostheses and orthodontic devices. Conventional resin-based dental materials containing antibacterial additives—particularly systems designed for controlled release or surface antibacterial functionalization—have demonstrated significant reductions in microbial colonization.[9,10] Recently, this concept has been extended to dental 3D-printed resins, where antibacterial fillers have been incorporated into the resin matrix to impart antibacterial activity.[11–14] For example, Salgado *et al.*[11] reported that graphene-enhanced printed resin inhibited the growth and biofilm formation of *Candida albicans* and *Streptococcus mutans*. Mangal *et al.*[12] demonstrated that nanodiamond incorporation reduced *S. mutans* adhesion on printed resin surfaces. Jin *et al.*[13] showed that a fluoride-doped resin effectively suppressed *S. mutans* proliferation through sustained fluoride release. Additionally, Khattar *et al.*[14] demonstrated that ZrO_2 incorporation inhibited *C. albicans* adhesion and growth in 3D-printed resins. These advances highlight the potential of antibacterial 3D-printed resins for dental applications.

However, previous studies have not comprehensively examined how incorporating antibacterial agents influences key performance characteristics specific to VPP resin systems—including printability, physicochemical behavior, mechanical integrity, and antibacterial efficacy. These material properties are critical determinants of the clinical success of 3D-printed dental devices. Therefore, a major remaining challenge is to understand how antibacterial additives influence the essential material properties of dental 3D-printed resins that determine their clinical performance.

To develop novel antibacterial photocurable resins for VPP 3D printing, cetylpyridinium chloride (CPC) was selected as the antimicrobial agent. CPC is a quaternary ammonium compound widely used in oral care products, including mouthwashes, denture cleansers, and toothpastes.[15] It exhibits broad-spectrum antibacterial and antifungal activity, along with favorable biocompatibility for intraoral applications. Several studies have investigated CPC-loaded dental polymeric materials and demonstrated their antibacterial performance.[16–25] For example, Namba *et al.*[17] incorporated CPC into methacrylate-based resins, reporting sustained antibacterial activity driven by CPC release into the surrounding environment. Yamamoto *et al.*[26] developed CPC–montmorillonite-loaded resin cement and demonstrated continuous anti-biofilm effects associated with controlled CPC release. However, CPC has not yet been incorporated into photocurable resin matrices used for VPP-based 3D printing in dental applications.

This study aims to develop a CPC-loaded photocurable resin for VPP 3D printing and to evaluate its feasibility for dental applications. A comprehensive assessment was performed, including analyses of printability, mechanical properties, antibacterial activities, and sustained CPC-release behavior of the printed resins.

2. Materials and methods

2.1. Experimental procedure

A schematic overview of the preparation process for CPC-loaded photocurable resins and the subsequent evaluations is shown in Figure 1.

2.2. Fabrication of cetylpyridinium chloride-loaded photocurable resins and vat photopolymerization 3D printing

2.2.1. Preparation of photocurable resin for vat photopolymerization 3D printing

The reagents used to prepare the photocurable resins are listed in Table 1. All procedures were performed at room temperature under ambient laboratory conditions. CPC was first dissolved in 2-hydroxyethyl methacrylate

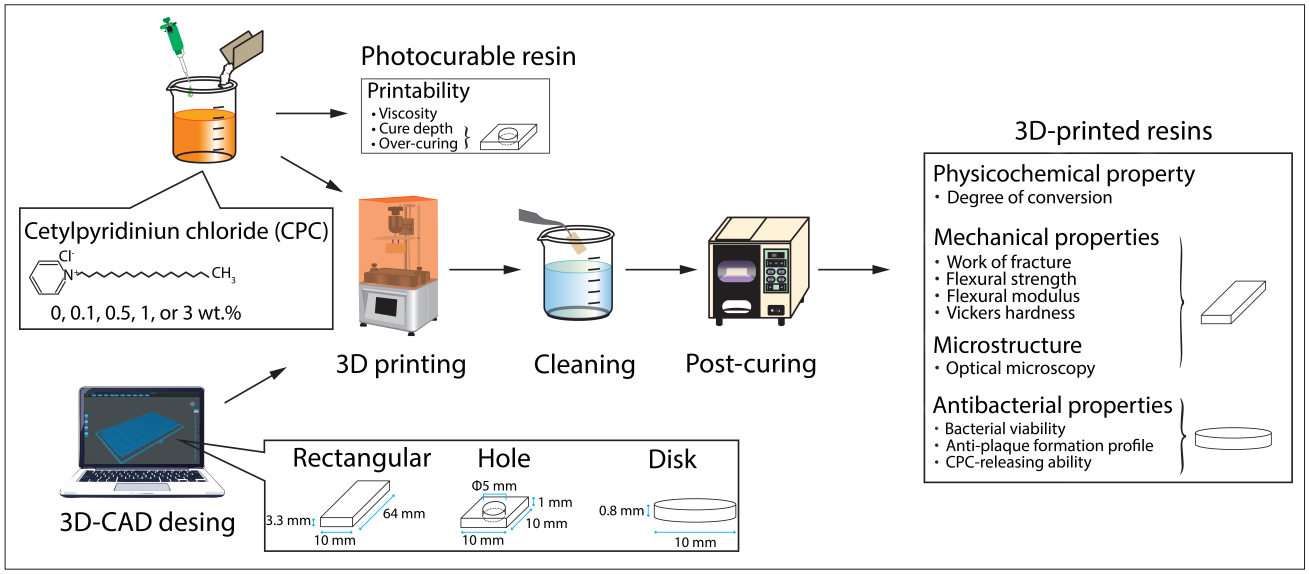


Figure 1. Schematic overview of the fabrication and evaluation workflow for CPC-loaded photocurable resins, highlighting the relationship between resin formulation, vat photopolymerization 3D printing, and subsequent evaluations of printability, mechanical properties, and antibacterial performance. Abbreviation: CAD, computer-aided design; CPC, cetylpyridinium chloride.

(HEMA) by magnetic stirring for 30 min. Separately, the remaining resin components were premixed using a planetary centrifugal mixer (ARE-310, THINKY Corp., Japan) at 2000 rpm for 4 min. The CPC-containing HEMA was then added to the premixed resin and mixed for an additional 2 min. Subsequently, the photo-initiator and photo-absorber were incorporated into the mixture and mixed for another 2 min, followed by a 1-min defoaming cycle to remove entrapped air. The resultant photocurable resin formulations containing 0, 0.1, 0.5, 1, and 3 wt.% CPC were prepared for subsequent experiments.

2.2.2. Computer-aided design model and slicing for 3D printing

Three geometries (rectangular bars, discs, and hole-pattern specimens, as shown in Figure 1) were designed using 3D CAD software (Tinkercad, Autodesk Inc., USA) and exported as STL files. The STL files were processed with slicer software (CHITUBOX Basic, Version 2.1.0, CBD-Tech, China) to generate layer-by-layer print data suitable for import into the 3D printer.

2.2.3. Vat photopolymerization 3D printing and post-treatment

The printing of the CPC-loaded photocurable resins was performed using an LCD-type VPP printer (ELEGOO Mars 3 Pro, ELEGOO, China) with a layer thickness of 0.05 mm and 5 s light exposure per layer. Printed objects were removed from the build platform and ultrasonically cleaned in isopropyl alcohol for 5 min. Post-curing was performed using a xenon-flash curing unit (Otoflash G171, BEGO, Germany) with two cycles of 2000 flashes

Table 1. Materials used for preparing the CPC-loaded photocurable resins for the vat photopolymerization 3D printing

Abbreviation	Material	Type	Weight (g)	Manufacturer
CPC	Celylpyridinium chloride	Antibacterial agent	0, 0.05, 0.25, 0.5, or 1.5	FUJIFILM Wako Pure Chemical Corp, Japan
HEMA	2-Hydroxyethyl methacrylate	CPC-loaded monomer	5.0	FUJIFILM Wako Pure Chemical Corp, Japan
UDMA	Urethane dimethacrylate	Main monomer	20.0	Sigma-Aldrich Co. LLC, Germany
TEGDMA	Triethyleneglycol dimethacrylate	Diluent monomer	20.0	FUJIFILM Wako Pure Chemical Corp, Japan
TMPTA	Trimethylolpropane triacrylate	Cross-linker	5.0	Tokyo Chemical Industry Co., Ltd., Japan
BAPO	Phenylbis(2,4,6-trimethylbenzoyl) phosphine oxide	Photo-initiator	0.25	Tokyo Chemical Industry Co., Ltd., Japan
TBT	2,5-Bis(5-tert-butyl-2-benzoxazolyl)triophene	Photo-absorber	0.05	Tokyo Chemical Industry Co., Ltd., Japan

under an N_2 atmosphere. The post-cured printed resins were subsequently used for the following evaluations.

2.3. Printability evaluation of cetylpyridinium chloride-loaded photocurable resins for vat photopolymerization 3D printing

2.3.1. Viscosity

Viscosities of the photocurable resins were measured at a shear rate of 10 s^{-1} using a rotational rheometer (MCR 92, Anton Paar GmbH, Austria) equipped with a cone-and-plate geometry at 25°C (n = 5).

2.3.2. Cure depth

The photocurable resins were poured into the printer vat and exposed to light for 5 s. The resulting polymerized films were removed, and their thickness was measured using a digital caliper (CD-15CPX, Mitutoyo Corp., Japan). The measured film thickness was defined as the cure depth of the photocurable resins in the VPP 3D printing process (n = 10).

2.3.3. Over-curing

Dimensional accuracy in the XY direction was evaluated using hole-pattern specimens. The diameter of each printed hole was measured with a digital microscope (VHX-600, Keyence Corp., Japan). Over-curing (overgrowth) was quantified as the difference between the designed hole diameter in the CAD model and the measured diameter of the printed specimen (n = 10).

2.3.4. Degree of conversion

Degree of conversion for the printed resins was determined using Fourier-transform infrared spectroscopy (FTIR; IRSpirit, Shimadzu Corp., Japan). The degree of conversion was calculated from the peak intensities at 1638 cm^{-1} (C=C stretch) and 1720 cm^{-1} (C=O stretch) in accordance with previous studies,[27] using the following equation:

$$\text{Degree of conversion (\%)} = \left(\frac{[A(C=C)/A(C=O)]_{\text{after polymerization}}}{[A(C=C)/A(C=O)]_{\text{before polymerization}}} \right) \times 100 \quad (1)$$

where A(C=C) and A(C=O) represent the absorbance intensities of the C=C and C=O bonds, respectively (n = 10).

2.4. Mechanical properties

2.4.1. Three-point bending test

The rectangular bar specimens were used for mechanical testing. The three-point bending test was conducted according to ISO 20795-2:2013 (Dentistry—Base Polymers—Part 2: Orthodontic Base Polymers). According to ISO 20795-2, flexural properties of dental polymer-based materials are evaluated based on load–deflection data obtained from three-point bending tests, and the corresponding mechanical parameters are derived from these measurements using standard beam theory. Testing was performed using a universal testing machine (AGS-H, Shimadzu Corp., Japan) with a support span of 50 mm and a crosshead speed of 5 mm/min (n = 10). Load–deflection curves were recorded to determine the mechanical properties. The work of fracture W (J/m^2) was calculated using:

$$W = \frac{A}{bh} \quad (2)$$

where A represents the area under the load–deflection curve (N·mm), b is the specimen width (mm), and h is the specimen thickness (mm). The flexural strength σ (MPa) was calculated using the following equation:

$$\sigma = \frac{3FL}{2bh^2} \quad (3)$$

where F is the maximum load (N), and L is the distance between the supports (mm). The flexural modulus E (GPa) was calculated from the initial linear region of the load–deflection curve using the following equation:

$$E = \frac{mL^3}{4bh^3} \quad (4)$$

where m is the slope of the initial linear region of the load–deflection curve (N/mm).

2.4.2. Vickers hardness test

The fractured specimens obtained from the three-point bending tests were used for Vickers hardness measurement (n = 10). Hardness was determined using a microhardness tester (HMV-G21ST, Shimadzu Corp., Japan) under a 200 g load applied for 15 s.

2.5. Optical microscopy

The microstructure of the CPC-loaded printed resin surfaces with different CPC contents (0–3 wt.%) was examined using the digital microscope.

2.6. Antibacterial properties

To evaluate the antibacterial properties of the CPC-loaded printed resins, two types of tests were conducted: the antibacterial activity test and the anti-plaque formation

test. Disc-shaped specimens of the printed resins were used in both tests. All printed specimens were sterilized by UV irradiation for 40 min prior to the antibacterial activity and anti-plaque formation tests. The cariogenic bacterium *S. mutans* NBRC 13955 was used as the test microorganism. The bacteria were precultured in brain–heart infusion (BHI) broth at 37°C for 48 h under aerobic conditions. After centrifugation, the bacterial pellet was washed twice with sterile phosphate-buffered saline (PBS) and resuspended in fresh BHI broth to prepare bacterial suspensions with concentrations of 3×10^4 or 3×10^8 CFU/mL. All antibacterial activity and anti-plaque formation tests were performed in five specimens per group ($n = 5$) under identical experimental conditions.

2.6.1. Antibacterial activity test

Each specimen was immersed in 1.0 mL of *S. mutans* suspension (3×10^4 CFU/mL) and incubated at 37°C for 48 h to allow bacterial attachment to the specimen surface. After incubation, the specimens were transferred to 10 mL of sterile PBS and ultrasonically cleaned for 5 min to detach adherent bacteria. The resulting bacterial suspensions were serially diluted, and 0.2 mL of each dilution was spread onto BHI agar plates. After incubation at 37°C for 48 h, the colonies were counted to determine the number of viable adherent bacteria. To quantitatively compare the antibacterial performance of the CPC-loaded printed resins with that of the CPC-free printed resins, the antibacterial activity value (R) was calculated using the following equation:

$$R = \log_{10} NB_0 - \log_{10} NB_n \quad (5)$$

where NB_0 and NB_n represent the numbers of viable bacteria obtained from specimens containing 0% and n% CPC, respectively ($n = 0.1$, 0.5, 1, or 3).

2.6.2. Anti-plaque formation test

To evaluate the sustained antibacterial activity of the CPC-loaded printed resins, plaque formation before and after CPC release from the specimens was investigated. CPC-free (0%) and 1% CPC-loaded printed resin specimens were used. To induce CPC release, the specimens were immersed in distilled water at 37°C for 14 days. After immersion, the specimens were rinsed with sterile PBS and then incubated in 1.0 mL of *S. mutans* suspension (3×10^8 CFU/mL) at 37°C for 48 h to allow plaque formation. After gentle rinsing with distilled water, the plaque formed on the upper surface area (0.785 cm^2) was stained using a plaque-disclosing agent (DENT Liquid Plaque Tester AR, Lion Dental Products Co., Japan). The stained specimens were photographed using a digital camera (EOS Kiss X7, Canon Inc, Japan), and the images were analyzed with ImageJ2 software (National Institutes of Health, Bethesda, USA). The stained area was quantified using a saturation threshold value of 102 in the hue, saturation, brightness color model. The plaque formation rate (%) was calculated using the following equation:

$$\text{Plaque formation rate}\,(\%) = \frac{\text{Plaque - stained area}}{\text{Total surface area}} \times 100 \quad (6)$$

2.7. Cetylpyridinium chloride-release behavior test

Disc-shaped specimens were immersed individually in 10 mL of distilled water at 37°C and stored for 14 days. The absorbance of the immersion solutions was measured every few days using a UV–visible (Vis) spectrophotometer (V-650S, JASCO Corp., Japan). CPC exhibits a characteristic absorption peak near 260 nm; therefore, a calibration curve was prepared using aqueous solutions of known CPC concentrations. The CPC concentration in each sample was calculated based on the absorbance at 260 nm ($n = 10$).

2.8. Statistical analysis

All data were analyzed using EZR statistical software (Saitama Medical Center, Jichi Medical University, Japan). For multiple group comparisons, one-way analysis of variance followed by Tukey's post-hoc test was performed. For pairwise comparisons, the Student's t-test was used. Statistical significance was set at $p < 0.05$ for all analyses.

3. Results

3.1. Printability of the photocurable resins

The printability of the photocurable resins for VPP 3D printing was evaluated in terms of viscosity, cure depth, over-curing behavior, and degree of conversion.

Figure 2A shows the viscosity of the photocurable resins measured using a rheometer at a shear rate of 10 s^{-1}. This shear rate reflects the resin flow behavior during the VPP process, as it corresponds to the fluidity of the resin in the vat.[28] The viscosity of the CPC-free photocurable resin was 554 ± 41 mPa·s, and it increased with increasing CPC content. The 3% CPC-loaded printed resin exhibited a viscosity of 667 ± 85 mPa·s.

Figure 2B presents the cure depth of the photocurable resins after light exposure in the printer vat. No significant differences in cure depth were observed among the formulations, indicating that CPC incorporation up to 3% did not impair photopolymerization efficiency under the selected exposure conditions.

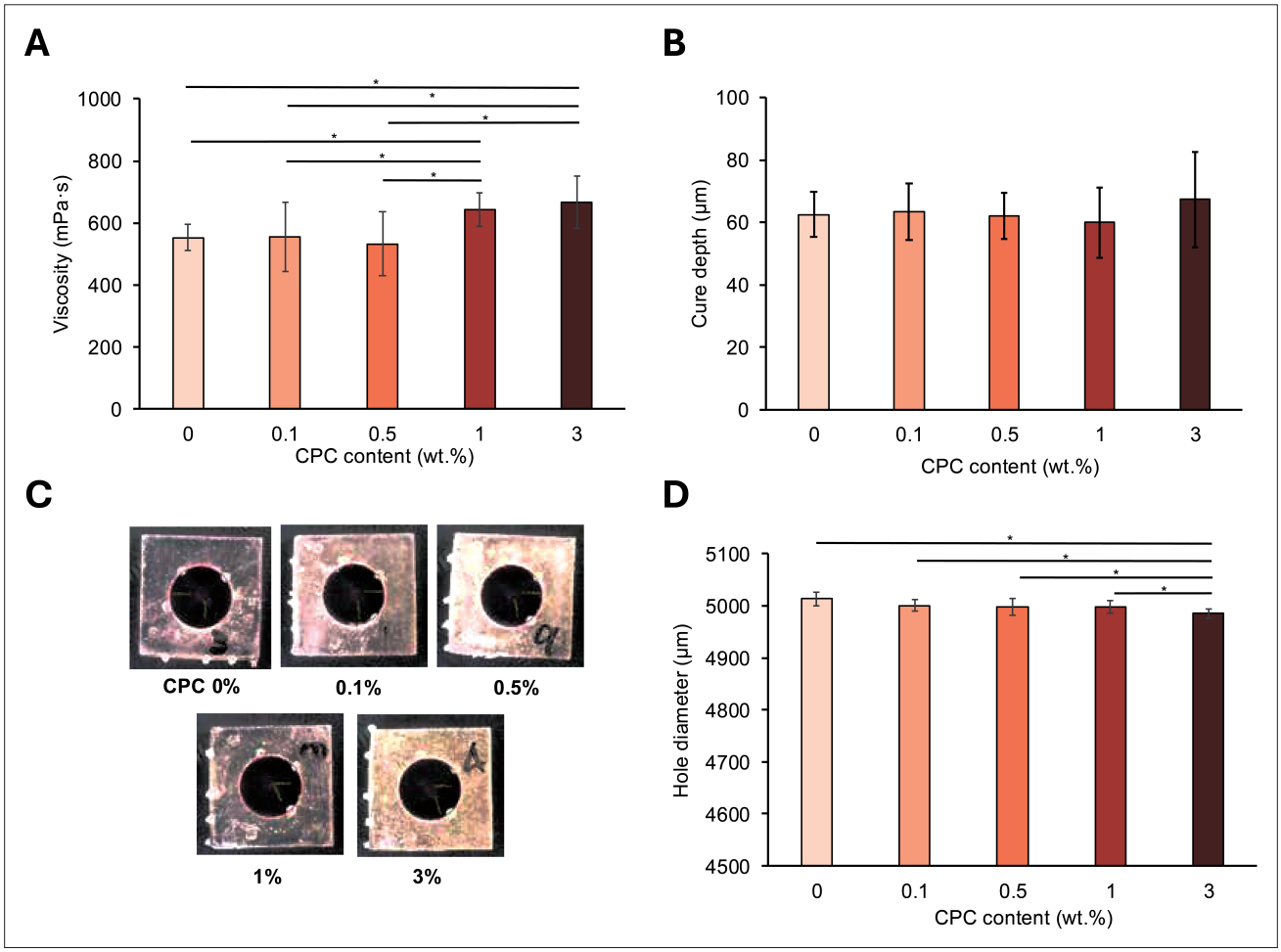


Figure 2. Printability of the photocurable resins for vat photopolymerization (VPP) 3D printing. (A) Viscosity of the photocurable resins with different cetylpyridinium chloride (CPC) contents. (B) Cure depth of the photocurable resins photopolymerized by 5 s of light exposure using the 3D printer. (C) Representative microscope images of the printed specimens with a hole pattern used to evaluate over-curing. (D) Quantification of over-curing calculated from the hole-pattern images shown in (C). These results indicate that CPC incorporation up to 1 wt.% maintains adequate resin flowability, curing behavior, and dimensional accuracy required for stable VPP 3D printing. Note: $*p < 0.05$.

Figure 2C shows representative microscopic images of hole-pattern printed resin specimens fabricated with different CPC concentrations, and Figure 2D quantifies over-curing based on the measured hole diameters. The hole diameter decreased with increasing CPC content. The CPC-free printed resin exhibited a hole diameter of 5013 ± 14 μm, whereas the 3% CPC-loaded printed resin showed a reduced diameter of 4984 ± 10 μm. A decrease in hole diameter indicates a greater degree of over-curing. Therefore, over-curing tended to increase as the CPC concentration increased. However, no significant difference was observed between the 0% and 1% CPC-loaded printed resins, indicating that CPC addition up to 1% does not significantly compromise lateral printing accuracy.

Figure 3 shows the degree of conversion of the printed resins. No significant differences were observed among the groups, indicating that CPC incorporation up to 3% did not adversely affect the polymerization efficiency of the photocurable resin.

3.2. Mechanical properties

The mechanical properties of the CPC-loaded printed resins, including work of fracture, flexural strength, flexural modulus, and Vickers hardness, are shown in Figure 4. The work of fracture, flexural strength, and Vickers hardness decreased with increasing CPC content. In particular, the 3% CPC-loaded printed resin showed significantly lower values compared with the CPC-free printed resin, whereas no significant differences were observed between the 0% and 1% CPC groups. In contrast, the flexural modulus

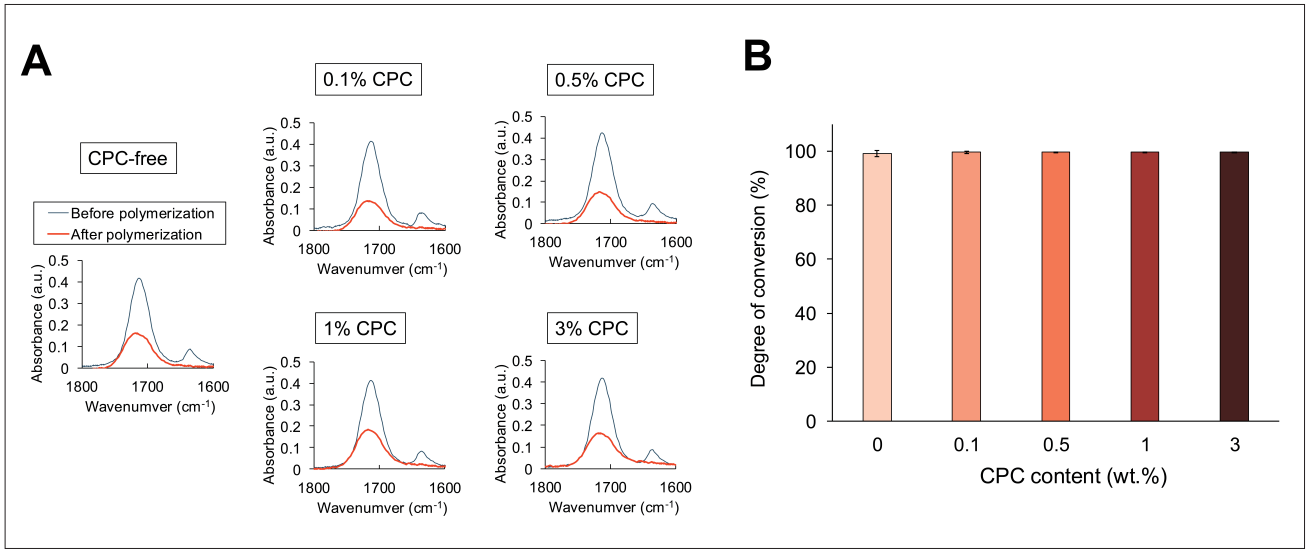


Figure 3. Degree of conversion of the printed resins. (A) Representative Fourier-transform infrared (FTIR) spectra of photocurable resins with different cetylpyridinium chloride (CPC) contents and their corresponding printed resins. (B) Degree of conversion determined by FTIR analysis. No significant differences are observed among the groups. This figure confirms that CPC incorporation does not interfere with the photopolymerization efficiency of the vat photopolymerization resin system.

was not affected by CPC incorporation. These findings indicate that CPC addition up to 1% does not adversely affect the mechanical properties of the printed resin, while higher CPC concentrations (e.g., 3%) reduce mechanical performance.

3.3. Microstructural observation

Figure 5 shows optical microscopy images of the printed resins with different CPC contents. No visible aggregates were observed in the CPC-free, 0.1%, 0.5%, or 1% CPC specimens, indicating a homogeneous microstructure. In contrast, the 3% CPC specimen exhibited distinct CPC-rich aggregates dispersed within the resin matrix, suggesting incomplete dissolution and phase separation.

3.4. Antibacterial properties

The antibacterial properties of the printed resins were evaluated by assessing both antibacterial activity and anti-plaque formation. Figure 6 shows the antibacterial activity of the printed resins, determined by quantifying the number of viable bacteria attached to each specimen. The number of surviving bacteria decreased markedly with increasing CPC content. The CPC-free printed resin exhibited approximately 10^7 CFU ($\log_{10}$NB ≈ 7), whereas the 1% CPC-loaded printed resin showed a substantial reduction to approximately 10^2 CFU ($\log_{10}$NB ≈ 2), which was significantly lower than that of the CPC-free printed resin ($p < 0.05$). The antibacterial activity value (R), defined as the logarithmic difference in bacterial counts between control (CPC-free) and CPC-loaded specimens, was 5.6 for 1% CPC and 7.4 for 3% CPC. According to ISO 22196,[29] an R value greater than 2 (corresponding to a 99% reduction compared with the control) indicates that the material possesses antibacterial activity. Therefore, both the 1% and 3% CPC-loaded printed resins demonstrated effective antibacterial performance.

Figure 7 shows the plaque formation rates, reflecting the sustained antibacterial effect of the 1% CPC-loaded printed resin. Figure 7A presents photographs of plaque-stained specimens. It is evident that the CPC-loaded printed resin exhibited visibly less staining than the CPC-free printed resin, even after the CPC release treatment. These plaque-stained images were further analyzed using image analysis to obtain quantitative values of plaque formation rates, as shown in Figure 7B. Before CPC release, a significant difference was observed between the CPC-loaded (14.6 ± 7.1%) and CPC-free (77.2 ± 20.9%) specimens. After CPC release, the plaque formation rates remained lower for the CPC-loaded specimens (22.7 ± 14.0%) than for the CPC-free samples (88.4 ± 18.1%), and the significant difference persisted ($p < 0.05$). These results indicate that the 1% CPC-loaded printed resin retained its anti-plaque formation activity even after CPC release, demonstrating sustained antimicrobial effectiveness.

3.5. Cetylpyridinium chloride-releasing ability

The CPC-releasing ability of the printed resins was evaluated by UV–Vis spectroscopy (Figure 8). Figure 8A shows the UV–Vis absorption spectra of CPC aqueous solutions with known concentrations used to establish the calibration curve. A characteristic absorption peak was observed at

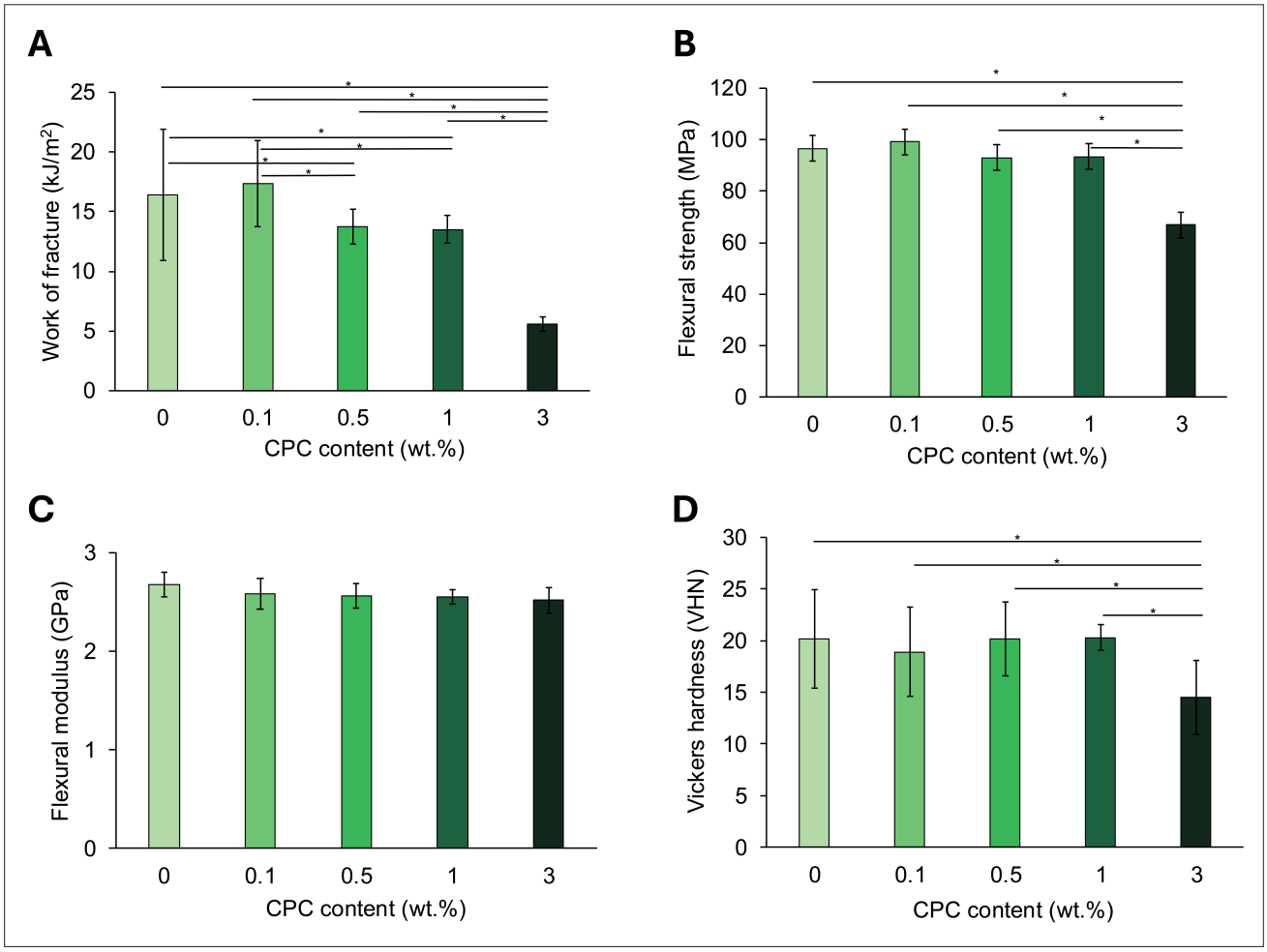


Figure 4. Mechanical properties of cetylpyridinium chloride (CPC)-loaded printed resins with varying CPC contents. (A) Work of fracture. (B) Flexural strength. (C) Flexural modulus. (D) Vickers hardness. The results show that CPC incorporation up to 1% maintains mechanical properties within the range required for dental polymer-based applications, whereas 3% CPC loading leads to a pronounced reduction in strength and fracture resistance. Note: $^*p < 0.05$.

approximately 260 nm, corresponding to CPC. This peak was used to quantify CPC concentrations in the immersion solutions of CPC-loaded printed resins, as shown in Figure 8B. Sustained CPC release was confirmed for specimens containing ≥0.5% CPC. The CPC concentration in the immersion medium gradually increased over time, indicating sustained CPC release from the printed resins throughout the 14-day test period. An initial release was observed at day 1, followed by a continued increase at days 7 and 14. For the 3% and 0.5% CPC-loaded printed resins, the CPC concentrations showed significant differences among the examined time points ($p < 0.05$), confirming sustained release throughout the observation period. A similar increasing trend was observed for the 1% CPC-loaded printed resin; however, the differences among time points were not statistically significant, suggesting a slower and more gradual release profile. In contrast, CPC release from the 0.1% CPC-loaded printed resin remained below the detection limit of the UV–Vis measurement under the present experimental conditions.

To evaluate the cumulative CPC release relative to the total CPC content in the resin, the amount of CPC released into the immersion medium after 14 days was estimated. Approximately 3.5% of the total CPC content was released from the 3% CPC-loaded printed resin, 2.6% from the 1% CPC-loaded printed resin, and 3.5% from the 0.5% CPC-loaded printed resin. These results indicate sustained CPC release without rapid depletion over the experimental period.

4. Discussion

This study aimed to develop a novel CPC-loaded photocurable resin for VPP 3D printing and to evaluate the

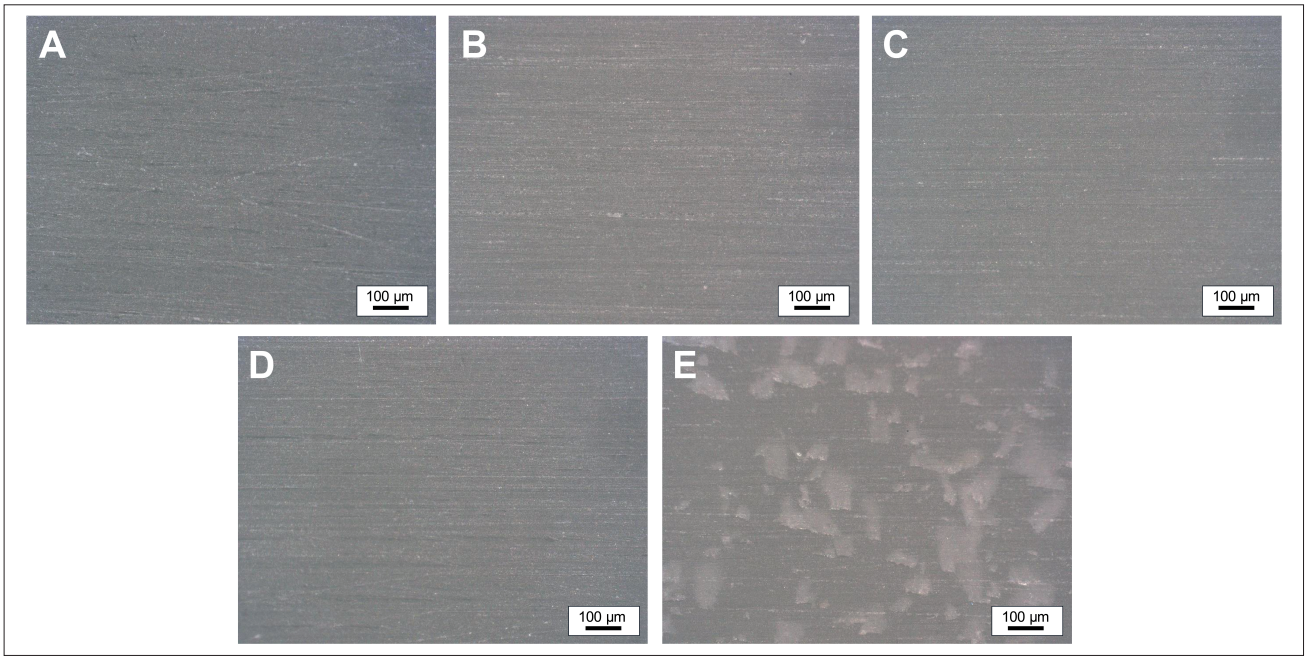


Figure 5. Microscope images of surfaces of the cetylpyridinium chloride (CPC)-loaded printed resins: (A) CPC-free, (B) 0.1% CPC, (C) 0.5% CPC, (D) 1% CPC, and (E) 3% CPC-loaded resins. Scale bars: 100 μm; magnifications: × 300. No visible CPC aggregates are observed in the resin matrices of the CPC-free, 0.1%, 0.5%, and 1% CPC-loaded resins. In contrast, distinct CPC aggregates are observed in the resin matrix of the 3% CPC-loaded resin, indicating incomplete dissolution and phase separation.

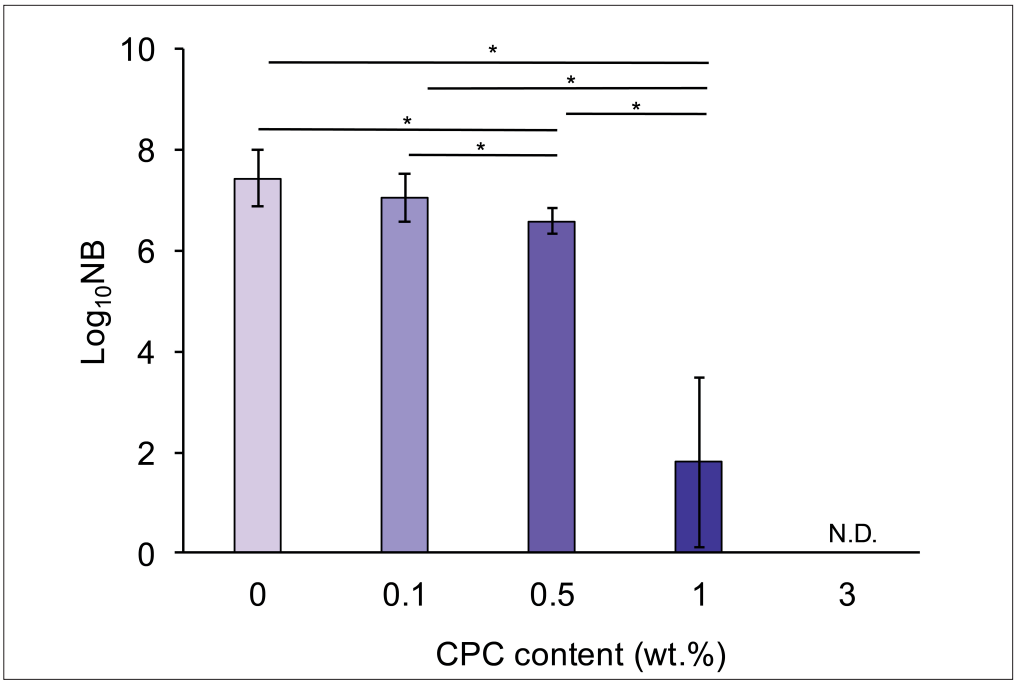


Figure 6. Antibacterial activity of CPC-loaded printed resins against *Streptococcus mutans*. Antibacterial activity was assessed based on bacterial viability, with antibacterial activity values (R) of 0.4 (63.0% reduction) for 0.1% CPC, 0.8 (90.6% reduction) for 0.5% CPC, 5.6 (> 99.99% reduction) for 1% CPC, and 7.4 (> 99.9999% reduction) for 3% CPC. This result indicates that 1% CPC-loading provides strong antibacterial activity exceeding the international performance criterion ($R \geq 2.0$), indicating its effectiveness for antibacterial dental applications. Note: $^*p < 0.05$. Abbreviations: NB, number of bacteria; N.D., not detected; CPC, cetylpyridinium chloride.

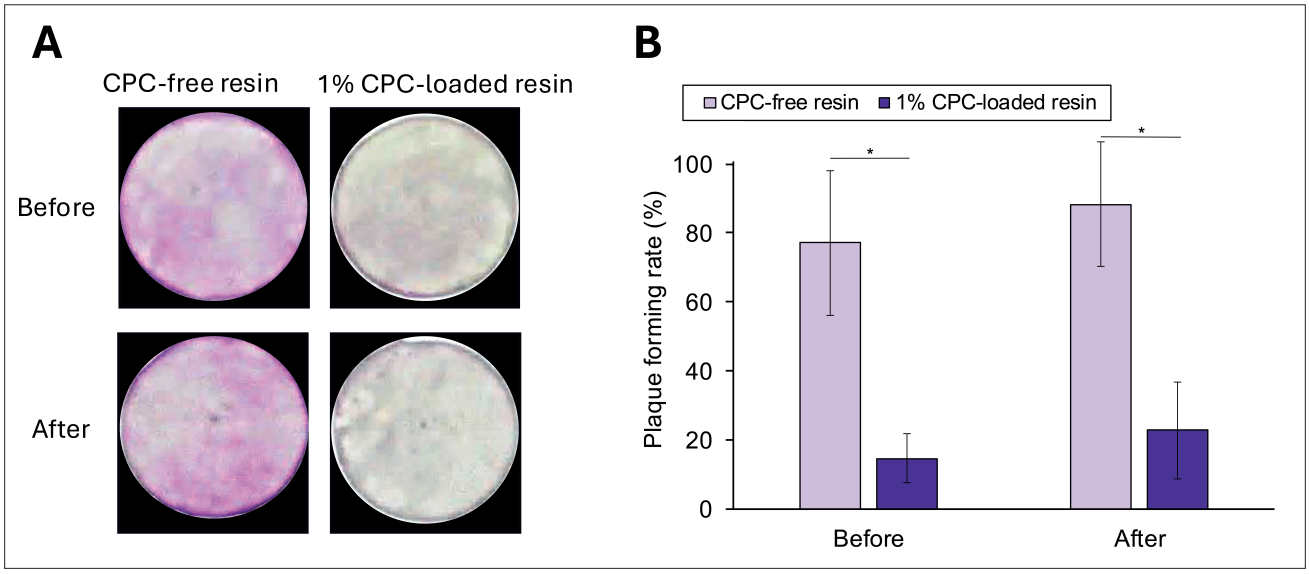


Figure 7. Anti-plaque formation on 1% cetylpyridinium chloride (CPC)-loaded and CPC-free printed resins. (A) Representative images of plaque-stained specimens (diameter: 10 mm) before and after CPC-release treatment by water immersion for 14 days. (B) Quantitative plaque formation rates obtained from the image analysis. These results indicate that the antibacterial effect of the CPC-loaded printed resin is sustained even after prolonged water immersion, suggesting continuous plaque-inhibition capability. Note: $*p < 0.05$.

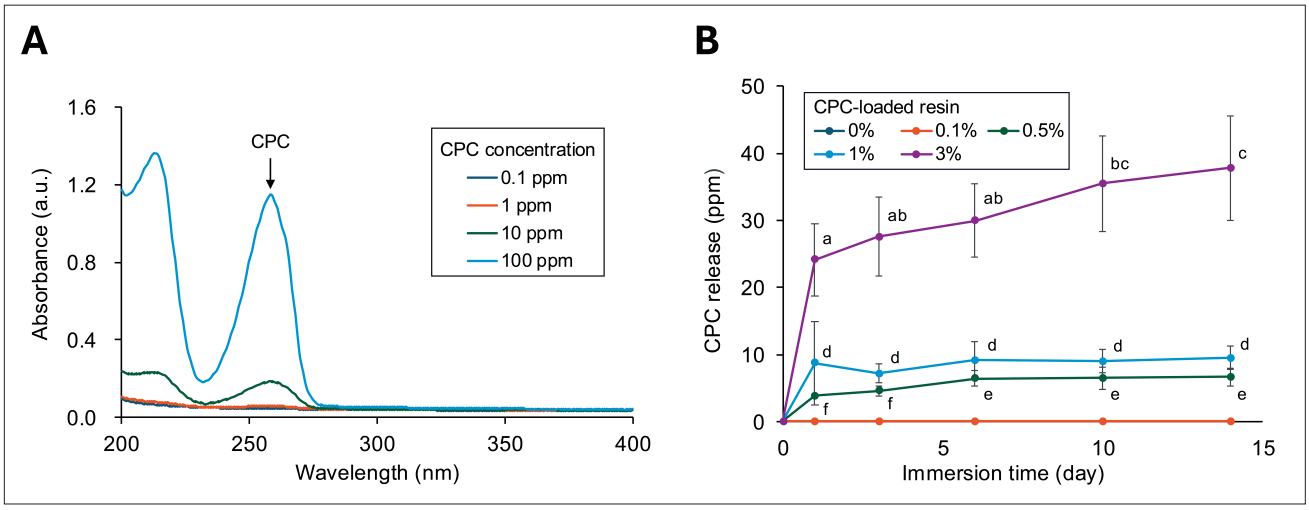


Figure 8. Cetylpyridinium chloride (CPC)-release behavior of CPC-loaded printed resins. (A) Representative UV-Vis spectra of standard aqueous CPC solutions. (B) CPC release profiles of CPC-loaded printed resins immersed in distilled water at 37°C, as determined by UV–Vis spectroscopy. These results confirm sustained CPC release from the printed resins over time, supporting the mechanism underlying their long-term antibacterial activity. Notes: Different letters indicate significant differences among groups at each time point ($p < 0.05$); Statistical analysis was performed within each CPC concentration, comparing CPC release amounts at different time points (days 1, 3, 7, 10, and 14). Different letters indicate significant differences among groups at each time point ($p < 0.05$).

effects of CPC incorporation on printability, mechanical properties, and antibacterial performance of the printed resins. The results demonstrated that the addition of CPC effectively imparted antibacterial activity when incorporated at concentrations of ≥1%, while maintaining acceptable printability and mechanical properties at 1%. These findings indicate that 1% CPC loading enables an optimal balance between antimicrobial function and material performance for the 3D-printed dental resins.

The photocurable resin formulation used consisted of urethane dimethacrylate (UDMA), triethyleneglycol dimethacrylate (TEGDMA), trimethylolpropane triacrylate (TMPTA), and HEMA as base monomers, all of which are commonly employed in dental polymer systems.[30]

In this formulation, each monomer played a distinct and essential role in achieving suitable performance for VPP 3D printing in dental applications. UDMA functioned as the primary backbone monomer, providing mechanical strength to the printed resin. TEGDMA served as a reactive diluent, reducing the viscosity of the photocurable resin and improving its flow behavior to ensure smooth recoating and layer formation during VPP 3D printing. TMPTA, an acrylate monomer with a high density of C=C functional groups, contributed to rapid polymerization and a high crosslink density under the relatively low-intensity light irradiation conditions of the LCD-type VPP printers. HEMA, a hydrophilic monomer containing hydroxyl groups, was critical for dissolving CPC uniformly within the resin matrix.[18] Our preliminary experiments revealed that CPC concentrations above 4% could not be completely solubilized in the monomer mixture, leading to apparent phase separation and compromised printability (data not shown). Therefore, the maximum CPC loading was limited to 3%.

In VPP 3D printing, the printability of resin-based materials is strongly influenced by parameters such as viscosity,[31] cure depth,[32] over-curing behavior,[33] and the photopolymerization characteristics of the resin.[34] Low-viscosity resins can readily flow and fill the narrow gap between the printed object and the vat, ensuring uniform layer formation during the printing process. Conversely, high-viscosity resins exhibit poor flowability, which can prevent complete filling of the gap between the object and the vat, leading to printing defects and poor surface accuracy. The optimal viscosity range for photocurable resins used in VPP printing is generally below 3000 mPa·s.[28] In the present study, the viscosity of all photocurable resins remained below 1000 mPa·s, well within the acceptable range for stable printing.

The cure depth of the photocurable resin is a key factor influencing the continuous stacking of layer-by-layer structures in the 3D printing process. In general, VPP 3D printing employs layer thicknesses of 10–50 μm to achieve high-precision fabrication. Therefore, continuous printing requires the cure depth of the resin to be sufficiently greater than the designated layer thickness to ensure complete interlayer polymerization.[35] The present photocurable resins exhibited a cure depth exceeding 60 μm, which was considered adequate for the continuous curing process required in VPP 3D printing.

Over-curing is an important factor that affects the dimensional accuracy of printed objects. During the light exposure process in VPP 3D printing, part of the irradiated light penetrates or scatters within the resin. Such light penetration and scattering can induce polymerization beyond the intended exposure area, resulting in undesirable over-curing.[36] This phenomenon leads to the overgrowth of the printed object and consequently reduces dimensional accuracy. In the present system, the photocurable resins exhibited increasing degrees of over-curing with higher CPC content, resulting in lateral overgrowth and reduced hole diameters. This phenomenon may be partially attributed to changes in the optical properties of the photocurable resin induced by CPC incorporation. CPC has been reported to exhibit a relatively high refractive index (estimated $n \approx 1.6$),[37] whereas typical methacrylate-based monomers such as UDMA show lower refractive indices (≈1.48).[30] Such a refractive index mismatch may enhance internal light scattering during photoirradiation, potentially contributing to increased over-curing. However, this interpretation should be regarded as a hypothesis, and further optical characterization—such as direct refractive index measurement or light scattering analysis—will be required to clarify the underlying mechanism. For further optimization of resin printability, the over-curing induced by CPC incorporation may be mitigated by adjusting the concentrations of photo-absorbers and photo-initiators, as well as by optimizing light exposure parameters such as irradiation time. Systematic optimization of these factors will be necessary to further improve dimensional accuracy in CPC-loaded resins.

The high degree of conversion observed in the printed resins can be attributed to the highly reactive monomer composition and the intensive post-curing procedure performed under a nitrogen atmosphere. It should be noted that the degree of conversion values, obtained by FTIR analysis, represent relative conversion levels and may approach high values under optimized curing conditions. CPC addition had no significant influence on the degree of conversion. However, increasing CPC content led to a reduction in the mechanical properties of the printed resins, including flexural strength, work of fracture, and Vickers hardness. In particular, the 3% CPC-loaded printed resin exhibited a marked decrease in these properties. This deterioration can be attributed to the non-polymerizable nature of CPC, which lacks reactive functional groups, such as C=C bonds, and therefore cannot be incorporated into the crosslinked polymer network. As shown in Figure 5, while the 1% CPC-loaded printed resin exhibited a homogeneous microstructure, the 3% CPC-loaded printed resin showed visible CPC aggregates, indicating incomplete dissolution and phase separation within the resin matrix. This aggregation potentially acted as a stress concentrator and disrupted the polymer network continuity, thereby contributing to the observed reduction in mechanical properties at 3% CPC loading. Similar reductions in mechanical performance have been reported in the CPC-

loaded methacrylate-based resins when excessive CPC is incorporated.[22,23] In contrast, the 1% CPC-loaded printed resin maintained adequate mechanical properties, meeting the requirements specified in ISO 20795-1:2013 for denture base polymers[38] and ISO 20795-2:2013 for orthodontic base polymers.[39] According to ISO 20795-1:2013, denture base polymers are required to exhibit a minimum flexural strength of 65 MPa and a flexural modulus of 2.0 GPa, whereas ISO 20795-2:2013 specifies minimum values of 50 MPa for flexural strength and 1.5 GPa for flexural modulus for orthodontic base polymers. In the present study, the 1% CPC-loaded printed resin exceeded all of these threshold values, thereby satisfying the mechanical requirements of both ISO standards. These findings suggest that the 1% CPC-loaded printed resin has potential applicability for removable dental prostheses such as dentures, orthodontic aligners, and retainers.

Regarding antibacterial activity, 1% CPC loading effectively inhibited *S. mutans* growth, yielding an *R*-value of 5.6—corresponding to more than 99.99% bacterial reduction—and surpassing the international antibacterial performance criterion ($R \geq 2.0$, 99% reduction).[29] CPC is a well-known cationic surfactant that electrostatically binds to the negatively charged *S. mutans* cell surface and adsorbs onto the cytoplasmic membrane. Its hydrophobic alkyl chain subsequently penetrates the lipid bilayer, resulting in membrane destabilization, increased permeability, and leakage of intracellular components. These events disrupt cellular energy metabolism and ultimately lead to bacterial death. Furthermore, CPC modifies bacterial surface characteristics and suppresses adhesion and biofilm formation. These mechanisms are consistent with the present antibacterial test results. The antibacterial effect observed in this study originated from the sustained release of CPC from the resin matrix, as demonstrated by the 14-day release profile. This gradual release is expected to provide prolonged antibacterial activity, indicating the potential for sustained plaque inhibition in intraoral environments.

To the best of our knowledge, this is the first study to develop a VPP 3D printing resin with intrinsic antibacterial functionality through CPC incorporation. CPC has been widely incorporated into conventional dental resin systems, including poly(methyl methacrylate)-based resins, adhesive materials, and restorative materials, where its antimicrobial efficacy has been well documented. However, these systems differ fundamentally from photocurable resins used in VPP 3D printing, which require precise control of rheological properties, photopolymerization behavior, cure depth, and dimensional accuracy during layer-by-layer fabrication. To date, the incorporation of CPC into VPP-compatible photocurable resin systems has not been systematically investigated. Although CPC was selected due to its established safety and efficacy in oral care products, future research may explore not only CPC but also other biocompatible antibacterial agents—such as isopropyl methylphenol and naturally derived antimicrobials—that may offer enhanced suitability for intraoral applications.[40] Additionally, alternative incorporation strategies, including microencapsulation and covalent immobilization, should be investigated to improve long-term stability and sustained antibacterial performance without compromising the printability or mechanical properties of the resin. The CPC-loaded VPP-printed resin developed in this study also requires further investigation regarding its potential for rechargeable antibacterial functionality, which could enhance its long-term clinical utility. Removable dental prostheses—such as dentures, aligners, and retainers—are routinely cleaned using aqueous cleaning solutions that often contain antimicrobial agents. This daily cleaning process may serve a dual purpose: not only removing accumulated biofilm but also replenishing the CPC content within the resin matrix. Kitagawa *et al.*[18] previously demonstrated that CPC-loaded poly(HEMA/TMPTA) resins were capable of releasing CPC and subsequently being recharged through immersion in CPC-containing solutions. Applying this concept to CPC-loaded VPP-printed resins could enable day-to-day recharging and prolonged antibacterial efficacy. Therefore, future studies should evaluate the CPC recharging capability of VPP-printed materials to establish their long-term antimicrobial performance in clinical use.

Despite the promising results, several limitations of the present study should be acknowledged. First, the photocurable resin formulation contains HEMA, which is known to increase hydrophilicity and water sorption in polymer networks. Increased water uptake may adversely affect dimensional stability and mechanical durability over time, particularly under long-term intraoral conditions. Second, the mechanical properties evaluated in this study represent initial values obtained after printing and post-curing. Long-term mechanical durability under aging conditions—such as prolonged water immersion, thermal cycling, or repeated mechanical loading—was not investigated and should be addressed in future studies to better predict clinical longevity. Third, with respect to biocompatibility, CPC has a well-established safety profile in oral-care products; however, the biocompatibility and cytotoxicity evaluations of CPC-loaded printed resins were not conducted in this study. Therefore, further *in vitro* and *in vivo* assessments will be required to determine the optimal CPC concentration that achieves effective antimicrobial activity without inducing adverse biological effects. Fourth, with respect to antibacterial activity, although the present

study demonstrated antibacterial activity against *S. mutans in vitro*, the oral cavity harbors a complex multispecies biofilm environment.[41] CPC has been reported to exhibit broad-spectrum antimicrobial activity against various oral microorganisms, including *C. albicans* and *Actinomyces* species; however, its penetration into mature biofilms is limited, whereas suppression of initial bacterial adhesion may indirectly inhibit early biofilm development.[21] To verify clinical applicability, future investigations should include antimicrobial assessments against multiple oral microorganisms, as well as *in vivo* evaluations of biofilm formation and plaque inhibition. Ultimately, such comprehensive studies—including preclinical and *in vivo* clinical investigations—will be essential not only for establishing CPC-loaded printed resins as clinically viable materials for antibacterial dental applications but also for validating their intraoral performance and clinical utility.

5. Conclusion

This study demonstrated that CPC can be effectively incorporated into VPP 3D-printed photocurable resins. CPC loading up to 1 wt.% maintained adequate printability. The 1% CPC-loaded printed resin exhibited comparable mechanical properties to the CPC-free printed resin while showing strong antibacterial activity and sustained CPC release. These results indicate that 1% CPC-loading provides an optimal balance among printability, mechanical performance, and antibacterial functionality for 3D-printed dental applications. This study was limited to *in vitro* evaluations using a single bacterial species and a short-term assessment of CPC release; therefore, further investigations are required to validate long-term antibacterial performance under clinically relevant oral conditions.

Acknowledgments

None

Funding

This work was supported by JSPS KAKENHI (grant number 25K20440).

Conflict of interest

The authors declare no conflicts of interest.

Author contributions

Conceptualization: Tomoe Nishikawa, Hiroshi Ikeda
Formal analysis: Jun J. Miyamoto
Funding acquisition: Yusaku Nishizawa, Yasuhiko Akama, Tatsuo Kawamoto
Investigation: Tomoe Nishikawa, Yuki Nagamatsu, Yasuhiko Akama, Yusaku Nishizawa
Methodology: Tomoe Nishikawa, Yusaku Nishizawa, Hiroshi Ikeda
Project administration: Hiroshi Ikeda
Supervision: Tatsuo Kawamoto, Hiroshi Ikeda
Validation: Jun J. Miyamoto, Kaori Gunjigake-Kometani
Writing–original draft: Tomoe Nishikawa, Yuki Nagamatsu, Hiroshi Ikeda
Writing–review & editing: Kaori Gunjigake-Kometani, Tatsuo Kawamoto

Ethics approval and consent to participate

Not applicable.

Consent for publication

Not applicable.

Availability of data

The data that support the findings of this study are available from the corresponding author upon reasonable request.

References

1. Caussin E, Moussally C, Le Goff S, *et al*. Vat photopolymerization 3D printing in dentistry: a comprehensive review of actual popular technologies. *Materials*. 2024;17(4):950. doi: 10.3390/ma17040950

2. Andjela L, Abdurahmanovich VM, Vladimirovna SN, Mikhailovna GI, Yurievich DD, Alekseevna MY. A review on vat photopolymerization 3D-printing processes for dental application. *Dent Mater*. 2022;38(11):e284-e296. doi: 10.1016/j.dental.2022.09.005

3. Jungbauer R, Sabbagh H, Janjic Rankovic M, Becker K. 3D printed orthodontic aligners—a scoping review. *Appl Sci*. 2024;14(22):10084. doi: 10.3390/app142210084

4. Turanoglu OF, Talay Cevlik E, Vural C. Investigation of adhesion status of *Candida* species to the surface of resin materials produced at different angles with additive manufacturing. *BMC Oral Health*. 2024;24(1):738. doi: 10.1186/s12903-024-04505-1

5. Ozer NE, Sahin Z, Yikici C, Duyan S, Kilicarslan MA. Bacterial adhesion to composite resins produced by additive and subtractive manufacturing. *Odontology*. 2024;112(2):460-471. doi: 10.1007/s10266-023-00862-5

6. Tseng CF, Sung CC, Yang YT, *et al*. Impacts of surface characteristics on biological responses and biofilm formation of 3D-printed denture base resins: an in vitro study. *J Dent Sci*. 2025;20(3):1716-1722.

doi: 10.1016/j.jds.2025.03.027

7. Ghezzi B, Artesani L, Giovati L, *et al*. Biological behavior of human gingival fibroblasts and formation of microbial biofilm on 3D-printed dental resin restorations. *Dent Mater*. 2025;41(10):1266-1276. doi: 10.1016/j.dental.2025.07.012

8. Meirowitz A, Rahmanov A, Shlomo E, Zelikman H, Dolev E, Sterer N. Effect of denture base fabrication technique on *Candida albicans* adhesion in vitro. *Materials*. 2021;14(1):221. doi: 10.3390/ma14010221

9. Zalega M, Bociong K. Antibacterial agents used in modifications of dental resin composites: a systematic review. *Appl Sci*. 2024;14(9):3710. doi: 10.3390/app14093710

10. Melo MAS, Garcia IM, Alluhaidan T, *et al*. The next frontier in antibacterial dental resins: a 20-year journey of innovation and expectations. *Dent Mater*. 2025;41(9):1045-1057. doi: 10.1016/j.dental.2025.06.013

11. Salgado H, Gomes A, Duarte AS, *et al*. Antimicrobial activity of a 3D-printed polymethylmethacrylate dental resin enhanced with graphene. *Biomedicines*. 2022;10(10):2607. doi: 10.3390/biomedicines10102607

12. Mangal U, Min YJ, Seo JY, *et al*. Changes in tribological and antibacterial properties of poly(methyl methacrylate)-based 3D-printed intra-oral appliances by incorporating nanodiamonds. *J Mech Behav Biomed Mater*. 2020;110:103992. doi: 10.1016/j.jmbbm.2020.103992

13. Jin G, Ravichandran V, Shim MS, Kim JE. Incorporating an artificially synthesized fluoride complex into urethane-acrylate-based 3D printing resin: effects on mechanical properties, cytotoxicity, antimicrobial actions, and its long-term fluoride-releasing properties. *J Dent*. 2024;150:105363. doi: 10.1016/j.jdent.2024.105363

14. Khattar A, Alghafli JA, Muheef MA, *et al*. Antibiofilm activity of 3D-printed nanocomposite resin: impact of ZrO_2 nanoparticles. *Nanomaterials*. 2023;13(3):591. doi: 10.3390/nano13030591

15. Mao X, Auer DL, Buchalla W, *et al*. Cetylpyridinium chloride: mechanism of action, antimicrobial efficacy in biofilms, and potential risks of resistance. *Antimicrob Agents Chemother*. 2020;64(8):166-191. doi: 10.1128/AAC.00576-20

16. Nezu T, Nagano-Takebe F, Endo K. Designing an antibacterial acrylic resin using the cosolvent method—effect of ethanol on the optical and mechanical properties of a cold-cure acrylic resin. *Dent Mater J*. 2017;36(5):662-668. doi: 10.4012/dmj.2016-222

17. Namba N, Yoshida Y, Nagaoka N, *et al*. Antibacterial effect of bactericide immobilized in resin matrix. *Dent Mater*. 2009;25(4):424-30. doi: 10.1016/j.dental.2008.08.012

18. Kitagawa H, Takeda K, Kitagawa R, *et al*. Development of sustained antimicrobial-release systems using poly(2-hydroxyethyl methacrylate)/trimethylolpropane trimethacrylate hydrogels. *Acta Biomater*. 2014;10(10):4285-95. doi: 10.1016/j.actbio.2014.06.016

19. Matsuo K, Yoshihara K, Nagaoka N, *et al*. Rechargeable antimicrobial adhesive formulation containing cetylpyridinium chloride montmorillonite. *Acta Biomater*. 2019;100:388-397. doi: 10.1016/j.actbio.2019.09.045

20. Kitagawa H, Kitagawa R, Tsuboi R, *et al*. Development of endodontic sealers containing antimicrobial-loaded polymer particles with long-term antibacterial effects. *Dent Mater*. 2021;37(8):1248-1259. doi: 10.1016/j.dental.2021.04.008

21. Otsubo S, Nakanishi K, Fukukawa K, *et al*. Development of autopolymerizing resin material with antimicrobial properties using montmorillonite and nanoporous silica. *Pharmaceutics*. 2023;15(2):544. doi: 10.3390/pharmaceutics15020544

22. Yoshihara K, Nagaoka N, Makita Y, Yoshida Y, Van Meerbeek B. Long-term antibacterial efficacy of cetylpyridinium chloride-montmorillonite containing PMMA resin cement. *Nanomaterials*. 2023;13(9):1495. doi: 10.3390/nano13091495

23. Khan S, Amin F, Amin R, Kumar N. Exploring the effect of cetylpyridinium chloride addition on the antibacterial activity and surface hardness of resin-based dental composites. *Polymers*. 2024;16(5):588. doi: 10.3390/polym16050588

24. Okazaki Y, Nakamori K, Yao C, *et al*. Antibacterial dental adhesive containing cetylpyridinium chloride montmorillonite. *Materials*. 2024;17(17):4368. doi: 10.3390/ma17174368

25. Yoshihara K, Kameyama T, Nagaoka N, *et al*. Development of an antimicrobial coating film for denture lining materials. *Pharmaceutics*. 2025;17(7):902. doi: 10.3390/pharmaceutics17070902

26. Yamamoto Y, Yoshihara K, Nagaoka N, Van Meerbeek B, Yoshida Y. Novel composite cement containing the antimicrobial compound CPC-montmorillonite. *Dent Mater*. 2022;38(1):33-43. doi: 10.1016/j.dental.2021.10.009

27. Perea-Lowery L, Gibreel M, Garoushi S, Vallittu P, Lassila L. Evaluation of flexible three-dimensionally printed occlusal splint materials: an in vitro study. *Dent Mater*. 2023;39(10):957-963. doi: 10.1016/j.dental.2023.08.178

28. Simunovic L, Brenko L, Maric AJ, Mestrovic S, Haramina T. Rheology of dental photopolymers for SLA/DLP/MSLA 3D printing. *Polymers*. 2025;17(19):2706.

doi: 10.3390/polym17192706

29. *ISO Standard 22196; Measurement of Antibacterial Activity on Plastics and Other Non-porous Surfaces*. Geneva, Switzerland: International Standards Organization; 2011.

30. Pratap B, Gupta RK, Bhardwaj B, Nag M. Resin based restorative dental materials: characteristics and future perspectives. *Jpn Dent Sci Rev*. 2019;55(1):126-138. doi: 10.1016/j.jdsr.2019.09.004

31. Taormina G, Sciancalepore C, Messori M, Bondioli F. 3D printing processes for photocurable polymeric materials: technologies, materials, and future trends. *J Appl Biomater Funct Mater*. 2018;16(3):151-160. doi: 10.1177/2280800018764770

32. Bennett J. Measuring UV Curing parameters of commercial photopolymers used in additive manufacturing. *Addit Manuf*. 2017;18:203-212. doi: 10.1016/j.addma.2017.10.009

33. Kolb C, Lindemann N, Wolter H, Sextl G. 3D-printing of highly translucent ORMOCER®-based resin using light absorber for high dimensional accuracy. *J Appl Polym Sci*. 2020;138(3):e49691. doi: 10.1002/app.49691

34. Khan K, Hussain MI, Tareen AK, Asghar A, Hamza M, Chen Z. Advances in vat photopolymerization 3D printing: multifunctional materials, process innovations, and emerging applications. *Mater Sci Eng R Rep*. 2026;167:101120. doi: 10.1016/j.mser.2025.101120

35. Hofstetter C, Orman S, Baudis S, Stampfl J. Combining cure depth and cure degree, a new way to fully characterize novel photopolymers. *Addit Manuf*. 2018;24:166-172. doi: 10.1016/j.addma.2018.09.025

36. Zakeri S, Vippola M, Levänen E. A comprehensive review of the photopolymerization of ceramic resins used in stereolithography. *Addit Manuf*. 2020;35:101177. doi: 10.1016/j.addma.2020.101177

37. ChemBK. *Cetylpyridinium Chloride*. https://www.chembk.com/en/chem/Cetylpyridinium%20chloride. Accessed September 20, 2025.

38. *ISO 20795-1; Dentistry—Base Polymers Part 1: Denture Base Polymers*. Geneva, Switzerland: International Standards Organization; 2013.

39. *ISO 20795-2; Dentistry—Base Polymers Part 2: Orthodontic Base Polymers*. Geneva, Switzerland: International Standards Organization; 2013.

40. Sakagami H, Tomomura M. Dental application of natural products. *Medicines*. 2018;5(1):21. doi: 10.3390/medicines5010021

41. Mosaddad SA, Tahmasebi E, Yazdanian A, *et al*. Oral microbial biofilms: an update. *Eur J Clin Microbiol Infect Dis*. 2019;38(11):2005-2019. doi: 10.1007/s10096-019-03641-9

ACCSCIENCE PUBLISHING

International Journal of Bioprinting

RESEARCH ARTICLE

A novel method to enhance acoustic droplet bioprinting quality through the analysis of parametric influence mechanisms

Qing Guo, Siyu Li, Dachao Li[1]*, and Haixia Yu[2]*

State Key Laboratory of Precision Measurement Technology and Instruments, Tianjin University, Tianjin, China.

Abstract

Three-dimensional bioprinting ushers a transformative change in tissue engineering, providing unparalleled opportunities for regenerative medicine by precisely fabricating intricate, biomimetic tissues. To achieve true organ-level *in vitro* tissue construction, various advanced bioprinting technologies have been developed. Among these, acoustic droplet bioprinting technology, owing to its excellent biocompatibility and multi-sample handling capabilities, offers an efficient, non-contact liquid-handling approach for tissue engineering applications. To meet the printing structure's geometric precision requirements, meticulous control of printing parameters is essential. However, the selection of acoustic droplet printing parameters still depends heavily on empirical values, which often leads to print outcomes that fall short of optimal standards. In this paper, a parameterized droplet dispensing method for multi-sample droplet excitation was established. This method introduces a unified scaling parameter based on the product of surface tension and viscosity, integrating acoustic stress and fluid response into a single dimensionless quantity, thereby enabling precise adjustment of droplet velocity. The relative error between the initial velocity measured using this method and the preset velocity was less than 6.7%. Next, we analyzed the effects of droplet overlap distance and the Weber and Ohnesorge numbers on printed line-width consistency. By employing optimized printing parameters, we achieved controllable printing of patterned hydrogel meshes suitable for cell culture. The results demonstrated that the lengths and widths of the nine sub-meshes exhibited high consistency. These advances move acoustic droplet bioprinting from an experience-driven process toward a more systematic, predictive, and reproducible parameter-optimization strategy.

Keywords: Acoustic droplet bioprinting; Bioprinting parameters optimization; Parameterized droplet dispensing method

***Corresponding authors:**
Dachao Li
(dchli@tju.edu.cn)

Haixia Yu
(hxy2081@tju.edu.cn)

Citation: Guo Q, Li S, Li D, Yu H. A novel method to enhance acoustic droplet bioprinting quality through the analysis of parametric influence mechanisms. *Int J Bioprint*. 2026;12(1):622-636. doi: 10.36922/IJB025470490

Received: November 21, 2025
Revised: December 27, 2025
Accepted: December 31, 2025
Published online: January 8, 2026

Copyright: © 2026 Author(s). This is an Open Access article distributed under the terms of the Creative Commons Attribution License, permitting distribution and reproduction in any medium, provided the original work is properly cited.

Publisher's Note: AccScience Publishing remains neutral with regard to jurisdictional claims in published maps and institutional affiliations.

1. Introduction

According to the latest statistics from the World Health Organization, nearly 2 million people worldwide require organ transplantation each year, whereas organ availability remains far below demand (supply–demand ratio < 1:20).[1] Organ shortages present the biggest challenge for organ transplant recipients. In recent years, the rapid advancement in

tissue engineering has shown great potential in addressing the "organ transplant crisis."[2] Tissue engineering, an emerging science developed in the late 1980s, involves the interdisciplinary fusion of clinical medicine, biomaterials, cell biology, bioengineering, and other fields.[3] It aims to establish three-dimensional (3D) complexes of cells and biomaterials using bioactive substances through *in vitro* cultivation or construction methods to replace or repair damaged organs.[4]

To achieve true organ-level *in vitro* tissue construction, researchers have developed various advanced 3D bioprinting technologies, including extrusion-based bioprinting,[5,6] inkjet bioprinting,[7,8] laser-assisted bioprinting,[9,10] and stereolithography bioprinting.[11,12] These technologies, characterized by high printing resolution, rapid fabrication speed, and advanced automation, are pivotal to the evolution of tissue engineering.[13] However, nozzle-dependent bioprinting methods, such as extrusion-based and inkjet bioprinting, typically face the following challenges: (i) High concentrations and viscosities of bioinks can lead to nozzle clogging, thereby reducing droplet distribution accuracy[14]; and (ii) the transient high pressure and shear forces generated at the nozzle during the distribution of biomolecules and cells can damage bioactive materials.[15,16] Conversely, while nozzles do not constrain laser-assisted and stereolithographic printing methods, residual reagents can readily cause biological materials to lose activity.[17]

Compared with other 3D bioprinting techniques, acoustic droplet bioprinting employs focused ultrasound to dispense bioinks in a non-contact manner with high spatial precision and without nozzle-induced constraints.[18] The absence of physical contact and shear-inducing nozzles minimizes mechanical stress on cells and biomaterials, thereby preserving bioactivity and viability. In addition, its capability to handle diverse bioinks without clogging enables flexible, multi-material deposition, which is particularly advantageous for constructing complex tissue and organ-like architectures.[19] Owing to these features, acoustic droplet bioprinting offers distinct advantages for tissue and organ printing and has attracted increasing attention in the field.

In 2021, Jentsch *et al.*[20] successfully fabricated complex 3D hydrogel structures laden with cells using acoustic droplet bioprinting technology, without adversely affecting the proliferation or differentiation capacity of stem cells. Xia *et al.*,[21] Chen *et al.*,[22] and Gong *et al.*[23] integrated personalized medicine with acoustic droplet bioprinting to construct reliable tumor models. These models not only closely mimic the *in vivo* tumor microenvironment but also enable objective and accurate assessment of drug efficacy and safety. However, the lack of precise optimization in the dynamic control of acoustic droplet bioprinting parameters results in poor consistency in multi-sample droplet ejection and challenges in achieving the desired structural precision of *in vitro* tissue models.[23]

Current studies on control methods rely predominantly on empirical observations. For example, Jentsch *et al.*[19] reported that the droplet impact velocity varies linearly with ultrasonic electrical input power, while the droplet diameter is inversely proportional to the ultrasonic frequency. In addition, Fang *et al.*[24] experimentally demonstrated that the droplet diameter increases with increasing pulse duration. Although these findings provide useful insights into the controllable dispensing of droplets in acoustic droplet bioprinting, they do not offer a systematic analysis of how the complex fluid properties of bioinks influence droplet generation and key characteristic parameters.

The commonly used input power control methods for acoustic droplet bioprinting include power scanning and dynamic fluid analysis methods. The method of power scanning involves a step-by-step incrementation of the acoustic energy until the ideal droplet initial velocity is obtained. Although implementation is straightforward, the process requires a substantial time investment.[24,25] In 2016, Hadimioglu *et al.*[18] developed a dynamic fluid analysis technique, which evaluates threshold power by analyzing the dynamic response of the liquid surface under focused acoustic energy. This method enables the automated assessment of the minimum input power needed for droplet excitation, but identifying the specific input power that matches the desired droplet initial velocities is difficult. The aforementioned studies fail to provide a viable solution for the controllable dispensing of multiple samples.

On the other hand, apart from ensuring stable droplet ejection, analyzing the impact of printing parameters on print quality, such as line width and its smoothness, is crucial for high-fidelity *in vitro* tissue construction. Gudapati *et al.*[26] emphasized in their review that the spreading characteristics of bioink droplets on the substrate significantly impact printing resolution and structural integrity. Gong *et al.*,[27] in their optimization study of linear bioprinting processes, found that droplet spreading characteristics are influenced by multiple factors, including substrate wettability, collision velocity, and droplet volume. Current research still lacks a correlation analysis of the impact of printing parameters on print quality. Relying solely on empirical methods makes it challenging to achieve high-precision and reproducible printing of *in vitro* tissue models.

Therefore, our method first introduces a unified scaling parameter based on the product of surface tension and viscosity, integrating acoustic stress and fluid response

into a single dimensionless quantity. By analyzing the correlations among input power, droplet velocity, and this liquid-property product, the input power required to excite droplets to a target velocity can be accurately predicted for bioinks with known properties. This capability enables controlled bioprinting of diverse bioinks, significantly reducing the reliance on extensive power scanning, thereby shortening experimental time and improving reproducibility.

Next, a direct correlation between input power and line width was established by analyzing the effects of input power and droplet characteristic parameters, as well as the influence of the droplet overlap distance, Weber number (*We*), and Ohnesorge number (*Oh*) on line width. To verify the feasibility, patterned hydrogel meshes for cell culture were printed. By integrating the predictive velocity control and optimized printing parameters, we demonstrated the fabrication of hydrogel mesh structures with high dimensional consistency. The lengths and widths of the nine subgrids exhibited excellent consistency.

2. Materials and methods

2.1. Experimental system

The acoustic droplet bioprinting system consists of four components: a liquid-depth measuring system, a droplet-excited system, a high-speed visualization system, and a target substrate (Figure 1). The liquid depth measuring system consists of an oscilloscope (DS7000, Rigol, China) and a pulser/receiver (5072PR, Olympus, Japan). They were utilized to measure the depth of the liquid within the wells and to align the transducer focal point onto the liquid surface. The droplet-excited system includes a power amplifier (75A250, Amplifier Research, USA), a 5-MHz-focused ultrasound transducer (V309S-SU, Olympus, Japan), and an arbitrary waveform generator (DG5000, Rigol, China), which were utilized for generating the required acoustic energy. The ultrasound transducer has an active aperture diameter of 12.7 mm and a focal length of 19.43 mm, corresponding to an f-number of 1.53. The focal zone was characterized by an axial length of 5.24 mm and a lateral diameter of 0.47 mm. The high-speed visualization setup (SA-X2, Photron, Japan) was used to record the entire process of droplet excitation, upward flight, and printing onto the target substrate at 12,500 fps.

Droplet diameter and velocity were measured using contour detection and centroid-extraction algorithms. During the experiments, 48-well plates (each well with a diameter of 11.5 mm and a depth of 17 mm) served as the source liquid wells, while glass slides measuring 26 × 76 mm with a thickness of 1 mm acted as the target substrate. The glass slide was positioned 0.50 cm above the liquid surface.

2.2. Reagents and materials

Gelatin methacrylate (GelMA) solutions (≥98% purity; Psaitong, China) at various concentrations, containing 10 μm polystyrene green fluorescent microspheres (G1000B, ThermoFisher, USA), were used as the experimental media (Table 1). GelMA is commonly used as a bioink due to its adjustable physicochemical properties, excellent biocompatibility, and close resemblance to natural extracellular matrices.[28,29] Polystyrene microspheres with sizes, shapes, and surface properties approximating those of cells were chosen as cell surrogates to simplify analysis.[19]

Because GelMA solutions are thermosensitive, viscosity decreases at 37°C, improving flowability and printability.

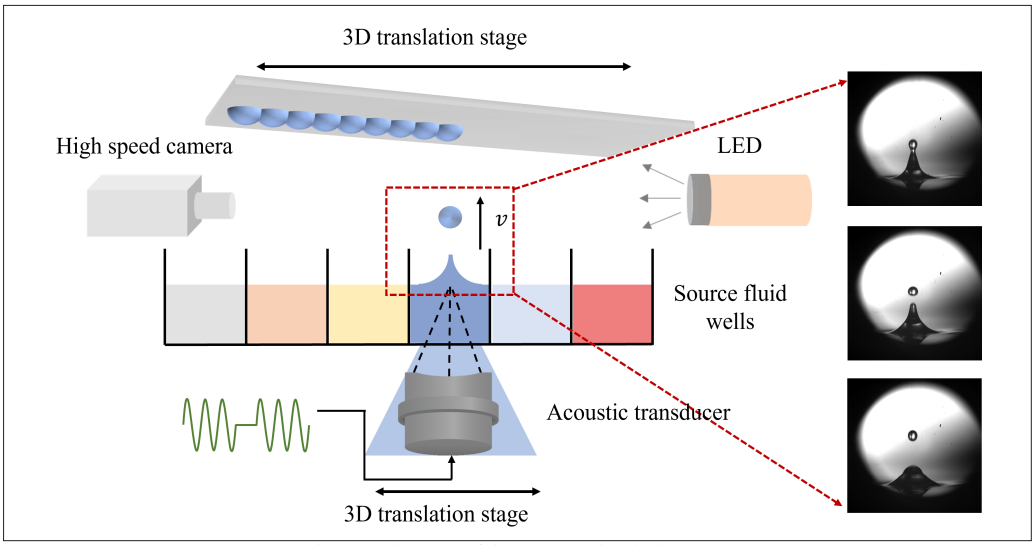


Figure 1. Schematic diagram of the acoustic droplet bioprinting system.

This characteristic makes GelMA hydrogel more suitable for bioprinting. Therefore, during the experimental process, a temperature control system (ED330, Jiangsu Huakai Electric Heating Appliances Co., Ltd., China) was utilized to heat the source fluid wells. The temperature control system consists of a polyimide heating film, an intelligent digital temperature controller, and a power adapter. The temperature control system achieves a precision of 0.1°C, with a temperature deviation not exceeding 0.5°C.

To develop a parameterized droplet dispensing method, it is crucial to measure the liquid properties in advance. The surface tension of bioink was measured by a surface tension instrument (CV-ZL1020, CVOK, China). The viscosity was measured by an automatic digital viscometer (DV3TLV, Brookfield, USA). Each value represents the mean of six measurements. During the measurements, a small heating plate was placed beneath the glass container holding the test reagent, maintaining the liquid temperature at 37°C. According to the measurements, the GelMA-based inks containing 10 or 20 μm polystyrene microspheres exhibited viscosities in the range of 8.36–10.91 cP and surface tensions between 36.82 and 50.52 mN/m. In addition, to ensure the uniform distribution of microspheres in the GelMA solution, both the printing and liquid properties measurement experiments were conducted within 10 min after stirring.

2.3. Statistical analysis

All quantitative data are expressed as mean ± standard deviation (SD). Each experimental condition was independently repeated at least five times ($n \geq 5$), as specified in the corresponding figure captions. Correlation analyses between printing parameters (e.g., acoustic input power, droplet overlap distance, *We*, and *Oh*) and printing outcomes (e.g., droplet velocity and printed line width) were performed using linear regression analysis. The goodness-of-fit was evaluated by the coefficient of determination (R^2). For comparisons involving variability in printed line width, the coefficient of variation (CV) was used as the primary quantitative metric to assess printing consistency. CV was calculated as the ratio of the SD to the mean value of the measured line width. Statistical analyses and data fitting were performed using Origin (version 2021, OriginLab Corporation, USA). Image analysis and quantitative measurements were conducted using ImageJ (version 1.53, National Institutes of Health, USA).

3. Results and discussion

3.1. Parameterized droplet dispensing method

Previous studies have shown that with increasing input power, the droplet diameter varies minimally, while the initial velocity is easily detectable and linearly increases.[18] Subsequent droplet excitation experiments were conducted on the reagents listed in Table 1, aiming to establish quantitative correlations between liquid properties (e.g., viscosity and surface tension), input power, and droplet initial velocity. Given the propensity of droplets to exhibit unstable excitation at lower input power and the potential for secondary droplet formation at excessively high input power, the input power control range needs to be defined within an interval extending from the threshold power, corresponding to the point of zero initial velocity, to the maximum power point, where the onset of secondary droplet formation occurs.

As shown in Figure 2, the linear correlation between velocity and input power was significantly influenced by the liquid properties. With the increase in microsphere concentration in the GelMA solution, the slope also varied. The linear correlations between droplet initial velocity and input power for the six reagents from A to F were as follows: $y = 0.57176x - 1.15969$ ($R^2 = 0.97$), $y = 0.38632x - 0.65024$ ($R^2 = 0.98$), $y = 0.34184x - 0.52587$ ($R^2 = 0.99$), $y = 0.32956x - 0.49615$ ($R^2 = 0.98$), $y = 0.29551x - 0.48313$ ($R^2 = 0.99$), and $y = 0.27658x - 0.44181$ ($R^2 = 0.99$).

This pattern can be attributed to the addition of microspheres, which results in a change in the liquid properties. The differences were primarily reflected in

Table 1. Characteristics of the experimental fluids

Liquid name	Density (g/cm^3)	Surface tension (mN/m)	Dynamic viscosity (cP)	Speed of sound (m/s)
A	1.03	36.82	8.36	1526
B	1.02	45.52	9.44	1523
C	1.01	46.11	9.52	1515
D	1.00	47.23	9.58	1497
E	0.98	49.88	10.12	1490
F	0.94	50.52	10.91	1526

Notes: A: 5% gelatin methacrylate (GelMA), B: 5% GelMA with 1.81×10^5 microspheres/mL, C: 5% GelMA with $5 \times 1.81 \times 10^5$ microspheres/mL, D: 5% GelMA with 1.81×10^6 microspheres/mL, E: 5% GelMA with $5 \times 1.81 \times 10^6$ microspheres/mL, F: 5% GelMA with 1.81×10^7 microspheres/mL.

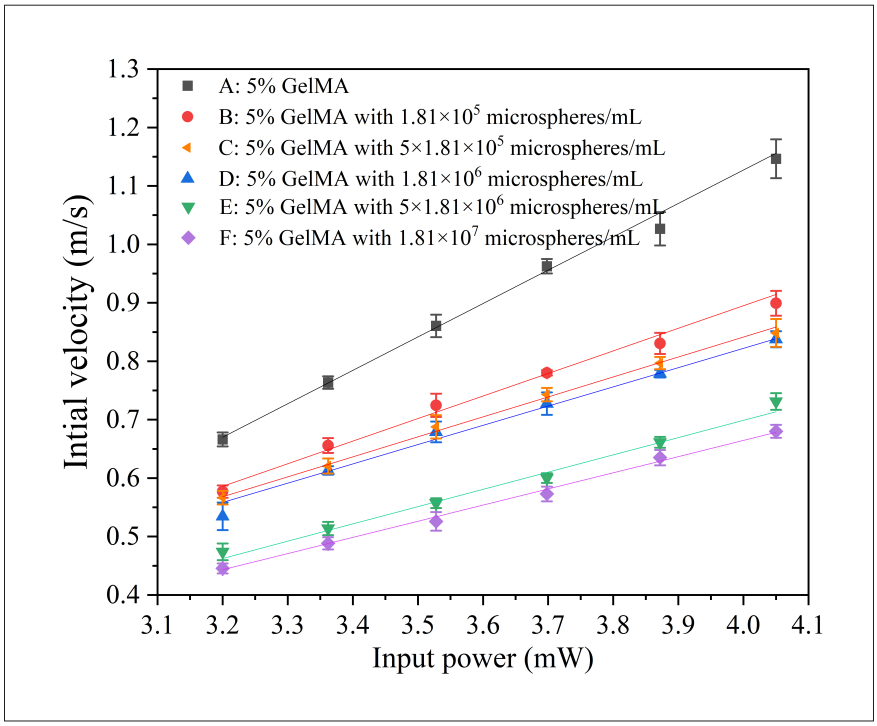


Figure 2. Correlation between droplet initial velocity and input power. Each experimental data point was obtained by averaging five repeated measurements. Abbreviation: GelMA, gelatin methacrylate.

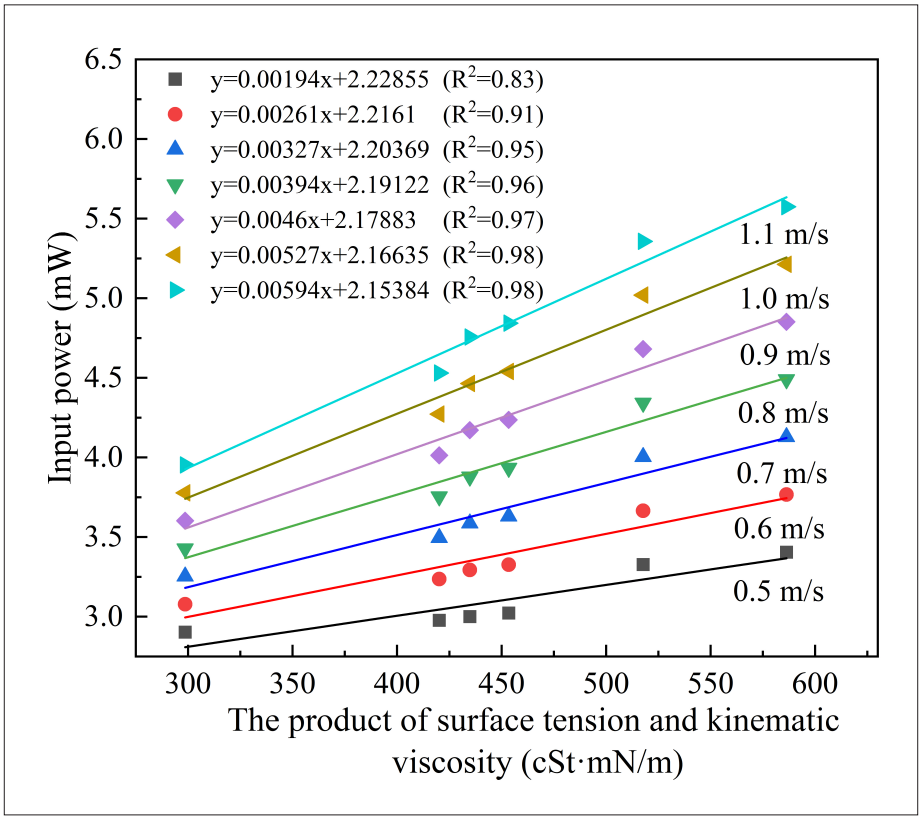


Figure 3. Correlation between input power and the product σv at specific initial velocities.

density, surface tension, and viscosity. Therefore, we introduced the product of surface tension σ and kinematic viscosity ν[30,31] and developed a parameterized droplet dispensing method by establishing the correlation between droplet initial velocity, input power, and the product $\sigma\nu$. The fluid's kinematic viscosity ν was calculated by dividing its dynamic viscosity by the fluid's density.

As the concentration of microspheres increases, the products $\sigma\nu$ of these reagents from A to F were determined to be 298.61, 420.15, 434.82, 453.41, 517.75, and 586.30 cSt·mN/m. With the increase in $\sigma\nu$, the internal resistance to flow and intermolecular forces also increase. This requires higher input power to achieve the target velocity. Therefore, for bioinks exhibiting a greater $\sigma\nu$, the slope of the linear fitting equation was smaller.

To examine the correlation between the $\sigma\nu$, velocity, and input power, we extracted input power data for initial droplet velocities (0.5–1.1 m/s) from Figure 2 and conducted a linear fit, as shown in Figure 3. Establishing this correlation is essential for developing the parameterized droplet dispensing method during acoustic droplet bioprinting. Based on these linear correlations, we predicted the input power corresponding to seven specific velocities by measuring the liquid properties of bioinks in advance. Furthermore, by refitting the linear correlations using seven velocity points and their corresponding predicted input powers, the input power for other velocities (0–1.1 m/s) can be determined under the given experimental system.

3.2. Verification of parameterized droplet dispensing method

To verify the accuracy of the parameterized droplet dispensing method, three test reagents were used: G (5% GelMA with 1.12×10^6 microspheres [20 μm]/mL), H (7.5% GelMA with 1.81×10^5 microspheres [10 μm]/mL), and I (7.5% GelMA with 1.81×10^7 microspheres [10 μm]/mL). The $\sigma\nu$ of the three reagents were measured as 303.51, 697.82, and 934.23 cSt·mN/m, respectively. Incorporating these liquid properties into the linear correlations shown in Figure 3, the required input power for specific initial velocities could be calculated. Using the calculated input power to eject droplets, the resulting initial droplet velocities closely matched the preset values, as shown by the black square in Figure 4.

To evaluate the predictive accuracy of the required input power at other velocities, droplet excitation experiments were conducted by randomly selecting six sets of input power. As shown by the blue square in Figure 4, the experimentally obtained average droplet initial velocities coincide perfectly with the preset values based on the linear fitting equation. The maximum relative error of velocities remained below 6.7%. This error primarily arises from inaccuracies in measuring surface tension and viscosity, temperature control deviations, and systematic errors.

3.3. Effect of droplet overlap distance on line width

For a bioprinted object, discrete droplets must be placed at a specific overlap distance to form a continuous line, which is then stacked to construct a patterned structure.[32] To ensure consistent bioprinting outcomes, we kept all other variables constant and specifically analyzed the influence of droplet overlap distance L on bioprinting quality after achieving controllable dispensing of multiple bioink droplets. L is defined as the center-to-center spacing of the droplets, or the step length of the stage movement. The bioprinting quality was evaluated by analyzing the CV of the line width. The steps for extracting line width and its CV are detailed below:

(i) A CCD camera (Model 1600, PCO AG, Germany) was installed on an inverted fluorescence microscope (Axio Observer A1, Zeiss, Germany) to capture fluorescent images of the printed structures following ultraviolet (UV) curing.

(ii) Image processing algorithms were applied to outline the edge contours of the fluorescent images, identifying the center points.

(iii) The center point was designated as the origin, and all line width values within the x-coordinate range of $-L/2 \times (n-1)$ to $L/2 \times (n-1)$ were extracted through 100 sampling points, where n represents the number of printed droplets.

(iv) Their mean and SD were computed, and the CV of the line widths was used as the final evaluation metric.

The experimental medium used for droplet printing was 5% GelMA with 1.81×10^6 microspheres (10 μm)/mL. The input power was set to 3.33 mW, resulting in an initial droplet velocity of 0.60 m/s and a droplet diameter of 385 μm. The spreading diameter D_s of the droplet onto the substrate surface was 660 μm.

To analyze the effect of L on line width, it is necessary to achieve coordinated control between the droplet-excited setup and the displacement platform. The displacement platform was purchased from Zolix Instruments Co., Ltd. (uKSA 100). It has a travel range of 100 μm along the x-axis and 50 μm along the y-axis, with a repeatability positioning accuracy of ±2 μm. While the transducer remained stationary, the substrate was translated along the x-axis at a speed of 10 mm/s with a delay time of 0.5 s and a motion of L mm. When the program was started, the transducer was

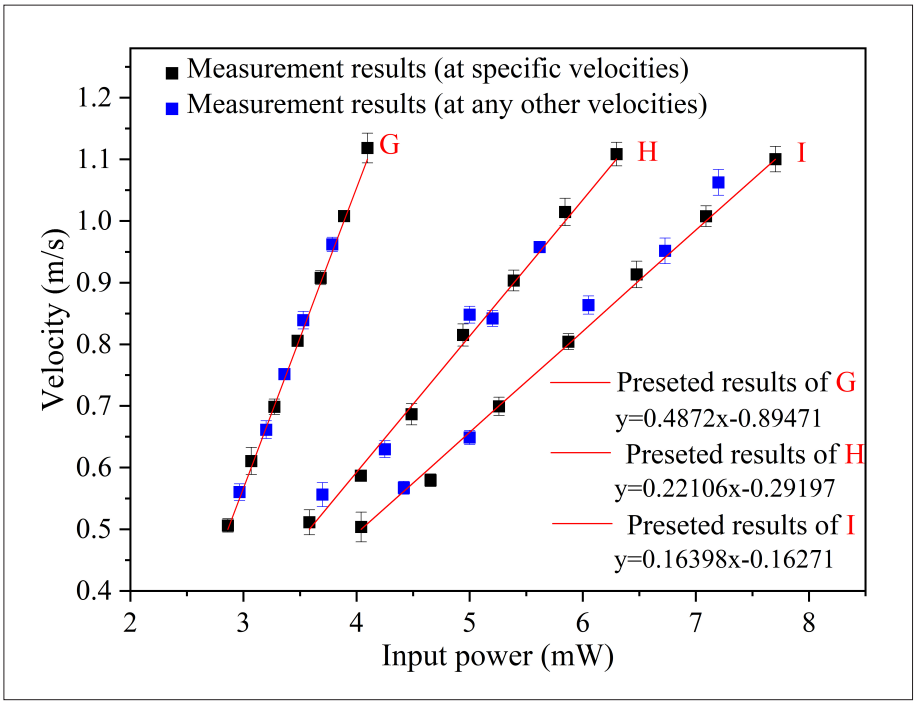


Figure 4. Correlation between input power and the product σv at specific initial velocities. Each experimental data point was obtained by averaging five repeated measurements.

triggered, with a time interval of 0.558 s between single pulses. Once the target substrate was positioned within 0.5 s based on the specific L, the second droplet collided and coalesced with the already printed one.

During the droplet collision, the surface tension promotes coalescence, and the viscosity resists shearing motion.[33,34] When the overlap distance L is small, the droplets have a larger contact area. Due to the initial kinetic energy of the upward flying droplets, the axial momentum during droplet collision is converted into radial momentum, causing the coalesced droplets to undergo expansion and enlargement along the center point. Under these printing conditions, the average line width will be relatively larger. As the L increases, the contact area between droplets decreases, leading to a more uniform distribution of material in the junction area and thereby smoothing the boundaries. When the L continues to increase, the connection gradually becomes concave, assuming a wavy shape, and the average line width decreases. The blue fluorescence images in Figure 5 show printing outcomes at different overlap distances.

As shown in Figure 5A, when the overlap distance was 0.50 mm ≤ L ≤ 0.66 mm, the line boundaries were smooth, and the SD of the line width was minimized, with all CVs being less than 1%. Binary-droplet printing is a building block for forming continuous lines. During multi-droplet printing, collisions and coalescence among droplets occur more frequently. The increased complexity of internal fluid dynamics in this process requires more precise control over the overlap distances between droplets to achieve smooth boundaries. To assess the suitability of the selected range of overlap distances for multi-droplet printing, we conducted continuous printing experiments using 5 and 10 droplets.

For the continuous printing of five droplets, the CV of the line width was less than 1% only within the overlap distance of 0.50 mm ≤ L ≤ 0.60 mm. In addition, it was verified that this overlap distance also applies to the continuous printing of 10 droplets, with no further reduction in the corresponding range (Figure 5B). Therefore, for multi-droplet printing, the range of 0.56–0.60 mm is considered the optimal selection. The optimal L results from the interplay of droplet size, impact velocity, liquid properties, and substrate wettability, which collectively regulate the balance between inertial spreading, capillary coalescence, and viscous dissipation under the present experimental conditions.

To extend printing parameters to a broader range of reagent compatibility, this study introduced the collision parameter P to normalize the collision overlap distance, enhancing parameter adaptability. P is given by the ratio L/D_s. The optimal overlap distance is 0.56–0.60 mm, corresponding to a collision parameter range of

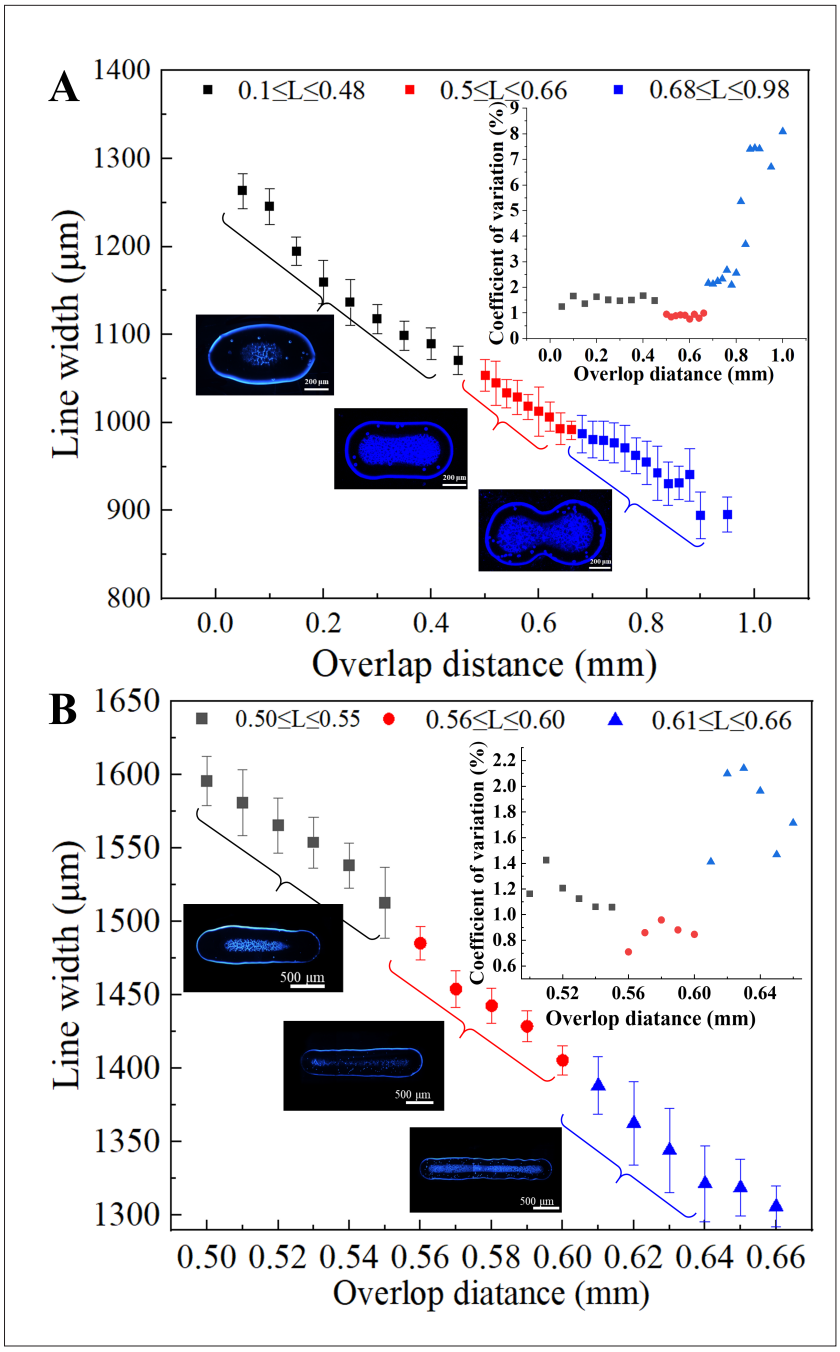


Figure 5. Correlation between droplet overlap distance and line width for (A) five-droplet and (B) 10-droplet printing. The inset graphs represent the coefficients of variation of line width under different droplet overlap distances. The inset blue fluorescent images indicate the printing effect under different droplet overlap distances (scale bars: [A] 200 μm, [B] 500 μm; magnifications: [A] 5×, [B] 5×). Each experimental data point was obtained by averaging five repeated measurements.

Table 2. Printing results of different bioinks

Reagent	Spreading diameter *Ds* (μm)	Collision parameter *P*	Average line width (μm)	Standard deviation	Coefficient of variation (%)
B	678	0.86	1462.35	9.87	0.67
F	634	0.88	1446.83	10.12	0.70

$0.85 \leq P \leq 0.91$. Next, the 10-droplet continuous printing experiment was conducted using reagents B and F to validate the applicability of the optimal L across different bioinks. Using the parameterized droplet dispensing method, the input power required to reach an initial velocity of 0.60 m/s was first determined as 3.24 and 3.77 mW for reagents B and F, respectively.

As shown in Table 2, the spreading diameters of the two bioinks, B and F, were 678 and 634 μm, respectively. Within the range of $0.85 \leq P \leq 0.91$, a set of parameters was selected for the 10-droplet continuous printing experiment. The results demonstrate that the line width's CV for both bioinks remained within 1%. Thus, the collision parameter range determined in this study not only accommodates various bioinks but also aids researchers in achieving smooth line printing more rapidly.

3.4. Effect of droplet characteristic parameters on bioprinting quality

In the process of 3D bioprinting, the characteristic parameters of droplets, such as velocity and volume, are also crucial to the interactions at the collision interface and the formation of the desired final pattern. The *We* is dimensionless, calculated as the ratio of inertial force to surface tension force. Using the *We*, we can normalize the effects of droplet velocity and volume, allowing for a more direct comparison of different printing conditions and the resulting print quality.

$$We = \frac{2\rho v^2 R_0}{\sigma} \quad (1)$$

where v and R_0 are the collision velocity and radius of the flying droplet, respectively, and ρ and σ are the density and surface tension of the droplets, respectively. The collision velocity of the droplet can be automatically extracted according to its initial velocity and flight height (0.5 cm). According to the experimental results in **Section 3.3**, as the droplet number increased to 10 or more, the resulting line width stabilized, showing no significant increase. Therefore, the subsequent analysis was confined to the line width resulting from the printing of 10 droplets. Under the $0.85 \leq P \leq 0.91$v, the experiment achieved droplet printing under varying collision *We*s by adjusting the input power. According to previous experimental results, it was found that higher input power leads to increased droplet ejection and collision velocities, and decreased droplet volume.

As shown in Figure 6A, for continuous 10-droplet printing, the line width decreased linearly as the *We* increased. This is mainly attributed to the reduction in droplet volume and its spreading diameter. The line widths' CVs were less than 1% for the three overlap distances. The results indicate that the collision parameter range established in **Section 3.3** is equally applicable under varying *We*s. On the other hand, according to the linear equation in Figure 6, it is possible to achieve controllable printing of specific line widths within the *We* range of stable droplet excitation.

However, when reagents were changed or ultrasonic transducers with different frequencies were used, resulting in variations in droplet size, achieving consistent printing of specific line widths becomes challenging. This is because the *We* exhibits low sensitivity to changes in droplet diameter and does not account for viscosity effects.

The *Oh* integrates viscosity, surface tension, and droplet size, offering a more comprehensive view of the droplet's resistance to deformation and spreading. The subsequent analysis was focused on the impact of the *Oh* on line width.

$$Oh = \frac{\mu}{\sqrt{2\rho\sigma R_0}} \quad (2)$$

Figure 7 shows a strong linear correlation between the *Oh* and line width.

By analyzing the effects of input power and droplet characteristic parameters in **Section 3.2**, as well as the influence of the *L*, *We*, and *Oh* numbers on line width, a direct correlation between input power and line width can be established. However, the current method for predicting line width is limited to a single reagent. To extend this method to other reagents, a preliminary 10-droplet printing experiment should first be conducted at a fixed *L* to establish the corresponding relationships between the *We*, *Oh*, and line width. Based on these correlations and the parameterized droplet dispensing method, printing with a targeted line width can then be achieved predictably.

3.5. Patterned hydrogel mesh printing

In this section, we leveraged the optimal parameter combination established in previous research to print a patterned hydrogel mesh structure designed for cell culture, thereby validating the effectiveness of the previously proposed printing control strategy.

The mesh structure mimics a basic scaffold, offering a porous framework that resembles the extracellular matrix in tissues.[35] This allows researchers to verify whether the printed structure can provide sufficient mechanical support and a suitable environment for cell adhesion and growth, key prerequisites for tissue engineering applications. The mesh, typically a simple crisscross pattern of intersecting

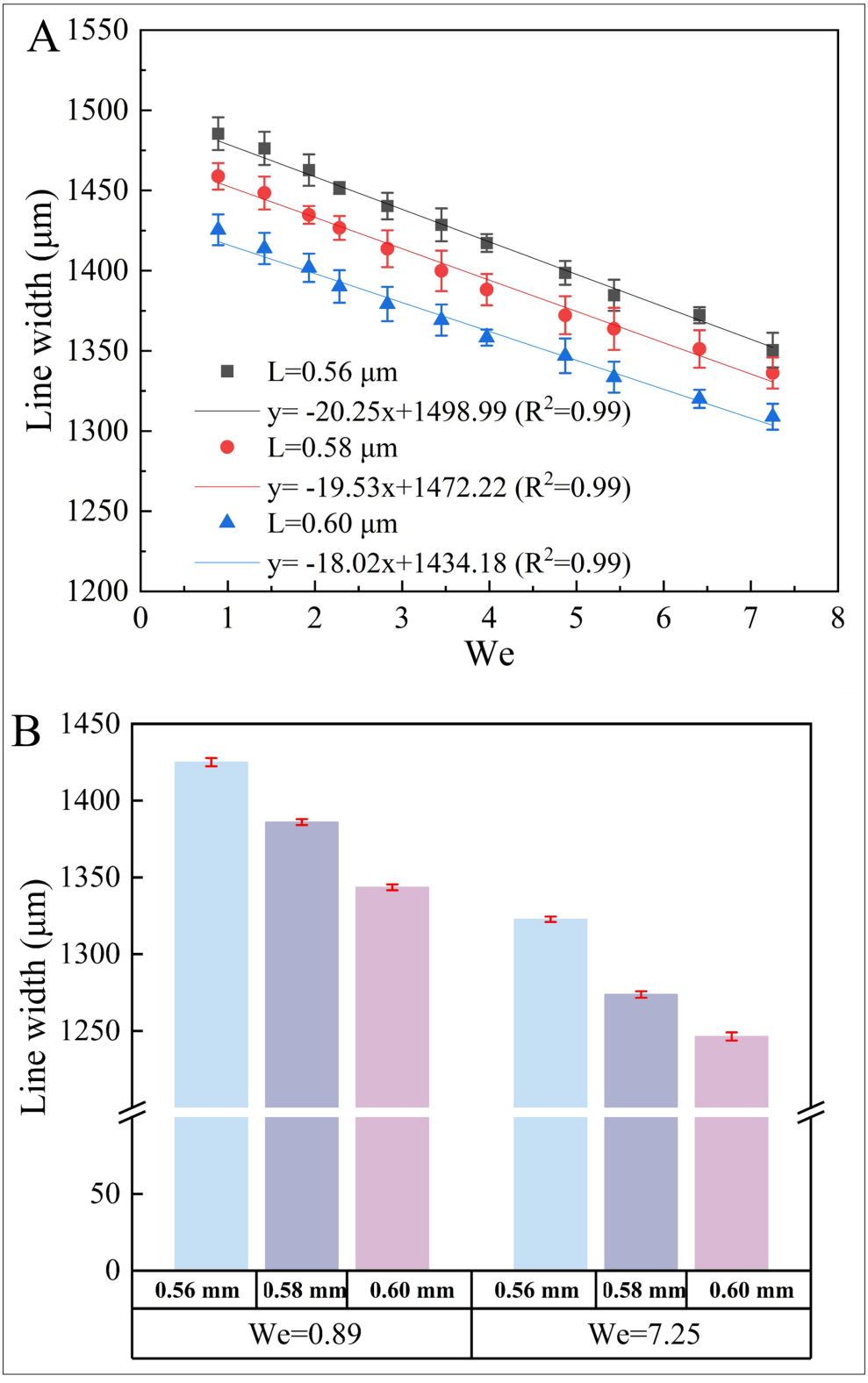


Figure 6. Quantitative evaluation of the influence of Weber number (*We*) on printing performance and stability. (A) Correlation between line width and *We*. (B) Repetitive experiments for the maximum and minimum *We* at the optimal droplet overlap distance. Each experimental data point was obtained by averaging five repeated measurements.

lines, along with evenly spaced horizontal and vertical lines, provides a clear benchmark for measuring line width, consistency of spacing, and dimensional accuracy.

The experimental medium was 5% GelMA (with photoinitiator) mixed with 1.81×10^6 polystyrene microspheres (10 μm)/mL, printed using acoustic excitation at 4.05 mW, with an L of 0.60 mm. As shown in Figure 8A, the first printing path involved depositing four lines, along the x-axis, with a center-to-center spacing d_1 of 2.5 mm. After printing, the first layer was UV-cured (5–10 s) to restrict liquid flow. Subsequently, the displacement platform was repositioned to the lower-left corner, and four lines were printed in the same manner along the y-axis with a center-to-center spacing d_2 of 2.5 mm, constituting the second layer.

The printed result shown in Figure 8B revealed that the first layer exhibited uniform and smooth lines, yet the second layer showed ink droplet aggregation, resulting in uneven line width. This phenomenon is mainly caused by ink droplets contacting both the hydrophobic cured first layer and the hydrophilic substrate during the second-layer printing process. The difference in wettability at the interface hinders normal droplet spreading at the junction, thus affecting the uniformity and smoothness of the second layer. An image processing approach was employed to detect the contours of each sub-mesh and fit minimum bounding rectangles, enabling the identification and measurement of the width and height of each sub-mesh. The results revealed that the lengths and widths of the nine sub-meshes exhibited poor consistency.

To improve the uniformity of the second layer, the printing path was optimized by implementing an intermittent printing approach. The initial printing position was redefined by setting a point 0.60 mm above the original y-axis coordinates as the starting point for the second-layer printing, followed by the continuous deposition of three droplets with a droplet overlap distance L' of 0.60 mm At an input power of 4.05 mW, employing the control method described in **Section 3.3**, the droplet initial velocity and collision velocity were calculated as 0.87 and 0.78 m/s, respectively, with a measured droplet diameter of 377.25 μm. Therefore, with a We of 4.87, the theoretical line width was determined to be 1346.42 μm based on the formula presented in Figure 6A.

When the d_1 was 2.5 mm, the dimensions of a single sub-mesh were 1.15 × 1.15 mm. Given that $L' < 1.15$ mm $< 2L'$, the consecutive printing of three droplets can ensure the formation of side walls of the sub-mesh.

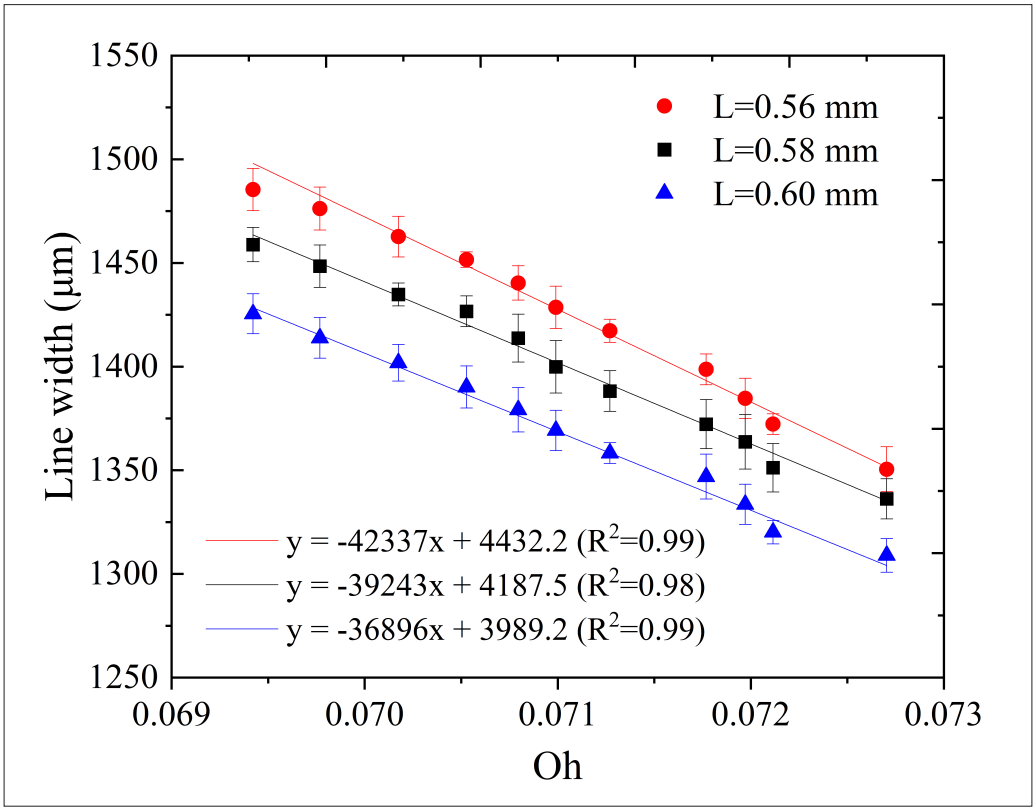


Figure 7. Correlation between line width and Ohnesorge number. Each experimental data point was obtained by averaging five repeated measurements.

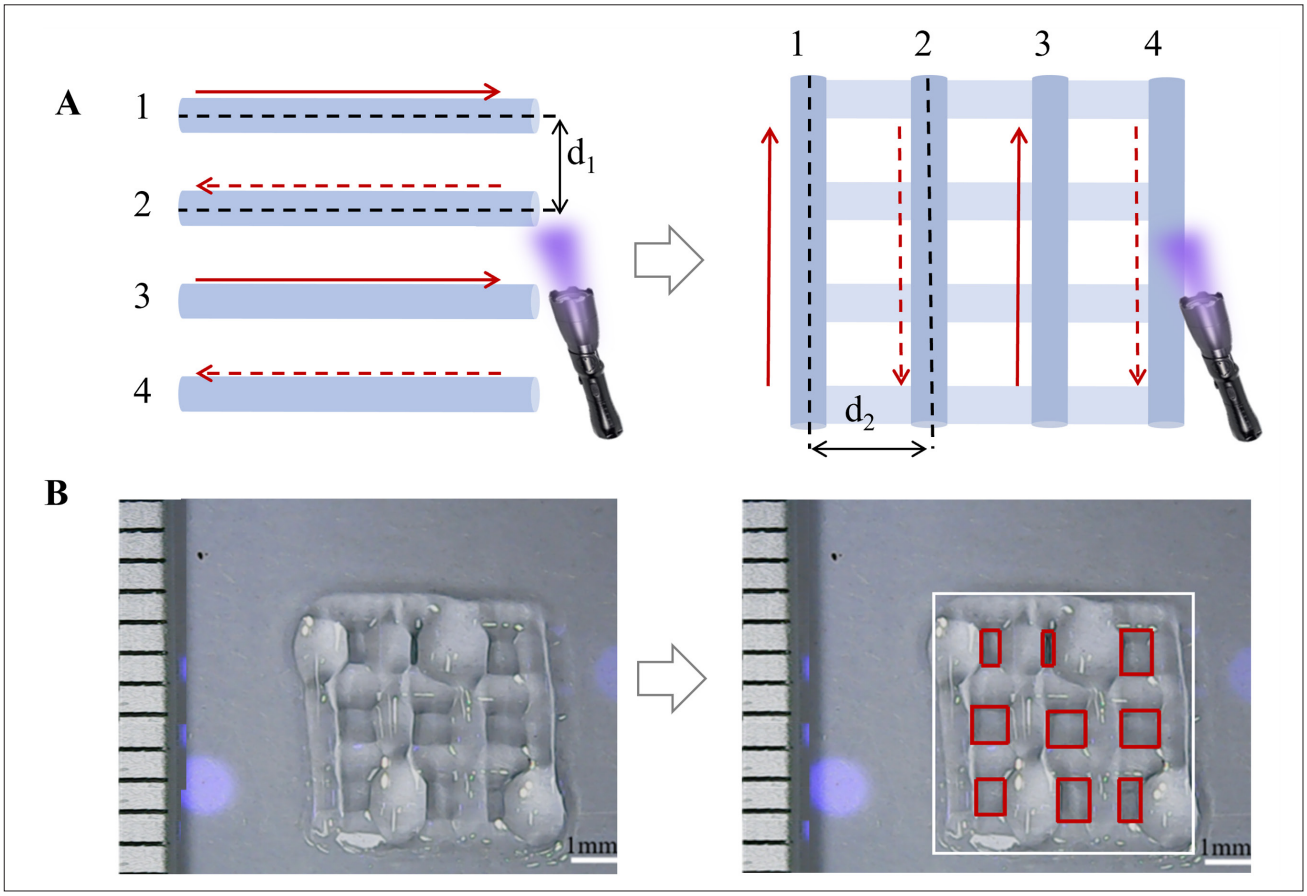


Figure 8. Schematic of the printing path for (A) the mesh scaffold structure and (B) photographs of the printed object.

Building on this foundation, by moving 2.5 mm along the *x*- and *y*-axes and sequentially printing the other eight sidewalls, the complete structure can be achieved. Following scheme optimization, the second-layer printing performance surpasses the results depicted in Figure 8B, exhibiting enhanced uniformity and smoothness in the overall structure, alongside a significant improvement in the consistency of mesh specifications (Figure 9). Next, five repeated printing experiments of the mesh structure were conducted, and the length and width of nine sub-meshes were extracted from each of the five experimental groups. Comparative analysis results revealed that the CV for both length and width in each group did not exceed 3%, with the relative error between measured and preset dimensions across all groups remaining below 6% (Table 3).

4. Conclusion

This study focused on addressing two fundamental challenges in acoustic droplet bioprinting: (i) poor consistency during multiple droplet generation, and (ii) low fidelity of printed structures under multi-parameter influences. To achieve controllable droplet excitation and obtain uniform linear structures, we first conducted experimental investigations to explore the correlation between the initial velocity of droplets and acoustic input power. By introducing a unified scaling parameter based on the product of surface tension and viscosity, a parameterized droplet dispensing method was established, allowing the prediction of the acoustic input power required to achieve specified droplet velocities for GelMA-based bioinks under the given acoustic configuration. The experimental validation results revealed that the relative errors between target droplet velocities and measured velocities using the selected excitation power, and the measured velocities were consistently less than 6.7%. Although this control strategy is not directly transferable to other acoustic systems without recalibration, the underlying theoretical scaling framework is general and can serve as a quantitative reference for efficient excitation parameter determination in future acoustic droplet printing studies.

Next, this study conducted a thorough analysis of the effects of droplet overlap distance (L), We, and Oh on line

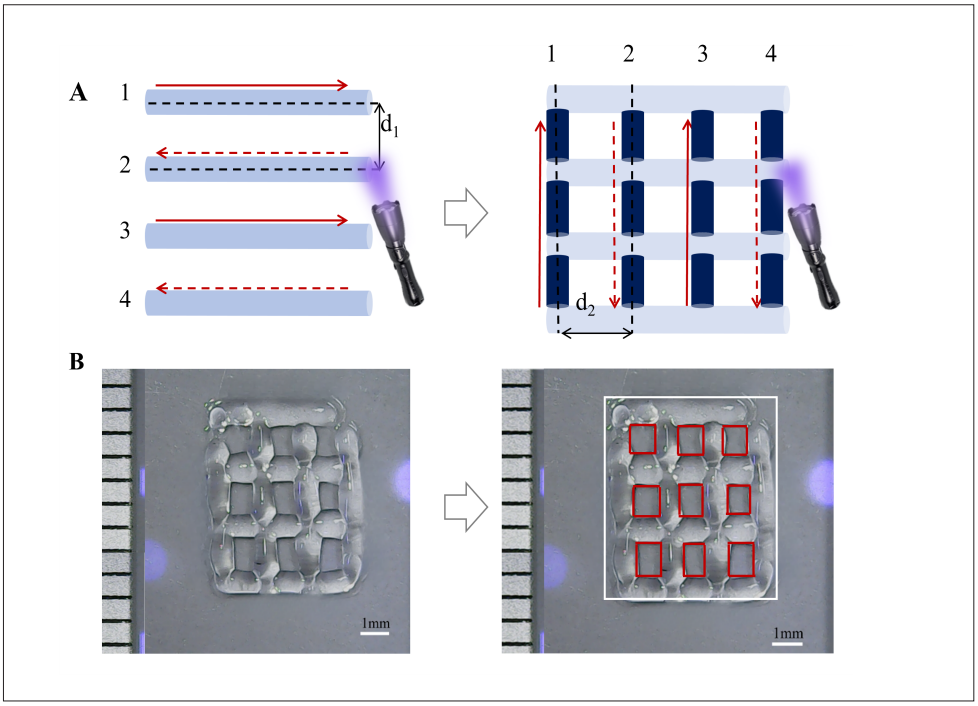


Figure 9. Schematic of improved printing path for (A) mesh scaffold and (B) photographs of the printed object.

Table 3. Dimensional statistic of sub-mesh across five experimental conditions

Experimental condition	Average length/width (mm)	CV of length/width (%)	Relative error (%)
1	1.18/1.10	1.94/1.87	2.41/−3.96
2	1.16/1.11	2.37/1.28	0.58/−3.09
3	1.11/1.12	1.58/1.41	−2.71/−2.61
4	1.15/1.11	2.29/1.69	0.19/−3.48
5	1.19/1.09	1.94/1.84	2.41/−5.51

Abbreviation: CV, coefficient of variation.

width and smoothness, establishing a direct correlation between input power and line width. This enables the controlled printing of lines with specific widths and smooth boundaries. Based on the developed printing parameter control method, mesh structures with individual unit dimensions of 1.15 × 1.15 mm were printed. The consistency of length and width across nine sub-meshes was evaluated by fitting a minimum bounding rectangle. The CVs for the lengths and widths of the nine sub-mesh units did not exceed 3%, and the relative errors between the measured and preset dimensions were less than 6%.

By integrating predictive droplet velocity control with optimized printing parameters, this work establishes a directly applicable parameter control strategy for acoustic droplet bioprinting. This strategy enables efficient selection of excitation and printing conditions, thereby improving printing efficiency while enhancing the fidelity and dimensional accuracy of printed structures. In addition, it provides a transferable methodological reference for extending acoustic droplet bioprinting to applications such as drug development, personalized medicine, and synthetic biology.

Acknowledgments

None.

Funding

This work is supported by the National Natural Science Foundation of China (No. 12304532) and the Natural Science Foundation of Tianjin (No. 23JCQNJC01320).

Conflict of interest

The authors declare no conflict of interest.

Author contributions

Conceptualization: Qing Guo, Dachao Li
Formal analysis: Qing Guo, Siyu Li
Investigation: Qing Guo, Siyu Li
Methodology: Qing Guo
Writing–original draft: Qing Guo
Writing–review & editing: Qing Guo, Dachao Li, Haixia Yu

Ethics approval and consent to participate

Not applicable.

Consent for publication

Not applicable.

Availability of data

Data are available from the corresponding author upon reasonable request.

References

1. Lechler RI, Sykes M, Thomson AW, Turka LA. Organ transplantation—how much of the promise has been realized? *Nat Med*. 2005;11(6):605-613.
doi: 10.1038/nm1251

2. Giwa S, Lewis JK, Alvarez L, *et al*. The promise of organ and tissue preservation to transform medicine. *Nat Biotechnol*. 2017;35(6):530-542.
doi: 10.1038/nbt.3889

3. Berthiaume F, Maguire TJ, Yarmush ML. Tissue engineering and regenerative medicine: history, progress, and challenges. *Annu Rev Chem Biomol Eng*. 2011;2(1):403-430.
doi: 10.1146/annurev-chembioeng-061010-114257

4. Van Blitterswijk C, De Boer J. Tissue Engineering. Cambridge, MA, USA: Academic Press; 2022.
doi: 10.1016/C2020-0-01481-7

5. Paxton N, Smolan W, Böck T, Melchels F, Groll J, Jungst T. Proposal to assess printability of bioinks for extrusion-based bioprinting and evaluation of rheological properties governing bioprintability. *Biofabrication*. 2017;9(4):044107.
doi: 10.1088/1758-5090/aa8dd

6. Ozbolat IT, Hospodiuk M. Current advances and future perspectives in extrusion-based bioprinting. *Biomaterials*. 2016;76(37):321-343.
doi: 10.1016/j.biomaterials.2015.10.076

7. Li X, Liu B, Pei B, *et al*. Inkjet bioprinting of biomaterials. *Chem Rev*. 2020;120(19):10793-10833.
doi: 10.1021/acs.chemrev.0c00008

8. Angelopoulos I, Allenby MC, Lim M, Zamorano M. Engineering inkjet bioprinting processes toward translational therapies. *Biotechnol Bioeng*. 2020;117(1):272-284.
doi: 10.1002/bit.27176

9. Guillotin B, Souquet A, Catros S, *et al*. Laser assisted bioprinting of engineered tissue with high cell density and microscale organization. *Biomaterials*. 2010;31(28):7250-7256.
doi: 10.1016/j.biomaterials.2010.05.055

10. Ventura RD. An overview of laser-assisted bioprinting (LAB) in tissue engineering applications. *Med Lasers Eng Basic Res Clin Appl*. 2021;10(2):76-81.
doi: 10.25289/ML.2021.10.2.76

11. Melchels FP, Feijen J, Grijpma DW. A review on stereolithography and its applications in biomedical engineering. *Biomaterials*. 2010;31(24):6121-6130.
doi: 10.1016/j.biomaterials.2010.04.050

12. Skoog SA, Goering PL, Narayan RJ. Stereolithography in tissue engineering. *J Mater Sci Mater Med*. 2014;25(3):845-856.
doi: 10.1007/s10856-013-5107-y

13. Murphy SV, Atala A. 3D bioprinting of tissues and organs. *Nat Biotechnol*. 2014;32(8):773-785.
doi: org/10.1038/nbt.2958

14. Krainer S, Smit C, Hirn U. The effect of viscosity and surface tension on inkjet printed picoliter dots. *RSC Adv*. 2019;9(54):31708-31719.
doi: 10.1039/c9ra04993b

15. Castro JO, Ramesan S, Rezk AR, Yeo LY. Continuous tuneable droplet ejection via pulsed surface acoustic wave jetting. *Soft Matter*. 2018;14(28):5721-5727.
doi: 10.1039/c7sm02534c

16. Guo Q, Su X, Zhang X, Shao M, Yu H, Li D. A review on acoustic droplet ejection technology and system. *Soft Matter*. 2021;17(11):3010-3021.
doi: 10.1039/d0sm02193h

17. Derakhshanfar S, Mbeleck R, Xu K, Zhang X, Zhong W, Xing M. 3D bioprinting for biomedical devices and tissue engineering: a review of recent trends and advances. *Bioact Mater*. 2018;3(2):144-156.
doi: 10.1016/j.bioactmat.2017.11.008

18. Hadimioglu B, Stearns R, Ellson R. Moving liquids with sound: the physics of acoustic droplet ejection for robust laboratory automation in life sciences. *J Lab Autom*. 2016;21(1):4-18.
doi: 10.1177/2211068215615096

19. Lagus TP, Edd JF. High-throughput co-encapsulation of self-ordered cell trains: cell pair interactions in microdroplets. *RSC Adv*. 2013;3(43):20512-20522.
doi: 10.1039/C3RA43624A

20. Jentsch S, Nasehi R, Kuckelkorn C, Gundert B, Aveic S, Fischer H. Multiscale 3D bioprinting by nozzle-free acoustic droplet ejection. *Small Methods*. 2021;5(6):2000971.
doi: 10.1002/smtd.202000971

21. Xia Y, Chen H, Li J, *et al*. Acoustic droplet-assisted superhydrophilic–superhydrophobic microarray platform for high-throughput screening of patient-derived tumor spheroids. *ACS Appl Mater Interfaces*. 2021;13(20):23489-23501.
doi: 10.1021/acsami.1c06655

22. Chen K, Jiang E, Wei X, *et al*. The acoustic droplet printing of functional tumor microenvironments. *Lab Chip*. 2021;21(8):1604-1612.
doi: 10.1039/d1lc00003a

23. Gong Z, Huang L, Tang X, *et al*. Acoustic droplet printing tumor organoids for modeling bladder tumor immune microenvironment within a week. *Adv Healthc Mater*. 2021;10(22):2101312.
doi: 10.1002/adhm.202101312

24. Fang Y, Frampton JP, Raghavan S, *et al*. Rapid generation of multiplexed cell cocultures using acoustic droplet ejection followed by aqueous two-phase exclusion patterning. *Tissue Eng Part C Methods*. 2012;18(9):647-657.
doi: 10.1089/ten.TEC.2011.0709

25. Guo Q, Shao M, Su X, Zhang X, Yu H, Li D. Controllable droplet ejection of multiple reagents through focused acoustic beams. *Langmuir*. 2021;37(51):14805-14812.
doi: 10.1021/acs.langmuir.1c02450

26. Gudapati H, Dey M, Ozbolat I. A comprehensive review on droplet-based bioprinting: past, present and future. *Biomaterials*. 2016;102:20-42.
doi: 10.1016/j.biomaterials.2016.06.012

27. Gong Y, Bi Z, Bian X, *et al*. Study on linear bio-structure print process based on alginate bio-ink in 3D bio-fabrication. *Bio Des Manuf*. 2020;3(2):109-121.
doi: 10.1007/s42242-020-00065-9

28. Xiao S, Zhao T, Wang J, *et al*. Gelatin methacrylate (GelMA)-based hydrogels for cell transplantation: an effective strategy for tissue engineering. *Stem Cell Rev Rep*. 2019;15(5):664-679.
doi: 10.1007/s12015-019-09893-4

29. Mamidi N, Ijadi F, Norahan MH. Leveraging the recent advancements in GelMA scaffolds for bone tissue engineering: an assessment of challenges and opportunities. *Biomacromolecules*. 2023;25(4):2075-2113.
doi: 10.1021/acs.biomac.3c00279

30. Lemmo AV, Fisher JT, Geysen HM, Rose DJ. Characterization of an inkjet chemical microdispenser for combinatorial library synthesis. *Anal Chem*. 1997;69(4):543-551.
doi: 10.1021/ac960808v

31. Gao H, Luo X, Cui D, *et al*. A study of film thickness and hydrodynamic entrance length in liquid laminar film flow along a vertical tube. *AIChE J*. 2018;64(6):2078-2088.
doi: 10.1002/aic.16081

32. Ji Y, Yang QZ, Huang GY, *et al*. Improved resolution and fidelity of droplet-based bioprinting by upward ejection. *ACS Biomater Sci Eng*. 2019;5(8):4112-4121.
doi: 10.1021/acsbiomaterials.9b00400

33. Qian J, Law CK. Regimes of coalescence and separation in droplet collision. *J Fluid Mech*. 1997;331:59-80.
doi: 10.1017/S0022112096003722

34. Brazier-Smith P, Jennings S, Latham J. The interaction of falling water drops: coalescence. *Proc R Soc Lond A Math Phys Sci*. 1972;326(1566):393-408.
doi: 10.1098/rspa.1972.0016

35. Cui Z, Feng Y, Liu F, Jiang L, Yue J. 3D bioprinting of living materials for structure-dependent production of hyaluronic acid. *ACS Macro Lett*. 2022;11(4):452-459.
doi: 10.1021/acsmacrolett.2c00037

ACCSCIENCE PUBLISHING

International Journal of Bioprinting

RESEARCH ARTICLE

Development of an *in situ* 3D bioprinting and laser-assisted wound care model: From leech regeneration to space medicine applications

Giada Loi[1], Mariagrazia Zaccara[1], Francesca Cialdai[2], Chiara Risaliti[2], Glenda Leggieri[2], Lorenzo Notari[2], Daniele Bani[3], Michele Conti[1,4*], and Monica Monici[2]

[1] Department of Civil Engineering and Architecture, University of Pavia, Pavia, Italy

[2] ASA campus Joint Laboratory, ASA Research Division, Department of Experimental and Clinical Biomedical Sciences "Mario Serio", University of Florence, Florence, Italy

[3] Department of Experimental and Clinical Medicine, University of Florence, Florence, Florence, Italy

[4] 3D and Computer Simulation Laboratory, IRCCS Policlinico San Donato, San Donato Milanese, Milan, Italy

(This article belongs to the *Special Issue*: *Emerging Bioprinting Techniques for Regenerative Medicine*)

Abstract

Wound healing is a complex process that ensures tissue recovery and survival, but remains challenging to manage, particularly in deep wounds and burns. Conventional treatments require specialized operators, repeated interventions, and high costs. In extreme environments, such as space, the absence of dedicated facilities and personnel further complicates wound care, highlighting the need for novel, automated, and easy-to-use therapeutic strategies. In this study, we developed and validated a protocol that combines *in situ* 3D bioprinting with near-infrared (NIR) laser irradiation to promote graft integration and accelerate wound repair. The approach was tested in the leech model of a skin wound with tissue loss, selected for its suitability in reproducing key aspects of tissue regeneration and for its relevance in space-oriented regenerative medicine experiments design comprised four steps: (i) identification of biomaterial inks compatible with the wound environment; (ii) application of an optimized *in situ* 3D bioprinting protocol; (iii) NIR laser irradiation to stimulate graft integration; and (iv) histological and immunofluorescence evaluation of healing outcomes compared to controls (bioprinting only, laser only, and untreated). Results demonstrated that the integrated protocol significantly improved wound healing, preventing fibrosis and enhancing re-epithelialization, fibroblast activation, and transdifferentiation. The combined treatment outperformed all control conditions, confirming the synergistic effect of *In situ* bioprinting and laser irradiation. This work introduces an advanced wound care strategy integrating biofabrication and photobiomodulation. The protocol shows high potential for clinical translation, with applications not only in conventional medical settings but also in extreme environments such as space.

Keywords: 3D *In situ* bioprinting; Wound healing; Near-infrared laser therapy; *In vivo* model

***Corresponding author:**
Michele Conti
(michele.conti@unipv.it)

Citation: Loi G, Zaccara M, Cialdai F, *et al.* Development of an *In situ* 3D bioprinting and laser-assisted wound care model: From leech regeneration to space medicine applications. *Int J Bioprint*. 2026;12(1):637-655. doi: 10.36922/IJB025400406

Received: September 29, 2025
Revised: December 5, 2025
Accepted: December 8, 2025
Published online: December 19, 2025

Copyright: © 2025 Author(s). This is an Open Access article distributed under the terms of the Creative Commons Attribution License, permitting distribution and reproduction in any medium, provided the original work is properly cited.

Publisher's Note: AccScience Publishing remains neutral with regard to jurisdictional claims in published maps and institutional affiliations.

1. Introduction

Wound healing is a highly conserved biological process that allows organisms to survive injuries. It is conventionally divided into three phases, namely inflammation, proliferation, and remodeling. However, it would be more accurate to define it as a set of complex mechanisms that follow one another and partially overlap within a defined timeline. Wound healing of the skin involves several cell types, including immune cells, fibroblasts, endothelial cells, and keratinocytes, whose activity is tightly regulated by a number of biochemical and mechanical factors.[1,2]

Among the cell populations involved in the healing process, fibroblasts play a pivotal role as they take part in all stages, orchestrating the activities of other cell populations by producing numerous soluble factors and mediating cell–cell cross-talk. During the inflammatory response to tissue injury, activated fibroblasts (stromal activation) promote events that occur during the proliferation phase, such as re-epithelialization and neoangiogenesis. Then, they transdifferentiate into myofibroblasts, capable of regulating connective tissue remodeling and wound closure by combining extracellular matrix (ECM) biosynthesis and intrinsic contractile properties through the development of an extended myofilament cytoskeleton.[3]

When the normal progression of one or more events leading to healing is altered quantitatively, qualitatively, or temporally, the whole process is impaired. The consequences of wound healing dysfunction range from healing delay and keloid scarring to much more severe and chronic conditions, such as chronic ulcers and fibrosis.[4,5] The management of healing dysfunction is an unmet clinical and socio-economic need. Reports on chronic wounds and their burden on national health systems show that in the United States (US), approximately 10 million patients (2.5% of the US population) are affected by chronic ulcers, with a significant impact on their quality of life and associated costs exceeding 20 billion dollars.[6] Similar numbers have been reported for other countries. Moreover, the prevalence of healing disorders is expected to increase further due to the aging population, rising diabetes and obesity, and the persistent problem of infections and antibiotic resistance.[7,8] All these reports indicate that one of the most effective ways to improve patients' quality of life and reduce the social costs of defective healing is to enhance wound care and prevent infections and wound-healing complications.

The management and care of severe wounds and burns are difficult and require precise wound diagnostics and complex therapeutic strategies aimed at promoting wound closure, including wound debridement, cleaning and disinfection, infection prevention, appropriate dressing, and pharmacological and non-pharmacological treatments, such as laser therapy and negative pressure therapy. When surgery is needed to merge the wound edges, remove the necrotic tissue, or prepare and apply a skin graft, as occurs in deep burn injuries, specialist intervention is required.[9,10]

Wound management and therapy are more complicated in extreme environments on Earth and in space, where hospital centers with adequate facilities, instruments, and skilled operators are lacking. Moreover, in extreme environments, the resilience of the organism to injury can be undermined by environmental stressors. During spaceflight, microgravity, radiation, and other stress factors induce significant pathophysiological alterations that could affect the efficiency of the healing process.[11–13] Therefore, it is necessary to make further efforts to search for new therapeutic strategies that are effective and also meet the requirements to be applied in extreme environments. In cases of severe injuries, ulcers, and burns, the aim is to automate and simplify medical and surgical procedures and to develop strategies that promote tissue regeneration. Substantial expectations are placed on the development of skin analogues that can mimic specific morpho-functional characteristics of the skin. These tissue analogues have several advantages: they allow the skin barrier to be rapidly restored, avoiding the need for cadaveric or heterologous transplants at risk of rejection and the removal of autologous skin flaps from the patient. Moreover, in the future, automated facilities could enable the preparation of tissue analogues even in extreme environments.[14]

Although it is complicated to recreate the morpho-functional complexity of the skin, interesting advances have recently been made in 3D bioprinting and tissue engineering techniques. Space agencies are developing systems for 3D bioprinting on board spacecraft or space stations, and one such facility has already been installed on the International Space Station (ISS).[15] These techniques could play a significant role in managing medical emergencies that may occur during future space exploration missions, in which, given the distance from Earth, an emergency medical evacuation with return to our planet would not be possible.

This study aims to develop a wound care model that, while accounting for the constraints and requirements imposed by extreme environments, can serve as a solid starting point for future wound management strategies in these settings. In particular, the protocol studied for the management of wounds with loss of substance consists of *in situ* 3D bioprinting a tissue construct (graft) using a biocompatible ink embedding human dermal fibroblasts, followed by the application of a near-infra red (NIR) laser source.

The wound care protocol was tested in an *in vivo* model of a wound with loss of substance in the leech. This invertebrate represents a fascinating model for studying wound healing and tissue regeneration[16-19] because its sequence of events leading to healing is highly similar to that of vertebrates. This is a remarkable example of the evolutionary conservation of critical physiological functions.[16] In addition to being a recognized model of wound healing, the leech was selected for its ease of management, including in future experiments on space platforms[20] and other extreme environments, due to its minimal husbandry requirements for long-term survival.

Although wound healing in *Hirudo verbana* proceeds faster than in humans, the sequence of events is conserved. Inflammatory cell recruitment and fibroblast activation occur within 24–48 h, followed by early collagen deposition within 3–5 days.[16] In the leech, healing relies on re-epithelialization and ECM remodeling, making its evolution comparable to human regenerative mechanisms despite the shorter timescale.

In designing this wound care protocol, two advantages were hypothesized: (i) the 3D bioprinting of the graft directly in the wound bed (*in situ*) would have immediately closed the dead space, temporarily replacing the skin barrier and protecting the integrity of the body from the external environment; (ii) the NIR laser radiation, modulating inflammation and stimulating tissue repair mechanisms, would have promoted the integration of the graft with the surrounding tissue, speeding up the wound healing process.

It is noteworthy that both *in situ* bioprinting and laser technologies can be automated, and the relatively small size of the instrumentation makes them suitable for use even in extreme environments, provided they are made compliant with the requirements for operating in such conditions.

2. Materials and Methods

2.1. Study design

The study involved the following steps (Figure 1):

(i) Preparation of the *in vivo* wound model through surgical removal of dorsal tegument tissues.

(ii) Pre-printing activities, which consisted of the selection, preparation, and testing of fibroblast-enriched bioinks compatible with the wound environment. They also involved the development and validation of a setting for *in situ* 3D bioprinting through monolayer, multilayer, and leech phantom tests.

(iii) Printing through the application of the developed *in situ* 3D bioprinting protocol in the model of a wound with loss of substance in the leech.

(iv) Treatment with an NIR dual-wavelength laser source to promote the integration of the graft into the surrounding tissues and shorten healing times.

(v) Post-care analysis through histology and immunofluorescence to evaluate graft integration and wound healing.

2.2. Preparation of the wound model with loss of substance in the leech

Leeches (*H. verbana*; Phylum: Annelida, Subclass: Hirudinea) about 6 cm long and 0.7 cm in diameter were purchased from Ricarimpex (Eysines, France). Since leeches are invertebrates, Animal Ethics Committee approval is not required for their use in research. However, in this study, the animals were treated in accordance with strict ethical principles to avoid suffering, and all procedures were performed under anesthesia.

The leeches were housed in aerated aquaria containing mineral water at about 20°C. Before surgical procedures, the leeches were anesthetized by immersion in a 10% ethanol solution (AppliChem GmbH, Germany).

An excised wound was created in the dorsal skin (at about the 14th metamere) of each leech with a surgical biopsy punch (Figure 1A). The original punch produced a cylindrical wound with a diameter of 3 mm and a depth of 7 mm. To avoid compromising the animal's internal organs and limit the excision to the skin (or integument) level, the punch was modified by an inner adapter to reduce the depth to 2 mm (Figure S8). The adapter was designed using the Autodesk Inventor CAD software (v.2023, Autodesk, Inc., US). It consisted of a hollow cylinder, 4 mm in diameter and 5.5 mm thick, suitable for insertion into the punch. The computer-aided design (CAD) model was exported as an STL file that was imported into Slic3r for printing. For this application, Nylon PA12 powder was used, and the 3D printing technology was binder jetting using an HP Multijet Fusion system (HP, US). The PA12 was selected due to its ability to be autoclaved (melting point of 220°C and autoclave temperature of 140°C). To create wounds, the punch was pressed and slightly rotated on the leech's back to cut and remove a circular skin biopsy. The wound was cylindrical, measuring 3 mm in diameter and 2 mm in depth.

2.3. Cell culture

Normal human dermal fibroblasts (nHDF) (ATCC, US) were cultured in Dulbecco's modified Eagle's medium (Sigma-Aldrich, Germany) supplemented with 10% fetal

bovine serum (Sigma-Aldrich, Germany), 100 IU/mL penicillin, 100 µg/mL streptomycin, and 2 mM glutamine (Sigma-Aldrich, Germany) at 37°C in a humidified atmosphere of 5% CO_2 in air.

2.4. Biomaterial ink selection and preparation

According to previous reports,[21-24] two different biomaterial inks suitable for inducing regeneration were preliminarily studied: one composed of alginate and gelatin (SA-GEL), and the other a commercial product (CELLINK Fibrin, see below).

2.4.1. Alginate and gelatin-based biomaterial ink

A hydrogel based on gelatin (GEL) and sodium alginate (SA) was prepared at a final concentration of 4% (w/v) and 8% (w/v), respectively, as described in previous papers.[22,25] First, the GEL powder (G9391, Sigma-Aldrich, Germany) was dissolved by vortexing in sterile phosphate-buffered solution (PBS) in a thermostatic bath and heated to +72°C. Then, SA powder (W201502, Sigma-Aldrich, Germany) was added to the GEL solution and vortex-mixed until completely homogenized. The hydrogel was centrifuged for 5 min at 2,000 rpm to remove air bubbles, then pasteurized in a thermostatic water bath at 72°C for 1 h. Finally, the hydrogel was transferred to a syringe and stored in a refrigerator at 4°C until use. All steps described were performed under sterile conditions.

2.4.2. Hydrogel

CELLINK Fibrin (IKC206000301, Sweden) is a commercially available nano-fibrillated cellulose (NFC)/alginate-fibrinogen-based hydrogel. The nanosized fibrils make the bioink semi-translucent, allowing cell imaging and analysis. Among the various biomaterials, fibrinogen-based hydrogels, extensively studied in the literature as biopolymers for tissue engineering applications, are particularly valued for their strong proangiogenic properties, outstanding biocompatibility and biodegradability, and customizable physicochemical characteristics.[26] This hydrogel offers significant advantages compared to other biomaterials, making it a highly suitable candidate for skin scaffold fabrication. In addition, the commercial kit includes an enhanced cross linking solution composed of an ionic binding agent ($CaCl_2$) to develop a compound network with improved printability and stability.

2.5. Preparation of the bioink containing human dermal fibroblasts

The bioink preparation was carried out under sterile conditions. After washing the cells with 5 mL of PBS, they were detached with 1 mL of trypsin and then centrifuged for 5 min at 1,200 rpm. The supernatant was discarded, and the cell pellet was resuspended in fresh culture medium at a final concentration of 3 $\times 10^7$/mL. The cell suspension was transferred into a syringe, which was then connected to a second syringe containing CELLINK Fibrin hydrogel, with a 1:10 ratio. The syringes were linked using a luer connector, and the bioink was prepared by passing the mixture between the two syringes until a visually uniform consistency was achieved (about eight passages). The bioink was then transferred to the printing cartridge, the needle was connected, and the cartridge was inserted into the printer head #1 (PH1).

2.6. Bioprinter

The 3D bioprinter used in this study is the Cellink INCREDIBLE+ (D16110010716, CELLINK, Sweden). This bioprinter features a pneumatic extrusion system with dual print heads (PHs), enabling the bioprinting of different types of cells and bioinks within the same structure without switching cartridges or pausing the process. PHs can be heated to 130°C, allowing the bioprinting of a wide range of biomaterials, from hydrogels (e.g., GEL, chitosan, hyaluronic acid, and alginate) to thermoplastic materials (e.g., polycaprolactone) and synthetic materials (such as Pluronic). PHs move along the x–y axes, while the print bed moves along the z-axis. The extrusion system consists of an external air compressor that generates an airflow in the cartridge–piston system, causing the material to extrude through the nozzle. The maximum pressure supported by the bioprinter is 700 kPa. The patented Clean Chamber Technology provides a sterile environment inside the bioprinter without the need for a laminar airflow hood. Moreover, behind the two PHs are two built-in UV light-emitting diodes with different wavelengths: 365 nm to sterilize the printing area and 405 nm to crosslink those hydrogels that require photo-crosslinking. Sterility was maintained using a high-efficiency H13 HEPA filter (retention rate > 99.95%) and a fan that creates positive air pressure inside the bioprinter chamber.

2.7. Setting for *in situ* bioprinting

To enable *in situ* 3D bioprinting, the first step involved generating a customized G-code. The purpose was to process an image of the printing plate and the cavity where printing would be performed to obtain a specific G-code. Three steps were employed to convert the acquired image to the final G-code. Different software was used for each step:

(i) Image segmentation with MATLAB (R2019b, MathWorks, US): The image was imported, segmented, and the coordinates of the wound area to be printed were extracted.

(ii) CAD model development with Autodesk Inventor: The CAD model was developed based on the

extracted wound coordinates, and the model was exported in STL format.

(iii) G-code generation with Repetier-Host (Hot-World GmbH & Co. KG, Germany) and Slic3r: The STL file was imported, and the printing options were set for the G-code generation. Before starting printing, the bioprinter settings were configured. The axes were homed, and the z-axis was calibrated. Finally, the correct printing pressure was set. PH1 was opened and, starting from 0 kPa, the pressure was gradually increased until the material was extruded.

2.7.1. Printing bed picture acquisition

Initially, a procedure for photographing the wounded leech on the printing plate was established. To outline the wound, we used a 3D-printed perforated disk that could be placed on the wound located on the leech's back. This disk, designed in Autodesk Inventor and printed in polylactic acid (PLA) using a fused deposition modeling 3D printer, had an inner diameter matching the wound diameter (3 mm), an outer diameter of 5 mm, and a height of 1 mm (Figure S1).

Then, a four-step procedure was followed for photographing (Figure 1B). First, the HEPA filter was removed from the top of the bioprinter. Second, using the bioprinter's Move axis function, the PHs were moved to the lowest coordinate on the x-axis and to the highest coordinate on the y-axis to frame the entire printing plate. Third, a digital camera was placed above the bioprinter to capture images of the whole printing plate. Finally, the photos were edited and cropped to the edges of the printing plate to segment and analyze only the objects of interest.

2.7.2. Image segmentation

In the second step, a code for image segmentation and processing was developed using MATLAB (Figure 1B) to obtain the coordinates of the wound outline on which bioprinting was to be performed. The procedure of image segmentation can be divided into the following five phases: image import, image binarization, selection of the contour pixel of interest, transformation of contour pixels into coordinates for 3D printing, and saving of the extracted coordinates in an XSLX format. To ensure high usability, an application based on the above-described steps was developed using MATLAB's App Designer. A summary of the MATLAB code's pseudocode is provided. More details on the MATLAB code are provided in **Section S1.2** and **Figures S2 and S3** in the **Supplementary Materials**.

```
# --- 1. Setup ---
clear_all()
close_all()
clc()
# --- 2. Load and preprocess image ---
picture = load_image('s_1.jpg')
image = extract_channel(picture, 'blue')
image = invert(image)
im_bw = binarize(image, threshold=0.5)
show(im_bw, title= 'Binarized image')
# --- 3. Find valid contours ---
all_contours = find_contours(im_bw)
B = [c for c in all_contours if size(c) > 20]
plot_contours(B, color= 'red', title= 'Contours')
# --- 4. Plate to real-world coordinates ---
plate = B[0]
plate_real_size = (128, 86) # mm (width, height)
pixel_bounds = get_bounds(plate)
scaling_x, scaling_y = compute_scaling
(pixel_bounds, plate_real_size)
x_plate, y_plate = convert_to_real(plate, pixel_bounds,
scaling_x, scaling_y)
plot(x_plate, y_plate, label= 'Plate')
# --- 5. Object transformation ---
coordinates = []
for obj in B[1:]:
    x_obj, y_obj = convert_to_real(obj, pixel_bounds,
    scaling_x, scaling_y)
    plot(x_obj, y_obj, label='Object')
    coordinates.append((x_obj, y_obj))
label_axes('x [mm]', 'y [mm]')
add_legend()
# --- 6. Export results ---
save_to_excel('s_1_0412.xlsx', coordinates)
```

2.7.3. CAD model development

The coordinates saved in the XLSX file, based on the printing plate coordinate system, were imported into Autodesk Inventor. Based on the shape given by the coordinates derived from the image, a 2D sketch was created and extruded. The CAD model was then exported as an STL file.

Table 1. Main printing parameters

Parameters	Value (mm)
Layer height	0.35
Default extrusion width	0.41
Bed size (x)	128
Bed size (y)	86
Origin (x)	63
Origin (y)	44

2.7.4. Option setting and G-code generation

A further step concerned the G-code generation and print settings (Figure 1B). Initially, the STL file was imported into Slic3r to set the printing parameters. The main parameters are summarized in Table 1, primarily the extrusion height (which defines the layer height), the extrusion width, and the printing bed dimensions and origins, which are necessary for correct printer calibration. Then, the G code was generated, and printing was started.

2.8. Software validation

Before using the above protocol in the animal model, it was optimized and validated in simpler scenarios using monolayer and multilayer assays and a surrogate animal model.

2.8.1. Monolayer assay

The monolayer validation replicated some flat geometrical shapes drawn on the printing plate. A picture of the shapes was taken and processed, following the protocol described in **Section 2.7**. Then, the printing was performed to verify the correct material deposition on the drawing. The procedure was optimized to correctly reproduce a rectangle, three straight lines, and a circle (Figure S4). In all these tests, the selected ink was the SA-GEL-based hydrogel.

2.8.2. Multilayer assay

The multilayer validation was performed by correctly depositing four layers of material within a support with a hole. The first one was a parallelepiped with dimensions 10× 10× 2 mm. In this case, a SA-GEL-based hydrogel was used as it is cross-linkable with a calcium chloride ($CaCl_2$)-based solution and extractable from the support to analyze the printed structure. Two different dyes were mixed with the hydrogel to verify the correct separation of the layers.

A second multilayer experiment was necessary to simulate the wound shape in the *in vivo* model. In particular, the correct gel deposition in a cylindrical model was evaluated. This cylinder-shaped hole had a diameter of 3 mm and a depth of 2 mm (Figure S5).

2.8.3. Leech phantom

Before being used on the actual animal model, the software was tested on a dummy model, termed "leech phantom" (Figure S6). It was made in ballistic GEL through a 3D-printed mold. The ballistic GEL was mixed with graphite, giving the phantom a black color, so that the surrogate animal model faithfully mimicked the actual

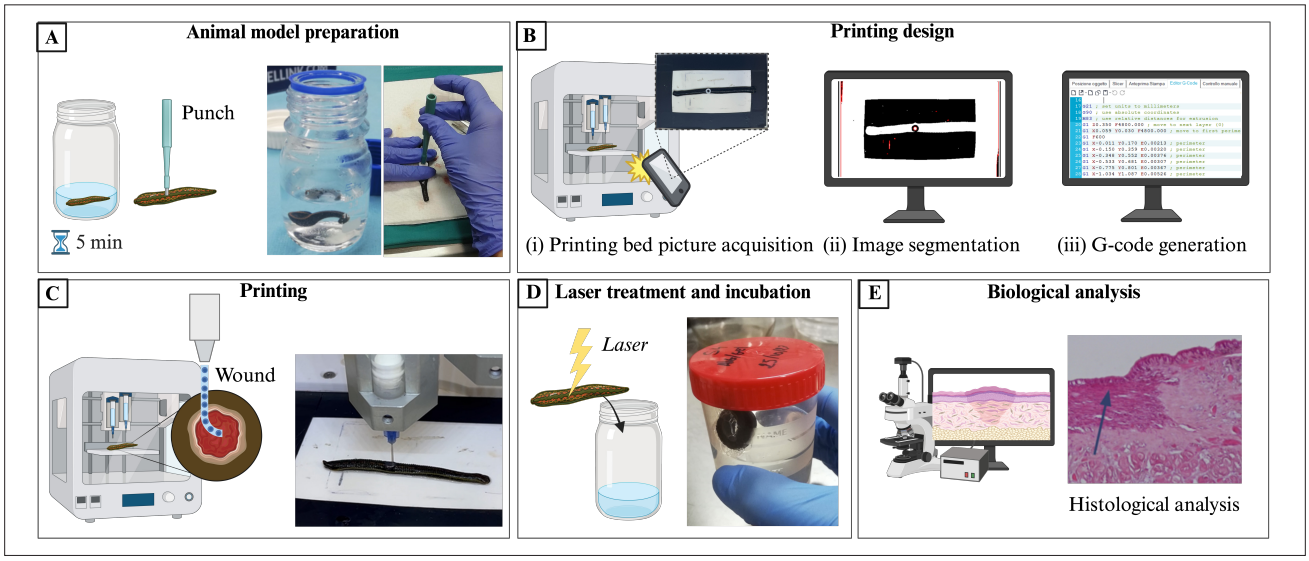


Figure 1. Schematic representation of the experimental procedures. (A) Animal model preparation. Leeches are anesthetized through immersion in 10% ethanol, and then a surgical tissue excision is made on the dorsal skin of each leech using a surgical biopsy punch. (B) Printing design. (i) Acquisition of digital images of the printing plate and the cavity to be filled by bioprinting. (ii) Image segmentation. (iii) G-code generation. (C) 3D printing of the bioink in the wound bed. (D) Laser treatment to promote graft integration, and incubation of the animals in separate aquarium boxes. (E) Post-treatment histological analyses.

wounded leech model. The mold was designed using a CAD model that reproduced the shape and dimensions of a leech with a cylindrical wound on the back. In particular, the phantom had a length of 6 cm and a diameter of 1 cm, whereas the wound had a diameter of 3 mm and a depth of 2 mm. The phantom was printed on a commercial FDM printer using PLA (Figure S7). The mold was first smeared with Vaseline for easy removal. Then, the ballistic GEL was melted and then poured into the mold. After 20 min of drying, the ready-to-use leech phantom was extracted from the mold. Initially, the wound was highlighted with white chalk to ease its identification by the software. Then, the leech phantom was placed on the printing plate, and a picture was taken. The above-described protocol was then applied: the software correctly elaborated the picture and generated the G-code for printing. In these tests, the SA-GEL-based hydrogel was employed.

2.9. *In situ* bioprinting in the *in vivo* model of wound with loss of substance in the leech

For the *in situ* bioprinting, anesthetized leeches were placed on the printing plate, and the procedure described in **Sections 2.7 and 2.8** was applied. Briefly, a circular-shaped object was put on the leech to highlight the wound, and a picture of the wounded leech on the printing plate was taken with a digital camera (Nikon D5200, Japan) (Figure S9A). The wound contour pixels were selected through the procedure developed in MATLAB (Figure S9B). The CAD model was designed in Autodesk Inventor for the extracted contours, and an STL file was generated (Figure S9 C). The STL file was imported into Slic3r, where the printing parameters were imposed, and the G-code was generated. Finally, the *in situ* 3D bioprinting into the wound was performed (Figures 1C and S9D). Immediately after printing, a $CaCl_2$ solution was added to the printed graft in the wound to crosslink the hydrogel for 3 min (Figure S9E). Before returning to water, the leeches were allowed to recover from anesthesia in a Petri dish with 5–6 mL of PBS for 5 min (Figure S9F). Then, each animal was placed in a separate small aquarium to prevent them from sticking to one another (Figure S9G).

The *in situ* 3D bioprinting procedure on the *in vivo* model was first validated using the SA-GEL hydrogel. On the other hand, the CELLINK Fibrin hydrogel containing human dermal fibroblasts was used for the final wound care protocol.

2.10. Near-infrared laser treatment

In this study, an NIR laser treatment was used to promote graft integration (Figure 1D). The laser source was a Multiwave Locked System laser (MLS-MiS; ASA S.r.l., Italy). It is a class IV NIR laser system with two synchronized sources. The first source is a pulsed laser diode emitting at 905 nm, with peak power ranging from 140 W ± 20% to 1 kW ± 20% and a pulse frequency of 1–2,000 Hz. The second source is a laser diode emitting at 808 nm wavelength that can operate in continuous (max power 6 W ± 20%) or frequency mode (pulse repetition rate 1–2,000 Hz, 50% duty cycle). The two laser beams work simultaneously and synchronously, with their propagation axes coincident.

Leeches were exposed to laser radiation every 24 h for four consecutive days, starting 24 h after the bioprinting procedure. To perform the laser treatment, the leech was placed in a plastic support, shaped like a half-tube, designed to securely and safely house a leech. The inner surface of the half-tube was smooth, facilitating gentle contact with the leech's skin and allowing it to extend comfortably along its length. The parameters used for the laser treatment were: frequency 10 Hz, intensity 50%, treatment time 10 s, and fluence 4.92 J/cm^2. The treatment parameters were chosen not only on the basis of the effects of laser treatment on fibroblasts, which have been extensively evaluated in previous studies on fibroblast cultures,[27-29] but also considering other aspects, such as the color of the animal's integument, the depth of treatment, and the duration of exposure based on the anesthesia given to the animal.

2.11. Tissue sampling, processing, and histological analysis

Six hours after the last MLS-MiS laser treatment, the leeches were anesthetized in a 10% ethanol solution. Once anesthetized, they underwent fixation by immersion in a fixative solution (ImmunoFix, phosphate-buffered, 4% paraformaldehyde, pH 7.4; Bio-Optica, Italy). The leeches were maintained in the fixative for 2 h at room temperature, then stored at 4°C for 48 h. The extremities of the animals were removed, preserving only the body segment that included the wound for dehydration in graded ethanol. Following dehydration, samples were cleared by two passages in Bio-Clear (Bio Optica, Italy), placed in paraffin oil, and finally embedded in paraffin wax (Bio-Optica, Italy) at 58°C overnight. Sections of 5-µm thickness were mounted on glass slides. Then, two histological staining were carried out (Figure 1E): (i) hematoxylin and eosin (H&E) to provide an overview of the general morphology and histological features; (ii) Picrosirius red staining (0.2% Picrosirius red solution for 60 min) to identify collagen fibers, which appear intensely red. The stained sections were dehydrated, cleared, and embedded in a permanent mounting resin under coverslips. Images of the stained sections were acquired using a Nikon DS F12 CCD camera (Japan) connected to a Nikon Eclipse E200 light microscope (Japan) at 4× and 20× magnification.

2.12. Collagen fiber morphometry

In each Picrosirius red-stained section, two photomicrographs of the connective tissue of the wound bed were taken at random using the Nikon DS F12 CCD camera connected to a Nikon Eclipse E200 light microscope at 40× magnification (each micrograph: 57,700 μm^2). On each image, four regions of interest (ROI), 10,000 μm^2 each, were randomly chosen: here, the surface area of the collagen fibers was selected by thresholding (to exclude the Picrosirius red-negative amorphous ground substance and cells) and measured using ImageJ 1.53k software (http://imagej.nih.gov/ij). Values are expressed as the percent area of collagen fibers over the whole ROI area.

2.13. Immunofluorescence analysis

Immunofluorescence staining was performed on 5 μm sections of the paraffin-embedded samples. After paraffin removal in Bio-Clear (Bio-Optica, Italy) and rehydration in graded ethanol, the sections were subjected to antigen retrieval by immersion in citrate buffer at 90°C for 10 min, followed by cooling to room temperature for 30 min. Then, after rinsing in isotonic PBS, the sections were incubated with 2 mg/mL glycine in PBS for 15 min and 5% bovine serum albumin (BSA) in PBS for 1 h to block non-specific antibody binding. A rabbit monoclonal anti- heat shock protein 47 (HSP47) immunoglobulin G (IgG) antibody (Millipore, US), diluted 1:50 in PBS + 3% BSA, was used to detect fibroblasts. A mouse monoclonal anti-alpha smooth muscle actin (α-SMA) IgG antibody (Millipore, US), diluted 1:100 in PBS + 3% BSA, was used to detect activated myofibroblasts. The slides were incubated with the primary antibodies at 4°C overnight, washed thoroughly with PBS, and incubated with the appropriate secondary antibodies: tetramethylrhodamine isothiocyanate (TRITC)-conjugated (red emission) goat anti-rabbit IgG (Millipore, US), diluted 1:100 in PBS + 3% BSA, to label HSP47 immunoreactivity; and fluorescein isothiocyanate (FITC)-conjugated (green emission) goat anti-mouse IgG (Millipore, US), diluted 1:200 in PBS + 3% BSA, to label α-SMA immunoreactivity. The secondary antibodies were incubated at room temperature for 2 h and then washed thoroughly in PBS. Finally, cell nuclei were counterstained with 4´,6-diamidino-2-phenylindole (DAPI) present in the mounting medium. Images were acquired using an Olympus BX63F fluorescence microscope (Japan).

2.14. Statistical analysis

Morphometric data are presented as means ± SD of the measurements of four individual animals, with four ROI (approximately 10,000 μm^2 each) per animal across the different experimental groups. Statistical comparison of differences between groups was performed using one-way analysis of variance (ANOVA) followed by Student's *t*- test for unpaired values, assuming $p \leq 0.05$ as significant. Calculations were performed using Prism 5.0 software (GraphPad Software, US). For immunofluorescence analysis, at least 10 random fields were scored per slide.

3. Results

3.1. Validation of the software for the 3D bioprinting protocol

Before employing the animal model, the developed protocol was tested and validated. First, tests on bioprinted monolayers were conducted. They consisted of replicating some planar geometrical shapes visible on the printing plate. These were digitally acquired and processed according to the developed protocol. Finally, the printing was made, and the correct material deposition on the drawing was verified. The procedure was optimized to correctly reproduce a rectangle, three separate straight lines, and a circle. Second, tests on bioprinted multilayers were performed to verify the correct deposition of four layers of bioink within a hole made into the supporting structure. The first 3D printout was a 10 ×10× 2 mm parallelepiped, while the second was a cylinder with a diameter of 3 mm and a depth of 2 mm, necessary to test conditions similar to those in the experimental tests with the animal model. The protocol successfully guaranteed the deposition of four layers of material in the correct coordinates. Finally, a test with a GEL-moulded leech phantom was performed to validate the software further. Initially, the wound was highlighted with white chalk to ease identification by the software. Then, the leech phantom was placed on the printing plate and processed according to the developed protocol, which successfully generated a conformal bio printed construct within the wound model created on the leech phantom.

3.2. Validation of the *in situ* 3D bioprinting procedure in the *in vivo* wound model

Two tests were conducted. The first was to validate the *in situ* 3D bioprinting procedure in the *in vivo* wound model, using the SA-GEL hydrogel bioink and the $CaCl_2$ crosslinking agent. The second aimed to validate the entire procedure using the more complex CELLINK Fibrin hydrogel bioink, with or without human dermal fibroblasts, and to optimize it for the wound care protocol. Again, $CaCl_2$ was used as a crosslinking agent. The fibrinogen-based hydrogel was chosen as a suitable environment for human dermal fibroblasts since, in previous experiments, it has been shown to preserve cell viability[26] and function better than the SA-GEL.[21] Human dermal fibroblasts were incorporated into the bioink to promote tissue repair, as they can release growth factors and cytokines that facilitate healing and enhance tissue regeneration.[30] Additionally, they can produce ECM components that

provide both structural support and biochemical signals essential for tissue repair.[31] Furthermore, fibroblasts can transdifferentiate into myofibroblasts, which play a critical role in the remodeling phase of wound healing by contributing to tissue contraction and ECM remodeling.[32]

For these tests, models of wounds with loss of substance were prepared in the leeches as described in **Section 2.2**. The animals (n=9) were then divided into three groups:

(i) Untreated animals (n=3), no *in situ* 3D bioprinting, served as a negative control.

(ii) Animals (n=3) that received an *in situ* 3D-bioprinted graft of SA-GEL hydrogel.

(iii) Animals (n=3) that received an *in situ* 3D-bioprinted graft of CELLINK Fibrin hydrogel containing human dermal fibroblasts.

The *in situ* 3D bioprinting procedure was successful with both the bioinks (SA-GEL and CELLINK Fibrin), as demonstrated by their precise deposition within the wounds and the stability of the grafts. The animals were monitored before and after receiving the *in situ* 3D-bioprinted grafts, and the results were compared with untreated wounded controls. Visual inspection did not reveal any adverse effects of the bioprinting procedure.

The next step was to analyze histologically the grafts in the wound beds and surrounding tissues taken 4 days after *in situ* bioprinting, and to compare them with the untreated wounds. Examination of the H&E-stained sections from the untreated controls (Figure 2A) showed a wound healing process at a very early stage: the surface epithelium was particularly thin, and the underlying connective tissue appeared as a loose meshwork containing a few cells and was distinct from the surrounding tissues (as shown in the inset). The sections from the leeches that received the SA-GEL graft (Figure 2B) showed a thin epithelial layer covering the whole graft, and the bioprinted graft appeared as a dense fibrous layer containing scattered cells and adhering firmly to the surrounding tissues. The sections from the leeches grafted with the CELLINK Fibrin hydrogel containing human dermal fibroblasts (Figure 2C) showed a thicker, multi layered epithelium over the whole graft; in some points at the wound margins, it formed buds extending toward the underlying stroma, conceivably representing proliferative cell compartments. The graft tissue appeared thinner but better organized than that of the other samples (Groups 1 and 2) and was often virtually indistinguishable from the adjacent tissues at the wound bed.

These results confirmed that both *in situ* bioprinted grafts can improve wound healing, fill the wound bed, and facilitate re-epithelization. These phenomena were particularly enhanced in the fibroblast-seeded CELLINK Fibrin hydrogel group, which showed superior performance in efficiently closing the wound and promoting the regrowth of the surface epithelium, thereby restoring a barrier to the external environment. Of note, no histological signs of adverse side effects induced by the graft were observed in the tissues surrounding the wound.

These findings confirmed that the bioink composed of CELLINK Fibrin hydrogel and human dermal fibroblasts is a suitable substrate for 3D bioprinting in wound care. Next, we applied it to test a new wound care model comprising *in situ* 3D grafting and NIR laser treatment.

3.3. Effectiveness of the new wound care protocol on graft integration and wound healing

The described protocol for wound management, based on *in situ* 3D bioprinting of the fibroblast-seeded (nHDF) CELLINK Fibrin hydrogel, followed by NIR laser treatment to promote graft integration and stimulate healing, was assessed. For these tests, the leeches (n=16) were subjected to standard tegument tissue wounds, as described in **Section 2.2**, and then divided into four groups:

(i) Untreated animals (n=4) with no *in situ* 3D bioprinting and NIR laser treatment, taken as negative controls.

(ii) Animals that received a graft of CELLINK Fibrin-nHDF produced through *in situ* 3D bioprinting (n=4; CELLINK Fibrin-nHDF).

(iii) Animals that received NIR laser treatment (n=4).

(iv) Animals that received a graft of CELLINK Fibrin-nHDF followed by NIR laser treatment (n=4; CELLINK Fibrin-nHDF+NIR laser).

Six hours after the last laser treatment, the animals were processed for histological sampling and analysis, as described in **Sections 2.11 and 2.12**.

3.3.1. Morphological analysis using hematoxylin and eosin staining

The morphological features at the wound site were first analyzed using the H&E-stained slides. The sections from the untreated controls showed features similar to those of the same controls of the previous experiment: the surface epithelium was extremely thin, and the underlying connective tissue formed a loose meshwork (Figure 3A). The sections from the leeches grafted with CELLINK Fibrin-nHDF showed a thicker, multi layered epithelium over a thin connective tissue containing newly formed blood capillaries (Figure 3B). The sections from the leeches treated with NIR laser alone showed a thin,

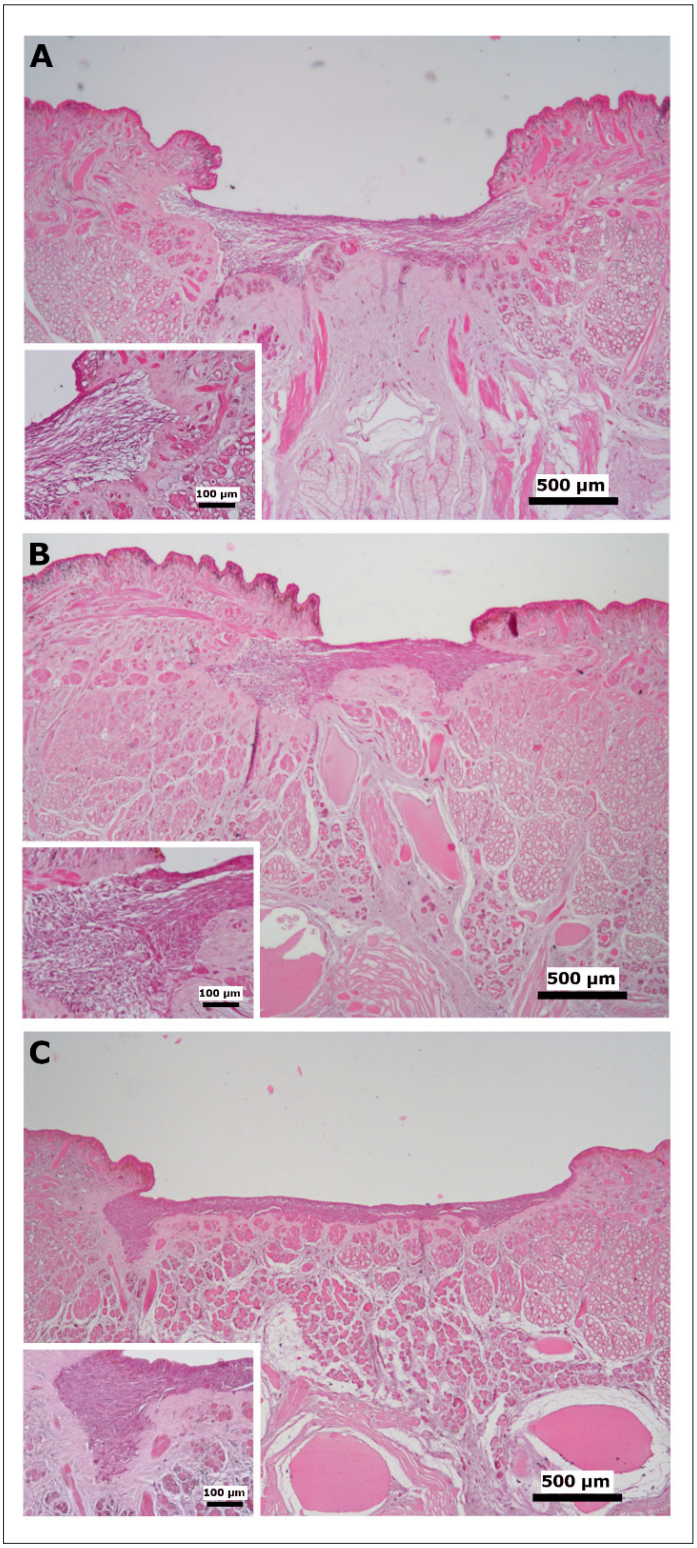


Figure 2. Validation of *in situ* 3D bioprinting procedure for leech wound healing using alginate and gelatin (SA-GEL) hydrogel and CELLINK Fibrin hydrogel containing normal human dermal fibroblasts. Comparative analysis of the different experimental conditions using hematoxylin and eosin staining. (A) Untreated control leech, showing early healing. (B) Leech grafted with SA-GEL hydrogel, showing a denser sub-epithelial supporting matrix. (C) Leech grafted with CELLINK Fibrin hydrogel containing human dermal fibroblasts, showing improved re-epithelization of the wound. Scale bars: 500 µm, insets:100 µm; magnifications: 4×, insets: 20×.

sometimes incomplete epithelium that, at the wound margins, formed buds of proliferating cells growing into the underlying stroma; it lay over a hyperplastic connective tissue featuring granulation tissue, rich in dilated blood capillaries (Figure 3C). The sections from the leeches grafted with CELLINK Fibrin-nHDF+NIR laser showed the most advanced wound healing, with a thick epithelium continuous with the perilesional tissue, overlaying connective tissue with a normal appearance similar to that beyond the wound margins (Figure 3D).

3.3.2. Analysis of collagen fibers

Collagens play a crucial role in the healing process by providing a scaffold that supports tissue regeneration, facilitates cell migration, and contributes to the mechanical strength and integrity of the newly formed ECM.[33] On the other hand, excessive formation of collagen fibers can lead to hypertrophic scars and fibrosis. Therefore, the network of collagen fibers at the wound site was studied using Picrosirius red staining. In untreated controls, the connective tissue surrounding the wound exhibited a dense network of collagen fibers, which thinned to an extremely thin layer at the wound bed (Figure 4A). In the sections from the CELLINK Fibrin-nHDF group, collagen fibers formed a well-defined, dense layer under the thickened surface epithelium (Figure 4B). In the NIR laser treatment group, collagen fibers also formed a well-defined layer under the epithelial buds and were abundant, albeit loosely arranged, in the granulation tissue at the wound area (Figure 4C). In the sections from the CELLINK Fibrin-nHDF + NIR laser group, a continuous layer of loosely woven collagen fibers was present under the newly formed epithelium, extending

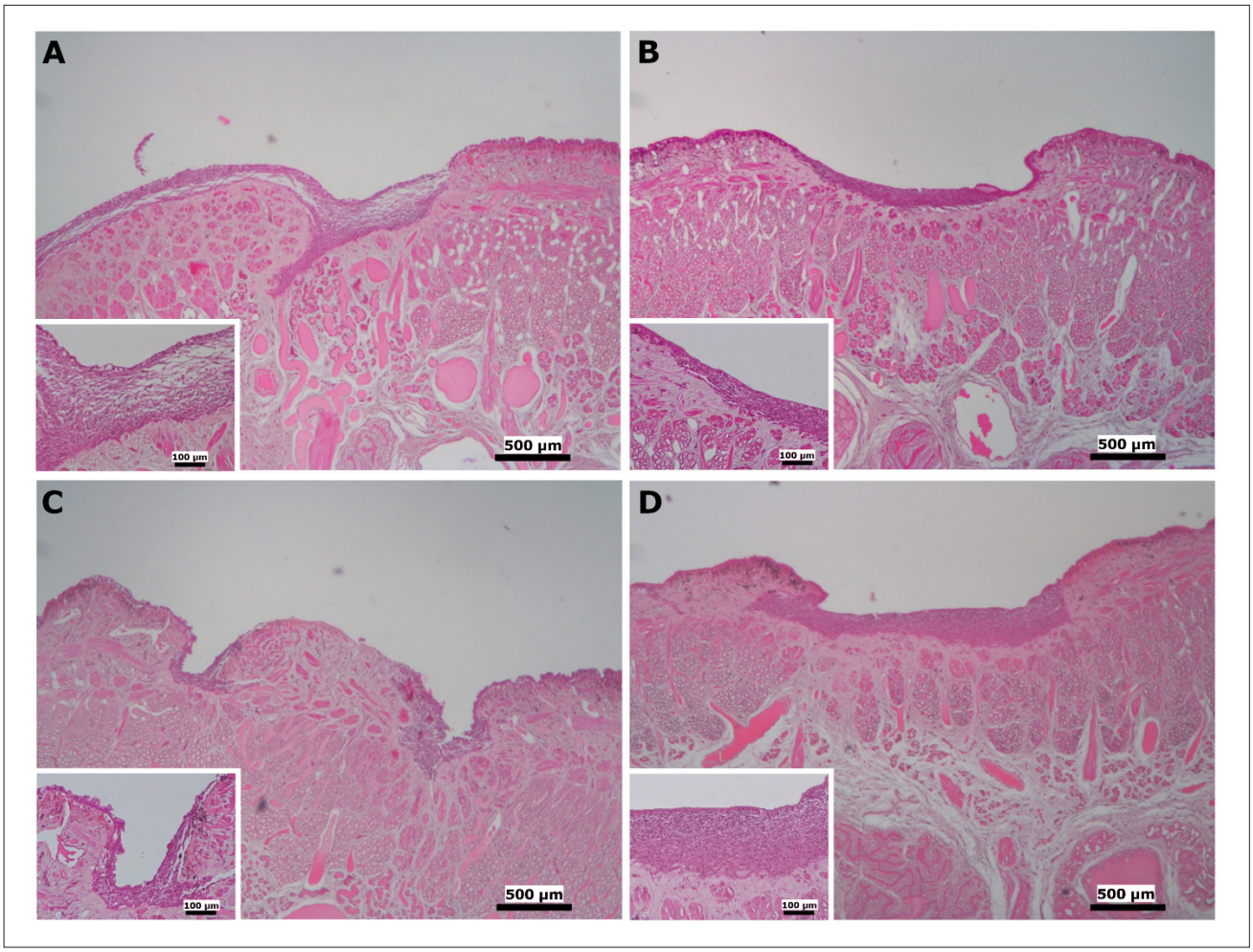


Figure 3. Effect of *in situ* 3D bioprinting procedure and near-infrared (NIR) laser treatment on leech wound healing. Comparative analysis of the different experimental conditions using hematoxylin and eosin staining. (A) Untreated control leech, showing early healing. (B) Leech grafted with CELLINK Fibrin-normal human dermal fibroblasts (nHDF), showing improved re-epithelialization of the wound. (C) Leech treated with NIR laser alone, showing marginal epithelial regrowth and neo-angiogenesis. (D) Leech grafted with CELLINK Fibrin-nHDF + NIR laser, showing markedly thicker surface epithelium and nearly normal underlying connective tissue. Scale bars: 500 µm, insets:100 µm; magnifications: 4×, insets: 20×.

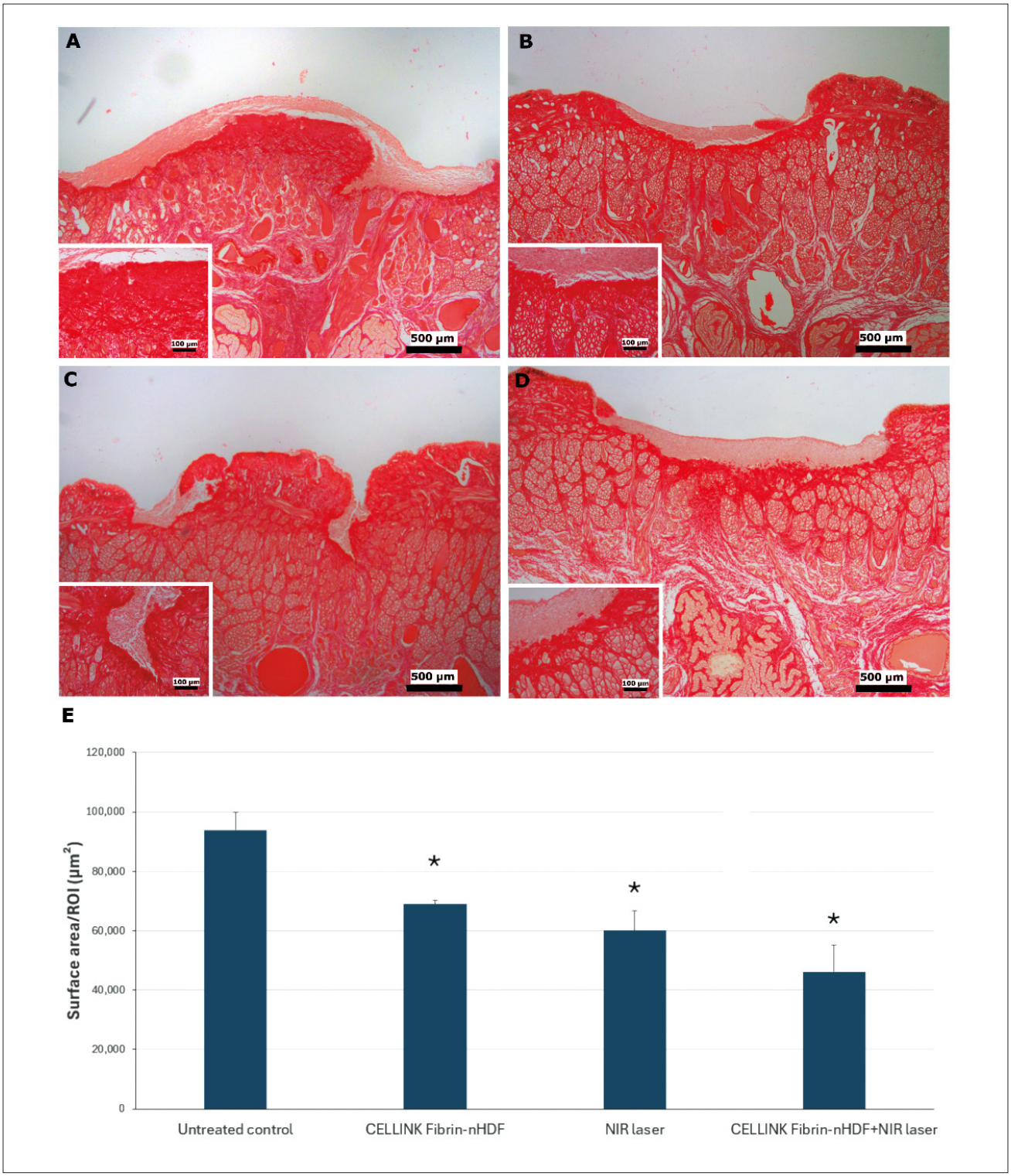


Figure 4. Effect of *in situ* 3D bioprinting procedure and near-infrared (NIR) laser treatment on leech wound healing. Comparative analysis of the Picrosirius red- stained collagen fiber network across experimental groups. (A) Untreated control. (B) Leech grafted with CELLINK Fibrin-normal human dermal fibroblasts (nHDF). (C) Leech treated with NIR laser radiation alone. (D) Leech grafted with CELLINK Fibrin-nHDF + NIR laser. See the text for details. Scale bars: 500 µm, insets:100 µm; magnifications: 4×, insets: 20×. (E) Morphometric analysis of the amount of collagen fibers across experimental groups. Notes: *$p < 0.05$, determined by one-way ANOVA followed by multiple comparison tests. All comparisons are made relative to the untreated control group. Abbreviation: ROI: Region of interest.

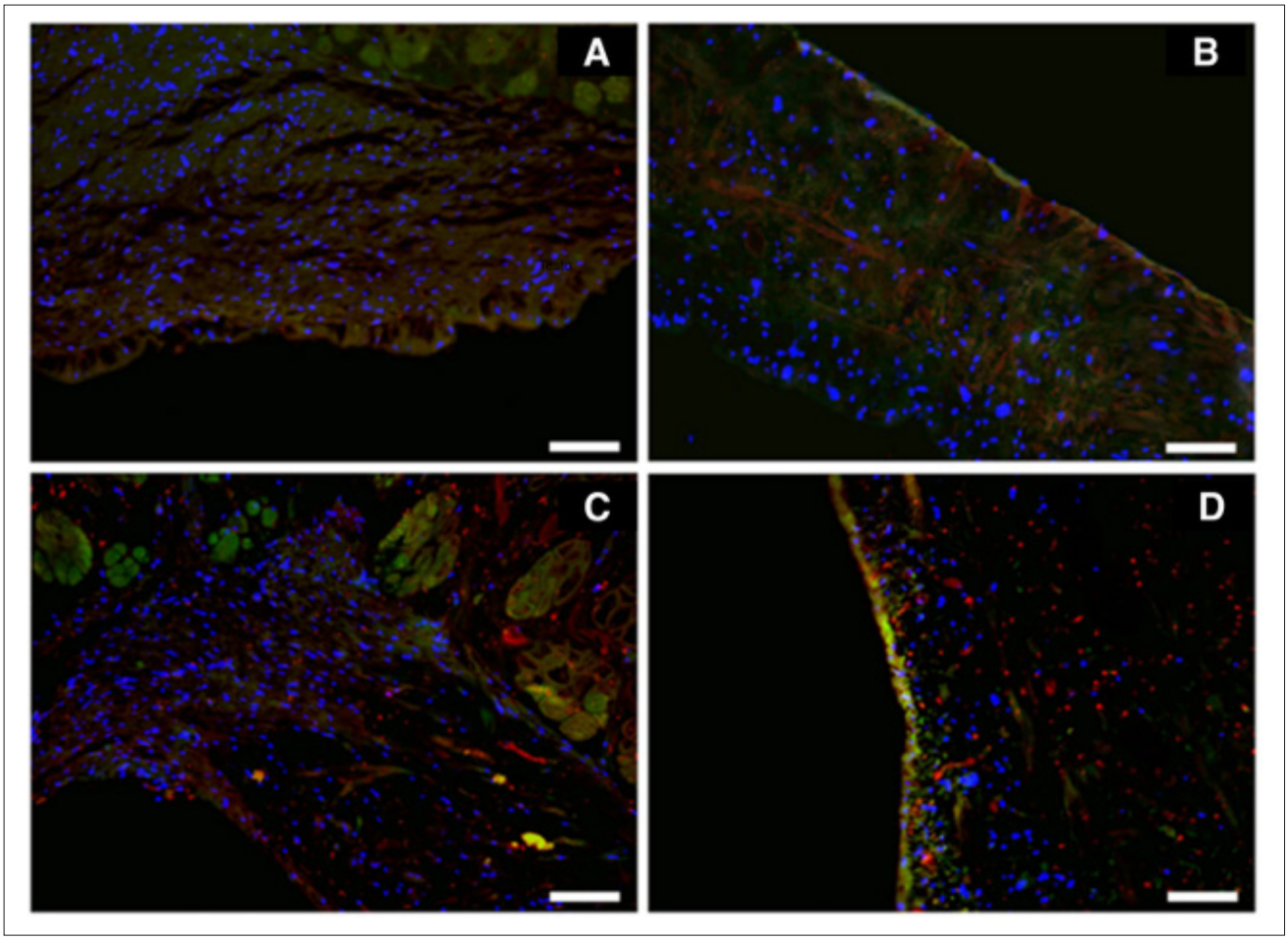


Figure 5. Effect of *in situ* 3D bioprinting procedure and near-infrared (NIR) laser treatment on leech wound healing. Immunofluorescent co-localization of HSP47 (red) and α-SMA (green) fibroblast activation markers across experimental groups. Cell nuclei are counterstained with DAPI (blue). (A) Untreated control. (B) Leech grafted with CELLINK Fibrin-normal human dermal fibroblasts (nHDF). (C) Leech treated with NIR laser radiation alone. (D) Leech grafted with CELLINK Fibrin-nHDF + NIR laser treatment shows well-detectable expression of HSP47 and α-SMA. Scale bars: 50 μm, magnifications: 20×. Abbreviations: α-SMA: Alpha smooth muscle actin; DAPI: 4´,6-diamidino-2-phenylindole; HSP47: Heat shock protein 47.

into the stroma of the deeper muscle tissues (Figure 4D). The collagen meshwork at the wound margins appeared continuous with that of the wound area, suggesting tissue integration. The absence of a dense collagen layer in this group suggests that this treatment could have reduced the local inflammatory response, potentially limiting fibrosis. The morphometric analysis of Picrosirius red-stained collagen fiber content in the wound area confirmed these observations (Figure 4E).

3.3.3. Analysis of fibroblast markers

Immunofluorescence analysis was performed to evaluate the expression of key fibroblast markers. HSP47, a collagen-specific chaperonin essential for proper folding, assembly, and secretion of collagen during ECM production and tissue repair,[34] is assumed to be a pan-fibroblast marker. Alpha-SMA is believed to be a marker for the fibroblast-to-myofibroblast switch, which is crucial for wound contraction and tissue remodeling, as well as for hypertrophic scarring and fibrosis.[35] The results showed that the samples from the negative controls (Figure 5A), the CELLINK Fibrin-nHDF group (Figure 5B), and the NIR laser treatment group (Figure 5C) did not exhibit significant fluorescence, except for a slight HSP 47- positive signal in the NIR laser treatment group, indicating that the cell expression of HSP47 (red) and α-SMA (green) was negligible in these groups. In contrast, the samples from the CELLINK Fibrin-nHDF + NIR laser group (Figure 5D) showed a substantial cell expression of HSP 47 and α-SMA. This finding suggests that in this group, fibroblast recruitment and activation occur to promote healing, a result in agreement with the data from conventional histology and collagen histochemistry.

4. Discussion

The advantages of *in situ* 3D bioprinting, compared to *in vitro* 3D bioprinting and subsequent grafting of the tissue construct into an organism, have been widely highlighted in recent literature.[36,37] It is well known that the culture and maturation of a biofabricated tissue are regulated by numerous biochemical and biophysical factors that can hardly be reproduced *in vitro*, especially considering the unavoidable time gap between printing and grafting. The physiological environment is dynamic, continuously evolving to maintain or restore homeostasis, which challenges attempts to mimic it accurately *in vitro*.[38] Furthermore, *in vitro* culture of biofabricated tissues requires dedicated facilities, prolonged timeframes, higher costs, and repeated handling of samples, all of which increase the risk of microbial contamination, loss of structural integrity, and compromised geometric fit with the recipient site.[39,40] Therefore, the *in situ* bioprinting technique was chosen for the development of the wound care model in this study.

The *in situ* 3D bioprinting procedure in the leech model was complex. The leech is an annelid; it has a wavy integument, and even under anesthesia, slight body movements can result in lengthening or shortening of the body, leading to deformation of the wound bed. Therefore, the *in situ* 3D bioprinting procedure used in the present study required careful preparation and a series of validation tests.

In preparation for the experiments with the animal model, the 3D bioprinting protocol software was successfully validated through 2D printing tests—producing differently shaped monolayers—and 3D printing tests, creating multilayered structures (four layers) of different shapes and sizes to simulate the grafts intended for the *in vivo* experiments. Following these preliminary tests, the *in situ* 3D bioprinting procedure was further validated using a leech phantom. This test showed that the developed protocol allowed a graft to be successfully printed within the wound model created on the phantom.

Before evaluating the effectiveness of the proposed wound care strategy (3D bioprinting followed by NIR laser irradiation), the *in situ* 3D bioprinting procedure was additionally tested on the animal model. Initially, a SA-GEL hydrogel crosslinked with $CaCl_2$ was used as the bioink. Then, a $CaCl_2$-crosslinked CELLINK Fibrin hydrogel mixed with human dermal fibroblasts was tested. Both tests confirmed the feasibility of the *in situ* 3D bioprinting procedure without adverse effects on the animals. In particular, the human dermal fibroblasts embedded in the CELLINK Fibrin hydrogel did not elicit a rejection response, as leeches have a rudimentary immune system. They lack a complex adaptive component and rely primarily on innate immunity, which is incapable of developing long-term immunological memory against specific antigens. Furthermore, as blood-sucking parasites, leeches have evolved tolerance to blood components from different species and produce anticoagulant substances in their saliva.

The fibrinogen-based hydrogel was chosen as a suitable environment for human dermal fibroblasts because previous experiments showed its superior ability to preserve cell viability[26] and function compared to SA-GEL.[21] Specifically, in the study by Cavallo *et al.*[26], a cell viability of 94 ± 4% was demonstrated using L929 fibroblasts embedded in a fibrinogen- and alginate-based hydrogel, with no cytotoxic effect from the biomaterial ink observed.

Histological analyses of tissue samples collected four days after 3D bioprinting demonstrated that: (i) graft deposition procedure within the wound was successful using both hydrogels; (ii) the SA-GEL-based graft improved wound healing compared to untreated wounds; and (iii) the CELLINK Fibrin hydrogel containing human dermal fibroblasts induced more effective activation of healing mechanisms compared to both untreated and SA-GEL-grafted wounds (Figure 2). On this basis, the CELLINK Fibrin hydrogel was selected for further *in vivo* experiments to validate the proposed wound care protocol.

In some protocols, the CELLINK Fibrin hydrogel is added with thrombin to convert fibrinogen into fibrin. However, the construct should then be washed thoroughly, as thrombin residues can affect cell viability.[26] Because *in situ* bioprinting only allows partial washing (on the exposed side), $CaCl_2$ crosslinking was preferred. Furthermore, a previous study showed that converting fibrinogen to fibrin did not significantly enhance cell viability and function preservation.[21]

As reported, the major advantage of *in situ* bioprinting over *in vitro* bio fabrication is that the graft is directly placed in its recipient area, within a physiological environment that provides the necessary biochemical and biophysical signals to support tissue maturation. However, this environment is highly dynamic and responds to wound damage and grafting. In response to injury, a complex repair process rapidly takes place through several phases, each partially overlapping and tightly regulated qualitatively, quantitatively, and temporally. Briefly, the immediate hemostatic phase is followed by the inflammatory phase, which prevents infection and induces stromal activation through the production of pro-inflammatory factors by innate and immune cells. The proliferative phase then occurs, characterized by neoangiogenesis, granulation

tissue formation, and re-epithelialization, involving fibroblasts, endothelial cells, and surface epithelial cells. Finally, during the remodeling phase, fibroblasts remodel the ECM of the newly formed tissue to improve its structure and function. Endothelial cells and the stem cell compartment of the surface epithelium are responsible for neoangiogenesis and re-epithelialization, respectively, whereas fibroblasts are involved in all phases of healing by orchestrating the process through continuous cross-talk with other cell populations. The transition between healing phases is primarily regulated by apoptosis: cell populations that have completed their function in the damaged area undergo programmed cell death and are replaced by newly recruited cell populations required for the next phase.[3,41]

When the graft is bioprinted into the wound bed, it is surrounded by tissues undergoing an inflammatory reaction, which can be exacerbated by the presence of engrafted exogenous material. Acute inflammation is required to initiate repair mechanisms and can facilitate graft maturation by promoting cell migration, neoangiogenesis, and ECM production. However, excessive or persistent inflammation can lead to abnormal stromal cell activation, excessive capillary formation, and ECM deposition, potentially resulting in the formation of fibrous tissue encapsulating the graft[42] and hindering its integration. In summary, an overly intense or prolonged inflammatory response jeopardizes repair mechanisms and compromises the interaction between the graft and the surrounding tissues. Therefore, several strategies have been proposed to control inflammation upon grafting.[42]

Based on our previous research on the anti-inflammatory properties of NIR laser radiation,[29] we hypothesized that NIR laser treatment could be an effective and easy-to-implement strategy to modulate inflammation at the graft site. Accordingly, the proposed wound care protocol, designed to improve the healing of wounds with loss of substance (in the leech model, loss of tegumental tissue), consists of two treatments: (i) *in situ* 3D bioprinting of a graft composed of CELLINK Fibrin hydrogel containing human dermal fibroblasts directly into the wound bed; (ii) additional treatment of the wound and surrounding tissues via irradiation with an NIR laser source. The working hypotheses were twofold: (i) the *in situ* bioprinting of the graft was hypothesized to promote tissue regeneration by protecting the wound from microorganisms and external factors, thus decreasing the risk of contamination. Moreover, by replacing lost tissue with a protein network and a nanofibrillated cellulose matrix containing dermal fibroblasts, the graft was expected to support cell repopulation and tissue remodeling. (ii) The adjunctive NIR laser treatment was hypothesized to promote graft integration with surrounding tissues, accelerate healing, and prevent fibrosis through its dual effects—inhibitory effects on inflammatory response and stimulatory effects on cell energy metabolism, production, and assembly of ECM molecules.[27,29]

To test the above hypotheses, four groups of differently treated animals were compared: (i) untreated controls, (ii) *in situ* 3D bioprinting only, (iii) NIR laser irradiation only, and (iv) the combined treatment. As hypothesized, the *in situ* bioprinted grafts significantly improved wound healing. Untreated controls showed a particularly thin surface epithelium and an underlying connective tissue that appeared as a loose meshwork containing few cells, clearly distinct from the surrounding tissues. In contrast, leeches grafted with the fibrinogen hydrogel containing human dermal fibroblasts showed a thicker, multilayered epithelium throughout the graft, accompanied by the formation of proliferative cellular compartments.

For this result, a crucial aspect is the choice of biomaterial ink and its degree of degradation, which must support proper wound filling and allow the gradual regeneration of the animal's native tissue. In this regard, the degradation of fibrinogen- and alginate-based hydrogels was studied in detail by Cavallo *et al.*[26] In their study, a mass loss of approximately 20% was observed in bioprinted samples during the first week of incubation (Figure S11). The mass remained nearly constant over the following three weeks, followed by an increase in degradation during the fifth week. In our application, this gradual degradation of the hydrogel ensured appropriate wound filling on the leech's back and provided protection from microorganisms and external factors, thus reducing the risk of contamination. Furthermore, by replacing the lost tissue with a network of proteins and a nanofibrillated cellulose matrix containing dermal fibroblasts, the graft, as hypothesized, promoted cell repopulation and subsequent tissue remodeling.

Conventional histological analysis, quantitative histochemical assay of the collagen fiber network, and immunofluorescence detection of activated fibroblasts in healing tissues concur to indicate that leeches that received the combined treatment—*in situ* bioprinting followed by laser treatment—showed favorable results in terms of the rate and quality of graft integration and tissue regeneration. In particular, re-epithelialization was nearly complete, and the underlying stromal tissue appeared well-structured, free from signs of fibrosis, and tightly connected to the surrounding tissues (Figure 4D).

In untreated animals and those receiving the *in situ* 3D-bioprinted graft, histochemical and morphometric analyses of collagen fibers revealed a thick fibrotic network extending into the adjacent tissues (Figure 4A and 4B). Fibrotic tissue is generally an expression of excessive

and/or prolonged inflammation. In the animals treated with laser radiation alone, fibrosis was reduced; however, a hyperplastic mass of granulation tissue —apparently impeding complete re-epithelization—was often observed (Figure 4C). These findings confirm the synergism between the *in situ* bioprinted grafts and NIR laser irradiation to achieve optimal healing effects. They also support previous observations that NIR laser treatment can effectively limit fibrosis, potentially through its modulatory effects on inflammation and on ECM protein deposition, including collagen.

As mentioned above, fibroblasts play a key role in wound healing. Once activated, they regulate the activity of the other cell populations that participate in the healing process. Furthermore, upon differentiation into contractile myofibroblasts, they induce wound contraction and ECM remodeling.[3,31] The findings on HSP47 and α-SMA expression, analyzed by immunofluorescence microscopy, suggest that this activation occurred only in animals receiving both *in situ* bioprinting and laser treatment, in which these markers were clearly detected, indicating a more advanced stage of healing. In the other experimental groups, no significant expression of these markers was detected, suggesting that fibroblast recruitment was still at an early stage or potentially impaired.

In situ 3D bioprinting is an emerging technology, whereas NIR laser therapy has been applied to promote the healing of acute and chronic lesions for several years. The pro-regenerative effects of NIR laser radiation have been widely reported in the literature, with extensive information spanning from the molecular to the clinical level.[3,43,44] However, to our knowledge, this is the first study to apply NIR laser irradiation to support the engraftment of a biofabricated tissue construct directly within the wound bed.

The main limitations of this study include: (i) the small number of animals per experimental group, which requires caution when generalizing the results; and (ii) the use of a small invertebrate animal model, in which the wound area and the volume of dead space are proportionate to body size. Nevertheless, the leech model has been recognized as a valuable tool for studying the regeneration of human skin,[16] and has the advantage of being particularly suitable for experiments conducted in extreme environments, such as space platforms.

In relatively small wounds, such as those adopted in this study, re-epithelialization occurs spontaneously from the wound margins, especially when aided by a graft that simulates dermal functions—particularly fibroblast activity, which promotes keratinocyte proliferation and migration through cytokine release.[2] In large wounds, the current model could be extended by printing an additional superficial layer containing keratinocytes, thereby mimicking the epidermis to further accelerate wound closure and restoration of the skin barrier. This is a key aspect in view of future clinical applications and will be investigated in future research.

Despite the promising results obtained with the proposed wound management protocol, clinical translation remains highly challenging. The main issues include: (i) the development of 3D bioprinters suitable for the clinical setting, ideally at the patient's bedside; and (ii) the fabrication of grafts large enough to cover extended wound areas or substantial tissue loss. Large wounds pose critical challenges related to re-epithelialization and vascularization. Vascularization is essential for graft survival, as passive transport mechanisms, such as diffusion, become insufficient once the graft exceeds a certain size. Re-epithelialization and vascularization will therefore be central topics in our future research aimed at improving the proposed model. Another challenge is that producing grafts of clinically relevant dimensions requires substantially more cells, making cell supply a significant bottleneck.

In summary, the scaling challenges for human applications include developing efficient cell-expansion protocols and strategies for printing complex grafts incorporating two or more distinct cell populations, such as fibroblasts, keratinocytes, and endothelial cells. Endothelial cells are essential for supporting the formation of a capillary network, which is crucial in larger constructs to ensure adequate nutrients and oxygen delivery.

Implementing this approach in extreme environments, particularly aboard space platforms, poses additional challenges, including: (i) the adaptation of equipment for use in space, i.e., the development of hardware (3D bioprinter and laser source) that meets safety and operational criteria in space; (ii) strict control over the 3D bioprinting process to ensure product quality and prevent biological contamination within the spacecraft environment; and (iii) the limited current knowledge of how space environment affects 3D-bioprinted constructs. To advance this knowledge, it may be useful to study the behavior of long-term (≥ 3 weeks) tissue-construct cultures under simulated microgravity. While microgravity favors the formation of cellular aggregates, the combined effects of microgravity and space radiation can profoundly alter cellular functions, including proliferation, differentiation, apoptosis, ECM production, and cell-to-cell cross-talk, potentially compromising the survival and proper maturation of the constructs. Therefore, detailed studies

are needed to assess the maturation of 3D-bioprinted constructs and the fate of the embedded cells.

5. Conclusion

The wound treatment protocol proposed in this study—combining *in situ* 3D bioprinting with NIR laser treatment—has demonstrated effectiveness in promoting the engraftment of 3D-printed tissue constructs and in activating intrinsic wound healing mechanisms. These findings may pave the way for innovative strategies for managing severe wounds and burns, for which current treatments are often complex and expensive, healing times are prolonged, and undesirable sequelae such as fibrosis are common. The implementation of new wound-healing therapies is particularly relevant in extreme environments—such as space platforms, submarines, and Arctic and Antarctic bases—or under extreme conditions, including military operations, terrorist strikes, and natural disasters, where the management of severe injuries becomes particularly challenging.

Acknowledgments

None.

Funding

This research was funded by the Italian Space Agency (ASI) under the projects GROWS (C-ASI No. 2021-16-U.0), WEAR ME! (ASI No. 2023-3-U.0), and SATURNO (ASI No. 2024-12-U.0). Support to this study was also provided by the European Space Agency (ESA) through the selection of the GROWS project and funding of the WHISPER project (No. 4000130928/20/NL/PG/pt). Additional support was provided by the European Union (ERC, EPEIUS, Grant Agreement No. 101125466). This study was also partially supported by the Ricerca Corrente funding from the Italian Ministry of Health to IRCCS Policlinico San Donato.

Conflict of interest

The authors declare they have no competing interests.

Author contributions

Conceptualization: Monica Monici, Michele Conti
Formal analysis: Francesca Cialdai, Chiara Risaliti, Lorenzo Notari, Daniele Bani
Funding acquisition: Monica Monici, Michele Conti
Investigation: Giada Loi, Mariagrazia Zaccara, Francesca Cialdai, Chiara Risaliti, Lorenzo Notari, Glenda Liggieri
Methodology: Monica Monici, Michele Conti, Daniele Bani
Supervision: Monica Monici, Michele Conti, Daniele Bani
Writing–original draft: Giada Loi, Mariagrazia Zaccara, Francesca Cialdai, Chiara Risaliti, Lorenzo Notari, Glenda Liggieri
Writing–review & editing: Monica Monici, Michele Conti, Daniele Bani

Ethics approval and consent to participate

Since leeches are invertebrates, Animal Ethics Committee approval is not required for their use in research. However, in this study, the animals were treated in accordance with strict ethical principles to avoid suffering, and all treatments were performed under anesthesia.

Consent for publication

Not applicable.

Availability of data

The data that support the findings of this study are available from the corresponding author upon reasonable request.

References

1. Sorg H, Sorg CGG. Skin Wound Healing: of Players, patterns, and processes. *Eur Surg Res.* 2023;64(2):141-157. doi: 10.1159/000528271
2. Peña OA, Martin P. Cellular and molecular mechanisms of skin wound healing. *Nat Rev Mol Cell Biol.* 2024;25(8):599-616. doi: 10.1038/s41580-024-00715-1
3. Cialdai F, Risaliti C, Monici M. Role of fibroblasts in wound healing and tissue remodeling on Earth and in space. *Front Bioeng Biotechnol.* 2022;10:958381. doi: 10.3389/fbioe.2022.958381
4. Darby IA, Hewitson TD. Fibroblast differentiation in wound healing and fibrosis. *Int Rev Cytol.* 2007;257:143-79. doi: 10.1016/S0074-7696(07)57004-X
5. Martin P, Pardo-Pastor C, Jenkins RG, Rosenblatt J. Imperfect wound healing sets the stage for chronic diseases. *Science*. 2024;386(6726):eadp2974. doi: 10.1126/science.adp2974
6. Sen CK. Human Wound and Its Burden: Updated 2022 Compendium of Estimates. *Adv Wound Care (New Rochelle).* 2023;12(12):657-670. doi: 10.1089/wound.2023.0150
7. Avishai E, Yeghiazaryan K, Golubnitschaja O. Impaired wound healing: facts and hypotheses for multi-professional considerations in predictive, preventive and personalised medicine. *EPMA J.* 2017;8(1):23-33. doi: 10.1007/s13167-017-0081-y

8. Hongying Z, Chunmei H, Lijuan C, *et al*. The current status and influencing factors of quality of life of chronic wound patients based on Wound-QoL scale: a cross-sectional study. *Medicine (Baltimore)*. 2025;104(27):e42961. doi: 10.1097/MD.0000000000042961

9. Harding K, Gray D, Timmons J, Hurd T. Evolution or revolution? Adapting to complexity in wound management. Int Wound J. 2007;4(Suppl 2):1-12. doi: 10.1111/j.1742-481X.2007.00329.x

10. Radzikowska-Büchner E, Łopuszyńska I, Flieger W, Tobiasz M, Maciejewski R, Flieger J. An overview of recent developments in the management of burn injuries. *Int J Mol Sci*. 2023;24(22):16357. doi: 10.3390/ijms242216357

11. Kirkpatrick AW, Ball CG, Campbell M, Williams DR, Parazynski SE, Mattox KL, Broderick TJ. Severe traumatic injury during long duration spaceflight: Light years beyond ATLS. *J Trauma Manag Outcomes*. 2009;3:4. doi: 10.1186/1752-2897-3-4

12. Balukoff NC, Houk G, Gonzalez T, *et al*. Out of this World: wound healing on earth and in space. *J Invest Dermatol*. 2025;145(8):1879-1895. doi:10.1016/j.jid.2024.12.024

13. Pantalone D. Surgery in the next space missions. *Life*. 2023;13(7):1477. doi: 10.3390/life13071477

14. Cubo-Mateo N, Gelinsky M. Wound and skin healing in space: the 3D Bioprinting Perspective. *Front Bioeng Biotechnol*. 2021;9:720217. doi: 10.3389/fbioe.2021.720217

15. Klarmann GJ, Rogers AJ, Gilchrist KH, Ho VB. 3D bioprinting meniscus tissue onboard the International Space Station. *Life Sci Space Res (Amst)*. 2024;43:82-91. doi: 10.1016/j.lssr.2024.09.004

16. Tettamanti G, Grimaldi A, Congiu T, Perletti G, Raspanti M, Valvassori R, de Eguileor M. Collagen reorganization in leech wound healing. *Biol Cell*. 2005;97(7):557-68. doi: 10.1042/BC20040085

17. Grimaldi A, Banfi S, Bianchi C, *et al*. The leech: a novel invertebrate model for studying muscle regeneration and diseases. *Curr Pharm Des*. 2010;16(8):968-77. doi: 10.2174/138161210790883417

18. Cialdai F, Colciago A, Pantalone D, *et al*. Effect of unloading condition on the healing process and effectiveness of platelet rich plasma as a countermeasure: study on *In vivo* and *In vitro* wound healing models. *Int J Mol Sci*. 2020;21(2):407. doi: 10.3390/ijms21020407

19. Baranzini N, Pulze L, Tettamanti G, Acquati F, Grimaldi A. *Hv*RNASET2 regulate connective tissue and collagen I remodeling during wound healing process. *Front Physiol*. 2021;12:632506. doi: 10.3389/fphys.2021.632506

20. Lotz RG, Baum P, Bowman GH, Klein KD, von Lohr R, Schrotter L. Test of a life support system with Hirudo medicinalis in a sounding rocket. *Life Sci. Space Res*. 1972;10:133–143.

21. Ronzoni FL, Aliberti F, Scocozza F, *et al*. Myoblast 3D bioprinting to burst *in vitro* skeletal muscle differentiation. *J Tissue Eng Regen Med*. 202216(5):484–495. doi: 10.1002/term.3293

22. Delgrosso E, Scocozza F, Cansolino L, *et al*. 3D bioprinted osteosarcoma model for experimental boron neutron capture therapy (BNCT) applications: Preliminary assessment. *J Biomed Mater Res B Appl Biomater*. 2023;111(8): 1571-1580. doi: 10.1002/jbm.b.35255

23. Loi G, Scocozza F, Aliberti F, *et al*. 3D Co-Printing and Substrate Geometry Influence the Differentiation of C2C12 Skeletal Myoblasts. *Gels*. 2023; 9(7):595. doi: 10.3390/gels9070595

24. Loi G, Scocozza F, Benedetti L, *et al*. Design, development, and benchmarking of a bioreactor integrated with 3D bioprinting: application to skeletal muscle regeneration. *Bioprinting*. 2024;42:e00352. doi: 10.1016/j.bprint.2024.e00352

25. Fantini V, Bordoni M, Scocozza F, *et al*. Bioink composition and printing parameters for 3D modeling neural tissue. *Cells*. 2019;8(8):830. doi: 10.3390/cells8080830

26. Cavallo A, Al Kayal T, Mero A, *et al*. Fibrinogen-Based Bioink for application in skin equivalent 3D Bioprinting. *J Funct Biomater*. 2023;14(9):459. doi: 10.3390/jfb14090459

27. Monici M, Basile V, Cialdai F, Romano G, Fusi F, Conti A. Irradiation by pulsed Nd: YAG laser induces the production of extracellular matrix molecules by cells of the connective tissues: a tool for tissue repair. Biophotonics: Photonic solutions for better health care. Edited by Popp Jürgen, Drexler Wolfgang, Tuchin Valery V, Matthews Dennis L. Proceedings of the SPIE. 2008;6991:10.

28. Monici M, Cialdai F, Romano G, Fusi F, Egli M, Pezzatini S. An *in vitro* study on tissue repair: impact of unloading on cells involved in the remodelling phase. *Microgravity Sci Technol*. 2011;23:391–401. doi:10.1007/s12217-011-9259-4

29. Genah S, Cialdai F, Ciccone V, Sereni E, Morbidelli L, Monici M. Effect of NIR laser therapy by MLS-MIS source on fibroblast activation by inflammatory cytokines in relation to wound healing. *Biomedicines*. 2021;9(3):307. doi: 10.3390/biomedicines9030307

30. Barrientos S, Stojadinovic O, Golinko MS, Brem H, Tomic-Canic M. Growth factors and cytokines in wound healing. Wound Repair Regen. 2008;16(5):585-601. doi: 10.1111/j.1524-475X.2008.00410.x

31. Moretti L, Stalfort J, Barker TH, Abebayehu D. The interplay of fibroblasts, the extracellular matrix, and inflammation in scar formation. *J Biol Chem.* 2022;298(2):101530. doi: 10.1016/j.jbc.2021.101530

32. Younesi FS, Miller AE, Barker TH, Rossi FMV, Hinz B. Fibroblast and myofibroblast activation in normal tissue repair and fibrosis. *Nat Rev Mol Cell Biol.* 2024;25(8):617-638. doi: 10.1038/s41580-024-00716-0

33. Gardeazabal L, Izeta A. Elastin and collagen fibres in cutaneous wound healing. *Exp Dermatol.* 2024;33(3):e15052. doi: 10.1111/exd.15052

34. Ito S, Nagata K. Roles of the endoplasmic reticulum-resident, collagen-specific molecular chaperone Hsp47 in vertebrate cells and human disease. *J Biol Chem.* 2019;294(6):2133-2141. doi: 10.1074/jbc.TM118.002812

35. McAndrews KM, Miyake T, Ehsanipour EA, *et al*. Dermal αSMA+ myofibroblasts orchestrate skin wound repair via β1 integrin and independent of type I collagen production. *EMBO J*. 2022;41(7):e109470. doi: 10.15252/embj.2021109470

36. Singh S, Choudhury D, Yu F, Mironov V, Naing MW. *In situ* bioprinting – Bioprinting from benchside to bedside? *Acta Biomaterialia.* 2020;101(2020):14–25 doi: 10.1016/j.actbio. 2019.08.045

37. Hu C, Wang C, Bian S, *et al*. *In situ* bioprinting: Tailored printing strategies for regenerative medicine. *Int J Bioprint*. 2024;10(5):3366. doi: 10.36922/ijb.3366

38. Ashammakhi N, Ahadian S, Pountos I, *et al*. *In situ* three-dimensional printing for reparative and regenerative therapy. Biomed Microdevices. 2019;21(2):42. doi: 10.1007/s10544-019-0372-2

39. Wang MY, He JK, Liu YX, *et al*. The trend towards *in vivo* bioprinting. *Int J Bioprinting*. 2015;1(1): 15–26. doi: 10.18063/IJB.2015.01.001

40. Chaudhry MS, Czekanski A. *In-situ* bioprinting of skin - a review. *Bioprinting*. 2023;e00271:1-15. doi: 10.1016/j.bprint.2023.e00271

41. Wallace HA, Basehore BM, Zito PM. Wound healing phases. In: StatPearls [Internet]. Treasure Island (FL): StatPearls Publishing; 2025.

42. Zhu W, Nie X, Tao Q, Yao H, Wang DA. Interactions at engineered graft-tissue interfaces: a review. *APL Bioeng.* 2020;4(3):031502. doi: 10.1063/5.0014519

43. Kuffler DP. Photobiomodulation in promoting wound healing: a review. *Regen Med.* 2016;11(1):107-22. doi: 10.2217/rme.15.82

44. Mosca RC, Ong AA, Albasha O, Bass K, Arany P. Photobiomodulation therapy for wound care: a potent, noninvasive, photoceutical approach. *Adv Skin wound care*. 2019;32(4):157-167. doi: 10.1097/01.ASW.0000553600.97572.d2

ACCSCIENCE PUBLISHING

International Journal of Bioprinting

RESEARCH ARTICLE

3D-printed nano-hydroxyapatite/polylactic acid scaffold with simvastatin-loaded hydroxyethyl methacrylate/sulfobetaine methacrylate hydrogel for accelerated bone repair

Yang Qu[1,2†], Ya-nan Wang[3†], Weiqing Kong[4], Xiaofan Du[1], Jianyi Li[1], Yukun Du[1], Guanghui Gu[1*], and Yongming Xi[1*]

[1]Department of Spinal Surgery, The Affiliated Hospital of Qingdao University, Qingdao, Shandong, China

[2]Key Laboratory of Trauma and Neural Regeneration, Ministry of Education and National Center for Trauma Medicine, Department of Orthopedics and Trauma, Peking University People's Hospital, Beijing, China

[3]Department of Nuclear Medicine, Xuzhou Central Hospital, Southeast University, Xuzhou, Jiangsu, China

[4]Department of Orthopedics, Xuzhou Central Hospital, Southeast University, Xuzhou, Jiangsu, China

[†]These authors contributed equally to this work.

***Corresponding authors:**
Guanghui Gu
(guguanghui@qdu.edu.cn)

Yongming Xi
(xym700118@qdu.edu.cn)

Citation: Qu Y, Wang Y, Kong W, *et al.* 3D-printed nano-hydroxyapatite/polylactic acid scaffold with simvastatin-loaded hydroxyethyl methacrylate/sulfobetaine methacrylate hydrogel for accelerated bone repair. *Int J Bioprint.* 2026;12(1):656-671. doi: 10.36922/IJB025490505

Received: December 2, 2025
Revised: January 1, 2026
Accepted: January 1, 2026
Published Online: January 14, 2026

Copyright: © 2026 Author(s). This is an Open Access article distributed under the terms of the Creative Commons Attribution License, permitting distribution, and reproduction in any medium, provided the original work is properly cited.

Publisher's Note: AccScience Publishing remains neutral with regard to jurisdictional claims in published maps and institutional affiliations.

Abstract

Bone defects resulting from trauma, infection, or tumor resection often exceed the self-healing capacity of bone tissue, requiring bioactive and mechanically robust repair materials. In this study, a composite scaffold was developed via *in situ* polymerization of a hydroxyethyl methacrylate/sulfobetaine methacrylate (HMSM) hydrogel with a three-dimensional-printed nano-hydroxyapatite/polylactic acid (NP) gradient scaffold to achieve controlled simvastatin (SIM) delivery and enhanced osteogenesis. The HMSM hydrogel served as a hydrophilic and biocompatible matrix, while the NP scaffold provided mechanical strength and structural support. SIM was incorporated into the hydrogel–scaffold composite (SIM@HMSM/NP) to establish a sustained drug-release system. The composite exhibited a smooth microstructure, uniform pore distribution, and a gradient architecture mimicking native bone. Mechanical testing demonstrated improved compressive strength compared with individual components, and *in vitro* studies revealed stable SIM release over 24 days with a degradation profile compatible with bone regeneration. The SIM@HMSM/NP demonstrated excellent cytocompatibility, promoting the proliferation and osteogenic differentiation of bone marrow mesenchymal stem cells, and significantly enhanced bone formation in a rat calvarial defect model. These findings suggest that the SIM@HMSM/NP scaffold provides a promising strategy for sustained drug delivery and accelerated bone regeneration in critical-sized bone defects.

***Keywords*:** Bone tissue engineering; Hydrogel–scaffold composite; Hydroxyethyl methacrylate/sulfobetaine methacrylate hydrogel; Nano-hydroxyapatite/polylactic acid scaffold; Simvastatin; Three-dimensional printing

1. Introduction

Bone defects remain a major challenge in orthopedic surgery, resulting from trauma, infection, tumor resection, or congenital malformation.[1] Although minor defects can undergo spontaneous regeneration owing to the intrinsic healing capacity of bone tissue, critical-sized defects often exceed this capacity and require surgical intervention to restore function and integrity.[2] Conventional bone repair materials, such as metallic implants, polyether ether ketone, and allograft bone, have shown certain success but still suffer from inherent limitations.[3] For instance, polyether ether ketone is bioinert and lacks osteoinductivity, often resulting in poor osseointegration and fibrous tissue encapsulation.[4] Metallic implants, for instance, exhibit mismatched elastic modulus and poor biodegradability, while allografts carry risks of immune rejection and limited integration.[5] Therefore, the development of advanced bone substitutes with controllable mechanical strength, bioactivity, and biodegradability remains a pressing need to improve clinical outcomes in bone defect repair.

Hydrogels have gained increasing attention in bone tissue engineering due to their tunable physicochemical properties, high water content, and biocompatibility. Their three-dimensional (3D) network allows for nutrient diffusion, cell adhesion, and potential incorporation of bioactive molecules, making them ideal matrices for tissue regeneration.[6–8] However, traditional hydrogels are hindered by low mechanical strength and insufficient mineralization, restricting their direct application in load-bearing environments.[9] Thus, integrating mechanically robust structures with bioactive hydrogels has emerged as an effective strategy to achieve both mechanical reinforcement and osteoconductive microenvironments for bone regeneration.

Among various hydrogel systems, hydroxyethyl methacrylate (HEMA) has been extensively utilized in biomedical applications due to its favorable mechanical stability and ease of fabrication.[10] However, its application in bone repair is often limited by insufficient hydrophilicity and bioactivity, which are crucial for nutrient transport and cell adhesion. On the other hand, zwitterionic polymers, such as sulfobetaine methacrylate (SBMA), have attracted significant attention for their ability to mimic cell membrane structures, creating a super-hydrophilic hydration layer that minimizes non-specific protein adsorption and inflammation.[11] Recent studies have indicated that the copolymerization of HEMA and SBMA can synergize the mechanical robustness of HEMA with the antifouling and biocompatible properties of SBMA, resulting in a composite hydrogel named HMSM. This HMSM hybrid system thus presents a compelling candidate for bone tissue engineering, offering a tunable microenvironment that supports cellular functions while maintaining structural integrity.

However, even optimized hydrogels often fail to meet the mechanical demands of load-bearing bone defects. To address this, we integrated the bioactive HMSM hydrogel with a mechanically robust 3D-printed nano-hydroxyapatite (nHAP)/polylactic acid (PLA) (NP) scaffold. This composite strategy aims to leverage the high compressive strength of the 3D-printed framework to protect the softer, drug-loaded hydrogel matrix, thereby achieving a balance between mechanical support and biological functionality.

3D printing technology has revolutionized scaffold fabrication by enabling precise control over geometry, pore size, and internal gradient structure.[12] This technique enables scaffolds to replicate the hierarchical architecture of natural bone, which comprises cortical and trabecular regions characterized by distinct porosity and mechanical gradients. In particular, 3D-printed scaffolds composed of biodegradable polymers, such as PLA, and inorganic fillers, like nHAP, have demonstrated excellent biocompatibility and osteoconductivity.[13,14] The inclusion of nHAP enhances mineral deposition and promotes cell-mediated osteogenesis, while PLA provides mechanical integrity and biodegradability. Moreover, the NP scaffold can better match the structural and mechanical transitions of native bone, offering an optimized environment for bone tissue remodeling.[15–19]

Simvastatin (SIM), a lipophilic statin widely used for hyperlipidemia and cardiovascular diseases, has recently been identified as an osteoinductive molecule.[20,21] It can enhance bone formation by stimulating osteoblast differentiation, upregulating bone morphogenetic protein-2 (BMP-2), and promoting angiogenesis.[22–24] However, the therapeutic application of SIM in bone repair is often limited by its poor water solubility and rapid release kinetics, which may lead to transient local effects and systemic side effects upon repeated administration.[25] Therefore, developing a localized, sustained delivery system for SIM remains a critical research focus.

In this study, we developed a composite scaffold that combines a 3D-printed NP scaffold with an HMSM hydrogel for sustained SIM delivery and bone regeneration (Figure 1). The HMSM hydrogel was designed as a hydrophilic matrix to infiltrate and coat the porous scaffold, while the 3D-printed NP provided structural support and osteoconductivity. SIM was incorporated into the hydrogel–scaffold composite (denoted as SIM@HMSM/NP) to achieve localized, controlled drug release. This integrated system aims to synergistically

enhance mechanical strength, osteogenic activity, and biodegradation compatibility.

A comprehensive evaluation was conducted to assess the physicochemical characteristics, drug release profile, mechanical properties, cytocompatibility, and osteogenic efficacy of the composite both *in vitro* and *in vivo* using a critical-sized rat calvarial defect model. We hypothesized that the SIM@HMSM/NP scaffold could provide a favorable microenvironment for bone tissue regeneration, supporting sustained SIM delivery while maintaining mechanical integrity during the healing process.

2. Materials and methodology

2.1. Reagents and materials

HEMA, SBMA, and ethylene glycol dimethacrylate were purchased from Macklin Biochemical Co., Ltd. (China). SIM, ammonium persulfate (APS), N,N,N',N'-tetramethylethylenediamine (TEMED), and tannic acid (TA) were obtained from Aladdin Reagent Co., Ltd. (China). nHAP and PLA powders for 3D printing were supplied by Jinan Daigang Biomaterial Co., Ltd. (China). Alpha minimum essential medium (α-MEM) was purchased from BasalMedia Technologies, China. Fetal bovine serum was purchased from Gibco (Thermo Fisher Scientific, USA). Penicillin–streptomycin solution was obtained from Yeasen Biotechnology Co., Ltd. (China). The osteogenic induction medium contained 10 mM β-glycerophosphate, 100 nM dexamethasone, and 0.2 mM ascorbic acid (Sigma-Aldrich, USA). Calcein acetoxymethyl ester/propidium iodide (PI) live–dead cell staining kit, alkaline phosphatase (ALP) staining kit, 5-bromo-4-chloro-3-indolyl phosphate/nitro blue tetrazolium (BCIP/NBT), and Alizarin Red S (ARS) staining kit were purchased from ServiceBio (China). Hematoxylin and eosin (H&E) and Masson's trichrome staining kits were obtained from Beijing Solarbio Science & Technology Co., Ltd., China. Dylight 488- (A23210) and 594- (A23420) conjugated secondary antibodies used for immunofluorescence staining were obtained from Abbkine Scientific Co., Ltd. (China). All other reagents and solvents were of analytical grade and used without further purification. Ultrapure water (18.2 MΩ·cm) was used in all experiments.

2.2. Preparation of hydroxyethyl methacrylate/sulfobetaine methacrylate hydrogel loaded with simvastatin

A room-temperature free-radical polymerization method was employed to prepare the HMSM hydrogel loaded with SIM. Briefly, a predetermined amount of SIM was dissolved in 100 μL of deionized water under magnetic

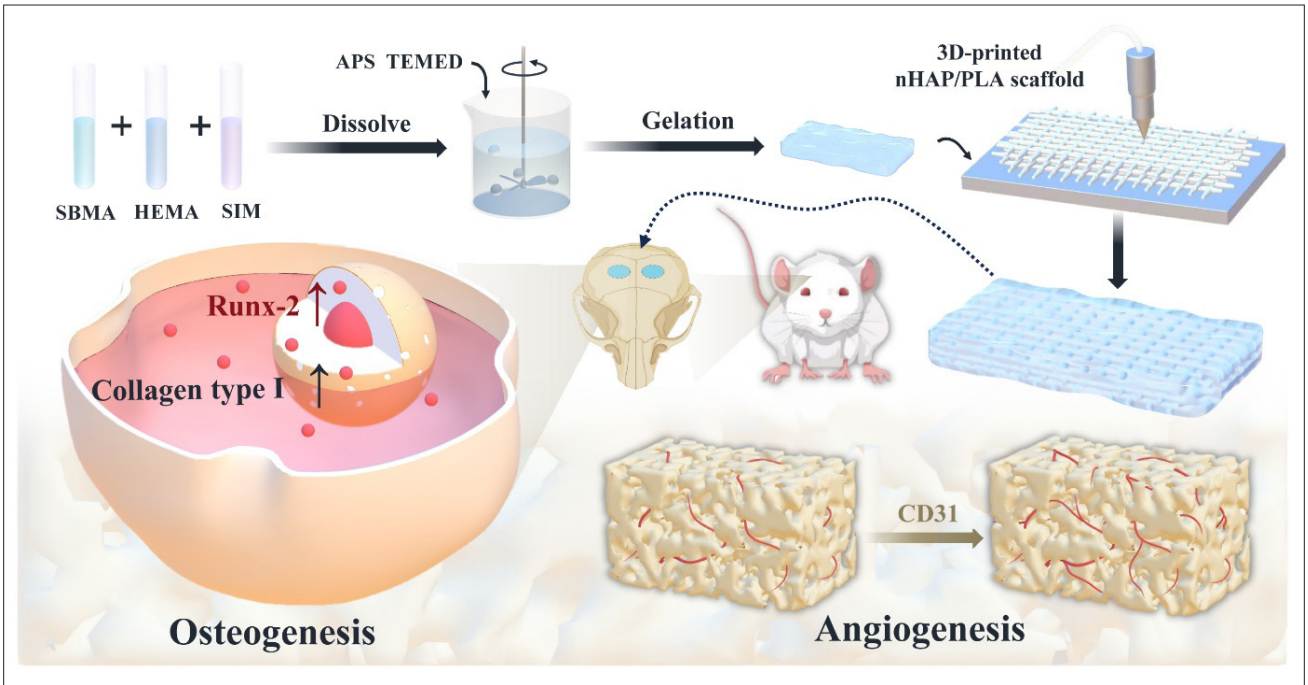


Figure 1. Schematic illustration of the SIM-loaded HEMA/SBMA hydrogel/nHAP/PLA composite scaffold for bone regeneration. The two blue dots on the rat skull indicate bilateral critical-sized calvarial defect sites. The composite scaffold promotes bone regeneration by enhancing osteogenesis, as indicated by the upregulation of Runx-2 and collagen type I, and angiogenesis, as evidenced by increased CD31 expression. Abbreviations: 3D, three-dimensional; APS, ammonium persulfate; CD, cluster of differentiation; TEMED, N,N,N',N'-tetramethylethylenediamine; SIM, simvastatin; HEMA, hydroxyethyl methacrylate; SBMA, sulfobetaine methacrylate; nHAP, nano-hydroxyapatite; PLA, polylactic acid; Runx-2, runt-related transcription factor 2.

stirring. A total of 300 μL of HEMA and 300 μL of SBMA were separately dissolved in 400 μL of Tris buffer (pH = 8.5; 10 mM) and stirred for 30 minutes at 300 rpm to obtain two solutions. Then, the two solutions were mixed and stirred for 30 minutes at 300 rpm to obtain a homogeneous solution. Subsequently, 40 μL of ethylene glycol dimethacrylate was added as a cross-linker and stirred for 15 minutes at 350 rpm. The 280 μL of SIM solution (1 mg/1 mL) was then introduced into the HEMA/SBMA mixture, followed by continuous stirring for 30 minutes at 500 rpm. Then, 5 mg of APS and 5 μL of TEMED were added as the initiator and accelerator, respectively, to initiate polymerization. Preliminary gelation occurred within 15 minutes of stirring at 150 rpm and 5 minutes of standing. All the reactions were placed at room temperature. After 24 hours of polymerization at room temperature, the hydrogel was removed, rinsed thoroughly with deionized water to eliminate unreacted monomers, and dried in an oven for further use.

2.3. *In vitro* drug release experiment of hydroxyethyl methacrylate/sulfobetaine methacrylate hydrogel loaded with simvastatin

The *in vitro* drug release behavior of the HMSM hydrogel was evaluated in phosphate-buffered saline (pH 7.4) at 37°C. Three samples of SIM-loaded hydrogels (1 g each) and three drug-free hydrogels were placed separately into 20 mL of phosphate-buffered saline solution and incubated on a constant-temperature shaker. At predetermined time intervals (0 hour, 1 hour, 3 hours, 6 hours, 9 hours, 12 hours, 18 hours, 24 hours, 3 days, 6 days, 9 days, 12 days, 18 days, and 24 days), 4 mL of the supernatant was collected and replaced with an equal volume of fresh phosphate-buffered saline. The absorbance of the withdrawn solution at 238 nm was recorded using a ultraviolet–visible spectrophotometer (Molecular Devices, USA). The cumulative release percentage of SIM was calculated based on the standard calibration curve, and the results were averaged from three independent samples.

2.4. Design and preparation of the nano-hydroxyapatite/polylactic acid scaffold

The NP scaffold was designed using computer-aided design software. Each printed scaffold had dimensions of 3 cm × 2 cm × 0.1 cm, with a line width of 300 μm and an initial pore size of 300 μm. The pore size increased by 25 μm per layer to form a gradient architecture, and each lower layer was offset by 250 μm to enhance structural stability. The scaffold was fabricated using a Low-temperature deposition manufacturing 3D printer (Bio-Architect, Regenovo, China). Before printing, PLA granules were dissolved in dichloromethane (DCM) to prepare a 15% (w/v) solution. nHAP powder was then added to the solution at a mass ratio of 1:9 (nHAP:PLA) and stirred magnetically for 24 hours to obtain a homogeneous printing ink. The printing process was conducted at room temperature with a speed of 12 mm/s and an extrusion pressure of 0.2–0.4 MPa. After printing, the scaffolds were subsequently dried at room temperature for 8 hours to allow the evaporation of DCM and at 4°C for 8 hours to remove residual solvents. Low-temperature drying was chosen because the boiling point of DCM (39.6°C) is relatively low; heating above this temperature would cause solvent boiling and potentially lead to structural defects.

2.5. Cross-linking of the drug-loaded hydrogel and the three-dimensional-printed gradient scaffold

After fabricating the 3D-printed scaffold, the SIM-loaded HMSM hydrogel precursor solution was prepared by mixing monomers, cross-linker, initiator, and SIM. TA was added to enhance interfacial adhesion. To fabricate the composite, the NP scaffold was fully immersed in the prepared SIM-loaded HMSM precursor solution (containing monomers and cross-linker) for 24 hours to ensure complete infiltration of the solution into the scaffold's micropores. Subsequently, the polymerization initiator APS and TEMED were added into the mixture to trigger *in situ* gelation. The system was allowed to react at room temperature for 24 hours, ensuring that the hydrogel formed a continuous network within and around the scaffold framework, reinforced by the addition of 2 mg of TA, for interfacial adhesion. The resulting composite (SIM@HMSM/NP) was retrieved and subjected to a rigorous purification process. Specifically, the scaffolds were immersed in a large volume of deionized water (200 mL) for 24 hours, with the water replaced every 8 hours to facilitate the diffusion and removal of unreacted monomers and residues. After washing, the scaffolds were dried in a vacuum oven for further analysis.

2.6. Scanning electron microscopy analysis

The surface morphology and microstructure of the scaffolds were characterized using scanning electron microscopy (SEM, Sigma 500, Carl Zeiss, Oberkochen, Germany). Prior to observation, the samples were freeze-dried and mounted on aluminum stubs using conductive carbon tape. All specimens were sputter-coated with a thin layer of gold to enhance electrical conductivity. SEM images were acquired at an accelerating voltage of 5–10 kV under high-vacuum conditions. Images were collected at different magnifications to evaluate the pore architecture, surface topography, and interconnectivity of the scaffolds.

2.7. Measurement of porosity

The porosity of the scaffolds was determined using the liquid displacement method based on Archimedes'

principle. Absolute ethanol was used as the displacement medium. The porosity was calculated using **Equation (1)**:

$$\text{Porosity} = (V_1 - V_3)/(V_2 - V_1) \times 100\% \quad (1)$$

where V_1 is the volume of ethanol before sample immersion, V_2 is the total volume after sample immersion, and V_3 is the remaining volume after sample removal. The calculated value represents the percentage of internal pore volume relative to the total scaffold volume.

2.8. Mechanical properties of the simvastatin@hydroxyethyl methacrylate/sulfobetaine methacrylate/nano-hydroxyapatite/polylactic acid scaffold

The mechanical properties of the HMSM hydrogel, the NP scaffold, and the composite scaffold (SIM@HMSM/NP) were tested using a universal mechanical testing machine (Zwick/Roell, Germany) under compression mode. The stress–strain curve was obtained for each sample, and the elastic modulus was calculated as the slope of the linear regression line fitted to the stress–strain data within the linear elastic region (strain range of 10–20%).

2.9. Preparation of extraction solutions of the simvastatin@hydroxyethyl methacrylate/sulfobetaine methacrylate/nano-hydroxyapatite/polylactic acid scaffold

The extraction of SIM@HMSM/NP composites was performed following a standardized protocol.[26] The HMSM hydrogel, NP scaffold, and SIM@HMSM/NP composite were cut into square specimens measuring 5 mm × 5 mm. After sterilization under ultraviolet light, each sample was immersed in complete culture medium at a surface area-to-volume ratio of 6 cm^2/mL and incubated at 37°C for 24 hours to obtain the extraction solutions. The extracts were subsequently collected, filtered through a 0.22 μm membrane to remove particulates, and stored at 4°C for subsequent biocompatibility and osteogenic evaluations.

2.10. Biocompatibility evaluation and live/dead staining

To evaluate cytocompatibility, the hydrogel and composite samples were pre-soaked in complete culture medium overnight to remove residual monomers. Bone marrow mesenchymal stem cells (BMSCs, 1×10^5 cells per well) were then seeded onto the surface of the SIM@HMSM/NP composites in 24-well plates and incubated under standard culture conditions. After 7 days of co-culture, cell viability was assessed using a calcein acetoxymethyl ester/PI staining kit, following the manufacturer's instructions. A Transwell indirect co-culture assay was further employed to assess potential cytotoxicity.[27] Briefly, hydrogel samples were placed in the upper chamber of a Transwell insert (pore size 3 μm; Cat. No. TCS019024, Jet Biofil, China), while BMSCs were seeded in the lower chamber. After 3 days of co-culture, live/dead staining was performed as described above. The stained cells were imaged using an inverted fluorescence microscope (ECLIPSE Ts2R, Nikon, Japan) or a confocal laser scanning microscope (STELLARIS 5, Carl Zeiss, Germany). To quantitatively assess cell proliferation, a Cell Counting Kit-8 (CCK-8) assay was performed. BMSCs were seeded on the scaffolds in 24-well plates at a density of 1×10^4 cells per well. At predetermined time points (1, 3, and 5 days), the culture medium was replaced with fresh medium containing 10% CCK-8 solution. After incubation for 2 hours at 37°C, the absorbance of the supernatant was measured at 450 nm using a microplate reader (Molecular Devices, USA). All experiments were performed in triplicate.

2.11. *In vitro* evaluation of osteogenic properties of the simvastatin@hydroxyethyl methacrylate/sulfobetaine methacrylate/nano-hydroxyapatite/polylactic acid scaffold

To evaluate the osteogenic potential of the composites, extraction solutions from different material groups were co-cultured with BMSCs. After 7 days of incubation, alkaline phosphatase staining was performed using a BCIP/NBT chromogenic substrate kit (ServiceBio, China) to visualize ALP activity and assess early-stage osteogenic differentiation. Mineralization was further evaluated on day 21 by ARS staining to detect calcium nodule formation under a light microscope. In addition, immunofluorescence staining was conducted to analyze the expression of osteogenesis-related proteins, including collagen type I (Col-I) and runt-related transcription factor 2 (Runx-2). Dylight 488- or 594-conjugated secondary antibodies (1:200) were used for fluorescent labeling, and images were captured using a fluorescence microscope (ECLIPSE Ts2R, Nikon, Japan).

2.12. Cell lines and animals

All animal procedures were reviewed and approved by the Laboratory Animal Management and Ethics Committee of Qingdao University (Approval No. 20220910) and conducted in accordance with the Guidelines for the Care and Use of Laboratory Animals (National Research Council, USA) and the Guidelines for the Ethical Review of Experimental Animals in the People's Republic of China (GB/T 35892-2018). Healthy male Sprague–Dawley (SD) rats (n = 48), aged approximately 8 weeks and weighing 250–300 g, were obtained from the Fushan Campus of Qingdao University. The animals were housed under standard laboratory conditions (temperature 22 ± 2°C,

relative humidity 55 ± 5%, 12 hours light/dark cycle) with free access to food and water. The rats were randomly divided into four groups (n = 12 per group): (i) blank group (Blank): defect left unfilled without any material implantation; (ii) hydrogel group (HMSM): implantation of HMSM hydrogel; (iii) scaffold group (NP): implantation of 3D-printed NP scaffold; and (iv) composite group (SIM@HMSM/NP): implantation of SIM-loaded hydrogel–scaffold composite. BMSCs were isolated from 4-week-old male SD rats following standard procedures. BMSCs were maintained in α-MEM supplemented with 10% fetal bovine serum and 1% penicillin–streptomycin under standard culture conditions (37°C, 5% carbon dioxide, humidified atmosphere). The culture medium was refreshed every 2 days. For osteogenic induction, BMSCs were cultured in α-MEM containing 10 mM β-glycerophosphate, 100 nM dexamethasone, and 0.2 mM ascorbic acid for the indicated time periods prior to further analysis.

2.13. *In vivo* bone formation assessment

A critical-sized cranial defect model was established in 8-week-old male SD rats (250–300 g) to evaluate *in vivo* bone formation as previously reported.[28] A full-thickness circular defect (5 mm in diameter) was created on the parietal bone using an electric trephine drill under continuous saline irrigation to avoid thermal injury. The defect sites were treated according to the experimental grouping: Blank, HMSM, NP, and SIM@HMSM/NP. After implantation, the periosteum and skin were sutured in layers. At 4 and 8 weeks postoperatively, the rats were euthanized, and the calvarial specimens were harvested and fixed in 10% paraformaldehyde. Micro-computed tomography (Micro-CT; Bruker, USA) was performed to assess new bone formation, and the data were analyzed using CTAn software (version 1.18.4.0) to quantify bone volume fraction (BV/TV). The fixed samples were then decalcified, dehydrated, and embedded in paraffin. Sections (5 μm thick) were prepared for histological analysis, including H&E and Masson's trichrome staining, to evaluate bone matrix deposition and collagen organization. Additionally, immunofluorescence staining was performed to detect osteogenic and angiogenic markers, including Col-I and cluster of differentiation 31 (CD31), using Dylight 488- and 594-conjugated secondary antibodies (1:200), respectively. Images were captured using a fluorescence microscope (ECLIPSE Ts2R, Nikon, Japan).

2.14. Statistical analysis

All data were expressed as mean ± standard deviation (mean ± SD). Differences among groups were evaluated by one-way analysis of variance followed by Tukey's post hoc multiple comparison test. A p-value of less than 0.05 was considered statistically significant. Statistical significance levels were denoted as $p < 0.05$. GraphPad Prism software (version 9.0, GraphPad software, USA) was used for data visualization and figure preparation.

3. Results and discussion

3.1. Preparation of hydroxyethyl methacrylate/sulfobetaine methacrylate hydrogel loaded with simvastatin

The development of an effective drug delivery matrix with mechanical robustness is essential for bone tissue engineering. Hydrogels have been widely explored as localized drug carriers owing to their high biocompatibility, adjustable cross-linking density, and ability to sustain therapeutic release.[29] However, single-component hydrogels such as HEMA or SBMA often face limitations: HEMA hydrogels provide good mechanical strength but poor water absorption, whereas SBMA hydrogels exhibit outstanding hydrophilicity yet insufficient mechanical integrity.[30,31]

By co-polymerizing HEMA and SBMA, the HMSM hydrogel combines the complementary advantages of both monomers, resulting in improved flexibility, enhanced water retention, and improved surface compatibility. The incorporation of SIM into the HMSM network enables localized drug loading, while integration with a 3D-printed NP scaffold further enhances mechanical stability and osteoconductivity. The SIM@HMSM/NP was constructed by integrating chemical polymerization and 3D-printing technologies. The free radical polymerization of HEMA and SBMA, initiated by APS/TEMED, led to the formation of a cross-linked HMSM hydrogel network capable of encapsulating SIM. The zwitterionic SBMA component imparted strong hydration and antifouling properties through electrostatic charge balance, while HEMA provided structural stability to the hydrogel matrix.

The pre-formed HMSM precursor was introduced into the 3D-printed NP scaffold, where *in situ* gelation occurred, filling the scaffold pores and ensuring intimate interfacial adhesion between the polymeric and inorganic phases. This hybrid design combines the high biocompatibility and sustained release capacity of the hydrogel with the mechanical strength and osteoconductivity of the NP framework.

In Figure 2A–I, the hydrogel exhibited a transparent, uniform texture, while the 3D-printed scaffold presented a well-defined gradient porous structure. SEM analysis confirmed smooth surfaces for HMSM, regular and interconnected pores for NP, and cohesive integration in the SIM@HMSM/NP without interfacial delamination. As shown in Figure 2C–D, the NP scaffold was designed using computer-aided design software and fabricated through

3D printing with precise control of pore geometry and filament arrangement. The scaffold exhibited a rectangular shape (3 cm × 2 cm × 0.1 cm) with a uniform, grid-like pattern. The surface layer was composed of printed filaments with a diameter of approximately 300 μm and a pore size of 300 μm, while the pore size gradually increased to 500 μm in the lower layers, with a 25 μm increment per layer. This gradient structural design was specifically engineered to validate the concept of bionic repair. By mimicking the transition from dense cortical bone to porous trabecular bone, the scaffold achieves a functional balance: the upper layers with smaller pores provide necessary mechanical shielding and structural integrity, while the lower layers with larger pores create an open microenvironment. This open structure is critical for minimizing resistance to nutrient diffusion and facilitating the deep ingrowth of blood vessels and bone tissue, as distinct from uniform scaffolds, which often suffer from necrotic cores due to poor perfusion. The success of this design is evidenced by the superior mechanical properties (Figure 3C) and the uniform bone formation observed in the critical-sized defect model. This programmed gradient created a hierarchical internal architecture with distinct layer-by-layer offsets, providing larger interspaces toward the base of the scaffold. Such a gradient configuration not only enhances the mechanical stability of the construct but also increases its capacity to retain and distribute hydrogel or drug molecules evenly within the pores.[2,32,33] The enlarged internal channels facilitate deeper penetration of the HMSM hydrogel during *in situ* gelation, which is expected to reduce the initial burst release and promote a more sustained and uniform drug delivery profile during subsequent degradation. These structural features collectively contribute to improved mechanical reinforcement and bioactivity, laying a robust foundation for effective bone tissue regeneration.

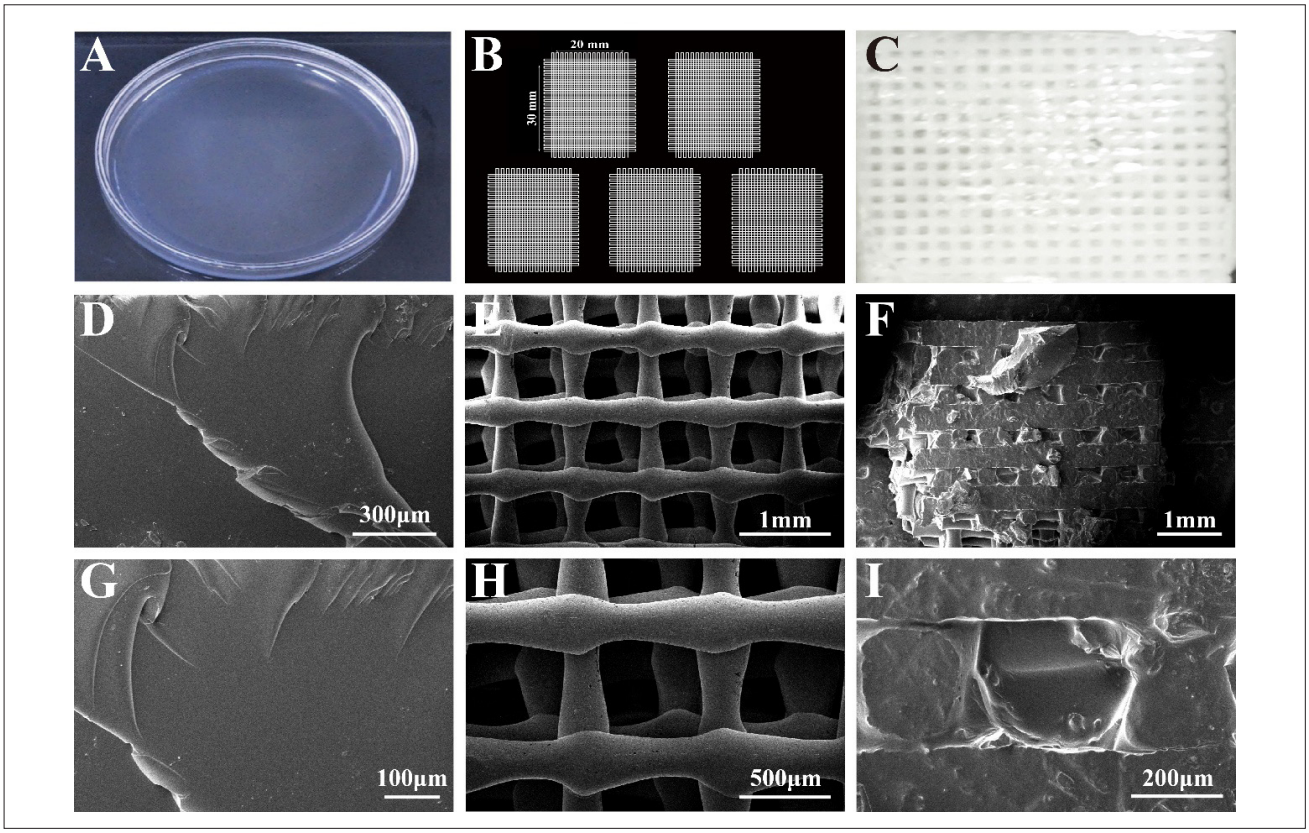


Figure 2. Fabrication process and morphological characterization of the SIM@HMSM/NP composite scaffold. (A) Photograph of the synthesized HMSM hydrogel exhibiting a transparent and homogeneous appearance. (B) Computer-aided design of the 3D-printed NP scaffold with precise pore control. (C) Optical image of the printed scaffold showing a uniform, interconnected framework. (D & G) SEM images of the HMSM hydrogel showing a smooth surface and dense polymeric morphology. Scale bars: 100 μm, 300 μm; magnifications: 200× & 1000×. (E & H) SEM images of the 3D-printed NP scaffold demonstrating well-ordered gradient pores and regular filament arrangement. Scale bars: 1 mm, 500 μm; magnifications: 1000× & 2000×. (F & I) SEM images of the SIM@HMSM/NP revealing tight interfacial bonding between the hydrogel and scaffold with continuous, integrated pore structures. Scale bars: 1 mm, 200 μm; magnifications: 200× & 2000×. Abbreviations: 3D, three-dimensional; HMSM, hydroxyethyl methacrylate/sulfobetaine methacrylate; NP, nano-hydroxyapatite/polylactic acid; SEM, scanning electron microscopy; SIM, simvastatin.

3.2. Characterizations of simvastatin @hydroxyethyl methacrylate/sulfobetaine methacrylate/nano-hydroxyapatite/polylactic acid hydrogel

The NP scaffold was fabricated with precisely controlled pore architecture and uniform layer alignment (Figure 3A–D). Mechanical testing revealed that the HMSM hydrogel exhibited an elastic modulus of 2.18 ± 0.287 MPa, while the NP scaffold reached 16.95 ± 2.36 MPa. Notably, the SIM@HMSM/NP composite showed the highest modulus of 24.17 ± 4.27 MPa, surpassing both human cancellous bone (3.2–12.8 MPa) and cortical bone (17–20 MPa), indicating sufficient mechanical strength for bone defect support. Based on the liquid displacement method, the porosity of the NP scaffold was calculated to be 46.22 ± 1.01%. This value falls well within the optimal range (40–70%) required for bone tissue engineering applications. Such a porous structure is conducive to nutrient transport and provides sufficient space for cell adhesion and proliferation, which is essential for facilitating subsequent neovascularization and bone ingrowth. Furthermore, the water absorption capability is a vital parameter for hydrogel-based composites, as it influences nutrient diffusion and metabolic waste removal. As shown in Figure 3E, the HMSM hydrogel exhibited a high swelling ratio due to its hydrophilic nature. The SIM@HMSM/NP composite also demonstrated significant water absorption. This swelling behavior ensures that the composite can effectively absorb tissue fluids upon implantation, creating a moist microenvironment conducive to cell survival and recruitment. In the degradation assay, the SIM@HMSM/NP composite exhibited a gradual mass loss of 42.82 ± 3.18% after 28 days (Figure 3D). Interestingly, this degradation rate was slightly higher than that of the pure HMSM hydrogel. This phenomenon can be attributed to the "restricted swelling" effect: the rigid NP scaffold constrains the volume expansion of the hydrophilic HMSM hydrogel. The resulting internal swelling stress may induce micro-cracking and accelerated fragmentation of the hydrogel network within the pores. Additionally, the porous architecture of the scaffold increases the specific surface area of the hydrogel exposed to the medium, further facilitating hydrolytic degradation. This degradation profile corresponds well with the pace of natural bone regeneration.[34] This controlled degradation ensures that the scaffold maintains temporary mechanical integrity while gradually providing space for new bone ingrowth.

The quantification of SIM concentration was determined using a standard calibration curve, which showed a good linear relationship (Figure 3A). Drug release analysis (Figure 3B) showed an initial mild release followed by a sustained phase over 24 days, suggesting that the hydrogel–scaffold composite effectively reduces early burst release and maintains long-term drug availability. It is important to note that the drug release behavior is intrinsically governed by the structural parameters of the composite system. In this study, the formulation was optimized to balance mechanical strength and biological activity. The release mechanism is twofold. First, the dense cross-linked network of the HMSM hydrogel acts as the primary diffusion barrier, regulating the migration of SIM molecules. Second, the 3D-printed NP scaffold imposes a geometric constraint. Unlike a free-swelling hydrogel, the hydrogel within the composite is confined within the scaffold struts, which limits the effective surface area exposed to the surrounding fluid. This structural confinement prevents rapid bulk degradation and burst release, thereby extending the therapeutic window. While varying the pore size or hydrogel cross-linking density could further tune the release kinetics, the current parameters were chosen to prioritize mechanical stability and a conducive pore size for osteoblast infiltration. Collectively, these findings confirm that the SIM@HMSM/NP composite achieves a desirable balance between mechanical stability, biodegradability, and sustained drug delivery, which are essential parameters for bone tissue regeneration.

3.3. Biocompatibility of composite materials

Good biocompatibility is a prerequisite for the application of hydrogels in tissue engineering, as it directly influences cellular behavior and regenerative outcomes.[35] To comprehensively assess the cytocompatibility of the HMSM hydrogel, NP scaffold, and SIM@HMSM/NP composite, both direct and indirect co-culture assays were performed (Figure 4A–C). In the direct co-culture setup, fluorescently labeled BMSCs were observed to be distributed as discrete punctate signals on the surface of SIM@HMSM/NP, indicating successful cell attachment and survival. Although the intrinsic fluorescence of the scaffold resulted in a green background signal, the presence of distinct cell-associated fluorescence confirmed the cytocompatibility of the composite scaffold (Figure 4B). In the Transwell indirect co-culture system, live/dead staining showed predominant green fluorescence across all groups, confirming high cell viability and minimal cytotoxicity (Figure 4C). This observation was further supported by quantitative analysis of the percentage of live cells (Figure 4E), which showed no significant differences among the control, HMSM, NP, and SIM@HMSM/NP groups.

Compared with the control, both HMSM hydrogel and NP scaffold maintained favorable cell survival, while the SIM@HMSM/NP composite exhibited excellent biocompatibility, supporting robust BMSC proliferation and uniform distribution similar to the control groups. These results indicate that the incorporation of SIM and

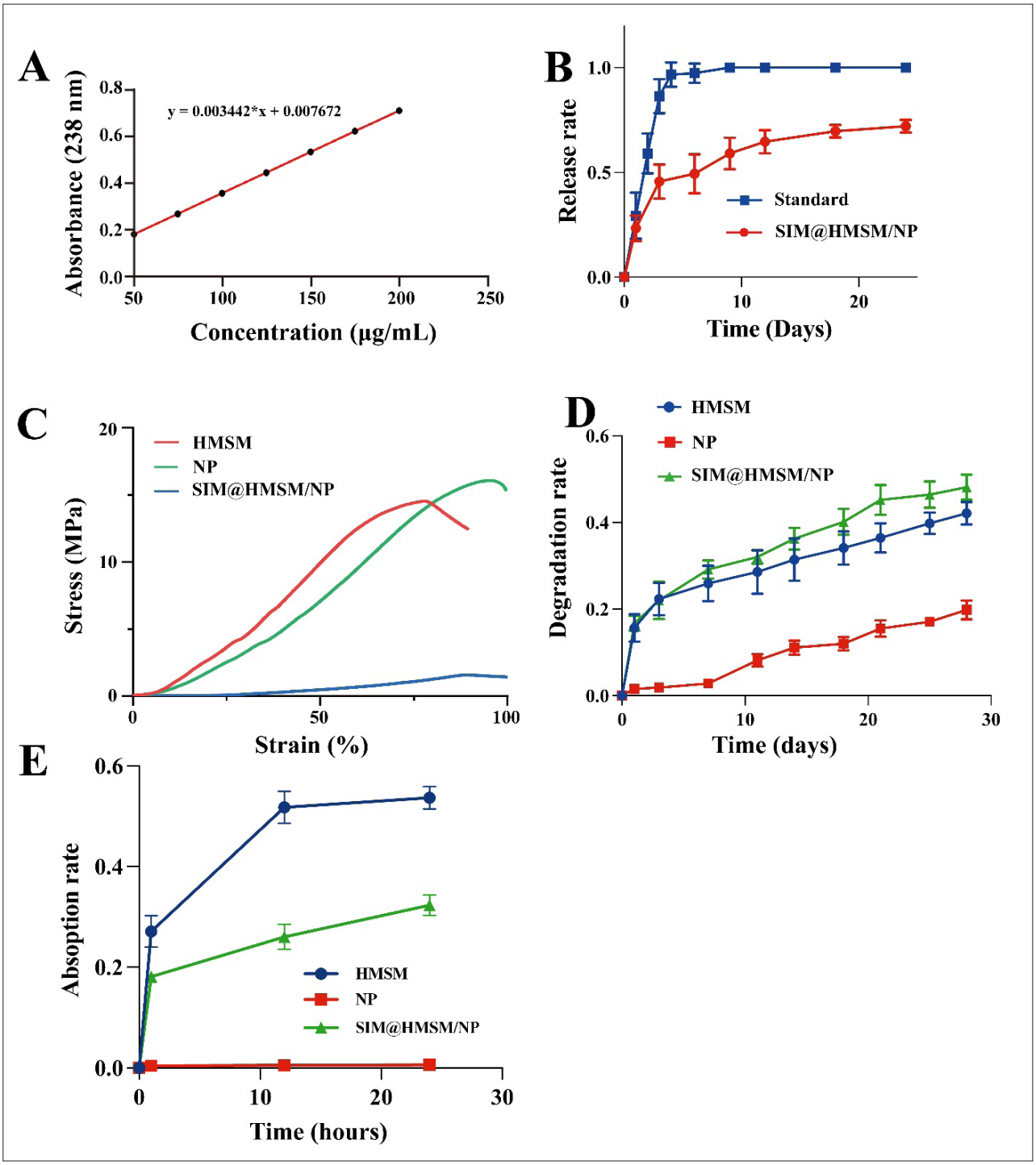


Figure 3. Physicochemical and mechanical characterization of HMSM hydrogel, NP scaffold, and SIM@HMSM/NP composite scaffold. (A) Standard calibration curve of SIM at 238 nm showing linear correlation between absorbance and concentration ($y = 0.003442 \times x + 0.007672$, $R^2 = 0.998$), confirming reliable quantification for release analysis. (B) Cumulative drug release profiles of SIM@HMSM/NP composite and free SIM standard solution over 24 days, indicating a sustained and controlled release behavior in the composite scaffold. (C) Compressive stress–strain curves of HMSM hydrogel, NP scaffold, and SIM@HMSM/NP composite. The composite exhibited the highest elastic modulus (24.17 ± 4.27 MPa), surpassing both individual components and aligning with the mechanical range of natural bone. (D) *In vitro* degradation profiles of HMSM hydrogel, NP scaffold, and SIM@HMSM/NP composite over 28 days. The composite displayed gradual mass loss (42.82 ± 3.18%), suggesting balanced biodegradability compatible with bone tissue regeneration. (E) Water absorption behavior of the scaffolds. The experiments were performed in triplicate. Data are presented as mean ± standard deviation ($n = 3$). Abbreviations: HMSM, hydroxyethyl methacrylate/sulfobetaine methacrylate; NP, nano-hydroxyapatite/polylactic acid; SIM, simvastatin.

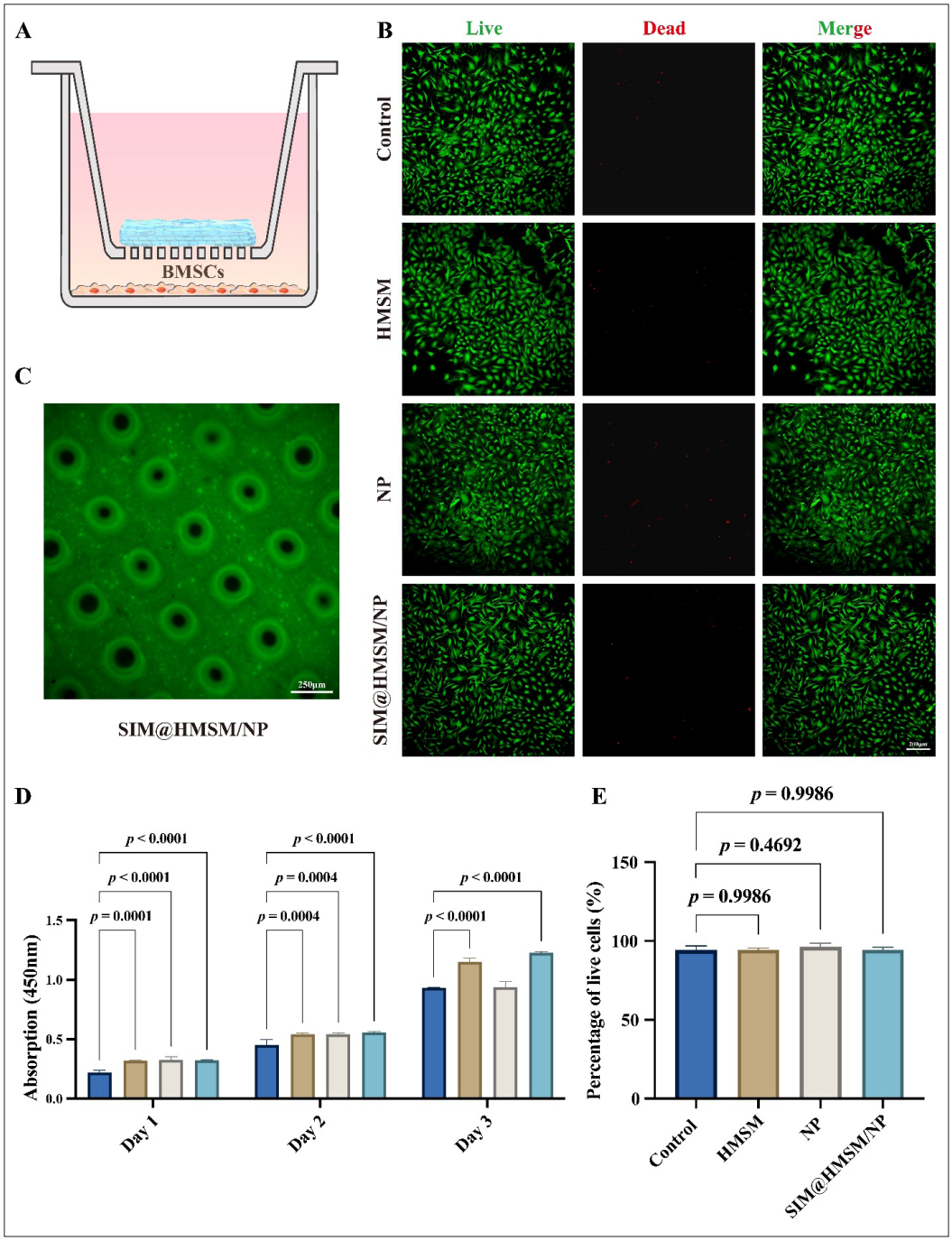


Figure 4. Cytocompatibility evaluation of HMSM hydrogel, NP scaffold, and SIM@HMSM/NP composite using calcein AM/PI staining. (A) Schematic illustration of the Transwell co-culture setup used for cytocompatibility testing. SIM@HMSM/NP composites were placed in the upper chamber, while BMSCs were cultured in the lower chamber to assess indirect cytotoxicity. (B) Live/dead staining of BMSCs directly co-cultured with the SIM@HMSM/NP composite, showing extensive cell survival and uniform cell attachment on the material surface. Scale bar: 250 μm; magnification: 10×. (C) Representative fluorescence images of BMSCs after 3 days of indirect co-culture with different material extracts (control, HMSM, NP, and SIM@HMSM/NP). Green fluorescence (calcein AM) indicates live cells, and red fluorescence (PI) indicates dead cells. Scale bar: 200 μm; magnification: 20×. (D) Quantitative analysis of BMSC proliferation evaluated by the CCK-8 assay at days 1, 2, and 3. The absorbance at 450 nm increased over time in all groups, demonstrating continuous cell proliferation and confirming that none of the materials inhibited cell growth. (E) Quantitative analysis of cell viability expressed as the percentage of live cells, showing no significant differences among the control, HMSM, NP, and SIM@HMSM/NP groups, further confirming excellent cytocompatibility. Data are presented as mean ± standard deviation (n = 3). Abbreviations: AM, acetoxymethyl ester; HMSM, hydroxyethyl methacrylate/sulfobetaine methacrylate; NP, nano-hydroxyapatite/polylactic acid; PI, propidium iodide; SIM, simvastatin; BMSCs, bone marrow-derived mesenchymal stem cells.

the hybridization of hydrogel with the 3D-printed scaffold did not compromise biocompatibility but provided a more conducive microenvironment for cell growth. Quantitative analysis via the CCK-8 assay (Figure 3D) further corroborated these findings. The optical density (OD) values in all groups increased continuously from day 1 to day 5, indicating active cell proliferation. The SIM@HMSM/NP group showed slightly higher OD values than the control group, demonstrating that the composite scaffold supports BMSC viability and proliferation.

3.4. *In vitro* osteogenic performance of composite materials

To assess the osteogenic potential of the composite materials, BMSCs were cultured in extraction solutions from different groups and subjected to ALP, ARS, and immunofluorescence analyses (Figure 5A–D). After 7 days, ALP staining revealed pronounced blue coloration in the SIM@HMSM/NP group, suggesting enhanced early osteogenic differentiation compared with HMSM and NP alone. By day 21, ARS staining showed dense red calcium nodules, indicating active mineralization and late-stage osteogenesis. Quantitative analysis confirmed that ALP activity in the SIM@HMSM/NP group was significantly higher than in the HMSM, NP, or control groups ($p < 0.0001$) (Figure 5B). Immunofluorescence results further validated these findings. As shown in Figure 5C, both Runx-2 and Col-I exhibited markedly increased fluorescence intensity in the SIM@HMSM/NP group. Statistical analysis (Figure 5D) demonstrated that Runx-2 expression increased approximately 2.8-fold and Col-I expression 3.1-fold compared with the control group ($p < 0.0001$). These results indicate that the composite scaffold not only supports cell survival but also effectively promotes osteogenic differentiation.

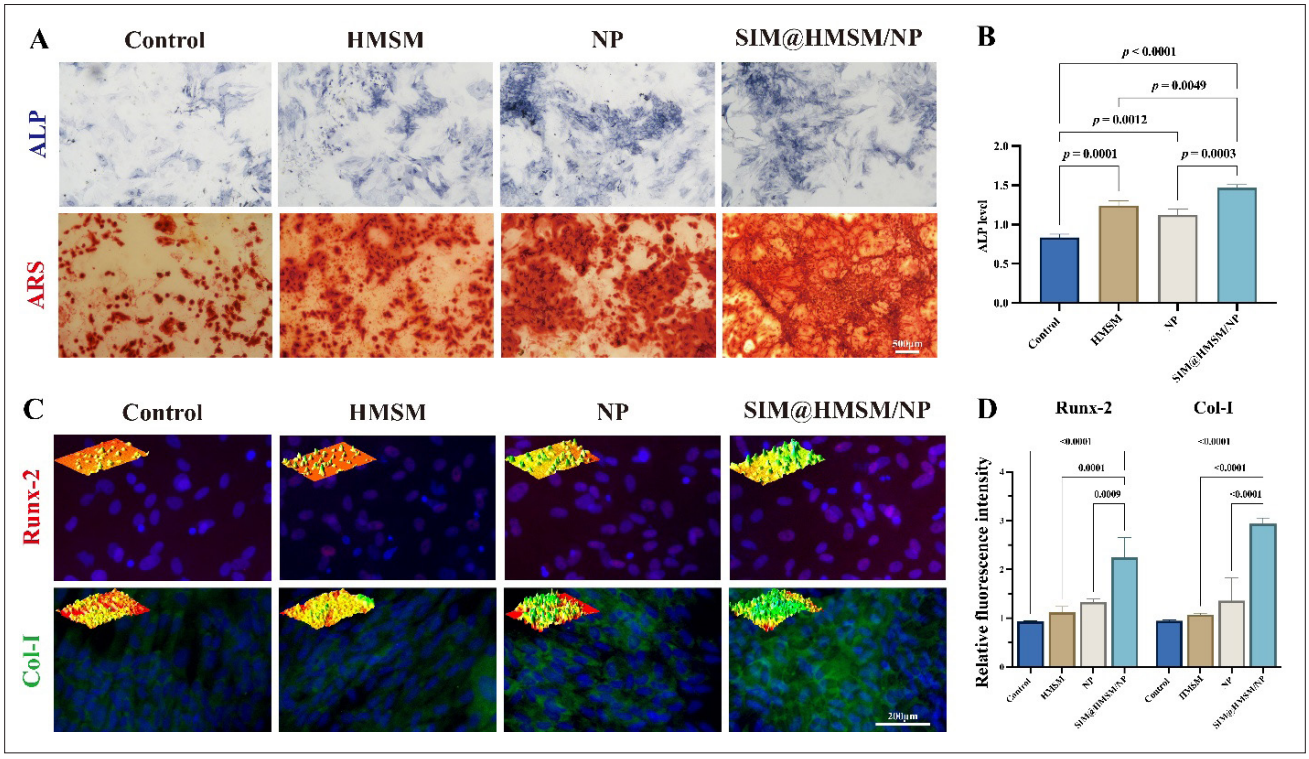


Figure 5. Osteogenic differentiation of BMSCs cultured with extracts from different materials. (A) Representative images of ALP staining at day 7 (upper panels) and ARS staining at day 21 (lower panels) in different extract groups (control, HMSM, NP, and SIM@HMSM/NP). In the ALP images, purple/blue coloration indicates ALP-positive regions, reflecting early osteogenic differentiation, while in the ARS images, red-stained areas represent calcium-rich mineralized nodules, indicating late-stage mineralization. Scale bar: 500 μm; magnification: 10×. (B) Quantitative analysis of ALP activity, showing significantly higher ALP levels in the SIM@HMSM/NP group compared with the other groups ($p < 0.0001$). (C) Immunofluorescence staining of osteogenic markers Runx-2 and Col-I in BMSCs after 14 days of culture. Protein expression is visualized using pseudo-colored fluorescence intensity maps, while cell nuclei were counterstained with DAPI (blue). Scale bar: 200 μm; magnification: 20×. (D) Quantification of fluorescence intensity demonstrating significantly increased Runx-2 and Col-I expression in the SIM@HMSM/NP group compared with the other treatments ($p < 0.0001$). Data are presented as mean ± standard deviation ($n = 3$). Abbreviations: ALP, alkaline phosphatase; ARS, Alizarin Red S; BMSCs, bone marrow-derived stem cells; Col-I, collagen type 1; DAPI, 4',6-diamidino-2-phenylindole; HMSM, hydroxyethyl methacrylate/sulfobetaine methacrylate; NP, nano-hydroxyapatite/polylactic acid; Runx-2, runt-related transcription factor 2; SIM, simvastatin.

This enhancement can be attributed to the synergistic effects of SIM and the bioactive NP framework. SIM is known to upregulate BMP-2 and activate Runx-2 signaling pathways, while nHAP provides osteoconductive cues that promote calcium phosphate deposition.[36] The incorporation of HMSM hydrogel further ensures localized, sustained release of SIM, maintaining effective concentrations at the cell–material interface. Together, these factors establish a favorable osteoinductive microenvironment conducive to bone tissue regeneration.

3.5. *In vivo* osteogenic performance of composite materials

To further assess the osteogenic performance of the composite materials *in vivo*, a critical-sized rat calvarial defect model was used to evaluate bone regeneration at 4 and 8 weeks post-implantation (Figure 6A–C). Micro-CT 3D reconstruction demonstrated that the control group retained large unhealed regions, while defects treated with HMSM or NP scaffolds exhibited limited bone ingrowth. In contrast, the SIM@HMSM/NP group showed continuous new bone formation and

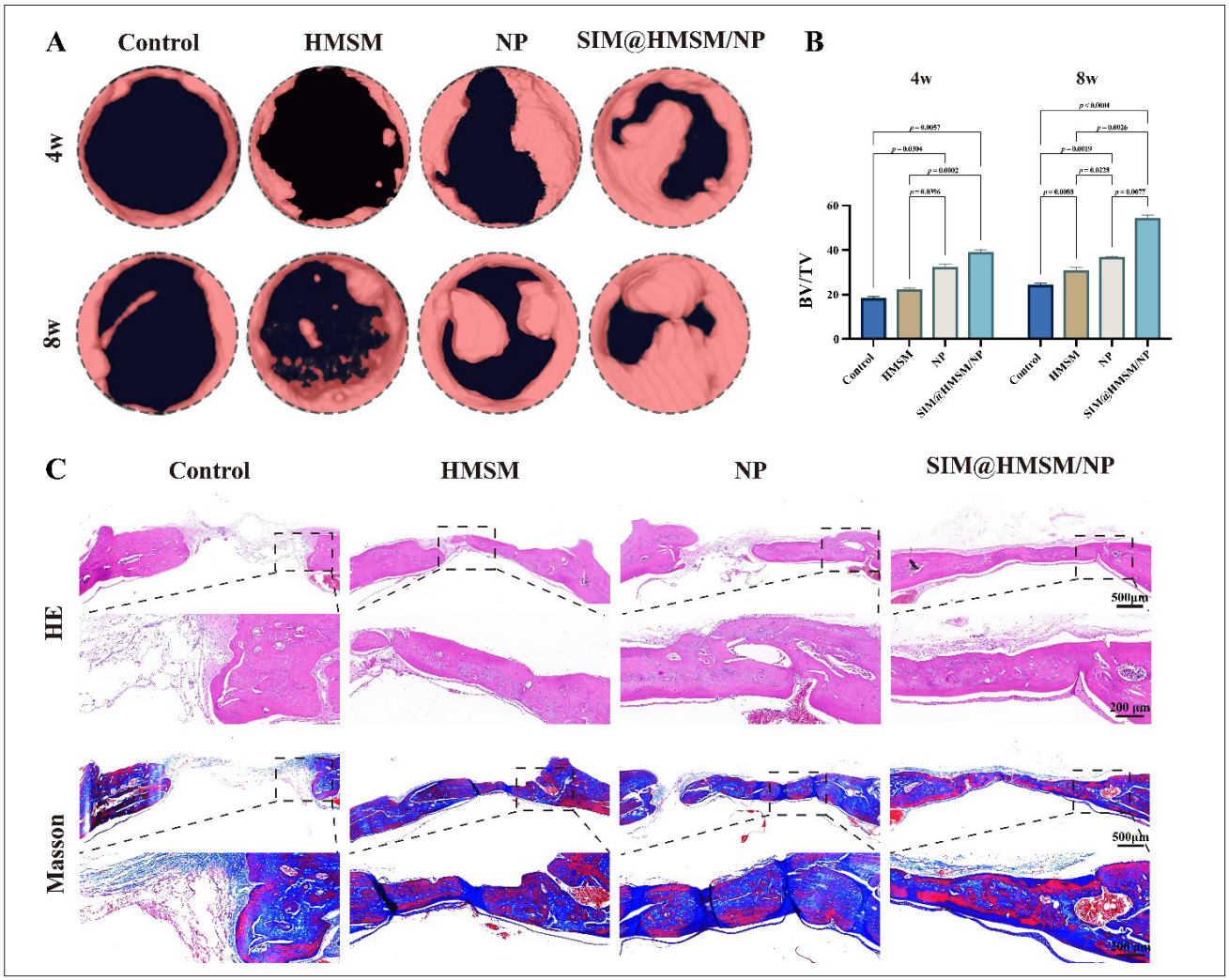


Figure 6 *In vivo* bone regeneration in rat calvarial defects treated with different materials. (A) Three-dimensional micro-CT reconstruction images of cranial bone defects at 4 and 8 weeks post-implantation in different treatment groups (control, HMSM, NP, and SIM@HMSM/NP). The SIM@HMSM/NP group exhibited markedly enhanced bone formation and defect bridging compared with other groups. (B) Quantitative analysis of BV/TV derived from micro-CT data, showing significantly higher bone regeneration in the SIM@HMSM/NP group than in the HMSM, NP, and control groups ($p < 0.001$). (C) Representative histological sections stained with H&E and Masson's trichrome at 8 weeks. H&E staining revealed abundant new bone trabeculae and well-integrated bone tissue in the SIM@HMSM/NP group, while Masson's staining confirmed dense collagen deposition and mature bone matrix formation. Scale bars: 200 and 500 μm; magnifications: 20× & 2×. Data are presented as mean ± standard deviation. For each group at each time point, $n = 6$ independent biological replicates were analyzed. Abbreviations: CT, computed tomography; HMSM, hydroxyethyl methacrylate/sulfobetaine methacrylate; NP, nano-hydroxyapatite/polylactic acid; SIM, simvastatin; BV/TV, bone volume fraction; H&E, hematoxylin and eosin; SIM, simvastatin.

near-complete bridging of the defect area by week 8. Quantitative micro-CT analysis revealed that the BV/TV in the SIM@HMSM/NP group was significantly higher than in the other groups at both 4 and 8 weeks ($p < 0.001$) (Figure 6B). These findings indicate that the incorporation of SIM markedly enhanced osteogenesis within the composite scaffold, consistent with its known ability to stimulate BMP-2 expression and activate the Runx-2 pathway. Histological staining further corroborated the imaging results. H&E staining revealed extensive formation of new trabecular bone with a well-organized structure in the SIM@HMSM/NP group, while the control and single-material groups showed only partial repair (Figure 6C). Masson's trichrome staining exhibited dense blue-stained collagen fibers and well-mineralized bone tissue in the SIM@HMSM/NP group, confirming active matrix deposition and tissue maturation.

Collectively, these results demonstrate that the SIM@HMSM/NP not only accelerates bone defect healing but also promotes the formation of mature, vascularized bone tissue, validating its potential for clinical application in bone regeneration. It is worth noting that while the current study demonstrated significant bone regeneration and near-complete defect bridging within 8 weeks, the complete remodeling of the calvarial defect may require a longer observation period. Future studies should extend the *in vivo* evaluation to 12 or 16 weeks to further investigate the long-term degradation behavior of the scaffold and the complete maturation process of the regenerated bone tissue.

3.6. Angiogenic and osteogenic coupling within regenerated bone tissue

Recent advances highlight that effective bone regeneration relies not only on osteogenic differentiation but also on coordinated vascularization, a process defined as angiogenic–osteogenic coupling.[37,38] For example, SIM-loaded scaffolds have been shown to simultaneously enhance new bone formation and neovascularization *in vivo*.[39] Scaffold designs that integrate angiogenic cues and osteogenic cues are thus emerging as a key strategy in bone tissue engineering.[40] To elucidate the interplay between angiogenesis and osteogenesis during bone repair, immunofluorescence staining for CD31 and Col-I was conducted on calvarial sections harvested at 8 weeks (Figure 7). In the control and single-material groups (HMSM and NP), only sparse CD31-positive vessels were observed within the defect area, suggesting limited

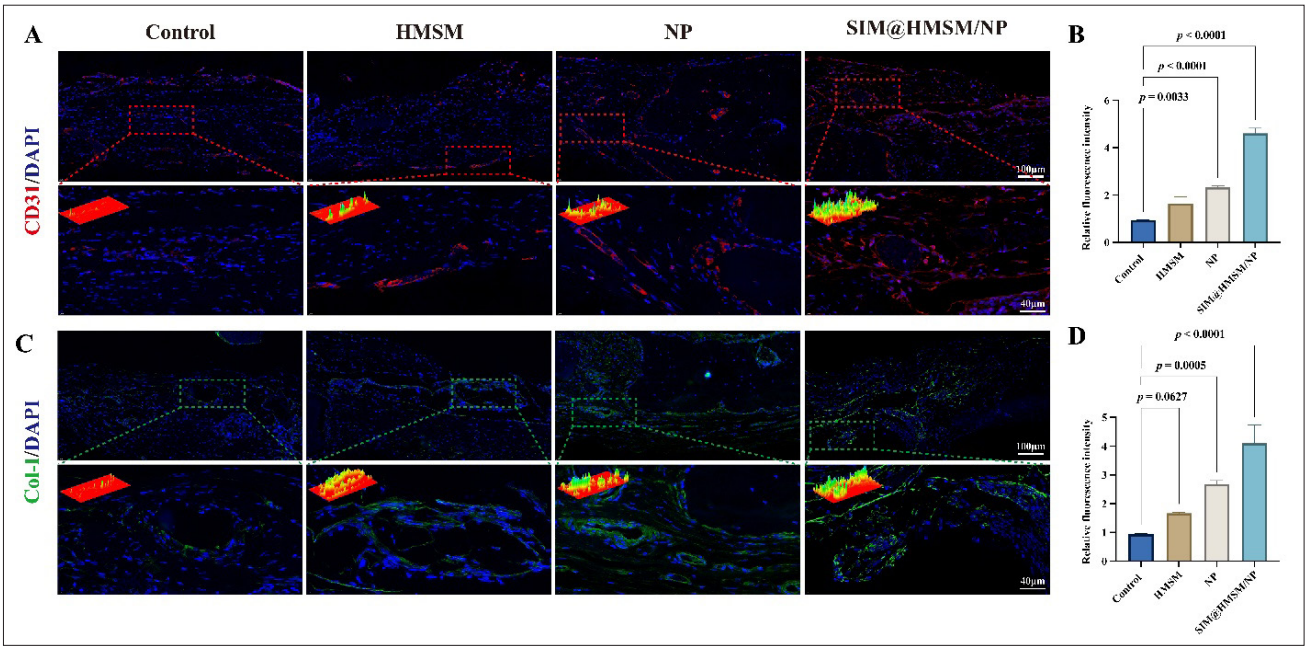


Figure 7. Immunofluorescence analysis of angiogenesis and bone matrix formation in regenerated calvarial tissue. (A) Representative immunofluorescence images of cranial defect sections stained for the vascular endothelial marker CD31 (red), with cell nuclei counterstained by DAPI (blue), showing neovascular distribution in different groups (control, HMSM, NP, and SIM@HMSM/NP). Scale bars: 40 & 100 μm; magnifications: 100× & 40×. (B) Quantitative analysis of relative CD31 fluorescence intensity. (C) Immunofluorescence staining of Col-I (green) with DAPI (blue), illustrating collagen deposition and bone matrix formation in the regenerated tissue. Scale bars: 40 & 100 μm; magnifications: 100× & 40×. (D) Quantitative analysis of relative Col-I fluorescence intensity. Data are presented as mean ± SD ($n = 6$), and statistical significance was determined by one-way analysis of variance. Abbreviations: CD, cluster of differentiation; Col-I, collagen type 1; DAPI, 4',6-diamidino-2-phenylindole; HMSM, hydroxyethyl methacrylate/sulfobetaine methacrylate; NP, nano-hydroxyapatite/polylactic acid; SIM, simvastatin.

neovascularization. In contrast, the SIM@HMSM/NP group exhibited extensive CD31 expression surrounding newly formed bone trabeculae, indicating the formation of a dense microvascular network that supports active tissue regeneration. Similarly, Col-I staining revealed markedly enhanced collagen deposition in the SIM@HMSM/NP group compared with the other groups, reflecting vigorous extracellular matrix production and maturation of regenerated bone tissue. The 3D fluorescence intensity analysis confirmed that both CD31 and Col-I signals were significantly upregulated in the SIM@HMSM/NP group, consistent with the micro-CT and histological results (Figures 6A–C).

These findings demonstrate that the SIM@HMSM/NP effectively promotes osteogenic–angiogenic coupling—a critical process for successful bone regeneration. The sustained release of SIM likely plays a dual regulatory role by upregulating vascular endothelial growth factor and BMP-2 pathways, thereby stimulating endothelial cell proliferation and osteoblast differentiation simultaneously. This coordinated effect enhances nutrient supply, matrix deposition, and tissue integration, collectively accelerating defect healing and functional bone restoration.

The SIM@HMSM/NP group exhibited significantly higher CD31 and Col-I expression compared with the other groups, indicating enhanced angiogenesis and bone matrix formation.

4. Conclusion

In recent years, increasing attention has been paid to advanced hydrogel systems for bone regeneration, including injectable and self-healing hydrogels, supramolecular hydrogels, and shape–memory hydrogels fabricated by 3D printing. These systems enable minimally invasive delivery, dynamic structural adaptation, and programmable drug release behavior, showing great potential for accelerating bone repair.[41] In this study, a novel SIM@HMSM/NP integrating a zwitterionic HMSM hydrogel with a 3D-printed NP scaffold was successfully developed for bone defect repair. The hydrogel component provided excellent biocompatibility, sustained drug release, and favorable water retention, while the NP scaffold offered mechanical stability and osteoconductivity. The incorporation of SIM further endowed the composite with osteoinductive and angiogenic properties, facilitating synergistic regulation of bone regeneration. *In vitro* analyses demonstrated that the SIM@HMSM/NP exhibited superior mechanical performance, controlled degradation, and sustained drug release, effectively promoting BMSC proliferation and osteogenic differentiation. In *in vivo* models, the SIM@HMSM/NP scaffold significantly enhanced new bone formation and collagen matrix deposition while simultaneously stimulating neovascularization within the defect area. These findings confirm that the integration of bioactive hydrogel and 3D-printed scaffold achieves a desirable balance between biodegradability, mechanical support, and biological activity.

Overall, this work provides a versatile strategy for the design of multifunctional scaffolds that enable osteogenic–angiogenic coupling and efficient bone defect repair. The SIM@HMSM/NP holds strong potential for future translational applications in bone tissue engineering and regenerative medicine.

Acknowledgments

None.

Funding

This study was supported by the Taishan Scholar Project of Shandong Province (No. tstp20250511).

Conflict of interest

The authors declare they have no competing interests.

Author contributions

Conceptualization: Jianyi Li; Yukun Du
Data curation: Yang Qu; Ya-nan Wang
Formal analysis: Yang Qu; Ya-nan Wang; Weiqing Kong; Xiaofan Du
Funding acquisition: Yongming Xi
Investigation: Yang Qu; Ya-nan Wang; Guanghui Gu
Methodology: Yang Qu; Ya-nan Wang
Project administration: Jianyi Li; Yukun Du
Supervision: Jianyi Li; Yukun Du; Guanghui Gu
Writing – original draft: Yang Qu; Ya-nan Wang
Writing – review & editing: Jianyi Li; Yukun Du
All authors have read and approved the final version of the manuscript.

Ethics approval and consent to participate

All animal procedures were reviewed and approved by the Laboratory Animal Management and Ethics Committee of Qingdao University (Approval No. 20220910) and conducted in accordance with the Guidelines for the Care and Use of Laboratory Animals (National Research Council, United States of America) and the Guidelines for the Ethical Review of Experimental Animals in the People's Republic of China (GB/T 35892-2018).

Consent for publication

Not applicable.

Availability of data

The data that support the findings of this study are available from the corresponding author upon reasonable request.

References

1. Xu JL, Bao G, Jia B, *et al*. An adaptive biodegradable zinc alloy with bidirectional regulation of bone homeostasis for treating fractures and aged bone defects. *Bioact Mater*. 2024;38:207-224. doi: 10.1016/j.bioactmat.2024.04.027
2. Kim J, Park S, Park JY, *et al*. Dual-phase blocks for regeneration of critical-sized bone defects. *Nano Today*. 2024;54:102120. doi: 10.1016/j.nantod.2023.102120
3. Lee J, Byun H, Madhurakkat Perikamana SK, Lee S, Shin H. Current advances in immunomodulatory biomaterials for bone regeneration. *Adv Healthc Mater*. 2019;8(4):e1801106. doi: 10.1002/adhm.201801106
4. Yuan B, Cheng Q, Zhao R, *et al*. Comparison of osteointegration property between PEKK and PEEK: effects of surface structure and chemistry. *Biomaterials*. 2018;170:116-126. doi: 10.1016/j.biomaterials.2018.04.014
5. Wang JC, Dou ZL, Xia L, Huang N. Metal-organic complex coating for enhanced corrosion control and biocompatibility on biodegradable magnesium alloy for orthopaedic implants. *J Mat Chem B*. 2024;12(23):5661-5677. doi: 10.1039/d4tb00347k
6. Hama R, Ulziibayar A, Reinhardt JW, Watanabe T, Kelly J, Shinoka T. Recent developments in biopolymer-based hydrogels for tissue engineering applications. *Biomolecules*. 2023;13(2):280. doi: 10.3390/biom13020280
7. Cao H, Duan L, Zhang Y, Cao J, Zhang K. Current hydrogel advances in physicochemical and biological response-driven biomedical application diversity. *Signal Transduct Target Ther*. 2021;6(1):426. doi: 10.1038/s41392-021-00830-x
8. Huang QT, Zou YJ, Arno MC, *et al*. Hydrogel scaffolds for differentiation of adipose-derived stem cells. *Chem Soc Rev*. 2017;46(20):6255-6275. doi: 10.1039/c6cs00052e
9. Gu GH, Cui ZC, Du XF, *et al*. Recent advances in biomacromolecule-reinforced 2D material (2DM) hydrogels: from interactions, synthesis, and functionalization to biomedical applications. *Adv Funct Mater*. 2024;34(48):8367. doi: 10.1002/adfm.202408367
10. Tzoumani I, Iatridi Z, Fidelli A, Krassa P, Kallitsis J, Bokias G. Room-temperature self-healable blends of waterborne polyurethanes with 2-hydroxyethyl methacrylate-based polymers. *Int J Mol Sci*. 2023;24(3):2575. doi: 10.3390/ijms24032575
11. He X, He S, Xiang G, *et al*. Precise lubrication and protection of cartilage damage by targeting hydrogel microsphere. *Adv Mater*. 2024;36(40):2405943. doi: 10.1002/adma.202405943
12. Rodzen K, O'Donnell E, Hasson F, *et al*. Advanced 3D printing of polyetherketoneketone hydroxyapatite composites via fused filament fabrication with increased interlayer connection. *Materials (Basel)*. 2024;17(13):3161. doi: 10.3390/ma17133161
13. Derby B. Printing and prototyping of tissues and scaffolds. *Science*. 2012;338(6109):92-926. doi: 10.1126/science.1226340
14. Shafiee A, Atala A. Printing technologies for medical applications. *Trends Mol Med*. 2016;22(3):254-265. doi: 10.1016/j.molmed.2016.01.003
15. Li JY, Li KK, Du YK, *et al*. Dual-nozzle 3D printed nano-hydroxyapatite scaffold loaded with vancomycin sustained-release microspheres for enhancing bone regeneration. *Int J Nanomedicine*. 2023;18:307-322. doi: 10.2147/IJN.S394366
16. Rajabi M, McConnell M, Cabral J, Ali MA. Chitosan hydrogels in 3D printing for biomedical applications. *Carbohydr Polym*. 2021;260:117768. doi: 10.1016/j.carbpol.2021.117768
17. Vijayavenkataraman S, Yan WC, Lu WF, Wang CH, Fuh JYH. 3D bioprinting of tissues and organs for regenerative medicine. *Adv Drug Deliv Rev*. 2018;132:296-332. doi: 10.1016/j.addr.2018.07.004
18. Mandrycky C, Wang ZJ, Kim K, Kim DH. 3D bioprinting for engineering complex tissues. *Biotechnol Adv*. 2016; 34(4):422-434. doi: 10.1016/j.biotechadv.2015.12.011
19. Anada T, Pan CC, Stahl AM, *et al*. Vascularized bone-mimetic hydrogel constructs by 3D bioprinting to promote osteogenesis and angiogenesis. *Int J Mol Sci*. 2019;20(5):1096. doi: 10.3390/ijms20051096
20. Duarte JA, de Barros ALB, Leite EA. The potential use of simvastatin for cancer treatment: a review. *Biomed Pharmacother*. 2021;141:111858. doi: 10.1016/j.biopha.2021.111858
21. Yao X, Xie R, Cao Y, *et al*. Simvastatin induced ferroptosis for triple-negative breast cancer therapy. *J Nanobiotechnol*. 2021;19(1):311. doi: 10.1186/s12951-021-01058-1
22. Sun TT, Huang J, Zhang W, *et al*. Simvastatin-hydroxyapatite coatings prevent biofilm formation and improve bone

formation in implant-associated infections. *Bioact Mater*. 2023;21:44-56.
doi: 10.1016/j.bioactmat.2022.07.028

23. Chiu KY, Huang JY, Su YH, Ou SF, Chen KK, Wang YH. A 3D-printed bioactive glass scaffold coated with sustained-release PLGA/simvastatin stimulates calvarial bone repair. *Mater Des*. 2024;241:112898.
doi: 10.1016/j.matdes.2024.112898

24. Dai BY, Li X, Xu JK, *et al*. Synergistic effects of magnesium ions and simvastatin on attenuation of high-fat diet-induced bone loss. *Bioact Mater*. 2021;6(8):2511-2522.
doi: 10.1016/j.bioactmat.2021.01.027

25. Chiu KY, Huang JY, Su YH, Ou SF, Chen KK, Wang YH. A 3D-printed bioactive glass scaffold coated with sustained-release PLGA/simvastatin stimulates calvarial bone repair. *Mater Des*. 2024;241:112898.
doi: 10.1016/j.matdes.2024.112898

26. Zhen J, Wan T, Sun G, Chen X, Zhang S. A ROS-responsive microsphere capsule encapsulated with NADPH oxidase 4 inhibitor ameliorates macrophage inflammation and ferroptosis. *Heliyon*. 2024;10(1):e23589.
doi: 10.1016/j.heliyon.2023.e23589

27. Liu XF, Gaihre B, Park S, *et al*. 3D-printed scaffolds with 2D hetero-nanostructures and immunomodulatory cytokines provide pro-healing microenvironment for enhanced bone regeneration. *Bioact Mater*. 2023;27:216-230.
doi: 10.1016/j.bioactmat.2023.03.021

28. Gu GH, Xu YY, He P, *et al*. Bioinspired composite hydrogels with osteogenic, angiogenic, and antioxidant properties for enhanced bone repair. *Small Struct*. 2025;6(4):2400462.
doi: 10.1002/sstr.202400462

29. Çetin D, Kahraman AS, Gümüsderelioglu M. Novel scaffolds based on poly(2-hydroxyethyl methacrylate) superporous hydrogels for bone tissue engineering. *J Biomater Sci Polym Ed*. 2011;22(9):1157-1178.
doi: 10.1163/092050610x501704

30. Moura D, Pereira AT, Ferreira HP, *et al*. Poly(2-hydroxyethyl methacrylate) hydrogels containing graphene-based materials for blood-contacting applications: from soft inert to strong degradable material. *Acta Biomater*. 2023;164:253-268.
doi: 10.1016/j.actbio.2023.04.031

31. Kim S, Shin BH, Yang C, *et al*. Development of poly(HEMA-Am) Polymer hydrogel filler for soft tissue reconstruction by facile polymerization. *Polymers*. 2018;10(7):772.
doi: 10.3390/polym10070772

32. Gao F, Xu ZY, Liang QF, *et al*. Direct 3D printing of high strength biohybrid gradient hydrogel scaffolds for efficient repair of osteochondral defect. *Adv Funct Mater*. 2018;28(13):1706644.
doi: 10.1002/adfm.201706644

33. Wang LL, Chen X, Wang XY, *et al*. Bio-inspired mineralized collagen scaffolds with precisely controlled gradients for the treatment of severe osteoarthritis in a male rabbit model. *Int J Biol Macromol*. 2025;300:139843.
doi: 10.1016/j.ijbiomac.2025.139843

34. Pathmanapan S, Periyathambi P, Anandasadagopan SK. Fibrin hydrogel incorporated with graphene oxide functionalized nanocomposite scaffolds for bone repair — in vitro and in vivo study. *Nanomed*. 2020;29:102251.
doi: 10.1016/j.nano.2020.102251

35. Xue X, Hu Y, Deng YH, Su JC. Recent advances in design of functional biocompatible hydrogels for bone tissue engineering. *Adv Funct Mater*. 2021;31(19):2009432.
doi: 10.1002/adfm.202009432

36. Zhou D, Yan X, Xiao L, Wang JL, Wei JC. Gold capped mesoporous bioactive glass guides bone regeneration via BMSCs recruitment and drug adaptive release. *Chem Eng J*. 2024;487:150546.
doi: 10.1016/j.cej.2024.150546

37. Jang HJ, Yoon JK. The role of vasculature and angiogenic strategies in bone regeneration. *Biomimetics*. 2024;9(2):75.
doi: 10.3390/biomimetics9020075

38. Schott NG, Friend NE, Stegemann JP. Coupling osteogenesis and vasculogenesis in engineered orthopedic tissues. *Tissue Eng Part B Rev*. 2021;27(3):199-214.
doi: 10.1089/ten.teb.2020.0132

39. Yu WL, Sun TW, Qi C, *et al*. Enhanced osteogenesis and angiogenesis by mesoporous hydroxyapatite microspheresderived simvastatin sustained release system for superior bone regeneration. *Sci Rep*. 2017;7:44129.
doi: 10.1038/srep44129

40. Saberi A, Kouhjani M, Mohammadi M, Hosta-Rigau L. Novel scaffold platforms for simultaneous induction osteogenesis and angiogenesis in bone tissue engineering: a cutting-edge approach. *J Nanobiotechnol*. 2023;21(1):351.
doi: 10.1186/s12951-023-02115-7

41. Pan Q, Zong Z, Li H, *et al*. Hydrogel design and applications for periodontitis therapy: a review. *Int J Biol Macromol*. 2025;284:137893.
doi: 10.1016/j.ijbiomac.2024.137893

ACCSCIENCE PUBLISHING

International Journal of Bioprinting

RESEARCH ARTICLE

Construction of gelatin methacryloyl-based artificial skin substitutes with "small-micro" vascular networks via hybrid double-crosslinked coaxial and extrusion bioprinting

Yichen Luo[1,2], Dan Li[3], Cai Lin[4], Bin Zhang[1,2*], Hao Ding[5,6*] and Xue Zhou[1,2*]

[1]State Key Laboratory of Fluid Power and Mechatronic Systems, Zhejiang University, Hangzhou, Zhejiang 310058, China

[2]School of Mechanical Engineering, Zhejiang University, Hangzhou, Zhejiang 310058, China

[3]Department of Electro-Hydraulic Technology and Equipment Research Center, Binhai Industrial Technology Research Institute, Zhejiang University, Tianjin 300457, China

[4]Department of Burn, The First Affiliated Hospital of Wenzhou Medical University, Wenzhou, Zhejiang 325000, China

[5]Department of Cardiology, The Second Affiliated Hospital, School of Medicine, Zhejiang University, Hangzhou, Zhejiang 310009, China

[6]Cardiovascular Key Laboratory of Zhejiang Province, The Second Affiliated Hospital, School of Medicine, Zhejiang University, Hangzhou, Zhejiang 310009, China

(This article belongs to the *Special Issue*: *Biofabrication Breakthroughs: Innovation and Application in Bioprinting, Biomaterials, and Organoid*)

Abstract

The repair of deep skin defects involving subcutaneous tissue urgently requires vascularized skin substitutes that can provide immediate blood perfusion. However, existing engineering strategies struggle to construct multi-level vascular networks *in vitro*. This study aims to develop a multi-layered skin substitute with both biomimetic structure and physiological function, incorporating a perfusable "small-micro" hierarchical vascular system. We employed a composite coaxial–extrusion bioprinting strategy. First, a composite bioink consisting of 2% sodium alginate and 5% gelatin methacryloyl was formulated and evaluated for its printability and biocompatibility. Subsequently, using an ionic-photo dual-crosslinking coaxial printing technique, we fabricated subcutaneous small vessels with controllable dimensions and adequate mechanical properties. Finally, small vessels were integrated with an extrusion bioprinted dermal microvascular network and an epidermal layer to form a complete "small-micro" vascular pathway. This multi-layered construct was designed to mimic the stratified characteristics of natural skin. *In vitro* functional experiments confirmed that the epidermis possesses an excellent barrier function, and the subcutaneous small vessels demonstrated an effective capability for delivering drug molecules. The dual-crosslinking coaxial printing and composite manufacturing strategy proposed in this proof-of-concept study successfully constructed vascularized skin with a hierarchical tubular structure, offering a new solution with clinical translation potential for treating full-thickness skin defects.

***Corresponding authors:**
Xue Zhou
(zhouxue@zju.edu.cn)

Hao Ding
(11818166@zju.edu.cn)

Bin Zhang
(zbzju@zju.edu.cn)

Citation: Luo Y, Li D, Lin C, Zhang B, Ding H, Zhou X. Construction of gelatin methacryloyl-based artificial skin substitutes with "small-micro" vascular networks via hybrid double-crosslinked coaxial and extrusion bioprinting. *Int J Bioprint*. 2026;12(1):672-688. doi: 10.36922/IJB025490504

Received: December 2, 2025
Revised: January 5, 2026
Accepted: January 12, 2026
Published online: January 16, 2026

Copyright: © 2026 Author(s). This is an Open Access article distributed under the terms of the Creative Commons Attribution License, permitting distribution, and reproduction in any medium, provided the original work is properly cited.

Publisher's Note: AccScience Publishing remains neutral with regard to jurisdictional claims in published maps and institutional affiliations.

***Keywords*:** Artificial skin; Blood vessel; Coaxial printing; Gelatin methacryloyl; Three-dimensional bioprinting

1. Introduction

Deep tissue defects in the human body typically involve the loss of the epidermis and dermis, as well as damage to or absence of subcutaneous structures, including blood vessels, nerves, and the muscle layer.[1,2] The lack of functional vascular networks in traditional grafts leads to low graft survival rates, delayed healing, and impaired function in the damaged area.[3,4] Addressing these challenges requires the development of advanced skin substitutes featuring a multi-layered, vascularized structure that can restore the anatomical and physiological properties of the damaged tissue.

Recent advancements in bioprinting have offered promise for constructing complex tissues.[5] Various three-dimensional (3D) bioprinting modalities now enable the precise fabrication of biomimetic artificial skin structures. These techniques could effectively replicate the stratified epidermis–dermis architecture of native skin and integrate functional components such as vascular networks.[6–8] This diverse technological landscape has significantly expanded applications in wound healing and drug testing.[9,10] Among the materials used, gelatin methacryloyl (GelMA)[11] is widely employed as a core matrix material due to its excellent biocompatibility and tunable physical properties.[12,13] Sodium alginate (SA),[14] renowned for its rapid ionic crosslinking capability, effectively enhances the immediate shape fidelity and mechanical stability of printed structures.[15,16] Their excellent hydrophilicity and biocompatibility help regulate the local microenvironment, creating favorable conditions for cell growth and tissue regeneration.[17] Utilizing these materials, researchers have successfully created skin models mimicking the epidermis–dermis structure via techniques such as extrusion[13,18] and photopolymerization,[12,19] and have attempted to incorporate pre-vascularized components.[6,20,21]

Current mainstream strategies for introducing vascular structures into skin substitutes primarily fall into three categories. The pre-vascularization approach involves co-printing vascular endothelial cells with fibroblasts and other supporting cells within a blended bioink, relying on their self-assembly capability *in vivo* or *in vitro* to form microvascular networks.[22,23] For instance, Nuutila *et al.*[24] used a handheld bioprinter to deposit vascular endothelial growth factor (VEGF)-containing GelMA ink directly onto wounds, significantly promoting wound healing and neovascularization. A second approach leverages endothelial self-assembly by creating a permissive microenvironment within the printed dermal layer, enabling spontaneous lumen formation.[7,20] Choi *et al.*[12] used silk fibroin–gelatin ink for digital light processing printing to construct a pre-vascularized layer containing human umbilical vein endothelial cells (HUVECs) and human dermal fibroblasts, demonstrating cell proliferation within the ink. A third approach creates channels via sacrificial materials or coaxial printing. In sacrificial printing, a removable template (e.g., gelatin) is printed and later removed to form conduits that are endothelialized[8,25]; alternatively, coaxial printing can directly construct hollow tubular structures.[26] Thomas *et al.*[27] used projection stereolithography to simultaneously print a degradable sacrificial ink and hyaluronic acid methacrylate bioink, forming perfusable channels lined with HUVECs with a diameter of up to 360 μm. Ramasamy *et al.*[28] embedded a 3D-printed polycaprolactone mesh within acellular collagen and then sequentially printed bioinks containing human dermal fibroblasts and human adult keratinocytes to construct a full-thickness skin equivalent.

However, these strategies generally share two major limitations. Firstly, pre-vascularization often relies on the spontaneous tubulogenesis of endothelial cells within hydrogels, making it difficult to form structurally stable, dimensionally controllable subcutaneous small vessels *in vitro* that meet the requirements for surgical anastomosis with host vasculature. Secondly, they lack a hierarchical design mimicking the architecture of the native cutaneous vascular system, thereby struggling to achieve graded perfusion from small vessels to microvessels. This ultimately limits their efficacy in repairing deep defects.

To overcome these bottlenecks, this study proposes an innovative hybrid bioprinting strategy. Building upon our previously published multi-material extrusion printing technology,[29] we investigated and integrated coaxial printing methods to construct a multi-layered skin substitute featuring a "small-micro" hierarchical vascular network. Specifically, this study employs coaxial printing combined with an ionic-photo dual-crosslinking mechanism to precisely fabricate subcutaneous small vessels with excellent mechanical strength. A T-shaped microvascular network is designed within the dermal layer via extrusion printing, serving as a bridge connecting the small vessels to the superficial tissue. The ultimate goal is to integrate and validate the functional performance of a full-thickness skin model with multi-level vascular

networks. This strategy aims to develop and validate a hybrid bioprinting strategy for the integrated fabrication of a multi-layered skin substitute that incorporates a perfusable, hierarchical vascular network prototype, thereby restoring its crucial barrier and nutrient transport functions, providing the structural foundation for subsequent functional maturation.

2. Materials and methods

2.1. Preparation of vascular hydrogel inks and flowability measurement

Based on previous research findings,[30] 2% SA (Sigma-Aldrich, USA) and 5% GelMA (Sigma-Aldrich, USA) were identified as the optimal concentrations for formability and biocompatibility, respectively. Accordingly, five groups of hybrid hydrogels were prepared with the following compositions: 1% SA/5% GelMA, 2% SA/5% GelMA, 3% SA/5% GelMA, 2% SA/3% GelMA, and 2% SA/10% GelMA. The rheological properties of the hybrid hydrogel samples were measured using an MCR302 rotational rheometer (Anton Paar, Austria). The storage modulus (G′) and loss modulus (G″) were determined under conditions of a fixed frequency of 1 Hz and a temperature decreasing from 40°C to 4°C at a rate of 5°C/min. Additionally, the influence of temperature on viscosity was recorded as the temperature varied from 40°C to 4°C at a fixed shear rate of 50/s.

2.2. Cell culture

HUVECs (Cell Bank of the Chinese Academy of Sciences, China) and human foreskin fibroblasts (Fenghui Bio, China) were cultured in Dulbecco's Modified Eagle Medium/Nutrient Mixture F-12 (Gibco, USA) supplemented with 10% fetal bovine serum (Gibco, USA) and 1% penicillin/streptomycin. Human epidermal keratinocytes (KCs, Fenghui Bio, China) were cultured in defined keratinocyte serum-free medium (Gibco, USA) supplemented with epidermal growth factor (EGF) and bovine pituitary extract. All cells were maintained at 37°C under 5% carbon dioxide. HUVECs and HFF-1 were routinely passaged in tissue culture flasks and discarded after 8 and 12 passages, respectively. Primary KCs were used between passages 2 and 4 to ensure the retention of their proliferative and differentiation potential. The culture medium was changed every 2 days, and the cells were passaged when they reached 80%–90% confluence.

2.3. Biocompatibility of sodium alginate/gelatin methacryloyl composite hydrogels

The SA/GelMA bioinks (1%/5%, 2%/5%, 3%/5%, 2%/3%, 2%/10%) were prepared and uniformly coated into well plates. After complete crosslinking via immersion in calcium chloride solution and exposure to 405 nm light, endothelial cell suspensions of equal concentration and volume were added onto the material surfaces. Cell status on the material surface was observed after 7 days of incubation. SA/GelMA bioinks (1%/5%, 2%/5%, 3%/5%, 2%/3%, 2%/10%) loaded with green fluorescent protein-labeled HUVECs (1×10^6 cells/mL) were prepared. The bioinks were first ionically crosslinked by immersion in calcium chloride ($CaCl_2$; Sigma-Aldrich, USA), followed by complete photocuring under 405 nm light. Subsequently, the samples were immersed in a 20 mM ethylenediaminetetraacetic acid (EDTA; Gibco, USA) solution for 5 min to thoroughly degrade the SA component. After washing three times with complete culture medium to remove EDTA, the samples were incubated for 7 days, and cell spreading behavior was observed.

2.4. Simulation analysis of the flow field inside the coaxial printing nozzle

During the coaxial printing process, Fluent software (ANSYS 2022 R1, USA) was used to simulate the inner and outer flow channels separately to analyze fluid flow behavior. To simplify the simulation, the following assumptions were made regarding the fluid flow characteristics:

i The ink conforms to mass conservation, i.e., it is an incompressible fluid.

ii The fluid state is laminar, with a no-slip and no-penetration condition relative to the channel walls.

iii The inertial forces during flow are neglected.

A coaxial nozzle assembly consisting of an inner 22G needle (inner diameter 0.40 mm, outer diameter 0.45 mm) and an outer 17G needle (inner diameter 1.07 mm) was selected as the simulation object. The inner and outer flow channel models were constructed in SolidWorks 2021 (Dassault Systèmes, USA) and imported into Fluent for tetrahedral meshing. The ink was modeled as 2% SA, and the crosslinker as an aqueous $CaCl_2$ solution. The multiphase volume of fluid method was employed for solving the flow field.

2.5. Analysis and optimization of coaxial printing process parameters

A composite hydrogel consisting of 2% SA and 5% GelMA was prepared and printed using four nozzle combinations (G11–G15, G13–G18, G15–G20, and G17–G22; Shenzhen Deli Precision Technology Co., Ltd., China). A 0.5% $CaCl_2$ solution was used for ionic crosslinking, with the flow rates for both the inner and outer channels controlled at 2 mL/min. Apart from nozzle specifications, the influence of material flow rate can be divided into two aspects: the absolute flow rate values and their ratio. The G17–G22

nozzle combination, which met the diameter requirements for constructing small vessels, was selected for further printing tests. The flow rates for the inner and outer channels were sequentially decreased starting from 2 mL/min. Regarding the hydrogel-to-$CaCl_2$ flow rate ratio parameter, this factor alters the printed lumen structure by influencing the anti-collapse relationship between the two phases, with its effect being more pronounced at lower flow rates. Printing tests were conducted using the following hydrogel-to-$CaCl_2$ flow rate ratios: 0.5:1, 0.5:0.1, 0.5:0.3, 0.5:0.5, and 0.7:0.1 mL/min.

2.6. Construction of the small vessel intima

The subcutaneous small vessel consists of a bilayered structure comprising the vascular endothelium and the vascular wall, which cannot be achieved by coaxial printing alone. In this study, the lumen surface of the printed small vessel was first coated with Matrigel (Corning, USA). Subsequently, an endothelial cell suspension was injected into the lumen using a syringe. The vessel was positioned horizontally to allow the endothelial cells to settle and adhere to the inner wall of the vessel. The vessel was then rotated 90° every 5 min, repeating this process 5–10 times, before being transferred to a culture dish for incubation. Following this, the printed small vessel was embedded in 5% (w/v) GelMA containing HFF-1 cells to construct a tissue block containing the vascular structure. After 10 days of culture, the samples were embedded, sectioned, and characterized to assess the cross-sectional morphology of the printed small vessels.

2.7. Integrated construction of the multi-layered vascularized skin substitute

To achieve the integrated construction of the multi-layered vascularized skin, this study was based on the extrusion-based 3D bioprinting system (design principle shown in Figure S1) from previous research,[29] and integrated the coaxial printing nozzle into the printing system, as shown in Figure 1. The material supply for this nozzle is independently controlled by syringe pumps (Leadfluid, China) and shares the *XY*-axis system with conventional extrusion printheads, allowing for the one-step printing of multi-layered, vascularized skin substitutes. A 5% GelMA hydrogel containing HFF-1 (1×10^6 cells/mL) was printed as the subcutaneous layer. Small vessel structures containing HUVECs (1×10^6 cells/mL) were fabricated via coaxial printing. Subsequently, a 5% GelMA hydrogel containing HFF-1 cells was printed above this to construct the dermal

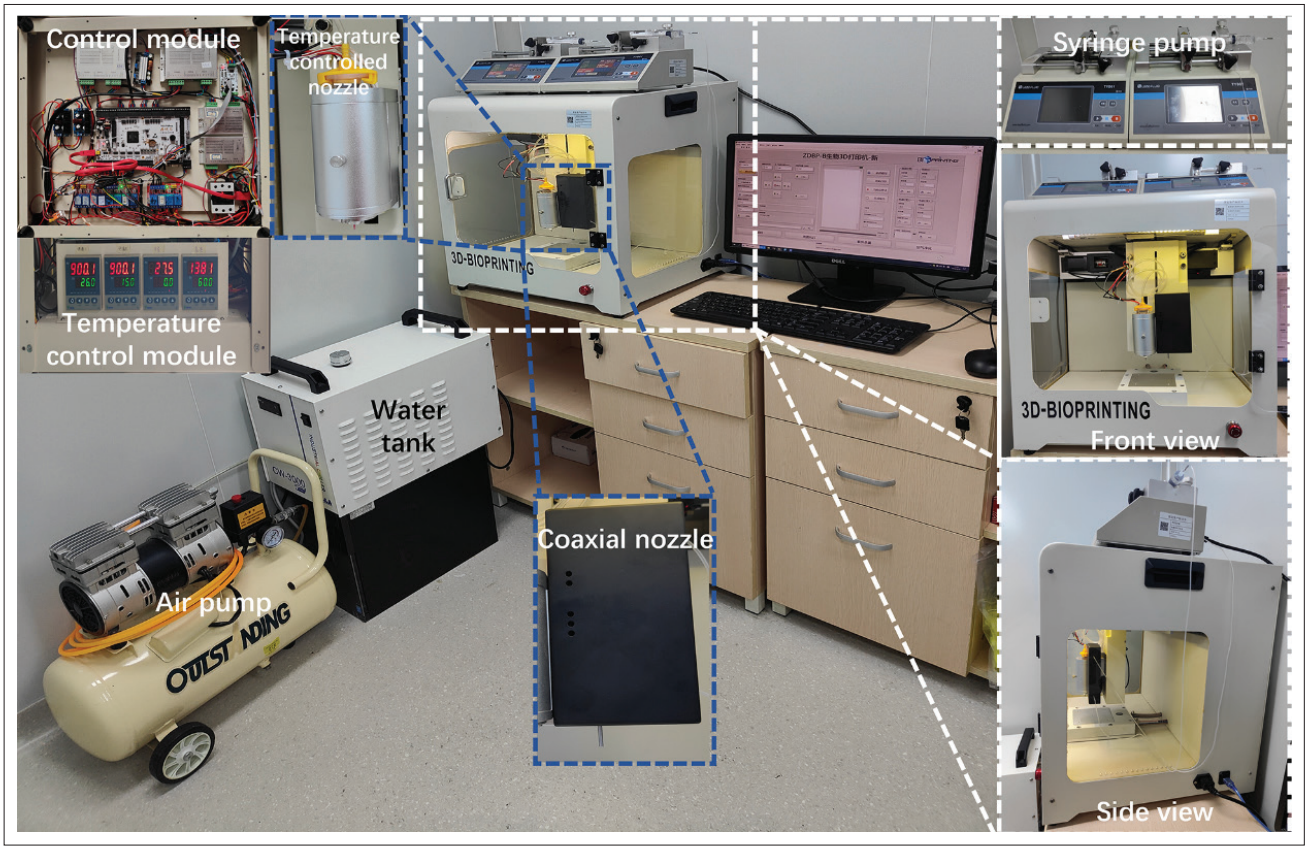


Figure 1. Composite construction system for the multi-layered vascularized skin substitute.

reticular layer. A 3% GelMA hydrogel containing HUVECs was extrusion-printed to form a microvascular network in the T-shaped papillary layer, serving as a bridge connecting the small vessels and the epidermis. Finally, a thin layer of 20% GelMA was printed as the epidermal base, onto which keratinocytes were seeded, while HUVECs were cultured within the vascular lumen.

2.8. Cell viability and morphology assessment

The HFF-1 cells (1.0×10^6 cells/mL) were added to 5%, 10%, 15%, and 20% concentrations of GelMA. Cell viability was assessed by measuring red or green fluorescent dye uptake using LIVE/DEAD® Viability/Cytotoxicity Kit (Abcam, UK). The samples were cultured in a humidified 5% carbon dioxide incubator at 37°C for 7 days. The fluorescence images of the cell-laden structures were collected using confocal laser scanning microscopy (ZEISS LSM780, Oberkochen, Germany). Cell proliferation was determined using Cell Counting Kit-8 assays (Medchemexpress, USA). The cells encapsulated in the GelMA were cultured in a humidified 5% carbon dioxide incubator at 37°C for 7 days. The samples were incubated at 37°C for 2 h, and cell viability was quantified by measuring absorbance at 450 nm using a microplate reader (RT-6100, Rayto, China).

2.9. F-actin fluorescent labeling

For the fluorescent staining of F-actin, the samples were washed twice in phosphate-buffered saline (PBS) and then fixed with 4% paraformaldehyde (Slarbio, China) for 10 min at room temperature. After a 3 × 10-min rinse with PBS, the samples were permeabilized with 5% Triton X-100 (Sigma-Aldrich, USA) for 3 min, washed thrice for 10 min in PBS, and stained with tetramethylrhodamine isothiocyanate phalloidin (Sigma-Aldrich, USA) for 30 min at 37°C in the dark. The samples were then washed three times for 5 min in PBS. The samples were then counterstained with 100 nM 4',6-diamidino-2-phenylindole (Solarbio, China) for 15 min at room temperature in the dark and then washed twice for 5 min in PBS. The images of the samples were observed using confocal stereo fluorescence microscope (M165FA, Leica, Germany) and analyzed using ImageJ version 1.54j (NIH, USA).

2.10. Barrier function assessment

2.10.1. Transepidermal water loss test

The vascularized skin was printed directly in Transwell inserts. After 14 days of culture, the inserts were removed. Surface culture medium was aspirated, and the inserts were inverted and placed into a sealed container. A predetermined amount of color-changing silica gel particles was placed at the bottom of the container, while deionized water was added to the porous membrane at the bottom of the inverted insert. The container was then sealed with sealing film. Silica gel particles were periodically removed to observe color changes and weighed.

2.10.2. Dextran–fluorescein isothiocyanate permeability assay

The vascularized skin was printed directly in Transwell inserts and cultured for 14 days. The original culture medium in the lower chamber was aspirated and replaced with PBS solution, ensuring the liquid level covered the skin's upper surface. A dextran–fluorescein isothiocyanate (Dextran-FITC; 40 kDa; Sigma-Aldrich, USA) solution prepared in PBS was added to the upper chamber. The fluorescent tracer permeated through the skin surface into the dermal layer and subsequently diffused into the lower chamber. The fluorescence intensity of the solution was measured at different time points under identical microscope parameters to analyze the barrier capacity of the skin samples.

2.10.3. Transepithelial electrical resistance measurement

Skin substitutes were printed directly in Transwell inserts and cultured for 14 days. Under sterile conditions, the old culture medium was aspirated from both the upper and lower chambers of the Transwell. Pre-warmed (37°C) fresh culture medium was added to both the upper and lower chambers, ensuring equal liquid levels. Transepithelial electrical resistance (TEER) measurements of the printed skin samples were performed using an EVOM voltohmmeter (Millicell ERS-2; Merck, USA).

2.11. Drug delivery function assessment

The vascularized skin was printed in Transwell inserts and cultured for 14 days. A 1 mg/mL solution of Dextran-FITC in PBS was prepared as a model drug molecule. Using a micro-syringe and flexible catheter, the Dextran-FITC solution was slowly injected into the inlet end of the constructed subcutaneous small vessel. Simultaneously with the initiation of perfusion, real-time time-lapse imaging of the vessel and the surrounding dermal matrix area was performed using stereo fluorescence microscope. Fluorescence images were captured at 0, 10, 20, and 30 min. ImageJ was used to measure the average fluorescence intensity within specific regions of interest outside the vessel in the captured image sequences and to quantify the diffusion rate of the fluorescent molecules.

2.12. Data processing methods

All data presented in this study were obtained from a minimum of three independent replicates. Experimental results are expressed as the arithmetic mean ± standard deviation of the mean (SEM). Outliers, defined as values

below Q1 − 1.5 × the interquartile range and above Q3 + 1.5 × the interquartile range, were excluded from the analysis. Statistical significance was analyzed using a one-way analysis of variance, with the Bonferroni method applied for multiple comparison corrections to adjust the *p*-values of individual tests. A *p*-value of ≤0.05 was considered statistically significant and marked with an asterisk (*). As the level of significance increased, the number of asterisks correspondingly increased.

3. Results and discussion

3.1. Rheological properties and biocompatibility of the composite hydrogel

The construction of stable and perfusable subcutaneous small vessels required a bioink that combines excellent printability/formability with good biocompatibility. To this end, we developed a composite hydrogel system comprising SA and GelMA and systematically evaluated its rheological properties and its ability to support HUVEC behavior. Rheological test results (Figure 2A) showed that all tested SA/GelMA composite hydrogel formulations exhibited typical thermosensitive behavior, with a defined gelation point (G' = G"). Figure 2B shows that the viscosity of all grouped inks decreased with increasing temperature, a property that can be utilized to control the extrusion behavior of the bioink by adjusting the temperature of the coaxial printhead. At the printing temperature, all formulated inks were in a flowing state with low viscosity, ensuring they could be smoothly extruded from the coaxial printhead and meeting the basic requirements for ink fluidity during the printing process.

Biocompatibility was another key criterion for ink screening. HUVEC adhesion experiments on the material surface are shown in Figure 2C. The results of Figure 2E indicate that when the SA proportion was too high (e.g., the 3% SA/5% GelMA and 2% SA/3% GelMA groups), cell adhesion rates were very low (all <0.6%), attributable to the inherent lack of cell adhesion sites in SA. In contrast, groups with higher GelMA content (1% SA/5% GelMA, 2% SA/5% GelMA, 2% SA/10% GelMA) exhibited relatively better cell adhesion, with the 2% SA/10% GelMA group showing the highest adhesion coverage (12.24 ± 1.41%), indicating that the RGD peptides in GelMA effectively promoted cell adhesion.

However, surface adhesion is only a two-dimensional characteristic; constructing 3D vascular structures requires investigation of cell spreading and tubulogenesis capability within the gel. We observed HUVEC tubulogenesis behavior after chelating and degrading the SA component with EDTA to expand the internal space of the gel. As shown in Figure 2D, after EDTA treatment, the 1% SA/5% GelMA, 2% SA/5% GelMA, and 2% SA/3% GelMA groups all supported significant HUVEC spreading and the formation of tubular structures. Notably, the 2% SA/3% GelMA group exhibited the best tubulogenesis capability, potentially due to its lower GelMA crosslinking density after pore expansion, which made it more conducive to cell extension and interaction (Figure 2F). In contrast, cells in the 2% SA/10% GelMA group mostly remained rounded, presumably because its crosslinked network was too dense; even after SA removal, the remaining cavity structure was insufficient to support cell spreading.

Integrating the above results, we balanced the ink's printability, cell adhesion, and 3D tubulogenesis capability. Although the 2% SA/3% GelMA group performed best in terms of intragel tubulogenesis, its low GelMA content might lead to insufficient mechanical strength of the final construct and poor surface cell adhesion. The 2% SA/10% GelMA group, while having good surface adhesion, had an internal structure unfavorable for 3D cellular functions. The 2% SA/5% GelMA formulation achieved the best balance among rheological properties, cell adhesion, and intragel tubulogenesis capability, and was therefore selected as the ideal bioink for subsequent coaxial printing.

3.2. Coaxial printing process optimization enables perfusable small vessels

We aimed to establish a stable and controllable coaxial printing process[31,32] to construct small vessels that met the dimensional requirements for subcutaneous vessels (lumen diameter 300–1000 μm) with structural integrity. After preliminary investigation of the ionic crosslinking process parameters between the SA/GelMA composite ink and the $CaCl_2$ solution, we found that an inappropriate flow rate ratio between the hydrogel and the $CaCl_2$ solution in the inner and outer channels prevented the stable formation of the tubular structure, potentially leading to clogging or fracture (Figure S2). Guided by simulations (Figure S3), we systematically investigated the effects of nozzle specifications, absolute flow rates, and the inner-to-outer flow rate ratio on the printed structure. The results indicated that the nozzle specification is the primary factor determining the vessel dimensions (Figure 3A). Using the G17–G22 nozzle combination at a flow rate of 2 mL/min, vessels with an outer diameter of 730.5 ± 14.9 μm and a wall thickness of 77.25 ± 5.26 μm could be stably fabricated, meeting the size and wall thickness requirements of small arteries. Maintaining the inner-to-outer flow rate ratio while decreasing the absolute flow rates effectively reduced the printed tube diameter (Figure 3B). This is attributed to fluid contraction being more susceptible to surface tension effects at lower flow rates, as Figure 3C intuitively illustrates. Furthermore, adjusting the flow rate ratio

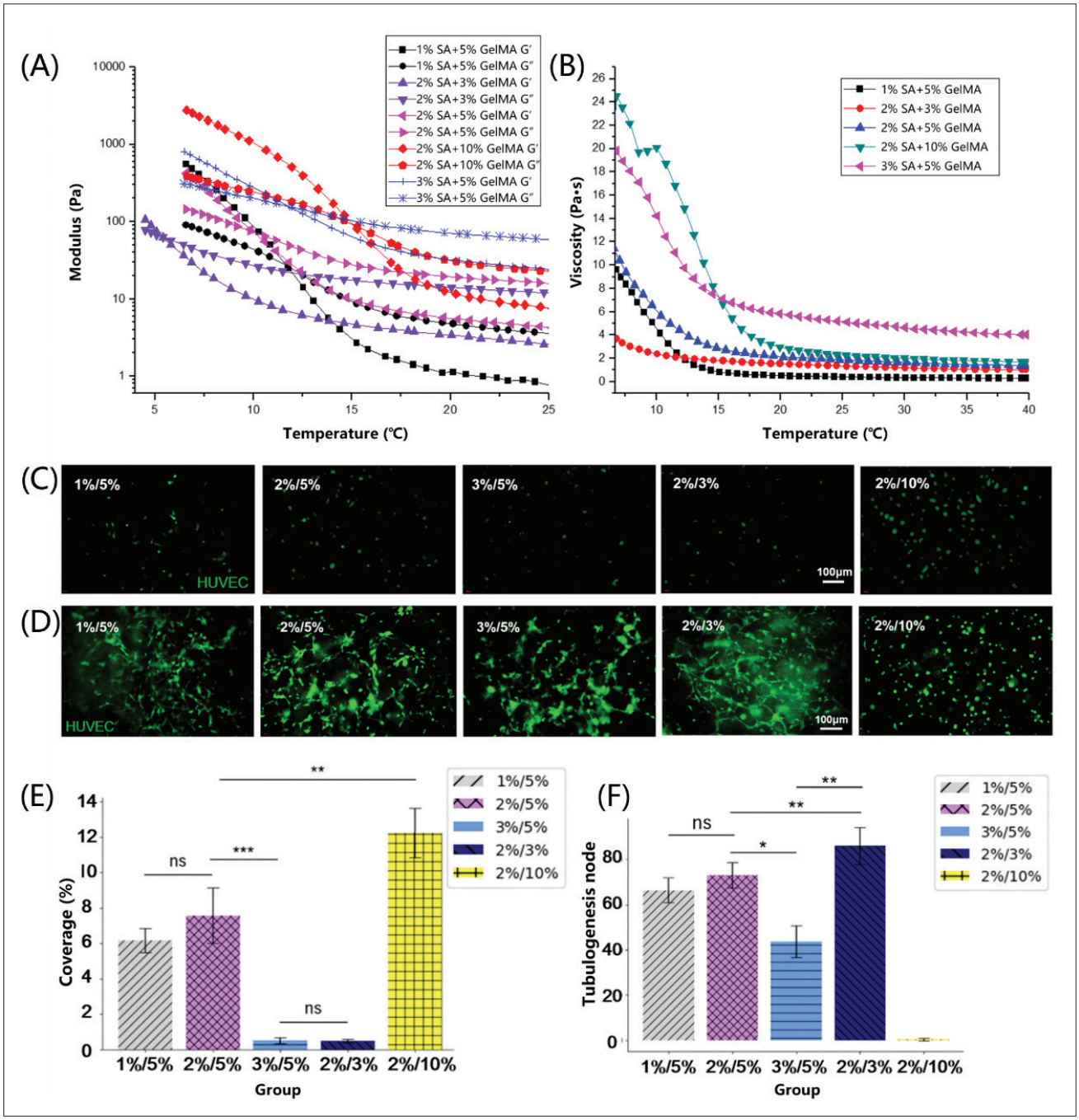


Figure 2. Biological characteristics of the composite hydrogels. (A) Modulus of different SA/GelMA hydrogels as a function of temperature. (B) Viscosity of different SA/GelMA hydrogels as a function of temperature. (C) HUVEC adhesion on the material surface. Scale bar: 100 μm; magnification: 100×. (D) HUVEC spreading within the hydrogels. (E) Coverage rate of HUVECs on the material surface. (F) The tubulogenesis node formed by HUVECs within the hydrogels. Data were analyzed using one-way analysis of variance and are presented as mean ± standard deviation (n = 3). Statistical significance determined at $^{*}p < 0.05$, $^{**}p < 0.01$, and $^{***}p < 0.001$, while ns indicates not significant. Abbreviations: GelMA, gelatin methacryloyl; HUVEC, human umbilical vein endothelial cell; SA, sodium alginate.

between the hydrogel and the crosslinker allowed precise modulation of the vessel wall thickness (Figure 3D). When the hydrogel flow rate was relatively high, the ability of the $CaCl_2$ stream to resist hydrogel retraction decreased, resulting in increased wall thickness; conversely, the wall thickness decreased as the flow rate decreased.

Formation relying solely on ionic crosslinking was still constrained by fluid surface tension at the nozzle, leading to lumen contraction and structural fluctuations.[33] To address this issue, we introduced an ionic-photo dual-crosslinking mechanism (Figure 3E). This strategy enabled the inner layer of the extruded hydrogel tube wall to undergo ionic crosslinking with $CaCl_2$, while the outer layer was simultaneously fixed by immediate photocuring, effectively counteracting the contraction effect (Figure 3F). Validation experiments showed that under the same printing parameters, the introduction of photocrosslinking increased the inner and outer diameters of the printed vessels by 18.5% and 18.8%, respectively, while the wall thickness remained unchanged (Figure 3G). Printing tests with varying flow rates yielded similar conclusions (Figure 3H). This characteristic can simulate the morphological differences between arteries and veins, offering the potential for constructing pathological models of arteriovenous malformations.

The dual-crosslinking strategy not only improved printing accuracy but also significantly enhanced the mechanical properties of the vessels. Tensile tests showed (Figure 4A) that the tensile modulus of the dual-crosslinked vessels reached 115.21 ± 6.34 kPa, representing a 119.49% increase compared to the 52.49 ± 4.79 kPa of the single-crosslinked vessels. Although this modulus is lower than that of human large arteries,[34] it meets the mechanical requirements for small animal vessels[35] and provides the necessary mechanical strength for subsequent surgery.[36] Meanwhile, we verified the patency and function of the printed vessels through dye perfusion experiments (Figure 4B). Red dye could completely perfuse an S-shaped lumen within 10 s without leakage, demonstrating its excellent liquid transport capability. In a small vessel grid scaffold constructed using this dual-crosslinking method, the dye also filled the entire network, indicating that this process maintains good lumen patency even when constructing complex, lengthy vascular structures (Figure 4C).

3.3. Construction and structural validation of the vascularized skin substitute

We further integrated coaxial printing with multi-material extrusion printing technology, aiming to achieve the integrated fabrication of a multi-layered skin substitute featuring a biomimetic "small-micro" vascular network (Figure 5A). The process involved printing a 5% GelMA hydrogel containing HFF-1 cells as the hypodermis/subcutaneous tissue layer. The small vessel structure containing HUVECs, obtained via coaxial printing, was embedded within this. Subsequently, a 5% GelMA hydrogel containing HFF-1 cells was printed above this to construct the dermal reticular layer. A 3% GelMA hydrogel containing HUVECs was then extrusion-printed to form a microvascular network in the papillary layer, specifically in a T-shaped zone, serving as the connection between the small vessels and the epidermis. Finally, a thin layer of 20% GelMA was printed as the epidermal base, onto which keratinocytes were seeded, while HUVECs were seeded on the surface of the vascular lumen, ultimately yielding the multi-layered, vascularized skin model (Figure 5B).

To evaluate the potential for endothelialization, we performed luminal seeding of HUVECs into the coaxially printed small vessels. The lumen surface was first coated with Matrigel to provide adhesion sites, followed by injection of a concentrated HUVEC suspension. Through a sequential rotation protocol, the cells were allowed to settle and adhere to the inner wall (Figure 6A(i)). After 5 days of culture, fluorescence staining revealed that HUVECs had adhered and spread across a substantial portion of the luminal surface, achieving a confluent cellular coverage (Figure 6A(ii, iii)). Quantitative analysis of the cell attachment area revealed that the attached area reached its peak after 5 days of culture, approximately four times the initial value, indicating that the intima had essentially formed (Figure 6A(iv)). This demonstrates the feasibility of our printed tubular structures as scaffolds for endothelial lining, highlighting their potential for subsequent vascular maturation. Embedding the printed small vessels within a fibroblast–GelMA matrix for sectioning and observation, 4',6-diamidino-2-phenylindol staining confirmed the presence of the hollow lumen structure (Figure 6B), although mechanical compression during sectioning caused slight distortion of its circularity.

Cross-sectional fluorescence analysis of the integrally printed construct confirmed the spatial organization achieved by our hybrid printing strategy (Figure 6C). The architecture displayed a multi-layered cellular distribution, suggesting it may correspond to the anatomical layers of skin: hypodermis, the cell-dense dermal layers, and the superficial epidermal layer. More importantly, the staining results clearly showed that the coaxially printed small vessels in the hypodermis were structurally connected to the T-shaped microvascular network formed by HUVECs via intervening cell clusters. This observation confirmed that our printing strategy successfully constructed a multi-level network ranging from the subcutaneous small

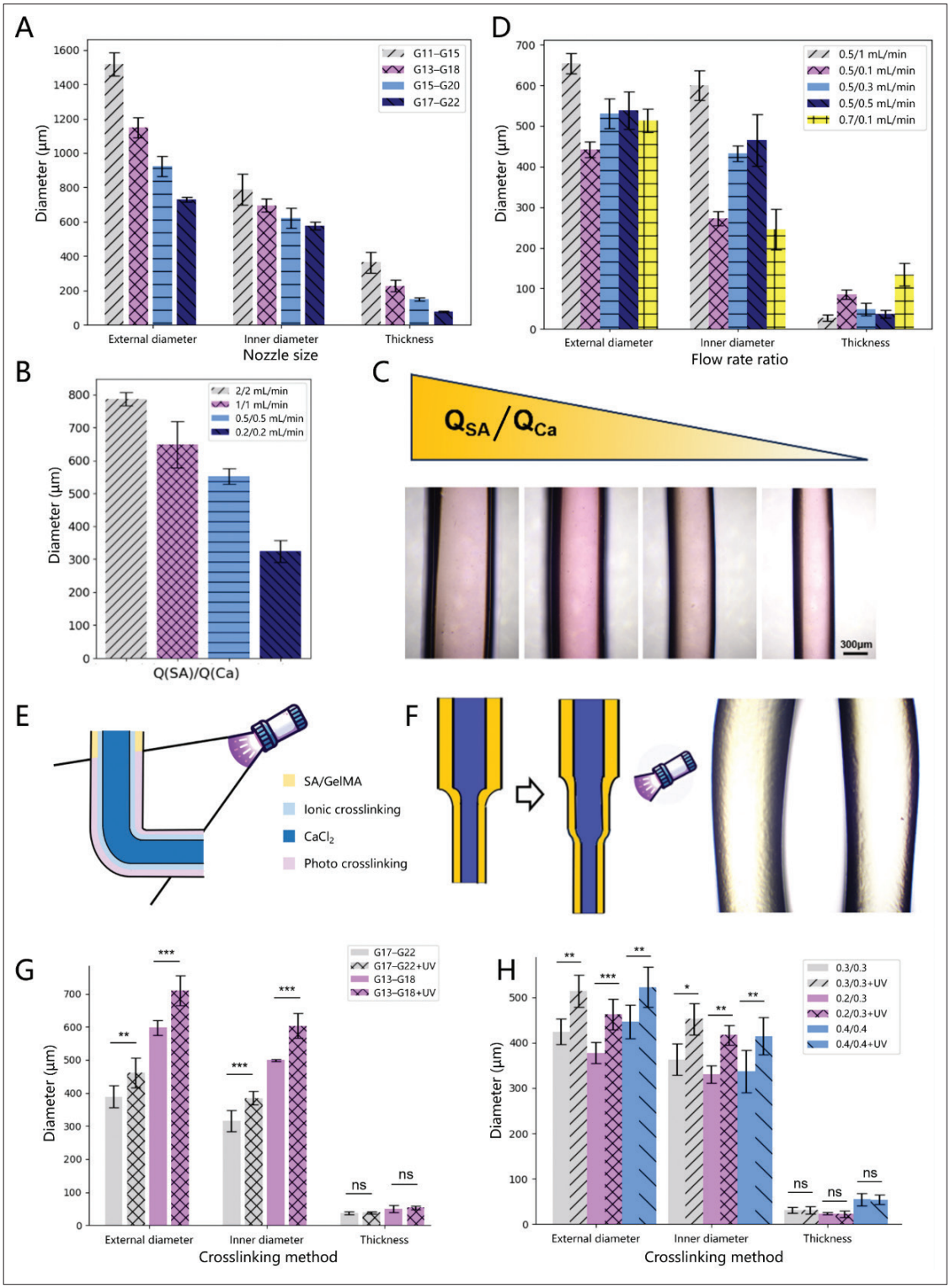


Figure 3. Optimization of coaxial printing nozzle parameters. (A) Vessel dimensions under different nozzle specifications and (B) different hydrogel flow rates. (C) Representative images of vessels printed at different hydrogel flow rates. Scale bar: 300 μm. (D) Vessel dimensions under different inner-to-outer flow rate ratios. (E) Ionic-photo dual-crosslinking schematic. (F) Comparison showing the enlarged lumen resulting from the dual-crosslinking strategy. (G) Vessel dimensions after introducing dual-crosslinking under different nozzle specifications and (H) different hydrogel flow rates. Data were analyzed using one-way analysis of variance and are presented as mean ± standard deviation ($n = 3$). Statistical significance determined at $^{*}p < 0.05$, $^{**}p < 0.01$, and $^{***}p < 0.001$, while ns indicates not significant. Abbreviations: $CaCl_2$, calcium chloride; GelMA, gelatin methacryloyl; SA, sodium alginate; UV, ultraviolet.

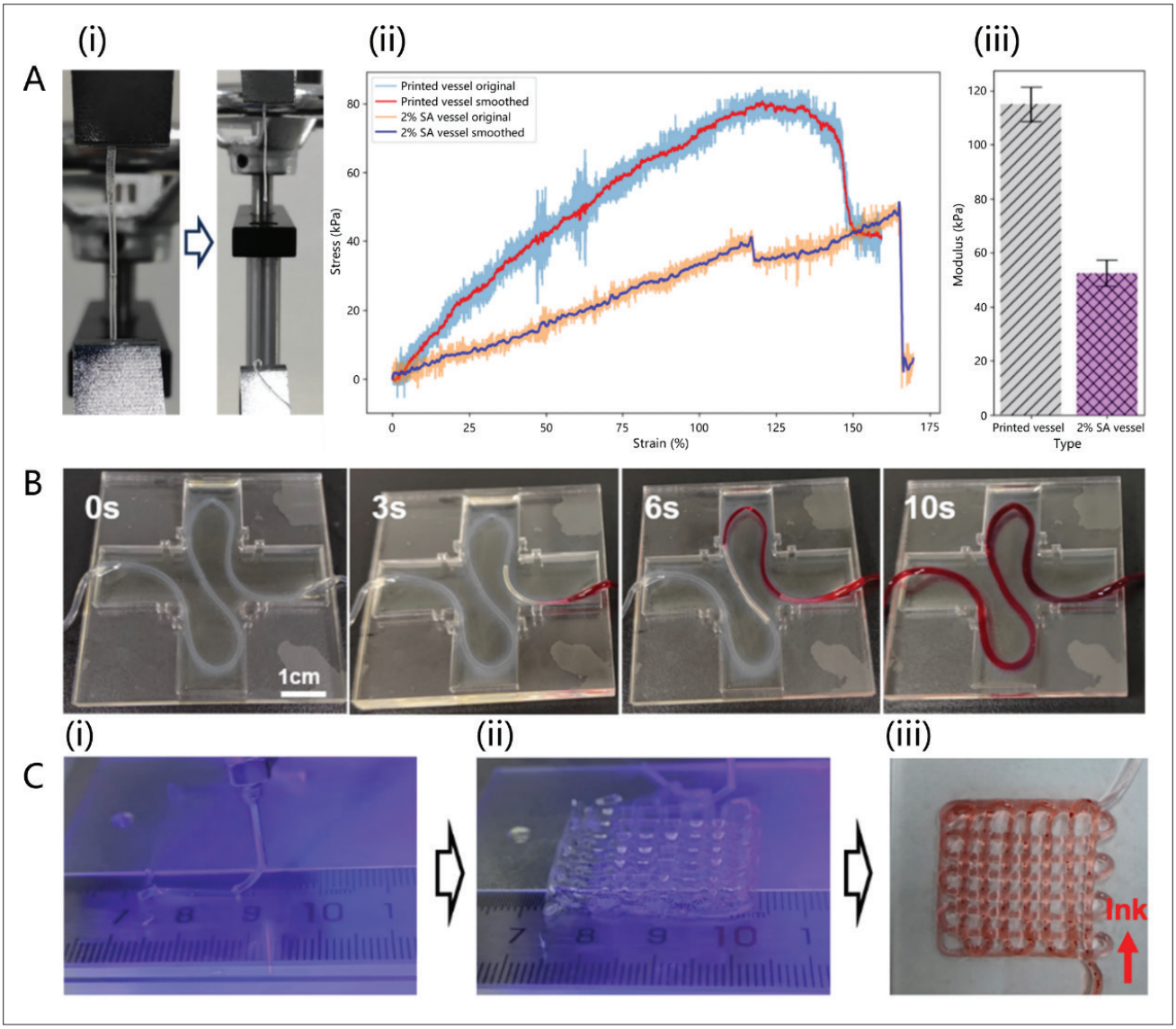


Figure 4. Characterization of coaxial-printed small vessel performance. (A) Mechanical properties of small vessels: (i) tensile testing, (ii) stress–strain curves, (iii) elastic modulus of the vessels. (B) Perfusion of vessels with red dye. Scale bar: 1 cm. (C) Small vessel grid scaffold: (i) printing initiation, (ii) upon printing completion, (iii) perfusion with red dye. Data were analyzed using one-way analysis of variance and are presented as mean ± standard deviation ($n = 3$). Statistical significance determined at $^{*}p < 0.05$, $^{**}p < 0.01$, and $^{***}p < 0.001$, while ns indicates not significant. Abbreviation: SA, sodium alginate.

vessels to the dermal microvessels, closely mimicking the hierarchical distribution of the vascular system in native skin. The current model provides the spatial organization of different cell types. However, achieving precise histological stratification and mature epidermal differentiation will be a key objective for the next stage of model refinement.

3.4. *In vitro* validation of the skin substitute

The structural biomimicry of the construct serves as the foundation for achieving its intended functions. To verify whether this multi-layered vascularized skin substitute possesses the key physiological functions of native skin, we conducted a series of *in vitro* experiments, focusing on evaluating its physical barrier function and the substance transport potential of the subcutaneous vascular network. The coaxial printing process developed in this work, combined with the previously reported layer-by-layer printing method,[29] forms a composite strategy for fabricating a multi-layered vascularized skin substitute, which was ultimately constructed and functionally validated. We established four experimental groups: the no epidermis group contained only the dermal layer, lacking

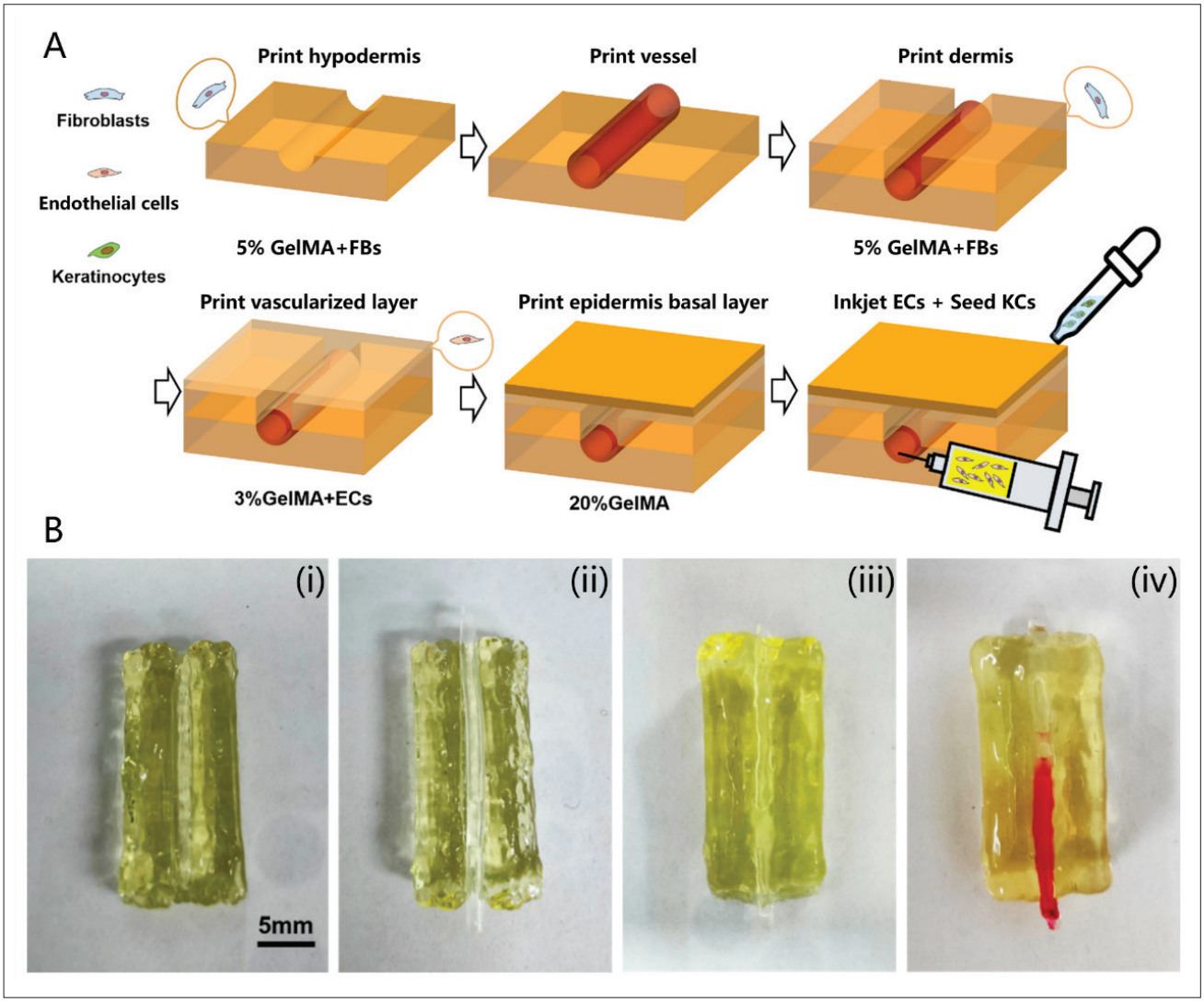


Figure 5. Construction of the multi-layered vascularized skin substitute. (A) Construction method. (B) Sequential construction of the (i) hypodermis, (ii) small vessels, and (iii) papillary and epidermal layers, resulting in a (iv) perfusable network. Scale bar: 5 mm. Abbreviations: EC, endothelial cell; F, fibroblast; GelMA, gelatin methacryloyl; KC, keratinocytes.

an epidermal structure. The incomplete epidermis group and the complete epidermis group were both fabricated on the basis of the no epidermis group. By adjusting the printing stage temperature and path spacing, we engineered a surface with either grooves or a continuous, dense, and smooth layer. The no skin sample group was used to account for interference from water vapor inside the container. Both the Incomplete epidermis and complete epidermis groups contained the "small-micro" vascular network.

We systematically evaluated the barrier function using transepidermal water loss (TEWL) measurements, a transdermal penetration assay with a fluorescent substance, and TEER testing. As shown in Figure 7A, the TEWL test based on water absorption by color-changing silica gel demonstrated that the water retention capability of the complete epidermis group was significantly superior to that of the incomplete epidermis and no epidermis groups. This demonstrates that the dense keratinocyte layer and the intercellular substances it secretes effectively block passive water evaporation, a crucial process for maintaining the internal water balance. The impaired function of the incomplete epidermis group directly correlates with its engineered micro-grooves, which provide pathways for TEWL and molecular permeation.

The transdermal penetration assay further corroborated this observation (Figure 7B). When Dextran-FITC was used as a model molecule, its penetration rate

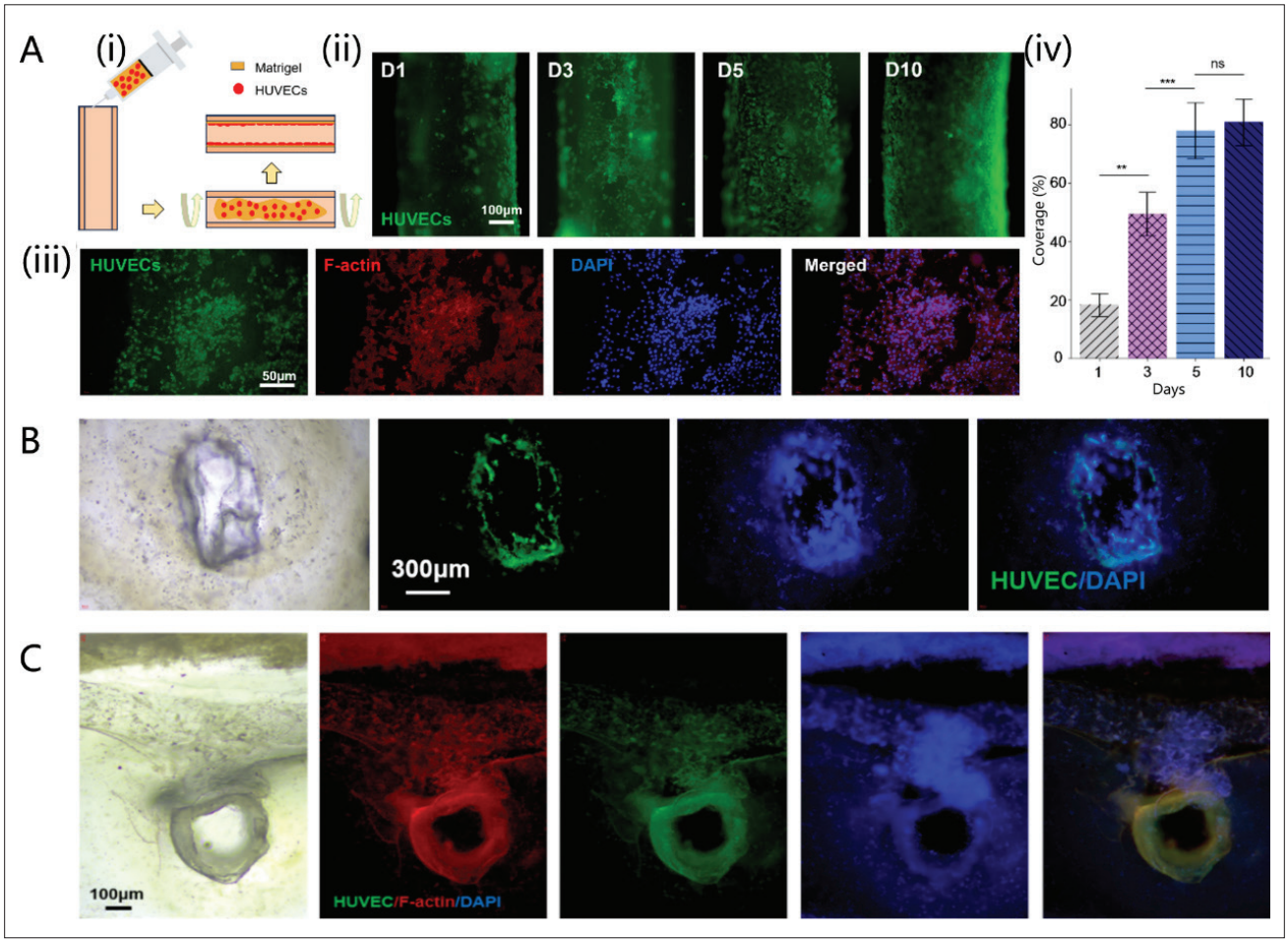


Figure 6. Characterization results of the multi-layered vascularized skin substitute. (A) Luminal adhesion of HUVECs: (i) schematic of the adhesion procedure, (ii) temporal changes in HUVEC adhesion, (iii) fluorescence staining of HUVECs, (iv) quantitative analysis of HUVEC coverage rate over time. Scale bars: 50, 100 μm; magnifications: 100×. (B) Characterization of HUVEC adhesion within the coaxial-printed small vessels. Scale bar: 300 μm; magnification: 50×. (C) Structure of the vascularized skin. Scale bar: 100 μm; magnification: 100×. Data were analyzed using one-way analysis of variance and are presented as mean ± standard deviation ($n = 3$). Statistical significance determined at $^{*}p < 0.05$, $^{**}p < 0.01$, and $^{***}p < 0.001$, while ns indicates not significant. Abbreviation: HUVEC, human umbilical vein endothelial cell.

through the complete epidermis group was the slowest, with the fluorescence intensity in the solution remaining consistently low. In contrast, the fluorescent molecules rapidly penetrated the no epidermis group, while the incomplete epidermis group showed an intermediate level, indicating that structural defects in the epidermis significantly impair its barrier efficacy. TEER testing provided electrophysiological evidence for this observation (Figure 7C). The TEER value of the complete epidermis group (3170 ± 162.35 Ω) was substantially higher than that of the incomplete epidermis group (1316 ± 182.06 Ω) and the blank control group (no skin sample) (199 ± 59.50 Ω). This 140.82% increase relative to the incomplete-epidermis group supports the conclusion that a complete and tightly connected epidermal layer is the decisive factor in establishing a high-impedance physical barrier. The results from these three experiments consistently demonstrate that the structural integrity of the epidermal layer is necessary for the engineered skin to exert an effective barrier function.

Beyond serving as a physical barrier, a functional skin substitute requires its subcutaneous vascular network to possess the capability for substance exchange. Therefore, we simulated the process of drug diffusion from blood vessels by injecting a Dextran-FITC solution into the coaxially printed small vessel within the construct and observing its extravasation behavior in real-time (Figure 7D). Time-lapse images clearly showed that the fluorescent molecules were initially confined to the vascular lumen and then gradually diffused into the surrounding extracellular matrix over time. Quantitative analysis of the

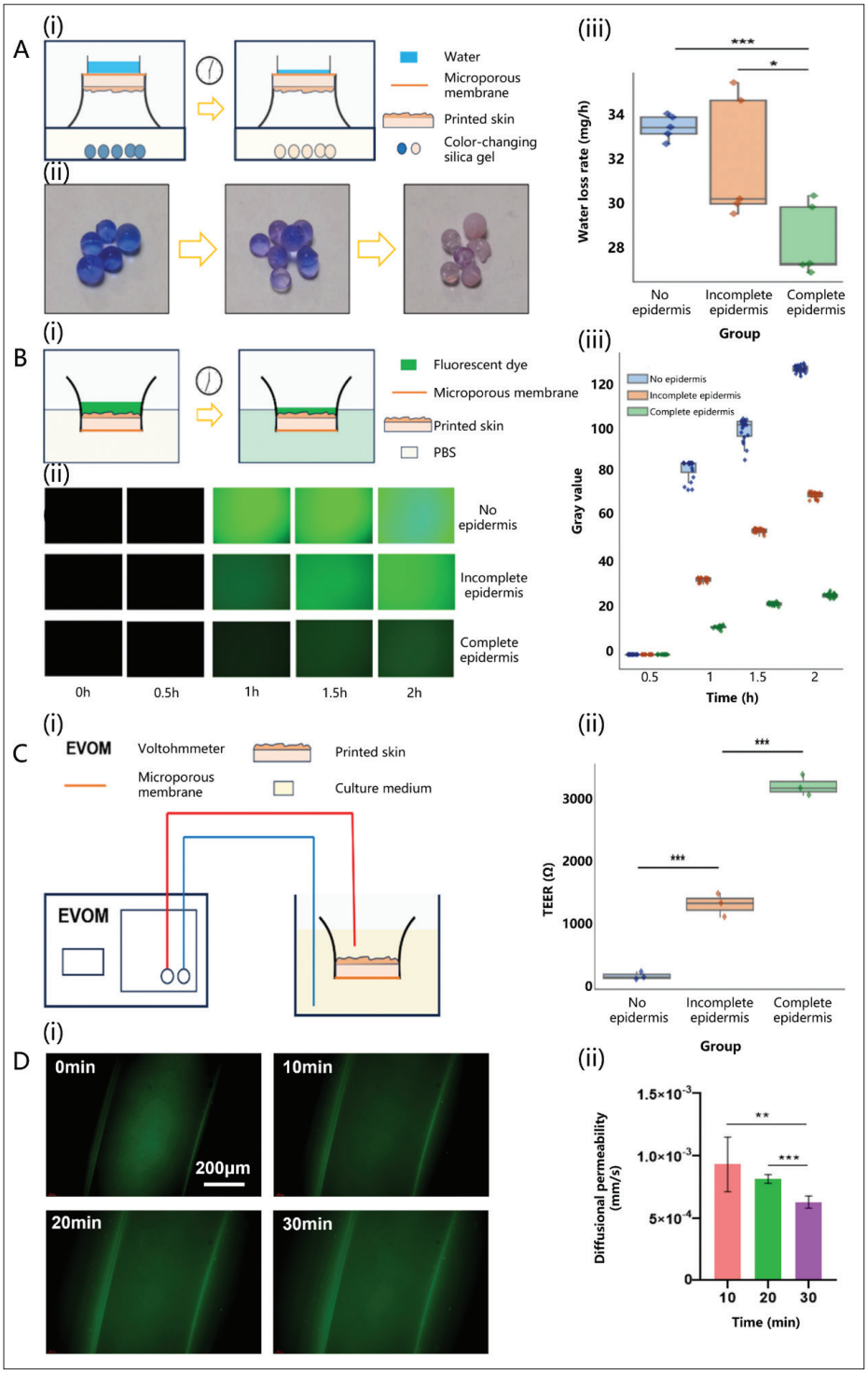


Figure 7. *In vitro* validation of the skin substitute. (A) TEWL measurement: (i) schematic of the test setup, (ii) color change of silica gel due to water absorption, (iii) water loss rate across different groups. (B) Transdermal penetration assay: (i) schematic of the test principle, (ii) fluorescence detection results, (iii) changes in fluorescence values across different groups. (C) TEER measurement: (i) schematic of the measurement principle, (ii) electrical resistance values across different groups. (D) Dextran-FITC permeability assay: (i) time-lapse images showing fluorescent molecule diffusion, (ii) quantification of diffusion rate. Scale bar: 200 μm. Data were analyzed using one-way analysis of variance and are presented as mean ± standard deviation ($n = 3$). Statistical significance determined at $^{*}p < 0.05$, $^{**}p < 0.01$, and $^{***}p < 0.001$, while ns indicates not significant. Abbreviations: Dextran-FITC, dextran–fluorescein isothiocyanate; EVO, epithelial voltohmmeter; PBS, phosphate-buffered saline; TEER, transepithelial electrical resistance; TEWL, transepidermal water loss.

diffusion rate indicated that the rate decreased over time, consistent with the classical Fick's law of diffusion,[37] where the driving force for diffusion naturally weakens as the concentration gradient across the vessel wall decreases. The hydrodynamic diameter of 40 kDa dextran is comparable to that of a key transport protein in the human body—serum albumin (approximately 66 kDa).[38] Albumin serves as the natural carrier for many hydrophobic drugs. Numerous therapeutic biomolecules, such as cytokines, enzymes, and antibody fragments, also fall within this molecular weight range. The permeation behavior of Dextran-FITC can be used to model the diffusion and clearance of these drug–protein complexes within the interstitial space and vascular system. For instance, Aflibercept (VEGF Trap),[39] a dimeric glycoprotein used to treat neovascular age-related macular degeneration, diabetic macular edema, and other angiogenic diseases, has a functional subunit size comparable to 40 kDa Dextran-FITC. Observing the diffusion of Dextran-FITC from the vascular network can directly simulate and predict the distribution kinetics and local clearance rate of drugs like Aflibercept in diseased skin tissue.

The *in vitro* functional validation demonstrates that our constructed multi-layered vascularized skin substitute not only successfully mimicked the anatomical structure of native skin but also replicated two of its core physiological functions: the excellent physical barrier function provided by the complete epidermis, and the substance transport and potential drug delivery function enabled by the multi-level hierarchical vascular network. This lays a solid foundation for its applications in wound repair, disease modeling, and *in vitro* drug screening.

3.5. Limitations and future perspectives

While the hybrid bioprinting strategy proposed in this study shows promise for constructing vascularized skin constructs, the current model still has several limitations, which also point the way for future research.

In terms of vascular function, although we achieved confluent endothelial coverage within the coaxially printed small vessels, the maturity and barrier integrity of this endothelium require further validation. For example, immunofluorescence staining for endothelial junctional proteins such as vascular endothelial cadherin and claudin-5, combined with perfusion assays using fluorescently labeled macromolecules like 70 kDa dextran, is needed to quantitatively assess vascular permeability.

Regarding tissue maturation and structural fidelity, although the current construct successfully achieved the designed spatial organization of multiple cell types, more in-depth histological analysis is still required to truly recapitulate the sophisticated layered architecture of native skin. In subsequent work, hematoxylin and eosin staining, Masson's trichrome staining, and immunohistochemical analysis should be performed to assess layer-specific markers quantitatively and evaluate tissue maturation and stratification. Relevant markers may include cytokeratin 10 for epidermal differentiation, collagen I/III in the dermal matrix, and cluster of differentiation 31 for vascular networks. Simultaneously, introducing melanocytes to model pigmentation or incorporating immune cells such as macrophages to confer immunocompetence would significantly enhance the biological relevance of this model for disease modeling and immunological studies.

For the drug delivery assessment, the diffusion kinetics of the 40 kDa Dextran-FITC model molecule provide valuable preliminary insights. However, to more accurately predict therapeutic efficacy, future studies need to directly investigate the transport and retention behaviors of clinically relevant agents. This includes small-molecule drugs, growth factors such as VEGF or basic fibroblast growth factor, as well as nanoparticle-based formulations. By analyzing the structural characteristics and permeability of the construct's vascular network and correlating them with the pharmacokinetic profiles of these agents, this model holds the potential to evolve from a structural platform into a predictive tool for preclinical drug screening.

Finally, the ultimate validation of any tissue-engineered construct lies in *in vivo* experimentation. Future work should focus on implanting these skin constructs into full-thickness skin defect models in small animals, such as mice or rats. Key evaluation metrics should include the anastomosis of the engineered vascular network with the host circulatory system, the long-term survival rate of the graft, perfusion monitoring via imaging techniques, and the wound healing efficacy compared to standard therapies. The outcomes of these experiments will lay the foundation for testing in larger, more clinically relevant animal models.

4. Conclusion

This study successfully developed a hybrid bioprinting strategy for the integrated fabrication of a multi-layered skin substitute featuring a biomimetic "small-micro" hierarchical vascular network. The 2% SA/5% GelMA composite hydrogel was optimized and validated as the coaxial printing ink. It achieved an optimal balance among rheological properties, cell adhesion, and 3D tubulogenesis capability, thus laying the material foundation for constructing functional vessels. Through systematic optimization of coaxial printing parameters combined with an ionic-photo dual-crosslinking mechanism, we achieved the automated fabrication of structurally

stable, dimensionally controllable, mechanically robust, and perfusable subcutaneous small vessels, effectively overcoming the challenges of structural contraction and instability associated with single-crosslinking methods. By integrating coaxial printing with extrusion printing technologies, we achieved, for the first time, the integrated fabrication of a full-thickness, biomimetic skin construct with designed layer compartments in a single manufacturing process. Structural characterization demonstrated that the printed construct formed a multi-level "small-micro" vascular structure and achieved the precise distribution of various cell types in their predefined locations. *In vitro* functional experiments demonstrated that the construct possessed both an effective physical barrier function and drug delivery potential enabled by the engineered vascular network, proving it to be a promising platform that integrates biomimetic architecture with initial barrier and transport functionalities.

In summary, the composite printing and dual-crosslinking strategy proposed in this study provided an effective technical solution for addressing the challenge of pre-vascularization and thick-walled tissue construction. The fabricated, multi-layered, vascularized skin substitute exhibits great potential for application in the repair of deep skin defects, disease modeling, and *in vitro* drug screening. Future work should focus on the long-term *in vivo* functional evaluation of this construct and its reparative efficacy in large animal models.

Acknowledgments

None.

Funding

This work was supported by the National Natural Science Foundation (Grant No. 82300566), the Key Science and Technology Program of Zhejiang Province (Grant No. 2023C03170 and 2023C03071), and the China Postdoctoral Science Foundation (Grant No. 2023M733095 and 2025T180562)

Conflict of interest

The authors declare no conflict of interest.

Author contributions

Conceptualization: Yichen Luo, Hao Ding, Xue Zhou
Data curation: Yichen Luo, Dan Li, Xue Zhou
Formal analysis: Yichen Luo
Funding acquisition: Bin Zhang
Investigation: Yichen Luo
Methodology: Yichen Luo, Cai Lin, Xue Zhou
Project administration: Bin Zhang
Resources: Yichen Luo
Software: Yichen Luo, Cai Lin, Xue Zhou
Supervision: Hao Ding, Xue Zhou
Validation: Yichen Luo, Dan Li, Cai Lin, Xue Zhou
Visualization: Yichen Luo, Dan Li
Writing – original draft: Yichen Luo, Dan Li
Writing – review & editing: Yichen Luo, Xue Zhou
All authors have read and agreed to the published version of the manuscript.

Ethics approval and consent to participate

Not applicable.

Consent for publication

Not applicable.

Availability of data

The data that support the findings of this study are available on request from the corresponding author.

References

1. Sen CK. Human wounds and its burden: updated 2020 compendium of estimates. *Adv Wound Care*. 2021;10(5):281-292.
doi: 10.1089/wound.2021.0026

2. Shlash SOA, Madani JOA, Deib JIE, *et al*. Demographic characteristics and outcome of burn patients requiring skin grafts: a tertiary hospital experience. *Int J Burns Trauma*. 2015;6(2):30-36.

3. Halim AS, Khoo TL, Yussof SJM. Biologic and synthetic skin substitutes: an overview. *Indian J Plast Surg*. 2010;43(Suppl):S23-S28.
doi: 10.4103/0970-0358.70712

4. Böttcher-Haberzeth S, Biedermann T, Reichmann E. Tissue engineering of skin. *Burns*. 2010;36(4):450-460.
doi: 10.1016/j.burns.2009.08.016

5. Murphy SV, Atala A. 3D bioprinting of tissues and organs. *Nat Biotechnol*. 2014;32(8):773-785.
doi: 10.1038/nbt.2958

6. Kim BS, Kwon YW, Kong JS, *et al*. 3D cell printing of invitro stabilized skin model and invivo pre-vascularized skin patch using tissue-specific extracellular matrixbioink: a step towards advanced skin tissue engineering. *Biomaterials*. 2018;168:38-53.
doi: 10.1016/j.biomaterials.2018.03.040

7. Zhang J, Yun S, Karami A, *et al*. 3D printing of a thermosensitive hydrogel for skin tissue engineering: a proof of concept study. *Bioprinting*. 2020;19:e00089.
doi: 10.1016/j.bprint.2020.e00089

8. Abaci HE, Guo Z, Coffman A, *et al*. Human skin constructs with spatially controlled vasculature using primary and iPSC-derived endothelial cells. *Adv Healthc Mater*. 2016;5(14):1800-1807.
doi: 10.1002/adhm.201500936

9. Hao L, Zhao S, Hao S, *et al*. Functionalized gelatin-alginate based bioink with enhanced manufacturability and biomimicry for accelerating wound healing. *Int J Biol Macromol*. 2023;240:124364.
doi: 10.1016/j.ijbiomac.2023.124364

10. Maggiotto F, Valle ED, Fietta A, Visentin LM, Giomo M, Cimetta E. 3D bioprinting of a perfusable skin-on-chip model suitable for drug testing and wound healing studies. *Mater Today Bio*. 2025;33:101974.
doi: 10.1016/j.mtbio.2025.101974

11. Yue K, Santiago TD, Alvarez MM, Tamayol A, Annabi N, Khademhosseini A. Synthesis, properties, and biomedical applications of gelatin methacryloyl (GelMA) hydrogels. *Biomaterials*. 2015;73:254-271.
doi: 10.1016/j.biomaterials.2015.08.045

12. Choi KY, Ajiteru O, Hong H, *et al*. A digital light processing 3D-printed artificial skin model and full-thickness wound models using silk fibroin bioink. *Acta Biomater*. 2023;164(000):16.
doi: 10.1016/j.actbio.2023.04.034

13. Daikuara L, Yue Z, Skropeta D, Wallace G. In vitro characterisation of 3D printed platelet lysate-based bioink for potential application in skin tissue engineering. *Acta Biomater*. 2021;123:286-297.
doi: 10.1016/j.actbio.2021.01.021

14. Lee KY, Mooney DJ. Alginate: properties and biomedical applications. *Prog Polym Sci*. 2012;37(1):106-126.
doi: 10.1016/j.progpolymsci.2011.06.003

15. Lee SJ, Lee JH, Park J, Kim WD, Park SA. Fabrication of 3D printing scaffold with porcine skin decellularized bio-ink for soft tissue engineering. *Materials (Basel)*. 2020;13(16):3522.
doi: 10.3390/ma13163522

16. Hakimi N, Cheng R, Leng L, *et al*. Handheld skin printer: in situ formation of planar biomaterials and tissues. *Lab Chip*. 2018;18(10):1440-1451.
doi: 10.1039/c7lc01236e

17. Gungor-Ozkerim PS, Inci I, Zhang YS, Khademhosseini A, Dokmeci MR. Bioinks for 3D bioprinting: an overview. *Biomater Sci*. 2018;6(5):915-946.
doi: 10.1039/C7BM00765E

18. Rúben P, Aureliana S, Barrias CC, Paulo B, Granja PL. A single-component hydrogel bioink for bioprinting of bioengineered 3D constructs for dermal tissue engineering. *Mater Horiz*. 2018;5(6):1100-1111.
doi: 10.1039/C8MH00525G

19. Hafa L, Breideband L, Ramirez Posada L, *et al*. Light sheet-based laser patterning bioprinting produces long-term viable full-thickness skin constructs. *Adv Mater*. 2024;36(8):e2306258.
doi: 10.1002/adma.202306258

20. Pontiggia L, Van Hengel IA, Klar A, *et al*. Bioprinting and plastic compression of large pigmented and vascularized human dermo-epidermal skin substitutes by means of a new robotic platform. *J Tissue Eng*. 2022;13:20417314221088513.
doi: 10.1177/20417314221088513

21. Kim BS, Gao G, Kim JY, Cho DW. 3D cell printing of perfusable vascularized human skin equivalent composed of epidermis, dermis, and hypodermis for better structural recapitulation of native skin. *Adv Healthc Mater*. 2019;8(7):e1801019.
doi: 10.1002/adhm.201801019

22. Huyan Y, Lian Q, Zhao T, Li D, He J. Pilot study of the biological properties and vascularization of 3D printed bilayer skin grafts. *Int J Bioprint*. 2020;6(1):246.
doi: 10.18063/ijb.v6i1.246

23. Ma J, Qin C, Wu J, *et al*. 3D Printing of strontium silicate microcylinder-containing multicellular biomaterial inks for vascularized skin regeneration. *Adv Healthc Mater*. 2021;10(16):e2100523.
doi: 10.1002/adhm.202100523

24. Nuutila K, Samandari M, Endo Y, *et al*. In vivo printing of growth factor-eluting adhesive scaffolds improves wound healing. *Bioact Mater*. 2022;8:296-308.
doi: 10.1016/j.bioactmat.2021.06.030

25. Kolesky DB, Truby RL, Gladman AS, Busbee TA, Homan KA, Lewis JA. 3D bioprinting of vascularized, heterogeneous cell-laden tissue constructs. *Adv Mater*. 2014;26(19):3124-3130.
doi: 10.1002/adma.201305506

26. Kim BS, Ahn M, Cho WW, Gao G, Jang J, Cho DW. Engineering of diseased human skin equivalent using 3D cell printing for representing pathophysiological hallmarks of type 2 diabetes in vitro. *Biomaterials*. 2021;272:120776.
doi: 10.1016/j.biomaterials.2021.120776

27. Thomas A, Orellano I, Lam T, *et al*. Vascular bioprinting with enzymatically degradable bioinks via multi-material projection-based stereolithography. *Acta Biomater*. 2020;117:121-132.
doi: 10.1016/j.actbio.2020.09.033

28. Ramasamy S, Davoodi P, Vijayavenkataraman S, *et al*. Optimized construction of a full thickness human skin equivalent using 3D bioprinting and a PCL/collagen dermal scaffold. *Bioprinting*. 2020;21:e00123.
doi: 10.1016/j.bprint.2020.e00123

29. Luo Y, Li D, Lin C, Zhou X, Ma J, Zhang B. Three-dimensional bioprinting of gelatin methacryloyl hydrogel with a tri-layered vascularized architecture for full-thickness skin regeneration. *Int J Bioprint*. 2025;11(4):328-349.
doi: 10.36922/IJB025090069

30. Zhang B, Gao L, Gu L, Yang H, Luo Y, Ma L. High-resolution 3D bioprinting system for fabricating cell-laden hydrogel scaffolds with high cellular activities. *Procedia CIRP*. 2017;65:219-224.
doi: 10.1016/j.procir.2017.04.017

31. Shao L, Gao Q, Zhao H, *et al*. Fiber-based mini tissue with morphology-controllable GelMA microfibers. *Small*. 2018;14(44):e1802187.
doi: 10.1002/smll.201802187

32. Gao Q, He Y, Fu J-z, Liu A, Ma L. Coaxial nozzle-assisted 3D bioprinting with built-in microchannels for nutrients delivery. *Biomaterials*. 2015;61:203-215.
doi: 10.1016/j.biomaterials.2015.05.031

33. Jia W, Gungor-Ozkerim PS, Zhang YS, *et al*. Direct 3D bioprinting of perfusable vascular constructs using a blend bioink. *Biomaterials*. 2016;106:58-68.
doi: 10.1016/j.biomaterials.2016.07.038

34. Riley WA, Barnes RW, Evans GW, Burke GL. Ultrasonic measurement of the elastic modulus of the common carotid artery. The Atherosclerosis Risk in Communities (ARIC) Study. *Stroke*. 1992;23(7):952-956.
doi: 10.1161/01.str.23.7.952

35. Yen RT, Fung YC, Bingham N. Elasticity of small pulmonary arteries in the cat. *J Biomech Eng*. 1980;102(2):170-177.
doi: 10.1115/1.3138218

36. Humphrey JD, Schwartz MA. Vascular mechanobiology: homeostasis, adaptation, and disease. *Annu Rev Biomed Eng*. 2021;23:1-27.
doi: 10.1146/annurev-bioeng-092419-060810

37. Fick A. On liquid diffusion. *J Membr Sci*. 1995;100(1):33-38.
doi: 10.1016/0376-7388(94)00230-V

38. Merlot AM, Kalinowski DS, Richardson DR. Unraveling the mysteries of serum albumin-more than just a serum protein. *Front Physiol*. 2014;5:299.
doi: 10.3389/fphys.2014.00299

39. Stewart MW. Aflibercept (VEGF Trap-eye): the newest anti-VEGF drug. *Br J Ophthalmol*. 2012;96(9):1157-1158.
doi: 10.1136/bjophthalmol-2011-300654

ACCSCIENCE PUBLISHING

International Journal of Bioprinting

RESEARCH ARTICLE

Structural design and multiphase biomechanical evaluation of a topology-optimized metal 3D-printed dual-compression plate for patellar fractures

Chi-Yang Liao[1,2], Shao-Fu Huang[3,4], Ya-Han Chan[4], Hsuan-Wen Wang[3,4], Yu-Pin Yang[4], and Chun-Li Lin[3,4]*

[1]Department of Orthopedics, Tri-Service General Hospital Songshan Branch, National Defense Medical University, Taipei, Taiwan

[2]Department of Surgery, Tri-Service General Hospital Songshan Branch, National Defense Medical University, Taipei, Taiwan

[3]Department of Biomedical Engineering, Innovation & Translation Center of Medical Device, National Yang Ming Chiao Tung University, Taipei, Taiwan

[4]Department of Biomedical Engineering, National Yang Ming Chiao Tung University, Taipei, Taiwan

(This article belongs to the *Special Issue*: *3D Printing for Advancing Orthopedic Applications*)

Abstract

Patellar fractures, especially transverse and comminuted types, often present mechanical challenges that exceed the capabilities of conventional fixation constructs. This study develops a topology-optimized metal three-dimensional-printed dual-compression patellar plate designed to improve fragment stability while maintaining appropriate intraoperative rigidity. The plate design was first refined using an original anatomically assembled thin bone plate, which underwent finite element analysis and topology optimization to preserve primary load-bearing paths and reduce excessive stiffness. The optimized structure was subsequently fabricated using selective laser melting with Ti-6Al-4V and mechanically evaluated in accordance with American Society for Testing and Materials F382 standards. Static four-point bending tests demonstrated a proof load (P) of 257.31 ± 5.40 N and structural bending stiffness of 1.10 ± 0.01 N·m^2. Fatigue testing revealed runout at 15% *P*, while failure occurred at higher load levels (25% *P* & 30% *P*), revealing two distinct modes: plate fracture at topology-optimized transition zones and locking-screw shear failure. Static tensile testing revealed that dual-compression fixation significantly ($p<0.05$) enhanced load-bearing capacity compared with single-compression fixation for both C1 (712 N vs. 517.5 N) and C3 (253.75 N vs. 205.25 N) fracture models. Dynamic knee-extension testing demonstrated that dual compression markedly reduced medial–lateral fracture micromotion, decreasing C3 gaps from 0.348–0.534 mm to 0.078–0.107 mm without increasing quadriceps reaction force. Overall, the topology-optimized dual-compression patellar plate provides mechanically validated interfragmentary stability, effective micromotion control, and a well-defined fatigue performance envelope, supporting its potential as an advanced fixation solution for clinically challenging patellar fractures.

Keyword: Biomechanics; Dynamic tests; Four-point bending; Patella; Three-dimensional printing

***Corresponding author:**
Chun-Li Lin
(cllin2@nycu.edu.tw)

Citation: Liao CY, Huang SF, Chan YH, Wang HW, Yang YP, Lin CL. Structural design and multiphase biomechanical evaluation of a topology-optimized metal 3D-printed dual-compression plate for patellar fractures. *Int J Bioprint*. 2026;12(1):689-706. doi: 10.36922/IJB025480494

Received: November 25, 2025
Revised: December 14, 2025
Accepted: December 26, 2025
Published online: January 8, 2026

Copyright: © 2026 Author(s). This is an Open Access article distributed under the terms of the Creative Commons Attribution License, permitting distribution, and reproduction in any medium, provided the original work is properly cited.

Publisher's Note: AccScience Publishing remains neutral with regard to jurisdictional claims in published maps and institutional affiliations.

1. Introduction

Patellar fractures account for approximately 0.5–1.5% of all fractures, primarily caused by direct impact or forceful quadriceps contraction.[1–8] Integrity of the patella is crucial for knee stability and lower limb movement due to its location at the lever center of the knee extensor system. Additionally, it plays a crucial role in transmitting pressure and tension between the quadriceps and patellar tendon.[1–8] Although traditional tension band wiring fixation can withstand tensile stress, it struggles to provide sustained and effective compression across the fracture interface. Bone fragment displacement, implant loosening, and subcutaneous irritation are common problems, with implant removal rates as high as 65%, demonstrating its inadequate mechanical control for dynamic compression stabilization.[9–18]

To enhance fixation stability, anterior locking plates have been increasingly adopted in clinical patellar reconstruction. This design provides direct anterior locking and compressive fixation[19–24]; however, given that the anterior surface of the patella has a highly complex curvature with substantial inter-individual variation, commercially available plates often require repeated intraoperative bending, fine-tuning, and locking by the surgeon to achieve proper conformity. In addition, the precision of conventional computer numerical control machining is limited when producing plates with multi-curvature surfaces, thin walls, or multi-axial screw trajectories, making fabrication challenging and costly and ultimately restricting the conformity and clinical operability of these implants.[19–23] Consequently, metal three-dimensional (3D) printing has emerged as an ideal solution, enabling accurate reconstruction of the patellar surface while integrating complex multi-functional design features.

An anatomically assembled thin bone plate (AATBP) fabricated using 3D printing has been proposed to improve the biomechanical performance of complex patellar fractures.[24,25] This plate incorporates a double-hook embracing structure and a ratchet-type height-adjustment mechanism, enabling adjustable fixation length based on patellar size and providing active compression. Finite element (FE) analysis and dynamic fatigue testing demonstrated that the AATBP obviously reduces fracture gap and bone stress while maintaining excellent stability under repeated loading. However, despite the use of 3D printing technology, the structural stiffness of the AATBP remains excessively high. Although this design offers strong operational stability, it limits implant light weighting and restricts flexible intraoperative adjustments. Therefore, the present study refines the previous design by introducing a topology-optimized, lightweight framework that reduces stiffness while preserving moderate elasticity and adaptive curvature, thereby improving clinical operability and achieving a balance between rigidity and adjustability.

Furthermore, clinical observations suggest that for patellar fractures located proximally in a transverse pattern or those that are highly comminuted,[14–18] relying solely on circumferential compression from the proximal and distal hooks, together with anterior screw fixation, may be insufficient. This limitation can result in displacement of the proximal fragment and uneven interfacial pressure. To address this mechanical deficiency, this study introduces a dual-compression design concept. Two micro distal-oriented fixation screws are incorporated into the proximal hook of the original AATBP. These screws extend distally to create a local bi-axial compression path. This design simultaneously generates downward pressure and inward clamping force, providing both circumferential and penetrating dual compression, thereby improving proximal fragment stability and shear resistance, particularly for proximal transverse and comminuted fracture patterns.

This study investigates the 3D-printed fabrication of a novel lightweight patellar fixation plate. Functional four-point bending static and fatigue tests were conducted to evaluate the structural rigidity, bending strength, and fatigue durability of the plate in accordance with the Food and Drug Administration (FDA) regulations and American Society for Testing and Materials (ASTM) F382 standards.[26] In parallel, the load-bearing capacity of proximal transverse and comminuted fractures within acceptable bone-healing gaps was evaluated under single-circumferential compression fixation and dual-compression fixation. Additionally, a biomechanical dynamic testing platform was utilized to replicate the repetitive loading conditions encountered during clinical knee extension. Dynamic fatigue tests were conducted to assess changes in fracture displacement and maximum reactive force under different fixation strategies, thereby determining the mechanical feasibility of the dual-compression patellar fixation plate.

2. Materials and methods

2.1. Novel bone plate design concept and finite element analysis

The novel 3D-printed patellar fixation plate is an extension and refinement of a previously published AATBP,[24,25] incorporating structural modifications based on the requirements of structural optimization and addressing unmet clinical needs for compression fixation. The AATBP was reconstructed using clinical patellar computed tomography morphology and features a modular configuration consisting of a proximal plate and a distal plate. These components were connected through a

ratchet-type compression adjuster, which allowed overall height adjustment according to patellar size. A dual-hook wrapping mechanism was included at both the proximal and distal ends to achieve circumferential coverage of the fracture margins and prevent slippage. The overall plate thickness was controlled at 1.6 mm to minimize subcutaneous irritation, and 0.6-mm-high conical bumps were incorporated on the posterior surface to enhance bone–implant friction and stability (Figure 1A).

The previously constructed computer-aided design (CAD) model of the patellar C3 comminuted fracture fixation AATBP and the associated ligaments/tendons were imported into ANSYS Workbench (version 22, Swanson Analysis, United States of America [USA]) for FE analysis. This analysis aimed to evaluate the mechanical behavior of the fixation under a standardized tensile loading condition. A quadratic 10-node tetrahedral solid element was used for meshing, resulting in 38,991 elements and 70,742 nodes (Figure 1A). To simulate contact behavior between bone–bone interfaces (fracture surfaces, friction coefficient = 0.45) and between the AATBP and bone (friction coefficient = 0.3), frictional contact elements reported in the literature were adopted. Cortical bone, cancellous bone, tendons, the AATBP, and fixation screws were all modeled as linear elastic and isotropic materials according to relevant literature.[24,25,27,28] The proximal (basal) nodes of the quadriceps tendon were fully constrained in all directions as boundary conditions. A tensile load of 150 N was applied along the longitudinal axis of the patellar tendon to simulate biomechanical testing conditions (Figure 1A).

Topology optimization was integrated with FE analysis to optimize the proximal plate structure.[29] The objective was to minimize compliance, i.e., maximize stiffness, while satisfying a 70% volume-retention constraint. This optimization aimed to achieve light weighting while maintaining an optimal distribution of structural material. The resulting topology maps indicated regions suitable for material removal, which were subsequently reconstructed in the CAD environment using SpaceClaim (version 22, Swanson Analysis, USA). Lateral wing structures were added to accommodate clinical micro-adjustments, allowing minor intraoperative shaping to match individual patellar curvatures on both sides (Figure 1A & B).

To provide proximal circumferential compression and alignment, holes were designed on both sides of the proximal plate at the hook platform locations, along the proximal–distal direction, to accommodate a locking screw (2.0 mm diameter, 17 mm length). The screw features continuous threading to lock its head into the hook platform, forming a dual-compression fixation pathway together with the screw originally inserted through the anterior curved surface of the plate. This mechanism provides dual-compression fixation for proximal transverse and comminuted fractures, thereby enhancing the overall stability of patellar fracture repair (Figure 2A).

The optimized plate was also evaluated via FE analysis using a C3 comminuted patellar fracture model, representing a clinically severe scenario, under identical loading and boundary conditions as the original AATBP. The optimized plate mesh model consisted of 110,855 elements and 159,971 nodes (Figure 1B). Bone maximum principal stress and plate von Mises stress were compared to evaluate differences in mechanical performance between the AATBP and the optimized plate.

2.2. Manufacturing of bone plate

The novel dual-compressive lightweight patellar bone plate was fabricated using metal 3D printing (additive manufacturing) technology. The components were produced using a selective laser melting (SLM) system, specifically the EOS M290 (EOS GmbH, Germany). The printing material used was a commercially available medical-grade Ti-6Al-4V alloy powder. Its chemical composition included titanium (balance), aluminum (5.5–6.5 wt%), vanadium (3.5–4.5 wt%), and controlled trace impurities such as oxygen (<0.13 wt%), carbon (≤0.08 wt%), and nitrogen (≤0.05 wt%). The particle size distribution ranged from 15 to 53 μm, meeting standard specifications for medical-grade powder bed fusion processing.[25] The SLM process employs a high-energy laser to selectively melt and solidify powder bed layers, enabling the fabrication of complex geometries and curved structures with high precision—an advantage particularly suited for orthopedic implants that require strict shape conformity.

For the manufacturing parameters, the laser power was set to 400 W, the scanning speed to 0.6 m/s, and the exposure time to 125 μs.[24,25,29] A layer thickness of 90 μm and a hatch spacing of 30 μm were selected to enhance component resolution and ensure dimensional stability. The overall manufacturing tolerance was controlled to approximately 30 μm. To minimize deformation caused by thermal accumulation, each plate was oriented along the edge of the patella contour, ensuring greater forming stability throughout the build process.

Post-processing was performed to improve surface quality after SLM fabrication. First, burrs were removed by hand, and then the surface was polished with a magnetic polishing system. The polishing medium consisted of stainless-steel pins (1 mm diameter, 3 mm length) that were operated at 2700 rpm. Residual powder and metallic debris were subsequently removed by ultrasonic cleaning, ensuring that surface cleanliness met clinical requirements.[24,25,29]

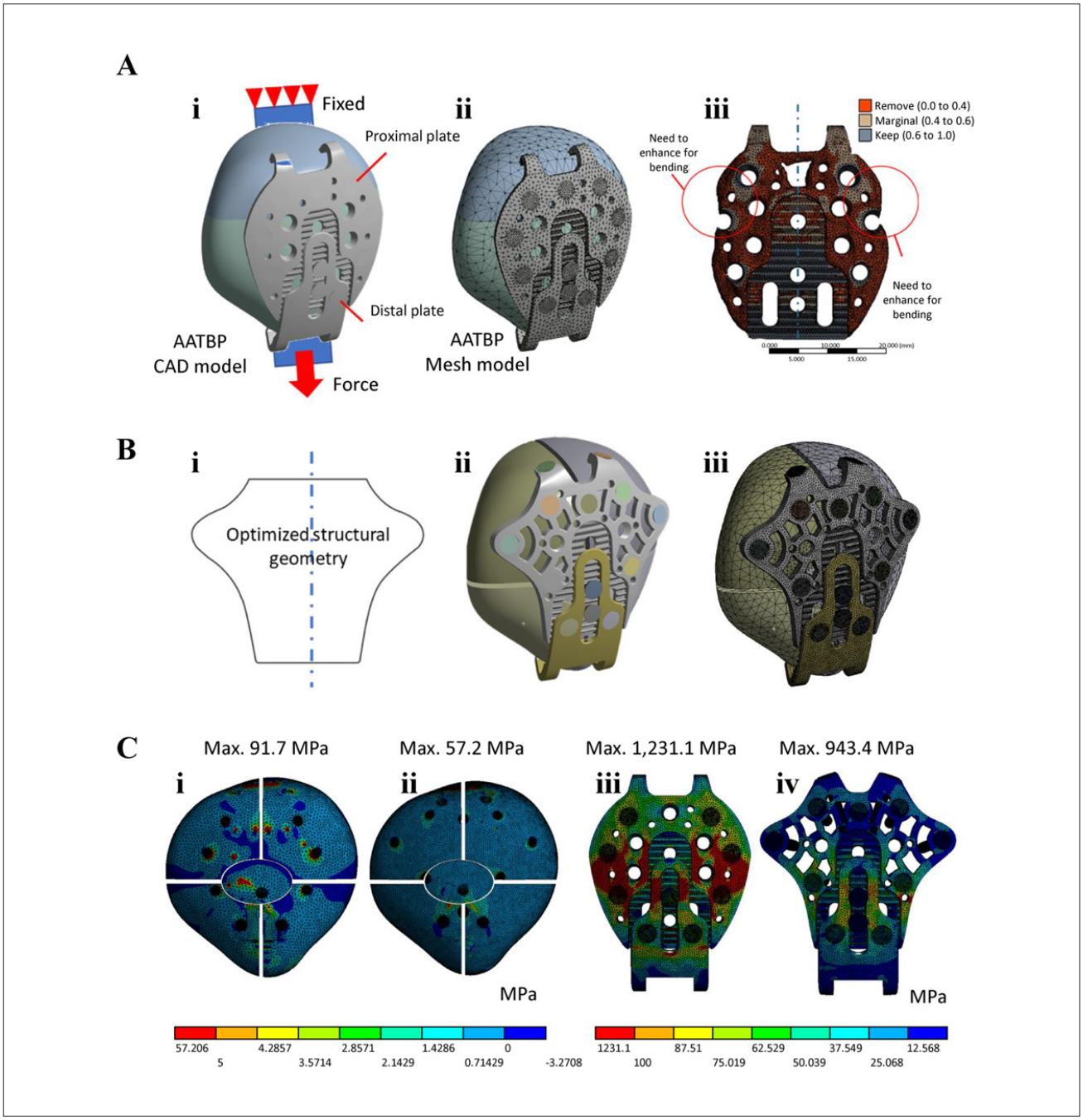


Figure 1. Topology-optimized and FE analysis of new plate. (A) Topology-optimized redesign of the proximal plate. The original anatomically assembled thin bone plate (AATBP) (i) computer-aided design (CAD) model and (ii) finite element (FE) mesh model are shown alongside the topology map, which indicates material retention and removal zones. (iii) The right part showed that critical load-bearing regions were preserved, and low-stress material was removed. (B) (i) Both lateral wing structures were added to accommodate minor intraoperative shaping. (ii) CAD and (iii) FE mesh models of the optimized plate, respectively. (C) (i) Bone principal stress patterns for AATBP and (ii) optimized plate, and corresponding maximum stress values. Plate von Mises stress patterns for (iii) AATBP and (iv) optimized plate, and corresponding maximum stress values.

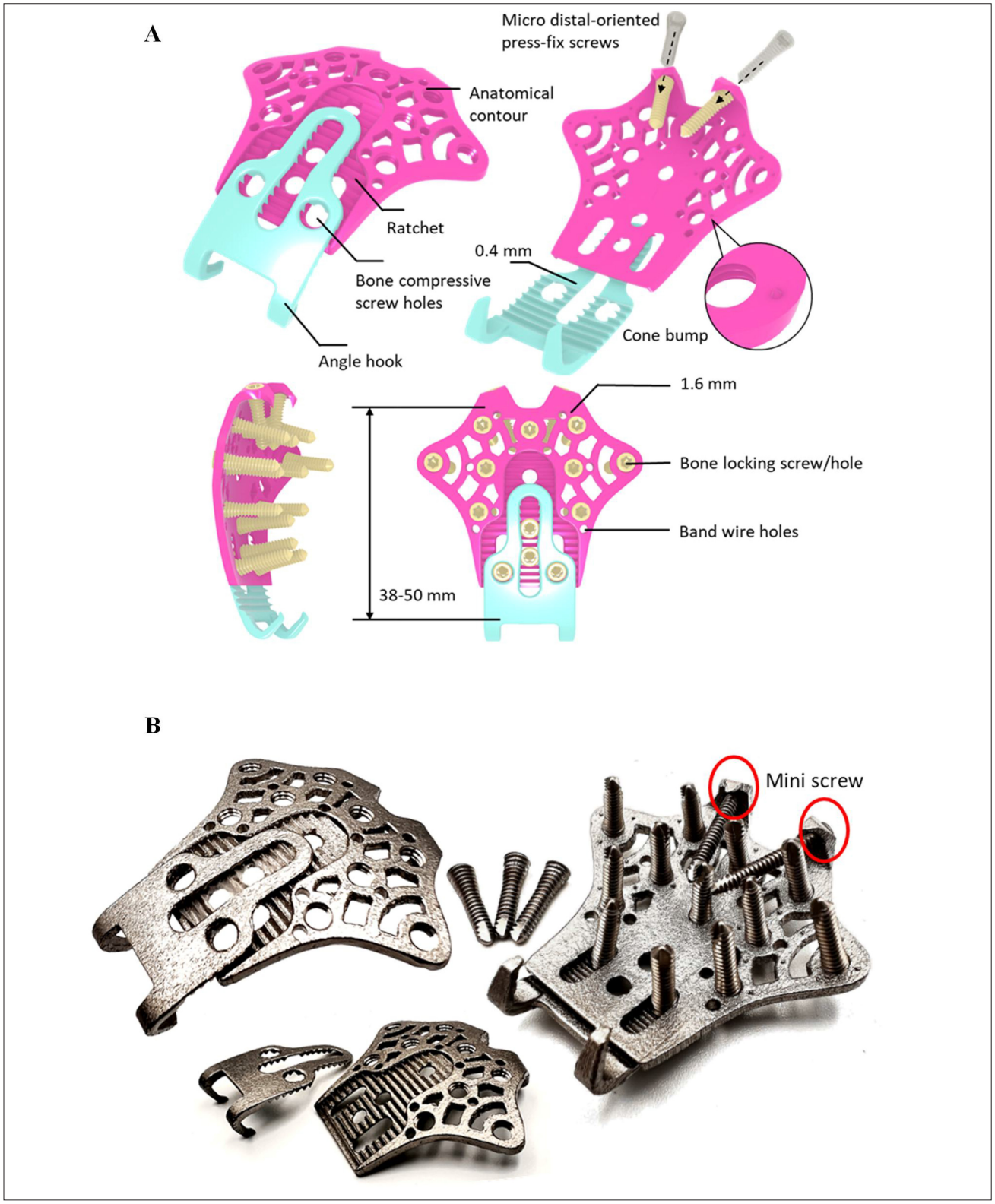


Figure 2. CAD and physical mode of the new patellar plate. (A) Final structural design of the topology-optimized patellar plate, featuring micro distal-oriented screws, ratchet adjustment mechanism, proximal and distal hooks, bone-contact cone bumps, and designated screw/wire holes. (B) Metal three-dimensional-printed components of the dual-compression patellar plate produced using selective laser melting.

To achieve the high geometric accuracy required for screw and wire holes, these features were not formed directly during the 3D printing process. Instead, their positions were predefined during the build and later finished by computer numerical control machining. This approach enabled the hole diameter tolerance to be maintained within 0.02 mm, ensuring compatibility with standard clinical screws. All of the holes were within clinically acceptable error limits (Figure 2B). This hybrid additive–subtractive manufacturing strategy combines the geometric freedom of 3D printing with the precision of conventional machining, resulting in a patellar plate that meets the functional and reliability standards required for clinical implantation.

2.3. Static and dynamic four-point bending tests of patellar plates

To provide a comprehensive mechanical reference for patellar plates used in skeletal fixation, static and dynamic four-point bending tests were conducted on the novel dual-compression lightweight patellar plate using an Instron 3000 testing machine (INSTRON, USA). The tests followed the ASTM F382-17 standard to evaluate bending stiffness, structural bending stiffness, bending strength, and fatigue strength.[26]

Since the patellar plate was a short and asymmetrical anatomical plate, it does not satisfy the standard roller-placement configuration specified in the regulation. Therefore, an alternative test setup was developed using rigid extension segments to effectively lengthen the plate and meet the geometric requirements of the four-point bending test. The patellar plate was secured to the customized extension segments at both ends using screws (Figure 3A). The extension segments were designed to avoid interfering with the actual deformation of the plate during bending. Both pairs of loading rollers and support rollers contacted only the extension segments rather than the plate itself, ensuring that the central region of the plate remained within the pure bending zone. In the test configuration, the span between the two loading rollers was set to a = 40 mm, and the distance between each loading roller and its adjacent support roller (loading span) was set to h = 40 mm, resulting in a total support span of 120 mm, consistent with the four-point bending geometry defined by ASTM F382. The roller diameter was 6 mm (Figure 3B).

Static testing was performed on three samples using a four-point bending fixture, with loading applied at a displacement rate of 0.05 mm/s until failure. For each test, the proof load (P), bending stiffness (K), and structural bending stiffness (EI_e) were calculated according to the standard, and the failure mode of each specimen was documented. The P was defined as the load corresponding to a 0.2% deviation from the linear region of the load–displacement curve, and the K was obtained from the slope of the linear portion of the load–displacement curve. The EI_e was calculated from the geometry of the four-point bending setup as shown in **Equation (1)**.

$$EI_e = \frac{(2h^3 + 3ha)Kh^2}{12} \quad (1)$$

Fatigue testing was conducted based on the P obtained from the static tests. Three maximum load levels were selected: 30% P, 25% P, and 15% P. Three specimens were tested at each load level. A sinusoidal cyclic load was applied at a constant frequency of 5 Hz, with the stress ratio (R-ratio) set to 0.1 (i.e., the minimum bending moment was 10% of the maximum). Each specimen was subjected to cyclic bending from initial loading until either an obvious fracture occurred or the cumulative cycle count reached 1×10^6 (runout), at which point the test was terminated. For each specimen, the maximum bending moment, termination cycle count, and failure mode and location were recorded to construct the moment–life (M–N) relationship.

2.4. Biomechanical static and dynamic tests

Common transverse patellar fractures (Arbeitsgemeinschaft für Osteosynthesefragen (AO) classification: 34-C1, denoted as C1) and complex comminuted five-part patellar fractures (AO classification: 34-C3, denoted as C3)[24,25] were selected as the test models. A 3D CAD model of the patella was reconstructed from skeletal computed tomography images. The model was simplified and segmented in CAD software (PTC Creo V6.0; PTC, USA) to simulate the two fracture types, leaving a passage for a 25-mm-wide polyester tension-band loop that simulated the quadriceps and patellar tendons (Figure 4A). Fabrication was performed using a 3D printer (Dimension 1200es SST; Stratasys, USA) with acrylonitrile–butadiene–styrene (ABS) copolymer (ABS-P430; Stratasys, USA) as the material. The novel dual-compression lightweight patellar plate could be adjusted via a ratchet mechanism to match the printed patellar height (approximately 40.0 mm). Fracture fragments were secured using corresponding hooks that passed through the straps. Before final fixation, the curvature of the plate was manually adjusted to match the anterior patellar surface as closely as possible. For C1 and C3 fractures, 2.4 × 12-mm locking screws (A Plus Biotechnology Co., Ltd., Taiwan) were inserted into the proximal plate. For dual-compression specimens, an additional locking screw was inserted on each side of the hook platform on the proximal plate. The screws were

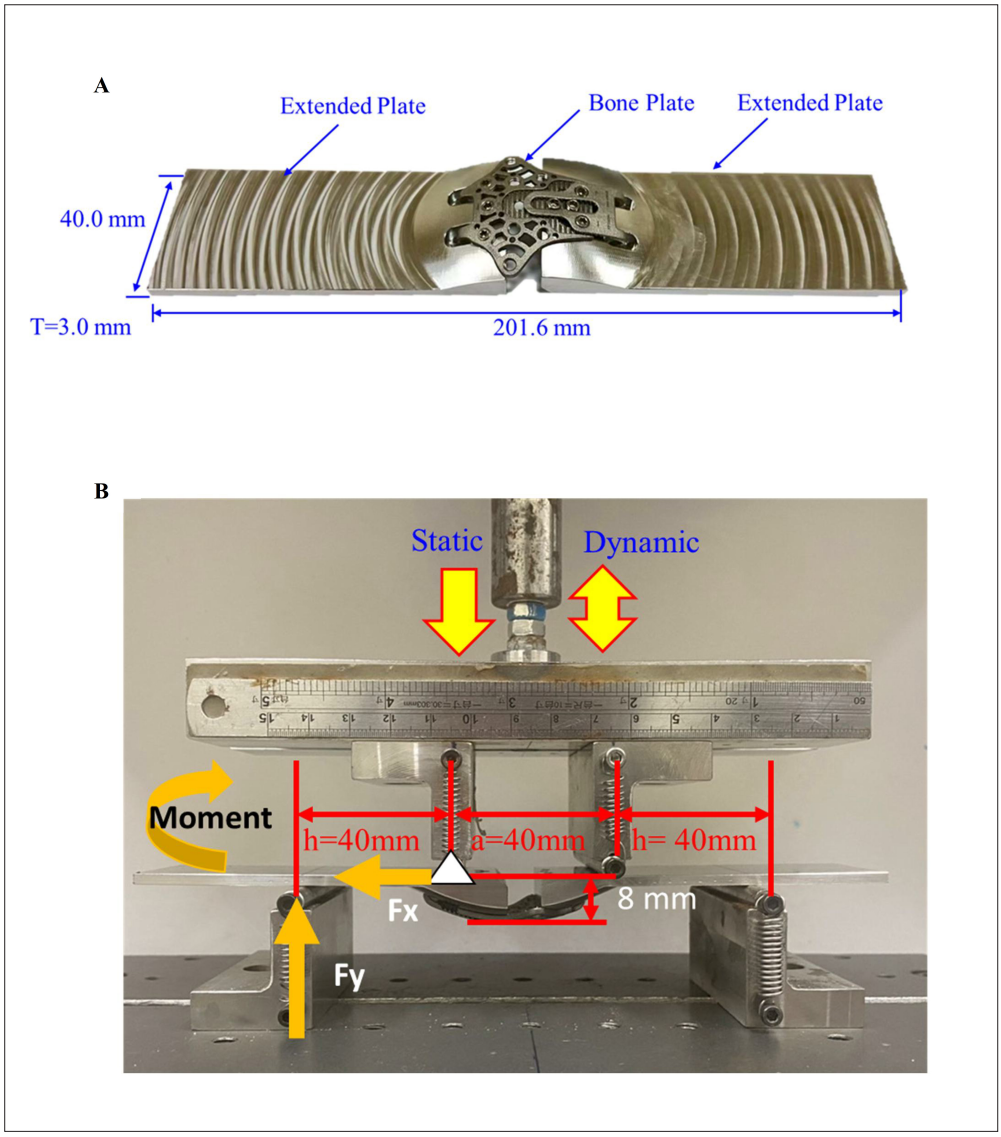


Figure 3. ASTM F-382 four-point bending testing. (A) Custom-designed extension plates used to satisfy American Society for Testing and Materials F382 standard four-point bending test geometry, enabling proper roller placement and establishing a pure bending region. (B) Four-point bending test setup showing applied forces, moment equilibrium calculations, loading span (h = 40 mm), total support span (120 mm), and the static proof-load determination (257.31 N).

evenly distributed with lateral symmetry to stabilize the fractured patella and effectively bypass the fracture gap (Figure 4B).

Static tensile failure tests were first conducted on both fracture types (C1 & C3) using single- and dual-compression fixation configurations. Three specimens were prepared for each test condition. Polyester tension bands simulating the quadriceps and patellar tendons at the proximal and distal ends were clamped to the upper and lower grips of the testing machine, respectively, ensuring the specimen's alignment and the loading direction. A measuring ruler was placed beside the specimen and parallel to the tension band to record crack opening on the medial and lateral sides after loading. The proximal tension band was then pulled upward at a rate of 3 mm/min until the medial or lateral crack opening exceeded 2 mm, at which point loading was stopped (Figure 4A). After removal, the medial and lateral crack openings were measured again using digital vernier calipers.

Twelve additional specimens were prepared for dynamic biomechanical testing, corresponding to two patellar fracture types and two fixation configurations

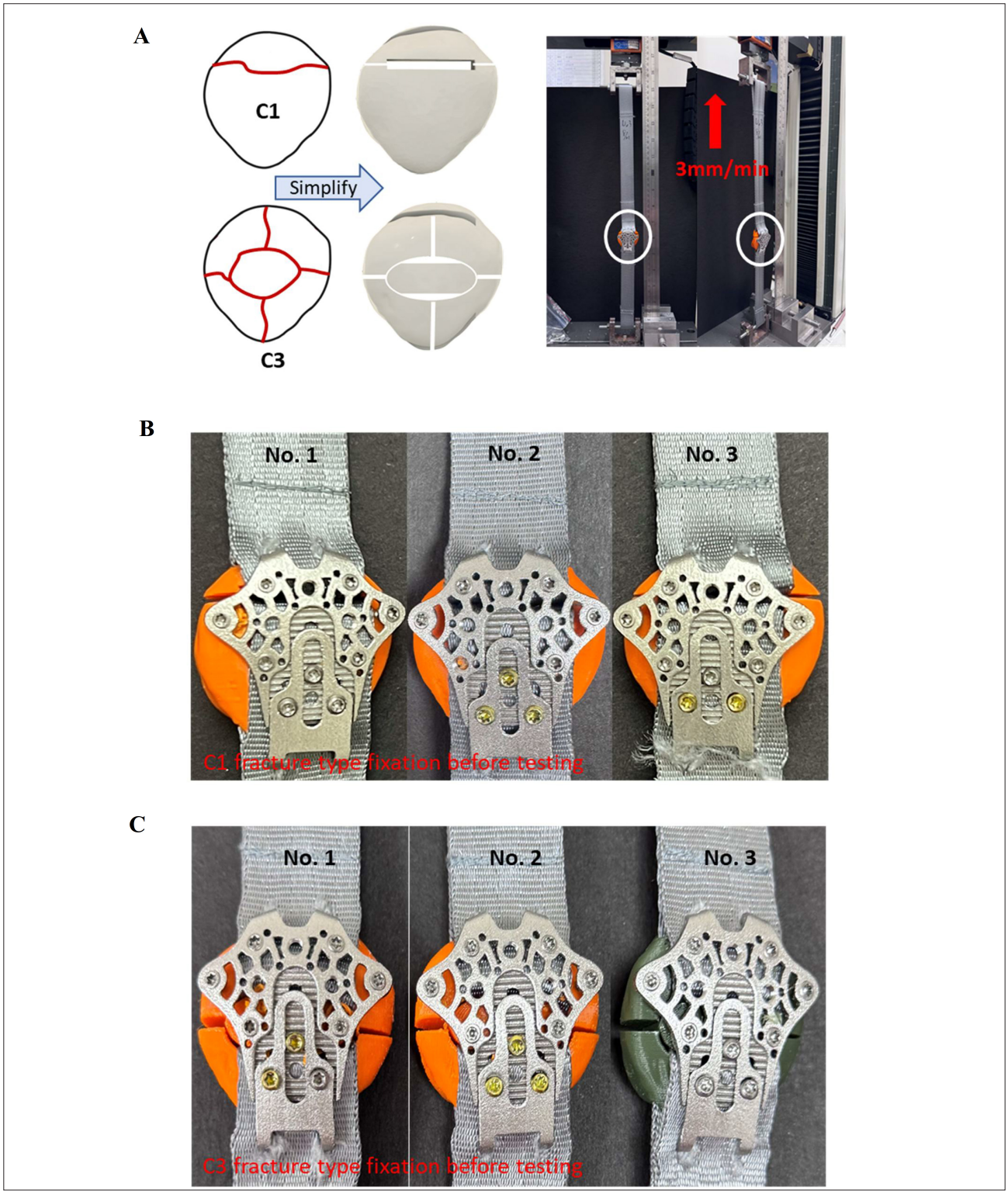


Figure 4. Static failure testing. (A) Computer-aided design-based reconstruction of C1 transverse and C3 comminuted patellar fractures and fabrication using acrylonitrile–butadiene–styrene three-dimensional printing. (B) Single and dual compression fixation configurations before static tensile loading for C1 fractures, showing specimen preparation. (C) Single and dual compression fixation configurations before static tensile loading for C3 fractures, showing specimen preparation. One sample exhibited a different color; however, the material composition was identical and did not affect the experimental results.

(single- and dual-compression) (n = 3 per group). All specimens were vertically clamped on the biomechanical testing platform previously developed by Liao *et al*[24,25] to simulate knee flexion at 90°. A femoral condyle model fabricated using ABS material via 3D printing served as the fulcrum, and a preload of 20 N was applied to ensure that the tension-band loop was fully stretched until the force–displacement curve entered the linear region (Figure 5A).

During dynamic testing, tensile loading was applied through polyester tension-band loops attached to the proximal end (quadriceps tendon) and distal end (patellar tendon). A vertical downward load of 15 kg (approximately 150 N) was added to simulate knee motion from 90° flexion to full extension at 0° (Figure 5A). Each cyclic loading test simulated the patellofemoral contact trajectory from 90° flexion (0 mm stroke) to 0° extension (50 mm stroke) at a constant speed of 5 mm/s. All specimens underwent 300 loading cycles, each controlled by a 50-mm position stroke. The relationship between quadriceps tendon force and flexion–extension displacement, measured using a force sensor, was recorded and plotted for each loading cycle (Figure 5A). Additionally, the fracture gap at the medial and lateral borders of each patella was measured using digital calipers before and after the final test cycle.

2.5. Statistical analysis

All recorded data in this study were organized and processed using Microsoft Excel (Microsoft 365, 2023; Microsoft, USA). Statistical comparisons among the five groups were performed using the Kruskal–Wallis test, due to the small sample size and non-normal data distribution, with analyses conducted using the Statistical Package for the Social Sciences software (version 22; IBM, USA).

3. Results

Figure 1A illustrates the geometric adjustments to material retention and removal based on the topology optimization results. Critical load-bearing regions were reinforced, while low-stress regions were removed. Lateral wing structures were added on both sides to accommodate minor intraoperative shaping, thereby completing the reconstruction and optimizing the implant design (Figure 1B). Figure 1C shows a comparison of FE analysis between AATBP and the new optimized plate, demonstrating that the maximum principal stress in the patella decreased from 91.7 MPa in the AATBP to 57.2 MPa in the new plate, indicating reduced stress transfer to the bone and a lower risk of secondary fracture or fixation failure. The plate's maximum equivalent stress also decreased from 1231.1 to 943.4 MPa, accompanied by a more uniform stress distribution. In contrast, the original AATBP exhibited a pronounced stress concentration in the central bridge region.

Figure 2A shows the final implant, redesigned according to the topology optimization results and manufactured using metal 3D printing. A locking screw can be inserted into the hook-platform region on both sides of the proximal plate, forming a "dual-compression" fixation pathway together with the screw originally inserted through the anterior plate surface. The right-side image of Figure 2B displays the actual screw-implantation configuration, confirming that no interference occurs between the newly added guide-screw hole and the original screw path, ensuring clinical feasibility and surgical convenience. The original AATBP structure weighed approximately 6 g, while the optimized bone plate weighed about 4.5 g, representing a reduction of roughly 25% (Figure 2B).

Figure 6Ai illustrates the load–displacement curve of the static four-point bending testing. The results showed that the mean (standard deviation) values of P, K, and EI_e were 257.31±5.40 N, 5.15±0.11 N/mm, and 1.10±0.01 N·m^2, respectively. The M–N curve from the dynamic fatigue four-point bending test is presented in Figure 6Aii. The results indicate that the plate cannot withstand one million loading cycles and fails under both 30% P and 25% P load levels (three specimens per group). Table 1 lists the relevant values. Figure 6B shows the appearance of the specimen after static testing. Figure 6C shows the fatigue–failure fracture morphology. Two failure modes were identified: Type I, characterized by an obvious fracture of the plate, and Type II, characterized by screw fracture without visible damage to the plate. The failure conditions of each specimen are summarized in Table 1.

Static biomechanical failure testing showed that, for both fracture types (C1 & C3), the dual-compression fixation method resulted in meaningfully higher failure loads—defined as a 2-mm increase in medial and lateral fracture-gap opening—than the single-compression method (Figure 7A). For both fracture types (C1 & C3), the higher failure-load values represent the dual-compression fixation method, and the lower values represent the single-compression method, reported as mean ± standard deviation. Specifically, for C1, the dual- and single-compression failure loads were 712 ± 31.51 N and 517.5 ± 29.05 N, respectively; for C3, the corresponding values were 253.75 ± 6.34 N and 205.25 ± 4.59 N (Figure 7B).

Dynamic biomechanical testing demonstrated that the maximum quadriceps-reaction force for all simulated conditions (Figure 5A) occurred within an extension-angle range of 62–66°. The average forces (**mean ± standard deviation**) for single- and dual-compression fixation were 293.92±38.4 N / 292±2.82 N for C1 and 262.13±22.63

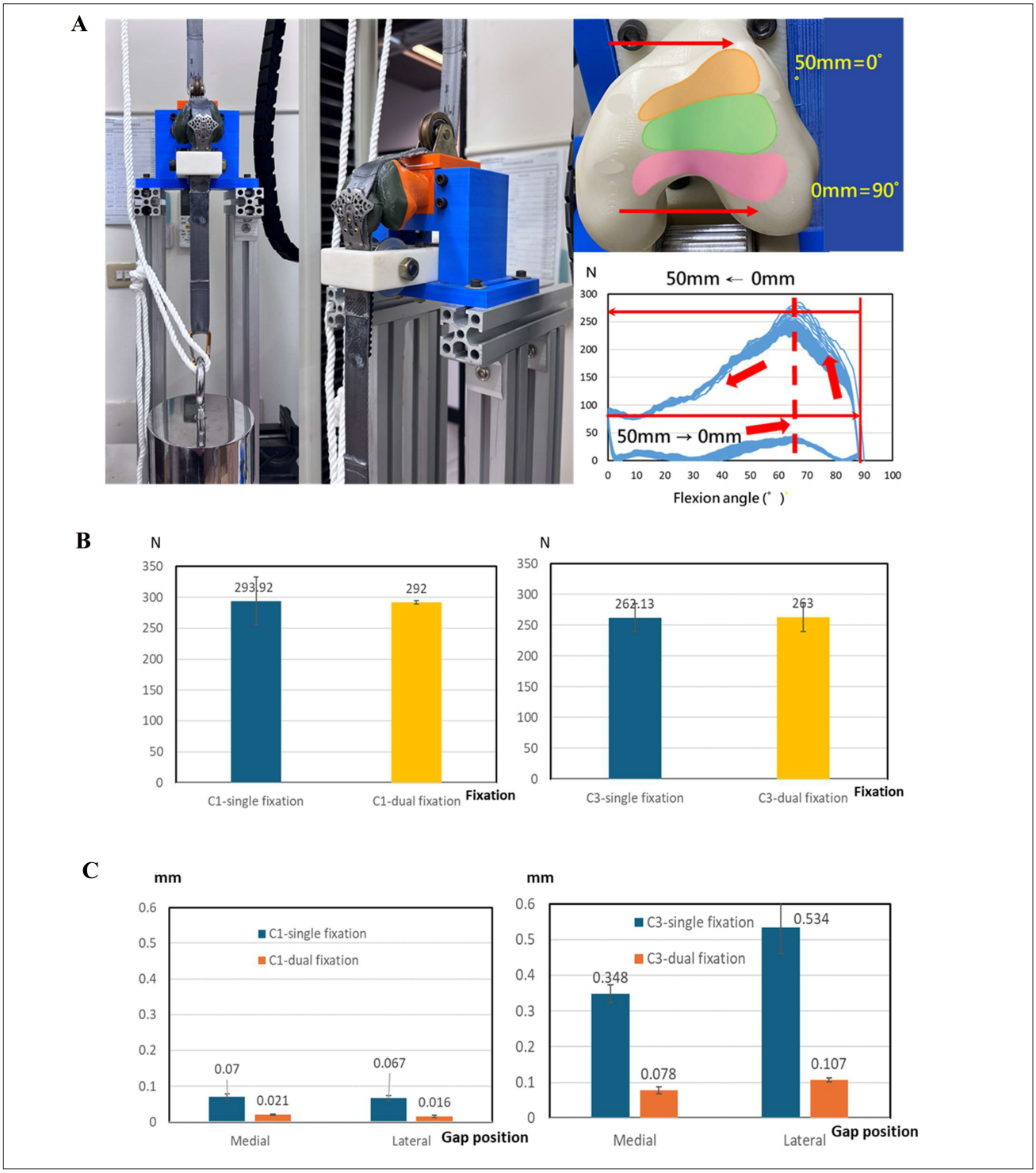


Figure 5. Dynamic test and results (A) Dynamic knee-extension biomechanical testing setup. Patella specimens were mounted at 90° knee flexion, and the femoral condyle model served as the fulcrum. The 50-mm stroke simulated patellofemoral motion from 90° flexion to 0° extension. (B) Quadriceps reaction forces for C1 and C3 fracture models under single- and dual-compression fixation, showing similar peak force ranges (62°–66° extension). (C) Interfragmentary gap measurements on medial and lateral fracture borders before and after dynamic loading, demonstrating significantly reduced micromotion under dual-compression fixation.

Table 1. Fatigue test results under different percentages of proof load

Sample	Percentage of proof load	Range of load (N)	Number of cyclic loads	Failure mode
4	30%	9.74–97.43	243,659	Type I
5	30%	9.74–97.43	19,770	Type II
6	30%	9.74–97.43	169,694	Type II
7	25%	8.12–81.19	666,352	Type II
8	25%	8.12–81.19	254,874	Type I
9	25%	8.12–81.19	690,677	Type II
10	15%	4.87–48.72	1,000,000	Pass
11	15%	4.87–48.72	1,000,000	Pass
12	15%	4.87–48.72	1,000,000	Pass

N / 263±22.9 N for C3 (Figure 5B), with no statistically significant differences (p>0.05).

Regarding interfragmentary gap measurements, both C1 and C3 fractures showed markedly smaller medial and lateral gap openings under dual-compression fixation than under single-compression fixation, and this improvement was statistically significant (p<0.05). For C1, the medial/lateral gaps under single vs. dual compression were 0.07 mm/0.067 mm (average 0.0685 mm) and 0.021 mm/0.016 mm (average 0.018 mm), respectively. The corresponding gaps for C3 were 0.348 mm/0.534 mm (average 0.441 mm) and 0.078 mm/0.107 mm (average 0.0925 mm) (Figure 5C). Additionally, C1 consistently exhibited smaller medial and lateral gaps than C3, regardless of the fixation configuration.

4. Discussion

This study reconfigured the material distribution of the anterior patellar plate through topology optimization to address the excessive stiffness of the original AATBP while preserving the structural integrity required for patellar fixation. The primary objective was to allow slight intraoperative bending without compromising the essential load-bearing framework. By applying a topology optimization algorithm constrained by a 70% volume fraction, material was preferentially retained along the primary tension and compression transmission paths in the bending core region, while low-stress peripheral material was removed to reduce overall stiffness and weight.

The 70% volume constraint was not arbitrarily selected; instead, it was determined based on convergence behavior and clinical design constraints. Since the original AATBP includes predetermined screw holes at fixed clinical positions, excessive material removal around these regions led to numerical instability and unrealistic geometries. An initial optimization attempt with 60% volume retention failed to converge, likely due to insufficient load-transfer pathways surrounding the constrained screw-hole regions. In contrast, stable convergence was achieved at a 70% volume retention rate, which was therefore selected as the lowest feasible and convergent constraint.

As a result, the plate mass was reduced from approximately 6.0 g for the original AATBP to 4.5 g for the optimized design, representing a 25% reduction in weight. In addition, lateral wing structures were incorporated to form locally thin-walled regions, enabling minor surgical contouring while maintaining the mechanical integrity of the core load-bearing region. Under identical loading and boundary conditions, FE analysis using a C3 comminuted patellar fracture model further demonstrated the mechanical advantages of the optimized design compared with the original AATBP. The maximum principal stress in the patella decreased from 91.7 MPa to 57.2 MPa, indicating reduced stress transfer to the bone and a lower risk of secondary fracture or fixation failure. The maximum equivalent stress in the plate also decreased from 1,231.1 MPa to 943.4 MPa, accompanied by a more uniform stress distribution, whereas the original AATBP exhibited pronounced stress concentration in the central bridge region. Collectively, these results confirm that the optimized AATBP achieved a 25% weight reduction while maintaining—and in some aspects improving—its mechanical performance, thereby supporting the core claim that the plate can be lightened without compromising structural stability.

Regarding the concept of proximal enhanced compression, this study proposed a reinforced dual-compression mechanism to enhance shear control and fragment coaptation. Two miniature locking screws were therefore added to the proximal hook platform. The compressive force generated by these screws provides additional axial compression and inward clamping on the proximal fragments, reducing the likelihood of

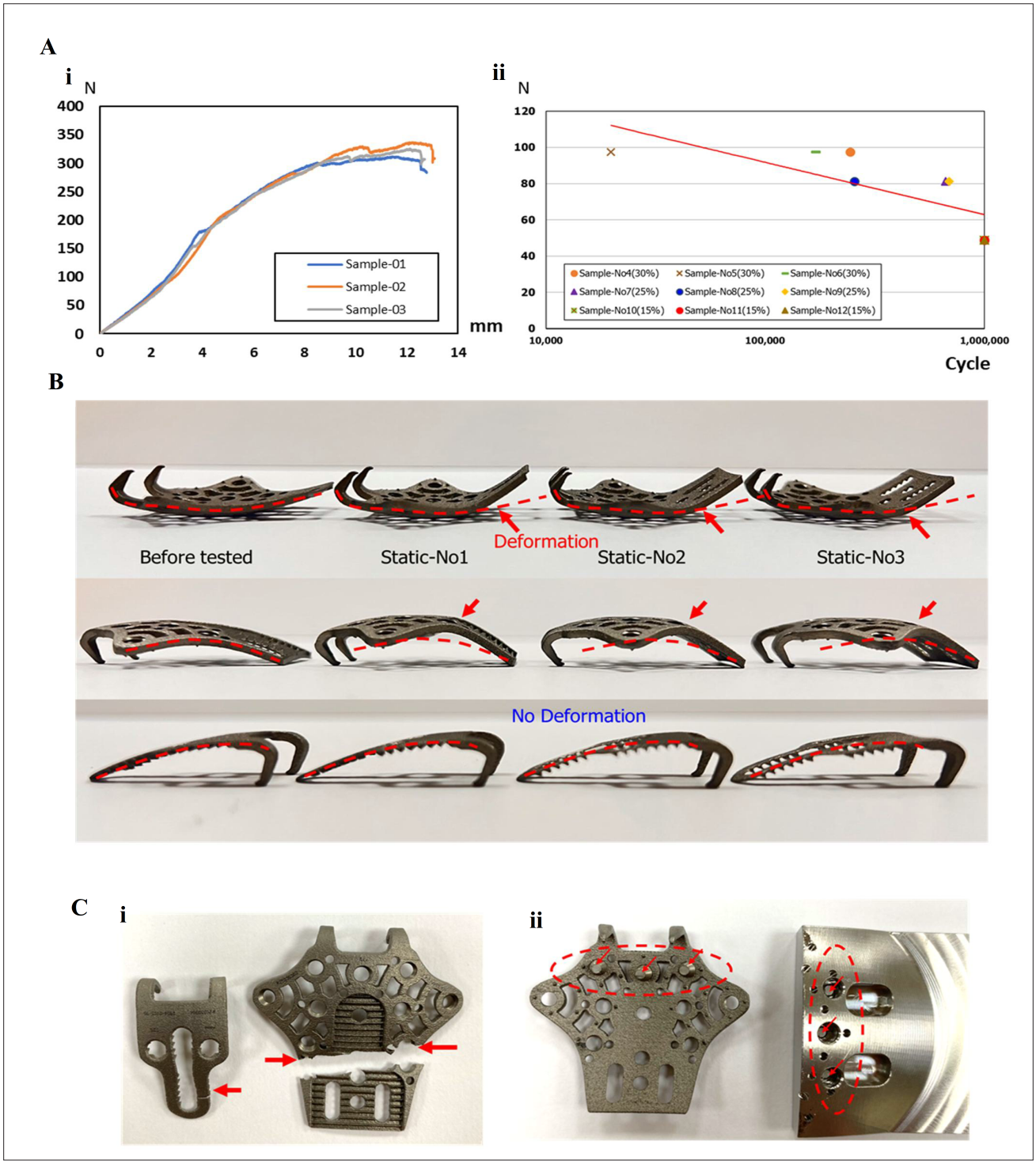


Figure 6. Results of four-point bending test. (A) Load–displacement curves and S–N (moment–life) fatigue curves from ASTM F382 testing. The plate failed before 1×10^6 cycles at 25% proof load and 30% proof load. (B) Static bending deformation patterns for three specimens, compared with the undeformed plate prior to testing. (C) Two fatigue-failure modes: (i) Type I—fracture of the plate at the topology-optimized transition zone; (ii) Type II—locking-screw fracture without visible plate damage.

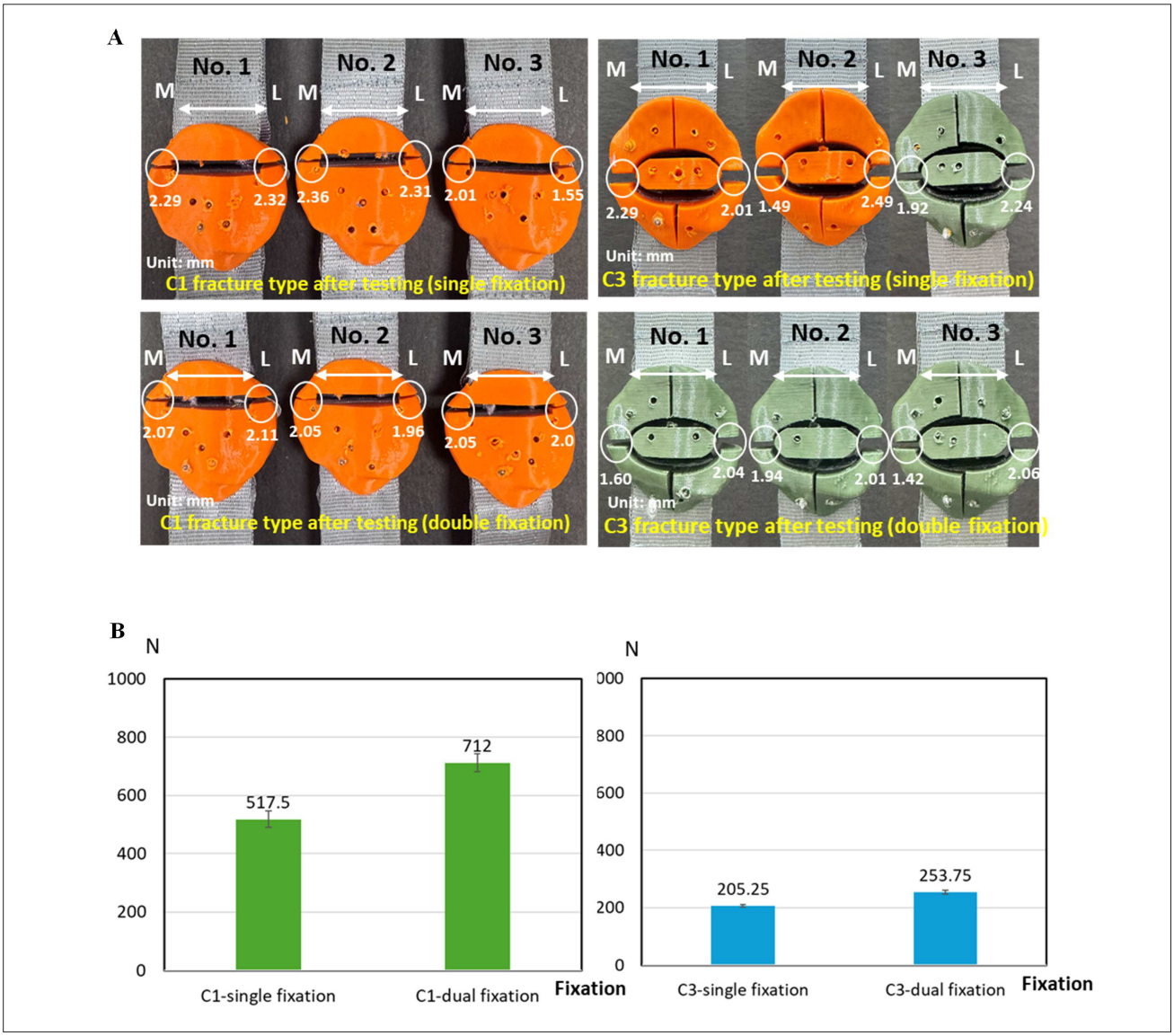


Figure 7. Results of dynamic biomechanical test. (A) Static tensile failure patterns for C1 and C3 fractures under single- and dual-compression fixation, showing medial and lateral gap openings at the 2-mm failure criterion. Some samples exhibited different colors; however, the material composition was identical and did not affect the experimental results. (B) Failure loads for C1 and C3 fractures, indicating significantly (*p<0.05) higher load-bearing capacity with dual-compression fixation compared with single-compression fixation.

slippage or valgus displacement under tensile loading. Static biomechanical tensile testing confirmed that, for both C1 and C3 fractures, dual compression resulted in a substantially higher failure load than single compression.

Dynamic knee-extension testing further demonstrated that dual compression significantly reduced micromotion at the fracture interface during functional loading. Using a dynamic platform capable of reproducing patellar sliding, rotation, and tension changed from 90° to 0° of knee extension, deformation across the medial and lateral fracture lines was quantified. The results showed that dual compression produced markedly reduced fracture-gap opening with improved bilateral symmetry; in C3 fractures, the gap decreased dramatically from 0.348–0.534 mm to 0.078–0.107 mm for the medial-lateral side. Literature indicates that maintaining interfragmentary micromotion within 0.2–1.0 mm provides a mechanically favorable environment for endochondral ossification and promotes stable bone healing.[30,31] Therefore, the dual-compression design demonstrated in this study provides an effective strategy for improving the biological healing environment without increasing quadriceps reaction

forces, confirming that the construct does not impose excessive mechanical constraint.

In this study, a comprehensive dynamic biomechanical comparison was further conducted among the topology-optimized single- and dual-compression plates, the previous AATBP design, and a commercially inspired anterior plate (ASP).[25] In terms of quadriceps reaction force, ASP exhibited the highest peak values in both C1 and C3 fracture models (334.5 N & 260.6 N, respectively), indicating the least stable force transmission behavior. In contrast, the AATBP demonstrated the lowest reaction forces (238.1 N for C1 & 198.3 N for C3), reflecting its high structural stiffness and efficient load transmission. The topology-optimized plates showed intermediate reaction forces between ASP and AATBP, with peak values of 293.92 N and 262.13 N for the single- and dual-compression configurations in C1 fractures, and 292 N and 263 N, respectively, in C3 fractures. These values were significantly ($p<0.05$) higher than those of AATBP (C1: $p = 0.045/0.010$; C3: $p = 0.006/0.006$), indicating a redistribution of load-sharing pathways rather than a reduction in fixation capability.

Unlike quadriceps reaction force, fracture gap displacement represents a more direct and clinically relevant indicator of fixation stability. As summarized in Table 2, C1 fractures showed a progressive reduction in average fracture gap in the order of ASP, AATBP, single-compression, and dual-compression fixation, with the dual-compression design achieving the smallest gap (0.018 mm) and thus the highest stability among all configurations. In C3 comminuted fractures, the AATBP exhibited an extremely small fracture gap (0.0274 mm), which can be attributed to its inherently high structural stiffness. However, even under these highly unstable and clinically challenging conditions, the topology-optimized dual-compression design limited fracture gap displacement to only 0.0925 mm, representing a substantial improvement compared with the ASP plate (1.93 mm). These findings demonstrate that the dual-compression configuration provides superior fragment control and shear stability relative to the commercial reference. Overall, this direct comparison confirms that the topology-optimized dual-compression plate not only advances the structural design beyond the previous AATBP but also delivers superior biomechanical fixation performance in fracture scenarios associated with the greatest clinical instability.

Four-point bending static and fatigue tests revealed that, although the plate structure still exhibited localized high-stress concentration, its overall mechanical performance satisfied baseline safety requirements. According to the ASTM F382 results, the static P, K, and EI_e all met the criteria for metallic bone plates. Under cyclic loading, the plate successfully withstood more than one million cycles without failure at 15% P, meeting FDA fatigue performance requirements for long-term use. However, the plate failed to reach one million cycles at higher load levels of 25% P and 30% P. According to the standard, failure includes not only a complete fracture but also visible crack formation or excessive displacement. Therefore, in our study, any noticeable cracking of the plate or screw was considered a failure to meet the 1×10^6 cycle requirement at that load level. Two distinct failure modes were found for all samples. Type I failure was characterized by fatigue crack initiation in the proximal–central transition region, where the topology-optimized material removal ratio was relatively high, suggesting that the local section modulus and effective EI_e in this area remained insufficient. Type II failure involved

Table 2. Comparison of medial and lateral fracture gap displacement in C1 and C3 fractures

Fracture	Image	ASP	AATBP	Single fixation	Dual fixation
C1		1.233±0.641/0.949±0.917	0.257±0.33/0.110±0.156	0.07±0.0081/0.067±0.0072	0.02±0.0015/0.016±0.0032
Average		1.091	0.2935	0.0685	0.018
C3		1.697±0.66/2.163±1.03	0.002±0.221/0.025±0.414	0.348±0.0249/0.519±0.0604	0.078±0.0098/0.107±0.0061
Average		1.93	0.027	0.4335	0.0925

Note: All data are presented as mean ±standard deviation of medial/lateral components. C1 fracture: ASP>AATBP>Single>Dual; C3 fracture: ASP>Single>Dual>AATBP.

Abbreviations: AATBP, anatomically assembled thin bone plate; ASP, commercially inspired anterior plate.

fracture of the locking screw due to excessive shear loading, indicating that load transfer between the plate and screws was not yet optimally balanced.

The observed fatigue behavior can be attributed to both structural and material factors. Although topology optimization effectively reduces weight by removing material from low-stress regions, it may also introduce stress risers around screw holes and locally thinned sections that reach fatigue limits earlier under high cyclic loads. In addition, the metal 3D-printed Ti-6Al-4V plates in this study did not undergo post-processing treatments such as hot isostatic pressing or annealing, which are known to reduce internal porosity and improve fatigue resistance. Consequently, the fatigue performance at higher load levels is expected to be lower than that of wrought or post-processed components, as reported in previous studies of additively manufactured implants. From a clinical perspective, the 15% *P* condition represents a conservative estimate of long-term postoperative loading under appropriate rehabilitation protocols, whereas the 25% *P* and 30% *P* conditions serve as stress–test scenarios, reflecting unexpected or extreme loading events, such as noncompliance, accidental falls, or high patient activity. These findings not only clarify the fatigue performance envelope of the current design but also provide clear directions for next-generation optimization, including reinforcing the proximal–central transition region, thickening selected struts, and redesigning screw-hole geometry to reduce stress concentration and enhance fatigue durability.

It is worth noting that the ASTM F382 testing completed in this study is not only scientifically meaningful but also represents a key milestone for future commercialization. Patellar fixation plates are classified as Class II medical devices, which do not require animal implantation studies but must pass the four-point bending static and fatigue tests specified in ASTM F382 to demonstrate adequate safety under functional loading conditions. In the static four-point bending test, the *P* was 257.31 N (*y*-direction). Using the left load application point as the fulcrum and applying the principle of moment equilibrium, F_y = 257.31/2 N, therefore:

$$128.655\ \text{N} \times 40\ \text{mm} = F_x \times 8\ \text{mm} \quad (2)$$

the reaction force at the fulcrum was calculated to be approximately 618.275 N (*x*-direction: F_x) (Figure 3B). This value exceeds the 517.5 N required in biomechanical tensile testing to produce an interfragmentary gap of more than 2 mm, thereby confirming that the plate provides sufficient structural strength. Furthermore, the test results provide comprehensive data on *K*, EI_e, fatigue life, and failure modes, all of which serve as important technical references for the FDA's safety evaluation. These data also offer objective benchmarks for comparison with existing commercially available patellar fixation plates.

The use of ABS 3D-printed patellar models for biomechanical testing was motivated by the advancement of 3D printing technology; consequently, many biomechanical studies now employ 3D-printed bone analogs to evaluate trend-level mechanical differences under highly controlled conditions.[25,32] The primary advantage of this approach is the ability to maintain identical geometry and material properties across specimens, thereby minimizing biological variability that could otherwise obscure fixation-related effects. Consistent with this rationale, the ABS 3D-printed patellae used in this study were not intended to replicate the absolute mechanical behavior of real bone. Instead, they were selected to provide a highly uniform testing substrate, ensuring that differences in fixation design (e.g., C1 vs. C3, single vs. dual compression) constituted the dominant source of mechanical variation. In contrast, natural patellae exhibit substantial inter-individual variability in cortical thickness and cancellous bone density, which could introduce experimental noise exceeding the true mechanical effects of the fixation constructs and thereby reduce the statistical power of between-group comparisons.

Although the elastic modulus and fracture toughness of ABS differ from those of human cortical and cancellous bone and may affect the absolute magnitudes of fracture gap or micromotion, all specimens in this study were fabricated using identical ABS material, printing parameters, and density, ensuring that relative mechanical differences and trends between fixation designs remain valid. To further verify the physiological relevance of these trends, an additional FE analysis using human bone material properties was performed for the single-fixation configuration, demonstrating that the optimized plate exhibited a larger average fracture gap (0.207 mm) than the AATBP (0.187 mm), consistent with the ABS experimental results.

The dynamic testing platform used in this study is a well-established and validated model for comparative patellar biomechanics. The applied 150 N compressive load and single-plane sliding trajectory were adapted from widely accepted protocols in the literature and have also been validated in our previous studies.[24,25] This setup was intentionally designed to provide a highly standardized and reproducible dynamic environment for comparing the relative mechanical performance of different fixation constructs, rather than to replicate the full 3D patellofemoral motion.

Although physiological patellofemoral mechanics involve multi-directional loading, incorporating such complexity would markedly reduce test repeatability and increase inter-specimen variability. While a simplified two-dimensional loading model may underestimate absolute fracture gap magnitude, all constructs—including both fracture types (C1 & C3) and fixation strategies (single & dual compression)—were tested under identical loading and kinematic conditions. This ensures that the observed between-group differences remain valid and reproducible. Future studies using cadaveric patellae and whole-joint biomechanical models under more physiologically representative 3D loading conditions are warranted to further validate the clinical applicability of the dual-compression design.

5. Conclusion

This study developed a topology-optimized, metal 3D-printed dual-compression patellar plate and demonstrated its mechanical feasibility. The optimized design preserved key load-bearing paths while reducing excessive stiffness, and the manufactured plate met ASTM F382 static requirements with runout at 15% *P* in fatigue testing. Two fatigue-failure modes—plate transition-zone cracking and locking-screw fracture—were identified, highlighting areas for structural reinforcement. Static tensile and dynamic knee-extension tests further showed that the dual-compression mechanism significantly improved fragment stability and reduced interfragmentary micromotion, especially in comminuted fractures, without increasing quadriceps reaction force. Overall, the dual-compression plate provides enhanced fixation stability and effective micromotion control, supporting its potential as an improved solution for challenging patellar fractures.

Acknowledgments

None

Funding

This study is supported in part by NSTC project 113-2622-E-A49 -027 and 114-2923-E-A49 -014 -MY2 Taiwan.

Conflict of interest

No potential conflict of interest was reported by the author(s).

Author contributions

Conceptualization, Methodology: Chi-Yang Liao
Methodology, Investigation: Shao-Fu Huang
Methodology: Hsuan-Wen Wang, Ya-Han Chan
Software: Yu-Pin Yang
Investigation, Conceptualization, Writing-Reviewing and Editing: Chun-Li Lin

Ethics approval and consent to participate

Not applicable.

Consent for publication

Not applicable.

Availability of data

The data that support the findings of this study are available from the corresponding author upon reasonable request.

References

1. Schmidt V, Möller Rydberg E, Krause M, Wolf O. Patient-reported outcomes following patella fractures: a nationwide observational study of 8,726 patients from the Swedish Fracture Register. *Bone Jt Open***.** 2025;6(9):1080-1089. doi: 10.1302/2633-1462.69.BJO-2025-0141.R1
2. Larsen P, Court-Brown CM, Vedel JO, Vistrup S, Elsoe R. Incidence and epidemiology of patellar fractures. *Orthopedics***.** 2016;39(6):e1154-e1158. doi: 10.3928/01477447-20160811-01
3. Larsen P, Vedel JO, Vistrup S, Elsoe R. Long-lasting hyperalgesia is common in patients following patella fractures. *Pain Med***.** 2018;19(3):429-437. doi: 10.1093/pm/pnx144
4. Fehske K, Berninger MT, Alm L, *et al*. Current treatment standard for patella fractures in Germany. *Unfallchirurg***.** 2021;124(10):832-838. doi: 10.1007/s00113-020-00939-8
5. Gwinner C, Märdian S, Schwabe P, Schaser KD, Krapohl BD, Jung TM. Fractures of the patella: current concepts review. *GMS Interdiscip Plast Reconstr Surg DGPW***.** 2016; 5:Doc01. doi: 10.3205/iprs000080
6. Singh S, Surana R, Rai A, Sharma D. Outcome analysis of fixed angle locking plate in patella fractures: a single centre experience from North India. *Indian J Orthop***.** 2021;55(3):655-661. doi: 10.1007/s43465-020-00302-4
7. Neumann-Langen MV, Sontheimer V, Näscher J, Izadpanah Z, Schmal H, Kubosch EJ. Incidence of postoperative complications in patellar fractures related to different osteosynthesis procedures. *BMC Musculoskelet Disord***.** 2023;24(1):871. doi: 10.1186/s12891-023-06998-3
8. Stoffel K, Zderic I, Pastor T, *et al*. Anterior variable-angle locked plating versus tension band wiring of simple and

complex patella fractures: a biomechanical investigation. *BMC Musculoskelet Disord*. 2023;24(1):279. doi: 10.1186/s12891-023-06394-x

9. Hung LK, Chan KM, Chow YN, Leung PC. Fractured patella: operative treatment using the tension band principle. *Injury*. 1985;16(5):343-347. doi: 10.1016/0020-1383(85)90144-5
10. Dy CJ, Little MTM, Berkes MB, *et al*. Meta-analysis of re-operation, nonunion, and infection after open reduction and internal fixation of patella fractures. *J Trauma Acute Care Surg*. 2012;73(4):928-932. doi: 10.1097/TA.0b013e31825168b6
11. Larsen P, Rathleff MS, Østgaard SE, Johansen MB, Elsøe R. Patellar fractures are associated with an increased risk of total knee arthroplasty: a matched cohort study with 14.3-year follow-up. *Bone Joint J*. 2018;100-B(11): 1477-1481. doi: 10.1302/0301-620X.100B11.BJJ-2018-0472.R1
12. Garner MR, Homcha B, Cowman T, Goss M, Reid JS, Lewis GS. Transverse patella fracture fixation: a cadaveric biomechanical comparison of cannulated screws and anterior tension band versus low-profile multiplanar mesh plating. *Injury*. 2024;55(6):111574. doi: 10.1016/j.injury.2024.111574
13. Gibert S, Kowaleski MP, Matthys R, Nützi R, Serck B, Boudrieau RJ. Biomechanical comparison of pin and tension-band wire fixation with a prototype locking plate fixation in a transverse canine patellar fracture model. *Vet Comp Orthop Traumatol*. 2016;29(1):20-28. doi: 10.3415/VCOT-15-07-0115
14. Wild M, Fischer K, Hilsenbeck F, Hakimi M, Betsch M. Treating patella fractures with a fixed-angle patella plate: a prospective observational study. *Injury*. 2016;47(8):1737-1743. doi: 10.1016/j.injury.2016.06.018
15. Siljander MP, Vara AD, Koueiter DM, Wiater BP, Wiater PJ. Novel anterior plating technique for patella fracture fixation. *Orthopedics*. 2017;40(4):e739-e743. doi: 10.3928/01477447-20170615-02
16. Lee KH, Lee Y, Lee YH, Cho BW, Kim MB, Baek GH. Biomechanical comparison of three tension band wiring techniques for transverse fracture of patella. *J Orthop Surg (Hong Kong)*. 2019;27(3):2309499019882140. doi: 10.1177/2309499019882140
17. Wagner FC, Neumann MV, Wolf S, *et al*. Biomechanical comparison of a 3.5-mm anterior locking plate to cannulated screws with tension band wiring in comminuted patellar fractures. *Injury*. 2020;51(6):1281-1287. doi: 10.1016/j.injury.2020.03.030
18. Kfuri M, Escalante I, Schopper C, *et al*. Comminuted patellar fractures: the role of biplanar fixed-angle plate constructs. *J Orthop Translat*. 2021;27:17-24. doi: 10.1016/j.jot.2020.09.003
19. Berninger MT, Frosch KH. Change in the treatment of patellar fractures. *Unfallchirurgie (Heidelb)*. 2022;125(7):518-526. doi: 10.1007/s00113-022-01167-y
20. Moore TB, Sampathi BR, Zamorano DP, Tynan MC, Scolaro JA. Fixed angle plate fixation of comminuted patellar fractures. *Injury*. 2018;49(6):1203-1207. doi: 10.1016/j.injury.2018.03.030
21. Wurm S, Augat P, Bühren V. Biomechanical assessment of locked plating for fixation of patella fractures. *J Orthop Trauma*. 2015;29(9):e305-e308. doi: 10.1097/BOT.0000000000000309
22. Ellwein A, Lill H, DeyHazra RO, Smith T, Katthagen JC. Outcomes after locked plating of displaced patella fractures: a prospective case series. *Int Orthop*. 2019;43(12): 2807-2815. doi: 10.1007/s00264-019-04337-7
23. Elsoe R, Thorninger R, Severinsen R, *et al*. Tension band versus locking plate fixation for patella fractures: protocol for a randomized controlled trial. *Dan Med J*. 2024;71(5):A12230753. doi: 10.61409/A12230753
24. Liao CY, Huang SF, Tsai WC, Zeng YH, Li CH, Lin CL. Biomechanical evaluation of an anatomical bone plate assembly for thin patella fracture fixation fabricated by titanium alloy 3D printing. *Int J Bioprint*. 2023;9(6):0117. doi: 10.36922/ijb.0117
25. Liao CY, Huang SF, Tsai WC, *et al*. Biomechanical comparison of traditional and 3D-printed titanium alloy anatomical anterior plating under three patellar fracture conditions. *Virtual Phys Prototyp*. 2024;19(1):e2404982. doi: 10.1080/17452759.2024.2404982
26. ASTM International. *ASTM F382-24: Standard Specification and Test Method for Metallic Bone Plates*. West Conshohocken, PA: ASTM International; 2024. doi: 10.1520/F0382-24
27. Chang CW, Chen CH, Li CT, *et al*. Role of an additional third screw in fixation of transverse patellar fracture with two parallel cannulated screws and anterior wire. *BMC Musculoskelet Disord*. 2020;21(1):752. doi: 10.1186/s12891-020-03744-x
28. Chen CH, Chen YN, Li CT, Chang CW, Chang CH, Peng YT. Roles of the screw types, proximity and anterior band wiring in the surgical fixation of transverse patellar fractures: a finite element investigation. *BMC Musculoskelet Disord*. 2019;20(1):99. doi: 10.1186/s12891-019-2474-7
29. Wang HW, Chen CH, Chen KH, Zeng YH, Lin CL. Designing a 3D-printed medical implant with macrostructural topology and microbionic lattices: a novel wedge-shaped spacer for high tibial osteotomy and biomechanical study. *Int J Bioprint*. 2024;10(1):1584.

doi: 10.36922/ijb.1584

30. Wen J, Zeng Y, Su S, *et al*. Magnesium degradation-induced variable fixation plates promote bone healing in rabbits. *J Orthop Traumatol***.** 2024;25:56.
doi: 10.1186/s10195-024-00803-0

31. Huxman C, Lewis G, Armstrong A, Updegrove G, Koroneos Z, Butler J. Mechanically compliant locking plates for diaphyseal fracture fixation: a biomechanical study. *J Orthop Res***.** 2025;43(1):217-227.
doi: 10.1002/jor.25968

32. Nägl K, Reisinger A, Pahr DH. The biomechanical behavior of 3D-printed human femoral bones based on generic and patient-specific geometries. *3D Print Med***.** 2022;8(1):35.
doi: 10.1186/s41205-022-00162-8

ACCSCIENCE PUBLISHING

CORRECTION

DOI: 10.36922/ijb.corr020725

Published Online: July 11, 2025

Correction 1

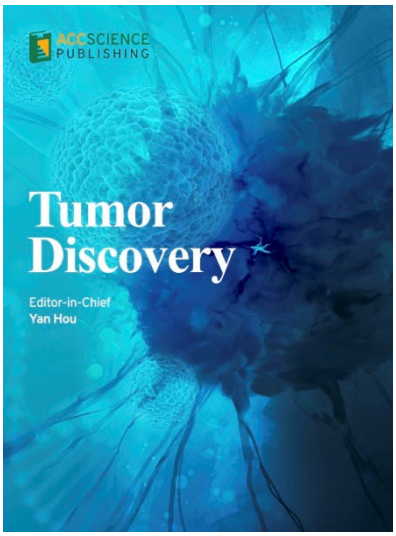
Bettendorf E, Schmid R, Horch RE, *et al*. Bioprinted keratinocyte and stem cell-laden constructs for skin tissue engineering. *Int J Bioprint*. 2024;10(6):3925. doi: 10.36922/ijb.3925

The author would like to incorporate statement on publication fulfilment as required by the corresponding university to obtain doctoral degree. To address this, the Acknowledgments section has been revised accordingly, as follows:

We would like to thank Stefan Fleischer for the excellent technical assistance during the study. The present work was performed in (partial) fulfillment of the requirements for obtaining the degree "Dr. med."

This modification has been reflected and integrated directly in the latest version of record for this article, and a brief statement flagging the modification made is displayed on the title page of said version of record.

Our Journals

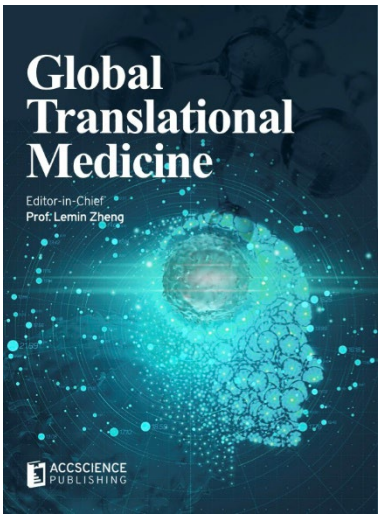


Tumor Discovery is a peer-reviewed and open-access journal that aims to present new cancer research with strong emphasis on fundamental and translational studies. *Tumor Discovery* covers topics, including but not limited to the following:

- Etiology and pathogenesis of cancer
- Mechanisms and molecular pathways underlying cancer initiation and progression
- Tumor metastasis
- Tumor evolution and heterogeneity
- Tumor microenvironment and tumor-host interactions
- Cancer genetics and genomics
- Cancer characterization using omics approaches
- Discovery and validation of cancer biomarker
- Discovery of new therapeutic targets
- New approaches of diagnostic and treatment modalities
- Statistical methods in cancer research

Global Translational Medicine is a quarterly journal that focuses on medicine, biological sciences, and biomaterials engineering. The goal of *Global Translational Medicine* is to provide a platform to researchers for showcasing their latest research works in translational medicine so as to advance the field towards the betterment of human health. Despite the advancement of omics and new technologies, the process of transforming these technologies and scientific research results into effective therapies and putting them into clinical use still has a long way to go. *Global Translational Medicine* provides a platform to fill the gaps in preclinical and inter-disciplinary research, to promote clinical translation of scientific research results, and to contribute to the conception of new and improved preventive measures as well as diagnostic and therapeutic techniques of diseases.

Global Translational Medicine covers the following themes: cardiovascular disease, metabolism/diabetes/obesity, neuroscience/neurology, cancer, biomaterials and their applications in medicine, proteomics/metabolomics, pharmacogenomics, biomarkers, bioinformatics and data mining, animal and clinical research, and medical methods arising from interdisciplinary crossover.



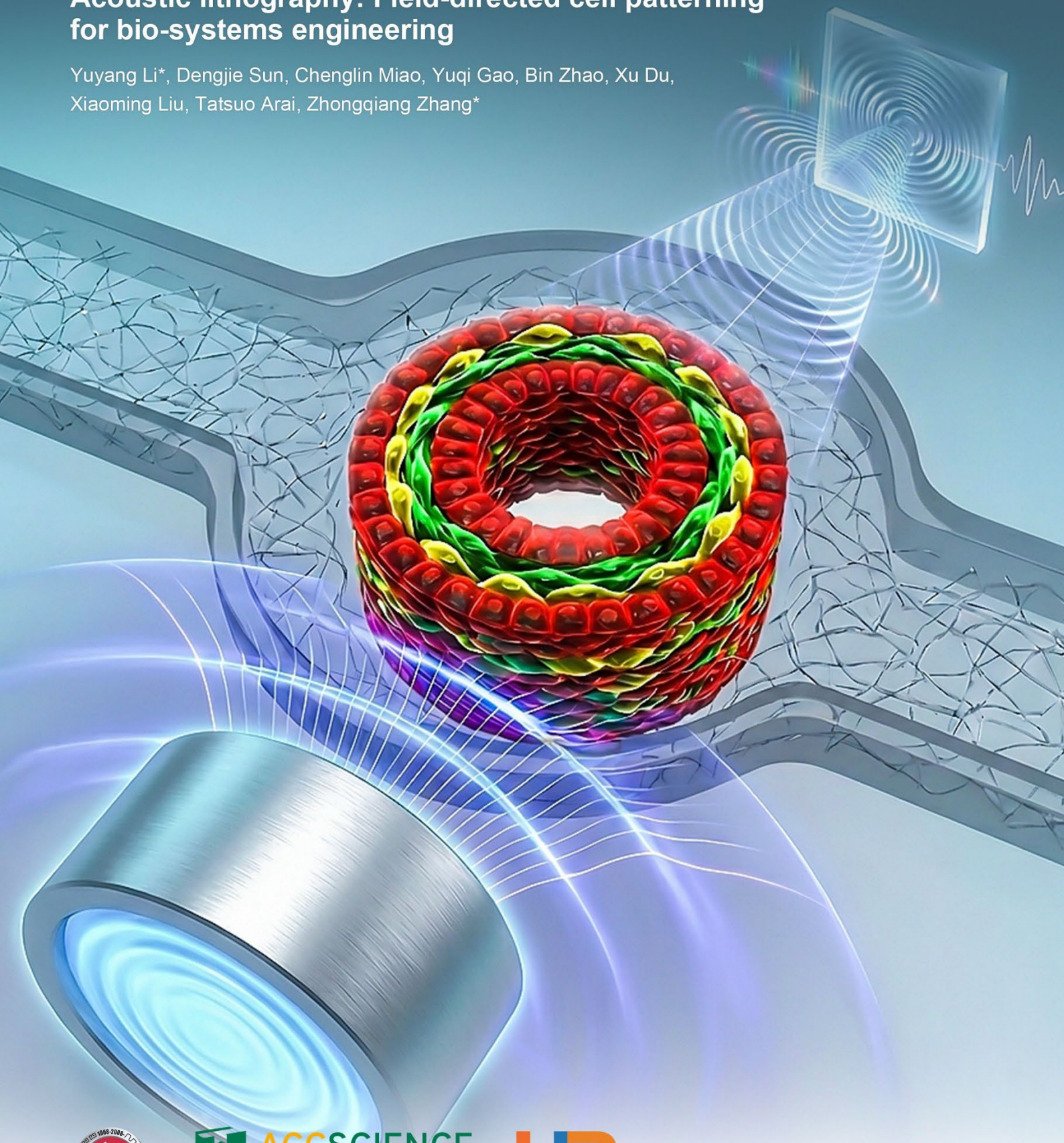
Start a new journal

Write to us via email if you are interested to start a new journal with AccScience Publishing. Please attach your CV, professional profile page and a brief pitch proposal in your email. We shall inform you of our decision whether we are interested to collaborate in starting a new journal.

Contact: info@accscience.com

Acoustic lithography: Field-directed cell patterning for bio-systems engineering

Yuyang Li*, Dengjie Sun, Chenglin Miao, Yuqi Gao, Bin Zhao, Xu Du, Xiaoming Liu, Tatsuo Arai, Zhongqiang Zhang*



ACCSCIENCE PUBLISHING

IJB

AccScience Publishing

ijb.office@accscience.sg

9 Raffles Place, Republic Plaza 1 #06-00 Singapore 048619